

ACOUSTICAL NEWS-USA		663
USA Meeting Calendar		668
ACOUSTICAL NEWS-INTERNATIONAL		671
International Meeting Calendar		671
BOOK REVIEWS		
Immersive Audio Signal Processing		673
REVIEWS OF ACOUSTICAL PATENTS		674
REVIEW ARTICLES		
Internal solitons in the ocean and their effect on underwater sound		695
Speech production knowledge in automatic speech recognition		723
LETTERS TO THE EDITOR		
Comment on "Analysis of the time-reversal operator for scatterers of finite size," by D. H. Chambers [J. Acoust. Soc. Am. 112, 411–419 (2002)] (L)	Xudong Chen	743
Analysis of voice source characteristics using a constrained polynomial representation of voice source signals (L)	Tokihiko Kaburagi, Kouji Kawai, Shinya Abe	745
Echolocation clicks from killer whales (<i>Orcinus orca</i>) feeding on herring (<i>Clupea harengus</i>) (L)	Malene Simon, Magnus Wahlberg, Lee A. Miller	749
GENERAL LINEAR ACOUSTICS [20]		
Scattering of a Bessel beam by a sphere	Philip L. Marston	753
An annular superposition integral for axisymmetric radiators	James F. Kelly, Robert J. McGough	759
Numerical evaluation of the acoustic radiation from planar structures with general baffle conditions using wavelets	R. S. Langley	766
NONLINEAR ACOUSTICS [25]		
Manipulation of micrometer sized particles within a micromachined fluidic device to form two-dimensional patterns using ultrasound	Stefano Oberti, Adrian Neild, Jürg Dual	778
Bubble interaction dynamics in Lagrangian and Hamiltonian mechanics	Yurii A. Ilinskii, Mark F. Hamilton, Evgenia A. Zabolotskaya	786

CONTENTS—Continued from preceding page

AEROACOUSTICS, ATMOSPHERIC SOUND [28]

- Mode detection in turbofan inlets from near field sensor arrays Fabrice O. Castres, Phillip F. Joseph 796

UNDERWATER SOUND [30]

- A single-scattering correction for large contrasts in elastic layers Elizabeth T. Küsel, William L. Siegmann, Michael D. Collins 808
- An equivalent roughness model for seabed backscattering at very high frequencies using a band-matrix approach Gorm Wendelboe, Finn Jacobsen, Judith M. Bell 814
- Evidence of dispersion in an artificial water-saturated sand sediment Preston S. Wilson, Allen H. Reed, Jed C. Wilbur, Ronald A. Roy 824
- Estimating parameter uncertainties in matched field inversion by a neighborhood approximation algorithm Kunde Yang, N. Ross Chapman, Yuanliang Ma 833
- Underwater implosion of glass spheres Stephen E. Turner 844

ULTRASONICS, QUANTUM ACOUSTICS, AND PHYSICAL EFFECTS OF SOUND [35]

- The effect of cavity geometry on the nucleation of bubbles from cavities Michael A. Chappell, Stephen J. Payne 853
- Model for continuously scanning ultrasound vibrometer sensing displacements of randomly rough vibrating surfaces Purnima Ratilal, Mark Andrews, Ninos Donabed, Ameya Galinde, Carey Rappaport, Douglas Fenneman 863
- Acoustoelastic analysis of reflected waves in nearly incompressible, hyper-elastic materials: Forward and inverse problems Hirohito Kobayashi, Ray Vanderby 879

STRUCTURAL ACOUSTICS AND VIBRATION [40]

- Granular layers on vibrating plates: Effective bending stiffness and particle-size effects Wonmo Kang, Joseph A. Turner, Florin Bobaru, Liyong Yang, Kitti Rattanadit 888
- A study of vibroacoustic coupling between a pump and attached water-filled pipes Bilong Li, Melinda Hodkiewicz, Jie Pan 897
- On the diffuse field reciprocity relationship and vibrational energy variance in a random subsystem at high frequencies R. S. Langley 913
- Radiation clusters and the active control of sound transmission into a symmetric enclosure Tsutomu Kaizuka, Nobuo Tanaka 922
- Use of principle velocity patterns in the analysis of structural acoustic optimization Wayne M. Johnson, Kenneth A. Cunefare 938

NOISE: ITS EFFECTS AND CONTROL [50]

- Optimization of a clamped plate silencer Chunqi Wang, Jun Han, Lixi Huang 949

ARCHITECTURAL ACOUSTICS [55]

- Comparison of two modeling approaches for highly heterogeneous porous media Giulio Pispola, Kirill V. Horoshenkov, Amir Khan 961

ACOUSTIC SIGNAL PROCESSING [60]

- Source characterization of a subsonic jet by using near-field acoustical holography Moohyung Lee, J. Stuart Bolton 967

CONTENTS—Continued from preceding page

PHYSIOLOGICAL ACOUSTICS [64]

Theory of forward and reverse middle-ear transmission applied to otoacoustic emissions in infant and adult ears	Douglas H. Keefe, Carolina Abdala	978
Basilar membrane tension calculations for the gerbil cochlea	Ram C. Naidu, David C. Mountain	994
Cochlear traveling-wave amplification, suppression, and beamforming probed using noninvasive calibration of intracochlear distortion sources	Christopher A. Shera, John J. Guinan, Jr.	1003
Physiological detection of interaural phase differences	Bernhard Ross, Kelly L. Tremblay, Terence W. Picton	1017

PSYCHOLOGICAL ACOUSTICS [66]

Differences in loudness of positive and negative Schroeder-phase tone complexes as a function of the fundamental frequency	Manfred Mauermann, Volker Hohmann	1028
Variability and uncertainty in masking by competing speech	Richard L. Freyman, Karen S. Helfer, Uma Balakrishnan	1040
Speech intelligibility in free field: Spatial unmasking in preschool children	Soha N. Garadat, Ruth Y. Litovsky	1047
The binaural performance of a cross-talk cancellation system with matched or mismatched setup and playback acoustics	Michael A. Akeroyd, John Chambers, David Bullock, Alan R. Palmer, A. Quentin Summerfield, Philip A. Nelson, Stuart Gatehouse	1056
Binaural interference and auditory grouping	Virginia Best, Frederick J. Gallun, Simon Carlile, Barbara G. Shinn-Cunningham	1070
The detection of differences in the cues to distance by elderly hearing-impaired listeners	Michael A. Akeroyd, Stuart Gatehouse, Julia Blaschke	1077
Effective compression and noise reduction configurations for hearing protectors	King Chung	1090

SPEECH PRODUCTION [70]

Coherent structures of the near field flow in a self-oscillating physical model of the vocal folds	Jürgen Neubauer, Zhaoyan Zhang, Reza Miraghaie, David A. Berry	1102
Influence of acoustic loading on an effective single mass model of the vocal folds	Matías Zañartu, Luc Mongeau, George R. Wodicka	1119
An acoustic description of the vowels of northern and southern standard Dutch II: Regional varieties	Patti Adank, Roeland van Hout, Hans van de Velde	1130
Acoustic cues discriminating German obstruents in place and manner of articulation	Julia Hoelterhoff, Henning Reetz	1142
Voice F_0 responses to pitch-shifted voice feedback during English speech	Stephanie H. Chen, Hanjun Liu, Yi Xu, Charles R. Larson	1157

SPEECH PERCEPTION [71]

Integration efficiency for speech perception within and across sensory modalities by normal-hearing and hearing-impaired individuals	Ken W. Grant, Jennifer B. Tufts, Steven Greenberg	1164
The effect of smoothing filter slope and spectral frequency on temporal speech information	Eric W. Healy, Heidi M. Steinbach	1177

MUSIC AND MUSICAL INSTRUMENTS [75]

Singing proficiency in the general population	Simone Dalla Bella, Jean-François Giguère, Isabelle Peretz	1182
---	--	------

CONTENTS—Continued from preceding page

BIOACOUSTICS [80]

A mechanistic analysis of stone fracture in lithotripsy	Oleg A. Sapozhnikov, Adam D. Maxwell, Brian MacConaghy, Michael R. Bailey	1190
The freshwater dolphin <i>Inia geoffrensis geoffrensis</i> produces high frequency whistles	Laura J. May-Collado, Douglas Wartzok	1203
Patterned burst-pulse vocalizations of the northern right whale dolphin, <i>Lissodelphis borealis</i>	Shannon Rankin, Julie Oswald, Jay Barlow, Marc Lammers	1213
Spatial release from masking of aerial tones in pinnipeds	Marla M. Holt, Ronald J. Schusterman	1219
Semi-analytical computation of the acoustic field of a segment of a cylindrically concave transducer in lossless and attenuating media	Başak Ülker Karbeyaz, Eric L. Miller, Robin O. Cleveland	1226
Method for detecting small changes in vibrotactile perception threshold related to tactile acuity	A. J. Brammer, J. E. Piercy, I. Pyykkö, E. Toppila, J. Starck	1238

ERRATA

Erratum: “The acoustic center of laboratory standard microphones” [J. Acoust. Soc. Am. 120(5), 2668–2675 (2006)]	Salvador Barrera-Figueroa, Knud Rasmussen, Finn Jacobsen	1248
---	--	------

JASA EXPRESS LETTERS

Focus in production: Tonal shape, intensity and word order	Martti Vainio, Juhani Järvikivi	EL55
Drive-point functions and modal density	Richard H. Lyon	EL62
On the effect of error correlation on matched-field geoacoustic inversion	Chen-Fen Huang, Peter Gerstoft, William S. Hodgkiss	EL64
Acoustic virtual mass of granular media	Nicholas P. Chotiros, Marcia J. Isakson	EL70
Loudness pattern-based speech quality evaluation using Bayesian modeling and Markov chain Monte Carlo methods	Guo Chen, Vijay Parsa	EL77
Discrimination of starting phase with sinusoidal envelope modulation	Stanley Sheft, William A. Yost	EL84
Unattended speech processing: Effect of vocal-tract length	Marie Rivenez, Christopher J. Darwin, Léonore Bourgeon, Anne Guillaume	EL90
Emergence of the acoustic Green’s function from thermal noise	Oleg A. Godin	EL96

CUMULATIVE AUTHOR INDEX

1251

Focus in production: Tonal shape, intensity and word order

Martti Vainio and Juhani Järvikivi

Department of Speech Sciences, University of Helsinki, P.O. Box 9 (Siltavuorenpenger 20), FIN-00014, Helsinki, Finland and Department of Psychology, University of Turku, Assistentinkatu 7, FIN-20014 Turku, Finland
martti.vainio@helsinki.fi, juhani.jarvikivi@utu.fi

Abstract: The effect of word order and prosodic focus on the tonal shape and intensity in the production of prosody was studied. The results show that the production of focus in Finnish follows a global pattern with regard to tonal features. The relative pitch height difference between contrasted words is the most important pitch-related factor in signaling narrow prosodic focus. Narrow focus is not localized to prosodically emphasized words only but relates to the utterance as a whole. It was also found that syntactic structure with respect to both intensity and tonal structure modulated relative prosodic prominence of individual words.

© 2007 Acoustical Society of America

PACS numbers: 43.70.Fq, 43.70.-h, 43.70.Bk [AL]

Date Received: August 14, 2006 **Date Accepted:** November 26, 2006

1. Introduction

The question investigated in the present study is whether and how prosody and syntactic structure interact in the production of information structure, particularly in the production of focus. Focusing is used to draw attention, to contrast or to emphasize the importance of a particular part of an utterance. In general, focus is signaled by the speaker by making one or another part of an utterance prominent either syntactically or prosodically. Focus, as understood here, pertains to new propositional information evoked by the focused element and what is pragmatically presupposed by the speaker and the hearer, i.e., to information which is not already presupposed or talked about, and thus not shared by the speaker and hearer. In this sense, focus is seen as an abstract proposition emerging from the combination of the presupposed or shared information and a sentence element that is marked as more prominent by prosody or syntax. In the present study the relation between syntactic and prosodic prominence and information structure in Finnish is exploited in investigating whether changes in syntactic structure together with different propositions are reflected in prosodic parameters of voice fundamental frequency (f_0) and intensity in production.

Finnish is an agglutinative-fusional language with flexible word order. The word order in Finnish frequently serves to signal information structure. For example, in an unmarked case, such as (1) “Menemme laivalla Jimille” (we go by boat to Jimi’s), the canonical order of the two adverbs *laiva+lla* (boat+with) and *Jimi+lle* (Jimi+to) (i.e., manner+place) conforms to its default information structure. Consequently, no propositions over and above what is already explicitly asserted is evoked by the word order. In contrast, changing the word order to marked (2) “Menemme Jimille laivalla” highlights the last element *laivalla* (with boat). Therefore, rather than just asserting that we are in fact going to Jimi’s, this presupposed information together with the marked position of “*laivalla*” evokes the proposition that it is by boat we are going to Jimi’s and not by a car, for example—as if it were an answer to a question “how do you go to Jimi’s?” For the pragmatic use of word order in Finnish, see, e.g., Ref. 1.

In addition to word order, prosody can be used to mark any constituent under the domain of focus even in the syntactically unmarked case by increasing the accent or stress on the part of an utterance that is intended to be brought into focus. Thus, a Finnish speaker can say “Menemme *Jimille* laivalla” as well as “Menemme Jimille *laivalla*” (italics depict prosodic focus). An important question is, then, whether and how the two main means available for

signaling focus in Finnish—syntactic and prosodic—interact in production when one or another part of an utterance needs to be prosodically marked as focused.

Prosodic (narrow) focus is usually achieved by the speaker by increasing the prominence of the focused constituent in the utterance. This is usually done by making the local f_0 excursions bigger and attenuating others. Usually these are accompanied by respective increases and decreases in intensity as well as segmental durations. The f_0 and intensity changes do not, however, correlate perfectly, and their interactions tend to be fairly complex. Thus, the perception of prominence is tightly coupled with the perception of pitch in speech. For instance, Pierrehumbert² showed that a later f_0 peak in an utterance has to be lower than the previous ones to be perceived as having an equally high pitch in English. This has since been shown to hold in many other languages (for instance Dutch³ and Finnish⁴). The situation in tone languages seems to be more complex, although declination has been attested for at least Mandarin Chinese.⁵

Vainio and Järvikivi⁴ studied the role of intensity and accentuation in the perception of prominence in Finnish. On one hand, they found that *ceteris paribus* a word order reversal had an effect on the perceived relative prominence of two words in a short Finnish utterance (verb followed by two nouns inflected to act as adverbials of place and manner; we will use only the term “noun” from now on except when we refer to both of them at once as an adverbial phrase). They explained this finding to reflect the fact that, since the word order reversal resulted in the latter word being syntactically marked for focus, the participants perceived it as being also prosodically more prominent, despite the fact that pitch and intensity were controlled with respect to the unmarked word order condition. On the other hand, they also found that the prominence of the two nouns in the utterance followed a so-called *flat-hat* pattern; i.e., the prominence of the earlier word related to the f_0 rise and the prominence of the latter words was related to the f_0 fall, with the relative heights of the peaks being the most important factor when subjects were asked to indicate which word (if any) they perceived as the most prominent. In other words, the fall of the earlier peak and the rise of the later peak (i.e., the transition between the peaks) did not contribute significantly to the perception of prominence of either peak, which both exhibit characteristic pointed-hat patterns.

We designed a production experiment to test hypotheses formed according to the findings above: (1) If the perceptual bias in the Vainio and Järvikivi study was caused by the change in information structure evoked by the change in word order, the same phenomenon should be reflected in production as compensation with regard to prominence, which should be significantly less pronounced with marked word order that already syntactically focuses one of the critical words, and (2) the different narrow focus conditions should form a pattern where the difference between the f_0 peaks (usually referred to as top-line declination) is the most important contributing factor together with a rise (in the case of “early focus”) and a fall (in the case of “late focus”). It is within these variables where the word order-induced compensation should be visible.

2. Materials

A simple declarative sentence starting with a verb and ending with an adverbial phrase whose word order could be reversed to mark the sentence for focus was used; the basic sentence “Menemme laivalla Jimille” (go-we boat-by Jimi’s-to) or with a reversed word order “Menemme Jimille laivalla” (go-we Jimi’s-to boat-by), allows for three different focus conditions with regard to the nouns *laiva*, and *Jimi*: broad focus (no specific prosodic marking for emphasis), narrow focus on the first noun, and narrow focus on the second noun. Two different words were used for the vehicle [“laiva” (boat) and “juna” (train)] and three proper nouns for the person to be visited (Jimi, Jani, and Lumi). With three different focus conditions and two different word order conditions, a set of 36 different sentences was created. Accordingly, a set of prompt questions matching the intended three focus conditions was created as follows: Broad focus; Mitä teette tänään (what do you do today)?, Narrow focus on “laivalla;” Millä menette Lumille (with what/How do you go to Lumi’s)?, and Narrow focus on “lumille;” Minne menette laivalla (where do you go by boat)?. The question prompts were then recorded by a female speaker to be

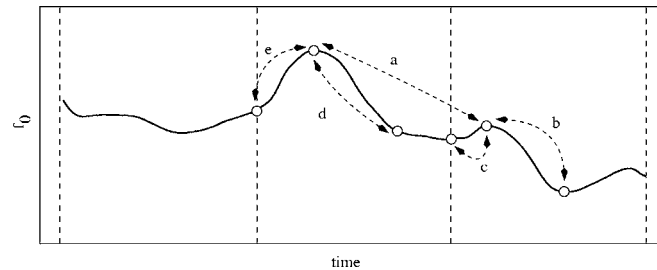


Fig. 1. A schematic illustration of the measured differences on an f_0 contour. Vertical lines depict word boundaries, and dotted lines with arrows marked with letters (a–e) show the differences (calculated in semitones) used in analyses. The pitch contour is a time-normalized average of the broad focus items used in the analyses.

presented to the participants in order to elicit the desired prosodic focus in the reply which was read from a sheet of paper.

2.1 Participants and procedure

Eight participants (seven female) took part in the experiment. All of the participants were choir members living in the Helsinki area with similar backgrounds in eastern Finland. None of the participants was familiar with speech research and none reported any hearing problems. All of the speakers spoke with a neutral Helsinki area dialect/accents.

The 36 prompt-reply pairs were randomized for each participant and he or she was given a sheet of paper with the corresponding replies. The focus was not indicated in any way on the paper as it was intended to be elicited by the type of question to be presented to the participants. The participants were not informed of the nature of the experiment and were asked to speak lively.

The prompt questions were played to the participants through a high-quality loudspeaker (Genelec 1029A) in a sound-treated recording studio at the Department of Speech Sciences at the University of Helsinki. The prompts were spaced so that the participants had ample time to reply. The replies uttered by the participants were recorded directly to a computer hard disk at 44.1-kHz sampling frequency and 16-bit quantization using a high-quality analog-to-digital converter (Digi002 by Digidesign) and a high-quality condenser microphone (AKG 4000B).

3. Results

Before data analyses each of the participants' responses was labeled and both intensity and f_0 were calculated using the PRAAT program.⁶ The utterances were then annotated manually. Three points of interest for each word in the utterance were marked on the f_0 curve and the segmental contents were labeled on a syllable basis. The three points for a given word corresponded to the basic pointed-hat pattern mainly used for accentuation in Finnish: the first point corresponding to the start of the f_0 rise, the second point to the peak, and the last point to the end of the f_0 fall. Both f_0 and intensity were measured at these points for subsequent statistical analyses. An example of the analysis points can be seen in Fig. 1.

Logistic regression analyses were conducted to determine which pitch-related factors contributed to the pitch contours' belonging to a given focus category. Several regression models were estimated using the pitch differences relevant to the formulated predictions. All models were cross validated (40 repetitions) and backwards elimination was used to determine the significant predictors. The predictors were also tested for nonlinearities using restricted cubic splines⁷ (all of the predictors turned out to behave in a linear fashion). We also tested the interactions between the predictors.

Before the analyses were conducted, the first author marked all utterances considered problematic with regard to f_0 patterns by visually inspecting the curves. In total, 36 utterances were identified as problematic and were played—together with the same number of filler

Table 1. Pitch differences semitones as used in the regression analyses: Means (upper part) and standard deviations (lower part).

Condition	peakdif a	lfall b	lrise c	ffall d	frise e
B	3.193	3.806	-1.179	3.311	-3.258
N1	6.928	1.406	-0.805	6.220	-3.784
N2	-1.437	6.275	-2.345	1.352	-2.275
B	2.139	2.399	1.493	2.392	2.463
N1	2.428	1.789	1.095	2.195	2.463
N2	2.215	2.067	1.169	1.337	1.581

utterances—to a group of 20 naive listeners who judged the focus condition of each utterance. Utterances whose focus was judged to be the intended one by fewer than four listeners were removed from the regression analyses as outliers. All in all, 12 trials used in the analyses were rejected this way (4% of the data). (Note that for the ANOVAs a different method of removing outliers was used.) The rises, falls, and peak height differences used in the statistical analyses were calculated in semitones. The intensities were calculated in decibels; the values were measured instantaneously at the peak f_0 points.

3.1 Tonal pattern

The following predictions concerning the tonal pattern of accentuation were tested: (1) the most important feature responsible for the focus conditions is the difference in peak heights of the two accented words (a in Fig. 1); (2) the rise of the first peak (line e) is more important than the fall (d in Fig. 1); and (3) the fall of the latter peak (b in Fig. 1) is more important than its rise (c in Fig. 1). The relative importance of the features was tested with logistic regression, using the different pitch-related features as predictors and the given focus condition as the dependent variable. Analysis was only performed on the two narrow focus conditions as there were no predictions with regard to the broad focus condition. The measurements (marked with letters from a to e) can be seen in Fig. 1. The semitone values are summarized in Table 1. The analyses of the narrow focus conditions are discussed separately below.

3.1.1 Early focus

The early focus (condition N1) was best explained by a model that included only the peak height difference (peakdif a), the last peak fall (lfall b), and their interaction. The most important predictor was the difference between the peak heights [$\chi^2(2)=42.99, p < 0.0001$], followed by the last fall [$\chi^2(1)=24.15, p < 0.0001$] and their interaction [$\chi^2(1)=20.28, p < 0.0001$]. The whole model was naturally highly significant [$\chi^2(3)=74.55, p < 0.0001, R^2(3)=0.735$]. That is, more than 70% of the categorization can be accounted for by pitch alone.

3.1.2 Late focus

The late focus condition (N2) turned out to be more complex requiring two additional predictors, mainly the ones describing the first peak (ffall d, and frise e). The main predictor was again the peak height difference [$\chi^2(2)=24.07, p < 0.0001$], followed by the last fall [$\chi^2(2)=10.24, p < 0.0060$], and their interaction [$\chi^2(1)=8.41, p < 0.0037$]. The first peak rise and fall were also highly significant [$\chi^2(1)=8.44, p < 0.0037$] and [$\chi^2(1)=6.41, p < 0.0113$], respectively. The overall model was again highly significant [$\chi^2(5)=44.46, p < 0.0001, R^2(5)=0.833$].

Figure 2 shows the f_0 contours in all focus conditions averaged over all speakers. The f_0 contours can be summarized in terms of pitch range adjustments from the broad focus in order

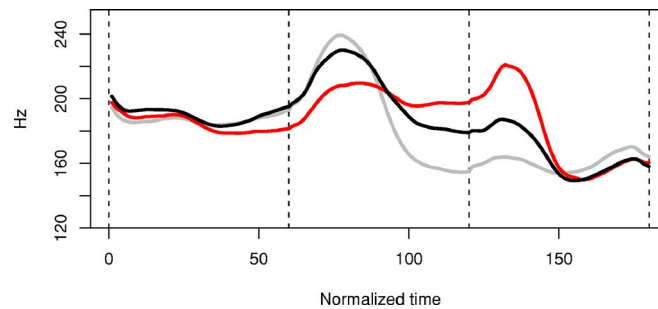


Fig. 2. (Color online) f_0 contours averaged over all focus conditions: broad focus; black line, narrow focus on first noun; light gray line, narrow focus on last word; red line. Word boundaries are depicted by vertical dashed lines. Each word was time normalized and averaged separately using 60 equidistant time points.

to maximize the difference between the peak heights without deaccenting the nonfocused word. That is, the basic tonal shape is preserved. Similar results have been found for English by Xu and Xu.⁸

3.2 Word order

To investigate whether the manipulation of word order interacted with intensity and tonal shape (pitch) in the production of focus, 2×3 analyses of variance (ANOVAs) with word order (marked, unmarked) and focus (broad, N1, N2) as factors were done with peak difference in decibels (intensity) and semitones (pitch) as the dependent measure. Both by-subject (participant means averaged over items— $F1$) and by-item analyses (item means averaged over participants— $F2$) are reported. Before analyzing the data for pitch, outliers were removed using 2.5 SDs below and above the condition means as a criterion. The outliers in the pitch experiment accounted for 2.8% of all data points. As these outliers were mostly caused by production errors, i.e., the speaker either interpreting the question incorrectly or producing a clearly unintended response, these outliers were also removed from the analyses of intensity. Additionally, all further data points 2.5 SDs over or above the condition means were removed from the analyses of intensity. These outliers accounted for a further 4.2% of the data. The condition means for intensity and pitch are summarized in Table 2. The results from all subsequent statistical analyses are given in Table 3.

In both analyses (pitch and intensity) word order (unmarked, marked) and focus (broad=B, noun 1=N1, noun 2=N2) were within variables in the subject analyses ($F1$). In the item analyses ($F2$) word order was a between-item factor. In what follows we discuss the results of each of the analyses separately.

3.2.1 Intensity

As expected there was a significant main effect of focus. In addition, however, the results also showed a significant interaction between word order and intended focus. Further pairwise com-

Table 2. Peak differences in decibels (intensity) and semitones (pitch) for the emphasized and nonemphasized prompts in the marked and unmarked word order conditions for broad focus (B), narrow focus on the first word (N1), and narrow focus on the second word (N2).

Condition	Pitch		Intensity	
	Unmarked	Marked	Unmarked	Marked
B	2.68 (2.00)	4.06 (2.52)	2.25 (2.21)	3.83 (2.26)
N1	7.01 (1.99)	7.17 (2.14)	7.50 (3.92)	6.95 (4.32)
N2	-1.25 (1.94)	-1.58 (2.00)	0.40 (3.67)	0.50 (3.71)

Table 3. Results from the overall analyses of variance with decibels (intensity) and semitones (tonality) as the dependent measures. Statistical significances are marked as follows: (*) $p < 0.1$, * $p < 0.05$, ** $p < 0.01$, *** $p < 0.001$.

Condition	Pitch		Intensity	
	F1	F2	F1	F2
WO.	3.768 (*)	1.116	<1	<1
Foc	103.62***	423.29***	31.29**	203.70***
WO × Foc	4.981*	4.595*	5.830*	3.645 (*)

parisons showed that the broad focus condition was significantly modulated by whether the word order was marked or not [$t1(7)=3.375, P=0.012$; $t2(5)=2.706, p=0.042$].

3.2.2 Pitch

Again the results showed a significant main effect of focus. Additionally, this effect was further qualified by a significant interaction between focus and word order. Pairwise contrasts showed that the interaction was mainly due to a significant difference between the marked and unmarked broad focus conditions [$t1(7)=3.062, p=0.018$; $t2(5)=2.274, p=0.072$], although the difference was not statistically significant, most likely due to a lack of power; the tendency to compensate for the word order reversal can be seen numerically in the N2 condition as well ($t's < 1.12, p's > 0.15$) as well as graphically in Fig. 3.

4. Discussion

The results presented in this paper reveal a complicated phenomenon relating to the production of focus in Finnish.⁴ First, the results regarding the overall tonal shape are in consonance with results on perception of prominence. That is, the production of narrow focus in Finnish follows a flat-hat pattern with regard to the tonal features used for increasing local prominence; a fall in the final word of an utterance and a rise on a nonfinal word. However, the patterns are somewhat more complex due to the fact that the participants mostly produced patterns with a so-called sagging transition (a clear valley between the two peaks) between the two peaks, as a real flat-hat pattern would signify a different pragmatic meaning in Finnish. More interestingly, the pattern for the early focus only depends on the peak height difference and the fall of the latter, final accent. It seems that in this case the speakers are controlling the pitch features in a holistic manner and concentrate on the attenuation of parts more than on the intensification. In summary, the production of prosodic focus is not localized to the prominent or emphasized word only but relates to the time domain of the whole utterance or at least to the part of it where the

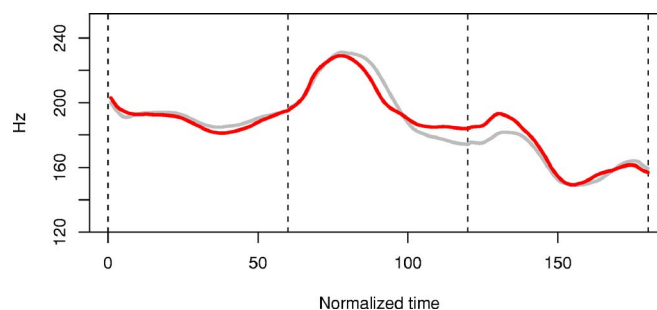


Fig. 3. (Color online) f_0 contours averaged over both word order conditions in the broad focus condition. Word boundaries are depicted by vertical dashed lines. Each word has been time normalized and averaged separately using 60 equidistant time points. The compensation described in Sec. IV can be seen in the marked word order contour (light gray line).

relative prominences are relevant; in our case the whole adverbial phrase. The results are, moreover, in accordance with a somewhat similar study by Xu and Xu on the realization of focus in English.⁸

Second, the results showed an effect of syntactic structure with respect to both intensity and, most importantly, tonal shape. In other words, the word order of the produced utterances modulated the difference between the two peaks, that is, their relative prominence. Whereas in perception, marked word order modulates *ceteris paribus* the perceived relative prominence of the two peaks by resulting in a decrease of prominence of the first peak and an increase of the second peak compared with the neutral unmarked case, in production speakers compensate, particularly in the broad focus condition, to keep the overall pattern neutral when the word order in fact signals a narrow focus on the later word. That is, they compensate to keep the whole utterance under sentence focus. The speakers clearly take into account the fact that the marked word order itself already signals focus, and compensate by enlarging the difference between the two peaks in the broad focus condition, in order to not end up unintentionally signaling a narrow focus on either word.

Whether the observed relation between syntax and prosody in focus assignment is specific to Finnish only remains for further investigation to find out. However, as Donati and Nespor⁹ argue, prosodic focus and syntactic structure tend to be related, in that the more prosodic prominence is allowed to move around in the phrase the more rigid the word order properties of the language tend to be. Thus, it may be that the interaction between syntax and prosody in focus assignment is at its clearest with languages such as Finnish, where the trade-off between intonation and syntactic structure for focus placement is sufficiently large due to the well-defined pragmatic functions of the word order changes. Accordingly, the interaction between syntactic structure and prosody in focus assignment may be less pronounced both in languages with either syntactically more constrained word order or syntactically free but pragmatically less-constrained word order.⁴ Be that as it may, the present study suggests that, as in the perception of prosodic prominence, higher order structural information, word order, interacts with the basic prosodic parameters in order to ensure a semantically and pragmatically coherent interpretation of the utterance.

Acknowledgments

Both authors have contributed equally to this paper. We would like to thank Mietta Lennes, Leena Wahlberg, and Anna Dannenberg for their help with obtaining and labeling the data for this study. We would also like to thank Stefan Werner for providing much help at earlier stages of the study reported here. We would also like to thank Daniel Hirst for his insightful comments on an earlier version of the manuscript. The present study was supported by Grant No. 107606 from the Academy of Finland to M. Vainio and Grant No. 106418 from the Academy of Finland to J. Järvikivi.

References and links

- ¹M. Viikuna, *Free Word Order in Finnish: Its Syntax and Discourse Functions* (Suomalaisen Kirjallisuuden Seura, Helsinki, 1989).
- ²J. Pierrehumbert, "The perception of fundamental frequency declination," *J. Acoust. Soc. Am.* **66**, 363–369 (1979).
- ³C. Gussenhoven, B. H. Repp, A. Rietveld, H. H. Rump, and J. Terken, "The perceptual prominence of fundamental frequency peaks," *J. Acoust. Soc. Am.* **102**, 3009–3022 (1997).
- ⁴M. Vainio and J. Järvikivi, "Tonal features, intensity, and word order in the perception of prominence," *J. Phonetics* **34**, 319–342 (2006).
- ⁵C. Shih, "A declination model of Mandarin Chinese," in *Intonation: Analysis, Modelling and Technology* (Kluwer Academic, Dordrecht, 2000), pp. 243–268.
- ⁶P. Boersma, "PRAAT, a system for doing phonetics by computer," *Glott International* **10**, 341–345 (2001).
- ⁷F. E. Harrell, *Regression Modeling Strategies* (Springer, New York, 2001).
- ⁸Y. Xu and C. X. Xu, "Phonetic realization of focus in English declarative intonation," *J. Phonetics* **33**, 159–197 (2005).
- ⁹C. Donati and M. Nespor, "From focus to syntax," *Lingua* **113**, 1119–1142 (2003).

Drive-point functions and modal density

Richard H. Lyon

*RH Lyon Corp, 60 Prentiss Lane, Belmont, Massachusetts, 02478 and Acentech, Inc., Cambridge, Massachusetts
rhlyon@lyoncorp.com*

Abstract: It is well known that the real part of a drive-point function, averaged in frequency, can be estimated from the modal density and mass of a structure. Furthermore, the results are often the same as when the modal overlap is large due to damping or when the system boundaries are infinitely extended. The present note examines the possible use of modal density in estimating the imaginary part of the same system drive-point function.

© 2007 Acoustical Society of America

PACS numbers: 43.40.At, 43.40.Dx, 43.20.Bi [JMD]

Date Received: October 23, 2006 Date Accepted: November 15, 2006

1. System conductance

A system that has mode shapes $\psi_m(x)$, density $\rho(x)$, resonance frequencies ω_m , and total mass M has a drive point admittance (mobility) function¹

$$Y(\omega) = \frac{V(\omega)}{F(\omega)} = \frac{j\omega}{M} \sum_m \frac{\psi_m^2(x)}{\omega_m^2 - \omega^2 + j\omega\omega_m\eta}, \quad (1)$$

where the mode shape functions are normalized so that $\langle \psi_m(x)^2 \rangle_\rho = 1$. The real part of this function is

$$G(\omega) = \frac{\omega^2}{M} \sum_m \frac{\psi_m^2(x)\omega_m\eta}{(\omega_m^2 - \omega^2)^2 + \omega^2\omega_m^2\eta^2}, \quad (2)$$

where η is the loss factor (the reciprocal of the quality factor Q and twice the critical damping ratio ζ). Each term in this expression has a “noise bandwidth” $\Delta_n = \pi\omega\eta/2$ and a peak value $\psi_m^2/\omega_m\eta M$.² Since the average number of modes that are resonantly excited (damping controlled) in the bandwidth Δ_n is the modal density times this bandwidth, then the average value of the sum in Eq. (2) is

$$\langle G \rangle = \langle \psi_m^2 \rangle n(\omega_m) \Delta_n / \omega_m \eta M = \pi n(\omega_m) / 2M, \quad (3)$$

which is the known result referred to above.³ It has been shown to be equal to the conductance when the system in question has its boundaries infinitely extended for a variety of mechanical and acoustical systems.

2. System susceptance

Now, we consider the imaginary part $B(\omega)$ of the admittance (or mobility) $Y = G - jB$. When $\omega_m < \omega$, the mode is driven above its resonance frequency and its response is mass controlled,

$$B_m^-(\omega) = \psi_m^2 / j\omega M. \quad (4)$$

Modes that are driven at a frequency below their resonance frequency are stiffness controlled with a stiffness value $\omega_m^2 M$.⁴

$$B_m^+(\omega) = j\omega \psi_m^2 / \omega_m^2 M. \quad (5)$$

We can then add up all of these nonresonant modes to obtain the total imaginary part of the admittance (excluding the bandwidth of resonant modes),

$$\langle B(\omega) \rangle = \frac{\langle \psi_m^2 \rangle}{j\omega M} \left[\int_0^{\omega - \Delta_n/2} n(\omega_m) d\omega_m - \int_{\omega + \Delta_n/2}^{\infty} \frac{\omega^2 n(\omega_m)}{\omega_m^2} d\omega_m \right]. \quad (6)$$

Many average modal densities can be expressed in terms of a simple power law, $n(\omega) \sim \omega^p$. If we use that fact and make the substitution $\xi \equiv \omega_m/\omega$, we get

$$\langle B \rangle = \frac{-j\langle \psi_m^2 \rangle n(\omega)}{M} \left[\int_0^{1 - \pi\eta/2} \xi^p d\xi + \int_{1 + \pi\eta/2}^{\infty} \xi^{p-2} d\xi \right]. \quad (7)$$

We note that the second integral will diverge for $p \geq 1$, which is no surprise since systems with such dependence of modal density on frequency (3D acoustical fields, membranes, elastic solids⁵) are known to have divergent reactances or susceptances (not resistances or conductances) for point-source excitation, although these become finite when transducer footprints are finite and the integrals in Eq. (7) are truncated accordingly. Evaluating the integrals in Eq. (7) and ignoring terms in η^2 yields the following:

$$\langle B \rangle = -j \frac{\langle \psi_m^2 \rangle n(\omega)}{M} R; \quad R = \frac{2p}{p^2 - 1}. \quad (8)$$

3. Discussion

When Eq. (1) refers to an admittance function (velocity/force), then a positive imaginary value of $\langle B \rangle$ indicates compliance and a negative value indicates a mass. The situation is reversed, for example, when we calculate an acoustical impedance (pressure/volume velocity). The susceptance vanishes for $n=0$, which is consistent with known results for 1D acoustical systems (pipes) and 2D flexural plates.⁶

The ratio $R = 2p/(p^2 - 1)$ is positive for $p < 0$ (mass-like; modal density decreases with frequency) and negative for $p > 0$ (stiffness-like; modal density increases with frequency) for admittance functions (opposite for impedance functions). When $p = -1/2$ (the modal density for flexural vibrations of a beam), this factor is $R = 4/3$. This result is not quite what we would expect because the admittance for an infinite beam has equal real and imaginary parts given by $R = \pi/2 = 1.57$, not 1.33.⁶ Some critical measurements could possibly resolve this uncertainty, although the difference is only 15%.

Although the power-law assumption for modal density may seem too restrictive, we note that many systems (rectangular rooms, plates with combinations of bending and in-plane modes, etc.) have modal densities that are sums of power law terms in the form

$$n(\omega) = \sum_i A_i \omega^{p_i}, \quad (9)$$

in which case, the reactive part of the drive-point function is

$$\langle B \rangle = -j \frac{\langle \psi_m^2 \rangle}{M} \sum_i A_i \omega^{p_i} R(p_i); \quad R(p_i) = \frac{2p_i}{p_i^2 - 1}. \quad (10)$$

References and links

¹These are standard relationships. A reference for the notation used is R. Lyon, *Machinery Noise and Diagnostics* (Butterworths, Boston, 1987), p. 79.

²Reference 1, p. 75.

³Reference 1, p. 82.

⁴Reference 1, p. 77.

⁵L. Kurzweil, "Seismic excitation of footings and footing-supported Structures," Ph.D. thesis (MIT ME Dept., September 1971).

⁶L. Cremer, M. Heckl, and E. Ungar, *Structure-Borne Sound* (Springer, New York, 1973), Chap. IV.

On the effect of error correlation on matched-field geoacoustic inversion

Chen-Fen Huang, Peter Gerstoft, and William S. Hodgkiss

*Marine Physical Laboratory, Scripps Institution of Oceanography, 9500 Gilman Drive,
La Jolla, California 92093-0238*

chenfen@mpl.ucsd.edu, gerstoft@ucsd.edu, wsh@ucsd.edu

Abstract: The effect of correlated data errors on matched-field geoacoustic inversion for vertical array data is examined. The correlated errors stem from the inability to model the inhomogeneities in the environment resulting in an additional error term beyond ambient noise. Simulated data with these correlated errors are generated and then inverted with or without using the proper covariance matrix. Results show that the correlated error has a negative impact on geoacoustic parameter estimation if not accounted for properly.

© 2007 Acoustical Society of America

PACS numbers: 43.30.Pc, 43.60.Pt [GD]

Date Received: August 13, 2006 Date Accepted: November 13, 2006

1. Introduction

In experimental data with high signal-to-noise ratio, error in modeling the parametrized environment is expected to be the dominant source of error in the inversion procedure. Because the modeling error may be correlated across receivers, the assumption of independent and identically distributed (IID) complex Gaussian error¹⁻³ in the likelihood function is no longer appropriate. Instead, a full data error covariance matrix C_D is needed. Some efforts have been made to estimate the error correlation, e.g., Dosso⁴ assumed the errors to be ergodic in space, leading to a Toeplitz structure of C_D .

We studied the effect of error correlation on matched-field geoacoustic inversion using simulated complex-valued pressure fields with correlated errors added. A Bayesian approach is adopted to solve the inversion where uncertainty in the inversion is described by the posterior density (PPD) of the estimated parameters. Since the primary interest is the effect of the error correlation on the geoacoustic inversion results, we assume the error covariance matrix is known and originates from uncertainty in modeling the inhomogeneities in the environment. These inhomogeneities could be due to a random environment such as internal waves (simulated here) or they could result from the chosen parametrization of the environment. For the latter case, the parametrization error must be so small that it can be modeled as a random field component. These environmental errors will cause a correlated error that presents a smooth, though random, shift in the fields.

Inversions were carried out first without, and subsequently with the full covariance matrix. In the former case, only the diagonal elements of the covariance matrix were assumed nonzero. As expected, inversions that did not take account of the full covariance matrix were poor, producing a deviation from the true solution for each environmental parameter. On the other hand, using the proper covariance matrix led to a substantially better result.

2. Theory

For matched-field geoacoustic inversion problems, the relationship between the observed complex-valued pressure field sampled at an N -element array and the predicted pressure field, at the frequency of interest, is described by the signal model

$$\mathbf{d} = \mathbf{D}(\mathbf{m}) + \mathbf{n}, \tag{1}$$

where \mathbf{d} is the observed data, $\mathbf{D}(\mathbf{m})$ is the modeled data based upon a parametrized environmental model, and the vector \mathbf{n} represents the error terms, that is, the residual variations in the data that are not deterministically reproducible.¹

Let the operator \mathcal{G}_{th} denote an exact forward modeling operator from model to data domain. The results of measurements that consist of the response of the physical system and the measurement errors can be described by

$$\mathbf{d} = \mathcal{G}_{\text{th}} + \mathbf{n}_{\text{obs}}, \tag{2}$$

where \mathbf{n}_{obs} is an unknown residual which may result from mechanisms that are not considered in the exact theory, such as ambient noise.

Another source of errors is that we never have access to \mathcal{G}_{th} . Thus, the simplified parametrization with model parameter \mathbf{m} of the true geoacoustic environment is the other source of error,

$$\mathcal{G}_{\text{th}} = \mathbf{D}(\mathbf{m}) + \mathbf{n}_{\text{mod}}. \tag{3}$$

Thus, from Eqs. (2) and (3), we obtain

$$\mathbf{d} = \mathbf{D}(\mathbf{m}) + \mathbf{n}_{\text{mod}} + \mathbf{n}_{\text{obs}}. \tag{4}$$

Therefore, the total error is the sum of modeling and observational errors, $\mathbf{n} = \mathbf{n}_{\text{mod}} + \mathbf{n}_{\text{obs}}$. The likelihood function $\mathcal{L}(\mathbf{m})$ is the conditional probability density function (pdf) of \mathbf{d} given \mathbf{m} and can be related to the pdf of the total error by

$$\mathcal{L}(\mathbf{m}) = p(\mathbf{d}|\mathbf{m}) \equiv p[\mathbf{d} - \mathbf{D}(\mathbf{m})] = p(\mathbf{n}_{\text{mod}} + \mathbf{n}_{\text{obs}}). \tag{5}$$

Suppose that \mathbf{n}_{mod} and \mathbf{n}_{obs} are Gaussians and statistically independent; then, the sum is also a Gaussian, in which the means and covariances add.⁵ Thus, the likelihood is

$$\mathcal{L}(\mathbf{m}) = \frac{1}{\pi^N |\mathbf{C}_D|} \exp\{-[\mathbf{d} - \mathbf{D}(\mathbf{m})]^\dagger \mathbf{C}_D^{-1} [\mathbf{d} - \mathbf{D}(\mathbf{m})]\}, \tag{6}$$

where $|\cdot|$ and \dagger denote, respectively, determinant and complex conjugate transpose. The data error covariance matrix, \mathbf{C}_D , is the sum of the modeling covariance matrix \mathbf{C}_{mod} and observational covariance matrix \mathbf{C}_{obs} ,

$$\mathbf{C}_D = \mathbf{C}_{\text{mod}} + \mathbf{C}_{\text{obs}}. \tag{7}$$

For a single deterministic signal, $\mathbf{D}(\mathbf{m})$ is represented by $\mathbf{w}(\mathbf{m})s$, where $\mathbf{w}(\mathbf{m})$ is the normalized signal field computed using an acoustic propagation model for a model \mathbf{m} and s is the complex source signature at the frequency of interest. The maximum likelihood (ML) estimate of \mathbf{m} and s is found by minimizing the exponent of Eq. (6).

We factorize the inverse of the data error covariance matrix, via the singular value decomposition expression of $\mathbf{C}_D = \mathbf{U}\mathbf{\Lambda}\mathbf{U}^\dagger$, as follows:

$$\mathbf{C}_D^{-1} = \mathbf{A}^\dagger \mathbf{A}, \tag{8}$$

where $\mathbf{A} = \mathbf{\Lambda}^{-1/2} \mathbf{U}^\dagger$, in which the columns of \mathbf{U} are the eigenvectors of \mathbf{C}_D and $\mathbf{\Lambda}$ has the corresponding eigenvalues along the main diagonal. Prewhitening \mathbf{d} and \mathbf{w} , via the transformation: $\tilde{\mathbf{d}} = \mathbf{A}\mathbf{d}$ and $\tilde{\mathbf{w}} = \mathbf{A}\mathbf{w}$, the likelihood function can be rewritten as

$$\mathcal{L}(\mathbf{m}, s) = \frac{1}{\pi^N |\mathbf{C}_D|} \exp[-(\tilde{\mathbf{d}} - \tilde{\mathbf{w}}s)^\dagger (\tilde{\mathbf{d}} - \tilde{\mathbf{w}}s)]. \tag{9}$$

The above equation has the same form as one in the IID case, except that the observed and replica vectors are replaced by their prewhitened counterparts. The ML estimate of s can be

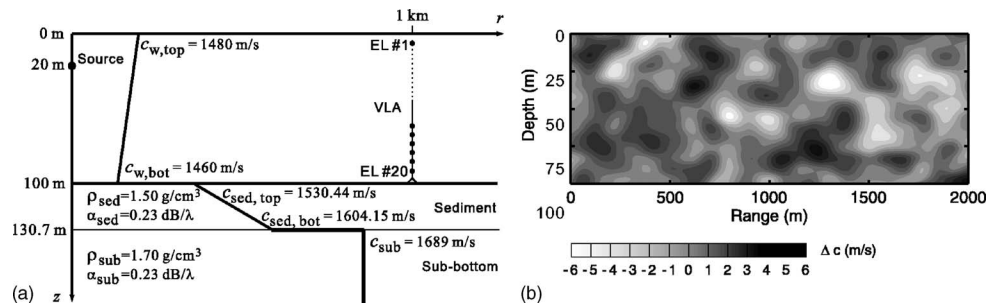


Fig. 1. (a) The sdc baseline environment from the Geo-Acoustic Inversion Workshop 1997 (Ref. 10). (b) One realization of the range-depth ocean sound-speed perturbation.

found by setting $(\partial/\partial s)\log \mathcal{L}(\mathbf{m}, s) = 0$, and the solution is $s_{ML} = \tilde{\mathbf{w}}^\dagger \tilde{\mathbf{d}} / \|\tilde{\mathbf{w}}\|^2$. After substituting this relationship into Eq. (9), the following equation is obtained:

$$\mathcal{L}(\mathbf{m}, \mathbf{C}_D) = \frac{1}{\pi^N |\mathbf{C}_D|} \exp[-\phi(\mathbf{m})], \tag{10}$$

where $\phi(\mathbf{m})$ denotes an objective function defined as

$$\phi(\mathbf{m}) = \mathbf{d}^\dagger \mathbf{C}_D^{-1} \mathbf{d} \left[1 - \frac{|\mathbf{w}^\dagger \mathbf{C}_D^{-1} \mathbf{d}|^2}{(\mathbf{d}^\dagger \mathbf{C}_D^{-1} \mathbf{d})(\mathbf{w}^\dagger \mathbf{C}_D^{-1} \mathbf{w})} \right]. \tag{11}$$

The second term in the braces is a generalization of the conventional Bartlett processor. When the error terms at the receivers are assumed IID, the objective function reverts to the Bartlett power objective function² for then \mathbf{C}_D is proportional to the identity matrix.

3. Setup: Background and perturbed environments

We use synthetic data so that the true environmental model is known in advance and can be compared with the inversion results. Figure 1(a) shows the baseline model that consists of a downward-refracting sound-speed profile overlying a positive-gradient sediment layer atop of a homogeneous subbottom layer.

3.1 Modeling uncertainty

An exact theory of the geoacoustic environment (deterministic) is highly complex, and requires unrealistic demand on our ability to model the environment. Stochastic descriptions are needed because many parameters are unknown. For example, the ocean sound-speed field might be better described statistically such as by use of the internal wave spectrum. The variations between acoustic fields generated from ocean sound-speed realizations constitute the modeling uncertainty. Inspired by Gouveia and Scales,⁶ the covariance matrix of data error [neglecting \mathbf{C}_{obs} in Eq. (7)] is assumed to be the sum of various sources of modeling error,

$$\mathbf{C}_D \approx \mathbf{C}_{mod} = \mathbf{C}_{mod}^{SSP} + \mathbf{C}_{mod}^{WD} + \mathbf{C}_{mod}^{SED} + \dots, \tag{12}$$

where the superscripts SSP, WD, and SED represent uncertainties not captured in the parametrized environment due to variations in ocean sound speed, water depth, and sediment sound speed, respectively. All the errors are assumed to be additive; the final \mathbf{C}_D matrix is the sum of the individual covariances.

Covariances are computed for each source of error by Monte Carlo simulation,

$$\mathbf{C}_{mod} = \langle (\mathbf{p} - \langle \mathbf{p} \rangle)(\mathbf{p} - \langle \mathbf{p} \rangle)^\dagger \rangle, \tag{13}$$

where \mathbf{p} is the acoustic field from a realization of the range-dependent environment.

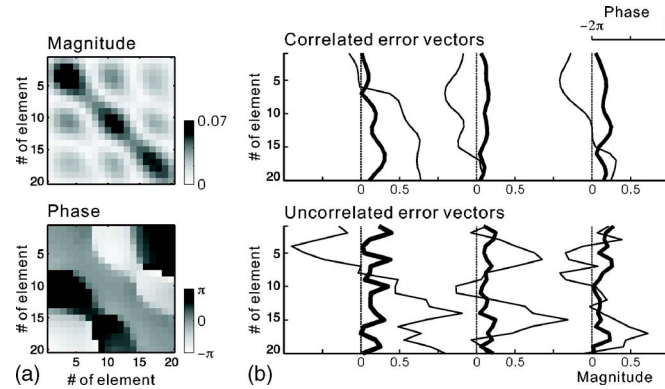


Fig. 2. (a) Magnitude (normalized by its trace) and phase for the error covariance matrix $\mathbf{C}_{\text{mod}}^{\text{SSP}}$ at the source-receiver range of 1 km for frequency of 100 Hz. (b) The correlated error vectors (top) resulting from the ocean sound-speed error for three realizations of the environment and the equivalent error vectors made IID (bottom). Heavy and light lines indicate the magnitude and phase, respectively.

To describe ocean sound-speed variability, we use the root mean square (rms) to measure the magnitude of deviation from its reference value and the correlation lengths to control the rate of change of deviation along the range (L_r) and depth (L_z). Figure 1(b) shows a realization of the range-depth ocean sound-speed perturbation, idealized from the internal wave spectrum, with an rms speed 2 m/s and a Gaussian correlation function of $L_r=100$ m and $L_z=10$ m.

3.2 Data uncertainty

Uncertainty due to a lack of knowledge of the sound speed is then mapped into the acoustic field. Data uncertainty induced from the random ocean sound speed is quantified via Eq. (13) with 1000 Monte Carlo runs. To propagate the acoustic field through the range-dependent environment, we use Collins' higher-order energy-conserving parabolic equation⁷ with 2.5-m range and 0.15-m depth grid spacing, and four Padé terms. The grid spacing is verified by using a finer grid spacing with the same result obtained. The acoustic fields are simulated on a vertical array with 20 hydrophones equally spaced over 95 m with first phone at 5-m depth, and the source located at 1-km range and 20-m depth, transmitting a 100-Hz tone.

Figure 2(a) shows the structure of data error covariance resulting from ocean sound-speed modeling uncertainty. The error-free signal to modeling error power ratio (SER) averaged across the array is 15 dB. Since the error covariance matrix is Hermitian, the magnitude of the covariance matrix is symmetric (top) about its diagonal elements and the phase is antisymmetric (bottom). Note that the error covariance matrix does not have a Toeplitz structure as assumed in Ref. 4.

Correlation in errors may result in a smoother (although random) pattern in the errors across the array. The top panel of Fig. 2(b) shows three realizations of the error vector resulting from ocean sound-speed modeling error. The bottom panel shows the same total error power distributed independently and identically across the array. The patterns in the top panel appear to be smooth, are intrinsically random, and could be interpreted as a component of the signal.

4. Impact of data error correlation on inversion results

To investigate the influence of data error covariance matrix on inversion in the presence of correlated errors, we consider three approaches for \mathbf{C}_D in Eq. (10).

- (1) diagonal matrix with equal variances ($\nu\mathbf{I}$);
- (2) diagonal matrix with unequal variances ($\text{diag}(\mathbf{C}_D)$);
- (3) full covariance matrix (\mathbf{C}_D).

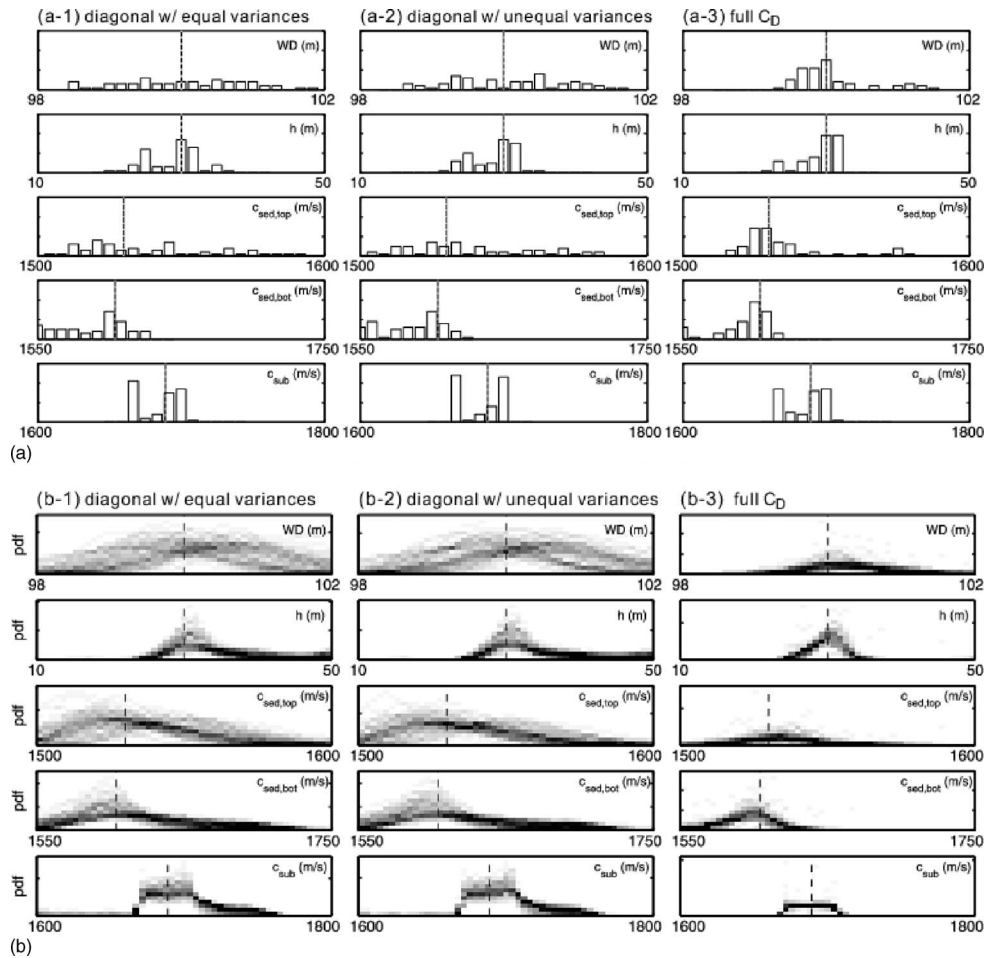


Fig. 3. (a) Histograms of the maximum *a posteriori* (MAP) estimates and (b) uncertainty of the marginal 1D posterior probability densities (PPDs) for the model parameters computed from 60 independent inversions. Vertical dotted line indicates the true value for the model parameter. The columns represent from left to right (1) diagonal C_D with equal variances; (2) diagonal C_D with unequal variances; and (3) full C_D , respectively.

To compare these three approaches, a total of 60 independent inversions is carried out for each approach. The solution of an inversion is represented by both the maximum *a posteriori* (MAP) estimate and 1D marginal PPD for each model parameter. For each inversion, the observed data vector is generated by computing the pressure field from the baseline environment and adding a realization of the correlated error vector from the full C_D in Fig. 2(a), e.g., the three realizations shown in the top panel of Fig. 2(b).

The estimated parameters are water depth WD , sediment thickness h , top and bottom sediment sound speeds $c_{sed,top}$ and $c_{sed,bot}$, and subbottom sound speed c_{sub} , with the search bounds being the same as the horizontal axis for each parameter in Fig. 3. Each inversion was carried out using Markov chain Monte Carlo sampling⁸ and ORCA (Ref. 9) was used for forward-field calculations.

Figure 3(a) shows histograms of the MAP estimates from all 60 inversions for each model parameter. Each column represents one of the above approaches for C_D . Using the full C_D [Fig. 3(a-3)], the MAP estimates have less spread. Without including the correlation structure in the objective function [Figs. 3(a-1 and 2)], the smooth pattern of the error vector can be mistaken as a component of the signal. The inversion process treats the error as signal, resulting

in a biased MAP estimate. With full C_D [Fig. 3(a-3)], the bias induced by the correlated error is eliminated; the MAP estimates are more centered around the true solution.

Figure 3(b) shows the superimposed 1D marginal PPDs for each of the model parameters from the 60 independent inversions. A gray scale is used to indicate the distribution of the PPD curves. The darker color represents more curves falling into a particular bin of the grid. It displays uncertainty of the marginal 1D PPDs for each model parameter. When the full error covariance matrix is properly accounted for in the likelihood function, the parameter uncertainty derived from an observed data set is more reliable.

5. Conclusions

We have described an approach for modeling data error correlations on matched-field geoacoustic inversion for vertical array data. The data error correlations considered here originate from inhomogeneities that are not included in the environmental model. These inhomogeneities could be due to a random environment or result from the chosen parametrization of the environment. We have only simulated modeling errors resulting from our inability to model the inhomogeneities in the ocean sound-speed structure.

In the presence of error correlation, the smooth pattern of the error vector can be mistaken as a component of the signal. This influences the posterior probabilities if not taken into consideration. By including the data error covariance matrix C_D in the likelihood function, the impact of the smooth pattern induced by the data errors may be reduced. Consistent 1D PPDs are obtained and MAP estimates are more centered around the true solution.

Multifrequency inversions might have a mitigating effect on the geoacoustic inversion results presented here. However, the environmental perturbations might result in cross frequency correlation.

References and links

- ¹P. Gerstoft and C. F. Mecklenbräuker, "Ocean acoustic inversion with estimation of *a posteriori* probability distributions," *J. Acoust. Soc. Am.* **104**, 808–819 (1998).
- ²C. F. Mecklenbräuker and P. Gerstoft, "Objective functions for ocean acoustic inversion derived by likelihood methods," *J. Comp. Acoust.* **8**, 259–270 (2000).
- ³C.-F. Huang, P. Gerstoft, and W. S. Hodgkiss, "Uncertainty analysis in matched-field geoacoustic inversions," *J. Acoust. Soc. Am.* **119**, 197–207 (2006).
- ⁴S. E. Dosso, P. L. Nielsen, and M. J. Wilmut, "Data error covariance in matched-field geoacoustic inversion," *J. Acoust. Soc. Am.* **119**, 208–219 (2006).
- ⁵A. Tarantola, *Inverse Problem Theory and Methods for Model Parameter Estimation* (SIAM, Philadelphia, 2005).
- ⁶W. P. Gouveia and J. A. Scales, "Bayesian seismic waveform inversion: Parameter estimation and uncertainty analysis," *J. Geophys. Res.* **103**, 2759–2779 (1998).
- ⁷M. D. Collins and E. K. Westwood, "A higher-order energy-conserving parabolic equation for range-dependent ocean depth, sound speed, and density," *J. Acoust. Soc. Am.* **89**, 1068–1075 (1991).
- ⁸P. Gerstoft, *SAGA Users guide 5.0, an inversion software package*, An updated version of "SAGA 2.0," SACLANT Undersea Research Centre, SM-333, La Spezia, Italy (1997).
- ⁹E. K. Westwood, C. T. Tindle, and N. R. Chapman, "A normal mode model for acoustoelastic ocean environments," *J. Acoust. Soc. Am.* **100**, 3631–3645 (1996).
- ¹⁰A. Tolstoy, N. R. Chapman, and G. Brooke, "Workshop'97: Benchmarking for geoacoustic inversion in shallow water," *J. Comp. Acoust.* **6**, 1–28 (1998).

Acoustic virtual mass of granular media

Nicholas P. Chotiros and Marcia J. Isakson

*Applied Research Laboratories, The University of Texas at Austin, Texas 78713-8029
chotiros@arlut.utexas.edu*

Abstract: Mechanical coupling between grains in a randomly packed unconsolidated granular medium is shown to cause an increase in the effective inertia, hence, a reduction in sound and shear wave speeds, relative to predictions by the standard expressions for a uniform elastic solid. The effect may be represented as a virtual mass term, and directly related to the scintillation index of the grain-to-grain contact stiffness.

© 2007 Acoustical Society of America

PACS numbers: 43.20.Hq, 43.20.Jr [JL]

Date Received: October 30, 2006 **Date Accepted:** December 3, 2006

An acoustic wave traveling through an unconsolidated granular medium is often modeled as an elastic wave in a uniform elastic solid, using the following expressions:

$$c_p^2 = \frac{K_{HM} + \frac{4}{3}G_{HM}}{\rho}, \quad c_s^2 = \frac{G_{HM}}{\rho}, \quad (1)$$

where G_{HM} is the shear modulus, K_{HM} bulk modulus, ρ density, c_p and c_s the pressure and shear wave speeds. It will be shown that this procedure will lead to significant inaccuracies because of grain-to-grain interactions in a randomly packed structure. The conservation of energy approach will be used because it is the most insightful. Starting with a propagating wave of the form

$$u = A_u \cos\left(\frac{\omega x}{c_p} - \omega t\right), \quad (2)$$

where u is the displacement in the $+x$ direction, A_u displacement amplitude, ω angular frequency, and t time, the kinetic and potential energies in an elastic solid are given by

$$E_{\text{kinetic}} = \frac{\rho}{2} \left(\frac{du}{dt}\right)^2 = \frac{\rho}{2} \omega^2 A_u^2 \sin^2\left(\frac{\omega x}{c_p} - \omega t\right), \quad (3)$$

$$E_{\text{potential}} = -\left(K_{HM} + \frac{4}{3}G_{HM}\right) \frac{u}{2} \frac{d^2u}{dx^2} = \left(K_{HM} + \frac{4}{3}G_{HM}\right) \frac{\omega^2}{2c_p^2} A_u^2 \cos^2\left(\frac{\omega x}{c_p} - \omega t\right). \quad (4)$$

In the lossless case, conservation of energy requires that the sum of the two energies be a constant. The resulting solution is the expression for the pressure wave speed in Eq. (1). A similar analysis yields the expression for the shear wave speed.

In a granular medium, with the same values of bulk and shear moduli (G_{HM} and K_{HM}), it is postulated that there are additional terms in the kinetic energy equation, due to orthogonal linear and angular motion at the grain level. To put this concept into its proper perspective, it is necessary to understand the underlying assumptions that are commonly used and their implications. A qualitative description will be given, with the aid of the diagrams in Fig. 1. A regular arrangement of five grains, in the equilibrium state, is shown in Fig. 1(a). The grains are spherical and each grain-to-grain contact region is outlined by a rectangular boundary. Consider the situation where the outer grains are pushed horizontally toward the center grain by external forces. If one assumes a homogeneous and elastic medium, the strain must be evenly distributed. The implication is that grains deform into ovals and the contact rectangles are compressed

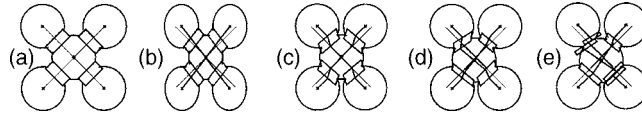


Fig. 1. Illustration of important classes of grain-to-grain interactions.

and slightly sheared, as illustrated in Fig. 1(b). The porosity remains constant and the Poisson's ratio of the frame is equal to that of the grain material. This assumption is often used in the application of Biot's theory to the modeling of porous rocks and sandstones,^{1,2} and it is implicit in Stoll's equations.³ This is usually referred to as the uniform, isotropic elastic frame assumption.

In practice, the grains are much stiffer than the contacts; therefore, they retain their spherical shape and almost all the strain is absorbed by the contacts, mostly in the form of additional shear deformation, as illustrated in Fig. 1(c). For small strains, this case corresponds to the Hertz-Mindlin model.⁴ It predicts a Poisson's ratio for the skeletal structure that is lower than that of the grain material, and the porosity changes as a function of volumetric strain. This case will be referred to as the symmetric elastic contact model. Due to randomness in packing and imperfections, contact stiffness is expected to vary randomly, strain is unevenly distributed, and the center grain will be subjected to rotation and displacement in random directions orthogonal to the applied forces, as illustrated in Fig. 1(d). In this illustration, the upper right contact is the stiffest, and consequently the center grain is displaced to the lower left and rotated anticlockwise. This case will be referred to as the asymmetric elastic contact model. It has some similarities to a micropolar material.⁵ Finally, if the number of contacts are more numerous than the minimum number necessary to determine its position and orientation, as is often the case, there will be additional stresses due to conflicts between the contact forces. The weaker contacts may be overcome by the stronger ones, and suffer plastic deformation and slippage. This case is illustrated in Fig. 1(e), in which two contacts are shown divided into two quadrilaterals with relative slip. The slippage is also a loss mechanism. The total frame resembles a complicated Maxwellian system.⁶ This case will be referred to as the asymmetric inelastic contact model. This study addresses the asymmetric elastic model of Fig. 1(d). The inelastic model and slippage will be addressed in a later study.

In comparison to Eq. (3), the expression for the kinetic energy of a sound wave in a granular medium is expected to include an additional term,

$$E_{\text{granular_kinetic}} = \frac{\rho}{2} \omega^2 A_u^2 \sin^2 \left(\frac{\omega x}{c_p} - \omega t \right) (1 + m_p), \quad (5)$$

where m_p represents the additional linear and angular kinetic energy in orthogonal directions at the grain level, as a fraction of the linear acoustic energy. It also has the appearance of a virtual mass term. The resulting expressions for wave speeds are of the form

$$c_{gp}^2 = \frac{K_{HM} + \frac{4}{3}G_{HM}}{\rho(1 + m_p)}, \quad c_{gs}^2 = \frac{G_{HM}}{\rho(1 + m_s)}. \quad (6)$$

The subscript "g" is added to distinguish the granular medium from the uniform elastic solid. The virtual mass coefficient m_s for the shear wave may have a different value than that of the pressure wave.

Expressions for the virtual mass coefficients will be derived, for a randomly packed granular medium with approximately spherical grains, by considering the coupling of translational and angular motion at the grain level. Each grain is mechanically connected to its neighbors at a number of contact points. If it were subjected to linear and angular displacements ($\Delta_x, \theta_z, \Delta_y,$

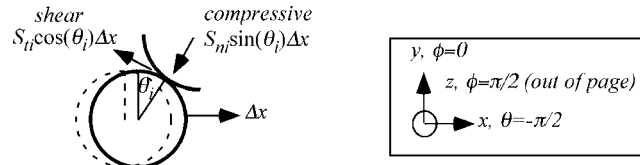


Fig. 2. Grain contact forces.

$\theta_x, \Delta_z, \theta_y$), it would experience a combination of reactive forces and torques ($F_x, T_z, F_y, T_x, F_z, T_y$). For small displacements, the vectors are related by a coupling matrix.

$$\begin{bmatrix} F_x \\ T_z \\ F_y \\ T_x \\ F_z \\ T_y \end{bmatrix} = \begin{bmatrix} b_{xx} & q_{zx} & b_{yx} & q_{xx} & b_{zx} & q_{yx} \\ a_{xz} & h_{zz} & a_{yz} & h_{xz} & a_{zz} & h_{yz} \\ b_{xy} & q_{zy} & b_{yy} & q_{xy} & b_{zy} & q_{yy} \\ a_{xx} & h_{zx} & a_{yx} & h_{xx} & a_{zx} & h_{yx} \\ b_{xz} & q_{zz} & b_{yz} & q_{xz} & b_{zz} & q_{yz} \\ a_{xy} & h_{zy} & a_{yy} & h_{xy} & a_{zy} & h_{yy} \end{bmatrix} \begin{bmatrix} \Delta_x \\ \theta_z \\ \Delta_y \\ \theta_x \\ \Delta_z \\ \theta_y \end{bmatrix}. \quad (7)$$

The inverse coupling matrix defines the displacements produced by applied forces and torques. Capital letters are used to distinguish the terms in the inverse matrix.

$$\begin{bmatrix} \Delta_x \\ \theta_z \\ \Delta_y \\ \theta_x \\ \Delta_z \\ \theta_y \end{bmatrix} = \begin{bmatrix} B_{xx} & Q_{zx} & B_{yx} & Q_{xx} & B_{zx} & Q_{yx} \\ A_{xz} & H_{zz} & A_{yz} & H_{xz} & A_{zz} & H_{yz} \\ B_{xy} & Q_{zy} & B_{yy} & Q_{xy} & B_{zy} & Q_{yy} \\ A_{xx} & H_{zx} & A_{yx} & H_{xx} & A_{zx} & H_{yx} \\ B_{xz} & Q_{zz} & B_{yz} & Q_{xz} & B_{zz} & Q_{yz} \\ A_{xy} & H_{zy} & A_{yy} & H_{xy} & A_{zy} & H_{yy} \end{bmatrix} \begin{bmatrix} F_x \\ T_z \\ F_y \\ T_x \\ F_z \\ T_y \end{bmatrix}. \quad (8)$$

In a perfectly regular crystalline structure or an elastic solid, all the contacts have identical stiffness and are evenly spaced over the grain's surface. A linear displacement Δ_x will only generate a collinear force F_x . Similarly, a rotation θ_z will cause only a collinear torque T_z . Conversely, a linear force will only generate a collinear displacement. Therefore, only the diagonal terms would be nonzero. The corresponding terms in the forward and inverse matrices can be shown to be inversely related, i.e., b_{xx} is equal to $1/B_{xx}$, etc.

In the case of a granular medium with random packing, such as sand, the contacts between each grain and its neighbors are not perfectly balanced. Consequently, the off-diagonal terms of the matrices are generally nonzero. Consider a grain connected at N points to its neighbors. The i th contact point (where “ i ” is a number between 1 and N) is at polar coordinates (r_i, θ_i, ϕ_i) relative to the center of the grain and it has a compressive stiffness S_{ni} and shear stiffness S_{ii} . Let the grain move a distance Δ_x from its equilibrium position. In this case, it is convenient to have the $+x$ direction coincident with $\theta_i = -\pi/2$, the $+y$ direction coincident with $\theta_i = 0$ and $\phi_i = 0$, and the $+z$ direction with $\theta_i = 0$ and $\phi_i = \pi/2$. Within the context of the coupling matrix, the collinear reactive force F_x is given by

$$F_x = b_{xx} \Delta_x. \quad (9)$$

With reference to Fig. 2, it can be shown that the diagonal terms b_{xx} and h_{xx} are given by

$$b_{xx} = \sum_{i=1}^N S_{ni} \sin^2(\theta_i) + S_{ti} \cos^2(\theta_i), \quad h_{xx} = \sum_{i=1}^N S_{ti} r_i^2 \cos(\theta_i). \quad (10)$$

Similar expressions may be derived for the remaining diagonal terms. Representative off-diagonal terms are given by

$$b_{xy} = \sum_{i=1}^N (S_{ni} - S_{ti}) \cos(\theta_i) \sin(\theta_i) \cos(\phi_i), \quad h_{xy} = \sum_{i=1}^N S_{ti} r_i^2 \cos(\theta_i) \sin(\theta_i) \cos(\phi_i), \quad (11)$$

$$a_{xy} = \sum_{i=1}^N S_{ti} r_i \cos(\phi_i) \sin(\theta_i), \quad q_{xy} = \sum_{i=1}^N S_{ti} r_i \cos(\theta_i) \sin(\phi_i). \quad (12)$$

Similar expressions may be derived for the remaining off-diagonal terms. For spherical grains, a linear force normal to the surface must pass through the center of the sphere and, therefore, cannot produce a collinear rotation, and vice versa. Therefore the remaining off-diagonal terms a_{xx} , a_{yy} , a_{zz} , q_{xx} , q_{yy} , and q_{zz} are zero. For approximately spherical grains, they will be nonzero but still negligible.

The dominant random variables are expected to be variations in the compressive and shear stiffnesses S_{ni} and S_{ti} . Experimental studies indicate that the variations are large. The contacts with higher values of stiffness are randomly connected in “force chains” and the magnitude of the contact stiffness appears to follow an exponential distribution.⁷ The contact points on each grain are more or less evenly distributed, because of the geometrical constraint that the separation between adjacent grains be at least one grain diameter. The probability density function (pdf) of the contact point angles, ϕ_i , and θ_i , may be represented by uniform probability densities,

$$dP(\phi_i) = d\phi_i / (2\pi), \quad \phi_i \text{ from } 0 \text{ to } 2\pi \quad (13)$$

$$dP(\theta_i) = \cos(\theta_i) d\theta_i / 2, \quad \theta_i \text{ from } -\pi/2 \text{ to } +\pi/2. \quad (14)$$

Integrating the product of each diagonal term with the appropriate pdf, one obtains the first moments.

$$\langle b_{xx} \rangle = \langle b_{yy} \rangle = \langle b_{zz} \rangle = \frac{N}{3} (\langle S_{ni} \rangle + 2\langle S_{ti} \rangle); \quad \langle h_{xx} \rangle = \langle h_{yy} \rangle = \langle h_{zz} \rangle = \frac{\pi N}{4} \langle S_{ti} \rangle r_o^2, \quad (15)$$

where $\langle \dots \rangle$ indicates the first moment or average value and r_o is the average value of r_i . Since spherical grains of approximately the same size are assumed, variations in the value of r_i are negligible to first order. Each off-diagonal term contains a multiplication by $\cos(\phi_i)$ or $\sin(\phi_i)$, and its average value must be zero. This means that a traveling wave is not refracted by the grain contact physics. The stiffnesses S_{ni} and S_{ti} at each contact point are related by the Poisson’s ratio ν of the contact material by the Hertz-Mindlin model,⁴

$$R_{nt} = \frac{S_{ti}}{S_{ni}} = 2 \frac{1 - \nu}{2 - \nu}. \quad (16)$$

At this point, it is convenient to consider the stiffness terms S_{ni} as the sum of an average value and a zero-mean random deviation,

$$S_{ni} = S_{no} + S_{ndi}, \quad (17)$$

such that

$$\langle S_{ni} \rangle = S_{no}, \quad \langle S_{ni}^2 \rangle = S_{no}^2 + \langle S_{ndi}^2 \rangle, \quad \langle S_{ndi} S_{ndj} \rangle = 0, \text{ except when } i = j. \quad (18)$$

It can be shown that the second moments of the diagonal terms are given by

$$\langle b_{xx}^2 \rangle = \frac{N^2}{9}(1 + 2R_{nt})^2 S_{no}^2 + \frac{N}{15}(8R_{nt}^2 + 4R_{nt} + 3)\langle S_{ndi}^2 \rangle, \quad \langle h_{xx}^2 \rangle = r_o^4 R_{nt}^2 \left(\frac{\pi^2 N^2}{16} S_{no}^2 + \frac{2N}{3}\langle S_{ndi}^2 \rangle \right). \quad (19)$$

The second moments of the off-diagonal terms are expressible as double integrals of the form

$$\langle b_{xy}^2 \rangle = N\langle S_{ndi}^2 \rangle(1 - R_{nt})^2 \int \cos^2(\theta_i)\sin^2(\theta_i)dP(\theta_i) \int \cos^2(\phi_i)dP(\phi_i). \quad (20)$$

The solutions are

$$\langle b_{xy}^2 \rangle = \langle b_{xz}^2 \rangle = \frac{N}{15}\langle S_{ndi}^2 \rangle(1 - R_{nt})^2, \quad \langle h_{xy}^2 \rangle = \langle h_{xz}^2 \rangle = \frac{N}{15}\langle S_{ndi}^2 \rangle r_o^4 R_{nt}^2, \quad (21)$$

$$\langle a_{xy}^2 \rangle = \langle a_{xz}^2 \rangle = \frac{N}{3}\langle S_{ndi}^2 \rangle r_o^2 R_{nt}^2, \quad \langle q_{xy}^2 \rangle = \langle q_{xz}^2 \rangle = \frac{N}{3}\langle S_{ndi}^2 \rangle r_o^2 R_{nt}^2. \quad (22)$$

Using these expressions, it is possible to formulate the kinetic energy in the orthogonal directions that must exist at the grain level and derive expressions for the virtual mass terms. Consider a wave traveling in the +x direction as defined by Eq. (2). The displacement of a particle of mass m relative to its neighbors is given by

$$u_f = m \frac{d^2 u}{dt^2} B_{xx}. \quad (23)$$

This displacement, in combination with the random imbalances in the contact stiffness, will couple into orthogonal directions. The coupled motion is incoherent from one grain to the next; therefore, it can only be treated statistically. For example, the mean-square linear force in the y direction is given by

$$\langle f_y^2 \rangle = \langle (b_{xy} u_f)^2 \rangle = \langle b_{xy}^2 \rangle \langle u_f^2 \rangle. \quad (24)$$

Since b_{xy} is a grain-level medium property, and u_f is the macroscopic result of an external force, they are uncorrelated. The corresponding mean-square kinetic energy is given by

$$\frac{m}{2} \langle v_y^2 \rangle = \frac{\langle f_y^2 \rangle}{2m\omega^2}, \quad (25)$$

where $\langle v_y^2 \rangle$ is the mean-square velocity in the y direction. It may be expressed as a fraction of the particle kinetic energy in the wave direction,

$$m_{ply} = \frac{\langle v_y^2 \rangle}{\langle (du/dt)^2 \rangle}. \quad (26)$$

This term represents a component of the virtual mass term m_p due to the linear kinetic energy in the y-direction, hence the subscript “ply.” Substituting from the above equations, one obtains an expression in terms of the second moments of the coupling coefficients,

$$m_{ply} = B_{xx}^2 \langle b_{xy}^2 \rangle. \quad (27)$$

For coupling of linear energy into angular motion about the y axis, a similar result is obtained,

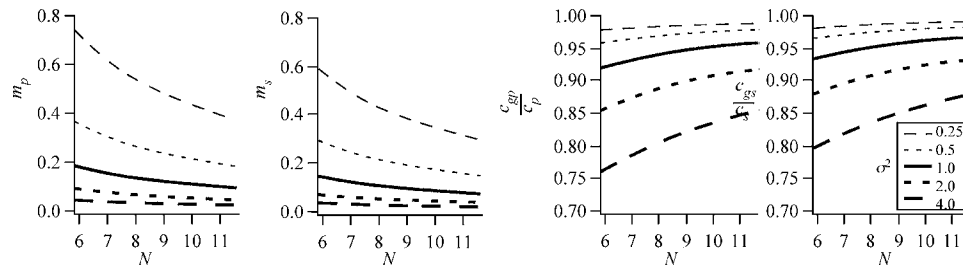


Fig. 3. Computed values of m_p , m_s , c_{gp}/c_p , and c_{gs}/c_s , as functions of N , at $\nu=0.08$, for a number of selected values of σ^2 .

$$m_{pay} = \frac{m\langle a_{xy}^2 \rangle}{\varphi b_{xx}^2}, \quad \varphi = \frac{3mr_o^2}{5}, \tag{28}$$

where φ is the moment of inertia of a spherical grain. The subscript “ l ” for linear motion is replaced by “ a ” to indicate angular motion. Finally, the small perturbation approximation is invoked, given that the off-diagonal terms in Eq. (7) are small compared to the diagonal terms,

$$B_{xx} \approx \frac{1}{b_{xx}}, \quad H_{xx} \approx \frac{1}{h_{xx}}, \text{ etc.} \tag{29}$$

In the case of an elastic solid, the off-diagonal terms would be zero and these relationships exact. The total virtual mass is given by the sum of the angular and linear kinetic energies in the orthogonal directions, as a fraction of the linear kinetic energy in the wave direction,

$$m_p = m_{ply} + m_{plz} + m_{pay} + m_{paz}. \tag{30}$$

By symmetry $m_{plz} = m_{ply}$ and $m_{paz} = m_{pay}$. The total is given by

$$m_p \approx \frac{\sigma^2(6[R_{nt} - 1]^2 + 50R_{nt}^2)}{5N(2R_{nt} + 1)^2}, \quad \sigma^2 = \frac{\langle S_{ndi}^2 \rangle}{S_{no}^2}, \tag{31}$$

where σ^2 is the scintillation index of the contact stiffness. For the shear wave, a similar analysis yields

$$m_s \approx \frac{128\sigma^2}{15N\pi^2}. \tag{32}$$

The virtual mass terms are proportional to the scintillation index σ^2 of the contact stiffness, and inversely proportional to the number of contacts per grain N . For an exponential distribution, which is common for positive random quantities, σ^2 is exactly 1. For spherical grains of the same size, the value of N has an upper limit of 12, which corresponds to tetrahedral close packing, and a lower limit of 6 for cubic packing. Most sands and bead packs have porosity values in between these limits. The value of m_p also depends on the ratio R_{nt} , which is related to the Poisson’s ratio of the grain material. For quartz, the Poisson’s ratio⁸ is 0.08, giving a value of 0.96 for R_{nt} . Since this is very close to 1, the coupling into orthogonal linear grain movement, as represented by b_{xy} and b_{xz} in Eq. (21), will be relatively small, compared to angular motion represented by a_{xy} and a_{xz} . Values of m_p and m_s from Eqs. (31) and (32), and the corresponding wave speed ratios c_{gp}/c_p and c_{gs}/c_s , are shown in Fig. 3, for a Poisson’s ratio of 0.08, and for values of σ^2 between 0.25 and 4, as a function of N .

Acknowledgment

This work is sponsored by the Office of Naval Research, Code 321 OA, Ocean Acoustics Program, under the management of Dr. Robert Headrick.

References and links

- ¹C. Gazanhes and J.-P. H erault, "Dispersion acoustique dans des roches poreuses (Acoustic dispersion in porous rocks)," *J. Phys. III* **3**, 2071–2086 (1993); Eq. (1) and associated text.
- ²M. A. Biot and D. G. Willis, "The elastic coefficients of the theory of consolidation," *J. Appl. Mech.* **24**, 594–601 (1957); Eqs. (23) and (24) and associated text.
- ³R. D. Stoll, *Sediment Acoustics* (Springer, New York, 1989), Eq. (1.11) and associated text.
- ⁴G. Mavko, T. Mukerji, and J. Dvorkin, *The Rock Physics Handbook* (Cambridge University Press, Cambridge, 1998), pp. 149–151.
- ⁵A. Cemal Eringen, *Microcontinuum Field Theories I. Foundations and Solids* (Springer, New York, 1999), p. 101.
- ⁶P. N. Hagin and M. D. Zoback, "Viscous deformation of unconsolidated reservoir sands. II. Linear viscoelastic models," *Geophysics* **69**, 742–751 (2004).
- ⁷C.-H. Liu, S. R. Nagel, D. A. Schecter, S. N. Coppersmith, S. Majumdar, O. Narayan, and T. A. Witten, "Force fluctuations in bead packs," *Science* **269**, 513–515 (1995), Eq. (1).
- ⁸P. Heyliger, H. Ledbetter, and S. Kim, "Elastic constants of natural quartz," *J. Acoust. Soc. Am.* **114**, 644–650 (2003).

Loudness pattern-based speech quality evaluation using Bayesian modeling and Markov chain Monte Carlo methods

Guo Chen and Vijay Parsa

*Department of Electrical and Computer Engineering and National Centre for Audiology; University of Western Ontario; London, Ontario N6A 5B9, Canada
guo.chen@nca.uwo.ca, parsa@nca.uwo.ca*

Abstract: This work presents a speech quality evaluation method which is based on Moore and Glasberg's loudness model and Bayesian modeling. In the proposed method, the differences between the loudness patterns of the original and processed speech signals are employed as the observed features for representing speech quality, a Bayesian learning model is exploited as the cognitive model which maps the features into quality scores, and Markov chain Monte Carlo methods are used for the Bayesian computation. The performance of the proposed method was demonstrated through comparisons with the state-of-the-art speech quality evaluation standard, ITU-T P.862, using seven ITU subjective quality databases.

© 2007 Acoustical Society of America

PACS numbers: 43.71.Gv, 43.72.Ar, 43.72.Kb, 43.72.Gy, 43.72.-p [DOS]

Date Received: July 17, 2006 **Date Accepted:** December 7, 2006

1. Introduction

Speech quality evaluation is an important topic in the field of speech processing. A good speech quality measure can be used as an effective assessment tool for analyzing and optimizing speech processing devices and algorithms. In general, speech quality can be measured through subjective listening trials, or through objective measurement. The most widely used subjective test is the absolute category rating (ACR) method,¹ which results in mean opinion score (MOS). While subjective opinions of speech quality are preferred as the most trustworthy criterion for speech quality, they are also time-consuming, expensive, and not readily reproducible. In contrast, objective measures, which assess speech quality using parameters extracted from the speech signal, are less expensive to administer, save time, and therefore are highly desirable in practical applications. In the past two decades, objective quality measures have received considerable attention.^{2,3} Generally objective measures can be divided into two groups. One is intrusive evaluation, which assesses speech quality by measuring the "distortion" between the input and output signals.⁴⁻⁶ The other is nonintrusive evaluation, which assesses speech quality only based on the output speech signal of a system under test.⁷⁻¹¹ Regardless of the type of measurement, there are two key issues for the objective quality evaluation: (i) the identification of a set of features extracted from the speech signal that effectively represent the perceived speech quality and (ii) the development of a cognitive model that maps the feature set into a corresponding speech quality score. Previous studies have shown that the speech features extracted using perceptual models exhibit a higher degree of correlations with subjective quality ratings.⁴⁻¹¹ The challenge is therefore to develop a model to transform the extracted features into speech quality scores. The main problem in developing this model is its complexity or dimensionality: a model with low complexity will not accurately capture the underlying relationship between the features and the quality scores, and a model with a high complexity will result in overfitting and reduced prediction accuracy. In this paper, we address this issue by developing a model based on Bayesian methodology that utilizes Markov chain Monte Carlo (MCMC) methods, which handles the model complexity issue in a natural and consistent way.

We propose an objective speech quality measure, termed loudness pattern-based Bayesian speech quality evaluation method (LP-BSQE), which employs features extracted using Moore and Glasberg's auditory model (the MG model)¹² and the aforementioned Bayesian modeling methodology.¹³

2. The LP-BSQE method

The speech quality evaluation is separated into two parts in the LP-BSQE method. In the first part, the loudness pattern distortions are extracted as the speech quality features based on the MG model. A description of the feature extraction procedure is given in Sec. III. In the second part, a cognitive model is developed to transform the extracted features into the speech quality scores. Essentially, the cognitive model determines the relationship between the quality score y and the observation features X , i.e., $y=Q(X)+\epsilon$, where ϵ is a zero-mean error distribution. The true function Q is unknown and needs to be approximated. To do this we must make use of the observed data set, D , which consists of n observed quality scores with the associated input features, i.e., $D=\{(y_i,X_i)\}, i=1,\dots,n$. The main difficulty in the modeling is how to control the complexity of the cognitive model, as a model with low complexity will not accurately capture the underlying relationship and a model with a high complexity will result in overfitting. In the LP-BSQE method, we develop a cognitive model by using Bayesian modeling and Markov chain Monte Carlo methods, which can elegantly handle the model complexity problem. The basic concept behind Bayesian modeling is to calculate the posterior predictive distribution of new output y_{n+1} for the new input X_{n+1} given the training data set D , i.e.,

$$p(y_{n+1}|X_{n+1},D)=\int p(y_{n+1}|X_{n+1},W)p(W|D)dW, \quad (1)$$

where W denotes all the model parameters and hyper-parameters of the prior structures, and $p(W|D)$ represents the posterior probability of the parameters of the model Q given the training data set D . Note that the hyper-parameters stand for the noninformation priors for the model parameters, such as the parameters a , b , and v as defined as in Eq. (6). The estimation of speech quality can be obtained by

$$\hat{y}_{n+1}=E(y_{n+1}|X_{n+1},D)=\int Q(X_{n+1},W)p(W|D)dW. \quad (2)$$

In the meantime, we also wish to take into account the uncertainty between models M of different dimension (e.g., the number of basis functions), and we make this fact explicit by writing the expectation as

$$\hat{y}_{n+1}=\sum_{j=1}^J \int Q(X_{n+1},W_j,M_j)p(W_j|D,M_j)p(M_j|D)dW_j, \quad (3)$$

where $M=\{M_1,\dots,M_J\}$ is the set of models considered. In order to achieve this goal, a reversible jump MCMC sampling strategy¹⁴ was exploited by the LP-BSQE to approximate the integrals in Eq. (3) when the dimensions of the set of models M are unknown. It is worth noting that the samples from the posterior distribution are drawn during the "learning phase," which may be computationally very expensive, but predictions for the new data can be calculated quickly using the same stored samples and Eq. (3).

3. The feature extraction

The block diagram of the feature extraction of the loudness pattern distortion is shown in Fig. 1. The time delay information is first estimated using the cross-correlation method.⁶ After the time delay information is calculated, both the original speech s and its processed version s' are then separately analyzed by identical operations, leading to what we shall refer to as the loudness

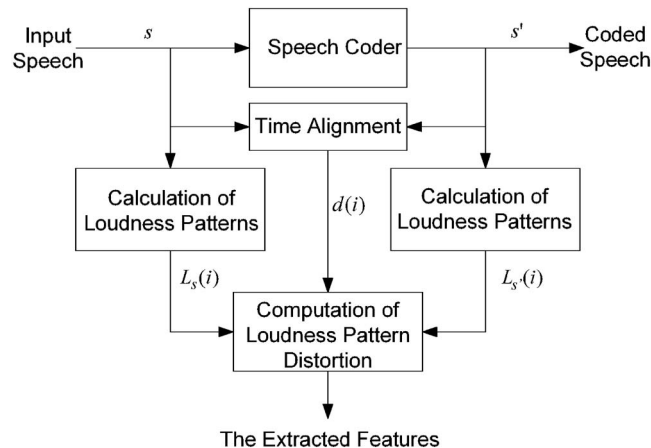


Fig. 1. The block diagram of the feature extraction.

patterns, L_s and $L_{s'}$, respectively. The quality features are then defined by an appropriate distance between these two specific loudness patterns. The procedure is briefly described as follows and details can be found in Ref. 6.

First, the level of the input speech is normalized and then the input speech signal was transformed into the frequency domain. The outputs are the short-time power spectral values, denoted by $P_1(i, k)$, where k and i represent the frequency scale and frame index, respectively. Next, the power spectrum is weighted by a frequency-dependent weighting function,⁶ which is used for simulating the transmission through the outer and middle ear. Using the weighted power spectrum $P_2(i, k)$, the excitation pattern can be calculated by $E(f_c) = \int_0^\infty \Phi(f, f_c, P_2) P_2(f) df$, where $\Phi(f, f_c, P_2)$ is the auditory filter and f_c is the center frequency of each auditory filter. Subsequently, the excitation patterns are transformed into the loudness patterns,⁶ denoted by $L(i, f_c)$. Finally, the loudness pattern distortions (i.e., the observed features) are obtained by

$$X(f_c) = \sqrt{\frac{\sum_{i=1}^I [L_s(i, f_c) - L_{s'}(i, f_c)]^2}{\sum_{i=1}^I [L_s(i, f_c)]^2}}, \tag{4}$$

where I is the total number of speech frames.

4. The cognitive model

In the LP-BSQE method, following the strategy introduced in Ref. 13, a Bayesian generalized linear model was chosen as the cognitive model and a reversible jump MCMC method was exploited for Bayesian computation. We assume that the known data consist of the n observations on the speech quality estimations $y = (y_1, \dots, y_n)'$ and the corresponding features $(X_1, \dots, X_n)'$, and that the cognitive model is represented by $y_i = Q(X_i) + \epsilon_i$, where Q is the regression function and the errors ϵ_i follow independent normal probability distributions $N(0, \sigma^2)$. The regression function Q is unknown, but we assume that it can be expressed as a linear combination of basis functions, B_j , i.e.,

$$y_i = \sum_{j=0}^k \beta_j B_j(X_i) + \epsilon_i \quad i = 1, \dots, n, \tag{5}$$

or, in matrix notation, $Y = \mathbf{B}\beta + \epsilon$. In general, there are many permissible forms of basis functions that the function $B(\cdot)$ can take. Three different types of radial basis functions (RBFs) (Ref.

15) were used in this work: (i) linear, $B(z)=z$; (ii) cubic, $B(z)=z^3$; and (iii) thin plate spline, $B(z)=z^2 \log(z)$, where $z=\|X_i-\mu_i\|$, μ_i is the knot or position of a RBF and $\|\cdot\|$ denotes a distance metric, usually the Euclidean distance.

Assuming that we have fully specified the set of basis functions, \mathbf{B} , the only unknown parameters in the model are the set of coefficients, β , and the regression variance σ^2 . It is convenient to choose mathematically convenient forms of prior distributions which result in computationally tractable posterior distributions.¹³ In the LP-BSQE method, we used a conjugate prior distribution for β and σ^2 , i.e., the normal inverse-gamma (NIG) distribution, which we shall denote by

$$\sigma^2 \sim \text{Inv-gamma}(a,b), \quad \beta|\sigma^2 \sim N(m,\sigma^2 V),$$

$$p(\beta, \sigma^2) = p(\beta|\sigma^2)p(\sigma^2) = \frac{b^a (\sigma^2)^{-a+(k/2)+1}}{(2\pi)^{k/2} |V|^{1/2} \Gamma(a)} \exp\left[-\frac{(\beta-m)' V^{-1} (\beta-m) + 2b}{2\sigma^2}\right], \quad (6)$$

where $V=vI$, I is the identity matrix, $\Gamma(\cdot)$ represents the standard gamma function, and a, b , and v are the hyper-parameters. Based on the above conjugate prior distribution, the likelihood $p(D|\beta, \sigma^2)$, or alternatively, $p(Y|X, \beta, \sigma^2)$, can be written as

$$p(D|\beta, \sigma^2) = N(B\beta, \sigma^2 I) = (2\pi\sigma^2)^{-n/2} \exp\left[-\frac{(Y-B\beta)'(Y-B\beta)}{2\sigma^2}\right]. \quad (7)$$

In terms of Bayes' theorem, the posterior distribution of the model parameters satisfies

$$p(\beta, \sigma^2|D) = \frac{p(D|\beta, \sigma^2)p(\beta, \sigma^2)}{p(D)}. \quad (8)$$

With the combination of Eqs. (6)–(8), we can obtain the posterior density as

$$p(\beta, \sigma^2|D) = \frac{(b^*)^a (\sigma^2)^{-a^*+(k/2)+1}}{(2\pi)^{k/2} |V^*|^{1/2} \Gamma(a^*)} \exp\left[-\frac{(\beta-m^*)' (V^*)^{-1} (\beta-m^*) + 2b^*}{2\sigma^2}\right], \quad (9)$$

where

$$m^* = (V^{-1} + B' B)^{-1} (V^{-1} m + B' Y), \quad V^* = (V^{-1} + B' B)^{-1},$$

$$a^* = a + n/2, \quad b^* = b + [m' V^{-1} m + Y' Y - (m^*)' (V^*)^{-1} m^*] / 2.$$

The marginal likelihood of a model M can also be obtained by

$$p(D|M) = \frac{|V^*|^{1/2} \Gamma(a^*) (b^*)^a}{|V|^{1/2} \Gamma(a) (b^*)^{a^*} \pi^{n/2}}. \quad (10)$$

In addition, it is often the case that a number of competing models exist to describe the relationship between the quality scores and the observation features. The Bayes factor¹³ is used to quantify the relative merits of model M_i over M_j , which can be expressed as

$$BF(M_i, M_j) = \frac{p(D|M_i)}{p(D|M_j)} = \frac{|V_j|^{1/2} |V_i^*|^{1/2} (b_j^*)^{a^*}}{|V_i|^{1/2} |V_j^*|^{1/2} (b_i^*)^{a^*}}. \quad (11)$$

In the Bayesian modeling approach, the complex integrals generally cannot be calculated using analytical methods. Instead, they are approximated by drawing samples from the joint probability distribution of all the model parameters, i.e., the Markov chain Monte Carlo (MCMC) methods.¹⁶ In the proposed LP-BSQE method, a reversible jump Metropolis-Hastings method¹⁴ was employed to approximate the integral in Eq. (3) where the number of basis functions of each model is unknown. This reversible jump sampling technique proceeds by augmenting the usual proposal step of a conventional Metropolis-Hastings sampler with a number of other

possible move types surrounding a change in the dimension of the density. At each iteration, in addition to the possibility of attempting a move within a particular parameter subspace, the sampler can propose to “jump” dimension, either up or down, by adding or removing a basis function from the cognitive model. We refer to these jumps as BIRTH, DEATH, and MOVE steps. The probability of attempting a BIRTH or DEATH or MOVE step when the current state has k basis functions is given by b_k , d_k , and m_k , respectively. In this work, we set the proposal probabilities as $b_k=d_k=m_k=1/3$ for $k=1, \dots, K-1$ and $b_k=d_0=m_0=0$, $b_0=1$, and $d_K=m_K=1/2$, where K is the maximum number of basis functions. Under this specification, the acceptance probability in the Metropolis-Hastings algorithm for a proposed move from a model M (of dimension k) to another model M' (of dimension k') can be derived to be

$$\text{Acceptance probability} = \min\left(1, \frac{p(D|M')}{p(D|M)} \times R\right), \quad (12)$$

where R is a ratio of probabilities given by $d_{k'}/b_k$ for a BIRTH, $b_{k'}/d_k$ for a DEATH, and $m_{k'}/m_k$ for a MOVE step. The detailed derivation can be found in Ref. 13. The reversible jump Metropolis-Hastings algorithm starts with one basis function with unity values for the input features. For each successive iteration, the MOVE step selects a basis function at random and resets its location to another value drawn randomly from the data set. The BIRTH step adds another basis function at a randomly selected point in the data set. The DEATH step selects just one basis at random and removes it. An initial portion of the chain (i.e., burn-in) is discarded to ensure convergence, and the final stored samples are used to make predictions using Eq. (3). The whole algorithm is written in pseudocode as follows:

```

Initialize:   Set  $t=1$ ,  $k=1$ ,  $a=0.01$ ,  $b=0.01$ ,  $v=100$ , and  $M^{(t)}$  with  $B_0(X)=1$ ;
              Calculate the initial mean of  $\beta$ ,  $m=(X'X)^{-1}X'Y$ ;
              Draw  $(\sigma^2)^{(t)}$  from Inv-Gamma( $a,b$ ) and draw  $\beta^{(t)}$  from  $N(m, \sigma^2 V)$ ;
              Calculate the marginal likelihood  $p(D|M^{(t)})$ ;
Repeat:      Set  $u_1$  to a draw from a  $U(0,1)$  distribution;
              IF ( $u_1 < b_k$ ) THEN  $M'=$ BIRTH step ( $M^{(t)}$ )
              IF ( $b_k < u_1 \leq b_k+d_k$ ) THEN  $M'=$ DEATH step ( $M^{(t)}$ )
              OTHERWISE  $M'=$ MOVE step ( $M^{(t)}$ )
              Calculate the marginal likelihood  $p(D|M')$ ;
              Set  $u_2$  to a draw from a  $U(0,1)$  distribution;
              IF ( $u_2 < \min(1, BF(M', M^{(t)}) \times R)$ ) THEN  $M^{(t+1)}=M'$ ;
              OTHERWISE  $M^{(t+1)}=M^{(t)}$ ;
              Updated the parameters to  $a^*$ ,  $b^*$ ,  $m^*$ ,  $V^*$  using Eq. (9)
              raw  $(\sigma^2)^{(t+1)}$  from Inv-Gamma( $a^*, b^*$ ) and draw  $\beta^{(t+1)}$  from  $N(m^*, (\sigma^2)^{(t+1)} V^*)$ 
               $t=t+1$  and store  $M^{(t)}$  after the initial burn-in;
End Repeat.

```

5. Experimental results and conclusions

The effectiveness of the proposed LP-BSQE method was demonstrated through comparisons with the state-of-the-art speech quality evaluation standard, ITU-T P.862 (PESQ).⁴ The experimental data consist of 1328 subjective MOS ratings that come from seven subjective MOS databases (English, French, Japanese, and Italian) obtained in the subjective listening tests which are described in experiment 1 (three databases) and experiment 3 (four databases) of the ITU-T P-Series supplement 23. Each of these databases contains a number of speech sentence pairs spoken by four talkers (two female and two male) and each sentence pair stands for one condition under test. In experiment 1, each database contains 44 sentence pairs while in experiment 3 each database contains 50 sentence pairs. The correlation coefficient (ρ) between sub-

Table 1. Performance of the LP-BSQE compared with the ITU-T P.862 (PESQ) using the correlation coefficient per-condition ρ and the standard deviation of error τ .

Database	PESQ		LP-BSQE(linear)		LP-BSQE(cubic)		LP-BSQE(thin plate)	
	ρ	τ	ρ	τ	ρ	τ	ρ	τ
Exp1A	0.918	0.421	0.953 (104%)	0.230	0.931 (101%)	0.278	0.941 (103%)	0.2560
Exp1D	0.937	0.251	0.920 (98%)	0.251	0.896 (96%)	0.284	0.905 (97%)	0.2722
Exp1O	0.941	0.316	0.960 (102%)	0.217	0.949 (101%)	0.245	0.953 (101%)	0.2342
Exp3A	0.865	0.378	0.908 (105%)	0.286	0.896 (104%)	0.302	0.893 (103%)	0.3065
Exp3D	0.940	0.269	0.903 (96%)	0.291	0.900 (96%)	0.296	0.903 (96%)	0.2910
Exp3O	0.913	0.332	0.920 (101%)	0.285	0.916 (100%)	0.291	0.918 (101%)	0.2886
Exp3C	0.928	0.422	0.913 (98%)	0.345	0.895 (96%)	0.375	0.893 (96%)	0.3791
Total	0.864	0.447	0.936 (108%)	0.275	0.925 (107%)	0.297	0.927 (107%)	0.2921

jective and objective values and the standard deviation of error (τ), which are widely used for evaluating the performance of an objective speech quality measure,² are employed in our experiments. Generally, a subjective MOS test contains different testing conditions and it is typical to use the correlation coefficient and the standard deviation of error per condition to demonstrate the resultant performance. These are obtained as

$$\rho = \frac{\sum_{i=1}^N (t_i - \bar{t})(d_i - \bar{d})}{\sqrt{\sum_{i=1}^N (t_i - \bar{t})^2 \sum_{i=1}^N (d_i - \bar{d})^2}} \quad \tau = \sqrt{\frac{\sum_{i=1}^N (t_i - d_i)^2}{(N-1)}}, \quad (13)$$

where t_i is the MOS ratings for condition i (averaged over all sentences and listeners), \bar{t} is the average over all t_i 's, d_i is the estimated quality by an objective measure for condition i , \bar{d} is the average of all d_i 's, and N is the number of conditions.

The performance of the LP-BSQE with three types of radial basis functions (i.e., linear, cubic, and thin plate) on the seven databases is shown in Table 1. It can be seen that the correlation coefficients of the LP-BSQE for all databases are above 0.89. In particular, the correlation coefficients of the LP-BSQE with linear radial basis function are all over 0.90. For comparison, the performance of the standardized ITU-T P.862 (PESQ) is also included in the table. The percentage within the parentheses in italic type shows the performance of the LP-BSQE relative to that of the PESQ, i.e., the ratio of the correlation coefficients of the LP-BSQE to those of the PESQ. As shown in Table 1, for four tests (Exp1A-French, Exp1O-English, Exp3A-French, and Exp3O-English), the performance of the LP-BSQE is superior to that of the PESQ. For the other three tests (Exp1D-Japanese, Exp3D-Japanese, and Exp3C-Italian), the performance of the LP-BSQE is slightly lower than that of the PESQ. Interestingly, it can be observed that the LP-BSQE performed better than the PESQ for the French and English databases but not for the Japanese and Italian databases. For the entire databases, the performance of the LP-BSQE shows the averaged correlation coefficient of about 0.929, which is better than 0.864 of the performance of the PESQ. These results show that the proposed LP-BSQE method can effectively predict the speech quality scores highly correlating with the subjective speech quality.

Acknowledgments

We gratefully acknowledge the financial support by the Oticon Foundation, Denmark, and the NSERC, Canada.

References and links

¹ITU, "Methods for subjective determination of transmission quality," ITU-T P.800 (1996).

²S. R. Quackenbush, T. P. Barnwel III, and M. A. Clements, *Objective Measures of Speech Quality* (Prentice-

Hall, Englewood Cliffs, NJ, 1988).

- ³A. Rix, "Perceptual speech quality assessment - A review," in *Proceedings IEEE Int. Conf. Acoustics, Speech and Signal Processing*, Vol. 3, 1056–1059, Montreal, Canada (2004).
- ⁴ITU, "Perceptual evaluation of speech quality," ITU-T P.862 (2001).
- ⁵G. Chen, S. N. Koh, and I. Soon, "Enhanced Itakura measure incorporating masking properties of human auditory system," *Signal Process.* **83**, 1445–1456 (2003).
- ⁶G. Chen, V. Parsa, and S. Scollie, "An ERB loudness pattern based objective speech quality measure," in *Proceedings of the International Conference on Spoken Language Processing*, 2174–2177, Pittsburgh, PA (2006).
- ⁷ITU, "Single ended method for objective speech quality assessment in narrow-band telephony applications," ITU-T P.563 (2004).
- ⁸D.-S. Kim, "Anique: An auditory model for single-ended speech quality estimation," *IEEE Trans. Speech Audio Process.* **13**, 821–831 (2005).
- ⁹G. Chen and V. Parsa, "Output-based speech quality evaluation by measuring perceptual spectral density distribution," *Electron. Lett.* **40**, 783–784 (2004).
- ¹⁰G. Chen and V. Parsa, "Non-intrusive speech quality evaluation using an adaptive neurofuzzy inference system," *IEEE Signal Process. Lett.* **12**, 403–406 (2005).
- ¹¹G. Chen and V. Parsa, "Bayesian model based non-intrusive speech quality evaluation," in *Proceedings IEEE Int. Conf. Acoustics, Speech and Signal Processing*, Vol. 1, 385–388, Philadelphia, PA (2005).
- ¹²B. C. J. Moore, B. Glasberg, and T. Baer, "A model for the prediction of thresholds, loudness, and partial loudness," *J. Audio Eng. Soc.* **45**, 224–239 (1997).
- ¹³D. Denison, C. C. Holmes, B. K. Mallick, and A. F. M. Smith, *Bayesian Methods for Nonlinear Classification and Regression* (Wiley, Chichester, England, 2002).
- ¹⁴P. Green, "Reversible jump Markov chain Monte Carlo computation and Bayesian model determination," *Biometrika* **82**, 711–732 (1995).
- ¹⁵C. C. Holmes and B. K. Mallick, "Bayesian radial basis functions of variable dimension," *Neural Comput.* **10**, 1217–1233 (1998).
- ¹⁶W. R. Gilks, S. Richardson, and D. J. Spiegelhalter, *Markov Chain Monte Carlo in Practice* (Chapman and Hall, London, 1996).

Discrimination of starting phase with sinusoidal envelope modulation

Stanley Sheft and William A. Yost

*Parmly Hearing Institute, Loyola University Chicago, 6525 North Sheridan Road, Chicago, Illinois 60626
ssheft@luc.edu, wyost@luc.edu*

Abstract: Modulation-filterbank models discard phase information above very low rates of amplitude modulation (AM). The present work evaluated this restriction by measuring thresholds for discriminating the starting phase of sinusoidal modulators of wideband-noise carriers. Results showed a low-pass characteristic with some listeners unable to perform the task once the modulation rate was greater than 12.5 Hz. For others, however, thresholds were obtained with AM rates of up to one to two octaves higher. Intersubject variability may in part relate to the presence of multiple discrimination cues, with only some based on comparison of the ongoing pattern of envelope fluctuation.

© 2007 Acoustical Society of America

PACS numbers: 43.66.Mk, 43.66.Ba [QJF]

Date Received: November 11, 2006 **Date Accepted:** December 8, 2006

1. Introduction

Current psychophysical models of auditory processing of amplitude modulation (AM) are often based on a modulation filterbank (MF). Following envelope detection, stimuli in MF models are processed by an array of broadly tuned, overlapping bandpass filters that span the range of envelope fluctuation rates detectable by human observers. Past work has shown MF models successful at accounting for a variety of results, including AM detection with various carrier types and bandwidths, AM depth discrimination, and modulation masking (Dau *et al.*, 1997, 1999; Verhey *et al.*, 2003; Ewert and Dau, 2004). While some model applications base decision statistics solely on integrated envelope power, others retain temporal response features of filterbank channels centered at 10 Hz and below. The basis of this low-pass restriction comes from work by Dau (1996), who for three listeners measured performance at discriminating envelope starting phase with sinusoidal modulators.

The temporal pattern of low-rate envelope fluctuation can play an important role in envelope perception, most notably with speech for which intelligibility depends on both the magnitude and phase of the low-rate modulation spectrum (Greenberg and Arai, 2004). Understanding of the basis and limitations of envelope-pattern processing can be important when applying MF models to complex stimulus configurations (Viemeister *et al.*, 2004). With variation of envelope starting phase, discrimination may be cued by either the temporal pattern of the envelope or processing of some related consequence of the stimulus manipulation (e.g., intensity discrimination between observation intervals at a specific stimulus time). The goal of the present work was to gain insight into the cues that listeners might use to discriminate envelope phase. To minimize possible involvement of specific cues, some conditions involved randomization of stimulus parameters. Either individually or in combination, possible randomizations included overall level, stimulus duration, and the starting phase of the reference modulator.

2. Method

Thresholds for discriminating the starting phase of sinusoidal modulators of gated wideband-noise carriers were measured in terms of radians. The modulation index was always 1.0. In the cued two-interval forced-choice task, the nonsignal interval repeated the cue modulator with the phase increment added to the signal-interval modulator. Independent noise samples were used for the carrier on each stimulus presentation. In the audio-frequency domain, the short-

term amplitude spectrum of a specific carrier varies with modulator phase. Use of independent noise carriers precludes this variation from providing a discrimination cue.

In each condition, the starting phase of the cue modulator was either fixed in sine phase or randomized across trials. Random phases were selected from a uniform distribution ranging from 0.0 to 2π radians. Duration and level were also either fixed or randomized. With duration randomization, the cue duration was always 400 ms, with the stimulus duration of each observation interval randomly selected from a uniform distribution extending from 200 to 600 ms. In conditions without duration randomization, the common duration of all stimulus presentations of a trial varied from 50 to 800 ms. Across AM rates, duration was limited so that a minimum of one full cycle of modulation was presented. The interstimulus interval was always 400 ms with all stimuli shaped with 5-ms \cos^2 rise/fall ramps. In the fixed-level conditions, overall stimulus level was 65 dB SPL, corresponding to a pressure spectrum level of 24.5 dB. Conditions with level randomization employed a 20-dB rove (± 10 dB) about a mean level of 65 dB SPL. Dell PCs with 24-bit Echo Gina 3G soundcards were used for stimulus generation and experimental control. Following analog conversion at a 44.1-kHz sampling rate, stimuli were low-pass filtered at 12 kHz and presented diotically through Sennheiser HD 520 II headphones, with the subjects seated in a double-walled soundproof booth.

Thresholds were measured with a three-down, one-up tracking procedure with feedback (Levitt, 1971). The initial tracking step size varied phase by a factor of 1.25. Following two reversals, the factor was reduced to 1.125. A run was terminated after 16 reversals with threshold estimated as the geometric mean of the last 12 reversals. Reported threshold values are the geometric mean of at least six threshold estimates. If the tracking procedure called for a phase increment equal to or greater than π radians, threshold was not calculated for that run. In Sec. 3, results which indicate that a threshold could not be obtained in a specific condition represent at least four attempts. Data were collected from six listeners, though only four participated in all conditions. Experimental protocol was approved by the Institutional Review Board of Loyola University Chicago.

3. Results and discussion

Individual differences characterized results from all conditions. Figure 1 shows individual thresholds as a function of AM rate with the cue modulator either in sine (circles) or random (triangles) phase. Stimulus duration was 400 ms. With increasing AM rate, the first rate at which threshold could not be obtained with the adaptive procedure is indicated by the appropriate symbol shape with a slash. For both configurations of cue-modulator phase, results indicate a low-pass characteristic, that is, threshold values rose with AM rate. The highest AM rate at which threshold could be obtained varied across subjects from 10 to 50 Hz. Except for subject S2, randomizing cue modulator phase had little effect on this upper cutoff rate. The low-pass result is in general agreement with the findings of Dau (1996). In that study, performance was measured for detecting a modulator-phase increment of π radians with randomization of the reference phase. Results showed that all three subjects were at chance performance once the modulation rate was increased to 12 Hz. The present work, however, indicates that for some subjects, the highest AM rate at which starting phase is discriminable can be one to two octaves higher, despite randomization of the reference phase angle.

In Fig. 1, the effect of phase randomization on threshold values was more pronounced than on rate limitation, and in almost all cases, covered the entire range over which individual thresholds could be measured. This result suggests that randomization of cue-modulator phase disrupted use of a discrimination cue(s) that was used at all AM rates. Potentially, there are multiple cues that could be used to discriminate envelope phase with the effect of phase randomization, or more generally starting phase angle *per se*, dependent on specific cue. Listeners could compare or cross correlate the temporal pattern of envelope fluctuation. Alternatively, they could focus on a specific stimulus time and attempt to detect a cross-interval intensity difference. Finally, the “effective” or perceived stimulus duration may vary with modulator phase if in some cases the envelope begins and ends near trough values. The effect of phase randomization may then be from either actual disruption of the information of a specific dis-

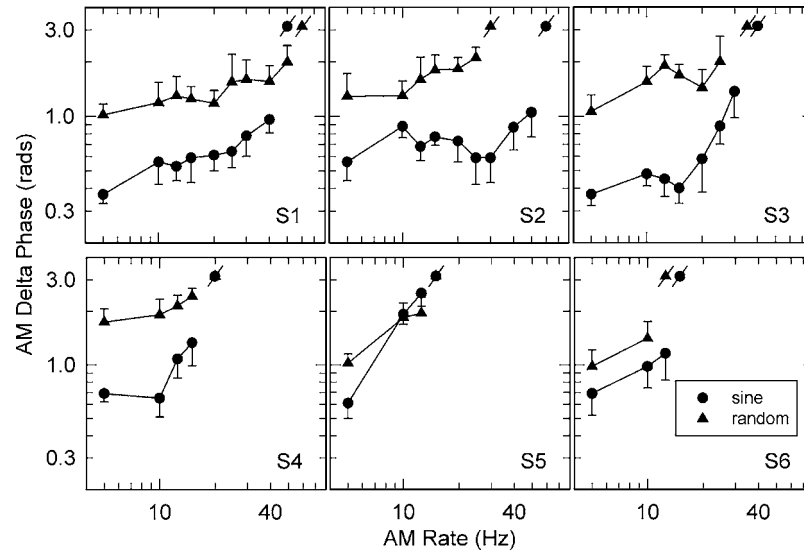


Fig. 1. Individual phase-discrimination thresholds as a function of AM rate with a 400-ms stimulus duration. The cue modulator was either in sine (circles) or random (triangles) phase. Unconnected symbols with a slash indicate that a threshold could not be obtained in that condition. Error bars represent 1 standard deviation (s.d.) of the mean threshold.

crimination cue or from a reduction in the frequency of occurrence of “optimal” cue presentation. While the present data sets do not distinguish these possibilities, the intent of the remaining conditions was to evaluate possible involvement of the various detection cues.

Dau *et al.* (1997) modeled AM detection with a decision statistic based on cross correlation of the signal with a stored template. Use of a correlation receiver for envelope-phase discrimination predicts that performance in terms of d' should improve by the square root of duration. Figure 2 shows thresholds obtained as a function of stimulus duration in conditions in which cue-modulator phase was randomized. The parameter is AM rate. With 20-Hz AM, conditions in which thresholds could not be measured were at the longer, not shorter, stimulus durations. In conditions with measurable thresholds, the functions were all relatively flat. Both results contrast with predictions based on discrimination by a correlation receiver. Dau (1996) reported no significant dependence of envelope-phase-discrimination performance on duration in the range of 300–700 ms. With duration discrimination showing an approximate Weber relationship (Abel, 1972), absence of an effect of duration in both past and present results discounts the suggestion of phase discrimination cued by change in perceived stimulus duration.

Cross-interval intensity discrimination at specific stimulus times is another potential cue that represents processing of a consequence of envelope modulation rather than of the ongoing modulation *per se*. In this scheme, listeners would for example estimate the time of the first peak of the cue modulator, and judge for which of the two observation intervals level has varied at the estimated time from stimulus onset. Results from the first data set indicated a substantial effect of randomizing the reference envelope phase. Though most likely having impact by varying from trial to trial the times relative to onset of the cue-modulator peaks, phase randomization does not eliminate the ability to base decisions on cross-interval intensity discrimination. Randomization of the overall level of each stimulus presentation of a trial can eliminate this cue. In the final condition set, level and duration were randomized, both individually and in combination with cue-modulator phase.

Results for three subjects are shown in Table 1. The ability to perform the task in conditions of parameter randomization varied dramatically among subjects. Subject S1 was able to complete all but two of the conditions, while for S2, thresholds could not be obtained in

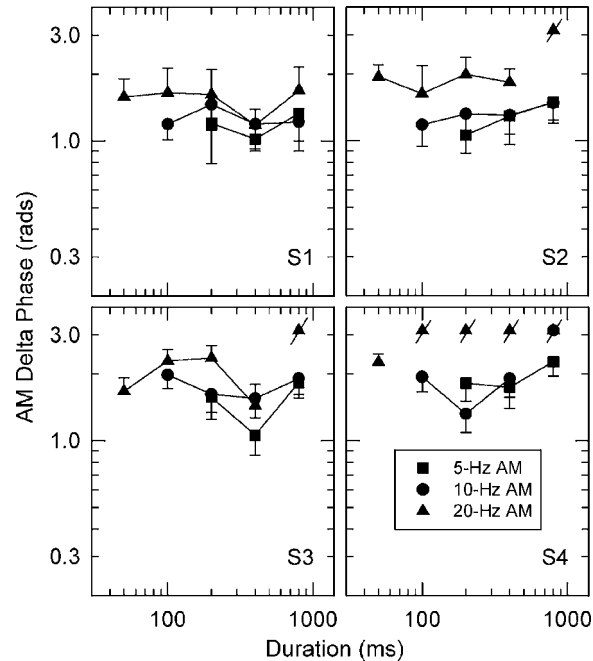


Fig. 2. Individual thresholds as a function of stimulus duration in conditions with randomization of cue-modulator phase. Symbol shape indicates AM rate of either 5 (squares), 10 (circles), or 20 (triangles) Hz. Unconnected symbols with a slash indicate that a threshold could not be obtained in that condition. Error bars represent 1 s.d. of the mean threshold.

18 of the 30 conditions that involved randomization. As observed in the data of Fig. 1, randomization affected sensitivity in a way that varied across subjects. For individual listeners, data trends were similar with either level or duration randomization. Though impoverished by phase or duration randomization, only level randomization eliminates the cross-interval intensity-discrimination cue. Results suggest that this cue was often not effectively used. Concurrent randomization of several stimulus parameters generally made the task more difficult. Results from conditions in which stimulus duration was varied (see Fig. 2) suggest that the effect of duration randomization relates to neither variation in threshold with duration nor loss of a duration-discrimination cue. Along with restricting potential involvement of various discrimination cues, randomization introduces uncertainty which can increase the variance of the discrimination process. Overall data trends suggest that by introducing uncertainty, randomization itself affects performance.

The absence of an effect of stimulus duration was interpreted as inconsistent with use of a decision statistic based on cross correlation. Alternatively, listeners may, at least in some conditions, perform a limited pattern matching of distinctive stimulus features. By subject report, one cue that varies with phase is irregularity of envelope pattern near stimulus onset. With periodic modulation, the time between envelope peaks is not dependent on starting modulator phase. However, the time from stimulus onset to the first envelope peak does vary with phase. This variation may be perceived as altering the regularity of the envelope pattern. Perception of envelope rhythm requires resolution of the individual envelope peaks, that is, a perception of envelope fluctuation rather than roughness. The low fluctuation strength associated with AM rates of greater than 20 Hz (see Fastl, 1983) is consistent with involvement of a rhythm cue in current results. It is unclear whether this cue would persist for AM rates of 30 Hz and greater for which some subjects were still able to perform the phase-discrimination task.

In the modulation domain, change in the starting phase of the modulator affects the short-term amplitude spectrum. At stimulus onset, the effect is observed in terms of amplitude

Table 1. Individual subject thresholds in radians. The conditions labeled “fixed” refer to the cue modulator in sine phase; labels “dB,” “ms,” and “rad” indicate randomization of level, duration, and starting phase, respectively. An asterisk indicates that threshold could not be measured adaptively in that condition.

Subj	Condition	AM Rate (Hz)				
		5	10	20	30	40
S1	fixed	0.37	0.56	0.61	0.78	0.96
	dB	0.42	0.69	0.83	0.9	1.21
	ms	0.92	0.52	0.77	0.75	0.84
	rad	1.02	1.19	1.18	1.60	1.56
	rad, dB	1.06	1.41	1.67	2.20	*
	rad, ms	1.46	1.27	1.01	1.41	1.92
	rad, dB, ms	1.46	1.24	1.89	1.88	*
S2	fixed	0.56	0.88	0.73	0.59	0.87
	dB	0.85	1.5	*	*	*
	ms	0.7	1.32	*	*	*
	rad	1.29	1.30	1.83	*	*
	rad, dB	1.08	1.66	*	*	*
	rad, ms	1.70	2.05	*	*	*
	rad, dB, ms	1.52	*	*	*	*
S3	fixed	0.37	0.48	0.58	1.37	*
	dB	0.74	1.11	0.96	1.14	*
	ms	1.11	0.98	0.85	1.16	1.33
	rad	1.06	1.55	1.44	*	*
	rad, dB	1.33	1.94	2.06	*	*
	rad, ms	1.89	1.80	*	*	*
	rad, dB, ms	*	*	*	*	*

splatter, which conceivably is discriminable with frequency-selective modulation processing. Sheft and Yost (2004) demonstrated that variation in the envelope-phase spectrum can be discriminated for durations as brief as roughly 16 ms (shorter durations were not considered). To evaluate the potential utility of short-term spectral cues at stimulus onset, simulations were run using the ten-channel MF-model parameters of Sheft and Yost (2004). To estimate best-case performance, model predictions ignored potential cross-MF-channel masking (see Sheft and Yost, 2004) with the decision statistic based solely on change in channel-output power calculated over a 10-ms window at stimulus onset. Without internal noise added to the simulations, model performance is limited solely by the intrinsic envelope fluctuations of the independent carrier samples. In conditions with the cue modulator in sine phase, model performance increased with AM rate in contrast to the trend for low-pass subject performance. At 40 Hz, the simulated d' value was 4.1 with a delta phase of π radians. However, model performance dropped to a d' value of no greater than 0.3 when adding the internal noise level needed to account for the discrimination results of Sheft and Yost (2004). Randomization of the cue-modulator starting phase also adversely affected simulations, with model performance never significantly exceeding chance performance. Overall, these results discount potential involvement of short-term spectral cues in the current discrimination conditions.

Along with cross-MF-channel masking of short-term spectral-amplitude differences, another source of likely masking is temporally based, that is masking of onset splatter by subsequent stimulation. Due to the intrinsic envelope fluctuations of the WBN carriers, wideband modulation is present throughout the stimulus duration and is not just a result of onset splatter. Temporal masking most likely would degrade the information derived from a 10-ms window at stimulus onset in the previous simulations. A second effect of intrinsic carrier fluctuations is the introduction of second-order modulation when the carrier is sinusoidally modulated. The higher

MF channels show significant response to the intrinsic carrier fluctuations. The Hilbert envelope of this response temporally follows the pattern of the lower-rate sinusoidal modulators, thus a function of modulator phase. As with onset cues considered above, the addition of internal noise into model simulations eliminated the efficacy of this potential discrimination cue.

From a modeling standpoint, the key issue concerning the present work is the extent to which MF models should retain envelope-phase information. Regardless of the specific discrimination cue(s) used by listeners, results are relevant to this concern as long as the decision statistic is based on MF output. MF models incorporate a low filter Q and shallow filter-skirt slopes. With significant response to stimuli well removed from the filter center frequency (CF), ability to discriminate envelope phase would be expected at AM rates which exceed the CFs of MF channels which retain temporal response features. The current results indicate a need for upward revision of the upper cutoff for preserving phase information in MF models. Using the model parameters of Sheft and Yost (2004) with one additional MF channel centered at 18 Hz preserving phase information, envelope-phase discrimination can be simulated for AM rates of up to 35 Hz. Preservation of phase information in a second additional channel is required to model the best performance of the current data set, that of subject S1. In either case, intersubject variability is assumed to represent suboptimal processing by some listeners.

In contrast to present results, both lateralization and synchrony-detection procedures demonstrate an ability to utilize envelope-phase information at moderate to high AM rates (e.g., Yost and Sheft, 1989; Bernstein and Trahiotis, 2002). Conceivably, the envelope processing required by these tasks may precede or operate in parallel to an MF stage. Alternatively, restrictions on MF models may be task dependent. Though modeling of auditory masking is often based on signal and masker power levels, the intent is not to argue for a general loss of fine-structure phase information that would leave lateralization ability unaccountable. A similar task dependency may be required when considering AM processing.

Acknowledgment

This research was supported by NIDCD grant numbers DC005423 and DC00625.

References and links

- Abel, S. M. (1972). "Duration discrimination of noise and tone bursts," *J. Acoust. Soc. Am.* **51**, 1219–1223.
- Bernstein, L. R., and Trahiotis, C. (2002). "Enhancing sensitivity to interaural delays at high frequencies by using 'transposed stimuli'," *J. Acoust. Soc. Am.* **112**, 1026–1036.
- Dau, T. (1996). *Modeling Auditory Processing of Amplitude Modulation* (BIS, Universität Oldenburg).
- Dau, T., Kollmeier, B., and Kohlrausch, A. (1997). "Modeling auditory processing of amplitude modulation. I. Detection and masking with narrow-band carriers," *J. Acoust. Soc. Am.* **102**, 2892–2905.
- Dau, T., Verhey, J., and Kohlrausch, A. (1999). "Intrinsic envelope fluctuations and modulation-detection thresholds for narrow-band noise carriers," *J. Acoust. Soc. Am.* **106**, 2752–2760.
- Ewert, S. D., and Dau, T. (2004). "External and internal limitations in amplitude-modulation processing," *J. Acoust. Soc. Am.* **116**, 478–490.
- Fastl, H. (1983). "Fluctuation strength of modulated tones and broadband noise," in *Hearing—Physiological Bases and Psychophysics*, edited by R. Klinke and R. Hartmann (Springer, Berlin).
- Greenberg, S., and Arai, T. (2004). "What are the essential cues for understanding spoken language?" *IEICE Trans. Inf. Syst.* E87-D, 1059–1070.
- Levitt, H. (1971). "Transformed up-down methods in psychoacoustics," *J. Acoust. Soc. Am.* **49**, 467–477.
- Sheft, S., and Yost, W. A. (2004). "Minimum integration times for processing of amplitude modulation," in *Auditory Signal Processing: Physiology, Psychoacoustics, and Models*, edited by D. Pressnitzer, A. de Cheveigne, S. McAdams, and L. Collet (Springer, New York).
- Verhey, J. L., Ewert, S. D., and Dau, T. (2003). "Modulation masking produced by complex tone modulators," *J. Acoust. Soc. Am.* **114**, 2135–2146.
- Viemeister, N. F., Stellmack, M. A., and Byrne, A. J. (2004). "The role of temporal structure in envelope processing," in *Auditory Signal Processing: Physiology, Psychoacoustics, and Models*, edited by D. Pressnitzer, A. de Cheveigne, S. McAdams, and L. Collet (Springer, New York).
- Yost, W. A., and Sheft, S. (1989). "Across-critical-band processing of amplitude-modulated tones," *J. Acoust. Soc. Am.* **85**, 848–857.

Unattended speech processing: Effect of vocal-tract length

Marie Rivenez

*Institut de Médecine Aéronautique du Service de Santé des Armées, France
mrivenez@imassa.fr*

Christopher J. Darwin

*Department of Psychology, University of Sussex, Brighton, United Kingdom
cjd@sussex.ac.uk*

Léonore Bourgeon

*Institut de Médecine Aéronautique du Service de Santé des Armées, France
lbourgeon@imassa.fr*

Anne Guillaume

*Institut de Médecine Aéronautique du Service de Santé des Armées, France
aguillaume@imassa.fr*

Abstract: Rivenez *et al.* [J. Acoust. Soc. Am. **119** (6), 4027–4040 (2006)] recently demonstrated that an unattended message is able to prime by 28 ms a simultaneously presented attended message when the two messages have a different F_0 range. This study asks whether a difference in vocal-tract length between the two messages rather than a difference in F_0 can also produce such priming. A priming effect of 13 ms was found when messages were in the same F_0 range but had different (15%–30%) vocal-tract length, suggesting that the processing of unattended speech strongly relies on the presence of perceptual grouping cues.

© 2007 Acoustical Society of America

PACS numbers: 43.66.Lj, 43.66.Rq, 43.71.Bp, 43.71.Gv [JH]

Date Received: August 9, 2006 **Date Accepted:** November 10, 2006

1. Introduction

It is established that speech intelligibility is largely influenced by perceptual cues differentiating the voices such as pitch, timbre, or level (see for instance Brungart, 2001; Brungart *et al.*, 2001; Darwin, Brungart, and Simpson, 2003). However, very few researches have investigated the implication of such cues on the processing of unattended speech. The purpose of this study was to extend this finding to the processing of an unattended message simultaneously presented with an attended message. Specifically, we asked whether a difference in the vocal-tract length between two speakers can improve the processing of an unattended message.

Since a thorough and influential review by Holender (1986), it has been generally accepted that there is no lexical processing of unattended speech. Claims that such processing *had* occurred were attributed to experimental paradigms that allowed attention to be switched transiently to the nominally unattended message. Further support for this consensual view came recently from Dupoux, Kouider, and Mehler (2003) using a lexical decision task. Listeners made lexical decisions on words presented in lists to the attended ear. Their decisions were primed (about 100 ms faster) when a lexically identical word (same word but different acoustically because of their respective pronunciation) rather than an unrelated word had just occurred on the unattended ear. However, such priming occurred only when the prime in the unattended ear was presented as an isolated word; it did not occur when the prime was part of a continuous sentence. According to the authors, the abrupt onset of words presented in isolation probably attracted an involuntary switch of attention.

This consensus has recently been challenged by Rivenez, Darwin, and Guillaume (2006). They used a dichotic priming paradigm similar to Dupoux's and found a small, but significant, priming effect of 28 ms when the priming word was presented as part of a sentence to the unattended ear. However, this priming effect was only found when the voices in the two ears had different fundamental frequency (F_0) ranges—their mean F_0 differed by 4.2 semitones. When the voices had the same F_0 range, there was no priming. Rivenez *et al.* (2006) postulated that the F_0 range difference increased the perceptual separation of the two messages and hence the clarity of the (20-dB quieter) unattended message.

It is well known that a difference in F_0 between two concurrent messages can enhance the simultaneous and the sequential grouping of speech signals (Assmann and Summerfield, 1990; Bird and Darwin, 1998; Broadbent and Ladefoged, 1957; Brokx and Nootboom, 1982; Darwin, 1981; Darwin, Brungart, and Simpson, 2003; Darwin and Hukin, 2000; Scheffers, 1983). If the effect of F_0 observed in Rivenez *et al.* (2006) is explained by an improvement in the perceptual organization of the unattended message when the messages are in a different F_0 range, then providing a different cue that distinguishes the attended and unattended messages should also improve the processing of the unattended message and increase the priming effect.

The intelligibility of two simultaneous messages can be improved if their voices differ sufficiently in vocal-tract (VT) length. The acoustic consequence of a modification of VT length is a modification in formant frequencies by a constant amount. Using two messages in the same F_0 range, speech intelligibility can be improved with a 13% (Darwin *et al.*, 2003) or a 20% VT length difference (Culling and Poster, 2004; Assmann, 1999). It is likely that a substantial part of the improvement produced by a difference in VT length relies on the ability to track a sound source across time by providing a qualitative difference between the two voices (Darwin and Hukin, 2000). A difference in VT length is less likely to be effective at grouping sounds simultaneously rather than sequentially (Assmann, 1999; Culling and Poster, 2004; Darwin *et al.*, 2003; Darwin and Hukin, 2000). In contrast, a difference in F_0 between voices can substantially aid both types of grouping (Bird and Darwin, 1998; Culling and Darwin, 1993). The relative effectiveness of VT length and F_0 differences in improving the intelligibility of a target message in the presence of a simultaneous competing message has been systematically explored by Darwin *et al.* (2003) using a task (coordinate response measure, CRM) that is very substantially weighted towards sequential rather than simultaneous perceptual grouping. When the target message was 6 dB quieter than the competing message, a difference of 4 semitones in the F_0 range of the voices produced an improvement of about 20% in task performance. Further increases in F_0 difference produced no additional improvement. For VT length, an 8% or a 16% difference gave only a small improvement of about 10% and performance only increased by around 20% for a VT length difference of 34%. Comparing these changes in F_0 and VT length with those found between male and female speakers indicates that natural differences in F_0 are more useful for sequential grouping than are differences in VT length: on average, female F_0 's are 70%–90% higher than male, and their VT 15%–20% shorter (Peterson and Barney, 1952). The 34% difference in VT length needed to obtain substantial improvement in the CRM task is an extreme difference, whereas the 4-semitone difference in F_0 is within the normal range of a single voice.

The purpose of this experiment was to assess the effect of a difference in VT length on the priming of an attended by an unattended message delivered with the same F_0 range using the dichotic priming paradigm developed by Rivenez *et al.* (2006). We anticipate that substantial differences in VT length will be needed to obtain performance changes comparable to those found previously with a 4-semitone difference in F_0 range.

2. Method

Each attended message was made up of a list of about 18 monosyllabic words presented at an average speed of 2.1 words per second. Each list included one or two target words belonging to a specific semantic category. Attended messages were recorded by a native English speaker (CJD). F_0 was held constant at its average value across the sentence (140 Hz), using the

PSOLA algorithm implementation running on PRAAT 4.1 (Kortekaas and Kohlrausch, 1999; Moulines and Charpentier, 1990), in order to increase the task difficulty in the attended ear and minimize the number of attentional switches to the unattended ear.

Each unattended message was made up of four nonsense sentences, adapted from Freyman *et al.*'s (1999) material, spoken with natural prosody by the same talker as for the attended messages (average $F_0=140$ Hz). They were not pitch flattened in order to avoid any signal degradation which could have decreased their perceptual clarity. Related primes could either be the same word as the target (primed condition), or a word totally unrelated to the target (unprimed condition). Unrelated primes were selected randomly among the other content words in the sentences. Related and unrelated primes were embedded into one of the unattended nonsense sentences. Further details of the materials used are given in Rivenez *et al.* (2006).

There were three VT length differences between the attended and unattended messages: 0%, 15%, and 30%. The data for the 0% difference have already appeared in Rivenez *et al.* (2006)¹. With the 15% difference, two experimental conditions were produced which increased the VT length of either the attended or the unattended message by 15%. To obtain the 30% difference, we chose to manipulate the VT length of the two messages by $\pm 15\%$ to minimize any degradation caused by the change of VT length (e.g., reduced naturalness of the voices due to a mismatch between F_0 and VT length parameters). Thus, there were four experimental conditions: (a) the VT length of the attended message was increased by 15% and the unattended message one was unchanged; (b) the VT length of the attended message was reduced by 15% and the unattended message one was unchanged; (c) the VT length of the attended message was increased by 15% and the unattended message one was reduced by 15%; and (d) the VT length of the attended message was reduced by 15% and the unattended message one was increased by 15%. Two sound files illustrate the conditions with a 0% and a 30% VT length [condition (c)] difference between the attended and unattended messages. Each participant was allocated to one of these four experimental conditions. Two lists of items were set up to counterbalance the priming factor (list A vs list B).

Mm 1. Sf 1. 0% VT length difference condition. This is a file of type .wav (715 KB).

Mm 2. Sf 2. 30% VT length difference condition. This is a file of type .wav (715 KB).

The apparent VT length of the talker was modified using the PRAAT 4.1 implementation of the PSOLA algorithm to change the F_0 and duration of the original speech material. The aim of the technique, which was previously used by Darwin and Hukin (2000), is to rescale the VT length (more precisely, the spectral envelope) without changing the F_0 or the duration of the speech (see Fig. 1). To achieve, say, a 15% increase in formant frequencies, the original speech has its F_0 lowered and its duration increased by 15% using PSOLA (leaving the formants unchanged) and is then resampled to give a 15% higher rate to bring the duration and F_0 back to their original values, resulting in a 15% increase in formant frequencies. A similar process is now built into the Change Gender... command of PRAAT.

Sounds were digitized in 16-bits quantization at 22.05-kHz sampling rate and were presented through an Audiomeia III Soundcard in a Macintosh G3 running PsyScope under MacOS 9.2 and played binaurally through Sennheiser HD 414 headphones at an average level of 72-dB SPL Lin (sound-pressure level) for the attended ear and 60-dB SPL Lin for the unattended ear, as measured with an artificial ear. Response times (RTs) were recorded through a PsyScope button box.

Participants were instructed to listen to the message in the left ear, while ignoring the message in the right ear, and press a button whenever they detected a word in the left ear belonging to a specific semantic category displayed on a computer screen in front of them. The next trial started 500 ms after the response. The order in which primed and unprimed conditions, as well as categories, were presented was randomized across trials and participants.

The 120 listeners in this study (for the conditions with a 15% and a 30% VT length difference) were student volunteers from the University of Sussex who were paid for their participation. They were native English speakers with no reported hearing, language, or attentional

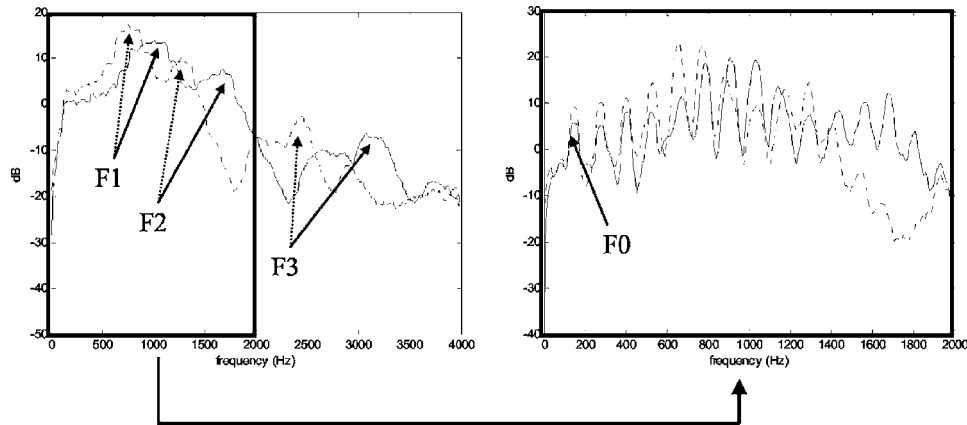


Fig. 1. Example of the effect of a VT length change on the spectrum envelope of the vowel/ə/ (like in “amend”). Dotted lines represent the original signal and solid lines represent the signal when the VT length was increased by 30%. The spectrum envelopes were obtained with a Fourier transform applied on the overall points of the signal to avoid window effects. On the left panel, a moving average filter over 28 points was applied to the spectrum in order to show the VT length of the two signals (first formant, F_1 , second formant, F_2 , and third formant, F_3). It is shown that the VT length was shifted between the two signals but that the spectral shape of their envelope was unchanged. On the right panel, the window of the moving average filter was of 8 points in order to show the fundamental frequency of the two signals. It appears that the fundamental was unchanged between the two signals.

impairment.

3. Results

For each participant’s RTs, we first discarded RTs that were above 1500 ms or below 300 ms, and then discarded RTs above or below 2 standard deviations from the new average, replacing the missing values by the average value for this condition. The purpose of this data cleaning was to discard the false detections (e.g., a short RT could be due to the detection of a word prior to the target). Five targets detected by less than 40% of the participants (averaged across each condition) were discarded from the analysis.

We first tested whether priming differed according to whether the attended or the unattended message received the 15% VT length increase. It did not; so, we then analyzed RTs as a function of the VT length difference between the attended and unattended messages (0% vs 15% vs 30%, between factor) and whether the trial was primed or not.

There was a significant main effect of priming ($F_1(1,137)=5.85;p<0.01;F_2(1,54)=12.69;p<0.001$) (Table 1); overall primed trials had faster RTs than unprimed. We also found a significant effect of the VT length difference on RTs in the item analysis [$F_2(2,108)$

Table 1. RTs (in ms) and percentage of correct detections for the primed and unprimed conditions (rows) and for the 0%, 15%, and 30% VT length difference (columns). The priming effect (RTs in the unprimed condition, RTs in the primed condition) for each VT length difference is given in the last line of the table. Standard deviation (SD) is shown in parentheses: the first number refers to the SD across participants and the second refers to the SD across items.

VT length difference	RTs (in ms)			% correct detections		
	0%	15%	30%	0%	15%	30%
Primed	762(61;56)	779(75;59)	787(64;57)	69	69	70
Unprimed	769(65;53)	790(66;51)	802(62;51)	65	68	68
Priming	7(51;60)	10(46;55)	16(45;45)			

=35.54; $p < 0.0001$]: planned comparisons showed that RTs were faster when there was no VT length difference (765 ms) than when there was a 15% difference (784 ms) [$F_2(1, 54) = 24.16; p < 0.0001$] and they were also faster for this last condition than when there was a 30% difference (794 ms) [$F_2(1, 54) = 12.91; p < 0.001$]. The slower RTs obtained with the increased VT length difference can be explained either by some small degradation in speech quality by the speech synthesis or by reduced naturalness in combining an altered VT length with the original F_0 . Such degradation impaired some listeners but not others, since this factor was not significant in the by-subjects analysis.

There was no significant interaction between priming and VT length difference. However, since we had predicted that priming should be greater with increasing VT length difference, we carried out planned comparisons on the different levels of the VT length difference factor. They showed that priming was not significant when there was no VT length difference [$F_1 < 1; F_2(1, 54) = 1.64; p = 0.2$], marginally significant for the participant analysis [$F_1(1, 137) = 2.84; p < 0.1$], and significant for the item analysis [$F_2(1, 54) = 5.54; p < 0.05$] when there was a 15% VT length difference and significant on both analyses when there was a 30% difference [$F_1(1, 137) = 6.95; p < 0.01; F_2(1, 54) = 14.21; p < 0.0005$]. These data thus provide some evidence to support the view that, when there is no difference in F_0 between concurrent messages, a VT length difference is sufficient to produce priming of the attended by the unattended message.

Conducting the same ANOVA on the participants' percentage of correct detections, we found that priming was significant in the by-subjects analysis: the percentage of correct detections was slightly higher in the primed (70%) than in the unprimed condition (67%) [$F_1(1, 137) = 4.08; p < 0.05$]. This difference could not be explained by a speed-accuracy trade-off since faster RTs were associated with larger percentage of correct detections in the primed condition. No other main effect or interaction was observed.

4. General discussion

In this study we have shown that significant (though small) priming of an attended word by an unattended one can be obtained when there is a difference in VT length between the voices of the attended and unattended messages. A 15% difference in VT length gave marginally significant priming of 10 ms, and a 30% difference a significant priming effect of 16 ms. No priming was obtained when there was no difference in VT length (in neither case was there a difference in F_0 range). This study complements our previous finding that this priming effect is statistically significant when the attended and unattended messages differ in F_0 range and not in VT length.

The way we manipulated the VT length of the messages could have resulted in an odd/formant relationship which may have increased attention to the nominally unattended message. We believe that this was not the case since Rivenez *et al.* (2006) have shown that the priming effect, as measured with the dichotic priming paradigm and the present material, can be replicated when participants were asked to perform a secondary task to maintain their attention to the attended message. Using voices differing in F_0 range, the authors found a priming effect of 26 ms when participants had to recall a word in the attended message presented simultaneously to the prime. The same priming effect was observed when the same participants did not have to perform the recall task, showing that the priming effect, as measured in our paradigm, does not require attention.

Although the present experiment found significant priming of attended words by unattended, a very substantial difference in VT length was required. This result echoes those from the CRM task discussed in the Introduction, which also showed that very substantial differences in VT length were required to obtain equivalent effect sizes to those produced by differences in F_0 range. Despite the large VT length difference required, this experiment has been successful in extending our knowledge of the conditions under which effective priming of attended by unattended speech can be obtained.

The present data and previous studies showed a similar pattern of results concerning the implication of the perceptual grouping cues in the processing of attended and unattended speech (strong effect of F_0 , weaker effect of VT length). These findings suggest that the perceptual grouping of speech is not solely necessary for processing attended speech but that it is also a prerequisite for the processing of unattended speech.

Acknowledgments

This research was supported by a Marie Curie Fellowship and a fellowship from the Délégation Générale pour l'Armement. These experiments were part of Marie Rivenez's Ph.D. conducted in Université Paris 5 - René Descartes. The authors are grateful to Lionel Pellieux for his assistance in the acoustic analyses.

References and links

¹In Rivenez *et al.* (2006), the condition with no VT length difference was run with an independent group of participants. The integration of these data to the present experiment was made possible by the fact that the conditions with a VT length difference were also run with independent groups.

- Assmann, P. F. (1999). "Vocal tract size and the intelligibility of competing voices," *J. Acoust. Soc. Am.* **106**, 2272.
- Assmann, P. F., and Summerfield, Q. (1990). "Modeling the perception of concurrent vowels: Vowels with different fundamental frequencies," *J. Acoust. Soc. Am.* **88**, 680–697.
- Bird, J., and Darwin, C. J. (1998). "Effects of a difference in fundamental frequency in separating two sentences," in *Hearing: Psychophysical and Physiological Advances*, edited by A. R. Palmer, A. Rees, A. Q. Summerfield, and R. Meddis (Eds), (Whurr: London), pp. 263–269.
- Broadbent, D. E., and Ladefoged, P. (1957). "On the fusion of sounds reaching different sense organs," *J. Acoust. Soc. Am.* **29**, 708–710.
- Brox, J. P. L., and Nootboom, S. G. (1982). "Intonation and the perceptual separation of simultaneous voices," *J. Phonetics* **10**, 23–36.
- Brungart, D. (2001b). "Informational and energetic masking effects in the perception of two simultaneous talkers," *J. Acoust. Soc. Am.* **109**, 1101–1109.
- Brungart, D. S., Simpson, B. D., Ericson, M. A., and Scott, K. R., (2001). "Informational and energetic masking effects in the perception of multiple simultaneous talkers," *J. Acoust. Soc. Am.* **110**, 2527–2538.
- Culling, J. F., and Darwin, C. J. (1993). "Perceptual separation of simultaneous vowels: Within and across-formant grouping by F_0 ," *J. Acoust. Soc. Am.* **93**, 3454–3467.
- Culling, J. F., and Poster, J. S. (2004). "Effects of differences in the accent and gender of interfering voices on speech segregation," in *Auditory Signal Processing: Physiology, Psychoacoustics and Models*, edited by D. Pressnitzer (Springer, Berlin), pp. 307–314.
- Darwin, C. J. (1981). "Perceptual grouping of speech component differing in fundamental frequency and onset-time," *Q. J. Exp. Psychol.* **33**, 185–208.
- Darwin, C. J., and Hukin, R. W. (2000). "Effectiveness of spatial cues, prosody and talker characteristics in selective attention," *J. Acoust. Soc. Am.* **107**, 970–977.
- Darwin, C. J., Brungart, D. S., and Simpson, B. D. (2003). "Effects of fundamental frequency and vocal-tract length on attention to one of two simultaneous talkers," *J. Acoust. Soc. Am.* **114**, 2913–2922.
- Dupoux, E., Kouider, S., and Mehler, J. (2003). "Lexical access without attention? Exploration using dichotic priming," *J. Exp. Psychol. Hum. Percept. Perform.* **29**, 172–184.
- Freyman, R. L., Helfer, K. S., McCall, D. D., and Clifton, R. K. (1999). "The role of perceived spatial separation in the unmasking of speech," *J. Acoust. Soc. Am.* **106**, 3578–3588.
- Holender, D. (1986). "Semantic activation without conscious identification in dichotic listening, parafoveal vision, and visual masking: A survey and appraisal," *Behav. Brain Sci.* **9**, 1–66.
- Kortekaas, R. W., and Kohlrausch, A. (1999). "Psychoacoustical evaluation of PSOLA. II. Double-formant stimuli and the role of vocal perturbation," *J. Acoust. Soc. Am.* **105**, 522–535.
- Moulines, E., and Charpentier, F. (1990). "Pitch synchronous waveform processing techniques for text-to-speech synthesis using diphones," *Speech Commun.* **9**, 453–467.
- Peterson, G. H., and Barney, H. L. (1952). "Control methods used in a study of the vowels," *J. Acoust. Soc. Am.* **24**, 175–184.
- Rivenez, M., Darwin, C. J., and Guillaume, A. (2006). "Unattended speech processing," *J. Acoust. Soc. Am.* **119**, 4027–4040.
- Scheffers, M. T. (1983). "Sifting vowels: Auditory pitch analysis and sound segregation," Unpublished doctoral dissertation, Groningen University, The Netherlands.

Emergence of the acoustic Green's function from thermal noise

Oleg A. Godin

*CIRES, University of Colorado and NOAA/Earth System Research Laboratory, DSRC, Mail Code R/PSD,
325 Broadway, Boulder, Colorado 80305-3328
oleg.godin@noaa.gov*

Abstract: The fluctuation-dissipation theorem is used to show how acoustic Green's functions corresponding to sound propagation in opposite directions between any two given points can be extracted from time series of thermal noise recorded at these points. The result applies to arbitrarily inhomogeneous, moving or motionless fluids with time-independent parameters, and demonstrates that the two-point correlation function of thermal noise contains as much information about the environment as can be obtained acoustically by placing transceivers at the two points.

© 2007 Acoustical Society of America

PACS numbers: 43.20.Bi, 43.40.Lc, 43.60.Rw [AN]

Date Received: October 10, 2006 **Date Accepted:** December 6, 2006

1. Introduction

Seminal experiments of Weaver and Lobkis demonstrated that cross correlation of time series of thermal^{1,2} and other³ diffuse acoustic fields recorded at two points gives the time-domain Green's function between the points; i.e., the wave field that would be observed at one point if a source were placed at the other. Correlation of random wave fields is an extremely promising technique of passive imaging, with demonstrated success in studying the interior of the Earth⁴⁻⁷ and the Sun^{8,9} as well as the ocean.^{10,11}

The relation between cross correlation of random fields in a stationary medium and the deterministic acoustic Green's function has been established theoretically using normal modes of a closed system,¹⁻³ time-reversal arguments,¹² stationary phase analysis,¹³ or reciprocity considerations;^{14,15} for a recent review see Weaver and Lobkis.¹⁶ Extension of this work to arbitrary inhomogeneous moving fluids showed that the cross correlation of an acoustic field due to random sources distributed on a surface gives a combination of acoustic Green's functions, which correspond to sound propagation in opposite directions between the two points, and contains information necessary to characterize both sound speed and flow velocity.¹⁷ Similar results but for a fluid with slow and weakly varying currents were independently obtained in Ref. 18.

These studies were preceded by much earlier work by Rytov.^{19,20} To our knowledge, in his investigation of thermal electromagnetic fields, Rytov was the first to prove that cross correlation of thermal noise is proportional to an appropriate deterministic Green's function. Rytov's approach relies on his spectral formulation¹⁹⁻²¹ of the fluctuation-dissipation theorem (FTD). In a remote sensing context, theoretical study of the two-point correlation of a thermal phonon field is motivated by recent experimental observations^{1,2} and the fact that thermal noise dominates the ambient noise at sufficiently high frequencies, e.g., above 50–200 kHz, depending on the sea state, in the ocean.²² Furthermore, investigation of thermal noise provides insights into diffuse acoustic fields of other origins. In this paper, we obtain an acoustic counterpart of Rytov's result and extend it to arbitrarily inhomogeneous moving fluid with time-independent parameters. In addition to accounting for fluid motion, this work differs from the earlier theory^{1,2} by being equally applicable to open systems, waveguides, and resonators.

2. Governing equations and the flow-reversal theorem

Linear acoustic fields in an inhomogeneous moving fluid with sound speed $c(\mathbf{x})$, mass density $\rho(\mathbf{x})$, and flow velocity $\mathbf{u}(\mathbf{x})$ are governed by the equations^{23,24}

$$\rho \frac{d^2 \mathbf{w}}{dt^2} + \nabla p + (\mathbf{w} \cdot \nabla) \nabla p_0 - \frac{\nabla p_0}{\rho c^2} (p + \mathbf{w} \cdot \nabla p_0) = \mathbf{F}, \quad (1)$$

$$\nabla \cdot \mathbf{w} + (p + \mathbf{w} \cdot \nabla p_0) / \rho c^2 = B, \quad d/dt \equiv \partial/\partial t + \mathbf{u} \cdot \nabla, \quad (2)$$

where p, p_0 , and \mathbf{w} are acoustic pressure, background pressure (i.e., the pressure in the absence of acoustic waves), and oscillatory displacement of fluid particles due to an acoustic wave. The acoustic wave is generated by sources with volume densities \mathbf{F} of force and dB/dt of volume velocity. For continuous waves (cw) we will assume and suppress the time dependence $\exp(-i\omega t)$. Equations (1) and (2) have been derived^{23,24} neglecting irreversible thermodynamic processes. It is common to model sound propagation in a medium with dissipation by formally attributing complex values of sound speed and mass density.²⁵ With complex $c(\mathbf{x})$ and $\rho(\mathbf{x})$, Eqs. (1) and (2) become model governing equations for acoustic fields in a moving fluid with dissipation. Note that assigning complex values to sound speed and mass density results in only an approximate description of the physical processes in the fluid with dissipation. In particular, the model does not account for viscous and thermal waves; see Brekhovskikh and Godin.²⁵ These rapidly attenuating waves are not important for long-range field correlations, which are the subject of this paper.

The linearized boundary conditions^{23,24} for the cw acoustic field at an impedance (i.e., locally reacting) surface S within a moving fluid are

$$\mathbf{u} \cdot \mathbf{N} = 0, \quad p + (\mathbf{N} \cdot \nabla p_0 - i\omega \zeta) \mathbf{w} \cdot \mathbf{N} = 0, \quad \mathbf{x} \in S, \quad (3)$$

where \mathbf{N} is a unit normal to S and $\zeta = \zeta(\mathbf{x}, \omega)$ is the impedance of the surface. Free and rigid boundaries can be viewed as special cases of the impedance surface corresponding to zero or infinite impedance, respectively.

The flow reversal theorem (FRT) (Refs. 23 and 24) relates the acoustic field $p^{(1)}, \mathbf{w}^{(1)}$ generated by a set $B^{(1)}, \mathbf{F}^{(1)}$ of sources in a medium with flow velocity $\mathbf{u}(\mathbf{x})$, with an acoustic field $p^{(2)}, \mathbf{w}^{(2)}$ generated by another set $B^{(2)}, \mathbf{F}^{(2)}$ of sources in a medium with the same sound speed and density and *reversed* flow with velocity $-\mathbf{u}(\mathbf{x})$,

$$\int_{\Omega} d^3 \mathbf{x} [B^{(2)} p^{(1)} - \mathbf{F}^{(2)} \cdot \mathbf{w}^{(1)} - B^{(1)} p^{(2)} + \mathbf{F}^{(1)} \cdot \mathbf{w}^{(2)}] = \int_{\partial \Omega} ds \mathbf{N} \cdot \mathbf{j}, \quad (4)$$

where Ω is an arbitrary domain with the boundary $\partial \Omega$, \mathbf{N} is an external unit normal to $\partial \Omega$, and

$$\mathbf{j} = p^{(1)} \mathbf{w}^{(2)} - p^{(2)} \mathbf{w}^{(1)} + \rho \mathbf{u}(\mathbf{w}^{(1)} \cdot \tilde{d}\mathbf{w}^{(2)}/dt + \mathbf{w}^{(2)} \cdot d\mathbf{w}^{(1)}/dt). \quad (5)$$

The tilde denotes quantities referring to a medium with reversed flow. In particular, $\tilde{d}/dt = \partial/\partial t - \mathbf{u} \cdot \nabla$. The boundary $\partial \Omega$ is not required to be simply connected. Parts of $\partial \Omega$ may be located at infinity. Below, we assume that the fluid is either unbounded or has free, rigid, or impedance boundaries. When Ω is chosen to be the entire volume occupied by the fluid, the right side of Eq. (4) vanishes.^{23,24} In the absence of currents ($\mathbf{u} \equiv 0$) FRT reduces to the acoustic reciprocity principle.

3. Acoustic Green's function

As in Ref. 17, we define the Green's function $G(\mathbf{x}, \mathbf{x}_1, t)$ as the acoustic pressure at \mathbf{x} due to a point source of volume velocity with $B = \delta(\mathbf{x} - \mathbf{x}_1) \delta'(t)$ and $\mathbf{F} = 0$. The oscillatory displacement in such an acoustic field will be denoted $\mathbf{g}(\mathbf{x}, \mathbf{x}_1, t)$. In the case of motionless fluid, the Green's function so defined corresponds to the field of a monopole sound source. The frequency spec-

trum $G(\mathbf{x}, \mathbf{x}_1, \omega)$ of the time-domain Green's function $G(\mathbf{x}, \mathbf{x}_1, t)$ has the meaning of the cw Green's function. In motionless fluid, $\mathbf{g}(\mathbf{x}, \mathbf{x}_1, \omega) = (\rho\omega^2)^{-1} \nabla G(\mathbf{x}, \mathbf{x}_1, \omega)$. For the Green's functions G and \tilde{G} in the original medium and in a medium with reversed flow, a simple symmetry relation follows from Eq. (4):

$$G(\mathbf{x}, \mathbf{x}_1, \omega) = \tilde{G}(\mathbf{x}_1, \mathbf{x}, \omega). \tag{6}$$

From the Green's function definition and FRT (4), we obtain

$$p(\mathbf{x}, \omega) = i\omega^{-1} \int d^3\mathbf{y} [B(\mathbf{y})\tilde{G}(\mathbf{y}, \mathbf{x}, \omega) - \mathbf{F}(\mathbf{y}) \cdot \tilde{\mathbf{g}}(\mathbf{y}, \mathbf{x}, \omega)] \tag{7}$$

for the acoustic field generated by cw sources of volume velocity and force that are distributed within the fluid with arbitrary densities B and \mathbf{F} .

Let an acoustic field be generated by random sound sources, which have zero statistical mean and are δ -correlated in space,

$$\langle B(\mathbf{x}) \rangle = 0, \langle \mathbf{F}(\mathbf{x}) \rangle = 0, \langle B(\mathbf{x})B^*(\mathbf{y}) \rangle = Q^{(1)}(\mathbf{x})\delta(\mathbf{x} - \mathbf{y}),$$

$$\langle B(\mathbf{x})F_j^*(\mathbf{y}) \rangle = Q_j^{(2)}(\mathbf{x})\delta(\mathbf{x} - \mathbf{y}), \langle F_m(\mathbf{x})F_j^*(\mathbf{y}) \rangle = Q_{mj}^{(3)}(\mathbf{x})\delta(\mathbf{x} - \mathbf{y}), \quad m, j = 1, 2, 3. \tag{8}$$

Here and below, angular brackets $\langle \cdot \rangle$ denote ensemble average. Acoustic pressure and oscillatory displacement in the random acoustic field are zero on average. For a two-point correlation function of acoustic pressure in a moving medium, from Eqs. (7) and (8) we find

$$\begin{aligned} \langle p(\mathbf{x}_1)p^*(\mathbf{x}_2) \rangle = & \omega^{-2} \int_{\Omega} d^3\mathbf{y} [Q^{(1)}(\mathbf{y})\tilde{G}(\mathbf{y}, \mathbf{x}_1)\tilde{G}^*(\mathbf{y}, \mathbf{x}_2) - Q_j^{(2)}(\mathbf{y})\tilde{G}(\mathbf{y}, \mathbf{x}_1)\tilde{g}_j^*(\mathbf{y}, \mathbf{x}_2) \\ & - Q_j^{(2)*}(\mathbf{y})\tilde{G}^*(\mathbf{y}, \mathbf{x}_2)\tilde{g}_j(\mathbf{y}, \mathbf{x}_1) + Q_{mj}^{(3)}(\mathbf{y})\tilde{g}_m(\mathbf{y}, \mathbf{x}_1)\tilde{g}_j^*(\mathbf{y}, \mathbf{x}_2)], \end{aligned} \tag{9}$$

where summation over repeated indexes $m, j=1, 2, 3$ is assumed. Here and below, where it cannot lead to confusion, the argument ω is suppressed for brevity.

The FRT relates acoustic fields in the original medium and in a medium with reversed flow. For future use, we now derive a similar identity that relates cw Green's function G and its complex conjugate G^* to the dissipative properties of the fluid. Consider first the motionless case. For brevity, designate $G_j \equiv G(\mathbf{x}, \mathbf{x}_j, \omega)$ and $\mathbf{g}_j \equiv \mathbf{g}(\mathbf{x}, \mathbf{x}_j, \omega)$. By calculating a volume integral of the sum of the dot product of \mathbf{g}_2^* and Eq. (1) for G_1 , the dot product of $-\mathbf{g}_1$ and Eq. (1) for G_2^* , the product of G_2^* and Eq. (2) for G_1 , and the product of $-G_1$ and Eq. (2) for G_2^* , we obtain

$$\begin{aligned} G(\mathbf{x}_2, \mathbf{x}_1) + G^*(\mathbf{x}_1, \mathbf{x}_2) = & \frac{i}{\omega} \int_{\partial\Omega} ds(\mathbf{x}) \mathbf{N} \cdot (G_2^* \mathbf{g}_1 - G_1 \mathbf{g}_2^*) \\ & - \frac{2}{\omega} \int_{\Omega} d^3\mathbf{x} \left[G_1 G_2^* \left(\text{Im} \frac{1}{\rho c^2} \right) + \omega^2 \mathbf{g}_1 \cdot \mathbf{g}_2^* (\text{Im} \rho) \right]. \end{aligned} \tag{10}$$

In the case of a moving medium, we will assume that mass density ρ is real. Then, the sound speed c is the only complex-valued environmental parameter in Eqs. (1) and (2). We calculate the same quantity as in the above derivation of Eq. (10), and after some algebra, find

$$\begin{aligned} G(\mathbf{x}_2, \mathbf{x}_1) + G^*(\mathbf{x}_1, \mathbf{x}_2) = & i \int_{\partial\Omega} ds(\mathbf{x}) \frac{\mathbf{N}}{\omega} \cdot [\rho \mathbf{u} (2i\omega \mathbf{g}_1 \cdot \mathbf{g}_2^* + \mathbf{g}_1 (\mathbf{u} \cdot \nabla) \mathbf{g}_2^* - \mathbf{g}_2^* (\mathbf{u} \cdot \nabla) \mathbf{g}_1) \\ & - G_1 \mathbf{g}_2^* + G_2^* \mathbf{g}_1] - \frac{2}{\omega} \int_{\Omega} d^3\mathbf{x} \left(\text{Im} \frac{1}{\rho c^2} \right) [G_1 G_2^* + G_1 \mathbf{g}_2^* \cdot \nabla p_0 \\ & + G_2^* \mathbf{g}_1 \cdot \nabla p_0 + (\mathbf{g}_1 \cdot \nabla p_0) (\mathbf{g}_2^* \cdot \nabla p_0)]. \end{aligned} \tag{11}$$

The algebraic transformations involved in derivation of the identity (11) parallel those used in the FRT derivation^{23,24} and will not be reproduced here. In the absence of dissipation ($\text{Im } \rho = 0, \text{Im } c = 0$), Eqs. (10) and (11) reduce to identities established in Refs. 14 and 17 for motionless and moving media, respectively. Surface integrals in Eqs. (10) and (11) vanish when the surface $\partial\Omega$ is located at infinity or is composed of pressure release and rigid surfaces or impedance surfaces with purely reactive impedance, i.e., $\zeta^* = -\zeta$ [see Eq. (3)].

4. Thermal noise and the fluctuation-dissipation theorem

A thermal acoustic field in fluids is produced by the chaotic thermal motion of microscopic particles such as atoms, ions, and electrons. The fluctuation-dissipation theorem (FDT) allows one to represent acoustic noise at thermal equilibrium as a field due to effective, random, macroscopic sound sources. Let small perturbations of a continuous system be described by a set $\{\xi_n(\mathbf{x}, t)\}$, $n=1, 2, 3, \dots, N$ of generalized coordinates, and macroscopic equations of motion can be written in terms of spectral components of the generalized coordinates as follows:

$$\sum_{m=1}^N \hat{A}_{nm}(\mathbf{x}, \omega) \xi_m(\mathbf{x}, \omega) = f_n(\mathbf{x}, \omega), \quad n = 1, 2, \dots, N. \tag{12}$$

Here, $\hat{A}_{nm}(\mathbf{x}, \omega)$ is a linear operator, and $f_n(\mathbf{x}, \omega)$ are spectral components of generalized forces. The generalized forces and generalized coordinates are also related by the requirement that the statistical average of volume density of the power created by a force $f_n(\mathbf{x}, t)$ is $\langle f_n(\mathbf{x}, t) \partial \xi_n(\mathbf{x}, t) / \partial t \rangle$. According to the FDT, thermal fluctuations of the system can be viewed as generated by random generalized forces with zero mean and the following correlation functions (Ref. 20, p. 119; Ref. 21, p. 273):

$$\langle f_n(\mathbf{x}) f_m^*(\mathbf{y}) \rangle = -\frac{i\Theta}{2\pi\omega} [\hat{A}_{mn}^*(\mathbf{x}, \omega) - \hat{A}_{nm}(\mathbf{y}, \omega)] \delta(\mathbf{x} - \mathbf{y}), \quad \Theta = \frac{\hbar\omega}{2} \coth \frac{\hbar\omega}{2\kappa T}, \tag{13}$$

where T is temperature, Θ is the mean energy of a quantum oscillator, and \hbar and κ are Planck’s and Boltzmann’s constants. In the classical (or high-temperature) limit, where $\hbar\omega \ll \kappa T$, $\Theta(T, \omega) \approx \kappa T$.

For acoustic fields in dissipative fluids, we choose $\xi_j = w_j, j=1, 2, 3; \xi_4 = p$. From the expression²⁴ $\int d^3\mathbf{x} [\mathbf{F}(\mathbf{x}, t) \cdot \partial \mathbf{w}(\mathbf{x}, t) / \partial t + p(\mathbf{x}, t) \partial B(\mathbf{x}, t) / \partial t]$ for acoustic energy production by sound sources, it follows that the generalized forces corresponding to the chosen generalized coordinates are $f_j = F_j, j=1, 2, 3; f_4 = -B$. In a motionless fluid, from Eqs. (1), (2), and (12) for the operators $\hat{A}_{nm}(\mathbf{x}, \omega)$, we find

$$\hat{A}_{ls} = -\omega^2 \rho \delta_{ls}, \quad \hat{A}_{s4} = -\hat{A}_{4s} = \partial / \partial x_s, \quad \hat{A}_{44} = -1/\rho c^2, \quad l, s = 1, 2, 3. \tag{14}$$

Substituting this result into general equation (13), for effective sources of thermal acoustic noise, we obtain Eq. (8) with

$$Q^{(1)} = (\pi\omega)^{-1} \Theta \text{Im} (1/\rho c^2), \quad Q_m^{(2)} = 0, \quad Q_{mn}^{(3)} = \pi^{-1} \omega \Theta \delta_{mn} \text{Im } \rho. \tag{15}$$

Similarly, in the case of a moving fluid with $\text{Im } \rho = 0$, we again arrive at Eq. (8) with

$$Q^{(1)} = \frac{\Theta}{\pi\omega} \text{Im} \frac{1}{\rho c^2}, \quad Q_m^{(2)} = -\frac{\Theta}{\pi\omega} \frac{\partial p_0}{\partial x_m} \text{Im} \frac{1}{\rho c^2}, \quad Q_{mn}^{(3)} = \frac{\Theta}{\pi\omega} \frac{\partial p_0}{\partial x_m} \frac{\partial p_0}{\partial x_n} \text{Im} \frac{1}{\rho c^2}. \tag{16}$$

Note that, at thermal equilibrium, the stronger the dissipation, the stronger are the effective sources of thermal fluctuations.

5. Green’s function retrieval from noise cross-correlation

With the properties of the effective sources of thermal noise described by Eqs. (8), (15), and (16), the two-point correlation function of pressure fluctuations is given by Eq. (9) within the

dissipative fluid and in adjacent fluid domains if the medium is composed of distinct fluids with and without (pronounced) dissipation. The result can be simplified greatly when the dissipative fluid is unbounded or there is no energy flux through its boundaries. We assume that the external boundaries, if there are any, are rigid, pressure release, or locally reacting ones with purely reactive impedance. Then, the surface integrals in Eqs. (10) and (11) vanish. Taking into account that Θ does not depend on position at thermal equilibrium, from Eqs. (9), (10), and (15) we find

$$\langle p(\mathbf{x}_1, \omega) p^*(\mathbf{x}_2, \omega) \rangle = - (2\pi\omega^2)^{-1} \Theta [G(\mathbf{x}_1, \mathbf{x}_2, \omega) + G^*(\mathbf{x}_2, \mathbf{x}_1, \omega)] \quad (17)$$

in the motionless case. Thus, in the frequency domain, the cross correlation of thermal noise equals the product of a temperature-dependent function, which does not depend on coordinates, and the real part of the cw Green's function between the two points. Remarkably, the parameters describing dissipative properties of the fluid drop out from the final result. Equation (17) expresses the acoustic counterpart of the result established much earlier for equilibrium thermal electromagnetic fields (Ref. 20, Sec. 3.9; Ref. 21, Sec. 15).

The same Eq. (17) is obtained in the case of a moving fluid by using the symmetry property (6) of the Green's function and comparing integrands in Eq. (9) [with $Q^{(s)}$ from Eq. (16)] and in the identity (11) written for fields in a medium with reversed flow.

In the high-temperature limit, Θ becomes independent of frequency: $\Theta(T, \omega) \approx \kappa T$, and Eq. (17) can be concisely written in the time domain. We define cross-correlation function $C(\mathbf{x}_1, \mathbf{x}_2, \tau)$ of statistically stationary fluctuations of pressure and the power spectrum $C(\mathbf{x}_1, \mathbf{x}_2, \omega)$ of the fluctuations in a standard way,

$$C(\mathbf{x}_1, \mathbf{x}_2, \tau) \equiv \langle p(\mathbf{x}_1, t - \tau) p(\mathbf{x}_2, t) \rangle = \int_{-\infty}^{+\infty} C(\mathbf{x}_1, \mathbf{x}_2, \omega) e^{-i\omega\tau} d\omega. \quad (18)$$

Then, $C(\mathbf{x}_1, \mathbf{x}_2, \omega) = \langle p^*(\mathbf{x}_1, \omega) p(\mathbf{x}_2, \omega) \rangle$, and from Eq. (17) we find

$$(\partial^2 / \partial \tau^2) C(\mathbf{x}_1, \mathbf{x}_2, \tau) = (2\pi)^{-1} \Theta [G(\mathbf{x}_1, \mathbf{x}_2, -\tau) + G(\mathbf{x}_2, \mathbf{x}_1, \tau)]. \quad (19)$$

Because of causality, $G(\mathbf{x}_1, \mathbf{x}_2, t) = 0$ at $t < 0$ and $G(\mathbf{x}_1, \mathbf{x}_2, -t) = 0$ at $t > 0$. Hence,

$$G(\mathbf{x}_2, \mathbf{x}_1, \tau) = \frac{2\pi}{\kappa T} \frac{\partial^2}{\partial \tau^2} C(\mathbf{x}_1, \mathbf{x}_2, \tau), \quad G(\mathbf{x}_1, \mathbf{x}_2, \tau) = \frac{2\pi}{\kappa T} \frac{\partial^2}{\partial \tau^2} C(\mathbf{x}_1, \mathbf{x}_2, -\tau), \quad \tau > 0. \quad (20)$$

In motionless fluid, cross-correlation function $C(\mathbf{x}_1, \mathbf{x}_2, \tau)$ is an even function of time delay τ ; in moving fluid, according to Eq. (20), the difference $C(\mathbf{x}_1, \mathbf{x}_2, \tau) - C(\mathbf{x}_1, \mathbf{x}_2, -\tau)$ provides a measure of acoustic nonreciprocity.

6. Conclusion

Following an approach originally developed by Rytov¹⁹⁻²¹ to study thermal electromagnetic fields, we have demonstrated that the deterministic time-domain Green's function of an arbitrarily inhomogeneous, moving or motionless, dissipative fluid can be found as the second derivative in time²⁶ of the two-point correlation function of thermal acoustic noise. The fluid is supposed to be in thermal equilibrium and can be unbounded or have rigid, pressure-release, or reactive impedance boundaries. Unlike an earlier theory,^{1,2} results apply equally to open systems, waveguides, and resonators, and allow for background fluid motion (currents). Extension to moving fluid has been made possible by use of the flow reversal theorem²³ and its corollaries.

In the case of thermal noise, an exact relation between the deterministic Green's function and the two-point correlation function of pressure fluctuations holds under much less restrictive conditions than in the case of sources distributed on an interface.^{14,17} Ultimately, this is because the thermal noise is perfectly diffuse at thermal equilibrium. In moving and motionless fluid, the two-point correlation function of thermal noise contains as much information about the environment as can be obtained acoustically by placing transceivers at the two points. In

particular, when the cross correlation of thermal noise can be measured reliably, it can be used to quantify flow-induced acoustic nonreciprocity and retrieve unknown current velocity.

It is clear from their derivation that the relationships (17) and (20) between cross correlation of acoustic pressure fluctuations and the deterministic Green's function hold not only for thermal noise but also other fields of delta-correlated volumetric random sources as long as their density is proportional to the local value of sound attenuation; see Eqs. (15) and (16). As a particular case where $\mathbf{u}=0$, $\rho=a_1$, $c^{-1}=a_2+i\omega a_3$, and a_j are positive constants, our theory includes the problem of the Green's function emergence from cross correlations of acoustic pressure due to delta-correlated random sources uniformly distributed in a homogeneous, dissipative fluid. This problem was considered by Roux *et al.*²⁷ Another particular case of our theory, where $\mathbf{u}=0$, $\text{Im } \rho=0$, and $\rho c^2=-i\omega a_4$, encompasses retrieval of the Green's function of the diffusion equation from the response to uniformly distributed, delta-correlated noise sources, which has been considered recently by Snieder.²⁸

Extensions of the theory presented above to thermal noise in solid and fluid-solid structures and to nonthermal noise will be reported elsewhere.

Acknowledgments

This work was supported in part by the Office of Naval Research. Discussions with A. G. Voronovich, R. I. Weaver, V. G. Irisov, O. I. Lobkis, and M. Charnotskii are gratefully acknowledged.

References and links

- ¹R. L. Weaver and O. I. Lobkis, "Ultrasonics without a source: Thermal fluctuation correlations at MHz frequencies," *Phys. Rev. Lett.* **87**, 134301 (2001).
- ²R. L. Weaver and O. I. Lobkis, "Elastic wave thermal fluctuations, ultrasonic waveforms by correlation of thermal phonons," *J. Acoust. Soc. Am.* **113**, 2611–2621 (2003).
- ³O. I. Lobkis and R. L. Weaver, "On the emergence of the Green's function in the correlations of a diffuse field," *J. Acoust. Soc. Am.* **110**, 3011–3017 (2001).
- ⁴M. Campillo and A. Paul, "Long-range correlations in the diffuse seismic coda," *Science* **299**, 547–549 (2003).
- ⁵N. M. Shapiro and M. Campillo, "Emergence of broadband Rayleigh waves from correlations of the ambient seismic noise," *Geophys. Res. Lett.* **31**, L07614 (2004).
- ⁶N. M. Shapiro, M. Campillo, L. Stehly, and M. Ritzwoller, "High resolution surface wave tomography from ambient seismic noise," *Science* **307**, 1615–1618 (2005).
- ⁷K. G. Sabra, P. Gerstoft, and P. Roux, "Extracting time-domain Green's function from ambient seismic noise," *Geophys. Res. Lett.* **32**, L03310 (2005).
- ⁸T. L. Duvall, Jr., S. M. Jefferies, J. W. Harvey, and M. A. Pomerantz, "Time-distance helioseismology," *Nature (London)* **362**, 430–432 (1993).
- ⁹J. E. Rickett and J. F. Claerbout, "Calculation of the Sun's impulse response by multidimensional spectral factorization," *Sol. Phys.* **192**, 203–210 (2000).
- ¹⁰P. Roux, W. A. Kuperman, and the NPAL Group, "Extracting coherent wave fronts from acoustic ambient noise in the ocean," *J. Acoust. Soc. Am.* **116**, 1995–2003 (2004).
- ¹¹K. G. Sabra, P. Roux, A. M. Thode, G. L. D'Spain, W. S. Hodgkiss, and W. A. Kuperman, "Using ocean ambient noise for array self-localization and self-synchronization," *IEEE J. Ocean. Eng.* **30**, 338–347 (2005).
- ¹²A. Derode, E. Larose, M. Tanter, J. de Rosny, A. Tourin, M. Campillo, and M. Fink, "Recovering the Green's function from field-field correlations in an open scattering medium," *J. Acoust. Soc. Am.* **113**, 2973–2976 (2003).
- ¹³R. Snieder, "Extracting the Green's function from the correlation of coda waves: A derivation based on stationary phase," *Phys. Rev. E* **69**, 046610 (2004).
- ¹⁴K. Wapenaar, "Retrieving the elastodynamic Green's function of an arbitrary inhomogeneous medium by cross correlation," *Phys. Rev. Lett.* **93**, 254301 (2004).
- ¹⁵R. L. Weaver and O. I. Lobkis, "Diffuse fields in open systems and the emergence of the Green's function," *J. Acoust. Soc. Am.* **116**, 2731–2734 (2004).
- ¹⁶R. L. Weaver and O. I. Lobkis, "Diffuse fields in ultrasonics and seismology," *Geophysics* **71**, S15–S19 (2006).
- ¹⁷O. A. Godin, "Recovering the acoustic Green's function from ambient noise cross correlation in an inhomogeneous moving medium," *Phys. Rev. Lett.* **97**, 054301 (2006).
- ¹⁸K. Wapenaar, "Nonreciprocal Green's function retrieval by cross correlation," *J. Acoust. Soc. Am.* **120**, EL7–EL13 (2006).
- ¹⁹S. M. Rytov, "On thermal fluctuations in distributed systems," *Dokl. Akad. Nauk SSSR* **110**, 371 (1956).
- ²⁰M. L. Levin and S. M. Rytov, *A Theory of Equilibrium Thermal Fluctuations in Electrodynamics* (Nauka, Moscow, 1967) [In Russian].

- ²¹S. M. Rytov, Yu. A. Kravtsov, and V. I. Tatarskii, *Principles of Statistical Radiophysics. 3: Elements of Random Fields* (Springer, Berlin, 1989), Chap. 3.
- ²²R. H. Mellen, "The thermal-noise limit in the detection of underwater acoustic signals," *J. Acoust. Soc. Am.* **24**, 478–480 (1952).
- ²³O. A. Godin, "Reciprocity and energy theorems for waves in a compressible inhomogeneous moving fluid," *Wave Motion* **25**, 143–167 (1997).
- ²⁴L. M. Brekhovskikh and O. A. Godin, *Acoustics of Layered Media. 2: Point Sources and Bounded Beams*. 2nd, extended ed. (Springer, Berlin, 1999), Chap. 8.
- ²⁵L. M. Brekhovskikh and O. A. Godin, *Acoustics of Layered Media. 1: Plane and Quasi-Plane Waves*. 2nd ed. (Springer, Berlin, 1998). Chap. 7.1.
- ²⁶The appearance of the relation between the noise correlation function and the Green's function depends on the definition of the latter. If the Green's function were defined as the field due to a source with $B = \delta(\mathbf{x} - \mathbf{x}_1) \delta(t)$ instead of $B = \delta(\mathbf{x} - \mathbf{x}_1) \delta'(t)$, first-order derivatives with respect to τ would appear in Eq. (20) instead of the second-order derivatives.
- ²⁷P. Roux, K. G. Sabra, and W. A. Kuperman, "Ambient noise cross correlation in free space: Theoretical approach," *J. Acoust. Soc. Am.* **117**, 79–84 (2005).
- ²⁸R. Snieder, "Recovering the Green's function of the diffusion equation from the response to a random forcing," *Phys. Rev. E* **74**, 046620 (2006).

Elaine Moran

Acoustical Society of America, Suite 1N01, 2 Huntington Quadrangle, Melville, NY 11747-4502

Editor's Note: Readers of the journal are encouraged to submit news items on awards, appointments, and other activities about themselves or their colleagues. Deadline dates for news and notices are 2 months prior to publication.

Preliminary Notice: 153rd Meeting of the Acoustical Society of America

The 153rd Meeting of the Acoustical Society of America will be held Monday through Friday, 4–8 June 2007 at the Hilton Salt Lake City Center, Salt Lake City, Utah, USA. A block of rooms has been reserved at the Hilton Salt Lake City Center.

Information about the meeting also appears on the ASA Home Page at (<http://asa.aip.org/meetings.html>). Online registration is available.

CHARLES E. SCHMID

Executive Director

Technical Program

The technical program will consist of lecture and poster sessions. Technical sessions will be scheduled Monday through Friday, 4–8 June.

Special Sessions

Acoustical Oceanography (AO)

Acoustics of bubble clouds
(Joint with Physical Acoustics)

Effects of collective bubble oscillations in the ocean

Acoustic sensing of the ocean and seabed using gliders and autonomous underwater vehicles (AUVs)
(Joint with Underwater Acoustics, Engineering Acoustics and Signal Processing in Acoustics)

Hank Medwin memorial session

(Joint with Physical Acoustics and Underwater Acoustics)

Contributions and influence of Hank Medwin in using acoustics to understand physical processes in the ocean

Animal Bioacoustics (AB)

Paleohearing

Inferring hearing function using fossil evidence

Seismic communications in animals

Behavior, physiology, and physics of the seismic communication channels used by animals

Architectural Acoustics (AA)

Advancements in speech privacy

(Joint with Noise, Speech Communication and ASA Committee on Standards)

Advancements in standards, measuring designing for, and reporting speech privacy in the built environment

Effects of rooms on the sound of organs

(Joint with Musical Acoustics)

How rooms for organ performance and organs interact

In situ measurements of absorption coefficients

(Joint with Noise, Engineering Acoustics and ASA Committee on Standards)

Current and new methods of making *in situ* measurements of absorption coefficients

Knudsen lecture

(Joint with Noise)

Theater crawl

Technical tour of theaters, auditoria, and concert halls in Salt Lake City

Troubleshooting in room acoustics

Identifying and correcting acoustical problems in listening environments

Workshop for AIA CEU presentation

Training and qualification process for delivery of AIA accredited presentation

Biomedical Ultrasound/Bioresponse to Vibration (BB)

Acceleration of blood clot dissolution with ultrasound

Results of efforts to use ultrasound to dissolve blood clots

Biomedical applications of acoustic radiation force imaging

Applications of and techniques for acoustic radiation force imaging in medicine

Bioresponse to vibration on the stage

Effects of performing arts practices and facilities in theater, dance, and music on performers

Coded excitation

Methods of electrical excitation (e.g., frequency chirps) of transducers to improve medical imaging or therapy

Modeling of acoustic cavitation *in vivo*

Calculation and simulation of acoustic cavitation in biological tissue

Engineering Acoustics (EA)

Acoustic technologies for coastal surveillance and harbor defense

(Joint with Underwater Acoustics and Signal Processing in Acoustics)

Acoustic technologies and systems for use in homeland security

Musical Acoustics (MU)

Choral singing

Acoustics of the singing voice in the context of large vocal ensembles, and signal analysis properties of choirs

Flow dynamics in musical instruments

(Joint with Physical Acoustics)

Measurement, simulation, and theory of wave propagation in musical instruments

Musical requirements for Western and non-Western worship spaces

(Joint with Architectural Acoustics)

Influence of architecture on the musicality and intelligibility of choirs versus solo voices

“Myths and Mysteries” in musical acoustics
Origins and current thought on “myths and mysteries” which have occurred in the field of musical acoustics

Voice production and pedagogy
Methods for improving vocal production based on acoustic principles

Noise (NS)

Engineering noise control for the mining industry
Measurements, strategies, further planning
Environmental noise in national parks
Review of measurements and policies in the U.S. park properties

Noise regulation and ordinances
(Joint with ASA Committee on Standards)
Review of current experiences and policies

Recent advances in active noise control
(Joint with Engineering Acoustics and Signal Processing in Acoustics)
Recent development in active noise control and overview of the current state-of-the-art

Workshop on standardization for soundscape techniques
Developing techniques and strategies building up an international working group on soundscapes

Physical Acoustics (PA)

Academic genealogy poster session
(Joint with Education in Acoustics)
Show us your siblings (fellow graduate students), parents (thesis advisor, committee members), grandparents (their advisors), as well as those from your post-graduate careers (post-doc advisor, your current and former graduate students) and show where they have gone, who they begot, etc. “Come to the session and discover long-lost members of your academic family”

Acoustic probes of planetary environments
(Joint with Engineering Acoustics)
A forum bringing together the acoustics and planetary science communities for exploring the potential that acoustics has to offer in planetary exploration, on both the scientific and engineering fronts

Physical acoustics demonstrations
(Joint with Education in Acoustics)
Explain and conduct a demo session in a period of 15 minutes. Geared for an audience of ASA conference attendees

Ultrasound in condensed matter, neutrons, nano-materials, magnetism
Papers that relate to ultrasound and inelastic neutron scattering to probe fundamental thermodynamics, nano-materials, magnetic and magnetostrictive effects for engineering and condensed matter

Psychological and Physiological Acoustics (PP)

The neural coding of pitch: Insights from psychophysics, neurophysiology, and brain imaging
Multidisciplinary findings relating to neural representations of pitch in brainstem and cortex

Topics and methods in environmental sound research
Provide a forum for a diverse group of researchers studying perception of environmental sounds, often from different theoretical perspectives and with different practical goals

Signal Processing in Acoustics (SP)

Acoustic signal processing: Signal processing and uncertainty
(Joint with Acoustical Oceanography and Underwater Acoustics)

Effects of randomness and uncertainty to performance of detection and classification

Diverse problems—Similar solutions
Diverse physical problems have similar mathematical and signal processing solutions

Topics in seismic signal processing
Modeling, processing, and interpretation of seismic signals

Speech Communication (SC)

Computational and experimental approaches to fluid dynamics of speech production
Recent advances in understanding, and methods of approach to fluid dynamics of speech production

Frontiers of spectrum analysis with speech applications
Focusing on improved spectrum visualization by increased information extraction from time-frequency transforms

Structural Acoustics and Vibration (SA)

Launch vehicle and space vehicle acoustical and vibration environments
How acoustics and vibration affect launch vehicle and space vehicle design and performance

Sound source localization
(Joint with Signal Processing in Acoustics)
Share new ideas and technologies for locating sound sources in a general, nonideal environment cost effectively

Underwater Acoustics (UW)

Passive imaging and monitoring using random wavefields
(Joint with Acoustical Oceanography)
Theoretical and experimental studies of the propagating medium using coherent processing of random wavefields (ambient noise, scattered fields, sources of opportunity)

Other technical events

Technical tours

A tour of the acoustics research facilities at Brigham Young University (BYU) in Provo, Utah will be conducted on Monday, 4 June 2007. Facilities and current research projects will be shown, as well as the carillon bell tower on the BYU campus. Facilities include a large and small anechoic chamber, two coupled reverberation chambers, and vibration laboratory with scanning laser Doppler vibrometer. Research is ongoing in areas such as active noise control, audio acoustics, energy-based acoustic measurements, nonlinear acoustics, and nearfield acoustic holography. The bus will leave the Hilton Salt Lake City Center at 1:30 p.m. and return at approximately 5:30 p.m. The fee for the Technical Tour is \$5.00. This fee will be waived for students who register for the tour by 28 May 2007. To register, please email asalc07@byu.edu. Registration is requested by 28 May 2007. After this date, registration will only be accepted if there is available space.

A technical tour of the LDS Conference Center and the Mormon Tabernacle will be conducted on Wednesday, 6 June 2007. The LDS Conference Center houses a large 21 000 seat auditorium that is used for both musical performances and the spoken word. Acoustical features will be shown, and some of the acoustical challenges will be discussed. The newly renovated Mormon Tabernacle is a unique listening space with its elliptically shaped ceiling, and some of the acoustical properties of this venue will be shown. Both of these facilities are a short walking distance (three blocks, about 8–10 min) from the Hilton Salt Lake City Center. A walking group will leave the Hilton at 10:00 a.m. and shuttle transportation will be provided shortly thereafter for those who need it. At the conclusion of the technical tour (12:00 noon), there will be an organ recital in the Mormon Tabernacle. Tour participants are welcome to stay and listen to the recital. This technical tour is free to those wishing to participate, but registration by 28 May 2007

is required. To register, please email asasc07@byu.edu. If you require shuttle transportation, mention that in your registration message for the tour.

Hot Topics

A "Hot Topics" session sponsored by the Tutorial Committees is scheduled covering the fields of Animal Bioacoustics, Musical Acoustics, and Noise.

Student Design Competition

The Technical Committee on Architectural Acoustics of the Acoustical Society of America and the National Council of Acoustical Consultants are sponsoring a Student Design Competition to be displayed and professionally judged at the Salt Lake City meeting. The 2007 competition involves the design of a performance hall primarily for opera performances.

Individual students or teams of a maximum of three may submit entries. Graduate and undergraduate entries are welcome. Attendance at the Salt Lake City meeting is not required for entry or award in the competition.

Submissions will be poster presentations that emphasize the general building acoustics design (room acoustics, noise control, and acoustic isolation).

An award of \$1,250.00 USD will be made to the submitter(s) of the entry judged "First Honors." Four awards of \$700.00 USD each will be made to submitters of entries judged "Commendation."

Registration deadline is 9 April 2007. Full details about registration, the competition, and the design scenario are available at (www.newmanfund.org) or can be requested by contacting Bob Coffeen: (913) 645-2381; coffeen@ku.edu.

Gallery of Acoustics

The Technical Committee on Signal Processing in Acoustics will sponsor the ninth Gallery of Acoustics at the Salt Lake City meeting. The objective of the Gallery is to enhance ASA meetings by providing a setting for researchers to display their work to all meeting attendees in a forum emphasizing the diversity, interdisciplinary, and artistic nature of acoustics. The Gallery of Acoustics provides a means by which we can all share and appreciate the natural beauty and aesthetic appeal of acoustic phenomena: This is a forum where science meets art.

The Gallery will consist of a multimedia collection of images, videos, audio clips, and narrations, of images and/or sounds generated by acoustic processes or resulting from signal and image processing of acoustic data. Images and videos can consist of actual visualizations of acoustic processes, or of aesthetically and technically interesting images resulting from various signal and image processing techniques and data visualization. Audio clips and segments should also have both aesthetic and technical appeal.

Entries must be submitted electronically, either by email attachment, CD, or DVD. The allowed electronic formats are:

- IMAGE/PHOTOGRAPH:
- PDF, EPS, TIFF, JPG (although lossless formats are encouraged)
- Video (3 minute limit STRICTLY ENFORCED)
- QuickTime, MPEG (with QuickTime compatible CODEC)
- SOUND CLIP: (3 minute limit)
- AU, WAV, MP3, AIFF

Each entry will be an individual chapter on a single multimedia DVD. Written posters, descriptions, and abstracts will be posted on the Gallery of Acoustics display surrounding the video monitor.

All entries must be accompanied by all authors' names and affiliations, a brief description of the entry and importance or interest of the entry (no more than 1000 words), and statement of permission to publish the entry in complete form or in parts.

A panel of referees will judge entries on the basis of aesthetic/artistic appeal, ability to convey and exchange information, and originality. A cash prize of \$350.00 USD will be awarded to the winning entry. The top three entries will be posted on the Gallery web site: www.sao.nrc.ca/ims/asa_sp/Gallery.html

Note that authors must give permission for publication in complete form or in part to be eligible.

The relevant deadlines are as follows:

2 March 2007: deadline for notice of intent to submit plus brief description of entry

6 April 2007: deadline for receipt of all entries with the brief abstracts

Entries, requests for information and all other communications regarding the Gallery should be directed to Dr. Sean K. Lehman, LLNL/EE/DSED, L-154, Lawrence Livermore National Laboratory, 7000 East Avenue, Livermore, CA 94550-9234 USA; Tel.: (925) 423-3580; FAX: (925) 423-3144; electronic mail: lehman2@llnl.gov

Signal Processing Student Challenge Problem

The Technical Committee on Signal Processing in Acoustics announces the 2007 Student Challenge Problem in Signal Processing. Details will be presented on the Committee's webpage (http://ims-ism.nrc-cnrc.gc.ca/asa_sp/StartHere.html) in May 2007. Students are encouraged to visit the web page for details and rules regarding the problem. This is a great way to learn new skills over the summer, earn an award and receive recognition for your contribution. There will be \$1,000.00 in prize money available. Student participation in the 2006 Student Challenge Problem was exceptional. Results will be posted on the website.

Mentoring Session for Early Career Acousticians

The Women in Acoustics (WIA) Committee will be offering an informal mentoring session for early career acousticians. Roundtable discussions will be led by WIA members on topics such as early academic careers, balancing family and career, interviewing for jobs, finding/handling post-doctoral research positions, and research management. Anyone is welcome to join us for these mentoring sessions. The session will be held immediately following the plenary session on Wednesday, 6 June, from approximately 5:30 p.m. to 6:30 p.m. We will adjourn at 6:30 p.m. so that students can proceed immediately to the students reception.

Charitable Giving Seminar

The Acoustical Society Foundation will hold a two-hour presentation on charitable giving. This will include ways of making gifts to organizations such as the Foundation. Gifts can provide tax deductions and income. There will also be presentations on estate planning. Preregistration will be required. To register contact Paul Ostergaard, General Secretary of the Foundation, 5071 Bear Creek Road, Fairview, PA 16415, or by email at leadoxide@alum.mit.edu.

Online Meeting Papers

The ASA has replaced its at-meeting "Paper Copying Service" with an online site which can be found at (<http://scitation.aip.org/asameetingpapers/>). Authors of papers to be presented at meetings will be able to post their full papers or presentation materials for others who are interested in obtaining detailed information about meeting presentations. The online site will be open for author submissions in April. Submission procedures and password information will be mailed to authors with the acceptance notices. Those interested in obtaining copies of submitted papers for this meeting may access the service at anytime. No password is needed.

Meeting Program

An advance meeting program summary will be published in the April issue of JASA and a complete meeting program will be mailed as Part 2 of the May issue. Abstracts will be available on the ASA Home Page (<http://asa.aip.org>) in April.

Tutorial Lecture

A tutorial presentation titled "Musical Acoustics: Science and Performance. An Evening with the Salt Lake City Jazz Orchestra" will be given by Uwe J. Hansen of Indiana State University and Jerry Floor, Director of the Salt Lake City Jazz Orchestra, on Monday, 4 June at 7:00 p.m.

The presentation will begin with a brief introduction of concepts of waves and vibrations as they relate to music and musical instruments lead-

ing into the science of the “String” sound with examples to include an illustration of the string wave form and a representative spectrum. This will be followed with a performance by the Salt Lake City Jazz Orchestra featuring the string bass. An introduction to the nature of sound production in woodwinds, including the nature of the reed, the bore, and pitch control will follow, including a performance featuring the woodwinds. Next will be a presentation about the physics of brasses to include the role of the mouthpiece, the bore, the bell, and the valves (or the slide), and again spectral examples will be shown. An appropriate performance featuring brass instruments will illustrate this section. The piano is next, emphasizing the nature of the struck excitation and the inharmonicity of piano strings, which will be illustrated by a spectrum. The piano will be featured in the illustrative performance example. The nature of the excitation and the overtone structure will be emphasized and illustrated for percussion instruments. A few comments about radiation directivity and interaction with the hall will then lead to the enjoyment of the rich sound of the well known Salt Lake City Jazz Orchestra.

To partially defray the cost of the lecture a registration fee is charged. The fee is \$15.00 USD for registration received by 7 May and \$25.00 USD at the meeting. The fee for students with current ID cards is \$7.00 USD for registration received by 7 May and \$12.00 USD at the meeting. To register, use the registration form in the printed call for papers or register online at (<http://asa.aip.org>).

Short Course

Architectural acoustics is the science of sound in and around buildings, with four primary concerns: isolation (airborne and structureborne), mechanical system noise and vibration control, surface treatments (absorption, reflection, and diffusion), and electroacoustics. This short course will emphasize architectural acoustics consulting, which is the art of applying the science in a timely and practical manner. The format is similar to that used with nonacoustical professionals like architects and engineers to provide the tools to make informed evaluations and decisions about acoustics, and to communicate efficiently with acoustical consultants, because every project has a unique set of details and challenges.

The objective of the course is to provide an overview of the fundamentals and terminology of architectural acoustics, a basis for general design decisions and evaluations, and confidence to navigate the oceans of information and propaganda about “acoustical” materials, products, and practices.

The instructor, Anthony Hoover, is a Principal with Cavanaugh Tocci Associates, Inc., Consultants in Acoustics, is an Assistant Professor at Berkeley College of Music, has taught at various colleges and institutions, and has served as an expert witness on Capitol Hill and in Federal Court. He is a Fellow of the ASA and a Board-Certified Member of the Institute of Noise Control Engineering. He is a past-president of the National Council of Acoustical Consultants, and a past-chair of ASA’s Technical Committee on Architectural Acoustics. Tony’s passions include outreach to nonacousticians and discovering future acousticians.

The course schedule is Sunday, 3 June 2007, 1:00 p.m. to 6:00 p.m.; Monday, 4 June 2007, 8:30 a.m. to 12:30 p.m.

The registration fee is \$300.00 USD and covers attendance, instructional materials, and coffee breaks. The number of attendees will be limited so please register early to avoid disappointment. Only those who have registered by 7 May will be guaranteed receipt of instructional materials. There will be a \$50.00 USD discount for registration made prior to 7 May. Full refunds will be made for cancellations prior to 7 May. Any cancellation after 7 May will be charged a \$25.00 USD processing fee. To register, use the form in the printed call for papers or register online at (<http://asa.aip.org>). If you miss the preregistration deadline and are interested in attending the course, please send an email to asa@aip.org.

Student Transportation Subsidies

A student transportation subsidies fund has been established to provide limited funds to students to partially defray transportation expenses to meetings. Students presenting papers who propose to travel in groups using economical ground transportation will be given first priority to receive subsidies, although these conditions are not mandatory. No reimbursement is intended for the cost of food or housing. The amount granted each student depends on the number of requests received. To apply for a subsidy, submit

a proposal (e-mail preferred) to be received by 30 April to: Jolene Ehl, ASA, Suite 1NO1, 2 Huntington Quadrangle, Melville, NY 11747-4502, Tel: 516-576-2359, Fax: 516-576-2377, E-mail: jehl@aip.org. The proposal should include your status as a student; whether you have submitted an abstract; whether you are a member of ASA; method of travel; if traveling by auto; whether you will travel alone or with other students; names of those traveling with you; and approximate cost of transportation.

Young Investigator Travel Grant

The Committee on Women in Acoustics (WIA) is sponsoring a Young Investigator Travel Grant to help with travel costs associated with presenting a paper at the Salt Lake City meeting. Young professionals who have completed their doctorate in the past five years are eligible to apply if they plan to present a paper at the Salt Lake City meeting, are not currently students, and have not previously received the award. Each award will be of the order of \$300 with three awards anticipated. Awards will be presented by check at the WIA luncheon at the meeting. Both men and women may apply. Applicants should submit a request for support, a copy of the abstract for their presentation at the meeting, and a current resume/vita which includes information on their involvement in the field of acoustics and in the ASA. Submission by e-mail is preferred to Dr. Lily Wang at (lwang4@unl.edu) or by regular mail to 101A Peter Kiewit Institute, 1110 S. 67th Street, Omaha NE 68182-0681; Tel: 402-554-2065; Fax: 402-554-2080. Deadline for receipt of applications is 23 April.

Students Meet Members for Lunch

The ASA Education Committee provides a way for a student to meet one-on-one with a member of the Acoustical Society over lunch. The purpose is to make it easier for students to meet and interact with members at ASA meetings. Each lunch pairing is arranged separately. Students who wish to participate should contact David Blackstock, University of Texas at Austin, by e-mail (dtb@mail.utexas.edu) or telephone 512-343-8248 (alternative number 512-471-3145). Please provide your name, university, department, degree you are seeking (BS, MS, or PhD), research field, acoustical interests, and days you are free for lunch. The sign-up deadline is ten days before the start of the meeting, but an earlier sign-up is strongly encouraged. Each participant pays for his/her own meal.

Plenary Session, Awards Ceremony, Fellows’ Lunch and Social Events

Buffet socials with cash bar will be held on Tuesday and Thursday evenings at the Hilton Salt Lake City Center. The Tuesday evening social will be held on the plaza behind the Hilton (weather permitting), while the Thursday evening social will be held in the Grand Ballroom of the Hilton.

The ASA Plenary session will be held on Wednesday afternoon, 6 June, in the Grand Ballroom of the Hilton Salt Lake City Center where Society awards will be presented and recognition of newly elected Fellows will be announced.

A Fellows Luncheon will be held on Thursday, 7 June, at 12:00 noon in the Rose-Wagner Hall, which is several hundred feet from the Hilton Salt Lake City Center (2–3 minute walk). This luncheon is open to all attendees and their guests. To register, use the form in the printed call for papers or register online at (<http://asa.aip.org>).

Women in Acoustics Luncheon

The Women in Acoustics luncheon will be held on Wednesday, 6 June. Those who wish to attend this luncheon must register using the form in the printed call for papers or online at (<http://asa.aip.org>). The fee is \$15 (students \$5) for preregistration by 7 May and \$20 (students \$5) at the meeting.

Transportation and Hotel Accommodations

Air Transportation

Salt Lake City is served by Salt Lake International Airport, (Airport Code SLC). The airport is a hub for Delta Airlines, but is also served by the following airlines: Air Canada, America West Airlines, American Airlines, Atlantic Southeast, Continental Airlines, Frontier Airlines, jetBlue Airways, Northwest Airlines, Southwest Airlines, United Airlines. For further information see (<http://www.slcairport.com>).

Ground Transportation

Transportation from the Salt Lake City International Airport to the Hilton Salt Lake City Center:

- **Ground Transportation:** There is a Ground Transportation Desk located at the far end of the baggage claim area in both terminals where ground transportation options and information can be obtained and where transportation can be arranged.
- **Car rental:** Most major car rental companies have rental counters at the Salt Lake City International Airport located on the ground floor of the short-term parking garage directly across from the terminal buildings. The self-parking rate at the Hilton Salt Lake City Center is \$10.00 USD per day and valet parking is \$14.00 USD per day.
- **Airport Shuttle Service, shared-ride, door-to-door service:** There are several shuttle companies that provide service from the Salt Lake City International Airport to the downtown area, including the Hilton Salt Lake City Center. Arrangements can be made at the Ground Transportation Desks, or by contacting individual shuttle companies, which can also be done in the baggage claim areas or online at (<http://www.slcairport.com>). Current rates for shuttle service are in the range of \$8.00–\$10.00 USD one way.
- **Taxicabs and limousines:** Taxis are available outside the terminal at Salt Lake City International Airport. The Hilton Salt Lake City Center is approximately 8 miles from the airport, and typically takes about 15 minutes driving time, with fares currently averaging about \$16.00 USD one way. All cab fares are metered. Please phone 801-363-5550, 801-359-7788, or 801-521-2100 for more information.
- **Public Transportation:** City bus service (UTA) is available to travel from the Salt Lake City International Airport to the Hilton Salt Lake City Center. Bus Route No. 50 leaves the airport every 30 minutes, and has a direct route to a bus stop located a half block south of the Hilton Salt Lake City Center. The current fare is \$1.50 USD. Further information can be obtained at (<http://www.utabus.com>).
- **Driving Information:** From I-15 (north or south), take the 600 S exit (Exit 306). Drive east 0.7 miles to West Temple. Turn left (north) and drive 0.5 miles to the Hilton Salt Lake City Center. The self-parking rate at the Hilton Salt Lake City Center is \$10.00 USD per day and valet parking is \$14.00 USD per day.

Hotel Accommodations and Reservations

The meeting and all functions will be held at the Hilton Salt Lake City Center. Please make your reservations directly with the hotel by phone, fax or online.

A block of guest rooms at discounted rates has been reserved for meeting participants at the Hilton Salt Lake City Center. **Early reservations are strongly recommended.** Note that the special ASA meeting rates are not guaranteed after 4 May 2007. The reservation cutoff date for the special discounted ASA rates is 4 May 2007; after this date, the conference rate will no longer be available. You must mention the Acoustical Society of America when making your reservations to obtain the special ASA meeting rates.

The Hilton Salt Lake City Center is located in the heart of the entertainment and business district of downtown Salt Lake City. The hotel features a fully equipped health club, indoor swimming pool, as well as a full service business center. For more details visit (<http://www.hilton.com/en/hi/hotels/index.jhtml?ctyhocn=SLCCCHH>).

Hilton Salt Lake City Center
255 S. West Temple
Salt Lake City, UT 84101
Tel.: 801-328-2000; Toll Free: 1-800-445-8667
FAX: 801-238-4888
Online: <http://www.saltlakecitycenter.hilton.com/ASA>
Rates (excluding taxes, currently 12.46%)
Single/Double: \$149.00
Triple: \$164.00
Quad: \$179.00

Room Sharing

ASA will compile a list of those who wish to share a hotel room and its cost. To be listed, send your name, telephone number, e-mail address, gender, smoker or nonsmoker preference, by 23 April to the Acoustical Society of America, preferably by e-mail: asa@aip.org or by postal mail to Acoustical Society of America, Attn.: Room Sharing, Suite 1NO1, 2 Huntington Quadrangle, Melville, NY 11747-4502. The responsibility for completing any arrangements for room sharing rests solely with the participating individuals.

Weather

June is generally one of the most beautiful months for weather in Utah, when spring is giving way to summer, but before the hot summer months. Enjoy warm sunny afternoons, with the evenings cooling off. Bright sunny skies characterize the typical weather at this time of year, and it is recommended that you wear a hat and sunscreen when staying outdoors for extended periods. The average high temperature in June is 83 degrees F, with average lows around 54 degrees F. Average precipitation for the month is 0.77 inches. For additional information on Salt Lake City weather, visit: (<http://www.weather.gov/climate/index.php?wfo=slc>).

Assistive Listening Devices

Anyone planning to attend the meeting who will require the use of an assistive listening device, is requested to advise the Society in advance of the meeting: Acoustical Society of America, Suite 1NO1, 2 Huntington Quadrangle, Melville, NY 11747-4502, asa@aip.org.

Accompanying Persons Program

Spouses and other visitors are welcome at the Salt Lake City meeting. The registration fee for accompanying persons is \$50.00 for preregistration by 7 May and \$75.00 at the meeting. A hospitality room for accompanying persons will be open at the Hilton Salt Lake City Center from 8:00 a.m. to 11:00 a.m. each day throughout the meeting where information about activities in and around Salt Lake City will be provided. Two accompanying persons tours are being organized, as described below. To register for either or both tours, please email asaapp07@byu.edu.

Crossroads of the West—City Tour

(Tuesday, June 5, 9:00 a.m.–12:00 noon)

Salt Lake City was built out of a desert by the industrious Mormon pioneers. This tour is a complete look at what makes Salt Lake City so unique. You will begin by seeing the historic downtown area, including the world-famous Mormon Temple Square, which took 40 years to build. Next, visit the beautifully restored 1908 Union Pacific Depot featuring French Renaissance architecture and original artwork. Then outside to enjoy the Olympic Legacy Plaza overlooked by a classic clock tower and featuring the “dancing waters” of the Olympic Snowflake Fountain. Next, we drive through historic downtown and the residential area known as the “Avenues” which is listed on the State and National Historic Registers. Now proceed to the University of Utah. The “U,” founded in 1850, was the first University built west of the Missouri River and site of the 2002 Winter Olympic Athletes Village. We continue past Fort Douglas, which was started during Abraham Lincoln’s administration in 1862 and on to “This is the Place Heritage Park.” This park is where Brigham Young and the Mormon Pioneers entered the valley in 1847 and Brigham Young said “This is the right place, drive on...” Afterward you will visit the Olympic Cauldron Park at Rice Eccles Stadium. Rice Eccles was the site of the Opening and Closing 2002 Winter Olympic Ceremonies. Finally, you return to your hotel knowing that you have had a top-notch overview of Salt Lake City! Price per person: \$25.00.

Alps of Utah

(Thursday, June 7, 9:00 a.m.–4:00 p.m.)

The Rocky Mountains are breathtaking as you make your way through Provo Canyon on your way to Robert Redford’s Sundance Resort, home of the Sundance Film Institute. Take time to walk around and enjoy the beautiful alpine splendor in the shadows of majestic Mt. Timpanogos. Upon

reboarding your motorcoach, your tour continues through the charming Swiss village of Midway, located in the very heart of the "Alps" of Utah. Your next stop will be the Homestead Resort, situated on a landscape of rolling hills dotted with natural hot springs at the base of the beautiful Wasatch Mountains in Utah's Heber Valley. You will enjoy a delicious lunch at this award-winning restaurant, highlighted by direct-from-garden vegetables, herbs and spices! Continuing on this delightful tour, you will find yourself in Utah's most famous resort town, Park City. You will appreciate time for exploring the many unique shops in Park City's Main Street historic district before returning to Salt Lake City. Price per person: \$75.00.

There are numerous sites and activities available in the Salt Lake City area that may be of interest to accompanying persons, and additional information will be provided in the hospitality room. Several such possibilities include skiing (depending on snow conditions at that time in 2007) at one of the ski resorts located within a half hour of Salt Lake City, Kennecott Copper Mine, Historic Gardner Village, historic sites in downtown Salt Lake City (within walking distance), and the Family History Library for those interested in exploring their family roots.

For those interested in pre- and postconference activities, there are five National Parks located in Utah, all within a 4–5 hour drive from Salt Lake City. With five national parks, Utah is America's national parks capital. The national parks include: Zion National Park, Arches National Park, Bryce Canyon, Canyonlands National Park, and Capitol Reef National Park. These national parks are located close together, allowing you to visit more than one, if desired. The parks provide opportunities to explore fascinating geological formations and witness the stunning vistas that can be found in Utah. Further information on these parks (and other sites of interest) can be found at <http://www.us-national-parks.net/state/ut.htm>, or at <http://www.utah.com/nationalparks>.

Registration Information

The registration desk at the meeting will open on Monday, 4 June, at the Hilton Salt Lake City Center. To register use the form in the printed call for papers or register online at <http://asa.aip.org>. **If your registration is not received at the ASA headquarters by 7 May you must register on-site.**

Registration fees are as follows:

Category	Preregistration	
	by 7 May	Onsite Registration
Acoustical Society Members	\$350	\$425
Acoustical Society Members One-Day	\$175	\$215
Nonmembers	\$400	\$475
Nonmembers One-Day	\$200	\$240
Nonmember Invited Speakers One-Day Only	Fee waived	Fee waived
Nonmember Invited Speakers (Includes one-year ASA membership upon completion of an application)	\$110	\$110
ASA Student Members (with current ID cards)	Fee waived	\$25
Nonmember Students (with current ID cards)	\$40	\$50
Emeritus members of ASA (Emeritus status pre-approved by ASA)	\$50	\$75
Accompanying Persons (Spouses and other registrants who will not participate in the technical sessions)	\$50	\$75

Nonmembers who simultaneously apply for Associate Membership in the Acoustical Society of America will be given a \$50 discount off their dues payment for the first year (2007) of membership. Invited speakers who are members of the Acoustical Society of America are expected to pay the registration fee, but **nonmember invited speakers** may register for one-day only without charge. A nonmember invited speaker who pays the full-week registration fee, will be given one free year of membership upon completion of an ASA application form.

Note: A \$25 processing fee will be charged to those who wish to cancel their registration after 7 May.

Online Registration

Online registration is available at asa.aip.org.

USA Meetings Calendar

Listed below is a summary of meetings related to acoustics to be held in the U.S. in the near future. The month/year notation refers to the issue in which a complete meeting announcement appeared.

2007

- 4–8 June 153rd Meeting of the Acoustical Society of America, Salt Lake City, Utah [Acoustical Society of America, Suite 1NO1, 2 Huntington Quadrangle, Melville, NY 11747-4502; Tel.: 516-576-2360; Fax: 516-576-2377; Email: asa@aip.org; WWW: <http://asa.aip.org>]. 2/07
- 22–24 Oct NoiseCon 2007, Reno, NV [Web: www.inceusa.org/nc07]
- 27 Nov–2 Dec 154th Meeting of the Acoustical Society of America, New Orleans, Louisiana (note Tuesday through Saturday) [Acoustical Society of America, Suite 1NO1, 2 Huntington Quadrangle, Melville, NY 11747-4502; Tel.: 516-576-2360; Fax: 516-576-2377; Email: asa@aip.org; WWW: <http://asa.aip.org>].

2008

- 29 Jun–4 Jul Acoustics 08, Joint Meeting of the Acoustical Society of America, European Acoustics Association and the Acoustical Society of France, Paris, France [Acoustical Society of America, Suite 1NO1, 2 Huntington Quadrangle, Melville, NY 11747-4502; Tel.: 516-576-2360; Fax: 516-576-2377; Email: asa@aip.org; WWW: <http://asa.aip.org>].
- 28 Jul–1 Aug 9th International Congress on Noise as a Public Health Problem (Quintennial meeting of ICBEN, the International Commission on Biological Effects of Noise). Foxwoods Resort, Mashantucket, CT [Jerry V. Tobias, ICBEN 9, Post Office Box 1609, Groton CT 06340-1609, Tel.: 860-572-0680; Web: www.icben.org. Email: icben2008@att.net].

Cumulative indexes to the Journal of the Acoustical Society of America

Ordering information: Orders must be paid by check or money order in U.S. funds drawn on a U.S. bank or by Mastercard, Visa, or American Express credit cards. Send orders to Circulation and Fulfillment Division, American Institute of Physics, Suite 1NO1, 2 Huntington Quadrangle, Melville, NY 11747-4502; Tel.: 516-576-2270. Non-U.S. orders add \$11 per index.

Some indexes are out of print as noted below.

Volumes 1–10, 1929–1938: JASA, and Contemporary Literature, 1937–1939. Classified by subject and indexed by author. Pp. 131. Price: ASA members \$5; Nonmembers \$10.

Volumes 11–20, 1939–1948: JASA, Contemporary Literature and Patents. Classified by subject and indexed by author and inventor. Pp. 395. Out of Print.

Volumes 21–30, 1949–1958: JASA, Contemporary Literature and Patents. Classified by subject and indexed by author and inventor. Pp. 952. Price: ASA members \$20; Nonmembers \$75.

Volumes 31–35, 1959–1963: JASA, Contemporary Literature and Patents. Classified by subject and indexed by author and inventor. Pp. 1140. Price: ASA members \$20; Nonmembers \$90.

Volumes 36–44, 1964–1968: JASA and Patents. Classified by subject and indexed by author and inventor. Pp. 485. Out of Print.

Volumes 36–44, 1964–1968: Contemporary Literature. Classified by subject and indexed by author. Pp. 1060. Out of Print.

Volumes 45–54, 1969–1973: JASA and Patents. Classified by subject and indexed by author and inventor. Pp. 540. Price: \$20 (paperbound); ASA members \$25 (clothbound); Nonmembers \$60 (clothbound).

Volumes 55–64, 1974–1978: JASA and Patents. Classified by subject and

indexed by author and inventor. Pp. 816. Price: \$20 (paperbound); ASA members \$25 (clothbound); Nonmembers \$60 (clothbound).

Volumes 65–74, 1979–1983: JASA and Patents. Classified by subject and indexed by author and inventor. Pp. 624. Price: ASA members \$25 (paperbound); Nonmembers \$80 (clothbound).

Volumes 75–84, 1984–1988: JASA and Patents. Classified by subject and indexed by author and inventor. Pp. 625. Price: ASA members \$30 (paperbound); Nonmembers \$80 (clothbound).

Volumes 85–94, 1989–1993: JASA and Patents. Classified by subject and indexed by author and inventor. Pp. 736. Price: ASA members \$30 (paperbound); Nonmembers \$80 (clothbound).

Volumes 95–104, 1994–1998: JASA and Patents. Classified by subject and indexed by author and inventor. Pp. 632. Price: ASA members \$40 (paperbound); Nonmembers \$90 (clothbound).

Volumes 105–114, 1999–2003: JASA and Patents. Classified by subject and indexed by author and inventor. Pp. 616. Price: ASA members \$50 (paperbound); Nonmembers \$90 (clothbound).

ACOUSTICAL NEWS—INTERNATIONAL

Walter G. Mayer

Physics Department, Georgetown University, Washington, DC 20057

International Meetings Calendar

Below are announcements of meetings and conferences to be held abroad. Entries preceded by an * are new or updated listings.

March 2007

13–15 **Spring Meeting of the Acoustical Society of Japan**, Tokyo, Japan (Acoustical Society of Japan, Nakaura 5th-Bldg., 2-18-20 Sotokanda, Chiyoda-ku, Tokyo 101-0021, Japan; Fax: +81 3 5256 1022; Web: www.asj.jp/index-en.html).

15–17 **AES 30th International Conference on Intelligent Audio Environments**, Saariselkä, Finland (Web: www.aes.fi/aes30/).

19–22 **German Acoustical Society Meeting (DAGA2007)**, Stuttgart, Germany (Web: www.daga2007.de).

April 2007

2–4 **International Conference on Emerging Technologies in Non-destructive Testing**, Stuttgart, Germany (Web: www.fa.asso.fr/secretariat/etech-flyerStuttgart.pdf).

9–12 **International Congress on Ultrasonics (2007 ICU)**, Vienna, Austria (Fax: +43 158801 13499; Web: www.icultrasonics.org).

10–12 **4th International Conference on Bio-Acoustics**, Loughboro, UK (Web: www.ioa.org.uk/viewupcoming.asp).

16–18 **29th International Symposium on Acoustical Imaging**, Shonan Village Center, Kanagawa Pref., Japan (Web: publicweb.shonan-it.ac.jp/ai29/AI29.html).

24–25 **Institute of Acoustics (UK) Spring Conference**, Cambridge, UK (Web: www.ioa.org.uk/viewupcoming.asp).

June 2007

1–3 **Second International Symposium on Advanced Technology of Vibration and Sound**, Lanzhou, China (Web: www.jsme.or.jp/dmc/Meeting/VSTech2007.pdf).

3–7 **11th International Conference on Hand-Arm Vibration**, Bologna, Italy (Web: associazioneitalianadiacustica.it/HAV2007/index.htm).

4–6 **Japan-China Joint Conference on Acoustics**, Sendai, Japan (Fax: +81 3 5256 1022; Web: www.asj.gr.jp/eng/index.html).

18–21 **Oceans07 Conference**, Aberdeen, Scotland, UK (Web: www.oceans07ieeearberdeen.org).

25–29 **2nd International Conference on Underwater Acoustic Measurements: Technologies and Results**, Heraklion, Crete, Greece (Web: www.uam2007.gr).

July 2007

2–6 **8th International Conference on Theoretical and Computational Acoustics**, Heraklion, Crete, Greece (Web: www.iacm.forth.gr/~ictca07).

3–5 **First European Forum on Effective Solutions for Managing Occupational Noise Risks**, Lille, France (Web: www.noiseatwork.eu).

4–7 **International Clarinet Association Clarinetfest**, Vancouver, British Columbia, Canada (E-mail: john.cipolla@wku.edu; Phone: 1 270 745 7093).

9–12 **14th International Congress on Sound and Vibration (ICSV14)**, Cairns, Australia (Web: www.icsv14.com).

16–21 **12th International Conference on Phonon Scattering in Condensed Matter**, Paris, France (Web: www.isen.fr/phonons2007).

August 2007

6–10 **16th International Congress of Phonetic Sciences (ICPhS2007)**, Saarbrücken, Germany (Web: www.icphs2007.de).

27–31 **Interspeech 2007**, Antwerp, Belgium (Web: www.interspeech2007.org).

28–31 **Inter-noise 2007**, Istanbul, Turkey (Web: www.internoise2007.org.tr).

September 2007

2–7 **19th International Congress on Acoustics (ICA2007)**, Madrid, Spain (SEA, Serrano 144, 28006 Madrid, Spain; Web: www.ica2007madrid.org).

9–12 **ICA Satellite Symposium on Musical Acoustics (ISMA2007)**, Barcelona, Spain (SEA, Serrano 144, 28006 Madrid, Spain; Web: www.ica2007madrid.org).

9–12 **ICA Satellite Symposium on Room Acoustics (ISRA2007)**, Sevilla, Spain (Web: www.ica2007madrid.org).

17–19 **3rd International Symposium on Fan Noise**, Lyon, France (Web: www.fannoise.org).

18–19 ***International Conference on Detection and Classification of Underwater Targets**, Edinburgh, UK (Web: ioa.org.uk).

19–21 **Autumn Meeting of the Acoustical Society of Japan**, Kofu, Japan (Acoustical Society of Japan, Nakaura 5th-Bldg., 2-18-20 Sotokanda, Chiyoda-ku, Tokyo 101-0021, Japan; Fax: +81 3 5256 1022; Web: www.asj.gr.jp/index-en.html).

24–28 **XIX Session of the Russian Acoustical Society**, Nizhny Novgorod, Russia (Web: www.akin.ru).

October 2007

9–12 ***2007 Canadian Acoustic Conference**, Montréal, Québec, Canada (Web: caa-aca.ca).

June 2008

30–4 **Acoustics'08 Paris: 155th ASA Meeting+5th Forum Acusticum (EAA)+9th Congrès Français d'Acoustique (SFA)**, Paris, France (Web: www.acoustics08-paris.org).

July 2008

7–10 **18th International Symposium on Nonlinear Acoustics (ISNA18)**, Stockholm, Sweden (Web: www.congrex.com/18th_isna/).

28–1 **9th International Congress on Noise as a Public Health Problem**, Mashantucket, Pequot Tribal Nation (ICBEN 9, P.O. Box 1609, Groton, CT 06340-1609, USA; Web: www.icben.org).

September 2008

22–26 **INTERSPEECH 2008–10th ICSLP**, Brisbane, Australia (Web: www.interspeech2008.org).

November 2008

1–5 **IEEE International Ultrasonics Symposium**, Beijing, China (Web: www.ieee-uffc.org/ulmain.asp?page=symposia).

September 2009

6–10 ***InterSpeech 2009**, Broughton, UK (Web: www.interspeech2009.org).

August 2010

23–27 **20th International Congress on Acoustics (ICA2010)**, Sydney, Australia (Web: www.ica2010sydney.org/).

Archives of Acoustics on the Web

The Polish Acoustical Society announced that volumes 25 through 30 (2000–2005) of their journal *Archives of Acoustics* are now available in pdf format, at no charge, at <http://acoustics.ippt.gov.pl>

Archives of Acoustics is an English-language peer-reviewed journal published in Poland. It publishes original research papers in all areas of acoustics as well as 200-word abstracts of papers presented at international conferences on various branches of acoustics organized regularly in Poland

(like the “International Symposia on Hydroacoustics,” “International Conferences on Speech Analysis, Synthesis, and Recognition,” and others).

German Acoustical Society elections

DEGA, the German Acoustical Society, held elections last Summer to replace the membership representatives on the Executive Council whose term in office had expired. There were 26 DEGA members who were listed as candidates. The election committee counted the mail ballots in November and announced the winners, those being the ten candidates who received the most votes. The elected representatives of the membership will serve for a term of 3 years, starting with the announcement of the winners.

The Executive Council has elected Prof. Dr.-Ing. Joachim Scheurer of Müller-BBM in Planegg as the new President of DEGA. He will serve from July 2007 to July 2010.

ICA admitted to ICSU

The International Council for Science (ICSU), having received the requisite support letters and no objections, has now formally admitted the International Commission for Acoustics (ICA) as a Scientific Associate. ICSU is nongovernmental and provides a forum for discussions of international science as it may be related to policy issues. The President of ICSU is Goverdhan Mehta (India) who succeeded Jane Lubchenco (USA). The secretariat of ICSU is in Paris and the next meeting of the Council will be held, in 2008, in Mozambique.

The International Commission for Acoustics (ICA) is an organization in which the Acoustical Society of America has been and still is actively involved. Larry Crum and Gilles Daigle are Past Presidents of ICA and Charles Schmid is now serving on the board of the Commission.

More information about ICSU and ICA can be found on websites www.icsu.org and www.icacommission.org

BOOK REVIEWS

P. L. Marston

Physics Department, Washington State University, Pullman, Washington 99164

These reviews of books and other forms of information express the opinions of the individual reviewers and are not necessarily endorsed by the Editorial Board of this Journal.

Editorial Policy: *If there is a negative review, the author of the book will be given a chance to respond to the review in this section of the Journal and the reviewer will be allowed to respond to the author's comments. [See "Book Reviews Editor's Note," J. Acoust. Soc. Am. 81, 1651 (May 1987).]*

Immersive Audio Signal Processing

Sunil Bharitkar and Chris Kyriakakis

Springer, 2006. 232 pp. Price: \$79.95 (hardcover). ISBN: 038728532

This book reports on recent and current research in audio-signal processing performed in Los Angeles at the Immersive Audio Laboratory, the Signal and Image Processing Institute (both at the University of Southern California) and the Audyssey Laboratories.

The main body of the book consists of six chapters, whereby five of them are marked as already published in journals or at conferences (Chaps. 4–7 and 9). These are preceded by three introductory chapters which deal with fundamentals of audio-signal processing; digital-filter design, acoustics, and psychoacoustics.

The focus of the book is clearly on digital-signal-processing methods, particularly for dealing with—almost exclusively linear—multichannel audio systems. The buzz word “immersive” in the book title denotes the fact that room-related systems for the creation of immersive auditory environments are usually multichannel ones. Yet, immersion as a perceptual effect—as currently heavily discussed among experts of virtual reality—is not dealt with.

The first of the main chapters (Chap. 4) starts with a virtual-microphone technique for creating surround sound, e.g., for deriving a plausible 5.1 audio perspective from two-channel stereo recordings. The possibility of parametric synthesis of musical sounds is discussed as a way out when virtual microphones in the traditional sense fail. Further, the well-known transaural technique for rendering binaural signals over loudspeakers is generalized for application with multiple listeners. Head tracking is not applied. The results of preliminary perceptual tests with realized systems are reported and a suggestion for further research is offered.

Chapter 5 elaborates on the theory of room equalization for multiple-listener positions in real time. The objective here is to design inverse filters for compensating the effects of loudspeakers and rooms. A pattern-recognition method is proposed to master the necessary simultaneous multichannel-equalization problem with low-order filters. Special emphasis is put on the evaluation of the robustness of the method to reverberation. A nonlinear projection method—the Sammon map, known from multidimensional scaling—is applied to visualize the results of the filter-design method used, i.e., a fuzzy clustering algorithm.

Chapter 6 regards practical problems of multichannel equalization, particularly, the selection of proper cross-over frequencies between loudspeakers. Specific topics are the equalization of phase differences between noncoincident loudspeakers and the design of multiposition bass-management filters. The very interesting results are evaluated by nonperceptual quality measures.

Chapter 7 concerns the effect of displacement on equalization, e.g., of listeners with regard to the measuring microphones. A mismatch analysis for spatial-average equalization is undertaken, resulting in observations of the

influence of distance and frequency on the equalization region, the steady-state equalization error depending on the listening distance and the influence of the reverberant-field correlation. For closer interpretation of these observations the reader is referred to future research.

Chapter 8 continues the topic of the preceding chapter, but from a different point of view. It reports on a simulation of a six-listener scenario using a statistical approach with modal equations for evaluating the robustness of equalization based on magnitude-response averaging. Perceptual verification of the results is suggested as a future project.

The last chapter (Chap. 9) takes on the problem of providing quiet zones within target spaces of audio systems. After a hardly convincing review of known methods to this end, the authors propose a novel approach based on eigenfilters. The properties of eigenfilters and their performance as a function of the filter order are discussed as well as performance sensitivity with respect to the lengths of the room responses. Perceptual tests are suggested as future work.

As most of the main body of the book has already been peer-reviewed in the process of prior publications, there is no reason for this reviewer to question the soundness of the results. The main part of the book can thus be seen as a proceedings report from the authors' laboratories.

The introductory part of the book starts with two chapters on fundamentals of digital signal processing. Although clearly written, they represent a syllabus rather than an introduction for readers not yet familiar with the basics of the field.

The third chapter regards fundamentals of acoustics and psychoacoustics. Here the suitability for teaching purposes must be seriously questioned. As to the acoustics, even if one agreed with the selection of topics, the presentation is inadequate. For example, many equations are written in such a way that letter symbols denote numbers instead of quantities. At some point even the good old “erg” celebrates a revival!

Regarding the psychoacoustics part, it is obvious that the authors are no experts in this field. Their explanation of the frequency selectivity in the cochlea is adventurous. This reviewer asked himself why the authors have included a psychoacoustics section at all, since this field is not actually applied in the main body of the book.

In the foreword, the expectation is expressed that this little book may be useful as a text for courses in digital audio-signal processing. This may well be the case, but prospective users are warned that they may need additional course material for this purpose.

The book, however, provides a compact overview on an important research area within digital audio-signal processing at large. For those who want to avoid the effort of collecting the original articles, this compilation is certainly a good buy.

JENS BLAUERT
Communications Acoustics
Ruhr University
Universtaetsstr 150
Bochum, D-44780 Germany

REVIEWS OF ACOUSTICAL PATENTS

Lloyd Rice

11222 Flatiron Drive, Lafayette, Colorado 80026

The purpose of these acoustical patent reviews is to provide enough information for a Journal reader to decide whether to seek more information from the patent itself. Any opinions expressed here are those of reviewers as individuals and are not legal opinions. Printed copies of United States Patents may be ordered at \$3.00 each from the Commissioner of Patents and Trademarks, Washington, DC 20231. Patents are available via the Internet at <http://www.uspto.gov>.

Reviewers for this issue:

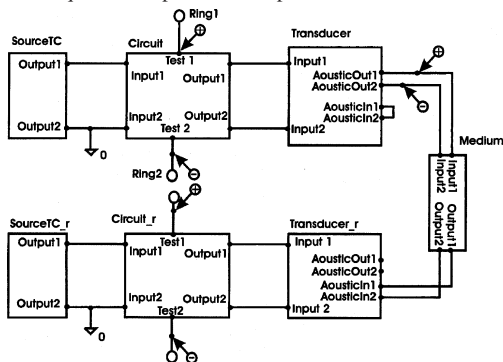
GEORGE L. AUGSPURGER, *Perception, Incorporated, Box 39536, Los Angeles, California 90039*
ANGELO CAMPANELLA, *3201 Ridgewood Drive, Hilliard, Ohio 43026-2453*
DIMITRI DONSKOY, *Stevens Institute of Technology, Castle Point on the Hudson, Hoboken, New Jersey 07030*
JOHN M. EARGLE, *JME Consulting Corporation, 7034 Macapa Drive, Los Angeles, California 90068*
SEAN A. FULOP, *California State University, Fresno, 5245 N. Backer Avenue M/S PB92, Fresno, California 93740-8001*
JEROME A. HELFFRICH, *Southwest Research Institute, San Antonio, Texas 78228*
MARK KAHRS, *Department of Electrical Engineering, University of Pittsburgh, Pittsburgh, Pennsylvania 15261*
DAVID PREVES, *Starkey Laboratories, 6600 Washington Ave. S., Eden Prairie, Minnesota 55344*
DANIEL R. RAICHEL, *2727 Moore Lane, Fort Collins, Colorado 80526*
NEIL A. SHAW, *Menlo Scientific Acoustics, Inc., Post Office Box 1610, Topanga, California 90290*
ERIC E. UNGAR, *Acentech, Incorporated, 33 Moulton Street, Cambridge, Massachusetts 02138*
ROBERT C. WAAG, *University of Rochester, Department of Electrical and Computer Engineering, Rochester, New York 14627*

7,079,450

43.35.Ae SYSTEM AND METHOD FOR ELIMINATING AUDIBLE NOISE FOR ULTRASONIC TRANSDUCERS

David S. Breed *et al.*, assignors to Automotive Technologies International, Incorporated
18 July 2006 (Class 367/138); filed 29 April 2004

Methods are provided for reducing clicking of ultrasonic air-coupled transducers. A mechanical filter that attenuates audible frequencies relative to ultrasonic frequencies is placed in the path of the ultrasonic waves as they



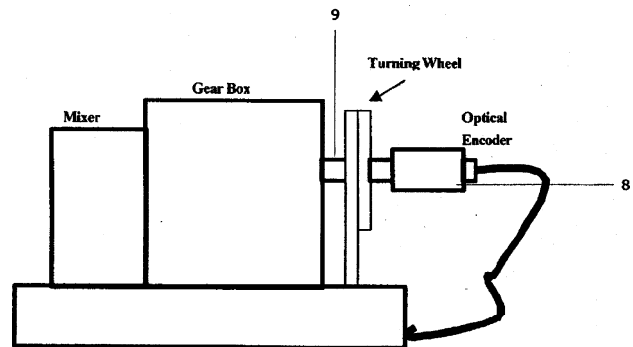
travel from the transducer to a target such as an object in a vehicle compartment.—DRR

7,080,556

43.35.Bf ULTRASONIC APPARATUS AND METHODS FOR THE MONITORING OF MELTING, MIXING AND CHEMICAL REACTION PROCESSES

Cheng-Kuei Jen *et al.*, assignors to National Research Council of Canada
25 July 2006 (Class 73/590); filed 12 June 2003

The device provides for inline monitoring of melting, mixing, and chemical reaction of materials in an enclosed chamber. At least one rotating



element is coupled to the chamber and a motor is coupled to the rotating element(s). At least one ultrasonic sensor measures transmitted and received ultrasonic signals, said sensor(s) bridging between the interior and exterior of the enclosed chamber. A position encoder coupled to the motor provides synchronization between such ultrasonic measurements and the position of the rotating element(s).—DRR

7,075,084

43.35.Ud ULTRASONIC THERMOGRAPHY INSPECTION METHOD AND APPARATUS

Jeffrey G. Thompson and Clyde T. Uyehara, assignors to The Boeing Company
11 July 2006 (Class 250/341.6); filed 20 December 2002

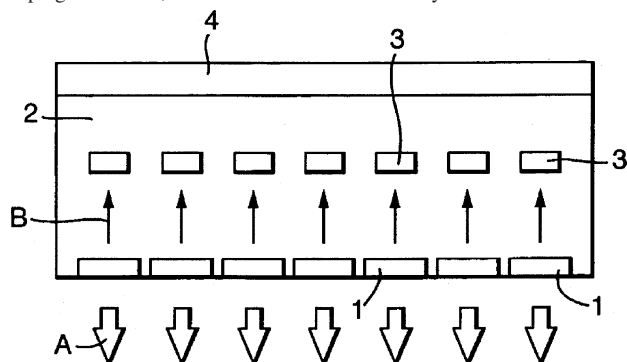
A portable thermal-imaging specimen analyzer includes a removable frame attachable to the specimen by vacuum and suction cups. The apparatus includes a sound source and thermal imaging camera that generates thermal images of the specimen, along with a controller connected to the sound source and imaging camera.—DRR

7,069,786

43.35.Yb ULTRASONIC TRANSDUCER STRUCTURES

Anthony K. Dunhill, assignor to Rolls-Royce PLC
4 July 2006 (Class 73/632); filed in United Kingdom 23 January 2003

An ultrasonic transducer structure is so arranged as to have a layer of transducer elements 1 on the front of the structure, backed up by a layer of damping material 2, within which is a second array of transducer elements



3. When the front layer of transducer elements sends ultrasonic signals from the front face, the sound energy traveling into the second layer of transducer elements 3 can be received and the size or amplitude or time delay can be monitored.—DRR

7,073,395

43.35.Yb ULTRASONIC FLOWMETER AND ULTRASONIC FLOW RATE MEASURING METHOD

Takehiko Suginochi and Masahiko Hashimoto, assignors to Matsushita Electric Industrial Company, Limited
11 July 2006 (Class 73/861.27); filed in Japan 26 November 2002

Described is an ultrasonic flowmeter. First and second ultrasonic transducers are arranged so that the ultrasonic propagation path is within the fluid flow path. A zero-crossing detection unit measures the propagation time of the ultrasonic wave after the zero-crossing counts are corrected for noise in the received signal. In a preferred embodiment, the correction unit corrects the flow volume of the fluid on the basis of the amplitude of the received signal.—DRR

7,079,132

43.35.Yb SYSTEM AND METHOD FOR THREE-DIMENSIONAL (3D) RECONSTRUCTION FROM ULTRASOUND IMAGES

Frank Sauer *et al.*, assignors to Siemens Corporate Research Incorporated
28 July 2006 (Class 345/419); filed 16 August 2002

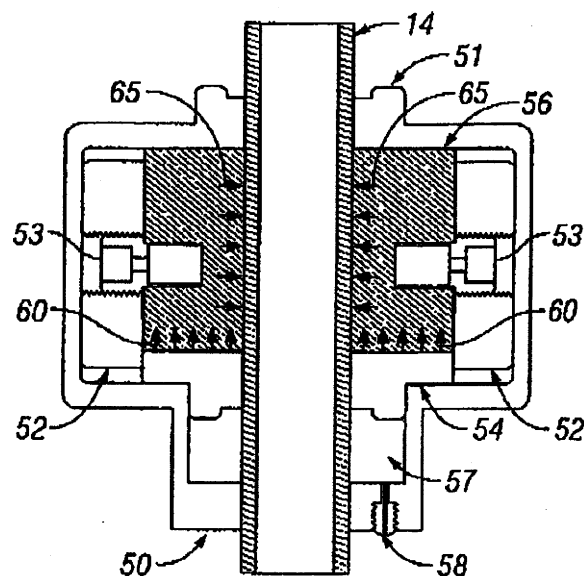
We have here a method for local 3D reconstruction from a series of 2D ultrasound images. The method includes deriving a 2D image of an object, defining a target region within said 2D image, defining a volume scan period, deriving further 2D images of the target region during the volume scan period, storing respective pose information for further 2D images, and reconstructing a 3D image representation for the target region by utilizing the 2D images and the respective pose information.—DRR

7,080,557

43.35.Yb METHOD AND APPARATUS FOR INSPECTING A TUBULAR USING ACOUSTIC SIGNALS

Sarmad Adnan, assignor to Schlumberger Technology Corporation
25 July 2006 (Class 73/622); filed 7 April 2004

A method for inspecting a tubular member involves the steps of contacting the tubular member with a coupling material, transmitting an acoustic signal, receiving a returned acoustic signal, and releasing the contact of



the coupling material with the tubular element. In specific embodiments, the acoustic signal may be an ultrasonic signal, the tubular member may be a coiled tubing, and the coupling material may be an elastomeric compound.—DRR

7,095,160

43.35.Zc PIEZOELECTRIC MOTOR AND METHOD OF EXCITING AN ULTRASONIC TRAVELING WAVE TO DRIVE THE MOTOR

Kenji Uchino *et al.*, assignors to The Penn State Research Foundation
22 August 2006 (Class 310/333); filed 26 May 2004

This patent discloses yet another way of converting linear motion into rotary motion. The basic methods described are the use of an eccentric hole in the rotor, and a swash plate rotor. These are both standard approaches that have been used and disclosed before.—JAH

7,087,264

43.38.Ar ULTRASONIC TRANSDUCER, METHOD FOR MANUFACTURING ULTRASONIC TRANSDUCER, AND ULTRASONIC FLOWMETER

Masaaki Suzuki *et al.*, assignors to Matsushita Electric Industrial Company, Limited
8 August 2006 (Class 427/100); filed in Japan 28 February 2001

The object of this device is to provide an ultrasonic transducer configured so as to reduce variation in its characteristics, thereby improving the precision and durability of an ultrasonic flowmeter. In order to attain this object, the transducer is configured so as to include a piezoelectric element and an acoustic matching layer, wherein the acoustic matching layer is made

of a dry gel of an inorganic oxide or an organic polymer. A solid skeletal part of the dry gel has been rendered hydrophobic. With this configuration, it is possible to feature an ultrasonic transducer with an acoustic matching layer that is very lightweight and has a small acoustic impedance due to the solid skeletal part of the dry gel. It is also possible to obtain an ultrasonic transducer that shows a narrow range of characteristic variation and is stable due to the high homogeneity of the dry gel.—DRR

7,089,069

43.38.Bs METHOD AND APPARATUS FOR RECONSTRUCTION OF SOUNDWAVES FROM DIGITAL SIGNALS

Kaigham Gabriel et al., assignors to Carnegie Mellon University
8 August 2006 (Class 700/94); filed 16 August 2002

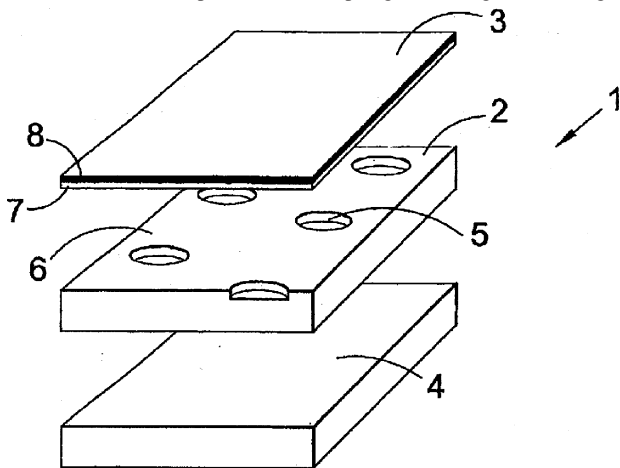
This patent discloses the use of “speakers” or tiny MEMS membranes as speakers in a digital sound reproduction scheme. The membranes described in this invention are 1.5 mm square, and have resonant frequencies in the 1.6-kHz range. The authors suggest configurations in which they are lined up in rows with lengths equal to the different powers of two. Thus, by the sixteenth bit, we would need 65 536 transducers lined up in a 100-m row, or in a 38-cm square. There are several problems with this idea that are not addressed in the patent, such as dynamic range limitations and limited frequency response. For more original thinking on this issue, the reader is advised to look at discussions by Meridian Audio and AT&T in the 1980s.—JAH

7,095,864

43.38.Bs ELECTROSTATIC AUDIO LOUSPEAKERS

Duncan Robert Billson and David Arthur Hutchins, assignors to University of Warwick
22 August 2006 (Class 381/191); filed 28 August 2000

Here we have another patent in which the abstract is at odds with the patent claims. In this case, the abstract describes “An electrostatic transducer, such as a loudspeaker or microphone...” whereas the claims are restricted to a loudspeaker only. Well, the general design is similar to an electret condenser microphone in that diaphragm 3 lies against an irregular



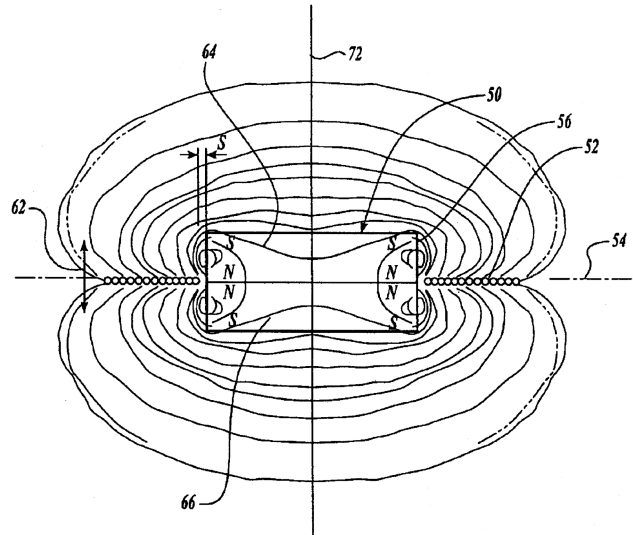
back plate 2, forming multiple smaller diaphragms with individual miniature back cavities. In this case, however, the irregular backing is an insulating layer sandwiched between the conductive diaphragm and conductive layer 4. Will this design really revolutionize the loudspeaker industry? Only time will tell.—GLA

7,058,195

43.38.Dv SPEAKER ASSEMBLY

Roland Pierre Trandafir, Seattle, Washington
6 June 2006 (Class 381/409); filed 13 May 2003

Take two ring or other topology magnets, 64 and 66, and arrange them so that like poles face each other as in 50. Wind a coil 52 using round or flat wire in one or multiple layers so that the coil is shaped like the rings of Saturn. Describe various embodiments of this general arrangement, also using what looks like conventional magnet arrangements, in 24 columns of



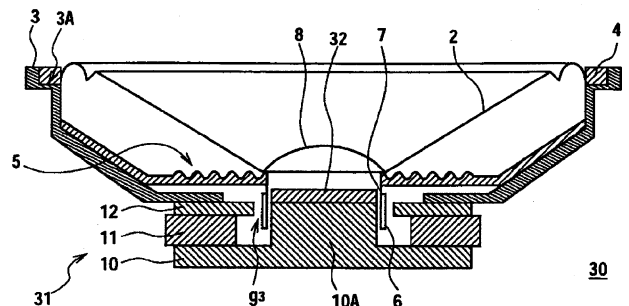
text and illustrate with 66 figures. While the invention ostensibly relates to these pancake-style voice coils and the purported benefits of same, nonlinearities in the response, power limitations due to the mechanical flexing of the coil, and those still-pesky inhomogeneities in the magnetic field appear immediately to this reviewer.—NAS

7,068,807

43.38.Dv SPEAKER DEVICE

Shinji Kobayashi, assignor to Sony Corporation
27 June 2006 (Class 381/412); filed in Japan 17 November 2003

By adding a submagnet 32 to the top of the pole piece 10A of magnet structure 31, the magnetic flux in gap g3 is extended by the thickness of the



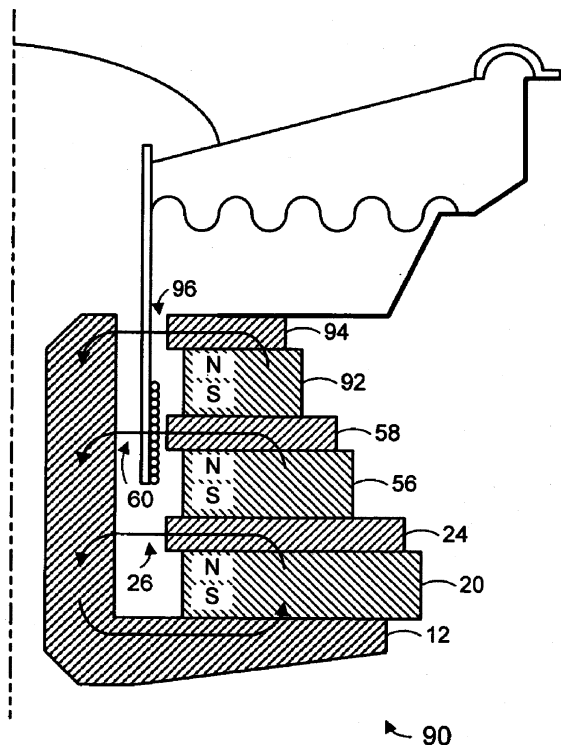
submagnet, thereby increasing the magnetic flux density in the gap, and so increasing the linear part of the travel by voice coil 6.—NAS

7,065,225

43.38.Dv ELECTROMAGNETIC TRANSDUCER HAVING A LOW RELUCTANCE RETURN PATH

Enrique M. Stiles, assignor to STEP Technologies, Incorporated
20 June 2006 (Class 381/412); filed 13 April 2005

This patent is a further development of the ideas stated in the inventor's earlier United States Patent 6,940,992 [reviewed in J. Acoust. Soc. Am. 119(4), 1908 (2006)] with the goal of increasing the linear portion of the magnetic field in which a voice coil operates. Various design combinations



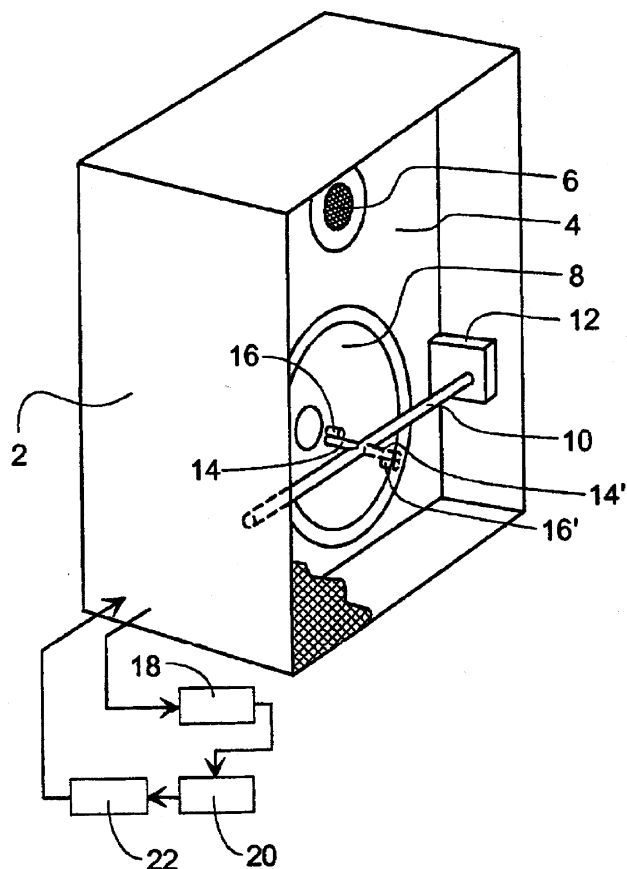
are described using one or two voice coils, two or three magnets, and various magnetic paths, with and without shielding. Some implementations use a nonmagnetic heat sink in the magnetic path. The specification section is quite readable.—NAS

7,092,535

43.38.Ew ENVIRONMENT ADAPTABLE LOUDSPEAKER

Jan Abildgaard Pedersen and Ole Ploug, assignors to Bang & Olufsen A/S
15 August 2006 (Class 381/96); filed in Denmark 6 October 1998

The measurement of sound intensity usually involves two matched-precision microphones spaced a known distance apart. Such equipment has been available from Brüel & Kjær for more than 20 years. More recently, that company has shown that the concept can also be used to measure radiation resistance at the cone of a low-frequency loudspeaker. The information can then be processed to create a loudspeaker system that automatically adapts to its acoustic environment. Now let us consider a somewhat simpler way to measure sound intensity. If conditions are stable long enough to run two frequency sweeps, then a less expensive single microphone can be sequentially located at two positions. This technique, using commercial



Time Delay Spectrometry test equipment, was demonstrated by Richard Heyser in the 1980s and has now been rediscovered by Brüel & Kjær. The patent describes several practical methods for repositioning a single microphone in front of a woofer.—GLA

7,081,577

43.38.Fx ELECTRONIC METRONOME

Fumiyoshi Nagakura, assignor to Seiko Instruments Incorporated
25 July 2006 (Class 84/484); filed in Japan 27 May 2003

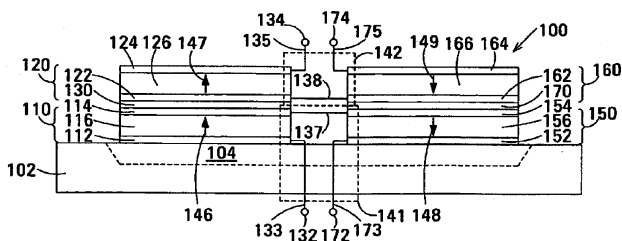
Learning absolute tempo changes for performance can be problematic. This metronome has a piezoelectric transducer that generates a vibration that the player can feel and not hear.—MK

7,091,649

43.38.Fx FILM ACOUSTICALLY-COUPLED TRANSFORMERS WITH TWO REVERSE C-AXIS PIEZOELECTRIC ELEMENTS

John D. Larson III and Yury Oshmyansky, assignors to Avago Technologies Wireless IP (Singapore) Pte. Limited
15 August 2006 (Class 310/324); filed 29 April 2004

This patent discloses the use of stacked film bulk acoustic resonators (FBARs) in a transformer design that is supposed to allow for impedance transformation as well as balanced-to-unbalanced conversion. The figure



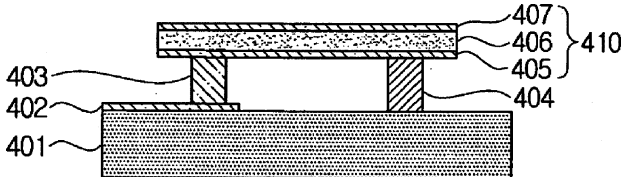
shows the electrical circuitry involved in this configuration. The ideas are nothing new, leaving only the details of the construction.—JAH

7,095,298

43.38.Fx FILM BULK ACOUSTIC RESONATOR HAVING SUPPORTS AND MANUFACTURING METHOD THEREFORE

Il-jong Song et al., assignors to Samsung Electronics Company, Limited
22 August 2006 (Class 333/187); filed in South Korea 29 May 2003

The authors disclose a method of isolation of a film bulk acoustic resonator from the substrate that involves elevating the resonator on legs,



three to be exact. The idea would certainly work, but is it worth the extra trouble of bringing the electrical leads up the legs as vias? One would think not.—JAH

7,098,758

43.38.Fx ACOUSTICALLY COUPLED THIN-FILM RESONATORS HAVING AN ELECTRODE WITH A TAPERED EDGE

Kun Wang et al., assignors to Avago Technologies Wireless IP (Singapore) Pte. Limited
29 August 2006 (Class 333/189); filed 3 November 2004

The authors disclose a method of coupling two adjacent film bulk acoustic resonators having a common substrate (such as silicon) by placing them close together and chamfering the electrodes to facilitate the transfer of acoustic energy between them. This, it is stated, is preferable to using wires to couple the energy electrically when it is desired to have two or more stages in cascade. It would appear that the design and control of this coupling is rather complicated, however.—JAH

7,092,539

43.38.Gy MEMS BASED ACOUSTIC ARRAY

Mark Sheplak et al., assignors to University of Florida Research Foundation, Incorporated
15 August 2006 (Class 381/114); filed 28 November 2001

The authors of this patent disclose how one can fabricate a MEMS microphone out of silicon using strain gauge sensors implanted in the membrane. They proceed to show how this allows inclusion of some of the signal conditioning electronics on the chip with the sensor, and how one can make many of these and deploy them in an array. Little of this is new, except the particulars of the integration of MEMS with amplification. This drove the use of amorphous silicon strain gauges as the sensors, and the microphones

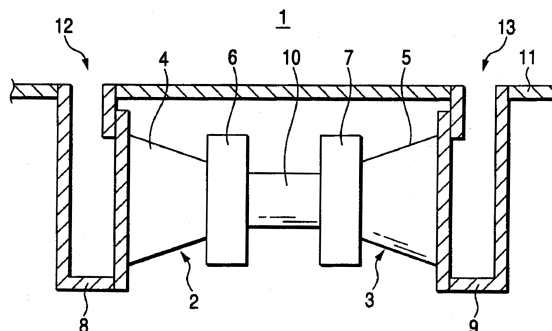
consequently can be expected to have rather poor noise performance. A fair amount of technical detail is included.—JAH

7,062,054

43.38.Hz SPEAKER DEVICE

Akira Nishikawa et al., assignors to Fujitsu Ten Limited
13 June 2006 (Class 381/182); filed in Japan 7 June 2002

By using a stilted dialect of English, that is, patentese, a means is disclosed of lowering the second and third harmonic distortion, without ever using these terms in any manner, in a trunk/rear-deck-mounted car audio low-frequency device 11. System 1 consists of electrodynamic transducers 6



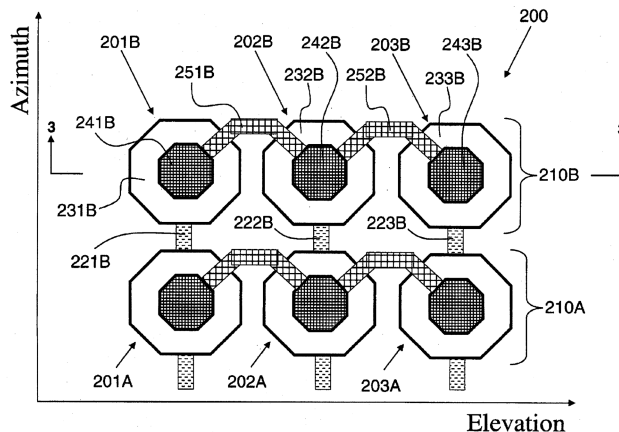
and 7, rod 10 which connects the driving systems, and acoustic loads 12 and 13, which are basically a slot and a cavity. The connecting rod is said to reduce vibrations by the speaker units, while the acoustic loads reduce the "resonance" frequency so that the passband of the unit is expanded.—NAS

7,087,023

43.38.Hz MICROFABRICATED ULTRASONIC TRANSDUCERS WITH BIAS POLARITY BEAM PROFILE CONTROL AND METHOD OF OPERATING THE SAME

Christopher M. W. Daft et al., assignors to Sensant Corporation
8 August 2006 (Class 600/459); filed 14 February 2003

The present device provides a means to control the phase profile of a capacitive microfabricated ultrasonic transducer (cMUT) element or array of elements by varying the spatial distribution of the bias voltage on the cMUT. The cMUT is arranged so that it can be focused in the elevation direction by varying the sign of the applied elevation bias. In one aspect of the device,



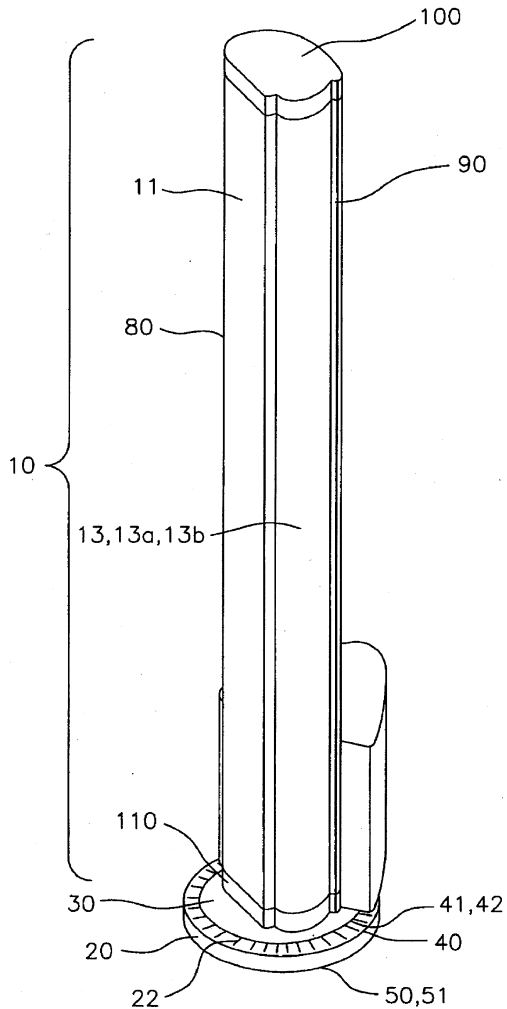
elevation focusing is achieved without the aid of a mechanical lens. The cMUT provides enhanced multirow focusing performance without the expense and complexity of the high-voltage switches required in multirow probes and without the signal degradation that occurs when the rf signal passes through these lossy, high-voltage switches.—DRR

7,090,047

43.38.Ja SURROUND SOUND POSITIONING TOWER SYSTEM AND METHOD

Noel Lee and Demian Martin, assignors to Monster Cable Products, Incorporated
 15 August 2006 (Class 181/199); filed 3 September 2003

To facilitate aiming, this tower loudspeaker system sits on a rotating base fitted out with angle markers. So far, so good, but the patent makes no mention of how the base itself is intended to be aligned to a reference axis.—GLA

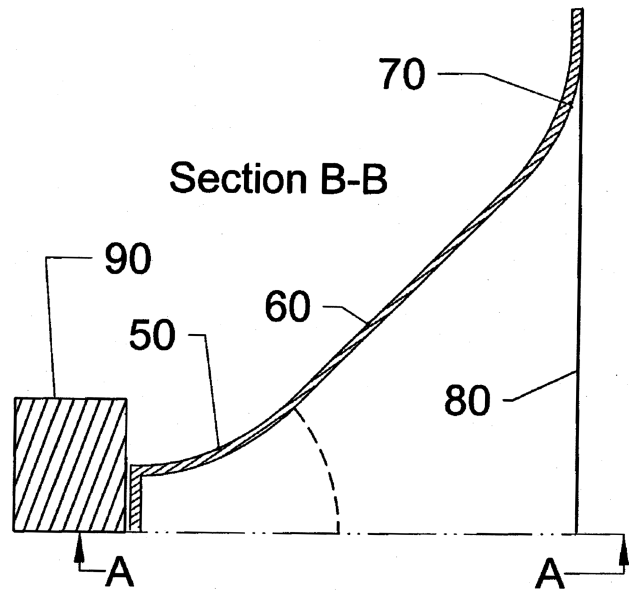


7,068,805

43.38.Ja ACOUSTIC WAVEGUIDE FOR CONTROLLED SOUND RADIATION

Earl Russell Geddes, Northville, Michigan
 27 June 2006 (Class 381/340); filed 11 July 2003

Asymmetric dispersion-pattern horns that use a diffraction slot cause reflections back to the source at the discontinuity. This causes ambiguity in the acoustic center as well as other deleterious artifacts. Horns based on an oblate spheroidal (OS) geometry cannot offer dispersion patterns with more than a 20°–30° difference. Plus, these OS-based horns want to have a circular mouth, and manipulation of the mouth geometry causes more deleterious effects. By using a prolate spheroidal (PS) section 50 from the horn



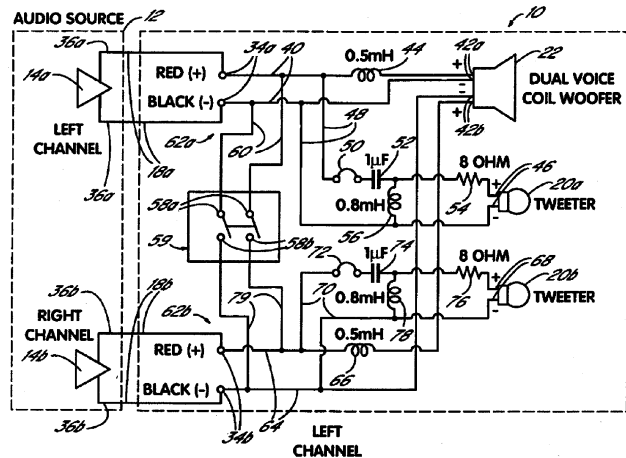
throat on, an elliptic cylindrical section 60 from the mouth back, and joining them (at, the patent says, any of many locations), a horn can be designed that eliminates, or at least mitigates, the problems associated with diffraction slots and OS sections. Flare 70 is designed to minimize the effects of diffraction and reflection at the mouth 80. Note: PS and EC are reversed in the reference numerals in the drawings chart.—NAS

7,088,827

43.38.Ja RECONFIGURABLE SPEAKER SYSTEM

Tejaswi Vishwamitra, assignor to Broan-NuTone LLC
 8 August 2006 (Class 381/1); filed 9 December 1999

It is common practice to create a synthetic center channel by combining left and right stereo channels in a dual-voice-coil loudspeaker. However, upgrading this concept to a two-way loudspeaker system is a little trickier because dual-voice-coil tweeters are not readily available. The solution described in this patent uses two identical tweeters for this application. If the



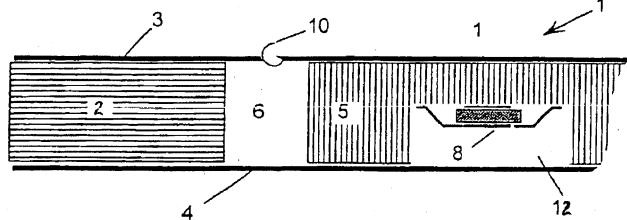
system is to be used for conventional left- or right-channel reproduction, then both woofer coils and both tweeters are paralleled. When the system is set to combine left and right channels (a kitchen loudspeaker, for example), then each input drives one woofer coil and one tweeter.—GLA

7,088,836

43.38.Ja DOOR WITH STRUCTURAL COMPONENTS CONFIGURED TO RADIATE ACOUSTIC ENERGY

Wolfgang Bachmann *et al.*, assignors to Harman Becker Automotive Systems GmbH
 8 August 2006 (Class 381/152); filed in Germany 20 September 1999

Hollow-core wooden doors are lightweight and stiff; by choosing suitable materials they should make good bending-wave loudspeakers. In the arrangement shown, transducer 8 is mounted in recess 12 to drive front panel 1. A "clamping device" 10 maintains suitable tension for optimum



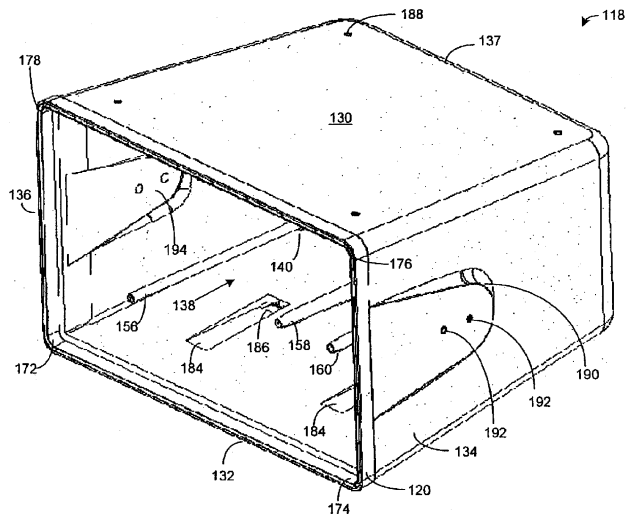
sonic performance. This illustration is found on the front page of the patent, but it is not what is actually patented. The patent claims require at least two transducers—one driving the front surface and one driving the rear surface of the door.—GLA

7,096,995

43.38.Ja POLYURETHANE FOAM CABINETS

David H. Cox and Chen-Hui Huang, assignors to Harman International Industries, Incorporated
 29 August 2006 (Class 181/199); filed 4 June 2003

A two-layer molded loudspeaker cabinet is described. The outer layer is a conventional plastic casing. The inner layer is a polyurethane foam that stiffens and damps the cabinet walls. The patent discusses material formulations and manufacturing processes in considerable detail. It should be



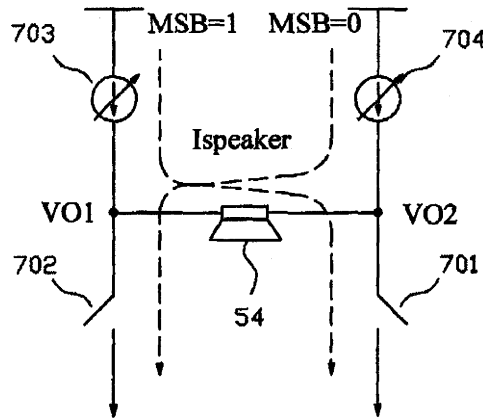
noted that the history of molded loudspeaker cabinets goes back at least 70 years and includes a wealth of prior art. In this patent, however, all 20 references were cited by the examiner.—GLA

6,992,607

43.38.Lc SPEECH SYNTHESIZER

Wuu-Trong Shieh and Ying-Pin Ho, assignors to Elan Microelectronics Corporation
 31 January 2006 (Class 341/144); filed in Taiwan 20 December 2000

The title of this patent is thoroughly misleading. The subject matter is not the construction of phonemes, words, or phrases, but rather, a type of D/A converter, for constructing a speech or audio waveform from digital data. The essence of the method seems to be that the most significant bit



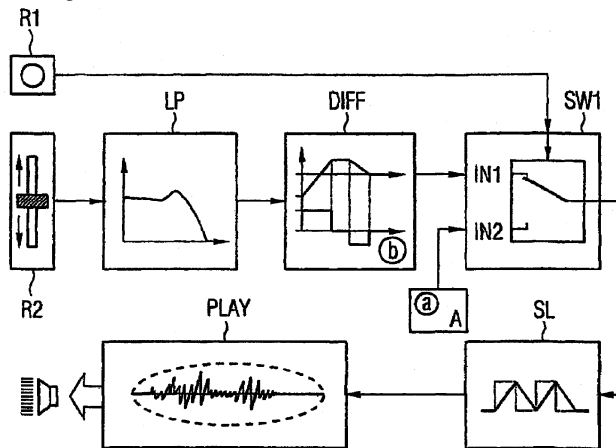
from each digital sample is used to switch a current mirror in a way that requires less power. The remaining bits of the digital sample are then converted in the usual way, but requiring a DAC with one bit less than would normally be needed. The DAC output is then flipped by the current mirror to produce the final analog waveform.—DLR

7,041,892

43.38.Md AUTOMATIC GENERATION OF MUSICAL SCRATCHING EFFECTS

Friedemann Becker, assignor to Native Instruments Software Synthesis GmbH
 9 May 2006 (Class 84/603); filed in Germany 18 June 2001

With the disappearance of the vinyl groove, scratchers are out of luck. Previous patents (see United States Patent 6,535,462 [reviewed in J. Acoust.



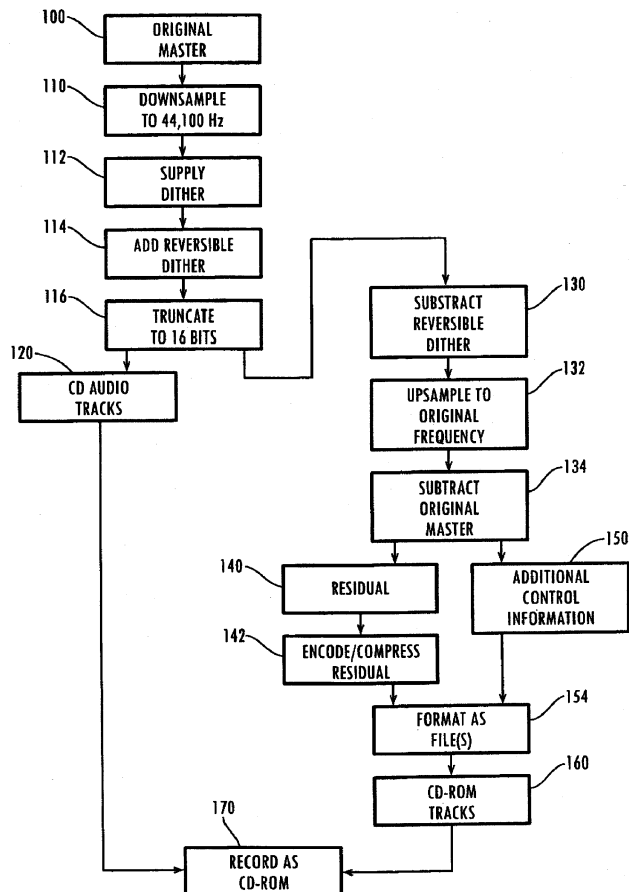
Soc. Am. 114(3), 1205 (2003)] have addressed the variable playback rate. This proposal uses beat detection along with switchable rate control of playback.—MK

7,043,312

43.38.Md CD PLAYBACK AUGMENTATION FOR HIGHER RESOLUTION AND MULTI-CHANNEL SOUND

James A. Moorer, assignor to Sonic Solutions
9 May 2006 (Class 700/94); filed 17 February 2000

Here's the problem: how can you increase the resolution of a standard 16-bit audio CD? The inventor's solution is well thought out: If it was oversampled, downsample to the standard CD rate (44.1 K samples per



second). Then dither and truncate to 16 bits. This forms the standard CD track. Next step: subtract the dither, upsample to the original rate, and subtract from the master: this forms the residual which is then encoded.—MK

7,047,201

43.38.Md REAL-TIME CONTROL OF PLAYBACK RATES IN PRESENTATIONS

Kenneth H. P. Chang, assignor to SSI Corporation
16 May 2006 (Class 704/503); filed 4 May 2001

In multimedia transmission, the issue always is how to pack a varying number of channels of varying rates into a fixed-rate channel. All this text maintains is that you can choose varying encoding schemes depending on how the data rate changes. All of the claims should be obvious to those "skilled in the art."—MK

7,053,290

43.38.Md MUSIC REPRODUCING APPARATUS AND MUSIC REPRODUCING METHOD

Junichi Tagawa *et al.*, assignors to Matsushita Electric Industrial Company, Limited
30 May 2006 (Class 84/609); filed in Japan 19 June 2003

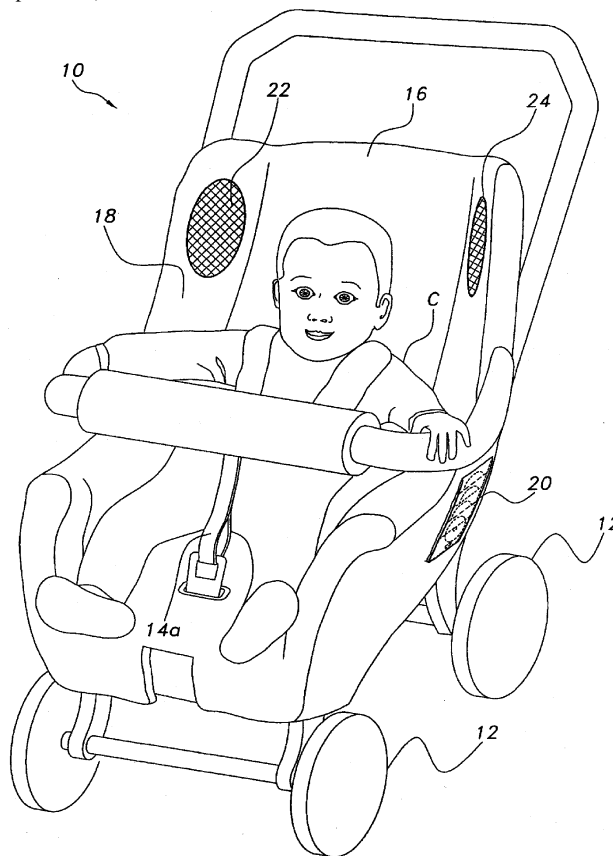
Supposedly, "emotionality" and "activeness" can be derived automatically by an algorithm (covered by a patent application in Japan). This 2D space can be searched by the listener to find a piece more suitable to the listener's current mood. Without validation of the space or the metrics, the whole process is suspect.—MK

7,077,405

43.38.Md STROLLER WITH CD PLAYER

Stacie Akpom, Arlington, Texas
18 July 2006 (Class 280/47.38); filed 6 January 2004

All city dwellers are used to the loud, drive-by vehicles with +120-dB sound pouring out of the windows. Now we may see the same phenomena with strollers (thanks to speakers 22 and 24 supplied by CD player with amplifier 20).—MK



7,079,014

43.38.Md DIGITAL SAMPLING PLAYBACK DOORBELL SYSTEM

Scott Steinetz, Sparta and Mike Palazzi, Mountain Lakes, both of New Jersey
18 July 2006 (Class 340/392.1); filed 8 May 2004

It had to happen. Doorbells are too boring. Instead of a mechanically actuated chime, a speaker is used to sound any number of different sound

tracks. Naturally, it can have any number of different computer interfaces as well. If only the doorbell could recognize the visitor!—MK

7,080,016

43.38.Md AUDIO INFORMATION REPRODUCTION DEVICE AND AUDIO INFORMATION REPRODUCTION SYSTEM

Masahiko Miyashita *et al.*, assignors to Pioneer Corporation
18 July 2006 (Class 704/278); filed in Japan 28 September 2004

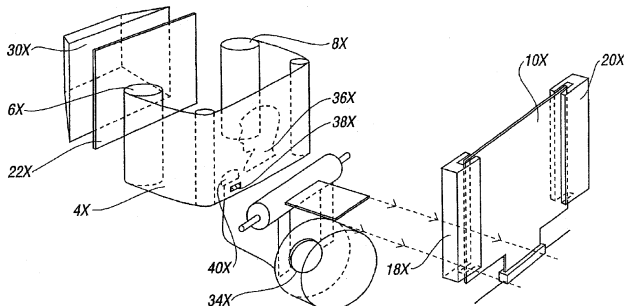
In order to form a perfect segue, a DJ smoothly mixes two pieces together by crossfading. This disclosure proposes using beat detection to alter the playback rate of the new piece to match the rate of the previous piece. At this rate, the slow dance will never arrive—the dancers will never get a break and the romantic moments never arrive.—MK

7,080,473

43.38.Md NOVELTY ANIMATED DEVICE WITH SYNCHRONIZED AUDIO OUTPUT, AND METHOD FOR ACHIEVING SYNCHRONIZED AUDIO OUTPUT THEREIN

Robert Kay, assignor to Virtual Video UK Limited
25 July 2006 (Class 40/454); filed in United Kingdom 24 May 2000

Imagine a roll of images 4X moved via motors 8X in a lenticular image display device. How can the motorized motion be synchronized with



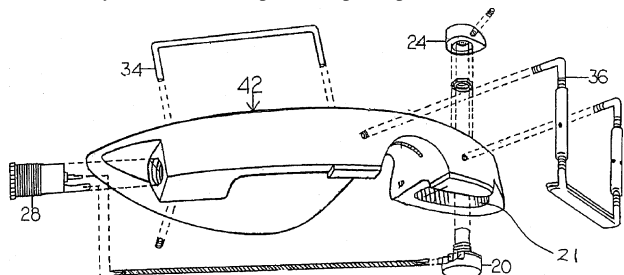
the audio (and vice versa)? Somehow, the microprocessor will control the motor speed (how is left unsaid in the text and claims) along with the audio playback.—MK

7,084,341

43.38.Md SOUND PICKUP SYSTEM FOR ACOUSTIC STRING INSTRUMENTS

Damon A. Barr, Medford, Oregon
1 August 2006 (Class 84/743); filed 14 January 2004

The only innovation is to place the preamp controls in the violin chin-



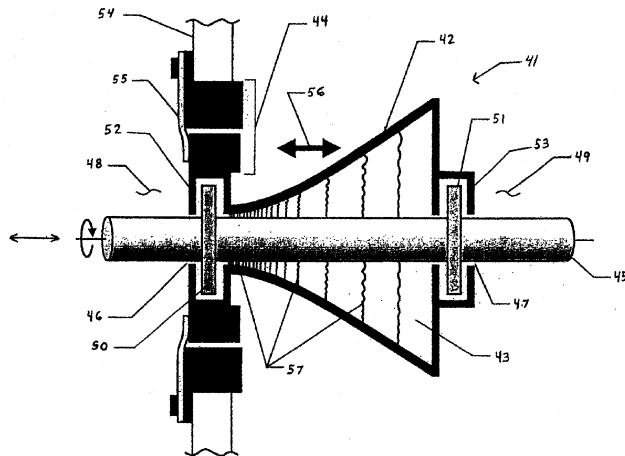
rest. The inventor believes that the sensitivity control will act as a low-pass filter to attenuate bow noise. Really?—MK

7,086,648

43.38.Pf ACOUSTIC SEAL

Bruce M. Steinetz, assignor to The United States of America as represented by the Administrator of the National Aeronautics and Space Administration
8 August 2006 (Class 277/409); filed 22 August 2003

Turbine fluid pump shaft 45 requires a pressure seal 46 between pressure 48 and low pressure 49. An oscillating transducer driver 44 causes sinusoidal fluid pressure variations 57 in fluid reservoir 42. Oscillation fre-



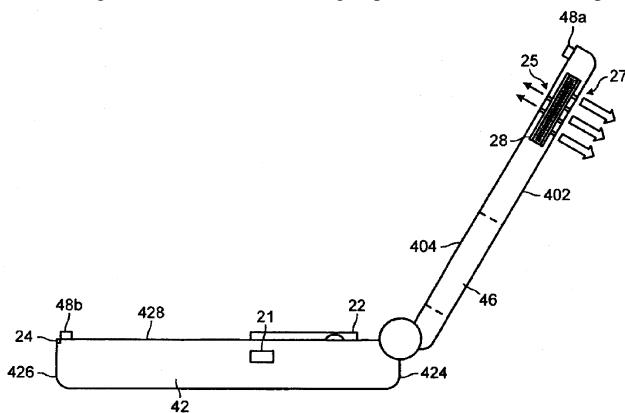
quency may be 500–4500 Hz and amplitude 0.0001–0.10 in. Asymmetric flow resistance at the choke point 57 (near barrier 50) causes a net fluid flow toward high pressure 48, thus effecting a pressure seal having little or no leakage.—AJC

7,092,745

43.38.Si PORTABLE ELECTRONICS DEVICE WITH VARIABLE SOUND OUTPUT

Winand D'Souza, assignor to Nokia Mobile Phones Limited
15 August 2006 (Class 455/575.1); filed in United Kingdom 8 October 1999

This cellular telephone houses an audio transducer whose main output emerges through rear openings 27. At the same time, some acoustic energy travels through the interior of the housing to produce an attenuated output at



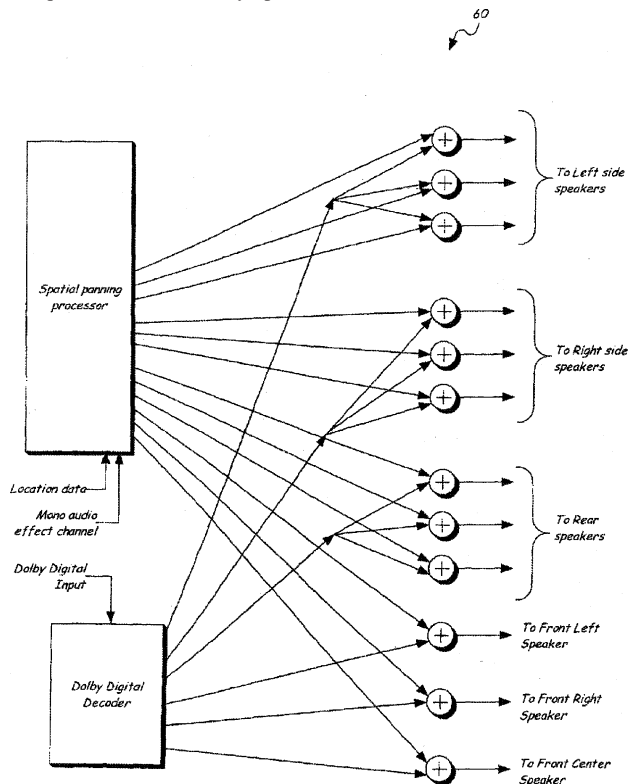
earphone openings 25. In addition, the user can switch power amplifier gain between hands-free (high power) and handset (low power) settings. Thus, hands-free operation is possible whether the phone is open or closed.—GLA

7,092,542

43.38.Vk CINEMA AUDIO PROCESSING SYSTEM

David Stanley McGrath, assignor to Lake Technology Limited
15 August 2006 (Class 381/307); filed 15 August 2001

This patent discusses methods for enhancing the performance of 5-channel discrete audio systems for multiple listeners. Added loudspeakers are required and are laterally spaced at the sides and rear of the listening



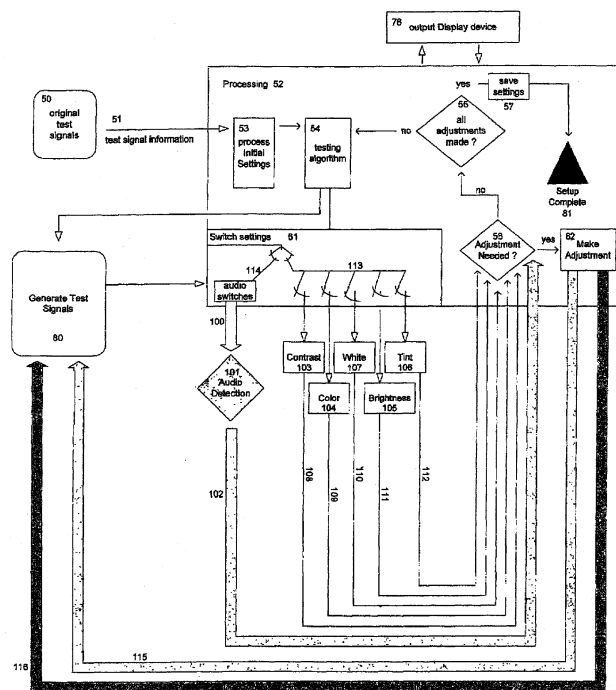
zone. A combination of amplitude and delay panning is then used to provide compensatory cues for the listeners, enabling them to sense more accurately the motion of sound sources around the sides and rear of the listening zone.—JME

7,095,455

43.38.Vk METHOD FOR AUTOMATICALLY ADJUSTING THE SOUND AND VISUAL PARAMETERS OF A HOME THEATRE SYSTEM

Richard J. Jordan and Omar M. Ahmad, assignors to Harman International Industries, Incorporated
22 August 2006 (Class 348/734); filed 21 March 2001

Today it is possible to buy a self-equalizing loudspeaker that uses an embedded computer to perform sophisticated acoustic tests and then carry out appropriate electronic adjustments. This patent explains such a program



in detail and expands the concept to include detection and adjustment of video parameters.—GLA

7,086,507

43.40.Tm CONTROLLABLE MAGNETO-RHEOLOGICAL ELASTOMER VIBRATION ISOLATOR

Gregory H. Hitchcock et al., assignors to The Board of Regents of the University and Community College System of Nevada on behalf of the University of Nevada, Reno
8 August 2006 (Class 188/267.2); filed 12 May 2004

This patent describes several vibration isolator configurations that make use of flexible elements which enclose a magneto-rheological elastomer. Coils attached at suitable locations provide magnetic fields for adjusting the elastomer's effective stiffness, thus controlling the stiffness of the isolator.—EEU

7,093,815

43.40.Tm VIBRATION QUENCHING SUBSTRATE FOR DIAGNOSTIC EQUIPMENT SUSCEPTIBLE TO VIBRATIONS

Steven Patrick Stofiel, assignor to Hitachi Medical Systems America, Incorporated
22 August 2006 (Class 248/633); filed 29 October 2001

This patent pertains to vibration isolation of magnetic resonance imaging devices and similar equipment. The isolation system described here consists of a structural under layer of reinforced concrete, an isolation layer consisting of an array of elastomeric elements, and a relatively massive reinforced concrete slab on which the device of concern is to be supported. The whole arrangement is intended to be located in a depression in the floor of the building that is to house the device, so that the base of the device is even with the adjacent floor. Conductors are included in the underlayer to provide electromagnetic shielding.—EEU

7,086,509

43.40.Tm VIBRATION ISOLATOR WITH ADJUSTABLE RESPONSE

John Cunningham, Saratoga Springs, New York and Robert E. Roemer, Bolton, Massachusetts
8 August 2006 (Class 188/378); filed 14 March 2002

This isolator consists in essence of a leaf spring that is supported at its two ends, with a load application point in the middle. Several mechanism designs are shown that use screw or cam arrangements to adjust the effective length of the leaf spring, thus adjusting the stiffness of the isolator.—EEU

7,094,478

43.40.Tm MAGNETIC DAMPING

Kevin W. Griffey *et al.*, assignors to Material Sciences Corporation, Engineered Materials and Solutions Group, Incorporated
22 August 2006 (Class 428/692.1); filed 13 September 2002

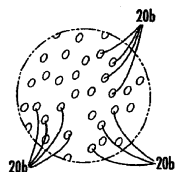
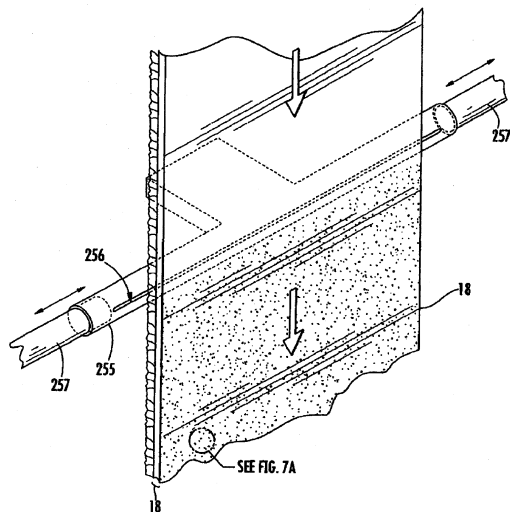
This patent describes a viscoelastic damping system of the constrained-layer type. In such a system, a viscoelastic material is sandwiched between two structural layers so that it dissipates energy as the result of shear that is induced in it as the sandwich assembly is flexed. The novel feature here is that one of the structural layers is of a magnetic material, enabling the damping system to be attached easily to surfaces of ferromagnetic structural elements.—EEU

7,097,723

43.50.Gf LIGHTWEIGHT ACOUSTIC AUTOMOTIVE CARPET

Timothy J. Allison *et al.*, assignors to Collins & Aikman Products Company
29 August 2006 (Class 156/72); filed 21 May 2004

Vehicle-floor-mat sound absorption is improved in production by drawing air through woven backing 18 via vacuum rail 255. The backing is coated with a polyethylene secondary layer heated to be flowable. Air drawn



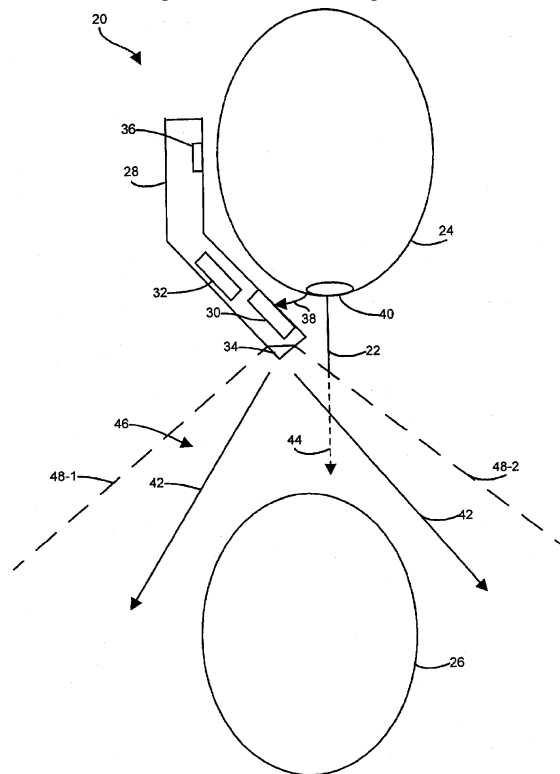
through the backing causes the polyethylene coating to flow into the backing weave, resulting in microscopic air channels whose air flow resistance improves sound absorption.—AJC

7,088,828

43.50.Ki METHODS AND APPARATUS FOR PROVIDING PRIVACY FOR A USER OF AN AUDIO ELECTRONIC DEVICE

Richard W. Bradford and Philip Jacobs, assignors to Cisco Technology, Incorporated
8 August 2006 (Class 381/71.1); filed 13 April 2000

Active noise suppression technology has reached the stage where it can be miniaturized and adapted to cellular telephones. In this version, an additional sensing microphone and speech-canceling loudspeaker are incorporated into the handset. The normal "talk" signal is inverted, delayed, and fed to the second loudspeaker to create an antispeech zone in the vicinity of



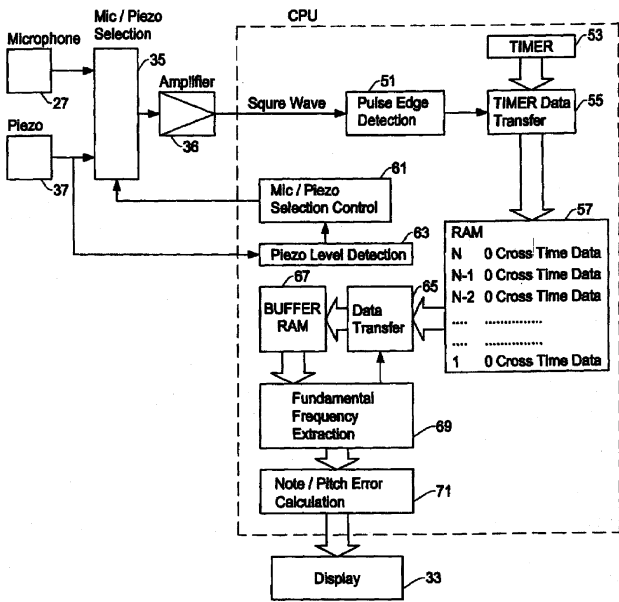
the user. A signal from the sensing microphone adjusts the delay dynamically to maintain optimum acoustic cancellation. It is interesting to note that the feedback feature is not mentioned in the abstract and appears as an optional embodiment in the explanatory text, yet seems to be included in all of the patent claims.—GLA

7,049,502

43.58.Hp MUSIC TUNER

Takeo Taku and Kousuke Higo, assignors to Korg, Incorporated
23 May 2006 (Class 84/454); filed 24 October 2003

There are two innovations in this electronic tuner: First, it automatically selects between microphone 27 and piezoelectric transducer 37 input



based on the piezoelectric signal amplitude and, second, it clips onto an instrument (think guitar neck). The rest is as expected.—MK

7,093,487

43.58.Kr ANGULAR-RATE DETECTING APPARATUS

Yoichi Mochida, assignor to Murata Manufacturing Company, Limited
22 August 2006 (Class 73/504.14); filed in Japan 29 September 2003

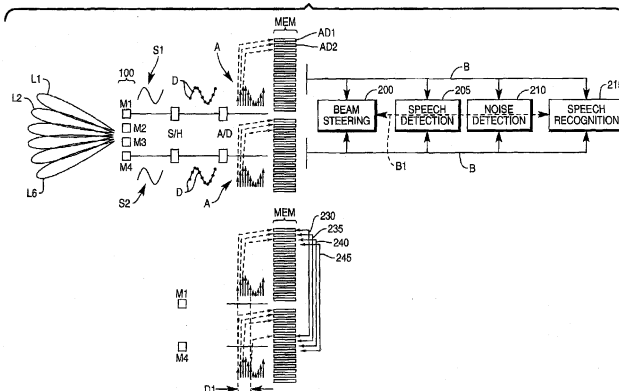
Angular rate detection is accomplished by measuring the relative displacement of vibrating masses acted upon by Coriolis forces. The masses vibrate in the opposite direction while being rotated in the same direction; therefore, the Coriolis forces act in the opposite direction on the respective mass and the resulting relative displacement is proportional to the angular rate. The vibrating masses are attached to a substrate which resonates at its natural frequency. This arrangement allows for stable and reliable angular rate measurements.—DMD

7,092,882

43.60.Dh NOISE SUPPRESSION IN BEAM-STEERED MICROPHONE ARRAY

Jon A. Arrowood and Michael S. Miller, assignors to NCR Corporation
15 August 2006 (Class 704/233); filed 6 December 2000

The patent discusses the use of traditional beam forming and modify-



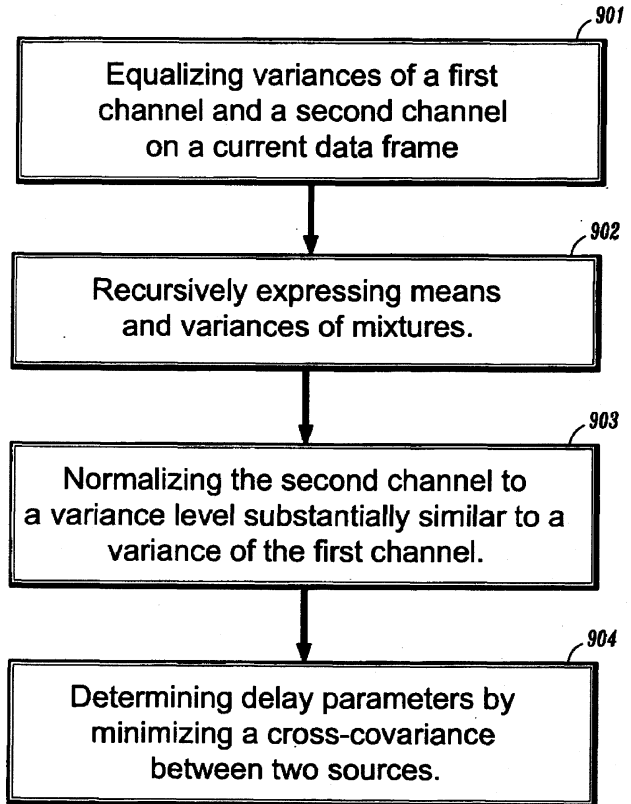
ing techniques to isolate the source of speech of a patron using a self-service kiosk, such as an ATM or general information station.—JME

7,088,831

43.60.Dh REAL-TIME AUDIO SOURCE SEPARATION BY DELAY AND ATTENUATION COMPENSATION IN THE TIME DOMAIN

Justinian Rosca *et al.*, assignors to Siemens Corporate Research, Incorporated
8 August 2006 (Class 381/92); filed 6 December 2001

With the increase in hands-free automotive communications systems we are seeing a proliferation of patents covering methods of isolating speech signals from background noise in the cab of a vehicle. A common approach is to use a microphone array from which both directional and level cues,



relative to a fixed source, can be determined. Further iterative and “learning” functions may then be applied to identify a given source. Most of the patents seen thus far rely on this as a basic operating approach, along with subtle refinements. This patent is typical.—JME

7,092,514

43.60.Dh AUDIBILITY ENHANCEMENT

Tõnu Trump and Anders Eriksson, assignors to Telefonaktiebolaget LM Ericsson (publ)
15 August 2006 (Class 379/390.03); filed 25 February 2004

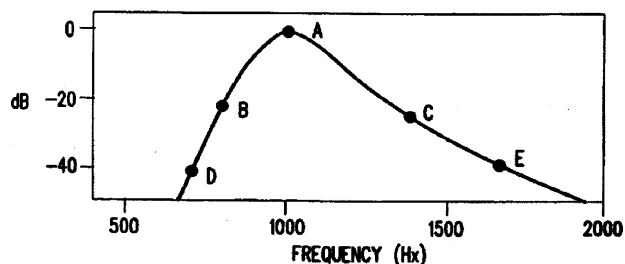
Prior art procedures for speech level and noise level estimation are combined in this patent to create a method whereby a mobile phone handset could automatically adjust the earpiece gain of the far end transmission in response to a noisy listener environment. The method here goes beyond merely increasing the volume, however, as that would also increase the “side-tone” volume (from the listener’s own mouthpiece), which would act to increase the transmission of the environmental noise to the listener’s ear.—SAF

7,089,181

43.60.Qv ENHANCING THE INTELLIGIBILITY OF RECEIVED SPEECH IN A NOISY ENVIRONMENT

Adoram Erell, assignor to Intel Corporation
8 August 2006 (Class 704/225); filed 30 January 2002

A system is described which would allow mobile phones to better adapt to noisy environments. The patent is brief and sketchy, but the general idea is to provide an automatic gain control on a handset that would be noise-sensitive, and which would eliminate the user's desire to manually turn up the speaker volume on their handset in a noisy setting.—SAF



cludes determining the user's audio profile and including this to create an overall tonal sensitivity curve. Two or more tones are then generated, spaced along a critical band scale. Assuming that a pager is always carried in a predetermined location and that background noise is always negligible, it just might work.—GLA

7,071,230

43.64.Gz THERAPEUTIC USE OF D-METHIONINE TO REDUCE THE TOXICITY OF NOISE

Kathleen C. M. Campbell, assignor to Board of Trustees of Southern Illinois University
4 July 2006 (Class 514/562); filed 23 July 2001

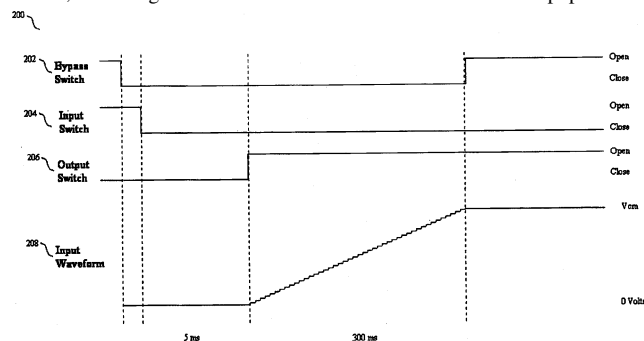
The patent describes methods of chemically preventing or reducing hearing or balance loss and damage to ear cells in patients who have been exposed to toxic levels of noise. These methods consist of administering an effective amount of a methionine protective agent, such as D-methionine, before, during, and/or after exposure to noise.—DRR

7,092,534

43.66.Lj METHOD AND SYSTEM FOR REDUCING POP NOISE OF A SOUND BROADCASTING INSTRUMENT

Yuhe Wang *et al.*, assignors to VIA Telecom Company, Limited
15 August 2006 (Class 381/94.5); filed 7 June 2004

In activities involving the routing of both analog and digital signal sources, switching transients can often cause loud "clicks" or "pops" which



are bothersome to the end user. The patent describes a method for "ramping up" signals so that these effects are minimized.—JME

7,081,085

43.64.Wn EEG FEEDBACK CONTROLLED SOUND THERAPY FOR TINNITUS

Erik Viirre *et al.*, assignors to The Regents of the University of California
25 July 2006 (Class 600/28); filed 5 February 2002

This is an automated method for treating tinnitus by habituation through the use of neurological feedback. It consists of connecting the patient through a headphone set to an electronic sound player which, in turn, is connected to a PC work station presenting sound examples to the patient. The patient can refine the sounds by manipulating a series of controls on the player, thereby making an electronic recording of the sound in digital music format, storing the recording in the computer, transferring the electronic sound to the patient's player, and generating an EEG signature of the patient's brain activity in response to the presented sound.—DRR

7,088,839

43.66.Ts ACOUSTIC RECEIVER HAVING IMPROVED MECHANICAL SUSPENSION

Onno Geschiere *et al.*, assignors to Sonion Nederland B.V.
8 August 2006 (Class 381/368); filed 3 April 2002

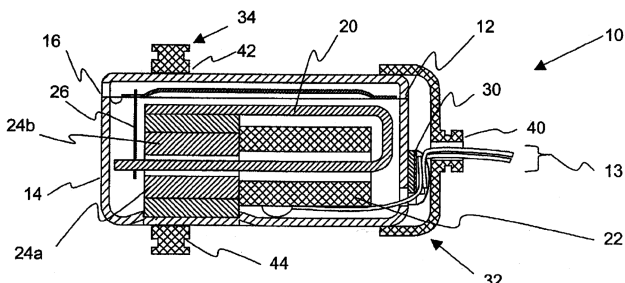
Several implementations are described of elastic suspension systems to isolate hearing aid receiver vibrations from the outside casing. Electronics

7,089,176

43.66.Lj METHOD AND SYSTEM FOR INCREASING AUDIO PERCEPTUAL TONE ALERTS

Marc Andre Boillot *et al.*, assignors to Motorola, Incorporated
8 August 2006 (Class 704/200.1); filed 27 March 2003

This patent starts out with a highly technical seven-page summary of perceptual loudness theory. It then applies information about critical bands, masking, and equal-loudness contours to the thorny problem of creating the loudest possible pager alert signal while drawing the least amount of power. Since different individuals have different hearing losses, the process in-



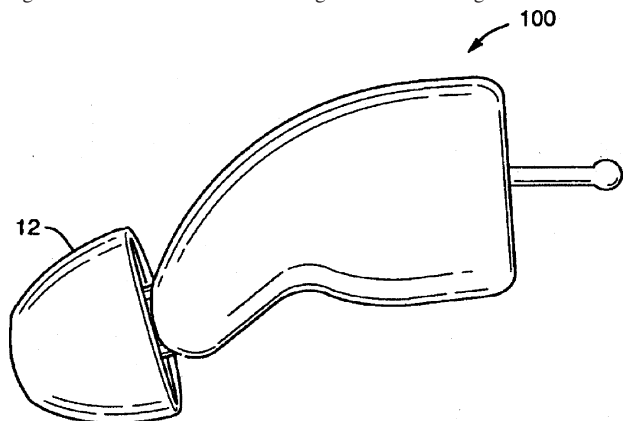
are included within the receiver housing to convert an electric audio signal to an acoustic output signal.—DAP

7,092,543

43.66.Ts ONE-SIZE-FITS-ALL UNI-EAR HEARING INSTRUMENT

Derek D. Mahoney *et al.*, assignors to Sarnoff Corporation
15 August 2006 (Class 381/328); filed 13 March 2000

A standard-size housing consisting of two half-shells joined together is designed to fit into either the left or right ear of a hearing aid wearer. A soft



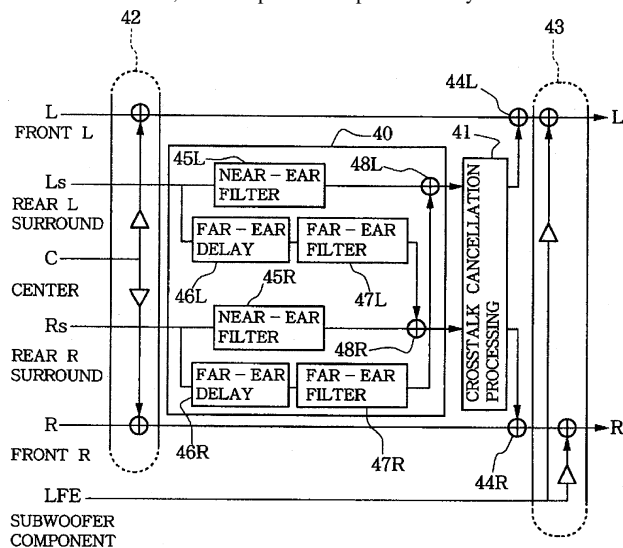
termination tip on the distal end of the hearing aid housing is intended to go very deep into the ear canal. The hearing aid receiver can be housed in the tip.—DAP

7,095,865

43.66.Yw AUDIO AMPLIFIER UNIT

Masaki Katayama and Hirofumi Onitsuka, assignors to Yamaha Corporation
22 August 2006 (Class 381/309); filed in Japan 4 February 2002

The abstract for this patent reads: "Face of a listener (user) is photographed by a CCD camera, and a face width and auricle size of the listener are detected on the basis of the picture of the listener's face. HRTFs ... are calculated, using the detected face width and auricle size as head shape data of the listener. Then, a filter process is performed by a DSP of a USB



amplifier unit so as to attain characteristics of the HRTFs, as a result of which sound image localization of the rear loudspeakers can be achieved via front loudspeakers." Supporting data suggest that this can be carried out with a fair degree of accuracy, thanks to what the authors refer to as the "measuring wizard!"—JME

7,089,177

43.72.Ar SYSTEM AND METHOD FOR CHARACTERIZING VOICED EXCITATIONS OF SPEECH AND ACOUSTIC SIGNALS, REMOVING ACOUSTIC NOISE FROM SPEECH, AND SYNTHESIZING SPEECH

Greg C. Burnett *et al.*, assignors to The Regents of the University of California
8 August 2006 (Class 704/203); filed 3 August 2005

This patent presents a mishmash of envisioned applications for a previously patented scheme of electromagnetic radar which can detect the cycling of the vocal cords through the neck tissues. The ability to accurately detect glottal opening and closing cycles is presented here as enhancing other speech technologies such as noise removal and speech synthesis, with several such applications briefly outlined. The only drawback appears to be the EM sensing equipment itself, which requires the speaker's neck to be in close proximity to the transmitter and receiver of the EM waves.—SAF

7,092,881

43.72.Ar PARAMETRIC SPEECH CODEC FOR REPRESENTING SYNTHETIC SPEECH IN THE PRESENCE OF BACKGROUND NOISE

Joseph Gerard Aguilar *et al.*, assignors to Lucent Technologies Incorporated
15 August 2006 (Class 704/233); filed 26 July 2000

This patent describes, in adequate detail, an improvement upon standard implementations of sinusoidal (also called harmonic) speech coding and resynthesis. The major innovations appear to be (1) the modeling of background noise along with the speech, and (2) the use of a multilayer neural network to improve the voicing-dependent spectrum estimation that is critical to the performance of sinusoidal speech coders.—SAF

7,089,182

43.72.Dv METHOD AND APPARATUS FOR FEATURE DOMAIN JOINT CHANNEL AND ADDITIVE NOISE COMPENSATION

Younes Souilmi *et al.*, assignors to Matsushita Electric Industrial Company, Limited
8 August 2006 (Class 704/234); filed 15 March 2002

This patent describes an improvement on a recently patented "Jacobian" approach to noise reduction in speech signals. The method to be improved accomplishes the adaptive simultaneous reduction of additive and convolutional signal noise by an approximation to the computationally expensive technique of parallel model combination, which is achieved by means of Jacobian matrices of certain model parameters. This approximate Jacobian method is known to perform poorly when test noise conditions are considerably different from training conditions. The patent describes a way of ameliorating this problem by a scheme of (linear or nonlinear) transformations applied to the matrices.—SAF

7,096,182

43.72.Dv COMMUNICATION SYSTEM NOISE CANCELLATION POWER SIGNAL CALCULATION TECHNIQUES

Ravi Chandran *et al.*, assignors to Tellabs Operations, Incorporated
22 August 2006 (Class 704/226); filed 28 February 2003

This patent, though not grammatically titled, is written with a rare attention to expository quality that makes it seem more like a published scientific paper. The general idea involves improvements to the prior art of

noise cancellation in speech using frequency-band decomposition and reassignment of band weights. The weighting factors are calculated by invoking a sophisticated approach to the estimation of signal power and noise power in each frequency band.—SAF

7,092,884

43.72.Fx METHOD OF NONVISUAL ENROLLMENT FOR SPEECH RECOGNITION

James R. Lewis *et al.*, assignors to International Business Machines Corporation
15 August 2006 (Class 704/243); filed 1 March 2002

Speaker-independent speech recognition software must undergo some training speech, known as “enrollment,” from each new user in order to perform to design specification. Normally, the user is asked to speak written text presented through the computer’s visual interface. Here, an idea is patented for using an audio-only interface for enrollment, in which the user would “shadow” (repeat as immediately as possible) the speech of a computer speech synthesizer speaking the enrollment text.—SAF

6,990,449

43.72.Ja METHOD OF TRAINING A DIGITAL VOICE LIBRARY TO ASSOCIATE SYLLABLE SPEECH ITEMS WITH LITERAL TEXT SYLLABLES

Eliot M. Case, assignor to Qwest Communications International Incorporated
24 January 2006 (Class 704/260); filed 27 March 2001

This speech synthesis system is one of the “segment concatenation” type, but with the proviso that the segments should be as large as possible, i.e., words, even phrases, whenever possible, and if (shudder) absolutely necessary, possibly a syllable or two. The strategy is to store an immense repertoire of natural speech units and to always find the most suitable unit and seldom or never do any adjustment or adaptation. The only discussion related at all to waveform or spectral details is a lengthy section on finding the portions of consonants where cuts and joins could best be made. One figure suggests that pitch patterns might be adapted or synthesized in some way, but no detail is given as to how this might be done. Instead, “each item in the digital voice library may be recorded in up to as many inflections as present in the inflection table.” There is no estimate of the number of terabytes required for this library.—DLR

6,990,450

43.72.Ja SYSTEM AND METHOD FOR CONVERTING TEXT-TO-VOICE

Eliot M. Case *et al.*, assignors to Qwest Communications International Incorporated
24 January 2006 (Class 704/260); filed 27 March 2001

This speech synthesis system is basically identical to that described in United States Patent 6,990,449, reviewed above, but it has a more extensive claims section, which spells out in greater detail the variety of recordings which will be needed to accomplish the synthesis operations.—DLR

6,990,451

43.72.Ja METHOD AND APPARATUS FOR RECORDING PROSODY FOR FULLY CONCATENATED SPEECH

Eliot M. Case and Richard P. Phillips, assignors to Qwest Communications International Incorporated
24 January 2006 (Class 704/260); filed 1 June 2001

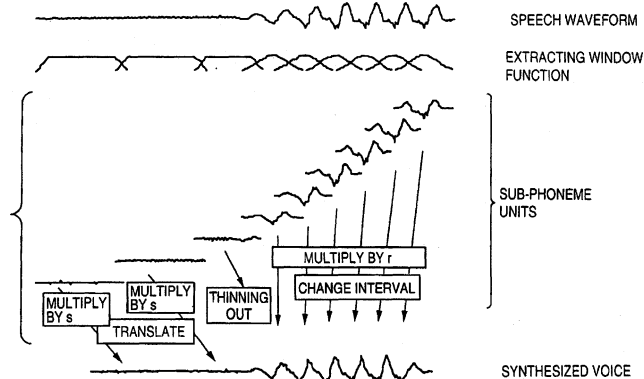
This speech synthesis system is basically identical to that described in United States Patents 6,990,449 and 6,990,450, both reviewed above, but now with emphasis on the recording process by which a suitable collection of speech recordings would be obtained. Details presented here include instructions to the speaker (the “talent”) by whose voice the desired collection of recordings may best be accomplished.—DLR

6,993,484

43.72.Ja SPEECH SYNTHESIZING METHOD AND APPARATUS

Masayuki Yamada *et al.*, assignors to Canon Kabushiki Kaisha
31 January 2006 (Class 704/261); filed in Japan 31 August 1998

The abstract of this speech synthesis patent describes the method using an elaborate construction of phrases involving “amplitude altering magnifications of subphoneme units.” If this phrase is replaced by descriptions of



gain control of pitch periods, the patent becomes much easier to understand. In fairness, it should also be said that the gain control is also applied to unvoiced portions of the speech signal. From there, the rest is fairly cut and dried.—DLR

7,089,186

43.72.Ja SPEECH INFORMATION PROCESSING METHOD, APPARATUS AND STORAGE MEDIUM PERFORMING SPEECH SYNTHESIS BASED ON DURATIONS OF PHONEMES

Toshiaki Fukada, assignor to Canon Kabushiki Kaisha
8 August 2006 (Class 704/258); filed in Japan 31 March 2000

The objective here is all about improving the prosody of a speech synthesizer by computing the durations of phonemes that would be required by the language in order to yield the most natural pronunciation. The phoneme durations are apparently supposed to be learned by the software using various basic *ad hoc* (atheoretical) calculations, but there is limited detail here.—SAF

7,089,187

**43.72.Ja VOICE SYNTHESIZING SYSTEM,
SEGMENT GENERATION APPARATUS FOR
GENERATING SEGMENTS FOR VOICE SYNTHESIS,
VOICE SYNTHESIZING METHOD AND
STORAGE MEDIUM STORING PROGRAM
THEREFOR**

**Reishi Kondo and Hiroaki Hattori, assignors to NEC Corporation
8 August 2006 (Class 704/267); filed in Japan 27 September 2001**

This inscrutable patent is written in poor English, but it attempts to present a number of related methods for reducing the size of an acoustic segment database employed in a speech synthesizer. The methods all invoke the idea of storing or decompressing a smaller number of compressed segments than would actually be needed for high-quality synthesis, with various ways suggested for calculating how to reuse previously decompressed and cached acoustic segments during a synthesis output.—SAF

7,092,878

**43.72.Ja SPEECH SYNTHESIS USING MULTI-MODE
CODING WITH A SPEECH SEGMENT
DICTIONARY**

**Masayuki Yamada, assignor to Canon Kabushiki Kaisha
15 August 2006 (Class 704/230); filed in Japan 3 August 1999**

This patent simply describes different versions of the idea of using different speech coding qualities (and thus compression rates) for different kinds of speech segments in a synthesizer. For example, some kinds of segments could be encoded in 7-bit μ -law, others in 8-bit μ -law, and still others could be stored “without encoding,” a notion that can only be interpreted to mean that one would resort to some default high-rate encoding like 16-bit PCM. The encoding decision would be made using a distortion threshold.—SAF

7,095,314

**43.72.Ja EVENT REPORTING SYSTEM WITH
CONVERSION OF LIGHT INDICATIONS
INTO VOICED SIGNALS**

**Jonathan T. Kemper, assignor to Directed Electronics,
Incorporated
22 August 2006 (Class 340/425.5); filed 27 February 2004**

The patent describes an idea whose time has surely come—using a simple light-sensing and pattern-interpreting computer and speech synthesizer to give voice to the light-blinking signals of security devices. In this way, the processor detects the flashes of, say, a car alarm, “determines from the look-up table that the sequence corresponds to a passenger compartment violation, and loads from the memory a speech synthesis segment” such as “WARNING! DOOR HAS BEEN OPENED. CHECK PASSENGER COMPARTMENT FOR INTRUDERS.” “These are of course merely exemplary events and announcements.”—SAF

7,096,183

**43.72.Ja CUSTOMIZING THE SPEAKING STYLE OF
A SPEECH SYNTHESIZER BASED ON
SEMANTIC ANALYSIS**

**Jean-Claude Junqua, assignor to Matsushita Electric Industrial
Company, Limited
22 August 2006 (Class 704/258); filed 27 February 2002**

This is one of those patents that lays claim to a pie in the sky and does not offer any details. In a couple of pages, the author patents the notion of modifying the speaking style of the speech synthesizer (by altering its prosodic parameters somehow) according to the result of topic analysis of the target text. For example, “if the topic is sports, then the speaking style of a sportscaster may be used to render the input text.” One wonders: Has the author ever heard a real speech synthesizer?—SAF

6,988,072

**43.72.Ne CONTROLLING THE LISTENING
HORIZON OF AN AUTOMATIC SPEECH
RECOGNITION SYSTEM FOR USE IN HANDSFREE
CONVERSATIONAL DIALOGUE**

**Eric Horvitz, assignor to Microsoft Corporation
17 January 2006 (Class 704/275); filed 7 July 2004**

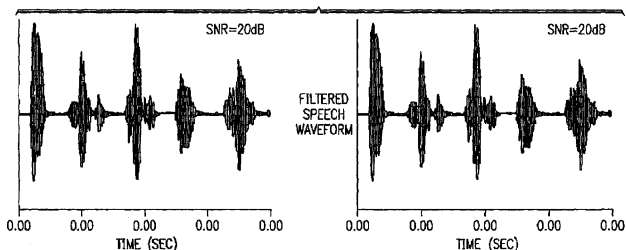
This patent deals with the issue of activating a speech recognition system in the manner that a push-to-talk switch is sometimes used and, in this case, trying to guess what the user wants to do next. The assumption is that it would be undesirable for various reasons to keep the recognizer operating all of the time. The scheme described here involves something called a “listening horizon,” a time period during which the computer will be listening for user input. The time period may be fixed or may be adjusted depending on the conversational state or other factors. The patent goes on to discuss various cases in which the horizon may be expanded, such as when a reply is expected to a computer action, or when the dialog sequence would indicate that a user utterance is expected. Other events that may extend the horizon include filled pauses, such as “ummm,” “uhhh,” etc. Certain definitive user inputs, such as “yes” or “no,” may abruptly terminate the horizon.—DLR

6,990,445

**43.72.Ne SYSTEM AND METHOD FOR SPEECH
RECOGNITION AND TRANSCRIPTION**

**Dung H. Ky, assignor to XL8 Systems, Incorporated
24 January 2006 (Class 704/235); filed 17 December 2001**

This patent proclaims the strategy of using syllable structure as a key element of a speech recognition system. However, when it gets down to the brass tacks, details are scarce. Several times, it is said that waveforms are stored in a reference waveform library. “Waveform parameters such as amplitude, frequency, period, etc., are used in the comparison.” Elsewhere, it is said that the syllables can easily be counted, such as for the five-syllable phrase, “Hello, Joshua,” as seen in the figure. Word identification is to be aided by counting the number of syllables in a word. But, this assumes that



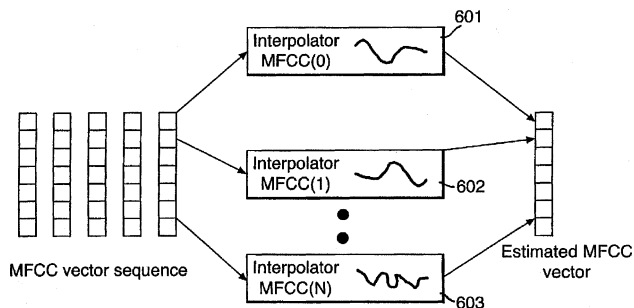
one can also easily find the word boundaries. How this is to be done is not clarified.—DLR

6,993,483

43.72.Ne METHOD AND APPARATUS FOR SPEECH RECOGNITION WHICH IS ROBUST TO MISSING SPEECH DATA

Benjamin P. Milner, assignor to British Telecommunications public limited company
31 January 2006 (Class 704/236); filed in the European Patent Office 2 November 1999

This speech recognition system is designed for use in a network environment in which spectral analysis packets in the form of feature vectors would be transmitted from the speech collection point to recognizer software running in a server. The emphasis here is on a method of interpolating



between the feature vectors such that data may be filled in to bridge across the gap in the case of missing data packets. The system is designed around the widely used Mel-frequency cepstral coding (MFCC) method, and the vector interpolation takes place in this coding domain.—DLR

7,089,178

43.72.Ne MULTISTREAM NETWORK FEATURE PROCESSING FOR A DISTRIBUTED SPEECH RECOGNITION SYSTEM

Harinath Garudadri *et al.*, assignors to Qualcomm Incorporated
8 August 2006 (Class 704/205); filed 30 April 2002

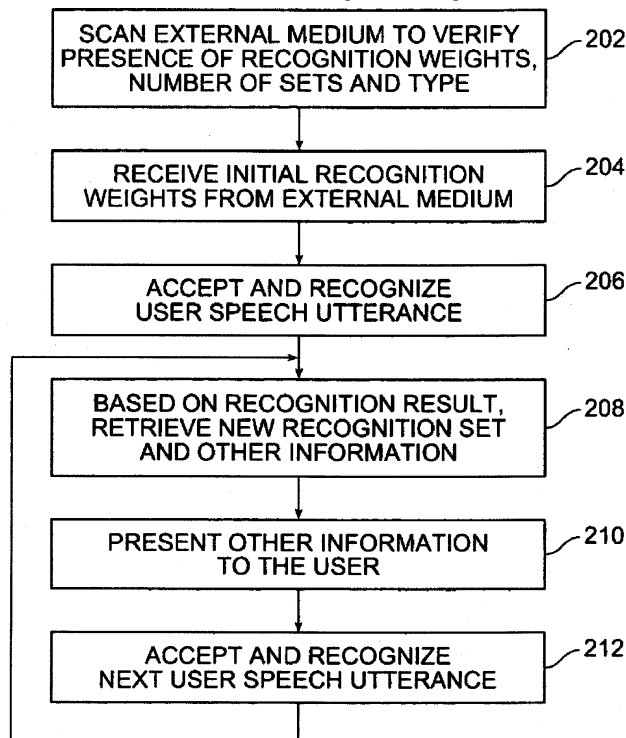
A method for processing, transmitting, receiving, and decoding speech separates and independently processes high-frequency (e.g., >4 kHz) and low-frequency components of the signal. Extracted features are transmitted with optional compression to a network using a cepstral stream, a nonlinear neural network stream, and a multiband temporal-pattern architecture stream.—DAP

7,092,887

43.72.Ne METHOD OF PERFORMING SPEECH RECOGNITION ACROSS A NETWORK

Todd F. Mozer and Forrest S. Mozer, assignors to Sensory, Incorporated
15 August 2006 (Class 704/270.1); filed 15 October 2003

A speaker-independent recognition engine is incorporated in a base unit such as a CD player, computer, telephone, video game, or TV set. An external medium, such as a CD or video game cartridge, is connected to the



base unit and interactively provides different data sets in two download steps for the recognition engine to recognize a spoken utterance from a limited set of utterances.—DAP

7,076,035

43.75.Bc METHODS FOR PROVIDING ON-HOLD MUSIC USING AUTO-COMPOSITION

Alan R. Loudermilk, assignor to MediaLab Solutions LLC
11 July 2006 (Class 379/101.01); filed 4 January 2002

Can anything beat the experience of being on hold and listening to the same music theme over and over (and over) again? So, why not use a pseudorandom noise generator to control a simple composition algorithm? The inventor could have augmented his idea by using genre selection to change the rules (“Press 1 for jazz, 2 for baroque...”) but he did not. MIDI output is proposed so one supposes performance nuance is not on the agenda.—MK

7,078,609

43.75.Bc INTERACTIVE DIGITAL MUSIC RECORDER AND PLAYER

Alain Georges, assignor to MediaLab Solutions LLC
18 July 2006 (Class 84/645); filed in France 19 October 1999

At issue is how to assist naive, untrained users in the composition of musical pieces. This kitchen sink proposal mixes digital-audio media players

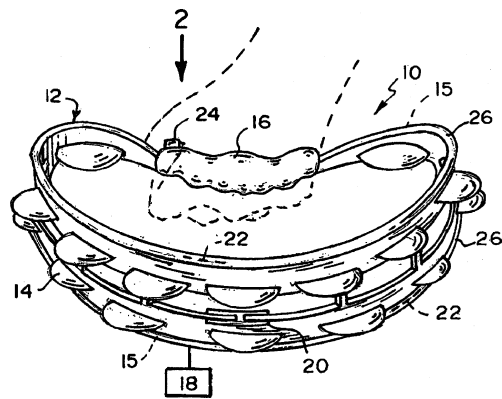
with a MIDI synthesizer with automatic composition algorithms (completely unspecified) with an FM radio receiver. This hodgepodge has a user interface, which is the only aspect described in any detail.—MK

7,078,605

43.75.Fg INVERSELY PROPORTIONED MOUTHPIECES

Robert Worth Love, Englewood, Ohio
18 July 2006 (Class 84/398); filed 8 December 2003

Brass mouthpiece patents are unusual. In this one, the inventor proposes using his “principle of inverse proportionality.” He says that (1) mouthpiece length is inversely proportional to the cup volume and (2) total air volume is constant with length as a design variable. Using these principles, the patent describes a number of related brass mouthpieces.—MK



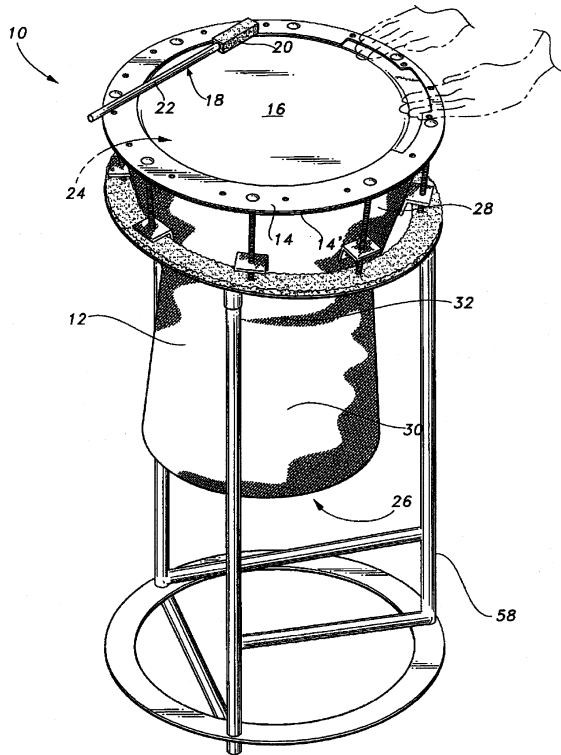
do not seem to realize that audio is not MIDI and so the needed power-conversion apparatus is missing.—MK

7,074,995

43.75.Hi UNIQUE SOUNDING DRUM

Yaser K. Barakat, Roanoke, Virginia
11 July 2006 (Class 84/411 R); filed 1 July 2004

It is not at all clear from the writing why this goblet drum should sound “unique,” as the inventor claims. Perhaps our hint is the “interior



chamber with a plurality of scratchings on it, which provide the drum assembly with a clearer sound and voice.” Which means what?—MK

7,045,697

43.75.Kk ELECTRONIC TAMBOURINE

Gina Covello and H. Edward Vega, both of Farmingville, New York
16 May 2006 (Class 84/418); filed 8 October 2004

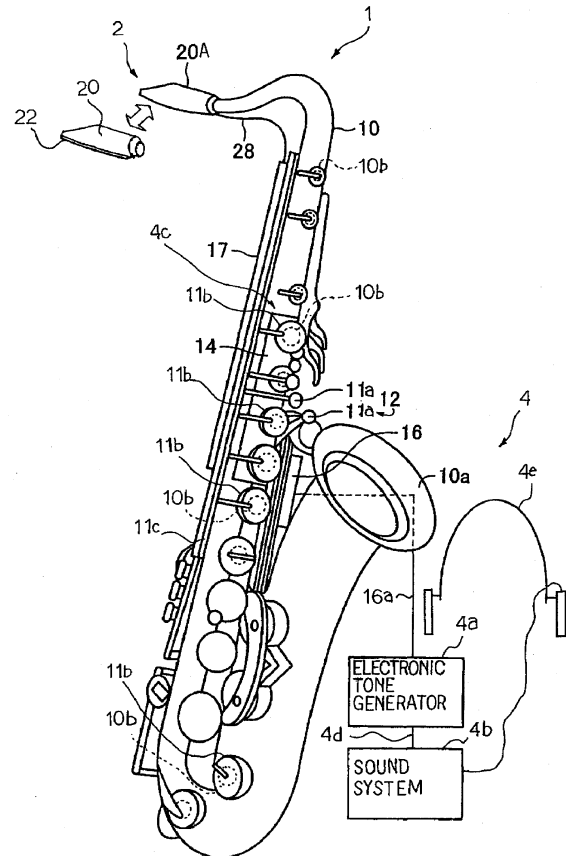
The inventors propose augmenting a tambourine by adding a MIDI port 24. They appear to be confused by calling 22 a “MIDI sensor”—they

7,049,503

43.75.Tv HYBRID WIND INSTRUMENT SELECTIVELY PRODUCING ACOUSTIC TONES AND ELECTRIC TONES AND ELECTRONIC SYSTEM USED THEREIN

Naoyuki Onozawa and Kazuhiro Fujita, assignors to Yamaha Corporation
23 May 2006 (Class 84/723); filed in Japan 31 March 2004

The Yamaha WX-7 was a very successful electronic clarinet: it used a velocity sensor mouthpiece and electronic switches to create a MIDI stream suitable for input to a MIDI synthesizer. In this update, Yamaha creates an



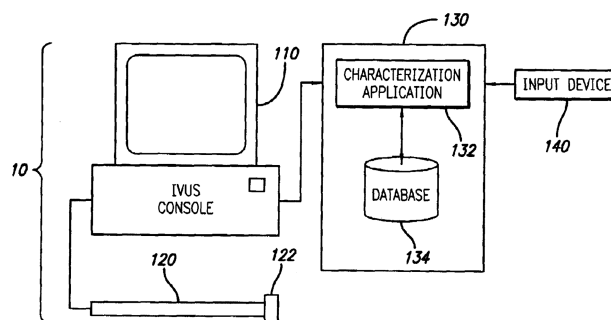
electronic saxophone. The most interesting aspect is the “tonguing sensor”—an infrared light is radiated back toward the player’s tongue and is then sensed. The ability to control reed vibration by biting on the reed is not addressed.—MK

7,045,700

43.75.Wx METHOD AND APPARATUS FOR PLAYING A DIGITAL MUSIC FILE BASED ON RESOURCE AVAILABILITY

Matti S. Hämäläinen and Timo Kosonen, assignors to Nokia Corporation
16 May 2006 (Class 84/645); filed 16 April 2004

It is well known that MIDI output devices have a limit to the maximum number of simultaneously sounding voices. A given MIDI file may exceed the maximum available, which mandates choosing a voice to delete. The question is, which voice should be muted? The complete algorithm is given inside the patent body, so it is possible to verify that the idea is reasonable.—MK



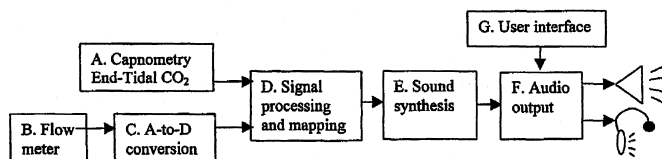
tissue of the vascular object. The IVUS data are then transmitted to the computing device and used (either by the computing device or the IVUS console) to generate an IVUS image.—DRR

7,070,570

43.80.Qf METHOD AND MEANS OF PHYSIOLOGICAL MONITORING USING SONIFICATION

Penelope Margaret Sanderson, St. Lucia and Marcus Watson, Sherwood, both of Australia
4 July 2006 (Class 600/532); filed in Australia 29 August 2001

This respiratory sonification system monitors a patient's respiration and uses a capnometric process for measuring carbon dioxide concentrations. A flowmeter measures gas flow and volume of gas. All of these measures are processed into digital information, which is sent into a sound-



system synthesizer where it is synthesized as audio output. In this manner, changes in respiratory flow during inhalation and exhalation, changes in end tidal carbon dioxide (ETCO₂) concentrations, and cumulative tidal volume (cumVt) of the patient can be represented as changes in synthesized sound heard through a loudspeaker, headphone, or earpiece.—DRR

7,074,188

43.80.Qf SYSTEM AND METHOD OF CHARACTERIZING VASCULAR TISSUE

Anuja Nair *et al.*, assignors to The Cleveland Clinic Foundation
11 July 2006 (Class 600/443); filed 25 August 2003

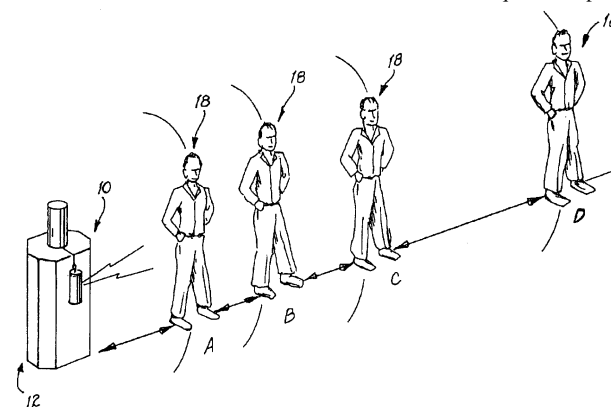
This device provides a method of using backscattered data together with known parameters to characterize vascular tissue. An ultrasonic device [e.g., an intravascular ultrasound (IVUS) console and catheter] is used to acquire rf backscattered data (i.e., IVUS data) from a blood vessel. For example, a transducer may be attached to the end of a catheter and carefully maneuvered through the patient's body to a point of interest. The transducer is then pulsed to acquire echoes or backscattered signals reflected from the

7,077,815

43.80.Qf METHOD FOR TREATING BODY TISSUE DISEASE WITH ACOUSTIC WAVES

Alphonse Cassone, Las Vegas, Nevada
18 July 2006 (Class 601/47); filed 19 July 2000

This is a rather simplistic and somewhat dubious method for treating inflammatory musculoskeletal connective tissue disorders by exposing the patient to acoustic waves from a transducer immersed in liquid. The patient



is preferably placed between 1 and 20 feet from the wave source and is exposed to waves at a frequency of about 600 Hz for approximately 25 min.—DRR

7,082,330

43.80.Qf IMPLANTABLE MEDICAL DEVICE EMPLOYING SONOMICROMETER OUTPUT SIGNALS FOR DETECTION AND MEASUREMENT OF CARDIAC MECHANICAL FUNCTION

Robert W. Stadler *et al.*, assignors to Medtronic, Incorporated
25 July 2006 (Class 607/17); filed 24 March 2004

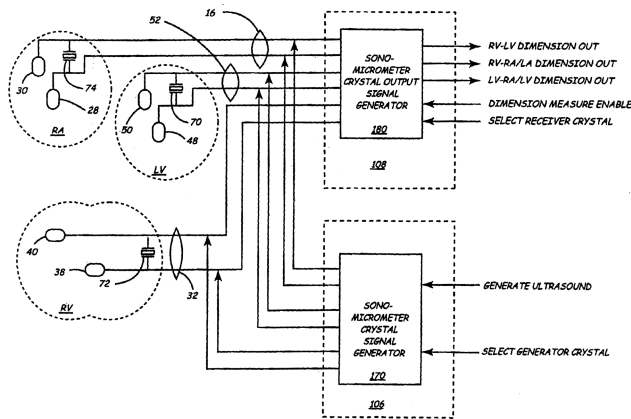
This is a system for detecting mechanical heart function and measuring mechanical heart performance of the upper and lower, left and right heart chambers. The use of a dimension sensor allows this to be done without intruding into the left heart chamber. The dimension sensor includes at least one sonomicrometer piezoelectric crystal mounted to a lead body implanted into or in relation to one heart chamber that operates as an ultrasound trans-

7,078,015

43.80.Sh ULTRASOUND IMAGING AND TREATMENT

Evan C. Unger, assignor to ImaRx Therapeutics, Incorporated
18 July 2006 (Class 424/9.52); filed 8 November 2004

A description is given of the methods and apparatus for preparing temperature-elevated, activated, gaseous-precursor-filled liposomes. The liposomes prepared by these methods are particularly useful, for example, in ultrasonic imaging applications and in therapeutic drug delivery systems. Gas, gaseous precursors, and perfluorocarbons are presented as novel potentiators for ultrasonic hyperthermia. These materials, which may be interstitially administered into the vasculature or into any body cavity, are designed to accumulate in cancerous and diseased tissues. When therapeutic ultrasonic energy is applied to the diseased region, heating is increased because of the greater effectiveness of sound energy absorption by these agents.—DRR



mitter when a drive signal is applied to it. At least one other sonomicrometer crystal mounted to a second lead body implanted into or in relation to a second heart chamber operates as an ultrasound receiver.—DRR

7,083,778

43.80.Qf ULTRASOUND CONTRAST AGENTS AND METHODS OF MAKING AND USING THEM

Michel Schneider *et al.*, assignors to Bracco International B.V.
1 August 2006 (Class 424/9.52); filed 12 March 2003

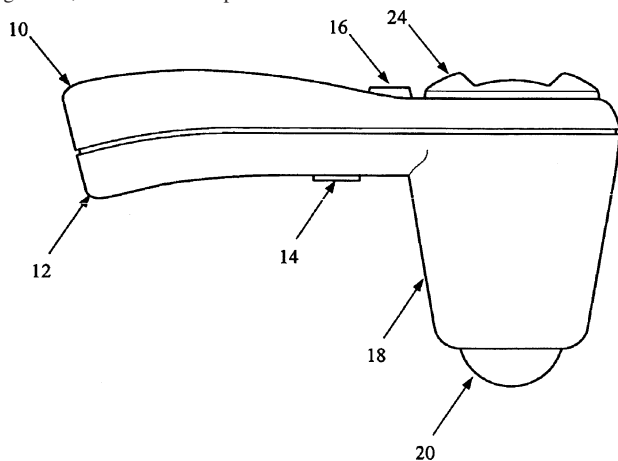
These contrast agents entail gas- or air-filled microbubble suspensions in aqueous phases usable as contrast imaging contrast agents in ultrasonic echography. They contain surfactants and, optionally, hydrophilic stabilizers. The surfactants may be in the form of liposomes. Methods of making them are also described in the patent.—DRR

7,087,022

43.80.Qf 3D ULTRASOUND-BASED INSTRUMENT FOR NON-INVASIVE MEASUREMENT OF AMNIOTIC FLUID VOLUME

Vikram Chalana *et al.*, assignors to Diagnostic Ultrasound Corporation
8 August 2006 (Class 600/449); filed 5 November 2003

Disclosure is made for a handheld ultrasound instrument for noninvasively and automatically measuring amniotic fluid volume in the uterus with minimal operator intervention. Through the use of a 2D image-processing algorithm, the instrument provides automatic feedback to the user about



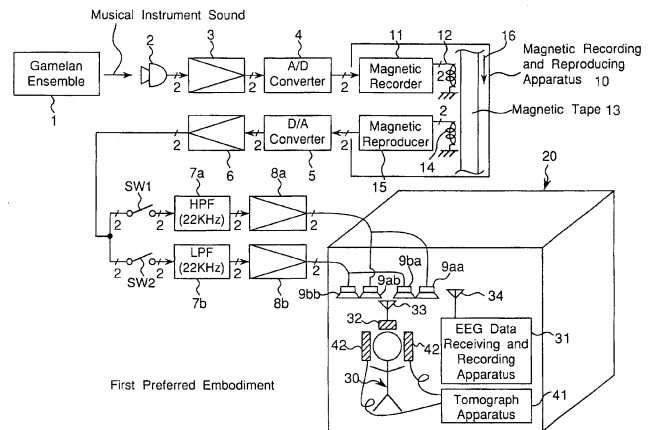
where to acquire the 3D image set. The user acquires one or more 3D data sets covering all the amniotic fluid in the uterus, and these data are then processed using an optimized 3D algorithm to output the total amniotic fluid volume correction for any fetal brain volume contributions.—DRR

7,079,659

43.80.Sh SOUND GENERATING APPARATUS AND METHOD, SOUND GENERATING SPACE AND SOUND, EACH PROVIDED FOR SIGNIFICANTLY INCREASING CEREBRAL BLOOD FLOWS OF PERSONS

Tsutomu Oohashi *et al.*, assignors to Advanced Telecommunications Research Institute International
18 July 2006 (Class 381/98); filed in Japan 26 March 1996

In a sound-generating apparatus, a sound is generated which has a frequency within a first frequency range beyond a predetermined audio frequency range and up to a predetermined maximum frequency, and which is nonstationary so as to change in a microtemporal area in a second frequency



range beyond 10 kHz. The generated sound is then applied to the patient, thereby increasing cerebral blood flows. This is said to cause improvement and enhancement of the person's state of mind and body, so as to relieve stresses, thereby causing the patient to relax.—DRR

7,087,020

43.80.Vj ULTRASOUND IMAGE RECONSTRUCTION WITH RECEIVE APERTURE CONTROL

Ching-Hua Chou *et al.*, assignors to Zonare Medical Systems, Incorporated
8 August 2006 (Class 600/437); filed 31 January 2005

The number of signals in a receive aperture is compared to the number of signals desired for beam formation. If the number of aperture signals is less than or equal to the number of signals desired for beam formation, all of

the aperture signals are used for beam formation. Otherwise, the aperture signals are processed to reduce the number of signals to the number desired for beam formation. The size of the desired receive aperture may be based on the direction or depth of a region of interest.—RCW

7,090,640

43.80.Vj SYSTEM AND METHOD FOR AUTOMATIC DETERMINATION OF A REGION OF INTEREST WITHIN AN IMAGE

Jacques Dov Barth *et al.*, assignors to Q-Vision
15 August 2006 (Class 600/443); filed 12 November 2003

The analysis of an ultrasonic image of a carotid artery is automated to identify a region of interest in a selected frame by searching for parallel boundaries of the carotid artery.—RCW

7,090,641

43.80.Vj ULTRASOUND IMAGE FOCUSING METHOD AND RELATIVE ULTRASOUND SYSTEM

Elena Biagi *et al.*, assignors to Actis Active Sensors S.r.l.
15 August 2006 (Class 600/443); filed in Italy 22 November 2002

Coherently demodulated signals received from elements of a linear array are Fourier transformed in the depth dimension, compensated for depth, inverse Fourier transformed in the depth dimension, Fourier transformed in the transverse direction, remapped, compensated in the transverse direction, and inverse Fourier transformed in the transverse direction to obtain an image with focusing.—RCW

7,090,642

43.80.Vj ULTRASONIC TRANSMITTING AND RECEIVING APPARATUS AND ULTRASONIC TRANSMITTING AND RECEIVING METHOD

Yoshiaki Satoh, assignor to Fuji Photo Film Company, Limited
15 August 2006 (Class 600/447); filed in Japan 30 September 2002

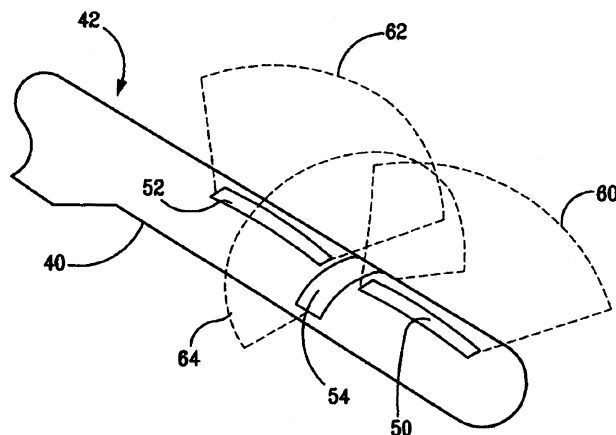
Sparse combinations of elements in a 2D ultrasonic array are used to form transmit and receive beam patterns that have reduced sidelobes in the product of transmit and receive beam patterns.—RCW

7,090,643

43.80.Vj ULTRASONIC IMAGING DEVICE. SYSTEM AND METHOD OF USE

Howard F. Fidel and Raul F. Gutierrez, assignors to 3G
Ultrasound, Incorporated
15 August 2006 (Class 600/447); filed 23 January 2004

Three arrays of transducer elements are used in an ultrasonic imaging probe. Two of the arrays are aligned with the longitudinal axis of the probe



and produce images parallel to the longitudinal axis. The third array is arranged to produce an image in a plane orthogonal to the plane of the other two images.—RCW

7,092,749

43.80.Vj SYSTEM AND METHOD FOR ADAPTING THE BEHAVIOR OF A DIAGNOSTIC MEDICAL ULTRASOUND SYSTEM BASED ON ANATOMIC FEATURES PRESENT IN ULTRASOUND IMAGES

Kenneth M. Fowkes and Lewis J. Thomas III, assignors to
Siemens Medical Solutions USA, Incorporated
15 August 2006 (Class 600/407); filed 11 June 2003

Rules of operation or the characteristics of an anatomic model are used to obtain anatomy-specific information for image processing. Images being acquired are modified automatically using this information. Alternatively, the operator may be prompted to make operational changes.—RCW

7,097,619

43.80.Vi ELEVATION BEAM PATTERN VARIATION FOR ULTRASOUND IMAGING

Patrick L. Von Behren and Paul D. Freiburger, assignors to
Siemens Medical Solutions USA, Incorporated
29 August 2006 (Class 600/447); filed 31 March 2003

A user-based or automatic search mode is used to obtain initial images with one or more beamwidths in elevation. A diagnosis mode is then used to obtain further images with a narrow elevation beamwidth. The modes employ arrays that have a coarse pitch in elevation.—RCW

Internal solitons in the ocean and their effect on underwater sound

John R. Apel^{a)}

Johns Hopkins University, Applied Physics Laboratory, Laurel, Maryland 20723

Lev A. Ostrovsky

Zel Technologies/NOAA Earth System Research Laboratory, Boulder, Colorado 80305

Yury A. Stepanyants

Australian Nuclear Science and Technology Organization, Menai (Sydney), NSW 2234, Australia

James F. Lynch

Applied Ocean Physics and Engineering Department, Woods Hole Oceanographic Institution, Woods Hole, Massachusetts 02543

(Received 24 March 2006; accepted 16 October 2006)

Nonlinear internal waves in the ocean are discussed (a) from the standpoint of soliton theory and (b) from the viewpoint of experimental measurements. First, theoretical models for internal solitary waves in the ocean are briefly described. Various nonlinear analytical solutions are treated, commencing with the well-known Boussinesq and Korteweg–de Vries equations. Then certain generalizations are considered, including effects of cubic nonlinearity, Earth's rotation, cylindrical divergence, dissipation, shear flows, and others. Recent theoretical models for strongly nonlinear internal waves are outlined. Second, examples of experimental evidence for the existence of solitons in the upper ocean are presented; the data include radar and optical images and *in situ* measurements of wave forms, propagation speeds, and dispersion characteristics. Third, and finally, action of internal solitons on sound wave propagation is discussed. This review paper is intended for researchers from diverse backgrounds, including acousticians, who may not be familiar in detail with soliton theory. Thus, it includes an outline of the basics of soliton theory. At the same time, recent theoretical and observational results are described which can also make this review useful for mainstream oceanographers and theoreticians. © 2007 Acoustical Society of America.

[DOI: 10.1121/1.2395914]

PACS number(s): 43.30.Ft, 43.30.Bp, 43.30.Pc [ADP]

Pages: 695–722

I. PREFACE

The first incarnation of this review paper appeared in 1995 as a Report of the Applied Physics Laboratory of John Hopkins University.¹ It was planned then to continue working on the material and publish it in a refereed journal. Unfortunately, these plans were frozen when one of the authors and the actual initiator of this project, Professor John Apel, passed away.

Recently, we received a suggestion to publish this material in *The Journal of the Acoustical Society of America*, with the motivation being that the acoustical monitoring of internal solitary waves had become one of the leading topics in acoustical oceanography. We agreed, realizing that both the theory and observations of internal solitons have progressed enormously since 1995. Thus, along with preserving most of the previous material of the paper, we tried to update it in order to reflect, at least briefly, the main new results in the area. This took another few years, and while doing that, we had to restrict ourselves in adding too many new parts; otherwise the text threatened to grow out of our control. As a result, the basic material and older results are still repre-

sented more comprehensively than the results of the last 8–10 years. Still we hope that, first, we managed to concisely present or at least mention most of the important new achievements and, second, that such an imbalance is not important to acousticians and other professionals who are not directly involved in ocean hydrodynamics. On the other hand, for those who are involved in physical oceanography, the paper can give some useful information regarding the present status of the problem and also the corresponding references. All this seems worth the effort due to the richness of the topic. Indeed, the internal solitary waves are arguably the most ubiquitously observed type of solitons in geophysics, and they affect many important oceanic processes, especially in the coastal zones. As a result, their studies by various means, including acoustic ones, is an exciting enterprise.

Due to journal space restrictions, this report is being presented here in a significantly abbreviated version. In particular, this concerns the reference list in which we had to restrict ourselves by those publications, from which the equations and figures were shown in the text below, plus a few books and reviews of a general character. The expanded text, with more figures and a full list of references has been published recently as a WHOI Technical Report.

^{a)}Deceased.

II. INTRODUCTION AND OVERVIEW

It has been known for over a century that in the island archipelagos of the Far East there are occasionally seen on the surface of the sea long, isolated stripes of highly agitated features that are defined by audibly breaking waves and white water. These features propagate past vessels at speeds that are at times in excess of two knots; they are not usually associated with any nearby bottom feature to which one might attribute their origin, but are indeed often seen in quite deep water. In the nautical literature and charts, they are sometimes identified as “tide rips.” In Arctic and sub-Arctic regions, especially near the mouths of fjords or river flows into the sea, analogous phenomena of lower intensity are known, dating back perhaps even to the Roman reports of “sticky water,” but certainly a recognized phenomenon since Viking times.

It is now understood that many of these features are surface manifestations of internal gravity waves, sometimes only weakly nonlinear but quite often highly nonlinear excitations in the form of “solitary waves” or “solitons.”² Their soliton-like nature (steady propagation, preserving shape) has only relatively recently been established, with two of us rhetorically questioning in 1989 whether internal solitons actually exist in the ocean.³ Now it is a widely accepted view that they (or at least structures close to solitary waves) exist as ubiquitous features in the upper ocean, and that they may be seen at scores of locations around the globe with a wide variety of *in situ* and remote sensors.

This paper sets forth (a) the basic theoretical formulations and characteristics of solitons in a stratified, sheared, rotating fluid and (b) some of the observational and experimental evidence for their existence.

Isolated nonlinear *surface* waves of great durability were first reported propagating in a shallow, unstratified Scottish canal by Scott Russell in 1838 and 1844, but their correct theoretical description was offered much later, in 1870s by Boussinesq and Rayleigh and in 1895 by Korteweg and de Vries. More recent reviews have set forth many of the interesting characteristics of solitons in general, such as their ability to preserve shapes and amplitudes upon interaction, as elastic particles do.⁴

Recognition of the nonlinear and, more specifically, the solitary character of oceanic *internal* waves on continental shelf waters appears to have first been made in the 1960s and early 1970s in the experiments by Lee, Ziegenbein, Halpern, and others, and extensive investigations into the phenomenon have since been made by many groups of workers. The bibliography includes references to these works that will be cited later in their proper contexts. A number of experimental data concerning internal wave (IW) solitons in the ocean may be found in, e.g., Ostrovsky and Stepanyants,⁵ Apel,⁶ and later in Duda and Farmer;⁷ see also the Internet Atlas of internal solitons.⁸

The creation of solitons relies on the existence of both intrinsic dispersion and nonlinearity in the medium. If, through nonlinear effects, the speed of the wave increases depending on the local displacement, the long wave (simple wave) steepens toward a shock-like condition. In a dispersive

system, however, unlike in nondispersive acoustics, this shock formation is resisted by dispersion, i.e., the difference between phase velocities of the various Fourier components making up the wave, which tends to broaden the steepening fronts. A soliton then represents a balance between these two factors, with a wave of permanent shape resulting that propagates at a speed dependent on its amplitude, the layer depths, and the density contrast, among other factors. In many cases, a soliton train (a “solibore”) is formed rather than a single soliton.

This simple picture, although providing a conceptual framework for discussing solitons, must be enriched by a more thorough theoretical treatment of the many facets of solitary waves.

In the recent years, the “family” of observed internal solitary waves has been significantly extended, and to address this and other issues, a special workshop on internal solitary waves was held in 1998.⁷ New observations have confirmed that internal solitary waves in coastal zones are often strongly nonlinear, so that the most usable weakly nonlinear theoretical models fail to describe them adequately.

The atmosphere also supports nonlinear internal waves, most notably the lee-wave/lenticular cloud phenomenon found downwind of sharp gradients in mountain ranges; we do not discuss atmospheric internal waves here, however.

The practical importance of IWs is evident, as strong IWs can provide an intensive mixing in both the upper ocean and in shallow areas, can affect biological processes, as well as radar signals, play a role in underwater acoustics and underwater navigation, etc. Military aspects of the problem seem to be of interest as well; apart from the seemingly anecdotal information circulated in 1970s on the IW role in submarine catastrophes, it should be noted that some recent publications have been supported under Naval auspices (see, e.g., the materials of the aforementioned workshop⁷).

We shall concentrate on internal solitons in the sea, with Sec. III developing the theoretical aspects, Sec. IV giving a summary of observational data (*in situ* and remote), and their discussion. Finally, Sec. V briefly outlines the impact of internal solitons on acoustic waves. Note that in the September issue of “Chaos” for 2005, a review of laboratory experiments with internal solitary waves is published⁵ so that we omit this important issue here.

III. THEORETICAL MODELS

A. Basic equations

The description of internal gravity waves in water is, in general, based on the equations of hydrodynamics for an incompressible, stratified fluid in a gravity field

$$\rho \left[\frac{\partial \mathbf{U}}{\partial t} + (\mathbf{U} \cdot \nabla) \mathbf{U} \right] + \nabla p + \rho(\mathbf{f} \times \mathbf{U}) = -\rho \mathbf{g}, \quad (1)$$

$$\frac{\partial \rho}{\partial t} + (\mathbf{U} \cdot \nabla) \rho = 0, \quad (2)$$

$$\nabla \cdot \mathbf{U} = 0. \quad (3)$$

Here the basic variables are $\mathbf{U}=(u,v,w)$ is the fluid velocity vector (w is its vertical component), p is the fluid pressure, ρ is its density, \mathbf{g} is the gravitational acceleration, and \mathbf{f} is the Earth's angular frequency vector.

In the ocean, the static density variations are very small, typically less than 1%. This enables one to somewhat simplify the problem by using the Boussinesq approximation. Let us represent the density field $\rho=\rho_0+\rho'$ as the sum of a large, equilibrium, depth-dependent part $\rho_0(z)$, and a small variable part $\rho'(\mathbf{r},t)$, where $\mathbf{r}=(x,y,z)$ is the position coordinate, with x and y lying in the horizontal plane, and z directed upward. According to Boussinesq approximation, vertical variations of the static density, $\rho_0(z)$, are neglected in all terms except the buoyancy term proportional to $d\rho_0/dz$ which is, in fact, responsible for the existence of internal waves. Boundary conditions of zero vertical displacement are applied at the bottom, $z=-H$, and at the horizontal surface $z=0$ that corresponds to the unperturbed water surface, (the "rigid lid" approximation, an analog of Boussinesq approximation for the boundary condition).

The hydrodynamical equations written in the Boussinesq approximation and its ancillary relationships then have the forms

$$\nabla \cdot \mathbf{u} + \frac{\partial w}{\partial z} = 0, \quad (4)$$

$$\rho_0 \frac{\partial \mathbf{u}}{\partial t} + \nabla p' + \rho_0(\mathbf{f} \times \mathbf{u}) = - \left[\rho_0 w \frac{\partial \mathbf{u}}{\partial z} + \rho_0(\mathbf{u} \cdot \nabla) \mathbf{u} \right] \equiv s_1, \quad (5)$$

$$\frac{\partial \rho'}{\partial t} + w \frac{d\rho_0}{dz} = - \left[w \frac{\partial \rho'}{\partial z} + (\mathbf{u} \cdot \nabla) \rho' \right] \equiv s_2, \quad (6)$$

$$\frac{\partial p'}{\partial z} + g\rho' = - \rho_0 \left[w \frac{\partial w}{\partial z} + (\mathbf{u} \cdot \nabla) w \right] - \rho_0 \frac{\partial w}{\partial t} \equiv s_3. \quad (7)$$

Here the variables are $\mathbf{u}=(u,v)$ is the horizontal fluid velocity vector; w is its vertical component; p' is the fluid pressure perturbation; $f=2\Omega \sin \varphi$ is the so-called Coriolis parameter or radian frequency; (φ is the geographic latitude and Ω is the angular velocity of the Earth's rotation),⁹ and ∇ is now the two-dimensional gradient operator acting on the horizontal plane (x,y). For the derivation of these relationships see, e.g., Phillips¹⁰ and Miropol'sky.¹¹

B. Shallow-water models

Most of the studies devoted to internal solitons deal with moderate-amplitude waves for which the velocity variations in the wave are small compared with the wave phase velocity; this permits us to take into account only linear and quadratic terms in the theory. It is also typically supposed that the characteristic horizontal scale of the wave is large compared with either the depth of the basin or the thickness of the layers where the perturbation mode is localized. In other words, dispersion and nonlinearity are relatively small and comparable in magnitude. These restrictions mean that the

right-hand parts of the previous equations specified as $s_{1,2,3}$ are small, which permits one to use perturbation theory.¹² We begin from this approximation, keeping in mind that strongly nonlinear processes also exist in the oceans, and they will be addressed further in this paper.

Let us represent the solution for the vertical velocity component, w , and horizontal velocity vector, \mathbf{u} , by an expansion in eigenmodes

$$w = \sum_{m=1}^{\infty} W_m(z) w_m(x,y,t), \quad \mathbf{u} = \sum_{m=1}^{\infty} C_m \frac{dW_m}{dz} \mathbf{U}_m(x,y,t), \quad (8)$$

and similarly for other variables. Vertical displacement of the isopycnal surfaces (those of equal density) is given by $\xi(x,y,z,t) = \sum_{m=1}^{\infty} \eta_m(x,y,t) W_m(z)$. Here C_m are constants. The orthogonal eigenfunctions W_m satisfy the boundary-value problem in the linear, nondispersive approximation

$$\frac{d^2 W}{dz^2} + \frac{N^2(z)}{c^2} W = 0, \quad (9)$$

with boundary conditions $W(0)=W(-H)=0$. From this, the eigenvalues $c=c_m$ and the eigenfunctions W_m can be found; note that c_m has the meaning of a long-wave velocity for each internal mode. The important quantity

$$N(z) = \sqrt{-\frac{g}{\rho_0} \frac{d\rho_0}{dz}} \quad (10)$$

is the Brunt-Väisälä or buoyancy frequency, the rate at which a stably stratified column of water oscillates under the combined influence of gravity and buoyancy forces.

Two simple cases are often considered for the modal problem. The first is the case $N=\text{constant}$, which occurs when the function $\rho_0(z)$ is an exponential. For small density variations, this exponential function can be considered as a linear one. In this case $W(z)$ is a harmonic function, and $c=c_m \approx NH/m\pi$, where $m=1,2,\dots$. From here it follows that the first mode is the fastest.

Another very useful model, which will be often considered below, is a fluid consisting of two layers, with upper layer having thickness h_1 and density ρ_1 , and the lower one, of thickness $h_2=H-h_1$ and density $\rho_2 > \rho_1$. This models a sharp jump of the density, a pycnocline, typical of many areas of the ocean. Again, the density difference, $\delta\rho=\rho_2-\rho_1$, is supposed small, $\delta\rho \ll \rho_{1,2}$. In this case, only one internal mode exists and has the following long-wave speed:

$$c = \sqrt{\frac{g\delta\rho}{\rho_{av}} \frac{h_1 h_2}{h_1 + h_2}}, \quad (11)$$

where $\rho_{av} = 1/2(\rho_1 + \rho_2)$ is the mean density of the fluid.

In the general case, after solving Eq. (9), approximate equations describing the dependence of physical values on x , y , and t in long waves can be derived with the use of different perturbation schemes. Here we briefly describe a rather general model suggested by Ostrovsky,¹³ that reduces the problem to the solution of a system of coupled evolution equations in a form analogous to the Boussinesq equations (which should not be confused with the Boussinesq approxi-

mation) for long, weakly nonlinear surface waves. A variable η is used that characterizes the vertical displacement of an isopycnal surface from their equilibrium levels. In the absence of any resonance interactions, each mode can be considered as independent, which yields the following system:

$$\frac{\partial \eta}{\partial t} + H(\nabla \mathbf{U}) + \frac{\sigma}{2}(\nabla \cdot \eta \mathbf{U}) = 0, \quad (12)$$

$$\begin{aligned} \frac{\partial \mathbf{U}}{\partial t} + \frac{c^2}{H} \nabla \eta + (\mathbf{f} \times \mathbf{U}) \left(1 - \frac{\sigma \eta}{2H}\right) \\ + \sigma \left[(\mathbf{U} \nabla) \mathbf{U} - \frac{1}{2H} \frac{\partial(\eta \mathbf{U})}{\partial t} \right] + DH \nabla \frac{\partial^2 \eta}{\partial t^2} = 0. \end{aligned} \quad (13)$$

Here σ and D are nondimensional parameters describing nonlinearity and high-frequency dispersion, respectively. For each mode, they are determined by

$$\begin{aligned} \sigma = \frac{H}{Q} \int_{-H}^0 \left(\frac{dW}{dz} \right)^3 dz, \quad D = \frac{1}{H^2 Q} \int_{-H}^0 W^2 dz, \\ Q = \int_{-H}^0 \left(\frac{dW}{dz} \right)^2 dz. \end{aligned} \quad (14)$$

Equations (12) and (13) are the extensions of the Boussinesq equations, well known for surface waves, to the internal modes. A known peculiarity should be noted here: for the case of $N(z)=\text{const}$, the nonlinear parameter σ is zero, so that the nonlinearity vanishes in these equations, and reveals itself only in either the next (cubic) approximation or by going beyond the Boussinesq and/or rigid lid approximations.

At small nonlinearity, only a weak mode coupling exists, that usually leads to small corrections to the shape of the soliton and to its velocity, as long as there is no resonant coupling between different modes, such as occurs, for instance, when their phase velocities are close to one another. If the latter is not the case, one may consider each mode separately. Note, however, that at more complex density profiles, several resonantly coupled modes must be included in these equations.

It is interesting that the system (12) and (13), which here describes internal wave modes, is also applicable to long-wavelength Rossby (or planetary/potential vorticity) waves that exist when the Coriolis parameter f depends on the horizontal coordinate y (the latitude) via $f=f_0+\beta y$. In this case, β describes the variation of Coriolis frequency with latitude (β -plane approximation).

1. The Korteweg–de Vries equation

Let us first examine the well-investigated case of internal waves propagating in an arbitrarily stratified but nonrotating fluid, thus taking $f=0$. Suppose that the associated linear eigenvalue problem has already been solved and that the modal speeds c_m are known. Let us now take into account small dispersion and small nonlinearity. Then for one-dimensional progressive waves propagating in the positive direction of axis x , the classical Korteweg–de Vries equation

widely discussed in literature (see, e.g., Whitham,¹⁴ Miropol'sky,¹¹ Ablowitz and Segur⁴) readily follows from the Boussinesq set of equations

$$\frac{\partial \eta}{\partial t} + c \frac{\partial \eta}{\partial x} + \alpha \eta \frac{\partial \eta}{\partial x} + \beta \frac{\partial^3 \eta}{\partial x^3} = 0, \quad (15)$$

the rescaled nonlinear and dispersion parameters (α and β , respectively) are

$$\alpha = \frac{3c\sigma}{2H}, \quad \beta = \frac{cDH^2}{2} \quad (16)$$

with σ and D given by Eq. (14). The important quantities α and β are known as environmental parameters and incorporate the effects of buoyancy (density stratification), shear currents in general (see below) and depth via their effects on the eigenfunction profiles, $W(z)$.

The well-known solitary solution to Eq. (15) is

$$\eta(x,t) = \eta_0 \operatorname{sech}^2 \frac{x-Vt}{\Delta}, \quad (17)$$

the nonlinear velocity V and the characteristic width Δ of this soliton being related to the linear speed c and the amplitude of the displacement η_0 by

$$V = c + \frac{\alpha \eta_0}{3}, \quad \Delta^2 = \frac{12\beta}{\alpha \eta_0}. \quad (18)$$

The dispersion parameter β is always positive for oceanic gravity waves (although for capillary waves on a surface of thin liquid films, this parameter may be negative). The sign of the nonlinear parameter α may be both positive and negative. The combination of parameters α and β determines the soliton polarity; namely, the sign of η_0 is such that Δ^2 in Eq. (18) is positive. Thus, if α is negative, so will be η_0 , i.e., the soliton is a wave of isopycnal depression. This appears to be the usual case where a shallow pycnocline overlies deeper water. However, in shallow seas with strong mixing, the reverse situation may occur, with the pycnocline being located near the bottom. In this case α and η_0 are both positive.

Let us consider the aforementioned two-layer model where $\rho(z)=\rho_1$ for $0 > z > -h_1$ and $\rho(z)=\rho_2 > \rho_1$ for $-h_1 > z > -H$. In this case we have

$$c = \left[\frac{g(\rho_2 - \rho_1)h_1h_2}{\rho_2h_1 + \rho_1h_2} \right]^{1/2} \approx \left[\frac{g\delta\rho}{\rho_{av}} \frac{h_1h_2}{h_1 + h_2} \right]^{1/2}, \quad (19)$$

$$\alpha = \frac{3c}{2h_1h_2} \frac{\rho_2h_1^2 - \rho_1h_2^2}{\rho_2h_1 + \rho_1h_2} \approx \frac{3}{2} \frac{c}{h_1h_2} \frac{h_1 - h_2}{h_1h_2}, \quad (20)$$

$$\beta = \frac{ch_1h_2}{6} \frac{\rho_1h_1 + \rho_2h_2}{\rho_2h_1 + \rho_1h_2} \approx \frac{ch_1h_2}{6}. \quad (21)$$

The relations on the right are valid for the ocean, where $\delta\rho = \rho_2 - \rho_1$ is always small. As seen from Eq. (20), solitons propagating on a thin upper layer over a deeper lower layer are always negative, i.e., depressions, whereas solitons riding on near-bottom layers are elevations.¹⁵

The one-dimensional KdV Eq. (15) can be derived directly from the hydrodynamic Eqs. (4)–(7) in their two-

dimensional form (see, e.g., Grimshaw *et al.*¹⁶ and references therein). However, the Boussinesq-type Eq. (12) and (13) have their own value. They are valid for arbitrary stratification and also allow various generalizations of the KdV equation, such as the Kadomtsev–Petviashvili equation shown below.

The KdV equation belongs to the class of completely integrable systems. It was a subject of intense study during the past five or so decades. Currently it is one of the most thoroughly studied nonlinear equations, and we shall not go into details which can be easily found in numerous books and reviews (see, e.g., Whitham,¹⁴ Ablowitz and Segur⁴). Rather, we will just list a few salient points of interest. Note first that it belongs to the class of exactly integrable equations for which an infinite set of integrals of motion exists. A remarkable process worth noting is the interaction of KdV solitons, from which they escape unchanged, similar to two colliding rigid particles, only acquiring an additional delay (phase shift) at a given distance (hence, the name of soliton). Another important feature of the KdV equation is that solitons can arise from arbitrary localized perturbations having the same polarity as a soliton. Moreover, if the “mass” of an initial perturbation, $M = \int_{-\infty}^{\infty} \eta(x,t) dx$, is nonzero and its sign coincides with the soliton polarity, at least one soliton will emerge, even for a small-amplitude and small-width perturbation. In particular, an initial delta impulse, $\eta(x,0) = \eta_0 \delta(x)$, where $\delta(x)$ is Dirac delta-function, always evolves into one soliton followed by a dispersive “tail.”⁴ Perturbations with the opposite sign of mass never generate solitons but rather disperse into a long oscillatory wave train, whose amplitude eventually tends to zero. The number and parameters of solitons produced by an initial pulse can be calculated exactly by the inverse scattering method or evaluated approximately by means of perturbation techniques (see, e.g., Ablowitz and Segur⁴). The result depends on the value of the Ursell parameter, $Ur = \alpha A_0 L_0^2 / \beta$, where A_0 and L_0 are the amplitude and characteristic width of the initial perturbation, respectively.¹⁷ Some examples of experimental observations of these processes will be illustrated in the forthcoming sections. Here we will only mention that for an actual KdV soliton (17) whose characteristic width, Δ , is related to the amplitude, η_0 , according to Eq. (18), the Ursell parameter is equal to 12, independent of the soliton amplitude.

Transient processes. The single pulse solution to the KdV equation in the form of Eq. (17) is very simple, and readily provides physical insight when examined. However, a common observation in the ocean is of wave trains consisting of several oscillations with wavelengths, crest lengths, and amplitudes varying from the front to the rear of the wave train (as schematically shown in Fig. 1 plotted from a simple theoretical model of evolution of an initial step function within the framework of the KdV equation). As these oscillations, especially the few frontal ones, are very close to being a series of solitons (indeed, each oscillation develops into independent soliton at infinity), and the entire perturbation represents an undular bore, it is sometimes called solibore.¹⁸

Korteweg and de Vries in 1895 had already found periodic solutions to their equation in the form of the so-called

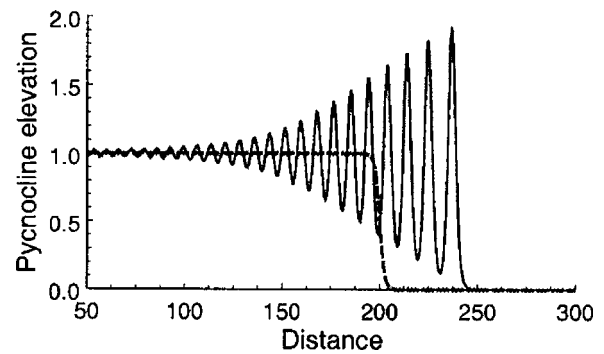


FIG. 1. Disintegration of a stepwise perturbation into a train of solitons within the framework of the KdV equation (a simplistic scheme of solibore formation). Axes are in arbitrary units.

“cnoidal” waves, which involve the Jacobi elliptic function $cn_s(x)$. This function has a nonlinear parameter, s , that characterizes the degree of nonlinearity, with $0 \leq s \leq 1$. For the KdV equation, the cnoidal solution is given by

$$\eta(x,t) = \eta_m + \eta_0 cn_s^2[k_0(x - Vt)]. \quad (22)$$

In the above solution η_0 is the wave magnitude, η_m is the constant background, and k_0 is the wave number; the soliton velocity V can be expressed in terms of these parameters. This solution reduces to a harmonic wave when $s \rightarrow 0$ and $cn_s x \rightarrow \cos x$, and to a solitary wave when $s \rightarrow 1$ and $cn_s x \rightarrow \text{sech}^2 x$. Thus, the soliton can be considered as a limit of a periodic wave train at $s=1$.

However, there is still some ocean phenomenology missing from the cnoidal solution. Specifically, it does not describe transient processes such as the onset and the long-term trailing edge displacement of the isopycnal surfaces behind the wave group. Using an approximate approach suggested by Whitham, Gurevich, and Pitaevskii¹⁹ have constructed a self-similar solution for the evolution of an initially stepwise perturbation into a train of oscillations with a slow variation of the nonlinear parameter s within the train. In the process of evolution, these oscillations become deep at the front of the perturbation forming a set of separated impulses, each close to a soliton, and eventually decrease to a constant trailing edge.

To describe an oceanic nonlinear wave train with oscillatory behavior at the leading edge and a constant depression at the trailing edge, Apel¹⁸ has applied the Gurevich and Pitaevskii’s approach to modeling the internal solibores. This approach is based on a slightly different representation of the periodic solution

$$\eta(x,t) = \eta_m + \eta_0 \{ dn_s^2[k_0(x - Vt)] - (1 - s^2) \}, \quad (23)$$

where $dn_s(x)$ is another periodic elliptic function (Jacobi delta amplitude) which tends to unity at $s \rightarrow 0$ and to $\text{sech}^2(x)$ when $s \rightarrow 1$. In accordance with the Whitham’s method, the parameters s and $V(s)$ are supposed to be slowly varying functions of x and t . For a stepwise initial impulse exerted on a fluid at $t=0$, the solution of the KdV equation is described locally by Eq. (23) in which $s(x,t)$ is close to 1 at the front and eventually decreases to zero at the rear. Thus, the solution represents a sequence of qua-

solitons at the frontal part and transforms to quasisinusoidal oscillations decreasing to a constant background. Figure 1 illustrates such a process.

This solution, which Apel has named the “dnoidal” wave, can be suitable for describing weakly nonlinear internal tides. Indeed, initial tidal perturbations have a finite duration and are relatively smooth. Thus, the process of soliton formation includes a stage of wave steepening and the subsequent formation of oscillations. The first stage may be described by the equation of a “simple wave” which is in fact a KdV equation with $\beta=0$ (the “dispersionless KdV equation”). Each point of such a wave propagates at its own velocity, $c+\alpha\eta$, until the wave front becomes steep (see the details in Apel¹⁸). At that point, the dispersion effects must be taken into account, which leads to the formation of solitons at the frontal zone of each tidal period. To accommodate the relaxation back to the equilibrium state, Apel¹⁸ introduced an “internal tide recovery function” $I(x,t)$, which multiplies the dnoidal solution. This function takes the dnoidal solution back to equilibrium, using just one adjustable parameter which is the time required for the relaxation to occur.

2. The extended and modified Korteweg–de Vries equations

It follows from the above that for $\rho_2 h_1^2 < \rho_1 h_2^2$ (that is practically $h_1 < h_2$ for the ocean), solitons cause the interface (the pycnocline) to descend, and vice versa if the inequality is reversed. Of some interest is the special case when $h_2^2/h_1^2 \approx \rho_2/\rho_1 \approx 1$, i.e., the interface is close to the middle of the water layer. In this case the nonlinear coefficient α is small or even equal to zero. As mentioned before, in this case one must either abandon the Boussinesq and rigid lid approximations or take into account higher-order nonlinear terms in the evolution equations. In the latter case, the extended Korteweg–de Vries (eKdV) equation (also called the combined KdV and Gardner equation), having both quadratic and cubic nonlinearities, results

$$\frac{\partial \eta}{\partial t} + (c + \alpha \eta + \alpha_1 \eta^2) \frac{\partial \eta}{\partial x} + \beta \frac{\partial^3 \eta}{\partial x^3} = 0, \quad (24)$$

where for the case of two-layer fluid the second nonlinear coefficient is

$$\begin{aligned} \alpha_1 &= \frac{3c}{h_1^2 h_2^2} \left[\frac{7}{8} \left(\frac{\rho_2 h_1^2 - \rho_1 h_2^2}{\rho_2 h_1 + \rho_1 h_2} \right)^2 - \frac{\rho_2 h_1^3 + \rho_1 h_2^3}{\rho_2 h_1 + \rho_1 h_2} \right] \\ &\approx -\frac{3}{8} c \frac{(h_1 + h_2)^2 + 4h_1 h_2}{h_1^2 h_2^2}. \end{aligned} \quad (25)$$

The last expression is again valid for the case of close densities which we shall consider below.

This equation, as well as its generalization containing a combination of higher-order nonlinear and dispersive terms, was derived by many authors starting from the paper by Lee and Beardsley.²⁰ A contemporary derivation, convenient for applications, can be found, e.g., in Grimshaw *et al.*¹⁶

As follows from Eq. (25), within the framework of the two-layer model, α_1 is always negative. However, in the general case the coefficient α_1 may be either negative or positive

(see, e.g., Talipova *et al.*²¹). In the latter case, solitons of both positive and negative polarities may exist. In addition, nonstationary solitons, called breathers, are also possible. The evolution of initial pulse-type perturbations may be fairly complex.

If the pycnocline is located just at the critical level so that the parameter α is exactly zero, Eq. (24) reduces to the well-known modified Korteweg–de Vries (mKdV) equation. In the geophysically most interesting case, when $\alpha_1 < 0$ and $\beta > 0$, this equation has no stationary solitary wave solutions asymptotically vanishing at $x \rightarrow \pm\infty$. However, it has a particular solution that is a type of stepwise transition, which can be considered to be a soliton in a more general sense. Such a solution is usually called a kink and has the form of a bore moving into a depression area.²²

$$\eta = \pm \eta_0 \tanh\left(\frac{x - vt}{\Delta}\right), \quad (26)$$

where now

$$V = c + \frac{\alpha_1 \eta_0^2}{3}, \quad \text{and } \Delta^2 = -\frac{6\beta}{\alpha_1 \eta_0^2}. \quad (27)$$

Note that the vertical velocity component $w \approx \partial \eta / \partial t$ has the form of a localized pulse, so that it may properly be treated as a soliton. The specific feature of such a kink is that its velocity, V , is always less than the linear velocity, c , due to $\alpha_1 < 0$.

The mKdV equation, Eq. (24) also has soliton-type solutions, but only those propagating on a constant nonzero pedestal. These solutions are interesting not so much by themselves as they are within the framework of the eKdV Eq. (24) with $\alpha \neq 0$ [note that under the transformation $\eta = u - \alpha/2\alpha_1$, Eq. (24) can be reduced to the mKdV form]. In this case the solitary solution of Eq. (24) can be written in the form of a kink-antikink pair of a stationary shape:

$$\eta(x,t) = -\frac{\alpha}{\alpha_1} \frac{\nu}{2} \left[\tanh\left(\frac{x - Vt}{\Delta} + \phi\right) - \tanh\left(\frac{x - Vt}{\Delta} - \phi\right) \right], \quad (28)$$

where ν is a free dimensionless parameter with the range $0 < \nu < 1$, and the remaining parameters are

$$\phi(\nu) = \frac{1}{4} \ln\left(\frac{1 + \nu}{1 - \nu}\right), \quad \Delta = \sqrt{\frac{-24\alpha_1\beta}{\alpha^2\nu^2}}, \quad V = c - \frac{\alpha^2\nu^2}{6\alpha_1}. \quad (29)$$

In contrast with the kink described by Eqs. (26) and (27), the velocity of this soliton is always greater than the linear velocity c . This family of solutions has rather interesting properties. The amplitude of the soliton, $\eta_0 = -(\alpha/\alpha_1)\nu \tanh \phi$, varies from zero up to a maximum of $|\alpha/\alpha_1|$, in contrast to the amplitude of the KdV soliton, which in principle can range from zero to infinity. When soliton amplitude approaches its maximum value, its width increases so that the soliton profile changes from the bell

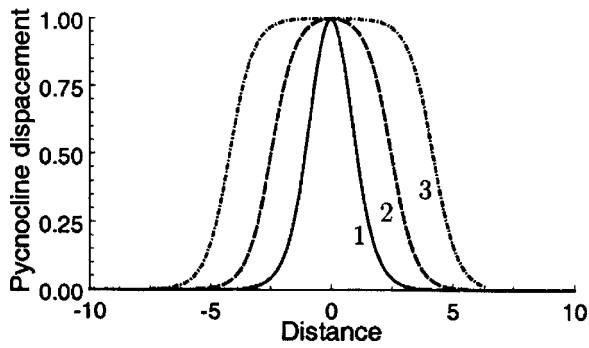


FIG. 2. Normalized wave shapes in the eKdV Eq. (28) for three values of the parameter $\varepsilon = 1 - \nu$: 1- $\varepsilon = 10^{-1}$ (close to the KdV case); 2- $\varepsilon = 10^{-4}$; 3- $\varepsilon = 10^{-7}$.

shape to the rectangular shape. In the limit $\nu \rightarrow 1$, the eKdV soliton tends to two infinitely separated kinks.

In the near-critical situation when $h_1 \approx h_2 = h$ and the eKdV equation is indeed applicable, the amplitude does not exceed $|h_2 - h_1|/2$, and the velocity cannot exceed the value of

$$V_{\max} = c - \frac{\alpha^2}{6\alpha_1} \approx c \left[1 + \frac{(h_2 - h_1)^2}{8h^2} \right]. \quad (30)$$

Note that if the ratio h_1/h_2 is as close to unity as ρ_2/ρ_1 , the latter ratio must be taken into account in these formulas. For example, the maximal soliton amplitude is $|\rho_2 h_1 - \rho_1 h_2|/2\rho_2$.

Furthermore, the solution (28) has in fact two spatial scales: that of the hyperbolic tangent profile, as characterized by the parameter Δ , and a distance between these profiles characterized by the parameter $S = \phi(\nu)\Delta$. In general, the actual width of the soliton is determined by these parameters, which in turn depend on the hydrodynamic environment and the amplitude through the free parameter ν . Figure 2 shows normalized shapes of solitons for three values of the modified free parameter $\varepsilon \equiv 1 - \nu$. The evolution from a classical KdV soliton when ν is small and the characteristic total width $D \approx 2\Delta$ to the flat-top kink-antikink construction at $\nu \rightarrow 1$, in which case $D \approx 2S$, is clear.

The width of the soliton increases in both limits: $\nu \rightarrow 0$ and $\nu \rightarrow 1$. Hence, for some $\nu = \nu_m$ there exists a minimum value of D . Figure 3 depicts $D_{0.5}$, the full width of the soliton at the half its maximum amplitude, as a function of the amplitude, η_0 . The minimum of $D_{0.5}$ occurs at $\nu \approx 0.9$, when the amplitude is about 0.56 of the maximum. A more detailed discussion of the dependency between D and η_0 both for weakly nonlinear perturbations, described by the eKdV equation, and for more intensive perturbations, described by the primitive Eulerian equations, can be found in the paper by Funakoshi and Oikawa.²²

From Eq. (29) it follows that:

$$\eta_0 = - \frac{\alpha\nu \sqrt{1+\nu} - \sqrt{1-\nu}}{\alpha_1 \sqrt{1+\nu} + \sqrt{1-\nu}}, \quad (31)$$

with ν related to ϕ and Δ by Eqs. (29).

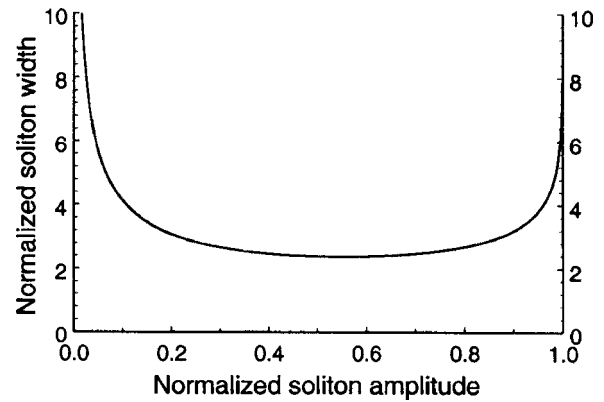


FIG. 3. Dependency of the characteristic width, $\bar{D}_{0.5}$, of eKdV solitons, Eq. (28), on amplitude $\bar{\eta}_0$ in dimensionless variables: $\bar{D}_{0.5} = D_{0.5}|\alpha|/(24\alpha_1\beta)^{1/2}$; $\bar{\eta}_0 = \eta_0\alpha_1/\alpha$.

Higher-order KdV equations containing corrections both to the nonlinear and dispersive terms have been derived for internal waves in a stratified shear flows in many papers beginning from the aforementioned pioneering paper by Lee and Beardsley.²⁰ For a rather general and convenient form of this derivation, see, e.g., Grimshaw *et al.*¹⁶

The mathematical theory of the eKdV equation has been developed in many papers for different combinations of signs of nonlinear and dispersion terms (see, e.g., Grimshaw *et al.*,²³ and references therein). It was shown that the eKdV equation and its reduced version, the mKdV equation, are also completely integrable equations as is the usual KdV equation. In particular, the evolution of an initial pulse was studied in detail and two-soliton interaction was analyzed for the case where the dispersion and cubic nonlinear coefficients of Eq. (24) are of opposite signs (i.e., $\beta > 0$ and $\alpha_1 < 0$).

Although the eKdV equation is valid for small nonlinearity and a specific stratification, sometimes it can be successfully applied to the description of strongly nonlinear internal solitons as a phenomenological model, whereas the usual KdV equation fails to approximate observational and laboratory data.²⁴⁻²⁶ The reason for this is a qualitative (but in general not quantitative!) correspondence of the eKdV solitons to those of strongly nonlinear solitary waves in a two-layer fluid. The correspondence relates, in particular, to the nonmonotonic dependence of their width on the amplitude and to the existence of a limiting amplitude.

3. The Benjamin-Ono equation

An important modification is needed if the wavelength is large compared with one (say, upper) layer but small compared with the other (lower) layer of the ocean, so that one can let $h_2 \rightarrow \infty$. These waves can be described by another completely integrable model, namely by the differential-integral Benjamin-Ono (BO) equation (see, e.g., Ablowitz and Segur⁴)

$$\frac{\partial \eta}{\partial t} + c \frac{\partial \eta}{\partial x} + \alpha \eta \frac{\partial \eta}{\partial x} + \frac{\beta}{\pi} \frac{\partial^2}{\partial x^2} \oint_{-\infty}^{\infty} \frac{\eta(x', t)}{x - x'} dx' = 0, \quad (32)$$

the symbol \oint indicates that the principal value of the integral should be taken, and the coefficients are

$$c = \sqrt{\frac{(\rho_2 - \rho_1)gh_1}{\rho_1}}, \quad \alpha = -\frac{3}{2} \frac{c}{h_1}, \quad \beta = \frac{ch_1 \rho_2}{2 \rho_1}. \quad (33)$$

Solitons described by this equation are also well known

$$\eta(x, t) = \frac{\eta_0}{1 + (x - Vt)^2/\Delta^2}. \quad (34)$$

Their amplitudes η_0 , velocities V , and half-widths Δ are related by

$$V = c + \frac{\alpha \eta_0}{4}, \quad \text{and } \Delta = \frac{4\beta}{\alpha \eta_0}. \quad (35)$$

The displacement of these solitons is a downgoing motion of the interface when the upper layer is thin, and conversely for the case when the thin layer lies near the bottom (there is a general thumb rule: pycnocline displacement induced by a soliton is directed to the deeper layer).

As in most integrable cases, the BO solitons restore their parameters after a collision. However, unlike the KdV case, the displacement in the BO soliton decreases algebraically, as x^{-2} , rather than exponentially (therefore they are often called ‘‘algebraic solitons’’). Another difference is that BO solitons do not acquire a phase shift after a collision. As was shown by Pelinovsky and Sulem in 1998, they are stable with respect to small perturbations and can emerge from arbitrary pulse-type initial perturbations of appropriate polarity, i.e., the polarity required for the existence of a BO soliton.

4. The Joseph–Kubota–Ko–Dobbs equation

Apparently, Whitham¹⁴ was the first to point out explicitly that a linear evolution equation can be constructed by applying the inverse Fourier transform to a dispersion relation known for a harmonic wave. Such an equation can be differential or, more generally, integro-differential. For finite-amplitude perturbations it can be supplemented by a nonlinear term derived in the nondispersive, long-wave approximation, and which accounts for a hydrodynamic nonlinearity of the type $\eta(\partial \eta / \partial x)$. This approach, albeit not quite consistent, leads to useful model equations in cases when the regular derivation is cumbersome or even impossible.

Based on this approach, a more general model, so-called Joseph–Kubota–Ko–Dobbs (JKKD) equation,²⁷ has been suggested. It is applicable to the case when the thickness of one of the layers, say the upper one, h_1 , is small in comparison with the thickness of lower layer, h_2 , i.e., $h_1/h_2 \ll 1$. At the same time, the perturbation wavelength, $\lambda \gg h_1$, may have an arbitrary relationship with h_2 , i.e., the total water layer can be either shallow or deep. The resulting evolution equation can be presented in a variety of equivalent forms; one of the simplest is (see, e.g., Ablowitz and Segur⁴)

$$\frac{\partial \eta}{\partial t} + c \frac{\partial \eta}{\partial x} + \alpha \eta \frac{\partial \eta}{\partial x} - \beta \frac{\partial^2}{\partial x^2} \oint_{-\infty}^{\infty} \frac{\eta(x'/h_2, t)}{\tanh\left(\frac{\pi x - x'}{2 h_2}\right)} dx' = 0, \quad (36)$$

where, for the two-layer model with a sharp density interface, the parameters c and α are the same as in Eq. (32) and $\beta = ch_1/(4h_2)$.

The dispersion relation corresponding to this equation and relating the wave number k with a frequency ω of the linear perturbations, $\eta \sim \exp(kx - \omega t)$, is

$$\omega = ck \left(1 - \frac{kh_1}{2 \tanh kh_2} \right). \quad (37)$$

In the shallow-water ($kh_2 \rightarrow 0$) and deep-water ($kh_2 \rightarrow \infty$) limits this reduces to the KdV and BO dispersion relations, respectively.

The JKKD equation has a solitary solution which has been obtained by many authors and presented in different forms. One of the forms convenient for practical applications is

$$\eta(x, t) = \frac{\eta_0}{1 + \frac{2}{1 + \cos \frac{2h_2}{\Delta}} \sinh^2 \frac{x - Vt}{\Delta}}, \quad (38)$$

where

$$\eta_0 = \frac{4 h_1^2}{3 \Delta} \frac{\sin \frac{2h_2}{\Delta}}{1 + \cos \frac{2h_2}{\Delta}}, \quad V = c \left(1 - \frac{h_1}{\Delta \tan \frac{2h_2}{\Delta}} \right). \quad (39)$$

Here Δ is a free parameter characterizing the soliton width.

Equations (38) and (39) reduce to a KdV soliton, Eqs. (17) and (18), in the limit of $h_2/\Delta \rightarrow 0$, for a fixed h_1/h_2 . Meanwhile, there is no smooth transition from the JKKD soliton to the BO soliton as $h_2 \rightarrow \infty$. This issue still remains unclear because Eq. (36) tends to either the KdV or the BO limit as $h_2 \rightarrow 0$ or $h_2 \rightarrow \infty$, respectively.

The main features of the initial perturbation dynamics within the framework of the JKKD equation are very similar to those described by the KdV model. It is worth noting here that all the models considered above, beginning from the KdV, are analytically integrable, possessing an infinite set of conservation laws and multisoliton solutions (see, e.g., Ablowitz and Segur⁴). Their properties have been thoroughly studied by mathematicians.

However, seemingly crude as it may be, the two-layer model often gives a good approximation to situations in which the density and velocity vary continuously but sharply with depth; this occurs especially for the first vertical mode in near-shore regions where moderate depths are the rule. This may be seen, for example, by comparison between the two-layer model and a more exact model based on a smooth density profile measured in the seas. An optimal adjustment of the two-layer model parameters which gives the best ap-

proximation for wave velocities and other observable wave characteristics in the real ocean is discussed in Nagovitsyn *et al.*²⁸ and Gerkema.²⁹ However, in other cases the parameters of the corresponding equations must be calculated from the expressions (16) and (14) corresponding to a general case of a continuously stratified fluid (see, e.g., Ostrovsky and Stepanyants,³ and references therein).

From an observational viewpoint, it is important to remember that a single measurement of a solitary-like formation does not guarantee that the entity is indeed a soliton. An initial impulse may quickly disintegrate afterward into something other than a solitary wave. In principle, it is necessary to follow such a wave out to a distance much greater than its spatial width to ensure that its shape remains stationary, which is not a simple task in real experiments. Another criterion for identification of a soliton is based on knowledge of the background density and horizontal velocity profiles. After a theoretical calculation of soliton parameters, one can compare these with the observational data. For example, the product of the characteristic wave width Δ and the square root of its height, $\sqrt{\eta_0}$, must not depend on that height [cf. Eq. (18)], provided the KdV equation is applicable to the situation considered.

C. Soliton propagation under perturbations

For the conditions generally existing in nature, the simple models considered above are rarely applicable without taking into account a number of perturbing factors, such as dissipation of various origins, wave front curvature, horizontal inhomogeneities, depth variation, and the like. However, these factors are often locally weak enough so that they strongly affect the wave only at distances large compared to a wavelength. Under these conditions, perturbation theory is generally applicable. Such an approach results in the appearance in the model equation of small additive terms, each responsible for a specific perturbing factor. As an example, for waves much longer than the total depth of the controlling layer, the three factors mentioned above may be taken into account within the framework of a generalized “time-like” KdV equation³⁰

$$\frac{\partial \eta}{\partial r} + \frac{1}{c} \frac{\partial \eta}{\partial t} - \frac{\alpha \eta}{c^2} \frac{\partial \eta}{\partial t} - \frac{\beta}{c^4} \frac{\partial^3 \eta}{\partial t^3} = -\frac{\eta}{2r} - \frac{\eta}{2c} \frac{dc}{dr} + R(\eta). \quad (40)$$

The terms on the right-hand side of Eq. (40) describe, respectively, the effects of cylindrical divergence (the distance r from the source is supposed to be much greater than the wavelength), slow variation of the long-wave speed c along the ray r due to spatial inhomogeneity (e.g., due to variation of the pycnocline depth), and dissipation.

The latter term depends on a specific mechanism of losses. In particular, a horizontal eddy (turbulent) viscosity A_h and a molecular viscosity ν_m result in dissipation that is described by a Reynolds-type term, $R = (\delta/c^2)(\partial^2 \eta / \partial t^2)$ (δ is proportional to the sum of A_h and ν_m , and usually $A_h \gg \nu_m$). Semiempirical models accounting for bottom friction are also used, resulting in the terms $R = \gamma_{Ra} \eta$ (Rayleigh dissipation) and $R = \gamma_{Ch} |\eta| \eta$ (Chezy dissipation) with γ_{Ra} , γ_{Ch} taken

as empirical coefficients.^{31,32} A more rigorous consideration of viscous effects in the laminar bottom boundary layer leads to the inclusion into Eq. (40) of a more complex integral term (see, e.g., Grimshaw³¹ or Ostrovsky and Stepanyants⁵ for references).

From Eq. (40), an ordinary differential equation for the slow variation of the soliton amplitude η_0 over large distances can be obtained. As follows from perturbation theory (see, e.g., Ref. 31), the first-order solution of Eq. (40) for the soliton amplitude may be obtained by multiplying it by η , substituting the soliton (17) and (18) with locally constant parameters, and then integrating over infinite limits in time, $-\infty < t < \infty$. One obtains

$$\frac{d\eta_0}{dr} = -\frac{2\eta_0}{3r} - \frac{2\eta_0}{3c} \frac{dc}{dr} - \frac{4\alpha\delta}{45\beta} \eta_0^2, \quad (41)$$

which describes slow variations of the soliton amplitude under the effect of small cylindrical divergence, horizontal inhomogeneity, and eddy and molecular viscosity. The variations of length and width of the soliton are then defined via the local relation, Eq. (18), as before.

As particular cases, we readily obtain the laws of soliton variability due to

(a) Cylindrical divergence ($\delta=0$, $c=\text{const}$):

$$\eta_0 \sim r^{-2/3}, \quad \Delta \sim r^{1/3}; \quad (42)$$

These dependencies were examined in laboratory experiments with surface and internal waves and very good agreement between the theory and experiment was obtained.

(b) A smooth horizontal variation of c in a plane wave

$$\eta_0 \sim c^{-2/3}. \quad (43)$$

(c) The separate effect of Reynolds losses results in the following damping law:

$$\eta_0(r) = \frac{\eta_0(0)}{1 + \eta_0(0)qr}, \quad (44)$$

where $\eta_0(0)$ is the initial soliton amplitude, and $q=4\alpha\delta/\beta$. From Eq. (44) it is seen that soliton damping is nonexponential because of the nonlinearity. Moreover, at large distances, $r \gg [\eta_0(0)q]^{-1}$, the soliton amplitude ceases to depend on its initial value at all,³³ $\eta_0(r) \sim (qr)^{-1}$. Chezy friction leads to the same law of soliton attenuation,³¹ whereas Rayleigh dissipation yields an exponential damping with an exponent different from that for linear waves.

As mentioned above, soliton decay due to energy dissipation in the laminar boundary layer at tank bottom and side-walls is described by an integral term

$$R(\eta) = -\delta_1 \int_{-\infty}^{+\infty} \frac{1 - \text{sgn}(t-t')}{\sqrt{|t-t'|}} \frac{\partial \eta(t',x)}{\partial t'} dt'. \quad (45)$$

The dissipation coefficient δ_1 depends, in general, on many parameters such as the depth, density, and viscosity of the fluid layers. However, in the Boussinesq approximation with the additional assumption that kinematic viscosities of layers are also equal, $\nu_1 = \nu_2 = \nu_m$, this coefficient may be presented in a relatively simple form

$$\delta_1 = \frac{1}{4c} \frac{\sqrt{\nu_m/\pi}}{h_1 + h_2} \left[b + \frac{(1+b)^2}{2b} + 2 \frac{h_2}{W} (1+b) \right], \quad (46)$$

where $b = h_1/h_2$ and W is the width of the tank. The applicability of this dissipation model requires the boundary-layer thickness to be much less than the total water depth.

For such dissipation, the following damping law for soliton amplitude follows from the adiabatic theory:

$$\eta_0(r) = \frac{\eta_0(0)}{(1 + r/r_{\text{ch}})^4}, \quad (47)$$

where r_{ch} is the characteristic spatial scale of soliton decay (see details in the references cited above). For $r \gg r_{\text{ch}}$ this formula gives $\eta_0(r) \sim r^{-4}$, and the soliton amplitude also ceases to depend on its initial value [because $r_{\text{ch}} \sim \eta_0^{-1/4}(0)$].

According to estimations by Grimshaw,³¹ for typical oceanic conditions Eqs. (44) and (47) allow lifetimes for internal solitary waves of several orders of magnitude greater than their intrinsic time scale.

The perturbed KdV and eKdV equations similar to Eq. (40) were used in numerical modeling of the internal tide transformation observed in several areas of the ocean, e.g., on the Australian northwest shelf, the Malin shelf edge (western coast of Scotland), and the Arctic shelf (Laptev's Sea) (see, e.g., Holloway *et al.*³²).

1. Refraction and diffraction of solitons

Various generalizations of the KdV equation have been suggested for nonlinear waves having smoothly curved phase fronts. One of the most popular is the Kadomtsev–Petviashvili (KP) equation, which is applicable to a weakly diffracted wave beam, and is based again on adding a small term to the KdV equation describing transverse variations

$$\frac{\partial}{\partial x} \left(\frac{\partial \eta}{\partial t} + c \frac{\partial \eta}{\partial x} + \alpha \eta \frac{\partial \eta}{\partial x} + \beta \frac{\partial^3 \eta}{\partial x^3} \right) = - \frac{c}{2} \frac{\partial^2 \eta}{\partial y^2}, \quad (48)$$

where y is the coordinate transverse to the propagation direction x . This equation is also known to be completely integrable. Its exact solutions have been studied in numerous papers and books (see, e.g., Ablowitz and Segur⁴). The main properties of solitary solutions to this equation as applied to oceanic waves (when the dispersion parameter is always positive, $\beta > 0$) are as follows. A plane soliton is stable with respect to transverse perturbations of its front. Multiple soliton interactions can occur when solitons propagate in different directions at small angles to each other. The zone of nonlinear interaction of two solitons can be fairly long in space (in a special resonant case, even infinite); the perturbation in this zone looks like a soliton and propagates steadily.

2. Internal waves on shear flows

The velocities of shear flows in the ocean are often of the same order of magnitude as the velocities of the IWs, so that energy exchange between these two types of motions may be very effective, and may even result in instabilities. As it is well known, the main parameter defining the crite-

rium for stability of a stratified fluid is the Richardson number, $Ri(z) = [N/U_0'(z)]^2$, where $U_0(z)$ is the horizontal mean flow speed (see, e.g., Phillips¹⁰ and Miropol'sky¹¹).

In the Boussinesq approximation, the modal structure of a linear perturbation is defined by the Taylor–Goldstein equation

$$\frac{d}{dz} \left[(U_0 - c)^2 \frac{dW}{dz} \right] + [N^2 - k^2(U_0 - c)^2]W = 0, \quad (49)$$

where the notation is the same as in Eq. (9).

According to the well-known Miles–Howard theorem, a flow with $Ri > 1/4$ is always stable in the linear approximation. For long IWs in stable flows, a KdV equation was obtained by many authors (see, e.g., Grimshaw *et al.*,¹⁶ and references therein). In the Boussinesq approximation, the expressions for the environmental coefficients of the KdV Eq. (15) can be presented in the form [cf. Eq. (16) via Eq. (14)]:

$$\alpha = \frac{3}{2Q} \int_{-H}^0 (U_0 - c)^2 \left(\frac{dW}{dz} \right)^3 dz,$$

$$\beta = \frac{1}{2Q} \int_{-H}^0 (U_0 - c)^2 W^2 dz,$$

$$Q = \int_{-H}^0 (U_0 - c)^2 \left(\frac{dW}{dz} \right)^2 dz. \quad (50)$$

The coefficients are calculated for a fixed internal mode with a given modal number n . Note that the above-mentioned situation in which $\alpha = 0$, is also possible here; the corresponding modes satisfy the mKdV equation rather than KdV. Of course, the eKdV equation can also be applicable in this environment. For some specific profiles of $N(z)$ and $U_0(z)$, boundary-value problem for the Taylor–Goldstein Eq. (49) can be analytically solved (see, e.g., Turner³⁴).

The situation becomes radically different when the basic flow is unstable, a condition that is possible if $Ri < 1/4$. Observational data testify that this does take place in the ocean, although it is difficult to tell how frequently. Typically, there are often near-critical conditions in which the Richardson number is close to $1/4$ because the surface wind stress drives the near-surface layers and causes significant vertical shear in the mean flow. Physical models of shear flows having smoothly varying density and velocity profiles are usually very difficult to handle in analytical form, even in the linear case. That is why simplifying approximations to the stratification and current, such as models having tangential discontinuities and piecewise-linear profiles, are often used in theory (see, e.g., Turner³⁴ and Redekopp³⁵).

An interesting finding was made by Thorpe in 1969 who showed that the fluid stratification can destabilize some shear flows known to be stable in the uniform fluid (see also in Turner³⁴). The physical interpretation of that phenomenon was given in terms of negative energy waves (see, e.g., Stepanyants and Fabrikant,³⁶ and references therein) when the total energy of a system containing wave perturbations is less than the energy of the system without perturbation. As a result of that, dissipation or any other losses lead to the in-

crease of wave energy modulus, which causes growth of the wave amplitude. This means that adding losses to the system may lead to an instability when the wave amplitude increases due to energy consumption from the shear flow.

A similar phenomenon is known in fluid mechanics since the 1920s, when Heisenberg discovered the destabilizing effect of viscosity in boundary layers. Analogously, radiation of bulk internal waves in an infinitely deep smoothly stratified fluid with a sharp density interface in the upper layer uniformly moving with respect to the lower one may result in a specific radiation instability (see, e.g., Ostrovsky³).

D. Effect of Earth's rotation on large-scale nonlinear waves

For the description of mesoscale processes having spatial scales of a few kilometers or more and time durations of an hour or more, the effects of the Earth's rotation become significant. There arise some radically new elements in the behavior of nonlinear waves in this case. The important new variable is the Coriolis parameter f which defines the lowest possible frequency of surface and internal gravity waves; these are also sometimes called gyroscopic or inertial gravity waves. For frequencies close to f , long-wave dispersion plays a major role.³⁷ It should be emphasized that we are restricting our attention to waves with frequencies above f , where f is assumed to be constant (f -plane approximation). As was already mentioned, Rossby waves for which the meridional dependence of the Coriolis force must be taken into account (β -plane approximation) also exist in a rotating fluid, but their frequencies lie below f .

Equations (12) and (13) may be used for the description of gyroscopic waves. Moreover, for waves with their frequency spectrum lying in the interval between f and the maximum Brunt-Väisälä frequency, N_{\max} , but not too close to either of these parameters, both the low- and high-frequency dispersion effects are small provided $N_{\max} \ll f$. An adequate partial differential equation may again be obtained from the dispersion relation for linear waves in the limit of weak dispersion, namely

$$\omega \simeq ck - \beta k^3 + \frac{f^2}{2ck}, \quad (51)$$

from which the evolution equation follows in the form:

$$\frac{\partial}{\partial x} \left(\frac{\partial \eta}{\partial t} + c \frac{\partial \eta}{\partial x} + \alpha \eta \frac{\partial \eta}{\partial x} + \beta \frac{\partial^3 \eta}{\partial x^3} \right) = \frac{f^2}{2c} \eta. \quad (52)$$

This equation was first derived by Ostrovsky¹³ and was then reproduced and analyzed in many subsequent papers. In the absence of rotation ($f=0$), it reduces to the KdV Eq. (15), so that Eq. (52) may be called rotationally modified KdV or briefly rKdV equation.³⁸ An analogous equation with $\beta=0$ was obtained for different types of waves (see, e.g., Ostrovsky and Stepanyants³⁹ and Grimshaw *et al.*⁴⁰ for references).

Unlike the above model equations, Eq. (52) is apparently not completely integrable. Still, for periodic and localized solutions, it possesses a series of useful integrals such as

an energy integral. It also has a “zero-mass” integral, $\int \eta dx = 0$ (for periodic solutions the integration is taken over the wave period whereas for solitary perturbation the integration is taken over the entire x axis). Note that for the previously considered equations, such as the KdV, mKdV, comb-KdV, BO, and JKKD equations, this “mass” integral is an arbitrary constant but not necessarily zero.

Exact analytical solutions for even the stationary version of Eq. (52) are unknown (except for the steady wave of the parabolic profile, see below). However, many of the solutions have been investigated numerically by now.

A relatively simple analysis can be performed if the high-frequency dispersion (the term with β) is neglected, which is possible for sufficiently long waves. Then, a second-order equation results, stationary solutions of which can be analyzed on the phase plane of the variables η and $d\eta/d\xi$ (see details in Ostrovsky¹³ and Grimshaw *et al.*⁴⁰). There exists a family of periodic solutions to this reduced equation whose shape varies from sinusoidal to parabolic. The wave of limiting amplitude has sharp crests and is represented by a periodical sequence of parabolic arcs. Note that each arc itself is also a solution of the full Eq. (52) with the high-frequency dispersion

$$\eta = \frac{f^2}{12\alpha c} \left[(\xi - \xi_0)^2 - \frac{\lambda^2}{12} \right], \quad -\frac{\lambda}{2} \leq \xi - \xi_0 \leq \frac{\lambda}{2}, \quad (53)$$

In 1996 Gerkema²⁹ derived a two-directional generalization of equation Eq. (52) for small-amplitude waves in two-layer fluid. Later, on the basis of Lee and Beardsley²⁰ approach, the same equation was derived by New and Esteban in 1999 for an arbitrarily stratified fluid. In terms of the horizontal component of the stream function, $A(x, t)$, this equation reads

$$\frac{\partial^2 A}{\partial t^2} - c^2 \frac{\partial^2 A}{\partial x^2} - s \frac{\partial^4 A}{\partial t^2 \partial x^2} + f^2 A = r \frac{\partial^2 A^2}{\partial x^2}. \quad (54)$$

For waves propagating in one direction this equation readily reduces to Eq. (52) with $\alpha=r/c$ and $\beta=cs/2$.

Internal waves in a two-layer rotating fluid were also studied by Plougonven and Zeitlin in 2003. Following the Shrira's approach (see, e.g., in Grimshaw *et al.*⁴⁰) developed for strongly nonlinear surface waves in a rotating fluid, they considered stationary periodic solutions for interfacial waves without high-frequency dispersion and then numerically constructed wave shapes.

As shown by Leonov in 1981 and then other authors, an important peculiarity of Eqs. (52) and (54) is that for the high-frequency dispersion characteristic of oceanic waves [when the coefficient β in Eq. (52) is positive], solitary waves in the form of stationary localized pulses cannot exist at all (see, e.g., Grimshaw *et al.*⁴⁰).

In addition to the stationary solutions mentioned above, some nonstationary solutions for the rKdV equation have also been studied, mostly numerically.^{39,40} It was observed, in particular, that the initial KdV-type solitary perturbation undergoes a “terminal decay,” i.e., it completely annihilates (more exactly, transforms into radiation) in a finite time.⁴⁰

Related equations were also obtained for deep rotating fluids. One of them is a generalization of the BO equation for a very deep ocean having a relatively thin pycnocline⁴⁰

$$\frac{\partial}{\partial x} \left[\frac{\partial \eta}{\partial t} + c \frac{\partial \eta}{\partial x} + \alpha \eta \frac{\partial \eta}{\partial x} + \frac{\delta}{\pi} \frac{\partial^2}{\partial x^2} \int_{-\infty}^{\infty} \frac{\eta(\zeta, t)}{x - \zeta} d\zeta \right] = \frac{f^2}{2c} \eta. \quad (55)$$

Estimates show that the role of rotation is important for real internal waves in the ocean that have lengths of a few kilometers and more and periods in excess of roughly 1 h.

E. Strongly nonlinear waves

In previous sections, both nonlinearity and dispersion were considered small in the sense that in, e.g., a two-layer fluid, the displacement of the pycnocline is significantly smaller than its equilibrium depth (or, for a pycnocline close to the bottom, than its height over the bottom). Along with a number of observations for which the weakly nonlinear models provide a good approximation, there is also a growing number of data for which they are evidently wrong (see also the experimental Sec. IV). Note that the transition from the KdV equation to the eKdV-type equation has been suggested by Lee and Beardsley²⁰ to improve theoretical description of Halpern's observations of strong solitons in 1971. As was mentioned above, the eKdV model sometimes may serve as a phenomenological model for strong solitons because, as in the more consistent theories, it predicts much wider solitons than those which follow from the KdV equation for strong waves.

A more consistent description of strongly nonlinear internal waves can be based on direct numerical simulation for the basic hydrodynamic equations. For two-dimensional, steady-state waves in the Boussinesq approximation, the basic Euler equations, Eqs. (4)–(7), can be reduced to a single equation for the stream function, Ψ , as shown as early as in 1930s by Dubriel-Jacotin and later independently by Long in 1953:

$$\frac{\partial^2 \Psi}{\partial \xi^2} + \frac{\partial^2 \Psi}{\partial z^2} + \frac{N^2(z - \Psi/V)}{V^2} \Psi = 0. \quad (56)$$

Here $\xi = x - Vt$, $N(z)$ is the known buoyancy frequency, and the velocity components are $u = \partial \Psi / \partial z$ and $w = -\partial \Psi / \partial x$. It is seen that at $N(z) = \text{const}$, the steady waves (but only them!) are described by a linear equation, as mentioned above for weakly nonlinear waves.

Many numerical works have considered steady waves in a two-layer fluid. For this case, the linear Laplace equation can be used for each layer. The first study using this approach was probably the paper by Amick and Turner.⁴¹ In addition to a detailed mathematical treatment of the problem, they have shown that there exists a limiting amplitude at which a soliton acquires a flat top and tends to two separated kinks, similar to the case of the eKdV equation but with different parameters. The amplitude and velocity of such a limiting soliton are

$$\eta_0 \lim = \frac{h_1 - h_2 \sqrt{a}}{1 + \sqrt{a}} \approx \frac{h_1 - h_2}{2}, \quad (57)$$

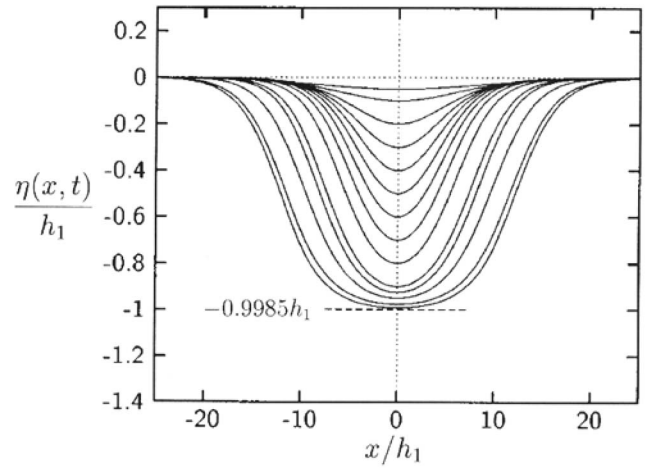


FIG. 4. Soliton profiles, $\eta(x)/h_1$ vs x/h_1 , for the two-layer fluid with $h_2/h_1=3$, $\rho_1/\rho_2=0.997$ (surface is at +1; bottom at -3 on the vertical axis). The profiles shown correspond to different soliton amplitudes, $-\eta_0/h_1 = 0.05, 0.1, 0.2, 0.3, 0.4, 0.5, 0.6, 0.7, 0.8, 0.9, 0.925, 0.95, 0.975, \text{ and } 0.99$. The dashed horizontal line marks the level of limiting amplitude wave. From Evans—see in Duda and Farmer (Ref. 7).

$$V_{\text{lim}} = \frac{\sqrt{g(1-a)(h_1+h_2)}}{1+\sqrt{a}} \approx \frac{\sqrt{g'(h_1+h_2)}}{2}, \quad (58)$$

where $a = \rho_1/\rho_2 < 1$, $g' = g(1-a)$, and positive displacement is upward. The relations on the right are valid for oceanic conditions where density variation is always small, i.e., $a \approx 1$.

Subsequently, direct numerical analysis of the two-layer case as applied to stationary solitary waves was performed by many authors (see, e.g., the paper by Evans in Duda and Farmer⁷ or Grue⁴²). As an example, Fig. 4 shows calculations of soliton profiles for the two-layer fluid using the parameters chosen by Evans.

In the recent years, some numerical calculations of strongly nonlinear waves in a sea with smooth stratification have been performed, including wave steepening, formation of soliton groups, and breaking, with the associated generation of turbulence. Such factors as wave shoaling over a sloping bottom in coastal areas, and formation of a trapped core were considered. The reader can be referred to, e.g., the papers by Vlasenko and Hutter⁴³ and Lamb.⁴⁴

In particular, Vlasenko *et al.*⁴⁵ calculated some practical cases, taking the data from observation. They considered a stratified layer with different density profiles, including those of a pycnocline type and some smoother ones, and calculated stationary soliton structures using the Euler equations for vorticity and density.

In the context of this paper, we shall concentrate on the long-wave models in which the explicit dependence on the vertical coordinate is eliminated. Indeed, direct numerical computations are usually time costly and, what is perhaps more important, it is often difficult to understand the qualitative pattern of the process. Although there is, strictly speaking, no *a priori* small parameters that could be used to simplify the problem, in many cases the soliton length remains larger than the thickness of one of the layers or of the total depth of the ocean, especially in coastal areas. For these

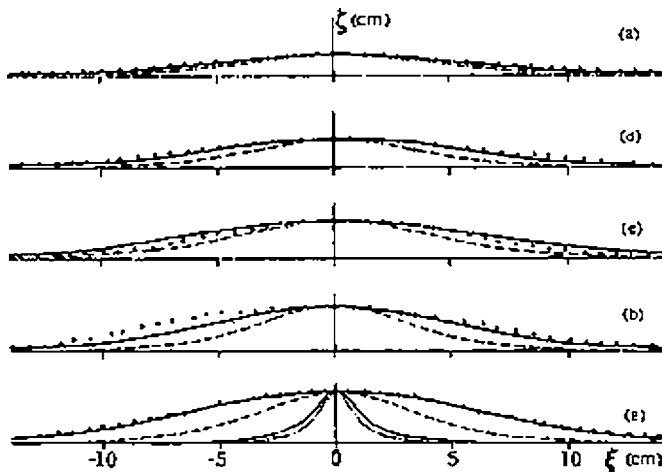


FIG. 5. Comparison of theoretical and experimental data for large-amplitude solitons. Dots are experimental points. Solid line—solitary wave from the long-wave Miyata’s model; broken line—KdV soliton; thin solid line—BO soliton; dot-dashed line—JKKD soliton. The latter two theoretical profiles are not shown in frames (b)–(e), but they are below the KdV profile. $\zeta(\xi)$ is equivalent to our $\eta(\xi)$, where $\xi = x - Vt$. (a) $-\eta_0/h_2 = 1.57$; (b) $-\eta_0/h_2 = 1.27$; (c) $-\eta_0/h_2 = 1.14$; (d) $-\eta_0/h_2 = 0.92$; (e) $-\eta_0/h_2 = 0.64$. From Miyata (see Ref. 46).

cases, a long-wave approximation can be constructed that uses the corresponding expansion of dispersive terms while keeping the nonlinearity strong. This basic approach was first suggested by Whitham in 1967 for surface waves based on the expansion of the Lagrangian.

For internal waves, Miyata^{46,47} was apparently the first who suggested (albeit without a detailed derivation) the long-wave equations for strongly nonlinear, weakly dispersive waves in a two-layer fluid, and analyzed a steady solitary solution of these equations. Miyata’s equations, together with other weakly nonlinear models, KdV, eKdV, BO, and JKKD, were examined against numerical calculations in Miyata⁴⁶ and Michallet and Barthélemy.²⁴ Figure 5 shows a comparison of experimental data for large-amplitude solitons against different theoretical models.

A detailed analysis of the same problem for a two-layer fluid was performed by Choi and Camassa.⁴⁸ For shallow water, these equations (essentially the same as those obtained by Miyata), being reduced to the case of a small density jump, $\Delta\rho \ll \rho_{1,2}$, can be represented in the form⁴⁹

$$\frac{\partial \eta}{\partial t} + \frac{\partial}{\partial x}[(h_1 + \eta)u_1] = 0, \quad (59)$$

$$-\frac{\partial \eta}{\partial t} + \frac{\partial}{\partial x}[(h_2 - \eta)u_2] = 0. \quad (60)$$

$$\begin{aligned} \frac{\partial(u_1 - u_2)}{\partial t} + u_1 \frac{\partial u_1}{\partial x} - u_2 \frac{\partial u_2}{\partial x} + g' \frac{\partial \eta}{\partial x} &= \frac{1}{3(h_1 + \eta)} \frac{\partial}{\partial x} \\ &\times \left\{ (h_1 + \eta)^3 \left[\frac{\partial^2 u_1}{\partial t \partial x} + u_1 \frac{\partial^2 u_1}{\partial x^2} - \left(\frac{\partial u_1}{\partial x} \right)^2 \right] \right\} \\ &- \frac{1}{3(h_2 - \eta)} \frac{\partial}{\partial x} \left\{ (h_2 - \eta)^3 \left[\frac{\partial^2 u_2}{\partial t \partial x} + u_2 \frac{\partial^2 u_2}{\partial x^2} \right] \right\} \end{aligned}$$

$$- \left(\frac{\partial u_2}{\partial x} \right)^2 \right\}. \quad (61)$$

Here the z axis is directed downward, and $u_{1,2}$ are the horizontal velocities in the layers, each averaged over the layer thickness.

For a stationary soliton propagating with a constant velocity V , this system can be reduced to a second-order ordinary differential equation that can be readily analyzed.

1. Nondispersive waves and evolution equations

The set of Eqs. (59)–(61) is two-directional and can be considered as a strongly nonlinear extension of the Boussinesq equations in the two-layer case. In applications, one usually deals with waves propagating in one direction from a source, such as a shelf break, transforming a part of the energy of the barotropic tides into internal waves propagating onshore. Hence, an important problem is to obtain an evolution equation for a wave propagating in one direction, i.e., a strongly nonlinear analog of the KdV or eKdV equations. Besides simplifying analytical considerations and making the result more physically clear, this may also significantly save computer time in practical applications. This seems to be especially attractive for strongly nonlinear waves, the equations of which are typically nonintegrable. This problem was discussed by Ostrovsky (see in Duda and Farmer⁷) and addressed in detail in Ostrovsky and Grue.⁵⁰ The approach starts from the exact nondispersive limit for long waves when the term D in Eq. (61) is neglected. In this case, a progressive (simple, or Riemann) nonlinear wave exists which propagates with a nonlinear velocity $c(\eta)$, and all variables are functionally related: $u_{1,2} = u_{1,2}(\eta)$, so that

$$\frac{\partial \eta}{\partial t} + C_{\pm}(\eta) \frac{\partial \eta}{\partial x} = 0. \quad (62)$$

Here, two possible simple wave velocities exist (e.g., Sandström and Quon⁵¹). In the explicit form these velocities are⁵²

$$\begin{aligned} C_{\pm}(\eta) = \pm c \left\{ 1 + 3 \frac{(h_1 - h_2)(h_1 - h_2 - 2\eta)}{(h_1 + h_2)^2} \right. \\ \left. \times \left[\sqrt{\frac{(h_1 - \eta)(h_2 + \eta)}{h_1 h_2}} - \frac{h_2 - h_1 + 2\eta}{h_2 - h_1} \right] \right\}, \quad (63) \end{aligned}$$

where c is the linear velocity of long waves given by Eq. (19).

The velocity of a simple wave reduces to the linear wave velocity in two cases, when the perturbation is infinitesimal, $\eta \rightarrow 0$, and when $\eta = (h_2 - h_1)/2$; it is worth noting that the latter formula determines the limiting amplitude, η_{lim} , of a soliton.

These results are exact for a nondispersive wave in a two-layer fluid. Similar to the gas dynamics case, the basic nondispersive equations can be rewritten in terms of Riemann invariants, I_{\pm} . As is known from the theory of hyperbolic equations, the progressive wave of Eq. (62) corresponds to the case when one of the invariants, e.g., I_{-} , turns to a constant, in our case zero.

Returning to the full set of Eqs. (59)–(61) in which the dispersive operator D is nonzero but small, for the wave propagating in a positive direction, the invariant I_- is also small, of order D . As a result, Eq. (62) is modified to give⁵⁰

$$\eta_t + C(\eta)\eta_x = \frac{D_1(\eta)}{dI_{\pm 0}/d\eta} = D(\eta) \frac{h_1 + \eta}{C_+(\eta) - C_-(\eta)} \frac{h_2 - \eta}{h_1 + h_2}. \quad (64)$$

Here $C_{\pm}(\eta)$ correspond to the signs in Eq. (63).

2. Simplified evolution equation (β model)

It should be emphasized that, unlike in the weakly nonlinear case, the long-wave approximations for surface and internal waves considered above (both two and one directional) are of a somewhat contradictory nature. Indeed, these equations combine strong nonlinearity and weak dispersion, whereas a soliton exists as a balance between the nonlinearity and dispersion, so that it is *a priori* unclear whether a strong soliton would be long enough to provide sufficiently small dispersion terms and thus secure the applicability of the shallow-water approximation. Considering this, in Ostrovsky and Grue⁵⁰ a different approach to obtaining an evolution equation was developed. Namely, the exact nondispersive operator is retained unchanged but a dispersive term is represented in a semiphenomenological form based on slowness of the displacement variation. For strongly nonlinear waves, along with the exact long-wave velocity $c(\eta)$ defined by Eq. (63), we introduce a local dispersion parameter corresponding to that in KdV, but with the instantaneous values of the layer depths: $\beta = \frac{1}{6}C(\eta)(h_1 + \eta)(h_2 - \eta)$. As a result, a strongly nonlinear evolution equation (β model) follows:

$$\frac{\partial \eta}{\partial t} + C(\eta) \frac{\partial \eta}{\partial x} + \frac{\partial}{\partial x} \left[\beta(\eta) \frac{\partial^2 \eta}{\partial x^2} \right] = 0. \quad (65)$$

Detailed comparisons between solitary solutions following from different long-wave models, direct fully nonlinear computations, and observational data, were presented in Ostrovsky and Grue.⁵⁰ An example is shown in Fig. 6. The particle velocity and soliton propagation velocity are approximated very well by the long-wave equations. As regards the soliton profile and width, for a moderate depth ratio, h_2/h_1 , both two-directional Choi–Camassa (CC) model and the evolution β model [but not always Eq. (64)] give quite satisfactory results.

Note that all one-directional models have a common disadvantage: they do not exactly conserve mass and energy at the same time. In particular, Eq. (64) conserves neither, and Eq. (65) conserves only mass (although energy is close to constant as well). Its modification, the “e model” also used in Ostrovsky and Grue⁵⁰ conserves energy but allows slight variations of mass. However, the solutions of the β and e equations are typically close to each other.

3. Deep lower layer

For a very large depth ratio the applicability of the “shallow-water” models is limited because the basin is not always shallow enough for the solitons. In these cases the

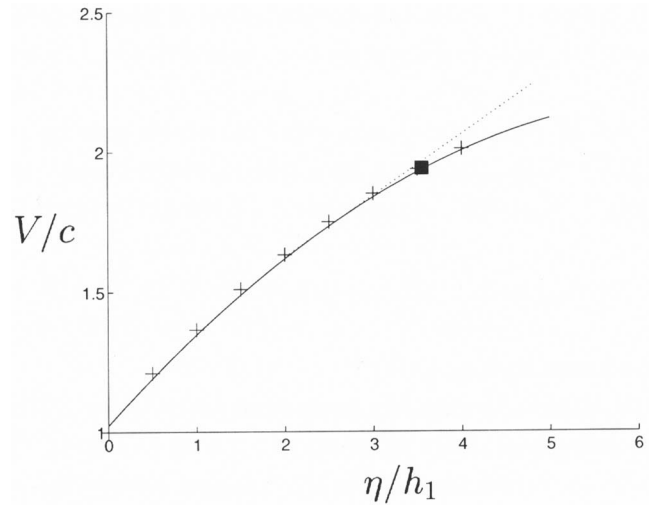


FIG. 6. Normalized soliton velocity versus normalized amplitude for $h_2/h_1=20.4$ (COPE). Solid line—fully nonlinear numerical solution, crosses— β model (CC model gives very close results), dotted line—fully nonlinear calculations for $h_2/h_1=500$ (i.e., practically infinitely deep lower layer). Filled square—observation. From Ostrovsky and Grue (see Ref. 50).

following model may work better. Namely, consider another limiting case when the lower layer is infinitely deep but the wave is still long as compared to the upper layer; for weak nonlinearity, this is the case for which the BO Eq. (32) has been derived. In a two-directional, weakly dispersive form the corresponding long-wave equations were obtained by Choi and Camassa.⁴⁸ They considered the upper layer nonlinear but nondispersive and the lower fluid dispersive but linear, and obtained the equations in the form (here we again use the limit of a small density jump across the density interface)

$$\frac{\partial \eta}{\partial t} + \frac{\partial}{\partial x} [(h_1 + \eta)u_1] = 0, \quad (66)$$

$$\frac{\partial u_1}{\partial t} + u_1 \frac{\partial u_1}{\partial x} + g' \frac{\partial \eta}{\partial x} = \frac{1}{\pi} \oint_{-\infty}^{\infty} \frac{\partial^2 \eta(t, \xi)}{\partial \xi^2} \frac{d\xi}{\xi - x}. \quad (67)$$

Here, the same restrictions on the applicability of the dispersive term should again be imposed. In Ostrovsky and Grue⁵⁰ an evolution equation generalizing the BO equation for strong nonlinearity has been suggested in the form

$$\frac{\partial \eta}{\partial t} + C(\eta) \frac{\partial \eta}{\partial x} + \frac{1}{\pi} \frac{\partial}{\partial x} \oint_{-\infty}^{\infty} \frac{\partial \eta(t, \xi)}{\partial x'} \frac{\gamma[\eta(t, \xi)]}{\xi - x} d\xi = 0, \quad (68)$$

where $C(\eta) = \sqrt{g'h_1(3\sqrt{1+\eta/h_1}-2)}$ is the simple wave velocity Eq. (63) taken in the limit of $h_1/h_2 \rightarrow 0$, and $\gamma(\eta) = \frac{1}{2}C(\eta)(h_1 + \eta)$ generalizes the corresponding parameter of the BO equation in the same manner as it has been done above for the β model. This equation gives a very good agreement with direct computations, at least for moderate soliton amplitudes, up to $\eta_0=0.8h_1$.

Considering the growing number of observations of strong solitons in the ocean (see the experimental part below)

and the increasing role of coastal areas, the theory of strongly nonlinear internal waves should be considered as an important branch of theoretical physical oceanography.

IV. EXPERIMENTAL OBSERVATIONS IN THE OCEANS

Observations of nonlinear internal waves close to solitons or their groups (solibores) are numerous and these measurements are being actively performed now. It is impossible to even mention all them. Here we discuss some examples, specifically a few of the pioneering ones and also a few recent experiments. More observational data can be found in Duda and Farmer⁷ and in the Jackson–Apel Atlas.⁸

A. Internal solitons near the continents

With the advent of satellites that carry high-resolution imaging systems (e.g., Landsat, Seasat, and subsequent spacecraft), it has been possible to obtain overviews of certain processes occurring in the sea that have distinguishable surface signatures. Such phenomena include coherent internal waves. The combination of the methods of satellite oceanography, underwater acoustics, and *in situ* measurements has enabled considerable progress to be made in understanding the kinematics and dynamics of these waves. The Olympian view provided by the satellite remote observations has allowed careful planning of subsequent *in situ* experiments to be done, with the result that a moderately detailed picture of the birth, evolution, propagation, and decay of the internal waves has been obtained. For those cases in which workers could achieve both (a) the synoptic view provided by satellites and (b) the detailed in-water view given by current meters and acoustic echo sounders, these coherent waves have most frequently proven to be soliton-like. As a consequence, when soliton characteristics are observed in satellite images for which no concurrent *in situ* data are available, one can assume with some confidence that a solitary wave is indeed being observed.⁵³ In addition, certain features unique to soliton interactions have been seen in satellite imagery, e.g., the spatial phase shifts that occur when two solitons pass through each other (see, e.g., in Apel *et al.*¹). Such observations are unambiguous proof of the solitary wave character of these oceanic internal waves.

Having established that internal solitons are fairly commonplace in the sea, we can then discuss the observations in that context without continually raising questions about the correctness of the interpretation.

Tidal interaction with bottom features appears to be the dominant mechanism for generation of the coherent oceanic internal waves near the continents; closer to shore, riverine canyons or glacial scours provide secondary generating mechanisms. Also, the boundaries of intense current systems such as the Gulf Stream appear to be sources of coherent wave packets that propagate at large angles to the current direction. Since tides, stratification, and bottom topography are global features, one expects tidally excited internal waves to be ubiquitous wherever stratified waters and shallow bathymetry exist.

At least two mechanisms have been advanced to explain the generation process at the shelf break. The first hypoth-

esizes that the barotropic (i.e., uniform in depth) tide will be scattered into baroclinic (i.e., varying with depth) modes at the shelf break. The second is a kind of lee-wave mechanism, wherein tidal flow directed offshore beyond the shelf break results in an oscillating depression of the pycnocline just offshore of the break. As the tidal current ellipse is swept out, the reversal of that current releases the lee wave from its down-current, phase-locked position. The wave of depression then propagates opposite to the earlier current direction, i.e., toward shore, where it evolves independently of further tidal action except for advective effects. There is some experimental support for both of these processes at the shelf edge, at sills or similar geometries, and different opinions exist concerning this.

Figure 7 is an image of the ocean made with the 6-cm-wavelength synthetic aperture radar (SAR) on the European Remote Sensing Satellite, ERS-1, taken southeast of New York near the edge of the continental shelf on 18 July 1992. The image is 90×90 km², and shows quasiperiodic internal wave signatures running diagonally across it, approximately parallel to the edge of the continental shelf. The waves occur in packets separated by some 20–25 km and propagate under refractive control of the shallow continental shelf in water depths between roughly 200–50 m. Each packet has been generated by the semidiurnal (12.5 h) and diurnal (25 h) tides during the phase when the tidal current is directed offshore. Initially, the offshore flow depresses the pycnocline just seaward of the continental shelf break. As it moves shoreward, the depression begins to steepen and develop undulations, most likely because of the dispersion at the leading edge of the depression which agrees with the description given in the theoretical part here. Within less than one semidiurnal tidal period, the pycnocline depression became fully modulated and has grown into a solitary wave train. It is these wave packets that are visible in Fig. 7, which shows perhaps six groups of waves that represent a history of soliton formation, propagation, and attenuation extending backward in time at least 75 h. Also visible in the lower right-hand corner is what is believed to be a nascent packet being formed just at the shelf break at the time of the satellite overpass. Note that in this and some other cases satellite images show more than one family of solitary wave packets that undergo collisions.

Figure 8 is an acoustic echo-sounder trace of solitary wave packets in the region of Fig. 7, taken with a 20 kHz downward-looking pulsed sonar. The nonlinear character of the waves is clearly visible, with only downgoing pulses appearing and with very little upgoing excursion. The towed echo sounder made repeated passes across the wave train, thereby allowing questions of stability and wave coherence to be addressed (see, e.g., Proni and Apel⁵⁴). Moored and towed current meters and temperature probes give similar detailed pictures of the behavior of the waves with time.

A schematic of the type of solitary waves appearing in Fig. 7 is given in Fig. 9; an overall vertical profile and a plan view are shown, along with the characteristic length scales. Such packets have strong tendencies for those individual solitons having the largest amplitudes, longest wavelengths, and longest crest lengths to be at the front of the group, with



FIG. 7. Image of New York Bight taken by the European Remote Sensing Satellite ERS-1 on 18 July 1992, showing several packets of internal solitons generated during six previous tidal cycles in the vicinity of the Hudson Canyon. Dimensions 100×100 km. Image courtesy of Chapman and the European Space Agency.

the ones having the smallest attributes appearing at the rear. In theory, the small solitons are followed by linear, dispersive wave trains, but such are difficult to distinguish from the trailing solitons.

Internal waves propagating shoreward on the continental shelf soon encounter shoaling bathymetry that affects their propagation speeds and amplitudes. Near the region where the pycnocline depth is roughly one-half the total depth, they

appear to undergo various transformations. These processes have been studied in numerous papers. Depending on local hydrological conditions and the incoming wave, different scenarios of subsequent wave evolution can occur, including the creation of sequences of secondary solitons, disperse wave trains, various types of billows, vorticity formation, or just turbulent spots. As mentioned, for the case of a mid-depth pycnocline, the extended KdV Eq. (24) works well; its

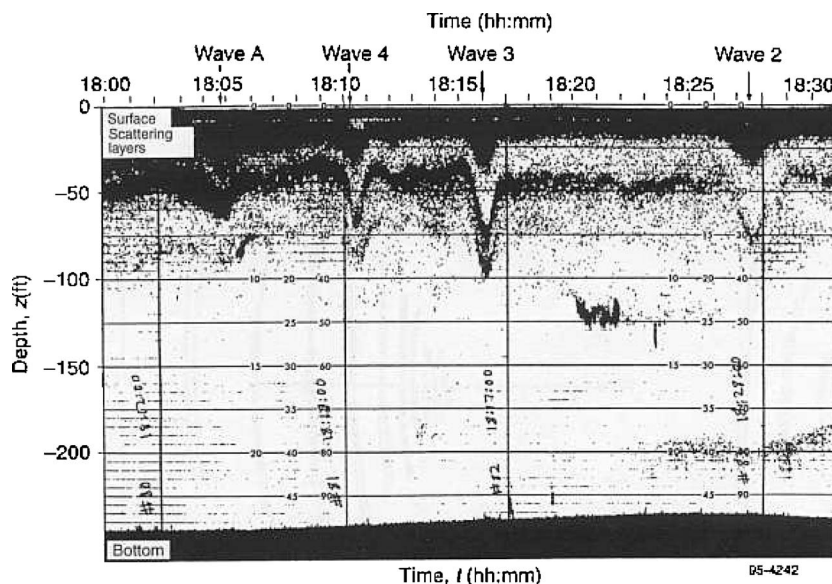


FIG. 8. Acoustic echo-sounder record of solitary wave displacements in the region of Fig. 7. From Gasparovich *et al.* (see Ref. 82).

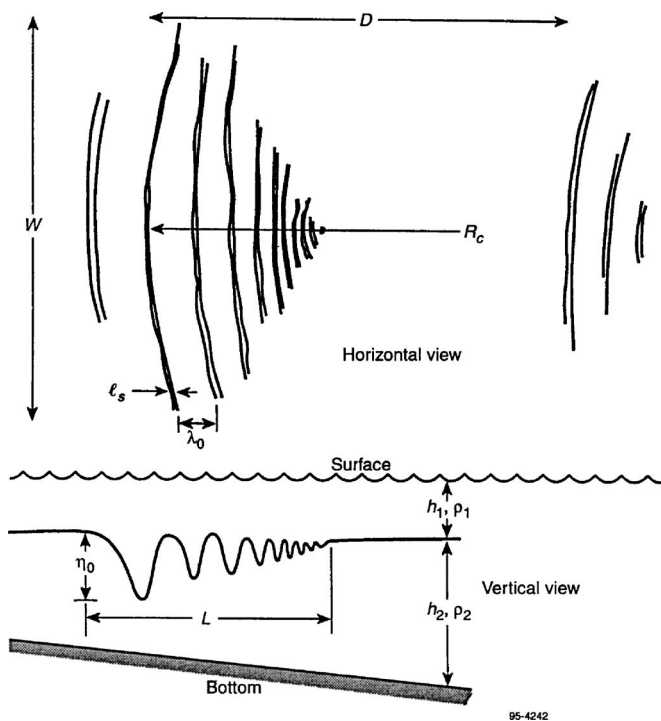


FIG. 9. Schematics of a soliton wave packet on the continental shelf, and some of its dimensions. From Apel (see Ref. 6).

application to the interpretation of observation data is described in, e.g., the paper by Holloway *et al.*³² Wave propagation through the point when the pycnocline crosses the middle of the layer due to the depth variation has been observed by, e.g., Orr and Mignerey.⁵⁵

In shallow regions, increased amounts of suspended sediments often exist due to solitons, as has been observed with acoustic echo sounders.⁵⁴ Since the bottom currents associated with these waves are large enough to resuspend sediments, the force due to bottom friction is large and the process of breaking on the sloping bottom may be what ultimately destroys the waves. Soliton signatures have generally disappeared from imagery taken in this shallow domain. Soliton processes also apparently inject large amounts of nutrients into the food chain in the shallow region,⁵⁶ and it is likely that other areas also benefit biologically from the effects of internal waves. Note that in a number of cases, satellite images show more than one family of solitary wave packets undergoing collisions.

For solitons in midlatitude continental shelf waters during summer conditions, typical scales of the waves (their order of magnitude) in terms of a two-layer approximation are given in Table I; note that deviations from these quantities can be large. The algebraic quantities appearing in the table are defined in Fig. 9. The distance D between successive packets is set by the nonlinear phase speed of the leading solitons in the packets. The radius of curvature R_c can be

TABLE I. Typical scales for continental shelf solitons. See Fig. 9 for notation.

L (km)	η_0 (m)	h_1 (m)	h_2 (m)	l_s (m)	λ_0 (m)	W (km)	D (km)	R_c (km)	$\Delta\rho/\rho$
1–5	0–30	5–25	100	100	50–500	0–30	15–25	15– ∞	0.001

TABLE II. Dynamical quantities.

Brunt–Väisälä frequency, $N/2\pi$	10 cycles/h
Radian frequency, ω	0.001–0.005 rad/s
Speed, c	0.20–1.0 m/s
Current velocity, U	0.10–1.0 m/s
Packet lifetime, τ_{life}	24–48 h
Interpacket period, τ_{gen}	12.5–25 h

of the order of the distance from the generation region, although in shallower water, the phase fronts become controlled by the bathymetry. Scales for dynamical quantities appear in Table II.

At the edge of the continental shelf, still other processes are active in generating internal waves. For example, upwelling, especially near regions of strong bathymetric relief such as submarine canyons, appears to be an important source. Such a disturbance was probably observed by the 10-cm-wavelength SAR on the Soviet/Russian spacecraft Almaz-1 (A. Smirnov, private communication). On the basis of preliminary calculations, those analyzing the data believe that the upwelling serves to excite internal disturbances in submarine canyons and similar regions of high relief, which then go on to develop into solitons.

A rather recent observation of large, shoaling deep-water nonlinear internal waves comes from the Asian Seas International Acoustics Experiment (ASIAEX), a joint acoustics and physical oceanography observational program conducted in the northeastern part of the South China Sea in 2001. In ASIAEX, numerous moored, shipboard, and RADARSAT observations were made of the nonlinear internal wave field, in support of the program's objective of determining the effect of nonlinear internal waves on acoustic propagation at low frequencies (50–1000 Hz) in shallow water (0–300 m). The nonlinear waves observed in ASIAEX were among the largest observed in the world's oceans. Emanating from the Luzon Strait, these waves had crests up to 200 km in lateral extent, and vertical amplitudes ranging from 29 to over 140 m. The ASIAEX experiment concentrated significant resources in studying the shoaling of these large waves, with heavily instrumented moorings extending from 30 to 70 m depth, as well as high frequency acoustic imaging. The interested reader is referred to, e.g., the article by Orr and Mignerey.⁵⁵

Finally, we present an example of a group of strongly nonlinear solitary waves observed in 1995 in the Coastal Ocean Probing Experiment (COPE) off the coast of northern Oregon. Presumably due to the proximity of Columbia River, a sharp and shallow (5–7 m deep) pycnocline was formed on which groups of very strong, tide-generated internal waves propagated. A highlight of this experiment was that the *in situ* observations were performed in two locations along onshore IW propagation direction separated by 20 km

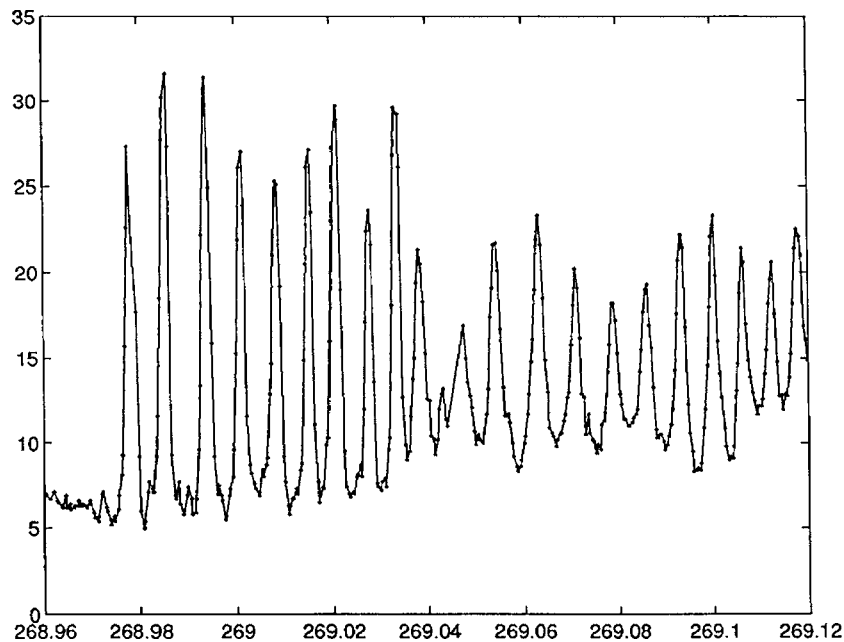


FIG. 10. Temporal record of depth of 14 °C isotherm for September 25–26, 1995 (the peaks are actually water depressions). From Kropfli *et al.* (see Ref. 58).

so that the soliton group evolution could be followed up. At the first site, with a depth of 150 m, measurements were carried out with a CTD probe from the floating platform (FLIP). In the second site, with a depth of 60 m, moored thermistor chains were used.⁵⁷ In both cases, the current velocity of the IW was measured. Remote images were also obtained from coastal X-band and Ka-band Doppler radars with horizontal and vertical polarizations.⁵⁸ Details of this experiment can be found in the cited publications.

Figure 10 presents the 14 °C isotherm displacement (actually a depression) at the FLIP site.²⁵ The isotherm depressions reach 25–30 m from its initial depth of 5–7 m. The same group of solitons was registered at the thermistor site after about 6.4 h of onshore propagation (M. V. Trevorror, private communication), so that mean propagation velocity was about 0.85 m/s. Peak particle velocity exceeded 0.7 m/s, only slightly smaller than the propagation velocity, which confirms that the nonlinearity was very strong. Clear radar images of this and other groups have been obtained by a coastal radar.⁵⁸ Amazingly, such images could be obtained even with strong sea surface roughness, at wind speeds of up to 13 m/s. The parameters of observed solitons are far from those predicted by the KdV equation (a bit better approximation can sometimes be given by the eKdV equation, as done in Stanton and Ostrovsky²⁵) but they can be satisfactorily approximated by the strongly nonlinear models discussed above.

More examples of strongly nonlinear solitons are given in Duda and Farmer.⁷ Note also an earlier observation in Celtic Sea by Pingree and Mardell in 1985 where soliton amplitudes reached 40 m.

The last, but not the least, interesting aspect of strong internal solitons in coastal zones is their environmental effects. Examples can be found in Duda and Farmer.⁷ In particular, Stanton observed a significant increase in turbulent

mixing in solitons, whereas Lennert-Cody and Franks observed strong phytoplankton luminescent activity in solitons.

B. Internal waves in the deep ocean

As a broader view of internal soliton activity on the continental shelves was obtained, the interest of researchers expanded to their study in the deep ocean. Various questions were asked: Do solitons exist in the deep sea? What are their typical and extreme parameters? Where are they encountered most frequently? Over what distances can they propagate? What fraction of the total internal wave field energy do they contain? Why are they so coherent as to be recognizable over a large span of space and time scales? What relation do they have to deep-ocean internal waves, whose spectra, as described by Garrett and Munk, imply that very little coherence exists, and that energy levels are approximately the same around the globe? We now know that solitary internal waves occur in a wide range of deep-ocean locales, in regions at least as far as 500 km from shore, and perhaps even farther.

Deep-water solitons are typically formed during strong tidal flow over relatively shallow underwater sills that protrude up into the permanent thermocline (e.g., 300–500 m); they then radiate away from their sources in narrow straits. The Strait of Gibraltar has been, perhaps, the most thoroughly studied case.⁵⁹ Figure 11 is a photograph taken from the US Space Shuttle showing three packets of solitons propagating into the western Mediterranean Sea following their generation at the Gibraltar sill by the combined tidal, surface, and subsurface flows of Mediterranean water out into the Atlantic Ocean.⁶⁰ The amplitude of these waves is of order 50 m and their intersoliton distance, or wavelength, is 500–2000 m. It should be emphasized that these internal waves may have significantly different characteristics from the continental shelf waves discussed above. The solitons can have larger amplitudes in deep water and much larger



FIG. 11. Photograph of solitons in the Strait of Gibraltar as observed by the U. S. Space Shuttle. Image courtesy of NASA and La Violette *et al.* (see Ref. 60).

scales both across and along their fronts. At the same time, due to the deeper pycnocline position and smoother stratification, the effective nonlinearity in such solitons may remain relatively small, whereas in the shelf zone it can reach significant values as discussed above.

A group of solitary waves having an intersoliton spacing of 20 km and a maximum crest length of over 90 km at a distance of 400 km from their source has been observed with the Landsat multispectral scanner in the Sulu Sea in the Philippines, where they radiate from a narrow sill approximately 2 km in width.⁶¹ In these South East archipelagos, a combination of complex geography, inland seas with differing tidal responses, and a deep pycnocline formed by the stress of the trade winds all work to cause the soliton populations in the region to be extraordinarily dynamic. These large, deep-water solitons have been studied in some detail. Several measurements in the Andaman Sea⁶² and Sulu Sea⁶¹ have shown that solitons exist with amplitudes of up to 70–90 m and phase speeds approaching 2.5 m/s, caused by strong tidal flow over underwater sills between islands. Although the unperturbed pycnocline depth is of order 125–150 m in that region of the ocean, waves having amplitudes of the order of the pycnocline depth can be generated by the lee-wave process. Such large amplitudes are accompanied by an appreciable nonlinear increase in phase speed, according to Eqs. (18). The observations of solitons with amplitudes up to 60 m were made by Pinkel in 1999 (see in Duda and Farmer⁷) during the TOGA-COARE experiment in the Western Pacific. Large waves have been detected in the areas of the Guiana Basin in Western Atlantic and of the Mascaren Ridge in Indian Ocean. The “champion” internal solitary

wave (ISW) of 120 m amplitude has apparently been observed in the Strait of Gibraltar by Bryden in the unpublished Cruise Report in 1998.

Detailed observations and analysis of solitary internal wave dynamics in the Sulu Sea were carried out by Apel *et al.*⁶¹ Some 14 days of measurements were made with current meters and thermistors at three locales along the direction of wave propagation, which had been determined earlier using satellite imagery (Fig. 12). Shipborne instruments, including radar, optical, and acoustic sensors, were also used to follow wave packets from their birth at a sill at the southern entrance to the Sulu Sea to their decay approximately 400 km across the sea. A tidal generation process was established during which (1) the tide initially produces a complex hydrodynamic perturbation at the sill; (2) the disturbance gradually becomes steeper as it propagates into deep water; and (3) the perturbation then forms into a soliton, i.e., an undulatory bore that becomes fully modulated into a group of several solitons by the time the packet reaches a distance of 200 km from the source region. At that distance, the modal differences in velocity of propagation [see Eq. (9)] have caused a separation of the internal waves by mode to have taken place, with only mode $n=1$ being observed at larger distances (although higher-order modes are detected closer to the source). Measurements of density, currents, and shear flow profiles allowed the evaluation of the coefficients of the solitary wave equations, Eqs. (17) and (18), or the like.

In the subsequent publications, the authors modeled these waves by a modified form of the JKKD equation that is similar to Eq. (36), but with modifications for cylindrical spreading and Reynolds-type dissipation [as in Eq. (40)]. They calculated the evolution of a wave packet over distances from 90 to 200 km using as the initial data the registered wave perturbation at the point located 90 km away from the source. To fit numerical and observational data for the 200-km site, the authors used an empirical value of the coefficient of horizontal eddy viscosity $A_h=10 \text{ m}^2/\text{s}$ and obtained fairly good agreement between the theoretical/numerical and experimental results. The calculations clearly demonstrate how the soliton packet evolves out of the initial disturbance into a rank-ordered train of pulses that decay in both amplitude and wavelength toward the rear of the group. Figure 13 shows a comparison of the phase speeds of 18 solitons in the Sulu Sea with the theoretical JKKD model [cf. Eq. (39)]; the dependence appears to be in accord with the theory. Such comparisons form quite reasonable tests of the soliton character of the waves.

Numerical models show that in addition to the tidally generated solitons which are formed near the continental shelves and which then propagate toward shore, a well-defined internal soliton packet that propagates into deep water can be generated. Some studies (e.g., Pingree *et al.*⁶³) suggest that the shelf-break generation process also launches an offshore-traveling disturbance that propagates down to the bottom, then reflects/refracts upward, and finally reappears near the surface a few hundred kilometers out to sea. If such generation actually occurs in nature, then the continental shelves can be considered to be global sources of deep-water internal waves. Indeed, the generation process is likely to be

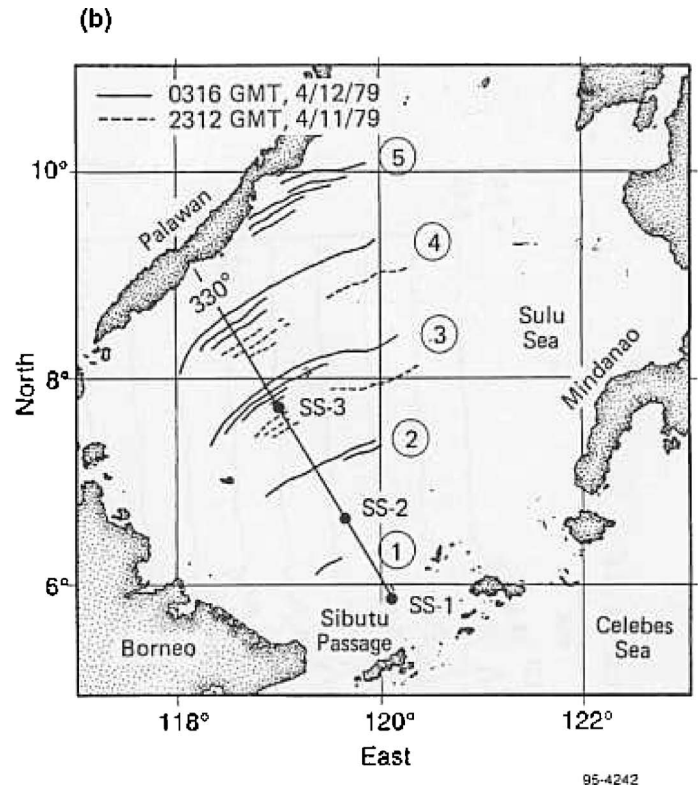
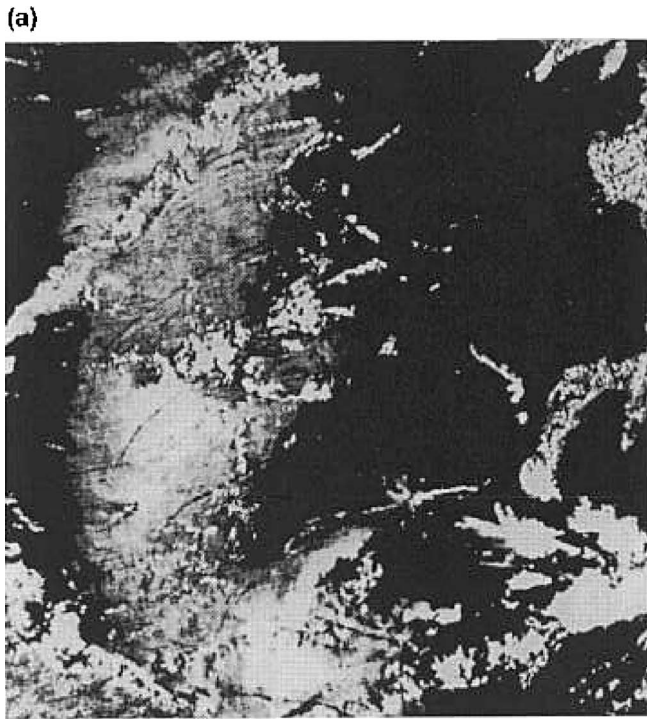


FIG. 12. (a) Internal solitons in the Sulu Sea in the Philippines' area, as observed with the Defence Meteorological Satellite, and seen in reflected sunlight. Borneo is at lower left. Visible are five packets of solitons generated by tidal action in the Sibutu Passage. (b) Schematic of phase fronts in frame (a) as observed on two consecutive days in 1979. Current meter moorings were emplaced at SS-1, SS-2, and SS-3 during 1981. From Apel *et al.* (see Ref. 61).

as widespread as is the combination of bathymetry, stratification, and current flow. If this is true, as it appears to be, then the entire rim and island population of an ocean basin can be sources of internal waves.

The energy in such internal waves ultimately derives from the rotational energy of the Earth-Moon-Sun system. Observations of the decay of orbital parameters, as well as measurements of solid-Earth tidal dissipation and bottom friction acting on oceanic tides in shallow seas, suggest that ocean tides by themselves are insufficient to account for the energy loss. Estimates of internal wave dissipation made using Seasat SAR data suggest that perhaps 5%–10% of the changes in the rotational energy budget could be attributed to internal wave excitation; thus it appears that this process can provide a small but significant fraction of the missing energy. Although this problem is beyond the scope of this paper, it is amusing to consider that space-based observations of events occurring beneath the sea and which have subtle surface signatures should yield information relevant to celestial mechanics.

A brief compilation of sightings of internal waves thought to be solitons is shown in Fig. 14. The signatures have been recorded by *in situ* sensors and, in some cases, observed and photographed simultaneously from aircrafts or satellites. The updated information on intense internal waves registered from satellites and the map of their sightings is presented in the Internet Atlas by Jackson and Apel.⁸ The global nature of the sightings demonstrates the widespread occurrence of intense internal waves and, among them, internal solitons and their trains—solibores. Note that the major-

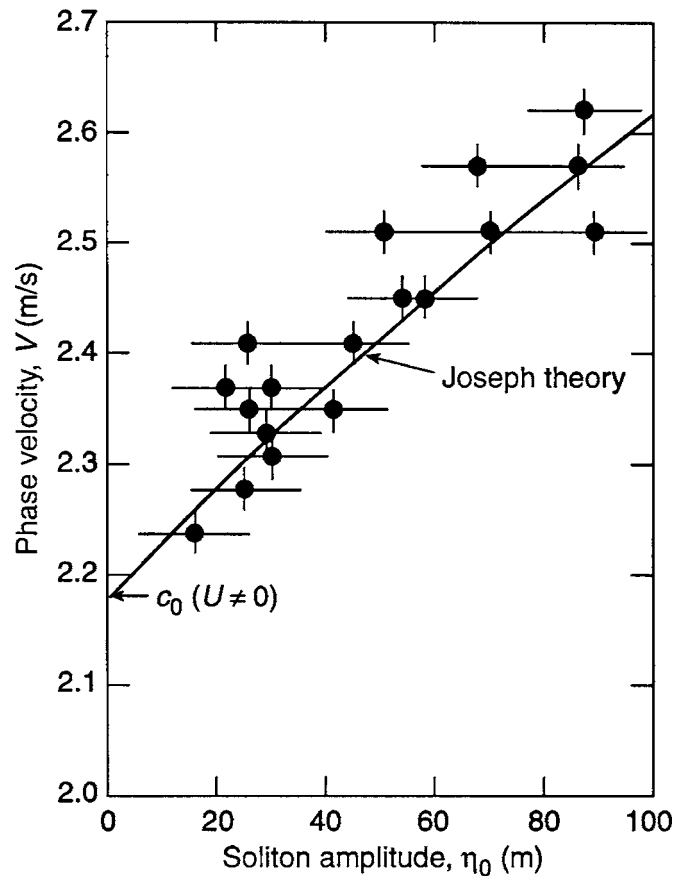


FIG. 13. Experimental versus theoretical phase speeds for solitons in the Sulu Sea. From Apel *et al.* (see Ref. 61).

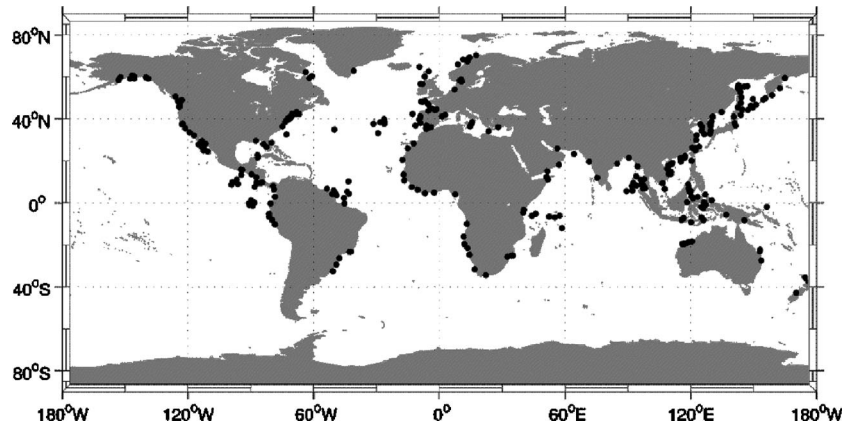


FIG. 14. Map showing sites where internal solitons have been reported (courtesy of Jackson).

ity of data reflected on the maps concerns primarily coastal zones and adjoin parts of deep ocean areas. Apparently, this confirms an important role of shelf breaks in the formation of intense nonlinear IWs.

C. Surface signatures of internal waves

The visibility of internal waves at the surface is due to the modification of the quasidequilibrium surface wave vector spectrum, $\Psi_{\text{eq}}(\mathbf{k})$, by the subsurface currents in the IW, to form a perturbed, nonequilibrium spectrum, $\Psi(\mathbf{k}; \mathbf{x}, t)$. In general, this spectrum depends on a number of parameters such as currents, wind, the presence of surfactants, long surface waves, etc. As a result, the problem of surface wave modulation is not completely solved yet. Detailed discussion of this problem is beyond the scope of this paper. Below we give only a short outline of some mechanisms forming the surface signatures of internal waves.

In the majority of cases, the basic motion affecting surface waves is the horizontal velocity of the IW current near the surface. This current changes the wave number and, generally, the energy of surface waves. The commonly used description of the modulation processes is grounded in the equation for the conservation of the wave action spectrum.^{10,64} The wave action spectral density, $N(\mathbf{k}, \mathbf{x}, t)$, is wave energy density per unit surface area divided by the Doppler frequency of the wave, $\omega_D = \omega - \mathbf{k} \cdot \mathbf{U}$, where \mathbf{U} is the horizontal current velocity at the surface. The balance equation for action spectral density can be derived from the Lagrangian description or from the energy density balance equation for surface waves.¹⁰ In the “relaxation time” approximation it states that the action spectrum changes along characteristics in (\mathbf{k}, \mathbf{x}) space according to

$$\frac{dN(\mathbf{k}, \mathbf{x}, t)}{dt} = \frac{\partial N}{\partial t} + \nabla_{\mathbf{k}} N \cdot \frac{d\mathbf{k}}{dt} + \nabla_{\mathbf{x}} N \cdot \frac{d\mathbf{x}}{dt} = - \frac{N(N - N_{\text{eq}})}{\tau}, \quad (69)$$

where $N_{\text{eq}}(k)$ is the equilibrium action density, and τ is the surface wave relaxation time, a phenomenological measure of how long a perturbed wave spectrum takes to relax back to its equilibrium state depending on the wind stress;⁶⁵ note that some models take N_{eq}^n with $n > 1$ which implies a sharper dependence of the process on wave am-

plitude. This equation may be integrated along its characteristics to describe perturbations of the surface wave spectrum (see, e.g., Hughes⁶⁵ for a treatment of the corresponding effects).

The signatures of strong internal waves can be considerably enhanced by the effect of “group synchronism,” when the phase velocity of internal wave is close to the group velocity of the surface waves responsible for the formation of radar and optical images.⁶⁶ This is because the phase speeds of the internal wave solitons are typically dozens of cm/s (sometimes over 1 m/s), with the corresponding wavelengths for surface waves lying between several decimeters and few meters. These waves, in turn, can affect the shorter gravity-capillary waves (cascade modulation).

For weakly nonlinear internal waves the solution of the action Eq. (69) without relaxation ($\tau \rightarrow \infty$) shows that the wave intensity is distributed according to the “strain rate,” $\partial u / \partial x|_{z=0}$. This strain rate causes alternating compressive and tensile effects on the surface wave spectrum, rendering the internal waves visible on the ocean surface as roughness changes.

As an example, Fig. 15 shows internal solitary waves in the New York Bight via (a) their surface signatures in a SAR image, (b) *in situ* current meter measurements made simultaneously with the SAR image, and (c) theoretical cross-sectional modulations computed using the formalism mentioned above.⁶⁷ The agreement between observation and theory is quite good, as may be seen by comparing the solid and dotted lines in Fig. 15.

For strongly nonlinear waves, however, the result can be quite different. For such solitons Bakhanov and Ostrovsky (2002) have shown that, instead of the strain rate maxima, the decrease of surface wave intensity (slicks) can shift toward the soliton peak (maximal depression) that is in agreement with the COPE observations mentioned above. Indeed, in Kropfli *et al.*,⁵⁸ the variations of scattering intensity and isotherm displacements were plotted together to show that for the strong solitons, the scattering minima are from the soliton peaks (Fig. 16). Note that a similar effect can be produced due to surfactant modulation by the IW current.

In all these cases, alternating regions of enhanced and diminished surface wave spectral density occur, i.e., regions that are rougher and smoother than the average. Electromag-

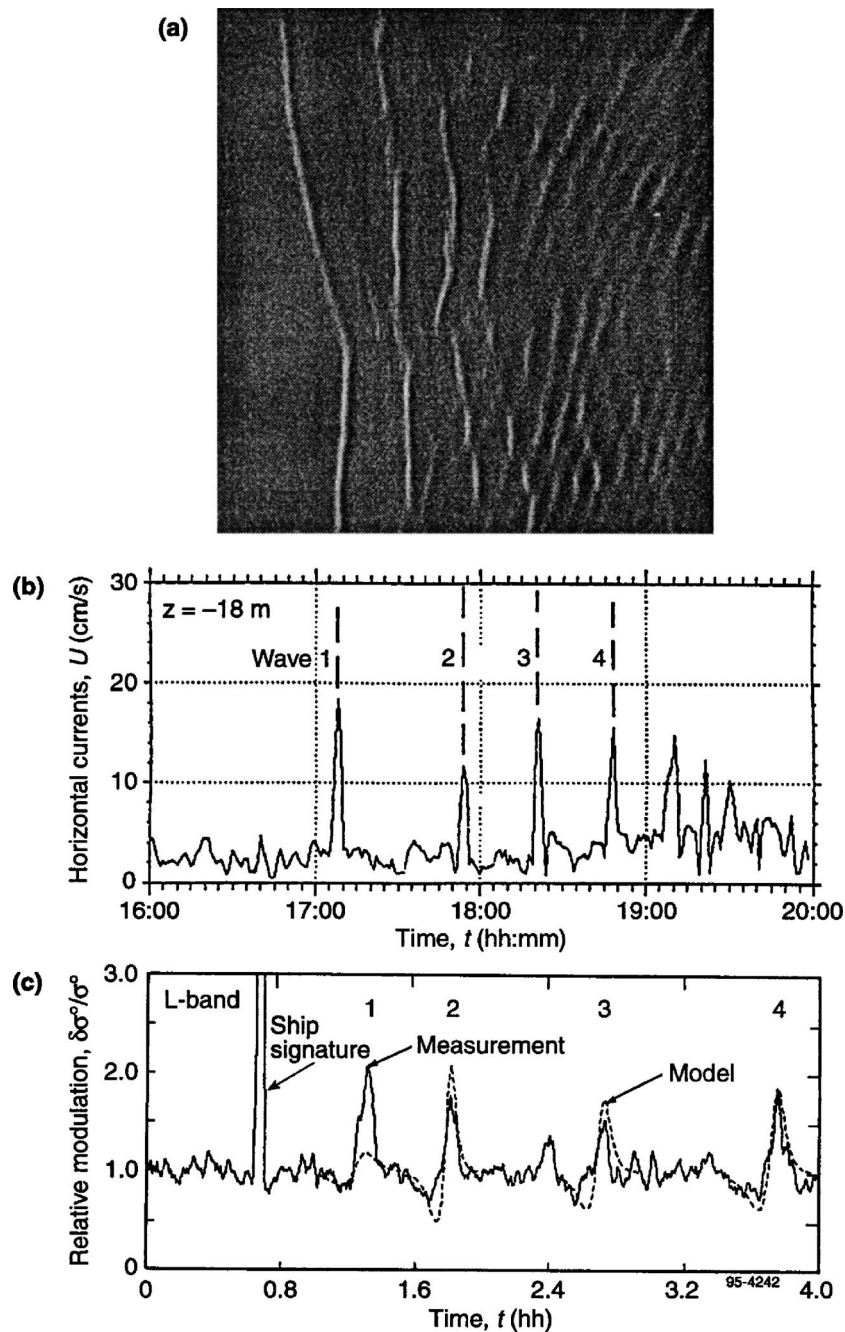


FIG. 15. (a) Internal solitons in the New York Bight as observed with SAR from Environmental Research Institute of Michigan flown on Canadian CV-580 aircraft. (b) In situ current measurements of internal wave packet in frame (a). (c) Fractional modulations of waves in radar image, comparing observation and theory of Eq. (69). From Gasparovich *et al.* (see Ref. 67).

netic radiation incident on the surface is thus scattered differentially by the rough and smooth portions, and an image constructed from such scattered radiation—say a photograph made in visible light or a radar image—will map the roughness variations. This map mainly mirrors the underlying internal currents.

Even more complex situation occurs for short gravity-capillary waves when the wind relaxation cannot be neglected. In this case the IW modulates air flow stress in the lower atmospheric boundary layer which, in turn, affects wave amplification by wind. Whereas the action of long surface waves on the low atmospheric boundary layer has been a subject of a number of papers, the effect of internal soliton

wavetrain on short surface waves via the wind perturbations has been considered in comparatively few publications.⁶⁸

Finally, internal waves can affect generation of ripples at the crests of longer gravity waves (“parasitic ripples”). This process is important when the gravity wave amplitude is close to its breaking value where the wave crest has a large curvature.⁶⁹ Due to the sensitivity of ripple generation to the curvature, even for a slight modulation of the “primary” long wave by the IW current, the ripple amplitude can change radically. This version of cascade modulation (IW → longer gravity wave → ripples) was observed in laboratory and described theoretically, for references see Charnotskii *et al.*⁷⁰.

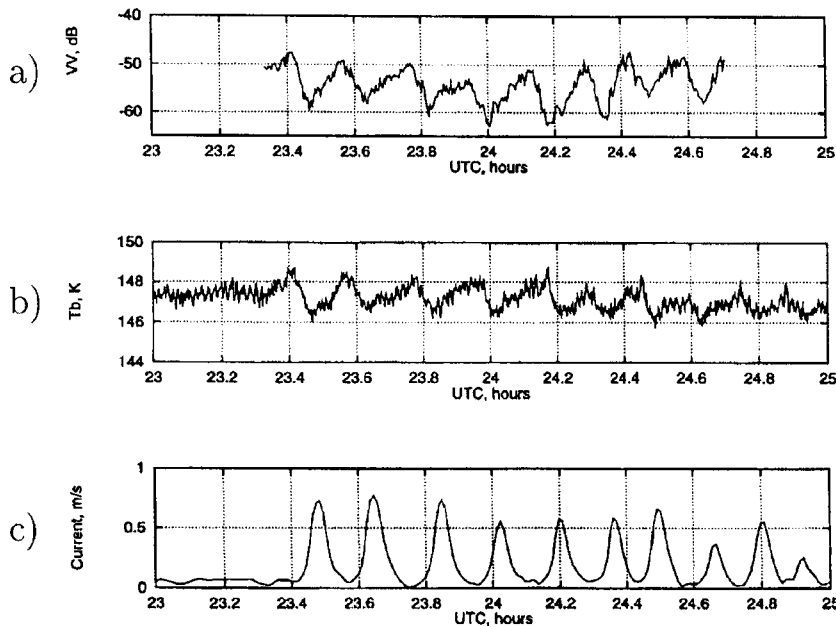


FIG. 16. Temporal records of (a) normalized radar cross-section at vertical polarization, (b) 37-GHz brightness temperature, and (c) current at 4.4 m depth for September 25–26, 1995. From Kropfli *et al.* (see Ref. 58).

V. EFFECTS OF NONLINEAR INTERNAL WAVES ON SOUND WAVES IN THE OCEAN

From the point of view of ocean acoustics, nonlinear internal waves are important scatterers of sound. This scattering is highly frequency dependent, unsurprising given the broad range of the scatterers scales. We first define what frequency bands are of interest. Based on experience, we consider three frequency bands: high frequency ($f \geq 50$ kHz), mid frequency ($1 \text{ kHz} \leq f \leq 50 \text{ kHz}$), and low frequency ($f \leq 1 \text{ kHz}$).

In the high frequency band, medium attenuation limits sound propagation to ranges on the order of a few meters to a kilometer. Thus for sonars at high frequencies, the monostatic backscatter geometry is found to be the most useful. Using high frequency sound also allows one to image an ensonified object with good resolution. In the past few decades, high frequency acoustic scattering has been used successfully for imaging the detailed structure of nonlinear internal waves. Such images have provided information on various parameters of the internal waves, including: snapshots of the detailed spatial structure of individual solitons; the space-time evolution of solitons, including their generation, propagation, dispersion, broadening by bathymetry changes, inversion at the so-called “critical depth;” and the dissipation of solitons via turbulent processes and wave breaking.

High frequency acoustic images also give views of how material such as sediment and biota are carried by the waves, which is important since these waves can provide non-zero mean transport of a “tracer” due to their nonlinearity. In terms of the acoustics problem for high frequency scattering by nonlinear internal waves, there are still a number of loose ends. Specifically, there is a well known, yet continually nagging problem of determining which tracer of the internal wave has scattered the acoustic signal. Is the scattering due to sound speed or density structure, biota, bubbles, or sediment? These tracers all highlight different parts of the internal wave, and if one is doing imaging, it is obviously neces-

sary to know what one is imaging. Moreover, one is also often interested in the tracers themselves; for example, one might like to know what type and size of biota are being carried along by the wave. The literature on high frequency scattering, while reasonably developed, is not yet overly extensive. We would refer the reader to the work of Farmer and Armi⁷¹ as one of the representative samples of this literature, from which one can find references to other work in the field.

Scattering of sound from internal waves at medium frequencies is, at this point in time, an under-developed area of research. The Strait of Gibraltar tomography study by Tiemann *et al.*^{72,73} is perhaps the most detailed look at scattering of midfrequency sound by internal soliton trains reported in the literature. Using frequency modulated sweeps from 1136 to 3409 Hz, the two transmission paths considered, of 14.6 and 20.1 km length, provided a “raypath-averaged” view of the solitons, from which the researchers were able to understand how tidal cycle variability affected both the internal wave wave field and its acoustic effect. The effects of ISW on medium frequency acoustics have also been seen in “acoustic navigation nets” working at 8–13 kHz, and Hedrick and Lynch⁷⁴ report significant travel time fluctuations of short paths (hundreds of meters to a kilometer) due to nonlinear internal waves. Henyey and Ewart and their collaborators looked at kilometer scale transmissions in shallow water at midfrequencies, only using moored towers to constrain observation of the energy to the water column.

Still, the corresponding literature is rather sparse. This paucity of results should not continue indefinitely, however, as there are good reasons to look at the scattering of midfrequency sound by internal solitary waves. For instance, if one is interested in the turbulence generated both in a nonlinear internal wave and in its wake, which could have scales from centimeters to tens of meters, looking for resonance Bragg scattering from midfrequency acoustics, which has the same span of wavelengths as the turbulence, might be a viable method. Short range tomography at mid-frequencies, which has been explored by Yamaoka *et al.*,⁷⁵ is also an interesting

possibility. Experiments which will look at midfrequency propagation and scattering in the midst of a strong internal wave field are being planned at present, so that it is probably just a matter of time before the literature in this area will expand.

By far the largest amount of research on the scattering of sound by internal solitary waves has been done in the low frequency regime, and in shallow water, where we operationally define shallow water to be the region from the tidal mixing front (≈ 30 m) to the continental shelf break (≈ 200 m). In shallow water, there is a well known “optimal” frequency of propagation, on the order of a few hundred Hertz, at which one sees a minimum in propagation loss.⁷⁶ This optimal transmission characteristic makes low frequency an ideal band for shallow water sonar systems. Since the continental shelves are also the home to a plethora of nonlinear internal waves, it becomes inevitable that the interaction between the sound waves and ocean internal waves is strongly observed.

When examining, the interaction of sound with the coastal soliton field, there are a number of different issues to address. First, we note that we must treat both the amplitude and phase of a scattered signal. This can to some extent be done separately, as the scattering characteristics for these two basic quantities are often independent, at least to first order. Also, in treating these variables, we further note that the most common acoustic measurements are of intensity and pulse travel time fluctuations, two secondary quantities, rather than of the amplitude and phase directly. Another important consideration in looking at the acoustic scattering by internal waves is that the acoustic scattering is very different for source-to-receiver geometries which go across the wave fronts of the internal wave packets as opposed to those geometries which are along the IW wave fronts. We will examine this next, in the context of acoustic normal mode theory, which is a natural and physically insightful descriptor for low frequency, shallow water sound. We will use two-dimensional (2D) range dependent mode theory here for notational simplicity, noting that a fully three-dimensional (3D) treatment of the acoustic field is needed for some of the effects we will discuss.

When dealing with a range dependent ocean acoustic waveguide, the Helmholtz equation is nonseparable; however, a variant of the usual separation of variables technique, called “partial separation of variables,” can be employed. Specifically, the range dependent Helmholtz equation is

$$\nabla^2 \psi(r, z) + k^2(r, z) \psi(r, z) = 0, \quad (70)$$

where z is the vertical coordinate, r is the horizontal range, $\psi(r, z)$ is the range dependent normal mode field, and $k(r, z) = \omega/c(z, r)$ is the total wave number, which carries within it the description of the range-dependent sound speed of the ocean.

For this case, we stipulate the partially separable (modal) solution:

$$\psi(r, z) = \sum_n R_n(r) \phi_n(r, z). \quad (71)$$

Inserting this solution into Eq. (70) results in a “local normal mode” equation

$$\left[\frac{\partial^2}{\partial z^2} + k^2(r, z) - k_n^2 \right] \phi_n(r, z) = 0 \quad (72)$$

and a set of coupled equations for the radial part of the solution

$$R_m''(r) + \frac{1}{r} R_m'(r) + k_m^2(r) R_m(r) = - \sum_n \left[A_{mn} R_n + B_{mn} \left(\frac{R_n}{r} + 2R_n' \right) \right], \quad (73)$$

where the prime signifies a range derivative and

$$A_{mn} = \int_0^\infty \rho(z) \phi_m(z, r) \phi_n''(z, r) dz \quad \text{and} \\ B_{mn} = \int_0^\infty \rho(z) \phi_m(z, r) \phi_n'(z, r) dz \quad (74)$$

are the mode coupling coefficients.

These “coupled mode equations” are well known in ocean acoustics, and so we will just refer the reader to some of the standard texts if more information is desired about them.^{76,77} The solutions to these equations are usually generated numerically, via codes like the well-known KRAKEN code.

It is worth noting the details of the weakly range dependent solution to the coupled mode equations, obtained by setting the A_{mn} and B_{mn} terms of Eq. (73) equal to zero. In this limit, the so-called “adiabatic mode” solution for pressure is as follows:

$$p(z, r) \sim \psi(z, r) = C \sum_m \underbrace{\frac{\phi_m(z_s) \phi_m(z_r)}{\sqrt{\int_0^R k_m(r) dr}}}_{\text{amplitude}} \underbrace{\exp \left\{ i \int_0^R k_m(r) dr \right\}}_{\text{phase}} \times \underbrace{\exp \left\{ - \int_0^R \alpha_m(r) dr \right\}}_{\text{attenuation}}. \quad (75)$$

This particular modal solution is germane to propagation along the internal wave front, where the range dependence of the medium parameters is slow, so that the coupling coefficients remain small. The adiabatic solution clearly shows how the variability of the ocean medium (in our case the internal waves) produces amplitude and phase (and thus travel time) fluctuations. For amplitude, the passage of the internal waves over the source and receiver positions produces a distortion of the normal modes at those positions, which thus changes the received pressure $p(z, r)$. For phase, $k_m(r)$ varies over the source to receiver range, which changes the phase, is $\phi_m = \int_0^R k_m(r) dr$. Such adiabatic amplitude and

phase fluctuation effects are well known and have been examined in detail for the case of surface gravity waves.

For the coupled mode (across the IW crest) propagation case, we get both the adiabatic effects noted above (since the adiabatic solution is, in essence, the lowest order coupled mode solution) as well as some additional effects. In the case of strong range dependency (i.e., large $\partial c_s(z, r)/\partial r \rightarrow$ large, where c_s is the sound speed in the water column and “large” means of the order of 10 m/s per km or more, the same order as the deep ocean vertical sound speed change), the normal modes exchange energy along the source-to-receiver track. This leads modal arrivals at a distant receiver which have shared characteristics of the modes along the path. As an example, consider the travel time of a mode one upon arriving at a receiver (assuming we can filter the signal so as to identify modes) in a waveguide that only supports two modes. For the case of no coupling, mode one arrives at its expected travel time, i.e., $t_1 = R/v_1^G$. However, with coupling, the mode one arrival can start out in mode two, travel to a point x where it encounters a soliton and couples into mode one, and then continues propagating to the receiver as that mode. This “coupled mode one” has the arrival time $t_1^{\text{CP}} = x/v_2^G + (R-x)/v_1^G$, which is intermediate between the uncoupled mode one and mode two arrival times. It is easy to see that, if there are scatterers densely distributed along the source-to-receiver path, one will see a mode one arrival which is spread out in time between the usual mode one and mode two arrival times. This “time spreading” is a well known phenomenon in shallow water pulse propagation, where the coupled mode arrival spreads between the arrival times of the fastest and slowest uncoupled modes.

Turning to soliton induced coupled mode effects on amplitude, it is found that the biggest contribution to amplitude fluctuation is caused by the difference in medium attenuation for different modes (or “differential attenuation”). In general (though exceptions can be found), the low-order trapped acoustic modes attenuate slowly, whereas the higher order trapped modes (and certainly the continuum modes) attenuate far more quickly, due to enhanced boundary interaction. Thus, if a low mode couples to a high mode, more propagation loss is seen—the opposite is true for a high mode coupling to a low mode.

We next look at ISW sound scattering effects on phase and travel time. “Pulse wander,” which is the variation in arrival time of a pulse with no change in the shape of the pulse, is mathematically the frequency derivative of the phase (fluctuation) integral shown in Eq. (75). It has been shown that pulse wander effects are significantly larger for along IW wave front propagation than for across wave front, an effect which is readily understood by examining the phase integral in Eq. (75). The integrand of that integral oscillates quickly and largely cancels for across IW wave front propagation, whereas it is relatively constant along an IW wave front. The wander also shows a distinct mode number dependence, which is associated with where the acoustic mode vertical turning points are located in relation to the maximum amplitude points of the internal wave modes (which are usually dominated by mode one, as previously discussed). Wander effects for path lengths of 25–50 km at frequencies of

100–500 Hz tend to be of order 10 ms (or less) along IW wave fronts, and about 1 ms (or less) across the wave fronts.

The travel time spread, which is caused by the mode coupling due to across IW wave front propagation, shows an interesting effect which has been dubbed “near receiver dominance.” Specifically, when an internal wave or packet of internal waves is between an acoustic source and receiver, and moreover when especially it is close to the receiver, then the time spread seen is a maximum. The explanation for this is easily seen by taking the limit $x \rightarrow R$ in our previous two mode simplistic example. In this limit, the arrival time difference between the undisturbed mode one and the coupled mode one is a maximum. This spreading effect was clearly seen in the 1995 SWARM experiment by Headrick and Lynch,⁷⁴ who showed an M2 tidal signal in the spread of pulsed signals due to the passage of the nonlinear internal tide by the receiver.

Let us return to the acoustic amplitude scattering effects of the internal waves. We will first look at the across IW wave front propagation geometry, simply because that was the geometry that was first examined experimentally and theoretically, and is better understood at this point in time. Undoubtedly the best known shallow water acoustics experiments on sound scattering by internal waves are the Yellow Sea series of experiments reported by Zhou *et al.*⁷⁸ In these experiments, Zhou reported seeing anomalously high propagation losses versus frequency, up to 30–40 dB, a huge amount. These anomalous losses were attributed to resonant Bragg scattering from a strong internal wave train with evenly spaced internal wave solitons. (This is not the usual soliton wave train one sees, but it is what exists in the Yellow Sea.) Resonant scattering occurs when projection of the IW wavelength along the acoustic path, Λ_{IW} , is equal to the acoustic mode interference distance (commonly called the “mode cycle distance”), Δ_{mn} , where $\Delta_{mn} = 2\pi/(k_m - k_n)$. The internal wave train then acts as a two-dimensional Bragg crystal lattice, which gives both frequency and azimuth dependence to the scattering field. At resonance, the predominantly lower mode energy created at the source was transferred to higher modes, which then attenuated more quickly, thus greatly increasing the total energy losses reported. (We again note that the opposite effect from this can happen, depending upon the depth of the source relative to the stratification of the ocean. If the source is in warmer, higher sound-speed water, higher acoustic modes are preferentially excited at the source. IW coupling then transfers much of their energy to the low modes, which decay more slowly, producing less loss.) This resonance mechanism is a robust and easily understandable one. Moreover, it can be generalized to nonregularly spaced internal wave trains, simply by examining the spatial wave number spectrum of a soliton wave train, and then matching these wave number components to the acoustic mode cycle distances. Preisig and Duda⁷⁹ have shown, via numerical simulations, the details of a second mechanism for strong scattering, specifically the resonance of pairs of acoustic modes with the widths of the individual solitons. This mechanism is universal and is, in fact, a more detailed version of the Bragg mechanism just discussed. Since strong IW scattering mechanisms exist in

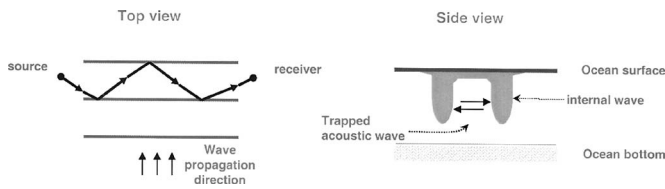


FIG. 17. Ducting of sound between internal waves.

nature, substantial across-wave front, coupled mode acoustic scattering is the rule, rather than the exception.

Next we come to propagation along IW wave front. This topic has been explored mostly theoretically, though recent experimental data has confirmed some of the theory. An interesting geometry which recently has been considered is the “along IW wave front” geometry shown in Fig. 17. This creates “horizontally ducted propagation” of acoustic normal modes between internal wave solitons. Two neighboring solitons in a wave train create high sound-speed regions, with a comparatively low speed region in between. This creates a horizontal duct (in the x - y plane) for each vertical acoustic normal mode. The detailed scattering by this duct was predicted via the theory and computer modeling and recently has seen a striking confirmation in the SWARM experimental data taken by Badiey *et al.*^{80,81} This ducting effect is a strong one, easily producing 6–8 dB level increases in low frequency, broadband transmissions. Moreover, since this is a fully three-dimensional effect, the focusing of energy gives amplitude fluctuations over and above the 5.6 dB that one expects from saturated normal mode multipath interference in two dimensions (in the x - z plane). Additionally, the description of such propagation requires fully 3D theory and numerics, and goes beyond the scope of the simple 2D equations presented previously.

There are two additional “along-internal-wave front” scattering effects that have been theoretically predicted, though not yet unambiguously observed. They are the so-called “Lloyd’s mirror”⁷⁷ and “whispering gallery mode” effects. In the first effect, one sees the interference between a direct arrival and a totally internally reflected arrival which has been glancingly reflected off an internal wave or the leading edge of a packet of internal waves. The second effect, the whispering gallery effect, is somewhat more complicated. To begin with, sound propagating along-shelf is being refracted seaward by seaward sloping bathymetry. Then internal waves just seaward of the acoustic paths reflect the acoustic energy back in the shoreward direction, given small grazing angle incidence. This results in the sound being trapped between the slope pushing it seaward and the IWs reflecting it shoreward. It is the ocean acoustic analog of a whispering gallery except that the curved rays act like the curved walls of a whispering gallery, whereas the IWs act as the wall reflector. This effect may have in fact been observed (though from a front, not internal waves) via the enhanced noise level at a receiver in the SWARM experiment; however, this evidence is preliminary at best, and detailed experiments are needed to verify this.

To conclude, we note that further oceanographic measurements of nonlinear internal waves are needed to better

understand the scattering of acoustic signals. To begin with, the fully 3D structure and evolution of internal wave trains in range variable bathymetry and hydrology needs to be understood, as this defines the basic scattering entity. Second, the turbulence generated by the nonlinear internal waves needs to be better measured, as it also promises to be important to midfrequency acoustic scattering. Finally, the relative strength of the coastal nonlinear versus linear internal wave field needs to be described, as both species of waves can be important to acoustic scattering.

VI. CONCLUDING REMARKS

In this review paper we tried to outline different aspects of ISWs including theoretical models, field data, and the ISW action on acoustic wave propagation. Natural observations confirm that intense ISWs or their trains (solibores) do exist both in shallow and deep ocean areas, and in many cases their parameters are close to those predicted theoretically. There is not only academic interest to ISWs: they are able to provide strong vertical mixing, transport particles, affect turbulence and biological life, and even possibly interfere with underwater navigation. They affect surface waves, thus creating surface “slicks” that are visible by optical devices and radars and sometimes by naked eye. They influence propagation of acoustic signals in water and may form specific conditions for ducting sound waves.

Intensive theoretical and observational studies over the last decade have confirmed that ISWs are a widespread phenomenon throughout the oceans, especially in coastal zones where they are generated by barotropic tides. They probably absorb a noticeable part of the total tidal energy. Internal solitons are, so to say, the “extremes” of the internal wave spectrum, their magnitudes possibly reaching many dozens of meters. They may be at least partially responsible for the fact that the IW spectrum in upper ocean differs from the Garrett–Munk spectrum characteristic of deeper water layers (the main thermocline area).

In spite of an impressive recent progress in studies of ISWs, some important questions remain unanswered or at least not completely clear. One of them is how the ISW are generated in the ocean. The main source of oceanic ISWs is apparently internal tides. However, the relative roles of specific mechanisms in their formation (shear-flow induced lee waves, scattering of barotropic tides by bottom features), as well as the Earth’s rotation, etc., that are discussed in literature, are not clear in many cases. Also the energy sinks for solitons (dissipation, scattering on bottom roughness, etc.) are also not always known quite well.

Another problem is the ISWs propagation along inhomogeneous paths, e.g., onshore propagation from the shelf break zone. There exist a number of theoretical models for these processes, especially for weakly nonlinear waves described by the KdV or KP equations with slowly varying parameters. Experimentally, however, most *in situ* observations cover one or, in few cases, two observation points, with little knowledge of what occurs at other points.⁸⁴ On the other hand, remote observations from aircraft and satellites can provide a panoramic pattern of the surface slicks but

without detailed *in situ* data. Some exceptions have been described above.

Other questions relate to statistical properties of solitons: where are most active zones of soliton generation located, what are the typical and extreme parameters of solitons in different areas, and, in cases when solitons are randomly distributed, what are their statistical and spectral characteristics. We already mentioned the Atlas of solitons available on the Internet, but it only describes several typical areas; perhaps a more comprehensive atlas could be created in the form of a map like that shown in Fig. 14 but much more detailed.

And certainly the numerous possible mechanisms of ISW interaction with the electromagnetic and acoustic fields must be better understood: indeed, the interpretation of remote sensing data crucially depends on the corresponding models.

Finally, the action of ISWs on other processes such as, e.g., biological life in upper ocean and shallow seas, has not been sufficiently addressed yet; this is a very promising and practically important area of oceanography.

Nonetheless, from we already know, we can arguably state that ISWs are the most regularly and clearly observed kind of solitons in natural conditions! One can foresee much further progress in this area of theoretical and experimental oceanography.

ACKNOWLEDGMENTS

The authors are indebted to A. Newhall for his enormous help with the manuscript preparation for publication. The authors are also thankful to E. Pelinovsky and V. Shrira for useful advice and discussions of some aspects of this review. This work was funded in part by the U.S. Office of Naval Research under Contract Nos. N00014-04-10146 and N00014-04-10720.

¹J. R. Apel, L. A. Ostrovsky, and Yu. A. Stepanyants, "Internal solitons in the ocean," Report MERCJRA0695, Milton S. Eisenhower Research Center, APL, The John Hopkins University, 1995. This report was recently updated, and we refer the reader to "Internal Solitons in the Ocean" by J. R. Apel, L. A. Ostrovsky, Y. A. Stepanyants, and J. F. Lynch, Woods Hole Oceanographic Institution Technical Report WHOI-2006-4, January 2006.

²Notwithstanding the common definition of solitons as nonlinear pulses which remain unchanged upon interaction we shall use the name soliton for any stable, nondissipative (or weakly dissipative) solitary formations, not only for brevity but also because we (and a number of others) believe that even if solitary waves interact by emitting some radiation (as is typically the case in nonintegrable mathematical models), they still reveal the properties of a particle which, which is the reason for the term "soliton."

³L. A. Ostrovsky and Yu. A. Stepanyants, "Do internal solitons exist in the ocean?," *Rev. Geophys.* **27**, 293–310 (1989).

⁴M. J. Ablowitz and H. Segur, *Solitons and the Inverse Scattering Transform* (SIAM, Philadelphia, 1981).

⁵L. A. Ostrovsky and Y. A. Stepanyants, "Internal solitons in laboratory experiments: Comparison with theoretical models," *Chaos* **15**, 037111 (2005).

⁶J. R. Apel, "Linear and nonlinear internal waves in coastal and marginal seas," in *Oceanographic Applications of Remote Sensing*, edited by M. Ikeda and F. Dobson (CRC Press, Boca Raton, 1995).

⁷"The 1998 WHOI/IOS/ONR Internal Solitary Wave Workshop: Contributed Papers," edited by T. F. Duda and D. Farmer, Technical Report WHOI-99-07, 1999. See also <http://www.whoi.edu/science/AOPE/ISW98workshop/text/>. Last viewed 1/19/2007.

⁸C. R. Jackson and J. R. Apel, "An Internet atlas of internal solitary-like

waves and their properties. Global Ocean Associates," 2nd ed. (2004); <http://www.internalwaveatlas.com>

⁹Here the so-called traditional approximation is used, where only the vertical component of \mathbf{f} is taken into account, which is valid for long waves (see the references cited in this paragraph).

¹⁰O. M. Phillips, *The Dynamics of the Upper Ocean*, 2nd ed. (Cambridge University Press, Cambridge, 1977).

¹¹Yu. Z. Miropol'sky, *Dynamics of Internal Gravity Waves in the Ocean* (Gidrometeoizdat, Leningrad, 1981, in Russian); [Engl. transl.: (Kluwer Academic, Dordrecht, 2001)].

¹²The "nonhydrostatic" linear term $\rho_0 \partial w / \partial t$ in s_3 is small provided the wavelength is large in comparison with the vertical scale.

¹³L. A. Ostrovsky, "Nonlinear internal waves in a rotating ocean," *Okeanologia* **18**, 181–191 (1978), (in Russian); [Oceanology (Engl. Transl.) **18**(2), 119–125 (1978)].

¹⁴G. B. Whitham, *Linear and Nonlinear Waves* (Wiley-Interscience, New York, 1974).

¹⁵Note that surface wave solitons in natural basins or estuaries would always be humps and never depressions. However, capillary solitons on a surface of thin films may be of negative polarity, i.e., they may represent surface depressions. Such solitons were recently observed in laboratory experiments (see Ref. 83).

¹⁶R. Grimshaw, E. Pelinovsky, and O. Poloukhina, "Higher-order Korteweg–de Vries models for internal solitary waves in a stratified shear flow with a free surface," *Nonlinear Processes Geophys.* **9**, 221–235 (2002).

¹⁷This parameter is known in nonlinear wave theory as the similarity parameter of the KdV equation [see, e.g., Ablowitz and Segur (Ref. 4)]. In this paper we use the term "Ursell parameter" from the surface-wave terminology and apply it to the general water waves.

¹⁸J. R. Apel, "A new analytical model for internal solitons in the ocean," *J. Phys. Oceanogr.* **33**, 2247–2269 (2003).

¹⁹A. V. Gurevich and L. P. Pitaevskii, "Nonstationary structure of a collisionless shock wave," *Zh. Eksp. Teor. Fiz.* **65**(2), 590–595 (1973), (in Russian); [Engl. transl.: *Sov. Phys. JETP* **38**, 291–297 (1974)].

²⁰Ch.-Y. Lee and R. C. Beardsley, "The generation of long nonlinear internal waves in a weakly stratified shear flows," *J. Geophys. Res.* **79**(3), 453–457 (1974).

²¹T. G. Talipova, E. N. Pelinovsky, K. Lamb, R. Grimshaw, and P. Holloway, "Cubic nonlinearity effects in the propagation of intense internal waves," *Dokl. Akad. Nauk* **365**(6), 824–827 (1999), (in Russian); [Engl. transl.: *Dokl. Earth Sci.* **365**(2), 241–244 (1999)].

²²M. Funakoshi and M. Oikawa, "Long internal waves of large amplitude in a two-layer fluid," *J. Phys. Soc. Jpn.* **55**(1), 128–144 (1986).

²³R. Grimshaw, D. Pelinovsky, E. Pelinovsky, and A. Slunyaev, "Generation of large-amplitude solitons in the extended Korteweg–de Vries equation," *Chaos* **12**, 1070–1076 (2002).

²⁴H. Michallet and E. Barthélemy, "Experimental study of interfacial solitary waves," *J. Fluid Mech.* **366**, 159–177 (1998).

²⁵T. P. Stanton and L. A. Ostrovsky, "Observations of highly nonlinear internal solitons over the continental shelf," *Geophys. Res. Lett.* **25**(14), 2695–2698 (1998).

²⁶Yu. A. Stepanyants, "On the theory of internal surges in shallow basins," *Morskoi Gidrofizicheskii Zhurnal* **2**, 19–23 (1990), (in Russian); [Engl. transl.: *Sov. J. Phys. Oceanogr.* **2**, 99–104 (1991)].

²⁷It is also called the intermediate long wave (ILW) or finite-depth (FD) equation.

²⁸A. P. Nagovitsyn, E. N. Pelinovsky, and Yu. A. Stepanyants, "Observation and analysis of solitary internal waves in the coastal zone of the Sea of Okhotsk," *Morskoi Gidrofizicheskii Zhurnal* **1**, 54–58 (1990), (in Russian); [Engl. transl.: *Sov. J. Phys. Oceanogr.* **2**, 65–70 (1991)].

²⁹T. Gerkema, "A unified model for the generation and fission of internal tides in a rotating ocean," *J. Mar. Res.* **54**, 421–450 (1996).

³⁰This term is used for the version of KdV equation with transposed temporal and spatial variables t and x . Such equation is relevant to the analysis of time series measured by point sensors in fixed spatial places.

³¹R. Grimshaw, "Internal solitary waves," in *Environmental Stratified Flows*, edited by R. Grimshaw (Kluwer Academic, Dordrecht 2002); Chap. 1, pp. 1–27.

³²P. Holloway, E. Pelinovsky, and T. Talipova, "Internal tide transformation and oceanic internal solitary waves," in *Environmental Stratified Flows*, edited by R. Grimshaw (Kluwer Academic, Dordrecht, 2002), Chap. 2, pp. 29–60.

- ³³A similar behavior is known in nonlinear acoustics for weak shock waves having a sawtooth form.
- ³⁴J. S. Turner, *Buoyancy Effects in Fluids* (Cambridge University Press, Cambridge, 1973).
- ³⁵L. G. Redekopp, "Elements of instability theory for environmental flows," in *Environmental Stratified Flows*, edited by R. Grimshaw (Kluwer Academic, Dordrecht, 2002), Chap. 2, pp. 223–281.
- ³⁶Yu. A. Stepanyants and A. L. Fabrikant, *Propagation of Waves in Shear Flows* (NaukaFizmatlit, Moscow, 1996) (in Russian); [Engl. transl.: A. L. Fabrikant and Yu. A. Stepanyants (World Scientific, Singapore, 1998)].
- ³⁷An analogous situation occurs for electromagnetic and acoustic waves in waveguides.
- ³⁸It is also referred to in many papers as the Ostrovsky equation.
- ³⁹L. A. Ostrovsky and Yu. A. Stepanyants, "Nonlinear surface and internal waves in rotating fluids," in *Nonlinear Waves 3, Proc. 1989 Gorky School on Nonlinear Waves*, edited by A. V. Gaponov-Grekhov, M. I. Rabinovich, and J. Engelbrecht (Springer, Berlin, Heidelberg, 1990), pp. 106–128.
- ⁴⁰R. H. J. Grimshaw, L. A. Ostrovsky, V. I. Shrira, and Y. A. Stepanyants, "Long nonlinear surface and internal gravity waves in a rotating ocean," *Surv. Geophys.* **19**(4), 289–338 (1998).
- ⁴¹C. J. Amick and R. E. L. Turner, "A global theory of internal solitary waves in two-fluid system," *Trans. Am. Math. Soc.* **298**, 431–484 (1986).
- ⁴²J. Grue, A. Jensen, P. O. Rusan, and J. K. Sveen, "Properties of large amplitude internal waves," *J. Fluid Mech.* **380**, 257–278 (1999).
- ⁴³V. I. Vlasenko and K. Hutter, "Numerical experiments on the breaking of solitary internal waves over a slope-shelf topography," *J. Phys. Oceanogr.* **32**, 1779–1793 (2002).
- ⁴⁴K. G. Lamb, "Shoaling solitary internal waves: on a criterion for the formation of waves with trapped cores," *J. Fluid Mech.* **478**, 81–100 (2003).
- ⁴⁵V. I. Vlasenko, P. Brandt, and A. Rubino, "On the structure of large-amplitude internal solitary waves," *J. Phys. Oceanogr.* **30**, 2172–2185 (2000).
- ⁴⁶M. Miyata, "Long internal waves of large amplitude," in *Nonlinear Water Waves*, edited by K. Horikawa and H. Maruo (Springer, Berlin, 1988), pp. 399–406.
- ⁴⁷M. Miyata, "A note on broad narrow solitary waves," IPRC Report 00–01, SOEST, University of Hawaii, Honolulu, 00–05, 2000.
- ⁴⁸W. Choi and R. Camassa, "Long internal waves of finite amplitude," *Phys. Rev. Lett.* **77**, 1759–1762 (1996).
- ⁴⁹This reduction has been done in Ostrovsky and Grue (see Ref. 50); it was also demonstrated in this work that the set of Eqs. (59)–(61) is a straightforward result of the long-wave expansion of the Lagrangian suggested by Whitham (see Ref. 14) for surface waves.
- ⁵⁰L. A. Ostrovsky and J. Grue, "Evolution equations for strongly nonlinear internal waves," *Phys. Fluids* **15**, 2934–2948 (2003).
- ⁵¹H. Sandström and C. Quon, "On time-dependent, two-layer flow over topography. I. Hydrostatic approximation," *Fluid Dyn. Res.* **11**, 119–137 (1993).
- ⁵²A. V. Slunyaev, E. N. Pelinovsky, O. E. Poloukhina, and S. L. Gavriluyuk, "The Gardner equation as the model for long internal waves," in *Topical Problems of Nonlinear Wave Physics, Proc. of the Intern. Symp., Inst. of Appl. Phys (RAS, Nizhny Novgorod, 2003)*, pp. 368–369.
- ⁵³J. R. Apel and F. I. Gonzalez, "Nonlinear features of internal waves off Baja California as observed from the SEASAT imaging radar," *J. Geophys. Res.* **88**, 4459–4466 (1983).
- ⁵⁴J. R. Proni and J. R. Apel, "On the use of high-frequency acoustics for the study of internal waves and microstructure," *J. Geophys. Res.* **80**, 1147–1151 (1975).
- ⁵⁵M. H. Orr and P. C. Mignerey, "Nonlinear internal waves in the South China Sea: Observations of the conversion of depression internal waves to elevation internal waves," *J. Geophys. Res.* **108**(C3), 3064 (2003).
- ⁵⁶H. Sandström and J. A. Elliott, "Internal tide and solitons on the Scotian Shelf: A nutrient pump at work," *J. Geophys. Res.* **89**, 6415–6426 (1984).
- ⁵⁷M. V. Trevorrow, "Observations of internal solitary waves near the Oregon coast with an inverted echo sounder," *J. Geophys. Res.* **103**(C4), 7671–7680 (1998).
- ⁵⁸R. A. Kropfli, L. A. Ostrovsky, T. P. Stanton, E. A. Skirta, A. N. Keane, and V. Irisov, "Relationships between strong internal waves in the coastal zone and their radar and radiometric signatures," *J. Geophys. Res.* **104**(C2), 3133–3148 (1999).
- ⁵⁹D. M. Farmer and L. Armi, "The flow of Atlantic water through the Strait of Gibraltar," *Prog. Oceanogr.* **21**, 1–105 (1988); L. Armi and D. M. Farmer, "The flow of Mediterranean water through the Strait of Gibraltar," *ibid.* **21**, 1–105 (1988).
- ⁶⁰P. E. La Violette, T. H. Kinder, and D. W. Green III, "Measurements of internal waves in the Strait of Gibraltar using a shore-based radar," Report 118, Naval Ocean Research and Development Activity, Stennis Space Center, MS, 1986.
- ⁶¹J. R. Apel, J. R. Holbrook, J. Tsai, and A. K. Liu, "The Sulu Sea internal soliton experiment," *J. Phys. Oceanogr.* **15**, 1625–1651 (1985).
- ⁶²A. R. Osborne and T. I. Burch, "Internal solitons in the Andaman Sea," *Science* **208**, 451–460 (1980).
- ⁶³R. D. Pingree, G. T. Mardell, and A. L. New, "Propagation of internal tides from the upper slopes of the Bay of Biscay," *Nature (London)* **321**, 154–158 (1986).
- ⁶⁴J. R. Apel, *Principles of Ocean Physics* (Academic, London, 1987).
- ⁶⁵B. A. Hughes, "The effect of internal waves on surface wind waves; Theoretical analysis," *J. Geophys. Res.* **83C**, 455–465 (1978).
- ⁶⁶A. Ya. Basovich, V. V. Bakhanov, and V. I. Talanov, "Transformation of wind-driven wave spectra by short internal wave trains," *Izv. Akad. Nauk SSSR, Fiz. Atmos. Okeana* **23**(7), 694–706 (1987), (in Russian); [Engl. transl.: *Izv., Acad. Sci., USSR, Atmos. Oceanic Phys.* **23**(7), 520–528 (1987)].
- ⁶⁷R. F. Gasparovic, J. R. Apel, and E. S. Kasichke, "An overview of the SAR internal wave signature experiment," *J. Geophys. Res.* **93**, 12304–12316 (1988).
- ⁶⁸K. A. Gorshkov, I. S. Dolina, I. A. Soustova, and Yu. I. Troitskaya, "Modulation of short wind waves in the presence of strong internal waves: The effect of growth-rate modulation," *Izvestiya, Atmospheric and Oceanic Physics.* **39**(5), 596–606 (2003).
- ⁶⁹M. S. Longuet-Higgins, "Parasitic capillary waves: a direct calculation," *J. Fluid Mech.* **301**, 79–107 (1995).
- ⁷⁰M. Charnotskii, K. Naugolnykh, L. A. Ostrovsky, and A. Smirnov, "On the cascade mechanism of short surface wave modulation," *Nonlinear Processes Geophys.* **9**, 281–288 (2002).
- ⁷¹D. Farmer and L. Armi, "The generation and trapping of solitary waves over topography," *Science* **283**, 188–190 (1999).
- ⁷²C. O. Tiemann, P. F. Worcester, and B. D. Cornuelle, "Acoustic scattering by internal solitary waves in the Strait of Gibraltar," *J. Acoust. Soc. Am.* **109**(1), 143–154 (2001).
- ⁷³C. O. Tiemann, P. F. Worcester, and B. D. Cornuelle, "Acoustic remote sensing of solitary internal waves and internal tides in the Strait of Gibraltar," *J. Acoust. Soc. Am.* **110**(2), 798–811 (2001).
- ⁷⁴R. Headrick, J. F. Lynch, and the SWARM Group, "Acoustic normal mode fluctuation statistics in the 1995 SWARM internal wave scattering experiment," *J. Acoust. Soc. Am.* **107**, 201–220 (2002); "Modeling mode arrivals in the 1995 SWARM experiment acoustic transmissions," *ibid.*, **107**, 221–236 (2002).
- ⁷⁵H. Yamaoka, A. Kaneko, J.-H. Park, H. Zheng, N. Gohda, T. Takano, X.-H. Zhu, and Y. Takasugi, "Coastal acoustic tomography system and its field application," *IEEE J. Ocean. Eng.* **27**(2), 283–295 (2002).
- ⁷⁶F. B. Jensen, W. A. Kuperman, M. B. Porter, and H. Schmidt, *Computational Ocean Acoustics* (American Institute of Physics, New York, 1994).
- ⁷⁷B. Katznelson and V. Petnikov, *Shallow Water Acoustics* (Praxis, Chichester, 2002).
- ⁷⁸J. X. Zhou, X. S. Zhang, and P. Rogers, "Resonant interaction of sound waves with internal solitons in the coastal zone," *J. Acoust. Soc. Am.* **90**(4), 2042–2054 (1991).
- ⁷⁹J. C. Preisig and T. F. Duda, "Coupled acoustic mode propagation through continental shelf internal solitary waves," *IEEE J. Ocean. Eng.* **22**(2), 256–269 (1997).
- ⁸⁰M. Badiéy, Y. Mu, J. F. Lynch, X. Tang, J. R. Apel, and S. Wolf, "Azimuthal and temporal dependence of sound propagation due to shallow water internal waves," *IEEE J. Ocean. Eng.* **27**(1), 117–129 (2002).
- ⁸¹M. Badiéy, B. G. Katznelson, J. F. Lynch, S. A. Pereselkov, and W. Siegmant, "Measurement and modeling of 3-D sound intensity variations due to shallow water internal waves," *J. Acoust. Soc. Am.* **117**(2), 613–625 (2005).
- ⁸²R. F. Gasparovic, J. R. Apel, D. R. Thompson, and J. S. Toscho, "A comparison of SIR-B synthetic aperture radar data with ocean internal wave measurements," *Science* **232**, 1529–1531 (1986).
- ⁸³E. Falcon, C. Laroche, and F. Fauve, "Observation of depression solitary waves on a thin fluid layer," *Phys. Rev. Lett.* **89**, 204501-1–204501-4 (2002).
- ⁸⁴P. D. Weidman, R. Zakhem, "Cylindrical solitary waves," *J. Fluid Mech.* **131**, 557–573 (1988).

Speech production knowledge in automatic speech recognition

Simon King^{a)} and Joe Frankel

*Centre for Speech Technology Research, University of Edinburgh, 2 Buccleuch Place,
Edinburgh EH8 9LW, United Kingdom*

Karen Livescu

*MIT Computer Science and Artificial Intelligence Laboratory, 32 Vassar Street, Room 32-G482, Cambridge,
Massachusetts 02139*

Erik McDermott

*Nippon Telegraph and Telephone Corporation, NTT Communication Science Laboratories,
2-4 Hikari-dai, Seika-cho, Soraku-gun Kyoto-fu 619-0237, Japan*

Korin Richmond and Mirjam Wester

*Centre for Speech Technology Research, University of Edinburgh, 2 Buccleuch Place,
Edinburgh EH8 9LW, United Kingdom*

(Received 13 October 2005; revised 1 November 2006; accepted 6 November 2006)

Although much is known about how speech is produced, and research into speech production has resulted in measured articulatory data, feature systems of different kinds, and numerous models, speech production knowledge is almost totally ignored in current mainstream approaches to automatic speech recognition. Representations of speech production allow simple explanations for many phenomena observed in speech which cannot be easily analyzed from either acoustic signal or phonetic transcription alone. In this article, a survey of a growing body of work in which such representations are used to improve automatic speech recognition is provided. © 2007 Acoustical Society of America. [DOI: 10.1121/1.2404622]

PACS number(s): 43.72.Ne, 43.70.Jt, 43.70.Bk [DOS]

Pages: 723–742

I. INTRODUCTION

There is a well-established body of knowledge about the speech production mechanism (e.g., Löfqvist, 1997), covering articulatory processes (e.g., Perkell, 1997), coarticulation (e.g., Farnetani, 1997), and so on. The movements of the articulators can be directly measured in real time and models of the articulatory system, particularly the tongue, have been built (e.g., Honda *et al.*, 1994; Kaburagi and Honda, 1996). Aside from actual articulatory data, other representations of speech production are available, including various kinds of feature systems, gestures, and landmarks. These expressive representations allow simple explanations for many phenomena observed in speech which cannot be easily analyzed from either the acoustic signal or the phonetic transcription alone.

Acoustic modeling for automatic speech recognition (ASR) currently uses very little of this knowledge and as a consequence speech is only modeled as a *surface* phenomenon. Generally, hidden Markov models (HMMs) link the phonetic level to the observed acoustic signal via a single discrete hidden variable, the state. The state space (i.e., the set of values the state variable can take, which may be many thousands) is a homogeneous layer with no explicit model of the structural differences or similarities between phones; the evolution of the state through time is modeled crudely. In this article we consider whether acoustic modeling for

speech recognition stands to benefit from the judicious use of knowledge about speech production.

The standard approach to acoustic modeling continues to be the “beads on a string” model (Ostendorf, 1999) in which the speech signal is represented as a concatenation of phones. The fact that the acoustic realization of phones is context-dependent—the consequence of coordinated motion of multiple, slow-moving physical articulators—is accounted for by the use of context-dependent models. Because the set of contexts is very large, statistical clustering techniques must be used. This approach is probably not optimal, and perhaps effective only for relatively constrained types of speech. Although these clustering techniques use articulatory/phonetic features, a direct use of these features as statistical factors may offer better performance. Variations in speech production (e.g., due to speaking rate) are either not modeled, or require the creation of situation-specific models, leading to a problem of robust estimation. There is some work on explicit modeling of pronunciation variation, but this is severely limited by the coarseness of the phone unit: another consequence of the beads on a string approach. Section II provides a full definition of what we mean by “speech production knowledge.” For now, we can take it to include data about articulation (recorded directly, or annotated by human labelers), automatic recovery of such data, or features derived from phonetic transcriptions.

A. The scope of this article

We aim to provide a comprehensive overview of the large body of speech recognition research that uses speech

^{a)}Electronic mail: Simon.King@ed.ac.uk

production knowledge: a road map for the reader that makes connections between the different approaches. This article was inspired by the Beyond HMM Workshop (2004) and had its genesis in a short paper by McDermott (2004).

Section I B makes the case for using speech production knowledge, Sec. I C acknowledges ways in which current systems already do, and Sec. I D gives some pointers to early work. Section II defines in detail just what is meant by speech production knowledge and discusses how it can be represented with a view to using it in speech recognition; we do not attempt a complete review of all work on speech production, nor do we consider theories of speech *perception* with a production basis (Lieberman and Mattingly, 1985). We will not consider formant frequencies in any depth (because they only give an incomplete picture of speech production) or prosody, source features or phrasal effects (because we are not aware of any production-based ASR system that uses them). In Secs. III and IV, we look at how this speech production knowledge can be obtained, whether it is from articulatory measurements, manual transcription, derivations from phonetic labels, or by machine-learning. Section V provides a survey of efforts to use production knowledge in acoustic modeling for automatic speech recognition. Finally, in Sec. VI, we highlight some ongoing work and suggest future directions.

B. The case for using speech production knowledge in speech recognition

Incorporating speech production knowledge into ASR may alleviate some of the problems outlined earlier and enable improved recognition of spontaneous speech, greater robustness to noise, and multilingual acoustic models (Rose *et al.*, 1996). In practice, it is hard to realize these benefits.

Most production representations use a *factored representation*: parallel “streams” of features/parameters. Since any given feature/parameter will typically be shared amongst many phoneme classes, the training data are used in a potentially more effective way. Low-frequency phonemes will share features with high-frequency ones, benefiting from their plentiful training data. Parameter tying for context-dependent HMMs already takes advantage of this property.

Rather than modeling complex *acoustic* effects of coarticulation, *explicit modeling* at the production level specifies precisely where, when, and how coarticulation occurs. Since production representations are easily interpreted, models that use them are more *transparent* than HMMs, where the hidden state defies any interpretation or post-hoc error analysis. Although our understanding of the modeling capabilities of HMMs has recently been advanced (Bilmes, 2004; Bridle, 2004; Tokuda *et al.*, 2004), there is still a long way to go before we are able to interpret current large systems.

The advantages of explicit modeling and a factored representation together imply better performance on *spontaneous or casual speech* because of the greater degree of coarticulation observed in this type of speech (Farnetani, 1997). We also expect production-based models to be *noise robust*. The factored representation means each feature/parameter is easier to recognize than, say, 61 phoneme classes, because features/parameters typically have far fewer than 61 possible

values. In a factored representation, errors for each factor are multiplied together, which could potentially make the situation worse, but each feature/parameter will be affected differently by noise, so we could expect that—provided there is a little redundancy, or a strong enough language model—in the presence of noise, sufficient features/parameters could still be identified (“islands of reliability”) to perform speech recognition. In order to take full advantage of the varying reliability of the different features, a confidence measure is required.

It is possible to construct production-based representations that are *multilingual* or perhaps even *language universal*. This is an underexplored area, deserving of further research. The International Phonetic Alphabet [IPA, International Phonetic Association (1999)] provides a phoneme set which is intended to be universal, but suffers from a number of problems, such as: A single IPA symbol may be pronounced somewhat differently in different languages; some symbols are very rare amongst the world’s languages. Features offer a powerful and language-universal system (Ladefoged, 1997). Some representations of speech production can be argued to be relatively *speaker independent*, compared to standard spectral features (Maddieson, 1997). Expressing *pronunciation variation* as phonemic transcriptions is problematic (Sec. V E). A factored feature representation is potentially both more expressive (e.g., it allows small variations that do not result in phonemes changing class) and more compact.

C. How much production knowledge do current HMM systems use?

Current systems, which are almost invariably HMM-based, use a little knowledge of speech production. One of the above advantages of a speech production representation—its factorial nature—is exploited, albeit to a limited extent and in somewhat opaque fashion, by standard HMM systems during decision tree-based parameter tying. Vocal tract length normalization (Cohen *et al.*, 1995) acknowledges a physiological fact of speech production, and is widely used. Jurafsky *et al.* (2001) suggest that models of triphones (context-dependent phones) can usually deal with phonetic substitutions, but not large-scale deletions.

1. Decision trees for state tying

Because the state space of a context-dependent HMM system is large (there are more parameters than can be learned from current data sets), it is necessary to share parameters within clusters of states. Bundles of discrete features, similar to the systems discussed in Sec. II B, are the usual representation used for phonetic context when building the decision trees used for tying the states of context-dependent HMMs such as triphone models (e.g., Young *et al.*, 2002). If phonemes were used to describe the left and right context, the power of state-tying would be severely restricted. For example, it would not be possible to identify the similar effect that nasals like [n] and [m] have on preceding vowels, or the similar formant transitions seen in vowels following bilabial stops like [p] and [b]. The fact that

[p] and [b] have the same values for some discrete features tells us that they are similar (in terms of production) and will have similar effects on neighboring phones. This use of features is still limited, because features are attached to phones (or HMM states), so the power of the modeling is still restricted by the beads on a string problem. To really exploit the power of features to describe contextual and pronunciation variation in speech, probably requires the model to retain an internal feature-based representation.

2. State tying gives structure to the state space

After state tying, the state space has structure. When a pair of states from different triphone models (the same base phone in different left and/or right contexts) are tied, the acoustics of these two triphones must be similar. Since the tying was guided by features that can be related to production knowledge, the underlying production of the two triphones must also be similar. A cluster of tied states thus connects a localized region of acoustic space with a localized region of articulatory space. Therefore, although the state-space structure (the set of clusters) formed by state tying is not at all easy to interpret, it forms a mapping from production to acoustics. Within a cluster, the mapping is approximately constant (all states in the cluster share the same values for some subset of the production-based features and all use the same output density); from cluster to cluster, the mapping changes, sometimes by a small amount (a smooth region in the global articulation-to-acoustic mapping), sometimes by a large amount (a discontinuity in the global articulation-to-acoustic mapping). However, little attempt is made to take any further advantage of this implicit mapping, by interpolating between clusters for example. Luo and Jelinek (1998) suggested “nonreciprocal data sharing” as a method for estimating HMM state parameters without hard state tying. This is, in essence, an interpolation between the clusters of states, but it does not explicitly use any articulatory information.

D. Historical perspective

Early attempts to use knowledge of speech production for speech recognition were limited. Since articulatory motion data were not easily available, knowledge had to be gleaned from human examination of the acoustic signal, from experiments on human reading of spectrograms (Cole *et al.*, 1980; Zue, 1985), from static x-ray images or introspection. This knowledge was then translated into rules or other classifiers that typically produced either a phoneme string or a phoneme lattice as output. Some highlights of this early work are mentioned in the following.

Fujimura (1986) proposed that certain, critical articulatory movements are more speaker-invariant than the acoustic signal. Cole *et al.* (1986) suggested that features (e.g., formant-related) were required to make fine phonetic distinctions and De Mori *et al.* (1976) used features attached to syllables. Lochschmidt (1982) used simple articulatory parameters to aid phonetic classification. Several systems have used a variety of acoustic-phonetic features, which often have some speech production basis. The CMU Hearsay-II

system (Goldberg and Reddy, 1976) and the CSTR Alvey recognizer (Harrington, 1987) made use of phonetic features. More recent work has continued this knowledge-based approach (Bitar and Espy-Wilson, 1995, 1996; Espy-Wilson and Bitar, 1995).

In this article, we will not further discuss these early (and often failed) attempts, which generally used knowledge-based “expert systems” methods. We will instead consider more recent work, which uses statistical/machine-learning techniques. One of the earliest attempts at a production-inspired model within a statistical machine-learning framework was the Trended HMM of Deng (1992) in which HMM states, instead of generating independent identically distributed observations, generate “trended” sequences of observations in the observation space. The model only accounts for one aspect of the acoustic consequences of speech production: piecewise smooth/continuous observation sequences. It does not attempt to explicitly model underlying production.

II. WHAT IS SPEECH PRODUCTION KNOWLEDGE?

In the following, we examine what various researchers mean by speech production knowledge, the linguistic theories which provide the original motivations, and how speech production can be represented, whether that is in a literal or abstract form.

A. Why the representation matters

For production knowledge to be useful for speech modeling and recognition, an encoding must be chosen. A variety of possibilities exist, ranging from continuous-valued measurements of vocal tract shape during speech, to the use of discrete-valued manually selected feature sets. The speech production parameters which appear in this survey can be broadly categorized as discrete or continuous. “Discrete” is used in this article to cover both categorical features and discretized positions (e.g., high/mid/low are the three possible values for the discrete feature “height” in some feature systems). As we will see, the form of the representation is crucial. If we adopt an approach that models the representation explicitly, the representation will directly determine the type of statistical or other model that can be used.

Generally, representations abstract away from the articulatory organs and lie somewhere between a concrete description of the continuous-valued physical positions and motions of the articulators and some higher-level symbolic, linguistic representation (e.g., phonemes). The motivations for each representation are quite different: a desire to explain coarticulation, or the atomic units in some particular phonological theory, for example. Likewise, the position of each representation along the *physical production space* ↔ *abstract linguistic space* axis is different. All of them claim to normalize articulation, within and particularly across speakers—they are more speaker-independent than measurements of tongue position, for example. Most also claim to be language independent (Ladefoged, 1997). Many claim to be able to explain phenomena that have complex acoustic consequences, such as coarticulation or phonological assimilation, quite simply, e.g., by overlapping or spreading of features

(Farnetani, 1997). These are all strong motivations for believing that production knowledge should be used in ASR.

Clearly, the degree of abstraction affects the usefulness of a representation for modeling purposes. While physical measurements of articulator positions might be most true to the reality of speech production, they pose significant problems for statistical modeling—for example, they are generally continuous-over-time trajectories and therefore require a different class of models and algorithms than frame-based data. At the other extreme, highly abstract representations might be simpler to model, but cannot express the details of speech production that might improve speech recognition accuracy. Typically, more abstract representations will tend to be discrete whereas concrete ones will tend to be continuous-valued. Discretization of continuous processes is common when formulating numerical models. In the case of speech production, the choice of symbols may be suggested by the feature system in use (e.g., a traditional place/manner system may have nine values for place and five for manner) or by quantizing articulatory measurements (e.g., Stephenson's work discussed in Sec. V A 3). We will use the terms *articulatory features* (AFs) to refer to discrete-valued representations and *articulatory parameters* to refer to continuous-valued representations.

B. Discrete representations of speech production

Discrete representations of speech production fall into two categories. In one, the number of features is usually small, with each feature taking a value from a set of possible values. It is possible for a feature to have an unspecified value (the set of features is then called “underspecified”). These features are often associated with a linguistic unit. A traditional system for describing phonemes using a small number of features, each of which can take multiple values, has as its two most important features manner and place. To these, various other features can be added; for example, the inventory used by Kirchhoff (1999) is manner (possible values: vowel, lateral, nasal, fricative, approximant, silence), place (dental, coronal, labial, retroflex, velar, glottal, high, mid, low, silence), voicing (voiced, voiceless, silence), rounding (rounded, unrounded, nil, silence), and front-back (front, back, nil, silence). Because the set of possible places of articulation depends on manner, the values that place can take may be made conditional on the value of manner (Chang *et al.*, 2005; Juneja and Espy-Wilson, 2003b). This is a frequently used representation for modeling, where the features are known as *pseudoarticulatory* features, or simply articulatory features. AF-labeled data are commonly produced using rule-based systems which map from existing labels to a corresponding articulatory configuration or sequence of configurations (see Sec. IV B 3). Other discrete parametrizations include quantizing measured articulatory data (Sec. V A 3).

The other category of representations uses a larger number of *binary* features; a vector of such features may be associated with a linguistic unit or, for the purposes of ASR, may be specified for every time frame. One influential phonological model (Chomsky and Halle, 1968) represents pho-

nemes as vectors of binary features, such as voiced/voiceless, nasal/non-nasal, or rounded/unrounded. These all have a physical production interpretation, although they were intended for use in phonological rules. Some approaches to ASR described in this article use this approach (Sec. V A 1). However, they generally adopt only the feature set and ignore the rule-based phonological component. They also generally specify the features every frame, rather than associating them with linguistic units because the features can thus be automatically recognized from the acoustic signal prior to hypothesizing linguistic unit boundaries. This is in contrast to “landmark” approaches, which first hypothesize linguistically important events, and then produce either acoustic features for each event or distinctive features defined at landmarks (Sec. IV C).

The key advantage of using features in phonology transfers directly to statistical modeling. Features are a *factored* representation and, through this factorization, feature values are shared by several phonemes. As we already mentioned in Sec. I, even in standard HMM-based recognition systems (e.g., Young *et al.*, 2002), this factored representation is extremely useful.

Chomsky and Halle's features are an abstract representation of speech production. After all, they were used in a *phonological* theory, in which only symbolic processes (e.g., assimilation) are of interest. In speech modeling, we wish to represent more acoustic detail than this. Fortunately, the feature set can be used to describe some acoustic (nonphonological) processes. For example, we could describe a nasalized version of an English vowel by simply changing its nasal feature value from $-$ to $+$. A simple extension of this feature system (see Sec. V A 1) changes the interpretation of the feature values to be probabilistic, with values ranging from 0 to 1, thus allowing *degrees* of nasalization, for example.

Speech as articulatory gestures. A separate and also influential perspective on speech organization was developed at Haskins Laboratories during the 1980s (e.g., Browman and Goldstein, 1992). A central tenet of the gestural approach is that speech percepts fundamentally correspond to the articulatory *gestures* that produced the acoustic signal. Gestures typically involve several articulators working together in (loose) synchrony. In the gestural view of speech production, a “gestural score” is first produced, from which a task dynamic model (Saltzman and Munhall, 1989) generates articulatory trajectories. The score is written using a finite number of types of gesture, such as “bilabial closure” and “velic opening.” An example gestural score, using Browman and Goldstein's *vocal tract variables*, is shown in Fig. 1. These gestures correspond directly to physical actions of the articulators.

The gestural approach provides an account of variation in spontaneous or casual speech. Instead of using complex phonological rules to account for phenomena such as lenition, reduction, and insertion, it uses simple and predictable changes in the relative timing of vocal tract variables (Browman and Goldstein, 1991). A vivid example of the representational power of the gestural approach is provided in Rubin and Vatikiotis-Bateson (1998) for the utterances “banana,”

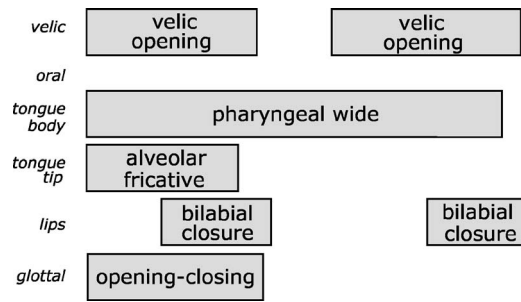


FIG. 1. Gestural score for the word “spam,” adapted from Browman and Goldstein (1991).

“bandana,” “badnana,” and “baddata” where it is shown that the differences between these utterances all come down to differences in the timing of velar movement.

C. Continuous-valued representations of speech production

In a few systems (e.g., Frankel, 2003; Wrench, 2001; Zlokarnik, 1995), a number of continuous-valued streams of data together give a smoothly varying description of speech production. These may consist of measured human articulation, parameters automatically recovered from acoustic input (Sec. IV A), or production-*inspired* parameters (Nix and Hogden, 1998; Richards and Bridle, 1999).

The relationship between articulation and acoustics is highly nonlinear. Measured articulatory parameters are smooth, slowly varying, and continuous (yet noisy), due to the highly constrained dynamics of speech production. By contrast, acoustic parameters display regions of smooth spectral change interspersed by sudden discontinuities such as found in plosives. Analysis of speaker-dependent electromagnetic articulograph (EMA) data from the MOCHA corpus (Wrench and Hardcastle, 2000) reported by Frankel (2003) shows that a linear predictor can explain much of the variation found in articulatory parameters, both within and between phone segments. On acoustic data, while a linear predictor is suitable within phones, a nonlinear predictor is required to model dependencies between phone segments.

III. MEASURING SPEECH PRODUCTION FROM THE ARTICULATORS

In the following, we look at ways of measuring speech production, then in Sec. IV we will cover methods that only require the acoustics (at least, at recognition time). We must make a distinction between “data” and “knowledge.” While data (e.g., articulation measured by electromagnetic articulography or magnetic resonance imaging) may be regarded as ground truth, it is not sufficient to build a *model*. Powerful machine-learning techniques are available for learning the parameters of a model and, increasingly, for selecting amongst a set of candidate models. These techniques use *data* but require the *model* (or model type) to be specified. Machine-learning cannot hypothesize new types of model for us; for that, we must apply *knowledge* of the problem. In this article, we concentrate on systems that follow this methodology: they use knowledge of speech production to hypoth-

esize a new type of model, then use machine-learning and data to learn its parameters.

A. Techniques for measuring articulation

Measuring articulation is frequently an invasive process. However, subjects generally manage to produce intelligible and reasonably natural speech despite the array of instruments to which they are attached.

An x-ray microbeam system involves attaching 2–3 mm gold pellets to the articulators which are tracked by a narrow, high-energy x-ray beam. The system described by Westbury (1994) achieves sampling rates of between 40 and 160 Hz depending on the articulator being tracked. The x-ray machinery produces appreciable levels of background noise, resulting in a noisy speech signal and also interfering with speech production—the Lombard effect (Junqua, 1993).

An EMA system uses small receiver coils, instead of gold pellets, which have threadlike wires attached. These interfere surprisingly little with speech production. Current is induced in the coils by alternating magnetic fields from fixed transmitter coils mounted on a helmet, and their position can be inferred. As with an x-ray microbeam system, only *x* and *y* coordinates of each sensor in the *midsagittal plane* are measured, although a recently developed three-dimensional version overcomes this limitation and additionally removes the need to attach the transmitter coils to the subject (Hoole *et al.*, 2003). EMA systems can be located in recording studios, produce little operating noise, and therefore offer very high quality audio; there are, however, some limitations on microphone type and placement, due to the electromagnetic field. In practice, the duration of recording sessions is limited because coils become detached or the subject tires.

A laryngograph, or electroglottograph (EGG), measures variation in conductance between transmitting and receiving electrodes positioned on either side of the larynx, which is related to the change in glottal contact. An electropalatograph (EPG) measures tongue/palate contact over the whole palate using a custom-made artificial palate which has electrodes embedded on the lower surface in a grid pattern. Because it is a few millimeters thick, this interferes substantially with speech production. However, articulatory compensation (Perkell, 1997) means that relatively natural speech can be produced if the speaker wears the palate for some time before the recording session starts. An overview of other articulation-measuring devices can be found in Stone (1997), including computed tomography, magnetic resonance imaging, ultrasound, electromyography, strain gauges, video tracking systems, various aerodynamic measurement devices, and so on.

B. Available corpora

Corpora large enough for training and evaluating ASR systems are scarce due to the expense and labor involved in data collection. We are aware of just two such data sets. The Wisconsin x-ray microbeam database (Westbury, 1994) consists of parallel articulatory and acoustic features for 60+ subjects, each of whom provide about 20 min of speech, including reading prose passages, counting and digit se-

quences, oral motor tasks, citation words, near-words, sounds and sound sequences, and read sentences. The MOCHA corpus (Wrench, 2001; Wrench and Hardcastle, 2000) was recorded at Queen Margaret University College, Edinburgh, and consists of parallel acoustic-articulatory recordings for a number of speakers, each of whom read up to 450 sentences from TIMIT (Garofolo *et al.*, 1993), plus 10 further sentences to cover the received pronunciation (RP) accent of British English. The measurements comprise EMA, EPG, and EGG. Data sets from the other measurement devices listed earlier do exist, but not usually in useful quantities. New data are gradually becoming available, including EMA and magnetic resonance imaging (MRI) video data from the University of Southern California.¹

IV. INFERRING SPEECH PRODUCTION FROM THE ACOUSTIC SIGNAL

In the absence of measurements of speech production, some method is required for recovering this information from the acoustic signal. Here, we discuss the tasks of articulatory inversion (Sec. IV A), articulatory feature recognition (Sec. IV B), and landmark detection (Sec. IV C). Articulatory inversion is concerned with faithful recovery of articulation or realistic, articulatorlike parameters. Articulatory feature recognition is the inference of discrete pseudoarticulatory states. Landmark detection aims to enhance feature detection by locating points in the signal at which reliable acoustic cues may be found.

A. Articulatory inversion

An inversion mapping seeks to invert the process of speech production: Given an acoustic signal, it estimates the sequence of underlying articulatory configurations. There is evidence that multiple articulatory configurations can result in the same or very similar acoustic signals: a many-to-one mapping. This makes the inversion mapping one-to-many, which is an *ill-posed* problem. For example, using the Wisconsin University x-ray microbeam database, Roweis (1999) showed that the articulatory data points associated with the nearest thousand acoustic neighbors of a reference acoustic vector could be spread widely in the articulatory domain, sometimes in multimodal distributions.

One method of inversion uses an analysis of the acoustic signals based on some mathematical model of speech production and the physical properties of the articulatory system (Krstulović, 1999; Wakita, 1979). Another technique uses articulatory speech synthesis models with an analysis-by-synthesis algorithm: Model parameters are adjusted so the synthesizer output matches the acoustic target (e.g., Shirai and Kobayashi, 1986). Synthesis models can be used to generate articulatory-acoustic databases, which can be used for performing the inversion mapping as part of a code-book inversion method (e.g., Atal *et al.*, 1978) or as training data for another data-driven machine-learning model (e.g., Rahim *et al.*, 1993). A fundamental problem facing the use of analytical methods and of articulatory synthesis models is the difficulty in evaluating the result with respect to real human articulation. From this point of view, measurements of hu-

man articulation can provide a huge advantage. (Section VI E considers the problem of evaluation more generally.)

Together with new data, the popularity of machine-learning methods has led to a recent increase in data driven methods, including extended Kalman filtering (Dusan and Deng, 2000), self-organizing HMMs (Roweis, 1999), codebooks (Hogden *et al.*, 1996), artificial neural networks (ANNs) such as the multilayer perceptron (Papcun *et al.*, 1992; Richmond *et al.*, 2003) and the mixture density network (Richmond *et al.*, 2003), Gaussian mixture models (Toda *et al.*, 2004), and an HMM-based speech production model (Hiroya and Honda, 2004).

Finally, there are approaches that do not rely on *articulatory* data: so-called latent variable models, such as the maximum likelihood continuity map (MALCOM) (Hogden *et al.*, 1998), which estimates the most likely sequence of hidden variables in accordance with an articulatorylike constraint, given a sequence of acoustic frames. The constraint is simply that the estimated motion of pseudoarticulators cannot contain frequency components above a certain cutoff frequency, e.g., 15 Hz. This is a direct use of the knowledge that articulator motion is smooth (more specifically, band-limited) to aid the inversion process.

Although Hogden *et al.* do not use articulatory data for training, they report that the trajectories of the hidden variables correlate highly with measured articulatory trajectories.

B. Articulatory feature recognition

Articulatory feature recognition can be incorporated directly into existing phone or word-based systems, or can provide a subtask on the way to building a full AF-based ASR system. Typically, separate models are trained to distinguish between the possible values of each feature. Kirchhoff (1999) proposes this approach because the complexity of each individual classifier will be less than that of a monolithic classifier, leading to improved robustness. Efficient use is made of training data, improving the modeling of infrequently occurring feature combinations. ANNs, HMMs, and dynamic Bayesian networks (DBNs) have all successfully been applied to the task of AF recognition.

Attempting the task of AF recognition, without actually performing word recognition, presents two inherent difficulties, both of which stem from deriving AF labels from phone labels: obtaining labels for the data and evaluating the system. If the AFs directly correspond to articulator positions, then they may be obtained by quantizing articulatory measurement data. If AF labels are produced from phonetic transcriptions, there is the possibility of merely having a *distributed* representation of phonemes without advantages of a truly *factored* representation. Embedded training (e.g., Wester *et al.*, 2004) can be used to address limitations in phone-derived AF labels, by allowing boundaries to be moved and labels potentially changed.

The following work on AF recognition all aims toward full ASR; AF recognition is merely a staging post along the way. There are two distinct categories of work here. The first uses AFs of the kind discussed earlier; we describe three different machine-learning approaches to recognizing the

values of AFs from speech. The second approach is that of landmarks. Evaluation of such systems can present some problems, which are discussed in Sec. VI E.

1. Articulatory feature recognition using neural networks

King and Taylor (2000) report articulatory feature recognition experiments on TIMIT using ANNs, comparing three feature systems: binary features based on the *sound pattern of English* (SPE) (Chomsky and Halle, 1968), multi-valued features using traditional phonetic categories such as manner, place, etc., and *government phonology* (GP) (Harris, 1994). The percentage of frames with all features simultaneously correct together was similar across feature systems: 52%, 53%, and 59% for SPE, multivalued, and GP, respectively (59%, 60%, and 61% when each frame was mapped to the nearest phoneme). Dalsgaard *et al.* (1991) aligned acoustic-phonetic features with speech using a neural network; the features were similar to the SPE set, but underwent principal components analysis to reduce correlation. It is not clear whether they retain linguistic meaning after this procedure. Kirchhoff (Kirchhoff, 1999; Kirchhoff *et al.*, 2002) used articulatory features to enhance a phone-based system. Wester *et al.* (2001) and Chang *et al.* (2005) used separate place classifiers for each value that manner can take. Omar and Hasegawa-Johnson (2002) used a maximum mutual information approach to determine subsets of acoustic features for use in AF recognition.

2. Articulatory feature recognition using hidden Markov models

A number of systems use HMMs for AF recognition, including Metze and Waibel (2002), who used the set of linguistically motivated questions devised for clustering context-dependent HMM phone models to provide an initial AF set. A set of feature detectors was then used to supplement an HMM system via likelihood combination at the phone or state level. Word error rate (WER) was reduced from 13.4% to 11.6% on a 40k word vocabulary Broadcast News task and from 23.5% to 21.9% on spontaneous speech from the Verbmobil task. An HMM approach was also taken by Eide (2001), and used to generate observations for further processing in a phone-based HMM system.

3. Articulatory feature recognition using dynamic Bayesian networks

In contrast to the use of ANNs and HMMs, the use of DBNs is motivated specifically by their particular capabilities for this task: the ability to transparently and explicitly model interdependencies between features and the possibility of building a single model that includes both AF recognition and word recognition.

Frankel *et al.* (2004) proposed DBNs as a model for AF recognition. As with the manner-dependent place ANNs discussed earlier, evaluation on the TIMIT corpus (Garofolo *et al.*, 1993) showed that modeling interfeature dependencies led to improved accuracy. The model is shown in Fig. 2. Using phone-derived feature labels as the gold standard, the

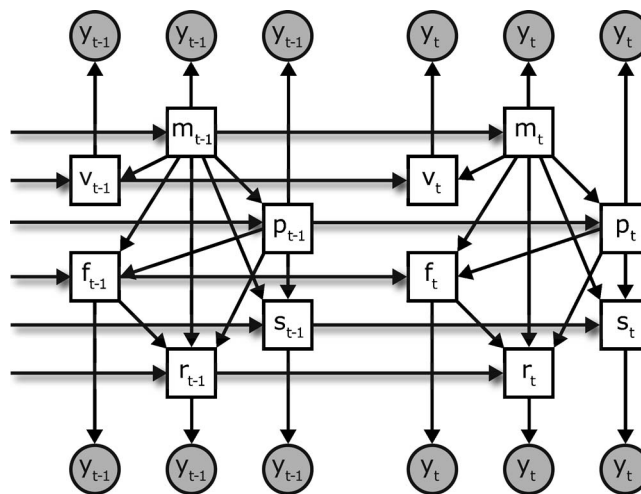


FIG. 2. A DBN for articulatory feature recognition, from Frankel *et al.* (2004), shown in graphical model notation where square/round and shaded/unshaded nodes denote discrete/continuous and observed/hidden variables, respectively. (Arcs between time slices are drawn here, and in all other DBN figures, with “drop shadows” for clarity, although they are otherwise no different than other arcs.) The discrete variables $m_t, p_t, v_t, f_t, s_t, r_t$ are the articulatory features (manner, place, voicing, frontback, static, rounding) at time t . The model consists of six parallel HMMs (e.g., consider only the variables m_t, m_{t-1} and their corresponding observations) plus a set of interfeature dependencies (e.g., the arc from m_t to p_t indicates that the distribution of p_t depends on the value of m_t). These interfeature dependency arcs allow the model to learn which feature values tend to co-occur. The continuous observation y_t is repeated six times (a product-of-Gaussians observation density).

overall framewise percent features correct was increased from 80.8% to 81.5% by modeling dependencies, and frames with all features simultaneously correct together increased dramatically from 47.2% to 57.8% (this result can be compared to 53% for King and Taylor’s multivalued feature system described in Sec. IV B 1, where the feature system was very similar).

To mitigate the problems of learning from phone-derived feature labels, an embedded training scheme (mentioned in Sec. IV B) was developed by Wester *et al.* (2004) in which a set of asynchronous feature changes was learned from the data. Evaluation on a subset of the OGI Numbers corpus (Cole *et al.*, 1995) showed that the new model led to a slight increase in accuracy over a similar model trained on *phone-derived* labels (these accuracy figures do not tell the whole story—see Section VI E 2 a). However, there was a threefold increase in the number of feature combinations found in the recognition output, suggesting that the model was finding some asynchrony in feature changes. Frankel and King (2005) describe a hybrid ANN/DBN approach, in which the Gaussian mixture model (GMM) observation process used by the original DBNs is replaced with ANN output posteriors. This gives a system in the spirit of hybrid ANN/HMM speech recognition (Bourlard and Morgan, 1993), combining the benefit of the ANN’s discriminative training with the interfeature dependency modeling offered by the DBN. The feature recognition accuracy on OGI Numbers was increased to 87.8%.

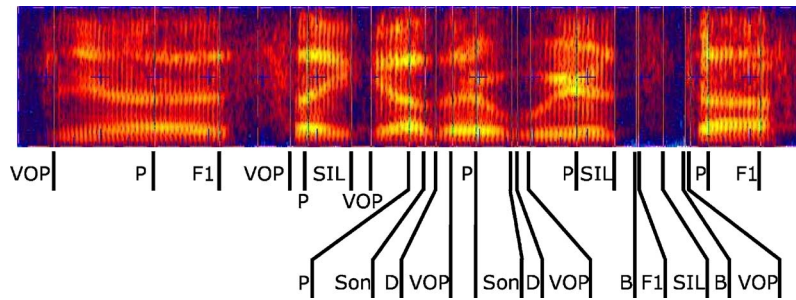


FIG. 3. (Color online) Landmarks for the utterance “Yeah it’s like other weird stuff.” Text labels correspond to the landmark to their right. F1: fricative onset; Son: sonorant consonant onset; P: vowel nucleus; D: syllabic dip; SIL: silence onset; B: stop burst onset; VOP: vowel onset point. Based on Fig. 4.2 in Hasegawa-Johnson *et al.* (2005).

C. Landmark-based feature detection

Feature-based representations have been used for a long time in the landmark-based recognition work of Stevens (2000, 2002) which models speech perception in humans; this work has inspired landmark-based ASR (e.g., Hasegawa-Johnson *et al.*, 2005; Juneja, 2004; Zue *et al.*, 1989). Stevens (2002) describes the recognition process as beginning with hypothesizing locations of *landmarks*, points in the speech signal corresponding to important events such as consonantal closures and releases, vowel centers, and extrema of glides (e.g., Fig. 3). The type of landmark determines the values of *articulator-free* features such as [sonorant] and [continuant]. Various cues (e.g., formant frequencies, spectral amplitudes, duration of frication), are then extracted around the landmarks and used to determine the values of *articulator-bound* distinctive features (e.g., place, vowel height, nasality). The set of hypothesized features is matched against feature-based word representations in the lexicon.

There is no system for automatic speech recognition of which we are aware that implements this theory fully, but modules implementing some aspects of the theory have been developed. Howitt (1999) reports on a method for vowel landmark detection using a simple multilayer perceptron; Choi (1999) presents knowledge-based cues and detectors for consonant voicing at manually labeled landmarks. Two complete ASR systems using landmarks—the MIT SUMMIT system and a system from the 2004 Johns Hopkins Summer Workshop—are described in Sec. V B. Juneja and Espy-Wilson (Juneja, 2004; Juneja and Espy-Wilson, 2003b) report related work, which combines support vector machine outputs with dynamic programming to locate landmarks and label manner features.

D. Comparison of AF and landmark approaches

In most AF-based systems, AF values are defined every time frame. This is compatible with any of the frame-based modeling techniques described in Sec. V, including generative models such as HMMs. These frame-based models compute the likelihood of an utterance given some hypothesized labels (e.g., a word sequence) by multiplying together frame-level likelihoods. It is also straightforward to compute a frame-level accuracy for these types of systems, so long as reference labels are available (Sec. VI E discusses this issue). In contrast, landmarks are *events*. Evaluation of landmark

accuracy requires a measure such as the F score which combines recall and precision, *plus* some measure of the temporal accuracy of the landmarks. For this reason, reports of landmark accuracy are less common, less consistent, and harder to interpret. For subsequent word recognition, landmarks are used to guide acoustic feature extraction, meaning that these acoustic features are not available at every time frame to any subsequent model.

V. ACOUSTIC MODELING USING PRODUCTION KNOWLEDGE

We now consider how speech production knowledge has been used to improve acoustic modeling for speech recognition. Some of the work builds on AF recognition described earlier. A simple way to use articulatory features is as a replacement for conventional acoustic observations. Alternatively, “landmarks” may be located in the signal, and acoustic parameters extracted at those locations. AFs can be used to perform phone recognition, where they have been shown to improve noise robustness, although this approach suffers from the phone “bottleneck” that AF approaches usually try to avoid. A rather different way to harness the power of articulatory information is to use it for model selection by, for example, defining the topology of an otherwise conventional HMM. Other models maintain an explicit internal representation of speech production, whether that be discrete or continuous. AFs have also been used in pronunciation modeling, and for recognition-by-synthesis using an articulatory speech synthesizer.

A. Articulatory features or parameters as observations

Articulatory parameters (continuous-valued or quantized) can be used directly as (part of) the observation vector of a statistical model. This requires access to measured or automatically recovered articulation.

1. Hidden Markov models

Zlokarnik (1995) used measured or automatically recovered articulatory parameters, appended to acoustic features, in an HMM recognizer. On VCV sequences, adding measured articulation to Mel-frequency cepstral coefficients (MFCCs) reduced WER by more than 60% relative. Articulatory parameters recovered using a multilayer perceptron (MLP) gave relative WER reductions of around 20%. The

additional information carried by the recovered articulation may be attributable either to the supervised nature of MLP training, or the use of 51 frames (approximately half a second) of acoustic context on the MLP inputs.

Similar experiments were conducted on a larger scale by Wrench. For a single speaker, augmenting acoustic features with measured articulatory parameters gave a 17% relative phone error rate reduction using triphone HMMs. The articulatory feature set was generated by stacking EMA, EGG, and EPG signals with their corresponding δ (velocity) and $\delta\delta$ (acceleration) coefficients and performing linear discriminant analysis (LDA) dimensionality reduction. However, when real articulation was replaced with articulatory parameters automatically recovered from the acoustics using a MLP, there was no improvement over the baseline acoustic-only result (Wrench, 2001; Wrench and Hardcastle, 2000; Wrench and Richmond, 2000).

Eide (2001) describes augmenting the MFCC observation vector for a standard HMM system with information about articulatory features. Mutual information between the true and estimated presence of features was used to reduce the original 14 features down to 4. In an evaluation on city and street names spoken in a car with the engine running at 0, 30, and 60 mph, the augmented observations gave 34%/22% relative word/string error rate reductions.

Fukuda *et al.* (2003) used a MLP to map from acoustic parameters to a 33-dimensional output vector representing 11 distinctive phonetic features (DPFs) at the current time frame along with inferred values at preceding and following contexts. The modeling of the MLP-derived DPFs was refined through the application of logarithmic feature transforms (Fukuda and Nitta, 2003a) and dimensionality reduction (Fukuda and Nitta, 2003b). Augmenting MFCC feature vectors with the MLP-derived DPFs gave accuracy increases over the baseline, particularly in the presence of noise.

King *et al.* (1998) and King and Taylor (2000) also report recognition experiments based on the combination of the output of a number of independent ANN classifiers. The work was primarily aimed at comparing phonological feature sets on which to base the classifiers, though the feature predictions were also combined to give TIMIT phone recognition results. Unlike Kirchoff, who used an ANN to combine the independent feature classifiers, the predicted feature values were used as observations in an HMM system. The resulting recognition accuracy of 63.5% was higher than the result of 63.3% found using standard acoustic HMMs, though not statistically significant. The need for an asynchronous articulatory model was demonstrated using classifications of a set of binary features derived from Chomsky and Halle (1968). In cases where features changed value at phone boundaries, allowing transitions within two frames of the reference time to be counted as correct, the percentage of frames where all features were correct (i.e., where the phone was correctly identified) rose from 52% to 63%. Furthermore, the accuracy with which features were mapped onto the nearest phone rose from 59% to 70%. This demonstrates the limiting nature of forcing hard decisions at phone bound-

aries onto asynchronous data. In both the King *et al.* and the Kirchoff systems, the individual feature classifiers were independent.

2. Hybrid HMM/ANN systems

Kirchoff (Kirchoff, 1999; Kirchoff *et al.*, 2002) showed that an AF-based system can increase robustness to noise. The OGI Numbers corpus (Cole *et al.*, 1995) was used to develop this approach, using the feature representation given in Sec. II B. Feature labels were generated from time-aligned phone labels using rules. As in Sec. IV B, a separate MLP for each feature was trained to estimate posterior probabilities, given the acoustic input. A further MLP was trained to map from the outputs of the five feature networks to phone class posteriors which were then used in a standard hybrid HMM/ANN recognition system.

On clean speech, the word error rates for the acoustic and articulatory models were comparable, 8.4% and 8.9%, respectively, though in the presence of a high degree of additive noise, the articulatory model produced significantly better results. At 0 dB (signal and noise have equal intensity), the word error rate for the acoustic model was 50.2% but was 43.6% for the articulatory system. When the outputs of the acoustic and articulatory recognizers were combined, the error rates were lower than for either of the two individually, under a variety of noise levels and also on reverberant speech. The framewise errors for the different articulatory feature groups showed that classification performance on the voicing, rounding, and front-back features do not deteriorate as quickly as for manner and place in the presence of noise. This result suggests that, by incorporating confidence scores when combining the outputs of individual classifiers, the system could be tailored to particular operating conditions, and supports the authors' suggestion that combining individual classifiers might lead to improved robustness over a monolithic classifier (i.e., one that recognizes all features simultaneously). Similar experiments were performed on a larger spontaneous dialog corpus (Verbmobil). Improvements were also shown when acoustic and articulatory features were combined, giving relative WER reductions of up to 5.6%.

3. Dynamic Bayesian networks

Stephenson *et al.* (2000, 2004) created a DBN which enhances the output mixture distribution of an HMM by including dependency on an articulator position. Figure 4(c) shows two time slices of the model. The articulator position is conditioned on its previous value and on the current subword state, providing an element of contextual modeling. Note that the decoding version of the model is shown in which the articulator position is hidden. During training, the articulator position may be observed. The Wisconsin x-ray microbeam database (Westbury, 1994) was used to provide parallel acoustic-articulatory data for an isolated word recognition task. The acoustic features were 12 MFCCs and energy along with their δ coefficients, and the articulatory features consisted of x and y coordinates for eight articulator positions (upper lip, lower lip, four tongue positions, lower front tooth, lower back tooth). Both acoustic and articulatory

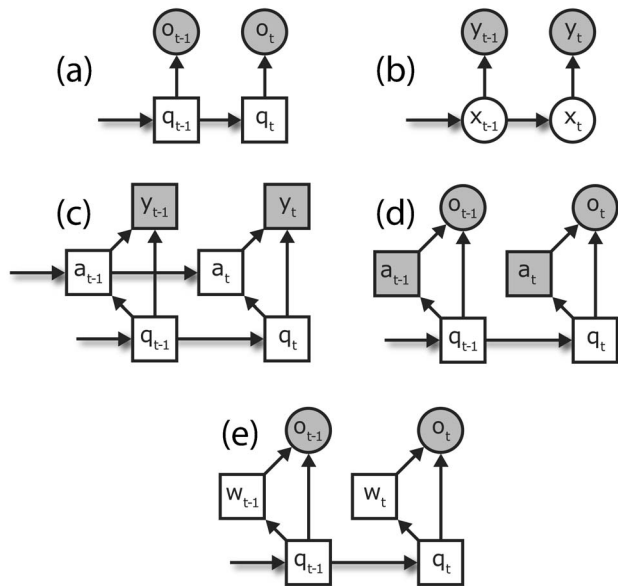


FIG. 4. (a) HMM in graphical model notation. q_t is the hidden discrete state at time t and o_t is the continuous-valued observation. This graph illustrates the conditional independence assumptions in this model, e.g., o_t is conditionally independent of everything except q_t , given q_t . (b) Linear dynamic model (LDM). x_t is the continuous hidden state and y_t is the continuous observation at time t . The model is similar to the HMM except the state is now continuous: its value is a vector of real numbers. Whereas the HMM stochastically chooses a state sequence, the LDM makes stochastic trajectories in its state-space. (c) DBN from Stephenson *et al.* (2000). q_t is the hidden state at time t , y_t is a discrete acoustic observation, and a_t is a discretized articulator position (which may be observed during training). This model is somewhat similar to the conventional HMM with a mixture-of-Gaussians output density in (e), except that the observation is discrete (for practical implementation reasons). The dependency of a_t on a_{t-1} models the dynamics of articulator movement. (d) Hybrid HMM/BN from Markov *et al.* (2003). q_t is the hidden state at time t , o_t is a discrete acoustic observation, and a_t is an observed, discretized articulator position. The model is very similar to that of Stephenson except the articulator position is always observed (so the dependency of a_t on a_{t-1} is not needed). (e) A conventional mixture-of-Gaussians continuous-density HMM. w_t is the hidden mixture component at time t (the probability mass function of w_t is constant: it is the set of mixture weights). The production-based models in (c) and (d) use a similar structure to achieve a mixture distribution over the observation.

observations were discretized by generating code-books using K-means clustering. The acoustic-only word error rate of 8.6% was reduced to 7.6% when the articulatory data were used during recognition. With the articulation hidden, the system gave a recognition word error rate of 7.8%, which is a 9% relative error decrease over the acoustic baseline.

4. Hybrid hidden Markov model/Bayesian network

Similar work is described in Markov *et al.* (2003), using a hybrid HMM plus Bayesian network (BN): an HMM in which the BN provides the observation process. The hybrid HMM/BN shown in Fig. 4(d) was used to implement a similar system to that in Stephenson *et al.* (2000), but without the dependency between successive articulator positions. By conditioning the GMM observation distributions on both the subword state and the (discrete) articulator value, the model is an HMM with a mixture output distribution where the mixture component (i.e., articulator position) is observed. Figure 4(e) shows a standard HMM with continuous obser-

variations and a mixture-of-Gaussians output density for comparison. As earlier, real articulatory data collected on an EMA machine were used for training the models, with the data first discretized. Unlike Stephenson *et al.* (2000), continuous-valued acoustic observations were used. Speaker-dependent experiments showed that the structure in the BN observation process makes it possible to support more mixture components than with standard GMMs (Markov *et al.*, 2003). Using 300 training sentences of parallel acoustic and articulatory data from 3 speakers, HMMs trained and tested on both acoustic and articulatory data significantly outperformed HMMs trained and tested on only acoustic data. HMM/BN models trained on both acoustic and articulatory data, even though performing recognition using only the acoustic parameters, gave similar performance to the HMMs trained and tested on both. These findings support those of Stephenson *et al.* (2000). Both these systems require articulatory measurement data for training.

5. Linear dynamic models

In the preceding work using HMMs and HMM/BNs, no attempt (other than the use of delta features) was made to model the continuous nature of articulator positions through time. Only Stephenson's model includes a dependency between the current articulatory state variable and its value at the preceding time, but this variable is discrete. All of these models use only discrete hidden state variable(s). In contrast, linear dynamic models (LDMs) use a *continuous* state variable.

Frankel *et al.* (Frankel, 2003; Frankel and King, 2001a,b; Frankel *et al.*, 2000) report the results of phone classification and recognition on the MOCHA corpus using LDMs. These are generative state-space models in which a continuous-valued hidden state variable gives rise to a time-varying multivariate Gaussian output distribution. Figure 4(b) shows two time slices of a LDM in graphical model notation. Frankel (2003) describes a phone classification task comparing various types of observation vectors derived from the MOCHA corpus. These include MFCCs, measured articulation (EMA), EGG, and EPG data. Acoustic-only observations gave higher accuracy than EMA alone, but when EGG (i.e., voicing information) and EPG data were added to EMA, the accuracy approaches that of the acoustic-only system. The acoustic-only phone error rate was reduced by 16.2% relative by adding EMA. Replacing measured EMA parameters with values recovered from the acoustics by a MLP (Richmond *et al.*, 2003) actually led to a slight reduction in accuracy, compared to the acoustic-only system. This may be due to the type of feed-forward MLP used in the inversion mapping, which estimates the conditional average articulatory parameters, given the acoustic inputs. Papcun *et al.* (1992) and Rose *et al.* (1996) observed that noncritical articulators tend to have higher associated variance than critical articulators. With no provision to model this variation, the MLP will introduce consistency where there should be none which may lead to an overemphasis on data streams corresponding to noncritical articulators. An alternative type of network might be better: in Richmond (2002) a mixture density network was applied to the inversion task. Such net-

works can model one-to-many relationships and account for variance, because their outputs are mixtures of probability density functions.

B. Landmark-based systems

The idea of locating landmarks in the speech signal, and using those locations to extract acoustic information, was introduced in Sec. IV C. The use of landmarks does not, in itself, imply the use of production knowledge or articulatory features, and has been used as part of both phone-based and articulatory feature-based recognition systems.

The MIT SUMMIT speech recognition system (Glass, 2003; Zue *et al.*, 1989) formalizes some of the ideas of Stevens' landmark-based approach (Stevens, 2002) in a probabilistic setting. SUMMIT locates potential phone-boundary landmarks and uses a phone-based dictionary to represent words. SUMMIT has used various landmark detection algorithms (Chang and Glass, 1997; Glass, 1988) and acoustic cues (Halberstadt and Glass, 1998; Muzumdar, 1996; Zue *et al.*, 1989). SUMMIT operates in either (or both) of two modes: a boundary-based mode, in which the acoustic cues around phonetic-boundary landmarks are explicitly modeled, and a segment-based mode, in which the regions between landmarks are modeled. Recent work by Tang *et al.* (2003) uses SUMMIT in a combined phone-feature approach to word recognition.

The 2004 Johns Hopkins Summer Workshop project on landmark-based speech recognition used an entirely feature-based representation of words rather than a phonetic one (Hasegawa-Johnson *et al.*, 2005). It also differed from SUMMIT in that it used support vector machines (SVMs) to detect both landmarks and the presence or absence of distinctive features. The outputs of these SVMs were combined into word scores and used to rescore word lattices produced by a baseline HMM-based recognizer. This project experimented with three ways of combining the SVM outputs into word scores. The first system used the approach of Juneja and Espy-Wilson (2003a), in which SVM discriminant scores are converted to likelihoods and modified Viterbi scoring is done using a phonetic baseform dictionary, mapped to distinctive features. The second system used an articulatory feature-based pronunciation model inspired by that of Livescu and Glass (Sec. V E) and the third used a maximum entropy model to classify words in a confusion network.

C. Articulatory features for HMM model selection

Articulatory features may also be used for the purposes of model selection, providing a prior on model topology by specifying the function of subword states. This is distinct from AFs providing the internal representation because, in the model selection approach, once the model is selected (e.g., the topology of an HMM is specified), the articulatory information is no longer required

1. Feature bundles

Deng and colleagues (e.g., Deng and Sun, 1994a,b; Sun *et al.*, 2000) have developed HMM systems where each state represents an articulatory configuration. Following Chomsky

and Halle's theory of distinctive features and Browman and Goldstein's system of phonology (Browman and Goldstein, 1992), they developed a detailed system for deriving HMM state transition networks based on a set of "atomic" units. These units represent all combinations of a set of overlapping articulatory features that are possible under a set of hand-written rules. Each phone is mapped to a static articulatory configuration (affricates and diphthongs each have a sequence of two configurations). Features can spread, to model long span dependencies. When articulatory feature bundles overlap asynchronously, new states are created for the intermediate portions which describe transitions or allophonic variation. On a TIMIT classification task, HMMs constructed from these units achieved an accuracy of 73% compared with context-independent HMMs of phones which gave an accuracy of 62%. The feature-based HMMs also required fewer mixture components. This suggests that a principled approach to state selection requires fewer parameters and therefore less training data, since each state is modeling a more consistent region of the acoustic space. This work was extended to include higher level linguistic information (Sun *et al.*, 2000), including utterance, word, morpheme and syllable boundaries, syllable onset, nucleus and coda, word stress and sentence accents. This time, results were reported on TIMIT phone recognition, rather than classification. A recognition accuracy of 73% was found using the feature-based HMM, which compares favorably to their baseline triphone HMM which gave an accuracy of about 71%, although this is not a state-of-the art accuracy.

2. Hidden articulator Markov model

Richardson *et al.* (2000a,b) drew on work by Erler and Freeman (1996) in devising the hidden articulator Markov model (HAMM), which is an HMM where each articulatory configuration is modeled by a separate state. The state transitions reflect human articulation: Static constraints disallow configurations which would not occur in American English, and dynamic constraints ensure that only physically possible movements are allowed. Asynchronous articulator movement is allowed: Each feature can change value independently of the others. On a 600 word PHONEBOOK isolated word, telephone speech, recognition task, the HAMM gave a significantly higher WER than a four-state HMM (7.56% vs 5.76%) but a combination of the two gave a WER of 4.56%: a relative reduction of 21% over the HMM system.

D. Articulatory information as internal structure

Articulatory information can be used to provide some or all of the internal model structure. This can take the form of decomposing subword states into a set of discrete articulatory features (Bilmes *et al.*, 2001; Livescu *et al.*, 2003), or using a continuous-valued articulatorylike representation which then generates acoustic parameters via some transform (Iso, 1993; Richards and Bridle, 1999; Russell and Jackson, 2005); some of the linear dynamic models of Frankel and colleagues (Sec. V A 5) can be seen as having a hidden continuous articulatorylike state variable which generates acoustic observations.

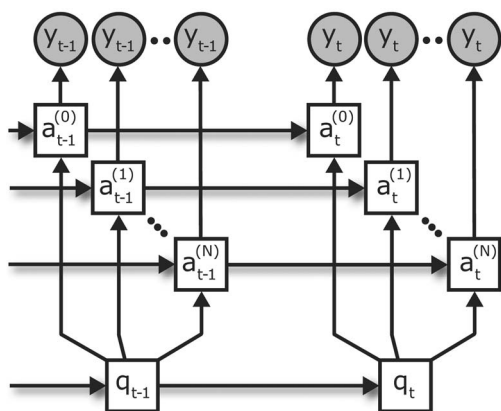


FIG. 5. A hidden feature model from Livescu *et al.* (2003) shown in graphical model notation. q_t is the (phonetic) hidden state, y_t is the acoustic observation, and $a_t^{(0)} \dots a_t^{(N)}$ are the articulatory variables, at time t . The dependency of the observation on the phone is mediated by the articulatory variables. Adding this intermediary layer allows for feature-based pronunciation modeling via the phone-to-feature dependencies.

1. Factoring the state into discrete articulatory features

Features provide a parsimonious framework within which to represent the variation present in natural speech. The following approaches use AF recognition (Sec. IV B 1) coupled with some method of mapping from features to sub-word or word units; thus, the AFs are explicitly present in the model's internal representation.

Eide *et al.* (1993) presents work in this vein, though phones are used to mediate between features and words, which compromises the benefits of a feature approach. Kirchhoff (1996) observes that articulatory asynchrony spans units longer than phones, and describes a system in which synchronization of feature streams is delayed to the syllable level. HMMs are used to infer values corresponding to each of six feature streams, and syllables are defined as parallel sequences of feature values. In evaluation on spontaneous German speech, a baseline triphone-based recognizer gave a phone accuracy of 54.81%. To allow comparison, recognized syllables were mapped to a phone sequence, and gave the substantially higher recognition accuracy of 68.3%, although it should be noted that this not a fair comparison because the syllable-based system benefits from the phonotactic constraints provided by the syllable models.

Bilmes *et al.* (2001) proposed a DBN-based approach to ASR with an AF internal representation. Livescu *et al.* (2003) continued this work and proposed a model that uses an articulatory feature factorization of the state space. A set of eight features is defined, with the value of each conditioned on the current phone state and its own previous value (Fig. 5). Dependencies may also be added between features in the same time slice. To overcome the problem of specifying an observation model for every possible combination of features, a product-of-mixtures-of-Gaussians model is used. Evaluation of the model on the Aurora 2.0 noisy digit corpus showed small accuracy increases over a phone-based HMM baseline in clean test conditions and more substantial improvements in some noise conditions. However, improvements over the baseline were only found when a phone-to-

observation edge was included, giving a system in which the feature and phone-based model likelihoods are effectively combined at the frame level. Only limited forms of such models were considered (for computational reasons), in which the interframe feature dependencies shown in Fig. 5 were omitted and features were conditionally independent of each other. Given the flexibility of the DBN framework, there is much scope for further development of this approach.

There have been other attempts to use a factored state representation. For example, Nock (2001) proposed "loosely-coupled HMMs" which have two or more Markov chains, each with its own observation variable. In Nock's work, the observations for each chain were derived from a different frequency band of the spectrum. Although it is clear that the acoustic consequences of speech production do not factor neatly into frequency bands, Nock's approach is inspired by the asynchronous nature of speech production and the loosely-coupled HMM may be more effective with observation streams that relate more directly to speech production (e.g., articulatory features).

2. Continuous articulatory internal representation

A number of researchers have investigated the use of continuous state-space representations, where the acoustic observations are modeled as the realization of some (possibly unobserved) dynamical system. Some of these approaches, such as the linear Gaussian systems described by Digalakis (1992), Frankel (2003), and Rosti (2004) are intended to reflect only the *general properties* of speech production and provide a compact representation of acoustic parameters (Sec. V A 5). Other studies, as described in the following, make a more explicit attempt to incorporate a model of the relationship between articulatory and acoustic domains.

a. Segmental HMM. Russell and Jackson (2005) describe a multilevel segmental hidden Markov model (MSHMM) in which formant frequencies are used to build an articulatorylike internal representation. Each state in the model generates a variable-duration noisy linear trajectory in articulatory space, which is projected into the acoustic space via a linear mapping. The articulatory-acoustic mappings are either on a per-phone basis or shared across phone classes. A number of tying strategies were compared, with greater numbers of mappings giving improved performance. Given the linear nature of the articulatory trajectories, and the linear mapping to the acoustic parameters, a theoretical upper bound on performance is given by a fixed linear-trajectory acoustic segmental HMM (FT-SHMM) (Holmes and Russell, 1999), which models the acoustic parameters directly. Experimental results show that this bound is met, and that where triphone models are employed, the MSHMM gives comparable performance to the FT-SHMM system with a 25% reduction in the number of free parameters. To overcome the limitation of using a linear mapping between articulatory and acoustic domains, Jackson *et al.* (2002) investigated the nonlinear alternatives of MLP and radial basis function (RBF), finding superior performance with the RBF (for background reading on these and other machine-learning techniques, see Sec. VI G).

b. Long-span contextual modeling. Attempting to capture long-span contextual effects along with the nonlinear relationship between articulatory and acoustic parameters has prompted models such as that of Iso (1993) and the hidden dynamic model (HDM) of Richards and Bridle (1999). The HDM uses a segmental framework in which a static target or series of targets in a hidden state space is associated with each phone in the inventory. A Kalman smoother is run over the targets to produce a continuous trajectory through the state space. These trajectories are connected to the surface acoustics by a single MLP. For an N -best rescoring task on the Switchboard corpus and a baseline WER of 48.2% from a standard HMM system, 5-best rescoring with the reference transcription included² using the HDM gave a reduced error rate of 34.7% (Picone *et al.*, 1999). An identical rescoring experiment using an HMM trained on the data used to build the HDM gave a word error rate of 44.8%. This suggests that the HDM was able to capture information that the HMM could not.

Deng and Ma (2000) describe a similar model in which the state is intended to model the pole locations of the vocal tract frequency response via vocal-tract-resonance (VTR) targets for each phone. Multiple switching MLPs are used to map from state to observations, though instead of the deterministic output distribution found in the HDM, filtering is implemented with an extended Kalman filter (EKF). To avoid the difficulties of training a nonlinear mapping and the inherent problems of the EKF, Ma and Deng (2004a,b) describe a system in which a mixture of linear models is used to approximate the nonlinearity, and demonstrate slight error reductions over an HMM baseline on a Switchboard rescoring task.

Zhou *et al.* (2003) describe a hidden-trajectory HMM (HTHMM) which also combines VTR dynamics with a mixture of linear projections to approximate a nonlinear state-to-observation mapping. However, the model is frame-based rather than segmental, and the state trajectories are deterministic, conditioned on the sequence of subword units, which in fact consist of HMM states. The model can be interpreted as an HMM in which the output distributions are adapted to account for long-span contextual information by conditioning on a continuous hidden trajectory. The deterministic continuous state obviates the need for filtering to infer state trajectories that, in combination with-frame-based computation, simplifies decoder implementation – described in Seide *et al.* (2003). Initial evaluation on TIDIGITS (Leonard, 1984) with a context-independent HTHMM system produced 0.37% WER and matched the 0.40% WER of a context-dependent triphone HMM system.

E. Articulatory feature modeling of pronunciation variation

The usual choice of subword unit is the phoneme and the usual representation of a word is as a string of phonemes. AFs are an alternative to phonemes and their use is motivated by difficulties in describing pronunciation variation using a string of phonemes. Spoken pronunciations often differ radically from dictionary baseforms, especially in conversational speech (Weintraub *et al.*, 1996). This contributes to the poor performance of ASR (Fosler-Lussier, 1999; McAllaster *et al.*, 1998; Saraclar *et al.*, 2000). Phoneme-based pronunciation models usually account for variability by expanding the dictionary with additional pronunciation variants (Hazen

et al., 2005; Riley and Ljolje, 1996; Shu and Hetherington, 2002; Wester, 2003). However, phoneme-based pronunciation models have numerous drawbacks. Saraclar *et al.* (2000) show that a phonetic realization is often somewhere between the intended phoneme and some other phoneme, rather than a phonemic substitution, insertion, or deletion. Phonemic changes can lead to increased confusability, e.g., “support” will be confusable with “sport” if it is allowed to undergo complete deletion of the schwa. In reality though, the [p] in “support” will be aspirated even if the schwa is deleted; the one in “sport” will not. Bates (2003) addresses these drawbacks by building a model of phonetic substitutions in which the probabilities of possible realizations of a phoneme are computed using a product model in which each product term involves a different AF or AF group.

Livescu and Glass (Livescu, 2005; Livescu and Glass, 2004a,b) generate pronunciation variants from baseforms through feature substitution and feature asynchrony using features based on Browman and Goldstein’s vocal tract variables (Browman and Goldstein, 1992). Effects that can be modeled include: *asynchrony only*: Nasal deletions as in *can’t* → [k ae_n t] are caused by asynchrony between the nasality and tongue closure features; *substitution only*: Incomplete stop closures, as in *legal* → [l iy g_fr ax l], can be described as the substitution of a complete velar closure with a critical closure, resulting in frication (the [g_fr] is a fricated [g]); *both asynchrony and substitution*: *everybody* → [eh r uw ay], which can be described as the substitution of narrow lip and tongue closures for critical or complete ones (accounting for the reduction of the [v], [b], and [dx]) and asynchrony between the tongue and lips in the middle of the word (accounting for [iy] → [uw] via early lip closure).³ Livescu and Glass represent this type of model using a DBN and show improved coverage of observed pronunciations and reduced error rate in a lexical access task on the phonetically transcribed portion of Switchboard (Greenberg *et al.*, 1996), relative to a phone-based pronunciation model.

There are a number of ways in which such a pronunciation model could be incorporated into a complete recognizer. One recent attempt was described in Sec. V B, in the context of landmark-based speech recognition. A similar pronunciation model has been applied to the task of visual speech recognition (i.e., lipreading) by Saenko *et al.* (2005a,b) and Lee and Wellekens (2001) describe a lexicon using phonetic features.

F. Recognition by articulatory synthesis

Blackburn and Young (2000) investigated an articulatory speech production model (SPM) in order to give an explicit model of coarticulation. Experiments using real articulatory data were carried out on the Wisconsin x-ray microbeam data (Westbury, 1994) and other experiments on the resource management (RM) corpus (Price *et al.*, 1988). The system rescored output from an HMM recognizer by resynthesizing articulatory traces from time-aligned phone sequences and mapping these into log-spectra using MLPs (one per phoneme). Errors between these and the original speech were used to reorder the N -best list. The model includes a notion

of articulatory effort that leads to an account of the varying strength of coarticulation. On the Wisconsin corpus, recognition performance was enhanced for all but one speaker in the test set using N -best lists with $2 \leq N \leq 5$. The SPM worked best for speakers with low initial word accuracy. On the RM corpus, N -best rescoring for small N offered modest gains, but performance deteriorated with $N=100$.

VI. DISCUSSION

A. The use of data

This article has given an overview of many approaches to using knowledge about speech production to improve automatic speech recognition. Some require articulatory measurement data, although perhaps only when training the models. Others use a more abstract representation, such as articulatory features or landmarks, which can be obtained more easily.

Approaches that require actual articulatory data will always have to deal with the problems of very limited corpora and with the challenge of doing without these data when actually performing recognition. Elegant solutions to the latter problem include Stephenson's use of DBN variables that are observed during training but hidden during recognition—a technique reminiscent of multitask training (Caruana, 1997). However, there is still more work to be done, because new (and less invasive) forms of articulatory measurement are becoming available, such as real-time magnetic resonance imaging (Narayanan *et al.*, 2004) or ultrasound. These systems offer great potential because they provide a complete contour of the tongue.

On the other hand, approaches that can utilize *knowledge* about articulation, such as articulatory features that can be initialized from phonetic transcriptions or models with kinematic constraints on (pseudo-)articulator movement, suffer less from the lack of corpora and so are perhaps more likely to transfer easily to larger tasks.

B. Explicit versus implicit modeling

The use of an explicit representation of speech production in the statistical model used for ASR allows the model to make a direct and interpretable account of the processes mentioned earlier. The behavior of such models is more easily analyzed than a large state-tied HMM system and therefore it is, in theory, possible to determine if the model is indeed learning to model specific speech processes.

The price paid for this transparency is typically that the wide variety of powerful techniques developed for HMMs are not immediately available. In some cases, this is merely for practical reasons: for example, algorithms for adaptation or discriminative training are currently more readily available for HMMs than DBNs. In other cases, there are theoretical difficulties: for example, the use of Gaussian *mixture* distributions in LDMs (Sec. V A 5) leads to intractable models.

A currently underexplored area of research is the marriage of speech production inspiration with standard models such as HMMs, DBNs, or ANNs. We have seen some initial work in this area: In Sec. IV B 1 we described systems which

first used ANNs to recover AFs from speech, then used HMMs to model these AFs either by deriving phone class posteriors (this is known as a hybrid HMM/ANN system) or by using the AFs as observations to be generated by the HMM. This latter method is essentially a Tandem system (Ellis *et al.*, 2001), but without the dimensionality reduction/decorrelation step. A true Tandem system using ANNs trained to recover AFs is a promising area to explore, as shown by Çetin *et al.* (2007), and may be particularly appropriate in a multilingual or language-independent situation. One can argue that it is far easier to devise a universal AF set than a universal phoneme set. So, while the explicit use of a speech production representation allows direct modeling of speech effects, implicit approaches like Tandem currently offer a better selection of powerful models and techniques.

C. Moving into the mainstream

There are two distinct routes by which the work we have discussed could move into the mainstream. The first is obvious: If these techniques can show real accuracy gains on the large vocabulary, very large corpus, conversational telephone speech tasks that drive research on conventional HMM-based systems then they may *replace* such systems. The second route is a little more subtle: Speech production-based models can *influence* HMMs-of-phones systems. For example, if it can be shown that a factored state representation provides a more structured or parsimonious state space and therefore allows more sophisticated parameter tying schemes, then this could be used directly in HMM systems, where the factored state is only required during training and can be “flattened” to a single hidden variable so that the model becomes a standard HMM (and can then be used in existing decoders—a major advantage). This transfer of techniques into the mainstream has the added practical advantage that the novel models can continue to be developed on smaller corpora than are currently in use in mainstream HMM research.

D. Ongoing work

In the work that we have mentioned, several strands of research can be identified that continue to be areas of active research. In particular, we wish to highlight DBNs as a very exciting framework (Zweig and Russell, 1998). With the advent of powerful toolkits such as the graphical models toolkit GMTK (Bilmes, 2002) and the Bayes Net Toolbox for Matlab (Murphy, 2001) it is now straightforward to quickly explore a very large family of models. Many of the models mentioned in this article can be implemented in the DBN framework, including all HMMs, the hybrid HMM/BN model in Sec. V A 4, linear dynamic models, factorial HMMs (Ghahramani and Jordan, 1995), and segmental models. Work in other formalisms continues too. For example, landmark-based systems, as described in Sec. V B are benefiting from the incorporation of classifiers such as SVMs. Indeed, the most successful speech production approaches to ASR generally follow the key principles of conventional techniques: Statistical models are used, parameters are learned from data; these models are used in a consistent

probabilistic framework, where evidence from all sources (e.g., the acoustic signal, the lexicon and the language model) is combined to reach the final decision.

E. Evaluation

Over the many decades of development of conventional ASR, a single standard evaluation methodology has emerged: systems are trained and evaluated on standard corpora, and compared using the standard measure of word error rate. While an imperfect measure in some regards, the universal use of WER makes cross-system comparison easy and fair.

For speech production-inspired systems, there is not yet a single evaluation methodology. This is a severe problem both in terms of the development of such methods and their acceptance into the mainstream. Those systems that perform the full ASR task and produce word transcriptions can, of course, be evaluated using WER. However, it is necessary to be able to evaluate systems under development: those that do not (yet) perform word transcription.

The lack of standard evaluation methods hampers development because it is difficult to make cross-system comparisons and thus identify the best approaches. In this paper, we have attempted to make these comparisons wherever possible, but have been limited by the lack of common corpora, task definitions, and error measures. In the following, we suggest ways in which future comparisons could be made easier.

1. Standard corpora

It is often the case that novel acoustic models cannot be developed on very large corpora (for computational reasons) and it is also often desirable to use relatively simple tasks, such as isolated words or small vocabularies (to make decoding times shorter, or error analysis easier, for example). Typical spontaneous speech corpora have vocabularies that are too large for this purpose. On the other hand, the spontaneous speech effects that production-inspired approaches aim to model are less prominent in read-text corpora (e.g., spoken digits, newspaper sentences). One solution is to construct a small vocabulary corpus from fragments of a large, spontaneous speech corpus, as has been done in the *SVitchboard 1* corpus (King *et al.*, 2005), which contains a number of manageable, yet realistic, benchmark tasks made from Switchboard 1 data.

2. Standard error measures

a. Directly measuring feature recognition accuracy.

Evaluation of AF recognition accuracy is problematic because comparing recognizer output to reference feature labels derived from phone labels will incorrectly penalize a number of the processes which the feature models are intended to capture but are not present in the reference transcription. Making comparisons at the frame level will penalize instances where the feature models change value asynchronously. This may be alleviated through the use of a recognition accuracy measure in which timing is ignored, though all feature insertions, deletions, and substitutions will still be counted as errors even where they are in fact correct.

Evaluation of landmark accuracy is also problematic since not only are both temporal and classification errors possible, there also is the possibility of insertion or deletion of landmarks. Each researcher currently appears to use a different measure.

Niyogi *et al.* (1999) use receiver operating characteristic (ROC) curves which show the trade off between false detections (landmark insertions) and false rejections (landmark deletions). Automatically detected landmarks are compared to the landmarks in the reference transcription within some time window to allow for small temporal misalignments. Juneja (2004) uses two measures. The first is the frame-level accuracy of a small number of binary manner classifiers. This measure gives a very incomplete picture of the system's performance. The second measure is for the sequence of recovered manner segments and uses the string measure "Percent correct," which does not take into account the large number of insertions that many event-based systems are prone to. "Accuracy" figures are not given. Hasegawa-Johnson *et al.* (2005) feed fragments of speech wave form (half of which contain a reference landmark, and half of which do not) to the landmark detector and the detection accuracy is measured.

b. Evaluating in terms of other linguistic units. One option for evaluation is to convert to either phones or syllables, and evaluate using a conventional WER-like measure. This can give some insights into system performance but care must be taken if a fair comparison is to be made. A conversion from AFs to phones at the frame level, as done by King and Taylor (2000), is straightforward, subject to the caveat above that phone-to-feature conversion penalizes some of the very properties of features that are thought to be most desirable.

However, if using a system that incorporates some model of the syllable or word, conversion to phones for evaluation purposes is unfair since the phonotactic constraints of syllables or words provide a strong language model that may not be part of the systems being compared to.

c. Evaluating pronunciation modeling. Measures of performance of a pronunciation model include *coverage*, the proportion of spoken pronunciations which the model considers to be allowable realizations of the correct word, and *accuracy*, the proportion of the test set for which the word is recognized correctly. Coverage can be increased trivially, by giving all possible pronunciations of every word a nonzero probability, but this would reduce accuracy by introducing confusability.

F. Future directions

Some powerful classifiers, such as SVMs, are inherently binary (that is, they can only solve two-class problems). In standard ASR systems, such classifiers can only normally be used by reformulating ASR as a two-class problem; for example, disambiguating confusable word pairs from confusion networks (e.g., Layton and Gales, 2004) or in event/landmark-based systems (Hasegawa-Johnson *et al.*, 2005; Juneja, 2004; Juneja and Espy-Wilson, 2003b). Some articulatory feature systems (e.g., SPE, Sec. II B) are naturally binary, so would be ideal for use with these classifiers.

The phonetic layer in most current systems is a bottleneck. As we have described, it is highly unsatisfactory for

describing many forms of pronunciation variation. Some of the feature-based systems we have described still use a phone-based representation between features and word. This clearly constrains the flexibility afforded by the features; for example, it will not allow modeling of highly reduced pronunciations such as the *everybody* → [eh r uw ay] example from Sec. V E because it prevents modeling asynchronous feature value changes. The problem of mediating between acoustic and word levels, while avoiding the phone(me) bottleneck, is addressed from a rather different angle by Gutkin and King (2005) who use a structural approach to discover hierarchy in speech data.

Finally, the potential for language-independent recognition systems based on AFs is huge. This is an almost unexplored area (Stüker, 2003).

G. Suggested background reading

Löfqvist (1997), Perkell (1997), and Farnetani (1997) are all chapters in Hardcastle and Laver (1997), which contains many other interesting articles, such as Steven's chapter on articulatory-acoustic relationships (Stevens, 1997), and a long bibliography. Extensive reading lists for many topics are available from Haskins Laboratories' "Talking Heads" website. For papers on novel approaches to ASR, the proceedings of the Beyond HMM Workshop (2004) are a good starting point. For general background on machine-learning and pattern recognition, we recommend: Bishop and Hinton (1995) and MacKay (2003); for dynamic Bayesian networks either Cowell *et al.* (1999) for the theory, or Bilmes and Bartels (2005) for the use of graphical models in ASR.

ACKNOWLEDGMENTS

J.F., K.R., and M.W. are funded by grants from the Engineering and Physical Sciences Research Council (EPSRC), UK and from Scottish Enterprise, UK. S.K. holds an EPSRC Advanced Research Fellowship. K.L. was funded by an NSF grant and a Luce Post-doctoral Fellowship. Thanks to Mark Hasegawa-Johnson for pointers to various landmark accuracy measures, and to the reviewers for many constructive suggestions.

¹<http://sail.usc.edu/span>. Last viewed 1/10/2007.

²Caution must be exercised when using such an " $N+1$ "-best list because, if the N hypotheses from the first pass are very poor, then even a bad second-pass model will be able to pick out the correct hypothesis (the "+1") quite easily. Picone *et al.* (1999) worked around this problem by also rescored the list with a standard HMM system for comparison.

³This example is taken from the phonetically transcribed subset of the Switchboard database (Greenberg, 1997; Greenberg *et al.*, 1996). All three examples use the ARPABET alphabet modified by diacritics as in the Switchboard phonetic transcriptions.

Atal, B. S., Chang, J. J., Mathews, M. V., and Tukey, J. W. (1978). "Inversion of articulatory-to-acoustic transformation in the vocal tract by a computer sorting technique." *J. Acoust. Soc. Am.* **63**, 1535–1555.

Bates, R. (2003). "Speaker dynamics as a source of pronunciation variability for continuous speech recognition models," Ph.D. thesis, Department of Electrical Engineering, University of Washington, Seattle, WA.

Bilmes, J. (2002). GMTK: The Graphical Models Toolkit, URL <http://ssli.ee.washington.edu/~bilmes/gmtk/>. Last viewed 1/10/2007.

Bilmes, J. (2004). "What HMMs can't do," in *Proceedings of the Institute of Electronics, Information and Communication Engineers Beyond HMM Workshop*, Kyoto, Japan, Vol. 104, SP2004-81-95.

Bilmes, J., and Bartels, C. (2005). "Graphical model architectures for speech recognition." *IEEE Signal Process. Mag.* **22**, 89–100.

Bilmes, J., Zweig, G., Richardson, T., Sandness, E., Jackson, K., Livescu, K., Xu, P., Holtz, E., Torres, K., Filali, J., and Brandman, Y. (2001). "Discriminatively structured graphical models for speech recognition," Johns Hopkins University, CSLP 2001 Summer Workshop Final Report.

Bishop, C. M., and Hinton, G. (1995). *Neural Networks for Pattern Recognition* (Clarendon, Oxford).

Bitar, N. N., and Espy-Wilson, C. Y. (1995). "A signal representation of speech based on phonetic features," in *Proceedings of the 1995 IEEE Dual-Use Technologies and Applications Conference*, SUNY Institute of Technology, Utica/Rome, NY, pp. 310–315.

Bitar, N. N., and Espy-Wilson, C. Y. (1996). "A knowledge-based signal representation for speech recognition," in *Proceedings ICASSP '96*, Atlanta, GA, pp. 29–32.

Blackburn, C. S., and Young, S. J. (2000). "A self-learning predictive model of articulator movements during speech production," *J. Acoust. Soc. Am.* **107**, 1659–1670.

Bourlard, H., and Morgan, N. (1993). *Connectionist Speech Recognition: A Hybrid Approach* (Kluwer Academic, Boston).

Bridle, J. S. (2004). "Towards better understanding of the model implied by the use of dynamic features in HMMs," in *Proceedings of the International Conference on Spoken Language Processing*, Jeju, Korea (CD-ROM).

Browman, C., and Goldstein, L. (1991). "Gestural structures: Distinctiveness, phonological processes, and historical change," in *Modularity and the Motor Theory of Speech Perception*, edited by I. Mattingly and M. Studdert-Kennedy (Erlbaum, Hillsdale, NJ), Chap. 13, pp. 313–338.

Browman, C., and Goldstein, L. (1992). "Articulatory phonology: An overview," *Phonetica* **49**, 155–180.

Caruana, R. (1997). "Multitask learning, machine learning," Ph.D. thesis, Carnegie Mellon University, Pittsburgh, PA.

Çetin, O., Kantar, A., King, S., Bartels, C., Magimai-Doss, M., Frankel, J., and Livescu, K. (2007). "An articulatory feature-based tandem approach and factored observation modeling," in *Proceedings of the IEEE International Conference on Acoustics, Speech, and Signal Processing (ICASSP-2007)* (submitted).

Chang, J., and Glass, J. (1997). "Segmentation and modeling in segment-based recognition," in *Proceedings of Eurospeech*, Rhodes, Greece (CD-ROM).

Chang, S., Wester, M., and Greenberg, S. (2005). "An elitist approach to automatic articulatory-acoustic feature classification for phonetic characterization of spoken language," *Speech Commun.* **47**, 290–311.

Choi, J.-Y. (1999). "Detection of consonant voicing: A module for a hierarchical speech recognition system," Ph.D. thesis, Department of Electrical Engineering and Computer Science, Massachusetts Institute of Technology.

Chomsky, N., and Halle, M. (1968). *The Sound Pattern of English* (Harper & Row, New York).

Cohen, J., Kamm, T., and Andreou, A. (1995). "Vocal tract normalization in speech recognition: Compensating for systematic speaker variability," *J. Acoust. Soc. Am.* **97**, 3246–3247.

Cole, R., Noel, M., Lander, T., and Durham, T. (1995). "New telephone speech corpora at CSLU," in *Proceedings of the Fourth European Conference on Speech Communication and Technology*, Vol. 1, pp. 821–824.

Cole, R., Stern, R. M., and Lasry, M. J. (1986). "Performing fine phonetic distinctions: Templates versus features," in *Invariance and Variability of Speech Processes*, edited by J. S. Perkell and D. Klatt (Erlbaum, Hillsdale, NJ), Chap. 15, pp. 325–345.

Cole, R. A., Rudnicky, A. I., Zue, V. W., and Reddy, R. (1980). "Speech as patterns on paper," in *Perception and Production of Fluent Speech*, edited by R. Cole (Erlbaum, Hillsdale, NJ), pp. 3–50.

Cowell, R., Dawid, A., Lauritzen, S., and Spiegelhalter, D. (1999). *Probabilistic Networks and Expert Systems*, Information Science & Statistics Series (Springer, New York).

Dalsgaard, P., Andersen, O., and Barry, W. (1991). "Multi-lingual label alignment using acoustic-phonetic features derived by neural-network technique," in *Proceedings of the IEEE International Conference on Acoustics, Speech, and Signal Processing*, ICASSP-91, pp. 197–200.

- De Mori, R., Laface, P., and Piccolo, E. (1976). "Automatic detection and description of syllabic features in continuous speech," *IEEE Trans. Acoust., Speech, Signal Process.* **24**, 365–379.
- Deng, L. (1992). "A generalized hidden Markov model with state-conditioned trend functions of time for the speech signal," *Signal Process.* **27**, 65–78.
- Deng, L., and Ma, J. (2000). "Spontaneous speech recognition using a statistical coarticulatory model for the vocal-tract-resonance dynamics," *J. Acoust. Soc. Am.* **108**, 3036–3048.
- Deng, L., and Sun, D. (1994a). "Phonetic classification and recognition using HMM representation of overlapping articulatory features for all classes of English sounds," in *Proceedings of the International Conference on Acoustics, Speech, and Signal Processing*, Adelaide, Australia, Vol. I, pp. 45–48.
- Deng, L., and Sun, D. X. (1994b). "A statistical approach to automatic speech recognition using the atomic units constructed from overlapping articulatory features," *J. Acoust. Soc. Am.* **95**, 2702–2719.
- Digalakis, V. (1992). "Segment-based stochastic models of spectral dynamics for continuous speech recognition," Ph.D. thesis, Boston University Graduate School, Boston, MA.
- Dusan, S., and Deng, L. (2000). "Acoustic-to-articulatory inversion using dynamical and phonological constraints," in *Proceedings of the fifth Seminar on Speech Production: Models and Data & CREST Workshop on Models of Speech Production: Motor Planning and Articulatory Modeling*, Kloster Seeon, Bavaria, Germany, pp. 237–240.
- Eide, E. (2001). "Distinctive features for use in an automatic speech recognition system," in *Proceedings of Eurospeech*, Aalborg, Denmark, pp. 1613–1616.
- Eide, E., Rohlicek, J., Gish, H., and Mitter, S. (1993). "A linguistic feature representation of the speech waveform," in *Proceedings of the International Conference on Acoustics, Speech, and Signal Processing*, Minneapolis, MN, pp. 483–486.
- Ellis, D., Singh, R., and Sivasdas, S. (2001). "Tandem acoustic modeling in large-vocabulary recognition," in *Proceedings of the IEEE International Conference on Acoustics, Speech, and Signal Processing (ICASSP-01)*, Salt Lake City, UT.
- Erler, K., and Freeman, G. H. (1996). "An HMM-based speech recogniser using overlapping articulatory features," *J. Acoust. Soc. Am.* **100**, 2500–2513.
- Espy-Wilson, C. Y., and Bitar, N. N. (1995). "Speech parametrization based on phonetic features: Application to speech recognition," in *Proceedings of Eurospeech*, Madrid, Spain, pp. 1411–1414.
- Farnetani, E. (1997). "Coarticulation and connected speech processes," in *The Handbook of Phonetic Sciences*, edited by W. J. Hardcastle and J. Laver (Blackwell, Oxford), Chap. 12, pp. 371–404.
- Fosler-Lussier, J. E. (1999). "Dynamic pronunciation models for automatic speech recognition," Ph.D. dissertation, University of California at Berkeley, Berkeley, CA.
- Frankel, J. (2003). "Linear dynamic models for automatic speech recognition," Ph.D. thesis, The Centre for Speech Technology Research, University of Edinburgh, Edinburgh, UK.
- Frankel, J., and King, S. (2001a). "ASR—Articulatory speech recognition," in *Proceedings of Eurospeech*, Aalborg, Denmark, pp. 599–602.
- Frankel, J., and King, S. (2001b). "Speech recognition in the articulatory domain: Investigating an alternative to acoustic HMMs," in *Proceedings of the Workshop on Innovations in Speech Processing*, Stratford-upon-Avon, UK (CD-ROM).
- Frankel, J., and King, S. (2005). "A hybrid ANN/DBN approach to articulatory feature recognition," in *Proceedings of Eurospeech*, Lisbon, Portugal (CD-ROM).
- Frankel, J., Richmond, K., King, S., and Taylor, P. (2000). "An automatic speech recognition system using neural networks and linear dynamic models to recover and model articulatory traces," in *Proceedings of the International Conference on Spoken Language Processing*, Beijing, China (CD-ROM).
- Frankel, J., Wester, M., and King, S. (2004). "Articulatory feature recognition using dynamic Bayesian networks," in *Proceedings of the International Conference on Spoken Language Processing*, Jeju, Korea (CD-ROM).
- Fujimura, O. (1986). "Relative invariance of articulatory movements: An iceberg model," in *Invariance and Variability of Speech Processes*, edited by J. S. Perkell and D. Klatt (Erlbaum, Hillsdale, NJ), Chap. 11, pp. 226–242.
- Fukuda, T., and Nitta, T. (2003a). "Noise-robust ASR by using distinctive phonetic features approximated with logarithmic normal distribution of HMM," in *Proceedings of Eurospeech*, Geneva, Switzerland, pp. 2185–2188.
- Fukuda, T., and Nitta, T. (2003b). "Noise-robust automatic speech recognition using orthogonalized distinctive phonetic feature vectors," in *Proceedings of Eurospeech*, Geneva, Switzerland, pp. 2189–2192.
- Fukuda, T., Yamamoto, W., and Nitta, T. (2003). "Distinctive phonetic feature extraction for robust speech recognition," in *Proceedings of the International Conference on Acoustics, Speech, and Signal Processing*, Vol. 2, pp. 25–28.
- Garofolo, J. S., Lamel, L. F., Fisher, W. M., Fiscus, J. G., Pallett, D. S., and Dahlgren, N. L. (1993). "DARPA TIMIT acoustic-phonetic continuous speech corpus CD-ROM," National Institute of Standards and Technology, Washington, DC, NISTIR 4930.
- Ghahramani, Z., and Jordan, M. I. (1995). "Factorial hidden markov models," in *Proceedings of the Conference of Advances in Neural Information Processing Systems*, edited by D. S. Touretzky, M. C. Mozer, and M. E. Hasselmo (MIT, Cambridge, MA), Vol. 8, pp. 472–478.
- Glass, J. (2003). "A probabilistic framework for segment-based speech recognition," *Comput. Speech Lang.* **17**, 137–152.
- Glass, J. R. (1988). "Finding acoustic regularities in speech: Applications to phonetic recognition," Ph.D. thesis, Massachusetts Institute of Technology, Cambridge, MA.
- Goldberg, H. G., and Reddy, D. R. (1976). "Feature extraction, segmentation and labelling in the Harpy and Hearsay-II systems," *J. Acoust. Soc. Am.* **60**, 1044–1067.
- Greenberg, S. (1997). "The switchboard transcription project," 1996 Large Vocabulary Continuous Speech Recognition Summer Research Workshop Technical Report Series Research Report 24, Center for Language and Speech Processing, Johns Hopkins University, Baltimore, MD.
- Greenberg, S., Hollenback, J., and Ellis, D. (1996). "Insights into spoken language gleaned from phonetic transcription of the Switchboard corpus," in *Proceedings of the International Conference on Spoken Language Processing*, Philadelphia, PA, pp. 24–27.
- Gutkin, A., and King, S. (2005). "Detection of symbolic gestural events in articulatory data for use in structural representations of continuous speech," in *Proceeding of the IEEE International Conference on Acoustics, Speech, and Signal Processing*, ICASSP-05, Philadelphia, PA, Vol. I, pp. 885–888.
- Halberstadt, A., and Glass, J. (1998). "Heterogeneous measurements and multiple classifiers for speech recognition," in *Proceedings of the International Conference on Spoken Language Processing*, Sydney, Australia, pp. 995–998.
- Hardcastle, W. J., and Laver, J., eds. (1997). *The Handbook of Phonetic Sciences* (Blackwell, Oxford).
- Harrington, J. (1987). "Acoustic cues for automatic recognition of English consonants," in *Speech Technology: A survey*, edited by M. A. Jack and J. Laver (Edinburgh University Press, Edinburgh), pp. 19–74.
- Harris, J. (1994). *English Sound Structure* (Blackwell, Oxford).
- Hasegawa-Johnson, M., Baker, J., Borys, S., Chen, K., Coogan, E., Greenberg, S., Juneja, A., Kirchoff, K., Livescu, K., Mohan, S., Muller, J., Sonmez, K., and Wang, T. (2005). "Landmark-based speech recognition: Report of the 2004 Johns Hopkins Summer Work-shop," Technical report, Johns Hopkins University.
- Hazen, T. J., Hetherington, I. L., Shu, H., and Livescu, K. (2005). "Pronunciation modeling using a finite-state transducer representation," *Speech Commun.* **46**, 189–203.
- Hiroya, S., and Honda, M. (2004). "Estimation of articulatory movements from speech acoustics using an HMM-based speech production model," *IEEE Trans. Speech Audio Process.* **12**, 175–185.
- Hogden, J., Lofqvist, A., Gracco, V., Zlokarnik, I., Rubin, P., and Saltzman, E. (1996). "Accurate recovery of articulator positions from acoustics: New conclusions based on human data," *J. Acoust. Soc. Am.* **100**, 1819–1834.
- Hogden, J., Nix, D., and Valdez, P. (1998). "An articulatorily constrained, maximum likelihood approach to speech recognition," Technical report, Los Alamos National Laboratory, Los Alamos, NM.
- Holmes, W. J., and Russell, M. (1999). "Probabilistic-trajectory segmental HMMs," *Comput. Speech Lang.* **13**, 3–37.
- Honda, K., Hirai, H., and Dang, J. (1994). "A physiological model of speech production and the implication of tongue-larynx interaction," in *Proceedings of the International Conference on Spoken Language Processing*, Yokohama, Japan, pp. 175–178.
- Hoole, P., Zierdt, A., and Geng, C. (2003). "Beyond 2D in articulatory data

- acquisition and analysis," in *Proceedings of the 15th International Congress of Phonetic Sciences*, Barcelona, Spain, pp. 265–268.
- Howitt, A. W. (1999). "Vowel landmark detection," in *Proceedings of Eurospeech*, Budapest, Hungary, Vol. 6, pp. 2777–2780.
- International Phonetic Association (1999). *Handbook of the International Phonetic Association: A Guide to the Use of the International Phonetic Alphabet* (Cambridge University Press, Cambridge, UK).
- Iso, K. (1993). "Speech recognition using dynamical model of speech production," in *Proceedings of the International Conference on Acoustics, Speech, and Signal Processing*, Minneapolis, MN, Vol. 2, pp. 283–286.
- Jackson, P., Lo, B.-H., and Russell, M. (2002). "Data-driven, non-linear, formant-to-acoustic mapping for ASR," *IEEE Electron Device Lett.* **38**, 667–669.
- Juneja, A. (2004). "Speech recognition based on phonetic features and acoustic landmarks," Ph.D. thesis, University of Maryland, College Park, MD.
- Juneja, A., and Espy-Wilson, C. (2003a). "An event-based acoustic-phonetic approach to speech segmentation and E-set recognition," in *Proceedings of the 15th International Congress of Phonetic Sciences*, Barcelona, Spain (CD-ROM).
- Juneja, A., and Espy-Wilson, C. (2003b). "Speech segmentation using probabilistic phonetic feature hierarchy and support vector machines," in *Proceedings of the International Joint Conference on Neural Networks*, Portland, OR.
- Junqua, J. (1993). "The Lombard Reflex and its role on human listeners and automatic speech recognisers," *J. Acoust. Soc. Am.* **93**, 510–524.
- Jurafsky, D., Ward, W., Jianping, Z., Herold, K., Xiuyang, Y., and Sen, Z. (2001). "What kind of pronunciation variation is hard for triphones to model?," in *Proceedings of the International Conference on Acoustics, Speech, and Signal Processing*, Vol. 1, Salt Lake City, UT, pp. 577–580.
- Kaburagi, T., and Honda, M. (1996). "A model of articulator trajectory formation based on the motor tasks of vocal-tract shapes," *J. Acoust. Soc. Am.* **99**, 3154–3170.
- King, S., Bartels, C., and Bilmes, J. (2005). "SVitchboard 1: Small vocabulary tasks from switchboard 1," in *Proceedings of Interspeech*, Lisbon, Portugal (CD-ROM).
- King, S., Stephenson, T., Isard, S., Taylor, P., and Strachan, A. (1998). "Speech recognition via phonetically featured syllables," in *Proceedings of the International Conference on Spoken Language Processing*, Vol. 3, Sydney, Australia, pp. 1031–1034.
- King, S., and Taylor, P. (2000). "Detection of phonological features in continuous speech using neural networks," *Comput. Speech Lang.* **14**, 333–353.
- Kirchhoff, K. (1996). "Syllable-level desynchronisation of phonetic features for speech recognition," in *Proceedings of the International Conference on Spoken Language Processing*, Vol. 4, pp. 2274–2276.
- Kirchhoff, K. (1999). "Robust speech recognition using articulatory information," Ph.D. thesis, University of Bielefeld, Bielefeld, Germany.
- Kirchhoff, K., Fink, G., and Sagerer, G. (2002). "Combining acoustic and articulatory feature information for robust speech recognition," *Speech Commun.* **37**, 303–319.
- Krstulović, S. (1999). "LPC-based inversion of the DRM articulatory model," in *Proceedings of Eurospeech*, Budapest, Hungary, Vol. 1, pp. 125–128.
- Ladefoged, P. (1997). "Linguistic phonetic descriptions," in *The Handbook of Phonetic Sciences*, edited by W. J. Hardcastle and J. Laver (Blackwell, Oxford), Chap. 19, pp. 581–618.
- Layton, M., and Gales, M. (2004). "Maximum margin training of generative kernels," Technical Report No. CUED/F-INFENG/TR.484, Cambridge University Engineering Department.
- Lee, K.-T., and Wellekens, C. J. W. (2001). "Dynamic lexicon using phonetic features," in *Proceedings of the Eurospeech*, Aalborg, Denmark.
- Leonard, R. (1984). "A database for speaker-independent digit recognition," in *Proceedings of the International Conference on Acoustics, Speech, and Signal Processing*, San Diego, Vol. 1, pp. 328–331.
- Lieberman, A. M., and Mattingly, I. G. (1985). "The motor theory of speech perception revised," *Cognition* **21**, 1–36.
- Livescu, K. (2005). "Feature-based pronunciation modeling for automatic speech recognition," Ph.D. thesis, MIT EECS Department, Cambridge, MA.
- Livescu, K., and Glass, J. (2004a). "Feature-based pronunciation modeling for speech recognition," in *Proceedings of the Human Language Technology Conference/North American Chapter of the Association for Computational Linguistics Annual Meeting*, Boston (CD-ROM).
- Livescu, K., and Glass, J. (2004b). "Feature-based pronunciation modeling with trainable asynchrony probabilities," in *Proceedings of the International Conference on Spoken Language Processing*, Jeju, South Korea (CD-ROM).
- Livescu, K., Glass, J., and Bilmes, J. (2003). "Hidden feature modeling for speech recognition using dynamic Bayesian networks," in *Proceedings of Eurospeech*, Geneva, Switzerland, Vol. 4, pp. 2529–2532.
- Lochschmidt, B. (1982). "Acoustic-phonetic analysis based on an articulatory model," in *Automatic Speech Analysis and Recognition*, edited by J.-P. Hayton (Reidel, Dordrecht), pp. 139–152.
- Löfqvist, A. (1997). "Theories and models of speech production," in *The Handbook of Phonetic Sciences*, edited by W. J. Hardcastle and J. Laver (Blackwell, Oxford), Chap. 13, pp. 405–426.
- Luo, X., and Jelinek, F. (1998). "Nonreciprocal data sharing in estimating HMM parameters," in *Proceedings of the International Conference on Spoken Language Processing*, Sydney, Australia.
- Ma, J., and Deng, L. (2004a). "A mixed-level switching dynamic system for continuous speech recognition," *Comput. Speech Lang.* **18**, 49–65.
- Ma, J., and Deng, L. (2004b). "Target-directed mixture linear dynamic models for spontaneous speech recognition," *IEEE Trans. Speech Audio Process.* **12**, 47–58.
- MacKay, D. J. C. (2003). *Information Theory, Inference and Learning Algorithms* (Cambridge University Press, Cambridge).
- Maddieson, I. (1997). "Phonetic universals," in *The Handbook of Phonetic Sciences*, edited by W. J. Hardcastle and J. Laver (Blackwell, Oxford), Chap. 20, pp. 619–639.
- Markov, K., Dang, J., Iizuka, Y., and Nakamura, S. (2003). "Hybrid HMM/BN ASR system integrating spectrum and articulatory features," in *Proceedings of Eurospeech*, Vol. 2, pp. 965–968.
- McAllaster, D., Gillick, L., Scattone, F., and Newman, M. (1998). "Fabricating conversational speech data with acoustic models: A program to examine model-data mismatch," in *Proceedings of the International Conference on Spoken Language Processing*, Sydney, Australia, Vol. 5, pp. 1847–1850.
- McDermott, E. (2004). "Production models for speech recognition," in *Proceedings of the Institute of Electronics, Information and Communication Engineers Beyond HMM Workshop*, Kyoto, Japan, Vol. 104, pp. 1–6, SP2004-81-95.
- Metze, F., and Waibel, A. (2002). "A flexible stream architecture for ASR using articulatory features," in *Proceedings of the International Conference on Spoken Language Processing*, Denver, CO (CD-ROM).
- Murphy, K. (2001). "The Bayes Net Toolbox for Matlab," *Computing Science and Statistics* (CD-ROM), Vol. 33.
- Muzumdar, M. (1996). "Automatic acoustic measurement optimization for segmental speech recognition," Master's thesis, MIT Department of Electrical Engineering and Computer Science, Cambridge, MA.
- Narayanan, S., Nayak, K., Lee, S., Sethy, A., and Byrd, D. (2004). "An approach to real-time magnetic resonance imaging for speech production," *J. Acoust. Soc. Am.* **115**, 1771–1776.
- Nix, D., and Hogden, J. (1998). "Maximum-likelihood continuity mapping (MALCOM): An alternative to HMMs," in *Proceedings of the Advances in Neural Information Processing Systems Conference, NIPS*, edited by M. Kearns, S.olla, and D. Cohn (MIT, Cambridge), Vol. 11, pp. 744–750.
- Niyogi, P., Burges, C., and Ramesh, P. (1999). "Distinctive feature detection using support vector machines," in *Proceedings of the IEEE International Conference on Acoustics, Speech, and Signal Processing, ICASSP-99*, Phoenix, AZ.
- Nock, H. J. (2001). "Techniques for modelling phonological processes in automatic speech recognition," Ph.D. thesis, Cambridge University Engineering Department, Cambridge, UK.
- Omar, M. K., and Hasegawa-Johnson, M. (2002). "Maximum mutual information based acoustic features representation of phonological features for speech recognition," in *Proceedings of the International Conference on Acoustics, Speech, and Signal Processing*, Vol. 1, Orlando, FL, pp. 1–81.
- Ostendorf, M. (1999). "Moving beyond the 'beads-on-a-string' model of speech," in *Proceedings of the IEEE Automatic Speech Recognition and Understanding Workshop*, Keystone, CO, Vol. 1, pp. 79–83.
- Papcun, G., Hochberg, J., Thomas, T. R., Laroche, F., Zachs, J., and Levy, S. (1992). "Inferring articulation and recognising gestures from acoustics with a neural network trained on x-ray microbeam data," *J. Acoust. Soc. Am.* **92**, 688–700.
- Perkell, J. (1997). "Articulatory processes," in *The Handbook of Phonetic Sciences*, edited by W. J. Hardcastle and J. Laver (Blackwell, Oxford), Chap. 11, pp. 333–370.

- Picone, J., Pike, S., Regan, R., Kamm, T., Bridle, J., Deng, L., Ma, Z., Richards, H., and Schuster, M. (1999). "Initial evaluation of hidden dynamic models on conversational speech," in *Proceedings of the International Conference on Acoustics, Speech, and Signal Processing*, Phoenix, AZ, Vol. 1, pp. 109–112.
- Price, P., Fisher, W. M., Bernstein, J., and Pallett, D. S. (1988). "The DARPA 1000-word resource management database for continuous speech recognition," in *Proceedings of the International Conference on Acoustics, Speech, and Signal Processing*, New York, Vol. 1, pp. 651–654.
- Rahim, M., Goodyear, C., Kleijn, W., Schroeter, J., and Sondhi, M. (1993). "On the use of neural networks in articulatory speech synthesis," *J. Acoust. Soc. Am.* **93**, 1109–1121.
- Richards, H. B., and Bridle, J. S. (1999). "The HDM: A segmental hidden dynamic model of coarticulation," in *Proceedings of the International Conference on Acoustics, Speech, and Signal Processing*, Phoenix, AZ, Vol. 1, pp. 357–360.
- Richardson, M., Bilmes, J., and Diorio, C. (2000a). "Hidden-articulator Markov models for speech recognition," in *Proceedings of ASR2000—Automatic Speech Recognition: Challenges for the new Millennium, ISCA Tutorial and Research Workshop*, Paris, France, pp. 133–139.
- Richardson, M., Bilmes, J., and Diorio, C. (2000b). "Hidden-articulator Markov models: Performance improvements and robustness to noise," in *Proceedings of the International Conference on Spoken Language Processing*, Beijing, China (CD-ROM).
- Richmond, K. (2002). "Estimating articulatory parameters from the acoustic speech signal," Ph.D. thesis, Centre for Speech Technology Research, University of Edinburgh, Edinburgh, UK.
- Richmond, K., King, S., and Taylor, P. (2003). "Modelling the uncertainty in recovering articulation from acoustics," *Comput. Speech Lang.* **17**, 153–172.
- Riley, M. D., and Ljolje, A. (1996). "Automatic generation of detailed pronunciation lexicons," in *Automatic Speech and Speaker Recognition: Advanced Topics*, edited by C.-H. Lee, F. K. Soong, and K. K. Paliwal (Kluwer Academic, Dordrecht), pp. 285–302.
- Rose, R. C., Schroeter, J., and Sondhi, M. M. (1996). "The potential role of speech production models in automatic speech recognition," *J. Acoust. Soc. Am.* **99**, 1699–1709.
- Rosti, A.-V. I. (2004). "Linear Gaussian models for speech recognition," Ph.D. thesis, Cambridge University Engineering Department, Cambridge, UK.
- Roweis, S. (1999). "Data driven production models for speech processing," Ph.D. thesis, California Institute of Technology, Pasadena, CA.
- Rubin, P., and Vatikiotis-Bateson, E. (1998). "Measuring and modeling speech production in humans," in *Animal Acoustic Communication: Recent Technical Advances*, edited by S. L. Hopp and C. S. Evans (Springer, New York), pp. 251–290.
- Russell, M., and Jackson, P. (2005). "A multiple-level linear/linear segmental HMM with a formant-based intermediate layer," *Comput. Speech Lang.* **19**, 205–225.
- Saenko, K., Livescu, K., Glass, J., and Darrell, T. (2005a). "Production domain modeling of pronunciation for visual speech recognition," in *Proceedings of the International Conference on Acoustics, Speech, and Signal Processing*, Vol. 5, pp. 473–476.
- Saenko, K., Livescu, K., Siracusa, M., Wilson, K., Glass, J., and Darrell, T. (2005b). "Visual speech recognition with loosely synchronized feature streams," in *Proceedings of the International Conference on Computer Vision*, Beijing, China (CD-ROM).
- Saltzman, E., and Munhall, K. G. (1989). "A dynamical approach to gestural patterning in speech production," *Ecological Psychol.* **4**, 333–382.
- Saraclar, M., Nock, H., and Khudanpur, S. (2000). "Pronunciation modeling by sharing Gaussian densities across phonetic models," *Comput. Speech Lang.* **14**, 137–160.
- Seide, F., Zhou, J., and Deng, L. (2003). "Coarticulation modeling by embedding a target-directed hidden trajectory model into HMM—MAP decoding and evaluation," in *Proceedings of the International Conference on Acoustics, Speech, and Signal Processing*, Hong Kong, China, Vol. 1, pp. 748–751.
- Shirai, K., and Kobayashi, T. (1986). "Estimating articulatory motion from speech wave," *Speech Commun.* **5**, 159–170.
- Shu, H., and Hetherington, I. L. (2002). "EM training of finite-state transducers and its application to pronunciation modeling," in *Proceedings of the International Conference on Spoken Language Processing*, Denver, CO (CD-ROM).
- Stephenson, T., Boulard, H., Bengio, S., and Morris, A. (2000). "Automatic speech recognition using dynamic Bayesian networks with both acoustic and articulatory variables," in *Proceedings of the International Conference on Spoken Language Processing*, Beijing, China, Vol. 2, pp. 951–954.
- Stephenson, T. A., Magimai-Doss, M., and Boulard, H. (2004). "Speech recognition with auxiliary information," *IEEE Trans. Speech Audio Process.* **12**, 189–203.
- Stevens, K. N. (1997). "Articulatory-acoustic-auditory relationships," in *The Handbook of Phonetic Sciences*, edited by W. J. Hardcastle and J. Laver (Blackwell, Oxford), Chap. 15, pp. 462–506.
- Stevens, K. N. (2000). "From acoustic cues to segments, features and words," in *Proceedings of the International Conference on Spoken Language Processing*, Beijing, China, Vol. 1, pp. A1–A8.
- Stevens, K. N. (2002). "Toward a model of lexical access based on acoustic landmarks and distinctive features," *J. Acoust. Soc. Am.* **111**, 1872–1891.
- Stone, M. (1997). "Articulatory processes," in *The Handbook of Phonetic Sciences*, edited by W. J. Hardcastle and J. Laver (Blackwell, Oxford), Chap. 1, pp. 12–32.
- Stüker, S. (2003). "Multilingual articulatory features," Master's thesis, Carnegie Mellon University, Pittsburgh, PA.
- Sun, J., Jing, X., and Deng, L. (2000). "Data-driven model construction for continuous speech recognition using overlapping articulatory features," in *Proceedings of the International Conference on Spoken Language Processing*, Beijing, China (CD-ROM).
- Tang, M., Seneff, S., and Zue, V. (2003). "Two-stage continuous speech recognition using feature-based models: A preliminary study," in *Proceedings of the IEEE Automatic Speech Recognition and Understanding Workshop*, U.S. Virgin Islands, pp. 49–54.
- Toda, T., Black, A., and Tokuda, K. (2004). "Acoustic-to-articulatory inversion mapping with Gaussian mixture model," in *Proceedings of the International Conference on Spoken Language Processing*, Jeju, Korea (CD-ROM).
- Tokuda, K., Zen, H., and Kitamura, T. (2004). "Reformulating the HMM as a trajectory model," in *Proceedings of the Institute of Electronics, Information and Communication Engineers Beyond HMM Workshop*, Kyoto, Japan, Vol. 104, SP2004-81-95.
- Wakita, H. (1979). "Estimation of vocal-tract shapes from acoustical analysis of the speech wave: The state of the art," *IEEE Trans. Speech Audio Process.* **ASSP-27**, 281–285.
- Weintraub, M., Taussig, K., Hunnicke-Smith, K., and Snodgrass, A. (1996). "Effect of speaking style on LVCSR performance," in *Proceedings of the International Conference on Spoken Language Processing*, Philadelphia, PA, pp. 16–19.
- Westbury, J. (1994). *X-Ray Microbeam Speech Production Database User's Handbook* (University of Wisconsin Press, Madison, WI).
- Wester, M. (2003). "Pronunciation modeling for ASR—Knowledge-based and data-derived methods," *Comput. Speech Lang.* **17**, 69–85.
- Wester, M., Frankel, J., and King, S. (2004). "Asynchronous articulatory feature recognition using dynamic Bayesian networks," in *Proceedings of the Institute of Electronics, Information and Communication Engineers Beyond HMM Workshop*, Kyoto, Japan, Vol. 104, pp. 37–42, SP2004-81-95.
- Wester, M., Greenberg, S., and Chang, S. (2001). "A Dutch treatment of an elitist approach to articulatory-acoustic feature classification," in *Proceedings of Eurospeech*, Aalborg, Denmark, pp. 1729–1732.
- Wrench, A. A. (2001). "A new resource for production modelling in speech technology," in *Proceedings of the Workshop on Innovations in Speech Processing*, Stratford-upon-Avon, UK (CD-ROM).
- Wrench, A. A., and Hardcastle, W. J. (2000). "A multichannel articulatory speech database and its application for automatic speech recognition," in *Proceedings of the Fifth Seminar on Speech Production: Models and Data & CREST Workshop on Models of Speech Production: Motor Planning and Articulator Modelling*, Kloster Seeon, Bavaria, Germany, pp. 305–308.
- Wrench, A. A., and Richmond, K. (2000). "Continuous speech recognition using articulatory data," in *Proceedings of the International Conference on Spoken Language Processing*, Beijing, China (CD-ROM).
- Young, S., Evermann, G., Kershaw, D., Moore, G., Odell, J., Ollason, P., Povey, D., Valtchev, V., and Woodland, P. (2002). "The HTK Book (for HTK Version 3.2)," Cambridge University Engineering Department, Cambridge, UK.
- Zhou, J., Seide, F., and Deng, L. (2003). "Coarticulation modeling by embedding a target-directed hidden trajectory model into HMM—Model and training," in *Proceedings of the International Conference on Acoustics, Speech, and Signal Processing*, Hong Kong, China, Vol. 1, pp. 744–747.

- Zlokarnik, I. (1995). "Adding articulatory features to acoustic features for automatic speech recognition," *J. Acoust. Soc. Am.* **97**, 3246.
- Zue, V. (1985). "The use of speech knowledge in automatic speech recognition," *Proc. IEEE* **73**, 1602–1615.
- Zue, V., Glass, J., Phillips, M., and Seneff, S. (1989). "The MIT SUMMIT speech recognition system: A progress report," in *Proceedings of the DARPA Speech and Natural Language Workshop*, Cape Cod, MA, pp. 126–134.
- Zweig, G., and Russell, S. J. (1998). "Speech recognition with dynamic Bayesian networks," in *Proceedings of the 15th National Conference on Artificial Intelligence and 10th Innovative Applications of Artificial Intelligence Conference*, Madison, WI, pp. 173–180.

LETTERS TO THE EDITOR

This Letters section is for publishing (a) brief acoustical research or applied acoustical reports, (b) comments on articles or letters previously published in this Journal, and (c) a reply by the article author to criticism by the Letter author in (b). Extensive reports should be submitted as articles, not in a letter series. Letters are peer-reviewed on the same basis as articles, but usually require less review time before acceptance. Letters cannot exceed four printed pages (approximately 3000–4000 words) including figures, tables, references, and a required abstract of about 100 words.

Comment on “Analysis of the time-reversal operator for scatterers of finite size,” by D. H. Chambers [J. Acoust. Soc. Am. 112, 411–419 (2002)] (L)

Xudong Chen^{a)}

Department of Electrical and Computer Engineering, National University of Singapore, Singapore, 117576, Singapore

(Received 21 August 2006; revised 5 October 2006; accepted 12 November 2006)

This letter concerns the paper “Analysis of the time-reversal operator for scatterers of finite size” [J. Acoust. Soc. Am. 112, 411–419 (2002)]. The number of possible eigenvalues and eigenfunctions of the time reversal operator for a finite sphere given in the paper is much more than the correct number, which is proven to be the total number of multipole moments induced inside the finite sphere. © 2007 Acoustical Society of America. [DOI: 10.1121/1.2405130]

PACS number(s): 43.20.Fn, 43.60.Pt [LLT]

Pages: 743–744

I. INTRODUCTION

Although the paper by Chambers¹ shows that the time reversal operator for a finite sphere has a large number of distinguishable eigenvalues and eigenfunctions, the present author believes that the total number of possible eigenvalues and eigenfunctions given there is incorrect. The purpose of this letter is to show that many eigenfunctions given in Ref. 1 are in fact linearly dependent so that the time reversal operator has a much lower total number of eigenvalues, which is proven to be the total number of multipole moments induced inside the finite sphere.

II. NUMBER OF TOTAL EIGENVALUES AND EIGENFUNCTIONS

The reduced scattering kernel is given by Eq. (11) in Ref. 1,

$$K(\xi', \eta', \xi, \eta) = \frac{1}{r_M r'_M} \sum_{n=0}^N A_n (-1)^n \left(\frac{\xi' \xi + \eta' \eta + z_M^2}{r'_M r_M} \right)^n, \quad (1)$$

where (ξ, η, z_M) and (ξ', η', z_M) denote the positions of the transmitter (\mathbf{r}) and receiver (\mathbf{r}') in the time-reversal mirror (TMR), respectively, and A_n are complex coefficients. For each integer n , the kernel is separated to $(n+1)(n+2)/2$ linearly independent terms, amounting to a total number of $T_0 = (N+3)(N+2)(N+1)/6$ linearly independent terms for all n

ranging from 0 to N . The reduced scattering kernel can be expressed by

$$K(\mathbf{r}'; \mathbf{r}) = \sum_{t=1}^{T_0} C_t f_t(\mathbf{r}') g_t(\mathbf{r}), \quad (2)$$

where C_t are complex coefficients related to the previous coefficients A_n .

For ease of presenting, the TMR is discretized into S parts, and the integers i and j index the receiver and transmitter. Thus, the scattering kernel becomes the scattering matrix K with elements

$$K_{i,j} = \sum_{t=1}^{T_0} C_t f_t(\mathbf{r}_i) g_t(\mathbf{r}_j), \quad i, j = 1, 2, \dots, S. \quad (3)$$

Thus the scattering matrix can be expressed as a sum of T_0 terms, each of which is an outer product of vectors

$$K = \sum_{t=1}^{T_0} C_t \mathbf{f}_t \mathbf{g}_t^T, \quad (4)$$

where $\mathbf{f}_t = [f_t(\mathbf{r}_1), f_t(\mathbf{r}_2), \dots, f_t(\mathbf{r}_S)]^T$, $\mathbf{g}_t = [g_t(\mathbf{r}_1), g_t(\mathbf{r}_2), \dots, g_t(\mathbf{r}_S)]^T$, and the superscript “ T ” stands for transpose. The singular value decomposition for the scattering matrix K is given by

$$K \phi = \mu \phi^*. \quad (5)$$

Substitution of Eq. (4) into Eq. (5) yields

^{a)}Electronic mail: elechenx@nus.edu.sg

$$\phi = \sum_{t=1}^{T_0} \mathbf{f}_t^* C_t^* \left(\frac{\mathbf{g}_t^T \phi}{\mu} \right)^* \quad (6)$$

Thus the eigenfunction can be expressed as a linear superposition of \mathbf{f}_t^* ,

$$\phi = \sum_{t=1}^{T_0} \alpha_t \mathbf{f}_t^* \quad (7)$$

where complex coefficients α_t are equal to $C_t^*(\mathbf{g}_t^T \phi / \mu)^*$.

Although the matrixes $\mathbf{f}_t \mathbf{g}_t^T$ are linearly independent, the vectors \mathbf{f}_t are not. An examination of Eq. (1) yields some examples. The i th ($i=1, 2, \dots, S$) components of \mathbf{f}_t for $n=0, 1, 2$ are listed as follows:

$$\begin{aligned} n=0: f_{1(i)} &= \frac{1}{r_i}, \\ n=1: f_{2(i)} &= \frac{\xi_i}{r_i^2}, \quad f_{3(i)} = \frac{\eta_i}{r_i^2}, \quad f_{4(i)} = \frac{z_M}{r_i^2}, \\ n=2: f_{5(i)} &= \frac{\xi_i^2}{r_i^3}, \quad f_{6(i)} = \frac{\eta_i^2}{r_i^3}, \quad f_{7(i)} = \frac{z_M^2}{r_i^3}, \\ f_{8(i)} &= \frac{\xi_i \eta_i}{r_i^3}, \quad f_{9(i)} = \frac{z_M \xi_i}{r_i^3}, \quad f_{10(i)} = \frac{z_M \eta_i}{r_i^3}. \end{aligned}$$

It is obvious that $f_{7(i)} = f_{1(i)} - f_{5(i)} - f_{6(i)}$, since $\xi_i^2 + \eta_i^2 + z_M^2 = r_i^2$. Thus \mathbf{f}_7 is linearly dependent on \mathbf{f}_1 , \mathbf{f}_5 , and \mathbf{f}_6 since the subscript i can be any of $\{1, 2, \dots, S\}$. Similarly, for $n > 2$, any vector with a power of z_M greater than 1 is linearly dependent on others. The number of terms with the zeroth and first powers of z_M are $n+1$ and n , respectively, amounting to a total of $2n+1$ linearly independent vectors \mathbf{f} . This result agrees with the total number of the n th order multipoles, which is seen from the spherical harmonic expansion for a general scattered field [Eq. (12) in Ref. 1],

$$P_S(r, \theta, \varphi) = \sum_{n=0}^{\infty} \sum_{l=-n}^n C_{ln} P_n^l(-\cos \theta) e^{il\varphi} h_n(kr). \quad (8)$$

There are $2n+1$ multipole terms for each n since l ranges from $-n$ to n . For $n=0, 1, \dots, N$, there are $T_1 = (N+1)^2$ linearly independent vectors \mathbf{f} in total, which is much less than $(N+3)(N+2)(N+1)/6$ as given by Ref. 1.

Equation (7) reduces to a new expression of the eigenfunction that is a superposition of linearly independent vectors \mathbf{f}_t ,

$$\phi = \sum_{t=1}^{T_1} \beta_t \mathbf{f}_t^* \quad (9)$$

where β_t are complex coefficients related to α_t . Substitution of Eq. (4) and Eq. (9) into Eq. (5) enables one to obtain up to T_1 eigenvalues μ and coefficients of their corresponding eigenfunctions $[\beta_1, \beta_2, \dots, \beta_{T_1}]^T$.

The actual number of eigenvalues may be less, depending on the configuration of the time-reversal mirror. For example, the two examples investigated in Sec. V of Ref. 1 use a linear array, where the values of η and η' are set to zero. It is easy to show that there are only two independent terms for each order n greater than zero, and one for $n=0$, amounting to $2N+1$ vectors for all terms up to N . Consequently, since the number N is set to the smallest integer greater than three plus the maximum ka of interest, the number of eigenvalues scales with $(ka)^2$ for planar arrays, and ka for linear arrays.

III. CONCLUSION

The number of possible eigenvalues and eigenfunctions of the time-reversal operators for a finite sphere is equal to the number of possible multipole moments induced in the sphere, which is much less than that presented in Ref. 1.

¹D. H. Chambers, "Analysis of the time-reversal operator for scatterers of finite size," J. Acoust. Soc. Am. **112**, 411–419 (2002).

Analysis of voice source characteristics using a constrained polynomial representation of voice source signals (L)

Tokihiko Kaburagi

Faculty of Design, Kyushu University, 4-9-1 Shiobaru, Minami-ku, Fukuoka, 815-8540 Japan

Kouji Kawai

Fujitsu Prime Software Technologies Limited, 1-16-38 Aoi, Higashi-ku, Nagoya-shi, Aichi 461-0004 Japan

Shinya Abe

Graduate School of Design, Kyushu University, 4-9-1 Shiobaru, Minami-ku, Fukuoka, 815-8540 Japan

(Received 2 August 2004; revised 21 June 2006; accepted 7 September 2006)

To analyze the characteristics of voice source signals from speech, a model is presented in the form of polynomial function by expanding the definition of the Rosenberg model. In combination with the all-pole assumption of the vocal-tract filter, methods are described for the pitch-synchronous speech analysis and temporal search of the glottal opening and closing instants. Because the source and filter models are both linear, the parameter estimation problem can be conveniently solved. In addition, the temporal search method can refine the locations of the glottal events and improve the accuracy of the parameter estimation. Analyses of non-nasalized voiced speech are conducted using an electroglottographic device from which the initial estimate of the temporal information is given. © 2007 Acoustical Society of America. [DOI: 10.1121/1.2359234]

PACS number(s): 43.72.Ar, 43.70.Gr [DOS]

Pages: 745–748

I. INTRODUCTION

To study the voice acoustics, a number of parametric models were proposed to represent voice source signals. Such models were also used to estimate the source and vocal-tract characteristics jointly from speech (Klatt and Klatt, 1990; Childers and Lee, 1991; Kaburagi and Kawai, 2003). However, some models have inconveniences for determining the values of model parameters. For example, determination of the α parameter of the LF model (Fant, 1986) results in a nonlinear problem giving rise to a large amount of computation, and there still exists a nonlinear equation constraining the time parameters of the R++ model (Veldhuis, 1998). Kasuya *et al.* (1999) therefore employed a simple RK model (Klatt and Klatt, 1990), because such nonlinearities are especially inconvenient for speech analysis. On the other hand, Milenkovic (1986, 1993) showed that complexities of the estimation problem can be reduced using linearized models formed as polynomial functions.

This paper presents a speech analysis method by combining models of the vocal tract and voice source signal. While the tract filter is modeled using the conventional all-pole assumption, the voice source signal is represented as a polynomial, constructed by overlapping multiple base signal. Also, these base signals are obtained by expanding the Rosenberg model (Rosenberg, 1971).

Speech analysis is then performed using procedures of the joint parameter estimation and temporal searching. The optimal values of the model parameters are uniquely determined as in Milenkovic (1986) when the instants of the glottal opening and closing events are given. In addition, the temporal search procedure efficiently refines the time locations of glottal events initially provided, for example, by an electroglottographic (EGG) device under an error criterion.

II. VOICE SOURCE REPRESENTATION AND SPEECH PARAMETER ESTIMATION

A polynomial expression is used to model the time-differentiated glottal flow as

$$g(t) = (2 + \alpha)t^{1+\alpha} - (3 + \alpha)t^{2+\alpha} \quad (1)$$

for a time interval ($0 \leq t \leq 1$) between the instants of glottal opening ($t=0$) and closing ($t=1$). When α , a parameter specifying the polynomial order, is zero, $g(t)$ is coincident with the model proposed by Rosenberg (1971). Irrespective of the value of α , the expression meets conditions

$$g(t) = \begin{cases} 0, & t = 0, \\ -1, & t = 1, \end{cases} \quad (2)$$

at both boundaries and satisfies an integral condition

$$\int_0^1 g(t)dt = 0. \quad (3)$$

A. Speech production model

It is assumed in this study that only non-nasalized voiced speech is considered as the object of the analysis. Then the speech production model can be represented as

$$\tilde{s}[n] = - \sum_{i=1}^p a_i s[n-i] + d[n], \quad (4)$$

where $s[n]$ and $\tilde{s}[n]$ respectively represent the actual and predicted samples of speech. a_i ($1 \leq i \leq p$) are the filter coefficients and p is the filter order. $d[n]$ represents the driving signal defined as

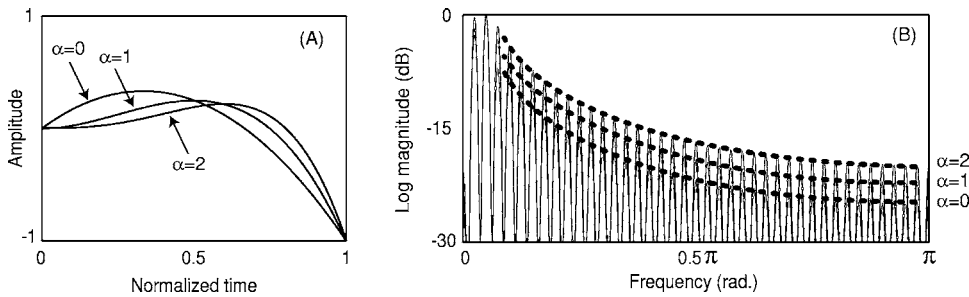


FIG. 1. Waveform and magnitude spectrum of the base polynomial model. In (a), $g(t)$ in Eq. (1) was sampled at $t=n/40$ ($0 \leq n \leq 40$) and interpolated linearly. In (b), the pitch period was set at 80 samples by adding 39 zero samples to each signal in (a) and a discrete Fourier transform was applied. The horizontal axis in (b) represents the frequency in the discrete-time domain.

$$d[n] = \sum_{j=1}^r \sum_{k=1}^m b_{jk} g_{jk}[n], \quad (5)$$

where r is the number of pitch periods within the analysis frame and m is that of overlapped base signals for each period. b_{jk} are parameters controlling the amplitude of base signals. Tracheal coupling can add poles and zeros to the transfer function of the vocal tract when the glottis is open. To reduce this coupling effect, speech samples should not be taken from the initial and final parts of a voiced segment for which the effect can be more prominently observed (Klatt and Klatt, 1990).

The base signal $g_{jk}[n]$ takes a nonzero value in the interval $n_{j1} \leq n \leq n_{j2}$ and becomes zero outside so that n_{j1} and n_{j2} respectively correspond to the instants of glottal opening and closing. Then $g_{jk}[n]$ can be constructed by sampling the function $g(t)$ in Eq. (1), where instants $t=0$ and $t=1$ respectively correspond to n_{j1} and n_{j2} .

In Fig. 1, $g(t)$ is shown in the left and the magnitude spectrum in the right. The envelope of the magnitude spectrum can be controlled by the order parameter: the slope of the spectral envelope is about -5.4 , -5.3 , and -5.2 dB/oct over 0.1π when α is 0, 1, and 2, respectively. In the speech analysis, parameters of the source model (r , m , and α) and the filter order (p) should be specified in advance. Also, the instants of glottal opening (n_{j1}) and closing (n_{j2}) should be given.

B. Joint estimation of the model parameters

The optimal values of a_i and b_{jk} in Eqs. (4) and (5) can be simultaneously determined so that the total squared error within the analysis frame,

$$E = \mathbf{e} \mathbf{e}^T, \quad (6)$$

is minimized, where the error $e[n] = s[n] - \hat{s}[n]$ between the actual sample $s[n]$ ($0 \leq n \leq N-1$) and the predicted one $\hat{s}[n]$ can be written in the vector form as $\mathbf{e} = \mathbf{s}_0 + \mathbf{q} \mathbf{G}^T$. T denotes the transposition. From the optimality condition $dE/d\mathbf{q} = 0$, the problem results in simultaneous linear equations as

$$\mathbf{q} \mathbf{G}^T \mathbf{G} = -\mathbf{s}_0 \mathbf{G} \quad (7)$$

and it can be solved explicitly. Here, $\mathbf{e} = (e[p], e[p+1], \dots, e[N-1])$, $\mathbf{s}_k = (s[p-k], s[p-k+1], \dots, s[N-k-1])$, and $\mathbf{q} = (a_1, \dots, a_p, -b_{11}, \dots, -b_{1m}, \dots, -b_{r1}, \dots, -b_{rm})$. \mathbf{G} is a matrix storing samples of speech and the voice source model as $\mathbf{G} = [(\mathbf{s}_1)^T, \dots, (\mathbf{s}_p)^T, (\mathbf{g}_{11})^T, \dots, (\mathbf{g}_{1m})^T, (\mathbf{g}_{21})^T, \dots, (\mathbf{g}_{2m})^T, \dots, (\mathbf{g}_{r1})^T, \dots, (\mathbf{g}_{rm})^T]$, where \mathbf{g}_{jk} is the vector $\mathbf{g}_{jk} = (g_{jk}[p], g_{jk}[p+1], \dots, g_{jk}[N-1])$ corresponding to the k th

base signal of the j th pitch period.

III. TEMPORAL DETERMINATION OF GLOTTAL EVENTS

This section presents a temporal search method of the glottal events. Suppose that the instants n_{j1} and n_{j2} are initially guessed using, for example, an electroglottographic (EGG) device. Then it is convenient to define the analysis frame in synchronization with them. Both ends of the analysis frame can be set at the instants of the glottal opening with the interval of L pitch periods as n_{01} and n_{L1} (Fig. 2). These end points are fixed and the positions of other $2L-1$ time points are searched in the vicinity of their initial estimates. In the following, the instants $\{n_{01}, n_{02}, \dots, n_{L1}\}$ are rewritten as $\{n_0, n_1, \dots, n_{2L}\}$ for simplicity.

A. Definition of the segmental error

The instants $\{n_1, n_2, \dots, n_{2L-1}\}$ are determined by fitting the voice source model to the residual signal obtained by inversely filtering the speech samples. Then the squared error within the frame is defined as

$$E = \sum_{l=1}^{2L} E_l(n_{l-1}, n_l), \quad (8)$$

where E_l is the error between $n = n_{l-1}$ and $n_l - 1$

$$E_l(n_{l-1}, n_l) = \sum_{n=n_{l-1}}^{n_l-1} (x[n] - d[n])^2. \quad (9)$$

$x[n]$ is the residual signal computed as $x[n] = \sum_{i=0}^p a_i s[n-i]$ ($a_0=1$), where a_i is the coefficient of the vocal-tract filter. In the segment for which the glottis is closed, $d[n]$ is set at zero and hence E_l is the sum of $x[n]$ squared. When the glottis is open, the voice source signal is represented as $d[n] = \sum_{k=1}^m b_k g_k[n]$, where b_k are unknown weighting parameters. Their optimal values are determined from the condition $dE_l/db_k = 0$ and expressed by $x[n]$. Then the segmental error can be written as $E_l(n_{l-1}, n_l) = \mathbf{e}_l \mathbf{e}_l^T$ when the glottis is open

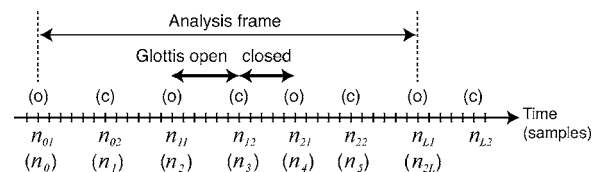


FIG. 2. Illustration of glottal opening (o) and closing (c) events and corresponding notations (n_{j1} and n_{j2}) of the voice source model. In the brackets, time markers used in the temporal search procedure are shown.

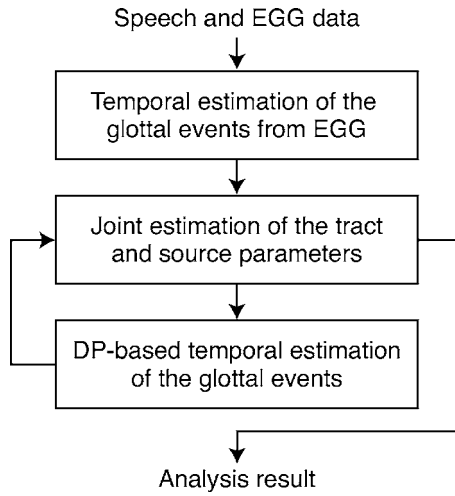


FIG. 3. The procedure for jointly determining the optimal values of source and tract parameters of the speech production model. DP stands for the dynamic programming used in Sec. III.

and $E_l(n_{l-1}, n_l) = \mathbf{x}_l \mathbf{x}_l^T$ when it is closed. $\mathbf{x}_l = (x[n_{l-1}], x[n_{l-1} + 1], \dots, x[n_l - 1])$ is the vector storing samples of the residual signal, $\mathbf{e}_l = \mathbf{x}_l \{I - G(G^T G)^{-1} G^T\}$ is the error vector when the residual signal is approximated by the voice source model, $G = [(\mathbf{g}_1)^T, (\mathbf{g}_2)^T, \dots, (\mathbf{g}_m)^T]$ is the matrix storing the base signals of the voice source model, and I is the unit matrix.

B. Dynamic programming solution

The instants $\{n_1, n_2, \dots, n_{2L-1}\}$ are determined so that the error E in Eq. (8) is minimized. The accumulated error along the search path is first computed as

$$D_1(n_1) = E_1(n_0, n_1),$$

$$D_l(n_l) = \min_{n_{l-1}} D_{l-1}(n_{l-1}) + E_l(n_{l-1}, n_l) \\ (l = 2, 3, \dots, 2L - 2),$$

$$D_{2L-1}(n_{2L-1}) = \min_{n_{2L-2}} D_{2L-2}(n_{2L-2}) + E_{2L-1}(n_{2L-2}, n_{2L-1}) \\ + E_{2L}(n_{2L-1}, n_{2L}), \quad (10)$$

where the search range of each time point is set as $n_l = n_l^0, n_l^0 \pm 1, \dots, n_l^0 \pm \delta n$ for the initial value (n_l^0) and the range parameter (δn). Then the solution can be obtained as

$$n_{2L-1}^* = \arg \min_{n_{2L-1}} D_{2L-1}(n_{2L-1}),$$

$$n_{l-1}^* = \arg \min_{n_{l-1}} D_l(n_{l-1}^*) \quad (l = 2L - 1, \dots, 2), \quad (11)$$

where n_l^* represents the optimal time position.

IV. SPEECH ANALYSIS EXPERIMENT

The speech analysis procedure is summarized as follows (Fig. 3). Audio signals were recorded at a sampling frequency of 8 kHz. EGG signals were recorded simultaneously and the initial estimates of n_{j1} and n_{j2} were obtained as zero-crossing points in time after the bias components were removed. Given the values of r , m , and α of the source model and p of the tract model, values of a_i and b_{jk} were determined by the joint estimation [Eq. (7)] for fixed glottal temporal alignments. After that, the temporal search procedure [Eq. (11)] was performed for fixed filter coefficients, where

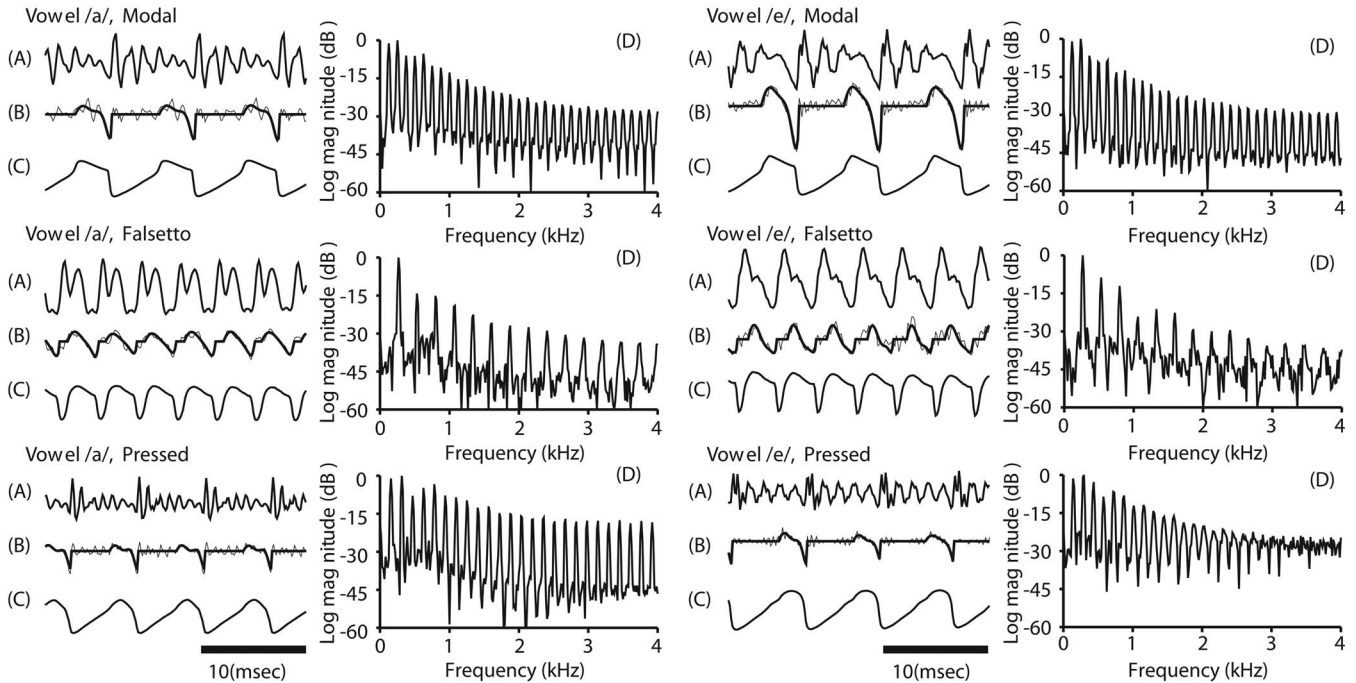


FIG. 4. The results of analyses of vowels /a/ and /e/ using three phonation conditions. Traces in each phonation condition show (a) speech $s[n]$, (b) voice source signal $d[n]$ (thick) and residual of speech (thin), and (c) EGG signal. In (d), the magnitude spectrum of the voice source signal is shown. The voice source signal was calculated using the expression given in Eq. (5), where the values of the model parameters were determined by the analysis procedure. The residual signal was obtained by inversely filtering the speech in (a) as explained in Sec. III A.

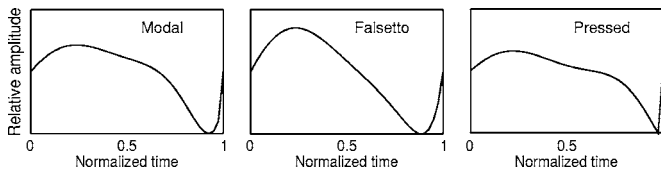


FIG. 5. Voice source signals reconstructed from the speech analysis results. The time axis was normalized so that zero and one respectively correspond to the instants of glottal opening and closing. The amplitude was also normalized arbitrarily to compare three signals in their waveforms.

the tract filter was used to obtain the residual signal. These procedures were alternatively used as long as the signal prediction error in Eq. (6) decreased. Finally, properties of the vocal tract and voice source signal were determined as the solution to the joint estimation problem.

Figure 4 shows analysis results of two vowels uttered by a male subject. Four base signals with the order parameter of 0, 2, 4, and 6 were used. The order of the tract filter and the frame length (number of pitch periods) were 14 and 2 for the modal and pressed voices and 10 and 3 for the falsetto. The range of the temporal search was set at $\delta n=3$. As a measure of the objective evaluation, signal-to-noise ratio (SNR) was 10 to 17 dB for these samples.¹ In Fig. 5, these source signals are illustrated. These results indicate that the source signal of the falsetto voice can be characterized by a rounded waveform and a large magnitude difference between the fundamental frequency and its second harmonic. In the pressed voice, the source signal forms a sharp edge in the vicinity of the glottal closure, and the magnitude spectrum is slowly decaying. The estimated open quotient (OQ) and speed quotient (SQ) are 0.44 and 2.2 for the modal, 0.74 and 1.2 for the falsetto, and 0.41 and 2.7 for the pressed on average.² These indicate that the falsetto voice has a long pulse width and a low pulse skewing and, in the pressed, they are opposite as described in Childers and Lee (1991).

On the other hand, parameters of the source model were empirically determined. Mean SNR of 13.3 dB for six utterances in Fig. 4 decreased to 11.2, 10.7, and 9.8 dB when m was reduced to 3 ($\alpha=0,2,4$), 2 ($\alpha=0,2$), and 1 ($\alpha=0$), respectively. Also, when m was 4 and $\alpha=0, 1, 2$, and 3, mean SNR was 11.5 dB. So the values of m and α used were superior to other parameter settings tested. Finally, the performance was about 16.9 dB on average when each of two females and two males spoke five Japanese vowels with the modal voice. Also, the mean SNR increased about 1 dB through the iterative use of the joint estimation and temporal search procedures, indicating that the initial temporal information from the EGG observation was effectively refined.

V. CONCLUSIONS

A method was proposed for the analysis of voice source dynamics. The voice source signal was constructed by a linear superposition of base polynomial models. The order of the polynomial model is variable while it was fixed at four in Milenkovic (1986). The spectral envelope of the overlapped

model can be controlled by adjusting the relative weights among the base signals, while a low-pass filter was employed in the RK model (Klatt and Klatt, 1990).

Due to the linearities of the source and tract models, the optimal value of every model parameter can be jointly determined. In the estimation method using the RK model (Kasuya *et al.*, 1999), on the other hand, complicated optimization procedures were required. Our signal model has a relatively large number of parameters such as the order parameters, weighting parameters, and temporal parameters of the glottal events. However, when the temporal information is given, the weights are uniquely determined for prescribed order parameters. Furthermore, the temporal search method was effective even when the EGG was used to estimate the glottal events initially.

Speech analyses revealed that the proposed method has a potential for capturing features of voice source signals. The results were generally in agreement with those in Childers and Lee (1991), but our method tended to estimate a relatively small open quotient. This might be caused by the tendency that the source signal approaches to zero in the return phase more quickly than the LF model as can be seen in Fig. 5. Further studies will be addressed to incorporating a frictional source model for capturing features of the breathy voice. Work supported by JSPS.

¹Speech samples were resynthesized as $\tilde{s}[n]$ where the values of the model parameters were estimated by analysis of the speech samples ($s[n]$). Then the SNR was calculated as $10 \log_{10} P_s/P_e$, where $P_s = \sum_{n=1}^M s[n]^2$, $P_e = \sum_{n=1}^M (s[n] - \tilde{s}[n])^2$, and M is the length of $s[n]$. Note that $s[n-i]$ should be replaced by $\tilde{s}[n-i]$ on the right side of Eq. (4) for the resynthesis.

²The OQ, the ratio of the open phase of the glottis to the pitch period, was calculated as $(n_{j2} - n_{j1}) / (n_{(j+1)1} - n_{j1})$ and SQ, the ratio of the opening phase to the closing phase, as $(n_c - n_{j1}) / (n_{j2} - n_c)$. n_c represents the instant at which the differentiated flow becomes zero, and it was determined as $n_c = \arg \min_n |d[n]|$ for $n_{j1} < n < n_{j2}$ where $d[n]$ is the source signal estimated by analysis in the form of Eq. (5).

- Childers, D. G., and Lee, C. K. (1991). "Vocal quality factors: Analysis, synthesis, and perception," *J. Acoust. Soc. Am.* **90**, 2394–2410.
- Fant, G. (1986). "Glottal flow: models and interaction," *J. Phonetics* **14**, 393–399.
- Kaburagi, T., and Kawai, K. (2003). "Analysis of voice source characteristics using a constrained polynomial model," *Proc. Eurospeech 2003*, pp. 461–464.
- Kasuya, H., Maekawa, K., and Kiritani, S. (1999). "Joint estimation of voice source and vocal tract parameters as applied to the study of voice source dynamics," *Proc. Int. Congress of Phonetic Science (ICPhS)*, pp. 2505–2512.
- Klatt, D. H., and Klatt, L. C. (1990). "Analysis, synthesis, and perception of voice quality variations among female and male talkers," *J. Acoust. Soc. Am.* **87**, 820–857.
- Milenkovic, P. (1986). "Glottal inverse filtering by joint estimation of an AR system with a linear input model," *IEEE Trans. Acoust., Speech, Signal Process.* **ASSP-34**, 28–42.
- Milenkovic, P. (1993). "Voice source model for continuous control of pitch period," *J. Acoust. Soc. Am.* **93**, 1087–1096.
- Rosenberg, A. E. (1971). "Effect of glottal pulse shape on the quality of natural vowels," *J. Acoust. Soc. Am.* **49**, 583–590.
- Veldhuis, R. (1998). "A computationally efficient alternative for the Liljencrants-Fant model and its perceptual evaluation," *J. Acoust. Soc. Am.* **103**, 566–571.

Echolocation clicks from killer whales (*Orcinus orca*) feeding on herring (*Clupea harengus*) (L)

Malene Simon^{a)}

Greenland Institute of Natural Resources, Post Box 570, 3900 Nuuk, Greenland and Institute of Biology, University of Southern Denmark, Campusvej 55, 5230 Odense M, Denmark

Magnus Wahlberg

Institute of Biological Sciences, University of Aarhus, C.F. Moellers Alle Building 131, 8000 Aarhus C, Denmark and Fjord&Bælt, Margrethes Plads 1, 5300 Kerteminde, Denmark

Lee A. Miller

Institute of Biology, University of Southern Denmark, Campusvej 55, 5230 Odense M, Denmark

(Received 21 June 2006; revised 25 October 2006; accepted 13 November 2006)

Echolocation clicks from Norwegian killer whales feeding on herring schools were recorded using a four-hydrophone array. The clicks had broadband bimodal frequency spectra with low and high frequency peaks at 24 and 108 kHz, respectively. The -10 dB bandwidth was 35 kHz. The average source level varied from 173 to 202 dB re $1 \mu\text{Pa}$ (peak-to-peak) @ 1 m. This is considerably lower than source levels described for Canadian killer whales foraging on salmon. It is suggested that biosonar clicks of Norwegian killer whales are adapted for localization of prey with high target strength and acute hearing abilities. © 2007 Acoustical Society of America.

[DOI: 10.1121/1.2404922]

PACS number(s): 43.80.Ka, 43.80.Lb, 43.30.Sf [WWA]

Pages: 749–752

I. INTRODUCTION

Toothed whales (Order: Odontoceti) listen for echoes from their intense, brief echolocation clicks to find prey. There have been many studies on the biosonar of captive odontocetes, but our understanding of how these animals use echolocation in the field is limited (Au, 2002). Killer whales (*Orcinus orca*) specialize in a large variety of prey species in different parts of the world. The acoustic properties of their biosonar signals have been described for the NE Pacific resident killer whales that feed mainly on salmon (Barrett-Lennard *et al.*, 1996; Au *et al.*, 2004). Comparing these data with those from other killer whale populations that feed on other prey species may reveal how the biosonar in this odontocete is adapted to different foraging situations and prey.

Here we present the first acoustic analysis of full-bandwidth hydrophone array recordings of echolocation clicks from wild killer whales foraging on Atlantic herring (*Clupea harengus*).

II. MATERIALS AND METHODS

Recordings of killer whales foraging on herring were made from October to December 2001 in Vestfjord and adjacent fjords, Norway. The rocky seabed of the recording site had a depth between 50 and 500 m. Foraging activity was defined as killer whales surfacing in different directions, arching their body before diving, seabirds taking fish at the site of diving and the presence of fish or fish parts at the surface (Similä and Ugarte, 1993). The boat was placed ap-

proximately 100 m upwind from the foraging whales and the engine switched off before recording in order to minimize disturbance of the whales and herring.

The recording system consisted of an array of four omnidirectional Reson (Copenhagen, Denmark) TC4034 hydrophones with a flat (± 3 dB) frequency response from 0.1 to 300 kHz (sensitivity $-218 \text{ dB} \pm 3 \text{ dB re } 1 \text{ V}/\mu\text{Pa}$). Three hydrophones were placed at the tips of an equilateral triangle, separated by 0.5 m from a fourth hydrophone in the center. The array was mounted on a pole and held from the side of the boat so that the center hydrophone was 1.5 m below the water surface (see Simon *et al.*, 2005). Each hydrophone was connected via a 26 dB amplifier and 1 Hz high-pass filter (Etec, Copenhagen, Denmark) to a Racal Store 4DS high-speed tape recorder (tape speed 30 in./s on $\frac{1}{4}$ -in. magnetic Ampex tapes). A calibration signal from a B&K pistonphone calibrator [250 Hz, 171 dB re $1 \mu\text{Pa}$ (pp)] was recorded on the tape and used for measuring the received level (see below). The analog recordings were played back eight times slower and digitized on a computer at a sampling rate of 48 kHz (20 kHz antialiasing filter), giving an effective sample rate of 384 kHz (recording software CoolEdit Pro, Syntrillium Software, Phoenix, AZ). The distance from the phonating whales to the array was calculated from the time-of-arrival differences of a click recorded at the four hydrophones (Au and Herzing, 2003; Schotten *et al.*, 2004). These differences were calculated by measuring the interval between highest-amplitude peaks of the envelope of cross-correlation curves between the center channel and each of the three outer channels (using a custom designed MATLAB program, The MathWorks, Inc., Cambridge, MA).

^{a)}Electronic mail: masi@natur.gl

The apparent source level (ASL) is defined as the sound pressure level 1 m away in any direction of the sound source (Møhl *et al.*, 2000). The ASL of the clicks, on all four hydrophones, was calculated as

$$\text{ASL} = \text{RL} + \text{TL} \quad [\text{Eq.(1)modified from Urick(1983)}],$$

where Received level, $\text{RL} = 20 \log(V_{\text{pp}}/V_{\text{ppcal}}) - \text{dBcal}$, Transmission loss, $\text{TL} = \text{Spherical spreading} + \text{absorption loss} = 20 \log(R) + \alpha \cdot R$, and V_{pp} =recorded peak-to-peak voltage of killer whale signal; V_{ppcal} =recorded peak-to-peak voltage of calibration signal; dBcal =peak-to-peak sound level of the calibration signal, 171 dB re 1 μPa (pp); R =calculated range in meters; and α =absorption coefficient=0.008 dB/m (Urick, 1983).

Measurements of the localization accuracy of the recording system revealed that source levels were underestimated by up to 5 dB at distances of less than 15 m from the array, mainly due to slight variations of tape speed in the analog tape recorder (Simon, 2004). Only clicks located at distances of less than 15 m in front of the array were chosen for further analysis. On-axis clicks were defined by having a higher or equally high ASL on the center hydrophone relative to the surrounding hydrophones.

The click duration (τ_{E97}) is defined as the time period containing 97% of the click energy (Simon *et al.*, 2005) and was measured according to Madsen *et al.* (2004). The frequency bandwidth and the center frequency f_0 were measured as in Au (1993). The signal analysis was performed using CoolEdit Pro (Syntrillium Software, Phoenix, AZ), BatSound Pro (Pettersen Elektronik, Upsala, Sweden), MATLAB and SIGPRO (Pedersen, Centre for Sound Communication, Denmark).

III. RESULTS

From 19 different recording sessions a total of 748 clicks were recorded on all four channels, 516 of which were found to be within 15 m from the array. Eighty-four of the clicks (recorded during seven sessions) were considered on-axis. Examples of clicks and their spectra are given in Fig. 1. The signal parameters of on-axis clicks were compared to similar measurements made by Au *et al.* (2004) of killer whales foraging on salmon (Table I). Although measured ranges of click parameters overlapped, echolocation clicks from herring-eating killer whales had mostly lower ASLs, center frequencies and frequency bandwidth than the echolocation clicks from salmon-eating killer whales. The click durations for herring-eating killer whales covered a broader range than those of salmon-eating killer whales, but this probably due to methodological differences (Table I).

IV. DISCUSSION

The method used in this study classified on-axis clicks as those with the highest or equally high source level on the center hydrophone compared to the surrounding hydrophones. Our method is similar, though more restrictive than that used by Au *et al.* (2004) and Au and Herzing (2003). Our method could include off-axis clicks if they are recorded from a direction where the apparent source level is not

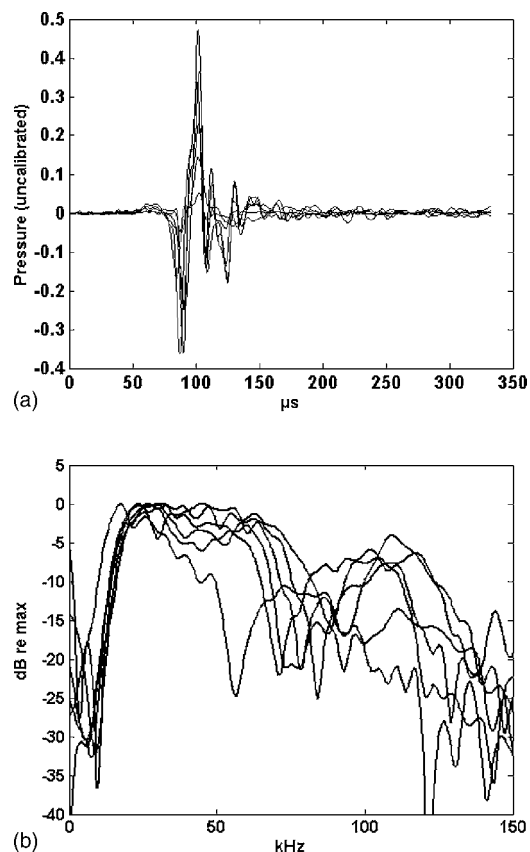


FIG. 1. (a) Wave form of six typical on-axis echolocation clicks recorded from feeding Norwegian killer whales (recording bandwidth: 150 kHz). (b) Normalized frequency spectra of the clicks in Fig. 1(a). (Rectangular window, fast Fourier transform window size: 128, frequency resolution: 2.3 kHz, spectra interpolated ten times).

changing substantially with the off-axis angle. However, our results can be compared to those reported by Au *et al.* (2004) from NE Pacific resident killer whale.

Even though the frequency characteristics and duration of Norwegian killer whale clicks are similar to those of the NE Pacific killer whales, the source levels are lower for the former (Table I). This may be explained by the fact that Norwegian and NE Pacific resident killer whales feed on prey with very different schooling behavior. NE Pacific resident killer whales feed on Chinook salmon (*Oncorhynchus tshawytscha*), which generally do not form schools (Ford *et al.*, 1998). Norwegian killer whales feed on Atlantic herring, which have a pronounced schooling behavior (Christensen,

TABLE I. Acoustic properties of on-axis clicks recorded from herring-eating (this study) and salmon-eating killer whales (from Au *et al.* 2004). [The mean and standard deviation are given in parenthesis as ($X \pm \text{SD}$).]

Killer whale ecotype	N	ASL, dB re 1 μPa (pp)	-10 dB bandwidth (kHz)	Center frequency f_0 (kHz)	Duration (μs)
Scandinavian herring-eaters	84	173–202 (189 \pm 7.1)	8–58 (35 \pm 15.9)	22–49 (38 \pm 6.7)	31–203 (89 \pm 51.0)
NE Pacific salmon-eaters	1185	195–224	35–50	45–80	80–120

In the Scandinavian study the duration was measured as τ_{E97} ; for the Salmon-eating study the method used is unknown.

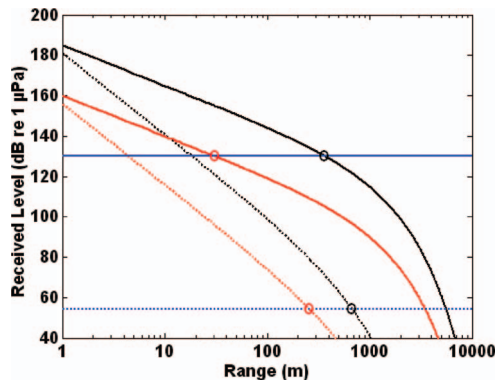


FIG. 2. Acoustic interactions between killer whales and herring. The black and red solid lines illustrate high and low level killer whale clicks (low-pass filtered at 5 kHz). The dashed black and red lines illustrate the broadband echo from high level and low level killer whale clicks, respectively. The rings show the maximum distance at which the received level is sufficient for the herring to detect the click (solid blue line) and for the killer whale to detect the echo of the herring (dashed blue line). Norwegian killer whales using low level clicks can detect the echo from a herring at greater distances than the herring can detect the whale's click giving the killer whale an advantage over the herring.

1982; Similä *et al.*, 1996; Nøttestad and Axelsen, 1999). A school of herring has much larger target strength than a single salmon (Simmonds and MacLennan, 2005). Pacific resident killer whales might therefore need a higher source level when locating their prey than do Norwegian killer whales. In addition, the Pacific killer whales recorded by Au *et al.* (2004) were searching for individual fish that presumably try to escape predation by swimming away. While swimming away, their target strength would be lowered by the skewed angle to the killer whale (Au *et al.*, 2004). Under such circumstances powerful, long-range sonar might be advantageous. In contrast, the Norwegian killer whales recorded in this study encircled relatively stationary schools of fish and powerful, long-range sonar was not necessary to detect the schools. Norwegian killer whales may actually benefit by producing low energy clicks when feeding on prey of high target strength and with good hearing. The hearing abilities of Atlantic herring (measured by Mann *et al.*, 2005) should be much better than those of Pacific salmon. Although the hearing abilities of Pacific salmon are unknown they are probably similar to those of Atlantic salmon (*Salmo salar*) that are insensitive to frequencies above 200–300 Hz (Hawkins and Johnstone, 1978).

The advantage of using different levels of echolocation clicks can be illustrated by modeling the echolocation performance of a killer whale while searching for prey. In Fig. 2 received levels are shown as a function of range of a 5 kHz low-pass-filtered click with a source level similar to that of a salmon-eating (black line, from Au *et al.*, 2004) and a herring-eating (red line, data from this paper) killer whale, respectively. The 5 kHz low-pass filter results in a 40 dB drop in the click source level and crudely imitates the frequency response of the herring auditory system (data from Mann *et al.*, 2005). The intersections between the solid lines and the herring hearing threshold (blue solid line, taken from Mann *et al.*, 2005 at 4 kHz) indicate the ranges at which the herring can hear the two different types of killer whale

clicks. Even though the hearing abilities of herring improve considerably below 1 kHz there is very little energy in the killer whale clicks at such low frequencies, which is the rationale of choosing the hearing threshold at 4 kHz for the calculations in Fig. 2.

The dashed red and black curves in Fig. 2 illustrate the intensity of echoes received by the killer whale from a herring at various ranges when using different click source levels, that of herring and that of salmon eating killer whales. These curves are calculated from the full-bandwidth click source levels, as the echoes are detected by a whale with a very large receiving bandwidth (Szymanski *et al.*, 1999). The target strength of the herring was chosen as -44 dB, corresponding to a 25 cm long herring (Foote, 1987). The killer whale hearing threshold is assumed to be limited by background noise integrated over the bandwidth of the click rather than by the hearing threshold measured in quiet conditions. Assuming a noise spectral density of 30 dB re $1 \mu\text{Pa}/\text{Hz}^{1/2}$ (which is approximately the ambient noise level at sea state 2 at 50 kHz; see Wenz, 1962), integrating the bandwidth of the click (35 kHz) and subtracting an assumed directionality index of 20 dB (estimated by Au *et al.*, 2004) we obtain a total received ambient noise level of $30 + 10 \log(35\,000) - 20 = 55$ dB re $1 \mu\text{Pa}$. Here, this is used as an approximate detection threshold for the killer whale, indicated in Fig. 2 with a blue dotted line. The intersections of the echoes with the killer whale hearing threshold (marked with a red and a black circle) are the maximum ranges at which a killer whale could detect a herring using echolocation.

The model shows that if the herring-eating Norwegian killer whales used clicks with the same high source levels as those used by salmon-eating NE Pacific killer whales, the herring would detect the clicks over much larger distances, giving little advantage to the killer whale (the two black circles in Fig. 2). However, by using lower source levels the killer whale can detect an echo from a herring at much greater distances than the herring can detect the predator (the two red circles in Fig. 2).

When exposed to click trains resembling those of foraging killer whales, Pacific herring (*Clupea pallasii*) react by increasing schooling density, swimming speed and depth (Wilson and Dill, 2002). Even though killer whales can dive to depths of more than 300 m (Similä *et al.*, 2002), they seem to be unsuccessful in herding herring schools to the surface if the herring are deeper than 180 m (Nøttestad *et al.*, 2002). Therefore, diving may be an effective antipredator strategy. Thus it may be crucial for the killer whales to detect the herring before the herring hear their echolocation clicks and increase their depth.

The patterns in Fig. 2 may change dramatically when considering variations in target strength, hearing thresholds, and other parameters. Nevertheless, Fig. 2 illustrates that it might be an advantage for an echolocating predator to reduce the source level when foraging on prey with sensitive hearing abilities. On the other hand, it is advantageous to use high source level echolocation clicks when foraging on prey with low hearing sensitivity (salmon), as a high source level will increase the search range. The hearing abilities of

salmon are restricted to low frequencies and killer whale clicks are probably not detectable by the salmon even at very high received levels. Similar arguments have been used to explain variations in source levels found in bats hunting for tympanate insects (Surlykke, 1988). More accurate data are needed on the acoustic interaction between killer whales and their prey to confirm that the mechanisms outlined in Fig. 2 are actually used by the whales in real life.

ACKNOWLEDGMENTS

The authors thank F. Ugarte for help throughout the study especially during fieldwork and valuable discussions and comments on the manuscript. Thanks to the following for assistance in the field: L. Briones, N. Eriksen, M. Rasmussen, B. Kjeldsberg, and Natasha. Thanks to P. T. Madsen for discussions on the subject, Kate Stafford for comments on the manuscript. The SIGPRO was developed by S. B. Pedersen, The Centre of Sound Communication, Denmark. The study was funded by Andenes Whale Safari, Andenes Cetacean Research Unit (ANCRU), the killer whale adoption program (T. Similä & G. McCallum), and the Danish National Research Council. M.S. was funded by a grant from the Oticon Foundation and M.W. by grants from the Danish National Research Council, the Office of Naval Research, the Oticon Foundation, and the Carlsberg Foundation.

Au, W. W. L. (1993). *The Sonar of Dolphins* (Springer, New York).
 Au, W. W. L. (2002). "Echolocation," in W. F. Perrin, B. Würsig, J.G.M. Thewissen, *Encyclopedia of Marine Mammals* (Academic Press, New York), pp. 358–367.
 Au, W. W. L., and Herzing, D. L. (2003). "Echolocation signals of wild Atlantic spotted dolphin (*Stenella frontalis*)," *J. Acoust. Soc. Am.* **113**, 598–604.
 Au, W. W. L., Ford, J. K. B., Horne, J. K., and Allman, K. A. N. (2004). "Echolocation signals of free-ranging killer whales (*Orcinus orca*) and modeling of foraging for chinook salmon (*Oncorhynchus tshawytscha*)," *J. Acoust. Soc. Am.* **115**(2), 901–909.
 Barrett-Lennard, L. G., Ford, J. K. B., and Heise, K. A. (1996). "The mixed blessing of echolocation: differences in sonar use by fish-eating and mammal-eating killer whales," *Anim. Behav.* **51**, 553–565.
 Christensen, I. (1982). "Killer whales in Norwegian coastal waters," *Rep. Int. Whal. Comm.* **32**, 633–672.
 Foote, K. (1987). "Fish target strengths for use in echo intergrator surveys," *J. Acoust. Soc. Am.* **82**, 981–987.
 Ford, J. K. B., Ellis, G. M., Barret-Lennard, L. G., Morton, A. B., Palm, R. S., and Balcomb, K. C. (1998). "Dietary specialization in two sympatric populations of killer whales (*Orcinus orca*) in coastal British Columbia

and adjacent waters," *Can. J. Zool.* **76**, 1456–1471.
 Hawkins, A. D., and Johnstone, A. D. F. (1978). "The hearing of the Atlantic salmon, *Salmo salar*," *J. Fish Biol.* **13**, 655–673.
 Madsen, P. T., Kerr, I., and Payne, R. (2004). "Echolocation clicks of two free-ranging, oceanic delphinids with different food preferences: false killer whales (*Pseudorca crassidens*) and Risso's dolphins (*Grampus griseus*)," *J. Exp. Biol.* **207**, 1811–1123.
 Mann, D. A., Popper, A. N., and Wilson, B. (2005). "Pacific herring hearing does not include ultrasound," *Biological Letters* **1**, 158–161.
 Møhl, B., Wahlberg, M., Madsen, P. T., Miller, L. A., and Surlykke, A. (2000). "Sperm whale clicks: Directionality and source levels revisited," *J. Acoust. Soc. Am.* **107**(1), 638–648.
 Nøttestad, L., and Axelsen, B. E. (1999). "Herring schooling maneuvers in response to killer whale attack," *Can. J. Zool.* **68**, 1209–1215.
 Nøttestad, L., Fernö, A., and Axelsen, B. E. (2002). "Digging in the deep: Killer whales' advanced hunting tactic," *Polar Biol.* **25**, 939–941.
 Schotten, M., Au, W. W. L., Lammers, M. O., and Aubauer, R. (2004). "Echolocation recordings and localizations of free-ranging spinner dolphins (*Stenella longirostris*) and pantropical spotted dolphins (*Stenella attenuata*) using a four hydrophone array," in *Echolocation in Bats and Dolphins*, edited by J. A. Thomas, C. F. Moss, and M. Vater (University of Chicago Press, Chicago), pp 393–400.
 Similä, T., and Ugarte, F. (1993). "Surface and underwater observations of cooperatively feeding killer whales in northern Norway," *Can. J. Zool.* **71**, 1494–1499.
 Similä, T., Holst, J. C., and Christensen, I. (1996). "Occurrence and diet of killer whales in northern Norway: Seasonal patterns relative to the distribution and abundance of Norwegian spring-spawning herring," *Can. J. Fish. Aquat. Sci.* **53**, 769–779.
 Similä, T., Holst, J. C., Øien, N., and Hanson, M. B. (2002). "Satellite tracking study of movements and diving behaviour of killer whales in the Norwegian Sea," *Proceedings of the 4th International Orca Symposium and Workshop, CEBC-CNRS, France*.
 Simmonds, E., and MacLennan, D. N. (2005). *Fisheries Acoustics: Theory and Practice* (Blackwell Science Ltd).
 Simon, M. (2004). "Sounds produced by foraging killer whales (*Orcinus orca*)," M.Sc. thesis, University of Southern Denmark-Odense.
 Simon, M., Wahlberg, M., Ugarte, F., and Miller, L. A. (2005). "Acoustic characteristics of underwater tail slaps used by Norwegian and Icelandic killer whales (*Orcinus orca*) to debilitate herring (*Clupea harengus*)," *J. Exp. Biol.* **208**, 2459–2466.
 Surlykke, A. (1988). "Interaction between echolocating bats and their prey," in *Animal Sonar: Processes and Performance*, edited by P. E. Nachtigall and P. W. B. Moore (Plenum, New York), pp. 551–566.
 Szymanski, M. D., Bain, D. E., Kiehl, K., Pennington, S., Wong, S., and Henry, K. R. (1999). "Killer whale (*Orcinus orca*) hearing: Auditory brainstem response and behavioural audiograms," *J. Acoust. Soc. Am.* **106**(2), 1134–1141.
 Urick, R. J. (1983). *Principles of Underwater Sound* (Peninsula Publishing, Los Altos).
 Wenz, G. M. (1962). "Acoustic ambient noise in the ocean: spectra and sources," *J. Acoust. Soc. Am.* **34**(12), 1936–1956.
 Wilson, B., and Dill, L. M. (2002). "Pacific herring respond to simulated odontocete echolocation sounds," *Can. J. Fish. Aquat. Sci.* **59**, 542–553.

Scattering of a Bessel beam by a sphere

Philip L. Marston^{a)}

Department of Physics and Astronomy, Washington State University, Pullman, Washington 99164-2814

(Received 2 August 2006; revised 9 November 2006; accepted 10 November 2006)

The exact scattering by a sphere centered on a Bessel beam is expressed as a partial wave series involving the scattering angle relative to the beam axis and the conical angle of the wave vector components of the Bessel beam. The sphere is assumed to have isotropic material properties so that the n th partial wave amplitude for plane wave scattering is proportional to a known partial-wave coefficient. The scattered partial waves in the Bessel beam case are also proportional to the same partial-wave coefficient but now the weighting factor depends on the properties of the Bessel beam. When the wavenumber-radius product ka is large, for rigid or soft spheres the scattering is peaked in the backward and forward directions along the beam axis as well as in the direction of the conical angle. These properties are geometrically explained and some symmetry properties are noted. The formulation is also suitable for elastic and fluid spheres. A partial wave expansion of the Bessel beam is noted. © 2007 Acoustical Society of America. [DOI: 10.1121/1.2404931]

PACS number(s): 43.20.Fn, 43.30.Gv, 43.40.Fz, 43.80.Qf [TDM]

Pages: 753–758

I. INTRODUCTION

Scalar wave Bessel beams are an exact solution of the linear wave equation proportional to $\exp[i(\kappa z - \omega t)]J_0(\mu\rho)$ where z and ρ denote the axial and radial coordinates, κ and μ denote the axial and radial wavenumbers, J_0 is a zero-order Bessel function, and $\kappa^2 + \mu^2 = k^2 = (\omega/c)^2$ where c denotes the phase velocity of the fluid. If such beams could be realized the beam would propagate without spreading.^{1,2} There has been considerable interest in the applications and properties of ultrasonic and optical approximations of such beams.^{3–9} The purpose of this paper is to describe the scattering by a sphere centered on the axis of such a beam and to explain aspects of the scattering from geometrical considerations. Though farfield scattering is emphasized, some consideration is given to analytical and geometric aspects of the nearfield properties. In practice, because of the finite width of sources realizable beams only retain their form over a finite propagation distance, however, in the discussion which follows the incident wave is taken to be an ideal Bessel beam. The results here are outside the scope of prior discussions of the scattering of Gaussian or flat-topped acoustic beams by spheres.¹⁰

It is anticipated that these results may be helpful not only for understanding the scattering but also in related investigations of the effects of Bessel beams on objects. Such applications include the radiation force imparted by a Bessel beam since the radiation force is related to the farfield scattering.¹¹ In a separate publication expressions for the scattering given here are applied to the calculation of the radiation force.¹²

II. PLANE-WAVE DECOMPOSITION OF BESSEL BEAMS

As reviewed by Redwood¹³ the synthesis of cylindrical waves by plane waves has long been used in the theory of

waveguides. Let the spatial dependence of the complex velocity potential of the Bessel beam be denoted by $\psi_B(z, \rho) = \psi_0 \exp(i\kappa z)J_0(\mu\rho)$ where ψ_0 determines the beam amplitude. For the azimuthal interval in Fig. 1 from ϕ' to $\phi' + d\phi'$ denote the incident wave contribution by $d\psi_B = (d\psi_B/d\phi')d\phi'$. Durnin's representation of the beam¹ may be interpreted as the following superposition of plane waves:

$$\psi_B(z, \rho) = \int_0^{2\pi} (d\psi_B/d\phi')d\phi', \quad (1)$$

$$d\psi_B/d\phi' = \psi_0(2\pi)^{-1} e^{i\kappa z} \exp(i\mu x \cos \phi' + i\mu y \sin \phi'), \quad (2)$$

where $x^2 + y^2 = \rho^2$ and ϕ' denotes the azimuthal direction of the plane wave component. The polar angle of each component relative to the z axis is $\theta' = \beta = \arcsin(\mu/k)$. The wave vector components form a cone having a conical angle β relative to the z axis.

III. SCATTERING BY EACH PLANE WAVE COMPONENT

Neglecting the absorption in the surroundings, the farfield scattering for each plane wave component of the incident wave by a sphere centered at $z=0$ and $\rho=0$ may be expressed using a complex dimensionless form function f using the relation^{14–19}

$$d\psi_S = (a/2r)f(ka, \cos \gamma)\exp(ikr)d\psi_B, \quad (3)$$

where $d\psi_B$ is evaluated at $z=0$, a denotes the radius of the sphere, r denotes the distance from the center of the sphere, and γ denotes the scattering angle of the field point relative to the local incident wave vector as shown in Fig. 1. The function f accounts for the dependence of the plane-wave scattering on the frequency and sphere size through the dependence on ka . The dependence on the relative scattering angle γ is expressed through the dependence on $\cos \gamma$. In the farfield the scattering amplitude decreases with increasing

^{a)}Electronic mail: marston@wsu.edu

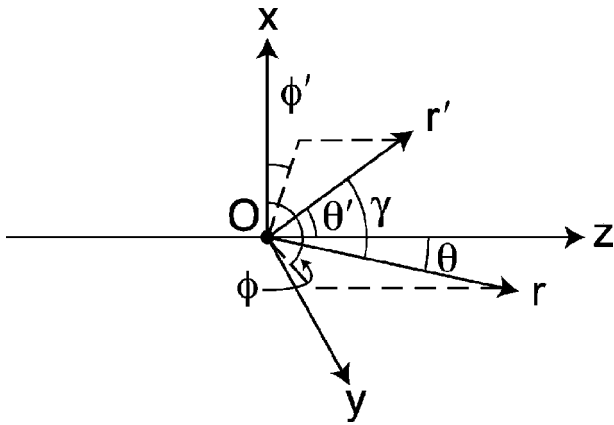


FIG. 1. Coordinate system used to analyze the scattering. The Bessel beam is incident along the z axis and the sphere is centered at the origin. The vector \mathbf{r}' denotes the direction of the incident plane-wave component having polar and azimuthal angles θ' and ϕ' . All of the incident components have $\theta' = \beta = \arcsin(\mu/k)$. The scattering is evaluated for \mathbf{r} in the θ, ϕ direction.

r in proportion to $1/r$. It is assumed that the sphere contains only isotropic materials, however, it may dissipate energy. When ka is large, the farfield condition is that $r \gg (1/2)ka^2$ but when ka is not large, the condition becomes $r \gg a$. The form function may be expressed in terms of a partial wave series¹⁷⁻¹⁹ for plane-wave incidence scattering

$$f(ka, \cos \gamma) = (-ika) \sum_{n=0}^{\infty} (2n+1)(s_n-1)P_n(\cos \gamma), \quad (4)$$

where P_n denotes a Legendre polynomial of the indicated argument, and the complex s_n depend on ka and are determined by the boundary condition and material properties. Instead of expressing the dependence on material properties through the factor (s_n-1) , a partial-wave coefficient having the form $a_n = (s_n-1)/2$ is typically used. The a_n and the s_n are known for a wide variety of spheres.¹⁴⁻¹⁹ When the sphere does not dissipate energy, s_n is unimodular.^{19,20} In that case, introducing the s_n enables the a_n to be expressed in a compact form. The s_n for rigid and soft spheres are noted in Sec. VI and the expression for s_n for fluid spheres was recently reviewed.¹² Partial-wave coefficients for quantum mechanical and electromagnetic scattering are commonly expressed as proportional to (s_n-1) where $|s_n|=1$ in the absence of absorption.²⁰ The case of acoustical scattering is directly analogous.¹⁹

While near-field expressions for the scattering are needed for the evaluation of the s_n , the derivation given below shows that once the s_n are found for the *plane-wave case* it is not necessary to repeat the nearfield analysis to construct the farfield scattering for a sphere centered on a *Bessel beam*. Nearfield scattering in the Bessel beam is discussed briefly at the end of Sec. VII.

IV. INTEGRATION OF THE SCATTERING COMPONENTS

The addition theorem of spherical harmonics²¹ allows each $P_n(\cos \gamma)$ to be expressed in terms of the direction θ and ϕ of the scattering

$$P_n(\cos \gamma) = [4\pi/(2n+1)] \sum_{m=-n}^n Y_{nm}(\theta, \phi) Y_{nm}^*(\theta', \phi'), \quad (5)$$

where Y_{nm} denotes standard spherical harmonics of the indicated angular arguments, $*$ denotes complex conjugation, and since all plane wave components of the incident wave lie on a cone, θ' is constant and is given by β . Insertion of Eq. (5) into (3) and (4) facilitates the desired integration:

$$\psi_s(r, \theta) = \int d\psi_s = (a/2r)\psi_0 F e^{ikr}, \quad (6)$$

$$F(ka, \cos \theta, \cos \beta) = (-ika) \sum_{n=0}^{\infty} (2n+1)(s_n-1)I_n, \quad (7)$$

$$I_n(\cos \theta, \cos \beta) = (2\pi)^{-1} \int_0^{2\pi} P_n(\cos \gamma) d\phi' \quad (8a)$$

$$= P_n(\cos \theta) P_n(\cos \beta). \quad (8b)$$

Equation (8b) follows from (8a) and (5) since only terms with $m=0$ survive the integration, and the spherical harmonics in that case reduce to²¹ $Y_{n0}(\theta, \phi) = [(2n+1)/4\pi]^{1/2} P_n(\cos \theta)$ and $Y_{n0}(\beta, \phi') = [(2n+1)/4\pi]^{1/2} P_n(\cos \beta)$. Combining (7) and (8b) gives the dimensionless form function for scattering by a Bessel beam

$$F(ka, \cos \theta, \cos \beta) = (-ika) \sum_{n=0}^{\infty} (2n+1) \times (s_n-1) P_n(\cos \theta) P_n(\cos \beta). \quad (9)$$

This function shows how the scattering in Eq. (6) depends on material parameters, on ka , on the scattering angle θ , and on the Bessel beam parameter β . The convergence is found to be similar to that of Eq. (4) so that the series may be terminated for n somewhat in excess of ka . Since the complex pressure is proportional to the velocity potential, ψ_s and ψ_0 in Eq. (6) may be replaced by complex pressures for the scattered and incident waves. Because the incident wave is assumed to be an ideal Bessel beam, shifting the sphere *along* the axis only alters the phase of the scattering. Shifting *off* of the axis will induce a dependence of the scattering on ϕ , however, that case is outside the scope of the present investigation.

V. FORM FUNCTION SYMMETRY PROPERTIES AND SPECIAL CASES

Comparison of (4) and (9) and standard properties of the Legendre polynomials gives the following special cases. For forward scattering along the Bessel beam axis, $\theta=0$, $\cos \theta=1$, and

$$F(ka, 1, \cos \beta) = f(ka, \cos \beta). \quad (10)$$

The scattering is given by f evaluated at a scattering angle β . For backscattering along the $-z$ axis, $\theta=\pi$, $\cos \theta=-1$, and

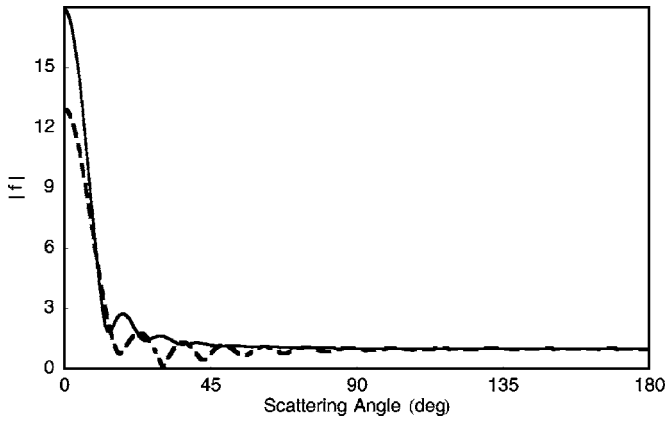


FIG. 2. For an incident plane wave the dimensionless form function $|f|$ is shown as a function of the scattering angle θ for soft (solid curve) and rigid (dashed curve) spheres with $ka=15$. See Sec. VI.

$$F(ka, -1, \cos \beta) = f(ka, -\cos \beta) \quad (11a)$$

$$= f(ka, \cos(\pi - \beta)). \quad (11b)$$

The scattering is given by f evaluated at a scattering angle $(\pi - \beta)$. Equation (11a) follows from the identity $P_n(-\cos \beta) = (-1)^n P_n(\cos \beta)$. Equations (10) and (11) also follow from symmetry considerations. Inspection of (9) also shows that

$$F(ka, \cos \theta, \cos \beta) = F(ka, \cos \beta, \cos \theta), \quad (12a)$$

$$F(ka, \cos \theta, 1) = f(ka, \cos \theta), \quad (12b)$$

where (12b) gives the plane-wave limit. Taking $\kappa=0$ gives $\beta=90^\circ$ so that the incident wave becomes a pure cylindrical wave. The terms in Eq. (9) vanish for odd n and the scattering becomes symmetric about the plane $z=0$ so that

$$F(ka, \cos \theta, 0) = F(ka, \cos(\pi - \theta), 0). \quad (13)$$

Under most circumstances^{16,22,23} when a gas bubble in a liquid is excited at the fundamental monopole resonance, the series in Eq. (4) is dominated by the term having $n=0$. For that situation the series in Eq. (9) will also be dominated by the term having $n=0$ so that $F \approx f$. Note, however, that for a gas bubble the function denoted here by s_0 has a modulus significantly less than unity as a consequence of thermal-viscous dissipation.^{22,23}

VI. REVIEW OF PLANE WAVE SCATTERING RESULTS

Prior to discussing results for Bessel beams it is helpful to review standard results for scattering by a perfectly soft sphere and a fixed rigid sphere.¹⁴ Understanding scattering by rigid and soft spheres is helpful for understanding scattering in other cases since they are often used as a background for isolating elastic effects.¹⁷ In the perfectly soft case^{14,19} $s_n = -h_n^{(2)}(ka)/h_n^{(1)}(ka)$ where h_n is a spherical Hankel function of the indicated kind. In the perfectly rigid case^{14,17} $s_n = -h_n^{(2)}(ka)' / h_n^{(1)}(ka)'$ where primes denote differentiation with respect to the indicated argument. Figure 2 shows the computed $|f|$ for soft and (dashed) rigid spheres having $ka=15$. The general features shown here are known to be

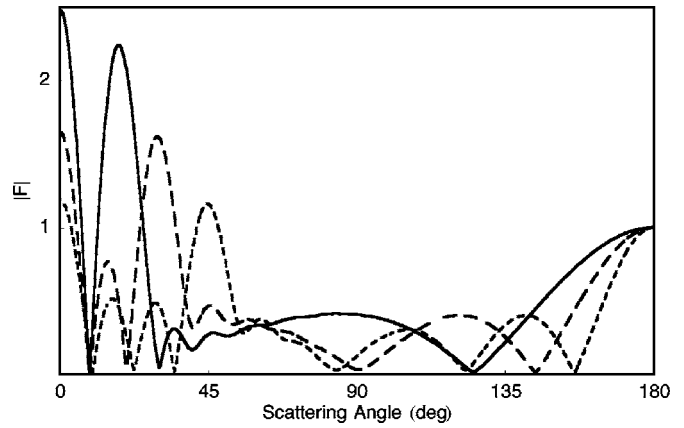


FIG. 3. Form function modulus $|F|$ from Eq. (9) for Bessel beam scattering by a soft sphere having $ka=15$ for β of 20° (solid curve), 30° (long dashes), and 45° (short dashes). The abscissa is the scattering angle θ .

present¹⁴ for ka greater than approximately 5. The flat region on the right side corresponds to specular reflection where $|f| \approx 1$. Here $|f|$ becomes closer to unity the greater the value of ka . This corresponds to the geometric optics limit where the modulus of the specular contribution for a sphere is independent of scattering angle and the normalization for f is such that $|f|=1$ for the specular contribution.^{19,24} In the forward region is a diffraction peak which narrows and grows with increasing ka . When ka is very large the forward scattering becomes¹⁴ $f(ka, 1) \approx ika$.

VII. BESSEL BEAM SCATTERING, GEOMETRICAL INTERPRETATION, AND DISCUSSION

Figure 3 shows $|F|$ as a function of θ for a perfectly soft sphere with $ka=15$. Three values of β are shown: 20° (solid curve), 30° (long dashes), and 45° (short dashes). Each curve has a peak in $|F|$ centered near $\theta=\beta$. This peak may be interpreted as associated with the superposition of the local forward scattering of the individual plane-wave components of the incident wave. Each curve also has a backscattering peak which becomes narrower for increasing β , and each has a forward directed peak at $\theta=0$ which narrows slightly for decreasing β . Aspects of these backward and forward directed peaks can be understood from geometric arguments

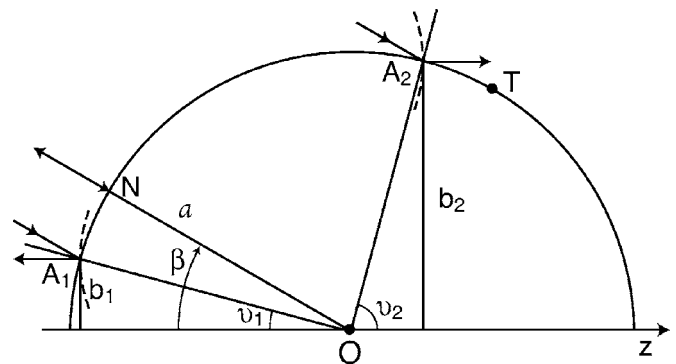


FIG. 4. Ray diagram for construction of geometric models of reflection contributions. The models are helpful for explaining some features of the exact results.

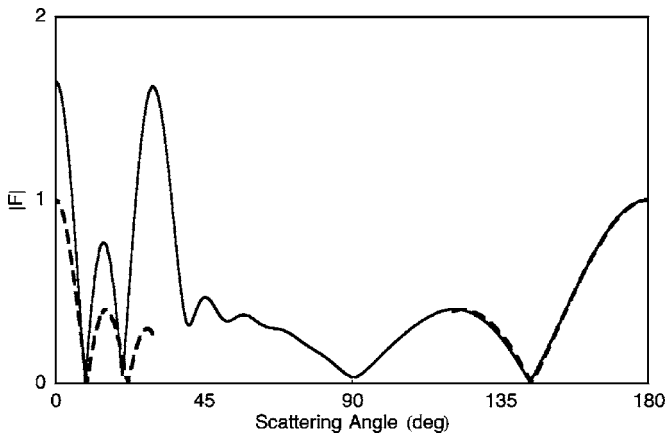


FIG. 5. The solid curve is $|F|$ from Eq. (9) for a soft sphere having $ka=15$ illuminated by a Bessel beam having $\beta=30^\circ$. The dashed curves are geometric models of specular contributions, Eq. (14). The dashed curve on the right is $|F_1|$ and the one on the left is $|F_2|$.

outlined below. This geometrical analysis is supportive of the analytical result in Eq. (9).

Figure 4 shows the ray optics of reflections from an impenetrable sphere where the incident wave vector is tilted from the z axis by an angle β , the cone angle of the Bessel beam. Rays having a local angle of incidence $v_1=\beta/2$ reflect to produce a ray traveling antiparallel to the z axis. The corresponding specular point is at A_1 where the offset from the axis is $b_1=a \sin(v_1)$. Associated with this reflected ray is a virtual wavefront that is curved along the dashed arc passing through A_1 . Similarly v_2 , A_2 , and b_2 denote corresponding properties of a forward-directed reflected ray where it is found that $b_2=a \cos(\beta/2)$. The specular point at A_2 is close to the shadow boundary at T where the incident wave vector is tangent to the sphere. At point N the ray is normally reflected.

Consider the scattering contribution associated with the ray reflected at A_1 and from similar points generated by rotating the figure around the z axis. It is shown in Appendix A that the superposed amplitudes produce a wavefront that has locally the shape of a circular torus. The Gaussian curvature of that wavefront vanishes on a ring of radius b_1 . It is a property of such wave fronts that for scalar waves the amplitude is approximately proportional to $J_0(kb_1(\pi-\theta))$ provided that $(\pi-\theta)$ is small and $kb_1 \gg 1$ ^{18,24-27} (see also Secs. 4.3-4.5 of Ref. 6). Since $b_1=a \sin(\beta/2)$, the resulting peak in the scattering becomes narrower for increasing β . Similarly the ray reflected at A_2 gives rise to a forward directed toroidal wavefront, however, in this case the width of the peak depends only weakly on β for $\beta \leq 45^\circ$ since $b_2=a \cos(\beta/2)$. Increasing β widens the forward peak.

When ka is large the magnitude of the backscattering at $\theta=180^\circ$ estimated from (11b) becomes the specular contribution to f giving $|F| \approx 1$. Similarly from (10), when $\theta=0$ the specular contribution to f gives $|F| \approx 1$ provided ka is very large and β is not small so that the forward diffraction peak does not contribute significantly to $f(ka, \cos \beta)$. These on-axis properties are shown from ray theory in Appendix A for Bessel beam reflection. When these approximations are applicable $|F|$ becomes

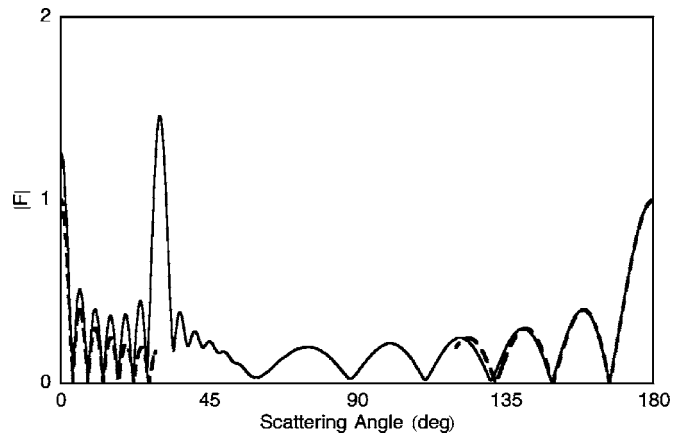


FIG. 6. Like Fig. 5 except that $ka=40$.

$$|F_j| = |J_0(kb_j\theta_j)|, \quad (14a)$$

$$\theta_1 = (\pi - \theta), \quad (14b)$$

$$\theta_2 = \theta, \quad (14c)$$

for the near-backward ($j=1$) and near-forward ($j=2$) contributions. This approximation will now be illustrated for soft and rigid spheres.

Figures 5 and 6 compare for $\beta=30^\circ$ the exact soft sphere result from (9) with the approximations from (14) for ka of 15 and 40. As expected from the restriction on the forward approximation, Eq. (14) is a more useful approximation in the backwards case. Figures 7 and 8 give similar comparisons for the corresponding case of a rigid sphere. In this case, however, (14) completely breaks down for $j=2$ where $ka=15$ so that $|F_2|$ is not shown. Inspection of Fig. 2 shows that $|f|$ is small for the rigid sphere near $\theta=30^\circ$ as a consequence of the forward diffraction and specular features so that from Eq. (10), $|F|$ is small for $\theta=0$ when $ka=15$. See also the discussion in Appendix A.

Ordinarily for toroidal wavefronts generated by the transmission of sound through fluid filled and solid elastic spheres, the form function $|f|$ descriptive of the farfield scattering of plane waves increases in proportion to $(ka)^{1/2}$ as a consequence of axial focusing.²⁴⁻²⁷ This is the reason why high refractive index fluid-filled focusing spherical targets

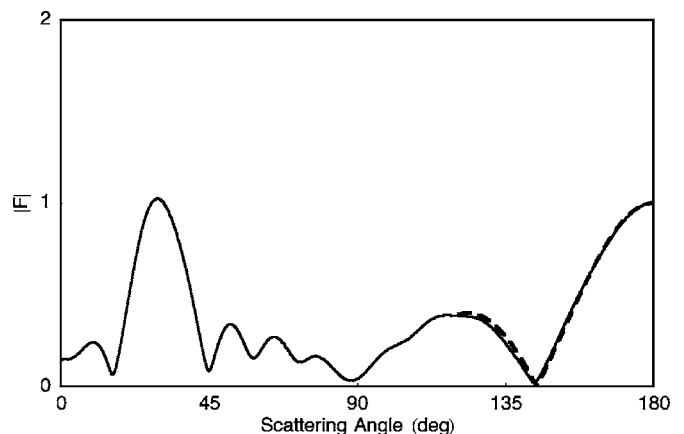


FIG. 7. Like Fig. 5 except that the sphere is rigid and $|F_2|$ is not shown.

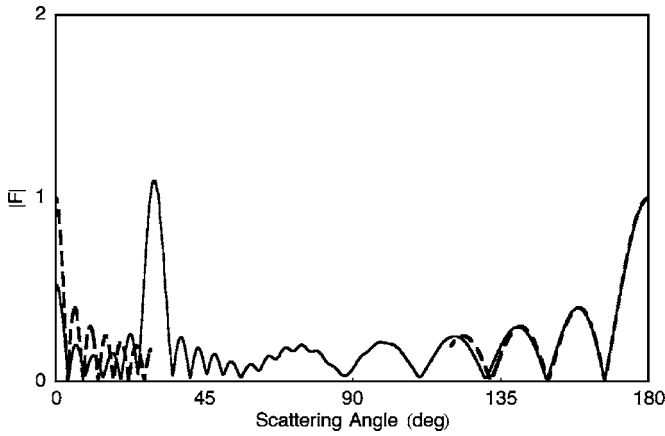


FIG. 8. Like Fig. 5 except that the sphere is rigid and $ka=40$.

are still useful with acoustical refractive indices somewhat less than 2 [see Sec. 4.8 of Ref. 6 for the $(ka)^{1/2}$ scaling by such targets]. Since the reflection of a Bessel beam by a soft or rigid sphere produces a toroidal wavefront, it may appear paradoxical that $|F_j|=1$ for the on-axis scattering when ka is large. This is resolved in Appendix A where it is found that the *amplitude* of the toroidal wavefront close to the sphere is proportional to $(ka)^{-1/2}$ in the Bessel beam case. In contrast, for the usual focusing sphere case the amplitude does not depend on ka when attenuation is neglected.

The discussion above of Fig. 3 emphasized the geometric interpretation of the scattering. Figure 3 also illustrates how the dependence on the ratio of beam size to sphere size influences the scattering. This may be seen by defining b such that $\mu b \approx 2.405$ is the first root of $J_0(\mu b)=0$. Consequently b denotes the half-width of the beam at the first radial pressure node of the beam. The ratio of the size of the sphere to the size of the beam is characterized by

$$a/b = \mu a / \mu b \approx (ka/2.405) \sin \beta.$$

In the *plane-wave limit* β and the ratio a/b both vanish when ka remains fixed. For the cases shown in Fig. 3 of $\beta=20^\circ$, 30° , and 45° , the respective values of a/b are 2.13, 3.12, and 4.41. While the scattering examples illustrated here are for the cases of soft and rigid spheres, some examples of the angular dependence of $|F|$ for fluid spheres were recently published¹² together with plots of how the back-scattering depends on ka . Plots were shown of $|F|$ for spheres having relatively small values of ka in beams with small values of a/b .¹²

The farfield restriction on (6) may be removed by taking the scattering ψ_s for $r \geq a$ to be an infinite sum of partial waves $\psi_{sn} = (\psi_0/2) i^n (2n+1)(s_n-1) P_n(\cos \theta) P_n(\cos \beta) h_n^{(1)}(kr)$. The result in (6) and (9) is recovered by approximating $h_n^{(1)}(kr)$ for large kr . Summing this ψ_s with Eq. (B2) gives the partial waves of the total velocity potential $\psi_T(r, \theta) = \psi_s + \psi_B$. It follows that as required $\psi_T(a, \theta) = 0$ when using the soft sphere $s_n = -h_n^{(2)}(ka)/h_n^{(1)}(ka)$. It also follows that as required $\partial \psi_T / \partial r = 0$ at $r=a$ when using the rigid sphere $s_n = -h_n^{(2)}(ka)' / h_n^{(1)}(ka)'$ where primes denote differentiation. This verifies that, in agreement with the analysis in Secs. III and IV, illumination by a Bessel beam does not alter

the s_n . While the nearfield properties could have been introduced at an earlier stage of the analysis, it was not necessary to do so since the *plane-wave scattering* is taken to be already known in Sec. III.

ACKNOWLEDGMENT

This research was supported by the Office of Naval Research. B. T. Hefner of APL (University of Washington) supplied helpful comments.

APPENDIX A: TOROIDAL WAVEFRONT AND AMPLITUDE

The reflected wave properties may be constructed by inspection of Fig. 4 and by using the methods of ray optics.^{6,24,26,27} For simplicity consider the properties of the wavefront reflected near point A_1 . For a specified incident wave vector component lying in the plane of Fig. 4, back-propagating the reflected wavefront to point A_1 while neglecting the presence of the sphere generates a virtual wavefront that is locally ellipsoidal. One of the principal planes of the reflected wavefront lies in the plane of Fig. 4 and the intersection of the virtual wavefront with that plane gives the dashed curve shown. At A_1 the associated principal radius is found from Eq. (1) of Ref. 24 to be $\alpha' = (a/2) \cos(v_1)$. At A_1 the orthogonal principal radius is found to be $\alpha'' = (a/2) / \cos(v_1)$. Consider the associated complex amplitude in a virtual exit plane perpendicular to the z axis which passes through A_1 . The local wavefront shape gives the amplitude as

$$d\psi_E = (\psi_0/2\pi) \exp[ik(s-b_1)^2/2\alpha' + iku^2/2\alpha'' + i\eta] d\phi', \quad (A1)$$

where s denotes the radial coordinate and u denotes the orthogonal coordinate perpendicular to the plane of Fig. 4. The phase constant η contains geometrical factors and it also depends on the sign of the reflection coefficient. The superposition for all wave vector components of the incident wave gives the exit-plane amplitude

$$\psi_E(s) = \int d\psi_E \approx \psi_0 (2\pi k b_1^2 / \alpha'')^{-1/2} \exp[ik(s-b_1)^2/2\alpha' + i\eta + i\pi/4], \quad (A2)$$

where in the integration over $d\phi'$, $u = b_1(\phi' - \phi_0')$ where ϕ_0' is the azimuthal angle of the slice shown in Fig. 4. The integration uses the stationary phase approximation. This confirms that the reflection of a Bessel beam generates a toroidal wavefront and that the amplitude is proportional to $k^{-1/2}$. A Rayleigh-Sommerfeld diffraction integral gives the on-axis magnitude of the contribution to the farfield form function for such a toroidal wavefront as [see Eq. (14) of Ref. 24 or Eqs. (248)–(250) of Ref. 6]

$$|F| \approx (2k/a) |\psi_0^{-1}| \int_0^\infty s \psi_E(s) ds. \quad (A3)$$

Application of the stationary phase approximation gives $|F| \approx (2/a) \sqrt{(\alpha' \alpha'')}$. The product $\alpha' \alpha''$ of the principal radii

is $(a/2)^2$ so that $|F| \approx 1$ for backscattering in agreement with (14).

Repeating this analysis for the reflection at A_2 gives $|F| \approx 1$ for forward scattering. In that case, however, α' is small and the specular point at A_2 lies close to the shadow edge at T in Fig. 4. Thus the result for $|F_2|$ in (14) and the stationary phase approximation of (A3) are only applicable when ka is very large.

APPENDIX B: PARTIAL WAVE EXPANSION OF A BESSEL BEAM

The following expansion in spherical coordinates facilitates the discussion at the end of Sec. VII. It is also used in the derivation of the radiation force given in Ref. 12. Application of the usual spherical-coordinate plane-wave expansion theorem (p. 119 of Ref. 20 or p. 471 of Ref. 21) to the plane-wave component $d\psi_B = (d\psi_B/d\phi')d\phi'$ gives

$$d\psi_B = (\psi_0/2\pi) \sum_{n=0}^{\infty} i^n (2n+1) j_n(kr) P_n(\cos \gamma) d\phi', \quad (\text{B1})$$

at a location specified by (r, θ, ϕ) in Fig. 1. Consequently the incident Bessel beam may be expanded in spherical partial waves as

$$\psi_B(r, \theta) = \int d\psi_B = \psi_0 \sum_{n=0}^{\infty} i^n \times (2n+1) j_n(kr) P_n(\cos \theta) P_n(\cos \beta), \quad (\text{B2})$$

by using Eq. (8). This expansion was verified numerically to converge to $\psi_0 e^{i\kappa z} J_0(\mu\rho)$.

¹J. Durnin, "Exact solutions for nondiffracting beams. I. The scalar theory," *J. Opt. Soc. Am. A* **4**, 651–654 (1987).

²J. Durnin, J. J. Miceli, Jr., and J. H. Eberly, "Diffraction-free beams," *Phys. Rev. Lett.* **58**, 1499–1501 (1987).

³D. K. Hsu, F. J. Margetan, and D. O. Thompson, "Bessel beam ultrasonic transducer: Fabrication method and experimental results," *Appl. Phys. Lett.* **55**, 2066–2068 (1989).

⁴J. A. Campbell and S. Soloway, "Generation of a nondiffracting beam with frequency-independent beamwidth," *J. Acoust. Soc. Am.* **88**, 2467–2477 (1990).

⁵J.-y. Lu and J. F. Greenleaf, "Ultrasonic nondiffracting transducer for medical ultrasonics," *IEEE Trans. Ultrason. Ferroelectr. Freq. Control* **37**, 438–447 (1990).

⁶P. L. Marston, "Geometrical and catastrophe optics methods in scattering," *Phys. Acoust.* **21**, 1–234 (1992), See Section 2.15 p. 44–47.

⁷P. R. Stepanishen and J. Sun, "Acoustic bullets: Transient Bessel beams generated by planar apertures," *J. Acoust. Soc. Am.* **102**, 3308–3318 (1997).

⁸K. B. Cunningham and M. F. Hamilton, "Bessel beams of finite amplitude in absorbing fluids," *J. Acoust. Soc. Am.* **108**, 519–525 (2000).

⁹D. McGloin and K. Dholakia, "Bessel beams: diffraction in a new light," *Contemp. Phys.* **46**, 15–28 (2005).

¹⁰G. C. Gaunaurd and H. Uberall, "Acoustics of finite beams," *J. Acoust. Soc. Am.* **63**, 5–16 (1978).

¹¹P. J. Westervelt, "The theory of steady forces caused by sound waves," *J. Acoust. Soc. Am.* **23**, 312–315 (1951).

¹²P. L. Marston, "Axial radiation force of a Bessel beam on a sphere and direction reversal of the force," *J. Acoust. Soc. Am.* **120**, 3518–3524 (2006).

¹³M. Redwood, *Mechanical Waveguides* (Pergamon Press, Oxford, 1960), pp. 286–287.

¹⁴J. J. Bowman, T. B. A. Senior, and P. L. E. Uslenghi, *Electromagnetic and Acoustic Scattering by Simple Shapes* (Taylor and Francis, Abingdon, 1988), pp. 354–380.

¹⁵V. C. Anderson, "Sound scattering from a fluid sphere," *J. Acoust. Soc. Am.* **22**, 426–431 (1950).

¹⁶K. A. Sage, J. George, and H. Uberall, "Multipole resonances in sound scattering from gas bubbles in a liquid," *J. Acoust. Soc. Am.* **65**, 1413–1422 (1979).

¹⁷G. C. Gaunaurd and H. Uberall, "RST analysis of monostatic and bistatic acoustic echoes from an elastic sphere," *J. Acoust. Soc. Am.* **73**, 1–12 (1983).

¹⁸S. G. Kargl and P. L. Marston, "Observations and modeling of the backscattering of short tone bursts from a spherical shell: Lambwave echoes, glory, and axial reverberations," *J. Acoust. Soc. Am.* **85**, 1014–1028 (1989).

¹⁹P. L. Marston, "Generalized optical theorem for scatterers having inversion symmetry: applications to acoustic backscattering," *J. Acoust. Soc. Am.* **109**, 1291–1295 (2001).

²⁰L. I. Schiff, *Quantum Mechanics*, 3rd ed. (McGraw-Hill, New York, 1968), pp. 131–133.

²¹J. D. Jackson, *Classical Electrodynamics*, 3rd ed. (Wiley, New York, 1999), Secs. 3.5–3.6, pp. 107–111.

²²R. Y. Nishi, "Scattering and absorption of sound-waves by a gas bubble in a viscous-liquid," *Acustica* **33**, 65–74 (1975).

²³A. Prosperetti, "Thermal effects and damping mechanisms in the forced radial oscillations of gas bubbles in liquids," *J. Acoust. Soc. Am.* **61**, 17–27 (1977).

²⁴P. L. Marston, "Quantitative ray methods for scattering" in *Encyclopedia of Acoustics*, edited by M. J. Crocker (Wiley, New York, 1997), Chap. 43, pp. 483–492.

²⁵H. C. van de Hulst, "A theory of the anti-coronae," *J. Opt. Soc. Am.* **37**, 16–22 (1947).

²⁶P. L. Marston and D. S. Langley, "Glory- and rainbow-enhanced acoustic backscattering from fluid spheres: models for diffracted axial focusing," *J. Acoust. Soc. Am.* **73**, 1464–1475 (1983).

²⁷W. P. Arnott and P. L. Marston, "Unfolding axial caustics of glory scattering with harmonic angular perturbations of toroidal wavefronts," *J. Acoust. Soc. Am.* **85**, 1427–40 (1989).

An annular superposition integral for axisymmetric radiators

James F. Kelly^{a)} and Robert J. McGough^{b)}

Department of Electrical and Computer Engineering, Michigan State University,
East Lansing, Michigan 48824

(Received 14 July 2006; revised 31 October 2006; accepted 5 November 2006)

A fast integral expression for computing the nearfield pressure is derived for axisymmetric radiators. This method replaces the sum of contributions from concentric annuli with an exact double integral that converges much faster than methods that evaluate the Rayleigh-Sommerfeld integral or the generalized King integral. Expressions are derived for plane circular pistons using both continuous wave and pulsed excitations. Several commonly used apodization schemes for the surface velocity distribution are considered, including polynomial functions and a “smooth piston” function. The effect of different apodization functions on the spectral content of the wave field is explored. Quantitative error and time comparisons between the new method, the Rayleigh-Sommerfeld integral, and the generalized King integral are discussed. At all error levels considered, the annular superposition method achieves a speed-up of at least a factor of 4 relative to the point-source method and a factor of 3 relative to the generalized King integral without increasing the computational complexity. © 2007 Acoustical Society of America. [DOI: 10.1121/1.2405124]

PACS number(s): 43.20.Rz, 43.20.Ei, 43.35.Bf [TDM]

Pages: 759–765

I. INTRODUCTION

Many radiators in biomedical ultrasonics, SONAR, and nondestructive testing have a spatially varying particle velocity on the piston surface. This variation in surface velocity, or apodization, significantly alters the beam pattern compared to a radiator with uniform velocity. In order to accurately model pressures generated by these transducers, this apodization must be considered.^{1,2} Although a formal solution to this problem is given by the Rayleigh-Sommerfeld diffraction integral³ or the King integral,⁴ these solutions can be poorly behaved numerically, especially near the source. In the case of the King integral, the integrand is singular, which leads to slow convergence relative to other integral expressions. Therefore, many specialized solutions have been developed to handle piston radiators, including series solutions in terms of spherical wave functions,^{5–7} single-integral expressions based on the impulse response,^{8–10} and transient single-integral expressions.¹¹ Recent series approaches have considered circular sources in finite baffles¹² and resilient disks¹³ with nonuniform surface velocity distributions.

To overcome the difficulties associated with the Rayleigh-Sommerfeld and generalized King integrals, an axisymmetric solution to the piston radiator problem is derived. Based on the fast nearfield method (FNM) for radiators with uniform surface velocity,^{14–16} the proposed annular superposition method calculates the pressure fields generated by apertures where the surface velocity is a function of the radial variable. As an extension of the FNM expression derived in Ref. 14, this annular superposition method has a numerically well-behaved integrand that rapidly converges within the nearfield region of the radiator. Unlike the impulse response or Schoch solutions, the resulting annular superpo-

sition integral is defined by a single expression that describes the pressure throughout the entire computational domain.

After classical solutions to the apodized piston problem are reviewed, the method based on the annular superposition integral is derived subject to an arbitrary axisymmetric surface velocity distribution. This new method is applied to the “smooth piston” model and polynomial apodization functions. In addition, the method is generalized to the case of transient excitations. Example fields are computed and the spectral content of apodized wave fields are examined. Transient wave fields are also presented. An error analysis and comparison of the annular superposition method to the standard point-source approach is performed. The results show that the annular superposition integral achieves a speed-up by a factor of 4 relative to the Rayleigh-Sommerfeld integral at all error levels considered.

II. NEARFIELD CALCULATIONS FOR A CIRCULAR PISTON

Before the annular superposition integral is derived, two classical solutions to the baffled piston problem are reviewed: the Rayleigh-Sommerfeld and King integrals. Both the Rayleigh-Sommerfeld and the generalized King integral will be quantitatively compared to the proposed method.

A circular aperture with radius a , located in the x - y plane, radiates into a homogeneous acoustic half-space with constant density ρ and sound speed c . Initially, the excitation is assumed to be single frequency with angular frequency ω . The velocity distribution is assumed symmetric with respect to the angle θ lying in the x - y plane, allowing all apodization and phasing information to be encoded in an *aperture function* $q(\sigma)$, where σ is radial distance. Figure 1 displays the geometry and notation used in the subsequent derivation. Since any realistic transducer has finite extent, q is assumed to be zero outside the interval $[0, a]$.

^{a)}Electronic mail: kellyja8@msu.edu

^{b)}Electronic mail: mcgough@egr.msu.edu

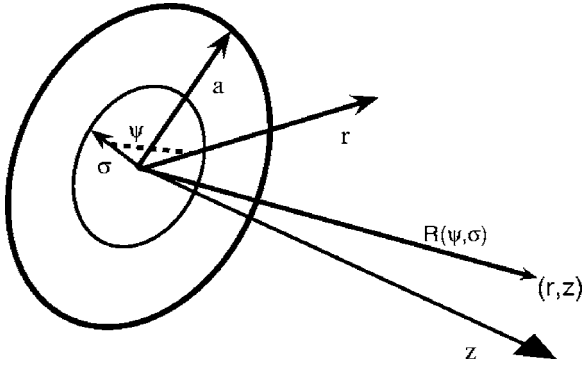


FIG. 1. Coordinate axis used in the derivation. A piston of radius a is excited by a radially varying particle velocity specified by an aperture function $q(\sigma)$, where σ is the radial position on the piston. The radiator is surrounded by an infinite rigid baffle in the $z=0$ plane. The angle ψ and relative distance $R(\psi, \sigma)$ correspond to the notation used in Eq. (1).

A. Rayleigh-Sommerfeld integral

The Rayleigh-Sommerfeld diffraction integral, evaluated with the point-source approach,³ is the standard method for evaluating pressure fields generated by acoustic radiators. The Rayleigh-Sommerfeld integral analytically sums spherical wave contributions from each point on the aperture. In cylindrical coordinates, the Rayleigh-Sommerfeld integral is given by

$$\hat{p}(r, z; \omega) = \frac{jk\rho c}{\pi} \int_0^a \sigma q(\sigma) \int_0^\pi \frac{e^{-jkR(\psi, \sigma)}}{R(\psi, \sigma)} d\psi d\sigma \quad (1)$$

with $R(\psi, \sigma) = \sqrt{z^2 + \sigma^2 + r^2 - 2r\sigma \cos \psi}$. Through the cylindrical symmetry of $R(\psi, \sigma)$, the integrand of Eq. (1) evaluated for $\psi \in [0, \pi]$ is replicated for $\psi \in [\pi, 2\pi]$, so the limits of integration are reduced to $[0, \pi]$. Note that Eq. (1) possesses a $1/r$ singularity.

B. Generalized King integral

The generalized King integral utilizes the spectral form of the Green's function to represent the pressure generated by an axisymmetric radiator as a single integral. However, the domain of integration is infinite and the integrand is weakly singular at wave number k . In cylindrical coordinates, the King integral is given by

$$\hat{p}(r, z; \omega) = \rho\omega \int_0^\infty \frac{\exp(-jz\sqrt{k^2 - \alpha^2})}{\sqrt{k^2 - \alpha^2}} \tilde{q}(\alpha) J_0(r\alpha) \alpha d\alpha, \quad (2)$$

where $\tilde{q}(\alpha)$ is the Hankel transform of the apodization function $q(\sigma)$ and $J_n(z)$ is the Bessel function of the first kind of order n . In the case of the uniform piston, $\tilde{q}(\alpha)$ is proportional to $aJ_1(\alpha a)/\alpha$, reducing Eq. (2) to the classical King integral [see Eq. (7) in Ref. 1]. Unlike the $1/r$ singularity present in Eq. (1), Eq. (2) contains a weak singularity at $\alpha = k$.¹⁷ Numerically, the integral is decomposed into two integrals ranging from $[0, k)$ and (k, ∞) and a trigonometric and hyperbolic substitution is performed on each integral, respectively. The integration from $[0, k)$ represents the propagating

spectrum, whereas the integration from (k, ∞) represents the evanescent spectrum.

C. Annular superposition integral

The single-frequency pressure $\hat{p}_a(r, z; \omega)$ generated by a circular piston a with spatially uniform velocity v_0 is given by the FNM¹⁴

$$\hat{p}_a(r, z; \omega) = \frac{\rho c a v_0}{\pi} \int_0^\pi \frac{r \cos \psi - a}{r^2 + a^2 - 2ar \cos \psi} \times (e^{-jk\sqrt{r^2 + a^2 + z^2 - 2ar \cos \psi}} - e^{-jkz}) d\psi, \quad (3)$$

where ρc is the characteristic acoustic impedance of the (homogeneous) medium, v_0 is the piston velocity, and (r, z) are the observation coordinates in cylindrical coordinates. As suggested in Ref. 10, the pressure field $\hat{p}(r, z; \omega)$ associated with the aperture function $q(\sigma)$ can be synthesized by decomposing the circle of radius a into N concentric annuli where the i th annulus has inner radius $(i-1)\sigma$ and outer radius $i\sigma$. After defining $p_i = \hat{p}_{i\Delta\sigma}(r, z; \omega)$ and $q_i = q(i\Delta\sigma)$ and a uniform spacing of annuli with $\Delta\sigma = a/N$, then the total pressure is written as

$$\hat{p}(r, z; \omega) \approx \sum_{i=1}^{N-1} p_i(q_i - q_{i+1}) + p_N q_N. \quad (4)$$

Taking $q_N = 0$ (since the aperture function vanishes on the boundary), Eq. (4) can be written as a Riemann sum

$$\hat{p}(r, z; \omega) \approx \sum_{i=1}^{N-1} -p_i \frac{q_{i+1} - q_i}{\Delta\sigma} \Delta\sigma. \quad (5)$$

Letting $N \rightarrow \infty$ and $\Delta\sigma \rightarrow 0$, the sum becomes an integral and the difference quotient becomes a derivative, yielding

$$\hat{p}(r, z; \omega) = - \int_0^a \hat{p}_\sigma(r, z; \omega) q'(\sigma) d\sigma. \quad (6)$$

Inserting Eq. (3) into Eq. (6) yields the following double integral for the apodized pressure field:

$$\hat{p}(r, z; \omega) = - \frac{\rho c v_0}{\pi} \int_0^a q'(\sigma) \int_0^\pi \frac{r \cos \psi - \sigma}{r^2 + \sigma^2 - 2\sigma r \cos \psi} \times (e^{-jk\sqrt{r^2 + \sigma^2 + z^2 - 2\sigma r \cos \psi}} - e^{-jkz}) d\psi d\sigma. \quad (7)$$

Equation (7) provides the basis for the axisymmetric superposition method. By choosing the appropriate complex-valued aperture function $q(\sigma)$, the acoustic field pressure $\hat{p}(r, z; \omega)$ is specified for all observation points (r, z) in the acoustic half-space. Since the derivative of $q'(\sigma)$ appears in Eq. (7), the aperture function $q(\sigma)$ must be at least weakly differentiable.

Physically, Eqs. (6) and (7) state that the total pressure generated by an apodized radiator consists of contributions from concentric annuli with uniform velocity. Note that Eq. (6) is valid for any pressure uniform pressure expression $\hat{p}_\sigma(r, z; \omega)$, such as the impulse response integral.⁸ However, other single-integral solutions are defined piecewise over the computational domain, making the integration over σ intrac-

table. The single integral expression developed for the fast nearfield method¹⁴ is ideal for those calculations due to rapid convergence in the nearfield region.

D. Pulsed circular radiator

The expression in Eq. (7) is also amenable to time-domain calculations of transient pressures generated by apodized circular pistons. The velocity distribution is assumed to be separable in radial coordinate σ and time t such that $u(\sigma, t) = v(t)q(\sigma)$. For a pulse $v(t)$ with a spectrum given by $\hat{v}(\omega)$, the transient pressure field is recovered by weighting Eq. (7) by the pulse spectrum $\hat{v}(\omega)$ and inverse Fourier transforming. These operations yield

$$p(r, z; t) = -\frac{\rho c}{\pi} \int_0^a q'(\sigma) \sigma \int_0^\pi \frac{r \cos \psi - a}{r^2 + \sigma^2 - 2\sigma r \cos \psi} \times (v(t - \tau_1) - v(t - \tau_2)) d\psi d\sigma, \quad (8)$$

where the delay times τ_1 and τ_2 are defined by

$$\tau_1 = \sqrt{r^2 + z^2 + \sigma^2 - 2a\sigma \cos \psi} / c, \quad (9a)$$

$$\tau_2 = z/c. \quad (9b)$$

III. APERTURE FUNCTIONS

In the following, double integral expressions are derived for the following aperture functions: uniform piston, smooth piston, and polynomial apodization. An expression for a pulsed, apodized piston is also derived.

A. Uniform piston

Note that for spatially uniform pressure, $q(\sigma) = H(a - \sigma)$, where $H(z)$ is the Heaviside function. Then the weak derivative $q'(\sigma) = -\delta(\sigma - a)$, where $\delta(z)$ is the Dirac delta function. Inserting $q'(\sigma) = -\delta(\sigma - a)$ into Eq. (7) yields the original expression for pressure given by Eq. (3).

B. Smooth piston

A piston model proposed in Ref. 18 provides a smooth tapering of surface particle velocity near the surrounding baffle. This smooth piston assumes an aperture function given by

$$q(\sigma) = \begin{cases} 1 & \text{if } \sigma \leq a \\ \frac{(1 + \delta)^2 - \sigma^2/a^2}{\delta(2 + \delta)} & \text{if } a < \sigma \leq a(1 + \delta) \\ 0 & \text{otherwise,} \end{cases} \quad (10)$$

where $\delta > 0$ is a unitless parameter that specifies a continuous transition region between piston-like motion and the rigid baffle. Note that the σ integral is evaluated over the thin semiannular region $a(1 + \delta) \leq \sigma \leq a$, which significantly reduces the computational complexity.

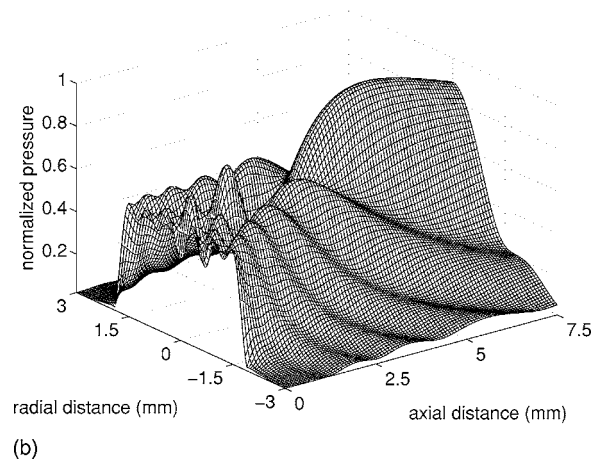
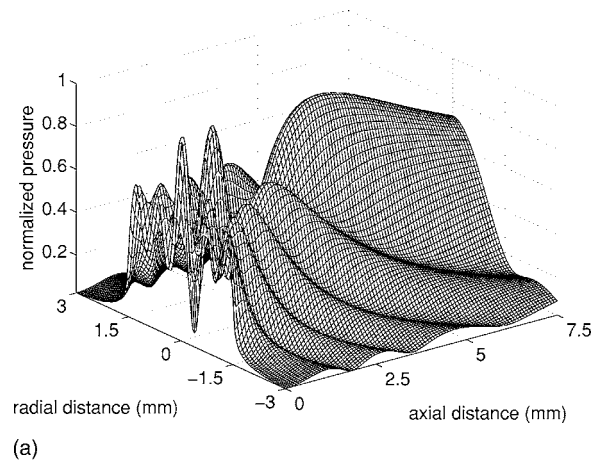


FIG. 2. Normalized pressure fields generated by “smooth” pistons modeled by Eq. (10). (a) The pressure produced by a piston with radius $a = 2.5\lambda$ with transition parameter $\delta = 0.05$, which closely resembles the field produced by a uniform piston. (b) The field generated by a piston with the same radius $\delta = 0.30$.

C. Polynomial apodization

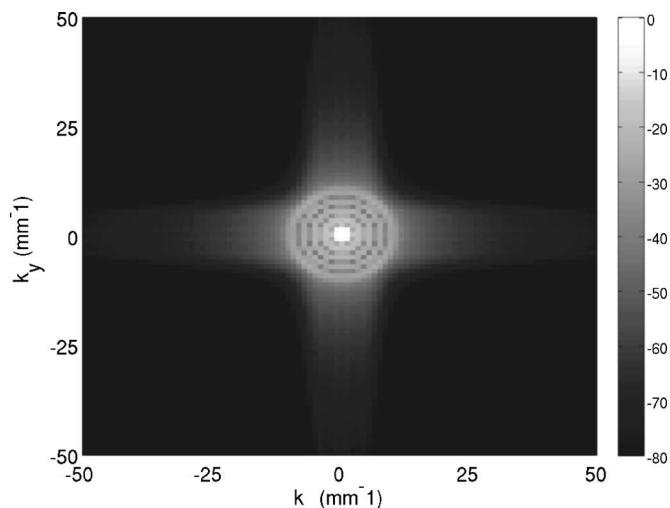
Previous studies of piston radiators have employed polynomial apodization functions^{2,19} to model the distribution of normal particle velocity across the face of the radiator. A general aperture function of the form

$$q(\sigma) = 1 - (\sigma/a)^n \quad (11)$$

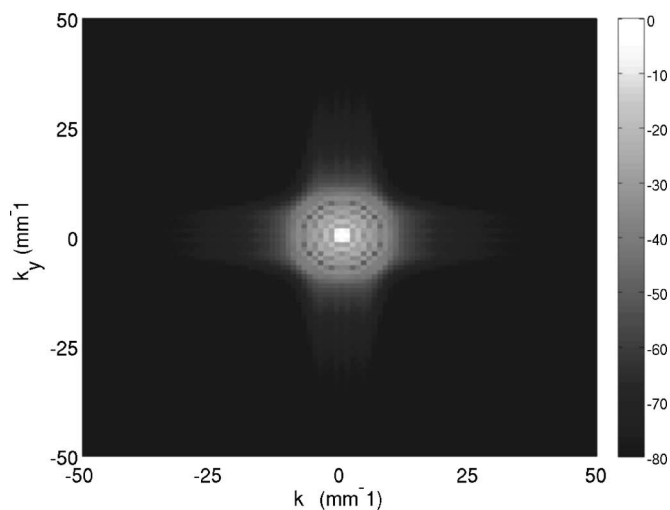
is considered for $\sigma < a$. The uniform rigid piston is recovered by letting $n \rightarrow \infty$, while linear, quadratic, and quartic apodizations are obtained for $n = 1$, $n = 2$, and $n = 4$, respectively. Evaluation of the on-axis pressure for $0 < n < \infty$ shows a reduction in on-axis nulls that characterize the nearfield of circular pistons.

IV. NUMERICAL RESULTS

Examples of continuous wave and pulsed fields are computed using the apodization and phasing schemes described in Sec. II. All double integrals were evaluated via Gauss-Legendre quadrature.²⁰ Since the region of integration for each of the integral expressions is a half-disc of radius a , the number of quadrature points for the i th ψ or θ integral is chosen as proportional to the radial variable σ_i . Thus, the computational cost is reduced by roughly a factor of 2 rela-



(a)

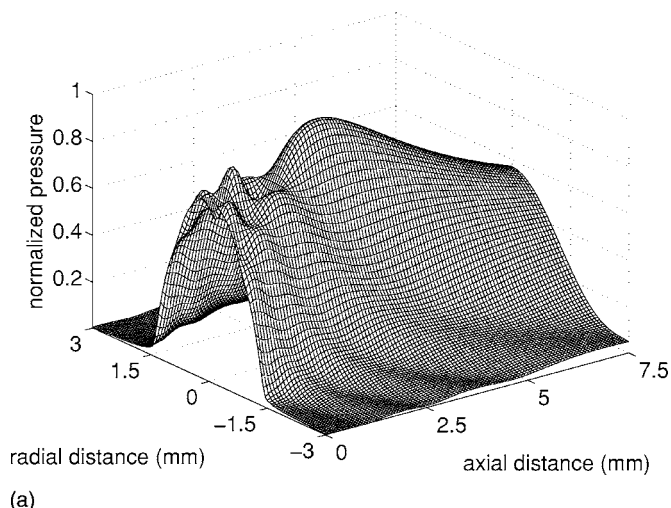


(b)

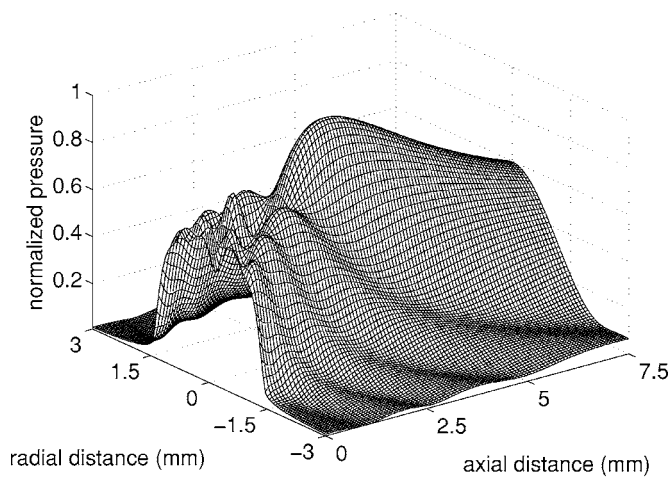
FIG. 3. Normalized magnitude spectrum of the “smooth piston” pressure fields displayed in Fig. 2. In each panel, the nearfield pressure is calculated in a transverse plane at $z=0.9375$ mm via Eq. (10) followed by a two-dimensional Fourier transform. (a) The magnitude spectrum, displayed on a normalized decibel scale, for a smooth piston with $\delta=0.05$. (b) The spectrum for a smooth piston with $\delta=0.30$. Panel (b) contains significantly less spectral information than (a) due to the wider transition band.

tive to direct application of Gauss-Legendre quadrature. The King integral, given by Eq. (2), was evaluated using the substitutions given in Ref. 17. Both the propagating and evanescent integrals were integrated using Gauss-Legendre quadrature with an equal number of abscissas.

A fixed computational grid and sampling frequency (in the case of transient fields) is used in all field computations. In the following simulations, a piston of radius $a=2.5\lambda=1.5$ mm is driven at a center frequency of 2.5 MHz in a homogeneous medium with sound speed $c=1.5$ mm/ μ s. The scaling factor v_0 in Eq. (7) is taken to be unity. A fixed computational grid with 121 samples in the radial direction and 101 samples in the axial direction is employed, which corresponds to $\lambda/4$ spacing. The computational grid is axially offset by $\lambda/4$ in order to facilitate comparison to the Rayleigh-Sommerfeld integral in Sec. IV. The resulting fields are normalized with respect to the peak pressure magnitude.



(a)



(b)

FIG. 4. Reference pressure fields for polynomial apodization given by Eq. (11). (a) The effect of quadratic apodization ($n=2$). (b) Quartic apodization ($n=4$).

A. Smooth piston fields

Figure 2 shows the normalized pressure fields produced by the “smooth” piston model given by Eq. (10). Figure 2(a) displays the pressure field associated with a relatively narrow transition region of $\delta=0.05$, whereas Fig. 2(b) displays the pressure fields associated with a wider transition region of $\delta=0.30$. Relative to the field in Fig. 2(a), the field in Fig. 2(b) contains less spatial variation resulting from less variation in the apodization function $q(\sigma)$. The spatial bandwidth for each piston is quantified in Fig. 3, which displays the magnitude spectrum in the transverse plane $z=0.9375$ on a normalized decibel scale. Comparing Figs. 2(a) and 2(b), the $\delta=0.05$ piston contains significantly more spectral information than the $\delta=0.3$ piston due to a shorter transition band in the normal surface velocity. This wider spectrum correlates with the greater spatial variation depicted in Fig. 2(a).

B. Polynomial apodization

Pressure fields resulting from the polynomial apodization given by Eq. (11) are evaluated on a fixed computational grid for $n=2$ and $n=4$. The resulting normalized pressure

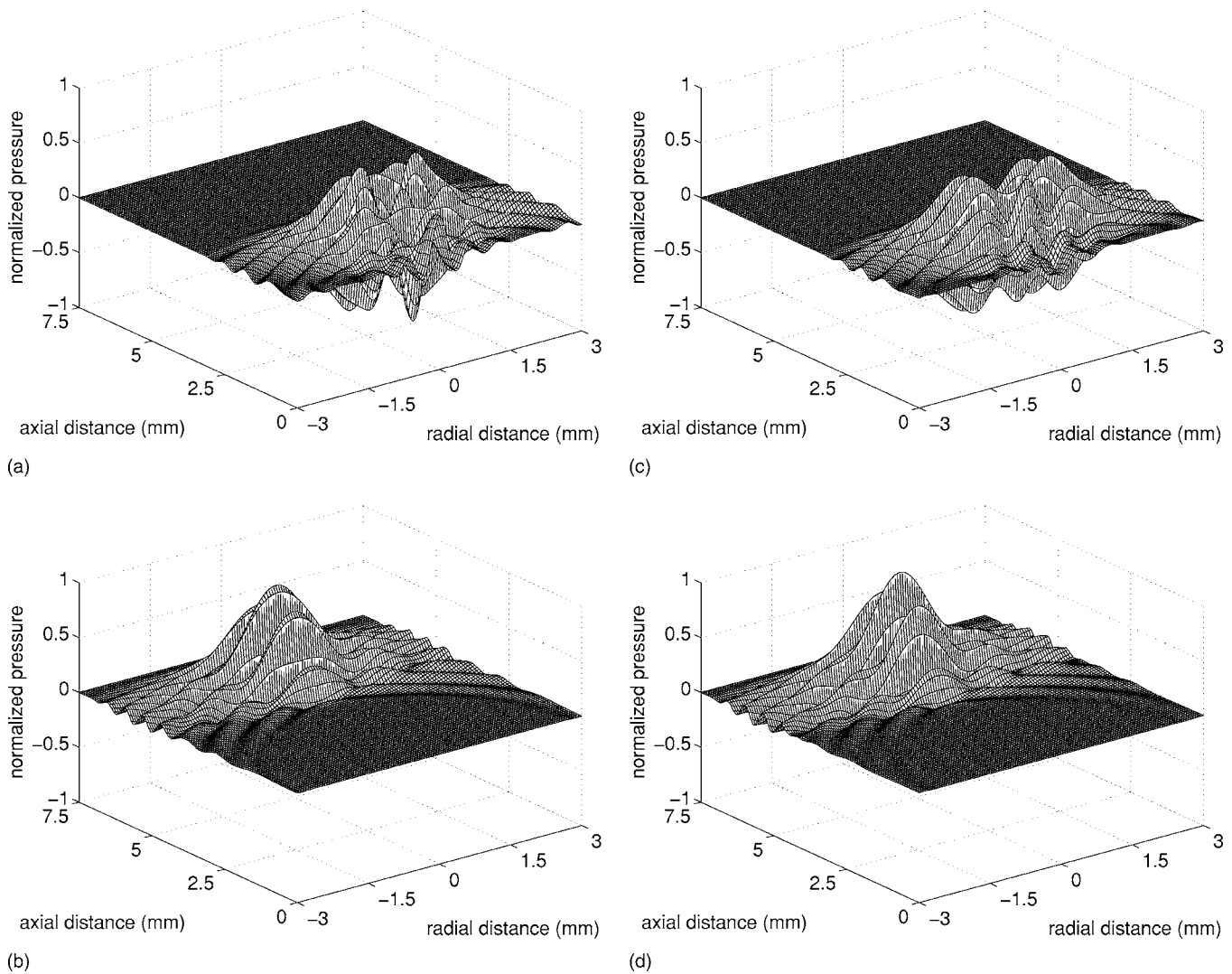


FIG. 5. Pulsed fields generated by smooth pistons with the same parameters used in Fig. 2. The time evolution for smooth pistons with $\delta=0.3$ and $\delta=0.05$ are compared. (a) and (b) Normalized pressure fields corresponding to $\delta=0.05$ at $t=2.50 \mu\text{s}$ and $t=5.00 \mu\text{s}$, respectively. (c) and (d) Normalized pressure fields corresponding to $\delta=0.30$ at $t=2.50 \mu\text{s}$ and $t=5.00 \mu\text{s}$, respectively.

fields are plotted in Fig. 4. Figure 4(a), displaying the effect of quadratic apodization, demonstrates the reduced spatial variation of the parabolic radiator compared to a uniform rigid piston with the same geometry (see Fig. 5 in Ref. 3). Spectral computations similar to those shown in Fig. 3 demonstrate the larger spatial bandwidth of the quartic apodization relative to the quadratic apodization. This greater bandwidth is observed qualitatively through the noticeable oscillations near the axial region in Fig. 4(b). These oscillations are produced by the rapid change in the apodization function near the piston boundary at $r=a$.

C. Pulsed fields

The time-domain pressure for the smoothed circular piston model was computed via Eqs. (8) and (10). The computational grid and piston parameters used in the continuous wave case were utilized in the pulsed case. Figure 5 displays the time evolution of the pulsed pressure fields associated with pistons having transition parameters $\delta=0.05$ and $\delta=0.30$. In both cases, a six-cycle Hanning-weighted tone burst with center frequency $f_0=2.5 \text{ MHz}$ models the excita-

tion pulse $v(t)$. Figures 5(a) and 5(c), which show, respectively, the normalized fields at $t=2.50 \mu\text{s}$ for $\delta=0.05$ and $\delta=0.30$ piston, exhibit significant disparity between the two fields. In particular, the $\delta=0.05$ piston exhibits an edge wave associated with the sharp change in surface velocity in the source plane; the edge wave for the $\delta=0.30$ piston is not as pronounced due to the more gradual change in surface velocity. Figures 5(b) and 5(d) display the normalized fields at $t=5.00 \mu\text{s}$ for $\delta=0.05$ and $\delta=0.30$; compared to Figs. 5(a) and 5(c), the two fields in Figs. 5(b) and 5(d) are very similar, indicating that the effects of spatial apodization are filtered out by space after a short propagation distance.

V. ERROR ANALYSIS

A. Reference field

The reference field was generated by applying a 20 000 point Gauss quadrature to the generalized King integral using quadratic apodization.⁴ This integration scheme resulted in a reference field that converged within 10^{-6} of machine precision.

B. Error metric

The spatial distribution of error is computed via the following metric:

$$\eta(r, z) = \frac{|\hat{p}(r, z; \omega) - \hat{p}_{\text{ref}}(r, z; \omega)|}{\max_{r, z} |\hat{p}_{\text{ref}}(r, z; \omega)|} \quad (12)$$

The peak error is then determined by taking the maximum of Eq. (12).

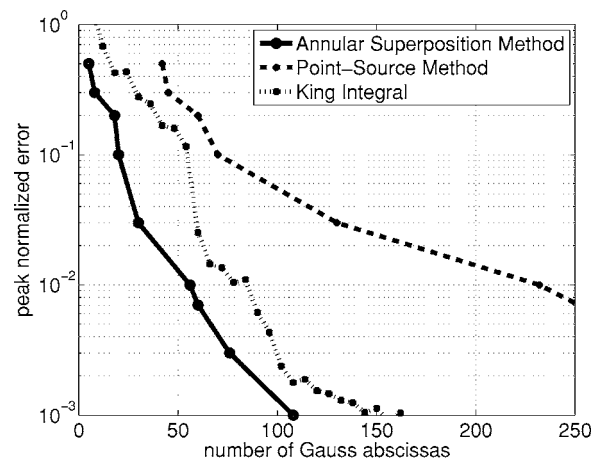
C. Error and time comparison

The annular superposition method, the point source method, and the generalized King integral were implemented in the C programming language and executed on a 3.0 GHz Pentium IV processor running RED HAT LINUX. The Bessel functions in the integrand of Eq. (2) were evaluated with the GNU Scientific Library.²¹ The annular superposition method, the point source method, and the generalized King integral subject to quadratic apodization, are evaluated with varying numbers of quadrature points and the computation times recorded at specified error levels. The resulting error and time analysis is summarized in Fig. 6. Figure 6(a) displays the number of quadrature points required to achieve a peak specified error, while Fig. 6(b) displays the associated computation times required for a specified error. Figures 6(a) and 6(b) demonstrate that the present superposition method converges significantly faster with respect to the point source approach and generalized King integral within the metric given by Eq. (12). For instance, at 10% peak specified error, the annular superposition method requires 20 quadrature points, while the point-source method requires 70 quadrature points and the generalized King integral requires 56 quadrature points. Comparing the computation times in Fig. 6(b), the superposition method requires 0.0486 s while the point-source requires 0.1946 s at the 10% peak error level. Hence, the annular superposition method achieves a speed-up by a factor of 4 at the 10% error level. Although the generalized King integral requires less quadrature points than point-source to achieve 10% maximum error, the computation time associated with Eq. (2) is about twice as long relative to point-source (0.3851 s vs 0.1946 s) due to evaluations of special functions.

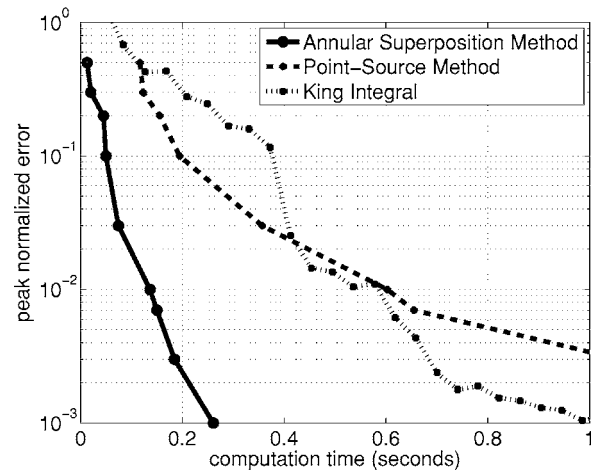
Similar speed-ups are observed at other specified peak error levels, with the speed-up increasing as the peak error decreases. At 1% peak error, the new method achieves a speed-up factor of 4.4 relative to the point-source approach and a speed-up factor of 3.7 relative to the generalized King integral.

VI. DISCUSSION

The farfield approximation is commonly employed to simplify cw and pulsed calculations of baffled radiators.²² Although the computational complexity of a problem is reduced by making this approximation, unacceptable error may be introduced if employed too close to the nearfield region. In the following, the farfield approximation applied to a parabolic radiator is analyzed.



(a)



(b)

FIG. 6. Number of Gauss abscissas vs specified peak error (a) and computation time vs specified peak error (b) for the annular superposition method, the Rayleigh-Sommerfeld integral, and the generalized King integral applied to a parabolic radiator. The annular superposition method achieves 10% peak error with the application of 20 abscissas, the Rayleigh-Sommerfeld approach requires 70 abscissas, and the generalized King integral requires 56 abscissas. Since the computation times are similar for each integral evaluated with the same number of abscissas, (b) demonstrates the present method's speed advantage compared to the Rayleigh-Sommerfeld approach and the generalized King integral at all error levels considered.

The farfield directivity pattern for a parabolic radiator, obtained from the Hankel transform of Eq. (11) using $n=2$, is given by

$$D(\theta) = \frac{2J_2(ka \sin \theta)}{k^2 \sin^2 \theta}, \quad (13)$$

where the angle $\theta = \sin^{-1}(r/z)$. The farfield pressure field is then proportional to Eq. (13) multiplied by the free-space Green's function. The error due to the farfield approximation was then computed relative to exact nearfield pressure. On-axis, the farfield error is less than 10% for all values of $z > 3.7a^2/\lambda$, where a^2/λ is the farfield transition distance. The farfield error on-axis is less than 1% for all values of $z > 11.8a^2/\lambda$.

The farfield approximation introduces greater error for the uniform piston. The farfield error is less than 10% for all values of $z > 4.9a^2/\lambda$, while the error is less than 1% for all

values of $z > 15.7a^2/\lambda$. In all cases examined, the farfield error at a fixed axial location z is less for the parabolic radiator than the uniform radiator. Thus, the apodization of the piston reduces the effective size of the nearfield by reducing the spectral content of the wave field.

VII. CONCLUSION

A new analytical integral expression for the wave fields generated by axisymmetric radiators mounted in a rigid baffle has been derived. Integral expressions are derived for several common apodization models, including apodized transient excitations. The effect of apodization on the resulting wave field has been examined for both cw and transient excitations. Compared to the classical Rayleigh-Sommerfeld integral, this new approach converges faster with respect to number of quadrature points by at least a factor of 4. Similar speed-up relative to the generalized King integral is observed. Unlike the generalized King integral, the annular superposition integral does not require the evaluation of special mathematical functions over an infinite range of integration. In short, the new method combines the ease of implementation of the point-source method with a more rapid convergence within the nearfield region of the radiator.

ACKNOWLEDGMENTS

The authors thank Xiaozheng Zeng and Donald Chorman of the Department of Electrical and Computer Engineering at Michigan State University for helpful discussions and insight. This work was funded in part by NIH Grant No. 1R01 CA093669.

¹G. R. Harris, "Review of transient field-theory for a baffled planar piston," *J. Acoust. Soc. Am.* **70**, 10–20 (1981).

²M. Greenspan, "Piston radiator: Some extensions of the theory," *J. Acoust. Soc. Am.* **65**, 608–621 (1979).

³J. Zemanek, "Beam behavior within the nearfield of a vibrating piston," *J. Acoust. Soc. Am.* **49**, 181–191 (1971).

⁴L. V. King, "On the acoustic radiation field of the piezo-electric oscillator and the effect of viscosity on transmission," *Can. J. Res.* **11**, 135–155

(1934).

⁵T. Hasegawa, N. Inoue, and K. Matsuzawa, "A new rigorous expansion for the velocity potential of a circular piston source," *J. Acoust. Soc. Am.* **74**, 1044–1047 (1983).

⁶R. C. Wittmann and A. D. Yaghjian, "Spherical-wave expansions of piston-radiator fields," *J. Acoust. Soc. Am.* **90**, 1647–1655 (1991).

⁷T. D. Mast and F. Yu, "Simplified expansions for radiation from a baffled circular piston," *J. Acoust. Soc. Am.* **118**, 3457–3464 (2005).

⁸J. C. Lockwood and J. G. Willette, "High-speed method for computing the exact solution for the pressure variations in the nearfield of a baffled piston," *J. Acoust. Soc. Am.* **53**, 735–741 (1973).

⁹J. A. Archer-Hall, A. I. Bashter, and A. J. Hazelwood, "Means for computing the Kirchhoff surface integral for a disk radiator as a single integral with fixed limits," *J. Acoust. Soc. Am.* **65**, 1568–1570 (1979).

¹⁰D. A. Hutchins, H. D. Mair, P. A. Puhach, and A. J. Osei, "Continuous-wave pressure fields of ultrasonic transducers," *J. Acoust. Soc. Am.* **80**, 1–12 (1986).

¹¹O. G. Kozina and G. I. Makarov, "Transient processes in the acoustic fields generated by a piston membrane of arbitrary shaped," *Sov. Phys. Acoust.* **7**, 39–43 (1961).

¹²T. Mellow and L. Kärkkäinen, "On the sound field of an oscillating disk in a finite open and closed circular baffle," *J. Acoust. Soc. Am.* **118**, 1311–1325 (2005).

¹³T. Mellow, "On the sound field of a resilient disk in an infinite baffle," *J. Acoust. Soc. Am.* **120**, 90–101 (2006).

¹⁴R. J. McGough, T. V. Samulski, and J. F. Kelly, "An efficient grid sectoring method for calculations of the nearfield pressure generated by a circular piston," *J. Acoust. Soc. Am.* **115**, 1942–1954 (2004).

¹⁵R. J. McGough, "Rapid calculations of time-harmonic nearfield pressures produced by rectangular pistons," *J. Acoust. Soc. Am.* **115**, 1934–1941 (2004).

¹⁶J. F. Kelly and R. J. McGough, "A time-space decomposition method for calculating the nearfield pressure generated by a pulsed circular piston," *IEEE Trans. Ultrason. Ferroelectr. Freq. Control* **53**, 1150–1159 (2006).

¹⁷A. O. Williams, Jr., "Acoustic field of a circular plane piston," *J. Acoust. Soc. Am.* **36**, 2408–2410 (1964).

¹⁸J. Naze Tjøtta and S. Tjøtta, "Nearfield and far-field of pulsed acoustic radiators," *J. Acoust. Soc. Am.* **71**, 824–834 (1982).

¹⁹W. A. Verhoef, M. J. T. M. Cloostermans, and J. M. Thijssen, "The impulse-response of a focused source with an arbitrary axisymmetric surface velocity distribution," *J. Acoust. Soc. Am.* **75**, 1716–1721 (1984).

²⁰P. J. Davis and R. P. Rabinowitz, *Numerical Integration* (Academic, New York, 1975), pp. 139, 140.

²¹M. Galassi, *GNU Scientific Library Reference Manual*, 2nd ed. (Network Theory, Bristol, UK, 2006).

²²E. G. Williams, *Fourier Acoustics: Sound Radiation and Nearfield Acoustical Holography* (Academic, London, 1999).

Numerical evaluation of the acoustic radiation from planar structures with general baffle conditions using wavelets

R. S. Langley^{a)}

Department of Engineering, University of Cambridge, Trumpington Street, Cambridge, CB2 1PZ, United Kingdom

(Received 28 July 2006; revised 3 November 2006; accepted 6 November 2006)

A method is presented for computing the acoustic radiation from baffled, unbaffled, or partially baffled planar structures. The surface displacement and the surface pressure are expressed in terms of wavelets, and the acoustic dynamic stiffness (baffled case) or the acoustic receptance (unbaffled case) between any two wavelets is derived in closed form. The wavelets are employed with translation only (i.e., no dilation), and the jinc function is used; the Hankel transform of this function is the Heavyside step function, and this feature greatly simplifies the analysis. There is a trivial mapping between the wavelet amplitudes and the physical motion of the structure, and hence the dynamic stiffness and receptance results can readily be used to derive the acoustic dynamic stiffness matrix (by inverting the receptance matrix in the unbaffled case) in any set of generalized coordinates. Partially baffled systems can then be studied by substructuring the dynamic stiffness matrix. A set of example problems is considered in which the method is used to compute the resistive and reactive radiation efficiency of a range of benchmark systems. © 2007 Acoustical Society of America. [DOI: 10.1121/1.2405125]

PACS number(s): 43.20.Rz, 43.30.Jx, 43.40.Rj [SFW]

Pages: 766–777

I. INTRODUCTION

There are many areas of engineering in which fluid-structure coupling is an important design issue, with regard to both the sound radiated into the fluid and the effect of the fluid on the vibrations of the structure. Examples include the study of interior noise in automotive, aerospace, and marine vehicles, and the effect of heavy external fluid loading on marine structures. The past two decades have brought remarkable developments in the computational modeling of this type of problem, and very complex structures can now be analyzed routinely by using commercial software that employs the boundary element method (BEM) and/or the finite element method. Such software, although very general purpose, is not always convenient for design studies where multiple calculations are required to identify an optimal design. This is particularly true for high frequency vibrations, where the short wavelength of the structural and acoustic displacements requires the use of very many degrees of freedom. In such cases it is helpful to have available a more efficient analysis method, which may be more approximate and/or limited in application, but which provides both physical insight and numerical results of quantitative utility. Similarly, when considering the feasibility of a new technology, such as, for example, the efficacy of new actuators for the active control of radiated sound, it is very useful to consider initially a relatively simple system and an efficient analysis method which allows the analyst to focus on the key issues of practical concern. An efficient fluid-structure analysis method which is compatible with these aims is developed here for the case of baffled, unbaffled, and partially baffled

planar structures. Before considering the method in detail, a brief review of previous methods that can also be categorized in this way is given.

The analysis of the sound radiated by a vibrating planar body has been the subject of research for many years, and a complete solution for a harmonically vibrating baffled planar structure is given by the Rayleigh integral (Rayleigh, 1896), which states

$$p(\mathbf{x}) = - \left(\frac{\rho\omega^2}{2\pi} \right) \int_A \left(\frac{e^{-ik_a r}}{r} \right) w(\mathbf{x}') d\mathbf{x}', \quad (1a)$$

$$r = |\mathbf{x} - \mathbf{x}'|. \quad (1b)$$

This equation relates the complex amplitude of the pressure $p(\mathbf{x})$ at a general location \mathbf{x} in space to the complex amplitude of the out-of-plane displacement $w(\mathbf{x}')$ at all locations \mathbf{x}' on the vibrating structure. The terms ρ and k_a are, respectively, the air density and the acoustic wave number, and ω is the frequency of the vibration. The region A represents the vibrating structure, which is taken to lie within a rigid planar baffle, so that the fluid velocity normal to the plane of the structure is zero at all points that lie outside A . Almost a century after Rayleigh, Williams and Maynard (1982) considered the numerical evaluation of the radiated pressure via the following wave number representation of Eq. (1):

$$p(\mathbf{x}) = \left(\frac{1}{4\pi^2} \right) \int_R \left(\frac{i\omega\rho c k_a}{\sqrt{k_a^2 - k^2}} \right) W(\mathbf{k}) e^{i\mathbf{k}\cdot\mathbf{x}} d\mathbf{k}, \quad (2a)$$

$$k = |\mathbf{k}|. \quad (2b)$$

Here $W(\mathbf{k})$ is the spatial Fourier transform of $w(\mathbf{x}')$, and the integration region R covers the whole of the two-dimensional wave number plane, with $\mathbf{k}=(k_1, k_2)$. Both $W(\mathbf{k})$ and $p(\mathbf{x})$

^{a)}Electronic mail: rsl21@eng.cam.ac.uk

can be computed very efficiently by using the fast Fourier transform (FFT) algorithm, and hence Eq. (2) allows the application of Eq. (1) to a wide range of baffled systems. The extension of this type of analysis to an unbaffled planar system was considered by Williams (1983), who developed an iterative FFT based method, and (for rectangular plate structures) by Atalla *et al.* (1996) using a variational approach based on the pressure jump across the plate. Each of these two approaches, although powerful, display numerical problems, respectively, at low and high frequencies. An alternative method has been presented by Laulagnet (1998) for a simply supported unbaffled plate based on expanding the pressure jump in terms of the plate modes. This approach, although limited to a simply supported plate, allows the effect of the baffle condition to be investigated over a wide frequency range.

The present approach differs from previous work in that the variable of interest (the displacement or pressure on the surface of the structure) is represented in terms of wavelets. The wavelets are translated across the structure, but no dilation is employed, and in this regard the current modeling approach has more in common with the techniques employed in smoothed particle hydrodynamics (Monaghan, 1992) than conventional wavelet analysis (Newland, 1993). A similar strategy has been employed by McWilliam *et al.* (2000) in the numerical solution of the Fokker-Planck-Kolmogorov equation which arises in random vibration, and in that case the wavelets employed were sinc functions. In the present work jinc functions are used; these functions have a band-limited Hankel transform, and are particularly well suited to work in planar acoustics. Furthermore, the mapping between the amplitudes of the jinc functions and the physical system displacement (or pressure) is trivial. Considering initially the case of baffled systems, it is shown that the acoustic dynamic stiffness matrix can be written in closed form when expressed in terms of jinc functions, and the matrix is then easily transformed to any set of generalized coordinates. For unbaffled systems a similar approach is used to obtain the receptance matrix in closed form, and this can then be inverted to yield the dynamic stiffness matrix. It is also shown that the approach can be extended to partially baffled systems, and there is no restriction on the shape of the planar structure under consideration. Given the acoustic dynamic stiffness matrix, the fluid-structure problem can readily be fully analyzed. The present approach is clearly less generally applicable than the boundary element method [see, for example, Petyt and Jones (2004)], but for planar structures it has numerous advantages, including the avoidance of any computational issues regarding the singularity in the acoustic Green's function, and the availability of closed form expressions for the acoustic stiffness or receptance matrix. The method is illustrated here by application to a number of benchmark problems: a baffled, unbaffled, and partially baffled plate, and an unbaffled circular disk.

II. BAFFLED SYSTEMS

A. The acoustic dynamic stiffness matrix

In the following a general expression is derived for the acoustic dynamic stiffness matrix associated with a baffled

planar structure that radiates into free space. The out-of-plane displacement $w(\mathbf{x})$ of the structure at the spatial location $\mathbf{x}=(x_1, x_2)$ is written in terms of a set of generalized degrees of freedom a_n ($n=1, 2, \dots, N$) in the form

$$w(\mathbf{x}) = \sum_n a_n u_n(\mathbf{x}), \quad (3)$$

where $u_n(\mathbf{x})$, $n=1, 2, \dots, N$, represents a set of prescribed shape functions. The motion of the system is taken to be harmonic with frequency ω , so that both $w(\mathbf{x})$ and a_n represent complex amplitudes, with the time-dependent response being given by $\text{Re}\{w(\mathbf{x})\exp(i\omega t)\}$ and $\text{Re}\{a_n \exp(i\omega t)\}$, respectively. The surface pressure due to the motion of the system can be written in the form

$$\begin{aligned} p(\mathbf{x}) &= \int_A g(\mathbf{x} - \mathbf{x}') w(\mathbf{x}') d\mathbf{x}' \\ &= \sum_n a_n \int_A g(\mathbf{x} - \mathbf{x}') u_n(\mathbf{x}') d\mathbf{x}', \end{aligned} \quad (4a)$$

$$g(\mathbf{x}) = -\frac{\rho\omega^2 e^{-ik_a|\mathbf{x}|}}{2\pi|\mathbf{x}|}, \quad (4b)$$

where A represents the surface of the system and $g(\mathbf{x} - \mathbf{x}')$ is the acoustic Green function, i.e., the pressure produced at location \mathbf{x} by a harmonic delta function displacement at location \mathbf{x}' , given that the motion is zero elsewhere. The region A can actually be replaced by the infinite plane, given that the system displacement is nonzero only within A ; this interpretation of A will be adopted in what follows. Equation (4a) represents the Rayleigh integral (Rayleigh, 1896), as presented in Eq. (1). The generalized force acting on degree of freedom a_m due to this pressure has the form

$$f_m = \int_A p(\mathbf{x}) u_m(\mathbf{x}) d\mathbf{x} = \sum_n D_{mn} a_n, \quad (5a)$$

$$D_{mn} = \int_A \int_A g(\mathbf{x} - \mathbf{x}') u_m(\mathbf{x}) u_n(\mathbf{x}') d\mathbf{x} d\mathbf{x}'. \quad (5b)$$

Here the terms D_{mn} are the entries of the acoustic dynamic stiffness matrix \mathbf{D} of the system, expressed in the generalized coordinates a_n . This result can be expressed in a more convenient form by writing the shape functions and the Green's function in terms of their Fourier transforms, $U_n(\mathbf{k})$ and $G(k)$, respectively, so that

$$u_n(\mathbf{x}) = \frac{1}{4\pi^2} \int_R U_n(\mathbf{k}) e^{i\mathbf{k}\cdot\mathbf{x}} d\mathbf{k}, \quad (6)$$

$$g(\mathbf{x}) = \frac{1}{4\pi^2} \int_R G(k) e^{i\mathbf{k}\cdot\mathbf{x}} d\mathbf{k}, \quad (7)$$

where $\mathbf{k}=(k_1, k_2)$ is the acoustic wave number vector with modulus $k=|\mathbf{k}|$, and R is the wave number plane $\{-\infty \leq k_1 \leq \infty, -\infty \leq k_2 \leq \infty\}$. Substituting Eqs. (6) and (7) into Eq. (5b) yields the acoustic dynamic stiffness matrix in the form

$$D_{mn} = \frac{1}{4\pi^2} \int_R G(k) U_m^*(\mathbf{k}) U_n(\mathbf{k}) d\mathbf{k} = i\omega Z_{mn}, \quad (8)$$

where the notation Z_{mn} is introduced to represent the entries of the acoustic impedance matrix \mathbf{Z} . The function $U_n(\mathbf{k})$ which appears in this result will depend on the shape functions employed in Eq. (3), while the function $G(k)$ is given by (see, for example, Cremer *et al.*, 1988, p. 527)

$$G(k) = \frac{i\omega\rho ck_a}{\sqrt{k_a^2 - k^2}}, \quad (9)$$

where ρ , c , and k_a are, respectively, the air density, the speed of sound, and the acoustic wave number. Equation (8) will be used in the sections that follow to develop an efficient method of computing the acoustic dynamic stiffness matrix of a baffled planar structure.

It can be noted for future reference that the time averaged power radiated by the structure can be written in terms of either the acoustic dynamic stiffness matrix or the impedance matrix as follows:

$$P_{\text{rad}} = (\omega/2) \mathbf{a}^{*T} \text{Im}\{\mathbf{D}\} \mathbf{a} = (\omega^2/2) \mathbf{a}^{*T} \text{Re}\{\mathbf{Z}\} \mathbf{a}. \quad (10)$$

B. The use of jinc shape functions

The usual approach to defining the shape functions $u_n(\mathbf{x})$ that appear in Eq. (3) is to use either a set of *global* shape functions that extend over the whole structure, such as a Fourier series, or to use *local* shape functions that are each restricted to a finite region of the structure, as in the finite element method. An alternative approach is adopted here which is analogous to a wavelet description of the motion of the system [see, for example, Newland, (1993)]. The n th shape function is written in the form

$$u_n(\mathbf{x}) = u(\mathbf{x} - \mathbf{x}_n), \quad (11)$$

where $u(\mathbf{x})$ is a function whose maximum lies at $\mathbf{x}=\mathbf{0}$. Equations (3) and (11) do not quite constitute a standard wavelet description of the response, which would rather have the more general form

$$w(\mathbf{x}) = \sum_n \sum_j a_{nj} u(\mathbf{s}_j \cdot \mathbf{x} - \mathbf{x}_n), \quad (12)$$

where \mathbf{s}_j is a scale factor. Equation (12) represents a series of translations and dilations of the function $u(\mathbf{x})$, whereas Eqs. (3) and (11) represent only a series of translations. Nonetheless, the present approach is similar to the modeling strategy adopted in the method of smoothed particle hydrodynamics (Monaghan, 1992), and convergence of the response description can be expected with the use of an increasing number of grid points \mathbf{x}_n .

Given Eq. (11), a mathematically convenient function $u(\mathbf{x})$ must be selected. One approach would be to use the Shannon wavelet (or sinc function) so that

$$u(\mathbf{x}) = \sin(k_s x_1) \sin(k_s x_2) / (k_s^2 x_1 x_2), \quad (13)$$

where k_s is a suitable wave number. This type of description has been used, for example, by McWilliam *et al.* (2000) in the numerical solution of the Fokker-Planck-Kolmogorov

equation. In the present application the function given by Eq. (13) has the disadvantage of not being radially symmetric: If the function is radially symmetric so that $u(\mathbf{x})=u(r)$ where $r=|\mathbf{x}|$, then Eq. (8) can be reduced from a two-dimensional integral to the following one-dimensional integral:

$$D_{mn} = \frac{1}{2\pi} \int_0^\infty G(k) |U(k)|^2 J_0(kr_{mn}) k dk, \quad r_{mn} = |\mathbf{x}_m - \mathbf{x}_n|, \quad (14)$$

where

$$U(k) = \int_A u(\mathbf{x}) e^{-i\mathbf{k}\cdot\mathbf{x}} d\mathbf{x} = 2\pi \int_0^\infty u(r) J_0(kr) r dr. \quad (15)$$

In deriving this result it has been noted that

$$u_n(\mathbf{x}) = u(\mathbf{x} - \mathbf{x}_n) \Rightarrow U_n(\mathbf{k}) = U(k) e^{-i\mathbf{k}\cdot\mathbf{x}_n}, \quad (16)$$

which allows Eq. (8) to be integrated over the variable $\theta = \tan^{-1}(k_2/k_1)$ to give Eq. (14). The result yielded by Eq. (14) depends only on the acoustic wave number k (and hence the frequency ω) and the distance between the two points \mathbf{x}_n and \mathbf{x}_m , giving a very convenient form of the dynamic stiffness matrix and thus providing strong motivation for the use of a radially symmetric function $u(\mathbf{x})$. The simplest form of radially symmetric function is a cylindrical piston, and this type of model has previously been used in the study of the active control of sound radiation (Elliott and Johnson, 1993). The use of the cylindrical piston function has been investigated by Shorter (2005). Despite the fact that the function has a sharp edge and is not a tile, it was found that an accurate and efficient estimate of the resistive (imaginary) part of the dynamic stiffness matrix could be obtained, although the reactive (real) part might be poorly estimated. An alternative function is employed here which does not have a sharp edge, and has the further advantage of having a band-limited Hankel transform, so that Eq. (14) becomes a finite integral. The function is the jinc function, $\text{jinc}(x)=J_1(x)/x$, so that $u(\mathbf{x})$ and $U(k)$ are given by

$$u(\mathbf{x}) = \frac{2J_1(k_s r)}{k_s r} = 2\text{jinc}(k_s r), \quad (17)$$

$$U(k) = \begin{cases} 0, & k > k_s \\ 4\pi/k_s^2, & k \leq k_s \end{cases}. \quad (18)$$

It can be noted that

$$\lim_{k_s \rightarrow \infty} \{k_s^2 u(\mathbf{x})\} = 4\pi \delta(x_1) \delta(x_2), \quad (19)$$

so that the jinc function behaves like the delta function at high wave number k_s . However the concern here is not with this limiting form of behavior but rather with the use of shape functions which produce a smooth and accurate approximation to the displacement of the system. A suitable choice of the wave number k_s can be deduced by considering the mapping between the nodal values of the displacement, $w(\mathbf{x}_n)$, and the generalized coordinates a_n . The simplest way to approach this relationship is by taking the points \mathbf{x}_n to be evenly spaced and considering Eq. (3) to be a trapezium

approximation to the following convolution integral

$$w(\mathbf{x}) = \int_A a(\mathbf{x}') u(\mathbf{x} - \mathbf{x}') d\mathbf{x}' / (dx_1 dx_2). \quad (20)$$

Here dx_1 and dx_2 are the grid spacings between the points \mathbf{x}_n . Taking the Fourier transform of each side of Eq. (20) and employing Eq. (18) yields

$$w(\mathbf{k}) = \begin{cases} 0, & k > k_s \\ 4\pi a(\mathbf{k}) / (dx_1 dx_2 k_s^2), & k \leq k_s. \end{cases} \quad (21)$$

Clearly this result can only be valid if $w(\mathbf{x})$ has no wave number content of modulus greater than k_s . If we put $dx_1 = dx_2$ then the shortest wave number that can be captured by the grid points \mathbf{x}_n is $k = \sqrt{2}(\pi/dx_1)$, corresponding to a half wavelength between each grid point. It follows that setting $k_s = \sqrt{2}(\pi/dx_1)$ will ensure the validity of the first part of Eq. (21), and it then follows from the second part of the equation that

$$w(\mathbf{k}) = (2/\pi)a(\mathbf{k}) \Rightarrow a_n = (\pi/2)w(\mathbf{x}_n). \quad (22)$$

Thus if we set $k_s = \sqrt{2}(\pi/dx_1)$ there is an immediate and simple mapping between the generalized coordinates a_n and the response of the system at the grid points $w(\mathbf{x}_n)$. One implication of this result is that, given the dynamic stiffness matrix \mathbf{D} , it is very easy to compute the power radiated by any arbitrary deflection shape $w(\mathbf{x})$ by first employing Eq. (22) to find the generalized coordinates \mathbf{a} , and then using Eq. (10) to compute the radiated power. Moreover, it is shown in the following section that the dynamic stiffness matrix \mathbf{D} can be evaluated in closed form. As an aside it can be noted that Eqs. (21) and (22) could have been obtained by taking the discrete Fourier transform of Eq. (3) rather than considering the convolution integral, Eq. (20).

The foregoing wavelet approach can be used to model any field variable, and in Sec. III it is used to describe the pressure distribution over an un baffled system. It can be noted from Eqs. (21) and (22) that the approach can fully match the system response on a regular grid of spacing $dx_1 = dx_2 = \sqrt{2}\pi/k_s$, and this provides an insight into the fidelity of the wavelet description. Any step discontinuity cannot be captured exactly but rather is smeared over an interval of size dx_1 , as would also be the case in a finite difference or finite element model. Consider for example the case of an infinite region in which the response is zero everywhere apart from a finite domain that has a unit response. If the plane is covered with a grid of points, then the modeled slope of the discontinuity is of order $1/dx_1$ rather than infinity. Furthermore, although the wavelet description will give a response of precisely zero at every grid point outside the finite domain, the fact that the jinc function has "infinite tails" will give the possibility of some small nonzero oscillation between the grid points. Thus, as with all numerical modeling approaches, the use of a finite number of degrees of freedom cannot provide a perfect description of the system response. However, the numerical examples described in what follows demonstrate that the description afforded by the use of wavelets provides an extremely good model.

C. Evaluation of the acoustic dynamic stiffness matrix

The dynamic stiffness matrix given by Eq. (14) can be rewritten in the form

$$D_{mn} = D(r_{mn}, \omega), \quad (23)$$

where it follows from Eqs. (9) and (18) that

$$D(r, \omega) = \frac{i8\pi\omega\rho ck_a}{k_s^4} \int_0^{k_s} \frac{J_0(kr)k}{\sqrt{k_a^2 - k^2}} dk \\ = \frac{i8\pi\omega\rho ck_a}{k_s^4} \left\{ \int_0^{k_a} \frac{J_0(kr)k}{\sqrt{k_a^2 - k^2}} dk + \int_{k_a}^{k_s} \frac{J_0(kr)k}{\sqrt{k_a^2 - k^2}} dk \right\}. \quad (24)$$

The first term on the right-hand side of this expression can be evaluated analytically (Gradshteyn and Ryzhik, 1994, formula 6.554.2) to yield

$$D(r, \omega) = \frac{i8\pi\omega\rho ck_a^2}{k_s^4} \{ \text{sinc}(k_a r) + if(k_a r) \}, \quad (25)$$

$$f(z) = \int_1^{k_s/k_a} \frac{J_0(zx)x}{\sqrt{x^2 - 1}} dx. \quad (26)$$

Now the function $f(z)$ can be rewritten as

$$f(z) = \int_1^{k_s/k_a} \frac{J_0(zx)x}{\sqrt{x^2 - 1}} dx = \int_1^\infty \frac{J_0(zx)x}{\sqrt{x^2 - 1}} dx - \int_{k_s/k_a}^\infty \frac{J_0(zx)x}{\sqrt{x^2 - 1}} dx \\ = \frac{\cos z}{z} - \int_{k_s/k_a}^\infty \frac{J_0(zx)x}{\sqrt{x^2 - 1}} dx, \quad (27)$$

where formula 6.554.3 of Gradshteyn and Ryzhik (1994) has been employed. Now given that k_a is the acoustic wave number and k_s is related to the system mesh density, it can be expected that $k_s/k_a \gg 1$. This means that $x \gg 1$ for the integration range considered in the final term in Eq. (27), and the function $f(z)$ can be approximated as

$$f(z) \approx \frac{\cos z}{z} - \int_{k_s/k_a}^\infty J_0(zx) dx \\ = \frac{\cos z}{z} - \int_0^\infty J_0(zx) dx + \int_0^{k_s/k_a} J_0(zx) dx \\ = \frac{\cos z - 1}{z} + \frac{1}{z} \int_0^{k_s/k_a} J_0(x) dx \\ = \frac{\cos z - 1}{z} + \frac{2}{z} \sum_{k=1}^\infty J_{2k+1}(zk_s/k_a), \quad (28)$$

where formulas 6.511.1 and 6.511.3 of Gradshteyn and Ryzhik (1994) have been employed. Although the final approximation is in closed form, it has been found to be numerically more efficient to tabulate the integral of $J_0(x)$ and use the penultimate expression in Eq. (28) to compute $f(z)$ rather than sum the series of Bessel functions. It can be noted that if $k_s \rightarrow \infty$ then Eq. (28) gives $f(z) \rightarrow (\cos z)/z$ and thus Eq. (25) yields $D(r, \omega) \rightarrow (16\pi^2/k_s^4)g(r)$, where $g(r)$ is the

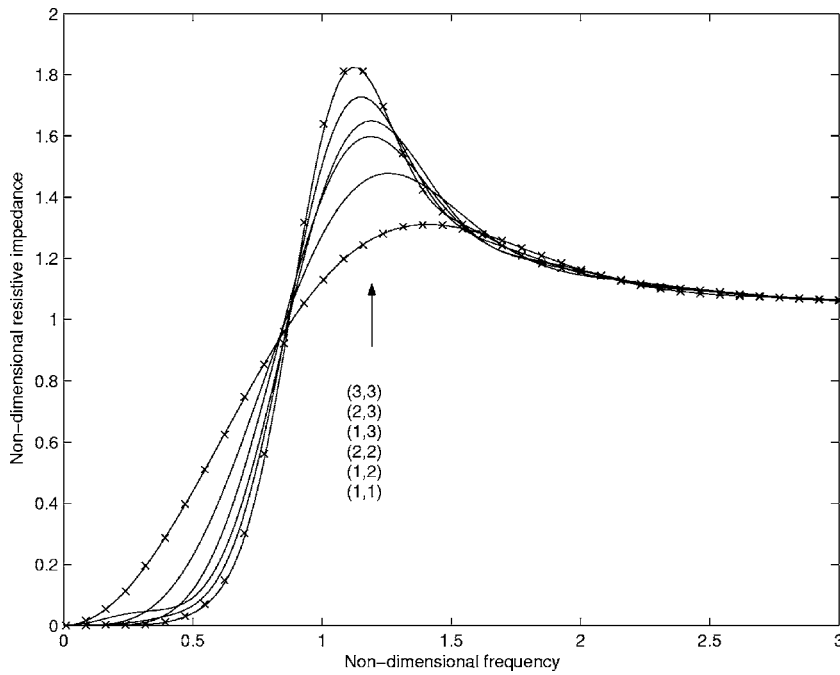


FIG. 1. Nondimensional resistive impedance (radiation efficiency), as defined by Eq. (30), for the first six modes of a baffled square plate, plotted against the non-dimensional frequency k_a/k_{nm} . Crosses represent benchmark results for the (1,1) and (3,3) modes, as given by the FFT method of Williams and Maynard (1982).

Green's function given by Eq. (4b). This result is consistent with the high wave number behavior of the jinc function: For $k_s \rightarrow \infty$ the function is proportional to the delta function, as noted in Eq. (19), and thus the dynamic stiffness should be expected to be proportional to the Green's function. With the use of a finite value of k_s the singularity in the Green's function which occurs when $r=0$ does not appear in $D(r, \omega)$, and thus the present formulation circumvents the singularity that appears in the Rayleigh integral, Eq. (1).

Equations (23), (25), and (28) allow the rapid computation of the dynamic stiffness matrix associated with jinc shape functions. As mentioned following Eq. (22), this result can readily be used to compute the dynamic stiffness and acoustic radiation associated with an arbitrary motion of the system; more generally the result can be transformed to give the dynamic stiffness matrix associated with any alternative set of generalized coordinates. These issues are illustrated in the following examples.

D. Example

The foregoing approach has been used to compute the acoustic radiation from a baffled simply supported square plate of side length L . The nm th mode of vibration of the plate is given by

$$w(x_1, x_2) = \sin(n\pi x_1/L) \sin(m\pi x_2/L), \quad (29)$$

and the nondimensional radiation efficiency σ and reactive acoustic impedance κ of this mode are defined by

$$\sigma = \frac{4 \operatorname{Re}\{Z\}}{\rho c L^2}, \quad (30)$$

$$\kappa = \frac{4 \operatorname{Im}\{Z\}}{\rho c L^2}, \quad (31)$$

$$Z = \mathbf{a}^T \mathbf{D} \mathbf{a} / (i\omega). \quad (32)$$

Here Z is the complex impedance associated with the modal deflection shape, and it can be noted that in Eq. (32) the generalized amplitudes \mathbf{a} are evaluated in terms of $w(\mathbf{x})$ via Eq. (22). The present method has been employed using a grid of $N \times N$ sample points \mathbf{x}_n over the surface of the plate, and results for $N=20$ are shown in Figs. 1 and 2 for various modes of vibration. The horizontal axis on Figs. 1 and 2 corresponds to the nondimensional acoustic wave number k_a/k_{nm} , where k_{nm} is the bending wavelength of the mode, given by $k_{nm} = (\pi/L) \sqrt{(n^2 + m^2)}$. Also shown in Figs. 1 and 2 are benchmark results for the (1,1) and (3,3) modes which have been obtained by using the FFT method to evaluate Eq. (8), as detailed by Williams and Maynard (1982). Excellent agreement with the benchmark results can be seen.

The convergence of the present method with the number of grid points N is shown in Fig. 3 for the two modes (1,1) and (3,3). Results are shown for two frequencies which lie on either side of the coincidence condition $k_a = k_{nm}$: $k_a/k_{nm} = 0.1$ and $k_a/k_{nm} = 1.1$. Below the coincidence condition the plate bending wavelength is shorter than the acoustic wavelength, and were the deflection shape extended over an infinite region then the impedance would be purely reactive. The fact that the resistive part of the impedance is actually non-zero is due to the finite size of the plate: The Fourier transform of the baffled deflection shape contains long wavelength components that radiate sound. This fact is of course well known, but it is mentioned here to explain why the present method converges more quickly for the reactive component than for the resistive component in the case $k_a/k_{nm} = 0.1$: the resistive component requires a more accurate description of the plate deflection shape. The situation is reversed for $k_a/k_{nm} = 1.1$, where the impedance of an infinitely extended system would be purely resistive, and hence the

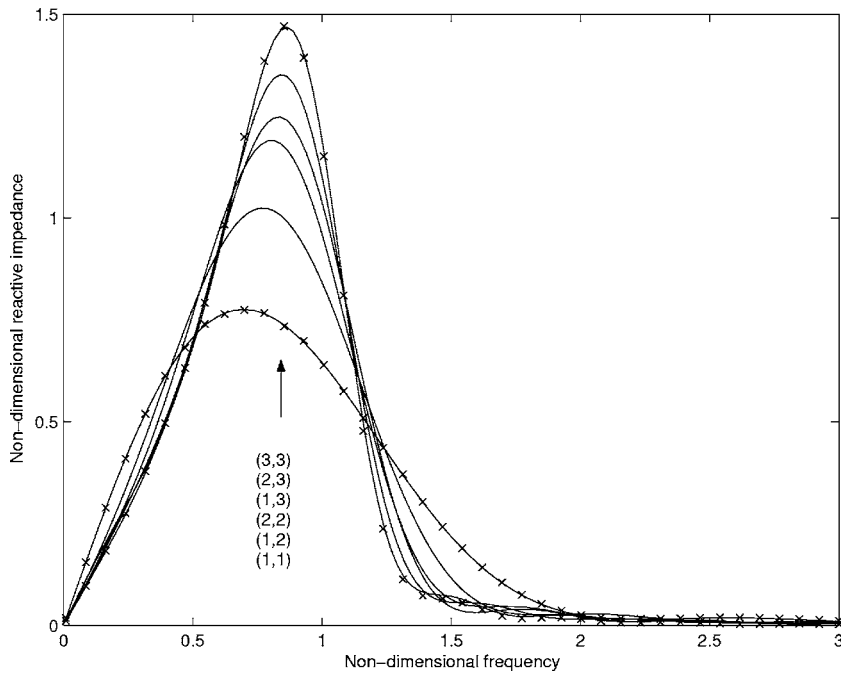


FIG. 2. Nondimensional reactive impedance, as defined by Eq. (31), for the first six modes of a baffled square plate, plotted against the nondimensional frequency k_a/k_{mn} . Crosses represent benchmark results for the (1,1) and (3,3) modes, as given by the FFT method of Williams and Maynard (1982).

reactive component requires a more accurate description of the plate deflection and displays a slower convergence with N . For each of the modes considered the results obtained are accurate to within 5% when there are eight or more sample points per half wavelength of structural deformation.

III. UNBAFFLED SYSTEMS

A. The acoustic receptance matrix

The acoustics of an un baffled planar structure can be analyzed most easily by considering initially the acoustic receptance matrix, rather than dynamic stiffness matrix. This is because an un baffled system has a pressure release boundary condition at all points in the plane of the system that lie outside of the vibrating structure, and thus pressure, rather

than displacement, is the most convenient fundamental variable. By analogy with Eqs. (1) and (16), the pressure at a location \mathbf{x} on the structure can be written in the form

$$p(\mathbf{x}) = \sum_n b_n u(\mathbf{x} - \mathbf{x}_n), \quad (33)$$

where $u(\mathbf{x})$ is twice the jinc function, as given by Eq. (17). Now by analogy with Eqs. (5a) and (14), the generalized displacement associated with grid point m on the structure can be written as

$$w_m = \int_A w(\mathbf{x}) u(\mathbf{x} - \mathbf{x}_m) d\mathbf{x} = \sum_n R_{mn} b_n, \quad (34)$$

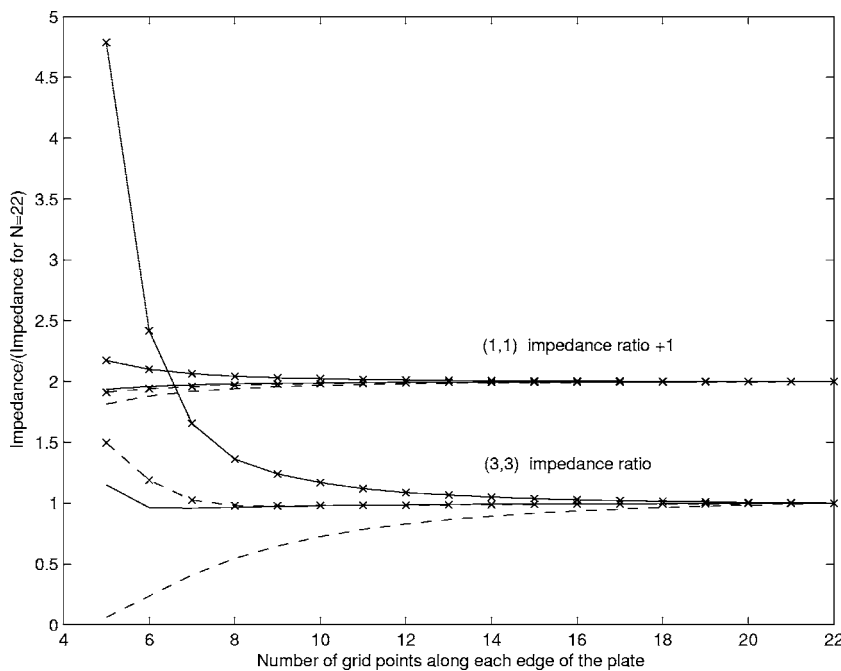


FIG. 3. Convergence of the computed acoustic impedance for the (1,1) and (3,3) modes of a baffled square plate with increasing grid dimension N . Solid lines: $k_a/k_{mn}=1.1$. Dashed lines: $k_a/k_{mn}=0.1$. No symbols: Resistive impedance. Crosses: Reactive impedance. The impedance ratio is offset by unity for the (1,1) mode for clarity.

$$R_{mn} = \frac{1}{2\pi} \int_0^\infty G^{-1}(k) |U(k)|^2 J_0(kr_{mn}) k dk, \quad r_{mn} = |\mathbf{x}_m - \mathbf{x}_n|, \quad (35)$$

where $U(k)$ is given by Eq. (18) and $G^{-1}(k)$ is the Fourier transform of the receptance Green's function $g_R(\mathbf{x}-\mathbf{x}')$; this Green's function is the fluid displacement (normal to the plane) produced at location \mathbf{x} by a harmonic delta function pressure at location \mathbf{x}' , given that the pressure is zero elsewhere. The function $G^{-1}(k)$ is the reciprocal of the function given in Eq. (9).

The term R_{mn} that appears in Eq. (34) is the m th entry of the receptance matrix \mathbf{R} , expressed in the generalized coordinates b_n . It can readily be shown from equations analogous to Eqs. (20)–(22) that $f_n = (dx_1 dx_2) (2/\pi)^2 b_n$, where f_n is defined by Eq. (5a), and also that $w_n = (dx_1 dx_2) (2/\pi)^2 a_n$, where a_n is the generalized coordinate that appears in Eq. (1). It then follows that the dynamic stiffness matrix \mathbf{D} , expressed in the generalized coordinates a_n , can be written in terms of \mathbf{R} in the form

$$\mathbf{D} = (dx_1 dx_2)^2 (2/\pi)^4 \mathbf{R}^{-1}, \quad (36)$$

and the radiated power associated with any given displacement field can be computed from Eq. (10). The detailed evaluation of the entries of the receptance matrix is considered in the following.

B. Evaluation of the acoustic receptance matrix

It follows from Eqs. (9), (18), and (35) that the entries of the acoustic receptance matrix can be written in the form

$$R_{mn} = R(r_{mn}, \omega) = \frac{-i8\pi}{\omega \rho c k_a k_s^4} \int_0^{k_s} \sqrt{k_a^2 - k^2} J_0(kr_{mn}) k dk. \quad (37)$$

This result can also be written as

$$R(r, \omega) = \frac{-i8\pi}{\omega \rho c k_a k_s^4} \left\{ \int_0^{k_a} \sqrt{k_a^2 - k^2} J_0(kr) k dk + \int_{k_a}^{k_s} \sqrt{k_a^2 - k^2} J_0(kr) k dk \right\}, \quad (38)$$

and the first part of this expression can be evaluated analytically (Gradshteyn and Ryzhik, 1994, formula 6.567.1) to yield

$$\begin{aligned} & \int_0^{k_a} \sqrt{k_a^2 - k^2} J_0(kr) k dk \\ &= k_a^3 \int_0^1 \sqrt{1 - x^2} J_0(k_a r x) x dx \\ &= k_a^3 \sqrt{2} \Gamma(3/2) (k_a r)^{-3/2} J_{3/2}(k_a r) \\ &= k_a^3 \left\{ \frac{\sin(k_a r)}{(k_a r)^3} - \frac{\cos(k_a r)}{(k_a r)^2} \right\}_{k_a r=0} \rightarrow k_a^3/3. \end{aligned} \quad (39)$$

The receptance matrix then becomes

$$R(r, \omega) = \frac{-i8\pi k_a^2}{\omega \rho c k_s^4} \left\{ \frac{\sin(k_a r)}{(k_a r)^3} - \frac{\cos(k_a r)}{(k_a r)^2} + i g(k_a r) \right\}, \quad (40)$$

$$g(z) = \int_1^{k_s/k_a} \sqrt{x^2 - 1} J_0(zx) x dx. \quad (41)$$

An approximation to the function $g(z)$ can be obtained by noting from Eqs. (26) and (41) that

$$f(k_a r) = k_a^{-1} \int_{k_a}^{k_s} \frac{J_0(kr) k dk}{\sqrt{k^2 - k_a^2}}, \quad (42)$$

$$g(k_a r) = k_a^{-3} \int_{k_a}^{k_s} J_0(kr) k \sqrt{k^2 - k_a^2} dk. \quad (43)$$

It follows from these expressions and Eq. (28) that

$$\begin{aligned} \frac{d}{dk_a} [k_a^3 g(k_a r)] &= -k_a \int_{k_a}^{k_s} \frac{J_0(kr) k dk}{\sqrt{k^2 - k_a^2}} = -k_a^2 f(k_a r) \\ &\approx -k_a^2 \left\{ \frac{\cos(k_a r) - 1}{k_a r} + \frac{1}{k_a r} \int_0^{k_s r} J_0(x) dx \right\}. \end{aligned} \quad (44)$$

Now integrating with respect to k_a yields

$$\begin{aligned} k_a^3 g(k_a r) &\approx -\frac{1}{r} \left\{ \frac{k_a \sin(k_a r)}{r} + \frac{\cos(k_a r)}{r^2} \right. \\ &\quad \left. - \frac{k_a^2}{2} \left(1 - \int_0^{k_s r} J_0(x) dx \right) \right\} + C, \end{aligned} \quad (45)$$

and the constant of integration C can be found by considering the behavior of the function at low values of k_a ; Eqs. (43) and (45) yield

$$\begin{aligned} \lim_{k_a \rightarrow 0} [k_a^3 g(k_a r)] &= \int_0^{k_s} k^2 J_0(kr) dk = \frac{1}{r^3} \int_0^{k_s r} x^2 J_0(x) dx \\ \Rightarrow C &= \frac{1}{r^3} \left\{ 1 + \int_0^{k_s r} x^2 J_0(x) dx \right\}. \end{aligned} \quad (46)$$

Thus

$$\begin{aligned} g(k_a r) &\approx -\frac{\sin(k_a r)}{(k_a r)^2} + \frac{1 - \cos(k_a r)}{(k_a r)^3} + \frac{1}{2k_a r} \\ &\quad \times \left(1 - \int_0^{k_s r} J_0(x) dx \right) + \frac{1}{(k_a r)^3} \int_0^{k_s r} x^2 J_0(x) dx. \end{aligned} \quad (47)$$

The two integrals that appear in this expression can be pre-computed and tabulated, thus yielding a numerically efficient approximation to $R(r, \omega)$ via Eq. (40), and hence the acoustic receptance matrix, via Eq. (37). As an aside, it can be noted that Eq. (47) yields

$$g(0) \approx (k_s/k_a)^3/3 - (k_s/k_a)/2, \quad (48)$$

whereas the exact result follows from Eq. (41) as

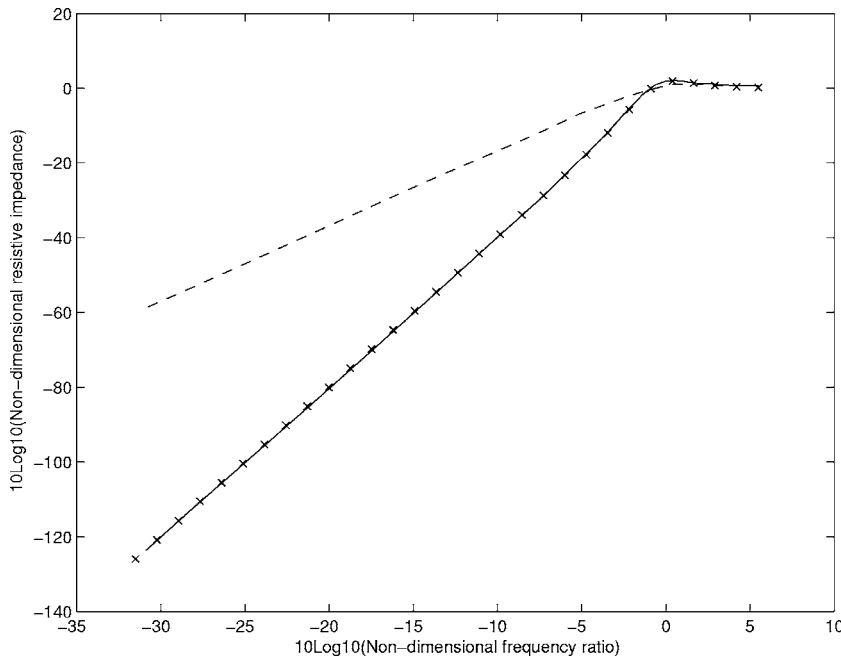


FIG. 4. Nondimensional resistive impedance (radiation efficiency), as defined by Eq. (30), for the (1,1) mode of a square plate, plotted against the nondimensional frequency k_a/k_{mn} . Solid line: Results of Laulagnet (1998) for an unbaffled plate. Crosses: Results of the present method for an unbaffled plate. Dashed line: Results of Laulagnet (1998) for a baffled plate.

$$g(0) = (1/3)[(k_s/k_a)^2 - 1]^{3/2}. \quad (49)$$

The difference between Eqs. (48) and (49) is of order $(k_a/k_s)^4$ compared to the leading order term, and thus Eq. (48) is an extremely accurate approximation, given that the condition $k_a \ll k_s$ must be met to ensure the acoustic wavelength is much greater than the grid point spacing. It can further be noted that if $k_s \rightarrow \infty$, so that the jinc function becomes proportional to the delta function, then Eq. (40) yields $R(r, \omega) \rightarrow -(4\pi/\rho\omega^2k_s^2)^2(1/r)\partial/\partial r\{g(r)/r\}$, where $g(r)$ is given by Eq. (4b). This is consistent with the fact that the point-to-point receptance function (the Green's function) between displacement and pressure, which is given by the Fourier transform of $G^{-1}(k)$, is proportional to $(1/r)\partial/\partial r\{g(r)/r\}$, being the fluid displacement field associated with a dipole.

C. Examples

The foregoing approach has been applied to an unbaffled simply supported square plate of side length L . A grid of $N \times N$ sample points was employed over the surface of the plate, arranged so that each point was located in the interior of the plate and not on the boundary, i.e., the x_1 coordinates (and the x_2 coordinates) of the points were $jL/(N+1)$ for $j = 1, 2, \dots, N$. This configuration ensures that a zero pressure condition is imposed on the plate boundary. Results for the nondimensional impedance of the (1,1) mode are shown in Figs. 4 and 5 for the case $N=31$; the nondimensional quantities plotted are the same as those considered in Figs. 1 and 2, and the results for the baffled plate are included for comparison. Also shown are results for the unbaffled plate which

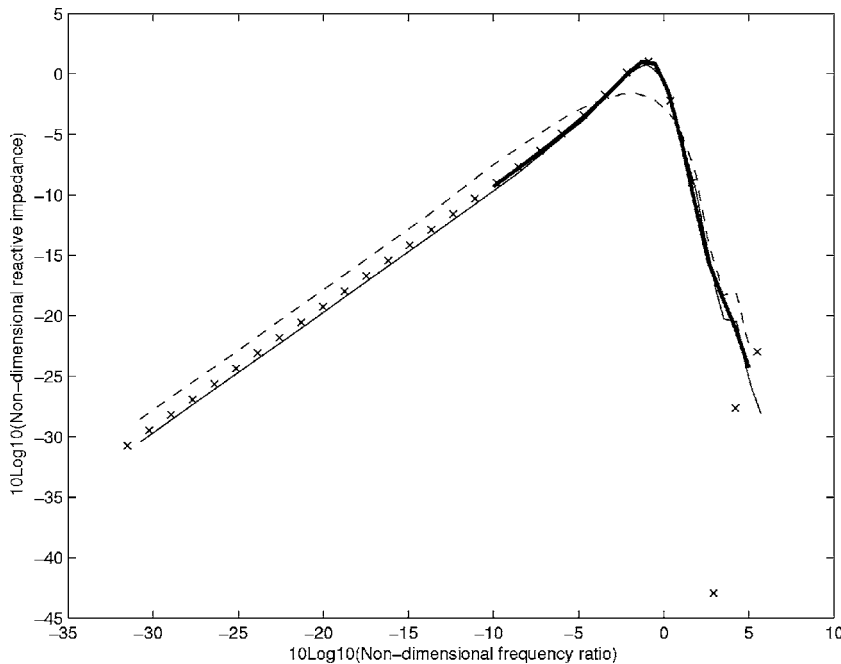


FIG. 5. Nondimensional reactive impedance, as defined by Eq. (31), for the (1,1) mode of a square plate, plotted against the nondimensional frequency k_a/k_{mn} . Light solid line: Results of Laulagnet (1998) for an unbaffled plate. Heavy solid line: Results of Cotoni (2006) for an unbaffled plate. Crosses: Results of the present method for an unbaffled plate. Dashed line: Results of Laulagnet (1998) for a baffled plate.

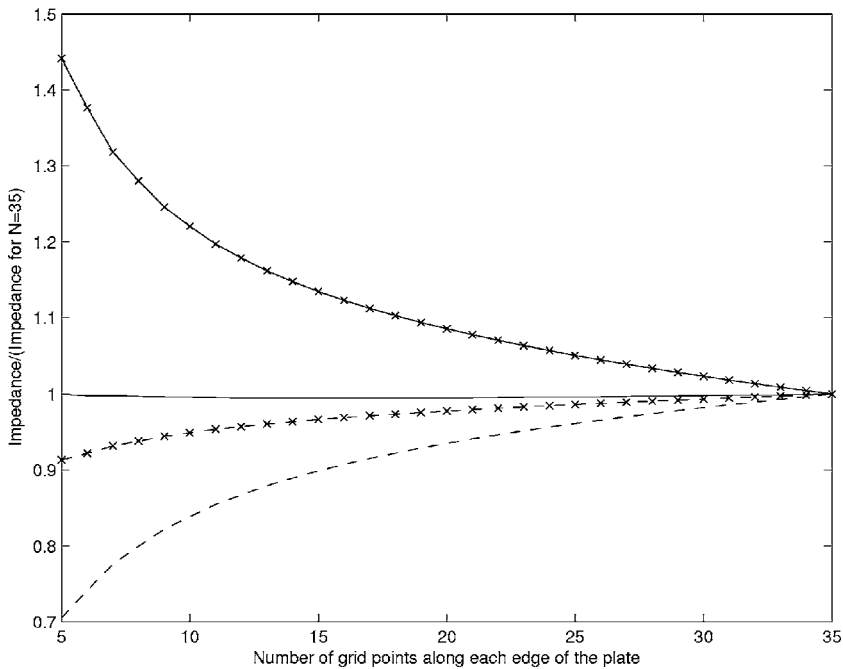


FIG. 6. Convergence of the computed acoustic impedance for the (1,1) mode of an un baffled square plate with increasing grid dimension N . Solid lines: $k_a/k_{nm} = 1.1$. Dashed lines: $k_a/k_{nm} = 0.1$. No symbols: Resistive impedance. Crosses: Reactive impedance.

have been scanned from the figures presented by Laulagnet (1998). The scanned results are in close agreement with the present results for the resistive impedance (Fig. 4) but there is a discrepancy of approximately 0.5 dB (12%) for the reactive impedance at low frequencies (Fig. 5). Also shown in Fig. 5 are results yielded by a high resolution Fourier transform approach (Cotoni, 2006). These results cover a limited frequency range, but appear to show closer agreement to the present results than the scanned results; the accuracy of the results presented in Fig. 5 will be reconsidered in Sec. IV B.

The convergence of the present results with increasing N is shown in Fig. 6. In agreement with the baffled case (Fig. 3), the resistive component converges more rapidly than the reactive component at frequencies below the coincidence condition ($k_a = k_{nm}$) while the situation is reversed above this condition. The convergence of the method is generally slower than for the baffled plate, and small changes in the results continue beyond $N=35$: For example, increasing N from 35 to 41 has been found to change the presented results by a minimum of 0.27% (the resistive component at $k_a/k_{nm} = 1.1$) and a maximum of 2.5% (the reactive component at $k_a/k_{nm} = 1.1$). The main reason for this is that the receptance matrix must be found to a sufficient accuracy for an accurate inverse to be computed, or to put this another way, the matrix inversion will amplify any errors present in the receptance matrix.

A second example application concerns the acoustic radiation of an un baffled circular disk undergoing oscillatory rigid body displacement. This case has been considered by Williams (1983) as an example of an iterative approach to computing the acoustic radiation from un baffled plates. The radius of the disk is taken to be a , and two vibration frequencies are considered, $k_a a = 2$ and $k_a a = 4\pi$. In this case the nondimensional pressure distribution across the disk is considered, defined by $p/(\rho c v)$, where v is the amplitude of the disk velocity. To employ the present method, the disk is centered on an $N \times N$ grid of sample points of dimension $2a$

$\times 2a$, and then those points that lie outside or on the boundary of the disk are removed from the analysis. The pressure is computed from Eq. (33), having used Eq. (34) to solve for the coefficients \mathbf{b} in terms of the prescribed displacement of the disk. Results for the reactive and resistive parts of the pressure at the two frequencies are shown in Fig. 7. In each case, two curves are shown, corresponding to $N=35$ and $N=41$, and further results scanned from Williams (1983) are denoted by symbols. As a point of detail, it can be noted that the results taken from Williams (1983) are the analytical results due to Beyer (1983) reported therein, rather than the very similar numerical results of Williams (1983). One source of inaccuracy in the present method arises from the use of a rectangular grid of sample points; with this approach the boundary of the disk is not a smooth arc but rather a jagged line lying between neighboring grid points that are, respectively, on and off the disk. This can be expected to affect the resistive pressure at the lower frequency and the reactive pressure at the high frequency, for reasons discussed in Sec. II D when considering the convergence of the method. There is some evidence of this loss of accuracy in Fig. 7, both in terms of the effect of increasing N from 35 to 41, and in the level of agreement with the results of Beyer (1983). It would be possible to modify the present approach to enforce the zero pressure condition precisely on the curved boundary, but this was not attempted given the generally good agreement displayed in Fig. 7.

IV. EXTENSION TO PARTIALLY BAFFLED SYSTEMS

A. General approach

In some cases it may be that an otherwise baffled system has regions over which there is a pressure release boundary condition—for example, a baffled plate containing holes. Problems of this type can be addressed by partitioning the total set of generalized coordinates \mathbf{a} into a set \mathbf{a}_1 covering the unmodified parts of the structure and a set \mathbf{a}_2 over which

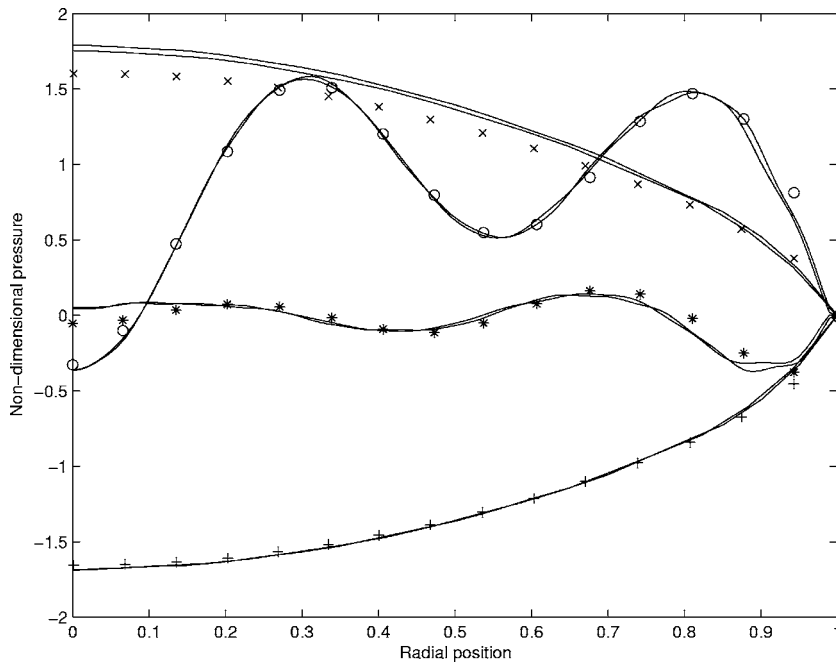


FIG. 7. Nondimensional pressure $p/(\rho cv)$ on the surface of an oscillating unbaffled circular disk as a function of the radial position r/a . The results of the present method for both $N=35$ and $N=41$ are shown as solid curves, and the symbols show the results of Beyer (1983) with the following notation. Plus signs: Reactive pressure at $k_a a=2$. Asterisks: Reactive pressure at $k_a a=4\pi$. Circles: Resistive pressure at $k_a a=4\pi$.

a pressure release boundary condition is to be applied, i.e., the “holes” in the structure. The baffled dynamic stiffness matrix of Sec. II can then be partitioned in the following way:

$$\begin{pmatrix} \mathbf{D}_{11} & \mathbf{D}_{12} \\ \mathbf{D}_{21} & \mathbf{D}_{22} \end{pmatrix} \begin{pmatrix} \mathbf{a}_1 \\ \mathbf{a}_2 \end{pmatrix} = \begin{pmatrix} \mathbf{f}_1 \\ \mathbf{f}_2 \end{pmatrix}. \quad (50)$$

The pressure release boundary condition at the holes can be enforced by putting $\mathbf{f}_2=0$, which yields

$$\mathbf{D}_{\text{red}} \mathbf{a}_1 = \mathbf{f}_1, \quad (51a)$$

$$\mathbf{D}_{\text{red}} = \mathbf{D}_{11} - \mathbf{D}_{12} \mathbf{D}_{22}^{-1} \mathbf{D}_{21}. \quad (51b)$$

The acoustic calculations can thus proceed by considering only the generalized coordinates \mathbf{a}_1 and using the reduced dynamic stiffness matrix \mathbf{D}_{red} . Generalizations of this approach can readily be developed; for example, a mainly unbaffled system with added baffled regions can be analyzed by partitioning the receptance matrix of Sec. III.

B. Example

Consider a baffled simply supported square plate of side length L . Suppose now that an air gap is introduced between each edge of the plate and the baffle, so that the plate is centered within a square aperture in the baffle. The radiation impedance of the plate can be calculated by using the foregoing method: A grid of sample points is placed over the square aperture, and those that lie within the plate are assigned to \mathbf{a}_1 while those that lie within the air gap are assigned to \mathbf{a}_2 . The system considered here is such that a total grid size of 40×40 points is employed of which the central 20×20 points lie on the plate; this corresponds to a square aperture of side length $1.91L$, where L is the side length of the plate. The radiation impedance of the (1,1) mode of the plate is shown in Figs. 8 and 9, where results for a baffled plate and an unbaffled plate are also shown for comparison.

Considering initially the resistive impedance, Fig. 8, it can be seen that the results are almost identical to those of an unbaffled plate at high frequencies, but are closer to those of a baffled plate at low frequencies. This behavior is consistent with the fact that the ratio of the size of air gap to the acoustic wavelength increases with increasing frequency. In the case of the reactive impedance, it can be seen from Fig. 9 that the result is close to the unbaffled case, as calculated by Laulagnet (1998), at all frequencies. This is consistent with the fact that the reactive impedance is associated with non-propagating acoustic waves, and is therefore governed mainly by the baffled/unbaffled condition in the immediate vicinity of the plate. It can be noted that the results shown in Fig. 9 are nearly identical to those shown in Fig. 5 for the unbaffled case as calculated by the method presented in Sec. III; the fact that two very different formulations of the present approach yield identical results adds credence to the accuracy of the results presented in Fig. 5, which differ by 12% from those of Laulagnet (1998) at low frequencies.

V. CONCLUDING REMARKS

In the present approach the acoustic dynamic stiffness matrix of a planar structure is derived by using a wavelet description of either the surface displacement or the surface pressure. For a baffled system the dynamic stiffness matrix is given by Eqs. (23), (25), and (28), while for an unbaffled system the receptance matrix is given by Eqs. (37), (40), and (47) and the dynamic stiffness matrix is then found via Eq. (36). The dynamic stiffness matrix of a partially baffled system is given by Eq. (51). All of these results are expressed in generalized wavelet coordinates, but given that the mapping between the wavelets and the system displacement is trivial, Eq. (22), the dynamic stiffness matrix can readily be transformed into any set of generalized coordinates. The method is numerically efficient and easy to apply, and it therefore offers an alternative to more complex (although also more

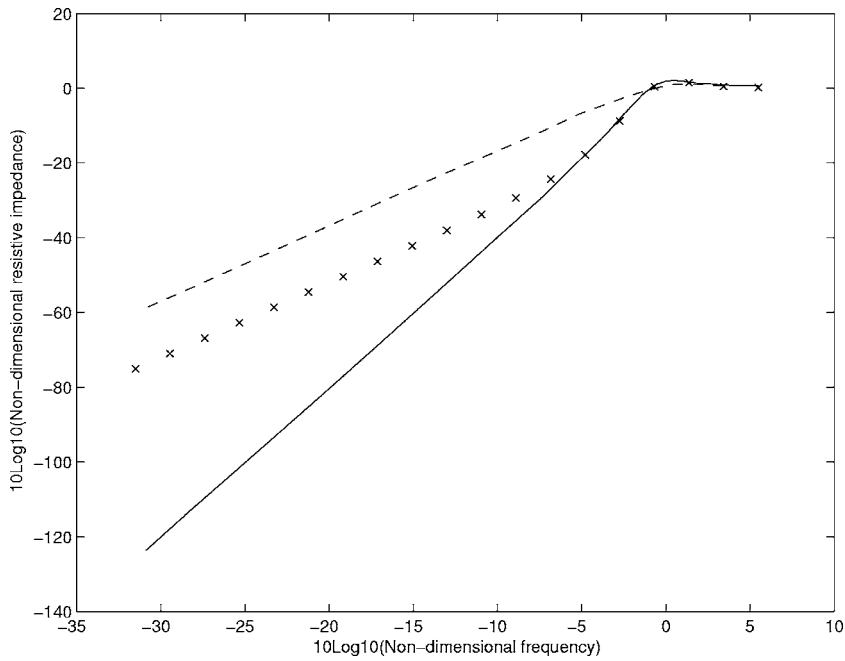


FIG. 8. Nondimensional resistive impedance (radiation efficiency), as defined by Eq. (30), for the (1,1) mode of a square plate, plotted against the nondimensional frequency k_a/k_{mn} . Solid line: Results of Laulagnet (1998) for an un baffled plate. Dashed line: Results of Laulagnet (1998) for a baffled plate. Crosses: Results of the present method for a partially baffled plate.

general) techniques such as the BEM. For baffled systems the method has similar capabilities to the FFT approach of Williams and Maynard (1982), although it obviates the need to calculate the Fourier transform of the shape functions used to describe the system deflection. For un baffled or partially baffled systems the method avoids the restrictions of other semianalytical (i.e., non-BEM) approaches, which are either limited to specific geometries or display convergence problems at low or high frequencies, as discussed in Sec. I.

Given the acoustic dynamic stiffness matrix, the sound generated by any form of surface motion can readily be calculated, and this has been demonstrated here by computing the resistive and reactive radiation efficiency for a range of example structures. Furthermore, the acoustic dynamic stiff-

ness matrix \mathbf{D} appears in the “diffuse field reciprocity relation” of Shorter and Langley (2005a), which states

$$\mathbf{S}_{ff} = \left(\frac{4E}{\pi\omega n} \right) \text{Im}\{\mathbf{D}\}. \quad (52)$$

Here \mathbf{S}_{ff} is the cross-spectral matrix of the forces exerted on the structure by a diffuse acoustic field, E is the energy contained in the acoustic field, and n is the modal density of the volume containing the acoustic field. Thus once \mathbf{D} is known, Eq. (52) provides an efficient way of computing the forces acting on the structure in a random acoustic environment. Equation (52) also provides the key to including random acoustic cavities in the hybrid finite element/statistical en-

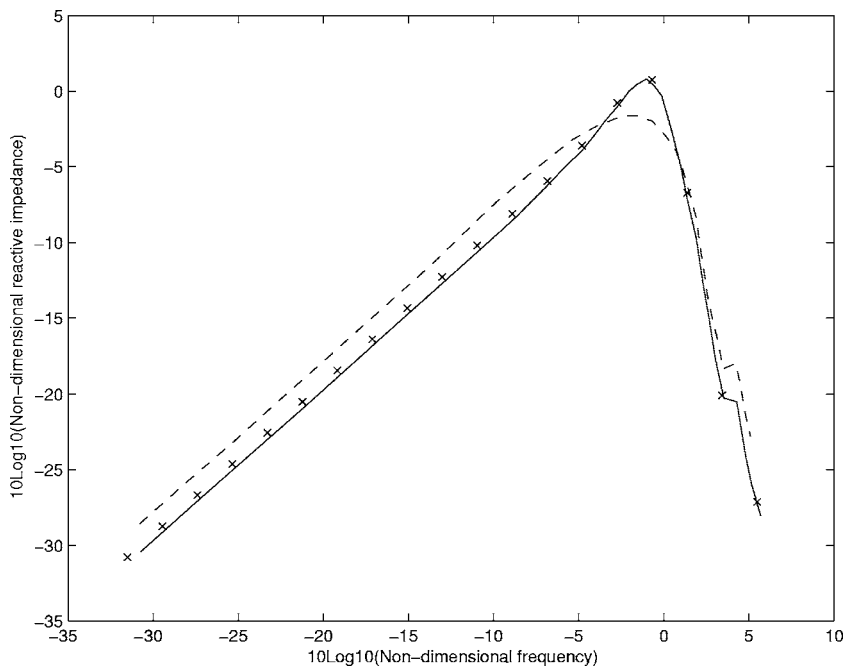


FIG. 9. Nondimensional reactive impedance, as defined by Eq. (31), for the (1,1) mode of a square plate, plotted against the nondimensional frequency k_a/k_{mn} . Solid line: Results of Laulagnet (1998) for an un baffled plate. Dashed line: Results of Laulagnet (1998) for a baffled plate. Crosses: Results of the present method for a partially baffled plate.

ergy analysis method of Shorter and Langley (2005b) and hence the present work has direct application in that context.

ACKNOWLEDGMENTS

This work was performed while the author was a visiting research scientist at ESI US R&D Inc., San Diego. The topic was suggested by Dr. Philip Shorter, who had developed an acoustic code for baffled systems based on piston functions rather than wavelets. Dr. Vincent Cotoni provided the electronic scans and the FFT results presented in the figures. Helpful conversations with Dr. Shorter and Dr. Cotoni are gratefully acknowledged.

- Atalla, N., Nicolas, J., and Gauthier, C. (1996). "Acoustic radiation of an unbaffled vibrating plate with general elastic boundary conditions," *J. Acoust. Soc. Am.* **99**, 1484–1494.
- Beyer, T. (1984). "Test of a nearfield acoustic holography technique using an unbaffled, uniformly oscillating disc." Master's thesis, The Pennsylvania State University, University Park, PA.
- Cotoni, V. (2006). (Private communication).
- Cremer, L., Heckl, M., and Ungar, E. E. (1988). *Structure Borne Sound: Structural Vibrations and Sound Radiation at Audio Frequencies*, 2nd ed. (Springer, Berlin).
- Elliott, S. J., and Johnson, M. E. (1993). "Radiation modes and the active control of sound power," *J. Acoust. Soc. Am.* **94**, 2194–2204.

- Gradshteyn, I. S., and Ryzhik, I. M. (1994). *Tables of Integrals, Series, and Products*, 5th ed., edited by A. Jeffrey (Academic, Boston).
- Laulagnet, B. (1998). "Sound radiation by a simply supported unbaffled plate," *J. Acoust. Soc. Am.* **103**, 2451–2462.
- McWilliam, S., Knappett, D. J., and Fox, C. H. J. (2000). "Numerical solution of the stationary FPK equation using Shannon wavelets," *J. Sound Vib.* **232**, 405–430.
- Monaghan, J. J. (1992). "Smoothed particle hydrodynamics," *Annu. Rev. Astron. Astrophys.* **30**, 543–574.
- Newland, D. E. (1993). *An Introduction to Random Vibrations, Spectral and Wavelet Analysis*, 3rd ed. (Longman Scientific and Technical, Harlow, United Kingdom).
- Petyt, M., and Jones, C. J. C. (2004). "Numerical methods in acoustics," in *Advanced Applications in Acoustics, Noise and Vibration*, edited by F. Fahy, and J. Walker (Spoon, London).
- Rayleigh, Lord (1896). *The Theory of Sound*, 2nd ed. (Dover, New York), Vol. **II**.
- Shorter, P. J. (2005). "Hybrid area junctions," ESI US R&D Inc., San Diego, Internal Report.
- Shorter, P. J., and Langley, R. S. (2005a). "On the reciprocity relationship between direct field radiation and diffuse reverberant loading," *J. Acoust. Soc. Am.* **117**, 85–95.
- Shorter, P. J., and Langley, R. S. (2005b). "Vibro-acoustic analysis of complex systems," *J. Sound Vib.* **288**, 669–700.
- Williams, E. G. (1983). "Numerical evaluation of the radiation from unbaffled, finite plates using the FFT," *J. Acoust. Soc. Am.* **74**, 343–347.
- Williams, E. G., and Maynard, J. (1982). "Numerical evaluation of the Rayleigh integral for planar radiators using the FFT," *J. Acoust. Soc. Am.* **72**, 2020–2030.

Manipulation of micrometer sized particles within a micromachined fluidic device to form two-dimensional patterns using ultrasound

Stefano Oberti,^{a)} Adrian Neild, and Jürg Dual
Center of Mechanics, ETH Zurich, CH-8092 Zurich, Switzerland

(Received 5 April 2006; revised 3 November 2006; accepted 12 November 2006)

Ultrasonic manipulation, which uses acoustic radiation forces, is a contactless manipulation technique. It allows the simultaneous handling of single or numerous particles (e.g., copolymer beads, biological cells) suspended in a fluid, without the need for prior localization. Here it is reported on a method for two-dimensional arraying based on the superposition of two in-plane orthogonally oriented standing pressure waves. A device has been built and the experimental results have been compared with a qualitative analytical model. A single piezoelectric transducer is used to excite the structure to vibration, which consists of a square chamber etched in silicon sealed with a glass plate. A set of orthogonally aligned electrodes have been defined on one surface of the piezoelectric. This allows either a quasi-one-dimensional standing pressure field to be excited in one of two directions or if both electrodes are activated simultaneously a two-dimensional pressure field to be generated. Two different operational modes are presented: two signals identical in amplitude and frequency were used to trap particles in oval shaped clumps; two signals with slightly different frequencies to trap particles in circular clumps. The transition between the two operational modes is also investigated. © 2007 Acoustical Society of America. [DOI: 10.1121/1.2404920]

PACS number(s): 43.25.Gf, 43.20.Ks, 43.25.Qp [MFH]

Pages: 778–785

I. INTRODUCTION

Manipulation of suspended particles (e.g., micrometer-sized solid objects, biological cells, droplets of an immiscible fluid) is relevant in several fields. Of particular interest are life sciences and microtechnology. For instance, holding living cells in distinct and multiple locations would be beneficial for screening the effect of new drugs in a parallel manner (so-called cell arrays^{1,2}); in a similar way, expression of proteins could be studied by holding beads coated with antibodies and flush them with different antigens (antibodies arrays³), this being advantageous in terms of binding area if compared with the standard arrays on planar solid surfaces. Furthermore, improved possibilities for the manipulation of micromachined components would enable the fabrication of hybrid microdevices, consisting of multiple microparts,⁴ frequently hindered by incompatible manufacturing processes.

Different techniques based on electrical,⁵ magnetic,⁶ or optical⁷ principles have been suggested. They all are characterized by the fact that periodic pattern of particles can only be created in an indirect way, by using multiple electrodes or multiple optical beams for instance, making the design of such systems complex. Here, we present a manipulation technique based on the force arising as a second-order effect when an ultrasonic wave generated by the vibration of a solid object in contact with the liquid interacts with a suspended particle. If second-order terms are retained, when the pressure is integrated over the surface of the sphere and time averaged, the result is the acoustic radiation force.⁸ The periodicity of the acoustic standing wave field can be exploited

for simultaneous positioning. This is due to the acoustic wavelength being different from the particle size typically by two or more orders of magnitude. Moreover, because the long range acoustic force field acts throughout the fluidic volume, it is not necessary to locate the particles prior to manipulation. The result is a higher freedom in the design of the fluidic chamber and dispensing with the need for multiple actuating sites.

A significant amount of work has been presented on acoustic devices consisting of multilayered resonators, so-called acoustic filters,^{9–12} for the separation of two phases, provided that at least one is liquid or gaseous. They create a standing pressure field in the fluid layer between a piezoelectric transducer and a reflector, with nodal planes parallel to them. Recently, thanks to the increasing importance of microtechnology, work on miniaturization of such devices has been done.^{13,14} By extending the concept of capturing particles in planes, further devices were made that collect particles in planes perpendicular to the bottom surface, with the advantage of allowing visual access to each plane. Furthermore, as the vertical dimension is usually kept small, particles can be observed throughout the nodal plane.^{15–19}

Haake *et al.* reported on two-dimensional particle²⁰ and cell²¹ manipulation in a fluid layer confined between a macrosized glass plate, excited to vibration by shear piezoceramic transducers attached along its edges, and a passive reflector. Excitation of two perpendicularly orientated transducers generates a two-dimensional displacement field in the plate, and by coupling the vibration to the adjacent fluid layer this results in concentrating particles in a two-dimensional pattern. In contrast, in the approach anticipated by Lilliehorn *et al.*²² an array of single transducers are placed

^{a)}Electronic mail: stefano.oberti@imes.mavt.ethz.ch

at the location of the desired trapping sites. Two-dimensional positioning of microorganisms in a square chamber has been demonstrated by Saito *et al.*,²³ by superimposing two standing waves acting in orthogonal direction excited by four cylindrical transducers positioned on the sides of the square chamber.

Here, we present the theoretical investigation of a novel approach to two-dimensional manipulation, which, exploiting the fact that a single actuator is sufficient to set up a pressure field throughout the fluidic chamber, combines the advantages in terms of fabrication of a simple design with the possibility of changing the distance between the trapping sites by simply varying the excitation signal frequency to the next resonance frequency. Furthermore, this design is well suited for further miniaturization of the device. Two different operation modes are illustrated in this work, which trap particles in oval shaped and circular shaped clumps, respectively.

Moreover, if the chamber is provided with multiple inlets bringing different types of particles, the possibility of switching between the one-dimensional and the two-dimensional field can be exploited to load the chamber in such a way that the one-dimensional field first traps similar particles in the same line and successively, by exciting an orthogonal electrode, they can be divided in clumps to then be treated with different chemicals, for instance.

II. DEVICE

The system presented here has been designed by extending the functionality of the device previously described by the same authors.¹⁸ It is based on the excitation to resonance of the fluid confined within a chamber, so that a standing pressure field is set up. The fluidic chamber ($5 \times 5 \times 0.2$ mm), shown in Figs. 1(a) and 1(b), has been manufactured by dry etching a 300- μm -thick silicon wafer to a depth of 200 μm and sealing it on the top with a 1-mm-thick glass slide, cut from a standard microscopy slide with a wafer saw. This allows visual access to the suspended particles within the cavity. As shown for one-dimensional systems, when $h < \lambda/2$, h being the channel depth and λ the acoustic wavelength, an essentially one-dimensional field can be set up¹⁹ which does not vary substantially in the vertical direction. As $h < \lambda/2$ is satisfied in this work, we treat the system as two dimensional.

A piezoceramic plate, measuring 5×5 mm ($x \times z$) with a thickness of 0.5 mm, has been glued beneath the silicon wafer, aligned with the fluidic cavity. As shown in Ref. 18, a quasi-one-dimensional pressure field can be set up by defining a strip electrode on the lower side of the piezoelectric, applying a voltage to it while grounding the two remaining electrodes. This is achieved by cutting the lower surface of the piezoelectric to a depth of 30 μm , so that a line of the metallic layer is removed along the whole length of the plate. The pressure field is then parallel to the direction of the strip electrode. The asymmetric configuration, in comparison to a full plate actuation, allows for a larger number of modes to be excited, as demonstrated previously.¹⁹ In that study it was shown that the wavelength across the channel is not neces-

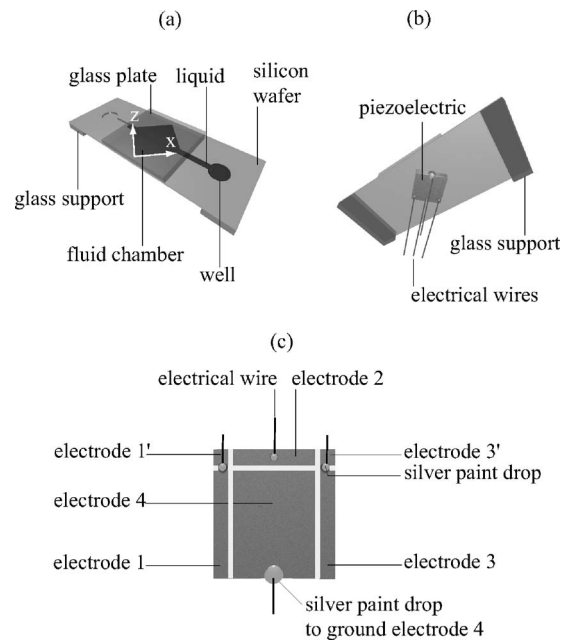


FIG. 1. Schematics of the ultrasonic manipulation device, top view (a) and bottom view (b). The system consists of a fluidic cavity ($5 \times 5 \times 0.2$ mm) etched in a 300- μm -thick silicon wafer and sealed on the top with a glass plate. A piezoelectric plate ($5 \times 5 \times 0.5$ mm) has been attached beneath the wafer, aligned with the fluid cavity. (c) Zoomed view of the piezoelectric lower surface, highlighting the electrode configuration used to generate a one-dimensional displacement field by applying an ac voltage to a single electrode (e.g., 1), or two dimensional by exciting two orthogonal electrodes (e.g., 1 and 2). In contrast, the upper piezoelectric surface, the one in contact with the wafer, has only one electrode, connected to the middle electrode on the lower side (electrode 4) and grounded. The device extends 30 mm in the x direction and 12 mm in the z direction and is supported at both ends.

sarily equal to λ based on $\lambda = c/f$, c being the speed of sound in the fluid and f the frequency of the sound wave, and is therefore better expressed as $\lambda_x = c_x/f$, c_x being the phase speed in the x direction.

Based on this principle, it is expected that a two-dimensional pressure field will be excited when the one-dimensional fields generated by two orthogonally orientated electrodes are superimposed. Figure 1(c) shows that three electrodes have been defined at the under side of the piezoelectric. First, two cuts were made 700 μm from the edge of the plate, then a third across the width of the plate. The result is then symmetric. In fact, only two of these electrodes were used for operation of the device. The small square areas at the extremities (electrodes 1' and 3') have been connected to the lateral ones (electrodes 1 and 3) in a single electrode by means of conductive paint, the reason being to achieve the highest active area possible. The middle electrode (electrode 4) has been connected with the electrode in contact with the silicon wafer by putting a droplet of conductive silver paint at one extremity and then both electrodes have been grounded. The whole device extends 30 mm in the x direction and 12 mm in the z direction, and is supported at both ends by means of glass supports.

Loading of the fluid chamber occurs by applying the particle suspension into one of the wells at each end of the device with a pipette and then waiting until the device is filled by capillary forces through the 1-mm-wide inlet chan-

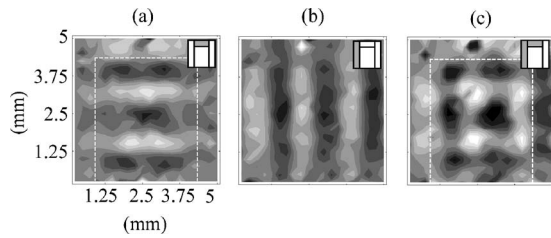


FIG. 2. Normalized displacement field in the $x \times z$ plane measured on the lower surface of the piezoelectric on a grid of 625 points spaced by $250 \mu\text{m}$ in both directions, the excitation voltage having an amplitude of 14 V at 1.971 MHz. (a), (b) The result when a single electrode is excited (marked in grey in the insert), pointing out how a displacement can be obtained only in the region having the same width as the strip electrode, delimited by the dotted line. The two dimension displacement is shown in (c).

nel. In this way, the device can be operated in nonflowing condition, an operational mode which is desirable for some of the applications.

The examination by laser interferometry of the displacement of the lower surface of the piezoelectric confirmed that the displacement field of the piezoelectric is in fact quasi-one-dimensional, when an electrical signal is applied to a single electrode, as shown in Fig. 2(a), and two dimensional when two orthogonally aligned electrodes are excited [Fig. 2(b)]. Furthermore, as has been noted previously,¹⁸ this result indicates that the wavelength in the structure is not necessarily equal either to $\lambda = c/f$, $\lambda_x = c_x/f$, or $\lambda_z = c_z/f$, as clearly demonstrated by comparing for instance Fig. 2(a) with the result presented later in Fig. 4, where the wavelength in the fluid corresponds to approximately $760 \mu\text{m}$, i.e., less than half of the wavelength in the structure.

III. RESULTS

In the experiments reported here, the device has been positioned under a microscope (Olympus ZSH) equipped with a CCD camera (Sony CCD-RISI, Model SSC-M370CE) connected to a PC frame grabber (National Instruments, PC-IMAQ 1408). The excitation of the piezoelectric was performed by means of a function generator (Stanford Research, DS345) connected to an amplifier (ENI, 2100L). To vary one of the voltages applied to the electrodes, the amplifier output signal was split in two. One wire has been connected directly to the first electrode, while the other was connected to the second electrode through a homebuilt voltage divider. This consisted of a series of ten ohmic resistors and a switch, the position ten corresponding to maximal voltage (i.e., $V_1 = V_2 = V$, V_1 being the voltages applied to electrode 1 or 3 and V_2 that applied to electrode 2), whilst the position one corresponds to one-tenth of the applied voltage (i.e., $V_1 = V$ and $V_2 = V/10$). Using the signal from the same function generator guaranteed that the electrodes are excited at the exact same frequency. In the case where two different signals needed to be applied, a second function generator and a second amplifier identical to the first ones completed the setup. In all experiments copolymer particles of either 9.6 or $26 \mu\text{m}$ suspended in de-ionized water (Duke Scientific) have been used.

A. Superposition of two standing waves (general case)

A two-dimensional standing pressure field can be set up by superimposing two planar standing waves with orthogonal wave vectors (x and z). For an arbitrary pressure field in a nonviscous fluid the position of a spherical particle with radius r_S and speed of sound c_S corresponds to the location of minimum force potential, expressed by the equation derived by Gor'kov:²⁴

$$\langle U \rangle = 2\pi r_S^3 \rho \left(\frac{1}{3} \frac{\langle p^2 \rangle}{\rho^2 c^2} f_1 - \frac{1}{2} \langle v^2 \rangle f_2 \right) \quad (1)$$

where $\langle p^2 \rangle = \langle (p_x + p_z)^2 \rangle$ and $\langle v^2 \rangle = \langle v_x^2 + v_z^2 \rangle$ are the mean square fluctuations of the fluid pressure and velocity at the particle's location; $f_1 = 1 - \rho c^2 / (\rho_S c_S^2)$ and $f_2 = 2(\rho_S - \rho) / (2\rho_S + \rho)$. Here, only the primary acoustic radiation force is considered; other effects, such as secondary acoustic forces acting between particles, acoustic streaming, gravity, and buoyancy are not taken into account.

It should be noted that Gor'kov assumes the particle is not near a wall and therefore the scattered field reflected at that surface is not considered. Such an assumption cannot be made for a microfluidic system, but it seems reasonable to further assume that any discrepancy between the existing theory and the microfluidic case is a difference in amplitude rather than a major change in the shape of the force field, the latter which is of interest in this work.

We define a standing pressure wave in the x and z directions as

$$p_x = p_{x0} \cos(k_x x) \cos(\omega_x t), \quad (2a)$$

$$p_z = p_{z0} \cos(k_z z) \cos(\omega_z t) = p_{z0} \cos(k_z z) \cos(\omega_x t + \Delta\omega t), \quad (2b)$$

where p_{x0} and p_{z0} are the peak amplitudes, $k_x = 2\pi/\lambda_x$ and $k_z = 2\pi/\lambda_z$ the wave numbers in the x and z directions, $\Delta\omega = \omega_z - \omega_x$ the difference of the angular frequencies, and t the time. The velocity field in the fluid can be derived through the velocity potential $v = [-\partial\phi/\partial x, -\partial\phi/\partial z]$ using the linear relation $\partial\phi/\partial t = p/\rho$.

The mean square fluctuation of the pressure averaged over one period of time is then

$$\begin{aligned} \langle p^2 \rangle &= \langle (p_x + p_z)^2 \rangle = \frac{p_{x0}^2 \cos^2(k_x x)}{2} + \frac{p_{z0}^2 \cos^2(k_z z)}{2} \\ &\quad + 2p_{x0}p_{z0} \cos(k_x x) \cos(k_z z) \langle \cos(\omega_x t) \cos(\omega_z t) \rangle \\ &= \frac{p_{x0}^2 \cos^2(k_x x)}{2} + \frac{p_{z0}^2 \cos^2(k_z z)}{2} \\ &\quad + p_{x0}p_{z0} \cos(k_x x) \cos(k_z z) \langle \cos(\Delta\omega t) \rangle, \end{aligned} \quad (3)$$

where the third term has been expanded to $p_{x0}p_{z0} \cos(k_x x) \cos(k_z z) \langle \cos(2\omega_x t + \Delta\omega t) + \cos(\Delta\omega t) \rangle$ using basic trigonometric relations and simplified then to $p_{x0}p_{z0} \cos(k_x x) \cos(k_z z) \langle \cos(\Delta\omega t) \rangle$ by taking into account that $\langle \cos(2\omega_x t + \Delta\omega t) \rangle = 0$. In the cases of interest, the period of the oscillatory term $\cos(\Delta\omega t)$ might exceed the period of the other terms $\cos(\omega_x t)$ and $\cos(\omega_z t)$, hence time

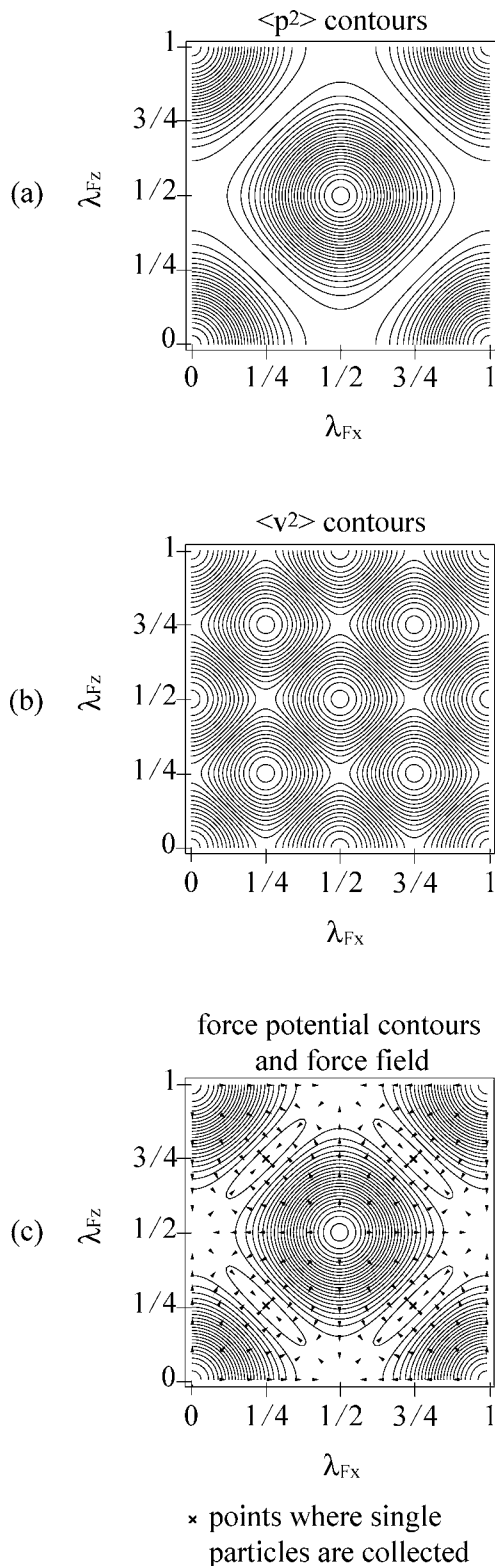


FIG. 3. The (a) $\langle p^2 \rangle$ and (b) $\langle v^2 \rangle$ terms of the force potential $\langle U \rangle$, resulting from the superposition of two in phase cosine functions with identical amplitude and frequency, plotted for a single wavelength λ_x by λ_z range as contour plot. The force potential field in $\langle U \rangle$ is depicted in (c) together with the force field displayed by arrows. Particles, according to Gor'kov's theory, are expected to collect at two positions per wavelength, where the force potential has its minima (locations marked by a cross). The potential wells are characterized by an oval shape.

average has been performed for the first two terms in Eq. (3) but not for the third one.

The mean square fluctuation of the velocity is given by

$$\langle v^2 \rangle = \langle v_x^2 + v_z^2 \rangle = \frac{1}{2\rho^2} \left[\frac{k_x^2 p_{x0}^2 \sin^2(k_x x)}{\omega_x^2} + \frac{k_z^2 p_{z0}^2 \sin^2(k_z z)}{\omega_z^2} \right]. \quad (4)$$

In the following sections several special cases are presented.

B. Superposition of two standing waves with same amplitude and frequency

1. Model

In the case under consideration here ω_x , the angular frequency excited in the x direction and ω_z , the corresponding term in the z direction, are equal. Equation (3) therefore reduces to

$$\langle p^2 \rangle = \langle (p_x + p_z)^2 \rangle = \frac{p_{x0}^2 \cos^2(kx)}{2} + \frac{p_{z0}^2 \cos^2(kz)}{2} + p_{x0} p_{z0} \cos(kx) \cos(kz) \quad (5)$$

with $k=k_x=k_z$, while the mean square fluctuation of the velocity can be rewritten as

$$\langle v^2 \rangle = \langle v_x^2 + v_z^2 \rangle = \frac{k^2}{2\rho^2 \omega^2} [p_{x0}^2 \sin^2(kx) + p_{z0}^2 \sin^2(kz)] \quad (6)$$

with $\omega = \omega_x = \omega_z$.

In Figs. 3(a) and 3(b) the $\langle p^2 \rangle$ term and the $\langle v^2 \rangle$ term in the $x \times z$ plane are represented separately for a single wavelength in both directions as contour lines (left-hand side) and as three-dimensional plots in arbitrary units in the vertical direction (right-hand side). The full force potential field $\langle U \rangle$ is shown in Fig. 3(c), together with the force field represented by the arrows. Particles collect at two positions per wavelength in a potential well of oval shape, at the locations marked with a cross.

It has been assumed here that the two pressure amplitudes are equal ($p_{x0} = p_{z0}$) and that copolymer particles ($c_S = 3000$ m/s, $\rho_S = 1050$ kg/m³) suspended in de-ionized water ($c = 1481$ m/s, $\rho = 998$ kg/m³) have been used. As the values of f_1 and f_2 are 0.7684 and 0.034, respectively, the $\langle p^2 \rangle$ term

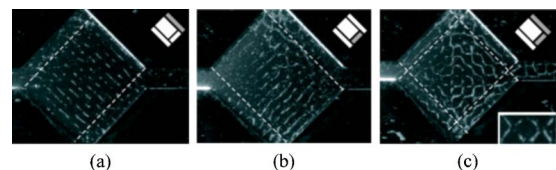


FIG. 4. (a), (b) 9.6 μ m copolymer particles collecting in lines parallel to the excited electrode, as marked in the insert. In contrast, when the same voltage is applied to orthogonal electrodes, particles collect in clumps with oval shape, as shown in the bottom insert (c). An excessive amount of particles cannot fill the potential wells and is therefore distributed along lines connecting the potential minima, as shown in the last image. The device has been excited with a 14 V amplitude signal at 1.971 MHz.

dominates over the $\langle v^2 \rangle$ term in Eq. (1). The dominant forces acting on the particles cause them to collect in the areas of $\langle p^2 \rangle = 0$, and more specifically within this area at the locations where the $\langle v^2 \rangle$ term is maximum. It is important to note that the areas of $\langle p^2 \rangle = 0$ are all connected (forming a grid), hence it is the relatively small $\langle v^2 \rangle$ term which keeps the particles, in adjacent clumps, apart.

2. Experimental results

As already mentioned in Sec. II, applying a voltage to a single electrode generates a parallel oriented pressure field, as confirmed by the result illustrated in Figs. 4(a) and 4(b), where the two electrodes have been excited separately in two different experiments with a 14 V amplitude signal at 1.971 MHz and the 26- μm -diam particles were randomly distributed at the beginning of the experiment. The inserts show the piezoelectric lower surface with the excited electrode in grey. Since the pattern of particles is maintained after the electrical signal is removed, between experiments the chamber has been refilled with particles; hence the concentration is not necessarily constant. The presence of the inlet and outlet channel hinders the formation of lines near the chamber walls. A standing pressure field cannot be set up outside the region delimited by the dotted line. This is acceptable for this proof of concept device but represents an issue to be solved in the future development of this system. The excitation of two orthogonal electrodes, as shown in Fig. 4(c), resulted in the collection of particles in oval clumps in a zig-zag pattern (i.e., each oval is at 90° to its direct neighbors in either direction) as predicted by the model, where it is however difficult to differentiate between single clumps.

The process of two-dimensional arraying of 9.6 μm particles previously aligned in a one-dimensional pattern is depicted in Fig. 5. At the sequence beginning the 2.562 MHz signal with 16 V amplitude has been applied to a second electrode.

C. Superposition of two standing waves with same frequency and different amplitude

The effect of two different voltages on the force potential field was explored next. It is not necessarily the case that the pressures in each direction have exactly the same amplitude, the reason being manufacturing errors, for instance. For this reason we explored this effect in the extreme case when the amplitude of one of the voltages is decreased down to one-tenth, starting with the same signal applied to both electrodes.

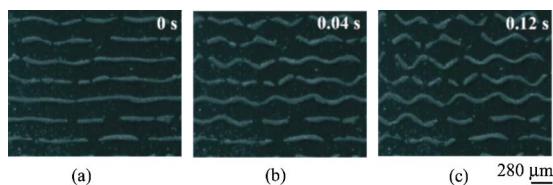


FIG. 5. Process of clump formation at 2.562 MHz starting with 9.6 μm copolymer particles collected into lines. At the beginning of the sequence, the 16 V signal has been applied to a second electrode, too, causing the particles to gather in the oval shaped potential wells.

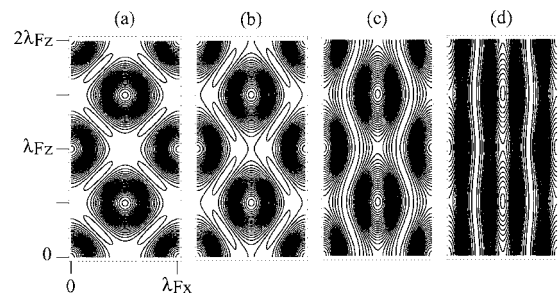


FIG. 6. Sequence of images illustrating the effect of a change in the voltage applied to the electrode in the x direction. The result is shown for four different steps corresponding to the four positions of the voltage divider, starting with $V_1 = V_2$ (a), 1 and 2 referring to the respective electrodes, and ending with $V_2 = 0.1V_1$ (d), each step being separated by 0.3 V.

1. Model

Figure 6 illustrates the change in the force potential field, when the voltage applied to the electrode in the x direction (electrode 2 in Fig. 1) is decreased in three steps to one-tenth of the voltage applied to the perpendicular electrode (electrode 1). The result is depicted for one wavelength in the x direction and two wavelengths in the z direction. The oval shape of the potential well is maintained, but the single clumps rotate around their centers to finally merge into lines, as the amplitude of the forces in z direction decreases.

It is conceivable that this operational method could be of use, for example, in the treating of various cell populations with different chemicals and subsequently allowing them to merge in order to study their interaction.

2. Experimental results

One voltage has been stepwise decreased by means of the voltage divider from position 10, corresponding to 16 V amplitude to position 1, corresponding to 1.6 V, the frequency being 2.6 MHz in all cases. The experimental result (Fig. 7) is in good agreement with the model.

It can be observed in this experiment [cf. Fig. 7(a)] and in the one described in Sec. III B [cf. Fig. 4(c)], that the single clumps of particles are not distinctly separated. This occurs when such a high particle concentration is chosen that the potential wells cannot accommodate all of them. This is detrimental to the device in applications where mixing between single clumps has to be avoided even when the num-

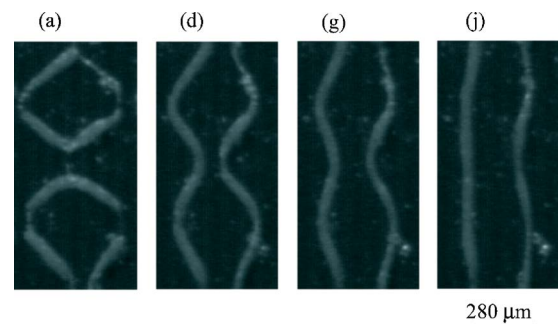


FIG. 7. Experimental result of the process illustrated in Fig. 6. When the amplitude of the signal applied to the electrode in the x direction decreases, the clumps start to rotate around their center to finally merge into lines.

ber of particles is excessive, as in the case of different cell populations. An operational mode which solves this problem is described in the following.

D. Superposition of two signals with different frequency and same amplitude

1. Model

When angular frequencies ω_x and ω_z differ so much that the period of the oscillatory term is shorter than the time scale of interest in the experiment, the term $\langle \cos(\Delta\omega t) \rangle$ in Eq. (3) time averages to zero. The mean square fluctuation of the pressure is then

$$\langle p^2 \rangle = \langle (p_x + p_z)^2 \rangle = \frac{p_{x0}^2 \cos^2(k_x x)}{2} + \frac{p_{z0}^2 \cos^2(k_z z)}{2}, \quad (7)$$

while the velocity mean square fluctuation is still described by Eq. (4).

The $\langle p^2 \rangle$ and the $\langle v^2 \rangle$ terms are plotted separately in Figs. 8(a) and 8(b) for one wavelength in both directions. It has been assumed again that the pressure amplitudes are equal ($p_{x0}=p_{z0}$) and that copolymer particles are used.

In comparison with the previous case, there is an additional peak here between two adjacent peaks, already present previously (see for instance the peak at $x=0$ and $z=\lambda_z/2$). This additional peak keeps the clumps apart. Furthermore, the maxima of $\langle p^2 \rangle$ and the minima of $\langle v^2 \rangle$ fall at the same position; thus the only effect the $\langle v^2 \rangle$ term has is that of increasing the depth of the potential wells; it is the larger $\langle p^2 \rangle$ term which keeps the particles apart.

It has to be noted that in Fig. 8 the force potential is plotted for a single wavelength λ_x by λ_z range. If λ_x were to be different from λ_z , for instance if two different modes are excited, then the circular clump become oval but remain dominated by the $\langle p^2 \rangle$ term.

2. Experimental results

Figure 9 shows the process of two-dimensional positioning starting from a one-dimensional pattern, when two signals of 2.562 MHz and 2.562 MHz+25 Hz, both with 16 V amplitude, are applied to the electrodes. This slight frequency difference has been seen to be enough to cause a change in the shape of the clumps formed.

As predicted by the model, a pattern of circular clumps is obtained. The size variation depends on the nonuniform particle concentration in the lines from which the circular clumps have been formed after the second electrode has been activated. Again, a small number of particles are stuck on the substrate.

E. Superposition of two standing waves with slightly different frequency and different amplitude

The reason why a slight frequency difference alters the pattern considerably is not intuitive and needs further explanation, therefore the region of transition between the two previously described operational methods has been investigated.

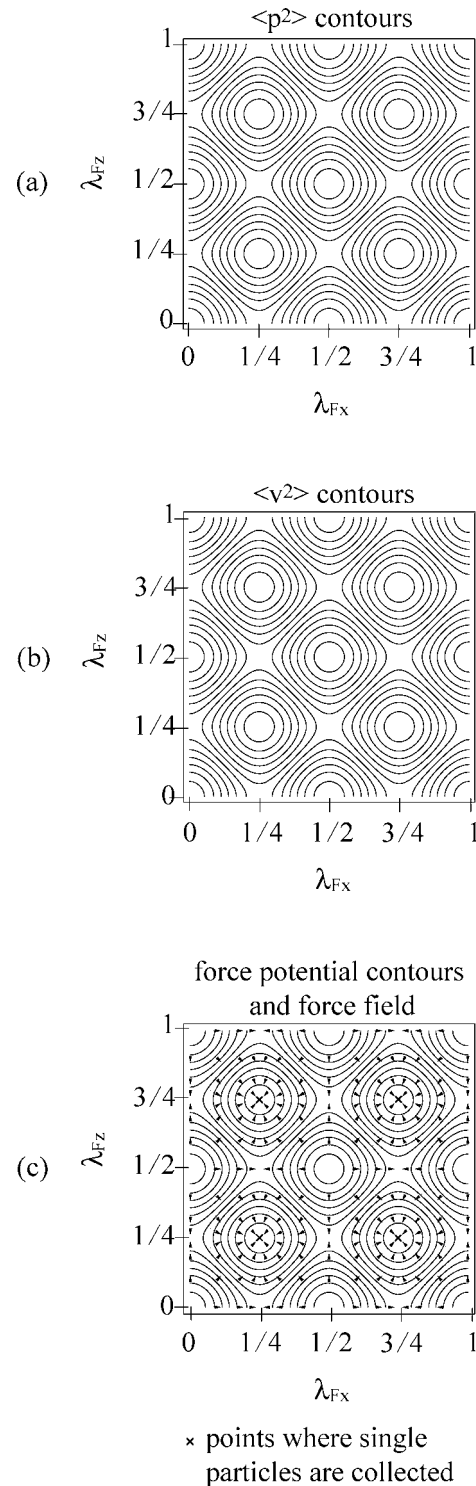


FIG. 8. (a), (b) A contour plot and three-dimensional plot of the $\langle p^2 \rangle$ and $\langle v^2 \rangle$ terms of the force potential $\langle U \rangle$, resulting from the superposition of two in phase cosine functions with identical amplitude but different frequency. The force potential field in $\langle U \rangle$ is depicted in (c) together with the force field.

When the two frequencies differ only slightly the period of the oscillatory term $\langle \cos(\Delta\omega t) \rangle$ in Eq. (3) might exceed the period of the other terms, and, therefore when averaged it does not vanish, contributing instead to the $\langle p^2 \rangle$ term. The oscillatory term shifts the force potential field between the two cases mentioned previously in Secs. III B and Sec. III D

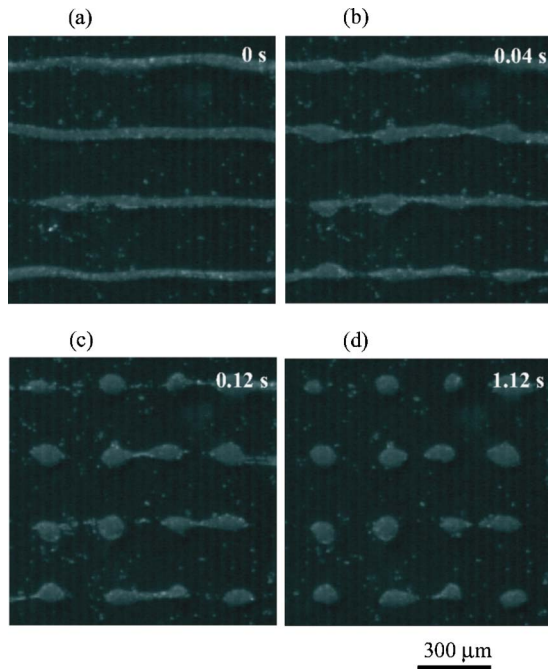


FIG. 9. Process of two-dimensional positioning from a one-dimensional field excited by a 16 V amplitude signal at 2.562 MHz. At the sequence beginning another 16 V amplitude signal at 2.562 MHz+25 Hz has been applied to the electrode in the z direction, causing the $9.6 \mu\text{m}$ particles to separate in circular clumps, the difference in their size being due to a non-uniform particle distribution in the original lines [cf. (a)].

back and forth. In this varying pressure field, the orientation of the oval potential well changes as well. The force potential field is shown in Fig. 10 at different time windows,

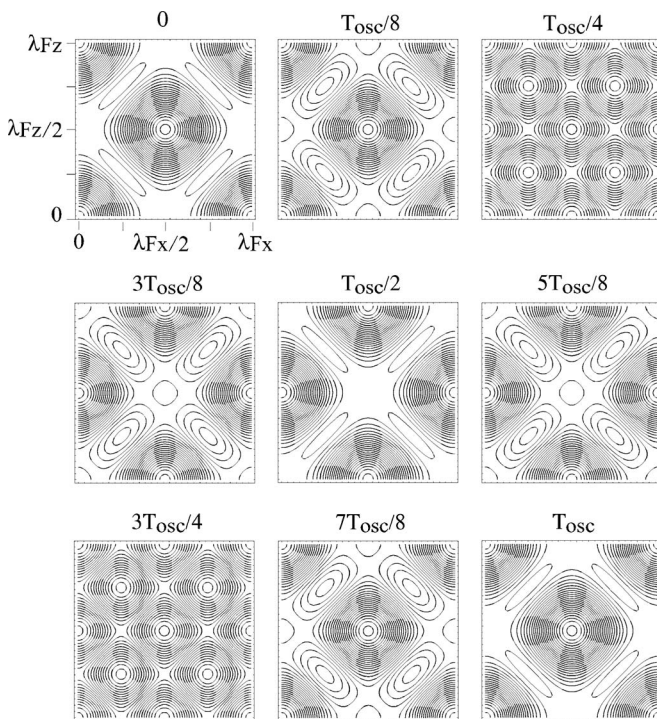


FIG. 10. When the frequency difference between the two excitation signals differs only slightly, the oscillatory term does not necessarily vanish. Therefore, if different time windows are considered, different contributions to the force potential result. In this sequence of images ($x \times z$ plane), the force potential is depicted for an increasing time window ($T_{\text{osc}}/8$).

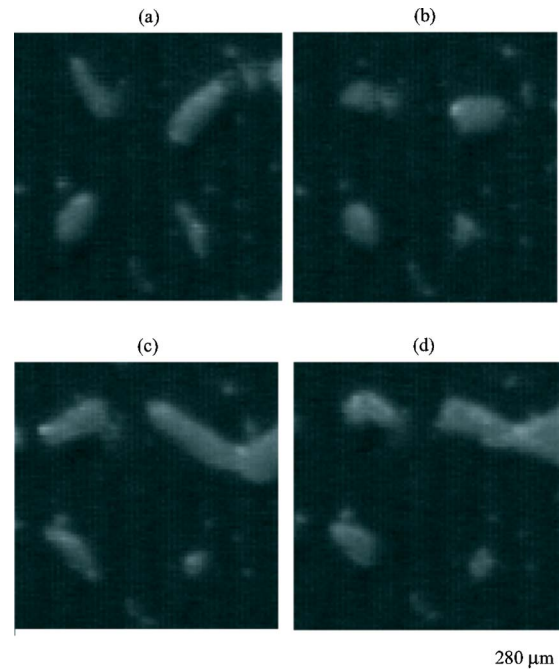


FIG. 11. When the frequencies differ by less than 5 Hz, the particle pattern visibly changes continuously from the oval shape potential well to the round shape wells and back. The orientation of the ovals changes as well.

spaced by $T_{\text{osc}}/8$, with $T_{\text{osc}} = 2\pi/\Delta\omega$ being the period of the oscillatory term, the white regions corresponding to the force potential maxima, the black ones to the minima.

When the period of oscillation lies in the time range of the experiment it can be visually followed, as the image capture rate of the camera is 25 frames/s and the typical length of sequence is 10 s. This corresponds to frequency differences ranging from 0.1 to 25 Hz. As the difference increases, the time scale of the experiment becomes bigger than the oscillation and the pressure field changes as such a high speed that the inertia and the viscous drag force of the clumps (the latter can be expected to dominate) prevent them from realigning in oval form with the new orientation; instead they stay in circular clumps.

This has been observed in experiments where the frequency of one signal was swept from -25 to $+25$ Hz around the frequency of the other signal of 2.6 MHz. We observed that when the two frequencies differ by less than 5 Hz, but do indeed differ, the pattern visibly changes continuously from the oval shape potential well to the round shape wells and back (Fig. 11). As the frequency difference increases, the motion becomes faster to the extent where jiggling can no longer be seen, this happening when the two frequencies are approximately 25 Hz apart.

The continuous movement of particles can be used in practical applications to keep clumps of cell in continuous motion and prevent them from attaching to the substrate.

IV. CONCLUSION

A method for forming two-dimensional arrays of particles within a micromachined fluidic square chamber has been presented. By superimposing the one-dimensional standing pressure waves generated by exciting strip elec-

trodes orthogonal to each other and defined on the surface of the piezoelectric, it has been possible to collect particles in oval shaped clumps, if two identical signals were applied, or circular clumps, by introducing a slight frequency difference between the signals. If this is small enough, the pattern continuously changes between the oval potential well and the circular one. By making the frequency difference greater than 25 Hz, the inertia and the viscous drag force of the clumps prevent them from visibly following this reorientation, so that they gather in circular clumps regardless of the particle concentration in the chamber, which is more advantageous from the application point of view.

- ¹A. Khademhosseini, J. Yeh, G. Eng, J. Karp, H. Kaji, J. Borenstein, O. C. Farokhzad, and R. Langer, "Cell docking inside microwells within reversibly sealed microfluidic channels for fabricating multiphenotype cell arrays," *Lab Chip* **5**, 1380–1386 (2005).
- ²H. Andersson and A. van den Berg, "Microfluidic devices for cellomics: A review," *Sens. Actuators B* **92**, 315–325 (2003).
- ³D. J. Cahill, "Protein and antibody arrays and their medical application," *J. Immunol. Methods* **250**, 81–91 (2001).
- ⁴A. O'Riordan, P. Dalaney, and G. Redmond, "Field configured assembly: Programmed manipulation and self-assembly at the mesoscale," *Nano Lett.* **4**, 761–765 (2004).
- ⁵N. Manaresi, A. Romani, G. Medoro, L. Altomare, A. Leopardi, M. Tartagli, and R. Guerrieri, "A CMOS chip for individual cell manipulation and detection," *IEEE J. Solid-State Circuits* **38**, 2297–2305 (2003).
- ⁶H. Lee, A. M. Purdon, and R. M. Westervelt, "Manipulation of biological cells using a microelectromagnet matrix," *Appl. Phys. Lett.* **85**, 1063–1065 (2004).
- ⁷E. R. Dufresne and D. G. Grier, "Optical tweezer arrays and optical substrates created with diffractive optics," *Rev. Sci. Instrum.* **69**, 1974–1977 (1998).
- ⁸M. Gröschl, "Separation of suspended particles. I. Fundamentals," *Acustica* **84**, 432–447 (1998).
- ⁹M. Gröschl, W. Burger, and B. Handl, "Ultrasonic separation of suspended particles. III. Application in biotechnology," *Acustica* **84**, 815–822 (1998).
- ¹⁰E. Benes, W. Burger, M. Groeschl, and F. Trampler, "Method for treating a liquid," Patent EP 0 633 049 A1, 1995.
- ¹¹M. Hill, Y. Shen, and J. J. Hawkes, "Modeling of layered resonators for ultrasonic separation," *Ultrasonics* **40**, 385–392 (2002).
- ¹²H. Nowotny and E. Benes, "General one-dimensional treatment of the layered piezoelectric resonator with two electrodes," *J. Acoust. Soc. Am.* **82**, 513–521 (1987).
- ¹³N. R. Harris, M. Hill, M. S. Beeby, Y. Shen, N. M. White, J. J. Hawkes, and W. T. Coakley, "A silicon microfluidic ultrasonic separator," *Sens. Actuators B* **95**, 425–434 (2003).
- ¹⁴N. Harris, M. Hill, Y. Shen, R. J. Townsend, S. Beeby, and N. M. White, "A dual frequency, ultrasonic, microengineered particle manipulator," *Ultrasonics* **42**, 139–144 (2004).
- ¹⁵G. M. Dougherty and A. P. Pisano, "Ultrasonic particle manipulation in microchannels using phased co-planar transducers," Proceedings of the 12th International Conference on Solid State Sensors, Actuators and Microsystems, Boston, 2003, pp. 670–673.
- ¹⁶M. Wiklund, C. Günther, R. Lemor, M. Jäger, G. Fuhr, and H. M. Hertz, "Ultrasonic features integrated into DEP chips," Proceedings of NanoTech 2005, Montreux.
- ¹⁷F. Petersson, A. Nilsson, C. Holm, H. Jönsson, and T. Laurell, "Continuous separation of lipid particles from erythrocytes by means of laminar flow and acoustic standing wave forces," *Lab Chip* **5**, 20–22 (2005).
- ¹⁸A. Neild, S. Oberti, A. Haake, and J. Dual, "Finite element modeling of a micro-particle manipulator," *Ultrasonics* (in press), Available online 9 June 2006, doi:10.1016/j.ultras.2006.05.168.
- ¹⁹A. Neild, S. Oberti, and J. Dual, "Design, modeling and characterization of microfluidic devices for ultrasonic manipulation," *Sensors and Actuators B: Chemical*, (in press). Corrected proof, available online 16 May 2006, doi:10.1016/j.snb.2006.04.065.
- ²⁰A. Haake and J. Dual, "Contactless micromanipulation of small particles by an ultrasound field excited by a vibrating body," *J. Acoust. Soc. Am.* **117**, 2752–2760 (2005).
- ²¹A. Haake, A. Neild, G. Radziwill, and J. Dual, "Positioning, displacement, and localization of cells using ultrasonic forces," *Biotechnol. Bioeng.* **92**, 8–14 (2005).
- ²²T. Lilliehorn, M. Nilsson, U. Simu, S. Johansson, M. Almqvist, J. Nilsson J, and T. Laurell, "Dynamic arraying of microbeads for bioassays in microfluidic channels," *Sens. Actuators B* **106**, 851–858 (2005).
- ²³M. Saito, N. Kitamura, and M. Terauchi, "Ultrasonic manipulation of locomotive microorganisms and evaluation of their activity," *J. Appl. Phys.* **92**, 7581–7586 (2002).
- ²⁴L. P. Gor'kov, "Forces acting on a small particle in an acoustic field within an ideal fluid," *Dokl. Akad. Nauk SSSR* **140**, 88–92 (1961).

Bubble interaction dynamics in Lagrangian and Hamiltonian mechanics

Yurii A. Ilinskii, Mark F. Hamilton,^{a)} and Evgenia A. Zabolotskaya

Applied Research Laboratories, The University of Texas at Austin, Austin, Texas 78713-8029

(Received 20 February 2006; revised 13 July 2006; accepted 13 November 2006)

Two models of interacting bubble dynamics are presented, a coupled system of second-order differential equations based on Lagrangian mechanics, and a first-order system based on Hamiltonian mechanics. Both account for pulsation and translation of an arbitrary number of spherical bubbles. For large numbers of interacting bubbles, numerical solution of the Hamiltonian equations provides greater stability. The presence of external acoustic sources is taken into account explicitly in the derivation of both sets of equations. In addition to the acoustic pressure and its gradient, it is found that the particle velocity associated with external sources appears in the dynamical equations. © 2007 Acoustical Society of America. [DOI: 10.1121/1.2404798]

PACS number(s): 43.25.Yw [AJS]

Pages: 786–795

I. INTRODUCTION

Theoretical investigations have been conducted to model the interactions of two^{1–4} and many^{5–8} gas bubbles in liquid. Our focus recently has been on the latter,^{9–11} motivated in large part by observations of collective interactions in bubble clusters generated during shock wave lithotripsy.¹² Most of the aforementioned investigations take into account translation as well as pulsation of the interacting bubbles.^{1,3–5,7–9,11}

In many situations, the bubbles are clustered sufficiently close to one another, and the characteristic time scale of external acoustic excitation is sufficiently long, that the motion of any one bubble may be considered to affect all others instantaneously. This is the underlying assumption for all of the models developed in Refs. 1–8, and it is in the present paper as well.

The present paper has two specific aims. One is to develop dynamical equations for an arbitrary number of interacting bubbles using Hamiltonian mechanics. The other is to show rigorously how to account for the effect of external acoustic sources.

Previous models of interacting bubble dynamics have been derived using primarily Lagrangian or Newtonian mechanics. With both approaches, the resulting coupled equations of motion are second order in the time derivative. For just a few bubbles, say two or three, the system of second-order differential equations may be reduced analytically to equations of first order that can be solved with standard numerical algorithms. However, a difficulty is encountered when solving these equations numerically for large numbers of bubbles. The equations cannot realistically be recast in the desired first-order form, with the result that a matrix inversion is required at each time step.¹⁰ The inversions result in the accumulation of substantial errors for large systems of equations, which in turn lead to instability. These errors are avoided by using Hamiltonian mechanics, because the equations of motion are automatically of first order, and therefore

matrix inversions are not required to solve them numerically. Thus for large numbers of bubbles, the Hamiltonian equations developed in the present paper result in increased numerical accuracy and stability compared with models based on Newtonian or Lagrangian mechanics.

Two earlier papers discuss bubble interaction models within the framework of Hamiltonian mechanics, but without obtaining our results. In the first, by Russo and Smereka,¹³ an explicit expression for the Hamiltonian is provided only for the translation (dipole) mode of the bubble motion, but not for the pulsation (monopole) mode. They refer to this as the point-bubble approximation. Our Hamiltonian accounts for pulsation as well as translation. In the second paper, by Teshukov and Gavriluk,¹⁴ the Hamiltonian is defined only implicitly, not as an explicit function of generalized displacements and momenta. It depends also on velocities, which must be eliminated before the Hamiltonian can be used in the canonical equations. Our Hamiltonian is an explicit function of displacements and momenta, with no dependence on velocities. As a result, our final dynamical equations are presented in explicit forms that can be integrated immediately. One reason the Hamiltonians in these earlier papers are inappropriate for our purposes may be that the focus of those papers is on development of kinetic theories for describing the statistical properties of collective bubble interactions. In contrast, our focus is on describing the dynamics of individual bubbles within the cluster.

A second specific aim of the present paper is formal derivation of the source terms required to account for an externally applied sound field. In all previous work that we know, the influence of an external acoustic source has been included *ad hoc* in the dynamical equations for interacting bubbles. In the equations of radial motion, the source term has been introduced as a perturbation of the pressure at infinity, exactly as it appears in the Rayleigh-Plesset equation.¹⁵ In the equations of translational motion, the source term has been introduced as a pressure gradient corresponding to the primary Bjerknes force.⁸ The derivation in the present paper shows explicitly how both the acoustic pressure and particle velocity produced by external sources

^{a)}Electronic mail: hamilton@mail.utexas.edu

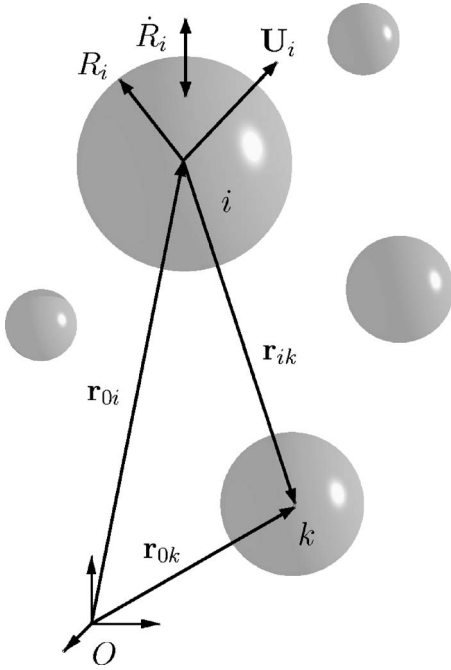


FIG. 1. Notation used to describe the motion of the bubbles.

appear in both the Lagrangian and Hamiltonian equations of motion.

The paper is structured as follows. The kinetic energy function is derived in Sec. II. Both pulsation and translation are taken into account. It is through the kinetic energy that the influence of external acoustic sources is taken into account. The dynamical equations based on Lagrangian and Hamiltonian mechanics are developed in Secs. III and IV, respectively, and a comparison of numerical simulations based on the two sets of equations is presented in Sec. V.

II. KINETIC ENERGY

We begin by deriving the kinetic energy of dynamically coupled bubbles in an inviscid incompressible liquid. Motion of the liquid is described by a velocity potential ϕ that satisfies Laplace's equation,

$$\nabla^2 \phi = 0. \quad (1)$$

It is assumed that the bubbles remain spherical in shape, and that the motion of the i th bubble is described by its radial velocity \dot{R}_i and translational velocity \mathbf{U}_i , where R_i is the instantaneous radius of the bubble, \mathbf{r}_{0i} the position of its center relative to a fixed origin, $\mathbf{U}_i = \dot{\mathbf{r}}_{0i}$, and dots over quantities indicate time derivatives; see Fig. 1.

It is convenient to first calculate the kinetic energy in the absence of external sources. This result is then used to determine the additional kinetic energy that results from the presence of external sources.

A. Source-free bubble interactions

The total kinetic energy of the liquid is the integral

$$\mathcal{K} = \frac{\rho}{2} \int_V |\nabla \phi|^2 dV \quad (2)$$

over the volume occupied by the liquid and excluding the bubbles, where ρ is the density of the liquid. For a liquid that is at rest at infinity, the integral can be rewritten as¹⁶

$$\mathcal{K} = -\frac{\rho}{2} \sum_i \int_{S_i} \phi \frac{\partial \phi}{\partial r_i} dS_i. \quad (3)$$

The surfaces S_i coincide with the bubble walls, r_i is the magnitude of the local coordinate vector \mathbf{r}_i that defines position relative to the center of the i th bubble, $r_i = |\mathbf{r}_i|$, and the summation is over all N bubbles in the cluster, $1 \leq i \leq N$. Calculation of the kinetic energy thus requires knowledge of the velocity potential and its normal derivative on the surface of each bubble.

The normal derivative on the surface of the i th bubble is determined by the boundary condition

$$\frac{\partial \phi}{\partial r_i} = \dot{R}_i + \mathbf{U}_i \cdot \mathbf{n}_i \quad \text{at } r_i = R_i, \quad (4)$$

where $\mathbf{n}_i = \mathbf{r}_i / r_i$ is the unit vector in the direction of \mathbf{r}_i . Equation (3) thus becomes

$$\mathcal{K} = -\frac{\rho}{2} \sum_i \int_{S_i} (\dot{R}_i + \mathbf{U}_i \cdot \mathbf{n}_i) \phi dS_i. \quad (5)$$

This expression is the usual starting point for calculating the kinetic energy of interacting bubbles. Our method for deriving an expression for the velocity potential in Eq. (5) is different from procedures used by others,¹⁻⁸ and in order to account for external sources in Sec. II B we require a higher-order approximation of the kinetic energy than has appeared in previous work.

The procedure begins with the solution of Eq. (1) for an isolated bubble in an infinite liquid, subject to the boundary condition given by Eq. (4):

$$\phi_{0i} = -\frac{R_i^2}{r_i} \dot{R}_i - \frac{R_i^3}{2r_i^2} \mathbf{U}_i \cdot \mathbf{n}_i, \quad (6)$$

which is the solution for the potential produced by a monopole source plus a dipole source. We consider the summation

$$\phi_0 = \sum_i \phi_{0i} \quad (7)$$

to be the zeroth-order solution for the potential produced by a system with more than one bubble. Equation (7) satisfies Eq. (1) but not Eq. (4). Only the i th term in the summation satisfies Eq. (4). Potentials created by all bubbles for which $k \neq i$ do not obey the boundary condition on the surface of the i th bubble.

A correction to the zeroth-order solution is needed. To determine this correction, the zeroth-order solution is expanded in the neighborhood of the i th bubble to obtain

$$\begin{aligned}\phi_0(\mathbf{r}_i) &= \phi_{0i}(\mathbf{r}_i) + \sum_{k \neq i} \phi_{0k}(\mathbf{r}_{ki} + \mathbf{r}_i) \\ &= \phi_{0i}(\mathbf{r}_i) + \sum_{k \neq i} [\phi_{0k}(\mathbf{r}_{ki}) + \mathbf{c}_{ki} \cdot \mathbf{r}_i + \dots],\end{aligned}\quad (8)$$

where $\mathbf{r}_{ki} = \mathbf{r}_{0i} - \mathbf{r}_{0k}$ and, from Eq. (6),

$$\begin{aligned}\mathbf{c}_{ki} &= \left(\frac{\partial \phi_{0k}(\mathbf{r}_k)}{\partial \mathbf{r}_k} \right)_{\mathbf{r}_k = \mathbf{r}_{ki}} \\ &= \frac{R_k^2}{r_{ki}^2} \dot{R}_k \mathbf{n}_{ki} - \frac{R_k^3}{2r_{ki}^3} [\mathbf{U}_k - 3(\mathbf{U}_k \cdot \mathbf{n}_{ki}) \mathbf{n}_{ki}].\end{aligned}\quad (9)$$

Equation (8) is truncated after the linear (dipole) term because all higher-order terms are orthogonal to the monopole and dipole terms in the integrand of Eq. (5), and therefore they cannot contribute to the kinetic energy.

The radial velocity at the surface of the i th bubble, based on the zeroth-order solution, is

$$\frac{\partial \phi_0}{\partial r_i} = \dot{R}_i + \mathbf{U}_i \cdot \mathbf{n}_i + \sum_{k \neq i} \mathbf{c}_{ki} \cdot \mathbf{n}_i \quad \text{at } r_i = R_i. \quad (10)$$

Comparison with Eq. (4) shows that the failure of ϕ_0 to satisfy the boundary condition on the i th bubble is due to the presence of the terms $\mathbf{c}_{ki} \cdot \mathbf{r}_i$ in Eq. (8). As seen from Eq. (9), the resulting error in the boundary condition is of order R^2/d^2 . Here and subsequently, $R = O(R_i)$ is the characteristic bubble radius and $d = O(r_{ik})$ is the characteristic distance between neighboring bubbles.

In the next approximation, which we write as

$$\phi = \phi_0 + \phi_1, \quad (11)$$

we seek a correction ϕ_1 that satisfies Eq. (1), and such that ϕ more accurately approximates the boundary conditions. The appropriate correction, expanded in the neighborhood of the i th bubble, is

$$\begin{aligned}\phi_1 &= \phi_{1i}(\mathbf{r}_i) + \sum_{i \neq i} \phi_{1k}(\mathbf{r}_{ki} + \mathbf{r}_i) \\ &= \phi_{1i}(\mathbf{r}_i) + \sum_{k \neq i} [\phi_{1k}(\mathbf{r}_{ki}) + \mathbf{d}_{ki} \cdot \mathbf{r}_i + \dots],\end{aligned}\quad (12)$$

which consists of the following dipole solutions of Eq. (1):

$$\phi_{1i}(\mathbf{r}_i) = \sum_{k \neq i} \frac{R_i^3}{2r_i^2} \mathbf{c}_{ki} \cdot \mathbf{n}_i, \quad (13)$$

$$\phi_{1k}(\mathbf{r}_{ki}) = \sum_{j \neq k} \frac{R_k^3}{2r_{ki}^2} \mathbf{c}_{jk} \cdot \mathbf{n}_{ki}. \quad (14)$$

Equation (13), which is the first term in Eq. (12), is the correction to the i th term in Eq. (8) that is required to cancel the terms $\mathbf{c}_{ki} \cdot \mathbf{n}_i$ in Eq. (10). The same correction must be applied consistently to all other bubbles, which results in the summation in Eq. (12).

Since $\mathbf{d}_{ki} = [\partial \phi_{1k}(\mathbf{r}_k) / \partial \mathbf{r}_k]_{\mathbf{r}_k = \mathbf{r}_{ki}}$ is of order R^5/d^5 , which is of higher order than we need, the terms $\mathbf{d}_{ki} \cdot \mathbf{r}_i$ and beyond in Eq. (12) are discarded to obtain

$$\phi_1 = \phi_{1i}(\mathbf{r}_i) + \sum_{k \neq i} \phi_{1k}(\mathbf{r}_{ki}). \quad (15)$$

Equation (11) now becomes, together with Eq. (8),

$$\begin{aligned}\phi(\mathbf{r}_i) &= \phi_{0i}(\mathbf{r}_i) + \phi_{1i}(\mathbf{r}_i) \\ &+ \sum_{k \neq i} [\phi_{0k}(\mathbf{r}_{ki}) + \phi_{1k}(\mathbf{r}_{ki}) + \mathbf{c}_{ki} \cdot \mathbf{r}_i].\end{aligned}\quad (16)$$

At this level of approximation one obtains

$$\frac{\partial \phi}{\partial r_i} = \dot{R}_i + \mathbf{U}_i \cdot \mathbf{n}_i + O(R^5/d^5) \quad \text{at } r_i = R_i. \quad (17)$$

Equation (16) is thus the desired velocity potential to an accuracy of order R^4/d^4 .

Evaluation of Eq. (16) on the surface of the i th bubble yields, through order R^4/d^4 ,

$$\begin{aligned}\phi|_{S_i} &= - \left(R_i \dot{R}_i + \frac{R_i}{2} \mathbf{U}_i \cdot \mathbf{n}_i \right) \\ &+ \sum_{k \neq i} \left\{ - \left(\frac{R_k^2}{r_{ik}} \dot{R}_k + \frac{R_k^3}{2r_{ik}^2} \mathbf{U}_k \cdot \mathbf{n}_{ki} \right) \right. \\ &+ \frac{3R_i R_k^2}{2r_{ik}^2} \dot{R}_k (\mathbf{n}_{ki} \cdot \mathbf{n}_i) \\ &\left. - \frac{3R_i R_k^3}{4r_{ki}^3} [\mathbf{U}_k \cdot \mathbf{n}_i - 3(\mathbf{U}_k \cdot \mathbf{n}_{ki})(\mathbf{n}_{ki} \cdot \mathbf{n}_i)] \right\} \\ &+ \sum_{\substack{j,k \\ k \neq i,j}} \frac{R_j R_k^3}{2r_{ik}^2 r_{jk}^2} \dot{R}_j (\mathbf{n}_{jk} \cdot \mathbf{n}_{ki}).\end{aligned}\quad (18)$$

The kinetic energy is calculated by substituting Eq. (18) in Eq. (5), making use of the identity

$$\int_{S_i} (\mathbf{a} \cdot \mathbf{n}_i)(\mathbf{b} \cdot \mathbf{n}_i) dS_i = \frac{4\pi}{3} R_i^2 (\mathbf{a} \cdot \mathbf{b}) \quad (19)$$

to evaluate integrals over products of dipole terms, and observing that $\int_{S_i} \mathbf{n}_i dS_i = \mathbf{0}$ due to the orthogonality of monopole and dipole terms. The result of this calculation is

$$\begin{aligned}\mathcal{K}_0 &= 2\pi\rho \left\{ \sum_i R_i^3 \dot{R}_i^2 + \frac{1}{6} \sum_i R_i^3 U_i^2 + \sum_{\substack{i,k \\ i \neq k}} \frac{R_i^2 R_k^2}{r_{ik}} \dot{R}_i \dot{R}_k \right. \\ &+ \frac{1}{2} \sum_{i,k} \frac{R_i^2 R_k^2}{r_{ik}^2} [R_i \dot{R}_k (\mathbf{U}_i \cdot \mathbf{n}_{ik}) + R_k \dot{R}_i (\mathbf{U}_k \cdot \mathbf{n}_{ki})] \\ &+ \frac{1}{4} \sum_{\substack{i,k \\ i \neq k}} \frac{R_i^3 R_k^3}{r_{ik}^3} [(\mathbf{U}_i \cdot \mathbf{U}_k) - 3(\mathbf{U}_i \cdot \mathbf{n}_{ik})(\mathbf{U}_k \cdot \mathbf{n}_{ik})] \\ &\left. + \frac{1}{2} \sum_{\substack{i,j,k \\ k \neq i,j}} \frac{R_i^2 R_j^2 R_k^3}{r_{ik}^2 r_{jk}^2} \dot{R}_i \dot{R}_j (\mathbf{n}_{ik} \cdot \mathbf{n}_{jk}) \right\},\end{aligned}\quad (20)$$

where the subscript on \mathcal{K}_0 has been introduced to distinguish this expression from contributions to the kinetic energy as-

sociated with external sources, which are considered in Sec. II B.

Except for the last term, which is of relative order R^4/d^4 , Eq. (20) coincides with Doinikov's⁸ Eq. (19) for the kinetic energy. Doinikov's expansion terminates at order R^3/d^3 . The term of order R^4/d^4 in Eq. (20) is needed to determine the additional kinetic energy due to an external sound source that excites the bubble cluster. Another distinction is that each of the double summations in Eq. (20) is written in symmetric form. Harkin *et al.*³ performed an analysis of coupled pulsation and translation through order R^4/d^4 , but only for two bubbles.¹⁷

Equation (20) may be interpreted as follows. The first and second terms are the kinetic energies due to isolated monopoles and dipoles, respectively. The third term is the energy due to monopole-monopole interactions, the fourth due to monopole-dipole interactions, and the fifth due to dipole-dipole interactions. The sixth term is the energy due to the interaction of two monopoles through a third monopole. Hydrodynamic energy associated with each of these interactions possesses a direct analogy with electrostatic energy associated with the interactions of charges and dipoles distributed on the surface of a sphere.¹⁸

B. External source

The acoustic pressure and particle velocity fields generated by an arbitrary external sound source that insonifies the bubble cluster are now taken into account. The first step is to calculate the increase in kinetic energy of the liquid due to an additional "bubble" whose motion is prescribed and is thus interpreted as the source. This $(N+1)$ th bubble, or source, is designated to have radius R_e , radial velocity \dot{R}_e , and remain in a fixed location, such that $\mathbf{U}_e = \mathbf{0}$. Equation (20) accounts for the kinetic energy in the absence of any sources. The total kinetic energy in the presence of the source becomes

$$\mathcal{K} = \mathcal{K}_0 + \mathcal{K}_e, \quad (21)$$

where the additional kinetic energy due to the interaction of the potential fields produced by the external source and the bubbles is

$$\mathcal{K}_e = 2\pi\rho \left[2 \sum_i \frac{R_i^2 R_e^2}{r_{ei}} \dot{R}_i \dot{R}_e - \sum_i \frac{R_i^3 R_e^2}{r_{ei}^2} \dot{R}_e (\mathbf{U}_i \cdot \mathbf{n}_{ei}) + \frac{1}{2} \sum_i \frac{R_i^3 R_e^4}{r_{ei}^4} \dot{R}_e^2 + \sum_{i,k} \frac{R_i^2 R_e^2 R_k^3}{r_{ik}^2 r_{ek}^2} \dot{R}_i \dot{R}_e (\mathbf{n}_{ik} \cdot \mathbf{n}_{ek}) \right]. \quad (22)$$

Equation (22) is obtained from Eq. (20) by retaining only bubble-source interaction terms, which arise when i, j , or k equals the $(N+1)$ th value identified by e . For example, the term $2\pi\rho R_e^3 \dot{R}_e^2$ was discarded because it is not a bubble-source interaction term and therefore does not contribute to the bubble dynamics.

The leading-order term in Eq. (22) can be rewritten as

$$\begin{aligned} 4\pi\rho \sum_i \frac{R_i^2 R_e^2}{r_{ei}} \dot{R}_i \dot{R}_e &= \rho \frac{d}{dt} \sum_i V_i \frac{R_e^2 \dot{R}_e}{r_{ei}} - \rho \sum_i V_i \frac{d}{dt} \left(\frac{R_e^2 \dot{R}_e}{r_{ei}} \right) \\ &= \rho \frac{d}{dt} \sum_i V_i \frac{R_e^2 \dot{R}_e}{r_{ei}} \\ &\quad - \sum_i V_i \left(\frac{\rho \ddot{V}_e}{4\pi r_{ei}} - \rho \mathbf{U}_i \cdot \mathbf{u}_{ei} \right), \end{aligned} \quad (23)$$

where $V_i = \frac{4}{3}\pi R_i^3$ is the volume of the i th bubble, $V_e = \frac{4}{3}\pi R_e^3$ is the volume of the source, and

$$\mathbf{u}_{ei} = \frac{R_e^2}{r_{ei}^2} \dot{R}_e \mathbf{n}_{ei} \quad (24)$$

is the fluid velocity generated by the source at the location of the i th bubble. The corresponding pressure generated by the source is thus⁶

$$p_{ei} = \frac{\rho \ddot{V}_e}{4\pi r_{ei}} - \frac{1}{2} \rho u_{ei}^2. \quad (25)$$

Next, it is noted that since a total time derivative of any function of the generalized coordinates and time does not contribute to Lagrange's equations,¹⁹ and by extension there is also no effect on Hamilton's canonical equations, the first term on the right-hand side of Eq. (23) is discarded. Employing definitions (24) and (25) in Eq. (22), one obtains

$$\mathcal{K}_e = \mathcal{K}_{e0} + \mathcal{K}_{e1}, \quad (26)$$

where

$$\mathcal{K}_{e0} = - \sum_i V_i \left(p_{ei} - \frac{1}{4} \rho u_{ei}^2 \right), \quad (27)$$

$$\mathcal{K}_{e1} = - \frac{\rho}{2} \sum_i V_i (\mathbf{U}_i \cdot \mathbf{u}_{ei}) + 2\pi\rho \sum_{\substack{i,k \\ i \neq k}} \frac{R_i^2 R_k^3}{r_{ik}^2} \dot{R}_i (\mathbf{u}_{ek} \cdot \mathbf{n}_{ik}). \quad (28)$$

Separation of the terms in the kinetic energy according to the definitions of \mathcal{K}_{e0} and \mathcal{K}_{e1} proves useful for calculation of the Hamiltonian in Sec. III.

It is seen that \mathcal{K}_e depends on the acoustic pressure p_{ei} and particle velocity \mathbf{u}_{ei} in the sound field radiated by the source, but it does not depend explicitly on the radius R_e or radial velocity \dot{R}_e characterizing the hypothetical monopole. The physical source of the acoustic pressure and particle velocity is no longer relevant. For example, the acoustic field might be a sound beam or a standing wave. The quantities p_{ei} and \mathbf{u}_{ei} account for the total variations in pressure and velocity presumed to be imposed on the bubbles by the sound field, including dc effects such as radiation pressure and acoustic streaming. Moreover, these external pressures and velocities need not be acoustical in nature. They are the field variables associated with any background flow.

Of course, the inclusion of acoustic source terms is an acknowledgment of compressibility, which in turn imposes a restriction on the validity of the model. The restriction is that

the wavelength must be large in comparison with the size of the bubble cluster, in which case one may still regard the fluid to be locally incompressible in the vicinity of the cluster.

As far as we know, only the acoustic pressure in Eq. (27) appears as a source term in dynamical equations for bubble interactions reported previously in the literature. Moreover, the applied sound pressure is typically introduced *ad hoc*. In the equations for radial motion it is introduced through the pressure at infinity, and in the equations for translational motion it is introduced as a Bjerknes force. It is not evident that any of the acoustic particle velocity terms in Eqs. (27) and (28) have been taken into account in previous models of bubble interactions.

III. LAGRANGIAN FORMALISM

The Lagrangian of the system is

$$\mathcal{L}(q, \dot{q}, t) = \mathcal{K}(q, \dot{q}, t) - \mathcal{V}(q), \quad (29)$$

where q and \dot{q} represent the sets of generalized displacements and velocities of the system, respectively, and \mathcal{V} is the potential energy. With R_i and \mathbf{r}_{0i} taken to be the generalized coordinates, Lagrange's equations describing the dynamics of the system become, for $1 \leq i \leq N$,

$$\frac{d}{dt} \left(\frac{\partial \mathcal{L}}{\partial \dot{R}_i} \right) = \frac{\partial \mathcal{L}}{\partial R_i}, \quad \frac{d}{dt} \left(\frac{\partial \mathcal{L}}{\partial \dot{\mathbf{r}}_{0i}} \right) = \frac{\partial \mathcal{L}}{\partial \mathbf{r}_{0i}}. \quad (30)$$

Equations (30) constitute a system of $4N$ second-order differential equations for the radius and three coordinates associated with each of the N bubbles.

The kinetic energy of the liquid is

$$\mathcal{K} = \mathcal{K}_0 + \mathcal{K}_{e0} + \mathcal{K}_{e1}, \quad (31)$$

where the terms on the right are given by Eqs. (20), (27), and (28). It remains to calculate the potential energy of the system, which may be expressed in terms of its differential

$$d\mathcal{V} = \sum_i (P_0 - P_i) dV_i, \quad (32)$$

where P_0 is atmospheric pressure. The pressure in the liquid acting on the surface of the i th bubble is taken to be, for simplicity,

$$P_i = \left(P_0 + \frac{2\sigma}{R_{i0}} \right) \left(\frac{R_{i0}}{R_i} \right)^{3\gamma} - \frac{2\sigma}{R_i}, \quad (33)$$

where γ is the ratio of specific heats, and σ is surface tension. Additional effects that contribute to this pressure, such as thermal damping, gas diffusion, and condensation, are not considered here. Rewriting bubble volume in terms of radius one obtains

$$d\mathcal{V} = 4\pi \sum_i (P_0 - P_i) R_i^2 dR_i, \quad (34)$$

which is in a form that is convenient for direct substitution in Eq. (30).

The first of Eqs. (30) yields for the radial motion, through order R^2/d^2 ,

$$\begin{aligned} R_i \ddot{R}_i + \frac{3}{2} \dot{R}_i^2 &= \frac{P_i - P_0}{\rho} + \frac{1}{4} U_i^2 - \sum_{k \neq i} \frac{R_k}{r_{ik}} (R_k \ddot{R}_k + 2\dot{R}_k^2) \\ &+ \frac{1}{2} \sum_{k \neq i} \frac{R_k^2}{r_{ik}^2} [\dot{R}_k (5\mathbf{U}_k + \mathbf{U}_i) \cdot \mathbf{n}_{ik} + R_k (\dot{\mathbf{U}}_k \cdot \mathbf{n}_{ik})] \\ &+ Q_i^R, \end{aligned} \quad (35)$$

where

$$\begin{aligned} Q_i^R &= -\frac{p_{ei}}{\rho} + \frac{1}{4} u_{ei}^2 - \frac{1}{2} (\mathbf{u}_{ei} \cdot \mathbf{U}_i) \\ &- \frac{1}{2} \sum_{k \neq i} \frac{R_k^2}{r_{ik}^2} [3\dot{R}_k (\mathbf{u}_{ek} + \mathbf{u}_{ei}) \cdot \mathbf{n}_{ik} + R_k (\dot{\mathbf{u}}_{ek} \cdot \mathbf{n}_{ik})] \end{aligned} \quad (36)$$

accounts for the external acoustic source. The second of Eqs. (30) yields for the translational motion, also through order R^2/d^2 ,

$$\dot{\mathbf{M}}_i = 4\pi\rho \sum_{k \neq i} \frac{R_i^2 R_k^2}{r_{ik}^2} \dot{R}_i \dot{R}_k \mathbf{n}_{ik} + \mathbf{Q}_i^{M1}, \quad (37)$$

where

$$\mathbf{M}_i = \frac{1}{2} \rho V_i \mathbf{U}_i + \frac{3}{2} \rho V_i \sum_{k \neq i} \frac{R_k^2}{r_{ik}^2} \dot{R}_k \mathbf{n}_{ik} + \mathbf{Q}_i^{M2} \quad (38)$$

is the generalized momentum of the i th bubble, and

$$\begin{aligned} \mathbf{Q}_i^{M1} &= -V_i \nabla \left[p_{ei} - \frac{1}{4} \rho u_{ei}^2 + \frac{1}{2} \rho \mathbf{u}_{ei} \cdot \mathbf{U}_i \right. \\ &\left. + \frac{3}{2} \rho \sum_{k \neq i} \frac{R_k^2}{r_{ik}^2} \dot{R}_k (\mathbf{u}_{ei} \cdot \mathbf{n}_{ik}) \right], \end{aligned} \quad (39)$$

$$\mathbf{Q}_i^{M2} = -\frac{1}{2} \rho V_i \mathbf{u}_{ei}, \quad (40)$$

account for the external source. Equations (35) and (37) comprise a coupled system of $4N$ equations for the N values of R_i and the three components of \mathbf{M}_i . The translational velocities are obtained from Eq. (38):

$$\mathbf{U}_i = \frac{2}{\rho V_i} (\mathbf{M}_i - \mathbf{Q}_i^{M2}) - 3 \sum_{k \neq i} \frac{R_k^2}{r_{ik}^2} \dot{R}_k \mathbf{n}_{ik}. \quad (41)$$

In the absence of an external source, in which case Q_i^R , Q_i^{M1} , and Q_i^{M2} are all zero, Eqs. (35) and (37) agree with Eqs. (22) and (23) of Donikov.⁸ His equations include terms of order R^3/d^3 , which are beyond the level of our approximation. He accounts for an external acoustic source by introducing pressure terms in Eqs. (35) and (37), without including any of the particle velocity terms.

The quantity \mathbf{M}_i defined in Eq. (38) is the generalized momentum of the i th bubble. Its first term, $\frac{1}{2} \rho V_i \mathbf{U}_i$, is the momentum of the induced mass associated with translational motion of the bubble in a liquid at rest. Its second term is the contribution to the induced mass due to the flow produced by

pulsations of all the other bubbles. The summation on the right-hand side of Eq. (37) accounts for the secondary Bjerknes forces.

Equation (35), without translation taken into account ($\mathbf{U}_i = \mathbf{0}$), was used previously to simulate the growth and collapse of 50 bubbles adjacent to a rigid surface and subjected to a shock wave.⁹⁻¹¹ The explosive bubble growths in these simulations required development of an algorithm to account for coalescence of bubbles that come in contact with one another. The coalescence algorithm is based on the five conservation rules described in Ref. 11.

A. Dynamical equations for a single bubble

For a single bubble, Eqs. (35) and (37) reduce to

$$R\ddot{R} + \frac{3}{2}\dot{R}^2 = \frac{P_l - P_0}{\rho} - \left(\frac{p_e}{\rho} - \frac{1}{4}|\mathbf{U} - \mathbf{u}_e|^2 \right), \quad (42)$$

$$\frac{d}{dt}[R^3(\mathbf{U} - \mathbf{u}_e)] = -2R^3 \nabla \left(\frac{p_e}{\rho} - \frac{1}{4}|\mathbf{U} - \mathbf{u}_e|^2 \right), \quad (43)$$

where P_l is the liquid pressure given by Eq. (33). The formulation on the right-hand side of Eq. (43) was obtained by noting that $\nabla|\mathbf{U} - \mathbf{u}_e|^2 = \nabla(u_e^2 - 2\mathbf{u}_e \cdot \mathbf{U})$ because $\nabla U^2 = \mathbf{0}$. These coupled equations may be compared with the corresponding model for an acoustically driven bubble that was developed recently by Reddy and Szeri.²⁰ The term $|\mathbf{U} - \mathbf{u}_e|^2$ on the right-hand side of both Eqs. (42) and (43) is missing from their equations for radial and translational motion.

B. Ordering parameter for large clusters

Here we address a potential concern that Eqs. (35) and (37) may lose validity when some bubbles in the cluster are close together, since the interaction terms are obtained as an expansion of the kinetic energy in powers of the small parameter R/d . While the relative order of successive terms in the expansions is characterized by R/d for small numbers of bubbles, another ordering parameter emerges for large numbers of bubbles.

Consider the first summation in Eq. (35), the individual terms of which are seen to be of order R/d relative to the quantity on the left-hand side of the equation. Now consider the terms in this summation collectively, and evaluate the series for a bubble in the center of a spherical cluster having radius R_{cl} , volume $V_{cl} = \frac{4}{3}\pi R_{cl}^3$, and containing N bubbles with similar radii, $R_k \approx R_i$:

$$\begin{aligned} \sum_{k \neq i} \frac{R_k}{r_{ik}} (R_k \ddot{R}_k + 2\dot{R}_k^2) &\sim R_i (R_i \ddot{R}_i + 2\dot{R}_i^2) \frac{N}{V_{cl}} \int_{V_{cl}} \frac{dV}{r} \\ &\sim \frac{NR_i}{R_{cl}} (R_i \ddot{R}_i + 2\dot{R}_i^2). \end{aligned} \quad (44)$$

Following summation this term is thus of order NR/R_{cl} , rather than of order R/d , relative to the left-hand side of Eq. (35). Performing a similar calculation for the second summation in Eq. (35) reveals that it is of relative order NR^2/R_{cl}^2 . For clusters containing many bubbles, the inter-

action terms in Eqs. (35) and (37) may be regarded as expansions not in powers of R/d , but instead in powers of the much smaller quantity R/R_{cl} . The physical explanation for this effect is that for a uniform distribution of bubbles, those farther away collectively exert greater influence because their number per unit volume increases as r^2 , which more than compensates for the influence of an individual bubble, whose effect decreases as $1/r$. For N sufficiently large, Eqs. (35) and (37) therefore remain valid even when R/d is of order one for isolated pairs of bubbles.

A similar argument can be made using the kinetic energy, and it therefore applies also to the Hamiltonian equations developed in Sec. IV.

C. Viscosity

Inclusion of viscosity in the dynamical equations for interacting bubbles, and in particular viscous drag forces associated with translational motion, has been covered by other authors. It is not our aim to evaluate existing models. Rather, our intention here is simply to explain where such forces appear in the dynamical equations, and to provide examples of representative analytical expressions that have been used for these forces in other recent models of bubble interaction.

The effect of viscosity on the radial motion is taken into account by including the term $-4\eta\dot{R}_i/R_i$ on the right-hand side of Eq. (33), where η is the shear viscosity coefficient.^{8,15} The effect of viscosity on the translational motion is taken into account by including a viscous drag force $\mathbf{F}_i^{\text{vis}}$ on the right-hand side of Eq. (37). For example, two expressions that have been used previously for this force are^{20,21}

$$\mathbf{F}_i^{\text{vis}} = -4\pi\eta R_i \mathbf{U}_{ri}, \quad \text{Re}_i \ll 1 \quad \text{and} \quad \mathcal{U}_i \text{Re}_i \ll 1 \quad (45)$$

$$= -12\pi\eta R_i \mathbf{U}_{ri}, \quad \text{Re}_i \gg 1 \quad \text{or} \quad \mathcal{U}_i \text{Re}_i \gg 1, \quad (46)$$

where

$$\mathbf{U}_{ri} = \mathbf{U}_i - \mathbf{u}_{ei} - \sum_{k \neq i} \frac{R_k}{r_{ki}} \dot{R}_k \mathbf{n}_{ki} \quad (47)$$

is the translational velocity of the i th bubble relative to the surrounding fluid, to order R^2/d^2 . As discussed by Magnaudet and Legendre,²¹ and subsequently by Reddy and Szeri,²⁰ the magnitude of the drag force depends on both the Reynolds number, $\text{Re}_i = \rho R_i U_{ri} / \eta$, and the ratio of radial to relative translational velocity, $\mathcal{U}_i = |\dot{R}_i| / U_{ri}$. These same authors also discuss inclusion of a Basset-Boussinesq term in Eq. (45) to account for drag due to the wake behind the bubble. Doinikov⁸ used Eq. (46) in his numerical simulations of three interacting bubbles in a sound field. Wang and Smereka,⁷ and also Gavriluk and Teshukov,²² proposed correction terms to include in Eq. (46) for interactions of many bubbles.

IV. HAMILTONIAN FORMALISM

A. The Hamiltonian

Whereas the Lagrangian is a function of generalized coordinates and velocities, the Hamiltonian is a function of generalized coordinates and momenta. The general expression for the Hamiltonian is¹⁹

$$\mathcal{H}(p, q, t) = \sum_s p_s \dot{q}_s - \mathcal{L}(q, \dot{q}, t), \quad (48)$$

where p_s are the generalized momenta of the system, with p , q , and \dot{q} representing the sets of all p_s , q_s , and \dot{q}_s for the entire system. Note that all \dot{q} on the right-hand side must ultimately be expressed as functions of p and q . The momenta of the system are defined by

$$p_s = \frac{\partial \mathcal{L}}{\partial \dot{q}_s}, \quad (49)$$

and the canonical equations are

$$\dot{q}_s = \frac{\partial \mathcal{H}}{\partial p_s}, \quad \dot{p}_s = -\frac{\partial \mathcal{H}}{\partial q_s}. \quad (50)$$

The generalized coordinates of the system are again R_i and \mathbf{r}_{0i} , and the generalized momenta are thus

$$G_i = \frac{\partial \mathcal{K}}{\partial \dot{R}_i}, \quad \mathbf{M}_i = \frac{\partial \mathcal{K}}{\partial \dot{\mathbf{U}}_i}, \quad (51)$$

where it was taken into account that \mathcal{V} in Eq. (29) depends only on displacements. The translational momentum \mathbf{M}_i is given by Eq. (38), and the radial momentum G_i is calculated in the following.

To evaluate the Hamiltonian we begin by using Eq. (49) to write the summation in Eq. (48) as

$$\sum_s p_s \dot{q}_s = \sum_s \frac{\partial \mathcal{K}}{\partial \dot{q}_s} \dot{q}_s. \quad (52)$$

The summation can now be expressed in closed form using Euler's theorem for homogeneous functions. In Eq. (31) for the kinetic energy, it is observed that in terms of the velocities \dot{R}_i and $\dot{\mathbf{U}}_i$, \mathcal{K}_0 is a homogeneous function of order two, \mathcal{K}_{e0} is order zero, and \mathcal{K}_{e1} is order one. The summation thus yields

$$\sum_s p_s \dot{q}_s = 2\mathcal{K}_0 + \mathcal{K}_{e1}, \quad (53)$$

and Eq. (48) becomes

$$\mathcal{H} = \mathcal{K}_0 - \mathcal{K}_{e0} + \mathcal{V}. \quad (54)$$

While \mathcal{K}_{e1} does not appear explicitly in this expression, it contributes to the dynamical equations through Eq. (51), as follows.

The next step is to express the velocities \dot{q}_s in terms of the displacements q_s and momenta p_s in order to evaluate the kinetic energies. Begin by using the first of Eqs. (51) to calculate the radial momentum:

$$G_i = 4\pi\rho \left[R_i^3 \dot{R}_i + \sum_{k \neq i} \frac{R_i^2 R_k^2}{r_{ik}} \dot{R}_k - \frac{1}{2} \sum_{k \neq i} \frac{R_i^2 R_k^3}{r_{ik}^2} (\mathbf{U}_k \cdot \mathbf{n}_{ik}) + \frac{1}{2} \sum_{k \neq i} \frac{R_i^2 R_k^3}{r_{ik}^2} (\mathbf{u}_{ek} \cdot \mathbf{n}_{ik}) \right], \quad (55)$$

which is to be solved for $\dot{R}_i = \dot{R}_i(R_i, \mathbf{r}_{ik}, G_i, \mathbf{M}_i)$. Note that only relative values of the coordinates \mathbf{r}_{0i} appear in the equations of motion, and specifically in the combination $\mathbf{r}_{ik} = \mathbf{r}_{0i} - \mathbf{r}_{0k}$ for $k \neq i$. Equation (55) is reorganized to place \dot{R}_i on the left-hand side:

$$R_i^3 \dot{R}_i = \frac{G_i}{4\pi\rho} - \sum_{k \neq i} \frac{R_i^2 R_k^2}{r_{ik}} \dot{R}_k + \frac{1}{2} \sum_{k \neq i} \frac{R_i^2 R_k^3}{r_{ik}^2} (\mathbf{U}_k \cdot \mathbf{n}_{ik}) - \frac{1}{2} \sum_{k \neq i} \frac{R_i^2 R_k^3}{r_{ik}^2} (\mathbf{u}_{ek} \cdot \mathbf{n}_{ik}). \quad (56)$$

Translational velocities must also be expressed in the form $\mathbf{U}_i = \mathbf{U}_i(R_i, \mathbf{r}_{ik}, G_i, \mathbf{M}_i)$, and therefore Eq. (38) is rewritten with \mathbf{U}_i on the left-hand side:

$$R_i^3 \mathbf{U}_i = \frac{3\mathbf{M}_i}{2\pi\rho} - 3 \sum_{k \neq i} \frac{R_i R_k^2}{r_{ik}^2} \dot{R}_k \mathbf{n}_{ik} + R_i^3 \mathbf{u}_{ei}. \quad (57)$$

Substitutions are now made iteratively in Eqs. (56) and (57) to eliminate the velocities \dot{R}_i and \mathbf{U}_i on the right-hand sides to obtain, through the same relative order R^2/d^2 ,

$$4\pi\rho \dot{R}_i = \frac{G_i}{R_i^3} - \sum_{k \neq i} \frac{G_k}{R_i R_k r_{ik}} + 3 \sum_{k \neq i} \frac{\mathbf{M}_k \cdot \mathbf{n}_{ik}}{R_i r_{ik}^2} + \sum_{\substack{j,k \\ k \neq i,j}} \frac{R_k G_j}{R_i R_j r_{ik} r_{kj}}, \quad (58)$$

$$4\pi\rho \mathbf{U}_i = \frac{6\mathbf{M}_i}{R_i^3} - 3 \sum_{k \neq i} \frac{G_k \mathbf{n}_{ik}}{R_k r_{ik}^2} + 4\pi\rho \mathbf{u}_{ei}. \quad (59)$$

Equations (58) and (59) are used to eliminate the velocities from the kinetic energy.

One can see that substitution of Eqs. (58) and (59) in Eq. (20) will generate a rather large number of terms. It is much easier to evaluate the summation in Eq. (48). We therefore use Eq. (53) to eliminate \mathcal{K}_0 from the Lagrangian in Eq. (48) to obtain

$$\mathcal{H} = \frac{1}{2} \sum_i G_i \dot{R}_i + \frac{1}{2} \sum_i (\mathbf{M}_i \cdot \mathbf{U}_i) - \mathcal{K}_{e0} - \frac{1}{2} \mathcal{K}_{e1} + \mathcal{V}. \quad (60)$$

Note that the summations simply require multiplication of Eqs. (58) and (59) by G_i and \mathbf{M}_i , respectively. The final expression for the Hamiltonian is, through order R^2/d^2 and expressed exclusively in terms of coordinates and momenta,

$$\begin{aligned} \mathcal{H} = & \frac{1}{4\pi\rho} \left[\frac{1}{2} \sum_i \frac{G_i^2}{R_i^3} + 3 \sum_i \frac{M_i^2}{R_i^3} - \frac{1}{2} \sum_{i \neq k} \frac{G_i G_k}{R_i R_k r_{ik}} \right. \\ & + 3 \sum_{i \neq k} \frac{G_i (\mathbf{M}_k \cdot \mathbf{n}_{ik})}{R_i r_{ik}^2} + \left. \frac{1}{2} \sum_{\substack{i,j,k \\ k \neq i,j}} \frac{R_k G_i G_j}{R_i R_j r_{ik} r_{kj}} \right] + \sum_i V_i p_{ei} \\ & + \sum_i (\mathbf{M}_i \cdot \mathbf{u}_{ei}) + \mathcal{V}. \end{aligned} \quad (61)$$

B. Dynamical equations

From Eqs. (50), the dynamical equations are

$$\dot{R}_i = \frac{\partial \mathcal{H}}{\partial G_i}, \quad \dot{\mathbf{r}}_{0i} = \frac{\partial \mathcal{H}}{\partial \mathbf{M}_i}, \quad \dot{G}_i = -\frac{\partial \mathcal{H}}{\partial R_i}, \quad \dot{\mathbf{M}}_i = -\frac{\partial \mathcal{H}}{\partial \mathbf{r}_{0i}}. \quad (62)$$

Equations (62) constitute a system of $8N$ first-order differential equations. Substitution of Eq. (61) yields

$$\begin{aligned} 4\pi\rho\dot{R}_i = & \frac{G_i}{R_i^3} - \sum_{k \neq i} \frac{G_k}{R_i R_k r_{ik}} + 3 \sum_{k \neq i} \frac{\mathbf{M}_k \cdot \mathbf{n}_{ik}}{R_i r_{ik}^2} \\ & + \sum_{\substack{j,k \\ k \neq i,j}} \frac{R_k G_j}{R_i R_j r_{ik} r_{kj}}, \end{aligned} \quad (63)$$

$$\begin{aligned} 4\pi\rho\dot{G}_i = & \frac{3}{2} \frac{G_i^2}{R_i^4} + 9 \frac{M_i^2}{R_i^4} - \sum_{k \neq i} \frac{G_i G_k}{R_i^2 R_k r_{ik}} + \sum_{\substack{j,k \\ k \neq i,j}} \frac{R_k G_i G_j}{R_i^2 R_j r_{ik} r_{kj}} \\ & - \frac{1}{2} \sum_{\substack{j,k \\ k \neq i,j}} \frac{G_i G_k}{R_k R_j r_{ki} r_{ij}} + 3 \sum_{k \neq i} \frac{G_i (\mathbf{M}_k \cdot \mathbf{n}_{ik})}{R_i r_{ik}^2} \\ & + 4\pi\rho(4\pi R_i^2)(P_i - P_0 - p_{ei}), \end{aligned} \quad (64)$$

$$\dot{\mathbf{r}}_{0i} = \frac{2}{\rho} \frac{\mathbf{M}_i}{V_i} - \frac{3}{4\pi\rho} \sum_{k \neq i} \frac{G_k \mathbf{n}_{ik}}{R_k r_{ik}^2} + \mathbf{u}_{ei}, \quad (65)$$

$$\dot{\mathbf{M}}_i = \frac{1}{4\pi\rho} \sum_{k \neq i} \frac{G_i G_k \mathbf{n}_{ik}}{R_i R_k r_{ik}^2} - V_i \nabla p_{ei} - \nabla (\mathbf{M}_i \cdot \mathbf{u}_{ei}). \quad (66)$$

Equations (63)–(66) are in the desired form for straightforward application of standard Runge-Kutta algorithms to obtain numerical solutions for R_i , G_i , \mathbf{r}_{0i} , and \mathbf{M}_i . The translational velocity is, by definition, $\mathbf{U}_i = \dot{\mathbf{r}}_{0i}$. Notice that the source terms in the Hamiltonian equations are much more simple than in the Lagrangian equations. Effects of viscosity are included in the same way as with the Lagrangian equations of motion, i.e., as discussed in Sec. III B. For a single bubble, Eqs. (63)–(66) reduce to

$$\dot{R} = \frac{G}{4\pi\rho R^3}, \quad (67)$$

$$\dot{G} = \frac{3(G^2 + 6M^2)}{8\pi\rho R^4} + 4\pi R^2(P_l - P_0 - p_e), \quad (68)$$

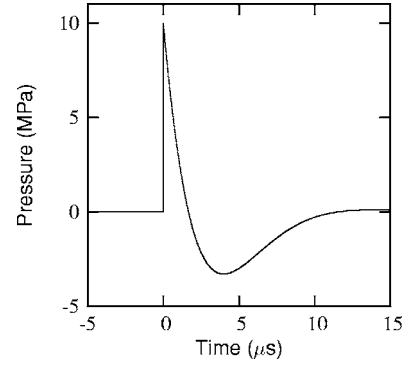


FIG. 2. Shock waveform used for simulations in Fig. 3.

$$\dot{\mathbf{r}} = \frac{3\mathbf{M}}{2\pi\rho R^3} + \mathbf{u}_e, \quad (69)$$

$$\dot{\mathbf{M}} = -\frac{4}{3}\pi R^3 \nabla p_e - \nabla (\mathbf{M} \cdot \mathbf{u}_e). \quad (70)$$

V. COMPARISON OF LAGRANGIAN AND HAMILTONIAN EQUATIONS

Equations (35) and (37) in the Lagrangian formulation are not identical to Eqs. (63)–(66) in the Hamiltonian formulation. The reason is that both systems of equations were obtained as expansions of the kinetic energy in powers of R/d , carried out through order R^2/d^2 , such that differences in the two formulations are of order R^3/d^3 . Except when R/d approaches unity, numerical simulations based on the two formulations agree to within graphical resolution.

An example that demonstrates agreement between the two formulations, and simultaneously illustrates rebound in the radial motion and the corresponding abrupt accelerations in the translational motion, is a bubble initially at rest near a plane rigid wall when it is subjected to a shock wave. In the absence of viscosity, by virtue of the method of images the response is dynamically equivalent to that of $N=2$ identical bubbles subjected to the same acoustical excitation. However, while viscosity is included in the calculations, in order to use the method of images we ignore the effect of viscosity on the liquid in contact with the wall.

The bubble has initial radius $R_0=10 \mu\text{m}$ and its center is initially 5 mm from the wall. The parameters are chosen for an air bubble in water at atmospheric pressure: $\gamma=1.4$, $\rho=1 \text{ g/cm}^3$, $\sigma=73 \text{ dyn/cm}$, $\eta=0.01 \text{ dyn s/cm}^2$, $P_0=10 \text{ dyn/cm}^2$. The shock waveform is defined for $t>0$ by

$$p_e(t) = 2p_{\text{sh}} e^{-\alpha t} \cos(\omega t + \pi/3) \quad (71)$$

for both external acoustic pressures p_{e1} and p_{e2} , with $p_e=0$ for $t<0$. The specific shock waveform used in the simulation is shown in Fig. 2. It is typical of waveforms encountered in shock wave lithotripsy, and it is obtained by setting $p_{\text{sh}}=10 \text{ MPa}$ for the amplitude of the shock, with the profile trailing the shock obtained by setting $\alpha=0.35 \mu\text{s}^{-1}$ and $\omega=0.1\pi \text{ rad}/\mu\text{s}$.

For the stated conditions, the growth-collapse time for the bubble pulsation is on the order of $100 \mu\text{s}$, whereas the duration of the source waveform is only $10 \mu\text{s}$. Therefore the

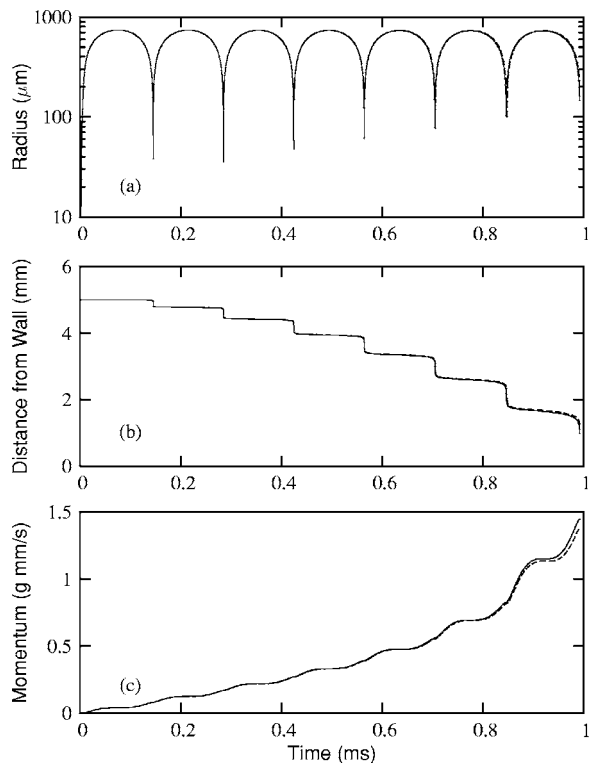


FIG. 3. Comparison of numerical simulations based on the Lagrangian equations (solid lines) and the Hamiltonian equations (dashed lines) for a bubble initially at rest with radius $R_0=10\ \mu\text{m}$ when it is subjected to the shock waveform in Fig. 2: (a) bubble radius; (b) distance from wall; and (c) generalized momentum.

excitation is essentially an impulse that determines the initial conditions for the subsequent free response. As our focus is on comparing Lagrangian and Hamiltonian descriptions of bubble interaction dynamics, for simplicity we ignore all source terms containing the particle velocity \mathbf{u}_e and pressure gradient ∇p_e , retaining only the pressure p_e in Eqs. (36) and (64). In reality, as a shock front sweeps over a bubble and reflects off a nearby wall at normal incidence, the bubble receives two “translational kicks” in rapid succession, in opposite directions, and of equal magnitude. The integrated effect of this translational impulse, which is taken into account by the particle velocities and pressure gradients, is negligible.

Results of the calculations are shown in Fig. 3. The curves calculated with the Lagrangian equations (solid lines) and with the Hamiltonian equations (dashed lines) are seen to be nearly identical for the (a) radial pulsation, (b) translation toward the wall, and (c) the generalized momentum of translation. The slight discrepancies near $t=1\ \text{ms}$ are not associated with time, but rather with proximity to the wall as $R/d \rightarrow 1$. This is a manifestation of the differences at order R^3/d^3 noted at the beginning of this section. Notice how the bubble jumps toward the wall with each rebound in order to conserve translational momentum as its size, and therefore effective mass, becomes very small. The gradual overall increase in the translational momentum seen in Fig. 3(c) corresponds to the gradual increase in the average translational velocity up until the bubble encounters the wall. In the absence of viscosity, and with the system considered in terms

of two identical bubbles rather than one bubble adjacent to a rigid wall, the total momentum of the system is conserved, and $\mathbf{M}_1 + \mathbf{M}_2 = \mathbf{0}$ at all times.

We emphasize that the simulation presented in Fig. 3 is nothing more than a simple example used to illustrate quantitatively the small differences in the Lagrangian and Hamiltonian formulations under conditions of strong variations in both the radial and translational motion. For example, the viscous drag law we used was Eq. (46) because of the high Reynolds numbers encountered when the bubble jumps forward with each rebound. One might argue that a more sophisticated viscous drag model is required. Likewise, the rebounding suggests that liquid compressibility and perhaps other effects should be taken into account, as well as non-spherical collapse when in close proximity to the wall. However, such refinements are unnecessary for the purpose of the comparison being made in this example.

VI. SUMMARY

Lagrangian and Hamiltonian mechanics were used to derive two alternative sets of dynamical equations for interacting bubbles that pulsate and translate. The derivations were carried out through order R^2/d^2 , although it is straightforward to continue the calculations to higher order. The presence of external acoustic sources is taken into account explicitly in the derivations. When solved numerically for large numbers of bubbles, the Hamiltonian equations hold a distinct advantage over the Lagrangian equations. The advantage is due to the fact that the Hamiltonian equations are of first order in the time derivatives. The second-order time derivatives in the Lagrangian equations make it necessary to perform a matrix inversion at each time step in the solution algorithm. For large systems of equations, the matrix inversions can introduce substantial numerical errors, and use of the Hamiltonian formulation can become essential for maintaining stability.

ACKNOWLEDGMENTS

The authors are grateful to Todd Hay for his comments on the manuscript. This work was supported by the IR&D Program at Applied Research Laboratories, and by the Office of Naval Research.

¹G. N. Kuznetsov and I. E. Shchekin, “Interaction of pulsating bubbles in a viscous liquid,” *Sov. Phys. Acoust.* **18**, 466–469 (1973).

²E. A. Zabolotskaya, “Interaction of gas bubbles in a sound field,” *Sov. Phys. Acoust.* **30**, 365–368 (1984).

³A. Harkin, T. J. Kaper, and A. Nadim, “Coupled pulsation and translation of two gas bubbles in a liquid,” *J. Fluid Mech.* **445**, 377–411 (2001).

⁴A. A. Donikov, “Translational motion of two interacting bubbles in a strong acoustic field,” *Phys. Rev. E* **64**, 026301-1–026301-6 (2001).

⁵O. V. Voinov and A. M. Golovin, “Lagrange equations for a system of bubbles of varying radii in a liquid of small viscosity,” *Fluid Dyn.* **5**, 458–464 (1970).

⁶Yu. A. Ilinskii and E. A. Zabolotskaya, “Cooperative radiation and scattering of acoustic waves by bubbles in liquid,” *J. Acoust. Soc. Am.* **92**, 2837–2841 (1992).

⁷N. Wang and P. Smereka, “Effective equations for sound and void wave propagation in bubbly fluids,” *SIAM J. Appl. Math.* **63**, 1849–1888 (2003).

⁸A. A. Donikov, “Mathematical model for collective bubble dynamics in strong ultrasound fields,” *J. Acoust. Soc. Am.* **116**, 821–827 (2004).

- ⁹E. A. Zabolotskaya, Yu. A. Ilinskii, G. D. Meegan, and M. F. Hamilton, "Bubble interactions in clouds produced during shock wave lithotripsy," Proceedings of the 2004 IEEE International UFFC Joint 50th Anniversary Conference, Montreal, Canada, pp. 890–893. The first two terms on the right-hand side of Eq. (10) should be divided by a factor of 6. The results in Fig. 5 were obtained using the corrected equation.
- ¹⁰M. F. Hamilton, Yu. A. Ilinskii, G. D. Meegan, and E. A. Zabolotskaya, "Interaction of bubbles in a cluster near a rigid surface," *ARLO* **6**, 207–213 (2005).
- ¹¹Yu. A. Ilinskii, M. F. Hamilton, E. A. Zabolotskaya, and G. D. Meegan, "Influence of compressibility on bubble interaction," in *Innovations in Nonlinear Acoustics*, Proceedings of the 17th International Symposium on Nonlinear Acoustics, edited by A. A. Atchley, V. W. Sparrow, and R. M. Keolian (AIP, New York, 2006), pp. 303–310.
- ¹²Yu. A. Pishchalnikov, O. A. Sapozhnikov, M. R. Bailey, J. C. Williams Jr., R. O. Cleveland, T. Colonius, L. A. Crum, A. P. Evan, and J. A. McAteer, "Cavitation bubble cluster activity in the breakage of kidney stones by lithotripter shockwaves," *J. Endourol.* **17**, 435–446 (2003).
- ¹³G. Russo and P. Smereka, "Kinetic theory for bubbly flow. I. Collisionless case," *SIAM J. Appl. Math.* **56**, 327–357 (1996).
- ¹⁴V. M. Teshukov and S. L. Gavriluk, "Kinetic model for the motion of compressible bubbles in a perfect fluid," *Eur. J. Mech. B/Fluids* **21**, 469–491 (2002).
- ¹⁵T. G. Leighton, *The Acoustic Bubble* (Academic, San Diego, 1994), Sec. 4.2.
- ¹⁶H. Lamb, *Hydrodynamics*, 6th ed. (Dover, New York, 1993), Art. 46.
- ¹⁷In Eqs. (2.1) and (2.2) of Harkin *et al.* (Ref. 3) the positions of the fourth-order terms $R_1^3 R_2^2 \dot{R}_2 / 2D^4$ and $R_2^3 R_1^2 \dot{R}_1 / 2D^4$ should be reversed. As a result, changes are required in the fourth-order terms of their Eqs. (3.3) and (3.5) for the radial motion. Sign changes are also required in the third-order terms of their Eqs. (3.5), (3.8), and (3.10) for the translational motion. However, subsequent calculations in the paper are based on equations in which terms above second order are discarded, and therefore the indicated changes are of no consequence to the conclusions in the paper.
- ¹⁸L. D. Landau and E. M. Lifshitz, *The Classical Theory of Fields*, 4th English ed. (Butterworth-Heinemann, Oxford, 2000), Sec. 42.
- ¹⁹L. D. Landau and E. M. Lifshitz, *Mechanics*, 3rd ed. (Butterworth-Heinemann, Oxford, 1993), Secs. 2 and 40.
- ²⁰A. J. Reddy and A. J. Szeri, "Coupled dynamics of translation and collapse of acoustically driven microbubbles," *J. Acoust. Soc. Am.* **112**, 1346–1351 (2002).
- ²¹J. Magnaudet and D. Legendre, "The viscous drag force on a spherical bubble with a time-dependent radius," *Phys. Fluids* **10**, 550–554 (1998).
- ²²S. L. Gavriluk and V. M. Teshukov, "Drag force acting on a bubble in a cloud of compressible spherical bubbles at large Reynolds numbers," *Eur. J. Mech. B/Fluids* **24**, 468–477 (2005).

Mode detection in turbofan inlets from near field sensor arrays

Fabrice O. Castres^{a)} and Phillip F. Joseph

Institute of Sound and Vibration Research, Southampton University, University Road, Highfield, Southampton SO17 1BJ, United Kingdom

(Received 26 May 2006; revised 22 November 2006; accepted 3 December 2006)

Knowledge of the modal content of the sound field radiated from a turbofan inlet is important for source characterization and for helping to determine noise generation mechanisms in the engine. An inverse technique for determining the mode amplitudes at the duct outlet is proposed using pressure measurements made in the near field. The radiated sound pressure from a duct is modeled by directivity patterns of cut-on modes in the near field using a model based on the Kirchhoff approximation for flanged ducts with no flow. The resulting system of equations is ill posed and it is shown that the presence of modes with eigenvalues close to a cutoff frequency results in a poorly conditioned directivity matrix. An analysis of the conditioning of this directivity matrix is carried out to assess the inversion robustness and accuracy. A physical interpretation of the singular value decomposition is given and allows us to understand the issues of ill conditioning as well as the detection performance of the radiated sound field by a given sensor array. © 2007 Acoustical Society of America. [DOI: 10.1121/1.2427124]

PACS number(s): 43.28.Py, 43.20.Ye, 43.20.Mv [NX]

Pages: 796–807

I. INTRODUCTION

The detection of the radiated modes from an aircraft engine can help in characterizing the in-duct sound field. This information provides a better understanding of noise generation mechanisms in the engine, and helps to develop strategies to control the radiated sound field. The knowledge of the modal content of the broadband noise generated by ducted fans is also very useful for determining the most appropriate mode distribution model for duct liner predictions and for sound power measurements of the radiated sound field. However, it is only in the last 10 years that techniques concerning the detection of modes radiated by a turbofan inlet have been addressed. This is perhaps because such techniques require the use of a large number of microphones resulting in a large number of simultaneous acquisition channels. These have only been available fairly recently. This paper is concerned with the detection of the amplitudes of the radiated modes from acoustic pressure measurements made in the radiated near field, for example, on the turbulence control screen (TCS). The TCS, shown in Fig. 1, consists of a spherical porous structure which is attached to the static inlet flare of the test engine for smoothing the ingested flow during ground tests. It offers a convenient platform for permanently locating microphones to deduce broadband mode amplitudes. The first documented approach dealing with the inversion of mode amplitudes using pressure measurements in the near field was performed on a circular hoop microphone array by Thomas *et al.*¹ and extended by Farasat, Nark, and Russel.² Their approach consisted of applying Fourier analysis of the far-field pressure in the azimuthal direction to deduce the spinning mode amplitudes. This circular sensor array was then rotated and the measurements

repeated. The radial modes within each spinning mode were then deduced by inverting a system of linear equations relating the pressure measurements to the mode amplitudes. While the conditioning of the matrix inverted was investigated and their technique was demonstrated to reliably detect radiated mode amplitudes, it requires an extensive number of measurements and it is only feasible for tonal noise and does not readily allow for the inversion of broadband mode amplitudes.

Another approach aimed at the inversion of duct mode amplitudes from TCS measurements is by Lan *et al.*³ They distributed an array of 40 microphones, which consisted of four rings of ten nonuniformly spaced microphones in each ring. Their approach was to ascertain, by computer simulation, microphone positions on the TCS for which the directivity matrix to be inverted is orthogonal so that, in effect, each microphone senses only one mode. The inversion of the directivity matrix in this case is then trivial and likely to be well conditioned. While the number of microphones required in this approach is equal to the number of modes to be inverted, the approach has a disadvantage that these microphone positions are difficult to find at any single frequency and probably impossible to obtain over a band of frequencies.

In this paper, the radiation problem from a ducted fan inlet is analyzed by expressing the sound field radiating from the inlet as a modal expansion, which involves modal directivity functions weighted by the corresponding amplitudes. A model directivity matrix is then inverted, which, together with the near field pressure measurements, is used to determine directly the amplitudes of the modes generated by the ducted fan inlet. The technique is readily extended to broadband noise. Such an inverse problem is ill posed and therefore its robustness to inaccuracies in the predicted model directivity matrix and in the pressure measurements is an essential issue to be considered. Fundamental modal radia-

^{a)}Author to whom correspondence should be addressed. Electronic mail: fc@isvr.soton.ac.uk



FIG. 1. (Color online) Turbulence control screen attached on a Rolls Royce Trent 700 during ground testing.

tion properties that affect the inversion robustness and hence the inversion accuracy are investigated in this paper. A physical interpretation of the singular value decomposition (SVD) is also given, which enables the cause of ill conditioning and the coupling between the radiated sound field and the measurement locations to be understood.

The paper begins with the theoretical background of duct mode radiation and a discussion of the SVD of the modal radiation problem. Section III deals with the inverse problem for the least square duct mode amplitudes and defines the perturbation bound which enables the error found in the least square solution due to noise contaminating the measurements to be assessed. Section IV investigates the conditioning of the inverse technique using a simple analytical case which involves the inversion of three modes from pressure measurements at three microphone positions. Section V gives an interpretation of the SVD of the directivity matrix, which describes the coupling between sensor geometry and modal radiation properties. Finally, this paper investigates a regularization technique to enhance the inversion conditioning.

II. MODAL RADIATION PROBLEM

At a single frequency, the sound field radiated at a point in space $\mathbf{r}=(r, \theta, \varphi)$ from a cylindrical duct of radius a may be written as the sum of modal components

$$p(\mathbf{r}) = \sum_{m=-\infty}^{+\infty} \sum_{n=1}^{+\infty} a_{mn} D_{mn}(\mathbf{r}), \quad (1)$$

where $D_{mn}(\mathbf{r})$ is the radiation directivity factor and a_{mn} is the complex pressure amplitude of a mode of spinning mode number m and radial mode number n , $k=\omega/c$ is the free space wave number, where c is the speed of sound. A good approximation to D_{mn} at radiation angles not too close to the sidelines ($\varphi < 70^\circ$) may be derived by the 1st Rayleigh integral as follows:

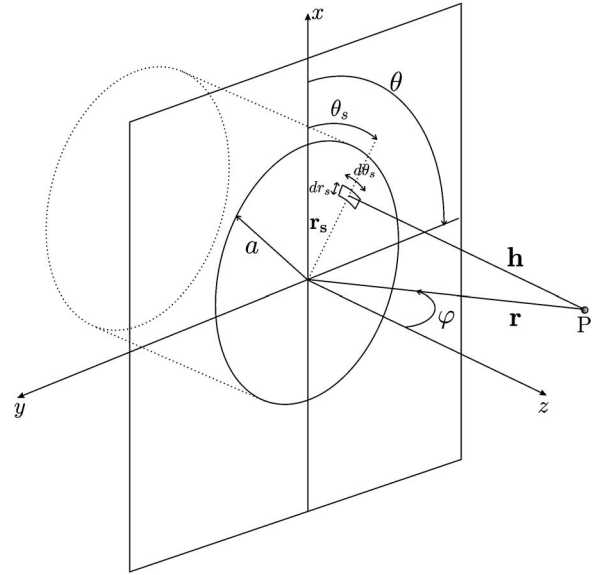


FIG. 2. Cylindrical coordinate system for inlet duct analysis and spherical coordinate system for radiation analysis.

$$D_{mn}(\mathbf{r}) = j \frac{k \sqrt{1 - \alpha_{mn}^2}}{2\pi} \int_S \Psi_{mn}(\mathbf{r}_s) \frac{e^{-jk h(\mathbf{r}|\mathbf{r}_s)}}{h(\mathbf{r}|\mathbf{r}_s)} r_s dr_s d\theta_s, \quad (2)$$

where h is the distance between the point $\mathbf{r}_s=(r_s, \theta_s)$ on the duct cross section and the location \mathbf{r} on the TCS (i.e., see Fig. 2), and is given by

$$h(\mathbf{r}|\mathbf{r}_s) = r \sqrt{1 + \left(\frac{r_s}{r}\right)^2 - 2 \frac{r_s}{r} \sin \varphi \cos(\theta - \theta_s)} \quad (3)$$

and where α_{mn} is the modal cut-on ratio defined by

$$\alpha_{mn} = \frac{\kappa_{mn}}{k}, \quad (4)$$

where κ_{mn} is the transverse modal wave number. Note that $\alpha_{mn} \mapsto 0$ for modes excited well above their cut-on frequencies and $\alpha_{mn} \mapsto 1$ as the cut-on frequency is approached from above. In the case of hard-walled circular duct, the mode shape functions are given by

$$\Psi_{mn}(\mathbf{r}_s) = \frac{1}{\sqrt{\Lambda_{mn}}} J_m(\kappa_{mn} r_s) e^{-jm\theta_s}, \quad (5)$$

where $J_m(x)$ is the Bessel function of first kind of order m and Λ_{mn} is chosen to ensure the normalization condition over the duct cross-section S

$$\frac{1}{S} \int_S |\Psi_{mn}(\mathbf{r}_s)|^2 dS = 1. \quad (6)$$

In this paper, Eq. (1) is restricted to cut-on modes only (i.e. $0 \leq \alpha_{mn} \leq 1$) and can now be expressed in matrix form

$$\mathbf{p} = \mathbf{D} \mathbf{a}, \quad (7)$$

where \mathbf{p} is a complex vector of radiated acoustic pressures at K sensors, \mathbf{a} is a complex vector of L modal amplitudes, and \mathbf{D} is the modal directivity matrix and contains the radiation properties of L modes at K sensor positions on the TCS.

Note the presence of the factor $\sqrt{1-\alpha_{mn}^2}$ in Eq. (2) for the modal directivity function, which suggests that modal radiation vanishes as cut-on is approached ($\alpha_{mn} \rightarrow 1$). This behavior will be shown to be the cause of ill conditioning of the inverse problem at frequencies close to the modal cut-on frequencies.

III. INVERSE PROBLEM FOR DUCT MODE AMPLITUDES

A. Least square estimate of mode amplitudes

A vector $\hat{\mathbf{p}}$ of K pressure measurements may be expressed as the sum of the modeled pressures given by Eq. (7) and a vector \mathbf{n} whose elements represent the departure of the measurements from the model and may also include, for example, the effect of contaminating noise at the sensors. Thus,

$$\hat{\mathbf{p}} = \mathbf{D}\mathbf{a} + \mathbf{n}. \quad (8)$$

We seek the vector of modal amplitudes $\hat{\mathbf{a}}$ that ensures the best least squares fit of the modeled acoustic pressures to the measured pressure data, i.e., that is which minimizes $\|\hat{\mathbf{p}} - \mathbf{D}\mathbf{a}\|_2^2$. The least squares solution $\hat{\mathbf{a}}$ minimizes the following cost function

$$J = \sum_{k=1}^K |n_k(\omega)|^2 = \mathbf{n}^H \mathbf{n} \quad (9)$$

such that $\partial J / \partial \mathbf{a} = 0$ is given by

$$\hat{\mathbf{a}} = \mathbf{D}^+ \hat{\mathbf{p}}, \quad (10)$$

where \mathbf{D}^+ is the pseudo-inverse of the modal directivity matrix \mathbf{D} given by

$$\mathbf{D}^+ = [\mathbf{D}^H \mathbf{D}]^{-1} \mathbf{D}^H, \quad (11)$$

where the superscript “**H**” denotes the Hermitian transpose operator. Eq. (10) can be readily extended for broadband sound fields. The least squares estimate for the cross-spectral matrix of mode amplitudes is given by

$$\mathbf{S}_{\hat{\mathbf{a}}\hat{\mathbf{a}}} = \lim_{T \rightarrow \infty} E \left[\frac{1}{T} \hat{\mathbf{a}} \hat{\mathbf{a}}^H \right] = \mathbf{D}^+ \mathbf{S}_{\hat{\mathbf{p}}\hat{\mathbf{p}}} \mathbf{D}^H, \quad (12)$$

where the $\mathbf{S}_{\hat{\mathbf{p}}\hat{\mathbf{p}}}$ is the cross-spectral matrix of pressure measurements defined by

$$\mathbf{S}_{\hat{\mathbf{p}}\hat{\mathbf{p}}} = \lim_{T \rightarrow \infty} E \left[\frac{1}{T} \hat{\mathbf{p}} \hat{\mathbf{p}}^H \right]. \quad (13)$$

Note that when the number of sensors equals the number of possible radiated modes (i.e., \mathbf{D} is square), the solution reduces to $\hat{\mathbf{a}} = \mathbf{D}^{-1} \hat{\mathbf{p}}$, which is the minimum number of sensors required for the inversion to be performed. No solution exists for the modal amplitudes for the case of an underdetermined system (i.e., when the number of sensors is smaller than the number of radiated modes $K < L$) unless some further constraint on the solution is imposed. This situation will not be studied in this paper since the inverse technique presented in this article only accounts for a system of overdetermined equations given in Eq. (7) (i.e., $K > L$).

Later it will be shown to be useful to express \mathbf{D} in terms of its singular values and singular vectors. The singular value decomposition (SVD) of \mathbf{D} is given by

$$\mathbf{D} = \mathbf{U} \mathbf{\Sigma} \mathbf{V}^H, \quad (14)$$

where \mathbf{U} is a $K \times K$ unitary matrix that contains the left singular vectors of \mathbf{D} equivalent to the eigenvectors of the Hermitian matrix $\mathbf{D}^H \mathbf{D}$, and \mathbf{V} is a $L \times L$ unitary matrix that contains the right singular vectors equivalent to the eigenvectors of the Hermitian matrix $\mathbf{D} \mathbf{D}^H$ and $\mathbf{\Sigma}$ is a $K \times L$ diagonal matrix of L real singular values σ_i so that $\mathbf{\Sigma}^+ = \mathbf{\Sigma}^{-1}$. These singular values are the square root of the eigenvalues of the Hermitian matrix $\mathbf{D}^H \mathbf{D}$.

Introducing Eq. (14) into Eq. (10) leads to the least squares solution in the form

$$\hat{\mathbf{a}} = \mathbf{V} \mathbf{\Sigma}^+ \mathbf{U}^H \hat{\mathbf{p}}. \quad (15)$$

B. Robustness of inversion

Even though the system of equations is assumed here to be overdetermined, similar problems to that of an underdetermined system may arise if the sensor array is unable to detect sufficient information relating to all modes to be inverted. This situation can occur in two ways:

1. The directivity patterns of different radiated modes are similar, for example, if their main radiation lobes are at the same polar angle (i.e., with similar cutoff ratios) so that their contribution to each of the many sensors will be similar. This leads to redundant, and therefore insufficient, information with which to perform the inversion. This behavior can be improved by increasing the number of sensors and improving the array geometry.
2. The modal radiation is inefficient and consequently the radiated pressures tend to zero as cut-on is approached. The behavior cannot be avoided.

In these two cases, the exact least squares solution to this problem of Eq. (15) is still valid, but the inversion accuracy is highly sensitive to the presence of noise and modeling errors. A suitable parameter for evaluating this sensitivity is the condition number of the modal directivity matrix \mathbf{D} . The condition number $\kappa(\mathbf{D})$ for a rectangular matrix $\mathbf{D} \in \mathbb{C}^{K \times L}$ is defined to be⁴

$$\kappa(\mathbf{D}) = \|\mathbf{D}\|_2 \|\mathbf{D}^+\|_2. \quad (16)$$

The condition number bounds the error $\mathbf{e} = \hat{\mathbf{a}} - \mathbf{a}$ in the solution due to the noise \mathbf{n} at the sensors

$$\frac{\|\mathbf{e}\|_2}{\|\hat{\mathbf{a}}\|_2} \leq \kappa(\mathbf{D}) \frac{\|\mathbf{n}\|_2}{\|\hat{\mathbf{p}}\|_2}. \quad (17)$$

Thus a large condition number will greatly amplify small perturbations in \mathbf{p} (i.e., noise) and hence implies an ill-conditioned inversion. In practical terms contaminating noise will have a disproportionately large effect on the solution for the modal amplitude vector $\hat{\mathbf{a}}$ if the matrix is “badly conditioned” with large condition number $\kappa(\mathbf{D})$. The acceptable value of the condition number is subjective and depends on the noise that contaminates the measurements and the result-

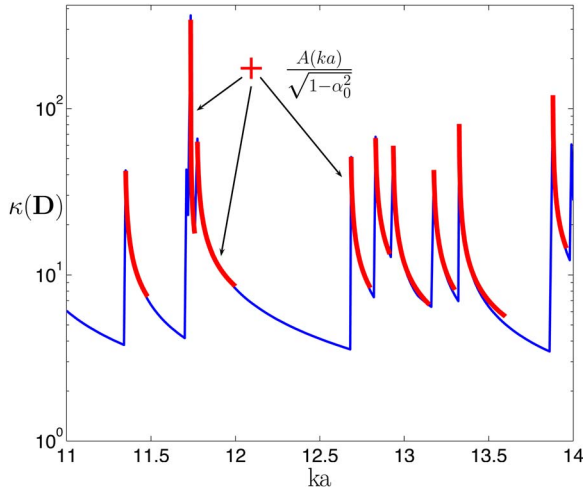


FIG. 3. (Color online) Variation with frequency of the condition number of \mathbf{D} accounting for the inversion of all cut-on modes by a geodesic sensor array. The function given by Eq. (24) is fitted at frequencies close to cut-on frequencies.

ing error in the mode amplitude reconstruction. The condition number can be related to the maximum and minimum singular values σ_{\max} and σ_{\min} of \mathbf{D} by

$$\kappa(\mathbf{D}) = \frac{\sigma_{\max}}{\sigma_{\min}}. \quad (18)$$

The condition number is the principal quantity used by the authors to investigate guidelines on sensor array geometries to be employed on the TCS that affords robust inversion. It was shown in Castres, Joseph and Astley⁵ that the condition number varies significantly with the number of sensors on the TCS and its positioning. It was also shown that at any single frequency a number of sensors satisfying $K/L \approx 1.3$ with a reasonably uniform distribution of microphones, both in the azimuthal and polar directions, were important requisites for robust inversion.

In this paper, numerical simulation results will be presented for a geodesic sensor array of 126 microphones, which leads to low values of the condition number.⁶ A geodesic array is one in which sensors are located on the vertices of a geodesic dome^{7,8} and so offers a perfectly uniform distribution of microphones in both angles on the TCS and $K/L \approx 1.15$ at $ka=20$.

Figures 3 and 4 show the variation of condition number $\kappa(\mathbf{D})$ with the nondimensional frequency ka . The κ spectrum contains a number of peaks coinciding with the modal cut-on frequencies. Away from the cut-on frequencies, κ increases slowly with ka . The reasons for this behavior are discussed in the next section.

IV. ANALYTICAL BEHAVIOR OF $\kappa(\mathbf{D})$

The behavior observed in Fig. 3 can be explained from the analysis of the simple case involving the inversion of three modes by three microphone measurements. Using the far-field approximation, Eq. (2) can be written analytically in the form⁹

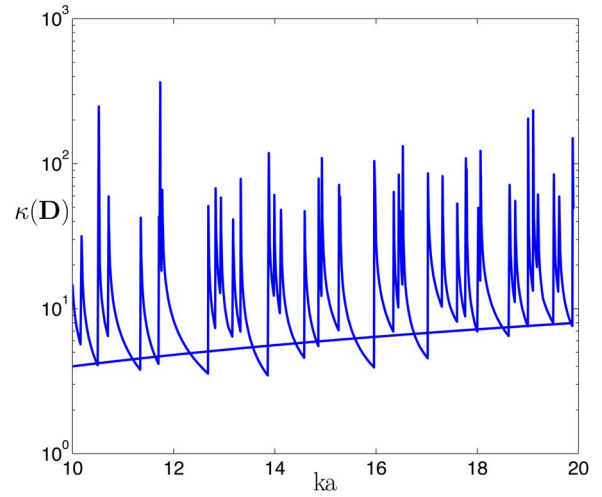


FIG. 4. (Color online) Variation with frequency of the condition number of \mathbf{D} accounting for the inversion of all cut-on modes by a geodesic sensor array. The function given by Eq. (31) follows the overall variation between cut-on frequencies.

$$D_{mn}(\mathbf{r}) = \sqrt{1 - \alpha_{mn}^2} F_{mn}(\mathbf{r}), \quad (19)$$

where

$$F_{mn}(\mathbf{r}) = j^{m+1} \frac{e^{-jkr}}{r} \frac{a \sin \varphi J'_m(ka \sin \varphi)}{\sqrt{\Lambda_{mn}} \alpha_{mn}^2 - \sin^2 \varphi}. \quad (20)$$

Here, $J'_m(x)$ is the derivative of the Bessel function with respect to its argument. The peaks of the condition number in Fig. 3 are caused by the presence of modes excited at their cutoff frequencies. Apart for axisymmetric modes (i.e., $m=0$), the modes occur in pairs such that for every (m,n) mode, there is a corresponding $(-m,n)$ mode. Consider the case in which there are just three modes. Two of these modes, a_1 and a_2 , are degenerate in the sense that they have equal and opposite spinning mode number m and hence $\alpha_{mn} = \alpha_{-mn} = \alpha_0$. These two modes are assumed to be excited close to their cut-on frequency. The third mode, a_3 , is assumed to be excited well away from its cut-on frequency and hence $\sqrt{1 - \alpha_{mn}^2} \approx 1$. Equation (7) for this case may be written as

$$\begin{bmatrix} p_1 \\ p_2 \\ p_3 \end{bmatrix} = \begin{bmatrix} \sqrt{1 - \alpha_0^2} F_{11} & \sqrt{1 - \alpha_0^2} F_{12} & F_{13} \\ \sqrt{1 - \alpha_0^2} F_{21} & \sqrt{1 - \alpha_0^2} F_{22} & F_{23} \\ \sqrt{1 - \alpha_0^2} F_{31} & \sqrt{1 - \alpha_0^2} F_{32} & F_{33} \end{bmatrix} \begin{bmatrix} a_1 \\ a_2 \\ a_3 \end{bmatrix}. \quad (21)$$

Following Eq. (18) and that the singular values σ_i of \mathbf{D} are related to the eigenvalues λ_i of $\mathbf{D}^H \mathbf{D}$ by $\lambda_i = \sigma_i^2$, the condition number $\kappa(\mathbf{D})$ can be rewritten as

$$\kappa(\mathbf{D}) = \sqrt{\frac{\lambda_{\max}}{\lambda_{\min}}}, \quad (22)$$

where λ_{\max} and λ_{\min} may be deduced from the following eigenvalue equation

$$\det(\mathbf{D}^H \mathbf{D} - \lambda \mathbf{I}) = 0, \quad (23)$$

where \mathbf{I} is the identity matrix. It is shown in the appendix that for this three-mode inversion the behavior of $\kappa(\mathbf{D})$ in the vicinity of cut-on frequencies is of the form

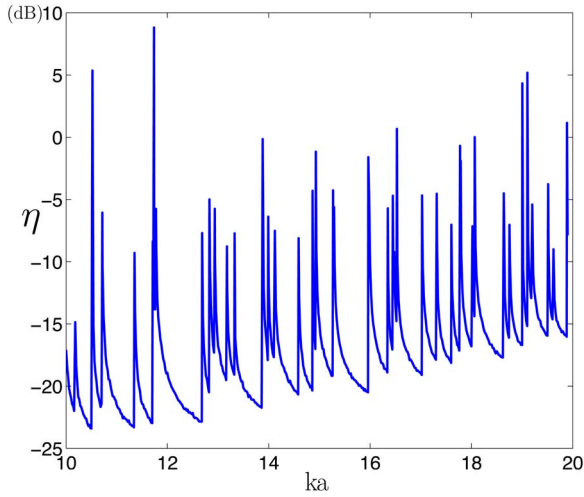


FIG. 5. (Color online) Variation with frequency of the reconstruction accuracy parameter η .

$$\kappa(\mathbf{D}) \mapsto \frac{A(ka)}{\sqrt{1 - \alpha_0^2}}, \quad \alpha_0 \mapsto 1, \quad (24)$$

where $A(ka)$ is a complicated factor involving combinations of Bessel functions and is a slowly varying function of frequency. Equation (24) is plotted in Fig. 3 for a number of modes close to their cut-on frequencies, where A is adjusted to give best fit to the exact variation in each case. This asymptotic dependence is found to be in close agreement with the exact variation of $\kappa(\mathbf{D})$ at frequencies in the vicinity of the cut-on frequencies. Even though this analysis is carried out for the inversion of just three modes with three sensors, Eq. (24) also applies to the inversion of a much larger number of modes and microphones. The singular behavior of κ poses a particular problem at high frequencies when the modal cut-on frequencies become increasingly closer together. The effect of measurement noise on the inversion accuracy of the modal amplitudes, in dB, can be quantified from

$$\eta = 20 \log_{10} \left(\frac{\|\hat{\mathbf{a}} - \mathbf{a}\|_2}{\|\mathbf{a}\|_2} \right). \quad (25)$$

Clearly, this parameter cannot be evaluated in practice since \mathbf{a} cannot be known *a priori*. The reconstruction accuracy parameter η versus frequency for a set of modes with unit amplitudes and a signal to noise ratio (SNR) of 20 dB is shown in Fig. 5. It is seen that at low ka , η is of similar values to the SNR. This is because as $ka \rightarrow 0$ and hence $K/L \rightarrow \infty$, the inversion of the modal amplitudes tends to be exact. Only the noise is therefore not inverted and hence $\eta \rightarrow \text{SNR}$. Consistent with Fig. 4, the reconstruction accuracy is poor at the cut-on frequencies.

We now investigate the frequency variation of $\kappa(\mathbf{D})$ at frequencies in between the cut-on frequencies. In the absence of flow, the number of modes L with cut-on frequencies below a frequency ka is approximately given by¹⁰

$$L(ka) \approx \frac{1}{2}ka + \left(\frac{1}{2}ka \right)^2. \quad (26)$$

The number of propagating modes ℓ within a unit frequency band is therefore given by

$$\ell(ka) = \frac{L(ka + \delta ka) - L(ka)}{\delta ka} \approx \frac{dL}{d(ka)} \approx ka. \quad (27)$$

It therefore follows that the average frequency separation between adjacent cut-on modes is

$$\Delta ka \approx \frac{1}{ka}. \quad (28)$$

Consider a single mode excited at its cut-on at frequency, $ka = \kappa_{mn}a$, such that $\alpha(ka) = 1$. Its cut-on ratio at the next average cut-on frequency $ka + \Delta ka$, from Eq. (28), is therefore given by

$$\alpha_{mn}(ka + \Delta ka) = \frac{\kappa_{mn}a}{ka + \Delta ka} \approx \frac{1}{1 + (1/ka)^2}. \quad (29)$$

Substituting Eq. (29) into Eq. (24) gives

$$\kappa(\mathbf{D})|_{ka+\Delta ka} \approx \frac{A(ka)}{[1 - (1 + (ka)^{-2})^{-2}]^{1/2}} \quad (\alpha_{mn} \neq 1). \quad (30)$$

Equation (30) can be written as a series expansion in ka , which to leading term, is of the form

$$\begin{aligned} \kappa(\mathbf{D})|_{ka+\Delta ka} &\approx \frac{A(ka)}{[1 - (1 - 2(ka)^{-2})]^{1/2}} \\ &\approx A(ka) \cdot ka \quad (\alpha_{mn} \neq 1). \end{aligned} \quad (31)$$

Putting $A(ka) = \text{constant}$, the function given by Eq. (31) is shown in Fig. 4 and is in good agreement with the variation of the lower envelope of $\kappa(\mathbf{D})$ versus frequency. At frequencies not too close to a cut-on frequency, the general trend in the condition number therefore increases as ka , which is slow compared to the rapid variation close to the cut-on frequencies.

V. INTERPRETATION OF POOR CONDITIONING BY THE USE OF THE SINGULAR VALUE DECOMPOSITION OF THE DIRECTIVITY MATRIX

The analysis of radiation problems using the SVD have been extensively investigated¹¹⁻¹⁶ by expressing the radiated pressure in terms of the velocity distribution on the source plane and a Green function matrix. In this paper, the radiation problem from a ducted fan inlet is analyzed using a different approach since the radiated pressure is directly related to mode amplitudes via a directivity matrix. The SVD of the directivity matrix \mathbf{D} is useful in providing greater insight into the physical cause of ill-conditioned mode inversion at frequencies in the vicinity of the cut-on frequencies. Introducing Eq. (14) into Eq. (7) and pre-multiplying by the unitary matrix \mathbf{U} (i.e. $\mathbf{U}^H \mathbf{U} = \mathbf{I}$) yields

$$\mathbf{U}^H \mathbf{p} = \mathbf{\Sigma} \mathbf{V}^H \mathbf{a}. \quad (32)$$

The unitary properties of \mathbf{U} and \mathbf{V} enable the investigation of the radiated pressures and mode amplitudes into another set

of basis functions. Denoting $\tilde{\mathbf{p}} = \mathbf{U}^H \mathbf{p}$ as a vector of transformed complex pressures and $\tilde{\mathbf{a}} = \mathbf{V}^H \mathbf{a}$ as a vector of transformed mode amplitudes, Eq. (32) shows that

$$\tilde{\mathbf{p}} = \tilde{\Sigma} \tilde{\mathbf{a}}. \quad (33)$$

The vectors of transformed mode amplitudes and acoustic pressures are related by the singular values of the directivity matrix. Thus $\tilde{\mathbf{p}}$ and $\tilde{\mathbf{a}}$ are both linear combinations of their respective original vectors \mathbf{p} and \mathbf{a} . These transformed vectors depend on the TCS sensor array and therefore determine how the modal distribution over the duct outlet is coupled with the sound field detected by the TCS sensor array. The right singular vectors contained in \mathbf{V} possess information about the modal distribution over the duct outlet cross section. Similarly the left singular vectors contained in the unitary matrix \mathbf{U} possess information relating to the radiated sound field. It should be noted that the transformation process associated with the SVD is dependent upon the geometry of the TCS array. It is therefore important to investigate the behavior of the singular values as well as the right and left singular vectors of the directivity matrix. The physical interpretation of these quantities is discussed below.

A. Interpretation of singular values

We now demonstrate that the singular values of \mathbf{D} , which in Sec. III B have been shown to be fundamental in determining the robustness of the inversion, relate directly to the radiation efficiency of the transformed modes. We recall that the time-averaged radiated acoustic power is approximately given by

$$W = \frac{1}{2\rho c} \mathbf{p}^H \mathbf{p} \delta S, \quad (34)$$

where ρ and c are the air density and speed of sound and δS is the average surface area occupied by a single microphone on the TCS. Noting that $\mathbf{p} = \mathbf{U} \tilde{\mathbf{p}}$, the unitary properties of the matrix \mathbf{U} lead to the expression for the radiated power of the form

$$W = \frac{1}{2\rho c} \tilde{\mathbf{p}}^H \tilde{\mathbf{p}} \delta S. \quad (35)$$

Equations (34) and (35) are analogous to Parseval's theorem in spectral analysis. Introduction of Eq. (33) into Eq. (35) gives

$$W = \frac{1}{2\rho c} \tilde{\mathbf{a}}^H \tilde{\Sigma}^T \tilde{\Sigma} \tilde{\mathbf{a}} \delta S \quad (36)$$

$$= \frac{\delta S}{2\rho c} \sum_{i=1}^L |\tilde{a}_i|^2 \sigma_i^2. \quad (37)$$

Equation (36) suggests that the total mean radiated acoustic power can be written as the sum of the acoustic powers \tilde{W}_i in each of the transformed modes

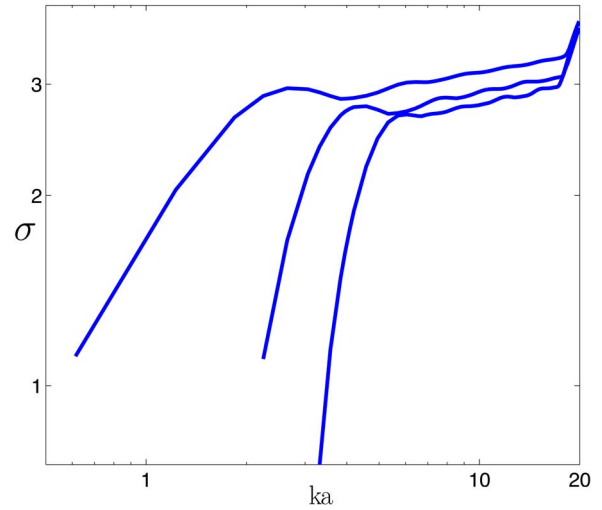


FIG. 6. (Color online) Variation with frequency of the three largest singular values for a geodesic sensor array.

$$W = \sum_{i=1}^L \tilde{W}_i. \quad (38)$$

The singular values σ_i may therefore be interpreted as a measure of radiation efficiencies of the transformed modes

$$\sigma_i^2 = \frac{\rho c \tilde{W}_i}{\tilde{a}_i^2 \delta S}, \quad (39)$$

where $\tilde{a}_i^2 = (1/2) |\tilde{a}_i|^2$. Figure 6 shows the variation frequency of the three largest singular values. These maximum singular values describe the radiation efficiency of transformed modes and have similar trend to the radiation efficiency of acoustic duct modes as shown in Morfey.¹⁷ On the other hand, the variation with frequency of the smallest singular value shown in Fig. 7 has a totally different behavior. This singular value decreases significantly at cut-on frequencies. This clearly demonstrates that this minimum singular value is responsible for the large order of magnitudes of the condition number at cut-on frequencies as shown in Fig. 4. The

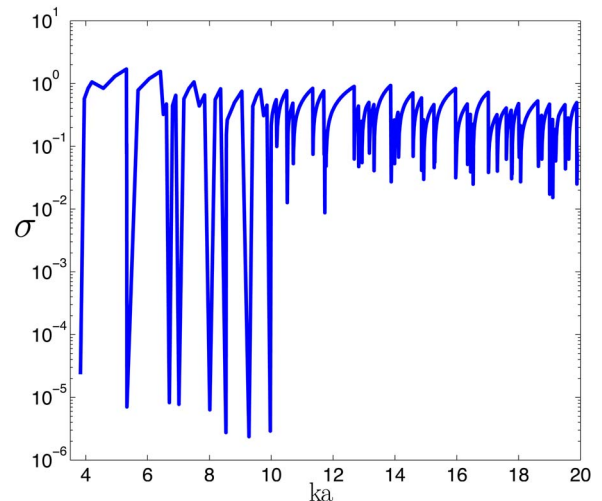


FIG. 7. (Color online) Variation with frequency of the smallest singular value for a geodesic sensor array.

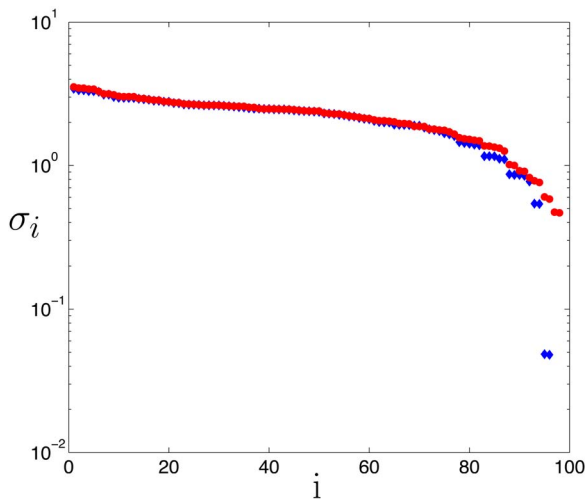


FIG. 8. (Color online) Spectrum of singular values for a geodesic array diamonds at the cut-on frequency $ka=18.64$ and circles away from cut-on frequency $ka=19$.

radiation efficiency of the transformed mode associated with this singular value is indeed very low at cut-on frequencies. The distribution of singular values is also important in determining which transformed modes dominate the sound field detected by the TCS array. Robust inversion will be achieved if the modal information detected by the TCS array is evenly distributed across these transformed mode amplitudes. The ideal case from Eq. (18) is that all singular values are equal and hence the condition number is equal to unity. Figure 8 shows the spectrum of singular values of the modal directivity matrix for a geodesic sensor array at a frequency very close to a cut-on frequency $ka=18.64$ (i.e., that is $\alpha=0.9999$) and at a frequency away from this cut-on frequency $ka=19$. At the cut-on frequency, the spectrum displays a gradual decay of singular values followed by a well-defined gap in the magnitudes of the very small σ values. At the frequency away from the cut-on frequency, a similar gradual decay in the spectrum of singular values can be observed but the magnitude of the very small σ values has been increased and the σ spectrum is now smooth. The gradual decay of the singular values is inherent in ill-posed problems. However, the well-defined gap found in the σ spectrum close to the cut-on frequency affects two singular values only. At frequencies away from the cut-on frequency, the modal information associated with these two very small singular values is no longer negligible. We now show below that each transformed mode associated with each singular value comprises comparatively few acoustic duct modes. This explains the reason for the different behavior in the singular value spectra shown in Fig. 8.

B. Interpretation of singular vectors

If \mathbf{v}_i denotes the i th column vector of the matrix \mathbf{V} , from Eqs. (32) and (33) the i th transformed mode amplitude is given by

$$\tilde{a}_i = \sum_{j=1}^L v_{ji}^* a_j. \quad (40)$$

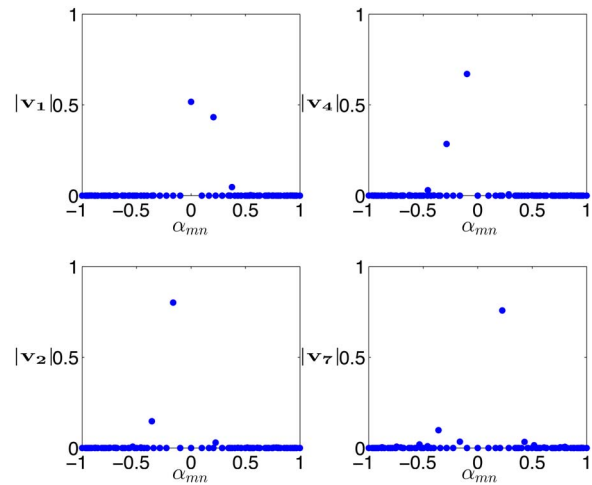


FIG. 9. (Color online) Content of acoustic modes within right singular vectors associated with large singular values at $ka=18.64$.

The j th element of the i th singular vector, v_{ji} , therefore quantifies the content of acoustic modes in the i th transformed mode. Thus only the first L transformed pressures contribute to the sound field. Acoustic modes associated with the first singular vector (i.e., with largest value σ_1) are those “best detected” by the TCS array. Conversely, the transformed mode associated with the smallest singular value σ_L is most weakly detected and is the cause of the poor conditioning of the inversion. It is therefore interesting to investigate the modal content of $\tilde{\mathbf{a}}$ to understand how acoustic modes are coupled with a particular sensor array as well as to understand which acoustic modes are responsible for ill conditioning. Figure 9 shows the modal content sorted with the cut-on ratio of the right singular vectors associated with large singular values (i.e., $i=1,2,4,7$) and Fig. 10 shows the modal content of the right singular vectors associated with the smallest singular values (i.e., $i=106, 107, 108, 109$) for a geodesic sensor array at $ka=18.64$ with 109 cut-on modes. Prior to analyzing the content of these singular vectors, it is important to note that, although such content differs with sensor arrays, the following properties are found with all the sensor ge-

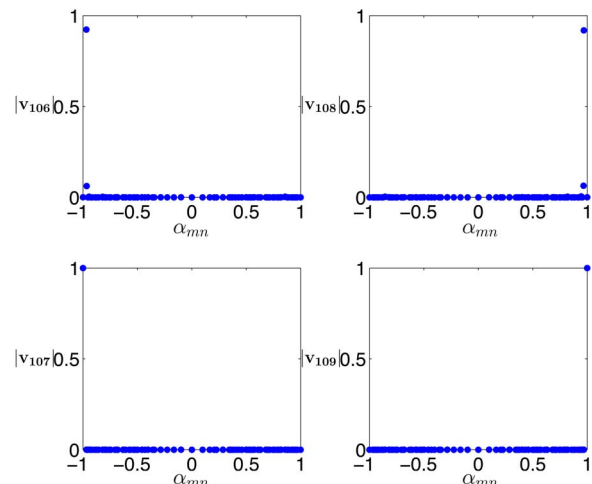


FIG. 10. (Color online) Content of acoustic modes within right singular vectors associated with small singular values at $ka=18.64$.

ometries studied by Castres, Joseph, and Astley.⁵ It is interesting to observe that each singular vector comprises only a few acoustic duct modes. Moreover, well cut-on modes are found within singular vectors associated with large singular values. Conversely, singular vectors associated with small singular values contain nearly cutoff modes. In particular, the singular vectors \mathbf{v}_{108} and \mathbf{v}_{109} associated with the two smallest singular values that are the cause of the ill conditioning (see Fig. 8) each contain only a single duct mode as shown in Fig. 10. These modes are found to be those with $\alpha=0.9999$.

By analogy with Eq. (40), the transformed mode shape functions over the duct cross section may be defined as follows:

$$\tilde{\psi}_i = \sum_{j=1}^L v_{ij}^* \psi_j. \quad (41)$$

With reference to Figs. 9(a) and 10(d), at $ka=18.64$, $\tilde{\Psi}_1$ is the mode shape function whose radiation is best detected by the sensor array while the radiation from $\tilde{\Psi}_{109}$ is the least well detected and hence is most sensitive to measurement noise. The transformed mode shape functions for a geodesic sensor array at $ka=18.64$ are shown in Figs. 11(a) and 12(a) for the 1st, 2nd, 4th and 7th largest singular values and the four smallest singular values, respectively. The radiation patterns of the transformed modes $i=1, 2$, and 4 have characteristics of monopolar, dipolar, and quadrupolar radiation, respectively, whereas $i=7$ has characteristics of higher order radiation. These modes are associated with the largest singular values and hence radiate with greatest efficiency. Conversely, the transformed modes $i=106 \rightarrow 109$ exhibit very high order radiation and therefore radiate very inefficiently. The contribution of these transformed mode shape functions to the overall sound field are represented by the transformed pressures, prescribed by the left singular vectors \mathbf{u}_i (i.e., the i th column vector of \mathbf{U}) and are shown in Figs. 11(b) and 12(b). From Figs. 11 and 12, there is a close relationship between the transformed mode shape functions defined in Eq. (41) and the left singular vectors \mathbf{u}_i .

VI. METHODS FOR IMPROVING INVERSION ROBUSTNESS

Previous sections have shown that modal inversion performed at frequencies close to the modal cut-on frequencies is very poorly conditioned. This results in poor reconstruction accuracy at these frequencies, as shown in Eq. (10). It is therefore necessary to constrain the solution to make it more stable to nonquantifiable errors and hence provide good inversion accuracy. The use of such procedures is aimed at constraining the original solution and is called regularization. The most common approach to regularization is to penalize the norm of the solution \mathbf{a} . This is called the Tikhonov regularization scheme. We seek the vector of modal amplitudes that ensures that $\|\hat{\mathbf{p}} - \mathbf{D}\mathbf{a}\|_2^2 + \beta\|\mathbf{R}\mathbf{a}\|_2^2$ is a minimum, i.e., $\delta J \delta \mathbf{a} = 0$, where J is the following cost function:

$$J = \sum_{k=1}^K |n_k(\omega)|^2 + \sum_{k=1}^P |y_k(\omega)|^2 = \mathbf{n}^H \mathbf{n} + \mathbf{y}^H \mathbf{y}, \quad (42)$$

where $\mathbf{y} = \sqrt{\beta} \mathbf{R}\mathbf{a}$ is the constraint on the magnitude of the solution and β is a specified weighting factor, often called the Tikhonov parameter. Here \mathbf{R} is the regularizing matrix that specifies the distribution of weighting between the various modes. If the constraint is applied uniformly on the solution, then $\mathbf{R} = \mathbf{I}$ and the Tikhonov regularization scheme is said to be in standard form. We have shown that the smallest singular values are due to modes very close to cut-off and are therefore very sensitive to measurement noise and modeling errors and consequently have a disproportionate influence on the solution, as shown in Eq. (15). As an attempt to prevent this from occurring, the following regularization matrix is defined:

$$\mathbf{R} = \begin{bmatrix} \mathbf{I}_{L-Q} & \mathbf{0} \\ \mathbf{0} & \mathbf{S}_Q \end{bmatrix} \quad \mathbf{S}_Q = \text{diag}(\mathbf{1}/\|\mathbf{D}_i\|). \quad (43)$$

Here, \mathbf{S}_Q is a diagonal matrix whose elements comprise the norm of the column vectors of \mathbf{D} for Q modes with $\alpha_i \geq 0.99$. Thus modes closest to cutoff are penalized most in the cost function since from Eq. (2), $\|\mathbf{D}_i\| \rightarrow 0$ as $\alpha_i \rightarrow 1$. The underlying idea of this scheme is that a regularized solution having a suitably small residual norm and satisfying the additional constraint will not deviate too far from the desired, unknown solution. It may be shown that the constrained least squares solution may be written as

$$\hat{\mathbf{a}}_{\mathbf{R}} = \mathbf{D}^{\#} \hat{\mathbf{p}}, \quad (44)$$

where

$$\mathbf{D}^{\#} = [\mathbf{D}^H \mathbf{D} + \beta \mathbf{R}^H \mathbf{R}]^{-1} \mathbf{D}^H. \quad (45)$$

The appropriate perturbation bound κ_{β} , which relates the error in the solution to errors found in the pressure measurements

$$\frac{\|\mathbf{e}\|}{\|\mathbf{a}\|} \leq \kappa_{\beta} \frac{\|\mathbf{n}\|}{\|\hat{\mathbf{p}}\|} \quad (46)$$

is now of the form^{18,19}

$$\kappa_{\beta} = \frac{\|\mathbf{D}\| \|\mathbf{R}^{-1}\|}{2\sqrt{\beta}}. \quad (47)$$

Since the constraint on the norm of the solution introduces some inaccuracies, the Hansen L-curve analysis²⁰ is performed to determine values of β that afford the best trade-off between the minimization of the residual error $\|\hat{\mathbf{p}} - \mathbf{D}\mathbf{a}\|$ and inaccuracies due to regularization. Figures 13 and 14 show the variation of κ and η before and after regularization, respectively. However, at frequencies at which Eq. (10) is well conditioned, the error found in the constrained least squares solution is larger than when unconstrained. Thus, regularization gives significant improvement in inversion accuracy at frequencies close to the cut-on frequencies and no improvement at frequencies well away from the cut-on frequencies.

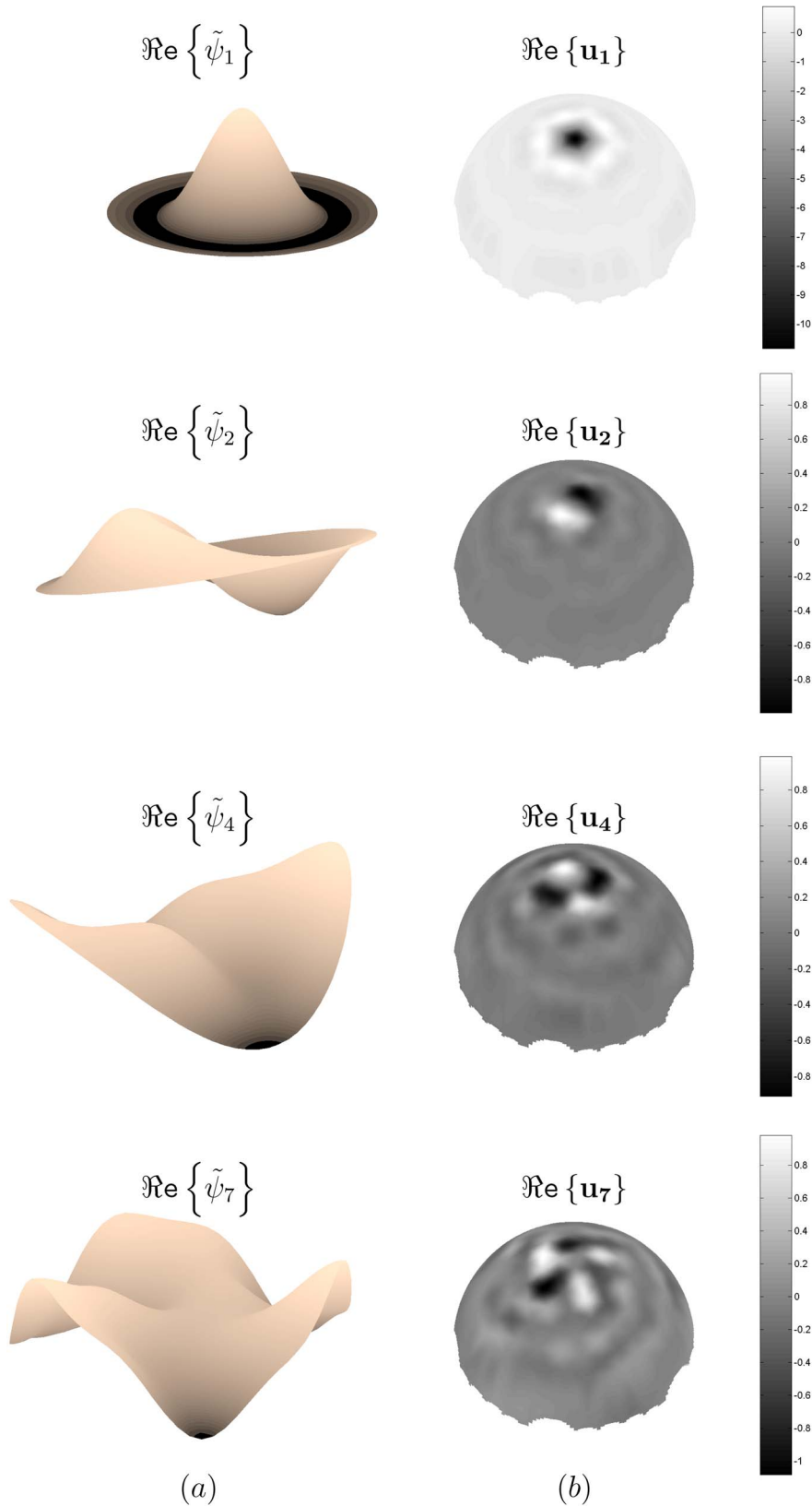


FIG. 11. (Color online) (a) Transformed mode shape functions as defined by Eq. (41) and (b) left singular vectors associated with the 1st, 2nd, 4th and 7th largest singular values.

VII. CONCLUSION

This paper has described an inverse technique for determining the least squares estimate of the mode amplitudes in a fan inlet from external pressure measurements. It was shown that the condition number of the modal directivity matrix to be inverted is an essential parameter in assessing

the robustness of this technique. Numerical simulations using a particular microphone arrangement on the TCS were performed to investigate the variation of the condition number of the directivity matrix over a broad range of frequencies. It was found that the mode inversion technique is highly sensitive to noise at the modal cut-on frequencies, which can

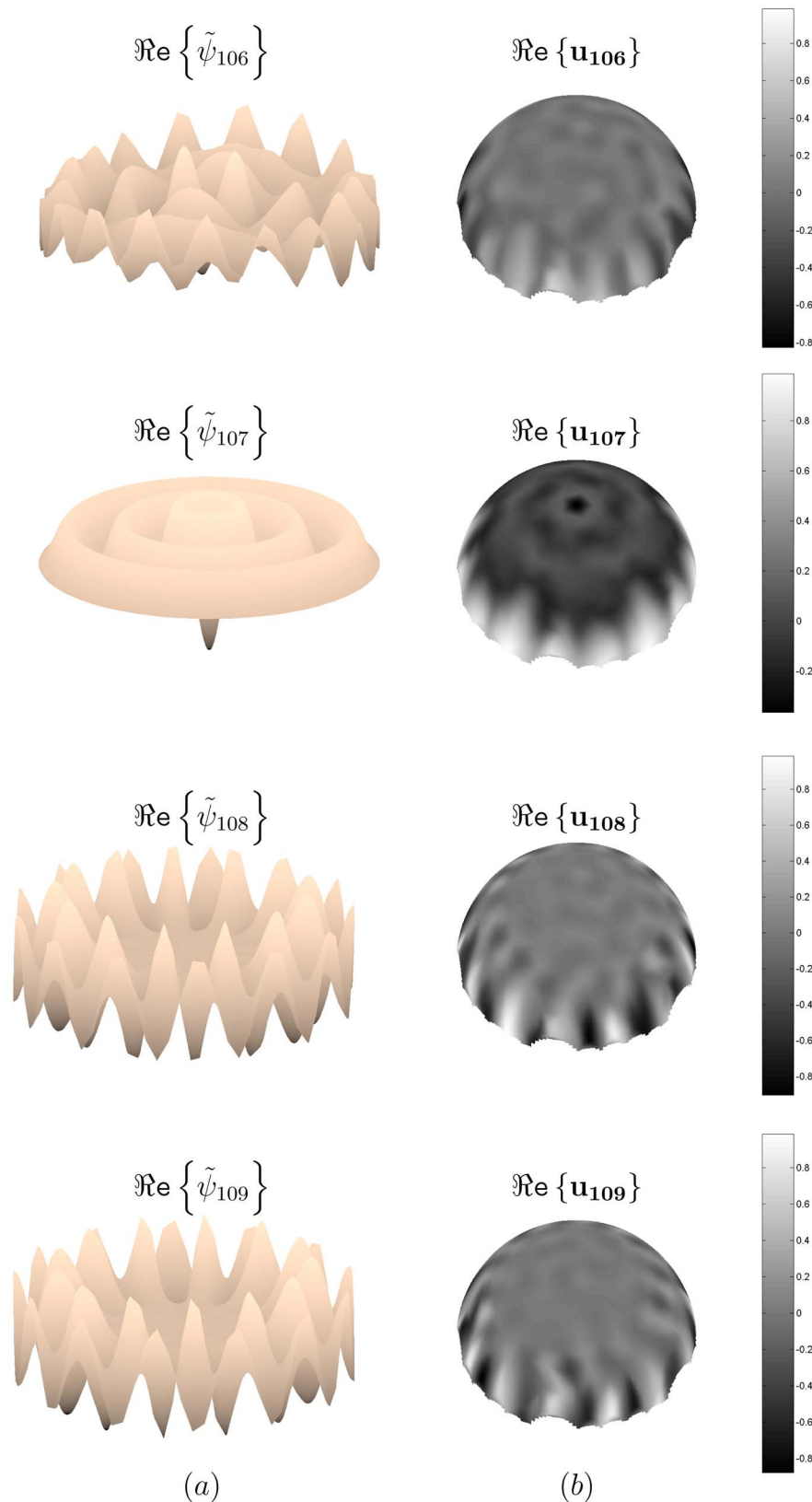


FIG. 12. (Color online) (a) Transformed mode shape functions as defined by Eq. (41) and (b) left singular vectors associated with the four smallest singular values.

be problematic at high frequencies when the modal cut-on frequencies become increasingly closer together. An analytical expression for the condition number in the simple case of inverting three modes by three microphones was investigated. It showed that the condition number is critically high at the cut-on frequencies, and increases slowly with fre-

quency between these cut-on frequencies. A reconstruction accuracy parameter has been defined to assess the inversion accuracy of the modal amplitudes. Although this parameter cannot be evaluated experimentally since it requires the *a priori* solution, it was shown to be consistent with the variations of the condition number of the directivity matrix. It was

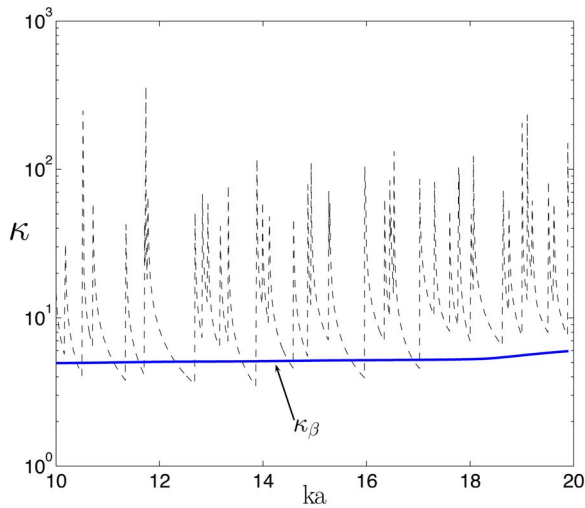


FIG. 13. (Color online) Variation with frequency of perturbation bounds for the unconstrained and the nonuniform constrained least squares solutions.

found that the modal inversion accuracy was poor in the vicinity of the modal cut-on frequencies. A physical interpretation of the SVD of the directivity matrix was also given in this paper. This has enabled an understanding of the reasons for the ill conditioning as well as the detection performance of the modal information radiated from the inlet by a given sensor array. It was shown to be useful to expand the radiated field at the sensors in terms of a new set of modes that are transformations of the original duct modes. Singular values were shown to give a measure of the radiation efficiencies of the transformed modes. Each of these transformed modes was found to have a specific content of acoustic modes which varies with frequency and sensor positioning. This content therefore determines the coupling between the radiated modal information and the sensor positioning. It was shown that efficiently radiating transformed modes contain well cut-on modes while inefficient ones contain modes close to cut-off. Transformed mode shape functions were defined and were found to have very efficient radiation patterns of monopole, dipole, and quadrupole behaviors. These trans-

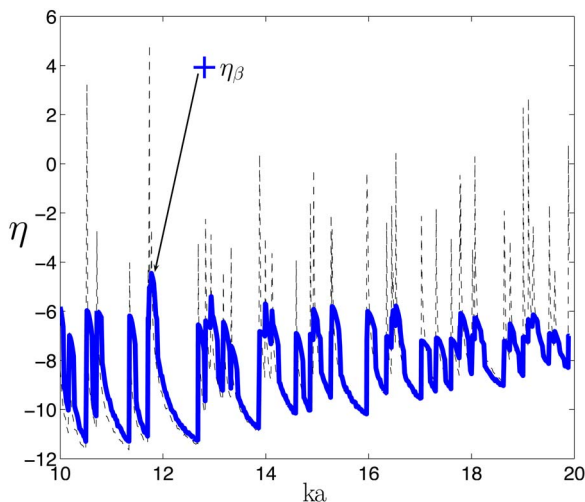


FIG. 14. (Color online) Variation with frequency of the reconstruction accuracy for the unconstrained and the nonuniform constrained least squares solutions.

formed mode shape functions were also found to be closely related to the transformed pressures prescribed by the left singular vectors of the directivity matrix. Finally, a regularization scheme was described and was shown to improve the inversion robustness at the cut-on frequencies. The experimental data obtained from external pressure measurements in the near field of a scale model fan rig will be presented in a subsequent paper. Generally, it was shown that TCS mounted microphone arrays are able to provide a valuable method for performing mode detection in ducts.

ACKNOWLEDGMENTS

The authors would like to acknowledge Dr. Rod Self of the ISVR for contributing to the investigation of the analytic behavior of the inversion conditioning. This work was supported in part by Rolls-Royce plc through the Rolls-Royce University Technology Centre in Gas Turbine Noise at ISVR, University of Southampton.

APPENDIX: ASYMPTOTIC BEHAVIOR OF THE CONDITION NUMBER

Consider the inversion of three modes by three microphones, with the pair of least cut-on modes of identical cut-on ratio $\alpha_1 = \alpha_2 = \alpha_0 \approx 1$. For this problem the directivity matrix \mathbf{D} is then given by Eq. (21), where F_{ij} is a factor deduced from Eq. (20) for the mode j at microphone i . From Eq. (18), $\kappa(\mathbf{D})$ is found from the ratio of the maximum to minimum singular values of \mathbf{D} . These singular values turn out to also be equal to eigenvalues of the Hermitian matrix $\mathbf{D}^H \mathbf{D}$, which can be written as

$$\begin{bmatrix} \gamma_0^2 H_1 & \gamma_0^2 H_4 & \gamma_0 H_5 \\ \gamma_0^2 H_4^* & \gamma_0^2 H_2 & \gamma_0 H_6 \\ \gamma_0 H_5^* & \gamma_0 H_6^* & H_3 \end{bmatrix}, \quad (\text{A1})$$

where $\gamma_0 = \sqrt{1 - \alpha_0^2}$ and the H_i 's are linear combinations of F_{ij} 's. The eigenvalues of this matrix are found from Eq. (23), namely

$$\det(\mathbf{D}^H \mathbf{D} - \lambda \mathbf{I}) = 0, \quad (\text{A2})$$

which leads to the following cubic characteristic equation:

$$\lambda^3 - (H_3 + \gamma_0^2 K_1) \lambda^2 + (\gamma_0^4 K_2 + \gamma_0^2 K_3) \lambda - \gamma_0^4 K_4 = 0, \quad (\text{A3})$$

where K_i 's are frequency dependent constants. In order to study how the behavior of the condition number is influenced by the pair of least cut-on modes, it is necessary to find an approximate solution for the eigenvalues as $\alpha_0 \rightarrow 1$ and therefore $\gamma_0 \rightarrow 0$. Expanding the solution of Eq. (A3) into a regular series in γ_0 ,

$$\lambda = \lambda_0 + \lambda_1 \gamma_0^2 + \lambda_2 \gamma_0^4 + \dots \quad (\text{A4})$$

introducing Eq. (A4) into Eq. (A3) and solving for the terms of order $O(\gamma_0^0)$ yields

$$\lambda_0^2 (\lambda_0 - H_3) = 0. \quad (\text{A5})$$

Solving for the coefficients of order $O(\gamma_0^0)$ yields the three eigenvalues

$$\lambda_0 = 0, 0, H_3. \quad (\text{A6})$$

Now solving for the terms of order $O(\gamma_0^2)$ yields

$$(3\lambda_0^2 - 2\lambda_0 H_3)\lambda_1 - \lambda_0(K_1\lambda_0 - K_3) = 0 \quad (\text{A7})$$

and therefore the coefficients of order $O(\gamma_0^2)$ of the three eigenvalues are

$$\lambda_1 = \frac{K_1\lambda_0 - K_3}{3\lambda_0 - 2H_3}. \quad (\text{A8})$$

The maximum and minimum eigenvalues to second order $O(\gamma_0^2)$ are found to be

$$\lambda_{\max} = H_3 + \frac{K_1 H_3 + K_3}{H_3} \gamma_0^2, \quad (\text{A9})$$

$$\lambda_{\min} = \frac{K_3}{2H_3} \gamma_0^2.$$

As $\gamma_0 \mapsto 0$, one can deduce from Eq. (A9)

$$\frac{\lambda_{\max}}{\lambda_{\min}} \approx \frac{2H_3^2}{K_3\gamma_0^2} + \frac{K_1 H_3 - K_3}{K_3}. \quad (\text{A10})$$

Therefore the behavior of the condition number of the directivity matrix in the vicinity of the cut-on frequencies is of the form

$$\kappa(\mathbf{D}) \mapsto \frac{A(ka)}{\sqrt{1 - \alpha_0^2}} \quad (\alpha_0 \mapsto 1). \quad (\text{A11})$$

¹R. Thomas, F. Farassat, L. Clark, C. Gerhold, J. Kelly, and L. Becker, "A mode detection using the azimuthal directivity of a turbofan model," in *Fifth AIAA/CEAS Aeroacoustics Conference*, Bellevue, WA (1999).

²F. Farassat, D. Nark, and H. Russel, "The detection of radiated modes from ducted fan engine," in *Seventh AIAA/CEAS Aeroacoustics Conference*, Maastricht, The Netherlands (2001).

³J. Lan, J. Premo, and D. L. Sutliff, "Inlet mode measurements with an

inflow control device microphone array," in *AIAA/CEAS Aeroacoustics Conference* (Breckenridge, CO, 2002).

⁴G. Golub and C. Van Loan, *Matrix Computations* (North Oxford Academic, Oxford, 1983).

⁵F. Castres, P. Joseph, and R. Astley, "Mode detection in turbofan inlets from acoustic pressure measurements in the radiated field," in *Tenth AIAA/CEAS Aeroacoustics Conference*, Manchester, UK (2003).

⁶F. Castres, "Mode detection from turbofan inlets," Ph.D. thesis, University of Southampton (2006).

⁷B. Fuller, "The age of the dome," *BUILD INTERNATIONAL* **2**, 7–15 (July/August 1969).

⁸H. Kenner, *Geodesic Math and How to Use It* (University of California Press, Berkeley, 1976).

⁹M. Tyler and T. Sofrin, "Axial flow compressor noise studies," *Soc. Automot. Eng. Trans.* **70**, 309–332 (1962).

¹⁰F. Bromwell, "Extended asymptotic eigenvalue distributions for bounded domains in n space," *J. Math. Mech.* **6**, 119–166 (1957).

¹¹G. Borgiotti, "The power radiated by a vibrating body in an acoustic fluid and its determination from boundary measurements," *J. Acoust. Soc. Am.* **88**, 1884–1893 (1990).

¹²G. Borgiotti and E. Rosen, "The determination of the far field of an acoustic radiator from sparse measurement samples in the near field," *J. Acoust. Soc. Am.* **92**, 807–818 (1992).

¹³G. Borgiotti and K. Jones, "The determination of the acoustic far field of a radiating body in an acoustic fluid from boundary measurements," *J. Acoust. Soc. Am.* **93**, 2788–2797 (1993).

¹⁴M. Currey and K. Cunefare, "The radiation modes of baffled finite plates," *J. Acoust. Soc. Am.* **98**, 1570–1580 (1995).

¹⁵P. Nelson and S. Yoon, "Estimation of acoustic source strength by inverse methods: Part i, conditioning of the inverse problem," *J. Sound Vib.* **233**, 643–668 (2000).

¹⁶E. Williams, B. Houston, and P. Herdic, "Fast Fourier transform and singular value decomposition formulations for patch near field acoustical holography," *J. Acoust. Soc. Am.* **114**, 1322–1333 (2003).

¹⁷C. Morfey, "A note on the radiation efficiency of acoustic duct modes," *J. Sound Vib.* **9**, 367–372 (1969).

¹⁸C. Hansen, "Perturbations bounds for discrete tikhonov regularization," *Inverse Probl.* **5**, L42–L44 (1989).

¹⁹C. Hansen, "Regularization, gsvd and truncated gsvd," *BIT* **29**, 491–504 (1989).

²⁰C. Hansen, "Rank-deficient and discrete ill-posed problems," *SIAM Monographs on Mathematical Modeling and Computation*, **243** (1998), tY-CHAP Compilation and indexing terms, Copyright 2005 Elsevier Engineering Information, Inc. U1-98024057146.

A single-scattering correction for large contrasts in elastic layers

Elizabeth T. Küsel^{a)} and William L. Siegmann
Rensselaer Polytechnic Institute, Troy, New York 12180

Michael D. Collins
Naval Research Laboratory, Washington, DC 20375

(Received 8 August 2006; revised 8 November 2006; accepted 8 November 2006)

The single-scattering solution is implemented in a formulation that makes it possible to accurately handle solid-solid interfaces with the parabolic equation method. Problems involving large contrasts across sloping stratigraphy can be handled by subdividing a vertical interface into a series of two or more scattering problems. The approach can handle complex layering and is applicable to a large class of seismic problems. The solution of the scattering problem is based on an iteration formula, which has improved convergence in the new formulation, and the transverse operator of the parabolic wave equation, which is implemented efficiently in terms of banded matrices. Accurate solutions can often be obtained by using only one iteration. © 2007 Acoustical Society of America. [DOI: 10.1121/1.2404627]

PACS number(s): 43.30.Bp, 43.30.Ma [AIT]

Pages: 808–813

I. INTRODUCTION

The parabolic equation method provides an excellent combination of accuracy and efficiency for many problems in ocean acoustics.¹ This approach is based on the assumption that outgoing energy dominates backscattered energy, which is neglected. One of the key unresolved issues is to improve accuracy for problems involving elastic layers in the sediment.^{2–5} Continuous depth dependence and horizontal interfaces can be handled accurately by working in the (u_x, w) formulation,⁶ where u_x is the horizontal derivative of the horizontal displacement and w is the vertical displacement. In this paper, we describe an approach based on the (u_x, w) formulation that accurately handles range dependence, such as sloping interfaces between solid layers.

Several approaches have proven to be effective for handling range dependence in purely acoustics problems. The standard approach is to approximate a range-dependent medium in terms of a series of range-independent regions, use the parabolic wave equation to propagate the field through each region, and apply an energy-conservation^{7,8} or single-scattering⁹ correction at the vertical interfaces between regions. Some progress has been made for problems involving elastic layers, but this case has not been fully resolved. An approximate energy-conservation correction provides improved accuracy.¹⁰ An improved energy-conservation correction has been proposed¹¹ but has not been successfully implemented. In its original form, the single-scattering correction for elastic media is only applicable to problems involving weak contrasts across interfaces.¹² Approaches based on coordinate mapping¹³ and rotation¹⁴ are applicable to a wide class of range-dependent problems, but they only address the issue of a sloping fluid-solid interface.

There is a need for a general approach for handling sloping interfaces between solid layers and range dependence within solid layers.

In this paper, we describe a single-scattering correction that is based on the (u_x, w) formulation, can handle large contrasts across interfaces, and should provide accurate solutions for a large class of seismic problems. The single-scattering approach is based on an iteration formula that has convergence problems in the original implementation.¹² We show that this limitation can be reduced by working in the (u_x, w) formulation and eliminated by approximating a large-contrast interface in terms of a series of small-contrast interfaces. The (u_x, w) formulation and the parabolic equation are discussed in Sec. II. The single-scattering solution is derived in Sec. III. The accuracy and capability of the approach are illustrated in Sec. IV.

II. THE PARABOLIC EQUATION

We work in the frequency domain and consider a two-dimensional problem, where z is the depth and the range x is the horizontal distance from a source. The compressional and shear wave speeds c_p and c_s are related to the density ρ and the Lamé parameters λ and μ by $\rho c_p^2 = \lambda + 2\mu$ and $\rho c_s^2 = \mu$. Attenuation is taken into account by allowing c_p and c_s to be complex. A problem is said to be range dependent when λ , μ , and ρ depend on x . Range dependence can be handled by approximating the medium in terms of a series of range-independent (or stratified) regions. The vertical interfaces between regions can be handled with the approach described in Sec. III.

In each range-independent region, the displacements u and w satisfy the equations,⁶

^{a)}Present Address: Graduate School Of Oceanography, University of Rhode Island, Narragansett, Rhode Island 02882.

$$(\lambda + 2\mu)\frac{\partial^2 u_x}{\partial x^2} + \frac{\partial}{\partial z}\left(\mu\frac{\partial u_x}{\partial z}\right) + \rho\omega^2 u_x + (\lambda + \mu)\frac{\partial^3 w}{\partial x^2 \partial z} + \frac{\partial \mu}{\partial z}\frac{\partial^2 w}{\partial x^2} = 0, \quad (1)$$

$$\mu\frac{\partial^2 w}{\partial x^2} + \frac{\partial}{\partial z}\left((\lambda + 2\mu)\frac{\partial w}{\partial z}\right) + \rho\omega^2 w + (\lambda + \mu)\frac{\partial u_x}{\partial z} + \frac{\partial \lambda}{\partial z}u_x = 0, \quad (2)$$

$$u_x \equiv \frac{\partial u}{\partial x}, \quad (3)$$

where ω is the circular frequency. These equations are derived from the standard equations of motion for an isotropic medium¹⁵ and are in the form

$$\left(L\frac{\partial^2}{\partial x^2} + M\right)\begin{pmatrix} u_x \\ w \end{pmatrix} = 0, \quad (4)$$

where the matrices L and M contain depth operators and the properties of the medium. Multiplying Eq. (4) by L^{-1} , we obtain

$$\left(\frac{\partial^2}{\partial x^2} + L^{-1}M\right)\begin{pmatrix} u_x \\ w \end{pmatrix} = 0. \quad (5)$$

Factoring the operator in Eq. (5), we obtain

$$\left(\frac{\partial}{\partial x} + i(L^{-1}M)^{1/2}\right)\left(\frac{\partial}{\partial x} - i(L^{-1}M)^{1/2}\right)\begin{pmatrix} u_x \\ w \end{pmatrix} = 0, \quad (6)$$

where the factors correspond to outgoing and backscattered energy. Assuming that outgoing energy dominates incoming energy, we obtain the (u_x, w) parabolic equation,

$$\frac{\partial}{\partial x}\begin{pmatrix} u_x \\ w \end{pmatrix} = i(L^{-1}M)^{1/2}\begin{pmatrix} u_x \\ w \end{pmatrix}, \quad (7)$$

which can be implemented numerically to efficiently propagate the field through each range-independent region.^{5,16}

III. VERTICAL INTERFACES

The displacements and the stresses,

$$\sigma_{xx} = (\lambda + 2\mu)\frac{\partial u}{\partial x} + \lambda\frac{\partial w}{\partial z}, \quad (8)$$

$$\sigma_{xz} = \mu\frac{\partial u}{\partial z} + \mu\frac{\partial w}{\partial x}, \quad (9)$$

must be conserved across a vertical interface between two range-independent regions. Since the tangential stress σ_{xz} vanishes at a free boundary and is conserved across a horizontal interface, it is necessary to implement the vertical interface conditions with care to avoid a singularity.¹² Since u is continuous across a vertical interface, so is its depth derivative, and an effective approach for eliminating the singularity is to add a multiple of this quantity to Eq. (9) to obtain

$$\sigma_{xz} + \lambda_0\frac{\partial u}{\partial z} = (\lambda_0 + \mu)\frac{\partial u}{\partial z} + \mu\frac{\partial w}{\partial x}, \quad (10)$$

where λ_0 is an arbitrary constant (such as a representative value of λ). From Eqs. (2), (9), and (10), we obtain

$$-\frac{\partial \sigma_{xz}}{\partial x} - \lambda_0\frac{\partial u_x}{\partial z} = \frac{\partial}{\partial z}\left((\lambda + 2\mu)\frac{\partial w}{\partial z}\right) + \rho\omega^2 w + (\lambda - \lambda_0)\frac{\partial u_x}{\partial z} + \frac{\partial \lambda}{\partial z}u_x. \quad (11)$$

From Eqs. (8) and (11), we obtain the following relations between the dependent variables and the quantities that must be conserved across vertical interfaces:

$$\begin{pmatrix} \sigma_{xx} \\ w \end{pmatrix} = R\begin{pmatrix} u_x \\ w \end{pmatrix}, \quad (12)$$

$$\frac{\partial}{\partial x}\begin{pmatrix} u \\ -\sigma_{xz} - \lambda_0\frac{\partial u}{\partial z} \end{pmatrix} = S\begin{pmatrix} u_x \\ w \end{pmatrix}, \quad (13)$$

$$R \equiv \begin{pmatrix} \lambda + 2\mu & \lambda\frac{\partial}{\partial z} \\ 0 & 1 \end{pmatrix}, \quad (14)$$

$$S \equiv \begin{pmatrix} 1 & 0 \\ (\lambda - \lambda_0)\frac{\partial}{\partial z} + \frac{\partial \lambda}{\partial z} & \frac{\partial}{\partial z}(\lambda + 2\mu)\frac{\partial}{\partial z} + \rho\omega^2 \end{pmatrix}. \quad (15)$$

We use the subscripts i , r , and t to denote the incident, reflected, and transmitted fields and the subscripts A and B to denote the regions on the incident and transmitted sides of the vertical interface. Conserving the quantities in Eqs. (12) and (13) and using Eq. (7) to eliminate the range derivative, we obtain

$$R_A\left[\begin{pmatrix} u_x \\ w \end{pmatrix}_i + \begin{pmatrix} u_x \\ w \end{pmatrix}_r\right] = R_B\begin{pmatrix} u_x \\ w \end{pmatrix}_t, \quad (16)$$

$$S_A(L_A^{-1}M_A)^{-1/2}\left[\begin{pmatrix} u_x \\ w \end{pmatrix}_i - \begin{pmatrix} u_x \\ w \end{pmatrix}_r\right] = S_B(L_B^{-1}M_B)^{-1/2}\begin{pmatrix} u_x \\ w \end{pmatrix}_t. \quad (17)$$

The negative sign in Eq. (17) accounts for the fact that the reflected field is incoming. Eliminating the transmitted field, we obtain

$$S_A(L_A^{-1}M_A)^{-1/2}\left[\begin{pmatrix} u_x \\ w \end{pmatrix}_i - \begin{pmatrix} u_x \\ w \end{pmatrix}_r\right] = S_B(L_B^{-1}M_B)^{-1/2}R_B^{-1}R_A\left[\begin{pmatrix} u_x \\ w \end{pmatrix}_i + \begin{pmatrix} u_x \\ w \end{pmatrix}_r\right]. \quad (18)$$

To obtain a solution that is easily implemented in terms of banded matrices, we rearrange Eq. (18) into the iteration formula,

$$\begin{pmatrix} u_x \\ w \end{pmatrix}_r = \frac{\tau-2}{\tau} \begin{pmatrix} u_x \\ w \end{pmatrix}_r + \frac{1}{\tau} \Lambda \left[\begin{pmatrix} u_x \\ w \end{pmatrix}_i + \begin{pmatrix} u_x \\ w \end{pmatrix}_r \right], \quad (19)$$

$$\Lambda \equiv I - (L_A^{-1} M_A)^{1/2} S_A^{-1} S_B (L_B^{-1} M_B)^{-1/2} R_B^{-1} R_A, \quad (20)$$

where $\tau \geq 2$ is a convergence parameter. This iteration formula converges when the contrast across the vertical interface is sufficiently small. When the contrast is relatively large, convergence can be improved by increasing τ . After the iteration converges, Eq. (16) is used to compute the transmitted field, which is used as the starting field in the next region.

When the contrast between layers is too large for the iteration formula to converge, the interface can be divided into a series of interfaces with smaller contrasts. This approach may break down when backscattering is significant (e.g., for the case of a strong reflector), but it should be accurate for gradually range-dependent problems in which outgoing energy dominates. For such problems, it should not matter how the medium is discretized as long as the sampling is sufficiently fine. In particular, a vertical interface can be approximated in terms of a series of vertical interfaces between arbitrarily thin regions. The single-scattering solution is then applied to each interface and multiple scattering is neglected.

IV. EXAMPLES

In this section, we present solutions that demonstrate the accuracy and capability of the single-scattering solution. Each of the examples involves a line source in plane geometry. For many seismic problems, it is necessary to use finer grid spacings than are commonly used in acoustics, especially when shear waves are important and energy couples between wave types and propagates at steep angles. We compare the single-scattering solution with the uncorrected solution that conserves (u_x, w) across vertical interfaces. Our purpose is to test these techniques rather than to consider realistic examples.

Example A involves a 25 Hz source at $z=100$ m in a medium with a sloping interface between two homogeneous layers. The thickness of the lossless upper layer is 200 m at $r=0$ and decreases linearly with range to 100 m at $r=4$ km. The compressional and shear attenuations are both 0.5 dB/ λ in the lower layer, which is modeled as a half space by artificially increasing the attenuation far below the interface. The density of the lower layer is 1.5 times the density of the upper layer. In the upper layer, we take $c_p=1500$ m/s and $c_s=700$ m/s. In the lower layer, we consider the cases $c_p=1700$ m/s and $c_s=800$ m/s, $c_p=2400$ m/s and $c_s=1200$ m/s, and $c_p=3400$ m/s and $c_s=1700$ m/s. For the numerical solution, we use the grid spacings $\Delta r=5$ m and $\Delta z=0.25$ m. For the rational approximation of the operator, we use eight terms and expand about the reference wave speed of 1000 m/s. We use one slice, iterate once for the case $\tau=2$, and iterate ten times for the case $\tau=4$. In Fig. 1, the $\tau=4$ solution is compared with the (u_x, w) conserving solution, which has significant errors for all three cases of the wave speeds. The $\tau=2$ and $\tau=4$ solutions are compared in

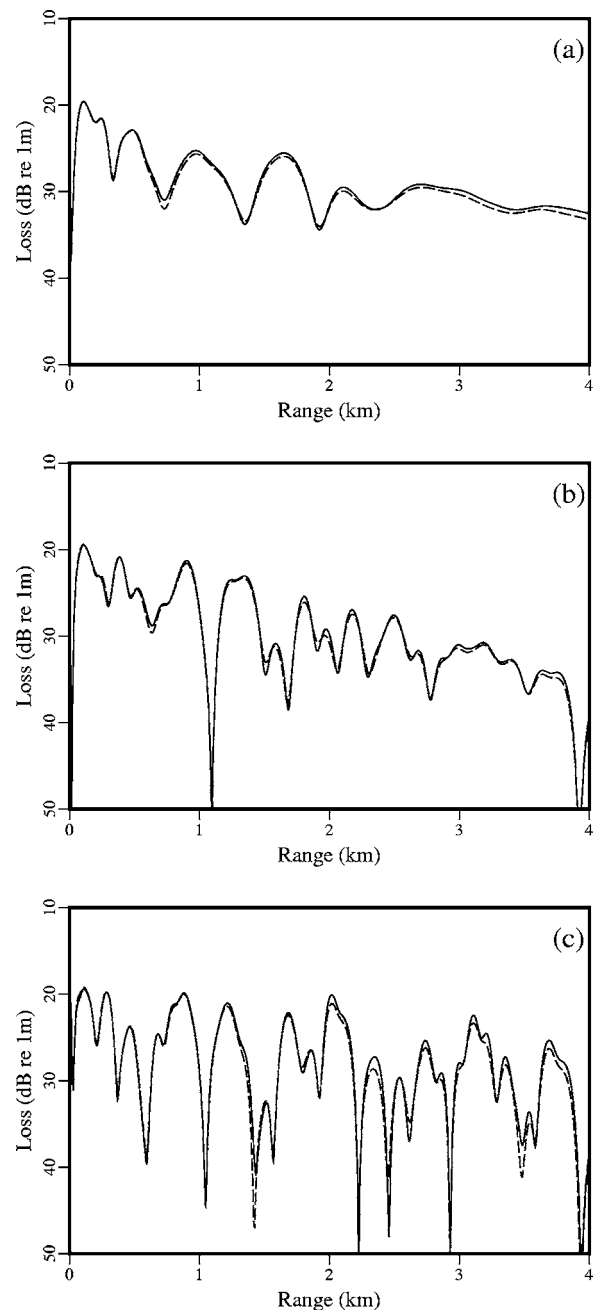


FIG. 1. Compressional wave transmission loss at $z=30$ m for example A. The dashed curves are the single-scattering solutions obtained using one slice, $\tau=4$, and ten iterations. The solid curves are the (u_x, w) conserving solutions. (a) The $c_p=1700$ m/s and $c_s=800$ m/s case. (b) The $c_p=2400$ m/s and $c_s=1200$ m/s case. (c) The $c_p=3400$ m/s and $c_s=1700$ m/s case. The errors in the (u_x, w) conserving solutions are typical of what has been observed in related problems involving only compressional waves (e.g., see Refs. 7 and 8).

Fig. 2. Although it takes several iterations for the iteration formula to converge over all depth, the single iteration solutions (which are much more efficient) are nearly identical to the multiple iteration solutions.

Example B is similar to example A, with the exception that the density ratio is 2.5. We only consider the $c_p=3400$ m/s and $c_s=1700$ m/s case for this example. We consider the case $\tau=4$ with 20 iterations for both two and four slices. We also consider the case $\tau=2$ with one slice and one iteration. Results for example B appear in Fig. 3. There

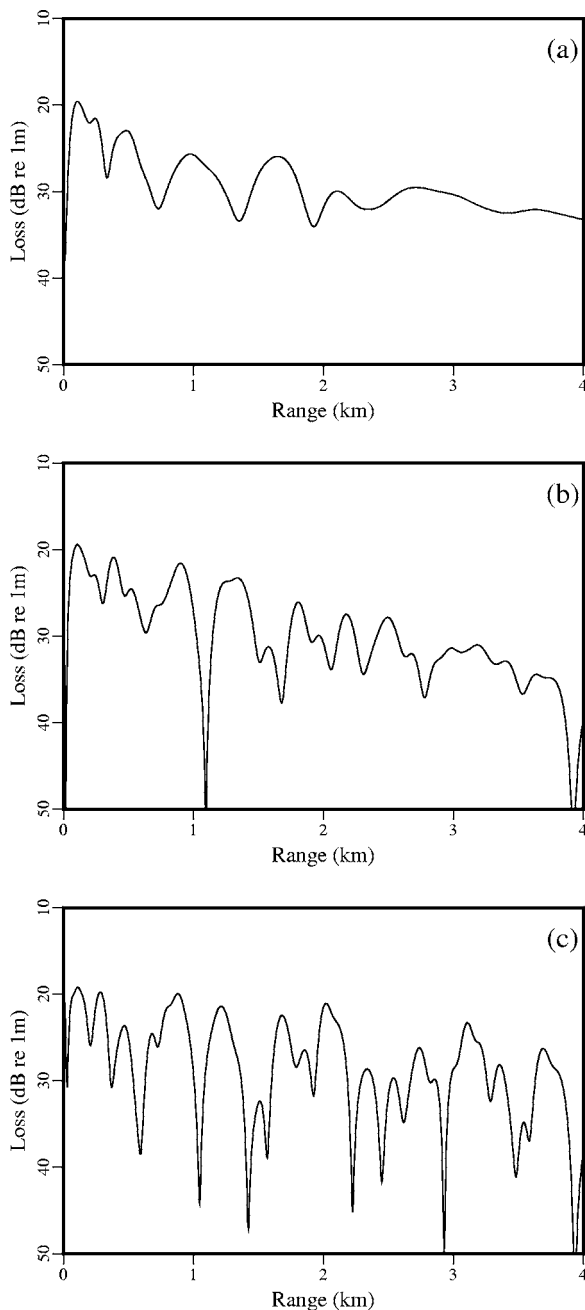


FIG. 2. Compressional wave transmission loss at $z=30$ m for example A. The dashed curves are the single-scattering solutions obtained using one slice, $\tau=4$, and ten iterations. The solid curves are the single-scattering solutions obtained using one slice, $\tau=2$, and one iteration. (a) The $c_p=1700$ m/s and $c_s=800$ m/s case. (b) The $c_p=2400$ m/s and $c_s=1200$ m/s case. (c) The $c_p=3400$ m/s and $c_s=1700$ m/s case. Although it takes several iterations for the scattered field to settle down, the solution obtained using only one iteration is essentially identical to the solution obtained using ten iterations.

are large errors in the (u_x, w) conserving solution. The $\tau=4$ solutions are nearly identical, which illustrates that vertical interfaces can be subdivided repeatedly when outgoing energy dominates backscattered energy. The $\tau=2$ solution is in excellent agreement with the $\tau=4$ solution despite the fact that the iteration formula diverges when there is only one slice. This is evidently an example of an asymptotic solution in which the first term is useful even though the series diverges.

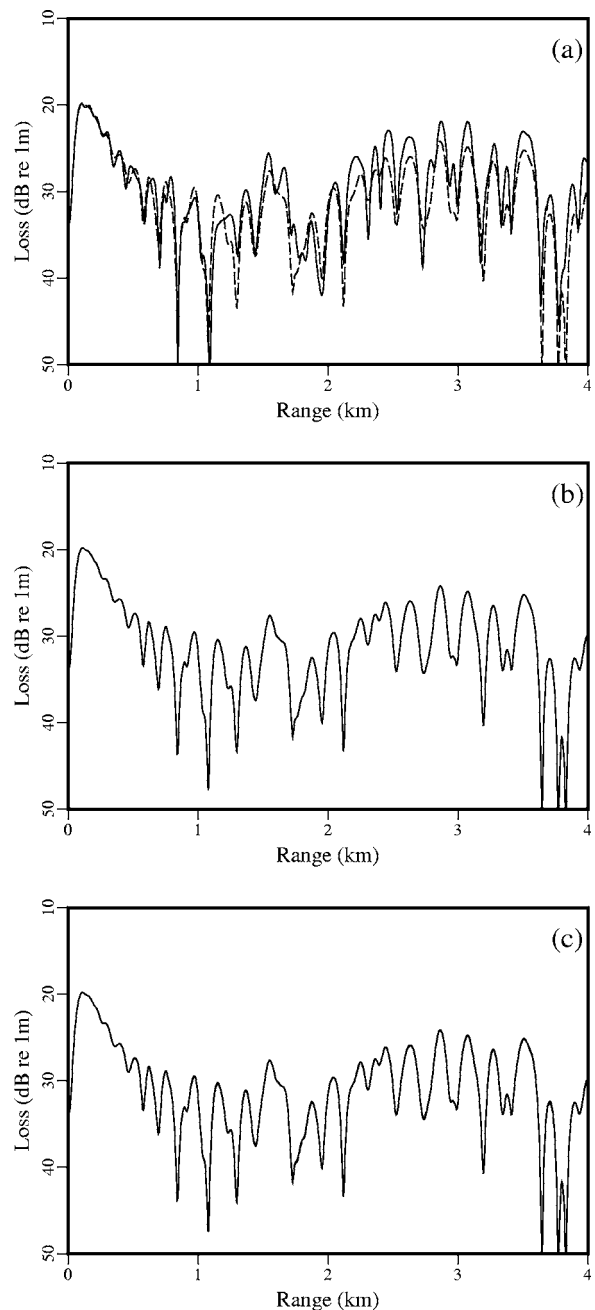


FIG. 3. Compressional wave transmission loss at $z=30$ m for example B. The dashed curves are the single-scattering solution obtained using two slices, $\tau=4$, and twenty iterations. The solid curves are (a) the (u_x, w) conserving solution, (b) the single-scattering solution obtained using four slices, $\tau=4$, and 20 iterations, and (c) the single-scattering solution obtained using one slice, $\tau=2$, and one iteration. There are significant errors in the (u_x, w) conserving solution. The fact that the solutions obtained using two and four slices are nearly identical illustrates that interfaces can be subdivided repeatedly when outgoing energy dominates. Although the iteration formula diverges for this problem when only one slice is used, the solution obtained using only one slice and one iteration is nearly identical to the solutions obtained using multiple slices.

Example C is a benchmark problem that is obtained by rotating a range-independent problem that consists of a 400 m thick elastic waveguide bounded above and below by elastic half spaces. The density is 1.5 times greater in the half spaces. The waves speeds are $c_p=2400$ m/s and $c_s=1200$ m/s in the half spaces and $c_p=1500$ m/s and c_s

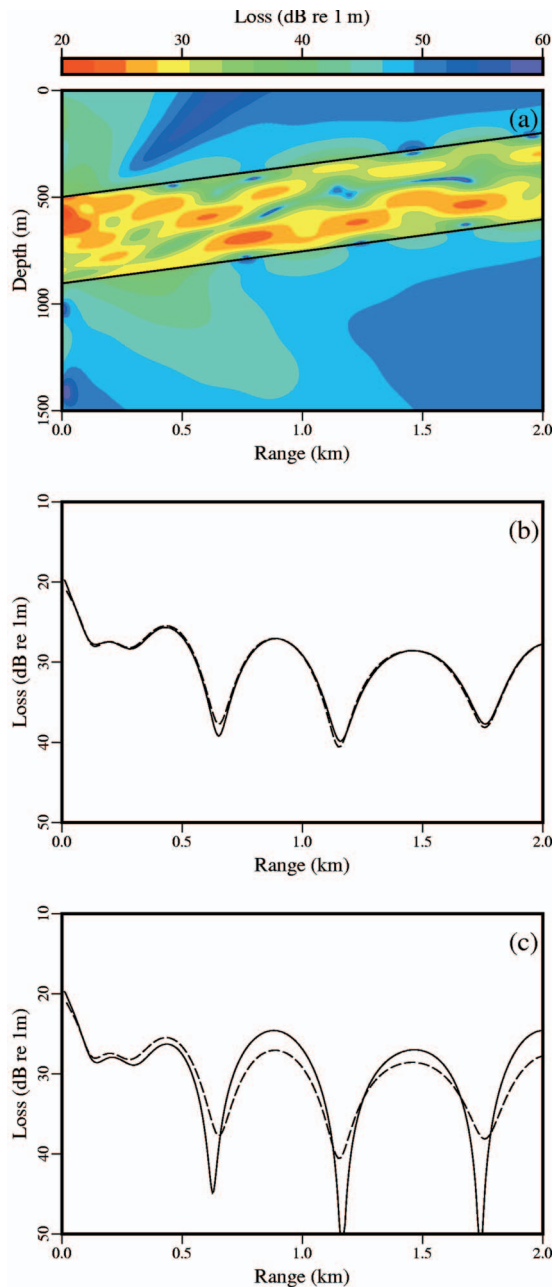


FIG. 4. Compressional wave transmission loss 100 m below the top boundary of the waveguide for example C. This range-dependent problem is equivalent to a range-independent problem that has been rotated. (a) The problem consists of a parallel elastic waveguide bounded above and below by elastic half spaces. The dashed curves are the solution of the equivalent range-independent problem. The solid curves are (b) the single-scattering solution and (c) the (u_x, w) conserving solution.

=850 m/s in the waveguide. There is no attenuation in the waveguide or the half spaces, with the exception of absorbing layers that are placed far above and below the waveguide. A 10 Hz source is placed 100 m below the top boundary of the waveguide. We obtain a reference solution by solving the unrotated problem, which is range independent. We obtain an equivalent range-dependent problem by rotating the medium so that the boundaries of the waveguide slope upward a total of 300 m over 2 km for an 8.53 deg slope. Results for example C appear in Fig. 4. There are large

TABLE I. Properties of the layers for example D, where β_p and β_s are the compressional and shear attenuations. The layers are numbered in order starting from the top.

Layer	c_p (m/s)	c_s (m/s)	ρ (g/cm ³)	β_p (dB/ λ)	β_s (dB/ λ)
1	1500	700	1.0	0.0	0.0
2	2000	950	1.2	0.1	0.2
3	2400	1200	1.4	0.1	0.2
4	2800	1600	1.7	0.2	0.4
5	3400	1700	2.0	0.5	0.5

errors in the (u_x, w) conserving solution. The single-scattering solution is in good agreement with the reference solution.

Example D involves a 2 Hz source at $z=2500$ m in a medium with five layers and sloping interfaces. The properties of the layers are listed in Table I. The single-scattering solution appears in Fig. 5. The second and third layers pinch off and disappear near 20 and 25 km but return near 35 and 40 km. There is significant interaction of seismic waves at all of the interfaces.

V. CONCLUSION

The single-scattering solution for range-dependent seismic problems has been improved by implementing in the (u_x, w) formulation and by using multiple slices to handle vertical interfaces with large contrasts. Convergence is greatly improved in this formulation and all convergence issues can be eliminated by using a sufficient number of slices. The accuracy of the single-scattering solution was tested for a range-dependent problem that was obtained by rotating a range-independent problem. Errors in the (u_x, w) conserving solution were illustrated for several problems. It was demonstrated that accurate solutions can often be obtained by using only one slice and one iteration. The single-scattering solution should be accurate for a large class of seismic problems.

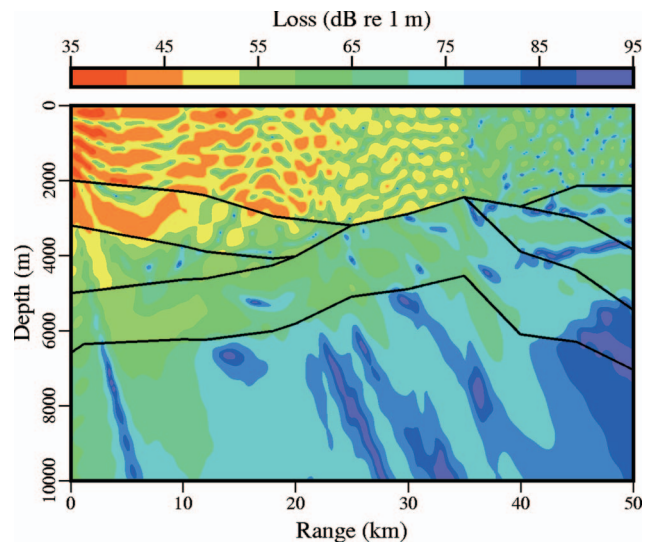


FIG. 5. Compressional wave transmission loss for example D, which involves a 2 Hz source and multiple layers with sloping interfaces. The properties of the layers are given in Table I.

Cases that have not yet been fully addressed are variable topography and the combination of fluid and solid layers.

ACKNOWLEDGMENT

This work was supported by the Office of Naval Research.

- ¹F. B. Jensen, W. A. Kuperman, M. B. Porter, and H. Schmidt, *Computational Ocean Acoustics* (American Institute of Physics, New York, 1994), pp. 343–412.
- ²R. R. Greene, “A high-angle one-way wave equation for seismic wave propagation along rough and sloping interfaces,” *J. Acoust. Soc. Am.* **77**, 1991–1998 (1985).
- ³M. D. Collins, “A higher-order parabolic equation for wave propagation in an ocean overlying an elastic bottom,” *J. Acoust. Soc. Am.* **86**, 1459–1464 (1989).
- ⁴B. T. R. Wetton and G. H. Brooke, “One-way wave equations for seismoaoustic propagation in elastic waveguides,” *J. Acoust. Soc. Am.* **87**, 624–632 (1990).
- ⁵M. D. Collins, “Higher-order parabolic approximations for accurate and stable elastic parabolic equations with application to interface wave propagation,” *J. Acoust. Soc. Am.* **89**, 1050–1057 (1991).
- ⁶W. Jerzak, W. L. Siegmann, and M. D. Collins, “Modeling Rayleigh and Stoneley waves and other interface and boundary effects with the para-

bolic equation,” *J. Acoust. Soc. Am.* **117**, 3497–3503 (2005).

- ⁷M. B. Porter, F. B. Jensen, and C. M. Ferla, “The problem of energy conservation in one-way models,” *J. Acoust. Soc. Am.* **89**, 1058–1067 (1991).
- ⁸M. D. Collins and E. K. Westwood, “A higher-order energy-conserving parabolic equation for range-dependent ocean depth, sound speed, and density,” *J. Acoust. Soc. Am.* **89**, 1068–1075 (1991).
- ⁹M. D. Collins and R. B. Evans, “A two-way parabolic equation for acoustic back scattering in the ocean,” *J. Acoust. Soc. Am.* **91**, 1357–1368 (1992).
- ¹⁰M. D. Collins, “An energy-conserving parabolic equation for elastic media,” *J. Acoust. Soc. Am.* **94**, 975–982 (1993).
- ¹¹M. D. Collins and W. L. Siegmann, “A complete energy conservation correction for the elastic parabolic equation,” *J. Acoust. Soc. Am.* **104**, 687–692 (1999).
- ¹²M. D. Collins, “A two-way parabolic equation for elastic media,” *J. Acoust. Soc. Am.* **93**, 1815–1825 (1993).
- ¹³M. D. Collins and D. K. Dacol, “A mapping approach for handling sloping interfaces,” *J. Acoust. Soc. Am.* **107**, 1937–1942 (2000).
- ¹⁴D. A. Outing, W. L. Siegmann, M. D. Collins, and E. K. Westwood, “Generalization of the rotated parabolic equation to variable slopes,” *J. Acoust. Soc. Am.* **120**, 3534–3538 (2006).
- ¹⁵H. Kolsky, *Stress Waves in Solids* (Dover, New York, 1963).
- ¹⁶M. D. Collins, “A split-step Padé solution for the parabolic equation method,” *J. Acoust. Soc. Am.* **93**, 1736–1742 (1993).

An equivalent roughness model for seabed backscattering at very high frequencies using a band-matrix approach

Gorm Wendelboe^{a)}

Danish Defense Research Establishment (DDRE), Ryvangs Allé 1, DK-2100 Copenhagen and Ørsted-DTU, Technical University of Denmark, Ørsted's Plads, Building 348, DK-2800 Kgs. Lyngby, Denmark

Finn Jacobsen^{b)}

Ørsted-DTU, Technical University of Denmark, Ørsted's Plads, Building 348, DK-2800 Kgs. Lyngby, Denmark

Judith M. Bell^{c)}

School of Engineering and Physical Sciences, Heriot-Watt University, Edinburgh, Scotland

(Received 10 August 2006; revised 28 November 2006; accepted 5 December 2006)

This work concerns modeling of very high frequency (>100 kHz) sonar images obtained from a sandy seabed. The seabed is divided into a discrete number of 1D height profiles. For each height profile the backscattered pressure is computed by an integral equation method for interface scattering between two homogeneous media as formulated by Chan [IEEE Trans. Antennas Propag. **46**, 142–149 (1998)]. However, the seabed is inhomogeneous, and volume scattering is a major contributor to backscattering. The SAX99 experiments revealed that the density in the unconsolidated sediment within the first 5 mm exhibits a high spatial variation. For that reason, additional roughness is introduced: For each surface point a stochastic realization of the density along the vertical is generated, and the sediment depth at which the density has its maximum value will constitute the new height field value. The matrix of the full integral equation is reduced to a band matrix as the interaction between the point sources on the seabed is neglected from a certain range; this allows computations on long height profiles with lengths up to approximately 25 m (at 300 kHz). The equivalent roughness approach, combined with the band-matrix approach, agrees with SAX99 data at 300 kHz. © 2007 Acoustical Society of America. [DOI: 10.1121/1.2427127]

PACS number(s): 43.30.Gv, 43.30.Hw, 43.30.Ft [SLB]

Pages: 814–823

I. INTRODUCTION

Very high frequency (>100 kHz) sonar plays a key role for naval mine detection and identification. This work is related to mines lying on the seabed, i.e., proud mines, and the goal is modeling of high frequency sonar images. Sonar images of a sandy seabed are contaminated with clutter, a term that refers to the noisy, or unwanted, component of the received sonar signal; its strength governs the detection performance of the backscattered pressure from an object, or, say, the signal-to-reverberation ratio. Hence, clutter has a key role in manually controlled as well as automated mine detection/identification systems since it can affect the false alarm rates.¹ Clutter is the result of an oscillating pressure signal scattered back from the seabed, where a complex wave interference on the water/sediment interface and in the sediment volume occur.

Wave scattering from random rough surfaces can be modeled by a field average over an ensemble of random surfaces where the scattered acoustic power is derived analytically (see, e.g., Ref. 2 and Ref. 3, Chap. 9.3). Alternatively, the scattered pressure can be computed numerically from a stochastic realization of the rough surface, that is, a

Monte Carlo approach (see e.g., Ref. 4). A combination of the average field method and the Monte Carlo approach has been applied in some sonar simulation models.^{5,6} However, such models generate energy-based reflectograms that do not represent the rapid phase variations obtained from real signals. The field scattered from a rough interface can be computed by the classical composite model,^{2,3} a combination of the Kirchhoff approximation and the small perturbation approximation, but the small slope approximation, a relatively new model, is valid for a broader range of surfaces (see, e.g., Ref. 3, Chap. 9.14 and Refs. 7 and 8). The full integral equation solution and approximate integral equation methods have been applied on 1D surfaces, see, e.g., Refs. 9–11. Meanwhile, models for interface scattering are not sufficient for acoustic field interaction with the seabed; acoustic waves penetrate into the sediment and inhomogeneities induce a scattered field. Jackson^{12–16} applied the small perturbation approximation for frequencies below 100 kHz, that is, for wavelengths greater than approximately 1.5 cm; for smaller wavelengths the model can fail.¹⁷ At 140 kHz, volume scattering from strongly inhomogeneous sediments can be the dominating scattering mechanism,¹⁸ a conclusion that also may be valid for the backscattering experiment at 300 kHz conducted at the Sediment Acoustic Experiment in 1999 (SAX99).¹⁹ Small scale measurements of the density and sound speed variability conducted at SAX99 tend to confirm that;²⁰ within the first centimeter the sediment is unconsoli-

^{a)}Electronic mail: gw@oersted.dtu.dk

^{b)}Electronic mail: fja@oersted.dtu.dk

^{c)}Electronic mail: j.bell@hw.ac.uk

dated and the geoacoustical parameters exhibit a significantly higher spatial variability than in the deeper parts of the sediment.

In the model presented here the rapid phase variations are required, and a stochastic seabed realization that covers all roughness scales, i.e., a full Monte Carlo approach, will be applied. The sandy seabed is approximated by a discrete number of 1D height profiles in planes similar to the sonar beams. The height profiles are synthesized by application of seabed roughness parameters acquired from stereo-photogrammetric measurements at SAX99. The scattering problem is solved by using the formulation by Chan,¹¹ where a rough interface divides two homogeneous fluids. Volume scattering is taken into account by introducing the equivalent roughness approximation: For each surface point a stochastic realization of the density along the vertical is generated and the sediment depth at which the density has its maximum value will constitute the new height profile value. The new height profile is subsequently filtered by an AR(1)-filter in order to generate correlation along the horizontal direction. The scattering matrix is reduced to a band matrix as interactions between point sources on the seabed are neglected from a certain range, and the reduction will allow computations of long height profiles. The number of nonzero diagonals are evaluated in terms of a tradeoff between accuracy and required height profile lengths. The equivalent roughness approach combined with the band-matrix approximation is compared with SAX99 data at 300 kHz (see Ref. 21).

All simulations are carried out with a 300-kHz sinusoid and the speed of sound in water is assumed to be $c_1 = 1500$ m/s, thus the acoustic wavelength in water is $\lambda = 0.5$ cm.

II. SEABED MODELING

In this section modeling of the rough water-sediment interface as well as modeling of the density variations in the upper sediment are described. The seabed is considered as a height field; hence, the height, h , is a function of the ground plane coordinates, x and y , i.e., $h=h(x, y)$. In this work, the sandy seabed is approximated by a discrete number of 1D height profiles in planes similar to the sonar beams. Thus, each height profile is given as

$$h = h(x), \quad (1)$$

where x is the ground range coordinate along the height profile. Simulations by George²² indicate that the backscattering characteristics are independent of sonar beam width, a result that supports the height profiles approximation.

A. Interface roughness

The seabed roughness is characterized in terms of its power spectrum, which according to, e.g., Briggs *et al.*,²³ is given by

$$P(f_s) = \frac{\phi}{f_s^\gamma}, \quad (2)$$

where f_s is the spatial frequency measured in cycles/cm, ϕ is the *spectral intercept* measured in cm^3 , and γ is the *spectral*

TABLE I. Applied interface roughness parameters.

Two-power law	f_s (cm^{-1})	γ	ϕ (cm^3)
Large scale	0.02–2.0	3.00	0.000 75
Small scale	2.0–4.0	3.81	0.001 31

exponent, which is dimensionless. Taking the logarithm on each side of Eq. (2) yields

$$\log_{10} P(f_s) = \log_{10}(\phi) - \gamma \log_{10}(f_s), \quad (3)$$

where the spectral intercept is found at $f_s=1$, i.e., at one cycle per centimeter. The power spectrum parameters are estimated by *in situ* experiments with stereo-photogrammetric equipment.^{1,23–25} The seabed may contain several power laws distributed over the different spatial frequencies. Here, a two-power-law spectrum is used,

$$P(f_s) = \begin{cases} \phi_1 f_s^{-\gamma_1}, & f_s^{(\min)} < f_s < f_s^{(\text{tr})}, \\ \phi_2 f_s^{-\gamma_2}, & f_s^{(\text{tr})} < f_s < f_s^{(\max)}, \\ 0, & \text{elsewhere,} \end{cases} \quad (4)$$

where ϕ_1 , γ_1 , and ϕ_2 , γ_2 are the spectral intercept and spectral exponent for the the first and second power laws, respectively. The minimum spatial frequency, $f_s^{(\min)}$, is governed by the size of the experimental area; $f_s^{(\text{tr})}$ is the transition frequency between the two power laws; and the maximum spatial frequency, $f_s^{(\max)}$, is related to the resolution of the stereo-photogrammetric system.

Throughout this work ϕ_1 , γ_1 , ϕ_2 , and γ_2 are based on data presented in Ref. 23 (BAMS, 5 Oct. N, Table II, p. 511). The parameters are listed in Table I. Note, the maximum spatial frequency is chosen to be $f_s^{(\max)} = 4$ cycles/cm, although the value is 5 cycles/cm in Ref. 23. This choice will become clear in the following.

The height profiles are synthesized in the frequency domain. Equation (4) is realized by suppressing frequencies below $f_s^{(\min)}$ by application of a tapered cosine window,

$$W_1(f_s) = \begin{cases} \frac{1}{2} [1 - \cos(\pi f_s f_s^{(\min)})], & |f_s| < f_s^{(\min)}, \\ 1, & \text{elsewhere,} \end{cases} \quad (5)$$

and, additionally, by suppressing frequencies above $f_s^{(\max)}$ by application of the following tapered cosine window,

$$W_2(f_s) = \begin{cases} \frac{1}{2} \left[1 - \cos\left(\pi \frac{f_g - f_s}{f_g - f_s^{(\max)}}\right) \right], & |f_s| > f_s^{(\max)}, \\ 1, & \text{elsewhere,} \end{cases} \quad (6)$$

where f_g is the Nyquist frequency. The Fourier transform of the synthetic height profile, $h(x)$, is

$$H(f_s) = N(f_s) W_1(f_s) W_2(f_s) \sqrt{P(f_s)}, \quad (7)$$

where $N(f_s)$ is the Fourier transform of a random Gaussian variable with unit variance. The first and second order de-

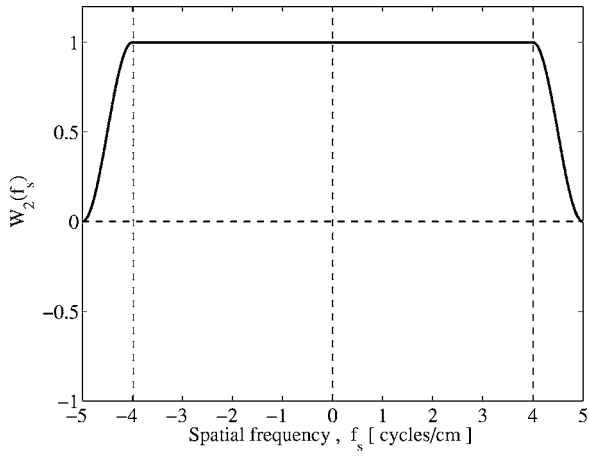


FIG. 1. The tapered cosine, frequency domain window, $W_2(f_s)$, see Eq. (6). It is applied on the surface, h , its derivative, dh/dx , and the second order derivative, d^2h/dx^2 .

derivatives of the height profile are required in the scattering formulation presented in Sec. III. Since

$$h(x) \leftrightarrow H(f_s), \quad (8)$$

the surface derivatives are given by

$$\frac{dh}{dx} \leftrightarrow 2\pi i f_s H(f_s), \quad (9)$$

$$\frac{d^2h}{dx^2} \leftrightarrow -4\pi^2 f_s^2 H(f_s). \quad (10)$$

If the equidistant step range along the ground range axis (the x axis) is equal to

$$\Delta x = 0.2\lambda = 0.1 \text{ cm}, \quad (11)$$

the spatial Nyquist frequency is

$$f_s^{(\text{Nyquist})} = 5 \text{ cycles/cm}. \quad (12)$$

The Bragg spatial frequency (or wave number) for backscattering at zero grazing angle is

$$f_s^{(\text{Bragg})} = 4 \text{ cycles/cm} \quad (13)$$

(see the Appendix); it is the maximum spatial frequency of the rough surface where reinforcement of the backscattered signal can occur. For a sonar model the grazing angle may vary between, say, $\theta=10^\circ$ and $\theta=75^\circ$, and consequently, the Bragg wave numbers will approximately lie between 1 to 3.9 cycle/cm.

Figures 1–3 show $W_2(f_s)$, $2\pi i f_s W_2(f_s)$, and $-4\pi^2 f_s^2 W_2(f_s)$, respectively. The tapered cosine window, $W_2(f_s)$, suppresses undesired high frequency content in $h(x_n)$ and its the first and second order derivative. The ground range resolution, specified in Eq. (11), has been selected such that $W_2(f_s)$ tapers off between the maximum Bragg wave number and the Nyquist frequency, and that explains why the implementation uses $f_s^{(\text{max})} = f_s^{(\text{Bragg})} = 4 \text{ cycles/cm}$ and not 5 cycles/cm as in Ref. 23.

In the literature Δx may vary from 0.2λ down to 0.05λ [see, e.g., Ref. 4 (Appendix 1, Table 1)]. Here, an analysis of convergence has shown that a resolution of 0.2λ yields back-

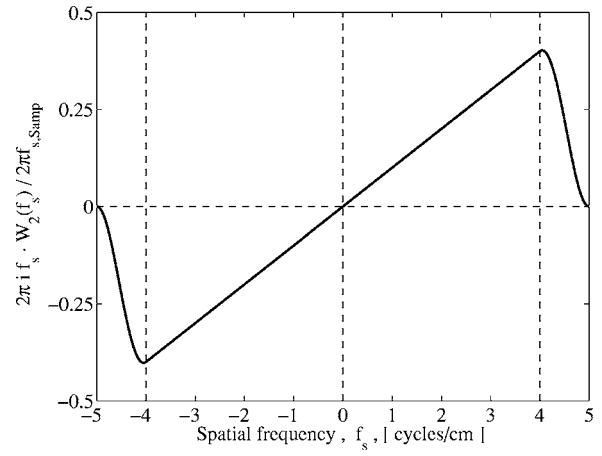


FIG. 2. Frequency domain window applied to obtain the surface first order derivative, dh/dx .

scattering strengths that nearly coincide with backscattering strengths obtained at a resolution of 0.1λ . Thus, a resolution of $\Delta x=0.2\lambda$ is applied. The distance between adjacent points on the rough surface, i.e., the arc-length of the n th height profile sample, $\Delta s(x_n)$, depends on the magnitude of the surface derivative, $\gamma(x_n)$, by

$$\Delta s(x_n) = \gamma(x_n) \Delta x, \quad (14)$$

where x_n is n th ground range sample, and where the magnitude of the surface derivative is given by

$$\gamma^2(x_n) = 1 + \left(\frac{dh}{dx} \right)^2 \Big|_{x=x_n}. \quad (15)$$

For very steep height variations in the profile the arc lengths become large. The simplest way to decrease Δs is by reducing Δx , but that will increase the computational workload drastically and include a large number of redundant or unnecessary surface points. Instead, extra points are inserted between points in the height profile when $\Delta s > \lambda/4$ (see, e.g., Ref. 26). The extra points are found by cubic spline interpolations and, consequently, Δx is no longer constant and Eq. (14) yields

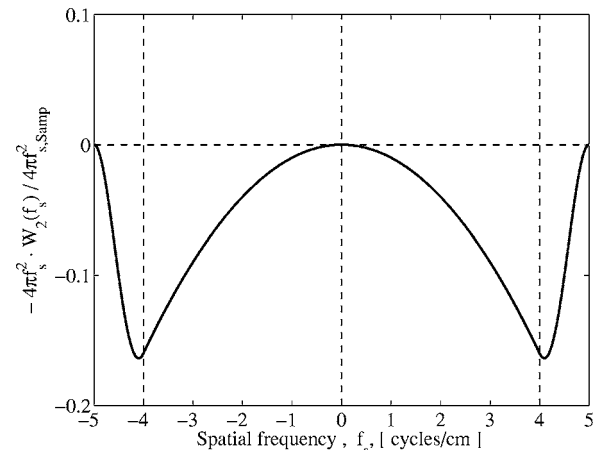


FIG. 3. Frequency domain window applied to obtain the surface second order derivative, d^2h/dx^2 .

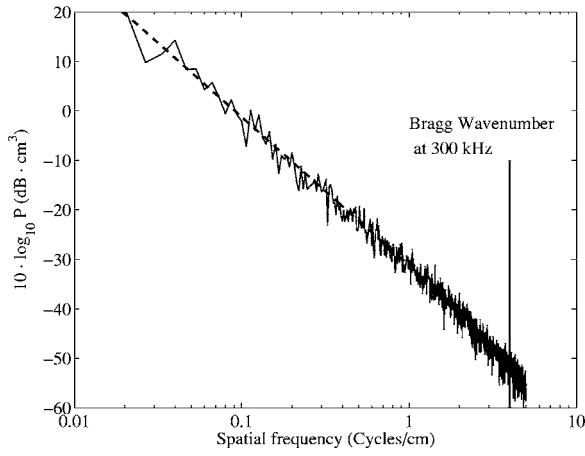


FIG. 4. Power spectrum of the interface roughness between the water and sediment; the spectrum has been acquired by optical means, i.e., stereophotogrammetric equipment. The dotted line represents the two-power law power spectrum according to Eq. (4) with the parameters listed in Table I. The solid, noisy, line is an average of five realizations.

$$\Delta s(x_n) = \gamma(x_n) \Delta x(x_n). \quad (16)$$

The number of extra points required depends inversely on minimum spatial frequency. If $f_s^{(\min)}$ decreases, the height profile will contain larger height values and arc lengths will increase. However, the minimum spatial frequency applied here only results in a few percent extra surface points. Equation (16) is applied in the implementation described in Sec. III.

Figure 4 shows the roughness power spectrum of the modeled interface; the spectrum shows an average of 5 roughness power spectra, and the maximum Bragg-wavenumber for backscattering at 300 kHz ($=4$ cycles/cm) is indicated by the solid vertical line.

B. Sediment density variations

The seabed may typically consist of sand, mud, stones, plants, and different animal species, but in this work only a sandy seabed sediment is considered. Experiments of the vertical and horizontal density variations have been carried out at the SAX99, and this section is solely based on results obtained by Tang *et al.*²⁰ The experiments showed that the density variations are strongest within the first 5 mm of the sediment, that is, the transition layer or unconsolidated sediment. For frequencies below 100 kHz, i.e., wavelengths above approximately 1.5 cm, the density inhomogeneities do not contribute to the scattering as the wavelength is greater than the thickness of the transition layer. At frequencies above 100 kHz inhomogeneities are believed to affect scattering significantly.

The 3D spatial variations in the upper sediment layer, that is, 0 to 6 cm, have been measured with an *in situ* measurement of porosity (IMP) system that measures the variability of the electrical conductivity within the sediment. The vertical density variations are considered in the following; Eqs. (17)–(21) are taken from Ref. 20 [Eqs. (11)–(15)]. For a sandy sediment the mean density as a function of depth is

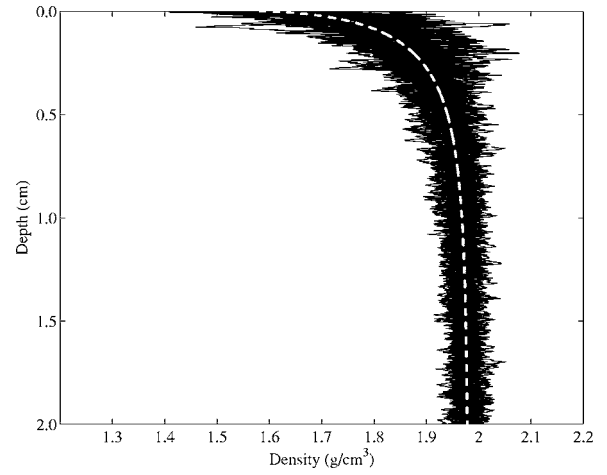


FIG. 5. A total of 32 synthetic density profiles based on density parameters listed in Table II and adopted from Ref. 20. The white dotted line represents the mean density profile, $\rho_m(z)$, given in Eq. (17).

$$\rho_m(z) = 1.98 - 0.4e^{-3.5z^{0.6}}, \quad (17)$$

where ρ is measured in g/cm^3 and the depth z in cm. The relative density variability,

$$\epsilon = \frac{\rho(x, y, z) - \rho_m(z)}{\rho_m(z)}, \quad (18)$$

is spatially nonstationary and follows the trend

$$\epsilon_m = 0.0152 - 0.096e^{-3.7z^{0.82}}. \quad (19)$$

The relative density variation is normalized by its trend profile, Eq. (19),

$$\eta = \frac{\epsilon(x, y, z)}{\epsilon_m(z)}, \quad (20)$$

where η is assumed to be a spatial stationary process. In the vertical direction the power law spectrum yields

$$P_z(f_s) = \frac{w}{f_s^{\gamma_\rho}}, \quad (21)$$

where $w = 6.76 \times 10^{-2} \text{ cm}^{1-\gamma_\rho}$ and $\gamma_\rho = 2.17$. The power law has been verified up to a spatial frequency of approximately $f_s = 20$ cycles/cm, which corresponds to a spatial resolution of 0.5 mm [see Ref. 20 (Fig. 14)]; above this frequency the noise floor of the IMP is reached. From these relations stochastic realizations of the sediment density are generated as a function of depth (see Fig. 5).

C. The equivalent roughness profile

The high density variations in the first millimeters below the water-sediment interface, i.e., the unconsolidated sediment, are believed to contribute significantly to the backscattered field. In order to include density variations in a model that only accounts for interface roughness scattering, an equivalent roughness approach is presented here. Considered from an acoustic point of view, there are numerous interfaces, or spatially distributed impedance contrasts, within the first 5 mm that contribute to the wave interaction. Here, the interface is redefined in terms of the density variations: For

TABLE II. Applied sediment density parameters.

Direction	Type	Parameters
Vertical	Power law	$\gamma_\rho=2.17$ $w=0.0676 \text{ cm}^{1-\gamma_\rho}$ $(f_s=0.3-30 \text{ cm}^{-1})$
Horizontal	AR(1)	$\kappa=0.45$

each point along the height profile a Monte Carlo realization like the ones shown in Fig. 5 is carried out, and the depth where the maximum density is found, $z(x_n, \rho_{\max})$, forms the new height profile value. At the present stage the equivalent roughness is defined as

$$h_{\text{eq}}(x_n) = h(x_n) - z(x_n, \rho_{\max}). \quad (22)$$

Along the horizontal direction the density variations also follow a power spectrum [see Ref. 20 (Fig. 15)], but experimental data are only provided in the frequency range 0.06 to 2 cycles/cm, and at a minimum depth of 1 cm. Here, we are interested in wave numbers up to 4 cycles/cm at sediment depths from 0 to 1 cm. Because $z(x_n, \rho_{\max})$ tends to be white noise along the horizontal direction, $h_{\text{eq}}(x_n)$ is filtered with an AR(1) low-pass filter (see, e.g., Ref. 27) with coefficient κ , that is,

$$h_{\text{eqft}}(x_n) = \kappa h_{\text{eqft}}(x_{n-1}) + (\kappa - 1)h_{\text{eq}}(x_n). \quad (23)$$

A single part of the results presented in Sec. IV is given in advance by anticipating that $\kappa=0.45$; this value gives an equivalent roughness profile, $h_{\text{eqft}}(x_n)$, that results in modeled backscattering strengths that approach experimental data. The parameters applied for the generation of equivalent roughness profiles are listed in Table II.

Figure 6 shows the spatial power spectra of the equivalent roughness profile together with the equivalent roughness interface in the case where the interface acquired by optical means is perfectly flat, that is, $h(x_n) \equiv x_0$. The optically acquired two-power law, i.e., Eq. (4), is also shown. The power

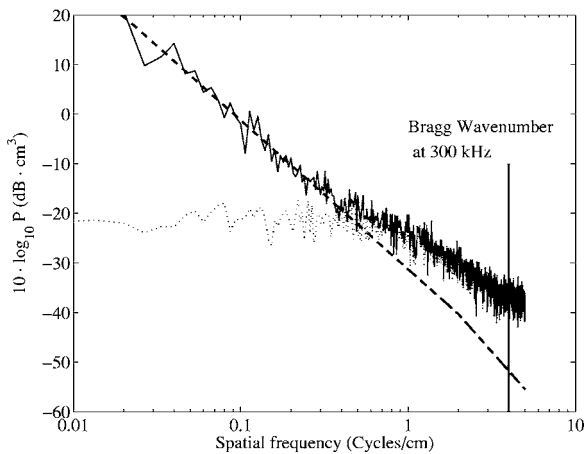


FIG. 6. Spatial power spectra obtained as an average of five equivalent roughness realizations based on spatial density parameters given in Table II. The solid line (—) is the equivalent roughness according to Eq. (23). The thin dotted line (·) is the roughness solely estimated from the density variations. The dashed line (--) is the two-power law, see Eq. (4), based on parameters listed in Table I.

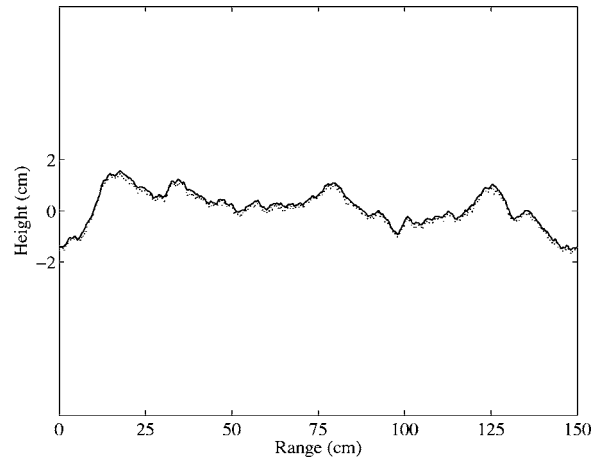


FIG. 7. Stochastic realizations of height profiles. The solid line (—) represents the interface roughness and the dotted line (·) the equivalent roughness.

spectra of the equivalent roughness profiles exhibit higher levels for large wave numbers, i.e., from 0.4 to 4 cycles/cm, than the optically acquired two-power law. Hence, an increase in the backscattering level is expected there.

Figure 7 is an example of a 1.5-m-long height profile based on optical data only, together with the corresponding equivalent roughness profile. Figure 8 is Fig. 7 zoomed to the range between 10 and 30 cm.

In the next section the field equations and the method applied to calculate the scattered field from the interface are presented.

III. FIELD EQUATIONS

In this work wave field propagation and scattering is considered in two dimensions, a consequence of the height-field to height-profiles approximation presented in beginning of Sec. II. The $e^{-i\omega t}$ time dependence is assumed. Hence, a two-dimensional diverging outgoing wave is described in terms of the Hankel function of the first kind, $H_0^{(1)}(z)$. A plane wave incident on the water-sediment interface on the

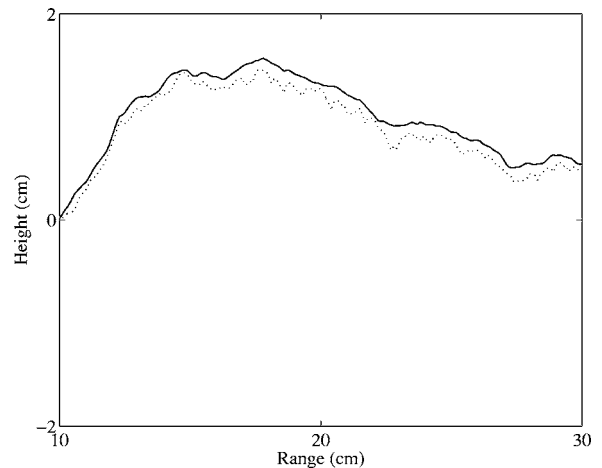


FIG. 8. The height profile realization from Fig. 7 zoomed. The solid line (—) represents the interface roughness and the dotted line (·) the equivalent roughness. Note, the equivalent roughness exhibits higher small scale variations.

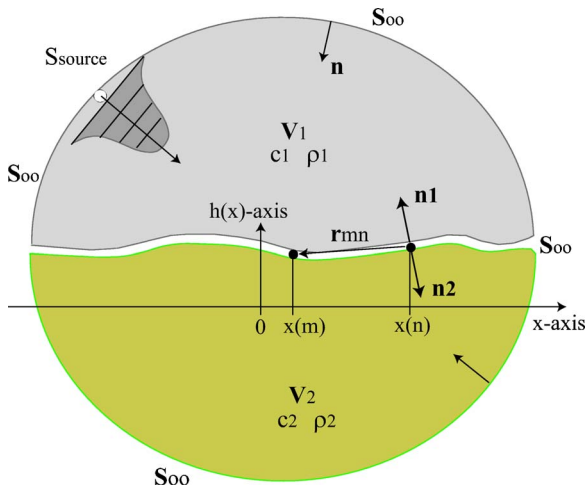


FIG. 9. The geometry applied for the fluid-fluid model represented by the coupled integral equations, Eqs. (24)–(26). In the water, i.e., medium 1, a tapered plane wave is incident from the infinity. Medium 2 represents the homogeneous sediment.

seabed is considered. The sediment is modeled as a fluid, i.e., the acoustic properties are fully described in terms of the mass density and sound speed. The backscattered pressure from the interface is the subject here. In Fig. 9 V_1 represents the water medium, with density ρ_1 and sound speed c_1 , and V_2 represents the sediment with density ρ_2 and sound speed c_2 . Within V_1 a source at infinity generates a plane wave incident on the interface between the water and sediment; the plane wave is tapered, i.e., it is of finite extent and excites only a limited part of the seabed.

The field on the surface, S_∞ , at infinity obeys Sommerfeld's radiation condition, i.e., the field vanishes here. The pressure p at an observation point \mathbf{r} within or on the boundary of V_1 can be expressed in terms of the Kirchhoff Helmholtz integral equation (see, e.g., Ref. 28):

$$\alpha_1 p(\mathbf{r}) = p^i(\mathbf{r}) + \frac{1}{4i} \int_{-\infty}^{\infty} \left(p(\mathbf{r}') \frac{\partial H_0^{(1)}(k_1 |\mathbf{r} - \mathbf{r}'|)}{\partial n'} - H_0^{(1)}(k_1 |\mathbf{r} - \mathbf{r}'|) \frac{\partial p(\mathbf{r}')}{\partial n'} \right) ds', \quad (24)$$

where the integral represents the field scattered from the interface s' , p^i is the incoming field, \mathbf{r}' is a point on s' and serves as an integration variable, $k_1 = \omega/c_1$ is the acoustic wave number in the water, and $\partial/\partial n' = \nabla \cdot \hat{\mathbf{n}}'$ is the gradient projected onto the surface normal vector $\hat{\mathbf{n}}'$ of unit length on s' . Finally, the constant α_1 on the left hand side of Eq. (24) is, for $j=1$, given by

$$\alpha_j = \begin{cases} 1, & \text{if } \mathbf{r} \text{ is inside } V_j, \\ \frac{1}{2}, & \text{if } \mathbf{r} \text{ is on the boundary of } V_j, \\ 0, & \text{if } \mathbf{r} \text{ is outside } V_j. \end{cases} \quad (25)$$

In the sediment, i.e., in V_2 , the integral equation becomes

$$-\alpha_2 p(\mathbf{r}) = \frac{1}{4i} \int_{-\infty}^{\infty} \left(p(\mathbf{r}') \frac{\partial H_0^{(1)}(k_2 |\mathbf{r} - \mathbf{r}'|)}{\partial n'} - H_0^{(1)}(k_2 |\mathbf{r} - \mathbf{r}'|) \frac{\partial p(\mathbf{r}')}{\partial n'} \right) ds', \quad (26)$$

where there is no incoming field from within V_2 , α_2 is defined in Eq. (25) with $j=2$, and the sign of the integral has been reversed due to a 180° reversal of the normal vector, $\hat{\mathbf{n}}'$ (see Fig. 9). The two integral equations, Eqs. (24) and (26), are coupled through the boundary conditions at the water-sediment interface as

$$p_1(\mathbf{r}') = p_2(\mathbf{r}'), \quad (27)$$

$$\frac{\partial p_1(\mathbf{r}')}{\partial n'} = \frac{1}{\mu} \frac{\partial p_2(\mathbf{r}')}{\partial n'}, \quad (28)$$

where $\mu = \rho_2/\rho_1$.

The gradient of the Hankel function projected onto the surface normal [the left term inside the integral of Eq. (24) and Eq. (26)] is considered next. The surface derivative of the zeroth-order Hankel function of the first kind projected onto the surface normal is

$$\frac{H_0^{(1)}(k|\mathbf{r} - \mathbf{r}'|)}{\partial n'} = k H_1^{(1)}(k|\mathbf{r} - \mathbf{r}'|) (\hat{\mathbf{r}} \cdot \hat{\mathbf{n}}'), \quad (29)$$

where $\hat{\mathbf{r}}' = (\mathbf{r} - \mathbf{r}')/|\mathbf{r} - \mathbf{r}'|$.

In the following, the position variables are written in terms of a discrete surface and, thus, the observation point vector \mathbf{r} is given by $(x_m, h(x_m))$, where $m=1, 2, \dots, N$; the integration variable \mathbf{r}' is given by $(x_n, h(x_n))$, where $n=1, 2, \dots, N$. The distance between the observation point m and integration point n is

$$r_{mn} = \sqrt{(x_m - x_n)^2 + [h(x_m) - h(x_n)]^2}, \quad (30)$$

and the unit vector pointing from n to m is

$$\hat{\mathbf{r}}_{mn} = \frac{1}{r_{mn}} \begin{bmatrix} x_m - x_n \\ h(x_m) - h(x_n) \end{bmatrix}. \quad (31)$$

The unit surface normal vector is given by

$$\hat{\mathbf{n}}(x_n) = \frac{1}{\gamma(x_n)} \begin{bmatrix} -(dh/dx)|_{x=x_n} \\ 1 \end{bmatrix}, \quad (32)$$

where $\gamma(x_n)$ is defined in Eq. (15). The n th line segment that points towards the m th observation point has an effective length of

$$\kappa_{mn} = \Delta s(n) \hat{\mathbf{n}}(x_n) \cdot \hat{\mathbf{r}}_{mn}, \quad (33)$$

and combining Eqs. (14), (31), and (32) in Eq. (33) yields

$$\kappa_{mn} = \Delta x(n) \frac{-(x_m - x_n) (dh/dx)|_{x=x_n} + [h(x_m) - h(x_n)]}{r_{mn}}, \quad (34)$$

a factor applied in the discretization of the first integrand in Eq. (26). In order to find the scattered pressure the pressure and pressure gradient on rough interface must be determined. The establishment of the matrix equations for the coupled

problem follows Chan,¹¹ who used the collocation method to obtain the following set of equations,

$$p^{(\text{inc})}(x_m) = \sum_{n=1}^N a_{mn} F_1(x_n) + \sum_{n=1}^N b_{mn} F_2(x_n), \quad (35)$$

$$0 = \sum_{n=1}^N c_{mn} F_1(x_n) + \sum_{n=1}^N d_{mn} F_2(x_n), \quad (36)$$

where $F_1(x) = p(x)$ and $F_2(x) = \gamma(x_n) \partial p(x) / \partial n$. For $m \neq n$,

$$a_{mn} = -\frac{ik_1}{4} \kappa_{mn} H_1^{(1)}(k_1 r_{mn}), \quad (37)$$

$$b_{mn} = \Delta x(n) \frac{i}{4} H_0^{(1)}(k_1 r_{mn}), \quad (38)$$

$$c_{mn} = \frac{ik_1}{4} \kappa_{mn} H_1^{(1)}(k_2 r_{mn}), \quad (39)$$

$$d_{mn} = -\mu \Delta x(n) \frac{i}{4} H_0^{(1)}(k_2 r_{mn}), \quad (40)$$

where κ_{mn} is defined by Eq. (34). For $m=n$ the coefficients become

$$a_{mm} = \frac{1}{2} - \frac{h''(x) \Delta x(m)}{4\pi \gamma_m^2}, \quad (41)$$

$$b_{mm} = \Delta x \frac{i}{4} H_0^{(1)}[k_1 \Delta x(m) \gamma_m / (2e)], \quad (42)$$

$$c_{mm} = \frac{1}{2} + \frac{h''(x) \Delta x(m)}{4\pi \gamma_m^2}, \quad (43)$$

$$d_{mm} = -\mu \Delta x(m) \frac{i}{4} H_0^{(1)}[k_1 \Delta x(m) \gamma_m / (2e)]. \quad (44)$$

In matrix form the following is obtained,

$$\begin{bmatrix} a_{11} & b_{11} & a_{12} & \dots & a_{1N} & b_{1N} \\ c_{11} & d_{11} & c_{12} & \dots & c_{1N} & d_{1N} \\ \vdots & \vdots & \ddots & \ddots & \vdots & \vdots \\ \vdots & \vdots & \dots & \dots & \dots & \dots \\ a_{N1} & b_{N1} & a_{N2} & \dots & a_{NN} & b_{NN} \\ c_{N1} & d_{N1} & c_{N2} & \dots & c_{NN} & d_{NN} \end{bmatrix} \begin{bmatrix} F_1(x_1) \\ F_2(x_1) \\ \vdots \\ \vdots \\ F_1(x_N) \\ F_2(x_N) \end{bmatrix} = \begin{bmatrix} p^i(x_1) \\ 0 \\ \vdots \\ \vdots \\ p^i(x_N) \\ 0 \end{bmatrix}. \quad (45)$$

When the pressure and the pressure gradient on the interface have been determined the resulting field at any observation point in the water column can be determined. The far field expression for the scattered field is

$$p_{sc}(\mathbf{r}) = \frac{1}{4i} \sum_{n=1}^N \sqrt{\frac{2}{\pi k_1 r_n}} e^{ik_1 r_n} e^{-i\pi/4} \left[ip(x_n) - \frac{\partial p}{\partial n}(x_n) \right] \times \Delta x(n), \quad (46)$$

where $r_n = |\mathbf{r} - \mathbf{r}_n|$.

IV. APPROXIMATIVE SOLUTION FOR LARGE SURFACES

For very long height profiles the matrix in Eq. (45) becomes extremely large since a sonar's field of view may cover several square meters. Suppose a height profile of length 20 m is required for modeling the sonar beam; a scattering computation of a 300-kHz wave requires a height field resolution equal to 1 mm, which yields a matrix of size $20\,000^2$ or 2.3 Gigabytes. Iterative solutions to Eq. (45) can be applied such as the conjugate gradient method (see Ref. 11) or the forward-backward method, similar to the Gauss-Seidel procedure (see Ref. 10). Here the direct method is maintained, but the matrix is reduced to a sparse band matrix by the insertion of zeros outside a certain number of diagonals,

$$\begin{bmatrix} a_{11} & b_{11} & \dots & b_{1M} & a_{1,M+1} & 0 & \dots & 0 \\ c_{11} & d_{11} & & & & & \ddots & \vdots \\ \vdots & & & & & & \ddots & \vdots \\ c_{K1} & & & & & & & 0 \\ a_{M+1,1} & & & & & & & 0 \\ 0 & \ddots & & & & & & \vdots \\ & 0 & & & & & & \vdots \\ \vdots & & \ddots & & & & & b_{NN} \\ & & \vdots & \ddots & & & & d_{NN} \\ 0 & 0 & 0 & 0 & 0 & \ddots & \dots & c_{NN} \end{bmatrix}, \quad (47)$$

with M diagonals below and M diagonals above the main diagonal. This choice is based on the fact that the Hankel function decays with range or, expressed in physical terms, the pressure at a given observation point on the surface mainly depends on the nearest neighbor points due to the geometrical spreading of the scattered waves.

V. RESULTS

The incoming field is formed as a tapered plane wave according to Ref. 9 [Eq. (11)], where the tapering parameter, g , of the incoming plane wave is equal to $L/4$, and L is the height profile length. Results are presented in terms of the scattering strength,

$$SS = 10 \log_{10} \sigma(\theta, \theta_s), \quad (48)$$

where $\sigma(\theta, \theta_s)$ is the dimensionless scattering cross section. For 2D wave propagation it is given by [see, e.g., Ref. 9, Eq. (13)]

$$\sigma(\theta, \theta_s) = \langle I_s(\theta_s) \rangle r / I_{\text{inc}} L, \quad (49)$$

where I_{inc} is the incident intensity and $\langle I_s(\theta_s) \rangle$ is the scattered intensity in the far field range r and averaged over numerous surface realizations in the direction θ_s . Finally, L is the profile length. Thus, σ is the ratio of the acoustic power scattered in direction θ_s to the power of the incoming field with grazing angle θ , and, hence, it is comparable with the scattering cross section applied for 3D scattering problems.

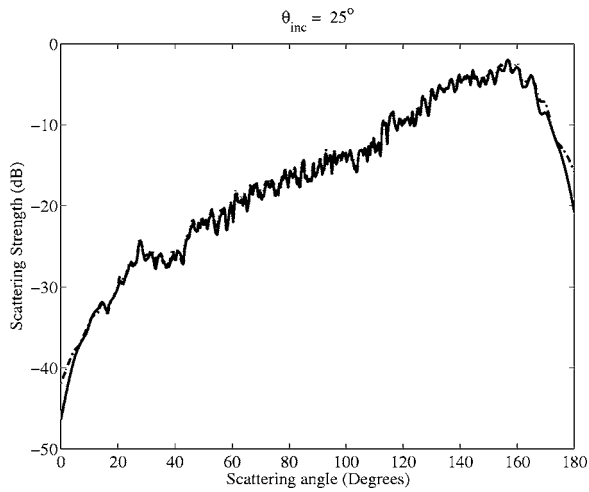


FIG. 10. Bistatic scattering strength for the equivalent roughness surface subject to a pressure release boundary condition. The incoming wave has a grazing angle of 25° . The solid line (—) is the full matrix solution and the dash-dot line (— · —) is the band-matrix solution with $M=80$.

The equivalent roughness profiles applied in the following correspond to the type of realizations shown in Figs. 7 and 8; the seabed parameters are depicted in Tables I and II. The AR(1)-parameter value, $\kappa=0.45$ [see Eq. (23)] is found to be an acceptable choice since the modeled backscattering strengths match the experimental data reasonably well (see below). The spatial ground range resolution of a height profile is $\lambda/5=1$ mm, and the acoustic parameters used in the simulations are, unless anything else is specified, as follows: the speed of sound in water $c_1=1500$ m/s, the sound speed ratio $\delta=c_2/c_1=1.165$, the water density $\rho_1=1$ g/cm³, and the homogeneous sediment density $\rho_1=1.8$ g/cm³.

Figure 10 shows the bistatic scattering strength for an incident field with a grazing angle, $\theta_i=25^\circ$, and a height profile length of 120λ . The interface has a pressure-release boundary condition, which is established by setting $\rho_2=10^{-5}$ g/cm³. For the scattering problem on a pressure release surface the Kirchoff-Helmholtz integral equation reduces to

$$p^i(\mathbf{r}) = \frac{1}{4i} \int_{-\infty}^{\infty} H_0^{(1)}(k_1|\mathbf{r}-\mathbf{r}'|) \frac{\partial p(\mathbf{r}')}{\partial n'} ds', \quad (50)$$

and the solution, given by Eqs. (4), (5), and (8) in Ref. 9, is applied as a first validation of the model presented here.

In Fig. 10 the full matrix solution based on Thorsos's solution is shown together with the solution provided by the band-matrix method, with $M=80$, where M is the number of nonzero diagonals to each side of the main diagonal. For the scattering angles in the range from 0° to 10° the error decreases from 5 dB down to approximately 1 dB. From 10° up to approximately 160° the solutions continue to coincide within 1 dB.

Figure 11 shows the backscattering error between the full matrix solution and the band matrix solution for different values of M , i.e., $M=20, 40, 80, 160, 320$. The grazing angles under consideration are $\theta=1^\circ, 5^\circ, 10^\circ, 20^\circ, 30^\circ, \dots, 90^\circ$, and each point is an average of 20 surface realizations of length $200\lambda=1$ m. The errors increase dramatically for grazing

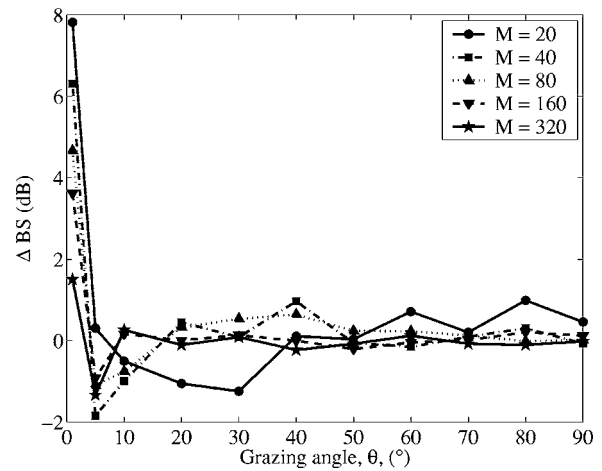


FIG. 11. Backscattering difference in dB between the full matrix solution and the band matrix solution for different values of M as a function of grazing angle. The curves are averages of 20 surface realizations of length 200λ .

angles below 5° , where the most sparse matrix solution, i.e., $M=20$, has a maximum error of approximately 8 dB at $\theta=1^\circ$. The smallest error, at $\theta=1^\circ$, is 1.8 dB for $M=320$. For grazing angles above 5° the error for $M=20$ is within 1.5 dB, 1 dB for $M=40$, and for higher values of M below 0.5 dB. Apart from computational accuracy, the computational efficiency is another aspect that must be taken into account: The capability of estimating the backscattered pressure from long height profiles is needed. Therefore, a band matrix with $M=20$ is chosen. It is unlikely that a sonar is directed toward the seabed with a grazing angle of less than 5° and, therefore, with $M=20$, an expected error of 1.5 dB is considered to be acceptable.

The required CPU time as a function of height profile length has been investigated on a 3 GHz Pentium4™ processor with 512 MB RAM, and computations have been made in Matlab™ on a Windows-XP™ operating system. The maximum profile length that can be computed on the current platform is $N=25\,000$, which takes approximately 95 s; larger matrices result in lack of workspace memory and cannot be carried out. The applied incremental ground range resolution is 1 mm, which yields a profile length of 25 m. The interpolation that is carried out when the distances between adjacent points on the height profile are larger than $\lambda/4$ typically increases the number of elements, N , by 3%, thus the actual matrix length is $N=25\,750$. Computation of a matrix of length $N=15\,000$, i.e., a profile length of 15 m, takes approximately 40 s, and a matrix with $N=5\,000$, i.e., a profile length of 5 m, takes approximately 15 s.

Figure 12 shows different backscattering strengths computed from equivalent roughness profiles; the grazing angle resolution is 0.5° , and each curve represents an average of 50 surface realizations. All band matrix solutions use $M=20$, i.e., 20 nonzero diagonals below and above the main diagonal of Eq. (47). The backscattering strengths from the equivalent roughness profiles of length $L_x=200\lambda$, i.e., 1 m, have been computed by the full matrix solution and the band matrix solution. Additionally, backscattering strengths from equivalent roughness profiles of length $L_x=2000\lambda$, i.e.,

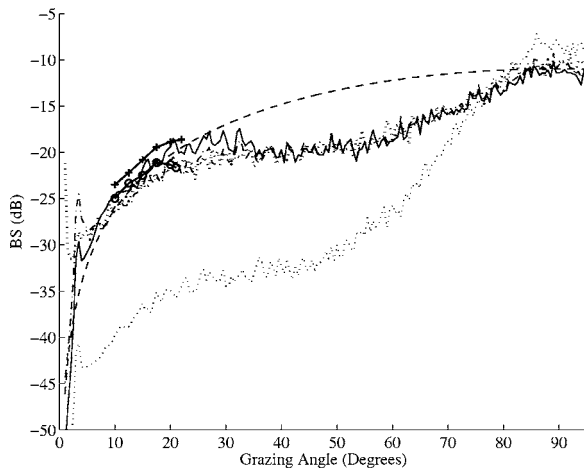


FIG. 12. Backscattering strength as a function of θ with $\Delta\theta=0.5^\circ$. All band matrix solutions (BMS) use $M=20$. The solid line (—) is the full band matrix solution, the dash-dot line (— · —) is the BMS, and both curves are based on the equivalent roughness profile (ERP). The thin dotted line (:) is the BMS from a height profile only based on stereo photogrammetry. The ERPs explained so far have a length of 200λ . The thick dotted line (:) is BMS, with an ERP length of 2000λ ; the cross and circle marked lines, i.e., (+), and (⊕), represent the SAX99 data; finally, the thin dashed line (—) is Lambert's law.

10 m, have been computed with the band matrix solution. The three solutions coincide within a few decibels with the SAX99 data, i.e., XBAMS and BAMS presented in Ref. 21 (Fig. 5, p. 10) for grazing angles between 10° and 22° . The backscattering strengths calculated from the interface found by optical means, i.e., the stereo-photogrammetric equipment, are for $\theta=5^\circ$ to 50° , approximately 15 dB weaker than the strengths found from the equivalent roughness profiles. For grazing angles between approximately 50° up to normal incidence, i.e., 90° , this difference decreases gradually. The model follows Lambert's law for small grazing angles as well as angles near normal incidence, i.e., for $\theta < 30^\circ$ and $\theta > 80^\circ$, respectively.

VI. DISCUSSION

Apart from a strong spatial variability of the density, experiments have also revealed a high spatial variability of the sediment sound speed (see, for example, Refs. 20 and 25), but sound speed variability is not included in the equivalent roughness approximation.

The scattering model presented in Sec. III is adopted from radar theory, where the interface between air and ground has a significant impedance contrast, which consequently yields a weak wave penetration into the ground. Hence, interface scattering is the dominant scattering mechanism, and the air and ground can be considered as homogeneous media. Prior to the development of the equivalent roughness approach it was attempted to vary the sediment density along each discrete surface point; that is, the density ratio μ , in Eqs. (40) and (44), was replaced by μ_n , with $n = 1, 2, \dots, N$, where N represents the total number of surface points. The same principle was applied by varying k_2 , i.e., the sediment sound speed, along the height profile. However, simulations did not show any change in the shape of the

backscattering curve, probably because the equations formulated in Sec. III are formulated strictly for interface roughness variations.

Another approach to compute the scattered field could be a finite element model, also for 1D height profiles, of the upper part of the sediment combined with a boundary value formulation for the interface. However, the method would probably become very computationally demanding and yet suffer from the lack of precise information regarding small scale density and sound speed variations in the upper part of the sediment.

It has also been attempted to apply the method presented by D. Kapp *et al.*,¹⁰ but it yields more inaccurate results for the zeroth-order Born term than the band matrix approximation applied here, and it does not converge for higher order iterations.

It is important to emphasize that the optically acquired roughness parameters, shown in Table I, probably not are measured at the same date and time as the acoustic data. Except for the fact that BAMS is the correct site, it is not quite clear which set of parameters in Ref. 23 must be applied. However, it does not change the fact that the equivalent roughness approach lifts the backscattering level up to the levels obtained from experiments.

VII. CONCLUSION

The equivalent roughness approximation yields, when $\kappa=0.45$, backscattering strengths at 300 kHz that agree with experimental data acquired at SAX99. The band-matrix approximation, with $M=20$, yields backscattering errors of 8 dB for $\theta=1^\circ$; for grazing angles above 5° backscattering errors are less than 1.5 dB. Sonar simulations are not expected to be carried out for grazing angles of less than 5° , and, hence, the model is considered to have a sufficient accuracy for $M=20$. Computations have been carried out in Matlab6.5TM on a PC with a Windows XPTM operating system, a 3 GHz (Pentium4TM) processor, and 512 MB RAM. The method allows computations of height profiles with 25 000 elements that correspond to 25 m when the resolution is one-fifth of the wavelength and the wavelength is $\lambda = 0.5$ cm. The equivalent roughness approach combined with the band matrix method is well suited to model sandy seabed backscattering for artificially very high frequency sonar images.

ACKNOWLEDGMENTS

The authors are grateful to Dajun Tang at Applied Physics Laboratory, University of Washington, for answers related to the seabed model, and to Eric Thorsos, Applied Physics Laboratory, University of Washington, for general advice regarding the scattering problem. The authors also gratefully acknowledge advice from Per Christian Hansen, Informatics and Mathematical Modeling (IMM), Technical University of Denmark, regarding the band matrix solution.

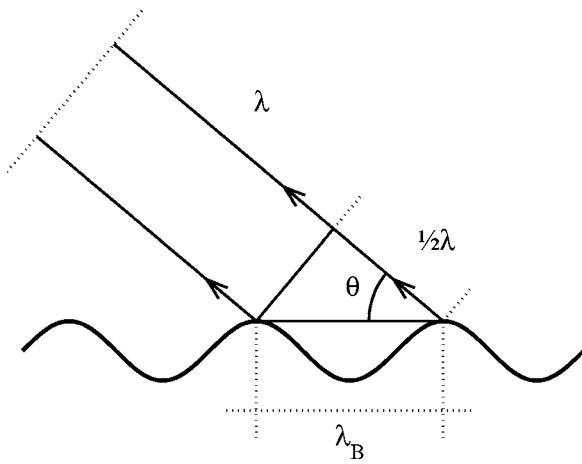


FIG. 13. Geometry applied to derive the Bragg wavelength.

APPENDIX: THE BRAGG WAVELENGTH

The Bragg wavelength, λ_B , for a rough interface is defined in terms of an incoming, monochromatic plane wave with wavelength, λ , and a grazing angle of incidence, θ , that is,

$$\lambda_B = \frac{\lambda}{2 \cos \theta} \quad (\text{A1})$$

(see Fig. 13). Equation (A1) is equivalent to the reinforcement criterion for backscattering described by Urick.²⁹ The Bragg frequency of the seabed roughness is

$$f_B = \frac{2 \cos \theta}{\lambda}. \quad (\text{A2})$$

At 300 kHz the wavelength is $\lambda=0.5$ cm when it is assumed that the sound speed is $c=1500$ m/s; thus at zero grazing angle, i.e., $\theta=0$, one has $f_B=4$ cycles/cm, which corresponds to the vertical lines indicated in Figs. 1–3.

¹E. Pouliquen, G. Canepa, L. Pautet, and A. P. Lyons, "Temporal variability of seafloor roughness and its impact on acoustic scattering," in Proceedings of the Seventh European Conference in Underwater Acoustics (ECUA2004), Delft, The Netherlands, 5–8 July 2004.

²J. A. Ogilvy, *Theory of Wave Scattering from Random Rough Surfaces* (IOP, London, 1991), Chap. 4.1.2.

³L. M. Brekhovskikh and Yu. P. Lysanov, *Fundamentals of Ocean Acoustics*. Third edition (AIP, Springer-Verlag, New York, 2003).

⁴E. I. Thorsos and D. R. Jackson, "Studies of scattering using numerical methods," *Waves Random Media* **3**, S165–S190 (1991).

⁵J. M. Bell, "Application of optical ray tracing techniques to the simulation of sonar images," *Opt. Eng. (Bellingham)* **36**, 1806–1813 (1997).

⁶T. Capron, G. Hayward, and R. Chapmann, "A 3D simulator for the design and evaluation of sonar system instrumentation," *Meas. Sci. Technol.* **10**, 1116–1126 (1999).

⁷E. I. Thorsos and S. L. Broschat, "An investigation of the small slope approximation for scattering from rough surfaces. Part I. Theory," *J. Acoust. Soc. Am.* **97**, 2082–2093 (1995).

⁸S. L. Broschat and E. I. Thorsos, "An investigation of the small slope approximation for scattering from rough surfaces. Part II. Numerical studies," *J. Acoust. Soc. Am.* **101**, 2615–2625 (1997).

⁹E. I. Thorsos, "The validity of the Kirchhoff approximation for rough surface scattering using a Gaussian roughness spectrum," *J. Acoust. Soc. Am.* **83**, 78–92 (1988).

¹⁰D. A. Kapp and G. S. Brown, "A new numerical method for rough surface scattering calculations," *IEEE Trans. Antennas Propag.* **44**, 711–721 (1996).

¹¹C. H. Chan, L. Tsang, and Q. Li, "Monte Carlo simulations of large scale one-dimensional random rough surface scattering at near-grazing incidence: Penetrable case," *IEEE Trans. Antennas Propag.* **46**, 142–149 (1998).

¹²D. R. Jackson, D. P. Winebrenner, and A. Ishmaru, "Application of the composite roughness model to high frequency bottom backscattering," *J. Acoust. Soc. Am.* **79**, 1410–1422 (1986).

¹³D. R. Jackson and K. B. Briggs, "High frequency bottom backscattering: Roughness versus sediment volume scattering," *J. Acoust. Soc. Am.* **92**, 962–977 (1992).

¹⁴P. D. Mourad and D. R. Jackson, "High-frequency sonar equation models for bottom backscatter and forward loss," in *Proceedings of OCEANS'89* (1989), pp. 1168–1175.

¹⁵D. R. Jackson, "Models for scattering from the sea bed," *Proc. IOA*, Vol. **16**, Part 6 (1994).

¹⁶K. L. Williams and D. R. Jackson, "Bistatic bottom scattering: Model, experiments, and model/data comparison," *J. Acoust. Soc. Am.* **103**, 169–181 (1998).

¹⁷S. Stanic, R. R. Goodman, K. B. Briggs, N. P. Chotiros, and E. T. Kennedy, "Shallow-water bottom reverberation measurements," *IEEE J. Ocean. Eng.* **23**, 203–210 (1998).

¹⁸E. Pouliquen and A. P. Lyons, "Backscattering from Bioturbated sediments at very high frequency," *IEEE J. Ocean. Eng.* **27**, 388–402 (2002).

¹⁹K. L. Williams, D. R. Jackson, E. I. Thorsos, D. Tang, and K. B. Briggs, "Acoustic backscattering experiments in a well characterized sand sediment: Data/model comparisons using sediment fluid and Biot models," *IEEE J. Ocean. Eng.* **27**, 376–387 (1998).

²⁰D. Tang, K. B. Briggs, K. L. Williams, D. R. Jackson, E. I. Thorsos, and D. B. Percival, "Fine scale volume heterogeneity measurements in sand," *IEEE J. Ocean. Eng.* **27**, 546–560 (2002).

²¹E. I. Thorsos, K. L. Williams, N. P. Chotiros, J. T. Christoff, K. W. Commander, C. F. Greenlaw, D. V. Holliday, D. R. Jackson, J. L. Lopes, D. E. McGehee, J. E. Piper, M. D. Richardson, and D. Tang, "An overview of SAX99: Acoustic measurements," *IEEE J. Ocean. Eng.* **26**, 4–25 (2001).

²²O. George and R. Bahl, "Simulation of backscattering of high frequency sound from complex objects and sand sea-bottom," *IEEE J. Ocean. Eng.* **20**, 119–130 (1995).

²³K. B. Briggs, D. Tang, and K. L. Williams, "Characterisation of interface roughness of rippled sand off Fort Walton Beach, Florida," *IEEE J. Ocean. Eng.* **27**, 505–514 (2002).

²⁴K. B. Briggs, "Microtopographical roughness of shallow-water continental shelves," *IEEE J. Ocean. Eng.* **14**, 360–367 (1989).

²⁵K. B. Briggs, M. Zimmer, and M. D. Richardson, "Spatial and temporal variations in sediment compressional wave speed and attenuation measured at 400 kHz for SAX04," in Proceedings of Boundary Influences in High Frequency, Shallow Water Acoustics, Bath, UK, September 2005.

²⁶E. I. Thorsos and M. D. Richardson, "Guest Editorial," *IEEE J. Ocean. Eng.* **27**, 341–345 (2002), p. 342, first column, lines 27–31.

²⁷J. G. Proakis and D. G. Manolakis, *Digital Signal Processing. Principles, Algorithms, and Applications*. Third edition (Prentice-Hall, Englewood Cliffs, NJ, 1996), Chap. 11.1.1.

²⁸E. G. Williams, *Fourier Acoustics. Sound Radiation and Nearfield Acoustical Holography* (Academic, London, 1999), Chap. 8.5, pp. 262–264.

²⁹R. J. Urick, *Principles of Underwater Sound*. Third edition (Peninsula, Los Altos, CA, 1983), Chap. 8.13.

Evidence of dispersion in an artificial water-saturated sand sediment

Preston S. Wilson^{a)}

Mechanical Engineering Department and Applied Research Laboratories, The University of Texas at Austin, Austin, Texas 78712-0292

Allen H. Reed

Seafloor Sciences Branch, Naval Research Laboratory, Stennis Space Center, Mississippi 39529-5004

Jed C. Wilbur and Ronald A. Roy

Department of Aerospace and Mechanical Engineering, Boston University, Boston, Massachusetts 02215

(Received 2 February 2006; revised 3 November 2006; accepted 3 November 2006)

A laboratory experiment was conducted to measure the speed of sound in an artificial water-saturated granular sediment composed of cleaned and sorted medium-grained sand and degassed distilled water. The experiment was conducted within a range of frequencies where dispersion is predicted by a number of existing models. Between 2 and 4 kHz, the sound speed was inferred from measurements of the resonance frequencies of a thin-walled cylindrical container filled with the material. An elastic waveguide model was used to account for the effect of the finite impedance of the walls, although this effect was found to be small. From 20 to 300 kHz, the sound speed was obtained directly from time-of-flight measurements within the sediment. Dispersion in close agreement with the Williams effective density fluid model [K. L. Williams, *J. Acoust. Soc. Am.* **110**, 2276–2281 (2001)] was observed. © 2007 Acoustical Society of America. [DOI: 10.1121/1.2404619]

PACS number(s): 43.30.Ma [RR]

Pages: 824–832

I. INTRODUCTION

A complete understanding of sound propagation in water-saturated granular sediments has not been achieved. A number of experimental studies have appeared in the literature that report either direct or indirect evidence of sound speed dispersion in this medium.^{1–6} Such results generally support the Biot-Stoll model (and its variants)^{7–12} for sound propagation. The Biot-derived models predict a low-frequency sound speed, followed by an increase to a higher sound speed beyond some transition frequency. There are also a number of experimental studies^{13,14} that found no evidence of sound speed dispersion and support Hamilton's dispersionless fluid model.¹⁵ The dispersion predicted by the Biot models occurs over a range of about two orders of magnitude in frequency (from around 100 Hz to 10 kHz for medium-grained sand, for example). It is experimentally difficult to obtain measurements on a uniform body of sediment using a single technique that spans the entire range of interest. Further, the predicted dispersion is on the order of 10% and achieving experimental accuracy significantly greater than this has been difficult. Surface and volume inhomogeneities in natural sediments also cause uncertainty in experimental measurements.^{4,16}

A series of laboratory experiments designed to overcome some of these difficulties were performed on a water-saturated sand sediment. The sediment was contained within a thin-walled cylindrical vessel large enough to permit time-

of-flight sound speed measurements within the bulk sediment above 20 kHz. Lower frequency sound speeds were inferred from the measured resonance frequencies of the cylindrical sediment-filled container. For this analysis, transverse waves within the sediment were ignored. The sediment was modeled as a fluid, but the sediment sound speed was not constrained to be constant. The walls of the cylinder were initially approximated as a pressure release boundary (details of the assumption's validity are discussed in the following). The cylinder was placed upon a layer of insulation foam, which yielded a pressure release lower boundary condition. The water/air interface provided a pressure release boundary at the top of the sediment. Therefore, a pressure release waveguide model was used to relate the measured resonance frequencies to the effective sediment sound speed. In order to identify individual modes, and hence infer frequency-dependent sound speeds from resonances, both symmetric and asymmetric excitation of the sediment cylinder was used. The spatially dependent phase of the acoustic pressure, relative to the drive signal, was employed to aid in mode identification. Dispersion was observed and these results are presented and compared to the effective density fluid model,¹² hereafter referred to as EDFM. The effect of the finite impedance imparted by the cylindrical wall of the sediment container is also discussed. A model of an elastic-walled waveguide was used to relate the sediment sound speeds that were inferred from axisymmetric modes in the tank to the values that would be observed in an unconfined free field. The effect was found to be small (less than 0.53%) at the lowest experimental frequency and decreased as the frequency increased.

^{a)}Electronic mail: pswilson@mail.utexas.edu

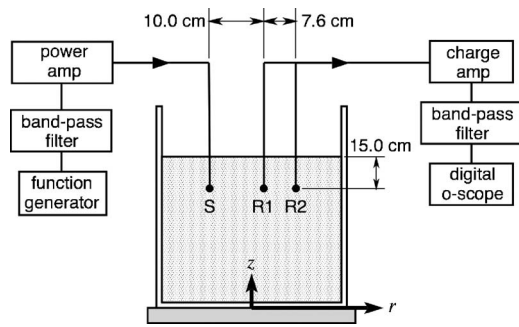


FIG. 1. A schematic diagram of the time-of-flight measurement apparatus.

II. DESCRIPTION OF THE EXPERIMENT

A. Sediment container

The sediment was contained in a right-circular-cylindrical tank possessing walls made of high-density polyethylene (HDPE). The mean inner diameter was 0.686 m, the height of the sediment within the vessel was 0.80 m, and the mean wall thickness was 0.48 cm. The tank, which had a flat bottom, was placed upon a 10-cm-thick styrofoam panel which, in turn, rested on a concrete floor.

The sediment was prepared in the following manner. Filtered fresh water was added to the tank and degassed *in situ* by heating it to 60 °C using several immersion heaters. Circulation was imposed during this process with a motorized stirring impeller. The water was kept at 60 °C for several hours during which time the dissolved gas concentration attained equilibrium. Then, approximately 500 kg of a commercial silica blasting sand was slowly added to the water, as the stirring continued. The sediment was then allowed to cool to room temperature, over a period of 24 h. As the system cooled, the water phase became undersaturated with gas and thus drew into solution any gas pockets entrained by the introduction of the sand, resulting in a fully saturated sediment. A sieve analysis conducted on approximately 500 ml of the sand yielded grain sizes ranging from 150 to 600 μm , with a mean size of 300 μm .

B. High-frequency time-of-flight measurements

The sound speed within the sediment was measured using a time-of-flight technique at 20, 50, 100, and 300 kHz. A schematic diagram of this experiment is shown in Fig. 1. The signal source was a function generator programmed to produce sinusoidal pulses of various length, depending upon the frequency, to avoid multipath interference. The source signal was bandpass filtered (24 dB/octave) at the pulse center frequency with a Krohn-Hite model 34A filter and then amplified by a Krohn-Hite model 7500 wide-band power amplifier and directed to a Brüel & Kjær model 8103 miniature hydrophone, operating as a source (labeled S in Fig. 1). Two more 8103 hydrophones were positioned 10.0 and 17.6 cm away from the source on a horizontal line (parallel to the sediment surface), at a depth of 15.0 cm. The latter two hydrophones acted as receivers (labeled R1 and R2 in Fig. 1). The relative positions of the source and receivers were constrained to within ± 0.25 mm by mounting each hydrophone and its cable inside a stiff stainless steel tube. These tubes were

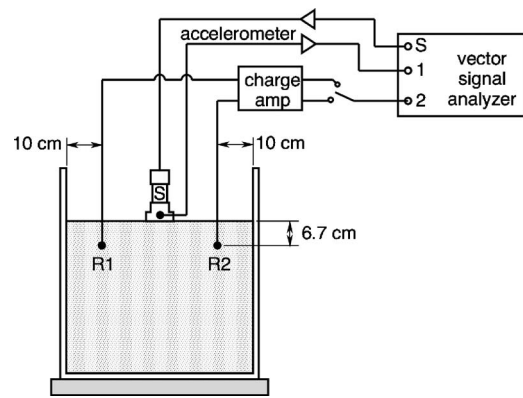


FIG. 2. A schematic diagram of the resonance frequency apparatus.

mounted to a steel frame and fastened securely in place. The R1–R2 separation distance was set and measured with a micrometer caliper prior to inserting the hydrophones into the sediment. The rigidity of the mounting scheme was sufficient to prevent caliper-measurable deflection during the inserting process. The hydrophone-enclosing tubes were filled with degassed water to minimize acoustic disturbance of the sediment.

The signals from R1 and R2 were conditioned with a Brüel & Kjær model 2692 charge amplifier, then bandpass filtered (24 dB/octave) at the pulse center frequency with Krohn-Hite model 34A filters. The filtered source and receive signals were acquired with a digital oscilloscope. At each frequency, 100 pings were collected and the averaged signals were sent to a computer for processing. The R1 and R2 signals were cross-correlated to obtain the time-of-flight and then sound speed was calculated from the known sensor separation distance. The uncertainty in sound speed was calculated from the previously stated position uncertainty, and the digitization sample rate and found to be between ± 6.6 and ± 9.9 m/s at 300 and 20 kHz, respectively.

C. Low-frequency resonance measurements

The apparatus for this portion of the experiment is shown in Fig. 2. A custom-fabricated Tonpiltz-type transducer was used as a source. It is described in Ref. 17 and has a circular-shaped radiating face with an accelerometer imbedded in it, and therefore can be driven at constant velocity amplitude by suitable monitoring of the accelerometer signal and modification of the excitation voltage amplitude. The source was placed face-down on the surface of the sediment in one of two positions, to be described later. The source signal was a band-limited (2–5 kHz) periodic chirp, provided by a Hewlett-Packard 89410A vector signal analyzer (VSA) and amplified by a Crown CE 1000 power amplifier. The chirp amplitude was modified onboard the VSA to produce a source velocity amplitude that was uniform across the frequency range, as discussed earlier. The acoustic pressure was measured in the sediment with B&K 8103 hydrophones at two positions, labeled R1 and R2 in Fig. 2. The depth was 6.7 cm and each sensor was positioned 10 cm from the vessel wall. When observed from above, R1–S–R2 formed a straight line. The signals from R1 and R2 were conditioned

TABLE I. Specific acoustic impedance of sediment and tank materials.

Material	Specific acoustic impedance (Pa s/m)
Sediment	3.5×10^6
Tank wall material, HDPE	2.5×10^6
Air	415

by the B&K 2692 charge amp, which included bandpass filtering from 10 to 10 kHz, and digitized by the VSA. The complex spectrum of each hydrophone signal (with phase referenced to the excitation signal) was calculated onboard the analyzer using 100 spectral averages and converted to complex acoustic pressure spectra using the calibrated hydrophone sensitivities.

III. ACOUSTIC MODEL OF SEDIMENT AND CONTAINER

An acoustic model of the sediment/container system is needed to infer sound speeds from measured resonance frequencies. In this analysis, the sediment was considered to be an effective fluid with wave number k , which is a valid approach for granular sediments.¹² We assume the phase speed can be frequency dependent, but $\text{Im}[k] \ll \text{Re}[k]$, so that the resonance frequencies depend primarily upon the phase speed and have weak dependence upon the attenuation. Transverse waves in the sediment were ignored.

Initially, we ignore the container walls and consider the sides of the cylinder to have a pressure-release boundary condition under the following justification. (1) Typical values of the specific acoustic impedance of the materials involved are given in Table I. Based on these values and the wall thickness (0.48 cm), the three-medium reflection coefficient R , given by Eq. 6.3.7 in Ref. 18 for pressure waves incident upon the wall, is $R = 1.00 \angle 176.5^\circ \pm 1.5^\circ$ between 2 and 5 kHz. (2) This was qualitatively verified by the observation of inverted reflections from the walls during the time-of-flight measurements, and (3) by the absence of plane-wave longitudinal mode resonances in the system. The air-sediment interface at the top of the container is clearly pressure release. Finally, the container was placed upon a 10-cm-thick styrofoam building insulation panel to approximate a pressure release boundary condition on the bottom. For the cylindrical coordinate system shown in Fig. 1 and sinusoidal excitation, the acoustic pressure in a right-circular cylinder with $p=0$ boundary conditions at all surfaces is

$$P_{mnN}(r, \theta, z, t) = A_{mnN} J_m(\alpha_{mn} r/a) \times \cos(m\theta - \theta_{0m}) \sin(N\pi z/h) e^{j\omega t}, \quad (1)$$

and has resonance frequencies

$$f_{mnN} = \frac{c}{2} \sqrt{\left(\frac{\alpha_{mn}}{\pi a}\right)^2 + \left(\frac{N}{h}\right)^2}, \quad (2)$$

where α_{mn} is the n th root of the Bessel function $J_m(x)$, c is the effective speed of sound in the sediment, a is the tank radius, h is the sediment height, A_{mnN} is the modal amplitude coefficient, and θ_{0m} is a phase angle which depends on the source condition. Equations (1) and (2) were adapted from

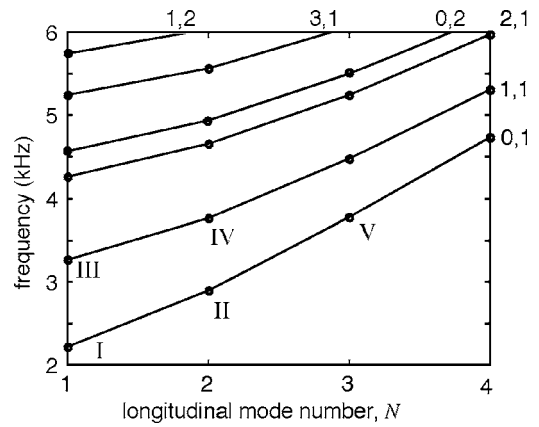


FIG. 3. The resonance frequencies for the six lowest-order mode families for a constant sound speed of 1730 m/s. The families are labeled m,n around the top and right-hand side of the plot. The plane wave mode would be $0,0,N$ if it existed.

Ref. 19. A plot of resonance frequencies versus longitudinal mode number N is shown in Fig. 3 for the six lowest-order mode families. Five modes, in order of ascending frequency, are labeled with roman numerals from I to V. Note that above mode III, multiple modes appear with similar eigenfrequencies.

Calculation of sound speed from a measured spectral peak requires one to identify the specific eigenmode and its m,n,N values. Mode family $0,1,N$ is axisymmetric and mode family $1,1,N$ is asymmetric about the center of the sediment cylinder, as shown in Fig. 4. These two modes were selectively excited by using the source positions shown in Fig. 4. To excite mode family $0,1,N$, the source was placed at the center of the sediment cylinder. To excite mode family $1,1,N$, the source was placed halfway between the center and the container wall. The relative phase of the acoustic pressure observed at R1 and R2 was used to help identify the mode associated with an observed resonance peak. For example, Eq. (1) yields acoustic pressures at R1 and R2 that are in phase for modes I, II, and V, and 180° out of phase for modes III and IV.

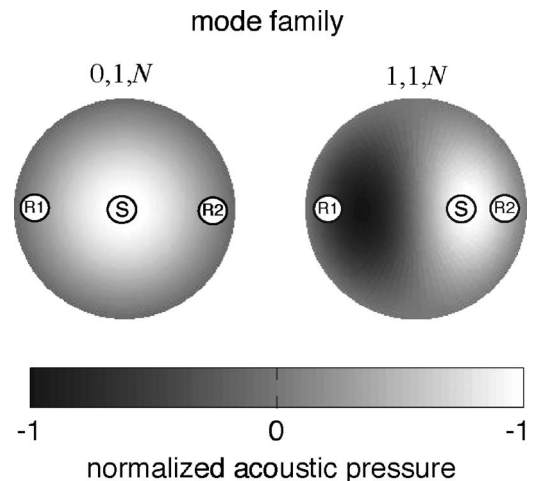


FIG. 4. The mode shapes given by Eq. (1) for two mode families. The source positions for each case are labeled S. The receiver positions, which remain the same in both cases, are labeled R1 and R2.

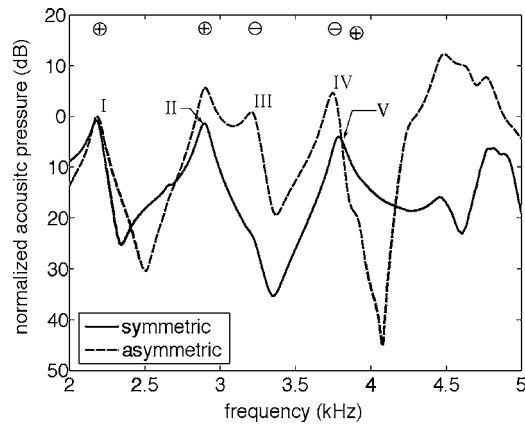


FIG. 5. Acoustic pressure spectra obtained at position R1 for both symmetric and asymmetric excitation. Spectra measured at position R2 were similar. The acoustic pressure measured between R1 and R2 was in phase (within $\pm 1^\circ$) at the resonance peaks labeled I, II, and V, and was out of phase (by 170°) at resonances III and IV, as indicated by \oplus and \ominus .

IV. RESULTS

A total of four averaged spectra were obtained during the resonance frequency experiment. These consisted of the acoustic pressure measured at R1 and R2, for both of the source positions shown in Fig. 4. The pressure spectra obtained at R1 are shown in Fig. 5. For the spectral peaks labeled I, II, and V, there was less than one degree phase difference between R1 and R2. These three spectral peaks are associated with mode family $0, 1, N$ and correspond with the symmetric eigenmodes labeled I, II, and V in Fig. 3. Returning to Fig. 5, the spectral peaks labeled III and IV exhibited an R1–R2 phase difference of 170° . These peaks correspond to the asymmetric modes III and IV, shown in Fig. 3 and associated with mode family $1, 1, N$. Effective sediment sound speeds c were calculated from each of the identified peaks in Fig. 5 using Eq. (2). Although not shown, similar results were obtained from the sensor at R2.

Both the resonance-based and time-of-flight-based sound speeds are shown in Fig. 6. The speeds are normalized by the speed of sound in distilled water at the ambient temperature ($23.5 \pm 0.5^\circ\text{C}$). The sound speed predicted by the effective density fluid model¹² is also shown in Fig. 6. The pertinent equations of the model are shown in the following for convenience. The sediment parameters used for the model calculation are shown in Table II. These were primarily taken from Ref. 12 but the following were obtained from measurements: The water sound speed was calculated from the experimental temperature. The porosity of four samples was determined by the water evaporation method. The permeability was measured using a Soiltest K-605 combination permeameter modified to accommodate a 13-cm-long, 6.1-cm-diam core. Ten constant-head permeability tests²⁰ were performed on each of two samples.

V. SEDIMENT SOUND SPEED FROM THE EFFECTIVE DENSITY FLUID MODEL

The effective density fluid model of sound propagation in water-saturated granular sediments is described in detail elsewhere,¹² but the equations for prediction of the sediment

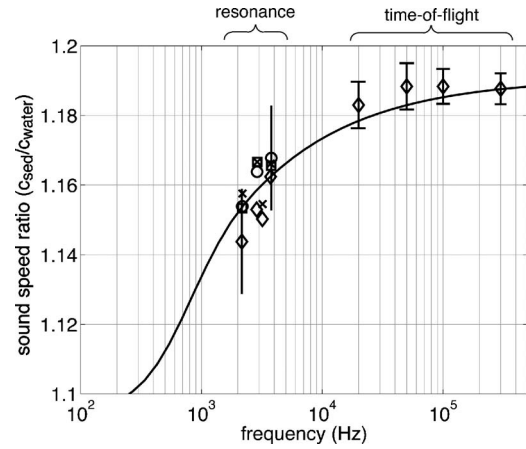


FIG. 6. Normalized sound speed measurements are compared to the EDFM (solid line). Resonance measurements are indicated with circles and squares (R1 and R2, respectively, with source in center) and crosses and diamonds (R1 and R2, respectively, source off-center, near R2). Vertical error bars near 2 and 4 kHz represent sound speed uncertainty due to uncertainties in the dimensions of the tank, but are only shown for the minimum and maximum sound speed measurements, so that the remaining data points are not obscured. For the time-of-flight measurements, the error bars represent sound speed uncertainty due to uncertainty in the sensor separation distance and the time resolution of the data acquisition. The EDFM was evaluated using the parameters in Table II and the mean values of porosity and permeability.

sound speed are repeated here for convenience. The EDFM considers a water-saturated granular sediment with a total mass density ρ , pore fluid mass density ρ_f , sediment particle mass density ρ_s , individual sediment grain bulk modulus K_r , pore fluid bulk modulus K_f , porosity β , tortuosity α , permeability κ , pore fluid viscosity η , and complex sound speed c . The sound speed is a function of angular frequency ω and is given by

$$c = \sqrt{\frac{H}{\rho_{\text{eff}}(\omega)}}, \quad (3)$$

where the compressibility is determined by a mixture rule

$$H = \left(\frac{1 - \beta}{K_r} + \frac{\beta}{K_f} \right)^{-1}, \quad (4)$$

and the effective density is

TABLE II. Material parameters used in the effective density fluid model (SI units). Parameters obtain from measurements on the sediment are in **BOLDFACE**. The mean value is followed by the range of variation among multiple measurements. The remaining parameters are from Ref. 12.

Porosity	0.370 (0.368–0.371)
Sand grain mass density	2650
Water mass density	998
Sand grain bulk modulus	3.6×10^{10}
Water sound speed	1492
Water viscosity	0.001
Permeability	4.58×10^{-11} (4.18×10^{-11} – 4.74×10^{-11})
Tortuosity	1.25

TABLE III. Material parameters used in the evaluation of Eq. (A1) (SI units).

Sediment mass density, ρ_L	2039
HDPE mass density, ρ_w	1000
HDPE compressive sound speed, c_l	2500
HDPE transverse sound speed, c_t	680

$$\rho_{\text{eff}}(\omega) = \rho_f \left(\frac{\alpha(1-\beta)\rho_s + \beta(\alpha-1)\rho_f + \frac{i\beta\rho F\eta}{\rho_f\omega\kappa}}{\beta(1-\beta)\rho_s + (\alpha-2\beta+\beta^2)\rho_f + \frac{i\beta F\eta}{\omega\kappa}} \right). \quad (5)$$

The parameter F represents a deviation from Poiseuille flow of the fluid within the pores and is given by

$$F(\epsilon) = \frac{\frac{\epsilon}{4}T(\epsilon)}{1 - \frac{2i}{\epsilon}T(\epsilon)}, \quad (6)$$

where the Bessel functions $J_\nu(x)$ are used in

$$T(\epsilon) = \frac{(-\sqrt{i})J_1(\epsilon\sqrt{i})}{J_0(\epsilon\sqrt{i})}, \quad (7)$$

where the quantity $\epsilon = a\sqrt{\omega\rho_f/\eta}$ in conjunction with $a = \sqrt{8\alpha\kappa/\beta}$ represents the pore size parameter. The sound speed measurements shown in Fig. 6 are compared to the model phase speed given by real part of Eq. (3) and the material parameters of Table II.

VI. EFFECT OF FINITE WALL IMPEDANCE

An exact analytic model²¹ for sound propagation in an elastic-walled, fluid-filled cylindrical tube was used to investigate the effects of finite wall impedance on the sound speeds inferred from the resonance frequency measurements for the axisymmetric modes. The model yields particle displacement field equations and a dispersion relation for the axisymmetric modes of an inviscid-liquid-filled cylindrical tube with arbitrary-thickness elastic walls, where the outermost radial boundary condition was approximated as pressure release. The dispersion relation has been verified for a variety of sizes and wall materials, including steel,¹⁷ aluminum, and PVC,²² and is presented in Eq. (A1).

The unconfined (intrinsic) sound speed of the material that fills the tube is an input parameter to Eq. (A1) and the admissible phase speeds are calculated. This model is limited to axisymmetric modes, so we applied it to the $0, 1, N$ modes and found that the maximum deviation of the sediment sound speed inferred from the pressure-release model was within 0.57% of the sound speed inferred from the elastic waveguide model and the minimum deviation was 0.18%. The material parameters used for the evaluation of Eq. (A1) are given in Table III and the resulting sediment sound speeds are given in Table IV. The corresponding sediment sound speeds obtained with the pressure-release model are also included in Table IV for comparison.

TABLE IV. Comparison between sediment sound speed values c of Fig. 6, which were inferred from the pressure-release model [Eq. (2)], and corrected sound speeds c_1 , obtained from the axisymmetric elastic waveguide model [Eq. (A1)].

Frequency (Hz)	c (m/s), Eq. (2)	c_1 (m/s), Eq. (A1)
Circle (○) data points		
2179	1721	1712
2892	1736	1731
3788	1742	1739
Square (□) data points		
2178	1721	1711
2899	1741	1735
3781	1739	1736
Cross (×) data points		
2186	1727	1717
2899	1741	1735
Diamond (◇) data points		
2160	1706	1697
2865	1720	1714

The relative size of the measurement uncertainty due to tank dimension uncertainty is compared to the finite wall impedance correction in Fig. 7. For clarity, this comparison is only shown for one of the data sets. The circle data points from Fig. 6 are repeated in Fig. 7 and their values after correction for the finite wall impedance are shown. The finite wall impedance biases the axisymmetric resonance measurements (circles and squares in Fig. 6) by +0.57% or less, but this is significantly less than the measurement uncertainty due to the tank dimensions.

An exact analytic model for asymmetric excitation of a liquid-filled waveguide with walls of arbitrary thickness is not available. We used an approximate model²³ which treats the wall as a shell and yields a dispersion relation Eq. (A6) for both axisymmetric and asymmetric modes. Otherwise, the corrections procedure is the same as for the axisymmetric case, discussed earlier. The dimensions of the sediment tank

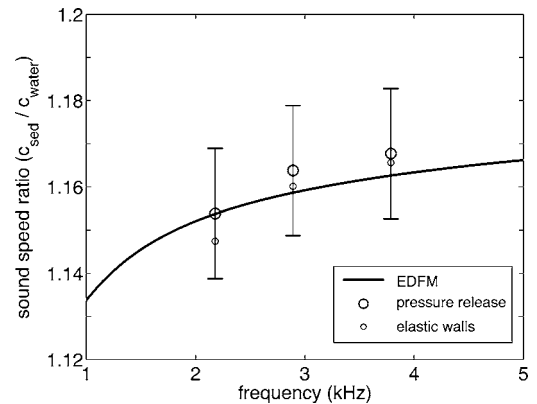


FIG. 7. The effect of ignoring the finite impedance of the tank walls is shown for the axisymmetric modes. The large circles are the sediment sound speeds inferred from a pressure-release model of the system, repeated here from Fig. 6, and the error bars represent the measurement uncertainty due to imperfect knowledge of the tank dimensions. The small circles are the sediment sound speeds inferred from a model which accounts for the finite impedance of the walls of the tank. Ignoring the finite impedance of the walls results in a maximum bias error of +0.53% at the lowest frequency measured.

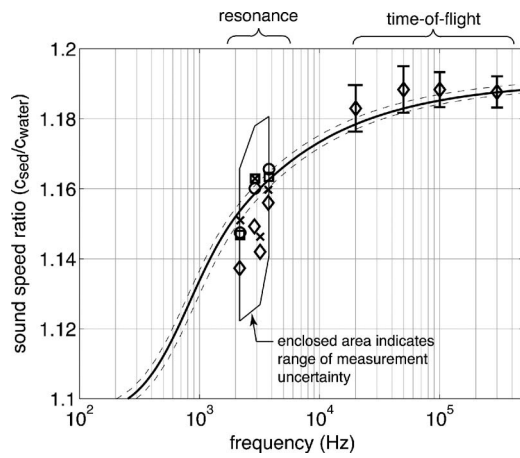


FIG. 8. The data and model prediction shown in Fig. 6 are repeated here, except that the resonance method measurements were corrected for the finite wall impedance of the tank. The extent of measurement uncertainty for the resonance-based measurements (due to sensor position and tank geometry uncertainty) is indicated by the closed polygon surrounding the data points. The solid curve is the EDFM prediction based on the mean porosity and mean permeability. The dashed curves above and below the solid curve represent the maximum and minimum EDFM predictions associated with the range of the porosity measurements and the standard deviation of the permeability measurements.

are well within the limits required by the shell approximation. To ensure continuity, we compared the phase speeds calculated by Eqs. (A1) and (A6) for the symmetric mode 0,1 and found excellent agreement. We are therefore confident that the approximate Eq. (A6) is accurate for the geometric and material properties used here. The data and model prediction presented in Fig. 6 are repeated in Fig. 8, but with the finite wall impedance correction applied to all the data from both axisymmetric and asymmetric modes. The asymmetric data before and after correction are presented in Table V, and shows a maximum correction of +0.76%. Note that the time-of-flight measurements are not biased by the presence of the tank walls because the environment appears to be a free field for the pulse lengths and frequencies used.

VII. CONCLUSIONS

Laboratory sound speed measurements were obtained in a water-saturated granular sediment composed of commercial silica blasting sand and fresh water. Above 20 kHz, a direct time-of-flight method was used and between 2 and 5 kHz, an indirect method was used to infer frequency-dependent sound speeds from measured resonance frequen-

TABLE V. Comparison between sediment sound speed values c of Fig. 6, which were inferred from the pressure-release model [Eq. (2)], and corrected sound speeds c_1 , obtained from the axisymmetric elastic waveguide model [Eq. (A6)].

Frequency (Hz)	c (m/s), Eq. (2)	c_1 (m/s), Eq. (A6)
Cross (×) data points		
3207	1723	1710
3747	1740	1730
Diamond (◇) data points		
3195	1716	1704
3735	1734	1725

cies. The pressure-release approximation yields a surprisingly good model for a thin-walled plastic tank filled with a water saturated sediment, as shown in Figs. 6–8. There is at maximum about 0.5% error in sound speeds inferred from the pressure release model.

Considering the more realistic analysis which does account for the finite impedance of the tank walls and is shown in Fig. 8, the EDFM model¹² describes the sound speed measurements very well. Most of the low-frequency measurements obtained with the resonance method are just lower than the predicted values, but the agreement between model and measurement is well within the measurement uncertainty. Three of the four high-frequency time-of-flight measurements are just higher than the prediction, but again, within the range of measurement uncertainty. The overall conclusion is that dispersion is clearly observed, as predicted by the Biot-derived models, and that the EDFM accurately describes the sound speed observed in this artificial laboratory sediment. Note that within the experimental frequency range, both measurements and model indicate about 4% dispersion. Evaluation of the EDFM from its low frequency asymptote (≈ 100 Hz) to its high frequency asymptote (≈ 1 MHz) yields a total of about 8% dispersion. A secondary conclusion can be drawn from the spread in the resonance-inferred data, which sampled the entire sediment volume, as compared to the high frequency measurements which only sampled a small portion of the volume. Even in a carefully prepared laboratory specimen, granular sediments are acoustically nonhomogeneous.

Overprediction of sediment sound speed by Biot-type models in the transition region between the low and high frequency asymptotes has been previously reported in Refs. 1 and 4. One explanation for this deviation in the previous work is the existence of undissolved air. In the present experiment, significant effort was expended to achieve a gas-free sediment, and it appears that if there was any remaining undissolved air (in microscopic crevices for instance) the effect was not acoustically significant.

ACKNOWLEDGMENTS

This work was supported by the U.S. Navy Office of Naval Research Ocean Acoustics program, Boston University, The University of Texas at Austin, and the ONR Coastal Geosciences program. This is NRL Contribution No. NRL/JA/7430-00-0014. The authors thank the reviewers for their astute suggestions.

APPENDIX

1. Axisymmetric dispersion relation

We considered sound propagation along the longitudinal axis of a lossless fluid cylinder enclosed by a lossless, arbitrary thickness, elastic cylindrical wall. Acoustic energy at angular frequency $\omega = 2\pi f$ propagating in this system (where f is the number of cycles per second) is governed by a set of exact wave theoretic equations given originally by Del Grosso²¹ and refined by Lafleur and Shields.²² The dispersion relation for this system is given in Eq. (A1). The ele-

ments of Eq. (A1) can be complex valued, but real values of $q_{0m} = \omega/c_{0m}$ that cause the left-hand side of Eq. (A1) to become zero lead to propagating modes that have phase speed c_{0m} . At any given frequency there can be multiple permissible modes, which are indexed by integer values of m . Since

the phase speed is frequency-dependent, at a given sediment cylinder resonance frequency $f_{0,m,N}$, the phase speed will attain a value denoted by $c_{0,m,N}$. The zero subscript that precedes the index m indicates that these are axisymmetric modes. The dispersion relation is

$$\begin{aligned}
 & 1 + [L_{11}(P_m)L_{00}(T_m)] \left(\frac{\pi^2 q_{0m}^2 b d P_m^2 T_m^2}{8 E_m^2} \right) + [L_{11}(T_m)L_{00}(P_m)] \left(\frac{\pi^2 b d E_m^2}{8 q_{0m}^2} \right) + [L_{10}(P_m)L_{01}(T_m) + L_{01}(P_m)L_{10}(T_m)] \\
 & \times \left(\frac{\pi^2 b d P_m^2 T_m^2}{8} \right) + [b L_{11}(P_m)L_{10}(T_m) + d(1 + Q_m b)L_{11}(P_m)L_{01}(T_m)] \left(\frac{\pi^2 P_m^2 T_m}{8 E_m} - \frac{\pi^2 P_m^2 q_{0m}^2 T_m}{8 E_m^2} \right) + [b L_{11}(T_m)L_{10}(P_m) \\
 & + d(1 + Q_m b)L_{11}(T_m)L_{01}(P_m)] \left(\frac{\pi^2 P_m E_m}{8 q_{0m}^2} - \frac{\pi^2 P_m}{8} \right) + [(1 + Q_m b)L_{11}(T_m)L_{11}(P_m)] \left(\frac{\pi^2 P_m}{8 q_{0m}^2} - \frac{\pi^2 P_m^2 q_{0m}^2}{8 E_m^2} - \frac{\pi^2 P_m^2}{4 E_m} \right) = 0,
 \end{aligned} \tag{A1}$$

where the following definitions have been used:

$$X_{0m} = b \sqrt{k_1^2 - q_{0m}^2}, \quad P_m = \sqrt{k_l^2 - q_{0m}^2}, \quad T_m = \sqrt{k_t^2 - q_{0m}^2}, \tag{A2}$$

$$q_{0m} = \omega/c_{0m}, \quad k_1 = \omega/c_1, \quad k_l = \omega/c_l, \quad k_t = \omega/c_t, \tag{A3}$$

$$E_m = q_{0m}^2 - k_t^2/2, \quad Q_m = \frac{\rho_L \omega^2 b J_0(X_{0m})}{2 \rho_W c_t^2 X_{0m} J_1(X_{0m})}, \tag{A4}$$

$$L_{mn}(\xi) = J_m(d\xi)Y_n(b\xi) - J_n(b\xi)Y_m(d\xi), \tag{A5}$$

and the geometric and material input parameters are: c_1 is the intrinsic sound speed in the inner liquid (the sound speed that the sediment would exhibit in the free field), c_l and c_t are the longitudinal and transverse (shear) speed for the wall material, ρ_L and ρ_W are the liquid and wall material densities, and b and d are the inner and outer radii of the pipe, respectively. $J_\nu(x)$ and $Y_\nu(x)$ are Bessel functions of the first and second kind, respectively.

2. Asymmetric dispersion relation

We modeled nonaxisymmetric sound propagation along the longitudinal axis of a lossless fluid cylinder enclosed by a lossless, finite thickness, shell-like cylindrical wall, using the formulation of Fuller and Fahy.²³ The dispersion relation is given in terms of a determinant

$$\det[L_{ij}] = 0 \tag{A6}$$

where

$$\begin{aligned}
 L_{11} &= -\Omega^2 + (k_{nm}b)^2 + \frac{1}{2}(1 - \nu)n^2, \\
 L_{12} &= \frac{1}{2}(1 + \nu)n(k_{nm}b), \quad L_{13} = \nu(k_{nm}b),
 \end{aligned} \tag{A7a}$$

$$\begin{aligned}
 L_{21} &= L_{12}, \quad L_{22} = -\Omega^2 + \frac{1}{2}(1 - \nu)(k_{nm}b)^2 + n^2, \quad L_{23} = n,
 \end{aligned} \tag{A7b}$$

$$L_{31} = L_{13}, \quad L_{32} = L_{23},$$

$$L_{33} = -\Omega^2 + 1 + \beta^2[(k_{nm}b)^2 + n^2] - FL. \tag{A7c}$$

In Eq. (A7), Ω is the dimensionless frequency, $\Omega = \omega b/c_l$, ν is the ratio of Poisson of the wall material, β is the wall thickness parameter $\beta^2 = h^2/12b^2$, h is the wall thickness, and FL represents fluid loading

$$FL = \Omega^2(\rho_L/\rho_W)(b/h)(1/k_m^r b)[J_n(k_m^r b)/J_n'(k_m^r b)]. \tag{A8}$$

The radial fluid wave number $k_m^r b$ and the axial wave number $k_{nm}b$ are related by

$$k_m^r b = [\Omega^2(c_l/c_1)^2 - (k_{nm}b)^2]^{1/2}. \tag{A9}$$

3. Illustration of finite wall impedance correction scheme

The effect of the finite wall impedance and the method of correction for this effect are demonstrated in Fig. 9 for the axisymmetric mode. The phase speed for the $0, 1, N$ mode is shown for both the pressure release model and the elastic waveguide model Eq. (A1). Note that the predicted phase speeds are similar, therefore we do not expect the corrections to be large. For a given experimentally observed resonance frequency $f_{0,1,N}$, the observed modal phase speed is calculated from

$$c_{0,1,N} = \lambda f_{0,1,N}, \tag{A10}$$

where $\lambda = 2h/N$. Then the effective sediment sound speed c_1 is varied in Eq. (A1) until the predicted modal phase speed is $c_{0,1,N}$. This procedure was repeated for each resonance frequency identified from an axisymmetric mode. The correction procedure is identical for the asymmetric modes, except Eq. (A1) is replaced by Eq. (A6). The results are reported in Table IV and shown in Fig. 8.

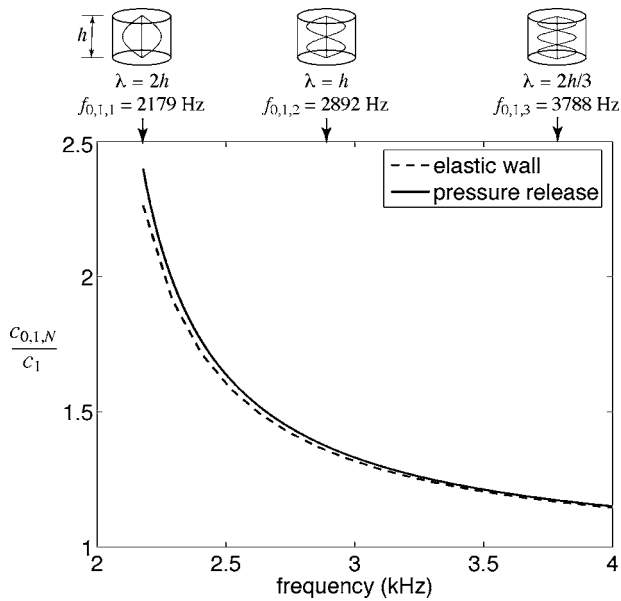


FIG. 9. The effect of the finite wall impedance on the modal phase speed $c_{0,1,N}$. The vertical axis is normalized by the sediment effective intrinsic sound speed c_1 . The basis for the procedure used to correct for the finite wall impedance is illustrated for one of the data sets (the open circles of Fig. 6). Integer multiples of one-half wavelength occupy the sediment cylinder along its height for the $0,1,N$ modes. Knowledge of these mode shapes from Eq. (1), the measured resonance frequencies $f_{0,1,N}$ and Eq. (A10) allow one to use Eq. (A1) to relate the measured value of $c_{0,1,N}$ to the intrinsic effective sediment sound speed c_1 that would be measured in the free field. The results of the correction are shown in Table IV.

4. Effect of neglecting viscosity in the wall impedance correction

The above-presented elastic waveguide models approximate the internal fluid as inviscid, therefore the fluid can slip at the boundary with the wall. In this section it is shown that neglecting the sediment viscosity in the waveguide models has an insignificant effect on the phase speeds in this experiment. This is due to the large size of the sediment tank in comparison to the boundary layer at the wall.

In this work, the sediment is approximated as an effective fluid and can be assigned an effective viscosity with respect to pipe wall interaction, as is done in the modeling of slurry flows,²⁴ and in acoustic studies of sediments in tubes.²⁵ For mixtures of liquids and sand with high solid volume concentrations (such as the present sediment) the effective mixture viscosity μ_{mix} is dependent upon the solid volume concentration ϕ as

$$\frac{\mu_{\text{mix}}}{\mu} = 1 + 2.5\phi + 10.05\phi^2 + 2.73 \times 10^{-3}\exp(16.6\phi), \quad (\text{A11})$$

where μ is the viscosity of the host liquid.²⁴ The sediment porosity in this work is 0.37 therefore $\phi=0.63$ and Eq. (A11) yields a viscosity ratio $\mu_{\text{mix}}/\mu=102$.

For acoustic waves propagating within a viscous fluid inside a pipe, an acoustic boundary layer is formed at the wall. The resulting acoustic effects can be modeled with a complex wave number²⁶

$$\tilde{k} = \frac{\omega}{c} + (1-i)\alpha_{\text{wall}}, \quad (\text{A12})$$

where c is the effective sound speed of the sediment inside the waveguide and $\omega/c \gg \alpha_{\text{wall}}$ is assumed. Thermal losses are considered negligible compared to the viscous losses, which are characterized by

$$\alpha_{\text{wall}} = \frac{1}{a} \sqrt{\frac{\mu_{\text{mix}}\omega}{2\rho c^2}}, \quad (\text{A13})$$

where a is the inner radius of the pipe and ρ is the total mass density of the sediment. Equation (A12) indicates a reduced phase speed inside the waveguide due to the viscous boundary layer. The effect of the viscosity on phase speed can be expressed in a ratio

$$\frac{\tilde{c}}{c} = \left(1 + \frac{c\alpha_{\text{wall}}}{\omega}\right)^{-1}, \quad (\text{A14})$$

where $\tilde{c} = \text{Re}[\omega/\tilde{k}]$ is normalized by the sound speed in absence of a viscous boundary layer, c .

Using the sediment mass density from Table III, the highest frequency in the resonance regime of the experiment (3788 Hz) and the mean sound speed observed inside the waveguide at the same frequency (1740 m/s), Eq. (A14) yields $\tilde{c}/c=0.99905$, which is a negligible systematic error in comparison to other sources of measurement uncertainty in this experiment and is ignored.

- ¹A. Turgut and T. Yamamoto, "Measurement of acoustic wave velocities and attenuation in marine sediments," *J. Acoust. Soc. Am.* **87**, 2376–2383 (1990).
- ²A. Maguer, E. Bovio, W. L. J. Fox *et al.*, "In situ estimation of sediment sound speed and critical angle," *J. Acoust. Soc. Am.* **108**, 987–996 (2000).
- ³I. Rosenfeld, W. M. Carey, P. G. Cable *et al.*, "Modeling and analysis of sound transmission in the Strait of Korea," *IEEE J. Ocean. Eng.* **26**, 809–820 (2001).
- ⁴K. L. Williams, D. R. Jackson, E. I. Thorsos *et al.*, "Comparison of sound speed and attenuation measured in a sandy sediment to predictions based on the Biot theory of porous media," *IEEE J. Ocean. Eng.* **27**, 413–428 (2002).
- ⁵R. D. Stoll, "Velocity dispersion in water-saturated granular sediment," *J. Acoust. Soc. Am.* **111**, 785–793 (2002).
- ⁶N. P. Chotiros, A. P. Lyons, J. Osler *et al.*, "Normal incidence reflection loss from a sandy sediment," *J. Acoust. Soc. Am.* **112**, 1831–1841 (2002).
- ⁷M. A. Biot, "Theory of propagation of elastic waves in a fluid-saturated porous solid. I. Low-frequency range," *J. Acoust. Soc. Am.* **28**, 168–178 (1956).
- ⁸M. A. Biot, "Theory of propagation of elastic waves in a fluid-saturated porous solid. II. Higher frequency range," *J. Acoust. Soc. Am.* **28**, 179–191 (1956).
- ⁹R. D. Stoll and T. K. Kan, "Reflection of acoustic waves at a water-sediment interface," *J. Acoust. Soc. Am.* **70**, 149–156 (1981).
- ¹⁰N. P. Chotiros, "Biot model of sound propagation in water-saturated sand," *J. Acoust. Soc. Am.* **97**, 199–214 (1995).
- ¹¹M. J. Buckingham, "Wave propagation stress relaxation and grain-to-grain shearing in saturated unconsolidated marine sediments," *J. Acoust. Soc. Am.* **108**, 2796–2815 (2000).
- ¹²K. L. Williams, "An effective density fluid model for acoustic propagation in sediments derived from Biot theory," *J. Acoust. Soc. Am.* **110**, 2276–2281 (2001).
- ¹³E. L. Hamilton, "Geoacoustic modeling of the sea floor," *J. Acoust. Soc. Am.* **68**, 1313–1340 (1980).
- ¹⁴E. L. Hamilton and R. T. Bachman, "Sound velocity and related properties of marine sediments," *J. Acoust. Soc. Am.* **72**, 1891–1904 (1982).
- ¹⁵E. L. Hamilton, "Prediction of in-situ acoustic and elastic properties of marine sediments," *Geophysics* **36**, 266–284 (1971).

- ¹⁶R. D. Stoll, G. M. Bryan, and E. O. Bautista, "Measuring lateral variability of sediment geoacoustic properties," *J. Acoust. Soc. Am.* **96**, 427–438 (1994).
- ¹⁷P. S. Wilson, R. A. Roy, and W. M. Carey, "An improved water-filled impedance tube," *J. Acoust. Soc. Am.* **113**, 3245–3252 (2003).
- ¹⁸L. E. Kinsler, A. R. Frey, A. B. Coppens *et al.*, *Fundamentals of Acoustics*, 4th ed. (Wiley, New York, 2000).
- ¹⁹D. T. Blackstock, *Fundamentals of Physical Acoustics* (Wiley, New York, 2000).
- ²⁰ASTM, Standard Designation D 2434-68: Standard Test Method for Permeability of Granular Soils (American Society for Testing and Materials, West Conshohocken, PA, 2006).
- ²¹V. A. Del Grosso, "Analysis of multimode acoustic propagation in liquid cylinders with realistic boundary conditions—Application to sound speed and absorption measurements," *Acustica* **24**, 299–311 (1971).
- ²²L. D. Laffleur and F. D. Shields, "Low-frequency propagation modes in a liquid-filled elastic tube waveguide," *J. Acoust. Soc. Am.* **97**, 1435–1445 (1995).
- ²³C. R. Fuller and F. J. Fahy, "Characteristics of wave propagation and energy distributions in cylindrical elastic shells filled with fluid," *J. Sound Vib.* **81**, 501–518 (1982).
- ²⁴B. E. Abulnaga, *Slurry Systems Handbook* (McGraw-Hill, New York, 2002).
- ²⁵S. R. Addison, "Study of sound attenuation in sediments," Ph.D. dissertation, University of Mississippi, 1984.
- ²⁶A. D. Pierce, *Acoustics: An Introduction to its Physical Principles and Applications* (American Institute of Physics, Woodbury, NY, 1994).

Estimating parameter uncertainties in matched field inversion by a neighborhood approximation algorithm

Kunde Yang^{a)}

College of Oceanic Engineering, Northwestern Polytechnical University, Xi'an, Shaanxi, P. R. China, 710072

N. Ross Chapman^{b)}

School of Earth and Ocean Sciences, University of Victoria, Victoria, B.C., V8W 3P6, Canada

Yuanliang Ma

College of Oceanic Engineering, Northwestern Polytechnical University, Xi'an, Shaanxi, P. R. China, 710072

(Received 12 July 2006; revised 25 November 2006; accepted 4 December 2006)

In Bayesian inversion, the solution is characterized by its posterior probability density (PPD). A fast Gibbs sampler (FGS) has been developed to estimate the multi-dimensional integrals of the PPD, which requires solving the forward models many times and leads to intensive computation for multi-frequency or range-dependent inversion cases. This paper presents an alternative approach based on a neighborhood approximation Bayes (NAB) algorithm. For lower dimension geoacoustic inversion, the NAB can approximate the PPD very well. For higher dimensional problems and sensitive parameters, however, the NAB algorithm has difficulty estimating the PPD accurately with limited model samples. According to the preliminary PPD estimation from the NAB, this paper developed a multi-step inversion scheme, which adjusts the parameter search intervals flexibly, in order to improve the approximation accuracy of the NAB and obtain more complete parameter uncertainties. The prominent feature of the NAB is to approximate the PPD by incorporating all models for which the forward problem has been solved into the appraisal stage. Comparison of the FGS and NAB for noisy synthetic benchmark test cases and Mediterranean real data indicates that the NAB provides reasonable estimates of the PPD moments while requiring significantly less computation time. © 2007 Acoustical Society of America. [DOI: 10.1121/1.2427125]

PACS number(s): 43.30.Pc, 43.60.Pt [AIT]

Pages: 833–843

I. INTRODUCTION

Geoacoustic inversion represents a strongly nonlinear inverse problem for which a direct solution is not available.^{1–10} From the Bayesian rule, the solution to an inverse problem is fully characterized by its posterior probability density (PPD), which combines prior information about the model parameters with information from an observed data set. The moments from the PPD including the mean, covariance, and marginal distributions can be extracted to provide parameter estimates and their uncertainties.

Computation of those moments involves multi-dimensional integrals, which are complicated to evaluate for multi-parameter geoacoustic models. Several methods have been developed, such as Monte Carlo integration and importance sampling based on genetic algorithm (GA), simulated annealing (SA), and hybrid techniques. Importance sampling by GA uses the final generation of GA inversions to sample the PPD, which is very efficient but quite empirical, biased, and not very precise.^{9,10} Monte Carlo integration and Gibbs sampling (GS) based on SA can provide an unbiased, asymptotically convergent sampling of the PPD.¹¹ However, they

are computationally slow. A fast Gibbs sampler (FGS) has been developed to increase the efficiency greatly, but it also requires solving the forward problem many times, at intensive computational cost.^{12–14}

Although much attention has been devoted to developing methods that efficiently search a parameter space for geoacoustic inversion, much less effort has been devoted to the problem of analyzing the resulting ensemble in a quantitative manner. Recently, Sambridge^{15–18} has proposed a neighborhood algorithm to estimate Bayesian information measures from an arbitrarily distributed ensemble. The essence of the approach is to use the information in the available ensemble to guide a resampling of the parameter space. This resampling is based on Voronoi cells (nearest neighbor regions) that represent all information contained in the input ensemble. Voronoi cells have been used in many areas of the physical sciences and more recently in geophysical inverse problems. The key idea is to replace the real PPD with a neighborhood approximate PPD, which requires no further solving of the forward problem. Then any Bayesian integral is evaluated by simply averaging over the resampled parameter ensemble.

Based on the neighborhood algorithm, a hybrid GA-GS method using Voronoi cells was developed in Ref. 19, which consists of three steps. First, it ran a classic GA to minimize the misfit function and saved all the populations and the

^{a)}Visitor at the University of Victoria from 22 February 2006 to 15 February 2007. Electronic mail: ykdzym@nwpu.edu.cn

^{b)}Electronic mail: chapman@uvic.ca

misfit values of all generations. Then it used GA samples and their likelihood values to construct Voronoi cells around each GA point. At last it ran a fast Gibbs sampler to approximate the PPD. The numerical simulation illustrated that the GA-GS worked well for a four-dimensional geoaoustic inversion problem.

The advantage of the neighborhood algorithm is that it can, in principle, extract Bayesian estimates from the samples generated by any search method, such as GA and SA. The disadvantage is that it can only extract what information exists in a given ensemble of models. If the available ensemble does not adequately represent (or sample) the acceptable region in parameter space, especially for higher dimensional problems, then the result will be biased.

The main objective of this study was to (1) overcome the difficulty of the neighborhood algorithm to approximate the PPD adequately in higher dimension inverse problems; (2) develop a scheme to estimate the PPD based on the models generated by the adaptive simplex simulated annealing (ASSA) algorithm;⁶ (3) evaluate the computation efficiency and accuracy of the neighborhood algorithm compared with the FGS.

The remainder of this paper is organized as follows. Section II describes briefly the matched field geoaoustic inversion problem with Bayesian formulation. In Sec. III, the basic principles of Bayes estimation with the neighborhood approximation are introduced, and its main features are analyzed. Section IV presents two inversion cases with the basic neighborhood approximation Bayes (NAB) algorithm. Section V presents a multi-step NAB inversion scheme in order to improve the approximation accuracy. Sections VI and VII examine the multi-step inversion scheme using synthetic data and Mediterranean experimental data. Finally, the results of this work are summarized and discussed.

II. BAYESIAN INVERSION

The Bayesian inference theory provides formalism to estimate parameter uncertainties for nonlinear inverse problems. In a Bayesian formulation, the solution is characterized by its posterior probability density. For data \mathbf{d} and model vectors \mathbf{m} considered to be random variables, the PPD $P(\mathbf{m}|\mathbf{d})$ is defined as follows by Bayes' rule,

$$P(\mathbf{m}|\mathbf{d}) \propto L(\mathbf{d}|\mathbf{m})P(\mathbf{m}), \quad (1)$$

where $L(\mathbf{d}|\mathbf{m})$ is the likelihood function and $P(\mathbf{m})$ is the prior distribution. Assuming that the random data errors are Gaussian distributed, the likelihood is of the form $L(\mathbf{d}|\mathbf{m}) \propto \exp[-E(\mathbf{m}, \mathbf{d})]$, where E is the appropriate error function for the inverse problem. The general form of the error function for multiple frequencies is given by

$$E(\mathbf{m}) = \sum_{f=1}^F B_f(\mathbf{m})|\mathbf{d}_f^{\text{obs}}|^2/v_f, \quad (2)$$

where v_f is the error variance for frequency f , which is often estimated by the maximum likelihood method.^{10,13} $B_f(\mathbf{m})$ represents the normalized Bartlett mismatch function defined by

$$B_f(\mathbf{m}) = 1 - \frac{|\mathbf{w}_f^+(\mathbf{m})\mathbf{d}_f^{\text{obs}}|^2}{|\mathbf{d}_f^{\text{obs}}|^2|\mathbf{w}_f(\mathbf{m})|^2}, \quad (3)$$

where “+” represents conjugate transpose, $\mathbf{w}_f(\mathbf{m})$ is the replica field vector computed via a numerical propagation model, and $\mathbf{d}_f^{\text{obs}}$ represents the observed data vector at frequency f . Complex pressure vectors are used to invert in this paper.

The moments of the PPD take the form

$$J = \int g(\mathbf{m})P(\mathbf{m}|\mathbf{d}) d\mathbf{m}, \quad (4)$$

where the $g(\mathbf{m})$ is used to define each integrand for calculating the mean, covariance, and one-dimensional marginal distributions.¹² A numerical estimate can be obtained using multidimensional Monte Carlo (MC) integration, that is,

$$\hat{J} = \frac{1}{Q} \sum_{k=1}^Q \frac{g(\mathbf{m}_k)P(\mathbf{m}_k|\mathbf{d})}{h(\mathbf{m}_k)}, \quad (5)$$

where Q is the number of discrete samples in the MC integration, \mathbf{m}_k is the k th model sample and, $h(\mathbf{m})$ is the density distribution of the importance sampling. Note that the importance sampling provides unbiased estimates of the integrals. Employing a Gibbs sampler at $T=1$ in importance sampling, the sampling function $h(\mathbf{m}_k)=P(\mathbf{m}_k|\mathbf{d})$ and Eq. (5) becomes

$$\hat{J} = \frac{1}{Q} \sum_{k=1}^Q g(\mathbf{m}_k). \quad (6)$$

Then an unbiased estimate of the integral is given by the mean value of $g(\mathbf{m})$. Although GS provides an attractive approach to estimate integral moments of the PPD, its basic form is computationally slow. Dosso^{12,13} developed a fast Gibbs sampling approach for Bayesian inversion, which provides an efficient, unbiased sampling of the PPD with a rigorous convergence criterion. In fact, the FGS increases the PPD estimation efficiency greatly, but it also requires solving the forward problem many times at intensive computational cost, especially for multi-frequency or range-dependent inverse problems.

III. NEIGHBORHOOD BAYES ESTIMATION

A. The neighborhood approximation of the PPD

The reconstruction of the PPD from a finite ensemble of samples is effectively an interpolation problem in a multidimensional space. In this paper the concept of Voronoi cells¹⁵ is applied to construct a multidimensional interpolation for matched-field inversion problems.

Given a set of n_p samples in model space for which the misfit function has been determined, Voronoi cells are defined in terms of a distance norm. Here the L_2 norm is used, and the distance between models \mathbf{m}_a and \mathbf{m}_b is given by

$$\|(\mathbf{m}_a - \mathbf{m}_b)\| = [(\mathbf{m}_a - \mathbf{m}_b)^+ \mathbf{C}_M^{-1} (\mathbf{m}_a - \mathbf{m}_b)]^{1/2}, \quad (7)$$

where \mathbf{C}_M is a matrix that removes the dimensionality of the variables. A simple choice would be a diagonal matrix with elements $1/s_i^2$. Here s_i can be interpreted as a scale factor for

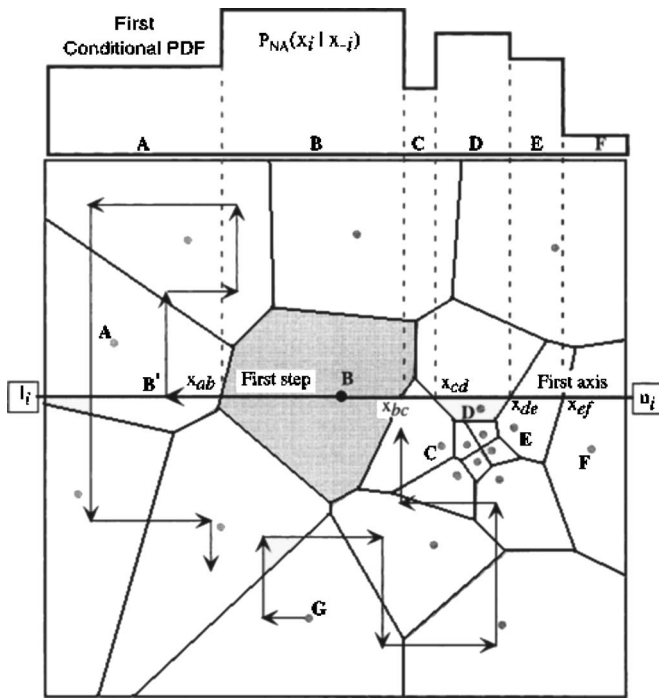


FIG. 1. Two independent random walks through the neighborhood approximation of the PPD.¹⁶ The Gibbs sampler is used. The first step (x direction) of the walk starts at cell B (shaded). The shape of the conditional PDF, $P_{NA}(x_i|x_{-i})$, is shown above the figure.

the i th parameter. In this case C_M is reduced to the identity matrix by rescaling each parameter axis.

A formal definition of the Voronoi cells follows: let $P = \{\mathbf{m}_1, \dots, \mathbf{m}_{n_p}\}$ be a set of points with dimension d , where $2 \leq n_p \leq \infty$, and let $\mathbf{m}_i \neq \mathbf{m}_j$ for $i \neq j$. The Voronoi cell about point \mathbf{m}_i is given by

$$V(\mathbf{m}_i) = \{\mathbf{x} \mid \|\mathbf{x} - \mathbf{m}_i\| \leq \|\mathbf{x} - \mathbf{m}_j\| \text{ for } j \neq i, (i, j = 1, \dots, n_p)\}. \quad (8)$$

Voronoi cells (shown in Fig. 1 for a two-dimensional example) have some useful properties that make them ideal for the basis of multi-dimensional interpolation. For any distribution of irregular points in any number of dimensions, they are unique, space-filling, convex polyhedra, whose sizes and shapes are automatically adapted to the distribution of the point set. Note that the size (volume) of each cell is inversely proportional to the density of the points. In order to construct an approximate PPD from a fixed ensemble, it is assumed that the PPD of each model is constant inside its Voronoi cell. It is called the neighborhood approximation to the PPD, and it can be written as $P_{NA}(\mathbf{m})$. Specifically, we have

$$P_{NA}(\mathbf{m}) = P(p_i), \quad (9)$$

where p_i is the model in the input ensemble that is closest to the point \mathbf{m} . With this approximation, the Bayesian integrals can then be evaluated by generating a new set of integration points in model space, $\mathbf{s}_k (k=1, \dots, N_r)$, whose distribution asymptotically tends towards $P_{NA}(\mathbf{m})$. It is called the “resampled ensemble.” Therefore, if the sampling is performed correctly, the sampling density $h(\mathbf{m})$ should satisfy

$$h(\mathbf{m}) \approx P_{NA}(\mathbf{m}) \approx P(\mathbf{m}). \quad (10)$$

So the Bayesian integral (4) becomes Eq. (6), which needs only simple averages over the resampled ensemble. Note that the approximate PPD no longer appears in Eq. (6) directly, but instead controls the distribution of the resampled ensemble.

B. Importance sampling of the neighborhood approximation

The resampled ensemble can be generated by a standard approach known as a Gibbs sampler.¹⁶ Figure 1 illustrates the procedure in two dimensions. The algorithm for generating new models can be summarized as follows.

The random walk starts at point \mathbf{m}_B , which is a model from the input ensemble. From this point it takes a series of steps along each parameter axis in turn. A step is performed by drawing a random deviate from the conditional probability density function (PDF) of $P_{NA}(\mathbf{m})$ along the i th axis. This function is written as $P_{NA}(x_i|x_{-i})$, where x_i is a position variable along the i th axis and x_{-i} denotes the fixed values of all other components of the model \mathbf{m}_B . The conditional $P_{NA}(x_i|x_{-i})$ is just the function $P_{NA}(\mathbf{m})$ sampled along the i th axis, which passes through point \mathbf{m}_B . Since $P_{NA}(\mathbf{m})$ is constant inside each Voronoi cell, the conditional is built from the PPD values inside each Voronoi cell intersected by the axis. A proposed step, x_i^p , is generated as a uniform random deviate between the endpoints of the axis, that is, in the interval (l_i, u_i) in Fig. 1. This proposed step is accepted if a second random variable, ξ , generated on the unit interval $(0, 1)$, satisfies

$$\xi \leq \frac{P_{NA}(x_i^p|x_{-i})}{P_{NA}(x_i^{\max}|x_{-i})}, \quad (11)$$

where $P_{NA}(x_i^{\max}|x_{-i})$ is the maximum value of the conditional PDF along the axis. If the proposed step is rejected, the whole procedure is repeated until an accepted step is produced. Note that the random walk can enter any of the Voronoi cells, and the probability of this occurring is determined by the product of the posterior probability density and the width of the intersection of the axis with the cell.

This approach is extendable to a multi-dimensional space,¹⁶ and it is assumed that after many iterations, the random walk will produce model space samples whose distribution asymptotically tends towards the target distribution, i.e., $P_{NA}(\mathbf{m})$.

C. Features of the neighborhood approximation of the PPD

- (1) An important feature of the resampling algorithm is that nothing is assumed about the distribution of the initial ensemble. In each Voronoi cell, the likelihood value is assumed to be constant with a value of its input sample. Therefore the likelihood of any point anywhere in the entire search space is known and there is no need for any

further forward model runs. This means that it can extract useful information from a complete ensemble, previously generated by any search method.

- (2) Three factors influence the computational time, T , of the algorithm, i.e., $T \propto N_r N_e d$, where N_r is the size of the resampled ensemble, N_e denotes the size of the input ensemble, and d is model dimension. So for practical inverse problems, it is necessary to compare both the speed and accuracy between the neighborhood approximation and other sampling approaches, like Monte Carlo integration and Gibbs sampling.
- (3) The accuracy of the approximation and hence the numerical integrals will, necessarily, depend on how well the input ensemble samples the regions of high data fit. Therefore ASSA or other optimizing methods should gather enough samples from the search space in order to construct Voronoi cells that allow adequate approximation of the PPD. The quality of the input ensemble will always be an issue.
- (4) The main difficulty that affects the sampling algorithm is that the minimum sample size is very sensitive to the dimension of the model parameter space. References 17 and 18 illustrate that the average saturated number of natural neighbors about each node, s , depends on dimension d exponentially, e.g., $s \approx d^{3.5}$, based on a uniform sampling. This suggests that increasingly greater numbers of samples will be needed as the dimension of the parameter space increases, in order to fill the Voronoi cell topology to the same degree. It turns out that, in higher dimensions, it is very difficult to obtain an adequate global sampling of the parameter space without drastically increasing the sample size to form a complete ensemble. This issue is discussed further below with reference to the geoaoustic inversion problem.

IV. BASIC INVERSION ALGORITHM

A. Basic inversion algorithm

The basic inversion process was summarized as the following steps.

- (1) With multi-frequency synthetic data and the ASSA hybrid optimization algorithm, the error variance for each frequency was estimated, which was used in the PPD estimation by FGS and NAB. A multi-frequency incoherent objective function, i.e., $\phi(\mathbf{m}) = \sum_{f=1}^F B_f(\mathbf{m})$, was used for the ASSA optimization. Note that in order to get enough model samples for NAB, all models generated outside and inside of the downhill simplex program in ASSA, either accepted or rejected, were saved. Meanwhile, the objective function for each frequency, $B_f(\mathbf{m})$, was saved. In order to consider the different error variances for each frequency, the error function E used to estimate the likelihood function in the neighborhood algorithm was computed by Eq. (2) after estimating the error variances. This process needs small computational cost because it uses the saved objective functions and does not require running the forward model.
- (2) The ensemble produced by ASSA is input to the NAB

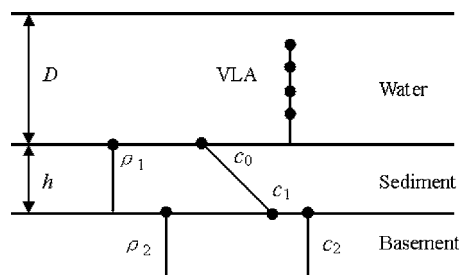


FIG. 2. Ocean environment model for WAa Benchmark test case. The attenuation both in sediment and basement are assumed to be 0.23 dB/ λ .

program, which resamples models and estimates the PPD according to the algorithm described in Sec. III.

- (3) The FGS is run to estimate the PPD that is considered as the true solution. An initial cooling stage in standard FGS is replaced by optimization results from ASSA in order to ensure that the Gibbs sampling begins in high probability regions of the model space.

B. Inversion results with the basic algorithm

The WAa test case from the 1997 Geoaoustic Inversion Workshop⁵ was chosen to evaluate the algorithms. The scenario for the test case WAa is shown in Fig. 2. The environment is range independent and consists of a sediment layer over a semi-infinite basement with nine geometric and geoaoustic parameters including water depth, D , source range and depth, r and z , sediment thickness, h , sound speeds at the top and bottom of the sediment layer, c_0 and c_1 , sound speed of the basement, c_2 , and the densities of the sediment and basement, ρ_1 and ρ_2 , respectively. A vertical linear array of 20 sensors equally spaced from 5 to 100 m was used to measure acoustic fields. Both synthetic fields and replica field vectors for inversion were generated by normal mode code SNAP.²⁰

Two inversion cases using the same scenario in Fig. 2 were applied to display the advantages and disadvantages of the NAB algorithm.

First, four relatively sensitive geoaoustic parameters including sediment thickness, h , sound speeds at the top and bottom of the sediment layer, c_0 and c_1 , and basement sound speed, c_2 , were inverted by synthetic data. Two frequency data with different signal-to-noise ratios (SNR), 50 Hz with 13 dB and 150 Hz with 11 dB, were used in case 1. White Gaussian noise was added to the simulated data. The estimated error variances for 50 and 150 Hz were 0.0072 and 0.0118, respectively. Figure 3 illustrates the 1-D marginal PPDs estimated by FGS and NAB, respectively. It shows that the two algorithms have very similar results. FGS had two independent runs and the convergence criterion was that the maximum difference between the cumulative marginal distributions for all parameters was less than 0.2 (Ref. 12 applied 0.1 to get more accurate results with longer time). NAB used 10k (1k=1000) input samples and produced 5k resamples to estimate the PPD, and converged reasonably well by monitoring the “potential scale reduction” factor.¹⁶ Both FGS and NAB required about 6 min on a 1.1 GHz PC with 512 MB random access memory.

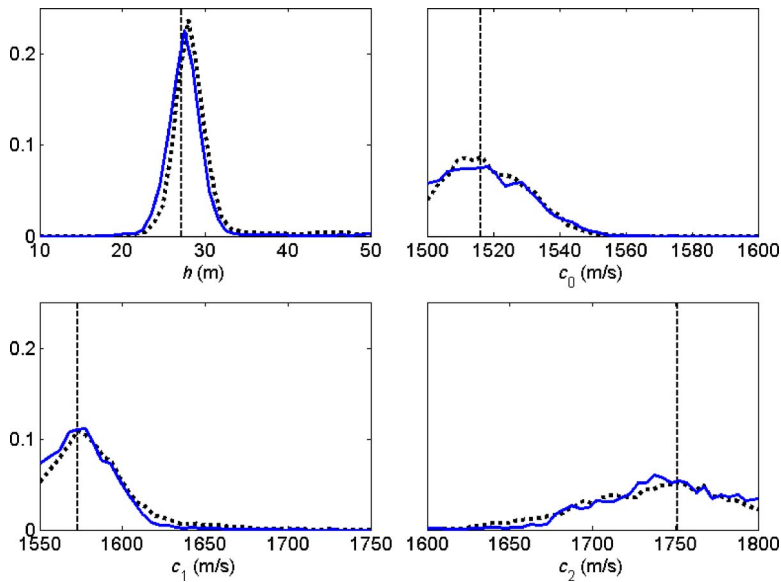


FIG. 3. (Color online) Estimated marginal PPDs by FGS (dotted lines) and basic NAB (solid lines) for case 1. Dashed vertical lines indicate the true parameter values.

Case 2 is to invert all nine parameters. The selected frequencies were 70, 100, 150, 200, and 300 Hz. The SNR values were selected as 9, 12, 13, 10, and 8 dB, respectively. The uncorrelated sensors¹³ used to estimate the error variances were selected to be 3, 4, 5, 6, and 7, and the corresponding error variances were 0.0319, 0.0099, 0.009, 0.0083, and 0.02, respectively. Ten thousand models generated by ASSA were used as input for the NAB and 5k resamples were produced to estimate the PPD. The results are shown in Fig. 4. Compared with FGS, there are obvious errors for NAB, especially for sensitive geometric parameters and sediment thickness. The inversion was carried out using 30k ASSA models to generate a resampled ensemble with the same size, to investigate if there was any improvement for

large initial samples. There were only minor changes in the resultant marginals, at a cost of considerable increase in computation time (120 min for NAB).

For the geoacoustic inversion problem, our simulation experiments show that if the parameter space dimension is small (less than about 6), the NAB approximation of PPD has comparable results with FGS for both sensitive and insensitive parameters. However, the NAB algorithm underestimates the marginal distributions for the sensitive parameters if the dimension is greater than about 6 and the sample is generated from a limited number of input samples. The results in Fig. 4 show that the PPD estimated by the NAB will be smoother than that of the FGS, which leads to broader regions of high probability density. It is consistent with the conclusion given by Refs. 17 and 18 that the NAB needs many more input samples and resamples in order to obtain a sufficient global sampling of the higher dimensional space. However, if a large number of samples is used, the computation time increases and there is no advantage in applying the neighborhood algorithm to approximate the PPD.

Fortunately, the NAB algorithm has comparable estimation results with FGS for less sensitive parameters, such as densities and speed values in sediment and basement shown in Fig. 4. This phenomenon suggests a means to modify the inversion method in order to overcome the disadvantages that the NAB algorithm has for higher dimensional problems.

V. MULTI-STEP BAYES ESTIMATION SCHEME

A. Reasons for modifying the NAB

The start points to modify the inversion scheme are based on the following analysis of the simulations.

- (1) The main objective to estimate the PPD is to provide uncertainty information for inverted parameters, which can be used to predict the uncertainties of transmission loss, or improve the performance of detection and localization. Therefore, the information about PPD values in

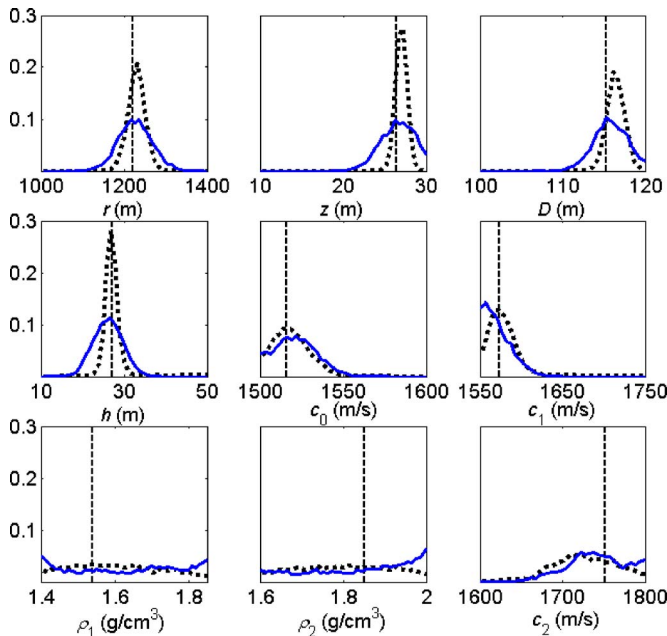


FIG. 4. (Color online) Estimated marginal PPDs by FGS (dotted lines) and basic NAB (solid lines) for case 2. Dashed vertical lines indicate the true parameter values.

the region of the highest probability density (HPD) is essential. If the prior information does not characterize the actual environment well enough, the HPD interval may not be adequately sampled. For instance, in Fig. 4 the inversion is limited by the prior bounds for the sediment top and bottom speeds, c_0 and c_1 , and the basement speed, c_2 . This suggests that the prior bounds should be broadened to get more complete distributions.

- (2) For the most sensitive parameters, the NAB has difficulty approximating the peak regions of the marginal PPDs without drastically increasing the number of input samples. But for the less sensitive parameters, the NAB can approximate the true PPD well. In general, the parameter sensitivity is defined relative to the search bounds. Therefore, for the most sensitive parameters like the geometric ones, if the search bounds are contracted using the preliminary PPD estimation from NAB, the sensitivity of geometric parameters will be reduced. This operation may allow the NAB to make a better approximation of the true PPD.
- (3) The boundary adjustment including contracting and broadening will provide more chances for ASSA to search the parameters in the high probability density interval and arrive at global optimization points, which is similar to the multi-step inversion scheme introduced in Refs. 21 and 22. Meanwhile it will generate higher quality model samples for the NAB.
- (4) Figure 4 shows that there are some errors for NAB if the true values are close to the bounds. This suggests that the NAB cannot approximate the PPD well near the bounds with limited samples. If the positions of true values are shifted to the middle of the range, the weakness may be avoided.

B. The method for adjusting the bounds

Based on the above analysis, a modified inversion scheme to estimate the marginal PPDs by the NAB is presented. The main objective is to estimate the PPD values faster than FGS, with reasonable approximation accuracy. The critical part in the approach is how to adjust the search bounds for different parameters according to the preliminary results estimated by NAB. For the example shown in Fig. 4, the following simple scheme is applied to change the boundary values.

- (1) First, threshold values are defined for the adjustment algorithm. The total sum of the 1-D marginal PPD values for each parameter is normalized to one. The mean distribution value ϵ is $1/M$, where M is the number of discrete samples for each parameter. For the sensitive parameters like the geometric parameters and sediment thickness, the threshold values are set to be $\epsilon/2$. For the remaining parameters, the threshold values are set to be $\epsilon/10$ in order to have wider bounds.
- (2) For parameters that have PPDs focusing on the middle of the parameter axis and have smaller PPD values than the threshold, such as source range, r , and sediment thickness, h , the intersection points between the PPD curves and the threshold are selected as the new bounds. For

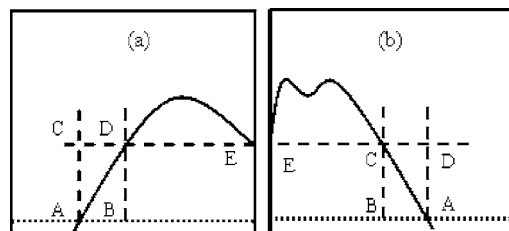


FIG. 5. The simple method to change the search bounds. (a) Broaden upper bound and (b) broaden lower bound. Dotted lines denote the threshold values.

example, in Fig. 5, the corresponding parameter values of intersection point A are selected as the new lower and upper bounds.

- (3) For the less sensitive parameters such as sediment density and basement density, ρ_1 and ρ_2 , whose PPD values are all higher than the threshold $\epsilon/10$, the search bounds are increased by 30% or 40%.
- (4) The remaining five parameters have unreasonable lower or upper bounds, which should be broadened in order to estimate the PPD more completely. Here a simple symmetric method shown in Fig. 5 was applied to broaden the bounds. If the new lower bound has been determined at point A in Fig. 5(a), and the PPD curve intersects the upper bound at point E, a line parallel to the horizontal axis is plotted, which will intersect with the PPD curve at point D. The horizontal interval between points A and B is added to the original upper bound to generate the new upper bound. A similar operation can be executed for parameters that have unreasonable lower bounds, according to Fig. 5(b).
- (5) In order to avoid the limitations from the assumption of symmetry, the new search intervals are increased by 30% or 40% for parameters whose bounds are adjusted based on Fig. 5.
- (6) Prior knowledge should be used to ensure that the bounds are physically reasonable.

C. Multi-step NAB algorithm

The steps in the modified multi-frequency inversion scheme are summarized below. Because the method runs NAB and ASSA two times to estimate the PPD, it is named the multi-step NAB inversion scheme.

- (1) With preliminary search intervals based on prior information, the ASSA is used to estimate the error variance for each frequency, and the model samples are saved. Then, the likelihood functions for each model sample are estimated by Eq. (2).
- (2) The marginal PPD values are estimated by the NAB with the model ensemble generated by the ASSA.
- (3) The search bounds are adjusted using the previously described method, which requires quite trivial computation cost.
- (4) The ASSA is run again with the new search intervals to store model samples for NAB.
- (5) The NAB is run again with the new search intervals and the new input ensemble to estimate the PPD.

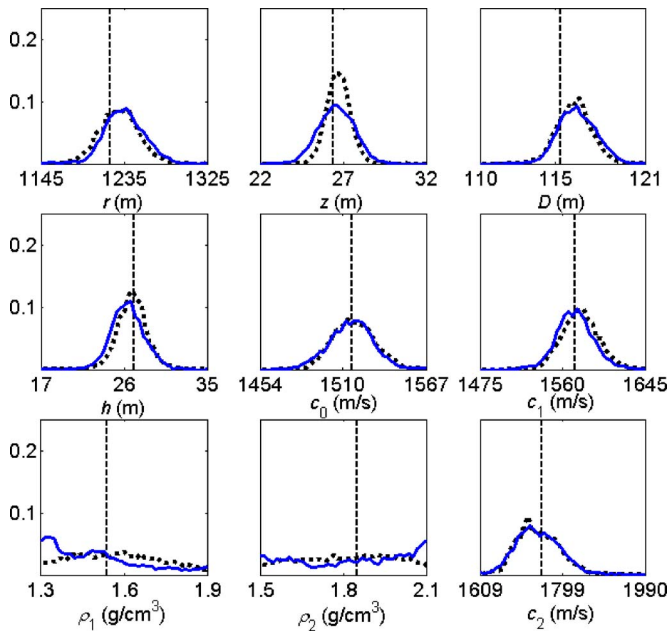


FIG. 6. (Color online) Estimated marginal PPDs by FGS (dotted lines) and multi-step NAB (solid lines) for case 2. Dashed vertical lines indicate the true parameter values.

The overall computation cost of the multi-step NAB scheme is about two times that needed by the basic NAB process. Performance comparisons of the multi-step NAB with the FGS are presented in the next two sections.

VI. INVERSION WITH SIMULATION CASES

A. Inversion results for range-independent case

The PPD values estimated by FGS and NAB with the new search intervals are shown in Fig. 6. The search bounds (the ranges of abscissa) for the source range and sediment thickness, r and h , were contracted. The sediment sound speeds, c_0 and c_1 , and the source depth and water depth, z and D , were shifted and broadened. The bounds of the remaining parameters were all broadened. Compared with the original estimates displayed in Fig. 4, the two curves in Fig. 6 have smaller differences. In Fig. 4, the maximum PPD errors between FGS and the basic NAB for nine parameters, r , z , D , h , c_0 , c_1 , ρ_1 , ρ_2 , and c_2 , are 0.1146, 0.1840, 0.0926, 0.1679, 0.0243, 0.0791, 0.0307, 0.0497, and 0.0301, respectively. However, in Fig. 6, the maximum PPD errors are 0.0261, 0.0516, 0.0189, 0.0263, 0.0112, 0.0169, 0.0418, 0.0433, and 0.0219, respectively. The PPD errors were reduced significantly with the multi-step scheme, except for sediment density, ρ_1 . Meanwhile, the peak regions of the PPD are shifted to the middle of the parameter axis, which provide more useful and complete estimates of parameter uncertainties.

Another objective of uncertainty analysis is to get the 95% HPD interval bounds,²³ which represent the intervals of the minimum width containing $\alpha\%$ of the area of 1-D marginal distribution. Tables I and II list the estimated HPD intervals before and after changing the search bounds.

In Table I, the HPD intervals of four sensitive parameters estimated by FGS and NAB have remarkable differ-

TABLE I. The 95% HPD interval bounds given by FGS and NAB before changing the search intervals for case 2.

Parameter	HPD by FGS	Intervals by FGS	HPD by NAB	Intervals by NAB
r (m)	1179.5–1282.1	102.6	1145–1325	180
z (m)	25.1–28.7	3.6	22.7–30	7.3
D (m)	114.1–119.2	5.1	110.7–120	9.3
h (m)	22–31	9	17.5–33.5	16
c_0 (m/s)	1500–1542.3	42.3	1500–1538.8	38.8
c_1 (m/s)	1550–1614	64	1550–1602.5	52.5
c_2 (m/s)	1648.7–1800	151.3	1677.5–1800	122.5

ences, because the NAB cannot approximate the PPD well. HPD uncertainties of the sound speed in sediment and basement do not have adequate information for use because of unreasonable search bounds. However, after applying the multi-step inversion scheme, the HPD intervals estimated by FGS and NAB are comparable, which are listed in Table II. Since the densities, ρ_1 and ρ_2 , are less sensitive, the HPD intervals are not listed in Tables I and II.

In case 2, the ASSA was run two times, before and after changing the search bounds, which converged with total 10×10^4 models for five frequencies requiring 20 min each time. At first, NAB used 10k input samples and 5k resamples with 6 min of computation time. For the second time, NAB used 20k input samples and 5k resamples with 15 min of computation time. The total time for the multi-step NAB inversion scheme was about 61 min. However, FGS was run 339 and 212 min before and after changing the bounds to converge to 0.2. If the complete PPD values in Fig. 6 were needed, the total run time was 551 min. It can be seen that after adjusting the search bounds with preliminary PPD distributions estimated by the NAB, the relatively accurate and more complete 1-D marginal distributions were obtained with $\frac{1}{9}$ of the computation time required by the FGS.

B. Inversion for range-dependent waveguide

Case 3 was used to evaluate the performance of the multi-step NAB scheme in a range-dependent environment. The test case 0 (the calibration case) from the geoacoustic inversion techniques workshop⁷ was applied in this study. The calibration case was a simple monotonic downslope environment, in which the water depth increased from 105 to 160 m over a range of 3 km. The geoacoustic model con-

TABLE II. The 95% HPD interval bounds given by FGS and NAB after changing the search intervals for case 2.

Parameter	HPD by FGS	Intervals by FGS	HPD by NAB	Intervals by NAB
r (m)	1184.2–1276.5	92.3	1191.2–1283.5	92.3
z (m)	25.2–28.3	3.1	24.3–28.9	4.6
D (m)	113.8–118.6	4.8	113.9–119.3	5.4
h (m)	22.8–31.0	8.2	22.5–30.4	7.9
c_0 (m/s)	1487.3–1548.2	60.9	1483–1546.7	63.7
c_1 (m/s)	1538.2–1621	82.8	1531.7–1614.5	82.8
c_2 (m/s)	1653–1858.1	205.1	1628.5–1853.2	224.7

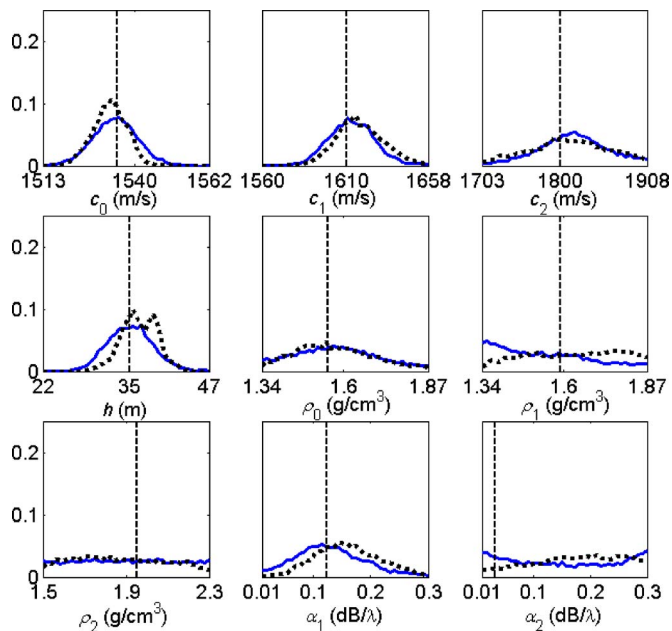


FIG. 7. (Color online) Estimated marginal PPDs by FGS (dotted lines) and multi-step NAB (solid lines) for case 3 (range-dependent environment). Dashed vertical lines indicate the true parameter values.

sisted of a 35-m constant sound speed gradient sediment layer over a basement half-space. The interface at the basement was parallel to the sea floor.

Nine geoacoustic parameters were inverted, which included sediment thickness, h , sound speeds at the top and bottom of the sediment layer, c_0 and c_1 , sound speed of the basement, c_2 , densities at the top and bottom of the sediment layer, ρ_0 and ρ_1 , density of the basement, ρ_2 , and the attenuation in sediment and basement, α_1 and α_2 . For geoacoustic inversion, 50-, 150-, and 300-Hz synthetic data were used. The vertical array contained 31 hydrophones spanning from 20 to 80 m at 2-m spacing. The SNR values were selected as 15, 13, and 11 dB, respectively. The data and replica field vectors were generated by the parabolic equation RAMGEO code.²⁴

Figure 7 displays the PPD estimates by FGS and NAB after adjusting the search bounds. The multi-step NAB algorithm obtained the comparable estimates with FGS for most of the parameters. In Fig. 7, the maximum PPD errors between FGS and the multi-step NAB for nine parameters are 0.0325, 0.0177, 0.0145, 0.0475, 0.0107, 0.0381, 0.0168, 0.0219, and 0.0289, respectively. However, the multi-step NAB did not get the same multi-modal distribution of sediment thickness as FGS.

In case 3, ASSA was run two times, before and after changing the search bounds, which converged with $21k \times 3$ models for three frequencies requiring 160 min each time. NAB used 20k input samples and 5k resamples with 15 min of computation time before and after adjusting the search bounds. The total time for the multi-step NAB inversion scheme was about 350 min. However, FGS was run about 37.3 and 22.5 h before and after changing the bounds to converge to 0.2. If the PPD values in Fig. 7 were needed, the total run time for FGS was about 62.5 h, which included the run time for estimating the error variances with ASSA. The

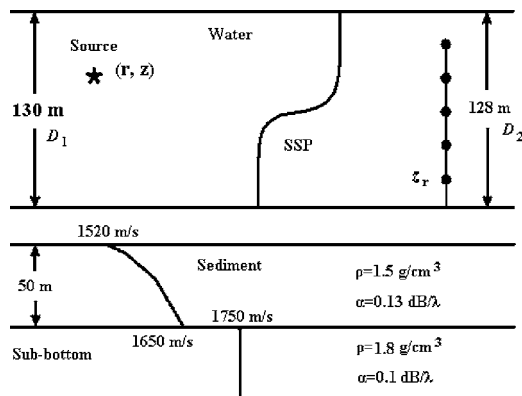


FIG. 8. The baseline environmental model for the North Elba experiment site.

multi-step NAB scheme obtained relatively accurate 1-D marginal PPD with $\frac{1}{11}$ of the computation time required by the FGS.

VII. EXPERIMENTAL DATA ANALYSIS

A. Experiment description and environmental model

The efficiency of the multi-step NAB inversion scheme described in Sec. V was examined using Mediterranean shallow-water benchmark data.^{25,26} The experimental data were collected over a 2-day period on 26 and 27 October 1993 in a shallow water area north of the island of Elba, off the Italian west coast, where the environmental conditions were known from earlier experiments. There are some differences about the baseline environment model between Refs. 25 and 26. The baseline model in Ref. 26 was used here, which is shown in Fig. 8 and Table III.

The bathymetry was measured to be approximately 128 m at the array site. The vertical array contained 48 hydrophones at 2-m spacing with a total aperture of 94 m. The bottom hydrophone was at a depth of 112.7 m and the top hydrophone at a depth of 18.7 m. The array was approximately vertical during the time period that these data were collected.

A stationary source was deployed at a depth of 80 m and approximately 5600 m due north of the array. The bathymetry at the source location was measured to be 130 m. Two signals were transmitted by the stationary source, both were continuous transmission of pseudorandom noise produced using a maximal length sequence. The center frequencies were 170 and 335 Hz. In this study the low frequency 170-Hz signals were used to invert the environmental parameters. The source signal was pseudo-random noise in a 20-Hz band around 170 Hz, whose -3 -dB bandwidth was approximately 12 Hz, and the sampling frequency was 1 kHz.

In Table III the receiver depth z_r is the depth of the hydrophone closest to the ocean bottom; this parameter controls the depth of all of the hydrophones. The array tilt t denotes the horizontal deviation at the top receiver. The following notations were used for the sound-speed profile in the sediment, c_0, c_5, c_{20} , and c_{50} , where the subscript denotes the depth of the profile point below the sediment interface. The

TABLE III. The baseline environmental model and search bounds before and after changing for Mediterranean data analysis.

Parameter	Baseline values	New bounds		
		Old bounds	RI-4 case	RD-4 case
Source range, r (m)	5600	5300–5900	5307–5608	5346–5639
Source depth, z (m)	80	72–82	72–78	72–79
Bathymetry-src, D_1 (m)	130	127–134	123–131	126–132
Bathymetry-rcv, D_2 (m)	128	127–134	...	125–132
Array tilt, t (m)	0	–3–3	–1.9–1.4	–2.0–1.5
Receiver depth, z_r (m)	112.7	110–115	110–115	...
Sediment speed, c_0 (m/s)	1520	1510–1560	1475–1546	1478–1566
Sediment speed, δ_1 (m/s)	30	0–100	0–100	0–100
Sediment speed, δ_2 (m/s)	50	0–100	0–100	0–100
Sediment speed, δ_3 (m/s)	50	0–100	0–100	0–100

sediment sound speeds were linked together using shape functions to perform more efficient optimization.²⁶ The shape functions were

$$c_5 = c_0 + \delta_1, \quad c_{20} = c_5 + \delta_2, \quad c_{50} = c_{20} + \delta_3. \quad (12)$$

The optimization was carried out over the three shape coefficients, δ_1 , δ_2 , and δ_3 , using the bounds listed in Table III.

Reference 26 tested many inversion models to obtain more accurate estimation. Since the main goal of this work is to compare the PPD results estimated by FGS and NAB with real noisy data, the 170-Hz band data were chosen to examine the efficiency of NAB.

Three frequencies with larger power were selected for inversion in order to achieve stable results. The selected frequencies were 164.6, 169.9, and 174.6 Hz. The input SNR along the array was about 15 dB. The frequency domain data vectors were formed using 4096 time samples, and two time epochs with a total time sample of approximately 8 s were computed to form data covariance matrix. According to the Table IV and V in Ref. 26, for the 170-Hz band, the range-independent model RI-4 and the range-dependent model RD-4 are the simplest models to use, based on Bartlett power.

B. Inversion results

First, the range-independent model RI-4 was used to evaluate the multi-step NAB inversion scheme. An additional parameter, receiver depth z_r , was included for the inversion. The original and new bounds of the nine parameters are listed in Table III. The bathymetry was assumed to be range independent. It is noted that, because the sediment speed at top interface, c_0 , was broadened, the remaining sediment speed increments, δ_1 , δ_2 , and δ_3 , would be unchanged due to the inner relationship in Eq. (12). Figure 9(a) displays the estimated marginal PPD by the FGS and the multi-step NAB after changing the bounds based on the preliminary estimates with basic NAB algorithm. The multi-step inversion scheme had comparable results with FGS. In Fig. 9(a), the maximum PPD errors between FGS and the multi-step

NAB for nine parameters are 0.0173, 0.0245, 0.0127, 0.0175, 0.0123, 0.0210, 0.0137, 0.0162, and 0.0266, respectively.

For the RI-4 case, FGS required $342k \times 3$ (three frequencies) forward models with computation time 255 min before changing the search intervals, and required $152k \times 3$ models with 113 min after changing the bounds. ASSA was run two times with 15 min for each time. NAB used 20k input samples and 5k resamples with computation time 15 min. Therefore the total time required by the multi-step inversion scheme was about 60 min, which was about $\frac{1}{6}$ of the total time required by FGS.

Another inversion case is the mildly range-dependent model RD-4 used in Ref. 26. The replica field was calculated by SNAPRD⁴ based on adiabatic normal mode theory. The inversion results are shown in Fig. 9(b) after changing the bounds. The maximum PPD errors between FGS and the multi-step NAB for nine parameters are 0.0261, 0.0177, 0.0154, 0.0129, 0.0214, 0.0132, 0.0162, 0.0166, and 0.0274, respectively.

For the RD-4 case, FGS converged to 0.2 and required $311k \times 3$ forward models with computation time 334 min before changing the search intervals, and $192k \times 3$ models with 210 min after changing the bounds. ASSA was run two times with 23 min for each time. NAB used 20k input samples and 5k resamples with computation time 15 min. Therefore the total time required by the multi-step NAB inversion scheme was about 76 min, which was about $\frac{1}{7}$ of the total time needed by FGS.

In Figs. 9(a) and 9(b), the optimizing results by ASSA have comparable values with Ref. 26 for geometric parameters. The estimates of the source range and depth in Fig. 9(a) for RI-4 case are 5419 and 75.5 m, which are comparable to the values in Ref. 26, 5490 and 76 m. The estimates in Fig. 9(b) for RD-4 case are 5435 m for range and 75.8 m for source depth, which are comparable to the values in Ref. 26, 5600 and 75 m. The estimated sound speed at sediment interface in this study, c_0 , is smaller than baseline value and that given in Ref. 26. Meanwhile, more complete parameter uncertainties were obtained by using FGS and NAB.

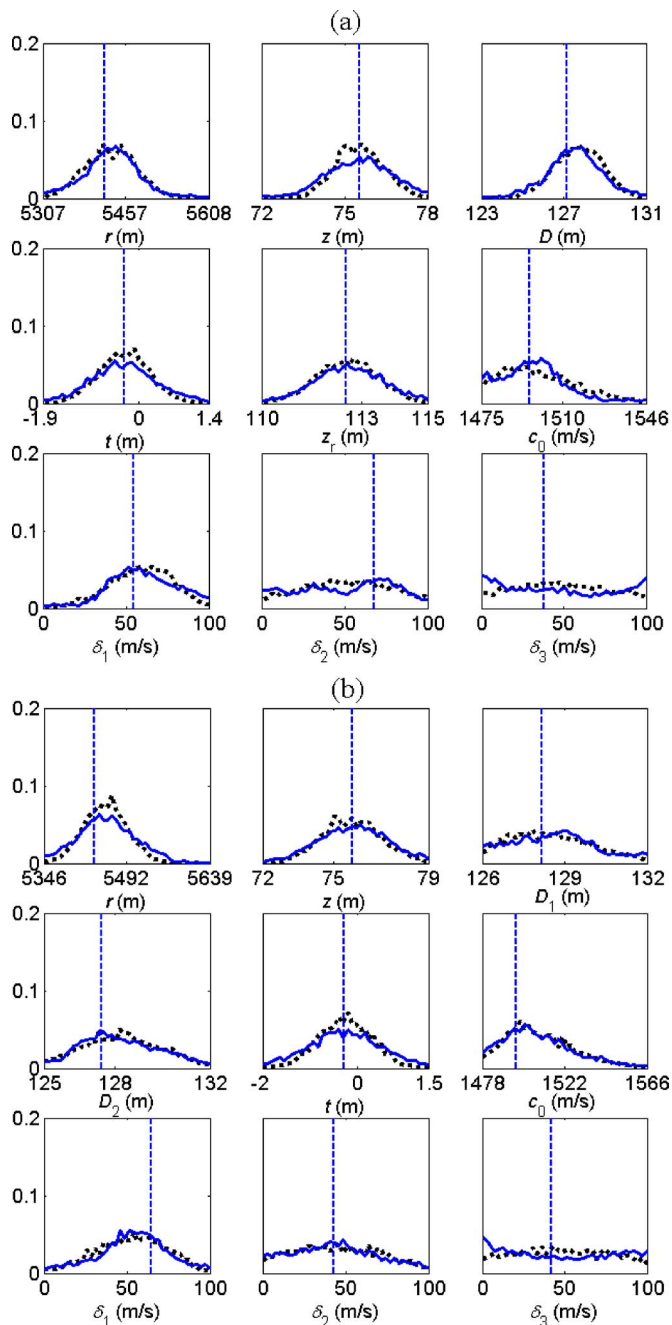


FIG. 9. (Color online) Estimated marginal PPDs by FGS (dotted lines) and multi-step NAB inversion scheme (solid lines) for North Elba experiment site: (a) RI-4 case and (b) RD-4 case. The vertical dashed lines represent the estimated parameter values by ASSA.

VIII. SUMMARY AND DISCUSSION

This paper introduces a neighborhood approximation Bayes algorithm for matched field inversion that concentrates on estimating parameter uncertainties. For low dimension inversion, the NAB approximates the true PPD very well. However, for higher dimensions than about six, it is very difficult for NAB to obtain accurate sampling of the marginal PPD without drastically increasing the input sample and resample sizes. The authors had tried several techniques including contracting perturbation sizes adaptively (like ASSA) to approximate the PPD and rotating the coordinates

to decouple the dependent parameters (like FGS). But these had little improvement due to the limitation of NAB as an approximation algorithm.

A multi-step inversion scheme was developed to overcome this problem. The core idea is to adjust the search intervals robustly based on the preliminary PPD estimation. The modified algorithm provides complete uncertainty information and improves the accuracy of the NAB.

The efficiency of the multi-step NAB inversion scheme was validated by the synthetic benchmark data and the real data collected in the Mediterranean shallow water environment. For the range-independent benchmark test cases of inverting nine parameters with five-frequency synthetic data, the multi-step NAB inversion scheme can obtain comparable PPD estimates, while requiring about one-ninth of the computation time needed by FGS. For the range-dependent benchmark test case with three-frequency data, the multi-step NAB required one-eleventh of computation time needed by FGS. For the real data with three frequencies, the NAB inversion scheme required one-sixth and one-seventh of the computation time needed by FGS for the range-independent and mildly range-dependent cases, respectively. Overall, the advantages of the NAB inversion method are greatest for application with range-dependent environments, where conventional matched field inversion techniques are severely constrained by the computation time of the forward models.

The weakness of NAB is that, even though the scheme of adjusting search bounds was introduced, it is difficult to reproduce the narrower peak regions and the microstructures of the true PPD. This will lead to HPD errors and should be investigated in future work. Despite this limitation, NAB provides a way of incorporating all models for which the forward problem has been solved into the appraisal stage, with significantly less computational cost.

ACKNOWLEDGMENTS

Kunde Yang would like to thank Yongmin Jiang at the University of Victoria for helpful discussions on inverse problems. This work was supported by the Natural Sciences and Engineering Research Council of Canada, the Chinese National Foundation of Sciences (Grant Nos. 10304015 and 60472073), and the Natural Foundation of Shaanxi province in China (2005F40).

¹M. D. Collins, W. A. Kuperman, and H. Schmidt, "Nonlinear inversion for ocean-bottom properties," *J. Acoust. Soc. Am.* **92**, 2770–2783 (1992).

²C. E. Lindsay and N. R. Chapman, "Matched field inversion for geoaoustic model parameters using adaptive simulated annealing," *IEEE J. Ocean. Eng.* **18**, 224–231 (1993).

³A. Tolstoy, "Using matched-field processing to estimate shallow water bottom properties from shot data in the Mediterranean Sea," *IEEE J. Ocean. Eng.* **21**, 471–479 (1996).

⁴P. Gerstoft, "SAGA Users guide 2.0, an inversion software package," SM-333, SACLANT Undersea Research Center, La Spezia, Italy (1997).

⁵A. Tolstoy, N. R. Chapman, and G. H. Brooke, "Workshop97: Benchmarking for geoaoustic inversion in shallow water," *J. Comput. Acoust.* **6**, 1–28 (1998).

⁶S. E. Dosso, M. J. Wilmut, and A.-L. S. Lapinski, "An adaptive hybrid algorithm for geoaoustic inversion," *IEEE J. Ocean. Eng.* **21**, 324–336 (2001).

⁷N. R. Chapman, S. Chin-Bing, D. King, and R. B. Evans, "Benchmarking geoaoustic inversion methods for range-dependent waveguides," *IEEE J.*

Ocean. Eng. **28**, 320–330 (2003).

- ⁸T. B. Neilsen and D. P. Knobles, “Geoacoustic inversion of range-dependent data with added Gaussian noise,” IEEE J. Ocean. Eng. **28**, 446–453 (2003).
- ⁹P. Gerstoft, “Inversion of seismoacoustic data using genetic algorithms and a *posteriori* probability distribution,” J. Acoust. Soc. Am. **95**, 770–781 (1994).
- ¹⁰P. Gerstoft and C. F. Mecklenbräuker, “Ocean acoustic inversion with estimation of a *posteriori* probability distributions,” J. Acoust. Soc. Am. **104**, 808–819 (1998).
- ¹¹M. K. Sen and P. L. Stoffa, “Bayesian inference, Gibbs sampler and uncertainty estimation in geophysical inversion,” Geophys. Prospect. **44**, 313–350 (1996).
- ¹²S. E. Dosso, “Quantifying uncertainty in geoacoustic inversion. I. A fast Gibbs sampler approach,” J. Acoust. Soc. Am. **111**, 129–142 (2002).
- ¹³S. E. Dosso and P. L. Nielsen, “Quantifying uncertainty in geoacoustic inversion. II. Application to broadband, shallow-water data,” J. Acoust. Soc. Am. **111**, 143–159 (2002).
- ¹⁴D. Battle, P. Gerstoft, W. S. Hodgkiss, W. A. Kuperman, and P. Nielsen, “Bayesian model selection applied to self-noise geoacoustic inversion,” J. Acoust. Soc. Am. **116**, 2043–2056 (2004).
- ¹⁵M. Sambridge, “Geophysical inversion with a neighbourhood algorithm I. Searching a parameter space,” Geophys. J. Int. **138**, 479–494 (1999).
- ¹⁶M. Sambridge, “Geophysical inversion with a neighbourhood algorithm II. Appraising the ensemble,” Geophys. J. Int. **138**, 727–745 (1999).
- ¹⁷M. Sambridge, “Exploring multi-dimensional landscapes without a map,” Inverse Probl. **14**, 427–440 (1999).
- ¹⁸M. Sambridge, “Finding acceptable models in nonlinear inverse problems using a neighbourhood algorithm,” Inverse Probl. **17**, 387–403 (2001).
- ¹⁹C. Yardim, P. Gerstoft, and W. S. Hodgkiss, “A fast hybrid genetic algorithm—Gibbs sampler approach to estimate geoacoustic parameter uncertainties,” The Conference of Underwater Acoustic Measurements, Crete, Greece (2005).
- ²⁰F. B. Jensen and F. C. Ferla, “SNAP: The SACLANTCEN normal-mode acoustic propagation model,” SM-121, SACLANT Undersea Research Center, La Spezia, Italy (1979).
- ²¹P. Ratilal, P. Gerstoft, and J. T. Goh, “Subspace approach to inversion by genetic algorithms involving multiple frequencies,” J. Comput. Acoust. **6**, 99–115 (1998).
- ²²Kunde Yang, Y. Ma, C. Sun, J. H. Miller, and G. R. Potty, “Multi-step matched field inversion for broadband data from ASIAEX2001,” IEEE J. Ocean. Eng. **29**, 964–972 (2004).
- ²³A.-L. S. Lapinski and S. E. Dosso, “Bayesian geoacoustic inversion for the inversion techniques 2001 workshop,” IEEE J. Ocean. Eng. **28**, 380–393 (2003).
- ²⁴M. D. Collins, “A split-step Padé solution for parabolic equation method,” J. Acoust. Soc. Am. **93**, 1736–1742 (1993).
- ²⁵D. F. Gingras and P. Gerstoft, “Inversion for geometric and geoacoustic parameters in shallow water: Experimental results,” J. Acoust. Soc. Am. **97**, 3589–3598 (1995).
- ²⁶P. Gerstoft and D. F. Gingras, “Parameter estimation using multifrequency range-dependent acoustic data in shallow water,” J. Acoust. Soc. Am. **99**, 2839–2850 (1996).

Underwater implosion of glass spheres

Stephen E. Turner^{a)}

Naval Undersea Warfare Center, 1176 Howell Street, Building 1246, Code 4121, Newport, Rhode Island 02841

(Received 22 December 2005; revised 10 September 2006; accepted 13 November 2006)

Underwater implosion experiments were conducted with thin-wall glass spheres to determine the influence that structural failure has on the pressure pulse. Four experiments were conducted with glass spheres having an outside diameter of 7.62 cm, thickness of 0.762 mm, and an estimated buckling pressure of 7.57 MPa. The experiments were performed in a pressure vessel at a hydrostatic pressure of 6.996 MPa. The average peak pressure of the implosion pressure pulse was 26.1 MPa, measured at a radial distance of 10.16 cm from the sphere center. A computational fluid structure interaction model was developed to assess how the failure rate of the glass structure influences the pressure time history. The model employed a specified glass failure sequence that is uniform in time and space. It was found that for the conditions of the test, a glass failure rate of 275 m/s provided a reasonable representation of the test data. The test data and the model results show that the failure time history of the structure has a significant influence on an implosion pressure pulse. Computational prediction of an implosion pressure pulse needs to include the failure time history of the structure; otherwise it will overpredict the pressure time history.

[DOI: 10.1121/1.2404921]

PACS number(s): 43.30.Zk, 43.30.Lz, 43.50.Pn [JGM]

Pages: 844–852

I. INTRODUCTION

An underwater implosion can occur upon failure of a structure that contains low-pressure gas and is surrounded by high pressure water. If the collapse rate is fast enough, the momentum of the in-rushing water causes the water to compress at the instant of closure. This compression manifests itself in an outward propagating pressure wave, which has the potential to be large. For many deep ocean applications, the resulting pressure pulse needs to be known to evaluate survivability of adjacent structures. Therefore, a series of tests has been conducted with thin-wall glass spheres in an effort to better understand the phenomenon and to provide data for comparison with computational models.

Historically, underwater implosion has been investigated in the context of cavitation bubbles and the bubble pulse from underwater explosions. In an effort to assess the magnitude of cavitation bubble collapse pressures, Rayleigh¹ proposed a theory for the collapse of a spherical cavity in an incompressible liquid. Solutions were given for the case of a spherical cavity having zero or constant internal pressure. The work of Gilmore,² Keller and Kolodner,³ Hickling and Plesset,⁴ and Plesset and Prosperetti⁵ led to solutions of the pressure and velocity fields in close proximity to a collapsing or expanding gas bubble, in which the liquid was modeled as a compressible fluid and the bubble contents modeled with the polytropic relationship. For larger bubbles, such as those caused by underwater explosions, buoyant effects become important. Hunter and Geers⁶ have developed a model for underwater explosion bubbles which accounts for the expansion due to explosion and the subsequent bubble oscillation, including the effects of buoyant translation. In each of the

above-mentioned cases, the analyses are restricted to one or two domain problems with spherical geometry.

There has been limited work in the past with respect to implosion experiments. Vanzant *et al.*⁷ imploded 27 aluminum spheres of 15.875 cm diameter having wall thicknesses of 0.91, 1.30, or 2.34 mm. Three interior configurations were tested: vacuum, charged with air at 1 atm, and filled with Styrofoam™ pellets. The near-field pressure time histories were measured and high-speed video was attempted during each event. The measured negative and positive pressure pulses were compared with gas bubble collapse theory. It was found that the experimental peak pressures were lower than the theoretical peak pressures and that the duration of the pulses was longer for the experiments than theory predicted. However, the impulse for the experiments was found to be in good agreement with theory. It was concluded that the energy required to break the metal sphere and accelerate the fragments inward was responsible for the lower peak pressures and longer event times. There was no attempt to identify factors that control failure of the aluminum shell.

Orr and Schoenberg⁸ conducted implosion experiments using glass spheres of 43.2, 33.0, and 23.5 cm diameter. Each sphere was preweakened by grinding a flat spot into the spherical surface. The spheres were submerged in the ocean until they imploded. The implosion depth (2600–3500 m) was found to be dependent on the thickness of glass at the flat. The acoustic signature of each implosion event was measured near the surface to assess the potential of imploding spheres as a nonexplosive broadband acoustic source. Peak pressures were reported in the range 3.31–13.6 MPa at a reference distance of 1 m. The measured pressure time histories were not compared with analytical predictions.

In another effort to develop an acoustic source without using explosives, Harben and Boro⁹ bundled five glass

^{a)}Electronic mail: stephen.e.turner1@navy.mil

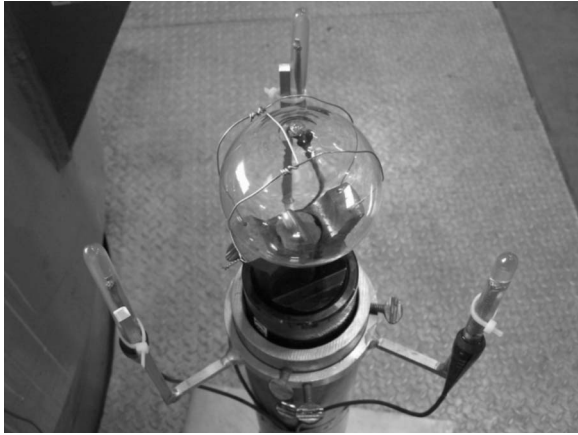


FIG. 1. Test stand with test sample and instrumentation installed.

spheres together to form an imploding source. Each sphere had a volume of 22 l and one of them was outfitted with a device to break the glass sphere at a predetermined depth. A peak pressure of 20 MPa at 1 m was measured for implosion of the bundle of spheres at a depth of 686 m.

A modeling approach is needed to address underwater implosion of arbitrarily shaped gas volumes separated from the ocean by a structure. The available theoretical models are for spherical gas bubbles and cannot account for a structure which may separate the gas and liquid. Further, the experimental work by Vanzant *et al.* indicates that the structure has a significant influence on the measured pressure pulse. The objectives of this paper are (1) to report near-field dynamic pressure data for hydrostatic implosion of spherical glass structures; and (2) to evaluate a fluid structure interaction modeling approach to the implosion event.

II. EXPERIMENTAL APPROACH

A. Test stand

The test stand consisted of an aluminum base plate with a 7.62 cm (3 in.) diameter pipe standing vertically. The test sample, instrumentation, and mechanical initiation device were mounted at the upper end of the pipe as shown in Fig. 1. The mechanical initiation device was a hydraulic piston with a blunt blade in contact with the glass. The piston/blade can be seen in Fig. 1 under the glass sphere. The glass sphere is secured to the mechanical initiation device by thin wires.

The test series reported in this paper was conducted in a 1.52 m diameter \times 3.66 m length (60 in. diameter \times 144 in. length) cylindrical pressure vessel, which was oriented vertically. The test stand was lowered by crane to a submerged platform and then the pressure vessel cap set in place and secured by a locking ring. A schematic of the test stand inside the pressure vessel is shown in Fig. 2. After purging the air from the cap, a water pump was used to increase the hydrostatic pressure. Even though there was no air in the pressure vessel, the decrease in hydrostatic pressure, resulting from the collapse, was less than 35 kPa, or 0.5% of the hydrostatic pressure.

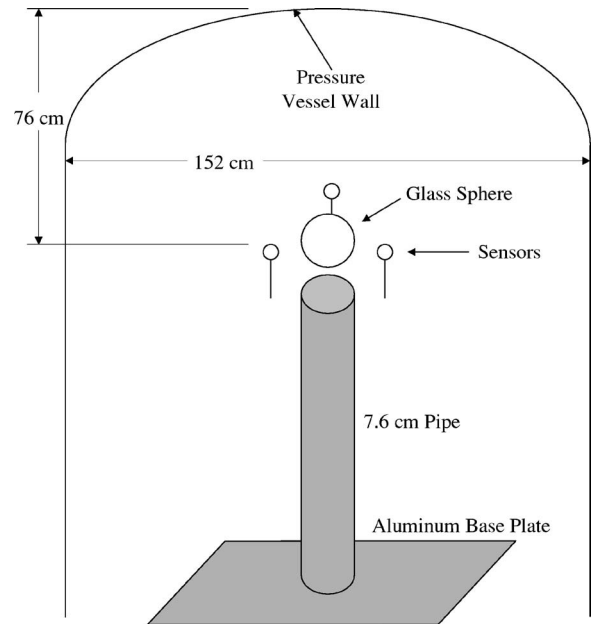


FIG. 2. Test stand schematic.

B. Instrumentation/recording equipment

The dynamic pressure sensors were PCB tourmaline underwater blast ICP pressure sensors (model W138A06, SN 6453, 6454, and 6455). The nominal sensitivity of each blast sensor was 0.145 mV/kPa over the measurement range of 0–34.474 MPa, and the uncertainty was ± 221 kPa. The three sensors were connected to a PCB model 481 sensor signal conditioner and recorded on a TEAC GX-1 recorder at a sample rate of 200 kHz. The sensors were positioned on a horizontal plane passing through the center of the sphere, at 120° increments around the circumference, and at a radial distance of 10.16 cm from the center. The sensor locations are shown in Fig. 3.

C. Test matrix

The test samples were borosilicate glass spheres with an outside diameter of 7.62 cm, a nominal wall thickness of

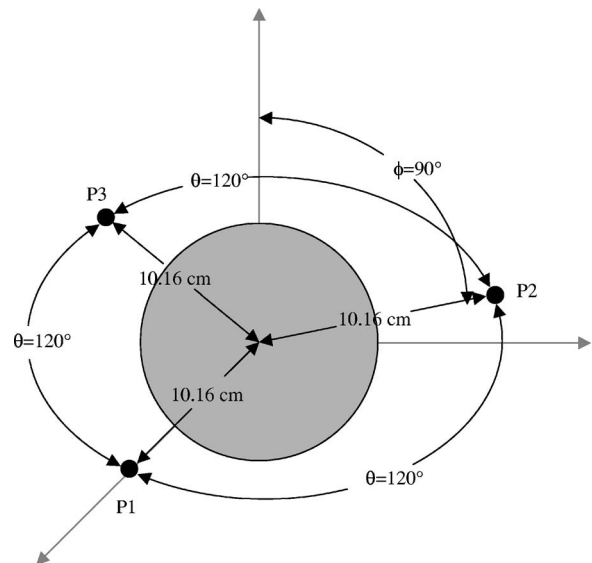


FIG. 3. Dynamic pressure sensor locations.

0.762 mm, and an internal volume of 218.0 cm³. Four tests were conducted at a hydrostatic pressure of 6.996 MPa (1014.7 psia). In the first test, the glass structure failed from hydrostatic instability at 6.996 MPa. In the remaining three tests, the mechanical initiation device was used to initiate the structural failure. The hydrostatic pressure was held constant for all four tests to evaluate the repeatability of the event and to assess the difference between initiated and uninitiated glass failures.

D. Test sequence

The test samples were prepared by securing the glass sphere in the wire frame above the mechanical initiation device (Fig. 1). Then, measurements were made to verify that each dynamic pressure sensor was 10.16 cm from the center of the sphere. After installing the test sample, the test stand was lowered into the pressure vessel and positioned at the centerline of the pressure vessel. Two locating pins on the pressure vessel platform were used to ensure the same test stand position relative to the pressure vessels for each test. The pressure vessel cap was secured and the pressure vessel was completely filled with water for the test. The hydrostatic pressure inside the pressure vessel was increased at a rate of 700 kPa/min using a water pump. The data acquisition was started when the hydrostatic pressure reached 4.8 MPa. The water pump continued to increase the hydrostatic pressure until either collapse occurred or until the pressure reached 6.996 MPa. After securing the water pump, the hydraulic pump was activated to slowly drive the blunt initiator into the test sample. After the test sample collapsed, the data acquisition was ceased.

E. Computational modeling

To better understand the experimental data, a fluid structure interaction model of the underwater implosion was developed. The models were developed using the Dynamic System Mechanics Analysis Simulation (DYSMAS) code, which was developed by the Naval Surface Warfare Center, Division Indian Head for underwater shock analysis. The DYSMAS code consists of two explicit solvers: an Eulerian fluid solver (GEMINI), and a Lagrangian finite element solver (DYNA-N); and a standard coupling interface, which passes interface data between the codes at each time step. GEMINI has fixed rectangular grids, through which fluid or the structure can move. Boundaries can be either free (nonreflecting) or fixed (reflecting, with zero normal flow). Conservation of mass, momentum, and energy are enforced at all grid boundaries. GEMINI was specifically built to solve underwater shock problems, so it incorporates compressible fluid models. However, GEMINI does not include heat transfer or viscous dissipation. It can be run in one, two, or three dimensions, and can be run on single or parallel processors. DYNA-N was developed at Lawrence Livermore National Laboratories for analysis of the transient dynamic response of solids.

Prior to solving the fluid structure interaction model, a comparison was made between the GEMINI fluid solver and an analytical solution for gas bubble oscillation developed by

Keller and Kolodner. This modified form of the Rayleigh-Plesset equation¹⁰ adds first-order compressibility effects to the liquid surrounding the gas bubble. The analysis case was similar to the experiments, except that there was no glass surrounding the gas bubble. A spherical gas bubble having a radius of 3.8 cm and pressure of 101.325 kPa is initially at rest in an infinite field of water at $P_{\text{hyd}}=6.996$ MPa. The bubble contains ideal gas with spatially uniform pressure, which follows an adiabatic, reversible process, $PV^\gamma = \text{constant}$ ($\gamma=1.4$). Surface tension, viscosity, and thermal effects are neglected. The GEMINI model has a nonreflecting boundary condition at $r=225$ cm. The instantaneous bubble radius was calculated by both models and is plotted in Fig. 4. There is essentially no difference between the curves. The GEMINI solution predicts the first bubble collapse will reach a minimum radius of 0.427 cm, or 11.24% of the initial bubble radius. The Keller-Kolodner solution predicts a minimum radius of 0.445 cm (11.71% of the initial bubble radius). In addition to the bubble radius, the pressure in the surrounding water was obtained from each model at a radial distance of 10.25 cm and is plotted in Fig. 5. The two pressure time histories are identical except for the magnitude of the first pressure pulse. The GEMINI solver predicts a peak pressure of 36.7 MPa, compared to 51.0 MPa for the Keller-Kolodner solution. The pressure pulse is a response of the in-rushing water to sudden compression as the bubble reaches a minimum radius. The Keller-Kolodner model uses a first-order compressibility model in which the density and speed of sound are constant. In the GEMINI model, the water is described by the Tillotson equation of state

$$P = P_0 + \omega\rho(e - e_0) + A\mu + B\mu^2 + C\mu^3, \quad (1)$$

which relates the pressure to density and internal energy. With constant density, the first-order approach is stiffer, leading to a higher estimate of the pressure. At all other times, the compressibility of the water is less significant, and good correlation between the two models is observed.

The one-dimensional GEMINI model contained 50 equally sized fluid cells within the initial bubble radius and 100 fluid cells between the initial bubble radius and the model boundary at $r=225$ cm (the cell size increased with radial distance from the bubble). To assess convergence, the model was run with a total of 2000 cells and again with 10,000 cells. The model results were identical for all three cases, so subsequent models contained 150 cells in the radial direction (50 within the initial bubble radius and 100 in the surrounding water).

A two-dimensional axisymmetric model was constructed with a fixed (reflecting) boundary condition on the axis of symmetry and free (nonreflecting) boundary conditions at the other boundaries. The pressure vessel was not modeled because the events of interest occur before reflected pressure waves come back to the test item or the sensors. Details of the fluid structure interaction model are provided in Fig. 6. The black half-circle represents the glass structure, modeled with 180 rigid elements of equal length. In the x (radial) direction, there are 50 cells of equal size within the radius of the sphere ($0 < x < 4$ cm), and 100 cells in the range $4 < x < 50$ cm (cell size increasing with radius). The cell density is

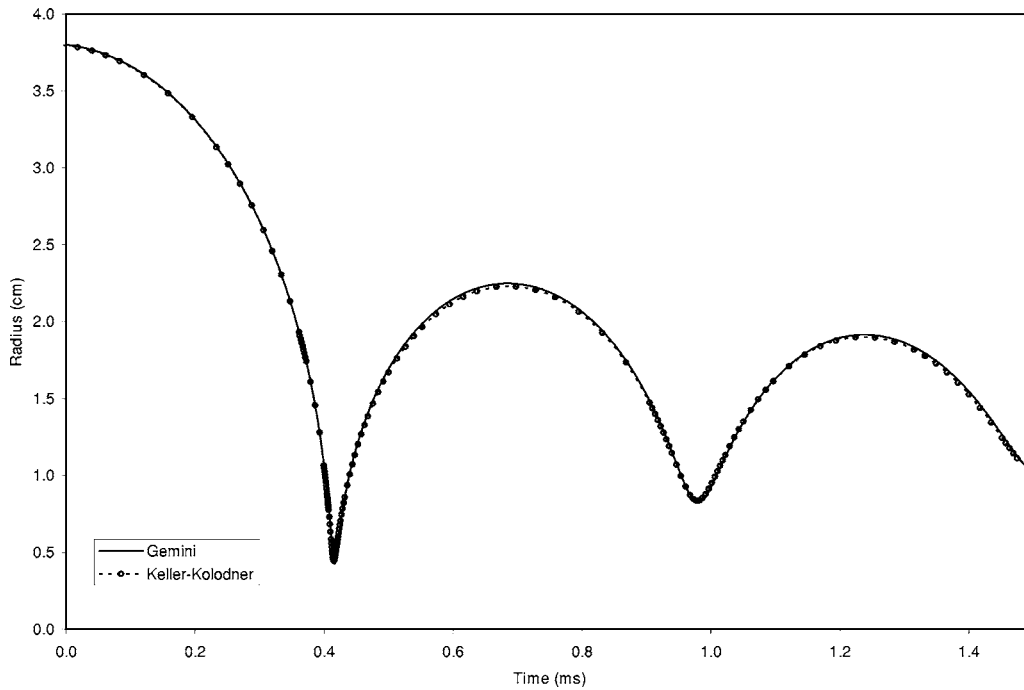


FIG. 4. Instantaneous bubble radius; oscillating bubble problem solved by GEMINI and Keller-Kolodner.

the same in the z direction, with respect to the center of the sphere. There are 100 cells across the diameter of the sphere ($-4 < z < 4$ cm), 100 cells from $4 < z < 50$ cm, and 100 cells from $-4 > z > -50$. The fluid cells inside the rigid elements contain air at 101.3 kPa, modeled as an ideal gas which undergoes an adiabatic, reversible process. Outside the rigid elements, the fluid cells contain water at 6.996 MPa, which was modeled as a compressible fluid with the Tillotson equation of state. The black cells shown below the half-circle are blocked cells, with reflecting boundaries, which represent the test stand/mechanical initiation device.

Material properties, including breaking stress and fracture characteristics, were not available to develop a fracture based material model for the glass. Instead, the glass was modeled with rigid elements. An element deletion rate was specified *a priori* to simulate the time-dependent failure of the glass structure. The initial conditions of the simulation are shown in Fig. 6. At time=0, the air pressure inside the sphere is 101.3 kPa and the water pressure outside the sphere is 6.996 MPa. During the simulation, the rigid elements were deleted, starting with the bottom of the sphere ($x=0$, $z=-3.81$ cm) and ending at the top. The element failure rate

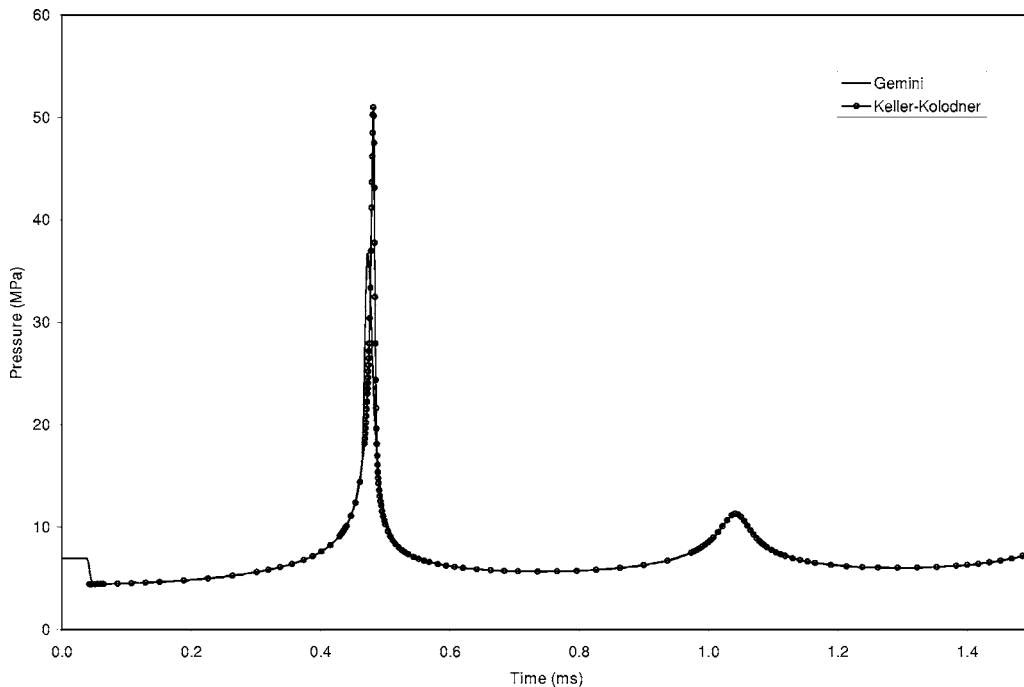


FIG. 5. Pressure calculated at 10.25 cm from center of sphere; oscillating bubble problem solved by GEMINI and Keller-Kolodner.

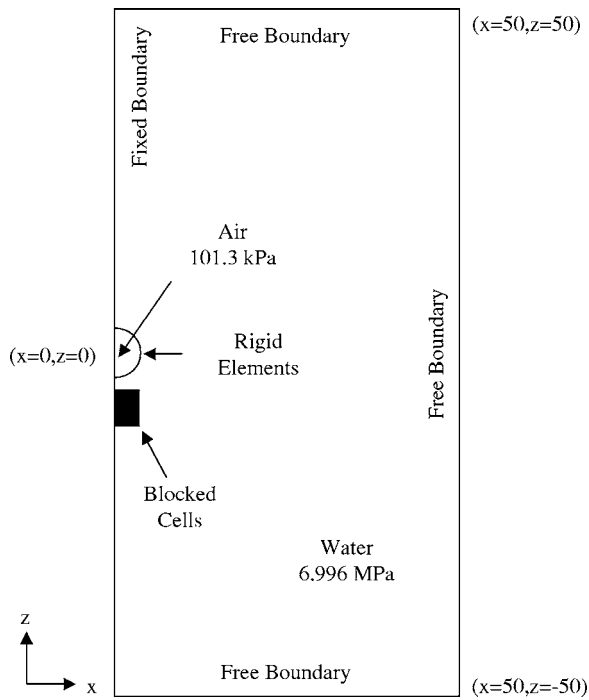


FIG. 6. Description of axisymmetric GEMINI model.

was specified in m/s measured around the circumference. As the rigid elements were deleted, the high pressure water flowed into the sphere, compressing the low pressure air. The flow area increased with time until all the rigid elements were deleted. The local water pressure at the sensors responded to the water in-rush, as the sphere filled, and to the sudden decrease in water velocity when the compressed air reached a minimum volume. Additionally, since the rigid elements have no thickness, the model included a 0.762-mm-thick layer of sand on the inside of the rigid elements. The sand represents the volume of incompressible glass after structure has failed. A P - α equation of state is used for the sand.¹¹

III. RESULTS

A. Glass failure by hydrostatic instability

Each of the four tests was conducted with glass spheres subject to an external hydrostatic pressure of 6.996 MPa and an internal pressure of 101.3 kPa. In test 1, structural instability occurred without activating the mechanical initiation device. Consequently, the point of failure initiation with respect to the sensors was unknown. The pressure time history for each sensor of test 1 is plotted in Fig. 7. Each curve was shifted in time by the same amount such that the peak pressure for sensor 1 occurs at 0.8 ms. Due to symmetry conditions, the pressure time histories of sensors 2 and 3 align with sensor 1 in time. The beginning of the collapse is observed as a decrease in the pressure at the sensors, which occurs between 0.12 and 0.16 ms. As the high pressure water rushes in to compress the low pressure gas, the local water pressure decreases by 1.6 MPa, according to Bernoulli's principle. The collapse phase ends when the gas reaches a minimum volume (closure); and the velocity of the water must go to zero. The large hydrostatic pressure used in these experiments caused the water to achieve a very high velocity during the collapse phase. Upon closure of the gas volume, the rapid change in water momentum caused compression of the water, and released a pressure wave in the outward radial direction. The pressure wave propagates toward the pressure vessel wall and then is reflected back toward the center. The distance between the sensors and the wall of the pressure vessel is 66 cm. In fresh water, the time for the pressure wave to travel from the sensor to the wall and back is about 0.9 ms. Therefore, the onset of reflections in the pressure time history is expected at 1.0 ms. Had the experiments been conducted at a lower hydrostatic pressure a lower peak pressure would be expected. The peak pressure is influenced by compression of the water and reexpansion of the compressed gas volume. The momentum of the in-rushing water during a collapse is dependent on the differential pressure (hydrostatic pressure minus initial gas pressure). Even if the momentum of the in-rushing water is not sufficient to cause the water to

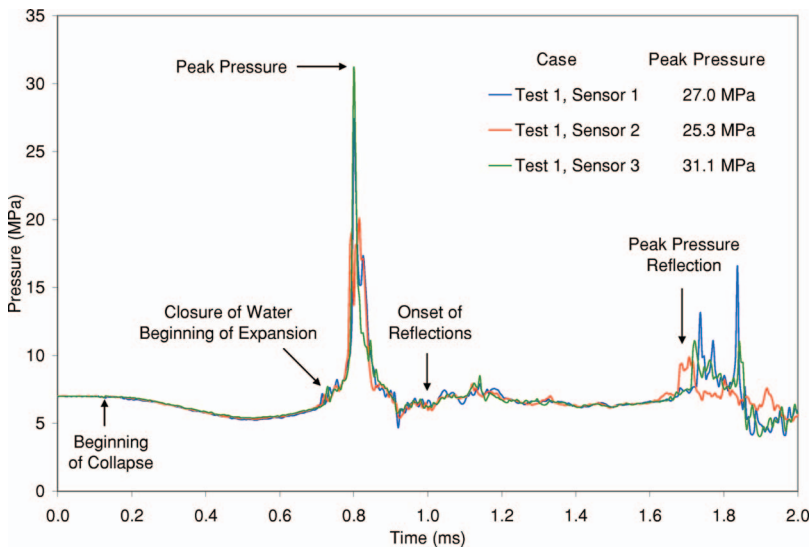


FIG. 7. Pressure time history for test 1.

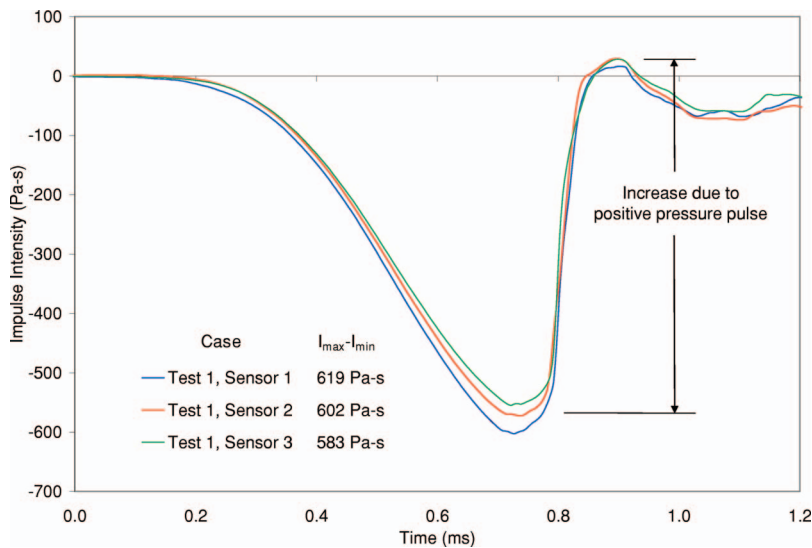


FIG. 8. Impulse time history for test 1.

compress at closure, the gas volume can still be compressed beyond the hydrostatic pressure, so that it has to reexpand.

During the collapse phase, the pressure time histories of sensors 1–3 are nearly identical. The curves begin to diverge as the pressure peak is reached at 0.8 ms. Sensor 3 recorded the highest peak pressure, but the duration of the pressure pulse was shorter than the other two sensors. It is often useful to integrate the dynamic pressure with respect to time to calculate the impulse, I , which is a measure of the momentum imparted to the water as the pressure wave passes through it.¹² Note that the dynamic pressure is obtained by subtracting the hydrostatic pressure from the absolute pressure, so that at $t=0$, the impulse is zero. In Fig. 8, the impulse is plotted for the three pressure time histories measured in test 1. For each time, t , between 0 and 1.2 ms, the pressure time history was integrated between 0 and t . The strength of the positive portion of the pressure pulse (where $P > P_{\text{hyd}}$) is the difference between the maximum impulse (occurring at about 0.9 ms) and the minimum impulse (occurring at about 0.73 ms). $I_{\max}-I_{\min}$ values of 619, 602, and 583 Pa s were calculated for sensors 1–3, respectively. For this test, the sensor-to-sensor difference between $I_{\max}-I_{\min}$ was 6%, whereas the difference for the peak dynamic pressure was

55%. The value of plotting the impulse is to show that the momentum imparted to the water in the three directions that were measured is uniform, even though there is local variation of the pressure time histories.

B. Glass failure by mechanical initiation

Tests 2–4 were conducted with glass spheres identical to test 1 at an external hydrostatic pressure of 6.996 MPa. Each glass sphere was caused to fail by activating the mechanical initiation device, which contacted the bottom of the sphere, 90° away from each sensor. The pressure time histories measured at sensor 1 for each test are shown in Fig. 9. For ease of comparison, the curves for each test were shifted in time to align the peak pressures at 0.8 ms. During the collapse phase, there is little deviation between the pressure time histories. However, the curves diverge at the peak pressure into four distinct curves. Still, the magnitudes of each peak pressure are within 5% of each other (25.8–27.2 MPa). Even though the failure location of test 1 is unknown, the pressure time history of test 1 is consistent with tests 2–4 with respect to the magnitude and duration of the collapse phase and the pressure peak.

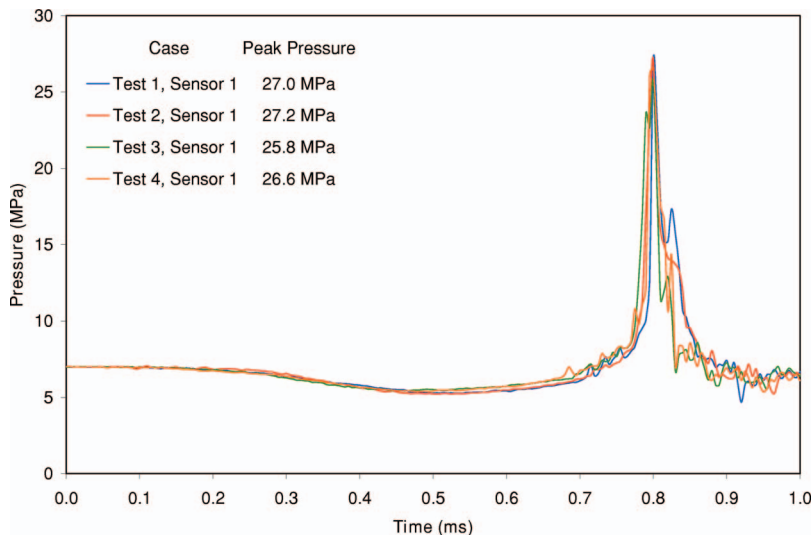


FIG. 9. Pressure time histories for tests 1–4, sensor 1.

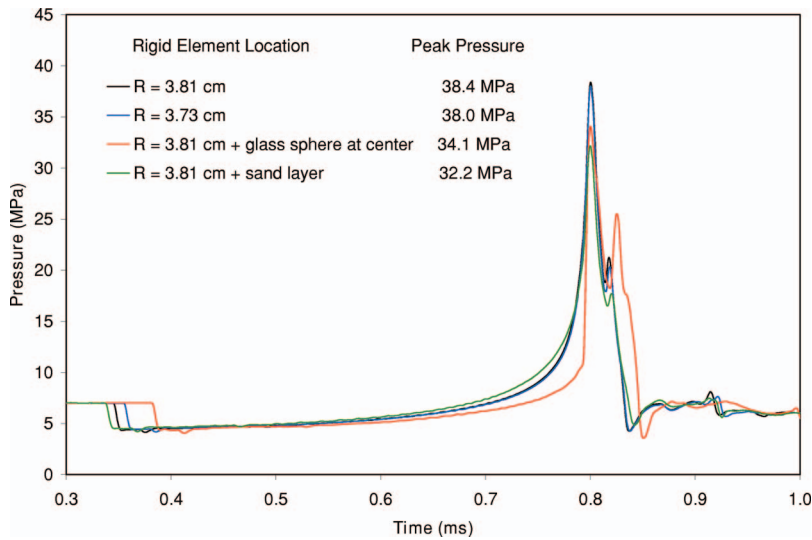


FIG. 10. Comparison of three computational models, each with an infinite glass failure rate.

C. Comparison with computational model

The primary variable in the computational model was the rate of glass failure. But before the parameter of glass failure rate was investigated, three different treatments of the glass volume were evaluated and compared against a baseline case, in which the zero thickness rigid elements were located at the outside radius of the glass sphere, $r=3.81$ cm. In the first case, the rigid elements were simply relocated to the inside radius of the glass sphere, $r=3.73$ cm. In case two, the rigid elements were relocated at $r=3.81$ cm, and a solid sphere having the same volume as the glass shell, was specified at the center. In the third case, the rigid elements were located at $r=3.81$ cm, and the glass shell thickness was modeled by a layer of sand against the inside of the rigid elements, so that after the rigid elements were deleted the influence of the glass particles would be included. The thickness of the sand layer was the same as the glass thickness. Each of the three cases is compared to the baseline case in Fig. 10. Figure 10 shows that the case modeled with the rigid elements at the outside radius with only gas on the inside of the sphere results in the largest pressure peak. Reducing the radius of the rigid elements to the inside radius of the glass

sphere has a minor influence on the peak pressure. There is a significant reduction in the peak pressure when the glass volume is modeled by the sphere or the layer of sand. Treatment of the glass volume with the layer of sand is more desirable since (1) it is more physically realistic to specify the initial location of the glass between the outer and inner radii; and (2) it represents the duration of the collapse phase better. In all the subsequent cases, the rigid elements were located at $r=3.81$ cm and the glass sphere was modeled by a layer of sand between the inner and outer radii of the glass sphere.

Eight cases were run with different glass failure rates. The first case represented a glass structure that shatters instantly (infinite failure rate); all the rigid elements were deleted at the same time. Seven additional cases were run with glass failure rates ranging from 1830 m/s, which corresponds to the maximum reported rate of crack propagation in glass,¹³ down to 200 m/s. The pressure time histories from the DYSMAS analyses are shown in Fig. 11. For ease of comparison, the curves were shifted in time to align the peak pressures at a common time of 0.8 ms. For the case of infinite failure rate, the pressure drops sharply from 6.99 to 4.21 MPa at 0.368 ms. Since all the rigid elements

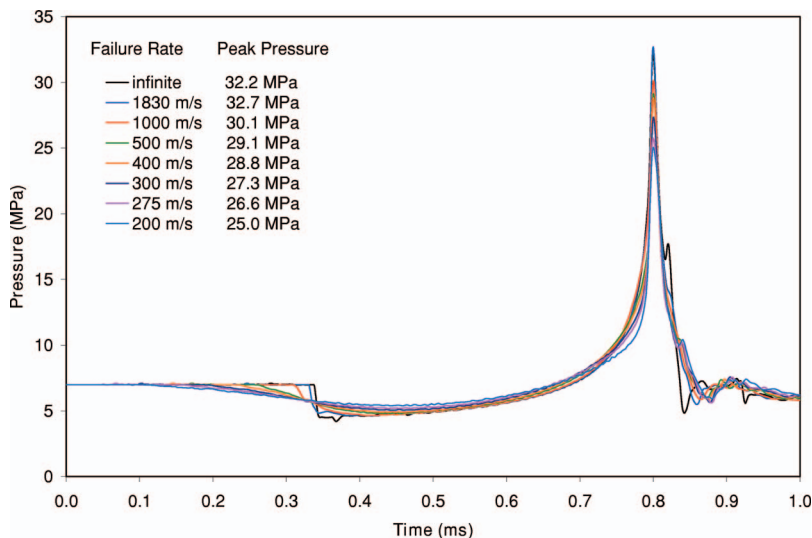


FIG. 11. Pressure time histories for DYSMAS calculations.

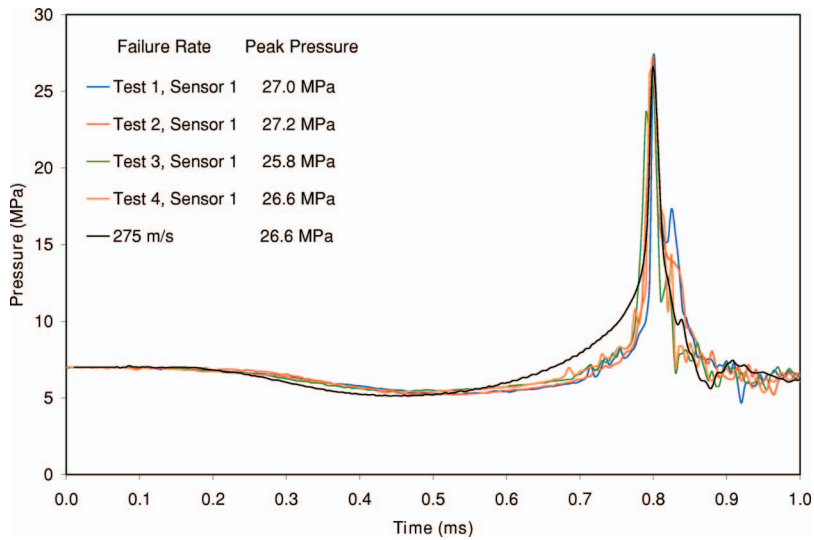


FIG. 12. Comparison of pressure time histories between experiments and DYSMAS calculation.

were deleted at one instant, allowing the water to instantly flow inward from all directions, the duration of the collapse is a minimum (0.462 ms). For the cases with finite glass failure rates, the presence of the elements restricts the in-rush of water, causing the collapse to take longer. It was found that as the glass failure rate was decreased, the peak pressure decreased. One exception is that the model results for the infinite failure rate predict a peak pressure of 32.2 MPa, which is 1.5% lower than the peak pressure for the 1830 m/s case (32.7 MPa). Further review of the model results indicated that the blocked cells located below the glass sphere restrict the in-rush of water from the bottom. For the infinite failure rate case, the water begins to flow inward from all directions the instant the rigid elements are deleted. There is limited water available between the blocked cells and the bottom of the glass sphere, which restricts the flow rate from the bottom. Consequently, the flow restriction causes the gas bubble to migrate toward the blocked cells. However, for the cases with finite failure rates, the first rigid elements to be deleted are at the bottom, causing the initial in-rush of water to be in the $+z$ direction. After all the rigid elements are deleted, the collapsing gas bubble has momentum in the $+z$ direction. The combination of an 1830 m/s element deletion rate starting at the bottom and the restricted flow rate from the bottom, simply produces a more symmetric collapse (and higher peak pressure) than is observed for the infinite failure rate case.

The computational analyses followed the simplifying assumption that the glass failure rate was uniform with respect to time and space, and that the rigid elements remain stationary until they are deleted. Even though these assumptions were not verified directly, the pressure time history for the 275 m/s glass failure rate provides a reasonable representation of the measured pressure time histories. The results for the 275 m/s analysis case are overlaid on the data from tests 1 to 4 in Fig. 12 (again, aligning the peak pressures at 0.8 ms). The 275 m/s case was selected because the peak pressure of 26.6 MPa matches the test data peak pressures (25.8–27.2 MPa). Additionally, the analysis matches the data with respect to the duration of the collapse, the pressure drop during the collapse, and the shape/duration of the posi-

tive pressure peak. The start of collapse was defined as the time at which the local pressure at the sensor drops below 99% of the hydrostatic pressure. The end of the collapse is considered to be the point at which the local pressure increases to the hydrostatic pressure. In each of the four tests, the duration of the collapse is between 0.505 and 0.6 ms. The 275 m/s analysis case had a slightly lower collapse time of 0.473 ms. The pressure drop for the test data (all three sensors and all four tests) is 1.624 MPa; for the analysis case, it is 1.87 MPa. Finally, the model results agree well with the test data with respect to the shape and duration of the positive pressure peak. Even the minor peak on the tail of the pressure peak is captured by the analysis. This corresponds to reflection from the test stand/mechanical initiator.

IV. CONCLUSIONS

The primary conclusion is that a computational model of an underwater implosion event must include the structure that separates the low pressure air from the high pressure water. If the structure is neglected, the model will overpredict the peak pressure. To support this conclusion, four experiments were conducted with glass spheres subject to hydrostatic pressure at, or near to, the failure load. The use of brittle glass was expected to result in near instantaneous structural failure. However, a computational model that does not account for the glass structure (instantaneous failure) was found to overpredict the peak pressure by 44%.

A uniform failure rate (in time and space) was implemented in the model to determine its influence on the pressure time history. Failure rates from the maximum crack propagation speed of 1830 down to 200 m/s were evaluated. Model results were found to agree with the test data when a structural failure rate of 275 m/s used. Since the rate of the collapse determines the momentum of the water as it approaches the point of closure, it is reasonable to expect good agreement with the peak pressure if the collapse rate has been determined.

Finally, the constant failure rate of 275 m/s is an effective value that only applies to the set of test conditions described. It is expected that the failure rate would change if

parameters such as glass thickness, sphere diameter, or hydrostatic pressure were changed. Further, it is expected that the actual failure time history of the glass structure varies in time and space. A more desirable approach would be a finite element description of the glass structure that reacts to mechanical forces of pressure and flow. Such a model would require detailed fracture and mechanical strength information for the glass material. While the above-described model is not suitable as a predictive capability, it does illustrate the influence the structure has on an underwater implosion.

ACKNOWLEDGMENTS

The authors would like to acknowledge support for this research from the Office of Naval Research and from the Naval Undersea Warfare Center, Division Newport. The Naval Surface Warfare Center, Division Indian Head provided valuable assistance for the fluid structure interaction modeling.

NOMENCLATURE

A, B, C	= constants
e_0	= reference energy
P	= pressure
P_0	= reference pressure
r	= radius
V	= Volume
ρ_0	= Reference density

γ = ratio of specific heats

μ = $(\rho/\rho_0) - 1$

ω = $\gamma - 1$

¹Lord Rayleigh, "On the pressure developed in a liquid during the collapse of a spherical cavity," *Philos. Mag.* **34**, 94–98 (1917).

²F. R. Gilmore, "The growth of collapse of a spherical bubble in a viscous compressible liquid," Report No. 26-4, Hydrodynamics Laboratory, California Institute of Technology, Pasadena, CA, 1952.

³J. B. Keller and I. I. Kolodner, "Damping of underwater explosion bubble oscillations," *J. Appl. Phys.* **27**, 1152–1161 (1956).

⁴R. Hickling and M. S. Plesset, "Collapse and rebound of a spherical bubble in water," *Phys. Fluids* **7**, 7–14 (1964).

⁵M. S. Plesset and A. Prosperetti, "Bubble dynamics and cavitation," *Annu. Rev. Fluid Mech.* **9**, 145–185 (1977).

⁶K. S. Hunter and T. L. Geers, "Pressure and velocity fields produced by an underwater explosion," *J. Acoust. Soc. Am.* **115**, 1483–1496 (2004).

⁷B. W. Vanzant, J. E. Russell, A. L. Schraeder, and R. C. DeHart, "Near-field pressure response due to a sphere imploding in water," Summary Technical Report No. 1938-1, Contract No. N00 140-66-C-0698, Southwest Research Institute, 1967.

⁸M. Orr and M. Schoenberg, "Acoustic signatures from deep water implosions of spherical cavities," *J. Acoust. Soc. Am.* **59**, 1155–1159 (1976).

⁹P. Harben and C. Boro, "Implosion source development and Diego Garcia reflections," 23rd Seismic Research Review: Worldwide Monitoring of Nuclear Explosions, 2–5, 23–31 October, 2001.

¹⁰C. E. Brennen, *Cavitation and Bubble Dynamics* (Oxford University Press, New York, 1995).

¹¹A. B. Wardlaw Jr., R. McKeown, and H. Chen, "Implementation and application of the P- α equation of state in the DYSMAS code," NSWCCD/TR-95/107, 1996.

¹²R. H. Cole, *Underwater Explosions* (Princeton University Press, Princeton, 1948).

¹³E. B. Shand, *Glass Engineering Handbook* (McGraw-Hill, New York, 1958).

The effect of cavity geometry on the nucleation of bubbles from cavities

Michael A. Chappell^{a)} and Stephen J. Payne

Department of Engineering Science, University of Oxford, Parks Road, Oxford, OX1 3PJ, United Kingdom

(Received 6 February 2006; revised 11 July 2006; accepted 8 November 2006)

The heterogeneous nucleation of gas bubbles from cavities in a surface in contact with a liquid is a widely recognized phenomenon. This process has previously been theoretically analyzed extensively for a conical crevice, although in practice a wide range of cavity geometries might be expected. The method of analysis originally presented by Atchley and Prosperetti [J. Acoust. Soc. Am. **86**, 1065–1084 (1989)] for the unstable growth of a gas-liquid interface in a conical crevice is here extended to any axisymmetric cavity geometry and four such different geometries are analyzed. Although the method presented neglects gas transfer, and therefore is most directly suitable for acoustic cavitations, this method is still valuable in comparing the nucleation behavior of different cavity types. It is found that once the interface has emerged outside the cavity, its behavior is determined by the size of the cavity's opening. Given that the behavior of the interface once it is outside the cavity will also be determined by the local flow conditions, the threshold for unstable growth of the interface inside the cavity leading to its emergence is the important value and will determine differences between cavity geometries in practice, as shown in the examples presented. © 2007 Acoustical Society of America. [DOI: 10.1121/1.2404629]

PACS number(s): 43.35.Ei, 43.25.Yw [AJS]

Pages: 853–862

I. INTRODUCTION

The nucleation of gas bubbles in a fluid can arise under a number of conditions: thermal expansion and phase change during boiling; supersaturation, for example in carbonated beverages or in the body during decompression, e.g., deep-sea divers; cavitation; acoustic pressure fluctuation, often referred to as acoustic cavitation. Four modes of nucleation have been identified (Jones *et al.*, 1999), the first two requiring homogeneous formation of bubbles either in the bulk of the liquid or catalyzed at the surface of some other material in contact with the liquid. These are unlikely to account for most observed nucleation, as these are associated with very high thresholds for nucleation: for example very high supersaturation is required for the homogeneous formation of bubbles in pure liquid. Instead heterogeneous nucleation is more likely; for many supersaturation nucleation phenomena, it is most likely to be nucleation as defined by Jones *et al.* (1999) as Type IV that is implicated.

This process involves preexisting gas pockets within cavities on the surface of materials in contact with the liquid. The geometry of these cavities permits the gas pockets to remain stable against collapse even, in the case of deep-sea divers, during an increase in the pressure of the liquid (i.e., subsaturation). On the application of supersaturation, typically a reduction in the liquid pressure (i.e., decompression), the gas pocket is no longer in equilibrium and begins to grow. Typically the growth will start off as stable, and will thus stop if the decompression is halted. However, if the threshold for unstable growth, the critical radius, is reached then nucleation would be expected to occur without any need

for further decompression. For nucleation from cavities, the picture can be more complex, as even if the critical radius for the gas pocket within the crevice is exceeded it does not guarantee that once the gas-liquid interface emerges from the cavity it will continue to grow and that ultimately a portion of gas will detach from the cavity to produce a free bubble in the liquid (Atchley and Prosperetti, 1989). The latter threshold for growth outside the cavity and detachment of a proportion of the gas may require a lower pressure (i.e., a larger decompression) than for emergence of the interface from the cavity.

The conical crevice was first proposed by Harvey *et al.* (1944) and has been widely used as a model site for heterogeneous nucleation, for example, Apfel (1970), Tikuisis (1986), Atchley and Prosperetti (1989), and Chappell and Payne (2006) and both the stability and the dynamic behavior of a gas pocket, including the effects of diffusion, in such a cavity have been considered. However, it is likely that nucleation may occur from cavities with different geometries from that of a conical pit. It would be valuable to have some method for comparing the behavior of different cavity geometries under decompression, since the precise geometry is often not known, and hence approximated, and the dependence of the nucleation behavior on the geometry has not been considered previously.

Dynamic models for the evolution of gas pockets within a conical crevice are relatively complex and depend upon a number of parameters beside those of the cavity geometry (Chappell and Payne, 2006). Although it is possible to derive similar models for other cavity geometry the complexity of the model rapidly increases as the geometry deviates away from the simple conical crevice. Hence in this work we seek to make comparisons between different cavity geometries us-

^{a)}Electronic mail: michael.chappell@eng.ox.ac.uk

ing a simpler approach, which is intended to predict and to compare the behavior of more complex cavity geometries with that of the simple conical crevice.

Previously Atchley and Prosperetti (1989) have presented a method via which the expansion of a pocket of gas held within a conical crevice under decompression can be examined. They considered both the thresholds for the emergence of the interface out of the crevice and for the further growth of the gas pocket outside the crevice along the external surface. Their model assumed that the mass of gas inside the pocket is constant during growth, which limits its direct application to situations where diffusion and phase change are negligible, such as acoustic cavitation. Acoustic cavitation might be expected to be associated with minimal gas transfer into the cavity as the time period for gas transfer for acoustic sources in the hundreds of kilohertz to megahertz range is less than 10^{-5} s, whereas the time constant for gas transfer into a crevice is likely to be of the order of tens of seconds (Chappell and Payne, 2006). Here we follow the same method, but generalize to any form of cavity whose width can be described as an explicit function of depth. We also consider the effects of an increase in the mass inside the gas pocket to simulate the effect of diffusion during growth.

II. THEORY

A. Laplace equation

For any gas pocket which has an interface with a liquid phase the balance of internal and external pressures and the normal stress due to surface tension can be found, in mechanical equilibrium, from the Laplace equation:

$$\sum_{i=1}^m p_i + p_v = p_L + \frac{2\sigma}{R}, \quad (1)$$

where the gas pocket has a spherical cap of radius R and there are m gases dissolved in the liquid each with partial pressure p_i , p_v is the partial pressure of the liquid vapor in the gas pocket, p_L is the pressure in the liquid, and σ is the surface tension. For a free bubble the radius of curvature must be positive: hence, for it to be stable, the pressure of gases inside the bubble must exceed the pressure in the liquid. This can only be achieved if the partial pressures of gases dissolved in the liquid exceed the pressure in the liquid, i.e., the liquid is supersaturated, which itself is not a stable condition unless the whole system is externally closed to gas transfer. However if the gas pocket resides inside a cavity the interface may take a range of values for R , both positive and negative, hence the gas pocket may be stable for both super- and subsaturated liquids, Fig. 1. The limits for the radius of curvature are set by the limits allowed for the contact angle, α , between the liquid-gas interface and the wall of the cavity. The contact angle may not exceed the advancing contact angle, α_A , or be smaller than the receding contact angle, α_R :

$$\alpha_A \leq \alpha \leq \alpha_R. \quad (2)$$

The values of these contact limits depend on all three phases: solid, liquid, and gas. Typically it is the interaction

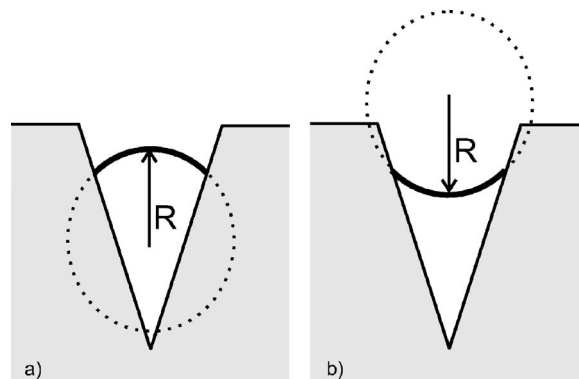


FIG. 1. A cavity can support a gas-liquid interface with both positive and negative radius of curvature.

between the liquid and the solid which is most significant. For example, for water on a surface defined as being hydrophilic it would have a low contact angle, typically in the range 10° – 30° , whereas on a hydrophobic surface it would have a larger contact angle, in the range 70° – 90° .

B. Nucleation process

Four phases of bubble growth during a nucleation event were considered by Atchley and Prosperetti as follows.

Growth within cavity:

1. Change in the radius of curvature by reduction in the contact angle, which proceeds until the receding contact angle is reached.
2. Movement of bubble interface up the cavity, with the interface contact angle at the receding value, which proceeds until the mouth of the cavity is reached.

Emergence outside cavity:

3. Change in the radius of curvature by reduction of the contact angle between the interface and the external surface, which proceeds until the receding contact angle is reached.
4. Growth of the gas pocket laterally along the external surface with the contact angle equal to the receding value.

At some point a proportion of the gas would be expected to detach and form a free bubble in the liquid, the conditions for this being set by the buoyancy of the gas pocket and any forces due to the flow of the liquid. Analysis and experiments for bubbles in carbonated beverages and the emergence of gas pockets from cavities into normal flows (Bai and Thomas, 2001; Liger-Belair *et al.*, 2002, 2005; Uzel *et al.*, 2006a,b) suggests that detachment typically occurs during the third phase, before the gas pocket begins to grow significantly along the external surface. For simplicity here we will adopt the definition of nucleation used by Atchley and Prosperetti as having occurred once the gas pocket interface is growing unstably along the surface outside the cavity, hence the evolution of the gas pocket will progress throughout all four phases listed.

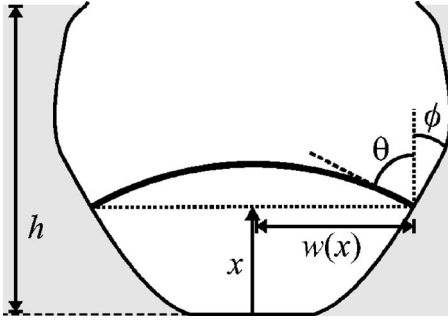


FIG. 2. Definition of parameters in a generic cavity.

C. Geometry

We define our cavity with axial symmetry and a half-width, w , which is a function of the height above the base of the cavity, x , as shown in Fig. 2. The contact angle between the interface and the cavity wall is composed of two angles:

$$\alpha = \theta + \phi, \quad (3)$$

where θ is the angle between the interface and the vertical and ϕ is the angle of the cavity wall to the vertical which is given by the slope of the cavity wall:

$$\phi = \arctan\left(\frac{dw(x)}{dx}\right), \quad (4)$$

hence

$$\theta(x, \alpha) = \alpha - \arctan\left(\frac{dw(x)}{dx}\right). \quad (5)$$

1. Inside the cavity

The radius of curvature of the interface when it is inside the cavity can be found by treating the interface as the spherical cap of a sphere with radius:

$$R_{\text{ini}}(x, \alpha) = \frac{w(x)}{\cos \theta(x, \alpha)}. \quad (6)$$

Likewise the volume can be found from the volume of the spherical cap described by the interface plus the volume of the cavity below the three-phase contact line:

$$V_{\text{ini}}(x, \alpha) = \frac{1}{3}\pi R_{\text{ini}}^3 [2 - (2 + \cos^2 \theta(x, \alpha)) \sin \theta(x, \alpha)] + \pi \int_{\lambda=0}^x w^2(\lambda) d\lambda. \quad (7)$$

2. Emergence outside the cavity

The radius of curvature is now given by the contact angle between the interface and the external surface, γ :

$$R_{\text{ext}}(\gamma) = \frac{w(x=h)}{\sin \gamma}. \quad (8)$$

The volume of the gas pocket can also be defined, until γ equals the receding contact angle and the interface starts to grow along the external surface, by

$$V_{\text{ext}}(\gamma) = \frac{1}{3}\pi R_{\text{ext}}^3 [2 + (2 + \sin^2 \gamma) \cos \gamma] + \pi \int_{\lambda=0}^h w^2(\lambda) d\lambda. \quad (9)$$

3. Lateral growth

The lateral growth of the gas pocket along the external surface can be defined in terms of a variable half-width, w' , which starts at the half-width of the cavity at its mouth. Hence the radius of curvature can be written as

$$R_{\text{ext}}(w') = \frac{w'}{\sin \alpha_R}, \quad (10)$$

with the volume being given by Eq. (9).

III. ANALYSIS

We initially assume that there is no transfer of gas into or out of the gas pocket during expansion so that the gas content of the pocket remains constant. For simplicity we consider only a single gas dissolved in the liquid and hence

$$p_G V = V_0 T_G, \quad (11)$$

where V is the volume of the gas pocket at any point during the expansion, V_0 is the initial volume, and T_G is the gas tension in the liquid. The gas tension describes the concentration of gas in the liquid in terms of its equivalent partial pressure. Hence the Laplace equation can be written as

$$\frac{V_0 T_G}{V} + p_v = p_L + \frac{2\sigma}{R}. \quad (12)$$

From Eq. (12) it is possible to determine the liquid pressure and saturation values required for the interface to be stable at any position within the cavity. For nucleation due to supersaturation we are interested in the condition where $p_L < T_G$. For example, postdecompression, where the liquid pressure was initially equal to T_G and in equilibrium with the gaseous atmosphere, or after the cap has been removed from the bottle of a carbonated beverage.

Of particular interest are the critical values of p_L which present a threshold to the growth of the gas pocket, hence a threshold to nucleation. This we analyze, following the procedure set down by Atchley and Prosperetti (1989). We assume that the gas pocket is stable before the liquid pressure is reduced, hence initially the interface is close to flat with a large radius of curvature (this may be either positive for marginally supersaturated solution or negative for an undersaturated solution).

A. First nucleation threshold

As has already been noted, the first phase of expansion of the gas pocket proceeds by a reduction of the interface contact angle with the cavity wall. This will result in a reduction in the radius of curvature. (Note that if the interface initially starts concave toward base of the cavity, then the initial radius of curvature will be negative and growth will proceed by increases in the negative magnitude of R until it

passes through infinity). The reduction in radius of curvature leads to an increase in the pressure due to surface tension until the receding contact angle is reached. Hence the receding contact angle can be regarded as a threshold to nucleation, as given by

$$p_L^A = p_v - \frac{2\sigma}{R_{\text{ini}}(x_0, \alpha_R)} + \frac{V_0 T_G}{V_{\text{ini}}(x_0, \alpha_R)}. \quad (13)$$

However, as noted by Atchley and Prosperetti, this will not represent an unstable threshold for growth of the gas pocket up the crevice unless the radius of curvature exceeds the critical radius. If it is not an unstable threshold, then further reduction in the liquid pressure, beyond p_L^A , will be required for the gas pocket to continue to grow.

The critical radius can be determined by considering the stability of the collapsing and expanding forces as described by the Laplace equation. The left-hand side of the Laplace equation gives the expanding forces, the right-hand side the collapsing: when they are equal there is equilibrium. The equilibrium is only stable if “the (negative) rate of change of the collapsing forces is larger than that of the expanding forces” (Atchley and Prosperetti, 1989):

$$\frac{d}{dR} \left(\frac{V_0 T_G}{V} + p_v \right) < \frac{d}{dR} \left(p_L + \frac{2\sigma}{R} \right). \quad (14)$$

When Eq. (14) holds with an equality sign this represents the transition between stable and unstable behavior. Thus the solution would give the critical radius, beyond which the growth of the gas pocket becomes unstable. Performing the required differentiation gives the critical radius as a solution of

$$\frac{T_G V_0 \frac{dV_{\text{ini}}(R, \alpha_R)}{dR}}{V_{\text{ini}}(R, \alpha_R)^2} = \frac{2\sigma}{R^2}. \quad (15)$$

Substituting back into the Laplace equation gives the corresponding pressure threshold:

$$p_L^B = p_v - \frac{2\sigma}{R_c} \left(1 - \frac{V_{\text{ini}}(R_c, \alpha_R)}{R_c \frac{dV_{\text{ini}}(R, \alpha_R)}{dR} \Big|_{R=R_c}} \right). \quad (16)$$

Note that we have taken the value of contact angle for this analysis to be the receding value, making the assumption that we only need to calculate this threshold during the second phase of growth, i.e., either the critical radius has already been exceeded by the time the receding contact angle has been reached at the end of the first phase, or it represents a further threshold to growth during the second phase. We discuss this assumption further later. For a conical crevice, as considered by Atchley and Prosperetti, V_{ini} can be written as a simple function of R^3 and thus Eq. (15) can be solved for the critical radius. However, for a more general cavity shape an explicit analytical solution is not guaranteed.

The next phase of growth of the gas pocket is movement of the interface up the cavity. If the critical radius has already been exceeded then unstable growth will proceed. Otherwise growth will remain stable, i.e., it will only continue as long

as the liquid pressure is sufficiently low. The smaller of the two of these pressure values is thus the threshold for unstable growth within the cavity and is defined by Atchley and Prosperetti as the first threshold for nucleation.

B. Second nucleation threshold

Once the interface has reached the cavity mouth there is a sharp change in the slope of the wall from the inside of the cavity to the external surface. The interface now has a “new” contact angle between itself and the external surface. As the value of this contact angle will be greater than the receding contact angle, growth of the gas pocket will proceed by the reduction in this external contact angle, γ . Thus a further threshold is expected at the point where $\gamma = \alpha_R$:

$$p_L^C = p_v - \frac{2\sigma}{R_{\text{ext}}(\alpha_R)} + \frac{V_0 T_G}{V_{\text{ext}}(\alpha_R)}. \quad (17)$$

Again this only represents a threshold to unstable growth if the radius of curvature is greater than the critical radius. Because the interface has emerged outside of the cavity there may be a smaller critical radius, and hence threshold on pressure, than that found earlier for inside the crevice. Once again the critical radius can be found by considering the transition from stable to unstable at the equilibrium point:

$$\frac{T_G V_0 \frac{dV_{\text{ext}}(R_{\text{ext}}, \alpha_R)}{dR_{\text{ext}}}}{V_{\text{ext}}(R_{\text{ext}}, \alpha_R)^2} = \frac{2\sigma}{R_{\text{ext}}^2}. \quad (18)$$

Unlike the volume of the gas pocket inside the cavity, the volume of the pocket once it has emerged can be given as a simple function of the radius of curvature from Eq. (9):

$$V_{\text{ext}}(\gamma) = \frac{1}{3} \pi [2 + (2 + \sin^2 \gamma) \cos \gamma] R_{\text{ext}}^3 + \pi \int_{\lambda=0}^h w^2(\lambda) d\lambda. \quad (19)$$

The critical radius is then a root of

$$2g(\alpha_R)^2 \sigma R_{\text{ext}}^6 - 3g(\alpha_R) T_G V_0 R_{\text{ext}}^4 + 4g(\alpha_R) V_c \sigma R_{\text{ext}}^3 + 2V_c^2 \sigma = 0. \quad (20)$$

Two approximate cases may be considered. In the first, $V_c \ll g(\gamma) R^3$, i.e., the volume of the spherical segment outside the cavity is much larger than the total volume of the cavity. Under these circumstances the radius of curvature, and hence the corresponding pressure threshold, can be found explicitly (Atchley and Prosperetti, 1989):

$$p_L^D \approx p_v - \frac{4\sigma}{3} \sqrt{\frac{2\sigma \gamma(\alpha_R)}{3V_0 T_G}}. \quad (21)$$

In the second case $V_c \gg g(\gamma) R^3$, the volume of the cavity exceeds that of the spherical segment outside the cavity. Under these conditions the Laplace equation simplifies to

$$\left(\frac{V_0}{V_c}\right)T_G + p_v = p_L + \frac{2\sigma}{R}, \quad (22)$$

which, once the stability of the equilibrium point is considered, gives an infinite critical radius, i.e., at a flat interface curvature. Hence, the growth would be unstable once the receding contact angle with the external surface is exceeded.

C. Critical radii

As has already been noted in calculating the critical radius within the crevice, it has been assumed that either it has been exceeded during the first phase of growth or it occurs during the second phase, where the contact angle equals the receding value. This is also true for the critical radius for growth outside the cavity in relation to the third and fourth phases. However, it is possible for the critical radius to occur during the first phase and to require a liquid pressure that is smaller than the value to reach the receding contact angle. According to the analysis presented so far under these conditions, no valid value of p_L^B would be found (the critical radius does not occur during the second phase) and so the value of p_L^A would be taken as critical, but it would be smaller than the true threshold. Strictly, therefore, it should be determined whether during the first phase there is a “critical contact angle” (with x fixed at the initial value) and, during the second phase a “critical length” (with α fixed at the receding value). The critical contact angle, α_c , is the solution of

$$\frac{d}{d\alpha} \left(\frac{V_0 T_G}{V_{\text{int}}(x_0, \alpha)} + p_v \right) = \frac{d}{d\alpha} \left(p_L + \frac{2\sigma}{R_{\text{int}}(x_0, \alpha)} \right). \quad (23)$$

A physically relevant solution only exists if $\alpha_0 \geq \alpha_c \geq \alpha_R$. Similarly the critical length, x_c , can be determined from

$$\frac{d}{dx} \left(\frac{V_0 T_G}{V_{\text{int}}(x, \alpha_R)} + p_v \right) = \frac{d}{dx} \left(p_L + \frac{2\sigma}{R_{\text{int}}(x, \alpha_R)} \right). \quad (24)$$

Again a physically relevant solution only exists for $x_0 \leq x_c \leq h$. If the solution to Eq. (24) is given by $x > h$, then the critical value lies beyond the height of the cavity, so under these conditions the critical length would correspond to the interface reaching the crevice mouth, i.e., $x_c = h$. The appropriate pressure thresholds can be determined by substitution back into the Laplace equation:

$$p_L^{B'} = p_v - \frac{2\sigma}{R_{\text{int}}(x_0, \alpha_c)} \left(1 - \frac{V_{\text{int}}(x_0, \alpha_c)}{R_{\text{int}}(x_0, \alpha_c) \frac{dV_{\text{int}}(x_0, \alpha)}{d\alpha} \Big|_{\alpha=\alpha_c}} \right), \quad (25)$$

$$p_L^B = p_v - \frac{2\sigma}{R_{\text{int}}(x_c, \alpha_R)} \left(1 - \frac{V_{\text{int}}(x_c, \alpha_R)}{R_{\text{int}}(x_c, \alpha_R) \frac{dV_{\text{int}}(x, \alpha_R)}{dx} \Big|_{x=x_c}} \right). \quad (26)$$

Note that p_L^B as determined by x_c in Eq. (26) will be the same as that defined in Eq. (16) when the critical radius, as defined

earlier, exists. Likewise the same should be done for the third and fourth phases to determine the critical values outside the cavity. Thus:

$$p_L^D = p_v - \frac{2\sigma}{R_{\text{ext}}(w'_c)} \left(1 - \frac{V_{\text{ext}}(\alpha_R, w'_c)}{R_{\text{ext}}(w'_c) \frac{dV_{\text{ext}}(\alpha_R, w')}{dw'} \Big|_{w'=w'_c}} \right), \quad (27)$$

where w'_c is the solution of

$$\frac{d}{dw'} \left(\frac{V_0 T_G}{V_{\text{ext}}(\alpha_R, w')} + p_v \right) = \frac{d}{dw'} \left(p_L + \frac{2\sigma}{R_{\text{ext}}(w')} \right), \quad (28)$$

the definition of R_{ext} in Eq. (10) being used and $w'_c > w(h)$. Additionally, a critical radius may be found before the receding contact angle with the external surface is reached at a liquid pressure of

$$p_L^{D'} = p_v - \frac{2\sigma}{R_{\text{ext}}(\gamma_c)} \left(1 - \frac{V_{\text{ext}}(\gamma_c)}{R_{\text{ext}}(\gamma_c) \frac{dV_{\text{ext}}(\gamma)}{d\gamma} \Big|_{\gamma=\gamma_c}} \right), \quad (29)$$

where γ_c is the solution of

$$\frac{d}{d\gamma} \left(\frac{V_0 T_G}{V_{\text{ext}}(\gamma)} + p_v \right) = \frac{d}{d\gamma} \left(p_L + \frac{2\sigma}{R_{\text{ext}}(\gamma)} \right), \quad (30)$$

with R_{ext} as defined in Eq. (8) and $(\alpha_R - \beta + \pi/2) > \gamma_c > \alpha_R$.

Atchley and Prosperetti do not make this distinction that we have made here; however, this may not be particularly significant given the conditions which they considered. The critical radius is determined both by the extent to which the volume has increased and the change in the pressure due to surface tension. During the first phase of expansion the change in volume is typically relatively small; hence the required liquid pressure is dominated by variations in the surface tension term. This term gets smaller as the radius of curvature increases with reduction in contact angle. Hence the critical value of pressure will occur at the limit of contact angle variation: the receding value. This is less likely to be the case once the interface has emerged outside the cavity, as during the third phase of growth variations in contact angle (now with the external surface) can lead to more significant variations in volume. However, if the volume of the cavity is much greater than that of the spherical segment, once again the significance of this volume change is small and it would be expected that if the critical radius occurred before the receding contact angle, it would be exceeded with a higher liquid pressure than that needed for reach the receding contact angle.

IV. NUMERICAL RESULTS

Atchley and Prosperetti noted that the picture that emerged from the analysis of nucleation in the conical crevice was very complex and this is no less the case for the analysis of more generalized crevice geometries presented earlier. To establish the threshold for nucleation it is strictly necessary to test all four of the thresholds considered earlier

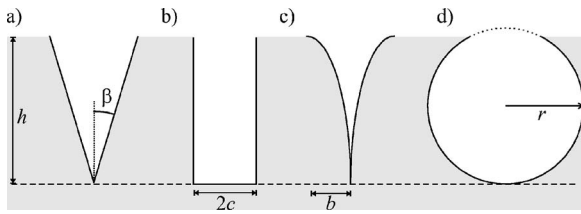


FIG. 3. Geometry of the four cavities.

to determine the limiting case. For the general case, this is complicated further because in two cases an analytic expression may not be available. Hence, like Atchley and Prosperetti, we will examine the behavior of different types of cavity using numerical analysis. The numerical results will be presented as plots of volume occupied by gas against the pressure in the liquid, showing the evolution of the gas pocket as the liquid pressure falls until the interface on the external surface has reached the receding contact angle and it has grown along the external surface up to twice the width of the cavity mouth. For comparison with previous work we will plot the quantity $p_v - p_L$ as the x ordinate and volume of the gas pocket as the y ordinate.

We consider four types of cavity.

1. Conical crevice, Fig. 3(a):

$$w(x) = x \tan(\beta). \quad (31)$$

The conical crevice is the most common form of cavity explored in nucleation analysis, as it has a relatively simple geometry and appears to be a reasonable simplification of the sort of imperfection that would be found on a surface.

2. Cylindrical cavity, Fig. 3(b):

$$w(x) = c. \quad (32)$$

The geometry is even simpler than that of the conical crevice, although it seems less likely that surface imperfections would take this form and hence are not commonly expected to be a good model for nucleation. However, this form of cavity has been used to model the formation of bubbles in carbonated beverages (Liger-Belair *et al.*, 2005; Uzel *et al.*, 2006a, b), as it has been found that nucleation occurs at hollow cylindrical fibers trapped on the walls of the glass (Liger-Belair *et al.*, 2002).

3. Elliptical crevice, Fig. 3(c):

$$w(x) = b \left(1 - \sqrt{1 - \frac{x^2}{h^2}} \right). \quad (33)$$

This has been proposed as a variation on the conical crevice by Tikuisis (1986), because in principle it is easier for the gas pocket to emerge from this form of cavity and the smooth transition between the inside of the cavity and outside surface may be a more realistic model of true nucleation sites.

4. Spherical cavity, Fig. 3(d):

$$w(x) = \sqrt{r^2 - (x-1)^2}, \quad (34)$$

with a penetration, fraction of the diameter of the sphere within the surface, given by $z = h/2r$. The spherical cavity is of particular interest to the nucleation of decompression

TABLE I. Geometric parameters used for the four cavities.

Geometric parameter		Value
	Conical crevice	
h		2
β		15°
	Cylindrical cavity	
h		2
c		0.536
	Elliptical crevice	
h		2
b		0.536
	Spherical cavity	
r		1.071
z		0.933

bubbles in the body. The site for the formation of the bubbles which are observed in the blood postdecompression has yet to be determined experimentally. However, caveolae have been proposed as a possible nucleation site (Brubakk, 2004). These caveolae are spherical invaginations into endothelial cells found on the lining of blood vessels, which are approximately modeled by the spherical cavity considered here. This cavity shape is also similar to the reservoir type of nucleation site, for example, Sluyter *et al.* (1991).

To compare these four cavity types, the dimensions are chosen so that they are all compatible: The height and size of opening onto the external surface of each is set equal to that of the conical crevice. The parameters used for the cavities are shown in Table I, a receding contact angle of 80° being used to make the cavity hydrophobic, and the interface starts one quarter of the way up the crevice, $x_0 = h/4$. Surface tension is taken to have a value of 0.03 N m⁻¹ as might be expected in biological media (Tikuisis, 1986; Chappell and Payne, 2006), which is lower than the value of 0.07 N m⁻¹ observed in water.

Figure 4 shows the evolution of the gas pocket for decompression from atmospheric pressure ($T_G = 1$ bar). For the two crevices there is no distinct p_L^B threshold, as the critical radius of curvature is reached when the receding contact angle is attained at p_L^A , growth of the interface after this point resulting in a reduction in the required pressure. The cylindrical cavity, however, never reaches the critical radius: Once the internal receding contact angle threshold is reached, the pressure continues to fall as the interface moves up the crevice, but no maximum is ever reached. The spherical cavity does have a p_L^B threshold, which occurs at the maximum pressure during the second phase of growth. For the conical and elliptical crevices and the spherical cavity there is also a $p_L^{D'}$ threshold at a smaller volume than the p_L^C value, i.e., the critical radius outside the cavity occurs during the third phase. The elliptical crevice behavior is particularly distinct because there is a smooth transition between the surface inside and outside the cavity; hence the interface is already at the receding contact angle once it emerges from inside the crevice. This means that unlike the other cavities the critical threshold for the elliptical crevice is p_L^A , i.e., once

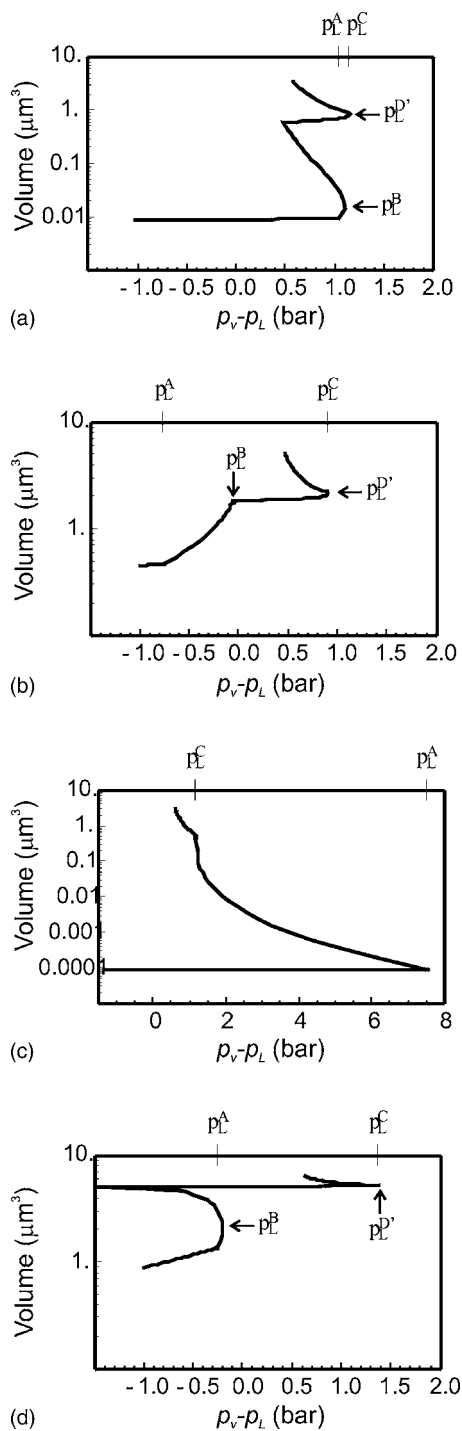


FIG. 4. The evolution of the gas pocket in the four different cavity types: (a) conical crevice, (b) cylindrical cavity, (c) elliptical crevice, and (d) spherical cavity.

the receding contact angle has been reached inside the crevice further growth of the gas pocket is unstable.

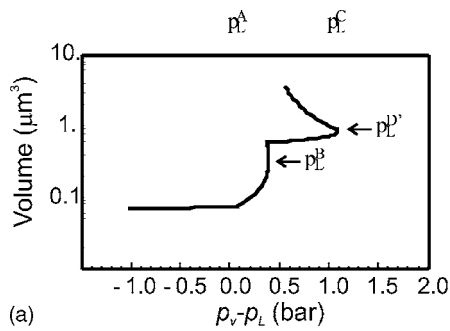
To compare the four cavity types: It is the elliptical cavity which has the lowest threshold value of liquid pressure for nucleation; hence it is the hardest in which to promote nucleation under these conditions. The other three have relatively similar minimum values for p_L , which is not surprising since once the interface has emerged outside of the cavity the behavior is primarily dominated by the surface tension term in the Laplace equation, the volume ratio term becoming

small as the total volume of the gas pocket increases. This means the behavior is dominated by the radius of curvature which will be the same for all these three cavities as they have been chosen to have the same radius of opening onto the external surface. Although the elliptical crevice is the hardest to promote to growth under these conditions, once the receding contact angle inside the crevice has been reached further growth is unstable. Thus the emergence of the gas pocket out of the cavity after this stage is easy, which is consistent with the predictions of Tikuisis (1986).

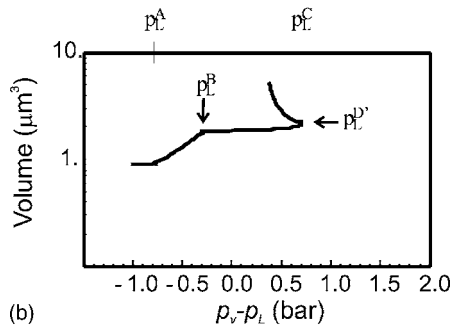
In all cases the value of liquid pressure that would be required for nucleation is negative, hence it would be impossible, under these conditions, to cause the gas pocket interface to reach the stage where it spreads outwards along the external surface. However, this may not be the most appropriate definition for nucleation in many circumstances. As has already been noted, the behavior of the gas pocket once it has emerged is also determined by the conditions in the liquid, for example, the presence of a flow. These conditions will dictate the nucleation behavior of the interface outside the cavity, and hence the threshold for the emergence of the interface may be most important. Under the conditions assumed here the interface cannot emerge from either the conical or the elliptical crevice; in both cases it is p_L^A that is critical. For the cylindrical cavity the critical radius inside the cavity is never reached, as the minimum value of p_L occurs once the interface reached the cavity mouth. This is unlike the spherical cavity which reaches the critical radius relatively early within the growth of the gas pocket and hence is relatively easy to promote to emergence out of the cavity.

Figure 5 shows the evolution of the gas pocket in the four cavities if the interface starts half-way up the inside of the cavity, $x_0 = h/2$. The cylindrical and spherical cavities are largely unaffected. However, the threshold for nucleation for the elliptical crevice is now substantially higher, hence easier to promote nucleation. The threshold for nucleation for the conical crevice is unaltered, although the behavior within the crevice has changed and it is now easier for it to emerge than previously. As with the examples in Fig. 4, for the elliptical crevice, cylindrical and spherical cavities the critical pressure for the second nucleation threshold is given by $p_L^{D'}$, although in this case this threshold is practically indistinguishable from p_L^C .

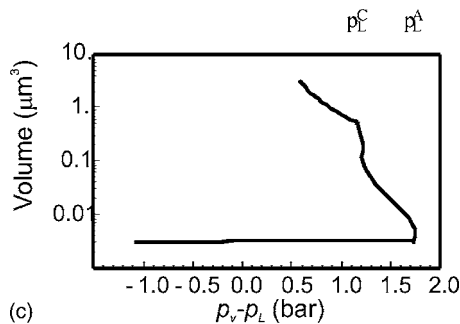
The difference in behavior between the cases where the interface starts half- and quarter-way up the cavity can be explained by the resultant variation in two important initial parameters of the gas pocket: volume and width of the interface. The effects can be seen on the variation in p_L^A with initial starting height of the interface illustrated in Fig. 6. For the cylindrical cavity, changes in the starting location of the interface do not result in very significant variation in the threshold p_L^A except if it starts very deep within the crevice. In this cavity shape there is no variation in the initial width of the interface with starting height, hence the changes in behavior can be attributed entirely to a change in initial volume, which implies that the effect of limiting the initial volume of the gas pocket is small on the nucleation behavior. The spherical cavity produces very similar results to the cy-



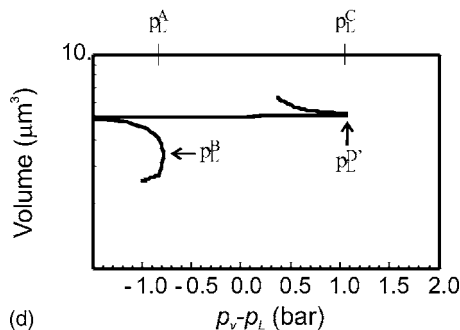
(a)



(b)



(c)



(d)

FIG. 5. Evolution for the gas pocket in the four different types of cavity, when the interface initially starts half-way up the cavity: (a) conical crevice, (b) cylindrical cavity, (c) elliptical crevice, and (d) spherical cavity.

lindrical cavity (not shown) because the variation in initial interface width with height is small over most of the range of the cavity height. The effect of variation of the initial width of the interface is, however, far more significant as illustrated by the two crevices. The reason of this variation is due to surface tension, which contributes to the pressure in the bubble as an inverse function of the radius of curvature. Hence for the gas pocket to attain the receding contact angle with the cavity wall a larger pressure reduction will be required if the width of the interface is smaller, as a far larger

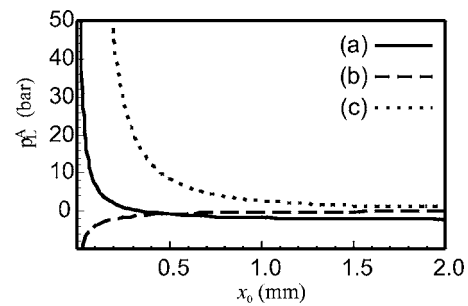


FIG. 6. Variation in the p_L^A threshold with the initial starting height of the interface within the cavity for (a) the conical crevice, (b) the cylindrical cavity, and (c) the elliptical crevice. The result for the spherical cavity is very close to (b) (not shown).

radius of curvature will be required. This effect is seen in the conical crevice, as the width of the crevice is a linear function of position within the crevice. However, the effect is most marked in the elliptical crevice, where deep with the cavity the width is very narrow. Hence the elliptical crevice for the above-considered conditions appears to be difficult to promote nucleation of a gas pocket. Although it becomes easier to promote nucleation as the interface starts further up the inside of the elliptical crevice, under the conditions considered here p_L^A never becomes negative, hence nucleation is strictly not possible.

V. DISCUSSION

A. Nonideal conditions

Inevitably the method presented here has considered an idealized smooth axially symmetric cavity and thus cannot predict all of the nucleation behavior that might be observed from a real cavity. For example inhomogeneities of the cavity surface might be expected to lead to contact line pinning: This process, by preventing the advance of the contact line between gas, fluid, and cavity wall, might be expected to increase the threshold decompression required for nucleation if it occurs near the limiting threshold. This may be particularly significant at the crevice mouth where advance of the interface occurs by contact line movement across a sharp change in surface gradient.

The buoyancy of the gas pocket has been neglected in the derivation presented here. This is reasonable given that for a $1 \mu\text{m}$ bubble in water the Bond number is of the order 10^{-7} implying that surface tension dominates over gravity effects. The effect of buoyancy would primarily be to deform the spherical cap of the gas pocket; however for the bubble sizes considered here this is likely to be small due to the high strength of the surface tension. Axial asymmetry is more likely to be introduced by more complex cavity geometry or, once the gas pocket has emerged, the effects of flow past the cavity. Under these conditions a simple one-dimensional description of the forces in the interface is no longer possible and the Laplace equation no longer holds in the form used here. It is likely that for gas pockets in axially asymmetric cavities a three-dimensional method would be required.

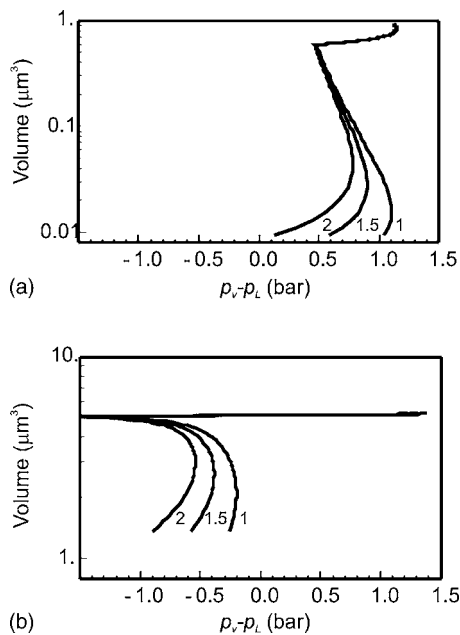


FIG. 7. Evolution of a gas pocket during the second and third phases, where the mass of gas in the pocket at the start of the second phase is a proportion k of the original mass, for (a) conical crevice, and (b) spherical cavity.

B. Effect of gas transfer

In this analysis it has been assumed that there is no gas transfer in or out of the gas pocket during growth. However, in many nucleation problems gas will enter the bubble either by diffusion or phase change, for example, it is diffusion that drives the nucleation of bubbles in carbonated beverages. Gas transfer is primarily a time dependent process and not readily amenable to the stability analysis used here. Ideally a dynamic model of the gas pocket's growth is required as has been done elsewhere for the conical cavity (Chappell and Payne, 2006). However, it is difficult to derive such a model for more complex geometries such as the spherical cavity. We thus propose a simple modification to the constant volume analysis used thus far which allows the change of behavior with gas transfer to be considered. The constant mass assumption embodied in Eq. (11) is replaced with

$$p_G V = k V_0 T_G, \quad (35)$$

where the total mass in the gas pocket is permitted to increase to a multiple, k , of the original value. Strictly gas transfer will be a gradual process over time and Eq. (35) cannot apply at the start of the evolution of the gas pocket. Hence the approximation will be taken that the increase in mass occurs during the first phase of growth, and there is no further transfer during the latter phases. The result of this for a range of values of k is shown in Fig. 7. The lines in Fig. 7 can be treated as iso- k -contours, hence it is possible to consider gas transfer by movement from smaller to larger k contours as time progresses. The effect of gas transfer is to reduce significantly the first nucleation threshold, for the interface to exit the cavity. Thus, if the decompression is insufficient for the first nucleation threshold to be reached, the effect of gas transfer will mean that interface will only become unstable once sufficient time has passed for an in-

crease in k to occur. The behavior outside the cavity is largely unaltered by gas transfer. Once again this can be understood by the reducing significance of the volume term in the Laplace equation once the gas pocket has grown outside the cavity.

Although gas transfer into the cavity appears to alter the behavior inside the cavity, it is likely that during this phase of growth the diffusion in many cases will be small, unless growth occurs over a long duration. Additionally, the presence of gas transfer does not appear to alter the fundamental differences in behavior between different cavity types, although the threshold for emergence is reduced in all cases.

VI. CONCLUSIONS

We have developed the method of Atchley and Prosperetti for the analysis of the nucleation in crevices to any axisymmetric geometry of cavity to permit the comparison of nucleation in cavities of differing geometries. The analysis is based on assuming that the gas content of the gas pocket remains constant, hence it is only directly applicable to nucleation where gas transfer is small, for example, acoustic cavitation. However, our results indicate that once the gas pocket has emerged from the cavity the effects of gas transfer during the growth inside the cavity are negligible. Additionally we have shown that the behavior of the gas pocket once it has emerged is practically independent of the shape of the cavity, as long as the interface starts deep within the cavity. Thus the behavior of a gas pocket outside of a cavity can be analyzed by considering the interface at a circular opening in a surface, without needing to specify accurately the cavity geometry. The second nucleation threshold, as considered here, may not be important in many nucleation situations, where the conditions of flow outside the cavity are important in determining the bubble behavior outside the cavity.

The first nucleation threshold remains important because it sets the pressure threshold for the interface to emerge out of the cavity. Our results suggest that this aspect of behavior is dependent upon the cavity geometry, a smaller decompression being required for emergence from the spherical cavity than nonreentrant cavities such as crevices. The nucleation behavior inside the cavity is primarily dependent upon the initial width of the interface, as this determines the relationship between radius of curvature, and thus surface tension, and contact angle. The result is that for cavities whose width is dependent upon the depth within the cavity, i.e., crevices, the nucleation behavior of the gas pocket is strongly dependent upon the initial starting height of the interface. Although the shape of the elliptical crevice means that emergence of the cavity is easier than other cavities, very large decompressions are required for nucleation if the interface starts deep with the crevice.

- Apfel, R. E. (1970). "The role of impurities in cavitation-threshold determination," *J. Acoust. Soc. Am.* **48**, 1179–1186.
 Atchley, A. A., and Prosperetti, A. (1989). "The crevice model of bubble nucleation," *J. Acoust. Soc. Am.* **86**, 1065–1084.
 Bai, H., and Thomas, B. G. (2001). "Bubble formation during horizontal gas injection into a downward flowing liquid," *Metall. Mater. Trans. B* **32**, 1143–1159.

- Brubakk, A. O. (2004). "Endothelium and bubble injury: The role of endothelium in decompression illness," 30th Annual Scientific Meeting of the European Underwater Baromedical Society, Ajaccio, Corsica, France, EUBS.
- Chappell, M. A., and Payne, S. J. (2006). "A physiological model of the release of gas bubbles from crevices under decompression," *Respiration Physiology & Neurobiology*, **153**, 166–180
- Harvey, E. N., Barnes, D. K., McElroy, W. D., Whiteley, A. H., Pease, D. C., and Cooper, K. W. (1944). "Bubble formation in animals. I. physical factors," *J. Cell. Comp. Physiol.* **24**, 1–22.
- Jones, S. F., Evans, G. M., and Galvin, K. P. (1999). "Bubble nucleation from gas cavities-A review," *Adv. Colloid Interface Sci.* **80**, 27–50.
- Liger-Belair, G., Vignes-Alder, M., Voisin, C., Robillard, B., and Jeandet, P. (2002). "Kinetics of gas discharging in a glass of champagne: The role of nucleation sites," *Langmuir* **18**, 1294–1301.
- Liger-Belair, G., Voisin, C., and Jeandet, P. (2005). "Modeling nonclassical heterogeneous bubble nucleation from cellulose fibers: Application to bubbling in carbonated beverages," *J. Phys. Chem. B* **109**, 14573–14580.
- Sluyter, W. M., Slooten, P. C., Copraij, C. A., and Chesters, A. K. (1991). "The departure size of pool-boiling bubbles from artificial cavities at moderate and high pressures," *Int. J. Multiphase Flow* **17**, 153–158.
- Tikuisis, P. (1986). "Modeling the observations of in vivo bubble formation with hydrophobic crevices," *Undersea Biomed. Res.* **13**, 165–180.
- Uzel, S., Chappell, M. A., and Payne, S. J. (2006a). "A model of the growth, detachment and transport of bubbles in blood vessels," *IEEE Trans. Biomed. Eng.* (in review).
- Uzel, S., Chappell, M. A., and Payne, S. J. (2006b). "Modelling the cycles of growth and detachment of bubbles in carbonated beverages," *J. Phys. Chem. B* **110**, 7579–7586.

Model for continuously scanning ultrasound vibrometer sensing displacements of randomly rough vibrating surfaces

Purnima Ratilal,^{a)} Mark Andrews, Ninos Donabed, Ameya Galinde, and Carey Rappaport
*Center for Subsurface Sensing and Imaging Systems, Northeastern University,
Boston, Massachusetts 02115*

Douglas Fenneman

*U.S. Army RDECOM CERDEC Night Vision and Electronic Sensors Directorate,
10221 Burbeck Road, Fort Belvoir, Virginia 22060*

(Received 20 June 2006; revised 4 November 2006; accepted 6 November 2006)

An analytic model is developed for the time-dependent ultrasound field reflected off a randomly rough vibrating surface for a continuously scanning ultrasound vibrometer system in bistatic configuration. Kirchhoff's approximation to Green's theorem is applied to model the three-dimensional scattering interaction of the ultrasound wave field with the vibrating rough surface. The model incorporates the beam patterns of both the transmitting and receiving ultrasound transducers and the statistical properties of the rough surface. Two methods are applied to the ultrasound system for estimating displacement and velocity amplitudes of an oscillating surface: incoherent Doppler shift spectra and coherent interferometry. Motion of the vibrometer over the randomly rough surface leads to time-dependent scattering noise that causes a randomization of the received signal spectrum. Simulations with the model indicate that surface displacement and velocity estimation are highly dependent upon the scan velocity and projected wavelength of the ultrasound vibrometer relative to the roughness height standard deviation and correlation length scales of the rough surface. The model is applied to determine limiting scan speeds for ultrasound vibrometer measuring ground displacements arising from acoustic or seismic excitation to be used in acoustic landmine confirmation sensing. © 2007 Acoustical Society of America.

[DOI: 10.1121/1.2404623]

PACS number(s): 43.35.Yb, 43.20.Fn [TDM]

Pages: 863–878

I. INTRODUCTION

Ultrasound based vibrometers are increasingly deployed to measure the displacement and velocity of vibrating surfaces, interfaces, or objects for a wide range of engineering applications.¹ For instance, in biomedical imaging, the ultrasound vibrometer is used to measure displacement of tissue stimulated to vibrate by various forms of mechanical or optical excitation.² The displacement measurement provides information regarding the elastic and other mechanical properties of the tissue from which its health can be inferred. In acoustic landmine detection,^{3–5} ultrasound vibrometers are being investigated as an imaging sensor that measures displacement and velocity of ground excited to vibrate at low acoustic or seismic frequencies in order to confirm the presence or absence of mine-like targets.^{6–8} In many applications, it is desirable for the vibrometer to be used in a *continuous* scan mode to rapidly comb through large areas of the surface or object under investigation. The presence of undulations or roughness on the surface often degrades the performance of the vibrometer for measuring surface displacements.

Here we develop analytic and numerical models to investigate the performance of an ultrasound vibrometer system to be used in *continuous* scan mode for measuring dis-

placements of a randomly rough vibrating surface. The motivation for this work is in acoustic land mine confirmation.^{3–5} Both plastic and metallic mines are highly compliant with complex mechanical structure compared to naturally occurring sediment or objects on the ground.^{3–5} When excited at low frequencies with acoustic or seismic waves, shallow buried mines vibrate with large amplitude oscillations and also exhibit resonance characteristics.⁵ The contrasting displacement amplitude of buried mines relative to their natural surroundings indicates their presence or absence in a given area. Laser vibrometers have been deployed to comb through the ground surface under investigation to create a displacement or velocity image of the area that is used to infer the horizontally projected size and shape of a mine.^{5,9} Laser-based vibrometers are susceptible to scattering by vegetation and ground roughness when used in continuous scan mode owing to the short wavelength of optical light. This degrades displacement estimation.⁷ In acoustic landmine detection applications, confirmation of the presence of a buried mine has been achieved when the laser vibrometer scans at speeds of 5 cm/s.¹⁰ Ultrasound vibrometers may provide advantages in situations where the scan speed is limited by speckle noise caused by the vibrometer scanning over the rough ground. This is because the ultrasound wavelength is roughly a thousand times larger than that of the laser and is therefore less susceptible to scattering from the rough ground. This has been verified experimen-

^{a)}Electronic mail: purnima@ece.neu.edu

tally in Ref. 7. Ultrasound vibrometers can also provide penetration through grass⁷ to directly image ground vibration without the need for these vibrations to be coupled to blades of grass as required¹⁰ for a laser vibrometer. Laser vibrometers are also costly to deploy in an array configuration since a suite of seven to ten of these sensors would be needed on a vehicle to comb through a region at least 1 m wide. Ultrasound vibrometers, on the other hand, are much less expensive to deploy. The models developed here are used to determine sonar design parameters and measurement geometry that can be used to enhance measurement of ground displacement and velocity with a continuously scanning ultrasound vibrometer.

The basics of an ultrasound vibrometer are as follows. The ultrasound source transducer transmits a signal at the carrier frequency that is incident on a surface or object. The signal is then reflected or scattered off the surface to a receiving transducer. The measurement can be either monostatic or bistatic. The moving surface or object causes phase modulation of the received field upon reflection or scattering. Laser based approaches¹¹ for signal processing such as coherent interferometry are commonly applied to extract information regarding the displacement and velocity of the surface. Ultrasound vibrometers may also use an incoherent approach of directly measuring the Doppler shift spectra.¹² Lasers have a narrow collimated beam and the angle incident on and reflected from the surface is often approximated as each traveling in one planar direction.¹¹ The resulting phase shift of the reflected field is then assumed to be linearly related to ground motion. Ultrasound transducers typically illuminate larger regions of the surface with finite spot sizes determined by the beam pattern of the transducer. This leads to multiple angles incident and reflected from the surface causing the phase shift in the reflected field to become nonlinearly related to the surface motion. Additional complexities arise when the vibrometer is used in continuous scan mode over a rough surface. The motion of the vibrometer adds temporally varying noise arising from scattering over the rough surface that randomizes the amplitude and phase of the received ultrasound signal. This causes a degradation of the signal spectrum as we will illustrate, rendering both coherent and incoherent processing extremely challenging when the surface being scanned is extremely rough.

Here, we apply Green's theorem to develop a full-field model for the time-dependent ultrasound field reflected and scattered off a randomly rough vibrating surface for a scanning, bistatic, ultrasound vibrometer system. Kirchhoff's approximation is used to model the local reflection and scattering from the rough surface. The model incorporates the beam patterns of both the transmitting and receiving ultrasound transducers as well as the statistical properties of the rough surface. The roughness heights on the surface are assumed to follow a spatial random process. The rough surface is characterized by its reflection coefficient and a correlation function that depends on the standard deviation of the roughness heights and their correlation length scales. The reflection coefficient takes into account any absorption losses on the rough surface. The theory developed here is general and applicable for analyzing the performance of other types of

wave-based vibrometers for sensing velocities and displacements of rough surfaces, including laser-based and radar-based^{4,13} systems.

The model is applied to determine the performance of a continuously scanning ultrasound vibrometer for measuring ground displacements under varying environmental conditions as a function of sonar design and measurement parameters. Simulations with the model indicate that scan speed and projected ultrasound wavelength are the two most sensitive parameters that determine the accuracy of the displacement measurement. When the ultrasound wavelength projected onto the surface is large in comparison to the surface roughness height standard deviation, the surface is considered to be smooth. Under such conditions, the ultrasound vibrometer can continuously scan the surface at relatively high speeds to yield accurate estimates of surface displacements using both coherent and incoherent data processing schemes. When the ultrasound wavelength projected onto the surface is small in comparison to the surface roughness height standard deviation, the surface is considered to be rough. Estimation of surface displacement can degrade significantly due to random scattering from the rough surface. The vibrometer system then has to be reconfigured to either transmit at lower frequencies so that the surface appears less rough or the scan speed has to be reduced. The model is applied to determine limiting scan speeds for an ultrasound vibrometer deployed as part of an acoustic landmine imaging sensor over naturally rough terrain consisting of either sand or gravel. Our analysis shows that for a 50 kHz ultrasound system, it is possible to attain scan speeds of 50 cm/s in coarse sand environments and 20 cm/s in gravel environments in order to detect ground displacements of at least $0.02 \mu\text{m}$. For medium and fine sands or silt environments, the scan speed can be larger than 50 cm/s.

The effects of rough surface scattering on the performance of laser and ultrasound vibrometers have been investigated experimentally by a number of researchers.^{7,10,14,15} These investigations all report on the severe degradation that vibrometer motion over a rough surface causes to surface displacement and velocity estimation. In addition to translation, some of these experimental investigations also study the effect of yaw, pitch, and roll on vibrometer performance. The previous *theoretical* studies of vibrometer performance conducted by Rothberg¹⁴ are based on using random number generators to simulate the time-dependent noise field received by a vibrometer from a rough surface. Their model is not based on scattering theory. They do not account for the full three-dimensional (3D) scattering interaction of the ultrasound wave field with the rough surface as we do here. As a consequence, these previous theories¹⁴ cannot provide a fundamental approach for analyzing speckle properties measured by a vibrometer as a function of the measurable statistical characteristic of a rough surface such as its roughness height standard deviation and correlation length scale.

In Sec. II, we develop the time-dependent full-field model for the ultrasound field reflected off a randomly rough vibrating surface. The coherent and incoherent signal processing schemes for estimating displacement and velocities from the received field are summarized in Sec. III. A statis-

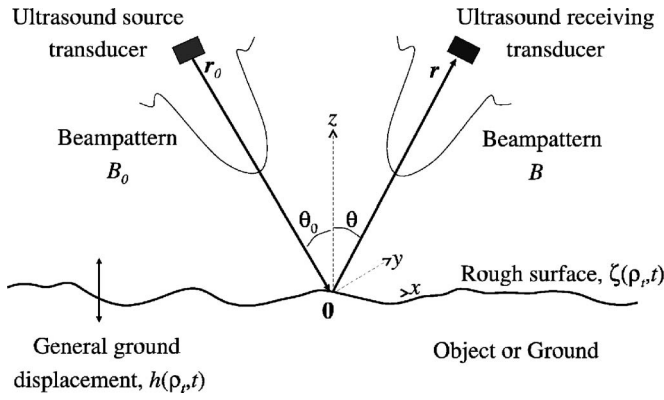


FIG. 1. Setup of a bistatic ultrasound vibrometer system. The origin of the coordinate system is located at the mean surface, at the intersection of the source and receiver beam-pattern axes.

tical description for the rough surface is provided in the Appendix and our approach for generating random realizations of the rough surface from its wave number spectrum is discussed in Sec. IV. Numerical simulations investigating the performance of the ultrasound vibrometer for application in landmine detection are provided in Sec. V.

II. FULL-FIELD MODEL FOR ULTRASOUND SIGNAL REFLECTED OFF MOVING SURFACE WITH RANDOM ROUGHNESS

In this section, we develop an analytic model for the time-dependent ultrasound field reflected off a randomly rough vibrating surface for a scanning ultrasound vibrometer in bistatic configuration. The origin of the coordinate system is located at the mean surface. The z axis is normal to the mean surface, while the x and y axes are on the mean surface as illustrated in Fig. 1. The source transducer is located at $\mathbf{r}_0 = (x_0, 0, z_0)$ and the axis of its main beam-pattern lobe makes an angle $\theta_0 = \tan^{-1}(x_0/z_0)$ with the surface normal. The receiving transducer is located at $\mathbf{r} = (x, 0, z)$ and its beam-pattern main lobe axis makes an angle $\theta = \tan^{-1}(x/z)$ with the surface normal. We will assume throughout the paper that the peak amplitudes of the source and receiver beam patterns intercept the surface at the origin of the coordinate system. For an ultrasound vibrometer in scan mode, the origin of the coordinate system moves with the vibrometer. Coordinates of points on the rough surface are denoted by $\mathbf{r}_t = (x_t, y_t, z_t)$. Spatial cylindrical (ρ, ϕ, z) and spherical (r, θ, ϕ) systems are defined by $x = r \sin \theta \cos \phi$, $y = r \sin \theta \sin \phi$, $z = r \cos \theta$, and $\rho^2 = x^2 + y^2$. The ultrasound frequency is denoted by f , with corresponding angular frequency $\omega = 2\pi f$ and wave number $k = \omega/c$ where c is the speed of sound in air.

For a continuously scanning ultrasound vibrometer, the surface imaged by the system within its resolution footprint can vary as a function of time as the vibrometer moves over the surface. Let the rough surface height at horizontal location $\boldsymbol{\rho}_t = (x_t, y_t)$ on the surface imaged by the system at time instance t be given by $\zeta(\boldsymbol{\rho}_t, t)$. The x and y components of the gradient of the surface are, respectively,

$$p(\boldsymbol{\rho}_t, t) = \frac{\partial \zeta(\boldsymbol{\rho}_t, t)}{\partial x_t} \quad (1)$$

and

$$q(\boldsymbol{\rho}_t, t) = \frac{\partial \zeta(\boldsymbol{\rho}_t, t)}{\partial y_t}. \quad (2)$$

The surface normal can then be expressed as

$$\mathbf{n}(\boldsymbol{\rho}_t, t) = \frac{(p, q, 1)}{\sqrt{p^2 + q^2 + 1}}. \quad (3)$$

A statistical description of the surface roughness height ζ is provided in the Appendix, along with its characterization in terms of a spatial correlation function and wave number spectrum.

For a vibrating rough surface, let $h(\boldsymbol{\rho}_t, t)$ be the vertical displacement of the surface at location $\boldsymbol{\rho}_t$ and at time t . Then the vertical position of the surface at $\boldsymbol{\rho}_t$ at any time instance t is $z_t = h(\boldsymbol{\rho}_t, t) + \zeta(\boldsymbol{\rho}_t, t)$. The surface displacement h is a function of both space and time to account for local variations in the displacement of the surface within the ultrasound resolution footprint. This occurs in acoustic landmine detection when the ground is excited by short wavelength acoustic signals.

The incident and reflected ultrasound wave vectors are denoted by $\mathbf{k}_i = k(\mathbf{r}_t - \mathbf{r}_0)/|\mathbf{r}_t - \mathbf{r}_0|$ and $\mathbf{k} = k(\mathbf{r} - \mathbf{r}_t)/|\mathbf{r} - \mathbf{r}_t|$, respectively. In general, these are functions of the source and receiver coordinates, respectively, as well as the coordinates of the surface since they determine the incident and reflected or scattered wave directions.

By application of Green's theorem, the time-dependent ultrasound field transmitted from a time harmonic source at \mathbf{r}_0 , reflected off the surface and received at \mathbf{r} is¹⁶

$$P(\mathbf{r}, t) = \Re \left\{ e^{-i\omega t} \int \int_S w(\boldsymbol{\rho}_t) [\Phi(\mathbf{r}_t | \mathbf{r}_0) \nabla_t G(\mathbf{r} | \mathbf{r}_t) - G(\mathbf{r} | \mathbf{r}_t) \nabla_t \Phi(\mathbf{r}_t | \mathbf{r}_0)] \cdot \mathbf{n}(\boldsymbol{\rho}_t, t) dS_t \right\}, \quad (4)$$

where $\Phi(\mathbf{r}_t | \mathbf{r}_0)$ is the total field on the surface, $G(\mathbf{r} | \mathbf{r}_t)$ is the free space Green function given by

$$G(\mathbf{r} | \mathbf{r}_t) = \frac{1}{4\pi} \frac{1}{|\mathbf{r} - \mathbf{r}_t|} e^{ik \cdot (\mathbf{r} - \mathbf{r}_t)}, \quad (5)$$

$w(\boldsymbol{\rho}_t)$ is a window function that depends on the beam pattern B of the receiver projected onto the surface,

$$w(\boldsymbol{\rho}_t) = B \left(\sin^{-1} \frac{\rho_t \cos \theta}{\sqrt{(x - x_t)^2 + y_t^2 + z^2}} \right), \quad (6)$$

and S is the region of the surface that contributes to the integrand in Eq. (4). The beam patterns of the source and receiving transducers provide natural window functions to limit the dominant region of the surface, that contributes to the received field, to be located where the two main lobes of the transducers intersect the surface. This approach avoids the need to worry about problems arising from edge effects

when considering plane wave scattering from infinite surfaces as discussed in Ref. 17.

We apply Kirchhoff's approximation to estimate the total field on the surface as the sum of the incident and locally reflected fields,

$$\Phi(\mathbf{r}_t|\mathbf{r}_0) = Q(4\pi)^2 w_0(\boldsymbol{\rho}_t)(1 + R(\mathbf{k}_i, \boldsymbol{\rho}_t))G(\mathbf{r}_t|\mathbf{r}_0), \quad (7)$$

where Q is the source amplitude, $w_0(\boldsymbol{\rho}_t)$ is the window function that determines the amplitude of the incident field at each point on the surface through the source beam pattern B_0 ,

$$w_0(\boldsymbol{\rho}_t) = B_0 \left(\sin^{-1} \frac{\rho_t \cos \theta_0}{\sqrt{(x_0 - x_t)^2 + y_t^2 + z_0^2}} \right), \quad (8)$$

and $R(\mathbf{k}_i, \boldsymbol{\rho}_t)$ is the local reflection coefficient on the surface. It depends on the intrinsic properties of the medium above and below the interface and the local curvature of the surface relative to the incident wave. For instance, in landmine detection applications, if the ground can be approximated as a homogeneous sediment, the reflection coefficient is

$$R(\mathbf{k}_i, \boldsymbol{\rho}_t) = \frac{\rho_2 \eta - \rho \sqrt{(k_2/k)^2 - (1 - \eta^2)}}{\rho_2 \eta + \rho \sqrt{(k_2/k)^2 - (1 - \eta^2)}}, \quad (9)$$

where ρ and ρ_2 are the densities of air and ground, respectively, $k_2 = 2\pi f/c_2$ is the ultrasound wave number on the ground, c_2 is the compressional wave speed of the ground, and

$$\eta(\boldsymbol{\rho}_t, t) = \frac{\mathbf{k}_i \cdot \mathbf{n}(\boldsymbol{\rho}_t, t)}{k_i} \quad (10)$$

is the cosine of the angle between the incident field and the surface normal. The reflection coefficient is complex in general. It accounts for an absorptive surface or a lossy layer such as a layer of dense vegetation when $|R| < 1$.

The derivative of the Green function and that of the total field on the surface are, respectively,

$$\nabla_t G(\mathbf{r}|\mathbf{r}_t) = -ikG(\mathbf{r}|\mathbf{r}_t), \quad (11)$$

and

$$\nabla_t \Phi(\mathbf{r}_t|\mathbf{r}_0) = Q(4\pi)^2 w_0(\boldsymbol{\rho}_t)G(\mathbf{r}_t|\mathbf{r}_0)i(\mathbf{k}_i + \mathbf{k}'R(\mathbf{k}_i, \boldsymbol{\rho}_t)), \quad (12)$$

where \mathbf{k}' is the wave vector in the local reflection direction determined solely by the local incident wave vector and the surface normal. The dot product of the local incident and reflected wave vectors with the surface normal satisfy

$$\mathbf{k}_i \cdot \mathbf{n}(\boldsymbol{\rho}_t) = -\mathbf{k}' \cdot \mathbf{n}(\boldsymbol{\rho}_t). \quad (13)$$

Substituting Eqs. (5), (7), (11), and (12) into Eq. (4), and applying Eq. (13), we find

$$P(\mathbf{r}, t) = \Re \left\{ e^{-i\omega t} Q \int \int_S i[R(\mathbf{k}_i, \boldsymbol{\rho}_t)(\mathbf{k}_i - \mathbf{k}) - (\mathbf{k}_i + \mathbf{k})] \cdot \mathbf{n}(\boldsymbol{\rho}_t, t) w_0(\boldsymbol{\rho}_t) w(\boldsymbol{\rho}_t) \times G(\mathbf{r}_t|\mathbf{r}_0)G(\mathbf{r}|\mathbf{r}_t) dS_t \right\}. \quad (14)$$

Expressing the Green's function in Eq. (14) in terms of the surface coordinates, the ultrasound field reflected off the vibrating surface becomes

$$P(\mathbf{r}, t) = \Re \left\{ e^{-i\omega t} Q \int \int_{S_0} i[R(\mathbf{k}_i, \boldsymbol{\rho}_t)(\mathbf{k}_i - \mathbf{k}) - (\mathbf{k}_i + \mathbf{k})] \cdot \mathbf{n}(\boldsymbol{\rho}_t, t) w_0(\boldsymbol{\rho}_t) w(\boldsymbol{\rho}_t) \times \frac{\exp(ik\sqrt{(x_t - x_0)^2 + y_t^2 + (h(\boldsymbol{\rho}_t, t) + \zeta(\boldsymbol{\rho}_t, t) - z_0)^2})}{\sqrt{(x_t - x_0)^2 + y_t^2 + (h(\boldsymbol{\rho}_t, t) + \zeta(\boldsymbol{\rho}_t, t) - z_0)^2}} \times \frac{\exp(ik\sqrt{(x - x_t)^2 + y_t^2 + (z - h(\boldsymbol{\rho}_t, t) - \zeta(\boldsymbol{\rho}_t, t))^2})}{\sqrt{(x - x_t)^2 + y_t^2 + (z - h(\boldsymbol{\rho}_t, t) - \zeta(\boldsymbol{\rho}_t, t))^2}} dS_t \right\}. \quad (15)$$

Note that in Eq. (15), the phase of the received signal is a nonlinear function of the surface displacement $h(\boldsymbol{\rho}_t, t)$. This is in contrast to the field measured using a narrow collimated laser beam where the received signal phase is often approximated to be a linear function of the surface displacement.¹¹ The wave numbers k in the argument of the exponential terms in Eq. (15) are complex to account for attenuation due to absorption in air. The surface displacement is an arbitrary function of time and can be used to describe surface motion arising from both sinusoidal and broadband excitation. Besides the ultrasound vibrometer, the theory developed here is also applicable to other wave-based displacement sensors, including both laser and radar^{4,13} vibrometers.

In order to illustrate the approaches for processing the received signal, we simplify Eq. (15) in the next section so that the received signal phase becomes a linear function of surface displacement. The conditions under which this simplification is valid for the ultrasound vibrometer is also discussed there. In Sec. V, we implement the full-field model in Eq. (15) for the general ultrasound vibrometer and numerically evaluate its performance for estimating surface displacement amplitudes and velocities under different environmental conditions and measurement scenarios.

Narrow beamwidth approximation. For an ultrasound vibrometer with a sufficiently narrow beamwidth such that the dominant ultrasound field incident on and reflected from the surface can each be approximated as traveling in one planar direction, much simplification can be obtained for the ultrasound field measured at the receiver. Let ρ_e be the radius of the patch of surface insonified by the transducer within its equivalent beamwidth, θ_e . The ultrasound fields incident upon and reflected from the surface are approximately planar if the phase variation within the insonified region is less than $\pi/4$. This occurs for vibrometer systems that satisfy $\theta_e < \sqrt{\lambda/r}$. This is the required condition for the vibrometer in order for the analysis in this section to be applicable. We also assume that the beam-pattern main lobe axis of the source and receiving transducers are symmetric about the z axis so that $\theta = \theta_0$, and the wave vectors are each planar, $\mathbf{k}_i \approx (k_x, 0, -k_z)$ and $\mathbf{k} \approx (k_x, 0, k_z)$, where $k_x = k \sin \theta$ and $k_z = k \cos \theta$.

The argument within the exponential phase terms in Eq. (15) can be simplified following $\mathbf{k}_i \cdot (\mathbf{r}_t - \mathbf{r}_0) = k\sqrt{(x_t - x_0)^2 + y_t^2 + (h(\boldsymbol{\rho}_t, t) + \zeta(\boldsymbol{\rho}_t, t) - z_0)^2} \approx -k_x x_0 - k_z(\zeta(\boldsymbol{\rho}_t) + h(t) - z_0)$, while the spherical spreading terms approximated following $|\mathbf{r}_t - \mathbf{r}_0| \approx r_0$. The weighting functions on the surface can be approximated as step functions over an area delimited by the equivalent beamwidth of the source and receiver, for instance,

$$P(\mathbf{r}, t) = -\Re \left\{ e^{-i\omega t} i Q 2k_z R_0 \int_0^{\rho_e} \int_0^{2\pi} \frac{1}{r_0} e^{-i[k_x x_0 + k_z(\zeta(\boldsymbol{\rho}_t, t) + h(t) - z_0)]} \frac{1}{r} e^{i[k_x x + k_z(z - \zeta(\boldsymbol{\rho}_t, t) - h(t))]} \rho_t d\phi_t d\rho_t \right\} \\ = -\Re \left\{ e^{-i\omega t} i (4\pi)^2 Q 2k_z R_0 G(\mathbf{0}|\mathbf{r}_0) G(\mathbf{r}|\mathbf{0}) e^{-i2k_z h(t)} \int_0^{\rho_e} \int_0^{2\pi} e^{-i2k_z \zeta(\boldsymbol{\rho}_t, t)} \rho_t d\phi_t d\rho_t \right\}, \quad (17)$$

where the last equality was obtained by applying Eq. (5).

We next denote the last factor in Eq. (17) which is the integrated random phase contribution to the reflected field due to scattering from roughness elements on the surface as

$$\mathcal{Z}_N(t) = A_N(t) e^{i\phi_N(t)} = \int_0^{\rho_e} \int_0^{2\pi} e^{-i2k_z \zeta(\boldsymbol{\rho}_t, t)} \rho_t d\phi_t d\rho_t. \quad (18)$$

Note that random scattering from surficial roughness affects both the amplitude and phase of the reflected signal so that both A_N and ϕ_N are random variables, or equivalently, \mathcal{Z}_N is a complex random variable. They may also be functions of time depending on whether the vibrometer is stationary in space or moving across the surface. Substituting Eq. (18) into Eq. (17), we obtain

$$P(\mathbf{r}, t) = \Re \{ B \mathcal{Z}_N(t) e^{-i(\omega t + 2k_z h(t))} \} \\ = \Re \{ B A_N(t) e^{-i[\omega t + 2k_z h(t) - \phi_N(t)]} \}, \quad (19)$$

where $B = -i(4\pi)^2 Q 2k_z R_0 G(\mathbf{0}|\mathbf{r}_0) G(\mathbf{r}|\mathbf{0})$.

Under the narrow beamwidth approximation, the phase of the received signal becomes a linear function of the surface displacement $h(t)$. This linear dependence is also obtained when one makes the far-field approximation.²⁵ Equation (19) is now directly amenable to both coherent and incoherent signal processing approaches for estimating surface displacement and velocity amplitudes as discussed next.

III. ULTRASOUND SIGNAL ANALYSIS FOR SURFACE DISPLACEMENT AND VELOCITY ESTIMATION

A review of approaches used to analyze ultrasound sensor data to estimate surface displacement and velocity for a wide range of applications is provided in the introduction of Ref. 12. They can be grouped into two main categories—either incoherent Doppler shift spectra or coherent interferometry. In the following, we discuss a version of each of these two main approaches for analyzing ultrasound sensor data by applying them analytically to the narrow beamwidth ultrasound system to estimate surface displacement. These

$$w(\boldsymbol{\rho}_t) = \begin{cases} 1 & \text{for } \rho_t < \rho_e \\ 0 & \text{elsewhere.} \end{cases} \quad (16)$$

We assume the local slopes on the surface are sufficiently small so that we can approximate the reflection coefficient over the insonified area as a constant, $R(\mathbf{k}_i, \boldsymbol{\rho}_t) = R_0$. Furthermore, we approximate $(\mathbf{k}_i - \mathbf{k}) \cdot \mathbf{n}_t \approx -2k_z$ and $(\mathbf{k}_i + \mathbf{k}) \cdot \mathbf{n}_t \approx 0$. Equation (15) for the field measured by the receiving transducer then becomes

approaches are also applied to analyze full-field data from the general larger beamwidth ultrasound system in the numerical simulation examples of Sec. V.

A. Incoherent Doppler shift spectra

This approach analyzes the signal received at the ultrasound transducer incoherently. For time-harmonic sinusoidal oscillations of the surface, it provides an estimate of the amplitude of the surface displacement from the spectrum of the received ultrasound field. We consider two specific motions of the surface—uniform translation and sinusoidal oscillation about a mean position.

For uniform translation of the surface, the speed v_g of the surface is a constant and the displacement can be expressed as

$$h(t) = v_g t. \quad (20)$$

Substituting Eq. (20) into Eq. (19), the field measured by the transducer becomes

$$P(\mathbf{r}, t) = \Re \{ B \mathcal{Z}_N(t) e^{-i(\omega + 2k_z v_g)t} \}. \quad (21)$$

In the absence of time-dependent scattering from the rough surface, the Fourier transform $P(\omega')$ of the received ultrasound signal defined as

$$P(\omega') = \int_0^T P(\mathbf{r}, t) e^{i\omega' t} dt \quad (22)$$

has a shift in the peak frequency from $\omega' = \omega$ to $\omega' = \omega + 2k_z v_g$. This Doppler shift in peak frequency $2k_z v_g = 2kv_g \cos \theta$ is directly proportional to the projected velocity $v_g \cos \theta$ of the surface in the direction of the transducer beam. For this approach to work, the projected surface velocity must be large enough to resolve the shift in peak frequency. In Eq. (22), T is the time duration of the signal used for computing its Fourier transform.

We next consider sinusoidal oscillations of the surface at angular frequency ω_g where the displacement can be expressed as

$$h(t) = h_0 \cos(\omega_g t + \phi_g). \quad (23)$$

Substituting Eq. (23) into Eq. (19), the field measured by the receiving transducer becomes

$$P(\mathbf{r}, t) = \Re\{B\mathcal{Z}_N(t)e^{-i[\omega t + 2k_z h_0 \cos(\omega_g t + \phi_g)]}\}. \quad (24)$$

Following the approach of Refs. 2, 11, and 7, we expand the sinusoidal phase term in Eq. (24) as a Bessel series of the form, $e^{ia \cos b} = \sum_{n=-\infty}^{\infty} i^n J_n(a) e^{inb}$, to obtain

$$P(\mathbf{r}, t) = \Re\left\{B\mathcal{Z}_N(t) \sum_{n=-\infty}^{\infty} i^n J_n(2k_z h_0) e^{i[(n\omega_g - \omega)t + n(\phi_g + \pi)]}\right\}. \quad (25)$$

We next take the Fourier transform of Eq. (25) following Eq. (22). Note that if the time-dependent variation in the scattering from the rough surface is negligible, the ratio of the Fourier transform peak magnitude at $\omega' = \omega$ to the n th order sideband at $\omega' = \omega \pm n\omega_g$ can be approximated as

$$\frac{|P(\omega' = \omega)|}{|P(\omega' = \omega \pm n\omega_g)|} = \frac{|J_0(2k_z h_0)|}{|J_n(2k_z h_0)|} \approx \frac{\Gamma(n+1)}{(h_0 k \cos \theta)^n}. \quad (26)$$

The last approximation uses the Bessel function expansion for small arguments¹⁸ and is therefore only valid when the ground displacement amplitude is small in comparison to the ultrasound wave number. We can obtain an estimate of the surface displacement amplitude \hat{h}_0 from the Fourier transform peak magnitude and any of the sidebands,

$$\hat{h}_0 = \frac{1}{k \cos \theta} \left[\frac{n! |P(\omega' = \omega \pm n\omega_g)|}{|P(\omega' = \omega)|} \right]^{(1/n)}. \quad (27)$$

The corresponding velocity amplitude is obtained from the displacement amplitude $\hat{v}_g = \omega_g \hat{h}_0$. The first-order sidebands $n = \pm 1$ at frequency $\omega' = \omega \pm \omega_g$ are the most prominent of the sidebands especially in the presence of surface roughness and estimates of surface displacements are usually based upon them.

B. Coherent interferometry

This is a coherent approach that uses data from both the transmitting and receiving ultrasound transducers. It has the potential to track both the amplitude and phase of the surface displacement. The version described here follows the approach of Ref. 12.

We first multiply the source signal,

$$P_0(t) = Q \cos \omega t, \quad (28)$$

to the received signal to obtain

$$M(t) = P(\mathbf{r}, t) P_0(t) = \Re\left\{\frac{1}{2}QB\mathcal{Z}_N(t)(e^{-i2k_z h(t)} + e^{-i2(\omega t + k_z h(t))})\right\}. \quad (29)$$

The first term is the only term needed for tracking the surface displacement. We next low-pass filter the data to remove the second, higher frequency term in Eq. (29) and obtain

$$M_f(t) = \Re\left\{\frac{1}{2}QB\mathcal{Z}_N(t)e^{-i2k_z h(t)}\right\}. \quad (30)$$

For small surface displacement amplitude compared to the ultrasound wavelength, we can approximate $e^{-2k_z h(t)} \approx 1 - i2k_z h(t)$. After removal of the mean or dc component of the filtered data, Eq. (30) simplifies to

$$\overline{M_f(t)} \approx -\Re\{iQB\mathcal{Z}_N(t)k_z h(t)\}. \quad (31)$$

In the absence of time-dependent scattering from the rough surface, the only time-varying quantity in Eq. (30) is $h(t)$. The temporal variation of the mean filtered data is therefore directly proportional to the ground displacement. This allows us to track both the amplitude and phase of the ground displacement.

It should be noted that the coherent approach can be applied to analyze ultrasound data reflected from both sinusoidal as well as general broadband ground displacements. For instance, for sinusoidal ground displacement with $h(t)$ satisfying Eq. (23), an estimate for the surface displacement amplitude is

$$\hat{h}_0 = \frac{1}{2k \cos \theta} \frac{\overline{\mathcal{M}_f(\omega' = \omega_g)}}{|P(\omega' = \omega)| |P_0(\omega' = \omega)|}, \quad (32)$$

where $\overline{\mathcal{M}_f(\omega')}$, $P(\omega')$, and $P_0(\omega')$ are the Fourier transforms of the mean low-pass filtered product signal, the received signal, and the source signal, respectively.

IV. GENERATING TWO-DIMENSIONAL SPATIAL REALIZATIONS OF THE ROUGH SURFACE

We assume the surface roughness heights follow a Gaussian random process that is locally stationary over the imaged area in the measurement time interval. They can be described by a Gaussian probability distribution function, as discussed in the Appendix. For the simulations in Sec. V, we further assume that the spatial correlation function of the roughness heights at any two horizontal locations $\boldsymbol{\rho}_t$ and $\boldsymbol{\rho}_{t'}$ on the surface is also Gaussian and can be expressed as

$$\begin{aligned} \langle \zeta(\boldsymbol{\rho}_t) \zeta(\boldsymbol{\rho}_{t'}) \rangle &= C_{\zeta\zeta}(\boldsymbol{\rho}_t - \boldsymbol{\rho}_{t'}) = C_{\zeta\zeta}(\mathbf{R}) \\ &= \sigma_{\zeta}^2 e^{-(1/2)(X^2/\ell_x^2 + Y^2/\ell_y^2)}, \end{aligned} \quad (33)$$

where $\mathbf{R} = (X, Y) = \boldsymbol{\rho}_t - \boldsymbol{\rho}_{t'} = (x_t - x_{t'}, y_t - y_{t'})$, σ_{ζ} is the standard deviation of the roughness heights on the surface, and ℓ_x and ℓ_y are the correlation lengths for the roughness heights in the x and y directions, respectively. For an isotropic rough surface, $\ell_x = \ell_y$. Following Eq. (A4), the two-dimensional (2D) Fourier transform of Eq. (33) yields the corresponding spatial wave number spectrum of the rough surface,

$$G(\boldsymbol{\kappa}) = \pi \sigma_{\zeta}^2 \ell_x \ell_y e^{-(\kappa_x^2 \ell_x^2 + \kappa_y^2 \ell_y^2)/4}. \quad (34)$$

The Gaussian probability distribution function is a good assumption for rough surfaces that are the result of a large number of local cumulative events or processes, and therefore obey Gaussian statistics by the central limit theorem.^{19,20}

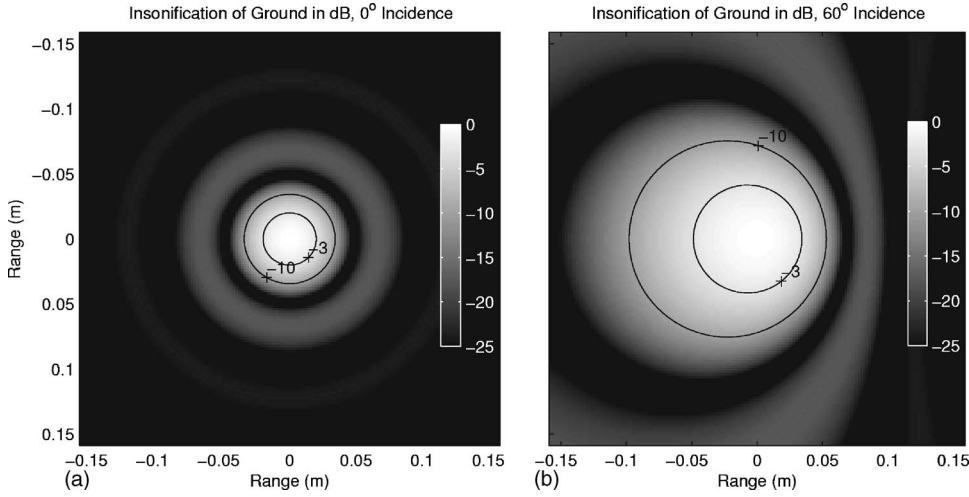


FIG. 2. Magnitude of ultrasound beam pattern in decibels at 50 kHz intercepted by a surface for (a) $\theta=0^\circ$, and (b) $\theta=60^\circ$ incidence of beam axis with surface. The transducer is a circular disk of diameter $D=3.5$ cm and is positioned 20 cm from the surface. The equivalent beamwidth of the transducer is approximately $4\lambda/\pi D=14^\circ$.

Naturally occurring terrain is an example of this.¹⁷ Other correlation functions and related wave number spectra can also be used to characterize the rough surface and the choice depends on the nature of the surface.

Following the approach in Refs. 21 and 17, we describe a procedure for generating spatial realizations of the 2D rough surface with a given wave number spectrum $G(\boldsymbol{\kappa})$. Given a rough surface, the 2D Fourier transform of the roughness heights over a finite spatial window with area S is

$$Z(\boldsymbol{\kappa}) = \int \int_S \zeta(\boldsymbol{\rho}_t) e^{i\boldsymbol{\kappa}\boldsymbol{\rho}_t} dS_t. \quad (35)$$

Here $Z(\boldsymbol{\kappa})$ is a zero-mean Gaussian random process due to its linear dependence on $\zeta(\boldsymbol{\rho}_t)$. According to Parseval's theorem,

$$\sigma_\zeta^2 = \frac{1}{S} \int \int_S \langle |\zeta(\boldsymbol{\rho}_t)|^2 \rangle dS_t = \frac{1}{S} \int \int \langle |Z(\boldsymbol{\kappa})|^2 \rangle \boldsymbol{\kappa} d\boldsymbol{\kappa} d\Theta. \quad (36)$$

From Eq. (A5), $\sigma_\zeta^2 = C_{\zeta\zeta}(0)$, so that

$$\langle |Z(\boldsymbol{\kappa})|^2 \rangle = \frac{S}{(2\pi)^2} \langle G(\boldsymbol{\kappa}) \rangle. \quad (37)$$

As S becomes arbitrarily large, delta-function correlation is achieved across the wave vector domain,

$$\langle Z(\boldsymbol{\kappa})Z(\boldsymbol{\kappa}') \rangle \approx \frac{G(\boldsymbol{\kappa})}{(2\pi)^2} \delta(\boldsymbol{\kappa} - \boldsymbol{\kappa}'),$$

indicating that components of $Z(\boldsymbol{\kappa})$ with wave vector separations exceeding $(2\pi)^2/S$ are uncorrelated. A random realization of the rough surface height $\zeta(\boldsymbol{\rho}_t)$ can be obtained as the inverse Fourier transform of $Z(\boldsymbol{\kappa})$ under the assumption that $Z(\boldsymbol{\kappa})$ are zero-mean Gaussian random variables that are uncorrelated when sampled at wave vector intervals of at least $(2\pi)^2/S$ and have variance $\langle G(\boldsymbol{\kappa}) \rangle S / (2\pi)^2$.

For the numerical simulation in Sec. V, we create the 2D rough surfaces by first generating the real and imaginary parts of a 2D matrix of complex Gaussian random variables

with zero mean and variance $\langle G(\boldsymbol{\kappa}) \rangle S / (2\pi)^2$. This matrix corresponds to $Z(\boldsymbol{\kappa})$. We apply the symmetry property of Fourier transforms of real signals to ensure that $Z(\boldsymbol{\kappa}) = Z(-\boldsymbol{\kappa})^*$. We then take the inverse Fourier transform of $Z(\boldsymbol{\kappa})$ to yield a purely real 2D rough surface with the required statistical property.

V. NUMERICAL SIMULATION

Here we investigate the performance of the ultrasound vibrometer for measuring surface displacement while continuously scanning a sinusoidally oscillating randomly rough ground. The performance of the system is investigated as a function of the ultrasound frequency, angle of incidence of the ultrasound beam, system scan velocity, and stand-off distance of the transducers from the surface. The stand-off distance determines the area of ground insonified by the system. We simulate different surface types, such as those of sand and gravel, by varying the roughness height standard deviation and correlation length scale of the surface. The performance of the system is quantified by examining the accuracy of the displacement estimation using both the coherent and incoherent data analysis schemes. In the examples to follow, the ultrasound source frequency is $f=50$ kHz, unless otherwise stated. The ground is assumed to be oscillating harmonically at a frequency of 120 Hz with a displacement amplitude of $h_0=2.5$ μm .

The transducer is modeled as a baffled circular disk of diameter $D=3.5$ cm. The equivalent beamwidth of the main lobe of the transducer is $\theta_e=4\lambda/\pi D=14^\circ$ and the far field for the transducer begins at $D^2/\lambda=18$ cm. The transducer is originally positioned at a distance of $r_0=r=20$ cm from the ground. The theoretical beam pattern is calculated based on the transducer dimensions. Figures 2(a) and 2(b) show the beam-pattern amplitude $w(\boldsymbol{\rho}_t)$ projected onto the ground for two different scenarios where the transducer main lobe axis makes the angle $\theta=0^\circ$ and $\theta=60^\circ$, respectively, with the surface normal. We observe that the dominant region of the surface insonified by the transducer is small, with a width of about $\rho_e=r\theta_e=4.9$ cm for 0° incidence. For 60° incidence, the beam pattern on the ground is asymmetric about the y axis and the dominant region insonified has a width of

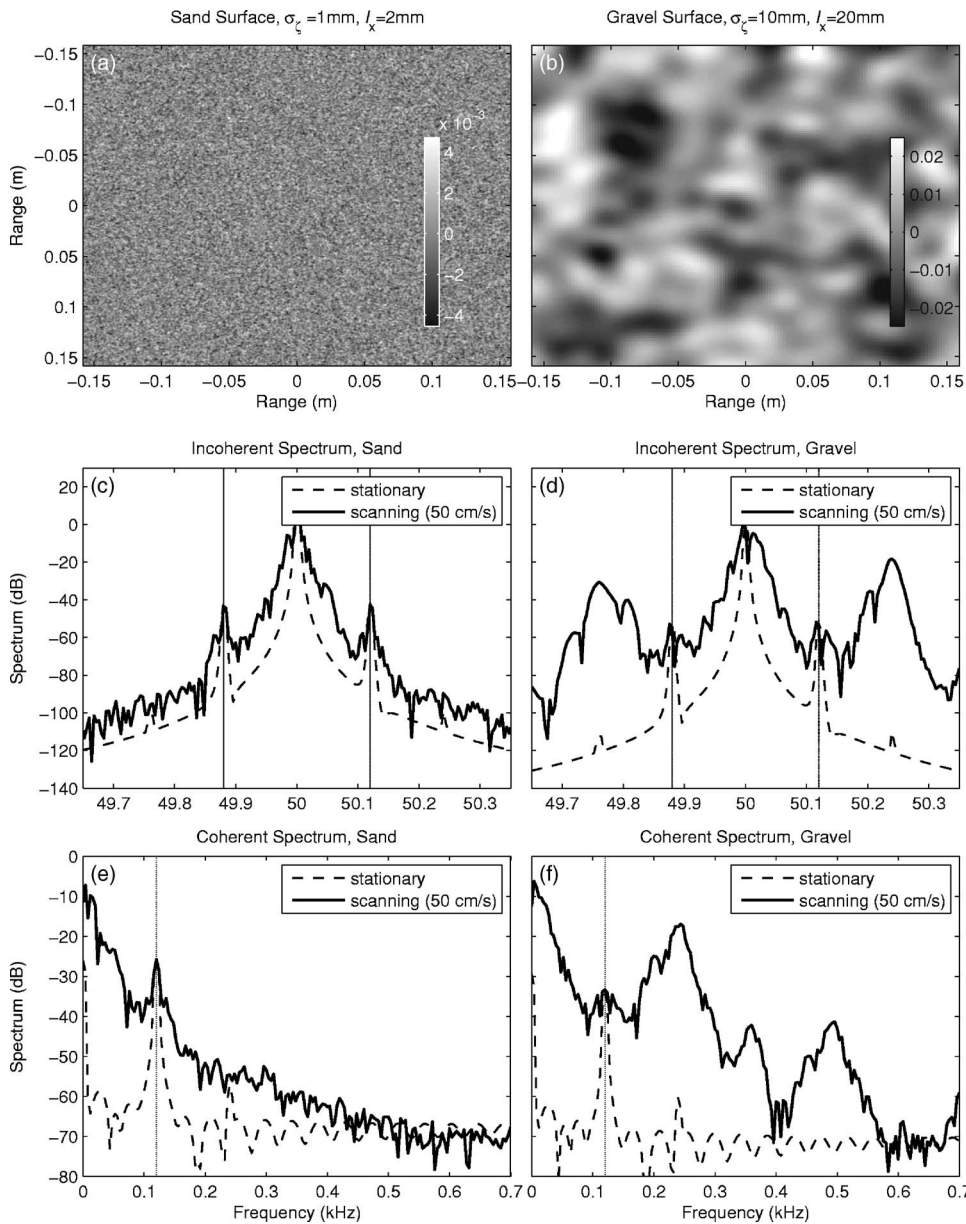


FIG. 3. Realizations of randomly rough (a) medium sand and (b) gravel surfaces. Spectrum of received ultrasound field, $10 \log_{10} |\mathcal{P}(\omega')|^2$, reflected and scattered off harmonically oscillating (c) medium sand and (d) gravel surfaces for an ultrasound vibrometer continuously scanning the surface at a speed of 50 cm/s. The corresponding results for the stationary vibrometer are plotted for comparison. (e) Medium sand and (f) gravel are the corresponding coherently processed spectrum of low-pass filtered mixed signal, $10 \log_{10} |\mathcal{M}_f(\omega')|$. The spectra are plotted for an ultrasound source level of 0 dB re 20 μ Pa at 1 m ($f=50$ kHz, $f_g=120$ Hz, $h_0=2.5$ μ m, $\theta=0^\circ$, $z=z_0=0.2$ m, $T=0.25$ s).

roughly $\rho_c/\cos \theta_c=9.8$ cm. The ground vibration wavelength at the acoustic excitation frequency of 120 Hz is roughly 2 m. This is much larger than the resolution footprint of the ultrasound system making lateral variations in ground vibration negligible in the measurement. Since the material density of the ground is much larger than in air, the reflection coefficient can be approximated as a constant, $R \approx 1$ from Eq. (9). In all the examples to follow, the results are plotted for a ultrasound system with source level of 0 dB re 20 μ Pa at 1 m.

A. Performance of scanning ultrasound vibrometer for varying surface types

In this section, the performance of the ultrasound vibrometer is studied as a function of roughness height standard deviation and correlation length scale of the rough surface. Figures 3(a) and 3(b) show realizations of isotropic rough surfaces for medium sand and gravel environments, respectively. The surface roughness is assumed to follow a Gauss-

ian random process with Gaussian correlation function as described in Sec. IV. The roughness height standard deviation and correlation length scales for medium sand are $\sigma_h=1$ mm, $\ell_x=2$ mm, and those for gravel are $\sigma_h=10$ mm, $\ell_x=20$ mm. Relative to the ultrasound wavelength of $\lambda=6.8$ mm, the sand surface is considered to be moderately rough with $k\sigma_z=0.9$, while the gravel surface is considered to be very rough with $k\sigma_z=9.2$.

Figures 3(c) and 3(d) plot the Fourier spectrum, $20 \log_{10} |\mathcal{P}(\omega')|$, of the received ultrasound field reflected and scattered off the oscillating rough surface for the sand and gravel environments, respectively. The received field is computed using Eq. (15) and a Hanning window was applied to the simulated data in time before calculating the spectrum. The results are plotted for the stationary ultrasound vibrometer as well as the vibrometer system continuously scanning the ground at a speed of $v_u=50$ cm/s. For the stationary vibrometer in both environments, we observe a peak in the spectrum at 50 kHz corresponding to the original ultrasound

transmitted frequency. We also observe the prominent first-order sidebands at 49.88 and 50.12 kHz which are Doppler shifts $f \pm f_g$ in the reflected signal caused by the harmonically oscillating ground. The second-order sidebands are also visible, but they have much smaller amplitudes. For the continuously scanning vibrometer, the spectrum of the received signal is degraded due to scattering from the rough surface. This degradation is small for the sand surface, but is significant for the gravel surface.

Incoherent signal analysis for the ground displacement amplitude is obtained from the ratio of the spectral peak to the first-order sidebands following Eq. (27). For the continuously scanning ultrasound vibrometer, we obtain $\hat{h}_0 \approx 2.46 \mu\text{m}$ for the medium sand surface, $\hat{h}_0 \approx 3.7 \mu\text{m}$ for the gravel surface. This corresponds to accuracies of 98% and 52% for the sand and gravel surfaces, respectively, with incoherent processing. These estimates are based on a single realization of the surface. The results after averaging over multiple realizations will be discussed in the next section.

Figures 3(e) and 3(f) show the Fourier spectrum of the filtered mix signal, $10 \log_{10} |M_f(\omega')|$, after removal of the mean and application of a Hanning window in time to the mix signal in the sand and gravel environments, respectively. The results are again plotted for both the stationary vibrometer and the vibrometer continuously scanning the ground at 50 cm/s. A prominent peak in the spectrum is observed in the sand and gravel environments at the ground oscillation frequency of 120 Hz when the vibrometer is stationary. For the continuously scanning system, the spectrum is randomized significantly in the gravel environment and no distinct peak can be observed at the desired frequency. Coherent signal analysis for the ground displacement amplitude is obtained by application of Eq. (32). For the continuously scanning vibrometer, we estimate $\hat{h}_0 \approx 2.8 \mu\text{m}$ for sand and $\hat{h}_0 \approx 1.79 \mu\text{m}$ for gravel. Corresponding accuracies are 89% and 72% for the sand and gravel surfaces, respectively, with coherent processing for a single realization of the surface.

The above-presented analysis indicates that when the vibrometer is stationary while acquiring data, it is expected to perform well in estimating surface displacement regardless of the rough surface condition. This is because random scattering from the rough surface is constant and does not add time-dependent noise to the measurement when the vibrometer is stationary. Since the sidebands for the stationary measurement stand above the background spectrum level by over 40 dB, in the absence of other sources of noise, the system is sensitive to displacements on the order of 0.1 nm. For the continuously scanning system, the 50 kHz vibrometer is expected to perform well in estimating surface displacements for sandy and other less rough surfaces at relatively high scan speeds. The performance of the 50 kHz vibrometer is degraded for gravel and other surfaces that are more rough indicating that these surfaces should not be continuously scanned at high speeds. In Sec. V D, we determine the limiting scan speeds for gravel and sandy environments for an ultrasound vibrometer to be used in acoustic landmine confirmation sensing.

B. Random spectral broadening in the continuously scanning vibrometer

Here we analyze the randomization in the spectrum that is caused by scattering from a randomly rough surface for the scanning ultrasound vibrometer. Figure 4(a) shows the spectrum of the received signal for a stationary ultrasound vibrometer reflected from a nonoscillating smooth surface. Nearly the same spectrum is obtained for the continuously scanning vibrometer over the same surface. Both systems measure the signal reflected from the smooth surface which has a peak in the spectrum at the ultrasound frequency of 50 kHz. For a smooth surface that is oscillating sinusoidally, Fig. 4(b) shows the introduction of sidebands at $f \pm n f_g$ to the spectrum of the received field for both the stationary and scanning systems. Here the sidebands up to $n=2$ are visible. When the surface becomes rough but is nonoscillating, the received signal differs for the stationary and continuously scanning ultrasound systems. For the stationary system, the received signal spectral peak at 50 kHz is reduced in amplitude due to nonspecular scattering of the field into other directions away from the receiving transducer as shown in Fig. 4(c). For the scanning system, Fig. 4(e), in addition to a reduction of the magnitude, there is also random broadening of the spectral peak. This spectral broadening around the peak is due to Doppler shifts caused by undulations on the rough surface as the transducer moves either toward or away from the roughness elements. When the rough surface oscillates harmonically, the effects noted for the nonoscillating rough surface now become applicable to both the spectral peak and sidebands for the harmonically oscillating rough surface. As shown in Fig. 4(d), for the stationary vibrometer, the level of both the peak and sidebands have been reduced due to scattering from the oscillating rough surface. In continuous scan mode, Fig. 4(f), the spectrum of the received field broadens for both the peak and sidebands in comparison to the stationary case.

The Doppler broadening of the spectrum is random and dependent on the particular realization of the rough surface. This can be noted in Figs. 5(a) and 5(b), which show the received signal spectrum obtained for the vibrometer with scan velocity of 50 cm/s for ten independent realizations of the sand and gravel surfaces, respectively. The average spectrum in Fig. 5 is found by incoherently averaging intensity of the individual spectra. When it is possible for the vibrometer to make several independent measurements of the surface in a given location, the estimation of surface displacement and accuracy can be improved. This would occur, for instance, when the vibrometer makes multiple passes in varying directions over a given location so that the scans can be approximated as independent. For the ten independent realizations of the surface shown in Fig. 5, there are two possible approaches for estimating h_0 . We can either estimate h_0 for each independent realization and then calculate the average, or estimate h_0 from the single averaged spectrum. In the former approach, we calculate the percentage root-mean-square (rms) error, e , for surface displacement estimation using

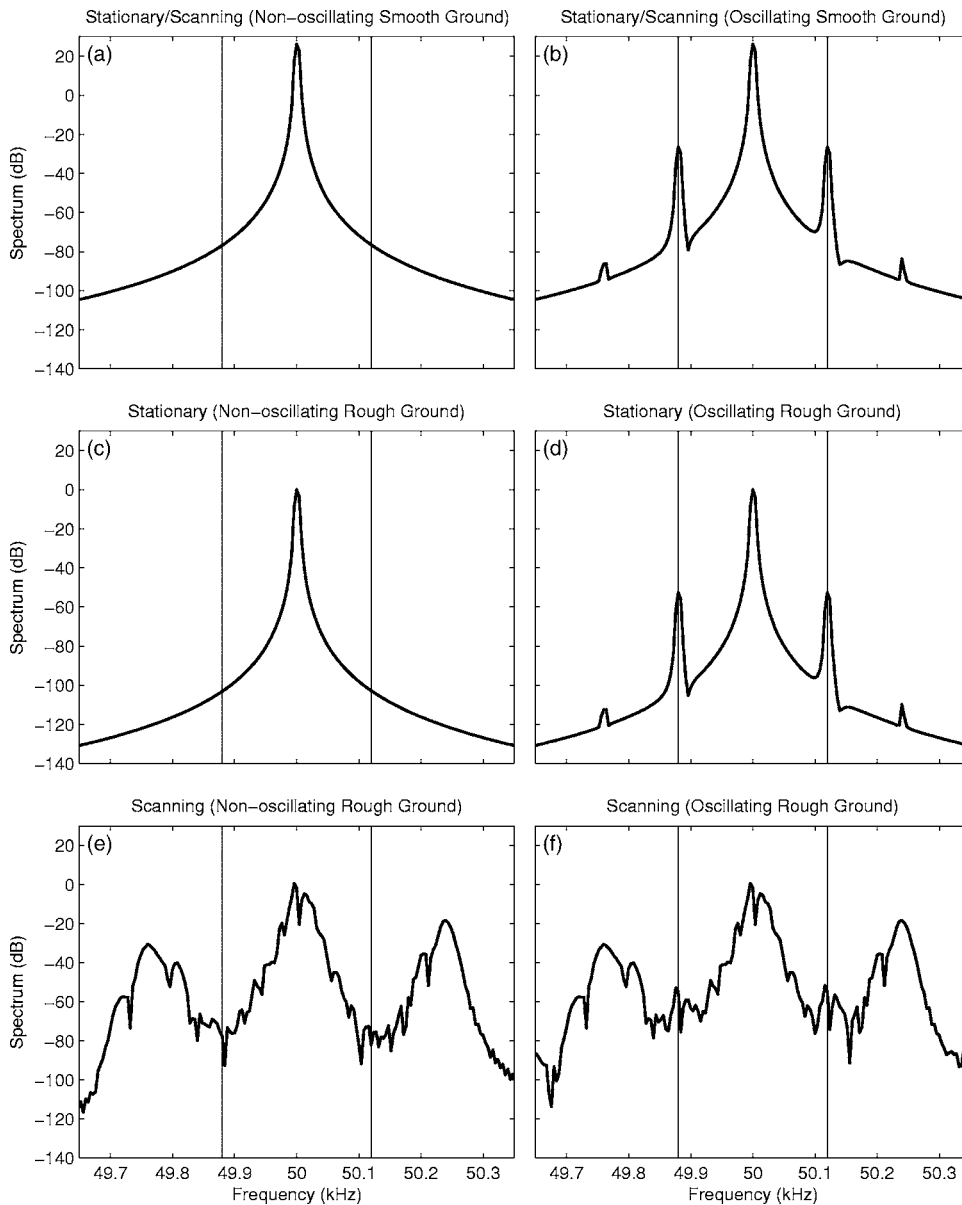


FIG. 4. Spectrum of ultrasound field at 50 kHz reflected and scattered at normal incidence off a (a) smooth and nonoscillating surface for the stationary vibrometer (same result for scanning system), (b) smooth and harmonically oscillating surface for stationary vibrometer (same result for scanning system), (c) nonoscillating rough gravel surface with stationary vibrometer, (d) oscillating rough gravel surface with stationary vibrometer, (e) nonoscillating rough gravel surface with scanning vibrometer, and (f) harmonically oscillating rough gravel surface with scanning vibrometer. In (a), (b), (e), and (f) the scanning vibrometer is moving at 50 cm/s. Unless otherwise specified, the sonar, measurement, and surface parameters are the same as in Fig. 3(d).

$$e = \frac{\sqrt{\langle (\hat{h}_0 - h_0)^2 \rangle}}{h_0} 100\% . \quad (38)$$

The results are summarized in Table I. The analysis indicates that surface displacement amplitude can be estimated with

higher accuracy and smaller standard deviation for sand surfaces than gravel with a vibrometer scan speed of 50 cm/s. Furthermore, averaging the results from multiple independent scans helps reduce the error in the displacement estimation, as expected.

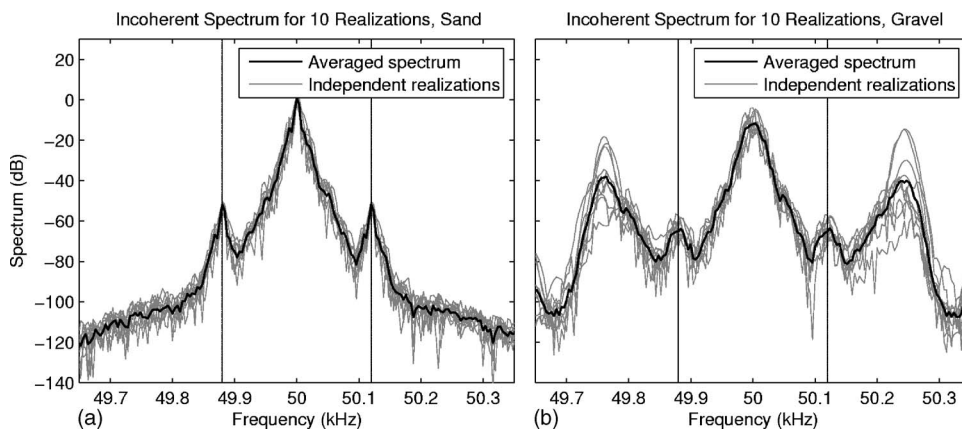


FIG. 5. Spectrum of received ultrasound field reflected and scattered off an oscillating (a) medium sand and (b) gravel surfaces. Results were for ten independent realizations of the sand and gravel surfaces, respectively. The average spectrum is obtained by incoherently averaging the intensity of the individual spectra. The ultrasound scan speed is 50 cm/s. Unless otherwise specified, the sonar, measurement, and surface parameters are the same as in Figs. 3(c) and 3(d), respectively.

TABLE I. Estimates of surface displacement amplitude from incoherent processing for a 50 kHz ultrasound vibrometer continuously scanning the surface at a speed of 50 cm/s. The estimates are obtained by either using data from a single scan, averaging h_0 estimates over ten independent scans at a given location, or estimating h_0 from the average spectrum for ten independent realizations. The quantities in parentheses are the accuracies for the estimation.

	Single realization	Averaged estimates from ten realizations	Averaged spectrum
Sand	2.46 (98%)	2.50 (99.8%, 0.7% rms error)	2.50 (99.8%)
Gravel	3.7 (52%)	2.55 (98%, 10% rms error)	2.68 (93%)

The time domain reflected signal from the harmonically oscillating sand and gravel surface is shown in Fig. 6 for the continuously scanning vibrometer at 50 cm/s speed. We observe time-dependent fluctuations in signal amplitude caused by interference of randomly scattered fields from the random rough surface, with severe fade-outs for the gravel surface at specific time instances. It should be noted that for the stationary vibrometer, scattering from the rough surface does not lead to time-dependent variations in the reflected signal amplitude. The statistical distribution for the amplitude and phase of the scattered ultrasound field is discussed in Ref. 19 and 26.

C. Effect of ultrasound frequency, measurement time, insonification area, angle of incidence, and scanning speed

Here we investigate the vibrometer system design and measurement parameters that can be adjusted to enhance the measurement of surface displacement for very rough surfaces, like that of gravel. Figure 7 compares the effect of lowering or raising the ultrasound source frequency from 50 kHz for the gravel surface. The spectral peak and sidebands of the received ultrasound signal are more pronounced at 20 kHz. There is less Doppler broadening of the signal spectrum because of reduced scattering from the rough surface with the longer ultrasound wavelength at 20 kHz, $k\sigma_\zeta = 3.7$, and the surface appears smoother. The spectrum worsens at 100 kHz when the ultrasound wavelength shortens leading to more significant scattering from the rough surface, $k\sigma_\zeta = 18.4$.

The effect of adjusting the measurement time or length of signal used in computing the signal spectrum is illustrated in Fig. 8(a) for the gravel surface. The measurement time change does not lead to significant changes in the signal spectrum. It should be noted that the measurement time T

along with the scan speed v_u determine the range resolution Δx of the vibrometer, $\Delta x = Tv_u$. For example, small antipersonnel mines require a smaller range resolution in comparison to larger antitank mines. Furthermore, inverse of the measurement time also determines the frequency resolution of the signal spectrum, $\Delta f = 1/T$. The frequency resolution should be set to clearly resolve the frequency sidebands due to ground oscillation and the ultrasound peak frequency. The frequency resolution and range resolution requirements then set a limit on the maximum scan speed such that $v_u \leq \Delta x \Delta f$.

Adjusting the distance of the ultrasound vibrometer system from the ground determines the area of ground insonified, and effects the spectrum of the received signal as shown in Fig. 8(b). Increasing the area of ground insonified improves the signal-to-noise ratio (SNR) of the sidebands slightly as more roughness elements are imaged, which statistically reduces the scattering noise level. Increasing the angle of incidence appears to have a more prominent effect on enhancing the signal spectrum. As illustrated in Fig. 8(c), the SNR for the sidebands improves when the grazing angle is increased from 0° to 60° incidence. The ultrasound wavelength projected onto the rough surface is larger at 60° incidence leading to reduced scattering from the rough surface since $k_z \sigma_\zeta = k \cos \theta \sigma_\zeta = 4.6$.

The most sensitive parameter for the scanning vibrometer is its scan velocity, v_u . We illustrate the effect of raising and lowering scan speeds on the received signal spectrum for sand and gravel in Figs. 9(a) and 9(b), respectively. The spectra shown were incoherently averaged over ten realizations of the rough surface types. When the scan speed is reduced from 1 m/s to 50 cm/s or 20 cm/s, the SNR for both the peak and sidebands are tremendously enhanced in sand and moderately in gravel. In the limit where the vibrometer becomes stationary, in comparison with Figs. 4(c) and

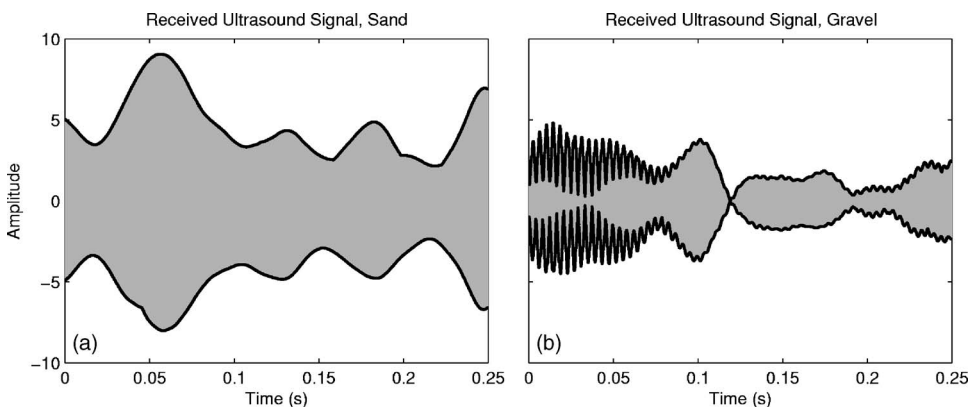


FIG. 6. Time domain wave form of ultrasound received field reflected and scattered off harmonically oscillating (a) sand and (b) gravel surface for the continuously scanning vibrometer. These were used to compute the spectra shown in Figs. 3(c) and 3(d) for the continuously scanning system.

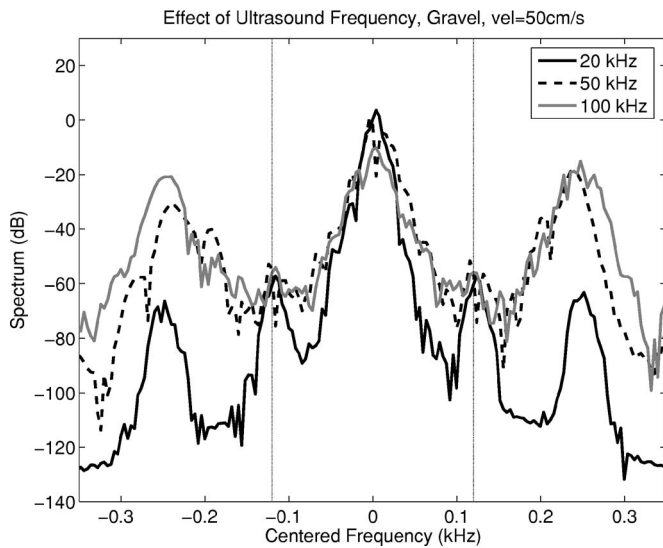


FIG. 7. Effect of adjusting the ultrasound source frequency on the spectrum of the received signal. The measurement setup is the same as in Fig. 3(d). The x axis should be scaled according to the ultrasound frequency for each of the cases.

4(d), the performance of the vibrometer is significantly improved. In Fig. 9(b) for gravel, we observe periodic local peaks in the spectrum in addition to the peak at the ultrasound frequency and sidebands at $f \pm n f_g$ due to ground oscillation. These additional periodic peaks are caused by Doppler shifts in the ultrasound frequency arising from motion of the vibrometer over the rough surface. As the surface height changes, it leads to frequency variations in the reflected ultrasound signal for the scanning vibrometer that is independent of ground oscillations, as can be seen by comparing

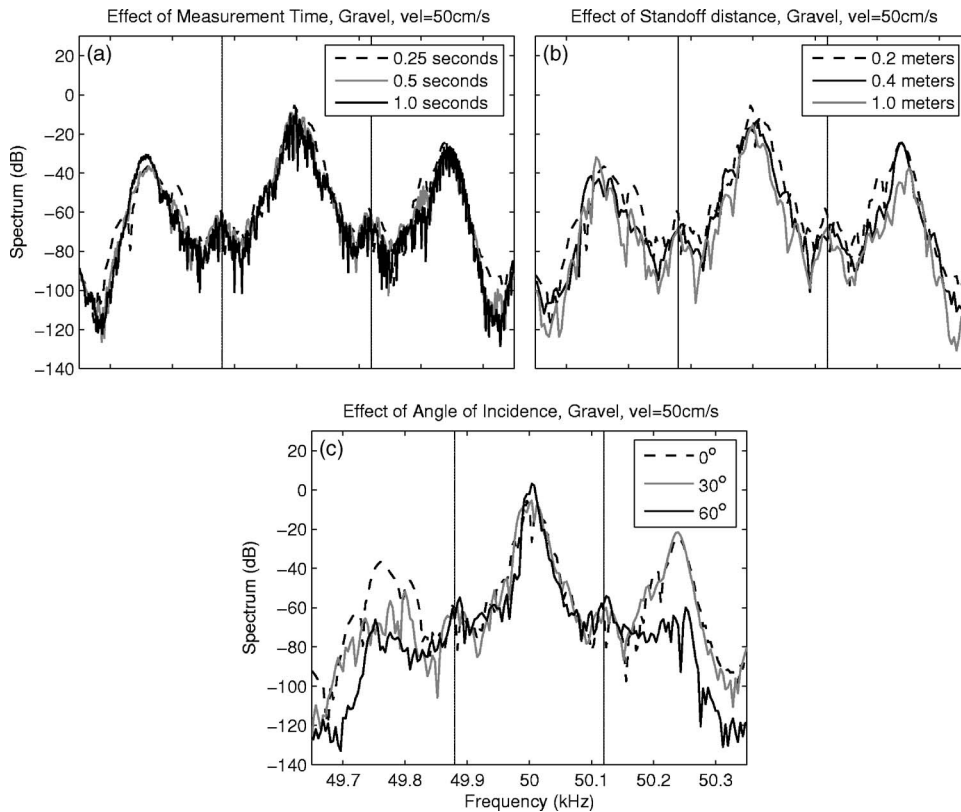


FIG. 8. Effect of adjusting the (a) measurement time T , (b) vibrometer stand-off distance z , and (c) angle of incidence θ , on the spectrum of the received signal. Unless otherwise specified, the measurement setup is the same as Fig. 3(d).

Figs. 4(e) and 4(f). Our analysis shows that their spacing in the frequency spectrum is directly proportional to the scan velocity and inversely proportional to the correlation length scale of the rough surface, v_u/ℓ_x . This factor determines the number of undulations on the rough surface traversed by the vibrometer per unit time. The amplitude of these periodic peaks depends on the surface gradient. For the sand surface, the roughness heights are not large enough to cause any significant Doppler shift of the ultrasound beam and so these additional peaks do not appear within the bandwidth illustrated in Fig. 9(a).

In an experimental scenario, when the periodic peaks due to rough surface scattering occur at the sidebands due to ground oscillation, one should alter the vibrometer scan speed or the frequency of ground oscillation so that the peaks due to rough surface scattering are moved out of the frequency sidebands of interest.

D. Limiting scan speed for acoustic landmine imaging

Here we investigate limiting scan speeds for an ultrasound vibrometer deployed as part of an acoustic landmine confirmation sensor over natural terrain. The ground surface oscillation amplitudes at the mine resonance frequency in areas containing mines are dependent on the type of mine, whether it is an antipersonnel mine or a larger antitank mine, burial depth of the mine, and the intensity with which the ground is excited at the low acoustic or seismic frequencies. For shallow buried mines, the ground is typically incident with acoustic field intensities that lead to surface velocity amplitudes of 40–500 $\mu\text{m/s}$ over areas enclosing mines at the mine resonance frequencies, and velocity amplitudes of

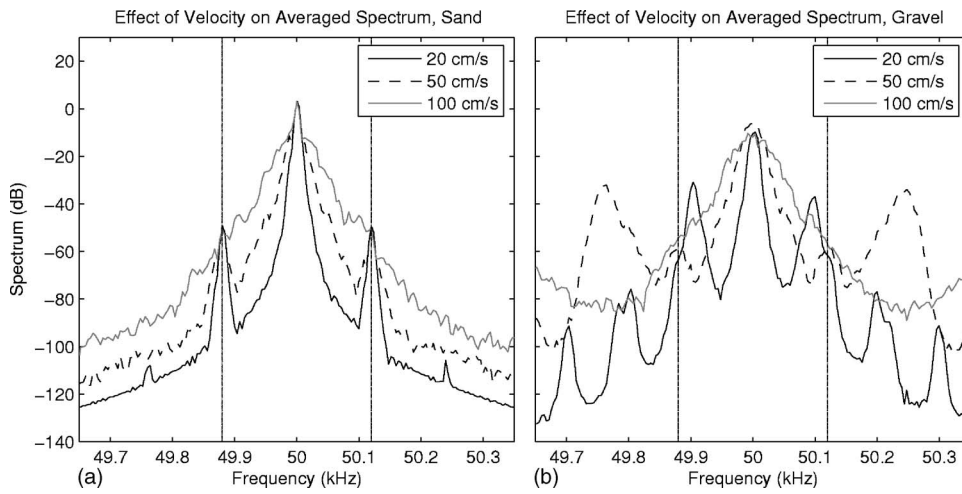


FIG. 9. Effect of adjusting the vibrometer scan velocity on the incoherently averaged spectrum of received signal from (a) sand and (b) gravel surfaces. All other parameters are the same as in Figs. 5(a) and 5(b).

roughly $20\text{--}50\ \mu\text{m/s}$ in areas devoid of mines.^{5,10} In order for the ultrasound system to clearly image a mine, it must distinguish surface velocity amplitudes in areas covering a mine from an area devoid of mines. The scattering noise floor level should not mask the Doppler shifted sideband levels caused by surface oscillation in the received signal spectrum. From all the spectra shown so far, we observe that the scattering noise floor level in the signal spectrum is a function of frequency. Here we illustrate results that are applicable to mine resonance frequencies of $f_g=140\ \text{Hz}$ and $f_g=400\ \text{Hz}$, which are the resonance frequencies typically observed and used for imaging mines of interest.^{5,10} For $f_g=140\ \text{Hz}$, the corresponding surface displacement amplitudes in areas that enclose a mine span from 0.05 to $0.5\ \mu\text{m}$, while at $f_g=400\ \text{Hz}$, the displacement amplitudes span from 0.02 to $0.16\ \mu\text{m}$.

In Figs. 10(a) and 10(b) we plot the scattering noise floor level measured by the received ultrasound transducer, as a function of scan speed for the sand and gravel surfaces, respectively, for a $50\ \text{kHz}$ ultrasound vibrometer at Doppler shift frequencies of $f_u \pm f_g$ for $f_g=140$ and $f_g=400\ \text{Hz}$. The

scattering noise floor levels were converted to equivalent displacement amplitudes using Eq. (27). In the sand environment, the curves were generated by first simulating the averaged spectrum for ten independent realizations of the rough surface for different ultrasound scan speeds from 20 to $160\ \text{cm/s}$. The corresponding noise floors at the required sideband frequencies were extracted and are shown as asterisks in the plot. We then fit a quadratic model to these points and the best fit curve is shown as a solid line. For the gravel environment, we first ignored the periodic Doppler shifted peaks due to significant rough surface scattering by interpolating the noise floor levels at frequencies outside of these periodic peaks. These noise floor levels are shown as asterisks with the corresponding quadratic curve fit. We did this because the frequency occurrence of the periodic peaks is a function of scan velocity and they do not occur continuously at a given sideband frequency of interest as scan velocity is varied. However, for the two resonance frequencies of interest, we indicate using circles the level of the periodic Doppler shifted peaks when they occur at the sidebands of

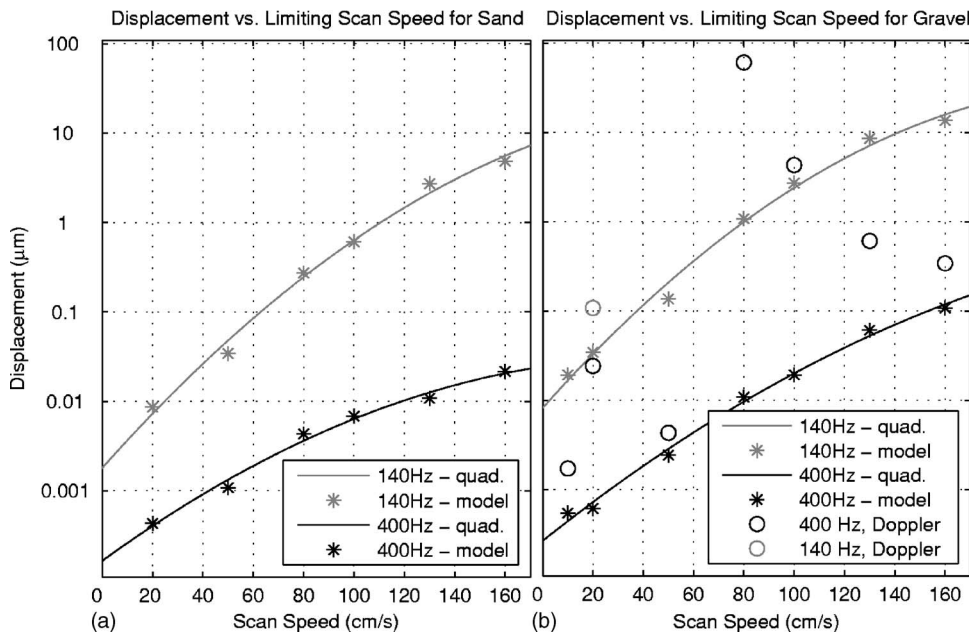


FIG. 10. Averaged spectrum of scattered noise level vs scan speed in (a) sand and (b) gravel for sidebands corresponding to ground resonance frequencies of 140 and $400\ \text{Hz}$ for a $50\ \text{kHz}$ ultrasound vibrometer. The scattered noise level is converted to equivalent displacement amplitude using Eq. (27).

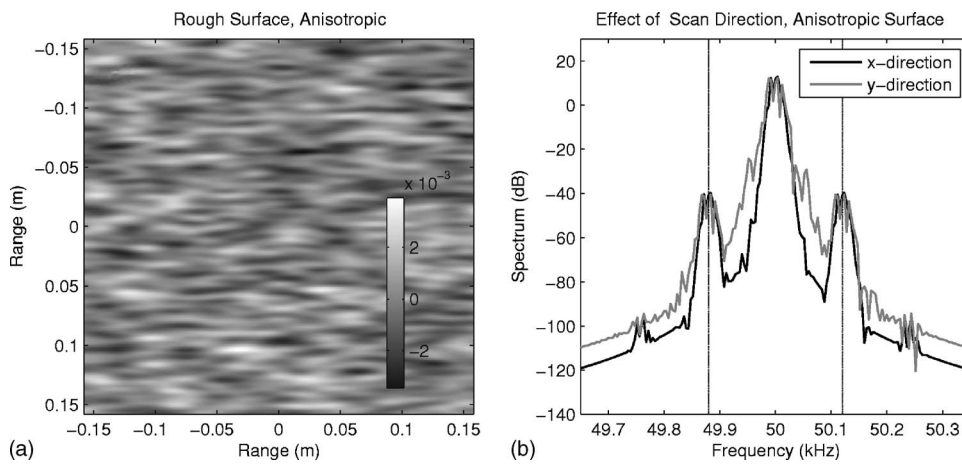


FIG. 11. (a) Anisotropic rough surface with five times longer correlation length in the x direction than in the y direction. (b) Similar to Fig. 3(d) but for the vibrometer continuously scanning in the x direction or y direction at 50 cm/s.

interest. These periodic Doppler shifted peaks are not present at the sidebands of interest for the sand surfaces.

We observe from Figs. 10(a) and 10(b) that the noise floor increases with scan speed as expected in both the sand and gravel environments. For the sand surface, the increase is monotonic at the mine resonance frequencies of interest. The limiting scan speed in sand is around 50 cm/s for the 140 Hz resonance frequency and 150 cm/s for the 400 Hz resonance. At scan speeds higher than this, the scattering noise floor is expected to mask the sidebands due to ground oscillation in the received signal spectrum. In the gravel environment, the increase is nonmonotonic due to the appearance of periodic peaks in the signal spectrum arising from Doppler shifts of the ultrasound frequency from rough surface scattering. The scan speeds are then limited to 20 cm/s at 140 Hz resonance and 60 cm/s for 400 Hz resonance. The limiting scan speeds may be further improved for the ultrasound system by lowering the ultrasound frequency. In addition to speckle noise, the vibrometer scan speed may also be limited by the range and frequency resolution requirement of the system as discussed in Sec. V C.

We should point out that the noise floor analysis in Ref. 10, Fig. 10, for the laser vibrometer was done experimentally with the laser scanning over a sheet of *paper*. It therefore cannot be compared to the noise floor analysis done here for the ultrasound vibrometer over natural terrain. The limiting scan speeds for the ultrasound vibrometer over the sand and gravel surfaces derived here should be much higher than that for a laser vibrometer over these same surfaces since the laser wavelength is a thousand times smaller than the ultrasound wavelength.

E. Anisotropic rough surfaces

For an anisotropic rough surface, such as sediment ripples formed by wind blowing in a specific direction over the surface, the performance of the vibrometer is dependent on the scan direction of the system. Figure 11(a) shows an anisotropic rough surface with a correlation length of 10 mm in the x direction and a smaller correlation length of 2 mm in the y direction. The roughness height standard deviation for this rough surface is 1 mm. We observe better performance for the ultrasound system when scanning in the direction with the larger correlation length. This is expected since the

rough surface gradients are much smaller in the x direction and therefore the spectral broadening due to Doppler, which is dependent on surface slope, is less significant.

VI. CONCLUSION

An analytic model for the ultrasound field reflected off a vibrating rough surface has been developed from Green's theorem for a scanning ultrasound vibrometer system. The model is bistatic and incorporates the beam patterns of both the transmitting and receiving ultrasound transducers, as well as the statistical properties of the rough surface. The ultrasound data from this model is then analyzed using two different processing schemes, coherent interferometry and incoherent Doppler shift spectra, to yield estimates of surface displacement amplitude for a sinusoidally oscillating rough surface. The model is applied to determine sonar design parameters and measurement geometry that can enhance performance of the scanning ultrasound vibrometer measuring ground displacements from acoustic/seismic excitation in acoustic landmine detection. Simulations with the model indicate that performance of the vibrometer is highly dependent on scan velocity, and vibrometer frequency, as well as statistical properties of the rough surface. The model has been applied to determine limiting scan speeds for an ultrasound vibrometer used for acoustic landmine imaging in natural terrain environments.

APPENDIX: STATISTICAL DESCRIPTION OF ROUGH SURFACE

Here we provide a statistical description of the randomly rough surface in terms of its probability distribution, correlation function, and spectrum of roughness heights following the approach of Refs. 21 and 17. We assume that the height $\zeta(\mathbf{r}_t)$ of the rough surface boundary at horizontal location \mathbf{r}_t follows a Gaussian random process in space with mean $\langle \zeta \rangle = 0$, and variance $\sigma_\zeta^2 = \langle \zeta^2 \rangle - \langle \zeta \rangle^2$. The probability density function of the rough surface height is

$$p_\zeta(\zeta) = \frac{1}{\sqrt{2\pi}\sigma_\zeta} \exp\left(-\frac{(\zeta - \langle \zeta \rangle)^2}{2\sigma_\zeta^2}\right). \quad (\text{A1})$$

The joint probability density function of the roughness height at horizontal locations \mathbf{r}_t and $\mathbf{r}_{t'}$ can be expressed as

$$p(\zeta(\mathbf{r}_t), \zeta(\mathbf{r}_{t'})) = \frac{1}{2\pi\sigma_{\zeta(\mathbf{r}_t)}\sigma_{\zeta(\mathbf{r}_{t'})}(1-\varrho^2)^{1/2}} \exp\left(-\frac{[(\zeta^2(\mathbf{r}_t)\sigma_{\zeta(\mathbf{r}_{t'})}^2 - 2\zeta(\mathbf{r}_t)\zeta(\mathbf{r}_{t'})\varrho\sigma_{\zeta(\mathbf{r}_t)}\sigma_{\zeta(\mathbf{r}_{t'})} + \zeta^2(\mathbf{r}_{t'})\sigma_{\zeta(\mathbf{r}_t)}^2)]}{2\sigma_{\zeta(\mathbf{r}_t)}^2\sigma_{\zeta(\mathbf{r}_{t'})}^2(1-\varrho^2)}\right), \quad (\text{A2})$$

where ϱ is the correlation coefficient defined as

$$\varrho = \frac{\langle \zeta(\mathbf{r}_t)\zeta(\mathbf{r}_{t'}) \rangle - \langle \zeta(\mathbf{r}_t) \rangle \langle \zeta(\mathbf{r}_{t'}) \rangle}{\sqrt{(\langle \zeta(\mathbf{r}_t) \rangle^2 - \langle \zeta(\mathbf{r}_t) \rangle^2)(\langle \zeta(\mathbf{r}_{t'}) \rangle^2 - \langle \zeta(\mathbf{r}_{t'}) \rangle^2)}}. \quad (\text{A3})$$

We assume that the roughness heights follow a locally stationary random process within the area imaged by the system for each measurement time interval. Its correlation function can then be expressed as a Fourier transform of its wave number spectrum $\mathcal{G}(\boldsymbol{\kappa})$ following²²

$$\begin{aligned} \langle \zeta(\mathbf{r}_t)\zeta(\mathbf{r}_{t'}) \rangle &= C_{\zeta\zeta}(\mathbf{r}_t - \mathbf{r}_{t'}) \\ &= \frac{1}{(2\pi)^2} \int_0^{2\pi} \int_0^\infty \mathcal{G}(\boldsymbol{\kappa}) e^{i\boldsymbol{\kappa} \cdot (\mathbf{r}_t - \mathbf{r}_{t'})} \kappa d\kappa d\Theta, \end{aligned} \quad (\text{A4})$$

where $\boldsymbol{\kappa} = (\kappa_x, \kappa_y) = (\kappa \cos \Theta, \kappa \sin \Theta)$ is the wave number vector with magnitude κ and azimuthal direction Θ . The roughness height standard deviation σ_ζ is then given by

$$\sigma_\zeta^2 = C_{\zeta\zeta}(0) = \frac{1}{(2\pi)^2} \int_0^{2\pi} \int_0^\infty \mathcal{G}(\boldsymbol{\kappa}) \kappa d\kappa d\Theta, \quad (\text{A5})$$

when $\langle \zeta \rangle = 0$, as with the present case.

The coherence length scale for the rough surface in the x and y directions and its coherence area A_c can be expressed in terms of its correlation function as given by Eqs. (7)–(10) of Ref. 21 or Eqs. (A7) and (A8) of Ref. 23. For instance, the correlation lengths ℓ_x and ℓ_y of the random process in the x and y directions, respectively, are

$$\ell_x = \ell_c(\Theta = 0) + \ell_c(\Theta = \pi), \quad (\text{A6})$$

and

$$\ell_y = \ell_c(\Theta = \pi/2) + \ell_c(\Theta = 3\pi/2), \quad (\text{A7})$$

where $\ell_c(\Theta)$ is the correlation length of the random process in any azimuthal direction Θ given by²⁴

$$\begin{aligned} \ell_c(\Theta) &= \frac{2(1/2\pi)^2 \int_0^\infty |G(\kappa, \Theta)|^2 \kappa d\kappa}{|(1/2\pi)^2 \int_0^{2\pi} \int_0^\infty G(\kappa, \Theta) \kappa d\kappa d\Theta|^2} \\ &= \frac{2(1/2\pi)^2 \int_0^\infty |G(\kappa, \Theta)|^2 \kappa d\kappa}{|C_{\zeta\zeta}(0)|^2}. \end{aligned} \quad (\text{A8})$$

The coherence length ℓ_c defines a shape function for the random process as its wave number spans the 2π azimuthal radians of Θ . The coherence area of the process is given by

$$\begin{aligned} A_c &= \frac{(1/2\pi)^2 \int_0^{2\pi} \int_0^\infty |G(\kappa, \Theta)|^2 \kappa d\kappa d\Theta}{\left| (1/2\pi)^2 \int_0^{2\pi} \int_0^\infty G(\kappa, \Theta) \kappa d\kappa d\Theta \right|^2} \\ &= \frac{(1/2\pi)^2 \int_0^{2\pi} \int_0^\infty |G(\kappa, \Theta)|^2 \kappa d\kappa d\Theta}{|C_{\zeta\zeta}(0)|^2}. \end{aligned} \quad (\text{A9})$$

Isotropic rough surface. For an isotropic rough surface, Eq. (A4) for the correlation function reduces to

$$\langle \zeta(\mathbf{r}_t)\zeta(\mathbf{r}_{t'}) \rangle = \frac{1}{2\pi} \int_0^\infty \mathcal{G}(\boldsymbol{\kappa}) J_0(\kappa|\mathbf{r}_t - \mathbf{r}_{t'}|) \kappa d\kappa, \quad (\text{A10})$$

since its wave number spectrum $\mathcal{G}(\boldsymbol{\kappa})$ is independent of the azimuth angle Θ . The coherence radius $\ell_c(\Theta)$ is a constant independent of azimuthal direction Θ so that the corresponding coherence lengths in the x and y directions and coherence area are simply given by $\ell_x = \ell_y = 2\ell_c$ and $A_c = \pi\ell_c^2$.

¹M. S. Young and Y. C. Li, "A high precision ultrasonic system for vibration measurements," *Rev. Sci. Instrum.* **63**, 5435–5441 (1992).

²Y. Yamakoshi, J. Sato, and T. Sato, "Ultrasonic imaging of internal vibration of soft tissue under forced vibration," *IEEE Trans. Ultrason. Ferroelectr. Freq. Control* **37**, 45–53 (1990).

³J. M. Sabatier and N. Xiang, "An investigation of acoustic-to-seismic coupling to detect buried antitank mines," *IEEE Trans. Geosci. Remote Sens.* **39**, 1146–1154 (2001).

⁴W. R. Scott, J. S. Martin, and G. D. Larson, "Experimental model for a seismic landmine detection system," *IEEE Trans. Geosci. Remote Sens.* **39**, 1155–1164 (2001).

⁵N. Xiang and J. M. Sabatier, "An experimental study on antipersonnel landmine detection using acoustic-to-seismic coupling," *J. Acoust. Soc. Am.* **113**, 1333–1341 (2003).

⁶J. S. Martin *et al.*, "Ultrasonic displacement sensor for the seismic detection of buried land mines," *Proc. SPIE* **4742**, 606–616 (2002).

⁷A. G. Petculescu and J. Sabatier, "Air-coupled ultrasonic sensing of grass-covered vibrating surfaces; qualitative comparisons with laser Doppler vibrometry," *J. Acoust. Soc. Am.* **115**, 1557–1564 (2004).

⁸D. Fenneman, B. Libbey, and J. Martin, "Evaluation of an ultrasonic displacement sensor," *J. Acoust. Soc. Am.* **115**, 2416 (2004).

⁹W. P. Arnott and J. M. Sabatier, "Laser-Doppler vibrometer measurements of acoustic to seismic coupling," *Appl. Acoust.* **30**, 279–291 (1990).

¹⁰V. Arunchuk, A. K. Lal, C. F. Hess, and J. M. Sabatier, "Multi-beam laser Doppler vibrometer for landmine detection," *J. Op. Eng.* **45**, 104302 (2006).

¹¹L. E. Drain, *The Laser Doppler Technique* (Wiley, Chichester, 1980).

¹²A. Kannath and R. J. Dewhurst, "Real-time measurement of acoustic field displacements using ultrasonic interferometry," *Meas. Sci. Technol.* **15**, N59–N66 (2004).

¹³W. R. Scott, J. C. Schroeder, and J. S. Martin, "An acousto-electromagnetic sensor for locating land mines," *Proc. SPIE* **3392**, 176–186 (1998).

¹⁴S. Rothberg and B. Halkon, "Laser vibrometry meets laser speckle," *Proc. SPIE* **5503**, 280–291 (2004).

¹⁵S. Rothberg, J. R. Baker, and N. A. Hallowell, "Laser vibrometry: pseudo-vibrations," *J. Sound Vib.* **135**, 516–522 (1989).

- ¹⁶P. M. Morse and K. U. Ingard, *Theoretical Acoustics* (Princeton University Press, Princeton, NJ, 1986).
- ¹⁷J. A. Ogilvy, *Theory of Wave Scattering from Random Rough Surfaces* (IOP, Bristol, 1991).
- ¹⁸M. Abramowitz and I. A. Stegun, *Handbook of Mathematical Functions* (Dover, New York, 1972).
- ¹⁹J. W. Goodman, *Statistical Optics* (Wiley, New York, 1985).
- ²⁰N. C. Makris, "The effect of saturated transmission scintillation on ocean acoustic intensity measurements," *J. Acoust. Soc. Am.* **100**, 769–783 (1996).
- ²¹T. Chen, P. Ratilal, and N. C. Makris, "Mean and variance of the forward field propagated through three-dimensional random internal waves in a continental-shelf waveguide," *J. Acoust. Soc. Am.* **118**, 3560–3574 (2005).
- ²²L. Mandel and E. Wolf, *Optical Coherence and Quantum Optics* (Cambridge University Press, New York, 1995).
- ²³P. Ratilal and N. C. Makris, "Mean and covariance of the forward field propagated through a stratified ocean waveguide with three-dimensional random inhomogeneities," *J. Acoust. Soc. Am.* **118**, 3532–3559 (2005).
- ²⁴B. R. Frieden, *Probability, Statistical Optics, and Data Testing* (Springer, New York, 1936).
- ²⁵P. Beckmann and A. Spizzichino, *The Scattering of Electromagnetic Waves from Rough Surfaces* (Pergamon/Macmillan, New York, 1963).
- ²⁶J. C. Dainty (editor), "Laser Speckle and Related Phenomena," *Topics in Applied Physics*, Vol. 9 (Springer-Verlag, Berlin 1975).

Acoustoelastic analysis of reflected waves in nearly incompressible, hyper-elastic materials: Forward and inverse problems

Hirohito Kobayashi^{a)} and Ray Vanderby

*Department of Orthopedics and Rehabilitation, Department of Biomedical Engineering,
University of Wisconsin—Madison, Madison, Wisconsin 53792*

(Received 28 March 2006; revised 13 November 2006; accepted 23 November 2006)

Many materials (e.g., rubber or biologic tissues) are “nearly” incompressible and often assumed to be incompressible in their constitutive equations. This assumption hinders realistic analyses of wave motion including acoustoelasticity. In this study, this constraint is relaxed and the reflected waves from nearly incompressible, hyper-elastic materials are examined. Specifically, reflection coefficients are considered from the interface of water and uni-axially prestretched rubber. Both forward and inverse problems are experimentally and analytically studied with the incident wave perpendicular to the interface. In the forward problem, the wave reflection coefficient at the interface is evaluated with strain energy functions for nearly incompressible materials in order to compute applied strain. For the general inverse problem, mathematical relations are derived that identify both uni-axial strains and normalized material constants from reflected wave data. The validity of this method of analysis is demonstrated via an experiment with stretched rubber. Results demonstrate that applied strains and normalized material coefficients can be simultaneously determined from the reflected wave data alone if they are collected at several different (but unknown) levels of strain. This study therefore indicates that acoustoelasticity, with an appropriate constitutive formulation, can determine strain and material properties in hyper-elastic, nearly incompressible materials.

© 2007 Acoustical Society of America. [DOI: 10.1121/1.2427112]

PACS number(s): 43.35.Zc, 43.20.Bi, 43.20.Fn [JMC]

Pages: 879–887

I. INTRODUCTION

Acoustoelasticity is a theory that describes wave propagation in statically deformed media. Because the acoustic characteristics of a material are strain dependent, acoustoelastic methods have the potential to determine strain distributions in complex structures under complex loadings. Modern acoustoelastic theory was initiated by Hughes and Kelly¹ and further defined by Toupin and Bernstein,² Truesdell,³ and Tokuoka and Iwashimizu.⁴ Pao, Sache, and Fukuoka⁵ studied and summarized many applications for acoustoelastic theory. To date, most applications calculate static prestrain distributions in typical engineering materials (e.g., steel, aluminum, etc.) based upon velocity changes in various acoustic waves comparing loaded to unloaded waves. Acoustoelastic analyses have also been performed on incompressible materials by Ogden,⁶ Erigen and Suhubi,⁷ and Fu.⁸ If, however, an elastic material is modeled as incompressible, then the theoretical propagation velocity of its dilatational wave becomes infinite. That is, an incompressible material cannot hold a dilatational wave, and acoustoelastic analysis is limited to the two shear waves. Although rubber is usually assumed incompressible, it is slightly compressible with a Poisson's ratio around 0.499 and does sustain dilatational waves.⁹ Similarly, biological tissues are often modeled as incompressible, but they too sustain dilatational waves.

Treating rubber and other “nearly incompressible” materials as “incompressible” is inconsistent with any analysis of dilatational wave propagation. Hence, Kobayashi and Vanderby¹⁰ relaxed the incompressibility constraint and studied the application of acoustoelasticity to hyper-elastic, nearly incompressible material. They showed a significant acoustoelastic effect in stretched rubber and formulated a new strain energy function that models this effect with fidelity.

In the current study, we evaluate the ability of strain energy functions to model reflected acoustic waves in nearly incompressible, prestressed materials. To our knowledge, no study has addressed this problem. We formulate both forward and inverse acoustoelastic problems relating reflection waves from the interface of a liquid and rubber, which is under a statically applied, uni-axial prestrain orthogonal to the direction of wave propagation. In the forward problem, reflection coefficients formulated with different strain energy functions use acoustic data to estimate strain. Results are compared to experimentally measured strains. Later, a general inverse problem is formulated and solved to compute both strains and normalized material properties only from reflected wave data that are measured at several levels of unknown strains. In the process, the following two mathematical equations are derived:

- (1) an equation relating an experimentally measured reflection coefficient to an unknown applied strain and an unknown normalized material coefficient for the target medium, and

^{a)}Electronic mail: koba@surgey.wisc.edu

- (2) an equation relating measured wave travel time (through a medium and reflected from the far surface) to a measured reflection coefficient and to the unknown applied strain.

Using these two equations repeatedly, each time with reflected wave data from a different unknown level of strain, provides sufficient information to compute normalized material coefficients and to quantify the levels of strain that were applied during the experiment.

II. NOTATIONS AND BASIC EQUATIONS

The theory of acoustoelasticity superposes small dynamic deformations of an ultrasonic wave onto a static, finite deformation. For convenience, three configurations are introduced:

- (1) The stress-free or *reference configuration* is defined with vector X_A to denote a material point in the body.
- (2) The initial, finite, static deformation is defined as the *deformed configuration* with position vector x_i .
- (3) The small dynamic wave deformation is defined as the *current configuration* with position vector x_i^* .

All Latin indices range from 1 to 3 and a repeated summation convention is assumed unless stated otherwise.

As defined in previous acoustoelastic studies,^{2,5} the equation of motion referred to as the *deformed configuration* is

$$\frac{\partial}{\partial x_j} \left[\bar{C}_{ijks} u_{k,s} + t_{js} \frac{\partial u_i}{\partial x_s} \right] = \rho \ddot{u}_i. \quad (1)$$

In above equation, \bar{C}_{ijks} and t_{js} respectively represent the fourth order stiffness tensor and Cauchy stress tensor caused by a finite static deformation. For a general compressible, hyper-elastic material, \bar{C}_{ijks} and t_{js} are related to the strain energy function $W(E_{AB})$, the deformation gradient tensor F_{jA} , and the finite Green strain tensor E_{AB} by

$$\bar{C}_{ijks} = \frac{1}{\det F_{jA}} F_{iA} F_{jB} F_{kC} F_{sD} \frac{\partial W}{\partial E_{AB}} \frac{\partial W}{\partial E_{CD}} \quad (2)$$

and

$$t_{js} = \frac{1}{\det F_{jA}} F_{jA} F_{sB} \frac{\partial W(E_{AB})}{\partial E_{AB}}, \quad (3)$$

where $F_{jA} = \partial x_j / \partial X_A$ and $E_{AB} = \frac{1}{2} (F_{iA} F_{iB} - \delta_{AB})$.

When prestress is zero, tensor \bar{C}_{ijks} becomes the stiffness tensor c_{ijks} for generalized Hooke's law, and Eq. (1) reduces to the wave equation. Due to symmetry of the strain and stress tensors, the tensor \bar{C}_{ijks} is symmetric as the Hookean stiffness tensor c_{ijks} , i.e.,

$$\bar{C}_{ijks} = \bar{C}_{ksij} = \bar{C}_{ijsk} = \bar{C}_{jiks}. \quad (4)$$

Finally, Cauchy stress in the current configuration can be written as

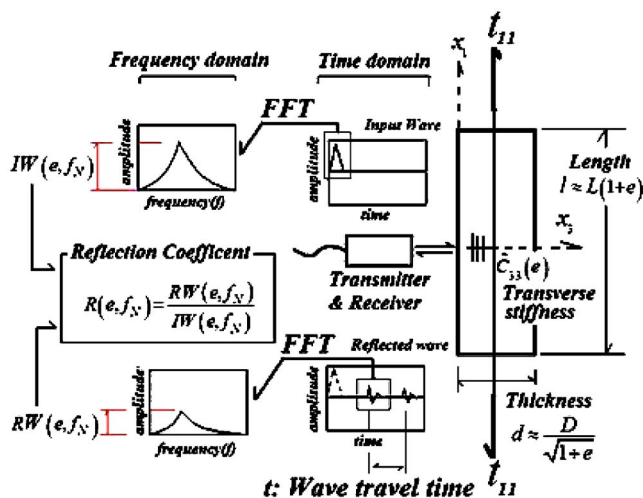


FIG. 1. (Color online) A hyper-elastic nearly incompressible rubber plate with original length L and thickness D is stretched in the x_1 direction. A dilatational wave in the transverse direction is excited by the ultrasonic transducer. Wave travel time (including both the left-to-right propagation and the right-to-left reflection) in the transverse direction x_3 can be measured by the peak distance between first reflected echo signal from near surface and the second echo signal from the far surface. The reflection coefficient of the experiment $R(e, f_N)$ is evaluated as the magnitude ratio of reflection wave over input wave at the nominal frequency f_N of the ultrasound transducer used. FFT represents fast Fourier transformation to convert the time domain wave signal into the frequency domain signal.

$$t_{ij}^* = \bar{C}_{ijks} u_{k,s} + (1 - u_{m,m}) t_{ij} + u_{i,k} t_{kj} + u_{j,s} t_{is}. \quad (5)$$

Due to symmetry, tensor \bar{C}_{ijks} is replaced hereafter with a 6 by 6 matrix \bar{C}_{pq} for convenience with the contracting subscript notations $1 \rightarrow 11, 2 \rightarrow 22, 3 \rightarrow 33, 4 \rightarrow 23, 5 \rightarrow 13, 6 \rightarrow 12$ to relate \bar{C}_{ijks} to \bar{C}_{pq} ($i, j, k, l = 1, 2, 3$ and $p, q = 1, 2, \dots, 6$). Pao, Sache, and Fukuoka⁵ provide a detailed derivation of the above equations.

III. FORMULATION OF THE FORWARD PROBLEM

In this section, we formulate the equations and analytically solve the forward wave reflection problem at the interface between fluid and the lateral surface of a prestretched, hyper-elastic, nearly incompressible rubber plate. The schematic relation between a uni-axially stretched rubber plate and an ultrasound transducer is presented in Fig. 1. The flow for evaluating the wave reflection coefficient from the measured wave signals is also presented.

For this problem, three equations of motion in three directions can be derived:

The acoustoelastic equation [Eq. (1)] for this problem is given in the x_1 direction as

$$\begin{aligned} (\bar{C}_{11} + t_{11}) \frac{\partial^2 u_1}{\partial x_1^2} + \bar{C}_{66} \frac{\partial^2 u_1}{\partial x_2^2} + \bar{C}_{55} \frac{\partial^2 u_1}{\partial x_3^2} + (\bar{C}_{12} + \bar{C}_{66}) \frac{\partial^2 u_2}{\partial x_1 \partial x_2} \\ + (\bar{C}_{13} + \bar{C}_{55}) \frac{\partial^2 u_3}{\partial x_1 \partial x_3} = \rho \frac{d^2 u_1}{dt^2}, \end{aligned} \quad (6a)$$

in the x_2 direction as

$$\begin{aligned}
& (\tilde{C}_{12} + \tilde{C}_{66}) \frac{\partial^2 u_1}{\partial x_1 \partial x_2} + (\tilde{C}_{66} + t_{11}) \frac{\partial^2 u_2}{\partial x_1^2} + \tilde{C}_{22} \frac{\partial^2 u_2}{\partial x_2^2} + \tilde{C}_{44} \frac{\partial^2 u_2}{\partial x_3^2} \\
& + (\tilde{C}_{23} + \tilde{C}_{44}) \frac{\partial^2 u_3}{\partial x_2 \partial x_3} = \rho \frac{d^2 u_2}{dt^2}, \quad (6b)
\end{aligned}$$

and in x_3 direction as

$$\begin{aligned}
& (\tilde{C}_{13} + \tilde{C}_{55}) \frac{\partial^2 u_1}{\partial x_1 \partial x_3} + (\tilde{C}_{23} + \tilde{C}_{44}) \frac{\partial^2 u_2}{\partial x_2 \partial x_3} + (\tilde{C}_{55} + t_{11}) \frac{\partial^2 u_3}{\partial x_1^2} \\
& + \tilde{C}_{44} \frac{\partial^2 u_3}{\partial x_2^2} + \tilde{C}_{33} \frac{\partial^2 u_3}{\partial x_3^2} = \rho \frac{d^2 u_3}{dt^2}. \quad (6c)
\end{aligned}$$

In above equations, \tilde{C}_{pq} and t_{11} represent the pq entries of the strain-dependent stiffness matrix and Cauchy stress in the x direction evaluated by Eq. (2) and (3), respectively.

The following eight sets of boundary conditions can be set up at both near and far interfaces:

(a) continuity of displacement at the surface $x_3=0, d$:

$$u_3 = u_3^f, \quad (7a)$$

(b) continuity of stresses at the surface $x_3=0, d$:

$$\tilde{C}_{55} \left(\frac{\partial u_3}{\partial x_1} + \frac{\partial u_1}{\partial x_3} \right) + t_{11} \frac{\partial u_3}{\partial x_1} = 0, \quad (7b)$$

$$\tilde{C}_{44} \left(\frac{\partial u_3}{\partial x_2} + \frac{\partial u_1}{\partial x_3} \right) = 0, \quad (7c)$$

$$\tilde{C}_{31} \frac{\partial u_1}{\partial x_1} + \tilde{C}_{32} \frac{\partial u_2}{\partial x_2} + \tilde{C}_{33} \frac{\partial u_3}{\partial x_3} = \lambda^F \left(\frac{\partial u_1^F}{\partial x_1} + \frac{\partial u_2^F}{\partial x_2} + \frac{\partial u_3^F}{\partial x_3} \right). \quad (7d)$$

In above relations, u_i^F ($i=1-3$) and λ^F represent displacements in the fluid and Lamé's constant of the fluid. Since we are only interested in wave propagation in the x_3 direction, the displacement fields can be assumed to be

$$\begin{Bmatrix} u_1 \\ u_2 \\ u_3 \end{Bmatrix} = \begin{Bmatrix} U_1 \\ U_2 \\ U_3 \end{Bmatrix} \exp \{i(Kx_3 \cdot x_3 - \omega t)\}. \quad (8)$$

By substituting these assumed displacements into Eqs. (6a)–(6c), the following eigenvalue equations are derived:

$$\begin{bmatrix} -\tilde{C}_{55}Kx_3^2 + \rho\omega^2 & 0 & 0 \\ 0 & -\tilde{C}_{44}Kx_3^2 + \rho\omega^2 & 0 \\ 0 & 0 & -\tilde{C}_{33}Kx_3^2 + \rho\omega^2 \end{bmatrix} \times \begin{Bmatrix} U_1 \\ U_2 \\ U_3 \end{Bmatrix} = 0. \quad (9)$$

The wave numbers in three distinctive directions are derived as eigenvalues as follows:

The dilatational wave with displacement in the x_3 direction is

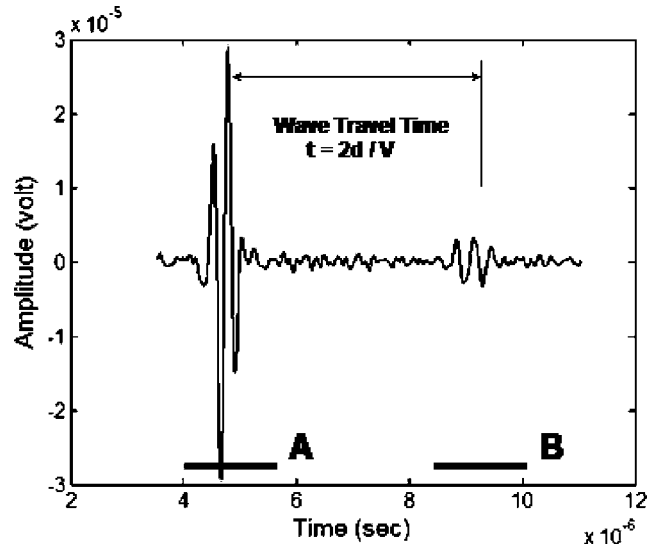


FIG. 2. A typical reflected wave signal from the interfaces of stretched rubber. Wave group A: Reflected wave from the near surface. Wave group B: Reflected wave from the far surface. The distance between two wave group peaks represents the time for propagation through and reflection back of the dilatational wave.

$$Kx_{3_D} = \omega \sqrt{\frac{\rho}{\tilde{C}_{33}}}, \quad (10a)$$

the shear wave with displacement in the x_3-x_2 direction is

$$Kx_{3_S1} = \omega \sqrt{\frac{\rho}{\tilde{C}_{44}}}, \quad (10b)$$

and the shear wave with displacement in the x_3-x_1 direction is

$$Kx_{3_S2} = \omega \sqrt{\frac{\rho}{\tilde{C}_{55}}}. \quad (10c)$$

Since wave propagation in water is purely dilatational with a displacement field (in this problem) only in the x_3 direction, only the dilatational wave can be excited in the solid. By introducing a relationship between wave velocity V , wave number Kx_3 , and wave frequency ω into above equations, that is,

$$V = \frac{\omega}{Kx_3}, \quad (11)$$

the wave velocity of the dilatational wave in the x_3 direction can be derived as

$$V_D = \sqrt{\frac{\tilde{C}_{33}}{\rho}}. \quad (12)$$

As presented in Fig. 2, the typical reflected wave signal has two distinct wave groups. Wave groups A and B represent the reflected echo signals from the near and far surfaces, respectively. The wave reflection problem at the surface of rubber can be solved by assuming the rubber is a semi-infinite medium, if only the first reflected wave group A is used in the analysis. Therefore, hereafter, the problem setting is now simplified as the wave reflection problem at the in-

terface of water and prestretched semi-infinite rubber only in the transverse direction. For this problem, displacement fields in both rubber and surrounding fluid are given by

$$u_3(x_3, t) = U_3 \exp [i(Kx_{3_D} \cdot x_3 - \omega t)] \quad (13a)$$

and

$$u_3^F(x_3, t) = \exp [i(K^F \cdot x_3 - \omega t)] - R \exp [i(-K^F \cdot x_3 - \omega t)]. \quad (13b)$$

In the above displacement fields, the magnitude of wave displacement in stretched rubber and the wave reflection coefficient at the surface are represented by U_3 and R , respectively. K^F designates the wave number in the surrounding fluid.

Substitution of displacement fields [Eqs. (13a) and (13b)] into boundary conditions [Eqs. (7a) and (7d)] yields

$$\begin{bmatrix} 1 & 1 \\ \tilde{C}_{33}Kx_{3_D} & -K^F\lambda^F \end{bmatrix} \begin{Bmatrix} U_3 \\ R \end{Bmatrix} = \begin{Bmatrix} 1 \\ K^F\lambda^F \end{Bmatrix}. \quad (14)$$

The reflection coefficient R is hence derived by solving the system [Eq. (14)] as

$$\begin{aligned} R(e) &= \frac{\tilde{C}_{33}(e)Kx_{3_D}(e) - K^F\lambda^F}{\tilde{C}_{33}(e)Kx_{3_D}(e) + K^F\lambda^F} \\ &= \frac{\tilde{C}_{33}(e)\sqrt{\rho/\tilde{C}_{33}(e)}\omega - \lambda^F\sqrt{\rho^F/\lambda^F}\omega}{\tilde{C}_{33}(e)\sqrt{\rho/\tilde{C}_{33}(e)}\omega + \lambda^F\sqrt{\rho^F/\lambda^F}\omega} \\ &= \frac{\sqrt{\tilde{C}_{33}(e)}\sqrt{\rho} - \sqrt{\lambda^F}\sqrt{\rho^F}}{\sqrt{\tilde{C}_{33}(e)}\sqrt{\rho} + \sqrt{\lambda^F}\sqrt{\rho^F}} = \frac{\sqrt{\tilde{C}_{33}(e)}\sqrt{\rho} - \rho^F V^F}{\sqrt{\tilde{C}_{33}(e)}\sqrt{\rho} + \rho^F V^F}. \quad (15) \end{aligned}$$

Since the stiffness [Eq. (2)] and Cauchy stress [Eq. (3)] are derived from a strain energy function, an appropriate strain energy function with well-defined parameters is essential. Doll and Schweizerhoff¹¹ conducted an extensive study on multiple strain energy functions for isotropic elastic compressible materials and proposed two. For this problem (see Fig. 1), the two strain energy functions proposed by Doll and Schweizerhoff¹¹ are chosen as candidates and compared with the strain energy function proposed by Kobayashi and Vanderby.¹⁰ The three strain energy functions under consideration are

$$W_1 = \frac{K}{2} [\exp(J-1) - \log J - 1] + C_1(\Gamma_1 - 3) + C_2(\Gamma_2 - 3), \quad (16a)$$

$$W_2 = \frac{K}{2} (J-1) \log J + C_1(\Gamma_1 - 3) + C_2(\Gamma_2 - 3), \quad (16b)$$

and

$$\begin{aligned} W_3 &= C_1(I_C - 3) + C_2(II_C - 3) + (C_1 + C_3)(III_C - 1) \\ &\quad + 2(-2C_1 - 2C_2 - C_3)(\sqrt{III_C} - 1) + C_4(\sqrt{III_C} - 1)^3, \end{aligned} \quad (16c)$$

where $\Gamma_1 = I_C/III_C^{1/3}$, $\Gamma_2 = II_C/III_C^{2/3}$, and $J = \sqrt{III_C}$, and I_C , II_C and III_C represent the first, second, and third invariants of

the Cauchy-Green tensor C_{ij} , respectively. The first and second functions (16a) and (16b) were proposed by Doll and Schweizerhoff,¹¹ while the third function (16c) was proposed in our previous study.¹⁰ All three functions add compressibility to the incompressible strain energy function proposed by Mooney and Rivlin,¹² that is,

$$W = C_1(I_C - 3) + C_2(II_C - 3). \quad (17)$$

With each of these strain energy functions, a strain-dependent stiffness tensor can be derived from Eq. (2). Since the rubber plate is stretched in the x_1 direction and ultrasound echo reflections are measured in the x_3 direction, only the stiffness $\tilde{C}_{33}(e)$ is considered in this study.

The detailed forms of the stiffness $\tilde{C}_{33}(e)$ from the three strain energy functions are derived and listed in the Appendix. In a state of zero strain, these three stiffness coefficients for $\tilde{C}_{33}(e)$ [Eqs. (A1)–(A3)] reduce to

$$\tilde{C}_{33}(e=0) = c_{33} = \frac{8(C_1 + C_2)}{3} + K \quad (18a)$$

for functions (16a) and (16b), and

$$\tilde{C}_{33}(e=0) = c_{33} = 4C_1 + 4C_2 + 2C_3 \quad (18b)$$

for function (16c).

The four material constants C_1 , C_2 , C_3 , and K used in these three strain energy functions were determined in the following manner. First, a strip of rubber ($L12 \text{ cm} \times W3 \text{ cm} \times T0.3 \text{ cm}$) was placed in a servo-hydraulic testing system (MTS 858 Bionix test system) and its stress versus stretch behavior was obtained and confirmed with repeated testing. This test determined basic material properties C_1 and C_2 by treating models (16a)–(16c) as incompressible. Next, dilatational wave velocity was measured in nonstretched rubber to determine parameters K of functions (16a) and (16b), and also C_3 of function (16c). Ultrasound wave travel time through thickness was measured directly from the peak distance between the first and second reflected waves in the recorded signal (Fig. 2). A 2.25-MHz (nominal frequency) ultrasonic transducer (PANAMETRICS-NDT™, 0.5 in diameter video scan immersion ultrasound transducer) was utilized. Dilatational wave velocity at the nonstretched state ($V_D|_{e=0}$) was computed from measured travel time divided by thickness measured by digital caliper. By substituting Eqs. (18a) and (18b) into Eq. (12), unknown parameters K and $2C_3$ can be evaluated as

$$K = V_D|_{e=0}^2 \rho - \frac{8(C_1 + C_2)}{3} \quad (19a)$$

and

$$2C_3 = V_D|_{e=0}^2 \rho - (4C_1 + 4C_2), \quad (19b)$$

where C_1 and C_2 were previously obtained.

In the forward problem, wave reflection coefficients from the stretched rubber plate at known applied strains are analytically evaluated from Eq. (15) with different transverse stiffnesses [Eqs. (A1)–(A3)]. All material constants were assumed to be known. Later, the analytically evaluated wave

reflection coefficients were compared with reflection coefficients that were calculated from measured wave signals.

The process for obtaining the reflection coefficient from the measured wave signals are presented in Fig. 1. First, the incident and reflected waves were recorded in time domain and converted to frequency domain with fast Fourier transformation (FFT). The experimental reflection coefficients at nominal frequency f_N of transducer were then calculated by

$$\text{Reflection coefficient: } R(e, f_N) = \frac{\text{Reflected wave: RW}(e, f_N)}{\text{Input wave: IW}(e, f_N)}. \quad (20)$$

IV. FORMULATION OF THE GENERAL INVERSE PROBLEM

In this section, a general inverse problem based on the proposed strain energy function (16c) is defined, and two key relations used for solving general inverse problem for the same prestretched rubber (Fig. 1) are derived. We define the general inverse problem to be as follows: *Evaluation of either (or both) applied strain or (and) material properties only from measured wave reflected signals.* Since measurable variables (e.g., reflection coefficient and material properties of surrounding fluid) and nonmeasurable variables (e.g., stiffness and density of target medium) are related in Eq. (15), this equation can be simplified with the following two assumptions:

- (1) Unknown material density is assumed to be constant at any deformed state.

$$\rho(e) \approx \rho(e=0) = \rho_0.$$

- (2) Material constants C_1 and C_2 are very small compared to C_3 :

$$C_3 \gg C_1, C_2 \quad \text{or} \quad \frac{C_1}{C_3} \approx 0 \quad \text{and} \quad \frac{C_2}{C_3} \approx 0.$$

The Poisson's ratio of nearly incompressible rubber is known to be very close to 0.5, hence the volume and density changes through static deformation are ignored for this part of the analysis. In a nearly incompressible rubber, the shear wave velocity $V_S = \sqrt{\mu/\rho_0} = \sqrt{2(C_1+C_2)/\rho_0}$ is reported to be (around 40–100 m/s)^{10,12,13} very slow compared to the velocity of the dilatational wave $V_D = \sqrt{(\lambda+2\mu)/\rho_0} = \sqrt{(4C_1+4C_2+2C_3)/\rho_0}$ (around 1500 m/s). From these, the order of C_1/C_3 and C_2/C_3 must be around 10^{-3} – 10^{-2} . Thus, our second assumption also appears valid.

In Eq. (15), the acoustic impedance square of the stretched rubber is given by

$$\begin{aligned} \rho_0 \tilde{C}_{33}(e) &= \rho_0 \left[4C_1 + 4C_2 + 2C_3 + (4C_1 + 4C_2 + 2C_3 + 6C_4) \right. \\ &\quad \times \left. \frac{e(C_1 + C_2 + C_1e - C_2e - C_2e^2)}{C_1 + C_2 + C_3 + 2C_1e + 2C_3e + C_1e^2 + C_3e^2} \right] \\ &= \left[\frac{(1+R(e))}{(1-R(e))} \rho^F V^F \right]^2 = \text{IPS}(e). \end{aligned} \quad (21)$$

For a nonstretched state, the impedance square becomes

$$\rho_0 \tilde{C}_{33}(e=0) = \rho_0 c_{33} = \left[\rho^F V^F \frac{(1+R_0)}{(1-R_0)} \right]^2 = \text{IPS}_0. \quad (22)$$

To eliminate the unknown material density ρ_0 , the ratio of Eq. (21) and Eq. (22) is taken as

$$\begin{aligned} \frac{\text{IPS}(e)}{\text{IPS}_0} &= \frac{\left[\rho^F V^F \frac{(1+R(e))}{(1-R(e))} \right]^2}{\left[\rho^F V^F \frac{(1+R_0)}{(1-R_0)} \right]^2} \\ &= \left[\frac{(1+R(e))}{(1-R(e))} \right]^2 \left[\frac{(1-R_0)}{(1+R_0)} \right]^2 \\ &\approx 12\alpha \frac{e}{1+e} + 12\beta \frac{e - e^2 - e^3}{(1+e)^2} + 1. \end{aligned} \quad (23)$$

In Eq. (23), e is the magnitude of the uni-axial applied strain. New normalized variables α, β are given by $\alpha = (C_1 C_4)/c_{33}^2$ and $\beta = (C_2 C_4)/c_{33}^2$. Since the density and wave velocity of the surrounding fluid are also eliminated simultaneously in this process, the material properties of surrounding fluid are not essential for the analysis and can be ignored. Equation (23) consists of three unknown parameters (α, β , and strain e), and it is not possible to retrieve all three variables with Eq. (23) alone. Therefore, an additional relation must be derived. As indicated in Fig. 1, reflection coefficients $R(e)$ are evaluated in the frequency domain. Hence Eq. (23) can be considered frequency domain information. The wave travel time between the near and far surfaces (across and back) (see Fig. 1) can easily be measured from the reflected echo signal by measuring the distance between the two peaks in the time domain. Therefore wave travel time is time domain information supplemental to the frequency domain information.

A time domain equation that relates measurable wave travel time to unknown properties can be derived in following manner. Let the wave velocity, thickness of the rubber, and travel time in nonstretched and stretched rubber be as follows:

For the nonstretched state, $e=0$,

$$\begin{aligned} \text{velocity } V_0 &= \sqrt{\frac{c_{33}}{\rho_0}}, \quad \text{thickness } D, \\ \text{measured travel time } T &= \frac{2D}{V_0}. \end{aligned} \quad (24a)$$

For the stretched state, $e \neq 0$,

$$\begin{aligned} \text{velocity } V &\approx \sqrt{\frac{\tilde{C}_{33}(e)}{\rho_0}}, \quad \text{thickness } d(e) \approx \frac{D}{\sqrt{1+e}}, \\ \text{travel time } t &= \frac{2d}{V}. \end{aligned} \quad (24b)$$

In relations (24b), the thickness in the stretched state is derived based on the assumption that thickness changes in nearly incompressible materials and in pure incompressible materials are almost the same. Taking the ratio of wave

travel times measured in the stretched and nonstretched states leads to

$$\left(\frac{T}{t}\right)^2 = \left(\frac{\tilde{C}_{33}(e)}{c_{33}}\right)(1+e) = \frac{\text{IPS}(e)}{\text{IPS}_0}(1+e). \quad (25)$$

Hence the applied strain e can be evaluated with

$$e = \frac{\text{IPS}_0}{\text{IPS}(e)} \left(\frac{T}{t}\right)^2 - 1. \quad (26)$$

This equation indicates that applied stretch can be evaluated simply from measured reflected wave signals. Since reflection coefficients $R(e)$ are evaluated only from waves reflected from the near surface of the stretched rubber (Fig. 1), the wave attenuation factor within the rubber should not affect the evaluation of Eqs. (23) and (26). Wave travel time is measured from the distance between peaks of first reflected wave and second reflected wave (Fig. 1). Again, wave attenuation in the rubber should not affect these measured wave travel times.

V. RESULTS

In this section, both forward and general inverse problems defined for the one-dimensional wave reflection problem at the surface of a stretched rubber plate (Fig. 1) are analyzed. In the forward problem, analytically evaluated reflection coefficient [Eq. (15)] with three different strain energy functions (16a)–(16c) are compared with the experimentally evaluated reflection coefficients (20). In the general inverse problem, two normalized material properties $\alpha = (C_1 C_4)/c_{33}^2$ and $\beta = (C_2 C_4)/c_{33}^2$ are evaluated from measured wave signals by utilizing Eqs. (23) and (26). These parameters are then compared with the same parameters determined from mechanical test results stretching the rubber specimen. For both forward and inverse problems, the following parameters are applied:

wave frequency=2.25 MHz,
 wave velocity for the water=1470 m/s,
 density of water=1000 kg/m³.

The following parameters were determined from the above mechanical tests:

density of rubber=971 kg/m³,
 parameters for strain energy functions:
 $C_1=8.60 \times 10^5$ Pa,
 $C_2=-1.55 \times 10^5$ Pa,
 $2C_3=2.18 \times 10^9$ Pa,
 $K=2.19 \times 10^9$ Pa.

The fourth parameter in the function (16c) was chosen to fit experimental data

$$C_4=3.0 \times 10^{11} \text{ Pa.}$$

As presented in our previous study,¹⁰ the analytically evaluated stress-strain behavior based on these parameters fits very closely to the stress-strain behavior obtained from the experiment. Analytically obtained reflection coefficients [Eq. (15)] using the three different strain energy functions

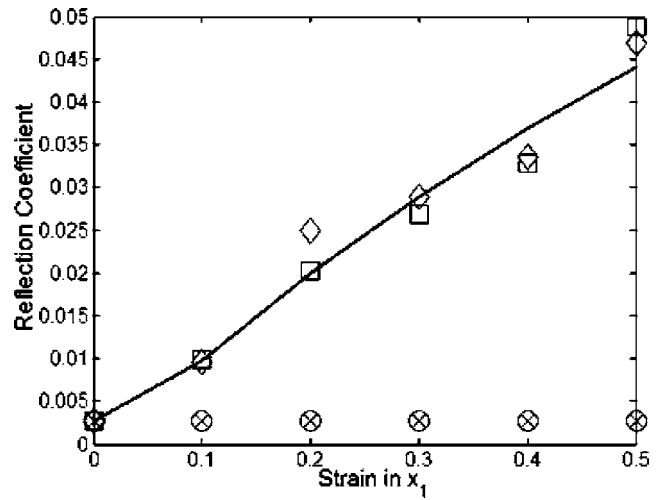


FIG. 3. Relation between reflection coefficient R and strain in x_1 direction for the experiment shown in Fig. 1. Square: Result from experiment 1. Diamond: Result from experiment 2. Solid line: Analytical result from function (16c). Circle: Analytical result from function (16a). Cross: Analytical result from function (16b). Results show a strain-dependent acoustoelastic effect in the experimental reflection coefficient, which can be modeled by Eq. (15) using the strain energy function (16c).

(16a)–(16c) and resulting stiffness coefficients [(A1)–(A3)] are compared to experimentally measured reflection coefficients [Eq. (20)] in Fig. 3. The experimental reflection coefficients are clearly strain dependent. They increase significantly with applied strain. This behavior shows the acoustoelastic effect in rubber, a nearly incompressible material. Figure 3 also indicates that this strain-dependent change in reflection coefficient is consistently represented by the acoustoelastic method of analysis if a proper strain energy function is used to release the constraint of incompressibility.

Reflection coefficients evaluated with three different strain energy functions are plotted in Fig. 3. Results using strain energy function (16c) predict the experimentally obtained reflection coefficients well and successfully simulate the acoustoelastic effect. These results indicate the importance of the higher order extra constitutive term governing volumetric change (third invariant III_C), which was included in function (16c).

Once strain is evaluated with Eq. (26), coefficients α and β can be evaluated with data from ratios of the reflection coefficients [Eq. (15)] computed from data measured at different strain levels. After curve fitting the measured data sets, smoothed data are used to evaluate the new variables. Since the parameters for materials C_1 through C_4 are known from mechanical testing, the same variables can also be evaluated with the acoustoelastic methods and compared. Results are presented in Table I and show the acoustoelastic method to estimate material properties within $\sim 7\%$ of measured values.

VI. DISCUSSION

Acoustic reflection coefficients from the interface of water and prestretched, nearly incompressible, hyper-elastic materials (like rubber or biological tissues) are analyzed in

TABLE I. Evaluation of normalized material properties α and β , comparison of properties from acoustoelastic approach using ultrasound data, and comparing them to the properties obtained from standard mechanical testing.

Material parameter	$\alpha=(C_1C_4)/C_{33}^2$	$\beta=(C_2C_4)/C_{33}^2$
Value from Eqs. (26) and (29) using only acoustic signals	0.0580	-0.0105
Value from C_1 through C_4 via mechanical testing	0.0543	-0.0098
Difference	6.40%	7.14%

this study. Results using the strain energy function proposed in our previous study¹⁰ [Eq. (16c)] fit experimental data better than results with the other strain energy functions [Eqs. (16a) and (16b)]. These results indicate the importance of a higher order term governing volume change in the strain energy function. In addition, the new method was successful in computing applied strain in the target material and estimated a normalized form of its material properties. The acoustoelastic method, presented here in a very simple load scenario, then appears to hold great promise for more general experimental strain analysis of statically loaded structures made from nearly incompressible, hyper-elastic materials. In addition to determining prestrain (i.e., solution of the forward acoustoelastic problem), results strongly suggest the possibility of using reflection coefficients to identify the material properties within these general structures (i.e., solution of the general inverse acoustoelastic problem). Such a technique could be extremely valuable for many applications including medical application of ultrasound.

The strain energy function used in this study is based on the well known ‘‘Moony-Rivlin’’ strain energy function. The Moony-Rivlin function is known to simulate small to medium size deformations well, but has less fidelity for large deformations. Therefore, the strain energy function used here [Eq. (16c)] is also not expected to accurately simulate acoustoelastic phenomena at large deformations. In our previous study,¹⁰ the volumetric part of our strain energy function [Eq. (16c)] satisfies the two physical requirements set forth by Doll and Sweitzhoff¹¹ as long as the material is nearly incompressible. They are

$$U(J) \geq 0 \quad (27)$$

and

$$\left. \frac{\partial^2 U}{\partial J^2} \right|_{J=1} = K = \lambda + \frac{2}{3}\mu. \quad (28)$$

In the above conditions, $U(J)$ represents the volumetric part of the strain energy function that is derived for function (16c):

$$U(J) = C_1(-4J + J^2 + 3J^{2/3}) + C_2(1 - 4J + 3J^{4/3}) + 6C_3(-1 + J)^2.$$

Our previous study¹⁰ also showed that the other mechanical properties (e.g., stress-strain relation and acoustoelastic effect in shear waves) evaluated with our function [Eq. (16c)]

are almost identical to those properties evaluated with the Moony-Rivlin function. These results indicate that this function [Eq. (16c)] can properly embody acoustoelastic effects in dilatational waves without disturbing the important mechanical characteristics inherited from the Moony-Rivlin function.

The methods presented here are corroborated by a limited amount of experimental data. Only the input-reflection case perpendicular to the material surface has been investigated. A more robust validation of the method should include experiments that excite all wave modes (e.g., incident waves at different azimuth and incident angles, other more complex loadings, etc.). In addition, the effect of damping on acoustic waves in this type of media should be further explored. Nevertheless, the preliminary evidence herein suggests that acoustoelasticity is a promising approach for the mechanical analysis of nearly incompressible materials (rubber, biological tissues, etc.).

VII. SUMMARY AND CONCLUSIONS

In this study, both forward and general inverse problems for the reflected waves from the interface of water and a uniaxially prestretched, hyper-elastic, nearly incompressible material were defined and analyzed.

The major features discussed in this study can be summarized as follows:

- (1) Materials that are typically assumed to be incompressible do sustain the propagation of dilatational waves. Acoustoelastic formulations can be created to model the behavior of these ‘‘incompressible materials’’ under deformation. The acoustoelastic effect can be measured in reflection coefficients evaluated at the interface between surrounding fluid and deformed medium. The reflection coefficients correlate with the magnitude of applied strain.
- (2) In the forward problem, the reflection coefficient $R(e)$ was derived as a function of material constants and applied axial strain e . Then, based on the material properties obtained from standard mechanical testing, strain-dependent reflection coefficients $R(e)$ were analytically evaluated and compared to experimental reflection coefficients from measured wave signals. It was shown that a higher order volumetric term in III_C is needed in the strain energy function to embody the acoustoelastic effect properly.
- (3) A general inverse problem was formulated to evaluate both applied strain and material properties from only the measured reflected acoustic waves from a deformed target medium. From the reflected waves, two key relations [Eqs. (23) and (26)] are derived in the frequency and time domains, respectively. From these two relations, both applied strains e and normalized material constants α and β can be evaluated. A major advantage for using relations (23) and (26) is that wave attenuation does not affect the values obtained in either relation. Thus, this technique can be used without having to simultaneously account for propagation losses due to wave attenuation.

APPENDIX

The detailed form of the stiffness $\tilde{C}_{33}(e)$ in the x_3 direction from the three strain energy functions are the following. For function (16a)

$$\tilde{C}_{33}(e) = \frac{1}{J} \left\{ \frac{[(24C_1 + 24C_2 + 9K) + (72C_1 + 96C_2 + 18K)e]}{9(1+e)^2} + \frac{[(96C_1 + 96C_2 + 9K)e^2 + 32(2C_1 + C_2)e^3 + 16C_1e^4]}{9(1+e)^2} - b_1(e)e \frac{[(48C_1 + 96C_2 + 27K) + (240C_1 + 192C_2 - 54K)e]}{54(1+e)^3} - b_1(e)e \frac{[(384C_1 + 192C_2 + 27K)e^2 + (256C_1 + 64C_2)e^3 + 64C_1e^4]}{54(1+e)^3} \right\}, \quad (A1)$$

where

$$b_1(e) = \frac{12(1+e)(C_1 + C_2 + C_1e)(3 + 3e + e^2)}{4C_1(3 + 9e + 12e^2 + 8e^3 + 2e^4) + 4C_2(3 + 3e + 3e^2 + e^3) - 9(1+e)^2K}.$$

For function (16b),

$$\tilde{C}_{33}(e) = \frac{1}{J} \left\{ \frac{[(24C_1 + 24C_2 + 9K) + (72C_1 + 96C_2 + 18K)e]}{9(1+e)^2} + \frac{[(96C_1 + 96C_2 + 9K)e^2 + 32(2C_1 + C_2)e^3 + 16C_1e^4]}{9(1+e)^2} - b_2(e)e \frac{[(48C_1 + 96C_2 + 27K) + (240C_1 + 192C_2 - 54K)e]}{54(1+e)^3} - b_2(e)e \frac{[(384C_1 + 192C_2 + 27K)e^2 + (256C_1 + 64C_2)e^3 + 64C_1e^4]}{54(1+e)^3} \right\}, \quad (A2)$$

where

$$b_2(e) = \frac{6(1+e)(C_1 + C_2 + C_1e)(3 + 3e + e^2)}{6C_1 + 6C_2 + 9K + (36C_1 + 24C_2 + 18K)e + (60C_1 + 24C_2 + 9K)e^2 + (40C_1 + 8C_2)e^3 + 10C_1e^4}.$$

For function (16c)

$$\tilde{C}_{33}(e) = \frac{1}{J} \left[4C_1 + 4C_2 + 2C_3 + b_3(e) \frac{2e(2C_1 + 2C_2 + C_3 + 3C_4)}{1+e} \right], \quad (A3)$$

where

$$b_3(e) = \frac{(1+e)[C_1(1+e) - C_2(-1+e+e^2)]}{C_2 + C_1(1+e)^2 + C_4(1+e)^2}.$$

In these relations, variables e and $b_i(e)$ ($i=1-3$) represent the applied strain and the magnitude of first order transverse shrinkage, respectively. The magnitude of shrinkage $b_i(e)$ is assumed to be a small perturbation of the width change in a nearly incompressible material that is defined in our previous study.¹⁰ The thickness $d(e)$ of the stretched incompressible material can be related to the original length of plate L and applied axial strain e by

$$d(e) = \frac{L}{\sqrt{1+e}}. \quad (A4)$$

For a nearly incompressible material, however, the thickness under stretch is assumed to be slightly more than the thickness of an incompressible material under stretch and can be evaluated by

$$d_n(e) = \frac{L}{\sqrt{1+(1-b(e))e}} = \frac{L}{\sqrt{1+e}} \frac{1}{\sqrt{1-b(e)e/(1+e)}} = d(e) \frac{1}{\sqrt{1-b(e)e/(1+e)}}. \quad (A5)$$

¹D. S. Hughes and J. L. Kelly, "Second-order elastic deformation of solids," *Phys. Rev.* **92**, 1145–1149 (1953).

²R. A. Toupin and B. Bernstein, "Sound waves in deformed perfectly elastic materials; the acoustoelastic effect," *J. Acoust. Soc. Am.* **33**, 216–225 (1961).

³D. Truesdell, "General and Exact Theory of Waves in Finite Elastic Strain," *Arch. Ration. Mech. Anal.* **8**, 263–296 (1961).

⁴T. Tokuoka and Y. Iwashimizu, "Acoustical Birefringence of Ultrasonic Waves in Deformed Isotropic Elastic Material," *Int. J. Solids Struct.* **4**, 383–389 (1968).

⁵Y. H. Pao, W. Sache, and H. Fukuoka, "Acoustoelasticity and Ultrasonic Measurement of Residual Stresses," in *Physical Acoustics* (Academic,

Orlando, 1984), Vol. XVII, Chap. 2.

⁶R. W. Ogden, *Non-Linear Elastic Deformations* (Dover, Mineola, NY, 1984), Chap. 6.4.

⁷A. C. Eringen and E. S. Suhubi, *Erastodynamics* (Academic, New York, 1974), Vol. 1, Chap. 4.

⁸Y. Fu, "On the propagation of nonlinear traveling waves in an incompressible elastic plate," *Wave Motion* **19**, 271–292 (1993).

⁹D. L. Folds, "Speed of sound and transmission loss in silicone rubbers at ultrasonic frequencies," *J. Acoust. Soc. Am.* **56**, 1295–1296 (1974).

¹⁰H. Kobayashi and R. Vanderby, "New Strain Energy Function for Acous-

toelasticity Analysis of Dilatational Waves in Nearly Incompressible, Hyper-Elastic Materials," *J. Appl. Mech.* **72**, 843–851 (2005).

¹¹S. Doll and K. Schweizerhof, "On the development of Volumetric Strain Energy Functions," *J. Appl. Mech.* **67**, 17–21 (2000).

¹²R. S. Rivlin, "Large Elastic Deformations of Isotropic Materials VI. Further Results in the Theory of Torsion, Shear and Flexure," *Philos. Trans. R. Soc. London* **242**(A845), 173–195 (1949).

¹³E. L. Madsen, H. J. Stahoff, and J. A. Zagzebski, "Ultrasound shear wave properties of soft tissues and tissue like materials," *J. Acoust. Soc. Am.* **74**, 1346–1355 (1983).

Granular layers on vibrating plates: Effective bending stiffness and particle-size effects

Wonmo Kang, Joseph A. Turner,^{a)} Florin Bobaru, Liyong Yang, and Kittu Rattanadit
*Department of Engineering Mechanics, University of Nebraska-Lincoln, W317.4 Nebraska Hall,
Lincoln, Nebraska 68588*

(Received 2 February 2006; revised 3 November 2006; accepted 9 November 2006)

Acoustic methods of land mine detection rely on the vibrations of the top plate of the mine in response to sound. For granular soil (e.g., sand), the particle size is expected to influence the mine response. This hypothesis is studied experimentally using a plate loaded with dry sand of various sizes from hundreds of microns to a few millimeters. For low values of sand mass, the plate resonance decreases with added mass and eventually reaches a minimum without particle size dependence. After the minimum, a frequency increase is observed with additional mass that includes a particle-size effect. Analytical nondissipative continuum models for granular media capture the observed particle-size dependence qualitatively but not quantitatively. In addition, a continuum-based finite element model (FEM) of a two-layer plate is used, with the sand layer replaced by an equivalent elastic layer for evaluation of the effective properties of the layer. Given a thickness of sand layer and corresponding experimental resonance, an inverse FEM problem is solved iteratively to give the effective Young's modulus and bending stiffness that matches the experimental frequency. It is shown that a continuum elastic model must employ a thickness-dependent elastic modulus in order to match experimental values. © 2007 Acoustical Society of America. [DOI: 10.1121/1.2404635]

PACS number(s): 43.40.At, 43.20.Tb, 43.40.Dx [JGM]

Pages: 888–896

I. INTRODUCTION

Interest in acoustic/seismic methods of detecting nonmetallic landmines has grown in recent years. Both linear^{1–4} and nonlinear^{5–8} detection methods have shown good success in laboratory and field tests. These methods rely on the vibration response of the top plate of the mine under excitation from an acoustic wave. This response is complex due to the interaction of the plate with the soil which lies above the mine. Thus, a clear understanding of the response of a plate-soil system is important for increasing the probability of detection and for reducing false alarms. The influence of a soil layer on the frequency response of a plate was recently examined experimentally by Korman and Sabatier⁹ for loess soil and by Zagrai *et al.*¹⁰ for moist sand. In all cases, it has been observed that the resonance decreases as the layer thickness increases, reaches a minimum and then increases. Here, a similar experiment is used to study the response of a plate loaded with sand. The emphasis is on the influence of particle size on the plate response. To explore the relation between particle size and the resonance analytically, a model based on effective medium theory and Hertzian contact is derived.

In addition, models of two-layer elastic plates are explored with regard to the measured data. First, the analytical solution of a two-layer plate is used and it is shown that such a model consistently overpredicts the observed resonant frequency. Next, a numerical model of the two-layer plate is used to describe the plate-sand behavior. The plate-sand sys-

tem examined experimentally is modeled as a thin-plate loaded by an equivalent elastic layer (EEL) which replaces the layer of sand. The nondissipative numerical model is then discretized by finite elements using shell elements for the thin metal plate and solid elements for the EEL. The equivalent elastic layer is defined as the layer that produces the shift/change in the first resonant frequency that matches the experimental measurements from the plate-sand system. This continuum-based model is selected due to its simplicity in evaluating effective elastic moduli for the granular layer. Its utility in evaluating the “bending stiffness” of a granular layer (a new concept defined here) is emphasized and the limits in capturing the interactions between the elastic plate and the real granular layer are examined.

In Sec. II, the experiments are described and results are presented. Then, the particle size effect observed experimentally is analyzed with an effective medium model for granular materials. In Sec. III, analytical and numerical models of the two-layer plate system are discussed. Also, the numerical method used to analyze the equivalent continuum three-dimensional system is described. Finally, a summary and conclusions are presented in Sec. IV. The results are expected to provide insight into the importance of particle size effects for acoustic landmine detection.

II. EXPERIMENTS AND EFFECTIVE MEDIUM MODELING

The experiments are designed to provide insight into the relation between the particle size of sand layer and the resonant behavior of the plate. The experimental setup used here is shown schematically in Fig. 1 and is based on that of Korman and Sabatier.⁹ The plate-sand system is created us-

^{a)}Author to whom correspondence should be addressed; electronic mail: jaturner@unl.edu

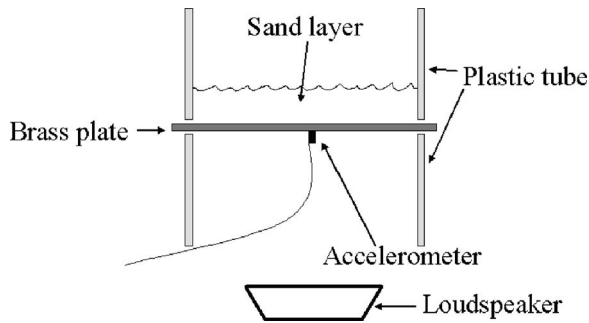


FIG. 1. Schematic of the cross section of the experimental setup. A thin brass plate is clamped between two plastic tubes and excited with a loudspeaker. The response is measured with an accelerometer mounted to the center of the plate.

ing a circular brass plate (mass=26.4 g, thickness =0.25 mm, radius=50.8 mm) clamped at the outer edge. Acoustic waves are generated by a loudspeaker positioned below the plate. A small input voltage of 50 mV is used to ensure that the response remained in the linear regime for all measurements. The response of the plate is measured using an accelerometer placed at the center of the plate. The natural frequency corresponding to the system is determined using an HP35670A Dynamic Signal Analyzer. The first bending resonance for the brass plate alone is approximately 170 Hz.

For this study, the influence of particle size is investigated. Thus, six different sizes of sand are used, all sieved from the same batch of dry sand. Additional measurements using the sand mixture are also made. The particle sizes and sample designations are shown in Table I. Note that all monodispersed samples have approximately the same effective density (the average density for S1–S6 is $1600 \pm 32.6 \text{ kg/m}^3$) indicating that the particles are packing essentially as spheres. However, the polydispersed sample (S-mix), from which the monodispersed samples were sieved, has an effective density $\sim 12\%$ higher than the monodispersed average. The first bending resonance of the plate-sand system is measured using 10 g increments of sand, with a maximum layer thickness of 3.3 cm.

A. Experimental results

The results of the experiments described above are presented in Fig. 2. The normalized resonant frequency, \tilde{f} is defined as the frequency of the loaded plate divided by the frequency of the unloaded plate. Figure 2 shows the dependence of \tilde{f} on the normalized mass of the sand layer. The overall trend of the resonance is similar to that observed for loess soil⁹ and moist sand.¹⁰ The resonance first decreases (region A), reaches a minimum and then increases (region B).

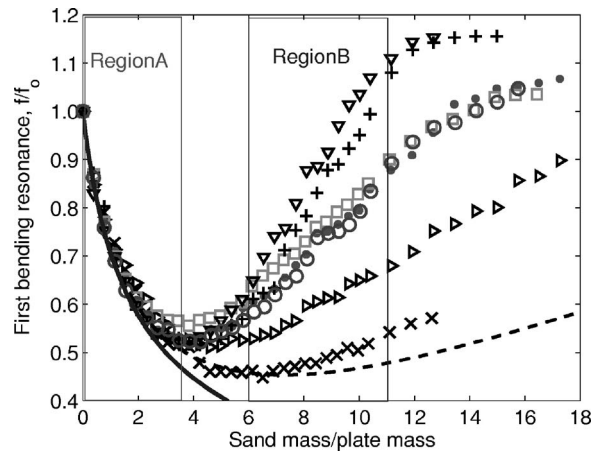


FIG. 2. Shift of the first bending resonance due to sand loading for seven samples of sand with various sizes (S1: ×, S2: ▷, S3: ●, S4: □, S5: ∇, S6: +, S-mix: ○, see Table I). The dashed line is based on Korman and Sabatier's data (Ref. 9), while the solid line is the behavior expected from mass loading alone as given by Eq. (3). In region A, there is no particle size effect observed. However, particle size becomes an important factor in region B.

B). It is clear from these results that the particle size is not relevant in Region A, but is important in region B. In addition, it is observed that larger particle sizes lead to higher resonant frequencies suggesting that the combined system is in some ways stiffer if larger particles are present. The universal nature of this response is discussed in the following. Another interesting result is also illustrated in Fig. 2. The curve denoted as S-mix is the result from the unsieved dry sand mixture (polydispersed). The size distribution of S-mix, shown in Table II, has an average particle size of 0.56 mm. The response of the plate when loaded with this polydispersed mixture corresponds to the same curve (0.3–0.6 mm) as a monodispersed layer with the same average particle size although their effective densities are slightly different. This result suggests that the behavior of the system in region B depends only on the average particle size of the layer and is not as sensitive to the distribution of particle sizes in the layer.

Region A is a mass-dominated regime in which the combined system behaves as a plate loaded by added mass. Some understanding of the resonant frequency in region A is attained from the analytical solution of a clamped plate. The first bending frequency from classical thin plate theory is given by¹¹

$$\omega_1 = \frac{\lambda_1^2}{\delta^2} \sqrt{\frac{D}{\rho}} = \frac{\lambda_1^2}{\delta^2} \sqrt{\frac{Eh^3}{12\rho(1-\nu^2)}}, \quad (1)$$

where $\lambda_1^2 (=10.2)$ is the eigenvalue associated with the first bending mode of a clamped plate, δ is radius of the plate, E is Young's modulus, h is the plate thickness, ρ is mass

TABLE I. Particle sizes and names of the samples of sand used for the experiments. All monodispersed samples (S1–S6) were sieved from the polydispersed mixture S-mix.

Name	S1	S2	S3	S4	S5	S6	S-mix
Size (mm)	<0.15	0.15–0.3	0.3–0.6	0.6–1.18	1.18–2.36	2.36–4.75	Unsieved sand
Density (kg/m ³)	1572	1574	1620	1660	1593	1570	1795

TABLE II. Particle size distribution of samples S-mix, the polydispersed sample.

Size	S1	S2	S3	S4	S5	S6
Weight (g)	17	209.3	344.4	156.7	41.4	5.1
Ratio (%)	2.2	27.05	44.50	20.25	5.35	0.66
Total weight of S-mix=773.9 g						

density per unit area of the plate, and ν is Poisson's ratio. Equation (1) also serves to define the plate bending stiffness D . It can be assumed that the mass of sand is the dominant parameter in region A. Thus, the first bending resonance in region A, ω_A , can be written as

$$\omega_A = \frac{\lambda^2}{\delta^2} \sqrt{\frac{D}{\rho_{\text{eff}}}} = \frac{\lambda^2}{\delta^2} \sqrt{\frac{D}{\rho_p(1+M)}}, \quad (2)$$

with an effective density defined as the average density of the plate-layer system $\rho_{\text{eff}} = \rho_p(1+M)$, where M is mass ratio (mass of the sand normalized by the mass of the plate) and ρ_p is the density of the brass plate per unit area ($=2.18 \text{ kg/m}^2$). Thus, \tilde{f} is given by

$$\tilde{f} = \frac{f}{f_0} = \sqrt{\frac{1}{1+M}}. \quad (3)$$

The solid line in Fig. 2 shows the trend expected from Eq. (3).

In region B, the thickness of the sand layer is sufficient so that it behaves in many ways as a plate itself. In this region, the sand layer is dominant such that the brass plate has only a minor influence on the response of the plate-sand system. In this case, the first bending resonance of the plate in region B, ω_B , is given by

$$\omega_B = \frac{\lambda^2}{\delta^2} \sqrt{\frac{Eh_{\text{eff}}^2}{12\rho_{\text{eff}}(1-\nu^2)}} \propto \sqrt{\frac{(h+M\rho_p/\rho_s)^3}{\rho_p(1+M)}}, \quad (4)$$

with the effective thickness of the plate-layer system given by $h_{\text{eff}} = (h+M\rho_p/\rho_s)$, where ρ_s is the density of the sand layer. Equation (4) shows that when M is sufficiently large, \tilde{f} is expected to depend linearly on M . Thus, the trends observed in region B are also expected from the standpoint of basic plate vibrations. The dependence of the slope of \tilde{f} on particle size in region B is discussed next, including expectations based on theoretical models of particle aggregates.

B. Particle-size dependence

As discussed earlier, the linear dependence of \tilde{f} on M is expected for the region of the measurements for which M varies from 6 to 11. However, the slopes of these curves are clearly dependent on the average particle size of the layer as well as other parameters. In order to quantify this dependence, the slope of each curve $\sigma = \partial\tilde{f}/\partial M$ in region B is extracted. The slopes are calculated by fitting the entire $\tilde{f}-M$ curve using the function⁹

$$\tilde{f} = [A/(M+1) + BM + CM^2]^{0.5}, \quad (5)$$

TABLE III. Slopes of the frequency curves for different particle sizes of sand.

Name	S1	S2	S3	S4	S5	S6
σ	0.0387	0.0424	0.0728	0.0686	0.1153	0.1077

where A , B , and C are fit coefficients. Then it is assumed that $\sigma = \sqrt{C}$ in the region of interest due to the relatively large value of M . The results are given in Table III. The dependence of σ on particle radius R is determined assuming a power-law relation. Thus, this dependence is given by

$$\sigma(R) = \alpha R^\beta, \quad (6)$$

where α and β are fit parameters obtained using the method of least squares. The results shown in Table III give a value for $\beta=0.305$ ($\alpha=0.08$). A plot of σ and R from the measurements are given in relation to Eq. (6).

The universality of this dependence is demonstrated using data from Korman and Sabatier.⁹ Their results are shown as the dashed line in Fig. 2 and are determined using Eq. (5) and their published coefficients ($A=1$, $B=0.0078$, and $C=0.0004$).⁹ The slope of their curve in region B is consistent with Eq. (6) for a particle size of $10.5 \mu\text{m}$. The soil used by Korman and Sabatier (S-KS) was loess soil, a mixture of clay and silt. The result seems reasonable in that the particle size of clay is less than $2 \mu\text{m}$ and that of silt is between 2 and $80 \mu\text{m}$.¹² The actual particle size of the S-KS soil was later confirmed as $10 \mu\text{m}$.¹³ Thus, it appears that the power-law dependence proposed is sufficiently general for a large range of particle radii. However, the bending vibration response of a granular layer has not yet been considered from a theoretical standpoint.

The effective elastic response of an aggregate of particles has been of interest for over two decades. Although previous attempts to model such aggregates using effective medium theories have met with limited success, some progress has been made. For example Digby,¹⁴ Walton,¹⁵ and more recently Jenkins *et al.*,¹⁶ have developed expressions for the effective elastic moduli of an aggregate of spherical

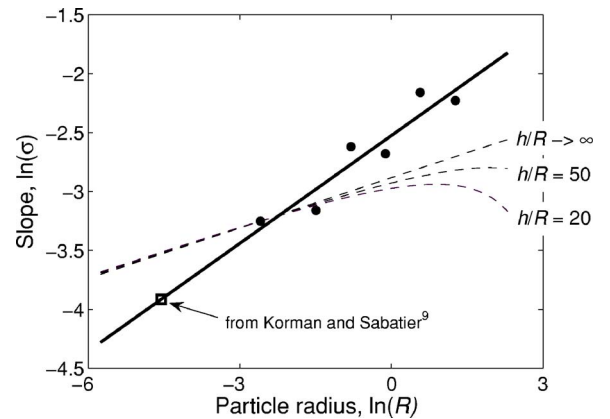


FIG. 3. Dependence of the slope of the resonance curves, σ , in region B on particle radius R . The experimental data from Table III are plotted as black circles. The power-law fit $\sigma = \alpha R^\beta$ is given by the solid line ($\alpha=0.08$, $\beta=0.305$). This curve matches with data from Korman and Sabatier (Ref. 9). The dashed lines correspond to the analytical model for three values of h/R .

particles under hydrostatic pressure. Here, their results are applied to the problem of interest such that the dependence of σ on R may be explored. As such, the resonant frequency of a circular plate of spherical particles with a clamped edge is assumed to have the form

$$\omega_B = \frac{\lambda_1^2}{\delta^2} \sqrt{\frac{\bar{E}h_s^3}{12\rho_s(1-\bar{\nu}^2)}}, \quad (7)$$

where \bar{E} is the effective Young's modulus and $\bar{\nu}$ is Poisson's ratio of the effective plate with h_s and ρ_s as the thickness and density of the layer. Considering a random packing of identical elastic spherical particles of radius R , the effective Lamé's constants $\bar{\lambda}$ and $\bar{\mu}$ may be written¹⁴

$$\bar{\lambda} = \frac{\mu C}{5\pi R} \left[\frac{a}{1-\nu} - \frac{2b}{2-\nu} \right],$$

$$\bar{\mu} = \frac{\mu C}{5\pi R} \left[\frac{a}{1-\nu} + \frac{3b}{2-\nu} \right], \quad (8)$$

where μ is shear modulus and ν is Poisson's ratio for the spheres. In addition, the packing has an average coordinate number $C=K\phi$, where K is average number of contacts of each sphere and ϕ is the packing fraction. Each pair of grains is assumed to be initially bonded with a contact radius b . Under an applied hydrostatic pressure, the packing increases resulting in an increase in contact area with radius a , such that $a \geq b$. For the experiments described here, it is assumed that the contact of two particles without load is negligible, such that $b=0$. For the sand layer considered, the pressure from loading that results in the contact radius a arises from the weight of the particles above the particle of interest. Thus, the effective Lamé constants may be rewritten in terms of the effective Young's modulus \bar{E} and Poisson's ratio $\bar{\nu}$ as

$$\bar{E} = \frac{\mu C}{\pi R} \frac{1}{2} \frac{a}{1-\nu},$$

$$\bar{\nu} = \frac{1}{4}. \quad (9)$$

Under the assumption of Hertzian contact between two particles, the contact radius is given by¹⁷

$$a = \left(\frac{3pR}{4E^*} \right)^{1/3}, \quad (10)$$

where p is the applied normal force at the point of contact. As noted previously,¹⁸⁻²⁰ no particle-size dependence results from this theory for a constant contact radius. To address this issue, it is assumed here that the contact force on a given particle contact is equal to the total weight of the particles above a given particle divided by the number of contacts over which the force is distributed. Thus, $p=p(z)=\rho_s g \pi(h-z)/(3zK\phi/4R^3)$, with z the depth in the layer that varies from 0 to h . The average contact area is then given by

$$\langle a \rangle = \left\langle \left(\frac{3p(z)R}{4E^*} \right)^{1/3} \right\rangle, \quad (11)$$

where the ensemble average $\langle \rangle$, is an integral through the thickness of the layer. Thus, Eq. (11) becomes

$$\langle a \rangle = \left(\frac{\rho_s g \pi}{E^* K \phi} \right)^{1/3} R^{4/3} \frac{1}{h} \int_R^h \left[\frac{h-z}{z} \right]^{1/3} dz,$$

where the reduced elastic modulus E^* of the contact is given by $E^*=2E/(1-\nu^2)$, with E and ν as the Young's modulus and Poisson's ratio of the particles, respectively. Then the ratio of $\langle a \rangle/R$ can be expressed by

$$\frac{\langle a \rangle}{R} = \left(\frac{\rho_s g \pi}{E^* K \phi} \right)^{1/3} R^{1/3} Q(R/h), \quad (12)$$

where

$$Q(R/h) = \int_{R/h}^1 \left(\frac{1-\tilde{z}}{\tilde{z}} \right)^{1/3} d\tilde{z}.$$

Finally, the dependence of resonant frequency, Eq. (7), on R is given by

$$\omega_B \propto \sqrt{R^{1/3} Q(R/h)}. \quad (13)$$

Thus, the final form given by Eq. (13) shows a dependence of the resonance on the size of particles in the layer. In order to put Eq. (13) in terms of the experimental results, the dependence of $\partial \tilde{f} / \partial M$ on R is needed. This quantity is

$$\sigma = \frac{\partial \tilde{f}}{\partial M} \propto \sqrt{R^{1/3} Q(R/h)}, \quad (14)$$

due primarily to the fact that the effective density of all particle sizes is equal. Example curves corresponding to Eq. (14) are shown in Fig. 3 for three values of h/R . It should be noted that for large layer thickness, $h/R \rightarrow \infty$ such that $Q(0)=2\pi/3\sqrt{3}$. In this case, the dependence of σ is $R^{1/6}$. The term \sqrt{Q} reduces the value of σ as shown. It is clear that Eq. (14) shows an increase in σ with R , but that the exponent of the power-law dependence does not match the experimental result. Just as effective medium theories for granular systems have not been able to predict average moduli accurately,¹⁶ Eq. (14) does not accurately predict the size dependence of the frequency for the plate-sand system, although the general trend (increasing σ for increasing R) is correct.

At this point it is unclear whether a more comprehensive effective medium approach, such as that developed by Jenkins *et al.*,¹⁶ would yield results more closely related to the experiments. It is likely that the difference between the analytical estimates provided by these well-bonded models (two grains originally in contact remain in contact after an external load is applied) and the experimental results can be explained by the failure²¹ of the well-bonded model to approximate accurately the bending motion in the vibration of the granular system.

In Sec. III, the plate/sand-layer system is analyzed with the multilayer Kirchoff plate theory and a finite element model. The notion of the bending stiffness of the granular layer is of particular interest here.

III. TWO-LAYER PLATE MODELS

It is clear from the experimental results shown above for the granular layer supported by a thin plate that a simple model is not sufficient to describe the observed behavior. Thus, additional aspects relevant for this system must be examined in order to identify the pertinent parameters that will allow predictive models to be developed. Toward that end, three different types of two-layer plate models are now explored. The first is an analytical model that describes the vibration behavior of a two-layer elastic plate.²² Such a model differs from the heuristic model presented previously¹⁰ for which the bending stiffnesses of the two layers were simply added. Unfortunately, the nature of the equation governing the vibrations of a multilayer plate does not support the approach in Ref. 10 from a physical standpoint. The second is a numerical approach using a finite element model (FEM). In this case, the upper layer is modeled using three-dimensional elements valid for thick plates. Finally, an inverse approach is presented for which the effective granular layer properties are extracted by matching the FEM results to the experimental results. This approach results in a thickness dependent modulus for the granular layer with corresponding bending stiffness (also thickness dependent).

A. Analytical model

The analytical solution for a two-layer elastic plate²² is now employed to model the system of interest. The top layer is considered as an EEL to study the dependence of the resonant frequency on the thickness of the granular layer. The majority of the derivation is not repeated here for brevity. The interested reader is referred to the original for more details.²² Both layers of the combined plate are modeled using Kirchhoff plate theory. The interface between the two layers is then assumed to be perfectly bonded such that there is continuity of displacement and stress. The boundary conditions of interest correspond to clamped conditions for both layers. Following standard vibration theory, harmonic solutions are sought and the spatial eigenvalue problem is derived. The solution of the eigenvalue problem results in the eigenfunctions (mode shapes) and allowable wave numbers (that are related to the natural frequencies) for the given geometry and boundary conditions. For the problem of interest here, the characteristic equation governing the natural frequencies is given by²²

$$\begin{vmatrix} J_0(\bar{\mu}_1\bar{a})/\bar{\mu}_1\bar{a} & J_0(\bar{\mu}_2\bar{a})/\bar{\mu}_2\bar{a} & -I_0(\bar{m}_3\bar{a})/\bar{m}_3\bar{a} \\ J_1(\bar{\mu}_1\bar{a}) & J_1(\bar{\mu}_2\bar{a}) & I_1(\bar{m}_3\bar{a}) \\ \frac{\bar{\mu}_1^2}{\bar{\alpha}^2 - \bar{\mu}_1^2}J_1(\bar{\mu}_1\bar{a}) & \frac{\bar{\mu}_2^2}{\bar{\alpha}^2 - \bar{\mu}_2^2}J_1(\bar{\mu}_2\bar{a}) & \frac{\bar{\mu}_3^2}{\bar{\alpha}^2 - \bar{\mu}_3^2}I_1(\bar{m}_3\bar{a}) \end{vmatrix} = 0, \quad (15)$$

where J_i and I_i are Bessel functions and modified Bessel functions of the first kind, respectively and $\bar{\alpha}^2 = R_0\bar{\omega}^2/\bar{A}$. Here, $\bar{\omega}$ is the natural frequency of the two-layer plate and \bar{a} is radius of the two-layer plate. Also, $R_0 = \rho_1 h_1 + \rho_2 h_2$ in

terms of the mass densities (ρ_i) of the plates and plate thicknesses (h_i). The parameter

$$\bar{A} = \frac{E_1}{1 - \nu_1^2}h_1 + \frac{E_2}{1 - \nu_2^2}h_2$$

is defined in terms of the moduli (E_i) and Poisson's ratios (ν_i) of the plates. The dimensionless quantities $\bar{\mu}_1\bar{a} > 0$, $\bar{\mu}_2\bar{a} > 0$, and $\bar{\mu}_3\bar{a} = \bar{m}_3\bar{a}i$ in Eq. (15) are not independent, but are the roots of the following sixth-degree [third-degree in $(\bar{\mu}\bar{a})^2$] polynomial

$$(1 - \bar{B}^2/\bar{A}\bar{D})(\bar{\mu}\bar{a})^6 - (R_0\bar{\omega}^2/\bar{A})\bar{a}^2(\bar{\mu}\bar{a})^4 - (R_0\bar{\omega}^2/\bar{D})\bar{a}^4(\bar{\mu}\bar{a})^2 + (R_0\bar{\omega}^2)^2\bar{A}\bar{D} = 0. \quad (16)$$

In Eq. (16) \bar{B} and \bar{D} are defined as

$$\bar{B} = -\frac{1}{2}\frac{E_1}{1 - \nu_1^2}h_1^2 + \frac{1}{2}\frac{E_2}{1 - \nu_2^2}h_2^2,$$

$$\bar{D} = \frac{1}{3}\frac{E_1}{1 - \nu_1^2}h_1^3 + \frac{1}{3}\frac{E_2}{1 - \nu_2^2}h_2^3,$$

where ρ_1 and ρ_2 are mass densities of the plates, h_1 and h_2 are the thicknesses, ν_1 and ν_2 are the Poisson's ratios, E_1 and E_2 are the Young's moduli, and $\bar{\omega}$ is frequency of the two-layer plate.²² Equations (15) and (16) must be solved numerically for the necessary natural frequencies of the two-layer plate. From the brief description included here it is clear that the vibrations of a two-layer plate are much more complicated than a single-layer plate. For example, the solutions of Eq. (16) show that $\bar{\mu}_1$, $\bar{\mu}_2$, and $\bar{\mu}_3$ have nonlinear dependencies on the thickness ratio h_1/h_2 as do the natural frequencies. The mode shapes that result from the two-layer plate are also slightly different from those of a single-layer plate with the specific mode shapes dependent on the thickness ratio as well. These points are made to highlight the differences between the analytical two-layer plate theory²² and the model of Zagrai *et al.*:¹⁰ The two-layer plate theory has a more complicated characteristic equation and gives different mode shapes, wave numbers, and corresponding natural frequencies than those associated with a single-layer plate. An example result is shown in Fig. 4 for which the two-layer plate solution (brass plate with a top layer having $E = 3$ MPa) is compared with Eq. (22) of Zagrai *et al.* Considerable differences are observed between the two results especially for most of the range of mass ratio.

Although the two-layer plate model discussed here has the appropriate qualitative behavior expected, it is not able to match the quantitative behavior of the experimental data. It is perhaps not too surprising since the Kirchhoff plate theory is valid for thin plates only (ratio of radius to thickness is at least 10–15). Thus, it is appropriate to explore a more applicable model that accounts for effects beyond the thin-plate theory.

B. Finite element model

The model discussed above is based on thin-plate theory. However, for much of the experimental data, the assumptions implicit in Eq. (4) are not expected to hold due to

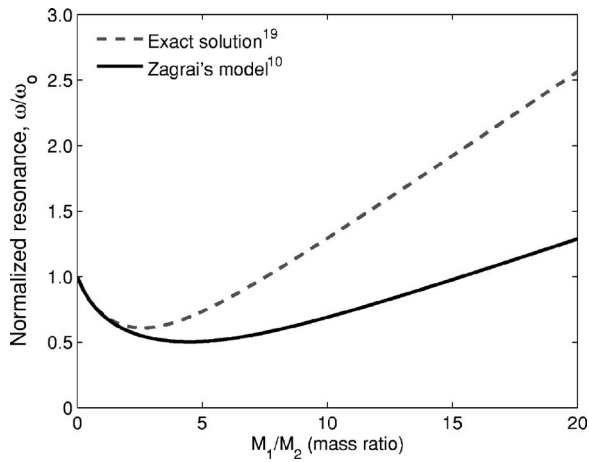


FIG. 4. Comparison between the exact solution (Ref. 22) for a two-layer plate and the heuristic model given in Ref. 10, Eq. (22).

thick-plate effects. In order to investigate the applicability of continuum models for this system further, the response of a thin plate loaded with an elastic layer is considered. The FEM is used to compute the first resonant mode of the two-layer system. The problem is axisymmetric such that axisymmetric elements can be used. Therefore, 57 SAX2 three-node axisymmetric shell elements and 115 CAX8R eight-noded biquadratic axisymmetric solid elements are used for the thin metal plate and the upper elastic layer, respectively.²³ The selection of the number of shell elements is based on a convergence study performed to match the exact solution for the first resonant frequency of the thin plate to six digits. The mesh generator in ABAQUS automatically selects the number of solid elements corresponding to the number of shell elements and the input data. The number of elements in the thickness direction varies with the thickness of the sand layer. For example, 14 elements are employed in the thickness direction in the case of mass ratio of 5. Due to the axisymmetry of the problem, the boundary condition corresponding to the center of the plate is chosen as rolling, while a clamped boundary condition is used for the plate outer edge. The boundary condition at the sand layer/tube interface (see Fig. 1) is expected to depend in some way on friction. The influence of this boundary condition on the numerical results is illustrated in Fig. 5, where results for both clamped and roller boundary conditions on the sand layer are compared. The results for a frictional boundary condition are expected to fall between these two extremes. The plots in Fig. 5 show that this boundary has only a minor influence on the predicted response for the regime of interest. Thus, a roller boundary condition is used for all simulations to follow. The condition along the interface between the plate and the EEL is rough friction (no slip occurs as relative horizontal motion of nodes in contact is prevented). Other interface conditions were examined as well but were found not to change results in any significant way.

The geometric and material properties of the plate are chosen to match the experimental system ($\delta=5.08 \times 10^{-2}$ m, $h=2.54 \times 10^{-4}$ m, $\rho=8575$ kg/m³, $E=103$ GPa, and $\nu=0.34$). Analytical results for a two-layer plate²² and the FEM results show that changes in Poisson's ratio from 0.05

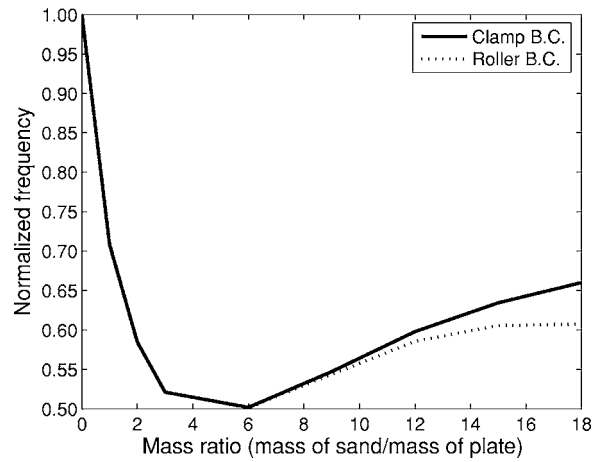


FIG. 5. Finite element results for the normalized first resonant frequency of the plate-EEL system for two types of boundary conditions (BC) applied at the interface between the tube walls and the EEL. The EEL replaces the granular layer of same thickness and density.

to 0.30 result in changes in the first resonant frequency smaller than 0.01%. Thus, it is concluded that the first resonant frequency is insensitive to changes in ν . Therefore, a Poisson's ratio of 0.25 is used for the EEL.

The ability of the numerical model to match the experimental results is first examined using a layer with the same density as that measured for the sand layer and with constant E . Numerical results are shown in Fig. 6 for $E=1, 3, 5$ MPa, together with the analytical result for a two-layer elastic plate ($E=3$ MPa) and three sets of experimental results (S1, S2, S5). In Fig. 6, the overall trends of the analytical two-layer plate theory and the three-dimensional FEM results are similar to the experiments: a decrease of the resonant frequency to a minimum then an increase with gradually decreasing rate as the thickness of the EEL increase. Note that the FEM result captures the leveling of the resonant frequency curve for large mass ratios. Such behavior is observed in the experiments but is impossible to obtain with the two-layer plate solution. However, neither the analytical solution for the two-layer plate nor the finite element models capture well the

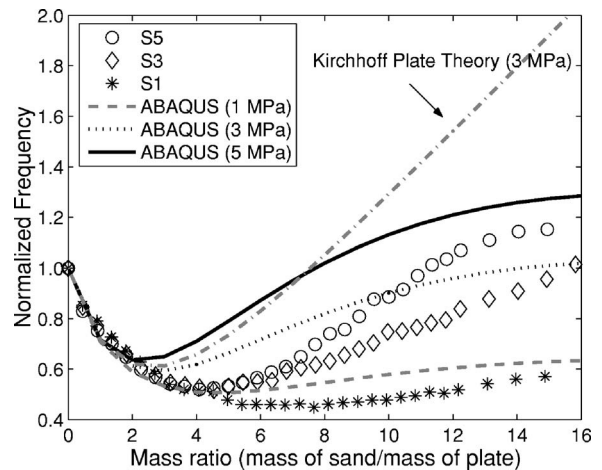


FIG. 6. Comparison of select experimental results with the two-layer plate model and the plate-EEL FEM model. The dash-dot line is obtained with the multilayer plate theory (Ref. 22) for $E=3$ MPa while the FEM results are obtained for equivalent elastic layers with $E=1, 3,$ and 5 MPa, respectively.

location of the minimum and the slope in the region of increasing frequency. In fact, the results shown in Fig. 6 suggest that the elastic modulus of the layer depends on its thickness. In order to study this effect further, the FEM is used in an inverse analysis to determine the effective elastic properties of the sand layer.

C. Thickness-dependent stiffness model

The results thus far, based on two-layer plate theory and finite element model that includes three-dimensional effects of the layer, clearly show that neither can adequately model the measured frequency shift as a function of layer thickness. It seems that the granular layer has an effective bending stiffness that changes with thickness. In order to determine the properties of an EEL that produces the same resonant frequencies as in the experiments, the problem is formulated as an inverse problem. The objective is to find the appropriate Young's modulus from a given experimental resonance and thickness using a procedure based on the shooting method.²⁴ For a given thickness of sand layer and the corresponding value of the first resonance from the experiment, the Young's modulus of an equivalent elastic layer of the same thickness is found as follows:

- (1) Two arbitrary values of the Young's modulus E_0 and E_1 are chosen and the finite element model of the EEL-plate system is solved for both cases giving two values for the first resonant frequency, ω_0 and ω_1 .
- (2) Subsequent values for the Young's modulus are computed using

$$E_{k+2} = E_k + \frac{\omega_k - \omega^*}{\omega_k - \omega_{k+1}} (E_{k+1} - E_k)$$

for $k=0,1,2,3,\dots$ where ω_k and ω_{k+1} are the resonant frequencies corresponding to E_k and E_{k+1} , respectively, with ω^* denoting the experimental resonance.

- (3) Iteration stops when the relative error between the experimental frequency and the frequency from the numerical model is less than a preset tolerance (here, 1%).

This procedure is repeated for all experimental measurements (all particles sizes and all layer thicknesses).

The results from these computations in terms of Young's modulus of the EEL for all experiments are shown in Fig. 7 over the range of mass ratio from 4 to 16. It should be noted that within the mass dominant regime for thin layers (region A in Fig. 2), the inverse problem of finding E for the EEL from the experimental frequencies is ill-posed due to the insensitivity of the resonant frequencies to variations in the Young's values of the EEL. That is, small perturbations in the input frequencies can induce large changes in Young's moduli.

The values obtained for E are in the range of several MPa for all sizes of sand examined, which is in the same range as those obtained by Yanagida *et al.*²⁵ for the "longitudinal elastic modulus" of sand using a different experiment when they analyzed properties of binary mixtures. The general trend observed is that layers of larger particles result in a larger effective E of the EEL. The results also show that the

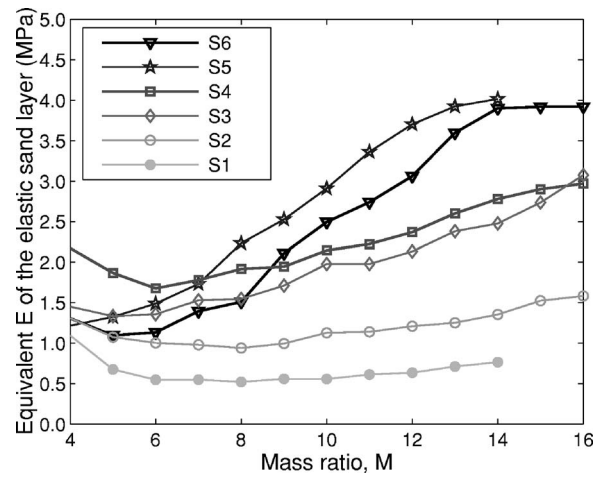


FIG. 7. Solution of the FEM-based inverse problem: computed values for the Young's modulus of an equivalent elastic layer that produces the same resonant frequency as the granular layer in the experiments (see Table I). Notice the general trend of increased elastic modulus with increase in particle size, as well as with the increase in thickness.

effective value of E increases with the layer thickness for all particle sizes. It may be conjectured that this increase is due to an increase in the interparticle pressure from the layer as outlined in the model described in Sec. II B. It is also interesting to note that the values of E shown in Fig. 6 are lower than might be expected based on wave speed measurements in sand (103–260 m/s),^{17,26} which would result in a range of E between 19 and 121 MPa.

In Fig. 8, the effective bending stiffness D of the EEL, normalized by the bending stiffness of the plate, is plotted as a function of mass ratio. The general observations for D are similar to those for E . However, when plotted in the context of the plate bending stiffness, the mass ratio necessary for the layer to become "stiffer" in bending than the metal plate is very clear. The results above the horizontal line ($D_{EEL}/D_p = 1$) denote granular layers that dominate the vibration response of the plate/granular layer system. In terms of the particle size dependence, the results in Fig. 8 show that

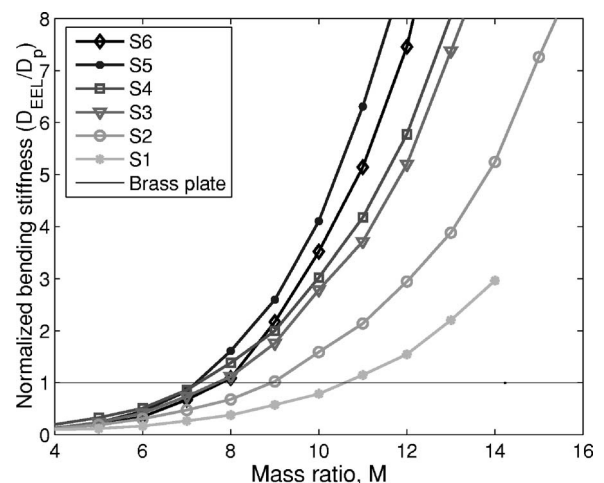


FIG. 8. Computed effective bending stiffness of the granular layer (see Table I) using the FEM-based inverse analysis for the equivalent elastic layer. Results are normalized by the bending stiffness of the metal plate.

the EEL for larger particles achieves the same effective D as the plate for layers that are thinner than the EEL for the smaller particles.

The inverse problem finite-element-based procedure described here provides a simple and effective means for computing the bending stiffness of a granular layer from experimental data. Such information is useful for the development of continuum models for granular media.

IV. SUMMARY

In this article, it has been shown that the vibration response of a sand-loaded plate has two primary regimes. For layers with mass that are less than approximately five times the mass of the plate, the resonance exhibits a mass-loading behavior as predicted theoretically. In this regime the resonance decreases with a dependence $(1+M)^{-1/2}$ with M as the mass ratio between the sand layer and plate. No dependence on particle size was observed. For higher values of M , the resonance reaches a minimum and then begins to increase with a clear dependence on average particle size: larger particles exhibit higher relative frequencies than smaller particles. The dependence on particle size is shown to behave according to a power law in particle radius. In addition, it was shown that the response to a polydispersed layer is equivalent to a monodispersed layer with the same average particle size. In other words, only the average particle size of a polydispersed layer appears to be important for this response. Attempts to understand this dependence based on effective moduli theories are qualitatively successful, but the value of the exponent in the power law does not match that of the experiments. The discrepancy between the observed exponent and the ones predicted by the well-bonded Hertzian models can perhaps be attributed to the failure of the model to include loss of contact and frictional dissipation in the bending motion induced by the vibration regime as well as other effects that are not clear at this time. This is the subject of future research.

In order to compute the bending stiffness of a granular layer a new methodology is proposed based on solving a sequence of inverse problems with the finite element method in which the metal-plate/granular layer system was replaced by an elastic shell/thick elastic layer numerical model. The nonlinear shooting method is used to obtain an elastic modulus for each thickness of the granular layer so that the equivalent elastic layer produces the same resonant frequency in the numerical model as that of the real system. It was shown that a single effective elastic modulus for the layers of a given particle size cannot be used to match the experimental results, but that a thickness-dependent modulus must be employed if the experimental data are to be matched.

These results show that layers of larger particles are "stiffer" than those made up of smaller particles for the same effective density. Modeling the dependence on particle size, however, remains to be elucidated since the effective medium theories based on well-bonded Hertzian models predict a value of the power law exponent that is half the size of that measured experimentally. At this point it is unclear if effec-

tive medium theories can resolve this issue. In the future discrete models will be used to include rotational degrees of freedom and frictional dissipation: two of the missing ingredients that may be responsible for the above-mentioned discrepancy. Such models are clearly important for an improved understanding of the vibration response of an elastic structure that interacts with a granular material. Quantitative methods of land mine detection by acoustic means will necessarily require a clear grasp of such fundamental behavior.

ACKNOWLEDGMENTS

The research was sponsored by the U.S. Army Research Laboratory under the RMAC-RTP Cooperative Agreement No. W911NF-04-2-0011. The authors also thank M. S. Korman and J. M. Sabatier for helpful discussions and information regarding the experimental setup and their data from the soil/plate oscillator. Finally, an anonymous reviewer is thanked for referring us to Refs. 18–20.

- ¹S. H. Lee, W. R. Scott, Jr., J. S. Martin, G. D. Larson, and G. S. McCall II, "Technical issues associated with the detection of buried land mines with high-frequency seismic waves," SPIE's Proceedings on Detection and Remediation Technologies for Mines and Minelike Targets VII, 2002, Vol. **4742**, pp. 617–628.
- ²J. M. Sabatier and N. Xiang, "Laser-Doppler based acoustic-to-seismic detection of buried mines," SPIE's Proceedings on Detection and Remediation Technologies for Mines and Minelike Targets IV, 2003, Vol. **3710**, pp. 215–222.
- ³W. R. Scott, Jr., S. H. Lee, G. D. Larson, J. S. Martin, and G. S. McCall II, "Use of high-frequency seismic waves for the detection of buried land mines," SPIE's Proceedings on Detection and Remediation Technologies for Mines and Minelike Targets VI, 2001, Vol. **4394**, pp. 543–552.
- ⁴N. Xiang and J. M. Sabatier, "An experimental study on antipersonnel landmine detection using acoustic-to-seismic coupling," J. Acoust. Soc. Am. **113**, 1333–1341 (2003).
- ⁵D. M. Donskoy, "Nonlinear vibro-acoustic technique for land mine detection," SPIE's Proceedings on Detection and Remediation Technologies for Mine and Minelike Targets III, 1998, Vol. **3392**, pp. 211–217.
- ⁶D. Donskoy, A. Ekimov, N. Sedunov, and M. Tsionskiy, "Nonlinear seismo-acoustic land mine detection and discrimination," J. Acoust. Soc. Am. **111**, 2705–2714 (2002).
- ⁷D. M. Donskoy and A. Ekimov, "Nonlinear vibrations of buried landmines," J. Acoust. Soc. Am. **117**, 690–700 (2005).
- ⁸A. Zagrai, D. Donskoy, and A. Ekimov, "Resonance vibrations of buried landmines," SPIE's Proceedings on Detection and Remediation Technologies for Mines and Minelike Targets IX, 2004, Vol. **5415**, pp. 21–29.
- ⁹M. S. Korman and J. M. Sabatier, "Nonlinear acoustic techniques for landmine detection," J. Acoust. Soc. Am. **116**, 3354–3369 (2004).
- ¹⁰A. Zagrai, D. Donskoy, and A. Ekimov, "Structural vibrations of buried land mines," J. Acoust. Soc. Am. **118**, 3619–3628 (2005).
- ¹¹W. Leissa, *Vibration of Plates* (Acoustical Society of America, 1993).
- ¹²J. K. Mitchell, *Fundamentals of Soil Behavior* (Wiley, New York, 1976).
- ¹³M. S. Korman (private communication).
- ¹⁴P. J. Digby, "The effective elastic moduli of porous granular rocks," J. Appl. Mech. **48**, 803–808 (1981).
- ¹⁵K. Walton, "The effective elastic moduli of a random packing of spheres," J. Mech. Phys. Solids **35**, 213–226 (1987).
- ¹⁶J. Jenkins, D. Johnson, L. LaRagione, and H. Makse, "Fluctuations and the effective moduli of an isotropic, random aggregates of identical, frictionless spheres," J. Mech. Phys. Solids **53**, 197–225 (2005).
- ¹⁷K. L. Johnson, *Contact Mechanics* (Cambridge University Press, New York, 1985).
- ¹⁸M. Prasad and R. Meissner, "Attenuation mechanisms in sands: Laboratory versus theoretical (Biot) data," Geophysics **57**, 710–719 (1992).
- ¹⁹R. Backrach, J. Dvorkin, and A. M. Nur, "Seismic velocities and Poisson's ratio of shallow unconsolidated sands," Geophysics **65**, 559–564 (2000).
- ²⁰M. Kimura, "Frame bulk modulus of porous granular marine sediments," J. Acoust. Soc. Am. **120**, 699–710 (2006).

- ²¹H. A. Makse, "Why effective medium theory fails in granular materials," *Phys. Rev. Lett.* **83**, 5070–5073 (1999).
- ²²Y. Stavsky and R. Loewy, "Vibration of isotropic composite circular plates," *J. Acoust. Soc. Am.* **49**, 1542–1550 (1971).
- ²³*ABAQUS V.6.4/Standard*.
- ²⁴C. F. Gerald and P. O. Wheatley, *Applied Numerical Analysis* (Pearson Education, 2004).
- ²⁵T. Yanagida, A. J. Matchett, B. N. Asmar, P. A. Langston, J. K. Walters, and J. M. Coulthard, "Dynamic response of well-mixed binary particulate systems subjected to low magnitude vibration," *Adv. Powder Technol.* **14**, 589–604 (2003).
- ²⁶M. L. Oelze, W. D. O'Brien, Jr., and R. G. Darmody, "Measurement of attenuation and speed of sound in soils," *Soil Sci. Soc. Am. J.* **66**, 788–796 (2002).

A study of vibroacoustic coupling between a pump and attached water-filled pipes

Bilong Li,^{a)} Melinda Hodkiewicz, and Jie Pan^{b)}

School of Mechanical Engineering, The University of Western Australia, 35 Stirling Highway, Crawley, WA6009 Australia

(Received 21 December 2005; revised 22 August 2006; accepted 9 November 2006)

This paper presents a model for the vibroacoustical behavior of a pump coupled with water-filled pipes. Coupling between (a) the pump and the inlet and outlet pipes, and (b) the pipe wall and the fluid contained in the pipe, is investigated through analytical modeling and numerical simulation. In the model, the pump is represented by a rigid body supported by multiple elastic mounts, and the inlet and outlet pipes by two semi-infinite water-filled pipes. The vibration characteristics of the coupled system under the excitation of mechanical forces and fluid-borne forces at the pump are calculated. The results enhance our understanding about how the input mechanical and fluid excitation energy at the pump is transmitted to the pipes and how to relate the piping vibroacoustical response to the excitations at the pump. This study assists in predicting dynamic stress in pipes for given excitations at the pump, and in developing methods to identify the nature (fluid or mechanical) of the excitation forces at the pump using the vibration and dynamic pressure measurements on the pump/pipe system. © 2007 Acoustical Society of America. [DOI: 10.1121/1.2405131]

PACS number(s): 43.40.Ey, 43.40.Rj, 43.40.Qi [JGM]

Pages: 897–912

I. INTRODUCTION

The dynamic behavior of pumps and associated piping systems is of practical interest due to its applications in industry noise and vibration control, and in pump condition monitoring, where vibroacoustical signals are often used for diagnosis purpose.

Research on pump and pipe vibration and internal hydrodynamics has traditionally focused on (a) modeling the hydroacoustic response in piping systems containing hydroacoustic excitation sources such as pumps,¹ (b) experimental studies on the effect of internal fluid excitation on the vibration response of the pump and pipes,^{2,3} or (c) modeling of the structural response of pipes to internal pipe hydroacoustic excitation.^{4–8} There is a need for a combined model to study the effects of fluid and mechanical excitation at the pump on the structural and hydroacoustic responses of the pipes. This is because the acoustical impedance presented by the fluid in, and structural mobility of, the pipes attached to the pump strongly affects the pump's vibration response. In addition, the dynamic loading of an elastically mounted pump at the end of a water-filled pipe also affects vibroacoustical response of the pipe.

Recently, Qi and Gibbs published two comprehensive papers addressing the problems of structure-borne sound transmission in a coupled pump/pipe domestic central heating system.^{9,10} Their work identifies the primary contribution by wave-type to structure-borne sound in semi-infinite and finite pipe systems and the effect of wave mode conversions at pipe junctions. The finite piping system in Ref. 10 comprises a radiator attached to a simple piping system. The

model relates the pump/pipe coupling effects to the point mobilities of pump/pipe junction, where the pump is treated as a mass, and the pipe is modeled as an equivalent beam.

In this paper, a model is developed to analyze the vibroacoustical coupling between a pump and attached water-filled pipes. The pump is simplified as a rigid body mounted on multiple elastic supports, and the associated inlet and outlet pipes as two semi-infinite water-filled pipes. The paper focuses on the calculation and examination of the modal characteristics and dynamic response of the pump/water-filled pipe system subjected to mechanical and fluid-borne excitations, and on the effect of vibroacoustical coupling between pump and pipes on these characteristics and response. The pipe model accommodates (a) all the higher order structural modes, (b) acoustical modes, and (c) their polarization angles due to nonsymmetrical feature of the pipe cross section. The analysis can be readily extended to more practical cases where pump casing is modally reactive and excitation of the fluid force may be spatially complicated (e.g., large double suction pump). Furthermore, the pump model allows (1) the pump to vibrate in six degrees-of-freedom and (2) a distributed connection (rather than a point connection) with pipes. This work has a potential application in predicting pipeline dynamic stress distribution due to pump excitation. The feasibility of identifying the excitation force (equivalent forcing function or input power) at the pump using the vibration and pressure information of the pipeline/pump system is also discussed.^{11,12}

II. A PUMP COUPLED WITH ONE WATER-FILLED PIPE

In the first part of this paper, we develop a model based on a single pipe coupled to a pump, as shown in Fig. 1. The pump is modeled as a rigid body supported by elastic mounts and the inlet pipe as a semi-infinite water-filled cylindrical

^{a)}Current address: Institute of Acoustics, Chinese Academy of Sciences, 100080, Beijing, P.R. China.

^{b)}Electronic mail: pan@mech.uwa.edu.au

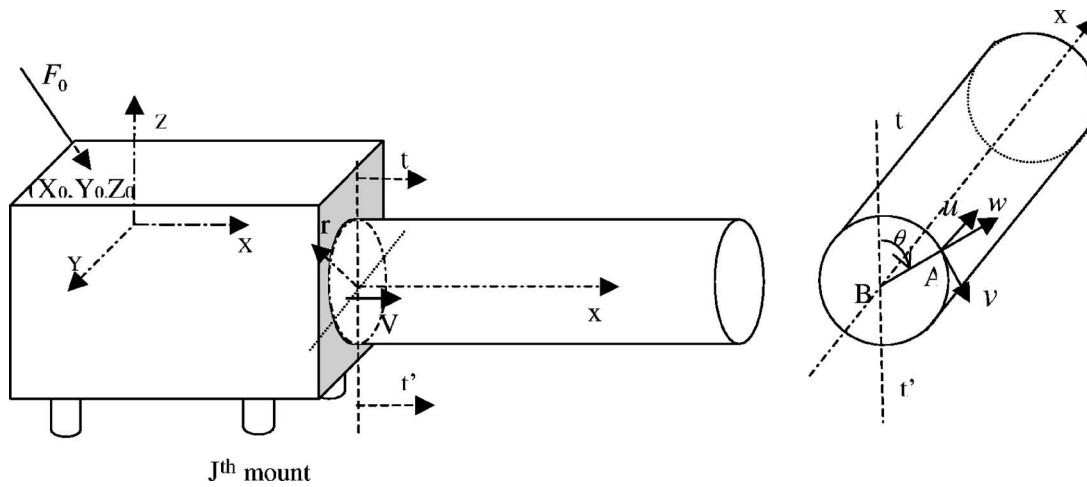


FIG. 1. A simplified model of pump/pipe coupled system.

pipe connected to the rigid body. The rigid body is referenced to a Cartesian coordinate (X, Y, Z) . The pipe is referenced to a cylindrical coordinate system (r, θ, x) , where x is taken in the axial direction of the shell, θ measures the angle in the circumferential direction, and r axis is directed outward along the radial direction. The pipe thickness and radius are h and a , respectively. The mechanical vibration source in the rigid body is described by a force vector $F_0 = (F_{0X} F_{0Y} F_{0Z})$ and a moment vector $M_0 = (M_{0X} M_{0Y} M_{0Z})$. The force and moment can be described by an external force matrix \mathbf{Q}_0 as follows:

$$\mathbf{Q}_0 = [F_{0X} \ F_{0Y} \ F_{0Z} \ M_{0X} \ M_{0Y} \ M_{0Z}]^T. \quad (1)$$

If the external force is a point force at $(X_0 \ Y_0 \ Z_0)$, \mathbf{Q}_0 can be written as

$$\mathbf{Q}_0 = \begin{bmatrix} 1 & 0 & 0 \\ 0 & 1 & 0 \\ 0 & 0 & 1 \\ 0 & Z_0 & -Y_0 \\ -Z_0 & 0 & X_0 \\ Y_0 & -X_0 & 0 \end{bmatrix} \begin{bmatrix} F_{0X} \\ F_{0Y} \\ F_{0Z} \end{bmatrix}. \quad (2)$$

The fluid-borne vibration source is described by a velocity V_0 located at the fluid cross section of the pipe/pump junction. The magnitude of the equivalent fluid-borne force acting on the rigid body may be approximated by

$$F_f = -\pi a^2 \rho_f c_f V_0, \quad (3)$$

where ρ_f and c_f are the density and the sound speed of fluid, respectively.

A. Rigid body (The pump model)

Using a similar approach described in Ref. 13, we define the origin of the coordinate system (X, Y, Z) at the center of gravity of the rigid body. The motion of this rigid body can be described by the displacement vector $\mathbf{s}_c = (u_c, v_c, w_c)$ of its center of gravity and angular displacement $\theta_c = (\theta_{cX}, \theta_{cY}, \theta_{cZ})$ around the X, Y, Z axes. The matrix expression describing these displacements is

$$\mathbf{D}_c = [u_c \ v_c \ w_c \ \theta_{cX} \ \theta_{cY} \ \theta_{cZ}]^T. \quad (4)$$

Figure 2 shows the coordinate system and the possible displacement vectors of the J th elastic mount. The bottom surface of the elastic mount is assumed to be rigid and with clamped boundary conditions. The displacement vectors at the top surfaces are expressed by \mathbf{D}_J^t ,

$$\mathbf{D}_J^t = [u_J^t \ v_J^t \ w_J^t \ \theta_{XJ}^t \ \theta_{YJ}^t \ \theta_{ZJ}^t]^T. \quad (5)$$

The elastic forces and moment acting on the rigid body at the top location of the J th mount can be written in a vector form as

$$\mathbf{Q}_J^t = [F_{XJ}^t \ F_{YJ}^t \ F_{ZJ}^t \ M_{XJ}^t \ M_{YJ}^t \ M_{ZJ}^t]^T. \quad (6)$$

The relation between the force vector \mathbf{Q}_J^t and the displacement vectors \mathbf{D}_J^t is

$$\mathbf{Q}_J^t = -\mathbf{K}_J \mathbf{D}_J^t, \quad (7)$$

where

$$\mathbf{K}_J = \text{diag}\{K_{XJ} \ K_{YJ} \ K_{ZJ} \ G_{XJ} \ G_{YJ} \ G_{ZJ}\}, \quad (8)$$

and $K_{XJ}, K_{YJ}, K_{ZJ}, G_{XJ}, G_{YJ}, G_{ZJ}$ are the complex elastic constants of the mount. For a cylindrical isotropic mount, $K_{XJ} = K_{YJ}$ and $G_{XJ} = G_{YJ}$.

The force \mathbf{Q}_E generated by all elastic supports is

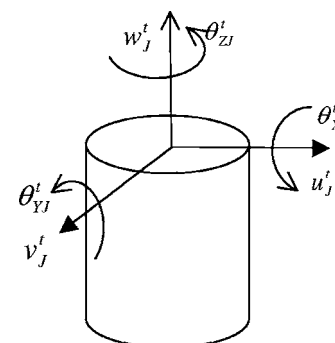


FIG. 2. The coordinate system and displacement components of the J th elastic mount.

$$\mathbf{Q}^P = \sum_n \mathbf{R}_n^{\theta 2} \mathbf{G}_n \mathbf{X}_n + [0, G_{0T}, 0, 0, 0]^T V_{0T}, \quad (22)$$

where

$$\mathbf{R}_n^{\theta 2} = \begin{cases} \text{diag}\{\cos(n\theta + \theta_{n0}), 0, \cos(n\theta + \theta_{n0}), \cos(n\theta + \theta_{n0}), \sin(n\theta + \theta_{n0})\}, & n = 0 \\ \text{diag}\{\cos(n\theta + \theta_{n0}), \sin(n\theta + \theta_{n0}), \cos(n\theta + \theta_{n0}), \cos(n\theta + \theta_{n0}), \sin(n\theta + \theta_{n0})\}, & n > 0, \end{cases} \quad (23)$$

$$\mathbf{X}_n = [W_{n1}, W_{n2}, \dots, W_{nm}]^T, \quad (24)$$

$$\mathbf{G}_n = [\mathbf{G}_n(1, m), \mathbf{G}_n(2, m), \mathbf{G}_n(3, m), \mathbf{G}_n(4, m), \mathbf{G}_n(5, m)]^T, \quad (25a)$$

where the elements of matrix \mathbf{G}_n are

$$\mathbf{G}_n(1, m) = \frac{Eh}{a(1 - \nu^2)} [\alpha_{n1}^U k_{n1} a + \nu n \alpha_{n1}^V + \nu, \dots, \alpha_{nm}^U k_{nm} a + \nu n \alpha_{nm}^V + \nu], \quad (25b)$$

$$\mathbf{G}_n(2, m) = -\frac{jEh}{2a(1 + \nu)} [n \alpha_{n1}^U + \alpha_{n1}^V k_{n1} a, \dots, n \alpha_{nm}^U + \alpha_{nm}^V k_{nm} a], \quad (25c)$$

$$\mathbf{G}_n(3, m) = -\frac{jEh^3}{12a^3(1 - \nu^2)} [(k_{n1} a)^3 + (2 - \nu)n^2 k_{n1} a, \dots, (k_{nm} a)^3 + (2 - \nu)n^2 k_{nm} a], \quad (25d)$$

$$\mathbf{G}_n(4, m) = \frac{Eh^3}{12a^2(1 - \nu^2)} [\nu n^2 + (k_{n1} a)^2, \dots, \nu n^2 + (k_{nm} a)^2], \quad (25e)$$

$$\mathbf{G}_n(5, m) = \frac{Eh^3}{12a^2(1 - \nu^2)} [n k_{n1} a, \dots, n k_{nm} a]. \quad (25f)$$

In Eq. (23), the second element of the diagonal matrix $\mathbf{R}_n^{\theta 2}$ is set to zero to exclude the torsional wave component contribution from the coupled expression for mode $n=0$. The contribution of torsional wave component for breathing mode is separately included in $G_{0T}V_{0T}$, where G_{0T} is given by

$$G_{0T} = -\frac{jEh}{2a(1 + \nu)} k_{0T} a. \quad (26)$$

At the pump/pipe junction $x=0$, the acoustic pressure inside the pipe is related to the displacement of the pipe wall by

$$p_f(r, \theta) = \sum_n P_n \cos(n\theta + \theta_{n0}) = \sum_n \mathbf{E}_n \mathbf{X}_n \cos(n\theta + \theta_{n0}), \quad (27)$$

where

$$\mathbf{E}_n = [E_n(1), E_n(2) \dots E_n(m)], \quad (28a)$$

$$E_n(m) = \alpha_{nm}^P J_n(k_m^r \sigma). \quad (28b)$$

C. Solution of the system response

To calculate the system response, it is necessary to expand the boundary conditions at the pipe/pump junction to determine (1) the six-degree-of-freedom motion of the rigid body, (2) the (n, m) th modal amplitude W_{nm} , and (3) the torsional modal amplitude V_{0T} of the pipe.

At the pipe/pump junction, the total forces acting on the rigid body from the pipe/pump junction are determined by the coupled motion of the pipe and the pump. Due to the rigid body assumption, only two pipe circumferential modes (breathing mode $n=0$ and beam mode $n=1$) couple with the rigid body motion of the pump. Therefore the total force \mathbf{Q}_T at the pipe/pump junction is given by

$$\mathbf{Q}_T = \mathbf{Q}_{T0} + \mathbf{Q}_{T1}, \quad (29)$$

where \mathbf{Q}_{T0} and \mathbf{Q}_{T1} represent forces contributed by breathing mode $n=0$ and beam mode $n=1$, respectively. These forces are related to modal amplitudes of the pipe wall (Appendix A), given by

$$\mathbf{Q}_{T0} = -\{\mathbf{R}_0^{\alpha 1} G_0(1, m) + \mathbf{R}_0^{\alpha 3}\} \mathbf{X}_0 - \mathbf{R}_{0T}^{\alpha} G_{0T} V_{0T}, \quad (30)$$

$$\mathbf{Q}_{T1} = -\{\mathbf{R}_1^{\alpha 1} \mathbf{G}_1 + \mathbf{R}_1^{\alpha 3}\} \mathbf{X}_1, \quad (31)$$

where $\mathbf{R}_n^{\alpha 3} = \int_0^a \mathbf{R}_n^{\alpha 2} \mathbf{E}_n r dr$, and the definition of the coefficient matrix $\mathbf{R}_n^{\alpha 1}$, $\mathbf{R}_n^{\alpha 2}$ and \mathbf{R}_{0T}^{α} are shown in Appendix C. For breathing mode $n=0$, Eq. (30) indicates that only the axial stress force N_{x0} and torsional shear stress $N_{x\theta 0}$ contribute to the motion of the rigid body. However if the elastic vibration on the pump casing is considered, participation of higher order pipe modes is possible in the coupling force and Eq. (22) should be used.

In Eqs. (30) and (31), the unknown coefficients \mathbf{X}_n and V_{0T} are determined by the continuity condition of the junction. At the pump/pipe junction, the displacement and the slope continuities suggest the following relation:

$$\begin{bmatrix} u & \nu & w & \frac{\partial w}{\partial x} \end{bmatrix}^T = \mathbf{R}^{AC} \mathbf{D}_c, \quad (32)$$

where \mathbf{R}^{AC} represents the location and coordinate conversion matrix given by Appendix B.

Substituting Eqs. (19) and (21) into Eq. (32), multiplying $\mathbf{R}_n^{\theta 3} = \text{diag}\{\cos(n\theta + \theta_{n0})\sin(n\theta + \theta_{n0})\cos(n\theta + \theta_{n0})\cos(n\theta + \theta_{n0})\}$ on both sides of the resultant equation and integrating it from 0 to 2π , results in

$$\alpha_n \mathbf{X}_n = \mathbf{R}_n^{\alpha 4} \mathbf{D}_c, \quad (33)$$

where

$$\mathbf{R}_n^{\alpha 4} = \Lambda^{-1} \int_0^{2\pi} \mathbf{R}_n^{\theta 3} \mathbf{R}_n^{\alpha 3} d\theta, \quad (34)$$

$$\Lambda = \int_0^{2\pi} \mathbf{R}_n^{\theta 3 2} d\theta, \quad (35)$$

$$\alpha_n = \begin{bmatrix} \alpha_{n1}^S & \alpha_{n2}^S & \cdots & \alpha_{nm}^S \\ -jk_{n1} & -jk_{n2} & \cdots & -jk_{nm} \end{bmatrix}. \quad (36)$$

For each circumferential mode, Eq. (33) provides four equations of coefficient \mathbf{X}_n . [The breathing mode $n=0$, where v is uncoupled with u and w , is excluded in the coupled expression of Eq. (33).] The remaining $(m-4)$ equations result from fluid boundary conditions at the junction. The particle velocity of the fluid at $x=0$ satisfies $\hat{v} = j(1/\rho\omega)(\partial p/\partial x)$. Using this relation, the remaining $(m-4)$ equations for particular circumferential mode can be written as⁸

$$\mathbf{E}_f^{s'} \mathbf{X}_n = \hat{V}_{ns'} \bar{\Lambda}_{ns'}, \quad (s' = 1, 2, \dots, m-4), \quad (37)$$

where $\hat{V}_{ns'}$ is modal amplitude for the assumed fluid volume source at $x=0$. It is related to the velocity of the fluid at the pump/pipe interface by

$$v_f|_{x=0} = \sum_{n,s} \hat{V}_{ns} \cos(n\theta + \theta_{n0}) J_n(k^s r) \quad (s = 1, 2, \dots, m-4), \quad (38)$$

where the velocity expression in the radial direction is expanded by the mode shape functions of sound pressure in a pipe with the rigid wall condition ($J_n'(k^s r)|_{r=a}=0$).

In Eq. (37), the matrix $\mathbf{E}_f^{s'}$ and the coefficients $\bar{\Lambda}_{ns'}$ and $\chi_{ns',nm}$ are given by

$$\mathbf{E}_f^{s'} = \frac{1}{\rho_f \omega} [k_{n1} \alpha_{n1}^P \chi_{ns',n1}, \quad k_{n2} \alpha_{n2}^P \chi_{ns',n2}, \quad \dots, \quad k_{nm} \alpha_{nm}^P \chi_{ns',nm}], \quad (39)$$

$$\bar{\Lambda}_{ns'} = \int_0^a J_n^2(k^{s'} r) r dr, \quad (40a)$$

$$\chi_{ns',nm} = \int_0^a J_n(k^{s'} r) J_n(k_m^s r) r dr. \quad (40b)$$

The combination of Eqs. (33) and (37) gives rise to

$$\mathbf{X}_n = \begin{bmatrix} \alpha_n \\ \hat{\mathbf{E}}_f \end{bmatrix}^{-1} \begin{bmatrix} \mathbf{R}_n^{\alpha 4} \mathbf{D}_c \\ \hat{\mathbf{V}}_n \end{bmatrix} = [\mathbf{F}_n^\alpha, \mathbf{F}_n^V] \begin{bmatrix} \mathbf{R}_n^{\alpha 4} \mathbf{D}_c \\ \hat{\mathbf{V}}_n \end{bmatrix}, \quad (41)$$

where the matrix $\mathbf{F}_n = [\mathbf{F}_n^\alpha, \mathbf{F}_n^V] = \begin{bmatrix} \alpha_n \\ \hat{\mathbf{E}}_f \end{bmatrix}^{-1}$ is introduced for the convenience of expression, and $\hat{\mathbf{V}}_n$ and \mathbf{E}_f are given by

$$\hat{\mathbf{V}}_n = [\hat{V}_{n1} \bar{\Lambda}_{n1} \quad \hat{V}_{n2} \bar{\Lambda}_{n2} \quad \cdots \quad \hat{V}_{ns'} \bar{\Lambda}_{ns'}]^T, \quad (42)$$

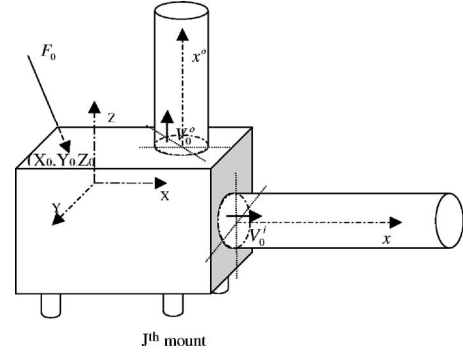


FIG. 3. A rigid body coupled with two semi-infinite water filled pipes.

$$\mathbf{E}_f = [E_f^1 \quad E_f^2 \quad \cdots \quad E_f^{s'}]^T. \quad (43)$$

The unknown coefficient V_{0T} for breathing mode is given by the continuity condition of the junction,

$$V_{0T} = a \theta_{cX} = \mathbf{R}_{0T}^{\alpha 2} \mathbf{D}_c. \quad (44)$$

The combination of Eqs. (16), (29)–(31), (41), and (44) leads to

$$(\mathbf{K}_r + \mathbf{K}_p - \omega^2 \mathbf{M}_r) \mathbf{D}_c = \mathbf{Q}_0 + \mathbf{Q}_f, \quad (45)$$

$$\mathbf{K}_p = \sum_{n=0}^1 \{ \mathbf{R}_n^{\alpha 1} \mathbf{G}_n + \mathbf{R}_n^{\alpha 3} \} \mathbf{F}_n^\alpha \mathbf{R}_n^{\alpha 4} + \mathbf{R}_{0T}^{\alpha 1} \mathbf{G}_{0T} \mathbf{R}_{0T}^{\alpha 2}, \quad (46)$$

$$\mathbf{Q}_f = - \sum_{n=0}^1 (\mathbf{R}_n^{\alpha 1} \mathbf{G}_n + \mathbf{R}_n^{\alpha 3}) \mathbf{F}_n^V \hat{\mathbf{V}}_n. \quad (47)$$

The response of the system can then be determined by solving Eqs. (41), (44), and (45).

III. A PUMP COUPLED WITH TWO WATER-FILLED PIPES

The extension of the above-discussed pump/pipe model to a pump coupled with inlet and outlet pipes is straightforward. Figure 3 shows an example of the rigid body pump coupled with two semi-infinite water-filled pipes. The pipe running parallel with the X axis of the rigid body represents the inlet pipe, and the pipe running parallel with Z of the rigid body corresponds to the outlet pipe. As with the model used in Sec. II, a mechanical force \mathbf{Q}_0 is imposed on the rigid body, and the fluid pulsation sources V_0 are located at the pump/pipe junctions. The superscripts i and o correspond to the inlet pipe and the outlet pipe, respectively. In Fig. 3, the x^i axis describing the inlet pipe runs parallel with X axis of the rigid body. The x^o axis describing the outlet pipe runs parallel with Z axis of the rigid body.

Following a similar procedure to that used in Sec. II and noting the location and coordination conversion matrix for the outlet pipe, the total forces acting on the rigid body at the rigid body/outlet pipe junction are described by

TABLE I. System parameters used in calculation.

a	0.0525 m	X_0	0
h	0.005 m	Y_0	0
ρ_s	7800 kg/m ³	Z_0	0.12 m
ρ_f	1000 kg/m ³	X_{c1}, X_{c2}	0.18 m
E	2.1×10^{11} N/m ²	X_{c3}, X_{c4}	-0.11 m
ν	0.3	Y_{c1}, Y_{c4}	0.11 m
m_c	105 kg	Y_{c2}, Y_{c3}	-0.11 m
η_p	0.01	$Z_{c1}, Z_{c2}, Z_{c3}, Z_{c4}$	-0.21 m
$\eta_{J,1-6}$	0.01	X_B^i	0.27 m
I_{XX}	1.57 kg m ²	Y_B^i	0
I_{YY}	3.03 kg m ²	Z_B^i	0
I_{ZZ}	2.74 kg m ²	X_B^o	0.18 m
I_{XY}	-0.0013 kg m ²	Y_B^o	0
I_{YZ}	-0.0078 kg m ²	Z_B^o	0.22 m
I_{XZ}	0.34 kg m ²		

$$\mathbf{Q}_T^o = - \sum_{n=0}^1 \{ \mathbf{R}_n^{o\alpha 1} \mathbf{G}_n^o + \mathbf{R}_n^{o\alpha 1} \} \mathbf{X}_n^o + \mathbf{R}_{0T}^{o\alpha 1} \mathbf{G}_{0T}^o \mathbf{V}_{0T}^o, \quad (48)$$

where \mathbf{X}_n^o and \mathbf{V}_{0T}^o may be derived by a similar procedure as Eqs. (41) and (44),

$$\mathbf{X}_n^o = \begin{bmatrix} \mathbf{F}_n^{o\alpha} \mathbf{R}_n^{o\alpha 4} \mathbf{D}_c \\ \mathbf{F}_n^{oV} \hat{\mathbf{V}}_n^o \end{bmatrix}, \quad (49)$$

$$\mathbf{V}_{0T}^o = \mathbf{R}_{0T}^{o\alpha 2} \mathbf{D}_c, \quad (50)$$

where the definition of coefficient matrices $\mathbf{R}_n^{o\alpha}$ and $\mathbf{R}_{0T}^{o\alpha}$ are shown in Appendix C.

Using Eqs. (48)–(50) and following the same procedure of the derivation of Eq. (45), the equation for the coupled system of rigid body/two pipes is

$$(\mathbf{K}_r + \mathbf{K}_p^i + \mathbf{K}_p^o - \omega^2 \mathbf{M}_r) \mathbf{D}_c = \mathbf{Q}_0 + \mathbf{Q}_f^i + \mathbf{Q}_f^o. \quad (51)$$

The definition of matrix \mathbf{K}_p and \mathbf{Q}_f in Eq. (51) follows the same procedure of Eqs. (46) and (47); the coefficient matrices shown in Appendices C and E are related to the inlet pipe and the outlet pipe, respectively.

IV. RESULTS AND DISCUSSIONS

Although an arbitrary number of mounts could be considered in the model, in this analysis we only use four mounts for the systems described in Figs. 1 and 3. The four mounts are assumed to be identical and modeled as isotropic cylindrical tubes. The parameters of pump, pipes, and mounts used for the calculation are listed in Tables I and II. In Table II E_J and ν_J are, respectively, Young’s modulus and Poisson’s ratio of the elastic material, and L_J , a_J , b_J are, respectively, the unloaded length, and the inside and outside radii of the mounts.

A. Pump coupled with the inlet pipe only

1. Modal characteristics of the pump

The modal characteristics of the pump/pipe system mounted on the mounts are determined from using Eq. (46) with $\mathbf{Q}_0=0$ and $\mathbf{Q}_f=0$,

TABLE II. Stiffness coefficients of mounts.

E_J		2.1×10^9 N/m ²
ν_J		0.4
a_J		0.02 m
b_J		0.03 m
L_J		0.05 m
$K_{J,1}, K_{J,2}$	$\frac{3\pi E_J (b_J^4 - a_J^4)}{4L_J^3}$	2.573×10^7 N/m
$K_{J,3}$	$\frac{\pi E_J (b_J^2 - a_J^2)}{L}$	6.6×10^7 N/m
$K_{J,4}, K_{J,5}$	$\frac{\pi E_J (b_J^4 - a_J^4)}{4L}$	2.144×10^4 N/m
$K_{J,6}$	$\frac{\pi E_J (b_J^4 - a_J^4)}{4(1 + \nu_J)L}$	1.532×10^4 N/m

$$(\mathbf{K}_r + \mathbf{K}_p - \omega^2 \mathbf{M}_r) \mathbf{D}_c = 0. \quad (52)$$

The matrix \mathbf{K}_p reflects the influence of pipe wave motion on the pump response. When $\mathbf{K}_p=0$, Eq. (52) represents the case where there is no inlet pipe attached to the pump. \mathbf{K}_p can be written as

$$\mathbf{K}_p = \mathbf{K}_p^T + \mathbf{K}_p^L + \mathbf{K}_p^B + \mathbf{K}_p^f. \quad (53)$$

\mathbf{K}_p^T and \mathbf{K}_p^L are the contributions to system stiffness matrix from the torsional wave motion and longitudinal wave motion of the pipe breathing mode, \mathbf{K}_p^B is the contribution from the bending wave motion of pipe beam mode. \mathbf{K}_p^f is due to sound wave in the pipe. They are expressed, respectively, as

$$\mathbf{K}_p^T = \mathbf{R}_{0T}^{\alpha 1} \mathbf{G}_{0T} \mathbf{R}_{0T}^{\alpha 2}, \quad (54a)$$

$$\mathbf{K}_p^L = \mathbf{R}_0^{\alpha 1} \mathbf{G}_0(1, m) \mathbf{F}_0^{\alpha} \mathbf{R}_0^{\alpha 1}, \quad (54b)$$

$$\mathbf{K}_p^B = \mathbf{R}_1^{\alpha 1} \mathbf{G}_1 \mathbf{F}_1^{\alpha} \mathbf{R}_1^{\alpha 4}, \quad (54c)$$

$$\mathbf{K}_p^f = \sum_{n=0}^1 \mathbf{R}_n^{\alpha 3} \mathbf{F}_n^{\alpha} \mathbf{R}_n^{\alpha 4}. \quad (54d)$$

The resonance frequencies and their corresponding modal shapes for the uncoupled rigid body and the coupled rigid body/pipe system are shown in Table III. If the matrix $\mathbf{K}_p^T \neq 0$, then the pump’s response is only affected by the torsional wave motion of the pipe. Table III shows that the motion consists of displacements in the six degrees of freedom, which are the three translation displacements and three rotational displacements ($T_X, T_Y, T_Z, R_X, R_Y, R_Z$). Since the mounts are not fully symmetrical with the centroid of the pump, each pump mode contains more than one component of the displacement. For the case of a pump uncoupled with the pipes, two groups of modes may be classified. The first group, described by (T_Y, R_X, R_Z) and including modes 1, 3, and 6, consists of contributions from the translation component in the Y direction and rotation components around the X direction and the Z direction. The second group, described by (T_X, T_Z, R_Y) and including modes 2, 4, and 5, consists of contributions from rotation components around the Y direc-

TABLE III. Modal characteristics of the pump.^a

No.	Rigid body only $\mathbf{K}_p=0$	Rigid body coupled with inlet pipe			
		$\mathbf{K}_p^T \neq 0$	$\mathbf{K}_p^L \neq 0$	$\mathbf{K}_p^B \neq 0$	$\mathbf{K}_p \neq 0$
1	95.0 Hz, (T_Y, R_X, R_Z), 0.34/1/0.23	Same	Same	96.2 Hz, (T_Y, R_X, R_Z), 0.35/1/0.89	96.2 Hz, (T_Y, R_X, R_Z), 0.35/1/0.89
2	108.8 Hz, (T_X, T_Z, R_Y), 0.41/-0.04/1	Same	Overdamping	Overdamping	Overdamping
3	183.4 Hz, (T_Y, R_X, R_Z), 0.02/0.13/-1	Same	Same	Overdamping	Overdamping
4	245.9 Hz, (T_X, T_Z, R_Y), 0.15/-0.69/1	Same	Same	245.5 Hz, (T_X, T_Z, R_Y), 0.13/-0.59/1	245 Hz, (T_X, T_Z, R_Y), 0.13/-0.59/1
5	322.3 Hz, (T_X, T_Z, R_Y), R_Y, T_X, T_Z 0.06/0.05/1	Same	Same	Overdamping	Overdamping
6	377.7 Hz, (T_Y, R_X, R_Z), 0.04/-1/0.09	Same	Same	Same	Same

^a R_X represents the rotation of the rigid body around the X direction, T_X is the translation of the rigid body in the X direction, etc.

tion and the translation components in the X direction and Z direction. The ratios of the displacement components are also given in Table III.

When the pump is coupled with the inlet pipe, the pipe's wave motion affects the pump vibration characteristics. Results are summarized as follows.

(a) The torsional wave motion of the pipe has no direct effect on the pump's natural frequencies and modal shape (Table III, column of $\mathbf{K}_p^T \neq 0$). For the matrix \mathbf{K}_p^T in Eq. 62(a), manipulation leads to a nonzero pure imaginary element, $K_p^T(4,4) = -j[\pi E h / (1 + \nu)] k_{0T} a^3$. Therefore, the pipe torsional wave motion presents a damping effect on the modes dominated by the rotation-dominant component around the X direction [Figs. 4(a)–4(d)].

(b) The longitudinal wave motion of the pipe also results in a damping effect on pump's response. The longitudinal input impedance of an infinite beam is represented by a pure real number.¹¹ As impedance is real, the corresponding stiffness term is imaginary and results in a damping on the coupled system. Table III and Figs. 4(b)–4(e) indicate that mode 2, which mainly contains the rotation component around the Y direction and translation component in the X direction, is over-damped and therefore unable to be excited when the pump couples with the longitudinal motion of the pipe. The modal characteristics of the remaining modes are unaffected by the longitudinal waves.

(c) The bending wave in the pipe has both stiffness and damping effects on the pump vibration. [The point input mobility of the bending wave in an infinite beam ($Y_b = (1 - j) / \rho S c_b$ (Ref. 11), has both real and imaginary parts.) Modes 2, 3, and 5, which are dominated by rotation component around the Z and Y directions, are not excited due to the heavy damping contribution from the pipe bending wave motion. Modes 1 and 4 are little affected by the bending

waves. Mode 6, which is also dominated by rotation component around the Y direction, is not affected by the pipe bending wave motion.

(d) The influence of pipe attachment on pump motion is the combination of effects from all the wave types. The damping due to pipe bending and longitudinal wave motions is the dominating effect in the pump/pipe coupling (see their effects on modes 2, 3, and 5). On the other hand, the damping due to the torsional wave motion has a slight effect on the pump vibration (see Table III).

Figure 4 shows an example of the influence of the pipe's individual wave motion on the rigid body response. The attached pipe significantly affects the rigid body motion. The resonance responses at modes 2, 3, and 5 are suppressed due to coupling effects of \mathbf{K}_p^L and \mathbf{K}_p^B ; mode 6 is slightly affected by \mathbf{K}_p^T . Figure 5 shows the rigid body response when the pump is coupled and uncoupled with the pipe. Once again, the significant coupling effect is evident on modes 2, 3, and 5.

2. System response characteristics

Fluid-borne noise and mechanical sources usually coexist in the pump/pipeline system. Fluid-borne noise can be produced by vortex formation in high-velocity flow, pulsations, cavitation, flashing, water hammer, flow separation, and impeller interaction with the pump cutwater. Examples of mechanical noise source may include the impeller and seal rubs, defective or damaged bearings, motor-pump coupling misalignment, looseness, and unbalanced rotating components. In condition monitoring, it is of practical interest to relate the system response to the excitation source type.

Table IV shows the force vectors used as excitation to the pump/inlet pipe system. The vector (F_{0X}, F_{0Y}, F_{0Z}) repre-

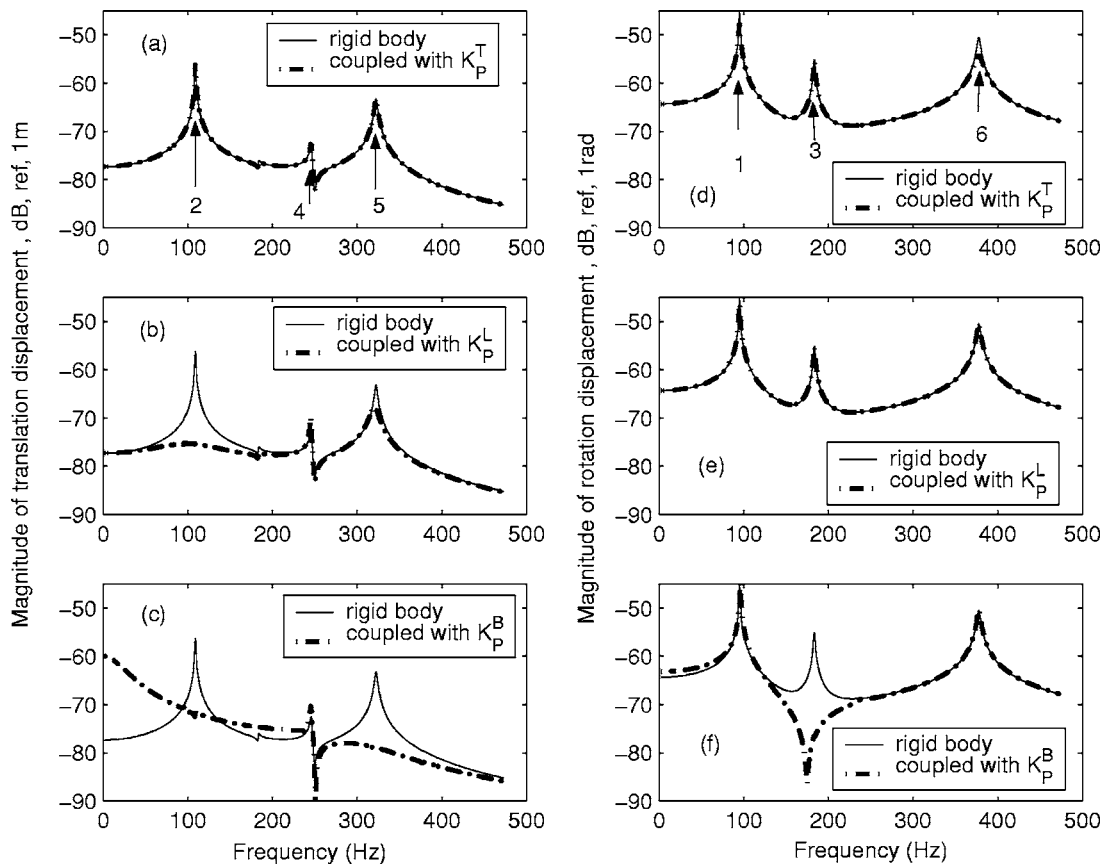


FIG. 4. Influence of wave type of the pipe motion on the displacement of the rigid body under the given force vector $[1 \ 1 \ 1 \ 1 \ 1 \ 1]^T$ exerted on its centroid, (a)–(c) u_c , (d)–(f) θ_{cX} .

sents the three components of an external point force acting on the coordinate $(0 \ 0 \ 0.12 \text{ m})$ of the rigid body, F_f^i represents the fluid-borne force generated by pulsating fluid velocity source at the pump/inlet pipe junction. The frequency range of the simulation is up to 5000 Hz; approximately 0.3 times the ring frequency of the pipe.

It is expected that the velocity magnitude of each component of the rigid body will depend upon the driving frequencies and force vector characteristics. Figure 6 shows the rigid body response for the given force vector. An external point force component in the X direction results in dominant response component in the same direction. The same results are observed for velocity in the Y direction and Z direction and the angular velocity around the X , Y , and Z direction, respectively. An equivalent fluid-borne force in the X direction generates a similar vibration level of the rigid body in comparison with that of the mechanic force component in the same direction.

The vibration response of the pipe wall due to the external force at the pump is shown in Fig. 7. For the breathing mode of the pipe, the vibration of the pipe wall is crucially related to source type [see Figs. 7(a)–7(c)]. This is further discussed in the following.

(a) Across the frequency range, a one unit equivalent fluid pulsatory source [fluid-borne force in Eq. (3)] in the X direction generates much larger radial velocity response in the pipe wall than that from one unit mechanical force in the same direction. We postulate that the reason may be ex-

plained like this: The axial mechanical force primarily excites longitudinal breathing mode, but due to coupling with the pipe wall displacement components, the longitudinal waves in the pipe produce only a small radial displacement. This is not like the acoustical source which produces pressure in the pipe's radial direction, therefore, the acoustical excitation is more effective in generating a larger radial movement of the pipe wall than an axial mechanical force at the pump/pipe junction. Further work is required to confirm that the same numerical value for equivalent fluid source strength and mechanical force result in similar input power into the pipe.

(b) For breathing type pipe motion, there are two propagating waves, structural longitudinal wave type and fluid plane wave type. These coexist and dominate the pipe response as shown in Fig. 8. We furthermore observe that the fluid pulsatory source generates predominantly a fluid plane wave type response, while an axial mechanical force generates predominantly a structural longitudinal wave type response (Fig. 8).

(c) Excitation forces in Y and Z directions do not excite the same magnitude of breathing type pipe motion as those in the X direction.

For beam wave motion of the pipe, the general frequency feature of the vibration response resulting from the mechanical dominated forces in the X , Y , and Z directions and the equivalent fluid pulsatory force in the X direction [see Figs. 7(d)–7(f)] are similar.

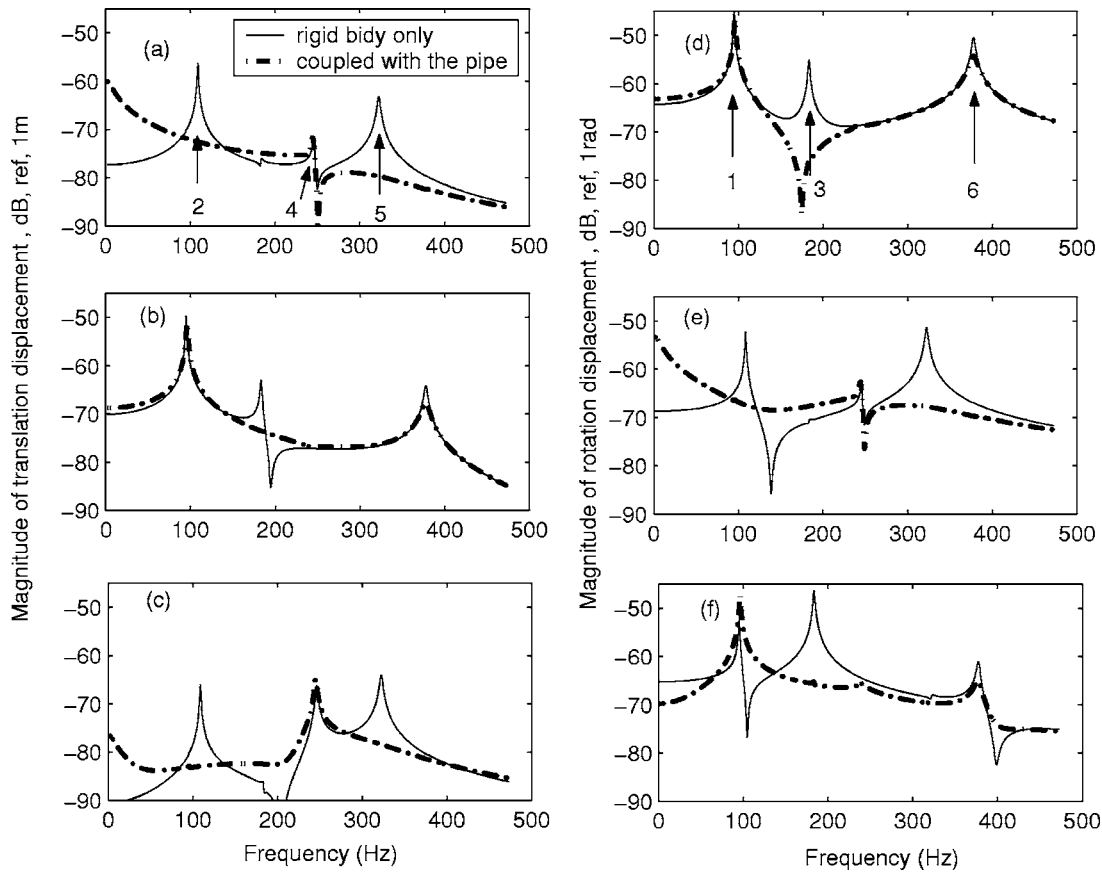


FIG. 5. Influence of pipe on the displacement of the rigid body under the given force vector $[1 \ 1 \ 1 \ 1 \ 1 \ 1]^T$ exerted on its centroid, (a) u_c , (b) v_c , (c) w_c , (d) θ_{cx} , (e) θ_{cy} , and (f) θ_{cz} .

For the pipe parameters at frequencies below 250 Hz, there is strong rapid decay in the magnitude of the vibration of the beam mode motion as the axial distance along the pipe increases. For this case, the axial wave number of the bending wave and fluid type wave have complex values. This indicates that the beam type pipe motion is an evanescent motion. When the frequency increases, there is cut-on for the beam type pipe motion, and the propagating bending wave dominates the pipe response.

The torsional wave motion of the pipe can be significant if it is excited by rotation dominant modes of the pump around the pipe axial direction (Fig. 9).

B. Numerical results of the pump coupled with the inlet and outlet pipes

When coupled with both inlet and outlet pipes (Fig. 3), the pump response to the force vector $[1 \ 1 \ 1 \ 1 \ 1 \ 1]^T$ ex-

erted on its centroid is shown in Fig. 10. As with the inlet pipe-only example, the longitudinal and beam wave motions of the outlet pipe will result in heavy damping on the pump motion. For example, although mode 6 identified in Fig. 10(d) is dominated by the rotation component around the X direction and influenced by the beam type motion of the inlet pipe, this mode is overdamped due to the beam type motion of the outlet pipe. Mode 1 has a dominant rotation component around the X direction, but also has a considerable contribution from the translation component in the Y direction. The combination of these two components may reduce the outlet pipe beam motion at the pipe/pump junction. As a result, mode 1 is less affected by the outlet pipe beam motion than mode 6. Figures 10(a) and 10(c) also show that mode 4 is slightly affected by the wave motion of the outlet pipe.

The pipe response to the force vector is shown in Table V. Figure 11 shows an example of pipe breathing mode un-

TABLE IV. The given force vectors used in excitation.

Excitation No.	External force vectors $[F_{0X}, F_{0Y}, F_{0Z}, F_j^i]$	Equivalent force vectors acting on the center of the rigid body $[F_{cX}, F_{cY}, F_{cZ}, M_{cX}, M_{cY}, M_{cZ}]$	Source type
1	$[1 \ 0 \ 0 \ 0]$	$[1 \ 0 \ 0 \ 0 \ 0.12 \ 0]$	Mechanical dominated source
2	$[0 \ 1 \ 0 \ 0]$	$[0 \ 1 \ 0 \ 0 \ 0.12 \ 0]$	
3	$[0 \ 0 \ 1 \ 0]$	$[0 \ 0 \ 1 \ 0 \ 0 \ 0]$	
4	$[0 \ 0 \ 0 \ 1]$	$[-1 \ 0 \ 0 \ 0 \ 0 \ 0]$	Fluid dominated source

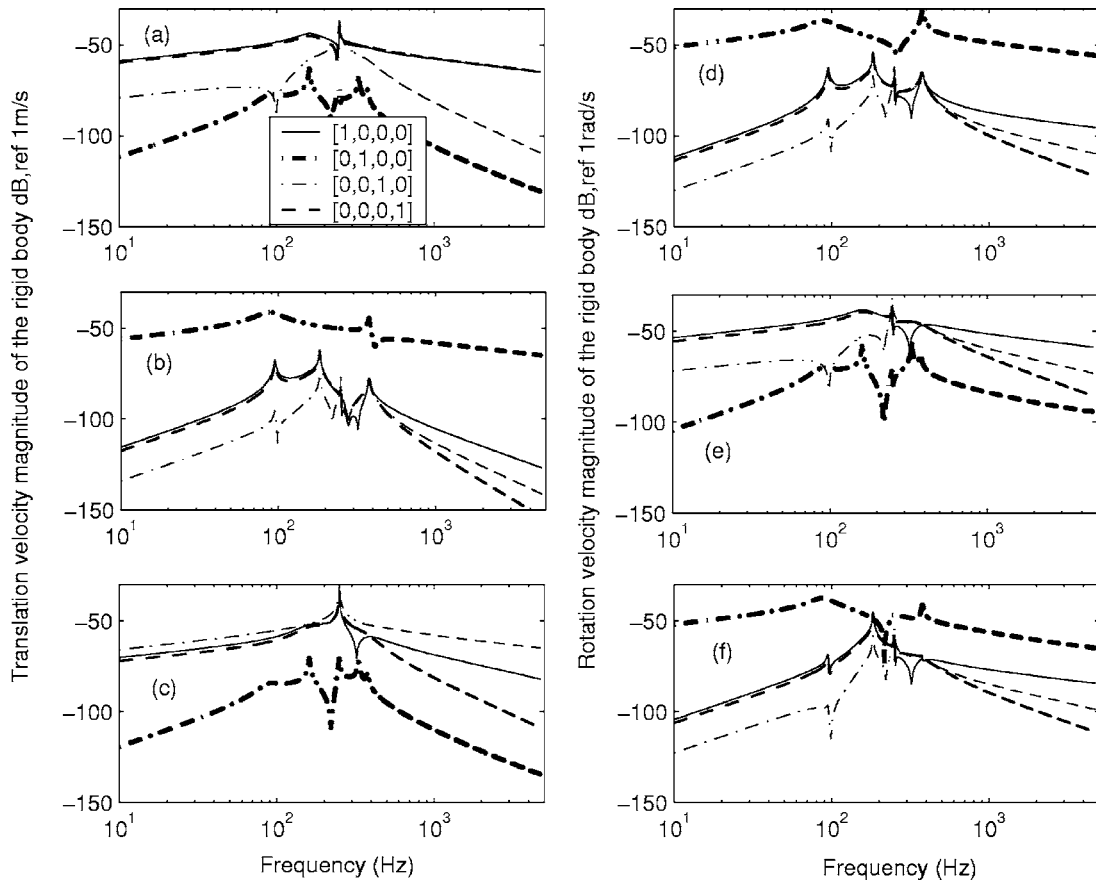


FIG. 6. Magnitude of six velocity components of the rigid body under the four types of excitations shown in Table IV. (a) $j\omega v_x$, (b) $j\omega v_y$, (c) $j\omega v_z$, (d) $j\omega\theta_x$, (e) $j\omega\theta_y$, and (f) $j\omega\theta_z$.

der the excitation of the given force vector. Again, we note that an equivalent fluid source in the pump/inlet pipe conjunction generates much larger radial velocity of the pipe wall than does a mechanical force in the X direction [Fig. 11(a)], and an equivalent fluid source in the pump/outlet pipe conjunction generates much larger radial velocity of the pipe wall than does a mechanical force in the Z direction [Fig. 11(b)]. We conclude that the response of pipe breathing mode is crucially related to the excitation source type.

Figure 12 shows examples of pipe beam mode under the given force vector. Once again, at low frequencies, we observe rapid decays in the response of the beam mode motion along the axial direction of the inlet and outlet pipes. This indicates that the beam type pipe motion is an evanescent motion. When the frequency increased, there is cut-on for the beam type pipe motion, and the propagating bending wave dominates the pipe's response.

V. CONCLUDING REMARKS

A theoretical model has been developed to analyze vibroacoustic coupling between a pump and attached water-filled pipes. This paper examines the effects of coupling between (1) the pump and the pipes, and (2) the pipe wall and the fluid contained in the pipe, on the pump's modal characteristics and pipe system response.

Torsional and longitudinal wave motions in the semi-infinite pipes result in damping effect on the pump's vibra-

tion response as both wave motions result in imaginary dynamic stiffness contribution to the pump's response. The bending wave motion of the pipe, on the other hand, results in both damping and stiffness contributions to the pump's response, and result in a change of natural frequency for certain pump modes. In general the longitudinal and beam wave motions of the pipe provide more damping to the pump motion than the torsional wave motion does. The effect of the pipe on the pump is also modally dependent. The pipe bending motion and longitudinal wave motion result in heavy damping effects on the second, third, and fifth pump modes as shown in Table III and Fig. 4. The pipe torsional wave motion has a small damping effect on the pump rotation modes around the axial direction of the pipe. The use of semi-infinite water-filled pipe in the pump/pipe coupled model is an approximation based on the assumption that the reflection of the radiated waves from the vibrating pump into the pipe can be ignored. If the pump is coupled with finite pipes, the resonance and modal damping of all wave types in the pipe will produce (in terms of the mobility functions) complex and frequency dependent loading on pump's response. As a result, the effect of the torsional and longitudinal waves will also present the pump with stiffness or mass (dependent on frequency) load contributions in addition to damping.

Due to the rigid body assumption for the pump, the radial vibration of the pipe cannot be excited directly. In the example presented, the pipe is excited by the pump through

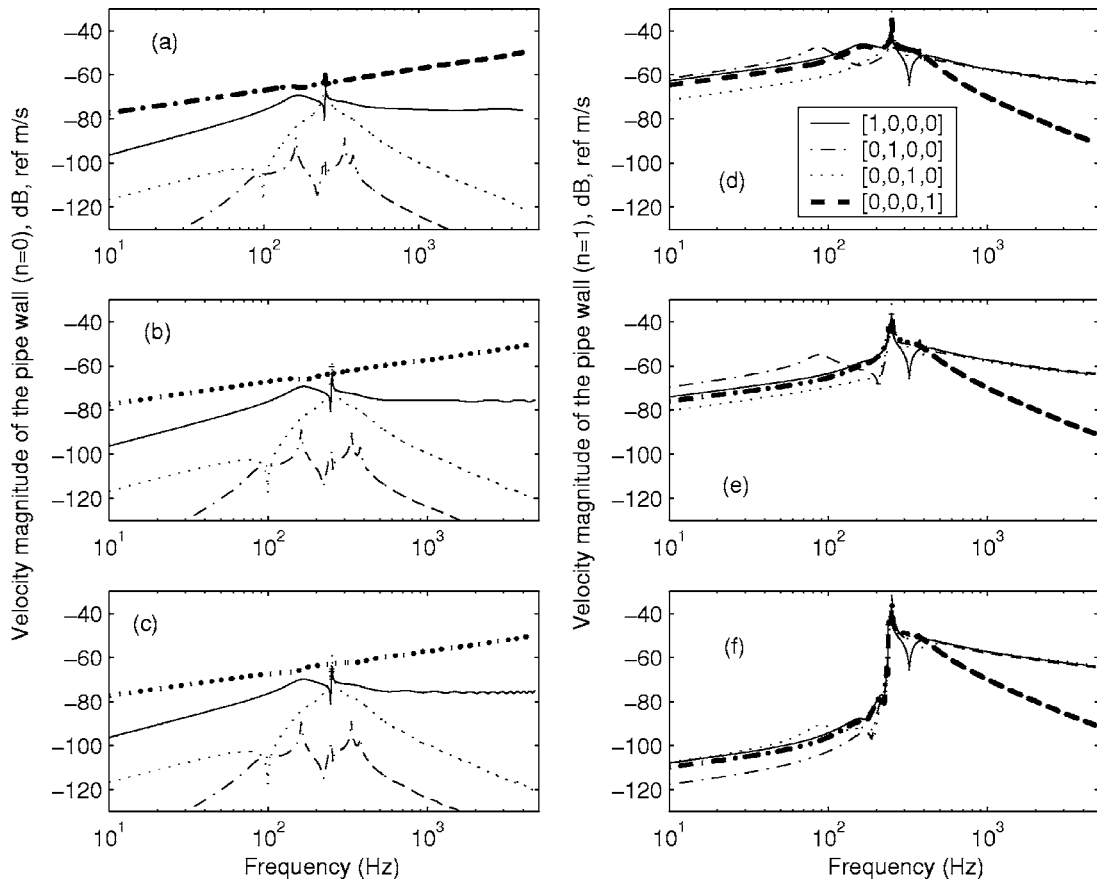


FIG. 7. Radial velocity magnitude of the pipe wall at different positions under the four types of excitations of the force shown in Table IV. (a)–(c) $n=0$, $j\omega w_0$, (c)–(e) $n=1$, $j\omega w_1$ ($\theta=-\theta_{10}$). (a), (d) $x=0.6$ m, (b), (e) $x=1.5$ m, (c), (f) $x=5$ m.

the bending, torsional, and axial coupling at the structural coupling interface, and by the direct acoustical excitation at the fluidal interface. Results indicate that the acoustical excitation is more effective in generating a larger radial movement of the pipe wall than an axial mechanical force at the

pump/pipe junction. The torsional wave motion of the pipe can be significant if it is excited by rotationally dominant modes of the pump around the pipe axial direction.

As demonstrated in the paper, the analysis of the coupled response of the pump/pipe system can be readily

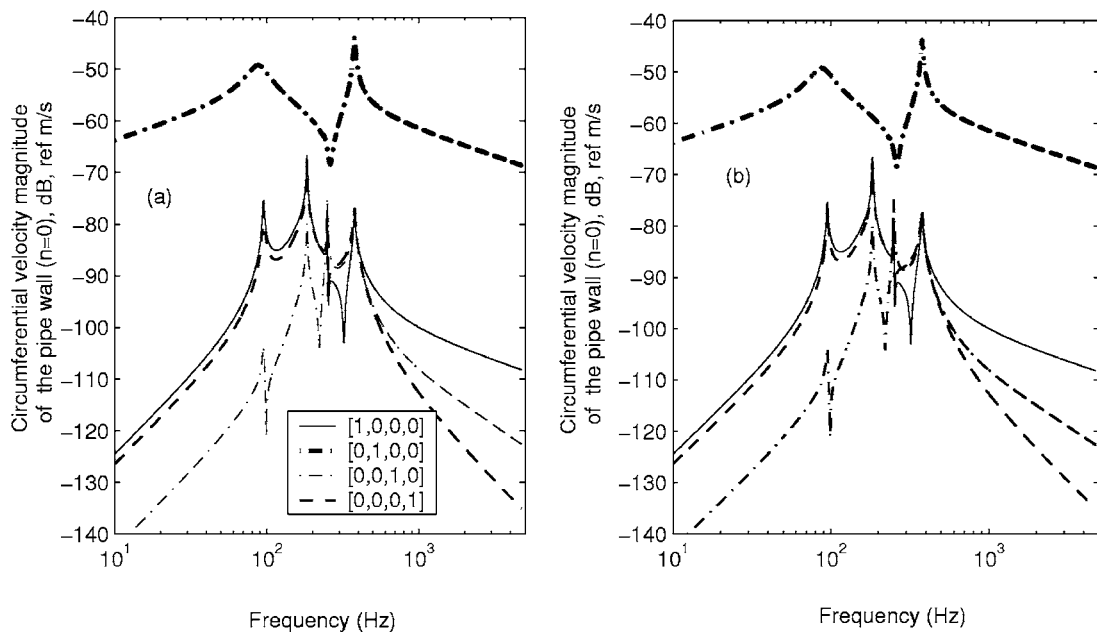


FIG. 8. Radial velocity magnitude of the different wave types of the pipe wall, $x=0.6$ m. Excitation force vector (a) $[1,0,0,0]$ and (b) $[0,0,0,1]$.

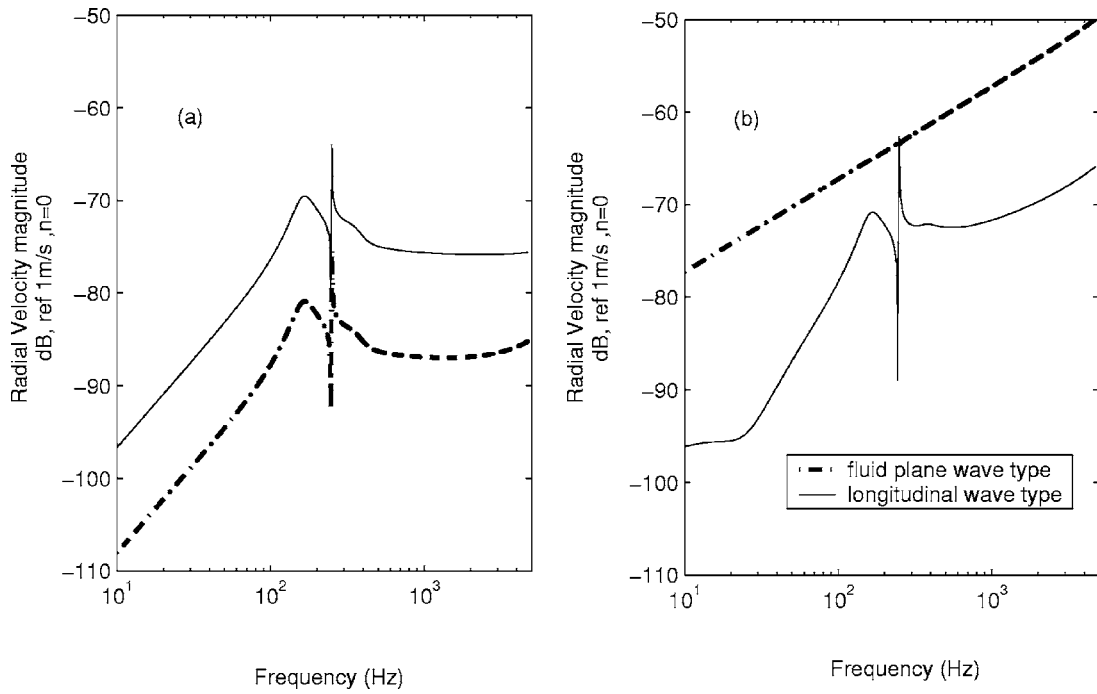


FIG. 9. Circumferential velocity magnitude of the pipe wall at the different positions under the four types of excitations shown in Table IV. $j\omega v_0$ (a) $x = 0.6$ m (b) $x = 1.5$ m.

extended to the case where a pump is connected with both inlet and outlet pipes. The wave motion in the different pipes affects the damping and stiffness of the pump modes differ-

ently because of the orientations of the pipes with respect to the pump. As a result of the combined contributions of the pipes, the pump response is significantly different from that

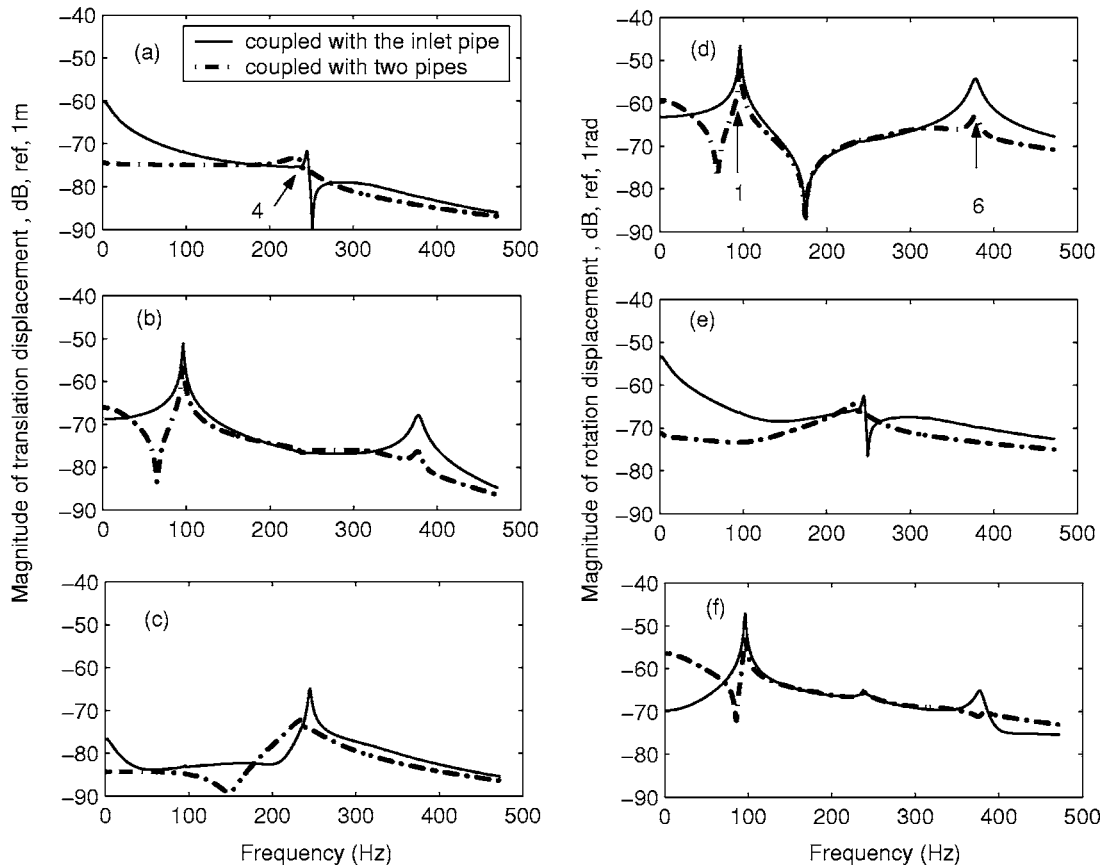


FIG. 10. Comparison of the displacement of the pump coupled with pipes under the given force vector $[1 \ 1 \ 1 \ 1 \ 1 \ 1]^T$ exerted on its centroid, (a) u_c , (b) v_c , (c) w_c , (d) θ_{cx} , (e) θ_{cy} , and (f) θ_{cz} .

TABLE V. The given force vectors used in excitation.

Excitation No.	External force vectors [$F_{0x}, F_{0y}, F_{0z}, F_j^i, F_j^o$]	Equivalent force vectors acting on the center of the rigid body	Source type
		[$F_{cx}, F_{cy}, F_{cz}, M_{cx}, M_{cy}, M_{cz}$]	
1	[1 0 0 0 0]	[1 0 0 0 0.12 0]	Mechanical dominated source
2	[0 0 1 0 0]	[0 1 0 0.12 0 0]	
3	[0 0 0 1 0]	[0 0 -1 0 0.18 0]	Fluid dominated source
4	[0 0 0 0 1]	[1 0 0 0 0 0]	

of a pump coupled with a single pipe. We observe similar behavior in pipe vibration response for the pump/inlet/outlet pipe and pump/inlet pipe configurations, when the pump is excited by mechanical and acoustical forces.

The results and method presented in this paper create a platform to assist engineers seeking to understand and separate mechanical and fluid excitation forces¹ contributions in pumps from the vibration response of their coupled piping systems. Further work is planned to (a) validate this theoretical model on an experimental system, (b) relate the results of the theoretical model to effects observed in “real” pump/pipe systems, and (c) identify how measurements of the pipe response may be used to identify the excitation source(s) strength by the inverse method.

ACKNOWLEDGMENT

The authors gratefully acknowledge the financial support of this work by CRC for Integrated Engineering Asset Manager (CIEAM) in Australia under research program ID201.

APPENDIX A

At the pipe/pump junction, the forces resulting from pipe wall stresses and fluid force acting on the rigid body can be obtained by the integration at the pipe cross section of the junction, viz.,

$$\mathbf{Q}_T = - \sum_n \int_0^{2\pi} \mathbf{R}^A \mathbf{R}^X \{ \mathbf{R}_n^{\theta 2} \mathbf{Q}_n^P + \mathbf{Q}_{0T}^P \} a d\theta - \sum_n \int_0^a \int_0^{2\pi} \mathbf{R}^f \cos(n\theta + \theta_{n0}) P_n r dr d\theta, \quad (A1)$$

where \mathbf{Q}_T are the total forces acting on the rigid body from the pump/pipe junction, $\mathbf{Q}_n^P = [N_{nx}, N_{nx\theta}, Q_{nx}, M_{nx}, M_{nx\theta}]^T$ is the stress resultant vector of the n th circumferential mode of the pipe at the junction, $\mathbf{Q}_{0T}^P = [0, N_{x\theta 0}, 0, 0, 0]^T$ is torsional stress resultant vector for breathing mode of the pipe, P_n is the acoustical pressure of the n th circumferential mode at the cross section of the pipe, \mathbf{R}^A and \mathbf{R}^f are location matrices, and \mathbf{R}^X is the coordinate conversion matrix, given by

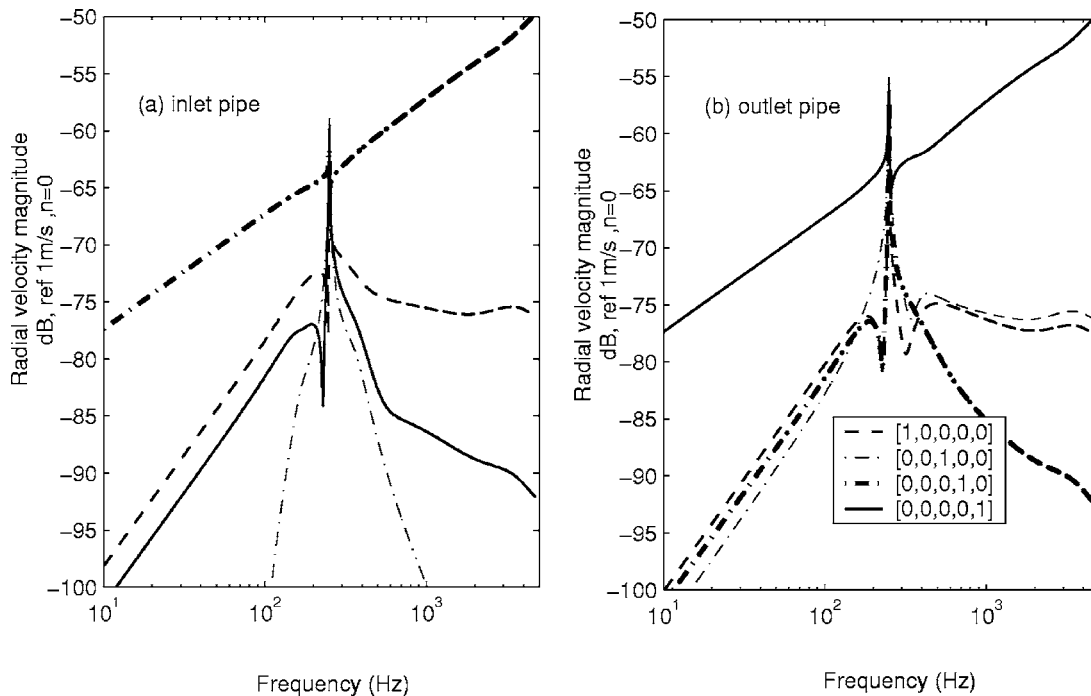


FIG. 11. Radial velocity magnitude of the pipe wall under the four types of excitation of force vector shown in Table V, $n=0, j\omega_0, x=0.6$ m.

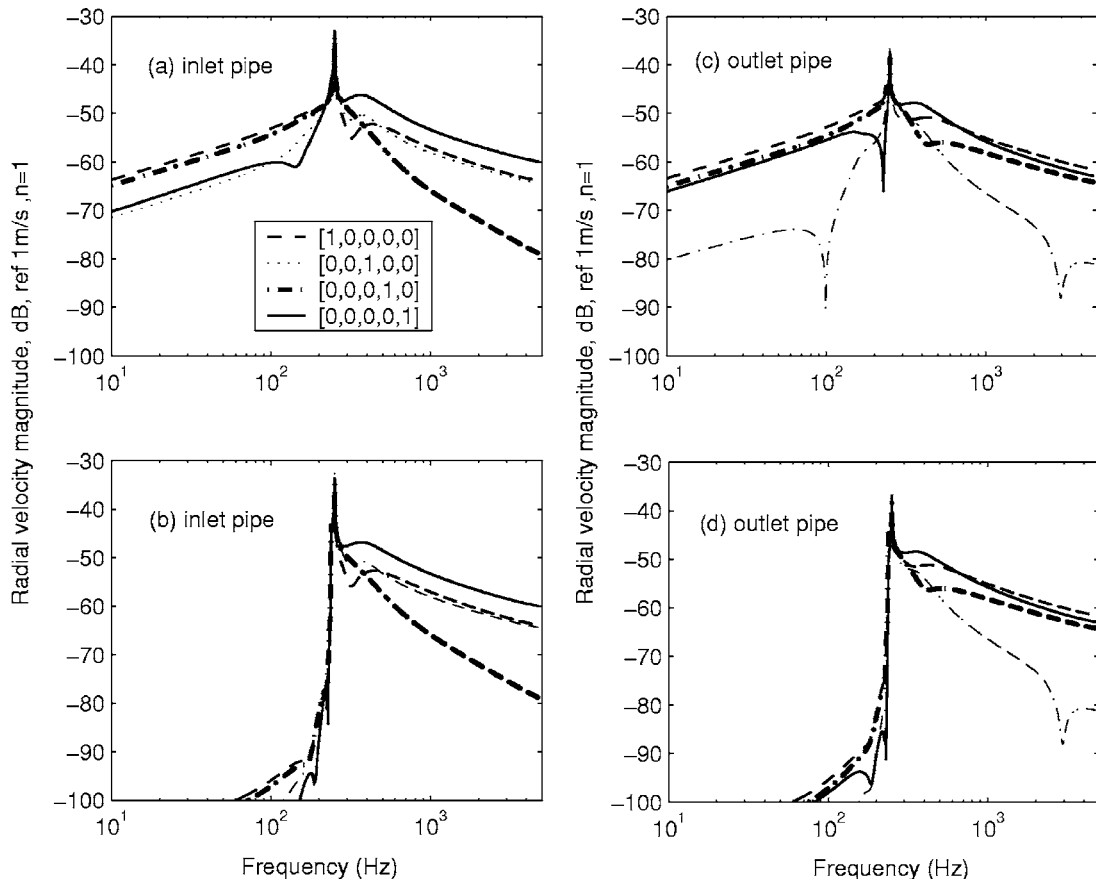


FIG. 12. Radial velocity magnitude of the pipe wall under the four types of excitation of given force vector shown in Table V, $n=1$, $j\omega w_1$ ($\theta=-\theta_{i0}$). (a), (c) $x=0.6$ m, (b), (d) $x=5$ m.

$$\mathbf{R}^A = \begin{bmatrix} 1 & & & & 0 \\ 0 & 1 & & & \\ 0 & 0 & 1 & & 0 \\ 0 & Z_B + a \cos \theta & -(Y_B + a \sin \theta) & 1 & \\ -(Z_B + a \cos \theta) & 0 & X_B & 0 & 1 \\ Y_B + a \sin \theta & -X_B & 0 & 0 & 0 & 1 \end{bmatrix}, \quad (\text{A2})$$

$$\mathbf{R}^f = [1 \quad 0 \quad 0 \quad 0 \quad -(Z_B + r \cos \theta) \quad Y_B + r \sin \theta]^T, \quad (\text{A3})$$

$$\mathbf{R}^X = \begin{bmatrix} 1 & 0 & 0 & 0 & 0 \\ 0 & \cos \theta & \sin \theta & 0 & 0 \\ & -\sin \theta & \cos \theta & 0 & 0 \\ 0 & 0 & 0 & 0 & 1 \\ 0 & 0 & 0 & \cos \theta & 0 \\ 0 & 0 & 0 & -\sin \theta & 0 \end{bmatrix}, \quad (\text{A4})$$

where the subscript B represents the point of the center of the pipe cross section at the junction. Rewriting Eq. (A1) as

$$\mathbf{Q}_T = -\sum_n \mathbf{R}_n^{\alpha 1} \mathbf{Q}_n^P - \sum_n \int_0^a \mathbf{R}_n^{\alpha 2} P_n r dr - \mathbf{R}_{0T}^{\alpha 1} \mathbf{Q}_{0T}^P, \quad (\text{A5})$$

where

$$\mathbf{R}_n^{\alpha 1} = \int_0^{2\pi} \mathbf{R}^A \mathbf{R}^X \mathbf{R}_n^{\theta 2} d\theta, \quad (\text{A6})$$

$$\mathbf{R}_{0T}^{\alpha 1} = \int_0^{2\pi} \mathbf{R}^A \mathbf{R}^X d\theta, \quad (\text{A7})$$

$$\mathbf{R}_n^{\alpha 2} = \int_0^{2\pi} \mathbf{R}^f \cos(n\theta + \theta_{n0}) d\theta. \quad (\text{A8})$$

In Eq. (A5), the forces acting on the rigid body resulting from the pump/pipe junction are related to the infinite circumferential modes of pipe movement. However, if the

pump is modeled as rigid body and the pipe is excited by the rigid body, one may expect that only limited circumferential modes ($n=0,1$) can be possibly excited, such expectation can be validated by straightforward calculation of coefficient matrices \mathbf{R}_n^α and \mathbf{R}_{0T}^α in Eqs. (A6)–(A8) and (34), given by

$$\begin{aligned} \mathbf{R}_0^{\alpha 1} &= 2\pi a [1 \ 0 \ 0 \ 0 \ -Z_B \ Y_B]^T, \quad \mathbf{R}_0^{\alpha 2} = \mathbf{R}_0^{\alpha 1}/a, \quad \mathbf{R}_0^{\alpha 4} = \mathbf{R}_0^{\alpha 1T}/2\pi a, \\ \mathbf{R}_{0T}^{\alpha 1} &= 2\pi a [0 \ 0 \ 0 \ a \ 0 \ 0]^T, \quad \mathbf{R}_{0T}^{\alpha 2} = \mathbf{R}_{0T}^{\alpha 1T}/2\pi a, \\ \mathbf{R}_1^{\alpha 1} &= \pi a \begin{bmatrix} 0 & 0 & 0 & 0 & 0 \\ 0 & \sin \theta_{10} & -\sin \theta_{10} & 0 & 0 \\ 0 & -\cos \theta_{10} & \cos \theta_{10} & 0 & 0 \\ 0 & Z_B \sin \theta_{10} + Y_B \cos \theta_{10} & -Z_B \sin \theta_{10} - Y_B \cos \theta_{10} & 0 & 0 \\ -a \cos \theta_{10} & -X_B \cos \theta_{10} & X_B \cos \theta_{10} & \cos \theta_{10} & 0 \\ -a \sin \theta_{10} & -X_B \sin \theta_{10} & X_B \sin \theta_{10} & \sin \theta_{10} & 0 \end{bmatrix}, \\ \mathbf{R}_1^{\alpha 2} &= \pi [0 \ 0 \ 0 \ 0 \ -\cos \theta_{10} \ -\sin \theta_{10}]^T, \\ \mathbf{R}_1^{\alpha 4} &= \mathbf{R}_1^{\alpha 1T}/\pi a, \quad \mathbf{R}_{n(n>1)}^\alpha = 0. \end{aligned} \quad (\text{A9})$$

For the circumferential mode ($n=0$), the polarization angle is adopted as zero in consideration of the rigidity ring contour of the rigid body/pipe conjunction. For the circumferential modes ($n>1$), the coefficient matrices, as shown in Eq. (A9), are all zero and independent of the polarization angles. For the circumferential mode ($n=1$), however, the polarization angle θ_{10} is crucially related to the external ex-

citation force vector. A way to determine polarization angle θ_{10} may start from Eq. (32), from which one may derive the following relation:

$$(u_{cY} - X_B \theta_{cZ}) \cos \theta_{10} + (w_{cZ} + X_B \theta_{cY}) \sin \theta_{10} = 0. \quad (\text{A10})$$

The combination of Eqs. (A10) and (46) can give rise to an extra equation in terms of polarization angle θ_{10} .

APPENDIX B

$$\mathbf{R}^{AC} = \begin{bmatrix} 1 & 0 & 0 & 0 & -(Z_B + a \cos \theta) & Y_B + a \sin \theta \\ 0 & \cos \theta & -\sin \theta & Z_B \cos \theta + Y_B + a & -X_B \sin \theta & -X_B \cos \theta \\ 0 & \sin \theta & \cos \theta & Z_B \sin \theta - Y_B \cos \theta & X_B \cos \theta & -X_B \sin \theta \\ 0 & 0 & 0 & 0 & \cos \theta & -\sin \theta \end{bmatrix}. \quad (\text{B1})$$

APPENDIX C

The coefficient matrices $\mathbf{R}_n^{\alpha\alpha}$ for the outlet pipe in Eqs. (56), (57), and (58) may follow the similar definition of Eq. (A9), while special attention should be paid to the location and coordination conversion matrix of the outlet pipe,

$$\mathbf{R}_0^{\alpha\alpha 1} = 2\pi a [0 \ 0 \ 1 \ -Y_{Bo} \ X_{Bo} \ 0]^T, \quad \mathbf{R}_0^{\alpha\alpha 2} = \mathbf{R}_0^{\alpha\alpha 1}/a, \quad \mathbf{R}_0^{\alpha\alpha 4} = \mathbf{R}_0^{\alpha\alpha 1T}/2\pi a,$$

$$\mathbf{R}_{0T}^{\alpha\alpha 1} = 2\pi a [0 \ 0 \ 0 \ 0 \ 0 \ a]^T, \quad \mathbf{R}_{0T}^{\alpha\alpha 2} = \mathbf{R}_{0T}^{\alpha\alpha 1T}/2\pi a,$$

$$\mathbf{R}_1^{o\alpha 1} = \pi a \begin{bmatrix} 0 & \sin \theta_{10} & -\sin \theta_{10} & 0 \\ 0 & -\cos \theta_{10} & \cos \theta_{10} & 0 \\ 0 & 0 & 0 & 0 \\ -a \cos \theta_{10} & -Z_{Bo} \cos \theta_{10} & Z_{Bo} \cos \theta_{10} & \cos \theta_{10} \\ -a \sin \theta_{10} & -Z_{Bo} \sin \theta_{10} & Z_{Bo} \sin \theta_{10} & \sin \theta_{10} \\ 0 & Y_{Bo} \sin \theta_{10} + X_{Bo} \cos \theta_{10} & -Y_{Bo} \sin \theta_{10} - X_{Bo} \cos \theta_{10} & 0 \end{bmatrix},$$

$$\mathbf{R}_1^{o\alpha 2} = \pi [0 \quad 0 \quad 0 \quad -\cos \theta_{10} \quad -\sin \theta_{10} \quad 0]^T,$$

$$\mathbf{R}_1^{o\alpha 4} = [\mathbf{R}_1^{o\alpha 1}]^T / \pi a, \quad \mathbf{R}_{n>1}^{o\alpha} = 0. \tag{C1}$$

¹G. Zrentkowski and S. Zbroja, "Experimental characterization of centrifugal pumps as an acoustic source at the blade-passing frequency," *J. Fluids Struct.* **14**, 529–558 (2000).

²M. R. Hodkiewicz and M. P. Norton, "The effect of change in flow rate on the vibration of double-suction centrifugal pumps," *Proceeding of Institute of Engineers Part E: J Process Mechanical Engineering* **216**, 47–58 (2002).

³M. R. Hodkiewicz and J. Pan, "Identification of transient axial vibration on double-suction pumps during partial flow operation," *Acoust. Aust.* **32**, 25–32 (2004).

⁴C. R. Fuller and F. J. Fahy, "Characteristic of wave propagation and energy distributions in cylindrical elastic shells filled with fluid," *J. Sound Vib.* **81**, 501–518 (1982).

⁵L. Feng, "Experimental study of the acoustic properties of a finite elastic pipe filled with water/air," *J. Sound Vib.* **189**, 511–524 (1996).

⁶R. Ming, J. Pan, and M. P. Norton, "The measurement of structural mobilities of a circular cylindrical shell," *J. Acoust. Soc. Am.* **107**, 1374–1382 (2000).

⁷B. Liu, J. Pan, X. D. Li, and J. Tian, "Sound radiation from a water-filled pipe with a plate attached to the pipe opening, Radiation into light fluid," *J. Acoust. Soc. Am.* **112**, 2814–2824 (2002).

⁸B. Liu, J. Pan, X. D. Li, and J. Tian, "Sound radiation from a water-filled pipe with an attached elastic plate, Radiation into heavy fluid," *Acta Acust.* **29**, 131–136 (2004) (in Chinese).

⁹N. Qi and B. M. Gibbs, "Circulation pumps as structure-borne sound sources: Emission to semi-infinite pipe," *J. Sound Vib.* **264**, 157–176 (2003).

¹⁰B. M. Gibbs and N. Qi, "Circulation pumps as structure-borne sound sources: Emission to finite-pipe system," *J. Sound Vib.* **284**, 1099–1118 (2005).

¹¹L. Cremer, M. Heckl, and E. E. Ungar, *Structure-borne Sound* (Springer, New York, 1998).

¹²R. Ming, J. Pan, and M. P. Norton, "The mobility functions and their application in calculating power flow in coupled cylindrical shells," *J. Acoust. Soc. Am.* **105**, 1702–1713 (1999).

¹³J. Pan, J. Q. Pan, and C. H. Hansen, "Total power flow from a vibrating body to a thin panel through multiple elastic mounts," *J. Acoust. Soc. Am.* **92**, 895–907 (1992).

¹⁴A. W. Lessia, "Vibration of Shells," NASA SP-288, 1973.

¹⁵M. C. Junger and D. Feit, *Sound, Structures and Their Interaction* (Acoustical Society of America, Melville).

¹⁶W. Soedel, *Vibrations of Shells and Plates* (Dekker, New York, 1981).

On the diffuse field reciprocity relationship and vibrational energy variance in a random subsystem at high frequencies

R. S. Langley^{a)}

Department of Engineering, University of Cambridge, Trumpington Street, Cambridge, CB2 1PZ, United Kingdom

(Received 7 February 2006; revised 17 November 2006; accepted 17 November 2006)

A recent paper has shown that under certain conditions the cross-spectral matrix of the forces exerted by a vibrational or acoustic wave field on its surrounding boundaries can be expressed in terms of (i) the energy of the wave field, and (ii) the direct field dynamic stiffness matrix of the boundary. This “diffuse field reciprocity relation” was derived using wave mechanics, and it is not immediately clear how the required wave field properties translate to conditions on the vibrational modes of the system or the applied forcing. This issue is addressed here by deriving an extended version of the reciprocity relation using modal methods, and the conditions required for the extended version to reduce to the existing relation are delineated. It is shown that the existing diffuse field reciprocity relation leads to an anomalous result when used to predict the energy variance of a subsystem, and that this anomaly is resolved by using the present extended version of the relation. A supplementary result arising from the analysis is that for systems with a sufficient degree of randomness the ensemble average of the dynamic stiffness matrix of a random subsystem is equal to the inverse of the ensemble average of the receptance matrix. © 2007 Acoustical Society of America. [DOI: 10.1121/1.2409484]

PACS number(s): 43.40.Hb, 43.20.Ks, 43.20.Rz, 43.30.Jx, 43.40.Qi [RLW] Pages: 913–921

I. INTRODUCTION

There is much practical interest in the dynamic response of structures that have uncertain properties due to variability in the manufacturing and assembly processes, with automotive structures being a prime example (Kompella and Bernhard, 1993). The potential difficulty in attempting to predict the response statistics of such structures is immense, due to the large number of physical variables which might be uncertain and the inevitable lack of data regarding the statistical distribution of these variables. However, significant progress has been made in recent years by recognizing that if the structure is “random enough” then the response statistics do not depend on the details of the underlying physical uncertainty. The reason for this is that, under a sufficient degree of randomness, the natural frequencies and mode shapes of the subcomponents (or “subsystems”) of the structure tend to conform to universal distributions derived in quantum theory and random matrix theory (Mehta, 1991). In particular, there is a large body of empirical evidence to suggest that the Gaussian orthogonal ensemble (GOE) provides a good description of the important features of the modal statistics of a random structure, and a discussion of this issue can be found in, for example, Mehta (1991), Weaver (1989), Bertlesen *et al.* (2000), Ellegaard *et al.* (2001), and Langley and Brown (2004). Among other advances, this fact has led to the development of an extended version of statistical energy analysis (SEA) which allows the ensemble mean and variance of the response of a complex structure to be computed without knowledge of the statistics of the physical uncertainties (Langley and Cotoni, 2004).

In stating that the GOE can provide a good description of the subsystem modal statistics, there is no intention to suggest that either: (i) the governing mass or stiffness matrices of the subsystem actually have the statistics of a GOE matrix, or (ii) *all* of the statistical properties of the subsystem natural frequencies and mode shapes conform to the GOE. Clearly these two statements cannot be fulfilled, since the GOE matrix is not positive definite, having an equal probability of positive or negative eigenvalues, and the matrix is therefore not physical in the context of structural dynamics. The important point is that the local statistics of the subsystem modes (i.e., the joint statistics of a group of neighboring modes, as measured by the low order correlation functions) conform to the GOE, in line with the random matrix principle of universality (see, for example, Hackenbroich and Weidenmüller, 1995). In the absence of any special symmetries, the condition for this to occur can be quantified in an approximate way by the statistical overlap factor S of the subsystem; this is defined as $S=2\sigma/\mu$, where σ is the standard deviation of a natural frequency and μ is the mean frequency spacing. If S is large (typically greater than unity) then a large degree of random coupling between the modes of a nominally perfect subsystem can be expected, which promotes the occurrence of universal statistics. The statistical overlap factor tends to increase with increasing frequency, and generally the GOE will not be applicable to the lower natural frequencies of the subsystems, where alternative models have been suggested (see, for example, Soize, 2003).

In many practical structures the conditions for the application of the GOE might be met by some components, such as thin panels, but not for others, such as beams and frames. In such cases it would be efficient to model the highly random parts of the structure using SEA and the remaining parts

^{a)}Electronic mail: rsl21@eng.cam.ac.uk

using a deterministic method such as the finite element (FE) method, possibly in combination with a parametric description of uncertainty. However SEA is based on energy flow and energy variables, while FE is based on physical displacements and equilibrium, so that the two approaches are not immediately compatible in a single model. This difficulty has been overcome recently by the development of a “diffuse field reciprocity relation” (Shorter and Langley, 2005a). The relation expresses the cross spectrum of the forces applied by a random subsystem on a deterministic structure in terms of (i) the subsystem energy and (ii) a computable matrix, known as the direct field dynamic stiffness matrix. This represents an extension of earlier studies presented by Smith (1962, 1981) and Shaw (1988) which were concerned with diffuse fields acting on single degree of freedom systems. The relation has been used to develop a coupled SEA-FE method (Shorter and Langley, 2005b) for the vibro-acoustic analysis complex systems across a broad frequency range, and it forms the main subject of the present work.

The derivation of the diffuse field reciprocity relation given by Shorter and Langley (2005a) is based on wave mechanics, and the conditions for the validity of the result were expressed in terms of the properties of the vibrational wave field. It was found that the wave field must be diffuse, as defined in a particular way: it is not immediately clear how this condition relates to conditions on the modal statistics of the subsystem or to conditions on the applied loading. This is one of the issues addressed here, and in the present work an extended version of the reciprocity relation is derived using modal methods, thus allowing the conditions for the applicability of the original relation to be explored in detail. In (unpublished) developments of the theory presented by Shorter and Langley (2005a), the author has found that an expression for the energy variance of a subsystem can be derived directly from the diffuse field reciprocity relation. The resulting formula for the relative variance of the energy is $1/\pi m$, where m is the modal overlap of the subcomponent. In comparison, Weaver (1989) and Langley and Brown (2004) have each presented a detailed analysis of energy variance based on GOE statistics, and at high m the result for the relative variance is $(\alpha-1)/\pi m$ where α is a parameter that depends upon the nature of the applied loading ($\alpha \approx 3$ for a point load). Clearly there is a significant discrepancy between the results yielded by the diffuse field reciprocity relation and the GOE, which raises concerns about the validity of one or other of the theoretical approaches. This issue is resolved here by demonstrating that the extended version of the reciprocity relation does in fact lead to the previous GOE based result for the energy variance.

As part of the present derivation an expression is derived for the ensemble averaged receptance matrix of a subsystem. It is shown that this matrix can be associated with a physical system, and it is further shown that the ensemble averaged dynamic stiffness matrix is equal to the inverse of the ensemble averaged receptance matrix.

The diffuse field reciprocity relation is reviewed in Sec. II, and a generalization of this result (together with a consideration of certain special cases) is presented in Sec. III. The application of the reciprocity relation to the prediction of

energy variance is considered in Sec. IV, and published numerical and experimental results which support the current findings are summarized in Sec. V. Concluding comments are made in Sec. VI.

II. DIFFUSE FIELD RECIPROCALITY RELATION

The following analysis is concerned with the harmonic vibration of a dynamic system under the action of external forces acting at frequency ω . The analysis is limited to systems that are homogeneous to the extent that they exhibit global modes, i.e., none of the mode shapes are confined to subregions of the system. Thus the concern is not with complete built-up engineering structures, but with a subcomponent, or subsystem, such as a beam, plate or enclosed acoustic volume, as considered by Shorter and Langley (2005a). Furthermore, the subsystem is taken to be random, and it will be assumed (in Sec. III onwards) that the statistical overlap S is high, which requires a high degree of randomness and/or a high frequency of excitation. These two assumptions represent the main restrictions of the analysis; all subsequent assumptions and approximations are generally a consequence of these restrictions.

The subsystem is considered to be modeled by a discretization scheme such as the finite element method, so that the degrees of freedom consist of displacement variables (or pressure variables for an acoustic subsystem) that describe the complete deformation of the subsystem. A selected subset of these displacement variables is referred to as the “boundary” degrees of freedom \mathbf{q} ; the key point is that other dynamic subsystems may be connected to the subsystem via these coordinates. In practice \mathbf{q} might relate to the physical perimeter of the subsystem, such as the edges of a plate, but equally \mathbf{q} could include other degrees of freedom, such as a point in the interior of the plate. If external forces \mathbf{f} are applied to the boundaries of the subsystem (defined as the regions associated with \mathbf{q}) then the governing equations of motion have the form

$$\mathbf{D}\mathbf{q} = \mathbf{f}, \quad (1)$$

where \mathbf{D} is the dynamic stiffness matrix of the subsystem and \mathbf{q} and \mathbf{f} represent complex amplitudes, so that, for example, the time dependent displacement vector is given by $\text{Re}[\mathbf{q} \exp(i\omega t)]$. The fact that \mathbf{q} represents only a subset of the total degrees of freedom of the subsystem implies that the dynamic stiffness matrix \mathbf{D} will in general be a transcendental function of frequency; furthermore, the principle of reciprocity implies that \mathbf{D} will be a symmetric matrix. The derivation of \mathbf{D} from the complete set of subsystem equations of motion is discussed in detail in Sec. III.

The present concern is with the statistics of the response of an ensemble of random subsystems, so that \mathbf{D} is a random matrix. In this case it is convenient to rewrite Eq. (1) in the form

$$\mathbf{D}_\infty \mathbf{q} = \mathbf{f} + \mathbf{f}_{\text{rev}}, \quad (2)$$

where \mathbf{D}_∞ is a constant (i.e., deterministic) matrix and the random vector \mathbf{f}_{rev} accounts for the remaining part of \mathbf{D} .

Equation (2) is true by definition, i.e., any constant matrix \mathbf{D}_∞ can be specified, and \mathbf{f}_{rev} is then *defined* as the balancing force required to reduce Eq. (2) to Eq. (1). The question is now how to select a value of \mathbf{D}_∞ that makes Eq. (2) a physically and mathematically useful description of the subsystem behavior. It might immediately be thought that the most suitable choice of \mathbf{D}_∞ would be the expected value of \mathbf{D} , but this is not necessarily the case. To consider this issue it is helpful to rewrite Eqs. (1) and (2) in the form

$$\mathbf{q} = \mathbf{H}\mathbf{f}, \quad (3)$$

$$\mathbf{q} = \mathbf{D}_\infty^{-1}\mathbf{f} + \mathbf{D}_\infty^{-1}\mathbf{f}_{\text{rev}}, \quad (4)$$

where $\mathbf{H} = \mathbf{D}^{-1}$ is the receptance matrix. The main criterion for the optimal choice of \mathbf{D}_∞ is that the random vector \mathbf{f}_{rev} should have the simplest possible statistics; for example, \mathbf{f}_{rev} should ideally have zero mean. This requirement on the mean is in fact sufficient to uniquely define \mathbf{D}_∞ , since taking the ensemble average of Eqs. (3) and (4) under the condition that the applied force \mathbf{f} is deterministic leads to

$$E[\mathbf{f}_{\text{rev}}] = 0 \Rightarrow \mathbf{D}_\infty = E[\mathbf{H}]^{-1}. \quad (5)$$

It is argued in Sec. III that under the appropriate conditions $E[\mathbf{D}] = E[\mathbf{H}]^{-1}$ so that \mathbf{D}_∞ does in fact correspond to the expected value of \mathbf{D} , but nonetheless Eq. (5) is taken here to represent the fundamental definition of \mathbf{D}_∞ . It can be noted that, although a deterministic force \mathbf{f} was considered to inform the selection of an appropriate value of \mathbf{D}_∞ , the applied force may in general be either deterministic or random.

Rewriting Eq. (1) in the form of Eq. (2) is only of practical use if something significant can be said about the statistical properties of \mathbf{f}_{rev} . This issue has been considered by Shorter and Langley (2005a), who showed that if the response of the subsystem constitutes a diffuse random wave field then

$$E[\mathbf{f}_{\text{rev}}\mathbf{f}_{\text{rev}}^{*T}] = \left(\frac{4E}{\pi\omega n} \right) \text{Im}(\mathbf{D}_\infty), \quad (6)$$

where E is the ensemble averaged vibrational energy of the subsystem and n is the modal density. Equation (6) makes a connection between the energetics of the subsystem and the elastic forces at the boundary, and as such it forms the key to coupling statistical analysis methods, such as statistical energy analysis (SEA), to deterministic analysis methods, such as the finite element method. In particular, this result underlies the hybrid vibro-acoustic analysis method presented by Shorter and Langley (2005b), and it can also be used to compute diffuse field acoustic loads on structures (Shorter and Langley 2005a). The existing proof of Eq. (6) is based on wave mechanics, wherein it is assumed a priori that the subsystem carries a diffuse wave field (as defined by Shorter and Langley 2005a) regardless of the nature of the loading. Moreover, in Shorter and Langley (2005a) the matrix \mathbf{D}_∞ is defined to be the dynamic stiffness matrix of the boundary when the remainder of the subsystem is “infinite,” so that no waves emanating from the boundary are reflected back to the boundary. Thus $\text{Im}(\mathbf{D}_\infty)$ determines the radiation properties of the boundary and for this reason Eq. (6) is referred to as the diffuse field reciprocity relation, in that it relates forc-

ing to radiation. The connection between the Shorter and Langley (2005a) definition of \mathbf{D}_∞ and Eq. (5) is not immediately obvious, but it is shown in what follows that the two definitions are in fact equivalent.

One of the aims of the present work is to provide a relatively simple derivation of Eq. (6) based on modal (rather than wave) considerations, and furthermore to generalize the result to cases where the subsystem does not carry a perfectly diffuse wave field in the sense of Shorter and Langley (2005a). This is done in the next section by expressing the equations of motion in terms of the free vibration modes of the subsystem.

III. GENERALIZATION OF THE RECIPROcity RELATION

A. Ensemble averaged receptance and dynamic stiffness matrices

Let ω_j and ϕ_j represent the j th natural frequency and mode shape of the subsystem described in the previous section, under boundary conditions that do not restrain the degrees of freedom \mathbf{q} . If u_j represents the complex amplitude of the response in the j th mode, then the equations of motion can be expressed in the standard form (see, for example, Meirovitch, 1986)

$$\mathbf{\Lambda}\mathbf{u} = \mathbf{g}, \quad (7)$$

$$\Lambda_{jk} = \delta_{jk}[\omega_j^2(1 + i\eta) - \omega^2], \quad (8)$$

where η is the loss factor, \mathbf{g} is the vector of generalized forces, and it has been assumed that the mode shapes ϕ_j are scaled to unit generalized mass. A hysteretic damping model has been adopted in Eqs. (7) and (8), which is consistent with the assumption of a near-homogeneous subsystem stated in Sec. II. Now the boundary degrees of freedom \mathbf{q} are linear functions of the modal amplitudes \mathbf{u} , and likewise the generalized forces \mathbf{g} depend linearly on the boundary forces \mathbf{f} . From the principle of reciprocity it can be deduced these relations have the form

$$\mathbf{q} = \mathbf{A}\mathbf{u}, \quad (9)$$

$$\mathbf{g} = \mathbf{A}^T\mathbf{f}, \quad (10)$$

where \mathbf{A} is a real rectangular matrix ($N \times R$ say, with $N < R$) such that A_{rj} is a linear function of the mode shape ϕ_j . It follows from Eqs. (7)–(10) that

$$\mathbf{q} = \mathbf{H}\mathbf{f}, \quad (11)$$

$$\mathbf{H} = \mathbf{A}\mathbf{\Lambda}^{-1}\mathbf{A}^T, \quad (12)$$

where \mathbf{H} is the receptance matrix at the boundary.

Equations (5) and (6) require the calculation of the ensemble averaged receptance matrix, and to this end Eq. (12) can be rewritten in the form

$$H_{rs} = \sum_j \frac{A_{rj}A_{sj}}{\omega_j^2(1 + i\eta_j) - \omega^2}, \quad (13)$$

where H_{rs} is the rs entry of \mathbf{H} . As discussed in Sec. II, the present concern is with random subsystems that have a large

statistical overlap factor, which implies that the statistics of the dynamic response can be derived without considering the detailed statistical properties of the underlying random physical parameters. The natural frequencies that appear in Eq. (13) can be viewed as a sequence of random points along the frequency axis, and random point process theory can be employed to derive the statistical properties of H_{rs} . The main results of this theory are summarized in the Appendix, and the application of Eq. (A3) to Eq. (13) yields

$$E[H_{rs}] = H_{\infty,rs} \approx \left(\frac{-i\pi n}{2\omega} \right) E[A_{rj}A_{sj}], \quad (14)$$

where the notation \mathbf{H}_{∞} will be used to represent $E[\mathbf{H}]$ in what follows. It is important to note that random point process theory employs a number of assumptions, and in the context of Eqs. (13) and (14) these are: (i) the subsystem modal density n is independent of frequency, and (ii) the numerators that appear in Eq. (13) are statistically independent and have the same mean value for each j . Clearly these conditions may not be met for a practical dynamic subsystem and the resulting implications regarding the validity of Eq. (14) must be carefully considered. Considering initially the imaginary part of H_{rs} , most of the contribution to Eq. (13) comes from resonant modes, i.e., those modes with $\omega_j \approx \omega$. In this case it is sufficient for conditions (i) and (ii) to be met locally over a limited frequency range in the vicinity of the excitation frequency, and Eq. (14) can therefore be expected to yield an accurate estimate of $\text{Im}(H_{rs})$. The situation is different for the real part of H_{rs} , where many nonresonant modes can make a contribution to Eq. (13); if Eq. (14) is to be accurate (i.e., the mean of the real part is zero) then conditions (i) and (ii) must apply over an extended frequency range, and this is not actually the case for many subsystems. This problem can be circumvented by noting that the receptance is a causal function and the real and imaginary parts must therefore form a Hilbert transform pair, in accordance with the Kramers-Kronig relation (Morfe 2001). Assuming that Eq. (14) is accurate for the imaginary part of H_{rs} it then follows that an accurate result for the complete function is given by

$$E[\text{Im}(H_{rs})] = \left(\frac{-\pi n}{2\omega} \right) E[A_{rj}A_{sj}], \quad (15)$$

$$E[\text{Re}(H_{rs})] = \left(\frac{1}{\pi} \right) \text{P. V.} \int_{-\infty}^{\infty} \frac{\text{Im}[H_{rs}(\omega')]}{(\omega - \omega')} d\omega'. \quad (16)$$

Given that $E[H_{rs}]$ is causal (as a direct result of the fact that H_{rs} is causal), it is interesting to consider whether Eqs. (15) and (16) correspond to the receptance of any physical subsystem. To this end it can be noticed that $E[H_{rs}]$ is independent of the subsystem loss factor η , whereas it is well known that the variance of H_{rs} decreases with increasing damping (see, for example, Lyon, 1969, or Langley and Brown, 2004). It can therefore be deduced that $E[H_{rs}]$ is the limiting value attained by H_{rs} for any member of the random ensemble as the damping is increased. With increasing damping the subsystem becomes “nonreverberant” in the sense that vibrational waves emanating from the boundary are damped out

before they can return to the boundary, and the boundary receptance becomes that due to the “direct field” only (i.e., the outgoing, nonreflected waves). For this reason $E[\mathbf{H}]$ (denoted as \mathbf{H}_{∞}) can be referred to as the direct field receptance matrix, and (in cases where such a geometry is conceptually feasible) it is equal to the receptance obtained when the subsystem extends infinitely away from the boundary.

In order to compare Eqs. (15) and (16) with existing work it is instructive to consider the case where the “boundary” consists of a single point within the subsystem, so that $A_{1j} = \phi_j(\mathbf{x})$ where \mathbf{x} is the location of the boundary point. Given that the modes are scaled to unit generalized mass it follows that $E[A_{1j}A_{1j}] = 1/M$, where M is the total mass of the subsystem, and thus Eq. (15) yields $E[\text{Im}(H_{11})] = (-\pi n / 2\omega M)$. According to the foregoing arguments, this expression should be equal to the imaginary part of the point receptance of an infinite subsystem. This is in fact correct, and the result agrees with earlier work presented by Cremer *et al.* (1990)—it can be noted that both n and M scale linearly with the size of the system, so that the expression is independent of the subsystem size. The average value of the real part of the receptance is given by Eq. (16), and the result obtained will depend on the frequency dependency of the modal density n . For a thin plate the modal density is constant, and Eq. (16) yields $E[\text{Re}(H_{11})] = 0$ for $\omega \neq 0$. For a beam the modal density is proportional to $\omega^{-1/2}$, and Eq. (16) yields $E[\text{Re}(H_{11})] = E[\text{Im}(H_{11})]$ for $\omega \neq 0$. In both cases the result is infinite for $\omega = 0$, representing the rigid body response of the unsupported system to a static point load. These results agree with the exact values given for infinite systems by Cremer *et al.* (1990), thus supporting the physical interpretation of the results represented by Eqs. (15) and (16).

A similar argument to that presented above for \mathbf{H} can be developed for the dynamic stiffness matrix \mathbf{D} by expressing the dynamics of the subsystem in terms of the boundary degrees of freedom plus the set of vibration modes associated with a clamped boundary (the “blocked” modes). The resulting expression for \mathbf{D} is similar to Eq. (13), and random point process theory can be applied to calculate the ensemble statistics. The key result (which can be anticipated from the above analysis) is that $E[\mathbf{D}]$ is independent of the subsystem loss factor while the variance reduces with increasing damping. It can then be deduced that $E[\mathbf{D}]$ relates to the same physical system as $E[\mathbf{H}]$, from which it follows that

$$E[\mathbf{D}] = E[\mathbf{H}]^{-1}. \quad (17)$$

Equations (5) and (17) imply that \mathbf{D}_{∞} , defined in Sec. II to enforce the condition $E[\mathbf{f}_{\text{rev}}] = 0$, is equal to the expected value of the dynamic stiffness matrix, which is in turn equal to the direct field dynamic stiffness matrix. These findings are consistent with the wave based analysis of Shorter and Langley (2005a).

B. Cross spectrum of the reverberant force vector

It follows from Eqs. (3), (4), and (17) that the reverberant force vector can be expressed in the form

$$\mathbf{f}_{\text{rev}} = \mathbf{D}_{\infty} \mathbf{H} \mathbf{f} - \mathbf{f} = \mathbf{D}_{\infty} (\mathbf{H} - \mathbf{H}_{\infty}) \mathbf{f}. \quad (18)$$

The rs component of the reverberant force cross-spectral matrix $E[\mathbf{f}_{\text{rev}}\mathbf{f}_{\text{rev}}^{*T}]$ is thus given by

$$E[f_{\text{rev},r}f_{\text{rev},s}^*] = \sum_{k,l,\alpha,\beta} D_{\infty,rk}D_{\infty,sl}^* \text{Cov}[H_{k\alpha}, H_{l\beta}^*] E[f_{\alpha}f_{\beta}^*], \quad (19)$$

where the notation is such that $f_{\text{rev},r}$ represents the r th component of \mathbf{f}_{rev} , and $\text{Cov}[x, y]$ represents the covariance of x and y . In deriving Eq. (19) the general case of random applied forces \mathbf{f} has been considered, with the natural assumption that the applied forces are statistically independent of the entries of the receptance matrix. Given that \mathbf{H} has the form of Eq. (13), random point process theory can be used to evaluate the covariance that appears in Eq. (19) and it follows from Eq. (A4) that

$$\text{Cov}[H_{k\alpha}, H_{l\beta}^*] = \left(\frac{\pi n}{2\eta\omega^3} \right) \{ E[A_{kj}A_{\alpha j}A_{lj}A_{\beta j}] + q(m)E[A_{kj}A_{\alpha j}]E[A_{lj}A_{\beta j}] \}. \quad (20)$$

Here $m = \omega\eta n$ is the modal overlap factor of the subsystem and the function $q(m)$ is detailed in the Appendix. The covariance of \mathbf{H} is dominated by contributions from modes that are resonant or close to resonance, and thus the complicating issues that are discussed below Eq. (14) do not arise for Eq. (13), i.e., it is sufficient for the assumptions of point process theory to be locally valid in the vicinity of ω , and there is no need to consider causality based corrections to allow for non-resonant contributions. The function $q(m)$ that appears in Eq. (13) is zero if the subsystem natural frequencies are assumed to constitute a Poisson point process, and nonzero if the natural frequencies are assumed to follow the GOE (tending to -1 at large values of m). In the case of the GOE, the mode shapes are theoretically Gaussian (Mehta, 1991), and given that the matrix \mathbf{A} is a linear function of the mode shapes it follows that \mathbf{A} will also be Gaussian. From the properties of Gaussian variables (see, for example, Lin, 1967) it follows that

$$E[A_{kj}A_{\alpha j}A_{lj}A_{\beta j}] = E[A_{kj}A_{\alpha j}]E[A_{lj}A_{\beta j}] + E[A_{kj}A_{\beta j}]E[A_{lj}A_{\alpha j}] + E[A_{kj}A_{lj}]E[A_{\alpha j}A_{\beta j}]. \quad (21)$$

The right hand side of Eq. (21) can be expressed in terms of the entries of the matrix \mathbf{H}_{∞} via Eq. (14). This result can then be substituted into Eq. (13) and subsequently into Eq. (19) to yield

$$E[\mathbf{f}_{\text{rev}}\mathbf{f}_{\text{rev}}^{*T}] = \left(\frac{2}{\pi m} \right) \{ \mathbf{D}_{\infty} \text{Im}(\mathbf{H}_{\infty}) (\mathbf{S}_{ff} + \mathbf{S}_{ff}^*) \text{Im}(\mathbf{H}_{\infty}) \mathbf{D}_{\infty}^* + \mathbf{D}_{\infty} \text{Im}(\mathbf{H}_{\infty}) \mathbf{D}_{\infty}^* \text{Tr}[\text{Im}(\mathbf{H}_{\infty}) \mathbf{S}_{ff}] + q(m) \mathbf{D}_{\infty} \text{Im}(\mathbf{H}_{\infty}) \mathbf{S}_{ff} \text{Im}(\mathbf{H}_{\infty}) \mathbf{D}_{\infty}^* \}, \quad (22)$$

where $\mathbf{S}_{ff} = E[\mathbf{f}\mathbf{f}^{*T}]$ is the cross spectral matrix of the applied forces and $\text{Tr}[\]$ represents the trace of the matrix. In deriving Eq. (22) it has been noted that all stiffness and receptance matrices are symmetric, while the force cross-spectral matrix is Hermitian. Equation (22) can be simplified by noting that

$$\mathbf{D}_{\infty} \text{Im}(\mathbf{H}_{\infty}) \mathbf{D}_{\infty}^* = -\text{Im}(\mathbf{D}_{\infty}), \quad (23)$$

$$P = (\omega/2) E[\text{Re}(i\mathbf{f}^{*T} \mathbf{H} \mathbf{f})] = -(\omega/2) \text{Tr}[\text{Im}(\mathbf{H}_{\infty}) \mathbf{S}_{ff}], \quad (24)$$

where Eq. (23) follows from Eq. (17), and P is the ensemble average of the power input by the applied forces. It can be noted that Eq. (23) is a matrix identity which is valid for any matrices \mathbf{D}_{∞} and \mathbf{H}_{∞} which satisfy $\mathbf{D}_{\infty} = \mathbf{H}_{\infty}^{-1}$, and it is employed extensively in the following analysis. The power input is related to the ensemble averaged vibrational energy E via $P = \omega\eta E$, and thus Eq. (22) can be rewritten in the form

$$E[\mathbf{f}_{\text{rev}}\mathbf{f}_{\text{rev}}^{*T}] = \left(\frac{4E}{\pi\omega n} \right) \text{Im}(\mathbf{D}_{\infty}) + \left(\frac{2}{\pi m} \right) \{ 2 \text{Re}(\mathbf{S}_{ff}^{\hat{\wedge}}) + q(m) \mathbf{S}_{ff}^{\hat{\wedge}} \}, \quad (25)$$

where

$$\mathbf{S}_{ff}^{\hat{\wedge}} = E[\hat{\mathbf{f}}\hat{\mathbf{f}}^{*T}], \quad (26)$$

$$\hat{\mathbf{f}} = i\mathbf{D}_{\infty} \text{Im}(\mathbf{H}_{\infty}) \mathbf{f}. \quad (27)$$

The first term on the right hand side of Eq. (25) is in agreement with the diffuse field reciprocity relation derived by Shorter and Langley (2005a), Eq. (6). The remaining terms arise from the fact that the vibrational field produced by the forcing may not be fully diffuse in the sense of Shorter and Langley (2005a), and a number of special cases are considered in the following section.

Equation (25) has been derived on the assumption that the natural frequencies and mode shapes of the subsystem have GOE statistics. If the natural frequencies are taken to be Poisson and the mode shapes are taken to be Gaussian, then the equation remains valid providing $q(m)$ is replaced by zero. For certain special geometries, such as rectangular systems, Poisson natural frequency statistics are accompanied by sinusoidal mode shapes, in which case $q(m) = 0$, and for point and line boundaries the right hand side of Eq. (25) must be multiplied by $(1/2)(3/2)^{d-1}$, where d is the physical dimension of the subsystem. For three-dimensional Poisson rectangular subsystems with area boundaries a number of other modifications must be made to Eq. (25), but this case is of limited practical interest and is not considered further here. The following analysis is concerned exclusively with GOE subsystems.

C. Special cases

Consider initially the case in which the ‘‘boundary’’ consists of a single point. In this case all of the matrices that appear in Eq. (25) reduce to scalar quantities, and it is readily demonstrated, noting Eqs. (23) and (24), that $\mathbf{S}_{ff}^{\hat{\wedge}} = 2\eta E \text{Im}(D_{\infty})$. Equation (25) then yields

$$E[f_{\text{rev}}f_{\text{rev}}^*] = \left(\frac{4E}{\pi\omega n} \right) \text{Im}(D_{\infty}) [3 + q(m)]. \quad (28)$$

Langley and Cotoni (2005) have shown that when a random subsystem is driven at a single point, the reverberant energy density at the forcing point is a factor of $3 + q(m)$ times the space averaged energy density. It is interesting that the same

factor appears in Eq. (28), and one interpretation is that Eq. (28) corrects the standard reciprocity relation, Eq. (6), to allow for the local increase in the energy density and hence in the reverberant force.

To investigate other special cases it is helpful to consider initially the eigenvalues and eigenvectors of the matrix $\text{Im}(\mathbf{H}_\infty)$. The matrix can be written in the form

$$\text{Im}(\mathbf{H}_\infty) = \mathbf{U}\mathbf{\Gamma}\mathbf{U}^T, \quad (29)$$

$$\mathbf{U}^T\mathbf{U} = \mathbf{I}, \quad (30)$$

where the j th eigenvector forms the j th column of the matrix \mathbf{U} , and the j th eigenvalue (γ_j say) is the j th diagonal entry of the diagonal matrix $\mathbf{\Gamma}$. Any applied force can be expanded in terms of the eigenvectors, so that

$$\mathbf{f} = \mathbf{U}\mathbf{b}, \quad (31)$$

where the vector \mathbf{b} contains the eigenvector amplitudes. The power input to the infinite system is thus

$$P = (\omega/2)\text{E}[\text{Re}\{\mathbf{f}^{*T}\mathbf{H}_\infty\mathbf{f}\}] = -(\omega/2)\sum_j \gamma_j \text{E}[|b_j|^2], \quad (32)$$

where it can be noted that each nonzero γ_j must be negative on physical grounds—any zero eigenvalues are omitted from Eq. (32) and all subsequent equations. With this notation, the cross spectrum that appears in Eq. (26) can now be written in the form

$$\mathbf{S}_{\hat{f}\hat{f}} = \mathbf{D}_\infty \mathbf{U} \mathbf{\Gamma} \text{E}[\mathbf{b}\mathbf{b}^{*T}] \mathbf{\Gamma} \mathbf{U}^T \mathbf{D}_\infty^*. \quad (33)$$

One interesting special case is that of random uncorrelated forcing which inputs an equal amount of power to each of the eigenvectors of $\text{Im}(\mathbf{H}_\infty)$. In this case it follows from Eq. (32) that

$$\text{E}[b_j b_k^*] = -\delta_{jk} \left(\frac{2P}{\omega \gamma_j N} \right) = -\delta_{jk} \left(\frac{2\eta E}{\gamma_j N} \right), \quad (34)$$

$$\mathbf{S}_{\hat{f}\hat{f}} = \left(\frac{2\eta E}{N} \right) \text{Im}(\mathbf{D}_\infty), \quad (35)$$

where N is the number of degrees of freedom at the boundary. Equation (25) then becomes

$$\text{E}[\mathbf{f}_{\text{rev}} \mathbf{f}_{\text{rev}}^{*T}] = \left(\frac{4E}{\pi \omega n} \right) \text{Im}(\mathbf{D}_\infty) \{1 + [2 + q(m)]/N\}. \quad (36)$$

Clearly this result approaches the standard reciprocity relation, Eq. (6), as the number of boundary degrees of freedom N becomes large. There is a close connection between Eq. (34) and the definition of a diffuse field employed by Shorter and Langley (2005a) and it is therefore not too surprising that this special case tends to the standard diffuse field result.

For more general applied loading (including all cases of deterministic loading) Eq. (34) will not apply. The diffuse field reciprocity relation will be a good approximation if

$$\mathbf{S}_{\hat{f}\hat{f}} \ll 2\eta E \text{Im}(\mathbf{D}_\infty), \quad (37)$$

since Eq. (25) will then be dominated by the first term on the right hand side. It should be noted that the inequality in Eq. (37) is to be interpreted in terms of the size of each matrix

entry, without regard to sign. By noting Eqs. (23), (24), and (29), this condition can be written in terms of eigenvalue and eigenvector notation as

$$\mathbf{D}_\infty \mathbf{U} \mathbf{\Gamma} \{ \text{E}[\mathbf{b}\mathbf{b}^{*T}] \mathbf{\Gamma} \} \mathbf{U}^T \mathbf{D}_\infty^* \ll \mathbf{D}_\infty \mathbf{U} \mathbf{\Gamma} \text{Tr}\{ \text{E}[\mathbf{b}\mathbf{b}^{*T}] \mathbf{\Gamma} \} \mathbf{U}^T \mathbf{D}_\infty^*, \quad (38)$$

where brackets have been inserted on the left hand side to emphasize an important matrix in the equation; the only difference between the two sides of the expression is that this matrix is replaced by its trace on the right hand side, which is equal to $-2\eta E$. One estimate of the relative size of the terms in Eq. (38) can be obtained by considering the trace of each side of the expression, excluding the presence of the matrix \mathbf{D}_∞ . This yields

$$\text{Tr}[\mathbf{U} \mathbf{\Gamma} \{ \text{E}[\mathbf{b}\mathbf{b}^{*T}] \mathbf{\Gamma} \} \mathbf{U}^T] = \sum_j \gamma_j^2 \text{E}[|b_j|^2], \quad (39)$$

$$\text{Tr}[\mathbf{U} \mathbf{\Gamma} \text{Tr}\{ \text{E}[\mathbf{b}\mathbf{b}^{*T}] \mathbf{\Gamma} \} \mathbf{U}^T] = \sum_k \gamma_k \sum_j \gamma_j \text{E}[|b_j|^2]. \quad (40)$$

Given that γ_j is always negative (to give positive power input to the subsystem), it is clear that the expression in Eq. (40) is always greater than that in Eq. (39), and significantly so if the set of eigenvalues consists of a large number (N_e say) of eigenvalues which are of similar modulus—in this case the ratio between the two expressions is $O(N_e)$. Under this condition it can be expected that Eq. (37) will be met in an average sense, although it is not guaranteed that the equation will be satisfied for every individual entry of the matrix $\mathbf{S}_{\hat{f}\hat{f}}$. In broad terms it can be stated that the diffuse field reciprocity relation will tend to be valid when the boundary has a large number of degrees of freedom and $\text{Im}(\mathbf{H}_\infty)$ has many eigenvalues of similar magnitude. Any deviation from the relation in a specific case can be studied by considering the more exact result, Eq. (25).

D. The a priori assumption of a diffuse field

The foregoing analysis has been concerned with a subsystem which is forced at the boundary. If alternatively there is no forcing at the boundary ($\mathbf{f}=\mathbf{0}$) but rather the system is forced on the nonboundary (or “internal”) degrees of freedom, then Eq. (1) no longer applies. The equation must be modified to include an additional term on the right hand side which is the *effective* boundary force arising from the internal excitation. In finite element notation, this force has the form $-\mathbf{D}_{\text{BI}} \mathbf{D}_{\text{II}}^{-1} \mathbf{f}_i$, where \mathbf{D}_{BI} and \mathbf{D}_{II} represent partitions of the finite element dynamic stiffness matrix, with “B” representing the boundary freedoms and “I” representing the internal freedoms, and \mathbf{f}_i is the force applied to the internal freedoms. The details of this additional force are not important to the present analysis, other than to note that the force exists and can be included in \mathbf{f}_{rev} , so that Eq. (2) (with $\mathbf{f}=\mathbf{0}$) remains valid for this case. Equations (2) and (9) then yield

$$\mathbf{f}_{\text{rev}} = \mathbf{D}_\infty \mathbf{q} = \mathbf{D}_\infty \mathbf{A} \mathbf{u}, \quad (41)$$

where \mathbf{u} is the vector of modal amplitudes. Consider now the case where it is assumed a priori that the internal forcing produces a diffuse field, i.e., the response is comprised of

vibration in N_r uncorrelated modes, and each mode is associated with an equal amount of (ensemble averaged) vibrational energy. The physical response due to a single mode j is $u_j \phi_j$, and, given that the mode shapes are scaled to unit generalized mass, the energy associated with this mode is $(\omega^2/2)|u_j|^2$. Given that the modes are equally energetic, the ensemble average of this result must be E/N_r , and hence it can be deduced that the modal amplitudes have the property

$$E[u_j u_k^*] = \delta_{jk} (2E/\omega^2 N_r), \quad j, k \in S_r, \quad (42)$$

where S_r is the set of N_r vibrating modes; by definition u_j will be zero if j does not belong to S_r . It now follows from Eqs. (41) and (42) that

$$\begin{aligned} E[f_{rev,r} f_{rev,s}^*] &= \left(\frac{2E}{\omega^2} \right) \sum_{k,l} D_{\infty,rk} D_{\infty,sl}^* \left\{ \left(\frac{1}{N_r} \right) \sum_{j \in S_r} E[A_{kj} A_{lj}^*] \right\} \\ &= \left(\frac{4E}{\pi \omega n} \right) \text{Im}(D_{\infty,rs}), \end{aligned} \quad (43)$$

where Eqs. (15) and (23) have been employed, and it has been assumed that the modal amplitudes are uncorrelated from the entries of the matrix \mathbf{A} . Equation (43) is in agreement with the standard diffuse field reciprocity relation, Eq. (6), and the present section provides, in combination with Eq. (15), perhaps the most straightforward and direct derivation of this result. However, the analysis rests on two assumptions: (i) the vibration field is diffuse and satisfies Eq. (42), and (ii) the modal amplitudes \mathbf{u} are uncorrelated from the entries of the matrix \mathbf{A} . Thus, even if the vibration field is perfectly diffuse, Eq. (6) could be invalidated by the failure of assumption (ii). Given that both the generalized forces (which produce \mathbf{u}) and the matrix \mathbf{A} depend on the mode shapes ϕ_j , any further assessment of the validity of assumption (ii) requires a more detailed consideration of the nature of the excitation forces. For example, if the excitation is random rain-on-the-roof loading then assumption (ii) is exactly satisfied. For other types of loading, such as a number of deterministic point loads, a very low degree of correlation between \mathbf{A} and \mathbf{u} would be expected if the excitation is remote from the boundary. The most direct approach to analyzing a particular situation would be to redefine the interior forcing points to be part of an extended boundary, and then employ Eq. (25), as in Sec. III C.

IV. DIFFUSE FIELD RECIPROCIITY AND ENERGY VARIANCE

The ensemble average of the power input is given by Eq. (24). To consider variance issues, it can be noted that the power input to any particular realization of the subsystem has the form

$$P_{in} = (\omega/2) \text{Re}(i \mathbf{f}^* \mathbf{T} \mathbf{q}) = (\omega/2) \text{Re}(i \mathbf{f}^{*T} \mathbf{H}_{\infty} \mathbf{f} + i \mathbf{f}^{*T} \mathbf{H}_{\infty} \mathbf{f}_{rev}). \quad (44)$$

For deterministic loading the variance of the power input is therefore given by

$$\begin{aligned} \text{Var}[P_{in}] &= E[\{(\omega/2) \text{Re}(i \mathbf{f}^{*T} \mathbf{H}_{\infty} \mathbf{f}_{rev})\}^2] \\ &= E[(\omega^2/8) \text{Re}(\mathbf{f}^{*T} \mathbf{H}_{\infty} \mathbf{f}_{rev} \mathbf{f}_{rev}^{*T} \mathbf{H}_{\infty} \mathbf{f} \\ &\quad - \mathbf{f}^{*T} \mathbf{H}_{\infty} \mathbf{f}_{rev} \mathbf{f}_{rev}^T \mathbf{H}_{\infty} \mathbf{f}^*)]. \end{aligned} \quad (45)$$

It follows from random point process theory that $E[\mathbf{f}_{rev} \mathbf{f}_{rev}^T] = 0$ (as discussed in the Appendix) and thus Eq. (45) yields

$$\text{Var}[P_{in}] = (\omega^2/8) \text{Re}\{\mathbf{f}^{*T} \mathbf{H}_{\infty} E[\mathbf{f}_{rev} \mathbf{f}_{rev}^*] \mathbf{H}_{\infty} \mathbf{f}\}. \quad (46)$$

It can be seen from this result that the variance of the input power (and hence the subsystem energy) is completely governed by the reverberant force cross spectrum. If the diffuse field reciprocity relation, Eq. (6), is adopted then it can readily be shown that Eq. (46) leads to a relative variance (i.e., the variance divided by the square of the mean) of $1/(\pi m)$, which is in disagreement with a result derived previously by Langley and Brown (2004). This apparent contradiction can be resolved by employing the more exact expression for the reverberant force cross spectrum, Eq. (25). The resulting expression for the relative variance is

$$\text{Relvar}(P_{in}) = \left(\frac{1}{\pi m} \right) \{ \alpha + q(m) \}, \quad (47)$$

$$\alpha = 2 + \left| \frac{\mathbf{f}^T \text{Im}(\mathbf{H}_{\infty}) \mathbf{f}}{\mathbf{f}^{*T} \text{Im}(\mathbf{H}_{\infty}) \mathbf{f}} \right|^2. \quad (48)$$

If the applied forces are real then $\alpha=3$; if the forces are complex, and \mathbf{f} is of large dimension, then it can be expected that $\alpha \approx 2$. By employing Eqs. (10), (15), and (21) it is possible to rewrite Eq. (48) in the form

$$\alpha = E[|g_j|^{4}] / E[|g_j|^2]^2, \quad (49)$$

where g_j is the generalized force acting in mode j . Equations (47) and (49) are in complete agreement with results obtained previously by Langley and Brown (2004), thus removing the apparent discrepancy between these results and the statistics of the reverberant force vector.

If the applied loading is random, rather than deterministic, then the variance of the power input cannot be expressed in terms of $E[\mathbf{f}_{rev} \mathbf{f}_{rev}^*]$, due to the fact that \mathbf{f} and \mathbf{f}_{rev} are statistically dependent in Eq. (45). The variance for this case has been derived by Langley and Brown (2004), but it is not considered further here, since $E[\mathbf{f}_{rev} \mathbf{f}_{rev}^*]$ is not the major determining factor.

V. SUPPORTING EVIDENCE

Various aspects of the foregoing theory have been validated previously by a range of authors, and therefore no new experimental or numerical results have been developed as part of the present work. The applicability of the GOE to structural dynamic subsystems has been discussed, with supporting numerical and experimental data, by (for example) Mehta (1991), Weaver (1989), Bertelsen *et al.* (2000), Ellegaard *et al.* (2001), and Langley and Brown (2004). The diffuse field reciprocity relation, Eq. (6), has been validated analytically by Shorter and Langley (2005a) for a number of wave bearing subsystems (beams and acoustic fields) under

the a priori assumption of a diffuse field. Furthermore, the relation has been employed in the hybrid FE-SEA analysis method to yield good predictions for the ensemble averaged response of a random structure when compared against direct numerical simulations or experimental results (Shorter and Langley, 2005b, Langley *et al.*, 2005). The structures considered in these references meet the requirements outlined in Sec. III C for the relation to be a good approximation: essentially a large value of N_e , as discussed below Eq. (40). The energy density concentration factor $3+q(m)$ that appears in Eq. (28) has been confirmed numerically by Langley and Cotoni (2005) for a random plate structure, and the relative variance predicted by Eq. (47) has been confirmed by Langley and Brown (2004) and Cotoni *et al.* (2005) both numerically and experimentally for a range of subsystems.

VI. CONCLUSIONS

This work has considered the response of a random subsystem that is forced at a set of “boundary” degrees of freedom, which constitute a subset of the total set of degrees of freedom. The main result is Eq. (25), which represents an extension of the diffuse field reciprocity relation, Eq. (6), to more general situations. The equation is applicable to a random subsystem which has statistically homogeneous global modes (for example, a beam, plate, or acoustic volume), and which has a high statistical overlap factor S , so that the natural frequencies can be considered to be a (locally) stationary random point process. The conditions under which Eq. (25) reduces to Eq. (6) have been discussed in Sec. III C, and two notable cases are:

- (i) Random excitation which inputs an equal amount of power into each eigenmode of $\text{Im}(\mathbf{H}_\infty)$. This leads Eq. (36), which reduces to Eq. (6) if the number of boundary degrees of freedom N is high.
- (ii) More general excitation which satisfies Eq. (38). As shown by Eq. (39), this result will tend to be satisfied on average (although not necessarily for each entry of the cross-spectral matrix) for any type of forcing providing $\text{Im}(\mathbf{H}_\infty)$ has a significant number of nonzero eigenvalues.

The further case of the a priori assumption of a diffuse field caused by nonboundary (i.e., internal) loading has been considered in Sec. III D. It was found that rain-on-the-roof excitation leads to Eq. (6), but otherwise a detailed consideration of the nature of the applied loading is required before a conclusion can be drawn. The concept of a boundary is used very loosely here, and Eq. (25) can readily be used to study the case of general internal loading by transferring the loaded degrees of freedom from the internal set to the boundary set.

It has also been shown in the present work that if the diffuse field reciprocity relation, Eq. (6), is used to predict the variance of the energy of a subsystem subjected to deterministic loading, then an erroneous result is obtained. This error is corrected by the use of the extended result, Eq. (25).

A subsidiary result yielded by the present analysis is that the ensemble average of the dynamic stiffness matrix is equal to the inverse of the ensemble average of the recep-

tance matrix, as stated by Eq. (17). Physically this is because each matrix corresponds to the same physical system, namely a heavily damped system in which waves emanating from the boundary do not return.

ACKNOWLEDGMENTS

The initial part of this analysis was performed while the author was Visiting Research Scientist, ESI US R&D Inc. This part of the work was funded by the Air Force Research Laboratory, Space Vehicles Directorate, Kirtland AFB, NM, USA under SBIR Phase II Contract No. F29601-02-C-0109. The author is grateful for helpful conversations with Dr. Vincent Cotoni and Dr. Phil Shorter of ESI US R&D Inc.

APPENDIX: RANDOM POINT PROCESS THEORY

Consider two random functions of frequency $x(\omega)$ and $y(\omega)$ that have the form

$$x(\omega) = \sum_j \frac{X_j}{\omega_j^2(1+i\eta) - \omega^2}, \quad (\text{A1})$$

$$y(\omega) = \sum_j \frac{Y_j}{\omega_j^2(1+i\eta) - \omega^2}. \quad (\text{A2})$$

Here the points ω_j form a stationary random sequence along the frequency axis, and the numerators X_j are statistically independent random variables each drawn from the same distribution. The numerators Y_j are similarly defined, although there is no requirement for Y_j to be statistically independent of X_j . It follows from random point process theory (for example, Stratonovich, 1963 Lin, 1967, Lyon, 1969, Langley and Brown, 2004) that

$$\text{E}[x(\omega)] = n\text{E}[X_j] \int_0^\infty \frac{d\omega_j}{\omega_j^2(1+i\eta) - \omega^2} \approx \left(\frac{-i\pi n}{2\omega}\right) \text{E}[X_j], \quad (\text{A3})$$

where n is the average density of the random points ω_j , i.e., the inverse of the mean spacing. It also follows from random point process theory (see, for example, Langley and Cotoni, 2005) that

$$\text{Cov}[x(\omega), y^*(\omega)] = \left(\frac{\pi n}{2\eta\omega^3}\right) \{ \text{E}[X_j Y_j^*] + \text{E}[X_j] \text{E}[Y_j^*] q(m) \}, \quad (\text{A4})$$

where Cov represents the covariance, $m = \omega\eta m$ and the function $q(m)$ depends on the statistics of the random point process. For Poisson points, $q(m)=0$, while for points conforming to the Gaussian orthogonal ensemble, Langley and Cotoni (2005) have shown that

$$q(m) = -1 + \left(\frac{1}{2\pi m}\right) (1 - e^{-2\pi m}) + E_1(\pi m) \left[\cosh(\pi m) - \left(\frac{1}{\pi m}\right) \sinh(\pi m) \right], \quad (\text{A5})$$

where E_1 is the exponential integral (Abramowitz and Ste-

gun, 1964). It can also be shown from random point process theory that $\text{Cov}[x(\omega), y(\omega)] = 0$.

- Abramowitz, M., and Stegun, I. A. (1964). *Handbook of Mathematical Functions* (Dover, New York).
- Bertelsen, P., Ellegaard, C., and Hugues, E. (2000). "Distribution of eigenfrequencies for vibrating plates," *Eur. Phys. J. B* **15**, 87–96.
- Cotoni, V., Langley, R. S., and Kidner, M. R. F. (2005). "Numerical and experimental validation of variance prediction in the statistical energy analysis of built-up systems," *J. Sound Vib.* **288**, 701–728.
- Cremer, L., Heckl, M., and Ungar, E. E. (1990). *Structure Borne Sound: Structural Vibrations and Sound Radiation at Audio Frequencies*, 2nd ed. (Springer-Verlag, Berlin).
- Ellegaard, C., Schaaf, K., and Bertelsen, P. (2001). "Acoustic chaos," *Phys. Scr.* **90**, 223–230.
- Hackenbroich, G., and Weidenmüller, H. A. (1995). "Universality of random matrix results for non-Gaussian ensembles," *Phys. Rev. Lett.* **74**, 4118–4121.
- Kompella, M. S., and Bernhard, B. J. (1993). "Measurement of the statistical variation of structural-acoustic characteristics of automotive vehicle," in *Proceedings of the SAE Noise and Vibration Conference*, Warrendale, PA.
- Langley, R. S., and Brown, A. W. M. (2004). "The ensemble statistics of the energy of a random system subjected to harmonic excitation," *J. Sound Vib.* **275**, 823–846.
- Langley, R. S., and Cotoni, V. (2004). "Response variance prediction in the statistical energy analysis of built-up systems," *J. Acoust. Soc. Am.* **115**, 706–718.
- Langley, R. S., and Cotoni, V. (2005). "The ensemble statistics of the vibrational energy density of a random system subjected to single point harmonic excitation," *J. Acoust. Soc. Am.* **118**, 3064–3076.
- Langley, R. S., Shorter, P. J., and Cotoni, V. (2005). "Predicting the response statistics of uncertain structures using extended versions of SEA," in *Proceedings of Inter-Noise*, Rio de Janeiro, Brazil.
- Lin, Y. K. (1967). *Probabilistic Theory of Structural Dynamics* (McGraw-Hill, New York).
- Lyon, R. H. (1969). "Statistical analysis of power injection and response in structures and rooms," *J. Acoust. Soc. Am.* **45**, 545–565.
- Meirovitch, L. (1986). *Elements of Vibration Analysis*, 2nd ed. (McGraw-Hill, New York).
- Mehta, M. L. (1991). *Random Matrices* (Academic, San Diego).
- Morfey, C. L. (2001). *Dictionary of Acoustics* (Academic, San Diego).
- Shaw, E. (1988). "Diffuse field response, receiver impedance, and the acoustical reciprocity principle," *J. Acoust. Soc. Am.* **84**, 2284–2287.
- Shorter, P. J., and Langley, R. S. (2005a). "On the reciprocity relationship between direct field radiation and diffuse reverberant loading," *J. Acoust. Soc. Am.* **117**, 85–95.
- Shorter, P. J., and Langley, R. S. (2005b). "Vibro-acoustic analysis of complex systems," *J. Sound Vib.* **288**, 669–700.
- Smith, P., Jr. (1962). "Response and radiation of structural modes excited by sound," *J. Acoust. Soc. Am.* **34**, 640–647.
- Smith, P., Jr. (1981). "Normal input admittance of a disk in a thin flat plate," *J. Acoust. Soc. Am.* **69**, 155–157.
- Soize, C. (2003). "Random matrix theory and non-parametric model of random uncertainties in vibration analysis," *J. Sound Vib.* **263**, 893–916.
- Stratonovich, R. L. (1963). *Topics in the Theory of Random Noise* (Gordon and Breach, New York), Vol. **1**.
- Weaver, R. L. (1989). "On the ensemble variance of reverberation room transmission functions, the effect of spectral rigidity," *J. Sound Vib.* **130**, 487–491.

Radiation clusters and the active control of sound transmission into a symmetric enclosure

Tsutomu Kaizuka^{a)} and Nobuo Tanaka

Department of Aerospace Engineering, Tokyo Metropolitan University, 6-6 Asahigaoka, Hino-city, Tokyo, 191-0065, Japan

(Received 24 April 2006; revised 11 October 2006; accepted 6 November 2006)

Radiation cluster control is proposed for the purpose of attenuating harmonic sound transmission into a symmetric enclosure using error signals derived from structural vibration sensors. The approach falls into a category of middle authority control, which is between LAC (low authority control: structural modal control) and HAC (high authority control: radiation modal control), possessing the benefit of practicality over LAC, while providing high control performance and some flexibility of control gain assignment similar to HAC. The structure of a radiation cluster control system is outlined, showing that it is possible to control a target cluster without affecting the other clusters. A design procedure for the radiation cluster control system is then proposed. Numerical results are also presented. © 2007 Acoustical Society of America. [DOI: 10.1121/1.2404621]

PACS number(s): 43.40.Rj, 43.40.Vn [SFW]

Pages: 922–937

I. INTRODUCTION

The use of structural control sources to minimize sound transmission through flexible structures into coupled enclosures offers advantages over the use of more conventional acoustic sources: fewer secondary sources are generally required for global noise attenuation of the enclosed acoustic field;¹ and surface mounted actuators are much less intrusive than bulky speaker/cabinet arrangements. However, the gains in system compactness are not necessarily realized in practice when microphones placed throughout the cavity are used to provide the controller error signals to achieve global attenuation. As an alternative, surface mounted structural sensors have also been used as error sensors to allow system compactness to be achieved in practice. Although a reduction in the vibration of the structure is achieved, a reduction in the enclosed acoustic field does not necessarily follow.^{2,3} Such a disproportionate relationship between vibration and sound level is caused by nonorthogonality of structural modes in the acoustic field.⁴

In 1993, it was shown that it is possible to describe a quantity from the vibration of the structure which is orthogonal with respect to the global potential energy in the enclosed acoustic field.⁵ One can sense the orthogonal contributors using structural error sensors; thus sound transmission from a structure into an enclosed space is successfully minimized even though error signals are derived from the vibration of the structure. It draws from the work of previous researchers who have investigated the acoustic power radiated into free space from vibrating beams,^{6–8} plates,^{9–13} and shells^{14–17} using orthogonal surface velocity patterns, commonly referred to as “radiation modes.” The approach involves decomposing the surface vibration, usually via singular value decomposition, into a number of surface velocity distributions which contribute independently to the radiated acoustic field. Sny-

der and Tanaka⁵ have extended the work to a brief study of the active control of sound transmission into a coupled enclosure. Further, Cazzolato and Hansen^{4,18} have discussed practical implementation issues of the active control of radiation modes in a coupled enclosure, and developed a practical methodology to construct radiation modal filters. Radiation modal filters consist of a weighted addition of outputs from multiple structural modal filters constructed by lumped parameter or distributed parameter sensors. Unfortunately, such a filtering system is difficult to implement, because structural and acoustic modal functions are required to be given *a priori* to construct structural modal filters as well as to design the additional weighting filter of structural modal filter outputs.

The primary objective of this paper is to describe a quantity from the vibration of the structure which replaces radiation mode as an orthogonal contributor with respect to global potential energy in the enclosed acoustic field. The orthogonal contributors presented in this paper are referred to as “radiation clusters” where emphasis is placed on specific clustering of structural modes of a symmetric enclosure. It is reasonable to assume that structural and acoustic modal functions are clustered to an even or an odd function when an enclosure has some symmetric structure, because structural modal functions of a symmetric enclosure and acoustic modal functions of the cavity enclosed by a symmetric enclosure are both also symmetric. Coupling is then found to occur in two ways as follows: coupling between structural clusters which belong to an even function and acoustic clusters which belong to an even function; coupling between structural clusters which belong to an odd function and acoustic clusters which belong to an odd function. This indicates orthogonality between structural and acoustic clusters. Hence, structural clusters can be regarded as orthogonal contributors with respect to the enclosed acoustic field, and referred to as “radiation clusters.” There is an essential difference between radiation modes and radiation clusters: radiation modes are the orthogonal contributors in units of

^{a)}Research Fellow of the Japan Society for the Promotion of Science; electronic mail: u6991501@cc.tmit.ac.jp

mode; and radiation clusters are the orthogonal contributors in units of cluster. Thus, from a viewpoint of particularity in an orthogonal contributor with respect to the enclosed acoustic field, radiation modes are superior to radiation clusters. In other words, minimizing the squared amplitudes of the radiation modes guarantees the reduction of the global potential energy in the enclosed acoustic field,⁴ while minimizing the amplitudes of the radiation clusters does not necessarily guarantee such a reduction of the global potential energy because the structural modes within the same radiation cluster couple to each other in the enclosed acoustic field. However, radiation clusters may still be reasonable error criteria for the active control of sound transmission, because minimizing the squared amplitudes of the radiation cluster which can couple with the dominant acoustic cluster in the enclosed acoustic field is reasonable compared to minimizing the squared amplitudes of all structural modes in a blind way, i.e., conventional vibration control with the error criterion being the structural modes. Moreover, radiation clusters provide superior practicality over radiation modes. As described later, measurement systems of radiation clusters are much simpler than those of radiation modes. Consequently, active control of radiation clusters falls into an eclectic strategy which arranges a compromise between particularity and practicality as an active control system of sound transmission into a coupled enclosure using structural error sensing.

The second objective is to develop mechanisms of filtering each radiation cluster using structural error sensors, referred to as “radiation cluster filters,” as well as actuating each radiation cluster using structural control sources, referred to as “radiation cluster actuators.” Combining radiation cluster filters and actuators, “radiation cluster control” can be performed. Radiation cluster control offers an advantage over radiation modal control in practice, since neither structural nor acoustic modal functions are required to construct measurement systems of radiation clusters.

The third objective is to numerically investigate the validity of radiation cluster control for sound transmission through a rectangular plate into a rectangular cavity. The plate-cavity coupled system was chosen because of the symmetry of the enclosure and the simplicity of the geometry. In addition, its modal behavior and characteristics are well understood, thus allowing effort to be concentrated on understanding the physical mechanisms involved in the control of sound transmission.

Section II begins by developing the general theory of sound transmission through a structure into a contiguous cavity. The transmitted acoustic field is derived in two formulations: one in terms of the amplitudes of the structural modes; and the other in terms of the amplitudes of the radiation modes. Throughout the structural modal formulation, nonorthogonality of the structural modes in the enclosed acoustic field is reviewed, and it is found that structural modal control is unsuitable for the control of sound transmission. In addition, throughout the radiation modal formulation, orthogonality of the radiation modes is reviewed, with the result that radiation modal control is found to be suitable for the control for sound transmission. Moreover, implementation of radiation modal control is discussed and the diffi-

culties in constructing radiation modal filters are pointed out. Much of the material presented in Secs. II A and II B is not new (as is indicated by the references throughout). It is represented here, with outline derivations when appropriate, in order to provide a self-contained and unified account of the base theory of the control of sound transmission through a structure into a cavity. Section II C specializes the theories of radiation cluster as well as those of radiation cluster control system. From a viewpoint of a feedforward control strategy, an optimal control law which minimizes the complex velocities of the radiation clusters is derived. Section III numerically verifies the effectiveness of radiation cluster control as the basis for attenuating the global potential energy in the enclosed acoustic field. Section IV summarizes significant conclusions of the work.

II. GENERAL THEORY

A. Structural modal control: Low authority control

An appropriate global error criterion for controlling the sound transmission into a coupled enclosure is the total time averaged frequency-dependent acoustic potential energy, $E_p(\omega)$, in the enclosure¹⁹

$$E_p(\omega) = \frac{1}{4\rho_0 c_0^2} \int_V |p(\mathbf{r}, \omega)|^2 d\mathbf{r}, \quad (1)$$

where $p(\mathbf{r}, \omega)$ is the complex sound pressure at some location \mathbf{r} in the enclosure, ρ_0 is the density of the acoustic fluid, c_0 is the speed of sound in the fluid, and V is the volume of the cavity. The dependence of the above-noted parameters on the frequency, ω , is assumed in the following analysis. Using the modal coupling approach,^{2,20} the acoustic pressure at any location within the cavity is expressed as a summation of M uncoupled acoustic modal functions and the associated modal pressure amplitudes of the cavity

$$p(\mathbf{r}, \omega) = \boldsymbol{\phi}^T(\mathbf{r})\mathbf{p}(\omega), \quad (2)$$

where the superscript T is the transpose, $\boldsymbol{\phi}(\mathbf{r})$ is the $(M \times 1)$ vector of the uncoupled acoustic modal functions, the m th term of which is $\phi_m(\mathbf{r})$, and $\mathbf{p}(\omega)$ is the $(M \times 1)$ vector of the acoustic modal pressure amplitudes, the m th term of which is $p_m(\omega)$. The modal expansion for the acoustic potential energy evaluated over M acoustic modes is then given by

$$E_p(\omega) = \mathbf{p}^H(\omega)\boldsymbol{\Lambda}\mathbf{p}(\omega) \quad (3)$$

where the superscript H denotes the Hermitian and $\boldsymbol{\Lambda}$ is the $(M \times M)$ diagonal weighting matrix, the diagonal terms of which are

$$\Lambda_{mm} = \frac{\Lambda_m}{4\rho_0 c_0^2}, \quad (4)$$

where Λ_m is the modal volume of the m th acoustic mode, defined as the volume integration of the square of the modal function,

$$\Lambda_m = \int_V \phi_m^2(\mathbf{r}) d\mathbf{r}. \quad (5)$$

The acoustic modal pressure amplitude vector, $\mathbf{p}(\omega)$, within the cavity, arising from the structural vibration are given by the product of N uncoupled structural modal functions at some location \mathbf{x} on the enclosure and the associated modal velocity amplitudes of the enclosure, that is,

$$\mathbf{p}(\omega) = \mathbf{Y}(\omega)\mathbf{B}\mathbf{v}(\omega), \quad (6)$$

where $\mathbf{Y}(\omega)$ is the $(M \times M)$ diagonal acoustic resonance matrix whose diagonal terms are given by

$$Y_{mm}(\omega) = \frac{j\rho_0 S \omega}{\Lambda_m(\kappa_m^2 - \kappa^2 + j\eta_m \kappa_m \kappa)}, \quad (7)$$

where S is the total surface area of the bounding structure, κ is the wave number of the sound in the cavity, and κ_m and η_m are the wave number and modal loss factor of the m th acoustic mode, respectively. \mathbf{B} is the $(M \times N)$ coupling coefficient matrix defined as

$$\mathbf{B} = \frac{1}{S} \int_S \boldsymbol{\phi}(\mathbf{x}) \boldsymbol{\psi}^T(\mathbf{x}) d\mathbf{x}, \quad (8)$$

where $\boldsymbol{\psi}(\mathbf{x})$ is the $(N \times 1)$ vector of uncoupled structural modal functions, the n th term of which is $\psi_n(\mathbf{x})$. $\mathbf{v}(\omega)$ is the $(N \times 1)$ vector of the structural modal velocity amplitudes, the n th term of which is $v_n(\omega)$. Substituting Eq. (6) into Eq. (3) gives an expression for the acoustic potential energy with respect to the normal structural vibration,

$$E_p(\omega) = \mathbf{v}^H(\omega) \boldsymbol{\Pi}(\omega) \mathbf{v}(\omega), \quad (9)$$

where the error weighting matrix $\boldsymbol{\Pi}(\omega)$ is given by

$$\boldsymbol{\Pi}(\omega) = \mathbf{B}^H \mathbf{Y}^*(\omega) \boldsymbol{\Lambda} \mathbf{Y}(\omega) \mathbf{B}. \quad (10)$$

It should be noted that the error weighting matrix is not necessarily diagonal, which implies that the normal structural modes are not orthogonal contributors to the enclosed acoustic field. Therefore the minimization of the squared amplitudes of the individual structural modes does not necessarily reduce the acoustic potential energy in the enclosure. We categorize structural modal control as LAC (low authority control) because it is unsuitable for the control of sound transmission into the enclosure.

B. Radiation modal control: High authority control

Snyder and Tanaka,⁵ and Cazzolato and Hansen⁴ derived the orthogonal contributors, termed radiation modes, with respect to the global potential energy in the enclosed acoustic field, developing the active feedforward control implementation to minimize the acoustic potential energy by suppressing only the significantly influential radiation modes. Here, it is worth overviewing the principle of radiation modal control in the enclosed acoustic field.

From Eqs. (9) and (10), the acoustic potential energy is reformulated to an expression for the acoustic potential energy as a function of an orthogonal radiation mode set,^{4,5}

$$E_p(\omega) = \mathbf{y}^H(\omega) \boldsymbol{\Omega}(\omega) \mathbf{y}(\omega), \quad (11)$$

where the $(M \times M)$ diagonal frequency-dependent weighting matrix, $\boldsymbol{\Omega}(\omega)$, is given by

$$\boldsymbol{\Omega}(\omega) = \mathbf{Y}^*(\omega) \boldsymbol{\Lambda} \mathbf{Y}(\omega), \quad (12)$$

and where the $(M \times 1)$ vector of the radiation modal velocity amplitudes, $\mathbf{y}(\omega)$, is given by

$$\mathbf{y}(\omega) = \mathbf{B}\mathbf{v}(\omega). \quad (13)$$

Equation (13) demonstrates that each radiation mode is made up of a linear combination of the normal structural modes, the ratio of which is defined by the coupling coefficient matrix. As the weighting matrix, $\boldsymbol{\Omega}(\omega)$, is diagonal, Eq. (11) may be written as

$$E_p(\omega) = \sum_{m=1}^M \Omega_{mm}(\omega) |y_m(\omega)|^2, \quad (14)$$

where $\Omega_{mm}(\omega)$ is the m th diagonal term of the weighting matrix, and $y_m(\omega)$ is the m th term of the radiation modal velocity amplitude vector.

The acoustic potential energy contribution from any radiation mode is equal to the square of its amplitude multiplied by the corresponding weight. The radiation modes are therefore orthogonal contributors to the acoustic potential energy, and hence the acoustic potential energy is directly reduced by minimizing the squared amplitude of any of the radiation modes. Therefore, we categorize radiation modal control as HAC (high authority control) because minimizing the squared amplitudes of the individual radiation modes guarantees the reduction of the acoustic potential energy.

To realize an active controller with the error criterion being the radiation modes, it is necessary to construct the radiation modal filters which can measure the amplitudes of the individual radiation modes. Equation (13) implies that the amplitudes of the radiation modes may be measured by a set of two kinds of filters: the structural modal filters to extract the amplitudes of the individual structural modes, $\mathbf{v}(\omega)$; and the weighting filters to linearly combine the amplitudes of the individual structural modes, \mathbf{B} . Note that the structural modal filters cannot be constructed without knowledge of the structural modal functions as presented in Refs. 21–23, and the weighting filters cannot be constructed without knowledge of both the structural and acoustic modal functions as is clear from Eq. (8). In this way, implementing the radiation modal control system is difficult in practice.

C. Radiation cluster control: Middle authority control

This section proposes a novel active control approach referred to as radiation cluster control where emphasis is placed on controlling designated groupings of the structural modes. As mentioned previously, the structural and acoustic modes are clustered to an even function or an odd function, when the enclosure has some symmetric structure. Figure 1 shows a schematic illustration of the shell of a car cabin as an example of symmetric enclosures along the x direction. The origin of the coordinate system is the gravity center of the enclosure. One can then find symmetric coordinates on the enclosure: $\mathbf{x}_1 = (x_x, x_y, x_z)$ is a coordinate in the range of $x \geq 0$; and $\mathbf{x}_2 = (-x_x, x_y, x_z)$ is the other coordinate in the range of $x \leq 0$ where x_x is assumed to be positive, as well as in the enclosed space: $\mathbf{r}_1 = (r_x, r_y, r_z)$ is a coordinate in the range of

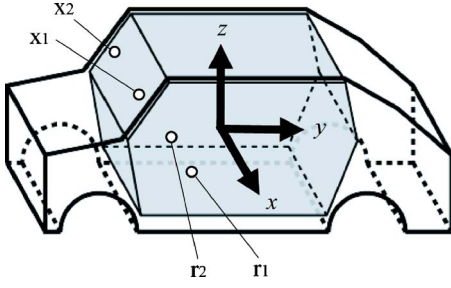


FIG. 1. An example of enclosures whose structure are symmetric along the x direction.

$x \geq 0$; and $\mathbf{r}_2 = (-r_x, r_y, r_z)$ is the other coordinate in the range of $x \leq 0$ where r_x is assumed to be positive. Note that the number of the symmetric coordinates is defined as $2^1=2$, thereby a pair of \mathbf{x}_1 and \mathbf{x}_2 can be found on the enclosure as well as a pair of \mathbf{r}_1 and \mathbf{r}_2 can be found in the enclosed space. If the enclosure was symmetric along the x and y directions, the number of the symmetric coordinates to be defined might be $2^2=4$. And if the enclosure was symmetric along the x , y , and z directions, the number of the symmetric coordinates to be defined might be $2^3=8$. For simplicity, this paper deals with symmetric enclosures whose symmetry is along the x direction only as shown in Fig. 1. However, the discussion may be expandable to any symmetric enclosure.

First, the acoustic modal functions are clustered as

$$\boldsymbol{\phi}(\mathbf{r}) = \begin{bmatrix} \boldsymbol{\phi}_e(\mathbf{r}) \\ \boldsymbol{\phi}_o(\mathbf{r}) \end{bmatrix} \quad (15)$$

where $\boldsymbol{\phi}_e(\mathbf{r})$ is the $(M_e \times 1)$ vector of the acoustic cluster which belongs to an even function, $\boldsymbol{\phi}_o(\mathbf{r})$ is the $(M_o \times 1)$ vector of the acoustic cluster which belongs to an odd function, and M_e and M_o denotes the number of the acoustic modal functions which belong to even and odd functions, respectively. Note that acoustic cluster, $\boldsymbol{\phi}_e(\mathbf{r})$ and $\boldsymbol{\phi}_o(\mathbf{r})$, satisfy

$$\boldsymbol{\phi}_e(\mathbf{r}_1) = \boldsymbol{\phi}_e(\mathbf{r}_2), \quad (16a)$$

$$\boldsymbol{\phi}_o(\mathbf{r}_1) = -\boldsymbol{\phi}_o(\mathbf{r}_2), \quad (16b)$$

In a similar fashion, the structural modal functions are clustered as

$$\boldsymbol{\psi}(\mathbf{x}) = \begin{bmatrix} \boldsymbol{\psi}_e(\mathbf{x}) \\ \boldsymbol{\psi}_o(\mathbf{x}) \end{bmatrix}, \quad (17)$$

where $\boldsymbol{\psi}_e(\mathbf{r})$ is the $(N_e \times 1)$ vector of the structural cluster which belongs to an even function, $\boldsymbol{\psi}_o(\mathbf{r})$ is the $(N_o \times 1)$ vector of the acoustic cluster which belongs to an odd function, and N_e and N_o denote the number of the structural modal functions which belong to even and odd functions, respectively. Note that the structural clusters, $\boldsymbol{\psi}_e(\mathbf{r})$ and $\boldsymbol{\psi}_o(\mathbf{r})$, satisfy

$$\boldsymbol{\psi}_e(\mathbf{x}_1) = \boldsymbol{\psi}_e(\mathbf{x}_2), \quad (18a)$$

$$\boldsymbol{\psi}_o(\mathbf{x}_1) = -\boldsymbol{\psi}_o(\mathbf{x}_2). \quad (18b)$$

Substituting Eqs. (15) and (17) into Eq. (8) yields

$$\mathbf{B} = \frac{1}{S} \int_S \begin{bmatrix} \boldsymbol{\phi}_e(\mathbf{x}) \boldsymbol{\psi}_e^T(\mathbf{x}) & \boldsymbol{\phi}_e(\mathbf{x}) \boldsymbol{\psi}_o^T(\mathbf{x}) \\ \boldsymbol{\phi}_o(\mathbf{x}) \boldsymbol{\psi}_e^T(\mathbf{x}) & \boldsymbol{\phi}_o(\mathbf{x}) \boldsymbol{\psi}_o^T(\mathbf{x}) \end{bmatrix} d\mathbf{x}. \quad (19)$$

Separating the domain of integration S into S_1 in the range of $x \geq 0$ and S_2 in the range of $x \leq 0$ leads to

$$\begin{aligned} \mathbf{B} = & \frac{1}{S_1} \int_{S_1} \begin{bmatrix} \boldsymbol{\phi}_e(\mathbf{x}_1) \boldsymbol{\psi}_e^T(\mathbf{x}_1) & \boldsymbol{\phi}_e(\mathbf{r}_1) \boldsymbol{\psi}_o^T(\mathbf{x}_1) \\ \boldsymbol{\phi}_o(\mathbf{x}_1) \boldsymbol{\psi}_e^T(\mathbf{x}_1) & \boldsymbol{\phi}_o(\mathbf{r}_1) \boldsymbol{\psi}_o^T(\mathbf{x}_1) \end{bmatrix} d\mathbf{x}_1 \\ & + \frac{1}{S_2} \int_{S_2} \begin{bmatrix} \boldsymbol{\phi}_e(\mathbf{x}_2) \boldsymbol{\psi}_e^T(\mathbf{x}_2) & \boldsymbol{\phi}_e(\mathbf{x}_2) \boldsymbol{\psi}_o^T(\mathbf{x}_2) \\ \boldsymbol{\phi}_o(\mathbf{x}_2) \boldsymbol{\psi}_e^T(\mathbf{x}_2) & \boldsymbol{\phi}_o(\mathbf{x}_2) \boldsymbol{\psi}_o^T(\mathbf{x}_2) \end{bmatrix} d\mathbf{x}_2. \end{aligned} \quad (20)$$

Considering Eqs. (16) and (18), Eq. (20) expands to

$$\mathbf{B} = \begin{bmatrix} \mathbf{B}_e & \mathbf{0} \\ \mathbf{0} & \mathbf{B}_o \end{bmatrix}, \quad (21)$$

where

$$\mathbf{B}_e = \frac{2}{S_1} \int_{S_1} \boldsymbol{\phi}_e(\mathbf{x}_1) \boldsymbol{\psi}_e^T(\mathbf{x}_1) d\mathbf{x}_1, \quad (22a)$$

$$\mathbf{B}_o = \frac{2}{S_1} \int_{S_1} \boldsymbol{\phi}_o(\mathbf{x}_1) \boldsymbol{\psi}_o^T(\mathbf{x}_1) d\mathbf{x}_1. \quad (22b)$$

Equation (21) implies the orthogonality between the structural and acoustic clusters. In other words, it is found that the structural-acoustic coupling can be independently discussed in two ways: the coupling between the structural and acoustic clusters, which are even functions; and the coupling between the structural and acoustic clusters, which are odd functions. Hence, the structural clusters are regarded as some orthogonal contributors with respect to the enclosed acoustic field, and referred to as radiation clusters in contrast with radiation modes. Moreover, the terms in the cluster coupling coefficient matrixes, \mathbf{B}_e and \mathbf{B}_o , are written as

$$B_{m_e n_e} = \frac{2}{S_1} \int_{S_1} \varphi_{m_e}(\mathbf{x}_1) \psi_{n_e}(\mathbf{x}_1) d\mathbf{x}_1 \begin{cases} \neq 0 \\ = 0, \end{cases} \quad (23a)$$

$$B_{m_o n_o} = \frac{2}{S_1} \int_{S_1} \varphi_{m_o}(\mathbf{x}_1) \psi_{n_o}(\mathbf{x}_1) d\mathbf{x}_1 \begin{cases} \neq 0 \\ = 0. \end{cases} \quad (23b)$$

When $B_{m_e n_e}$ equals zero, the m_e th structural mode does not couple with the n_e th acoustic mode. When $B_{m_o n_o}$ equals zero, the m_o th structural mode does not couple with the n_o th acoustic mode. However, the structural clusters are still the orthogonal contributors with respect to the enclosed acoustic field because Eq. (21) is satisfied, and it should be noted that the case of $B_{m_e n_e} = 0$ or $B_{m_o n_o} = 0$ is rare.

Next, substituting Eq. (21) into Eq. (10) yields

$$\begin{aligned} \boldsymbol{\Pi}(\omega) = & \begin{bmatrix} \boldsymbol{\Pi}_e(\omega) & \mathbf{0} \\ \mathbf{0} & \boldsymbol{\Pi}_o(\omega) \end{bmatrix} \\ = & \begin{bmatrix} \mathbf{B}_e^H \mathbf{Y}_e^*(\omega) \boldsymbol{\Lambda}_e \mathbf{Y}_e(\omega) \mathbf{B}_e & \mathbf{0} \\ \mathbf{0} & \mathbf{B}_o^H \mathbf{Y}_o^*(\omega) \boldsymbol{\Lambda}_o \mathbf{Y}_o(\omega) \mathbf{B}_o \end{bmatrix}, \end{aligned} \quad (24)$$

where $\boldsymbol{\Lambda}_e$ and $\boldsymbol{\Lambda}_o$ are, respectively, the $(M_e \times M_e)$ and $(M_o \times M_o)$ diagonal matrixes associated with Eq. (4) in a cluster

form, and $\mathbf{Y}_e(\omega)$ and $\mathbf{Y}_o(\omega)$ are, respectively, the ($M_e \times M_e$) and ($M_o \times M_o$) diagonal matrixes associated with Eq. (7) in a cluster form. Substituting Eq. (24) into Eq. (9) gives an expression for the acoustic potential energy with respect to the amplitudes of the radiation clusters,

$$E_p(\omega) = E_{p,e}(\omega) + E_{p,o}(\omega), \quad (25)$$

where

$$E_{p,e}(\omega) = \mathbf{v}_e^H(\omega) \mathbf{\Pi}_e(\omega) \mathbf{v}_e(\omega), \quad (26a)$$

$$E_{p,o}(\omega) = \mathbf{v}_o^H(\omega) \mathbf{\Pi}_o(\omega) \mathbf{v}_o(\omega) \quad (26b)$$

and where \mathbf{v}_e and \mathbf{v}_o are the ($N_e \times 1$) and ($N_o \times 1$) vectors of the radiation cluster velocity amplitudes, i.e., the vectors of the structural modal velocity amplitudes in a cluster form. Equation (25) implies that the acoustic potential energy radiated from the even and odd radiation clusters are independent of each other. Note that structural modes within the same cluster couple in the enclosed acoustic field because $\mathbf{\Pi}_e(\omega)$ and $\mathbf{\Pi}_o(\omega)$ are generally off-diagonal terms, thus minimizing the squared amplitudes of the individual radiation clusters does not necessarily guarantee the reduction of the acoustic potential energy. In short, radiation cluster control provides a less direct way in controlling the acoustic potential energy compared with that of radiation modal control. However, radiation cluster control may still be a reasonable strategy for the active control of sound transmission, because minimizing the squared amplitude of the radiation cluster which can couple with the dominant acoustic cluster in the enclosed acoustic field is reasonable compared to minimizing the sum of the squared amplitudes of all structural modes in a blind way, i.e., structural modal control.

To implement a radiation cluster control system, it is necessary to measure and control the individual radiation clusters. The processes of both filtering and actuating the individual radiation clusters are presented here. In what follows, we consider simplistic control systems, SISO (single input single output) arrangements based on feedforward control. Subsequently, we will expand the arrangements for MIMO (multiple input multiple output) implementations.

First, consider SISO arrangements of the radiation cluster control system. The number of the sensor points and the number of the actuator points are assumed to be set to two, which is similar to the number of radiation clusters, respectively. The sensor points are located at the symmetric coordinates \mathbf{x}_{s1} and \mathbf{x}_{s2} . In a similar fashion, the actuator points are located at symmetric coordinates \mathbf{x}_{a1} and \mathbf{x}_{a2} . The following formulas are then satisfied:

$$\boldsymbol{\psi}_e(\mathbf{x}_{s1}) = \boldsymbol{\psi}_e(\mathbf{x}_{s2}), \quad (27a)$$

$$\boldsymbol{\psi}_o(\mathbf{x}_{s1}) = -\boldsymbol{\psi}_o(\mathbf{x}_{s2}), \quad (27b)$$

$$\boldsymbol{\psi}_e(\mathbf{x}_{a1}) = \boldsymbol{\psi}_e(\mathbf{x}_{a2}), \quad (28a)$$

$$\boldsymbol{\psi}_o(\mathbf{x}_{a1}) = -\boldsymbol{\psi}_o(\mathbf{x}_{a2}). \quad (28b)$$

Then, the (2×1) vector of the complex velocities at the measurement points is given by

$$\begin{bmatrix} \nu(\mathbf{x}_{s1}, \omega) \\ \nu(\mathbf{x}_{s2}, \omega) \end{bmatrix} = \begin{bmatrix} \boldsymbol{\psi}_e^T(\mathbf{x}_{s1}) & \boldsymbol{\psi}_o^T(\mathbf{x}_{s1}) \\ \boldsymbol{\psi}_e^T(\mathbf{x}_{s2}) & \boldsymbol{\psi}_o^T(\mathbf{x}_{s2}) \end{bmatrix} \begin{bmatrix} \mathbf{v}_e(\omega) \\ \mathbf{v}_o(\omega) \end{bmatrix}. \quad (29)$$

At this point, consider a simple arithmetic processing as

$$\begin{bmatrix} 1 & 1 \\ 1 & -1 \end{bmatrix} \begin{bmatrix} \nu(\mathbf{x}_{s1}, \omega) \\ \nu(\mathbf{x}_{s2}, \omega) \end{bmatrix} = \begin{bmatrix} \nu(\mathbf{x}_{s1}, \omega) + \nu(\mathbf{x}_{s2}, \omega) \\ \nu(\mathbf{x}_{s1}, \omega) - \nu(\mathbf{x}_{s2}, \omega) \end{bmatrix}, \quad (30)$$

where the row vectors of the coefficient matrix in Eq. (30), respectively, the (2×1) polar character vectors associated with in-phase and out-of-phase between the complex velocities at the symmetric sensor points as shown in Eq. (27). Inserting Eq. (27) into Eq. (30) leads to

$$\begin{aligned} & 2 \begin{bmatrix} \boldsymbol{\psi}_e^T(\mathbf{x}_{s1}) & \mathbf{0} \\ \mathbf{0} & \boldsymbol{\psi}_o^T(\mathbf{x}_{s1}) \end{bmatrix} \begin{bmatrix} \mathbf{v}_e(\omega) \\ \mathbf{v}_o(\omega) \end{bmatrix} \\ &= 2 \begin{bmatrix} \boldsymbol{\psi}_e^T(\mathbf{x}_{s1}) \mathbf{v}_e(\omega) \\ \boldsymbol{\psi}_o^T(\mathbf{x}_{s1}) \mathbf{v}_o(\omega) \end{bmatrix} \\ &= \begin{bmatrix} \nu_e(\mathbf{x}_{s1}, \omega) \\ \nu_o(\mathbf{x}_{s1}, \omega) \end{bmatrix}. \end{aligned} \quad (31)$$

Note that given values $\nu_e(\mathbf{x}_{s1}, \omega)$ and $\nu_o(\mathbf{x}_{s1}, \omega)$ are the complex velocities of the radiation clusters at the sensor point \mathbf{x}_{s1} . The above-noted filtering mechanisms are referred to as radiation cluster filters.

Next, the vector of the structural modal velocity amplitudes due to the disturbance force, $f_d(\mathbf{x}, \omega)$, and a pair of the control forces at the symmetric actuator points, $f_1(\omega)$ and $f_2(\omega)$, is given by²

$$\begin{aligned} \mathbf{v}(\omega) = \mathbf{Z}^{-1}(\omega) \left\{ \int_S \boldsymbol{\psi}(\mathbf{x}) f_d(\mathbf{x}, \omega) d\mathbf{x} + \right. \\ \left. \times \begin{bmatrix} \boldsymbol{\psi}(\mathbf{x}_{a1}) & \boldsymbol{\psi}(\mathbf{x}_{a2}) \end{bmatrix} \begin{bmatrix} f_1(\omega) \\ f_2(\omega) \end{bmatrix} \right\}, \end{aligned} \quad (32)$$

where $\mathbf{Z}(\omega)$ is the ($N \times N$) structural modal input impedance matrix, the terms of which are

$$\begin{aligned} Z_{nn}(\omega) = S^2 \sum_{m=1}^M Y_{mm}(\omega) B_{mm}^2 \\ - \frac{j\Lambda_n(\omega_n^2 - \omega^2 + j\eta_n\omega_n\omega)}{\omega} \quad \text{diagonal terms,} \end{aligned} \quad (33a)$$

$$Z_{nr}(\omega) = S^2 \sum_{m=1}^M Y_{mm}(\omega) B_{mn} B_{mr} \quad (33b)$$

off-diagonal terms $n \neq r$,

where ω_n and η_n are, respectively, the natural frequency and modal loss factor of the n th structural mode, and Λ_n is the modal mass of the n th structural mode, defined as the surface integration of the square of the modal function,

$$\Lambda_n = \int_S m(\mathbf{x}) \psi_n^2(\mathbf{x}) d\mathbf{x} \quad (34)$$

in which $m(\mathbf{x})$ is the surface density. The matrix $\mathbf{Z}(\omega)$ is rewritten in a cluster form as

$$\mathbf{Z}(\omega) = \begin{bmatrix} \mathbf{Z}_e(\omega) & \mathbf{0} \\ \mathbf{0} & \mathbf{Z}_o(\omega) \end{bmatrix}, \quad (35)$$

where $\mathbf{Z}_e(\omega)$ is the $(N_e \times N_e)$ matrix, the terms of which are

$$Z_{n_e n_e}(\omega) = S^2 \sum_{m_e=1}^{M_e} Y_{m_e m_e}(\omega) B_{m_e n_e}^2 - \frac{j\Lambda_{n_e}(\omega_{n_e}^2 - \omega^2 + j\eta_{n_e} \omega_{n_e} \omega)}{\omega} \quad \text{diagonal terms,} \quad (36a)$$

$$Z_{n_e r_e}(\omega) = S^2 \sum_{m_e=1}^{M_e} Y_{m_e m_e}(\omega) B_{m_e n_e} B_{m_e r_e} \quad (36b)$$

off-diagonal terms $n_e \neq r_e$,

and where $\mathbf{Z}_o(\omega)$ is the $(N_o \times N_o)$ matrix, the terms of which are

$$Z_{n_o n_o}(\omega) = S^2 \sum_{m_o=1}^{M_o} Y_{m_o m_o}(\omega) B_{m_o n_o}^2 - \frac{j\Lambda_{n_o}(\omega_{n_o}^2 - \omega^2 + j\eta_{n_o} \omega_{n_o} \omega)}{\omega} \quad \text{diagonal terms,} \quad (37a)$$

$$Z_{n_o r_o}(\omega) = S^2 \sum_{m_o=1}^{M_o} Y_{m_o m_o}(\omega) B_{m_o n_o} B_{m_o r_o} \quad \text{off-diagonal terms } n_o \neq r_o. \quad (37b)$$

Note that the orthogonality in Eq. (21) has been used for deriving Eq. (35). Substituting Eq. (35) into Eq. (32) yields

$$\mathbf{v}(\omega) = \begin{bmatrix} \mathbf{v}_e(\omega) \\ \mathbf{v}_o(\omega) \end{bmatrix} = \begin{bmatrix} \mathbf{Z}_e^{-1}(\omega) & \mathbf{0} \\ \mathbf{0} & \mathbf{Z}_o^{-1}(\omega) \end{bmatrix} \times \left\{ \int_S \begin{bmatrix} \boldsymbol{\psi}_e(\mathbf{x}) f_d(\mathbf{x}, \omega) \\ \boldsymbol{\psi}_o(\mathbf{x}) f_d(\mathbf{x}, \omega) \end{bmatrix} d\mathbf{x} + \begin{bmatrix} \boldsymbol{\psi}_e(\mathbf{x}_{a1}) & \boldsymbol{\psi}_e(\mathbf{x}_{a2}) \\ \boldsymbol{\psi}_o(\mathbf{x}_{a1}) & \boldsymbol{\psi}_o(\mathbf{x}_{a2}) \end{bmatrix} \times \begin{bmatrix} f_1(\omega) \\ f_2(\omega) \end{bmatrix} \right\}. \quad (38)$$

At this point, consider a simple arithmetic processing as described for the radiation cluster filters,

$$\begin{bmatrix} 1 & 1 \\ 1 & -1 \end{bmatrix} \begin{bmatrix} f_1(\omega) \\ f_2(\omega) \end{bmatrix} = \begin{bmatrix} f_e(\omega) \\ f_o(\omega) \end{bmatrix}. \quad (39)$$

Substituting Eqs. (28) and (39) into Eq. (38) yields

$$\mathbf{v}(\omega) = \begin{bmatrix} \mathbf{v}_e(\omega) \\ \mathbf{v}_o(\omega) \end{bmatrix} = \begin{bmatrix} \mathbf{Z}_e^{-1}(\omega) \left\{ \int_S \boldsymbol{\psi}_e(\mathbf{x}) f_d(\mathbf{x}, \omega) d\mathbf{x} + \boldsymbol{\psi}_e(\mathbf{x}_{a1}) f_e(\omega) \right\} \\ \mathbf{Z}_o^{-1}(\omega) \left\{ \int_S \boldsymbol{\psi}_o(\mathbf{x}) f_d(\mathbf{x}, \omega) d\mathbf{x} + \boldsymbol{\psi}_o(\mathbf{x}_{a1}) f_o(\omega) \right\} \end{bmatrix}. \quad (40)$$

Note that the control forces $f_e(\omega)$ and $f_o(\omega)$ obtained through the process of Eq. (39) can control the even and odd radiation clusters, independently. The above-noted actuating mechanisms are referred to as radiation cluster actuators.

Finally, integrating the radiation cluster filters and actuators, SISO radiation cluster control systems can be described as

$$\begin{bmatrix} \nu_e(\mathbf{x}_{s1}, \omega) \\ \nu_o(\mathbf{x}_{s1}, \omega) \end{bmatrix} = 2 \begin{bmatrix} \boldsymbol{\psi}_e^T(\mathbf{x}_{s1}) \mathbf{Z}_e^{-1}(\omega) \left\{ \int_S \boldsymbol{\psi}_e(\mathbf{x}) f_d(\mathbf{x}, \omega) d\mathbf{x} + \boldsymbol{\psi}_e(\mathbf{x}_{a1}) f_e(\omega) \right\} \\ \boldsymbol{\psi}_o^T(\mathbf{x}_{s1}) \mathbf{Z}_o^{-1}(\omega) \left\{ \int_S \boldsymbol{\psi}_o(\mathbf{x}) f_d(\mathbf{x}, \omega) d\mathbf{x} + \boldsymbol{\psi}_o(\mathbf{x}_{a1}) f_o(\omega) \right\} \end{bmatrix}. \quad (41)$$

Equation (41) implies that there is no cross talk between the radiation cluster filter sets $\nu_e(\mathbf{x}_{s1}, \omega)$ and $\nu_o(\mathbf{x}_{s1}, \omega)$, and the radiation cluster actuator sets $f_e(\omega)$ and $f_o(\omega)$; $f_e(\omega)$ and $f_o(\omega)$ are, respectively, transmitted to $\nu_e(\mathbf{x}_{s1}, \omega)$ and $\nu_o(\mathbf{x}_{s1}, \omega)$ without causing any spillover.

Furthermore, consider MIMO arrangements of the radiation cluster control system which are constructed by N_s sets of the radiation cluster filters and N_a sets of the radiation cluster actuators. Equation (41) is then expanded as

$$\begin{bmatrix} \tilde{\nu}_e(\omega) \\ \tilde{\nu}_o(\omega) \end{bmatrix} = \begin{bmatrix} \boldsymbol{\Psi}_{e,s}^T \mathbf{Z}_e^{-1}(\omega) \left\{ \int_S \boldsymbol{\psi}_e(\mathbf{x}) f_d(\mathbf{x}, \omega) d\mathbf{x} + \boldsymbol{\Psi}_{e,a} \tilde{\mathbf{f}}_e(\omega) \right\} \\ \boldsymbol{\Psi}_{o,s}^T \mathbf{Z}_o^{-1}(\omega) \left\{ \int_S \boldsymbol{\psi}_o(\mathbf{x}) f_d(\mathbf{x}, \omega) d\mathbf{x} + \boldsymbol{\Psi}_{o,a} \tilde{\mathbf{f}}_o(\omega) \right\} \end{bmatrix}, \quad (42)$$

where

$$\tilde{\nu}_e(\omega) = [\nu_e(\mathbf{x}_{s1,1}, \omega) \cdots \nu_e(\mathbf{x}_{s1,i}, \omega) \cdots \nu_e(\mathbf{x}_{s1,N_s}, \omega)]^T, \quad (43a)$$

$$\tilde{\nu}_o(\omega) = [\nu_o(\mathbf{x}_{s1,1}, \omega) \cdots \nu_o(\mathbf{x}_{s1,i}, \omega) \cdots \nu_o(\mathbf{x}_{s1,N_s}, \omega)]^T, \quad (43b)$$

$$\begin{aligned} \begin{bmatrix} \nu_e(\mathbf{x}_{s1,i}, \omega) \\ \nu_o(\mathbf{x}_{s1,i}, \omega) \end{bmatrix} &= \begin{bmatrix} 1 & 1 \\ 1 & -1 \end{bmatrix} \begin{bmatrix} \nu(\mathbf{x}_{s1,i}, \omega) \\ \nu(\mathbf{x}_{s2,i}, \omega) \end{bmatrix} \quad (i \\ &= 1, 2, \dots, N_s), \end{aligned} \quad (44)$$

$$\Psi_{e,s} = 2 \begin{bmatrix} \psi_e(\mathbf{x}_{s1,1}) & \cdots & \psi_e(\mathbf{x}_{s1,i}) & \cdots & \psi_e(\mathbf{x}_{s1,N_s}) \end{bmatrix}, \quad (45a)$$

$$\Psi_{o,s} = 2 \begin{bmatrix} \psi_o(\mathbf{x}_{s1,1}) & \cdots & \psi_o(\mathbf{x}_{s1,i}) & \cdots & \psi_o(\mathbf{x}_{s1,N_s}) \end{bmatrix}, \quad (45b)$$

$$\Psi_{e,a} = \begin{bmatrix} \psi_e(\mathbf{x}_{a1,1}) & \cdots & \psi_e(\mathbf{x}_{a1,j}) & \cdots & \psi_e(\mathbf{x}_{a1,N_a}) \end{bmatrix}, \quad (46a)$$

$$\Psi_{o,a} = \begin{bmatrix} \psi_o(\mathbf{x}_{a1,1}) & \cdots & \psi_o(\mathbf{x}_{a1,j}) & \cdots & \psi_o(\mathbf{x}_{a1,N_a}) \end{bmatrix}, \quad (46b)$$

$$\begin{aligned} \begin{bmatrix} \sum_{i=1}^{N_s} |\nu_e(\mathbf{x}_{s1,i}, \omega)|^2 \\ \sum_{i=1}^{N_s} |\nu_o(\mathbf{x}_{s1,i}, \omega)|^2 \end{bmatrix} &= \begin{bmatrix} \tilde{\mathbf{v}}_e^H(\omega) \tilde{\mathbf{v}}_e(\omega) \\ \tilde{\mathbf{v}}_o^H(\omega) \tilde{\mathbf{v}}_o(\omega) \end{bmatrix} \\ &= \begin{bmatrix} \tilde{\mathbf{f}}_e^H(\omega) \mathbf{A}_e^H(\omega) \mathbf{A}_e(\omega) \tilde{\mathbf{f}}_e(\omega) + \tilde{\mathbf{f}}_e^H(\omega) \mathbf{A}_e^H(\omega) \mathbf{b}_e(\omega) + \mathbf{b}_e(\omega)^H \mathbf{A}_e(\omega) \tilde{\mathbf{f}}_e(\omega) + \mathbf{b}_e(\omega)^H \mathbf{b}_e(\omega) \\ \tilde{\mathbf{f}}_o^H(\omega) \mathbf{A}_o^H(\omega) \mathbf{A}_o(\omega) \tilde{\mathbf{f}}_o(\omega) + \tilde{\mathbf{f}}_o^H(\omega) \mathbf{A}_o^H(\omega) \mathbf{b}_o(\omega) + \mathbf{b}_o(\omega)^H \mathbf{A}_o(\omega) \tilde{\mathbf{f}}_o(\omega) + \mathbf{b}_o(\omega)^H \mathbf{b}_o(\omega) \end{bmatrix}, \end{aligned} \quad (49)$$

where

$$\begin{bmatrix} \mathbf{A}_e(\omega) \\ \mathbf{A}_o(\omega) \end{bmatrix} = \begin{bmatrix} \Psi_{e,s}^T \mathbf{Z}_e^{-1}(\omega) \Psi_{e,a} \\ \Psi_{o,s}^T \mathbf{Z}_o^{-1}(\omega) \Psi_{o,a} \end{bmatrix}, \quad (50)$$

$$\begin{bmatrix} \mathbf{b}_e(\omega) \\ \mathbf{b}_o(\omega) \end{bmatrix} = \begin{bmatrix} \Psi_{e,s}^T \mathbf{Z}_e^{-1}(\omega) \int_S \psi_e(\mathbf{x}) f_d(\mathbf{x}, \omega) d\mathbf{x} \\ \Psi_{o,s}^T \mathbf{Z}_o^{-1}(\omega) \int_S \psi_o(\mathbf{x}) f_d(\mathbf{x}, \omega) d\mathbf{x} \end{bmatrix}. \quad (51)$$

Note that $\mathbf{A}_e(\omega)$ and $\mathbf{A}_o(\omega)$ are the transfer functions between the radiation cluster actuators and the radiation cluster filters, and $\mathbf{b}_e(\omega)$ and $\mathbf{b}_o(\omega)$ are the product of the disturbance force and the transfer functions between the disturbance force and the radiation cluster filters. Expressed in this form, the optimum set of the control forces, which produce the unique global minimum value of the quadratic function in Eq. (49), may be defined by the relationship²

$$\begin{bmatrix} \tilde{\mathbf{f}}_e(\omega) \\ \tilde{\mathbf{f}}_o(\omega) \end{bmatrix} = - \begin{bmatrix} \{\mathbf{A}_e^H(\omega) \mathbf{A}_e(\omega)\}^{-1} \mathbf{A}_e^H(\omega) \mathbf{b}_e(\omega) \\ \{\mathbf{A}_o^H(\omega) \mathbf{A}_o(\omega)\}^{-1} \mathbf{A}_o^H(\omega) \mathbf{b}_o(\omega) \end{bmatrix}. \quad (52)$$

One advantage of radiation cluster control is that the orthogonal contributors with respect to the enclosed acoustic field can be independently measured and controlled by using structural sensors and actuators. A further advantage is that

$$\tilde{\mathbf{f}}_e(\omega) = [f_{e,1}(\omega) \cdots f_{e,j}(\omega) \cdots f_{e,N_a}(\omega)]^T, \quad (47a)$$

$$\tilde{\mathbf{f}}_o(\omega) = [f_{o,1}(\omega) \cdots f_{o,j}(\omega) \cdots f_{o,N_a}(\omega)]^T, \quad (47b)$$

$$\begin{bmatrix} f_{e,j}(\omega) \\ f_{o,j}(\omega) \end{bmatrix} = \begin{bmatrix} 1 & 1 \\ 1 & -1 \end{bmatrix} \begin{bmatrix} f_{1,j}(\omega) \\ f_{2,j}(\omega) \end{bmatrix} \quad (j = 1, 2, \dots, N_a) \quad (48)$$

and where $\mathbf{x}_{s1,i}$ and $\mathbf{x}_{s2,i}$ are the i th set of the symmetric sensor points, $\mathbf{x}_{a1,j}$ and $\mathbf{x}_{a2,j}$ are the j th set of the symmetric actuator points, and $f_{1,j}(\omega)$ and $f_{2,j}(\omega)$ are the j th set of the control forces located at the j th set of the symmetric actuator points, respectively.

Consider the case when the complex velocities of the radiation clusters are minimized at the discrete sensor points by using control forces. From Eq. (42), the sum of squared complex velocities of the radiation clusters at N_s locations can be expressed as

of simplicity: The radiation cluster filters and actuators can be achieved via simple arithmetic processes such as addition and subtraction without the structural and acoustic modal functions being given. Equation (52) shows that the optimal set of the control forces can be determined without the knowledge of the structural and acoustic modal functions, because $\mathbf{A}_e(\omega)$, $\mathbf{A}_o(\omega)$, $\mathbf{b}_e(\omega)$, and $\mathbf{b}_o(\omega)$ can be obtained from direct measurements. Consequently, radiation cluster control is positioned as part of MAC (middle authority control) which arranges a compromise between particularity to HAC (high authority control: radiation modal control) and practicality to LAC (low authority control: structural modal control) as an active control system of sound transmission into a coupled enclosure.

III. RADIATION CLUSTER CONTROL OF THE RECTANGULAR PLATE-CAVITY MODEL

The general theory of radiation cluster control in Sec. II enables a prediction to be made of the optimum control forces which will minimize the sum of squared complex velocities of the radiation clusters. In the following section, these theoretical models will be specialized to the plate-cavity coupled model to be used later in the study of control mechanisms.

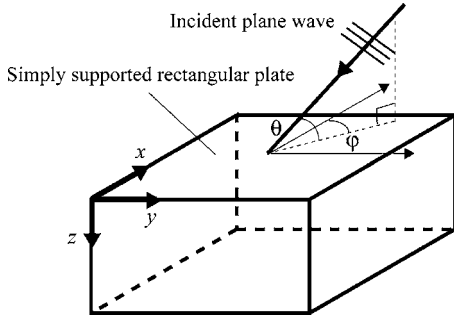


FIG. 2. A rectangular enclosure with one simply supported rectangular plate on the top surface on which external plane wave is incident with the angles of $\varphi = \pi/4$ and $\theta = \pi/4$.

A. Specialization of general theory for the rectangular plate-cavity model case

The model of interest is a rectangular enclosure shown in Fig. 2. This arrangement has a flexible top comprising a simply supported rectangular plate and five rigid walls, i.e., the structural-acoustic coupled model which consists of both a simply supported rectangular plate and a rigid rectangular cavity. This model has been considered, both theoretically and experimentally, in a number of papers in which active control by using structural and acoustic control sources has been examined.^{2,24–26} Note that radiation cluster control is applicable in the symmetric structural-acoustic coupled model where the symmetry of the structural model and the symmetry of the acoustic model match each other. If the x directional boundary conditions of the rectangular plate were symmetric and the y directional boundary conditions of the plate were not symmetric, radiation cluster control could still work for the x direction when the x directional boundary conditions of the rectangular cavity would be symmetric regardless of the y directional boundary conditions of the cavity, and radiation cluster control could not work when the x directional boundary conditions of the cavity would not be symmetric regardless of the y directional boundary conditions of the cavity. Note again that this section covers the purely symmetric structural-acoustic coupled model which consists of both a simply supported rectangular plate and a rigid rectangular cavity as just an example.

As mentioned in Sec. II, clusters can be defined as the basis for even and odd functions into which structural and acoustic modal functions fall. Further, the assumption of modal coupling implies that the response of the coupled system can be described by the uncoupled response of the structural component, the uncoupled response of the acoustic component, and the coupling between the two. For the system shown in Fig. 2, the uncoupled structural modal functions of a simply supported rectangular plate are,²⁴

$$\psi_n(\mathbf{x}) = \psi_{n_x n_y}(x, y) = \sqrt{\frac{4}{L_x L_y}} \sin \frac{n_x \pi x}{L_x} \sin \frac{n_y \pi y}{L_y},$$

$$n_x = 1, 2, 3, \dots, N_x, \quad n_y = 1, 2, 3, \dots, N_y, \quad (53)$$

where L_x, L_y are the dimensions of the plate, n_x and n_y are the structural modal indices, and N_x and N_y are the total number of the structural modes of interest. The origin of the coordi-

nate system is the leftmost corner of the plate shown in the figure. Considering even and odd function properties in both the x and y axes, the structural clusters are given by

$$\psi_{n_{e/e}}(\mathbf{x}) = \psi_{n_{x,o}/n_{x,o}}(x, y) = \sqrt{\frac{4}{L_x L_y}} \sin \frac{n_{x,o} \pi x}{L_x} \sin \frac{n_{y,o} \pi y}{L_y},$$

$$n_{x,o} = 1, 3, 5, \dots, N_{x,o}, \quad n_{y,o} = 1, 3, 5, \dots, N_{y,o} \quad (54a)$$

$$\psi_{n_{e/o}}(\mathbf{x}) = \psi_{n_{x,o}/n_{x,e}}(x, y) = \sqrt{\frac{4}{L_x L_y}} \sin \frac{n_{x,o} \pi x}{L_x} \sin \frac{n_{y,e} \pi y}{L_y},$$

$$n_{x,o} = 1, 3, 5, \dots, N_{x,o}, \quad n_{y,e} = 2, 4, 6, \dots, N_{y,e}, \quad (54b)$$

$$\psi_{n_{o/e}}(\mathbf{x}) = \psi_{n_{x,e}/n_{x,o}}(x, y) = \sqrt{\frac{4}{L_x L_y}} \sin \frac{n_{x,e} \pi x}{L_x} \sin \frac{n_{y,o} \pi y}{L_y},$$

$$n_{x,e} = 2, 4, 6, \dots, N_{x,e}, \quad n_{y,o} = 1, 3, 5, \dots, N_{y,o}, \quad (54c)$$

$$\psi_{n_{o/o}}(\mathbf{x}) = \psi_{n_{x,e}/n_{x,e}}(x, y) = \sqrt{\frac{4}{L_x L_y}} \sin \frac{n_{x,e} \pi x}{L_x} \sin \frac{n_{y,e} \pi y}{L_y},$$

$$n_{x,e} = 2, 4, 6, \dots, N_{x,e}, \quad n_{y,e} = 2, 4, 6, \dots, N_{y,e}. \quad (54d)$$

The $(N \times 1)$ vector of the uncoupled structural modal functions is then expressed as

$$\boldsymbol{\psi}(\mathbf{x}) = \begin{bmatrix} \boldsymbol{\psi}_{e/e}(\mathbf{x}) \\ \boldsymbol{\psi}_{e/o}(\mathbf{x}) \\ \boldsymbol{\psi}_{o/e}(\mathbf{x}) \\ \boldsymbol{\psi}_{o/o}(\mathbf{x}) \end{bmatrix}, \quad (55)$$

where

$$\boldsymbol{\psi}_{e/e}(\mathbf{x}) = [\psi_{1/1}(\mathbf{x}) \cdots \psi_{n_{x,o}/n_{y,o}}(\mathbf{x}) \cdots \psi_{N_{x,o}/N_{y,o}}(\mathbf{x})]^T, \quad (56a)$$

$$\boldsymbol{\psi}_{e/o}(\mathbf{x}) = [\psi_{1/2}(\mathbf{x}) \cdots \psi_{n_{x,o}/n_{y,e}}(\mathbf{x}) \cdots \psi_{N_{x,o}/N_{y,e}}(\mathbf{x})]^T, \quad (56b)$$

$$\boldsymbol{\psi}_{o/e}(\mathbf{x}) = [\psi_{2/1}(\mathbf{x}) \cdots \psi_{n_{x,e}/n_{y,o}}(\mathbf{x}) \cdots \psi_{N_{x,e}/N_{y,o}}(\mathbf{x})]^T, \quad (56c)$$

$$\boldsymbol{\psi}_{o/o}(\mathbf{x}) = [\psi_{2/2}(\mathbf{x}) \cdots \psi_{n_{x,e}/n_{y,e}}(\mathbf{x}) \cdots \psi_{N_{x,e}/N_{y,e}}(\mathbf{x})]^T \quad (56d)$$

and $\boldsymbol{\psi}_{e/e}(\mathbf{x})$ is the $(N_{e/e} \times 1)$ vector of the uncoupled structural modal functions which belong to the even/even cluster as shown in Eq. (56a), $\boldsymbol{\psi}_{e/o}(\mathbf{x})$ is the $(N_{e/o} \times 1)$ vector of the uncoupled structural modal functions which belong to the even/odd cluster as shown in Eq. (56b), $\boldsymbol{\psi}_{o/e}(\mathbf{x})$ is the $(N_{o/e} \times 1)$ vector of the uncoupled structural modal functions which belong to the odd/even cluster as shown in Eq. (56c), and $\boldsymbol{\psi}_{o/o}(\mathbf{x})$ is the $(N_{o/o} \times 1)$ vector of the uncoupled structural modal functions which belong to odd/odd cluster as shown in Eq. (56d).

Then, the uncoupled acoustic modal functions of the rigid rectangular cavity are²⁴

$$\begin{aligned} \phi_m(\mathbf{r}) &= \phi_{m_x/m_y/m_z}(x,y,z) \\ &= \sqrt{\frac{2^{(\epsilon_x+\epsilon_y+\epsilon_z)}}{L_x L_y L_z}} \cos \frac{m_x \pi x}{L_x} \cos \frac{m_y \pi y}{L_y} \cos \frac{m_z \pi z}{L_z}, \end{aligned}$$

$$\epsilon_x = \begin{cases} 0 \cdots m_x = 0 \\ 1 \cdots m_x \neq 0 \end{cases},$$

$$\epsilon_y = \begin{cases} 0 \cdots m_y = 0 \\ 1 \cdots m_y \neq 0 \end{cases},$$

$$\epsilon_z = \begin{cases} 0 \cdots m_z = 0 \\ 1 \cdots m_z \neq 0 \end{cases},$$

$$\begin{aligned} m_x &= 0, 1, 2, \dots, M_x, & m_y &= 0, 1, 2, \dots, M_y, & m_z &= 0, 1, 2, \dots, M_z, \end{aligned} \quad (57)$$

where L_x , L_y , and L_z are the dimensions of the cavity, m_x , m_y , and m_z are the acoustic modal indices, and M_x , M_y , and M_z are the total number of the acoustic modes of interest. Considering even and odd function properties in both the x and y axes, the acoustic clusters are given by

$$\begin{aligned} \phi_{m_{e/e}}(\mathbf{r}) &= \phi_{m_{x,e}/m_{y,e}/m_z}(x,y,z) = \sqrt{\frac{2^{(\epsilon_x+\epsilon_y+\epsilon_z)}}{L_x L_y L_z}} \cos \frac{m_{x,e} \pi x}{L_x} \cos \frac{m_{y,e} \pi y}{L_y} \cos \frac{m_z \pi z}{L_z}, \\ m_{x,e} &= 0, 2, 4, \dots, M_{x,e}, & m_{y,e} &= 0, 2, 4, \dots, M_{y,e}, & m_z &= 0, 1, 2, \dots, M_z, \end{aligned} \quad (58a)$$

$$\begin{aligned} \phi_{m_{e/o}}(\mathbf{r}) &= \phi_{m_{x,e}/m_{y,o}/m_z}(x,y,z) = \sqrt{\frac{2^{(\epsilon_x+\epsilon_y+\epsilon_z)}}{L_x L_y L_z}} \cos \frac{m_{x,e} \pi x}{L_x} \cos \frac{m_{y,o} \pi y}{L_y} \cos \frac{m_z \pi z}{L_z}, \\ m_{x,e} &= 0, 2, 4, \dots, M_{x,e}, & m_{y,o} &= 1, 3, 5, \dots, M_{y,o}, & m_z &= 0, 1, 2, \dots, M_z, \end{aligned} \quad (58b)$$

$$\begin{aligned} \phi_{m_{o/e}}(\mathbf{r}) &= \phi_{m_{x,o}/m_{y,e}/m_z}(x,y,z) = \sqrt{\frac{2^{(\epsilon_x+\epsilon_y+\epsilon_z)}}{L_x L_y L_z}} \cos \frac{m_{x,o} \pi x}{L_x} \cos \frac{m_{y,e} \pi y}{L_y} \cos \frac{m_z \pi z}{L_z}, \\ m_{x,o} &= 1, 3, 5, \dots, M_{x,o}, & m_{y,e} &= 0, 2, 4, \dots, M_{y,e}, & m_z &= 0, 1, 2, \dots, M_z, \end{aligned} \quad (58c)$$

$$\begin{aligned} \phi_{m_{o/o}}(\mathbf{r}) &= \phi_{m_{x,o}/m_{y,o}/m_z}(x,y,z) = \sqrt{\frac{2^{(\epsilon_x+\epsilon_y+\epsilon_z)}}{L_x L_y L_z}} \cos \frac{m_{x,o} \pi x}{L_x} \cos \frac{m_{y,o} \pi y}{L_y} \cos \frac{m_z \pi z}{L_z}, \\ m_{x,o} &= 1, 3, 5, \dots, M_{x,o}, & m_{y,o} &= 1, 3, 5, \dots, M_{y,o}, & m_z &= 0, 1, 2, \dots, M_z. \end{aligned} \quad (58d)$$

The $(M \times 1)$ vector of the uncoupled acoustic modal functions is then expressed as

$$\boldsymbol{\phi}(\mathbf{r}) = \begin{bmatrix} \boldsymbol{\phi}_{e/e}(\mathbf{r}) \\ \boldsymbol{\phi}_{e/o}(\mathbf{r}) \\ \boldsymbol{\phi}_{o/e}(\mathbf{r}) \\ \boldsymbol{\phi}_{o/o}(\mathbf{r}) \end{bmatrix}, \quad (59)$$

where

$$\begin{aligned} \boldsymbol{\phi}_{e/e}(\mathbf{r}) &= [\phi_{0/0/0}(\mathbf{r}) \cdots \phi_{m_{x,e}/m_{y,e}/m_z}(\mathbf{r}) \cdots \phi_{M_{x,e}/M_{y,e}/M_z}(\mathbf{r})]^T, \end{aligned} \quad (60a)$$

$$\begin{aligned} \boldsymbol{\phi}_{e/o}(\mathbf{r}) &= [\phi_{0/1/0}(\mathbf{r}) \cdots \phi_{m_{x,e}/m_{y,o}/m_z}(\mathbf{r}) \cdots \phi_{M_{x,e}/M_{y,o}/M_z}(\mathbf{r})]^T, \end{aligned} \quad (60b)$$

$$\begin{aligned} \boldsymbol{\phi}_{o/e}(\mathbf{r}) &= [\phi_{1/0/0}(\mathbf{r}) \cdots \phi_{m_{x,o}/m_{y,e}/m_z}(\mathbf{r}) \cdots \phi_{M_{x,o}/M_{y,e}/M_z}(\mathbf{r})]^T, \end{aligned} \quad (60c)$$

$$\begin{aligned} \boldsymbol{\phi}_{o/o}(\mathbf{r}) &= [\phi_{1/1/0}(\mathbf{r}) \cdots \phi_{m_{x,o}/m_{y,o}/m_z}(\mathbf{r}) \cdots \phi_{M_{x,o}/M_{y,o}/M_z}(\mathbf{r})]^T, \end{aligned} \quad (60d)$$

and where $\boldsymbol{\phi}_{e/e}(\mathbf{r})$ is the $(M_{e/e} \times 1)$ vector of the uncoupled acoustic modal functions which belong to the even/even cluster as shown in Eq. (60a), $\boldsymbol{\phi}_{e/o}(\mathbf{r})$ is the $(M_{e/o} \times 1)$ vector of the uncoupled acoustic modal functions which belong to the even/odd cluster as shown in Eq. (60b), $\boldsymbol{\phi}_{o/e}(\mathbf{r})$ is the $(M_{o/e} \times 1)$ vector of the uncoupled acoustic modal functions which belong to the odd/even cluster as shown in Eq. (60c), and $\boldsymbol{\phi}_{o/o}(\mathbf{r})$ is the $(M_{o/o} \times 1)$ vector of the uncoupled acoustic modal functions which belong to the odd/odd cluster as shown in Eq. (60d).

Then, the radiation cluster control system can be described as

$$\begin{aligned}
& \begin{bmatrix} \sum_{i=1}^{N_s} |v_{ele}(\mathbf{x}_{s1,i}, \omega)|^2 \\ \sum_{i=1}^{N_s} |v_{elo}(\mathbf{x}_{s1,i}, \omega)|^2 \\ \sum_{i=1}^{N_s} |v_{ole}(\mathbf{x}_{s1,i}, \omega)|^2 \\ \sum_{i=1}^{N_s} |v_{olo}(\mathbf{x}_{s1,i}, \omega)|^2 \end{bmatrix} = \begin{bmatrix} \tilde{\mathbf{v}}_{ele}^H(\omega) \tilde{\mathbf{v}}_{ele}(\omega) \\ \tilde{\mathbf{v}}_{elo}^H(\omega) \tilde{\mathbf{v}}_{elo}(\omega) \\ \tilde{\mathbf{v}}_{ole}^H(\omega) \tilde{\mathbf{v}}_{ole}(\omega) \\ \tilde{\mathbf{v}}_{olo}^H(\omega) \tilde{\mathbf{v}}_{olo}(\omega) \end{bmatrix} \\
& = \begin{bmatrix} \tilde{\mathbf{f}}_{ele}^H(\omega) \mathbf{A}_{ele}^H(\omega) \mathbf{A}_{ele}(\omega) \tilde{\mathbf{f}}_{ele}(\omega) + \tilde{\mathbf{f}}_{ele}^H(\omega) \mathbf{A}_{ele}^H(\omega) \mathbf{b}_{ele}(\omega) + \mathbf{b}_{ele}^H(\omega) \mathbf{A}_{ele}(\omega) \tilde{\mathbf{f}}_{ele}(\omega) + \mathbf{b}_{ele}^H(\omega) \mathbf{b}_{ele}(\omega) \\ \tilde{\mathbf{f}}_{elo}^H(\omega) \mathbf{A}_{elo}^H(\omega) \mathbf{A}_{elo}(\omega) \tilde{\mathbf{f}}_{elo}(\omega) + \tilde{\mathbf{f}}_{elo}^H(\omega) \mathbf{A}_{elo}^H(\omega) \mathbf{b}_{elo}(\omega) + \mathbf{b}_{elo}^H(\omega) \mathbf{A}_{elo}(\omega) \tilde{\mathbf{f}}_{elo}(\omega) + \mathbf{b}_{elo}^H(\omega) \mathbf{b}_{elo}(\omega) \\ \tilde{\mathbf{f}}_{ole}^H(\omega) \mathbf{A}_{ole}^H(\omega) \mathbf{A}_{ole}(\omega) \tilde{\mathbf{f}}_{ole}(\omega) + \tilde{\mathbf{f}}_{ole}^H(\omega) \mathbf{A}_{ole}^H(\omega) \mathbf{b}_{ole}(\omega) + \mathbf{b}_{ole}^H(\omega) \mathbf{A}_{ole}(\omega) \tilde{\mathbf{f}}_{ole}(\omega) + \mathbf{b}_{ole}^H(\omega) \mathbf{b}_{ole}(\omega) \\ \tilde{\mathbf{f}}_{olo}^H(\omega) \mathbf{A}_{olo}^H(\omega) \mathbf{A}_{olo}(\omega) \tilde{\mathbf{f}}_{olo}(\omega) + \tilde{\mathbf{f}}_{olo}^H(\omega) \mathbf{A}_{olo}^H(\omega) \mathbf{b}_{olo}(\omega) + \mathbf{b}_{olo}^H(\omega) \mathbf{A}_{olo}(\omega) \tilde{\mathbf{f}}_{olo}(\omega) + \mathbf{b}_{olo}^H(\omega) \mathbf{b}_{olo}(\omega) \end{bmatrix}, \quad (61)
\end{aligned}$$

where

$$\begin{aligned}
& \tilde{\mathbf{v}}_{ele}(\omega) \\
& = [v_{ele}(\mathbf{x}_{s1,1}, \omega) \quad \cdots \quad v_{ele}(\mathbf{x}_{s1,i}, \omega) \quad \cdots \quad v_{ele}(\mathbf{x}_{s1,N_s}, \omega)]^T, \quad (62a)
\end{aligned}$$

$$\begin{aligned}
& \tilde{\mathbf{v}}_{elo}(\omega) \\
& = [v_{elo}(\mathbf{x}_{s1,1}, \omega) \quad \cdots \quad v_{elo}(\mathbf{x}_{s1,i}, \omega) \quad \cdots \quad v_{elo}(\mathbf{x}_{s1,N_s}, \omega)]^T, \quad (62b)
\end{aligned}$$

$$\begin{aligned}
& \tilde{\mathbf{v}}_{ole}(\omega) \\
& = [v_{ole}(\mathbf{x}_{s1,1}, \omega) \quad \cdots \quad v_{ole}(\mathbf{x}_{s1,i}, \omega) \quad \cdots \quad v_{ole}(\mathbf{x}_{s1,N_s}, \omega)]^T, \quad (62c)
\end{aligned}$$

$$\begin{aligned}
& \tilde{\mathbf{v}}_{olo}(\omega) \\
& = [v_{olo}(\mathbf{x}_{s1,1}, \omega) \quad \cdots \quad v_{olo}(\mathbf{x}_{s1,i}, \omega) \quad \cdots \quad v_{olo}(\mathbf{x}_{s1,N_s}, \omega)]^T, \quad (62d)
\end{aligned}$$

$$\begin{bmatrix} v_{ele}(\mathbf{x}_{s1,i}, \omega) \\ v_{elo}(\mathbf{x}_{s1,i}, \omega) \\ v_{ole}(\mathbf{x}_{s1,i}, \omega) \\ v_{olo}(\mathbf{x}_{s1,i}, \omega) \end{bmatrix} = \begin{bmatrix} +1 & +1 & +1 & +1 \\ +1 & +1 & -1 & -1 \\ +1 & -1 & -1 & +1 \\ +1 & -1 & +1 & -1 \end{bmatrix} \begin{bmatrix} v(\mathbf{x}_{s1,i}, \omega) \\ v(\mathbf{x}_{s2,i}, \omega) \\ v(\mathbf{x}_{s3,i}, \omega) \\ v(\mathbf{x}_{s4,i}, \omega) \end{bmatrix} \quad (63)$$

($i = 1, 2, \dots, N_s$),

$$\begin{bmatrix} \mathbf{A}_{ele}(\omega) \\ \mathbf{A}_{elo}(\omega) \\ \mathbf{A}_{ole}(\omega) \\ \mathbf{A}_{olo}(\omega) \end{bmatrix} = \begin{bmatrix} \Psi_{ele,s}^T \mathbf{Z}_{ele}^{-1}(\omega) \Psi_{ele,a} \\ \Psi_{elo,s}^T \mathbf{Z}_{elo}^{-1}(\omega) \Psi_{elo,a} \\ \Psi_{ole,s}^T \mathbf{Z}_{ole}^{-1}(\omega) \Psi_{ole,a} \\ \Psi_{olo,s}^T \mathbf{Z}_{olo}^{-1}(\omega) \Psi_{olo,a} \end{bmatrix}, \quad (64)$$

$$\begin{bmatrix} \mathbf{b}_{ele}(\omega) \\ \mathbf{b}_{elo}(\omega) \\ \mathbf{b}_{ole}(\omega) \\ \mathbf{b}_{olo}(\omega) \end{bmatrix} = \begin{bmatrix} \Psi_{ele,s}^T \mathbf{Z}_{ele}^{-1}(\omega) \int_S \boldsymbol{\psi}_{ele}(\mathbf{x}) f_d(\mathbf{x}, \omega) d\mathbf{x} \\ \Psi_{elo,s}^T \mathbf{Z}_{elo}^{-1}(\omega) \int_S \boldsymbol{\psi}_{elo}(\mathbf{x}) f_d(\mathbf{x}, \omega) d\mathbf{x} \\ \Psi_{ole,s}^T \mathbf{Z}_{ole}^{-1}(\omega) \int_S \boldsymbol{\psi}_{ole}(\mathbf{x}) f_d(\mathbf{x}, \omega) d\mathbf{x} \\ \Psi_{olo,s}^T \mathbf{Z}_{olo}^{-1}(\omega) \int_S \boldsymbol{\psi}_{olo}(\mathbf{x}) f_d(\mathbf{x}, \omega) d\mathbf{x} \end{bmatrix}, \quad (65)$$

$$\Psi_{ele,s} = [\boldsymbol{\psi}_{ele}(\mathbf{x}_{s1,1}) \quad \cdots \quad \boldsymbol{\psi}_{ele}(\mathbf{x}_{s1,i}) \quad \cdots \quad \boldsymbol{\psi}_{ele}(\mathbf{x}_{s1,N_s})], \quad (66a)$$

$$\Psi_{elo,s} = [\boldsymbol{\psi}_{elo}(\mathbf{x}_{s1,1}) \quad \cdots \quad \boldsymbol{\psi}_{elo}(\mathbf{x}_{s1,i}) \quad \cdots \quad \boldsymbol{\psi}_{elo}(\mathbf{x}_{s1,N_s})], \quad (66b)$$

$$\Psi_{ole,s} = [\boldsymbol{\psi}_{ole}(\mathbf{x}_{s1,1}) \quad \cdots \quad \boldsymbol{\psi}_{ole}(\mathbf{x}_{s1,i}) \quad \cdots \quad \boldsymbol{\psi}_{ole}(\mathbf{x}_{s1,N_s})], \quad (66c)$$

$$\Psi_{olo,s} = [\boldsymbol{\psi}_{olo}(\mathbf{x}_{s1,1}) \quad \cdots \quad \boldsymbol{\psi}_{olo}(\mathbf{x}_{s1,i}) \quad \cdots \quad \boldsymbol{\psi}_{olo}(\mathbf{x}_{s1,N_s})], \quad (66d)$$

$$\Psi_{ele,a} = [\boldsymbol{\psi}_{ele}(\mathbf{x}_{a1,1}) \quad \cdots \quad \boldsymbol{\psi}_{ele}(\mathbf{x}_{a1,j}) \quad \cdots \quad \boldsymbol{\psi}_{ele}(\mathbf{x}_{a1,N_a})], \quad (67a)$$

$$\Psi_{elo,a} = [\boldsymbol{\psi}_{elo}(\mathbf{x}_{a1,1}) \quad \cdots \quad \boldsymbol{\psi}_{elo}(\mathbf{x}_{a1,j}) \quad \cdots \quad \boldsymbol{\psi}_{elo}(\mathbf{x}_{a1,N_a})], \quad (67b)$$

$$\Psi_{ole,a} = [\boldsymbol{\psi}_{ole}(\mathbf{x}_{a1,1}) \quad \cdots \quad \boldsymbol{\psi}_{ole}(\mathbf{x}_{a1,j}) \quad \cdots \quad \boldsymbol{\psi}_{ole}(\mathbf{x}_{a1,N_a})], \quad (67c)$$

$$\Psi_{olo,a} = [\psi_{olo}(\mathbf{x}_{a1,1}) \cdots \psi_{olo}(\mathbf{x}_{a1,j}) \cdots \psi_{olo}(\mathbf{x}_{a1,N_a})], \quad (67d)$$

$$\tilde{\mathbf{f}}_{ele}(\omega) = [f_{ele,1}(\omega) \cdots f_{ele,j}(\omega) \cdots f_{ele,N_a}(\omega)]^T, \quad (68a)$$

$$\tilde{\mathbf{f}}_{elo}(\omega) = [f_{elo,1}(\omega) \cdots f_{elo,j}(\omega) \cdots f_{elo,N_a}(\omega)]^T, \quad (68b)$$

$$\tilde{\mathbf{f}}_{ole}(\omega) = [f_{ole,1}(\omega) \cdots f_{ole,j}(\omega) \cdots f_{ole,N_a}(\omega)]^T, \quad (68c)$$

$$\tilde{\mathbf{f}}_{olo}(\omega) = [f_{olo,1}(\omega) \cdots f_{olo,j}(\omega) \cdots f_{olo,N_a}(\omega)]^T, \quad (68d)$$

$$\begin{bmatrix} f_{ele,j}(\omega) \\ f_{elo,j}(\omega) \\ f_{ole,j}(\omega) \\ f_{olo,j}(\omega) \end{bmatrix} = \begin{bmatrix} +1 & +1 & +1 & +1 \\ +1 & +1 & -1 & -1 \\ +1 & -1 & -1 & +1 \\ +1 & -1 & +1 & -1 \end{bmatrix} \begin{bmatrix} f_{1,j}(\omega) \\ f_{2,j}(\omega) \\ f_{3,j}(\omega) \\ f_{4,j}(\omega) \end{bmatrix} \quad (69)$$

$$(j = 1, 2, \dots, N_a),$$

$$\begin{aligned} \mathbf{x}_{s1,i} &= (x_{s1,i}, y_{s1,i}), & \mathbf{x}_{s2,i} &= (L_x - x_{s1,i}, y_{s1,i}), & \mathbf{x}_{s3,i} &= (L_x \\ & - x_{s1,i}, L_y - y_{s1,i}), & \mathbf{x}_{s4,i} &= (x_{s1,i}, L_y - y_{s1,i}), \end{aligned} \quad (70)$$

$$\begin{aligned} \mathbf{x}_{a1,j} &= (x_{a1,j}, y_{a1,j}), & \mathbf{x}_{a2,j} &= (L_x - x_{a1,j}, y_{a1,j}), & \mathbf{x}_{a3,j} &= (L_x \\ & - x_{a1,j}, L_y - y_{a1,j}), & \mathbf{x}_{a4,j} &= (x_{a1,j}, L_y - y_{a1,j}) \end{aligned} \quad (71)$$

and where $\mathbf{Z}_{ele}(\omega)$ is the $(N_{ele} \times N_{ele})$ matrix, the terms of which are

$$\begin{aligned} Z_{n_{ele}n_{ele}}(\omega) &= S^2 \sum_{m_{ele}=0}^{M_{ele}} Y_{m_{ele}m_{ele}}(\omega) B_{m_{ele}n_{ele}}^2 \\ & - \frac{j\Lambda_{n_{ele}}(\omega_{n_{ele}}^2 - \omega^2 + j\eta_{n_{ele}}\omega_{n_{ele}})}{\omega} \end{aligned} \quad (72a)$$

$$Z_{n_{ele}r_{ele}}(\omega) = S^2 \sum_{m_{ele}=0}^{M_{ele}} Y_{m_{ele}m_{ele}}(\omega) B_{m_{ele}n_{ele}} B_{m_{ele}r_{ele}} \quad (72b)$$

off-diagonal terms $n_A \neq r_A$

In a similar fashion, $\mathbf{Z}_{elo}(\omega)$, $\mathbf{Z}_{ole}(\omega)$, and $\mathbf{Z}_{olo}(\omega)$ are also defined,

$$\omega_n = \omega_{n_x n_y} = \sqrt{\frac{D}{\rho_s h} \left\{ \left(\frac{n_x \pi}{L_x} \right)^2 + \left(\frac{n_y \pi}{L_y} \right)^2 \right\}}, \quad (73)$$

$$D = \frac{Eh^3}{12(1-\nu^2)}, \quad (74)$$

where E is the Young's modulus of the plate, ρ_s is the density of the plate, ν is the Poisson ratio of the plate, h is the

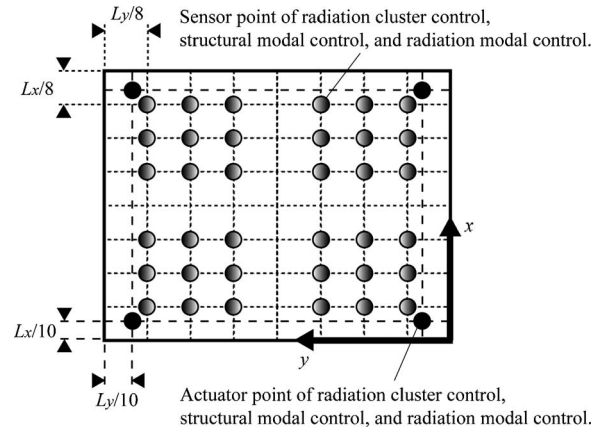


FIG. 3. A rectangular plate with locations of both sensors and actuators.

thickness of the plate, and η_n is the modal loss factor of the n th structural mode. Since Eq. (61) is the Hermitian quadratic form of the complex control force vector,² the optimum set of the control forces, which uniquely produce the global minimum value of the quadratic function, is given by

$$\begin{bmatrix} \tilde{\mathbf{f}}_{ele}(\omega) \\ \tilde{\mathbf{f}}_{elo}(\omega) \\ \tilde{\mathbf{f}}_{ole}(\omega) \\ \tilde{\mathbf{f}}_{olo}(\omega) \end{bmatrix} = - \begin{bmatrix} \{\mathbf{A}_{ele}^H(\omega)\mathbf{A}_{ele}(\omega)\}^{-1}\mathbf{A}_{ele}^H(\omega)\mathbf{b}_{ele}(\omega) \\ \{\mathbf{A}_{elo}^H(\omega)\mathbf{A}_{elo}(\omega)\}^{-1}\mathbf{A}_{elo}^H(\omega)\mathbf{b}_{elo}(\omega) \\ \{\mathbf{A}_{ole}^H(\omega)\mathbf{A}_{ole}(\omega)\}^{-1}\mathbf{A}_{ole}^H(\omega)\mathbf{b}_{ole}(\omega) \\ \{\mathbf{A}_{olo}^H(\omega)\mathbf{A}_{olo}(\omega)\}^{-1}\mathbf{A}_{olo}^H(\omega)\mathbf{b}_{olo}(\omega) \end{bmatrix}. \quad (75)$$

B. Numerical Results: Radiation cluster control versus both structural modal control and radiation modal control

In this section, the active control of sound transmission in the case of the plate-cavity coupled model shown in Fig. 2 is investigated to verify the validity of radiation cluster control presented in the work. The dimensions of the rectangular enclosure are $L_x=0.38$ m, $L_y=0.30$ m, and $L_z=0.25$ m, respectively. The top of the enclosure consists of a 1.3-mm-thick, simply supported aluminum plate. The Young's modulus of the plate is $E=71$ GPa, the density of the plate is $\rho_s=2720$ kg/m³, the Poisson ratio of the plate is $\nu=0.33$, and the modal loss factor of the structural and acoustic modes are uniformly $\eta_n=0.002$ and $\eta_m=0.002$, respectively. The sound speed in the air is $c_0=343$ m/s, and the density of the air is $\rho_0=1.21$ kg/m³. An external acoustic field excites the top plate, which, in turn, radiates sound into the cavity. The external acoustic field is a plane wave with an amplitude of 1 Pa, the incident angles are $\theta=\pi/4$, the elevation from the horizontal, and $\varphi=\pi/4$, the azimuth from the x axis (See Fig. 2). The numbers of the structural modes and acoustic modes to be considered in the simulation are $N_x=6$, $N_y=6$, $M_x=3$, $M_y=2$, and $M_z=2$.

Nine sets of the radiation cluster filters, 36 point sensors at symmetric coordinates, and a set of the radiation cluster actuators, 4 point forces at symmetric coordinates, are used as shown in Fig. 3. Note that the arrangement of the above-mentioned radiation cluster control system is interpreted as

TABLE I. Natural frequency and radiation cluster attribute of the structural modes of the plate.

Modal index	Natural freq (Hz)	Cluster attribute
1/1	58	Even/even
2/1	124	Odd/even
1/2	164	Even/odd
2/2	230	Odd/odd
3/1	234	Even/even
1/3	341	Even/even
3/2	341	Even/odd
4/1	389	Odd/even
2/3	407	Odd/even
4/2	495	Odd/odd
3/3	518	Even/even
5/1	588	Even/even
1/4	589	Even/odd
2/4	656	Odd/odd
4/3	673	Odd/even
5/2	694	Even/odd
3/4	766	Even/odd

TABLE II. Natural frequency and acoustic cluster attribute of the acoustic modes of the cavity.

Modal index	Natural freq (Hz)	Cluster attribute
0/0/0	0	Even/even
1/0/0	451	Odd/even
0/1/0	572	Even/odd
1/1/0	728	Odd/odd

SIMO (single input multiple output), i.e., 1 input 9 outputs, when the error criterion is a single radiation cluster. Though the number and location of both the error sensors and control forces have a significant effect upon the control performance,

the number and location in the simulation are not specially optimized because such a problem is not the main issue in this paper. To compare the control performance of radiation cluster control with those of traditional control methods, both structural modal control and radiation modal control are conducted. In the case of structural modal control, the error criterion is defined as the sum of squared amplitudes of the structural modes corresponding to the global kinetic energy of the plate. To implement the structural modal control system, the structural modal filters composed of 36 point sensors shown in Fig. 3, which can estimate the amplitudes of the individual structural modes, are built. Note that the structural modal filters in this simulation provide the estimates with high precision because the number of the point sensors equals the number of the structural modes, thus the performance of structural modal control is not deteriorated due to

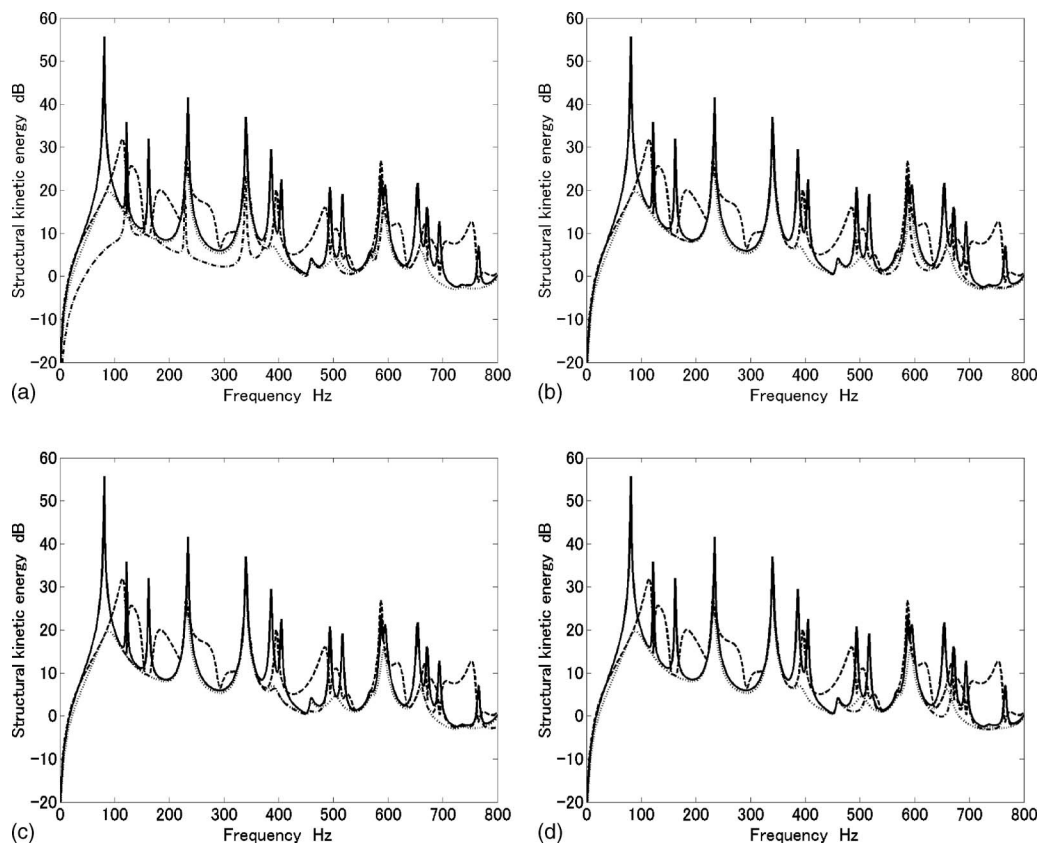


FIG. 4. Global kinetic energy of the plate (dB ref= 10^{-9} J) before (solid line) and after the SIMO arrangement of radiation cluster control (chained line), structural modal control (dotted line), and radiation modal control (dashed line). (a) Global kinetic energy of the plate, before and after radiation cluster control with the error criterion being the even/even radiation cluster, structural modal control, and radiation modal control. (b) Global kinetic energy of the plate, before and after radiation cluster control with the error criterion being the even/odd radiation cluster, structural modal control, and radiation modal control. (c) Global kinetic energy of the plate, before and after radiation cluster control with the error criterion being the odd/even radiation cluster, structural modal control, and radiation modal control. (d) Global kinetic energy of the plate, before and after radiation cluster control with the error criterion being the odd/odd radiation cluster, structural modal control, and radiation modal control.

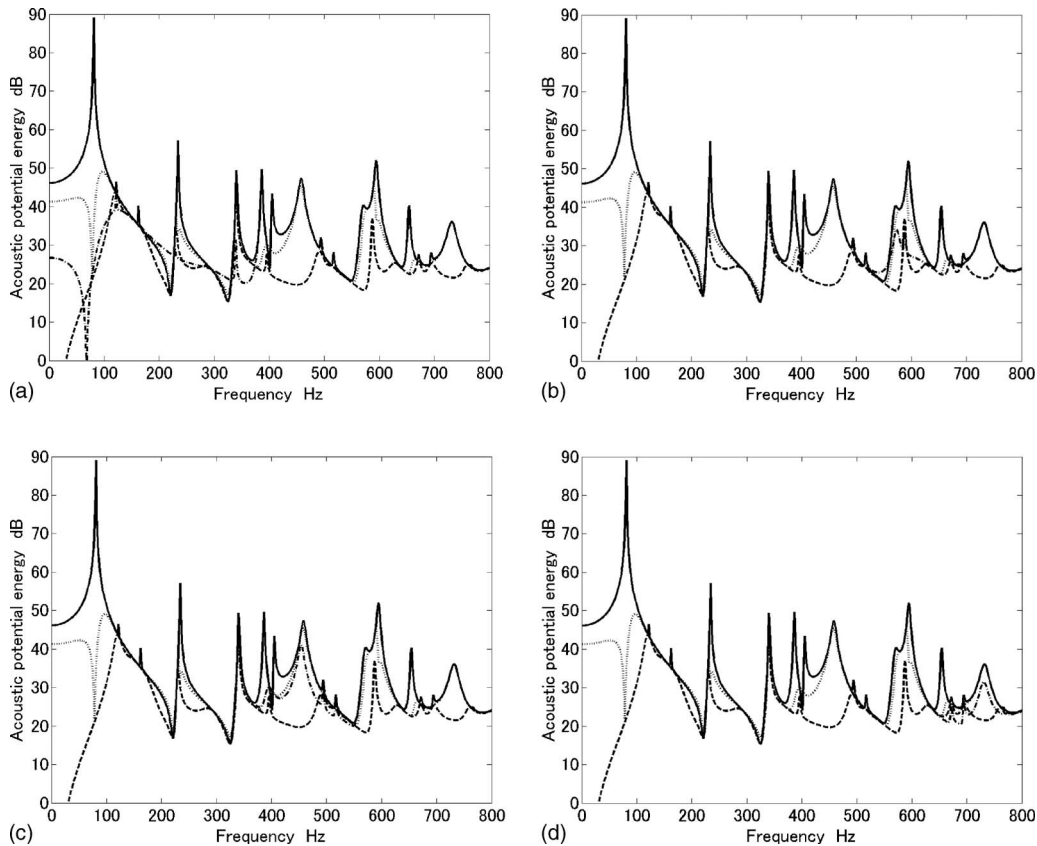


FIG. 5. Global potential energy in the enclosed acoustic field (dB ref= 10^{-12} J) before (solid line) and after the SIMO arrangement of radiation cluster control (chained line), structural modal control (dotted line), and radiation modal control (dashed line). (a) Global potential energy in the enclosed acoustic field, before and after radiation cluster control with the error criterion being the even/even radiation cluster, structural modal control, and radiation modal control. (b) Global potential energy in the enclosed acoustic field, before and after radiation cluster control with the error criterion being the even/odd radiation cluster, structural modal control, and radiation modal control. (c) Global potential energy in the enclosed acoustic field, before and after radiation cluster control with the error criterion being the odd/even radiation cluster, structural modal control, and radiation modal control. (d) Global potential energy in the enclosed acoustic field, before and after radiation cluster control with the error criterion being the odd/odd radiation cluster, structural modal control, and radiation modal control.

the estimation errors.²¹ A point force acts at one of the symmetric actuator points in radiation cluster control, ($L_x/10$, $L_y/10$), as shown in Fig. 3. Note that the arrangement of the above-mentioned structural modal control system is regarded as SIMO, i.e., 1 input 36 outputs. In the case of radiation modal control, the error criterion is defined as the sum of squared amplitudes of the radiation modes corresponding to the global potential energy in the enclosed acoustic field. To implement the radiation modal control system, radiation modal filters which can estimate the amplitudes of the individual radiation modes are constructed by combining the above-mentioned structural modal filters and the weighting filters corresponding to the coupling coefficient matrix. A point force acts at one of the symmetric actuator points in radiation cluster control, ($L_x/10$, $L_y/10$), as shown in Fig. 3. Note that the arrangement of the above-mentioned radiation modal control system is regarded as SIMO, i.e., 1 input 36 outputs.

The uncoupled structural natural frequencies of the plate and the uncoupled acoustic natural frequencies of the cavity are shown in Tables I and II, respectively. Comparing Tables I and II, it can be seen that at frequencies below 800 Hz (the case considered here) there are many more structural modes than acoustic modes.

Figures 4 and 5 present the kinetic energy of the plate and the acoustic potential energy in the enclosure before and after radiation cluster control with the error criterion being a single radiation cluster, structural modal control, and radiation modal control, respectively. The following are clear from Fig. 4: Radiation cluster control independently reduces the kinetic energy which the designated radiation cluster contributes; structural modal control reduces the kinetic energy which all structural modes contribute; whereas radiation modal control does not reduce the kinetic energy. Note that the reduction of the kinetic energy which the individual radiation cluster contributes by radiation cluster control with the error criterion being the associated radiation cluster is much greater than that by structural modal control. The observed behavior can be explained by taking into consideration that radiation cluster control can independently measure and control the designated radiation cluster without causing spillover between the individual radiation clusters, while structural modal control measures and controls all structural modes causing spillover between the individual radiation clusters. It is possible in structural modal control that a set of the structural modes which contribute the kinetic energy are excited out of phase with another set of the structural modes which also contribute the kinetic energy such

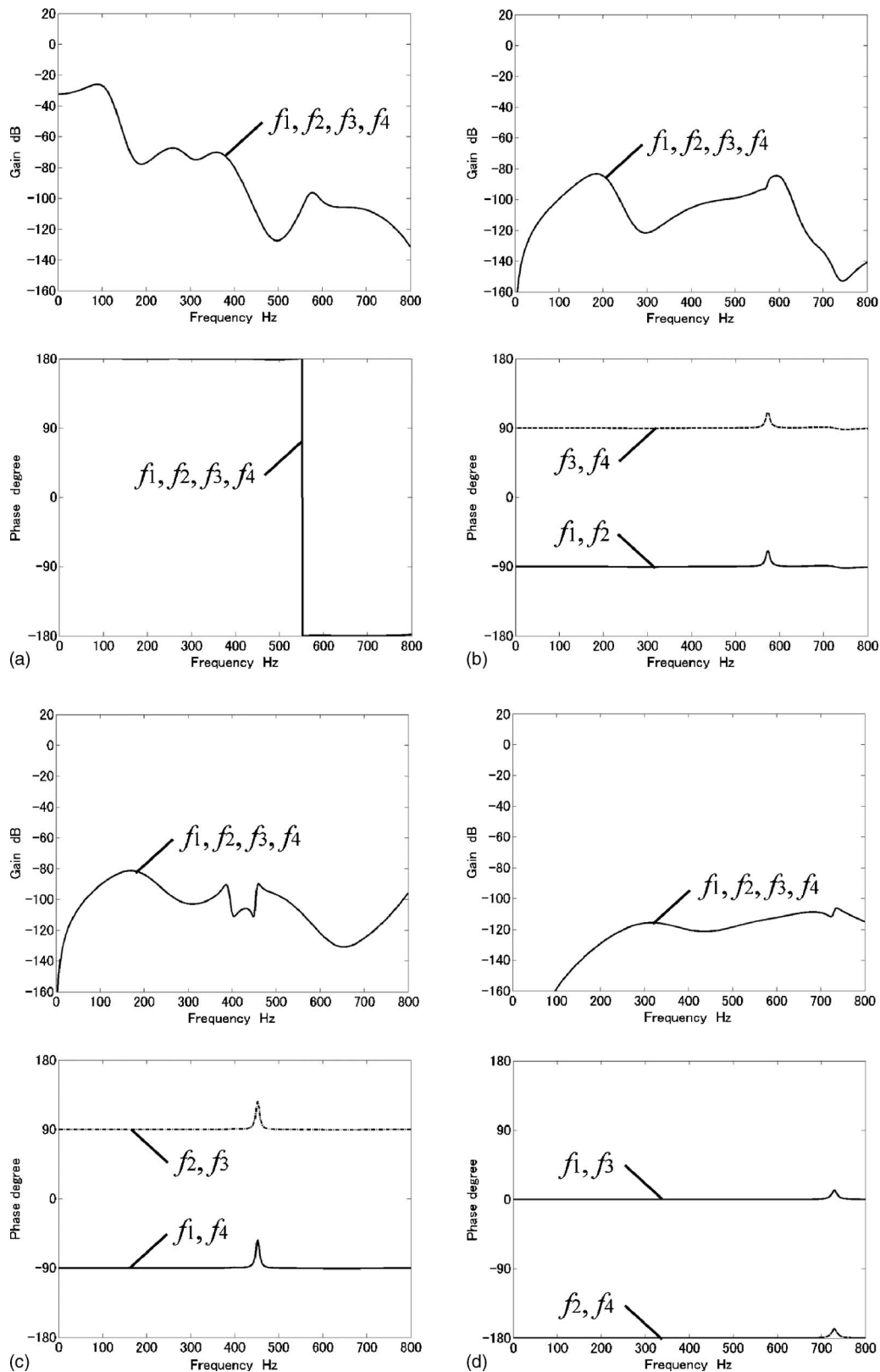


FIG. 6. Optimal gains (dB ref=incident acoustic pressure amplitude) and phases of the control forces in the SIMO arrangement of radiation cluster control: the control force at $(L_x/10, L_y/10)$, f_1 (solid line); the control force at $(9L_x/10, L_y/10)$, f_2 (chained line); the control force at $(9L_x/10, 9L_y/10)$, f_3 (dotted line); and the control force at $(L_x/10, 9L_y/10)$, f_4 (dashed line). (a) Optimal gains and phases of the control forces in radiation cluster control with the error criterion being the even/even radiation cluster. (b) Optimal gains and phases of the control forces in radiation cluster control with the error criterion being the even/odd radiation cluster. (c) Optimal gains and phases of the control forces in radiation cluster control with the error criterion being the odd/even radiation cluster. (d) Optimal gains and phases of the control forces in radiation cluster control with the error criterion being the odd/odd radiation cluster.

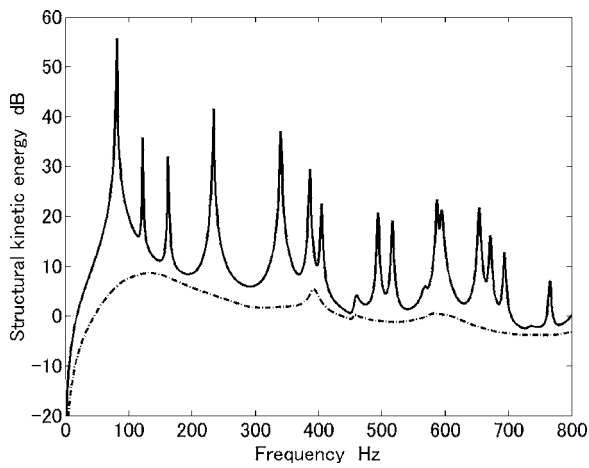


FIG. 7. Global kinetic energy of the plate (dB ref= 10^{-9} J) before (solid line) and after the four-parallel-SIMOs arrangement of radiation cluster control (chained line).

that their contributions largely cancel each other. Under these circumstances, structural modal control cannot decrease one of the sets of the structural modes because it causes an increase in the other set of the structural modes. On the other hand, radiation cluster control may overcome such a problem in the cluster sense, thereby decreasing the designated radiation cluster. As seen from Figs. 4 and 5, the radiation efficiency of the radiation cluster, which can couple with a dominant acoustic cluster at some frequencies, is higher than those of the other radiation clusters which cannot couple with the dominant acoustic cluster. This allows us to get an insight into the active control of sound transmission based upon structural error sensing: The radiation cluster which can couple with the dominant acoustic cluster should be preferentially measured and controlled. The following are clear from Fig. 5: Radiation cluster control with the error criterion being the radiation cluster which can couple with a dominant acoustic cluster at some frequencies achieves the greater reduction of the acoustic potential energy than structural modal control; and radiation modal control steadily achieves the reduction of the acoustic potential energy while the other two

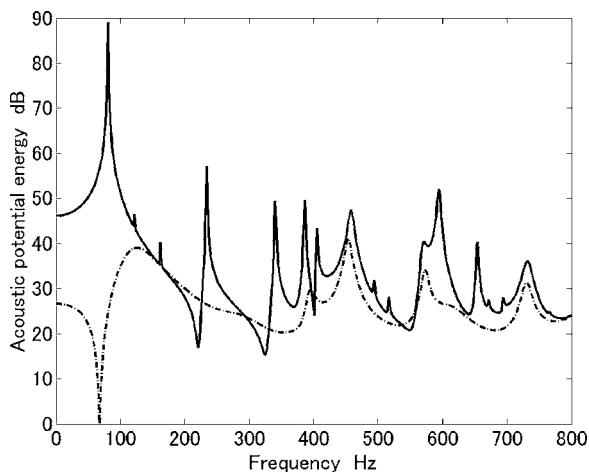


FIG. 8. Global potential energy in the enclosed acoustic field (dB ref= 10^{-12} J) before (solid line) and after the four-parallel-SIMOs arrangement of radiation cluster control (chained line).

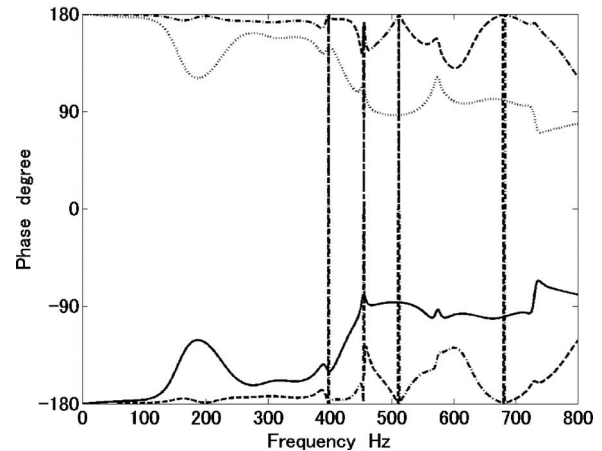
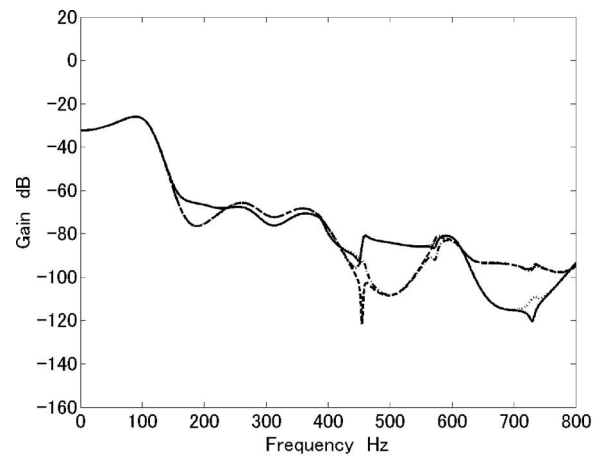


FIG. 9. Optimal gains (dB ref=incident acoustic pressure amplitude) and phases of the control forces in the four-parallel-SIMOs arrangement of radiation cluster control: the control force at $(L_x/10, L_y/10)$ (solid line); the control force at $(9L_x/10, L_y/10)$ (chained line); the control force at $(9L_x/10, 9L_y/10)$ (dotted line); and the control force at $(L_x/10, 9L_y/10)$ (dashed line).

control methods cause an increase of the acoustic potential energy at some off-resonance frequencies, as expected. Moreover, Fig. 6 shows the gains and phases of the optimal control forces in radiation cluster control with the error criterion being a single radiation cluster.

Figures 7 and 8 present the kinetic energy of the plate and the acoustic potential energy in the enclosure before and after radiation cluster control with the error criterion being all the radiation clusters, i.e., the four-parallel-SIMOs arrangement of radiation cluster control. Moreover, Fig. 9 shows the gains and phases of the optimal control forces in radiation cluster control with the error criterion being all the radiation clusters. It is clear from the figures that the performance of the four-parallel-SIMOs radiation cluster control achieves the overall reduction of both the kinetic energy and the acoustic potential energy up to 800 Hz.

IV. CONCLUSIONS

For the purpose of controlling sound radiation into a symmetric enclosure, radiation cluster control has been presented, the relationship between conventional structural modal control, radiation modal control, and radiation cluster control being clarified. Using the radiation cluster filters,

cluster information with some common property of structural modal functions of a symmetric enclosure may be extracted. Due to the reciprocity principle, cluster actuators allow one to explicitly excite the target radiation cluster without causing control spillover. Employing both the radiation cluster filters and the radiation cluster actuators, a radiation cluster control system is constructed, which falls into a category of MAC (middle authority control), possessing the benefit of implementation simplicity over LAC (low authority control: structural modal control), while providing particular controllability of the enclosed acoustic field to HAC (high authority control: radiation modal control). With a view to verifying the validity of radiation cluster control, numerical simulations have been conducted using a rectangular plate-cavity model, demonstrating a significant control effect for suppressing global acoustic potential energy in the enclosure.

ACKNOWLEDGMENT

This work was supported by Japan Society for the Promotion of Science.

- ¹F. Charette, C. Guigou, and A. Berry, "Development of volume velocity sensors for plates using pvdf film," in *Active 95*, pp. 241–252 (1995).
- ²S. D. Snyder and C. H. Hansen, "The design of systems to control actively periodic sound transmission into enclosed spaces. 1. Analytical models," *J. Sound Vib.* **170**, 433–449 (1994).
- ³S. D. Snyder and C. H. Hansen, "The design of systems to control actively periodic sound transmission into enclosed spaces. 2. Mechanisms and trends," *J. Sound Vib.* **170**, 451–472 (1994).
- ⁴B. S. Cazzolato and C. H. Hansen, "Active control of sound transmission using structural error sensing," *J. Acoust. Soc. Am.* **104**, 2878–2889 (1998).
- ⁵S. D. Snyder and N. Tanaka, "On feedforward active control of sound and vibration using vibration error signals," *J. Acoust. Soc. Am.* **94**, 2181–2193 (1993).
- ⁶W. T. Baumann, W. R. Saunders, and H. H. Robertshaw, "Active suppression of acoustic radiation from impulsively excited structures," *J. Acoust. Soc. Am.* **90**, 3202–3208 (1991).
- ⁷K. A. Cunefare, "The minimum multimodal radiation efficiency of baffled finite beams," *J. Acoust. Soc. Am.* **90**, 2521–2529 (1991).
- ⁸K. Naghshineh and G. H. Koopmann, "Material tailoring of structures to achieve minimum radiation condition," *J. Acoust. Soc. Am.* **92**, 841–855 (1992).
- ⁹S. J. Elliott and M. E. Johnson, "Radiation modes and the active control of sound power," *J. Acoust. Soc. Am.* **94**, 2194–2204 (1993).
- ¹⁰M. N. Currey and K. A. Cunefare, "The radiation modes of baffled finite plates," *J. Acoust. Soc. Am.* **98**, 1570–1580 (1995).
- ¹¹A. P. Berkhoff, "Sensor scheme design for active structural acoustic control," *J. Acoust. Soc. Am.* **108**, 1037–1045 (2000).
- ¹²A. P. Berkhoff, "Broadband radiation modes: Estimation and active control," *J. Acoust. Soc. Am.* **111**, 1295–1305 (2002).
- ¹³G. P. Gibbs, R. L. Clark, D. E. Cox, and J. S. Vipperman, "Radiation modal expansion: Application to active structural acoustic control," *J. Acoust. Soc. Am.* **107**, 332–339 (2000).
- ¹⁴G. V. Borgiotti, "The power radiated by a vibrating body in an acoustic fluid and its determination from boundary measurements," *J. Acoust. Soc. Am.* **88**, 1884–1893 (1990).
- ¹⁵G. V. Borgiotti and K. E. Jones, "Frequency independence property of radiation spatial filters," *J. Acoust. Soc. Am.* **96**, 3516–3524 (1994).
- ¹⁶K. A. Cunefare and M. N. Currey, "The radiation efficiency grouping of free-space acoustic radiation modes," *J. Acoust. Soc. Am.* **109**, 203–215 (2001).
- ¹⁷T. Chanpheng, H. Yamada, T. Miyata, and H. Katsuchi, "Application of radiation modes to the problem of low-frequency noise from a highway bridge," *Appl. Acoust.* **65**, 109–123 (2004).
- ¹⁸B. S. Cazzolato and C. H. Hansen, "Structural radiation mode sensing for active control of sound radiation into enclosed spaces," *J. Acoust. Soc. Am.* **106**, 3732–3735 (1999).
- ¹⁹P. A. Nelson, A. R. D. Curtis, S. J. Elliott, and A. J. Bullmore, "The active minimization of harmonic enclosed sound fields. 1. Theory," *J. Sound Vib.* **117**, 1–13 (1987).
- ²⁰L. D. Pope, "On the transmission of sound through finite closed shells: Statistical energy analysis, modal coupling, and nonresonant transmission," *J. Acoust. Soc. Am.* **50**, 1004–1018 (1971).
- ²¹D. R. Morgan, "An adaptive modal-based active control system," *J. Acoust. Soc. Am.* **89**, 248–256 (1990).
- ²²R. L. Clark, "Adaptive feedforward modal space control," *J. Acoust. Soc. Am.* **98**, 2639–2650 (1995).
- ²³N. Tanaka, Y. Kikushima, and N. Fergusson, "One-dimensional distributed modal sensors and the active modal control for planar structures," *J. Acoust. Soc. Am.* **104**, 217–225 (1998).
- ²⁴J. Pan, C. H. Hansen, and D. A. Bies, "Active control of noise transmission through a panel into a cavity. 1. Analytical study," *J. Acoust. Soc. Am.* **87**, 2098–2108 (1990).
- ²⁵S.-M. Kim and M. J. Brennan, "Active control of harmonic sound transmission into an acoustic enclosure both structural and acoustic actuators," *J. Acoust. Soc. Am.* **107**, 2523–2534 (2000).
- ²⁶I. Hagiwara, D. W. Wang, Q. Z. Shi, and R. S. Rao, "Reduction of noise inside a cavity by piezoelectric actuators," *ASME J. Vib. Acoust.* **125**, 12–17 (2003).

Use of principle velocity patterns in the analysis of structural acoustic optimization

Wayne M. Johnson^{a)}

Engineering Studies, Armstrong Atlantic State University, Savannah, Georgia 31419-1997

Kenneth A. Cunefare

The George W. Woodruff School of Mechanical Engineering, Georgia Institute of Technology, Atlanta, Georgia 30332-0405

(Received 11 October 2005; revised 11 September 2006; accepted 9 November 2006)

This work presents an application of principle velocity patterns in the analysis of the structural acoustic design optimization of an eight ply composite cylindrical shell. The approach consists of performing structural acoustic optimizations of a composite cylindrical shell subject to external harmonic monopole excitation. The ply angles are used as the design variables in the optimization. The results of the ply angle design variable formulation are interpreted using the singular value decomposition of the interior acoustic potential energy. The decomposition of the acoustic potential energy provides surface velocity patterns associated with lower levels of interior noise. These surface velocity patterns are shown to correspond to those from the structural acoustic optimization results. Thus, it is demonstrated that the capacity to design multi-ply composite cylinders for quiet interiors is determined by how well the cylinder can be designed to exhibit particular surface velocity patterns associated with lower noise levels. © 2007 Acoustical Society of America. [DOI: 10.1121/1.2404632]

PACS number(s): 43.40.Sk [JGM]

Pages: 938–948

I. INTRODUCTION

The tailoring of composite material properties for maximum strength, stiffness, and the like has been addressed quite often in the literature. However, the design of structures for optimal acoustic properties has been limited and even more so for composite structures. Of the few works addressing structural acoustic optimization of composites, none fully explain how or why certain designs of the properties lead to an improved acoustic environment enclosed by structures such as cylindrical shells. Further, it is unclear as to what mechanisms and design trends control the interior acoustic environment. In light of these uncertainties, this paper intends to interpret the optimization of a composite cylindrical shell using the decomposition of the interior acoustic potential energy.

The approach employed in this paper consists of performing structural acoustic optimizations of a composite cylindrical shell subject to external single-frequency harmonic monopole excitation. The ply angles of the composite cylinder are used for the optimization design variables. The objective of the optimization problem is to minimize the acoustic pressure inside the cylinder. The results of the optimization will then be interpreted based on the singular value decomposition of the interior acoustic potential energy. The decomposition of the acoustic potential energy will provide velocity patterns on the cylinder surface associated with lower levels of interior noise. It will be shown that these surface velocity patterns correspond to those from the structural acoustic optimization results. In this way, it will be

demonstrated that the ability to design multi-ply composite cylinders for quiet interiors would be determined by how well the cylinder could be designed to exhibit particular surface velocity patterns associated with lower noise levels.

This work will show that lower interior noise levels can be ensured by matching the surface velocity of the cylinder with those from the acoustic potential energy decomposition, namely the principle velocity patterns. This would significantly reduce the modeling complexity and computation times associated with structural acoustic optimization. The remainder of this section consists of a discussion of structural acoustic optimization in enclosed spaces using passive noise control and the use of principle velocity patterns in both exterior and interior fields. These patterns provide a means to prescribe surface velocity distributions that independently contribute to the radiated acoustic power for the exterior case and the acoustic potential energy in the interior case.

Passive noise control involves the modification of structural design parameters, such as structural member sizes, changing acoustic cavity shapes, applying vibration absorbing mounts, treating surfaces with damping coatings, and applying mass loading. An application of passive noise control is shape optimization, where the surface of the structure is modified to improve acoustic performance. An example of shape optimization is by Robinson,¹ who devised an approach to minimize the interior noise levels of a cylinder. This was achieved by optimizing the honeycomb core thickness of the shell subject to turbulent boundary layer excitation. The core thickness was formulated as a continuous cosine series in the circumferential direction with the coefficients of the expansion serving as design variables.

^{a)}Electronic mail: wj27@drake.armstrong.edu

Analytical formulations for the turbulent boundary layer, cylinder and enclosed cavity responses were developed for the constrained optimization problem. Two separate optimizations were run for the frequency ranges of 125–175 and 240–290 Hz. The first range had a reduction in the objective of 5.9 dB. Also, based on an examination of the structural resonances, the optimized cylinder was, for a given mode shape, stiffer than the unoptimized cylinder. The thickness variation on the circumference went from a somewhat arbitrary pattern to a uniform circumferential variation attributed to the final design vector having only one nonzero coefficient. The second frequency range had a noise reduction of only 0.59 dB. Unlike the first frequency range, there were many more structural modes in this frequency range potentially making it more difficult to reduce the objective. Overall, Robinson suggests that shape optimization can be used to reduce interior noise levels although more study is needed. Indeed, there was no effort made to correlate the acoustic cavity response with the structural response and the results of the optimization.

The use of multi-ply laminated composite materials in aircraft fuselages has increased dramatically recently. The notable examples of its use are the Beech Starship, the Raytheon Premier 1 business jet, and the Bell/Augusta Aerospace BA609 commercial tiltrotor. This is undoubtedly a result of composite material's high strength-to-weight and stiffness-to-weight ratio, corrosion resistance, durability, and damage tolerance.² Furthermore, laminated composite materials offer a unique capability over isotropic materials because they can be designed or tailored to exhibit particular properties.

The tailoring of composite material properties for maximum strength, stiffness, and the like has been addressed quite often in the literature as noted in a survey paper by Abrate.³ However, the design of composite structures for optimal acoustic properties, i.e., interior noise levels, has been limited to a study by Fernholz and Robinson⁴ in which they successfully demonstrated the influence of ply orientations on the interior noise of aircraft. The design sensitivity and optimization solution of a finite element tool was used exclusively in this study to determine the optimum lay up to minimize the interior noise of the Beech Starship. The entire fuselage was modeled, including stringers and stiffeners; however, the wings, trim panel, and floor were not included. They modeled the air inside the cabin with linear finite elements. Structure-borne noise from the engines was used for the excitation mechanism. The results of their work illustrated a 4 dB reduction of the interior sound pressure level over 185–210 Hz, for the eight-ply composite fuselage. In general, the optimization shifted the ply orientation from a symmetric layup to an unsymmetrical layup. Specifically, the inner four plies approached a cross-ply orientation shifted by 35°, i.e., 35/125/35/125, while the outer four plies all approached a ply angle of 40°. The authors did not provide any explanation about the nature of the trends. Also, their study considered only point force excitation, and they did not allow the ply angle design variables to vary along the length or circumference. This additional variation would be advanta-

geous as it would broaden the design space thereby improving the possibility of finding the optimal solution.

The principal velocity patterns employed in this work follow from the radiation modes concept. Radiation modes are based on the formulation of a radiation functional or operator, which maps a boundary value quantity to some other property or quantity in the radiated field. The boundary value is typically the normal surface velocity distribution and the radiated quantity is the acoustic pressure in the field. Borgiotti⁵ was one of the first to use the singular value decomposition technique to decompose a radiation functional of a body vibrating in a fluid. Borgiotti formulated the radiation operator using the Helmholtz integral equation. Thus, he was able to relate the normal velocity distribution on the surface to the radiated power in a specified far field region. The eigenvalue decomposition of the operator results in a set of orthogonal "singular velocity patterns" for the eigenvectors, as well as corresponding radiation efficiencies (eigenvalues).⁵ The radiation efficiencies are ordered in terms of decreasing efficiency. Similar to the structural or vibratory modes of a system, the exterior principle velocity patterns (PVPs) can be used to reconstruct any surface velocity pattern using an expansion theorem. However, unlike the vibratory modes, multiple principle velocity patterns exist at each frequency.

Cunefare and Currey⁶ examined the exterior acoustic radiation modes of a baffled beam using a modal style approach. They characterized the singular velocity patterns as *acoustic radiation modes*. Like, Borgiotti,⁵ they noted the direct correlation of the magnitudes of the eigenvalues, or singular values, with the radiation efficiencies of each corresponding acoustic radiation mode. Moreover, they discussed the similarities and differences of the radiation acoustic modes and structural vibration modes. One similarity is the need for a large number of terms to ensure convergence of higher ordered structural modes, or less efficient acoustic radiation modes.⁶ As they note, this heuristic is of particular interest to studies wishing to exploit the least efficient acoustic radiation modes.

Similar to the decomposition of the external radiation functional, we can perform a singular value decomposition on an internal acoustic functional. This internal functional relates the surface vibration of the enclosing structure to the acoustic potential energy of the cavity. The link between these two quantities is commonly referred to as the error weighting matrix;^{7,8} however it may be more informative to refer to this as the acoustic potential energy transfer matrix. The decomposition yields frequency dependent singular values that peak at selected cavity resonances. The singular vectors in this case are actually participation factors. When combined with the structural modal matrix, these participation factors select or filter the structural modes contributing to the actual PVP. The formulation and a more detailed discussion of the interior principle velocity patterns will be provided in Sec. III.

Cazzolato and Hansen⁷ used the transformed modal velocity amplitudes in a simulated active control scheme to reduce the interior acoustic potential energy for a stiffened cylindrical shell. The transformed modal velocities are the

amplitudes of the interior PVPs and contribute orthogonally to the interior acoustic potential energy; their minimization ensures reductions in the interior noise levels. To evaluate the effectiveness of this minimization approach, they modeled a longitudinally stiffened cylinder subject to point force excitation and with a single control force applied to the shell interior. Their results show that the acoustic potential energy can be reduced over a finite frequency range using the transformed modal velocity. The physical implementation of this approach would use shaped piezoelectric film sensors to estimate the transformed modal velocities and thus could be used as the error sensors in the control system.

The next section of this paper presents a description of the structural acoustic optimization design tool (SAOPT), and the finite and boundary element models used in this work as well as the design optimization approach. The principle velocity patterns are then discussed in more detail in the subsequent section. Principle velocity patterns allow the characterization of the surface velocity patterns that contribute to the interior acoustic potential energy, and specifically the interior noise levels. The results of the optimization cases for the ply angle design variable formulations are then provided along with their interpretation using the principle velocity patterns.

II. MODELING AND DESIGN OPTIMIZATION APPROACH

The SAOPT modeling and optimization design tool was originally developed in a joint Lockheed Martin/Georgia Tech research program. SAOPT incorporates a UNIX script with a finite element modeling package (MSC/NASTRAN), for the structural finite element model, a boundary element modeling (BEM) tool, (COMET/Acoustics), for the boundary element model acoustics, and CONMIN/COMPLEX for optimization. Although the SAOPT design tool can be used for the structural acoustic optimization of any structure, it was used to optimize an aircraft fuselage represented as a cylindrical shell. All optimizations were performed on a DEC Alphastation 500. A more detailed description of SAOPT can be found in the literature.⁹⁻¹²

There are three models used in the work at hand, the structural finite element model and exterior and interior boundary element models. The structural model consists of an unstiffened eight-ply graphite epoxy laminated composite cylinder clamped at both ends. The cylinder has a length of 3.66 m and a radius of 0.838 m. These dimensions and boundary conditions are consistent with previous structural acoustic optimization analyses on an aluminum shell.^{10,13,14} Each ply has a thickness of 0.2125 mm for a total shell thickness of 1.7 mm. The material properties of the graphite epoxy plies are: $E_{11}=135.6$ GPa, $E_{22}=9.9$ GPa, $G_{12}=4.2$ GPa, $\nu_{12}=0.3$, $\rho=1415$ kg/m³, where E_{ij} is the elastic modulus, G_{ij} is the modulus of rigidity, ν_{ij} is Poisson's ratio, and ρ is the density. The structural damping is 0.6%, which is consistent with other works using the same material.^{4,15} The finite element model uses 3200 linear quadrilateral plate elements. Note that plate elements are being used in lieu of shell elements to model the cylindrical shell, as shell elements are not

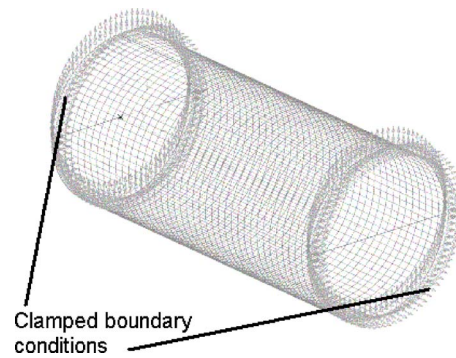


FIG. 1. Structural finite element model with clamped boundary conditions applied at ends.

available within most commercial finite element packages. Thus, the plate elements are modeling the cylindrical shell using a *faceted* approach. Figure 1 shows the structural finite element model with applied boundary conditions.

Two separate external and internal boundary element models are used. The external boundary element model consists of 2080 linear quadrilateral boundary elements and 3200 data recovery elements (linear quadrilateral). As shown in Fig. 2, the external BEM is subject to two monopole acoustic sources (in phase) located at 1.006 m from each side of the shell surface at the midpoint of the cylinder length. These sources operate at a frequency of 147.5 Hz.

The internal boundary element model consists of 2536 linear quadrilateral boundary elements. Two separate 30 and 60 element (linear quadrilateral) data recovery meshes are used with SAOPT's dynamic remeshing capability. The dynamic remeshing feature allows the user to specify two separate data recovery meshes. An initial optimization is performed with the coarser of the two meshes. Upon convergence with the coarse mesh, a second optimization is performed with the fine mesh. This approach provides significant reductions in the computation time for the interior boundary element analysis. The internal boundary element model and the fine and coarse data recovery meshes are shown in Fig. 3. Both meshes are located at a radius of 0.75 m. The remainder of this section will discuss the optimization approach employed in this work.

The analysis frequency of 147.5 Hz corresponds to the (2,1) structural mode of the composite cylinder with a ply

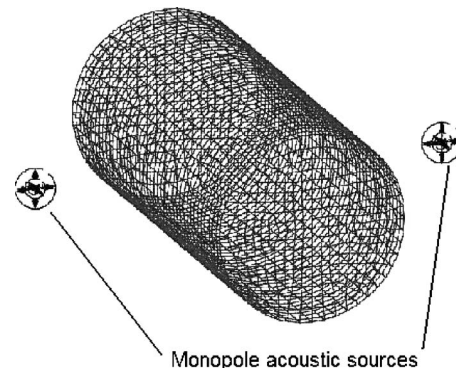


FIG. 2. External boundary element model with external monopole acoustic sources.



FIG. 3. Internal boundary element model and data recovery meshes.

layout of $[10/35/45/90]_s$. Several initial design states were selected for analysis. These cases are shown in Table I. The motivation for using multiple design states stems from the presence of multiple local minima in the design space which is quite common for multidisciplinary design optimization problems such as the one at hand.

The objective function minimized for the work at hand was the sum of the squared pressure amplitude at the data recovery nodes inside the cylinder. The only constraints on the system were side constraints on the ply angle design variables. The formal statement of the optimization problem is as follows.

Minimize

$$f(x) = \frac{\sum_{i=1}^N |p_i(x)|^2}{(\sum p_{\text{ref}}^2)} \quad (1)$$

subject to

$$x_L \leq x \leq x_U, \quad (2)$$

where x represents the ply angles as the design variables, $p_i(x)$ is the acoustic pressure at data recovery node i , p_{ref} is an arbitrary acoustic reference pressure, N represents the number of data recovery nodes, and the lower and upper limits of the ply angles are $x_L=0^\circ$ and $x_U=180^\circ$. Note this range was selected based on the precedence of the work by Fernholz and Robinson,⁴ and the traditional range of ply angles varying between -90° and 90° could have equivalently been used.

Three design variable (DV) formulations were studied. The first formulation was the uniform design variable formulation, where only the angle of each ply in the cylinder was allowed to vary for a total of eight design variables. The second formulation was the circumferential strip DV formulation depicted in Fig. 4, where the cylinder was divided into 10 equal length circumferential strips along the cylinder length for a total of 80 design variables. Finally, the third formulation depicted in Fig. 5 was the longitudinal strip DV formulation, where the cylinder was divided into 10 equal length longitudinal strips about the cylinder circumference for a total of 80 design variables. Note that the initial design states listed in Table I correspond to eight plies; thus, this ply orientation sequence is repeated for the 10 strips in the lon-

TABLE I. Initial ply angle design states.

Case	Ply orientation
1	$[10/35/45/90]_s$
2	$[0/90]_4$
3	$[90]_8$

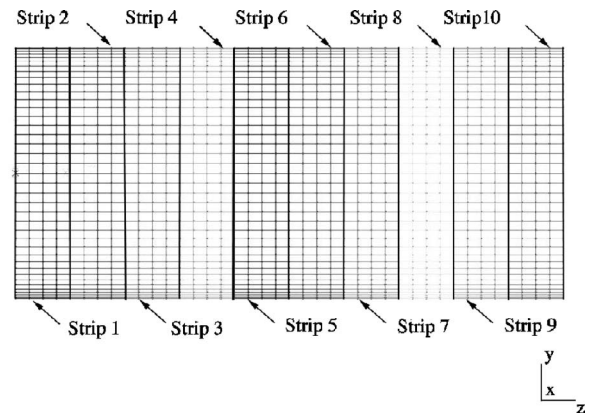


FIG. 4. Circumferential strip design variable formulation.

gitudinal and circumferential strip DV formulations.

III. PRINCIPLE VELOCITY PATTERNS

The PVPs¹⁶ allow us to characterize the surface velocity patterns that contribute to the interior acoustic potential energy and specifically the interior noise levels. The identification of the surface velocity patterns associated with interior noise levels can then be used to establish an understanding of the results of a structural acoustic optimization of a composite cylindrical shell. In this section we will formulate a quadratic function for the acoustic potential energy, decompose the function using singular value decomposition (SVD), the modal coupling coefficient, and the acoustic cavity modes, and study the resulting principle velocity patterns. All calculations will be based on a right circular cylinder with dimensions consistent with the structural finite element model discussed in Sec. II.

A. Acoustic potential energy based on the impedance matrix

We begin with the acoustic potential energy (APE) of an interior cavity as

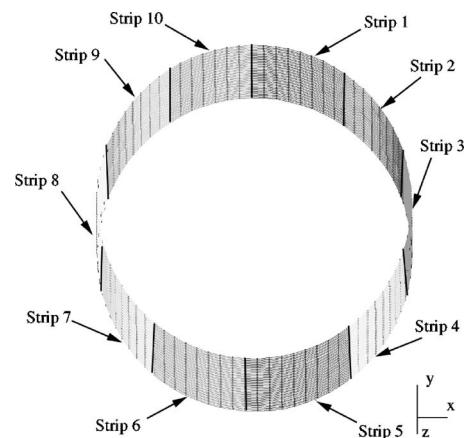


FIG. 5. Longitudinal strip design variable formulation.

$$E_p = \frac{1}{4\rho c^2} \int |p(x)|^2 dV, \quad (3)$$

where E_p is the APE, ρ is the density of the enclosed fluid, c is the speed of sound in the fluid, $p(x)$ is the acoustic pressure at some point x in the fluid field, and the integration is performed over the enclosed volume V . Using superposition, we can express the acoustic pressure as the superposition of rigid walled cavity modes $\phi_i(x)$ such that

$$p(x) = \sum_{i=1}^{\infty} p_i \phi_i(x), \quad (4)$$

where p_i is the pressure amplitude of the i th acoustic mode of the cavity. We can then substitute Eq. (4) into Eq. (3) to obtain

$$E_p = \frac{1}{4\rho c^2} \int \left(\sum_{i=1}^{\infty} p_i \phi_i(x) \right) \left(\sum_{j=1}^{\infty} p_j \phi_j(x) \right) dV. \quad (5)$$

But, due to modal orthogonality, we can simplify Eq. (5) as

$$E_p = \frac{1}{4\rho c^2} \sum_{i=1}^{N_a} \Gamma_{ii} |p_i|^2 dV, \quad (6)$$

where N_a is the number of acoustic modes considered, and Γ_{ii} is the acoustic volume normalization factor,

$$\int \phi_i \phi_j dV = \begin{cases} 0 & i \neq j \\ \Gamma_{ii} & i = j \end{cases}. \quad (7)$$

Finally, we can express Eq. (6) as a quadratic function of the modal pressure amplitudes

$$E_p = \mathbf{p}^H \mathbf{L} \mathbf{p}, \quad (8)$$

where \mathbf{p} is an $(N_a \times 1)$ vector of modal pressure amplitudes and \mathbf{L} is an $(N_a \times N_a)$ matrix. This matrix has been referred to as a diagonal weighting matrix.^{7,8} Its terms are

$$\mathbf{L}(i, i) = \frac{1}{4\rho c^2} \Gamma_{ii}. \quad (9)$$

However, we would ultimately like to express the APE in terms of a quadratic function of structural modal velocities. This facilitates the characterization of the coupling between the structure and the enclosed acoustic cavity. In order to accomplish this we need to establish the relationship between the modal acoustic pressure amplitudes and structural surface velocity amplitudes \mathbf{v} . This relationship can be gleaned from the structural-acoustic transfer function or impedance matrix \mathbf{Z}_{sa} , such that

$$\mathbf{p} = \mathbf{Z}_{sa} \mathbf{v}. \quad (10)$$

The impedance matrix has the dimensions $(N_a \times N_s)$ where N_s is the number of structural modes considered. The impedance relationship can be obtained from the Kirchhoff Helmholtz integral equation (KHIE). For the case of a rigid walled enclosure without any sources in the field, the KHIE simplifies to¹⁷

$$p(x) = \tilde{1} \rho \omega \int v(r_s) G(x/r_s) dS, \quad (11)$$

where $G(x/r_s)$ is the interior acoustic Green's function, r_s is a point on the vibrating surface, and $\tilde{1} = \sqrt{-1}$. The interior Green's function used in this work is based on the rigid walled cavity modes. A detailed derivation of this Green's function is available in Fahy¹⁸ and Koopman and Fahline.¹⁹ The rigid walled cavity mode formulation of the interior Green's function has been traditionally used in the literature.^{7,8,18,19} The only drawback from using this formulation is the requirement of many more modes to achieve convergence compared to the rigid walled cavity mode formulation. The Green's function for this case is expressed as

$$G(x/r_s) = \sum_{i=1}^{\infty} \frac{\phi_i(x) \phi_i(r_s)}{\Gamma_{ii}(\kappa_i^2 - k^2)}, \quad (12)$$

where κ_i is the wave number of the i th acoustic mode with resonant frequency ω_i and k is the acoustic wave number at the frequency of excitation ω .

As was done with the acoustic pressure, we can express the structural velocity $v(r_s)$ as the superposition of structural modes $\psi_j(r_s)$. Thus,

$$v(r_s) = \sum_{j=1}^{N_s} v_j \psi_j(r_s), \quad (13)$$

where v_j is the structural modal velocity amplitude. Substitution of Eqs. (12) and (13) into Eq. (11) yields

$$p(x) = \tilde{1} \rho \omega \sum_{i=1}^{N_s} \left[\sum_{j=1}^{N_a} \frac{v_j}{\Gamma_{ii}(\kappa_i^2 - k^2)} \int \phi_i(r_s) \psi_j(r_s) dS \right] \phi_i(x). \quad (14)$$

We should note that it has the same form as Eq. (4). We can also isolate the integral of the structural and acoustic modes evaluated at the surface as the modal coupling matrix B_{ij} such that

$$B_{ij} = \frac{1}{S} \int \phi_i(r_s) \psi_j(r_s) dS, \quad (15)$$

where S is the surface area of the enclosing structure. We can then formally define the impedance matrix introduced in Eq. (10) as

$$\mathbf{Z}_{sa_{ij}} = \frac{\tilde{1} \rho \omega S}{\Gamma_{ii}(\kappa_i^2 - k^2)} B_{ij}. \quad (16)$$

Finally, we can express the acoustic potential energy as a quadratic function in terms of the error weighting matrix $\mathbf{\Pi}$,^{7,8,20} and a column vector of structural modal velocity amplitudes \mathbf{v} , such that

$$E_p = \mathbf{v}^H \mathbf{Z}_{sa}^H \mathbf{L} \mathbf{Z}_{sa} \mathbf{v} = \mathbf{v}^H \mathbf{\Pi} \mathbf{v}. \quad (17)$$

The reference to $\mathbf{\Pi}$ as the error weighting matrix (EWM) stems from the term's use as the *error criteria* in active noise control schemes.^{7,8,20,21} The error weighting matrix is real and symmetric, but not necessarily positive semidefinite.

This means that the determinant of the matrix is zero, and thus the matrix is singular. This will have an effect on how we can decompose or diagonalize the error weighting matrix as explained in the following section.

B. Singular value decomposition of the error weighting matrix

SVD has been used extensively for the generation of exterior principle velocity patterns or acoustic radiation modes discussed in Sec. I.^{5,6,22} The key part of this process is the inversion of the error weighting matrix [see Eq. (17)], which is singular. SVD facilitates the decomposition of a singular matrix into the product of a pair of unitary matrices and a diagonal matrix. For example, using SVD, any matrix \mathbf{Q} can be expressed as the product of a column orthogonal matrix \mathbf{U} , a diagonal matrix \mathbf{S} of singular values, and the transpose of another orthogonal matrix \mathbf{V} . Stated mathematically, we have

$$\mathbf{Q} = \mathbf{U}\mathbf{S}\mathbf{V}^T. \quad (18)$$

The orthogonal matrices are known as left- and right-hand side singular vectors.²³ If \mathbf{Q} is real and symmetric, we can redefine Eq. (18) as

$$\mathbf{Q} = \mathbf{U}\mathbf{S}\mathbf{U}^T. \quad (19)$$

We have, then, essentially an eigenvalue problem. For example, if we define the eigen decomposition of \mathbf{Q} as

$$\mathbf{Q} = \mathbf{P}^T\mathbf{D}\mathbf{P}, \quad (20)$$

where \mathbf{P} is the column matrix of eigenvectors and \mathbf{D} is the diagonal matrix of eigenvalues, then we can express $\mathbf{Q}^T\mathbf{Q}$ as

$$\mathbf{Q}^T\mathbf{Q} = (\mathbf{P}^T\mathbf{D}\mathbf{P})^T\mathbf{P}^T\mathbf{D}\mathbf{P} = \mathbf{P}^T\mathbf{D}^2\mathbf{P}. \quad (21)$$

Therefore, the eigenvectors are the same as the singular vectors from \mathbf{U} and the singular values are, as previously stated, the square root of the eigenvalues or the diagonal of the \mathbf{D}^2 matrix in Eq. (21). Having presented the equivalence between the singular values and vectors to the eigenvalues and vectors, respectively, any subsequent references to singular values and vectors should be acknowledged as being the same as the eigenvalues and vectors.

Returning to the problem at hand, as stated in the previous section, the error weighting matrix is singular and so we may implement the SVD to diagonalize the EWM. Based on Eq. (19), we can diagonalize $\mathbf{\Pi}$ to obtain

$$E_p = \mathbf{v}^H\mathbf{\Pi}\mathbf{v} = \mathbf{v}^H\mathbf{U}\mathbf{S}\mathbf{U}^T\mathbf{v}. \quad (22)$$

Since $\mathbf{\Pi}$ is an $(N_s \times N_s)$ matrix, both \mathbf{U} and \mathbf{S} will have the same dimensions of $(N_s \times N_s)$. The \mathbf{U} and \mathbf{S} matrices take on a specific meaning as applied to the decomposition of the EWM. The singular values allow us to characterize the contribution of each singular vector and ultimately, each principle velocity pattern, to the acoustic potential energy. Bessac²⁴ suggests that for coupled problems such as this, the singular values characterize the level of coupling between the structure and enclosed acoustic cavity—the larger the value, the greater efficiency of the coupling between structure and the acoustic cavity. The singular vectors map the contributions of the structural modes to the acoustic potential

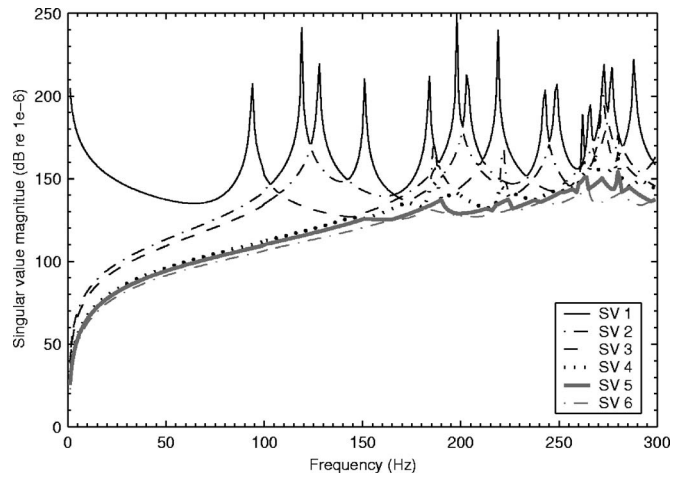


FIG. 6. Unsorted singular values of error weighting matrix.

energy. This will be elucidated in Sec. III B 3. In what follows, the sorting, convergence, and general significance of the singular values and vectors will be discussed.

1. Sorting of singular values and vectors

A singular vector, and ultimately the PVP, is associated with a specific singular value. But one drawback of SVD is that the rank-ordering of singular values as produced by the SVD algorithm does not yield the same ordered list of singular vectors at each frequency. This occurs because the magnitude of the singular values for singular vectors may cross; the SVD algorithm tracks the magnitude of the singular value at each frequency, not the singular vector. For example, as depicted in Fig. 6, singular value (SV) 1 is not continuous, and instead appears to have the largest magnitude compared to the other singular values over the range of frequencies. The same is true for the other singular values considered in Fig. 6. Therefore, in order to determine the frequency dependency of a given singular value and its respective singular vector, we must be able to discriminate it uniquely within the ordered listing produced by the SVD. A technique to sort the singular values and vectors will now be presented. As mentioned at the beginning of this section, all calculations are based on a right circular cylindrical geometry.

The sorting algorithm is based on the orthogonality of the singular vectors with respect to each other at a given frequency. The approach uses the dot product of the singular vectors at the first frequency of the analysis to sort the vectors over the entire frequency range. Figure 7 shows the sorted singular vectors, 1–6. Note how SV 1 is now continuous over the frequency range, but it does not necessarily have the greatest magnitude.

2. Discussion of singular values and vectors

Although this is a single frequency optimization analysis, it is important to illustrate that the singular values are frequency dependent. That is, the importance (magnitude) of a given singular value relative to other singular values will vary with frequency. The sorted singular values in Fig. 7 peak at the cavity resonances of the cylindrical volume.

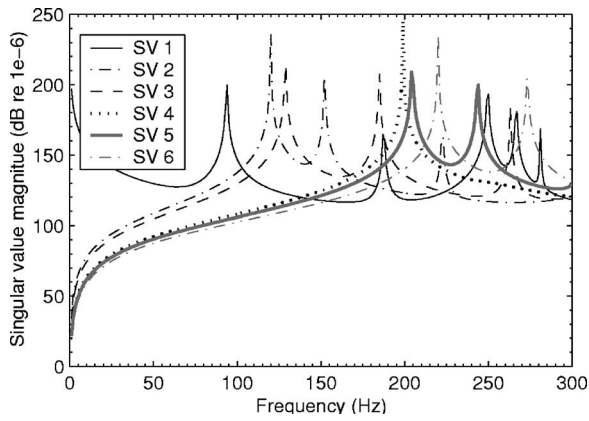


FIG. 7. Sorted singular values of error weighting matrix.

These modes are summarized in Table II. The acoustic mode indices (m, n, p) listed in Table II correspond to the indices of the axial, circumferential, and radial components of the cylindrical geometry mentioned earlier. A derivation of the acoustic mode shape and natural frequencies for cylindrical cavity is available in Blackstock.²⁵ Although not shown, similar peaks occur at the cavity modes associated with higher frequencies and singular values, i.e., beyond 300 Hz and for singular values greater than the sixth singular value. An important aspect of Table II is that specific cavity modes can be identified with each singular value and the corresponding singular vector and PVP. Another observation regarding Fig. 7 is that the singular values do not peak at all cavity modes within the frequency range considered. This is because these cavity modes do not couple with any structural modes considered.

Representative plots of the singular vectors at 147 Hz are shown in Fig. 8. Recall that the SVD is performed for each frequency. While the singular values varied over the frequency range, the singular vectors did not in terms of the mapping of the specific structural modes that ultimately contribute to the acoustic potential energy. This behavior is actually used to sort the singular values as discussed in the previous section. It has been shown in the literature⁷ that the level of contribution of a specific structural mode will have some variation with frequency. The frequency of 147 Hz was selected as it corresponded to the analysis frequency for the design optimizations in Sec. IV. The singular vectors in Fig. 8 are plotted over the number of structural modes considered, N_s . The singular vectors in Fig. 8 only peak for one to two structural mode indices. This is because modal coupling

TABLE II. Indices (m, n, p) of cavity modes corresponding to peaks in singular values 1–6.

No. 1	No. 2	Sing. vector				No. 6
		No. 3	No. 4	No. 5		
(0,0,0)	(0,1,1)	(1,1,1)	(0,2,1)	(1,2,1)	(2,2,1)	
(2,0,0)	(2,1,1)	(3,1,1)		(3,2,1)	(4,2,1)	
(4,0,1)	(4,1,1)	(5,1,1)		(5,2,1)		
(0,0,2)						
(2,0,2)						
(6,0,0)						

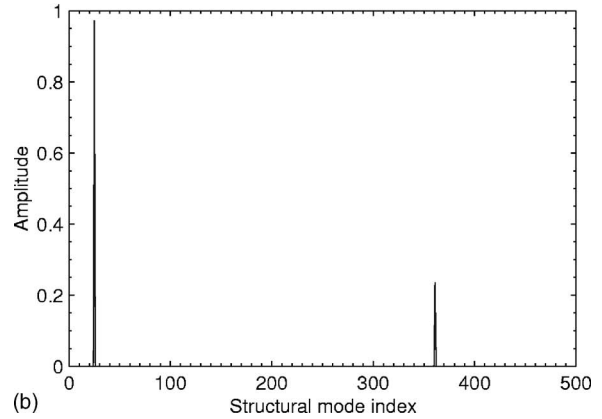
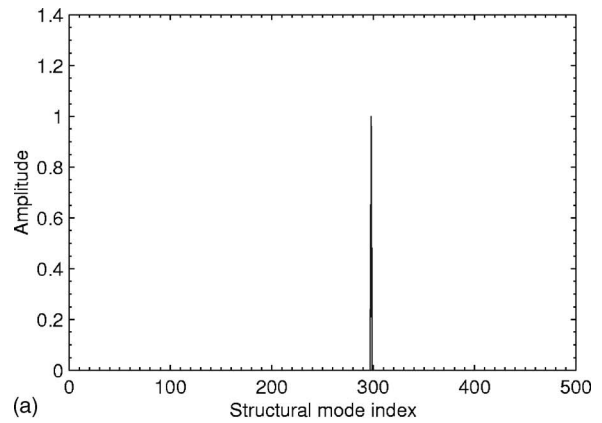


FIG. 8. Sorted singular vectors 1 and 4 based on SVD of error weighting matrix at 147 Hz. (a) Singular vector 1 and (b) singular vector 4.

for a cylindrical volume is significantly more selective than, for example, a rectangular cavity.⁸ The highly selective nature results in the need to consider many structural modes to achieve convergence.

3. Derivation of PVPs based on singular vectors

Continuing with Eq. (22), we can define the velocity amplitude or participation coefficients of the principle velocity pattern ν_{PVP} , as⁸

$$\nu_{\text{PVP}} = \mathbf{U}^T \mathbf{v}. \quad (23)$$

Similarly, we can define the surface velocity distribution as

$$\mathbf{v}_{r_s} = \mathbf{\Psi} \mathbf{v}, \quad (24)$$

where $\mathbf{\Psi}$ is the structural modal matrix. If we solve Eq. (24) for the modal velocity amplitudes \mathbf{v} and substitute this into Eq. (24), we obtain

$$\nu_{\text{PVP}} = \mathbf{U}^T \mathbf{\Psi}^{-1} \mathbf{v}_{r_s}. \quad (25)$$

Finally we can express the distribution of surface velocity as the superposition of principle velocity patterns, \mathbf{Y} , by inversion such that

$$\mathbf{v}_{r_s} = [\mathbf{\Psi} \mathbf{U}] \nu_{\text{PVP}} = \mathbf{Y} \nu_{\text{PVP}}. \quad (26)$$

The orthogonality of \mathbf{U} , i.e., $\mathbf{U}^T = \mathbf{U}^{-1}$, is a key aspect in the derivation of the principle velocity patterns based on the matrix of singular vectors. An examination of Eq. (26) reveals

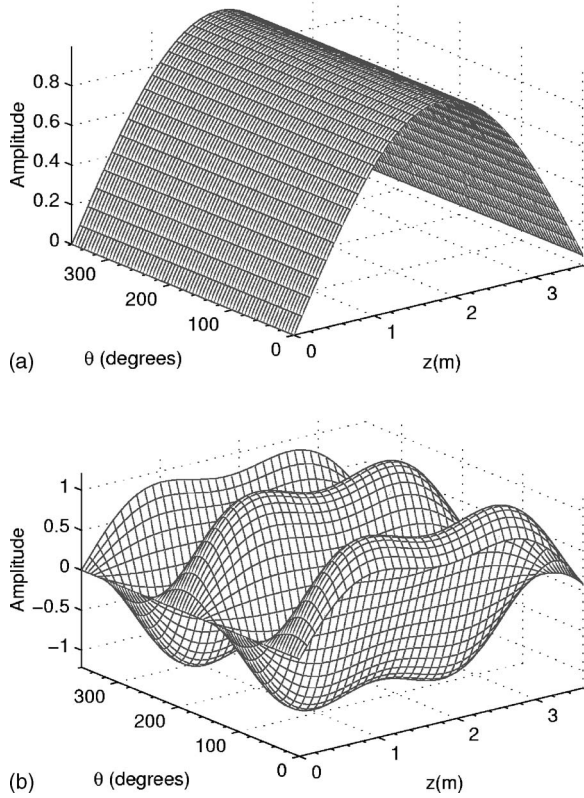


FIG. 9. Principle velocity patterns 1 and 4 based on SVD. (a) PVP 1. (b) PVP 4.

that each structural mode in Ψ can potentially contribute to a given PVP. These contributions will be governed by the l th singular vector, \mathbf{u}_l .

Returning to the acoustic potential energy, Eq. (22) can now be expressed as a function of the singular values S and PVP participation coefficients ν_{PVP} as

$$E_p = \nu_{\text{PVP}}^H S \nu_{\text{PVP}}. \quad (27)$$

Thus we see that reductions in participation coefficients lead directly to reductions in the acoustic potential energy. The singular values, as previously stated, characterize the efficiency of the coupling between the structure and acoustic cavity.

4. Discussion of principle velocity patterns

Figure 9 illustrates the principle velocity patterns 1 and 4, based on Eq. (26) at 147 Hz. These plots were generated by combining the singular vectors with the cylindrical structural modes. The azimuthal coordinate is unwrapped, i.e., it is plotted on a Cartesian coordinate instead of a polar coordinate. Five hundred (500) structural modes were used to formulate these PVPs. Although not shown, the PVPs at several other cavity modes and also nonresonant frequencies were calculated and plotted, all of which were the same. It is observed in these figures that the patterns have increasing levels of complexity with increasing PVP number. This behavior is consistent with the exterior PVPs discussed by several researchers.^{6,21,26} These interior patterns represent the surface velocity distributions that can be used to decouple or

TABLE III. Final normalized objective reductions for ply angle optimization.

Case	Uniform DV Circ.	Strip DV Long	Strip DV
1	-2.6	-4.8	-2.5
2	-3.9	1.4	-4.9
3	-2.2	-4.4	-4.2

diagonalize the error weighting matrix in Eq. (17). In other words, these PVPs represent the orthogonal contributors to the acoustic potential energy.

The following section present the results of the ply angle design optimization and interpretation using the principle velocity patterns for cases 1–6. For all ply angle design optimization cases presented, the objective function [see Eq. (1)] is normalized with respect to the initial objective value for case 1. This same normalization scheme is used for all subsequent objective value results. This scheme is used such that all the ply angle design optimization cases can be compared with each other. Moreover, it is only the final level of the objective that is relevant and comparable among design cases since each case will have a different initial level and subsequent reduction from that level. Any subsequent mention of *reduction* is relative to the initial objective value for case 1.

IV. DESIGN OPTIMIZATION ANALYSES

Table III provides a summary of the normalized objective reductions for all three cases (see Table I) and DV formulations. Of the three design cases considered, the circumferential strip design variable formulation achieved the largest objective reduction twice, while the longitudinal design variable formulations had the largest objective reductions once. This suggests that no single DV formulation is necessarily superior over another. Even the uniform DV formulation had the second largest objective reduction in cases 1 and 2. This is surprising since it was expected that the added design freedom of the longitudinal or circumferential design variable formulations would typically have the largest objective reductions. The variety of objective reductions for the different cases for a given DV formulation certainly confirms the presence of minima in the design space. Recall that reductions are the final design objective values relative to the initial objective value of case 1.

Cases 1 and 3 had some semblance of ply angle symmetry for their respective final design states for the circumferential and longitudinal DV formulations. However, this symmetry was not maintained for the uniform DV formulation for these two cases. The final ply orientations for all the other cases and DV formulations were also unsymmetrical. This is despite the symmetric loading applied to the cylinder. All the DV formulations for case 3 had very interesting final ply orientations in that several of the strips exhibited a sequential ordering. It was observed for many of the cases and design variable formulations that several ply angles had little change between the initial and final design states. While this

may very well be how the optimizer is able achieve reductions in the objective, it certainly suggests the need to explore other design variable formulations.

A. Interpretation of ply angle results using PVPs

The following presents an analysis of the ply angle results using the principle velocity patterns to decompose the structural velocities. The intent of this is to establish a physical understanding of the optimization results. Specifically, we would like to determine which principle velocity patterns contribute to the preoptimized and postoptimized composite cylinder. In what follows, we will discuss the decomposition approach, and then apply this method to examine the optimization results.

1. Decomposition of the cylinder velocity

Recall from Eq. (26) in Sec. III, that the surface velocity can be expressed as the superposition of the principle velocity patterns, whose level of contributions are governed by the velocity amplitudes of the principle velocity pattern ν_{PVP} . These can also be considered the participation coefficients. By solving for ν_{PVP} in Eq. (26), we have

$$Y^T \mathbf{v}_{r_s} = \nu_{PVP}. \quad (28)$$

By examining these participation coefficients for a particular surface velocity, we can establish which PVPs are responsible for that particular velocity distribution. The magnitude of the participation coefficient for a given PVP is directly proportional to that PVP's contribution to the surface velocity distribution. Applying this decomposition to our optimization results will show that the postoptimized cylinder will have more significant contributions from the higher order PVPs compared to the preoptimized cylinder. This will be evident by comparing the participation coefficients of the preoptimized and postoptimized cylinders.

The velocity on the right circular cylindrical shell obtained from the finite element analysis tool was reformulated in terms of a matrix. The size of this matrix was based on the element discretization in the azimuthal and longitudinal directions of the cylinder. Using modal analysis, the complex surface velocity \tilde{v}_{r_s} can be expressed explicitly as

$$[\tilde{v}_{r_s}] = [\Psi]\{\tilde{v}\}, \quad (29)$$

where Ψ is the structural modal matrix defined as

$$[\Psi] = [\{\psi_1\}\{\psi_1\}\{\psi_1\} \cdots \{\psi_N\}]. \quad (30)$$

Each mode ψ_i in its unwrapped state is a two-dimensional shape, but expressed in Eq. (30) as a vector for consistency with traditional modal analysis.²⁷ The vector of modal amplitudes $\{\tilde{v}\}$ is complex since the surface velocity is complex. Thus, Eq. (29) can be expressed as two equations, for the real and imaginary parts. Solving the real part of Eq. (29) for the modal amplitudes, we obtain

$$[\Psi]^T [v_{r_sR}] = [\Psi]^T [\Psi] \{v_R\} = [\text{ID}] \{v_R\}, \quad (31)$$

where $[\text{ID}]$ is a diagonal matrix. Likewise, solving for the imaginary part of Eq. (29) yields

$$[\Psi]^T [v_{r_sI}] = [\Psi]^T [\Psi] \{v_I\} = [\text{ID}] \{v_I\}. \quad (32)$$

In the same fashion, we can decompose the complex surface velocity \tilde{v}_{r_s} using the principle velocity patterns and compare the resulting participation coefficients, $\nu_{PVP R}$ and $\nu_{PVP I}$ for the preoptimized and postoptimized cylinder. Using the matrix of PVP's Y , Eqs. (31) and (32) become

$$[Y]^T [v_{r_sR}] = [Y]^T [Y] \{v_{PVP R}\} = [\text{ID}] \{v_{PVP R}\}, \quad (33)$$

and

$$[Y]^T [v_{r_sI}] = [Y]^T [Y] \{v_{PVP I}\} = [\text{ID}] \{v_{PVP I}\}. \quad (34)$$

The real and imaginary participation coefficients can be normalized by $[\text{ID}]$, and then combined by taking the complex modulus to obtain the participation coefficient ν_{PVP} defined as

$$\nu_{PVP} = \sqrt{v_{PVP R}^2 + v_{PVP I}^2}. \quad (35)$$

The initial and final participation coefficients for cases 1–6 will now be presented and discussed. The first ten PVPs were used to decompose the cylinder velocity from the finite element analysis tool. In using these PVPs for the decomposition, it will be desirable to observe a reduced emphasis on lower-index PVPs and a greater emphasis on the higher-index PVPs in the final design state. This is due to the lower-index PVPs having a greater impact on the interior acoustic potential energy and thus interior noise levels, relative to the higher-index PVPs. Recall from Sec. III that the singular values for the PVPs are associated with the efficiency of the coupling between the structure and the enclosed acoustic cavity. The lower-index PVPs will typically have a greater singular value and therefore greater influence on reducing the acoustic potential energy than the higher-index PVPs. What is more, the PVPs are ordered in decreasing levels of contribution to the acoustic potential energy. As a result, an overall increase in structural velocity at the final design state is not necessarily undesirable if it is dominated by higher-index PVPs.

2. Results

Figure 10 shows the participation coefficients for the initial and final design states for case 1 for the uniform, circumferential, and longitudinal DV formulations. All three DV formulations have the same initial velocity distribution, and can thus be represented with the same value in Fig. 10 as well as the other cases. Most of the participation coefficients (PCs) for the uniform DV formulation showed a reduction in value except PC 7, which actually increased in value, indicating a greater weighting on PVP 7. The circumferential and longitudinal DV formulations have more increases and decreases in the PC values. However, the increases for the circumferential DVs were biased toward PC 3 and greater, while the longitudinal DVs had increases associated with PC 4 and greater. In any case, this demonstrates that the optimizer is indeed selecting PVPs consistent with lower levels of acoustic energy and energy transfer between the structure and the enclosed acoustic cavity.

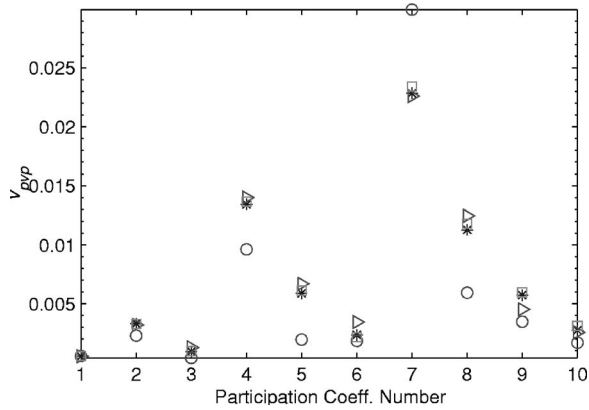


FIG. 10. Initial and final participation coefficients for case 1. (*) Initial DS, (o) final DS: Uniform DV, (\triangleright) final DS: Circumferential DV, (\square) final DS: Longitudinal DV.

The participation coefficients for the initial and final design states for case 2 are illustrated in Fig. 11. The uniform DV formulation had a similar distribution of reductions and increases in the PCs compared to case 1. For example, PC 7 showed an increase in the final design state, while the majority of the other PCs, especially PCs 2 and 4, had decreases in their respective values. The circumferential PCs remained unchanged between initial and final design states as expected since there was limited change in the DVs, and thus, in the objective function. The longitudinal DV formulation had a reduction in PC 2 like the uniform DV formulation for this case. But PC 4 was increased, and PC 7 displayed only a slight increase in value at the final design state.

Figure 12 shows the participation coefficients for the initial and final design states for case 3. The uniform DV formulation had significant reduction in PC 2 and increase in PC 7. There was also a greater contribution for PC 8 at the final design state. The circumferential DVs had a distribution similar to the uniform DV formulation for this case for PCs 2, 7, 8, and 9. But it also had an increase in PC 4 at the final design state. The longitudinal DV formulation also had a distribution similar to the uniform DV formulation, except for the decrease in PC 8 at the final design state.

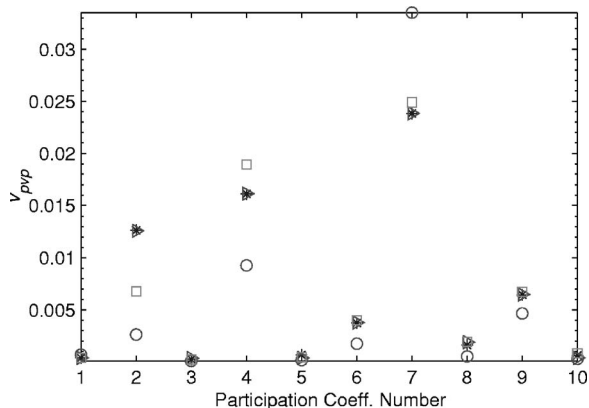


FIG. 11. Initial and final participation coefficients for case 2. (*) Initial DS, (o) final DS: Uniform DV, (\triangleright) final DS: Circumferential DV, (\square) final DS: Longitudinal DV.

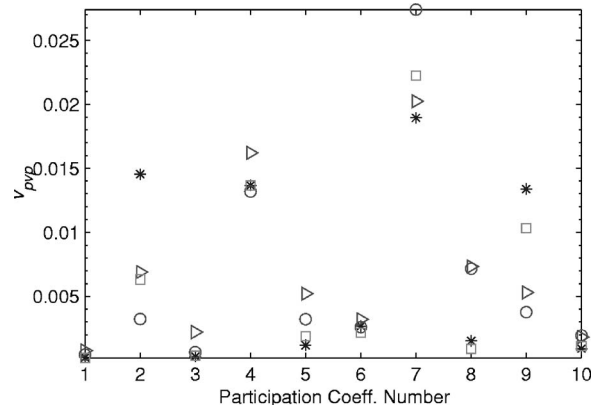


FIG. 12. Initial and final participation coefficients for case 3. (*) Initial DS, (o) final DS: Uniform DV, (\triangleright) final DS: Circumferential DV, (\square) final DS: Longitudinal DV.

B. Summary of PVP results

In terms of the PVP decomposition results based on an examination of the participation coefficients for each case and design variable formulation, it was found that increases in PC 7 and thus, PVP 7, were clearly favored by the optimizer to reduce interior noise levels. What is more, while PCs 1–6 had approximately the same number of increases as decreases in value, PC 7–10 clearly had more increases in value at the final design state for all the design variable formulations and cases considered. This reinforces the notion that the optimizer is selecting PVPs associated with reduced levels of energy transfer between the structure and acoustic cavity, and thus lower levels of acoustic potential energy.

A larger implication of this is that the ability to now design multi-ply composite cylinders for quiet interiors could be based on how well the cylinder can be designed to exhibit particular surface velocity patterns, associated with lower noise levels—these patterns would of course be the higher order principle velocity patterns. Based on this, the structural acoustic optimization approach implemented in this paper could be replaced with only a structural velocity optimization to match the surface velocity of the cylinder with those PVPs associated with lower levels of acoustic potential energy. This would significantly reduce the computation time by effectively limiting the necessity of the interior boundary element analysis to the initial and final design states to verify the results.

V. CONCLUSION

The principle velocity patterns have been used to analyze the results of a structural acoustic optimization of a composite cylindrical shell. The design optimization was carried out using a structural acoustic optimization design tool based on finite and boundary element analyses and the method of feasible directions optimization algorithm. The cylinder was subject to single frequency external monopole excitation. The objective of the optimization was the minimization of the sum of the squares of the acoustic pressure amplitudes.

The design variable formulations included uniform variation of the ply angles, circumferential strip variation of

the ply angles along the length of the cylinder, and longitudinal strip variation of the ply angles on the circumference of the cylinder. Three different initial design cases were considered. The majority of the cases achieved some level of reduction in interior noise levels. The ply angles of the optimized composite cylinders maintained limited ply angle symmetry for four of the nine design variable formulations considered. Otherwise, the optimized cylinder had unsymmetrical ply angles. It was also observed that in several design cases there was little change in the ply angles between the initial and final design states. In order to develop further insight into why the optimizer selected certain designs over others for the ply angle optimization, the principle velocity patterns were used to decompose and compare the initial and final cylinder surface velocities. The PVPs are orthogonal contributors to the interior acoustic potential energy, and are ordered in decreasing levels of contribution.

The examination of the participation coefficients with respect to the objective reductions revealed that optimizer selects designs with PVPs associated with reduced levels of acoustic potential energy. The broader implication of this work is the capacity to achieve interior noise reductions by matching the surface velocity distributions of the cylinder with those PVPs associated with lower levels of acoustic potential energy.

ACKNOWLEDGMENTS

W.M.J graciously acknowledges the assistance of Dr. Sergio Francesco and Michael Michaux for their assistance in completing this work. This work was supported initially by a NASA GSRP Fellowship.

- ¹J. H. Robinson, "Shape optimization of cylindrical shell for interior noise," in *OptiCON* (available at <http://hdl.handle.net/2002/15505>) (1999).
- ²D. C. Walden, "Applications of composites in commercial airplanes," in *Proceedings of the sixth Annual ASM/ESD Advanced Composites Conference* (Springer, Detroit, 1990), Vol. **10/08-11/90**, pp. 77–79.
- ³S. Abrate, "Optimal design of laminated plates and shells," *Compos. Struct.* **29**, 269–286 (1994).
- ⁴C. M. Fernholz and J. H. Robinson, "The influence of lamination angles on interior noise levels of an aircraft," NASA Tech. Memo. (1996).
- ⁵G. V. Borgiotti, "The power radiated by a vibrating body in an acoustic fluid and its determination from boundary measurements," *J. Acoust. Soc. Am.* **88**, 1884–1893 (1990).
- ⁶K. A. Cunefare and M. N. Currey, "On the exterior acoustic radiation

- modes of structures," *J. Acoust. Soc. Am.* **96**, 2302–2312 (1994).
- ⁷B. S. Cazzolato and C. H. Hansen, "Active control of sound transmission using structural error sensing," *J. Acoust. Soc. Am.* **104**, 2878–2889 (1998).
- ⁸S. D. Snyder and N. Tanaka, "On feedforward active control of sound and vibration using vibration error signals," *J. Acoust. Soc. Am.* **94**, 2181–2193 (1993).
- ⁹W. M. Johnson and K. A. Cunefare, "Structural acoustic optimization of a composite cylindrical shell using feb/bem," *J. Vib. Acoust.* **124**, 410–412 (2002).
- ¹⁰S. Crane, K. A. Cunefare, S. P. Engelstad, and E. A. Powell, "A comparison of optimization formulations for design minimization of aircraft interior noise," *J. Aircr.* **34**, 236–243 (1997).
- ¹¹S. P. Engelstad, K. A. Cunefare, E. A. Powell, and V. Biesel, "Stiffener shape design to minimize interior noise," *J. Aircr.* **37**, 167–171 (2000).
- ¹²K. A. Cunefare, S. P. Crane, S. P. Engelstad, and E. A. Powell, "Design minimization of noise in stiffened cylinders due to tonal external excitation," *J. Aircr.* **36**, 563–570 (1999).
- ¹³S. P. Crane, "Structural acoustic design optimization of cylinders using fem/bem," Masters thesis, Georgia Tech, 1995.
- ¹⁴S. P. Engelstad, K. A. Cunefare, S. Crane, and E. A. Powell, "Optimization strategies for minimum interior noise and weight using fem/bem," in 1995 International Conference on Noise Control Engineering, Proceedings of the 1995 International Conference on Noise Control Engineering, Newport Beach, 1995, 1205–1208.
- ¹⁵W. C. Gibson and E. M. Austin, "Analysis and design of damped structures," *Finite Elem. Anal. Design* **114**, 337–351 (1993).
- ¹⁶J. H. Ginsberg (private communication, 1999).
- ¹⁷P. A. Nelson and S. J. Elliott, *Active Control of Sound*, 2nd ed. (Academic, San Diego, 1992).
- ¹⁸F. Fahy, *Sound and Structural Vibration* (Academic, London, 1985).
- ¹⁹G. H. Koopman and J. B. Fahline, *Designing Quiet Structures* (Academic, San Diego, 1997).
- ²⁰B. S. Cazzolato and C. H. Hansen, "Structural radiation mode sensing for active control of sound radiation into enclosed spaces," *J. Acoust. Soc. Am.* **106**, 3732–3735 (1999).
- ²¹N. Tanaka, S. Snyder, and C. Hansen, "Distributed parameter modal filtering using smart sensors," *Trans. ASME, J. Vib. Acoust.* **118**, 630–640 (1996).
- ²²D. M. Photiadis, "The relationship of singular value decomposition to wave-vector filtering in sound radiation problems," *J. Acoust. Soc. Am.* **82**, 1152–1159 (1990).
- ²³G. H. Golub and C. F. Van Loan, *Matrix Computations* (Johns Hopkins University Press, Baltimore, 1983).
- ²⁴F. Bessac, L. Gagliardini, and J. L. Guyader, "Coupling eigenvalues and eigenvectors: A tool for investigating the vibroacoustic behaviour of coupled vibrating systems," *J. Sound Vib.* **191**, 881–889 (1996).
- ²⁵D. T. Blackstock, *Fundamentals of Physical Acoustics* (Wiley, New York, 2000).
- ²⁶S. Elliott and M. Johnson, "Radiation modes and the active control of sound power," *J. Acoust. Soc. Am.* **94**, 2194–2204 (1993).
- ²⁷J. H. Ginsberg, *Mechanical and Structural Vibrations: Theory and Applications* (Wiley, New York, 2001).

Optimization of a clamped plate silencer

Chunqi Wang, Jun Han,^{a)} and Lixi Huang^{b)}

Department of Mechanical Engineering, The Hong Kong Polytechnic University, Kowloon, Hong Kong

(Received 8 June 2006; revised 4 December 2006; accepted 5 December 2006)

A previous theoretical study [L. Huang, *J. Acoust. Soc. Am.* **119**, 2628–2638 (2006)] shows that, in a duct, a simply supported plate covering a side-branch rigid cavity can function effectively as a wave reflector over a broad range of low to medium frequencies. In this study, analytical formulation is extended to the boundary condition of clamped plate, which is easier to implement in practice. The theoretical model is tested experimentally using balsawood, which has a very high stiffness to mass ratio. The spectral peaks and shapes of the measured TL are in agreement with those calculated theoretically, attempts are also made to account for the considerable sound absorption in the rig. Further numerical studies based on the validated model show that, for a uniform plate, the optimal stopband is narrower and the lower band limit is worse than that of the simply supported configuration. However, a wave reflector using nonuniform, clamped plates with thinner ends out-performs the simply supported configuration in every aspect. Analyses show that the improvement is attributed to the increased acoustic radiation efficiency over the bulk length of the nonuniform plate, which behaves more like a rigid plate. © 2007 Acoustical Society of America. [DOI: 10.1121/1.2427126]

PACS number(s): 43.50.Gf, 43.20.Tb, 43.20.Ks [KA]

Pages: 949–960

I. INTRODUCTION

Low frequency duct noise is difficult to deal with by traditional methods such as porous duct lining and expansion chamber. Lining a duct with porous sound absorbing material is a very mature and reliable technique that can tackle the medium to high frequency noise easily (Mechel and Vér, 1992; Ingard, 1994). However, it does not work well for very low frequencies. An expansion-chamber-type muffler may be used to reflect the low frequency noise, but such a device is usually bulky and passbands exist. Aiming for a broadband passive noise control device that works effectively in the low-to-medium frequency range, Huang (2002) introduced the concept of a drumlike silencer. It consists of an expansion chamber with two side-branch cavities covered by light membranes under a fairly high tension. The predicted noise reduction performance has been verified without flow (Choy and Huang, 2002) and with flow (Choy and Huang, 2005). In addition to the broad bandwidth in the low frequency region, such a device has two other merits. First, it is fiber-free, hence more environmentally friendly than the porous duct lining. Second, because the membranes are flush-mounted with the duct and there is no sudden change of duct area, the flow can pass the silencer smoothly without causing any extra noticeable pressure loss.

In a recent study, Huang (2006) replaced the membranes used in the drumlike silencer described above by a simply supported plate (simply supported plate silencer, hereinafter). Theoretical study has shown that the proposed plate silencer can achieve a much wider logarithmic bandwidth than the

drumlike silencer of the same cavity geometry due to the changed intermodal acoustic interference between the odd and even *in vacuo* vibration modes. Besides, the plate silencer carries other advantages over the drumlike silencer. As discussed in the study of Choy and Huang (2002), the optimal tension plays an important role in achieving the desired performance. However, it is not an easy job to tune or to maintain the tension at the optimal value in practice, and the tension may vary due to membrane relaxation or the change of ambient temperature. The plate uses its natural bending moment as the sole structural restoring force. Thus, both the installation and the maintenance of the plate silencer are simplified.

The use of a plate or the tensioned membrane in noise abatement may not be new, but its use as a side-branch wave reflector is. For example, panel absorbers were used in broadcasting studios and other architectural practices (Brown, 1964; Ford and McCormick, 1969; Sakagami *et al.*, 1996; Horoshenkov and Sakagami, 2001); membrane absorbers were also used as a splitter silencer in the form of arrays of Helmholtz resonators (Frommhold *et al.*, 1994). However, in all these applications, the panel, or membrane, is a component of resonator, which works for a narrow frequency band, and the structural mass is a means to achieving a low resonance frequency. For the plate silencer, the most desirable properties of the plate are the high stiffness and low density, which contrast with the characteristics of the existing use of plate in noise control.

In this study, the leading and trailing edges of the plate are clamped instead of simply supported, which leads to a fixed-end plate silencer, or clamped plate silencer. The motivation for this change is given as follows. The simply supported ends described in Huang (2006) can be easily modeled in theoretical study and a model with such boundary conditions can be conveniently analyzed as well. However, it

^{a)}Current address: Ray W. Herrick Laboratories, Purdue University, 140 S. Intramural Drive, West Lafayette, IN 47907-2031.

^{b)}Corresponding author. Current address: Dept. of Mechanical Engineering, The University of Hong Kong, Pokfulam Road, Hong Kong. Electronic mail: lixi.huang@hku.hk

is usually difficult to implement such a boundary condition in an acoustic system, especially in a system like the plate silencer discussed here. One reason is that the elements in the acoustic system are usually so light in mass that the methods to implement the simply supported ends in a real device often result in effective clamped ends. Hence, it represents a step forward to replace the ideal simply supported boundary conditions by a more practical one. During the course of this study, it is found that when the bending stiffness and mass distribution of the clamped plate are constant along the length of the plate (a uniform plate, hereinafter), the stopband of the plate silencer turns out to be narrower than that of a simply supported one. One qualitative explanation is that the clamped-clamped boundary condition reduces the effective radiation length of the plate when it vibrates in response to the incident sound. To release the additional restrictions caused by the clamped ends, it is proposed to use a plate with variable bending stiffness and mass distribution along the length of the plate, namely, a nonuniform plate. The problem of sound scattering of similar structures has been studied before. For example, Fernyhough and Evans (1996) compared a step approximation to an exact solution of acoustic scattering in an acoustic waveguide with nonuniform wall impedance; Grant and Lawrie (2000) studied the acoustic scattering by a duct in which the bending stiffness varies smoothly with distance along the plate. Huang (2001) also presented a two-dimensional theoretical analysis of a membrane of varying compliance in the passive control of duct noise. As far as the current study is concerned, the employment of the nonuniform plate is mainly motivated by reducing the restrictions due to the clamped ends and thus increasing the radiation length of the plate. Hence, a nonuniform plate with two softer ends is preferred.

In what follows, Sec. II outlines the analytical formulation for the clamped plate silencer with both uniform and nonuniform plate. The transmission loss (TL) of the clamped plate silencer with uniform plate is first examined and optimized in Sec. III. It shows that the performance of such a plate silencer is a little better than that of the drumlike silencer of the same geometry but not as good as that of the simply supported plate silencer. Then the optimization of the nonuniform plate is conducted and the results show that, with a proper distribution of bending stiffness along the plate, the clamped nonuniform plate performs better than the simply supported plate. In Sec. IV, the basic theoretical model for the clamped plate silencer is validated experimentally.

II. ANALYTICAL FORMULATION

A. The theoretical model

Figure 1 shows the two-dimensional configuration of a side-branch plate silencer. It has a two dimensional duct of height h^* , with two plates (beams) flush-mounted on the wall. The asterisks denote dimensional variables while the corresponding dimensionless ones are introduced shortly without asterisks. The leading and trailing edges of the two plates are clamped to the rigid duct at the two edges of $|x^*| = L^*/2$, respectively, and are backed by a rigid-walled

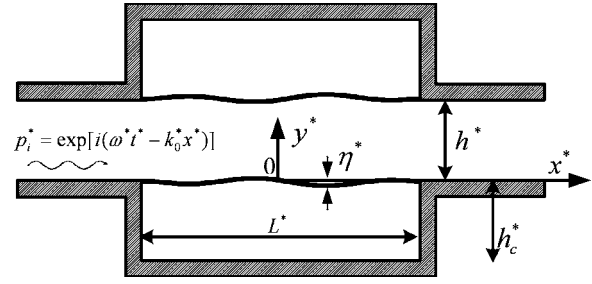


FIG. 1. Theoretical model of sound wave reflection by two cavity-backed plates forming part of the otherwise rigid duct walls.

cavity of depth h_c^* . The two lateral edges of the plates are set free and the three-dimensional plate is reduced to a two-dimensional beam. A plane incident wave comes from the left-hand side of the duct with a unit amplitude

$$p_i^* = \exp [i(\omega^* t^* - k_0^* x^*)] \quad (1)$$

and it causes the plate to vibrate with a transverse displacement of complex amplitude $\eta^*(x)$ and velocity $V^*(x)$ with the same time dependence, $\exp(i\omega^* t^*)$, which is henceforth omitted. The vibration radiates sound and imposes a radiation pressure on the plate surface. The problems of acoustics and plate vibration are fully coupled.

Before quantifying the plate dynamics, all variables are nondimensionalized as follows by three basic quantities, air density ρ_0^* , duct height h^* , and speed of sound in free space c_0^* :

$$x = \frac{x^*}{h^*}, \quad y = \frac{y^*}{h^*}, \quad t = \frac{c_0^* t^*}{h^*}, \quad L = \frac{L^*}{h^*}, \quad \eta = \frac{\eta^*}{h^*},$$

$$f = \frac{h^* f^*}{c_0^*}, \quad \omega = k_0 = 2\pi f, \quad (2)$$

$$p = \frac{p^*}{\rho_0^* (c_0^*)^2}, \quad m = \frac{m^*}{\rho_0^* h^*}, \quad T = \frac{T^*}{\rho_0^* (c_0^* h^*)^2},$$

$$B = \frac{B^*}{\rho_0^* (c_0^*)^2 (h^*)^3}.$$

Here, m is the plate-to-air mass ratio, B is the bending stiffness of the plate, which may vary with x , and T is the tension of membrane. According to the above normalization scheme, the dimensionless first cut-on frequency of the rigid-walled duct is $f=0.5$. Other variables will be explained when they are used.

Assume that the bending stiffness B and mass ratio m are functions of the coordinate along the plate, that is, x . The dynamics of the lower plate vibration is governed by

$$\frac{\partial^2}{\partial x^2} \left(B(x) \frac{\partial^2 \eta}{\partial x^2} \right) + m(x) \frac{\partial^2 \eta}{\partial t^2} + (p_i + \Delta p) = 0, \quad (3)$$

where p_i is the dimensionless incident wave and $\Delta p = p_+ - p_-$ is the fluid loading acting on the upper (+) and lower (-) sides of the plate induced by the plate vibration itself. When a uniform plate is used, bending stiffness B and mass

ratio m are then constant along the plate, and Eq. (3) is simplified as

$$B \frac{\partial^4 \eta}{\partial x^4} + m \frac{\partial^2 \eta}{\partial t^2} + (p_i + \Delta p) = 0. \quad (4)$$

Note that the effect of damping is excluded in the theoretical studies since sound reflection is dominant in the plate silencer. The effect of damping that necessarily exists in experiment is modeled and discussed in Sec. IV.

B. Modal dynamics of the sound-plate interaction

For harmonic vibration, the plate normal vibration velocity is $V = \partial \eta / \partial t = i\omega \eta$. Equation (3) then becomes

$$\frac{1}{i\omega} \left[\frac{\partial^2}{\partial x^2} \left(B(x) \frac{\partial^2 V}{\partial x^2} \right) \right] + m(x) i\omega \cdot V + (p_i + \Delta p) = 0. \quad (5)$$

The vibration mode shapes of a uniform clamped beam are available in textbooks such as (Inman, 2001) and, by introducing local variable ξ below, it is rewritten as

$$\begin{aligned} \varphi_j(\xi) = & A_{1,j} e^{\beta_j \xi} + A_{2,j} e^{-\beta_j \xi} + A_{3,j} \sin(\beta_j \xi) \\ & + A_{4,j} \cos(\beta_j \xi), \quad \xi = (x/L + 1/2), \end{aligned} \quad (6)$$

where

$$A_{1,j} = \frac{1}{2}(1 - \sigma_j), \quad A_{2,j} = \frac{1}{2}(1 + \sigma_j), \quad A_{3,j} = \sigma_j, \quad A_{4,j} = -1, \quad (7)$$

$$\sigma_j = \frac{\cosh(\beta_j) - \cos(\beta_j)}{\sinh(\beta_j) - \sin(\beta_j)}, \quad \tan(\beta_j) + \tanh(\beta_j) = 0.$$

The coupled dynamics Eq. (5) can be solved via the standard Galerkin procedure, in which V is expanded as a series of *in vacuo* modes $\varphi_j(\xi)$ of the clamped-clamped uniform plate with modal amplitudes V_j :

$$V = \sum_{j=1}^{\infty} V_j \varphi_j(\xi). \quad (8)$$

Equation (5) is then transformed as

$$\sum_{l=1}^{\infty} V_l L_{jl} + \int_0^1 (p_i + \Delta p) \varphi_j(\xi) d\xi = 0, \quad (9)$$

where the dynamic matrix L_{jl} is given by

$$\begin{aligned} L_{jl} = & \int_0^1 \left\{ \frac{1}{i\omega L^4} [B(\xi) \varphi_l^{(4)}(\xi) + 2B^{(1)}(\xi) \varphi_l^{(3)}(\xi) \right. \\ & \left. + B^{(2)}(\xi) \varphi_l^{(2)}(\xi)] + i\omega m(\xi) \varphi_l(\xi) \right\} \varphi_j(\xi) d\xi. \end{aligned} \quad (10)$$

When a uniform plate is used, the dynamic matrix $[L_{jl}]$ reduces to a diagonal matrix with element

$$L_{jj} = mi\omega + \frac{B}{i\omega} \left(\frac{j\pi}{L} \right)^4. \quad (11)$$

In order to solve Eq. (9), the fluid loading $(p_i + \Delta p)$ has to be related to the modal vibration velocity amplitude V_j . In other words, a modal impedance Z_{jl} must be found, Z_{jl} being defined as

$$Z_{jl} = \int_0^1 \varphi_l(\xi) \Delta p_j(x) d\xi, \quad (12)$$

where $\Delta p_j(x)$ is the fluid loading caused by the j th modal vibration of unit amplitude. A detailed method of solution to determine the modal impedance of the drumlike silencer was given in Huang (2002). The same procedure is followed here. Issues unique to the current model are (1) the mode $\sin(j\pi\xi)$ is replaced by $\varphi_j(\xi)$ defined in Eqs. (6) and (2) the fluid loading inside the cavity is found by the cavity modes to simplify the formulation. As said before, p_i is the incident wave, and the fluid loading induced by the plate vibration, Δp , may be divided into two parts:

$$\Delta p = p_{+\text{rad}} - p_{\text{cav}}, \quad (13)$$

where $p_{+\text{rad}}$ is the radiation sound pressure in the main duct and p_{cav} is the pressure inside the cavity acting on the lower plate surface. The formulation for $p_{+\text{rad}}$ is well known (Doak, 1973), and is rewritten in 2D dimensionless form

$$\begin{aligned} p_{+\text{rad}}(x, y) = & \frac{L}{2} \sum_{n=0}^{\infty} c_n \psi_n(y) \int_0^1 \psi_n(y') V(x') \\ & \times [H(x - x') e^{-ik_n(x-x')} + H(x' - x) e^{+ik_n(x-x')}] d\xi', \end{aligned} \quad (14)$$

where H is the Heaviside function, c_n , k_n , and ψ_n are, respectively, the modal phase speed, the modal wave number, and the modal velocity potential:

$$c_n = \frac{i}{\sqrt{(n\pi/\omega)^2 - 1}}, \quad k_n = \frac{\omega}{c_n}, \quad \psi_n(y) = \sqrt{2 - \delta_{0n}} \cos(n\pi y); \quad (15)$$

and δ_{0n} is the Kronecker delta. Hence, suppose the radiation pressure caused by the j th modal vibration of unit amplitude φ_j is $p_{+\text{rad},j}$. Then the modal impedance contributed by the radiation pressure in the main duct is defined as follows,

$$\begin{aligned} Z_{+jl} = & \int_0^1 \varphi_l(\xi) p_{+\text{rad},j}(x, 0) d\xi \\ = & \frac{L}{2} \sum_{n=0}^{\infty} c_n (2 - \delta_{0n}) \sum_{p=1}^4 \sum_{q=1}^4 A_{p,l} A_{q,j} I_{p,q}, \end{aligned} \quad (16)$$

where $A_{q,j}$ and $A_{p,l}$ are the coefficients defined in Eq. (7) and $I_{1,1} - I_{4,4}$ are given in the Appendix .

The acoustic pressure inside a lightly damped cavity can be expressed in terms of "rigid wall" modes of the cavity (Kuttruff, 2000). For the two-dimensional configuration considered here, the normalized pressure inside the cavity p_{cav} can be written as

$$\begin{aligned} p_{\text{cav}}(x, y) = & \sum_{m,n} \frac{-i\omega \phi_{m,n}(x, y)}{Lh_c(\kappa_{m,n}^2 - k^2 + 2i\zeta_{m,n} \kappa_{m,n} k)} \\ & \times \int_0^1 V(x', 0) \phi_{m,n}(x', 0) d\xi', \end{aligned} \quad (17)$$

where $V(x', 0)$ is the normal velocity over the flexible panel,

$\zeta_{m,n}$ is the damping ratio of the (m,n) th acoustic mode $\phi_{m,n}(x,y)$, L is the length of the cavity, h_c is the height of the cavity, and $\kappa_{m,n}$ is the corresponding acoustic wave number of the (m,n) th acoustic mode $\phi_{m,n}(x,y)$, with $\phi_{m,n}(x,y)$ and $\kappa_{m,n}$ given as

$$\phi_{m,n}(x,y) = \sqrt{(2 - \delta_{0m})(2 - \delta_{0n})} \cos\left(\frac{m\pi x}{L}\right) \cos\left(\frac{n\pi y}{h_c}\right), \quad (18)$$

$$\kappa_{m,n}^2 = \left(\frac{m\pi}{L}\right)^2 + \left(\frac{n\pi}{h_c}\right)^2. \quad (19)$$

Therefore, the cavity pressure caused by the j th modal vibration of unit amplitude, $p_{cav,j}(x,y)$, can be found and the cavity modal impedance becomes

$$\begin{aligned} Z_{cav,jl} &= - \int_0^1 \varphi_l(\xi) p_{cav,j}(x,0) d\xi \\ &= \sum_{m=0}^{\infty} \sum_{n=0}^{\infty} \frac{ik(2 - \delta_{0m})(2 - \delta_{0n})}{h_c(\kappa_{m,n}^2 - k^2 + 2i\zeta_{m,n}\kappa_{m,n}k)} \\ &\quad \times \left(\sum_{p=1}^4 A_{p,j} I_{cj,p} \sum_{q=1}^4 A_{q,l} I_{cl,q} \right), \end{aligned} \quad (20)$$

where $I_{cj,p}(I_{cj,1}-I_{cj,4})$ and $I_{cl,q}(I_{cl,1}-I_{cl,4})$ are given in the Appendix .

With the modal impedances due to p_{+rad} and p_{cav} found, the dynamics Eq. (5) becomes a set of linear equations for the modal vibration amplitude, V_j ,

$$\{L_{jl} + Z_{+jl} - Z_{cav,jl}\} \{V_j\} = -\{I_j\}, \quad (21)$$

where $\{V_j\}$, $\{I_j\}$ are column vectors, and the modal coefficient of the incident wave, I_j , is defined as

$$I_j = \int_0^1 p_i \varphi_j(\xi) d\xi. \quad (22)$$

Equation (21) can be solved via the inversion of matrix. In the actual calculation, modal truncation is necessary. The plate modes are truncated to 25. For instance, the subscripts of j and l in Eqs. (12), (16), and (20) range from 1 to 25, and the final impedance matrix $[Z_{jl}]$ is then of the size 25×25 . For the duct acoustic mode ψ_n in Eq. (14) and the cavity acoustic mode $\phi_{m,n}$ in Eq. (17), m and n are from 0 to 50. Numerical results show that the number of modes is normally enough as further increase in the number does not make significant difference for the purpose of this study.

The total sound pressure transmitted to the downstream is found by adding the incident wave, p_i , to the far-field radiation wave, p_{+rad} , which can be found from Eq. (14) by taking only the plane wave mode $n=0$ for $x > L/2$,

$$p_t = p_{+rad}|_{n=0, x \rightarrow +\infty} + p_i. \quad (23)$$

Similarly, the reflected wave is

$$p_r = \frac{p_{+rad}|_{n=0, x \rightarrow -\infty}}{e^{ik_0 x}}, \quad (24)$$

and the TL and the sound energy reflection coefficient β are

$$TL = 20 \log_{10} \frac{|p_i|}{|p_r|}, \quad (25)$$

and

$$\beta = \frac{|p_r|^2}{|p_i|^2}, \quad (26)$$

respectively.

III. SILENCER PERFORMANCE AND ITS OPTIMIZATION

The main objective of this study is to develop a broadband wave reflector, which works preferably in the low frequency range. Thus, the performance of the plate silencer can be characterized by the widest stopband that can be achieved. Following the previous study (Huang, 2002), the stopband here is defined as the frequency range, $f \in [f_1, f_2]$, in which the TL is above a criterion value, TL_{cr} , over the whole frequency band. As recommended in Huang (2004), the criterion value may be chosen as the peak TL for an expansion chamber whose cavity volume is three times the actual cavity volume in the silencer. For a silencer with two cavities of depth h and length $L=5h$, the value can be calculated and rounded up to 10 dB. For the purpose of comparison with previous studies, the same configuration of cavity is adopted in the current study, and $TL_{cr}=10$ dB is chosen as the threshold level.

A. Uniform clamped plates

The performance of a side-branch plate silencer using uniform clamped plates is investigated. The default cavity shape is chosen as $L=5$ and $h_c=1$. For a given structure-to-air mass ratio, m , the performance of the silencer is optimized by searching for the optimal bending stiffness B_{opt} so that the bandwidth is maximum by varying other parameters such as the bending stiffness and, for the nonuniform plate described below, the thickness distribution. Since special emphasis is put on the low frequency noise, the cost function for the optimization is set as the ratio of the band limits, f_2/f_1 , namely, the logarithmic bandwidth, instead of f_2-f_1 . Results of the performance optimization are shown in Fig. 2.

Figure 2(a) compares the overall TL of the clamped plate silencer (solid line) with the drumlike silencer (dashed line). The mass ratios of the two models are both equal to 1. For $B_{opt}=0.0698$, the lower and upper bandwidth limits of the plate silencer are $f_{1c}=0.0445$ and $f_{2c}=0.125$, respectively, and $f_{2c}/f_{1c}=2.81$. For the drumlike silencer with optimal tension $T_{opt}=0.475$, the lower and upper bandwidth limits and bandwidth are $f_{1d}=0.054$, $f_{2d}=0.141$, and $f_{2d}/f_{1d}=2.6$, respectively. Clearly, with the same mass ratio $m=1$, the optimal performance of the clamped plate silencer is better than that of the drumlike silencer in terms of the lower band limit and the achievable bandwidth. Figures

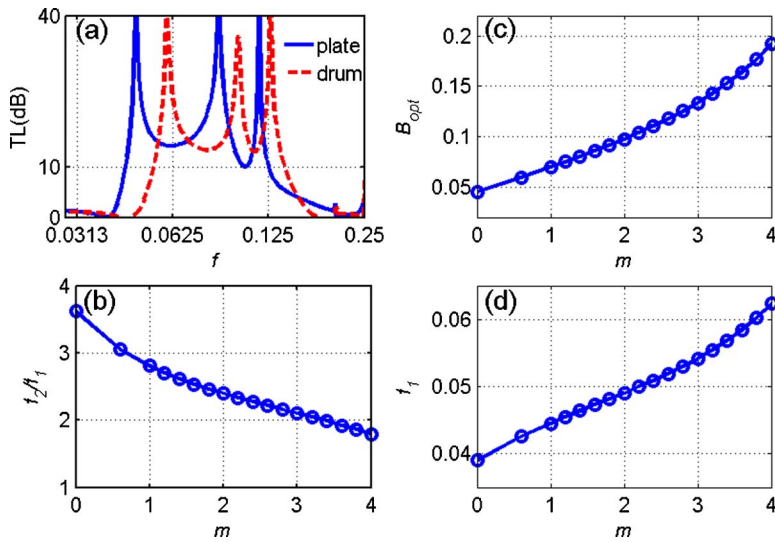


FIG. 2. (Color online) Performance optimization of the clamped plate silencer. (a) Comparison of the performance of the plate silencer (solid curve) with drumlike silencer (dashed curve) with the same cavity geometry of $L=5h$, $h_c=h$, and the same mass ratio of $m=1$. (b) Bandwidth f_2/f_1 . (c) Dimensionless optimal bending stiffness B_{opt} . (d) Dimensionless lower band limit f_1 .

2(b)–2(d) show the maximum bandwidth, the optimal bending stiffness, and the lower band limit as functions of m for the clamped plate silencer. As shown in Fig. 2(b), when the plate mass increases, the maximum achievable bandwidth f_2/f_1 decreases gradually. When the mass ratio m reaches 3, the maximum bandwidth is 2.1, which is still larger than one octave. Figure 2(c) suggests that the optimal bending stiffness increases with the plate mass, in much the same way as the simply supported plate silencer (Huang, 2006). However, since the clamped-clamped boundary conditions at the leading and trailing edges impose additional restrictions on the plate motion, the optimal bending stiffness required by the clamped-clamped plate is smaller than that of the corresponding simply supported plate of the same mass ratio. As shown in Fig. 2(c), the optimal bending stiffness for $m=1$ is $B_{opt}=0.0698$. For the simply supported plate, the corresponding $B_{opt}=0.1289$. When the plate mass increases, the lower band limit f_1 increases too, as shown in Fig. 2(d). Compared with the simply supported plate silencer, the lower band limit f_1 is a little higher when the clamped plate is adopted. This effect is undesirable for the plate silencer designed for low-frequency noise control. Nevertheless, the lower band limits are still within the low frequency region. For example, when $m=3$, $f_1=0.054$. For a duct with a height of 20 cm, the dimensional lower band limit is $f_1^*=92$ Hz.

Generally speaking, the performance of the clamped plate silencer using uniform plates is good, but it is not as attractive as that of the simply supported plate silencer. As presented in Huang (2006), when $m=1$, a simply supported plate silencer can achieve a stopband of $f_2/f_1=4.25$ with $f_1=0.0353$. For the current model the two corresponding indi-

cators are 2.81 and 0.0445. The performance degradation of the clamped plate silencer may be attributed to the clamped conditions applied to the leading and trailing edges of the plate. Such a boundary condition brings additional restrictions to portions of the plate near the ends, which in turn prevents the plate from vibrating and radiating reflection sound effectively. To further increase the stopband and reduce the lower band limit f_1 , the use of a nonuniform plate with softer ends is explored. In the next subsection, the optimal bending stiffness distribution along the length of the plate is investigated, and the optimal TL is analyzed and compared with that of the simply supported plate silencer.

B. Nonuniform plate

The so-called optimization of nonuniform distribution $B(x)$ is realized by choosing one shape from a set of possibilities that can yield the widest stopband. When constructing $B(x)$, the following two factors are taken into considerations. First, the purpose of introducing the nonuniform plate is to release the structural restrictions near the clamped ends; therefore, the bending stiffness near the two ends should be smaller than that in the middle. Second, the lower vibration modes (especially the first two) of the plate are dominant in the reflection of sound. Based on the above two considerations, it is appropriate to construct $B(x)$ as

$$B(x) = B_0 d(x), \quad (27)$$

where B_0 is a constant ratio to be determined, and $d(x)$ is the shape function of the bending stiffness. One such distribution is shown in Fig. 3(a) and is described below,

$$d(\xi) = \begin{cases} h_1 + \frac{\arctan(\alpha_1 \xi_1) + \arctan[\alpha_1(\xi - \xi_1)]}{\arctan(\alpha_1 \xi_1) + \arctan[\alpha_1(\xi_0 - \xi_1)]} (1 - h_1), & 0 < \xi \leq \xi_0, \\ h_2 + \frac{\arctan[\alpha_2(1 - \xi_2)] - \arctan[\alpha_2(\xi - \xi_2)]}{\arctan[\alpha_2(1 - \xi_2)] - \arctan[\alpha_2(\xi_0 - \xi_2)]} (1 - h_2), & \xi_0 < \xi < 1, \end{cases} \quad (28)$$

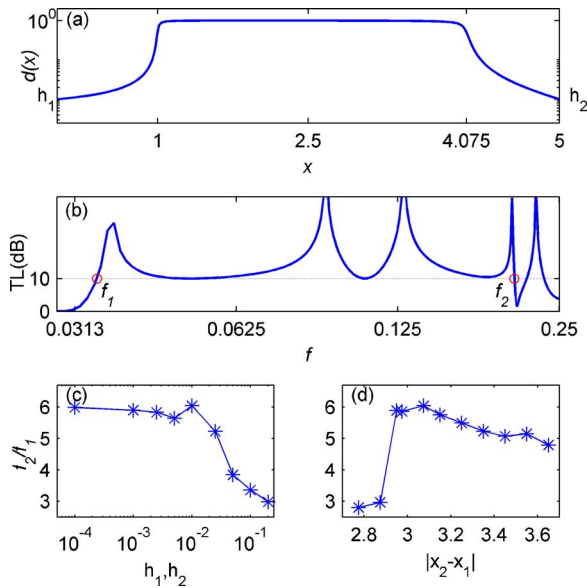


FIG. 3. (Color online) Optimization of the nonuniform plate. (a) Optimal distribution of the bending stiffness along the length of the plate. (b) TL. (c) Bandwidth f_2/f_1 with respect to the relative bending stiffness at the two thin ends. (d) Bandwidth f_2/f_1 with respect to the length of the thick part of the plate. The cavity geometry is $L=5h$, $h_c=h$; average mass ratio $\bar{m}=1$.

where $\xi=(x/L+1/2)$, as defined in Eq. (6). There are seven control parameters in the above-defined function $d(\xi)$, namely, α_1 , α_2 , h_1 , h_2 , ξ_0 , ξ_1 , and ξ_2 , where α_1 , α_2 control the slope of the resulting curve; h_1 , h_2 control the heights of the curve at the two ends; and ξ_0 , ξ_1 , and ξ_2 control the horizontal positions of the two segments. Since $B(x)$ plays a more important role in the dynamics of the plate than $m(x)$ does, the distribution of mass ratio, $m(x)$, is simply taken as

$$m(x) = m_0 \sqrt[3]{d(x)}. \quad (29)$$

The cavity geometry is still assumed to be $h_c=1$ and $L=5$. The ranges of the seven controlling parameters are $h_1, h_2 \in [0.0001, 0.2]$, $\alpha_1, \alpha_2 \in [1, 1500]$, $\xi_0 \in [0.3, 0.6]$, $\xi_1 \in [0.05, 0.25]$, and $\xi_2 \in [0.75, 0.95]$. During the optimization, the seven parameters vary step by step within the ranges given above. The TL is calculated for each given set of parameters, and the set of parameters that results in the widest stopband is chosen as the optimal one. The corresponding $B(x)$ is then the optimal distribution of the bending stiffness. In order to facilitate the comparison of the TL spectrum for each $B(x)$, the total mass along the plate is kept as a constant during the optimization,

$$\int_0^L m(x) dx = \bar{m}L, \quad (30)$$

where $\bar{m}=1$ is chosen in the example given. For the nonuniform plate, \bar{m} is the average mass ratio along the length of the plate. The maximum stopband $f \in [0.0343, 0.2062]$ is found with the following parameters:

$$\begin{aligned} \xi_0 &= 0.35, & \xi_1 &= 0.2, & \xi_2 &= 0.815, & \alpha_1 &= 300, \\ \alpha_2 &= 100, & h_1 &= h_2 &= 0.01. \end{aligned} \quad (31)$$

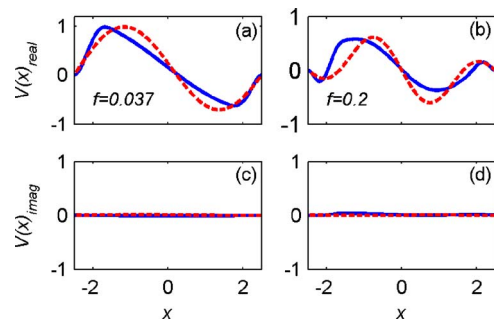


FIG. 4. (Color online) Comparison of the vibration velocity distribution $V(x)$ between the clamped nonuniform plate (solid lines) and the simply supported plate (dashed lines). (a) $f=0.037$, real parts. (b) $f=0.2$, real parts. (c) $f=0.037$, imaginary parts. (d) $f=0.2$, imaginary parts.

The constant B_0 is determined as 0.4935. The results of the optimization are shown in Fig. 3.

Figure 3(a) gives the optimal distribution of the bending stiffness along the length of the plate. Parameters h_1 and h_2 represent the relative bending stiffness at the two edges, and both of them are equal to 0.01 in this case. As expected, the two ends of the plate are much softer than the portion in the middle and the additional restriction due to the clamped boundary conditions is thus released. The length of the thick portion in the middle can be roughly characterized as $|\xi_2 - \xi_1|$, which is 0.615 in this case. Suppose the plate material is homogeneous. Such a distribution can be realized approximately by making the thickness of the plate into the shape of $\sqrt[3]{d(x)}$. Figure 3(b) shows the overall TL using a logarithmic scale. The stopband begins from $f_1=0.0343$ and ends at $f_2=0.2063$, the bandwidth being $f_2/f_1=6.02$. Four peaks can be observed in the stopband. Figure 3(c) shows the maximum bandwidth as a function of h_1 and h_2 . Here, values of other parameters given in Eq. (31) are used. A softer end can help reduce the restriction due to the clamp condition. However, it does not follow that the softer the two ends are, the better the performance is. As shown in Fig. 3(c), when $h_1, h_2=0.01$, the bandwidth reaches the maximum of 6.02. Further decrease in h_1 and h_2 does not make any noticeable improvement of the bandwidth. Figure 3(d) shows the bandwidth f_2/f_1 as a function of the length of the thick portion, $|\xi_2 - \xi_1|$, while other parameters are kept as the optimal values given in Eq. (31). As $|\xi_2 - \xi_1|$ decreases from the optimal point, the performance drops and approaches the behavior of a uniform plate.

Figure 4 compares the vibration velocity distribution $V(x)$ between the clamped nonuniform plate (solid lines) and a simply supported plate (dashed lines) at $f=0.037$ (the first peak) and $f=0.2$ (near the fourth peak). The real parts are shown in Figs. 4(a) and 4(b). Since the plate vibrations are almost in-phase over the entire length, the imaginary parts of $V(x)$ shown in Figs. 4(c) and 4(d) are almost zero. As expected, the clamped plate with softer ends responds in a similar way to the simply supported plate, but the peaks and troughs are much closer to the clamped ends. The effect of this difference is as follows. The plate vibration is dominated by a mode shape that is close to a dipolelike pattern of sound radiation. Much of the sound radiated by the leading edge portion of the plate with $V(x) > 0$, cf. Fig. 4(a), is cancelled

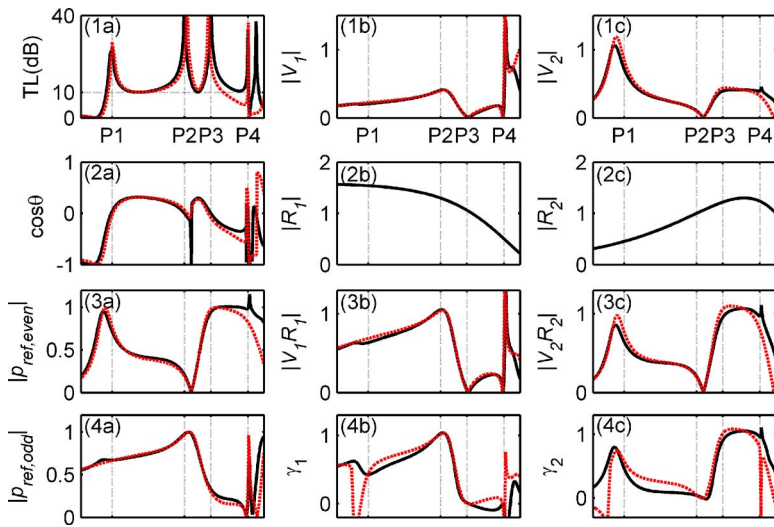


FIG. 5. (Color online) Comparison of the clamped non-uniform plate with the simply supported uniform plate (solid lines: nonuniform plate; dashed lines: simply supported). The cavity geometry is $L=5h$, $h_c=h$, and the average mass ratio $\bar{m}=1$. (1a) TL. (2a) Odd-even modal interference index. (3a) Sound reflected by the even modes. (4a) Sound reflected by the odd modes. The second and third columns compare the modal amplitude, $|V_j|$, the modal reflection coefficient, $|R_j|$, the single mode reflection, $|V_j R_j|$, and the modal contribution γ_j of the two plate silencers. The four peak positions are identified in all the subfigures.

by that from the trailing edge portion where $V(x) < 0$. When $f \rightarrow 0$, this cancellation would be rather complete since the plate length is negligible compared with the wavelength of sound in air. The length between the peaks and troughs in Figs. 4(a) and 4(b) thus determines the radiation efficiency of the plate for a finite frequency. In other words, a clamped plate with much of the length behaving like a rigid plate has a higher capability to reflect sound, in a dipolelike mode that is not prohibited by the cavity stiffness.

The performance of the nonuniform clamped plate silencer with that of the simply supported plate is compared and shown in Fig. 5. The cavity geometry and the mass ratio of the two silencers are the same, namely, $L=5$, $h_c=1$, and $\bar{m}=1$. The optimal bending stiffness B_{opt} of the simply supported plate is 0.129 (Huang, 2006). The results for the nonuniform plate silencer are shown in solid lines and those of the simply supported plate silencer in dashed lines. The first column compares the TL spectrum, odd-even modal interference index, and reflection sound due to odd and even modes. P1 through P4 identify the four peak positions. As shown in Fig. 5(1a), the performance of the clamped nonuniform plate silencer can be even better than that of the model using simply supported uniform plates. The difference mainly comes from the relatively high frequency region, namely, from P3 to P4. From P1 to P3, the reflection sound and odd-even modal interference index of the two silencers are almost identical, which results in a similar TL for the two silencers. The second and third columns compare the modal amplitude, $|V_j|$, modal reflection coefficient, $|R_j|$, the single mode reflection, $|V_j R_j|$, and the modal contribution, γ_j , of the first two modes. Here, R_j is the complex amplitude of the reflected sound by the induced vibration of the j th mode with unit amplitude. To facilitate the comparison, the vibration mode of a simply supported plate, $\sin(j\pi\xi)$, is used for both silencers. Hence, the expression for R_j given in Huang (2002) still applies. The γ_j represents the contribution of each single mode, denoted as $V_j R_j$, towards the total reflected sound p_r . When a nonuniform plate is used, the local peaks of both γ_1 and γ_2 near the first peak point P1 are pushed to lower frequency, which results in a smaller lower bound f_1 . The high TL between the third peak point P3 and the upper bound f_2

are mainly due to the increased $|V_2|$, $|V_2 R_2|$ and γ_2 , as shown in Figs. 5(1c), 5(3c), and 5(4c). Therefore, compared with the uniform plate, a properly designed nonuniform plate can greatly enhance the performance of the clamped plate silencer.

IV. EXPERIMENTAL VALIDATION

The main objective of the experimental study is to validate the basic theoretical model established. The TL of a prototyped clamped plate silencer was measured and compared with the theoretical prediction. In doing so, a number of issues that might complicate the task are put aside at this stage. One of these issues is the modeling of the dynamics of a plate of nonuniform thickness and the actual preparation of such thickness distribution for a thin plate. The following experiment is therefore limited to the test of a uniform plate. The issue of structural damping is another difficult one, but it cannot be avoided altogether. An attempt is made to simulate the damping effect towards the end of this section.

A. Experimental rig

The TL of the plate silencer was measured by the four-microphone, two-load method similar to the one described by Munjal and Doige (1990), as shown in Fig. 6. The incident noise is simulated by a loudspeaker connected to the duct through a contraction cone. The output signal from the DA converter (NI. PCI-M10-16E-1) was passed to the loudspeaker via a power amplifier (B&K's LAB Gruppen 300). Two pairs of 1/2-in., phase-matched microphones (B&K type 4187), labelled as M1 through M4, were used together with conditioning amplifier (B&K Nexus 2691). The separation distances between the microphones and their exact locations are indicated in Fig. 6. Signals from the four microphones were acquired via the AD converter (NI. PCI-4452). Both A/D and D/A processes were controlled by an NI Labview program and the test was run by a loop of discrete frequencies from 40 to 800 Hz with an increment of 10 Hz. Two linearly independent experiments with different downstream loading conditions were conducted to determine the TL of the tested silencer. In the current study, the first downstream

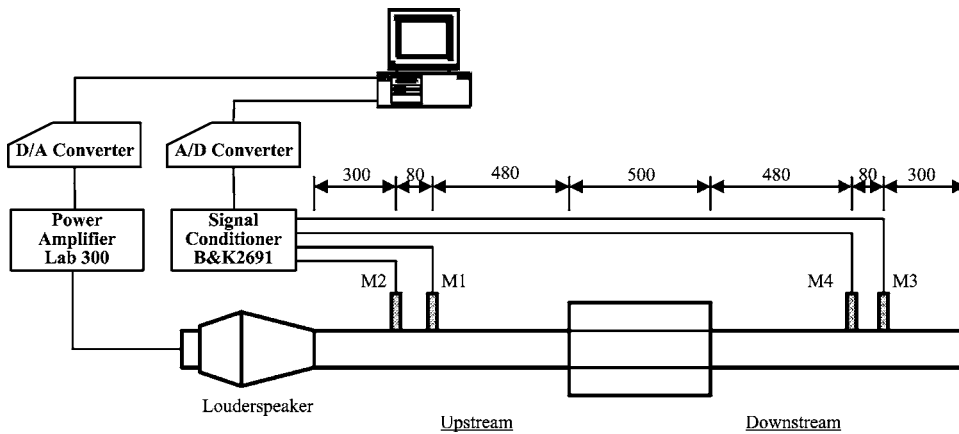


FIG. 6. The four-microphone, two-load measurement system (dimensions in mm).

boundary condition was a simple “rigid ending.” The other one was “absorption ending,” which was implemented by connecting the downstream end of the duct to an absorptive chamber.

The duct wall was made of 15-mm-thick acrylic and was considered to be acoustically rigid. The cross-section of the duct was $100 \times 100 \text{ mm}^2$. The two cavities also had a cross section of $100 \times 100 \text{ mm}^2$ and the length was 500 mm. With the geometry given, the first cut-on frequency in the rigid duct is about 1700 Hz, which is much higher than the upper limit of the measurement frequency range. Two pieces of balsawood plates were installed flush with the duct wall. The plates were 517 mm long, 102 mm wide, and 2 mm thick. The leading and trailing edges of the plates were clamped, and the final effective length of the plates was 500 mm. The two lateral edges of the plates were inserted into a thin gap between the two constituent plates of the cavity walls. The clearance between the lateral edges of the plates and the cavity walls was less than 0.5 mm. Such a configuration was adopted to make sure that the plates could vibrate freely and simulate the two-dimensional behavior of a beam while the leakage of noise from the main duct to the cavities via the gap was minimized.

The physical and mechanical properties of balsawood vary greatly depending on the origin and growth conditions. According to Chart 1 given in Ashby (2005), the density of balsawood ranges from 100 to 220 kg/m^3 , and the Young’s modulus from 2 to 5 GPa. Since the bending stiffness of the plate is one of the most crucial design factors, a three-point bending test was conducted to determine it experimentally. Figure 7(a) shows the schematic of the three-point bending test. The sample plate was of the size $90 \times 32 \times 2 \text{ mm}^3$, and the support span L was 50 mm. An axial static testing machine was used to apply the load gradually. The relationship between the applied load and the extension at the middle point of the plate is shown in Fig. 7(b). The response of the plate was rather linear as the extension increases from 0 to 1.5 mm. Hence, the measured data within this region were used to find the Young’s modulus. For a simply supported beam given in this test, the extension at the middle point and the applied load should satisfy the relationship

$$y = \frac{FL^3}{48EI}, \quad (32)$$

where y is the extension, F is the load applied, E is the Young’s modulus, and I is the second moment of inertia. According to Fig. 7(b), the Young’s modulus E can be estimated as 2.6 GPa. The measured density of the balsawood plate was 208 kg/m^3 . Therefore, the dimensionless bending stiffness and mass ratio of the plate in the silencer can be calculated by the scheme described in Eq. (2), and the final results are $B=0.0123$ and $m=3.4$.

Before measuring the TL of the plate silencer, the TL of the whole measurement system without the balsawood plates was first measured. This measurement serves two purposes. One is to calibrate the measurement system, and the other is to check the damping level of the duct and the cavity. The TL spectrum, the energy absorption coefficient α , and the energy reflection coefficient β were measured and compared with the theoretical predictions in Fig. 8. With the plate absent, the plate silencer became a rectangular expansion chamber. The theoretical results were obtained by assuming both the mass ratio and bending stiffness to be zero. Figure 8(a) indicates that the measured TL (the line with open circles) compares with the theoretical solution well on the whole, except

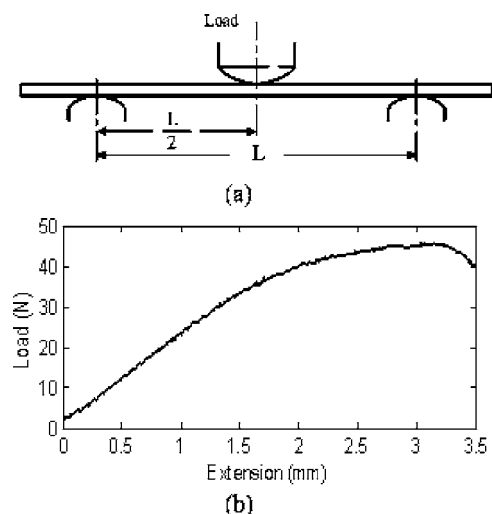


FIG. 7. Three-point bending test of the balsawood plate. (a) Schematic of the bending test. (b) Load versus extension at the middle point.

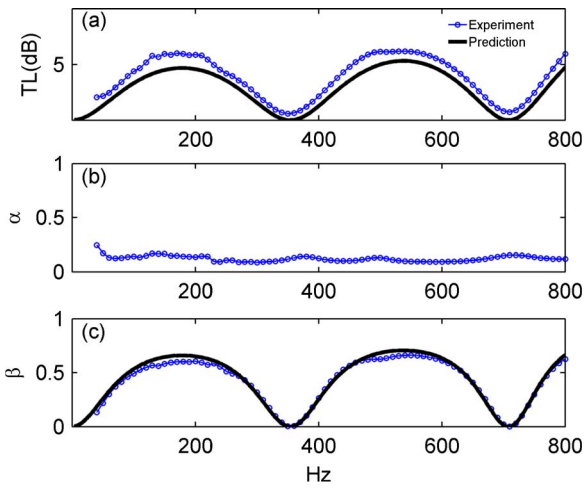


FIG. 8. (Color online) Comparison of the measured data (with open circles) with theoretical solution (without open circles) for the expansion chamber. (a) TL. (b) The absorption coefficient α . (c) The reflection coefficient β .

that the measured TL is 0.5 dB higher than the prediction. The discrepancy is mainly due to the energy dissipation mechanisms, which are necessarily present in the rig but excluded in the theory. As shown in Fig. 8(b), the overall energy absorption coefficient of the expansion chamber is around 0.1. The possible damping mechanism includes the cavity damping, wall vibration, etc.

B. Results analysis

The TL and the corresponding energy reflection coefficient β of the tested plate silencer were first calculated using the parameters found in the last section ($B=0.0123$, $m=3.4$). The predicted results are shown in Figs. 9(a) and 9(c) in solid curves. Since the damping effect was not considered in the theoretical model, the predicted absorption coefficient was zero. The frequency positions of the six predicted peaks in Fig. 9(a) are 54, 109, 224, 306, 415, and 727 Hz. Because the bending stiffness of the plate used is much smaller than the optimal one [see Fig. 2(c)], the TL between the first and

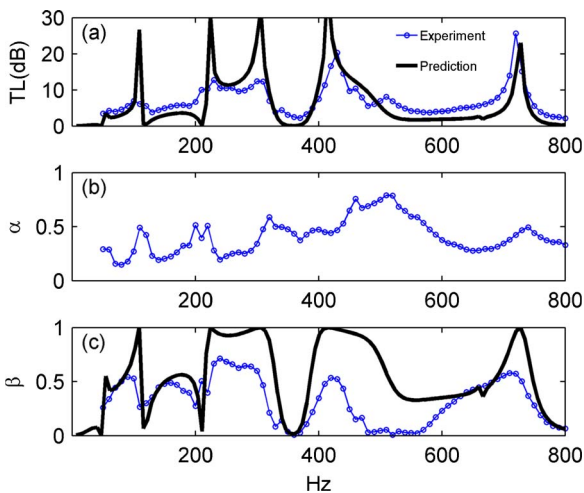


FIG. 9. (Color online) Comparison of experimental data (solid curves with open circles) with theoretical solution (solid curves without open circles). (a) TL. (b) The absorption coefficient α . (c) The reflection coefficient β . The dimensionless bending stiffness $B=0.0123$, the mass ratio $m=3.4$.

second peaks is low, and the widest stopband begins from 218 Hz and ends at 318 Hz, consisting of the third and fourth peaks, but it suffices to serve the objective of model validation. Note that the balsawood used here is relatively heavy and soft in the whole range of balsawood available. For better performance of the plate silencer, a lighter and stiffer balsawood may be used.

Figure 9(a) compares the measured TL (solid curves with open circles) with the predicted one. Evidently, the spectral peaks and the overall spectral shapes of the measured TL match those of the theoretical results. This means that the basic theoretical model is correct for the experimental rig. However, the predicted TL curve has sharp peaks while that from the experiment is quite smooth. This, again, implies significant energy dissipation mechanisms in the experimental rig, which are excluded in the theoretical model. As shown in Fig. 9(b), the measured absorption coefficient α ranges from 0.15 to 0.5 in the low frequency region (say, below 400 Hz) and from 0.3 to 0.8 in the relative high frequency region (above 400 Hz). Note that the sound absorption coefficient is only around 0.1 when the balsawood plates are absent. It is reasonable to assume that the main energy dissipation mechanism in the plate silencer is the structural damping in the plate. Figure 9(c) compares the energy reflection coefficient β . Obviously, the level of the measured reflection coefficient is lower than prediction. One explanation for this phenomenon is that the structural damping reduces the vibration level of the balsawood plates, which in turn results in a lower level of sound reflection. On the other hand, the existence of sound absorption also lowers the chances of the incident noise being reflected. Nevertheless, comparison between Figs. 9(b) and 9(c) shows that the mechanism of sound reflection still dominates over the sound absorption in the low frequency range. To summarize, the experimental results are in agreement with the theoretical prediction, but the damping effect, which is excluded previously, should be considered in the theoretical model to better represent the real physics behind the plate silencer.

The damping effect is now considered in the theoretical model by the Rayleigh damping model, and the coupled dynamics Eq. (3) becomes, for harmonic vibration of time dependence $e^{i\omega t}$,

$$\frac{\partial^2}{\partial x^2} \left(B(x) \frac{\partial^2 \eta}{\partial x^2} \right) (1 + i\sigma_s) + m(x) \frac{\partial^2 \eta}{\partial t^2} (1 - i\sigma_m) + (p_i + \Delta p) = 0, \quad (33)$$

where σ_s and σ_m are, respectively, the stiffness and mass damping coefficients. Two cases with different damping coefficients are investigated. In the first case, $\sigma_m=0.15$ and $\sigma_s=0$. The TL, absorption coefficient, and reflection coefficient are shown in Figs. 10(1a)–10(1c), respectively. It can be observed that the experimental data are in good agreement with the theoretical results when the frequency is below 360 Hz. However, the absorption coefficient is underestimated in high frequency. In the other case, the damping coefficients are chosen as $\sigma_m=\sigma_s=0.05$, and the results are shown in Figs. 10(2a)–10(2c). With such a combination of σ_m and σ_s , the measured TL, absorption

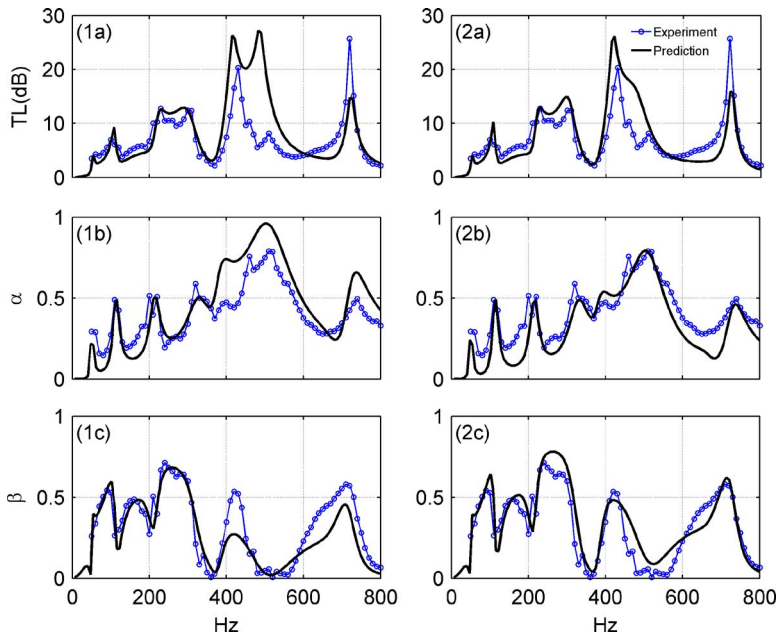


FIG. 10. (Color online) Modeling of plate damping mechanisms with two set of damping factors. (1a) and (1b), and (1c) show the results with $\sigma_m=0.15$, $\sigma_s=0$. (2a), (2b), and (2c) are the results with $\sigma_m=0.05$, $\sigma_s=0.05$.

coefficient, and reflection coefficient are all in agreement with the theoretical results on the whole. But in the frequency range of 240 to 300 Hz, the reflection coefficient is overestimated slightly. Since low frequency noise is of major interest in this study, the first damping model may be more suitable for design purposes.

V. CONCLUSIONS

It is easy to realize a side-branch plate silencer with the plate clamped at both the leading and trailing edges in practice. Theoretical study reveals that such a plate silencer can function effectively as a low frequency wave reflector over a broad frequency band. When uniform plates are used, a stopband above one octave can be achieved if the plate-to-air mass ratio is less than 3.5. The performance of the clamped plate silencer can be further enhanced by using plates with softer ends. Optimization study shows that, with a proper distribution of the bending stiffness along the plate, the widest stopband of the clamped plate silencer may be up to $f_2/f_1=6.0$ for a mass ratio of $m=1$, which is even wider than that of a simply supported plate silencer.

When excited by the incident wave, the clamped nonuniform plate responds in a similar way to the simply supported plate, but the displacement peaks and troughs are much closer to the clamped ends. The extended length between the peaks and troughs makes the nonuniform plate

more capable of reflecting sound in a dipolelike mode, which is not prohibited by the cavity. Comparison of the modal reflections between the clamped nonuniform plate and the simply supported plate shows that the second *in vacuo* plate mode contributes most to the expansion of the stopband of the nonuniform plate silencer, especially in the high frequency region, which, to some extent, conforms to the above explanation.

Experimental study demonstrated that the basic model of the clamped plate silencer is correct. The spectral peaks and the shapes of the measured TL are in agreement with those calculated theoretically. In the low frequency range, say, below 400 Hz, the sound reflection still dominates over the sound energy dissipation. Significant sound absorption exists in the plate silencer, especially at high frequencies. A Rayleigh damping model is adopted to represent the plate damping in the testing rig. Results show that with a proper combination of mass and stiffness damping coefficients, the simulated damping effect is in close agreement with the experimental data.

ACKNOWLEDGMENTS

The project is supported by a research grant from the Hong Kong SAR government (PolyU 5298/03E). The first two authors thank the Hong Kong Polytechnic University for the research studentships.

APPENDIX: RESULTS OF $I_{p,q}$, $I_{c_j,p}$, AND $I_{cl,q}$

When $j \neq l$, 9 out of the 16 components of $I_{p,q}$ ($I_{1,1} \sim I_{4,4}$) are given below:

$$I_{1,1} = \frac{2ik_n L(1 - e^{\beta_j + \beta_l})}{[\beta_j^2 + (k_n L)^2](\beta_j + \beta_l)} - \frac{e^{\beta_l - ik_n L} - 1}{(\beta_j + ik_n L)(\beta_l - ik_n L)} + \frac{e^{\beta_j + \beta_l} - e^{\beta_j - ik_n L}}{(\beta_j - ik_n L)(\beta_l + ik_n L)}, \quad (A1)$$

$$I_{1,3} = \frac{\beta_j(e^{\beta_l - ik_n L} - 1)}{(\beta_l - ik_n L)[\beta_j^2 - (k_n L)^2]} + \frac{2ik_n L[(\beta_l \sin \beta_j - \beta_j \cos \beta_l)e^{\beta_l} + \beta_j]}{(\beta_j^2 + \beta_l^2)[\beta_j^2 - (k_n L)^2]} - \frac{(e^{\beta_l} - e^{-ik_n L})(ik_n L \sin \beta_j + \beta_j \cos \beta_l)}{(\beta_l + ik_n L)[\beta_j^2 - (k_n L)^2]}, \quad (A2)$$

$$I_{1,4} = \frac{2ik_n L}{\beta_j^2 - (k_n L)^2} \left[\frac{(\beta_j \sin \beta_j + \beta_l \cos \beta_j) e^{\beta_l} - \beta_l - \frac{e^{\beta_l - ik_n L} - 1}{2(\beta_l - ik_n L)}}{\beta_j^2 + \beta_l^2} \right] + \frac{(e^{\beta_l} - e^{-ik_n L})(\beta_j \sin \beta_j - ik_n L \cos \beta_j)}{(\beta_l + ik_n L)[\beta_j^2 - (k_n L)^2]}, \quad (A3)$$

$$I_{3,1} = \frac{2ik_n L[(\beta_l \cos \beta_l - \beta_j \sin \beta_l) e^{\beta_j} - \beta_l]}{(\beta_j^2 + \beta_l^2)[\beta_j^2 + (k_n L)^2]} + \frac{(ik_n L \sin \beta_l - \beta_l \cos \beta_l) e^{\beta_j} + \beta_l e^{\beta_j - ik_n L}}{(\beta_j - ik_n L)[\beta_l^2 - (k_n L)^2]} - \frac{\beta_l - (ik_n L \sin \beta_l + \beta_l \cos \beta_l) e^{-ik_n L}}{(\beta_j + ik_n L)[\beta_l^2 - (k_n L)^2]}, \quad (A4)$$

$$I_{3,3} = \frac{\beta_j[\beta_l - (ik_n L \sin \beta_l + \beta_l \cos \beta_l) e^{-ik_n L}]}{[\beta_j^2 - (k_n L)^2][\beta_l^2 - (k_n L)^2]} + \frac{ik_n L}{\beta_j^2 - (k_n L)^2} \left[\frac{\sin(\beta_j - \beta_l)}{\beta_j - \beta_l} - \frac{\sin(\beta_j + \beta_l)}{\beta_j + \beta_l} \right] - \frac{(ik_n L \sin \beta_j + \beta_j \cos \beta_j)[(ik_n L \sin \beta_l - \beta_l \cos \beta_l) + \beta_l e^{-ik_n L}]}{[\beta_j^2 - (k_n L)^2][\beta_l^2 - (k_n L)^2]}, \quad (A5)$$

$$I_{3,4} = \frac{ik_n L[(ik_n L \sin \beta_l + \beta_l \cos \beta_l) e^{-ik_n L} - \beta_l]}{[\beta_j^2 - (k_n L)^2][\beta_l^2 - (k_n L)^2]} + \frac{ik_n L}{\beta_j^2 - (k_n L)^2} \left[\frac{1 - \cos(\beta_j + \beta_l)}{\beta_j + \beta_l} - \frac{1 - \cos(\beta_j - \beta_l)}{\beta_j - \beta_l} \right] + \frac{(\beta_j \sin \beta_j - ik_n L \cos \beta_j)[(ik_n L \sin \beta_l - \beta_l \cos \beta_l) + \beta_l e^{-ik_n L}]}{[\beta_j^2 - (k_n L)^2][\beta_l^2 - (k_n L)^2]}, \quad (A6)$$

$$I_{4,1} = \frac{(\beta_l \sin \beta_l + ik_n L \cos \beta_l) e^{\beta_j} - ik_n L e^{\beta_j - ik_n L}}{(\beta_j - ik_n L)[\beta_l^2 - (k_n L)^2]} - \frac{(\beta_l \sin \beta_l - ik_n L \cos \beta_l) e^{-ik_n L} + ik_n L}{(\beta_j + ik_n L)[\beta_l^2 - (k_n L)^2]} - \frac{2ik_n L}{\beta_j^2 + (k_n L)^2} \times \left[\frac{(\beta_l \sin \beta_l + \beta_j \cos \beta_l) e^{\beta_j} - \beta_j}{\beta_j^2 + \beta_l^2} \right], \quad (A7)$$

$$I_{4,3} = \frac{\beta_j[(\beta_l \sin \beta_l - ik_n L \cos \beta_l) e^{-ik_n L} + ik_n L]}{[\beta_j^2 - (k_n L)^2][\beta_l^2 - (k_n L)^2]} + \frac{ik_n L}{\beta_j^2 - (k_n L)^2} \left[\frac{1 - \cos(\beta_j + \beta_l)}{\beta_j + \beta_l} + \frac{1 - \cos(\beta_j - \beta_l)}{\beta_j - \beta_l} \right] - \frac{(ik_n L \sin \beta_j + \beta_j \cos \beta_j)[(\beta_l \sin \beta_l + ik_n L \cos \beta_l) - ik_n L e^{-ik_n L}]}{[\beta_j^2 - (k_n L)^2][\beta_l^2 - (k_n L)^2]}, \quad (A8)$$

$$I_{4,4} = \frac{(\beta_j \sin \beta_j - ik_n L \cos \beta_j)[(\beta_l \sin \beta_l + ik_n L \cos \beta_l) - ik_n L e^{-ik_n L}]}{[\beta_j^2 - (k_n L)^2][\beta_l^2 - (k_n L)^2]} + \frac{ik_n L}{\beta_j^2 - (k_n L)^2} \left[\frac{\sin(\beta_j + \beta_l)}{\beta_j + \beta_l} + \frac{\sin(\beta_j - \beta_l)}{\beta_j - \beta_l} \right] - \frac{ik_n L[(\beta_l \sin \beta_l - ik_n L \cos \beta_l) e^{-ik_n L} + ik_n L]}{[\beta_j^2 - (k_n L)^2][\beta_l^2 - (k_n L)^2]}. \quad (A9)$$

The remaining seven components are determined based on the above results. $I_{1,2}$ is obtained by replacing β_j with $(-\beta_j)$ in Eq. (A1); $I_{2,1}$ is obtained by replacing β_l with $(-\beta_l)$ in Eq. (A1); $I_{2,2}$ is obtained by replacing β_j and β_l with $(-\beta_j)$ and $(-\beta_l)$, respectively, in Eq. (A1); $I_{2,3}$ is obtained by replacing β_l with $(-\beta_l)$ in Eq. (A2); $I_{2,4}$ is obtained by replacing β_l with $(-\beta_l)$ in Eq. (A3); $I_{3,2}$ is obtained by replacing β_j with $(-\beta_j)$ in Eq. (A4); and $I_{4,2}$ is obtained by replacing β_j with $(-\beta_j)$ in Eq. (A7). When $j=l$, four items in Eqs. (A1)–(A9) become 0/0 type and should be replaced by the finite values given below:

$$\frac{1 - e^{\beta_l - \beta_j}}{\beta_j - \beta_l} = 1, \quad \frac{e^{\beta_j - \beta_l} - 1}{\beta_j - \beta_l} = 1, \quad (A10)$$

$$\frac{\sin(\beta_j - \beta_l)}{\beta_j - \beta_l} = 1, \quad \frac{1 - \cos(\beta_j - \beta_l)}{\beta_j - \beta_l} = 0.$$

Note that for frequency below the first cut-on of the duct, only the plane wave mode, $n=0$, has real wave number k_0 , and there are chances that $k_0 L \rightarrow \beta_j$ and/or β_l . In such case, some items in Eqs. (A1)–(A9) will also become 0/0 type. This problem can be avoided numerically easily, hence, it is not addressed here.

The $I_{c_j,p}$, and $I_{c_l,q}$ (p, q from 1 to 4) are given below:

$$I_{c_j,1} = \frac{\beta_j[\cos(m\pi)e^{\beta_j} - 1]}{\beta_j^2 + (m\pi)^2}, \quad I_{c_j,2} = \frac{\beta_j[1 - \cos(m\pi)e^{-\beta_j}]}{\beta_j^2 + (m\pi)^2},$$

$$I_{c_j,3} = \frac{\beta_j[1 - \cos(\beta_j + m\pi)]}{\beta_j^2 - (m\pi)^2}, \quad I_{c_j,4} = \frac{\beta_j \sin(\beta_j + m\pi)}{\beta_j^2 - (m\pi)^2},$$

$$I_{c_l,1} = \frac{\beta_l[\cos(m\pi)e^{\beta_l} - 1]}{\beta_l^2 + (m\pi)^2}, \quad I_{c_l,2} = \frac{\beta_l[1 - \cos(m\pi)e^{-\beta_l}]}{\beta_l^2 + (m\pi)^2},$$

$$I_{cl,3} = \frac{\beta_l [1 - \cos(\beta_l + m\pi)]}{\beta_l^2 - (m\pi)^2}, \quad I_{cl,4} = \frac{\beta_l \sin(\beta_l + m\pi)}{\beta_l^2 - (m\pi)^2}. \quad (\text{A11})$$

- Ashby, M. F. (2005). *Material Selection in Mechanical Design*, 3rd ed. (Butterworth Heinemann, Oxford).
- Brown, S. (1964). "Acoustic design of broadcasting studios," *J. Sound Vib.* **1**, 239–257.
- Choy, Y. S., and Huang, L. (2002). "Experimental studies of a drumlike silencer," *J. Acoust. Soc. Am.* **112**, 2026–2035.
- Choy, Y. S., and Huang, L. (2005). "Effect of flow on the drumlike silencer," *J. Acoust. Soc. Am.* **118**, 3077–3085.
- Doak, P. E. (1973). "Excitation, transmission and radiation of sound from source distributions in hard-walled ducts of finite length. I. The effects of duct cross-section geometry and source distribution space-time pattern," *J. Sound Vib.* **31**, 1–72.
- Fernyhough, M., and Evans, D. V. (1996). "Comparison of a step approximation to an exact solution of acoustic scattering in a uniform-width pipe with non-uniform wall impedance," *Q. J. Mech. Appl. Math.* **49**, 419–437.
- Ford, R. D., and McCormick, M. A. (1969). "Panel sound absorbers," *J. Sound Vib.* **10**, 411–423.
- Frommhold, W., Fuchs, H. V., and Sheng, S. (1994). "Acoustic performance of membrane absorbers," *J. Sound Vib.* **170**, 621–636.
- Grant, A. D., and Lawrie, J. B. (2000). "Propagation of fluid-loaded structural waves along a duct with smoothly varying bending characteristics," *Q. J. Mech. Appl. Math.* **53**, 299–321.
- Horoshenkov, K. V., and Sakagami, K. (2001). "A method to calculate the acoustic response of a thin, baffled, simply supported poroelastic plate," *J. Acoust. Soc. Am.* **110**, 904–917.
- Huang, L. (2001). "A theoretical study of passive control of duct noise using panels of varying compliance," *J. Acoust. Soc. Am.* **109**, 2805–2814.
- Huang, L. (2002). "Modal analysis of a drumlike silencer," *J. Acoust. Soc. Am.* **112**, 2014–2025.
- Huang, L. (2004). "Parametric studies of a drumlike silencer," *J. Sound Vib.* **269**, 467–488.
- Huang, L. (2006). "Broadband sound reflection by plates covering side-branch cavities in a duct," *J. Acoust. Soc. Am.* **119**, 2628–2638.
- Ingard, K. U. (1994). "Notes on the sound absorption technology," Noise Control Foundation, Poughkeepsie, NY.
- Inman, D. J. (2001). *Engineering Vibration* (Prentice Hall, Englewood Cliffs, N.J.).
- Kuttruff, H. (2000). *Room Acoustics* (E & FN Spon, New York).
- Mechel, F. P., and VÉR, I. L. (1992). *Noise and Vibration Control Engineering: Principles and Applications*, edited by L. L. Beranek and I. L. VÉR (Wiley, New York), Chap. 8.
- Munjal, M. L., and Doige, A. G. (1990). "Theory of a two source-location method for direct experimental evaluation of the four-pole parameters of an aeroacoustic element," *J. Sound Vib.* **141**, 323–333.
- Sakagami, K., Kiyama, M., Morimoto, M., and Takahashi, D. (1996). "Sound absorption of a cavity-backed membrane: A step towards design method for membrane-type absorber," *Appl. Acoust.* **49**, 237–247.

Comparison of two modeling approaches for highly heterogeneous porous media

Giulio Pispola^{a)}

Department of Industrial Engineering, University of Perugia, via G. Duranti 67, 06125 Perugia, Italy

Kirill V. Horoshenkov^{b)} and Amir Khan

School of Engineering, Design and Technology, University of Bradford, Bradford BD7 1DP, United Kingdom

(Received 18 May 2006; revised 23 November 2006; accepted 24 November 2006)

The purpose of this paper is to study the acoustic behavior of highly heterogeneous, low density porous structures having a complex pore size distribution using two distinct theoretical approaches. The first approach requires the direct numerical integration of the Biot viscosity correction function. The main requirement here is a knowledge of the probability density function of the pore size, which can be achieved by an optical pore-counting technique. The fact that the observed pore size distribution in these materials could be distinctively split into two parts suggested the use of the second approach based upon the double-porosity theory by Olny and Boutin [J. Acoust. Soc. Am. **114**(1), 73–89 (2003)]. The latter approach assumes a low permeability contrast between the two porous scales so that the acoustic properties could be estimated using the semi-phenomenological models of Johnson and Lafarge for the viscous and thermal dynamic permeabilities. Numerical results predicted by the two models are then compared with impedance tube experimental data showing good accuracy of the selected prediction methods. © 2007 Acoustical Society of America. [DOI: 10.1121/1.2427114]

PACS number(s): 4355Ev, 4320Bi, 4320Jr [KA]

Pages: 961–966

I. INTRODUCTION

There is an increasing demand for acoustic materials that are sustainable from environmental and economic points of view. This is the “driving force” for the development of new poroelastic materials from industrial and domestic polymeric waste. Traditional solutions based on virgin materials can be replaced with alternative sustainable products that offer equivalent or superior acoustic performance. The success of this work depends heavily on our understanding of acoustic wave propagation in heterogeneous porous media and on the availability of accurate prediction tools for engineering optimization.

Considerable heterogeneity frequently occurs in porous media manufactured by consolidating particles with widely different geometries and dimensions. In the present study, this is achieved through an optimization of the process parameters of a cold extrusion manufacturing method developed by Khan *et al.*¹ An analysis of the experimental data suggests that the observed high acoustic absorption performance of these products is largely attributable to their highly heterogeneous structure¹ with a broad, complex pore size distribution. Although analytical approximations are available for predicting the acoustical properties of porous materials with a log-normal pore size distribution,² the pore size distributions in the materials of interest are far from log-normal. Two distinct approaches were chosen to deal with this problem. The first, which will be called the arbitrary

pore size distribution (APSD) method, is based on the numerical integration of the viscosity correction function for known pore size distribution data.³ We use the term “arbitrary pore size distribution” to denote a pore size distribution that cannot be described by a simple analytical function. The second approach, called the double porosity (DP) model, is based on the fact that the observed pore size distributions can be split into two distinct regions, one around 10^{-4} m (the so-called “microscale”) and the other around 10^{-3} m (the so-called “mesoscale”), suggesting that wave propagation could be analogous to that observed in a double porosity medium with low permeability contrast.⁴ Finally, the predictions by these two models are validated against the experimental data measured using the standard standing wave apparatus.⁵

II. HIGHLY HETEROGENEOUS EXTRUDED MATERIALS

A controlled cold extrusion process was employed to manufacture the samples. A thorough description of the process has been provided by Khan *et al.*¹ The technique, widely used in polymer production, was tailored to mix polymer grains and fibers, reclaimed from textile waste, with a binder and water in controlled proportions. The fiber/grain mass content was kept constant for all the samples (60% of grains, 40% of fibers) without the loss in the acoustic absorption performance. A diphenylmethane diisocyanate (MDI) binder was chosen to create bonds between the granular and fibrous parts and, at the same time, react with water producing carbon dioxide. The structure of the bonded grains and fibers may be considered responsible for the lower pore sizes, while the CO₂ bubble coarsening accounts for the big-

^{a)}Electronic mail: pispola.unipg@ciriaf.it

^{b)}Electronic mail: k.horoshenkov@bradford.ac.uk

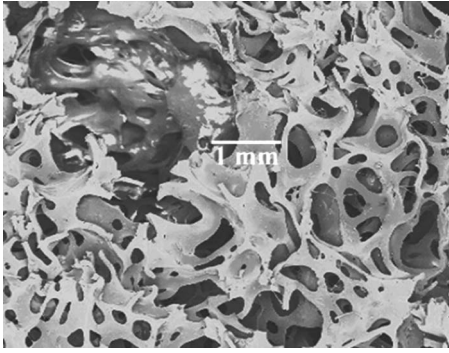


FIG. 1. Micrograph of material ES02 (see Table I).

ger pores (see Fig. 1). It was observed that an increase of the water/binder ratio gave rise to a wider pore size distribution and raised the probability density of the larger pores.

After an appropriate curing time, the samples were optically analyzed through a microscope employing a “pore-counting” technique in order to estimate their porosities and probability density functions (PDFs) of pore size¹ (see Fig. 2). Three materials were manufactured with different water/binder ratios. Five images per each material were analyzed by fitting circles to each pore to determine its size: the “effective radius” of the pore is that of a circle with an area equivalent to the actual area of the pore. The nonacoustical macroscopic parameters, the flow resistivity, porosity, and tortuosity, were estimated with standard testing methods⁶ and their values are summarized in Table I. Specifically, the method of the ultrasonic time of flight was adopted to determine the tortuosity. Finally, the characteristic impedance and complex wave number were measured using a four-microphone impedance tube (diameter 29 mm, overall length from source to acoustic termination 950 mm) and the transfer-matrix method proposed by Song *et al.*⁵ in the frequency range of 200–6400 Hz.

III. MODELING MEDIA WITH COMPLEX PORE SIZE DISTRIBUTION

A. Arbitrary pore size distribution approach

The viscosity correction function, originally introduced by Biot,⁷ is the ratio of the average viscous friction force on the capillary walls per unit bulk volume to the average seepage velocity per unit bulk cross-sectional area and measures the deviation from the Poiseuille flow friction. For a porous material modeled as a stack of circular cylindrical pores of radius s with probability density function $e(s)$, the viscosity correction function F is given by the following expression²

$$F(\omega) = \frac{1}{4} \frac{\int_0^\infty \kappa T(\kappa) e(s) ds}{\int_0^\infty [1 - 2\kappa^{-1} T(\kappa)] e(s) ds}, \quad T(\kappa) = \frac{I_1(\kappa)}{I_0(\kappa)}, \quad (1)$$

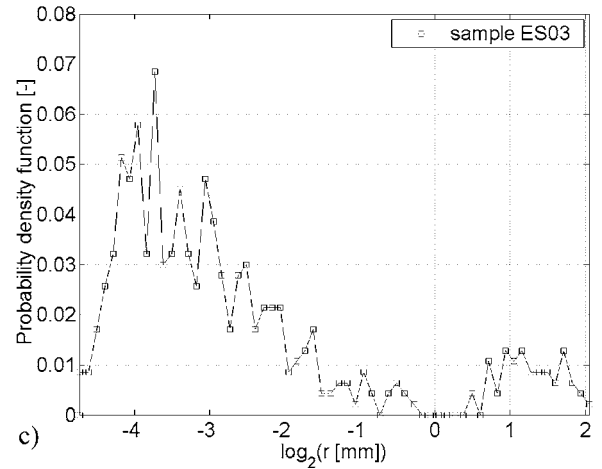
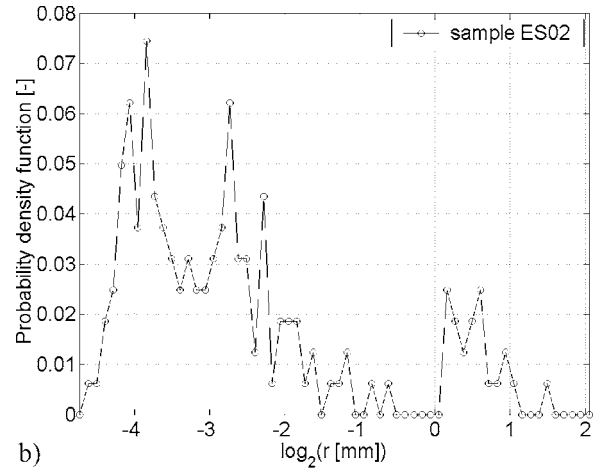
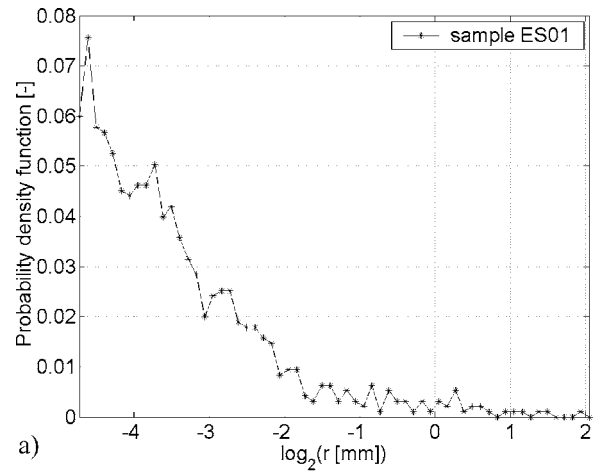


FIG. 2. Probability density functions of the pore size: (a) sample ES01, (b) sample ES02, and (c) sample ES03.

$$\kappa = s \sqrt{\frac{\omega \rho_0}{\eta}},$$

where I_1 and I_0 are the modified Bessel functions (of the first kind) of the first- and zeroth-order, respectively, ρ_0 is the equilibrium density of air, and η the dynamic viscosity of air. The sign convention $e^{-j\omega t}$ has here been adopted, ω being the angular frequency. The estimation of the viscosity correction function through a direct numerical integration approach only requires data on the probability density function of the

TABLE I. Nonacoustical properties of the tested samples.

Sample (designation)	ES01	ES02	ES03
Flow resistivity, σ_{db} (Pa s m ⁻²)	6500	4000	1300
Open porosity, Ω_{db}	0.81	0.81	0.80
Tortuosity, q_{db}	1.58	1.73	1.26
Bulk density (kg m ⁻³)	124	96	82
Plate thickness, d (m)	0.0425	0.038	0.036
Flow resistivity of the microscale, σ_m (Pa s m ⁻²)	25000	25000	20000
Open porosity of the microscale, Ω_m , within the pore size range $\{s_{\min}, s_{\max}\}$ (mm)	0.70 {0.04, 1.64}	0.23 {0.04, 0.65}	0.14 {0.04, 0.82}
Open porosity of the mesoscale, Ω_p , within the pore size range $\{s_{\min}, s_{\max}\}$ (mm)	0.36 {1.91, 3.83}	0.75 {1.12, 2.82}	0.77 {1.41, 4.14}

pore size distribution.³ The complex dynamic density ρ_b and complex dynamic compressibility C_b are then computed by the following relations, provided that the porosity, Ω , flow resistivity, σ , and tortuosity, $q^2 = \alpha_\infty$, of the material are known:

$$\rho_b(\omega) = \frac{q^2}{\Omega} \left(\rho_0 - \frac{\Omega \sigma}{j \omega q^2} F(\omega) \right), \quad (2)$$

$$C_b(\omega) = \frac{\Omega}{\gamma P_0} \left(\gamma - \frac{\gamma - 1}{[1 - (\Omega \sigma / j \omega q^2 \rho_0 \text{Pr})] F(\omega \text{Pr})} \right), \quad (3)$$

where γ is the ratio of specific heats, P_0 is the ambient atmospheric pressure, and Pr is the Prandtl number. Finally, the dynamic density and the complex compressibility can be used to compute the normalized characteristic impedance z_c , the complex wave number k_c , and the normalized surface impedance z_s for a hard-backed sample of thickness d :

$$z_c = \frac{1}{\rho_0 c} \sqrt{\frac{\rho_b}{C_b}}, \quad (4)$$

$$k_c = \omega \sqrt{\rho_b C_b}, \quad (5)$$

$$z_s = z_c \coth(-jk_c d), \quad (6)$$

where c is the sound speed in air.

B. Double porosity approach

The general double porosity theory developed by Olny and Boutin⁴ can be employed to model the acoustic behavior of materials with two distinct pore scales: meso-porous scale, l_p , and micro-porous scale, l_m . We adopt the subscripts p , m , db to denote the quantities related to meso-pores, micro-pores, and the multi-scale medium, respectively.

The following assumptions were made in order to facilitate this approach;

- (a) There is low permeability contrast,⁴ i.e., there is a low ratio (l_p/l_m) between the characteristic dimensions of the meso- and micro-porous parts of the medium;
- (b) Macroscopic nonacoustical quantities can be used to characterize the micro- and meso-porous parts.

From a close examination of the optical analysis PDF data¹ for the pore size distribution in materials ES02 and ES03 (see Fig. 2), it can be argued that there is a middle region of pore sizes for which the value of the PDF is relatively small, i.e., the region between 0.5 and 1 mm for sample ES02 and the region between 1 and 1.5 mm for sample ES03. This region was then considered as the separating limit between the micro- and meso-pores so that the ratio between the characteristic dimensions of the meso- and micro-porous parts was set to $l_p/l_m \approx 10$. In this case assumption (a) is fully valid. It was not possible to clearly discriminate the pore size limits for sample ES01 [see Fig. 2(a)]. However, by comparison with the other two materials, this porous structure can be considered as a limiting case with a very low proportion of meso-pores.

PDF data can, in principle, be used to determine the macroscopic values of the porosity, tortuosity, and flow resistivity. According to the expressions presented in the work by Olny and Boutin,⁴ the porosities can be computed by the aforementioned optical technique by which the overall areas attributed to the micro- and the meso-pores can be discriminated. Denoting the areas of sample occupied by micro- and meso-pores A_{fm} and A_{fp} , respectively, and employing Eq. (14) in Ref. 4 we obtain

$$\Omega_{db} = \Omega_p + \Omega_m(1 - \Omega_p) = \frac{A_{fp}}{A} + \left(1 - \frac{A_{fp}}{A} \right) \frac{A_{fm}}{(A - A_{fp})}, \quad (7)$$

where A is the total area of the sample surface.

In determining the flow resistivity σ , it is possible to consider the micro- and meso-pores as tubes acting in parallel.⁴ Therefore, according to Eq. (84) in Ref. 4,

$$\frac{1}{\sigma_{db}} = \left[\frac{(1 - \Omega_p)}{\sigma_m} + \frac{1}{\sigma_p} \right]. \quad (8)$$

A rough estimation of the flow resistivity of the micro-porous media could be obtained from the following [see exp. (3.61) in Ref. 8]:

$$\sigma_m = \frac{8\eta q_m^2}{\langle s_m \rangle^2 \Omega_m}, \quad \langle s_m \rangle^2 \equiv \int_{s_{\min}}^{s_{\max}} s_m^2 e(s_m) ds, \quad (9)$$

where $\langle s_m \rangle$ is the mean micro-pore size calculated from the PDF of the micro-pores within the effective pore size range, $\{s_{\min}, s_{\max}\}$.

In the case of materials with a structure similar to that shown in Fig. 1 it is difficult to determine the separate values of the tortuosity in the mixed meso- and micro-pores. As a first approximation, the tortuosity can be considered to be equal at the scales of both the meso- and micro-pores. Such an assumption is justified by assuming that both the micro- and meso-pores are the consequence of the same process of gas release, bubble formation, and collapse.

The semi-phenomenological models of Johnson *et al.*⁹ and Lafarge *et al.*¹⁰ were adopted to estimate the viscous and thermal dynamic permeabilities, Π and Θ , respectively, i.e.,

$$\Pi_i(\omega) = \Pi_i(0) \left(\left(1 - j \frac{M_i}{2} \frac{\omega}{\omega_{v,i}} \right)^{1/2} - j \frac{\omega}{\omega_{v,i}} \right)^{-1}, \quad (10)$$

$$\omega_{v,i} = \frac{\eta \Omega_i}{\rho_0 q_i^2 \Pi_i(0)} \quad (i = m, p),$$

$$\Theta_i(\omega) = \Theta_i(0) \left(\left(1 - j \frac{M'_i}{2} \frac{\omega}{\omega_{t,i}} \right)^{1/2} - j \frac{\omega}{\omega_{t,i}} \right)^{-1}, \quad (11)$$

$$\Theta_i(0) = \frac{\chi q_i^2 \Pi_i(0)}{C_p \eta} \quad (i = m, p),$$

where χ is the thermal conductivity of air, C_p is the specific heat of air at constant pressure, and $\Pi_i(0)$ and $\Theta_i(0)$ are the viscous and thermal static permeabilities, respectively. As a first approximation, it was assumed that the thermal characteristic frequencies $\omega_{t,i}$ matched their viscous counterparts $\omega_{v,i}$ and that the dimensionless shape factors M and M' were unity in order to avoid the ambiguity in defining the thermal static permeability. The complex dynamic density, ρ_{db} , and complex dynamic compressibility, C_{db} , of the double porosity medium were then computed through the expression suggested by Olny and Boutin [see Eqs. (85) and (80) in Ref. 4]:

$$\rho_{db}(\omega) = j \frac{\eta}{\omega} ((1 - \Omega_p) \Pi_m(\omega) + \Pi_p(\omega))^{-1}, \quad (12)$$

$$K_i(\omega) = \frac{\gamma P_0}{\Omega_i} \left(\gamma + j(\gamma - 1) \frac{\Theta_i(\omega)}{\delta_i^2 \Omega_i} \right)^{-1}, \quad (13)$$

$$\delta_i^2 = \frac{\chi}{\rho_0 C_p \omega} \quad (i = m, p),$$

$$C_{db}(\omega) = \left(\frac{(1 - \Omega_p)}{K_m(\omega)} + \frac{1}{K_p(\omega)} \right), \quad (14)$$

where δ_i is the thermal skin depth. Characteristic and surface impedances, together with the complex wave number, can then be calculated using Eqs. (4)–(6).

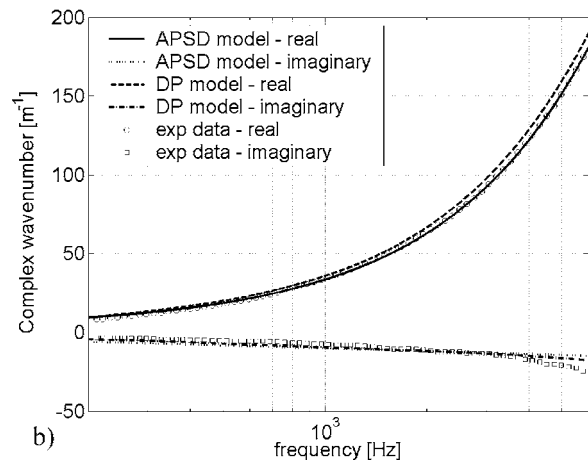
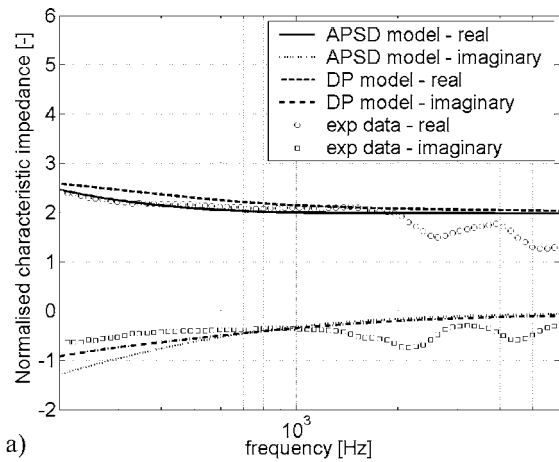


FIG. 3. Comparison between the experimental data (four-microphone impedance tube) and the theoretical predictions (APSD and DP models) for sample ES01: (a) normalized characteristic impedance and (b) complex wave number.

IV. RESULTS

In Figs. 3–5, comparisons between experimental data and theoretical predictions are reported for the three tested samples in terms of the characteristic impedance and complex wave number. These properties are fundamental and, if accurately modeled by the adopted methods, can be used to predict the absorption coefficient of a material layer of any arbitrary thickness and with any boundary conditions at the back.

The data presented in Figs. 3–5 show that some discrepancies between the experimental and the predicted values of the characteristic impedance are noticeable in the high frequency range. This could be attributed to the rather limited ratio between the wavelength and the characteristic size of the heterogeneities at the higher frequencies and to the circumferential gap effect.¹¹ The pore size ranges, $\{s_{\min}, s_{\max}\}$, in which the nonacoustic parameters were determined for meso- and micro-pores in materials ES01–ES03 are listed in Table I. It must be noticed that the choice of such ranges for samples ES02 and ES03 was essentially qualitative, determining a sensible boundary from the observed PDFs, which ensured a proper scale separation. It is evident that the approaches used have similar predictive capabilities despite the somewhat arbitrary method used by the authors to estimate

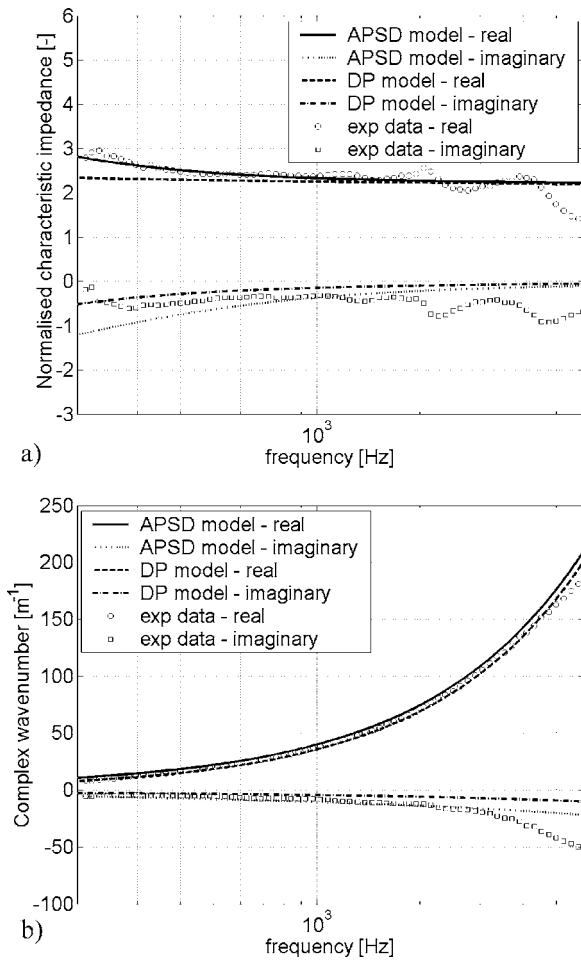


FIG. 4. Comparison between the experimental data (four-microphone impedance tube) and the theoretical predictions (APSD and DP models) for sample ES02: (a) normalized characteristic impedance and (b) complex wave number.

the nonacoustical properties of the microscale for the DP model. The results demonstrate that highly heterogeneous materials with low permeability contrast ($l_p/l_m \approx 10$) can be modeled reliably using either of the two models. Specifically, the Olny-Boutin approach⁴ can be based upon the viscous characteristic frequency formulation proposed by Johnson *et al.*⁹ In this case, full coupling between the oscillatory flows in the pores of the two different scales is assumed. This degree of coupling can be described using either expressions (80) and (85) in Ref. 4 or the APSD model based on the pore size distribution data.³ Neither of these two models relies upon the characteristic length data, which can be difficult or impossible to estimate and relate to the specific microstructural pore geometry.

V. CONCLUSIONS

Two distinct methodologies were applied for modeling materials with a broad, complex pore size distribution, which were manufactured through a recently developed mixing and binding process (cold extrusion) of polymer grains and fibers. Both the methods produce accurate predictions of the acoustic behavior while being suitable for different purposes. The arbitrary pore size distribution technique requires a

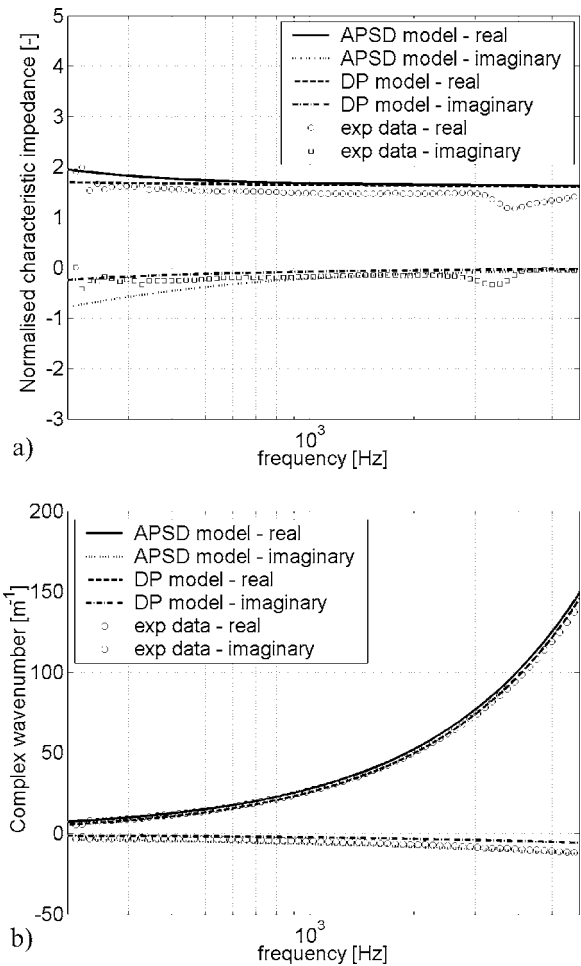


FIG. 5. Comparison between the experimental data (four-microphone impedance tube) and the theoretical predictions (APSD and DP models) for sample ES03: (a) normalized characteristic impedance and (b) complex wave number.

knowledge of the pore size probability density function, which is determined objectively using an optical pore-counting technique. Thus, this approach may be appropriate for a detailed material optimization in which a unique link between the material microstructure and the resultant acoustic performance can be established. On the other hand, a semi-phenomenological approach requiring only macroscopic quantities, such as pore permeabilities, could be more easily correlated to the manufacturing process parameters, but may not provide a unique link between the observed acoustic performance and the actual material microstructure (i.e. see Fig. 16 of Ref. 12). The scale separation observed in the pores of the tested samples ($l_p/l_m \approx 10$) means that it is possible to describe the wave propagation in terms of that occurring in a double porosity medium. Apart from the measured nonacoustical properties of the multi-scale medium, the double porosity model requires an estimation of the properties of either the micro- or meso-porosity. The estimation of these quantities was achieved in this case from the pore size distribution. Further work is needed to relate more rigorously the pore size distribution data and the fundamental nonacoustic characteristics of micro- and meso-pores.

- ¹A. Khan, K. V. Horoshenkov, and H. Benkreira, "Controlled extrusion of porous media for acoustic applications," on the CD-ROM: Lyon, December 7–9 2005, *Symposium on the Acoustics of Poro-Elastic Media (SAPEM 2005)*, available from Laboratoire des Sciences de l'Habitat, ENTPE (Ecole Nationale des Travaux Publics de l'Etat), 2 rue Maurice Audin, 69518 Vaulx-en-Velin Cedex, France.
- ²K. V. Horoshenkov, K. Attenborough, and S. N. Chandler-Wilde, "Padé approximants for the acoustical properties of rigid framed porous media with pore size distributions," *J. Acoust. Soc. Am.* **104**(3), 1198–1209 (1998).
- ³K. V. Horoshenkov, I. Rushforth, and M. J. Swift, "Acoustic Properties of Granular Materials with Complex Pore Size Distribution," on the CD-ROM: Kyoto, April 4–9 2004, *The 18th Int. Congress on Acoustics (ICA 2004)*, available from The Acoustical Society of Japan, Vol. **II**, pp. 1211–1214.
- ⁴X. Olny and C. Boutin, "Acoustic wave propagation in double porosity media," *J. Acoust. Soc. Am.* **114**(1), 73–89 (2003).
- ⁵B. H. Song and J. S. Bolton, "A transfer-matrix approach for estimating the characteristic impedance and wave numbers of limp and rigid porous materials," *J. Acoust. Soc. Am.* **107**(3), 1131–1152 (2000).
- ⁶K. V. Horoshenkov, "Characterisation of acoustic porous materials—Tyndall Medal paper," on the CD-ROM: Southampton, UK, 3–4 April 2006, *Proc. Spring Conference 2006*, available from the Institute of Acoustics.
- ⁷M. A. Biot, "Theory of propagation of elastic waves in a fluid-saturated porous solid, Part II: Higher frequency range," *J. Acoust. Soc. Am.* **28**, 179–191 (1956).
- ⁸K. V. Horoshenkov, "Control of traffic noise in city streets," Ph.D. thesis, University of Bradford, Bradford, UK, December 1996.
- ⁹D. L. Johnson, J. Koplik, and R. Dashen, "Theory of dynamic permeability and tortuosity in fluid-saturated porous media," *J. Fluid Mech.* **176**, 379–402 (1987).
- ¹⁰D. Lafarge, P. Lemarinier, J. F. Allard, and V. Tarnow, "Dynamic compressibility of air in porous structures at audible frequencies," *J. Acoust. Soc. Am.* **102**(4), 1995–2006 (1997).
- ¹¹D. Pilon, R. Panneton, and F. Sgard, "Behavioral criterion quantifying the effects of circumferential air gaps on porous materials in the standing wave tube," *J. Acoust. Soc. Am.* **116**(1), 344–356 (2004).
- ¹²C. Zwikker and C. W. Kosten, *Sound Absorbing Materials* (Elsevier, Amsterdam, 1949), p. 21.

Source characterization of a subsonic jet by using near-field acoustical holography

Moohyung Lee^{a)} and J. Stuart Bolton^{b)}

Ray W. Herrick Laboratories, School of Mechanical Engineering, Purdue University,
140 S. Intramural Drive, West Lafayette, Indiana 47907-2031

(Received 28 April 2006; revised 31 October 2006; accepted 8 November 2006)

In the present study, patch near-field acoustical holography was used in conjunction with a multireference, cross-spectral sound pressure measurement to visualize the sound field emitted by a subsonic jet and to predict its farfield radiation pattern. A strategy for microphone array design is described that accounts for the low spatial coherence of aeroacoustic sources and for microphone self-noise resulting from entrained flow near the jet. In the experiments, a 0.8-cm-diameter burner was used to produce a subsonic, turbulent jet with a *Mach* number of 0.26. Six fixed, linear arrays holding eight reference microphones apiece were disposed circumferentially around the jet, and a circular array holding sixteen, equally spaced field microphones was traversed along the jet axis to measure the sound field on a 30-cm-diameter cylindrical surface enclosing the jet. The results revealed that the jet could be modeled as a combination of eleven uncorrelated dipole-, quadrupole-, and octupole-like sources, and the contribution of each source type to the total radiated sound power could be identified. Both the total sound field reconstructed in a three-dimensional space and the farfield radiation directivity obtained by using the latter model were successfully validated by comparisons to directly measured results. © 2007 Acoustical Society of America.

[DOI: 10.1121/1.2404626]

PACS number(s): 43.60.Sx, 43.28.Ra [EGW]

Pages: 967–977

I. INTRODUCTION

The term “jet noise” is often used to describe the total sound radiated from aircraft exhaust systems. Among the various source components of jet noise, that related to turbulent mixing of the jet exhaust with the ambient fluid (thus, referred to as “jet mixing noise”) is considered to be the most fundamental. In the early 1950s, Lighthill showed, in his theory referred to as “Lighthill’s acoustic analogy,” that jet mixing noise is generated in a free jet by the action of the fluctuating Reynolds shear stress, and that the sound generation process can be modeled in terms of a volume distribution of equivalent acoustic sources (i.e., a collection of elemental quadrupole sources) that are assumed to be embedded in a uniform medium at rest.^{1,2} Related work was performed by Powell: In his “vortex sound theory,”³ quadrupole sound radiation in the farfield was explained by the leapfrogging of vortex rings.⁴

Various computational methods have been developed for the prediction of jet noise, e.g., the linearized Euler equations,⁵ *k*-epsilon modeling,⁶ direct numerical simulation,⁷ large eddy simulation,⁸ and so on. These methods allow, in principle, all flow quantities of interest to be computed, but are so computationally expensive even for moderate Reynolds number flows that only relatively short-time-period simulations are possible; that in turn hampers the application of the usual Fourier analysis and time-averaging

methods required to obtain robust spectral estimates, with the result that making meaningful comparisons with experimental data is difficult.

Experimental approaches have also been used to attempt to measure the turbulence statistics associated with Lighthill’s theory. At an early stage, hot-wire anemometers were used for measuring turbulence,⁹ but, due to their fragile nature, applications were restricted to low Mach number flows and low temperature jets. To overcome this problem, particle image velocimetry, a nonintrusive measurement technique based on the use of optical measurement tools, has been developed.^{10,11}

When focusing directly on the sound emitted by a jet, jet noise source localization in terms of explicit or implicit elemental sources has been performed by using various types of one-dimensional farfield arrays, e.g., the acoustic mirror,^{12,13} the acoustic telescope,^{12,14} and the polar correlation technique.^{12,15} The use of one- or two-dimensional phased arrays, based on beamforming, have also been explored for jet noise source localization and in wind tunnel measurements.^{16–21} The latter method allows the source probability distribution to be mapped. However, when applied to the visualization of jet noise, conventional beamforming techniques can result in significant errors since farfield array methods are best suited to spatially well-separated sources, and since their accuracy is degraded by refraction and Doppler effects. To address the latter problems, new beamforming algorithms have been proposed.^{22,23}

However, the array-based methods just mentioned have not, thus far, allowed accurate source localization and farfield sound predictions to be made over extended regions. That deficiency may result from oversimplifying the prob-

^{a)} Author to whom correspondence should be addressed; electronic mail: leemoohy@ecn.purdue.edu

^{b)} Electronic mail: bolton@ecn.purdue.edu

lem, for example, by decomposing the source into a small number of elemental sources, with the result that imaging accuracy is dependent upon the way in which the source is modeled, either explicitly or implicitly. In addition, existing techniques are typically based on farfield measurements and so impose a limit on the spatial resolution with which a source can be visualized.

The purpose of the present work was to address these various concerns by developing an alternative source visualization procedure based on near-field acoustical holography (NAH).²⁴ Compared to the above-described techniques, NAH is capable of providing results with higher spatial resolution and greater accuracy since this technique is based on nearfield measurements and can be used to visualize the sound field in a three-dimensional volume based on the use of basis functions that satisfy the Helmholtz equation without making any implicit or explicit assumption as to the nature of the sources.

In previous work, cylindrical NAH was applied in combination with a scan-based, cross-spectral measurement²⁵ to visualize the sound field radiated by an axial fan.²⁶ Here, the procedure implemented in the latter work was expanded to suit jet noise measurements.

First, a strategy for microphone array design was established. In the case of jet noise measurements, microphone arrays must be designed with care since a jet typically features high speed flows that are coherent only in limited spatial regions, thus imposing restrictions on the placement of array microphones. Recently, it was shown that the use of a relatively large number of reference microphones in a holography measurement can suppress the effects of additive noise included in the reference signals.²⁷ The latter method is particularly appropriate for jet noise measurements since it allows reference microphones to be placed close to a jet plume where the measured reference signals are likely to be partially corrupted by the effects of entrained flow. Also, it is shown here that reference microphones should be positioned to cover the whole source region due to the limited spatial coherence of jet noise.

Second, a partial field decomposition procedure that suppresses the spurious effects resulting from both nonstationary source level and measurement noise was implemented,²⁷ and third, patch NAH was implemented to mitigate the error resulting from the truncation of the sound field that is usually inevitable due to the spreading nature of a jet plume.²⁸⁻³¹

This article is organized in a following manner. In Sec. II, the theoretical background of the procedures used in this work is presented. In Sec. III, the experimental setup is described. A test jet was created by using a burner nozzle, and a reference microphone array and a field microphone array comprising 48 and 16 microphones, respectively, were constructed to measure the cross-spectral properties of the sound field. In Sec. IV, the reconstructed sound field and predicted farfield radiation pattern are presented along with comparisons to directly measured results. In Secs. V and VI, additional discussion and conclusions are presented.

II. THEORY

A. Near-field acoustical holography for the visualization of a sound field (Ref. 24)

A sound pressure vector, $\hat{\mathbf{p}}$, measured on a hologram surface and an acoustical property vector, $\hat{\mathbf{a}}$, to be reconstructed on a surface of interest can be related, in general, by a transfer matrix, \mathbf{T} , at every frequency, i.e.,

$$\hat{\mathbf{p}} = \mathbf{T}\hat{\mathbf{a}}. \quad (1)$$

Note that the caret denotes, in particular, a spatially coherent property since the latter relation is established based on the homogeneous, time-independent Helmholtz equation.

In the wave number description of a sound field, \mathbf{T} is decomposed as $\mathbf{T} = \mathbf{F}^{-1}\mathbf{G}\mathbf{F}$, where \mathbf{F} and \mathbf{F}^{-1} denote the forward and inverse two-dimensional discrete Fourier transform (DFT) operators, respectively, and $\mathbf{G} = \text{diag}(\tau_1, \dots, \tau_N)$ represents the propagation characteristics of each wave number component. The τ_i 's are determined explicitly depending both on the measurement geometry and the acoustic property to be reconstructed. In a cylindrical geometry, as implemented in the present work, the τ_i 's corresponding to a sound pressure and radial particle velocity on a surface of interest are given by²⁴

$$\tau_i \rightarrow \tau_{nk} = \begin{cases} \frac{H_n^{(1)}(k_{rk}r_h)}{H_n^{(1)}(k_{rk}r)} & \text{for sound pressure} \\ \frac{i\rho ck H_n^{(1)}(k_{rk}r_h)}{k_{rk} H_n^{(1)'}(k_{rk}r)} & \text{for radial partial velocity,} \end{cases} \quad (2)$$

where r and r_h represent the radius of the surface of interest and of the hologram surface, respectively, c is the ambient sound speed, ρ is the ambient density, $k = \omega/c$ is the acoustic wave number, the subscript k represents the discretization of the wave number spectrum (thus, $k_{rk} \equiv \sqrt{k^2 - k_{zk}^2}$ and k_{zk} represent the discretized radial and axial wave numbers, respectively), $H_n^{(1)}$ is the Hankel function of the first kind, and $\{\cdot\}'$ denotes the first derivative of a function with respect to its argument. Note that τ_{nk} corresponds to τ_i depending on the way that the sound pressure measured on a two-dimensional surface is transformed to a one-dimensional column vector, and that a harmonic time dependence of $e^{-j\omega t}$ is assumed in this development.

The holographic projection that reconstructs an acoustical property from the measured sound pressure is achieved by inverting Eq. (1). The latter procedure is a discrete, ill-posed inverse problem³² due to the existence of rapidly decaying, evanescent wave components. Thus, it is required to filter out noise-related, high wave number components to stabilize the inverse solution, especially when backprojecting toward the source. Therefore, the inverse solution of Eq. (1) is best expressed by incorporating a diagonal matrix, \mathbf{R}^α , that acts as a k -space filter, i.e.,

$$\hat{\mathbf{a}} = \mathbf{F}^{-1}\mathbf{R}^\alpha\mathbf{G}^{-1}\mathbf{F}\hat{\mathbf{p}}. \quad (3)$$

As implemented in previous NAH work,³³ \mathbf{R}^α can be constructed by using various regularization methods that de-

termine the filter shape and optimal cutoff in an automated way. In the present work, modified Tikhonov regularization was implemented, which results in³³

$$\mathbf{R}^\alpha = \text{diag} \left(\cdots |\tau_i|^2 \left/ \left(|\tau_i|^2 + \alpha^2 \left(\frac{\alpha^2}{\alpha^2 + |\tau_i|^2} \right)^2 \right) \cdots \right), \quad i = 1, 2, \dots, N, \quad (4)$$

and the Morozov discrepancy principle^{32,33} was used to determine the optimal value of the regularization parameter, α .

When implementing Eq. (3), the wave number spectrum of $\hat{\mathbf{p}}$ is calculated first by taking the two-dimensional DFT (i.e., $\hat{\mathbf{p}}_F = \mathbf{F}\hat{\mathbf{p}}$), and the projection is then performed based on element-by-element multiplication of each wave number component by the corresponding propagator (which is defined as the reciprocal of τ_i), rather than by a full matrix calculation as shown in Eq. (3), since each of the orthogonal wave number components can be projected independently, i.e.,

$$(\hat{a}_F)_i = \frac{R_i^\alpha}{\tau_i} (\hat{p}_F)_i, \quad i = 1, 2, \dots, N. \quad (5)$$

The spatial distribution of the projected property is finally obtained by evaluating the inverse two-dimensional DFT of the resulting wave number spectrum (i.e., $\hat{\mathbf{a}} = \mathbf{F}^{-1}\hat{\mathbf{a}}_F$).

The procedure described above, referred to as DFT-based NAH, is computationally efficient, but it is required that measurements be performed over a sufficiently large region (which will be referred to as a “complete” region in later sections) to avoid windowing effects. Thus, $\hat{\mathbf{p}}$ and N appearing in this article specifically represent a sound field satisfying the latter requirement and the number of discrete points where $\hat{\mathbf{p}}$ is measured, respectively.

B. Holography measurement and data processing

1. Multireference, cross-spectral measurement

In holography measurements of sources comprising a number of uncorrelated or partially correlated subsources, as is the case for a jet, it is necessary to implement a cross-spectral procedure based on the use of a set of reference microphones (whose number should be at least equal to the number of incoherent subsources) to identify the phase distribution of the partial fields on the hologram surface unequivocally. In the latter procedure, the cross-spectral matrix between the reference signals, \mathbf{C}_{rr} , and the cross-spectral matrix between the reference and field microphone signals, \mathbf{C}_{rp} , are measured. The sound field on the hologram surface, \mathbf{C}_{pp} , is then expressed by using multi-input/multi-output signal relations,³⁴ i.e.,

$$\mathbf{C}_{pp} = \mathbf{C}_{rp}^H \mathbf{C}_{rr}^{-1} \mathbf{C}_{rp} \quad (6a)$$

$$= \mathbf{H}_{rp}^H \mathbf{C}_{rr} \mathbf{H}_{rp}, \quad (6b)$$

where $\mathbf{H}_{rp} = \mathbf{C}_{rr}^{-1} \mathbf{C}_{rp}$ represents the acoustic transfer matrix that relates the reference and field microphone signals, the superscript H denotes the Hermitian operator, and the inverse represents the generalized inverse to accommodate rank-deficient matrices. The cross-spectral matrices are defined in

such a way that $\mathbf{C}_{rp} = \mathbf{E}[\mathbf{r}^* \mathbf{p}^T]$ where the superscripts T and * denote the transpose and complex conjugate operators, respectively, and $\mathbf{E}[\cdot]$ represents the expectation operator.

In many practical NAH measurements, a scan-based procedure in which a subarray is scanned over a number of patches in sequence (while simultaneously making measurements at an array of fixed reference microphones) has been adopted to measure the sound field on the entire hologram surface since this procedure allows the number of microphones required to perform a complete measurement to be reduced.²⁵

2. Partial field decomposition with correction for scan-to-scan source level variation (Ref. 27)

The composite sound field obtained by using the cross-spectral procedure must be decomposed into a set of spatially coherent partial fields that are mutually incoherent to enable the projection of the sound field as described in Sec. II A. The signals measured by the references, which are assumed to be linearly related to the source signals, are used as the basis for the decomposition since the source signals themselves cannot be measured directly in most practical cases.

When scan-based measurements are performed, as many reference cross-spectral matrices are obtained during the course of the measurement as there are scans performed. To help minimize statistical error, it is desirable to use the reference cross-spectral matrix averaged over all the scans for the decomposition. When using a virtual coherence method, the decomposition can be performed by using singular value decomposition (SVD), i.e.,

$$\mathbf{C}_{rr(\text{avg})} = \mathbf{U}_{(\text{avg})} \mathbf{\Sigma}_{(\text{avg})} \mathbf{V}_{(\text{avg})}^H = \mathbf{U}_{(\text{avg})} \mathbf{\Sigma}_{(\text{avg})} \mathbf{U}_{(\text{avg})}^H, \quad (7)$$

where the subscript (avg) denotes properties averaged over all the scans [while properties estimated during each individual scan are denoted in the following by the subscript (scan)], $\mathbf{\Sigma}$ is a diagonal matrix composed of the singular values, \mathbf{U} and \mathbf{V} are unitary matrices that comprise the left and right singular vectors, respectively, and \mathbf{U} and \mathbf{V} are identical here since \mathbf{C}_{rr} is a positive semi-definite Hermitian matrix.

The partial fields $\hat{\mathbf{P}}$ (which are subject to the condition that $\mathbf{C}_{pp} = \hat{\mathbf{P}}^* \hat{\mathbf{P}}^T$) can be calculated by using either Eq. (6a) or (6b) in conjunction with Eq. (7). However, in the case of scan-based measurements, the source level usually varies slightly from scan-to-scan in practical cases. When the latter variation is significant, the partial fields calculated based on the use of Eq. (6a) (i.e., $\hat{\mathbf{P}} = \mathbf{C}_{rp(\text{scan})}^T \mathbf{U}_{(\text{avg})}^* \mathbf{\Sigma}_{(\text{avg})}^{-1/2}$) are corrupted by a spatially distributed error. In contrast, the acoustic transfer matrix, \mathbf{H}_{rp} , calculated during each scan is essentially independent of source level since it represents amplitude and phase information relative to the sources. Thus, the effect of source level variation can be avoided by using Eq. (6b) when performing partial field decomposition,²⁷ i.e.,

$$\begin{aligned} \hat{\mathbf{P}} &= \mathbf{H}_{rp(\text{scan})}^T \mathbf{U}_{(\text{avg})}^* \mathbf{\Sigma}_{(\text{avg})}^{1/2} = [\mathbf{C}_{rr(\text{scan})}^+ \mathbf{C}_{rp(\text{scan})}]^T \mathbf{U}_{(\text{avg})}^* \mathbf{\Sigma}_{(\text{avg})}^{1/2} \\ &= [\mathbf{U}_{(\text{scan})} \mathbf{\Sigma}_{(\text{scan})}^+ \mathbf{U}_{(\text{scan})}^H \mathbf{C}_{rp(\text{scan})}]^T \mathbf{U}_{(\text{avg})}^* \mathbf{\Sigma}_{(\text{avg})}^{1/2}, \end{aligned} \quad (8)$$

where each column of $\hat{\mathbf{P}}$ represents a single partial field, the

multiplication by $\Sigma_{(\text{scan})}^+$ and $\Sigma_{(\text{avg})}^{1/2}$ implements the correction for source level variation from scan-to-scan, and $+$ represents the regularized inverse that implements the generalized inverse in general cases when signals include noise effects. When implemented in Eq. (8), the regularized inverse is calculated by discarding small, noise-related singular values (i.e., truncated singular value decomposition)³² as

$$\Sigma^+ = \begin{bmatrix} \Sigma_s & \mathbf{0} \\ \mathbf{0} & \Sigma_n \end{bmatrix}^+ \equiv \begin{bmatrix} \Sigma_s^{-1} & \mathbf{0} \\ \mathbf{0} & \mathbf{0} \end{bmatrix}. \quad (9)$$

The number of noise-related singular values, Σ_n , to be discarded is determined by finding the number of significant partial fields contributing to the total sound field, which can be identified most easily by examining the sum of the virtual coherence functions.²⁷

Once the partial fields are calculated, a number of projections equal to the number of significant partial fields contributing to the total sound field are performed as described in Sec. II A, and the total sound field can then be obtained as the quadratic sum of the projection results.

Recall that negative harmonic time dependence of a signal is assumed in this work while in the implementation of commercial FFT analyzers, a positive time dependence is usually assumed. Thus, care should be taken when processing data to ensure consistency in the choice of Fourier transform sign convention since the propagation direction depends on the resulting phase information when the sound field is projected from one surface to another.²⁶

3. Strategy for microphone array design

Unlike structure-borne noise sources, aeroacoustic sources are usually accompanied by a mean flow which may impinge on either the reference or field microphones or both. When microphones are exposed to flow, the measured data contain the self-noise generated by the interaction of the flow and the microphones as well as the desired signal. It is important that the reference cross-spectral matrix, in particular, not be contaminated by measurement noise since the partial field decomposition is performed based on the latter matrix. The effects of measurement noise included in the reference cross-spectral matrix appear in various ways. For example, the number of significant partial fields contributing to the total sound field may appear to be greater than the actual number of subsources, and, especially when the levels of noise autospectra are large, the levels of the decomposed partial fields are underestimated, with the result that the magnitude of the total sound field is also underestimated. The latter problem can be addressed by the proper placement of the microphones.³⁵ First, the reference microphones should be placed in a region *out of* the flow, and, second, the reference microphones should not sense flow noise generated by the interaction of the flow with the field microphones.

The strictness of the first requirement can be relieved by increasing the number of references used in the measurements since the use of a relatively large number of references results in a clearer separation between the source- and noise-related singular values, thus allowing the source-related sin-

gular values to approach those that would be obtained in a noise-free case.²⁷ As a result, the reference microphones can be positioned without regard to the first condition, at least to some extent. However, when microphones are exposed to a very high speed flow (e.g., when the reference microphones are placed in the jet plume), a very large number of reference microphones are required to cause the results to converge to those obtained from noise-free measurements. Thus, in a practical sense, the placement of the reference microphones is still, at least partially, subject to the first requirement in the jet case. That is, it is suggested that reference microphones be placed out of the main jet plume; but they can be placed in regions *close* to the jet plume even if the reference signals measured in that region are likely to be corrupted to some extent by the effects of entrained flow exterior to the main jet plume.

When SVD is used for partial field decomposition, reference microphones can be positioned arbitrarily (but, preferably, close to the component source locations when *a priori* information about the sources is available) so long as the members of the reference set between them sense all the signals radiated by all the sources. In a holographic measurement of a jet, however, more care should be taken due to the limited spatial coherence and the highly directional nature of jet noise, i.e., a reference array should cover the whole jet circumference and extend axially beyond all possible source regions to sense all the spatially localized subsources contributing to the total sound field.

4. Extension of the hologram pressure measured over a finite aperture (Ref. 31)

When the sound field emitted by a jet is scanned on a cylindrical hologram surface, as in the present work, the degree to which the hologram surface can be extended axially without intruding into the expanding jet plume is limited, thus possibly resulting in the truncation of the sound field in the jet's downstream direction. In the latter case, the direct use of the decomposed partial fields for holographic projection causes reconstruction results to be degraded by the windowing effect related to the use of the DFT. The latter problem can be alleviated by extending the sound field (i.e., each partial field) into the unmeasured region based on the use of an iterative data recovery algorithm, thus increasing the effective size of the measurement aperture, before holographic projection is performed. The latter procedure is referred to as patch NAH,²⁸⁻³¹ and can be applied to each partial field in turn, as necessary.

The iterative patch holography procedure is derived as follows. Let $\hat{\mathbf{p}}_w = \hat{\mathbf{p}}_w(\vec{r})$ denote the sound pressure truncated (or windowed) by a finite measurement aperture that extends over the region, Γ_m . Then, $\hat{\mathbf{p}}_w$ can be related to the complete (i.e., nontruncated) sound pressure by

$$\hat{\mathbf{p}}_w(\vec{r}) = \begin{cases} \hat{\mathbf{p}}(\vec{r}) & \text{when } \vec{r} \in \Gamma_m \\ 0 & \text{when } \vec{r} \notin \Gamma_m, \end{cases} \quad (10)$$

where $\vec{r} = (r_1, r_2)$ represents the two-dimensional position vector on the hologram surface. The relation shown in Eq. (10) can be expressed in matrix-vector form as $\hat{\mathbf{p}}_w = \mathbf{W}\hat{\mathbf{p}}$

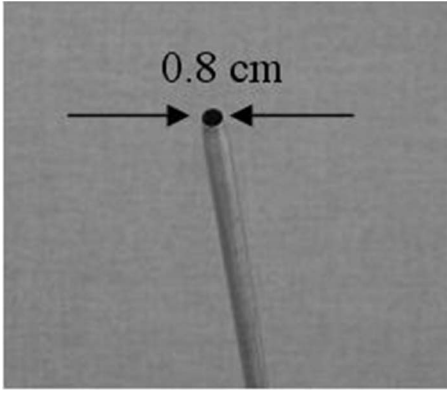


FIG. 1. Burner nozzle used in the measurement.

where \mathbf{W} , referred to as the spatial windowing operator, is a diagonal matrix whose diagonal terms are given by

$$W_{ii}(\vec{r}) = \begin{cases} 1 & \text{when } \vec{r} \in \Gamma_m \\ 0 & \text{when } \vec{r} \notin \Gamma_m \end{cases}, \quad i = 1, 2, \dots, N. \quad (11)$$

To enable data recovery from partially known information, an additional constraint must be imposed on the nature of the signals. Suppose a sound pressure over a complete region is band-limited to a finite k -space region, Ω_m . In that case, the sound pressure satisfies the expression $\hat{\mathbf{p}} = \mathbf{B}\hat{\mathbf{p}} = \mathbf{F}^{-1}\mathbf{L}\mathbf{F}\hat{\mathbf{p}}$, where \mathbf{B} is referred to as the band-limiting operator, and \mathbf{L} is a diagonal matrix acting as a k -space, low-pass filter whose diagonal terms are defined by

$$L_{ii}(\vec{k}) = \begin{cases} 1 & \text{when } \vec{k} \in \Omega_m \\ 0 & \text{when } \vec{k} \notin \Omega_m \end{cases}, \quad i = 1, 2, \dots, N, \quad (12)$$

where $\vec{k} = (k_1, k_2)$ represents the two-dimensional wave number vector. Since evanescent components decay relatively quickly, the hologram pressure usually (at least weakly) satisfies the latter condition.

From the relations noted above, $\hat{\mathbf{p}}_w$ and $\hat{\mathbf{p}}$ can be related to each other by $\hat{\mathbf{p}}_w = \mathbf{W}\mathbf{B}\hat{\mathbf{p}}$. A rearrangement of the latter relation gives $\hat{\mathbf{p}} = (\mathbf{I} - \mathbf{W})\mathbf{B}\hat{\mathbf{p}} + \hat{\mathbf{p}}_w$, where \mathbf{I} denotes the identity matrix, and $\hat{\mathbf{p}}$ can be restored iteratively from $\hat{\mathbf{p}}_w$ by using a method of successive approximations,³¹ i.e.,

$$\tilde{\mathbf{p}}^{(i+1)} = (\mathbf{I} - \mathbf{W})\mathbf{B}\tilde{\mathbf{p}}^{(i)} + \hat{\mathbf{p}}_w, \quad i = 1, 2, \dots, \quad \tilde{\mathbf{p}}^{(1)} = \hat{\mathbf{p}}_w, \quad (13)$$

where $\tilde{\mathbf{p}}^{(i+1)}$ denotes the extended pressure after the i th iteration.

The iteration can start with $\tilde{\mathbf{p}}^{(1)} = \hat{\mathbf{p}}_w$ which is, in practice, obtained by adding zeros to the decomposed partial field. When implemented in planar geometry, zero-padding can be applied to an arbitrary degree in both in-plane directions. When implemented in cylindrical geometry, however, the number of zeros to be added in the circumferential direction is necessarily finite to account for the periodic nature of the sound field in that direction,³⁰ i.e., in the wave number description of NAH, the total number of data points in the circumferential direction after zero-padding must be equal to 2π divided by the angular sample spacing (in radians).

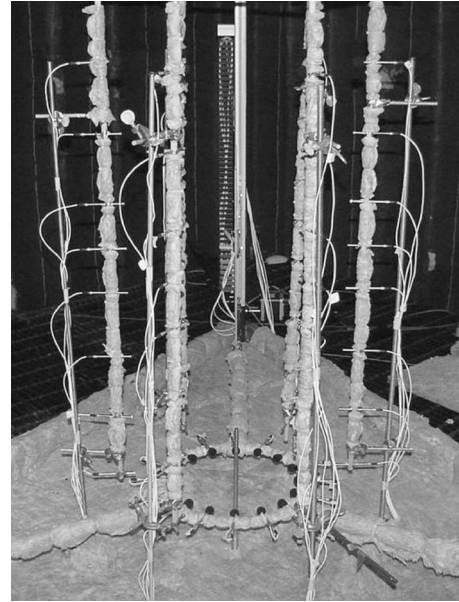


FIG. 2. Overview of an experimental setup (reference and field microphone arrays comprise six linear arrays and a circular array, respectively).

Equation (13) represents a “smooth-and-replace” procedure, as described in previous patch NAH articles, and the latter procedure is repeated until a convergence criterion, $\|\tilde{\mathbf{p}}^{(i+1)} - \tilde{\mathbf{p}}^{(i)}\| \leq \epsilon$ (where ϵ is an *ad hoc* convergence factor), is satisfied. In principle, the extended pressure approaches the complete pressure as the number of iterations increases (i.e., $\lim_{i \rightarrow \infty} \tilde{\mathbf{p}}^{(i)} = \hat{\mathbf{p}}$), but the latter convergence cannot be achieved over a complete region due to the effects of the

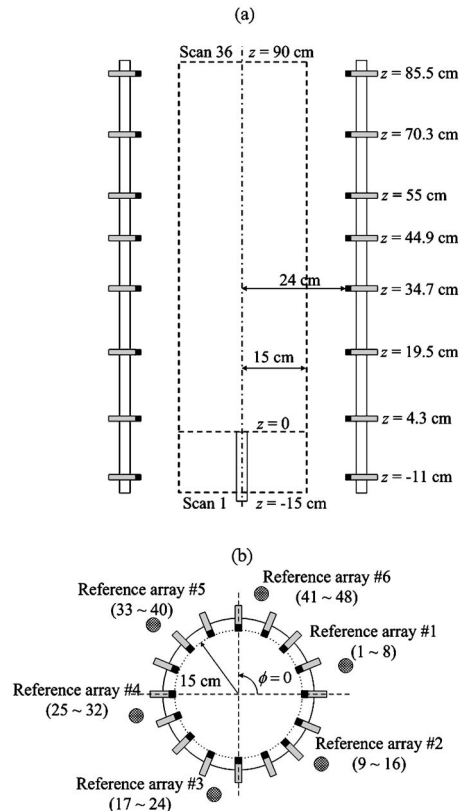


FIG. 3. Detailed layout of array: (a) side view; (b) top view.

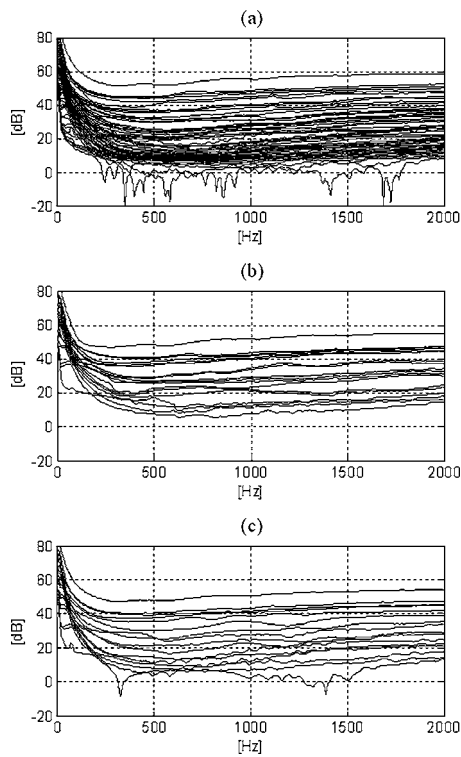


FIG. 4. Singular values of the reference cross-spectral matrix averaged over all the scans: (a) in the 48-reference case; (b) in the 18-reference case; (c) in the 16-reference case.

artificial truncation of the infinite domain, the discretization of continuous functions, and measurement noise.³¹

III. EXPERIMENTAL APPARATUS

A 0.8-cm-diameter burner nozzle with a sharp exit (see Fig. 1) was used to generate a subsonic ($Ma=0.26$) jet. Air was provided by a shop air supply, and an expansion chamber and air drier were installed to regulate flow and to remove moisture in the air, respectively. The reference array was designed to satisfy the conditions discussed earlier. Six fixed, linear arrays holding eight reference microphones (Larson Davis TMS426B01) apiece were positioned vertically at a radius of 24 cm so as to be external to the main jet plume, and eight reference microphones on each linear array were placed at heights of $-11, 4.3, 19.5, 34.7, 44.9, 55, 70.3,$ and 85.5 cm with respect to the jet exit. The reference microphones were spaced relatively closely in the vicinity of the expected main radiation lobe (i.e., the fourth, fifth, and sixth references from the bottom). A circular array holding 16, equally spaced field microphones (Larson Davis TMS426B01) was traversed axially from $z=-15$ cm with respect to the jet exit in 3 cm increments to sample the sound field on a 30-cm-diameter cylindrical hologram surface in 36 steps. The jet exit was 36 cm above the floor, and the floor and rig surfaces were covered by a sound absorbing material (see Figs. 2 and 3). The measurement bandwidth was 8192 Hz with a frequency resolution of 8 Hz.

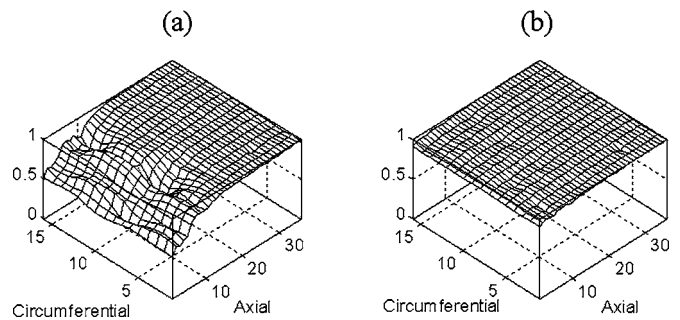


FIG. 5. Sum of the virtual coherence functions at 1 kHz in the 48-reference case: (a) when the first 5 partial fields were used; (b) when the first 11 partial fields were used.

IV. RESULTS

A. Effects of reference array configuration

The effects of reference array configuration are illustrated by a comparison of results obtained when various configurations were used. First, forty-eight references were used as described in Sec. III. Second, three references (the second, fifth, and seventh microphones from the bottom of the linear array) were chosen from each of the six linear arrays, thus giving eighteen references in total. Third, sixteen references were selected from two linear arrays (Nos. 1 and 2 in Fig. 3). Results are presented at 1 kHz.

In Fig. 4, the singular values of the reference cross-spectral matrix averaged over all scans are shown. In the 48 reference case, the singular values decrease in magnitude until they fall to the apparent noise level, at approximately 0 dB. By comparison with the latter results, it can be observed that the separation between the source-related singular values and the noise level were decreased when 18 and 16 references were used [compare Figs. 4(b) and 4(c) with Fig. 4(a)]. From the latter observation, it may be expected that the singular values in the 48-reference case are less affected by measurement noise than in the other two cases. The singular values might themselves be inspected to establish the sufficiency of the reference set. In the 48- and 16-reference cases, in particular, the smallest singular values dropped close to the noise level. Therefore, it might be concluded that the number of references used in either case was sufficient. However, it must be established in addition that all signals from all the sources are sensed by the references.

The sum of the virtual coherence functions can be used to check the latter condition. In Figs. 5–7, the sums of the virtual coherence functions calculated by using various numbers of partial fields for the three reference sets previously defined are shown. When 48 references were used, the sum of the virtual coherence functions clearly shows that the first 5 partial fields are not sufficient to describe the sound field, particularly in the region close the jet exit [see Fig. 5(a)]. In contrast, the sum of the first 11 partial fields was close to unity over all measurement points [see Fig. 5(b)], thus no significant benefit would result from the addition of further partial fields. Therefore, it was concluded that the first 11 partial fields were the main contributors to the sound field (i.e., the sound field could be modeled as being created by 11 independent, incoherent sources operating simultaneously),

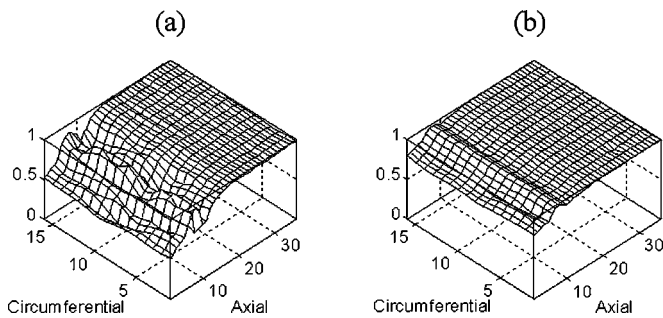


FIG. 6. Sum of the virtual coherence functions at 1 kHz in the 18-reference case: (a) when the first 5 partial fields were used; (b) when 18 partial fields were used.

and that the reference array configuration in the 48-reference case was appropriate and sufficient. In contrast, the sum of the virtual coherence functions calculated by using the 18 and 16 partial fields in the 18- and 16-reference cases, respectively, were smaller than that calculated by using the first 11 partial fields generated when using 48 references [compare Figs. 6(b) and 7(b) with Fig. 5(b)] even though the numbers of references used in those cases were still larger than the number of significant partial fields as judged based on the 48-reference measurement. In the 18-reference case, the summed coherence close to the jet exit and in the jet's upstream direction was relatively low since the reference microphones were relatively widely spaced in that region. The summed coherence was, however, nearly uniform in the circumferential direction since the reference array completely encompassed the jet in that case. In the 16-reference case, it is interesting to note that although the smallest singular value dropped to the noise level, the sum of the virtual coherence functions was less than unity especially at the field positions circumferentially remote from the references [see Fig. 7(b)]. This apparently contradictory conclusion results from the fact that the latter 16-element reference array was not suitable to represent the limited-spatial-coherence sound field since all the references were located on one side of the jet in this case.

From the results discussed above, it can be concluded that the "position" as well as the "number" of references is an important factor in reference array design, especially when the subsources are spatially localized and directional; it has also been confirmed that the number of the "virtual" references (or partial fields) required to construct the total

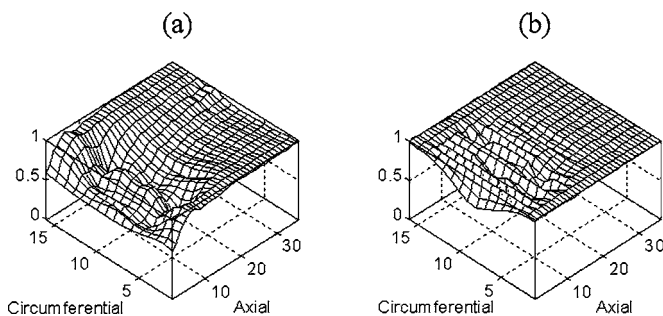


FIG. 7. Sum of the virtual coherence functions at 1 kHz in the 16-reference case: (a) when the first 5 partial fields were used; (b) when 16 partial fields were used.

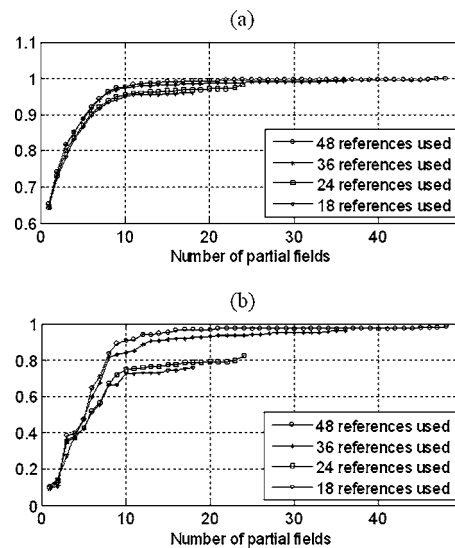


FIG. 8. Comparison of the sums of the virtual coherence functions obtained when various numbers of references were used with respect to the numbers of partial fields at 1 kHz: (a) the averaged value over all measurement positions; (b) the smallest value among all measurement positions.

sound field does not generally correspond to the number of physical references required to perform an accurate measurement in any particular instance.

In Fig. 8, the sums of virtual coherence functions obtained when the various numbers of references were used are presented as a function of the number of partial fields used in the calculation. The comparisons were made for four cases: 48, 36, 24, and 18 references (i.e., 8, 6, 4, and 3 references from each of the six linear arrays). The references were selected so as to cover uniformly the axial and circumferential extent defined by the reference array. The results shown in Figs. 8(a) and 8(b), respectively, represent the value averaged over all measurement positions and the smallest value among all the measurement positions. In all cases, it can be seen that the sum of the virtual coherence functions grew progressively closer to unity as the number of references was increased. This result confirms experimentally the suggestion that the use of a relatively large number of references is beneficial.

From these results, it can also be said that the reference array comprising the 48 microphones was close to optimal for this measurement since the smallest value of the summed coherence over all measurement points was larger than 0.9 when the first 11 partial fields were used. Therefore, the addition of further references could be expected to result in only slight improvement. In all cases, it was judged that the first 11 partial fields were the significant contributors to the total sound field since only a slight improvement in the summed coherence was obtained by adding further partial fields. However, when a smaller number of physical references were used, it was necessary to include a correspondingly larger number of partial fields to achieve comparable values of the coherence. For example, when 36 references were used, 20 partial fields must be processed by using the NAH procedure to achieve the same results as those obtained when using only the first 11 partial fields obtained when 48 references were used.

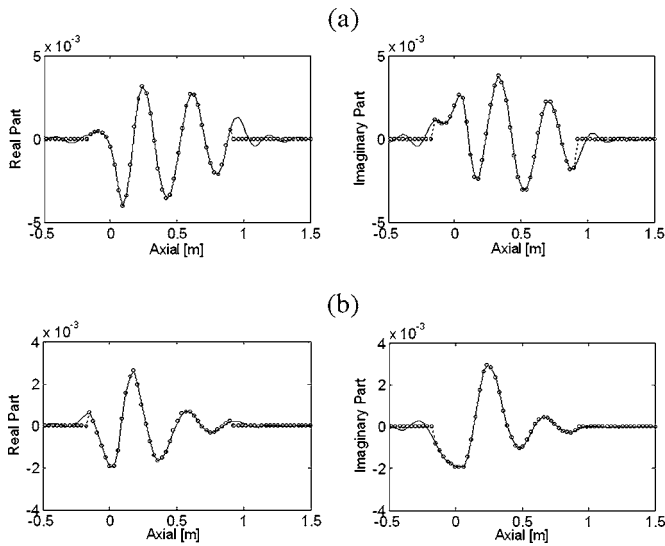


FIG. 9. Comparison of the extended partial fields to those with initial zero-padding: (a) the first partial field; (b) the second partial field. Each result is shown in a section, and the solid line depicts the extended result.

B. Partial fields and reconstruction of the sound field

The first 11 partial fields that were found to be the main contributors to the sound field at 1 kHz are presented here. Before performing holographic projections, the partial fields were extended beyond the measurement aperture by using the patch NAH procedure to reduce the finite measurement aperture effect. The initial pressures for the iteration procedure were constructed by applying zero-padding in both axial directions, i.e., 220 zeros were added to create an axial aperture of 256 points. The sixth scan position that corresponded to the position of the jet exit was located at the center of the extended aperture. In Fig. 9, the extended pressures of the first and second partial fields are presented, for example. It was particularly important to apply the latter procedure to the first partial field since its sound field was significantly truncated by the measurement aperture [see Fig. 9(a)].

In Fig. 10, the three-dimensional sound pressure distributions of the first 11 partial fields after extension are shown. The sound pressures were constructed in the radial region between $r=0.1$ and 1.5 m, and the cylindrical surface in these figures represents the surface defined by $r=0.1$ m. The downstream section of the first partial field was found to resemble radiation from an axial dipole, i.e., it was axisymmetric, and its main lobe was oriented to the jet's downstream direction. However, the amplitude contour plot differed from that of an ideal dipole, especially in the angular region near the jet exit, owing to the effect of the finite measurement aperture (see the discussion in Sec. IV C). The second, third, seventh, and eighth partial fields were found to correspond to the sound fields radiated from lateral quadrupole-like sources lying on planes parallel to the jet axis. The fourth, fifth, and sixth partial fields were also lateral quadrupole-like, but they lay on the plane perpendicular to the jet axis. In this case, the separation was not perfect. The fifth and sixth partial fields constituted the sound field that was a complement of the fourth partial field, and thus

the sum of the latter and the fourth partial fields yielded an axisymmetric sound field. The tenth and eleventh partial fields were octupole-like. The ninth partial field was not clear in character, but here is considered to be dipole-like.

The characteristics of each of the just-described partial fields can also be identified by examining the corresponding wave number spectra. In Fig. 11, the wave number spectra of the first, second, fourth, and tenth partial fields are presented. From the wave number spectrum of the first partial field [see Fig. 11(a)], it is clear that the first partial field was axisymmetric in its radiation pattern since only the $n=0$ circumferential component was observed. Also, the axial wave number components were similar to those of an axial dipole, but note that the negative k_z components were absent since only one lobe was observed in the jet's downstream direction. The second and fourth partial fields corresponded closely to the forms expected for lateral quadrupoles oriented at right angles to each other [see Figs. 11(b) and 11(c)]. Finally, the wave number spectrum of the tenth partial field was similar to that expected for an octupole. In the wave number spectra, the effect of convection can also be observed, i.e., all the wave number spectra were slightly shifted towards the positive k_z direction compared to those expected when those types of sources radiate into a still medium, and, as a result, the radiation pattern was "tilted" in the jet's downstream direction.

In Fig. 12, the sound powers of various source mechanisms are compared. It can be seen that the dipole-like (i.e., the first and ninth partial fields) and the quadrupole-like (i.e., partial fields from the second to eighth) components were the main contributors to the radiated sound power in this case.

C. Verification of projection results

The total sound field and farfield radiation pattern predicted by NAH were verified by comparisons to the directly measured results. The total sound field was obtained by adding quadratically the first 11 partial fields presented earlier. Together they exhibited an axisymmetric characteristic, as expected for a sound field generated by a circular flow. A comparison between the reconstructed and directly measured sound field was made on the plane defined by $\phi=225^\circ$ (see Fig. 13). It can be seen that the reconstructed result agreed well with the measured result. In Fig. 14, the far-field radiation pattern predicted by using NAH is compared with the directly measured result. The comparison was made on an arc 96 cm ($r/D=120$ where D is the diameter of a nozzle) from the jet exit [see Fig. 14(a)]. The two directivity results compared well, but the differences at angles close to the jet axis (i.e., $-20^\circ \leq \theta \leq 20^\circ$) were relatively large compared to the differences at other angles due, in particular, to the truncation of the axial dipole-like component (i.e., the first partial field). The error could be reduced by extending the partial fields, but not completely eliminated, since the extension of the sound field can be achieved only over a limited region

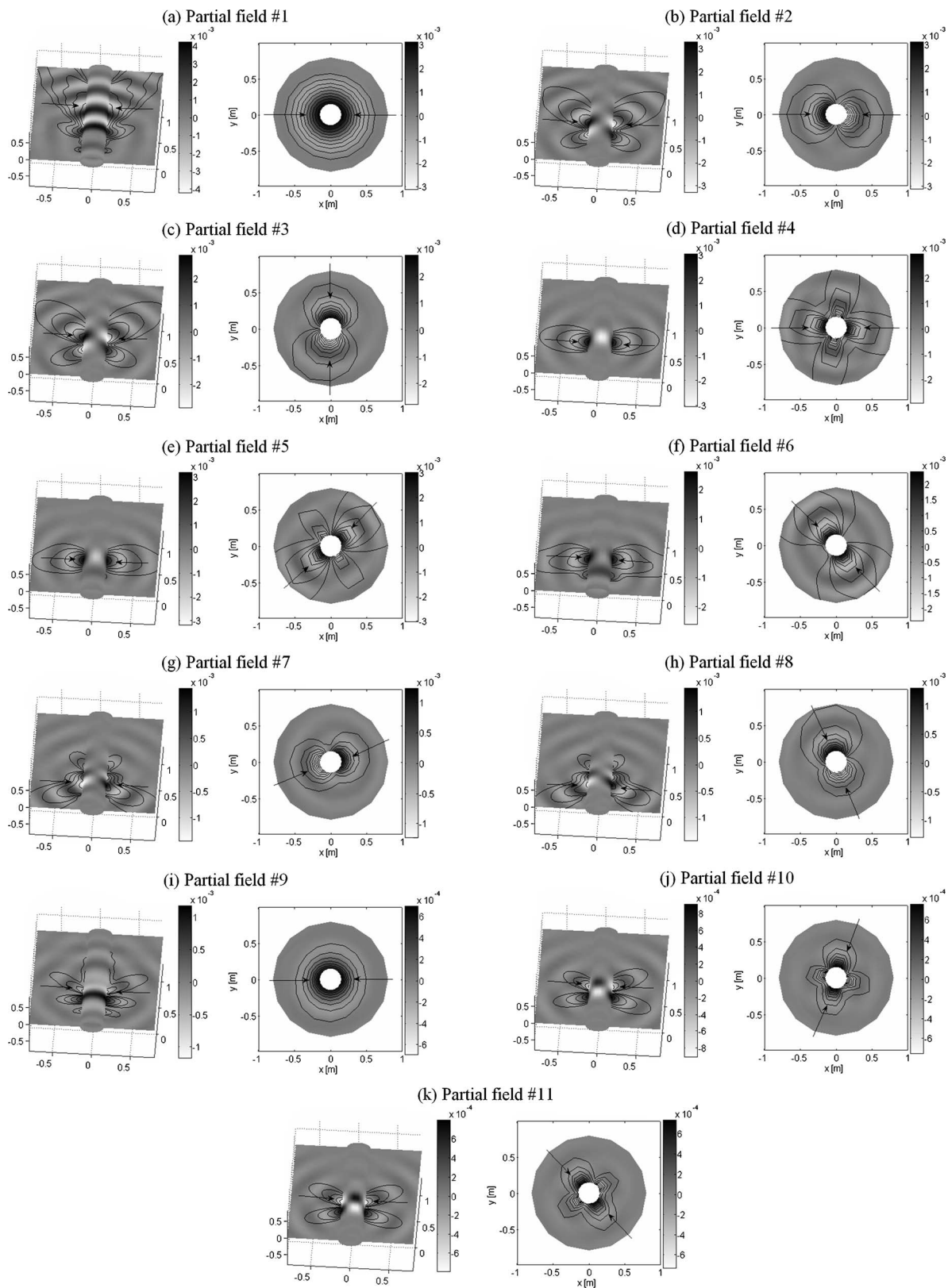


FIG. 10. Three-dimensional sound pressure distributions of the first 11 partial fields (real parts are plotted along with amplitude contours, and the arrows indicate the sections where the results are shown).

near the measurement aperture as noted earlier. In this measurement, however, the measurement aperture was extended axially to sense all subsources, thus allowing far-field prediction at angles close to the jet axis to be within 2 dB after applying the extrapolation procedure.

V. DISCUSSION

In this experiment, a shop air supply and a simple expansion chamber were used to create and regulate the jet flow, respectively. As a result, the flow conditions at the jet

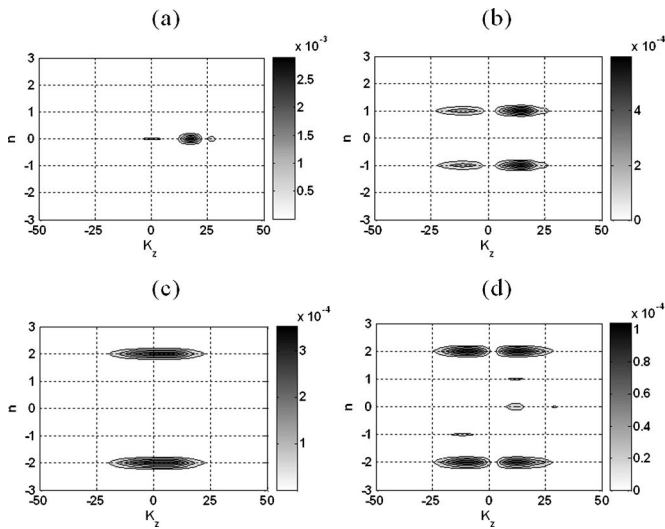


FIG. 11. Wave number spectra of the partial fields: (a) the first partial field (axial dipole); (b) the second partial field (lateral quadrupole lying on the plane parallel to a jet axis); (c) the fourth partial field (lateral quadrupole lying on the plane perpendicular to a jet axis); (d) the tenth partial field (octupole).

exit were not particularly uniform, thus creating sources within the jet pipe and close to the jet exit in addition to the expected quadrupole-like jet mixing noise. In general, the additional sources, usually referred to as excess noise, may be monopole- or dipole-like.³⁶ If a carefully designed flow facility was used, quadrupole-like jet mixing noise would likely be the main contributor to the radiated field. In the case when the contribution of a dipole-like component aligned parallel to a jet axis is small, the spatial truncation effects could be more effectively suppressed by an extension of the partial fields, and the resulting farfield directivity prediction could be expected to be more accurate at angles close to the jet axis than that presented here.

The results presented above have shown that the multi-reference NAH procedure can be used to separate independent source mechanisms, and that a finite number of independent sources can be used to model jet noise sources. Even though the present work does not provide clear evidence that the partial fields identified here correspond to the physically meaningful source mechanisms of the jet under test, the source decomposition capability is nonetheless important. A complete jet has on occasion been represented by a collection of vortex rings interacting with each other, and attempts to relate the vortex rings to the radiated sound field have been made based on the quadrupole radiation only. However,

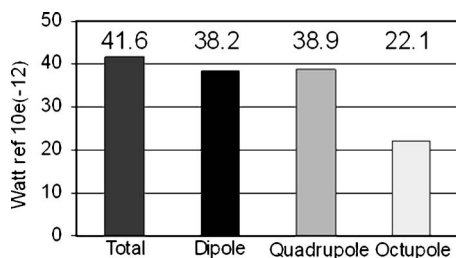


FIG. 12. Comparison of the sound powers associated with each source mechanism at 1 kHz.

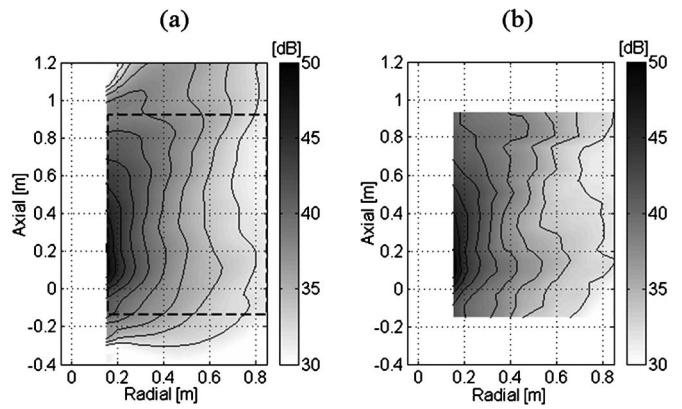


FIG. 13. Comparison of the total sound field at 1 kHz: (a) reconstructed by NAH (the first 11 partial fields were used); (b) directly measured.

the latter model has not provided accurate prediction of sound radiation directivity. To address the latter problem, the study of the role of octupole components in sound radiation has been increasing recently.³⁷ The quadrupole-octupole model can predict more accurately the sound radiation of a jet modeled simply as vortex rings, but, of course, the actual physical phenomenon is more complex than the model, i.e., the latter simplification of the jet's structure still results in prediction errors. The detailed dynamic processes of a jet may be too complex in character to be modeled or measured in complete detail. For accurate predictions, however, it is required that a sound field including, at least, the averaged properties of those processes be obtained and then be separated into a set of relatively simple sources (whether they are real or conjectural). Therefore, whether the decomposed partial fields are physically meaningful is not of great importance for the prediction of sound radiation, but may be useful for quantifying the contribution of vortex rings to the total sound field.

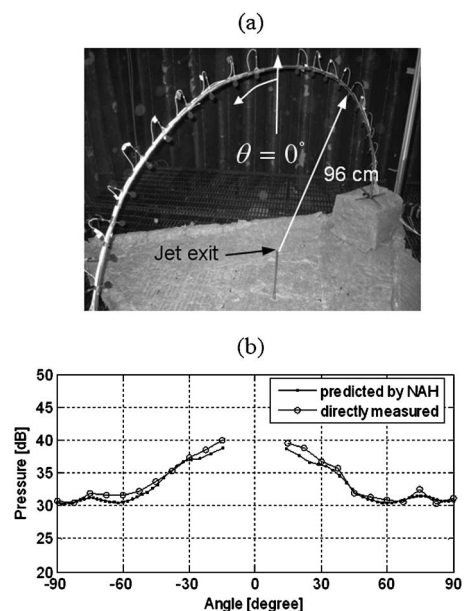


FIG. 14. Comparison of the far-field radiation directivity at 1 kHz: (a) measurement array; (b) sound pressure at $r=96$ cm.

VI. CONCLUSIONS

In the present study, cylindrical patch near-field acoustical holography was applied in conjunction with a cross-spectral sound pressure measurement to characterize the sound field radiated by a jet and to predict its farfield radiation pattern. The restrictions imposed on the positioning of microphones due to the existence of a high speed flow and the limited spatial coherence of the source were described. The latter causes the number of references required for a successful measurement to be relatively large. The reconstructions were performed by implementing various procedures: partial field decomposition with source level variation correction and noise rejection, extension of the sound field measured over a finite region, and holographic projection with regularization. In the test, a subsonic jet was generated by using a shop air passing through a burner nozzle. The sound field generated by the latter jet was decomposed into various components (i.e., dipole-, quadrupole-, and octupole-like), and it was found that the dipole- and quadrupole-like components were dominant. The total sound field and farfield radiation pattern were predicted based on the decomposed, uncorrelated sources; those results were compared with directly measured results, and good agreement was found.

- ¹M. J. Lighthill, "On sound generated aerodynamically. I. General theory," *Proc. R. Soc. London, Ser. A* **211**, 564–587 (1952).
- ²M. J. Lighthill, "On sound generated aerodynamically. II. Turbulence as a source of sound," *Proc. R. Soc. London, Ser. A* **222**, 1–32 (1954).
- ³A. Powell, "Theory of vortex sound," *J. Acoust. Soc. Am.* **36**, 177–195 (1964).
- ⁴A. Powell, "Some aspects of aeroacoustics: From Rayleigh until today," *J. Vib. Acoust.* **112**, 145–159 (1990).
- ⁵C. Bogey, C. Bailly, and D. Juvé, "Computation of flow noise using source terms in linearized Euler's equations," *AIAA J.* **40**, 235–243 (2002).
- ⁶P. J. Morris and F. Farassat, "Acoustic analogy and alternative theories for jet noise prediction," *AIAA J.* **40**, 671–680 (2002).
- ⁷B. E. Mitchell, S. K. Lele, and P. Moin, "Direct computation of the sound generated by vortex pairing in an axisymmetric jet," *J. Fluid Mech.* **383**, 113–142 (1999).
- ⁸W. Zhao, S. H. Frankel, and L. Mongeau, "Large eddy simulations of sound radiation from subsonic turbulent jets," *AIAA J.* **39**, 1469–1477 (2001).
- ⁹P. O. A. L. Davies, M. J. Fisher, and M. J. Barratt, "The characteristics of the turbulence in the mixing region of a round jet," *J. Fluid Mech.* **15**, 337–367 (1963).
- ¹⁰J. M. Seiner, L. Ukeiley, and M. K. Ponton, "Jet noise source measurements using PIV," 5th AIAA/CEAS Aeroacoustics Conference and Exhibit, Bellevue, WA, AIAA Pap. 99-1869 (1999).
- ¹¹C. F. Schram, "Aeroacoustics of subsonic jets: Prediction of the sound produced by vortex pairing based on particle image velocimetry," Ph.D. dissertation, Technische Universiteit, Eindhoven, 2003.
- ¹²H. V. Fuchs, "On the application of acoustic 'mirror,' 'telescope' and 'polar correlation' techniques to jet noise source location," *J. Sound Vib.* **58**, 117–126 (1978).
- ¹³M. Schaffar, "A localized study of the density of a jet-noise source in its

- mixing zone using an elliptical acoustic mirror associated with a laser velocimeter," *Acustica* **50**, 180–188 (1982).
- ¹⁴J. Billingsley and R. Kinns, "The acoustic telescope," *J. Sound Vib.* **48**, 485–510 (1976).
 - ¹⁵M. J. Fisher, M. Harper-Bourne, and S. A. L. Glegg, "Jet engine noise source location: The polar correlation technique," *J. Sound Vib.* **51**, 23–54 (1977).
 - ¹⁶M. Mosher, "Phased arrays for aeroacoustic testing: Theoretical development," 2nd AIAA/CEAS Aeroacoustics Conference, State College, PA, AIAA Pap. 96-1713 (1996).
 - ¹⁷W. M. Humphreys, T. F. Brooks, W. W. Hunter, Jr., and K. R. Meadows, "Design and use of microphone directional arrays for aeroacoustic measurements," 36th Aerospace Sciences Meeting and Exhibit, Reno, NV, AIAA Pap. 98-0471 (1998).
 - ¹⁸P. Sijtsma and H. Holthuisen, "Source location by phased array measurements in closed wind tunnel test sections," 5th AIAA/CEAS Aeroacoustics Conference and Exhibit, Bellevue, WA, AIAA Pap. 99-1814 (1999).
 - ¹⁹R. P. Dougherty, "Beamforming in acoustic testing," in *Aeroacoustic Measurements*, edited by T. J. Mueller (Springer, Berlin, 2002).
 - ²⁰J. R. Underbrink, "Aeroacoustic phased array testing in low speed wind tunnel," in Ref. 19.
 - ²¹S. S. Lee and J. Bridges, "Phased-array measurements of single flow hot jets," 11th AIAA/CEAS Aeroacoustics Conference (26th AIAA Aeroacoustics Conference), Monterey, CA, AIAA Pap. 2005-2842 (2005).
 - ²²T. Suzuki and G. W. Butler, "New beam-forming algorithm for high speed jet flows," Eighth AIAA/CEAS Aeroacoustics Conference, Breckenridge, CO, AIAA Pap. 2002-2505 (2002).
 - ²³S. R. Venkatesh, D. R. Polak, and S. Narayanan, "Beamforming algorithm for distributed source localization and its application to jet noise," *AIAA J.* **41**, 1238–1246 (2003).
 - ²⁴E. G. Williams, *Fourier Acoustics: Sound Radiation and Nearfield Acoustical Holography* (Academic, London, 1999).
 - ²⁵J. Hald, "STSF – A unique technique for scan-based near-field acoustic holography without restrictions on coherence," B&K Technical Review No. 1 (1989).
 - ²⁶M. Lee, J. S. Bolton, and L. Mongeau, "Application of cylindrical near-field acoustical holography to the visualization of aeroacoustic sources," *J. Acoust. Soc. Am.* **114**, 842–858 (2003).
 - ²⁷M. Lee and J. S. Bolton, "Scan-based near-field acoustical holography and partial field decomposition in the presence of noise and source level variation," *J. Acoust. Soc. Am.* **119**, 382–393 (2006).
 - ²⁸K. Saijyou and S. Yoshikawa, "Reduction methods of the reconstruction error for large-scale implementation of near-field acoustical holography," *J. Acoust. Soc. Am.* **110**, 2007–2023 (2001).
 - ²⁹E. G. Williams, "Continuation of acoustic near-fields," *J. Acoust. Soc. Am.* **113**, 1273–1281 (2003).
 - ³⁰M. Lee and J. S. Bolton, "Patch near-field acoustical holography in cylindrical geometry," *J. Acoust. Soc. Am.* **118**, 3721–3732 (2005).
 - ³¹M. Lee and J. S. Bolton, "Reconstruction of source distributions from sound pressures measured over discontinuous regions: Multi-patch holography and interpolation," *J. Acoust. Soc. Am.* (to be published).
 - ³²P. C. Hansen, *Rank-Deficient and Discrete Ill-Posed Problems* (SIAM, Philadelphia, 1998).
 - ³³E. G. Williams, "Regularization methods for near-field acoustical holography," *J. Acoust. Soc. Am.* **110**, 1976–1988 (2001).
 - ³⁴J. S. Bendat and A. G. Piersol, *Random Data: Analysis and Measurement Procedures*, 3rd ed. (Wiley, New York, 2000).
 - ³⁵M. Nakamura, T. Komine, M. Tsuchiya, and J. Hald, "Measurement of aerodynamic noise using STSF," B&K Application Note (1990).
 - ³⁶H. H. Hubbard, *Noise Sources, Aeroacoustics of Flight Vehicles: Theory and Practice*, Vol. 1 (Acoustical Society of America, Woodbury, 1995).
 - ³⁷V. F. Kopeiev and S. A. Chernyshev, "Octupole radiation of localized vortex," 11th AIAA/CEAS Aeroacoustics Conference, AIAA Pap. 2005-2955 (2005).

Theory of forward and reverse middle-ear transmission applied to otoacoustic emissions in infant and adult ears

Douglas H. Keefe^{a)}

Boys Town National Research Hospital, 555 North 30th Street, Omaha, Nebraska 68131

Carolina Abdala

House Ear Institute, Los Angeles, California 90057

(Received 2 August 2006; revised 5 December 2006; accepted 5 December 2006)

The purpose of this study is to understand why otoacoustic emission (OAE) levels are higher in normal-hearing human infants relative to adults. In a previous study, distortion product (DP) OAE input/output (I/O) functions were shown to differ at $f_2=6$ kHz in adults compared to infants through 6 months of age. These DPOAE I/O functions were used to noninvasively assess immaturities in forward/reverse transmission through the ear canal and middle ear [Abdala, C., and Keefe, D. H., (2006). *J. Acoust. Soc. Am.* **120**, 3832–3842]. In the present study, ear-canal reflectance and DPOAEs measured in the same ears were analyzed using a scattering-matrix model of forward and reverse transmission in the ear canal, middle ear, and cochlea. Reflectance measurements were sensitive to frequency-dependent effects of ear-canal and middle-ear transmission that differed across OAE type and subject age. Results indicated that DPOAE levels were larger in infants mainly because the reverse middle-ear transmittance level varied with ear-canal area, which differed by more than a factor of 7 between term infants and adults. The forward middle-ear transmittance level was -16 dB less in infants, so that the conductive efficiency was poorer in infants than adults.

© 2007 Acoustical Society of America. [DOI: 10.1121/1.2427128]

PACS number(s): 43.64.Jb, 43.64.Ha, 43.64.Kc [BLM]

Pages: 978–993

I. INTRODUCTION

This report evaluates the role of normal ear-canal and middle-ear functioning on the interpretation of otoacoustic emission (OAE) responses produced within a healthy cochlea. Based on the hypothesis that the cochlear mechanics are mature at birth and ear-canal and middle-ear mechanics are immature, Abdala and Keefe (2006) used measurements of distortion product (DP) OAE input/output (I/O) functions in infants and adults to calculate a relative forward transfer-function level ΔL_F and a relative reverse transfer-function level ΔL_R between the ear canal and the base of the cochlea. These levels assessed differences in acoustic ear-canal and middle-ear transmission in infants compared to adults. Each level in infants from newborn to 6 months of age was defined relative to an adult group. The ΔL_F in term infants was found to be -15 dB lower than adults and ΔL_R in term infants was 13 dB higher than adults for a DPOAE at 4 kHz. The higher ΔL_R in infants is responsible for DPOAE levels being higher in a healthy newborn relative to an adult ear. The goal of this report is to explain this 28 dB relative difference between term infants and adults in their combined forward and reverse transmission of sound.

A one-dimensional scattering-matrix theory of the acoustical-mechanical functioning of the ear canal, middle ear and cochlea (Shera and Zweig, 1992b) is introduced and extended to include ear-canal and maturational effects as well as incorporating the energy-reflecting properties of the

ear-canal probe (Secs. II A through II I). Theoretical predictions are summarized in Section II J for the reader specifically interested in the results concerning the effect of immaturities in ear-canal and middle-ear functioning on DPOAEs. Using the above-described results of Abdala and Keefe (2006), along with newly reported measurements of ear-canal reflectance that were obtained in the same groups of subjects, the theory is applied to analyze the effects of immaturities in ear-canal and middle-ear functioning on the forward and reverse transmission of DPOAEs.

II. THEORY OF DPOAE GENERATION AND TRANSMISSION

A. General model and pressure variables

The DPOAE source model is based on a one-dimensional transmission-line model of acoustical/mechanical signal flow in the external, middle and inner ears (see Fig. 1). A probe consisting of one or more sound sources and a microphone is inserted into the ear canal a distance ℓ from the tympanic membrane (TM). The pressure at a given location in the ear canal or cochlea is the sum of a forward pressure signal P_e^+ (each forward signal denoted by a superscript +) directed into the ear and a reverse pressure signal P_e^- (each reverse signal denoted by a superscript -) directed away from the TM and towards the probe. The pressure P_e measured by the microphone is decomposed into $P_e = P_e^+ + P_e^-$. A reverse signal P_e^- directed toward the probe leads to a reflected forward signal P_e^+ according to

^{a)}Author to whom correspondence should be addressed. Electronic mail: keefe@boystown.org

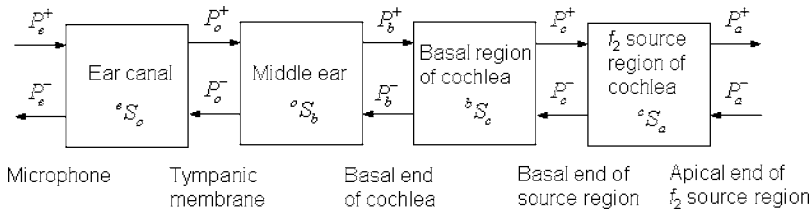


FIG. 1. Signal flow diagram in external, middle, and inner ears. On pressure variables and S matrices, a superscript + denotes wave in forward direction, and superscript - denotes wave in reverse direction.

$$P_e^+ = R_s P_e^- \quad (1)$$

in which R_s is the source reflectance of the probe. The acoustic propagating mode in the ear canal is coupled to the middle ear by the pressure $P_o = P_o^+ + P_o^-$ acting over the TM. The middle-ear energy is coupled into the cochlea, in which a pressure difference $P_b = P_b^+ + P_b^-$ acts across the basal end of the cochlear partition.

In a DPOAE test, two sinusoidal tones are presented at frequencies f_1 and f_2 with $f_2/f_1 \approx 1.2$, and the DPOAE is measured at frequency $f_{DP} = 2f_1 - f_2$. The model of cochlear function is assumed to be one-dimensional along the cochlear partition. For a low-level, sinusoidal excitation at frequency f_2 , the forward traveling wave on the basilar membrane has its maximum displacement at its tonotopic place. The cochlear model is decomposed into a set of connected regions (see Fig. 1): (1) a basal region, in which the basilar-membrane displacement varies approximately linearly with the stimulus amplitude, (2) a f_2 -source region, in which the basilar-membrane displacement varies nonlinearly with a stimulus amplitude at f_2 , and (3) an apical region, which includes the tonotopic place of f_{DP} , and more apical locations. A cochlear pressure $P_c = P_c^+ + P_c^-$ acts at the boundary between basal and f_2 -place regions, while a cochlear pressure $P_a = P_a^+ + P_a^-$ acts at the apical side of the f_2 -source region.

The theory of one-dimensional acoustic transmission lines to represent energy flow in the external, middle, and inner ear can be formulated using a variety of equivalent representations. One representation of one-dimensional transmission lines is the ABCD matrix approach. This has the property that spatially connected regions are represented by matrices that are concatenated together by the ordinary rules of matrix multiplication. Another representation of one-dimensional transmission lines is the scattering (S) matrix approach used in the present report. The S-matrix is advantageous for analyzing bidirectional energy flow in what can be called forward and reverse directions through a transmission line. The bidirectional model in terms of propagating signals in the forward and reverse directions is well suited to understanding effect of middle-ear transmission on the process of OAE generation, because the underlying parameters of a S matrix model, which are reflectances and transmittances, are applied in a simple manner to each of the stimulus and OAE response signals. The ABCD and S-matrix representations are equivalent representations of the same system, i.e., results obtained using a S matrix can also be obtained using an ABCD matrix.

It should be cautioned that neither the ABCD matrix nor the S-matrix representation is a detailed model of middle-ear mechanics. What each representation provides is a frame-

work for relating measurements at the tympanic membrane to measurements at the oval and round windows. A more detailed model of middle-ear mechanics would have the goal of explaining the ABCD or S-matrix parameters in terms of variables related to middle-ear structures. Such a goal was outside the scope of the present study.

B. Scattering matrix properties

Figure 1 shows a set of four networks drawn as boxes, with each network represented by a S matrix that relates the acoustic pressure at locations on either side of the network. The S matrix transforms the incoming waves into outgoing waves. For example, the forward and reverse components of the ear-canal pressures P_e and P_o are related by the S-matrix eS_o in Fig. 1, which represents sound propagation in the ear canal. For this network, the incoming waves are P_e^+ from the left and P_o^- from the right, and the outgoing waves are P_e^- to the left and P_o^+ to the right. The incoming and outgoing waves are each represented by a two-element column vector, and the ear-canal S matrix is a two-by-two matrix of complex coefficients:

$$\begin{pmatrix} P_e^- \\ P_o^+ \end{pmatrix} = {}^eS_o \begin{pmatrix} P_e^+ \\ P_o^- \end{pmatrix} \quad (2)$$

A general S-matrix 1S_2 relating location 1 on the left and location 2 on the right is written

$${}^1S_2 = \begin{pmatrix} r^+ & t^- \\ t^+ & r^- \end{pmatrix}, \quad \begin{pmatrix} P_1^- \\ P_2^+ \end{pmatrix} = {}^1S_2 \begin{pmatrix} P_1^+ \\ P_2^- \end{pmatrix} = \begin{pmatrix} r^+ & t^- \\ t^+ & r^- \end{pmatrix} \begin{pmatrix} P_1^+ \\ P_2^- \end{pmatrix} \quad (3)$$

The r^+ is the (pressure) reflectance, and t^+ is the (pressure) transmittance of an incoming, or incident, forward wave P_1^+ in the absence of an incoming reverse wave ($P_2^- = 0$). The r^- is the (pressure) reflectance, and t^- is the (pressure) transmittance of an incoming reverse wave P_2^- in the absence of an incoming forward wave ($P_1^+ = 0$).

A cascaded network is one in which the output from one network is the input to the following network. Suppose that a S-matrix 1S_3 is the cascade of scattering matrices 1S_2 followed by 2S_3 , with 2S_3 defined by

$${}^2S_3 = \begin{pmatrix} R^+ & T^- \\ T^+ & R^- \end{pmatrix} \quad (4)$$

The 1S_3 is calculated using a product operator \otimes , which is defined using Eqs. (3) and (4) by (Shera and Zweig, 1992b)

$$\begin{aligned} {}^1S_3 &= {}^1S_2 \otimes {}^2S_3 \\ &= \frac{1}{1 - r^- R^+} \begin{pmatrix} r^+ - R^+ \det {}^1S_2 & t^- T^- \\ t^+ T^+ & R^- - r^- \det {}^2S_3 \end{pmatrix}, \end{aligned}$$

$$\det {}^1S_2 = r^+r^- - t^+t^-,$$

$$\det {}^2S_3 = R^+R^- - T^+T^-. \quad (5)$$

The off-diagonal terms are simple products of the transmittances through the individual S matrices, while the diagonal terms are complicated by the presence of reflection sites within each element. Fortunately, the present model has few such reflection sites so that the resulting products remain relatively simple in form.

A one-dimensional transmission line can be represented using a pair of variables, one of which is a generalized force and the other is a generalized velocity. For the acoustic transmission line used herein, the acoustic pressure is the generalized force and the acoustic volume velocity is the generalized velocity. This type of transmission line falls into the class of systems that satisfy reciprocity (Strutt, 1873). Middle-ear functioning is reciprocal to the extent that it is adequately described by such a system of generalized forces and velocities. Middle-ear mechanics has been assumed to satisfy reciprocity in previous studies (Shera and Zweig, 1991; Shera and Zweig, 1992a; Puria, 2003; Voss and Shera, 2004) as in this study.

Consider a general S matrix 1S_2 terminated on the left by an acoustic transmission line with characteristic impedance Z_1 and on the right by a line with characteristic impedance Z_2 . Reciprocity in a one-dimensional S-matrix model implies (Shera and Zweig, 1992b)

$$t^- = \alpha t^+, \quad \alpha = \frac{Z_1}{Z_2}. \quad (6)$$

Reciprocity directly relates reverse and forward transmission with a coefficient α equal to the ratio of the characteristic impedances at the ends.

C. S-matrix formulation of ear-canal/middle-ear/cochlear model

A time dependence of $e^{j2\pi ft}$ with unit imaginary number j , frequency f , and time t is used throughout (the symbol t is frequently used elsewhere to denote a transmittance, but the meaning is always clear from the context). The S-matrix between the ear-canal microphone and the basal end of the cochlea for the model in Fig. 1 is ${}^eS_c = {}^eS_o \otimes {}^oS_b \otimes {}^bS_c$. If the cross-sectional area of the ear canal is slowly varying along its midline relative to its wavelength, then any forward or reverse incident wave travels without reflection. The resulting ear-canal S matrix over a distance ℓ is parametrized by the forward (t_ℓ^+) and reverse (t_ℓ^-) ear-canal transmittances

$${}^eS_o = \begin{pmatrix} 0 & t_\ell^- \\ t_\ell^+ & 0 \end{pmatrix}. \quad (7)$$

For constant ear-canal area, the transmittances satisfy

$$t_\ell^+ = t_\ell^- = e^{-jk\ell}, \quad k = 2\pi f/c, \quad (8)$$

in which c is the acoustical phase velocity. The ear-canal length ℓ is sufficiently short that viscothermal wall loss in the ear canal can be neglected, although additional losses are likely present due to motion of the ear-canal walls in young infants (Keefe *et al.*, 1993).

The stimulus levels are assumed sufficiently low that middle-ear muscle reflex effects are absent, so that the middle ear acts as a linear system. The middle-ear S matrix is parametrized according to the general form of Eq. (3) by

$${}^oS_b = \begin{pmatrix} R^+ & T^- \\ T^+ & R^- \end{pmatrix}. \quad (9)$$

It follows from Eq. (6) that

$$T^- = \alpha_M T^+, \quad \alpha_M = \frac{\zeta}{Z_{Cb}}, \quad \zeta = \rho c/A^{ec}, \quad (10)$$

in which the acoustical characteristic impedance in the ear canal is ζ with ear-canal cross-sectional area A^{ec} and equilibrium density of air ρ . The characteristic impedance associated with the cochlear traveling wave at the basal end of the cochlea is Z_{Cb} . If α_M is real, then Eq. (10) predicts that T^+ and T^- have equal phase responses. Because the phase of Z_{Cb} may differ from zero, the reverse middle-ear transmittance phase is the difference in the forward middle-ear transmittance phase and the phase of Z_{Cb} .

Because the basilar-membrane mechanics are linear in the basal end of the cochlea, the forward and reverse pressure waves travel therein without reflection, so that bS_c has the form

$${}^bS_c = \begin{pmatrix} 0 & t^- \\ t^+ & 0 \end{pmatrix}. \quad (11)$$

Reciprocity implies that

$$t^- = \alpha_C t^+, \quad \alpha_C = \frac{Z_{Cb}}{Z_{Cc}}, \quad (12)$$

in which the cochlear impedance at the cochlear vestibule Z_{Cb} and that at the basal boundary of the f_2 source region (location c in Fig. 1) in the cochlea is Z_{Cc} . The long-wavelength approximation to cochlear mechanics is thought to be accurate in the basal region (Zweig, 1991).

For modeling DPOAEs, the S-matrix cS_a in the f_2 -source region is assumed to have the same form as in Eq. (11), but in which the transmittances may vary with signal level (Shera and Zweig, 1992b). The dependence on signal level is indicated here and elsewhere, where needed for clarity, by a tilde over the variable. This S matrix is

$${}^cS_a = \begin{pmatrix} 0 & \tilde{t}^- \\ \tilde{t}^+ & 0 \end{pmatrix}. \quad (13)$$

The S-matrix ${}^eS_c = {}^eS_o \otimes {}^oS_b \otimes {}^bS_c$ between the probe microphone and the basal boundary of the f_2 source region in the cochlea is written using Eqs. (5) and (7)–(12) as

$$\begin{pmatrix} P_e^- \\ P_e^+ \end{pmatrix} = {}^eS_c \begin{pmatrix} P_c^+ \\ P_c^- \end{pmatrix},$$

$${}^eS_c = \begin{pmatrix} e^{-2jk\ell} R^+ & e^{-jk\ell} t^- T^- \\ e^{-jk\ell} t^+ T^+ & R^- t^+ t^- \end{pmatrix} = \begin{pmatrix} e^{-2jk\ell} R^+ & \alpha e^{-jk\ell} t^+ T^+ \\ e^{-jk\ell} t^+ T^+ & \alpha_C R^- t^+ t^- \end{pmatrix},$$

$$\alpha = \alpha_C \alpha_M = \frac{\zeta}{Z_{C_c}}. \quad (14)$$

This is the most general S matrix needed for subsequent analyses.

D. Forward transmission

The ear-canal source generates a forward incident pressure $P_c^+(f)$. Its forward transmission is analyzed between the stimulus pressure P_e in the ear canal and the cochlear pressure P_c at the basal end of the f_2 -source region.

1. SFOAE effects on ear-canal reflectance and the forward cochlear wave

If the stimulus frequency (SF) OAE source lies in the tonotopic region of the cochlea, a reverse cochlear SFOAE source P_c^- is related to the cochlear forward stimulus signal P_c^+ and an apical cochlear reflectance R_{SF} by

$$P_c^- = R_{SF} P_c^+. \quad (15)$$

The coherent reflection emission theory predicts a specific form of R_{SF} (Zweig and Shera, 1995), but the representation in Eq. (15) applies to any source mechanism apical to node c in Fig. 1. The ${}^e S_c$ in Eq. (14) is analyzed with Eq. (15) to solve for the reverse ear-canal pressure P_e^- in terms of the ear-canal stimulus P_e^+ with the result

$$P_e^- = \tilde{R}_e^+ P_e^+, \quad \tilde{R}_e^+ = e^{-2jk\ell} R^+ + \frac{e^{-2jk\ell} t^- T^- R_{SF} T^+ t^+}{1 - R^- t^+ t^- R_{SF}}. \quad (16)$$

The term R_e^+ (without a tilde) is the ear-canal reflectance in the absence of any SFOAE, and is given by the first term on the right-hand side of the above

$$R_e^+ = e^{-2jk\ell} R^+. \quad (17)$$

This is the product of round-trip travel in the ear canal and the reflectance at the eardrum. It is the commonly measured ear-canal reflectance, whose squared magnitude (called energy reflectance) is also commonly interpreted as a middle-ear response by neglecting the OAE contribution in Eq. (16).

The last term on the right-hand side of Eq. (16) represents the effect of SFOAEs on the reflectance measurement through its dependence on the apical cochlear reflectance R_{SF} . The denominator describes the effect of multiple internal reflections of the SFOAE within the cochlea. In the experiments to be described, the ear-canal reflectance was measured using a wideband click, so that the OAE generated is a transient evoked (TE) OAE, which is spectrally decomposed here into its SFOAE component at f . TEOAEs in human ears are likely generated through the process of coherent reflection emissions. Because of basilar-membrane compression, the relative contribution of the TEOAE in Eq. (16) to the measured ear-canal reflectance decreases with increasing stimulus level (Keefe, 1997; Burns and Keefe, 1998). The effect of the TEOAE on the reflectance spectrum in the ear canal produces a ripple in the response that is otherwise dominated by the middle-ear reflectance and the ear-canal phase delay.

The \tilde{P}_c is the cochlear pressure at the stimulus frequency that includes the effect of the SFOAE. The S-matrix ${}^e S_c$ is further analyzed with Eqs. (15)–(17) to solve for \tilde{P}_c in terms of the ear-canal stimulus P_e and the SFOAE (via R_{SF}) as follows:

$$\tilde{P}_c = P_c \left[\frac{1 + R_{SF}}{1 + \frac{t^- R_{SF} t^+}{1 + R_e^+} [-R^- + e^{-2jk\ell} (T^- T^+ - R^- R^+)]} \right], \quad (18)$$

in which the cochlea pressure P_c in the absence of any SFOAE is

$$P_c = \tilde{P}_c |_{R_{SF}=0} = \frac{e^{-jk\ell} T_F}{1 + R_e^+} P_e, \quad T_F = t^+ T^+. \quad (19)$$

The $T_F(f)$ is the forward pressure transfer function through the middle ear and the basal region of the cochlea to the location where $P_c(f)$ is defined.

2. Forward stimuli for DPOAEs

In a DPOAE test, the sinusoidal stimuli at primary frequencies f_1 and f_2 lead to cochlear pressures $\tilde{P}_c(f_1)$ and $\tilde{P}_c(f_2)$. If the SFOAEs at the primary frequencies are neglected, then the cochlear pressures $P_c(f_1)$ and $P_c(f_2)$ are found from Eq. (19) to be

$$P_c(f_1) = \frac{e^{-2\pi i f_1 \ell / c} T_F(f_1)}{1 + R_e^+(f_1)} P_e(f_1), \quad (20)$$

$$P_c(f_2) = \frac{e^{-2\pi i f_2 \ell / c} T_F(f_2)}{1 + R_e^+(f_2)} P_e(f_2).$$

When testing at stimulus levels near the DPOAE threshold, the SFOAE contributions to $\tilde{P}_c(f_1)$ and $\tilde{P}_c(f_2)$ in Eq. (18) may be relevant in interpreting the low-level DPOAE responses. For example, DPOAE I/O functions recorded in individual ears with $f_2/f_1=1.2$ are sometimes nonmonotonic even when the signal to noise ratio appears adequate (Gorga *et al.*, 1994), even though the I/O functions averaged across ears may be monotonic. Aside from these low-level effects near threshold, it suffices in the following to interpret the DPOAE using $P_c(f_1)$ and $P_c(f_2)$ given in Eq. (20).

E. DPOAE generator source model

The resulting DPOAE source pressure $P_c^-(f_{DP})$ was calculated by Shera and Zweig (1992b) as

$$P_c^-(f_{DP}) = \frac{\tilde{P}_c^- + \tilde{P}_a^+ \tilde{R}_a^- \tilde{t}^-}{1 - R_c^- \tilde{t}^+ \tilde{t}^- \tilde{R}_a^-} \quad (21)$$

in which each term on the right-hand side is evaluated at f_{DP} . This equation represents a two-source model of DPOAE generation. The first source \tilde{P}_c^- is generated within the f_2 -source region and travels in the reverse direction towards the ear canal. The second source \tilde{P}_a^+ is generated within the f_2 -source region, and travels in the forward direction to the more apical DP tonotopic place where it is reflected back. The \tilde{P}_a^+ is multiplied by the apical cochlear

reflectance \tilde{R}_a , measured with respect to the most apical region in Fig. 1. This reflectance is defined by $\tilde{P}_a^- = \tilde{R}_a \tilde{P}_a^+$. The \tilde{t}^- is the reverse transmittance defined in Eq. (13) across the f_2 -source region. The denominator of Eq. (21) includes \tilde{R}_a and transmittances defined in Eq. (13) as well as $R_c^-(f_{DP})$, which is described below.

Equation (21) is analyzed in the limit of small internal reflections, i.e., $|R_c^- \tilde{t}^+ \tilde{t}^- \tilde{R}_a| \ll 1$. Each reflectance and transmittance in this inequality has a magnitude between zero and one (ignoring any spontaneous OAEs present at f_{DP}). The inequality is typically satisfied so that Eq. (21) can be approximated using a first-order Taylor series as $P_c^-(f_{DP}) = (\tilde{P}_c^- + \tilde{P}_a^+ \tilde{R}_a \tilde{t}^-) [1 + R_c^- \tilde{t}^+ \tilde{t}^- \tilde{R}_a]$. The first term in parentheses on the right-hand side is the two-source term and is independent of middle- and external-ear functioning. The second term in brackets has terms representing cochlear nonlinearity and R_c^- , which depends on middle- and external-ear functioning. Consider averaging over a group of subjects, in which the effect of the total internal reflections would tend to average out. The group mean of $[1 + R_c^- \tilde{t}^+ \tilde{t}^- \tilde{R}_a]$ would be approximately equal to 1. It follows that the group mean of the magnitude $|P_c^-(f_{DP})|$, which is denoted by G , is a function only of the source terms as follows:

$$G = |\tilde{P}_c^- + \tilde{P}_a^+ \tilde{R}_a \tilde{t}^-| = G\left(f_1, f_2, \left| \frac{T_F(f_1)}{1 + R_e^+(f_1)} P_e(f_1) \right|, \left| \frac{T_F(f_2)}{1 + R_e^+(f_2)} P_e(f_2) \right| \right). \quad (22)$$

The DP source at f_{DP} is created by a nonlinear function G of the cochlear overlap of the two primaries [as described by Eq. (20)], and each primary input depends on the forward transmittance and the ear-canal reflectance. The second row shows the explicit dependence of G on f_1 and f_2 , which accounts for frequency-dependent variations in the DP source strength, and on their corresponding cochlear pressure amplitudes.

F. Reverse transmission

The DPOAE pressure at the probe microphone is calculated using Eq. (14). The DPOAE $P_c^-(f_{DP})$ in the cochlea is specified as the driving source. The boundary condition at the probe is that of Eq. (1), so that $P_e^+(f_{DP}) = R_s(f_{DP}) P_c^-(f_{DP})$. At frequency f_{DP} , Eq. (14) becomes

$$\begin{pmatrix} P_e^- \\ P_c^+ \end{pmatrix} = \begin{pmatrix} e^{-2jk\ell} R^+ & e^{-jk\ell} t^- T^- \\ e^{-jk\ell} t^+ T^+ & R^- t^+ t^- \end{pmatrix} \begin{pmatrix} R_s P_e^- \\ P_c^- \end{pmatrix}. \quad (23)$$

Using the top row of this equation and the fact that $P_e(f_{DP}) = [1 + R_s(f_{DP})] P_c^-(f_{DP})$, the resulting probe microphone pressure P_e is

$$P_e(f_{DP}) = \frac{[1 + R_s(f_{DP})] e^{-j2\pi f_{DP} \ell / c} T_R(f_{DP})}{[1 - R_s(f_{DP}) R_e^+(f_{DP})]} P_c^-(f_{DP}),$$

$$R_e^+(f_{DP}) = e^{-j4\pi f_{DP} \ell / c} R^+(f_{DP}), \quad (24)$$

$$T_R(f_{DP}) = t^-(f_{DP}) T^-(f_{DP}).$$

The middle equation is that of Eq. (17) evaluated at f_{DP} . The DPOAE pressure is proportional to $T_R(f_{DP})$, which is the reverse pressure transmittance at the TM. Using Eqs. (14) and (19), the reverse and forward transmittances at the TM are related by

$$T_R(f_{DP}) = \alpha(f_{DP}) t^+(f_{DP}) T^+(f_{DP}) = \alpha(f_{DP}) T_F(f_{DP}). \quad (25)$$

The bottom row of Eq. (23) with Eq. (22) provides the traveling wave ratio $R_e^-(f_{DP})$, which occurred in the denominator of Eq. (21), i.e.

$$R_e^-(f_{DP}) = \frac{P_c^+(f_{DP})}{P_c^-(f_{DP})} = t^+ R^- t^- + \frac{t^+ T^+ e^{-j4\pi f_{DP} \ell / c} R_s T^- t^-}{1 - R_e^+ R_s}. \quad (26)$$

G. Predicting forward and reverse transmission

For analyzing a group set of DPOAE I/O functions, the source term $|P_c^-|$ is replaced by its group mean G . The magnitude of Eq. (24) is expressed as

$$|P_e(f_{DP})| = H_R(f_{DP}) G,$$

$$H_R(f_{DP}) = E_R(f_{DP}) |T_R(f_{DP})| = \alpha E_R(f_{DP}) |T_F(f_{DP})|, \quad (27)$$

$$E_R(f_{DP}) = \frac{|1 + R_s(f_{DP})|}{|1 - R_s(f_{DP}) R_e^+(f_{DP})|}.$$

The reverse transfer function H_R is a product of the magnitudes of the reverse middle-ear transfer function and a reverse ear-canal transfer-function E_R , which depends on the ear-canal reflectance and the source reflectance of the probe.

The forward transfer function H_F is defined for use in Eq. (22) by

$$H_F(f) = E_F(f) |T_F(f)|, \quad E_F(f) = \frac{1}{|1 + R_e^+(f)|}. \quad (28)$$

The transfer function E_F varies with ear-canal reflectance. Magnitudes are converted to levels, i.e., the defined levels are L_1 and L_2 for stimuli, L_{DP} for DPOAEs, L_F for forward transfer function, L_R for reverse transfer function, and L_α for the reciprocity factor:

$$L_1 = 20 \log \frac{|P_e(f_1)|}{P_0}, \quad L_2 = 20 \log \frac{|P_e(f_2)|}{P_0},$$

$$L_{DP} = 20 \log \frac{|P_e(f_{DP})|}{P_0}, \quad L_F(f) = 20 \log |H_F(f)|, \quad (29)$$

$$L_R(f_{DP}) = 20 \log |H_R(f_{DP})| = L_\alpha + 20 \log E_R(f_{DP}) + 20 \log |T_F(f_{DP})|,$$

$$L_\alpha = 20 \log |\alpha|.$$

The reference pressure is $P_0 = 0.00002$ Pa.

Using Eqs. (22), (27), and (29), L_{DP} is expressed using a DPOAE source level g as

$$L_{\text{DP}}(f_1, f_2, L_1, L_2) = L_R(f_{\text{DP}}) + g[f_1, f_2, L_1 + L_F(f_1), L_2 + L_F(f_2)], \quad (30)$$

$$g = 20 \log \frac{G}{P_0}.$$

This simplifies in measurements with fixed frequency ratio f_2/f_1 and fixed level difference $\Delta L = L_1 - L_2$. Because $f_2/f_1 = 1.2$ is close to 1, the forward transmittance and ear-canal reflectance are assumed to vary sufficiently slowly that $L_F(f_1) \approx L_F(f_2)$. The resulting DPOAE level is the same as in the model of Abdala and Keefe (2006)

$$L_{\text{DP}}(L_2)|_{\text{fixed } f_2/f_1, \Delta L} = L_R(f_{\text{DP}}) + g[f_2, L_2 + L_F(f_2)]. \quad (31)$$

The explicit dependence of g on f_2 may be omitted in the following because the DPOAEs of Abdala and Keefe were measured at a single f_2 , i.e., $g(f_2, L_2 + L_F(f_2)) = g(L_2 + L_F)$.

H. Cochlear maturity and external/middle ear immaturity

In testing the hypothesis that cochlear functioning is mature in infants, Abdala and Keefe used a particular form of g in Eq. (31) to fit the mean adult DPOAE data in units such that the mean reverse transfer-function level L_R^a in adults and the mean forward transfer-function L_F^a in adults were each normalized to zero, i.e.

$$L_{\text{DP}}^a = L_{\text{DP}}(L_2)|_{\text{fixed } f_2/f_1, \Delta L} = g(L_2). \quad (32)$$

A superscript a on any variable denotes the adult group and i denotes any infant group. The infant DPOAE I/O functions L_{DP}^i were fitted with the same function g as in adults (consistent with the hypothesis of mature cochlear function), and their forward transfer-function level ΔL_F and reverse transfer-function level ΔL_R were calculated with respect to the adult level.

With Eqs. (19) and (28), the forward transfer function is decomposed into

$$H_F = |t^+ T^+| E_F. \quad (33)$$

The ratio ΔH_F of the forward transfer-function magnitude in infants re: adults is

$$\Delta H_F = \frac{H_F^i}{H_F^a} = \frac{|t^{+,i} T^{+,i}| E_F^i}{|t^{+,a} T^{+,a}| E_F^a} = \frac{|T^{+,i}| E_F^i}{|T^{+,a}| E_F^a}. \quad (34)$$

The hypothesis that cochlear functioning is adult-like was used in the above, so that the basal-region cochlear transmittance [see Eq. (11)] is the same in infants and adults ($t^{+,i} = t^{+,a}$). The term ΔH_F is expressed as a relative level ΔL_F by

$$\Delta L_F = 20 \log \Delta H_F = \Delta L_{\text{FE}} + \Delta L_{\text{FM}}, \quad (35)$$

$$\Delta L_{\text{FE}} = 20 \log \frac{E_F^i}{E_F^a}, \quad \Delta L_{\text{FM}} = 20 \log \frac{|T^{+,i}|}{|T^{+,a}|}.$$

The relative forward transfer-function level ΔL_F is expressed as a sum of a relative forward ear-canal level ΔL_{FE} and a relative forward middle-ear transmittance level ΔL_{FM} . The measurements of ear-canal reflectance in infants and adults

provide a measurement of ΔL_{FE} via Eq. (28). Combining this measured ΔL_{FE} with the measured ΔL_F by Abdala and Keefe (2006) provides an estimate of ΔL_{FM} , which quantifies the effects of maturation on forward middle-ear transmittance.

Concerning reverse transmission, reciprocity was expressed in Eq. (29) in terms of $\alpha = \alpha_C \alpha_M$. If cochlear functioning is mature in infants, then α_C in the basal cochlear region is the same in infants and adults. Thus, ΔL_α in infants re: adults is given using Eq. (10) by

$$\Delta L_\alpha = 20 \log_{10} \frac{\alpha^i}{\alpha^a} = 20 \log_{10} \frac{\alpha_M^i}{\alpha_M^a} = 20 \log \frac{A^a}{A^i}, \quad (36)$$

in which A^a is the cross-sectional area of the ear canal in adults, and A^i in infants. The above used the fact that Z_{Cb} is mature in infants with the hypothesis of mature cochlear function in full-term infants. The ΔL_α varies with the ratio of the average ear-canal areas in adults and infants. The relative reverse transmittance ΔL_R in infants compared to adults is defined based on the middle row of Eqs. (27), (35), and (36):

$$\begin{aligned} \Delta L_R(f_{\text{DP}}) &= 20 \log \left(\frac{H_R^i}{H_R^a} \right) \\ &= \Delta L_{\text{RE}}(f_{\text{DP}}) + \Delta L_{\text{FM}}(f_{\text{DP}}) + \Delta L_\alpha, \end{aligned} \quad (37)$$

$$\Delta L_{\text{RE}}(f_{\text{DP}}) = 20 \log \frac{E_R^i(f_{\text{DP}})}{E_R^a(f_{\text{DP}})}.$$

The relative level ΔL_{RE} is calculated using the ear-canal and source reflectances [see bottom row of Eq. (27)]. The relative level ΔL_R is a sum of relative levels involving the area, the ear-canal and source reflectances, and the forward middle-ear transmittance.

The reverse middle-ear transmittance T^- is related by reciprocity in Eq. (10) to the forward middle-ear transmittance T^+ . Converting that equation to a form showing the relative level difference between infants and adults, the relative reverse middle-ear transmittance level ΔL_{RM} is given by

$$\Delta L_{\text{RM}} = 20 \log \left| \frac{T^{-,i}}{T^{-,a}} \right| = \Delta L_{\text{FM}} + \Delta L_\alpha. \quad (38)$$

The second row of the above is based on the assumed maturity of the characteristic impedance Z_{Cb} in infant ears that occurs in Eq. (10), the bottom equation in Eqs. (35) and (36). It follows from Eqs. (37) and (38) that $\Delta L_R(f_{\text{DP}}) = \Delta L_{\text{RE}}(f_{\text{DP}}) + \Delta L_{\text{RM}}(f_{\text{DP}})$, which is the analog for reverse transmission to the top Eq. (35) for forward transmission. Thus, ΔL_{RM} is directly measured using

$$\Delta L_{\text{RM}}(f_{\text{DP}}) = \Delta L_R(f_{\text{DP}}) - \Delta L_{\text{RE}}(f_{\text{DP}}). \quad (39)$$

I. Acoustic estimate of ear-canal area

The ear-canal area needed to calculate ΔL_α in Eq. (36) was acoustically estimated using the following procedure. The reflectance R_e^+ in the ear canal was measured according to methods described in Sec. III B, in particular, based on the area A^{cal} of a calibration tube. Its corresponding characteris-

tic impedance was $\zeta^{\text{cal}} = \rho c / A^{\text{cal}}$. The ear-canal acoustic impedance $Z_e^+[k]$ at the probe tip was calculated in the k th frequency bin by

$$Z_e^+[k] = \zeta^{\text{cal}}(1 + R_e^+[k]) / (1 - R_e^+[k]). \quad (40)$$

The click response was recorded at a sample rate f_s using N samples; the k th frequency was $f_k = (k/N)f_s$ ($f_s = 22.05$ kHz, $N = 1024$). If the area A of a particular ear were measured, then the characteristic impedance of that ear canal would be $\zeta = \rho c / A$. Using this ζ , a new reflectance R_{ec}^+ can be defined such that the acoustic impedance takes the form

$$Z_e^+[k] = \zeta(1 + R_{\text{ec}}^+[k]) / (1 - R_{\text{ec}}^+[k]). \quad (41)$$

The invariance in impedance in Eqs. (40) and (41) is possible because the plane-wave impedances on opposite sides of an area discontinuity are equal (Morse and Ingard, 1968). This expression can be rearranged into $Z_e^+[k] = \zeta + R_{\text{ec}}^+[k](\zeta + Z_e^+[k])$, and expressed in the time domain as a recursive function of sample number n by (Sondhi and Resnick, 1983; McIntyre *et al.*, 1983)

$$z_e^+[n] = \zeta \delta[n] + r_{\text{ec}}^+[n] * (\zeta \delta[n] + z_e^+[n]). \quad (42)$$

The asterisk denotes time-domain convolution and $\delta[n]$ equals 1 for $n=0$, and 0 otherwise. The time-domain impedance $z_e^+[n]$ and reflectance $r_{\text{ec}}^+[n]$ in Eq. (42) are defined using the N -sample inverse discrete Fourier transform (DFT) by

$$z_e^+[n] = \frac{1}{N} \sum_{k=0}^{N-1} Z_e^+[k] e^{-j2\pi nk/N}, \quad (43)$$

$$r_{\text{ec}}^+[n] = \frac{1}{N} \sum_{k=0}^{N-1} R_{\text{ec}}^+[k] e^{-j2\pi nk/N}.$$

The $r_{\text{ec}}^+[n]$ is causal so that $r_{\text{ec}}^+[0] = 0$. It follows from Eq. (42) at $n=0$ that $z_e^+[0] = \zeta$. Combining this with the top equation of Eq. (43) at $n=0$ leads to

$$\begin{aligned} \zeta &= \frac{1}{N} \sum_{k=0}^{N-1} Z_e^+[k] \\ &= \frac{1}{N} \left(\text{Re } Z_e^+[0] + \text{Re } Z_e^+[N/2] + 2 \sum_{k=1}^{N/2-1} \text{Re } Z_e^+[k] \right). \end{aligned} \quad (44)$$

The latter form of the above uses DFT symmetry properties for the case that $\zeta = \rho c / A^{\text{ec}}$ is real. Its right-hand side is expressed in terms of the real part of the impedance. The $Z_e^+[N/2]$ converges to ζ at high frequencies, and $Z_e^+[0]$ is approximated as ζ (an improved theory would introduce a complex ζ at frequencies < 0.25 kHz), so that

$$\zeta = \frac{1}{N/2 - 1} \sum_{k=1}^{N/2-1} \text{Re } Z_e^+[k] = \langle \text{Re}(Z_e^+) \rangle. \quad (45)$$

Thus, the ear-canal area A was calculated in terms of the frequency average of the real part of the impedance $\langle \text{Re}(Z_e^+) \rangle$ by

$$A = \frac{\rho c}{\langle \text{Re}(Z_e^+) \rangle}. \quad (46)$$

Keefe *et al.* (1992) reported this relation with an incorrect coefficient, although this reference and Keefe *et al.* (1993) used the correct equation (46) to calculate the area. Huang *et al.* (2000) correctly reported this relation. Its practical application may be limited in that the bandwidth of the averaging of $\langle \text{Re}(Z_e^+) \rangle$ was limited to 0.25–8 kHz. Nevertheless, this finite-bandwidth approximation gave accurate area estimates for calibration tubes to within a couple of percent, so it is likely to be acceptable for area estimates in ears as well.

Any $\text{Re}(Z_e^+) < 0$ were reset to 0 but included in the average. Such negative values may have occurred due to small inaccuracies in reflectance calibration, errors related to a probe-tip placement close to the ear-canal wall, or by partial or complete blockage of the tip by cerumen. This procedure differed slightly from that of Huang *et al.* (2000), who omitted frequencies from the average at which $\text{Re}(Z_e^+) < 0$. The two procedures were compared across infant ears, and the differences in area estimates were within 10% in 88 of 106 ears. The maximum procedural difference for any ear was 44%, but this case involved a measurement with significant artifact. The median difference in estimating the area was zero for infants and 1.3% for adults. Thus, the acoustic area estimate was judged sufficiently accurate for use in interpreting reverse middle-ear transmission differences across age. The within-ear area differences attributable to choice of procedure were smaller than the between-ear differences.

This area estimation procedure assumed that the ear-canal walls were rigid. However, neonatal ear canals have nonrigid walls that move in response to sound below 1 kHz (Keefe *et al.*, 1993), which would introduce some error. The fact that the average extended over a wider frequency range (up to 8 kHz) would suggest that the contribution of nonrigid walls did not have a major effect in data from young infants, but the size of this error is unknown.

J. Summary of model predictions

For interpreting the relative forward (ΔL_F) and reverse (ΔL_R) transfer-function levels derived from measured DPOAE I/O functions, the main result of the model is to partition these levels in infants relative to adults into ear-canal and middle-ear components by

$$\Delta L_F(f_2) = \Delta L_{\text{FE}}(f_2) + \Delta L_{\text{FM}}(f_2), \quad (47)$$

$$\begin{aligned} \Delta L_R'(f_{\text{DP}}) &= \Delta L_{\text{RE}}(f_{\text{DP}}) + \Delta L_{\text{FM}}(f_{\text{DP}}) + \Delta L_\alpha \\ &\approx \Delta L_{\text{RE}}(f_{\text{DP}}) + \Delta L_{\text{FM}}(f_1) + \Delta L_\alpha, \end{aligned} \quad (48)$$

$$\Delta L_R(f_{\text{DP}}) = \Delta L_{\text{RE}}(f_{\text{DP}}) + \Delta L_{\text{RM}}(f_{\text{DP}}). \quad (49)$$

The ΔL_F is determined in Eq. (47) from DPOAE measurements (Abdala and Keefe, 2006), and ΔL_{FE} from reflectance measurements, so that the relative forward middle-ear transmittance level $\Delta L_{\text{FM}}(f_2) = \Delta L_F(f_2) - \Delta L_{\text{FE}}(f_2)$ may be calculated at f_2 .

The $\Delta L'_R$ in Eq. (48) is the predicted relative reverse transmission level, which is compared with the measured ΔL_R from DPOAE measurements (Abdala and Keefe, 2006). The $\Delta L_{RE}(f_{DP})$ was calculated from reflectance data, and ΔL_α from the ratio of the adult to the infant ear-canal cross-sectional area, as estimated acoustically. Because forward transmission was measured by Abdala and Keefe across the stimulus frequencies f_1 and f_2 , but not at f_{DP} , $\Delta L_{FM}(f_{DP})$ in Eq. (48) was approximated using $\Delta L_{FM}(f_1)$, i.e., it was calculated based on measurements at the stimulus frequency f_1 closest to f_{DP} . This $\Delta L_{FM}(f_1)$ was calculated using a relation similar to Eq. (47) at f_1 , i.e., $\Delta L_{FM}(f_1) \approx \Delta L_F(f_2) - \Delta L_{FE}(f_1)$. The level difference ε in predicted and measured relative reverse transmission levels was defined as

$$\varepsilon(f_{DP};f_1) = \Delta L'_R(f_{DP}) - \Delta L_R(f_{DP}). \quad (50)$$

The notation $\varepsilon(f_{DP};f_1)$ means that the dominant difference is compared at f_{DP} , but that the prediction of $\Delta L_R(f_{DP})$ depends on $\Delta L_{FM}(f_1)$ at f_1 . The level difference in $\varepsilon(f_{DP};f_1)$ was judged with respect to the reported 28 dB difference in terms infants between ΔL_R and ΔL_F .

By analogy with the above discussion of forward transmission, the $\Delta L_R(f_{DP})$ is determined in Eq. (49) from DPOAE measurements (Abdala and Keefe, 2006), and $\Delta L_{RE}(f_{DP})$ from reflectance measurements, so that the relative reverse middle-ear transmittance level $\Delta L_{RM}(f_{DP}) = \Delta L_R(f_{DP}) - \Delta L_{RE}(f_{DP})$ may be calculated at f_{DP} .

III. METHODS

This section describes the methods used to measure ear-canal reflectance in the same set of subjects in whom DPOAE responses were collected. DPOAE methodology and results for infant and adult subjects are completely described in Abdala and Keefe (2006).

A. Subjects

Ten normal-hearing adults and 35 normal-hearing infants participated as subjects in this part of the study. The adults had a mean age of 27.5 years and audiometric thresholds <15 dB HL for frequencies from 250 to 8000 Hz. Of the infant subjects, 21 were term born and 14 were infants born prematurely (mean age at birth=35 postconceptional weeks) but tested after they reached term-like status, i.e., 37–41 postconceptional weeks. Infants had a mean birth weight of 2920 g and mean apgar scores of 7.7 and 8.7. Other than premature birth, none of the infants had high-risk factors for hearing loss; the hearing in all infant subjects was within normal limits. Subjects included both males and females, and data were collected in one ear per subject. Each age group included both right and left test ears.

Ear-canal reflectance was analyzed in a subset of these ears. Inasmuch as some data were obtained longitudinally, data were dropped if the DPOAE in the same subject dropped by 10 dB or greater from one test session to another and parent reported the infant to be sick or congested, which indicated a possible upper respiratory infection. Data were dropped if the energy reflectance was close to zero and/or if the equivalent volume was extremely negative at low fre-

quencies (≤ 1 kHz). The presence of either or both conditions indicated a likely leak of the probe in the ear canal (Keefe *et al.*, 2000). Data were dropped if the energy reflectance at high frequencies (6–8 kHz) exceeded 1.2. In the absence of spontaneous OAEs, the energy reflectance should not exceed 1.0, but data with energy reflectances between 1.0 and 1.2 were retained in the data set, even though there was some artifact present in the measurement. We preferred to retain data with modest amounts of artifact at some frequencies rather than to discard all the subject's data. This artifact may have been due to a partially blocked probe tip by cerumen or resulting from placement near the ear-canal wall, or reflectance calibration errors at high frequencies. The final numbers of subjects analyzed in each age group was seven term infants, eight of age 1.5 months, nine at each of ages 3, 4, and 5 months, 13 at age 6 months, and ten adults.

B. Reflectance procedures

An Etymotic ER10C probe was used with two receivers and a microphone, with a manufacturer's modification to provide +20 dB additional gain to each receiver. This same probe was used in Abdala and Keefe (2006). DPOAE and reflectance responses were acquired, whenever possible, based on the same ear-canal insertion. Receiver 1 delivered a brief "click" approximating a band-limited impulse from 0.25 to 8 kHz. Receiver 1 was driven by the output of a digital to analog converter (DAC) of a computer sound card (CardDeluxe) using custom-written software. The microphone output was synchronously recorded using an analog to digital converter (ADC) on the sound card. The sample rate was 22.05 kHz using a DAC and ADC buffer length of 1024 samples.

The response was a time average of eight ADC buffers in each infant's ear and 16 ADC buffers in each adult's ear. The shorter test duration in infants provided a response when the infant was judged by the operator to be quiet. Up to six responses were stored so that the operator could acquire multiple responses and choose the "best" response afterwards.

The ear-canal reflectance R_e^+ was calculated based on the click response and a calibration procedure performed before the subject was tested. The calibration used click responses recorded in a long and a short cylindrical, rigid-walled tube, with each tube closed at its far end. The calibration was based on a model of viscothermal wave propagation in each tube. The two main outputs from the calibration were the incident pressure response and the source (pressure) reflectance of the probe [see Eq. (1)]. The incident pressure was the acoustic click response in the absence of reflections. The adult probe was calibrated using a pair of large-diameter tubes (of nominal lengths 292 and 8.2 cm) with a diameter (7.94 mm) close to that of the adult ear. The infant probe was calibrated using a pair of small-diameter tubes (of lengths 237 and 5.9 cm) with a diameter (4.76 mm) close to that of the infant ear canal.

Other calibration outputs, which are further described in Keefe and Simmons (2003), included the root-mean-squared error ΔR in the calibration and a final estimated value of a dimensionless parameter χ , which equaled one if the actual

viscothermal loss was the same as the model wall loss, and otherwise slightly exceeded one, indicating that the measured loss exceeded the model loss. A reflectance calibration was valid for the adult probe if $\Delta R \leq 0.014$ and $1 \leq \chi \leq 1.11$, and valid for the infant probe if $\Delta R \leq 0.014$ and $1 \leq \chi \leq 1.09$. These validity criteria were set after analyzing preliminary results. After calibration, the ear-canal reflectance was calculated based on the incident pressure, the source reflectance and the ear-canal pressure.

The procedure was similar to previous work except for the following. Keefe and Simmons erroneously stated that ear-canal reflectance was calculated [in their Eq. (13)] using an additional input, the “measured ear-canal area” based on the size of the probe tip. In fact, their ear-canal reflectance results were calculated using their Eq. (8), in which the “nominal pressure reflectance” was normalized to the area of the tube set used in calibration. This error was fortuitous, because it is inaccurate to estimate the ear-canal area by the area of the probe tip (Keefe, 2004). The present ear-canal reflectance results were calculated using Eq. (8) of Keefe and Simmons (2003). In Keefe and Simmons, the source reflectance was calculated as a weighted average of the source reflectances measured in the short and long tubes. In the present study, the source reflectance was that measured using the short tube. An iterative loop within the calibration procedure was used to improve the model fit to the data by adjusting the estimates of tube lengths and χ .

Distributions of source reflectance measurements using adult and infant probes were collected based on calibrations on different days, and are plotted in Fig. 2. The median source reflectance magnitude of the adult probe exceeded that of the infant probe at all frequencies. This may be due to the fact that the sum of the areas of the two receiver ports and of the microphone port is the same for both probes, but their summed port area relative to the ear-canal area was smaller in the adult than the infant probe. This would result in a larger reflection amplitude from the adult probe. The median source reflectance phase remained within ± 35 degrees for both probes at all frequencies. The median reflectance magnitudes of both probes were relatively high across frequency except for minima near 2.6 and 5 kHz. If the probe functioned as an ideal closed-end termination, its source reflectance would have a magnitude of 1 and a phase of 0° . The R_s of the adult probe was more similar than that of the infant probe to this idealized source reflectance.

The source reflectance phase ϕ_s for the adult probe showed a positive slope that was repeatable (see box and whiskers plot at 6 kHz for the adult probe in Fig. 2). The ϕ_s of 35° at 8000 Hz is expressed as a phase advance τ_s by $\phi_s = 2\pi f\tau_s$, with $\tau_s = 12 \mu\text{s}$. The source of the phase advance may have been an effect of higher-order evanescent modes. These modes describe the nonplane-wave coupling between source and receiver at the probe surface. Such evanescent-mode effects should be more pronounced in the adult than infant probe, because, as described earlier, there is a larger discontinuity for the adult-sized calibration tubes between the summed port area compared to the calibration-tube area. At frequencies (such as in the present study) for which the highest analysis frequency was much less than the lowest

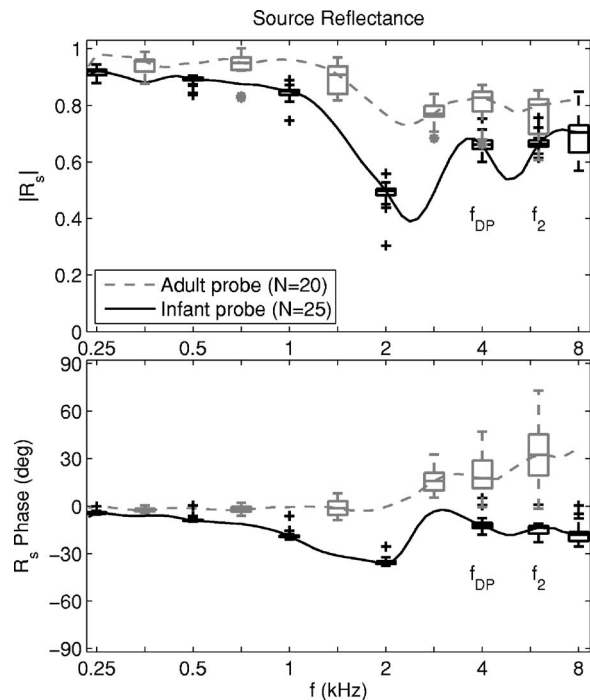


FIG. 2. The median source reflectance is shown for the probe used in infant (black solid line) and adult measurements (gray dashed line), while the distribution of source-reflectance responses is shown by the corresponding box and whisker plots spaced an octave apart. Box and whiskers plots are also shown at each of the f_{DP} and f_2 frequencies. The magnitude of the source reflectance is shown in the top panel and the phase of the source reflectance is shown in the bottom panel. The distribution of responses was based on $N=20$ calibrations of the adult probe and $N=25$ calibrations using the infant probe, with each calibration performed on a separate day.

cutoff frequency of any higher-order mode (Morse and Ingard, 1968), the impedance measured at the probe tip is the sum of the impedance of the plane-wave mode [as in Eq. (40)] plus an inductance that includes the effect of all the evanescent higher-order modes. The inductance impedance is parametrized as $j\zeta Eka$ in terms of the ear or calibration-tube radius a and a dimensionless evanescent mode factor E . The E depends on the specific geometry of source and receiver, but a typical value is of order 1 or less (Keefe and Benade, 1981). This means that evanescent-mode effects on acoustic pressure (e.g., inside the ear canal) are important only within an axial distance of order Ea from the probe surface. Taking $E=1$ as an estimate and $a \approx 4$ mm for the adult probe, the corresponding characteristic time associated with this inductance is of order $\tau_e = Ea/c \approx 7 \mu\text{s}$. This is similar in magnitude to $\tau_s = 12 \mu\text{s}$. The inductance would act as a perturbation in calculations of the incident pressure signal, the acoustic estimates of the lengths of the calibration tubes, and thus the source reflectance, but more study is needed.

Regarding the distributions of source reflectance data in Fig. 2, each box in a box and whiskers plot includes the inter-quartile range (IQR) between the 25th and 75th percentiles of responses, and each whisker above and below a box extends to the lesser of 1.5 IQR or the maximum data range. Individual outliers outside the whiskers were plotted with a black + for the infant probe and a gray * for the adult probe. The maximum number of outliers in magnitude or phase at any frequency never exceeded 3 out of a population of N

=20 adult-probe and $N=25$ infant-probe calibrations. The variability in source reflectance was smaller for the infant than the adult probe, as assessed by the narrower IQRs. This is likely due to the compressible foam eartip used in the adult probe, which differed in compression for each calibration. Sometimes when compressed, the foam was also slightly pushed out at its ends, which may have contributed to the variability. The variability increased slightly (i.e., the IQRs were wider) with increasing frequency. The particular f_2 and f_{DP} frequencies from the DPOAE data set are indicated in Fig. 2, and the median source reflectance at f_{DP} was used in calculating $\Delta L_{RE}(f_{DP})$.

The click stimulus to measure reflectance was delivered at a fixed voltage level to the receiver in each adult ear, and at a slightly different fixed level in each infant ear. The click amplitude in each ear was assessed in terms of the peak-to-peak pressure amplitude of the response. This pressure amplitude had a mean and standard deviation (SD) of 640 ± 151 mPa in adults, and a mean and SD of 588 ± 264 mPa in infants. The mean amplitudes expressed as peak sound pressure levels (pSPLs) were 90.1 dB for adults and 89.4 dB for infants. These are slightly less than the 85–95 dB pSPL click level used in typical measurements of a TEOAE using the nonlinear differential stimulus method (Kemp *et al.*, 1990). The pSPL does not adequately characterize the stimulus: the bandwidth of the click in the present study was broader (up to 8 kHz) than that used in typical TEOAE tests (up to 5–6 kHz), and the input voltage waveform was designed so that the acoustic stimulus was a band-limited impulse (Keefe and Simmons, 2003), whereas that used in typical TEOAE measurements is an electrical finite-duration impulse. The resulting click level in reflectance measurements had slightly lower spectral energy at frequencies where TEOAEs are typically measured. This emphasizes the fact that the reflectance stimulus did elicit TEOAE responses, which show up as a ripple on the individual-ear reflectance responses [see Eq. (16)].

C. Assessment of variability

Variability in measuring ΔL_F and ΔL_R from DPOAE I/O functions and variability in measuring the reflectance-based functions ΔL_{FE} , ΔL_{RE} and ΔL_α produced variability in derived estimates of ΔL_{FM} and ΔL_R . The effects of these sources of variability on estimating ΔL_{FM} and ΔL_R were assessed by calculating a (bootstrap) standard error (SE) of the mean for each variable across the population of responses using the methods of Efron and Tibshirani (1986).

The bootstrap method analyzed 1000 synthetic data sets (using the MATLAB Statistics Toolbox), in which each synthetic data set was created by randomly sampling N_d observations at a time with replacement from the actual N_d observations in each data set. This involved independent sampling of the DPOAE and reflectance data sets. The DPOAE data set comprised the set of DPOAE SPLs in each ear for each age group at each L_2 , and the reflectance data set comprised the set of reflectances and impedances measured in each ear for each age group.

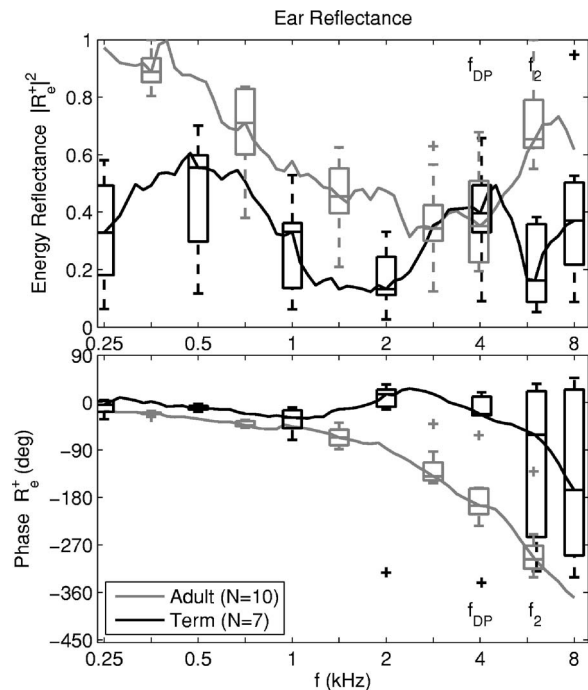


FIG. 3. The median ear-canal reflectance (average in frequency over each 1/12th octave) is shown for the adult group (gray line) and the full-term infant group (black line). The distribution of ear-canal reflectance responses in each group is also shown by box and whisker plots spaced an octave apart. Box and whisker plots are shown at each of the f_{DP} and f_2 frequencies. The ear-canal energy reflectance is shown in the top panel and its unwrapped phase is shown in the bottom panel.

IV. RESULTS

A. Ear-canal reflectance

The distribution of ear-canal energy reflectance ($|R_e^+|^2$) and unwrapped R_e^+ phase responses is plotted as 1/12th octave averages in Fig. 3 for the term-infant and adult groups. The energy reflectance was plotted rather than $|R_e^+|$ because it has often been reported in previous studies. The averaging partially smoothed out the ripples in R_e^+ that were a signature of a TEOAE response superimposed on the middle-ear reflectance, but some effects of OAE ripple remained. The 1/12th octaves were chosen because they include 4.00, 5.04 and 5.99 kHz, which are close to the DPOAE frequencies of f_{DP} (4 kHz), f_1 (5 kHz) and f_2 (6 kHz), respectively. Reflectance values at some of these frequencies were used in subsequent modeling.

The median energy reflectance was larger in adults than in term infants except at 4 kHz. The median reflectance phase delay was much larger in adults than term infants, mainly due to the larger distance between the probe tip and tympanic membrane in adults. The IQRs were more variable in the reflectance of term infants than in adults, especially in the energy reflectance at low (0.25 and 0.5 kHz) and high (6 and 8 kHz) frequencies. This increased variability in term infants was likely a result of differing maturational rates of ear-canal and middle-ear functioning. The variability in reflectance phase was small below 1 kHz in term infants and adults. At high frequencies in term infants, some reflectance phase responses required unwrapping and others did not, which increased the variability at 6 and 8 kHz. Each reflectance phase response was unwrapped in the adult group.

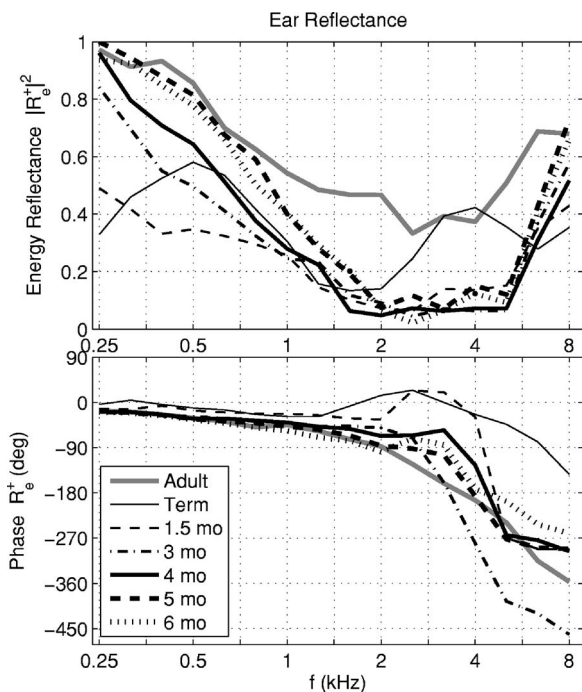


FIG. 4. The median ear-canal reflectance (average in frequency over each 1/3 octave) is shown for the adult group (gray line) and six infant groups (black lines). The magnitude of the ear-canal reflectance is shown in the top panel and its unwrapped phase is shown in the bottom panel. The line style and line thickness for each age group is listed in the legend.

The median energy reflectance and unwrapped phase delay of R_e^+ were plotted in Fig. 4 for the adult group (gray line) and infant groups ranging in age from full term to 1.5, 3, 4, 5, and 6 months. These reflectances were plotted as 1/3 octave averages to more fully remove the TEOAE-induced ripple. Except for full-term infants, which differed from the older infant age groups, the energy reflectance increased at low frequencies with increasing age. The energy reflectance in adults and infants of 1.5 months age and older had a minimum near 2–4 kHz, but the minimum energy reflectance was approximately 0.4 in adults versus 0.1 in infants. The unwrapped phase of R_e^+ had increasing delay with increasing frequency from 0.25 to 1.2 kHz in all age groups, with larger age variations above 2 kHz.

B. Ear-canal effects on forward and reverse transfer functions

The theory presented in Sec. I decomposed the forward and reverse transfer functions into ear-canal, middle-ear, and cochlear components. The measurement of ear-canal and source reflectances provided the ear-canal components of these transfer functions. Using Eqs. (28) and (33), a forward ear-canal transfer-function level L_{FE} (in dB) is

$$L_{FE} = 20 \log E_F = -20 \log |1 + R_e^+|. \quad (51)$$

Using Eq. (27), a reverse ear-canal transfer function level L_{RE} is

$$L_{RE} = 20 \log E_R = 20 \log \left| \frac{1 + R_s}{1 - R_s R_e^+} \right|. \quad (52)$$

The forward L_{FE} is relevant to interpreting ear-canal transmission in any hearing test that uses an insert earphone to

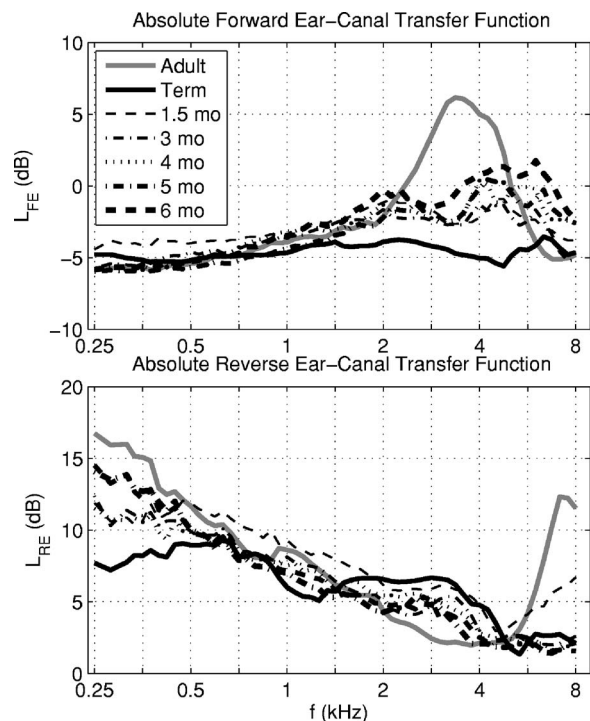


FIG. 5. The absolute level of the median forward ear-canal transfer function is shown in the top panel for the adult group (gray line) and six infant groups (black lines). The line style and line thickness are listed in the legend for each infant age group. The corresponding absolute level of the median reverse ear-canal transfer function is shown in the bottom panel.

deliver sound, and is relevant to a DPOAE test at stimulus frequencies f_1 and f_2 . The reverse L_{RE} is relevant to interpreting an OAE test outcome at the OAE frequency. The median $L_{FE}(f)$ and $L_{RE}(f)$ are plotted in Fig. 5 for infant and adult groups.

The forward level L_{FE} in the adult group had a well-defined maximum at frequencies in the range from 3 to 4 kHz—e.g., L_{FE} was 5 dB at 4 kHz, but only –2 dB at 2 kHz and –3 dB at 6 kHz. The L_{FE} in the adult and infant groups were similar at frequencies up to approximately 1.4 kHz. The full-term infant group had a relatively constant L_{FE} close to –5 dB at all frequencies. The infant groups at ages between 1.5 and 6 months had relatively small differences in L_{FE} . Their L_{FE} were between the adult and term-infant group levels between 2 and 4 kHz, and exceeded the adult and term-infant levels at and above 6 kHz.

The reverse level L_{RE} decreased with a slope of approximately –3 dB/octave between 0.6 and 5 kHz. The L_{RE} varied only slightly with age in this mid-frequency range, except for a 5 dB boost in term infants relative to adults near 2.8 kHz. In a common DPOAE screening procedure with f_2 of 4 kHz and f_2/f_1 of 1.2, the corresponding f_{DP} is 2.7 kHz. Thus, full-term infants received a boost relative to adults in the DPOAE response at this frequency due to reverse ear-canal transmission, while the adult received a larger boost relative to the full-term infant due to forward ear-canal transmission. Above 5 kHz, L_{RE} increased rapidly with increasing frequency up to approximately 7–8 kHz in adults. It remained approximately constant in infants, except for a small increase at high frequencies in the 1.5 month group. Below 0.6 kHz, L_{RE} varied significantly with age; the level at 0.25 kHz in the

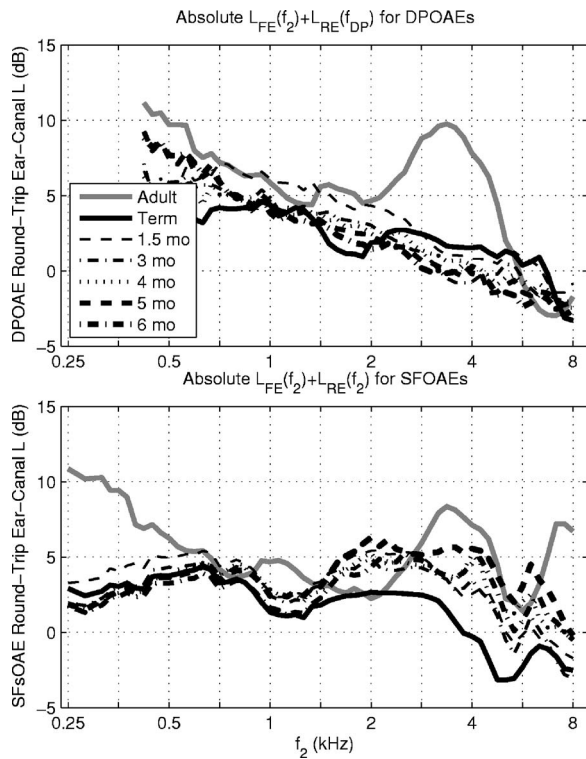


FIG. 6. Top panel: a round-trip ear-canal transfer function for a DPOAE test with $f_2/f_1=1.2$ is plotted vs f_2 as the sum of the medians of the forward ear-canal transfer function level $L_{FE}(f_2)$ and the reverse ear-canal transfer function level $L_{RE}(f_{DP})$. Bottom panel: a round-trip ear-canal transfer function for a SFOAE test is plotted vs its stimulus frequency (denoted f_2) as the sum of the medians of the forward ear-canal transfer-function level $L_{FE}(f_2)$ and the reverse ear-canal transfer-function level $L_{RE}(f_2)$. Results are shown for differing age groups with line styles as in Fig. 5.

adult group was approximately 9 dB larger than that in the term-infant group. This result may be related to the presence of ear-canal wall motion at low frequencies in younger infants. This effect contributes with the presence of their higher noise levels to the difficulties of measuring DPOAEs at low frequencies in young infants. These forward and reverse ear-canal levels interact differently in a DPOAE test in contrast to a SFOAE or TEOAE test. This is because forward transmission in a DPOAE test occurs at the f_2 (and f_1) frequencies and the DPOAE returns at the f_{DP} frequency.

The round-trip effect of these ear-canal transfer functions in a DPOAE test with $f_2/f_1=1.2$ (so that $f_{DP}=2f_2/3$) was represented by plotting $L_{FE}(f_2)+L_{RE}(f_{DP})$ (see top panel of Fig. 6). The most salient feature of this plot was that the adult group round-trip level had a maximum near 3.4 kHz. In a SFOAE test or a frequency-specific comparison in a TEOAE test, forward and reverse transmission occur at the same stimulus frequency. The round-trip effect of these ear-canal transfer functions in a SFOAE test was represented by plotting $L_{FE}(f_2)+L_{RE}(f_2)$ at the same stimulus frequency f_2 (see bottom panel of Fig. 6). The actual round-trip ear-canal level for the SFOAE test was somewhat flatter across frequency than for the DPOAE test within each age group (except for adults below 0.5 kHz, at which SFOAEs are rarely measured). It should be cautioned that the respective OAE levels are not strictly proportional to these sums of L_{FE} and L_{RE} , because the forward level is modified by cochlear non-linearity.

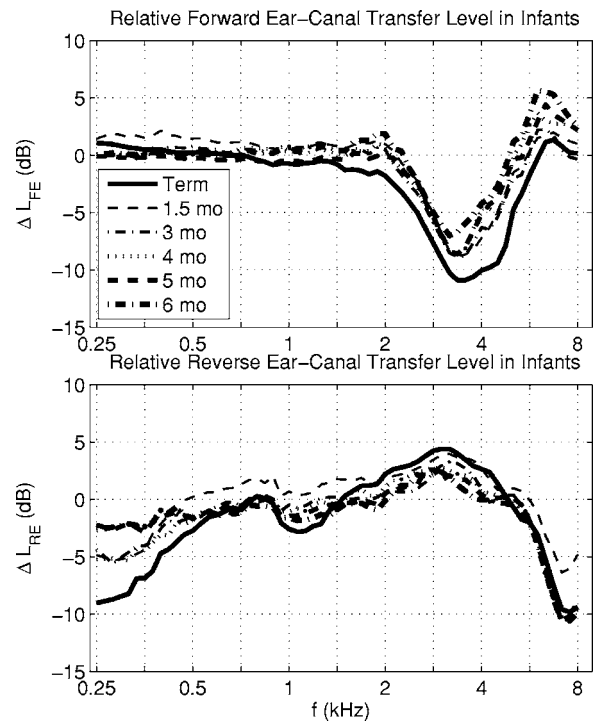


FIG. 7. Top panel: the level of each infant group relative to the adult group of the median forward ear-canal transfer function is plotted. The line style and line thickness are listed in the legend for each infant age group. Bottom panel: The corresponding level of each infant group relative to the adult group of the median reverse ear-canal transfer function is plotted.

The age differences in forward and reverse ear-canal transmission are revealed by defining the relative forward ear-canal transfer-function level ΔL_{FE} and relative reverse ear-canal transfer-function level ΔL_{RE} in infants compared to adults by

$$\Delta L_{FE} = L_{FE}^i - L_{FE}^a, \quad \Delta L_{RE} = L_{RE}^i - L_{RE}^a. \quad (53)$$

These definitions are equivalent to Eqs. (35) and (37). These relative levels in the infant groups are plotted in Fig. 7 in terms of the levels plotted in Fig. 5. The age effects in forward transmission were less than 2 dB at frequencies up to 2 kHz and above 6 kHz, but infant groups showed forward attenuation of up to 11 dB relative to adults at frequencies in the 3–4 kHz range. The relative reverse level in infants was attenuated below 0.6 kHz, boosted between 1.4 and 5 kHz, and attenuated above 5 kHz by as much as –10 dB at 8 kHz.

The theory in the Introduction identified the cross-sectional area A of the ear canal as important to reverse transmission of OAEs. The areas A^a in adults and A^i in infants were acoustically estimated using Eq. (46). The distributions of these areas were plotted in Fig. 8 using box and whiskers plots. The right vertical axis of the plot shows the approximate equivalent ear-canal diameter (equal to $\sqrt{4A/\pi}$) for the area A labeled on the left vertical axis at each tick mark. The median ear-canal area was only 8 mm² in the term-infant group and increased monotonically with increasing age to 31 mm² in 6 month olds, a value that was approximately half the median adult area of 58 mm². The IQR in each infant group was narrower than the adult IQR, although the IQRs relative to their medians were more similar. No

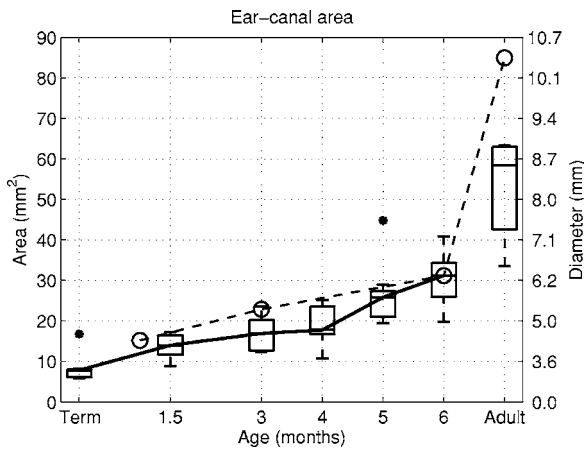


FIG. 8. The median of the acoustic estimate of the cross-sectional area of the ear canal is plotted as a function of age for infants and adults (solid line). Box and whisker plots show the distribution of measured areas in the present study with asterisks denoting an outlier in the term-infant group and in the 5 month group. The right-hand axis expresses this area as the diameter (in mm) of the equivalent circular cross section. The acoustic estimate of the ear-canal area from Keefe *et al.* (1993) are shown in a dashed line with circles as markers.

more than one outlier was present at any age. The acoustic estimates of ear-canal area from Keefe *et al.* (1993) are also shown in Fig. 8 (dashed line) at infant ages 1, 3, and 6 months, and in adults.

The relative area level $\Delta L_\alpha = 20 \log(A^a/A^i)$ introduced in Eq. (36) controlled the difference in reverse transmission between infants and adults. The distributions of ΔL_α in the infant groups were plotted in Fig. 9 as a set of box and whiskers plots. These box and whiskers plots were constructed for the distributions of infant ear-canal area relative to the median adult area (shown in Fig. 8). The median area level was 17 dB for term infants (corresponding to an adult area seven times larger than the infant area), and decreased with increasing age to 5 dB at 6 months.

The model-based decomposition of the relative forward level ΔL_F into an ear-canal component (ΔL_{FE}) and a middle-ear component ($\Delta L_{FM} = \Delta L_F - \Delta L_{FE}$) is shown in the top

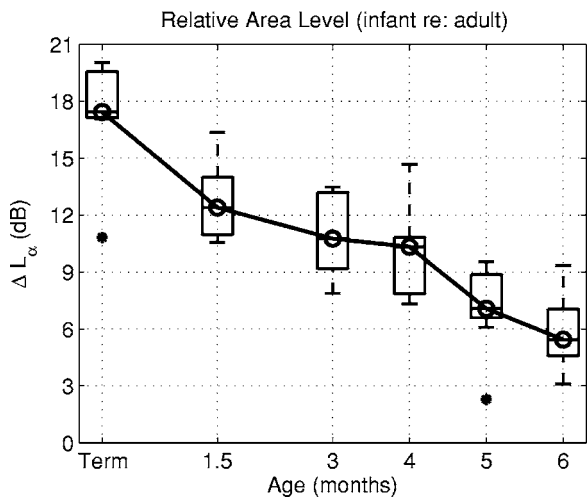


FIG. 9. The box plots of the median and IQR of relative area level ΔL_α (in dB) are plotted as a function of age based on the ratio of the median adult ear-canal area to the distribution of ear-canal areas in each infant age group.

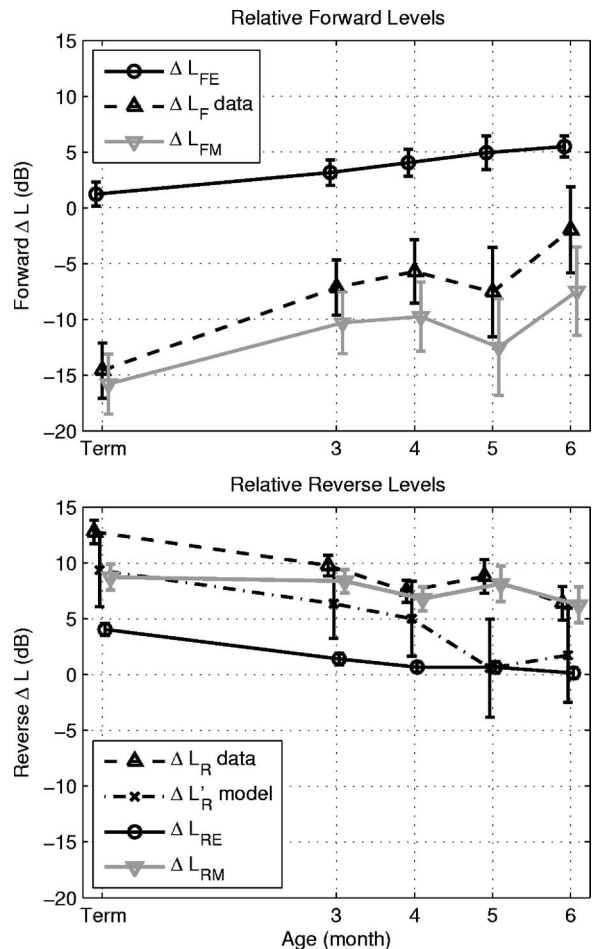


FIG. 10. Top panel: the relative forward transfer-function level ΔL_F data of Abdala and Keefe (2006) (dashed line, upwards triangle marker) and the ear-canal component ΔL_{FE} (solid black line, circle marker) are used to estimate the relative forward middle-ear transmittance level ΔL_{FM} (solid gray line, downwards triangle marker) at $f_2=6$ kHz as a function of infant age. Bottom panel: the relative reverse transfer-function level ΔL_R data of Abdala and Keefe (2006) (dashed line, upwards triangle marker) are plotted as a function of infant age at $f_{DP}=4$ kHz, as is its ear-canal component ΔL_{RE} (solid black line, circle marker), and its middle-ear component ΔL_{RM} (solid gray line, downwards triangle marker). The ΔL_R is compared to the model estimate $\Delta L'_R$ plot (dashed-dotted line, \times marker). The error bars in each estimate are shown as ± 1 SE. Some data are slightly offset horizontally to improve clarity in viewing error bars.

panel of Fig. 10. The mean ΔL_F results are derived from Abdala and Keefe (2006), and the mean ΔL_{FE} is evaluated at f_2 , (see corresponding median response in the top panel of Fig. 7). The mean ΔL_{FM} at f_2 showed an attenuation of 16 dB in term infants relative to adults; the attenuation decreased with increasing age to 7 dB in 6 month olds. The variability in each estimate was calculated as ± 1 SE. The variability in ΔL_{FE} across reflectance measurements was small compared to that in ΔL_F derived from DPOAE measurements, so that the variability obtained in ΔL_{FM} was similar to that in ΔL_F . Forward middle-ear transmission was not yet adult-like at age 6 months, and, in fact, the ΔL_{FE} was the least adult-like at the oldest age. This is evidence that the processes of ear-canal and middle-ear immaturity are far from complete at age 6 months.

The relative reverse level ΔL_R was compared with its ear-canal component ΔL_{RE} and the predicted $\Delta L'_R$ [see Eq. (48)] in the bottom panel of Fig. 10. The ΔL_{RE} was 4 dB in

term infants and decreased to 0 dB in 6 month olds relative to adults. The variability in ΔL_{RE} was smaller than that of ΔL_R . However, the variability in the mean of the model $\Delta L'_R$ was larger than either, because its calculation was based in part on $\Delta L_{FM}(f_1)$, which had similar variability to that of $\Delta L_{FM}(f_2)$ shown in the top panel of Fig. 10. The dominant contributor to variability was that associated with the measurement of ΔL_F in Abdala and Keefe (2006). The mean measured and predicted relative reverse levels were within measurement variability at all ages except at age 5 months. However, the trend was that the $\varepsilon(f;f_1) < 0$ at all ages [see Eq. (50)], with a mean difference of -4 dB. The relative reverse middle-ear level $\Delta L_{RM}(f_{DP})$ in the bottom panel of Fig. 10 was calculated using Eq. (49), and its variability was only slightly larger than that of ΔL_R and ΔL_{RE} . The $\Delta L_{RM}(f_{DP})$ had a gain of 9 dB in full-term infants, which decreased with increasing age to 6 dB in six month olds. Reverse middle-ear transmission was not yet adult-like at age 6 months, due mainly to immaturities in ear-canal area and in forward middle-ear transmission.

V. DISCUSSION

A. Maturation effects

A model of acoustical and mechanical transmission through the ear canal, middle ear, and cochlea was applied to interpret DPOAE and reflectance measurements in infants and adults. This allowed the estimation not only of the relative forward and reverse transmission levels in infants compared to adults, but also decomposed each of these forward and reverse levels into ear-canal and middle-ear components. The model to account for maturational differences in DPOAEs was based on the hypothesis that cochlear function and anatomy are adult-like in term infants. If this hypothesis were false, then at least some of the resulting model predictions would be expected to differ from measured data. Results from an analysis of human DPOAE I/O functions (Abdala and Keefe, 2006) suggested that cochlear function was, indeed, adult-like in newborns. The present analyses added a more refined test and further supports this hypothesis, inasmuch as the model assumed that several cochlear variables were adult-like in infant ears. These variables included: (1) the cochlear DPOAE source level g [see Eq. (30)], which was the cochlear variable that was assumed adult-like in infant cochleae by Abdala and Keefe, (2) the transmittance t^* in the basal region of the cochlea [see Eq. (34)], and (3) the characteristic impedances of the cochlea in basal and more apical regions [see Eqs. (10) and (12)]. Cochlear immaturity in any of these variables would have resulted in inaccuracies in model predictions. No gross inaccuracies were observed; the residual inaccuracies were likely due to assuming that each of ear-canal and middle-ear transmission were approximately constant over the frequency range between f_{DP} and f_2 (see below).

Regarding forward transmission near the stimulus frequencies of $f_1 = 5$ and $f_2 = 6$ kHz, there was a forward attenuation ΔL_F of -15 dB of sound between a probe microphone in the ear canal and the cochlea in term infants relative to adults (Abdala and Keefe, 2006). After partitioning out the

effect of ear-canal acoustics, the relative forward attenuation in middle-ear transmission in term infants compared to adults was ΔL_{FM} of -16 dB (see top panel of Fig. 10). This 16 dB of additional attenuation in the forward middle-ear transmittance of term infants relative to adults affects not only DPOAE measurement, but any OAE measurement, and, in fact, any hearing experiment in which sound is delivered through the middle ear to the cochlea. The presence of immaturity in middle-ear forward transmission has significance for the study of hearing in young infants.

As described further in a brief review of middle-ear maturation in Abdala and Keefe (2006), the observed age dependence of ear-canal area is unrelated to the size of the tympanic membrane, which is of adult size in term infants. The plane of the tympanic membrane is more horizontal in infants than in adults (Ikui *et al.*, 1997), which accommodates the smaller ear-canal area in infants. There were similarities and differences in the ear-canal area results reported in the present study compared to those in Keefe *et al.* (1993). The average area in 1 month olds in Keefe *et al.* was consistent with the present median estimates at term and 1.5 months. The area in 3-month-olds in Keefe *et al.* (1993) was slightly elevated above the IQR of the present study, and the results agreed in 6-month-olds. A large discrepancy in adult ears was identified by Keefe *et al.*, who reported an average area (and standard deviation) of 85 ± 33 mm². The median adult area in the present study was 58 mm² with an IQR from 43 to 63 mm². The present results are in good agreement with measured cross-sectional areas in adult earmolds at a location corresponding to a 10-mm insertion depth into the ear canal: the average earmold area was approximately 50 mm² with a range from 30 to 70 mm² (Stinson and Lawton, 1989). The adult area estimates of Keefe *et al.* (1993) were likely contaminated by either a lack of accuracy in measuring the acoustic impedance or an atypical distribution of adults with larger ear canals.

Regarding reverse transmission ΔL_R at $f_{DP} = 4$ kHz, Abdala and Keefe (2006) reported a 13 dB increase in total DPOAE level in newborn infants compared to adults (see bottom panel, Fig. 10), and this relative DPOAE gain decreased with increasing age. The increase in reverse transmission in infants is what accounts for their large OAE levels compared to adults. The reverse ear-canal component ΔL_{RE} accounted for 4 dB of this increase in newborns, partitioning the remaining 9 dB of ΔL_R into ΔL_{RM} . The model explained most of this difference as due to reciprocity in middle-ear mechanics, which predicts that the reverse middle-ear transmittance is equal to the product of the forward middle-ear transmittance and the ratio of the ear-canal characteristic impedance to the cochlear characteristic impedance [see Eq. (10)]. The reciprocal relation between forward and reverse middle-ear transmittance appears helpful in understanding the relationships between forward and reverse middle-ear transfer-function measurements in human-cadaver temporal bones and in nonhuman mammalian ears *in vivo*, but a review of this subject is outside the scope of this report. Nevertheless, maturation effects have been reported in young postnatal gerbils in the form of an attenuation of forward middle-ear transmission (Overstreet and Ruggero, 2002).

Such effects are similar to those that were observed noninvasively in the present study in human infants.

The fact that ΔL_R and $\Delta L'_R$ agreed overall in Fig. 10 to within 4 dB confirmed the basic theory that maturational differences in DPOAEs are controlled by maturation in external- and middle-ear functioning. The additional discrepancy at 5 months was likely due in part to inaccuracies in estimating ΔL_F and ΔL_R (Abdala and Keefe, 2006), which showed the least accurate fits in the same 5-month and 6-month age groups in which the largest magnitudes of $\varepsilon(f; f_1)$ were found. Other sources of this discrepancy might include error in the reflectance measurements or model accuracy, and any difference in the effect of immaturity on forward transfer of energy at f_{DP} relative to that at f_1 and f_2 . These immaturity effects might be further investigated by measurements in infants and adults over a broader frequency range.

The model accounted for approximately 24 dB of the 28 dB difference between ΔL_R and ΔL_F in term infants relative to adults. The immaturity in ear-canal area (see Fig. 9) accounted for 17 dB of this difference. Most of the remaining relative level was explained by reverse transmission ($\Delta L_{RE}=4$ dB, bottom panel, Fig. 10).

Consider the responses for newborns (i.e., the ‘‘Term’’ infant data in Fig. 10). The $\Delta L_{FM}(f_2)=-16$ dB (top panel, Fig. 10) and $\Delta L_{RM}(f_{DP})=9$ dB (bottom panel, Fig. 10) represent an attenuation in forward middle-ear transmission and a gain in reverse middle-ear transmission in the ears of newborns relative to adults. The round-trip difference was $\Delta L_{RM}(f_{DP})-\Delta L_{FM}(f_2)=9-(-16)=25$ dB. While not plotted in Fig. 10, the difference using forward transmission at f_1 was $\Delta L_{RM}(f_{DP})-\Delta L_{FM}(f_1)=9-(-11)=20$ dB in newborns. If these were measured at the same frequency, then the model would predict [see Eqs. (37) or (48)] that $\Delta L_{RM}(f_{DP})-\Delta L_{FM}(f_{DP})=\Delta L_\alpha=17$ dB. It appears that the difference is converging towards ΔL_α as the frequency at which forward transmission is assessed moves towards f_{DP} . Thus, immaturity in middle-ear mechanics in infants results in the attenuation of the forward-directed stimulus through the middle ear (at 5–6 kHz), while immaturity in the ear-canal area size results in an overall gain in the reverse-directed DPOAE (at 4 kHz) measured in the ear canal. These effects of immature function in infant ears are an attenuation of a sound stimulus to a lower effective level on the basilar membrane, but a boost in the resulting OAE level in the small ear canal of the infant.

The decomposition in Fig. 10 of forward and reverse transmission effects in infant ears relative to adults strictly applies to only one particular set of DPOAE frequencies. Forward transmission was assessed at $f_2=6$ kHz and $f_1=5$ kHz primaries, and reverse transmission was assessed at the 4 kHz DP frequency. The extent to which these results generalize to other frequencies is unknown. It should be noted that the restriction in this study to a single DPOAE frequency was required because a time-consuming DPOAE suppression protocol was implemented with each infant subject. Because of the length of this protocol, it was not possible to collect DPOAE I/O data at other frequencies. It would be useful to apply the procedures of the present study

across a wide range of DPOAE frequencies to assess maturational differences in DPOAEs in terms of maturational differences in ear-canal and middle-ear functioning.

The results in Fig. 10 show that the 6 month old is not yet adult-like in terms of both ear-canal and middle-ear functioning. An unexpected finding from the ΔL_{FE} results (Fig. 10) is that ΔL_{FE} in older infants up to age six months was more different from adults than ΔL_{FE} in younger infants. While this is only a 5 dB effect, it helps make the point that maturation of DPOAEs due to ear-canal and middle-ear development continues in infants older than 6 months. This is consistent with the reports that ear-canal and middle-ear functioning, as assessed by acoustic reflectance and impedance measurements, is not yet adult-like at age 24 months (Keefe *et al.* 1993), and ear-canal impedance is not yet adult-like even at age 11 years (Okabe *et al.* 1988). It may be that the remaining maturation after age 11 years and through puberty is related to increases in ear-canal area and the distance from the probe-tip location from the tympanic membrane (which might involve both area and ear-canal length changes), but more study in older children is needed.

B. Ear-canal transfer functions for different OAE types

Ear-canal reflectance and probe source reflectance measurements were used to calculate forward and reverse ear-canal transfer-function levels in adults and infants, and forward and reverse levels were combined to simulate the linear-systems effect of round-trip ear-canal transmission in a DPOAE measurement, and in a TEOAE or SFOAE measurement. In addition to their significance for understanding maturational effects, these ear-canal transfer function measurements have significance for interpreting differences in OAE type. The dominant effect of ear-canal acoustics occurred for adults in DPOAE measurements for f_2 in the range of 3–4 kHz in the forward ear-canal transfer-function level in Fig. 5, and in the round-trip level shown in Fig. 6. This effect was not undone by the reverse ear-canal transfer-function level. This increased stimulus transmission in a DPOAE measurement near a f_2 of 4 kHz in adults is shown in the frequency dependence of $L_{FE}(f_2)$ in Fig. 5. This increase may explain why DPOAEs were better able than TEOAEs to classify a population of test ears of adult and older children (≥ 3 years of age) as having normal or a sensorineural hearing loss at 4 kHz (Gorga *et al.* 1993). This advantage also may explain why SFOAEs in adult ears had a similar test performance to DPOAEs for predicting sensorineural hearing loss at octave frequencies from 1 to 8 kHz, except at 4 kHz where DPOAEs had better test performance (Ellison and Keefe, 2005). There is no such pronounced effect of ear-canal acoustics in newborns on DPOAEs for f_2 in the range of 3–4 kHz or at other frequencies in the range from 0.5 to 8 kHz compared to TEOAEs or SFOAEs (see Figs. 5 and 6). This is consistent with the finding of no difference in test performance of DPOAEs and TEOAEs at any frequency in classifying infant ears as normal or hearing impaired (Norton *et al.*, 2000). The longer ear-canal length in adults is one important factor in this effect. Thus, the predicted effect of differences in ear-canal and middle-ear functioning on OAE signal levels is consistent with differences

observed in test performance across OAE test type in adult ears, and with the absence of an effect of OAE test type in infant ears.

VI. CONCLUSIONS

Using a one-dimensional scattering matrix model of energy transmission in the ear canal, middle ear and cochlea, the forward and reverse transfer functions describing bidirectional sound transmission between the ear canal and cochlea were decomposed into ear-canal and middle-ear components. This decomposition was based on DPOAE and ear-canal reflectance responses measured in the same infants and adults.

The reflectance was sensitive to frequency-dependent effects of ear-canal and middle-ear transmission that differed across subject age groups and between DPOAE and SFOAE test types. A notable outcome in adult ears was that the frequency dependence of forward transmission appears to account for the better performance at 4 kHz of DPOAEs compared to TEOAEs and SFOAEs in classifying ears as normal or as having a sensorineural hearing loss.

Regarding the main goal of the study, the immaturities in DPOAE I/O functions observed by Abdala and Keefe (2006) in infants ranging from newborn to 6 months of age were explained in terms of immaturities in ear-canal and middle-ear functioning. For the $2f_1-f_2$ DPOAE measured at $f_1=5$ kHz and $f_2=6$ kHz, the results show a relative attenuation (in infants compared to adults) of 16 dB in the forward-transmitted stimulus energy through the middle ear. The results provide evidence that DPOAEs are larger in infant than adult ears, mainly because of the effect of ear-canal area growth, which contributes a 17 dB increase in the DPOAE measured in the newborn compared to the adult ear. Neither ear-canal nor middle-ear functioning were adult-like at age 6 months.

ACKNOWLEDGMENTS

This research was supported by the NIH (NIDCD Grant Nos. DC003784, DC003552, and DC006607), and the House Ear Institute. The authors would like to thank Dr. Ellen Ma and Sandy Oba for collection of infant data. The lead programmer in implementing the reflectance software at BTNRH was Dr. Denis F. Fitzpatrick.

Abdala, C., and Keefe, D. H. (2006). "Effects of middle-ear immaturity on distortion-product otoacoustic emission suppression tuning in infant ears," *J. Acoust. Soc. Am.* **120**, 3832–3842.

Burns, E. M., and Keefe, D. H. (1998). "Energy reflectance can exceed unity near SOAE frequencies," *J. Acoust. Soc. Am.* **103**, 462–474.

Ellison, J. C., and Keefe, D. H. (2005). "Audiometric predictions using stimulus-frequency otoacoustic emissions and middle ear measurements," *Ear Hear.* **26**, 487–503.

Efron, B., and Tibshirani, R. (1986). "Bootstrap methods for standard errors, confidence intervals, and other measurements of statistical accuracy," *Stat. Sci.* **1**, 54–77.

Gorga, M. P., Neely, S. T., Bergman, B. M., Beauchaine, K. L., Kaminski, J. R., Peters, J., Schulte, L., and Jesteadt, W. (1993). "A comparison of transient-evoked and distortion product otoacoustic emissions in normal-hearing and hearing-impaired subjects," *J. Acoust. Soc. Am.* **94**, 2639–2648.

Gorga, M. P., Neely, S. T., Bergman, B. M., Beauchaine, K. L., Kaminski, J.

R., and Liu, Z. (1994). "Towards understanding the limits of distortion product otoacoustic emission measurements," *J. Acoust. Soc. Am.* **96**, 1494–1500.

Huang, G. T., Rosowski, J. J., Puria, S., and Peake, W. T. (2000). "A non-invasive method for estimating acoustic admittance at the tympanic membrane," *J. Acoust. Soc. Am.* **108**, 1128–1146.

Ikui, A., Sando, I., Sudo, M., and Fujita, S. (1997). "Postnatal change in angle between the tympanic annulus and surrounding structures," *Acta Otol. Rhinol. Laryngol.*, **106**, 33–36.

Keefe, D. H. (1997). "Otoreflectance of the cochlea and middle ear," *J. Acoust. Soc. Am.* **102**, 2849–2859.

Keefe, D. H. (2004). "Using reflectance phase to estimate acoustic response at the tympanic membrane," *J. Acoust. Soc. Am.* **115**, 2499 (Abstract).

Keefe, D. H., and Benade, A. H. (1981). "Impedance measurement source and microphone proximity effects," *J. Acoust. Soc. Am.* **69**, 1489–1495.

Keefe, D. H., Bulen, J. C., Hoberg Arehart, K., and Burns, E. M. (1993). "Ear-canal impedance and reflection coefficient of human infants and adults," *J. Acoust. Soc. Am.* **94**, 2617–2638.

Keefe, D. H., Folsom, R. C., Gorga, M. P., Vohr, B. R., Bulen, J. C., and Norton, S. J. (2000). "Identification of neonatal hearing impairment: Ear-canal measurements of acoustic admittance and reflectance in neonates," *Ear Hear.* **21**, 443–461.

Keefe, D. H., Ling, R., and Bulen, J. C. (1992). "Method to measure acoustic impedance and reflection coefficient," *J. Acoust. Soc. Am.* **91**, 470–485.

Keefe, D. H., and Simmons, J. L. (2003). "Energy transmittance predicts conductive hearing loss in older children and adults," *J. Acoust. Soc. Am.* **114**, 3217–3238.

Kemp, D. T., Ryan, S., and Bray, P. (1990). "A guide to the effective use of otoacoustic emissions," *Ear Hear.* **11**, 93–105.

McIntyre, M. E., Schumacher, R. T., and Woodhouse, J. (1983). "On the oscillations of musical instruments," *J. Acoust. Soc. Am.* **74**, 1325–1345.

Morse, P. M., and Ingard, K. U. (1968). *Theoretical Acoustics* (McGraw-Hill, New York).

Norton, S. N., Gorga, M. P., Widen, J. E., Folsom, R. C., Sininger, Y., Cone-Wesson, B., Vohr, B. R., Mascher, K., and Fletcher, K. (2000). "Identification of neonatal hearing impairment: Evaluation of transient evoked otoacoustic emission, distortion product otoacoustic emission, and auditory brain stem response test performance," *Ear Hear.* **21**, 508–528.

Okabe, K., Tanaka, S., Hamada, H., Miura, T., and Funai, H. (1988). "Acoustic impedance measurement on normal ears of children," *J. Acoust. Soc. Jpn. (E)* **9**, 287–294.

Overstreet III, E. H., and Ruggero, M. A. (2002). "Development of wide-band middle ear transmission in the Mongolian gerbil," *J. Acoust. Soc. Am.* **111**, 261–270.

Puria, S. (2003). "Measurements of human middle ear forward and reverse acoustics: Implications for otoacoustic emissions," *J. Acoust. Soc. Am.* **113**, 2773–2789.

Shera, C. A., and Zweig, G. (1991). "Phenomenological characterization of eardrum transduction," *J. Acoust. Soc. Am.* **90**, 253–262.

Shera, C. A., and Zweig, G. (1992a). "Middle-ear phenomenology: The view from the three windows," *J. Acoust. Soc. Am.* **92**, 1356–1370.

Shera, C. A., and Zweig, G. (1992b). "Analyzing reverse middle-ear transmission: Noninvasive *Gedankenexperiments*," *J. Acoust. Soc. Am.* **92**, 1371–1381.

Sondhi, M., and Resnick, J. (1983). "The inverse problem for the vocal tract: Numerical methods, acoustical experiments and speech synthesis," *J. Acoust. Soc. Am.* **73**, 985–1002.

Stinson, M. R., and Lawton, B. W. (1989). "Specification of the geometry of the human ear canal for the prediction of sound-pressure level distribution," *J. Acoust. Soc. Am.* **85**, 2492–2503.

Strutt, J. W. (1873). "Some general theorems relating to vibration," *London Mathematical Society*, **IV**, 357–368. Reprinted in *Scientific Papers by Lord Rayleigh* (Dover, New York, 1964), Vol. 1, pp. 170–181.

Voss, S. E., and Shera, C. A. (2004). "Simultaneous measurement of middle-ear input impedance and forward/reverse transmission in cat," *J. Acoust. Soc. Am.* **116**, 2187–2198.

Zweig, G., and Shera, C. A. (1995). "The origin of periodicity in the spectrum of evoked otoacoustic emissions," *J. Acoust. Soc. Am.* **98**, 2018–2047.

Zweig, G. (1991). "Finding the impedance of the organ of Corti," *J. Acoust. Soc. Am.* **89**, 1229–1254.

Basilar membrane tension calculations for the gerbil cochlea

Ram C. Naidu

Hearing Research Center, Boston University, Boston, Massachusetts 02215 and Department of Biomedical Engineering, Boston University, Boston, Massachusetts 02215

David C. Mountain

Hearing Research Center, Boston University, Boston, Massachusetts 02215, Department of Biomedical Engineering, Boston University, Boston, Massachusetts 02215 and Department of Otolaryngology, Boston University, Boston, Massachusetts 02215

(Received 16 March 2006; revised 7 November 2006; accepted 10 November 2006)

Anatomical studies suggest that the basilar membrane (BM) supports a radial tension, which is potentially important in cochlear mechanics. Assuming that the tension exists, we have calculated its magnitude from measurements of BM stiffness, longitudinal coupling, and geometry using a BM model. Results for the gerbil cochlea show that the tension decreases from the base to the apex of the cochlea and generates a tensile stress that is comparable in magnitude to the stress generated in other physiological systems. The model calculations are augmented by experiments that investigate the source of BM tension. The experimental results suggest that BM tension is maintained by the spiral ligament. © 2007 Acoustical Society of America. [DOI: 10.1121/1.2404916]

PACS number(s): 43.64.Kc, 43.64.Bt [BLM]

Pages: 994–1002

I. INTRODUCTION

Anatomical studies suggest that the basilar membrane (BM) is structurally designed to support a radial tension (Engström, 1955; Henson and Henson, 1988). Figure 1(a) is a schematic view of the BM supporting the organ of Corti. Figure 1(b) shows the BM in the base of the gerbil cochlea as viewed through a light microscope. The BM is composed of a homogeneous, soft ground substance that is traversed radially by fibers, which extend between the spiral lamina and the spiral ligament. The BM can be divided into two regions based on the arrangement of the fibers: The lateral pectinate zone, where the fibers are grouped into bundles; and the arcuate zone, where the bundles separate into individual fibers (Iurato, 1967). The parallel arrangement of fiber bundles in the pectinate zone suggests that the bundles are under a radial tension (Engström, 1955). Studies also suggest that such a tension is maintained by the spiral ligament. Henson *et al.* (1984) have shown that the spiral ligament fibers are anchored to the bony cochlear wall by fibroblasts. Fibroblasts contain fibers composed of contractile proteins and have been shown to create tension (Harris *et al.*, 1981). In the spiral ligament, the configurations in which fibroblasts are arranged and oriented suggest that these cells actively maintain a radial tension in the BM (Henson and Henson, 1988).

Anatomical changes along the length of the cochlea further suggest the presence of a radial tension gradient. The density of the fiber bundles and fibroblasts (Henson and Henson, 1988) decreases from base to apex of the cochlea. The density gradient is accompanied by a visible decrease in the cross-sectional area of the spiral ligament. The variation in fibroblast density, together with the variation in the cross-sectional area of the spiral ligament, both suggest that tension, if present, decreases from the cochlear base towards the apex.

The anatomical evidence certainly suggests a role for tension induced by fibroblasts. However, such a claim is difficult to substantiate with direct measurements of BM tension. In fact, von Békésy's (1960) experimental results can be used to argue directly against the presence of BM tension. Von Békésy made fine slits in the BM of cadaver cochleae while simultaneously observing the experimental location under a microscope. He reported that the edges of the BM did not draw apart at the location of the slits. He, therefore, concluded that the BM was not under tension. However, von Békésy's results are difficult to interpret because limited information is available on the condition of the cochleae that were used in his experiments. It is, therefore, unclear whether the results obtained from the cadaver cochlea can be readily extrapolated to the pristine cochlea, especially since we know that rapid physiological changes occur within the cochlea following the death of an experimental animal (Rhode, 1973).

From a purely structural mechanics perspective, the architecture of the BM is remarkably similar to the architecture of a reinforced slab of concrete. The ground substance may be considered analogous to the concrete and the fiber bundles analogous to reinforcing steel bars as shown in Fig. 1(c). Using the above analogy, we argue that the preferential reinforcement of the BM along its width is designed to particularly enhance the, otherwise poor, ability of the BM ground substance to support large radial forces. This is similar to the manner by which reinforcing steel bars greatly increase the tensile strength of concrete along the direction of reinforcement.

The present study assumes, given the anatomical arguments, that the BM supports a radial tension. The tension is calculated from measurements of point stiffness of the BM using a model that exploits the reinforced structure of the BM. The model parameters are directly obtained or derived from experimental measurements of anatomy, point stiffness,

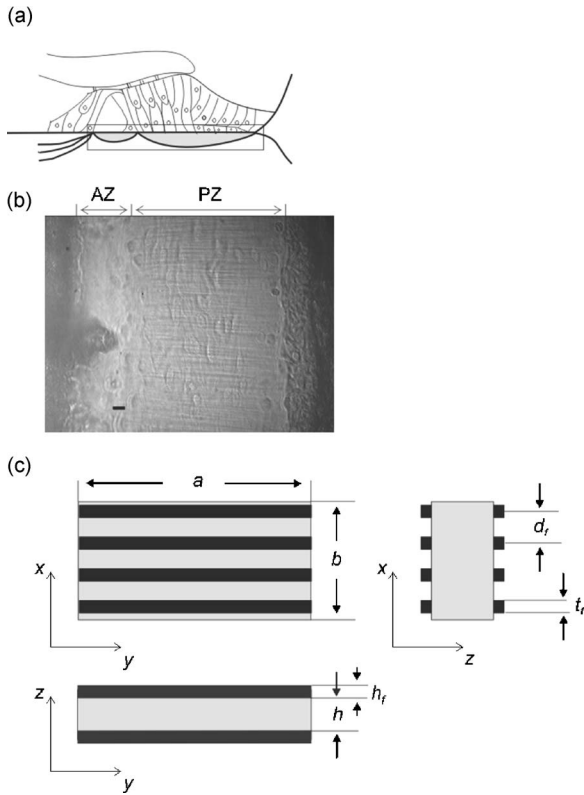


FIG. 1. (a) BM underlying the OC. (b) Microscope view of the BM from an excised cochlea. The fiber bundles traverse the pectinate zone (PZ). In the arcuate zone (AZ), the bundles separate into individual fibers that enter the spiral lamina (Iurato, 1962). (c) Equivalent plate model of the basilar membrane with stiffeners that represent the fiber bundles, oriented along the y direction. The plate has a length a , width b , thickness h , and is under tension, N_y , along its width. The fiber bundles have a height h_f , thickness t_f , and a spacing d .

and longitudinal coupling. In addition, experimental measurements are performed to investigate the source of BM tension.

The following is a summary of our results. We find that the calculated tension decreases along the cochlea and generates a tensile stress that is comparable in magnitude to the stress generated in other physiological environments. The results are reconciled with the experiments of von Békésy (1960) by showing that the tension is not large enough to cause a visible retraction of the BM when the BM is cut. Experimental measurements show that BM stiffness decreases following damage to the spiral ligament. This result supports the hypothesis that BM tension is maintained by the spiral ligament.

The study is organized as follows. Section II provides a description of the BM model and a qualitative description of the model solution, which is used to determine BM tension and the model results. Section III provides a description of the experiments, which were performed to locate the source of BM tension and the experimental results. The implications of the model and experimental results are discussed in Sec. IV. The mathematical details of the model equations are presented in the Appendix.

II. DESCRIPTION OF THE BM MODEL

At any given location along the cochlea, the BM is modeled as a plate as shown in Fig. 1(c). The dimensions of the

plate change with position along the cochlea. The width of the plate is oriented along the radial direction (x) of the cochlea. The length of the plate is oriented along the length (y) of the cochlear spiral.

The BM plate is composed of two components: (a) An isotropic plate of BM ground substance; and (b) two sets of fiber bundles, which travel along the top and bottom of the plate in order to preferentially reinforce the plate along its width. Due to the preferential reinforcement by the fiber bundles along the y direction, the plate is anisotropic, whereby it has different mechanical properties along its width and length.

A. Assumptions

The tension is calculated at multiple locations along the cochlea. The following simplifying assumptions are used in the model to describe the BM locally at each given location.

- (1) The organ of Corti (OC) is neglected.
- (2) The plate is rectangular. Therefore, the variation in BM width across the length of the plate is neglected. The curvature of the BM along the cochlear spiral is neglected.
- (3) The plate is simply supported at its edges. As a result of this edge condition, the deflection of the plate must decrease to zero at the edges while the slope of the deflection profile is not constrained to be zero at zero deflection. Additionally, the moment about the edge of the plate is zero.
- (4) The thickness of the plate is constant along its length and width.
- (5) The tension is distributed uniformly along the thickness of the plate. Therefore, the tension is carried by the entire plate and not by the BM fiber bundles alone.
- (6) The separation of fiber bundles in the arcuate zone is neglected. Instead, the bundles traverse the entire width of the plate.
- (7) The fiber bundles are rectangular in cross section. The top and bottom fiber bundles are of equal cross section.

B. Determination of BM plate dimensions

At a given position, x , along the cochlea, the dimensions of the plate are determined as follows. The width of the plate, a , is equal to the width of the BM, $w(x)$. The length of the plate, b , is calculated as

$$b(x) = 5\lambda_c(x), \quad (1)$$

where $\lambda_c(x)$ is the space constant that describes the amount of BM longitudinal coupling (Naidu and Mountain, 2001). The length of the plate in Eq. (1) is determined as follows. The deflection profile of the BM in response to the application of a local force decreases exponentially with increasing distance from the excitation as shown in Fig. 2 (Naidu and Mountain, 2001). The space constant, $\lambda_c(x)$, characterizes the rate of exponential decrease of displacement along the cochlea. As the deflection falls to less than 10% of the maximum deflection within a distance of $2.5\lambda_c(x)$ on either side of the point of excitation, we assume that deflections smaller

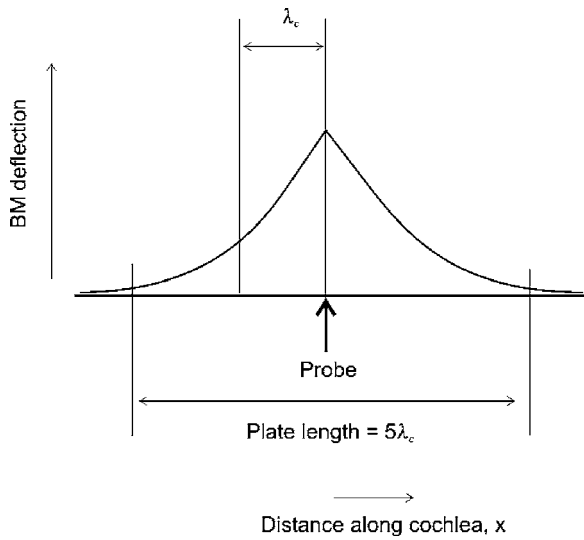


FIG. 2. BM deflection decreases exponentially with increasing distance from the site of excitation along the cochlea due to longitudinal coupling. The effective length of the BM plate is, therefore, determined from the space constant, λ_c , that characterizes the decay to be $5\lambda_c$ as shown.

than 10% of the maximum deflection can be neglected in our calculations. Therefore, the effective length of BM that determines the mechanics at a given location along the cochlea is $5\lambda_c(x)$. Therefore, we choose the length $b(x)$ of the plate to equal $5\lambda_c(x)$.

The effective thickness, $h(x)$, of the plate is calculated as the cross-sectional area of the BM divided by its width.

C. Determination of BM plate material properties

The deflection equation of a plate is determined by its flexural rigidities, D_x , D_y , and H , which are functions of the plate architecture, the elasticity of the fibers, and the elasticity of the ground substance. Given the preferential reinforcement of the plate along the radial (x) direction, the flexural rigidities, D_x , D_y , and H , of the plate can be calculated (Timoshenko and Woinowsky-Kreiger, 1959) to be

$$D_x(x) = \frac{E_g h^3(x)}{12(1 - \nu^2)}, \quad (2)$$

$$D_y(x) = \frac{E_g h^3(x)}{12(1 - \nu^2)} + \frac{E_f I_f(x)}{d_f(x)}, \quad (3)$$

$$H(x) = D_x(x), \quad (4)$$

where E_g and E_f represent the elasticity moduli of the ground substance and fiber bundles, respectively, ν is Poisson's ratio of the ground substance, $h(x)$ is the thickness of the BM plate, $d_f(x)$ is the spacing between fiber bundles, and $I_f(x)$ is the moment of inertia of each set of fiber bundles (top and bottom) with respect to the middle axis of the cross section of the plate calculated as

$$I_f(x) = \frac{1}{12} t_f(x) h^3(x) \left[1 - \left(1 - 2 \frac{h_f(x)}{h(x)} \right)^3 \right] \\ \cong \frac{1}{2} t_f(x) h^2(x) h_f(x), \quad (5)$$

where $h_f(x)$ is the height of fiber bundles and $t_f(x)$ is the thickness of fiber bundles.

D. Parameter estimation

The model was used to determine BM tension at six locations along the cochlea. Table I lists the experimental measurements which were used to calculate the model dimensions and mechanical properties.

Anatomical dimensions of the BM and OC along the cochlea were obtained from Schweitzer *et al.* (1996) and Edge *et al.* (1998). Note that an extra distance of 0.86 mm was added to the longitudinal distances measured by Edge *et al.* (1998) to include the length of the hook region, which is the extreme basal end of the BM. The corrected distances are marked using asterisks (*). The height of the BM was obtained by dividing the measured cross-sectional area of the BM by the measured width of the BM. At each given cochlear location, anatomical dimensions that were unavailable were estimated (shown by italics) using linear regression lines fit through the data that were measured at other locations. The length of the gerbil cochlea was determined to be 1.3 cm (Plassmann *et al.*, 1987).

Anatomical dimensions of the fiber bundles were obtained as follows. The thickness and height of the fiber bundles were determined from Schweitzer *et al.* (1996). At

TABLE I. Model parameters used to calculate BM tension at several locations along the cochlea. The distances marked with asterisks have been corrected to include the length of the hook region. The values in italics were determined using regression fits to the data in the unshaded cells. References used: A: Measured by the authors. (1) Edge *et al.* (1998); (2) Schweitzer *et al.* (1996); (3) Naidu and Mountain (2001); (4) Naidu and Mountain (1998b); (5) Lai-fook *et al.* (1976).

Parameter	Symbol	Value						Reference	mm
Location from base	x	1.3	3.61*	4.55	6.86*	7.54	11.26*	1*, 2	mm
BM width	a	149	168	194	211	231	259	A, 2	μm
Coupled length	b	54	67	83	96	110	136	3	μm
BM height	h	8.54	12.5	<i>13.1</i>	15.0	<i>15.9</i>	17.7	1	μm
Bundle thickness	h_f	1.5	<i>1.02</i>	0.77	<i>0.57</i>	0.59	<i>0.28</i>	2	μm
Bundle width	t_f	1.37	<i>1.13</i>	1.03	<i>0.80</i>	0.73	0.35	2	μm
Bundle spacing	d_f	1.58	<i>1.60</i>	<i>1.61</i>	<i>1.62</i>	1.63	1.67	A	μm
Point stiffness	k_p	1.98	1.26	0.72	0.46	0.28	0.12	4	N/m
Poisson's ratio	ν	0.4	0.4	0.4	0.4	0.4	0.4	5	N/m

each location of interest, the average thickness of the fiber bundles was calculated as the mean of the measured thickness of the upper and lower fiber bundles. We measured the spacing of the fiber bundles at locations in the three turns using digitized images of the BM in excised turns of gerbil cochlea.

The stiffness at the center of the BM was estimated from the measurements of Naidu and Mountain (1998b) as being equal to one-half the stiffness of the OC as measured under the outer hair cell region. The stiffness was experimentally measured at a BM deflection of z_0 approximately equal to $5 \mu\text{m}$. Measurements of longitudinal coupling of the BM were obtained from Naidu and Mountain (2001). Poisson's ratio of the ground substance of the BM was estimated to be 0.4 from measurements on dog lung tissue by Lai-Fook *et al.* (1976).

The ratio of the elasticity of the fibers to the elasticity of the ground substance was estimated to be 100. As discussed in Sec. IV, this ratio value makes the BM weakly anisotropic in the apex, which is consistent with the experimental measurements of Naidu and Mountain (1998a).

E. Model solution

An overview of the model solution is presented in this section. The relevant mathematical equations are presented in the Appendix. The model is used to calculate BM tension by simulating the experimental measurements of BM stiffness (Naidu and Mountain, 1998b). An analytical expression is derived for the deflection profile of the plate in response to a concentrated force, which is applied at the center of the BM. The deflection profile is a function of the elasticity of the fibers and ground substance, and the radial tension. Since the ratio of the elasticity of the fibers and ground substance is assumed to be 100, the deflection profile is only a function of two unknown variables, the elasticity of the ground substance and the radial tension. Therefore, only two equations, instead of three, are required to solve the tension of the BM.

The two equations are determined as follows. The first equation is obtained by equating the calculated stiffness to the stiffness as measured experimentally. The second equation is derived from the constraint that edges of the BM are not observed to move towards each other when the BM is deflected during the experimental stiffness measurement. Mathematically, the constraint is equivalent to balancing the strain developed in the BM due to deflection by the strain developed in the BM due to tension. The two equations formulated as described above are solved simultaneously to calculate the tension in the BM.

F. Model results

Figure 3(a) shows the calculated BM tension $N_y(x)$ plotted as a function of position along the length of the cochlea. The tension decreases by about two orders of magnitude from a value of about 0.76 N/m at the base to about 0.001 N/m at the apex. The continuous variation in tension, in units of N/m , with distance x along the cochlea is described by a regression fit to the predicted values, which is given by the function

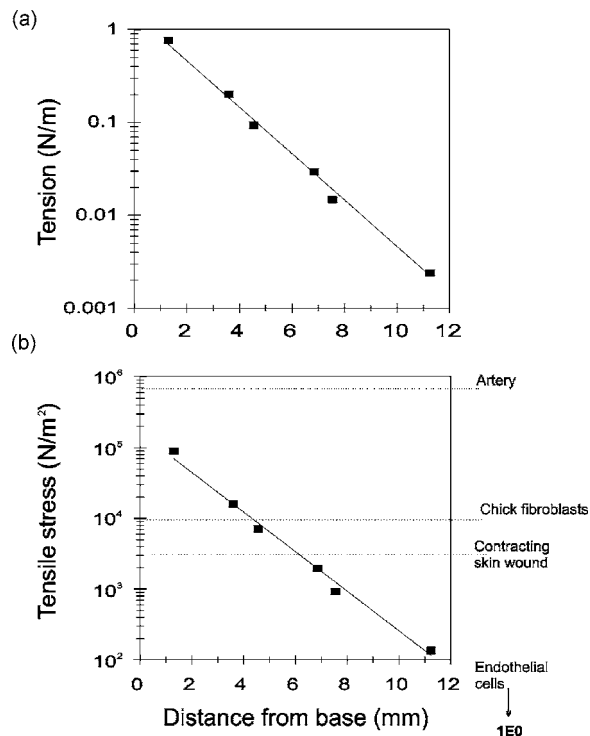


FIG. 3. (a) The variation of tension as a function of position along the cochlea. (b) Variation of BM tensile stress along the cochlea. The tensile stress is compared with stress developed in other physiological systems.

$$N_y(x) = 1.51e^{-0.58x}, \quad (6)$$

where x is specified in units of mm.

The corresponding tensile stress $\sigma_y(x)$ acting on the BM was calculated by dividing $N_y(x)$ by the effective height, $h(x)$, of the BM plate. Figure 3(b) shows the calculated tensile stress as a function of position along the length of the cochlea. The continuous variation in tensile stress, in units of N/m^2 , with distance x along the cochlea is described by a regression fit to the predicted values, which is given by the function

$$\sigma_y(x) = 1.67166 \times 10^5 e^{-0.65x}, \quad (7)$$

where x is specified in units of mm.

The predicted flexural rigidities of the plate, D_x and D_y , are plotted as a function of position along the cochlea in Fig. 4. The continuous variation in D_x and D_y , in units of Nm , with distance x along the cochlea are described by the regression fit to the predicted values, which are given by the functions

$$D_x(x) = 3 \times 10^{-11} e^{-0.01x}, \quad (8)$$

$$D_y(x) = 3.3 \times 10^{-9} e^{-0.33x}, \quad (9)$$

where x is specified in units of mm.

III. EXPERIMENTS

A. Preparation of excised cochleae

Experiments were performed to study whether BM tension is maintained by the spiral ligament. Specifically, we studied whether BM stiffness changed as a result of damage

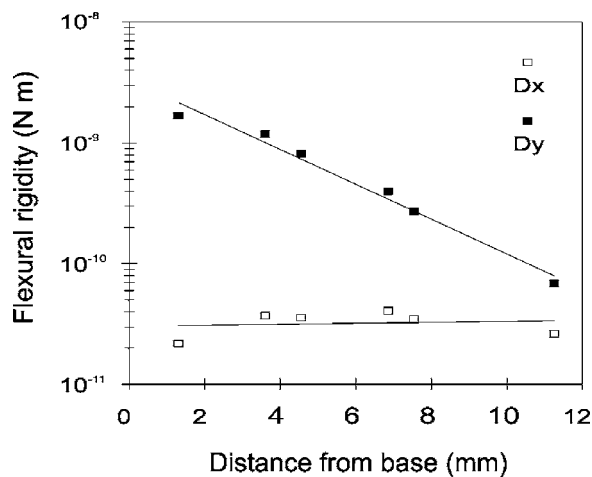


FIG. 4. Predicted flexural rigidities, D_x and D_y , plotted as a function of distance along the cochlea.

to the spiral ligament. The experiments were performed in morphologically stable excised preparations of the basal turn of the gerbil cochlea according to the protocol described in Naidu and Mountain (1998b).

A total of five excised basal turns were prepared using the following experimental procedure. Mongolian gerbils were deeply anaesthetized using a mixture of ketamine (0.16 mg/g) and xylazine (0.008 mg/g) and decapitated. The temporal bone was excised and placed in cold oxygenated culture medium (Leibovitz L-15). The bulla was opened to expose the cochlea. The cochlea was carefully opened by scoring a thin line above the basal turn. The higher turns were then removed to isolate basal turn. The round window membrane was opened to access the underside of the BM. Reissner's membrane was opened at the location of interest. The OC was mechanically removed using a fine micro-hook. The preparation was mounted on the stage of an inverted microscope. The experimental location was viewed through a CCD camera (Hamamatsu), which was mounted on the inverted microscope.

B. Stiffness measurements

Stiffness of the BM was measured using the protocol described in Naidu and Mountain (1998b) at several locations along its width as shown in Fig. 5(a). The measurements were performed with the force probe described in Olson and Mountain (1991) using a flat tip with a circular cross section $10 \mu\text{m}$ in diameter. The view from the camera was used to record the location of the probe and to measure the distance of each measurement location with respect to the spiral lamina. Two sets of measurements were performed as follows. In the first set of measurements, BM stiffness was measured before the spiral ligament was damaged. Following the first set of measurements, the spiral ligament was damaged by mechanical abrasion using a fine micro-hook at the location shown by the arrow in Fig. 5(a). A second set of measurements was then performed wherein the stiffness of the BM was remeasured at the locations at which stiffness was measured during the first set of measurements.

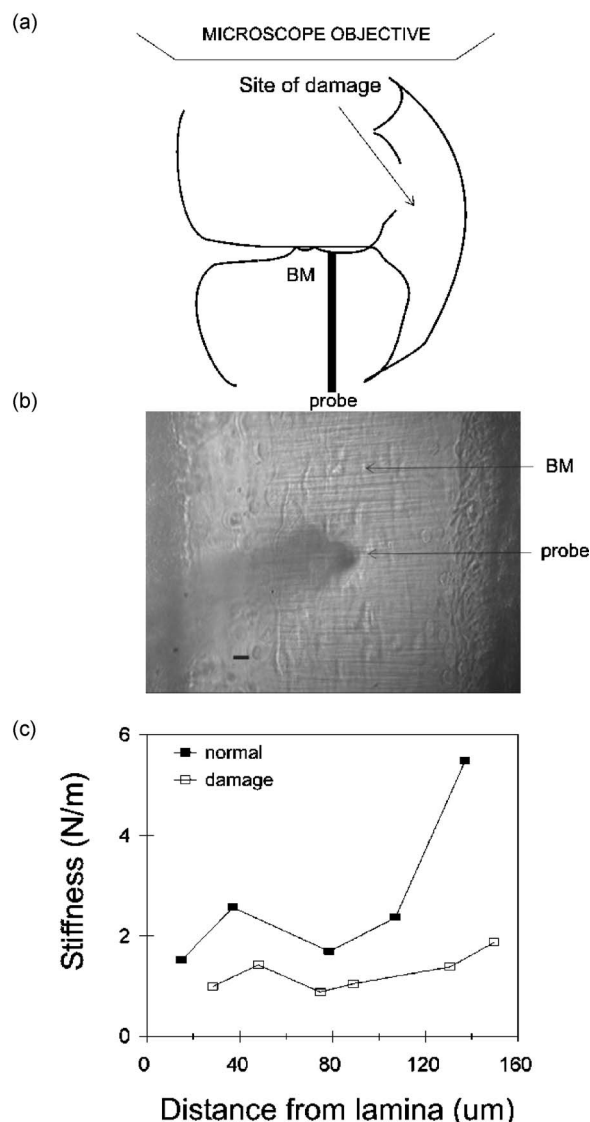


FIG. 5. (a) Schematic diagram of the measurement of BM stiffness using the force probe. The arrow shows the site of damage to the spiral ligament. (b) Microscope view of the experimental location during the measurements taken from the side of the organ of Corti. The force probe is visible as a dark shadow at the center of the basilar membrane. (c) Stiffness values measured at several locations along the width of the BM before and after damage to the spiral ligament in experiment 110598. The x -axis represents the distance of each measurement location from the spiral lamina.

The stiffness at each experimental location was determined using the following procedure as described in Olson and Mountain (1991) and Naidu and Mountain (1998b). The experimental data obtained at each measurement location consisted of stiffness measurements measured for deflections, z , of the BM between 0 and $15 \mu\text{m}$. The data were fit to the parabolic function $k_o + k_2(z - z_o)^2$. The constant term, k_o , determined from the fit was chosen as the stiffness of the measurement location.

C. Experimental results

Representative results from experiment 110 598 are presented in Fig. 5. Figure 5(a) shows the schematic cross section of the OC during the measurements. Figure 5(c) shows the measured stiffness plotted as a function of radial position

TABLE II. Variability of stiffness measured at the center of the BM determined from the results of five experiments performed in the basal turn of the gerbil cochlea.

Experimental condition	Mean (μ)	Standard deviation (σ)
Before damage	2.41	0.49
After damage	1.31	0.24

along the BM. The filled squares show the stiffness of the BM measured before the spiral ligament was damaged. The unfilled squares show the stiffness of the BM measured after the spiral ligament was damaged. In both cases, the measured stiffness increases towards the spiral ligament. However, the magnitude of the measured stiffness of the BM decreases after damage to the spiral ligament.

Table II lists the mean and standard deviation of the stiffness measured at the center of the BM before and after damage to the spiral ligament. The mean and standard deviation were determined from the results of five experiments.

IV. DISCUSSION

A. Model validity

The BM is modeled as a plate for the following reasons. In response to the application of a local force, the BM deflects in a two-dimensional pattern along its width as well as along the length of the cochlea (Naidu and Mountain, 2001). The deflection profile decreases gradually along the length of the cochlea because the BM is longitudinally coupled. From a structural mechanics perspective, the deflection is consistent with plate-like behavior (Timoshenko and Woinowsky-Krieger, 1959).

We have neglected nonlinear effects in our model for the following reason. The stiffness measurements are obtained according to the procedure described by Olson and Mountain (1991). The stiffness is measured as a function of BM deflection and the data are fit to a parabolic function. The constant term from the parabolic fit is chosen as the stiffness of the BM. The constant term is the stiffness of BM when the deflection measured in response to a force is linear. Since, our model calculated tension using the stiffness as determined above, the BM deflection model is chosen to be linear. Therefore, we assume that nonlinear effects associated with stretching the BM can be neglected.

In order to simplify the model, we have assumed that the BM is uniform in thickness along its width at any given location along the cochlea. Therefore, we neglect the effects of any variations in thickness with a radial position along the BM. For the gerbil, we note that this assumption may be less accurate towards the apex of the cochlea where the pectinate zone of the basilar membrane shows a large radial variation in the thickness (Plassmann *et al.*, 1987).

B. Choice of E_f/E_g

The ratio E_f/E_g was estimated to be equal to 100. The ratio was fixed based on the following argument. Naidu and Mountain (1998a) have previously studied the pattern of BM

deflection along the cochlea and shown that the BM is nearly isotropic at the apex. For the BM to be nearly isotropic, the ratio of the flexural rigidities, D_y/D_x , must be close to unity. Equations (6)–(8) can be combined to calculate D_y/D_x as a function of E_f/E_g given by

$$\frac{D_y(x)}{D_x(x)} = 1 + \left(\frac{E_f}{E_g} \right) G(x), \quad (10)$$

where $G(x)$ is a geometry term, given by

$$G(x) = \left(\frac{6(1 - \nu^2)t_f(x)h_f(x)}{h(x)d_f(x)} \right). \quad (11)$$

The value of $G(x)$ was calculated at the cochlear locations listed in Table I. The variation of $G(x)$ with x was fit using the function

$$G(x) = 1.26e^{-0.387x}. \quad (12)$$

The BM in the gerbil is about 13 mm long (Plassmann *et al.*, 1987). At $x=13$ mm, $G(x)$ is equal to 0.81. Therefore, (E_f/E_g) was chosen to be 100 so that the ratio D_y/D_x was evaluated to equal 1.81.

C. Range of values

Figure 3(b) compares the predicted tensile stress in the BM with the tensile stress generated in other physiological environments. The large tensile stress at the base of the cochlea is almost comparable with the stress generated by the walls of a pulsating artery (Herlihy and Murphy, 1973). The tensile stress at the apex, though smaller than the stress developed in a contracting skin wound (Higton and James, 1964), is still much larger than the stress generated by individual cells (Wang and Ingber, 1994). The comparison indicates that the model predicts values of tensile stress that are of the same magnitude as the stress developed in other environments. The comparison also indicates that the tension is probably maintained by groups of cells rather than by individual cells.

D. Will the BM retract when cut?

Von Békésy (1960) reported that when small slits were made in the BM, the slit edges did not draw apart. We used the BM plate model to predict the outcome of von Békésy's experiments by calculating the expected retraction of the cut BM using the procedure described by Gummer and Johnstone (1983). Before the BM is cut, its measured width, $w(x)$, is equal to its strained width. Let the strain $\varepsilon_y(x)$ result from an extension $e(x)$ caused by the tension. When the BM is cut, the strain is reduced to zero. Therefore, the cut edges should retract so that the BM returns to its unstretched width, $w(x) - e(x)$. The strain in the BM due to tension can then be calculated by using Eq. (A7) in the Appendix. The extension, $e(x)$, may then be determined using the expression

$$\varepsilon_y(x) = \frac{e(x)}{w(x) - e(x)}. \quad (13)$$

Table III lists the calculated strain and the predicted retraction along the cochlea. The predicted magnitude of the re-

TABLE III. Calculated strain in the BM and predicted retraction in BM length when the BM is cut.

Location from base (mm)	Calculated strain (%)	Predicted retraction (μm)
1.3	0.28	0.41
3.61	0.22	0.37
4.55	0.16	0.32
6.86	0.14	0.29
7.54	0.12	0.27
11.26	0.09	0.24

traction is less than $1 \mu\text{m}$. It is very difficult to detect a retraction of this magnitude with a light microscope, even at high magnification, unless the cut is exceptionally clean without ragged edges. We, therefore, believe that von Békésy would not have been able to detect the expected retraction and that his experiments cannot be used to prove the absence or presence of BM tension.

E. Elasticity moduli of the BM fibers and ground substance

The modulus of elasticity, E_g , of the ground substance was determined from Eq. (6) to be $1.4 \times 10^5 \text{ Pa}$. Since E_f/E_g was chosen to be equal to 100, the elasticity modulus for the fiber bundles is calculated to be $1.4 \times 10^7 \text{ Pa}$. This value lies in the range between the moduli determined for elastin ($6 \times 10^5 \text{ Pa}$) and collagen ($1 \times 10^9 \text{ Pa}$) (Fung, 1993).

In the BM plate model, the elasticity of the ground substance and the fibers are constant with position along the cochlea since elasticity is an intrinsic property of the tissue. However, the resulting flexural rigidities, D_x and D_y , change with position along the cochlea because they depend not only upon the elasticity but also upon the dimensions of the BM and the fiber bundles (see Appendix). The changing stiffness is, therefore, produced by the synergistic combination of the changing tension and the changing dimensions of the BM.

F. Source of BM tension

Henson and Henson (1988) have proposed, on the basis of extensive anatomical studies, that the spiral ligament is responsible for generating and maintaining tension in the BM. Our experimental measurements show that the measured stiffness of the BM decreases when the spiral ligament is damaged. Since our model assumes that the stiffness of the BM is a function of the radial tension, the decrease in measured stiffness is consistent with a decrease in existing tension. Therefore, the experimental results support the hypothesis that the spiral ligament is involved in maintaining the BM tension.

One may argue that the decrease in stiffness produced by damage to the spiral ligament can be explained by a change in the boundary condition. If the boundary condition changed from being simply supported to a free boundary condition, the measured stiffness would decrease with proximity to the ligament. However, our experiments show that, while the magnitude of the stiffness decreases after damage to the ligament, the measured stiffness shows the same radial

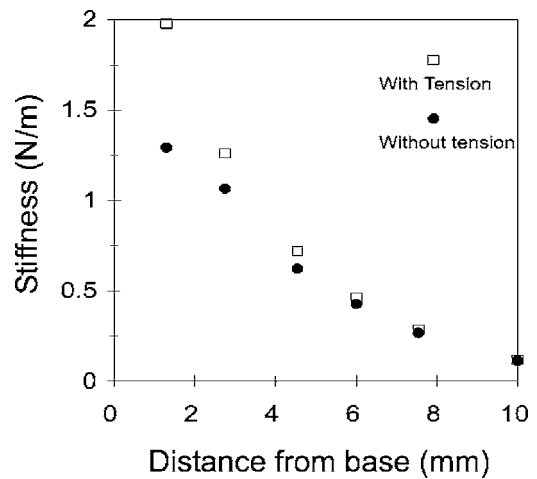


FIG. 6. Predicted changes in BM stiffness caused by loss of radial tension. The unfilled squares show the stiffness as measured along the cochlea. The filled circles show the predicted stiffness associated with a loss of tension at each location.

variation as the stiffness measured before damage and continues to increase with proximity to the spiral ligament. Therefore, we believe that the decrease in stiffness following damage to the spiral ligament is not caused by a change in the boundary condition on the edge of the plate.

We also predicted the change in stiffness that is caused by a loss of BM tension without changing the boundary conditions. The reduced stiffness is calculated by setting the tension term α in Eq. (A6) to zero. The results are shown in Fig. 6. At the base of the cochlea, a loss of tension results in a 35% decrease in stiffness, which agrees with the measured 45% decrease in stiffness calculated using Table II. In the middle of the cochlea, the loss of tension results in a 10%–15% decrease in stiffness. At the apex of the cochlea, we predict only a 3% decrease in stiffness due to a loss of tension. These results show that the contribution of the BM tension in determining the stiffness is largest in the base of the cochlea.

G. Implications for cochlear mechanics

Results from the model and experiments can be used to speculate on the role of BM tension and the spiral ligament in cochlea mechanics. The model results show that BM tension decreases from base to apex. The experimental results suggest that the spiral ligament is involved in maintaining BM tension. Combining the model and experimental results, we derive that changes in the spiral ligament alter BM tension, which in turn alters BM stiffness. Specifically, changes that strengthen the spiral ligament are expected to increase BM tension and thereby increase BM stiffness and vice versa. The characteristic frequency of the OC is a function of the BM stiffness. Therefore, an increase in BM stiffness will increase the resonant frequency of the OC. During development, changes that strengthen the spiral ligament occur when the cochlea matures (Henson and Rubsamen, 1996). Such changes imply that the tension gradient must also increase. The resulting increase in the stiffness gradient will cause the

frequency map to expand to encompass a larger frequency range in a manner that is consistent with the observed shift in the frequency map as the cochlea matures.

APPENDIX: CALCULATION OF THE BM TENSION

This Appendix describes the equations that are used to calculate the tension at a location x along the cochlea. All of the parameters and results are functions of x . Therefore, for simplicity of presentation, the dependence of each variable on x is omitted.

The general equation describing the deflection, $z(x, y)$, of the anisotropic BM plate in response to a generalized load, $q(x, y)$, and tension, N_y , along the y direction is given by

$$D_x \frac{\partial^4 z(x, y)}{\partial x^4} + 2H \frac{\partial^4 z(x, y)}{\partial x^2 \partial y^2} + D_y \frac{\partial^4 z(x, y)}{\partial y^4} - N_y \frac{\partial^2 z(x, y)}{\partial y^2} = q(x, y), \quad (\text{A1})$$

where the flexural rigidities D_x , D_y , and H are given by Eqs. (2)–(4).

The deflection in response to a concentrated force, P , applied at the center of the plate may be then obtained from Eq. (A1) in the form of a trigonometric series (Timoshenko and Woinowsky-Krieger, 1959).

$$z(x, y) = \frac{4P}{ab\pi^4} \times \sum_{n=1,3,\dots}^{\infty} \sum_{m=1,3,\dots}^{\infty} \frac{\sin \frac{m\pi}{2} \sin \frac{n\pi}{2}}{\left[D_x \frac{m^4}{b^4} + 2D_x \frac{m^2 n^2}{a^2 b^2} + D_y \frac{n^4}{a^4} + \frac{N_x m^2}{\pi^2 a^2} \right]} \times \sin \frac{m\pi x}{b} \sin \frac{n\pi y}{a}, \quad (\text{A2})$$

where H has been substituted by D_x using Eq. (4). For simplicity, we approximate the series by the largest term. The deflection profile is then given by the expression

$$z(x, y) = \frac{4Pab}{K\pi^4 D_x (1 + \alpha)} \sin \frac{\pi x}{a} \sin \frac{\pi y}{b}, \quad (\text{A3})$$

where

$$K = \left(\frac{D_y b^2}{D_x a^2} + 2 + \frac{a^2}{b^2} \right) \quad (\text{A4})$$

and

$$\alpha = \frac{N_y b^2}{\pi^2 D_x K}. \quad (\text{A5})$$

Two constraints are then applied to calculate the BM tension. First, the physiological stiffness, k_p , is measured experimentally at the center of the BM at a deflection, z_o in response to a force, P . The measured stiffness must be equal to the stiffness at the center of the plate calculated from the deflection profile using Eq. (A3) as follows:

$$\frac{1}{k_p} = \left. \frac{dz(a/2, b/2)}{dP} \right|_{z_p} = \frac{z_o(a/2, b/2)}{P} = \frac{4ab}{K\pi^4 D_x (1 + \alpha)}. \quad (\text{A6})$$

Second, during deflection, the tensile strain must balance the strain due to deflection. The strain, ε_y , generated in the plate by the tensile stress, σ_y , is then

$$\varepsilon_y = \frac{\sigma_y}{E_y} = \frac{N_y (1 - \nu^2)}{hE_y}, \quad (\text{A7})$$

where E_y represents the equivalent elasticity modulus along the y direction, which is related to the flexural rigidity D_y by

$$D_y = \frac{E_y h^3(x)}{12}. \quad (\text{A8})$$

The strain, ε_d , due to deflection is given by

$$\varepsilon_d = \frac{1}{2a} \int_0^a \left(\frac{dz(b/2, y)}{dy} \right)^2 dy, \quad (\text{A9})$$

where the right hand side of the equation is the ratio of the plate extension produced by deflection to the width a of the plate (Timoshenko, 1955). The plate extension is approximated by the difference between the arc length of the deflection profile and a .

Equating the tensile strain and strain due to deflection, we get

$$\frac{N_y (1 - \nu^2)}{hE_y} = \frac{1}{2a} \int_0^a \left(\frac{dz(b/2, y)}{dy} \right)^2 dy. \quad (\text{A10})$$

Substituting for $z(b/2, y)$ using Eq. (A3), and substituting for E_y using Eq. (A8), Eq. (A10) becomes

$$\frac{N_y h^2}{3D_y} = \left[\left(\frac{4Pab}{K\pi^4 D_x} \right) \left(\frac{1}{1 + \alpha} \right) \right]^2 \left(\frac{\pi}{a} \right)^2. \quad (\text{A11})$$

By dividing Eq. (A11) by Eq. (A6) and substituting for N_y using Eq. (A5), the value of α is calculated as

$$\alpha = \frac{3}{Kh^2} z_o^2 \left(\frac{b}{a} \right)^2 \left(\frac{D_y}{D_x} \right). \quad (\text{A12})$$

The tension, N_y is then be obtained from α by dividing Eq. (A5) by Eq. (A6)

$$N_y = \frac{4a}{\pi^2 b} \frac{\alpha}{(1 + \alpha)} k_p. \quad (\text{A13})$$

D_x and D_y may then be calculated from Eqs. (A5), (3), and (4).

NOMENCLATURE

x = coordinate along the longitudinal direction of the cochlea
 y = coordinate along the radial direction of the cochlea
 $a(x)$ = length of BM plate
 $b(x)$ = width of BM plate
 $d_f(x)$ = distance between fiber bundles
 $e(x)$ = extension of the BM at location x
 $h(x)$ = thickness of BM plate
 $h_f(x)$ = height of fibers
 $D_x(x)$ = flexural rigidity along x
 $D_y(x)$ = flexural rigidity along y
 $E_f(x)$ = modulus of elasticity of the BM fibers
 $E_g(x)$ = modulus of elasticity of the BM ground substance
 $E_y(x)$ = effective modulus of elasticity along y
 $G(x)$ = geometry factor
 $I_f(x)$ = moment of inertia of the fiber bundles
 $k_p(x)$ = point stiffness of the BM
 $N_y(x)$ = radial tension
 $q(x, y)$ = applied force
 $t_f(x)$ = thickness of fibers
 $w(x)$ = width of the BM at location x
 $z(x, y)$ = plate deflection at (x, y)
 z_o = deflection at which experimental stiffness is measured
 σ_x = stress along x
 σ_y = stress along y
 $\lambda_c(x)$ = longitudinal coupling space constant
 ν = poisson's ratio of the ground substance

Edge, R. M., Evans, B. N., Pearce, M., Richter, C. P., Hu, X., and Dallos, P. (1998). "Morphology of the unfixed cochlea," *Hear. Res.* **124**, 1–16.
 Engström, H. (1955). "The structure of the basilar membrane," *Acta Otorhinolaryngol. Belg.* **9**, 531–542.
 Fung, Y. C. (1993). *Biomechanics: Mechanical properties of living tissues* (Springer-Verlag, New York), p. 251.
 Gummer, A. W., and Johnstone, B. M. (1983). "State of stress within the basilar membrane: A re-evaluation of the membrane misnomer," *Hear.*

Res. **12**, 353–366.
 Harris, A. K., Stopak, D., and Wild, P. (1981). "Fibroblast traction as a mechanism for collagen morphogenesis," *Nature (London)* **290**, 249–251.
 Henson, M. M., Henson, Jr., O. W., and Jenkins, D. B. (1984). "Tension fibroblasts and the connective tissue matrix of the spiral ligament," *Hear. Res.* **16**, 231–242.
 Henson, M. M., and Henson, Jr., O. W. (1988). "Tension fibroblasts and the connective tissue matrix of the spiral ligament," *Hear. Res.* **35**, 237–258.
 Henson, M. M., and Rübsamen, R. (1996). "The postnatal development of tension fibroblasts in the spiral ligament of the horseshoe bat, *Rhinolophus rouxi*," *Aud. Neurosci.* **2**, 3–13.
 Herlihy, J. T., and Murphy, R. A. (1973). "Length-tension relationship of smooth muscle of the hog carotid artery," *Circ. Res.* **33**, 275–283.
 Highton, D. I. R., and James, D. W. (1964). "The force of contracting wounds," *Br. J. Surg.* **51**, 462–466.
 Iurato, S. (1962). "Functional implications of the nature and submicroscopic structure of the tectorial and basilar membranes," *J. Acoust. Soc. Am.* **34**, 1386–1395.
 Lai-Fook, S. J., Wilson, T. A., Hyatt, R. E., and Rodarte, J. R. (1976). "Elastic constants of inflated lobes of dog lungs," *J. Appl. Physiol.* **40**, 508–513.
 Naidu, R. C., and Mountain, D. C. (1998a). "Can longitudinal coupling within the organ of Corti be neglected?" *Proceedings of the Assoc. Res. Otolaryngol* **21**, 718.
 Naidu, R. C., and Mountain, D. C. (1998b). "Measurements of the stiffness map challenge a basic tenet of cochlear theories," *Hear. Res.* **124**, 124–131.
 Naidu, R. C., and Mountain, D. C. (2001). "Longitudinal coupling within the basilar membrane and reticular lamina," *J. Assoc. Res. Otolaryngol.* **2**, 257–267.
 Olson, E. S., and Mountain, D. C. (1991). "In vivo measurement of basilar membrane stiffness," *J. Acoust. Soc. Am.* **89**, 1262–1275.
 Plasmann, W., Peetz, W., and Schmidt, M. (1987). "The cochlea in gerbilline rodents," *Brain Behav. Evol.* **30**, 82–101.
 Rhode, W. S. (1973). "An investigation of postmortem cochlear mechanics using the Mössbauer effect," in *Basic Mechanisms of Hearing*, edited by A. R. Møller (Academic, New York).
 Schweitzer, L., Lutz, C., Hobbs, M., and Weaver, S. P. (1996). "Anatomical correlates of the passive properties underlying the developmental shift in the frequency map of the mammalian cochlea," *Hear. Res.* **97**, 84–94.
 Timoshenko, S. (1955). *Strength of Materials*, 3rd ed. (R. E. Krieger, Malabar, Florida), Chap. V.
 Timoshenko, S., and Woinowsky-Krieger, S. (1959). *Theory of Plates and Shells* (McGraw-Hill, New York).
 Von Békésy, G. (1960). *Experiments in Hearing* (McGraw-Hill, New York).
 Wang, N., and Ingber, D. E. (1994). "Control of cytoskeletal mechanics by extracellular matrix, cell shape, and mechanical tension," *Biophys. J.* **66**, 2181–2189.

Cochlear traveling-wave amplification, suppression, and beamforming probed using noninvasive calibration of intracochlear distortion sources

Christopher A. Shera^{a)} and John J. Guinan, Jr.

Eaton-Peabody Laboratory, Massachusetts Eye & Ear Infirmary, 243 Charles Street, Boston, Massachusetts 02114 and Department of Otolaryngology, Harvard Medical School, Boston, Massachusetts 02115

(Received 12 September 2006; revised 3 November 2006; accepted 3 November 2006)

Originally developed to estimate the power gain of the cochlear amplifier, so-called “Allen–Fahey” and related experiments have proved invaluable for probing the mechanisms of wave generation and propagation within the cochlea. The experimental protocol requires simultaneous measurement of intracochlear distortion products (DPs) and ear-canal otoacoustic emissions (DPOAEs) under tightly controlled conditions. To calibrate the intracochlear response to the DP, Allen–Fahey experiments traditionally employ invasive procedures such as recording from auditory-nerve fibers or measuring basilar-membrane velocity. This paper describes an alternative method that allows the intracochlear distortion source to be calibrated noninvasively. In addition to the standard pair of primary tones used to generate the principal DP, the noninvasive method employs a third, fixed tone to create a secondary DPOAE whose amplitude and phase provide a sensitive assay of the intracochlear value of the principal DP near its characteristic place. The method is used to perform noninvasive Allen–Fahey experiments in cat and shown to yield results in quantitative agreement with the original, auditory-nerve-based paradigm performed in the same animal. Data obtained using a suppression-compensated variation of the noninvasive method demonstrate that neither traveling-wave amplification nor two-tone suppression constitutes the controlling influence in DPOAE generation at close frequency ratios. Rather, the dominant factor governing the emission magnitude appears to be the variable directionality of the waves radiated by the distortion-source region, which acts as a distortion beamformer tuned by the primary frequency ratio. © 2007 Acoustical Society of America. [DOI: 10.1121/1.2404620]

PACS number(s): 43.64.Kc, 43.64.Jb, 43.64.Yp, 43.58.Ry [BLM]

Pages: 1003–1016

I. INTRODUCTION

Allen–Fahey and related paradigms use cochlear nonlinearities to create a calibrated intracochlear distortion source that can be moved along the organ of Corti by varying the frequencies of the stimulus tones. The power of the paradigm derives from the calibration of the distortion source—that is, from the ability to hold the distortion-source output constant within the cochlea while simultaneously measuring the sound produced in the external ear canal, where the distortion appears as an evoked otoacoustic emission (a DPOAE). Because of this tight control, the Allen–Fahey paradigm has been used extensively to probe the nonlinear mechanisms of wave generation, propagation, and amplification within the cochlea (e.g., Fahey and Allen, 1985; Allen and Fahey, 1992; Kanis and de Boer, 1993; Shera, 2003; de Boer *et al.*, 2005; Ren and Nuttall, 2006; Shera *et al.*, 2007).

In their original experiments, Allen and Fahey calibrated the intracochlear distortion product (DP) by using an auditory-nerve fiber (ANF) tuned to the DP frequency (Fahey and Allen, 1985; Allen and Fahey, 1992). More recently, de Boer and colleagues have extended the procedure by using laser interferometry to measure and control the DP component of

basilar-membrane (BM) velocity at the DP place (de Boer *et al.*, 2005), and one can imagine other variations on the theme, such as measuring DP components of intracochlear pressure (Dong and Olson, 2005). Unfortunately, these methods all employ invasive procedures that largely preclude their application in human and other subjects for whom the necessary surgeries are prohibitive. In this paper we describe an alternative method that allows the intracochlear distortion source to be calibrated noninvasively.

Interpretation of Allen–Fahey or other experiments performed using calibrated intracochlear distortion sources requires controlling for effects such as two-tone suppression that influence the result. For example, the original and most extensively discussed application of the Allen–Fahey paradigm is the estimation of the power gain of the cochlear amplifier at the DP frequency. Interpreting the results as a measure of power gain, however, is complicated by suppression. In particular, the primary tones used to produce the distortion source suppress the DP amplifier. Since it reduces the gain of the amplifier, suppression has been hypothesized to explain what is perhaps the most unexpected result of the Allen–Fahey experiment: The downturn in the measured DPOAE—suggesting strong power absorption, rather than amplification—in the region just basal to the peak of the traveling wave. Needless to say, it is precisely this region basal to the peak where other measures of cochlear amplifi-

^{a)}Electronic mail: shera@epl.meei.harvard.edu

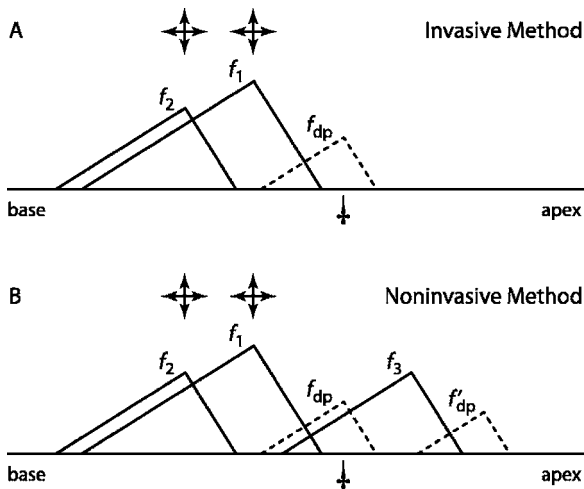


FIG. 1. Schematics showing the primary tones and distortion products employed for generating and calibrating intracochlear distortion sources. Both panels show stylized BM excitation patterns arrayed along the cochlear tonotopic axis. The solid lines show stimulus tones presented using earphones; dashed lines show distortion products created within the cochlea. Crossed double arrows (\oplus) indicate stimulus tones whose amplitude and frequency are varied during the measurement; the other stimulus tones are held fixed. Inverted daggers (\ddagger) mark the peak of the f_{dp} excitation pattern (x_{dp}) where the response is calibrated (e.g., held constant during Allen–Fahey experiments). (A) Stimulus paradigm used in the invasive calibration procedure. Intermodulation distortion between primary tones at frequencies f_1 and f_2 produces the distortion product $f_{dp}=2f_1-f_2$ whose amplitude is measured at x_{dp} using auditory-nerve recordings or laser interferometry. (B) Stimulus paradigm used in the noninvasive calibration procedure. The distortion product f_{dp} combines with the fixed primary f_3 to produce the secondary DP at frequency $f'_{dp}=2f_3-f_{dp}$. In this case, the peak of the f_{dp} excitation pattern (\ddagger) locates the approximate center of the f'_{dp} generation region; the level of the secondary DPOAE (L'_{dp}) therefore provides a measure of the amplitude of f_{dp} near its characteristic place.

cation [most tellingly, solutions the cochlear inverse problem (e.g., Zweig, 1991; de Boer, 1995; de Boer and Nuttall, 2001)] indicate that cochlear power amplification is strongest.

Broadly speaking, the paper has three parts.¹ In the first part, we briefly outline the noninvasive method and illustrate its application to Allen–Fahey experiments in cat. In the second part, we validate the noninvasive method by comparing its results to invasive, auditory-nerve experiments performed in the same animal. We find that the two methods are in strong quantitative agreement. Finally, in the third part, we apply the noninvasive method to explore the role of two-tone suppression in producing the decrease in ear-canal DPOAEs characteristic of Allen–Fahey experiments at close ratios. Although suppression appears strong, our results establish that neither suppression nor traveling-wave amplification constitutes the dominant factor shaping the response.

II. THE NONINVASIVE METHOD IN A NUTSHELL

Figure 1(A) shows a schematic of the stimulus tones widely used to generate sources of intracochlear distortion. When the ear is driven by two primary tones P_1 and P_2 with frequencies $f_2 > f_1$, intermodulation distortion products (e.g., $f_{dp}=2f_1-f_2$) are generated within the cochlea in a region near the f_2 place, where the overlap between the stimulus

excitation patterns is greatest. Although most distortion experiments measure the output of the distortion source at only a single location (usually in the ear canal, where the signal is most accessible), Allen–Fahey and related paradigms provide an additional level of experimental control by simultaneously calibrating the distortion-product level *inside* the cochlea (e.g., at its characteristic place, x_{dp}). Until now, invasive methods such as auditory-nerve recording or laser interferometry have been needed to calibrate the DP response within the cochlea (Fahey and Allen, 1985; Allen and Fahey, 1992; de Boer *et al.*, 2005).

The noninvasive calibration procedure is illustrated in Fig. 1(B). Rather than using a microelectrode or laser, the method employs a “secondary” distortion product to monitor the intracochlear excitation at frequency f_{dp} near x_{dp} .² More specifically, the noninvasive method assumes that the response to f_{dp} near x_{dp} can be calibrated by using it to generate a secondary DP at frequency $f'_{dp}=2f_3-f_{dp}$ through the interaction of f_{dp} with a third primary tone of fixed frequency ($f_3 < f_{dp}$) and level. Because f_{dp} acts as the high-frequency “primary” for the generation of f'_{dp} , the peak of the f_{dp} excitation pattern locates the approximate center of the f'_{dp} generation region. The level of the secondary DPOAE (L'_{dp}) therefore provides a measure of the amplitude of f_{dp} near its characteristic place. In particular, by monitoring the secondary DPOAE in the ear canal and adjusting the primaries P_1 and P_2 appropriately, one can keep the amplitude and phase of the f_{dp} traveling wave constant near x_{dp} . We write “near” here because the secondary DPOAE is generated over a region straddling x_{dp} , not at x_{dp} exclusively; as a result the noninvasive method is less tightly controlled than the ANF- or BM-based methods.

As an important caveat, we note that the uncontrolled introduction of additional primary tones can create a frightful cascade of “catalyzed” distortion products and other contaminating interactions (e.g., Fahey *et al.*, 2000). For example, since the frequency $f'_{dp}=2f_3-f_{dp}=2f_3-2f_1+f_2$ can be written in the form $(3f_3-2f_1)+(f_2-f_3)$, the secondary DPOAE at $2f_3-f_{dp}$ can in principle be contaminated by contributions from the even-order sum tone that arises from nonlinear interactions between the fifth-order DP at $3f_3-2f_1$ and the second-order DP at f_2-f_3 . Fortunately, at low and moderate levels most of these contaminating combination tones are small and appear to make little if any significant contribution to the measured DPOAE unless the additional “interfering” tones (in this case, they would be the primaries f_1 and f_2 themselves) are an octave or more above the DP frequency (Fahey *et al.*, 2000). For this reason, we generally restrict our attention to frequencies within an octave of f'_{dp} , avoiding high-frequency “lobes” whenever possible.

For simplicity, our nutshell description of the noninvasive method has ignored complications arising from the mixing of distortion and reflection components in the measured DPOAEs (reviewed in Shera and Guinan, 1999). For example, the secondary DPOAE monitored in the ear canal presumably contains not only distortion components originating near x_{dp} (i.e., within the principal generation region), but also reflection components arising via subsequent scat-

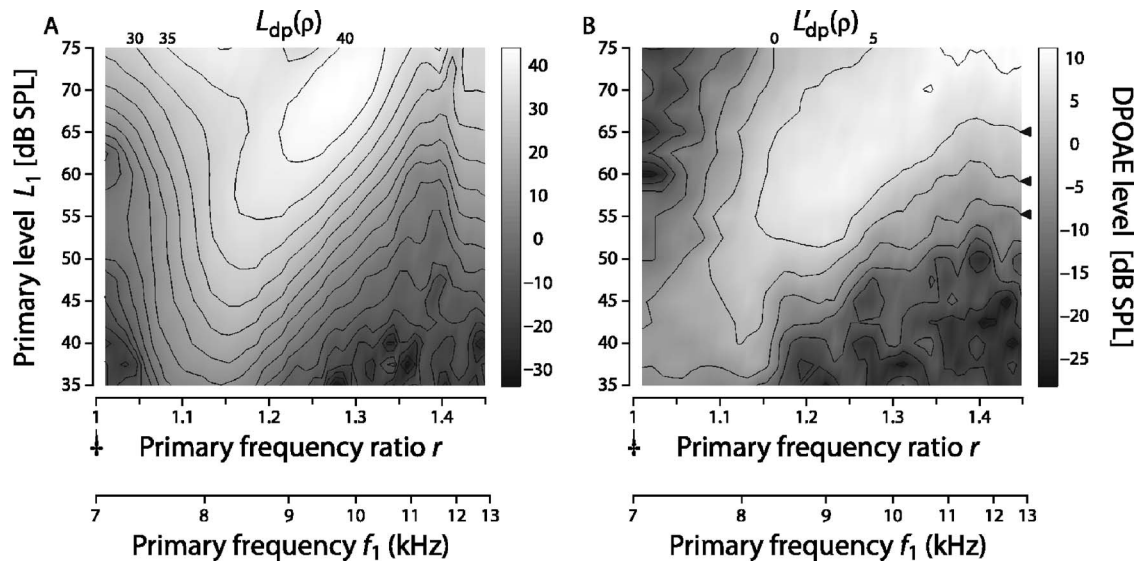


FIG. 2. DPOAE level maps measured using the noninvasive method in cat. The stimulus protocol is illustrated in Fig. 1(B). Each panel gives the primary frequency ratio r along the abscissa and the level L_1 along the ordinate. DPOAE level is coded using the gray scale indicated by the bar adjacent to each panel; contour lines are spaced at intervals of 5 dB SPL. Both r and f_1 increase along the abscissa [with $f_1 = f_{dp}/(2-r)$]. In all measurements, the frequency f_{dp} was fixed at 7 kHz, corresponding to $r=1$ (\dagger). (A) Principal DPOAE level map $L_{dp}(\rho)$ measured by varying the primary frequencies and intensities. The primary level L_2 was varied according to $L_2=L_1-15$ dB SPL. The data were obtained in the presence of a third primary, P_3 , defined so that $f_{dp}/f_3=1.15$ and $L_3=45$ dB SPL. Contour lines corresponding to DPOAE levels of $\{30, 35, 40\}$ dB SPL are labeled along the top margin. (B) Secondary DPOAE level map $L'_{dp}(\rho)$ measured simultaneously with the principal level map $L_{dp}(\rho)$ shown in (A). Triangles along the right margin mark iso- L'_{dp} contours corresponding to $\{5, 0, -5\}$ dB SPL.

tering near x'_{dp} (e.g., Kalluri and Shera, 2001). Although the measurements reported here were performed in cat, a species for which the relative amplitude of contaminating reflection components generally appears small, DPOAE source mixing may play a more significant role in humans and other species with large DPOAE microstructure. We note, however, that even when mixing is strong, both of the two f'_{dp} components depend on the amplitude of the f_{dp} wave near its peak. We therefore expect that complications due to mixing will not significantly compromise the utility of using L'_{dp} as an assay of intracochlear DP excitation near x_{dp} .

III. APPLICATION TO NONINVASIVE ALLEN-FAHEY EXPERIMENTS

The noninvasive method of calibrating the intracochlear distortion source is perhaps best illustrated by an example application: the Allen–Fahey experiment. Allen–Fahey experiments consist of measuring the ear-canal DPOAE as a function of the primary frequency ratio $r \equiv f_2/f_1$ while the intracochlear DP response is held constant at x_{dp} (the DP frequency f_{dp} remains fixed throughout the measurement). We denote the DPOAE sound-pressure level measured under these conditions by $L_{dp}^\dagger(r)$, where the superscripted dagger signifies the microelectrode originally employed to monitor the intracochlear distortion product. For clarity, we sometimes write $L_{dp}^\dagger(r)$, which we will refer to as the “Allen–Fahey function,” in the form $L_{dp}^\dagger(r; C)$, where the parameter C represents the imposed iso-response constraint. The parameter C will typically be either a constant value of L'_{dp} (denoted $L_{dp}^{\dagger\prime}$) or a constant increase in neural firing rate (ΔR^\dagger).

A. Mapping out the territory

Figure 2 shows typical data collected while using the method to perform a noninvasive Allen–Fahey experiment in cat. Similar experiments were performed at seven f_{dp} frequencies ranging from 2.5 to 8 kHz in two cats with good hearing. Additional experiments in four cats were used to develop the methods. Except when there were obvious problems with the acoustic calibrations, qualitatively similar results were found in all cases.

Although Allen–Fahey experiments are traditionally performed using a real-time feedback loop to maintain a constant response at x_{dp} , we took advantage of the additional freedom offered by the noninvasive method to “map out” the territory under open-loop conditions.³ The data are displayed in the form of DPOAE level maps⁴ that show the dependence of L_{dp} and L'_{dp} on the frequency ratio and level of the primaries. We thus regard the maps as functions of $\rho \equiv (r, L_1)$, which represents an ordered pair of independent variables that together define the “ ρ plane.” The maps were constructed by interpolation from data collected by randomized sampling on a rectangular grid (50 frequencies, 17 levels). For reference, iso-DPOAE level contours are spaced at intervals of 5 dB SPL.

The map $L_{dp}(\rho)$ evinces a characteristically snout-shaped main lobe that peaks at a primary frequency ratio $r_{opt} \approx 1.2$ [panel (A)]. Note, however, that the value of r_{opt} is clearly level dependent, ranging from $r_{opt} \approx 1.13$ at 35 dB SPL to $r_{opt} \approx 1.28$ at 70 dB SPL. At higher ratios ($r > 1.35$), the first in a series of notches and lobes appears, perhaps as the result of wave interference effects. Although overall levels are reduced, the map $L'_{dp}(\rho)$ is qualitatively similar in form [panel (B)].

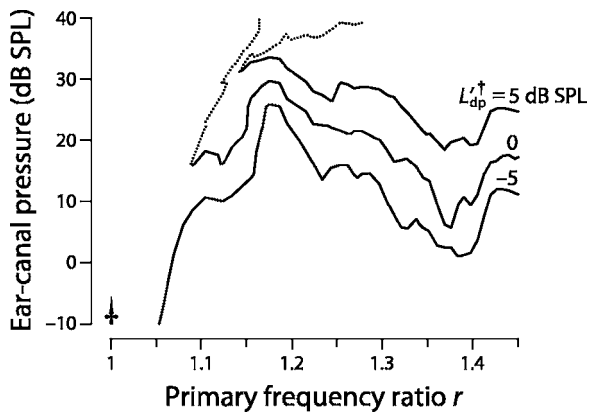


FIG. 3. Results for the noninvasive Allen–Fahey experiment. The lines show measured Allen–Fahey functions, $L_{dp}^\ddagger(r; L'_{dp}{}^\ddagger)$ defined as the level of the principal DPOAE (at f_{dp}) measured when the secondary DPOAE (at f'_{dp}) is held constant at $L'_{dp}{}^\ddagger$. The Allen–Fahey functions were obtained by evaluating $L_{dp}(\rho)$ from Fig. 2(A) along the three iso- L'_{dp} contours marked with triangles (\blacktriangle) in Fig. 2(B) ($L'_{dp}{}^\ddagger = \{5, 0, -5\}$ dB SPL). The inverted dagger (\ddagger) denotes the constant value of f_{dp} corresponding to $r=1$. The dotted lines show secondary branches of $L_{dp}^\ddagger(r; L'_{dp}{}^\ddagger)$ obtained when an iso- L'_{dp} contour loop backs on itself at $r < r_{opt}$.

B. Allen–Fahey experiments by inspection

The big-picture view provided by the maps $L_{dp}(\rho)$ and $L'_{dp}(\rho)$ in Fig. 2 frees us from the tyranny of the feedback loop—we can impose any auxiliary conditions we chose (e.g., the constant-response criterion mandated by the Allen–Fahey paradigm) after all measurements have been collected. Indeed, the level maps allow noninvasive Allen–Fahey experiments to be performed almost by inspection.

One begins by choosing a constant criterion value of L'_{dp} , which we will call $L'_{dp}{}^\ddagger$. The value $L'_{dp}{}^\ddagger$ defines an iso- L'_{dp} contour, $C_0(L'_{dp}{}^\ddagger)$, in the ρ plane. Contours C_0 corresponding to three different values of $L'_{dp}{}^\ddagger$ are shown marked by triangles in Fig. 2(B). For each value of $L'_{dp}{}^\ddagger$, the corresponding Allen–Fahey function $L_{dp}^\ddagger(r; L'_{dp}{}^\ddagger)$ can be obtained simply by extracting values from the map $L_{dp}(\rho)$ [Fig. 2(A)] along the contour $C_0(L'_{dp}{}^\ddagger)$:

$$L_{dp}^\ddagger(r; L'_{dp}{}^\ddagger) = L_{dp}[C(L'_{dp}{}^\ddagger)]. \quad (1)$$

The function $L_{dp}^\ddagger(r; L'_{dp}{}^\ddagger)$ obtained in this way represents the level of the principal DPOAE (at frequency f_{dp}) when the level of the secondary DPOAE (at f'_{dp}) is held constant (at $L'_{dp} = L'_{dp}{}^\ddagger$). According to the premise of the noninvasive method, holding L'_{dp} constant in the ear canal approximates holding the intracochlear response to f_{dp} constant near its characteristic place.

Figure 3 shows Allen–Fahey functions $L_{dp}^\ddagger(r; L'_{dp}{}^\ddagger)$ obtained by evaluating $L_{dp}(\rho)$ from Fig. 2(A) along the three marked iso- L'_{dp} contours from Fig. 2(B); the three contours correspond to $L'_{dp}{}^\ddagger = \{5, 0, -5\}$ dB SPL. Over most of the measured frequency range, the three different criterion values of $L'_{dp}{}^\ddagger$ all yield functions $L_{dp}^\ddagger(r; L'_{dp}{}^\ddagger)$ with a “bandpass” shape whose qualitative form is not especially sensitive to the value of $L'_{dp}{}^\ddagger$. As r decreases towards 1, the ear-canal amplitude of $L_{dp}^\ddagger(r; L'_{dp}{}^\ddagger)$ generally increases to a maximum and then decreases as r falls below $r_{opt} \cong 1.2$. Note, however, that at the two higher values of $L'_{dp}{}^\ddagger$ the decrease at close

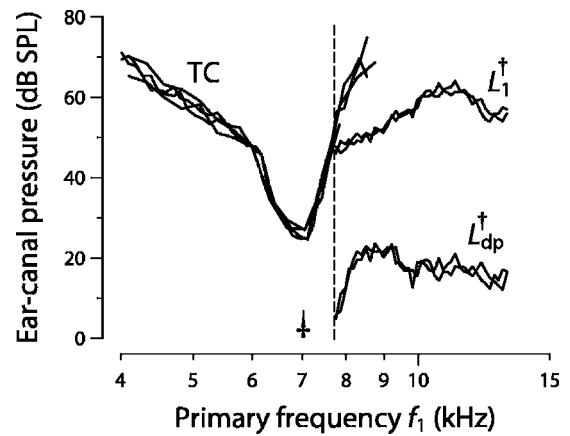


FIG. 4. Allen–Fahey experiment performed using the ANF-based method. The data are from the same animal and use the same f_{dp} frequency as the noninvasive results shown in Fig. 3. The figure shows measurements of the Allen–Fahey function, $L_{dp}^\ddagger(r; \Delta R^\ddagger)$, defined as the level of the principal DPOAE (at f_{dp}) measured when the DP response response at x_{dp} was held at neural threshold ($\Delta R^\ddagger = 20$ spikes/s above the spontaneous rate) using the auditory-nerve fiber whose threshold tuning curve (TC) is shown; the DP frequency f_{dp} was fixed at the fiber’s CF (\ddagger). The data are plotted versus f_1 (on a log scale) rather than r so that the tuning curve has its conventional form. For reference, the f_1 tick-mark frequencies $\{7, 8, 9, 10\}$ correspond to r values of approximately $\{1, 1.125, 1.22, 1.3\}$, respectively. The curve labeled L_1^\ddagger shows the corresponding level of the f_1 primary (with $L_2 = L_1 - 15$ dB SPL). The dashed vertical line indicates the frequency below which the f_1 primary drives the fiber so that the constant-DP condition cannot reliably be maintained. The acoustic noise floor was approximately -20 dB SPL. Multiple traces illustrate the reproducibility of the measurements.

ratios is cut short because the corresponding iso- L'_{dp} contours turn back on themselves at values of r less than r_{opt} [Fig. 2(B)]. For these values of $L'_{dp}{}^\ddagger$, the function $L_{dp}^\ddagger(r; L'_{dp}{}^\ddagger)$ remains undefined at close ratios.

Before exploring the origins of the bandpass form of $L_{dp}^\ddagger(r; L'_{dp}{}^\ddagger)$ —and of the undefined values at higher values of $L'_{dp}{}^\ddagger$ —we first compare the results obtained with the noninvasive method to those obtained using the original, auditory-nerve-based paradigm.

IV. COMPARISON WITH THE AUDITORY-NERVE-BASED METHOD

To test the validity of the noninvasive method, we also performed Allen–Fahey experiments using the original ANF-based paradigm. Figure 4 shows the ANF-derived $L_{dp}^\ddagger(r; \Delta R^\ddagger)$ measured at the same frequency and in the same cat employed for the noninvasive experiments shown in Fig. 3. In the invasive version of the experiment, the DP response at x_{dp} was adjusted to produce a threshold-level change, ΔR^\ddagger , in the firing rate of an auditory-nerve fiber with CF matching the DP frequency. Note that the ANF-based method cannot measure $L_{dp}^\ddagger(r; \Delta R^\ddagger)$ at close ratios: Once the primary P_1 crosses the tuning curve into the fiber’s response area, the primaries drive the fiber and the constant-DP condition can no longer reliably be maintained.⁵ Nevertheless, within their overlapping domains the invasive and noninvasive methods give qualitatively similar results. In particular, the two methods agree on the overall bandpass shape of $L_{dp}^\ddagger(r)$, as well as on some of the microstructural details (e.g., the peak location).

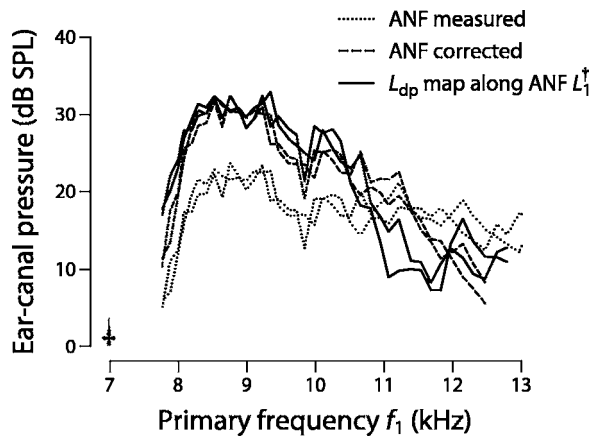


FIG. 5. ANF-based Allen–Fahey functions compensated for changes in the strength of the intracochlear distortion source. The curves show measured and corrected values of $L_{dp}^{\dagger}(r; \Delta R^{\dagger})$ versus the primary frequency f_1 . The dotted lines show the measured Allen–Fahey functions from Fig. 4; the dashed lines show the same measurements adjusted for frequency-dependent changes in the DP-gram that occurred during the interval between the noninvasive and ANF-based measurements. The multiple traces illustrate the reproducibility of the measurements. Solid lines show values from the noninvasive map $L_{dp}(\rho)$ [Fig. 2(A)] extracted along the ANF-based trajectory $L_1^{\dagger}(r)$ (Fig. 4). For reference, the f_1 tick-mark frequencies $\{7, 8, 9, 10, 11, 12, 13\}$ correspond to r values of approximately $\{1, 1.125, 1.22, 1.3, 1.36, 1.42, 1.46\}$, respectively.

A. Compensating for changes in distortion-source output

To provide a more quantitative comparison between the two methods, the data need to be corrected for differences in the physiological state of the ear, as manifest through the effective strength of the distortion source. Although the measurements in Figs. 3 and 4 were performed at the same frequency and in the same animal, the data were collected at different times. During the interval between the two measurements (approximately 17 h), noninvasive level maps were measured at other frequencies, the animal was prepared for neural recording by surgically exposing the auditory nerve, and recordings were made on about 30 fibers. These activities were accompanied by slow but significant changes in the state of the cochlea, as assayed using distortion-product “audiograms” (DP-grams). Meaningful quantitative comparisons between the two methods require that we “correct” the ANF-based results from Fig. 4 in order to estimate the value of $L_{dp}^{\dagger}(r; \Delta R^{\dagger})$ we would have measured had the neural recordings been made simultaneously with the noninvasive measurements of Fig. 3.

Fortunately, two independent means of performing the needed correction are available. The most straightforward approach is to adjust the ANF-based amplitude of $L_{dp}^{\dagger}(r; \Delta R^{\dagger})$ up or down by an amount equal to the measured shift in the DP-gram. The dashed lines in Fig. 5 show the results of applying this frequency-dependent adjustment for distortion-source output. As indicated by the size and direction of the shifts, the change in the DP-gram varied considerably across the measured range. Whereas for $f_1 < 11$ kHz, the distortion-source output decreased over time (the upward shift reflects the stronger DP generation at the earlier time), at higher frequencies the effective DPOAE source output in-

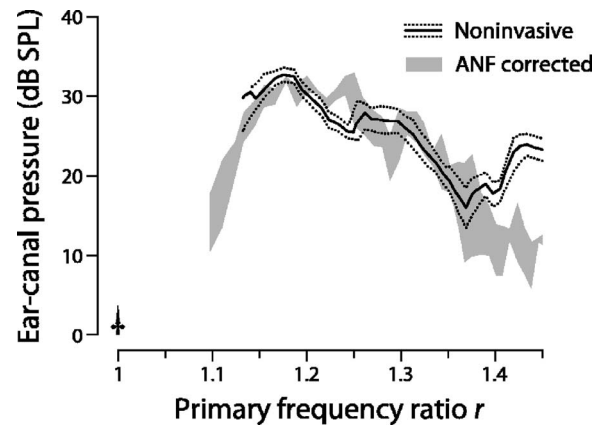


FIG. 6. Comparison of noninvasive and ANF-based Allen–Fahey functions. The solid line and flanking dotted uncertainties give Allen–Fahey functions $L_{dp}^{\dagger}(r; L'_{dp}{}^{\dagger})$ measured using the noninvasive method with iso- L'_{dp} contours of $L'_{dp}{}^{\dagger} = 4 \pm 1$ dB SPL. The shaded region shows the range of corrected ANF values from Fig. 5.

creased slightly during the interval (and the corrected curve shifts down). Because our standard DP-grams were recorded at a primary frequency ratio and level ($r=1.2$ and $\{L_1, L_2\} = \{50, 40\}$ dB SPL) roughly comparable to those that pertain near the peak of $L_{dp}^{\dagger}(r; L'_{dp}{}^{\dagger})$ measured along the $L'_{dp}{}^{\dagger} = 5$ dB SPL contour, the correction should be most reliable in this region.

The second strategy for correcting the ANF result is to evaluate $L_{dp}(\rho)$ using the noninvasive map in Fig. 2(A) along the “primary-level-trajectory” measured during the ANF experiment (i.e., along the curve labeled L_1^{\dagger} in Fig. 4). Henceforth we refer to this curve simply as the “ L_1 -trajectory,” since the primary levels L_1 and L_2 vary together. The solid lines in Fig. 5 show the resulting values of $L_{dp}^{\dagger}(r; L_1^{\dagger})$, where $L_1^{\dagger} = L_1^{\dagger}(r; \Delta R^{\dagger})$ is the L_1 trajectory. This approach assumes that although the distortion-source output level may vary somewhat during the experiment (e.g., according to the status of the outer hair cells), the *shape* of the iso-response contours varies much less. In other words, the correction presumes that despite an ongoing modulation in the overall level of intracochlear distortion, contours that produced constant distortion early in the experiment continue to yield constant (albeit usually reduced) distortion as the state of the cochlea varies (usually deteriorates) with time.

Figure 5 shows that the two correction methods yield very nearly the same results. Agreement is especially good near the peak of $L_{dp}^{\dagger}(r)$, where we expect the DP-gram correction to be most reliable.

B. Comparison between the methods

The compensation for intervening changes in distortion-source output allows us to compare the noninvasive and ANF-based results more quantitatively. Figure 6 directly overlays values of $L_{dp}^{\dagger}(r)$ measured using the two methods. The noninvasive values were obtained using iso- L'_{dp} contours of $L'_{dp}{}^{\dagger} = 4 \pm 1$ dB SPL; the ANF values correspond to the range of corrected results from Fig. 5.

The noninvasive contours used in the comparison ($L'_{dp}{}^{\dagger} = 4 \pm 1$ dB SPL) were chosen with reference to Fig. 7, which

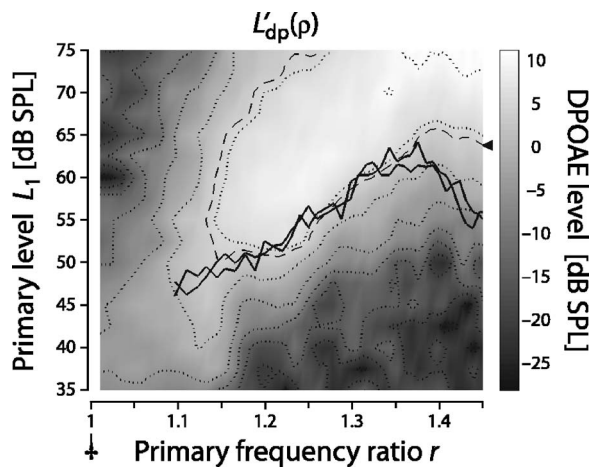


FIG. 7. Comparison between iso- L'_{dp} and ANF-derived constant-response contours. The L_1^\dagger curves from Fig. 4 (thick solid lines) are shown overlaid on the map $L'_{dp}(\rho)$ from Fig. 2(B). For reference, the dashed line marked with a triangle (\blacktriangleleft) shows the contour $L_{dp}=4$ dB SPL.

shows the ANF-derived L_1^\dagger curve (Fig. 4) overlaid on the noninvasive L'_{dp} map [Fig. 2(B)]. Except at the largest and smallest ratios, the L_1^\dagger curve closely parallels the iso- L'_{dp} contours, with the value $L'_{dp} \dagger \cong 4$ dB SPL providing a good overall match. The matching value $L'_{dp} \dagger$ depends on the threshold and rate response function of the auditory-nerve fiber. The L_1^\dagger curve for a more sensitive (lower threshold) fiber would presumably track iso- L'_{dp} contours corresponding to smaller values of $L'_{dp} \dagger$. (Unfortunately, we did not encounter a more sensitive 7 kHz CF fiber in this cat and are therefore unable to test this expectation directly.)

Although the invasive and noninvasive Allen–Fahey functions $L'_{dp}(r)$ —and their corresponding iso-response contours—differ at high frequencies, where the higher-order lobes in the map $L_{dp}(\rho)$ reside, the agreement within the main lobe is quite respectable. (Both methods yield functions that remain undefined at close ratios: The noninvasive curve terminates at ratios below $r \cong 1.13$ where the best matching $L'_{dp} \dagger$ contour turns back on itself; the ANF curve terminates near $r \cong 1.1$ where the trajectory L_1^\dagger crosses the tuning curve.) Thus, within the main lobe, the noninvasive criterion of constant L'_{dp} yields results in strong quantitative agreement with the invasive criterion of constant ANF response.

We performed similar ANF-based Allen–Fahey experiments in five cats and measured Allen–Fahey functions on approximately 27 fibers (partial results were obtained on many other fibers with which electrode contact was lost before data collection was complete). In two of the five cats, noninvasive methods were also employed. Although the data and control experiments required for full, CF-matched comparisons between the invasive and noninvasive methods exist for only a single fiber (see above), the data from other fibers appear consistent with at least a good qualitative match between the two methods. Taken together, our comparisons demonstrate a good correspondence between the methods and indicate that possible complications arising from the introduction of a third primary tone are small, at least within the main lobe of the response. Our results therefore support

the basic assumption of the noninvasive method, namely that the secondary DPOAE provides a useful assay of the amplitude of the principal DP near its characteristic place.

V. THE ROLE OF SUPPRESSION IN ALLEN–FAHEY EXPERIMENTS

We now apply the noninvasive method to probe the mechanisms responsible for the shape of the Allen–Fahey function, $L'_{dp}(r)$. The assumptions underlying Allen and Fahey’s (1992) analysis imply that the shape of $L'_{dp}(r)$ reflects the spatial variation of the integrated power gain of the cochlear amplifier at frequency f_{dp} . In this interpretation, segments along the abscissa in which $L'_{dp}(r)$ increases as one moves left toward $r=1$ correspond to regions of net power gain (i.e., amplification by the organ of Corti) and segments in which $L'_{dp}(r)$ decreases correspond to regions of net power loss (absorption by the organ of Corti). Interpreted in this way, the location of the maxima in the $L'_{dp}(r)$ curves (Figs. 3–6) indicates that the integrated power gain of the amplifier peaks at a location almost 2 mm basal to the peak of the f_{dp} excitation pattern, a distance equivalent to about one-half octave of CF.⁶ Furthermore, the downward trend in $L'_{dp}(r)$ at values $r < r_{opt}$ implies that strong power absorption—rather than amplification—occurs in the region just basal to the peak of the traveling wave. This conclusion conflicts with solutions to the cochlear inverse problem (e.g., Zweig, 1991; de Boer, 1995; de Boer and Nuttall, 2001), which indicate (based on different data and assumptions) that the integrated power gain peaks are much closer to x_{dp} .⁷

Other than the possibility that the emperor has no clothes (i.e., that the cochlear amplifier has negative gain), the most frequently cited explanation for the downturn in $L'_{dp}(r)$ at close ratios involves the suppressive influence of the primaries (e.g., Allen and Fahey, 1992; Kanis and de Boer, 1993; de Boer *et al.*, 2005). The idea is that at close ratios the primaries powerfully suppress the f_{dp} amplifier, causing the apparent gain measured by the Allen–Fahey function to plummet. In this section we apply the noninvasive method to test this explanation for the downturn in $L'_{dp}(r)$.

A. Measuring suppression by the primaries

To explore the role of suppression in shaping the Allen–Fahey function we devised a measurement paradigm that allows us to quantify the effects of suppression. In Allen and Fahey’s analysis, varying the primary frequency ratio r has only one effect: It moves the DP source around inside the cochlea, allowing the experiment to probe different parts of the DP amplification region. In principle, however, changing r also changes the amount of suppression of the DP amplifier by the primaries. Our strategy was to separate these two (and perhaps other) effects of changing r by producing the stimulus for BM motion at the DP frequency *outside* the cochlea (i.e., by using an earphone). When the DP sound is generated in the ear canal, the only effect of changing the primary frequencies on the DP-frequency BM motion is to change the amount of suppression.

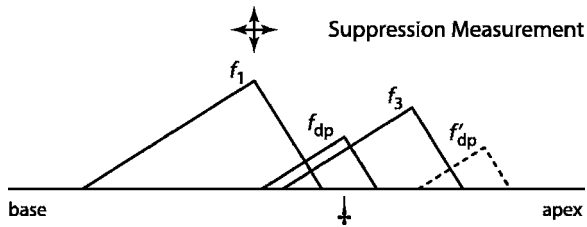


FIG. 8. Schematic showing the stimulus paradigm employed in the suppression measurements. The format is described in the caption to Fig. 1. The measurements determine the suppressive influence of the f_1 primary on the generation of the secondary DP at frequency f'_{dp} . The f_1 and f_3 primaries are identical to those used in the noninvasive method [Fig. 1(B)], but the f_2 primary has been turned off. Rather than being generated inside the cochlea, the excitation at frequency f_{dp} is produced in the ear canal using the earphone that previously generated f_2 .

To quantify the role of suppression in our noninvasive Allen–Fahey experiment, we adopted the stimulus protocol shown in Fig. 8. We measured the suppressive influence of the f_1 primary on the generation of the secondary DP by removing the intracochlear DP source at frequency f_{dp} (by turning off P_2) and presenting f_{dp} as an external tone.⁸ By presenting f_{dp} as an external tone we hold the location of the f_{dp} source constant (i.e., in the ear canal) and therefore fix the (un-suppressed) amplification of the f_{dp} traveling wave. We denote the level of the secondary DPOAE measured under these conditions by \hat{L}'_{dp} .

Figure 9 shows the substantial suppressive effect of the primary P_1 on the secondary DPOAE. As expected, the data show that suppression by P_1 increases both at higher intensities and at closer frequencies (as r decreases, f_1 draws closer to f_{dp}). Although observed here in the secondary DPOAE at frequency f'_{dp} , the suppression we measure in Fig. 9 presumably arises predominantly through the suppressive

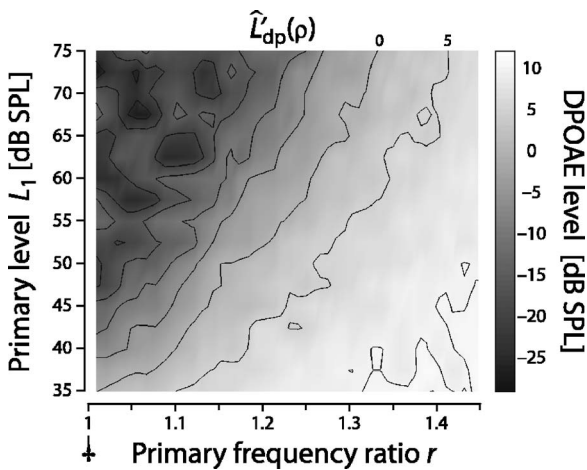


FIG. 9. Level map $\hat{L}'_{dp}(\rho)$ showing suppression of the secondary DPOAE by the f_1 primary. Shown in the same format as the maps $L_{dp}(\rho)$ and $L'_{dp}(\rho)$ in Fig. 2, the map $\hat{L}'_{dp}(\rho)$ was measured using the stimulus protocol illustrated in Fig. 8 by varying the frequency and level of P_1 , which acts here as a suppressor tone. The primary P_2 was turned off, and the tone at frequency f_{dp} was presented in the ear canal at a fixed level (25 dB SPL) chosen so that the secondary DPOAE near r_{max} had a level similar to L'_{dp} [see Fig. 2(B)]. The primary P_3 was the same used during the measurement of $L_{dp}(\rho)$ and $L'_{dp}(\rho)$.

action of P_1 on the f_{dp} excitation pattern (recall that f_{dp} is the high-frequency “primary” for the generation of f'_{dp}). As such, similar suppression would occur in *any* method of performing the Allen–Fahey experiment. Suppressive effects unique to the noninvasive method (such as direct suppression of P_3 , or of f'_{dp} itself, by P_1) are likely to be weaker but must also contribute.

B. Compensating for suppression

Now that we have quantified suppression and found it to be strong at close ratios, we would like to understand its contribution to the Allen–Fahey function, $L_{dp}^\dagger(r)$. Our approach will be to remove the effects of suppression from $L_{dp}^\dagger(r)$ by adjusting the constant-response criterion to compensate for the measured tuning of suppression. Compensation is necessary because the same cochlear nonlinearities that generate the DP also affect the sensitivity of the “detector” (i.e., the ANF fiber or the secondary DPOAE) used to monitor its intracochlear level. Rather than adopting a *constant* criterion, L'_{dp}^\dagger , we seek instead to adjust the criterion with r in such a way that the effects of suppression on the calibration of the intracochlear detector are subtracted out.

1. The suppression reference point

We begin by selecting $\rho_{ref}(L'_{dp}^\dagger)$, a suppression reference point along the iso- L'_{dp} contour $\mathcal{C}_0(L'_{dp}^\dagger)$ in the ρ plane. The suppression reference point defines the location with respect to which changes due to suppression will be measured. In the examples that follow, we take $\rho_{ref}(L'_{dp}^\dagger)$ to be the $r=1.36$ point of the contour $\mathcal{C}_0(L'_{dp}^\dagger)$ [i.e., the point where $\mathcal{C}_0(L'_{dp}^\dagger)$ intersects the line $r=1.36$; for $f_{dp}=7$ kHz, this ratio occurs at $f_1=11$ kHz]. A glance at Fig. 2(B) shows that $\rho_{ref}(L'_{dp}^\dagger) \cong (1.36, 64$ dB SPL) for the $L'_{dp}^\dagger=5$ dB SPL contour and $\rho_{ref}(L'_{dp}^\dagger) \cong (1.36, 60$ dB SPL) for the $L'_{dp}^\dagger=0$ dB SPL contour. Although none of our conclusions depend on the value of $\rho_{ref}(L'_{dp}^\dagger)$, our choice is convenient because it resides within the main lobe of $L_{dp}(\rho)$ [Fig. 2(A)] but is sufficiently far from $r=1$ not to manifest strong suppression (Fig. 9).

Relative to its value at $\rho_{ref}(L'_{dp}^\dagger)$, the suppression of the secondary DPOAE can be found from the map

$$S'_{dp}(\rho) \equiv \hat{L}'_{dp}(\rho_{ref}) - \hat{L}'_{dp}(\rho). \quad (2)$$

The suppression map $S'_{dp}(\rho)$ is 0 at ρ_{ref} (by definition) and its value generally increases as one moves closer to $r=1$ along $\mathcal{C}_0(L'_{dp}^\dagger)$. Evaluating $L_{dp}(\rho)$ along the contour $\mathcal{C}_0(L'_{dp}^\dagger)$ —defined by the constant response criterion $L'_{dp}(\mathcal{C}_0)=L'_{dp}^\dagger$ —includes effects due both to changes in DP source location (e.g., to changes in the amplification of forward and reverse DP waves) and to changes in the amount of suppression by the primaries.

2. Contour iteration

To approximate a suppression-compensated Allen–Fahey function, one might begin by evaluating $L_{dp}(\rho)$ along the modified contour \mathcal{C}_1 , defined as the curve along which

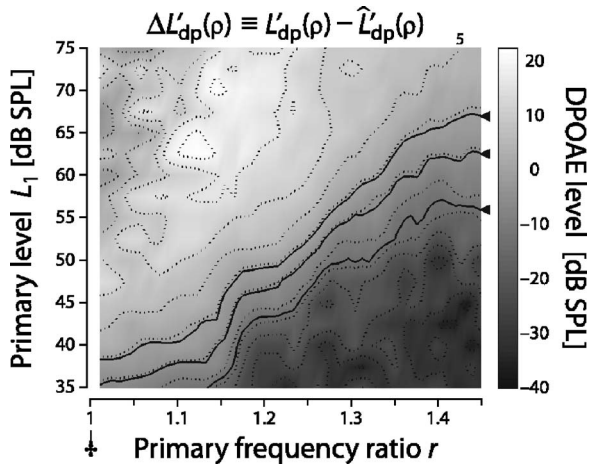


FIG. 10. Difference map $\Delta L'_{dp}(\rho) \equiv L'_{dp}(\rho) - \hat{L}'_{dp}(\rho)$ computed from the maps in Figs. 2(B) and 9. The solid lines marked with triangles (▲) are contours C_∞ along which $\Delta L'_{dp}(\rho) = \Delta L'_{dp}^\dagger$, where $\Delta L'_{dp}^\dagger = \{-0.75, -5.6, -12.9\}$ dB SPL. The ratio r of the reference point $\rho_{\text{ref}}(L'_{dp}^\dagger)$ is fixed at 1.36 (or $f_1 = 11$ kHz). For this choice of reference ratio, the three contours correspond to the marked contours at $L'_{dp}^\dagger = \{5, 0, -5\}$ dB SPL from Fig. 2(B).

$$L'_{dp}(C_1) = L'_{dp}^\dagger - S'_{dp}(C_0). \quad (3)$$

The quantity on the right-hand side represents an adjusted (r -dependent) criterion from which changes in $L'_{dp}(\rho)$ due to suppression along the original contour, C_0 , have been “subtracted out.” Although certainly an improvement, this approximation remains imperfect because the suppression along the modified contour C_1 generally differs from the suppression along C_0 that we subtracted out. To improve the approximation further we could iterate the process, subtracting out changes in suppression along C_1 to obtain another new contour, C_2 :

$$L'_{dp}(C_2) = L'_{dp}^\dagger - S'_{dp}(C_1). \quad (4)$$

By iterating in this way ad infinitum we obtain a sequence of contours $\{C_0, C_1, C_2, C_3, \dots\}$ whose limit, C_∞ , satisfies

$$L'_{dp}(C_\infty) = L'_{dp}^\dagger - S'_{dp}(C_\infty). \quad (5)$$

The limiting contour C_∞ is fully “suppression-compensated” in the sense that its defining criterion [the right-hand side of Eq. (5)] varies in just the right way so that changes in suppression along its path are removed.⁹

By using the definition of $S_{dp}(\rho)$ from Eq. (2) one can prove by algebra that the limiting contour satisfies

$$[L'_{dp} - \hat{L}'_{dp}](C_\infty) = L'_{dp}^\dagger - \hat{L}'_{dp}(\rho_{\text{ref}}), \quad (6)$$

where the right-hand side is constant. Thus, the suppression-compensated contour C_∞ is simply the contour along which

$$\Delta L'_{dp}(C_\infty) = \Delta L'_{dp}^\dagger \quad \text{where} \quad \begin{cases} \Delta L'_{dp}(\rho) \equiv L'_{dp}(\rho) - \hat{L}'_{dp}(\rho) \\ \Delta L'_{dp}^\dagger \equiv L'_{dp}^\dagger - \hat{L}'_{dp}(\rho_{\text{ref}}). \end{cases} \quad (7)$$

In other words, suppression-compensated contours C_∞ are just iso-level contours of the difference map, $\Delta L'_{dp}(\rho)$; different contour lines correspond to different values of L'_{dp}^\dagger and $\rho_{\text{ref}}(L'_{dp}^\dagger)$.

Figure 10 shows the difference map $\Delta L'_{dp}(\rho)$ computed from the maps $L'_{dp}(\rho)$ and $\hat{L}'_{dp}(\rho)$ [Figs. 2(B) and 9]. The

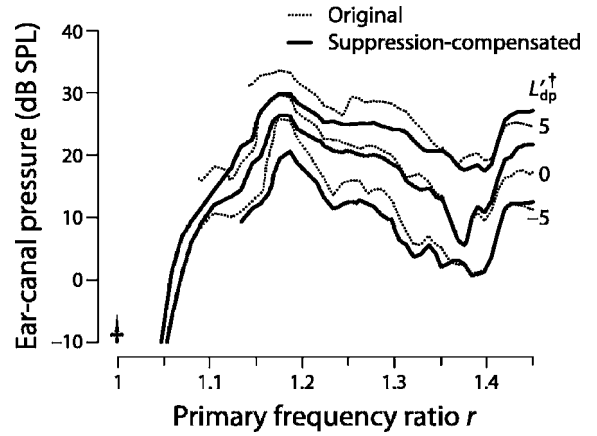


FIG. 11. Noninvasive Allen–Fahey functions with and without compensating for suppression. The solid lines show suppression-compensated functions $L'_{dp}^\dagger(r; \Delta L'_{dp}^\dagger)$ obtained by evaluating $L_{dp}(\rho)$ from Fig. 2(A) along the three marked iso- $\Delta L'_{dp}$ contours from Fig. 10. For comparison, the dotted lines show “original” (uncompensated) values of $L'_{dp}^\dagger(r; L'_{dp}^\dagger)$ reproduced from Fig. 3. The corresponding values of L'_{dp} are given on the right margin. Each pair of functions intersect at $r=1.36$, the frequency ratio of the suppression reference points, $\rho_{\text{ref}}(L'_{dp}^\dagger)$.

difference map $\Delta L'_{dp}(\rho)$ is noisy in the upper-left and lower-right corners [corresponding to small values of $\hat{L}'_{dp}(\rho)$ and $L'_{dp}(\rho)$, respectively] but is well determined along the intervening diagonal. The terminal triangles mark iso- $\Delta L'_{dp}$ contours corresponding to the three iso- $\Delta L'_{dp}$ contours marked in Fig. 2(B) (i.e., $L'_{dp}^\dagger = \{5, 0, -5\}$ dB SPL).

Note that unlike many of the iso- L'_{dp} contours in Fig. 2(B), the iso- $\Delta L'_{dp}$ contours C_∞ do not turn back on themselves at close ratios. Functions evaluated along the suppression-compensated contours are therefore well defined at all values of r . We interpret this difference between the original and suppression-compensated contours as indicating that at close ratios suppression is sufficiently strong that an iso- L'_{dp} criterion cannot always be maintained: Compensating for suppression is then the only way to obtain a solution.¹⁰

C. Suppression-compensated Allen–Fahey experiments

Figure 11 compares Allen–Fahey functions at three different response criteria before and after compensating for suppression. The dotted lines show the three uncompensated (“original”) functions $L'_{dp}^\dagger(r; L'_{dp}^\dagger)$ from Fig. 3; the solid lines show the corresponding functions $L'_{dp}^\dagger(r; \Delta L'_{dp}^\dagger)$ compensated for suppression by evaluating $L_{dp}(\rho)$ [Fig. 2(A)] along the marked iso- $\Delta L'_{dp}$ contours from Fig. 10. Because suppression reference points $\rho_{\text{ref}}(L'_{dp}^\dagger)$ were located at $r=1.36$, each pair of functions intersects at this ratio.

The comparison in Fig. 11 demonstrates that removing suppression *decreases* the function $L'_{dp}^\dagger(r)$ at values of r below the suppression reference point and increases it above the reference. Thus, the contribution of suppression to Allen–Fahey experiments is not to *decrease* the apparent gain measured by the paradigm, but to *increase* it. This is, of course, exactly the opposite of the intuitive and predicted result (e.g., Allen and Fahey, 1992; Kanis and de Boer, 1993; de Boer *et al.*, 2005)—it demonstrates that the downturn at close ratios in $L'_{dp}^\dagger(r)$ generally seen in Allen–Fahey experiments is *not*

due to suppression. Indeed, removing contributions from suppression evidently makes the downturn even more pronounced.

VI. DISCUSSION

We have shown that secondary distortion products can be used to calibrate an intracochlear distortion source. The method allows experiments that measure both intracochlear DPs and ear-canal DPOAEs (e.g., Allen–Fahey and related paradigms) to be performed noninvasively. We validated the method by using it to perform noninvasive Allen–Fahey experiments in cat, comparing the results with measurements made using the original, auditory-nerve based paradigm at the same frequency and in the same animal. Although the comparison has so far been made rigorously in only a single preparation, the quantitative similarity between the results— together with the strong qualitative similarities observed in other preparations— supports the assumption that the secondary DPOAE provides a useful assay of the principal DP near its characteristic place.

A. Pros and cons of noninvasive calibration

Because the noninvasive calibration method employs secondary distortion products, which arise from a *region* straddling x_{dp} , rather than at x_{dp} alone, the method is inherently less tightly controlled than methods based on ANF or BM measurements. Nevertheless, the noninvasive method has several nice features that help compensate for the lack of precise control. First and foremost, the procedure is—as its name implies—entirely noninvasive and can therefore be performed in a wide variety of species, including humans. Second, the procedure can be performed at any frequency (unlike, for example, the BM method which can be employed only at a rather limited number of surgically accessible locations within the cochlea). In addition, unlike the ANF-based method, the noninvasive method can be applied at primary-frequency ratios close to 1. Furthermore, the noninvasive method obviates the need to maintain contact with single neurons and therefore affords one the luxury of “mapping out” the territory under open-loop conditions (cf. Fig. 2). Consequently, the noninvasive method can provide a “big-picture” view: Mapping out the global structure permits the exploration of alternative constraints and greatly enhances the interpretive power.

B. Suppression in Allen–Fahey experiments

Contrary to intuitive expectations, our results indicate that suppression actually *increases* the apparent gain measured by the Allen–Fahey paradigm (Fig. 11). To understand why this is so, we need briefly to review Allen and Fahey’s (1992) argument that $L_{dp}^{\dagger}(\rho)$ measures the integrated power gain of the cochlear amplifier at frequency f_{dp} .

The argument goes as follows: The DP source generates waves that propagate away in both directions. As r decreases toward 1 the DP source moves apically toward x_{dp} and further into the region of presumed DP amplification. As the source advances further into the amplifier, the size of the amplification region for the forward wave shrinks, and the

amplitude of the DP at x_{dp} decreases. Since the DP amplitude is falling at x_{dp} , the source strength must be boosted correspondingly (e.g., by increasing the primary levels) in order to maintain the constant criterion response at x_{dp} . Now, as the amplification region for the forward wave shrinks, the amplification region for the reverse wave grows, and the reverse wave therefore propagates through ever larger regions of the amplifier on its way to the stapes. Thus, whereas the integrated amplification of the forward-traveling DP decreases as $r \rightarrow 1$, the integrated amplification of the reverse DP increases. Two effects therefore combine to increase the DPOAE amplitude as $r \rightarrow 1$: (a) the boost in source strength necessary to maintain a constant response at x_{dp} and (b) the increased amplification of the reverse wave. The net result is that $L_{dp}^{\dagger}(\rho)$ varies as the square of the power gain experienced by a wave traveling between the stapes and the DP source location (near x_2). This conclusion that $L_{dp}^{\dagger}(\rho)$ varies as the square of the gain presumes isotropic wave propagation within the cochlea, ignores suppression and internal reflections, and assumes that the intracochlear distortion source can be approximated as a point source whose “radiation field” is independent of r (Allen and Fahey, 1992; Shera and Zweig, 1992; Shera, 2003).

How does suppression modify this result? One might expect suppression to reduce the effective gain measured by the experiment (e.g., Allen and Fahey, 1992), in which case the variation of $L_{dp}^{\dagger}(r)$ would underestimate the actual, un-suppressed gain. But this intuitive analysis ignores the frequency dependence (tuning) of suppression. Moving the DP source region apically moves the primaries toward x_{dp} , increasing their suppressive effect on the forward-traveling DP wave. At x_{dp} the monitored response to the DP therefore decreases not only because the forward-traveling DP now travels through a smaller region of amplification, but also because suppression by the primaries has increased. Consequently, in order to maintain a constant response at x_{dp} , the DP source strength must be boosted even more than is necessary in the absence of suppression. Since boosting the source strength increases the ear-canal DPOAE, suppression of the DP response by the primaries increases the value of $L_{dp}^{\dagger}(r)$. In the Allen–Fahey paradigm, tuned suppression masquerades as power gain; unless controlled for, two-tone suppression actually *increases* the apparent gain.

By adopting an adjusted response criterion from which the effects of suppression have been subtracted out, we verified this counterintuitive result experimentally. In addition, our results demonstrate that suppression is not the cause of the pronounced downturn in $L_{dp}^{\dagger}(r)$ seen at close ratios. Neither, of course, is the downturn due to amplification; acting alone, amplification causes the curve to rise. If the behavior of $L_{dp}^{\dagger}(r)$ at close ratios results neither from amplification nor from suppression (both of which go the wrong way), how does the downturn arise?

C. Distortion beamforming and the Allen–Fahey function

We conjecture that the downturn in the Allen–Fahey function results from the emergence of a pronounced “direc-

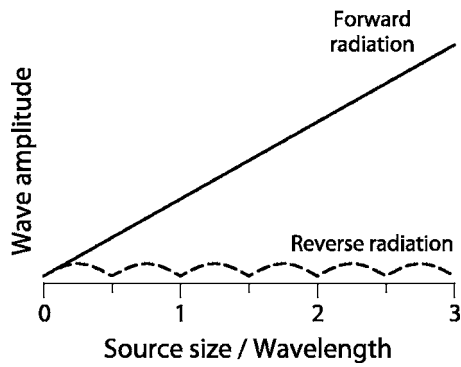


FIG. 12. The emergence of source directionality from phase interactions in a transmission line. The magnitudes of the waves radiated in the forward and reverse directions from a distributed source of uniform amplitude are shown. Although the source strength is uniform (constant per unit length), the source phase varies linearly with position, mirroring the phase of a plane wave traveling along the transmission line (i.e., as $e^{-2\pi ix/\lambda}$ where λ is the wavelength of the waves propagating in the line). The radiated wave magnitudes are plotted as a function of the size of the source region, whose length (relative to the wavelength) is given along the abscissa. Except when the source region is much smaller than a wavelength, the distributed source is highly directional, radiating much more in the forward direction than in the reverse.

tionality” to the waves radiated by the DP source (Shera, 2003; de Boer *et al.*, 2005). Contrary to the simplifying assumptions employed in the Allen–Fahey analysis of $L_{dp}^{\dagger}(r)$, the “DP source” cannot be a simple point source but must, in effect, consist of many point sources spread out over a region almost certainly a large fraction of a wavelength or more in extent. Because the source region is distributed, substantial phase differences can develop among the many sources arrayed along its length; these phase differences, which are created by and largely mirror the phase lags of the primary tones, vary with r and become especially large at close ratios. As $r \rightarrow 1$, the phase lag of the induced distortion sources increases significantly over the region of strong distortion; as a result of these spatial phase changes, the distortion-source region “radiates” much more in the forward direction than it does in the reverse (Shera and Guinan, 2007). The source region acts as a phased array or beamformer whose phasing, and therefore dominant beam direction (forward or reverse), is determined by the f_2/f_1 ratio.¹¹

1. Simulated distortion beamforming

By way of illustration, Fig. 12 shows an example of source directionality induced by wave interference effects in a simple model example: a uniform transmission line (Shera and Guinan, 2007). As detailed in Appendix B, the line is assumed to contain a distributed source region (i.e., a spatial array of point sources) that radiates waves in both directions. The wave amplitudes radiated in the two directions can be found by summing the wavelets generated by all the sources in the region, taking care to account for phase changes due to propagation. Whereas the source strength (per unit length) is assumed constant, the source phase is made to vary systematically over the source region. Variations in source phase are expected when the sources themselves are induced by a stimulus wave (or waves) propagating along the line. Figure 12 shows the magnitudes of the forward and reverse waves

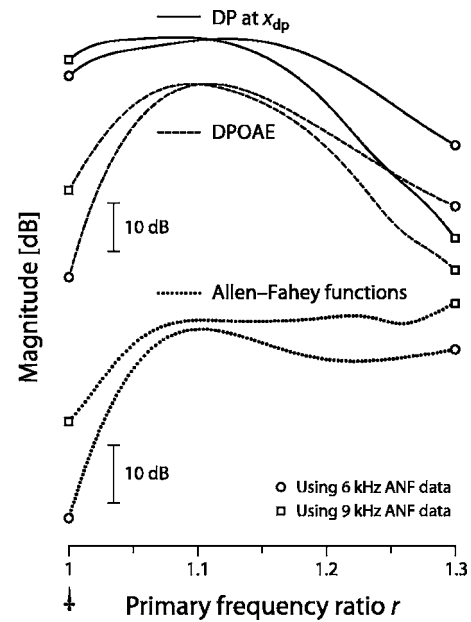


FIG. 13. Distortion beamforming simulated in the cat. DP magnitudes at x_{dp} (top pair of solid lines) and DPOAEs in the ear canal (middle pair of dashed lines) computed in a one-dimensional transmission-line model of the cat cochlea are shown. Stimulus intensities were held constant and the DP frequency was fixed at 7 kHz; responses were computed as a function of the primary frequency ratio, whose value increases along the abscissa. The top scale bar applies to both solid and dashed lines. The corresponding Allen–Fahey functions are shown on a slightly expanded vertical scale (bottom pair of dotted lines and secondary scale bar). The model was customized for cat by solving the inverse problem (Shera *et al.*, 2005) using ANF-derived measurements of the amplitude and phase of cochlear tuning (van der Heijden and Joris, 2003). Each pair of curves shows model results based on tuning measurements at CFs of 6 and 9 kHz (\circ and \square , respectively). All model responses have been offset vertically and grouped for clarity.

radiated by the source region as a function of its size (spatial extent). When the source region is small (i.e., much less than a wavelength), the forward and reverse wave amplitudes are nearly the same: the source region radiates equally in the two directions. But as the source region grows in size, and the total phase variation along its length increases, a pronounced asymmetry develops. In the forward direction, the individual wavelets from the many sources in the region always combine in phase, and the amplitude of the net forward wave grows rapidly. But in the reverse direction, destructive interference among the constituent wavelets causes strong cancellation within the source region, and the amplitude of the net reverse wave remains small. (Indeed, whenever the source length matches an integral number of half wavelengths, internal cancellation is complete and the net reverse wave is zero.) Although each individual source within the distribution radiates equally in the two directions, phase interactions induce a strong directionality on the distribution as a whole.

Model calculations performed using a simple quasilinear model of DP generation (e.g., Kanis and de Boer, 1997; Talmadge *et al.*, 1998; Shera, 2003) suggest that analogous beamforming takes place within the cochlea. Figure 13 shows DP magnitudes in the ear canal and at x_{dp} computed as a function of the primary frequency ratio using constant intensity primary tones (see Appendix B for details). Note that the curves have been grouped and offset vertically for clar-

ity; only their shapes have physical significance. To make the model computations as realistic as possible, we based them on BM mechanical responses estimated for the cat using ANF-derived measurements of the amplitude and phase of cochlear tuning (van der Heijden and Joris, 2003). To highlight effects due to wave interference, mutual and self-suppression among the primaries and the DP have been neglected. Because both the amplitude and the phase of the DP sources vary with position, the cochlear computation is rather more complicated than the transmission-line example discussed earlier. Nevertheless, the directional effects of phased beamforming are clearly evident at close ratios. Whereas the forward-radiated DP at x_{dp} plateaus or decreases only slightly for $r < 1.1$, the reverse-radiated DPOAE falls sharply, a decrease due almost entirely to destructive interference among wavelets emanating from the distributed generators.¹² Since suppression is neglected in this example, the Allen–Fahey function can be obtained simply by computing the ratio of the DPOAE and DP curves evaluated at constant intensity. The resulting functions $L_{dp}^{\dagger}(r)$ are shown as the bottom pair of curves in Fig. 13. As conjectured, destructive interference creates the fall-off evident in the Allen–Fahey function at close ratios.

2. Beamforming and the “DP filter”

As our measurements and simulations indicate, Allen–Fahey experiments are closely related to the so-called DP filter, which also has a characteristic bandpass shape (Brown *et al.*, 1992; Allen and Fahey, 1993). As Fig. 2(A) makes clear, the DPOAE level along almost any single-valued contour that traverses the map $L_{dp}(\rho)$ from left to right will manifest an approximately bandpass form—the DP filter function, typically measured using a procedure that amounts to evaluating $L_{dp}(\rho)$ along a horizontal (constant-level) contour, is just an especially simple case. Our beamforming explanation for the shape of $L_{dp}^{\dagger}(r)$ is thus consistent with a number of theoretical studies that trace the form of the DP filter to interference effects within the distributed source region (van Hengel, 1996; Talmadge *et al.*, 1998; Kemp and Knight, 1999; Shera, 2003). Fahey *et al.* (2006) have recently provided experimental evidence supporting the suggestion that the decrease in DPOAE amplitude as $r \rightarrow 1$ arises primarily from vector cancellation among multiple sources. In addition, measurements of the relative amplitudes of the distortion and reflection components of DPOAEs (e.g., Knight and Kemp, 2000) provide additional experimental evidence for changes in distortion-source “directionality” as a function of r (reviewed in Shera and Guinan, 2007). Thus, neither amplification nor suppression, but the shape of the DP radiation field and its variation with r may well be the most important determinant of the DP filter and the results of the Allen–Fahey experiment.

ACKNOWLEDGMENTS

We gratefully acknowledge the efforts of Leslie Liberman for her help with animal care and preparation. We thank Christopher Bergevin, Egbert de Boer, Nigel Cooper, Paul Fahey, Elizabeth Olson, Carrick Talmadge, Arnold Tubis,

Robert Withnell, and two anonymous reviewers for their helpful comments on the manuscript. We also thank Marcel van der Heijden for graciously sharing his data. This work was supported by Grant Nos. R01 DC03687 and F32 DC00108 to C.A.S. and R01 DC00235 to J.J.G. from the NIDCD, National Institutes of Health.

APPENDIX A: EXPERIMENTAL METHODS

This Appendix details the experimental methods used for performing the experiments described in the text. All procedures were conducted in accordance with National Institutes of Health guidelines and were approved by the animal care committees at the Massachusetts Eye and Ear Infirmary and the Massachusetts Institute of Technology.

1. Animal care and preparation

All measurements were in Dial-anesthetized cats; details of the surgery and auditory-nerve recording have been described elsewhere (e.g., Guinan and Gifford, 1988; Guinan and Stanković, 1996). The physiological condition of the animals (including body temperature, heart rate, breath rate, expired CO₂ levels, and EEG) was monitored continually throughout the experiment. Tone-evoked compound-action-potential (CAP) thresholds recorded with a silver-wire electrode near the round window and distortion-product “audiograms” (DP-grams) recorded from the ear canal were measured at regular intervals as assays of hearing function.

2. Stimulus generation and acquisition

Stimulus wave forms were generated and responses acquired and averaged digitally using a Spectrum Signal Processing PC/C31 DSP Board with two Burr-Brown analog daughter modules providing eight channels of 16 bit synchronized analog I/O (four in/four out). We used sampling rates of approximately 59.94 kHz. Output wave forms were filtered using 8-pole butterworth low-pass filters with corner frequencies of 30 kHz. Input signals were high- and low-pass filtered using a Rockland “brick-wall” filter. The hardware was computer controlled using a custom designed data-acquisition system implemented in LabVIEW and supplemented with hand-coded time-domain artifact-rejection and synchronous-averaging routines (Shera and Guinan, 1999). All measurements were performed in a sound- and vibration-isolated, electrically shielded chamber (Ver *et al.*, 1975).

The ear was driven by up to four simultaneous signals. To minimize spurious intermodulation distortion, each signal was presented through a separate earphone. Acoustic signals were transduced using calibrated Etymotic Research ER10c DPOAE Probe systems with earpieces adapted to allow simultaneous presentation of the four independent stimulus wave forms. In addition to the two earphone channels in the ER-10c, a pair of ER-3 earphones drove the two additional output channels employed by the noninvasive method. Control experiments in a small cavity indicate that the measurement-system distortion was at or below the noise floor, which was typically less than -20 dB SPL.

Absolute sound-level calibrations were performed prior to each experiment, and in-the-ear calibrations were performed frequently throughout in order to detect and control for changes in the acoustic calibrations caused, e.g., by possible fluid build-up in the ear canal.

3. Auditory-nerve recording

Tuning curves were measured using the standard Kiang-Moxon paradigm (Lieberman, 1978), thereby determining the unit's threshold and characteristic frequency (CF). In addition, spontaneous rate was recorded over an interval of 15–30 s.

4. Measurement of distortion products

Stimuli were windowed acoustic tone bursts consisting of two primary frequencies, f_1 and f_2 , with $f_2 > f_1$. Frequencies were quantized (typically with a resolution of roughly 29 Hz) so that the analysis window contained an integral number of stimulus periods. The pressures P_1, P_2 , and P_{dp} were extracted from the measured ear-canal pressure using 2048-point discrete Fourier transforms. Values at neighboring frequencies were recorded to provide an estimate of the noise floor. Measurements were made at frequency intervals small enough to resolve any standing-wave patterns due to interference effects. To maximize the overall level of distortion and minimize possible suppression by P_2 we used unequal primaries ($L_2 = L_1 - 15$ dB SPL). Our standard DP-grams, measured at the frequency ratio $r = 1.2$ using primary levels $\{L_1, L_2\} = \{50, 40\}$ dB SPL, were an exception to this rule.

In the auditory-nerve paradigm, the primary frequencies were chosen so that $f_{dp} \cong CF$, where $f_{dp} \cong 2f_1 - f_2$. Spike times were recorded and used to control a computer-automated feedback loop based on a modified Kiang-Moxon paradigm that adjusted the primary levels until the established neural criterion, defined with respect to the response during surrounding intervals of silence, was satisfied.

In the noninvasive paradigm, DPOAE level and suppression maps were measured using the stimulus paradigms illustrated in Figs. 1 and 8. Data were collected by randomized sampling on a rectangular grid (50 frequencies, 17 levels). Each data point in the map represents the average of 64 response buffers for a total averaging time of about 2.2 s per point. Measurement of the level maps shown in Figs. 2 and 9 took a combined total of roughly 90 min. The maps were gently smoothed using Savitzky-Golay filters (e.g., Press *et al.*, 1992) and then interpolated to find values along any desired contour (e.g., C_∞).

APPENDIX B: SIMULATED BEAMFORMING

1. Beamforming in a uniform transmission line

Figure 12 illustrates simple beamforming by showing the magnitude of the total voltage at both ends of a section of uniform transmission line produced by an array of distributed ac voltage sources whose relative phases vary system-

atically with position. Since a more systematic derivation can be found elsewhere (Shera and Guinan, 2007), we only briefly summarize the key steps here.

We begin by denoting the complex source strength per unit length by $\tilde{v}_{src}(x)$. If the source region resides on the interval $x \in [0, L]$, the net forward wave at $x = L$ is

$$\text{forward wave at } L \propto \int_0^L \tilde{v}_{src}(x)G(x|L)dx, \quad (B1)$$

where the complex function $G(x|L)$ acts to “propagate” each generated wavelet from its point of origin (i.e., x) to the point of observation (i.e., $x = L$). Similarly, the net reverse wave at $x = 0$ is

$$\text{reverse wave at } 0 \propto \int_0^L \tilde{v}_{src}(x)G(x|0)dx. \quad (B2)$$

For a uniform transmission line, the propagator has the form $G(x|x') = e^{-ik|x'-x|}$, where $k = 2\pi/\lambda$ and λ is the wavelength of the waves propagating in the line at the ac driving frequency.

We now evaluate the integrals, assuming that $\tilde{v}_{src}(x) = v_0 e^{-ikx}$ (i.e., constant amplitude and linear phase). For the forward wave we find that

$$\text{forward wave at } L \propto v_0 L, \quad (B3)$$

whose amplitude grows linearly with L . For the reverse wave, by contrast,

$$\text{reverse wave at } 0 \propto \frac{v_0}{2ik}(1 - e^{-2ikL}), \quad (B4)$$

whose amplitude remains bounded with L , oscillating with a period $\lambda/2$. The waves radiated in the two directions are of comparable magnitude only when the source size, L , is small compared to the wavelength ($L \ll \lambda/4\pi$).

2. Distortion beamforming in the cat

Figure 13 illustrates distortion beamforming in the cochlea by showing the magnitude of the total distortion product at both ends of a section of cochlear transmission line. The cochlea is assumed to contain an array of distributed DP sources whose relative amplitudes and phases are determined by those of the primary traveling waves and therefore vary systematically with position. Although the computations differ somewhat in detail, closely related calculations and further discussion can be found elsewhere (e.g., Talmadge *et al.*, 1998; Shera, 2003).

The cochlea was modeled as a one-dimensional hydro-mechanical transmission line containing an array of stimulus-dependent DP sources (e.g., Kanis and de Boer, 1997; Talmadge *et al.*, 1998; Shera, 2003). At each point x the complex-valued pressure-difference source at frequency $f_{dp} = 2f_1 - f_2$ was assumed proportional to the product $Z_{BM}(x; f_{dp})V_{dp}(x; f_1, f_2)$, where $Z_{BM}(x; f)$ is the impedance of the cochlear partition, $\tilde{V}_{dp}(x; f_1, f_2) \equiv V_{BM}^2(x; f_1)V_{BM}^*(x; f_2)$, and $V_{BM}(x, f)$ is basilar-membrane velocity (the traveling wave) at the indicated frequency. Stimulus intensities were assumed low enough that the nonlinearity could be approximated by the cubic term in a power-series expansion in the

local BM velocity. Suppression between the primaries was neglected and the DP, once generated, was assumed to propagate without further interaction with the primaries.

Using these assumptions, we calculated the DP at x_{dp} by evaluating the integral

$$\text{DP at } x_{dp} \propto \int_0^{x_{dp}} \tilde{V}_{dp}(x; f_1, f_2) G(x|x_{dp}) dx, \quad (\text{B5})$$

where $G(x|x_{dp})$ is the cochlear traveling-wave pressure propagator at the DP frequency (e.g., Shera *et al.*, 2005). The DPOAE was calculated as the integral

$$\text{DPOAE} \propto \int_0^{\infty} \tilde{V}_{dp}(x; f_1, f_2) G(x|0) dx, \quad (\text{B6})$$

where the upper limit of integration indicates that the summation extends throughout the cochlea. In both calculations, overall constants of proportionality and slowly varying factors that do not appreciably affect the final result (e.g., filtering by the middle ear) were neglected for simplicity. When reflections from the stapes are ignored, the traveling-wave pressure propagator $G(x|x')$ is given by

$$G(x|x') \propto W_l(x_{<}) W_r(x_{>}), \quad (\text{B7})$$

where $x_{<} \equiv \min(x, x')$ and $x_{>} \equiv \max(x, x')$. The $W_{r,l}(x)$ are the forward- and reverse-traveling pressure basis waves at the DP frequency (Shera *et al.*, 2005); they are analogous to the complex exponentials $e^{\pm ikx}$ in the uniform transmission line. Note that our notation intentionally camouflages much of the complicating detail in order to highlight the close formal similarity between Eqs. (B5) and (B6) and their counterparts for the uniform transmission line [Eqs. (B1) and (B2)].

To simulate the cat cochlea as faithfully as possible, we estimated BM traveling waves [e.g., $V_{BM}(x; f_1)$ and $V_{BM}(x; f_2)$] by converting ANF-derived measurements of the amplitude and phase of cochlear tuning (van der Heijden and Joris, 2003) to spatial responses using the assumption of local scaling (e.g., Zweig, 1976). The pressure basis waves were obtained using formulas derived from the Wentzel-Kramers-Brillouin approximation (Shera *et al.*, 2005):

$$W_r(x; f) \propto k^2(x; f) V_{BM}(x; f) \quad (\text{B8})$$

and

$$W_l(x; f) \propto k^{-3}(x; f) V_{BM}^{-1}(x; f). \quad (\text{B9})$$

In these equations, $k(x; f)$ represents the complex wave number of the traveling wave; it was obtained from a slightly smoothed version of $V_{BM}(x; f)$ using the wave number inversion formula derived elsewhere (Shera *et al.*, 2005).

¹A preliminary account of this work was presented at the 20th Midwinter Meeting of the Association for Research in Otolaryngology (Shera and Guinan, 1997).

²Secondary distortion products have been used by others to establish that distortion products propagate within the cochlea much like traveling waves excited by external tones (e.g., Goldstein *et al.*, 1978; Whitehead *et al.*, 1993).

³Before appreciating the value of measuring the maps $L_{dp}(\rho)$ and $L'_{dp}(\rho)$, we took the traditional route and implemented a feedback control loop that automatically adjusted the primary levels to maintain a constant criterion

value of L'_{dp} . The results were similar to those obtained using the maps, albeit somewhat noisier because of the additional uncertainty introduced by the adaptive search routine.

⁴Although we neither show nor discuss them here, each level map has a corresponding “phase map.”

⁵This restriction might be circumvented at DP frequencies in the phase-locking range by using a synchrony- rather than a rate-based measure of neural activity to distinguish the response to the DP from the responses to the primaries using Fourier analysis (Goldstein and Kiang, 1968). The use of a synchrony criterion has additional advantages: It permits measurement of the phase of the response at x_{dp} , rather than just the amplitude, and it allows the use of lower primary levels, since neural synchrony thresholds are typically 20 dB lower than rate thresholds (Evans, 1975). Using lower primary levels would help reduce the magnitude of two-tone suppression between the primaries and the distortion product and would sharpen the primary response envelopes, thereby more tightly localizing the distortion-product source along the organ of Corti.

⁶Since $L'_{dp}(r)$ peaks near r_{opt} , the distance is approximately $-l \ln[2/r_{opt}-1]$, where $l=5$ mm is the exponential “space constant” of the cat cochlear map (Liberman, 1982).

⁷Although the conclusion also conflicts with other estimates of the location of the amplifier (e.g., Cody, 1992) inverse solutions provide the strongest evidence for actual *power* gain in the mammalian cochlea.

⁸We turned off P_2 and focused on suppression by P_1 because we expected P_1 to have the greater effect: P_1 is both closer to the DP frequency and higher in level than P_2 . By removing the intracochlear DP source using another method that did not require us to turn off P_2 , we verified that any additional suppression caused by P_2 is small. Specifically, we removed the intracochlear source at f_{dp} by shifting f_2 slightly in frequency so that $f_{dp} \neq 2f_1 - f_2$. We found that removing the intracochlear f_{dp} source by changing the P_2 frequency produced results almost identical to turning off P_2 completely. This result differs from that of de Boer *et al.* (2005), who found that the two primaries together produced significantly greater suppression than either one alone. The difference, we suspect, can be traced to the different primary levels used in the two studies: Whereas de Boer *et al.* used equal-level primaries ($L_1=L_2$), we used an L_2 significantly lower than L_1 ($L_2=L_1-15$ dB SPL) in an attempt to maximize the overall level of distortion at low and moderate intensities.

⁹The “suppression-compensated” contour C_{∞} is only compensated for suppression relative to $\rho_{ref}(L'_{dp})$; it is not “free of suppression” because the net suppression at $\rho_{ref}(L'_{dp})$ is generally nonzero.

¹⁰The possibility of multiple-valued solutions raises a little discussed complication in the Allen-Fahey paradigm: For any given iso-response constraint there is no guarantee that a unique solution (or indeed any solution) exists for all interesting values of r . Since multiple solution “branches” may exist, once the desired branch has been located it is imperative that the experiment proceed by taking relatively small steps in the ρ plane, especially when using adaptive procedures to apply the iso-response constraint in real-time under closed-loop conditions. For example, when using the automated feedback loop we occasionally observed “bizarre” values of $L'_{dp}(r)$ that we now suspect reflect the multiple-valued nature of the solution.

¹¹For an early discussion of “directional coupling,” written before DPOAEs had even been discovered, see Schroeder (1975).

¹²Approximately 1 dB of the decrease at close ratios can be attributed to r -dependent changes in the strength with which DPs have been assumed to couple into the propagating pressure-difference wave.

Allen, J. B., and Fahey, P. F. (1992). “Using acoustic distortion products to measure the cochlear amplifier gain on the basilar membrane,” *J. Acoust. Soc. Am.* **92**, 178–188.

Allen, J. B., and Fahey, P. F. (1993). “A second cochlear-frequency map that correlates distortion product and neural tuning measurements,” *J. Acoust. Soc. Am.* **94**, 809–816.

Brown, A. M., Gaskill, S. A., and Williams, D. M. (1992). “Mechanical filtering of sound in the inner ear,” *Proc. R. Soc. London, Ser. B* **250**, 29–34.

Cody, A. R. (1992). “Acoustic lesions in the mammalian cochlea: Implications for the spatial distribution of the ‘active process,’” *Hear. Res.* **62**, 166–172.

de Boer, E. (1995). “The ‘inverse problem’ solved for a three-dimensional model of the cochlea. II. Application to experimental data sets,” *J. Acoust. Soc. Am.* **98**, 904–910.

de Boer, E., and Nuttall, A. L. (2001). “Power gain of the cochlear ampli-

- fier," in *Physiological and Psychological Bases of Auditory Function*, edited by D. J. Breebaart, A. J. M. Houtsuma, A. Kohlrausch, V. F. Prijs, and R. Schoonhoven (Shaker, Maastricht), pp. 1–7.
- de Boer, E., Nuttall, A. L., Hu, N., Zou, Y., and Zheng, J. (2005). "The Allen–Fahey experiment extended," *J. Acoust. Soc. Am.* **107**, 1260–1266.
- Dong, W., and Olson, E. S. (2005). "Two-tone distortion in intracochlear pressure," *J. Acoust. Soc. Am.* **117**, 2999–3015.
- Evans, E. F. (1975). "Cochlear nerve and cochlear nucleus," in *Handbook of Sensory Physiology*, edited by W. D. Keidel and W. D. Neff (Springer, Berlin), Vol. V/2, pp. 1–108.
- Fahey, P. F., and Allen, J. B. (1985). "Nonlinear phenomena as observed in the ear canal and at the auditory nerve," *J. Acoust. Soc. Am.* **77**, 599–612.
- Fahey, P. F., Stagner, B. B., Lonsbury-Martin, B. L., and Martin, G. K. (2000). "Nonlinear interactions that could explain distortion product interference response areas," *J. Acoust. Soc. Am.* **108**, 1786–1802.
- Fahey, P. F., Stagner, B. B., and Martin, G. K. (2006). "Mechanism for bandpass frequency characteristic in distortion product otoacoustic emission generation," *J. Acoust. Soc. Am.* **119**, 991–996.
- Goldstein, J. L., Buschsbaum, G., and Furst, M. (1978). "Compatibility between psychophysical and physiological measurements of aural combination tones," *J. Acoust. Soc. Am.* **63**, 474–485.
- Goldstein, J. L., and Kiang, N. Y. S. (1968). "Neural correlates of the aural combination tone $2f_1 - f_2$," *Proc. IEEE* **56**, 981–991.
- Guinan, J. J., and Gifford, M. L. (1988). "Effects of electrical stimulation of efferent olivocochlear neurons on cat auditory-nerve fibers. I. Rate versus sound level functions," *Hear. Res.* **33**, 97–114.
- Guinan, J. J., and Stanković, K. M. (1996). "Medial efferent inhibition produces the largest equivalent attenuations at moderate to high sound levels in cat auditory-nerve fibers," *J. Acoust. Soc. Am.* **100**, 1680–1690.
- Kalluri, R., and Shera, C. A. (2001). "Distortion-product source unmixing: A test of the two-mechanism model for DPOAE generation," *J. Acoust. Soc. Am.* **109**, 622–637.
- Kanis, L. J., and de Boer, E. (1993). "The emperor's new clothes: DP emissions in a locally-active nonlinear model of the cochlea," in *Biophysics of Hair Cell Sensory Systems*, edited by H. Duifhuis, J. W. Horst, P. van Dijk, and S. M. van Netten (World Scientific, Singapore), pp. 304–314.
- Kanis, L. J., and de Boer, E. (1997). "Frequency dependence of acoustic distortion products in a locally active model of the cochlea," *J. Acoust. Soc. Am.* **101**, 1527–1531.
- Kemp, D. T., and Knight, R. (1999). "Virtual DP reflector explains DPOAE 'wave' and 'place' fixed dichotomy," *Assoc. Res. Otolaryngol. Abs.* **22**, 396.
- Knight, R. D., and Kemp, D. T. (2000). "Indications of different distortion product otoacoustic emission mechanisms from a detailed f_1, f_2 area study," *J. Acoust. Soc. Am.* **107**, 457–473.
- Liberman, M. C. (1978). "Auditory-nerve response from cats raised in a low-noise chamber," *J. Acoust. Soc. Am.* **63**, 442–455.
- Liberman, M. C. (1982). "The cochlear frequency map for the cat: Labeling auditory-nerve fibers of known characteristic frequency," *J. Acoust. Soc. Am.* **72**, 1441–1449.
- Press, W. H., Teukolsky, S. A., Vetterling, W. T., and Flannery, B. P. (1992). *Numerical Recipes in C: The Art of Scientific Computing* (Cambridge University Press, Cambridge).
- Ren, T., and Nuttall, A. L. (2006). "Cochlear compression wave: An implication of the Allen–Fahey experiment," *J. Acoust. Soc. Am.* **119**, 1940–1942.
- Schroeder, M. R. (1975). "Amplitude behavior of the cubic difference tone," *J. Acoust. Soc. Am.* **58**, 728–732.
- Shera, C. A. (2003). "Wave interference in the generation of reflection- and distortion-source emissions," in *Biophysics of the Cochlea: From Molecules to Models*, edited by A. W. Gummer (World Scientific, Singapore), pp. 439–453.
- Shera, C. A., and Guinan, J. J. (1997). "Measuring cochlear amplification and nonlinearity using distortion-product otoacoustic emissions as a calibrated intracochlear sound source," *Assoc. Res. Otolaryngol. Abs.* **20**, 51.
- Shera, C. A., and Guinan, J. J. (1999). "Evoked otoacoustic emissions arise by two fundamentally different mechanisms: A taxonomy for mammalian OAEs," *J. Acoust. Soc. Am.* **105**, 782–798.
- Shera, C. A., and Guinan, J. J. (2007). "Mechanisms of mammalian otoacoustic emission," in *Active Processes and Otoacoustic Emissions*, edited by G. A. Manley, B. L. Lonsbury-Martin, A. N. Popper, and R. R. Fay, in press (Springer, New York).
- Shera, C. A., Tubis, A., and Talmadge, C. L. (2005). "Coherent reflection in a two-dimensional cochlea: Short-wave versus long-wave scattering in the generation of reflection-source otoacoustic emissions," *J. Acoust. Soc. Am.* **118**, 287–313.
- Shera, C. A., Tubis, A., Talmadge, C. L., de Boer, E., Fahey, P. F., and Guinan, J. J. (2007). "Allen–Fahey and related experiments support the predominance of cochlear slow-wave otoacoustic emissions," *J. Acoust. Soc. Am.* (in press).
- Shera, C. A., and Zweig, G. (1992). "Analyzing reverse middle-ear transmission: Noninvasive Gedankenexperiments," *J. Acoust. Soc. Am.* **92**, 1371–1381.
- Talmadge, C. L., Tubis, A., Long, G. R., and Piskorski, P. (1998). "Modeling otoacoustic emission and hearing threshold fine structure," *J. Acoust. Soc. Am.* **104**, 1517–1543.
- van der Heijden, M., and Joris, P. X. (2003). "Cochlear phase and amplitude retrieved from the auditory nerve at arbitrary frequencies," *J. Neurosci.* **23**, 9194–9198.
- van Hengel, P. W. J. (1996). "Emissions from cochlear modelling," Ph.D. thesis, Rijksuniversiteit Groningen.
- Ver, I. L., Brown, R. M., and Kiang, N. Y. S. (1975). "Low-noise chambers for auditory research," *J. Acoust. Soc. Am.* **58**, 392–398.
- Whitehead, M. L., Lonsbury-Martin, B. L., and Martin, G. K. (1993). "Measurement of $2f_1 - f_2$ excitation at the distortion-frequency place in the cochlea using ear-canal distortion products," *Assoc. Res. Otolaryngol. Abs.* **16**, 395.
- Zweig, G. (1976). "Basilar membrane motion," in *Cold Spring Harbor Symposia on Quantitative Biology* (Cold Spring Harbor Laboratory Press, Cold Spring Harbor, NY), Vol. XL, pp. 619–633.
- Zweig, G. (1991). "Finding the impedance of the organ of Corti," *J. Acoust. Soc. Am.* **89**, 1229–1254.

Physiological detection of interaural phase differences

Bernhard Ross^{a)}

Rotman Research Institute, Baycrest Center and University of Toronto, Toronto, M6A 2E1 Canada

Kelly L. Tremblay

Department of Speech and Hearing Sciences, University of Washington, Seattle, Washington 98105-6246

and Rotman Research Institute, Baycrest Center and University of Toronto, Toronto,

M6A 2E1 Canada

Terence W. Picton

Rotman Research Institute, Baycrest Center and University of Toronto, Toronto M6A 2E1, Canada

(Received 18 July 2006; revised 23 October 2006; accepted 10 November 2006)

Auditory evoked cortical responses to changes in the interaural phase difference (IPD) were recorded using magnetoencephalography (MEG). Twelve normal-hearing young adults were tested with amplitude-modulated tones with carrier frequencies of 500, 1000, 1250, and 1500 Hz. The onset of the stimuli evoked P1m-N1m-P2m cortical responses, as did the changes in the interaural phase. Significant responses to IPD changes were identified at 500 and 1000 Hz in all subjects and at 1250 Hz in nine subjects, whereas responses were absent in all subjects at 1500 Hz, indicating a group mean threshold for detecting IPDs of 1250 Hz. Behavioral thresholds were found at 1200 Hz using an adaptive two alternative forced choice procedure. Because the physiological responses require phase information, through synchronous bilateral inputs at the level of the auditory brainstem, physiological “change” detection thresholds likely reflect the upper limit of phase synchronous activity in the brainstem. The procedure has potential applications in investigating impaired binaural processing because phase statistic applied to single epoch MEG data allowed individual thresholds to be obtained. © 2007 Acoustical Society of America.

[DOI: 10.1121/1.2404915]

PACS number(s): 43.64.Ri, 43.66.Pn, 43.66.Nm [WPS]

Pages: 1017–1027

I. INTRODUCTION

Localization of sound sources in the horizontal plane is mainly based on neural comparison of the sounds arriving at each ear, with the primary cues being interaural time and intensity differences. Other binaural cues used for sound localization include interaural spectral differences associated with head transfer functions and changes in the sound field observed with small head movements. The acoustic cues are likely analyzed in separate neural networks in the brain (Yin, 2002), with some species having particular specializations in these networks.

The ability to localize sound is highly dependent on the ability to detect interaural time differences (ITD) for low frequencies, and interaural intensity differences (IID) for higher frequencies (Stevens, 1936). For steady signals, such as pure tones, the ITD is equivalent to the interaural phase difference (IPD). When presented in free field sound localization becomes ambiguous if the wavelength of the sound is equal to or smaller than the distance between the ears (i.e., $IPD \geq 2\pi$). For instance, the distance between ears in adult humans is less than 20 cm. Given this distance, maximum ITD is 0.7–0.9 ms (depending on frequency and distance of the sound) (Brungart and Rabinowitz, 1999) which corresponds to the period of 1100–1400 Hz tones.

According to behavioral studies, the upper frequency limit for IPD detection is between 1100 and 1300 Hz. For example, Garner and Wertheimer (1951) reported that the upper frequency limit for IPD detection was 1100 Hz for tones presented at 50 dB and 1300 Hz for tones presented at 90 dB. Zwislocki and Feldman (1956) found the upper frequency limit for perceiving IPDs to be 1300 Hz for pure tones presented at 75 dB SL. Schiano *et al.* (1986) reported that the sensitivity for sound lateralization decreases rapidly above 1100 Hz.

IPD processing requires that the phase information of the acoustical signal is preserved in the neural activity at the place of processing. However, phase locked encoding degrades along the ascending auditory pathway. Therefore, neural networks in the early part of the auditory brainstem that receive bilateral input are candidates for processing IPDs. The medial part of the superior olivary complex (MSO) is a likely candidate because it is the first station in the ascending mammalian auditory system that receives bilateral input from both ears. It is believed that MSO neurons likely act as coincidence detectors proposed in Jeffress' model for binaural hearing (Jeffress, 1948). A requirement of this model, that the bipolar MSO cells receive phase-locked input from both ears, seems fulfilled, at least for low frequencies. For example, auditory nerve fibers tuned to low frequencies fire synchronized with particular phases of the sine wave cycle, often at intervals of several cycles (Rose *et al.*, 1967). This phase-locked response to low frequencies is

^{a)}Author to whom correspondence should be addressed. Fax: +1(416) 785 2862. Electronic mail: bross@rotman-baycrest.on.ca

enhanced in those cells of the cochlear nucleus that project to the MSO (Joris *et al.*, 1994). When the IPD of pure tones is varied, MSO neurons respond best to a specific IPD. The specialization of MSO neurons to certain IPDs is expressed in highly facilitated responses to favorable IPDs with spike rates significantly exceeding the sum of separate ipsilateral and contralateral stimulation. Additionally, the responses to these IPDs exhibit a far higher degree of phase-locking than to unfavorable IPDs (Batra *et al.*, 1997). As the auditory information is processed beyond the superior olive to the nuclei of the lateral lemniscus and the inferior colliculus, the relative timing information is preserved, but the ability of the neurons to phase lock to the tones decreases (Kuwada *et al.*, 2006).

The aim of our study was to learn more about the encoding of binaural information in the auditory system and how this is reflected in auditory evoked responses. We developed a procedure for the recording of evoked responses to changes in IPD and used these responses to find individual physiological thresholds for the frequency in which binaural information can be processed based on IPD. We used magnetoencephalography (MEG) to record evoked cortical activity in response to binaural stimuli containing phase changes. Our aims were to determine whether IPD transitions evoke physiological “change” responses, and how well physiological IPD thresholds correspond with behavioral thresholds. Discriminating IPD changes would clearly be related to sound localization. Furthermore, our hypothesis was that the responses to IPD changes are limited to the frequency range of phase locked representation of the acoustical input in the auditory brainstem. Thus, the upper frequency limit for processing IPD in dichotic sound could give an indirect measure for phase locking in the auditory pathway. During normal aging or as a result of brain dysfunction phase locked neural encoding may be degraded. In general this threshold may indicate the upper frequency limit for phase locked processing in hearing. The obtained threshold could be an important indicator for the performance in sound localization and for other auditory processes requiring rapid waveform identification for the perception of speech and music.

II. METHODS

A. Subjects

Twelve healthy subjects (seven females), with a mean age of 26.8 years (std dev. 3.1 yrs), provided their informed consent before participating in the study, which was approved by the Research Ethics Board at Baycrest Center. Each participant had normal hearing, defined as thresholds <20 dB HL. For frequencies below 2000 Hz absolute threshold differences between left and right ear were less than or equal to 10 dB (mean absolute difference 3.5 dB).

B. Auditory stimuli for the physiological test

A specific stimulus signal was developed for recording auditory evoked responses to transitions in the IPD. Sinusoidal amplitude modulated tones were repeatedly presented for 4.0 s duration with stimulus onset asynchrony uniformly randomized between 7.5 and 8.5 s [Fig. 1(a)]. At 2.0 s after

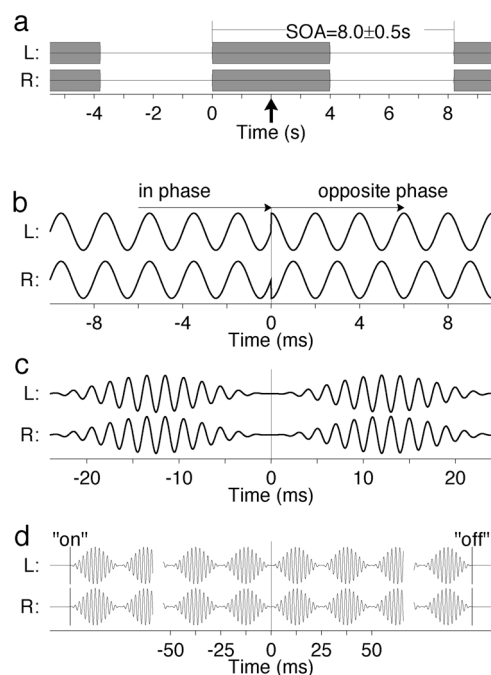


FIG. 1. Description of the auditory stimuli used during MEG testing. (a) The stimulus sequence was comprised of tonebursts (4 s in duration) presented dichotically with a SOA of 7.5–8.5 s. The arrow at 2 s after stimulus onset indicates the time point of the change in the IPD. (b) The 90 degree phase shifts, opposite in direction, result in a polarity reversal between left (L) and right (R) ears. (The time scale is adjusted to the phase shift.) (c) The phase shift occurs at the minimum point of the 40 Hz amplitude modulation (d) The 40 Hz AM envelope defines the shape of stimulus onset, the phase shift, and the stimulus offset.

stimulus onset, sudden phase shifts in the carrier signal of +90° in the left and –90° in the right ear, equivalent to 180° IPD, were introduced. Thus, during the first two seconds both ears received the identical tones, but during the last two seconds of stimulation the tones were of opposite polarity in the two ears [Fig. 1(b)]. Participants described the diotic portion of the stimulus during the first two seconds as sound arising from a single source in the center of the head. In contrast, the dichotic portion of the stimulus during the last two seconds was described as sound from separate sources in space without specific localization. A similar method of presenting sounds with different phases from two loudspeakers was used in the early days of sound reproduction to create the illusion of spatially distributed sound sources from a single audio signal and was termed quasi-stereophony (Schroeder, 1961).

To prevent the subject from perceiving a discontinuity in the sound at the moment of the phase-shift, the tones were amplitude modulated and the phase-shift was set to occur at the minimum point of modulation [Figs. 1(c) and 1(d)]. In a previous study we demonstrated that 90° diotic phase-shifts (in the same direction in both ears) at the minimum of the AM, did not elicit an evoked response (Ross *et al.*, 2004). Only when the dichotic phase-shift caused a change in the IPD, an evoked response was elicited. In addition, the 12.5 ms onset slope of the modulation envelope eliminates any differences in the onset time as a possible binaural cue. The modulation frequency of 40 Hz was chosen in order to

elicit the strongest auditory steady-state responses. The effect of IPD changes on the steady-state responses will be reported separately.

The experimental parameter in the current study was the carrier frequency of the stimulus, which was set to 500, 1000, 1250, and 1500 Hz. Since the phase change was always half a period, the introduced ITD was 1.0, 0.5, 0.4, and 0.33 ms, respectively. The frequencies were chosen being clearly below (500 and 1000 Hz) and around (1250 and 1500 Hz) the expected frequency threshold. One hundred stimuli with the same carrier frequency were presented in each experimental block of 13 min duration, and each block was repeated once. The eight experimental blocks were randomly presented across two experimental sessions of about one hour duration each on two subsequent days.

Stimuli were presented through Etymotic ER3A transducers connected with 1.5 m of length matched plastic tubing and foam earplugs to the subject's ears. The sound transducer had to be placed in sufficient distance to the MEG sensor in order to avoid any interference between the stimulus signal and the recorded brain activity. Below 2000 Hz the frequency characteristic of the sound transmission system was relatively flat (± 6 dB) and the phase characteristic was linear. The stimuli in the current study were defined on a narrow frequency band and, thus, were not distorted by the sound transmission tubes. The phase relation between acoustic signals at both earplugs was tested using a 2 cc coupler.

The stimulus intensity was set to 60 dB above individual sensation thresholds, which were measured immediately before each MEG recording. Insert-earphones provide typically interaural attenuation of more than 75 dB at the frequencies used in this study (Sklare and Denenberg, 1987). Thus, no effects of interaural cross talk were expected.

C. MEG data acquisition and analysis

MEG recordings were performed in a quiet, magnetically shielded room using a 151-channel whole-head neuro-magnetometer (VSM-Medtech, Port Coquitlam, BC, Canada). The detection coils of this MEG device are almost equally spaced on the helmet shaped surface and are configured as axial first-order gradiometers (Vrba and Robinson, 2001). After low-pass filtering at 200 Hz, the magnetic field data were sampled at the rate of 625 Hz and stored continuously.

MEG data were collected during passive listening, meaning, that the subjects did not need to attend to the stimuli or execute a task. In order to control for confounding changes in vigilance, the subjects watched a closed captioned movie of their choice, while the auditory stimuli were being presented. Compliance was verified using video monitoring. The subjects were in supine position with the head resting inside the helmet shaped MEG sensor. Head movements were verified to be less than 8 mm during each recording block using three detection coils attached to the subject's nasion and the pre-auricular points. No data had to be rejected because of excessive head movements.

D. MEG data analysis

Each block of continuously recorded MEG data was subdivided into 100 stimulus related epochs of 6000 ms duration including 1000 ms pre- and post-stimulus intervals. For artifact rejection, a principal component analysis was performed on each epoch of magnetic field data. This approach is effective for removing artifacts with amplitudes larger than the brain signals of interest (Lagerlund *et al.*, 1997). Principal components, which exceeded the threshold of 2 pT in at least one channel, were subtracted from the data. This procedure removed artifact primarily related to dental metal and eye-blinks, which are substantially larger than the brain activity (Bardouille *et al.*, 2006). After artifact removal, the magnetic field data were averaged and magnetic source analysis was applied to the ± 10 ms time interval around the maximum of the N1m wave, the most prominent response 100 ms after stimulus onset. Source analysis was based on the model of spatio-temporal equivalent current dipoles (ECD) in a spherical volume conductor. A head based Cartesian coordinate system was established by the x -axis pointing from the midpoint between the pre-auricular points to the nasion, the y -axis running from right to left in the plane formed by the three fiducials and the z -axis pointing in superior direction.

Single dipoles in both hemispheres were fit simultaneously to the 151-channel magnetic field distribution. First, the data were modeled with a mirror symmetric pair of dipoles. The resulting source coordinates were then used as starting points to fit the dipole in one hemisphere while the coordinates in the other hemisphere remained fixed. We then switched between hemispheres and repeated the last step until the source coordinates showed no further change. Dipole fits were accepted if their calculated fields explained at least 85% of the variance of the measured magnetic field. Eight estimates (four stimulus frequencies times two repetitions) of the N1m source location were obtained for each subject. The mean spatial coordinates and orientations were used as individual models to measure the source waveforms for the auditory evoked responses. The transient P1m-N1m-P2m components and sustained responses were obtained from source-space projection based on the source coordinates of the N1m "onset" response. To evaluate the validity of this approach, the linear regression of the actual magnetic field at each time point versus the magnetic field observed at the time of the N1m "onset" response was performed on the grand averaged data. This analysis tested how well the magnetic field distribution, at any time point, could be explained with the field distribution of the N1m onset response.

Data were analyzed primarily on dipole moment waveforms representing the source activity in the auditory cortices. MEG responses were modeled by single dipoles in left and right auditory cortices. Previous analyses, using a beamformer approach (Vrba and Robinson, 2001) with no *a priori* assumptions about the source configuration, demonstrated that single dipoles are sufficient to describe the activation of the auditory cortex (Herdman *et al.*, 2003). In this case, magnetic field waveforms of cortical source activity $\mathbf{q}(t)$ are detected by each of the 151 sensors with a distinct sensitivity

depending on the orientations and distances between the source and the sensors. If the sensitivities of all sensors at position \mathbf{R} for the source activity at location \mathbf{r} are given in matrix notation by the lead-field matrix $\mathbf{L}(\mathbf{r}, \mathbf{R})$ (Sarvas, 1987) the detected magnetic field $\mathbf{B}(\mathbf{R}, t)$ can be described by $\mathbf{B}(\mathbf{R}, t) = \mathbf{q}(\mathbf{r}, t) \cdot \mathbf{L}(\mathbf{r}, \mathbf{R})$. The pseudo-inverse of the lead-field matrix can then be used to obtain the cortical source activity from the measured magnetic field: $\mathbf{q}(\mathbf{r}, t) = \mathbf{B}(\mathbf{R}, t) \cdot \mathbf{L}^{-1}(\mathbf{r}, \mathbf{R})$. This operation, termed source space projection (Ross *et al.*, 2000; Tesche *et al.*, 1995), combines the 151 waveforms of magnetic field strength into a single waveform of a magnetic dipole moment measured in nanoAmpere-meter (nAm). The dipole moment is most sensitive for the localized area in the brain and less sensitive to electro-magnetic sources at other locations. Furthermore, this method of source space projection results in waveforms with higher signal-to-noise ratio than the magnetic field waveforms (Ross *et al.*, 2000).

A further advantage of analysis in source domain is that the dipole moment is independent of the sensor position. The position of the subject's head relative to the MEG sensor can change between sessions and will also be different between subjects. Combination of magnetic field data for group analysis is, therefore, not feasible. In contrast, the waveforms of cortical source activity can be combined across repeated sessions for a subject and across the group of subjects.

Statistical tests for detecting response components were based on the phase distribution of a Morlet wavelet transform with half-maximum-width corresponding to 2.5 periods of the test frequency applied to single trial source waveforms for each subject. The null hypothesis was that the signal phase is uniformly distributed across all trials if the signal contains no stimulus-related components. An evoked response either caused by an additive time-locked signal or by time-locked phase-synchronization is reflected as deviation from uniformly distributed signal phase. The Rayleigh test statistic R_{ij} was calculated for each point in time (i) and frequency (j) as $R_{ij} = \text{abs}(\langle c_{ij} / |c_{ij}| \rangle)$ where c is the complex coefficients obtained from the wavelet transform, c divided by its absolute value gives sine and cosine of the phase, and $\langle \rangle$ denotes calculation of the mean across all trials. Because the distribution of the Rayleigh statistic is known, p -values could be calculated by numerical approximation for all time-frequency coefficients (Fisher, 1993). This method has been successfully used to detect cortical evoked near threshold responses in objective audiometry (Ross *et al.*, 1999). Also, studies have demonstrated that phase tests may be more sensitive than amplitude tests (Sturzebecher and Cebulla, 1997). The minimum p -value for all coefficients in the time interval between 2.0 and 2.4 s and the frequency range from 3 to 10 Hz obtained from left and right hemisphere responses served as the test statistic for detecting a response to the change in the IPD. The selected time-frequency interval contained 1000 coefficients (25 frequencies \times 40 time points).

To correct the p -values for the multiple tests, we needed to estimate the degrees of freedom (the maximum number of independent time-frequency components). The frequency resolution of the Morlet transform was largest at 3 Hz with $\Delta f = 1.25$ Hz and the temporal resolution at 10 Hz with a

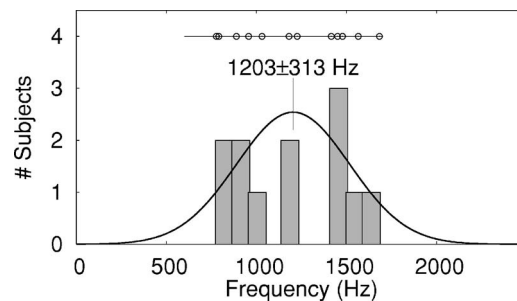


FIG. 2. Distribution of behavioral thresholds ($n=12$). The mean threshold was 1203 Hz, with standard deviation of 313 Hz.

sample interval of $\Delta t = 50.0$ ms. Therefore, the total degrees of freedom were estimated as 44.8 $[(10-3)/1.25 * 400/50]$. Being conservative we estimated the degree of freedom as 50 and rejected the null hypothesis (absence of a response) on the nominal level of 0.1% corresponding to the corrected $\alpha = 5\%$ level.

E. Behavioral stimuli and procedure

An adaptive two-alternative forced choice (2AFC) procedure was used for psycho-acoustical testing. Stimuli were sinusoidal amplitude modulated (AM) tones presented through Etymotic ER3A transducers. Two 40 Hz AM tones, 1.0 s in duration, either in phase or out of phase, were presented to both ears with 900 ms inter-stimulus interval. During an initial training phase the subjects learned that the two stimuli could be perceived as sound from a single source (diotic sound with the same interaural phase) or spacious sound in both ears (dichotic sound with different interaural phase). The order of stimuli was randomized during the test and the subjects were asked to identify if the first or the second stimulus sounded like two stimuli in separate ears. Immediately after the subject responded with a button press the next pair of stimuli was presented.

Initially the carrier frequency was 250 Hz; however, the carrier frequency increased by a quarter octave if two responses in a row were correct and decreased if a single response was incorrect (two-down, one-up procedure, Levitt, 1970). Visual feedback was provided, in the form of a green (correct) or red (incorrect) square on the computer screen. One hundred trials were presented in each run, lasting about 10 min. Each run was repeated once.

III. RESULTS

A. Behavioral results

The group mean behavioral threshold was 1203 Hz with a standard deviation of 313 Hz. The distribution of obtained thresholds can be found in Fig. 2. Figure 3(a) shows the time-course of threshold changes, for two individuals, using the adaptive 2AFC procedure. For subject 1, the time-course of frequency threshold changes stabilized immediately after the initial slope, and then oscillated around the assumed threshold. Figure 3(b) illustrates the estimated threshold for this subject (e.g., 1682 Hz). The solid line connecting the black squares denotes the cumulative percentage of downward steps in the graph of Fig. 3(a). The observed curve was

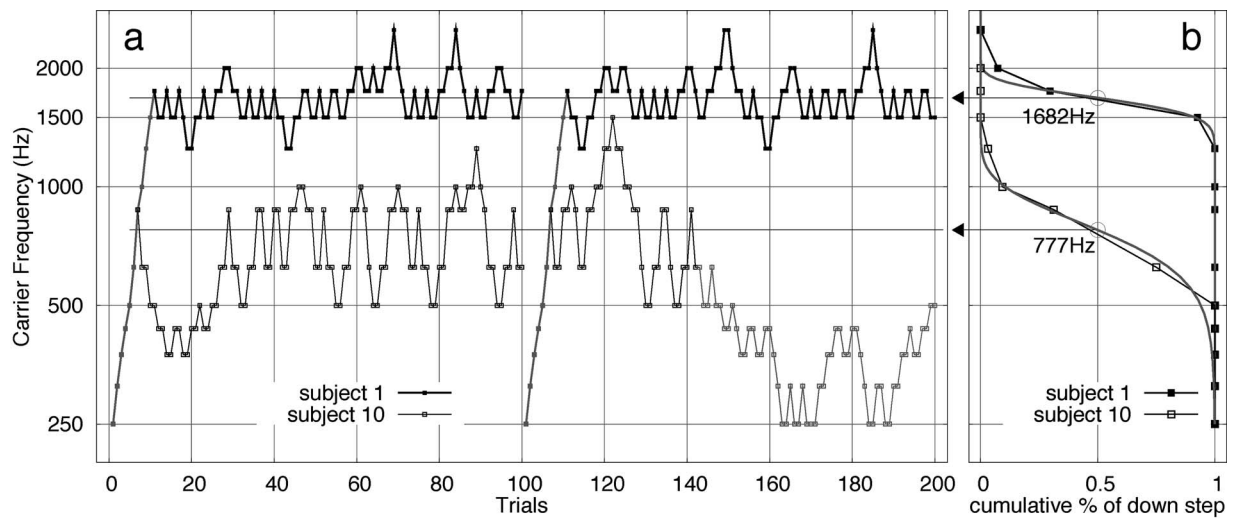


FIG. 3. Behavioral results for two sample subjects. (a) The time course of the test frequency using an adaptive procedure. Both subjects performed two blocks of 100 trials each. The initial phase, before the first reversal (gray line), was excluded from analysis. Whereas subject 1 performed consistently throughout the whole test, subject 10 showed larger fluctuations. Decreases in performance, toward the end of the test, may have resulted from fatigue or reduced alertness. Thus, trials 140–200 (gray line) were not included in the data analysis. (b) Cumulative percentage of downward steps during the adaptive procedure. The observed characteristics were approximated by a normal CDF and the threshold was defined as the 50% value of the CDF.

approximated by a cumulative normal distribution function (CDF) defined by the mean and standard deviation. The mean, equivalent to the 50% of the CDF, was accepted as an estimate for the threshold. When threshold is defined in this manner, it corresponds to the 70% point on the subject's psychometric function (Levitt, 1970).

The second subject in Fig. 3(a) was much more variable than the first subject. Although a relatively consistent threshold was observed in the first block, the performance deteriorated substantially during the second half of the second block. This might have been an effect of fatigue or decreased concentration. Therefore, in this instance, the last 60 trials were excluded from further analysis [shaded in gray in Fig. 3(a)].

B. Auditory evoked fields

Auditory evoked responses, from a sample individual subject, are shown in Fig. 4. Group results are shown in Fig.

5. At all stimulus frequencies, clear P1m-N1m-P2m “onset” and “offset” waveforms are evident. The presence of a P1m-N1m-P2m response signals the physiological detection of a change in the acoustical environment. In this experiment, the response waveforms indicate the onset from silence to sound, the change in IPD, and the offset from sound to silence. Of particular importance is that the presence of the P1m-N1m-P2m “change” response, signaling the physiological detection of phase changes, is absent at 1500 Hz but present at all lower frequencies. For example, on top of the sustained response an additional P1m-N1m-P2m response occurred after the sudden change in the IPD, at 2.0 s after stimulus onset. This change response has about the same amplitude as the onset response at 500 Hz. However, the amplitude of the IPD change response becomes smaller at 1000 Hz and is barely visible at 1250 Hz. Note there is no change response, for this subject, in the 1500 Hz frequency condition.

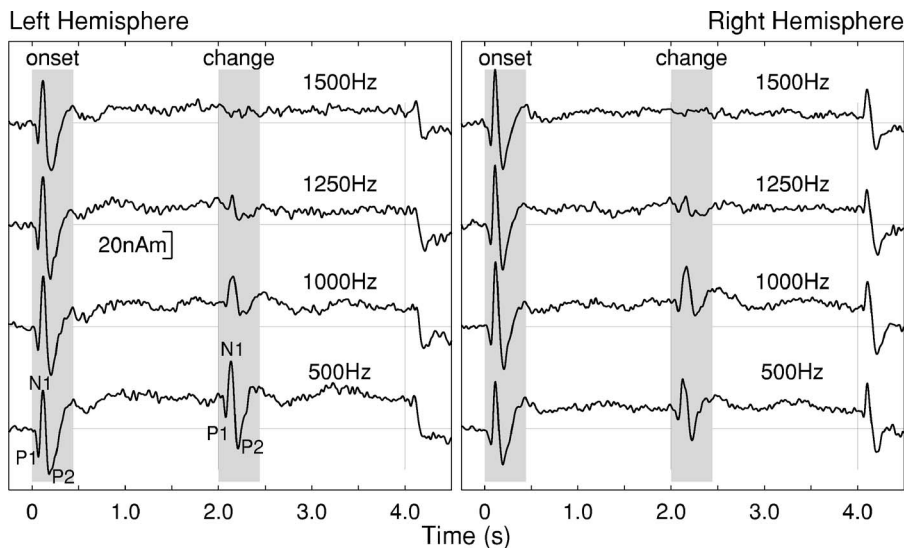


FIG. 4. Individual waveforms of 24 Hz lowpass filtered auditory evoked responses in the left and right hemisphere for each frequency tested. The response waveform at 500 Hz exhibits clear P1m-N1m-P2m responses to the stimulus onset and IPD change (at 2.0 s). Also sustained responses, continuing for the stimulus duration, and N1-P2 offset responses can be seen. Whereas the onset responses are fairly consistent across all stimulus frequencies, the phase change response clearly diminishes with increasing stimulus frequencies and is absent at 1500 Hz.

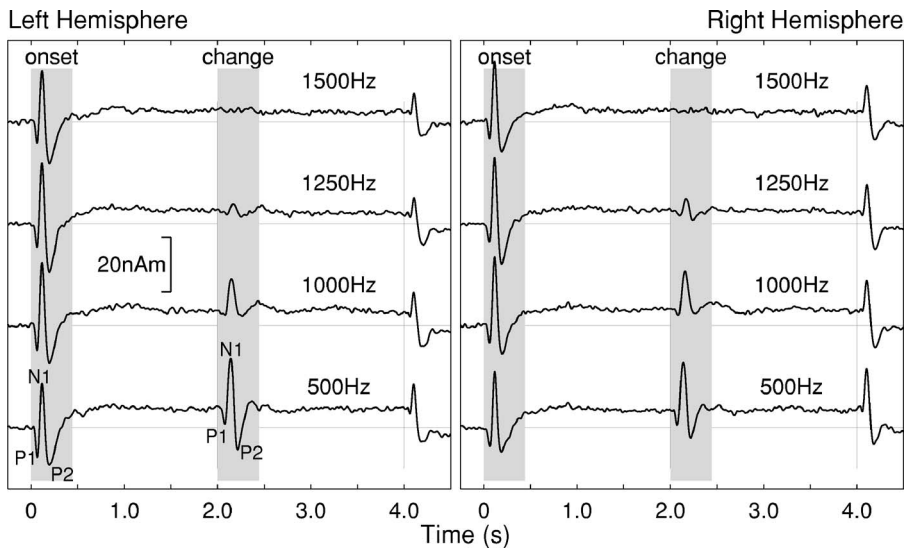


FIG. 5. Grand averaged ($n=12$) waveforms of 24 Hz lowpass filtered auditory evoked responses in the left and right hemisphere for four different stimulus frequencies.

Grand averaged waveforms of the onset and change responses are also shown in Fig. 6(a). This figure shows that the latencies for P1m, N1m, and P2m onset responses did not change across frequency conditions. In contrast, latencies of the change response increased, and amplitudes decreased, when higher frequency stimuli were used to evoke P1m, N1m, and P2m responses. At 500 Hz, the change response was similar in amplitude to the onset response but slightly delayed. For example, P1m latencies of the change response were delayed by about 14 ms when compared to the corresponding onset responses. Detailed information about peak latencies and amplitudes of the P1m-N1m-P2m onset and change responses at 500 Hz stimulus frequency are given in Table I. Differences in the group mean values of the onset and IPD change response peak amplitudes were not significant because of inter subject variability. However, the amplitude ratio of change versus onset response was larger in the left (1.6) than in the right hemisphere (0.6) ($t(11)=2.5$, $p < 0.03$) indicating that the IPD “change” response was more left lateralized compared to the onset response.

A summary of N1m amplitude results, as a function of stimulus frequency, is provided in Fig. 6(b). Whereas, ampli-

tudes of the N1m IPD change response decreased monotonically with increasing stimulus frequency; the N1m onset response showed an inverse u-shaped characteristic. From 500 to 1000 Hz the N1m onset response increased significantly [$t(11)=2.87$, $p < 0.015$]. The onset N1m amplitude decreased significantly between 1000 and 1500 Hz [$t(11)=2.56$, $p < 0.027$] and between 1250 and 1500 Hz [$t(11)=3.52$, $p < 0.005$].

C. Source coordinates

Sources of N1m onset responses were localized in all subjects with a goodness of fit larger than 85% (mean square difference between measured and modeled magnetic field). Group mean N1m source locations were converted into Talairach coordinates. N1m sources were found in left and right Planum temporale at ($x=49.2$, $y=-21.5$, $z=5.8$ mm) in the right and at ($x=-47.1$, $y=-26.4$, $z=6.3$ mm) in the left hemisphere with 95% confidence limits for the group means of less than 4 mm in any direction. The source locations represent centers of activity. Because of limited spatial resolution of MEG for simultaneous active sources, the possibility of

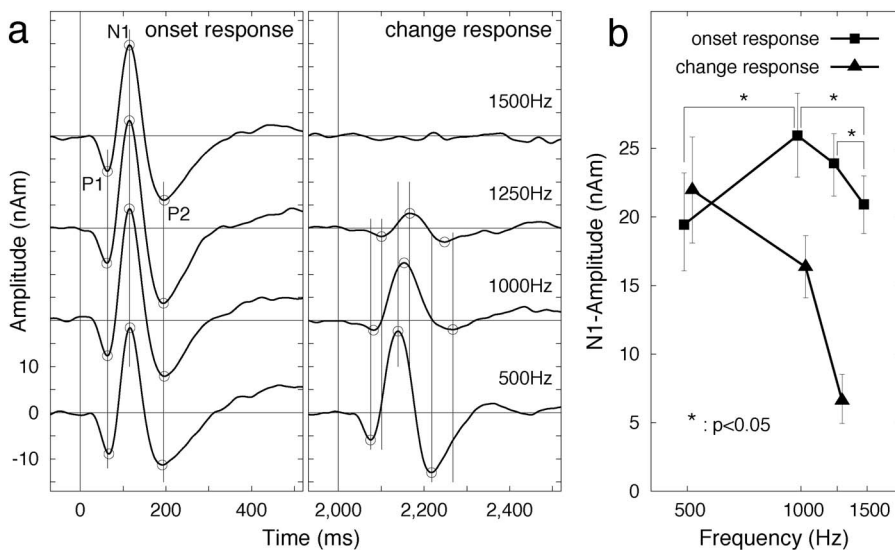


FIG. 6. (a) Averaged waveforms, across left and right hemispheres, for the P1m-N1m-P2m onset (left) and change (right) responses for the four stimulus frequencies. (b) N1m amplitude of the phase change response is affected by stimulus frequency.

TABLE I. Latencies and Amplitudes of onset and phase change responses at 500 Hz.

	Latency (ms)		Amplitude (nAm)	
	onset	phase change	onset	phase-change
P1m right	53±7	65±9*	8.5±4.4	7.0±6.0
P1m left	58±6	74±15*	10.7±3.0	5.9±4.2
N1m right	106±4	129±12*	23.4±9.6	22.4±9.2
N1m left	107±5	133±16*	15.6±6.5	21.4±10.6
P2m right	185±3	219±26*	10.5±9.5	10.4±9.4
P2m left	200±25	214±25	15.2±2.8	15.5±4.8

*Denotes a significant ($p < 0.05$) difference between onset and phase change response.

additional contributions from sources in Heschl's gyrus cannot be excluded. The hemispheric asymmetry of a 5 mm more anterior N1m source in the right hemisphere was significant in the group [$t(11)=2.7, p < 0.02$]. Source locations for the N1m phase change responses were not different from the onset responses suggesting generation of both response types in common or overlapping neural populations. The linear regression analysis applied to the grand averaged magnetic field data revealed that the field variance of the N1m change response could be explained with $r^2=0.956$ by the magnetic field at the maximum of N1m onset response.

D. Individual thresholds

A time-frequency representation of the p -values resulting from the Rayleigh test, applied to all time-frequency coefficients, is shown in Fig. 7. Gray shaded areas in the graphs denote time-frequency regions with p -values less than 0.1% (corrected $< 5\%$).

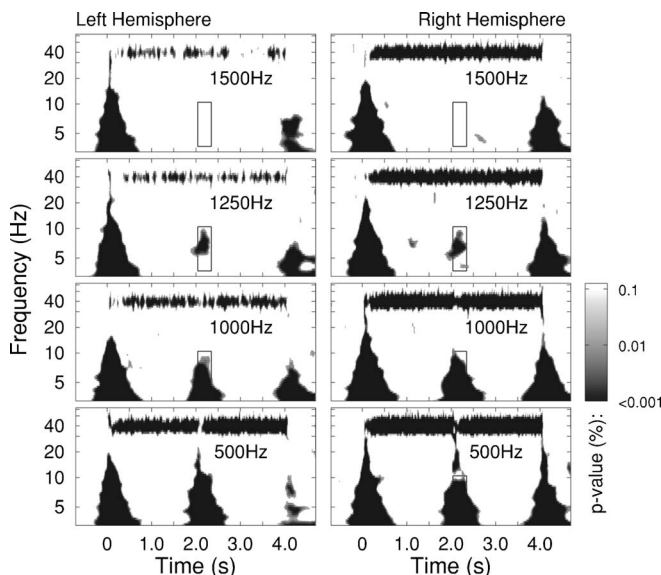


FIG. 7. Individual results of the Rayleigh test applied to the coefficients of a time-frequency decomposition of the response waveforms. The gray shaded areas denote p -values less than 0.1%. At 500 Hz, the most prominent response contributions are: the onset, the phase change, and the offset response. Also seen is the 40 Hz steady-state response, seen as a horizontal band of activity at 40 Hz. Rectangular boxes in the 2.0–2.4 s and 3–10 Hz region indicate the range of coefficients used to test for a response to the IPD change.

Characteristic patterns in the time-frequency maps can be related to corresponding time intervals in the response waveforms from the same subject shown in Fig. 4. For instance, the triangular area at the zero time-point (on the x -axis) represents the onset response. The triangular shape is partially caused by the temporal resolution of the wavelet transform, which decreases toward low frequencies. A similar pattern can be identified for the offset response at 4.0 s. For this particular subject the offset response is larger in the right than left hemisphere, consistent with the response waveforms shown in Fig. 4. The horizontal bar around 40 Hz reflects the frequency content of the auditory steady-state response evoked by the 40 Hz amplitude modulation. Once again it is more prominent over the right hemisphere, a finding that was consistent across subjects. The 40 Hz steady state response is not seen in Fig. 4, because the waveforms in Fig. 4 were low-pass filtered.

Consistent with the IPD change response shown in Fig. 4, significant time-frequency coefficients are seen at 500 and 1000 Hz stimulus frequency. At 1250 Hz, a smaller but significant set of response coefficients is seen. Upon further analysis, the phase change response was restricted to the 2.0–2.4 s time and 3–10 Hz frequency interval (rectangular boxes in Fig. 7). The boxes in the 1500 Hz region indicate that there was no significant response detected at this stimulus frequency.

The Rayleigh test results in these time-frequency boxes are summarized for all subjects in Fig. 8. Here, the results from left and right auditory cortices have been combined by showing the minimum of the two p -values for each time-frequency coefficient. At 500 and 1000 Hz, all twelve subjects showed clearly significant IPD change responses. At 1250 Hz nine subjects showed significant responses and no responses were detected at 1500 Hz. That means that for the subjects 6, 8, and 11, thresholds were above 1000 and below 1250 Hz. For the other nine subjects, thresholds were above 1250 and below 1500 Hz.

A comparison between the physiological and behavioral thresholds is given in Fig. 9. The histogram for the physiological thresholds contains four points on the x -axis because four frequencies were tested. The physiologic CDF approximation shows a group mean threshold close to 1250 Hz. The cumulative histogram of behavioral thresholds demonstrates the larger range of individual thresholds. Thresholds fell between 770 and 1682 Hz. The CDF approximation corresponds to the distribution given in Fig. 2, with a group mean of 1203 Hz.

IV. DISCUSSION

We recorded cortical evoked auditory responses to sudden changes in IPD and found the group mean upper frequency limit at 1250 Hz. This physiological threshold corresponded well with the group mean behavioral threshold of 1203 Hz. Both thresholds fall within the 1100–1300 Hz range, commonly reported in the literature as upper frequency limit for ITD/IPD detection.

Cortical responses to changes in ITD have been recorded in EEG studies using noise stimuli (Jones *et al.*,

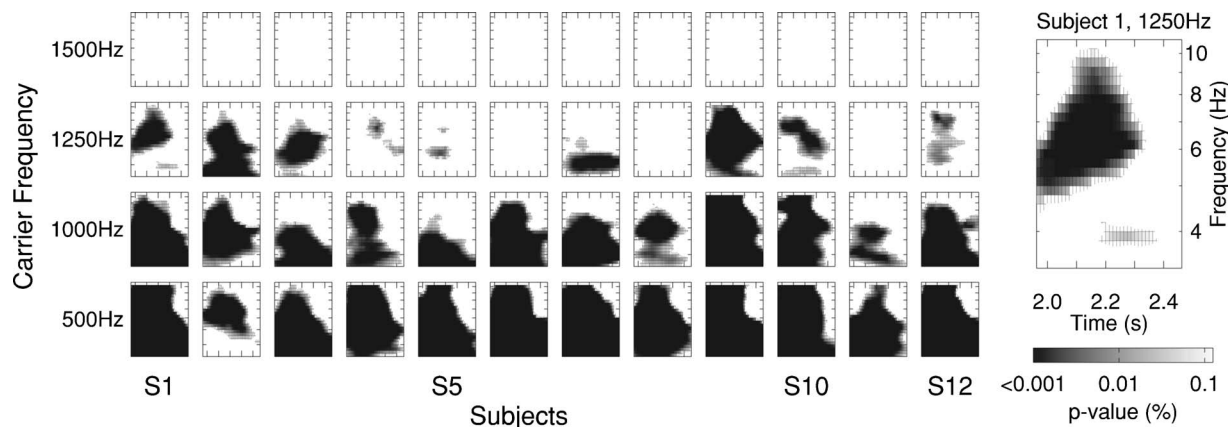


FIG. 8. P -values obtained with the Rayleigh test for time-frequency coefficients 3–10 Hz, 0–500 ms after the phase change. Data from subject 1, at 1250 Hz, is shown in the right enlarged panel, as an example. All subjects showed a significant phase change response at 500 and 1000 Hz, nine of twelve subjects showed a response at 1250 Hz and no subject responded to the phase change in the 1500 Hz tone.

1991; McEvoy *et al.*, 1991a, b; McEvoy *et al.*, 1990; Picton *et al.*, 1991). Like in our study, cortical responses were found for interaural changes between noncoherent and fully coherent noise sounds (Chait *et al.*, 2005; Dajani and Picton, 2006; Jones *et al.*, 1991). Several parallels exist between the responses elicited by changes in interaural coherence or ITD and changes in IPD in our study. In all cases the evoked P1-N1-P2 complex was several tens of milliseconds delayed compared to the response to sound onset; suggesting that discriminating changes in interaural disparity requires additional processing time than the mere detection of sound onset. Regardless of stimulus type, strongest effects were found at low frequencies.

A. Possible neural mechanisms underlying the IPD processing

The classical model for processing of ITDs, as proposed by Jeffress (1948), consists of an array of neurons that act as coincidence detectors, responding maximally to synchronous bilateral inputs. Furthermore, the model requires that the neurons receive delayed input from both ears. Such a network creates a topographical representation of the ITD. Recently, an alternative model of sound localization had been

proposed, which uses broadly tuned networks of ITD sensitive neurons in the left and right hemisphere and coding of neural firing rate instead of a place code (Harper and McAlpine, 2004; McAlpine, 2005). Common to all models is that they require phase locked bilateral input at the place of binaural computation.

Our MEG data do not directly answer the question of underlying structure and cannot directly tell us where or how IPD cues are processed in the brain. Localizing IPD change responses in the auditory cortex could have formally provided evidence for cortical processing of binaural input. However, the upper frequency limit for IPD processing seems too high for a cortical network that directly compares phase information from bilateral auditory inputs. We assume that the IPDs are processed most likely in medial (Yin and Chan, 1990) and lateral (Tollin and Yin, 2005) superior olivary nuclei. Outputs are then projected along the afferent auditory pathway to the cortex. We further speculate that the limitation of useful frequency range for IPD processing occurs at or below the point where bilateral phase locked neural activity converges. An explanation for the upper frequency limit is that phase locked neural activity has a limited temporal acuity. Thus, the thresholds we obtained may reflect the limited phase locking ability in the auditory brainstem or below.

B. Common generators for the change and onset response

The dependency of the N1m onset amplitudes on the stimulus frequency was affected by the presence of a change response. In general we would expect monotonic decrease in N1m amplitude with increasing stimulus frequency (Antinoro *et al.*, 1969; Naatanen and Picton, 1987). In contrast, the N1m amplitude increased between 500 and 1000 Hz (where the change response was largest) and decreased at higher frequencies. A possible explanation is that the onset and change responses share common neural resources. The 500 Hz stimulus elicited the largest IPD change response and could incur increased refractoriness in neural population common for onset and change response. Thus, reduced resources were available for the following onset response. This

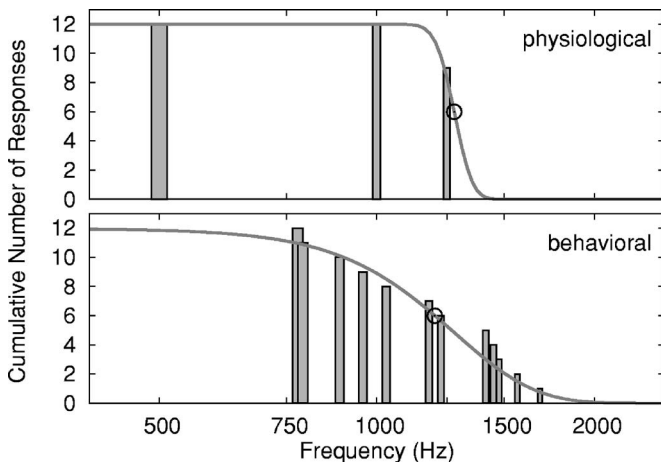


FIG. 9. Cumulative number of responses obtained with the physiological (top) and behavioral (bottom) tests.

situation changed for higher stimulus frequencies where smaller change responses were elicited and the generation of the onset response was unaffected. Thus, we interpret the observed frequency dependency of the onset response as evidence for common neural populations generating both types of responses. The finding that the magnetic field distribution at the peak of the N1m onset response could explain 95% of the variance in the magnetic field at the peak of the change response supports this interpretation.

C. Alternative interpretations

Stimulus frequency was the independent variable in our study. Because the phase change was always a half period, the ITD varied from 1.0 ms at 500 Hz to 0.4 ms at 1250 Hz. It is, therefore, reasonable to question whether the observed threshold reflects the shortest detectable ITD or an upper frequency limit for binaural processing based on ITDs. The ITDs in our study were at least one magnitude larger than those reported in literature for sound localization at corresponding frequencies. According to Zwislocki and Feldman (1956), the threshold for a noticeable change in the ITD of a 1000 Hz pure tone is 20 μ s, when tones are presented close to the midline in the horizontal plane. Because of those large differences it seems unreasonable to explain the observed frequency thresholds with the threshold for ITD discrimination. Consequently, we interpret our results as limits for the frequency range that is usable for IPD detection in steady tones.

We should also acknowledge that the current study did not evaluate the effect of stimulus intensity on the detection of IPD changes, because it was not feasible. Therefore, all tests (physiological and behavioral) were conducted using stimulus presentation levels of 60 dB SL. It is reasonable, however, to question if the thresholds obtained in our study would differ with different stimulus intensity levels. Because behavioral performance in sound localization has been shown to be similar, with stimulus intensities between 40 and 90 dB SL, and the upper frequency limit did not change (Zwislocki and Feldman, 1956), we expect that our behavioral thresholds do not depend strongly on intensity. Similarly, McEvoy *et al.* (1991a) showed that EEG responses to changes in the ITD of noise do not change when the stimulus intensity is varied between 55 and 75 dB SL. Thus it is likely that the observed IPD change response is widely independent of the stimulus intensity.

D. Physiological approaches to studying binaural hearing

Two main points should be emphasized. First is the small inter-subject variability in the physiological data, relative to the behavioral data. Second is the good agreement between the group mean results in physiological and behavioral tests even though different stimuli were used. The MEG portion of the study did not involve a behavioral task and instead examined the physiological detection of IPD change contained within the ongoing stimulus. The intention behind using a shorter stimulus, during the behavioral test, was to shorten the test time and prevent subject fatigue. However, a

psychoacoustic test that involves discriminating a short tone with or without a change in IPD would be another approach for future studies.

The behavioral threshold data were much more variable than the physiological data. Large inter subject variability in the behavioral data might be explained by the different strategies used by different subjects; individual motivation levels; or varying abilities to attend to the task. Performance variability might have been reduced if we had used highly trained subjects, as is commonly practiced in many psychoacoustical studies. However, we were interested in testing naive listeners under conditions comparable to those that would occur in a clinical test situation. Because physiological results can be less variable, there is interest in developing new techniques for assessing binaural processing in clinical populations with various types of hearing disorders.

Physiological tests, such as the one used in this study, are largely unaffected by the subject's motivation or attention span. For this reason, physiological procedures for assessing binaural interaction components (BIC), in populations with auditory disorders, have been described in the literature. Most BIC tests use auditory evoked brainstem responses to compute the difference between binaurally evoked responses and the sum of left and right monaurally evoked responses (Dobie and Berlin, 1979). The BIC reflects physiological processes underlying ITDs for click stimuli (Furst *et al.*, 1990, 1985) and has been used to assess children with central auditory processing disorders (CAPD) (Delb *et al.*, 2003). However, the brainstem BIC is small and often difficult to record (Stollman *et al.*, 1996). Furthermore, the BIC is derived from responses to click stimuli and likely related to a specific subsystem of binaural processing in the auditory pathway. For these reasons, recording cortical evoked responses to IPDs using low frequency tones, could improve the assessment of central sound processing.

Formally, the BIC could be derived from middle- and long-latency cortical responses and those BIC have larger amplitudes than the brainstem BIC (McPherson and Starr, 1993). However, cortical responses are reasonably well activated by either left or right ear input alone and do not increase to almost twice the size with binaural stimulation (Picton *et al.*, 1985). Thus, it is questionable whether the underlying assumption of linearity for calculating the BIC is valid and cortical BIC could truly represent binaural processing. Because no assumptions about linearity were made, paradigms like the one used in this study might be advantageous for investigating binaural hearing.

The presented method could potentially be used to assess central hearing abilities in individual subjects. One important step toward such application was to demonstrate a statistical test for the significance of individual responses. Another necessary step for clinical application of the paradigm is to demonstrate correlation between individual behavioral and physiological thresholds. Such regression analysis would require larger variation of individual thresholds than those reported in our study. Testing a broad range of individuals with different types of hearing disorders would also permit the opportunity to determine the sensitivity and specificity of this technique. For these reasons, a goal of future

studies is to investigate the physiological detection of IPD in people with various age groups, and with different types of hearing disorders.

V. CONCLUSIONS

Using cortical evoked potentials (P1m-N1m-P2m), we were able to record physiological change responses reflecting IPD processing. The responses could be recorded with stimulus frequencies below an upper limit, which closely approximated the behavioral threshold. Because the physiological responses require phase information through synchronous bilateral inputs at the level of the auditory brainstem, physiological change detection thresholds likely reflect the upper limit of phase synchrony in the brainstem. Therefore, this new approach to studying IPD holds promise for studying normal and disordered physiological processes underlying binaural hearing.

ACKNOWLEDGMENTS

The study was supported by grants from The Hearing Foundation of Canada, the Canadian Institutes for Health Research, and the Canada Foundation for Innovation.

- Antinoro, F., Skinner, P. H., and Jones, J. J. (1969). "Relation between sound intensity and amplitude of the AER at different stimulus frequencies," *J. Acoust. Soc. Am.* **46**(6), 1433–6.
- Bardouille, T., Picton, T. W., and Ross, B. (2006). "Correlates of eye blinking as determined by synthetic aperture magnetometry," *Clin. Neurophysiol.* **117**(5), 952–8.
- Batra, R., Kuwada, S., and Fitzpatrick, D. C. (1997). "Sensitivity to interaural temporal disparities of low- and high-frequency neurons in the superior olivary complex. I. Heterogeneity of responses," *J. Neurophysiol.* **78**(3), 1222–36.
- Brungart, D. S., and Rabinowitz, W. M. (1999). "Auditory localization of nearby sources. Head-related transfer functions," *J. Acoust. Soc. Am.* **106**(3 Pt 1), 1465–79.
- Chait, M., Poeppel, D., de Cheveigne, A., and Simon, J. Z. (2005). "Human auditory cortical processing of changes in interaural correlation," *J. Neurosci.* **25**(37), 8518–27.
- Dajani, H. R., and Picton, T. W. (2006). "Human auditory steady-state responses to changes in interaural correlation," *Hear. Res.* **219**(1-2), 85–100.
- Delb, W., Strauss, D. J., Hohenberg, G., and Plinkert, P. K. (2003). "The binaural interaction component (BIC) in children with central auditory processing disorders (CAPD)," *Int. J. Audiol.* **42**(7), 401–12.
- Dobie, R. A., and Berlin, C. I. (1979). "Binaural interaction in brainstem-evoked responses," *Arch. Otolaryngol.* **105**(7), 391–8.
- Fisher, N. I. (1993). *Statistical Analysis of Circular Data* (Cambridge University Press, Cambridge).
- Furst, M., Eyal, S., and Korczyn, A. D. (1990). "Prediction of binaural click lateralization by brainstem auditory evoked potentials," *Hear. Res.* **49**(1-3), 347–59.
- Furst, M., Levine, R. A., and McGaffigan, P. M. (1985). "Click lateralization is related to the beta component of the dichotic brainstem auditory evoked potentials of human subjects," *J. Acoust. Soc. Am.* **78**(5), 1644–51.
- Garner, W. R., and Wertheimer, M. (1951). "The effects of interaural phase differences on the perception of pure tones," *J. Acoust. Soc. Am.* **23**(6), 664–7.
- Harper, N. S., and McAlpine, D. (2004). "Optimal neural population coding of an auditory spatial cue," *Nature (London)* **430**(7000), 682–6.
- Herdman, A. T., Wollbrink, A., Chau, W., Ishii, R., Ross, B., and Pantev, C. (2003). "Determination of activation areas in the human auditory cortex by means of synthetic aperture magnetometry," *Neuroimage* **20**(2), 995–1005.
- Jeffress, L. A. (1948). "A place theory of sound localization," *J. Comp. Physiol. Psychol.* **41**, 35–39.
- Jones, S. J., Pitman, J. R., and Halliday, A. M. (1991). "Scalp potentials following sudden coherence and dis coherence of binaural noise and change in the inter-aural time difference: A specific binaural evoked potential or a "mismatch" response?" *Electroencephalogr. Clin. Neurophysiol.* **80**(2), 146–54.
- Joris, P. X., Carney, L. H., Smith, P. H., and Yin, T. C. (1994). "Enhancement of neural synchronization in the anteroventral cochlear nucleus. I. Responses to tones at the characteristic frequency," *J. Neurophysiol.* **71**(3), 1022–36.
- Kuwada, S., Fitzpatrick, D. C., Batra, R., and Ostapoff, E. M. (2006). "Sensitivity to interaural time differences in the dorsal nucleus of the lateral lemniscus of the unanesthetized rabbit: Comparison with other structures," *J. Neurophysiol.* **95**(3), 1309–22.
- Lagerlund, T. D., Sharbrough, F. W., and Busacker, N. E. (1997). "Spatial filtering of multichannel electroencephalographic recordings through principal component analysis by singular value decomposition," *J. Clin. Neurophysiol.* **14**(1), 73–82.
- Levitt, H. (1970). "Transformed up-down methods in psychoacoustics," *J. Acoust. Soc. Am.* **49**, 467–477.
- McAlpine, D. (2005). "Creating a sense of auditory space," *J. Physiol. (London)* **566**(Pt 1), 21–8.
- McEvoy, L. K., Picton, T. W., and Champagne, S. C. (1991a). "Effects of stimulus parameters on human evoked potentials to shifts in the lateralization of a noise," *Audiology* **30**(5), 286–302.
- McEvoy, L. K., Picton, T. W., and Champagne, S. C. (1991b). "The timing of the processes underlying lateralization: Psychophysical and evoked potential measures," *Ear Hear.* **12**(6), 389–98.
- McEvoy, L. K., Picton, T. W., Champagne, S. C., Kellett, A. J., and Kelly, J. B. (1990). "Human evoked potentials to shifts in the lateralization of a noise," *Audiology* **29**(3), 163–80.
- McPherson, D. L., and Starr, A. (1993). "Binaural interaction in auditory evoked potentials: brainstem middle- and long-latency components," *Hear. Res.* **66**(1), 91–8.
- Naatanen, R., and Picton, T. (1987). "The N1 wave of the human electric and magnetic response to sound: A review and an analysis of the component structure," *Psychophysiology* **24**(4), 375–425.
- Picton, T. W., McEvoy, L. K., and Champagne, S. C. (1991). "Human evoked potentials and the lateralization of a sound," *Acta Oto-Laryngol., Suppl.* **491**, 139–43; discussion 144.
- Picton, T. W., Rodriguez, R. T., Linden, R. D., and Maiste, A. C. (1985). "The neurophysiology of human hearing," *Human Communication Canada* **9**, 127–136.
- Rose, J. E., Brugge, J. F., Anderson, D. J., and Hind, J. E. (1967). "Phase-locked response to low-frequency tones in single auditory nerve fibers of the squirrel monkey," *J. Neurophysiol.* **30**(4), 769–93.
- Ross, B., Borgmann, C., Draganova, R., Roberts, L. E., and Pantev, C. (2000). "A high-precision magnetoencephalographic study of human auditory steady-state responses to amplitude-modulated tones," *J. Acoust. Soc. Am.* **108**(2), 679–91.
- Ross, B., Herdman, A. T., Wollbrink, A., and Pantev, C. (2004). "Auditory cortex responses to the transition from monophonic to pseudo-stereo sound," *Neurol. Clin. Neurophysiol.* **2004**, 18.
- Ross, B., Lutkenhoner, B., Pantev, C., and Hoke, M. (1999). "Frequency-specific threshold determination with the CERAGram method: Basic principle and retrospective evaluation of data," *Audiol. Neuro-Otol.* **4**(1), 12–27.
- Sarvas, J. (1987). "Basic mathematical and electromagnetic concepts of the biomagnetic inverse problem," *Phys. Med. Biol.* **32**(1), 11–22.
- Schiano, J. L., Trahiotis, C., and Bernstein, L. R. (1986). "Lateralization of low-frequency tones and narrow bands of noise," *J. Acoust. Soc. Am.* **79**(5), 1563–70.
- Schroeder, M. R. (1961). "Improved quasi-stereophony and 'colorless' artificial reverberation," *J. Acoust. Soc. Am.* **33**, 1061–1064.
- Sklare, D. A., and Denenberg, L. J. (1987). "Interaural attenuation for tube-earphone insert earphones," *Ear Hear.* **8**(5), 298–300.
- Stevens, S. S. (1936). "The localization of actual sources of sound," *Am. J. Psychol.* **48**(2), 297–306.
- Stollman, M. H., Snik, A. F., Hombergen, G. C., Nieuwenhuys, R., and ten Koppel, P. (1996). "Detection of the binaural interaction component in the auditory brainstem response," *Br. J. Audiol.* **30**(3), 227–32.
- Sturzebecher, E., and Cebulla, M. (1997). "Objective detection of auditory evoked potentials. Comparison of several statistical tests in the frequency domain on the basis of near-threshold ABR data," *Scand. Audiol.* **26**(1), 7–14.

- Tesche, C. D., Uusitalo, M. A., Ilmoniemi, R. J., Huutilainen, M., Kajola, M., and Salonen, O. (1995). "Signal-space projections of MEG data characterize both distributed and well-localized neuronal sources," *Electroencephalogr. Clin. Neurophysiol.* **95**(3), 189–200.
- Tollin, D. J., and Yin, T. C. (2005). "Interaural phase and level difference sensitivity in low-frequency neurons in the lateral superior olive," *J. Neurosci.* **25**(46), 10648–57.
- Vrba, J., and Robinson, S. E. (2001). "Signal processing in magnetoencephalography," *Methods* **25**(2), 249–71.
- Yin, T. C., and Chan, J. C. (1990). "Interaural time sensitivity in medial superior olive of cat," *J. Neurophysiol.* **64**(2), 465–88.
- Yin, T. C. T. (2002). *Neural Mechanism of Encoding Localization Cues in the Auditory Brainstem. Integrative Functions in the Mammalian Auditory Pathway*, edited by D. Oertel (Springer, New York), pp. 99–159.
- Zwislocki, J., and Feldman, R. S. (1956). "Just noticeable differences in dichotic phase," *J. Acoust. Soc. Am.* **28**(5), 860–864.

Differences in loudness of positive and negative Schroeder-phase tone complexes as a function of the fundamental frequency^{a)}

Manfred Mauermann^{b)} and Volker Hohmann

Medizinische Physik, Universität Oldenburg, D-26111 Oldenburg, Germany

(Received 14 July 2005; revised 20 November 2006; accepted 21 November 2006)

Tone complexes with positive ($m+$) and negative ($m-$) Schroeder phase show large differences in masking efficiency. This study investigated whether the different phase characteristics also affect loudness. Loudness matches between $m+$ and $m-$ complexes were measured as a function of (1) the fundamental frequency (f_0) for different frequency bands in normal-hearing and hearing-impaired subjects, and (2) intensity level in normal-hearing subjects. In normal-hearing subjects, the level of the $m+$ stimulus was up to 10 dB higher than that of the corresponding $m-$ stimulus at the point of equal loudness. The largest differences in loudness were found for levels between 20 and 60 dB SL. In hearing-impaired listeners, the difference was reduced, indicating the relevance of active cochlear mechanisms. Loudness matches of $m+$ and $m-$ stimuli to a common noise reference (experiment 3) showed differences as a function of f_0 that were in line with direct comparisons from experiment 1 and indicated additionally that the effect is mainly due to the specific internal processing of $m+$. The findings are roughly consistent with studies pertaining to masking efficiency and can probably not be explained by current loudness models, supporting the need for incorporating more realistic cochlea simulations in future loudness models. © 2007 Acoustical Society of America.

[DOI: 10.1121/1.2409772]

PACS number(s): 43.66.Cb, 43.66.Nm [AJO]

Pages: 1028–1039

I. INTRODUCTION

For a long time our understanding of auditory processing was dominated by spectral analysis, while the influence of the phase characteristics of auditory filters was neglected. More recently, the influence of temporal properties and phase characteristics of the stimuli on perception and the interaction of the phase characteristics of stimuli and auditory filters has been investigated in a number of studies. Many experiments in this field have investigated the masking effectiveness of Schroeder-phase tone complexes (Schroeder, 1970). In the current study, the influence of the phase characteristics of those tone complexes on loudness perception is investigated in some detail. Schroeder-phase tone complexes can be seen as trains of linear frequency sweeps with falling ($m+$) or rising ($m-$) instantaneous frequency with a very flat Hilbert envelope. Corresponding $m+$ and $m-$ tone complexes have the same power spectrum and the same Hilbert envelope. Their waveforms are time-reversed and inverted versions of each other. Nevertheless, they can produce differences in masking of up to 20 dB (e.g., Smith *et al.*, 1986; Kohlrausch and Sander, 1995). Typically $m+$ stimuli are less effective maskers than $m-$ tone complexes. Also, masked thresholds of short tone pulses in an $m+$ masker can differ by as much as 20 dB depending on the position of the test tone

within the masker period, while the masking by the $m-$ stimuli varies only slightly with the test tone position.

Differences in the masking produced by $m+$ and $m-$ complexes have been explained in terms of an interaction between the phase characteristics of the masking stimulus and the phase characteristics of the response at the respective place on the basilar membrane (BM), i.e., in the respective auditory filter (e.g., Kohlrausch and Sander, 1995; Oxenham and Dau, 2001).

Briefly, the negative phase curvature of the basilar membrane is thought to counteract the positive phase curvature of the $m+$ stimulus to produce a complex where all components are in phase, leading to a highly modulated, or peaky waveform. These assumptions, based on psychoacoustical data, are supported by recent physiological measurements of BM motion in chinchillas (Recio and Rhode, 2000) and guinea pigs (Summers *et al.*, 2003). In both studies the BM displacement or velocity response envelopes were peakier for $m+$ than for $m-$ tone complexes. Furthermore, Recio and Rhode (2000) found a higher energy output of the BM responses for $m-$ stimuli than for the $m+$ stimuli. This may indicate that the peakier BM responses associated with $m+$ stimuli obtain less gain from the compressive cochlear non-linearity than $m-$ stimuli. If loudness reflects the overall energy of BM vibration, the differences observed by Recio and Rhode (2000) should be reflected in loudness differences between $m+$ and $m-$ stimuli. There is some evidence that loudness is affected by the temporal properties and phase characteristics of the stimulating sounds. For instance, recent studies demonstrate that amplitude-modulated narrowband sounds are slightly softer than their unmodulated counter-

^{a)}Parts of this study were presented at the Meeting of the Deutsche Gesellschaft für Audiologie (DGA), 2005 in Göttingen, Germany, and at the 149th meeting of the Acoustical Society of America 2005 in Vancouver, Canada [J. Acoust. Soc. Am. (2005), 117(4), p. 2597(A)].

^{b)}Author to whom correspondence should be addressed. Electronic mail: manfred.mauermann@uni-oldenburg.de

parts (Grimm *et al.*, 2002). For broadband stimuli amplitude modulation at medium rates increases the loudness slightly (Zhang and Zeng, 1997; Moore *et al.*, 1999; Grimm *et al.*, 2002). The differences in loudness in these studies correspond to changes in level of about 1 dB.

Gockel *et al.* (2003) compared the loudness of broadband cosine-phase tone complexes with the loudness of random-phase tone complexes possessing the same power spectrum, as well as with the loudness of Gaussian noise that was filtered in the same way as the tone complexes. The random-phase tone complexes and the noise have a relatively flat temporal envelope, or low crest factor, while the cosine-phase tone complexes have a high crest factor and are expected to produce a highly modulated output over a wide frequency range on the BM. If BM compression were an important factor it would be predicted that the “peaky” (in the stimulus waveform as well as on the BM excitation) cosine-phase tone complexes are perceived as softer than the random-phase tone complexes or the noise. In contrast to this prediction, the cosine-phase tone complexes were perceived as being louder than both the random-phase-tone complexes and the Gaussian noise. Gockel *et al.* (2003) observed differences in loudness for a fundamental frequency (f_0) of the tone complexes of 62.5 Hz that corresponded to changes in level of approximately 7 dB. These data suggest that a large crest factor can lead to an increase in the loudness of broadband stimuli. Such results, that stimuli associated with a more peaky BM excitation are perceived as louder, is inconsistent with the findings of Carlyon and Datta (1997). Carlyon and Datta compared, qualitatively, the loudness of a subset of frequency components around 1100 Hz within tone complexes with $m-$ and $m+$. The tone complexes ranged from 200 to 2000 Hz with a fundamental frequency f_0 of 100 Hz. The subset of frequency components, whose loudness were judged, covered the frequency range between 900 and 1300 Hz. The frequency components within the $m-$ stimuli were perceived as louder than those within the $m+$ tone complexes. Thus, the results of Carlyon and Datta (1997) are in agreement with the idea that peaky BM responses associated with $m+$ stimuli obtain less gain from the compressive cochlear nonlinearity relative to the $m-$ stimuli.

In the current study we investigated the influence of the stimulus-phase curvature on loudness perception. In experiment 1 the differences in loudness between $m+$ and the corresponding $m-$ stimuli were investigated in four different frequency bands as a function of the phase curvature. The phase curvature was altered by varying the f_0 of the tone complexes. The same measurements were done in hearing-impaired subjects with loudness recruitment (Steinberg and Gardner, 1937; Fowler, 1950) to investigate the role of cochlear compression, which may affect the BM excitation produced by the Schroeder-phase tone complexes. In experiment 2 the level dependence of the level difference at the point of equal loudness (PEL) between $m+$ and $m-$ stimuli was investigated in normal-hearing subjects. Finally, in experiment 3, the loudness of all $m+$ and $m-$ stimuli with different phase curvatures were matched with the same noise as a reference stimulus in three normal-hearing subjects. The experiment was performed as an additional test of the hy-

pothesis that the differences in loudness between $m+$ and $m-$ stimuli are associated with a higher peakiness of $m+$ stimuli at certain f_0 , as is generally assumed to be a reason for the differences in masking efficiency between $m+$ and $m-$ maskers.

II. EXPERIMENT 1: LOUDNESS MATCHING OF TONE COMPLEXES WITH POSITIVE AND NEGATIVE SCHROEDER PHASE

A. Rationale

Several studies have demonstrated the relevance of phase curvature for the effectiveness of tone complex maskers (e.g., Lentz and Leek, 2001; Oxenham and Dau, 2001). In the current experiment we investigated whether loudness differences between $m+$ and $m-$ stimuli are observed for different phase curvatures in normal-hearing subjects. We also determined the absolute phase curvature for which the loudness differences are maximum. Loudness matches between $m+$ and the corresponding $m-$ stimuli were performed in four frequency bands (geometric mean frequencies 665, 1330, 2660, and 5320 Hz) with a bandwidth of 1.6 octaves. The same loudness matches were also performed in hearing-impaired subjects with loudness recruitment, to investigate the relevance of compression in more detail. In the current study f_0 was varied in order to systematically change the phase curvature of the tone complexes.

In masking experiments using a sinusoidal test tone (target), target detection is mainly determined by the auditory filter centered at the frequency of the test tone, whereas the loudness of a stimulus with a bandwidth of about 1.6 octaves, as used here, is determined by the output of several adjacent auditory filters. However, the phase curvature is thought to vary only slowly across adjacent filters.

In line with widely accepted explanations for the different masking capabilities of $m+ / m-$ stimuli (e.g., Kohlrausch and Sander, 1995; Oxenham and Dau, 2001), an $m+$ stimulus is expected to be perceived as softer than the corresponding $m-$ stimulus, if the respective f_0 is related to a phase curvature that has compensated for the phase curvature of the cochlear traveling wave. In turn, the loudness between $m+$ and $m-$ is expected to be similar if the phase curvature of the $m+$ stimulus does not compensate for the curvature in excited auditory filters.¹

A potential difference in loudness between $m+$ and $m-$ could be caused by the compressive nonlinearity of the auditory system differentially affecting the variety of peaky responses on the BM. Cochlear compression is thought to become manifest at stimulus levels of about 35 dB SPL in normal-hearing subjects, as indicated by physiological studies (for review see, e.g., Robles and Ruggero, 2001; Cooper, 2004), psychoacoustical studies (Plack and Oxenham, 1998), and otoacoustic emission measurements (Epstein and Florentine, 2005). In the current study, the loudness of the $m+$ stimuli was matched to the corresponding reference $m-$ stimulus, which was kept fixed in level. The reference levels L_r , i.e., the levels of the respective $m-$ reference stimuli, were adjusted individually to equal loudness across subjects to allow a comparison between normal-hearing and subjects

with mild-to-moderate hearing loss at a common reference. At the same loudness, a comparable BM excitation is expected across subjects if no loss of inner hair cells is assumed.

An adaptive categorical loudness scaling procedure called ACALOS (Brand and Hohmann, 2002) was used to determine the reference level for each subject and frequency band individually. As reference levels in the loudness-matching procedures, those levels were taken for which the loudness of noise-like stimuli—with identical bandwidths and windowing as the respective $m+$ / $m-$ stimuli—were scaled as “soft” (15 categorical units—cu).² In addition, the results of the loudness scaling indicate a frequency-specific loudness recruitment in the hearing-impaired subjects. A slope of the loudness growth function in the low-to-moderate level range (including the level corresponding to the loudness category soft) that is higher than typically observed in normal-hearing subjects provides a fairly good indicator of the loss of compression (Brand and Hohmann, 2002). That means that in frequency bands with an increased slope of the loudness growth function, we would expect reduced effects of active cochlear mechanisms in comparison to normal-hearing subjects.

B. Setup

A PC/MATLAB (Ver. 6.5, Math Works) controlled setup was used for the loudness matching measurements. The signals were generated digitally with a word length of 32 bits and a sampling rate of 48 kHz, and were sent through a RME Digi96/8 PAD digital I/O card to a RME ADI8 Pro 24 bit DA converter. After amplification (Tucker Davies Technologies headphone buffer HB7), the signals were presented monaurally via Sennheiser HD580 headphones. The output levels of the headphones were calibrated for each frequency band investigated in the study using an artificial ear (Type 4152, Bruel and Kjaer). Since the HD580 shows a sufficiently flat frequency response (on the artificial ear) within each of the frequency bands, no frequency specific correction was performed. The same hardware setup was used for the categorical loudness scaling which was performed with the Oldenburg measurement software OMA (HörTech).

C. Subjects

The measurements were carried out in the left ears of eight subjects with normal-hearing (6 male, 2 female). Seven subjects had thresholds in quiet of 15 dB HL or better at all audiometric frequencies (125–8 kHz), and one subject (MM) had a slightly increased hearing threshold of 25 dB HL at 8 kHz but no recruitment detected in the loudness scaling. The subjects ranged in age from 22 to 41 years. In addition, three hearing-impaired subjects, between 52 and 72 years of age participated in the study. All had a hearing loss of at least 25 dB at all audiometric frequencies, at least one frequency with a hearing loss of 50 dB or more and a clear indication of recruitment as quantified by categorical loudness scaling in at least one of the investigated frequency bands.

Most of the normal-hearing subjects had previous experience in loudness matching and scaling measurements. All

hearing-impaired subjects had taken part in previous psychoacoustical studies and had at least basic experience in loudness scaling procedures.

D. Stimuli

All tone complexes used for loudness matching were generated digitally as the sum of equal-amplitude sinusoids with a common fundamental frequency f_0 . The starting phase θ_n of each frequency component was computed according to Eq. (1), either with positive ($C=1$) or negative ($C=-1$) Schroeder phase (Schroeder, 1970; see also Lentz and Leek, 2001; Oxenham and Dau, 2001),

$$\theta_n = C\pi \frac{n(n-1)}{N}, \quad C = \pm 1, \quad (1)$$

where N is the total number of frequency components, n is the index, and θ_n is the starting phase of the n th frequency component of the tone complex. The phase curvature of the tone complex is given by the second derivative with respect to the frequency of Eq. (1) (see also Lentz and Leek, 2001; Oxenham and Dau, 2001)

$$\frac{d^2\theta}{df^2} = C \frac{2\pi}{Nf_0^2}. \quad (2)$$

The stimuli were generated for four different frequency bands with the geometric mean frequencies at 665, 1330, 2660, and 5320 Hz, respectively, and a bandwidth of about 1.6 octaves [i.e., about the same bandwidth that Oxenham and Dau (2001) used for their maskers]. The exact parameters of the stimuli are listed in Table I. With increasing mean frequency the f_0 was varied from 2 up to 192, 384, 768, or 1536 Hz, respectively. The phase curvature for a fixed frequency range is nearly doubled when halving the fundamental frequency, since the number of frequency components is nearly doubled as well.

For the categorical loudness scaling procedure, low-noise noise (LNN) with the same spectral bandwidth as the tone complexes was used.³ Each stimulus had a total duration of 500 ms including 5 ms Hanning-shaped ramps.

E. Procedures

Loudness matching between the $m+$ and $m-$ stimuli was performed using a two-alternative forced-choice paradigm. The measurements for each frequency band were performed in blocks of seven to ten interleaved tracks (e.g., Verhey and Kollmeier, 2002) with different f_0 . The number of tracks in each block increased with the geometric mean frequency of the respective frequency band (see Table I), since in the higher frequency bands an increasing number of different f_0 s were measured. The order of the tracks with different f_0 was randomized in each block as well as the order of test and reference stimulus in each trial. The $m-$ stimulus was always used as a reference signal. The reference and test stimuli (or vice versa) were presented in consecutive intervals separated by an interstimulus interval of 500 ms. Each presentation interval was marked visually on the computer screen. The subject had to decide which of the two stimulus intervals was louder. The reference stimuli were held fixed in level while

TABLE I. Properties of the Schroeder-phase tone complexes. Frequency range and geometric mean frequency in Hz, fundamental frequency f_0 , number of frequency components N , phase curvature in rad/Hz^2 , and dimensionless or normalized curvature related to the respective geometric mean frequency.

Bandwidth geometric mean (Hz)	f_0 (Hz)	N	Phase curvature (rad/Hz^2)	Normalized phase curvature
384-1152 665	192	5	$3.41E-05$	2.40
	96	9	$7.58E-05$	5.33
	48	17	$1.60E-04$	11.29
	24	33	$3.31E-04$	23.27
	12	65	$6.71E-04$	47.26
	6	129	$1.35E-03$	95.26
1536-4608 2660	2	385	$4.08E-03$	287.25
	768	5	$2.13E-06$	2.40
	384	9	$4.73E-06$	5.33
	192	17	$1.00E-05$	11.29
	96	33	$2.07E-05$	23.27
	48	65	$4.20E-05$	47.26
768-2304 1330	24	129	$8.46E-05$	95.26
	12	257	$1.70E-04$	191.25
	6	513	$3.40E-04$	383.25
	2	1537	$1.02E-03$	1151.25
	384	5	$8.52E-06$	2.40
	192	9	$1.89E-05$	5.33
3072-9216 5320	96	17	$4.01E-05$	11.29
	48	33	$8.26E-05$	23.27
	24	65	$1.68E-04$	47.26
	12	129	$3.38E-04$	95.26
	6	257	$6.79E-04$	191.25
	2	769	$2.04E-03$	575.25
3072-9216 5320	1536	5	$5.33E-07$	2.40
	768	9	$1.18E-06$	5.33
	384	17	$2.51E-06$	11.29
	192	33	$5.16E-06$	23.27
	96	65	$1.05E-05$	47.26
	48	129	$2.11E-05$	95.26
	24	257	$4.24E-05$	191.25
	12	513	$8.51E-05$	383.25
	6	1025	$1.70E-04$	767.25
	2	3073	$5.11E-04$	2303.25

the test stimuli followed an adaptive 1-up, 1-down procedure. The measurements for each $m+/m-$ pair with the same f_0 started with level steps of 6 dB, which were decreased to 4, 2, and finally 1 dB steps at each upper reversal. The median of the final eight reversals (with constant level changes of 1 dB) of the overall 15–16 reversals was taken as the preliminary estimate of equal loudness. Within one session, each block was repeated three times with different starting levels (L_r and $L_r \pm 8$ dB, respectively) of the test stimuli. The mean of the resulting three median values was taken as the final estimate for the level of equal loudness. The duration of each measurement block was about 10–20 min. Thus, the duration of a complete session for a single frequency band was about 60–75 min, including breaks. Each subject performed at least one training block before the regular measurements. A session was discarded if the results led to an average standard deviation of 1.2 dB or higher for the re-

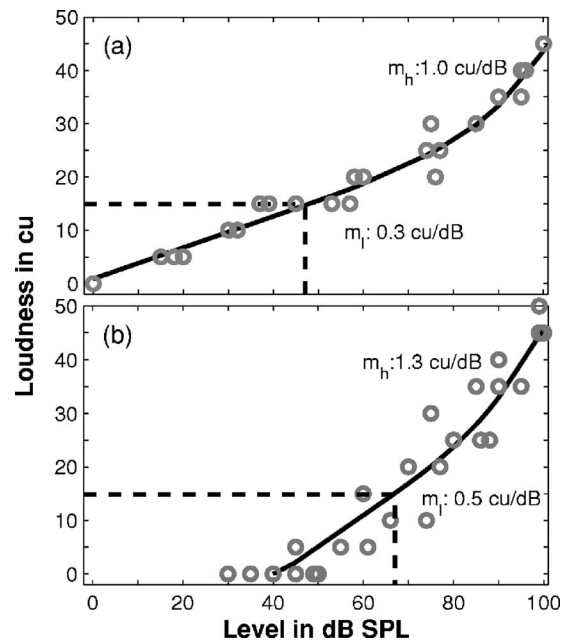


FIG. 1. Categorical loudness scaling—examples for typical results from the categorical loudness scaling, (a) from a normal-hearing subject (subject KW, at the 665 Hz frequency band) and (b) from a hearing-impaired subject (subject SK, at the 665 Hz frequency band). The gray circles indicate the individual loudness judgments given by the subjects during the adaptive procedure. The data points are fitted by the solid black line. The fit consists of two linear parts with independent slope values m_l and m_h and a transition region smoothed by a Bezier fit. The slopes are indicated in the plots in categorical units (cu) per dB. The m_l values are given in Table II as an indicator of loudness recruitment for all subjects. The reference level for the loudness matches was derived individually from the loudness scaling data as the level which corresponds to 15 cu indicated by the dotted black line.

peated measurement points. In all these cases the subjects reported lacking concentration during the measurement. The data from one normal-hearing subject (MMW) were excluded from further analysis because he failed the 1.2 dB standard deviation criterion for three of the four frequency bands and there was no time to repeat the sessions within the project’s time scope.

The categorical loudness scaling was performed by each subject using an interleaved procedure (Brand and Hohmann, 2002) for the four frequency bands investigated in the current study.⁴ The subjects judged the loudness of the presented stimulus on a scale of 11 categories from “inaudible” (0 cu) to “too loud” (50 cu) after hearing the stimulus. The loudness scaling data were fitted by a model function (see Fig. 1 for an example), which consists of two linear parts with independent slope values m_l (low to moderate level range) and m_h (high level range) and a transition region smoothed by a Bezier fit (for details see Brand and Hohmann, 2002; Brand, 2000). The slope m_h , which is typically increased in hearing-impaired subjects in comparison to the slope found in normal-hearing subjects, is used as an indicator for a loss of compression in the auditory system [compare Figs. 1(a) and 1(b) for a comparison of typical results from a normal-hearing and a hearing-impaired subject]. The levels L_r that correspond to the loudness category soft (15 cu) in the fitted model function were used as individual reference levels of the $m-$ tone complex in the loudness matching measurements (see the dotted lines in Fig. 1).

TABLE II. Individual reference levels L_r (in dB SPL) for loudness matches and slopes m_l (in cu/dB) as recruitment indicator. Boldface subject labels indicate the subjects shown in Fig. 2. *Italic* subject labels indicate hearing-impaired subjects.

Frequency	Subject																					
	DB		FJ		MM		KW		RD		MG		MMW		RP		<i>FL</i>		<i>MR</i>		<i>SK</i>	
	L_r	m_l	L_r	m_l	L_r	m_l	L_r	m_l	L_r	m_l	L_r	m_l	L_r	m_l	L_r	m_l	L_r	m_l	L_r	m_l	L_r	m_l
665	53	0.3	38	0.3	52	0.3	48	0.3	46	0.3	54	0.4	52	0.2	53	0.3	65	0.5	67	0.6	60	0.5
1330	50	0.3	37	0.3	48	0.3	47	0.3	45	0.3	56	0.3	48	0.3	50	0.3	69	0.5	71	0.6	61	0.3
2660	50	0.3	38	0.3	51	0.3	40	0.3	49	0.3	55	0.3	51	0.2	51	0.3	70	0.6	65	0.6	67	0.4
5320	60	0.4	47	0.3	59	0.3	49	0.3	57	0.3	60	0.3	59	0.3	55	0.2	76	0.6	65	0.4	81	0.5

F. Results and discussion

Table II shows the relevant results from categorical loudness scaling for all subjects in each tested frequency band. The reference levels L_r (derived as the presentation level producing a loudness of 15 cu) varies over a range of 37–60 dB SPL in the normal-hearing subjects and between 60 and 81 dB SPL in the hearing-impaired subjects. This corresponds to about a 9 dB lower level within 1/3 octave—as an approximation for the effective level within one auditory filter. In all normal-hearing subjects we see a slope m_l of 0.3 cu/dB or lower with two exceptions. The subjects DB and MG show a slope of 0.4 cu/dB at 5320 and 665 Hz, respectively. The three hearing-impaired subjects typically show a slope of 0.5 cu/dB or higher except for the subject MR at 5320 Hz (0.4 cu/dB) and the subject SK at 1330 and 2660 Hz (0.4 and 0.3 cu/dB, respectively). We would expect some remaining auditory compression for these hearing-impaired subjects in the frequency bands with these “normal” slopes while for the other subjects and frequency bands it can be assumed that effects of active cochlear mechanisms are clearly reduced.

Figures 2 (individual data) and 3 (averaged data) show the results of loudness matches associated with $m+$ / $m-$ signals as a function of f_0 and frequency bands (665, 1320, 2640, and 5320 Hz, respectively) for seven normal-hearing subjects. Positive level differences indicate that the level of

the $m+$ stimulus was higher than the level of the reference stimulus $m-$ at the PEL. The observed level differences between the $m+$ and $m-$ tone complexes at the PEL show a characteristic hump as a function of f_0 in all of the normal-hearing subjects. This result means that the level of the $m+$ tone complexes for these f_0 s had to be adjusted to higher levels than the $m-$ stimuli to be perceived as equally loud, i.e., the $m+$ stimuli were perceived as softer at the same overall rms level. The maximum level differences between $m+$ and $m-$ are about 4 dB in the frequency band around 665 Hz and about 5–6 dB in the three higher frequency bands (see Fig. 2). In individual cases the level differences can be as much as 10 dB. A one-way analysis of variance (ANOVA) was calculated separately for each frequency band with the factor f_0 for the seven normal-hearing subjects included in the analysis. The ANOVA indicates that the loudness differences are not identical for all f_0 s, i.e., there is an effect of f_0 ($p < 0.01$). The data points in Fig. 3 that are marked with circles are significantly different ($p < 0.05$) from the data point that is closest to 0 dB level difference (indicated by a post hoc LSD test). The data points in Fig. 3 marked with closed circles show a significant difference ($p < 0.05$) from the data point with the maximum level difference at the PEL. The open circles indicate those level differ-

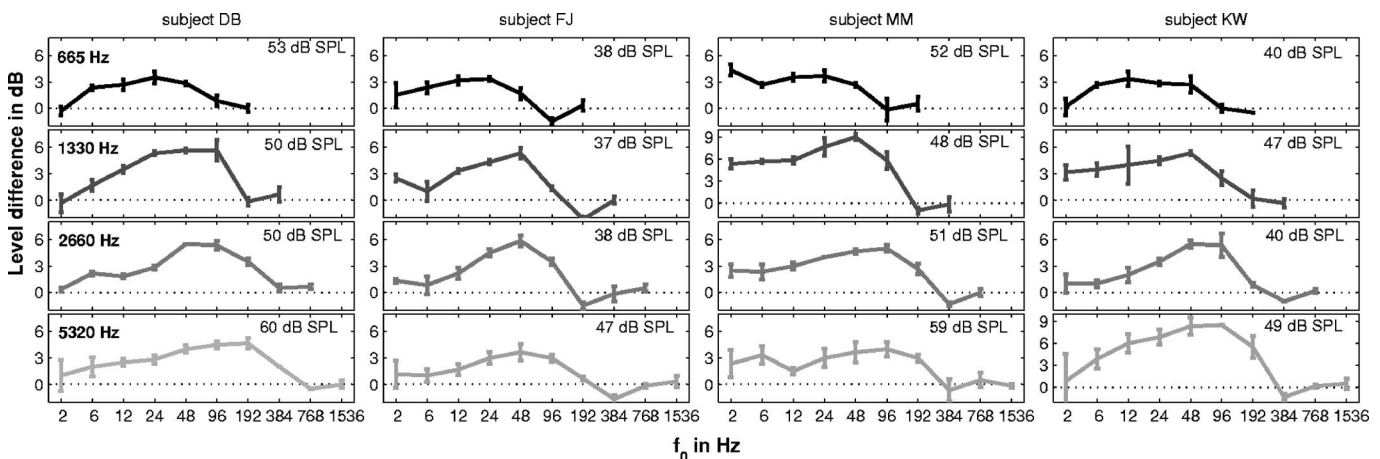


FIG. 2. Experiment 1—individual data of four normal-hearing subjects. The panels in the first to fourth rows show the results from loudness matching of $m+$ / $m-$ stimuli in different frequency bands (the respective center frequencies of each row are indicated in the upper left corner of each panel in the first column). Positive differences indicate that the level of the test stimulus ($m+$) was higher than the level of the reference stimulus ($m-$) at the PEL. The individually determined reference levels of the $m-$ stimuli are given in the upper right corners of the panels (see also Table II). The error bars give the standard deviation of three repetitions of the measurements with different start levels of the test stimuli. Note the different scaling of the ordinate for subject MM (third column) at 1330 Hz and KW (fourth column) at 5320 Hz.

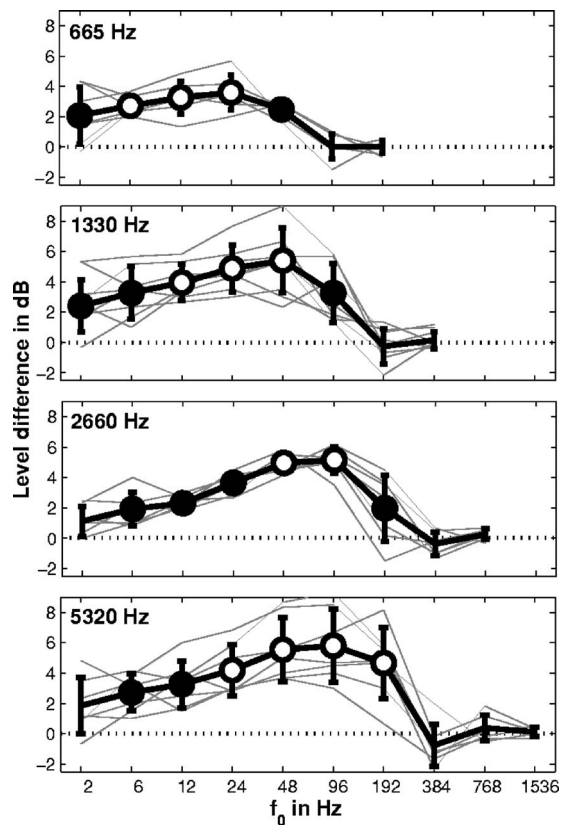


FIG. 3. Experiment 1—averaged data from seven normal-hearing subjects. The thin grey lines show the results of individual loudness matches between $m+$ / $m-$ from seven normal-hearing subjects for different frequency bands (panels from top to bottom for the center frequencies 665, 1320, 2640, and 5320 Hz, respectively). The black line gives the mean data and the error bars the standard deviation of the loudness matching data. Positive differences indicate that the level of the $m+$ stimulus was higher than the level of the reference stimulus $m-$ at the PEL. The data points marked with circles are statistically different ($p < 0.05$) from the data point that is closest to 0 dB level difference. The data points marked with closed circles are significantly different ($p < 0.05$) from the data point with the maximum level difference at the PEL. The open circles indicate those level differences that cannot be distinguished from the data point with the maximum level difference.

ences that cannot be distinguished from the maximum level difference. The level differences decrease at higher and lower f_0 s.⁵

The maximum level difference for the averaged data (see Fig. 3) was found for a fundamental frequency f_0 of 24 Hz in the 665 Hz band and shifts to higher f_0 (48, 96, and 96 Hz) for the higher frequency ranges (1330, 2660, and 5320 Hz). The f_0 of the individual level-difference maximum in each frequency band varies across subjects. Therefore, the mean over the f_0 s corresponding to the maxima from the individual curves may provide a better indicator for the shift of the level-difference maxima than the f_0 s obtained from the maxima of the averaged curves. The computation of the mean of the f_0 s indicates that the level-difference maximum of the 665 Hz frequency band is at an f_0 of 26 Hz, and for the frequency bands around 1330, 2660, and 5320 Hz at a f_0 of 50, 75, and 110 Hz, respectively.⁶ The estimated phase curvatures for these f_0 s vary between -3.31×10^{-4} rad/Hz² for the filters in the frequency band around 665 Hz ($f_0=26$ Hz) and -9.3×10^{-6} rad/Hz² for the frequency band around 5320 Hz ($f_0=110$ Hz). Oxenham and

Dau compared data from different studies by comparing the dimensionless phase curvature as suggested by Shera (2001). The dimensionless phase curvature is defined as the phase curvature originally in units of rad/Hz² multiplied by $f_s^2/2\pi$ (Shera, 2001), where f_s is the stimulus frequency. Since there is no specific stimulus frequency available in the current loudness experiment we used the geometric mean frequencies of the tone complexes as a coarse guess for the “stimulus frequencies” f_s . In a scaling invariant cochlea the dimensionless phase curvature is expected to be constant. Oxenham and Dau found dimensionless phase curvatures of the auditory filters changing from about -20 at 8 kHz to -8 at 1 kHz. They found a steeper slope of change toward lower stimulus frequencies (up to -4 at 500 Hz and close to 0 at 125 Hz). Other authors found comparable estimates for the dimensionless phase curvature. Kohlrausch and Sander (1995) found values between -4.5 and -6.3 at 1100 Hz. Estimates of dimensionless curvature obtained from the findings by Lentz and Leek (2001) are in the range of -7 and -12 at 2000 Hz or between -16 and -26 at 4000 Hz, respectively. The dimensionless phase curvatures estimated from the loudness data obtained in the current study changes from about -42 at 5320 Hz, to -31 , -23 , and -22 at 2660, 1330, and 665 Hz, respectively. Above 1 kHz these values differ by a factor of 2 to 3 from the estimates obtained by masking experiments in previous studies. The dimensionless phase curvature estimated from the loudness matching data for the frequency band around 665 Hz is -22 , i.e., it does not show the distinct increase found in the estimates from masking experiments. Furthermore, in comparison to the findings of Oxenham and Dau (2001) at 500 Hz (estimate of dimensionless phase curvature: -4), the dimensionless phase curvature found here differs by more than a factor of 5. Oxenham and Dau (2001) assumed a factor of 2 to give the bounds of measurement uncertainty in the masking experiments. Furthermore, the parameter f_s is not exactly known for the broadband stimuli used in the current loudness experiments. Thus, the magnitude of the curvature values found here for frequencies above 1 kHz can be seen as being roughly in the same order of magnitude as the findings reported from masking experiments. This finding may support the idea of common underlying mechanisms for differences in masking efficiency and loudness of corresponding $m+$ and $m-$ complexes, whereas the mismatch of the estimated phase curvatures for lower frequencies (here: 665 Hz) may indicate that different mechanisms are responsible for the differences in loudness and masking efficiency of corresponding Schroeder-phase tone complexes. However, the tone complex in the 665 Hz spectral region includes frequencies above 1 kHz (384–1152 Hz) and the weighting of auditory filters contributing to the differences in loudness is unclear. Future studies, including measurements at lower frequencies, may help to clarify if the observed effect is related to the differentially weighted contribution of auditory filters.

Another important aspect that might be relevant for the current findings is that the measurements of loudness differences at PEL between $m+$ and $m-$ tone complexes are influenced by the occurrence of resolved harmonics, at least for tone complexes with higher f_0 s. As the number of spectrally

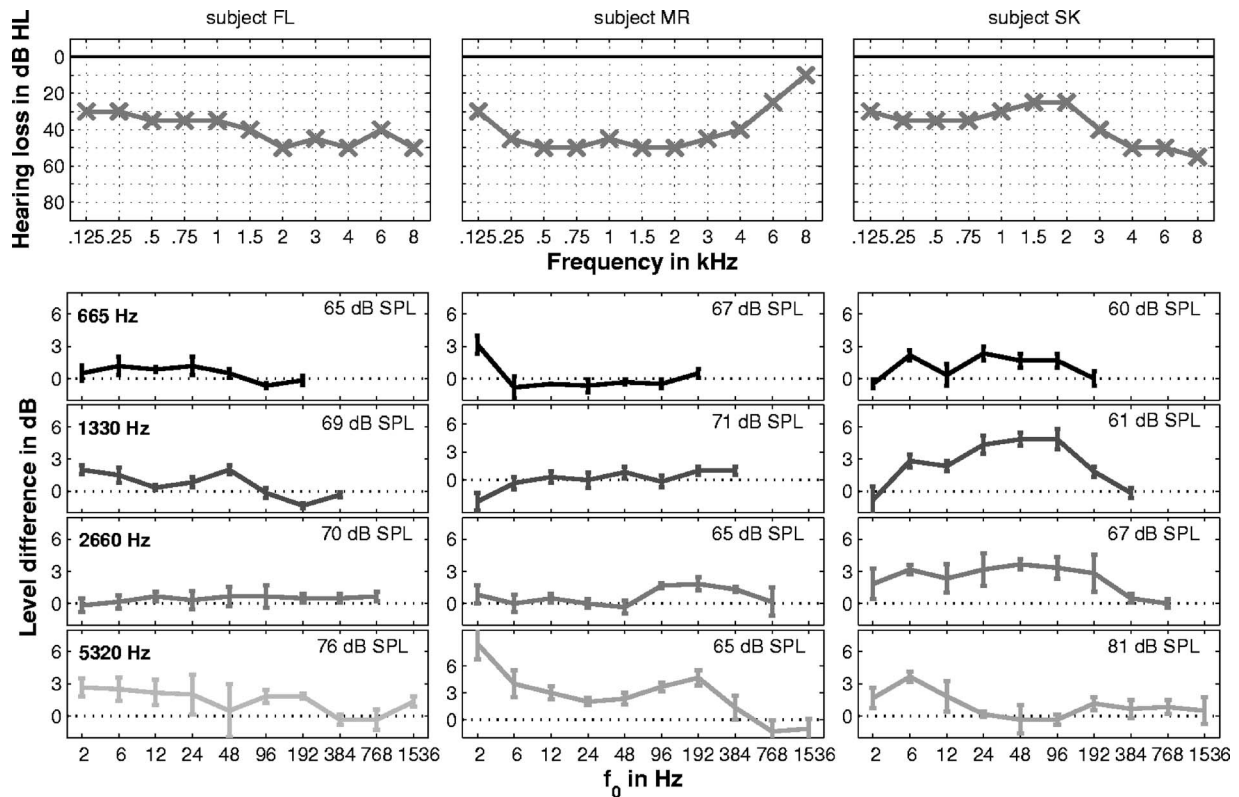


FIG. 4. Experiment 1—results from $m+/m-$ loudness matching in hearing-impaired subjects—individual data of three subjects. The first row shows the pure tone audiograms. The second to fifth rows show results from loudness matching of $m+/m-$ stimuli in different frequency bands (from top to bottom at the center frequencies 665, 1330, 2660, and 5320, respectively). Positive differences indicate that the level of the $m+$ stimulus was higher than the level of the reference stimulus $m-$ at the PEL.

resolved frequency components of the tone complex increases, the phase relation of the frequency components in the tone complex becomes less and less likely to have an effect on loudness because there is insufficient interaction between adjacent frequency components within the auditory filters. This would mean that either no or only reduced loudness differences between corresponding Schroeder phase tone complexes would occur. Most studies suggest that the first five to eight harmonics can be resolved (Plomp, 1964; Plomp and Mimpen, 1968; Moore and Ohgushi, 1993), but recent results suggest that harmonics up to the tenth may be aurally resolved under certain conditions (Bernstein and Oxenham, 2003). Under this assumption, the tone complexes around 665 Hz (384–1152 Hz) would contain at least some resolved harmonics for f_0 of 48 Hz and for higher f_0 s (96 and 192 Hz). Higher f_0 s are related to lower phase curvatures of the stimuli. If the differences in loudness between $m+$ and $m+$ tone complexes at higher f_0 s are reduced due to resolved harmonics this would mean that the prediction of phase curvature from the current loudness measurements would only mark the upper limit of the absolute values of phase curvature of the auditory filters. Hence, the “true” phase curvature might be closer to zero than predicted from the maxima in loudness differences of corresponding $m+$ and $m-$ in the current experiment. The influence of resolved harmonics would mostly affect the loudness differences for the 665 Hz tone complexes with higher f_0 s. These are the tone complexes for which the largest discrepancy occurs between the phase-curvature predictions from the current data and

masking data from the literature. Therefore, the differences in loudness of $m+$ and $m-$ might be based on the different internal peakiness of the stimuli. However, the loudness effects are possibly reduced at higher f_0 s because of the presence of resolved harmonics. In future studies similar measurements as done in the current study but using stimuli with variable c value to change the curvature [compare Eq. (1)]—instead of varying f_0 —could help to clarify if resolved harmonics have an influence on the results in the current experiment.

The loudness differences in the 665 Hz band are slightly less than those associated with the other three frequency bands. This observation might be related to the effect that the phase curvature in the auditory filters in this frequency range is changing more rapidly with frequency. The presence of resolved harmonics is another potential factor.

The relevance of active cochlear mechanisms for the loudness differences becomes obvious from the loudness matching data from the three hearing-impaired subjects (Fig. 4). The loudness differences between $m+$ and $m-$ are drastically reduced in frequency ranges where the thresholds in quiet are above 40 dB HL, and the results from categorical loudness scaling clearly indicate recruitment ($m_l \geq 0.5$, see Table II). In these regions the active nonlinear mechanisms in the cochlea are clearly reduced. In less impaired frequency regions (see, e.g., subject MR at 5320 Hz, and SK at 1330 and 2660 Hz in Fig. 4; compare m_l values in Table II) level differences between $m+$ and $m-$ are still observed. The observations associated with the hearing-impaired subjects are

in good agreement with the findings of Summers and Leek (1998) and Oxenham and Dau (2004). Both studies found a clearly reduced difference in masking of $m+$ / $m-$ stimuli or tone complexes with different c values [see Eq. (2)], respectively, in hearing-impaired subjects, which was interpreted as an effect of reduced active gain resulting from cochlear damage.

III. EXPERIMENT 2: EFFECTS OF REFERENCE LEVEL

A. Rationale

The individual reference levels in experiment 1 varied between 37 and 60 dB SPL for the 1.6 octave bandwidth signals. At these sound pressure levels there was approximately 6 dB difference between the $m+$ and $m-$ stimuli required to achieve the sensation of equal loudness among normal-hearing listeners. It is reasonable to assume that there is a level dependency of the observed effect resulting from the nonlinear input/output characteristic of cochlear processing and a decrease of the difference in BM excitation for $m+$ and $m-$ stimuli with increasing intensity (Summers *et al.*, 2003). The equal-loudness intensity-level difference (for the 2660 Hz frequency band) was investigated as a function of the reference level (5–80 dB SPL) in order to investigate the relationship between the $m+$ / $m-$ stimulus loudness differences and such factors as cochlear compression, changes in phase characteristics with level and psychophysical masking.

B. Subjects, setup, procedures, and stimuli

Four of the normal-hearing subjects from experiment 1 (DB, MG, JF, RP) and an additional normal-hearing subject (BS) participated in this experiment. Loudness matches were measured between $m+$ and $m-$ in the frequency band around 2660 Hz for a fixed f_0 of 48 Hz. The same setup and interleaved procedure was used as in experiment 1. Instead of sets of interleaved tracks with variable f_0 , seven tracks with different reference levels (5, 10, 20, 40, 60, 70, and 80 dB SL) were measured. The individual threshold in quiet for the $m-$ reference stimulus was measured using a self-adjusting procedure as described in detail by Mauermann *et al.* (2004). In this procedure the subject can switch the stimulus on and off via a play button and adjust the level via a slider on the computer screen using the mouse or a touch screen. The slider jumps immediately back to the starting position when unclipping it to avoid anchor effects. The subjects were instructed to adjust the signal level so that the stimulus is just audible. This level was used as a preliminary estimate of threshold in quiet. The mean of three repetitions was used as the final estimate of the threshold in quiet for the $m-$ stimulus.

The loudness matches between $m+$ and $m-$ stimuli were measured with the tone complexes around 2660 Hz and with a f_0 of 48 Hz, because these parameters provided a high level difference at the PEL for all subjects in experiment 1 and relatively low intra- and interindividual variability of the data.

C. Results and discussion

The loudness matching data and individual thresholds in quiet are illustrated in Fig. 5. The thresholds vary between

2.5 and 6.5 dB SPL. Loudness matches for all five subjects show a clear dependence on reference level. The maximum level differences of $m+$ and $m-$ at the PEL were determined for reference levels of the $m-$ stimulus at about 40 dB SL for most subjects. The maximum level differences were in the range of 4–9 dB. A clear decrease in the level differences was observed for the lower (5–10 dB SL) and higher reference levels (70–80 dB SL). Four out of five subjects exhibited a level difference at 20 dB SL (roughly around 25 dB SPL for the entire stimulus, i.e., about 16 dB SPL 1/3 octave band level), which was nearly as large as the maximum level difference observed. The fifth subject showed a clearly decreased level difference at 20 dB SL. If the differences in internal excitation of $m+$ and $m-$ are nearly level independent, and if the patterns are differentially affected by compression, then the loudness differences associated with the PEL suggest that a reasonable amount of compression occurs down to levels of about 16 dB SPL. Some physiological (animal) studies indicate BM compression down to 25 dB SPL (see, e.g., Cooper, 2004); however, compression at levels as low as 16 dB SPL would appear to contradict these physiological findings and psychoacoustical studies in humans. Thus, compression most probably cannot account for the differences between $m+$ and $m-$ found at reference levels of 20 dB SL. The conclusion that compression is not an important factor in accounting for the current results is also supported by the fact that there is no increase in level difference for levels above 40 dB SPL, where compression is common. Moreover, there is almost complete reduction of the level difference at levels as low as 80 dB SL. The reduction in level differences around 70–80 dB SL might be affected by the phase-sensitive elicitation of the acoustic reflex (Kubli *et al.*, 2005; Müller-Wehlau *et al.*, 2005). A consistent explanation of the current findings can be given by the idea of level-dependent cochlear excitation characteristics that become more similar for $m+$ and $m-$ with increasing level, i.e., the different temporal properties in the local auditory filters themselves cause differences in loudness rather than assuming that different peaky internal waveforms of the stimuli are differentially affected by the compressive cochlear nonlinearity: In guinea pigs, Summers *et al.* (2003) found that differences in BM excitation associated with $m+$ and $m-$ signals decreased steadily with increasing intensity above 75 dB SPL (see Fig. 4 in their study). The levels in the study by Summers were always computed relative to an octave range between 10 and 20 kHz, i.e., the effective levels in 1/3 octave range around the characteristic frequency of the cochlear site investigated is almost 8 dB lower than the nominal level. Such reductions in peakiness, and in peakiness differences, reflect changes in both the magnitude and phase response of BM filtering as a function of sound pressure level. A reduced curvature in the BM phase response at high intensities would tend to make responses to $m+$ and $m-$ stimuli more similar (see Summers *et al.*, 2003, p. 303). Increasingly similar internal patterns of the $m+$ and $m-$ stimuli with increasing level should result in the loudness of the two stimuli being judged as more similar. Given that the respective phase changes are probably associated with reduced active gain at high levels and that active gain is also

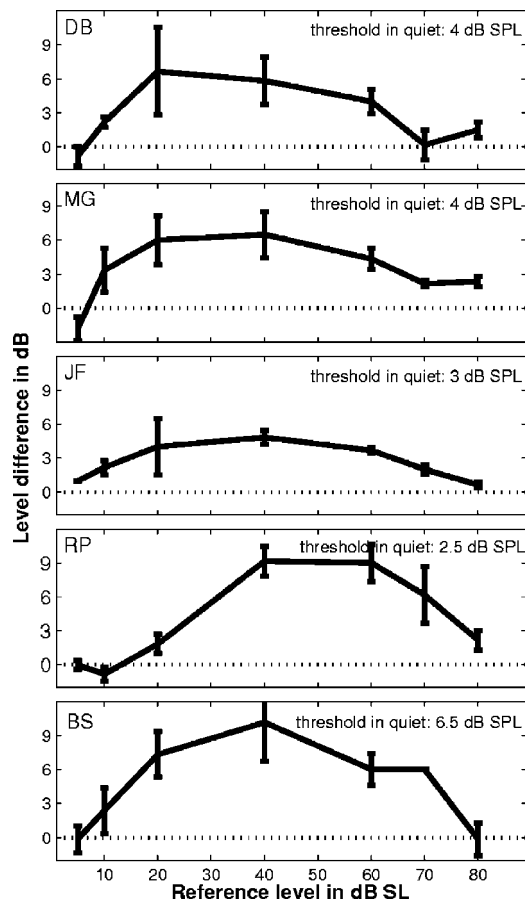


FIG. 5. Experiment 2—individual data from five subjects. The data show the level differences at the points of equal loudness between the $m+$ and the respective $m-$ stimuli for several fixed reference levels in the range from 5 to 80 dB SL. The individual thresholds in quiet for the reference $m-$ stimulus are given in the upper right corners of the panels. The data points give the mean and the error bars the standard deviation of the results from three measurement blocks.

reduced for hearing-impaired listeners, the BM phase curvature would presumably be reduced as a result of hearing loss, as found in experiment 1.

It should be noted that the reduction of loudness differences at higher levels is in contrast with the findings on level effects in the masking experiments mentioned earlier. These showed the largest masking-efficiency differences for stimulus levels at and above 60 dB SPL.

The reduction in differences of the level at PEL at the lowest levels tested here (5, 10 dB SL) might reflect a reduced filter bandwidth at these very low levels or the reduced audibility of some of the components in the tone complexes. Both effects would lead to reduced interaction of components within an auditory filter that would result in reducing the phase-related effects which are observed at higher levels.

IV. EXPERIMENT 3: LOUDNESS MATCHING OF A FIXED REFERENCE STIMULUS AND SCHROEDER-PHASE TONE COMPLEXES WITH DIFFERENT f_0

A. Rationale

In experiments 1 and 2, an $m+$ stimulus was adjusted in level so that it was as loud as the corresponding $m-$ signal

possessing the same envelope and f_0 . This paradigm has the advantage that most of the stimulus properties affecting loudness are the same for test and reference signals except for the phase curvature. In this closed experimental design it is possible to measure the impact of the phase curvature on loudness. However, the $m+/m-$ PEL differences do not indicate whether the observed f_0 -related differences are the result of a relative decrease in loudness of the $m+$ stimulus or to an increase in loudness of the $m-$ stimulus or both. Loudness matching of the $m+$ and the $m-$ stimuli across f_0 s with a single reference stimulus may provide additional insight into the mechanisms underlying the observed differences.

Assuming there is an “optimal” f_0 capable of creating the most peaky internal response of the respective $m+$ stimuli, and that this optimum peaky response results in reduced loudness, we would expect there to be a relative decrease in loudness of the $m+$ signal and no relative change in loudness of the $m-$ stimulus at the optimal f_0 (compared to the nonoptimal f_0 s). In other words, loudness matches with a fixed reference stimulus would be expected to show a decrease in loudness (i.e., an increased level at the PEL) for $m+$ at those f_0 s corresponding to the largest level differences found in experiment 1. No effect of f_0 would be expected for the $m-$ stimuli matched with the same reference.

When matching $m+$ and $m-$ stimuli with one and the same reference stimulus the phase effects on loudness might be superimposed by loudness changes due to other stimulus properties changing with f_0 (e.g., a result of an increasing number of resolved harmonics). However, such effects are likely to exhibit similar trends for both $m+$ and $m-$ stimuli. If these potential effects are continuous across f_0 and not too strong compared to the phase effects, sudden changes in loudness observed in the expected f_0 region would be expected to reflect the effect of stimulus phase on loudness.

B. Subjects, stimuli, and procedure

Three of the normal-hearing subjects from experiment 1 also participated in this experiment (JF, MM, and KW). Loudness matching was performed between $m+$ tone complexes with variable f_0 and a noise-like reference stimulus, as well as between $m-$ tone complexes at varying f_0 s and the same reference stimulus. $m+$ and $m-$ stimuli centered around 2660 Hz (the same as used in experiment 1) were used. The LNN stimulus from the loudness scaling procedure was used as the reference signal. This stimulus had the same bandwidth and center frequency as the Schroeder-phase tone complexes. The same loudness-matching procedure was used as described in experiment 1. The reference level was individually selected as the level judged as soft in the categorical loudness scaling (i.e., 38, 51, 40 dB SPL) for subjects JF, MM, and KW, respectively.

C. Results and discussion

Figure 6 shows the results for all three subjects. The first row shows loudness matches between $m+$ and LNN, and the second row illustrates the matches between $m-$ and LNN. For one of the subjects (MM), the level differences at the PEL (which depend on f_0) show a characteristic hump in the

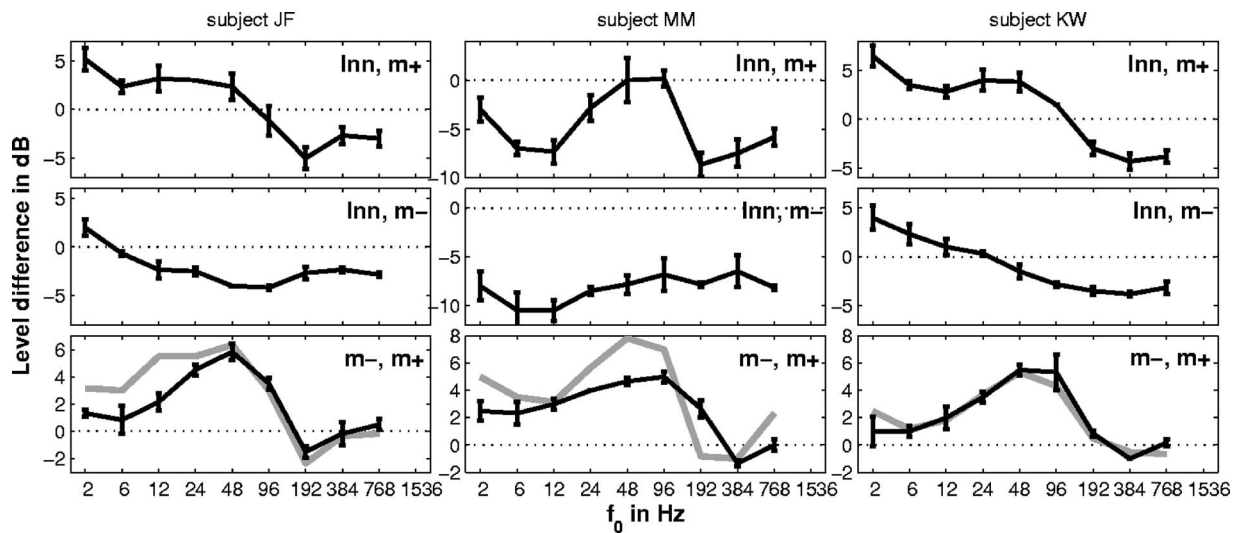


FIG. 6. Experiment 3—results from loudness matches between $m+$ /LNN and $m-$ /LNN stimuli. The first row shows the results from adjusting the level of an $m+$ complex so that it was equally loud as a LNN of the same bandwidth and the same center frequency of 2660 Hz for three normal-hearing subjects. The fundamental frequency (f_0) of the tone complexes was varied in the range from 2 to 768 Hz. The second row shows the results from adjusting an $m-$ complex to be equally loud as the LNN. The reference levels of the LNN were individually fixed at 38, 51, and 40 dB SPL for the subjects JF, MM, and KW, respectively. The third row gives the differences in level at the PEL that would be expected for loudness matches of $m+$ / $m-$ stimuli obtained by subtracting the results of the $m-$ /LNN matching from the results of the $m+$ /LNN matching (see the gray line). The black lines in the panels show the results of the direct loudness matching between $m+$ and $m-$ stimuli. These were obtained from the same subjects in experiment 1. Positive differences indicate that the level of the $m+$ or $m-$ stimulus was higher than the level of the reference stimulus (LNN) at the PEL.

data associated with loudness matches between $m+$ and LNN (Fig. 6, first row, second column). In contrast, there is no clear hump or dip in the loudness matches between the $m-$ and LNN stimuli (Fig. 6, second row, second column). The data of subjects JF and KW show an overall trend for the $m-$ /LNN matching (see Fig. 6, second row, first and last column) of a continuous decrease in level differences with increasing f_0 up to 192 Hz. A relatively constant (or even slightly increasing) difference is observed for higher f_0 s. The level differences obtained from the $m+$ /LNN loudness matching exhibit a similar trend to the differences from the $m-$ /LNN matching. However, a discontinuity toward higher level differences arises in the $m+$ /LNN data for f_0 s between 12 and 96 Hz.

The f_0 s of the hump in the $m+$ /LNN matching data from subject MM and the specific discontinuities in the two other subjects correspond closely to the f_0 s of the hump observed in the direct comparison of $m+$ and $m-$ in experiment 1. These findings indicate that the typical hump in the loudness differences between $m+$ and $m-$ (as found in experiment 1) is predominantly caused by a decrease of loudness of the $m+$ for “optimized” f_0 rather than an increase of loudness of the corresponding $m-$ stimuli. Overall the idea is supported that the loudness of $m+$ stimuli is clearly decreased for f_0 s or phase curvatures that result in a highly modulated internal response in the auditory filters.

The gray lines in the last row of Fig. 6 illustrate the differences between the loudness matching data of $m+$ /LNN (Fig. 6, first row) and of $m-$ /LNN (Fig. 6, second row); these data reflect the indirectly measured level differences of $m+$ and $m-$ at the PEL. For comparison, the black lines in the same row show the results from the direct loudness matching between $m+$ and $m-$ from experiment 1. If the loudness matching associated with the $m+$ /LNN and

$m-$ /LNN signals is affected in the same way by parameters other than phase, the difference between the curves (i.e., the indirect measurement of the $m+$ / $m-$ level difference at the PEL) should be the same as the direct measurement from experiment 1. The comparison of the gray and black lines in Fig. 6 (last row) shows a good agreement of both curves for each subject. This indicates (1) that potential additional effects (such as roughness, annoyance, and pitch), which possibly influence the subject’s judgments, affected the $m+$ /LNN and $m-$ /LNN measurements in the same way, and (2) that the subject’s loudness judgments across the different measurements are consistent.

Except for low f_0 s up to 24 Hz, the sound pressure level of the $m-$ stimuli at PEL is about 5 dB lower than the SPL of the LNN reference, which indicates that $m-$ stimuli appear to be louder than LNN. The same holds for $m+$ stimuli, except for optimized f_0 s that lead to a reduction in loudness of the respective $m+$ stimuli. This finding might reflect the influence of pitch strength on the subjects’ loudness judgments. As pointed out by Gockel *et al.* (2003), “...the existence of a strong residue pitch might increase the loudness of a sound relative to one with the same power spectrum but a weak or absent pitch.” The pitch strength of corresponding $m+$ and $m-$ signals should be similar and is likely greater than the pitch strength of the LNN. Furthermore, the lack of an $m+$ / $m-$ effect at high f_0 s (192 Hz and higher) might be explained by the occurrence of at least some resolved harmonics. Because resolved harmonics produce a stronger sensation of pitch, the fact that the $m+$ / $m-$ complexes were always judged louder than the LNN for high f_0 s suggests that subjects find it hard to separate loudness from pitch strength.

The current findings for the $m-$ /LNN matching are in good agreement with the findings by Gockel *et al.* (2003) for the loudness matching of cosine phase tone complexes with

either noise or random phase tone complexes. However, the current findings for the loudness matches of $m+$ /LNN deviate from this agreement at optimized f_0 s. Gockel *et al.* (2003) used tone complexes with f_0 s of 62.5 and 250 Hz and zero phase curvature (cosine phase). Since the phase curvature of the cosine phase complexes are always in between the phase curvature of corresponding $m+$ and $m-$ stimuli we would assume that the cosine phase complexes used by Gockel *et al.* (2003) do not match the optimal parameters associated with a maximum peakiness in the local auditory filters. Thus, the loudness effects observed by Gockel *et al.* (2003) presumably reflect a loudness increase related to pitch strength rather than a loudness decrease related to maximum peakiness in the local auditory filters. Both effects can separately be identified in the data of the current experiment.

V. SUMMARY AND CONCLUSIONS

A tone complex with Schroeder positive ($m+$) phase is the temporally inverted version of the corresponding tone complex with Schroeder negative phase ($m-$). Both have the same power spectrum and the same temporal envelope, but for a given frequency range and at certain f_0 s they show level differences of up to 10 dB at the PEL in normal-hearing subjects (experiment 1).

A clear reduction of the loudness differences between corresponding $m+$ and $m-$ stimuli in hearing-impaired subjects with recruitment suggests that active cochlear mechanisms are important for the phase effects associated with loudness perception (experiment 1).

The dimensionless phase curvature of the $m+$ stimuli resulting in the maximum level difference at PEL is a factor of about 2 to 3 greater (for the 665 Hz band the factor is even 5) than the phase curvature of $m+$ stimuli least effective in masking. Although these findings show only a rough correspondence, a common underlying mechanism for masking and loudness experiments (i.e., differentially peaky internal responses of $m+$ and $m-$ stimuli) cannot be ruled out since the phase curvature estimation from the data in experiment 1 might be affected by resolved harmonics in the tone complexes with high f_0 s.

The observed differences in level at the PEL are most likely related to differences in the temporal modulation of the internal patterns themselves in combination with a temporal loudness integration process rather than reflecting a different compression of the variably modulated internal patterns. This conclusion is consistent with the large level differences at PEL at low reference levels of 20 dB SL (corresponding roughly to about 16 dB SPL in a single auditory filter), where compression is unlikely to occur. It is consistent with the clear reduction of differences at levels of 70–80 dB SL, which are still in the compressive range of the auditory periphery (experiment 2).

The results from the loudness matches in experiment 3 of $m+$ and $m-$ tone complexes with the same noise-like reference stimulus (LNN) indicate that the loudness differences associated with the $m+$ and $m-$ signals at moderate reference levels are mainly due to a decrease in loudness of the $m+$ stimuli at certain f_0 s, rather than a relative change in loudness of the $m-$ stimuli.

Data from experiment 3 also suggest that cues other than loudness alone, such as pitch strength, might influence the loudness matching results. These cues may be superimposed on the loudness effects related to differences in the peakiness of the internal response to the different stimuli.

An interesting aspect of the current results is the fact that no loudness model, as far as we know, has the potential to explain the level differences at equal loudness between $m+$ and $m-$ described in this study. Most loudness models are based on the power spectrum of the stimulus (e.g., Fletcher and Munson, 1933; Zwicker and Scharf, 1965; Moore, 1997). These models predict well for steady sounds while failing to predict loudness for fluctuating stimuli such as amplitude-modulated sounds. Some models take the peak values of the stimuli into account to explain the effects of slow modulations on loudness. However, the stimuli compared here have the same temporal envelope and the same long term spectrum. Even short-time spectra down to a time scale of about 10 ms provide no clear distinction of the stimuli for f_0 s related to the largest level differences at the PEL. Even a more recent loudness model applicable to time-varying sound suggested by Glasberg and Moore (2002) most probably will fail to explain the differences in loudness of stimuli with different phase curvature like $m+$ and $m-$ stimuli because of a phase-insensitive filter bank used as input stage. The results of the current study support the suggestion by Glasberg and Moore (2002) that a more realistic cochlea model at the input stage is needed in future loudness models to explain the influence of stimulus phase characteristics on loudness perception.

ACKNOWLEDGMENTS

This study was supported by Deutsche Forschungsgemeinschaft, DFG Ho 1697/2-3 and DFG SFB TR31. We want to thank Stefan Uppenkamp and Jesko Verhey for helpful comments on an earlier version of the manuscript. We thank Monica Wagner for proofreading earlier versions of the manuscript and Steven Greenberg for proofreading and giving helpful suggestions to improve the clarity and conciseness of the final manuscript. We gratefully acknowledge Van Summers and an anonymous reviewer as well as the Associate Editor Andrew Oxenham for their valuable comments on the manuscript.

¹The loudness measurements should not be seen as a tool to estimate the phase curvature precisely. Rather the method is likely to be even less precise than measurements of masked thresholds. First, loudness matches show a higher variability than measurements of masked thresholds. Second, the loudness perception of the stimuli used here is thought to be affected by the output of multiple auditory filters, whereas the masked threshold of a sinusoid is essentially determined by a single filter. The contribution of the different filters to the overall loudness perception might be differentially weighted. Thus, the “stimulus frequency” f_s —that is well defined for sinusoidal targets—is essentially arbitrary in the case of loudness matches of stimuli with broader bandwidth. This means that for the loudness-matching experiments the phase curvature of a given phase complex is not necessarily related to the geometric mean frequency used in this study to parameterize the tone complexes (leading to variability in phase curvature estimates associated with the current loudness measurements).

²Normal-hearing subjects typically select the category soft for stimulus levels roughly in the range between 40 and 60 dB SPL. Pilot tests indicated that reference levels around 50 dB SPL for the loudness matches of the

corresponding Schroeder-phase tone complexes result in reasonable level differences at the PEL and are sufficiently comfortable, even for longer measurement duration. Furthermore, this level range should be clearly affected by cochlear compression. For subjects with moderate hearing loss the loudness category soft is typically related to levels at which remaining effects of cochlear compression might still be observable.

³For the loudness scaling one-time iterated low-noise noise (Pumplin, 1985; Kohlrausch *et al.*, 1997) was used to obtain a sufficient dynamic range for digital attenuation. This is the type of stimuli typically used with the ACALOS procedure. LNN computed with only a single iteration sounds still very noise-like. The advantage is that the crest factor is reduced, typically, by about 6 dB in comparison to the initial Gaussian noise (the one time iterated LNN shows a rms value in the range of about -7 to -8 dB re full scale). The RME-ADI8 Pro 24 bit DA converters provide a usable dynamic range of about 110 dB. Using LNN stimuli the given hardware thus provides a dynamical range of about 100 dB with purely digital attenuation and without the need of any programmable attenuators. A dynamic range of nearly 100 dB is sufficient for a reliable measurement of categorical loudness. A low-noise noise is generated by (1) generating a Gaussian noise, (2) restricting the bandwidth by setting the magnitude of the Fourier coefficients to zero outside the desired passband, (3) dividing the time signal by its Hilbert envelope, and (4) restricting the bandwidth of the resulting signal as described in (2). Steps (2) and (3) will be repeated according to the number of iterations minus one.

⁴The levels were limited to a maximum of 100 dB SPL.

⁵While in the average data the level differences at higher f_0 s clearly decrease toward zero, there remains a difference on the order of 2 dB for an f_0 of 2 Hz. Although a clear decrease of the level difference down to zero is observed for f_0 equal to 2 Hz in some subjects (e.g., DB), other subjects show an increase of loudness differences for f_0 s between 6 and 2 Hz (e.g., FJ at 1230 Hz, MM and MG at 665 Hz). This effect can be observed as well in the hearing-impaired subject MR. All subjects reported that the matching of loudness became more difficult when the stimuli could be easily identified as up and down chirps because the clearly perceived differences in pitch change provided an additional cue to differentiate between the two matched stimuli. At low f_0 s it is easy to identify the up and down chirps. Thus, a bias toward judging the tone complexes with decreasing instantaneous frequency ($m+$) as softer than the tone complexes with increasing instantaneous frequency ($m-$) might be responsible for the loudness differences observed at the lower f_0 s.

⁶In three individual curves the absolute maximum of level difference was found at 2 Hz (see Footnote 5). In these cases it is reasonable to take the maximum out of the f_0 s above 2 Hz for the computation of the mean f_0 corresponding to the maximum level difference of the respective frequency band.

Bernstein, J. G., and Oxenham, A. J. (2003). "Pitch discrimination of diotic and dichotic complexes: Harmonic resolvability or harmonic number?," *J. Acoust. Soc. Am.* **113**, 3323–3324.

Brand, T. (2000). "Analysis and optimization of psychoacoustical procedures in audiology," Ph.D. thesis, BIS, University of Oldenburg, Germany.

Brand, T., and Hohmann, V. (2002). "An adaptive procedure for categorical loudness scaling," *J. Acoust. Soc. Am.* **112**, 1597–1604.

Carlyon, R. P., and Datta, A. J. (1997). "Excitation produced by Schroeder-phase complexes: Evidence for fast-acting compression in the auditory system," *J. Acoust. Soc. Am.* **101**, 3636–3647.

Cooper, N. P. (2004). "Compression in the peripheral auditory system," in *Compression—from Cochlea to Cochlear Implants*, Springer Handbook of auditory Research, edited by S. P. Bacon, R. R. Fay, and A. N. Popper (Springer, New York).

Epstein, M., and Florentine, M. (2005). "Inferring basilar-membrane motion from tone-burst otoacoustic emissions and psychoacoustic measurements," *J. Acoust. Soc. Am.* **117**, 263–274.

Fletcher, H., and Munson, W. A. (1933). "Loudness, its definition, measurement and calculation," *J. Acoust. Soc. Am.* **5**, 82–108.

Fowler, E. P. (1950). "The recruitment of loudness phenomenon," *Laryngoscope* **60**, 680–695.

Glasberg, B. R., and Moore, B. C. J. (2002). "A model of loudness applicable to time-varying sounds," *J. Audio Eng. Soc.* **50**, 331–342.

Gockel, H., Moore, B. C., Patterson, R. D., and Meddis, R. (2003). "Louder

sounds can produce less forward masking: Effects of component phase in complex tones," *J. Acoust. Soc. Am.* **114**, 978–990.

Grimm, G., Hohmann, V., and Verhey, J. L. (2002). "Loudness of fluctuating sounds," *Acta. Acust. Acust.* **88**, 359–368.

Kohlrausch, A., and Sander, A. (1995). "Phase effects in masking related to dispersion in the inner ear. II. Masking period patterns of short targets," *J. Acoust. Soc. Am.* **97**, 1817–1829.

Kohlrausch, A., Fassel, R., van der Heijden, M., Kortekaas, R., van de Par, S., Oxenham, A., and Pschel, D. (1997). "Detection of tones in low-noise noise: Further evidence for the role of envelope fluctuations," *Acust. Acta Acust.* **83**, 659–669.

Kubli, L. R., Leek, M. R., and Dreisbach, L. E. (2005). "Acoustic reflexes to Schroeder-phase harmonic complexes in normal-hearing and hearing-impaired individuals," *Hear. Res.* **202**, 1–12.

Lentz, J. J., and Leek, M. R. (2001). "Psychophysical estimates of cochlear phase response: Masking by harmonic complexes," *J. Assoc. Res. Otolaryngol.* **2**, 408–422.

Mauermann, M., Long, G. R., and Kollmeier, B. (2004). "Fine structure of hearing threshold and loudness perception," *J. Acoust. Soc. Am.* **116**, 1066–1080.

Moore, B. C. J., Vickers, D. A., Baer, T., and Launer, S. (1999). "Factors affecting the loudness of modulated sounds," *J. Acoust. Soc. Am.* **105**, 2757–2772.

Moore, B. C. J. (1997). *An Introduction to the Psychology of Hearing*, 4th ed. (Academic, San Diego).

Moore, B. C. J., and Ohgushi, K. (1993). "Audibility of partials in inharmonic complex tones," *J. Acoust. Soc. Am.* **93**, 452–461.

Müller-Wehlau, M., Mauermann, M., Dau, T., and Kollmeier, B. (2005). "The effects of neural synchronization and peripheral compression on the acoustic-reflex threshold," *J. Acoust. Soc. Am.* **117**, 3016–3027.

Oxenham, A. J., and Dau, T. (2001). "Towards a measure of auditory-filter phase response," *J. Acoust. Soc. Am.* **110**, 3169–3178.

Oxenham, A. J., and Dau, T. (2004). "Masker phase effects in normal-hearing and hearing-impaired listeners: Evidence for peripheral compression at low signal frequencies," *J. Acoust. Soc. Am.* **116**, 2248–2257.

Plack, C. J., and Oxenham, A. J. (1998). "Basilar-membrane nonlinearity and the growth of forward masking," *J. Acoust. Soc. Am.* **103**, 1598–1608.

Plomp, R. (1964). "The ear as a frequency analyzer," *J. Acoust. Soc. Am.* **36**, 1628–1636.

Plomp, R., and Mimpen, A. M. (1968). "The ear as a frequency analyzer II," *J. Acoust. Soc. Am.* **43**, 764–767.

Pumplin, J. (1985). "Low-noise noise," *J. Acoust. Soc. Am.* **78**, 100–104.

Recio, A., and Rhode, W. S. (2000). "Basilar membrane responses to broadband stimuli," *J. Acoust. Soc. Am.* **108**, 2281–2298.

Robles, L., and Ruggero, M. A. (2001). "Mechanics of the mammalian cochlea," *Physiol. Rev.* **81**, 1305–1352.

Schroeder, M. R. (1970). "Synthesis of low peak-factor signals and binary sequences with low autocorrelation," *IEEE Trans. Inf. Theory* **16**, 85–89.

Shera, C. A. (2001). "Frequency glides in click responses of the basilar membrane and auditory nerve: Their scaling behavior and origin in traveling-wave dispersion," *J. Acoust. Soc. Am.* **109**, 2023–2034.

Smith, B. K., Sieben, U. K., Kohlrausch, A., and Schroeder, M. R. (1986). "Phase effects in masking related to dispersion in the inner ear," *J. Acoust. Soc. Am.* **80**, 1631–1637.

Steinberg, J. C., and Gardner, M. B. (1937). "The dependency of hearing impairment on sound intensity," *J. Acoust. Soc. Am.* **9**, 11–23.

Summers, V., de Boer, E., and Nuttall, A. L. (2003). "Basilar-membrane responses to multicomponent (Schroeder-phase) signals: Understanding intensity effects," *J. Acoust. Soc. Am.* **114**, 294–306.

Summers, V., and Leek, M. R. (1998). "Masking of tones and speech by Schroeder-phase harmonic complexes in normally hearing and hearing-impaired listeners," *Hear. Res.* **118**, 139–150.

Verhey, J. L., and Kollmeier, B. (2002). "Spectral loudness summation as a function of duration," *J. Acoust. Soc. Am.* **111**, 1349–1358.

Zhang, C., and Zeng, F. G. (1997). "Loudness of dynamic stimuli in acoustic and electric hearing," *J. Acoust. Soc. Am.* **102**, 2925–2934.

Zwicker, E., and Scharf, B. (1965). "A model of loudness summation," *Psychol. Rev.* **72**, 3–26.

Variability and uncertainty in masking by competing speech

Richard L. Freyman,^{a)} Karen S. Helfer, and Uma Balakrishnan

Department of Communication Disorders, University of Massachusetts, Amherst, Massachusetts 01003

(Received 2 May 2006; revised 3 October 2006; accepted 28 November 2006)

This study investigated the role of uncertainty in masking of speech by interfering speech. Target stimuli were nonsense sentences recorded by a female talker. Masking sentences were recorded from ten female talkers and combined into pairs. Listeners' recognition performance was measured with both target and masker presented from a front loudspeaker (nonspatial condition) or with a masker presented from two loudspeakers, with the right leading the front by 4 ms (spatial condition). In Experiment 1, the sentences were presented in blocks in which the masking talkers, spatial configuration, and signal-to-noise (S-N) ratio were fixed. Listeners' recognition performance varied widely among the masking talkers in the nonspatial condition, much less so in the spatial condition. This result was attributed to variation in effectiveness of informational masking in the nonspatial condition. The second experiment increased uncertainty by randomizing masking talkers and S-N ratios across trials in some conditions, and reduced uncertainty by presenting the same token of masker across trials in other conditions. These variations in masker uncertainty had relatively small effects on speech recognition. © 2007 Acoustical Society of America.

[DOI: 10.1121/1.2427117]

PACS number(s): 43.66.Dc, 43.66.Pn, 43.66.Qp, 43.71.Es [GDK]

Pages: 1040–1046

I. INTRODUCTION

There is accumulating evidence in the literature that when speech is presented in a competing speech environment, masking processes can exist beyond those normally attributable to traditional “energetic” masking. Carhart *et al.* (1969) called these additional processes “perceptual masking.” More recently the term “informational masking” has been used, in part because patterns in the data share several features with the classic informational masking studies conducted with nonspeech stimuli (e.g., Watson *et al.*, 1976; Leek *et al.*, 1991; Kidd *et al.*, 1994). Similar to nonspeech informational masking, significant interference between competing and target speech can occur even when their spectra have minimal overlap (e.g., Arbogast *et al.*, 2002, 2005; Gallun *et al.*, 2005). Also, substantial spatial release from masking has been demonstrated in competing speech situations where simulated or actual reflections minimize the advantages that can be realized from binaural interaction and head shadow cues (e.g., Freyman *et al.* 1999, 2001; Kidd *et al.*, 2005a; Brungart *et al.*, 2005; Rakerd *et al.*, 2006). The same spatial configurations do not produce sizable advantages when the masker is continuous or modulated noise. Presumably, perceptual spatial differences distinguish target from masker in specific competing speech situations, which helps to overcome the nonenergetic components of the masking. These spatial perceptual distinctions are not useful or necessary with noise maskers.

Two principles, similarity and uncertainty, are generally considered to be closely associated with informational masking (e.g., Kidd *et al.*, 2002; Durlach *et al.*, 2003a, 2003b; Watson, 2005). When applied to speech recognition in com-

peting speech situations, similarity appears to be an important prerequisite if substantial nonenergetic masking is to be observed. For example, masking by a single interfering talker appears to be most effective if the interfering talker is the same sex as the target talker. While some of this effect may be due to differences in energetic masking resulting from the degree of spectral overlap, the effect of matching the sex of target and masking talkers can be so large that perceptual similarity between target and masker is almost certainly an important factor (Brungart *et al.*, 2001). The role of uncertainty in masked speech recognition is less well understood. In general, the more one knows about the *target* ahead of time, the better performance will be (Kidd *et al.*, 2005b). However, the role of *masker* uncertainty is not as clear. A reasonable intuition is that reducing uncertainty of the masker would reduce informational masking, in that listeners could quickly learn to ignore maskers that they were certain about ahead of time and focus their attention on the target. However, with the Coordinate Response Measure corpus, Brungart and Simpson (2004) found surprisingly little effect of manipulations of masker uncertainty. They speculated that some of their conclusions may have been specific to the particular stimulus set and task, which was a color and number identification format with limited choices for both masker and target. One purpose of the present investigation was to study the role of masker uncertainty with a more difficult open-set speech recognition paradigm in which the speech of two masking talkers was presented simultaneously with the target.

The task for the listener was to repeat a sentence that was presented together with a mixture of competing sentences spoken by two masking talkers. Over the course of two experiments the uncertainty of the masker was manipulated by blocking the trials in several different ways. Maskers ranged from a most certain condition in which the

^{a)}Author to whom correspondence should be addressed. Electronic mail: rlf@comdis.umass.edu

subject received a fixed masking token from trial to trial, to a most uncertain condition in which the masking talkers, masking tokens, and signal-to-noise (S-N) ratio varied from trial to trial. The effect of these manipulations on informational masking was examined by comparing speech recognition performance in a nonspatial condition to a condition in which the precedence effect was employed to shift the spatial image of the masker away from the target. We assume that in the nonspatial condition both energetic and informational masking can limit subjects' speech recognition when the masker and target are from same-sex talkers. The purpose of the precedence effect manipulation is to create different spatial perceptions for target and masker without affecting energetic masking. However, informational masking is presumed to be largely released because these spatial differences cause the target and masker to be less confusable.

II. EXPERIMENT 1. VARIABILITY AMONG MASKING TALKERS

In order to examine the effect of uncertainty in the masker, it was necessary to create different maskers and know their individual and collective masking efficiency under conditions of fixed uncertainty. Only then would we be able to attribute changes in performance to changes in uncertainty in later experiments. For this purpose, five different masking signals, each of which was comprised of two talkers, were generated. Intelligibility of the target talker was examined for each of the five maskers as a function of S-N ratio for two different spatial conditions.

A. Method

1. Stimuli

The target stimuli were a set of 320 "nonsense sentences" that were syntactically but not semantically correct, e.g., "The moon could play your love." Each sentence included three key words, as underlined in the example. These sentences, recorded by a female talker, have been used in several earlier studies (Helfer, 1997; Freyman *et al.*, 1999, 2001, 2004, 2005; Li *et al.*, 2004). A full description of the recording methodology can be found in Helfer (1997) or Freyman *et al.* (1999). The maskers were nonsense sentences recorded by ten different female talkers. The sentences recorded were different across masking talkers and also different from the target sentences. The recordings were made in a sound-treated room, sampled at 20 000 Hz, and stored on a computer disk. Although the talkers monitored their vocal output via a VU meter in order to maintain a consistent level, no adjustments were made to equate rms amplitude across sentences. Using waveform editing software, pauses between sentences were removed to create approximately 35-s-long continuous streams of sentences. The streams were matched in rms amplitude and combined digitally to make five waveforms, each of which was comprised of a mixture of two voices. The initial sentences from each of the two talkers began simultaneously but because of different sentence lengths, speaking rates, etc., the rest of the sentences from the two talkers were not aligned. One two-talker masker (sstk) was used in previous studies (e.g., Freyman *et al.*,

TABLE I. Average fundamental frequencies (in Hz) for the target talker and each of ten masking talkers. Masking talkers are grouped to reflect the pairing used to make the two-talker maskers for the experiment. Values were averaged over 30 vowel segments over the duration of each masker.

Target	Maskers									
	sstk		ajhb		eash		cclm		jskc	
JF	SS	TK	AJ	HB	EA	SH	CC	LM	JS	KC
189	188	202	240	242	175	176	195	199	207	214

2001), so those two masking talkers were kept together as a pair. The selections of the other pairings were made roughly according to similarity in fundamental frequency. The average fundamental frequency of each masking talker was determined from the Fast Fourier Transforms of 30 vowels spread through the 35 s stream of sentences. Table I displays the average fundamental frequency of the target along with the average fundamental frequencies of the masking talkers.

2. Environment and apparatus

The experiment was conducted in a large double-walled sound-treated room (IAC No. 1604) measuring 2.76 × 2.55 m. Reverberation times measured in this room ranged from 0.12 s at 6.3 and 8.0 kHz to 0.24 s at 125 Hz (Nerbonne *et al.*, 1983). A previous study conducted in this room (Helfer and Freyman, 2005) showed the same kinds of spatial release that have been found in an anechoic chamber (e.g., Freyman *et al.*, 2001). The listener sat on a chair placed with its back against one wall of the room. Two loudspeakers (Realistic Minimus 7), at a distance of 1.3 m from the center of the head when seated in the chair and a height of 1.2 m (the approximate height of the ears of a typical listener) delivered the target and masking stimuli. One loudspeaker was placed at 0° azimuth, directly in front of the listener; the second loudspeaker was at 60° to the right. The target and masking stimuli were mixed digitally at the appropriate S-N ratio on a computer before presentation from two channels of the computer's sound card, attenuated (TDT PA4), amplified (TDT HBUF5), power amplified (TOA P75D), and delivered to the loudspeakers. In the F-F condition, target and masker were presented from the front loudspeaker. In the F-RF condition, the target was presented from the front loudspeaker and the masker from both loudspeakers, with the right leading the front by 4 ms. The F-RF masking configuration creates the perception (due to the precedence effect) that the masker is to the right, well separated from the front target. The 4 ms delay version of this F-RF configuration was shown by Freyman *et al.* (1999), by Brungart *et al.* (2005), and by Rakerd *et al.* (2006) to create little or no release from masking for speech targets in the presence of noise maskers, indicating no energetic masking release. Further, Helfer and Freyman (2005) demonstrated no energetic masking release for this configuration in the same sound-treated room used for the current studies. It is assumed, therefore, that when masking release occurs for the F-RF configuration in a competing speech task, the release from masking is due to non-

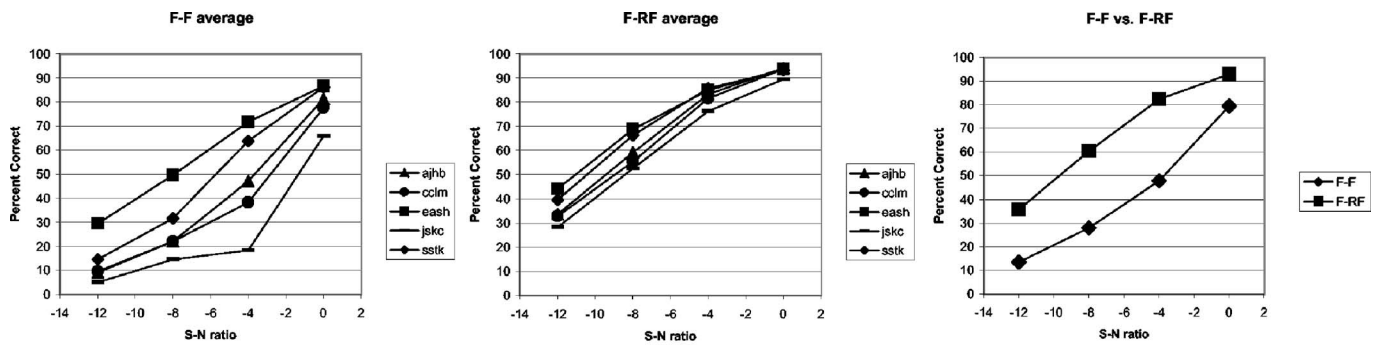


FIG. 1. Percent correct recognition of key words as a function of S-N ratio for five two-talker maskers. The left panel shows data for the F-F configuration, the middle panel for the F-RF condition. The right panel shows FF and F-RF data combined across all five maskers.

energetic effects, where perceptual spatial differences make it easier to extract the target from the complex mixture of voices.

3. Procedures

Subjects were seated in a chair and instructed to face the front loudspeaker but were not physically restrained. At the beginning of each trial the word “Ready” appeared on a computer screen in front of the subject. The presentation of the masker was then initiated, followed by the presentation of the target 0.6–1.2 s later. At the conclusion of the target sentence, the masker was terminated simultaneously. The listener repeated the target sentence out loud, and the experimenter, monitoring in a control room, scored the three key words as correct or incorrect.

On each trial a section of a particular two-talker masker waveform was selected randomly from the 35 s stream. The masker onset could occur anywhere in the stream, e.g., at the beginning of a sentence for one of the two talkers, in the middle for the other talker, etc. As noted above, the target sentence began slightly after the beginning of the masker. Subjects were told that they could use this delay as a cue for directing attention to the target speech in the presence of the masker. They were also presented with five (nontarget) sentences spoken by the target talker in quiet before testing began to help familiarize them with her voice.

A total of 40 conditions were presented to each of ten young normal-hearing listeners (audiometric thresholds ≤ 20 dB HL at 500 through 4000 Hz). There were five different two-talker maskers, two spatial configurations (F-F and F-RF), and four S-N ratios (–12, –8, –4, and 0 dB) in a completely crossed design. The S-N ratios were defined as target rms amplitude relative to the rms amplitude of the two-talker masking complex. S-N ratios were manipulated by changing the level of the masker for a fixed level target, which was always presented at 44 dBA (calibrated using a speech-spectrum noise with the same rms as the target sentences). The 320 target sentences were selected at random, without replacement, and with a different random order for each listener. The conditions were divided into 40 blocks of eight sentences each. The S-N ratio, masker, and spatial configuration were all fixed within a block. Across sets of four blocks (32 trials), only the S-N ratio changed (randomly), while the spatial configuration and masker were fixed. A sec-

ond set of four blocks followed where the spatial configuration switched from F-F to F-RF or vice versa. After eight blocks were presented (64 trials), the masker changed and the process was repeated until all five maskers had been presented for 64 trials. The spatial configuration simply alternated after every 32 trials (four blocks). Half the subjects received F-F first and the other half F-RF first. The order of presentation of the five masking talkers within a set of 320 trials was random and different for each listener. Subjects completed the experiment in one listening session.

B. Results and Discussion

The average results across listeners are plotted in Fig. 1; the individual masker data are shown for the F-F configuration in the left panel and for the F-RF configuration in the middle panel. Each line represents the results for a different two-talker masker. Each data point was based on 240 scored key words (ten listeners \times 8 sentences \times 3 key words per sentence). For the F-F condition, the five two-talker combinations varied widely in their masking effectiveness. The largest differences occurred at –4 dB S-N ratio, where listener performance ranged from less than 20% correct for the most effective masker to more than 70% correct for the least effective masker. As shown in the middle panel, the variability was far less with the F-RF configuration, although the ordering of effectiveness across maskers was similar. The right panel of Fig. 1 displays the data averaged over five maskers (1200 scored key words per data point) for the spatial (F-RF) and nonspatial (F-F) conditions. A clear advantage for the spatial condition is seen. The effect is about 5 dB at a performance level of 50% correct.

Our interpretation of differences in variability seen in the left and middle panels is linked to the working hypothesis that masking in the F-F condition includes both energetic and nonenergetic (“informational” or “perceptual”) factors, whereas the F-RF condition involves mostly energetic masking. The latter hypothesis arises from the fact that differences in the spatial percepts of target and masker create dissimilarity between them and reduce confusability. Because similarity is an important factor in informational masking (Durlach *et al.*, 2003b) the interference produced by the masker in the F-RF condition is likely to reflect primarily traditional energetic masking. Hence, we assume that the limited variability in the F-RF data reflects variability mostly

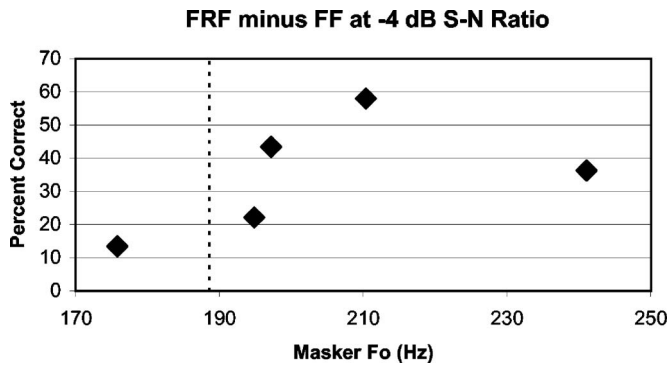


FIG. 2. F-RF vs F-F difference in percent correct at the -4 dB S-N ratio as a function of the mean Fo of the two talkers in each masker. The mean Fo of the target talker is shown by the vertical dashed line.

in energetic masking. While this small variability in energetic masking may also contribute to the spread of the F-F data in the left panel, most of the variability for the F-F configuration is likely due to nonenergetic factors. At the moment it is not possible to determine the degree to which these five selected maskers are representative of the larger population. However, there is a strong suggestion that variability in nonenergetic masking among different masking talkers of the same sex can be quite large.

It will be difficult to determine what factors influenced this variability, which as shown in Fig. 1, occurred mostly in the F-F condition. If this indeed reflects variability in nonenergetic aspects of the masking, i.e., in the perceptual extraction of the target voice from the mixture of three voices, then a logical place to look is at the average fundamental frequency, as there was a fairly wide variation across masking talkers (see Table I). Several previous studies have shown that fundamental frequency is an important factor in attending to the speech of one talker in the presence of another (e.g., Brox and Nooteboom, 1982; Bird and Darwin, 1998; Darwin *et al.*, 2003). One might expect that when the fundamental frequencies of target and masker are close, perceptual extraction of the target would be most difficult in nonspatial conditions and would show the largest release from masking when spatial differences are provided. Figure 2 plots the F-RF versus F-F difference in percent correct at the -4 dB S-N ratio as a function of the mean fundamental frequency of the two talkers in each masker. The average fundamental frequency of the target talker is shown by the vertical dashed line. The positive values of the symbols show that a benefit of the spatial condition occurred for all five two-talker maskers, although not to an equal degree. There appears to be a rough ordering related to the fundamental frequency of the maskers. Proximity, per se, of the target and masker fundamentals does not appear to be the only important variable as the masker with a lower but still reasonably close fundamental showed only a 13 percentage point benefit. The sample size is too small to be more definitive. One cannot rule out the possibility that other factors, such as perhaps voice quality, vocal tract size, prosodic or temporal properties, etc., are responsible for the variability (see Darwin and Hukin, 2000).

TABLE II. Grid showing the design of Experiment 2. Data for Condition B were taken from Experiment 1.

Condition	Token	Talkers	S-N Ratio	Spatial condition
A	Fixed	Fixed	Fixed	Fixed
B	Random	Fixed	Fixed	Fixed
C	Random	Random	Fixed	Fixed
D	Random	Random	Random	Fixed

III. EXPERIMENT 2. THE EFFECT OF MASKER UNCERTAINTY

The purpose of Experiment 2 was to explore the influence of the uncertainty of the masker. Classic conceptualizations of informational masking are tied to the idea of uncertainty, although recent discussions (Durlach *et al.*, 2003b; Watson, 2005) have stressed instead the importance of similarity for some tasks that have been called informational masking. It is not yet clear how the concept of uncertainty applies to the masking of speech by other speech. In separate conditions, the amount of masker uncertainty was both increased and decreased relative to the uncertainty in Experiment 1. As in Experiment 1, the amount of informational masking was estimated by the difference in performance in the spatial and nonspatial conditions.

A. Methods

The general approach in this experiment was to manipulate the manner in which the masker varied from trial to trial. As explained earlier, in Experiment 1 the selection of which of the five maskers was presented was fixed for 64 trials, the spatial configuration changed every 32 trials, and the S-N ratio changed every eight trials. In the reporting of the current study, that level of uncertainty will be called Condition B. In the current experiment three other levels of uncertainty were created (see Table II). Conditions C and D increased the uncertainty, while Condition A decreased the uncertainty. In Condition C, the S-N ratio and spatial configuration were fixed in each of 32 blocks of ten trials, but each of the five maskers was presented twice during each block, with a randomly shuffled order of maskers within the block of ten. After one block of ten trials the S-N ratio was changed. After four blocks, the spatial configuration was changed. After eight blocks, the entire process was repeated with a new ordering of S-N ratios. The spatial configuration simply alternated every four blocks. In Condition D, both S-N ratio and choice of two-talker masker were completely randomized within an initial block of 160 trials in which the only fixed variable was the spatial configuration (F-F or F-RF). A second 160-trial block followed with the opposite spatial configuration.

In Condition A, the uncertainty was *decreased*. The blocking was the same as Condition B (Experiment 1), but the same token from each masker was presented each time that masker was used. The masker tokens were extracted at a point that began exactly 10 s into each of the five 35-s-long maskers. The presentation of the target was initiated exactly 1 s after the initiation of the masker. Recall that the blocking in Condition B preserved the masker for 64 consecutive trials

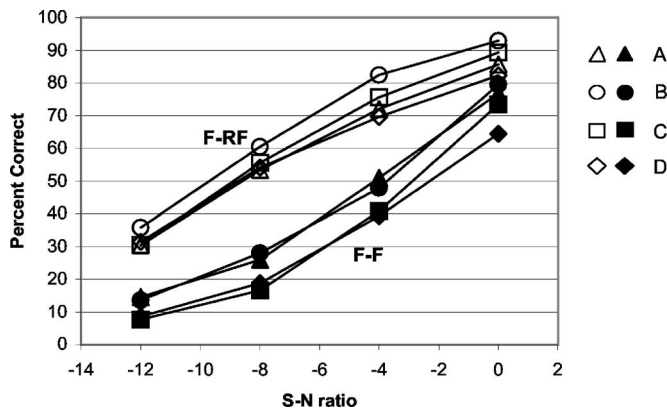


FIG. 3. Percent correct as a function of S-N ratio for four different uncertainty conditions. The filled symbols show the data for the F-F condition, and the open symbols the F-RF condition.

before switching to another masker. With the same blocking in Condition A, this meant the exact same masking token was presented for 64 consecutive trials. The spatial configuration switched after 32 trials, although it was not thought that the degree of uncertainty in spatial configuration would be important, as Jones and Litovsky (2005) reported no effect. Though Condition A was run last, we anticipated running this condition and sprinkled trials with the same specific masking tokens sparsely into each of the other uncertainty conditions (B, C, and D) when those experiments were run. These frozen masking tokens appeared ten times out of the 320 trials run for each subject. There was one presentation of the token for each of the five maskers in both spatial configurations, always at the -4 dB S-N ratio. This allowed some ability to compare performance with the same masking tokens across uncertainty conditions.

Three new sets of ten normal-hearing listeners were used for this study, one group for each of the conditions A, C, and D. Experiment 1 (Condition B) was not repeated, and the data from that experiment were used for comparison. The range of subject ages for all participants (across the four conditions) was 19 to 39 years, with a mean of approximately 22 years.

B. Results and Discussion

Psychometric functions of the averaged data across ten listeners are plotted in Fig. 3. The filled symbols show the data for the F-F condition, and the open symbols the F-RF condition. The relationship between F-F and F-RF configurations for each uncertainty condition is a within-subject comparison, whereas each of the different uncertainty conditions was from a different group of ten subjects. It was not expected that the effect of uncertainty would be very large for the F-RF condition, because presumably this reflects primarily energetic masking. Indeed the results for the F-RF condition show very little effect of uncertainty. In our view, the most striking aspect of the data was the small influence of uncertainty for the F-F conditions, where we assume there was a large informational masking component. Analysis of variance showed no significant effect of conditions A–D, and the difference across conditions is only about 2 dB at 50%

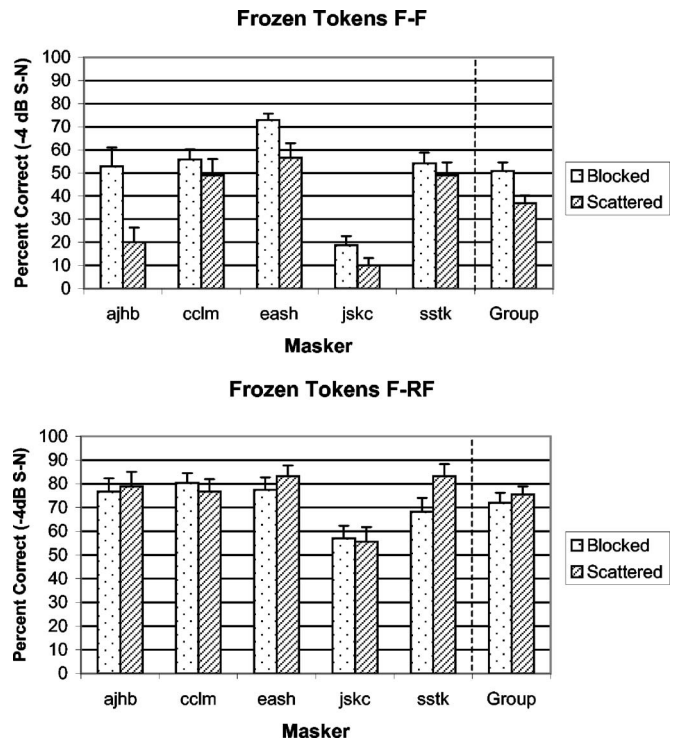


FIG. 4. Target recognition performance with frozen masker tokens in the blocked condition (left bar in each pair) and with frozen masker tokens scattered throughout trials of the three more uncertain masker conditions (right bar in each pair). Mean scores across the five two-talker maskers are shown on the right. Vertical lines illustrate one standard error of the mean across the group of 30 listeners for the three scattered conditions and ten listeners for the blocked condition.

correct. The randomization of the masking talkers and of the S-N ratio from trial to trial apparently had very little effect. Most surprising was that the repetition of the same exact token of masker for 64 consecutive trials seemed not to help the listener very much in the task of perceptually extracting and correctly perceiving the target. Subjects were informed about the repetition and were told to ignore the repeated masker. One might have expected that this would have helped the listener focus on the target. Nevertheless, recognition of the target sentences was not markedly better than it was in the other uncertainty conditions. There was still a large difference in performance between the F-RF and F-F spatial configurations. To the extent that the F-F versus F-RF difference reflects informational masking, it suggests that masker uncertainty is not required to demonstrate the presence of informational masking.

Somewhat greater benefit of the fixed token condition was found when the comparison was made with performance with the same frozen masking tokens scattered throughout the trials of the other three uncertainty conditions at the -4 dB S-N ratio. These trials consisted of a total of 450 scored items for both the F-F and F-RF conditions (five masking talkers \times 30 listeners \times three scored words per trial). The comparison of the frozen-token results in the blocked condition (A) with the results of the same tokens sprinkled through the more uncertain masker conditions is shown in Fig. 4. The results for the individual tokens are shown to the left of the dashed line, and the means across the five two-

talker maskers are shown to the right. For the F-F spatial configuration, mean performance in Condition A (fixed token) was better than in the three scattered conditions. However, this difference did not reach statistical significance ($p=0.053$). A nonsignificant difference was also found for the F-RF condition ($p=0.767$). Results for the individual masking tokens do show some strong improvements in the blocked condition for individual tokens, especially the ajhb masker. Overall performance in the blocked frozen-token F-F configuration was still much poorer than that for the F-RF configuration for the same tokens, suggesting that nonenergetic masking was present in this condition even when masker uncertainty was removed.

The overall result indicating a relatively small effect of masker uncertainty is consistent with data from Brungart and Simpson (2004) despite the difference in target and masker stimuli and general experimental approach. They found that fixing the masking token within a block was effective in reducing masking, but even then listeners were apparently often unable to use the strategy of ignoring the repeated masker and responding to the target. They also found that fixing just the masking *talker* within a block was not effective in reducing masking, as our data seem to show too (Fig. 4).

Although it is not clear how nonenergetic aspects of masking by competing speech are related to nonspeech informational masking tasks, it may be instructive to compare our studies to relevant studies conducted with nonspeech stimuli, particularly with regard to the relative importance of similarity and uncertainty. Following their study in which the effects of similarity of signal and masker were manipulated as a means of counteracting uncertainty, Durlach *et al.* (2003b) posed a question about whether dissimilarity of target and masker would provide release from masking even if masker uncertainty had been eliminated. Our Experiment 2, Condition A indeed produced that very result. Perceived spatial dissimilarity provided a release from masking even though uncertainty was held at a minimum in the fixed-masker-token condition.

Perhaps the most interesting of comparisons are with those studies where the uncertainty of the masker was directly manipulated (Watson *et al.*, 1976; Wright and Saberi, 1999; Richards and Neff, 2004; Richards *et al.*, 2004; Durlach *et al.*, 2005). For example, Durlach *et al.* (2005) investigated how listeners' sensitivity to a 1000 Hz tone in the presence of a multitone complex was affected by whether ten different exemplars of the multitone masker were fixed or presented randomly from trial to trial. The difference between the fixed and random masker conditions showed great intersubject variability, but four of the five subjects showed clear improvement with a nonrandomized masker. Using a similar tone detection in multitone complex task, Wright and Saberi (1999) found a 9 dB improvement in detection when masker uncertainty was reduced by limiting the number of masker exemplars. Richards and Neff (2004) and Richards *et al.* (2004) reduced masker uncertainty by providing a preview of the masker before the signal plus masker was presented during the test trial. The results showed that the benefit of giving a preview of masker was quite large (about

14 dB), as large as the benefit of providing a preview of the target (Richards and Neff, 2004). However, the improvement disappeared when the target frequency was randomized from trial to trial (Richards *et al.*, 2004). This last result could be relevant to our own finding. In a sense the repetition of the masker in our fixed-masker-token condition represents an extreme version of supplying a preview because subjects heard the same masker for 64 consecutive trials. Because our target stimuli varied from trial to trial, the absence of a large improvement is consistent with the results of Richards *et al.* (2004) with the uncertain target. Furthermore, the "preview" resulting from our repetition of the masker was always accompanied by the target. Richards *et al.* (2004) found that the signal-plus-masker previews were ineffective in improving signal detection.

Although we have not provided a pure preview of the masker in our previous speech recognition studies, we have provided a direct preview of the target (Freyman *et al.*, 2004). From this we learned that hearing or even seeing a printed version of the target message immediately preceding the target plus masker trial makes the target stand out against the background. It not only helps segregate target and masker, but it seems to help draw attention toward the target and away from the masker. In this same way, the continual repetition of the masker in our fixed token trials may have made it difficult for subjects to ignore it, although the intention was exactly the opposite. We cannot rule out the possibility that this had an influence on the results of the fixed-token experiment, or those of Brungart and Simpson (2004).

IV. SUMMARY AND CONCLUSIONS

1. With a single female talker target, considerable variability in masking effectiveness was found across five different two-female-talker maskers.
2. The variability was far greater in the F-F condition, where target and masker were presented from the same front loudspeaker, than in the F-RF condition in which target and masker appeared to be spatially separated. In the nonspatial F-F condition, presumably both energetic and nonenergetic forms of masking were present. This was interpreted as showing a greater variability in informational components of masking than in purely energetic masking.
3. Whether the masking tokens, masking talkers, or S-N ratios were fixed or randomized across trials had little effect on performance in either spatial or nonspatial conditions. Substantial advantages of perceived spatial separation remained even when the same token of masker was repeated for 64 consecutive trials. Masker uncertainty appears not to be required to observe spatial release from informational masking in speech recognition.

ACKNOWLEDGMENTS

This research was supported by a grant from the National Institute on Deafness and other Communicative Disorders (DC01625). The authors would like to thank Laurel Slongwhite, Lauren Sullo, Beth Ann Jacques, Ackland Jones,

and Sugata Bhattacharjee for assistance in data collection and analysis for these experiments, and Dr. Nathaniel Whitmal III for engineering support.

- Arbogast, T. L., Mason, C. R., and Kidd, G. Jr. (2002). "The effect of spatial separation on informational and energetic masking of speech," *J. Acoust. Soc. Am.* **112**, 2086–2098.
- Arbogast, T. L., Mason, C. R., and Kidd, G. Jr. (2005). "The effect of spatial separation on informational masking of speech in normal-hearing and hearing-impaired listeners," *J. Acoust. Soc. Am.* **117**, 2169–2180.
- Bird, J., and Darwin, C. J. (1998). "Effects of a difference in fundamental frequency in separating two sentences," in *Psychophysical and Physiological Advances in Hearing*, edited by A. R. Palmer, A. Rees, A. Q. Summerfield, and R. Meddis (Whurr, London), pp. 263–269.
- Brox, J. P. L., and Nootboom, S. G. (1982). "Intonation and the perceptual separation of simultaneous voices," *J. Phonetics* **10**, 23–36.
- Brungart, D. S., and Simpson, B. D. (2004). "Within-ear and across-ear interference in a dichotic cocktail party listening task: Effects of masker uncertainty," *J. Acoust. Soc. Am.* **115**, 301–310.
- Brungart, D. S., Simpson, B. D., Ericson, M. A., and Scott, K. R. (2001). "Informational and energetic masking effects in the perception of multiple simultaneous talkers," *J. Acoust. Soc. Am.* **110**, 2527–2538.
- Brungart, D. S., Simpson, B. D., and Freyman, R. L. (2005). "Precedence-based speech segregation in a virtual auditory environment," *J. Acoust. Soc. Am.* **118**, 3241–3251.
- Carhart, R., Tillman, T. W., and Greets, E. S. (1969). "Perceptual masking in multiple sound backgrounds," *J. Acoust. Soc. Am.* **45**, 694–703.
- Darwin, C. J., and Hukin, R. W. (2000). "Effectiveness of spatial cues, prosody and talker characteristics in selective attention," *J. Acoust. Soc. Am.* **107**, 970–977.
- Darwin, C. J., Brungart, D. S., and Simpson, B. D. (2003). "Effects of fundamental frequency and vocal-tract length changes on attention to one of two simultaneous talkers," *J. Acoust. Soc. Am.* **114**, 2913–2922.
- Durlach, N. I., Mason, C. R., Kidd, G., Arbogast, T. L., Colburn, H. S., and Shinn-Cunningham, B. G. (2003). "Note on informational masking," *J. Acoust. Soc. Am.* **113**, 2984–2987.
- Durlach, N. I., Mason, C. R., Shinn-Cunningham, B. G., Arbogast, T. L., Colburn, H. S., and Kidd, G. (2003b). "Informational masking: Counteracting the effects of stimulus uncertainty by decreasing target-masker similarity," *J. Acoust. Soc. Am.* **114**, 368–379.
- Durlach, N. I., Mason, C. R., Gallun, F. J., Shinn-Cunningham, B. G., Colburn, H. S., and Kidd, G. (2005). "Informational masking for simultaneous nonspeech stimuli: Psychometric functions for fixed and randomly mixed maskers," *J. Acoust. Soc. Am.* **118**, 2482–2497.
- Freyman, R. L., Balakrishnan, U., and Helfer, K. S. (2001). "Spatial release from informational masking in speech recognition," *J. Acoust. Soc. Am.* **109**, 2112–2122.
- Freyman, R. L., Balakrishnan, U., and Helfer, K. S. (2004). "Effect of number of masking talkers and auditory priming on informational masking in speech recognition," *J. Acoust. Soc. Am.* **115**, 2246–2256.
- Freyman, R. L., Helfer, K. S., and Balakrishnan, U. (2005). "Spatial and spectral factors in release from informational masking," *Acta. Acust. Acust.* **91**, 537–545.
- Freyman, R. L., Helfer, K. S., McCall, D. D., and Clifton, R. K. (1999). "The role of perceived spatial separation in the unmasking of speech," *J. Acoust. Soc. Am.* **106**, 3578–3588.
- Gallun, F. J., Mason, C. R. and Kidd, G. Jr. (2005). "Binaural release from informational masking in a speech identification task," *J. Acoust. Soc. Am.* **118**, 1614–1625.
- Helfer, K. S. (1997). "Auditory and auditory-visual perception of clear and conversational speech," *J. Speech Lang. Hear. Res.* **40**, 432–443.
- Helfer, K. S., and Freyman, R. L. (2005). "The role of visual speech cues in reducing energetic and informational masking," *J. Acoust. Soc. Am.* **117**, 842–849.
- Jones, G., and Litovsky, R. Y. (2005). "Role of masker predictability in the cocktail party effect," *Presented at the Association for Research in Otolaryngology Conference*, February, New Orleans.
- Kidd, G. Jr., Mason, C. R., Deliwal, P. S., Woods, W. S., and Colburn, H. S. (1994). "Reducing informational masking by sound segregation," *J. Acoust. Soc. Am.* **95**, 3475–3480.
- Kidd, G. Jr., Mason, C. R., and Arbogast, T. L. (2002). "Similarity, uncertainty, and masking in the identification of nonspeech auditory patterns," *J. Acoust. Soc. Am.* **111**, 1367–1376.
- Kidd, G. Jr., Mason, C. R., Brughera, A., and Hartmann, W. M. (2005a). "The role of reverberation in release from masking due to spatial separation of sources for speech identification," *Acta. Acust. Acust.* **91**, 526–536.
- Kidd, G. Jr., Mason, C. R., Arbogast, T. L., and Mason, C. R. (2005b). "The advantage of knowing where to listen," *J. Acoust. Soc. Am.* **118**, 3804–3815.
- Leek, M. R., Brown, M. E., and Dorman, M. F. (1991). "Informational masking and auditory attention," *Percept. Psychophys.* **50**, 205–214.
- Li, L., Daneman, M., Qi, J. G., and Schneider, B. A. (2004). "Does the information content of an irrelevant source differentially affect spoken word recognition in younger and older adults?" *J. Exp. Psychol. Hum. Percept. Perform.* **30**, 1077–1091.
- Nerbonne, G. P., Ivey, E. S., and Tolhurst, G. C. (1983). "Hearing protector evaluation in an audiometric testing room," *Sound Vib.* **17**, 20–22.
- Rakerd, B., Aaronson, N. L., and Hartmann, W. M. (2006). "Release from speech-on-speech masking by adding a delayed masker at a different location," *J. Acoust. Soc. Am.* **119**, 1597–1605.
- Richards, V. M., Huang, R., and Kidd, G., Jr. (2004). "Masker-first advantage for cues in informational masking," *J. Acoust. Soc. Am.* **116**, 2278–2288.
- Richards, V. M., and Neff, D. L. (2004). "Cueing effects for informational masking," *J. Acoust. Soc. Am.* **115**, 289–300.
- Watson, C., Kelly, W., and Wroton, H. (1976). "Factors in the discrimination of tonal patterns. II. Selective attention and learning under various levels of stimulus uncertainty," *J. Acoust. Soc. Am.* **60**, 1176–1185.
- Watson, C. (2005). "Some comments on informational masking," *Acta. Acust. Acust.* **91**, 502–512.
- Wright, B., and Saberi, K. (1999). "Strategies used to detect auditory signals in small sets of random maskers," *J. Acoust. Soc. Am.* **105**, 1765–1775.

Speech intelligibility in free field: Spatial unmasking in preschool children

Soha N. Garadat and Ruth Y. Litovsky^{a)}

Waisman Center, University of Wisconsin-Madison, Madison, Wisconsin 53705

(Received 16 January 2006; revised 22 November 2006; accepted 22 November 2006)

This study introduces a new test (CRISP-Jr.) for measuring speech intelligibility and spatial release from masking (SRM) in young children ages 2.5–4 years. Study 1 examined whether thresholds, masking, and SRM obtained with a test designed for older children (CRISP) and CRISP-Jr. are comparable in 4 to 5-year-old children. Thresholds were measured for target speech in front, in quiet, and with a different-sex masker either in front or on the right. CRISP-Jr. yielded higher speech reception thresholds (SRTs) than CRISP, but the amount of masking and SRM did not differ across the tests. In study 2, CRISP-Jr. was extended to a group of 3-year-old children. Results showed that while SRTs were higher in the younger group, there were no age differences in masking and SRM. These findings indicate that children as young as 3 years old are able to use spatial cues in sound source segregation, which suggests that some of the auditory mechanisms that mediate this ability develop early in life. In addition, the findings suggest that measures of SRM in young children are not limited to a particular set of stimuli. These tests have potentially useful applications in clinical settings, where bilateral fittings of amplification devices are evaluated. © 2007 Acoustical Society of America. [DOI: 10.1121/1.2409863]

PACS number(s): 43.66.Dc, 43.66.Pn, 43.71.Ft, 43.71.Gv [AJO]

Pages: 1047–1055

I. INTRODUCTION

Auditory environments in which children spend a majority of their time are typically acoustically complex; multiple acoustic signals are likely to coincide in time, location, and spectrum. In general, to achieve a high level of performance, children must segregate multitudes of signals into their basic components to make sense of the “what” and “where” aspects of the auditory environment. The phenomenon by which the auditory system extracts a distinct message in the presence of other competing sounds is known in general terms as the “cocktail party effect” (Cherry, 1953; Pollack and Pickett, 1958). During the many years since the problem was originally described there has been increasing interest in identifying the mechanisms by which the auditory system teases apart co-occurring sounds and facilitates speech understanding in noisy environments.

Given the complex nature of the “listening-in-noise” problem, it is important to better understand the mechanisms by which children are able to navigate in a complex auditory environment, a good example of which is a classroom. The vast majority of what is known about this ability is derived from studies on adult listeners. A number of studies that simulated aspects of complex auditory environments have shown that speech recognition in noise improves when the target source is spatially separated from the competing sounds (e.g., Hirsh, 1950; Dirks and Wilson, 1969; Plomp, 1976; Bronkhorst and Plomp, 1988; Festen and Plomp, 1990; Yost *et al.*, 1996; Peissig and Kollmeier, 1997; Noble *et al.*, 1997; Freyman *et al.*, 1999; Drullman and Bronkhorst, 2000). This improvement has been referred to as spatial re-

lease from masking (SRM), which has been shown to incorporate both binaural and monaural components of auditory processing (Kidd *et al.*, 1998; Culling *et al.*, 2004; Hawley *et al.*, 1999, 2004; Lin and Feng, 2003).

In contrast, little is known about how it is that children succeed in resolving auditory information in complex environments, and the developmental time course of this ability. This ability most likely includes mechanisms that mediate simple aspects of spatial hearing known to reach full maturation in early childhood. One example is the mechanism that contributes to discrimination of sound location for single-source sounds, which is adult-like by 5 years of age (Litovsky, 1997). Other examples exist for abilities that are not inherently spatial, such as frequency resolution, which is adult-like by age 6 (Allen *et al.*, 1989; Hall and Grose, 1991). On the other hand, mechanisms that are still developing are likely to limit children’s performance, such that they would appear to be poorer at extracting auditory information compared with adults. In particular, measures that focus on temporal resolution abilities suggest a more protracted developmental progression that extends into middle-to-late childhood. These include gap detection (Wightman *et al.*, 1989), backward masking (Hartley *et al.*, 2000), amplitude modulation detection at various rates (Hall and Grose, 1994), and masking level difference (Hall and Grose, 1990).

Studies that focused on auditory masking suggest that children have poorer performance in the presence of competing noise compared to that in *quiet* conditions. In general, it has been reported that children require a higher signal-to-noise ratio (SNR) than adults for comparable performance, in other words, they exhibit a greater degree of masking (Elliott *et al.*, 1979; Papsa and Blood, 1989). Children also appear to have greater difficulty than adults in extracting a target signal embedded in background noise when listening to multiple

^{a)}Electronic mail: litovsky@waisman.wisc.edu

sound sources (Hall *et al.*, 2002) or under conditions of perceptual masking and signal uncertainty (Allen and Wightman, 1995; Oh *et al.*, 2001; Wightman *et al.*, 2003).

Despite the rich and growing literature on auditory development, an area of research that remains relatively unexplored concerns how children exploit spatial cues in segregating complex signals. In a recent study, Litovsky (2005) showed that children 4.5–7 years of age are able to take advantage of spatial cues to segregate target speech in the presence of competing speech or modulated speech-shaped-noise. Although the children's average speech reception thresholds (SRTs) were higher than those of adults, the amount of masking (differences in SRT between quiet thresholds and conditions in which competitors are present) and SRM (differences in SRTs between masking when the competitors were in front versus on the side) were similar in children and adults, suggesting that by the time children reach school-age some aspects of source segregation are well developed. In a follow-up study, Johnstone and Litovsky (2006) found that, when the maskers consist of time-reversed speech, the novelty of the stimulus rendered the task significantly more difficult for the children, but not for adults, suggesting the importance of nonsensory factors such as informational masking in this task. Further work is needed to determine the robustness of these findings in younger children, and the developmental ontogeny of spatial unmasking. This area of research can not only give some insight into how children perform in environments such as classrooms, but might also be able to provide appropriate tools for evaluating children's performance using listening prostheses such as hearing aids and cochlear implants (Litovsky *et al.*, 2004, 2006).

The present study evaluated SRTs, masking, and SRM in two groups of children, ages 3 and 4–5 years. Although age-appropriate tests for measuring language and vocabulary development are available (e.g., the Reynell Developmental Language Scales III; Ball, 1999), none are geared toward measuring speech intelligibility in a challenging masked situation. In addition, the test used by Litovsky (2005), known as CRISP, uses spondees as targets (e.g., “cowboy,” “bluejay,” and “bird-nest”). That test was geared toward children with a minimum of 4 years and contains vocabulary that is not age-appropriate for the average younger child. In order to evaluate speech unmasking and SRM in younger children, the design of a novel stimulus set was required. A new test named CRISP-Jr. was developed for this purpose, with a corpus of target words that are estimated to be within the vocabulary of typically developing, normal-hearing 2.5 year olds. Ultimately, this test can also be extended to populations of children who may be older but whose language skills are delayed relative to their age-matched peers.

This paper presents results from two studies. The first study was designed to compare values of SRTs, masking, and SRM using the new set of stimuli (CRISP-Jr.) and the previously used corpus (CRISP). In a second study, the CRISP-Jr. test was extended to a group of 3-year-old children, in order to better understand the developmental trajectory of sound source segregation.

II. STUDY 1

This study utilized two sets of stimuli to measure SRTs, masking, and SRM in a group of 4- to 5-year-old children. Stimuli were the spondees from the CRISP test (Litovsky, 2005) and a new corpus of words designed for measuring speech intelligibility in children as young as 2.5 years of age, otherwise known as CRISP-Jr. The main purpose of this study was to determine whether perceptual measures are comparable and can be generalized across the two different tests and sets of stimuli. The differences were in the auditory stimuli with the matching pictures, as well as the animations and feedback that are used to entertain and engage the children during testing. Otherwise, algorithms for varying sound level, threshold estimation, and stimulus delivery are identical in the two tests. SRTs were measured in a group of 4- to 5-year-old children. For each test, three conditions were used that enabled estimation of masking and SRM.

A. Method

1. Participants

Ten subjects, 4 females and 6 males, all native speakers of English, participated. The age range was 4 years, 2 months to 5 years, 6 months (mean age of 4 years, 11 months). All subjects had normal hearing sensitivity as indicated by pure-tone, air conduction thresholds of 20 dB or better for frequencies ranging from 500 to 8000 Hz, and normal tympanograms. None of the children had ear infection or known illness, nor were any of the children taking medication on the day of testing (as reported by the parent/guardian). All subjects were also reported to be healthy and free of neurological disorders, and were right-handed. Every one of the recruited participants was able to complete the required measurements, with no exceptions, drop-outs, or replacements for other reasons.

2. Stimuli

The target stimuli in the CRISP test consist of a closed set of 25 words from the Children's Spondee list (CID W-1 test) recorded with a male voice. Targets in the CRISP-Jr. test consist of a closed set of 16 words, recorded with a different male voice. The target words in CRISP-Jr. were chosen to be within the receptive language and vocabulary of average 2.5- to 3.0-year-old children, and therefore consist of names of objects and/or body parts. The word list was inspired by the well-known Mr. Potato Head® game, in which the player can attach or remove body parts onto a toy shaped like a potato. This game has been used in some clinical and research settings with live voice to evaluate language acquisition of very young children (e.g., Robbins, 1994; Svirsky *et al.*, 2004). Here we used a computerized “listening game,” based on a similar platform to that described by Litovsky (2003, 2005), with the presumption that young children who have normal hearing and cognitive abilities can easily identify body parts and related items. The test, however, was developed for the purpose of measuring SRTs, and the words being tested are *known* to each child prior to testing (see Sec. II A 4). Appendices A and B include lists of the words used in the two tests, respectively. It is important to note that the

CRISP-Jr. list included 12 monosyllabic and 4 bi-syllabic words. Although this may not be ideal, we felt that it was important to increase the size of the target corpus. During individual trials, the options presented to the child on the computer screen in the 4-AFC procedure (see the following) were set up such that all the words had the same number of syllables. Although systematic testing was not conducted to determine whether some of the words were more difficult than others to identify, the procedures ensured that subjects were well familiarized with all targets prior to testing.

The competitor stimuli in both tests were sentences from the Harvard IEEE corpus (Rothausser *et al.*, 1969), recorded with a female voice. Examples of sentences are: “Glue the sheet to the dark blue background,” “Two blue fish swam in the tank” and “The meal was cooked before the bell rang.” Thirty such sentences were strung together, and segments were randomly chosen and played for a duration of 6 s during each trial. The timing was such that the target words occurred approximately 1.5 s after the onset of the competing sentence. All stimuli for this study were pre-recorded and digitized using a sampling rate of 44.1 kHz and stored on a laptop computer. The levels for all stimuli were rms equalized using MATLAB software.

3. Test setup and procedure

Testing was conducted in a carpeted double-walled sound booth (2.75 m × 3.25 m) with reverberation time (T_{60}) = 250 ms. Subjects were seated in the middle of the room with speakers mounted on a stand at a distance of 1.2 m from the center of the subject’s head. The target and the competitor stimuli were fed to separate audio channels of a laptop computer, amplified (Crown D-75) and played through separate loudspeakers (Cambridge Soundworks, Center/Surround IV). The target stimuli were always presented from the front (0° azimuth), while the competitor was presented from either the front (0° azimuth) or the right (90° azimuth). Prior to each testing session, stimuli were calibrated (Larsen-Davis System 824). A computer monitor was placed directly below the speaker at 0° azimuth (to avoid obstruction with wave propagation in the room). The child sat on a chair in front of a small table (covered with foam), on which the computer mouse and keyboard were placed. During testing the child was engaged in a computerized “listening game” and all visual stimuli (e.g., picture representations of the targets, puzzles, and animations) were presented from the monitor, which was particularly helpful in maintaining the head centered and minimizing head movements.

For both tests, the task involved 4-AFC. On each trial, following the target presentation, four randomly selected pictures, including the target, appeared simultaneously on the screen. The pictures were arranged in a 2 × 2 grid of equal-size squares, and the square containing the target picture was randomly chosen from trial to trial. A defined set of rules was applied in order to eliminate the possibility of words with similar initial sounds occurring in the same interval (e.g., “hands” and “hat”). On each trial a leading phrase such as “point to the...” or “show me...” preceded the target presentation. Subjects were instructed to listen to the target word (male voice) on each trial, and to select the one picture on

the computer monitor that matched the heard word. A verbal response was also required to ensure subjects’ correct identification of the targets, and the answer was entered into the computer by an examiner. In the unlikely event that a child pointed to one picture but verbally reported another, the trial was repeated (with a new stimulus). Feedback was provided for both correct and incorrect responses. Following each correct response, a brief musical clip was presented or a missing piece from a puzzle was added to the computer display. Following incorrect responses a phrase such as “that must have been difficult” or “let’s try a different one” was presented from the front speaker.

Using the aforementioned setup, measurements were obtained from each child on the two tests. For each test the following three conditions were included: (1) *quiet* with target at 0° azimuth and no competitor, (2) *front* with target and competitor both at 0° azimuth, and (3) *right* with target at 0° azimuth and competitor at 90° azimuth. For each subject, the order of the test (CRISP or CRISP-Jr.) was randomized using a Latin-square design, and the order of the three conditions (quiet, front, and right) within each test was then also randomized. The study was completed in one session that lasted approximately 2 h per subject, including frequent breaks.

4. Familiarization

Prior to each test, children underwent a familiarization procedure that lasted 5–10 min. First, the target words were each presented along with their associated pictures, and then the child was tested on his/her ability to correctly identify the targets. Words that were not easily identified were eliminated from that subject’s target corpus. In a typical case, a child was already familiar with all targets, or was able to quickly associate the auditory stimulus with the matching picture. In three cases one to two targets were discarded from the CRISP-Jr. corpus and in eight cases one to four targets were discarded from the CRISP corpus due to incorrect identification after the familiarization step.

5. Stimulus levels and threshold estimation

The level of the competitor was fixed at 60 dB SPL. Both tests incorporated an adaptive tracking procedure to vary the level of the target signal. The target level was set to 60 dB SPL (0 dB SNR) at the beginning of each adaptive track. The algorithm for varying the target level included a set of rules that are outlined in greater detail elsewhere (Litovsky, 2005). Briefly, during the initial portion of the adaptive track, the target level was decreased by 8 dB following each correct response. After the first incorrect response, a modified adaptive three-down/one-up algorithm was used, with the following rules: Following each reversal, the step size is halved, with the minimum step size set to 2 dB. If the same step size is used twice in a row in the same direction, the next step size is doubled in value. Testing is terminated following four reversals.

Thresholds were estimated using a constrained maximum-likelihood method of parameter estimation (MLE) which has been described by Wichmann and Hill (2001a, b). On average, the MLE approach has been shown to yield

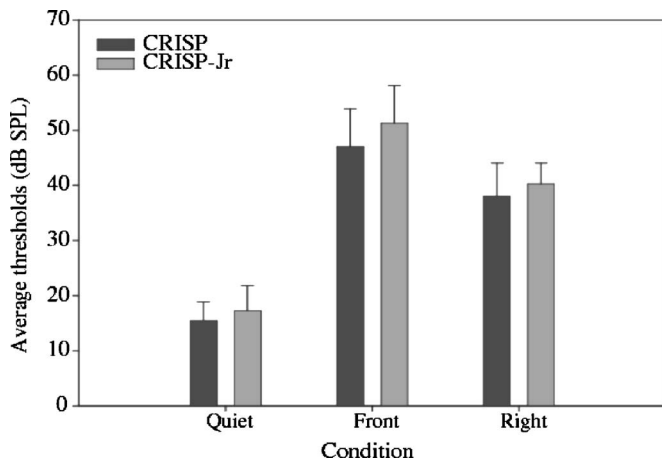


FIG. 1. Speech reception thresholds (SRTs in dB SPL) \pm s.d. are plotted for the quiet, front, and right conditions for ten subjects aged 4 to 5 years. Dark bars represent data collected with CRISP and light bars show data collected with CRISP-Jr.

comparable results to the traditional approach which estimates thresholds based on the average of certain number of reversal points; however, the MLE method has the advantage of producing smaller group variances (Litovsky, 2005). This approach is particularly suitable in pediatric research given that a smaller number of reversals can be obtained. In addition, because lapses of attention can lead to incorrect responses when the child would otherwise provide a correct response, values obtained on single trials can have disproportionate weighting in reversal-based threshold estimation. By using MLE, these issues can be minimized given that thresholds are estimated via a method that places greater weight on levels with the largest number of trials visited at a given adaptive track.

In this study, all the data from each experimental run for each participant were fit to a logistic function. Thresholds were calculated by taking the level of the speech signal at a specific probability level. Given that an adaptive, three-down/one-up procedure was employed, thresholds were estimated targeting performance level of 79.4% on the psychometric function (as estimated by Levitt, 1971).

B. Results

Group average SRTs are compared for the three conditions and two tests in Fig. 1. The results were subjected to a two-way repeated measures analysis of variance (ANOVA) with test (CRISP and CRISP-Jr.) and condition (quiet, front, and right) as within-subject variables. A main effect was found for test [$F(1,9)=8.872$; $p<0.05$], suggesting that CRISP-Jr. yielded higher SRTs than CRISP. In addition, there was a main effect for condition [$F(2,9)=109.463$, $p<0.0001$]. Scheffe's post hoc comparisons showed that SRTs were lower for *quiet* than *right* [$F(2,9)=100.23$, $p<0.0001$] and *front* [$F(2,9)=208.54$, $p<0.0001$]. This indicates that masking occurred for both competitor locations. SRTs were also significantly higher for *front* than *right* [$F(2,9)=19.62$, $p<0.001$], which suggests that SRM occurred and that these children benefited from the spatial separation of the target and competitor. There was no significant interaction between test and condition, suggesting that the effects described thus far occurred similarly for CRISP and CRISP-Jr.

The amount of masking for the two conditions is defined as the difference in SRTs between *front* or *right*, and *quiet*, respectively (e.g., $SRT_{front} - SRT_{quiet}$ and $SRT_{right} - SRT_{quiet}$). Figure 2 shows both individual and group data for the amount of masking on each test in the *front* and *right* conditions. A two-way repeated-measure ANOVA (test \times competitor location) revealed no statistically significant difference between the two tests. However, masking was significantly greater in *front* than *right* [$F(1,9)=51.735$; $p<0.0005$]. There was no significant interaction effect, which suggests that the amount of SRM (front masking – right masking) was similar for the CRISP and CRISP-Jr. tests, averaging 9.02 and 11.09 dB, respectively. An interesting finding, discussed later, is that subjects are not always consistent in their performance across the two tests; while some subjects exhibited higher thresholds with CRISP, others showed the opposite. This is highlighted for select cases by connecting the masked threshold lines in the two tests in Fig. 2.

In summary, results thus far suggest that the CRISP-Jr.

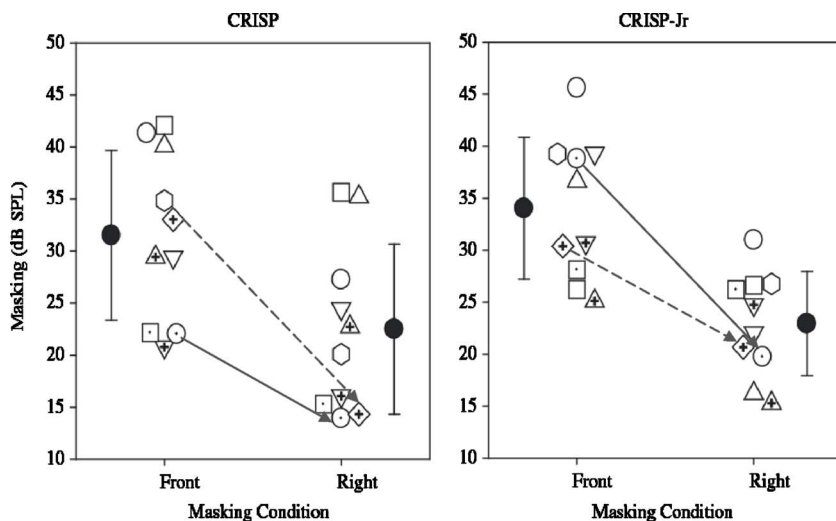


FIG. 2. Amounts of masking for front and right conditions are displayed for both CRISP (left panel) and CRISP-Jr. (right panel). Each subject's data are represented by a different symbol; closed circles represent group data (\pm s.d.) for each condition. The connecting lines are used to demonstrate examples of individual subjects' masking in the front vs right conditions. Comparisons across the two panels shows these subjects' inconsistent performance across the two tests; while some children exhibited higher masked thresholds with CRISP, for others CRISP-Jr. elicited higher thresholds.

test produces similar results to those obtained with CRISP, in particular for measures of masking and SRM. This testing paradigm may, therefore, provide a useful tool for investigating these same effects in younger children.

III. STUDY 2

This study was aimed at extending the CRISP-Jr. testing tool to a group of children under the age of four. Results from this young age group were compared to those obtained from the older group on the same test (CRISP-Jr.).

A. Method

1. Participants

Ten children (3 females and 7 males) participated in this study. All children were native speakers of English and were in the age range of 3 years, 4 months to 3 years, 10 months (mean age of 3 years, 7 months). Thresholds measurements were obtained separately in each ear using a standard audiometric clinical approach, whereby the child was asked to lift a finger or say "I hear it" every time that a tone was heard. A one-down one-up rule was used to adaptively vary the tone level. None of the children had ear infection or known illness, or were taking medication on the day of testing as reported by parents. Nine children were reported to be right handed and one was left handed. In order to obtain 10 participants 11 children were recruited (one child was unable to complete the necessary measurements due to lack of cooperation or lack of interest in the task). Otherwise, there was no need for averaging, exclusion, or filling in of missing data points.

B. Stimuli and procedure

Stimuli and testing apparatus were identical to those described in detail in experiment 1. Each child was tested on three conditions: *quiet*, *front*, and *right*, with the order of conditions randomized. The study was completed in one session that lasted approximately 1 h, including breaks.

1. Results

CRISP-Jr. SRTs were calculated using the same MLE procedure described in study 1. Average SRTs for the two age groups are shown in Fig. 3. Results were subjected to a two-way ANOVA, with age as the between-subjects variable and condition as the within-subjects variable. A significant main effect for age was found [$F(1, 18)=24.582$; $p < 0.0005$] such that across conditions, SRTs were an average of 10 dB higher in the 3-year-old age group compared with the 4 to 5 year olds. This finding suggests that children's ability to identify speech in a forced-choice paradigm improves with a small increase in age during the preschool years. A significant main effect for condition was also found [$F(2, 18)=114.43$, $p < 0.0005$], with Scheffe's post hoc contrasts showing that SRTs in the *quiet* condition were lower than *front* [$F(2, 18)=216.55$, $p < 0.0001$] as well as *right* [$F(2, 18)=108.09$, $p < 0.0001$]. As was found in study 1, this result suggests again the occurrence of masking regardless of the location of the competing sound. Finally, SRTs were sig-

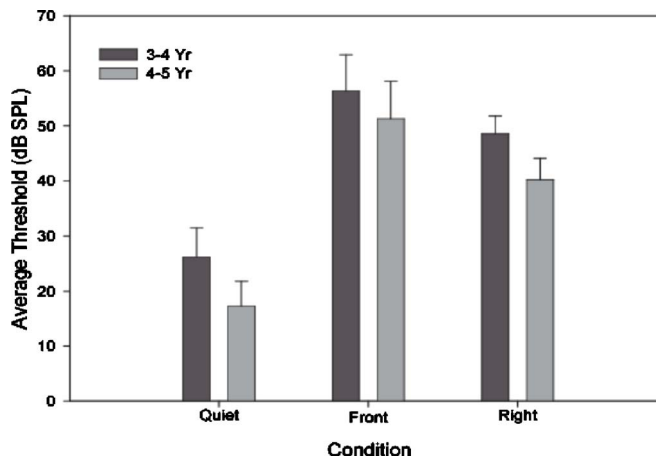


FIG. 3. Speech reception thresholds (SRTs in dB SPL) \pm s.d. elicited with CRISP-Jr. are plotted for the quiet, front, and right conditions for children grouped into two age groups, 3 and 4 to 5 year olds. Dark bars represent data collected from the younger group and light bars show data collected from the older group.

nificantly higher in *front* compared with *right* [$F(2, 18) = 18.65$, $p < 0.0001$]. No significant interactions were found.

Amount of masking was computed by subtracting SRTs in the *front* and *right* from *quiet*. A two-way ANOVA (age \times competitor location) showed no statistically significant difference between the two age groups in the amount of masking. A main effect of competitor location was found [$F(1, 18)=35.035$; $p < 0.0005$], with masking from the front being higher than the right. This finding, together with the result that SRTs were higher in the front than right, indicates the occurrence of SRM. The lack of interaction suggests that SRM was similar in both groups, or that the variability was too large to reveal age-related effects. Average SRM values of the 3 and 4 to 5 year olds were 7.7 (± 7.2 s.d.) dB, and 11 (± 7.1 s.d.) dB, respectively. These are plotted in Fig. 4 along with the individual subjects' results, to demonstrate the large intersubject variability within each group.

A regression analysis was conducted between the amount of SRM and SRTs obtained when the competitor was in one of the two masking conditions (*front* or *right*). Results plotted in Fig. 5 (left panel) support the statistical finding of

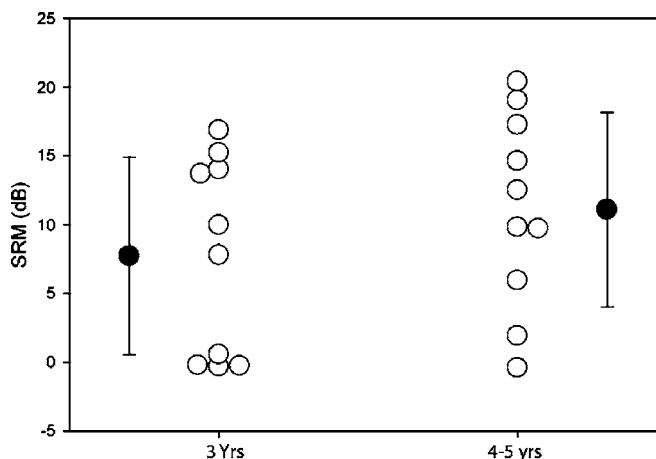


FIG. 4. Individual SRM values (open circles) and mean data (closed circles) are plotted for 20 children distributed into two age groups 3 years and 4 to 5 years old tested on CRISP-Jr.

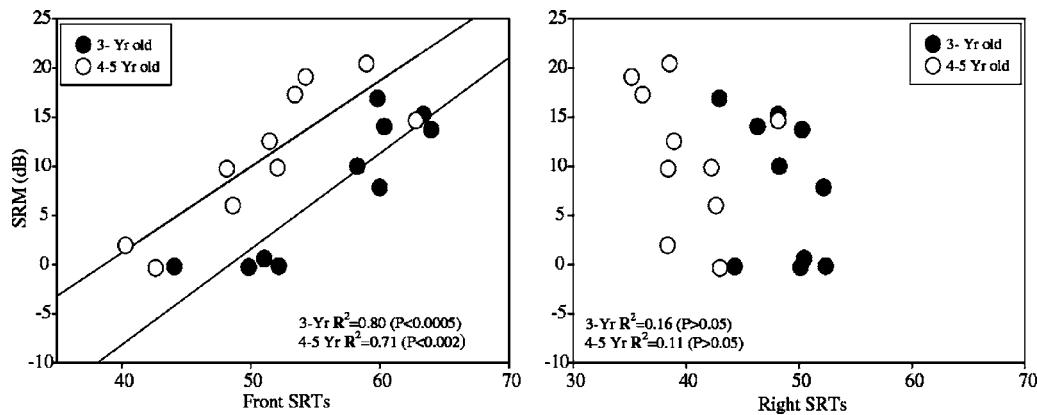


FIG. 5. Left panel displays SRM (in dB SPL) plotted against SRTs in the front condition. The right panel displays SRM against SRTs in the right condition. Data are shown for 20 subjects ranging in age between 3 and 5 years. The results of the regression analysis are shown at the bottom of each panel.

a significant regression with the *front* for both the 3-year-old ($p<0.0005$) and the 4- to 5-year-old ($p<0.002$) groups. Furthermore, two distinct regression lines can be noted due to the higher SRTs exhibited by the younger group of children. A similar analysis (Fig. 5, right panel) when the competitor was on the *right* was nonsignificant ($p>0.05$) for both age groups. This suggests that spatial separation between the target and masking source is particularly beneficial for children whose SRTs are high when both target and competitor are in front (i.e., in absence of spatial cues). In contrast, children whose *front* SRTs are initially low do not gain much extra benefit when spatial cues are introduced in the *right* condition.

IV. DISCUSSION

When listeners are faced with a complex array of sounds in a room, one of the ways in which they can separate important speech signals from noise is if the two sources arrive from different locations. In adults, spatial separation of speech from noise provides 3–12 dB improvement in SRT, depending on the type of stimulus, task, and whether stimuli are presented under binaural or monaural listening modes (e.g., Bronkhorst, 2000; Culling *et al.*, 2004; Hawley *et al.*, 2004). To the extent that spatial hearing mechanisms are well-developed in young children, similar benefits might also be observed. This is an important issue to determine, given the vast number of hours that children spend in noisy multi-source situations. In addition, there may be insights into potential benefits of amplification fitting strategies in hearing impaired children who receive bilateral hearing aids and/or cochlear implants (e.g., Litovsky *et al.*, 2004, 2006). For these reasons, the present study was aimed at extending the testing age to a younger group to evaluate the developmental trajectory of sound source segregation.

A. Speech reception thresholds and masking

SRTs measured here suggest that 3 year olds perform worse than 4 to 5 year olds. Our other work (Litovsky, 2005; Johnstone and Litovsky, 2006) suggest that SRTs continue to improve beyond age 7 compared with adults. However, on these tasks the amount of masking appears to be adult-like at the youngest ages. The overall increase in thresholds is con-

sistent with other findings on age-related changes in thresholds (e.g., Lenihan *et al.*, 1971; Fior, 1972; Roche *et al.*, 1978; Schneider *et al.*, 1986; Werner, 1996). Generally, it is believed that children's poor performance on certain auditory tasks is reflective of immaturity at central levels in the auditory pathway, as neurodevelopmental research suggests that central maturation continues throughout childhood (Ponton *et al.*, 2000; Moore and Guan, 2001; Rakic and Yakovlev, 1968). The neuroanatomical and physiological measures do not however identify which specific mechanisms are immature, and leave open the question as to what might account for the age differences in SRTs seen here.

Performance is most likely influenced by a complex interaction between various processes, including those borne in the auditory system, as well as attention, working memory, and other nonsensory factors. To the extent that differences in thresholds across age groups may be attributable to maturational changes in auditory processes, it is noteworthy that, despite the increased mean for the younger children, variance was generally similar in the two age groups (Fig. 3).

It is unlikely, however, that the results shown here are affected by age-related differences in language acquisition. Although language measures were not obtained, this factor and its effects were minimized if not eliminated by employing the familiarization procedure which ensured that all target words were known by each participant prior to testing.

The two groups showed similar amount of elevation in thresholds in the presence of competing speech. Although this study did not evaluate adults' performance on CRISP-Jr., differences in performance between adults and children is assumed because two previous studies that applied the CRISP testing paradigm have shown adults' performance to be significantly better than the children on the masked conditions, even when task difficulty is equated (Litovsky *et al.*, 2005; Johnstone and Litovsky, 2006). Other paradigms have also demonstrated that children are more susceptible to noise than adults, and that they require more favorable SNR than adults for comparable performance (e.g. Elliott *et al.*, 1979; and Nittrouer and Boothroyd, 1990). Children appear to adopt nonoptimal listening strategies when distracting noise is present (Allen and Wightman, 1994; Lutfi *et al.*, 2003) and they are very likely to have poor processing efficiency caused by higher internal noise than adults (Hill *et al.*, 2004).

The mechanism for suppressing this central noise has been suggested to improve with age as demonstrated in improved ability to segregate sounds with similar acoustical characteristics (Allen and Nelles, 1996).

B. Spatial release from masking

The results from the present study showed that by age three children can use spatial cues to segregate different auditory streams, and the amount of SRM for that age group was not statistically different from that of the older group. Previous studies (Litovsky, 2005; Johnstone and Litovsky, 2006), in which SRM was measured with CRISP, showed that children ages 4.5–7 did not differ significantly from adults. By extension, studies on this subject imply that by 3 years of age some of the auditory mechanisms that mediate SRM are well developed.

These current findings appear to be at variance with previous reports that showed a protracted developmental period when the task involves segregation of multiple auditory signals (e.g. Oh *et al.*, 2001; Hall *et al.*, 2005; Wightman *et al.*, 2003; Wightman and Kistler, 2005). In an attempt to explain the difference between the present findings and previous reports several possibilities should be considered. First, the differences may be due to the testing paradigm. Previous studies investigated speech unmasking in children under dichotic conditions in which *spatial cues* are limited to a single cue, inter-ear separation. By comparison, SRM as measured here was most likely influenced by a multitude of spatial cues that include both inter-aural binaural cues, as well as monaural cues such as level and spectra. The results from these two different paradigms are therefore not directly comparable, nor are they inconsistent with one another. A fuller exploration of the cues that mediate source segregation would thus help resolve some of these issues. Second, discrepancies in the results across studies may also be attributable to differences in the testing tools utilized across studies. The current study was aimed at using a very engaging testing tool that was especially developed for preschoolers. The tool was very successful in attracting the preschoolers and maintaining their attention throughout the testing. Other published work has also been successful at demonstrating that with the use of age-appropriate tests children can selectively attend to specific auditory information and suppress competing information, an ability that seems to emerge in early life and it is somewhat adult-like as early as 3 years of age (Sanders *et al.*, 2006).

Findings from this study also showed that individual subjects vary in amount of SRM. For instance, while some children showed SRM values that are greater than 15 dB, others had values near 0 dB, and a small group of children showed negative SRM (better SRTs in the front condition). This variability is consistent with previous reports on children's performance on auditory tasks (Litovsky, 1997; Buss *et al.*, 1999; Oh *et al.*, 2001; Litovsky, 2005). However, given that each SRM data point obtained in the current study represents a single adaptive track, the extent of the contribution of intrasubject variability to these results cannot be addressed or ruled out. Future studies should address this important issue.

For both groups of children there appeared to be a robust relationship between individuals' performance in *front* (when the target and the competitor are spatially near) and the amount of SRM. That is, SRM was generally greater when performance in front was worse. It is possible that young children adopt different listening strategies under nonoptimal listening situations. While some children are likely to use both spatial and perceptual cues such as differences in speakers' fundamental frequencies (F0), others are unable to exploit such nonspatial cues and for those children spatial cues are more potent. It is important to note that for those children who are good users of nonspatial cues, it is less likely to see robust SRM since the effect of spatial separation is minimized by the low (better) *front* SRTs. However, the extent to which children could differ in taking advantage of these perceptual cues or when this ability emerges needs to be investigated by future studies.

C. Effect of test

In the 4- to 5-year-old group, SRTs were somewhat higher when using CRISP-Jr. compared with CRISP. This result could be attributed to differences in the speech material; CRISP-Jr. contains primarily single-syllabic words while the stimuli in CRISP are bi-syllabic (spondees). Although the monosyllabic words are simpler, and therefore suitable for young children, they may require higher signal level to be fully identifiable. This is consistent with reports that monosyllabic words are the least understandable on the continuum of meaningful words (e.g., Hirsh *et al.*, 1954), and that speech intelligibility (i.e., SRTs measured in the present study) is expected to improve as the number of syllables per word increases. This does not negate the utility of the CRISP-Jr. test as an appropriate tool for testing very young children, because of the limited vocabulary of most young children. This issue was successfully overcome here. In fact, using single-syllabic words has the advantage of minimizing the redundancy of the speech signal, which eventually makes the test more sensitive for certain measures such as binaural integration (Smith and Resnick, 1972).

The SRT issue is also less fundamental when one considers the fact that the amounts of masking and SRM were similar for the CRISP-Jr. and the CRISP tests. This finding suggests that masking and SRM in young children are both robust phenomena that do not depend on the exact stimulus corpus or stimulus presentation platform. Similarly, the individual variability in amount of SRM was not restricted to one test. Most interesting perhaps is the finding that, while some children were better able to use spatial cues in the CRISP-Jr. test, for other children the CRISP test was more effective in eliciting SRM (see Fig. 2). It is possible that this type of inconsistent performance across the two tests emerged out of perceptual elements triggered by the difficulty of particular stimuli for some children but not for others. This may have elements akin to informational masking, whereby SRM increases when the challenge to the auditory system is greater. One aspect of informational masking is the stimulus uncertainty that occurs when the background masker is unknown or unpredictable (e.g., Durlach *et al.*,

2003; Brungart and Simpson, 2004; Hawley *et al.*, 2004). Each of the tasks used here placed the children in a somewhat different complex auditory environment, and it is possible that each child's approach to the problem varied in ways that created more uncertainty for some children in one task, and for other children on the alternate task. These differences may have led to increased informational masking in situations that caused greater uncertainty. Resolving this potential issue is beyond the scope of the present study, but is an issue that can be better addressed with more extensive testing in future work.

V. SUMMARY AND CONCLUSIONS

This study was aimed at evaluating the developmental ontogeny of sound source segregation in young children, ages 3 through 5 years, using child-friendly testing tools (CRISP and CRISP-Jr.). Results showed that there are age-related differences in SRTs, but not in amount of masking or SRM. In addition, the two tests yielded similar amount of SRM, which indicates that SRM is a robust phenomenon that does not depend on the exact stimulus corpus or stimulus presentation platform. These findings further suggest that children as young as 3 years old are able to use spatial cues to segregate different auditory streams, implying that some of the mechanisms that mediate spatial source segregation develop by early childhood. However, in complex auditory environments, individual children seem to adopt different listening strategies; while some children use both spatial and nonspatial cues, others seem to rely more heavily on spatial cues, which might be primarily monaural, although that remains to be better understood. These results underscore the importance of spatial separation between the target and the competing noise in educational settings such as classrooms. Furthermore, because CRISP and CRISP-Jr., can be used to evaluate benefits of spatial cues in source segregation, these tests may prove to be useful for evaluating hearing aids and cochlear implant fitting for usage in noisy environments. Finally, the CRISP-Jr. test could further be used for evaluating speech intelligibility in noise in children whose receptive language is delayed compared with age-matched peers.

ACKNOWLEDGMENTS

The authors are grateful to Diana Brown and Shelly Godar for helping in subjects' recruitment, and to Patti Johnstone and Gary Jones for helping with data analysis. We would also like to thank all of the parents and children who participated in the listening games, without whom this work would not be possible. This work was supported by NIH-NIDCD (Grant Nos. R01-DC003083 and R21-DC05469 to R.Y.L.).

APPENDIX A: LIST OF 25 SPONDEE WORDS USED IN CRISP

Hotdog
Ice cream
Birdnest
Cowboy
Dollhouse

Barnyard
Scarecrow
Railroad
Sidewalk
Rainbow
Cupcake
Birthday
Airplane
Eyebrow
Shoelace
Toothbrush
Hairbrush
Highchair
Necktie
Playground
Football
Baseball
Bluejay
Bath tub
Bedroom

APPENDIX B: LIST OF TARGET WORDS USED IN CRISP-JUNIOR

Mouth
Nose
Eyes
Cheeks
Hat
Feet
Ears
Hands
Socks
Shoes
Hair
Ball
Eyebrows
Toy car
Glasses
Balloons

- Allen, P., and Nelles, J. (1996). "Development of auditory information integration abilities," *J. Acoust. Soc. Am.* **100**, 1043–1051.
- Allen, P., and Wightman, F. (1994). "Psychometric functions for children's detection of tones in noise," *J. Speech Hear. Res.* **37**, 205–215.
- Allen, P., and Wightman, F. (1995). "Effects of signal and masker uncertainty on children's detection," *J. Speech Hear. Res.* **38**, 503–511.
- Allen, P., Wightman, F. L., Kistler, D. J., and Dolan, T. R. (1989). "Frequency resolution in children," *J. Speech Hear. Res.*, **32**, 317–322.
- Ball, M. J. (1999). "Reynell developmental language scales III: A quick and easy LARSP," *Int. J. Lang Commun. Disord.* **34**, 171–174.
- Bronkhorst, A. (2000). "The cocktail party phenomenon: A review of research on speech intelligibility in multiple-talker conditions," *Acust. Acta Acust.* **86**, 117–128.
- Bronkhorst, A. W., and Plomp, R. (1988). "The effect of head-induced interaural time and level differences on speech intelligibility in noise," *J. Acoust. Soc. Am.* **83**, 1508–1516.
- Brungart, D. S., and Simpson, B. D. (2004). "Within-ear and across-ear interference in a dichotic cocktail party listening task: Effects of masker uncertainty," *J. Acoust. Soc. Am.* **115**, 301–310.
- Buss, E., Hall, J. W., III, Grose, J. H., and Dev, M. B. (1999). "Development of adult-like performance in backward, simultaneous, and forward masking," *J. Speech Lang. Hear. Res.* **42**, 844–849.
- Cherry, E. C. (1953). "Some experiments on the recognition of speech, with

- one and two ears," *J. Acoust. Soc. Am.* **25**, 975–979.
- Culling, J. F., Hawley, M. L., and Litovsky, R. Y. (2004). "The role of head-induced interaural time and level differences in the speech reception threshold for multiple interfering sound sources," *J. Acoust. Soc. Am.* **116**, 1057–1065.
- Dirks, D. D., and Wilson, R. H. (1969). "The effect of spatially separated sound sources on speech intelligibility," *J. Speech Hear. Res.* **12**, 5–38.
- Drullman, R., and Bronkhorst, A. (2000). "Multichannel speech intelligibility and talker recognition using monaural, binaural, and three-dimensional auditory presentation," *J. Acoust. Soc. Am.* **107**, 2224–2235.
- Durlach, N. I., Mason, C. R., Shinn-Cunningham, B. G., Arbogast, T. L., Colburn, H. S., and Kidd, G. Jr. (2003). "Informational masking: Counteracting the effects of stimulus uncertainty by decreasing target-masker similarity," *J. Acoust. Soc. Am.* **114**, 368–379.
- Elliott, L. L., Conners, S., Kille, E., Levin, S., Ball, K., and Katz, D. (1979). "Children's understanding of monosyllabic nouns in quiet and in noise," *J. Acoust. Soc. Am.* **66**, 12–21.
- Festen, J. M., and Plomp, R. (1990). "Effects of fluctuating noise and interfering speech on the speech-reception threshold for impaired and normal hearing," *J. Acoust. Soc. Am.* **88**, 1725–1736.
- Fior, R. (1972). "Physiological maturation of auditory function between 3 and 13 years of age," *Audiology* **11**, 317–321.
- Freyman, R. L., Helfer, K. S., McCall, D. D., and Clifton, R. K. (1999). "The role of perceived spatial separation in the unmasking of speech," *J. Acoust. Soc. Am.* **106**, 3578–3588.
- Hall, J. W., III, Grose, J. H., Buss, E., and Dev, M. B. (2002). "Spondee recognition in a two-talker masker and a speech shaped noise masker in adults and children," *Ear Hear.* **23**, 159–165.
- Hall, J. W., III, and Grose, J. H. (1990). "The masking level difference in children," *J. Am. Acad. Audiol.* **1**, 81–88.
- Hall, J. W., III, and Grose, J. H. (1991). "Notched noise measures of frequency selectivity in adults and children using fixed masker level and fixed signal level presentation," *J. Speech Hear. Res.* **34**, 651–660.
- Hall, J. W., III, and Grose, J. H. (1994). "Development of temporal resolution in children as measured by the temporal resolution transfer function," *J. Acoust. Soc. Am.* **96**, 150–154.
- Hall, J. W., III, Buss, E., and Grose, J. H. (2005). "Informational masking release in children and adults," *J. Acoust. Soc. Am.* **118**, 1605–1613.
- Hartley, D. E., Wright, B. A., Hogan, S. C., and Moore, D. R. (2000). "Age-related improvements in auditory backward and simultaneous masking in 6- to 10-year-old children," *J. Speech Lang. Hear. Res.* **43**, 1402–1415.
- Hawley, M. L., Litovsky, R. Y., and Culling, J. F. (2004). "The benefits of binaural hearing in a cocktail party: Effect of location and type of interferer," *J. Acoust. Soc. Am.* **115**, 833–843.
- Hawley, M. L., Litovsky, R. Y., and Colburn, H. S. (1999). "Speech intelligibility and localization in a multi-source environment," *J. Acoust. Soc. Am.* **105**, 3436–3448.
- Hill, P. R., Hartley, D. E., Glasberg, B. R., Moore, B. C., and Moore, D. R. (2004). "Auditory processing efficiency and temporal resolution in children and adults," *J. Speech Lang. Hear. Res.* **47**, 1022–1029.
- Hirsh, I. J. (1950). "The relation between localization and intelligibility," *J. Acoust. Soc. Am.* **22**, 196–200.
- Hirsh, I. J., Reynolds, E. G., and Joseph, J. (1954). "Intelligibility of different speech material," *J. Acoust. Soc. Am.* **26**, 530–538.
- Johnstone, P., and Litovsky, R. (2006). "Effect of masker type and age on speech intelligibility and spatial release from masking in children and adults," *J. Acoust. Soc. Am.* **120**, 2177–2189.
- Kidd, G., Mason, C. R., Rohla, T. L., and Deliwala, P. S. (1998). "Release from masking due to spatial separation of sources in the identification of nonspeech auditory patterns," *J. Acoust. Soc. Am.* **104**, 422–431.
- Lenihan, J. M. A., Christie, J. F., Russell, T. S., Orr, N. M., Hamilton, M. D., and Konx, E. C. (1971). "The threshold of hearing in school children," *J. Laryngol. Otol.* **85**, 375–385.
- Levitt, H. (1971). "Transformed up-down methods in psychoacoustics," *J. Acoust. Soc. Am.* **49**, 467–477.
- Lin, W. Y., and Feng, A. S. (2003). "GABA is involved in spatial unmasking in the frog auditory midbrain," *J. Neurosci.* **23**, 8143–8151.
- Litovsky, R. Y. (1997). "Developmental changes in the precedence effect: Estimate of minimum audible angle," *J. Acoust. Soc. Am.* **102**, 1739–1745.
- Litovsky, R. Y. (2003). "Method and system for rapid and reliable testing of speech intelligibility in children," U.S. Patent No. 6,584,440.
- Litovsky, R. Y., Parkinson, A., Arcaroli, J., Peters, R., Lake, J., Johnstone, P., and Yu, G. (2004). "Bilateral cochlear implants in adults and children," *Arch. Otolaryngol. Head Neck Surg.* **130**, 648–655.
- Litovsky, R. Y. (2005). "Speech intelligibility and spatial release from masking in young children," *J. Acoust. Soc. Am.* **117**, 3091–3099.
- Litovsky, R. Y., Johnstone, P., and Godar, S. (2006). "Benefits of bilateral cochlear implants and/or hearing aids in children," *Int. J. Audiol.* **45**, 78–91.
- Lutfi, R. A., Kistler, D. J., Oh, E. L., and Callahan, M. R. (2003). "One factor underlies individual differences in auditory informational masking within and across age groups," *Prog. Aerosp. Sci.* **65**, 396–406.
- Moore, J. K., and Guan, Y. L. (2001). "Cytoarchitectural and axonal maturation in human auditory cortex," *J. Assoc. Res. Otolaryngol.* **2**, 297–311.
- Nittrouer, S., and Boothroyd, A. (1990). "Context effects in phoneme and word recognition by young children and older adults," *J. Acoust. Soc. Am.* **87**, 2705–2715.
- Noble, W., Byrne, D., and Ter-Horst, K. (1997). "Auditory localization, detection of spatial separateness, and speech hearing in noise by hearing-impaired listeners," *J. Acoust. Soc. Am.* **102**, 2343–2352.
- Oh, E. L., Wightman, F., and Lutfi, R. A. (2001). "Children's detection of pure-tone signals with random multitone maskers," *J. Acoust. Soc. Am.* **109**, 2888–2895.
- Papso, C. F., and Blood, I. M. (1989). "Word recognition skills of children and adults in background noise," *Ear Hear.* **10**, 235–236.
- Peissig, J., and Kollmeier, B. (1997). "Directivity of binaural noise reduction in spatial multiple noise-source arrangements for normal and impaired listeners," *J. Acoust. Soc. Am.* **101**, 1660–1670.
- Plomp, R. (1976). "Binaural and monaural speech intelligibility of connected discourse in reverberation as a function of azimuth of a single competing sound source (speech or noise)," *Acustica* **34**, 200–211.
- Pollack, I., and Pickett, J. M. (1958). "Stereophonic listening and speech intelligibility against voice babble," *J. Acoust. Soc. Am.* **30**, 131–133.
- Ponton, C. W., Eggermont, J. J., Kwong, B., and Don, M. (2000). "Maturation of human central auditory system activity: Evidence from multi-channel evoked potentials," *Clin. Neurophysiol.* **111**, 220–236.
- Rakic, P., and Yakovlev, P. I. (1968). "Development of the corpus callosum and cavum septi in man," *J. Comp. Neurol.* **132**, 45–72.
- Robbins, A. M. (1994). "The Mr. Potato head task," Indiana University School of Medicine, Indianapolis.
- Roche, A. F., Siervogel, R. M., Himes, J. H., and Johnson, D. L. (1978). "Longitudinal study of hearing in children: Baseline data concerning auditory thresholds, noise exposure, and biological factors," *J. Acoust. Soc. Am.* **64**, 1593–1601.
- Rothauser, E. H., Chapman, W. D., Guttman, N., Nordby, K. S., Silbigert, H. R., Urbanek, G. E., and Weinstock, M. (1969). "IEEE recommended practice for speech quality measurements," *IEEE Trans. Audio Electroacoust.* **17**, 227–246.
- Sanders, L. D., Stevens, C., Coch, D., and Neville, H. J. (2006). "Selective auditory attention in 3- to 5-year-old children: An event-related potential study," *Neuropsychologia* **44**, 2126–2138.
- Schneider, B. A., Trehub, S. E., Morriongiolo, B. A., and Thorpe, L. A. (1986). "Auditory sensitivity in preschool children," *J. Acoust. Soc. Am.* **79**, 447–452.
- Smith, B. B., and Resnick, D. M. (1972). "An auditory test for assessing brainstem integrity: Preliminary report," *Laryngoscope* **82**, 414–424.
- Svirsky, M., Teoh, S., and Neuburger, H. (2004). "Development of language and speech perception in congenitally, profoundly deaf children as a function of age at cochlear implantation," *Audiol. Neuro-Otol.* **9**, 224–233.
- Werner, L. A. (1996). "The development of auditory behavior (or what the anatomists and physiologists have to explain)," *Ear Hear.* **17**, 438–446.
- Wichmann, F. A., and Hill, J. (2001a). "The psychometric function. I. Fitting, sampling, and goodness of fit," *Percept. Psychophys.* **63**, 1293–1313.
- Wichmann, F. A., and Hill, J. (2001b). "The psychometric function. II. Bootstrap-based confidence intervals and sampling," *Percept. Psychophys.* **63**, 1314–1329.
- Wightman, F., Allen, P., Dolan, T., Kistler, D., and Jamieson, D. (1989). "Temporal resolution in children," *Child Dev.* **60**, 611–624.
- Wightman, F. L., and Kistler, D. J. (2005). "Informational masking of speech in children: Effects of ipsilateral and contralateral distracters," *J. Acoust. Soc. Am.* **118**, 3164–3176.
- Wightman, F. L., Callahan, M. R., Lutfi, R. A., Kistler, D. J., and Oh, E. (2003). "Children's detection of pure-tone signals: Informational masking with contralateral maskers," *J. Acoust. Soc. Am.* **113**, 3297–3305.
- Yost, W. A., Dye, R. H., and Sheft, S. (1996). "A simulated 'cocktail party' with up to three sound sources," *Percept. Psychophys.* **58**, 1026–1036.

The binaural performance of a cross-talk cancellation system with matched or mismatched setup and playback acoustics

Michael A. Akeroyd^{a)}

MRC Institute of Hearing Research (Scottish Section), Glasgow Royal Infirmary, Alexandra Parade, Glasgow G31 2ER, United Kingdom

John Chambers, David Bullock, Alan R. Palmer, and A. Quentin Summerfield^{b)}

MRC Institute of Hearing Research, University Park, Nottingham NG7 2RD, United Kingdom

Philip A. Nelson

Institute of Sound and Vibration Research, University of Southampton, Highfield, Southampton SO17 1BJ, United Kingdom

Stuart Gatehouse

MRC Institute of Hearing Research (Scottish Section), Glasgow Royal Infirmary, Alexandra Parade, Glasgow G31 2ER, United Kingdom

(Received 24 January 2006; revised 7 November 2006; accepted 8 November 2006)

Cross-talk cancellation is a method for synthesizing virtual auditory space using loudspeakers. One implementation is the “Optimal Source Distribution” technique [T. Takeuchi and P. Nelson, *J. Acoust. Soc. Am.* **112**, 2786–2797 (2002)], in which the audio bandwidth is split across three pairs of loudspeakers, placed at azimuths of $\pm 90^\circ$, $\pm 15^\circ$, and $\pm 3^\circ$, conveying low, mid, and high frequencies, respectively. A computational simulation of this system was developed and verified against measurements made on an acoustic system using a manikin. Both the acoustic system and the simulation gave a wideband average cancellation of almost 25 dB. The simulation showed that when there was a mismatch between the head-related transfer functions used to set up the system and those of the final listener, the cancellation was reduced to an average of 13 dB. Moreover, in this case the binaural interaural time differences and interaural level differences delivered by the simulation of the optimal source distribution (OSD) system often differed from the target values. It is concluded that only when the OSD system is set up with “matched” head-related transfer functions can it deliver accurate binaural cues. © 2007 Acoustical Society of America.

[DOI: 10.1121/1.2404625]

PACS number(s): 43.66.Pn, 43.60.Pt, 43.38.Md [AK]

Pages: 1056–1069

I. INTRODUCTION

Cross-talk cancellation systems have been proposed and described many times (e.g., Bauer, 1961; Atal and Schroeder, 1962; Cooper and Bauck, 1989; Møller, 1989; Kryiakakis, 1998; Ward and Elko, 1999; Foo *et al.*, 1999; Sæbø, 2001; Lentz *et al.*, 2005; Bai *et al.*, 2005; Bai and Lee, 2006). Their performance is often impressive, and they can give compelling demonstrations. In order to be a useful tool for experiments on spatial hearing, however, such systems need to be able to deliver accurately and reliably the interaural-time-difference (ITD) and interaural-level-difference (ILD) cues that underlie binaural analysis. This paper reports a set of computational tests of the degree to which a cross-talk cancellation system can perform binaurally. We conducted these evaluations as we had a requirement for an experimental facility that could replicate in the laboratory the spatial acous-

tics of real-world scenes; we were planning to study the relationships between spatial hearing and auditory disability or handicap in elderly adults (e.g., Gatehouse and Noble, 2004; Noble and Gatehouse, 2004), and we considered that a cross-talk cancellation system offered a potentially exact and convenient method for doing this.

Damaske (1971) first demonstrated the binaural capability of cross-talk cancellation, using two loudspeakers at azimuths of $\pm 30^\circ$ placed in an anechoic chamber. The listeners were required to report the location of a virtual source that was generated by binaural recordings using a dummy head of a talker speaking in an anechoic chamber. Localization performance was good, with the mean error being 10° at worst, and remarkably few front-back errors were reported. Performance was impaired if the sounds were reproduced in a reverberant room, and dramatically so if the listener was 17 cm from the optimum position in front of the loudspeakers. Nelson and colleagues (Takeuchi *et al.*, 2001; Rose *et al.*, 2002) have studied the binaural performance of a cross-talk cancellation system with two loudspeakers placed at azimuths of $\pm 5^\circ$ in a large anechoic chamber. They found accurate localizations for target azimuths ahead of the listener, although

^{a)}Author to whom correspondence should be addressed; electronic mail: maa@ihr.gla.ac.uk

^{b)}Current address: Department of Psychology, University of York, Heslington, York, YO10 5DD, United Kingdom.

back-to-front errors were again observed, and targets with large azimuths (near $\pm 90^\circ$) were often mislocated. Similar results were reported for other two-loudspeaker systems by Foo *et al.* (1999) and by Sæbø (2001). Bai *et al.* (2005) observed large numbers of back-to-front errors in their subjective tests of a two-loudspeaker system, although Lentz *et al.* (2005) found remarkably few back-to-front errors with a four-loudspeaker system, two of which were behind the listener.

Takeuchi (2001) tested the binaural performance of a six-loudspeaker system, placed in three left/right pairs at azimuths of $\pm 90^\circ$, $\pm 16^\circ$, and $\pm 3.1^\circ$ presenting frequencies of, respectively, less than 450 Hz, 450–3500 Hz, and greater than 3500 Hz. This system—termed the “optimal source distribution” (“OSD”) system (Takeuchi and Nelson, 2002)—showed encouraging results, in that it gave smaller overall localization errors, as well as fewer back-to-front errors, than a standard two-loudspeaker system with $\pm 5^\circ$ separation. The OSD system also avoids a problem that can be common to two-loudspeaker systems, as at some frequencies the cross-talk cancellation will require more power than the loudspeaker can supply (e.g., Yang *et al.*, 2003; Nelson and Rose, 2005; Orduna-Bustamante *et al.*, 2001). The values of these frequencies are inversely dependent upon the azimuthal span of the loudspeakers (Takeuchi and Nelson, 2002); they are avoided in the OSD system by a careful choice of loudspeaker spans and the frequencies they reproduce.

In order to perform cross-talk cancellation it is necessary to know what needs to be canceled. This can be found by measuring the head-related impulse response or “HRIR” (which in the frequency domain is the head-related transfer function or “HRTF”) between the loudspeakers and the ears of the listener. From these HRIRs a set of digital filters can be calculated which will perform the cancellation (see Sec. II A). It is well known that the HRIRs of individuals differ considerably (e.g., Wightman and Kistler, 1989; Middlebrooks, 1999a, b). Accordingly, the ideal method would be to measure these HRIRs—and also calculate cross-talk cancellation filters—for each individual listener. In many circumstances, however, it may be more practical to optimize the system in advance using a single set of HRIRs, perhaps from an accurately placed manikin, and then calculate from those a set of cross-talk cancellation filters which would be used for all the listeners (e.g., Damaske, 1971; Møller, 1989; Sæbø, 2001; Foo *et al.*, 1999; Takeuchi *et al.*, 2001; Lentz *et al.*, 2005; Bai *et al.*, 2005). In this situation there will be a difference between the listener/manikin for whom the system is set up and the listener/manikin to whom the final sounds are played back. This distinction is crucial to understanding the actual performance of cross-talk cancellation systems, as it corresponds to a distinction between the HRIRs used to calculate the cross-talk cancellation filters and the HRIRs of whomever is listening to the putatively canceled sounds. We will refer to the two sets of HRIRs as, respectively, the “setup” and the “playback” HRIRs. The ideal, individualized situation, where both are the same, represents a matched-HRIR system; the other, nonindividualized situation in which the system is optimized in advance is a mismatched-HRIR system. A mismatched cross-talk cancellation system can

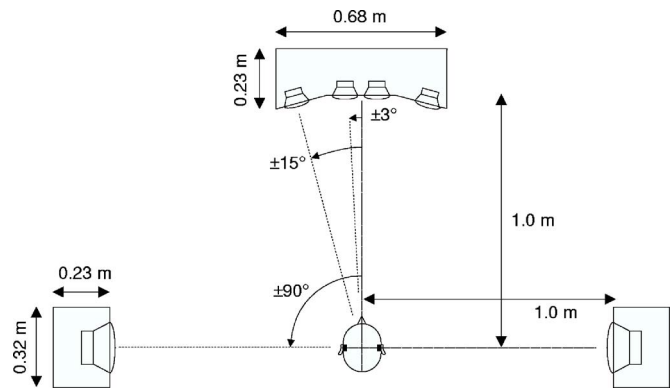


FIG. 1. Scale diagram of the six-loudspeaker, $\pm 3^\circ / \pm 15^\circ / \pm 90^\circ$ OSD system. The $\pm 3^\circ$ loudspeakers were used for frequencies above 3500 Hz, the $\pm 15^\circ$ loudspeakers between 500 and 3500 Hz, and the $\pm 90^\circ$ loudspeakers below 500 Hz.

only be useful for binaural experiments if it can tolerate the differences between the HRIRs of different individuals.

We implemented a computational simulation of the OSD system in order to study the binaural performance of matched-HRIR and mismatched-HRIR systems. First, we validated the simulation against an acoustic system with a manikin (see Sec. II); next we measured the amount of cancellation it gave in matched and mismatched situations (Sec. III), and finally we measured its ability to reproduce ITDs and ILDs, again in matched and mismatched situations (Sec. IV). We used a computational database (Blauert *et al.*, 1998) of seven individual HRIRs to investigate the effects of matching or mismatching the setup and playback HRIRs.

II. VALIDATION OF THE COMPUTATIONAL SIMULATION

In order to validate our computational simulation of the OSD system we compared it to a real acoustic system (Fig. 1). In the initial setup stage, the cross-talk cancellation filters were calculated from a set of HRIRs measured at the ears of the manikin for each of the loudspeakers. Its performance was quantified in the subsequent playback stage using a target signal that was white noise at one ear but silence at the other. Figure 2 shows a schematic illustration of each step involved in playback: first the target signals were digitally convolved with the cross-talk cancellation filters H , then summed to create the left and right signals v_L and v_R , passed through the frequency-crossover system and so split into three frequency bands. Each band was presented through a separate loudspeaker, and the signals thus obtained at the ears of the manikin were recorded for offline analysis.

The computational system simulated the playback stage by digitally convolving the processed signals with the measured HRIRs of the loudspeakers to microphones. Computational simulations have been used before to measure the amount of cancellation and the ITDs of a wave form (e.g., Takeuchi *et al.*, 2001; Hill *et al.*, 2000; Rose *et al.*, 2002; Orduna-Bustamante *et al.*, 2001; Lentz *et al.*, 2005; Bai and Lee, 2006). They tend to predict large amounts of cancellation; for instance, both Takeuchi (2001) and Bai and Lee (2006) predicted over 40 dB. Such performance would have

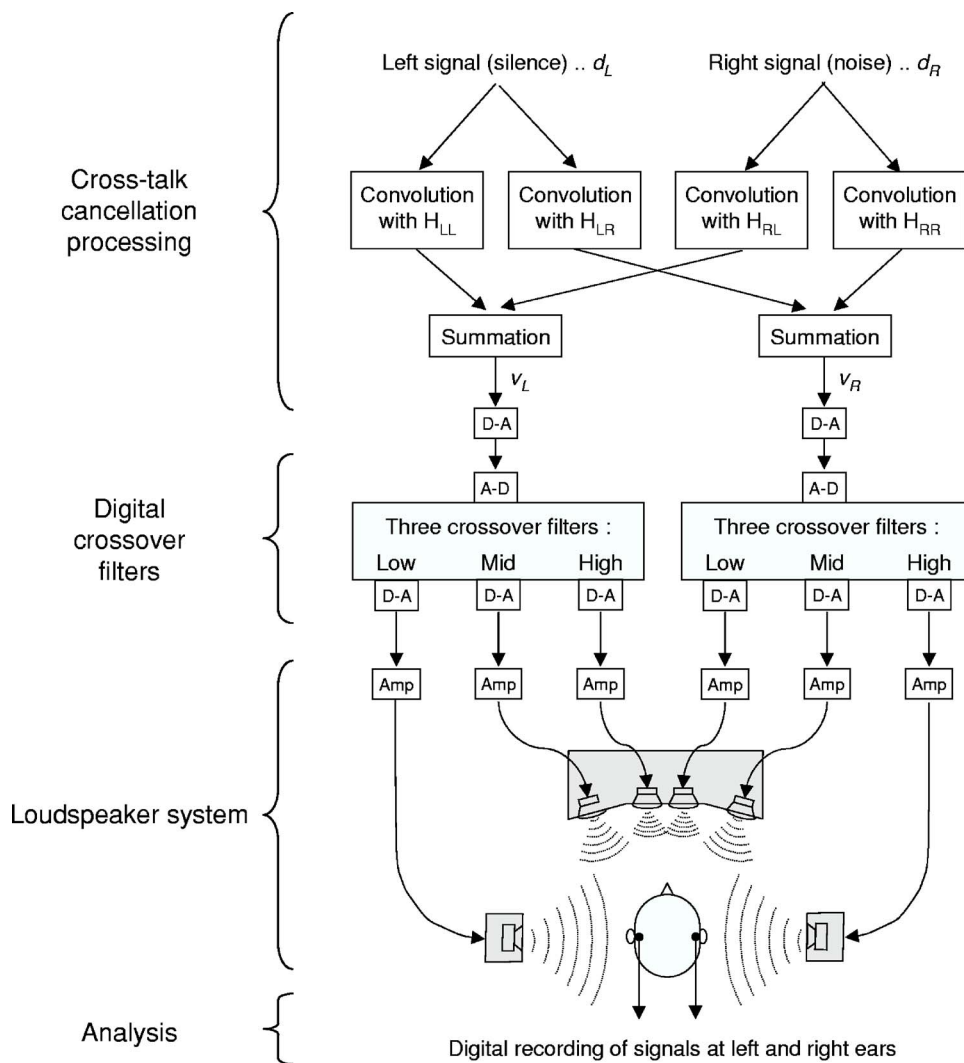


FIG. 2. Schematic illustration of each step involved in the *acoustic* cross-talk cancellation system. The first step (the cross-talk cancellation processing) was performed on a personal computer while the second step (cross-over filters) was performed on a separate digital-signal processing board; note the D/A and A/D converters between them. The final step was the loudspeaker presentation of the signals to an acoustic manikin, acting as the listener, with a subsequent off-line analysis of the actual signals received at its ears.

been more than sufficient for binaural experiments, as it is greater than the 25–30 dB of ILD that is the maximum that is usually encountered (e.g., Blauert, 1997).

A. Acoustical methods

Six loudspeakers were used, placed in three pairs at azimuths of $\pm 3^\circ$, $\pm 15^\circ$, and $\pm 90^\circ$ and built into two cabinets (Fig. 1, top panel). The cabinets were placed 1 m away from the center of an acoustic manikin (Brüel and Kjær, model 4100D), and were carefully measured to be left/right symmetric about the manikin. The manikin was fitted with silicone pinnae and with 1/2 in. condenser microphones placed at the entrance to each ear canal; the microphones were approximately 1 m above the floor of the room, and were level with the center of the loudspeakers. All the apparatus was placed in the center of a small acoustic chamber (4 m width, 1.8 m depth, 2 m height), whose surfaces were covered with foam wedges. The reverberation time of the room was less than 40 ms between 250 and 8000 Hz. All of the signal presentations were controlled by a host computer (Toshiba P4000). After D-A conversion (using the inbuilt converter of the computer) at a sampling rate of 22 050 Hz, the signals were passed through a real-time, digital frequency-crossover system. This consisted of three, 396 sample, 22 050 Hz

sampling-rate finite-impulse-response (FIR) digital filters (Trinder, 1982) running on a digital signal-processing board. The outputs of the amp crossover system were then amplified individually (three stereo amplifiers, Denon PMA-255UK) to form the feeds to the individual loudspeakers. The three filters were set to 0–500 Hz (“low;” $\pm 90^\circ$ loudspeakers), 500–3500 Hz (“mid;” $\pm 15^\circ$ loudspeakers), and 3500–11 025 Hz (“high;” $\pm 3^\circ$ -loudspeakers).

The cross-talk cancellation filters were calculated from measurements of the impulse responses of the transfer functions from the left loudspeakers to the left manikin microphone (C_{LL}), left to right (C_{LR}), right to left (C_{RL}), and right to right (C_{RR}).¹ The impulse responses were obtained using the maximum-length-sequence (“MLS”) method (e.g., Davies, 1966; for more on our implementation, see Thornton *et al.*, 2001, 1994, and Chambers *et al.*, 2001). The sampling rate was 44.1 kHz, and, as the MLS signals were passed through the frequency-crossover system and presented simultaneously through the three loudspeakers on the left (or right), the whole of each impulse response was obtained at the same time. Figure 3 shows the MLS recording of the C_{LL} impulse response. The large pulse was the direct sound, and its fine structure is due to both the FIR response of the cross-

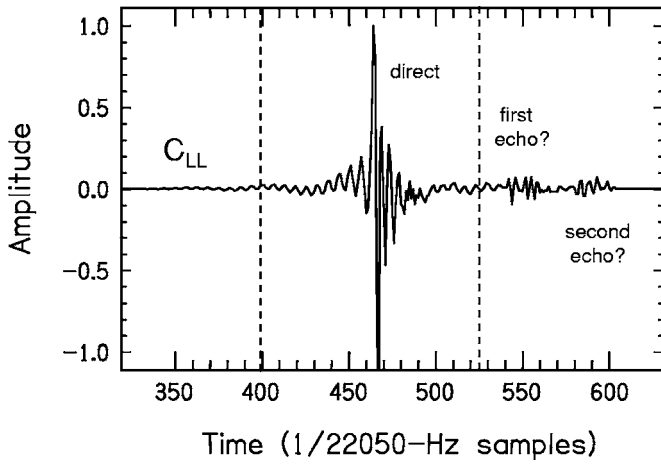


FIG. 3. The left-loudspeaker-to-left-microphone (C_{LL}) impulse response, measured using the MLS method in the $\pm 3^\circ / \pm 15^\circ / \pm 90^\circ$ cross-talk cancellation system. The direct sound is marked, along with two putative reflections, which were removed in subsequent modifications.

over filters and the HRTF of the manikin, whilst the subsequent, less-intense pulses were probably due to reflections from the loudspeaker cabinets.

The first step in the calculation of the four cross-talk cancellation filters was to digitally convolve each of the four impulse responses with a sharp, 11 kHz antialiasing digital filter. They were then downsampled to 22 050 Hz and edited to a 128 sample (5.8 ms) window, centered on the main pulse in order to remove the subsequent reflections (shown by the dashed lines in Fig. 3). Next, a 4096-point fast-fourier transform (FFT; 5.4 Hz resolution) was applied after suitable zero padding, and then the coefficients of the filters were calculated for each of the 4096 frequencies independently using

$$\begin{pmatrix} H_{LL,k} & H_{RL,k} \\ H_{LR,k} & H_{RR,k} \end{pmatrix} = \left(\begin{pmatrix} C_{LL,k} & C_{RL,k} \\ C_{LR,k} & C_{RR,k} \end{pmatrix} \right)^H \times \begin{pmatrix} C_{LL,k} & C_{RL,k} \\ C_{LR,k} & C_{RR,k} \end{pmatrix} + \beta \begin{pmatrix} 1 & 0 \\ 0 & 1 \end{pmatrix}^{-1} \times \begin{pmatrix} C_{LL,k} & C_{RL,k} \\ C_{LR,k} & C_{RR,k} \end{pmatrix}^H \times \exp\left(\frac{-j2\pi(k-1)D}{4096}\right) \quad (1)$$

[cf. Hill *et al.*, 2000, Eq. (6); Takeuchi and Nelson, 2002, Eq. (17)], where k is the frequency index (1-4096), $C_{LL,k}$, $C_{LR,k}$, $C_{RL,k}$, and $C_{RR,k}$ are the Fourier coefficients of the four loudspeaker-microphone transfer functions at the k th frequency, $H_{LL,k}$, $H_{LR,k}$, $H_{RL,k}$, and $H_{RR,k}$ are the Fourier coefficients of the corresponding cross-talk cancellation filters at the k th frequency, D (=1500 samples) is a modeling delay, β (=0.001) is a regularization parameter for ensuring a stable inversion, and H is the Hermitian operator (i.e., the transpose of the complex conjugate of a matrix).² The impulse responses of each of the four final cross-talk cancellation filters was obtained by applying an inverse FFT and then, to remove any minor imaginary components due to rounding errors, taking the real part.

The amount of cross-talk cancellation was measured using a 5 s test signal whose right channel d_R was a 8 kHz low-pass filtered white noise and whose left channel d_L was

silence. These signals (d_L and d_R) were digitally convolved with the impulse responses of the four cross-talk cancellation filters:

$$v_L = H_{LL} * d_L + H_{RL} * d_R, \quad (2)$$

$$v_R = H_{LR} * d_L + H_{RR} * d_R. \quad (3)$$

Raised-cosine gates (10 ms duration) were subsequently applied to smooth the onset and offset. The resulting signals were presented by the host computer through the frequency-crossover system and the six-loudspeaker array. The sounds w_L and w_R reaching the manikin's microphones were recorded using a digital recorder (Marantz PMD690). They differ from the presented signals by the action of the loudspeaker-microphone transfer functions, i.e.,

$$w_L = C_{LL} * v_L + C_{RL} * v_R, \quad (4)$$

$$w_R = C_{LR} * v_L + C_{RR} * v_R. \quad (5)$$

If the cross-talk cancellation had been perfect, then w_R and w_L would have matched d_R and d_L (i.e., on 8 kHz low-pass-filtered noise and silence).

The majority of analyses were based on the average of ten 10 ms Hanning windowed DFTs (1920 point, 25 Hz resolution) of the received sounds. The amount of cross-talk cancellation achieved was defined as the difference between the left and right power spectra (in decibels). For convenience, a single-number value was used to summarize performance. Termed the "wideband average cancellation," it was calculated as the average of the cross-talk cancellation at every discrete spectral frequency between 100 and 8000 Hz.

B. Acoustical results

The top panel of Fig. 4 shows the power spectra of the signals received at the two microphones of the manikin during playback. The spectrum at the right ear was close to the desired 8 kHz low-pass noise, but the spectrum at the left ear was not the desired silence. The bottom panel shows the amount of cross-talk cancellation that was found (i.e., the difference between those power spectra). At some frequencies, as much as 30 dB was obtained, but at other frequencies it was as little as 10 dB. The wideband average cancellation was 20 dB.

This amount of cancellation was less than we expected from other experimental studies of cross-talk cancellation; for instance, Bai *et al.* (2005), Lentz *et al.* (2005), and Bai and Lee (2006) obtained up to about 30 dB. We noted, however, two possible reflections in the loudspeaker-manikin HRIRs that may have affected performance: one was a reflection from the $\pm 90^\circ$ loudspeaker cabinets, corresponding to an additional distance of 1.4 m, or about 90 samples, whilst the other was a reflection from the manikin and then the $\pm 15^\circ / \pm 3^\circ$ loudspeaker cabinet, at a distance of 2 m, or 130 samples (see Fig. 3).³ We attempted to reduce both of these by removing the $\pm 90^\circ$ loudspeaker cabinets, moving the other cabinet further away, to a distance of 1.6 m, and presenting all the sounds through the middle pair of loud-

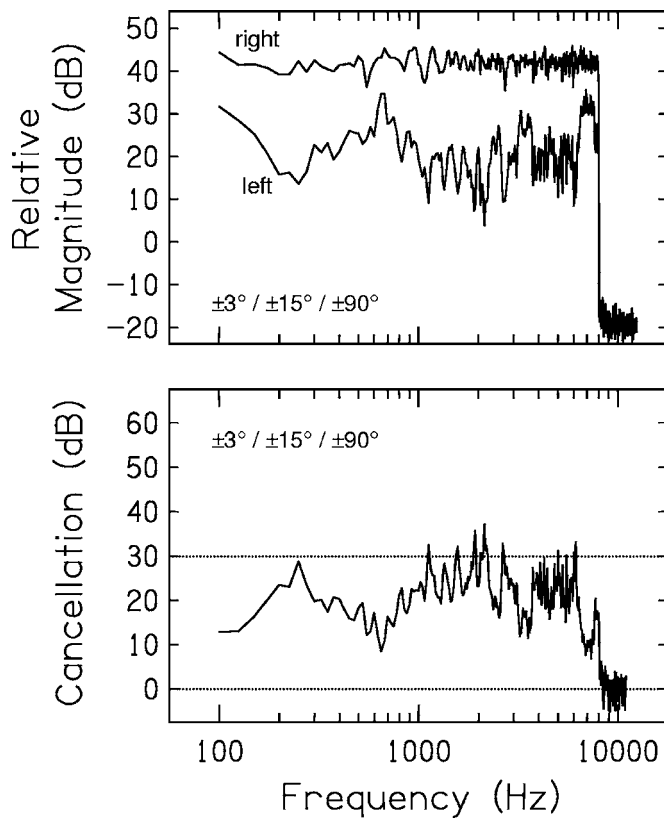


FIG. 4. The top panel shows the magnitude spectra of the signals delivered to the microphones of the manikin by the $\pm 3^\circ / \pm 15^\circ / \pm 90^\circ$ cross-talk cancellation system. The right-ear target was a 0–8 kHz white noise, while the left ear target was silence. The bottom panel shows the amount of cross-talk cancellation achieved, which was defined as the difference in those magnitude spectra.

speakers (which, due to the change in distance, subtended $\pm 9^\circ$ instead of $\pm 15^\circ$; see Fig. 5, top panel). These modifications gave us a minor improvement in wideband cancellation to 23 dB (Fig. 5, bottom panel). The best performance was found between about 2000 and 4000 Hz, where we obtained 30 dB of cancellation.

C. Computational methods

Our goal here was to simulate digitally, as closely as possible, the playback operation of the acoustical OSD system. Figure 6 shows a schematic illustration of the method: the same target signals as were used acoustically were defined, they were digitally convolved with the cross-talk cancellation filters (H_{LL} , etc.) to get the processed signals v_L and v_R , and those were then digitally convolved with the playback HRIRs of the four acoustic paths (C_{LL} , etc.) to get the signals that would have been received at the manikin microphones. These were then subjected to the same analysis procedures as before.

Table I lists the simulations that we tested. We attempted to predict both the full, six-loudspeaker OSD system (simulations A and B) and the reduced-echo, two-loudspeaker system (C and D). In simulations A and C we set the playback HRIRs to be exactly the same as the setup HRIRs, and so were short enough—128 samples (5.8 ms)—to encompass only the direct sound. In simulations B and D the playback

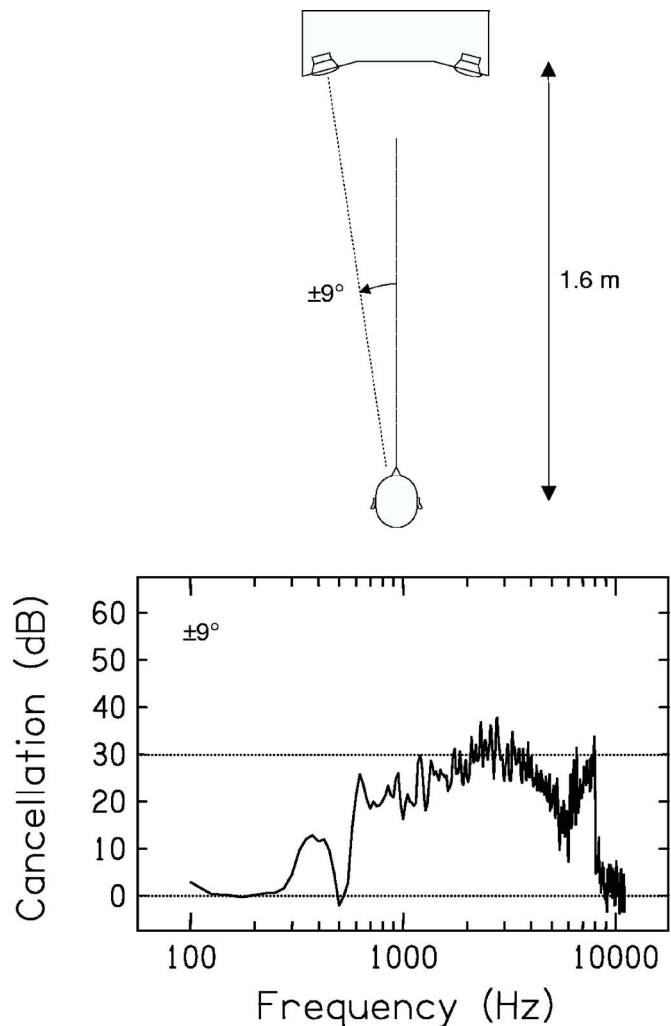


FIG. 5. A scale diagram of the modified acoustic system, using two loudspeakers at $\pm 9^\circ$ (cf. Fig. 1), and the amount of cross-talk cancellation it gave (cf. Fig. 4).

HRIRs were the *full*, 731 sample (33.2 ms) MLS recordings from which the setup HRIRs had been extracted; they were long enough to include the earliest reflections from the loudspeaker cabinets and the initial acoustic decay of the room. Simulation E is described later.

D. Computational results and discussion

The bold lines on the four panels of Fig. 7 show the amounts of cross-talk cancellation predicted by each of the four simulations, whilst the faint lines show the corresponding results from the acoustic system (Fig. 4). Both simulations A and C gave considerably more cross-talk cancellation than the acoustic measurements; the wideband cancellations were, respectively, 58 and 56 dB, whereas the corresponding acoustic values were 20 and 23 dB. In both of these simulations the playback HRIRs included the direct sound *only*. The results of the two simulations that had also incorporated the initial reflections into the playback HRIRs were a much closer match (simulation B gave 22 dB and simulation D gave 29 dB). Simulation B reproduced with fair accuracy its spectral profile of acoustic cancellation. The fit was less good

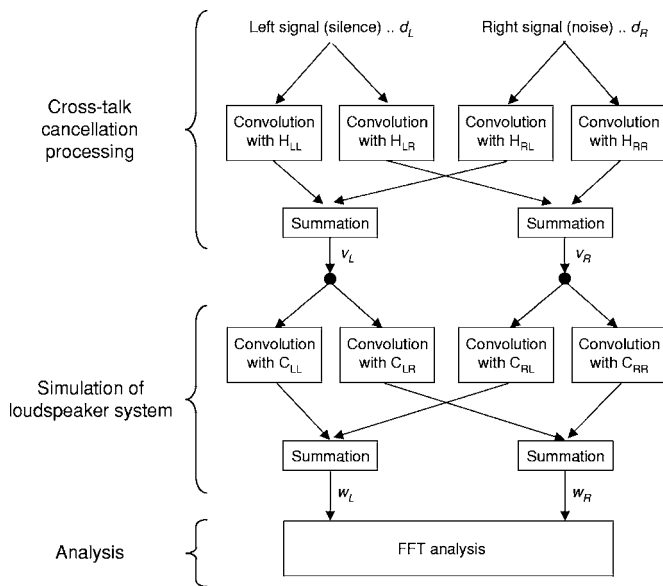


FIG. 6. Schematic illustration of each step involved in the *computational* simulations of cross-talk cancellation. The steps follow the acoustic system (Fig. 2), except that the loudspeaker presentation is simulated by a set of digital convolution and summations. The illustration represents simulations C, D, and E (Table I), as the digital crossover filters are not shown; simulations A and B included them.

for simulation D, although it did reproduce the broad dip near 6000 Hz that was seen acoustically.

The extreme amount of cancellation observed in simulations A and C is of interest. It is likely that it was due to the setup HRIRs being numerically identical to the playback HRIRs as well as to excluding all reflections; this accords with Takeuchi's (2001) results, who obtained similar ideal performance from simulations which used the same HRIRs (taken from KEMAR; Gardner and Martin, 1995) for setup and playback. We ran another simulation to study this (simulation E). Here the playback HRIRs were taken from a *second* run of the MLS algorithm; thus both the setup and playback HRIRs were measures of the same loudspeaker-manikin transfer functions, but, being independent recordings, they were numerically slightly different. The results of this simulation are shown in the bottom panel of Fig. 7. The match between the simulated and acoustic spectral profiles was impressive, especially between about 1000 and 6000 Hz.

The best matches between the simulation and the acoustic measurements were obtained only after including many of

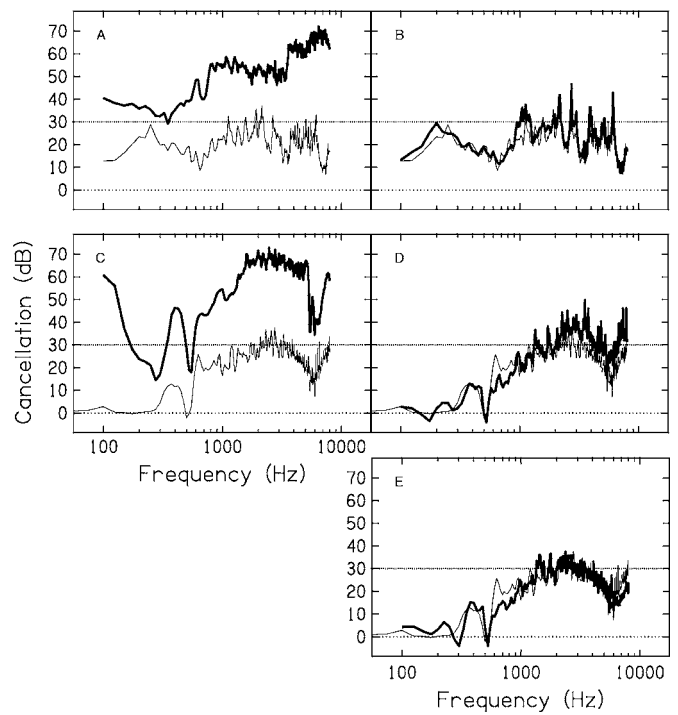


FIG. 7. The results of the five computational simulations of cross-talk cancellation. The parameters of each simulation are reported in Table I. The bold lines in each panel show the amount of cross-talk cancellation predicted by the simulations, and the faint lines show the corresponding acoustical measurements.

the decay characteristics of the experimental room. This implies that if the goal of a simulation is to predict accurately the performance of a real system, then it is necessary to include in the simulations the acoustics of the room used for playback and, ideally, to ensure that the playback HRIRs are recorded independently of the setup HRIRs. Furthermore, our results indicate that the performance of the real cross-talk cancellation system was probably limited by the reflections and reverberation of the playback room. This is consistent with Damaske (1971), who used a two-loudspeaker, $\pm 30^\circ$ azimuth system, and observed near-ideal localization in an anechoic space but an increase in back-to-front confusions in a room with a reverberation time of 0.5 s, and also with Sæbø (2001), who found performance compromised by reflections in tests with a system using two closely spaced loudspeakers placed in an anechoic room with and without additional reflecting surfaces [but it should be noted there are some conflicting data on the effects of reverberation; com-

TABLE I. Summary of the computational simulations used in validating the computational model. The sampling rate was 22.05 kHz and so the 5.8 ms duration impulse responses corresponded to 128 points, and the 33.2 ms responses to 731 points.

Simulation	Loudspeaker azimuths (deg)	Loudspeaker-to-manikin distance (m)	Duration of setup HRIRs (ms)	Duration of playback HRIRs (ms)	Relationship of HRIRs
A	$\pm 3, \pm 15, \pm 90$	1	5.8	5.8	Identical
B	$\pm 3, \pm 15, \pm 90$	1	5.8	33.2	Setup edited from playback
C	± 9	1.6	5.8	5.8	Identical
D	± 9	1.6	5.8	33.2	Setup edited from playback
E	± 9	1.6	5.8	33.2	Independent measurements

pare Cooper and Bauck (1989) to Sæbø (2001)]. In another condition Sæbø extended the setup HRIRs—and so the cross-talk cancellation filters—to include a reflection from a wall, and, although this offered some benefit, it did not return performance to the anechoic level. Any other fixed extraneous sounds, such as nonfrontal radiation from the loudspeakers or any reverberation, would similarly be expected to lead to a reduction in cross-talk cancellation (Takeuchi and Nelson, 2002), and it would always be necessary to exclude any dynamic or random sound from the setup HRIRs, as a cross-talk cancellation system can only ever remove static sounds.

In summary, it was clear that the acoustical data could be accurately matched by the simulation. The validation procedure was therefore successful, and we felt justified in using the simulation to study the amount of cross-talk cancellation given by and the binaural performance of matched and mismatched systems.

III. AMOUNTS OF CANCELLATION IN MATCHED AND MISMATCHED SYSTEMS

We used the computational simulation to investigate the degree to which the cross-talk cancellation system could tolerate the differences between the HRIRs of individuals. These tests were conducted using a database of HRIR recordings from seven individuals (Blauert *et al.*, 1998). We also studied performance when a set of nonindividual HRIRs were used for the calculation of the cross-talk cancellation filters, as such methods have been commonly used in subjective tests of the localization performance of cross-talk cancellation, be it either from analytic models of the head (e.g., Hill *et al.* 2000; Rose *et al.* 2002) or from manikin measurements (e.g., Foo *et al.*, 1999; Sæbø, 2001; Takeuchi *et al.*, 2001; Lentz *et al.*, 2005; Bai *et al.*, 2005).

A. Individual-listener HRIRs

The method followed closely that of the earlier simulations, differing only in that we needed to recreate the HRIRs for each listener as if he or she had been in the OSD system. The basis for this calculation was the seven individual HRIRs in the “AUDIS” database (Blauert *et al.*, 1998), which were recorded in an anechoic chamber at azimuth intervals of 15° around the head, for a loudspeaker-listener separation of 2.5 m. The recordings were taken at both ears, so incorporating the natural asymmetries of real people, and were 9 ms (400 samples at 44 100 Hz) in duration. We took the $\pm 90^\circ$ and $\pm 15^\circ$ HRIRs from the database and calculated the $\pm 3^\circ$ HRIRs by a linear, frequency-domain interpolation of the level and unwrapped phase spectra of the HRIRs at 0° and $+15^\circ$ or 0° and -15° (cf. Hartung *et al.*, 1999; Langendijk and Bronkhorst, 2000). They were downsampled to 22 050 Hz, then convolved with the three digital crossover filters, summed, and finally windowed to 128 samples (5.8 ms) approximately centered on the main impulse. We did not incorporate any reflections or reverberation, and so these simulations represented an ideal situation.

For the first set of simulations, the setup and playback HRIRs were matched. The top panel of Fig. 8 shows the magnitude spectra of the predicted signals at the ears for one

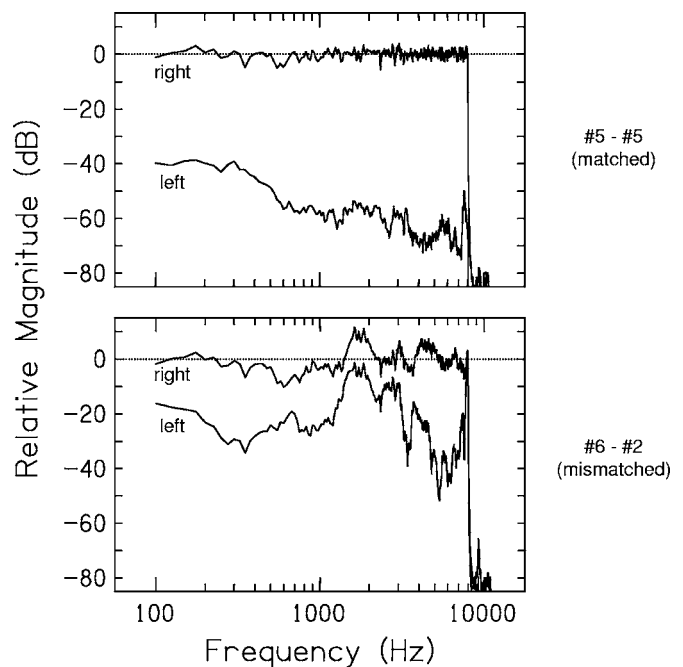


FIG. 8. The magnitude spectra of the signals at the microphones of the manikin calculated from the computational simulation. The top panel shows the results for a matched-HRIR system, the bottom panel for a mismatched-HRIR system.

of these simulations (both the setup HRIRs were from listener 5). The spectrum at the right ear was extremely close to the desired 0–8 kHz flat-spectrum noise, and the spectrum at the left ear was at least 40 dB lower, and was over 60 dB lower for frequencies above about 1000 Hz. The wideband average cancellation was 61 dB; the range across all seven matched-HRIR combinations was 61–71 dB (see Table II).

A second set of simulations studied mismatched HRIRs. The bottom panel of Fig. 8 shows the left and right magnitude spectra for the case when the setup HRIRs came from listener 6 and the playback HRIRs from listener 2. Neither of the signals at the right or left ears were those desired—both were quite modulated—and it is clear that the amount of cross-talk cancellation was far less than that found in the matched-HRIR simulations; the wideband average cancellation was 25 dB. This combination was chosen for illustration as it was the *best* of the mismatched simulations; the worst value across the 42 combinations was 10 dB, and the group mean was 17 dB (Table II). Figure 9 shows the spectral profile of cancellation for each of 49 combinations of HRIRs in the database. All of the matched combinations (top panel) gave cancellations of 40 dB or more at all frequencies up to 5000 Hz, and some were 70 dB or more at many frequencies. The mismatched combinations (bottom panel) occasionally reached 40 dB but most gave substantially less cancellation than this, and, for a broad band of midfrequencies (about 800–2500 Hz), the majority gave less than 20 dB of cancellation.

These simulations were conducted with HRIRs that were recorded in an anechoic room, and which were further windowed to 5.8 ms. We had noted earlier (Sec. II D) that HRIRs that excluded all of the decay characteristics of the playback room gave unrealistically good cross-talk cancellation

TABLE II. The values of simulated wideband cancellation for each of the 49 combinations of listener in the AUDIS database. The seven matched-HRIR conditions are along the main diagonal; the others are the 42 mismatched-HRIR conditions. The row means and column means (both underlined) are for the *mismatched* conditions only. Also shown are the values when the HRIRs were taken from Gardner and Martin's (1995) database for the KEMAR manikin.

Setup HRIR	Playback HRIR							<u>Mean</u>	KEMAR
	1	2	3	4	5	6	7		
1	68.1	16.1	14.4	14.9	16.5	13.2	13.5	<u>14.8</u>	12.6
2	10.2	62.7	17.6	13.4	24.4	21.5	17.1	<u>17.4</u>	21.9
3	11.7	21.0	64.6	16.5	21.9	19.9	17.6	<u>18.1</u>	17.9
4	12.1	16.7	16.6	62.1	17.4	14.7	12.5	<u>15.0</u>	13.4
5	10.3	24.6	18.6	14.0	60.8	21.5	17.9	<u>17.8</u>	22.1
6	10.2	24.7	19.7	14.4	24.5	70.5	17.0	<u>18.4</u>	21.4
7	12.5	22.4	19.4	14.2	23.0	19.0	62.3	<u>18.4</u>	17.7
<u>Mean</u>	<u>11.2</u>	<u>20.9</u>	<u>17.7</u>	<u>14.6</u>	<u>21.3</u>	<u>18.3</u>	<u>15.9</u>	<u>17.1</u>	<u>18.1</u>
KEMAR	9.2	24.9	17.3	12.9	24.8	21.1	15.3	17.5	64.6

performance, and the corresponding values found there (58 and 56 dB) with short, matched HRIRs are only slightly reduced from the range calculated here for matched HRIRs (61–71 dB). It is therefore likely that the present matched-HRIR simulations represent a computational ideal, and so even the reduced performance seen with the mismatched-HRIRs may be difficult to obtain in any real acoustic system operating in a real room.

Table II also reports the row and column means of the cancellations found in the mismatched combinations. It can be seen that the amount of cancellation was relatively constant across setup listener (a range of 3.4 dB) but depended

substantially upon playback listener (a range of 10.1 dB). These results suggest that the variations in performance are due more to variations in the playback HRIR than in the setup HRIR. Individual differences in head and ear dimensions can be substantial—heads differ by about ± 1 cm, ear sizes by about ± 0.5 cm, ear orientations by about $\pm 7^\circ$ (Al-gazi *et al.*, 2001; see also Burkhard and Sachs, 1975, and Middlebrooks, 1999a)—and it is likely that the variations across the seven listeners in the AUDIS database represent some of this individuality. Furthermore, unless some form of head-restraint was included listeners may also not place their heads exactly at the required point, and would be unlikely to stay stationary across the course of an experiment. Indeed, it is perhaps not surprising that cross-talk cancellation reduces dramatically when mismatches exist between the setup and playback HRIRs, as successful cancellation requires the signal presented from the right loudspeaker to match accurately, in *both* phase and amplitude, the signal from the left loudspeaker when both arrive at the ears. Any individual differences in the head or ear dimensions, and any movements or mislocations in position, must lead to differences in the phase or amplitude at the ears.

B. Manikin HRIRs

We tested whether a set of nonindividual HRIRs would be more successful by rerunning the simulations using the Gardner and Martin (1995) database of HRIRs for the KEMAR manikin. These were recorded using its small ears, which are replicas of an individual whose pinna dimensions are similar to the mean of the population (Burkhard and Sachs, 1975; Maxwell and Burkhard, 1979), and were 128 samples in duration. We simulated a matched system, in which the KEMAR HRIRs were used for both set up and playback, and mismatched systems, in which the KEMAR HRIRs were used for set up but the individual HRTFs from earlier were used for playback, or vice versa.

The results are reported in the last row and column of Table II. When used as the setup HRIR, the overall cancellation (17.5 dB) was as good as that found with many of the AUDIS HRIRs. The *range* of cancellation seen (11–21 dB)

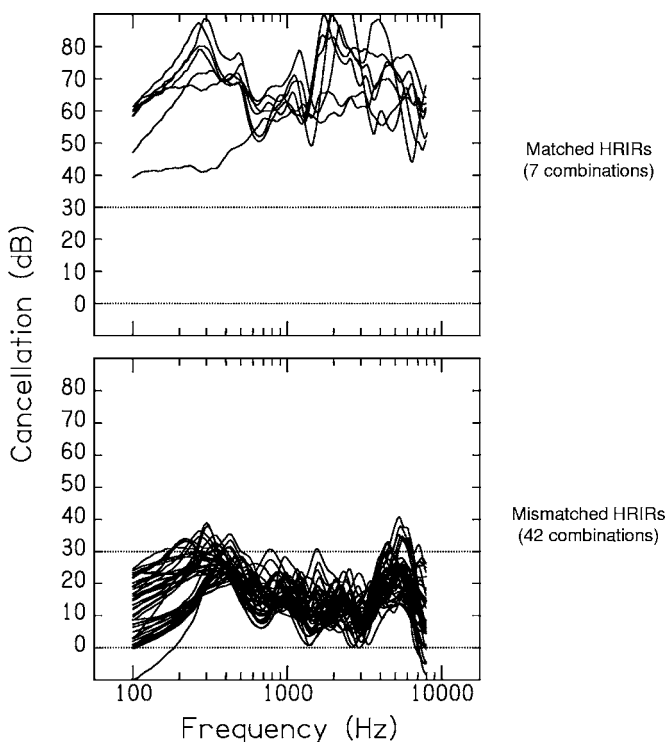


FIG. 9. The amounts of cross-talk cancellation calculated from the computational simulation, for each of the 7 matched-HRIR systems (top panel) and each of the 42 mismatched-HRIR systems (bottom panel). The values of wideband cancellation for each system are reported in Table II.

suggests, however, that some listeners—presumably those whose HRIRs are poor matches to KEMAR’s—would gain little benefit. These results support Takeuchi (2001). In some of his experiments on subjective localization with a two-loudspeaker, $\pm 5^\circ$ azimuth system, he compared cross-talk cancellation filters calculated from a manikin with those calculated from the individual HRIRs of his listeners. He noted better localization performance and a reduction in back-to-front errors in the individualized conditions, and a subsequent analysis showed that these errors were related to the individual spectral details of the HRIRs.

In summary, the results of these simulations clearly indicate that there is a severe reduction in the amount of cross-talk cancellation when the HRIRs used for setup are mismatched from those used for playback. It is likely that the amount of cancellation—on average, some 10–20 dB, depending upon the choice of setup HRIRs—would be insufficient for most binaural cues to be recreated sufficiently accurately (this is considered in more detail in Sec. IV). Furthermore, the cancellation that is obtained is idiosyncratic to each individual, and so, without a knowledge of someone’s HRIR, it would be impossible to know exactly what sounds were reaching them. But if these HRIRs were measured for each individual using the cross-talk cancellation loudspeakers, then the setup HRIRs would be matched to the playback HRIRs and so performance would be expected to be improved.

IV. BINAURAL PERFORMANCE OF MATCHED AND MISMATCHED SYSTEMS

We used the computational simulation to study the accuracy of the delivery of the ITDs and ILDs that underlie the perception of spatial angle. As the preceding simulations showed that the amount of cancellation dropped considerably in the mismatched-HRIR conditions, we expected that the binaural performance would be similarly compromised. In particular, if the mismatch was sufficiently large that the amount of cancellation was *less* than the target ILD, we expected that the delivered ITDs and ILDs would bear no resemblance to the target values but would instead be determined by the characteristics of the cross-talking sound (any nonperfect cancellation would, of course, mean that some of the sound intended for one ear would remain, uncanceled, at the other ear, and if this sound was greater than that actually intended for the other ear, it would determine the ITDs and ILDs).

We measured binaural performance in individual frequency channels. For low frequencies, we applied an analysis of ongoing ITDs and ILDs. For high frequencies, we analyzed the envelope ITDs and ILDs, as there is growing evidence from experiments with “transposed stimuli” of the sensitivity of the binaural system to the interaural cues carried by envelopes (e.g., Bernstein and Trahiotis, 2002, 2003).

A. Ongoing ITDs and ILDs

The test signal was a white noise with the required target ITD and ILD (see the following). This signal was passed through the computational simulation of the six-loudspeaker

(azimuths of $\pm 3^\circ$, $\pm 15^\circ$, and $\pm 90^\circ$) system, with HRIRs taken from the AUDIS database. The ITDs and ILDs of the signals that would have been received at the listener’s ears were obtained from a simplified computational model of binaural hearing (e.g., Shackleton *et al.*, 1992; Stern and Trahiotis, 1997; Akeroyd and Summerfield, 2000; Akeroyd, 2001). First, the signals were passed through two gammatone filters, one for the left channel and one for the right channel, each set to the required center frequency (see the following) and a bandwidth of 1 ERB (Patterson *et al.*, 1995; Glasberg and Moore, 1999). This filtering approximated peripheral auditory frequency analysis, but excluded any nonlinear effects and the action of the inner hair cells. Second, the binaural normalized correlation was computed on the outputs of the filters (Bernstein and Trahiotis, 1996) as a function of a delay applied to one wave form, giving the within-channel cross-correlation function at delays from -750 to $+750 \mu\text{s}$.⁴ Third, the largest peak in each cross-correlation function was found, and its position was taken as the delivered value of the ongoing ITD of the test signal. Fourth, the powers of the outputs of the left and right gammatone filters were measured, and the difference between the two was taken as the delivered ILD of the test signal. The binaural model was run at a sampling rate of 48 kHz.

For the first set of simulations we tested every combination of target ITD and target ILD in the ranges -600 to $+600 \mu\text{s}$ (in $100 \mu\text{s}$ steps) and -25 to $+25$ dB (in 5 dB steps) for a small number of matched-HRIR and mismatched-HRIR combinations. The auditory-filter frequency was fixed at 1000 Hz. The results are shown in Fig. 10. Each point is for a separate target ITD/ILD combination, with the lines connecting points with the same target ILD. The abscissa of each panel is the delivered ILD, the ordinate is the delivered ITD. The left panel shows the results for one of the matched-HRIR simulations (68 dB wideband average cancellation). The results are near-perfect: the rms errors between the target and delivered values were only $13 \mu\text{s}$ and 0.1 dB. We took this as a successful validation of the analysis method for ongoing ITDs and ILDs, but it also showed that the OSD system can reliably deliver any combination of ITD and ILD, provided that the setup and playback HRIRs are matched.

The middle panel plots the results for one of the mismatched-HRIR simulations, which gave a wideband average cancellation of 16 dB. Here, the OSD system failed to reliably recreate ongoing ITDs and ILDs: the rms errors were $296 \mu\text{s}$ and 8.5 dB. Furthermore, a “convergence” of ITD was observed, in that for target ILDs less than -5 dB, the delivered ITD was never larger than $\pm 250 \mu\text{s}$, despite the target ITDs being as large as $\pm 600 \mu\text{s}$. It was as though the delivered ITDs converged on one value—about $0 \mu\text{s}$ —no matter what the target ITDs were. Both the pattern of the results and the point of convergence varied with the choice of HRIRs in the mismatched simulations. The right panel plots the results for a different mismatched HRIR simulation (14 dB wideband average cancellation), in which the convergent point for negative target ILDs was at about $-100 \mu\text{s}$.

In a second set of simulations we tested all 42 combinations of mismatched HRIRs for two target ITD and ILDs

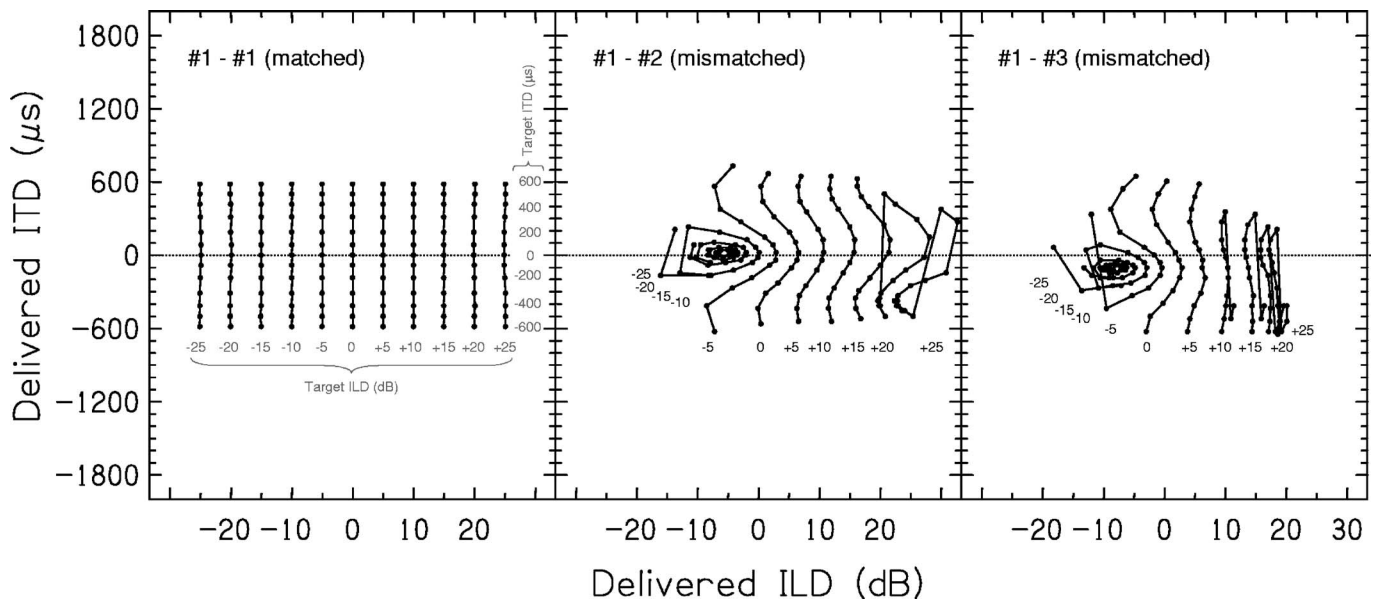


FIG. 10. The binaural performance of the computational simulation of cross-talk cancellation, calculated for a matched-HRIR system (left panel) and two mismatched-HRIR systems (middle and right panels). Each panel shows the ongoing ITD (ordinate) and ILD (abscissa) delivered by the simulation for a large set of combinations of target ITD and ILDs (parameters); the lines join points with the same target ILD. The analysis was run at an auditory-filter frequency of 1000 Hz.

pairs of $-500 \mu\text{s}/0 \text{ dB}$ and $+500 \mu\text{s}/0 \text{ dB}$. Auditory-filter frequencies between 100 and 1000 Hz were used. The results are shown in Fig. 11. The top-left panel shows the delivered ITDs for the $-500 \mu\text{s}/0 \text{ dB}$ target. At each frequency most of the combinations gave ITDs in one cluster, for which the solid points and error bars mark the means and standard deviations; those combinations that gave exceptional results—an ITD on the wrong side of the head—are plotted

as open circles. The mean ITD ($-498 \mu\text{s}$) was close to the target value of $-500 \mu\text{s}$. There was, however, a wide distribution across mismatched-HRIR combination; the standard deviation was, on average, $100 \mu\text{s}$. A similar result held for the $+500 \mu\text{s}/0 \text{ dB}$ target (top-right panel). The delivered ILDs are shown in the bottom-left and bottom-right panels. Again, the mean delivered ILD was almost exactly the target ILD, but the average standard deviation was 4 dB.

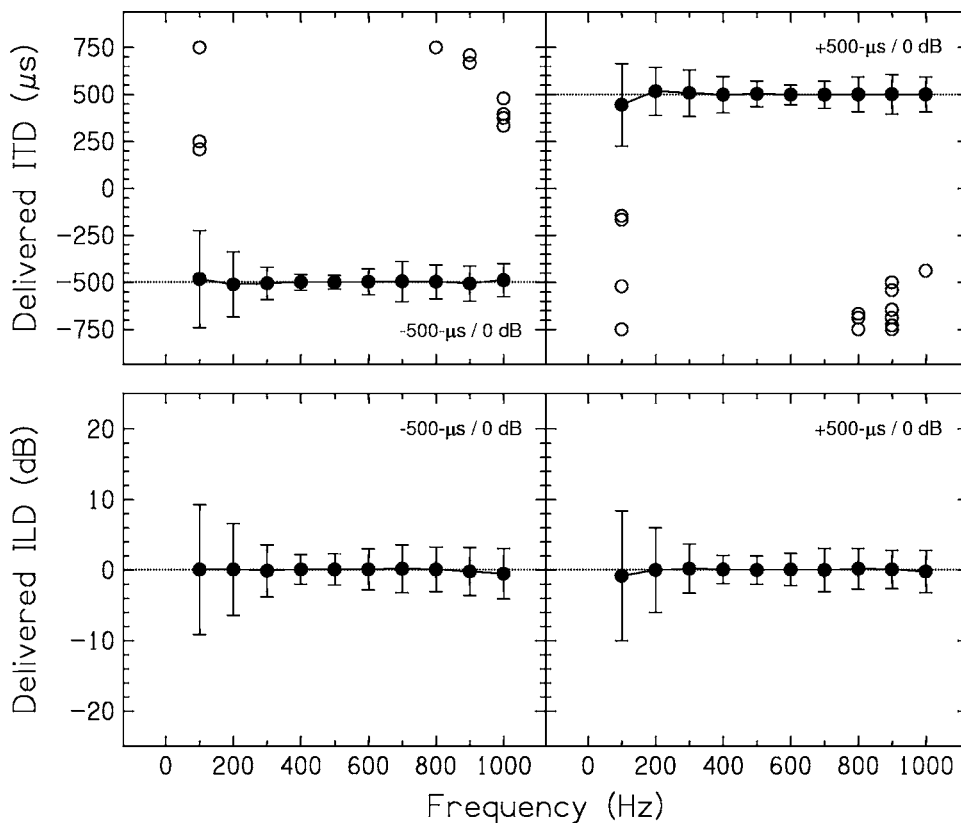


FIG. 11. The results of the ongoing-ITD and ongoing-ILD analyses of the computational simulation as a function of auditory-filter frequency. Each point plots the mean across all 42 mismatched-HRIR systems (the error bars show the standard deviations). For the top-left and bottom-left panels, the target ITD/ILD was $-500 \mu\text{s}/0 \text{ dB}$; for the top-right and bottom-right panels, the target were $+500 \mu\text{s}/0 \text{ dB}$. The few mismatched-HRIR systems that gave exceptional ITDs (taken as being on the wrong side) are plotted as open circles.

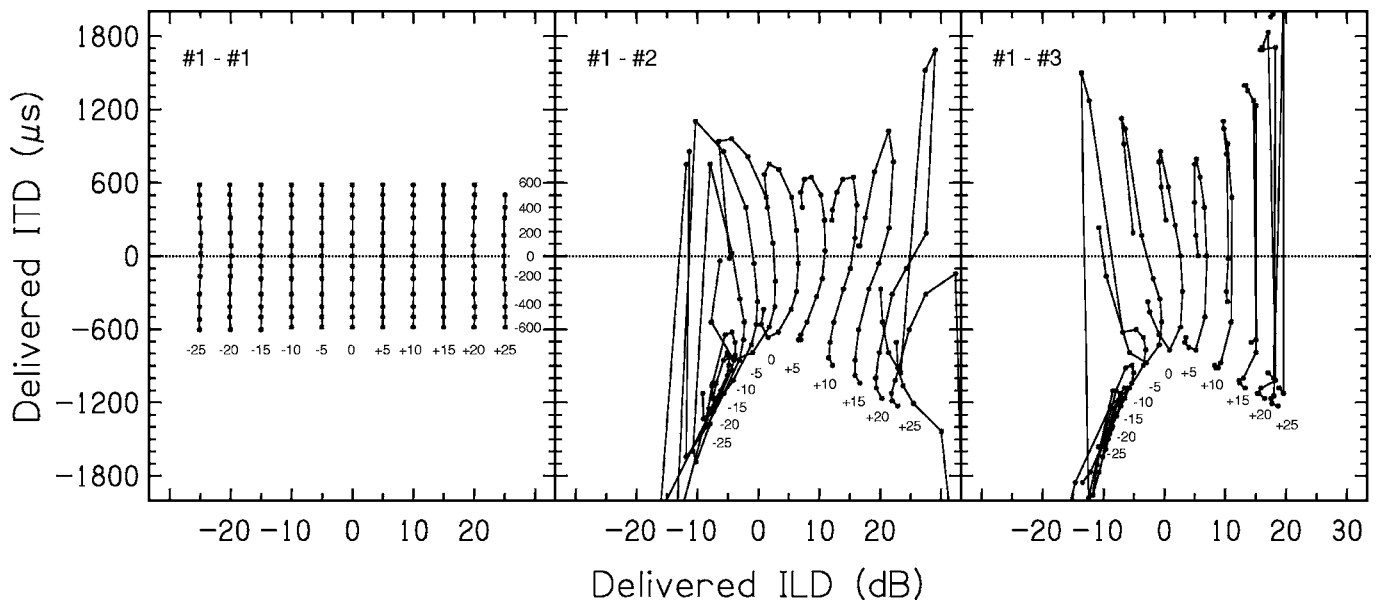


FIG. 12. The binaural performance of the computational simulations for the envelope ITD and ILD at 1000 Hz. The format is the same as Fig. 10.

B. Envelope ITDs and ILDs

The test signal was a single-sample click. It was passed through the same OSD simulation and then the same gammatone filters. Next, the envelopes of the outputs of the left and right gammatone filters were found (by calculating the analytic signal via the MATLAB “Hilbert” function and then taking its complex modulus), and the time of the peak of the envelope in each channel was measured. The left-right difference in peak time was taken as the delivered envelope ITD. The heights of the peaks were also measured, and this left-right difference was taken as the delivered value of the envelope ILD. Again the model was run at a sampling rate of 48 kHz.

Figure 12 shows the delivered envelope ITDs and ILDs at a center frequency of 1000 Hz, plotted in the same format as the earlier ongoing analysis (Fig. 10). The effects that were found there were also found here. First, for the matched-HRIR combination (left panel), the results were again remarkably accurate; the rms error on the measured ITDs was just 14 μs , whilst for the ILDs it was only 0.1 dB. Again, we took this as a successful verification of the analysis method and a demonstration of the ability of the OSD system to deliver the correct envelope ITDs and ILDs when the HRIRs are matched. Second, for the mismatched-HRIR combinations (middle and right panels), the delivered ITDs and ILDs were again quite dissimilar to the target values. There were not, however, any obvious similarities between the delivered ongoing ITDs and the delivered envelope ITDs that were shown in Fig. 10: the envelope ITDs reached much larger values—especially for the more extreme target ILDs—and the points of convergence were different.

Figure 13 shows the mean and standard deviations, across all the mismatched-HRIR combinations, of the delivered ITDs (top row) and ILDs (bottom row) as a function of frequency and for the three targets of 500 $\mu\text{s}/0$ dB (left column), 500 $\mu\text{s}/10$ dB (middle column), and 500 $\mu\text{s}/20$ dB (right column). The standard deviation of the ITDs, averaged

across all conditions, was 430 μs , and so was much larger than that found for the corresponding ongoing analysis shown in Fig. 11. The standard deviation of the ILDs was 4 dB and was therefore comparable to that found earlier. Furthermore, the delivered ITDs and ILDs were inaccurate when the target ILD was 20 dB; the mean errors from the target values of -500 μs and 20 dB were, respectively, $+160$ μs and -5 dB, respectively.

C. Discussion

These simulations show that a cross-talk cancellation system can reliably recreate accurate binaural ITDs and ILDs only when the playback HRIRs are matched to the setup HRIRs. It is likely that this is due to the large amount of cancellation found in the matched conditions—generally over 50 dB (Fig. 9, top panel)—so giving sufficient “headroom” to preserve the ITDs and ILDs of the target (Takeuchi *et al.*, 2001). In mismatched conditions—such as would be found if the system was set up in advance using an accurately measured HRIR from a manikin, and then used to present sounds to a population of listeners—the delivered ITDs and ILDs were often different from the targets, and it could not be guaranteed that a given target ITD was indeed being delivered. The difference depended on frequency, ILD, whether envelope or ongoing ITDs were being considered, and the setup versus playback combination of HRIRs used. The error was largest when the target ILD was 20 dB, which is consistent with the suggestion that the amount of cancellation headroom was indeed limiting performance. The standard deviation of the ongoing ITDs, across setup/playback combination, was 100 μs . Only if a random error of this magnitude can be tolerated could a mismatched system be useful for binaural experimentation. Moreover, the convergence phenomenon demonstrates that certain combinations of ITDs and ILDs can *never* be obtained (e.g., for the middle panel of Fig. 10, a target ITD larger than about 250 μs simultaneously with a target ILD of -10 dB or less). We ex-

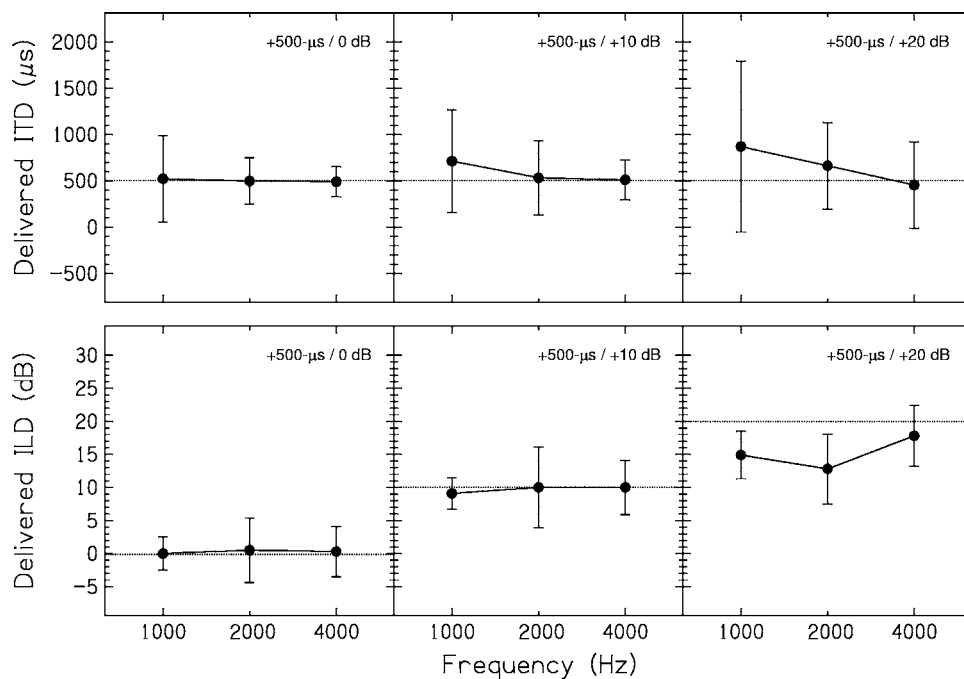


FIG. 13. The results of the envelope-ITD and envelope-ILD analyses of the computational simulation as a function of auditory-filter frequency. Each point plots the mean across all 42 mismatched-HRIR systems (the error bars show the standard deviations). The six panels are for target ITD/ILDs of +500 μ s/0 dB (top left and bottom left), +500 μ s/10 dB (top middle and bottom middle), and +500 μ s/20 dB target (top right and bottom right).

pect that such effects will occur in any mismatched system; an experimenter would not know in advance quite what ITDs or ILDs were being delivered to a given listener.

It should be noted that all these binaural simulations used a database of short-duration HRIRs measured in an anechoic room. Our experience with the acoustic system described in Sec. II and our validation of its computational simulation indicated that cancellation performance would be reduced if the acoustic characteristics of the playback were not anechoic or if there were any extraneous reflections or sounds amongst the loudspeakers. We expect the same caution to apply here, and so the binaural simulations probably represent an ideal performance. A real, acoustic cross-talk cancellation system, in which the HRIRs would be changed by room acoustics or listener movement, may deliver binaural cues that bear even less resemblance to the target values, and either would limit the gain to be had from measuring individualized HRIRs and using those to set up the cross-talk cancellation filters.

V. SUMMARY

We used a series of computational simulations to study the binaural performance of a cross-talk cancellation system in order to evaluate its suitability for binaural experimentation. First, we constructed an acoustic system and used that to validate the simulation. This six-loudspeaker system gave a wideband average cancellation of 20 dB, which was improved to 23 dB after modifications to remove the major reflections from the loudspeaker cabinets. A computational simulation of this system showed that when the playback and setup HRIRs were numerically identical, and both were short enough to exclude the acoustical characteristics of the playback room, then the wideband cancellation was over 50 dB. This situation represented a computational ideal, however, and was unrealistic. Instead, a close match between acoustic and computational results was found when the playback HR-

IRs were longer, so incorporating the early part of the acoustics of the room (and there was no gain in simulated performance from including this in the setup HRIRs). When run with HRIRs from a database of seven listeners, the simulation demonstrated that performance was reduced when the playback HRIR was from a different listener to the setup HRIR; the average amount of cancellation in these mismatched simulations was only 17 dB, and varied little with the choice of setup HRIR but depended substantially upon the playback HRIR.

The binaural analyses demonstrated that the cross-talk cancellation system could not be guaranteed to deliver the targeted ITDs and ILDs when the HRIRs were mismatched. The errors in ongoing ITDs and ILDs at low frequencies were random with a standard deviation of 100 μ s or 4 dB, respectively; those for envelope ITDs and ILDs were 430 μ s and 4 dB. At the largest ILDs usually encountered, the high frequency envelope ITDs and ILDs also had a systematic error, and, moreover, a “convergence” of delivered ITD was observed: for some values of target ILD, the delivered ITD was always the same value, no matter what the target ITD was. The convergent value differed across playback listener and if envelope or ongoing ITDs were measured.

Although cross-talk cancellation can give impressive demonstrations, and experiments on the angle perception of simple, static noise bursts can often give compelling results, the errors in ITD and ILD demonstrated here will affect any use of mismatched cross-talk cancellation for experiments that rely on accurate binaural cues. Takeuchi *et al.* (2001) noted that the poorest listeners in their subjective localization experiment were those whose HRIRs had the largest differences to the manikin HRIRs used to set up their system. Our own results support this, confirming that such mismatching of HRIRs is an important source of the inaccuracies in the final delivery of binaural cues.

ACKNOWLEDGMENTS

We would like to thank Dr. Takashi Takeuchi (Institute of Sound and Vibration Research, Southampton) for helping us get started and also in supplying the cross-talk cancellation algorithms, Dr. Jones Braasch (McGill University, Montreal) for supplying the “AUDIS” HRIR database, the Department of Engineering of the University of Nottingham for allowing us to use their acoustic chamber, Dr. Silvia Cirstea for help with the HRTF interpolation, David McShefferty for running some of the simulations, and Helen Lawson for her comments on the manuscript. We also thank the Associate Editor (Dr. Armin Kohlrausch) and the three anonymous reviewers for their valuable and insightful comments during the review process. The computational work was performed in MATLAB (www.mathworks.com), The Scottish Section of the IHR is co-funded by the Medical Research Council and the Chief Scientist’s Office of the Scottish Executive Health Department.

¹Our nomenclature follows that used by Takeuchi and Nelson (2002), where \mathbf{C} is the matrix of source-receiver functions and \mathbf{H} is the matrix of cross-talk-cancellation (inverse) filters.

²In our acoustic measurements we did not study the effects of varying the regularization parameter β or the size of the FFT. Subsequent investigations with one of the computational simulations showed that the chosen value of β (0.001) was well chosen: The wideband average cancellations were 15.5, 21.1, 21.8, 21.8, and 21.4 dB for values of β of 1, 0.1, 0.01, 0.001, and 0.0001, respectively (also, β was frequency-independent; see Bai and Lee (2006) for a frequency-dependent β). Similarly, the chosen FFT size (4096 points) was again justifiable: the cancellations were 11.0, 20.3, 19.2, 20.1, 21.7, and 21.8 dB for sizes of 128, 256, 512, 1024, 2048, and 4096 points, respectively.

³The front of the mid/high cabinet was shaped like a segmented arc of circle of 1 m radius. Although not a perfect reflector, it would still be expected to focus some of the sound to the center of the circle, which was where the manikin was placed (see Fig. 1). This may contribute to the strength of the reflection, and we found that moving the manikin away from that point reduced it.

⁴The model’s ITD range was slightly larger than the range of the stimuli in order to allow for the possibility that the cross-talk cancellation system might deliver an ITD larger than expected.

Akeroyd, M. A. (2001). “A binaural cross-correlogram toolbox for MATLAB,” software downloadable from <http://www.ihr.mrc.ac.uk/scottish/products/matlab.php> (last viewed December 20, 2006).

Akeroyd, M. A., and Summerfield, Q. (2000). “The lateralization of simple dichotic pitches,” *J. Acoust. Soc. Am.* **108**, 316–334.

Algazi, V. R., Duda, R. O., Thompson, D. M., and Avendano, C. (2001). “The CIPIC HRTF database,” in Proceedings of the 2001 IEEE Workshop on Applications of Signal Processing to Audio and Electronics, New Paltz, New York, pp. 99–102.

Atal, B. S., and Schroeder, M. R. (1962). “Apparent sound source translator,” US Patent No. 3236949 [reviewed in *J. Acoust. Soc. Am.* **41**, 263–264 (1967)].

Bai, M. R., and Lee, C.-C. (2006). “Development and implementation of cross-talk cancellation system in spatial audio reproduction based on sub-band filtering,” *J. Sound Vib.* **290**, 1269–1289.

Bai, M. R., Tung, C. W., and Lee, C. C. (2005). “Optimal design of loudspeaker arrays for robust cross-talk cancellation using the Taguchi method and the genetic algorithm,” *J. Acoust. Soc. Am.* **117**, 2802–2813.

Bauer, B. B. (1961). “Stereophonic earphones and binaural loudspeakers,” *J. Audio Eng. Soc.* **9**, 148–151.

Bernstein, L. R., and Trahiotis, C. (1996). “On the use of the normalized correlation as an index of interaural envelope correlation,” *J. Acoust. Soc. Am.* **100**, 1754–1763.

Bernstein, L. R., and Trahiotis, C. (2002). “Enhancing sensitivity to interaural delays at high frequencies by using ‘transposed’ stimuli,” *J. Acoust. Soc. Am.* **112**, 1026–1036.

Bernstein, L. R., and Trahiotis, C. (2003). “Enhancing interaural-delay-based extents of laterality at high frequencies by using ‘transposed’ stimuli,” *J. Acoust. Soc. Am.* **113**, 3335–3347.

Blauert, J. (1997). *Spatial Hearing: The Psychophysics of Human Sound Localization* (MIT Press, Cambridge MA).

Blauert, J., Brüggem, M., Bronkhorst, S. W., Drullman, R., Reynaud, G., Pellioux, L., Krebber, W., and Sottek, R. (1998). “The AUDIS catalogue of human HRTFs,” *J. Acoust. Soc. Am.* **103**, 3082 (see also <http://www.eaa-fenestra.org/Products/Documenta/Publications/09-de2>; last viewed November 6, 2006).

Burkhard, M. D., and Sachs, R. M. (1975). “Anthropometric manikin for acoustic research,” *J. Acoust. Soc. Am.* **58**, 214–222.

Chambers, J., Akeroyd, M. A., Summerfield, A. Q., and Palmer, A. R. (2001). “Active control of the volume acquisition noise in functional magnetic resonance imaging: Method and psychoacoustical evaluation,” *J. Acoust. Soc. Am.* **110**, 3041–3054.

Cooper, D. H., and Bauck, J. L. (1989). “Prospects for transaural recording,” *J. Audio Eng. Soc.* **37**, 3–19.

Damaske, P. (1971). “Head-related two-channel stereophony with loudspeaker reproduction,” *J. Acoust. Soc. Am.* **50**, 1109–1115.

Davies, W. T. (1966). “Generation and properties of maximum-length-sequences,” *Control* **10**, 364–365.

Foo, K. C. K., Hawksford, M. O. J., and Hollier, M. P. (1999). “Optimization of virtual sound reproduced using two loudspeakers,” in Proceedings of the 16th AES International Conference: Spatial Sound Reproduction, Rovaniemi, Finland, pp. 366–378.

Gardner, W. G., and Martin, K. D. (1995). “HRTF measurements of a KEMAR,” *J. Acoust. Soc. Am.* **97**, 3907–3908.

Gatehouse, S., and Noble, W. (2004). “The speech, spatial, and qualities of hearing scale (SSQ),” *Int. J. Audiol.* **43**, 85–99.

Glasberg, B. R., and Moore, B. C. J. (1999). “Derivation of auditory filter shapes from notched-noise data,” *Hear. Res.* **47**, 103–138.

Hartung, K., Braasch, J., and Sterbing, S. (1999). “Comparison of different methods for the interpolation of head-related transfer functions,” in Proceedings of the 16th AES International Conference: Spatial Sound Reproduction, Rovaniemi, Finland, pp. 319–329.

Hill, P. A., Nelson, P. A., Kirkeby, O., and Hamada, H. (2000). “Resolution of front-back confusion in virtual acoustic imaging systems,” *J. Acoust. Soc. Am.* **108**, 2901–2910.

Kyriakakis, C. (1998). “Fundamental and technological limitations of immersive audio systems,” *Proc. IEEE* **86**, 941–951.

Langendijk, E. H. A., and Bronkhorst, A. W. (2000). “Fidelity of three-dimensional-sound reproduction using a virtual auditory display,” *J. Acoust. Soc. Am.* **107**, 528–537.

Lentz, T., Assenmacher, I., and Sokoll, J. (2005). “Performance of spatial audio using dynamic cross-talk cancellation,” Proceedings of the 119th Audio Engineering Society Convention, New York, preprint 6541.

Maxwell, R. J., and Burkhard, M. D. (1979). “Larger ear replica for KEMAR manikin,” *J. Acoust. Soc. Am.* **65**, 1055–1058.

Middlebrooks, J. C. (1999a). “Individual differences in external-ear transfer functions reduced by scaling frequency,” *J. Acoust. Soc. Am.* **106**, 1480–1492.

Middlebrooks, J. C. (1999b). “Virtual localization improved by scaling non-individualized external-ear transfer functions in frequency,” *J. Acoust. Soc. Am.* **106**, 1493–1510.

Møller, H. (1989). “Reproduction of artificial-head recordings through loudspeakers,” *J. Audio Eng. Soc.* **37**, 30–33.

Nelson, P. A., and Rose, J. F. W. (2005). “Errors in two-point reproduction,” *J. Acoust. Soc. Am.* **118**, 193–204.

Noble, W., and Gatehouse, S. (2004). “Interaural asymmetry of hearing loss, speech, spatial, and qualities of hearing (SSQ) disabilities, and handicap,” *Int. J. Audiol.* **43**, 100–114.

Orduna-Bustamante, F., Lopez, J. J., and Gonzalez, A. (2001). “Prediction and measurement of acoustic crosstalk cancellation robustness,” Proceedings Acoustics, Speech and Signal Processing (ICASSP 2001), Vol. 5, pp. 3349–3352.

Patterson, R. D., Allerhand, M. H., and Giguère, C. (1995). “Time-domain modeling of peripheral auditory processing: A model architecture and a software platform,” *J. Acoust. Soc. Am.* **98**, 1890–1894.

Rose, J., Nelson, P., Rafaely, B., and Takeuchi, T. (2002). “Sweet spot size of virtual acoustic imaging systems at asymmetric listener locations,” *J. Acoust. Soc. Am.* **112**, 1992–2002.

Sæbø, A. (2001). “Influence of reflections on crosstalk cancelled playback

- of binaural sound," Ph.D. thesis, Norwegian University of Science and Technology, Trondheim, Norway.
- Shackleton, T. M., Meddis, R., and Hewitt, M. J. (1992). "Across frequency integration in a model of lateralization," *J. Acoust. Soc. Am.* **91**, 2276–2279.
- Stern, R. M., and Trahiotis, C. (1997). "Models of binaural perception," in *Binaural and Spatial Environments*, edited by R. H. Gilkey and T. R. Anderson (LEA, Mahwah, NJ).
- Takeuchi, T. (2001). "Systems for virtual acoustic imaging using the binaural principle," Ph.D. thesis, University of Southampton, Southampton, UK.
- Takeuchi, T., Nelson, P., and Hamada, H. (2001). "Robustness to head misalignment of virtual sound imaging systems," *J. Acoust. Soc. Am.* **109**, 958–971.
- Takeuchi, T., and Nelson, P. (2002). "Optimal source distribution for binaural synthesis over loudspeakers," *J. Acoust. Soc. Am.* **112**, 2786–2797.
- Thornton, A. R. D., Folkard, T. J., and Chambers, J. D. (1994). "Technical aspects of recording evoked otoacoustic emissions using maximum length sequences," *Scand. Audiol.* **23**, 225–231.
- Thornton, A. R. D., Shin, K., Gottesman, E., and Hine, J. (2001). "Temporal non-linearities of the cochlear amplifier revealed by maximum length sequence stimulation," *Clin. Neurophysiol.* **112**, 768–777.
- Trinder, J. R. (1982). "Hardware-software configuration for high-performance digital filtering in real time," *Proceedings Acoustics, Speech and Signal Processing (ICASSP 1982)*, Vol. 2, pp. 687–690.
- Ward, D. B., and Elko, G. W. (1999). "Effect of loudspeaker position on robustness of acoustic crosstalk cancellation," *IEEE Signal Process. Lett.* **6**, 106–108.
- Wightman, F. L., and Kistler, D. J. (1989). "Headphone simulation of free-field listening. I. Stimulus synthesis," *J. Acoust. Soc. Am.* **85**, 858–867.
- Yang, J., Gan, W.-S., and Tan, S.-E. (2003). "Improved sound separation using three loudspeakers," *ARLO* **4**, 47–52.

Binaural interference and auditory grouping

Virginia Best and Frederick J. Gallun

Hearing Research Center, Boston University, Boston, Massachusetts 02215

Simon Carlile

Department of Physiology, University of Sydney, Sydney, NSW, Australia

Barbara G. Shinn-Cunningham^{a)}

Hearing Research Center, Boston University, Boston, Massachusetts 02215

(Received 18 April 2006; revised 16 November 2006; accepted 17 November 2006)

The phenomenon of binaural interference, where binaural judgments of a high-frequency target stimulus are disrupted by the presence of a simultaneous low-frequency interferer, can largely be explained using principles of auditory grouping and segregation. Evidence for this relationship comes from a number of previous studies showing that the manipulation of *simultaneous* grouping cues such as harmonicity and onset synchrony can influence the strength of the phenomenon. In this study, it is shown that *sequential* grouping cues can also influence whether binaural interference occurs. Subjects indicated the lateral position of a high-frequency sinusoidally amplitude-modulated (SAM) tone containing an interaural time difference. Perceived lateral positions were reduced by the presence of a simultaneous diotic low-frequency SAM tone, but were largely restored when the interferer was “captured” in a stream of identical tones. A control condition confirmed that the effect was not due to peripheral adaptation. The data lend further support to the idea that binaural interference is affected by processes related to the perceptual organization of auditory information. Modifications to existing grouping-based models are proposed that may help account for binaural interference effects more successfully. © 2007 Acoustical Society of America.

[DOI: 10.1121/1.2407738]

PACS number(s): 43.66.Pn, 43.66.Qp, 43.66.Dc [AJO]

Pages: 1070–1076

I. INTRODUCTION

Several investigations over the past 30 years have revealed that sensitivity to binaural parameters may be degraded by the presence of simultaneous energy in remote spectral regions. So-called “binaural interference” has been demonstrated for tasks involving discrimination of interaural parameters as well as lateralization on the basis of these cues (McFadden and Pasanen, 1976; Zurek, 1985; Dye, 1990; Trahiotis and Bernstein, 1990; Buell and Hafter, 1991; Woods and Colburn, 1992; Stellmack and Dye, 1993; Buell and Trahiotis, 1994; Bernstein and Trahiotis, 1995; Heller and Trahiotis, 1995, 1996; Hill and Darwin, 1996). The phenomenon is intriguing because it is difficult to reconcile with evidence that simultaneous sounds can be localized quite accurately (Good and Gilkey, 1996; Good *et al.*, 1997; Lorenzi *et al.*, 1999; Best *et al.*, 2005), and with the intuition that listeners have a relatively robust spatial percept of their auditory surroundings.

It is generally agreed that binaural interference results from an obligatory combination of binaural information from spectrally remote components. While some researchers have discussed their data explicitly in terms of auditory object formation (Woods and Colburn, 1992), others do not explain binaural interference in this way. Here we review the binaural interference literature, and show that the bulk of the data is consistent with the idea that binaural interference is a by-

product of grouping processes that combine information likely to come from the same auditory object.

A. The basic phenomenon

Binaural interference was first described by McFadden and Pasanen (1976), who observed that just-noticeable differences in interaural time difference (ITD) for a high-frequency narrowband noise were elevated by the presence of a simultaneous low-frequency noise presented diotically. Reduced sensitivity to target ITD was also seen if the target was narrowband and flanked by broadband diotic noise (Zurek, 1985; Trahiotis and Bernstein, 1990), or if the target was a high-frequency sinusoidally amplitude-modulated (SAM) tone in the presence of a low-frequency SAM tone (Heller and Trahiotis, 1995). Furthermore, when presented with a low-frequency tone complex, listeners showed reduced sensitivity to the ITD in one component when one or more components were diotic (Dye, 1990; Woods and Colburn, 1992; Stellmack and Dye, 1993). Binaural interference has also been demonstrated in the detection of interaural level differences (ILDs; Bernstein and Trahiotis, 1995). In general, the data are consistent with the idea that judgments of perceived location underlie the effect. When binaural information is combined across frequencies, the resultant perceived location is only weakly influenced by the target ITD and ILD, and listeners have reduced sensitivity to changes in these parameters.

^{a)}Electronic mail: shinn@cns.bu.edu

B. The influence of simultaneous grouping cues

Several studies have noted that binaural interference only occurs in certain circumstances. A careful review of the literature reveals that binaural interference is most likely to occur when grouping cues support perceiving the target and interferer energy as one object. In particular, many examples show that there is less binaural interference when *simultaneous grouping* cues such as synchronous onsets or harmonicity do not drive the target and masker to be perceptually integrated.

Several studies increased the duration of the interferer such that the target turned on and off during the ongoing interferer rather than being gated on and off simultaneously with it (Trahiotis and Bernstein, 1990; Heller and Trahiotis, 1995). These studies showed that asynchronous gating almost completely eliminated the interference. However, smaller onset asynchronies have produced mixed results. Woods and Colburn (1992) measured ITD discrimination thresholds for a 600-Hz tone target in the presence of two interferer bands (400 and 800 Hz), and found that two out of four of their subjects benefited from an onset asynchrony of 250 ms, but two did not. Using a similar stimulus paradigm but with shorter asynchronies (ranging from 25 to 200 ms), Stellmack and Dye (1993) reported no release from binaural interference due to onset asynchrony. Interestingly, in both of these studies, subjects reported that the pitch of the target component was more salient when there was an onset asynchrony between the target and interferers, suggesting that the asynchrony made it easier to “hear out” the target from the interferer. Thus, subjects segregated the target from the interferers, but did not necessarily perceive it at a different intracranial position. In contrast, Hill and Darwin (1996) showed that listeners could independently lateralize the center component of a tonal complex if the component was delayed by only 80 ms relative to the other components. In their lateralization task, the complex was located on one side of the head, but target localization cues were consistent with a source on the opposite side of the head. It may be that at short onset asynchronies, a larger difference in ITD between the target and the interferers is required to ensure the components are heard at unique locations. The ITD discrimination task used by Woods and Colburn (1992) and Stellmack and Dye (1993) asked listeners to discriminate a small change in target ITD from a reference ITD of zero, in the presence of a diotic interferer. Given the similarity between the target and interferer spatial cues, relatively long onset asynchronies may be required for the target to be localized to a position that is perceptually distinct from that of the interferer (as in the continuous interferer conditions of Trahiotis and Bernstein, 1990, and Heller and Trahiotis, 1995).

Buell and Hafter (1991) assessed the influence of harmonicity on how binaural information is combined across frequency. They presented two low-frequency tones simultaneously, and found that interference only occurred when the tones were harmonically related. When the tones were not harmonically related, listeners were able to ignore the interferer and discriminate the target ITD as accurately as in the target-alone condition. The authors suggested that tones

bearing a simple harmonic relation are functionally grouped and their binaural information combined to form the perceived location of the composite object. This conclusion was confirmed by Hill and Darwin (1996), who reported that the perceived lateral position of a target tone is affected when it is played simultaneously with a harmonically related tonal complex, but not in the presence of an inharmonic complex. However, a study by Stellmack and Dye (1993) produced contrasting results, where significant interference was observed even when the target and interferer tones were inharmonic. As the tones used by Stellmack and Dye were more closely spaced in frequency, Hill and Darwin (1996) suggested that some monaural interference may have occurred. In addition, however, Hill and Darwin used competing locations on opposite sides of the head, whereas Stellmack and Dye used competing locations near the midline. As was noted for segregation based on onset asynchrony, the binaural system may require stronger evidence from harmonic segregation rules when binaural conflicts are small across frequency.

C. The influence of sequential grouping cues

If binaural interference is related to how listeners perceptually organize a sound mixture into objects, then sequential grouping rules (as well as simultaneous grouping rules) should influence the strength of the interference observed. The experiment presented in this paper was conducted to examine whether a target and interferer pair (with common onsets and offsets) could be “ungrouped” by capturing the interferer in a repeating auditory stream. This manipulation is similar in its philosophy to the “continuous interferer” stimulus in previous studies (Trahiotis and Bernstein, 1990; Heller and Trahiotis, 1995), but it preserves the local structure of the target/interferer pair (including common onsets and offsets). Thus, any effect of the sequential stream on binaural interference implicates grouping and streaming mechanisms that operate over relatively long time scales. Sequential capture has been shown previously to successfully promote the segregation of complex sounds. For example, it reduced the contribution of a component to the pitch and timbre of a harmonic complex (Darwin *et al.*, 1989; 1995) and it reduced modulation detection interference (Oxenham and Dau, 2001). It should be noted that observing a reduction in interference when the interferer is captured into a separate stream does not necessarily demonstrate that interference is caused by grouping of the target and interferer. However, it emphasizes that binaural interference is influenced by the perceptual organization of the components involved.

D. Measuring perceived location

Most studies of binaural interference measured it using an ITD discrimination task in the presence of a diotic interferer. The results are largely consistent with a model in which binaural information is combined in an obligatory fashion across frequencies in the absence of strong cues to allow the target to be heard as an independent object. An interaurally uncorrelated interferer (i.e., containing no con-

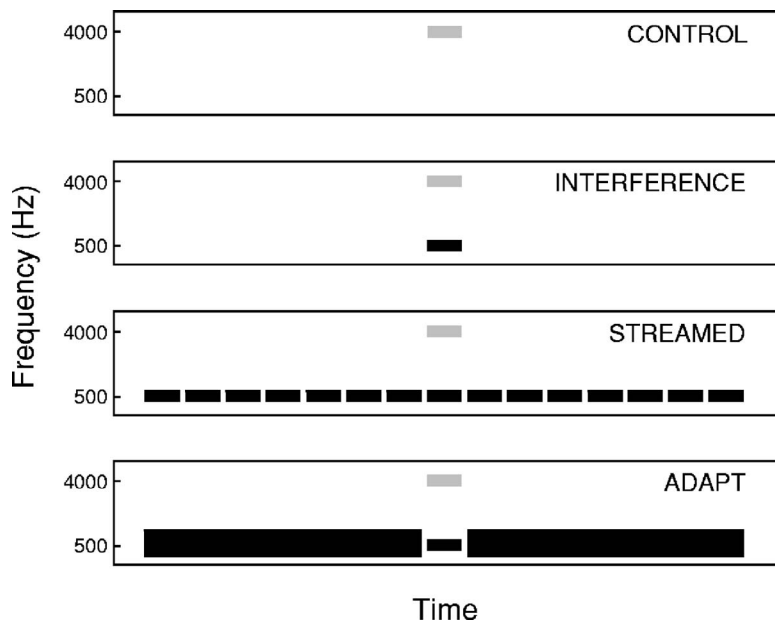


FIG. 1. Schematic illustration of the experimental stimuli. In the control condition, the high-frequency target was presented in isolation. In the interference condition, a simultaneous low-frequency interferer was presented. In the streamed condition, the interferer was flanked on either side by seven identical captor tones. In the adapt condition, the flanker tones were replaced by a sustained narrowband noise that spanned the frequency range of the flanker tones but was different in quality (and hence unlikely to be grouped with the interferer).

sistent binaural information) was shown to cause far less interference than a diotic interferer (Trahiotis and Bernstein, 1990). This is to be expected if spatial information is combined across frequencies. The target binaural information will dominate when the interferer has no strong spatial information, which will allow small changes in target ITD to cause relatively large changes in the perceived location of the composite object. However, a stronger test is to directly measure the perceived lateral position of a target in cases where there is an interferer present and examine whether the perceived location is predicted from the combination of spatial cues present in the target and interferer.

Only two of the studies discussed above directly measured perceived location under binaural interference conditions (Heller and Trahiotis, 1996; Hill and Darwin, 1996). These data confirm that the perceived laterality of the target is influenced by the lateral position of the interferer when binaural interference occurs. It appears that a synchronous interferer “attracts” the perceived target location either fully (in the case of a pure-tone target embedded in a seven-component tonal complex; Hill and Darwin, 1996) or partially (in the case of a high-frequency target and a single low-frequency interferer; Heller and Trahiotis, 1996). We know of no investigations that have examined the effect of lateralized interferers on the perceived lateral position of a target near the midline (although lateralized interferers do reduce ITD sensitivity in targets similar to diotic interferers; Buell and Hafter, 1991). In the experiment described in this paper, perceived target laterality was measured directly using a paradigm similar to that of Heller and Trahiotis (1996).

II. METHODS

A. Subjects

Eight listeners participated in the experiment (one female, seven male). All had normal audiograms and four had previous experience in psychophysical listening (S1–S4; S1

was the first author). All subjects gave informed consent to participate, required by the Boston University Charles River Campus Institutional Review Board.

B. Stimuli

The target stimulus was a high-frequency SAM tone (4-kHz carrier, 250-Hz modulation rate, 250-ms duration, 10-ms raised-cosine ramps at onset/offset). It was presented in four different conditions (see Fig. 1). In the “control” condition the target was presented with no interferer. In the “interference” condition, the target was presented with a single simultaneous interferer. The interferer was a low-frequency SAM tone (500-Hz carrier, 250-Hz modulation rate, 250-ms duration, 10-ms raised-cosine ramps at onset/offset). The “streamed” condition was identical to the interference condition, except the interferer was flanked temporally by identical tones (seven preceding and seven following, giving 15 tones in the stream in total). The interferer tones were separated by 50 ms of silence. As a control for any adaptation that might be caused by the flanking tones, an “adaptation” condition was included. In this condition, a narrowband noise was presented in place of the seven leading (and trailing) tones. The noise was bandpass filtered between 100 and 1000 Hz, and was scaled to be 6 dB higher in level than the stream of tones in a one-third-octave band centered at 500 Hz. It was assumed that the noise would cause at least as much adaptation as the stream of tones,¹ but would not group with the interferer tone.

The target was presented with an ITD that varied from trial to trial, taking one of seven values (0 μ s, \pm 200 μ s, \pm 400 μ s, or \pm 600 μ s). ITDs were created by delaying the entire waveform (both envelope and fine structure) in one ear. The interferer, when present, was presented diotically (0 μ s ITD).

C. Procedures

Subjects were seated in a sound-treated booth in front of a PC terminal. Digital stimuli were generated on the PC, sent to Tucker-Davis Technologies hardware for D/A conversion and attenuation, and presented over insert earphones (Ety-motic Research ER-2).

The four different conditions were tested in separate blocks of trials. Each block consisted of five trials at each of the seven ITD values, for a total of 35 trials. On each trial, subjects were presented with a random stimulus, and their task was to indicate the perceived location of the target using an ILD pointer. The ILD pointer was a high-frequency SAM tone identical to the target, whose lateral position was adjusted by increasing the level of the signal going to one ear. The pointer was presented (with an initial ILD of 0 dB) immediately after the initial presentation of the stimulus. Subjects used a graphical user interface displayed on the PC monitor to move the pointer to align it with the perceived lateral position of the target in the test stimulus. “Left” or “right” buttons increased or decreased the pointer tone ILD by 1 dB. A “replay” button allowed replay of the test stimulus followed by the pointer tone. Subjects moved the pointer tone and replayed the test stimulus until they were satisfied that the lateral positions matched.

Before commencing the test blocks, subjects were given detailed verbal instructions about the task. They were told to listen for the lateral position of the high-pitched target and were given a short practice test to familiarize them with the matching task. The practice test consisted of 14 trials of the control stimulus (two at each of the seven target positions, presented in a random order). Subjects were also given a description of the different conditions, and were played examples of each. They were instructed to ignore the low-pitched sounds when they were present. They were told that if they could not distinguish the simultaneous high- and low-pitched sounds then they should simply locate the sound they heard.

Two blocks of each of the four conditions were completed by each subject in a random order, with the constraint that one block of each condition was completed before any condition was revisited.

III. RESULTS

For each subject in each block of trials, mean position responses over the five repetitions were calculated for the seven target locations. In some cases, subjects showed a small lateral bias in their mean response to stimuli presented diotically (0- μ s ITD), which may have been due to earphone placement or small asymmetries in the ears. To correct for this bias, the mean perceived ILD for diotic stimuli was subtracted from all responses in that block (see Bernstein and Trahiotis, 1985). Responses to target positions left of midline were then mirror-flipped and combined with responses to target positions right of midline. Finally, zero-adjusted and mirror-flipped data from the two blocks in each condition were pooled for each subject.

Figure 2 shows results for the individual subjects in the control, interference, and streamed conditions.² Lateral esti-

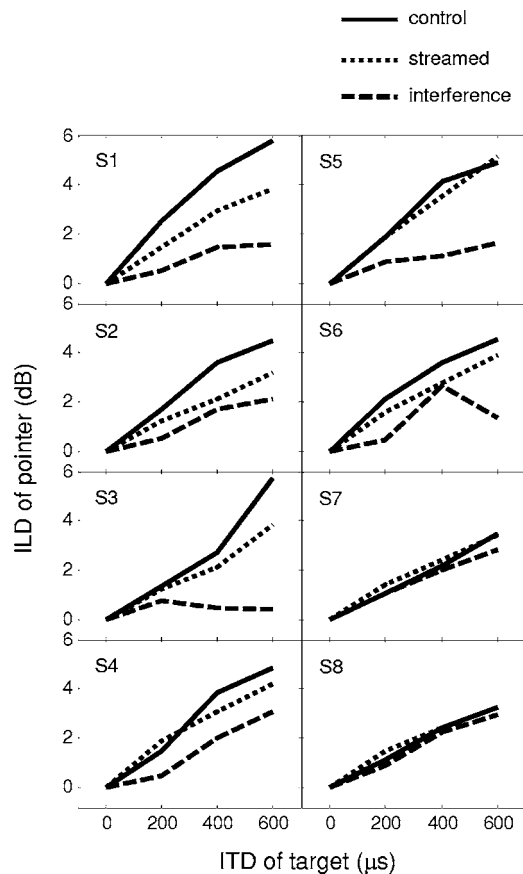


FIG. 2. Lateralization results for the eight individual subjects. Perceived lateral position of the target (indicated by matching to an ILD pointer) is shown as a function of target ITD. Different lines indicate mean responses for the control condition (solid lines), the interference condition (dashed lines), and the streamed condition (dotted lines).

mates are on the whole greatest in the control condition (solid lines) and tended to be reduced in the interference condition (dashed lines). These results are consistent with Heller and Trahiotis (1996), and consistent with the idea that binaural information is combined across the two frequency regions to give rise to a composite perceived location. However, there are substantial individual differences in the amount of interference that occurred. In particular, subjects S7 and S8 showed essentially no interference (and, interestingly, showed the smallest extents of laterality in the control condition). For all listeners who did show interference, the presence of the leading and trailing tones in the streamed condition reduced this interference (dotted lines). For some subjects (e.g., S5), lateral percepts were restored almost completely, and responses were close to the control condition. For other subjects (e.g., S2), the interference was reduced but not fully eliminated. The mean data, pooled across subjects, are shown in Fig. 3 and summarize these effects. Also shown in Fig. 3 are the mean data from the adapt condition (dash-dot lines). In this condition, responses were almost identical to the interference condition. A two-way repeated measures ANOVA was conducted on the mean data with factors of condition (control, interference, streamed, and adapt) and target location (all except 0 μ s). The main effect of condition was significant [$F(3, 21)=19.78, p < 0.001$], as was the main effect of location [$F(2, 14)=220.56, p < 0.001$] and the two-

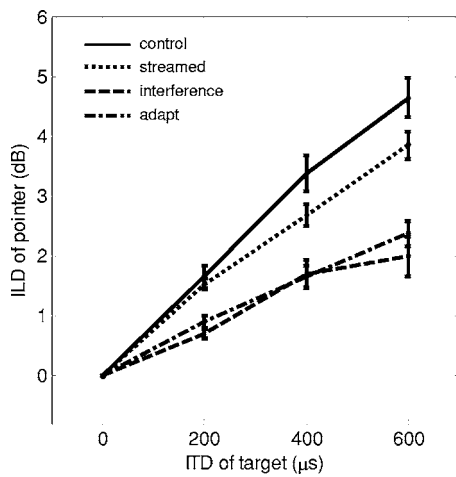


FIG. 3. Mean lateralization results pooled across subjects. Perceived lateral position of the target (indicated by matching to an ILD pointer) is shown as a function of target ITD. Different lines indicate mean responses for the control condition (solid lines), the interference condition (dashed lines), the streamed condition (dotted lines), and the adapt condition (dash-dot lines). Error bars represent standard errors of the across-subject mean.

way interaction [$F(6,42)=7.42, p<0.001$]. As the effect of condition was of primary interest, pairwise comparisons were done across conditions. These revealed that the control condition was significantly different from all other conditions ($p<0.05$). The interference condition was significantly different from both the control and streamed conditions ($p<0.01$), but was not different from the adapt condition ($p=0.16$), supporting the idea that binaural interference was abated by the sequential stream but not by the adapting noise. Further confirming this point, mean responses in the streamed and adapt conditions were significantly different ($p<0.01$).

IV. DISCUSSION

The key condition of interest in this experiment was the streamed condition. The fact that responses in this condition are more similar to responses in the control condition than the interference condition indicates that when the interferer was presented in the context of a sequential stream, the ability to assess the ITD of the target improved compared to when there were no flanking tones. The fact that a similar reduction in interference did not occur for the narrowband noise flankers in the adapt condition indicates that the reduction cannot be due merely to the presence of leading and trailing energy in the frequency region of the interferer. In other words, the effect of the sequential stream does not appear to be due to peripheral adaptation that reduces the neural representation of the interferer. Rather, the most parsimonious explanation is that the sequential stream (including the interferer) formed a perceptual object, allowing the target to be perceived and processed as a distinct object. Consistent with this idea, subjects who showed release from interference reported that they could hear out the target far more easily in the streamed condition than in the interference and adapt conditions.

These results support previous evidence suggesting that auditory grouping cues play a strong role in determining how

spatial information is combined across frequency. It appears that binaural interference is the result of obligatory grouping that occurs when there are no cues indicating the presence of two distinct sound sources (other than the spatial cues themselves). This is consistent with evidence that spatial information in isolation is a relatively weak cue for promoting the segregation of simultaneous sounds (Culling and Summerfield, 1995; Darwin and Hukin, 1999). However, introducing strong segregation cues (asynchronous onsets, inharmonicity, a sequential stream) reduces the obligatory grouping across frequency and improves the ability to independently access binaural information from sounds in different frequency regions.

Surprisingly, there has been no attempt to fully develop a scene-analysis-based explanation of binaural interference phenomena, perhaps because of what at first glance appear to be puzzling exceptions to such an account. First, it is clear that segregation of sounds does not always give perfect release from binaural interference; extraneous energy can still influence binaural processing in a clearly segregated sound. Indeed, for the majority of the subjects in the current study, interference was reduced but not eliminated in the streamed condition. One possible reason for this residual influence is that listeners do not perform optimally in complex tasks of this nature. Good evidence for this idea comes from the fact that binaural interference increases when the target frequency region is uncertain (Buell and Trahiotis, 1994). Furthermore, in many cases where listeners exhibit nonoptimal strategies for coping with “central” forms of interference, there also tend to be large individual differences. Consistent with this, a striking feature of binaural interference studies is the large amount of variation across individuals (Woods and Colburn, 1992; Heller and Trahiotis, 1995; present study). It is likely that listeners differ in their ability to isolate and attend selectively to the target interaural delays even when there are clear cues supporting segregation of target and interferer. Individual differences in this ability to listen “analytically” have been observed for binaural discrimination (Dye *et al.*, 1996; Stellmack and Lutfi, 1996). Furthermore, Dye and colleagues (2005) showed that these individual differences predict individual performance in a monaural discrimination task. The ability to weight different frequency regions selectively is also highly relevant in many studies of informational masking (Durlach *et al.*, 2003; Alexander and Lutfi, 2004; Richards and Neff, 2004), and in such studies, as in binaural interference studies, large individual differences are observed. In short, it is likely that different perceptual strategies influence the amount of interference observed in binaural interference studies. Finally, there are suggestions in the literature that listener exposure can affect susceptibility to interference (Woods and Colburn, 1992; Stellmack and Dye, 1993; Hill and Darwin, 1996), suggesting that experience with a particular task can lead to a more refined ability to hear out a target from a complex mixture.

A second puzzle concerns the fact that low-frequency sounds interfere much more strongly with high-frequency targets than vice versa (McFadden and Pasanen, 1976; Zurek, 1985; Trahiotis and Bernstein, 1990; Heller and Trahiotis, 1995). However, it is well known that low-frequency

ITDs are more potent than high-frequency ITDs (Henning, 1980; Bernstein and Trahiotis, 1982; Shinn-Cunningham *et al.*, 1995), and thus might be expected to be weighted more heavily when information is grouped across frequency. Indeed, “transposed tones” (which provide high-frequency channels with ITD information that is as potent as low-frequency ITDs) appear to be immune to binaural interference from a low-frequency noise interferer (Bernstein and Trahiotis, 2004, 2005). It is somewhat surprising that no interference occurs for these pairs, as their simultaneous onsets and offsets would predict some obligatory grouping. It is worth noting, however, that transposed tones have unusual spectral and temporal characteristics, including the exaggerated temporal envelope fluctuations that provide the basis for the robust ITD cues. It may be that the envelope of a transposed tone differs so much from that of the low-frequency noise that they are not perceptually grouped into the same object (McFadden, 1987; Hall *et al.*, 2006). It would be useful to contrast monaural and binaural interference for these stimuli (e.g., see Dye *et al.*, 2005) to determine how much grouping does in fact occur.

A final concern that has been raised in discussions trying to relate binaural interference phenomena directly to grouping processes is that models based on grouping have failed to explain the data completely. Models based on an obligatory weighted combination of binaural information across frequency have done quite well at predicting ITD thresholds under conditions of binaural interference (Buell and Hafter, 1991; Heller and Trahiotis, 1996). However, predicting “release” from binaural interference when segregation cues are introduced has proven more challenging. Woods and Colburn (1992) extended the Buell and Hafter model to include a stage where frequency channels are parsed according to the object with which they are associated. When applied to three-tone complexes, the model generally overpredicted performance (i.e., predicted less interference) in the case where the central target component was segregated on the basis of onset asynchrony. Importantly, their model assumed perfect parsing with no residual interference between frequency channels when computing perceived locations. The authors acknowledged that a “central noise source,” perhaps related to imperfect segregation of the tone or poor focus of attention, might be required. Indeed, in order to account for the aforementioned individual differences in results, such a stage is not only necessary, but must incorporate individualized nonoptimal weightings in the manner of Dye and colleagues (2005). An important observation made by Woods and Colburn was that perceptual segregation (“hearing out” the target tone) occurred reliably with asynchronous onsets even in cases where binaural interference persisted. Their conclusion was that it is necessary but not sufficient to hear out the target as a separate object for release from binaural interference to occur (a conclusion supported by the streamed condition of the current study). A complete grouping-based model of binaural perception may involve two decision stages; one stage determining the number of objects present, and another where the objects are localized (for a related idea see Litovsky and Shinn-Cunningham, 2001). In order to hear the different objects and distinct lo-

cations, the magnitude of the spatial disparity required may be inversely related to the weight of evidence supporting the presence of multiple objects.

ACKNOWLEDGMENTS

This work was supported by a grant from the National Institutes of Deafness and Communication Disorders (NIDCD) to Barbara G. Shinn-Cunningham (R01 DC05778-02). Frederick Gallun was supported by F32 DC006526 from NIDCD. Laura Stupin collected a large amount of preliminary data that shaped the final experiment. Andrew Oxenham, Toby Dye, and one nearly anonymous reviewer (CJD) provided extremely valuable feedback on previous versions of the manuscript.

¹In a recent study, Roberts and Holmes (2006) demonstrated that the addition of simultaneous frequency components to a pure tone reduces the effective level of the tone (presumably via broadband inhibition). In light of this, it is possible that increasing the bandwidth of the leading portion resulted in a less effective stimulus at 500 Hz. While the fact that we increased the level of the noise by 6 dB may have counteracted this effect, we cannot know with full certainty that the effective level of the noise at 500 Hz (and hence its ability to adapt) was as great as the sequential tones. ²It is worth pointing out that the pointer estimates fall into a relatively compressed range overall (± 6 -dB ILD). These values are smaller than those reported by Heller and Trahiotis (1996), who also used an ILD pointer to indicate the location of similar target stimuli. We believe the difference lies in the characteristics of the pointer stimulus: Heller and Trahiotis used a narrowband noise centered at 500 Hz, while in the current study we used a 4000-Hz SAM tone. Our experience with the high-frequency pointer is that it saturates relatively quickly, such that further increases in ILD do not give rise to substantial increases in perceived lateral displacement. The small range of pointer ILDs suggests that listeners restricted their responses to most useful region of the dynamic range.

- Alexander, J. M., and Lutfi, R. A. (2004). “Informational masking in hearing-impaired and normal-hearing listeners: Sensation level and decision weights,” *J. Acoust. Soc. Am.* **116**, 2234–2247.
- Bernstein, L. R., and Trahiotis, C. (1982). “Detection of interaural delay in high-frequency noise,” *J. Acoust. Soc. Am.* **71**, 147–152.
- Bernstein, L. R., and Trahiotis, C. (1985). “Lateralization of low-frequency, complex waveforms: The use of envelope-based temporal disparities,” *J. Acoust. Soc. Am.* **77**, 1868–1880.
- Bernstein, L. R., and Trahiotis, C. (1995). “Binaural interference effects measured with masking-level difference and with ITD- and IID-discrimination paradigms,” *J. Acoust. Soc. Am.* **98**, 155–163.
- Bernstein, L. R., and Trahiotis, C. (2004). “The apparent immunity of high-frequency transposed stimuli to low-frequency binaural interference,” *J. Acoust. Soc. Am.* **116**, 3062–3069.
- Bernstein, L. R., and Trahiotis, C. (2005). “Measures of extents of laterality for high-frequency transposed stimuli under conditions of binaural interference,” *J. Acoust. Soc. Am.* **118**, 1626–1635.
- Best, V., van Schaik, A., Jin, C., and Carlile, S. (2005). “Auditory spatial perception with sources overlapping in frequency and time,” *Acta Acust. Acust.* **91**, 421–428.
- Buell, T. N., and Hafter, E. R. (1991). “Combination of binaural information across frequency bands,” *J. Acoust. Soc. Am.* **90**, 1894–1900.
- Buell, T. N., and Trahiotis, C. (1994). “Detection of interaural delay in bands of noise: Effects of spectral interference combined with spectral uncertainty,” *J. Acoust. Soc. Am.* **95**, 3568–3573.
- Culling, J. F., and Summerfield, Q. (1995). “Perceptual separation of concurrent speech sounds: Absence of across-frequency grouping by common interaural delay,” *J. Acoust. Soc. Am.* **98**, 785–797.
- Darwin, C. J., and Hukin, R. W. (1999). “Auditory objects of attention: The role of interaural time differences,” *J. Exp. Psychol.* **25**, 617–629.
- Darwin, C. J., Hukin, R. W., and al-Khatib, B. Y. (1995). “Grouping in pitch perception: Evidence for sequential constraints,” *J. Acoust. Soc. Am.* **98**, 880–885.
- Darwin, C. J., Pattison, H., and Gardner, R. B. (1989). “Vowel quality

- changes produced by surrounding tone sequences," *Percept. Psychophys.* **45**, 333–342.
- Durlach, N. I., Mason, C. R., Kidd, G., Jr, Arbogast, T. L., Colburn, H. S., and Shinn-Cunningham, B. G. (2003). "Note on informational masking," *J. Acoust. Soc. Am.* **113**, 2984–2987.
- Dye, R. H. (1990). "The combination of interaural information across frequencies: Lateralization on the basis of interaural delay," *J. Acoust. Soc. Am.* **88**, 2159–2170.
- Dye, R. H., Stellmack, M. A., and Jurcin, N. F. (2005). "Observer weighting strategies in interaural time-difference discrimination and monaural level discrimination for a multi-tone complex," *J. Acoust. Soc. Am.* **117**, 3079–3090.
- Dye, R. H., Stellmack, M. A., Grange, A. N., and Yost, W. A. (1996). "The effect of distractor frequency on judgments of laterality based on interaural delays," *J. Acoust. Soc. Am.* **99**, 1096–1107.
- Good, M. D., and Gilkey, R. H. (1996). "Sound localization in noise: The effect of signal-to-noise ratio," *J. Acoust. Soc. Am.* **99**, 1108–1117.
- Good, M. D., Gilkey, R. H., and Ball, J. M. (1997). "The relation between detection in noise and localization in noise in the free field," in *Binaural and Spatial Hearing in Real and Virtual Environments*, edited by R. H. Gilkey and T. R. Anderson (Erlbaum, Hillsdale, NJ), pp. 349–376.
- Hall, J. W., Buss, E., and Grose, J. H. (2006). "Comodulation detection differences for fixed-frequency and roved-frequency maskers," *J. Acoust. Soc. Am.* **119**, 1021–1028.
- Heller, L. M., and Trahiotis, C. (1995). "Interference in detection of interaural delay in a sinusoidally amplitude-modulated tone produced by a second, spectrally remote sinusoidally amplitude-modulated tone," *J. Acoust. Soc. Am.* **97**, 1808–1816.
- Heller, L. M., and Trahiotis, C. (1996). "Extents of laterality and binaural interference effects," *J. Acoust. Soc. Am.* **99**, 3632–3637.
- Henning, G. B. (1980). "Some observations on the lateralization of complex waveforms," *J. Acoust. Soc. Am.* **68**, 446–454.
- Hill, N. I., and Darwin, C. J. (1996). "Lateralization of a perturbed harmonic: Effects of onset asynchrony and mistuning," *J. Acoust. Soc. Am.* **100**, 2352–2364.
- Litovsky, R. Y., and Shinn-Cunningham, B. G. (2001). "Investigation of the relationship among three common measures of precedence: Fusion, localization dominance, and discrimination suppression," *J. Acoust. Soc. Am.* **109**, 346–358.
- Lorenzi, C., Gatehouse, S., and Lever, C. (1999). "Sound localization in noise in normal-hearing listeners," *J. Acoust. Soc. Am.* **105**, 1810–1820.
- McFadden, D. (1987). "Comodulation detection differences using noise-band signals," *J. Acoust. Soc. Am.* **81**, 1519–1527.
- McFadden, D., and Pasanen, E. G. (1976). "Lateralization at high frequencies based on interaural time differences," *J. Acoust. Soc. Am.* **59**, 634–639.
- Oxenham, A. J., and Dau, T. (2001). "Modulation detection interference: Effects of concurrent and sequential streaming," *J. Acoust. Soc. Am.* **110**, 402–408.
- Richards, V. M., and Neff, D. L. (2004). "Cuing effects for informational masking," *J. Acoust. Soc. Am.* **115**(1), 289–300.
- Roberts, B., and Holmes, S. D. (2006). "Asynchrony and the grouping of vowel components: Captor tones revisited," *J. Acoust. Soc. Am.* **119**, 2905–2918.
- Shinn-Cunningham, B. G., Zurek, P. M., Durlach, N. I., and Clifton, R. K. (1995). "Cross-frequency interactions in the precedence effect," *J. Acoust. Soc. Am.* **98**, 164–171.
- Stellmack, M. A., and Dye, R. H. (1993). "The combination of interaural information across frequencies: The effects of number and spacing of components, onset asynchrony, and harmonicity," *J. Acoust. Soc. Am.* **93**, 2933–2947.
- Stellmack, M. A., and Lutfi, R. A. (1996). "Observer weighting of concurrent binaural information," *J. Acoust. Soc. Am.* **99**, 579–587.
- Trahiotis, C., and Bernstein, L. R. (1990). "Detectability of interaural delays over select spectral regions: Effects of flanking noise," *J. Acoust. Soc. Am.* **87**, 810–813.
- Woods, W. S., and Colburn, H. S. (1992). "Test of a model of auditory object formation using intensity and interaural time difference discrimination," *J. Acoust. Soc. Am.* **91**, 2894–2902.
- Zurek, P. M. (1985). "Spectral dominance in sensitivity to interaural delay for broadband stimuli," *J. Acoust. Soc. Am.* **78**, S18.

The detection of differences in the cues to distance by elderly hearing-impaired listeners

Michael A. Akeroyd^{a)} and Stuart Gatehouse

MRC Institute of Hearing Research (Scottish Section), Glasgow Royal Infirmary, Alexandra Parade, Glasgow, G31 2ER, United Kingdom

Julia Blaschke

Institute of Hearing Technology and Audiology, University of Applied Sciences, Oldenburg/Ostfriesland/Wilhelmshaven, Ofener Str. 16-19, D-26121 Oldenburg, Germany

(Received 14 March 2006; revised 10 November 2006; accepted 14 November 2006)

This experiment measured the capability of hearing-impaired individuals to discriminate differences in the cues to the distance of spoken sentences. The stimuli were generated synthetically, using a room-image procedure to calculate the direct sound and first 74 reflections for a source placed in a 7×9 m room, and then presenting each of those sounds individually through a circular array of 24 loudspeakers. Seventy-seven listeners participated, aged 22–83 years and with hearing levels from –5 to 59 dB HL. In conditions where a substantial change in overall level due to the inverse-square law was available as a cue, the elderly hearing-impaired listeners did not perform any different from control groups. In other conditions where that cue was unavailable (so leaving the direct-to-reverberant relationship as a cue), either because the reverberant field dominated the direct sound or because the overall level had been artificially equalized, hearing-impaired listeners performed worse than controls. There were significant correlations with listeners' self-reported distance capabilities as measured by the "Speech, Spatial, and Qualities of Hearing" questionnaire [S. Gatehouse and W. Noble, *Int. J. Audiol.* **43**, 85–99 (2004)]. The results demonstrate that hearing-impaired listeners show deficits in the ability to use some of the cues which signal auditory distance. © 2007 Acoustical Society of America. [DOI: 10.1121/1.2404927]

PACS number(s): 43.66.Qp, 43.66.Sr, 43.55.Ka [AK]

Pages: 1077–1089

I. INTRODUCTION

A recent self-report study has shown that hearing-impaired listeners report deficits in their capability to perceive the distance or motion of sound sources, and that those reports are related to the hearing handicap experienced by the listeners (Gatehouse and Noble, 2004). The questionnaire used, the "Speech, Spatial, and Qualities of Hearing" test (SSQ), enquired about many real-world aspects of listening, of which distance perception was one. Two of the questions (see the Appendix) were concerned with distance directly (e.g., "Do the sounds of people or things that you hear, but cannot see at first, turn out to be closer than expected?"), four others with the distance of dynamic sounds (e.g., "Can you tell from the sound whether a bus or truck is coming towards you?"), and one question with location in general ("Do you have the impression of sounds being exactly where you would expect them to be?"). Gatehouse and Noble (2004) calculated the partial correlation between the scores on these SSQ questions and an independent measure of hearing handicap, controlling for better-ear and worse-ear averages, across a sample of 153 unaided patients (mean age 71 years, mean better-ear-average 39 dB). They found that the four dynamic-distance questions correlated with hearing handicap ($r=0.3-0.5$), as did the "further-than-expected"

question ($r=0.26$). As similar amounts of correlation were found for the other items that are traditionally associated with auditory deficit,¹ it was clear that both distance and motion have prominent associations with hearing handicap.

The primary objectives of the present study were to test if such deficits in distance perception could be demonstrated experimentally, and to inquire if the experimental measures corresponded to the self-report data. Accordingly, we felt it was important for the experiment to use ecologically valid stimuli in a context that was commonly experienced by hearing-impaired listeners. Voices form one of the distance topics directly asked in the SSQ, and so the experiment measured the discrimination of the distance of static, spoken sentences in a room; both of the other two topics—footsteps and traffic—are primarily dynamic situations, whose reproduction in the laboratory would have needed quite-complex signal processing.

The cues to distance perception were reviewed by Coleman (1963), Blauert (1997), and Zahorik *et al.* (2005). One cue is the intensity or overall level of a sound; in an anechoic room, it reduces at a rate of 6 dB per doubling of distance by the inverse-square law, while in any nonanechoic room the rate is somewhat less; for instance, it was about 4 dB in both Simpson and Stanton's (1973) 3.5×3.8 m room and for Zahorik's (2002a) $12 \text{ m} \times 14 \text{ m}$ auditorium. A second cue is based on a distinction between the first sound to arrive and all the subsequent sounds. The first sound is the "direct" sound, and it is independent of the properties of the room; its

^{a)}Author to whom correspondence should be addressed; Electronic mail: maa@ihr.gla.ac.uk

level always changes at a rate of 6 dB per doubling of distance. The subsequent sounds are all reflections from the surfaces of the room and any objects within it. As their total level is dependent much less upon distance (in the small auditorium used by Zahorik, 2002a, it decreased at 1 dB per doubling of distance), the relationship between the direct sound and the reverberation is a second cue to distance.² This relationship is often measured by the ratio of the level of the direct sound to the total level of the reverberant sounds: this “direct-to-reverberant ratio” is larger for a closer source than a further source (the exact values depend upon both the room and the distance, but, as an example, Zahorik’s values for his small auditorium were approximately +12 dB at 1 m and 0 dB at 10 m). Both of these two cues were contrasted in our experiment, as we expected them to be characteristic of the range of distances commonly encountered by hearing-impaired people in domestic or public rooms. Two other distance cues were excluded, as they would only be informative for much larger or much smaller distances: the effect on the spectrum due to the differential absorption of the air across frequency, which only becomes substantial above 15 m or more (Blauert, 1997), and the effect on the sound’s interaural time difference (ITD) and interaural level difference (ILD) of the listener being close to the source, which is only important for distances closer than about 1 m (Brungart *et al.*, 1999).

As the environments inquired about in the SSQ questionnaire are quite general and often complex, we developed a synthetic method that had the potential for recreating in the laboratory the acoustics of many different environments. Our system—termed the “room-image/circular-loudspeaker-array” system (“RI-CLA”)—used a computational method to calculate the acoustics of a medium-sized, virtual room and combined that with a circular array of loudspeakers placed in a smaller, laboratory room. For computational simplicity the virtual room was set to be rectangular, with dimensions of 7 m wide by 9 m long by 2.5 m high (volume=158 m³). It was chosen to be representative of a normal room that might be commonly encountered by a listener; its size was also close to that of the 7.6 m×8.75 m real classroom used by Nielsen (1993). Each wall of the virtual room was given an absorption value of 0.5 (i.e., 3 dB loss per reflection), but the floor and ceiling were made perfect absorbers as there were no loudspeakers above or below the listener in our array. The overall reverberation time of the virtual room was about 250 ms (Sabine, 1964).

This method contrasts with the more obvious one of using loudspeakers placed at different distances in a real environment, such as an anechoic room (e.g., Nielsen, 1993), a nonanechoic room (e.g., Nielsen, 1993), or outdoors on an open field (e.g., Ashmead *et al.*, 1995). Such environments, however, offer limited flexibility or generality, whereas synthetic environments avoid these problems, and can be created using loudspeakers or headphones. Three studies have investigated distance synthetically using headphone presentation allied to the techniques of “virtual auditory space” (e.g., Wightman and Kistler, 1993, 2005): Zahorik (2002a) recorded the acoustics of a small auditorium using binaural in-ear microphones and then presented those over headphones, while Bronkhorst and Houtgast (1999) and

Bronkhorst (2001) used a computational model to calculate the acoustic environment of a room, which they then convolved with a set of head-related-transfer functions (“HRTFs”). We deliberately chose loudspeakers for the final presentation so that we could compare the present data with future experiments on the benefits or drawbacks of aided listening, as placing headphones over hearing-aids would have severely compromised the frequency characteristics and the directivity patterns of the aids.

We used an implementation of the “room-image” procedure (e.g., Allen and Berkeley, 1979; Peterson, 1986; Kompis and Dillier, 1993) to calculate the acoustic characteristics of the room. This procedure was used by Bronkhorst and Houtgast (1999; Bronkhorst, 2001) in their studies of distance perception, as well as in nondistance studies that required the acoustic environment of a room (e.g., Culling *et al.*, 2003; Zurek, 2004). It calculates a list of all the sounds that reach a single point in space—the virtual “listener”—each labeled with an arrival direction, time, and level. We then presented each one of these sounds, individually, from the loudspeaker whose azimuth was closest to the arrival direction, at the arrival level, and after waiting for its arrival time. The result is a recreation at the center of the loudspeaker array of the acoustics experienced by the virtual listener in the virtual room.³

II. METHOD

A. Design

Psychometric functions were measured for the distance discrimination of spoken sentences in a virtual room. A two-interval forced-choice procedure was used to measure the psychometric functions. In one interval, a sentence was simulated to be at a reference distance, while in the other interval, a different sentence was simulated to be at some comparison distance. One of the sentences was spoken by a man, the other by a woman. The task was to decide which of the two sentences was furthest. The two reference distances that were chosen—2 m and 5 m—represented typical real-life situations. The comparison distances were either closer-than or further-than the reference. This design gave psychometric functions for four tasks: closer-than 2 m (“2-Closer”), further-than 2 m (“2-Further”), closer-than 5 m (“5-Closer”), and further-than 5 m (“5-Further”).

Each of the four psychometric functions was measured for two conditions of the overall level of the stimuli. In one set (“Normal-Level”), the levels of the sound were those calculated by the room-image procedure. For these, both the overall level and the relationship between the direct and the reverberant sounds (here characterized by the direct-to-reverberant ratio) were available to determine which of the two sentences was further away. In the second set of conditions (“Equalized-Level”), the overall level of the comparison interval was equalized to that of the reference, and so the direct-to-reverberant relationship was the primary cue to the relative distance of the two sentences.

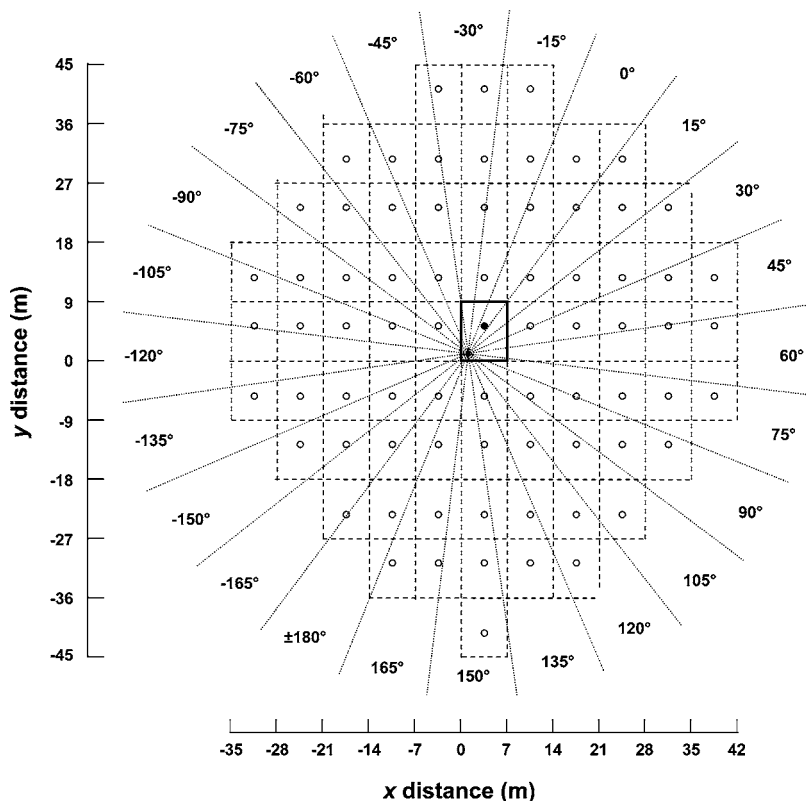


FIG. 3. Schematic illustration of the image method for calculating the echoes. The original virtual room is shown by the solid rectangle together with the receiver (cross) and source (filled circle). Each of the image rooms are shown by the dashed rectangles, with the image source in each shown by the open circles. The angles are quantized to 15° intervals (dotted lines) for presentation over the array. The *x*- and *y*-axes mark the scale, in meters.

listener, was set to be 1 m in from one corner, at a height of 1 m, while the virtual sources were set to be at distances of 1 to 8 m from the listener (at steps of either 1/3 or 1 m), at an angle of 30° relative to the long wall, and again at a height of 1 m. The virtual receiver faced the line of sources: from its perspective, it was looking diagonally across the virtual room, and all the virtual sources were directly ahead of it. This was done to ensure that there was some left/right asymmetry in the sounds. Each of the walls of the virtual room had an absorption value of 0.5, corresponding to a 3 dB loss per reflection. Because our loudspeaker array was installed in the horizontal plane, we set the absorption value of the floor and ceiling to be 1.0 (i.e., an infinite loss), so that all echoes coming from nonhorizontal directions were removed. The Sabine equation gave a reverberation time for the virtual room of 250 ms (Sabine, 1964).

An implementation of Allen and Berkeley's (1979) room-image procedure was used to calculate the direct and the first 74 reflected sounds in the virtual room; we felt that 75 sounds was a suitable compromise between the complexity of the presentation—mainly limited by the speed of the array-control computer—and the accuracy of the simulation (cf. Bronkhorst and Houtgast, 1999). Figure 3 illustrates the calculations for a virtual distance of 5 m. The solid rectangle shows the original, virtual room, with the cross marking the location of the receiver and the filled circle marking the location of the virtual source. Each of the dashed rectangles represents one of the room images, in which an open circle represents its image source. A straight line drawn from any image source to the receiver represents the path of a sound: the length corresponds to the distance traveled—which determines both the inverse-square law reduction in level and the travel time—the angle the arrival angle, and the number

of dashed or solid lines crossed the number of times the sound has reflected at a wall. The angle of each sound was then quantized into 15° sectors, and the sound presented through that sector's loudspeaker at the required time and at a level determined by the sum of the inverse-square law and the number of wall reflections.⁵

The sound levels generated were measured *in situ* by placing a microphone at the center of the loudspeaker array. The top panels of Fig. 4 show the overall level of the signals for each of the Normal-Level conditions (filled circles), as well as the level of the direct sound alone (asterisks) and the level of all the reverberant sound (i.e., everything *but* the direct sound; open circles). The level of the direct sound showed the expected inverse-square dependence on distance. The reverberant sounds showed much less of a dependence on distance. The two were approximately equal at a distance of 4 m; for distances less than this, the overall level was dominated by the direct sound, while for distances greater, it was dominated by the reverberant sound. The bottom panels of Fig. 4 show the corresponding plots for the Equalized-Level conditions. For these, the overall level from each distance was corrected so that the sounds at the comparison distances were at the same overall level as those at the two reference distances. These correction factors were calculated directly from the results of the room-image simulation, and the acoustic measurements showed the equalization had matched the levels to within 1 dB. This equalization meant that the change in level of the direct sound with distance was necessarily much reduced (i.e., there was no longer an inverse-square dependence for the asterisks), while the level of the reverberant sounds now *increased* with distance (open circles). Figure 5 shows the direct-to-reverberant ratio for each of the distances. The open circles are derived from the

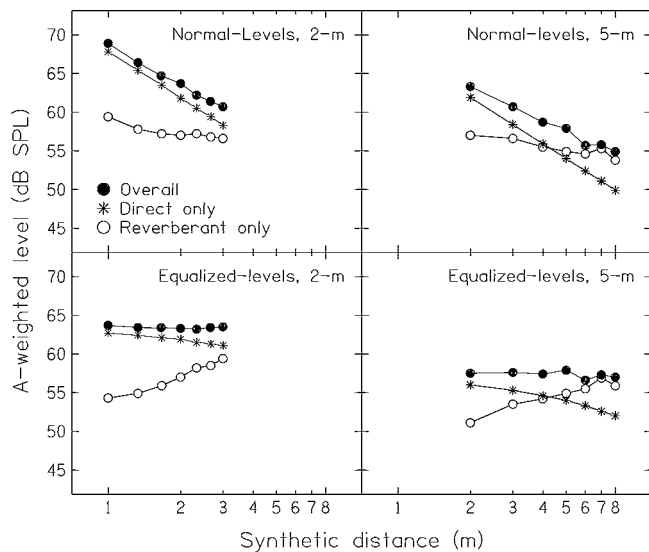


FIG. 4. The measured levels produced at the center of the array, for each of the virtual sources, as a function of the virtual distances. The asterisks mark the level of the direct sound, the open circles the level of all the other (reverberant) sounds, and the filled circles the combined level. The four panels are for the reference distance (2 or 5 m) crossed by the condition (normal or equalized level).

acoustical measurements, while the asterisks are the computational values. This ratio depended upon the distance of the source, being almost +8 dB at a distance of 1 m but about -4 dB at a distance of 8 m. For three of the four conditions (2-Closer, 2-Further, 5-Closer), the direct-to-reverberant ratio was positive, while for one (5-Further), it was negative. The dependence of direct-to-reverberant ratio with log distance was well fitted by a straight line, which gave a rate of change of about -4 dB per doubling in distance.

D. Procedures

The experiment was conducted across two visits, each of about 2 h. At the beginning of the first visit, each listener participated in a short demonstration so they became used to the loudspeaker array and the distance simulation. The listener was told to imagine that he/she was sitting in a large classroom, and a sequence of five sentences was then presented, with the virtual distance of the sentence either ap-

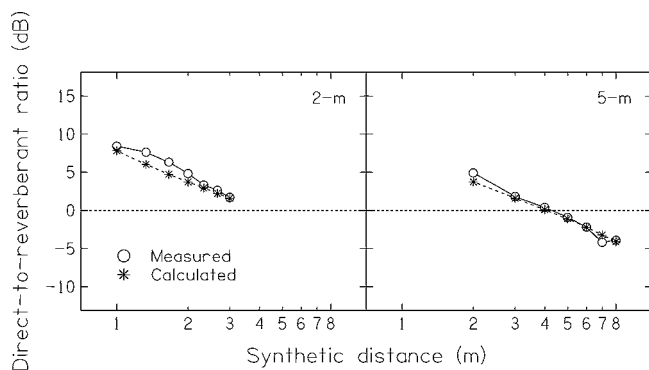


FIG. 5. The direct-to-reverberant ratios for each of the virtual sources. The circles are derived from the measured levels reported in Fig. 4; the asterisks are computed directly from the results of the image-source method. The dashed line marks a direct-to-reverberant ratio of 0 dB.

proaching or receding as the sequence progressed. The listener was asked if he/she felt the talker move, and, if so, whether the talker approached towards or receded away from him/herself. These sequences ranged between virtual distances of 1 and 8 m. Next, single sentences were presented, and each listener was asked how far away the talker was, if the talker was in front or behind, and what the sentence was.

A progressive training scheme was then used to train the listener in the experimental procedure. A two-interval, forced-choice method was used, in which two sentences were presented, one simulated to be at the reference distance, the other simulated to be at the comparison distance. One sentence was chosen at random, without replacement, from the ASL set (and so spoken by a male), the other was similarly chosen from the BKB set (spoken by a female). The listener task was to decide if the female was further than the male or vice versa. No feedback was given. The target interval and sex were counterbalanced across trials. In the training phase, the listener first undertook 16 trials of the 2 m reference, Normal-Level conditions, followed by 32 trials of the 5 m reference, Equalized-Level conditions, and then 64 trials of the 2 m reference, Equalized-Level conditions.

In the remainder of the first session the listener completed an experimental block for the 2 m reference distance followed by an experimental block for the 5 m distance. Each block lasted about 20 minutes and consisted of 168 trials (one reference distance times seven comparison distances times Equalized-Level or Normal-Level, presented 12 times each and in a random order). In the second session, the listener completed two more of each of the experimental blocks. The results were based on the results from all the experimental blocks, and so there were 36 trials for each point on each psychometric function.

E. Listeners

The listeners were patients and volunteers from the local population as well as members of staff. Seventy-eight listeners took part; one listener was removed as his *best* discrimination score was just 64%; in contrast, the best discrimination scores of the other 77 listeners were 86% or better. They were aged between 22 and 83 years (mean 54 years; standard deviation 14 years). Their hearing levels (defined as the average of the audiogram values at 500, 1000, 2000, and 4000 Hz, in their better ears) ranged from -5 to 59 dB HL (mean=20 dB; standard deviation=16 dB). Figure 6 shows a plot of their hearing loss against age. The open circles mark those listeners who had completed a SSQ questionnaire (see below); the asterisks those who did not. As the distribution was similar to the UK National Study of Hearing (Davies, 1995), which is shown by the solid line, the sample of listeners was a fair representation of the UK population.

For some of the analyses we divided the listeners into three equal-sized groups, according to age and hearing loss (see Table I). We defined an older hearing-impaired group, an older normal-hearing control group, and a younger, normal-hearing control group. The two older-adult groups were matched for age; it was not possible to match the hearing-levels of the two normal-hearing groups. Fifteen of

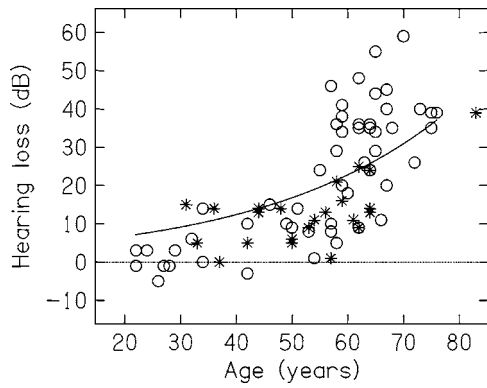


FIG. 6. The mean hearing loss in their better ear of the 77 listeners who took part in the experiment, plotted as a function of their age. The values are the average of 500, 1000, 2000, and 4000 Hz. The open circles are those listeners who completed a SSQ questionnaire; the asterisks are those who did not. The solid line plots the mean hearing loss from the UK National Study of Hearing (Davies, 1995).

the 19 individuals in the older, hearing-impaired group had sensorineural losses (defined by air-bone gaps ≤ 10 dB), the other four had mixed losses.

Two-thirds (53/77) of the listeners also completed the SSQ questionnaire (Gatehouse and Noble, 2004; Noble and Gatehouse, 2004). They formed a representative selection of our population, although there was an under-sampling of people aged between about 30 and 60 (Fig. 6). As our focus was the distance questions of the SSQ, we generated three summary measures of the SSQ responses (see Appendix): “expected-distance” (items 15 and 16); “expected location” (17), and “dynamic-distance” (8, 9, 12, 13). Each response to a question was marked from 0 to 10, with 0 representing complete inability or absence of a quality, and 10 representing complete ability or presence of a quality.

III. RESULTS

A. Group results

The average psychometric functions for the three groups of listeners in the Normal-Level conditions are shown in the panels of Fig. 7. Within each panel, the four tasks of 2-Closer, 2-Further, 5-Closer, and 5-Further are marked by open circles, filled circles, open hourglasses, and filled hourglasses, respectively. The error bars mark the $\pm 95\%$ -confidence intervals for each point of the psychometric functions; a score of 50% corresponds to chance. The left column plots the data as a function of the *difference in distance* between the two intervals of each trial, Δr ; the right column plots the same data as a function of the *percentage change* from the closest of the two distances, $\Delta r/r_{\min}$. The lines show psychometric functions fitted to the group data,

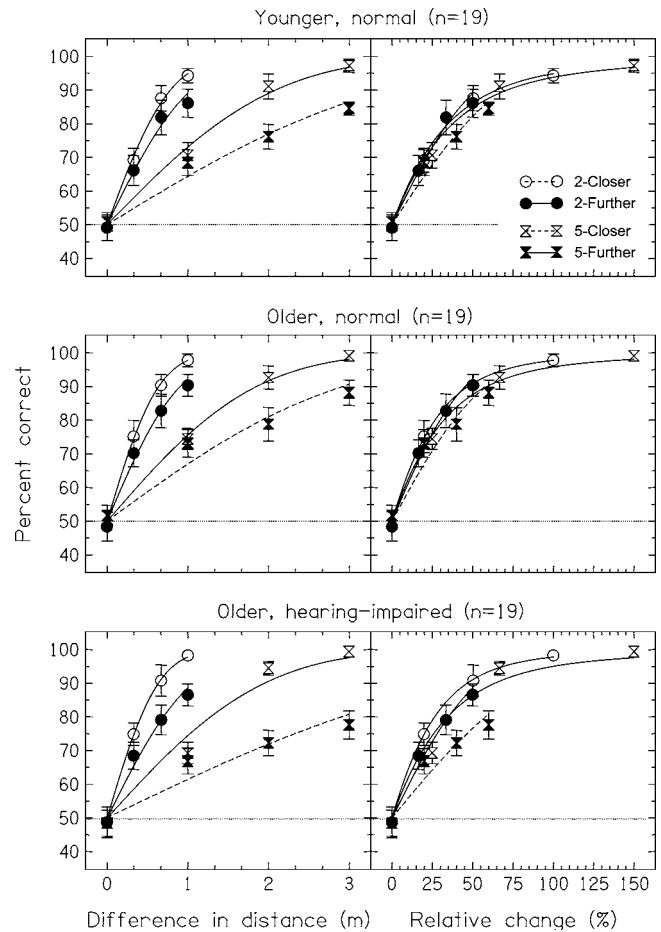


FIG. 7. Average psychometric functions for the Normal-Level conditions from each of the three groups of listeners (young normal, older normal, and older hearing impaired). The four functions in each panel are for the four tasks of “2-Closer,” “2-Further,” “5-Closer,” and “5-Further.” In the left column the data are plotted as a function of the difference in distance between the two trials, Δr ; in the right column the same data are plotted as a function of the percentage change in distance, $\Delta r/r_{\min}$. The lines show psychometric functions fitted to the group data, assuming that d' was proportional to Δr ; the 5-Further psychometric functions are shown by dashed lines to differentiate them from the others. Chance performance is 50%.

and assume that d' was proportional to Δr ; the 5-Further psychometric functions are shown by dashed lines to differentiate them from the others.

In the left-hand panels it can be seen that there was a clear advantage for the 2-Closer task over the 2-Further task and for the 5-Closer task over the 5-Further task, and also that both the 2 m tasks were easier than either of the 5 m tasks. That is, the listeners found distance discrimination to be easier for a closer target than for a further target when expressed as Δr ; for example, 1 vs 2 m was easier than 2 vs 3 m, and both were easier than 4 vs 5 m or 5 vs 6 m. These results reflect the well-known result that discrimination

TABLE I. The age and hearing-loss classifications used to define the three groups.

Group	N	Age, years		Hearing loss, dB	
		Conditional	Mean	Conditional	Mean
Younger, normal hearing	19	<45	33	≤ 25	5
Older, normal hearing	19	56–69	61	≤ 25	14
Older, hearing impaired	19	56–69	63	>25	38

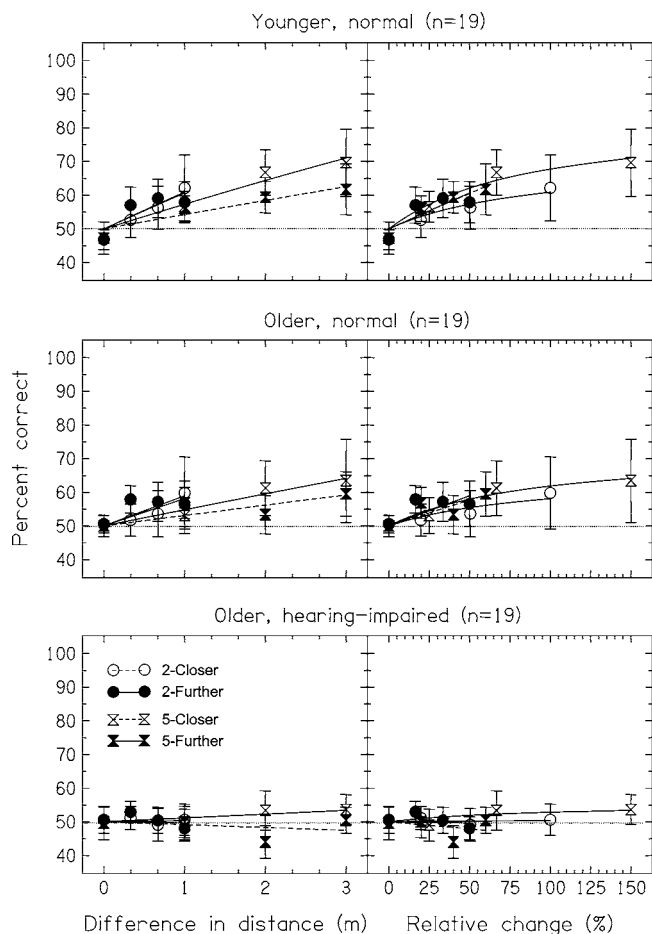


FIG. 8. As Fig. 7 but for the Equalized-Level conditions.

thresholds for distance are generally larger for further source distances (see review by Zahorik *et al.*, 2005). The right-hand panels show that the data are almost invariant across task when plotted as a function of $\Delta r/r_{\min}$; discrimination threshold (taken as 75% correct) corresponded to a $\Delta r/r_{\min}$ of about 25%. The exception was the 5-Further task, which generally gave lower performance than the other tasks. This was especially so for the older-impaired group (bottom-right panel); here discrimination threshold corresponded to a $\Delta r/r_{\min}$ of approximately 50%.

Figure 8 plots the corresponding data for the Equalized-Level conditions. Performance was lower overall, and many of the psychometric functions—especially those for the older-impaired group—were near chance. The invariance with distance ratio was mostly observed, although here it was the 2-Closer task (open circles) that appeared to give lower performance than the other tasks. None of the average functions reached threshold (75%), but an extrapolation of the functions would give a discrimination threshold of, at best, a $\Delta r/r_{\min}$ of somewhere around 200%.

In order to formally compare the results across groups we calculated the average score across the three points with nonzero $\Delta r/r_{\min}$ in each of the psychometric functions. The results for the Normal-Level conditions are shown by the histogram bars in the top panel of Fig. 9. The arrows mark the significant comparisons, with a criterion for significance of $p < 0.05$. Nonparametric statistical tests showed that there

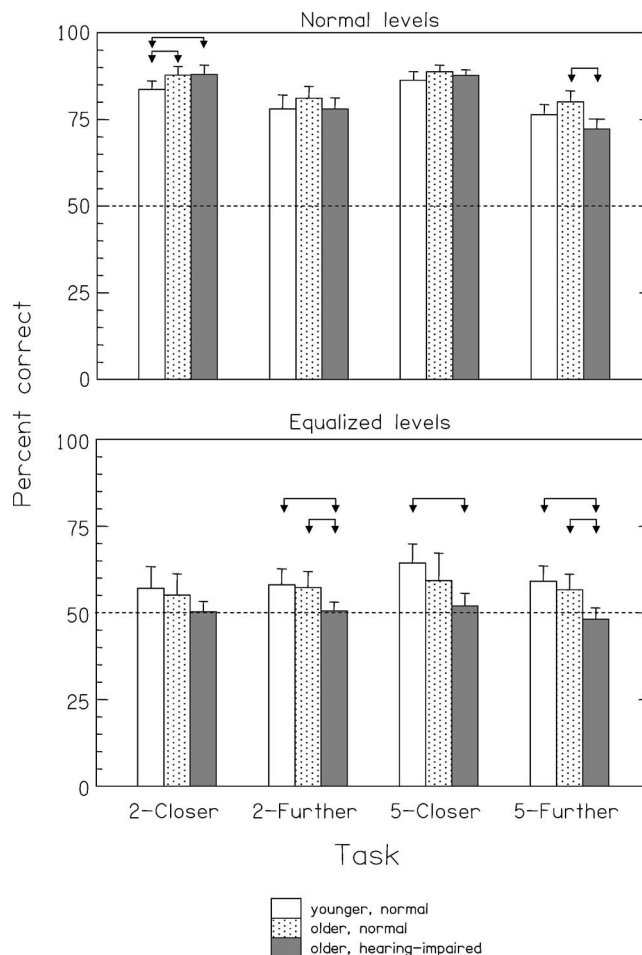


FIG. 9. Top panel: Average discrimination thresholds for each of the three groups of listeners for the four tasks in the Normal-Level conditions. The error bars are the 95% confidence intervals. The discrimination thresholds were calculated for $d' = 1$. Bottom panel: Average percent correct for each of the three groups of listeners for the four tasks in the Equalized-Level conditions and in the Normal-Level conditions. The values are the averages of the three right-most points in each psychometric function plotted in Figs. 7 and 8. The error bars are the 95% confidence intervals. Chance performance is 50%. In both panels the arrows mark the significant comparisons reported in the main text.

was an overall effect of listener group for the 2-Closer and 5-Further tasks (respectively, Kruskal-Wallis $H = 8.0$, $p < 0.05$ and $H = 9.7$, $p < 0.01$); within these, the younger-control group gave significantly lower scores than the older-control and older-impaired groups for the 2-Closer task (respectively, Mann-Whitney $Z = 2.2$, $p < 0.05$, and $Z = 2.5$, $p < 0.05$), while the older-impaired group gave significantly lower scores than the older control group in the 5-Further task ($Z = 3.1$, $p < 0.01$). Neither the 2-Further nor 2-Closer tasks gave a significant overall effect (respectively, $H = 1.8$, not significant; $H = 1.8$, not significant). The equivalent results for the Equalized-Level conditions are shown in the bottom panel of Fig. 9. Significant effects of listener group were found for the 2-Further, 5-Closer, and 5-Further tasks (respectively, $H = 8.2$, $p < 0.05$; $H = 8.4$, $p < 0.05$; $H = 14.0$, $p < 0.01$). In all three tasks, the older-impaired group performed worse than the younger-control group (respectively, $Z = 2.6$, $p < 0.01$; $Z = 3.1$, $p < 0.01$; and $Z = 3.5$, $p < 0.01$), but the older-impaired group performed worse than the older-

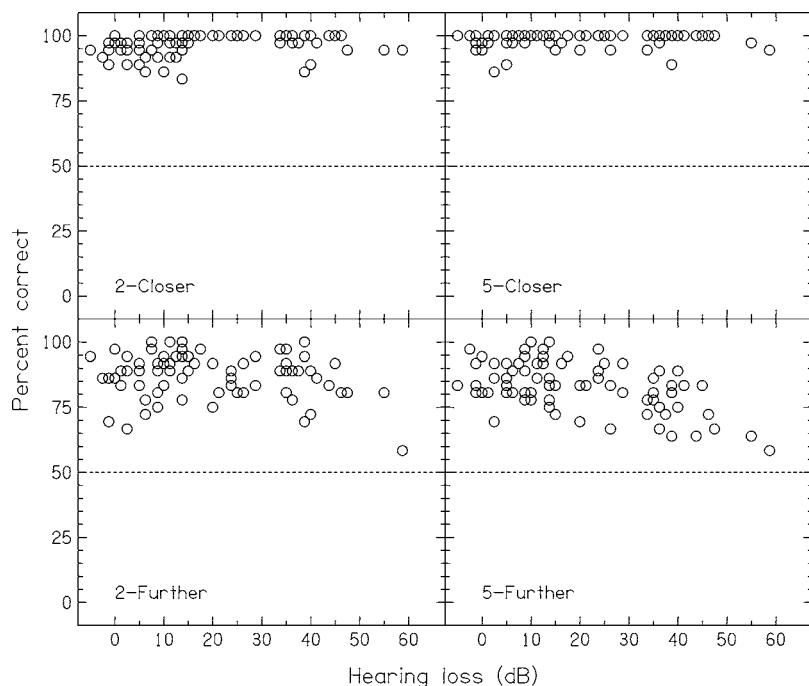


FIG. 10. Individual scores in the best (right-most point) in each of the psychometric functions, plotted as a function of each individual's hearing loss for the Normal-Level conditions.

control group in only the 2-Further and 5-Further tasks (respectively, $Z=2.3$, $p<0.05$; $Z=2.8$, $p<0.01$). No effect was found for the 2-Closer condition ($H=3.0$; not significant).

B. Individual results

Further insight into the results can be found from considering the individual data. The four panels of Fig. 10 show, for each of the normal-level tasks, each individual's score in the *last* point of the psychometric function as a function of their hearing loss (in 92% of the cases, this point gave the highest score on the psychometric function), for which the absolute difference in distance Δr was either ± 1 (2 m tasks) or ± 3 m (5 m tasks). As each point was based on 36 trials, the expected $\pm 95\%$ confidence interval about a score of 50% was a score range of $\pm 17\%$. In the 2-Closer and 5-Closer tasks (top row), most of the listeners were performing the task at ceiling for this point (for the 2-Closer task, 54/77 listeners either scored maximum or made one mistake in the 36 trials; for the 5-Closer task, 67/77 listeners did the same). Nevertheless, in the 2-Closer task (top-left panel), there was a surprising number of *normal-hearing* listeners who performed lower than ceiling. In the 2-Further and 5-Further tasks (bottom row), the results were more variable; only a minority of listeners performed at ceiling (the corresponding counts were 11/77 and 6/77), while even at the lowest levels of hearing loss there were some listeners who performed notably poorly. The nonparametric correlations (Spearman's rho) of performance with hearing loss for the four tasks, in the order 2-Closer, 2-Further, 5-Closer and 5-Further, were, respectively, $+0.27$, -0.11 , -0.01 , and -0.39 ($p<0.02$, not significant, not significant, $p<0.01$).

The corresponding plots for the Equalized-Level conditions are shown in Fig. 11. In all four tasks there was a significant nonparametric correlation with hearing loss (respectively, $r=-0.25$, -0.34 , -0.42 , -0.49 ; $p<0.03$, <0.01 ,

<0.01 , <0.01). Inspection of the graphs showed that the correlations were probably due to a relative lack of listeners who had high hearing losses *and* who performed well; at the lowest levels of hearing loss, the range of performances found was generally from 50% to 100%, but at the higher levels of hearing loss (25 dB or more), no one performed above 75%.

C. SSQ results

Table II reports the nonparametric correlations between the three summary measures of the SSQ distance questions and the average scores in each of the experimental conditions (columns 1–4) and with the average score across all the conditions (column 5). Apart from the 5-Further task with the “expected distance” summary measure, none of the Normal-Level data correlated significantly with any of the SSQ responses. In contrast, the majority of the correlations of the Equalized-Level data with the SSQ responses *were* significant; the correlation coefficients with the “expected distance” and “expected location” summary measures were about equal, although the correlation coefficients with the “dynamic-distance” summary measure were slightly less. That the signs of the significant correlations were all positive was expected: a higher mark on a SSQ item represented a better self-reported capability than a lower mark, while a higher score on the experimental test represented better distance discrimination than a lower score.

IV. DISCUSSION

A. Experimental results

We measured distance discrimination in a virtual 7 m \times 9 m room for a population of normal-hearing and hearing-impaired listeners. When the levels of the sentences were “normal,” in that the differences in overall level due to the effect of the inverse-square law were available, the threshold

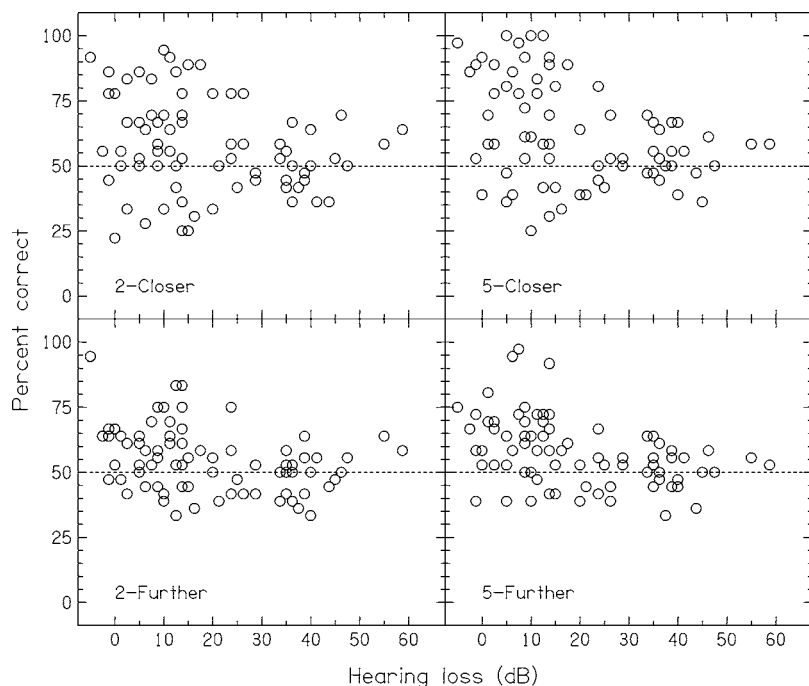


FIG. 11. As Fig. 10, but the individual scores for the Equalized-Level conditions.

(taken at 75% correct) corresponded to a relative change in distance $\Delta r/r_{\min}$ of about 25%. Only for the “further-than” task with the 5 m reference distance did a group of elderly hearing-impaired individuals perform worse than an age-matched normal-hearing group; there the threshold $\Delta r/r_{\min}$ was about 50%. These thresholds were derived from psychometric functions that assumed d' was proportional to the absolute change in distance Δr , which, apart from one condition, gave good fits to the data (the fits were worst for the 5-Further task). When the level of the sentences was equalized, in that the effect of the inverse-square law was removed, performance was substantially worse in every condition. Everyone with a hearing loss more than about 25 dB performed at chance, and there was substantial individual variation even in the normal-hearing listeners: some were able to discriminate the distances well, while others were also at chance. Thresholds could not be reliably determined for these cases, but visual inspection suggested they would be of the order of 200%.

The previous studies of distance discrimination were reviewed by Zahorik *et al.* (2005). There is little agreement on threshold values, and both the methods used and the acoustic

environment affect the results. The smallest values have been found for anechoic or pseudo-anechoic (outdoor) environments; for instance Ashmead *et al.* (1990) reported a threshold change as small as 6% using an anechoic chamber with reference distances of 1- and 2-m and with a 500 ms broadband noise. A useful comparison may be made with Simpson and Stanton’s (1973) study who, like us, were also interested in normal situations of indoor listening. They used a 3.5×3.8 m sound-treated room, which they described as acoustically complex with some reverberant sound, and which gave a rate of change of overall level of 4 dB per doubling of distance; they did not report its reverberation time. A 1600 Hz pulse train served as the stimulus, which was continually presented while the loudspeaker was moved until the listener reported that it had moved. For a reference distance of 2.3 m they found difference limens of 13% and 15% (expressed as $\Delta r/r_{\min}$; the first value is for a target closer-than the reference, the second for further-than). We are unsure why this value is lower than what we found, but it may relate to our use of spoken sentences as stimuli. These were chosen specifically because they are typical and because speech is a prominent topic in the SSQ questionnaire; had we adopted

TABLE II. Correlations of the summary measures of the SSQ items with the experimental data.

SSQ summary measure	Condition	Task				All
		2-Closer	2-Further	5-Closer	5-Further	
Expected distance (15, 16)	Normal Level	-0.03	0.20	0.25	0.28 ^a	0.21
Expected location (17)	Normal Level	0.06	0.17	0.05	0.24	0.14
Dynamic distance (8, 9, 12, 13)	Normal Level	-0.16	-0.11	-0.04	0.12	-0.05
Expected distance (15, 16)	Equalized Level	0.32 ^a	0.47 ^b	0.40	0.25	0.40 ^b
Expected location (17)	Equalized Level	0.30 ^a	0.39 ^b	0.36 ^b	0.26	0.37 ^b
Dynamic distance (8, 9, 12, 13)	Equalized Level	0.22	0.30 ^a	0.29 ^a	0.14	0.28 ^a

^aSignificance level <0.05.

^bSignificance level <0.01.

other stimuli, we might have compromised the relationship between the experimental measure and the questionnaire data. But spoken sentences have fast, dynamic, unpredictable variations in level, and the mean level of each sentence in the present databases also varied by about 1–1.5 dB. It is possible that both effects contributed to a detriment on the psychophysical performance, as stimulus-specific effects have been observed before in distance studies: for instance, Zahorik (2002a) noted that listeners placed more weight on the direct-to-reverberant ratio for a noise-burst stimulus than for a single spoken-syllable stimulus.

Most of the listeners suffered considerable difficulties in comparing the distances of sounds in situations where changes in the overall level were unavailable and the primary cue to distance was the relationship between the direct and the reverberant sounds. We estimated a $\Delta r/r_{\min}$ of somewhere around 200% in the Equalized-Level conditions, which compares poorly to the excellence of distance discriminability when overall level was the primary cue (e.g. Simpson and Stanton, 1973; Strybel and Perrott, 1984; Ashmead *et al.*, 1990). It is also somewhat larger than that found by Zahorik (2002b), who determined the discrimination threshold for distance via measurements of the discrimination thresholds for the direct-to-reverberant ratio itself using a virtual-acoustic, headphone-presentation method. His results gave a direct-to-reverberant discrimination threshold of about 5 dB, corresponding to a distance-discrimination threshold of 2.59 when expressed as a factor of the reference distance or 159% when expressed as $\Delta r/r_{\min}$. Zahorik also noted that it was similar to the factor (2.04, or a $\Delta r/r_{\min}$ of 104%) that he independently derived from a consideration of the variability in listeners' reports of apparent distance that he had collected in an earlier experiment in a small auditorium with a reverberation time of around 700 ms (Zahorik, 2002a).

There was considerable individual variability in the Equalized-Level conditions, however, and inspection of the results shown in Fig. 11 shows that some listeners may have been performing significantly *worse* than chance. This would suggest that they were using the total level of the reverberant sounds as a cue, rather than the direct-to-reverberant ratio: as can be seen from Fig. 4 (open circles), in the Equalized conditions this *increased* with distance, so, if a listener was deciding on the furthest away of the stimuli in the two intervals by choosing that with a lower level, he/she would be marked wrong. To quantify this possibility, we fitted psychometric functions (as before, assuming $d' \propto \Delta r$) to each of the individual datasets and calculated the distribution of the slopes of the functions; any listener who responded on the basis of the direct sound would give a negative slope, any listener who randomly guessed would give a zero slope, and any listener who responded on the basis of the direct-to-reverberant ratio would give a positive slope. The results are plotted as asterisks in Fig. 12; it can be seen that there were a substantial number of listeners who gave negative slopes. Some of these slopes will have happened by chance, however; to estimate these, we simulated 10 000 "chance" psychometric functions, in each of which the score for each of the four points was obtained from 36 trials of random guess-

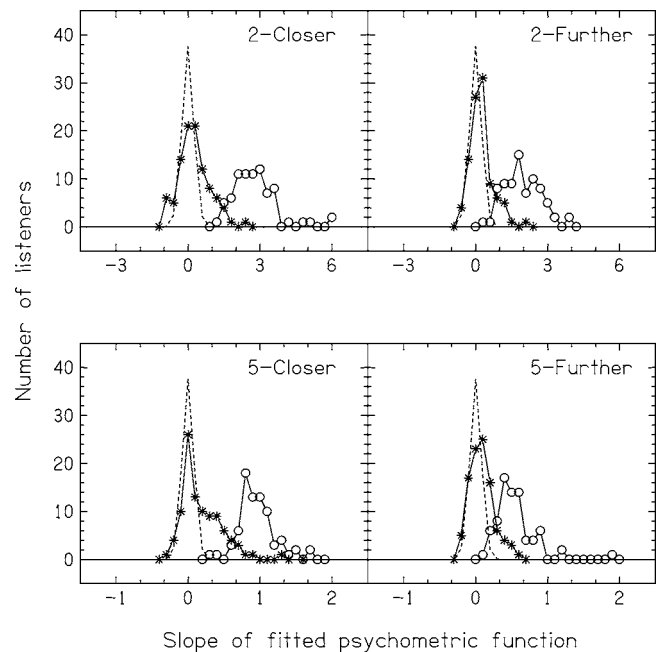


FIG. 12. Top left panel: Distribution of the slopes of the individual psychometric functions for the 2-Closer task in the Normal-Level condition (open circles) and in the Equalized-Level conditions (asterisks). The dashed line plots the expected distribution given chance performance, found using a computer simulation. Other panels: corresponding results for the other conditions of the experiment. Note that the abscissa for the bottom panels is different from the abscissa for the top panels.

ing, and fitted psychometric functions to those. The simulated distribution is shown by the dashed line in each panel of Fig. 12. On the upper side of the distributions, there are always more listeners than expected from the simulation who gave positive slopes; this indicates that some listeners could do the task and responded on the basis of the direct-to-reverberant ratio. Only in the lower side of one distribution (2-Closer; top-left panel) were there more listeners—about 5 out of 77—than expected who gave negative slopes. That is, about 6% of listeners in this condition appear to have responded on the basis of the level of the reverberant sounds.

The open circles in Fig. 12 plot the results of the corresponding analysis of the Normal-Level conditions; as expected, all the listeners showed positive slopes, indicating they were responding on the basis of overall level.

One of the principle objectives of the present experiment was to determine if there were any effects of hearing impairment on distance perception. With the Normal-Level stimuli, we found poorer performance only for the 5-Further task. As this was a condition where the change in the reverberant field dominated, it suggests that hearing-impaired listeners may have a reduced capacity to discriminate distances using the relationship between the direct sound and the reverberant field. This interpretation is consistent with the data from the Equalized-Level conditions, where performance of the hearing-impaired group was essentially at chance (but note that a substantial number of the *non*-impaired listeners also performed near chance in these conditions).⁶ It parallels the common experience that hearing-impaired listeners endure many problems in reverberant or noisy environments. It also suggests that listeners with sensorineural hearing loss rely

primarily on changes in overall level as a cue to differences in distance. If so, then any signal processing and fitting features in hearing aids or cochlear implants which can compromise overall level—for example, aggressively applied, fast-acting multi-channel wide-dynamic-range compression, or adaptive directional microphones—might carry penalties in distance perception. Such features are usually designed to offer advantages in simple speech intelligibility, but for some patients distance perception (and spatial listening in general) is an important contributor to their experience of hearing handicap: for them, any feature that changes overall level may actually be disadvantageous.

In a room the level of the direct sound reduces at 6 dB per doubling of distance while the level of the reverberant sound often reduces at a rate of the order of 1 dB. Thus it would be expected that distance perception would become more problematic for hearing-impaired listeners the further away the target was. The point at which the levels of the direct sound and reverberant field are equal—the critical distance—depends upon the size of the room and its acoustic properties. For our virtual room, the critical distance was 4 m (Fig. 5). Although the direct-to-reverberant ratios in our room were similar to those measured in a real classroom of approximately the same size (Nielsen, 1993, reported values at 1 and 5 m of 8.3 and -3.4 dB; ours were $+8$ and -1 dB), our room had a relatively short reverberation time for its size (Nielsen's value was about 500 ms; ours was about 250 ms). Longer reverberation times would reduce the critical distance, and so extend the range of difficult distances for hearing-impaired listeners.

The second principle objective was to determine if the experimental measure of distance perception was related to the self-report data from the SSQ questionnaire. Although the experimental method was much more controlled and constrained than the topics included in the SSQ, the data do provide some support in the performance domain for those self-reports.⁷ For the Normal-Level conditions, there was only one significant correlation; the 5-further task with the “expected distance” SSQ score. That the overall-level cue was weakest in that 5-further condition, and that the majority of correlations between the Equalized-Level data and the SSQ scores were statistically significant, suggests that listeners' subjective ratings of distance capability may be determined by their experience in environments dominated by direct-to-reverberant ratio rather than by overall level. There was little distinction between the “expected distance” and “expected location” summary measures, which was perhaps to be expected given the similarity in the questions. The correlations with the “dynamic distance” summary measure were, on average, the least. This may have been due our use of *static* sentences; a dynamic experiment, incorporating moving stimuli, may be required to reveal strong correlations with those SSQ items.

B. Distance simulation with a 24-loudspeaker array

The methods used in previous distance experiments have either presented stimuli from loudspeakers at differing distances in real rooms or outdoors (e.g., Nielsen, 1993; Ash-

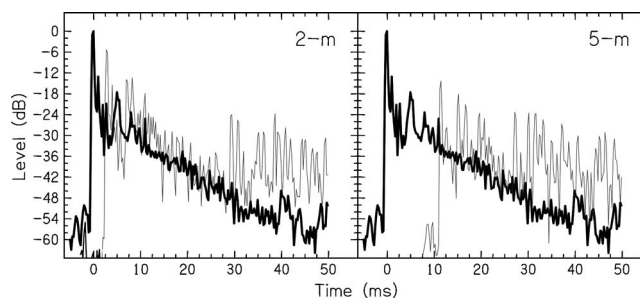


FIG. 13. The instantaneous level of the impulse response of the loudspeakers in the array, recorded in three conditions: 2 m virtual source (left panel, gray line); 5 m virtual source (right-panel, gray line), and a real source at 1 m (both panels, solid line). The recordings have been bandpass filtered between 200 and 12 000 Hz to avoid the background noise in the room, and are the result of time aligning the responses to ten individual clicks and then averaging.

mead *et al.*, 1995), or from headphones using virtual-acoustic techniques (e.g., Bronkhorst and Houtgast, 1999; Zahorik, 2002a). We do not know of any published studies that have used a synthetic loudspeaker-based system similar to our RI-CLA system, while we know of only one study that has used the more-complex method of wave-field synthesis (Kerber *et al.*, 2004). Our system differs from that in the emphasis on one point in space—wave-field synthesis (e.g., Berkhout *et al.*, 1993) attempts to recreate an accurate sound field across a substantial portion of space—and in accepting the curvature of the wave fronts that results from the loudspeakers being quite close to the listener. The system is similar to the “Simulated Open Field Environment” developed by Hafter and Seeber (2004) and Seeber and Hafter (2005), which uses a rectangular array of 48 loudspeakers instead of a circular ring of 24. All the loudspeaker methods have the advantage that the listener only uses their own HRTFs: there are no complications with nonindividualized HRTFs; nor are there any difficulties with the weak externalization of the percepts that can sometimes occur with headphone-presented virtual acoustics. Experimental time need not be spent measuring individual HRTFs for each listener, nor are there complications if the experimental design requires the listener to use hearing aids or cochlear implants. Furthermore, the computational analysis can be extended to generate the acoustics of most environments, so allowing considerable generality in future studies.

Our own experiences of the RI-CLA system—and those of visitors to the laboratory—were that the sounds were indeed at distance, and certainly further than the loudspeakers of the array. We have collected some acoustic and perceptual data that supports these experiences.

A set of acoustic measurements showed that the sounds actually found at the center of the loudspeaker array were, as required, dominated by the echoes calculated by the room-image method, but with the addition of reverberation from within the loudspeaker array and the experimental room. The solid line in both panels of Fig. 13 shows the instantaneous level (calculated via convolution with a 0.25 ms Hanning window) of the impulse response of the whole apparatus, measured by placing a single microphone at the center of the array, and recording the response to ten clicks (to avoid the

background noise in the room, the recordings were high-pass filtered from 200 to 12 000 Hz). The largest pulse was the direct sound, followed by a set of individual reflections, of which the clearest was at 5.4 ms and which was due to the sound reflecting from the opposite side of the array to the source loudspeaker, and then followed by a decaying response, at a rate of approximately -0.75 dB per ms. The gray lines in each panel show the equivalent recordings for the 2 m virtual source (left panel) and the 5 m virtual source (right panel). Both of these contain substantially more reflections than the impulse room of the apparatus itself, and demonstrate the dependence of the level and delay of the direct sound on distance. The results show that the present method is suitable for recreating complex acoustic environments, despite the nonideal acoustics of the loudspeaker array and the room.

Additional perceptual data showed that, on average, the apparent distance of a spoken sentence was underestimated in comparison to the virtual distance the sentence was synthesized to be at; this result is consistent with the commonly observed underestimation of the distance of a *real* source (see meta-analyses by Zahorik, 2002a, and Zahorik *et al.*, 2005). During the initial, demonstration part of the experiment we asked listeners to report the apparent distance of a 5 m sentence: 81% of the listeners reported it as further than the actual loudspeakers, and 24% reported it as *outside* the experimental room. The listeners were also asked to estimate numerically the apparent distance of sources at 2, 5 and 8 m: the mean responses were 1.5, 3, and 4 m. Although our listeners had few visual markers with which to calibrate their numerical estimates of distance, and that the purpose of the demonstration was to provide structured practice and training to the listeners instead of formal experimental data, the data are suggestive that the RI-CLA system provided a good experience of auditory distance.

Nevertheless, there are some limitations in the present system, primarily due to the design and loudspeaker array and to the computer model used to calculate the acoustic environment of the room. First, we noticed occasional (7%) front/back errors in the demonstration phase of the experiment. Second, as the radius of the array is only 1 m, the wave fronts of the sounds will still be somewhat curved when they reach the listener. An application of the inverse-square law gives a reduction in intensity at the far ear compared to the near ear, of, at most, 1.8 dB, and so would be minor in comparison to the expected interaural level differences of up to about 30 dB. Third, the apparent direction of the virtual source would tend towards the direction of one of the loudspeakers if the listener does not sit at the exact center of the array. If one sets as a criterion a difference between apparent and required angles of 10° —a reasonable value for a nonexperienced hearing-impaired listener to notice a misalignment in azimuth—then a geometric calculation shows that for a virtual distance of 8 m, the listener must sit within ± 20 cm of the center of the array. This size of this “sweet spot” is inversely dependent on the virtual distance; for a 2 m virtual source, it is ± 40 cm. Finally, our implementation of Allen and Berkeley’s (1979) room-image procedure was deliberately restricted in its acoustic complexity, primarily in

not using frequency-dependent absorption coefficients. It is clear that the final performance of any distance-synthesis system will be dependent upon the accuracy of the computational model; for instance, frequency-dependent effects were included by Bronkhorst (2001) in his calculation of the acoustics of a virtual room. We are presently exploring more complex algorithms.

C. Summary

The experimental results demonstrated that listeners with sensorineural hearing loss show deficits in the ability to use some of the cues—primarily the direct-to-reverberant ratio—that underpin distance perception, and the comparisons between the experimental data and the questionnaire responses suggest that hearing-impaired listeners may be thinking of environments dominated by direct-to-reverberant ratio when reporting their distance capabilities. Although the synthetic-distance paradigm used was simplified from the complexities and richness of everyday listening situations, the correspondence between performance on our constrained experimental task and a listener’s self-reported capability was encouraging. We plan on future studies that will address the challenges of making the environments more realistic while retaining experimental tractability, and expect to study the advantages and potential penalties of signal processing in hearing aids and cochlear implants.

ACKNOWLEDGMENTS

This study was conducted while Julia Blaschke was an intern in the MRC Institute of Hearing Research, Glasgow, for which she was supported by a Leonardo da Vinci Scholarship from the European Union. The loudspeaker array was constructed by the Nottingham University Section of the MRC Institute of Hearing Research; the room-image program was developed by Dr. Joseph Desloge with support from a grant from the Air Force Office of Scientific Research held by Professor Barbara Shinn-Cunningham of Boston University. We thank the Associate Editor (Dr. Armin Kohlrausch) and two anonymous reviewers for their incisive and informative comments during the review process, Trevor Agus and Dr. Gaetan Gilbert for comments on an earlier draft of this manuscript, David McShefferty for his help in making the acoustical measurements, and Ross Deas, Cheryl Glover, Pat Howell, and Helen Lawson for their assistance in collecting the experimental data. The Scottish Section of the IHR is co-funded by the Medical Research Council and the Chief Scientist’s Office of the Scottish Executive Health Department.

APPENDIX: DISTANCE QUESTIONS FROM THE SSQ QUESTIONNAIRE

The “Speech, Spatial, and Qualities of Hearing” Questionnaire was described by Gatehouse and Noble (2004) and Noble and Gatehouse (2004). Its 49 items include speech perception in noisy and/or dynamic environments, the direction and/or distance of sound sources, the clearness or naturalness of sounds, and the effort or concentration needed to listen or to distinguish sounds. Distance perception is a topic

in seven of the 49 items. Items 15 and 16 refer to distance in general (“expected distance”), 8, 9, 12, and 13 to the distance of dynamic sounds (“dynamic distance”), and 17 to location in general (“expected location”):

8. In the street, can you tell how far away someone is, from the sound of their voice or footsteps?

9. Can you tell how far away a bus or truck is, from the sound?

12. Can you tell from their voice or footsteps whether the person is coming towards you or going away?

13. Can you tell from the sound whether a bus or truck is coming towards you or going away?

15. Do the sounds of people or things you hear, but cannot see at first, turn out to be closer than expected?

16. Do the sounds of people or things you hear, but cannot see at first, turn out to be further than expected?

17. Do you have the impression of sounds being exactly where you would expect them to be?

¹For instance, the partial correlation of this speech-domain question with handicap was also 0.26: “You are talking with one other person in a quiet, carpeted lounge room. Can you follow what the other person is saying?”

²The rate-of-decay of 1 dB is for the combined level of the reverberation; each individual sound in the reverberation decays individually at 6 dB per doubling of distance.

³The present method was our second attempt at a loudspeaker-based synthesis. We had previously tried a cross-talk-cancellation system, but we found fundamental limitations in its ability to reproduce accurately the ITD and ILD information underlying spatial perception. This work is described separately (Akeroyd *et al.*, 2007).

⁴We did not take any steps to prevent the listeners from seeing the loudspeaker array, because its design and placement in the room would have made it impractical to install any curtains or blinds. Our own experiences of valid distance percepts were obtained while being able to see the array.

⁵Note that the whole loudspeaker array was rotated by 30° relative to the virtual room, and so the direct path was always presented from the 0° loudspeaker.

⁶Curiously, the younger, normal-hearing listeners performed worse than the others in the 2-Closer task. We are at a loss to explain this.

⁷Although the sizes of the correlations are modest, they were not unusual in other studies that have compared performance tests to self-report data (e.g., Gatehouse, 1991).

Akeroyd, M. A., Chambers, J., Bullock, D., Palmer, A. R., Summerfield, Q., Nelson, P. A., and Gatehouse, S. (2007). “The binaural performance of a cross-talk cancellation system with matched or mismatched setup and playback acoustics,” *J. Acoust. Soc. Am.* **121**, 1056–1069.

Allen, J. B., and Berkley, D. A. (1979). “Image method for efficiently simulating small-room acoustics,” *J. Acoust. Soc. Am.* **65**, 943–950.

Ashmead, D. H., Davis, D. L., and Northington, A. (1995). “Contribution of listeners’ approaching motion to auditory distance perception,” *J. Exp. Psychol. Hum. Percept. Perform.* **21**, 239–256.

Ashmead, D. H., LeRoy, D., and Odom, R. D. (1990). “Perception of the relative distances of nearby sound sources,” *Percept. Psychophys.* **47**, 326–331.

Bench, J., and Bamford, J. (1979). *Speech-Hearing Tests and the Spoken Language of Hearing Impaired Children* (Academic, London).

Berkhout, A. J., de Vries, D., and Vogel, P. (1993). “Acoustic control by wave field synthesis,” *J. Acoust. Soc. Am.* **93**, 2764–2778.

Blauert, J. (1997). *Spatial Hearing, The Psychophysics of Human Sound Localization* (MIT Press, Cambridge, MA).

Bronkhorst, A. W. (2001). “Effect of stimulus properties on auditory dis-

tance perception in rooms,” in *Physiological and Psychological Bases of Auditory Function*, edited by D. J. Breebaart, A. J. M. Houtsma, A. Kohlrausch, V.F. Prijs, and R. Schoonhoven (Shaker, Maastricht, The Netherlands), pp. 184–191.

Bronkhorst, A. W., and Houtgast, T. (1999). “Auditory distance perception in rooms,” *Nature* (London) **397**, 517–520.

Brungart, D. S., Durlach, N. I., and Rabinowitz, W. M. (1999). “Auditory localization of nearby sources. II. Localization of a broadband source,” *J. Acoust. Soc. Am.* **106**, 1956–1968.

Coleman, P. (1963). “An analysis of cues to auditory depth perception in free space,” *Psychol. Bull.* **60**, 302–315.

Culling, J. F., Hodder, K. I., and Toh, C. Y. (2003). “Effects of reverberation on perceptual segregation of competing voices,” *J. Acoust. Soc. Am.* **114**, 2871–2876.

Davies, A. (1995). *Hearing in Adults* (Whurr, London).

Gatehouse, S. (1991). “The role of non-auditory factors in measured and self-reported disability,” *Acta Oto-Laryngol., Suppl.* **476**, 249–256.

Gatehouse, S., and Noble, W. (2004). “The speech, spatial and qualities of hearing scale (SSQ),” *Int. J. Audiol.* **43**, 85–99.

Haftner, E., and Seeber, B. (2004). “The simulated open field environment for auditory localization research,” *Proceedings of the 18th Int. Congress on Acoustics*, Kyoto, Japan, Vol. 5, pp. 3751–3754.

Kerber, S., Wittek, H., Fastl, H., and Theile, G. (2004). “Experimental investigations into the distance perception of nearby sound sources: Real vs. WFS virtual nearby sources,” *Proceedings of the 7th Congrès Français d’Acoustique/30th Deutsche Jahrestagung für Akustik (CFA/DAGA 04)* (Strasbourg, France), pp. 1041–1042.

Kompis, M., and Dillier, N. (1993). “Simulating transfer functions in a reverberant room including source directivity and head-shadow effects,” *J. Acoust. Soc. Am.* **93**, 2779–2787.

MacLeod, A., and Summerfield, Q. (1987). “Quantifying the contribution of vision to speech perception in noise,” *Br. J. Audiol.* **21**, 131–141.

Nielsen, S. H. (1993). “Auditory distance perception in different rooms,” *J. Audio Eng. Soc.* **41**, 755–770.

Noble, W., and Gatehouse, S. (2004). “Interaural asymmetry of hearing loss, Speech, Spatial and Qualities of Hearing Scale (SSQ) disabilities and handicap,” *Int. J. Audiol.* **43**, 100–114.

Peterson, P. M. (1986). “Simulating the response of multiple microphones to a single acoustic source in a reverberant room,” *J. Acoust. Soc. Am.* **80**, 1527–1529.

Sabine, W. C. (1964). *Collected Papers on Acoustics* (Dover, New York).

Schroeder, M. R. (1965). “New method of measuring reverberation time,” *J. Acoust. Soc. Am.* **37**, 409–412.

Seeber, B., and Haftner, E. (2005). “Redesign of the simulated open-field environment and its application in audiological research,” Abstracts of the 28th Annual Midwinter Meeting, Assoc. Res. Otolaryngol., p. 339.

Simpson, W. E., and Stanton, L. D. (1973). “Head movement does not facilitate perception of the distance of a source of sound,” *Am. J. Psychol.* **86**, 151–159.

Strybel, T. Z., and Perrott, D. R. (1984). “Discrimination of relative distances in the auditory modality: The success and failure of the loudness discrimination hypothesis,” *J. Acoust. Soc. Am.* **76**, 318–320.

Wightman, F. L., and Kistler, D. J. (1993). “Sound localization,” in *Human Psychophysics*, edited by W. A. Yost, A. N. Popper, and R. R. Fay (Springer-Verlag, New York), pp. 155–192.

Wightman, F. L., and Kistler, D. J. (2005). “Measurement and validation of human HRTFs for use in hearing research,” *Acta. Acust. Acust.* **91**, 429–439.

Zahorik, P. (2002a). “Assessing auditory distance perception using virtual acoustics,” *J. Acoust. Soc. Am.* **111**, 1832–1846.

Zahorik, P. (2002b). “Direct-to-reverberant energy ratio sensitivity,” *J. Acoust. Soc. Am.* **112**, 2110–2117.

Zahorik, P., Brungart, D. S., and Bronkhorst, A. W. (2005). “Auditory distance perception in humans: A summary of past and present research,” *Acta. Acust. Acust.* **91**, 409–420.

Zurek, P. M., Freyman, R. L., and Balakrishnan, U. (2004). “Auditory target detection in reverberation,” *J. Acoust. Soc. Am.* **115**, 1609–1620.

Effective compression and noise reduction configurations for hearing protectors

King Chung^{a)}

Department of Speech, Language, and Hearing Sciences, Purdue University, West Lafayette, Indiana 47907

(Received 27 June 2006; revised 20 November 2006; accepted 21 November 2006)

The author proposed to adopt wide dynamic range compression and adaptive multichannel modulation-based noise reduction algorithms to enhance hearing protector performance. Three experiments were conducted to investigate the effects of compression and noise reduction configurations on the amount of noise reduction, speech intelligibility, and overall preferences using existing digital hearing aids. In Experiment 1, sentence materials were recorded in speech spectrum noise and white noise after being processed by eight digital hearing aids. When the hearing aids were set to 3:1 compression, the amount of noise reduction achieved was enhanced or maintained for hearing aids with parallel configurations, but reduced for hearing aids with serial configurations. In Experiments 2 and 3, 16 normal-hearing listeners' speech intelligibility and perceived sound quality were tested when they listened to speech recorded through hearing aids with parallel and serial configurations. Regardless of the configuration, the noise reduction algorithms reduced the noise level and maintained speech intelligibility in white noise. Additionally, the listeners preferred the parallel rather than the serial configuration in 3:1 conditions and the serial configuration in 1:1 rather than 3:1 compression when the noise reduction algorithms were activated. Implications for hearing protector and hearing aid design are discussed. © 2007 Acoustical Society of America. [DOI: 10.1121/1.2409859]

PACS number(s): 43.66.Vt, 43.66.Ts, 43.71.Gv, 43.60.Mn, 43.60.Dh [BLM] Pages: 1090–1101

I. INTRODUCTION

Exposure to hazardous noise levels is an international health concern for workers in noisy industries. A consequence of such noise exposure is noise-induced hearing loss. While noise-induced hearing loss is mostly preventable by using hearing protectors, many workers do not wear hearing protectors because they feel that hearing protectors interfere with communication and reduce the audibility of warning signals, especially for those who already have hearing loss (Kahan and Ross, 1994; Morata *et al.*, 2001; Morata *et al.*, 2005). The author proposes to adopt the adaptive multichannel modulation-based noise reduction and wide dynamic range compression algorithms that are commonly used in digital hearing aids to provide speech- and level-dependent signal processing and to enhance the performance of hearing protectors. As the compression and noise reduction algorithms can be implemented in different configurations, the focus of this study was to investigate effective compression and noise reduction configurations for the use of hearing protection. The effects of different configurations on objective speech intelligibility and subjective preferences were also examined.

Hearing aid studies reported that adaptive multichannel modulation-based noise reduction algorithms improved sound quality and reduced the overall level of noise without compromising speech understanding in speech spectrum noise or in noises with limited temporal fluctuations (Alcantara *et al.*, 2003; Bentler, 2005; Bentler and Chiou, 2006;

Boymans *et al.*, 1999; Boymans and Dreschler, 2000; Bray and Nilsson, 2001; Ricketts and Dhar, 1999; Valente *et al.*, 1998; Walden *et al.*, 2000; Ricketts and Hornsby, 2005). The implications for hearing protector use are that these noise reduction algorithms can reduce the overall noise exposure and at the same time maintain speech intelligibility.

Multichannel wide dynamic range compression is typically used in hearing aids to provide more amplification for low-level sounds and less amplification for high-level sounds. It can also provide different amounts of amplification for sounds in different frequency regions. When applied to hearing protectors, wide dynamic range compression can limit the output of high-level sounds while simultaneously providing low-level amplification to workers with hearing loss and/or enhancing the low-level sounds to preattenuated levels so that workers can still hear sounds they would normally hear without them. It is possible that if adaptive multichannel noise reduction and wide dynamic range compression algorithms are applied to hearing protectors, workers will be more willing to wear hearing protectors knowing that their ability to communicate with others and to hear low-level sounds will not be compromised.

While hearing aids could theoretically be modified to become hearing protectors by simply adding attenuators at the hearing aid input and/or output, the successful utilization of the noise reduction and wide dynamic range compression algorithms in hearing protectors requires careful consideration of the interactions between the two systems. Chung (2004) showed that a noise reduction algorithm greatly enhanced the modulation depth of a speech-in-noise signal when a hearing aid was set to linear (i.e., the noise reduction algorithm reduced the noise level and enhanced the modula-

^{a)}Electronic mail: kingchung@purdue.edu

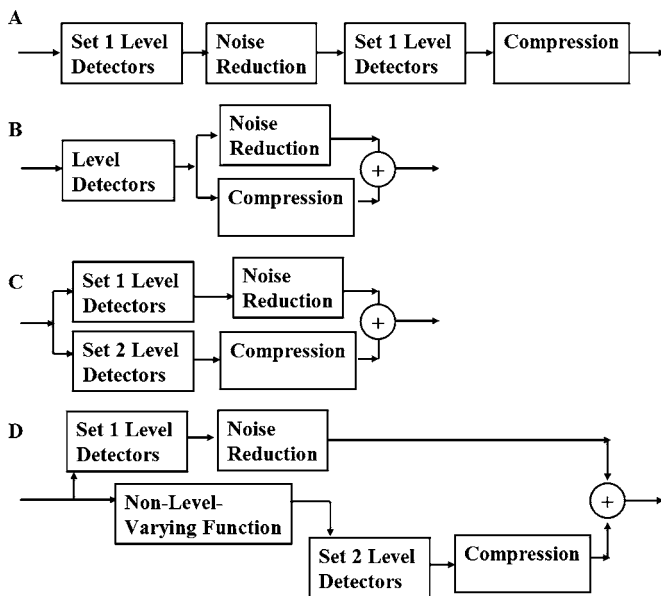


FIG. 1. Simplified diagrams of two possible configurations of the noise reduction and the compression systems: (A) series, (B)–(D) parallel.

tion depth of the speech envelope). When the hearing aid was set to 3:1 compression, however, the modulation depth of the speech envelope was greatly reduced compared to the linear (i.e., 1:1) setting. This indicated that the noise level was increased and the speech level was decreased when compression was activated, which is clearly undesirable.

The problem could be due to the serial implementation of the noise reduction and the compression algorithms in the test hearing aid used by Chung (2004) [Fig. 1(A)]. Noise reduction algorithms are designed to reduce the level of noise and, ideally, to leave the level of speech unaltered. On the other hand, compression is designed to reduce the level of high-level sounds and to increase the levels of low-level sounds. Both algorithms depend on level detectors which estimate the levels of the incoming signal, to determine their subsequent actions. If the noise reduction algorithm and the compression algorithm have their own level detectors and they are implemented in series, the noise reduction algorithm reduces the level of noise, and when the signal enters the compression algorithm, the noise (now a low-level signal) is amplified and speech (now a high-level signal) is reduced. Thus, the overall level of noise is increased and the overall level of speech is reduced.

An alternative configuration is to implement the noise reduction and the compression configurations in parallel, which means the two systems may share the same level detectors [Fig. 1(B)], use level detectors with different characteristics to detect the signal at the same point in the signal processing path [Fig. 1(C)], or implement level detectors at different points in the signal processing path with non-level varying functions in between [Fig. 1(D)]. In these configurations, the amount of gain provided by each frequency channel is a joint decision of both systems. Theoretically, the parallel configuration can avoid one system counteracting the actions of the other and produce a more desirable result (either the relative levels of speech and noise remain the same or increase with compression). Yet, few research studies have

addressed this issue and little is known about how the two different configurations affect the noise levels of the outputs, speech intelligibility, or perceived sound quality, all of which would contribute to the decision of whether the resulting system is more desirable for hearing protector use.

The purposes of this study were: (1) to determine the desirable configuration of the noise reduction and the compression algorithms (i.e., serial or parallel) that would result in a reduction of the overall level of noise with or without compression; and (2) to investigate if speech intelligibility and overall sound quality preferences were affected by the configurations of the compression and the noise reduction algorithms.

II. EXPERIMENT 1

In this experiment, the effects of different compression and noise reduction configurations were investigated using eight commercial digital hearing aids. Recordings of hearing aid output were made by using a Knowles Electronic Manikin for Acoustic Research (KEMAR) fitted with digital hearing aids and placed in a three-dimensional sound field. The noise levels of the recordings were measured in conditions with and without wide dynamic range compression or noise reduction algorithms when speech and two types of noises were presented to KEMAR at four signal-to-noise ratios (SNRs). The differences in the amount of noise reduction when the compression algorithms were set to 1:1 and 3:1 compression ratios were compared.

A. Calibration of the sound field

A three-dimensional speaker array was placed in an anechoic chamber with four speakers on the ceiling, four at ear level, and four on the floor. The ceiling and floor speakers were placed at 45°, 135°, 225°, and 315° azimuths and they were tilted so that the surface of the speakers faced the center of the speaker array. The ear-level speakers were placed at 0°, 90°, 180°, and 270° azimuths. Speech was presented to the ear-level speaker located at 0° azimuth (Speaker 1) and noise was presented to all speakers including Speaker 1. The two background noises used in this study were the speech spectrum noise from the Hearing in Noise Test (HINT, Nilsson *et al.*, 1994) and a white noise with flat spectrum up to 10 kHz.

During the calibration process, speech and noise were presented using Adobe AUDITION 1.0 wave-editing software from Computer 1 (2.39 GHz Pentium 4 with 1 Gbytes of RAM) to the speakers via 2 Delta 1010 (M audio) sound cards. The speech signal was sent to Speaker 1, a Mackie HR824 powered speaker with a ± 1.5 dB frequency response from 0.039 to 20 kHz and a maximum output of 100 dB SPL. Uncorrelated noise signals were sent to the Mackie speaker and through power amplifiers to 11 Hafler M5 speakers (Speakers 2–12), which have a frequency response of 0.07–21 kHz ± 3 dB and a maximum output of 100 dB SPL. The power amplifiers were two four-channel Crown 4210 and one Ressund eight-channel power amplifier.

The noise signals sent to Speakers 1–12 were calibrated to be 59 dB SPL to generate an overall sound pressure level of 70 dB when measured at the center of the speaker array in

TABLE I. A summary of the hearing aid characteristics.

	Group I				Group II			
	A	B	C	D1	D2	E1	E2	F
Hearing aid model	15	20	10	14	17	9	16	8
Number of noise reduction channels	15	20	4	14	17	9	16	8
Number of compression channels	ITE	ITE	ITE	ITE	BTE	ITE	BTE	ITE
Hearing aid style	Unknown	Unknown	Parallel	Parallel	Series	Series	Series	Series
Compression and noise reduction configuration								

the absence of KEMAR. Speech (Speaker 1) was calibrated to be 80, 75, 70, and 65 dB SPL to generate sound field signal-to-noise ratios of +10, +5, 0, and -5 dB, respectively. Then, KEMAR was placed at the center of the speaker array.

B. Hearing aid characteristics

The characteristics of eight digital hearing aids from six manufacturers are summarized in Table I. Hearing aids from the same manufacturer were designated the same letter with the older model named 1 and the newer model named 2. These eight hearing aids were chosen because they have adaptive multichannel modulation-based noise reduction algorithms that detect slow modulations of speech (i.e., modulations in the temporal envelope of speech generated by the opening and closing of the supralaryngeal vocal tract) and use the estimated speech-to-noise ratio to determine the amount of amplification in each frequency channel.

No hearing aid with curvilinear compression was chosen because its compression ratios changed with the input level and it was thus impossible to determine its compression ratio for a level-varying signal such as speech. In addition, hearing aids with noise reduction algorithms that utilized Wiener filters were not included because the noise levels at the output of these hearing aids were higher when the noise reduction algorithms were activated than when deactivated (Chung and Acker, 2006), and thus were not suitable for use in hearing protectors.

The eight digital hearing aids were programmed to have 1:1 and 3:1 compression with a flat frequency response (i.e., within 5 dB variation from 0.25 to 5 kHz at 80 dB SPL input) when the hearing aids were worn in KEMAR. The 3:1 compression ratio was chosen for the compression conditions because this is the typical upper limit for wide dynamic range compression hearing aids. The input-output functions of the digital hearing aids were also double-checked in the Fonix 7000 Hearing Aid Analyzer using the ANSI 1996 testing protocol.

Other advanced signal processing features such as directional microphones and feedback reduction algorithms were deactivated. In addition, the reserve gain was set to the minimum and the maximum power output was set to the maximum in order to avoid the testing materials being processed by the high-level compression limiting algorithm which typically have compression ratios higher than 5:1.

C. Recording of the stimuli

The equipment used in the recording process was identical to that used in the calibration process, except that a reference microphone (ER11) was hung above KEMAR's

head to record unprocessed sounds in the sound field. The outputs of the eight digital hearing aids were recorded at SNRs of +10, +5, 0, and -5 dB in speech spectrum noise and white noise when the hearing aids were set to linear or 3:1 compression at four settings:

1. No noise reduction (NR-Off),
2. Low noise reduction (NR-Low),
3. Medium noise reduction (NR-Medium),
4. High noise reduction (NR-High).

The NR conditions were recorded by activating the noise reduction algorithm in the hearing aid fitting software (i.e., all parameters in the hearing aids were identical in the NR-Off and NR conditions except the activation of the noise reduction algorithm). A total of 64 conditions were recorded for each of the eight hearing aids (i.e., 4 hearing aid settings \times 2 compression settings \times 4 SNRs \times 2 noises).

HINT lists 1 to 3 with sentence spacing identical to the original HINT were used to simulate an environment in which a co-worker of the hearing protector users was speaking sentences one by one with pauses in-between. Concatenated sentences (lists 1-3) were also recorded to simulate the environments where the co-worker spoke in paragraphs. During the recording process, the speech was presented roughly 10 s after the presentation of continuous noise to allow time for the noise reduction algorithms to adapt. The hearing aid output and the reference microphone output were recorded in the left and right channels of Computer 2 (1.8 GHz Intel Pentium M processor with 512 Mbytes RAM).

To ensure all speech signals were presented in the region with the intended compression ratio (i.e., below the compression limiting threshold), the 1:1 NR-Off condition at +10 dB SNR was always recorded first. The noise level in the left (hearing aid processed signal) and right (reference signal) channels were then equalized off-line to eliminate any difference caused by the gain of the hearing aid. Then, the overall levels of the concatenated speech were compared. If the overall level in the hearing aid output is more than 1 dB lower than that in the reference, it is likely that some of the speech components were recorded in the output limiting range of the hearing aid, which compressed speech peaks and lowered the overall output levels. In such case, the overall gain of the hearing aid was reduced. In the final recording, the level differences between the outputs of the hearing aid and the reference microphone were within 1 dB for all eight test hearing aids.

Figure 2 shows the output of two hearing aids, C and E1, when the hearing aid was set to NR-Off, NR-Low, NR-

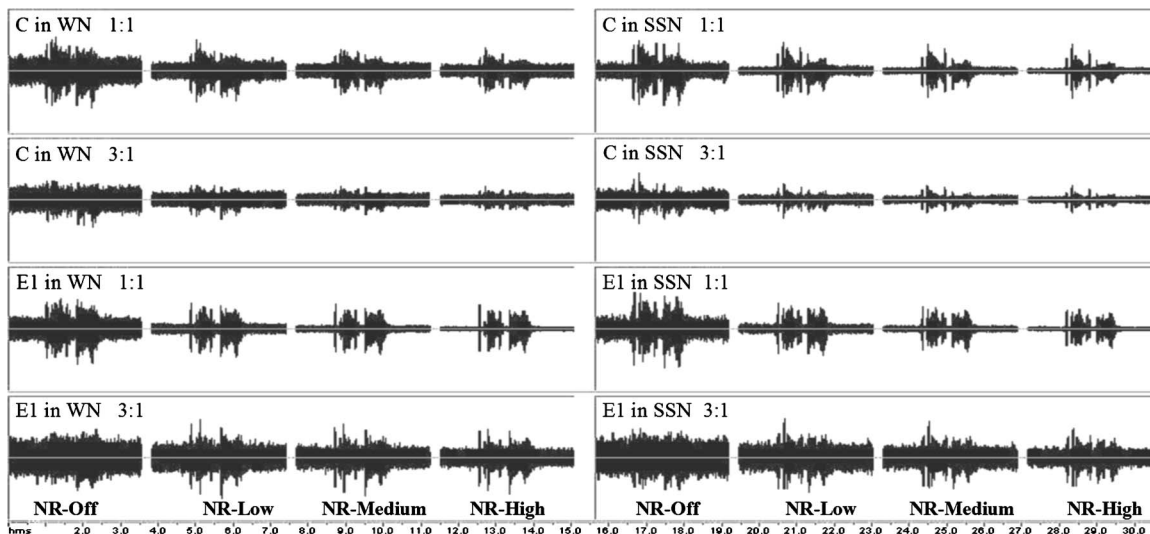


FIG. 2. The outputs of a hearing aid from Group I (C) and a hearing aid from Group II (E1) recorded when the hearing aids were set to no noise reduction (NR-Off), low noise reduction (NR-Low), medium noise reduction (NR-Medium), and high noise reduction (NR-High) at SNR 10 dB in white noise (WN) and in speech spectrum noise (SSN).

Medium, and NR-High. The recordings were recorded in the linear and 3:1 compression conditions at a SNR of +10 dB. For each condition, 1 s of noise precedes and follows the sentence “The team is playing well.” The lower the noise level, the more effective the noise reduction algorithm was for hearing protection. The higher the speech peaks, the higher the estimated overall speech level was.

D. Data analysis

The noise levels in the recordings were measured for each of the eight digital hearing aids. The noise level for each experimental condition was measured between sentences at approximately 0.5, 1, 2, and 3 min between sentences after the onset of the noise. The noise levels for most hearing aids stabilized within 1 dB of the steady state level within 1 min after the onset of the noise, with the exception of Hearing Aid A, which stabilized within 3 min. Thus, an additional measurement was taken at 4 min for Hearing Aid A. The average noise level of an experimental condition was estimated by averaging the measurements at 1, 2, and 3 min for the hearing aids. The average noise levels of Hearing Aid A were estimated by averaging the measurements at 3 and 4 min. The amount of noise reduction offered by the noise reduction algorithms was defined by the difference between the noise levels estimated in the NR-Off and the NR conditions.

E. Results

Based on the differences in noise reduction between the 1:1 and the 3:1 compression conditions, hearing aids with similar or negative noise level differences are assigned to Group I and hearing aids with positive differences are assigned to Group II. Tables II and III summarize the results in speech spectrum noise and white noise, respectively. The differences in the amount of noise reduction between the 1:1 and 3:1 conditions mainly reflected the interaction between the compression and the noise reduction algorithms. The noise levels in the 3:1 conditions of Group I hearing aids

were equal or similar to that in the linear conditions. This meant that the performance of these noise reduction algorithms was either not affected (i.e., 0 difference) or enhanced (i.e., negative difference) by the activation of 3:1 compression. Both scenarios are desirable for hearing protection applications. On the other hand, the amount of noise reduction in the 3:1 compression conditions of Group II hearing aids was lower than that in the linear conditions. This indicated that the noise reduction effect was reduced when the 3:1 compression was activated. As all the hearing aids in Group II had serial compression and noise reduction configurations, it is concluded that the serial configuration is undesirable for hearing protection applications.

Note that the speech level was expected to decrease for both hearing aids when the 3:1 compression was activated because all the recordings were made with speech peaks presented at a level higher than that of the noise level (see the temporal envelopes in Fig. 2). The effects of compression and noise reduction on the overall amplitude of speech at the hearing aid output are further discussed in Experiment 2.

F. Discussion

In this experiment, the interactions between the compression and the noise reduction algorithms were examined for eight hearing aids. Compared to the linear conditions, the 3:1 conditions yielded an equal or higher amount of noise reduction for Group I hearing aids and lesser amount of noise reduction for Group II hearing aids. From a practical point of view, noise reduction algorithms that yielded similar or higher amounts of noise reduction when compression was activated would be more desirable for hearing protection devices. As many hearing aid manufacturers keep information on the compression and noise reduction algorithm configuration proprietary, the configurations of some test hearing aids were unknown. From the available information in Table I, it is speculated that the parallel configurations were more desirable than the serial configurations.

TABLE II. The average amount of noise reduction in the linear (1:1) and 3:1 compression conditions in speech spectrum noise. All the values were calculated by subtracting the noise levels measured in the NR conditions in those in the NR-Off conditions.

NR settings	Group I												Group II												
	A			B			C			D1			D2			E1			E2			F			
	1:1 ^a	3:1 ^b	Diff ^c	1:1	3:1	Diff	1:1	3:1	Diff	1:1	3:1	Diff	1:1	3:1	Diff	1:1	3:1	Diff	1:1	3:1	Diff	1:1	3:1	Diff	
SNR=-5 in sound field																									
Low	6.9	82	-1.3	2.5	2.7	-0.3	5.9	5.6	0.4	3.1	3.4	-0.3	2.5	0.9	1.6	8.0	2.7	5.3	-0.2	-1.3	1.2				
Medium	11.8	13.2	-1.4	3.9	3.7	0.2	8.0	8.6	-0.7	5.0	5.7	-0.7	5.3	1.9	3.4	12.0	4.3	7.7	3.8	0.3	3.5	3.1	0.4	2.7	
High	9.2	10.7	-1.5	5.8	5.9	-0.1	11.1	9.9	1.2	7.5	8.1	-0.6	8.0	3.0	5.0	16.0	6.1	9.9	7.2	1.8	5.4				
SNR=0 dB in sound field																									
Low	5.2	5.9	-0.7	2.7	2.9	-0.1	5.1	5.4	-0.3	2.9	3.4	-0.5	2.6	0.9	1.7	7.8	2.7	5.1	-0.2	-1.3	1.1				
Medium	10.0	10.7	-0.7	4.3	3.8	0.5	7.2	7.4	-0.2	4.8	5.6	-0.8	5.3	1.9	3.4	11.9	4.1	7.7	3.5	0.2	3.2	3.2	0.3	2.9	
High	7.2	8.0	-0.8	5.6	5.8	-0.2	8.9	9.1	-0.1	7.3	8.1	-0.9	7.9	3.1	4.8	15.9	6.1	9.8	7.1	1.8	5.3				
SNR=+5 dB in sound field																									
Low	3.6	5.7	-2.1	2.4	2.7	-0.3	5.3	5.4	-0.1	2.9	3.5	-0.6	2.8	0.9	1.8	7.7	2.8	4.9	0.0	-1.4	1.4				
Medium	9.0	10.5	-1.5	3.5	3.6	-0.1	7.2	7.3	-0.1	4.8	5.6	-0.8	5.6	1.9	3.7	12.0	4.3	7.7	3.7	0.2	3.5	3.1	0.9	2.2	
High	5.5	7.8	-2.3	5.4	5.4	0.0	9.0	8.9	0.1	7.3	8.1	-0.8	8.3	3.0	5.4	15.7	6.0	9.7	7.3	1.9	5.5				
SNR=+10 dB in sound field																									
Low	3.7	5.8	-2.1	2.8	2.8	0.0	5.3	5.3	0.0	1.8	3.4	-1.6	2.6	0.9	1.7	7.9	2.7	5.2	-0.1	-1.4	1.4				
Medium	8.5	10.2	-1.7	3.8	3.5	0.3	7.2	7.3	-0.1	4.6	5.6	-1.0	5.4	1.8	3.5	11.8	4.2	7.6	3.8	0.3	3.5	2.0	0.4	1.5	
High	6.0	7.7	-1.8	5.4	5.1	0.4	9.0	9.9	-1.0	7.1	8.3	-1.1	8.1	3.0	5.1	15.7	11.6	4.1	7.2	1.7	5.5				

^aThe higher the values under 1:1 and 3:1 columns, the higher the amount of noise reduction.

^bIf the amount of noise reduction in 3:1 is less than that in 1:1 conditions, the addition of compression enhanced the level of noise which is undesirable for the application to hearing protectors.

^cThe higher the values in the Diff columns, the more adverse the effects of compression on noise reduction.

It appears that not all hearing aid manufacturers are aware of the potential problems of implementing the compression and the noise reduction algorithms in series. For example, Hearing Aids D1 and D2 were marketed roughly 4 years apart by the same hearing aid manufacturer. D1, the older model, has the more desirable parallel configuration yet the recently launched D2 has the serial configuration. It is unknown how many other hearing aids currently on the market also have the serial configuration. Although the percep-

tual effects arising from interactions between the noise reduction and compression algorithms have not been examined, it is presumably the case that hearing aid users might find it more preferable to listen to sounds with a lower level of background noise, making the parallel configuration more desirable for hearing aid use. In addition, Nabelek *et al.* (2006) reported that good hearing aid users have a higher tolerance of noise level than nonusers or occasional users. It is possible that the parallel configuration can provide ampli-

TABLE III. The average amount of noise reduction in the linear (1:1) and the 3:1 compression conditions in white noise.

NR settings	Group I												Group II												
	A			B			C			D1			D2			E1			E2			F			
	1:1	3:1	Diff	1:1	3:1	Diff	1:1	3:1	Diff	1:1	3:1	Diff	1:1	3:1	Diff	1:1	3:1	Diff	1:1	3:1	Diff	1:1	3:1	Diff	
SNR=-5 in sound field																									
Low	5.9	5.8	0.2	3.1	2.7	0.4	4.3	4.4	-0.1	3.8	3.8	0.0	2.5	0.8	1.7	7.3	2.6	4.8	-0.1	-1.5	1.4				
Medium	10.8	9.4	1.4	4.7	4.0	0.6	5.6	6.3	-0.7	6.4	6.3	0.1	5.3	1.8	3.5	10.5	4.0	6.5	3.4	0.1	3.3	5.2	1.4	3.8	
High	7.9	7.5	0.4	6.9	6.0	1.0	7.0	6.3	0.7	8.9	8.8	0.1	8.2	2.8	5.4	14.8	6.1	8.7	7.0	2.2	4.8				
SNR=0 dB in sound field																									
Low	6.1	5.9	0.2	3.0	2.8	0.3	4.1	4.9	-0.8	4.0	3.8	0.1	2.7	0.8	1.8	7.0	2.5	4.5	-0.1	-1.5	1.3				
Medium	10.8	10.2	0.6	4.7	3.8	0.8	5.3	6.2	-0.9	6.6	6.3	0.2	5.5	1.8	3.7	10.6	4.2	6.4	3.5	0.1	3.4	5.1	1.4	3.7	
High	7.8	7.5	0.3	6.7	5.9	0.9	6.5	7.7	-1.2	9.1	8.8	0.2	8.3	2.8	5.5	14.7	6.1	8.6	7.1	2.2	4.9				
SNR=+5 dB in sound field																									
Low	6.0	5.9	0.1	3.1	2.7	0.3	4.3	4.6	-0.3	4.0	3.8	0.1	2.6	0.8	1.7	7.1	2.4	4.7	-0.1	-1.5	1.4				
Medium	10.4	9.9	0.5	4.6	3.9	0.7	5.6	6.2	-0.5	6.6	6.3	0.3	5.4	1.8	3.6	10.5	3.9	6.6	3.5	0.1	3.4	4.7	1.3	3.4	
High	7.5	7.1	0.4	6.4	5.6	0.9	6.6	7.8	-1.1	9.1	8.8	0.2	8.3	2.8	5.4	14.7	5.7	9.1	7.1	2.2	4.9				
SNR=+10 dB in sound field																									
Low	5.6	5.6	0.0	3.0	2.8	0.2	4.1	4.6	-0.5	4.0	3.8	0.1	2.4	0.7	1.7	7.1	2.6	4.5	-0.2	-1.5	1.3				
Medium	9.6	9.1	0.5	4.3	3.9	0.3	5.1	6.1	-1.0	6.5	6.3	0.2	5.3	1.8	3.5	10.7	4.2	6.5	3.5	0.0	3.5	4.3	1.2	3.1	
High	6.7	6.4	0.3	6.2	5.2	0.9	6.3	7.7	-1.4	9.0	8.8	0.2	8.0	2.8	5.2	14.8	6.1	8.6	7.2	2.2	4.9				

fication with a consistently lower noise level regardless of the compression ratio and thus can enhance the acceptance of hearing aid use.

There are several other observations regarding the amount of noise reduction (see Tables II and III for details). First, some hearing aids in Group I had a higher amount of noise reduction in the 3:1 condition as compared to some hearing aids in Group II (i.e., Hearing Aid E1 in the 3:1 conditions reduced noise to an equal or greater degree than Hearing Aid B in both speech spectrum noise and white noise). This means that a hearing aid with a parallel configuration is not guaranteed to provide superior noise reduction effects compared to a hearing aid with a serial configuration. Second, the noise reduction algorithms implemented in the newer hearing aid models do not necessarily generate a higher amount of noise reduction than the older models. For example, E1 had a greater amount of noise reduction than E2. This could be due to a change in the manufacturer's philosophy of how much noise reduction is appropriate for hearing aids or other factors in the hearing aid implementation.

Third, a higher level of the noise reduction setting does not necessarily increase the amount of noise reduction. For example, the medium noise reduction setting of Hearing Aid A yielded the highest amount of noise reduction among the three settings. Fourth, the amount of noise reduction in speech spectrum noise and white noise need not be the same. For example, Hearing Aid C had more noise reduction in speech spectrum noise than in white noise but this pattern was reversed for Hearing Aid D1. The differences in noise reduction of different noises could be due to various factors in the hearing aids, e.g., the amount of noise reduction applied to different frequency bands and the manufacturer's assumption of the typical listening environments that the hearing aids encounter. The implication for hearing protectors is that it should be possible to tailor the parameters of the noise reduction algorithms to effectively reduce noises with different frequency spectra.

The noise level used in this experiment (i.e., 70 dB SPL) was relatively low compared to real-world noise levels encountered in noisy factories to avoid the high-level compression limiting algorithms implemented in some hearing aids. Should the compression and the noise reduction algorithms be used in hearing protectors, either the threshold of the compression limiting range can be set at a much higher level or an attenuator can be used to reduce the level of the input signal so that the input would not reach the compression limiting range. Thus, the same noise reduction actions that we see in this experiment can also be realized in hearing protectors even if the noise level in the real-world environments is much higher.

A caution in interpreting the above-mentioned findings is that the eight test hearing aids had different time constants (i.e., attack time and release time) in their compression algorithms and noise reduction algorithms. It was assumed that the pauses between the sentences (5–6 s) were much longer than the release times of the hearing aids so that the level of the following sentence was not affected by the presence of the previous sentence. In addition, as the amount of noise

reduction was compared between the 1:1 and 3:1 conditions, it was assumed that the effects created by the time constants of the noise reduction algorithm were canceled out for each hearing aid. However, the exact interactions of the time constants of compression and noise reduction algorithms are unknown at this time and should be a subject of future studies.

Overall, the measurements made in this experiment indicated that noise reduction algorithms utilizing modulation detection and gain reduction could be applied successfully to hearing protective devices to effectively reduce the noise level. Although different noise reduction algorithms varied in their effectiveness in reducing the noise level in speech spectrum noise and white noise, up to 15 dB of noise reduction in speech spectrum noise and 14.8 dB in white noise were possible compared to the NR-Off conditions. Additionally, the parallel configurations of the compression and the noise reduction algorithms allow the noise reduction algorithms to work in conjunction with compression so that the amount of noise reduction is maintained or enhanced when both algorithms are activated.

III. EXPERIMENT 2

The purpose of this experiment was to investigate the effects of compression, noise reduction and configurations of the compression and the noise reduction algorithms on speech intelligibility. Normal-hearing listeners' speech intelligibility was tested when they listened to recordings of speech in white noise testing materials which were processed by two hearing aids with known parallel (P) and serial (S) configurations of compression and noise reduction algorithms. P was Hearing Aid C and S was Hearing Aid E1 in Experiment I.

White noise was chosen to be the background noise because many machine noises resemble the attributes of white noise and few studies have tested the effectiveness of adaptive multichannel modulation-based noise reduction algorithms in white noise. As speech has less energy in the high frequency region, it is relatively more difficult for noise reduction algorithms to detect modulations in high-frequency channels in white noise than in speech spectrum noise due to lower SNRs in those channels. If the noise reduction algorithms reduce gain too much, they can potentially compromise speech intelligibility which is highly dependent on the audibility of high frequency speech components.

A. Subjects

Sixteen normal-hearing listeners between the ages of 18 and 31 (mean=25) years participated in this study. Their hearing thresholds were tested to be less than or equal to 20 dB HL in octave intervals between 0.25 and 8 kHz. All listeners had normal middle ear function (i.e., Type A tympanometry). They listened to speech processed by Hearing Aids P and S monaurally through a GSI 61 audiometer in an IAC sound-treated room.

B. Hearing aid characteristics

Hearing Aids P and S were selected for this experiment because their noise reduction algorithms were tested to pro-

TABLE IV. The r.m.s. presentation levels of speech and noise for Hearing Aids P and S and the effects of noise reduction algorithms and compression on the levels of speech and noise, the overall signal-to-noise ratios (SNR), and the change in overall SNR (Δ SNR). In general, the less negative or more positive the values in the speech and the Δ SNR columns and the more negative the values in the noise column, the better the noise reduction or compression effects.

Conditions	Presentation level				Noise reduction effect ^a			Compression effect ^b		
	Overall	Speech	Noise	SNR	Speech	Noise	Δ SNR	Speech	Noise	Δ SNR
P_1:1_NRoff	77.7	74.4	74.9	-0.5						
P_1:1_NR	72.4	71.5	64.9	6.6	-2.9	-10.0	7.1			
P_3:1_NRoff	75.6	67.6	74.9	-7.3				-6.8	0.0	-6.8
P_3:1_NR	69.6	67.9	64.7	3.2	0.3	-10.2	10.5	-3.6	-0.2	-3.4
S_1:1_NRoff	77.7	73.6	75.5	-1.9						
S_1:1_NR	71.3	70.3	64.3	6.0	-3.3	-11.2	7.9			
S_3:1_NRoff	76.0	65.9	75.5	-9.6				-7.7	0.0	-7.7
S_3:1_NR	73.1	69.2	70.9	-1.7	3.3	-4.6	7.9	-1.1	6.6	-7.7

^aCalculated by subtracting the levels in the NRoff conditions from that of the corresponding NR conditions. For example, the effect of noise reduction on speech for P_1:1_NR=71.5 (in P_1:1_NRoff condition)-74.4 (in P_1:1_NR condition)=-2.9 dB (i.e., noise reduction reduced the level of speech by 4.1 dB).

^bCalculated by subtracting the levels in the 1:1 conditions from those of the corresponding 3:1 conditions.

vide similar speech levels and amounts of noise reduction compared to their no noise reduction settings in 1:1 compression. In this study, P was set to maximum noise reduction and S was set to medium noise reduction during the recording process in order to achieve comparable noise reduction performance in 1:1 conditions.

C. Preparation of the testing stimuli

1. Recording of the test stimuli

Speech and white noise were presented to the sound field using the same equipment and recording procedures described in Experiment 1. The difference was that both speech and noise were presented from Speaker 1 to eliminate head shadow and body baffle effects. Sixteen HINT sentence lists (lists 9–16) and 30 concatenated sentences (HINT lists 1–3) were recorded in each experimental condition: (1) 1:1_NRoff, (2) 1:1_NR, (3) 3:1_NRoff, and (4) 3:1_NR. The HINT sentences and white noise were calibrated at 75 and 70 dB SPL, respectively (i.e., SNR=+5 dB in the sound field).

2. Characteristics of the test stimuli

As the amounts of gain provided by P and S were not the same, the overall level differences between the 1:1_NRoff conditions were measured using AUDITION. The overall level of all the conditions processed by the same hearing aid was adjusted by the amount of the difference to eliminate the differences in amplification between the two hearing aids. In addition, the amount of amplification provided by the 1:1 and 3:1 conditions were not equal in Hearing Aids P and S. Subsequently, the difference in the noise level of the 1:1_NRoff and 3:1_NRoff conditions was measured for each hearing aid and then the 3:1_NRoff and 3:1_NR conditions were amplified for the amount of the difference (see Table IV for details). Recall that the speech levels and the amount of noise reduction were equated in the 1:1 NR conditions for the two hearing aids. This meant that after adjusting for the gain differences between the hearing aids and between the 1:1 and 3:1 conditions, any differences in the amount of noise reduction (i.e., the noise level in NR minus

that in NRoff conditions) between the 1:1 and the 3:1 settings of the same hearing aid were due to the interactions between the compression and noise reduction algorithms.

The overall speech and noise levels of the test stimuli and the effects of the compression and the noise reduction algorithms are summarized in Table IV. The speech level was determined by subtracting the intensity of the noise level measured between sentences from the intensity of the corresponding concatenated sentences (overall level) using

$$I_{Sp} = I_{Sp+N} - I_N, \quad (1)$$

$$Sp = 10 \log[\log^{-1}(Sp + N)/10 - \log^{-1}(N)/10], \quad (2)$$

where I =intensity, Sp =level of speech in dB, N =level of noise in dB, and $Sp+N$ =level of speech plus noise in dB.

In general, the noise levels in the noise reduction (NR) conditions were lower than the no-noise reduction (NRoff) conditions. For P, the amount of noise reduction in the 1:1 and the 3:1 conditions were comparable because of the parallel configuration. For S, the amount of noise reduction in the 3:1 conditions were higher than those in the 1:1 conditions due to the serial configuration as described in Experiment 1. As expected, the speech level was generally reduced when a 3:1 compression was activated for both hearing aids.

D. Speech recognition test

During the test, the presentation orders of the hearing aids, hearing aid settings, and the allocation of the sentence lists to experimental conditions were counterbalanced across the subjects. The test stimuli were presented to normal-hearing listeners monaurally via an ER3-A insert earphone to their better ear or to the ear that they preferred. The listeners were instructed to repeat the sentence after listening to each sentence and they were encouraged to guess if they were not sure. Each listener listened to eight sentence lists in eight experimental conditions (i.e., 2 hearing aids \times 4 settings). The key words were generated and scored using the same procedures described in Chung *et al.* (2006). Speech recognition scores in percent correct were calculated for each experimental condition and each listener off-line.

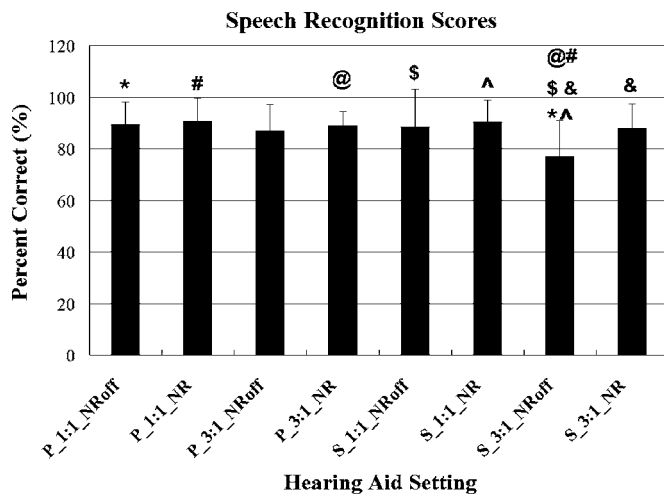


FIG. 3. The average speech recognition scores and standard deviations of speech recorded at SNR=+5 dB after being processed by Hearing Aids P and S at different combinations of noise reduction off (NRoff), noise reduction algorithm activated (NR), and compression ratios (i.e., 1:1 or 3:1). The symbols above the bars indicated significantly different conditions.

E. Results

The average speech recognition scores and standard deviations are plotted in Fig. 3. An ANOVA with repeated measure on the hearing aid setting factor was performed. Significant differences in speech recognition scores were found among the conditions ($F[15, 7]=3.927, p=0.0008$). Post hoc Bonferroni/Dunn tests indicated that the score obtained in the S_3:1_NRoff condition was significantly lower than the scores obtained in all other conditions ($p < 0.0018$, probability adjusted for the number of tests conducted) except the P_3:1_NRoff condition. These results indicated that the activation of the noise reduction and the compression algorithms did not affect the speech intelligibility for Hearing Aid P. For Hearing Aid S, the 3:1 compression without a noise reduction algorithm lowered the speech intelligibility and the activation of the noise reduction algorithm offset the degrading effects of compression.

F. Discussion

1. Effects of compression

A compression effect was observed for Hearing Aid S in the speech recognition scores. The activation of 3:1 compression slightly reduced the speech recognition scores obtained by S but did not affect the scores for P. As the speech in noise materials were presented at suprathreshold levels (i.e., 69.4 to 77.5 dB SPL), the audibility of the speech components should not have an effect on speech intelligibility for the normal-hearing listeners.

Previous studies reported that compression systems, as compared to linear systems, usually did not degrade speech intelligibility for normal-hearing listeners if the compression system had (1) compression ratios of equal to or less than 3:1, (2) low number of compression channels (i.e., ≤ 4 channels), and/or (3) long release times (i.e., ≥ 100 ms) (Yund and Buckles, 1995, (a)–(c)) Souza and Turner, 1998; Humes *et al.*, 1999; Boike and Souza, 2000, Hansen, 2002). However, studies using hearing aids with more frequency chan-

nels (i.e., ≥ 8 channels) and fast time constants (i.e., release time ≤ 100 ms) suggested that the speech recognition scores of normal-hearing listeners decreased with compression ratios as compared to linear amplification (Hohmann and Kollmeier, 1995; Yund and Buckles, 1995a–c; Hornsby and Ricketts, 2001). The reduction in speech recognition in these compression conditions was reportedly due to the reduction in the temporal and spectral contrasts between speech and noise, resulting in a lower overall SNR in the hearing aid output than in the input signal (Plomp, 1994; Crain and Yund, 1995; Hohmann and Kollmeier, 1995; Souza *et al.*, 2006). In Fig. 2, the 3:1 conditions clearly show a less distinctive temporal envelope for the speech signal than the 1:1 conditions for both hearing aids.

The difference in speech recognition scores for the conditions with 3:1 compression and no noise reduction (i.e., P_3:1_NRoff and S_3:1_NRoff) is probably due to the differences in the combination of the number of channels and the time constants implemented in the two hearing aids. P has four compression channels with adaptive time constants (i.e., the release time is less than 100 ms for brief/impact sounds and 800–900 ms for longer duration sounds) whereas S has nine compression channels with fast time constants (i.e., release times ≤ 35 ms in all compression channels). Our results showing that S_3:1_NRoff decreased speech recognition scores slightly while P_3:1_NRoff did not, are consistent with previous studies that the combination of high compression ratios (i.e., $\geq 3:1$), fast time constants and a high number of compression channels reduced the speech recognition scores of normal-hearing listeners.

The above-mentioned results also suggested that it is desirable to have different numbers of channels for the compression algorithm and the noise reduction algorithm in hearing devices. It is theoretically sound to implement more noise reduction channels because they allow for finer separation of speech and noise and thus result in better noise reduction effects. Yet, it is undesirable to have too many channels for the compression algorithm, especially if they have fast time constants. Future studies are needed to investigate the optimal combinations of the number of noise reduction and compression channels.

Compression has been reported to effectively enhance the audibility of low-level sounds, improve the speech intelligibility of low-level speech, and reduce harmonic distortions of high-level speech for listeners with hearing loss (Humes and Wilson 2004; Larson *et al.*, 2000; Lippmann *et al.*, 1981; Shanks *et al.*, 2002; Moore *et al.*, 1999; Souza, 2002; Souza and Turner, 1996, 1998; Souza and Kitch, 2001; Yund and Buckles, 1995a–c). It is expected that the above-mentioned results would also be true if compression were applied to hearing protectors.

2. Noise reduction algorithm

The speech recognition scores of normal-hearing listeners indicated that the activation of noise reduction algorithms did not degrade the speech intelligibility for either P or S. These results indicated that the noise reduction algorithms included in this experiment effectively reduced noise level without compromising the speech intelligibility in white

noise. It appears that although white noise has higher frequency contents than the speech signal, the noise reduction algorithms did not reduce the gain of the hearing aids excessively to compromise the intelligibility of the speech signals.

An interesting result is that although the activation of the noise reduction algorithms did not improve speech recognition compared to the 1:1_NRoff conditions for either hearing aid, the activation of the noise reduction algorithm offset the negative effects of 3:1 compression for Hearing Aid S. Chung *et al.* (2006) calculated the speech transmission index of signals processed with and without the noise reduction algorithm implemented in S in another study. They found that the noise reduction algorithm greatly increased the speech intelligibility index which implied that the modulation depth of the temporal envelope was greatly enhanced. A similar phenomenon was also observed in Fig. 2 in this study. As previous studies indicated that speech temporal envelope cues are important for speech understanding, especially at low SNRs (Drullman, 1995; Hohmann and Kollmeier, 1995; Shannon *et al.*, 1995; Noordhoek and Drullman, 1997; van der Horst *et al.*, 1999; Smith *et al.*, 2002; Healy and Warren, 2003; Souza and Boike, 2006), it is speculated that the restoration of the speech recognition scores in the S_3:1_NR condition occurred because the noise reduction algorithms enhanced temporal envelope cues and the normal-hearing listeners were able to use these envelope modulations for speech understanding in this particular listening condition.

Another possibility for the increased speech recognition scores in the S_3:1_NR condition is that the noise reduction algorithm reduced forward and backward masking of the low-level speech sounds compared to the S_3:1_NRoff condition. Further studies are needed to determine the underlying mechanism(s) involved.

3. Compression and noise reduction algorithm configuration

The configurations of the compression and the noise reduction algorithms do not seem to have an effect on speech intelligibility. The conditions with compression and noise reduction algorithms (P_3:1_NR and S_3:1_NR) yielded similar speech recognition scores as the conditions without compression or noise reduction for both hearing aids. However, the differences in the noise level at the hearing aid output did support the use of the parallel configuration for hearing protection applications.

IV. EXPERIMENT 3

In this experiment, normal-hearing listeners rated the overall sound quality preferences of A-B comparison pairs in a combined paired-comparison and categorical rating paradigm. Previous studies reported that sound quality is a multidimensional phenomenon (Gabrielsson and Sjogren, 1979, Gabrielsson *et al.*, 1988). Overall sound quality preference, instead of different sound quality dimensions, was used to allow the listeners to respond according to their own weightings of quality dimensions.

A. Subjects

The 16 normal-hearing listeners recruited for Experiment II also participated in this study.

B. Preparation of the testing stimuli

Six sentences from the sentence lists recorded in Experiment 2 were chosen to generate A-B comparison pairs. These sentences were chosen because they contained all the English vowels and consonants except “zh” as in pleasure. Each of the six sentences formed two reference combinations that are composed of the same sentence recorded at the same hearing aid settings (i.e., P_1:1_NR-P_1:1_NR and S_1:1_NRoff-S_1:1_NRoff) and seven test combinations that were composed of the same sentence recorded at different hearing aid settings (i.e., P_1:1_NRoff-P_3:1_NRoff, S_1:1_NRoff-S_3:1_NRoff, P_1:1_NR-P_3:1_NR, S_1:1_NR-S_3:1_NR, S_3:1_NRoff-P_3:1_NRoff, S_1:1_NR-P_1:1_NR, and S_3:1_NR-P_3:1_NR). Each sentence was preceded with 500 ms of noise and followed by 200 ms of noise. A 300 ms silence was inserted between the sentences to mark the boundary of the conditions. The order of occurrence for the test combinations were reversed in half of the sentences (e.g., three sentences were presented as P_1:1_NRoff-P_3:1_NRoff and another 3 as P_3:1_NRoff-P_1:1_NRoff). There were a total of 54 comparison pairs (i.e., 6 sentences × 9 combinations).

C. Procedures

During the test, the listeners were instructed to imagine that they were working in a noisy environment for 8 h a day and listening to their co-workers. After listening to a pair of sentences, they ranked the preferred condition (Condition 1 or Condition 2) and quantified the magnitude of preference using the overall sound quality preference rating scale depicted in Fig. 4. If a listener preferred Condition 1 and rated the magnitude of preference as 3, a 3 was assigned to Condition 1 and a 0 was assigned to Condition 2. This procedure recorded the differences in preference ratings for the comparison pairs. The presentation orders of the comparison pairs were randomized and the listeners were blinded to the conditions presented.

D. Results

A summary of the group mean differences in overall sound quality preference ratings are shown in Fig. 5. To examine if any combinations yielded significant differences between the conditions, the statistical analyses were carried out in five steps: (1) Calculate the *individual means* of each hearing aid setting in each combination by averaging the scores

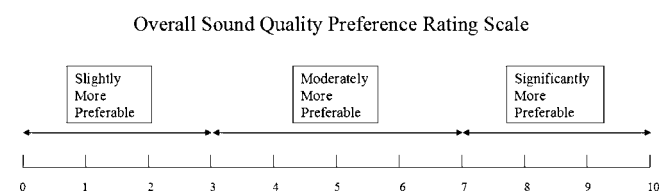


FIG. 4. The overall sound quality preference rating scale used in the combined paired-comparison and categorical rating paradigm.

Group Mean Differences in Overall Sound Quality Preferences

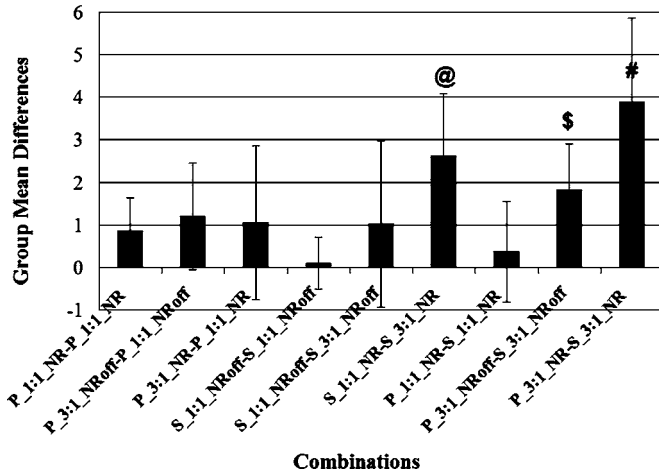


FIG. 5. Summary of the group mean differences in overall sound quality preference ratings for the nine combinations. The symbols indicate the combinations with mean differences significantly different from that of the reference.

given to each setting in the six sentences (e.g., the individual means for Settings A and B in Combination A–B); (2) calculate the *group means* by averaging the individual means for Settings A and B in each combination; (3) calculate the *individual mean difference* by subtracting the condition with a lower group mean (e.g., Setting A) from the condition with a higher group mean (e.g., Setting B) in each combination for each listener (i.e., the *individual mean difference* for Combination B–A); (4) conduct a repeated measure ANOVA to examine if there were any significant differences among the group mean differences of the nine combinations (note that all the *group mean differences* which are the average of individual mean differences for the different combination pairs, are positive); and (5) conduct post hoc tests if a significant main effect was found in Step 4.

The ANOVA results showed a significant main effect ($F[15, 8]=12.309, p < 0.0001$). Bonferroni/Dunn post hoc tests were conducted to compare the group mean differences

in preference ratings for the seven combinations and the average of group mean differences of the reference pairs. The group mean differences between P_3:1_NR–S_3:1_NR, S_1:1_NR–S_3:1_NR, and P_3:1_NRoff – S_3:1_NRoff were found to be significantly different from that of the reference pairs (i.e., difference $> 2.04, p < 0.0063$, with probability adjusted for eight t-tests conducted at 0.05 level of significance). These results indicated that the listeners preferred Hearing Aid P to Hearing Aid S if both 3:1 compression and noise reduction algorithms were activated. They also preferred Hearing Aid S in the linear setting more than the 3:1 compression setting when the noise reduction algorithm was activated. Additionally, the listeners preferred P rather than S in the 3:1_NRoff setting.

Besides ANOVA, regression analyses were performed between the group mean differences in preference ratings and the differences in overall sound pressure level, speech level, noise level, and speech-to-noise ratio between the two settings of the nine combinations. The correlation coefficients between these factors indicated that the group mean differences were inversely proportional to the differences in overall sound pressure level ($r=-0.69, p < 0.05$) and the level of noise ($r=-0.85, p < 0.01$), directly proportional to the difference in speech-to-noise ratios (i.e., correlation coefficient=0.47, $p=0.20$), and not correlated to the differences in the level of speech (i.e., correlation coefficient=–0.06, $p=0.89$) (see Table V for details). These results suggested that lower overall sound pressure levels and lower noise levels have significantly contributed to the sound quality preferences of the normal hearing listeners.

E. Discussion

In this experiment, the subjective sound quality preferences of normal-hearing listeners on the effects of activating the 3:1 compression were tested on hearing aids with serial and parallel configurations of their compression and noise reduction algorithms. Two reference conditions were included for reliability checks and for estimation of the vari-

TABLE V. The differences in overall sound quality preferences, overall sound pressure level, speech level, noise level, and SNR and between the comparison pairs and the correlation coefficients among these factors. The differences in preferences, overall SPL, speech level, noise level, and SNR were calculated by subtracting the values of Condition 2 from those of Condition 1.

Comparison pairs	Differences in preferences	Differences in			
		Overall SPL (dB)	Speech (dB)	Noise (dB)	SNR (dB)
P_1:1_NR–P_1:1_NR	0.9	0.0	0.0	0.0	0.0
P_3:1_NRoff–P_1:1_NRoff	1.2	–2.2	–10.7	1.0	–11.7
P_3:1_NR–P_1:1_NR	1.0	–2.8	–3.3	0.4	–3.7
S_1:1_NRoff–S_1:1_NRoff	0.1	0	0	0	0
S_1:1_NRoff–S_3:1_NRoff	1.0	1.9	5.3	0.6	4.7
S_1:1_NR–S_3:1_NR	2.6	–2.0	1.2	–8.5	9.7
P_1:1_NR–S_1:1_NR	0.4	0.9	1.1	–0.4	1.5
P_3:1_NRoff–S_3:1_NRoff	1.8	–0.5	–4.0	0.0	–4.0
P_3:1_NRS–S_3:1_NR	3.9	–3.9	–1.1	–8.5	7.4
Correlation		–0.69*	–0.06	–0.85*	0.47

* $p < 0.05$.

ability of the rating tasks. The group mean differences and the standard deviations of the reference pairs were less than or equal to 0.85 on a 10 point scale. This indicated that the listeners who participated in this study were reliable in the sound quality preference rating tasks and the variability was low.

The normal-hearing listeners rated the P_3:1_NRoff condition to be slightly more preferable than the S_3:1_NRoff condition. Previous studies reported that clarity was often the most highly weighted dimension of sound quality among normal-hearing and hearing-impaired listeners (Gabrielsson *et al.*, 1988; Balfour and Hawkins, 1992; Preminger and Van Tasell, 1995; Neuman *et al.*, 1998) and that clarity was highly correlated to the objective speech intelligibility scores (Jerlvall *et al.*, 1983; Gabrielsson *et al.*, 1988). As S_3:1_NRoff obtained lower speech recognition scores than other conditions, it is possible that the listeners preferred the P_3:1_NRoff condition because of higher perceived clarity.

Additionally, the P_3:1_NR and S_1:1_NR conditions were rated to be between slightly and moderately more preferable than the S_3:1_NR condition. Recall that none of these conditions yielded significantly different speech recognition scores in Experiment 2, yet the regression analysis showed a strong relationship between preference and lower noise level and a moderate relationship between preference and lower overall level. It is likely that the listeners preferred P_3:1_NR and S_1:1_NR more than S_3:1_NR because they had lower overall sound pressure levels and lower noise levels than the S_3:1_NR condition. In addition, the fact that P_1:1_NR and P_3:1_NR had similar overall noise levels and that they did not yield a significant difference in preference further supported that compression implemented in parallel with a noise reduction algorithm did not adversely affect subjective sound quality preferences of normal-hearing listeners. The parallel configuration of compression and noise reduction algorithm is, therefore, more preferable for the application of hearing protectors if both are activated. The same results can also be applied to hearing aids.

V. SUMMARY AND FUTURE STUDIES

The author proposed to adopt the adaptive multichannel modulation-based noise reduction and wide dynamic range compression algorithms to enhance hearing protector performance: Reducing noise level and, at the same time, allowing effective communication with peers via an acoustic medium. The results of this series of experiments indicated that when compression was activated, parallel implementation of the compression and the noise reduction algorithms provided an equal amount of noise reduction yet serial implementation reduced the amount of noise reduction compared to the linear conditions. In addition, adaptive multichannel modulation-based noise reduction algorithms did not degrade speech in white noise whether compression was activated or whether it was implemented in parallel or in series with the compression algorithm. Further, a noise reduction algorithm implemented in parallel with the compression algorithm reduced noise level and increased overall sound quality preference

and, at the same time, maintained speech recognition scores of normal-hearing listeners in white noise. Taken together, adaptive multichannel noise reduction algorithms and wide dynamic range compression should be implemented in parallel in hearing protectors for effective noise reduction.

The utilization of the compression and the noise reduction algorithms in hearing protectors can potentially solve many problems associated with current hearing protectors. For example, workers who fear being unable to communicate with their co-workers or to hear warning calls, do not fully insert the hearing protector, or simply do not wear the hearing protectors. If they knew their hearing protectors would not compromise their ability to hear speech, it is possible that they would be more willing to wear them. Further, these algorithms can potentially reduce the inconvenience of taking the hearing protectors in and out of the users' ears because they can communicate with their co-workers without the need to remove their hearing protectors.

Despite the promising effects of the compression and the noise reduction algorithms, future studies are needed in several areas. First, the effectiveness of these noise reduction algorithms needs to be examined using real-world noises which are likely to have more temporal fluctuations than the white noise used in this study and the noises reported in other hearing aid studies. Second, localization of speech and warning signals have been cited as one of most important concerns of workers using hearing protectors (Kahan and Ross, 1994; Morata *et al.*, 2001, 2005). Future studies need to address the effect of adaptive multichannel noise reduction algorithms on the localization ability of hearing protector users. Third, as the actions of noise reduction algorithms are controlled by multiple parameters, future studies are also needed to tailor the settings of these parameters so that the amount of noise reduction, speech intelligibility, and the users' localization ability will be maximized for different noisy environments. Fourth, many advanced hearing aid signal processing algorithms may be applicable to hearing protectors (e.g., directional microphones and automatic telecoil switches). Future studies are needed to explore which signal processing algorithms are suitable for hearing protectors.

ACKNOWLEDGMENTS

I would like to thank Dr. Jun Xie for providing statistical consultation and Drs. Patricia Davis, Dr. Alex Francis, and Dr. Jennifer Tufts for providing constructive comments on the initial versions of this manuscript. I would also like to thank Rachael Fischer and Meghan Matthews for data measurement, Kyle Acker for technical support, Lance Nelson for data collection, and Tarez Graban for editorial help.

- Alcantara, J. L., Moore, B. C., Kuhnelt, V., and Launer, S. (2003). "Evaluation of the noise reduction system in a commercial digital hearing aid," *Int. J. Audiol.* **42**, 34–42.
- Balfour, P. B., and Hawkins, D. B. (1992). "A comparison of sound quality judgments for monaural and binaural hearing aid processed stimuli," *Ear Hear.* **13**, 331–339.
- Bentler, R. A. (2005). "Effectiveness of directional microphones and noise reduction schemes in hearing aids: A systematic review of the evidence," *J. Am. Acad. Audiol.* **16**, 473–484.
- Bentler, R. A., and Chiou, L.-K. (2006). "Digital noise reduction: An overview," *Trends Amplif.* **10**, 67–81.

- Boike, K. T., and Souza, P. E. (2000). "Effect of compression ratio on speech recognition and speech-quality ratings with wide dynamic range compression amplification," *J. Speech Lang. Hear. Res.* **43**, 456–468.
- Boymans, M., Dreschler, W., Shoneveld, P., and Verschuure, H. (1999). "Clinical evaluation in a full-digital in-the-ear hearing instrument," *Audiology* **38**, 99–108.
- Boymans, M., and Dreschler, W. A. (2000). "Field trials using a digital hearing and with active noise reduction and dual-microphone directionality," *Audiology* **39**, 260–268.
- Bray, V., and Nilsson, M. (2001). "Additive SNR benefits of signal processing features in a directional DSP aid," *Hear Rev.* **8**, 48–51, 62.
- Chung, K. (2004). "Challenges and recent developments in hearing aids. I. Speech understanding in noise, microphone technologies and noise reduction algorithms," *Trends Amplif.* **8**, 83–124.
- Chung, K., and Acker, K. (2006). "A high-tech hearing protector to maximize attenuation and speech understanding," National Hearing Conservation Association at Tampa, FL.
- Chung, K., Zeng, F.-G., and Acker, K. (2006). "Effects of directional microphone and adaptive multi-channel noise reduction algorithm on cochlear implant performance," *J. Acoust. Soc. Am.* **120**, 2216–2227.
- Crain, T. R., and Yund, E. W. (1995). "The effect of multichannel compression on vowel and stop-consonant discrimination in normal-hearing and hearing-impaired subjects," *Ear Hear.* **16**, 529–543.
- Drullman, R. (1995). "Temporal envelope and fine structure cues for speech intelligibility," *J. Acoust. Soc. Am.* **97**, 585–592.
- Gabrielsson, A., Schenkman, B., and Hagerman, B. (1988). "The effects of different frequency responses on sound quality judgments and speech intelligibility," *J. Speech Hear. Res.* **31**, 166–177.
- Gabrielsson, A., and Sjögren, H. (1979). "Perceived sound quality of sound-reproducing systems," *J. Acoust. Soc. Am.* **65**, 1019–1033.
- Hansen, M. (2002). "Effects of multi-channel compression time constants on subjectively perceived sound quality and speech intelligibility," *Ear Hear.* **23**, 369–380.
- Healy, E. W., and Warren, R. M. (2003). "The role of contrasting temporal amplitude patterns in the perception of speech," *J. Acoust. Soc. Am.* **3**, 1676–1688.
- Hohmann, V., and Kollmeier, B. (1995). "The effect of multichannel dynamic compression on speech intelligibility," *J. Acoust. Soc. Am.* **97**, 1191–1195.
- Hornsby, B. W. Y., and Ricketts, T. A. (2001). "The effects of compression ratio, signal-to-noise ratio, and level on speech recognition in normal-hearing listeners," *J. Acoust. Soc. Am.* **109**, 1973.
- Humes, L. E., Christensen, L., Thomas, T., Bess, F. H., Headley-Williams, A., and Bentler, R. A. (1999). "A comparison of the aided performance and benefit provided by a linear and a two-channel wide dynamic range compression hearing aid," *J. Speech Lang. Hear. Res.* **42**, 65–79.
- Humes, L. E., and Wilson, D. L. (2004). "A comparison of single-channel linear amplification and two-channel wide-dynamic-range-compression amplification by means of an independent-group design," *Am. J. Audiol.* **13**, 39–53.
- Jervall, L., Almqvist, B., Ovegård, A., and Arlinger, S. (1983). "Clinical trial of in-the-ear hearing aids," *Scand. Audiol.* **12**, 63–70.
- Kahan, E., and Ross, E. (1994). "Knowledge and attitudes of a group of South African mine workers towards noise induced hearing loss and the use of hearing protective devices," *S Afr. J. Commun. Disord.* **41**, 37–47.
- Larson, V. D. *et al.* (2000). "Efficacy of 3 commonly used hearing aid circuits: A crossover trial," *JAMA, J. Am. Med. Assoc.* **284**, 1806–1813.
- Lippmann, R. P., Braida, L. D., and Durlach, N. I. (1981). "Study of multichannel amplitude-compression and linear amplification for persons with sensorineural hearing loss," *J. Acoust. Soc. Am.* **69**, 524–534.
- Moore, B. C. J., Peters, R. W., and Stone, M. A. (1999). "Benefits of linear amplification and multichannel compression for speech comprehension in backgrounds with spectral and temporal dips," *J. Acoust. Soc. Am.* **105**, 400–411.
- Morata, T. C., Fiorini, A. C., Fischer, F. M., Krieg, E. F., Gozzoli, L., and Colacioppo, S. (2001). "Factors affecting the use of hearing protectors in a population of printing workers," *Noise Health* **4**, 25–32, 38.
- Morata, T. C., Themann, C. L., Randolph, R. F., Verbsky, B. L., Byrne, D. C., and Reeves, E. R. (2005). "Working in noise with a hearing loss: Perceptions from workers, supervisors, and hearing conservation program managers," *Ear Hear.* **26**, 529–545.
- Nabelek, A. K., Freyaldenhoven, M. C., Tampas, J. W., Burchfield, S. B., and Muenchen, R. A. (2006). "Acceptable noise level as a predictor of hearing aid use," *J. Am. Acad. Audiol.* **17**, 626–639.
- Neuman, A., Bakke, M.H., Mackersie, C., Hellman, S., and Levitt, H. (1998). "The effect of compression ratio and release time on the categorical rating of sound quality," *J. Acoust. Soc. Am.* **103**, 2273–2281.
- Nilsson, M., Soli, S. D., and Sullivan, J. A. (1994). "Development of a hearing in noise test for the measurement of speech reception thresholds in quiet and in noise," *J. Acoust. Soc. Am.* **95**, 1085–1099.
- Noordhoek, I. M., and Drullman, R. (1997). "Effect of reducing temporal intensity modulations on sentence intelligibility," *J. Acoust. Soc. Am.* **101**, 498–502.
- Plomp, R. (1994). "Noise, amplification and compression: Considerations of three main issues in hearing aid design," *Ear Hear.* **15**, 2–12.
- Preminger, J. E., and Van Tasell, D. J. (1995). "Measurement of speech quality as a tool to optimize the fitting of a hearing aid," *J. Speech Hear. Res.* **38**, 726–736.
- Ricketts, T. A., and Dhar, S. (1999). "Aided benefit across directional and omni-directional hearing aid microphones for behind-the-ear hearing aids," *J. Am. Acad. Audiol.* **10**, 180–189.
- Ricketts, T. A., and Hornsby, B. W. Y. (2005). "Sound quality measures for speech in noise through a commercial hearing aid implementing 'digital noise reduction'," *J. Am. Acad. Audiol.* **16**, 270–277.
- Shanks, J. E., Wilson, R. H., Larson, V., and Williams, D. (2002). "Speech recognition performance of patients with sensorineural hearing loss under unaided and aided conditions using linear and compression hearing aids," *Ear Hear.* **23**, 280–290.
- Shannon, R. V., Zeng, F. G., Kamath, V., Wygonski, J., and Ekelid, M. (1995). "Speech recognition with primarily temporal cues," *Science* **270**, 303–304.
- Smith, Z. M., Delgutte, B., and Oxenham, A. J. (2002). "Chimaeric sounds revealed dichotomies in auditory perception," *Nature (London)* **416**, 87–90.
- Souza, P. E. (2002). "Effects of compression on speech acoustics, intelligibility, and sound quality," *Trends Amplif.* **6**, 131–165.
- Souza, P. E., and Boike, K. T. (2006). "Combining temporal-envelope cues across channels: Effects of age and hearing loss," *J. Speech Lang. Hear. Res.* **49**, 138–149.
- Souza, P. E., Jenstad, L. M., and Boike, K. T. (2006). "Measuring the acoustic effects of compression amplification on speech in noise (L)," *J. Acoust. Soc. Am.* **119**, 41–44.
- Souza, P. E., and Kitch, V. J. (2001). "Effect of preferred volume setting on speech audibility in different hearing aid circuits," *J. Am. Acad. Audiol.* **12**, 415–422.
- Souza, P. E., and Turner, C. W. (1996). "Effects of single-channel compression on temporal speech information," *J. Speech Hear. Res.* **39**, 901–911.
- Souza, P. E., and Turner, C. W. (1998). "Multichannel compression, temporal cues, and audibility," *J. Speech Lang. Hear. Res.* **41**, 315–326.
- Valente, M., Fabry, D., Potts, L., and Sandlin, R. (1998). "Comparing the performance of the Widex Senso digital hearing aid with analog hearing aids," *J. Am. Acad. Audiol.* **9**, 342–360.
- Van der Horst, R., Leeuw, A. R., and Dreschler, W. A. (1999). "Importance of temporal-envelope cues in constant recognition," *J. Acoust. Soc. Am.* **105**, 1801–1809.
- Walden, B. E., Surr, R. K., Cord, M. T., Edwards, B., and Olson, L. (2000). "Comparison of benefits provided by different hearing aid technologies," *J. Am. Acad. Audiol.* **11**, 540–560.
- Yund, E. W., and Buckles, K. M. (1995a). "Enhanced speech perception at low signal-to-noise ratios with multichannel compression hearing aids," *J. Acoust. Soc. Am.* **97**, 1224–1240.
- Yund, E. W., and Buckles, K. M. (1995b). "Discrimination of multichannel-compressed speech in noise: Long-term learning in hearing-impaired subjects," *Ear Hear.* **16**, 417–427.
- Yund, E. W., and Buckles, K. M. (1995c). "Multichannel compression hearing aids: Effect of number of channels on speech discrimination in noise," *J. Acoust. Soc. Am.* **97**, 1206–1223.

Coherent structures of the near field flow in a self-oscillating physical model of the vocal folds

Jürgen Neubauer^{a)} and Zhaoyan Zhang

The Laryngeal Dynamics Laboratory, UCLA School of Medicine, 31-24 Rehabilitation Center, 1000 Veteran Ave., Los Angeles, California 90095

Reza Miraghaie

Department of Mechanical and Aerospace Engineering, UCLA, Los Angeles, California 90095

David A. Berry

The Laryngeal Dynamics Laboratory, UCLA School of Medicine, 31-24 Rehabilitation Center, 1000 Veteran Ave., Los Angeles, California 90095

(Received 3 January 2006; revised 17 October 2006; accepted 19 November 2006)

Current theories of voice production depend critically upon knowledge of the near field flow which emanates from the glottis. While most modern theories predict complex, three-dimensional structures in the near field flow, few investigations have attempted to quantify such structures. Using methods of flow visualization and digital particle image velocimetry, this study measured the near field flow structures immediately downstream of a self-oscillating, physical model of the vocal folds, with a vocal tract attached. A spatio-temporal analysis of the structures was performed using the method of empirical orthogonal eigenfunctions. Some of the observed flow structures included vortex generation, vortex convection, and jet flapping. The utility of such data in the future development of more accurate, low-dimensional models of voice production is discussed. © 2007 Acoustical Society of America. [DOI: 10.1121/1.2409488]

PACS number(s): 43.70.Aj, 43.70.Bk, 43.70.Jt, 43.28.Ra [AL]

Pages: 1102–1118

I. INTRODUCTION

Traditionally, according to the linear source-filter theory of voice production, the glottal volume velocity is considered to be the sound source of the human voice (Fant, 1960; see, e.g., Stevens (1998), for extensive review). However, this theory relies heavily on assumptions about the voice source, the vocal tract filter, and the independence of the source and filter, which have never been formally validated for normal (modal) phonation, and much less for nonmodal states of phonation such as may occur in dysphonia, or at phrase and sentence boundaries in English. In addition to neglecting possible source-tract interactions, another critical limitation of the linear source-filter theory of voice production may be its dependence on one-dimensional, scalar field theory. McGowan (1988) maintained that a full three-dimensional description of the fluid velocity field at glottal exit was required to accurately model the voice source. First, he argued that a nonacoustic (rotational, incompressible) component of the glottal velocity field, separate from the glottal volume velocity, was required to accurately predict the oral acoustic output. Second, he argued that vortex structures in the glottal near field produced a fluctuating force on the vocal folds. In particular, he contended that vortex structures were produced during glottal opening, and that the roll-up, acceleration and downstream convection of such structures resulted in an upstream force on the vocal folds. Thus, McGowan (1988) proposed a flow feedback mechanism, which directly impacted

vocal fold dynamics, and hence sound generation within the larynx. Krane (2005) proposed a similar mechanism for unvoiced speech production.

Similarly, Hirschberg *et al.* (1996) has argued that the flow separation point and the area of the glottal jet, as assumed by most advanced computational models of vocal fold vibration, are only crude, first-order approximations. They contend that the flow separation point and the area of the glottal jet cannot be accurately approximated without a full knowledge of the near field flow structures immediately downstream of the glottis. Indeed, based on major discrepancies between theory and experiment, Hofmans *et al.* (2003) concluded that “the structure of the jet flow” was critical for modeling the sound source, and predicting the oral acoustic output. Indeed, many investigators have probed the possible contributions of three-dimensional source mechanisms in voice production (Barney *et al.*, 1999; Hirschberg, 1992; Hofmans, 1998; Hofmans *et al.*, 2001a, b; Howe and McGowan, 2005; Krane, 2005; McGowan, 1988; McGowan and Howe, 2006; Shadle *et al.*, 1999; Zhang *et al.*, 2002).

Despite such investigations, only a few attempts have been made to quantify the near field flow structures immediately downstream of the glottis. The primary measurement technique which has been used to quantify particle velocities in this region has been single-fiber, hot-wire anemometry, a method which assumes that particle velocities are nonzero only in the inferior-superior direction, and that in this direction, the velocities are non-negative. However, if complex three-dimensional fluid structures were to exist within the

^{a)}Author to whom correspondence should be addressed. Electronic mail: jneubauer@mednet.ucla.edu

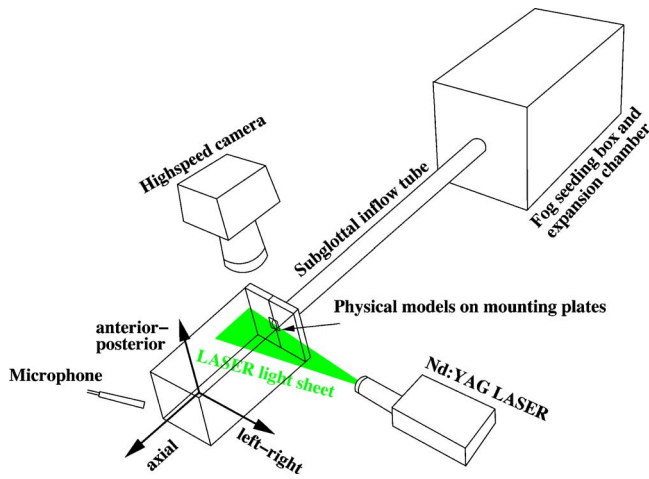


FIG. 1. (Color online) Experimental setup for flow visualization of glottal jet: Expansion chamber with the theatrical fog machine for flow seeding, straight cylindrical inflow tube, pair of physical vocal fold models, high speed camera, and Nd:YAG LASER with LASER sheet module. The axial direction is perpendicular to the plane of the mounting plates. Note that for the digital particle image velocimetry (DPIV) experiments we mounted a large rectangular duct downstream from the mounting plates to increase mixing and thus seeding density in the entrainment region of the glottal jet (duct dimensions: 25.4 cm \times 12.7 cm \times 12.7 cm).

near field flow, then hot-wire anemometry would not be an appropriate technique to quantify such structures.

In order to circumvent possible problems with the technique of hot-wire anemometry, we use the methods of flow visualization and particle image velocimetry to study the near field flow structures of a self-oscillating, physical model of the vocal folds, with a vocal tract attached. Using the method of empirical eigenfunctions, we conduct a spatio-temporal analysis of the near field flow structures. Specifically, we address the following questions: what are the most significant spatio-temporal structures of the near field flow? Are these structures similar to ones which have been reported previously for static models of the glottis? Do these structures suggest feedback mechanisms between the near field flow and the larynx? And what possible implications do such structures have on voice production?

II. MATERIALS AND METHODS

A. General experimental setup

The general setup for our experiments is shown in Fig. 1. It consisted of an expansion chamber, a straight inflow tube, a pair of physical models of the vocal folds, a LASER light sheet, and a high speed camera. The volumetric flow rate of the pressurized air supplied to the expansion chamber was measured with a precision mass flowmeter (type 558A, MKS). The expansion chamber was used to acoustically terminate the inflow tube on the upstream side with a defined acoustical impedance. It could be regarded as an experimental equivalent to the bronchi and lungs in humans. It was made of 1.27-cm-thick Plexiglas, was about 50.8 cm long, and had an inner cross section of 23.5 cm \times 25.4 cm (volume: approx. 30.3 l). A theatrical fog machine (Chauvet Hurricane Fogger F-650) inside the expansion chamber was used to seed the air flow with tracer particles for flow visualization

and digital particle image velocimetry (DPIV) measurements. Downstream from the expansion chamber, we placed a straight cylindrical PVC tube (inner diameter 2.54 cm). We used two inflow tube lengths, a 69-cm-long tube with quarter-wavelength frequency of approx. 125 Hz and an 81-cm-long tube with a quarter-wavelength frequency of about 106 Hz. The ratio of the cross-sectional areas of the expansion chamber and the subglottal inflow tube was approx. 117. Therefore, we assumed that on the upstream side the inflow tube had an acoustic termination equivalent to an ideal open end. The measured reflection factor reported in Zhang *et al.* (2006) confirmed this assumption.

The physical models glued into grooves in two acrylic mounting plates were placed at the downstream end of the subglottal inflow tube. Details on the fabrication and dynamic characteristics of the physical model were reported elsewhere (Thomson, 2004; Thomson *et al.*, 2005, 2004). In brief, they were made from a two-component liquid polymer solution mixed with a liquid flexibilizer solution. The models were approx. 1.2 cm high (superior-inferior dimension) and 0.8 cm wide (medial-lateral direction). The model lengths (in anterior-posterior direction) were 1.7 and 2.3 cm, respectively. The physical properties of both sets of models were identical and as reported in Thomson *et al.* (2005). Note that the oscillation frequencies of both sets were similar to the quarter-wavelength resonance frequency of the used subglottal inflow tube. For a detailed report on the influence of the acoustics of the subglottal inflow system see Zhang *et al.* (2006).

The sound pressure downstream from the physical model was measured with a 1.27-cm-diam microphone (4193-L-004, B&K, Denmark). The microphone was connected to a conditioning amplifier (NEXUS 2690, B&K, Denmark) where the signal was bandpass filtered between 20 Hz and 22.4 kHz. The filtered signal was monitored with a digital storage oscilloscope and recorded with a standard PC sound card at a sampling rate of 100 kHz and 24 bit resolution for a voltage range of ± 1.0 V. The microphone was calibrated with a B&K sound level calibrator (type 4231).

During the flow visualization and DPIV experiments with a double-pulsed LASER, the LASER pulses were not locked to specific phases of the model oscillation. Instead, we simultaneously recorded the far field sound pressure and a trigger signal generated from the LASER unit before each double pulse. As shown in Fig. 2, the far field sound pressure spectrum was harmonic. Thus, *a posteriori* we could select series of “snapshots” where the oscillating flow was repeatedly illuminated at approx. similar phases. The selected snapshots were “quasi-phase-locked” representations of the time-dependent periodic flow field. As the fundamental frequency f_0 depended weakly on the subglottal flow rate, we recorded a different number N_T of phases per period T due to the repetition rate f_{rep} of the double-pulsed LASER. The fundamental frequency f_0 was $f_0 = f_{\text{rep}}(n + 1/N_T)$ where the integer n is the number of oscillation cycles between consecutive double pulses of the LASER (f_{rep} is the repetition rate of the double pulses.).

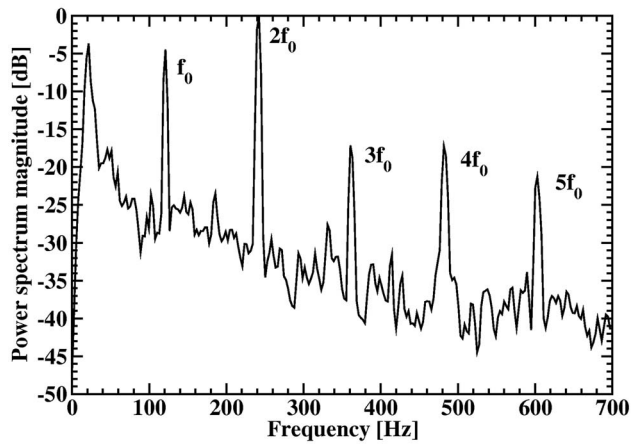


FIG. 2. Normalized power spectrum of the sound pressure signal during the flow visualization measurements. Note that the second harmonic ($2f_0$) is significantly stronger than the fundamental frequency (f_0). The peak at about 20 Hz is an artifact due to high-pass filtering of the microphone signal. ($f_0 \approx 122$ Hz, volumetric flow rate approx. 480 ml/s, subglottal inflow tube: 69 cm, physical model length: 1.7 cm).

B. Quasi phase-locked flow visualization with LASER light sheet

A qualitative analysis of coherent flow structures of the glottal jet was done using the images from the quasi phase-locked flow visualization experiments. Typical for flow visualization, the seeding density was high in the seeded flow regions and low outside. In flow regions where the mixing was small, the scattered LASER light from the seeded flow showed mainly the dynamics of the boundaries between seeded and unseeded flow. In flow regions with large mixing, boundaries between seeded and unseeded flow disappeared and only the motion of large-scale patches of seeded flow (“blobs”) could be identified by eye as “coherent structures” (see Fig. 3).

For flow visualization with a LASER light sheet, the beam from a double-pulsed Nd:YAG LASER (Solo III PIV 15, New Wave Research, Fremont, CA) was shaped into a thin light sheet (approx. 1 mm thick) with a light sheet module (Dantec Dynamics, Denmark) mounted to the LASER head. Each pulse from the double-pulse LASER had about 5 mJ light energy and a pulse duration of about 3–5 ns. The interpulse interval of the double pulses of the LASER was $\Delta t = 0.25$ ms or $\Delta t = 0.5$ ms, respectively. The repetition rate of the double-head LASER was 15 Hz. The scattered light from the tracer particles in the seeded glottal jet was observed with a high speed camera (Fastcam-Ultima APX, Photron USA, San Diego) and a 58 mm lens (Noct NIKKOR, Nikon, USA) with one 14 mm extension ring. The CMOS array of the camera contained 1024×1024 pixels to capture the scattered light from the selected field of view downstream from the physical model. The recording frame rate of the high speed camera was 2000 frames/s (for interpulse interval $\Delta t = 0.5$ ms) and 4000 frames/s (for $\Delta t = 0.25$ ms), respectively. Two light sheet orientations with respect to the physical model and the glottal jet were used for the illumination of the seeded jet flow: First, the light sheet was placed in an axial and left-right direction to observe the

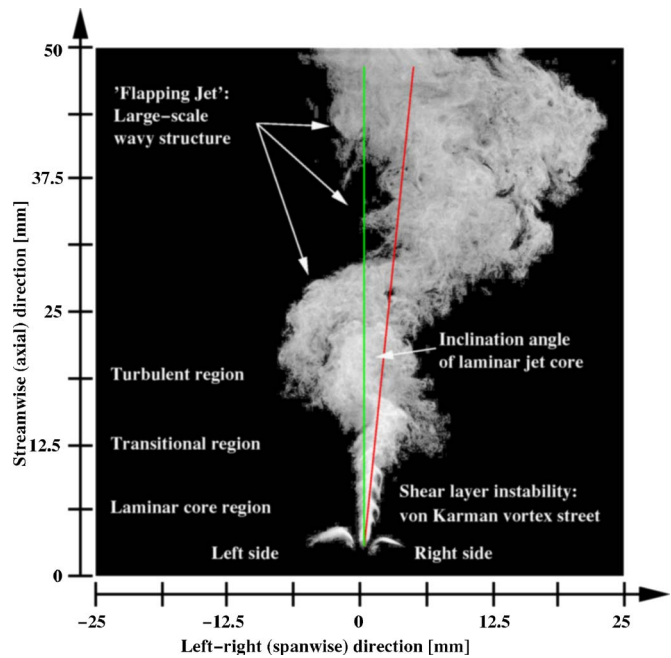


FIG. 3. (Color online) Representative flow visualization image during model oscillation: The superior edges of the left and right model sides were illuminated by the LASER light sheet. The direction of the streamwise jet axis is indicated by the red line. (volumetric flow rate about 480 ml/s, subglottal inflow tube length: 69 cm, physical model length: 1.7 cm).

medial-lateral dynamics of the glottal jet at the midline of the physical model (shown in Figs. 3, 5, 7, and 9). Second, the glottal jet flow in anterior-posterior direction was observed with a light sheet oriented in an axial and anterior-posterior direction to assess the three-dimensional structure of the glottal near field flow (shown in Fig. 10).

Figure 3 shows one representative flow visualization image where some general flow features can be seen. Note that at the bottom of Fig. 3, the superior edges of the left and the right sides of the physical model can be seen being illuminated by the LASER light sheet. The glottal jet within some small part of the glottal exit channel was also visible.

C. Digital particle image velocimetry (DPIV)

We used DPIV measurements to quantitatively observe coherent flow structures in the glottal near field flow. In contrast to flow visualization, the flow velocity field in the entrainment region outside the laminar core region could also be observed. The field of view of the DPIV measurements was restricted to about half the size of the flow visualization images. Therefore, we focused on the dynamics of the laminar core region with the roll-up of large-scale vortices and the convection of these vortices into the turbulent region (see Fig. 4). Thus, DPIV is an extension of flow visualization in both the resolved region of air flow and the flow field information in terms of flow velocities instead of only seeding density or seeding boundaries.

For planar DPIV, we used a double-pulse Nd:YAG LASER (Solo 120, New Wave Research, Fremont, CA) with a light sheet module (LaVision, MI) to illuminate a thin slice (about 1 mm thick) of the seeded jet flow. The light sheet was oriented in the axial and left-right direction. The energy

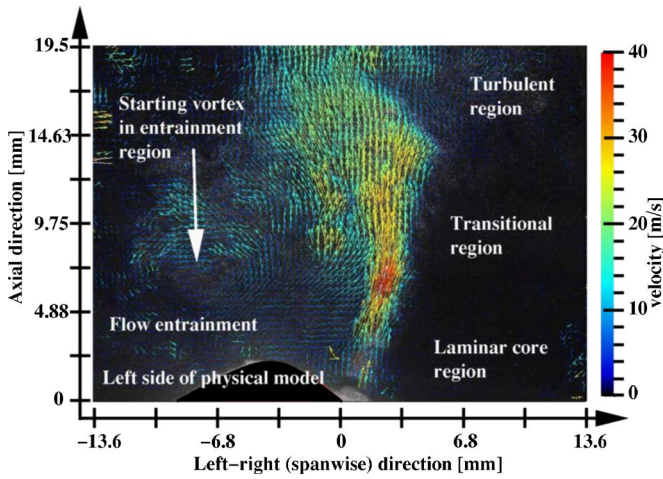


FIG. 4. (Color online) Representative velocity field from DPIV measurement of (slightly confined) glottal jet: The left side of the physical model was illuminated by the LASER light sheet. A vortex-like structure of the starting jet is visible on the left side in the entrainment region. The flow field on the right side of the model could not be resolved due to the low scattered light intensity in the shadow of the jet flow. The left and right walls of the confining downstream duct were located at approx. -63 and 63 mm in left-right direction, respectively. (volumetric flow rate approx. 480 ml/s, fundamental frequency $f_0 \approx 99.99$ Hz, subglottal inflow tube length: 81 cm, physical model length: 2.3 cm).

of each LASER pulse was about 5 – 10 mJ. The interpulse interval of the double pulses was $\Delta t = 5 \mu\text{s}$. A double-shutter camera (Image Intense, LaVision Inc., MI) with an inter-frame interval of $5 \mu\text{s}$ and a repetition rate of 4.95 double frames/s together with a 60 mm lens (NIKKOR, Nikon USA) was used to capture the scattered light from the tracer particles in the LASER light sheet. The CCD array of the camera contained 1376×1040 pixels that were used to capture a field of view of $27.2 \text{ mm} \times 19.5 \text{ mm}$.

For increased seeding particle density in the downstream region outside the core of the glottal jet (i.e., in the entrainment region), a rectangular acrylic duct was mounted downstream from the physical model. This also helped to isolate the jet flow from air disturbances from the laboratory environment. The duct was 25.4 cm long (in axial direction) and had a inner cross section of $12.7 \text{ cm} \times 12.7 \text{ cm}$. Therefore, the ratio of the duct width and the maximum glottal opening width ($W_{\text{max}} \approx 1$ mm) was approx. 127 . This expansion ratio was large, so that influences of the confining duct wall on the glottal jet dynamics could be neglected.

Flow velocity vector fields were calculated from image pairs that were obtained from LASER double pulses. For a detailed description of the theory of DPIV we refer to, e.g., Adrian (1991); Westerweel (1997). In our experiments, the processing was done with the software package DaVis (LaVision, Inc. MI) using a multi-pass algorithm. Two passes with an interrogation window size of 64×64 pixels were followed by two passes at 32×32 pixels. The overlap of the interrogation windows was 50% .

Figure 4 shows one representative velocity field obtained from two-dimensional DPIV measurements of the glottal jet through the physical model. Only the left side of the physical model was visible in these DPIV images. The confining duct walls in Fig. 4 were located at approx. -63

and 63 mm in left-right direction. The maximum jet core velocity was approx. 40 m/s. Note that the flow vector field immediately downstream from the right model could not be resolved, because there the intensity of the scattered LASER light was too low due to low seeding density and low LASER light intensity.

D. Extraction of coherent flow structures

Coherent structures are spatially and temporally organized flow structures that are found even in turbulent flow. They are the building blocks for large-scale motions in fully developed turbulence (Holmes *et al.*, 1997; Theodorsen, 1952; Townsend, 1976). Qualitatively, coherent flow structures could be identified using the “eyeball norm” to identify small- and large-scale structures in the scattered light from the seeding concentration fields in flow visualization experiments (Sirovich *et al.*, 1990): Using a high speed camera and a double-pulsed LASER light sheet with exposure times of about 3 – 5 ns, we effectively “froze” the motion of the glottal jet at two time instances. If the time delay between two consecutive LASER pulses is short enough compared to the flow velocities in the observed flow field, then the trajectories of seeding structures (such as blobs and “hook-like and wave-like boundaries”) can be tracked by visual inspection. This is useful especially for the characterization of small-scale, high-frequency shear layer vortices.

The technique of “principal component analysis” (PCA) can be used as an objective method to numerically extract coherent flow structures from seeding concentration fields in flow visualization experiments and from flow vector fields in DPIV experiments (Berkooz *et al.*, 1993; Holmes *et al.*, 1996; Lumley, 1967; Sirovich *et al.*, 1990). PCA provides a rational framework to decompose organized flow structures. PCA is a statistical procedure that identifies coherent, i.e., correlated dynamics in spatio-temporal patterns. As the recorded images from the flow visualization experiments and the DPIV measurements captured a superior part of the physical model, we could relate the dynamics of the coherent flow structures (here defined as the PCA eigenfunctions) to the vibrational behavior of the physical vocal fold model.

Coherent flow structures of a spatio-temporal flow field (“movie”) were defined as the empirical orthonormal functions $\psi_\ell(\mathbf{x})$ (EOFs) obtained from PCA. The scalar-valued or vector-valued movie $f(\mathbf{x}, t)$ ($\mathbf{x} \in \mathbf{R}^2$, $t \in \mathbf{R}$) is written as

$$f(\mathbf{x}, t) = \sum_{\ell=1}^N \sigma_\ell \varphi_\ell(t) \psi_\ell(\mathbf{x}). \quad (1)$$

The functions $\psi_\ell(\mathbf{x})$ capture the coherent spatial structures of the flow field movie, the functions $\varphi_\ell(t)$ are the corresponding temporal coefficients (“amplitudes”) of the coherent structure, and σ_ℓ were the weights of the coherent structures with respect to the total dynamics of the spatio-temporal flow field. We use the terms “topos” to refer to the spatial functions $\psi_\ell(\mathbf{x})$, “chronos” to refer to the temporal functions $\varphi_\ell(t)$, and “energy” to refer to σ_ℓ^2 (Aubry *et al.*, 1991). For a detailed description of coherent structures based on PCA, we refer to the Appendix.

III. RESULTS

At a subcritical flow rate of approx. 300 ml/s, in which the physical model was stationary (“prephonatory standstill”), the open model glottis discharged a steady open jet. Light sheet illumination of a left-right and axial plane in the center of the jet showed that the jet axis was inclined by approx. 8° away from the normal direction of the mounting plates towards the right model side. This side protruded less far downstream than the left model side. These observations hinted that the direction of the glottal duct during prephonatory standstill was oblique as the left and right physical models were deformed asymmetrically by the applied subglottal flow. Scherer *et al.* (2001) and Shinwari *et al.* (2003) found inclined jet axis directions for both symmetric and oblique rigid vocal fold models. They also showed that the pressure distribution in the glottal channel was asymmetric. In our experiments with deformable physical models, the model geometry during prephonatory standstill was the result of a static equilibrium of pressure forces on the physical model walls and the elastic forces of the models. Even if the elastic properties of the left and right physical model were identical, it is possible that the asymmetry in the pressure distribution on the left and right model walls would lead to an asymmetric oblique direction of the glottal channel during standstill.

For a supercritical flow rate above approx. 480 ml/s, the typical far field sound pressure of the model oscillations is as shown in Fig. 2. With this kind of physical model, we typically observed a significantly larger sound pressure amplitude at the second harmonic ($2f_0$) than for the fundamental frequency (f_0).

A. Oscillation of laminar jet core axis

Figure 5 shows an enlarged view of the seeded jet flow in the laminar core region. This cycle of double-frame images of the scattered LASER light revealed different stages of attachment and detachment of the laminar core from the physical model walls. We found this behavior to be consistent in our experiments with the physical model. At the beginning of the cycle (frame 0), when the flow rate was minimal and the model glottis was almost closed, the seeded flow stayed attached to the left side of the model (upper side in Fig. 5). This side protruded downstream further than the opposite right side, probably due to asymmetries of the mounting of the physical models onto the holding plates. During the opening phase (frames 1 and 2), when the flow rate increased, the laminar core width increased while the jet flow stayed attached to the right side of the model (lower side in Fig. 5). During maximum opening (frames 3 and 4), the jet core axis moved slightly to the center of the glottis, and the flow detached from the divergent exit wall of the right model. During the closing phase (frames 5 and 6), when the jet flow rate decreased, the laminar core width decreased and the flow reattached to the right model wall.

During maximum opening and during the closing phase (frames 3–6), the laminar core region downstream of the glottis exit was straight. During the opening phase, we observed a strongly curved flow downstream of the glottis exit: Just before opening of the model glottis (frames 0 and 7), the

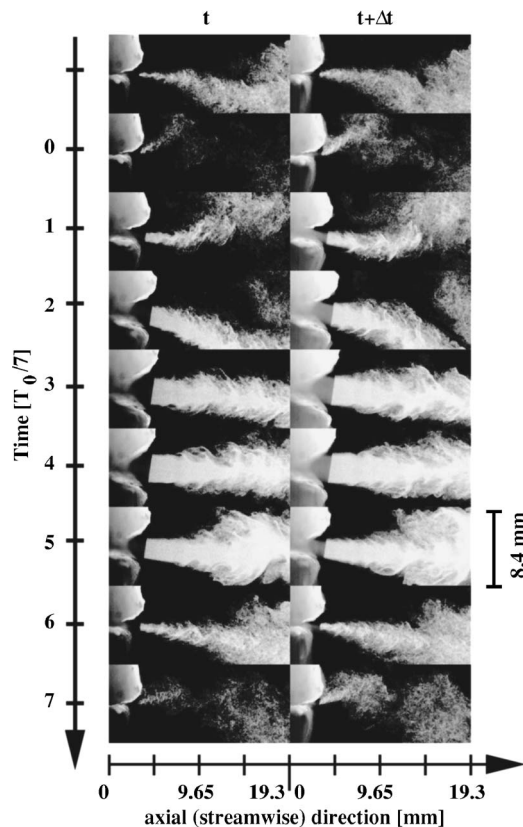


FIG. 5. Magnified view of image pairs showing the laminar core region and the transitional region for one oscillation cycle. The jet core axis oscillated in the left-right direction: During opening the flow stayed attached to the right model (lower side). It detached from the right side, while the direction of the jet core rotated to the left side. During closing, the flow reattached to the right side of the model. ($\Delta t=0.25$ ms, $f_{\text{rep}}=15$ Hz, volume flow rate approx. 630 ml/s, fundamental frequency $f_0 \approx 122$ Hz, subglottal inflow tube length: 81 cm, physical model length: 2.3 cm).

flow downstream from the almost closed glottis was bent towards the left model side. This might be due to the leftover recirculation from the flow in the previous cycle. This curved flow structure was convected downstream (frame 1) and the curvature changed towards the right side in a later opening phase (frame 2). The changing curvature is probably due to the influence of the jet flow in the beginning of the cycle which may produce circulation opposite to the one in frames 0 and 7.

For one oscillation cycle, we estimated the instantaneous width of the laminar core region and the instantaneous inclination angle of the laminar core axis with respect to the axial direction (the normal direction to the mounting plates) (Fig. 6). These values were measured visually from images of the seeded jet flow within and just downstream of the exit of the model glottis (as seen in Fig. 5). Positive inclination angles indicated inclination to the right model side. Figure 6 shows that the laminar jet width oscillated quasi-sinusoidally at the fundamental frequency ($T_0=1/f_0$). The observed core width varied between about 0.4 and 1.5 mm. The inclination angle varied about a mean value of approx. 8° with an amplitude of approx. 4° . Over one oscillation cycle, it showed a double-peak behavior: starting from about 4° at the beginning of the cycle ($t=0$), the inclination angle increased to about 12° at about one quarter of the cycle ($t=T_0/4$). Then the angle

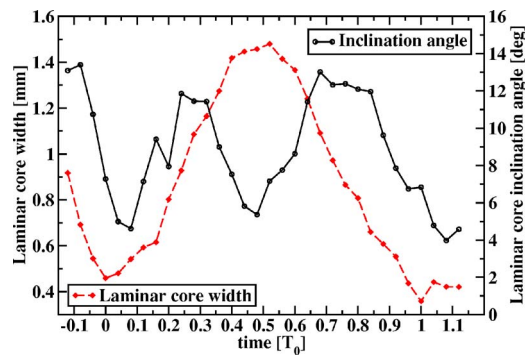


FIG. 6. (Color online) Inclination angle and width of the laminar core downstream from the physical model. The inclination angle was defined as the angle between the axial direction (perpendicular to the mounting plate of the physical model, see Fig. 1) and the instantaneous laminar core direction. Positive angles indicated a rotation towards the right side. While the width of the laminar core varied quasi-sinusoidally with the fundamental frequency, the inclination angle showed a double-peak behavior. During opening and closing (flow acceleration and deceleration), the jet axis stayed at the right side of the physical model. ($f_0=1/T_0=f_{\text{rep}}(n+1/N_T)=120.6$ Hz, where $N_T=25$, $n=8$, $f_{\text{rep}}=15$ Hz, volumetric flow rate approx. 480 ml/s, subglottal inflow tube length: 69 cm, physical model length: 1.7 cm).

decreased to about 5° at $t=T_0/2$. In the second half of the cycle, the inclination angle increased again to about 12° at about $t=3T_0/4$ and finally returned to about 4° at the end of the cycle. Note that the double-peak behavior was also present in the far field sound pressure as indicated by the dominant second harmonic in Fig. 2.

B. Shear layer structure

Downstream from the physical model exit, the laminar core was surrounded by a von Kármán-like vortex street indicated by the hook-like structure of the boundary of the seeded flow (Figs. 3 and 7). The width of this vortex street increased with increasing distance from the physical model, until the left and right shear layers merged and the visible hook-like structure disappeared. This widening of the shear layer was due to the convection and growth of the shear layer vortices. The flow within the glottal channel was laminar for the flow rates used in our experiments (here up to about 630 ml/s).

C. Flapping of turbulent region

Figure 7 shows the seeded jet flow in both the laminar and the turbulent region during one oscillation cycle. The disparity of image pairs recorded with a delay of $\Delta t=0.5$ ms allowed us to visually track flow patterns in the plane of the LASER light sheet. As shown in Fig. 7, the jet flow in the transitional region reorganized into small-scale turbulent behavior organized in a large-scale wave-like pattern in the turbulent region. This wave-like pattern in the turbulent region has been termed a “flapping jet” (see Gordeyev and Thomas (2000); Thomas and Brehob (1986)). It stems from early interpretations that the jet “flaps like a flag” which would imply left-right oscillations of the instantaneous axial velocity profile. In static planar jets, the “flapping jet phenomenon” is now understood in terms of large-scale coherent structures in the turbulent region organized in

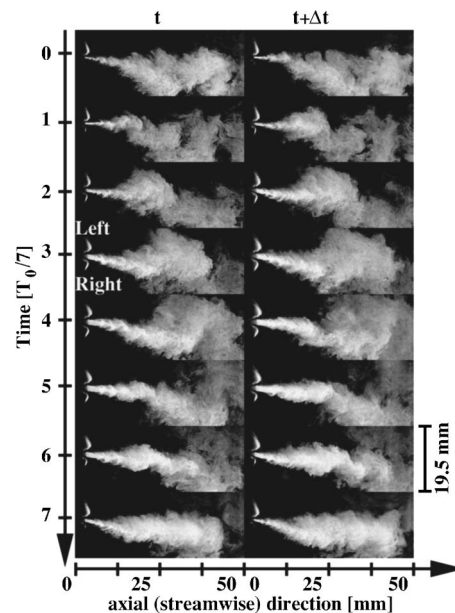


FIG. 7. Quasi phase-locked observation of the seeded open glottal jet during one oscillation cycle. A von Kármán-like vortex street in the shear layer of the laminar core and the flapping of the jet in the turbulent region can be observed. ($\Delta t=0.5$ ms, volumetric flow rate approx. 480 ml/s, $f_{\text{rep}}=15$ Hz, $f_0=f_{\text{rep}}(n+1/N_T)=121.875$ Hz, $N_T=8$ different phases, $n=8$, field of view: 50 mm \times 50 mm, inflow tube length: 69 cm, physical model length: 1.7 cm).

an antisymmetric array of counter-rotating vortices (Gordeyev and Thomas, 2000; Thomas and Brehob, 1986). This antisymmetric vortex array convects downstream into the turbulent region while new vortex structures are created in the transitional region. Visualizing such a velocity field with seeding particles in a light sheet, the seeded flow seems to “flap” in the left-right direction.

The experiments with DPIV confirmed the observations made from flow visualization. In Fig. 8 we show a sequence of velocity vector fields for one oscillation cycle. There, the flapping of the jet in the turbulent region due to the convection of a vortex structure can be clearly seen (frames 1–3). The vortex structure downstream from the left model side was created during the opening phase. As shown above in Fig. 5, at minimal opening the flow downstream from the model was bent towards the left side. This bend then convected downstream (frame 1 in Fig. 8) and led to the observation that the jet flapped to the right side (frame 2 and 3). In frame 4, a small, wavy undulation of the jet core in the transitional and turbulent region can be seen.

The convection of large-scale plume-like structures during one cycle was visualized by spatio-temporal plots constructed by concatenating axial slices from flow visualization image pairs (Fig. 9). This spatio-temporal plot contained 49 pixel=2.4-mm-wide slices taken from the center region of the double-pulse flow visualization images. It showed the temporal behavior of the glottal flow near field in an axial slice centered about the center of the glottal channel. Due to the convection of large-scale plumes of seeded flow and the flapping of the jet in the turbulent region, we observed inclined stripes of seeded flow in the spatio-temporal plot. The convection velocity of the large-scale structures initiated dur-

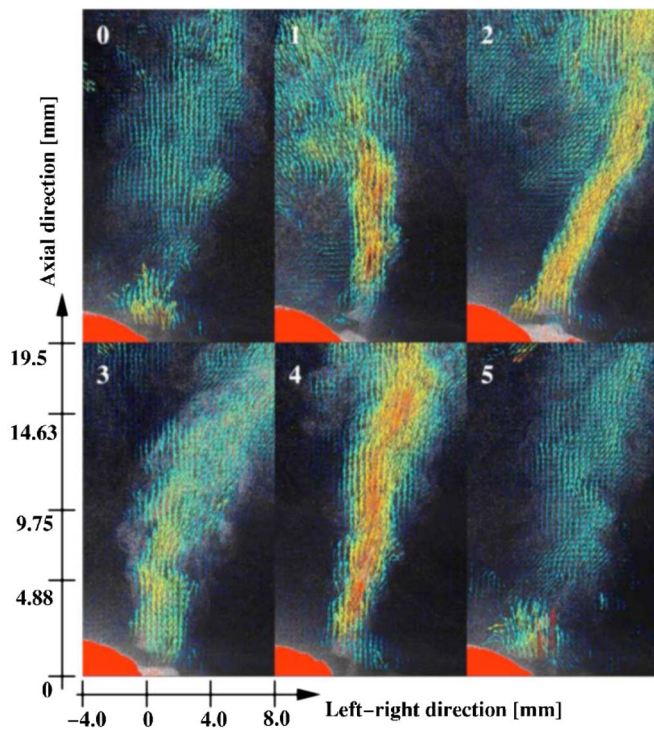


FIG. 8. (Color online) Magnified image sequence of velocity vector fields from DPIV experiments: Frame 1 corresponds to the velocity field shown in Fig. 4. In frames 0 and 5, the model glottis is minimal, but not closed. Residual flow from the previous oscillation cycle could be seen downstream from the glottal exit (frames 0 and 5). In frame 1, the glottis opened and the jet flow velocities in the laminar core increased, while the direction of the laminar core axis moved to the right side. In frames 2 and 3, the jet axis in the turbulent region flapped to the right side. In frame 3, the laminar core widened significantly while the direction of the laminar jet core axis moved back towards the left side. The largest flow velocities in the jet over the entire jet length occurred in frame 4. (volume flow rate approx. 480 ml/s, $f_0 = f_{rep}(n+1/N_T) = 99.99$ Hz where $N_T = 5$, $n = 20$, $f_{rep} = 4.95$ Hz, subglottal tube length: 81 cm, physical model length: 2.3 cm).

ing the opening phase could be estimated from the slope of the stripe-like patterns. We found convection velocities of approx. 9.7 m/s compared with jet core velocities of about 40 m/s. The convection velocity of flow structures in the middle of the oscillation cycle could be estimated as about 7.5 m/s. Note that for the location of the observation slice there were two inclined stripes for each oscillation cycle. Therefore, an observer at a fixed location in the turbulent region would observe a double-peaked seeding concentration signal for each oscillation cycle.

D. Three-dimensional flow features

Our study used only two-dimensional slices of the full three-dimensional glottal flow structure. The degree to which the glottal jet has three-dimensional features was illustrated with flow visualization experiments with the LASER light sheet in an axial and anterior-posterior plane (Fig. 10): First, we observed vortex structures in the shear layer at the anterior and posterior boundaries of the laminar core (frame 1). Second, downstream from the axially convected vortex structures, the anterior-posterior jet width decreased abruptly (frame 1). Third, at maximum opening (frame 2), we observed a converging laminar jet flow, which might be related

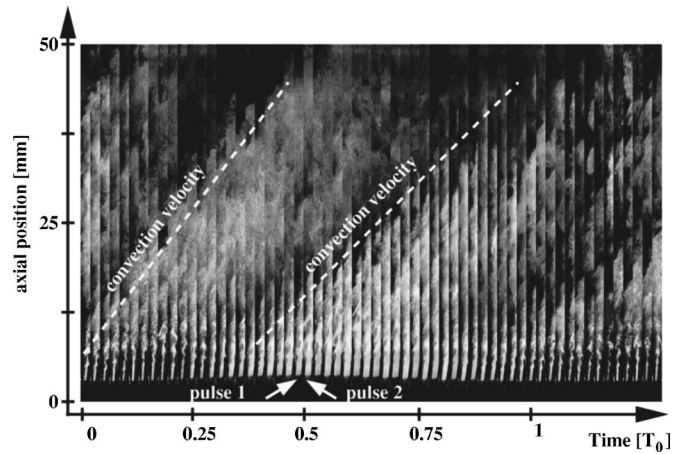


FIG. 9. Spatio-temporal plot from seeding density image pairs constructed from axial slices revealing convection of plume-like flow structures and flapping of the flow in the turbulent region: The jet flaps through the axial slices. For this cycle, the corresponding variation of the laminar core width and the inclination angle of the laminar core axis were shown above in Fig. 6. The convection velocity of the first plume-like structure could be estimated as about 9.7 m/s, the second as about 7.5 m/s. (width of concatenated slices: 49 pixel=2.4 mm, $\Delta t = 0.5$ ms, $f_{rep} = 15$ Hz, $f_0 = 1/T_0 = 120.6$ Hz with $N_T = 25$, volume flow rate approx. 480 ml/s, inflow tube length: 69 cm, physical model length: 1.7 cm).

to the axis switching phenomenon known from noncircular jets (Gutmark and Grinstein, 1999). And fourth, during closing (frame 4), the flow in the light sheet just downstream from the model broke up into two parts, one anterior and one posterior jet flow. Therefore, the flow downstream from the physical model was found to be essentially three dimensional and it showed typical features of jet flows through static noncircular orifices (Gutmark and Grinstein, 1999).

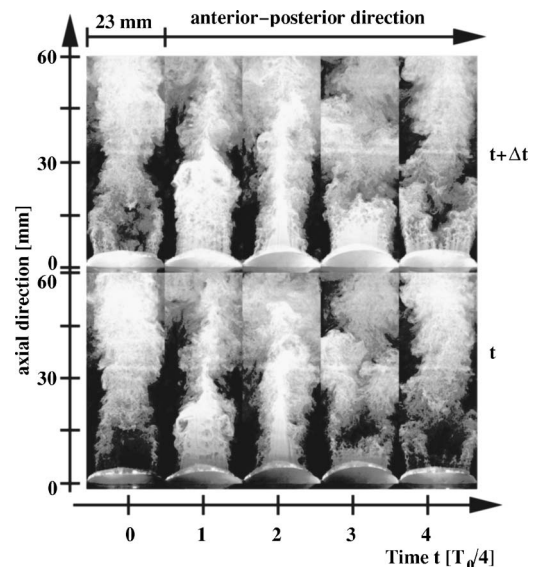


FIG. 10. Three-dimensional features estimated with flow visualization with LASER sheet aligned in anterior-posterior direction. One oscillation cycle of the quasi-phase-locked flow fields is shown. The jet flapped through the LASER sheet in medial-lateral direction and the jet axis was slightly inclined towards one side of the physical model. Hence, at certain parts of the glottal jet the light sheet did not intersect the seeded jet flow. ($\Delta t = 0.5$ ms, $f_{rep} = 15$ Hz, $f_0 = f_{rep}(n+1/N_T) = 123.75$ Hz, with $N_T = 4$ and $n = 8$, volume flow rate: 1050 ml/s, inflow tube length: 81 cm, physical model length: 2.3 cm).

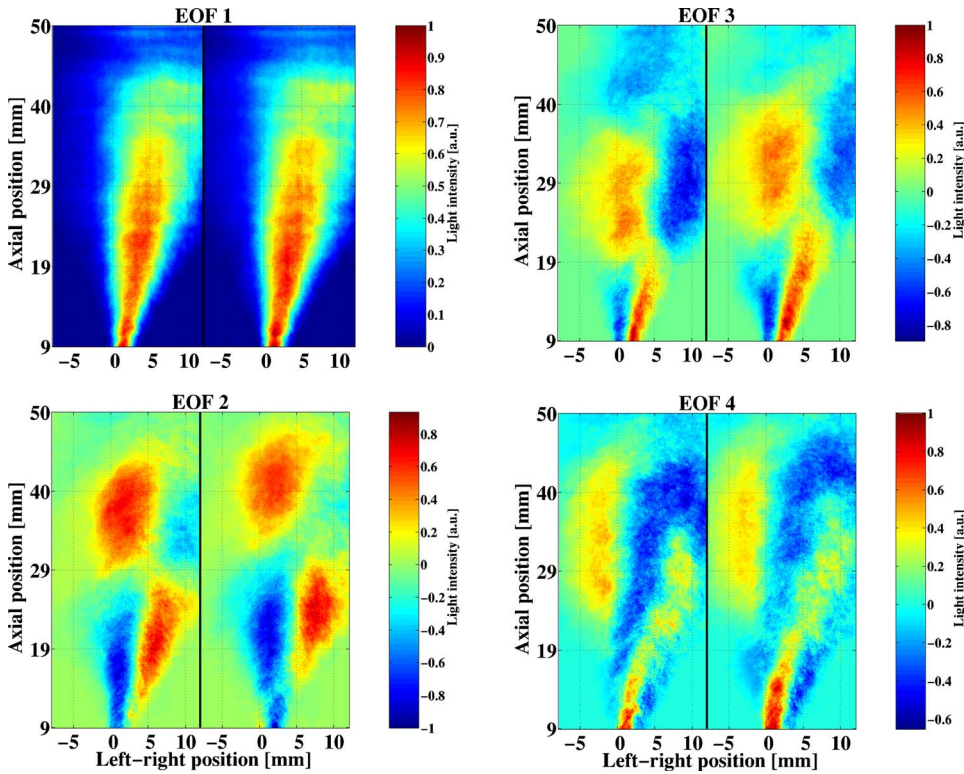


FIG. 11. (Color online) First four spatial coherent structures (topos) of the seeding concentration field from paired visualization images downstream from the oscillating physical model. The decomposition into coherent structures of paired images was similar to the decomposition of the flow velocity field of the glottal near field. The disparity of the image pairs of each topos contained the information about the underlying velocity field. Note that EOFs 2 and 3 (and EOFs 4 and 5 (not shown)) are approx. spatially shifted versions of each other. Thus, EOFs 2 and 3 (and EOFs 4 and 5) described traveling wave structures in the seeding concentration field.

E. Linear correlations between laminar core and turbulent region dynamics

1. Coherent structures from seeding concentration fields

We used PCA to objectively extract patterns of correlated flow behavior of the seeding density field in the laminar core region and the turbulent region. In this way, coherent structures were constructed by PCA by finding organized correlated behavior of flow structures.

The snapshot method was used to construct coherent flow structures (in terms of empirical orthogonal functions, EOFs). We used 51 image pairs of seeding concentration fields obtained with double-pulsed light sheet illuminations of the near field of the glottal jet flow. These 51 image pairs captured about seven cycles of the model vibration, similar to the one shown in Fig. 7. Before applying PCA we excluded the downstream protruding superior part of the physical models from the image pairs. In this way, we suppressed the influence of coherent scattered light patterns from the physical model on the construction of coherent flow patterns. The image pairs with a resolution of 800×850 pixels were treated as one image and analyzed together. The disparity between the image pairs is related to the glottal flow velocity field within the light sheet. Therefore, the constructed topos of pairs of seeding concentration fields could be associated with coherent structures of the flow velocity fields downstream from the physical model.

Figure 11 shows the first four spatial coherent structures of image pairs from the seeding concentration field. The corresponding spectra of the chronos are shown in Fig. 12 and the relative eigenvalues are given in Table I. Table I shows that some coherent structures (EOFs) appeared roughly in pairs with respect to their relative contributions to the total

variance (total kinetic energy). Paired eigenvalues were observed previously in other applications of PCA, e.g., see Deane *et al.* (1991); Leonardy *et al.* (1996); Ma and Karniadakis (2002); Ma *et al.* (2003); Noack *et al.* (2003). A theoretical explanation for paired eigenvalues from PCA can be found, e.g., in Glegg and Devenport (2001). In brief, for spatio-temporal systems with homogeneous directions (spatially or temporally translationally invariant directions) PCA modes resemble Fourier modes. Therefore, in spatially ideally homogeneous systems two identical PCA eigenvalues would appear (degenerate case) that are related to sine and cosine functions in space and time. Combined appropriately, paired topos and chronos could describe standing and travel-

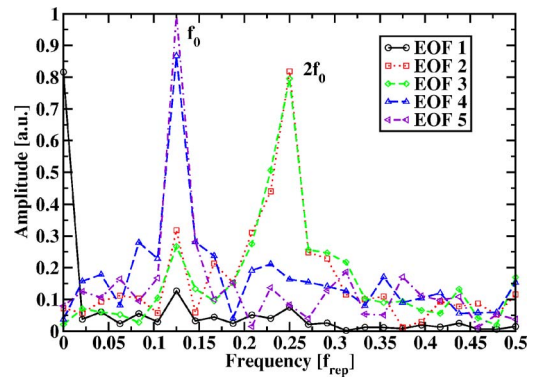


FIG. 12. (Color online) Normalized amplitude spectra of the first five chronos of the coherent structures from the seeding concentration field downstream from the oscillating physical model. The first five chronos could be approximated as: $\varphi_1(t) \propto \text{const.} - \cos(\omega_0 t)$, $\varphi_2(t) \propto \sin(2\omega_0 t)$, $\varphi_3(t) \propto \cos(2\omega_0 t)$, $\varphi_4(t) \propto \sin(\omega_0 t)$, and $\varphi_5(t) \propto \cos(\omega_0 t)$ ($\omega_0 = 2\pi f_0$, $f_{\text{rep}} = 15$ Hz, $f_0 = f_{\text{rep}}(n + f_{\text{exp}}) \approx 122$ Hz, where $f_{\text{exp}} \approx 0.125$ and $n = 8$).

TABLE I. Relative contributions of coherent structures of the near field of the flow visualization experiments to the total kinetic energy, the total mean energy, and the total fluctuating energy. More than 21 components were necessary to explain more than 95% of the total energy. The first component was sufficient to explain more than 95% of the total mean energy, whereas more than 31 components had to be included to recover more than 95% of the total fluctuating energy. ($E_{\text{mean}}/E_{\text{tot}}=43.2\%$, $E_{\text{fluct}}/E_{\text{tot}}=56.8\%$, see Appendix for a theoretical description of these expressions).

PCA index k	Relative contributions of coherent structures to total:		
	kinetic energy $\lambda_k=\langle\Psi_k^2(x)\rangle_x$ [%]	mean energy $\langle\Psi_k(x)\rangle_x^2$ [%]	fluctuating energy $\text{Var}_x(\Psi_k(x))$ [%]
1	76.9	99.6	59.7
2	4.6	$<10^{-1}$	8.0
3	4.1	$<10^{-1}$	7.2
4	1.8	$<10^{-1}$	3.2
5	1.1	$<10^{-1}$	1.9

ing waves. Here, paired eigenvalues of coherent structures were indicative of convection of flow structures in the near field of the glottal jet flow.

The first coherent structure captured approx. 77% of the total kinetic energy, about 100% of the total mean kinetic energy, and 60% of the total fluctuating kinetic energy. The first chronos could be approximated as $\varphi_1(t) \propto \text{const.} - \cos(\omega_0 t)$ ($\omega_0 = 2\pi f_0$, $f_0 \approx 122$ Hz). The first topos could be interpreted as the mean jet flow component that was inclined towards the right model side and oscillated in amplitude at the fundamental frequency of the model vibration.

The second and third coherent structures had similar values for their relative contributions to the total kinetic energy ($\lambda_2 \approx 5\%$, $\lambda_3 \approx 4\%$) and total fluctuating kinetic energy ($\text{Var}_x(\Psi_2(x)) \approx 8\%$, $\text{Var}_x(\Psi_3(x)) \approx 7\%$). Their contributions to the total mean kinetic energy were negligible. The corresponding chronos of these paired coherent structures could be approximated as $\varphi_2(t) \propto \sin(2\omega_0 t)$ and $\varphi_3(t) \propto \cos(2\omega_0 t)$, respectively. Therefore, the dominant frequency component for EOFs 2 and 3 was at the second harmonic ($2\omega_0$). As a pair, EOFs 2 and 3 described the convection of large-scale structures in the turbulent region, as their topos were approx. spatially shifted versions of each other. These two coherent structures showed that the dynamics of flow structures in the right (left) shear layer was strongly correlated with the dynamics of flow structures on the left (right) side of the turbulent region. They captured the correlated motion of the oscillation of the laminar core axis and the jet flapping of the flow in the turbulent region. This interpretation was consistent with our previous observation of the double-peaked behavior of the inclination angle of the laminar core direction (Fig. 6).

The fourth and fifth coherent structures also appeared as a pair with respect to their relative contributions to the total kinetic energy ($\lambda_4 \approx 2\%$, $\lambda_5 \approx 1\%$) and total fluctuating kinetic energy ($\text{Var}_x(\Psi_4(x)) \approx 3\%$, $\text{Var}_x(\Psi_5(x)) \approx 2\%$). Their contributions to the total mean kinetic energy were negligible. Their chronos could be approximated as $\varphi_4(t) \propto \sin(\omega_0 t)$ and $\varphi_5(t) \propto \cos(\omega_0 t)$, with the main frequency component at the fundamental frequency. Their topos (only the topos for the fourth coherent structure is shown here) were again spatially shifted versions of each other. They

showed spatial patterns with three antinodes in the left-right direction compared to two antinodes in left-right direction for the second and third coherent structures. Therefore, they captured smaller-scale details of the oscillation of the laminar core axis and of the flapping of the flow in the turbulent region. Similarly, higher-order coherent structures showed correlated behavior of flow structures on a smaller and smaller spatial scale.

2. Coherent structures from DPIV velocity fields

We used the snapshot method to decompose 50 two-dimensional DPIV velocity fields into coherent flow structures. The field of view for the DPIV observations was about half the size of the flow visualization experiments. In this way, we could focus on the coherent structures only in the immediate downstream near field of the glottal flow. The first four topos are shown in Fig. 13, the magnitude spectra of the corresponding chronos are given in Fig. 14. Table II shows the relative contributions of the coherent structures to the total kinetic energy, the total mean kinetic energy, and the total fluctuating kinetic energy. Similar to the coherent structures found in the seeding density images, coherent structures of the DPIV velocity fields appeared in pairs with respect to their relative contributions to the total kinetic energy. Thus, traveling wave structures, such as convected vortex structures, could be constructed from these paired coherent structures.

The first coherent structure contained about 64% of the total kinetic energy, about 97% of the total mean kinetic energy, and approx. 58% of the total fluctuating kinetic energy. The first topos described the mean jet flow with the mean jet axis inclined towards the right model side. The width of the mean jet flow stayed almost constant over the axial length of about one jet width. Then it widened along the axial direction. The chronos of the first coherent structure showed small amplitude oscillations about a large mean value. Thus, the first coherent structure described a pulsatile mean jet flow downstream from the physical model.

The second coherent structure contained about 8%, 2%, and about 9% of the total kinetic, mean kinetic, and fluctuating kinetic energy, respectively. The corresponding topos showed an antisymmetric velocity field with respect to the

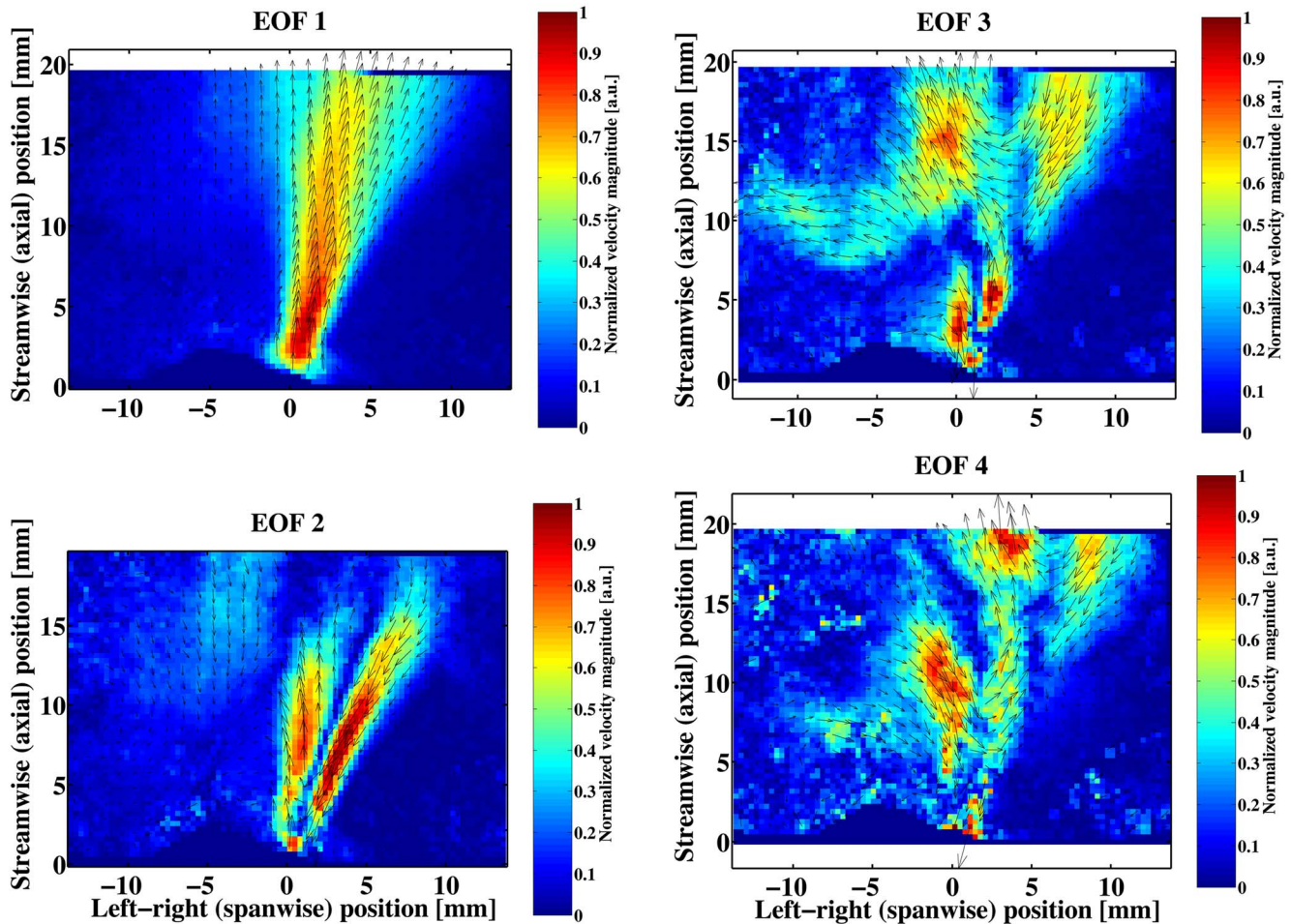


FIG. 13. (Color online) Velocity field and magnitude of the first four topos of the DPIV measurement (every third velocity vector shown): The topos of EOF 1 shows approx. the average velocity field with a mean laminar core width of approx. 2 mm. The topos of EOF 2 captured the left-right oscillation of the jet core location and direction. The topos of EOF 3 and 4 are approx. spatially shifted versions of each other. They showed vortex-like structures convecting downstream. Together, they described the flapping of the jet axis in the turbulent region.

mean jet axis: While the vector field on the left side of the jet core was directed downstream, the vector field on the right jet side was directed upstream (and *vice versa* for the second half of the oscillation cycle). The major frequency component of the corresponding chronos was at the fundamental frequency (f_0) of the model vibration. Therefore, this coher-

ent structure captured the left-right oscillation of the direction of the jet core axis.

The third and fourth coherent structures were approximately spatially shifted versions of each other. They contained about 6% and 2% of the total kinetic energy, and about 7% and 3% of the total fluctuating kinetic energy, respectively. Also the fifth and the sixth coherent structures were spatially shifted versions of each other (not shown here). The topos of EOFs 3 and 4 showed a downstream convecting vortex structure: a vortex-like structure has its center at about $(x, y) = (3, 18)$ mm in the topos of EOF 3. The corresponding vortex-like structure can be found at about $(x, y) = (6, 21)$ mm in the topos of EOF 4. This vortex rotated in clockwise direction. In the topos of EOF 3, an anti-clockwise rotating vortex-like structure was observed centered at about $(x, y) = (5, 5)$ mm downstream from the left side of the model. The major frequency component of the third coherent structure was at the fundamental frequency (f_0). A slightly smaller amplitude was found at the second harmonic ($2f_0$). The fourth coherent structure had its major frequency component at the second harmonic and a slightly weaker component at the fundamental frequency. Thus, the

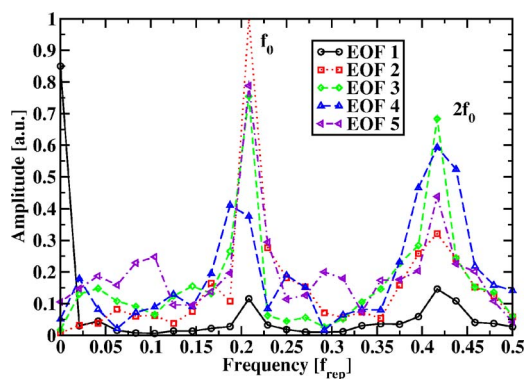


FIG. 14. (Color online) Normalized amplitude spectra of the first five chronos of the velocity field from the DPIV measurement. ($f_0 = (n + f_{\text{exp}})f_{\text{rep}} \approx 100$ Hz, where $f_{\text{exp}} \approx 0.21$, $f_{\text{rep}} = 4.95$ Hz and $n = 20$).

TABLE II. Relative contributions of coherent structures in the PIV experiments to the total kinetic energy, the total mean energy, and the total fluctuating energy. To recover more than 95% of the total variance of the velocity field, the first 30 EOFs had to be included. The first component was sufficient to explain more than 95% of the total mean energy. More than 32 component had to be included to explain more than 95% of the total fluctuating energy. The total mean energy contains about $E_{\text{mean}}/E_{\text{tot}}=16.9\%$ of the total kinetic energy, whereas the total fluctuating energy contains about $E_{\text{fluct}}/E_{\text{mean}}=83.1\%$ of the total energy. (see Appendix for a theoretical description of these expressions).

PCA index k	Relative contributions of coherent structures to total:		
	kinetic energy $\lambda_k = \langle \Psi_k^2(x) \rangle_x$ [%]	mean energy $\langle \Psi_k(x) \rangle_x^2$ [%]	fluctuating energy $\text{Var}_x(\Psi_k(x))$ [%]
1	64.3	96.5	57.8
2	7.7	2.0	8.9
3	6.1	1.2	7.0
4	2.1	$<10^{-1}$	2.6
5	1.4	$<10^{-1}$	1.7
6	1.3	$<10^{-4}$	1.6

third and fourth coherent structures explained the left-right jet flapping in the turbulent region as the convection of vortex structures. They also captured the roll-up of a starting vortex downstream from the left model side.

3. Comparison of coherent structures from seeding concentration fields and DPIV velocity fields

The presented coherent structures from the seeding concentration fields and from the planar DPIV velocity fields were obtained from different sizes of the fields of view: the fields of view for the seeding concentration fields were about twice as large as for the DPIV experiment. Therefore, the DPIV experiment only captured the immediate flow near field downstream from the physical model (the laminar core region, the transitional region, and the beginning of the turbulent region), whereas the flow visualization experiments included a larger part of the turbulent region. Therefore, the coherent structures of the flow visualization experiment captured correlated behavior between the immediate near field and the turbulent region. In this respect, the topos of EOFs 2 and 3 of the flow visualization experiment corresponded to the topos of EOF 2 of the DPIV experiment.

IV. DISCUSSION

In this paper, we used two experimental methods to qualitatively and quantitatively characterize the near field of the glottal flow through a self-sustained oscillating physical model of vocal folds: First, we used the scattered light intensity from a double-pulsed LASER light sheet to qualitatively measure the seeding density field in a single plane of the glottal jet. From the disparity of seeding density patterns of the paired flow visualization images we could estimate the motion of flow patterns. Second, we applied digital particle image velocimetry (DPIV) to quantitatively measure the in-plane flow velocity field in a single plane of the glottal jet.

Due to the limited repetition rate of the double-pulsed LASER we could only obtain a few quasi phase-locked image pairs per glottal jet oscillation. In the future, methods should be developed to increase the number of observable vibration phases. All qualitative and quantitative visualiza-

tion measurements were done for single planes either in axial and left-right direction or in axial and anterior-posterior direction. Thus, we observed that the flow near field is essentially three dimensional. Further experiments have to be done to, first, obtain out-of-plane velocity fields and, second, to get whole-volume measurements of the three-dimensional velocity field of the pulsating glottal jet.

As we used a fairly wide downstream duct (expansion ratio about 127) in our DPIV experiments to increase the seeding density, our DPIV measurements could be considered as open jet experiments. Using DPIV and PCA to extract coherent flow structures from flow velocity fields, future studies could be done on the influence of smaller expansion ratios on the dynamics of the glottal jet. In the human larynx, the ventricular folds could provide such a small expansion ratio. Recently, flow visualization experiments and DPIV measurements with static and driven vocal fold models including the ventricular folds have been reported in Triep *et al.* (2005) and Kucinschi *et al.* (2006).

A. Flow separation and unsteady Coanda effect

1. Asymmetric flow separation inside the glottis

The laminar core axis of the pulsatile glottal jet oscillated in the left-right direction. The jet flow stayed attached at one model side during opening. It then detached and moved to the center of the model glottis while its width increased. During closing, the jet flow reattached to the model side where it was attached during opening. This indicates that the flow separation points within the glottal channel occurred at different axial (inferior-superior) positions on the left and right medial surface of the physical model: The separation points within the glottal channel oscillated in axial direction, and the temporal variation of the jet separation location was different on the left and right model wall. In our experiments, the left and right model sides did not oscillate symmetrically with respect to the medial-lateral and inferior-superior vibration amplitude and phase, although left and right model oscillations were always synchronized to the same fundamental frequency. The asymmetries in amplitude and phase were presumably due to left-right asymmetric

pressure forces related to the asymmetric flow separation points and due to asymmetries in the mounting of the physical models.

We conclude that the flow separation points depended on the detailed instantaneous flow channel geometry. We hypothesize that once the separation points become asymmetric between left and right side, then left-right asymmetric flow pressure forces would act on the glottal channel walls. This would lead to left-right asymmetric vocal fold geometry, even if the visco-elastic vocal fold properties and the initial vocal fold geometry were identical and perfectly symmetric. The asymmetric vocal fold geometry in turn would affect the flow structure, thus completing a flow-structure feedback loop within the glottal channel. Thus, this flow-structure feedback loop inside the glottal channel affects the symmetry of the coupled fluid-structure system. Therefore, this flow-structure feedback could always render the left-right symmetric fluid-structure behavior unstable.

In general, human vocal folds show a similar behavior: Left-right asymmetries are inherent to the visco-elastic and geometric properties of human vocal folds. However, due to nonlinear coupling (such as from the glottal air stream) human vocal folds typically synchronize to a common fundamental frequency during phonation. For large left-right asymmetries in pathological conditions, such as recurrent nerve paralysis, left and right human vocal folds can de-synchronize and oscillate at different frequencies (Mergell *et al.*, 2000; Neubauer *et al.*, 2001; Steinecke and Herzel, 1995). Vocal fold asymmetries in healthy normal vocal folds can be induced voluntarily to desynchronize their oscillation. Thus, biphonation and chaotic behavior can be generated by asymmetries (Mergell and Herzel, 1997; Neubauer *et al.*, 2001; Steinecke and Herzel, 1995).

2. Unsteady Coanda effect

We provide further experimental evidence that the ‘unsteady Coanda effect’ can occur during vocal fold vibration. The term “unsteady Coanda effect” is used in analogy to the “Coanda effect” in stationary flows (Coanda, 1936; Panitz and Wasan, 1972). As our physical model of vocal folds was deformable, the divergence angle of the glottis [corresponds to include angle in Scherer *et al.* (2001); Shinwari *et al.* (2003)] and the glottal channel direction [termed obliquity in Scherer *et al.*, 2001; Shinwari *et al.*, 2003] were dynamic variables, in contrast to previous experiments where they were only control parameters (Erath, 2005; Pelorson *et al.*, 1994; Shinwari *et al.*, 2003; Triep *et al.*, 2005; Vilain *et al.*, 1999). Dynamically, maximum divergence angles typically occurred when the volume flow was maximal. The divergence angles of the left and right model at the downstream side of the model were asymmetric due to the construction of the physical model.

Measurements by Pelorson *et al.* (1994) and Vilain *et al.* (1999) with static and driven vocal fold models and starting or pulsatile flow found that the Coanda effect might not occur during phonation due to its large buildup time compared to the oscillation period. Recently, Erath (2005) and Erath and Plesniak (2006a, b, c) found that the unsteady Coanda effect occurs in pulsatile flows through static glottal channels

with different divergence angles at their outlet. In a recent DPIV study on a driven vocal fold model, Triep *et al.* (2005) found that the unsteady Coanda effect occurred during the opening of the driven glottis.

Our observations show that an unsteady Coanda effect can occur under unsteady oscillatory conditions, as we observed attached jet flow to only one model side, predominantly during glottal opening and closing. Our hypothesis is that the unsteady Coanda effect may be induced by flow structures downstream from the vocal folds.

B. Feedback/feedforward mechanisms in the glottal flow

1. Flapping of the turbulent jet region

In our flow visualization experiments, the jet axis in the transition region and the turbulent region showed wavy undulations in axial direction: The jet appeared to be flapping like a flag in the left-right direction. Our flow visualization experiments and DPIV measurements showed that large-scale vortex structures were generated and convected downstream into the transitional and turbulent region. The starting jet flow at the beginning of the oscillation cycle might have initiated the roll-up of these large-scale vortex structures. Note that this roll-up might be also influenced by the remaining flow structures from the previous cycle. The particular spatial alignment of large-scale vortex structures would result in an apparent flapping motion of the seeded jet flow. Analogous to planar jet experiments (Gordeyev and Thomas, 2000; Thomas and Brehob, 1986; Thomas and Prakash, 1991), we note that the term flapping jet is a misnomer in the context of glottal jets. We propose that the glottal jet axis in the turbulent region is undulated due to antisymmetric large-scale vortex structures that are convected downstream. Therefore, at a fixed axial position the jet axis appears to be oscillating in the left-right direction. Applying PCA to flow visualization fields and DPIV velocity fields, we found paired coherent structures that indicated sine and cosine-like flow patterns in the axial direction. The superposition of these patterns explained the flapping turbulent jet similar to a traveling wave. This corroborated our hypothesis that flapping was caused by convecting vortex structures in the transitional and turbulent region.

2. Coherent structures reveal correlations of the laminar core region and the turbulent region

Coherent flow structures were extracted from the near field flow. By construction from PCA, coherent flow structures revealed spatio-temporal patterns that showed correlated flow motion of the laminar core region, the surrounding shear layer, and the turbulent region. Coherent, i.e., correlated behavior might indicate a coupling mechanism, a “feedback/feedforward coupling” of the glottal flow and its downstream near field. Such a feedback/feedforward coupling of the shear layer mode with the jet column mode (i.e., the large-scale vortices in the transitional and turbulent region), has been found previously in planar jet experiments. In analogy to these planar jet experiments through static planar orifices (Huang and Hsiao, 1999; Thomas and Chu,

1989; Thomas and Prakash, 1991), it is possible that the free shear layers around the laminar core region and the boundary layers within the glottis may be strongly influenced by an acoustic and hydrodynamic interaction with the roll-up of large-scale vortex rings. Such a mechanism was already discussed by McGowan (1988).

Based on our extracted coherent flow structures, we hypothesize that there could be different mechanisms that could induce left-right asymmetric fluid-structure oscillatory behavior in oscillating physical models. Highly correlated regions within the first few dominant coherent structures were located on opposite sides of the axial jet centerline: The left (right) shear layer dynamics was positively correlated to the dynamics of the right (left) turbulent region. This observation may indicate that pulsatile glottal jets may be dynamically similar to planar jets (Gordeyev and Thomas, 2000; Thomas and Brehob, 1986; Thomas and Prakash, 1991). Spatial correlations in planar jets from symmetric static slit-like orifices explaining jet flapping (Thomas and Chu, 1989; Thomas and Prakash, 1991) were similar to the coherent structures observed in our physical model.

This dynamic similarity would imply that an interaction mechanism exists in pulsatile glottal jets that couples the shear layers around the laminar core region with the roll-up of large-scale vortices in the transition region. Thus, jet flapping in the turbulent region would be coupled with the shear layer dynamics (i.e., the shear layer mode). As explained above, jet flapping could be explained by an antisymmetric staggered array of large-scale vortex structures in the turbulent region. In analogy to static planar jet experiments (Thomas and Chu, 1989; Thomas and Prakash, 1991), we use the term “jet column mode” for this flow structure.

The buildup of this jet column mode in the transitional region could create an acoustic dipole due the vortex generation in the transition region. Following Thomas and Prakash (1991), the pressure waves from this dipole could disturb the shear layer mode (i.e., the von Kármán-like vortex street) close to the glottal discharge plane (feedback mechanism). In turn, disturbances of the shear layers would convect downstream until they would reach the transitional region to affect the vortex generation (feedforward mechanism).

Furthermore, the shear layers could affect the flow separation points in the glottis (feedback mechanism). Hence, the unsteady Coanda effect (i.e., asymmetric flow separation locations) discussed above might be even induced by the feedback interaction of the jet column mode with the shear layer mode. Disturbances in the shear layer might affect the boundary layers in the glottis. Thus, this might help to break the symmetry of the flow in the glottal channel. In turn, this might again influence the jet column mode and the flapping jet. Overall, this might close a feedback/feedforward loop comprising the glottal wall geometry (and the glottal viscoelastic properties), the flow pressure distribution in the glottal channel, and the near field of the glottal jet. Hence, the glottal dynamics would not only be affected by the flow in the glottal channel, but also by the near field of the glottal jet. Future experiments should further explore this hypothesis.

3. Influence of acoustic pressure field on glottal jet structures and dynamics

When the glottis is open, the glottal jet could be affected by the acoustic pressure in the subglottal, upstream system. It has been shown that the coherent structures of acoustically excited jets through static orifices behave different from “natural” unexcited jets (Faghani *et al.*, 1999; Kang *et al.*, 1998; Olsen *et al.*, 2003; Schram *et al.*, 2005; Thomas and Brehob, 1986; Thomas and Chu, 1989; Thomas and Prakash, 1991; Zhao *et al.*, 2001). Confined jets through static orifices can also be affected by the downstream acoustics. Maurel *et al.* (1996) showed that the downstream cavity length facilitated self-sustained jet oscillations (jet flapping) at a frequency determined by the cavity length. Studies on forced jets (e.g., Hsiao and Huang, 1990a, b; Huang and Hsiao, 1999; Peacock *et al.*, 2004) showed that oscillations of the jet orifice walls or acoustic pressure fluctuations at the trailing edge of the nozzle can control the symmetry of the instability mode in the shear layer around the laminar core region. Symmetric and antisymmetric modes could be selected using different oscillation frequencies of the orifice wall or acoustic pressure disturbance at the trailing edge of the nozzle. Moreover, the dynamics of the turbulent jet region can be affected by such acoustic or mechanic excitations of the shear layers in the laminar core region (Reynolds *et al.*, 2003).

C. Reduced-order dynamic models for glottal fluid-structure oscillator

Our study could be regarded as an extension of the work by Shinwari *et al.* (2003). In particular, they used flow visualization to qualitatively study the steady glottal jet flow through static glottal models. They used divergent glottal channel geometries that were either left-right symmetric or oblique (asymmetric). In two schematic drawings they qualitatively sketched the coherent flow structures of the flow near field downstream from the flow separation points. Here, we used PCA to quantify coherent flow patterns found in our self-sustained oscillating physical model. We also propose that in studies with static glottal models, coherent structures in terms of empirical orthogonal eigenfunctions should be extracted with PCA. This approach would allow a quantitative comparison of the flow structures found in experiments with static and self-sustained oscillating models.

More important, relevant mechanisms for the interaction of the glottal near field with the intraglottal flow can be parameterized using coherent flow structures: Reduced-order models can be constructed by “projecting” the governing equations of fluid dynamics onto a dynamically dominant subset of empirical coherent structures. This approach, sometimes called the “empirical Galerkin method” (Lumley and Blossey, 1998; Noack *et al.*, 2004), has been used in classical systems in unsteady fluid dynamics, e.g., cylinder wake flow (Ma and Karniadakis, 2002; Ma *et al.*, 2003; Noack *et al.*, 2003; Sirisup *et al.*, 2004), airfoils (Dowell and Hall, 2001), and two-dimensional unsteady flows in complex geometries (Deane *et al.*, 1991). Therefore, coherent structures could

facilitate the development of reduced-order dynamic models of the near field flow in static, driven, and self-sustained oscillating models of vocal fold vibration.

D. Interpretation of two-dimensional flow field representations

In this paper we presented two-dimensional velocity field measurements of a pulsatile glottal jet. We used measurement planes that intersected the glottal jet in different directions. Therefore, we showed that the glottal jet downstream from a physical model of vocal folds has an inherently three-dimensional structure. We found that the glottal flow near field of a self-sustained oscillating model of vocal folds was essentially three-dimensional and unsteady (time dependent). Caution has to be taken in the interpretations of two-dimensional flow visualization experiments where the time-dependent flow field images represent only two-dimensional slices of the flow. Azimuthal structures with out-of-plane motion and therefore three-dimensional effects were neglected in our study. For regular vocal fold oscillations, traversing measurement planes in future experiments could resolve the dynamics of the glottal jet in different layers. Thus, three-dimensional coherent flow structures could be observed. New developments in high speed DPIV (e.g., tomographic DPIV) would allow to also study glottal jets during nonstationary and irregular vocal fold oscillations. This would be especially important to further understand pathological voice production.

E. Interpretation of seeding density fields

Flow visualization measurements should be interpreted with caution, as the images only represent concentration fields of the seeding particles and the dynamics of the underlying velocity and pressure fields are unknown. If the seeding density is high as in our experiments, only the boundaries between the seeded glottal flow and the unseeded surrounding air could be detected in the near field. Therefore, the classic Kelvin-Helmholtz roll-up of the shear layers resulting in von Kármán-like vortex streets could be visually observed (Winter *et al.* (1987)). Flow visualization might not be able to show staggered vortex arrays in the transitional and turbulent region, as the seeding particles diffuse too fast for any discrete vortical structures to be visible after some distance downstream from the glottis. Nevertheless, Kirby *et al.* (1990) and Sirovich *et al.* (1990) showed that concentration field patterns can still be interpreted in terms of the actual fluid motion. Kirby *et al.* (1990) used computer simulations of steady open jet flows to compare the coherent structures (in terms of EOFs) from the flow velocity and pressure fields with the EOFs from the corresponding mass fraction field. The mass fraction is related to the seeding density and thus the scattered light intensity captured in flow visualization experiments. They showed that principal component analysis of the mass fraction field still yielded qualitatively similar information about the coherent flow patterns.

F. Preliminary studies and directions for future research

Using a physical rubber model of vocal folds, we showed the existence of coherent structures in this artificial glottal jet. In preliminary experiments on excised human and canine larynges we confirmed the existence of a flapping jet structure and of the left-right oscillation of the laminar core. The presented experiments on the jet flow through a physical model of vocal folds appeared to be qualitatively similar to these preliminary observations. Future work with excised larynx preparations using the presented experimental and analytical techniques should explore this behavior further.

V. CONCLUSION

Using methods of flow visualization and digital particle image velocimetry (DPIV), this study measured the near field flow structures immediately downstream of a self-oscillating, physical model of the vocal folds, with a vocal tract attached. A spatio-temporal analysis of the structures was performed using the method of empirical orthogonal eigenfunctions. Some of the observed flow structures included vortex generation, vortex convection, and jet flapping. Jet flapping was observed, presumably due to antisymmetric (staggered) arrays of large-scale vortices in the streamwise direction in the turbulent region. In the transition region of the glottal jet, large-scale vortices were generated, presumably from the growing instability waves in the free shear layer surrounding the laminar core region. It is hoped that this paper will stimulate the development of low-order models, as well as more detailed experiments regarding the interaction of coherent structures with each other and the vibrating vocal folds.

ACKNOWLEDGMENTS

This research was supported by Grant No. R01 DC004688 from the National Institute on Deafness and Other Communication Disorders (NIDCD). The authors also thank Dr. Scott Thomson and Dr. Luc Mongeau for providing the physical rubber model used in this study. The authors also thank the Fusion Science and Technology Center at UCLA for providing the LASER for flow visualization experiments, and Dr. Steven Anderson of LaVision Inc. for assisting with DPIV measurements.

APPENDIX: COHERENT STRUCTURES CONSTRUCTED FROM PRINCIPAL COMPONENT ANALYSIS (PCA)

Principal component analysis (PCA) was used to extract mutually decorrelated (orthogonal) spatio-temporal structures from measured complex spatio-temporal flow velocity fields $\mathbf{V}(\mathbf{x}, t)$, $\mathbf{x} \in \mathbb{R}^2$, $t \in \mathbb{R}$. PCA is also commonly referred to as “empirical orthogonal function analysis,” “biorthogonal decomposition,” “Karhunen-Loève expansion,” “proper orthogonal decomposition,” “principal factor analysis,” “singular value analysis,” and the “singular spectrum analysis” (Berry *et al.*, 1994). Consider the discretized velocity field “movie” $\mathbf{V}(x_k, y_\ell, t_i)$ describing the measured spatio-

temporal velocity field. Here, x_k , $k=1, \dots, N_x$, y_l , $l=1, \dots, N_y$, indicate the spatial coordinates (in left-right and anterior-posterior direction), and t_i , $i=1, \dots, M$ is the time index. We used the ‘‘snapshot method’’ (Sirovich, 1987) to analyze the spatio-temporal flow velocity fields obtained from flow visualization and digital particle image velocimetry (DPIV). The covariance matrix \mathbf{K} measures linear correlations of the velocity field $\mathbf{V}(x_k, y_l, t_i)$ by comparing on average the behavior of the measured field variable at all different measured time instances (snapshots) t_i :

$$K(t_k, t_\ell) = \frac{1}{N} \sum_{i=1}^N \mathbf{V}(\mathbf{x}_i, t_k) \cdot \mathbf{V}(\mathbf{x}_i, t_\ell) = \langle \mathbf{V}(\mathbf{x}_i, t_k) \cdot \mathbf{V}(\mathbf{x}_i, t_\ell) \rangle_{\mathbf{x}_i} \quad (\text{A1})$$

with $k, l=1, \dots, M$ and $N=N_x \cdot N_y$. The symbol $\langle \cdot \rangle_{\mathbf{x}_i}$ denotes a spatial average. We do not exclude the spatial or the temporal mean of the velocity field $\mathbf{V}(x_k, y_l, t_i)$ before calculating the covariance matrix, as this would introduce artificial correlations to the measured spatio-temporal field (Aubry *et al.*, 1991). The covariance matrix is a real, symmetric and positive semidefinite matrix. Therefore, it can be diagonalized and has real and non-negative eigenvalues:

$$\mathbf{K} \varphi_\ell = \lambda_\ell \varphi_\ell. \quad (\text{A2})$$

The normalized eigenvectors $\varphi_l(t)$, $l=1, \dots, M$, correspond to the empirical orthogonal functions (EOFs). Sometimes they are called ‘‘chronos’’ to indicate their chronological meaning (Aubry *et al.*, 1991). The eigenvalues λ_l are the ‘‘weights’’ of the normalized EOFs. They reflect the contributions of the EOFs to the overall variance. The eigenfunctions define a set of orthogonal directions in the 2M-dimensional state space $\{\mathbf{V}(t_i)\}$, and the eigenvalues are the variances of the measured velocity field movie $\mathbf{V}(\mathbf{x}, t)$ projected onto the EOF directions. The eigenfunctions are sorted with respect to their variances.

The total variance E_{tot} (total kinetic energy (Aubry *et al.*, 1991)) of the set of states $\{\mathbf{V}(\mathbf{x}_k, t_i)\}$ is given by the sum of the eigenvalues λ_j :

$$E_{\text{tot}} = \sum_{\ell=1}^N \lambda_\ell = \langle \mathbf{V}(\mathbf{x}_k, t_i) \cdot \mathbf{V}(\mathbf{x}_k, t_i) \rangle_{\mathbf{x}_k, t_i}, \quad (\text{A3})$$

where λ_i is the variance of one single spatio-temporal structure. As the EOFs φ_l establish an ortho-normal system ($\langle \varphi_k(t) \varphi_l(t) \rangle_t = \delta_{kl}$), the ‘‘movie’’ $\mathbf{V}(\mathbf{x}_k, t_i)$ can be written as a linear superposition:

$$\mathbf{V}(\mathbf{x}_k, t_i) = \sum_{\ell=1}^M \Psi_\ell(\mathbf{x}_k) \varphi_\ell(t_i). \quad (\text{A4})$$

The spatial expansion coefficients $\Psi_l(\mathbf{x}_i)$ are determined by the projection of the movie onto the eigenfunctions:

$$\Psi_\ell(\mathbf{x}_i) = \sum_{k=1}^M \mathbf{V}(\mathbf{x}_i, t_k) \varphi_\ell(t_k) = \langle \mathbf{V}(\mathbf{x}_i, t) \varphi_\ell(t) \rangle_t. \quad (\text{A5})$$

Sometimes, the spatial coefficients are called ‘‘topos,’’ as they express the topological importance of the associated chronos (Aubry *et al.*, 1991). They also can be regarded as

spatial eigenfunctions corresponding to their associated chronos that can be thought of as temporal eigenfunctions. Finally, the velocity field movie can be decomposed as

$$\mathbf{V}(\mathbf{x}_k, t_i) = \sum_{\ell=1}^M \sigma_\ell \psi_\ell(\mathbf{x}_k) \varphi_\ell(t_i) \quad (\text{A6})$$

with $\psi_l(\mathbf{x}_k)$ defined as

$$\Psi_\ell(\mathbf{x}_k) = \sigma_\ell \psi_\ell(\mathbf{x}_k), \quad (\text{A7})$$

$$\sigma_\ell = \sqrt{\lambda_\ell}. \quad (\text{A8})$$

Here, we used the following:

$$\langle \Psi_k(\mathbf{x}_i) \cdot \Psi_\ell(\mathbf{x}_i) \rangle_{\mathbf{x}_i} = \lambda_k \delta_{k\ell} = \sigma_k \sigma_\ell \langle \psi_k(\mathbf{x}_i) \cdot \psi_\ell(\mathbf{x}_i) \rangle_{\mathbf{x}_i}. \quad (\text{A9})$$

Thus, the normalized topos $\psi_l(\mathbf{x}_i)$ also establish an ortho-normal system of empirical spatial eigenfunctions.

Another useful property of the topos $\psi_k(\mathbf{x}_i)$ and the weights (total kinetic energy) λ_k can be derived using the general relationship between the variance of a function $\mathbf{f}(x)$ and its first two moments:

$$\text{Var}_x(\mathbf{f}(x)) = \langle (\mathbf{f} - \langle \mathbf{f} \rangle_x)^2 \rangle_x = \langle \mathbf{f}^2 \rangle_x - \langle \mathbf{f} \rangle_x^2. \quad (\text{A10})$$

Therefore, we can write

$$\text{Var}_x(\Psi_k(\mathbf{x})) = \langle \Psi_k^2(\mathbf{x}) \rangle_x - \langle \Psi_k(\mathbf{x}) \rangle_x^2. \quad (\text{A11})$$

Together with $\langle \Psi_k(\mathbf{x}) \cdot \Psi_l(\mathbf{x}) \rangle_x = \lambda_k \delta_{kl}$, we arrive at

$$\lambda_k = \langle \Psi_k(\mathbf{x}) \rangle_x^2 + \text{Var}_x(\Psi_k(\mathbf{x})). \quad (\text{A12})$$

With $E_{\text{tot}} = \langle \mathbf{V}(\mathbf{x}_k, t_i) \cdot \mathbf{V}(\mathbf{x}_k, t_i) \rangle_{\mathbf{x}_k, t_i} = \sum_{k=1}^M \lambda_k$ for the total kinetic energy, we can further write

$$E_{\text{tot}} = \sum_{k=1}^M \langle \Psi_k(\mathbf{x}) \rangle_x^2 + \sum_{k=1}^M \text{Var}_x(\Psi_k(\mathbf{x})) = E_{\text{mean}} + E_{\text{fluct}} \quad (\text{A13})$$

Thus, the contribution λ_k/E_{tot} of each EOF $\varphi_k(t)$ (chronos) to the total variance (the total kinetic energy) of the spatio-temporal velocity field movie $\mathbf{V}(\mathbf{x}, t)$ can be separated into the contribution to the total mean kinetic energy $\langle \Psi_k(\mathbf{x}) \rangle_x^2/E_{\text{mean}}$ and to the total fluctuating kinetic energy $\text{Var}_x(\Psi_k(\mathbf{x}))/E_{\text{fluct}}$.

$$\sum_{k=1}^M \frac{\lambda_k}{E_{\text{tot}}} = \frac{E_{\text{mean}}}{E_{\text{tot}}} \sum_{k=1}^M \langle \Psi_k(\mathbf{x}) \rangle_x^2 / E_{\text{mean}} + \frac{E_{\text{fluct}}}{E_{\text{tot}}} \sum_{k=1}^M \text{Var}_x(\Psi_k(\mathbf{x})) / E_{\text{fluct}}. \quad (\text{A14})$$

- Adrian, R. J. (1991). ‘‘Particle-imaging techniques for experimental fluid mechanics,’’ *Annu. Rev. Fluid Mech.* **23**, 261–304.
- Aubry, N., Guyonnet, R., and Lima, R. (1991). ‘‘Spatiotemporal analysis of complex signals: Theory and application,’’ *J. Stat. Phys.* **64**, 683–739.
- Barney, A., Shadle, C. H., and Davies, P. O. A. L. (1999). ‘‘Fluid flow in a dynamic mechanical model of the vocal folds and tract. I. Measurements and theory,’’ *J. Acoust. Soc. Am.* **105**, 444–455.
- Berkooz, G., Holmes, P., and Lumley, J. L. (1993). ‘‘The proper orthogonal decomposition in the analysis of turbulent flows,’’ *Annu. Rev. Fluid Mech.* **25**, 539–575.

- Berry, D. A., Herzel, H., Titze, I. R., and Krischer, K. (1994). "Interpretation of biomechanical simulations of normal and chaotic vocal fold oscillations with empirical eigenfunctions," *J. Acoust. Soc. Am.* **95**, 3595–3604.
- Coanda, H. (1936). "Device for deflecting a stream of elastic fluid projected into an elastic fluid," U.S. Patent No. 2,052,869, Sept. 1.
- Deane, A. E., Kevrekidis, I. G., Karniadakis, G. E., and Orszag, S. A. (1991). "Low-dimensional models for complex geometry flows: Application to grooved channels and circular cylinders," *Phys. Fluids* **3**, 2337–2354.
- Dowell, E. H., and Hall, K. C. (2001). "Modeling of fluid-structure interaction," *Annu. Rev. Fluid Mech.* **33**, 445–490.
- Erath, B. D. (2005). *An Experimental Investigation of Velocity Fields in Divergent Glottal Models of the Human Vocal Tract*, Master's thesis, Purdue University.
- Erath, B. D., and Plesniak, M. W. (2006a). "An investigation of bimodal jet trajectory in flow through scaled models of the human vocal tract," *Exp. Fluids* **40**, 683–696.
- Erath, B. D., and Plesniak, M. W. (2006b). "An investigation of jet trajectory in flow through scaled vocal fold models with asymmetric glottal passages," *Exp. Fluids* **41**, 735–748.
- Erath, B. D., and Plesniak, M. W. (2006c). "The occurrence of the Coanda effect in pulsatile flow through static models of the human vocal folds," *J. Acoust. Soc. Am.* **120**, 1000–1011.
- Faghani, D., Sévrain, A., and Boisson, H.-C. (1999). "Physical eddy recovery through bi-orthogonal decomposition in an acoustically forced plane jet," *Flow, Turbul. Combust.* **62**, 69–88.
- Fant, G. (1960). *Acoustic Theory of Speech Production* (Hague Mouton, The Netherlands).
- Glegg, S. A. L., and Devenport, W. J. (2001). "Proper orthogonal decomposition of turbulent flows for aeroacoustic and hydroacoustic applications," *J. Sound Vib.* **239**, 767–784.
- Gordeyev, S. V., and Thomas, F. O. (2000). "Coherent structure in the turbulent planar jet. Part 1. Extraction of proper orthogonal decomposition eigenmodes and their self-similarity," *J. Fluid Mech.* **414**, 145–194.
- Gutmark, E. J., and Grinstein, F. F. (1999). "Flow control with noncircular jets," *Annu. Rev. Fluid Mech.* **31**, 239–272.
- Hirschberg, A. (1992). "Some fluid dynamic aspects of speech," *Bulletin de la Communication Parlée* **2**, 7–30.
- Hirschberg, A., Pelorson, X., Hofmans, G., van Hassel, R. R., and Wijnands, A. P. J. (1996). "Starting transient of the flow through an in-vitro model of the vocal folds," in *Vocal Fold Physiology: Controlling Complexity and Chaos*, edited by P. J. Davies, and P. J. Fletcher (Singular, San Diego), pp. 31–46.
- Hofmans, G. C. J. (1998). *Vortex Sound in Confined Flows*, Ph.D. thesis, Technische Universiteit Eindhoven, The Netherlands.
- Hofmans, G. C. J., Boot, R. J. J., Durrieu, P. P. J. M., Auregan, Y., and Hirschberg, A. (2001a). "Aeroacoustic response of a slit-shaped diaphragm in a pipe at low Helmholtz number, 1: Quasi-steady results," *J. Sound Vib.* **244**, 35–56.
- Hofmans, G. C. J., Groot, G., Ranucci, M., Graziani, G., and Hirschberg, A. (2003). "Unsteady flow through in-vitro models of the glottis," *J. Acoust. Soc. Am.* **113**, 1658–1675.
- Hofmans, G. C. J., Ranucci, M., Ajello, G., Auregan, Y., and Hirschberg, A. (2001b). "Aeroacoustic response of a slit-shaped diaphragm in a pipe at low Helmholtz number, 2: Unsteady results," *J. Sound Vib.* **244**, 57–77.
- Holmes, J. D., Lumley, J. L., and Berkooz, G. (1996). *Turbulence, Coherent Structures and Symmetry* (Cambridge University Press, Cambridge, UK).
- Holmes, P. J., Lumley, J. L., Berkooz, G., Mattingly, J. C., and Wittenberg, R. W. (1997). "Low-dimensional models of coherent structures in turbulence," *Phys. Rep.* **287**, 337–384.
- Howe, M. S., and McGowan, R. S. (2005). "Aeroacoustics of [s]," *Proc. R. Soc. London, Ser. A* **461**, 1005–1028.
- Hsiao, F.-B., and Huang, J.-M. (1990a). "Near-field flow structures and sideband instabilities of an initially laminar plane jet," *Exp. Fluids* **9**, 2–12.
- Hsiao, F.-B., and Huang, J.-M. (1990b). "On the evolution of instabilities in the near field of a plane jet," *Phys. Fluids A* **2**, 400–412.
- Huang, J.-M., and Hsiao, F.-B. (1999). "On the mode development in the developing region of a plane jet," *Phys. Fluids* **11**, 1847–1857.
- Kang, Y., Karagozian, A. R., and Smith, O. I. (1998). "Transport enhancement in acoustically excited cavity flows, part 1: Nonreactive flow diagnostics," *AIAA J.* **36**, 1562–1567.
- Kirby, M., Boris, J., and Sirovich, L. (1990). "An eigenfunction analysis of axisymmetric jet flow," *J. Comput. Phys.* **90**, 98–122.
- Krane, M. H. (2005). "Aeroacoustic production of low-frequency unvoiced speech sounds," *J. Acoust. Soc. Am.* **118**, 410–427.
- Kucinschi, B. R., Scherer, R. C., DeWitt, K. J., and Ng, T. T. M. (2006). "Flow visualization and acoustic consequences of the air moving through a static model of the human larynx," *J. Biomater. Appl.* **128**, 380–390.
- Leonardy, J., Kaiser, F., Belić, M. R., and Hess, O. (1996). "Running transverse waves in optical phase conjugation," *Phys. Rev. A* **53**, 4519–4527.
- Lumley, J., and Blossey, P. (1998). "Control of turbulence," *Annu. Rev. Fluid Mech.* **30**, 311–327.
- Lumley, J. L. (1967). "The structure of inhomogeneous turbulent flows," in *Atmospheric Turbulence and Radio Wave Propagation*, edited by A. M. Yaglom, and V. I. Tatarski (Nauka, Moscow), pp. 166–178.
- Ma, X., and Karniadakis, G. E. (2002). "A low-dimensional model for simulating three-dimensional cylinder flow," *J. Fluid Mech.* **458**, 181–190.
- Ma, X., Karniadakis, G. E., Park, H., and Gharib, M. (2003). "DPIV-driven flow simulation: A new computational paradigm," *Proc. R. Soc. London, Ser. A* **459**, 547–565.
- Maurel, A., Ern, P., Zielinska, B. J. A., and Wesfreid, J. E. (1996). "Experimental study of self-sustained oscillations in a confined jet," *Phys. Rev. E* **54**, 3643–3651.
- McGowan, R. S. (1988). "An aeroacoustic approach to phonation," *J. Acoust. Soc. Am.* **83**, 696–704.
- McGowan, R. S., and Howe, M. S. (2006). "Compact Green's functions extend the acoustic theory of speech production," *J. Phonetics* (in press).
- Mergell, P., and Herzel, H. (1997). "Modelling biphonation—the role of the vocal tract," *Speech Commun.* **22**, 141–154.
- Mergell, P., Herzel, H., and Titze, I. R. (2000). "Irregular vocal fold vibration—High-speed observation and modeling," *J. Acoust. Soc. Am.* **108**, 2996–3002.
- Neubauer, J., Mergell, P., Eysholdt, U., and Herzel, H. (2001). "Spatio-temporal analysis of irregular vocal fold oscillations: Biphonation due to desynchronization of spatial modes," *J. Acoust. Soc. Am.* **110**, 3179–3192.
- Noack, B. R., Afanasiev, K., Morzynski, M., Tadmor, G., and Thiele, F. (2003). "A hierarchy of low-dimensional models for the transient and post-transient cylinder wake," *J. Fluid Mech.* **497**, 335–363.
- Noack, B. R., Tadmor, G., and Morzyński, M. (2004). "Low-dimensional models for feedback flow control. Part I: Empirical Galerkin models," in *Second AIAA Flow Control Conference*, Portland, OR, p. 2408.
- Olsen, J. F., Rajagopalan, S., and Antonia, R. A. (2003). "Jet column modes in both a plane jet and a passively modified plane jet subject to acoustic excitation," *Exp. Fluids* **35**, 278–287.
- Panitz, T., and Wasan, D. T. (1972). "Flow attachment to solid surfaces: The Coanda effect," *AIChE J.* **18**, 51–57.
- Peacock, T., Bradley, E., Hertzberg, J., and Lee, Y.-C. (2004). "Forcing a planar jet flow using MEMS," *Exp. Fluids* **37**, 22–28.
- Pelorson, X., Hirschberg, A., van Hassel, R. R., and Wijnands, A. P. J. (1994). "Theoretical and experimental study of quasisteady-flow separation within the glottis during phonation. Application to a modified two-mass model," *J. Acoust. Soc. Am.* **96**, 3416–3431.
- Reynolds, W. C., Parekh, D. E., Juvet, P. J. D., and Lee, M. J. D. (2003). "Bifurcating and blooming jets," *Annu. Rev. Fluid Mech.* **35**, 295–315.
- Scherer, R. C., Shinwari, D., Witt, K. J. D., Zhang, C., Kucinschi, B. R., and Afjeh, A. A. (2001). "Intraglottal pressure profiles for a symmetric and oblique glottis with a divergence angle of 10 degrees," *J. Acoust. Soc. Am.* **109**, 1616–1630.
- Schram, C., Taubnitz, S., Anthoine, J., and Hirschberg, A. (2005). "Theoretical/empirical prediction and measurement of the sound produced by vortex pairing in a low Mach number jet," *J. Sound Vib.* **281**, 171–187.
- Shadle, C. H., Barney, A., and Davies, P. O. A. L. (1999). "Fluid flow in a dynamic mechanical model of the vocal folds and tract: II. Implications for speech production studies," *J. Acoust. Soc. Am.* **105**, 456–466.
- Shinwari, D., Scherer, R. C., DeWitt, K. J., and Afjeh, A. A. (2003). "Flow visualization and pressure distributions in a model of the glottis with a symmetric and oblique divergent angle of 10 degrees," *J. Acoust. Soc. Am.* **113**, 487–497.
- Sirisup, S., Karniadakis, G. E., Yang, Y., and Rockwell, D. (2004). "Wave-structure interaction: Simulation driven by quantitative imaging," *Proc. R. Soc. London, Ser. A* **460**, 729–755.
- Sirovich, L. (1987). "Turbulence and the dynamics of coherent structures. I—Coherent structures. II—Symmetries and transformations. III—Dynamics and scaling," *Q. Appl. Math.* **45**, 561–571.
- Sirovich, L., Kirby, M., and Winter, M. (1990). "An eigenfunction approach

- to large scale transitional structures in jet flow," *Phys. Fluids A* **2**, 127–136.
- Steinecke, I., and Herzel, H. (1995). "Bifurcations in an asymmetric vocal fold model," *J. Acoust. Soc. Am.* **97**, 1571–1578.
- Stevens, K. N. (1998). *Acoustic Phonetics* (MIT Press, Cambridge, MA).
- Theodorsen, T. (1952). "Mechanism of turbulence," in *Second Midwestern Conference on Fluid Mechanics* (Ohio State University, Columbus, OH).
- Thomas, F. O., and Brehob, E. G. (1986). "An investigation of large-scale structure in the similarity region of a two-dimensional turbulent jet," *Phys. Fluids* **29**, 1788–1795.
- Thomas, F. O., and Chu, H. C. (1989). "An experimental investigation of the transition of a planar jet: Subharmonic suppression and upstream feedback," *Phys. Fluids A* **1**, 1566–1587.
- Thomas, F. O., and Prakash, K. M. K. (1991). "An experimental investigation of the natural transition of an untuned planar jet," *Phys. Fluids A* **3**, 90–105.
- Thomson, S. L. (2004). *Fluid-Structure Interactions Within the Human Larynx*, Ph.D. thesis, Purdue University, West Lafayette, Indiana.
- Thomson, S. L., Mongeau, L., and Frankel, S. H. (2005). "Aerodynamic transfer of energy to the vocal folds," *J. Acoust. Soc. Am.* **118**, 1689–1700.
- Thomson, S. L., Mongeau, L., Frankel, S. H., Neubauer, J., and Berry, D. A. (2004). "Self-oscillating laryngeal models for vocal fold research," in *Proceedings of the Eighth International Conference on Flow-Induced Vibrations* (Ecole Polytechnique, Paris, France), Vol. 2, pp. 137–142.
- Townsend, A. A. (1976). *The Structure of Turbulent Shear Flow*, 2nd ed. (Cambridge University Press, Cambridge, UK).
- Triep, M., Brücker, C., and Schröder, W. (2005). "High-speed PIV measurements of the flow downstream of a dynamic mechanical model of the human vocal folds," *Exp. Fluids* **39**, 232–245.
- Vilain, C., Pelorson, X., and Thomas, D. (1999). "Effects of an induced asymmetry on the flow through the glottis in relation to voice pathology," in *Proc. 1st Int. Workshop on Models and Analysis of Vocal Emission for Biomedical Applications (MAVEBA)*, edited by A. Manfredi (University of Florence, Italy).
- Westerweel, J. (1997). "Fundamentals of digital particle image velocimetry," *Meas. Sci. Technol.* **8**, 1379–1392.
- Winter, M., Lam, J. K., and Long, M. B. (1987). "Techniques for high-speed digital imaging of gas concentrations in turbulent flows," *Exp. Fluids* **5**, 177–183.
- Zhang, Z., Mongeau, L., and Frankel, S. H. (2002). "Experimental verification of the quasi-steady approximation for aerodynamic sound generation by pulsating jets in tubes," *J. Acoust. Soc. Am.* **112**, 1652–1663.
- Zhang, Z., Neubauer, J., and Berry, D. A. (2006). "The influence of subglottal acoustics on laboratory models of phonation," *J. Acoust. Soc. Am.* **120**, 1558–1569.
- Zhao, W., Frankel, S. H., and Mongeau, L. (2001). "Large eddy simulations of sound radiation from subsonic turbulent jets," *AIAA J.* **39**, 1469–1477.

Influence of acoustic loading on an effective single mass model of the vocal folds

Matías Zañartu^{a)}

School of Electrical and Computer Engineering and Ray W. Herrick Laboratories, Purdue University,
140 S. Intramural Drive, West Lafayette, Indiana 47907

Luc Mongeau^{b)}

School of Mechanical Engineering and Ray W. Herrick Laboratories, Purdue University,
West Lafayette, Indiana 47907

George R. Wodicka

Weldon School of Biomedical Engineering and School of Electrical and Computer Engineering,
Purdue University, West Lafayette, Indiana 47907

(Received 10 July 2006; revised 8 November 2006; accepted 20 November 2006)

Three-way interactions between sound waves in the subglottal and supraglottal tracts, the vibrations of the vocal folds, and laryngeal flow were investigated. Sound wave propagation was modeled using a wave reflection analog method. An effective single-degree-of-freedom model was designed to model vocal-fold vibrations. The effects of orifice geometry changes on the flow were considered by enforcing a time-varying discharge coefficient within a Bernoulli flow model. The resulting single-degree-of-freedom model allowed for energy transfer from flow to structural vibrations, an essential feature usually incorporated through the use of higher order models. The relative importance of acoustic loading and the time-varying flow resistance for fluid-structure energy transfer was established for various configurations. The results showed that acoustic loading contributed more significantly to the net energy transfer than the time-varying flow resistance, especially for less inertive supraglottal loads. The contribution of supraglottal loading was found to be more significant than that of subglottal loading. Subglottal loading was found to reduce the net energy transfer to the vocal-fold oscillation during phonation, balancing the effects of the supraglottal load. © 2007 Acoustical Society of America. [DOI: 10.1121/1.2409491]

PACS number(s): 43.70.Bk, 43.70.Aj [AL]

Pages: 1119–1129

I. INTRODUCTION

Mathematical models of human voice production may be used to study normal and pathologic phonation, to predict the effects of phonosurgery, or to aid voice therapy. Source-resonator coupling, produced by fluid-sound interactions at the glottis, is a key factor in the production of self-oscillations. Fluid-sound interactions affect voice efficiency, color the spectra of the voice source, and modify the stability of the dynamic voice production system, resulting in a change in oscillation frequency and onset pressure. Control of efficiency and spectral content can be used in singing (Titze, 2004). The instabilities produced by the flow-sound interaction could help to explain irregular phonation (Mergell and Herzel, 1997). The effects of subglottal tract loading may be critical, especially in studies involving excised larynx and synthetic models of the vocal folds, where the subglottal tract used to supply the flow may play a comparatively large role (Austin and Titze, 1997; Zhang *et al.*, 2006).

A. Mathematical models of voice production

Early models of vocal-fold vibrations were based on myoelastic-aerodynamic theory (Van den Berg, 1958). In the single-mass model of Flanagan and Landgraf (1968), the absence of the vocal tract made it impossible to obtain self-sustained oscillations. Earlier excised larynx experiments showed that self-sustained oscillation can be obtained in the absence of a vocal tract (Van den Berg and Tan, 1959). The effects introduced by the delay between the upper and lower portion of the vocal folds during oscillation were subsequently incorporated to create the well-known two-mass model (Ishizaka and Flanagan, 1972). This model allowed for acoustic feedback and self-sustained oscillations with or without the presence of acoustic loading. Multimass models have been developed to better account for the asymmetry between the lower and upper parts of the folds, and the presence of a mucosal wave. The “body-cover model” (Titze and Story, 1997) allowed the effects of acoustic loading on the volumetric flow rate to be considered using a wave reflection analog approach (Kelly and Lochbaum, 1962; Liljencrants, 1985; Rahim, 1994; Story, 1995). The flow model used in these investigations was shown to be stable and able to handle time-varying flow and irregular geometries (Titze, 1984). Fulcher *et al.* (2006) designed a so-called “effective one-mass model,” i.e., a single-mass model of the vocal folds

^{a)}Author to whom correspondence should be addressed. Electronic mail: mzanartu@purdue.edu

^{b)}Present address: Department of Mechanical Engineering, McGill University, 817 Sherbrooke Street West, Montreal, Quebec, Canada, H3A 2K6.

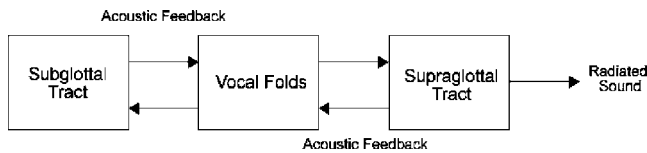


FIG. 1. Diagram of an interactive voice production system.

excited by a negative Coulomb damping force. The negative Coulomb damping force was assumed to be equivalent to the aerodynamic forces on the vocal folds, thus keeping the driving force in phase with tissue velocity. The pressure force for the inward, closing phase of the cycle was smaller by a factor of two than that for the outward opening phase. The model exhibited self-sustained oscillations without the need for acoustic loading. This model was conceptually accurate, but did not include a quantitative flow model, acoustic loading, or collision effects.

High-order models with thousands of degree of freedom (e.g., finite-element models) have provided additional insight on phonation mechanisms that are not captured by low-order models. The modal response of simplified vocal-fold models (Berry and Titze, 1996) and fluid-structure interactions (Thompson *et al.*, 2005) have been studied using the finite-elements method. Such models often use an incompressible flow formulation, and ignore acoustic loading effects. Simplified, unrealistic boundary conditions such as constant pressure or constant velocity are typically imposed at the inflow and outflow boundaries of the computational domain, ignoring the effects of sound waves in the subglottal and supraglottal spaces on transglottal pressures.

B. Previous observations of acoustic coupling in phonation

A schematic illustrating the acoustic coupling problem in voice production is shown in Fig. 1. The interactions between fluid flow through the glottis and radiated sound waves are regulated by the impedances of the glottis and the vocal tract (Rothenberg, 1981; Fant and Lin, 1987; Titze and Story, 1997). The impedance of the supraglottal tract has been argued to be primarily governed by the impedance of the lower tract, i.e., the epilarynx. Narrow entry sections in the vocal tract result in a high impedance, comparable with the impedance of the glottis, which favors flow-sound interactions, (Titze and Story, 1997). It has been shown that under these conditions, flow-sound interactions affect the volumetric flow rate waveform. Skewing, ripple or depressions in the open phase, as well as short-term variations of formant frequencies and bandwidths, were observed in cases with strong interactions (Rothenberg, 1981; Fant and Lin, 1987). Phonation is known to be facilitated by the combined effects of the time-varying geometry of the orifice and a delayed vocal-tract response. The effective damping of vocal-fold vibration decreases with vocal-tract inertance (positively reactive) and increases with vocal-tract resistance. In addition, a net compliant vocal-tract load (negatively reactive) tends to squelch oscillation (Titze, 1988).

Subglottal tract coupling effects are less well understood. Experimental studies using excised larynges (Austin

and Titze, 1997) and physical rubber models (Zhang *et al.*, 2006) indicate that a subglottal tract length much longer than the physiological length is required to obtain self-sustained oscillations. Different subglottal tract configurations were found to affect the phonation threshold pressure. Strong interactions between laryngeal dynamics and subglottal acoustics were observed. The results of these studies show the importance of including the subglottal tract in laryngeal dynamics.

C. Research objectives

In the present study, the factors that control the coupling between the vibration of the vocal folds, the sound field in the subglottal and supraglottal tracts, and the airflow through the larynx were investigated. The goal was to determine how significant acoustic loading effects were relative to the time-varying flow resistance of the glottis during normal phonation. The individual contributions of the vocal tract and the subglottal tract to the overall acoustic load impedance were identified. In order to achieve these goals, a dynamic model of phonation that included the effects of the sound field in the vocal tract and the supraglottal tract for several configurations was developed.

II. EFFECTIVE SINGLE-DEGREE-OF-FREEDOM MODEL

A. Model description

An enhanced version of the “effective one-mass model” of Fulcher *et al.* (2006) was used. The driving force associated with the negative Coulomb damping was defined based on the aerodynamic forces acting on the vocal folds. Fluid-structure interactions, fluid-sound interactions, and collision effects were included. Figure 2(a) shows schematics of the vocal-fold model. The motion of the folds was assumed to be bilaterally symmetric. The equation of motion for each fold is given by

$$m\ddot{y} + b\dot{y} + k(y - y_o) = F_p + F_H, \quad (1)$$

where m is the body mass of one vocal fold, y is the displacement of the mass at the glottal end, y_o is the equilibrium position of the mass without the action of external forces, b is the viscous damping constant, and k is the spring constant. The terms F_p and F_H are fluid pressure and impact forces, as described in detail in the following sections.

B. Pressure force

The net medial-lateral fluid pressure force, F_p , applied to the walls of the vocal folds is the main driving force for the oscillator. The wall pressure is affected by fluid-sound interactions, which cause instantaneous changes in transglottal pressures, and the air flow. The flow was assumed to be inviscid, irrotational, and approximately incompressible. The “quasi-steady approximation” was made, i.e., the time-varying flow was treated as a sequence of stationary flows for similar geometries and boundary conditions at each time step. Under these conditions, Bernoulli’s equation is valid along a streamline in the region from the subglottal to the

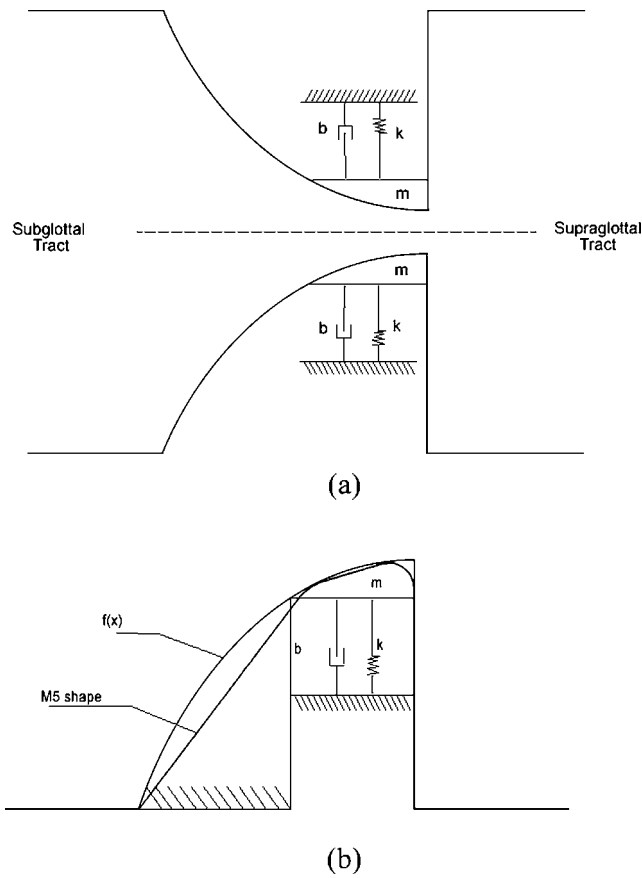


FIG. 2. Basic diagram of the single-degree-of-freedom. (a) Symmetric representation. (b) Comparison with M5 model profile (Scherer *et al.*, 2001).

glottal opening. The flow is assumed to be detached from the wall at the orifice discharge to form a jet. Aerodynamic effects after/at the glottal opening (pressure recovery, dynamic head loss, momentum diffusion, etc.) are included through the use of time-varying orifice discharge coefficient (herein referred to as ODC). The wave reflection analog supplies the subglottal and supraglottal acoustic pressures used in the calculations. From conservation of mass, the relation between subglottal and glottal flow velocities is

$$A_s u_{up} = A_g(x) u_{cl}(x), \quad (2)$$

where A_s and u_{up} are subglottal cross-sectional area and upstream (subglottal) pressure. $A_g(x)$ and $u_{cl}(x)$ are functions that describe cross-sectional area and centerline velocity along the depth of the folds (or length in the flow direction). For simplicity, the function that describes the glottal area $A_g(x)$ is assumed to be quadratic. This area is obtained using a shape function $f(x)$, such that $A_g(x)$ is equal to $f(x)$ times the length of the folds. A 2D comparison between this geometry and the M5 geometry of Scherer *et al.* (2001) is shown in Fig. 2(b). To relate pressure and velocity, Bernoulli's equation was used along the centerline (or symmetry line) between the subglottal section [$x=d$ in Fig. 3(a)] and the opening of the vocal folds [$x=0$ in Fig. 3(a)]. The pressure distribution and centerline velocity along the depth of the folds, $p_{cl}(x)$ and $u_{cl}(x)$, are related through

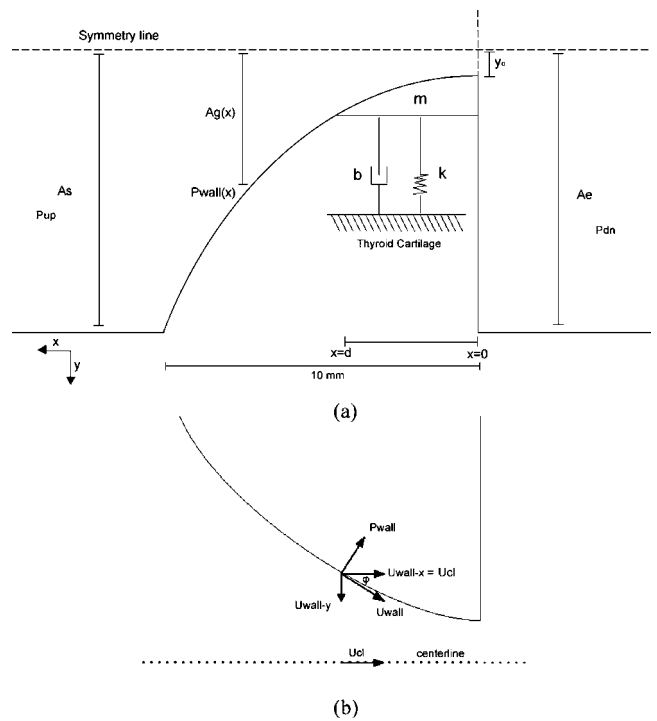


FIG. 3. Details considered to compute the pressure force. (a) Areas and pressures in the glottis. (b) Pressure and velocity along the wall.

$$\frac{1}{\rho} p_{cl}(d) + \frac{1}{2} u_{cl}^2(d) = \frac{1}{\rho} p_{cl}(0) + \frac{1}{2} u_{cl}^2(0), \quad (3)$$

where ρ is the air density. The total pressure at the different locations is known to be the sum of static and dynamic pressures (Mongeau *et al.*, 1997; Zhang *et al.*, 2002; Thompson *et al.*, 2005; Park and Mongeau, 2007). Thus, assuming the total head at $x=d$ is equal to the subglottal head, and that the centerline pressure at $x=0$ is equal to the supraglottal value, Eq. (3) can be rewritten as

$$\frac{1}{\rho} (p_{up} + p'_{up}) + \frac{1}{2} u_{up}^2 = \frac{1}{\rho} (p_{dn} + p'_{dn}) + \frac{1}{2} u_{cl}^2(0), \quad (4)$$

where p_{up} and p'_{up} are the upstream steady and upstream acoustic pressures, u_{up} is the upstream flow velocity, and p_{dn} and p'_{dn} are the downstream steady and downstream acoustic pressures. Using Eq. (4) to relate centerline velocities between the orifice and the subglottal section, and defining β as the area ratio, then

$$u_{up} = u_{cl} \frac{A_g}{A_s} = u_{cl} \beta, \quad (5)$$

where for simplicity $u_{cl} = u_{cl}(0)$ and $A_g = A_g(0)$. Note that all equations up to this point correspond to ideal flow. Thus, substitution of Eq. (5) in Eq. (4) yields the ideal velocity at the glottal opening,

$$u_{cl(ideal)} = \sqrt{\frac{2\Delta p + (p'_{up} - p'_{dn})}{\rho(1 - \beta^2)}}, \quad (6)$$

where Δp is the difference between the static pressure upstream and downstream. Since the volumetric flow rate Q

must be constant across the system, it can be computed at the glottal opening as

$$Q = u_{cl(ideal)} A_g. \quad (7)$$

Aerodynamic effects that occur after/at the glottal opening, such as pressure recovery, dynamic head loss, and momentum diffusion may be characterized through the use of an empirical ODC (Zhang *et al.*, 2002; Park and Mongeau, 2007). The actual volumetric flow rate is

$$Q = c_d(t) u_{cl} A_g, \quad (8)$$

where $c_d(t)$ is the time-varying ODC. Using Eq. (6), the flow velocity at the opening, from Eq. (7) is

$$u_{cl(actual)} = c_d(t) \sqrt{\frac{2\Delta p + (p'_{up} - p'_{dn})}{\rho(1 - \beta^2)}}. \quad (9)$$

This last expression was used with Eqs. (5) and (2) to obtain corrected expressions for the upstream flow velocity, u_{up} , and center velocity along the flow direction, $u_{cl}(x)$. Bernoulli's flow equation between the subglottal section and any point in the glottis along the centerline yields the centerline pressure distribution as a function of the position in the glottis,

$$p_{cl}(x) = p_{up} + p'_{up} + \frac{\rho}{2}(u_{up}^2 - u_{cl}^2(x)). \quad (10)$$

The axial flow velocity is approximately constant along x , which implies that the x component of the flow velocity near the wall is the same as along the centerline, as illustrated in Fig. 3(b). The relation between centerline velocity (u_{cl}) and the wall velocity (u_{wall}) can be obtained from the wall geometry, as shown in Fig. 3(b), yielding

$$u_{cl}(x) = u_{wall}(x) \cos \varphi, \quad (11)$$

$$\tan \varphi = \frac{d}{dx}(f(x)) = f'(x), \quad (12)$$

$$u_{wall}(x) = \frac{u_{cl}(x)}{\cos(\arctan(f'(x)))}. \quad (13)$$

Using Bernoulli's flow equation again for any pair of points in the glottis, the wall pressure over the folds as function of position, $p_{wall}(x)$, is

$$p_{wall}(x) = p_{up} + p'_{up} + \frac{\rho}{2}(u_{up}^2 - u_{wall}^2(x)). \quad (14)$$

The pressure force acting on the folds in Eq. (1) is the integral of the normal pressure $p_{wall}(x)$ over the surface of the folds. Therefore,

$$F_p = L \int_0^d p_{wall}(x) dx. \quad (15)$$

C. Orifice discharge coefficient (ODC)

Experimental data are available for the ODC of typical glottal orifices (Park and Mongeau, 2007; Zhang *et al.*, 2002; Scherer *et al.*, 2001). Values for the discharge coefficient

were selected from Park and Mongeau (2007) for an opening converging case and a closing divergent case. Values were selected for $Re=7000$ since the quasi-steady approximation was found to be accurate for that range. Peak values of the discharge coefficient were $c_d=0.85$ for the opening phase and $c_d=1.34$ for the closing phase, i.e.,

$$c_d(t) = \begin{cases} 0.85, & v(t) > 0 \\ 1.34, & v(t) \leq 0. \end{cases} \quad (16)$$

Such a step function change is physiologically unrealistic, but consistent with the Coulomb force excitation in Fulcher's original model. The following smoothing function was used in the present study to make the time evolution of the ODC more regular:

$$c_d(t) = 1.095 - 3.55 \frac{v}{|v_{max}|}, \quad v_{max} \neq 0. \quad (17)$$

D. Collision force

A Hertz impact force (Stronge, 2000) was used to describe the collision force, F_H in Eq. (1). The impact force on each fold is given by

$$F_H = \frac{4}{3} \delta^{3/2} (1 + b_H \dot{\delta}) \left(\frac{E \sqrt{r}}{1 - \mu^2} \right), \quad (18)$$

where δ is the penetration of each vocal fold through the contact plane, which corresponds to the absolute value of the position of the mass from the centerline $y=0$. Similarly, $\dot{\delta}$ is the magnitude of the velocity of the mass during collision. The relevant vocal-fold material properties are the damping constant b_H , the Young modulus E , and the Poisson ratio μ . The parameter r is the radius of curvature of the colliding surface, which is approximately the depth of the folds, d . The values of the parameters required to compute F_H are shown in Table I. An increment in the damping ratio η_H of the oscillator was included following the guidelines suggested by Story and Titze (1995). The damping ratio, η_H , was incremented by 40% with respect to its normal value. Note that the damping ratio defines the damping constant b , as expressed during collision as

$$b_H = 2 \eta_H \sqrt{mk}. \quad (19)$$

The pressure force was adjusted, since it acts onto part of the folds surface during collision. The pressure force during collision was assumed to be the product of the upstream pressure and the effective surface in contact with the fluid. From the model geometry, shown in Fig. 2, the supraglottal pressure does not affect the vibration of the vocal folds during collision. This is in contrast with models allowing convergent/divergent modes of vibration (e.g., the two-mass model or the body-cover model), in which both subglottal and supraglottal pressures can act over the vocal-fold surface during this phase of the cycle.

E. Parameter values

The values for the parameters used in the model were largely taken from previous studies (Titze, 2002; Story and

TABLE I. Parameters and constants used in the vocal-fold model for the numerical simulations.

Parameter	Symbol	Nominal value
Length of the vocal folds	L	0.015 [m]
Depth of the vocal folds	d	0.003 [m]
Equilibrium position of the mass	y_o	0.0001 [m]
Mass of one fold	m	2×10^{-4} [kg]
Stiffness (spring constant)	k	200 [N/m]
Damping ratio	η	0.1
Damping ratio (collision)	η_H	0.5
Subglottal lung pressure	p_{up}	800 [Pa]
Supraglottal pressure	p_{dn}	0 [Pa]
Density of air	ρ	1.15 [kg/m ³]
Speed of sound	c	350 [m/s]
Young modulus of the folds	E	8 [kPa]
Poisson ratio	μ	0.4

Titze, 1995; Berry and Titze, 1996). These values are shown in Table I. The values for the areas of the supraglottal tract were from Story *et al.* (1996). A simplified flow diagram of the source model is shown in Fig. 4.

III. IMPLEMENTATION OF THE WAVE REFLECTION ANALOG TECHNIQUE

The wave reflection analog technique (Kelly and Lochbaum, 1962; Liljencrants, 1985; Rahim, 1994; Story, 1995) is

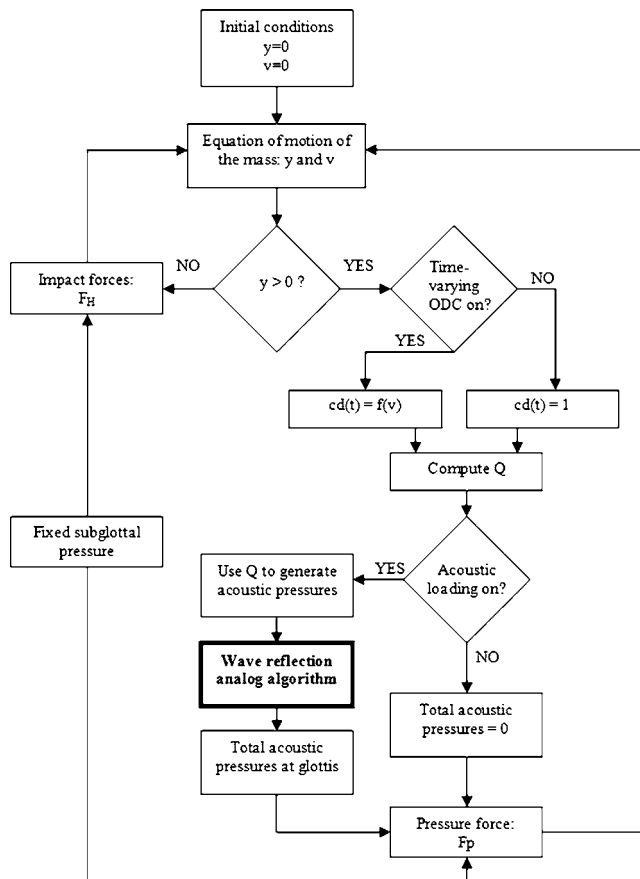


FIG. 4. Simplified flow diagram of the source model computation.

a time-domain description of the propagation of one-dimensional, planar acoustics waves through a collection of uniform, consecutive cylindrical tubes. Little has been done to model sound in the subglottal system using this technique, contrasting the wealth of information for the vocal tract. A subglottal area function along with an adequate subglottal attenuation factor are proposed in this section.

A. Subglottal area function

The area function for the subglottal tract was based on anatomical studies of the respiratory system (Weibel, 1963), in which the total cross-sectional area of the airways was measured as a function of the distance from the larynx using silicone rubber casts and excised adult lungs. Based on these data, an equivalent area function with no tube branching was denned. Although tube branching can potentially be included using a wave reflection analog approach, it was not included in this study. To compensate the absence of branching, a boundary correction (the boundary appears partially closed), first introduced by Titze (1984), was imposed at the terminal section of the equivalent subglottal model. The area denned for the terminal section produces a reflection coefficient ($r \approx 0.8$) that yielded the targeted subglottal resonances and bandwidths. Table II shows the values of the area function for 62 cylindrical sections of length 3.9683 [mm] and a sampling frequency of 44.1 [kHz].

TABLE II. Proposed subglottal area function with uniform sections of length 3.9683 [mm].

Section	Cross-sectional area in [cm] ²
1-10	2.7; 2.7; 2.7; 2.7; 2.7; 2.7; 2.7; 2.7; 2.7; 2.7;
11-20	2.7; 2.7; 2.7; 2.7; 2.7; 2.7; 2.7; 2.7; 2.7; 2.7;
21-30	2.7; 2.7; 2.7; 2.7; 2.7; 2.7; 2.7; 2.7; 2.7; 2.7;
31-40	2.2; 2.2; 2.2; 2.2; 2.2; 2.2; 2.2; 2.2; 2.2; 2.2;
41-50	2.2; 2.0; 2.0; 2.0; 2.0; 2.0; 2.0; 1.8; 1.8; 1.8;
51-60	2.7; 2.7; 2.7; 3.6; 3.6; 3.6; 4.9; 4.9; 6.7; 6.7;
61-61	9.8; 1.1;

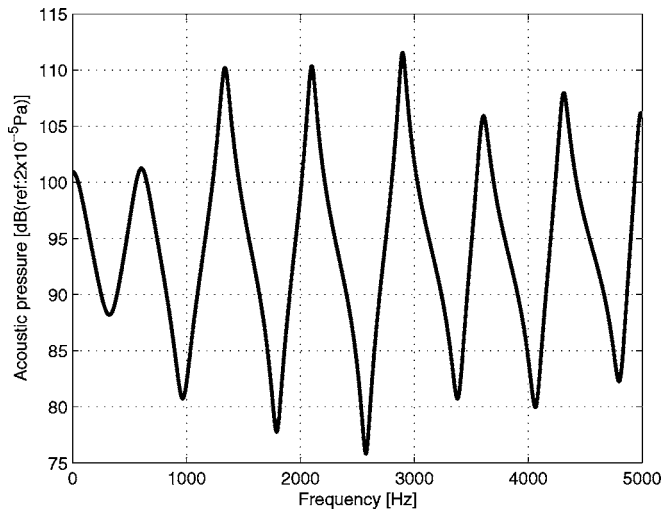


FIG. 5. Subglottal tract: Spectrum of the acoustic pressure at the glottis. Tract excited by a 1-Pa impulse.

B. Subglottal attenuation factor

Yielding walls, viscous dissipation, and heat conduction losses are the main sources of sound energy dissipation within the tracts. Following a procedure similar to that for the vocal tract (Rahim, 1994), heat conduction losses were characterized by an exponential attenuation factor. Viscous friction and heat conduction were assumed to be the same as for the vocal tract. Assuming that the main yielding walls losses in the subglottal tract are observed below 3000 Hz, the average attenuation factor was assumed to be

$$\alpha \approx \frac{0.0112}{\sqrt{A_K}}, \quad \text{and} \quad (20)$$

$$\gamma_K = e^{l\alpha_K} \approx 1 - l\alpha_K, \quad (21)$$

where α_K is the attenuation factor in cm^{-1} , A_K is the cross-sectional area of the k th section, γ_K is the propagation loss factor for the k th section, and l is the length of all sections.

C. Subglottal transfer function and verification studies

Figure 5 shows the transfer function of the subglottal system, constructed using the impulse response of the tract at the glottis with a sampling frequency of 44.1 KHz. It can be observed that the subglottal resonances are 613, 1341, 2100, and 2896 Hz; the half-power band widths are between 200 and 300 Hz for all formants. These values are in agreement with the findings of previous studies of subglottal acoustics (Harper *et al.* 2001, 2003; Stevens, 2000). The accuracy of the wave reflection analog scheme was evaluated through comparisons with predictions from harmonic wave propagation in tubes with simple geometries. The effects of different boundary conditions, including termination impedances, were evaluated as well as the effects of the loss factor. Acoustic coupling effects between subglottal and supraglottal tracts on vowel spectra were investigated. The details of these studies are available from Zañartu (2006).

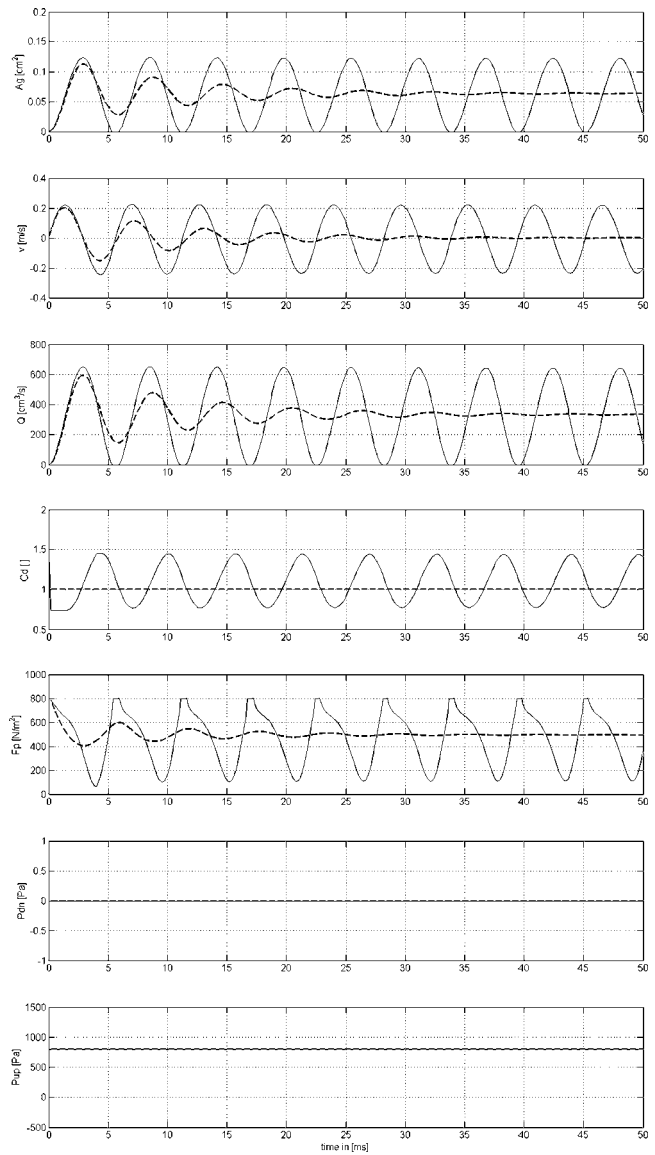


FIG. 6. Time history of key variables with no acoustic loading. A_g : glottal area [cm^2]; v : velocity of the mass [m/s]; Q : volumetric flow rate [cm^3/s]; c_d : orifice discharge coefficient; F_p : pressure force [N/m^2]; P_{dn} : downstream pressure [Pa]; P_{up} : upstream pressure [Pa]. Nomenclature: —: with ODC; - - -: without ODC.

IV. RESULTS

Section IV A describes the relative importance of aerodynamic and acoustic pressures with respect to flow-induced oscillations. Section IV B describes the contribution of each tract to the overall acoustic pressure excitation.

A. Relative influence of aerodynamic factors and acoustic coupling on stability

Three different acoustic loads were considered: (1) no acoustic loading; (2) subglottal tract and a close front unrounded vowel /i/ (IPA 301); and (3) subglottal tract and an open back unrounded vowel /a/ (IPA 305). These vowels were selected because their first formants are significantly different. The corresponding area functions were taken from Story *et al.* (1996). The area function describing the subglot-

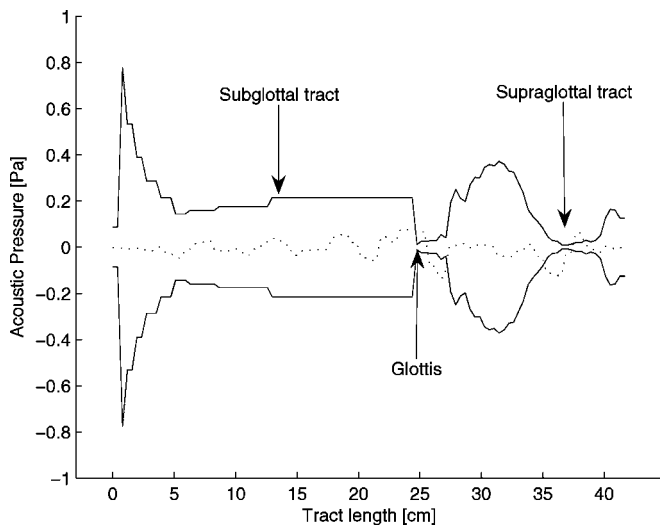


FIG. 7. Complete system geometry using the vowel /i/ with a snapshot of the acoustic pressure amplitude vs position at $t=5$ ms superimposed.

tal tract is shown in Table I. Results were obtained with and without the effects of the time-varying ODC.

1. No acoustic loading

The time history of key variables is presented in Fig. 6 for cases with and without the effect of the time-varying ODC. The subglottal static pressure was maintained at 800 Pa. In Fig. 6 (A_g) corresponds to the glottal opening obtained from the displacement of the mass. The volumetric flow rate (Q) was computed using several variables of the model as in Titze (1984, 2002). The ODC (c_d) and the pressure force (F_p) were computed using Eqs. (17) and (15). The downstream pressure (p_{dn}) is the acoustic pressure in the vocal tract at the glottis. The upstream pressure (p_{up}) was obtained as for the subglottal tract, but adding the static lung pressure. The fundamental frequency (f_0) was 180 Hz. This frequency was greater than the natural frequency of oscillation, which was expected to be 160 Hz. Self-oscillations were only obtained when the time-varying ODC was used. From the time history, it can be seen that the time-varying ODC is in phase with the velocity of the mass. Collision effects were not significant. Since there was no acoustic loading, the acoustic pressures upstream and downstream were negligible.

2. Vowel /i/ with subglottal tract

The supraglottal acoustic loading defined by the vowel /i/ had a first formant at 225 Hz and a second at 2486 Hz. The fact that the first formant is relatively close to the fundamental frequency makes this case particularly interesting. The vowel /i/ presents a loading that appears to be closer to a resistive loading than an inertive one. From Story *et al.* (1996), the section connected to the glottis is very narrow, with area 0.33 cm². This produces high vocal-tract impedance and strong coupling, given that the acoustic pressure within the tract is large. The subglottal tract had its first two resonances at 613 and 1341 Hz, and a cross-sectional area of 2.7 cm² at the glottis (see Table I). The model geometry is

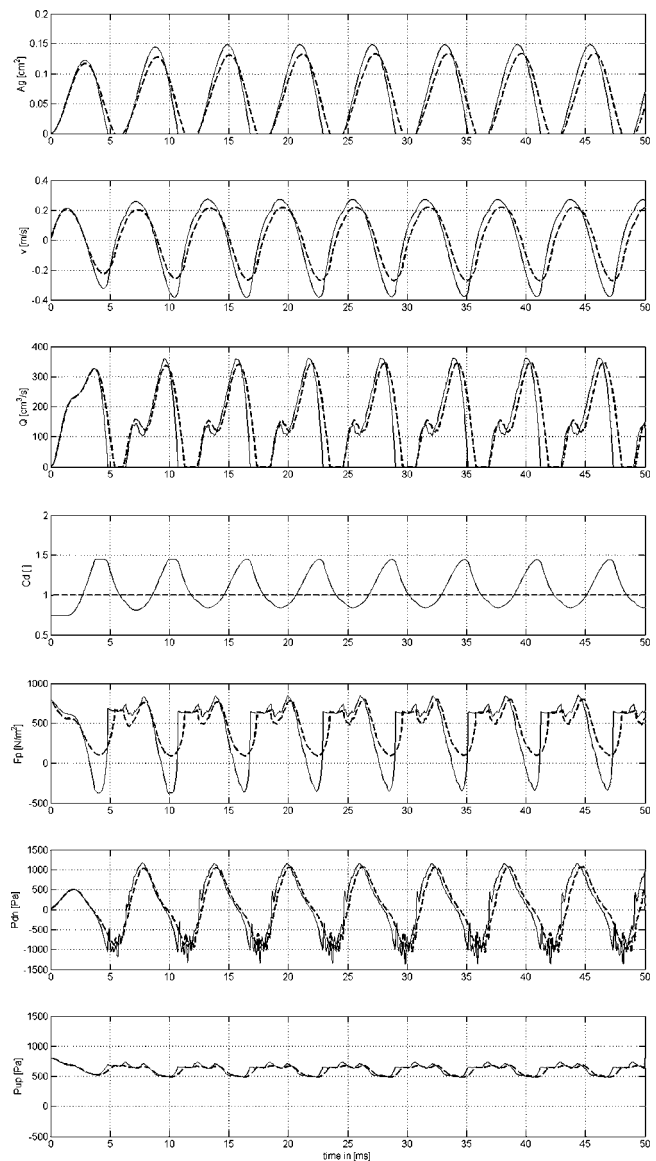


FIG. 8. Time history of key variables for vowel /i/ with subglottal tract. A_g : glottal area [cm²]; v : velocity of the mass [m/s]; Q : volumetric flow rate [cm³/s]; c_d : orifice discharge coefficient; F_p : pressure force [N/m²]; P_{dn} : downstream pressure [Pa]; P_{up} : upstream pressure [Pa]. Nomenclature: —: with ODC; - - -: without ODC.

illustrated in Fig. 7. The time history of key variables is presented in Fig. 8, using the same nomenclature as before. The oscillation reached a steady state after the second cycle, regardless of the effects of the time-varying ODC. This indicates that acoustic loading was the main factor that led to self-sustained oscillations. The collisions were larger than for the no-load case. A decrease (relative to the no-load case) in fundamental frequency, which was 170 Hz, was observed. The amplitude of the flow rate was reduced and its waveform was slightly skewed rightward in time. A depression was observed in the flow rate during the opening phase, mainly caused by the large peak in the downstream pressure. This peak is associated with the pressure oscillation associated with the low-frequency, first supraglottal formant. Although the subglottal tract was not responsible for the production of this depression, simulations without the subglottal tract suggested a significant contribution. The presence of the sub-

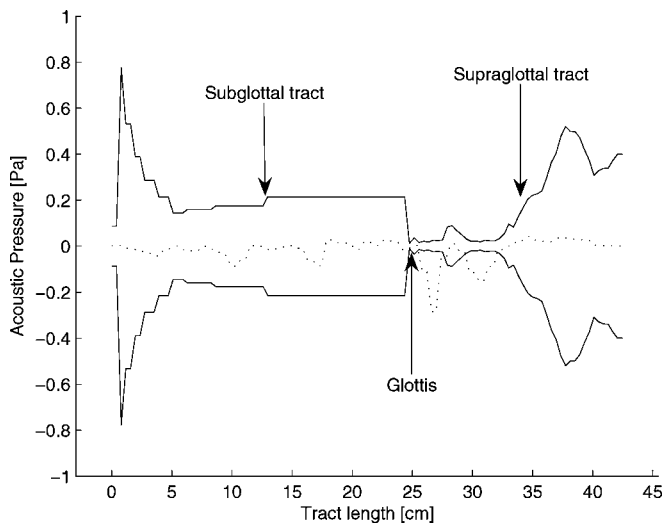


FIG. 9. Complete system geometry using the vowel /a/ with a snapshot of the acoustic pressure amplitude vs position at $t=5$ ms superimposed.

glottal system slightly reduced the depth of this depression, suggesting that it may have a damping effect on the volumetric flow rate oscillations. The contribution of each tract is studied in Sec. IV B. The coupling between source and tracts was evaluated by comparing the pressure force with the downstream and upstream pressures. During the opening phase, the downstream pressure reached a peak value and decayed almost in phase with the pressure force and the mass velocity, with a slight time lead. During collision, faster oscillations in the downstream pressure occurred, mostly associated with the high second formant frequency of the supraglottal tract. A clear coupling between source and subglottal tract was observed during collision.

The data obtained using the time-varying ODC were in close agreement with those from other interactive models of voice production (Rothenberg, 1981; Fant and Lin, 1987; Alipour *et al.*, 2000; Story and Titze, 1995; Story, 2002). The introduction of the time-varying ODC did not have a significant impact on most of the variables. This suggests that the effects of the fluid-structure interactions were less significant than the fluid-sound interaction in this simulation.

3. Vowel /a/ with subglottal tract

The supraglottal load given by the vowel /a/ has a first formant at 786 Hz and a second at 1147 Hz. From Story *et al.* (1996), the cross-sectional area at the glottis was 0.45 cm^2 . The first formant is much greater than the fundamental frequency of oscillation, implying that the supraglottal load impedance is inertive. The subglottal tract was the same as in the previous case. A schematic of the system and its sound field is shown in Fig. 9. The time history of several variables is shown in Fig. 10. As for the previous case, the oscillation reached a steady state after the second cycle. The collisions were comparable, and the fundamental frequency of oscillation was 190 Hz. A ripple during the opening phase of the volumetric flow rate was evident, in place of the large depression previously observed. This phenomenon can be explained by the increased inertance of the supraglottal tract due to the greater first formant frequency. As for the vowel

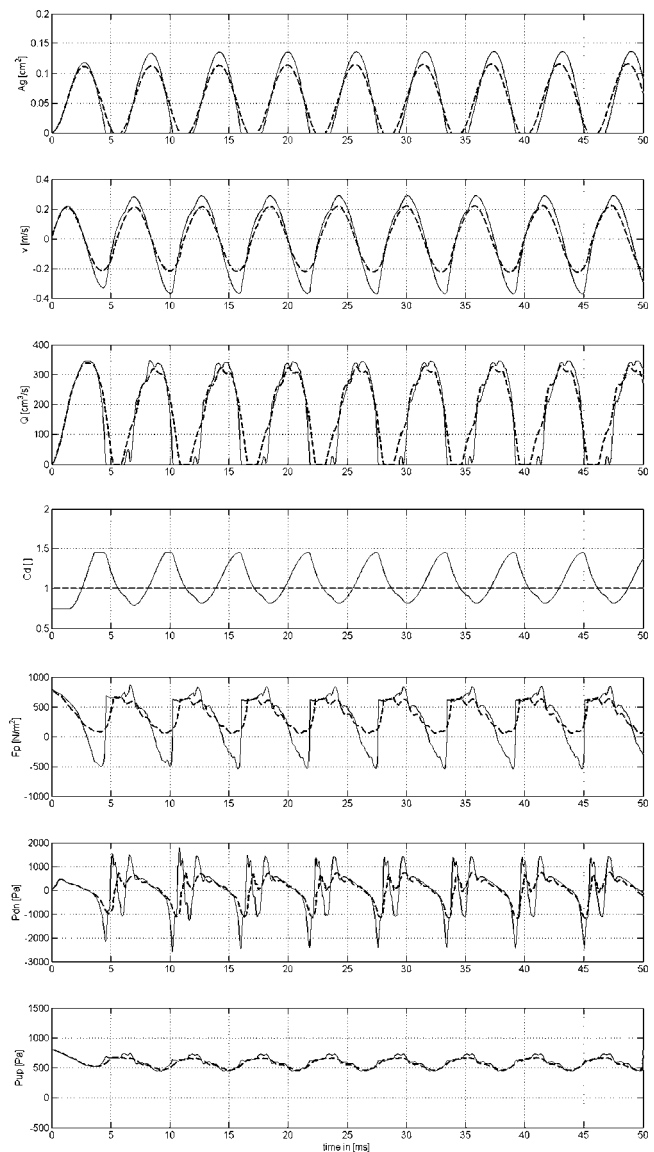


FIG. 10. Time history of key variables for vowel /a/ with subglottal tract. A_g : glottal area [cm^2]; v : velocity of the mass [m/s]; Q : volumetric flow rate [cm^3/s]; c_d : orifice discharge coefficient; F_p : pressure force [N/m^2]; P_{dn} : downstream pressure [Pa]; P_{up} : upstream pressure [Pa]. Nomenclature: —: with ODC; - - -: without ODC.

/i/, the reduced variation in the upstream pressure confirmed that the subglottal tract did not affect the production of the ripple, but it did reduce its magnitude. A detailed analysis of the contribution of the subglottal tract is presented in Sec. IV B. In comparison with the previous vowel, a higher degree of coupling with the supraglottal tract was observed since the structure of the downstream pressure closely resembled that of the pressure force.

Acoustic loading yielded self-sustained oscillations. Only minor variations were observed when the effects of fluid-structure interactions were added. The data were again in excellent agreement with those reported in other interactive models of voice production. The better coupled load (inertive vocal tract) produced less pronounced variations in the volumetric flow rate, thus introducing fewer changes in the sound source due to acoustic coupling.

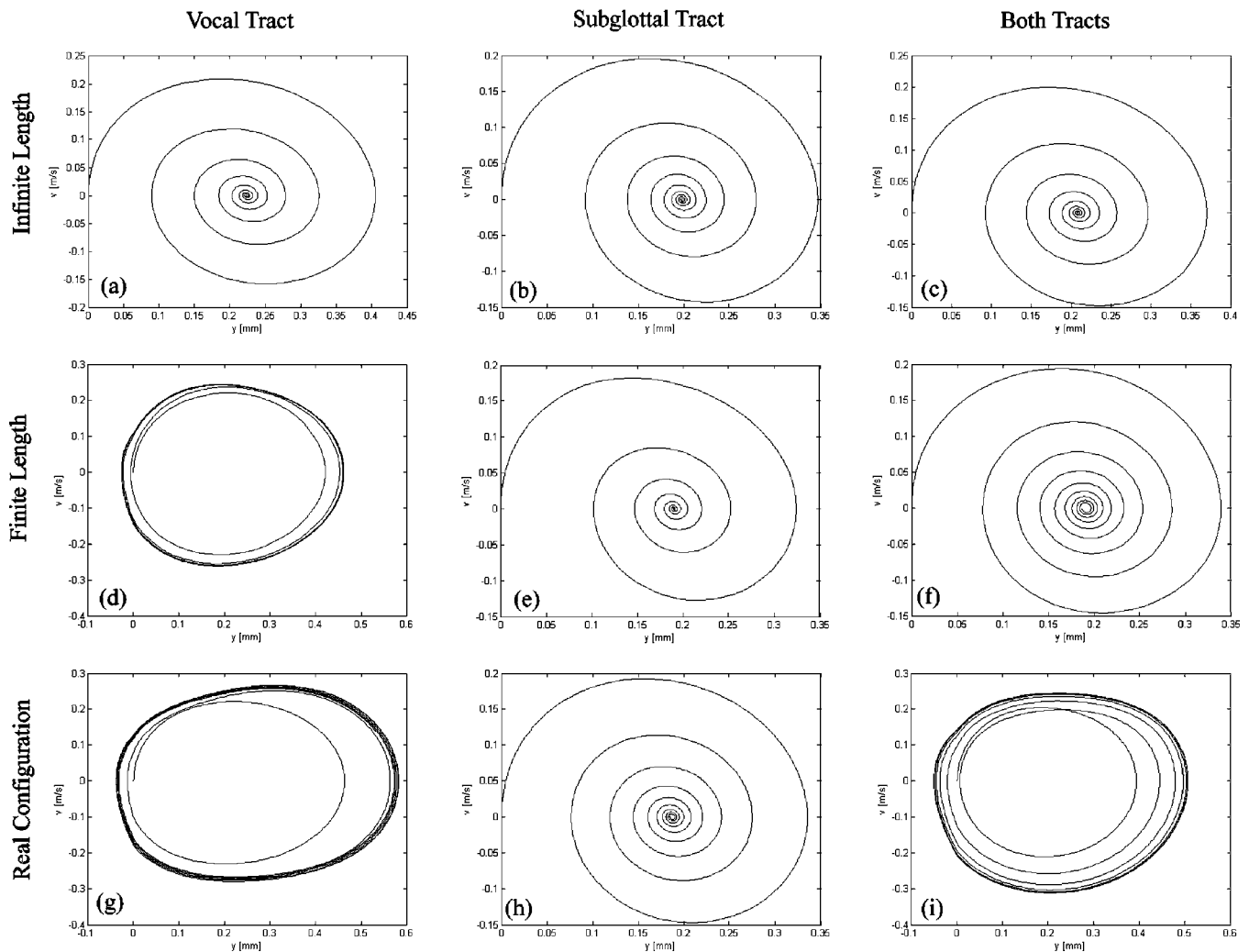


FIG. 11. Phase plots for different acoustic loadings. (a) Supraglottal: Infinitely long tube; (b) Subglottal: Infinitely long tube; (c) Both: Infinitely long tubes; (d) Supraglottal: Uniform tube, length 17 [cm] and area 1 [cm²]; (e) Subglottal: Uniform tube, length 17 [cm] and area 1 [cm²]; (f) Both: Uniform tube, length 17 [cm] and area 1 [cm²]; (g) Supraglottal: MRI vowel /i/; (h) Subglottal: Proposed subglottal design; (i) Both: MRI vowel /i/ and proposed subglottal design.

B. Contributions of subglottal and supraglottal loading on stability

To evaluate the contribution of each tract (subglottal and supraglottal) to the overall dynamic stability of the system, the sound field in each tract was selectively activated and deactivated, while keeping the ODC constant. The same loads used in the previous section were included, as well as other acoustic loads, strategically selected to illustrate the contribution of the sound field in each tract.

Phase plots were used to illustrate the behavior of the system for each specific acoustic load. The phase plot or phase portrait is a geometric representation of the trajectories of a dynamical system in the phase plane (displacement vs velocity). This representation was used to identify limiting cycles and to evaluate stability. Self-sustaining oscillations were easily identified as a closed loop in the phase plot. Phase plots for the three types of loads and for three different locations are shown in Fig. 11. Every row in the group represents a loading case (infinitely long tubes, finite uniform tubes, and realistic loads). For each load, supraglottal and subglottal tracts were tested separately, and together. Every

column represents the configuration of the acoustic load (supraglottal, subglottal, and both together). From the first row of Fig. 11, it can be observed that compliant loads (such as long tubes with low first formant frequencies) did not result in a steady state for any configuration. Inertive loads (such as the finite uniform tube, second row in Fig. 11) yielded self-sustained oscillations only if located supraglottally. The last row of Fig. 11 presents realistic loading profiles. The vowel /i/ led to a steady state in absence of subglottal loading. The addition of a subglottal load quenched the oscillations, indicating a damping effect or negative energy transfer.

V. DISCUSSION

Fluid-sound interactions appear to be more significant than fluid-structure interactions in maintaining self-sustained oscillations, particularly for more resistive supraglottal loads. For the subglottal tract, the acoustic field affects the aerodynamics of phonation, but not as significantly as the acoustic field of the vocal tract. The results indicate that (1) the acoustic field in the subglottal system reduces the effects intro-

duced by the vocal tract, and (2) if there is no presence of fluid-structure interactions, subglottal tract configurations (in the absence of a vocal tract) do not yield self-sustained oscillations. Subglottal loading may hamper the net energy transfer to the vocal folds oscillation during phonation, counterbalancing the effects introduced by the vocal tract. Expanding upon the behavior recently noted by Zhang *et al.* (2006), the results suggest that the inertance theory of acoustic loading (Titze, 1988) does not directly apply to the subglottal loading. The subglottal tract impedance closely resembles the behavior of a net compliant vocal-tract load, increasing the effective damping and reducing vocal-fold vibration. Product of the dipole source, the subglottal tract is driven by an acoustic pressure with an opposite polarity to that of the vocal tract. This change of sign in the subglottal impedance is consistent with the proposition that an inertive subglottal tract behaves like a compliant vocal tract, and vice versa. More work needs to be done, however, to completely understand the effects of subglottal impedance on oscillatory conditions.

Similar questions need to be investigated using more complex and extensive interactive models of phonation. More accurate numerical and experimental models of the subglottal system including several levels of tube branching, yielding walls, and other losses should be incorporated. The predictions of the current model need to be explained analytically and verified experimentally. Further research should evaluate the importance of acoustic loading under time-varying vocal-tract shapes (e.g., consonant followed by a vowel). Fast transitions observed for the vocal tract in real articulation could produce fast changes in the sound source that are likely to produce irregular patterns of vibration.

VI. CONCLUSIONS

The influence of arbitrary acoustic loading on the self-oscillation characteristics of an effective single mass model of the vocal folds was investigated. Numerical models for sound wave propagation in the subglottal tract and the vocal tract were developed based on a wave reflection analog method. A single-degree-of-freedom model with adjustable orifice discharge coefficient was designed to model vocal-fold vibrations and the airflow through the larynx, improving the model proposed by Fulcher *et al.* (2006). These models were fully coupled to study complex flow-structural-sound interactions, or how the sound field in the tracts affects source properties. The role of fluid-sound interactions was investigated by activating and deactivating some of the features of the model. The results indicated that fluid-sound interactions are generally more significant than fluid-structure interactions in maintaining self-sustained oscillation, although specific vocal-tract shapes can yield different trends. The results suggested that the acoustic field in the subglottal tract plays a less significant role than in vocal tract. However, subglottal loading tends to absorb energy when the energy transfer to the vocal-fold oscillation from hydrodynamic and vocal-tract coupling is positive, possibly damping oscillations. These findings underline the need of

further research on the acoustic field in the subglottal system and acoustic interactions with the sound source.

ACKNOWLEDGMENTS

This study was supported by the research grant No. R01 DC05788 from the National Institute of Deafness and Other Communication Disorders, National Institutes of Health. The first author of this paper also acknowledges the support provided by the Fulbright Program and the Institute of International Education.

- Alipour, F., Berry, D. A., and Titze, I. R. (2000). "A finite-element model of vocal-fold vibration," *J. Acoust. Soc. Am.* **108**(6), 3003–3012.
- Austin, S. F., and Titze, I. R. (1997). "The effect of subglottal resonance upon vocal fold vibration," *J. Voice* **11**(4), 391402.
- Berry, D. A., and Titze, I. R. (1996). "Normal modes in a continuum model of vocal fold tissues," *J. Acoust. Soc. Am.* **100**(5), 3345–3354.
- Fant, G., and Lin, Q. (1987). "Glottal source - vocal tract acoustic interaction," *Speech Transmission Laboratory Quarterly Progress and Status Report*, Royal Institute of Technology, Stockholm, pp. 013–027.
- Flanagan, J. L., and Landgraf, L. L. (1968). "Self-oscillating source for vocal tract synthesizers," *IEEE Trans. Audio Electroacoust.* **AU-16**, 57–64.
- Fulcher, L. P., Scherer, R. C., Melnykov, A., and Gateva, V. (2006). "Negative Coulomb damping, limiting cycles, and self-oscillation of the vocal folds," *Am. J. Phys.* **74**(5), 386–393.
- Harper, V. P., Kraman, S. S., Pasterkamp, H., and Wodicka, G. R. (2001). "An acoustic model of the respiratory tract," *IEEE Trans. Biomed. Eng.* **48**, 543–550.
- Harper, V. P., Pasterkamp, H., Kiyokawa, H., and Wodicka, G. R. (2003). "Modeling and measurement of flow effects on tracheal sounds," *IEEE Trans. Biomed. Eng.* **50**, 1–10.
- Ishizaka, K., and Flanagan, J. L. (1972). "Synthesis of voiced sounds from a two mass model of the vocal cords," *Bell Syst. Tech. J.* **51**, 1233–1268.
- Kelly, J. L., and Lochbaum, C. C. (1962). "Speech synthesis," *Proceedings of the Fourth International Congress on Acoustics*, Copenhagen, pp. 1–4.
- Liljencrants, J. (1985). "Speech Synthesis with a Reflection-type Line Analog," D.S. dissertation, Dept. of Speech Commun. and Music Acoust., Royal Inst. of Tech., Stockholm, Sweden.
- Mergell, P., and Herzel, H. (1997). "Modeling biphonation - The role of the vocal tract," *Speech Commun.* **22**, 141154.
- Mongeau, L., Francheck, N., Coker, C. H., and Kubli, R. A. (1997). "Characteristics of a pulsating jet through a small modulated orifice, with application to voice production," *J. Acoust. Soc. Am.* **102**(2), 1121–1133.
- Park, J. B., and Mongeau, L. (2007). "Instantaneous orifice discharge coefficient of a physical, driven model of the human larynx," *J. Acoust. Soc. Am.* **121**(1), 442–455.
- Rahim, M. G. (1994). *Artificial Neural Networks for Speech Analysis/Synthesis*, (Kluwer Academic, New York).
- Rothenberg, M. (1981). "Acoustic interaction between the glottal source and the vocal tract," in *Vocal Fold Physiology*, edited by K. N. Stevens and M. Hirano (University of Tokyo Press, Tokyo).
- Scherer, R. C., Shinwari, D., DeWitt, K. J., Zhang, C., Kucinschi, B. R., and Afjeh, A. A. (2001). "Intraglottal pressure profiles for a symmetric and oblique glottis with a divergence angle of 10 degrees," *J. Acoust. Soc. Am.* **109**(4), 1616–1630.
- Stevens, K. N. (2000). *Acoustic Phonetics*, 1st ed. (The MIT Press, Boston).
- Story, B. H. (1995). "Physiologically-Based Speech Simulation using an Enhanced Wave-Reflection Model of the Vocal Tract," Ph.D. dissertation, University of Iowa.
- Story, B. H. (2002). "An overview of the physiology, physics and modeling of the sound source for vowels," *Acoust. Sci. & Tech.* **23**(4), 195–206.
- Story, B. H., and Titze, I. R. (1995). "Voice simulation with a body-cover model of the vocal folds," *J. Acoust. Soc. Am.* **97**(2), 1249–1260.
- Story, B. H., Titze, I. R., and Hoffman, E. A. (1996). "Vocal tract are functions from magnetic resonance imaging," *J. Acoust. Soc. Am.* **100**(1), 537–554.
- Stronge, W. J. (2000). *Impact Mechanics*, 1st ed. (Cambridge University Press, New York).
- Thompson, S. L., Mongeau, L., and Frankel, S. H. (2005). "Aerodynamic

- transfer of energy to the vocal folds," *J. Acoust. Soc. Am.* **118**(3), 1689–1700.
- Titze, I. R. (1984). "Parametrization of glottal area, glottal flow and vocal fold contact area," *J. Acoust. Soc. Am.* **75**(2), 570–580.
- Titze, I. R. (1988). "The physics of small-amplitude oscillation of the vocal folds," *J. Acoust. Soc. Am.* **83**, 1536–1552.
- Titze, I. R. (2002). "Regulating glottal airflow in phonation: Application of the maximum power transfer theorem to a low dimensional phonation model," *J. Acoust. Soc. Am.* **111**(1), 367–376.
- Titze, I. R. (2004). "A theoretical study of f_0 - f_1 interaction with application to resonant speaking and singing voice," *J. Voice* **18**(3), 292–298.
- Titze, I., and Story, B. (1997). "Acoustic interactions of the voice source with the lower vocal tract," *J. Acoust. Soc. Am.* **101**, 2234–2243.
- Van den Berg, J. W. (1958). "Myoelastic-aerodynamic theory of voice production," *J. Speech Hear. Res.* **1**, 227–244.
- Van den Berg, J. W., and Tan, T. S. (1959). "Results of experiments with human larynxes," *Pract. Otorhinolaryngol. (Basel)* **21**, 425–450.
- Weibel, E. R. (1963). *Morphometry of the Human Lung*, 1st ed. (Springer, New York).
- Zañartu, M. (2006). "Influence of Acoustic Loading on the Flow-Induced Oscillations of Single Mass Models of the Human Larynx," M.S. thesis, School of Electrical and Computer Engineering, Purdue University.
- Zhang, Z., Mongeau, L., and Frankel, S. H. (2002). "Experimental verification of the quasi-steady approximation for aerodynamic sound generation by pulsating jets in tubes," *J. Acoust. Soc. Am.* **112**(4), 1652–1663.
- Zhang, Z., Neubauer, J., and Berry, D. A. (2006). "The influence of subglottal acoustics on laboratory models of phonation," *J. Acoust. Soc. Am.* **120**(3), 1558–1569.

An acoustic description of the vowels of northern and southern standard Dutch II: Regional varieties^{a)}

Patti Adank^{b)}

F.C. Donders Centre for Cognitive Neuroimaging, Kapittelweg 29, 6525 EN Nijmegen, The Netherlands

Roeland van Hout

Centre for Language Studies, Radboud University Nijmegen, Erasmuslaan 1, PO Box 9103, 6500 HD, Nijmegen, The Netherlands

Hans van de Velde

Utrecht Institute of Linguistics OTS, University of Utrecht, Trans 10 3512 JK Utrecht, The Netherlands

(Received 3 May 2006; revised 20 November 2006; accepted 20 November 2006)

An analysis is presented of regional variation patterns in the vowel system of Standard Dutch as spoken in the Netherlands (Northern Standard Dutch) and Flanders (Southern Standard Dutch). The speech material consisted of read monosyllabic utterances in a neutral consonantal context (i.e., /sVs/). The analyses were based on measurements of the duration and the frequencies of the first two formants of the vowel tokens. Recordings were made for 80 Dutch and 80 Flemish speakers, who were stratified for the social factors gender and region. These 160 speakers were distributed across four regions in the Netherlands and four regions in Flanders. Differences between regional varieties were found for duration, steady-state formant frequencies, and spectral change of formant frequencies. Variation patterns in the spectral characteristics of the long mid vowels /e o ø/ and the diphthongal vowels /ɛi œy ɔu/ were in accordance with a recent theory of pronunciation change in Standard Dutch. Finally, it was found that regional information was present in the steady-state formant frequency measurements of vowels produced by professional language users. © 2007 Acoustical Society of America. [DOI: 10.1121/1.2409492]

PACS number(s): 43.70.Fq, 43.70.Kv, 43.72.Ar [AL]

Pages: 1130–1141

I. INTRODUCTION

This paper describes the vowel system of Standard Dutch as spoken in the Netherlands and Flanders and examines regional patterns of variation in the acoustic characteristics of the 15 vowels of Dutch /a e i ɪ ɔ u y e o ø ɔu ɛi œy/. The reasons for describing these regional variation patterns were twofold.

First, in recent years it has become generally accepted that a language's vowel system is better characterized when its description includes regional varieties than when it includes only a single idealized set of acoustic-phonetic characteristics (Clopper *et al.*, 2005; Hagiwara, 1997). Earlier studies on the vowel system of Standard Dutch (Adank, van Hout, and Smits, 2004; Pols *et al.*, 1973; Van Nierop *et al.*, 1973) are therefore limited in that they do not include regional varieties. Pols *et al.* describe the acoustic characteristics of vowel tokens produced by 50 male speakers from the Netherlands, who spoke Standard Dutch, while Van Nierop *et al.* provide a description of vowel tokens produced by 25 female Standard Dutch speakers from the Netherlands. Adank *et al.* describe the acoustic characteristics (duration,

f_0 , and formant frequencies F_1 through F_3) of realizations of the vowels of Standard Dutch for ten male and ten female speakers from the Netherlands and ten male and ten female speakers from Flanders. Although Adank *et al.*'s description is an improvement over Pols *et al.*'s and Van Nierop *et al.*'s in the sense that speakers from Flanders are included as well, it is limited because it excludes regional varieties.

Second, it is at present not feasible to establish neither how the pronunciation of the vowels of Dutch varies across the Dutch language area, nor how this pronunciation of these vowels evolves over time, as no previous acoustic descriptions are available. This paper attempts to fill this gap by providing a comprehensive overview of the extent to which Dutch vowels vary in their acoustic characteristics across regional varieties in the Netherlands and Flanders. In doing so, this overview could serve as a point of reference for further studies on the vowel system of Standard Dutch.

The present study builds on Adank *et al.*, who describe recordings of 40 professional users of Standard Dutch (i.e., teachers of the Dutch language). These recordings were made using a sociolinguistic interview in which vowels and consonants were elicited through a wide variety of tasks. Adank *et al.*'s vowel tokens were recorded through a formal reading task, i.e., reading nonsense words in carrier sentences from a computer screen. Of the 40 speakers, 20 were from the socioeconomic core area (the culturally and economically dominant region) in the Netherlands and 20 were from Flanders' socioeconomic core area.

^{a)}Portions of this work were presented as "Distinguishing Regional Varieties of Dutch" at The International Conference on Language Variation in Europe (ICLaVE3) 2005 and as "Regional Variation Patterns in the Vowel System of Standard Dutch" at the Workshop on Accent, Variation and Change on March 3, 2006 at the UCL Centre for Human Communication.

^{b)}Author to whom correspondence should be addressed; electronic mail: patti.adank@fcdonders.ru.nl

TABLE I. The selected towns per speech community, for each of the eight selected regions.

Speech community	Region	Name	Selected towns
Netherlands Central	N-R	Randstad	Alphen aan de Rijn, Gouda
Intermediate	N-M	South-Gelderland	Tiel, Veenendaal, Ede, Culemborg, Elst
Peripheral 1	N-S	Limburg	Sittard, Geleen, Roermond
Peripheral 2	N-N	Groningen	Assen, Veendam, Winschoten
Flanders Central	F-B	Brabant	Lier, Heist-op-den berg
Intermediate	F-E	East-Flanders	Oudenaarde, Zottegem, Ronse, Brakel
Peripheral 1	F-L	Limburg	Tongeren, Bilzen
Peripheral 2	F-W	West-Flanders	Ieper, Poperinge

Originally, 160 speakers were recorded through Adank *et al.*'s sociolinguistic interview. The present study describes the remaining 120 speakers, who were distributed across six regional varieties of Standard Dutch, with ten female and ten male speakers per variety. In the description it is first established whether the variation patterns reported for the two standard varieties described in Adank *et al.* are representative for regional varieties of Standard Dutch and, second, the variation patterns across the six varieties are identified.

II. MATERIALS

A. Database design, recordings, and acoustic measurements

1. Speech communities, resigns, and towns

In each country, also referred to as "speech community," four regions were distinguished, a central region, and three noncentral regions: an intermediate region and two peripheral regions. Twenty speakers were recorded per region. The central region in each speech community was the socioeconomic core area of that community. It was thought that the speech from the speakers in the central region would reflect the most prestigious variety of Northern Standard Dutch, or NSD, (spoken in the Netherlands) and Southern Standard Dutch, or SSD, (spoken in Flanders) in both communities. In Adank *et al.*, the vowel tokens of the two central regions are described.

Regional pronunciation variation in Standard Dutch is directly influenced by the dialects of the regions in question. The more the regional dialects differ from Standard Dutch, the stronger the accent of that region is present when speaking the standard language (e.g., Chambers, 2003; Labov, 1972). Covering the range of pronunciation variation implies selecting peripheral areas. In both speech communities two peripheral regions were selected that were maximally distant geographically from each other and from the core area. The intermediate region was a region geographically next to the central region. The regional dialects of the intermediate region are closer to the standard language.

For NSD, the central region was the west, consisting of the provinces Northern-Holland, Southern-Holland, and Utrecht, also known as "the Randstad" and referred to as "N-R" (Netherlands-Randstad). The cities Amsterdam, Rotterdam, Utrecht, and The Hague are part of the Randstad. The intermediate region for NSD enclosed the southern part of the province Gelderland and part of the province Utrecht. This region is referred to as "N-M" (Netherlands-Middle).

The two peripheral regions for NSD were the province Limburg, or "N-S" (Netherlands-South), in the south of the Netherlands, and the province Groningen, or "N-N" (Netherlands-North), in the north of the Netherlands.

In SSD, the central region was "Brabant," denoted as "F-B" (Flanders-Brabant). Brabant enclosed the provinces Antwerpen and Flemish-Brabant, with the cities of Antwerpen and Leuven, respectively. The intermediate region was the province East-Flanders, referred to as "F-E" (Flanders-East). The two peripheral regions for SSD were the provinces (Flemish) Limburg, or "F-L" (Flanders-Limburg), and West-Flanders, or "F-W" (Flanders-West).

Several towns were selected per region, following three criteria. First, the selected towns in each region had a comparable socioeconomic profile. Second, they belonged to the same dialect group. Third, the Dutch spoken in the towns was regarded as characteristic of that region. No major cities were selected, because it was expected that the Dutch spoken in major cities is influenced by dialects (or languages) other than those spoken in the surrounding region, due to migration. Table I lists the selected towns per region and Fig. 1 shows the location of these towns in the Netherlands and Flanders.

2. Speakers

All 160 speakers were Dutch teachers at secondary education institutes at the time the interview was recorded. Dutch teachers were selected because they are professional language users who are expected to speak standard Dutch on a daily basis. Furthermore, they are instructors of the standard language and may therefore be regarded as having a normative role. A final reason for selecting Dutch teachers was that it was assumed that their speech would show more regional variation than broadcasters' (whose speech is generally used in pronunciation studies of the standard language, cf. Bell, 1983).

The teachers who participated in the interview taught at schools for secondary education in the selected towns. They had to meet the following requirements. First, at the time of the interview, they all lived in one of the selected towns, or near that town in the dialectal region characteristic for that region. Second, they were born in the region or moved there before their eighth birthday. Third, they had lived in the region for at least eight years prior to their 18th birthday. Finally, the speakers were divided into two age groups, a younger group and an older group. The speakers in the



FIG. 1. Map of the Netherlands and Flanders, showing all selected towns, ‘)’ shows the location of each town.

younger group were between 22 and 44 years old at the time of the interview and speakers in the older group were between 45 and 50 years old. Each region in Table I was thus represented by 20 speakers: five young men, five older men, five younger women, and five older women. Note that speaking a regional dialect or not was not a criterion for selection. It was assumed that growing up in a specific region implies that regional features of the standard language play a role in the acquisition and socialization process.

3. Carrier sentences

Dutch vowels have traditionally been divided into phonologically short vowels, /a ε ɪ ɔ ʏ/, phonologically long vowels /a e ɪ ø o u y/, and diphthongs, /eɪ ou œy/ (Booij, 1995). All target vowels were produced in a carrier sentence. The sentences had the following generic structure for the short vowels (“V” indicates the target vowel):

In sVs en in sVsse zit de V
 /ɪn sVs ən ɪn sVsə zɪt də V/
 [In sVs and in sVsse is the V]

The sentences had the following structure for the long vowels and the diphthongs:

In sVs en in sVze zit de V
 /ɪn sVs ən ɪn sVzə zɪt də V/
 [In sVs and in sVze is the V]

Of the three different consonantal contexts (CVC, CVCV, or V), the CVC contexts were selected for further processing. The CVC-structure /sVs/ can be regarded as a neutral context for Dutch vowels.

4. Recording procedure

The vowels were elicited through the sentences that were presented to the speaker on a computer screen, with a 3 s interval between sentences. When the speaker made a mistake, the interviewer interrupted the computer program and went back at least two sentences and asked the speaker to repeat these sentences. This task was performed twice. A total of 4800 vowel tokens were thus recorded: two tokens of each of the 15 vowel categories of Dutch, produced by 160 speakers.

5. Acoustic measurements: Duration, F_1 and F_2

The start and end times for the duration of each token were labeled manually in the digitized speech wave. Labels were placed at zero crossings at the onset and offset of the glottal vibrations of the vocalic portion of the /sVs/ syllable. When labeling it was ensured that the surrounding speech sounds were not audible in the remaining signal. The duration of each vowel segment was defined as the interval between the segment labels at the start and end of the vocalic portion.

The frequencies of F_1 and F_2 were stored at nine points of the vowel token’s duration, with the first point at the start of the vocalic portion and the ninth point at the end of the vocalic portion, and the remaining points spaced at equal-sized intervals, relative to the absolute duration. The nine monophthongal vowels /a a ε ɪ i ɔ u ʏ y/ were represented at one time point only, i.e., at 50%—the fifth of the nine time points—as Adank *et al.* (2004) report that these vowels can be separated fairly well based on their steady-state characteristics for their first two formants only. The diphthongal vowels /eɪ œy ou/ and the long mid vowels /e o ø/ were represented at two time points, i.e., 25% and 75%, or the third and seventh time point, as Adank *et al.* report that these vowels cannot be adequately separated unless information about their dynamic characteristics is supplied. They suggest that

the three long mid vowels for Dutch should not be treated as monophthongal vowels, but instead as semidiphthongal vowels, when describing Dutch vowels acoustically, especially for NSD. The monophthongal vowels, semidiphthongal vowels, and full diphthongal vowels were analyzed separately.

Finally, Adank *et al.* provided a description of the measurements of the fundamental frequency for the two central regions. However, as they found no differences between these two regions, it was decided to exclude the analysis of the fundamental frequency in the present paper. For further specifics of the acoustic measurements, see Adank, van Hout, and Smits (2004).

III. RESULTS

A. Duration

1. Duration variation within speech communities

Figure 2 shows the average duration measurements for all vowels across the four regions in the both speech communities and Figure 3 shows the average durations per region for both genders pooled across both speech communities.

A repeated-measures analysis of covariance (ANOVA) was run on the duration measurements for each vowel token, with vowel category as the within-subject factor and with the speaker's regional background (region) and gender as between-subjects factors. The analysis was carried out per speech community.

The analysis for NSD showed a significant main effect of the within-subjects factor vowel ($F[6.228, 104]=1253.32$, $p<0.05$, Huynh-Feldt corrected). Furthermore, effects were found for between-subjects factors region ($F[3,152]=8.91$, $p<0.05$) and gender ($F[1,152]=8.45$, $p<0.05$), whereas the region \times gender interaction was not significant. This suggests that the duration of some vowels varied across the four NSD regions. Second, the effect for gender indicates that the female speakers produced longer vowels than male speakers, as can be observed in Fig. 3. A post-hoc analysis was carried out on region to further investigate the differences between NSD regions. The p value was set to 0.001 to correct for the large number of analyses. The results showed that the vowels of the central region N-R were overall shorter than for N-M and N-N (cf. Fig. 2). The results for SSD revealed an effect of the within-subjects factor vowel ($F[5.118, 104]=1256.81$, $p<0.05$, Huynh-Feldt corrected) and a significant main effect of the between-subjects factor gender ($F[1,152]=20.45$, $p<0.05$), while region and the region \times gender interaction were not significant. Again, the female speakers showed longer durations than the male speakers (cf. Fig. 3).

2. Duration variation between speech communities

Figure 4 shows the average duration per speech community, pooled across the four regions in each community. To establish which vowels varied in their duration measurements across both communities, a univariate ANOVA was carried out for each vowel separately. The duration measurements per vowel token served as the dependent variable, and community served as the independent variable. Two univariate ANOVAs were run: one for the two central regions and

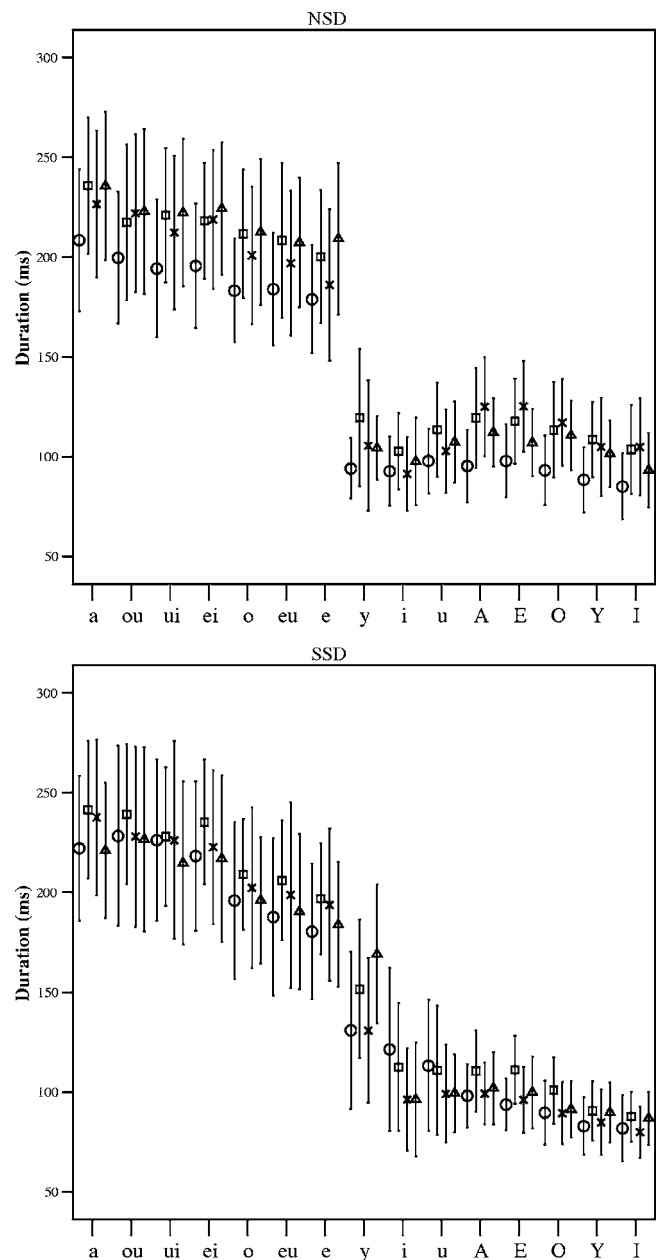


FIG. 2. Error bars (bars represent one standard deviation) of average duration in ms per vowel, for the 80 NSD speakers (top panel) and the SSD speakers (bottom panel). (“ou”= $/\text{ou}/$, “ui”= $/\text{y}/$, “eu”= $/\text{ø}/$, “A”= $/\text{a}/$, “O”= $/\text{ɔ}/$, “Y”= $/\text{ɣ}/$, “I”= $/\text{i}/$; o=central region, \square =intermediate region, x=peripheral I, and Δ =peripheral II).

one with the three noncentral regions nested under community, for NSD and SSD separately. Because of the large number of analyses, p was set to 0.001.

The analysis for the two central regions indicated that the durations for $/\text{æy}/$ ($F[1,78]=14.46$, $p\leq 0.001$) $/\text{y}/$ ($F[1,78]=30.52$, $p\leq 0.001$) and $/\text{i}/$ ($F[1,78]=16.62$, $p\leq 0.001$) were different for both communities. The analysis for the six noncentral regions showed that the duration of $/\text{y}/$ ($F[1,78]=84.84$, $p\leq 0.001$) was shorter for NSD and that the durations of $/\text{a}/$ ($F[1,78]=30.76$, $p\leq 0.001$), $/\text{ɛ}/$ ($F[1,78]=30.55$, $p\leq 0.001$), $/\text{ɔ}/$ ($F[1,78]=65.75$, $p\leq 0.001$), $/\text{ɣ}/$ ($F[1,78]=50.76$, $p\leq 0.001$), and $/\text{i}/$ ($F[1,78]=44.17$, $p\leq 0.001$) were all longer for NSD. There-

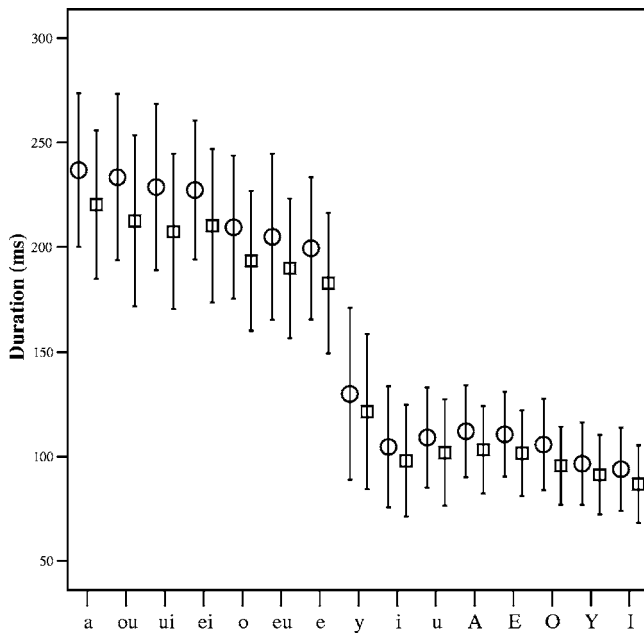


FIG. 3. Error bars (bars represent one standard deviation) of average duration in ms per vowel, for the 80 female speakers (circles) and 80 male speakers (squares) per region; (“ou”= ɔu ,”ui”= ɛy ,”eu”= ø ,”A”= a ,”O”= ɔ ,”Y”= ɣ ,”I”= ɪ).

fore, additional variation patterns were observed when the six noncentral regions were taken into account, especially for /a ɛ ɔ ʏ ɪ y/ .

Second, Adank, van Hout, and Smits (2004) report that the vowels for the two central regions can be divided into two durational groups, long $\text{/a e o ø ɔ u ɛɪ œy/}$ and short /a ɛ ɪ ɪ ɔ u ʏ y/ . To establish whether the same division would be found across all NSD and SSD regions, a series of t tests was carried out (cf. Adank *et al.*). A total of 105 pairwise comparisons were run for the 15 vowels. These 105

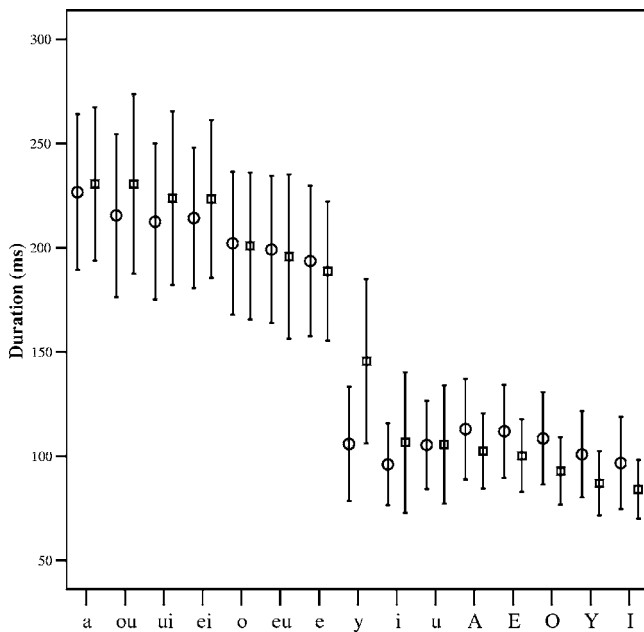


FIG. 4. Error bars (bars represent one standard deviation) of average duration in ms per vowel, for NSD (circles) and SSD (squares); (“ou”= ɔu ,”ui”= ɛy ,”eu”= ø ,”A”= a ,”O”= ɔ ,”Y”= ɣ ,”I”= ɪ).

analyses were repeated for the eight regions. The vowels $\text{/a e o ø ɔ u ɛ ɪ œy/}$ displayed significantly ($p \leq 0.001$) longer durations than /a ɛ ɪ ɪ ɔ u ʏ y/ for all four NSD regions and for SSD’s central region (F-B). The regions F-E, F-L, and F-W displayed a different pattern. For F-E and F-L, the vowels could be divided into three groups depending on their duration; long: $\text{/a e ɪ ɔ u o ø œy/}$, half-long: /y/ and short: /a ɛ ɪ ɪ ɔ u ʏ/ . For F-W, the vowels could be divided into two groups; long: $\text{/a e o ø ɔ u ɛɪ œy y/}$ and short: /a ɛ ɪ ɪ ɔ u ʏ/ .

The duration analysis shows that the division of vowels into phonetically long and short vowels was not identical in the two communities. A caveat must be made for F-B; this region’s division into long and short vowels is not representative for the three noncentral SSD regions. Instead, it resembles the pattern found for all NSD regions.

B. Formant frequencies: Steady state

1. Steady-state variation within speech communities

The nine monophthongal vowels $\text{/a a ɛ ɪ ɪ ɔ u ʏ y/}$ were represented by the formant measurements at 50% of each vowel token’s duration. The formant frequencies were transformed using Lobanov’s (1971) normalization procedure to enable comparison of formant frequencies across genders. Formant frequencies usually vary greatly across male and female speakers due to anatomical and physiological differences between both genders (Peterson and Barney, 1952). Therefore, Lobanov’s normalization procedure was applied as it effectively reduces anatomical and physiological gender-related variation in formant measurements, while adequately preserving variation related to the speaker’s regional background (Adank, Smits, and van Hout, 2004).

Two multivariate ANOVAs were run on the pooled measurements of F_1 and F_2 for each vowel token, one for NSD and one for SSD. In both analyses, the multivariate dependent variable consisted of pooled measurements of normalized F_1 (zF_1) and normalized F_2 (zF_2) for the nine monophthongal vowels, and region and gender were included as between-subjects factors. NSD showed a significant effect for region ($F[3,152]=11.44, p < 0.05$), while gender and the region \times gender interaction were not significant. This indicates that the shape of the vowel systems varied across the four NSD regions. A post-hoc analysis on region (Tukey, $p \leq 0.001$) indicated that N-S differed significantly from N-R and N-M. SSD showed an effect for region ($F[3,152]=16.74, p < 0.05$). The post-hoc analysis for region showed that F-E and F-W differed significantly from central region F-B, and that F-W differed from F-L. These results indicate that the shapes of the vowel systems varied regionally in both speech communities and that speaker gender did not affect these measurements.

It was decided to use the raw (un-normalized) data for further analyses, as it is presumed (Clopper *et al.*, 2005; Disner, 1980) that Lobanov’s normalization procedure may introduce artifacts when used for measurements based on vowel systems that differ in their overall size and shape (cf. Clopper *et al.*, 2005). In addition, as female speakers are not

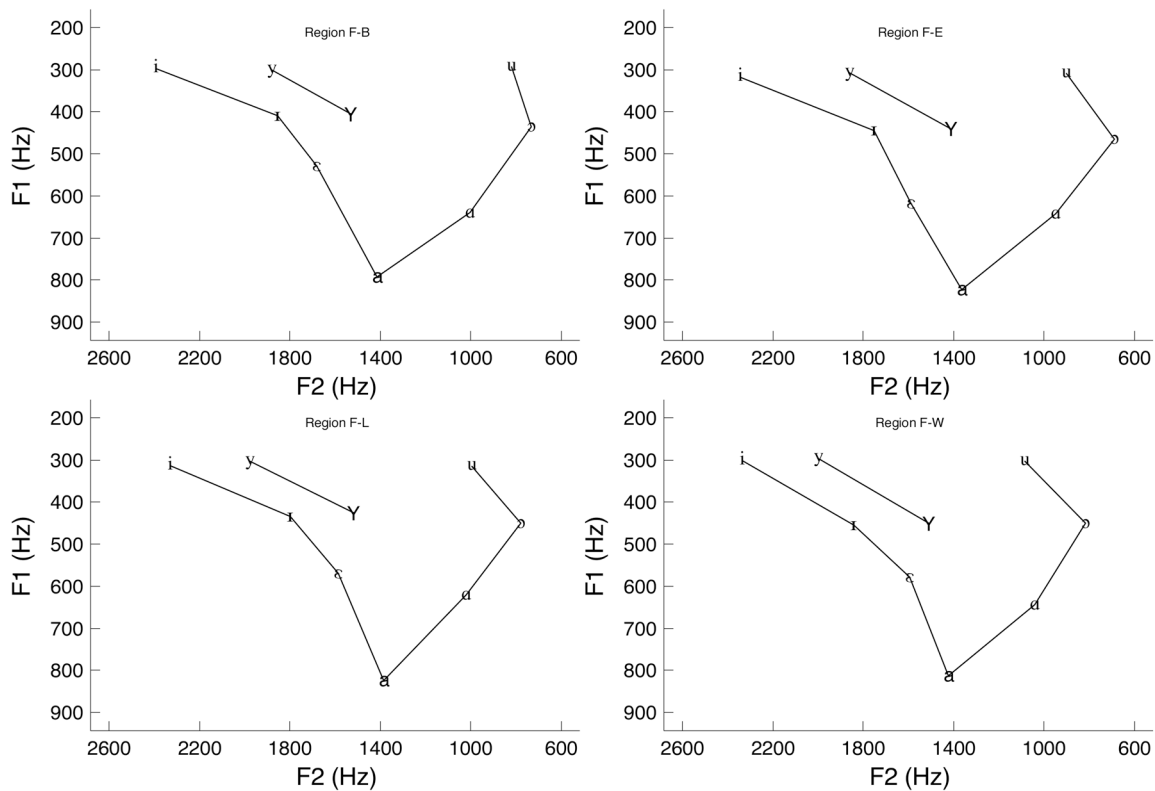


FIG. 6. Vowel diagram showing average formant frequencies for all monophthongal vowels for SSD. Averages taken at 50% of the duration. N per symbol is 40.

at 75%. The analyses were run on the pooled values for ΔF_1 and ΔF_2 and the four regions (region) served as the independent variable in all four analyses. The results showed one significant effect, for the female NSD speakers ($(F[3,76] = 5.83, p < 0.05)$). A post-hoc analysis ($p \leq 0.001$) on region showed that regions N-M and N-S differed, indicating some spectral-change differences between these two regions for the female speakers in Fig. 7 for the full diphthongs. No other effects were found.

The four multivariate repeated-measures ANOVAs for /e o ø/ used the same design as for /ɛi œy ɔu/. Effects were found for NSD only, for the female ($F[3,76] = 6.41, p < 0.05$) and male speakers ($F[3,76] = 2.20, p < 0.05$). A post-hoc analysis (Tukey, $p \leq 0.001$) indicated that N-M differed

from N-S for the female speakers. Figure 7 shows longer spectral change trajectories for the three long mid vowels for N-M than N-S.

Onset and offset frequencies. Figures 7 and 8 show both spectral change and onset and offset frequencies. Eight multivariate repeated-measures ANOVAs were run to ascertain the significance of the differences observed in both figures. The first four were run on the onsets for /ɛi œy ɔu/, repeated for F_1 and F_2 and for NSD and SSD. The within-subjects factor vowel category was made up of the formant measurements at 25% of the vowel's steady-state portion, and the eight regions served as the between-subjects factor region in each analysis. The results for F_1 showed no effects for NSD, but a significant main effect of region was found for SSD

TABLE II. Partial η^2 for the significant effects ($p \leq 0.001$) for REGION for the ANOVAs on frequencies for F_1 and F_2 for the nine monophthongal vowels.

Vowel	NSD		SSD	
	F_1	F_2	F_1	F_2
/a/	...	0.208
/a/
/ɛ/	0.413	0.181	0.126	...
/ɪ/	0.174	0.132
/i/
/ɔ/	0.169	0.151	...	0.125
/u/	...	0.213	...	0.179
/ɜ/	...	0.130
/y/

TABLE III. Partial η^2 for the significant effects ($p \leq 0.001$) for COMMUNITY for the ANOVAs on frequencies for F_1 and F_2 for the nine monophthongal vowels.

Vowel	Two regions		Six regions	
	F_1	F_2	F_1	F_2
/a/	0.048
/a/
/ɛ/	0.100
/ɪ/	0.046	0.096
/i/
/ɔ/
/u/	...	0.202	...	0.111
/ɜ/
/y/	0.169

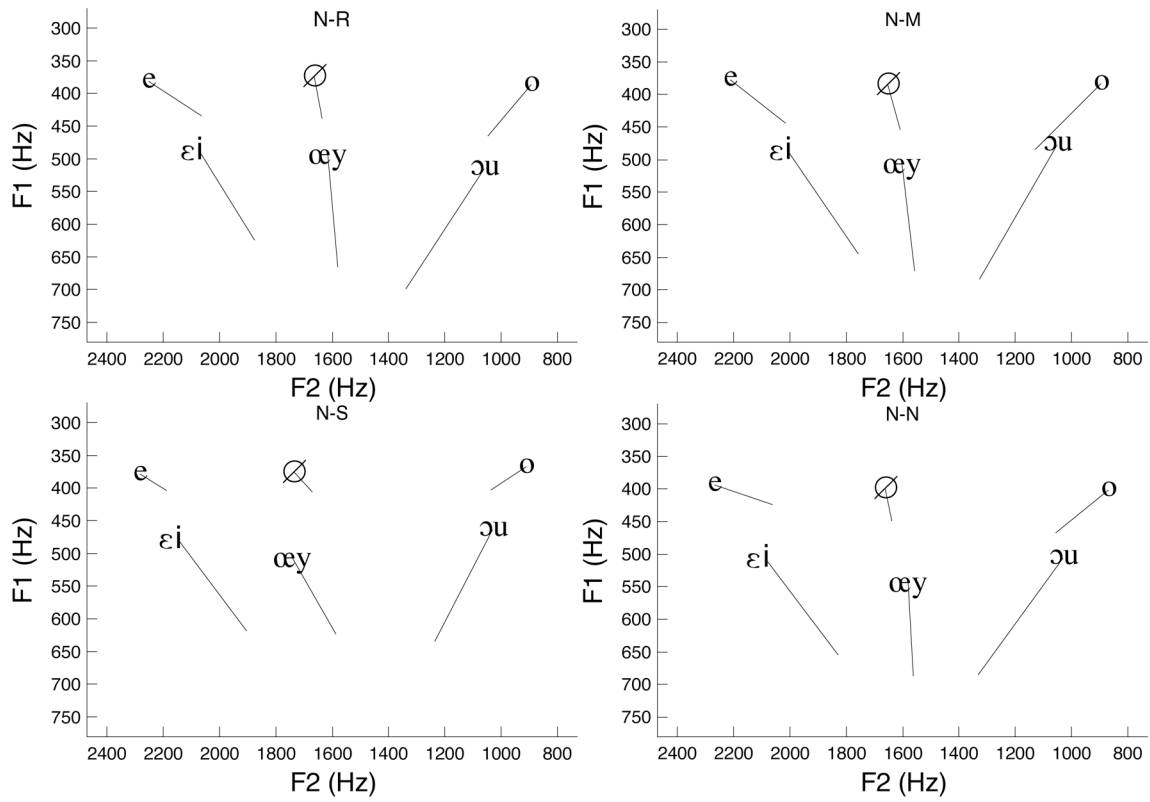


FIG. 7. Spectral change patterns for NSD. The phonetic symbol is plotted at the average formant frequency at 75% of the duration and the line originates from the average formant frequencies at 25% of the duration. N per symbol is 40.

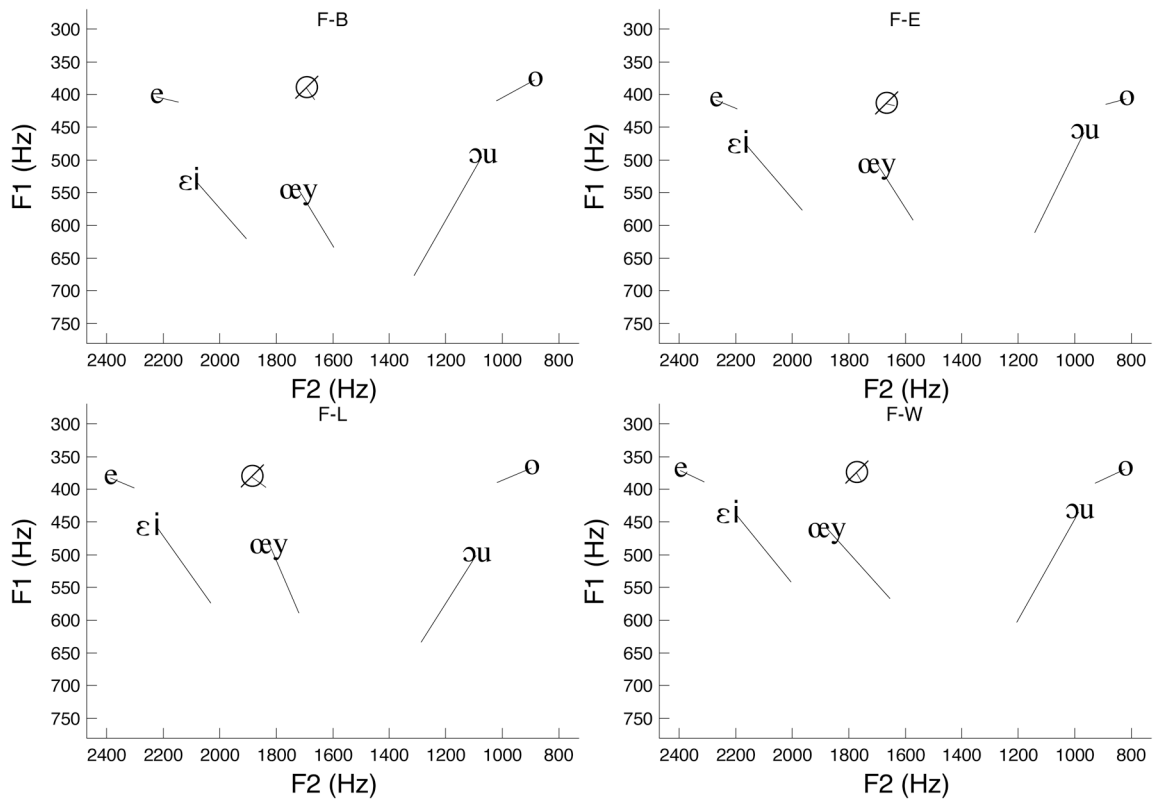


FIG. 8. Spectral change patterns for SSD. The phonetic symbol is plotted at the average formant frequency at 75% of the duration and the line originates from the average formant frequencies at 25% of the duration. N per symbol is 40.

D. Discriminant analyses

1. Steady-state measurements

Following Adank *et al.*, a quadratic discriminant analysis (QDA) was carried out to establish whether individual formant measurements show regional variation that allowed the speakers to be assigned to the corresponding region. The formant frequencies (F_1 and F_2) per vowel token for all nine monophthongal vowels were entered simultaneously as predictors. The QDA was set to classify each speaker into one of the eight regions, setting the chance level to 12.5%. A high percentage of correctly classified speakers suggests that regional accents are highly discriminable. The results showed that 72.2% of the speakers could be classified correctly. The formant frequencies of the speakers thus contained sufficient information about the speaker's regional background to allow the majority of the speakers to be assigned to the correct region.

A second QDA was carried out with community as the variable to be predicted (chance level 50%), with the F_1 and F_2 values of the nine monophthongal vowels entered simultaneously as predictors. The results showed that 84.4% of the speakers were classified correctly, meaning that the majority of speakers could be correctly assigned to either NSD or SSD.

2. Spectral change

Two QDAs were carried out to establish whether the speakers could be classified into the corresponding region or speech community based on the spectral change patterns in the formant frequencies of / ϵ i œ y ɔ u e o \emptyset /. In the first analysis, ΔF_1 and ΔF_2 , pooled for all 160 speakers for / ϵ i œ y ɔ u e o \emptyset / served as predictors, and region served as the dependent variable. This QDA showed that 48.8% of the speakers were classified correctly, which is above chance level (12.5%), but considerably lower than the percentages found for the monophthongal vowels. A second analysis was run with the same set of predictors, this time with community as the dependent variable, setting the chance level to 50%. The results showed that 78.4% of the speakers could be classified correctly.

These results indicate that the spectral change measurements contained sufficient information for a large proportion of the speakers to be assigned to the corresponding region or speech community, although the spectral change information conveyed less regional information than the steady-state measurements.

IV. DISCUSSION

A. Duration

First, considerable within-community differences were found for NSD, but not for SSD. The duration of the vowels from N-M and N-N was overall longer than for N-R. Furthermore, the division of vowels into phonetically long and short vowels was not identical for NSD and SSD. For the intermediate region (N-M) and the two peripheral regions (N-S and N-N) in NSD, the statistical analysis classified the vowels into two groups: / ϵ i œ y ɔ u e o \emptyset a/ and / α ϵ i ɔ u y

y/. Figure 2 shows that there is hardly any overlap between these two groups, especially for NSD, with longer durations for all vowels for the former group. The three noncentral SSD regions show a different pattern: for the intermediate region (F-E) and the peripheral I region (F-L), the vowels were divided into three groups, longer, / α ϵ ɛ i ɔ u o \emptyset œ y/, half-long: /y/ and shorter: / α ϵ i ɔ u y/. and for peripheral II, the vowels were divided into two groups, i.e., longer: / α e o \emptyset ɔ u ɛ œ y/ and shorter: / α ϵ i ɔ u y/. This pattern could be explained by variation in the duration of /y/; it was either phonetically long, or half long in the nonjcentral SSD varieties of Dutch, while it was phonetically short in NSD and in SSD's central region (F-B). The duration analysis revealed one further pattern within the Flanders speech community: the division into longer and shorter vowels in SSD's central region (F-B) was identical to the division in the four NSD regions, but differed from the three noncentral SSD regions. The division in Flanders' central variety was thus not representative for all SSD regions. The duration division for NSD and SSD's central regions was generally in agreement with phonological descriptions of the duration of Dutch vowels (Rietveld *et al.*, 2004). The results for regions F-E and F-L were more in accordance with the description of Koopmans-van Beinum (1980), who classifies /y/ as a half-long vowel. Nevertheless, the results for F-E and F-L did not fully comply with Koopmans-van Beinum's analysis as she classifies /i/ and /u/ as half-long, while they were short for F-L and F-E.

Second, the analysis indicated between-community differences for /y/ and / α ϵ ɛ ɔ y i/; /y/ was found to be significantly longer for SSD than for NSD, while / α ϵ ɛ ɔ y i/ were significantly longer for NSD (cf. Fig. 4).

Third, the duration results show longer overall durations for female speakers across all central and noncentral regions, and this gender-specific variation pattern was especially prominent for NSD's intermediate region (N-M). A similar difference between male and female speakers was previously reported for American English vowels (cf. Hillenbrand *et al.* 1995; Clopper *et al.*, 2005) and for Swedish vowels, in read speech as well as in more natural speaking styles (Simpson, 2001). It is not clear what causes their gender-related differences, although some authors suggest physiological explanations. For instance, Simpson proposes that these differences may be partly explained by differences in the synchronization of tongue body and tongue tip movements in female and male speakers.

B. Steady-state F_1 and F_2

The analysis for the steady-state measurements for the nine monophthongal vowels first showed within-community differences. The analyses per vowel showed regional differences across the majority of NSD's monophthongal vowels, i.e., for / α ϵ i ɔ u y y/. For SSD, regional differences were only found for three vowels, / ϵ ɔ u/. The vowels / ϵ ɔ u/ thus showed the most within-community variation as they show differences within both speech communities. Overall, the monophthongal vowels in both speech communities varied mostly in their tongue position, and less in their tongue

height, especially for SSD. Adank *et al.* reported that the central regions' vowel systems are anchored on the point vowels /a i u/, which were largely unaffected by language changes between the two central regions. However, the non-central varieties appeared to be anchored on /a/ and /i/ alone, as /u/ showed substantial variation in its F_2 dimension. Figures 6 and 7 show that /u/ was relatively backed in regions N-R, N-N and F-B, but fronted in the five remaining regions. The vowel /u/ may be undergoing a pronunciation change and become more fronted in certain regional varieties in NSD as well as SSD.

The analysis of the steady-state measurements showed some differences between speech communities as well. More differences were found between the three noncentral regions of NSD and SSD than between the two central regions. Differences between the two central regions were found for the two vowels /u/, while differences between the six noncentral regions were found for six vowels, i.e., /a ε ɪ u ʏ y/.

C. Spectral change of F_1 and F_2

For the long mid vowels /e o ø/ and the diphthongs /ei œy ou/, the spectral change, or diphthongization, was investigated for F_1 and F_2 . For the two central regions, Adank *et al.* reported considerably more diphthongization for /e o ø/ for N-R than for F-B for both formants. An effect of gender was also found: /ei œy ou/ showed greatest F_1 -diphthongization for the female speakers. The analyses first revealed some differences within NSD for /e o ø/; which showed more diphthongization in the intermediate region in the Netherlands than in the peripheral I region (N-S). No differences in diphthongization were found within the SSD speech community, neither for the diphthongal vowels nor for the long mid vowels.

The analysis indicated between-community effects only for the female speakers for /ei œy ou/, which was also reported in Adank *et al.* It was found that the female NSD speakers showed more diphthongization than the female SSD speakers. Furthermore, /e o ø/ were more diphthongized in NSD than in SSD, for all speakers. These findings are also in agreement with Adank *et al.*

The analysis of the onset and offset frequencies showed a prominent between-community difference for the long mid vowels: most NSD speakers started their long mid vowels at a more open position than the SSD speakers. This result is in agreement with one of the predictions of a recent theory on pronunciation change in Standard Dutch (Jacobi *et al.*, 2004; van Heuven *et al.*, 2002; Stroop, 1998). This theory states that a new sociolect of Dutch, "Polder Dutch" is evolving in the Netherlands. Stroop (1998) claims that this variety is typical of (relatively) young, highly educated, progressive Dutch women, but that men are most likely to follow suit. Stroop further claims that Polder Dutch is not based on any existing regiolect (regional variety) of Dutch and is spoken throughout the Dutch language area. The most conspicuous characteristics of Polder Dutch are a more open pronunciation of /ei œy ou/, and a more open pronunciation and increased diphthongization of the long mid vowels /e o ø/. The analysis of the onsets of /ei œy ou/ indicated that

the NSD speakers started these vowels at a more slightly more open position than the SSD's peripheral II speakers, but these effects should not be overrated as they were relatively small. The results for the long mid vowels displayed more aspects of Polder Dutch, as they showed considerably more diphthongization for the NSD speakers than for the SSD speakers. Furthermore, the analysis indicated that the NSD speakers started these vowels at a more open position than the SSD speakers. However, to establish whether Polder Dutch is emerging in the Netherlands, more extensive analyses on, preferably, more spontaneous recording material are required.

D. Differences between and within speech communities

The results showed differences between as well as within speech communities. Overall, it seems that more within-community variation patterns were found for NSD than for SSD; for NSD regional differences were found for duration, the steady-state measurements, and the spectral change measurements for the long mid vowels. The results indicated that the vowels of Standard Dutch show more regional variation in the Netherlands than in Flanders. A similar difference between the Netherlands and Flanders was described in Van de Velde *et al.* (1997). Van de Velde *et al.* suggest that the difference in uniformity originated from a divergence in the pace at which the standard variety evolves in the two speech communities, with NSD changing more rapidly than SSD.

E. Regional traces

The results of the discriminant analyses indicated that there was sufficient regional variation present in the measurements of the steady-state formant frequencies to allow most of the speakers to be classified into the appropriate region or speech community. When the analyses were run on the measurements for the long mid vowels and the diphthongal vowels, a similar pattern was found in the results (although the percentages were lower). This is noteworthy, given the specific speaking style used for recording the vowel tokens, i.e., reading aloud nonsense sentences from a computer screen. It is well documented (Chambers, 2003; Labov, 1972) that speakers tend to use more lower-prestige utterances (e.g., more dialect words) in more informal speaking styles such as spontaneous conversation. In more formal speaking styles, they tend to use more high-prestige utterances (i.e., more variants in the standard language). The interview was conducted in a relatively formal setting and the vowels were pronounced in nonsense sentences. When reading aloud words, especially in nonsense sentences, speakers are generally over conscious of their speaking style and tend to carefully monitor their pronunciation. The formal setting in conjunction with the specific task used may have induced them to monitor their speech in such a way that relatively little regional traces were present. However, the results illustrated that regional traces may very well be present in the speech from professional language users, even when the speech is recorded in a formal setting. It would therefore be

interesting to compare the present results with acoustic measurements of vowels recorded in one of the more informal tasks present in the sociolinguistic interview. This may lead to even more extensive regional variation patterns to be uncovered between these eight varieties of Standard Dutch. Another prospect would be to compare the classifications of the statistical analyses with classification scores from listeners, to establish whether listeners can perceive the reported regional differences as well. Alternatively, a perceptual similarity test could be run that presents listeners with a pair of vowel tokens and requires them to decide whether the two tokens were produced by speakers of different regional varieties (cf. Clopper *et al.*, 2006). Clopper *et al.* used a paired comparisons similarity task to estimate the perceptual distance between six regional varieties of Standard American-English. The results from such a perceptual similarity test may lead to more insights in the perceived linguistic distances between specific regional varieties in the Dutch language area.

F. Final remarks

It seems justified to conclude that the differences between the two central regions of NSD and SSD as described in Adank *et al.* were, to a large extent, also found for the noncentral regions within each speech community. However, the analysis revealed additional variation patterns within and between NSD and SSD. Most notably, the fronting of /u/ in five of the noncentral regions across NSD and SSD and the lengthening of /y/ in the three SSD varieties F-E, F-L, and F-W. Second, the analysis indicated that SSD was more uniform with respect to the variation in the vowel system than NSD. Furthermore, regional variations patterns in the production of long mid vowels /e oø/ supported a recent theory on an emergent sociolect of Standard Dutch in the Netherlands. Finally, the present study illustrated that distinct regional variation patterns can be observed in the speech of relatively highly educated (i.e., university level or comparable), professional users of the standard language.

ACKNOWLEDGMENTS

This research was supported by the Netherlands Organization for Research (NWO) through the Flemish Netherlands Committee (VNC) under Project No. 205-41-069 and by the Economic & Social Research Council (ESRC) under Project

No. PTA-026-27-1218.

- Adank, P., van Hout, R., and Smits, R. (2004). "An acoustic description of the vowels of Northern and Southern Standard Dutch," *J. Acoust. Soc. Am.* **116**, 1729–1738.
- Adank, P., Smits, R., and van Hout, R. (2004). "A comparison of vowel normalization procedures for language variation research," *J. Acoust. Soc. Am.* **116**, 3099–3107.
- Bell, A. (1983). "Broadcast news as language standard," *Int. J. Soc. Lang.* **40**, 29–42.
- Booij, G. (1995). *The Phonology of Dutch*. (Clarendon, Oxford).
- Chambers, J. K. (2003). *Sociolinguistic Theory: Linguistic Variation and its Social Significance*, 2nd ed. (Blackwell, Oxford).
- Clopper, C. G., Pisoni, D., and de Jong, K. (2005). "Acoustic characteristics of the vowel systems of six regional varieties of American English," *J. Acoust. Soc. Am.* **118**, 1161–1676.
- Clopper, C. G., Levi, S. V., and Pisoni, D. B. (2006). "Perceptual similarity of regional varieties of American English," *J. Acoust. Soc. Am.* **119**, 556–574.
- Disner, S. (1980). "Evaluation of vowel normalization procedures," *J. Acoust. Soc. Am.* **67**, 253–261.
- Hagiwara, R. (1997). "Dialect variation and formant frequency: The American English vowels revisited," *J. Acoust. Soc. Am.* **102**, 655–658.
- Hillenbrand, J., Getty, L. A., Clark, M. J., and Wheeler, K. (1995). "Acoustic analysis of American English vowels," *J. Acoust. Soc. Am.* **97**, 3099–3111.
- Jacobi, I., Pols, L. W. C., and Stroop, J. (2004). "Polder Dutch: Aspects of the [Ei]-lowering in Standard Dutch," in *Proceedings Eurospeech 2005*, Lisbon, 2877–2880.
- Koopmans-van Beinum, F. (1980). "Vowel Contrast Reduction," Ph.D. thesis, University of Amsterdam.
- Labov, W. (1972). *Sociolinguistic Patterns* (University of Pennsylvania Press, Philadelphia).
- Lobanov, B. M. (1971). "Classification of Russian vowels spoken by different speakers," *J. Acoust. Soc. Am.* **49**, 606–608.
- Peterson, G. E., and Barney, H. L. (1952). "Control methods used in the study of the vowels," *J. Acoust. Soc. Am.* **24**, 175–184.
- Pols, L. C. W., Tromp, H. R. C., and Plomp, R. (1973). "Frequency analysis of Dutch vowels from 50 male speakers," *J. Acoust. Soc. Am.* **53**, 1093–1101.
- Rietveld, T., Kerkhoff, J., and Gussenhoven, C. (2004). "Word prosodic structure and vowel duration in Dutch," *J. Phonetics* **32**, 349–371.
- Simpson, A. P. (2001). "Dynamic consequences of differences in male and female vocal tract dimensions," *J. Acoust. Soc. Am.* **109**, 2153–2164.
- Stevens, K. N. (1998). *Acoustic Phonetics* (MIT Press, Cambridge).
- Stroop, J. (1998). *Poldernederlands, waardoor het ABN verdwijnt* ('Polder' Dutch: The cause of the disappearance of 'Standard Civilized Dutch') (Bakker, Amsterdam).
- Van de Velde, H., van Hout, R., and Gerritsen, M. (1997). "Watching Dutch change," *J. Sociolinguistics* **1**, 361–391.
- van Heuven, V. J., Edelman, L., and van Bezooijen, R. (2002). "The pronunciation of /ei/ by male and female speakers of avant-garde Dutch," *Linguistics in the Netherlands*, 62072.
- Van Nierop, D. J. P. J., Pols, L. W. C., and Plomp, R. (1973). "Frequency analysis of Dutch vowels from 25 female speakers," *Acustica* **29**, 110–118.

Acoustic cues discriminating German obstruents in place and manner of articulation

Julia Hoelterhoff^{a)} and Henning Reetz

Universität Konstanz, Fachbereich Sprachwissenschaft, D-186, 78457 Konstanz, Germany

(Received 20 December 2005; revised 27 November 2006; accepted 4 December 2006)

This study focuses on the extraction of robust acoustic cues of labial and alveolar voiceless obstruents in German and their acoustic differences in the speech signal to distinguish them in place and manner of articulation. The investigated obstruents include the affricates [pf] and [ts], the fricatives [f] and [s] and the stops [p] and [t]. The target sounds were analyzed in word-initial and word-medial positions. The speech data for the analysis were recorded in a natural environment, deliberately containing background noise to extract robust cues only. Three methods of acoustic analysis were chosen: (1) temporal measurements to distinguish the respective obstruents in manner of articulation, (2) static spectral characteristics in terms of logarithmic distance measure to distinguish place of articulation, and (3) amplitudinal analysis of discrete frequency bands as a dynamic approach to place distinction. The results reveal that the duration of the target phonemes distinguishes these in manner of articulation. Logarithmic distance measure, as well as relative amplitude analysis of discrete frequency bands, identifies place of articulation. The present results contribute to the question, which properties are robust with respect to variation in the speech signal. © 2007 Acoustical Society of America. [DOI: 10.1121/1.2427122]

PACS number(s): 43.70.Jt, 43.70.Fq, 43.72.Ar [AL]

Pages: 1142–1156

I. INTRODUCTION

The aim of this paper is to distinguish German voiceless obstruents [pf, ts, p, t, f, s] in manner and place of articulation by making use of their physical differences: Obstruents are produced by a constriction of the articulators while the air escapes from the lungs. They include affricates, fricatives, and stops. Affricates contain acoustic features of both stops and fricatives. The closures of affricates and stops have the same acoustic properties while the frication of affricates is produced as in fricatives by a narrow constriction (cf. Stevens, 1998, p. 379). Stop consonants build up a substantial pressure of air during the closure of the vocal tract that is released. According to Stevens (1998, p. 348), the release is characterized by a transient, followed by the frication and aspiration (if aspiration is present at all). In comparison to the release of stops, fricatives have a much weaker energy onset causing the amplitude of noise to rise slower than in a stop. At the same time, the duration of the fricatives' noise portion is definitely longer compared to that of stops.

The experiments described in this article are designed to discriminate manner *and* place of articulation of labial and alveolar German obstruents in word-initial and word-medial position. The investigated obstruents, the fricatives [f] and [s], the stops [p] and [t], and the affricates [pf] and [ts], form a complete labial-alveolar contrast over three different manners of articulation. The completeness of this series is provided by the affricate [pf] that, apart from German, is only found in two of the Niger-Kordofanian languages in Zaire (cf. Maddieson, 1984). A velar pendant does not exist in

Standard High German. Only Swiss German and some South German dialects contain the velar affricate [kx].

To distinguish manner of articulation of affricates and fricatives, Howell and Rosen (1983) measured *rise time* by calculating the time interval between the onset of a fricative or affricate to its amplitude maximum. Their studies were based on one of the earliest acoustic investigations considering affricates being conducted by Gerstman (1957, as reported by Howell and Rosen, 1983). Overall, the findings of Howell and Rosen (1983) and Gerstman (1957) were the same, namely, that the mean rise time for affricates was significantly shorter compared to that of fricatives. This finding was independent of whether the affricate/fricative appeared in word-initial, word-medial or word-final position, or whether the measurements were conducted in isolated words or in a sentence context.

Shinn (1985) investigated manner and place of articulation for voiced and voiceless obstruents in German, Czech, and Mandarin. He tested six different acoustic parameters, taking account of temporal and energy measures: *VOT*, *rise time*, *energy change*, *attack* (high-frequency energy at the consonant onset in comparison to the amount of energy 20–70 ms after the onset), *fall time and noise duration*. The results of Shinn supported the findings of Gerstman (1957) and Howell and Rosen (1983), but he applied this metric not only to affricates and fricatives, but also to stops. *Rise time* appeared to be the most appropriate and stable parameter to distinguish affricates, fricatives, and stops. Stops had the shortest rise time with a mean of only 7.8 ms, followed by affricates, with a mean rise time of 49.3 ms and then the average fricatives rise time was 90 ms (Shinn, 1985, p. 128). Moreover, Shinn (1985) was able to distinguish place of articulation by the parameter *rise time* as well although the distinction between [ts] and [pf] in German was not possible.

^{a)}Author to whom correspondence should be addressed. Electronic mail: julia.hoelterhoff@uni-konstanz.de

Apart from *rise time* Shinn investigated the *noise duration* (i.e., the duration of the frication in affricates and fricatives and the part of the signal following the closure in stops) and found temporal boundaries within obstruents that allowed their classification. The frication noise is perceived as belonging to stops when its duration is below 75 ms, to affricates when the noise duration is between 75 and 130 ms, and to fricatives when it is above 130 ms.

Kluender and Walsh (1992) conducted two perceptual experiments testing the importance of the parameters' *rise time* against *noise duration* to distinguish American English voiceless affricates from fricatives. In each experiment one of these variables (i.e., either the duration of the rise time or the duration of the noise portion) was manipulated and their effects on the perception of [tʃ] versus [ʃ] were analyzed. They found that *rise time* alone was not a sufficient parameter to perceive the sounds correctly, but that a variation of the frication duration alone was.

Repp, Liberman, Eccardt, and Pesetsky (1978) investigated the perceptual relevance of temporal acoustic cues for the affricate - fricative (and stop) distinction. They varied the noise and silence durations in the stimuli "gray chip" and measured whether listeners perceived the fricative [ʃ] as in "great ship" or an affricate [tʃ] as in "great chip." They concluded that the silence and noise portions are interdependent acoustic cues that need to be related for the appropriate percept. With an identical duration of the silence portion, a shorter noise duration resulted in the perception of an affricate (gray chip), whereas a longer noise duration triggered the perception of a fricative (great ship). The findings of Repp *et al.* (1978) suggested that the closure and frication durations (or noise, respectively) of affricates are shorter compared to those in fricatives and stops. They pointed out that the identification of a sound as an affricate was not based on a single cue, but on the proportion of closure and frication duration of affricates—two acoustic events occurring one after the other. From a perceptual point of view, the relative and therefore dynamic processing of acoustic events seems to be important for proper speech recognition. To summarize, the perceptual distinction of manner of articulation of affricates, fricatives, and stops seems to be possible based on temporal measurements, either on duration alone or acoustic cues, like rise time, as well.

However, the studies on noise duration and rise time of affricates and fricatives showed that the individual duration depends on the context. In agreement with these findings, Klatt (1976) conveyed that the duration of fricatives is highly dependent on the context. A consonant such as [s] can range from 200 ms in a phrase final position to less than 50 ms in a consonant cluster. For example, the consonants [p] or [s] are longer in combination with an adjacent vowel than in the consonant cluster [sp]. Looking at affricates as simple consonant clusters, the components of affricates (i.e., closure and frication duration) should be shorter than the corresponding portions in fricatives and stops. Klatt (1976) also reported that stress patterns have a great influence on duration.

In several studies, *relative amplitude* was shown to differentiate place of articulation in fricatives. This function

measures the amplitude in a particular frequency region at the vowel center relative to the obstruent center. For example, Stevens (1985) found in several perceptual experiments that amplitude alone is not a relevant indicator to perceptually discriminate different types of fricatives. Instead, the spectrum amplitude in relation to the neighboring vowel determined the correct perception. Stevens' findings were supported by Gurlekian (1981), who detected the same correlation for the perception of Spanish fricatives.

One of the most comprehensive studies investigating fricatives was conducted by Jongman, Wayland, and Wong (2000). They tested several methods of analysis to distinguish place of articulation for American English fricatives, carrying out spectral, amplitudinal, and temporal measurements. They tested *spectral peak location* by calculating fast Fourier transform (FFT) and LPC spectra with a 40 ms Hamming window in the middle of the frication portion. The spectral peak (data sampled at 22 kHz) was defined as highest amplitude point of the FFT spectrum. Furthermore, they calculated *spectral moments*, performing FFTs with a 40 ms Hamming window at four different locations in the fricative (onset, middle, end, and center of fricative offset). The moments (*mean, variance, skewness, and kurtosis*) were calculated from Bark and linear scales. The authors reported no difference between the two types of scales and therefore used only the linear scale. They found spectral peak location and spectral moments to distinguish all four investigated places of articulation. The best results were achieved by computing the *normalized* and *relative amplitude*. Normalized amplitude refers to the difference between fricative and vowel amplitude. To measure the relative amplitude, a discrete Fourier transform (DFT) at the vowel onset was taken and the amplitude of the F3 and F5 region compared to the respective region in the fricative by subtracting both values.

To distinguish place of articulation in stop consonants, Stevens and Blumstein (1981) searched for invariant acoustic correlates in the spectral shape. They obtained spectra with a window length of 26 ms starting with the release of the stop sampled at 10 kHz, smoothed by linear prediction algorithm. For the labial [p], the spectrum was found to be flat because the frication noise source at the lips excites all formants equally. F2 and all higher formants show a downward shift compared to a neutral spectrum. The alveolar stops, however, showed upward shifts for F2, F3, and F4 compared to the neutral spectrum (the positions of the neutral position are located at 1500, 2500, and 3500 Hz for F2, F3, and F4, respectively) and excitation noise especially at the higher frequencies and weak acoustic excitation at the lower frequencies.

In contrast to the findings of Stevens and Blumstein (1981), Lahiri, Gewirth, and Blumstein (1984) found that invariant static acoustic properties do not serve to distinguish "diffuse" stop consonants in Malayalam, French, and English. The term diffuse refers to the fact that no incisive energy shape is observable in the spectrum. Labial and dental stop consonants were not distinguishable because the energy of those sounds is distributed in a diffuse and flat manner in the noise portion. Instead, Lahiri, Gewirth, and Blumstein (1984) discriminated these sounds by the ratio of the relative

change from the beginning of the release to the beginning of voicing measured in the low-frequency range (1500 Hz) and the high-frequency range (3500 Hz).

Miller (1989) proposed an auditory-perceptual approach correlating spectral prominences to defined locations in an auditory perceptual space for vowels. For this approach three *sensory formants*, SF1, SF2, and SF3 were located (representing the center frequencies of the first three significant prominences of a short term spectrum, briefly, referring to F1, F2, and F3) and a *sensory reference* (SR), serving as a normalizing factor (155 Hz for male and 185 Hz for female speakers, cf. Miller, 1989). He successfully described the speech sounds in a three-dimensional perceptual space that was composed of the logarithmic distances $\log(F1/SR)$, $\log(F2/F1)$, and $\log(F3/F2)$. This approach was taken up by Jongman and Miller (1991) to discriminate place of articulation in syllable initial stops. Since stops, unlike vowels, are characterized by an absence of low-frequency energy, it is difficult to obtain a BF1 value (i.e., burst frication sensory formant, analogous with the SF1 in the vowel investigation), and this is why the BF1 was set equal with the SR. As a consequence, the $\log(BF1/SR)$ value is zero, leaving only a two-dimensional perceptual space. To compute the formants, an LPC analysis was used with a 24 ms Hamming window centered over the burst onset. The metric was tested on a new set of speech data containing eight different speakers and allowed place discrimination with 70% of accuracy.

Unlike stops and fricatives, affricates are rarely investigated with respect to their place of articulation because English has only one place for affricates. Moreover, it was assumed that those cues distinguishing place of articulation of affricates are similar to those of stops, which had been well studied in English. The question remains open whether the results gained for English are applicable to German as well. The current investigation focuses on speech production, whereas most of the studies investigating obstruents have been perceptual ones.

For the manner and place distinction of the German obstruents [pf, ts, f, s, p, t], labial and alveolar manners of articulation ought to be discriminated by temporal measurements (cf. Klatt, 1976, Shinn, 1985). Since the studies mentioned revealed that duration itself is a variable parameter (e.g., depending on different contexts, inclusive stress), the test words of the present investigation are designed in a way that the target obstruent is always located in the stressed syllable (two of the test words form an exception to this rule—details are given in Sec. II A).

To distinguish place of articulation within fricatives, stops, and affricates, two types of metrics are chosen. First of all, *relative amplitude* as a dynamic approach (Jongman *et al.*, 2000) is tested. The positive results gained by the calculation of the *relative amplitude* for fricatives appear to be quite promising for the present study and the technique seems applicable to stops and affricates as well. Second, *logarithmic distance measure* (cf. Miller, 1989, Jongman and Miller, 1991) is applied as a static approach. Although the latter approach was not completely successful, this metric seems to have important potential for the needs of the present study. Jongman and Miller (1991) reported that the

burst frication sensory formants were hard to localize and proposed a dynamic approach to deal with this problem. Instead of computing a single frame from the spectrum, they proposed to compute a frame for every millisecond of the speech signal and generate a path through the auditory perceptual space. The great advantage of this metric is its ability to normalize across speakers.

All of the metrics mentioned above are developed in a way to fit with the needs of the FUL (*Featurally Underspecified Lexicon*, Lahiri and Reetz, 2002) speech recognition system. The characteristics found within this study will be combined and then implemented in the acoustic front end of the FUL automatic speech recognizer. The FUL speech recognition system is based on underlying phonological features providing robustness to variations in the speech signal. Apart from noise robustness, the FUL system is also meant to cope with dialectal and speaker variation. To embark on the strategy of extracting robust acoustic cues from the speech signal only, the speech data used for analysis in the present experiments was recorded in a natural and therefore noisy environment. Occasional background noise in the speech data is the main reason why *rise time* is not used as a parameter in the present investigation, since the peak of energy would have been problematic to localize. However, the duration of frication noise was reported to be more stable metric anyway (cf. Shinn, 1985; Kluender and Walsh, 1992). The details about the parameters used are described in Sec. II C.

II. EXPERIMENT

German obstruents are investigated to obtain robust acoustic cues from the speech signal. In order to analyze data with realistic background noise, as well as to avoid a hypercorrect speaking style, as it is sometimes found in read speech, the recordings of ten speakers were taken in standard living rooms. Two different tasks were designed to record the speech data: (1) a reading task and (2) a task with nearly spontaneous speech (cf. Sec. II C).

The study consists of three subtests. In the first test case, manner of articulation is discriminated in labial and alveolar obstruents by *temporal measurements*. The second and third test scenarios both deal with place distinctions. The second test case uses *logarithmic distance measure* as a static approach, whereas in the third test case a dynamic approach—*relative amplitude in discrete formant frequency regions*—is applied to distinguish place of articulation in the investigated obstruents. Since the experiments are designed to detect acoustic cues that are relevant for speech recognition rather than validating the results of prior studies mentioned above, metrics from prior studies were used and adapted for the present investigation.

Throughout this investigation, the two different affricate components are referred to as closure and frication segments. In the context of this investigation “segment” is understood as a part of a phoneme, characterized by the structure of the respective portion of the signal. An affricate is therefore composed of the closure and the frication, whereas a stop is characterized to consist of the closure and the release. Fricatives contain the frication segment only.

A. Materials

Six obstruents [pf], [ts], [f], [z] or [s] (depending on word the position, cf. last paragraph of this section), [p] and [t] are investigated in the environment of *seven* different vowels [ɪ], [ɛ], [a], [ɔ], [ʊ], [ʏ] and [œ]. In some cases, the short or lax vowel had to be replaced by the long or tense vowel because no respective vowel-obstruent combination was found in German. In the following, the IPA symbols for the short vowels are used, although some words with long vowels occur in the speech data.

The obstruents are distinguished by manner of articulation, separating affricates from fricatives and stops and also by place of articulation, distinguishing labial or alveolar obstruents. The German labial obstruents can be divided into labiodentals [pf, f] and bilabials [p], but are referred to as “labials” in the context of this investigation.

Each target sound was recorded in *two* word positions: word-initially and word-medially ($6 \times 7 \times 2 = 84$). For each of the word positions, *three* exemplary words were chosen ($84 \times 3 = 252$), for example, [pf] followed by the vowel [a] in word-initial position was represented by *Pfarrer* [pfaʁɐ] “priest,” *Pfanne* [pfaɲə] “pan,” and *Pfaffe* [pfafa] “cleric.” For the same phoneme combination in word-medial position (the relevant vowel precedes the consonant), the respective words were *Apfel* [apfəl] “apple,” *Stapfen* [ʃtapfən] “footprint,” and *Zapfer* [tsapfɐ] “tapster.” All test items, apart from *Sand* [zant] “sand” and *Pfuhl* “puddle” [pfu:l], were bisyllabic. It was not possible to use a CV (consonant vowel) combination in word-medial position (as it was done for the initial position), because only very few combinations can be found in German. The test words were again recorded in *two* different tasks, ($252 \times 2 = 504$). Ten speakers contributed to the data collection, summing up to a total of 5040 items ($504 \times 10 = 5040$).

Some of the test words contained the ending “-el” after the voiceless stop consonant, as in *Zettel* “slip of paper” [tʃɛtəl]. While labeling the soundfiles, it was checked that the subjects produced the schwa and did not delete the latter to produce only a syllabic [l], as in [tʃɛtl]. If the schwa had been deleted, which happened in less than 0.5% of the data, the soundfiles were not used for the present investigation.

In Standard High German, the voiced fricative [z] occurs word-initially and word-medially, whereas the voiceless fricative [s] does not occur word-initially, apart from some loan words. As a consequence, the voiced alveolar fricative [z] was used word-initially, whereas in word-medial position, the voiceless [s] was used. It was expected that [s] and [z] would differ to some extent in their duration. Baum and Blumstein (1987) measured the duration of syllable-initial fricative consonants in English and found that voiced [z] is shorter, although the authors reported some overlap in the distributions of duration of the voiced versus the voiceless fricatives. Moreover, the presence or absence of voicing influences the spectral characteristics of fricatives. Due to the vocal folds vibration of the voiced [z], the latter contains more energy in the lower frequency regions. The laryngeal vibrations modulate at the same time the turbulence noise, consequently, less energy can be found in the higher fre-

quency regions of [z] compared to the spectral distribution of [s]. The voiceless fricative [s] is characterized by the absence of low-frequency energy, but has noise energy in the higher-frequency regions (cf. Stevens, 1998). The complete set of materials is listed in the Appendixes A and B.

B. Participants

Ten speakers of Standard High German with no remarkable difference in their dialect were recorded. The five female and five male participants reported no speech impairment. All subjects had an academic, but nonlinguistic background and were not aware of the purpose of this investigation. The participants’ age ranged from 25 to 60 years.

C. Method

Two different recording tasks, (1) a reading task and (2) a sentence-composing task were chosen, in order to exclude effects elicited by the tasks themselves. The reading task is meant to induce a more formal pronunciation than the more spontaneous sentence-composition task.

For the reading task, the participants were asked to read the sentences appearing on a laptop screen at intervals of 1 s. The word containing the target sound was always positioned in the nominal phrase preceded by the definite articles *die* [di:] “the” (FEM) or *der* [deɐ̯] “the” (MASC). The German neuter definite article *das* [das] “the” was not used at all. Finally, the whole sentence structure consisted of a definite article and its subject followed by a verb and an object. The sentence context was different for each word, for example, the contextual frame for the word *Pfaffe* “cleric” was *der Pfaffe hat Hunger* “the cleric is hungry” and for *Zapfer* “tapster” *der Zapfer hat Spass* “the tapster is having fun.” For the sentence-composing task, the subjects were asked to compose sentences with two randomly mixed target words, appearing simultaneously on the laptop screen. The words were the same as in the first task. It was emphasized that there was no need to form a meaningful sentence. The words were presented at intervals of 4 s to gain an almost natural speaking style. An illustration sentence (that made no sense) was presented to the subjects before the session began. For example, the words *Apfel* “apple” and *Katze* “cat” were presented to the participants and could result in a sentence such as *der Apfel liegt auf der Katze*, “the apple lies on the cat.” Naturally, the responses varied among the subjects, and therefore the preceding sound or word was not predictable as it depended on the subjects’ creativity.

The stimuli were presented to the subjects by using Microsoft PowerPoint. The items within each recording scenario were presented randomly to avoid priming effects and to conceal the goal of the investigation. The data were recorded on a Sony DAT recorder TCD-D100 using the Sony ECM-MS 957 condenser microphone. The microphone was placed on the left side of the laptop on a stand, at an approximately 45° angle, about 30 cm away from the speaker, directed to the speakers’ mouth. Hence, the airflow was not directly hitting the membrane of the microphone. The recordings were made in various furnished rooms with little reverberation. During the recordings, background noise, for

example, that of other people, traffic, doors, naturally occurred because the aim was to collect almost natural speech data. Another positive effect was that the subjects acted more relaxed in their familiar environments.

A recording rate of 44.1 kHz and a 16 bit resolution were chosen. The speech data were downsampled to 22.05 kHz on hard disk, using an anti-aliasing filter.

III. ANALYSIS

The speech data were analyzed with respect to duration, logarithmic distance of formant frequencies and relative amplitude in discrete frequency bands. The details are discussed in the following sections. The speech data were manually labeled using `KAYLAB Multispeech 2.5.1`. All speech data were labeled by one person. Regularly, a set of data was controlled by another person to ensure the consistency. The manual labeling was performed on the basis of the wave form and the spectrogram. Criteria used to determine the onset (offset) of the obstruents were the attenuation (increase) of the amplitude of the signal and disappearing of higher frequency components at the onset and appearing of a clear formant structure at the offset. Nevertheless, an uncertainty of plus/minus one glottal pulse can exist at the segment boundaries also because the wave form and spectrogram display in `Multispeech` are not completely time aligned. The following phonemes and their segments were labeled:

- *Affricates*: Closure - Frication
- *Fricatives*: Frication
- *Stops*: Closure - Release
- *Vowel*

The frication measured in affricates also contained noise from the release of the closure. Both noise components were not separable, due to the background noise superimposing the speech signal. The closure of affricates and stops had the same structure. In addition to the obstruents and their segments, the neighboring vowel was labeled as well. Word-initially, the vowel following the obstruent was measured, whereas word-medially, the vowel preceding the obstruent was taken into account. The examples in Fig. 1 show how the word-initial labial obstruents were labeled.

The LPC analysis for the *logarithmic distance measure* (cf. Sec. III B) and *relative amplitude* (cf. Sec. III C) were both performed with `MATLAB 7.0 (R14)`. The statistical analysis was performed with the software suite `JMP 5.0.1` of the SAS Institute Inc.

A full-factorial repeated measures analysis of covariance (ANOVA) was computed. The nonsignificant interactions and factors were removed and finally the relevant factors interpreted. The following factors were chosen for the full-factorial model:

- *Obstruent* ([pf], [ts], [f], [z] or [s], [p], [t])
- *Vowel quality* ([ɪ], [ɛ], [a], [ɔ], [u], [y], [œ])
- recording *Task* (reading, sentence building)
- *Subject* set as random factor (ten speakers)

The variable test *Word* was nested under factors *Obstruent* and *Vowel*. The factors were the same for each analy-

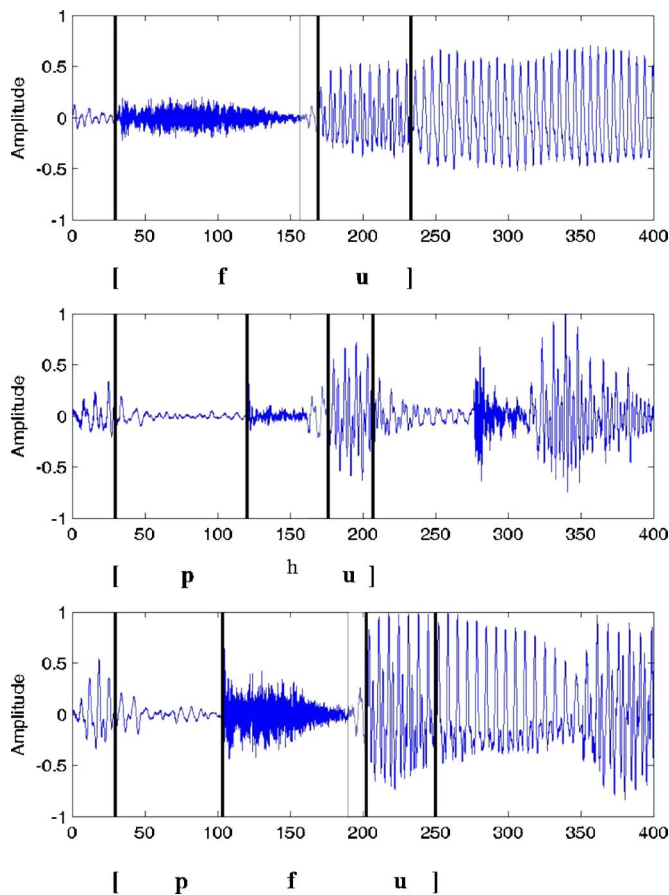


FIG. 1. (Color online) Demonstration of word-initial labial obstruent labels—indicated by the black vertical lines. The gray colored fields indicate the position of the Hamming window applied for the LPC analysis to compute the formant frequencies.

sis. The standard least square design with *Restricted Maximum Likelihood Estimation* (REML) was used. The application of a random effect for the variable *Subject* is compatible with a “by subject analysis:” the REML estimation does not substitute missing values by estimated means, hence no synthetic denominators are needed. If the results revealed a significant *Obstruent* effect, *post hoc* tests were performed. The *post hoc* tests used in `JMP` build a contrast of a set of linear combinations of parameters in terms of the least squares means of the effect. If an *Obstruent* × *Vowel* interaction was found to be significant, Tukey *post hoc* tests were applied. If an effect was found to be not significant ($\alpha=0.5$), this was not reported.

The variable *Obstruent* was not grouped with respect to manner or place, rather obstruents were tested against each other for the contrasts of interest (e.g., [f] against [p], and [pf] or [f], against [f] and [s]). By this procedure, the grouping of phonemes with structural differences was avoided.

The influence of *Gender* on the results was also statistically evaluated. The factor *Gender* showed no significant differences concerning all of the parameters investigated within the scope of this study and therefore will not be further discussed in the following sections.

A. Temporal analysis

The position of the labels in the soundfiles was extracted and then transferred to `JMP` to calculate the absolute duration

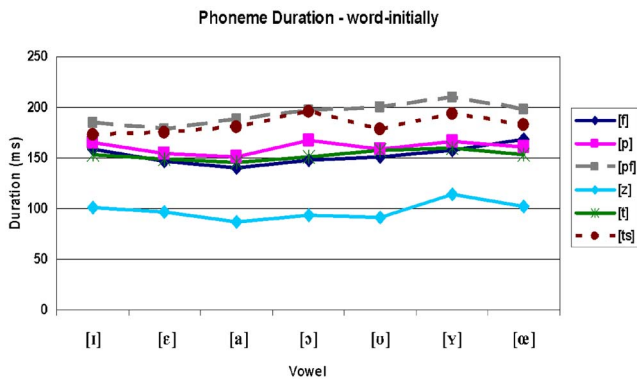


FIG. 2. (Color online) Comparison of mean duration of the obstruents per vowel in word-initial position.

of the phonemes as well as the duration of the segments. The temporal measurements were structured as such: The phoneme duration of affricates was compared to that of stops on the one hand and fricatives on the other. In addition, the sounds were compared according to the duration of their segments. For the segmental comparison of affricates and stops, the closure duration was evaluated. For the comparison of affricates and fricatives, the frication was analyzed. It has to be kept in mind that the closure of affricates and stops has the same phonetic status, whereas the frication of affricates and fricatives does not have the same quality. The frication of affricates follows a closure segment, therefore much more energy is present than in regular frication. The release of stops was also measured but not taken into account for the statistical analysis.

This study concentrates on duration only. Some cues that are known to influence the duration of certain segments were not taken into account, such as overall speaking rate, syllabic as well as stress patterns. However, the speaking rate was varied indirectly because two different tasks were chosen. All but two mono-syllabic words (*Pfuhl* “puddle,” *Sand* “sand”) had two syllables and initial stress (cf. Sec. II A and the Appendixes for the complete word lists).

B. Formant frequency analysis

For the automatic formant extraction, the speech data were downsampled to 12 kHz. An autocorrelation LPC analysis was chosen, using the root solving procedure to compute the first four formant frequencies (in the following referred to as F1, F2, F3, F4). One explicit goal of the present investigation was to compute the formants automati-

TABLE I. Mean duration (ms) of the target phonemes in word-initial and word-medial positions and their ratio (*obstruent-middle/obstruent-initial*).

Obstruent	Initial	Medial	Ratio
[f]	153	120	0.78
[p]	160	122	0.76
[pf]	193	205	1.06
[z],[s]	99	128	1.29
[t]	153	112	0.73
[ts]	183	197	1.08

cally with a routine programmed in MATLAB 6.5.1.

The LPC analysis uses a filter (finite impulse response) with the number of coefficients set to 8. Since the resonances of the back cavities are attenuated by the constriction of the fricatives, we expect only two to three front cavities and Helmholtz resonances, so that eight coefficients are appropriate to obtain smooth spectra.

It is known that automatic formant extraction has its difficulties, and therefore different parameter settings for the LPC analysis were tested. The testing of the parameter settings included the variation of the window size (10, 15, and 20 ms), as well as the placement of the window in the respective CV or VC transition, but here we will report only on those settings that were applied in the final analysis. The optimal configuration for the formant frequency estimation required different parameters for the soundfiles in word-initial and word-medial positions: word-initially, a 10 ms Hamming window was placed at the CV transition, measuring the last 10 ms of the obstruent before the beginning of the vowel (cf. Fig. 1). The reason for not placing the window at the vowel portion—although one would expect to find the formants there—was that there is already a formant structure in the last 10 ms of the obstruent before the beginning of the vowel. With the beginning of the vowel, the formants are dominated by the vowels rather than the obstruents under investigation.

Word-medially, a 20 ms Hamming window was used for analysis at the vowel-obstruent transition, placed exactly 10 ms before and 10 ms after the boundary between the vowel and the following obstruent. Word-medially, the transition was captured differently compared to the procedure applied in word-initial position, because some word-medial obstruents (i.e., affricates and stops) begin with a closure, containing no or little spectral information. The transition of the vowel reflects the spectral change and therefore implies information about the obstruents’ place of articulation. As mentioned above, in word-initial position, the formant structure of the vowel had an interfering influence on the automatic formant frequency estimation. Once the formant frequencies were obtained, the *logarithmic distance*, as proposed by Miller (1989) and Jongman and Miller (1991), was calculated in a modified way (no sensory formant was used). The logarithmic distance was calculated between two formants, for example, between F2 and F1, $\log_{10}(F2_{\text{transition}}/F1_{\text{transition}})$, from now on $\log_{10}(F2/F1)$. The following metrics were chosen:

- $\log_{10}(F2/F1)$
- $\log_{10}(F3/F2)$
- $\log_{10}(F4/F3)$

Word-initially, the formants were measured at the transition proportionate to the following vowel (CV sequence), word-medially the measurements were taken the other way round (VC sequence). Since the logarithmic distance metric is obtained at one point in time in the signal, it is referred to as a static metric. Miller (1989) tested different types of scales and came to the conclusion that linear scales produce nearly equivalent results with respect to the normalized formant ra-

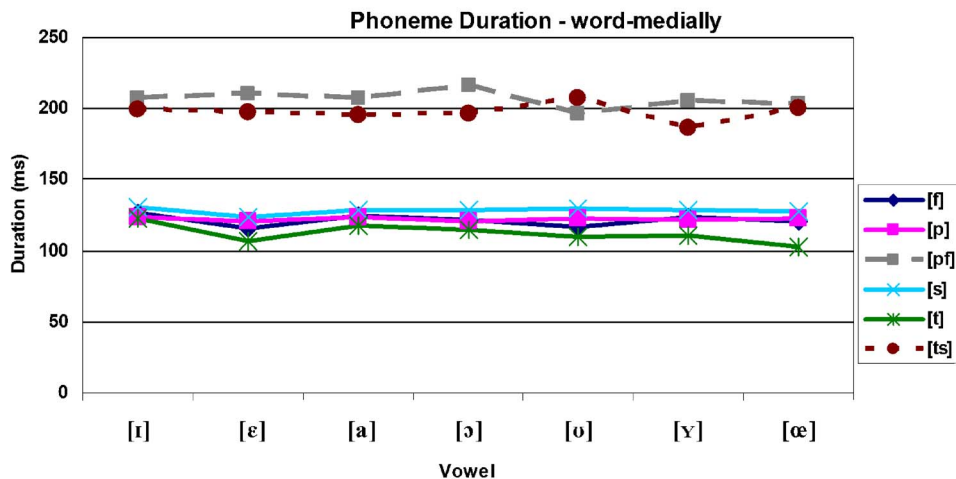


FIG. 3. (Color online) Comparison of mean duration of the obstruents per vowel in word-medial position.

tios compared to the nonlinear ones (e.g., Bark scale), which is why only linear scales were used in this investigation.

C. Energy analysis

Two-short-time Fourier transformations using a 30 ms Hamming window were taken, one at the center of the vowel and the other at the center of the relevant obstruent portion. For the affricates [pf] and [ts] and the fricatives [f] and [s], a 30 ms window was placed around the center of the frication portion. For the stops [p] and [t], the 30 ms window was placed around the center of the release portion.

To get an estimation of the distribution of energy across frequencies, the amplitude was taken from frequency bands divided into eight different regions in steps of 1000 Hz, starting from 0 to 1000 Hz and ending with the frequency band between 7000 and 8000 Hz (from now on abbreviated by 0–1 kHz, 7–8 kHz, etc.). Within each frequency band, the mean magnitude of the energy was calculated and then transformed to its amplitude (dB). The relative amplitude (dB) was subsequently calculated as the difference between the amplitude at the center of the vowel and at the center of the respective obstruent portion in the same frequency region.

IV. RESULTS

A. Duration

A full-factorial ANOVA (*Obstruent* × *Vowel* × *Subject* × *Task*) was calculated for the duration of the (1) complete obstruents, (2) frication, and (3) closure duration. The ANOVA on the absolute length of the obstruents revealed a main obstruent effect [$r^2=0.73, F(5, 45)=101.59, p < 0.0001$] in word-initial position, as well as in word-medial position [$r^2=0.82, F(5, 45)=335.6, p < 0.0001$]. *Post hoc* tests revealed significant differences ($t < 0.0001$) in manner of articulation for all tested conditions ([pf] and [ts] versus [f] and [s] and versus [p] and [t]), word-initially and word-medially.

Averaged across speakers, tasks and vowel contexts, word-initially, the mean duration of affricates is longer ([ts] 183 ms, [pf] 194 ms, cf. dotted lines in Fig. 2) compared to

that of fricatives and stops (around 153 and 160 ms, respectively). The voiced initial fricative [z] can be found at the bottom of Fig. 2 with a mean duration of 98 ms, averaged over all vowels (cf. Table I), being shorter compared to all other phonemes. The stops [p] and [t] and the fricative [f] have approximately the same duration.

Post hoc tests for the manner distinction in word-medial position indicated (under the same conditions as applied for word-initial position) that alveolar and labial affricates are significantly different than the respective fricatives and stops ($t < 0.0001$). Affricates are nearly twice as long (cf. Fig. 3, the two dotted lines represent the affricates) as fricatives and stops.

The mean duration, averaged across speakers, tasks and vowel contexts of the word-initial and word-medial obstruents is presented in Table I.

The present data reveal that fricatives and stops have essentially the same intrinsic duration (cf. Figs. 2, 3 and Table I), in word-initial as well as word-medial positions, apart from initial [z], which is shorter. The word-initial fricatives and stops show longer durations compared to those recorded in word-medial position (except initial [z]). For example, the phoneme duration ratio of word-medial [f] compared to word-initial [f] is 0.79. For stops, quite a similar ratio was observed, in that [p] showed a ratio of 0.76 and [t] one of 0.73. This ratio indicates that the duration of word-medial [t] is 73% of the duration of word-initial [t]. However, affricates do not show this kind of ratio. For [pf], the ratio is 1.07 and for [ts] 1.08, demonstrating that the medial affricates are longer than the initial ones. The reverse ratio proportion of affricates compared to that of stops and fricatives leads to the assumption that there must be a structural difference between word-medial affricates and word-medial fricatives and stops. This effect is also underlined by the fact that affricates in word-medial position turn out to be nearly twice as long as the respective fricatives and stops (above 80 ms mean difference), whereas initial affricates, are just slightly longer (around 30 ms). The comparison of middle and initial obstruents can be seen in Table I.

In word-initial position, the ANOVA revealed an *Ob-*

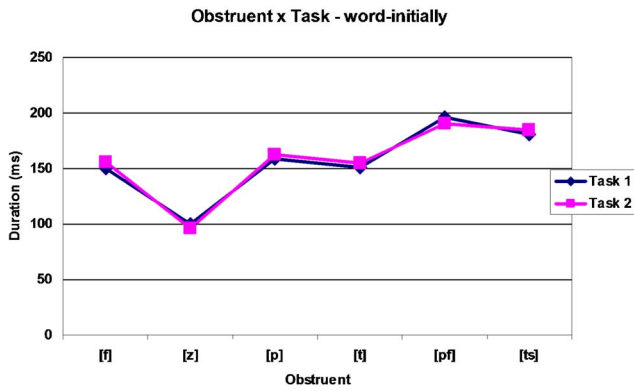


FIG. 4. (Color online) Mean phoneme duration (ms) averaged over all obstruents as a function of the two different tasks in word-initial position.

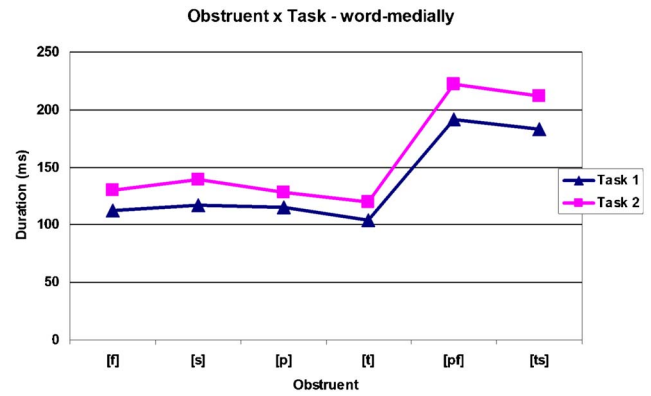


FIG. 5. (Color online) Mean phoneme duration (ms) averaged over all obstruents as a function of the two different tasks in word-medial position.

struent × *Vowel* interaction [$r^2=0.73, F(30, 2193)=3.51, p < 0.0001$], as well as in word-medial position [$r^2=0.82, F(30, 2286)=2.84, p < 0.0001$]. Nevertheless, this interaction was not found to be consistent. The Tukey *post hoc* tests showed no systematic results since nearly every contrast was significant. One could speculate that the low vowel [a] in word-initial position shortens the preceding obstruent. Word-medially, no systematic vowel influence could be found in the Tukey *post hoc* tests at all, which is also indicated by the graphs in Figs. 2 and 3.

The two different *Tasks* showed an interaction with the *Obstruent* in word-medial position ($[r^2=0.82, F(5, 2286)=11.91, p < 0.0001]$), but not in word-initial position. This interaction can be seen in Fig. 5. In the second task, all obstruents show a longer duration. The average duration of word-initial obstruents is nearly the same in both tasks, as can be seen in Fig. 4.

In addition to the phoneme duration, the duration of the segments was evaluated. A full-factorial ANOVA (*Obstruent* × *Vowel* × *Subject* × *Task*) revealed a main obstruent effect with respect to the frication duration of labial and alveolar obstruents in word-initial position [$r^2=0.70, F(3, 27)=46.64, p < 0.0001$]. *Post hoc* tests indicated that the frication of labial and alveolar affricates and fricatives is significantly different ([pf] vs [f] and [z], [ts] vs [f] and [z], all $t < 0.0001$). The frication of word-initial affricates is shorter than that of the fricative [f] ([z] is again shorter compared to all others, due to its voicing feature as discussed above). In word-medial position, however, the ANOVA revealed no sig-

nificant difference [$r^2=0.58, F(3, 27)=2.73, p < 0.0637$]. Word-medially, the frication of affricates and fricatives is very similar with respect to labial and alveolar place of articulation (cf. Table II).

The same pattern is observed analyzing the closure durations of affricates and stops in word-initial position. The ANOVA indicated a clear difference in manner of articulation for labial and alveolar obstruents [$r^2=0.56, F(3, 27)=22.05, p < 0.0001$]. *Post hoc* tests exposed that the closure of [pf] vs [p] and [t], and [ts] vs [p] and [t] is significantly different ($t < 0.0001$). The closure of labial and alveolar affricates is clearly shorter compared to that of the respective stops. However, in word-medial position, the ANOVA also revealed a significant difference in the closure duration [$r^2=0.56, F(3, 27)=9.58, p \leq 0.0002$]. *Post hoc* tests disclosed a significant difference under all tested conditions ([pf] vs [p], $t \leq 0.0422$; [pf] vs [t], $t \leq 0.0036$; [ts] vs [p], $t \leq 0.0116$; [ts] vs [t], $t \leq 0.0144$ are significantly different). The closure of [pf] and [ts] is shorter than that of [p], but longer than that of [t] (cf. Table II). In fact, the closure duration of labial and alveolar affricates and stops is significantly different. Nevertheless, the closure duration of word-medial affricates is found to be in between those measured for stops. All in all, this leads to the assumption that the closure and frication segments of affricates in word-medial position behave like the complete fricative and stop phonemes.

The obstruents showed no place difference, apart from [z] and [f] in word-initial position.

TABLE II. Mean segment and phoneme duration (ms) in word-initial and word-medial positions. The standard deviation is enclosed in brackets.

Word-initial	[pf]	[p]	[f]	[ts]	[t]	[z]
Closure-duration	64 (36)	107 (27)		71 (25)	93 (28)	
Frication-duration	129 (31)		153 (35)	112 (28)		99 (30)
Release-duration		53 (18)			60 (17)	
Phoneme-duration	193 (41)	160 (34)	153 (35)	183 (37)	153 (35)	99 (30)
Word-medial	[pf]	[p]	[f]	[ts]	[t]	[s]
Closure-duration	81 (22)	90(19)		79 (25)	68 (18)	
Frication-duration	124 (30)		120 (24)	119 (26)		128 (24)
Release-duration		32 (14)			44 (14)	
Phoneme-duration	205 (39)	122 (23)	120 (24)	197 (36)	112 (23)	128 (24)

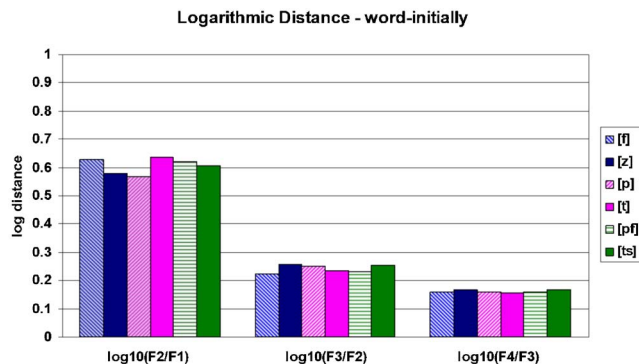


FIG. 6. (Color online) Mean logarithmic distance of all obstruents word-initially.

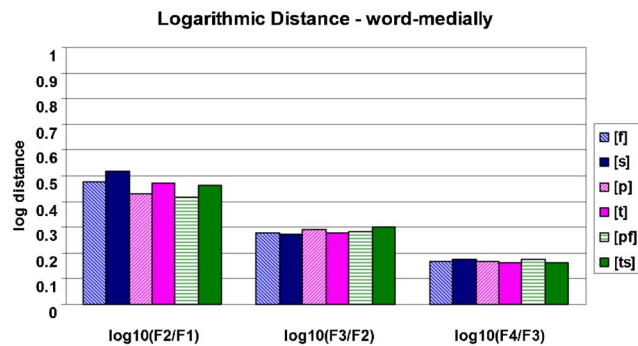


FIG. 7. (Color online) Mean logarithmic distance of all obstruents word-medially.

1. Summary

The comparison of the duration of the obstruents revealed that manner of articulation can be robustly distinguished in word-initial and word-medial positions. Affricates were always significantly longer than the corresponding stops and fricatives. In word-initial position, the difference was around 30 ms; in word-medial position, affricates were nearly twice as long as the corresponding fricatives and stops. Above all, word-initial and word-medial affricates revealed a structural difference. Fricatives and stops have more or less the same intrinsic duration in word-initial and word-medial positions. Fricatives and stops are longer in initial position than in medial position. Word stress is a considerable influencing factor that goes hand in hand with the increased duration at the word boundary. Since all test words were stressed on the first syllable containing the initial obstruents, these have longer durations, whereas the word-medial obstruents were in the unstressed syllable. The ratio of fricatives and stops in word-medial versus word-initial position (e.g., duration of medial [p] divided by initial [p]) revealed that word-initial fricatives and stops are approximately 30% longer than the medial ones (apart from the [z] versus [s] ratio, due to the added voicing feature of [z]). This proportion was not found for affricates. Initial affricates are even slightly shorter (around 1%) than medial ones. The different ratio of affricates compared to that of fricatives and stops indicates a structural difference. This is also underlined by the results of the segmental comparison. Word-initially, the closure and friction durations of stops and fricatives are significantly longer than the affricate equivalents, confirming the findings of Shinn (1985)—apart from initial [z]. As expected, fricatives have the longest friction duration as their segmental duration is identical with the phoneme duration. The comparison of the closure segments of stops and affricates shows a similar result; stops have a longer closure duration than affricates. In word-medial position, one would have expected the same pattern, namely that the stop and fricative segments are again longer than those of affricates. However, this is not the case. Affricates have segments, which are similar or even longer in duration compared to the corresponding segments of fricatives and stops. Moreover, fricatives and stops show the tendency that their intrinsic, as well as their segmental duration, is longer in word-initial

position. Conversely, affricates have a longer intrinsic and segmental duration in word-medial position. This systematic difference between initial and medial affricates versus fricatives and stops can be subsumed as follows: medial affricates are nearly twice as long as the medial stops and fricatives, whereas the same comparison in word-initial position reveals only a minor difference.

A possible explanation could be provided looking at the historical development of German affricates: the word-initial affricates [pf] and [ts] developed from the singletons [p] and [t], respectively (*Pfund* “pound,” (O.Fris.: “pund,” or *Zunge* “tongue” O.Fris.: “tunge”), giving evidence that initial affricates are monosegmental. Contrastively, word-medial affricates have a bisegmental nature; [-pf] and [-ts] developed from the geminates [-pp] and [-tt] (*Apfel* “apple” vs O.Fris.: “appel” or *Katze* “cat,” W.Gmc: “kattuz”). Since [z] was the only voiced sound in this investigation and has a strikingly shorter duration than the voiceless fricatives and stops, the shorter intrinsic phoneme duration must be due to voicing.

B. Formant frequencies

The results of the formant frequency analysis revealed significant differences to distinguish place of articulation in relation to the respective groups of sounds word-initially and word-medially. The different sounds were distinguished by the *logarithmic distance* of different formants.

Word-initially, the four-way ANOVA (*Obstruent* \times *Vowel* \times *Subject* \times *Task*) showed a main effect of *Obstruent* with respect to the logarithmic distance between F2 and F1 $\log_{10}(F2/F1)$ [$r^2=0.18$, $F(5, 45)=5.43$, $p \leq 0.0005$]. *Post hoc* tests revealed that [p] and [t] differ significantly from each other ($t \leq 0.0002$), as is the case with [f] and [z] ($t \leq 0.0038$), although they show no consistent pattern. For fricatives, the labial [f] has a greater logarithmic distance, whereas for stops the alveolar [t] has the greater distance. The affricates [pf] and [ts] could not be statistically separated by the $\log_{10}(F2/F1)$ and the mean value reveals that the logarithmic distance is greater for the labial affricate (cf. Fig. 6). An *Obstruent* \times *Vowel*, interaction [$r^2=0.18$, $F(30,270)=2.14$, $p \leq 0.0008$] was also found. Tukey *post hoc* tests indicated that most of the significant interactions involved the consonant-vowel combination [p] and [a]. Since no interaction between the other labials [pf] and [f] in combination

with the low vowel [a] was found, the conclusion was drawn that there was no systematic effect between labiality and low vowels.

The $\log_{10}(F3/F2)$ metric also showed a main *Obstruent* effect [$r^2=0.23$, $F(5315)=5.66$, $p<0.0001$] and no *Obstruent* \times *Vowel* interaction. *Post hoc* tests indicated significant difference between [f] and [z] ($t<0.0001$) and [pf] and [ts] ($t\leq 0.0025$). [p] versus [t] showed no significant difference. The logarithmic distance between F3 and F2 is greater for alveolar fricatives and affricates and therefore contrasts with the results gained with the $\log_{10}(F2/F1)$ metric exposing a greater logarithmic distance for the labial phonemes.

The logarithmic distance between F4 and F3 showed a main *Obstruent* effect [$r^2=0.10$, $F(5,45)=4.53$, $p\leq 0.0020$] and an *Obstruent* \times *Vowel* interaction [$r^2=0.10$, $F(30\ 2293)=1.66$, $p\leq 0.0141$]. Again, the *post hoc* tests revealed a significant difference for affricates and fricatives: [f] and [z] ($t\leq 0.0106$) and [pf] and [ts] ($t\leq 0.0277$). Stops did not differ significantly. Once more, the alveolar affricates and fricatives showed a greater logarithmic distance compared to the labial ones, being consistent with the results of the $\log_{10}(F3/F2)$ metric. For stops, the results were vice versa, but nevertheless nearly equivalent. Tukey *post hoc* tests indicated no systematic effects concerning the *Obstruent* \times *Vowel* interaction. Only very few significant differences were found that allowed no interpretation into any direction.

Word-medially, the result pattern was in some points similar compared to that in word-initial position: the logarithmic distance is greater between F2 and F1 than for F3/F2 and F4/F3. The logarithmic distance between F2 and F1 showed a main *Obstruent* effect [$r^2=0.47$, $F(5,45)=12.96$, $p<0.0001$] and also a strong *Obstruent* \times *Vowel* interaction [$r^2=0.47$, $F(30\ 270)=3.04$, $p<0.0001$]. *Post hoc* tests indicated that all labial and alveolar obstruents were distinguished significantly in manner of articulation by the following metric: [p] contrasted with [t] ($t\leq 0.0057$); [f] with [s] ($t\leq 0.0056$) and [pf] with [ts] ($t\leq 0.0025$). For all of the tested groups (i.e., affricates, fricatives and stops), alveolars had a greater logarithmic distance compared to the labial obstruents (cf. Fig. 7). Concerning the *Obstruent* \times *Vowel* interaction, Tukey *post hoc* tests revealed that the obstruents in combination with the back vowels [a] and [ɔ] had a significantly smaller logarithmic distance compared to the same obstruents in combination with the front vowels [i] and [y].

The logarithmic distance between F3 and F2 was not as effective as the other metrics in discriminating place of articulation with respect to the factor *Obstruent* [$r^2=0.39$, $F(5,45)=2.66$, $p\leq .0212$] and the *post hoc* tests showed no significant difference. The *Obstruent* \times *Vowel* interaction showed a strong effect [$r^2=0.39$, $F(30,270)=3.78$, $p<0.0001$]. However, Tukey *post hoc* tests of the six consonants with the seven vowels revealed no systematic results in the single contrasts.

The $\log_{10}(F4/F3)$ metric again produced more stable results. The ANOVA exposed a main effect [$r^2=0.23$, $F(5,45)=3.89$, $p\leq 0.0051$] for the variable *Obstruent*. *Post hoc* tests revealed significant results contrasting [f] and [s] ($t\leq 0.0274$) and [pf] and [ts] ($t\leq 0.0073$). [p] and [t] were

not significantly different. The logarithmic distance was again greater for the alveolar fricatives. Affricates showed the reverse result pattern; here the labial affricate showed a greater logarithmic distance. A main effect was also revealed for the *Obstruent* \times *Vowel* interaction [$r^2=0.23$, $F(30,270)=1.96$, $p<0.0029$]. Tukey *post hoc* tests showed a significant difference between some obstruent-vowel combinations, but not as clear and systematic as indicated by the $\log_{10}(F2/F1)$. Especially [pf] and [s], in combination with the vowel [ɔ], had a significantly greater logarithmic distance than nearly all other combinations. Also [pf] and [p], in combination with the vowel [a], revealed a significantly greater logarithmic distance compared to the other obstruents in combination with the vowels [i] and [y].

1. Summary

The *logarithmic distance* of specific formant frequencies at a particular point in time is a reliable dimension to distinguish place of articulation within affricates, fricatives and stops. Nevertheless, the parameter settings used for the LPC analysis play an important role. The size of the Hamming window, as well as its placement at the transition, influences the quality of the results.

Word-medially, a 20 ms Hamming window was placed exactly at the vowel-obstruent transition. With the latter configuration, the obstruents in word-medial position were distinguished solidly by the $\log_{10}(F2/F1)$ metric. Word-initially, the configuration had to be different. The best results were achieved with the 10 ms Hamming window placed at the end of the obstruent portion. The $\log_{10}(F2/F1)$ estimation was successful for stops and fricatives. However, affricates and also fricatives could be discriminated by the $\log_{10}(F4/F3)$ and $\log_{10}(F3/F2)$ ratios. Unlike in word-initial position, the vowel had a systematic effect on the obstruents, especially when discriminated by the $\log_{10}(F2/F1)$ metric and less systematic by the $\log_{10}(F4/F3)$ metric. This can be explained by the different windows applied in word-initial and word-medial positions. In word-initial position, it was placed at the obstruent portion only, whereas in word-medial position it was placed half at the obstruent portion and half at the vowel portion. The authors had assumed that measurements at a particular point in time provide good information about place of articulation as indicated, for example, by the results of Miller (1989). It turned out that normalization seems to be more robust when it is calculated over two time windows, as it was practiced for the relative amplitude in discrete frequency bands (cf. Sec. IV C). Normalization is one of the main goals to make speech recognition independent of variation in the signal, such as speaker variation or noise.

C. Relative amplitude in discrete frequency bands

The two places of articulation, labial and alveolar, were clearly distinguishable by their relative amplitude in discrete frequency bands within the respective obstruent groups, word-initially and word-medially. Very good results were found in the higher formant frequency regions to distinguish

TABLE III. ANOVA on the variable *Obstruent* in word-initial position per frequency band. The three columns on the right show the results of place distinction by the *post hoc* tests. The abbreviation “n.s.” is used for “not significant.”

Freq. band	ANOVA	Post hoc tests		
	Variable <i>obstruent</i>	[pf] vs [ts]	[f] vs [z]	[p] vs [t]
0–1 kHz	$r^2=0.63, F(5,45)=53.10, p<0.0001$	n.s.	$t<0.0001$	$t\leq 0.0492$
1–2 kHz	$r^2=0.77, F(5,45)=32.27, p<0.0001$	$t\leq 0.0048$	$t<0.0001$	n.s.
2–3 kHz	$r^2=0.73, F(5,45)=33.06, p<0.0001$	$t\leq 0.0015$	$t<0.0001$	$t\leq 0.0005$
3–4 kHz	$r^2=0.67, F(5,45)=19.36, p<0.0001$	n.s.	$t<0.0001$	$t<0.0001$
4–5 kHz	$r^2=0.79, F(5,45)=19.09, p<0.0001$	$t\leq 0.0004$	n.s.	$t<0.0001$
5–6 kHz	$r^2=0.76, F(5,45)=47.21, p<0.0001$	$t<0.0001$	$t\leq 0.0296$	$t<0.0001$
6–7 kHz	$r^2=0.72, F(5,45)=123.09, p<0.0001$	$t<0.0001$	$t\leq 0.0161$	$t<0.0001$
7–8 kHz	$r^2=0.77, F(5,45)=138.91, p<0.0001$	$t<0.0001$	n.s.	$t<0.0001$

place of articulation for stops, fricatives and affricates, corresponding to the results of former investigations (cf. Jongman *et al.*, 2000).

The four-way ANOVA (*Obstruent* × *Vowel* × *Subject* × *Task*) revealed a main effect for the variable *Obstruent* for all of the frequency bands in word-initial and word-medial positions (cf. Tables III and IV). The results of the *post hoc* tests for the word-initial obstruents are presented in Table III.

The *post hoc* tests indicated that place of articulation can be distinguished within affricates and stops in the higher frequency bands between 4 and 5 kHz up to 7–8 kHz. Fricatives show different results in word-initial position; the best results are achieved in the lower frequency regions between 0 and 1 kHz up to 3–4 kHz. The difference between fricatives on the one hand and affricates and stops on the other is due to the voicing feature of [z] contrasting with the voiceless [f]. Nevertheless, place distinction of fricatives is also possible in the frequency bands between 5 and 6 kHz and 6–7 kHz. In the lower frequency regions between 0 and 1 kHz up to 3–4 kHz, the relative amplitude values are positive indicating that the amount of energy is higher at the vowel center, whereas at the center of frication only little energy is measurable. In the higher frequency regions, alveolar phonemes have a greater relative amplitude compared to labial ones. This applies for nearly all frequency bands. The actual results are illustrated in Fig. 8.

Word-medially, the ANOVA calculated for the relative amplitude of discrete frequency bands revealed a main effect concerning the variable *Obstruent*. The *post hoc* tests expose,

a clear pattern. As in word-initial position, the higher frequency regions (4–5 kHz up to 7–8 kHz) show the ability to distinguish place of articulation in all obstruent groups. Again, the alveolar obstruents have greater relative amplitude values compared to labial obstruents (cf. Fig. 9 and Table IV).

The results of the relative amplitude calculation for the obstruents word-initially and word-medially revealed the same tendencies. In general, obstruents are preferably distinguished by their relative amplitude in the frequency region between 4 and 5 kHz up to 7–8 kHz. For example, in the frequency band between 5 and 6 kHz, the relative amplitude is –10.5 dB for [pf] and –23.7 dB for [ts]. Place of articulation in stops is also significantly different in the frequency bands between 2 and 3 kHz and 3–4 kHz, in both word-initial and word-medial positions. Affricates do not show the same pattern disclosing significant place differences in the frequency bands between 1 and 2 kHz and 2–3 kHz in word-initial and word-medial positions. Fricatives show the same pattern as affricates in word-medial position. A significant place difference is observed in the frequency bands between 1 and 2 kHz and 2–3 kHz. In word-initial position, all lower frequency regions show the possibility of significant place distinction for fricatives. Significance was proven for every place contrast evaluated by the *post hoc* tests. Alveolar obstruents have a greater relative amplitude than labial obstruents (apart from the frequency band between 0–1 kHz).

TABLE IV. ANOVA on the variable *Obstruent* in word-medial position per frequency band. The three columns on the right show the results of place distinction by the *post hoc* tests. The abbreviation “n.s.” is used for “not significant.”

Freq. band	ANOVA	Post hoc tests		
	Variable	[pf] vs [ts]	[f] vs [s]	[p] vs [t]
0–1 kHz	$r^2=0.72, F(5,45)=25.83, p<0.0001$	n.s.	n.s.	n.s.
1–2 kHz	$r^2=0.73, F(5,45)=10.98, p<0.0001$	$t<0.0001$	$t<0.0001$	n.s.
2–3 kHz	$r^2=0.69, F(5,45)=24.70, p<0.0001$	$t<0.0001$	$t<0.0001$	$t<0.0001$
3–4 kHz	$r^2=0.70, F(5,45)=19.36, p<0.0001$	n.s.	n.s.	$t<0.0001$
4–5 kHz	$r^2=0.83, F(5,45)=27.55, p<0.0001$	$t\leq 0.0008$	$t\leq 0.0002$	$t<0.0001$
5–6 kHz	$r^2=0.85, F(5,45)=63.04, p<0.0001$	$t<0.0001$	$t<0.0001$	$t<0.0001$
6–7 kHz	$r^2=0.82, F(5,45)=165.11, p<0.0001$	$t<0.0001$	$t<0.0001$	$t<0.0001$
7–8 kHz	$r^2=0.80, F(5,45)=214.28, p<0.0001$	$t<0.0001$	$t<0.0001$	$t<0.0001$

Relative Amplitude - word-initially - all frequency bands

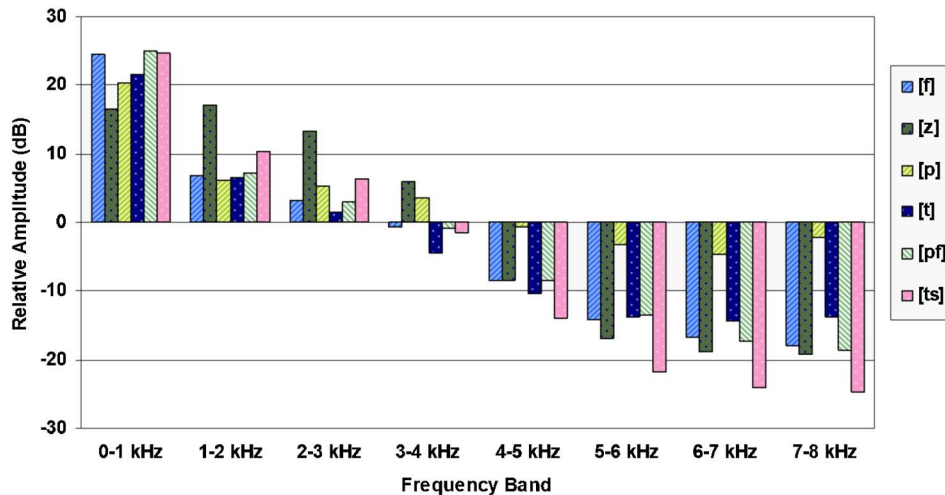


FIG. 8. (Color online) Mean relative amplitude as a function of place of articulation across all frequency bands (0–1 kHz up to 7–8 kHz), word-initially.

1. Summary

Within the settings of this investigation, relative amplitude serves as the most stable and reliable function to distinguish place of articulation of affricates, fricatives, and stops. Highly significant results were achieved word-initially as well as word-medially, demonstrating that relative amplitude in the higher frequency bands distinguishes place of articulation. All frequency bands between 4 and 5 kHz up to 7–8 kHz were adequate. It was found that the relative amplitude is smaller for labials compared to alveolars, regardless of the frequency band.

The results for the relative amplitude measurements support the findings of Jongman *et al.* (2000) with respect to the ability for place distinction in fricatives. The validity of these results was even extended to stops and affricates.

In contrast to the static approach of the logarithmic distance measure, relative amplitude calculation is a dynamic approach. Two events that are spread across two phonemes (the obstruent and the vowel) are related to each other. Unlike the formant frequency analysis, no influence of the se-

quence of these phonemes was found. The results were the same no matter whether a CV (word-initially) or VC sequence (word-medially) was analyzed. Therefore, the results gained by relative amplitude calculation in discrete frequency bands were even more stable in distinguishing place of articulation than those of the logarithmic distance measure.

V. CONCLUSIONS

The investigation of the speech production data of ten speakers indicates that acoustic analysis of temporal, spectral, and amplitudinal cues can identify place and manner of articulation of the German obstruents [pf, ts, f, z/s, p, t] word-initially and word-medially. Temporal measurements provide critical information to separate labial and alveolar affricates from fricatives and stops. Thus, duration is a reliable and robust cue to distinguish between these manners of articulation. Affricates turned out to be significantly longer compared to fricatives and stops, in both word-initial and word-medial positions. The comparison of the phoneme segments also revealed significant differences. Word-initially, the phoneme duration of affricates turned out to be just slightly longer than that of fricatives and stops, whereas the closure and frication portions of affricates were shorter compared to the respective fricative and stop segments—apart from initial [z], being the only investigated voiced phoneme. Word-medially, however, another pattern was observed. The affricate segments were found to be longer or to have around the same length as the corresponding segments of fricatives and stops. Correspondingly, the phoneme duration of affricates is clearly longer compared to that of fricatives and stops. Word-medial affricates are nearly twice as long compared to the corresponding fricatives and stops, giving evidence for the assumption of a systematic difference between initial and medial affricates. The comparison with the results of Shinn (1985) supports this hypothesis. The results obtained in word-initial position show the same pattern as those

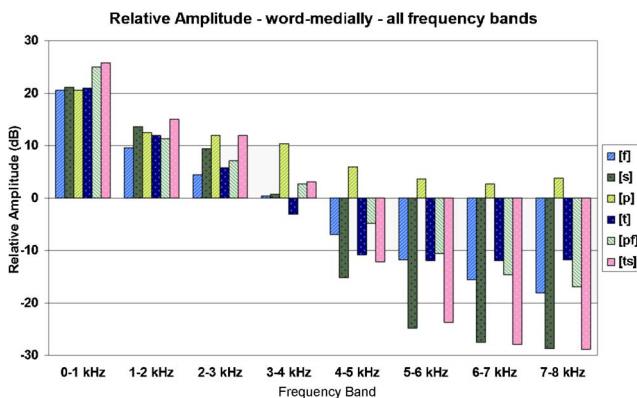


FIG. 9. (Color online) Mean relative amplitude as a function of place of articulation across all frequency bands (0–1 kHz up to 7–8 kHz), word-medially.

of Shinn (1985), the frication of affricates being shorter compared to that of fricatives, neglecting the voiced [z]. In word-medial position, however, affricates have around the same frication duration as fricatives. This structural divergence of German affricates is supported by the actual findings that word-initial fricatives and stops are longer compared to word-medial ones, presumably to mark the word boundary (cf. Repp *et al.*, 1978) and being influenced by stress patterns. However, the duration of word-medial affricates is not in agreement with the latter hypothesis, as word-medial affricates turned out to be longer compared to the initial ones. These results are also supported by diachronic facts. Word-initial [pf] and [ts] developed from the singletons [p] and [t], for example, *Pfanne* “pan” from Old English *Panne*, whereas word-medial [-pf] and [-ts] evolved from the geminates [-tt] and [-pp], for example, *Stapfen* “footprint” from Old English *Staeppan*.

Spectral and amplitudinal cues suggest a high potential for robustly distinguishing place of articulation of the investigated obstruents. The logarithmic distance between formants measured at a particular point in time was found to distinguish labial and alveolar place of articulation of the investigated obstruents. The present results support the approach of Jongman and Miller (1991). They already showed that the logarithmic distance within the auditory-perceptual space supplies the possibility of distinguishing place of articulation in stops with 70% of accuracy. However, the metric in the present investigation was modified without wanting to classify the investigated obstruents in an auditory perceptual space. Therefore, no sensory reference was used. Instead, the aim was to measure the formant distance using an auditory-perceptual metric, which can be applied automatically by computer analysis. However, it was found that the fine tuning of the parameters *window size* and *window placement* for the LPC analysis plays an important role. Word-initially, the last 10 ms of the signal of the obstruent were measured, indicating that stops can be robustly distinguished by the $\log_{10}(F2/F1)$ metric. Again, affricates and fricatives are discriminated by the $\log_{10}(F3/F2)$ and $\log_{10}(F4/F3)$ metrics. The different performance of the metrics with respect to stops on the one hand and affricates and fricatives on the other hand can be explained by the similarity of the signal portions taken for affricates and fricatives. Word-medially, the results are much easier to generalize. The $\log_{10}(F2/F1)$ metric revealed a highly significant difference between the labial and alveolar obstruents. The actual results gained in word-initial and word-medial positions go along with the findings of Liberman *et al.* (1952), Stevens (1985), Stevens and Blumstein (1981), among others, that information about place of articulation can be found at the obstruent-vowel boundary.

Relative amplitude in discrete frequency bands proved to be a very reliable and robust method to distinguish place of articulation of the investigated obstruents. The dynamic measurement of calculating the amplitude ratio of the obstruent in comparison to a neighboring vowel is another analysis technique to distinguish labial from alveolar obstruents. The difference between logarithmic distance and relative amplitude approach is found in their temporal rela-

tion. The latter describes a relation between two temporal points in the speech signal (transition and center of vowel), whereas the logarithmic distance, as a static approach, is fixed to one point in the signal only (the transition).

As in previous investigations (cf. Stevens, 1985, Jongman *et al.*, 2000), relative amplitude was found to be rather successful, although the metric chosen in this investigation differed in comparison to the classical approach. Usually, relative amplitude is extracted in the region of F3 (for [s, z]) and F5 (for [f]) and is expressed by the difference to the amplitude of same component of the vowel. Jongman *et al.* (2000) found that relative amplitude in the F5 region is smaller for labials than that of alveolars in the F3 region. Although the approach to measure relative amplitude in discrete frequency bands is a completely different one (because relative amplitude is measured in the same frequency region for all types of sounds, not associating F3 with alveolars and F5 with labials), the present results lead to the same conclusion: labial phonemes have a smaller relative amplitude compared to the alveolar obstruents in the higher-frequency regions. The present approach proved to be a stable function to distinguish place of articulation of the investigated obstruents because automatic formant estimation sometimes fails. For example, F0 is sometimes recognized as a formant—and as a consequence all higher formants shift up and, for instance, F4 was in fact F3. If frequency regions are defined independently of formants measuring the energy within them, these effects are minimized and even in “unclean” speech, obstruents remain distinguishable in place of articulation. Especially, the frequency bands between 4 and 5 kHz up to 7–8 kHz provide useful information to discriminate labial and alveolar obstruents. In either initial or medial word positions, the labial obstruents turn out to have a smaller relative amplitude compared to the alveolar ones (comparing them in their respective groups affricates, stops, fricatives). The initial fricative contrast between [f] and [z] is an exception, with the voiced alveolar [z] having a smaller relative amplitude.

The present study indicates that place discrimination of the investigated obstruents is possible by calculation of the logarithmic distance of particular formant frequencies, as well as by taking the relative amplitude in discrete frequency bands. However, in the context of the present investigation, relative amplitude showed more stable and robust results. It would be interesting to know for future research, whether amplitudinal information might contribute to distinguish manner of articulation. Another potential perspective is the analysis of the acoustic cues found in this study and their contribution to speech perception research.

ACKNOWLEDGMENTS

This work was supported by the *Sonderforschungsbereich 471*, funded by the *Deutsche Forschungsgesellschaft*. Our thanks go especially to Aditi Lahiri for bringing in her valuable ideas and to Allard Jongman for helpful reviews and comments. All errors are our own.

APPENDIX A: WORDS CONTAINING TARGET SOUNDS IN WORD-INITIAL POSITION

V/C	[pf]	[ts]	[p]	[t]	[f]	[z]
[ɪ]	pfiffe Pfingsten Pfirsich	Zipfel Zinker Ziffer	Pille Pinne Pisse	Tinte Tipper Tische	Finne Finken Filme	Sitze Sitte Siffe
[ɛ]	Pfeffer Pfennig Pferde	Zecke Zelle Zettel	Pelle Petze Pepper	Teller Teckel Tester	Felle Fette Faesser	Seppel Sessel Setter
[a]	Pfaffe Pfanne Pfarrer	Zander Zacke Zapfer	Panda Panther Pappe	Tante Tatze Tasse	Fakten Falke Fackel	Sache Sand Sattel
[ɔ]	Pforte Pfote Pfoeten	Zottel Zobel Zone	Polle Posse Popper	Toffee Tonne Topfen	Vollen Vogel Foto	Sorte Socke Sonne
[œ]	Pfoetchen Pfoertner Pfoestchen	Zoellner Zoepfe Zoegling	Poebel Poekel Poette	Toepfer Toeffel Toene	Foene Foeten Foerde	Soehne Soeldner Soege
[ʊ]	Pfuhl Pfunde Pfuscher	Zunge Zucker Zupfer	Putte Putzer Puffer	Tusse Tunnel Tupfer	Funde Funke Fummel	Summe Suppe Sultan
[ʏ]	Pfuehle Pfuetze Pfuendchen	Zuechter Zuender Zuenfte	Pueppchen Puerzel Pueffe	Tuepfel Tuecke Tuerme	Fuesse Fuechse Fuelle	Suesse Suende Suelze

APPENDIX B: WORDS CONTAINING TARGET SOUNDS IN WORD-MEDIAL POSITION

V/C	[pf]	[ts]	[p]	[t]	[f]	[s]
[ɪ]	Zipfel Wipfel Gipfel	Hitze Witze Sitze	Kippe Wippe Tipper	Mitte Ritte Sitte	Pfiffe Ziffer Siffe	Risse Wissen Pisse
[ɛ]	Schnepfe Naepfe Aepfel	Petze Hetze Netze	Pepper Steppe Seppel	Setter Fette Zettel	Neffe Treffer Pfeffer	Naesse Sessel Faesser
[a]	Apfel Stapfen Zapfer	Katze Tatze Glatze	Pappe Rappe Kappe	Ratte Sattel Natter	Affe Waffe Pfaffe	Tasse Kasse Masse
[ɔ]	Opfer Topfen Stopfen	Glotze Rotze Kotze	Kloppe Popper Koppel	Zottel Motte Schotte	Koffer Stoffe Toffee	Rosse Bosse Posse
[œ]	Toepfer Schoepfer Zoepfe	Goetze Kloetze Doetze	Kloepfel Moepfel Koeffe	Spoetter Goetter Poette	Loeffel Schoeffen Toeffel	Stoessel Floesse Groesse
[ʏ]	Tuepfel Huepfer Knuepfer	Scheutze Pfuetze Suelze	Knueppel Krueppel Schueppe	Huette Muetter Schuette	Bueffel Pueffe Trueffel	Nuesse Schuesse Kuesse
[ʊ]	Kupfer Tupfer Zupfer	Nutzen Putzer Stutzen	Kuppel Suppe Schnuppe	Kutte Putte Mutter	Muffel Puffer Knuffel	Busse Tusse Husse

- Baum, S. R., and Blumstein, S. E. (1987). "Preliminary observations on the use of duration as a cue to syllable-initial fricative consonant voicing in English," *J. Acoust. Soc. Am.* **82**, 1073–1077.
- Gerstman, L. J. (1957). *Perceptual Dimensions for the Frication Portions in Certain Speech Sounds* (unpublished Ph.D. dissertation, New York University); as cited by Howell, P., and Rosen, S. (1983). "Production and perception of rise time in the voiceless affricate/fricative distinction," *J. Acoust. Soc. Am.* **73**, 976–984.
- Gurlekian, J. A. (1981). "Recognition of the Spanish fricatives /s/ and /ʃ/," *J. Acoust. Soc. Am.* **109**, 1624–1627.
- Howell, P., and Rosen, S. (1983). "Production and perception of rise time in the voiceless affricate/fricative distinction," *J. Acoust. Soc. Am.* **73**, 976–984.
- Jongman, A., and Miller, J. D. (1991). "Method for the location of burst-onset spectra in the Auditory-Perceptual Space: A study of place of articulation in voiceless stop consonants," *J. Acoust. Soc. Am.* **89**, 867–873.
- Jongman, A., Wayland, R., and Wong, S. (2000). "Acoustic characteristics of English fricatives," *J. Acoust. Soc. Am.* **108**, 1252–1263.
- Klatt, D. H. (1976). "Linguistic uses of segmental duration in English: Acoustic and perceptual evidence," *J. Acoust. Soc. Am.* **59**, 1208–1221.
- Kluender, K. R., and Walsh, M. A. (1992). "Amplitude rise time and the perception of the voiceless affricate/fricative distinction," *Percept. Psychophys.* **51**, 328–333.
- Lahiri, A., Gwirth, L., and Blumstein, S. E. (1984). "A reconsideration of acoustic invariance for place of articulation in diffuse stop consonants: Evidence from a cross-language study," *J. Acoust. Soc. Am.* **76**, 391–404.
- Lahiri, A., and Reetz, H. (2002). "Underspecified recognition," in *Laboratory Phonology VII*, edited by C. Gussenhoven and N. Warner (Mouton, Berlin), pp. 637–675.
- Liberman, A. M., Delattre, P. C., and Cooper, F. S. (1952). "The role of selected stimulus variables in the perception of unvoiced stop consonants," *Am. J. Psychol.* **65**, 497–516.
- Maddieson, I. (1984). *Patterns of Sounds* (Cambridge University Press, Cambridge).
- Miller, J. D. (1989). "Auditory-perceptual interpretation of the vowel," *J. Acoust. Soc. Am.* **85**, 2114–2134.
- Repp, B. H., Liberman, A. M., Eccardt, T., and Pesetsky, D. (1978). "Perceptual integration of acoustic cues for stop, fricative and affricate manner," *J. Exp. Psychol. Hum. Percept. Perform.* **4**, 621–637.
- Shinn, P. C. (1985). *A cross language investigation of the stop, affricate and fricative manners of articulation* (Ph.D. dissertation, University Microfilms, Ann Arbor).
- Stevens, K. N., and Blumstein, S. E. (1981). "The search for invariant acoustic correlates of phonetic features," in *Perspectives on the Study of Speech*, edited by P. D. Eimas and J. L. Miller (Lawrence Erlbaum, Hillsdale), pp. 1–38.
- Stevens, K. N. (1985). "Evidence for the role of acoustic boundaries in the perception of speech sounds," in *Phonetic Linguistics. Essays in the honor of Peter Ladefoged*, edited by V. A. Fromkin (Academic, Orlando), pp. 243–255.
- Stevens, K. N. (1998). *Acoustic Phonetics* (MIT Press, Cambridge).

Voice F_0 responses to pitch-shifted voice feedback during English speech

Stephanie H. Chen

Feinberg School of Medicine, Northwestern University, 440 North McClurg Ct. #604, Chicago, Illinois 60611

Hanjun Liu

Department of Communication Sciences and Disorders, Northwestern University, 2240 Campus Drive, Evanston, Illinois 60208

Yi Xu

Department of Phonetics and Linguistics, University College London, London, United Kingdom

Charles R. Larson^{a)}

Department of Communication Sciences and Disorders, Northwestern University, 2240 Campus Drive, Evanston, Illinois 60208

(Received 1 June 2006; revised 3 November 2006; accepted 8 November 2006)

Previous studies have demonstrated that motor control of segmental features of speech rely to some extent on sensory feedback. Control of voice fundamental frequency (F_0) has been shown to be modulated by perturbations in voice pitch feedback during various phonatory tasks and in Mandarin speech. The present study was designed to determine if voice F_0 is modulated in a task-dependent manner during production of suprasegmental features of English speech. English speakers received pitch-modulated voice feedback (± 50 , 100, and 200 cents, 200 ms duration) during a sustained vowel task and a speech task. Response magnitudes during speech (mean 31.5 cents) were larger than during the vowels (mean 21.6 cents), response magnitudes increased as a function of stimulus magnitude during speech but not vowels, and responses to downward pitch-shift stimuli were larger than those to upward stimuli. Response latencies were shorter in speech (mean 122 ms) compared to vowels (mean 154 ms). These findings support previous research suggesting the audio vocal system is involved in the control of suprasegmental features of English speech by correcting for errors between voice pitch feedback and the desired F_0 . © 2007 Acoustical Society of America. [DOI: 10.1121/1.2404624]

PACS number(s): 43.70.Mn, 43.72.Dv, 43.70.Bk [AL]

Pages: 1157–1163

I. INTRODUCTION

Little is known about neural mechanisms controlling voice fundamental frequency (F_0) during speech. In English and other nontonal languages, F_0 , along with amplitude and duration, are all increased for stressed syllables and at the end of a phrase or sentence to indicate a question (Alain, 1993; Cooper *et al.*, 1985; Eady and Cooper, 1986; Lieberman, 1960; Xu and Xu, 2005). F_0 is thus important in the overall goal of speech communication and to convey emotional expression (Bänziger and Scherer, 2005; Chuenwatanapranithi *et al.*, 2006). In some types of neurologically based voice disorders, voice F_0 is often abnormal and interferes with communication (Duffy, 1995). Understanding mechanisms of F_0 control during speech is important for treatment and prevention of some types of voice disorders.

Theoretical discussions of speech motor control in the past have focused primarily on segmental features of speech. To this end, suggestions have been advanced that segmental features may be controlled by an internal model or a motor plan guided in part by sensory feedback (Fairbanks, 1954;

Gracco and Abbs, 1985; Munhall *et al.*, 1994). Several studies in recent years have also demonstrated through the use of the perturbation paradigm that auditory feedback is important for the on-line control of voice F_0 during sustained vowels (Bauer and Larson, 2003; Hain *et al.*, 2000; Larson *et al.*, 2001; Sivasankar *et al.*, 2005), glissandos (Burnett and Larson, 2002), singing (Natke *et al.*, 2003), nonsense syllables produced by German speakers (Donath *et al.*, 2002; Natke *et al.*, 2003; Natke and Kalveram, 2001), and during prolonged vowels in the context of Mandarin phrases (Jones and Munhall, 2002). A simple mathematical model based on negative feedback accounts for the main features of these responses (Bauer *et al.*, 2006; Hain *et al.*, 2000). It was also found in normal Mandarin speech that the magnitudes of F_0 responses to pitch perturbations were larger in phrases in which there was a subsequent fall in F_0 (high-falling or high-rising phrases) compared to a phrase where the F_0 remained relatively constant (high-high phrase). These observations suggest that there is task-dependent modulation of pitch-shift responses in Mandarin (Xu *et al.*, 2004a). Similarly, Natke *et al.* (2003) provided evidence that pitch-shift responses are modulated according to the demands of the vocal task by showing that responses to pitch perturbations were larger in

^{a)}Electronic mail: clarson@northwestern.edu

singing compared to speaking nonsense syllables. To date, no studies have demonstrated whether there is task-dependent modulation of the pitch-shift response magnitude in a non-tonal language such as English.

In a recent study of normal English speech, it was found that perturbations in voice pitch auditory feedback led to changes in the timing of suprasegmental features (Bauer, 2004). When the direction of the pitch-shift stimulus (e.g., down) was opposite to that of the F_0 change in direction for the inflected syllable (e.g., up), the timing of the peak in the F_0 contour for the inflected syllable was delayed. When the direction of the shift was in the same direction as the inflected syllable, there was no delay. Along with this timing change, response latencies to the pitch-shifted feedback were modulated so as to occur during the peak of the inflection. Possible changes in response magnitude were obscured by the relatively large variations in F_0 corresponding to the suprasegmental features of the sentence.

The present study was designed to explicitly test whether the magnitudes and latencies of responses to pitch-shifted voice feedback are modulated during English speech by using a phrase that did not have the very large variations in the F_0 contour as reported by Bauer (2004). In the present study, subjects were instructed to repeat a phrase in which the F_0 contour was relatively flat and then rose at the very end, as in a question. It was hypothesized that responses to pitch-shifted voice feedback that were presented during speech would be larger than those presented during a sustained vowel task because control of F_0 during speech is important for conveying information to the listener, while control of F_0 during a sustained vowel has no such goal and hence is inherently less meaningful than during speech. Results confirmed that responses to pitch-shifted feedback during speech were larger and faster than those produced during a sustained vowel task.

II. METHODS

A. Subjects

Twenty subjects (10 males and 10 females) between the ages of 19 and 21 were recruited. All subjects reported that English was the first language they learned. All subjects reported normal hearing, and none reported a history of speech or language problems or neurological disorder. All subjects signed informed consent approved by the Northwestern University Institutional Review Board.

B. Apparatus

Subjects were seated in a sound-attenuated chamber for the testing. Sennheiser headphones (model HMD 280) with an attached microphone were placed on the subject. The microphone signal was amplified (Mackie mixer model 1202), shifted in pitch with an Eventide Eclipse Harmonizer, mixed with 40 dB SPL masking noise (low-pass filtered from 10 to 5000 Hz), and then amplified to 10 dB SPL greater at the Sennheiser headphones than at the microphone. Subjects monitored their voice amplitude on a Dorrrough Loudness monitor (located 0.5 m in front of the subject) in an attempt to keep their vocal level near 70 dB SPL. Voice, feedback,

and TTL control pulses (generated by a locally fabricated circuit and controlled by MIDI software) were digitized at 10 kHz (5000 Hz low pass filter) on a laboratory computer. Acoustic calibrations were made with a Brüel & Kjær sound level meter (model 2250) and in-ear microphones (model 4100).

C. Procedures

Subjects were first instructed that they would hear a phrase (“you know Nina?”) spoken over headphones (female voice), and that they should repeat the phrase within 1 s in exactly the same manner as that of the sample. Because the phrase was spoken as a question, it started with a flat F_0 trajectory and then rose on the final syllable “...na” (Eady and Cooper, 1986).

The MIDI program initiated a trial by first presenting the voice recording to the subject. The onset of the subject’s voice then caused the MIDI program to activate the harmonizer and deliver the pitch-shift stimulus to the subject with a delay of 200 ms following voice onset. This delay time was chosen, based on measurements of the model phrase, so that the stimulus and response would begin before the rise in F_0 for the final syllable (na). It was necessary for the response to begin before the rise in F_0 so that we could measure it independently of the rise in F_0 (see the following). There was a 1500 ms intertrial interval. Subjects repeated this task 60 times, which took about 5 min. On one-third of the trials, an upward (increasing pitch) pitch-shift stimulus was presented, on one-third a decreasing pitch-shift stimulus was presented, and on one-third no stimulus (control) was presented. Since in the block of 60 trials, the sequence of stimuli was randomized, subjects could not predict which type of stimulus would occur on any given trial. Across 3 blocks of 60 trials, the stimulus magnitude was varied at ± 50 , 100, and 200 cents (200 ms duration). Stimulus durations of 200 ms were chosen because longer stimuli elicit voluntary responses by the subject (Burnett *et al.*, 1998).

Subjects were also tested with pitch-shifted voice feedback while repeating sustained vowel phonations. Subjects were instructed to say the vowel /u/ for a duration of approximately 5 s at their conversational pitch level and 70 dB SPL amplitude. During each vocalization, a randomized mixture of five control (no pitch-shift stimulus) or pitch-shift stimuli (± 50 , 100, or 200 cents) were presented at randomized times. Previous research has shown that this method of testing yields results that are identical to the presentation of one stimulus during each vocalization (Bauer and Larson, 2003). Thus, with each sequence of 12 vocalizations, 60 control or pitch-shift stimuli were presented. During any one block of trials, the pitch-shift magnitude was constant.

For data analysis, the voice, voice feedback, and TTL pulses were digitized at 10 kHz using Chart software (AD-Instruments). The voice wave form was then processed in Praat using an autocorrelation method to produce a train of pulses corresponding to the fundamental period of the voice waveform. This pulse train was then converted into an analog wave in Igor Pro (Wavemetrics, Inc., Lake Oswego, OR). The F_0 signals were then converted to a cents scale using the

following equation: $\text{cents} = 100 (39.86 \log_{10} (f_2/f_1))$ where f_1 equals an arbitrary reference note at 195.997 Hz (G4) and f_2 equals the voice signal in hertz. The F_0 wave form and TTL pulses were displayed on a computer screen, and the beginning and end points of the F_0 wave for each vocalization were marked with cursors. All the vocalizations in a block of 60 trials were then time-normalized. The time-normalization process was done by first calculating the average duration of all 60 vocalizations in a block of trials and then changing the durations of each of the F_0 traces and the accompanying trace representing the stimulus to the average duration of the entire group. By doing this normalization, the stimulus pulses maintained their alignment with the respective F_0 trace, and the pitch contours of the entire group were aligned in such a way that variability in the averaging process was reduced. Then, the F_0 trace for each vocalization was time-aligned with the TTL pulse representing the pitch-shift stimulus for each trial and an average trace was calculated separately for the two different stimulus directions in a block of 60 trials. An average of the control trials was produced in the same way, only in this case the TTL pulses were not accompanied by any change in voice pitch feedback. Thus, an average F_0 trace was constructed separately for downward stimuli, for upward stimuli and control trials for each subject and for each experimental condition.

After averaging, a statistical test was performed to determine if the average of the control wave differed significantly from the average of the test wave for the upward and downward stimulated trials. A point-by-point series of t-tests were run between all control and all test waves for a given condition and subject (see Xu *et al.*, 2004a). This process yielded an array of “ p ” values indicating the level of significant difference between the control and test waves. Response latencies were defined as the time point where the p values decreased below 0.02 and remained decreased for at least 50 ms. Rather than using a statistical correction factor to prevent spurious statistical significance from occurring (e.g., Bonferroni correction), we reasoned that physiological criteria provided a more valid approach. It is known from previous studies that a finite time of at least 60 ms occurs between a pitch-shift stimulus and a F_0 response (Burnett *et al.*, 1998; Burnett and Larson, 2002; Burnett *et al.*, 1997; Hain *et al.*, 2000; 2001; Larson 1998; Larson *et al.*, 2001; 1997, 2000). Also, it is known that the fastest contraction speeds of a muscle such as the cricothyroid, which is important for voice F_0 control, is about 30 ms to peak contraction (Perlman and Alipour-Haghighi, 1988), and a change in voice F_0 occurs 20–30 ms later (Kempster *et al.*, 1988; Larson *et al.*, 1987). Therefore, by limiting minimal latencies to 60 ms and response durations to 50 ms, this method guarded against significant changes in the voice F_0 that were not due to activity of the neuromuscular system. If we had employed a correction factor such as Bonferroni, some very short latencies or short duration responses could have been included in the set of acceptable responses.

A “difference wave” was then calculated by subtracting the average control wave from the averaged upward and downward stimulus test waves for each subject and each condition. The difference wave was used to measure the re-

TABLE I. Numbers of following (FOL), nonresponses (NR), and opposing responses (OPP) for the speech and nonspeech vocal conditions.

	Speech	Vowel	Total
FOL	16	5	21
NR	10	2	12
OPP	94	113	207
Total	120	120	240

sponse magnitude, which was measured as the greatest value of the difference wave following the latency and before the time where the p wave recrossed the 0.02 value indicating the end of the response. Response latency and magnitude measures were submitted to significance testing using a repeated-measures ANOVA (SPSS, v. 11.0).

III. RESULTS

Out of the 240 possible responses, there were 12 nonresponses that did not register a significant difference between the control and test wave, and 10 of these occurred in the speech condition (see Table I). Of the remaining 228, 21 responses were in the “following” direction (the response change in F_0 was in the same direction as the stimulus) and 207 in the opposing direction (response and stimulus waves changed in opposite directions). Sixteen of the “following” responses were in the speech condition, and 5 in the vowel condition. A chi-square test revealed a statistically greater number of nonresponses and “following” responses in the speech condition compared to the vowel condition ($\chi^2 = 12.84$, $df=2$; $p < 0.002$). The distribution of opposing, “following,” and nonresponses was even across the upward and downward stimulus directions and the stimulus magnitudes.

Figures 1–3 show examples of responses to pitch-shifted feedback during speech and vowel productions. Figure 1 illustrates responses to a downward 50 cents perturbation in voice pitch feedback on the left and an upward perturbation on the right. The top row shows responses produced during

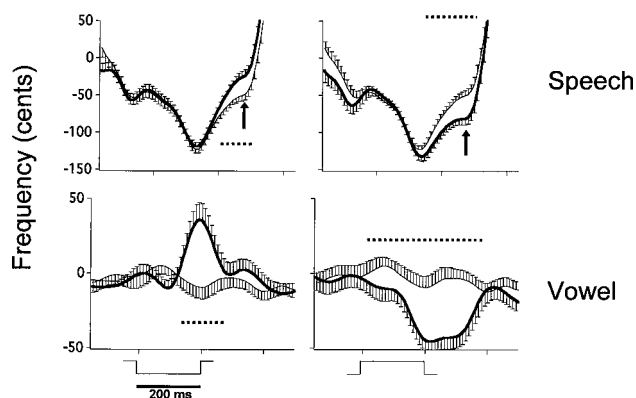


FIG. 1. F_0 contours for speech (top) and vowels (bottom). Traces for downward pitch-shift stimuli are on the left (indicated by square brackets at the bottom) and upward pitch-shift stimuli on the right. Contours with heavy lines are for stimulated trials, and light lines for control trials. Error bars represent 1 s.d. of the mean. Arrows indicate time where response magnitudes for speech contours were measured. Horizontal dashed lines indicate time when the control and test waves differed significantly. Stimulus magnitudes were ± 50 cents.

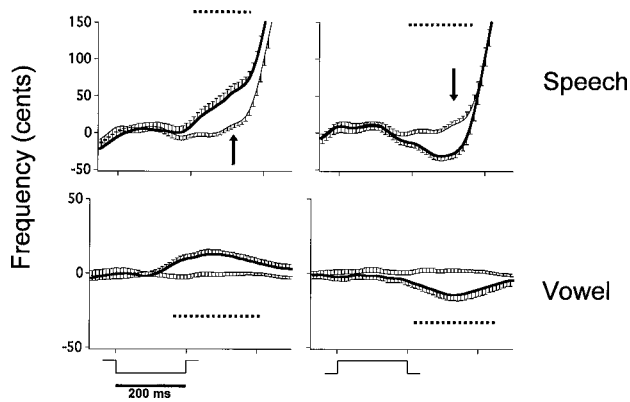


FIG. 2. F_0 contours for speech and vowel productions with ± 100 cents stimuli.

speech and the bottom row responses during a vowel. For each graph, the heavy line represents the average of the responses to the pitch perturbation and the light line the control responses. In each case, the responses to the pitch perturbation are in the opposite direction to the stimulus and occur within 200 ms of the onset of the stimulus. It is also clear that the responses during speech began before the rise in the F_0 trajectory of the final syllable and merged with the rising trajectory. In making the measurements of response magnitude, we noted the point of inflection of the F_0 trace that was part of the elevation at the end of the syllable and used this time as a cutoff point for measuring response magnitude from the difference wave. We compared this manual method with local peaks of acceleration of the F_0 trace and found no more than 20 ms disagreement. By making the measurements in this way, we attempted to reduce the likelihood that the response magnitude measures would be exaggerated by the rising F_0 at the end of the phrase. Arrows on the curves in Figs. 1–3 indicate the times where the measures were made. For the examples in Fig. 1, the responses produced during the vowel were larger than those produced during speech. Figures 2 and 3 show similar results for different subjects for the 100 and 200 cents perturbations, respectively. In these examples, as well as those for most of the subjects, all responses produced during speech were larger than those produced during vowels.

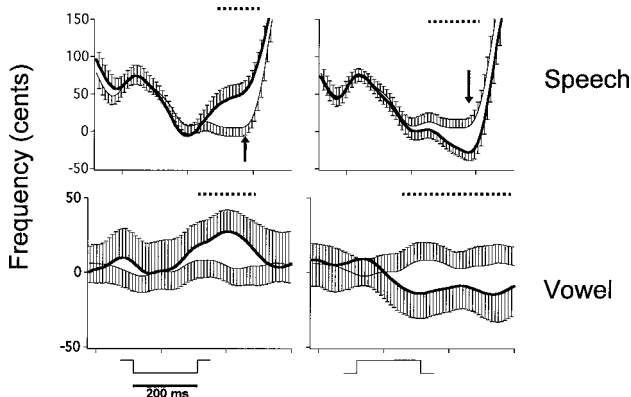


FIG. 3. F_0 contours for speech and vowel productions with ± 200 cents stimuli.

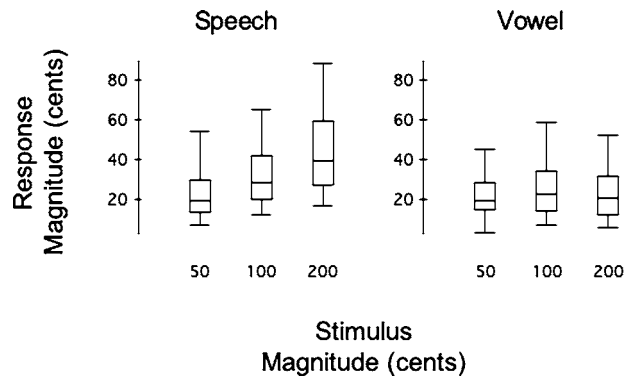


FIG. 4. Boxplots indicating response magnitudes for speech (left) and vowels (right) across stimulus magnitudes of ± 50 , 100, and 200 cents. Box definitions: Middle line is median, top and bottom of boxes are the 75th and 25th percentiles, whiskers extend to limits of main body of data defined as high hinge +1.5 (high hinge–low hinge), and low hinge –1.5 (high hinge–low hinge) (Data Desk; Data Description).

A three-way repeated-measures ANOVA was performed on the response magnitude of opposing responses with task, stimulus magnitude, and stimulus direction. Significant main effects on response magnitude were found for task ($F(1,114)=7.813$, $p<0.01$), stimulus magnitude ($F(2,114)=10.036$, $p<0.001$), and stimulus direction ($F(1,114)=28.332$, $p<0.001$). Responses in the speech condition (mean 31.5 ± 18.7 cents) were larger than those in the vowel condition (mean 21.6 ± 11.7). Significant interactions were between stimulus magnitude and stimulus direction ($F(2,38)=11.330$, $p<0.001$) and between stimulus magnitude and task ($F(2,114)=8.868$, $p<0.001$). Figure 4 shows box plots of response magnitude across the three stimulus magnitudes for all subjects for the speech and vowel conditions. Two-way repeated-measures ANOVAs (stimulus magnitude and stimulus direction) were performed on the magnitude for the speech and vowel conditions, respectively. As can be seen, there was a clear increase in response magnitude as a function of the stimulus magnitude for the speech ($F(2,57)=17.722$, $p<0.001$) but not for the vowel condition. Figure 5 shows box plots of response magnitude for the downward and upward stimuli for both speech and vowels. Here a clear effect of the stimulus magnitude can be seen for the downward stimuli during speech ($F(2,57)=25.996$, $p<0.001$), but not for the upward stimuli. No changes in response magnitudes for the vowels were observed.

A three-way repeated-measures ANOVA was also performed on the response latency with task, stimulus magnitude, and stimulus direction. There was a significant main effect for task, where latencies for speech (mean 122 ± 63 ms) were significantly shorter than those produced during the vowel task (mean 154 ± 79 ms) ($F(1,114)=13.195$, $p<0.0001$). There were no other significant latency effects.

IV. DISCUSSION

The present study was designed to test the hypothesis that the pitch-shift reflex would generate larger responses in an English speech task compared to a nonspeech task. This hypothesis is based on previous observations that reflexive

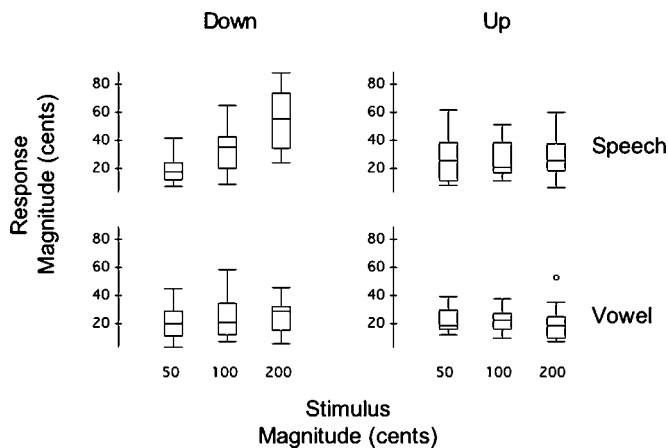


FIG. 5. Boxplots showing response magnitudes for ± 50 , 100, and 200 cents stimuli separately for downward (left) and upward stimuli (right). Upper row shows results from the speech condition and bottom row for the vowel condition. Box definitions: Middle line is median, top and bottom of boxes are 75th and 25th percentiles, whiskers extend to limits of the main body of data defined as high hinge $+1.5$ (high hinge-low hinge), and low hinge -1.5 (high hinge-low hinge) (Data Desk; Data Description).

mechanisms reflect neural connections between sensory feedback and motor control mechanisms (Houk, 1978; Stein, 1980). In other sensorimotor systems, when sensory feedback is important for the successful execution of a task, the controlling mechanisms generate compensatory responses to perturbations in sensory feedback (Gracco and Abbs, 1989; Munhall *et al.*, 1994; Shaiman, 1989; Tremblay *et al.*, 2003). As a subject is performing a motor task, the changes in the execution of the task that are measured in response to sensory perturbation reflect the neural mechanisms that are normally involved in completing the task. In this sense, the value of such studies lies in the knowledge they impart regarding neural mechanisms that control behavior.

In the present study, speakers produced a phrase in which the F_0 was held relatively stable across several syllables, and then elevated at the end of the phrase. This elevation was a suprasegmental adjustment in speech that made the phrase sound like a question. It is one of many ways in which nontonal languages use suprasegmental adjustments to express meaning (Bänziger and Scherer, 2005; Eady and Cooper, 1986; Lieberman, 1960; Xu and Xu, 2005). This particular experimental paradigm was necessitated by the difficulty in eliciting highly consistent intonation patterns from English subjects. In a pilot test, subjects were found to use variable intonation patterns for the sentences. This was probably because the English orthography does not implicitly specify any contrastive pitch patterns, as does the Chinese orthography. This variability could potentially be so large as to make the comparisons impossible. To avoid this problem, we used a prerecorded sentence as a model for the subjects. For each trial, they were asked to speak in the same way as the model sentence. No specific instructions were given, however, as to what aspects of the model they should imitate. This was to guarantee that they would not focus only on maintaining the pitch pattern. A similar imitation paradigm has been used previously in a study of Mandarin intonation (Xu *et al.*, 2004b). Because people's ability to con-

sciously analyze and imitate pitch is highly variable (Dankovicova *et al.*, in press), what is likely involved in performing the task is subjects' linguistic ability rather than their musical ability. Such linguistic ability, though also requiring highly accurate pitch control, involves only the control of relative pitch rather than exact pitch as in singing (Xu, 2005). Thus the larger responses observed in the speech condition compared to the vowel condition may indicate that auditory feedback is used on-line to help control suprasegmental features of speech production.

Additional evidence supporting this conjecture comes from the findings that responses were larger for downward stimuli compared to upward stimuli. The downward pitch perturbation was opposite in direction to the planned upward F_0 trajectory. It is known that questions in English manifest a rising intonation, particularly at the end of the sentence (Bolinger, 1989; Eady and Cooper, 1986; McRoberts *et al.*, 1995; Pell, 2001). Thus the downward pitch-shift would have made it sound to the subject as if his/her voice F_0 was changing in the wrong direction, away from the intended rise. In order to achieve the rising intonation, a greater upward response magnitude would be required compared to nonperturbed (control) trials. Moreover, the fact that the response magnitudes increased along with the magnitude of the downward directed pitch-shift stimuli, indicates that the system not only recognizes errors but is also capable of assessing their relative magnitudes and increasing the magnitude of the compensatory responses. By comparison, upward pitch perturbations, which were in the same direction as the planned inflection pattern, did not interfere with the inflection pattern. In this condition, as well as in the vowel productions, the response magnitudes were smaller than for downward directed stimuli presented during speech, suggesting the need for a corrective response was likely not as great.

Although there were far more opposing than "following" or nonresponses, there were a statistically greater number of "following" and nonresponses in the speech condition compared to the vowel condition. There may be two reasons for this difference. First, during speech, the F_0 trajectories of the control and test trials were dynamically changing, which made it more difficult to measure responses. Because of this, some responses may have been small and did not meet our criteria for acceptance. A second explanation may be that during the speech task, the audio-vocal system misinterpreted the direction of the stimulus and produced a "following" response in error. It is possible that if pitch shift stimuli are small (50–200 cents) and short in duration (200 ms), the system does not always recognize them. Providing larger magnitude and/or longer duration stimuli may reduce the number of nonresponses. It is more difficult to explain the higher percentage of "following" responses since there is still no clear explanation of their cause. However, it is possible that during speech, when F_0 is changing dynamically, subjects may misperceive the direction of the pitch-shift stimuli and respond inappropriately.

In this and previous pitch-shifting (Bauer and Larson, 2003; Burnett *et al.*, 1998; Burnett and Larson, 2002; Donath *et al.*, 2002; Elman, 1981; Hain *et al.*, 2000; Jones and Munhall, 2002; Kawahara, 1995; Natke *et al.*, 2003; Sivasankar

et al., 2005; Xu *et al.*, 2004a) and loudness-shifting (Bauer *et al.*, 2006; Heinks-Maldonado and Houde, 2005) studies, and studies of the Lombard response or side-tone amplification (Lane and Tranel, 1971), response magnitudes rarely achieved parity with stimulus magnitude. These findings reveal, as was suggested previously (Burnett *et al.*, 1998), that the audio-vocal system appears to be optimized for fine-tuning of voice F_0 or amplitude. The fact that the system can respond to 25 cent stimuli with a response of 26 cents shows that the system is optimally suited for correcting small errors in voice F_0 output (Larson *et al.*, 2001). It is also known that the system will respond to sounds other than those of the speaker (Sivasankar *et al.*, 2005). If the system responded to acoustical perturbations with responses of the same magnitude as the perturbation itself, environmental sounds could exert a predominant influence over the voice. Instead, by responding only partially to auditory feedback perturbations, the system allows for voluntary and cognitive mechanisms to be the most important factors controlling the voice. Moreover, the fact that response magnitudes can increase in certain speaking or singing conditions (Bauer *et al.*, 2006; Natke *et al.*, 2003; Xu *et al.*, 2004a), reveals the flexible nature of the audio-vocal system.

In comparing this study with previous ones, it was found that both the timing and magnitude of responses to pitch-shifted voice feedback are modulated during speech. In the present study, response latencies were shorter and magnitudes were greater in the speech condition compared to the vowel condition. Xu *et al.* (2004a) found that in Mandarin speech, response latencies were shorter and magnitudes were larger in speech conditions in which the stimulus direction (down) was introduced prior to a planned drop in voice F_0 (high-rising) compared to the condition where the F_0 contour was relatively stable (high-high phrase). Although the present study provides no evidence that response latencies may be differentially modulated according to different speech contexts, the fact that Bauer (2004) reported latencies to be increased in some English speech contexts and not others, suggests that the timing of voice F_0 responses to perturbations in auditory feedback can be modulated according to variations in the suprasegmental patterns of English speech just as with lexical contrasts in Mandarin. It is also important to note that the latency changes in speech are most likely due to the demands of speech since they have not been observed in other studies on sustained vowel productions (Bauer and Larson, 2003; Burnett *et al.*, 1998; Hain *et al.*, 2000). Thus data from this and previous studies indicate that during speech, both the timing and magnitude of responses to auditory feedback can be adjusted. These adjustments depend on the direction of the pitch-shift stimulus and the context of the speech at the time of the perturbation. The lack of such adjustments during vowels may reflect the fact that there is no differential importance to either an increase or decrease in voice pitch feedback.

Thus, experiments in both English and Mandarin have shown that pitch-shift reflex magnitudes and latencies are modulated during speech. Since Mandarin is a tone language and English is a nontonal language, the findings that the modulations in voice F_0 based on perturbations in voice

pitch feedback in both languages are similar suggest that the neural mechanisms underlying these responses are similar in tonal and nontonal languages as well as for segmental and suprasegmental features of speech production.

V. CONCLUSION

The present study demonstrated that neural control of voice F_0 during suprasegmental features of speech production is accomplished with the aid of auditory feedback of voice pitch. Moreover, results demonstrate that the control mechanisms are modulated according to task demands. The response magnitudes in speech were larger than in a non-speech task and for downward pitch-shift stimuli compared to upward stimuli. Since these responses occurred just before the inflection of voice F_0 associated with a question, it is suggested that the mechanisms controlling responses to voice pitch-shifted feedback are sensitive to the planned inflection in voice F_0 . As the subject is planning a rise in F_0 , a downward perturbation in voice pitch-feedback elicits a response that attempts to prevent F_0 from going in the wrong direction, so that the forthcoming rise in F_0 can be accurately made.

ACKNOWLEDGMENTS

This study was completed as part of an Undergraduate Honors Research Thesis in the Dept. of Communication Sciences and Disorders, Northwestern University. We acknowledge the contribution of Kaavya Paruchuri and Christine Lin for their assistance in data analysis. This study was supported by NIH Grant No. DC006243-01A1.

- Alain, C. (1993). "The relation among fundamental frequency, intensity, and duration varies with accentuation," *J. Acoust. Soc. Am.* **94**, 2434–2436.
- Bänziger, T., and Scherer, K. R. (2005). "The role of intonation in emotional expressions," *Speech Commun.* **46**, 252–267.
- Bauer, J. J. (2004). "Task dependent modulation of voice F_0 responses elicited by perturbations in pitch of auditory feedback during English speech and sustained vowels," Ph.D. dissertation, Northwestern University, Evanston, IL.
- Bauer, J. J., and Larson, C. R. (2003). "Audio-vocal responses to repetitive pitch-shift stimulation during a sustained vocalization: Improvements in methodology for the pitch-shifting technique," *J. Acoust. Soc. Am.* **114**, 1048–1054.
- Bauer, J. J., Mittal, J., Larson, C. R., and Hain, T. C. (2006). "Vocal responses to unanticipated perturbations in voice loudness feedback: An automatic mechanism for stabilizing voice amplitude," *J. Acoust. Soc. Am.* **119**, 2363–2371.
- Bolinger, D. (1989). *Intonation and Its Uses—Melody in Grammar and Discourse* (Stanford University Press, Stanford, CA).
- Burnett, T. A., Freedland, M. B., Larson, C. R., and Hain, T. C. (1998). "Voice F_0 responses to manipulations in pitch feedback," *J. Acoust. Soc. Am.* **103**, 3153–3161.
- Burnett, T. A., and Larson, C. R. (2002). "Early pitch shift response is active in both steady and dynamic voice pitch control," *J. Acoust. Soc. Am.* **112**, 1058–1063.
- Burnett, T. A., Senner, J. E., and Larson, C. R. (1997). "Voice F_0 responses to pitch-shifted auditory feedback; A preliminary study," *J. Voice* **11**, 202–211.
- Chuenwattanapranithi, S., Xu, Y., Thipakorn, B., and Maneewongvatana, S. (2006). "Expressing anger and joy with the size code," *Transactions on Engineering, Computing and Technology* **11**, 222–227.
- Cooper, W. E., Eady, S. J., and Mueller, P. R. (1985). "Acoustical aspects of contrastive stress in question-answer contexts," *J. Acoust. Soc. Am.* **77**, 2142–2156.
- Donath, T. M., Natke, U., and Kalveram, K. T. (2002). "Effects of

- frequency-shifted auditory feedback on voice F_0 contours in syllables," *J. Acoust. Soc. Am.* **111**, 357–366.
- Duffy, J. R. (1995). *Motor Speech Disorders* (Mosby, St. Louis).
- Eady, S. J., and Cooper, W. E. (1986). "Speech intonation and focus location in matched statements and questions," *J. Acoust. Soc. Am.* **80**, 402–416.
- Elman, J. L. (1981). "Effects of frequency-shifted feedback on the pitch of vocal productions," *J. Acoust. Soc. Am.* **70**, 45–50.
- Fairbanks, G. (1954). "Systematic research in experimental phonetics. 1. A theory of the speech mechanism as a servosystem," *J. Speech Hear. Res.* **19**, 133–140.
- Gracco, V. L., and Abbs, J. H. (1985). "Dynamic control of the perioral system during speech: Kinematic analyses of autogenic and nonautogenic sensorimotor processes," *J. Neurophysiol.* **54**, 418–432.
- Gracco, V. L., and Abbs, J. H. (1989). "Sensorimotor characteristics of speech motor sequences," *Exp. Brain Res.* **75**, 586–598.
- Hain, T. C., Burnett, T. A., Kiran, S., Larson, C. R., Singh, S., and Kenney, M. K. (2000). "Instructing subjects to make a voluntary response reveals the presence of two components to the audio-vocal reflex," *Exp. Brain Res.* **130**, 133–141.
- Hain, T. C., Burnett, T. A., Larson, C. R., and Kiran, S. (2001). "Effects of delayed auditory feedback (DAF) on the pitch-shift reflex," *J. Acoust. Soc. Am.* **109**, 2146–2152.
- Heinks-Maldonado, T. H., and Houde, J. F. (2005). "Compensatory responses to brief perturbations of speech amplitude," *ARLO* **6**, 131–137.
- Houk, J. C. (1978). "Participation of reflex mechanisms and reaction-time processes in the compensatory adjustments to mechanical disturbances," in *Cerebral Motor Control in Man: Long Loop Mechanisms*, edited by J. E. Desmedt (Karger, Basel) Vol. **4**, pp. 193–215.
- Dankovicova, A. C., House, J. J., and Jones, K. (In Press). "The Relationship between musical skills, music training, and intonation analysis skills," *Lang. & Speech*.
- Jones, J. A., and Munhall, K. G. (2002). "The role of auditory feedback during phonation: Studies of Mandarin tone production," *J. Phonetics* **30**, 303–320.
- Kawahara, H. (1995). "Hearing voice: Transformed auditory feedback effects on voice pitch control," *Computational Auditory Scene Analysis and International Joint Conference on Artificial Intelligence*, Montreal.
- Kempster, G. B., Larson, C. R., and Kistler, M. K. (1988). "Effects of electrical stimulation of cricothyroid and thyroarytenoid muscles on voice fundamental frequency," *J. Voice* **2**, 221–229.
- Lane, H., and Tranel, B. (1971). "The Lombard sign and the role of hearing in speech," *J. Speech Hear. Res.* **14**, 677–709.
- Larson, C. R. (1998). "Cross-modality influences in speech motor control: The use of pitch shifting for the study of F_0 control," *J. Commun. Disord.* **31**, 489–503.
- Larson, C. R., Burnett, T. A., Bauer, J. J., Kiran, S., and Hain, T. C. (2001). "Comparisons of voice F_0 responses to pitch-shift onset and offset conditions," *J. Acoust. Soc. Am.* **110**, 2845–2848.
- Larson, C. R., Burnett, T. A., Freedland, M. B., and Hain, T. C. (1997). "Voice F_0 responses to manipulations in pitch feedback stimuli," *First International Conference on Voice Physiology and Biomechanics*, Evanston, IL.
- Larson, C. R., Burnett, T. A., Kiran, S., and Hain, T. C. (2000). "Effects of pitch-shift onset velocity on voice F_0 responses," *J. Acoust. Soc. Am.* **107**, 559–564.
- Larson, C. R., Kempster, G. B., and Kistler, M. K. (1987). "Changes in voice fundamental frequency following discharge of single motor units in cricothyroid and thyroarytenoid muscles," *J. Speech Hear. Res.* **30**, 552–558.
- Lieberman, P. (1960). "Some acoustic correlates of word stress in American English," *J. Acoust. Soc. Am.* **32**, 451–454.
- McRoberts, G. W., Studdert-Kennedy, M., and Shankweiler, D. P. (1995). "The role of fundamental frequency in signaling linguistic stress and affect: Evidence for a dissociation," *Percept. Psychophys.* **57**, 159–174.
- Munhall, K. G., Löqvist, A., and Kelso, J. A. S. (1994). "Lip-larynx coordination in speech: Effects of mechanical perturbations to the lower lip," *J. Acoust. Soc. Am.* **95**, 3605–3616.
- Natke, U., Donath, T. M., and Kalveram, K. T. (2003). "Control of voice fundamental frequency in speaking versus singing," *J. Acoust. Soc. Am.* **113**, 1587–1593.
- Natke, U., and Kalveram, K. T. (2001). "Effects of frequency-shifted auditory feedback on fundamental frequency of long stressed and unstressed syllables," *J. Speech Lang. Hear. Res.* **44**, 577–584.
- Pell, M. D. (2001). "Influence of emotion and focus on prosody in matched statements and questions," *J. Acoust. Soc. Am.* **109**, 1668–1680.
- Perlman, A. L., and Alipour-Haghighi, F. (1988). "Comparative study of the physiological properties of the vocalis and cricothyroid muscles," *Acta Oto-Laryngol.* **105**, 372–378.
- Shaiman, S. (1989). "Kinematic and electromyographic responses to perturbation of the jaw," *J. Acoust. Soc. Am.* **86**, 78–88.
- Sivasankar, M., Bauer, J. J., Babu, T., and Larson, C. R. (2005). "Voice responses to changes in pitch of voice or tone auditory feedback," *J. Acoust. Soc. Am.* **117**, 850–857.
- Stein, R. B. (1980). *Nerve and Muscle* (Plenum, New York).
- Tremblay, S., Shiller, D. M., and Ostry, D. J. (2003). "Somatosensory basis of speech production," *Nature (London)* **423**, 866–869.
- Xu, Y. (2005). "Speech melody as articulatorily implemented communicative functions," *Speech Commun.* **46**, 220–251.
- Xu, Y., Larson, C., Bauer, J., and Hain, T. (2004a). "Compensation for pitch-shifted auditory feedback during the production of Mandarin tone sequences," *J. Acoust. Soc. Am.* **116**, 1168–1178.
- Xu, Y., and Xu, C. X. (2005). "Phonetic realization of focus in English declarative intonation," *J. Phonetics* **33**, 159–197.
- Xu, Y., Xu, C. X., and Sun, X. (2004b). "On the temporal domain of focus," *Proceedings of the International Conference on Speech Prosody 2004*, Nara, Japan.

Integration efficiency for speech perception within and across sensory modalities by normal-hearing and hearing-impaired individuals

Ken W. Grant^{a)}

Walter Reed Army Medical Center, Army Audiology and Speech Center, Washington, D.C. 20307-5001

Jennifer B. Tufts

Department of Communication Sciences, University of Connecticut, Storrs, Connecticut 06269

Steven Greenberg

Silicon Speech, 46 Oxford Drive, Santa Venetia, California 94903

(Received 22 October 2006; revised 9 November 2006; accepted 15 November 2006)

In face-to-face speech communication, the listener extracts and integrates information from the acoustic and optic speech signals. Integration occurs within the auditory modality (i.e., across the acoustic frequency spectrum) and across sensory modalities (i.e., across the acoustic and optic signals). The difficulties experienced by some hearing-impaired listeners in understanding speech could be attributed to losses in the extraction of speech information, the integration of speech cues, or both. The present study evaluated the ability of normal-hearing and hearing-impaired listeners to integrate speech information within and across sensory modalities in order to determine the degree to which integration efficiency may be a factor in the performance of hearing-impaired listeners. Auditory-visual nonsense syllables consisting of eighteen medial consonants surrounded by the vowel [a] were processed into four nonoverlapping acoustic filter bands between 300 and 6000 Hz. A variety of one, two, three, and four filter-band combinations were presented for identification in auditory-only and auditory-visual conditions: A visual-only condition was also included. Integration efficiency was evaluated using a model of optimal integration. Results showed that normal-hearing and hearing-impaired listeners integrated information across the auditory and visual sensory modalities with a high degree of efficiency, independent of differences in auditory capabilities. However, across-frequency integration for auditory-only input was less efficient for hearing-impaired listeners. These individuals exhibited particular difficulty extracting information from the highest frequency band (4762–6000 Hz) when speech information was presented concurrently in the next lower-frequency band (1890–2381 Hz). Results suggest that integration of speech information within the auditory modality, but not across auditory and visual modalities, affects speech understanding in hearing-impaired listeners. [DOI: 10.1121/1.2405859]

PACS number(s): 43.71.An, 43.71.Ky, 43.71.Es [ADP]

Pages: 1164–1176

I. INTRODUCTION

The ability to understand speech relies to a considerable degree on the integration of spectro-temporal information from different regions of the acoustic frequency spectrum. This cross-spectral integration is especially important for individuals using multichannel hearing aids and cochlear implants. Such auditory prostheses partition the spectrum into separate channels and subject them to various forms of signal processing. However, because most spoken conversations involve face-to-face interaction, visual speech information is often available in addition to auditory information. In these cases, listeners integrate information from both the auditory and visual modalities. This cross-modal integration occurs in tandem with the cross-spectral integration occurring entirely within the auditory modality. The present study evaluated the

efficiency of cross-modal and cross-spectral integration of speech information in normal-hearing and hearing-impaired listeners. This was done by analyzing error patterns in consonant identification tests consisting of spectrally sparse stimuli presented in auditory-only and auditory-visual conditions. A visual-only condition was also included.

When speech is presented acoustically, it is spectrally filtered in the auditory pathway into many overlapping frequency channels. Information about specific speech sounds may be distributed broadly across many different frequency channels or may be concentrated within a limited number of channels. Information distributed across many frequency channels may be helpful for decoding the speech signal, particularly in noisy and reverberant conditions. Early work on speech vocoder systems (Hill *et al.*, 1968) showed that speech recognition improved as the number of discrete frequency channels increased from three to eight (for frequencies between 180 and 4200 Hz). More recently, Shannon *et al.* (1995) demonstrated that the temporal information contained in as few as four broad spectral regions is sufficient

^{a)} Author to whom correspondence should be addressed. 301 Hamilton Avenue, Silver Spring, Maryland 20901. Telephone: 202-782-8596. Electronic mail: grant@tidalwave.net

for good speech recognition in ideal listening conditions. These studies were conducted in quiet using normal-hearing subjects whose abilities to integrate information across spectral channels were not in doubt. However, it is unclear whether individuals with sensorineural hearing loss are able to integrate information across spectral channels as efficiently as normal-hearing listeners do, especially if the hearing loss varies widely across the speech frequency range. Turner *et al.* (1999) addressed this issue, using speech signals composed primarily of temporal cues from different spectral bands. They assessed the intelligibility of 1, 2, 4, and 8-channel conditions. They hypothesized that normal-hearing and hearing-impaired listeners would perform similarly when speech was limited to a small number of spectral channels. As more spectral channels were used to represent the speech information, and the frequency resolution of the hearing-impaired listeners became a limiting factor, intelligibility for hearing-impaired listeners would fall below that of normal-hearing listeners. The results showed that normal-hearing and hearing-impaired listeners performed similarly when only one spectral channel was used, as expected. However, contrary to prediction, the hearing-impaired listeners were significantly poorer than normal-hearing listeners at identifying the speech tokens for all other conditions, including the two-band condition where frequency resolution would not be expected to be a problem. These results are consistent with those of Friesen *et al.* (2001) comparing speech recognition performance for normal-hearing subjects and cochlear implant (CI) patients as a function of the number of spectral channels. Friesen *et al.* (2001) demonstrated that most CI subjects were unable to utilize fully the spectral information provided by the electrodes used in their implants.

As Turner *et al.* (1999) point out, these results are difficult to interpret. Hearing-impaired and normal-hearing listeners have seemingly comparable abilities to extract temporal cues from the speech envelope derived from a single auditory channel (though single-channel speech decoding is poor for both groups of listeners). However, when even minimal amounts of spectral information are introduced into the speech signal (as when temporal envelopes from two different spectral regions are combined), hearing-impaired listeners perform more poorly than normal-hearing listeners. Although hearing-impaired listeners usually have poorer-than-normal spectral resolution, there are no models of hearing impairment that limit listeners with moderate sensorineural hearing loss to a single auditory channel. Thus, it is unclear why, once audibility has been taken into account, hearing-impaired listeners fail to benefit from the addition of a second channel of speech information to the same degree as normal-hearing listeners.

One explanation offered by Turner *et al.* (1999) was that greater overlap between adjacent bands may have existed due to broader critical bands in hearing-impaired listeners. This overlap can be likened to a third channel that introduces noise or unusable temporal cues. To test this hypothesis, Turner *et al.* (1999) interposed a band-reject region between 1000 and 2000 Hz that separated the two spectral bands. In this way, energetic interference between the two spectral

bands would be greatly reduced. It was anticipated that the speech recognition performance of the hearing-impaired listeners would improve in this condition. However, performance in both conditions (with and without spectrally contiguous channels) was essentially the same. A second explanation for the failure of hearing-impaired listeners to take advantage of additional spectral channels of information posited the existence of some form of central auditory deficit in these listeners due to their greater age (45–70 years) compared with the normal-hearing subjects (22–48 years).

The question remains as to why hearing-impaired listeners fail to benefit from the addition of a second channel of speech information to the same degree as normal-hearing listeners. It is possible that, although the hearing-impaired listeners were able to extract similarly useful information from the individual channels, they were not able to integrate the information across these channels as efficiently as the normal-hearing listeners. Healy and colleagues (Healy and Bacon, 2002; Healy, Kannabiran and Bacon, 2005) have presented additional evidence that hearing-impaired listeners have difficulty integrating temporal speech information presented in different frequency regions. They tested word recognition of normal-hearing and hearing-impaired listeners using two sinusoidal signals (750 and 3000 Hz) modulated by one-third octave bands of speech and presented either synchronously or asynchronously. Word recognition was essentially zero for either channel presented alone. The frequencies of the sinusoids were chosen to maximize channel isolation, and the presentation levels were chosen to ensure audibility. Listeners with hearing impairment performed more poorly than listeners with normal hearing, even at comparable sensation levels, suggesting that a deficit existed in their ability to integrate temporal speech information across different frequency regions. Furthermore, when between-band asynchrony was introduced, the performance of the hearing-impaired listeners fell far more precipitously than that of the normal-hearing listeners, and more sharply than predicted based on correlations of the envelopes of the two bands (Healy, Kannabiran and Bacon, 2005). These results provide further evidence for a deficit in cross-spectral integration separate from other effects of sensorineural hearing loss such as reduced audibility and broadened auditory filters.

Combining speech cues derived from multiple sources of information has been a topic of considerable discussion and research, primarily with respect to integration of cues across the auditory and visual sensory modalities (Massaro, 1987, 1998; Braida, 1991; Grant and Seitz, 1998; Massaro and Cohen, 2000; Grant, 2002). Auditory-visual integration refers to the process of combining information that has been extracted from the auditory and visual channels (Grant, 2002). All other things being equal, greater skill at integrating auditory and visual cues, or higher integration efficiency, will almost always lead to better performance in auditory-visual tasks (Grant, Walden, and Seitz, 1998). Highly efficient integrators are assumed to be better at using cues from multiple sources for speech recognition.

Models of auditory-visual integration conceptualize the extraction and integration of cues as independent processes

that operate serially. The models also assume no interference across modalities in the extraction of cues. However, listeners may not function this way in the real world. Sommers *et al.* (2005a) presented evidence that auditory-visual integration, as assessed with the Prelabeling Model of Integration model (Braida, 1991; see Sec. II for further information on this model), varied depending on the signal-to-noise ratio (SNR) at which the speech materials were presented. Sommers *et al.* (2005a) interpreted these results to mean that the processes of extraction and integration of unimodal cues interacted to determine overall auditory-visual benefit. Their conclusion appears related to that of Ross *et al.* (2006), who assessed unimodal and auditory-visual word recognition over a wide range of SNRs. They argued that auditory-visual integration is most effective for intermediate SNRs. That is, a minimum amount of auditory information is required before word recognition can be most effectively enhanced by visual cues. In extremely favorable or unfavorable SNRs, in which one modality is clearly dominant over the other, listeners may rely less heavily on the integration of cues across modalities to understand speech. Instead, they may switch to a strategy in which a strong bias exists for cues from the dominant modality, and information from the less-dominant modality is discarded. This form of "interference" in cue extraction across modalities would not be accounted for by current models and would lead to the appearance of sub-optimal auditory-visual integration. Nevertheless, models of auditory-visual integration assess cue extraction and integration independently. This is necessary because, in the absence of a comprehensive understanding of the interactions that may occur across such processes, integration cannot be validly assessed without first determining which cues are available for integration.

Models that were originally developed for assessing auditory-visual integration efficiency can also be applied to cross-spectral integration in the auditory pathway (Greenberg *et al.*, 1998; Silipo *et al.*, 1999; Müsch and Buus, 2001; Greenberg and Arai, 2004). In either the cross-modal or cross-spectral case, predictions of an optimal processing model are compared to actual performance, and the differences are used as an index of integration efficiency. For example, if observed performance is just slightly worse than predicted performance, then integration efficiency is considered nearly, but not quite, optimal. By examining the differences between observed and predicted performance, it may be possible to shed light on why listeners with sensorineural hearing loss do not benefit as much as expected by the addition of information in other spectral channels.

In the present study, the integration efficiency of normal-hearing and hearing-impaired listeners was compared both within and across modality. Nonsense syllable (VCV) tokens were spectrally filtered into four non-overlapping bands. These bands were combined in various ways and then presented to normal-hearing and hearing-impaired subjects for identification. Auditory-only and auditory-visual conditions were examined. The spectral band configurations have been used in earlier, studies of spectro-temporal integration (Greenberg *et al.*, 1998; Silipo *et al.*, 1999; Greenberg and Arai, 2004) and were chosen so as to preclude ceiling effects

when several bands were combined or when visual cues were available in addition to information in one or more of the bands.

Previous research (Grant and Walden, 1996; Grant *et al.*, 1998) has shown that speech-reading conveys significant information about consonantal place of articulation (i.e., [b] versus [d]), relatively little information about manner of articulation (e.g., [b] versus [m], especially once place cues have been accounted for), and virtually no information about voicing (e.g., [p] versus [b]). Acoustically, place information is usually associated with second and third formant transitions (Pickett, 1999) in the range between 1000 and 2500 Hz. Thus, the information conveyed by visual cues is essentially redundant with that provided by the acoustic signal in the mid-frequency region. If mid-frequency acoustic information is removed, but visual cues are available, efficient cross-modal integration should result in good speech recognition performance. Conversely, if only mid-frequency acoustic information is available along with visual cues, even the most efficient cross-modal integration would be expected to produce only modest gains in performance. The auditory-visual conditions of the experiment were designed with these expectations in mind. The purpose of the study was to address the following question: Are decrements in speech recognition performance in hearing-impaired listeners attributable to a deficit solely in the extraction of speech cues, or is the decrement due to a deficit in integration efficiency within and/or across sensory modalities, or both?

II. METHODS

A. Subjects

Four normal-hearing (mean age=43 years, range =29–55 years) and four hearing-impaired subjects (mean age=71 years, range=65–74 years) were recruited from the staff and patient population of the Army Audiology and Speech Center, Walter Reed Army Medical Center. Pure tone thresholds for right and left ears at frequencies between 250 and 8000 Hz are shown in Table I. For normal-hearing subjects, thresholds were 20 dB HL or better at all test frequencies, with the exception of one subject who had a threshold of 25 dB HL at 8000 Hz (ANSI, 1989). For hearing-impaired subjects, the mean three-frequency threshold at 500, 1000, and 2000 Hz was 39.2 and 33.3 dB HL for right and left ears, respectively. The average high-frequency threshold at 3000, 4000, and 6000 Hz was 72.1 and 75 dB HL for right and left ears, respectively. Recent audiometric evaluations showed immittance measures within normal limits and no significant air-bone gaps, indicating that the hearing loss was sensorineural in origin. The hearing-impaired subjects were experienced hearing-aid users who had received audiological examinations and hearing-aid fittings at the Army Audiology and Speech Center, Walter Reed Army Medical Center. All subjects were native speakers of American English with normal or corrected-to-normal vision (visual acuity equal to or better than 20/30 as measured with a Snellen chart). Subjects were compensated for their participation, as permitted by federal regulations. Each subject read and signed an informed consent form prior to beginning the

TABLE I. Pure tone thresholds (dB HL) for four normal-hearing subjects (NH) and four hearing-impaired subjects (HI).

	RIGHT EAR									LEFT EAR								
	250	500	1000	1500	2000	3000	4000	6000	8000	250	500	1000	1500	2000	3000	4000	6000	8000
NH1	5	10	5	15	15	15	0	5	25	5	10	0	10	10	15	5	5	5
NH2	15	15	10	10	15	20	15	15	20	10	5	5	10	10	15	10	20	15
NH3	5	0	5	5	0	5	10	5	20	10	5	5	5	0	0	10	10	10
NH4	5	5	5	5	15	15	5	10	10	5	0	0	5	20	10	5	0	15
HI1	20	20	20	15	35	55	65	70	70	20	15	15	35	40	95	95	100	90
HI2	20	25	40	45	55	70	80	80	80	20	20	25	40	35	60	65	80	80
HI3	10	25	50	50	45	50	60	105	120	20	15	45	45	40	55	60	75	75
HI4	40	40	45	70	70	75	75	80	75	30	35	45	65	70	70	70	75	70

study. The methods used in this study were approved by the Institutional Review Board at the Walter Reed Army Medical Center.

B. Stimuli

Consonant recognition in a vowel-consonant-vowel context was evaluated using spectrally sparse acoustic stimuli consisting of one, two, three, or four narrow (1/3-octave) spectral bands separated by an octave (e.g., the upper edge of one band was an octave below the lower edge of its higher-frequency neighbor). The stimuli consisted of the consonants /b,p,g,k,d,t,m,n,f,v,θ,ð,s,z,ʃ,ʒ,tʃ,dʒ/ surrounded by the vowel /a/. Ten unique productions of each nonsense syllable were spoken by a female speaker of American English and recorded audiovisually using a three-tube Ikegami color camera and stored on optical disk (Panasonic TQ-3031F). Two of these ten tokens were selected for training and the remaining eight tokens were reserved for testing. The speech tokens were then processed through a MATLAB© routine to create filtered speech tokens containing one to four spectrally distinct 1/3-octave bands. FIR filters were used with attenuation

rates that were, at minimum, 100 dB/octave (and usually between 500 dB/octave and 2000 dB/octave). The four-band auditory condition ($A_{1,2,3,4}$) consisted of filter pass-bands of 298–375 Hz (band 1), 750–945 Hz (band 2), 1890–2381 Hz (band 3), and 4762–6000 Hz (band 4) presented simultaneously. Four additional auditory conditions were tested, which included band 1 alone (A_1), bands 1 and 4 combined ($A_{1,4}$), bands 2 and 3 combined ($A_{2,3}$), and bands 1, 2, and 3 combined ($A_{1,2,3}$). Two separate auditory-visual conditions were tested in which subjects viewed a video image of the talker presented synchronously with either the two fringe bands ($AV_{1,4}$) or the two middle bands ($AV_{2,3}$). An eighth condition (V) examining visual-only speech recognition (i.e., speechreading) was also tested. The experimental conditions are listed in Table II.

The audio portion of each production was digitized at a sampling rate of 20 kHz with 16-bit amplitude resolution. The digitized samples were ramped on and off (using a 50 ms raised cosine function), lowpass-filtered at 8.5 kHz, and normalized in level so that all stimuli had the same average rms amplitude. One effect of this normalization was to alter the levels of the bands in the sub-band conditions relative to the $A_{1,2,3,4}$ condition. A sixth auditory condition ($A_{1,2,3,4sum}$) was added later to evaluate the effect of these band-level differences. This condition is the sum of the $A_{1,4}$ and $A_{2,3}$ conditions, and was not normalized in level. Thus, the band levels in this condition are equal to the band levels in the $A_{1,4}$ and $A_{2,3}$ conditions, but are more intense than the band levels in the $A_{1,2,3,4}$ condition. Table III shows the relative band levels for each of the auditory conditions. For auditory-visual presentations, the digitized computer audio

TABLE II. Experimental conditions. Performance was predicted for the conditions marked in parenthesis using Braida’s Prelabeling Model of Integration. Predicted and obtained results were then compared to derive Integration Efficiency measures (i.e., Obtained /Predicted × 100). See text for further explanation.

Condition	Description
1 ($A_{1,2,3,4}$)	Consonants filtered into four non-overlapping narrow filter bands: Band 1 (298–375 Hz), Band 2 (750–945 Hz), Band 3 (1890–2381 Hz), and Band 4 (4762–6000 Hz).
2 $A_{1,4}$	Consonants filtered into two bands: Bands 1 and Band 4.
3 $A_{2,3}$	Consonants filtered into two bands: Bands 2 and Band 3.
4 A_1	Consonants filtered into one band: Band 1.
5 $A_{1,2,3}$	Consonants filtered into three bands: Band 1, Band 2, and Band 3.
6 $A_{1,2,3,4sum}$	Additive sum of Condition 2 and Condition 3. This condition was more intense than the $A_{1,2,3,4}$ condition, especially for Bands 1 and 4. See text for further explanation.
7 ($AV_{1,4}$)	Condition 2 presented auditory-visually.
8 ($AV_{2,3}$)	Condition 3 presented auditory-visually.
9 V	Consonants were presented visually only (i.e., speechreading).

TABLE III. Relative band levels for each of the four filtered-speech bands in the six auditory conditions.

CONDITION	RELATIVE BAND LEVELS (dB)			
	BAND 1	BAND 2	BAND 3	BAND 4
A_1	-8.04			
$A_{1,4}$	-9.42			-22.22
$A_{2,3}$		-9.13	-27.26	
$A_{1,2,3}$	-17.05	-10.52	-28.71	
$A_{1,2,3,4}$	-17.46	-10.59	-29.55	-30.76
$A_{1,2,3,4sum}$	-9.45	-10.15	-28.40	-22.30

and optical disk video portions of each production were realigned using custom auditory-visual control software. Alignments were verified using a dual-trace oscilloscope to compare the original and digitized productions of each utterance and were found to be accurate within ± 2 ms. Video signals from the optical disk were routed through a digital time-base corrector (FOR. A FA-310) before being sent to a 21" color monitor (SONY PVM 2030) situated approximately 1.5 m from the subject. When active, the video monitor displayed a life size image of the talker's face, neck, and shoulders.

C. Procedure

Subjects were seated in a double-walled sound-attenuating booth. A touch-screen terminal was placed within easy reach of the subject and displayed the full set of 18 consonants used. All audio test signals were output through a 16-bit DAC (TDT DD1) and routed through an 8.5 kHz anti-aliasing filter (TDT FLT3), separate programmable attenuators (TDT PA4), mixer (TDT ADD1), head phone driver (TDT HBUF3), and stereo headphones (Beyer Dynamic DT770). Speech signals were presented binaurally at approximately 85 dB SPL for normal-hearing subjects and at a comfortable level (between 95 and 105 dB SPL depending on the subject) for hearing-impaired subjects. A third-octave band analysis was conducted on the speech stimuli for condition $A_{1,2,3,4}$ calibrated to 85, 95, and 105 dB SPL in order to determine the audibility of the bands. At these presentation levels, all of the speech information in bands 1, 2, and 3 would have been audible to the hearing-impaired subjects (with the exception of the weaker portions of the signal in band 3 for subject ECC). Given the severity of the hearing losses in the higher frequencies, it is likely that band 4 was not fully audible in some cases. Specifically, the mean rms SPL in band 4 (approximately 71–81 dB, depending on presentation level) was close to the thresholds of some of the hearing-impaired subjects; thus, while the speech peaks in band 4 would have been audible, the weaker portions of the speech signal may have been inaudible. Each trial began by first informing the subject of the test modality (auditory, visual, or auditory-visual) and then by playing a warning tone followed by one of the nonsense syllables (drawn from the set of eight unique productions of each syllable). Subjects responded by pressing one of the 18 consonants displayed on the touch screen, and then pressed a second touch area marked with the word "continue" when they were ready for the next trial. Subjects could change their responses as often as they wished until the continue button was pressed. Each block consisted of 72 trials of a single condition (four repetitions of each consonant \times 18 consonants). Each condition with the exception of $A_{1,2,3,4sum}$ was tested ten times, yielding a total of 40 trials (four repetitions \times 10 blocks) per consonant per condition. The order of auditory, visual, and auditory-visual conditions was randomized for each subject. No feedback was provided. Subject responses were stored in the form of stimulus-response confusion matrices for subse-

TABLE IV. Feature classification for voicing, manner, and place categories.

<u>VOICING</u>	
Voiced:	b,d,g,m,n,v,ð,z,ʒ,dʒ
Unvoiced:	p,t,k,f,θ,s,ʃ,tʃ
<u>MANNER OF ARTICULATION</u>	
Stop:	b,p,g,k,d,t
Nasal:	m,n
Fricative:	v,f,ð,θ,z,s,ʒ,ʃ
Affricate:	dʒ,tʃ
<u>PLACE OF ARTICULATION</u>	
Bilabial:	b,p,m
Alveolar:	d,t,n,s,z
Labio-Dental:	v,f
Dental:	ð,θ
Palatal:	ʒ,ʃ,dʒ,tʃ
Velar:	g,k

quent analysis. Testing and analysis of the control condition $A_{1,2,3,4sum}$ was completed following the other eight conditions.

D. Data analysis and model fits

For each of the conditions listed in Table II, excluding $A_{1,2,3,4sum}$, performance measures were computed for overall consonant recognition, and information transmission (Miller and Nicely, 1955) for the articulatory-acoustic features of voicing, manner of articulation, and place of articulation. Information-transmission rates for the phonetic features listed in Table IV were obtained using the SINFA algorithm (Wang, 1976), with values taken from the summary table for unconditional feature information.

A common metric for evaluating auditory-visual benefit, and sometimes auditory-visual integration (Sommers *et al.*, 2005b), is the relative benefit measure (RB) described by Sumbly and Pollack (1954). This metric evaluates the improvement in information transmission that occurs when auditory and visual information is available, relative to the case when only auditory or only visual information is available. Given an auditory-visual condition and some reference condition (either auditory-only or visual-only), the RB is the observed percent improvement in the amount of information transmitted for the auditory-visual condition compared with the information transmitted for the reference condition, divided by the theoretically possible percent improvement [e.g., $(AV-A)/(100-A)$], where AV is the percent information transmitted in the auditory-visual condition and A is the percent information transmitted in the auditory-only reference condition. Maximum RB is one. The RB is described here because of its historical importance as a measure of auditory-visual benefit, and because it offers an opportunity to examine why large auditory-visual benefit does not necessarily imply good auditory-visual integration, and vice versa. Consider a hypothetical auditory-only condition in which only place-of-articulation information is conveyed to the listener and a score of A ($A \ll 100\%$) is obtained. Next, consider the addition of visual cues to the auditory-only condi-

tion. Since speech-reading conveys primarily place cues, the auditory and visual information will be highly redundant. Little to no information about voicing or manner will be conveyed in the auditory-visual condition. A score of 100% information transmission is not possible in this case (Grant *et al.*, 1998). Therefore, the theoretically possible improvement is not 100-A, but some smaller number Y-A, $Y < 100$. If the listener perfectly integrates all of the available auditory and visual information, he or she will only obtain a score of Y and a corresponding RB of $(Y-A)/(100-A)$. Note that the denominator in the RB measure is 100-A, not Y-A, yielding an RB less than one. If RB is used as a measure of AV integration, this listener will appear to have less-than-optimal integration ability, when in actuality he or she has performed as optimally as possible in that condition.

Furthermore, the use of whole-word percent correct scores, as in the RB measure, does not provide enough information to calculate the theoretically possible improvement. A finer analysis of error patterns in terms of the phonetic features of voicing, manner and place of articulation is required.

Models for assessing integration efficiency have been developed that do not share these limitations (Massaro, 1987; Blarney *et al.*, 1989; Braida, 1991). In the present study, integration efficiency was assessed with the prelabeling (PRE) model of integration (Braida, 1991). In this model, the information the listener has extracted from the signal and which is available for integration is recovered by analyzing the error patterns generated in unimodal (i.e., auditory-only and visual-only) conditions. Next, this information is combined using an "optimal" decision rule that assumes perfect integration of the available information, and that also assumes an unbiased receiver with no interference across auditory frequency channels or across auditory and visual modalities. The resulting AV score is a prediction of optimal performance in the auditory-visual condition, given the information extracted from the auditory-only and visual-only channels. By comparing predicted and obtained scores, a metric for integration efficiency is computed. The PRE model subjects the confusion matrices from the unimodal conditions to a special form of multidimensional scaling (MDS) that is interpreted within a theory of signal detection (e.g., Green and Swets, 1966; Macmillan *et al.*, 1988). The model provides a spatial interpretation of the ability to distinguish between consonants, analogous to that derived from traditional MDS (Borg and Lingoes, 1987). However, unlike traditional MDS, the scaled distances between consonants in the separate condition spaces are converted to a common metric, d' , which explicitly reflects the correctness of response (and thus compensates for potential response bias). The decision rule assumes a comparison between stimulus attributes (modeled as a multidimensional vector of cues, \vec{X}) and prototypes or response centers (\vec{R}) in memory. Subjects are assumed to respond R_k if the distance from the observed vector of cues \vec{X} to \vec{R}_k is smaller than the distance to any other prototype. A subject's sensitivity $d'(i, j)$ in distinguishing stimulus S_i from stimulus S_j is given by

$$d'(i, j) = \|\vec{S}_i - \vec{S}_j\| = \sqrt{\sum_{k=1}^D (S_{ik} - S_{jk})^2}, \quad (1)$$

where $\|\vec{S}_i - \vec{S}_j\|$ is the distance between the D -dimensional vector of cues generated by stimuli S_i and S_j .

In the present study, estimates of stimulus and response centers that best fit a given confusion matrix were obtained iteratively using a KYST procedure (Kruskal and Wish, 1978). For the first iteration, \vec{S} and \vec{R} are assumed to be aligned. Subsequent iterations attempted to improve the match between predicted and obtained matrices (using a χ^2 measure) by displacing slightly both stimulus and response centers. Each iteration assumed 5120 presentations per consonant token yielding a total of 92, 160 trials per matrix (i.e., 18 consonants \times 5120 presentations). This number was selected to reduce the stimulus variability in each MDS fit to approximately 1/10th of the variability in the data. The MDS fits were further optimized by choosing either two- or three-dimensional solutions depending on which gave the best fit to the unimodal matrix.

PRE model predictions for $A_{1,2,3,4}$, $AV_{1,4}$, and $AV_{2,3}$ performance were made solely on the basis of performance in the $A_{1,4}$, $A_{2,3}$, and V conditions. Assuming that speech cues from different frequency bands and from the visual signal are combined optimally, the decision space for the combined conditions is the Cartesian product of the space for each of the component conditions. Thus, the relation between a subject's sensitivity in an auditory-visual condition (e.g., $AV_{1,4}$) and the corresponding unimodal sensitivities (e.g., $A_{1,4}$ and V), assuming no perceptual interference (e.g., masking or distraction) across modalities, is given by

$$d_{AV_{1,4}}(i, j) = \sqrt{d_{A_{1,4}}(i, j)^2 + d_V(i, j)^2}. \quad (2)$$

Similar equations may be written to describe model predictions for the $AV_{2,3}$ and $A_{1,2,3,4}$ conditions.

Predictions for the $A_{1,2,3,4}$, $AV_{1,4}$, and $AV_{2,3}$ conditions were compared to actual performance exhibited by individual subjects. Since the PRE model is an optimum-processor model, predicted scores should always equal or exceed observed scores. A subject's integration efficiency, as calculated by the model, is given by the ratio between observed and predicted recognition scores expressed as a percentage (with 100% indicating perfect integration).

III. RESULTS

Consonant recognition scores for the eight different conditions listed in Table II (excluding $A_{1,2,3,4sum}$) are illustrated in Fig. 1. The top panel shows the mean data for the five auditory-only conditions whereas the bottom panel shows the mean data for the visual-only and auditory-visual conditions. Not surprisingly, auditory-only recognition performance for the hearing-impaired subjects was worse than that of the normal-hearing subjects for all conditions except for A_1 . The band in the A_1 condition was in a spectral region (298–375 Hz) where threshold differences between the normal-hearing and hearing-impaired groups were relatively small. In spite of the reduced recognition scores of the hearing-

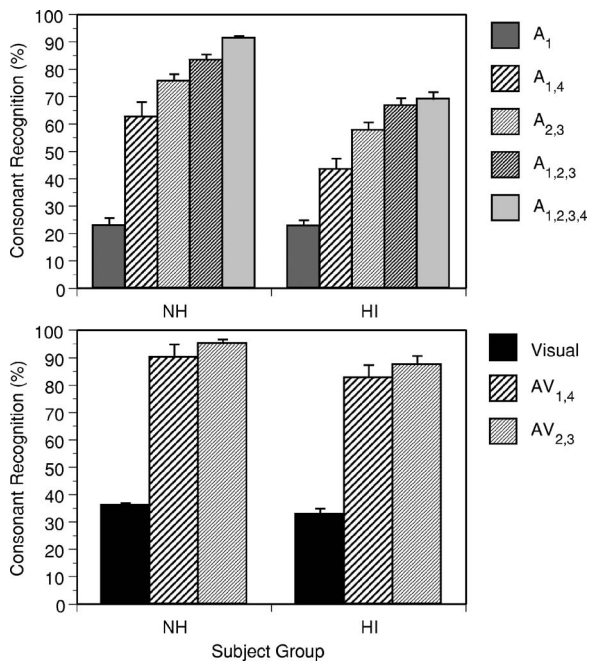


FIG. 1. Average consonant recognition scores for the five auditory conditions (top) and the three visual and auditory-visual conditions (bottom). Data are for four normal-hearing (NH) subjects and four hearing-impaired (HI) subjects. Error bars show +1 standard error.

impaired subjects in the other auditory-only conditions, the overall pattern of performance between the two groups was generally similar. However, hearing-impaired subjects showed proportionally less benefit than normal-hearing subjects when band 4 was added to either band 1 alone (i.e., $A_{1,4}$ compared to A_1) or to bands 1, 2, and 3 combined (i.e., $A_{1,2,3,4}$ compared to $A_{1,2,3}$). In particular, the amount of benefit afforded by band 4 in the context of the first three bands (i.e., $A_{1,2,3,4}$ versus $A_{1,2,3}$) was negligible for the hearing-impaired listeners. The bottom panel of Fig. 1, on the other hand, shows that visual-only and auditory-visual recognition performance was comparable across subject groups, suggesting that most of the hearing deficit was overcome when speechreading was combined with even limited auditory information.

The data displayed in Fig. 1 were subjected to a repeated-measures ANOVA with group (normal-hearing or hearing-impaired) as a between-subjects factor and condition as a within-subjects factor. Two separate analyses were conducted, one for the auditory-only conditions and one for the visual-only and auditory-visual conditions. For the auditory-only conditions, the main factors of group and condition, as well as their interaction, were all significant [group: $F(1,6) = 19.48, p = 0.005$; condition: $F(4,24) = 250, p < 0.001$; group*condition: $F(4,24) = 8.99, p < 0.001$]. The significant interaction arises from the already noted difference in the ability of listeners to make use of the information in band 4, with hearing-impaired listeners deriving less advantage than normal-hearing listeners. For the three conditions involving speechreading (V , $AV_{1,4}$, and $AV_{2,3}$), only the effect of condition was significant [$F(1,6) = 444, p < 0.001$], this being driven by the large differences between the visual-only and the two auditory-visual conditions. *Post hoc* tests indicated

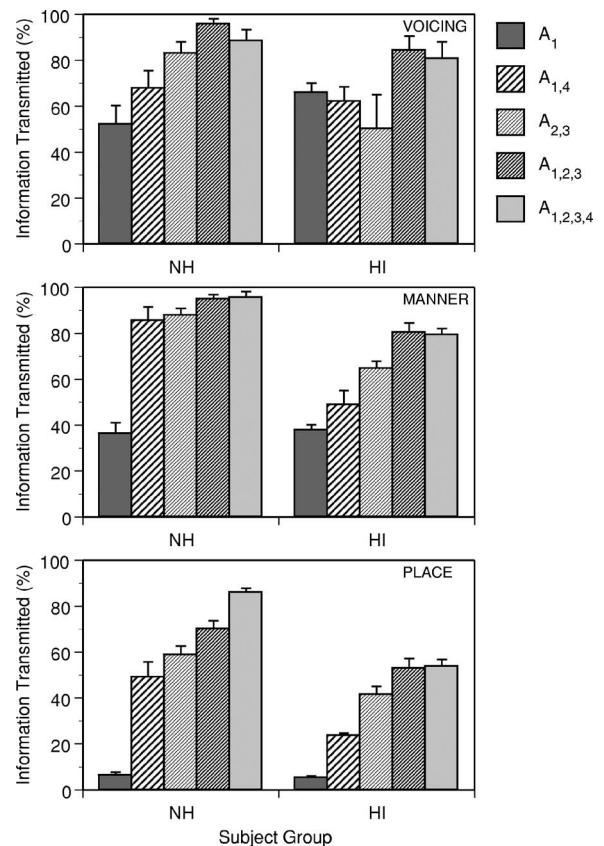


FIG. 2. Percent information transmitted in the five auditory conditions for the speech features voicing (top), manner-of-articulation (middle), and place-of-articulation (bottom). Data are for four normal-hearing (NH) subjects and four hearing-impaired (HI) subjects. Error bars are +1 standard error.

that there were no significant differences between the groups for either auditory-visual condition, or between the separate auditory-visual conditions within groups. Thus, in spite of significant differences in auditory-only recognition performance across the two subject groups (as seen in the upper panel of Fig. 1), once the visual signal was combined with the acoustic speech signal, all subjects recognized the consonants with nearly equal accuracy (as seen in the lower panel of Fig. 1). For example, although the hearing-impaired subjects' mean score in condition $A_{1,4}$ was significantly lower than the mean score for the normal-hearing subjects, their mean score in condition $AV_{1,4}$ (in which visual cues were added to $A_{1,4}$) was not significantly different from the normal-hearing subjects' mean score. This finding also held for conditions $A_{2,3}$ and $AV_{2,3}$. This apparent increase in auditory-visual benefit for the hearing-impaired subjects relative to the normal-hearing subjects (i.e., equivalent auditory-visual and visual-only performance across groups but reduced auditory-only performance in the hearing-impaired listeners) is discussed below.

Figures 2 and 3 show the relative information transmission (Miller and Nicely, 1955) for the features of voicing, manner, and place of articulation for the auditory-only conditions (Fig. 2) and for the visual-only and auditory-visual conditions (Fig. 3), respectively. In Fig. 2, information transmission for auditory place is lower than for either auditory

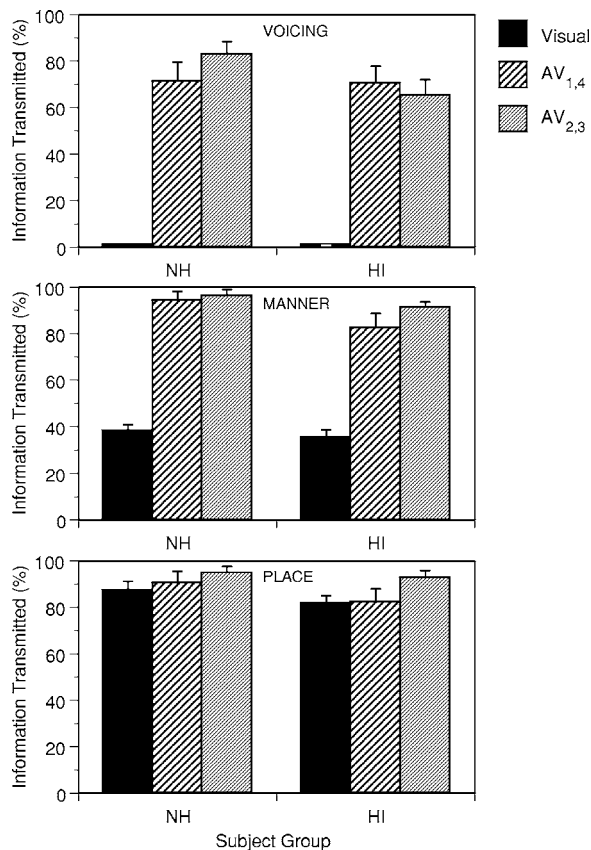


FIG. 3. Percent information transmitted in the three visual and auditory-visual conditions for the speech features voicing (top), manner-of-articulation (middle), and place-of-articulation (bottom). Data are for four normal-hearing (NH) subjects and four hearing-impaired (HI) subjects. Error bars are +1 standard error.

voicing or auditory manner in all conditions for both subject groups. This is consistent with place of articulation requiring greater acoustic bandwidth for optimum information transmission than either voicing or manner (Miller and Nicely, 1955). The two subject groups performed comparably in condition A_1 for all three features; however, the hearing-impaired subjects showed decrements in information transmission in most other conditions, most notably in the 2-, 3-, and 4-band conditions for the feature of place, in the two-band conditions for the feature of manner, and in the $A_{2,3}$ condition for the voicing feature. For the visual-only and auditory-visual conditions shown in Fig. 3, performance of the normal-hearing and hearing-impaired subjects was quite comparable. Voicing scores for both subject groups in the visual-only condition were nearly 0%, while mean manner scores were close to 40%, and place scores generally fell between 80% and 90%. This pattern is consistent with previous research described earlier (Grant and Walden, 1996; Grant *et al.*, 1998) showing that speechreading alone provides significant information about place of articulation, relatively little information about manner, and virtually no information about voicing. For the auditory-visual conditions, information transmission for voicing, manner, and place was similar across groups, despite decrements in auditory-alone performance of the hearing-impaired subjects (see, for example, the hearing-impaired subjects' gain in information

transmission for the manner feature in conditions $AV_{1,4}$ and $AV_{2,3}$ compared with their performance in conditions $A_{1,4}$ and $A_{2,3}$). This finding is most likely related to the fact that good transmission of visual place information, combined with even limited voicing and manner information, will yield both high feature and high overall consonant recognition scores (Grant *et al.*, 1998; Christiansen *et al.*, in press).

Integration efficiency was calculated for the $A_{1,2,3,4}$, $AV_{1,4}$, and $AV_{2,3}$ conditions using Braida's PRE model, as described in the Methods section (Braida, 1991; Grant and Seitz, 1998). Recall that the integration of speech cues from different spectral regions or from different modalities is confounded by individual subject performance in the constituent conditions. In the case of the $A_{1,2,3,4}$ condition, the constituent conditions were $A_{1,4}$ and $A_{2,3}$. For the $AV_{1,4}$ condition, the constituent conditions were $A_{1,4}$ and V , and for the $AV_{2,3}$ condition, they were $A_{2,3}$ and V .

The PRE model analyzes the information received from the constituent conditions and combines the information in an optimal manner. The model then predicts the best possible recognition score that could be obtained given the subject's proficiency on the constituent conditions. For example, the model predicts the recognition scores obtained in condition $A_{1,2,3,4}$ by taking into account observed errors in conditions $A_{1,4}$ and $A_{2,3}$ and assuming perfect integration. Thus, it is possible to estimate the subject's skill at integrating information (as shown by the integration efficiency index), independent of the subject's ability to extract information (as shown by scores in the constituent conditions). This knowledge may be valuable for developing strategies for rehabilitation, whether they are based primarily on signal-processing schemes to aid the *extraction* of speech cues, or on training programs to improve the *integration* of speech cues.

The top panel of Fig. 4 shows the model predictions and observed scores for overall consonant recognition. Each point represents a single subject in one of the three predicted conditions, $A_{1,2,3,4}$, $AV_{1,4}$, and $AV_{2,3}$. Filled symbols show the data for normal-hearing subjects and unfilled symbols show results for hearing-impaired subjects. The diagonal line in the figure indicates equality between observed and predicted scores. Points above this line are cases where predicted scores are greater than obtained scores, and by definition, indicate sub-optimal integration. The largest deviations between predicted and observed scores occurred for hearing-impaired subjects, especially in the auditory-only condition $A_{1,2,3,4}$.

The bottom panel of Fig. 4 shows the average integration efficiency (observed/predicted * 100) for both groups of subjects. For normal-hearing subjects, integration efficiency was high (>90%) regardless of whether the condition was auditory-only or auditory-visual. For hearing-impaired subjects, integration efficiency appears to be reduced, especially in the auditory-only condition $A_{1,2,3,4}$. A repeated-measures ANOVA was carried out with group as a between-subjects factor and condition as a within-subjects factor. The results showed a main effect for group [$F(1,6)=10.66, p=0.02$], condition [$F(2,12)=11.27, p=0.002$], and a group*condition interaction [$F(2,12)=13.33, p<0.001$]. However, when a similar analysis was conducted on just the auditory-visual

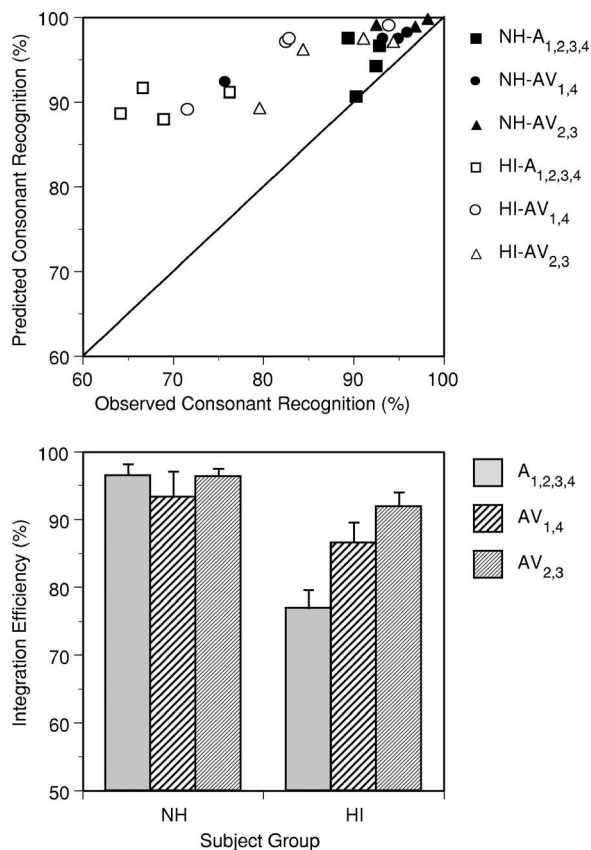


FIG. 4. (Top) Observed and predicted consonant recognition scores for $A_{1,2,3,4}$, $AV_{1,4}$, and $AV_{2,3}$ conditions. Scores for hearing-impaired (HI) subjects are shown by open symbols. The line indicates equality of observed and predicted scores. All scores to the left of this line indicate less than optimal integration. The greater the deviation from the diagonal line, the worse the subject is at integrating information from the different channels. (Bottom) Integration efficiency (IE) for NH and HI subjects. Integration efficiency is defined as the ratio between observed and predicted recognition performance. The difference in IE measures between NH and HI subjects was significant only for the $A_{1,2,3,4}$ condition. Error bars are +1 standard error.

conditions $AV_{1,4}$, and $AV_{2,3}$, none of the factors proved significant. This analysis indicates that the hearing-impaired subjects were able to integrate auditory-visual speech cues with the same relative efficiency as normal-hearing subjects, but had difficulty integrating auditory speech cues across spectral regions.

In interpreting the modeling results, the potential effects of band amplitude levels should be considered. Table III shows the RMS levels for each of the bands in each of the six auditory conditions. Recall that each of the first five auditory conditions was normalized in level to have the same overall rms amplitude as any other auditory condition. This normalization had the effect of altering the band levels depending on which bands were included in a given condition. For example, the levels of bands 1 and 4 were higher in the $A_{1,4}$ condition than they were in the $A_{1,2,3,4}$ condition. These differences in band levels are important for predictions made using the PRE model since the predictions are based on the information contained in the constituent conditions. Thus, if the band levels in the $A_{1,4}$ condition were higher than in the $A_{1,2,3,4}$ condition (as they were), then subjects could potentially extract more information from bands 1 and 4 when

presented in the $A_{1,4}$ condition than from these same bands when presented in the $A_{1,2,3,4}$ condition, due to potential differences in audibility. This would lead to a model prediction that would exceed the actual scores by a greater amount and give the impression of reduced integration efficiency. To address this issue, the hearing-impaired subjects were re-tested on the original $A_{1,2,3,4}$ condition and on a new condition, $A_{1,2,3,4sum}$, which was created by adding the $A_{1,4}$ and $A_{2,3}$ signals together without subsequently normalizing the overall level. Because $A_{1,2,3,4sum}$ was not normalized, its overall amplitude was higher than $A_{1,2,3,4}$. Specifically, compared to $A_{1,2,3,4}$, this new signal had higher levels for band 1 (approximately 8 dB) and band 4 (approximately 8.5 dB), and roughly equal levels for bands 2 and 3 (see Table III). The subjects were tested first on ten blocks of 72 trials on the new $A_{1,2,3,4sum}$ condition, and then for three blocks each on the original $A_{1,2,3,4}$ condition and the $A_{1,2,3,4sum}$ condition, presented in random order. As expected, the results showed slightly better performance (roughly 5% absolute) for the more intense $A_{1,2,3,4sum}$ signal. However, this difference was not significant for any of the four hearing-impaired subjects. Therefore, it is unlikely that subjects' performance was affected by the differences in the specific magnitudes of the band levels.

IV. DISCUSSION

Normal-hearing and hearing-impaired subjects' performance on a consonant recognition task was evaluated under a variety of auditory, visual, and auditory-visual presentation conditions. Significant differences between the groups were observed in overall consonant recognition and feature transmission scores in the auditory-only conditions. However, performance was comparable for the two groups in the visual-only and auditory-visual conditions. Observed scores for a subset of the conditions were compared to predicted scores, using an optimum-processor model of integration. Differences between predicted and observed scores were used to estimate the efficiency with which subjects were able to integrate auditory cues across the frequency spectrum, or auditory and visual cues across sensory modalities.

With regard to place cues, hearing-impaired listeners extracted less information in the auditory-only conditions $A_{1,4}$ and $A_{2,3}$ than the normal-hearing listeners did (see the bottom panel of Fig. 2). However, place cues are transmitted very well visually, and hearing-impaired subjects performed as well as normal-hearing subjects in the visual-only condition, V (see the bottom panel of Fig. 3). Therefore, it is likely that the hearing-impaired listeners were able to overcome the deficit in auditory place information by making use of visual cues. Seen in this way, the similar performance of the groups for the place feature in conditions $AV_{1,4}$ and $AV_{2,3}$ in Fig. 3 is not surprising.

Unlike place cues, manner and voicing cues are not transmitted well visually. Voicing information, especially, is highly complementary with visual information and contributes greatly to auditory-visual speech recognition (Grant *et al.*, 1998). In the present study, the hearing-impaired listeners fared much worse at extracting voicing cues in condition $A_{2,3}$

than did the normal-hearing listeners (see the top panel of Fig. 2). Yet, in the $AV_{2,3}$ condition, which combines speechreading with $A_{2,3}$, voicing scores and overall consonant recognition were nearly comparable across groups. This finding may seem somewhat puzzling at first glance, in light of the expected adverse impact of limited voicing information on auditory-visual performance (Grant *et al.*, 1998; Erber, 2002). However, the features of voicing, manner and place are not independent of one another; good place identification, as in the visual-only condition, can aid in the identification of voicing and manner cues (Christiansen *et al.*, 2005; Christiansen *et al.*, in press).

Unlike their efficiency in auditory-visual integration, hearing-impaired listeners had difficulty combining information across widely separated audio-frequency channels, independent of their ability to extract information from these channels. This is shown in Fig. 4 by the reduced integration efficiency for condition $A_{1,2,3,4}$ compared to the normal-hearing subjects. One explanation for this finding concerns the possibility of upward spread of masking interfering with band 4. Some hearing-impaired listeners, especially those with broadened auditory filters and poor frequency selectivity, are known to exhibit excessive amounts of upward spread of masking (Gagné, 1988). It is possible that information contained in band 4 was partially masked when embedded in the $A_{1,2,3,4}$ condition. The PRE model cannot take into account such interactions that may occur between bands as a result of being presented concurrently. Instead, the model assumes that the information extracted from the $A_{1,4}$ condition has the full contribution of band 4 without any interference from mid-frequency auditory information. If masking of band 4 did occur, this could account for the fact that the hearing-impaired subjects obtained much lower scores than predicted in condition $A_{1,2,3,4}$ and, therefore, had poorer integration efficiency. The frequency bands used in this study were separated by an octave from one another in order to reduce such band-on-band interactions. However, given the broadened auditory filters that typically accompany sensorineural hearing loss, energy presented in band 3 may have provided enough masking to interfere with the phonetic information contained band 4.

Another possible explanation for the finding of reduced cross-spectral integration efficiency concerns the extent of the hearing loss in the vicinity of band 4 (4762–6000 Hz) and the possibility of “off-frequency” listening (i.e., responding to the energy in band 4 through the excitation of neurons tuned to lower frequencies where the hearing loss was not as great). Because the hearing-impaired subjects had extensive hearing loss in the band 4 region, some of the information in band 4 (e.g., low-intensity fricative energy) would have been inaudible (see Sec. II C for additional information). Based on the hearing thresholds shown in Table I, this would have been true for band 4 in the $A_{1,2,3,4}$ condition as well as in the $A_{1,4}$ condition. However, in condition $A_{1,4}$, there was no signal energy in frequency channels just below 4762 Hz (the low-frequency edge of band 4). It is possible that some of the information contained in band 4 could have been partially obtained by listening off-frequency, using less impaired auditory channels below 4762 Hz (Moore, 2004). When all

four bands were presented in condition $A_{1,2,3,4}$, these same “off-frequency” channels may have been less able to extract the relevant information from band 4 because neurons tuned to the region just below band 4 were responding to frequency information associated with band 3, due to upward spread of masking. PRE model predictions of performance in condition $A_{1,2,3,4}$ were made under the assumption that all information extracted in the constituent conditions $A_{1,4}$ and $A_{2,3}$ was available for integration. This of course would not have been the case if the “off-frequency” listening hypothesis were correct. Thus, the poorer integration efficiency of the hearing-impaired listeners in condition $A_{1,2,3,4}$ may actually reflect an inability to extract and use high-frequency information when mid-frequency information is presented simultaneously.

This hypothetical scenario is not unlike previous suggestions (e.g., Doherty and Turner, 1996; Hogan and Turner, 1998) that hearing-impaired individuals have difficulty extracting and integrating high-frequency information from a broadband speech signal. More specifically, previous studies have claimed that high-frequency speech information may be useless for some hearing-impaired listeners with moderately severe to profound high-frequency hearing losses (e.g., Ching *et al.*, 1998; Hogan and Turner, 1998; Turner and Cummings, 1999). In particular, listeners with high-frequency “dead regions” in the cochlea (Moore, 2004) may be unable to make use of speech information that falls well within the dead region. The data in the present study conflict to a certain extent with these claims. The subjects in this experiment all had moderately severe to profound losses of between 60 and 105 dB HL in the region between 4000 and 6000 Hz (though they were not tested for the presence of dead regions). Yet, they were able to obtain selective benefit from high-frequency speech information, depending on the condition tested. In the studies previously referenced, high-frequency information was added to a broadband, lowpass-filtered speech signal. The lack of benefit seen when high-frequency information was added was interpreted to mean that listeners were unable to make any use of this information at all. Conditions $A_{1,2,3}$ and $A_{1,2,3,4}$ in the present study come closest to replicating the conditions in the previous studies. Indeed, limited benefit is seen by adding band 4 to bands 1, 2, and 3. However, the hearing-impaired listeners did benefit from band 4 when it was added to band 1 alone. This condition is unlike those in previous studies in that no mid-frequency information was presented along with band 4. Thus, amplified high-frequency speech information can be beneficial for listeners with significant high-frequency hearing loss, but only in contexts where no signal is presented in mid-frequency spectral regions.

More recently, studies have cast doubt on the notion that people with high-frequency hearing loss are unable to make use of amplified high-frequency speech information (Turner and Henry, 2002; Hornsby and Ricketts, 2003, 2006). In these studies, speech materials were presented in spectrally shaped noise or multitalker babble in various low-pass, high-pass or bandpass conditions. The high sound pressure levels required by the hearing-impaired listeners to ensure audibility may have reduced the utility of high-frequency speech

information to some extent. Nevertheless, the performance of the hearing-impaired listeners increased, albeit slightly in many cases, with the addition of high-frequency speech information. Listeners in these studies had hearing losses ranging up to 90 dB HL, but they were either not assessed for the presence of dead regions (Turner and Henry, 2002) or were found not to have dead regions (Hornsby and Ricketts, 2003, 2006). Certainly, it appears reasonable that if high-frequency information is presented to a dead region, then this information is only beneficial insofar as other, less damaged regions can make use of it. However, the results of these studies and the present study, which show that hearing-impaired listeners can benefit from high-frequency speech information in selected conditions, suggest caution with respect to limiting high-frequency amplification for listeners based solely on audiometric thresholds or audiometric configuration.

A third, and perhaps most likely, explanation for the hearing-impaired listeners' reduced cross-spectral integration efficiency may be related to an explanation suggested by Turner and Henry (2002) as to why their hearing-impaired subjects were able to make use of high-frequency speech information while other studies showed no benefit. In their study, consonant recognition performance was relatively poor, even in the broadest bandwidth condition, due to the presence of multitalker babble. The addition of high-frequency information to the various low-pass filter conditions may have provided listeners with enough additional information to decipher the "easier" features of speech, such as voicing. In earlier studies of speech in quiet (e.g., Hogan and Turner, 1998), much of the speech signal was already audible to the hearing-impaired listeners. Thus, additional high-frequency information was not as helpful to these listeners in deciphering more "difficult" features, such as place of articulation. In the present study, overall consonant recognition scores for band 1 alone were low (<30%). Analogous to the results of Turner and Henry (2002), the addition of band 4 to band 1 may have boosted scores considerably by providing information related to easier speech cues, whereas the addition of band 4 to bands 1, 2, and 3 may not have provided enough additional information to allow listeners to resolve the remaining, more difficult speech cues. As with the previous two explanations, an inability to make use of speech information in band 4 when it was presented concurrently with bands 1, 2, and 3 would give the appearance of reduced integration efficiency.

The reduced cross-spectral integration efficiency of the hearing-impaired listeners may not simply be a product of confounding the extraction and integration of information, but may in fact be evidence of a real deficit in the across-frequency processing of temporal information. As described in the Introduction, Healy and Bacon (2002) found that listeners with sensorineural hearing loss were less successful than normal-hearing listeners in integrating temporal speech information across two widely separated frequency channels. This finding is especially convincing, since their stimuli were designed to eliminate other confounding effects of sensorineural hearing loss such as broadened auditory filters and audibility.

Although age effects were not specifically assessed in this study, it is worthy of mention that the hearing-impaired subjects in the present study were all over 65 years of age, while the normal-hearing subjects were all 55 years of age and younger. Previous investigators (e.g., Spehar *et al.*, 2004; Sommers *et al.*, 2005b) have reported poorer consonant and word recognition in visual-only conditions for older versus younger adults. In contrast, the visual-only performance of older (hearing-impaired) and younger (normal-hearing) adults in the present study was comparable. This contrasting finding may be a reflection of differences in the ages of the "younger" subjects in each study. In the studies previously referenced, the younger adults were in their early- to mid-twenties, while those in the present study ranged in age from 29 to 55 years.

The auditory-visual integration abilities of older versus younger adults have been assessed using subject groups that were matched either for peripheral hearing sensitivity (Cienkowski and Carney, 2002, 2004) or for auditory-only performance (Sommers *et al.*, 2005b). Despite their poorer speechreading abilities, older adults' auditory-visual integration abilities appeared to be comparable to those of younger adults. Auditory-visual integration was assessed by analyzing responses to variations of a McGurk paradigm (Cienkowski and Carney, 2002, 2004) or by calculating measures of auditory and visual enhancement similar to the Sumbly and Pollack (1954) relative benefit measure (Sommers *et al.*, 2005b). As discussed previously, without taking into account individual phoneme confusions in the unimodal conditions, such measures may not provide an accurate assessment of listeners' integration abilities. Nevertheless, the findings of these studies do corroborate the indirect finding in the present study of no age effects in auditory-visual integration ability.

Finally, experiments with time-compressed *auditory* speech have revealed age effects suggestive of a slowing in central auditory processing (e.g., Gordon-Slant and Fitzgibbons, 1999). However, Spehar *et al.* (2004) found no such age effects for temporally altered *visual* speech signals. Spehar *et al.* (2004) finding suggests that the slowing of central processing with age may be modality-specific. While not conclusive in and of itself, the finding does leave open the possibility that the normal cross-modal but abnormal cross-spectral integration observed in the hearing-impaired subjects may have been partially due to differences in the effects of age on the speed of central processing across modalities. However, a recent study by Souza and Boike (2006) suggests that age may not be a significant factor in cross-spectral integration, at least with respect to speech signals composed of mostly temporal cues. Specifically, these authors examined the effect of age on the ability to combine temporal-envelope information across frequency channels. They assessed consonant identification in 1-, 2-, 4-, and 8-channel conditions processed to restrict spectral cues, as well as in an unprocessed condition. Results revealed a significant trend toward poorer performance with increasing age in all conditions except the unprocessed condition, suggestive of an age-associated deficit in the use of temporal-envelope information. However, no age-associated deficit was observed in combining information across frequency channels. There-

fore, it seems unlikely that age differences between the normal-hearing and hearing-impaired subjects in this study contributed significantly to the differences seen in their cross-spectral integration abilities.

Aural rehabilitation options for improving speech recognition should exploit the good use of visual cues that the hearing-impaired individuals were able to make. Despite poorer auditory-only performance compared with normal-hearing subjects, listeners with hearing loss were able to use the visual speech signal to overcome these deficits and achieve normal auditory-visual consonant recognition. Therefore, aural rehabilitation efforts that emphasize environmental and behavioral alterations to make better use of visual speech cues are likely to greatly aid the hearing-impaired listener in understanding speech, particularly in noisy or reverberant conditions. Furthermore, this study and previous studies have shown that hearing-impaired listeners are able to benefit from the provision of high-frequency speech information in certain impoverished audio conditions (e.g., due to noise or to spectral filtering). These results suggest caution with respect to limiting high-frequency amplification for listeners based solely on audiometric thresholds or audiometric configuration.

V. CONCLUSIONS

Comparisons of within-modality (auditory-only) and across-modality (auditory-visual) integration efficiency demonstrated that both normal-hearing and hearing-impaired subjects had little trouble integrating auditory-visual information. However, hearing-impaired listeners showed difficulty integrating spectral information across widely separated audio frequency channels. Specifically, high-frequency speech information (4762–6000 Hz) was found to be useful when combined with low-frequency speech information (298–375 Hz), but was less useful when mid-frequency speech information (1890–2381 Hz) was also present. These results support the contention that amplified high-frequency speech information can be beneficial for listeners with significant high-frequency hearing loss in quiet, particularly in contexts where no signal is presented in adjacent lower-frequency spectral regions. Future tests comparing the information content of the different spectral bands should help further our understanding of the auditory integration difficulties observed in hearing-impaired subjects. In the absence of clear evidence contraindicating the amplification of high-frequency speech information, such amplification combined with the use of visual cues is recommended to improve speech understanding for individuals with severe high-frequency sensorineural hearing loss in adverse listening conditions.

VI. ACKNOWLEDGMENTS

This research was supported by the Clinical Investigation Service, Walter Reed Army Medical Center, under Work Unit #00-2501, Grant No. DC 00792 from the National Institute on Deafness and Other Communication Disorders, Grant No. SBR 9720398 from the Learning and Intelligent Systems Initiative of the National Science Foundation to the

International Computer Science Institute, and the Oticon Foundation, Copenhagen, Denmark. We would also like to thank Rosario Silipo for assistance in creating the auditory stimuli, Mary Cord for assistance in data collection, and Louis Braida for his help fitting the Prelabeling Model of Integration to our data. The opinions or assertions contained herein are the private views of the authors and are not to be construed as official or as reflecting the views of the Department of the Army or the Department of Defense.

- American National Standards Institute (1989). Specifications for audiometers (ANSI S3.6-1989). (ANSI, New York).
- Blamey, P. J., Cowan, R. S. C., Alcantara, J. I., Whitford, L. A., and Clark, G. M. (1989). "Speech perception using combinations of auditory, visual, and tactile information," *J. Rehabil. Res. Dev.* **26**, 15–24.
- Borg, I., and Lingoes, J. (1987). *Multidimensional Similarity Structure Analysis* (Springer-Verlag, New York).
- Braida, L. D. (1991). "Crossmodal integration in the identification of consonant segments," *Q. J. Exp. Psychol.* **43**, 647–677.
- Ching, T., Dillon, H., and Byrne, D. (1998). "Speech recognition of hearing-impaired listeners: Predictions from audibility and the limited role of high-frequency amplification," *J. Acoust. Soc. Am.* **103**, 1128–1140.
- Christiansen, T. U., Dau, T., and Greenberg, S. (in press). "Spectro-temporal processing of speech—An information-theoretic framework," 14th International Symposium on Hearing.
- Christiansen, T. U., and Greenberg, S. (2005). "Frequency selective filtering of the modulation spectrum and its impact on consonant identification," 21st Danavox Symposium: Hearing Aid Fitting, **21**, 585–599.
- Cienkowski, K. M., and Carney, A. E. (2002). "Auditory-visual speech perception and aging," *Ear Hear.* **23**, 439–449.
- Cienkowski, K. M., and Carney, A. E. (2004). "The integration of auditory-visual information for speech in older adults," *J. Speech Lang. Path. Aud.* **28**, 166–172.
- Doherty, K. A., and Turner, C. W. (1996). "Use of a correlational method to estimate a listener's weighting function for speech," *J. Acoust. Soc. Am.* **100**, 3769–3773.
- Erber, N. P. (2002). "Hearing, vision, communication, and older people," *Seminars in Hearing* **23**, 35–42.
- Friesen, L. M., Shannon, R. V., Baskent, D., and Wang, X. (2001). "Speech recognition in noise as a function of the number of spectral channels: Comparison of acoustic hearing and cochlear implants," *J. Acoust. Soc. Am.* **110**, 1150–1163.
- Gagné, J. P. (1988). "Excess masking among listeners with a sensorineural hearing loss," *J. Acoust. Soc. Am.* **83**, 2311–2321.
- Gordon-Salant, S., and Fitzgibbons, P. J. (1999). "Profile of auditory temporal processing in older listeners," *J. Speech Lang. Hear. Res.* **42**, 300–311.
- Grant, K. W. (2002). "Measures of auditory-visual integration for speech understanding: A theoretical perspective (L)," *J. Acoust. Soc. Am.* **112**, 30–33.
- Grant, K. W., and Seitz, P. F. (1998). "Measures of auditory-visual integration in nonsense syllables and sentences," *J. Acoust. Soc. Am.* **104**, 2438–2450.
- Grant, K. W., and Walden, B. E. (1996). "Evaluating the articulation index for auditory-visual consonant recognition," *J. Acoust. Soc. Am.* **100**, 2415–2424.
- Grant, K. W., Walden, B. E., and Seitz, P. F. (1998). "Auditory-visual speech recognition by hearing-impaired subjects: Consonant recognition, sentence recognition, and auditory-visual integration," *J. Acoust. Soc. Am.* **103**, 2677–2690.
- Green, D. M., and Swets, J. A. (1966). *Signal Detection Theory and Psychophysics* (Wiley, New York).
- Greenberg, S., and Arai, T. (2004). "What are the essential cues for understanding spoken language?" *IEICE Trans. Inf. Syst.* **87D**, 1059–1070.
- Greenberg, S., Arai, T., and Silipo, R. (1998). "Speech intelligibility from exceedingly sparse spectral information," *Proc. Int. Conf. Spoken Lang. Processing*, Sydney, Australia, 74–77.
- Healy, E. W., and Bacon, S. P. (2002). "Across-frequency comparison of temporal speech information by listeners with normal and impaired hearing," *J. Speech Lang. Hear. Res.* **45**, 1262–1275.
- Healy, E. W., Kannabiran, A., and Bacon, S. P. (2002). "An across-frequency processing deficit in listeners with hearing impairment is sup-

- ported by acoustic correlation," *J. Speech Lang. Hear. Res.* **48**, 1236–1242.
- Hill, F. J., McRae, L. P., and McClellan, R. P. (1968). "Speech recognition as a function of channel capacity in a discrete set of channels," *J. Acoust. Soc. Am.* **44**, 13–18.
- Hogan, C. A., and Turner, C. W. (1998). "High-frequency audibility: Benefits for hearing-impaired listeners," *J. Acoust. Soc. Am.* **104**, 432–441.
- Hornsby, B. W. Y., and Ricketts, T. (2003). "The effects of hearing loss on the contribution of high- and low-frequency speech information to speech understanding," *J. Acoust. Soc. Am.* **113**, 1706–1717.
- Hornsby, B. W. Y., and Ricketts, T. (2006). "The effects of hearing loss on the contribution of high- and low-frequency speech information to speech understanding. II. Sloping hearing loss," *J. Acoust. Soc. Am.* **119**, 1752–1762.
- Kruskal, J. B., and Wish, M. (1978). *Multidimensional Scaling* (Sage, Beverly Hills, CA).
- Macmillan, N. A., Goldberg, R. F., and Braida, L. D. (1988). "Vowel and consonant resolution: Basic sensitivity and context memory," *J. Acoust. Soc. Am.* **84**, 1262–1280.
- Massaro, D. W. (1987). *Speech Perception by Ear and Eye: A Paradigm for Psychological Inquiry* (Lawrence Erlbaum Hillsdale, NJ).
- Massaro, D. W. (1998). *Perceiving Talking Faces: From Speech Perception to a Behavioral Principle* (MIT Press, Cambridge, MA).
- Massaro, D. W., and Cohen, M. M. (2000). "Tests of auditory-visual integration efficiency within the framework of the fuzzy logical model of perception," *J. Acoust. Soc. Am.* **108**, 784–789.
- Miller, G. A., and Nicely, P. E. (1955). "An analysis of perceptual confusions among some English consonants," *J. Acoust. Soc. Am.* **27**, 338–352.
- Moore, B. C. J. (2004). "Dead regions in the cochlea: Conceptual foundations, diagnosis, and clinical applications," *Ear Hear.* **25**, 98–116.
- Müsch, H., and Buus, S. (2001). "Using statistical decision theory to predict speech intelligibility. II. Measurement and prediction of consonant-discrimination performance," *J. Acoust. Soc. Am.* **109**, 2910–2920.
- Pickett, J. M. (1999). *The Acoustics of Speech Communication* (Allyn and Bacon, Boston, MA).
- Ross, L. A., Saint-Amour, D., Leavitt, V. M., Javitt, D. C., and Foxe, J. J. (2006). "Do you see what I am saying? Exploring visual enhancement of speech comprehension in noisy environments," *Cerebral Cortex Advance Access*, published June 19, 2006 at <http://cercor.oxfordjournals.org/cgi/reprint/bhl024v1>
- Shannon, R. V., Zeng, F. G., Kamath, V., Wygonski, J., and Ekelid, M. (1995). "Speech recognition with primarily temporal cues," *Science* **270**, 303–304.
- Silipo, R., Greenberg, S., and Arai, T. (1999). "Temporal constraints on speech intelligibility as deduced from exceedingly sparse spectral representations," *Proc. Eurospeech*, Budapest, Hungary, 2687–2690.
- Sommers, M. S., Spehar, B., and Tye-Murray, N. (2005a). "The effects of signal-to-noise ratio on auditory-visual integration: Integration and encoding are not independent (A)," *J. Acoust. Soc. Am.* **117**, 2574.
- Sommers, M. S., Tye-Murray, N., and Spehar, B. (2005b). "Auditory-visual speech perception and auditory-visual enhancement in normal-hearing younger and older adults," *Ear Hear.* **26**, 263–275.
- Souza, P. E., and Boike, K. T. (2006). "Combining temporal-envelope cues across channels: Effects of age and hearing loss," *J. Speech Lang. Hear. Res.* **49**, 138–149.
- Spehar, B., Tye-Murray, N., and Sommers, M. (2004). "Time-compressed visual speech and age: A first report," *Ear Hear.* **25**, 565–572.
- Summy, W. H., and Pollack, I. (1954). "Visual contribution to speech intelligibility in noise," *J. Acoust. Soc. Am.* **26**, 212–215.
- Turner, C. W., and Cummings, K. J. (1999). "Speech audibility for listeners with high-frequency hearing loss," *Am. J. Audiol.* **8**, 47–56.
- Turner, C. W., and Henry, B. A. (2002). "Benefits of amplification for speech recognition in background noise," *J. Acoust. Soc. Am.* **112**, 1675–1680.
- Turner, C. W., Chi, S. L., and Flock, S. (1999). "Limiting spectral resolution in speech for listeners with sensorineural hearing loss," *J. Speech Lang. Hear. Res.* **42**, 773–784.
- Wang, M. (1976). "SINFA: Multivariate uncertainty analysis for confusion matrices," *Behav. Res. Methods Instrum.* **8**, 471–472.

The effect of smoothing filter slope and spectral frequency on temporal speech information^{a)}

Eric W. Healy^{b)} and Heidi M. Steinbach

Department of Communication Sciences and Disorders, The Norman J. Arnold School of Public Health,
University of South Carolina, Columbia, South Carolina 29208

(Received 24 August 2005; revised 14 August 2006; accepted 15 August 2006)

It is known that information contained within the filter skirts can provide cues important to speech intelligibility. However, the role of filter slope during temporal smoothing has received little attention. In experiment 1, smoothing filter slope angle was found to have a large effect on the intelligibility of sentences represented by three amplitude-modulated sinusoids. In experiment 2, the use of temporal cues above 16 Hz was examined across various regions of the spectrum. When increases in rate were presented to individual spectral bands, intelligibility only increased when presented in the higher spectral region. This result suggests a greater reliance on higher-rate cues in this region. However, intelligibility was greatest when these cues were distributed across the spectrum, indicating that their effective use is not restricted solely to this region. © 2007 Acoustical Society of America. [DOI: 10.1121/1.2354019]

PACS number(s): 43.71.Es, 43.71.An, 43.66.Mk, 43.66.Ba [KWG]

Pages: 1177–1181

I. INTRODUCTION

Temporal information in speech is often classified according to the rate at which the amplitude fluctuations occur. Envelope fluctuations exist below approximately 50 Hz; periodicity (voicing) fluctuations occur between approximately 50 and 500 Hz; and fine structure fluctuations exist above these rates (Rosen, 1992). The typical method for limiting temporal information to a maximum rate involves low pass filtering (smoothing) of the rectified speech signal (Horii *et al.*, 1971). It is known that even relatively-steep filter skirts can contribute substantially to intelligibility when filtering in the spectral domain (Healy, 1998; Warren and Bashford, 1999; Warren *et al.*, 2004). Figure 1 shows the long-term average spectra for everyday sentences filtered to a 1/3-octave band having increasingly-steep slopes. Despite that the bands all share the same nominal bandwidth, the resulting intelligibility scores ranged from below 20% to over 95%.

However, the influence of filter slope in the temporal domain (smoothing) has received little attention. A wide variety of smoothing filter slope values has been employed and, even in studies directly targeting the influence of various temporal rates, relatively shallow slopes have been employed. Values employed have included 6 dB/octave (Shannon *et al.*, 1995, 1998; Fu *et al.*, 1998), 12 dB/octave (Dorman *et al.* 1997, 1998; Qin and Oxenham, 2003; Xu *et al.*, 2005; Nie *et al.*, 2006), 18 dB/octave (Shannon *et al.*, 2001), 24 dB/octave (Grant *et al.*, 1991; Lou and Fu, 2004), and 48 dB/octave (Van Tasell *et al.*, 1987; Faulkner *et al.*, 2000; Fu and Shannon, 2000; Apoux and Bacon, 2004). Although

the slope value employed is typically reported, conclusions regarding the use of temporal cues have generally been based only on filter cutoff values without regard to slope. The availability of information at rates above the cutoff and systematically attenuated by the slope of the smoothing filter may make difficult the accurate assessment of temporal information. The goal of the first experiment was to examine the influence of the temporal smoothing filter slope on recognition of sentences represented by a limited number of temporal patterns, and to establish the slope necessary to eliminate the contribution of information within the temporal filter skirt.

Another aspect of processing that has received relatively little attention involves the use of temporal information in different regions of the speech spectrum. To the extent that temporal processing is limited by the auditory periphery, it may be assumed that the ability to encode higher temporal rates will improve in higher regions of the speech spectrum where the critical band is wider (in Hz). Apoux and Bacon (2004) examined the relative contribution of temporal cues across the spectrum by removing each of four spectral bands in turn and examining consonant identification based upon the remaining three, and by modifying the signal to noise ratios of the individual bands. It was found that temporal information was distributed evenly across spectral bands below approximately 3000 Hz, but that information in the highest spectral band provided a greater contribution to identification. This result is in accord with that of Lorenzi *et al.* (1999), who observed that expansion of the temporal envelope improved consonant identification only when applied to a highest spectral band.

However, because temporal information was extracted using a single fixed low-pass (LP) cutoff for each spectral band, these studies do not allow the evaluation of different temporal rates across different regions of the spectrum. Silipo *et al.* (1999) found that limiting the rate of lower

^{a)}Portions of this work were presented in "Effect of Smoothing Filter Slope Angle on Temporal Speech Information," Proceedings of the 29th Midwinter Research Meeting of the Association for Research in Otolaryngology, Baltimore, Maryland, February, 2006.

^{b)}Electronic mail: ewh@sc.edu

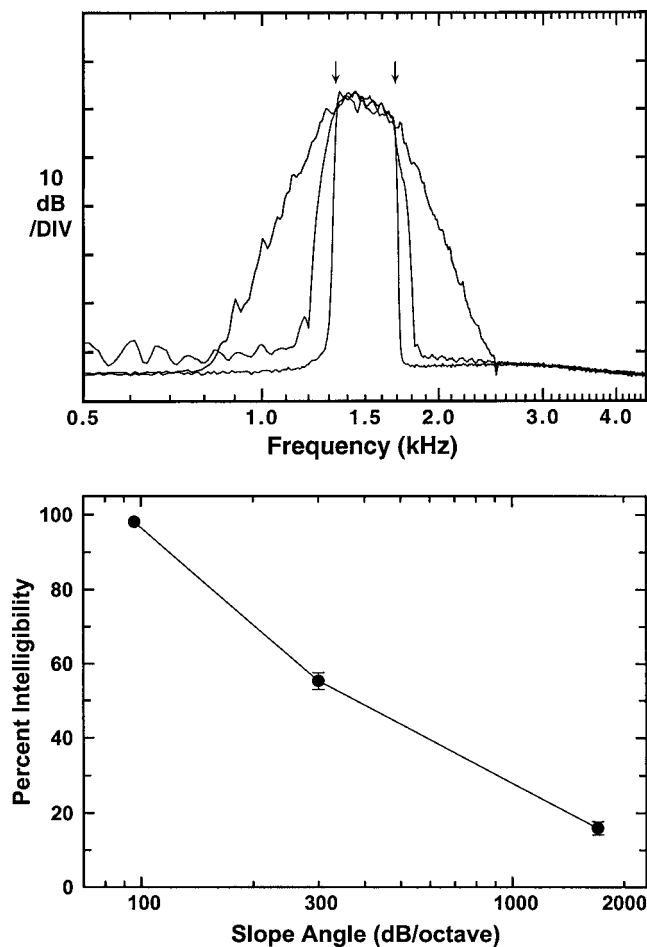


FIG. 1. The upper panel shows overlaid average spectra for 100 CID sentences filtered to a 1/3-octave band centered at 1500 Hz and having filter slopes of approximately 100, 300, and 1700 dB/octave (digital FIR filters having orders of 82, 275, and 2000). The nominal bandwidth is indicated by arrows. The lower panel shows corresponding mean intelligibility scores and standard errors from three separate groups of 20 normal-hearing listeners who each heard all 100 sentences (from Healy, 1998).

spectral bands (below approximately 1500 Hz) to 15 Hz had little effect on sentence intelligibility. However, scores were reduced by approximately 10% when spectral bands above 1500 Hz were similarly limited, suggesting that rates above approximately 15–20 Hz may be especially useful in the higher spectral regions. Whereas the examination of temporal rates by Silipo *et al.* was limited to approximately 20 Hz and below, the use of higher-rate information was examined in the current study. The goal of experiment 2 was to examine the use of higher-rate temporal cues across various regions of the speech spectrum by performing temporal smoothing differently across spectral bands.

II. EXPERIMENT 1: EFFECT OF LOW-PASS SMOOTHING SLOPE

A. Method

1. Subjects

Thirty-six subjects were recruited from courses at the University of South Carolina and received money or course credit for participating. They were native speakers of English having a mean age of 24 years and audiometric thresholds of

15 dB HL or better at standard audiometric frequencies from 250 to 8000 Hz (ANSI, 1996). Care was taken to ensure that none of the subjects had any prior exposure to the sentences employed.

2. Stimuli

The stimuli were derived from the 100 Central Institute for the Deaf (CID) everyday American speech sentences (Davis and Silverman, 1978). They were produced by a male speaker and recorded at 22-kHz sampling and 16-bit resolution. An additional 10 practice sentences were drawn from the high-predictability subset of the Speech Perception In Noise test (SPIN; Kalikow, Stevens, and Elliot, 1977). The sentences were first whitened using a high-pass filter at 1000 Hz and 6 dB/octave. This helped ensure that temporal cues in the higher spectral regions would be audible and not masked by energy in lower spectral regions. The level of each sentence was then scaled by equating the peaks of the slow-response rms average.

The signal was partitioned into three bands using cutoff frequencies of 100–800, 800–2500, and 2500–8000 Hz. The use of 2000-order FIR filters allowed sharp partitioning of at least several hundred dB/octave. Temporal information from each partition was extracted using half-wave rectification and LP filtering. Of primary interest in the current experiment was the slope of the LP smoothing filters. The orders of these digital Butterworth filters were 1, 2, 4, 8, 16, and 32, producing slopes of 6, 12, 24, 48, 96, and 192 dB/octave. Cutoff frequencies of both 16 and 100 Hz were employed. Temporal envelopes extracted from speech partitions one, two, and three were used to amplitude modulate pure tones at 450, 1650, and 3250 Hz respectively, and the resulting modulated tones were mixed. This processing was performed in MATLAB. All three amplitude-modulated tones comprising a condition shared a common envelope cutoff and slope parameter. The stimuli were converted to analog form using an Echo Gina 24 digital to analog converter, set to play back at a slow-peak level of 65 dBA in a flat-plate coupler (Larson Davis 800B and AEC101), and delivered diotically over Sennheiser HD 250II headphones.

3. Procedure

Separate groups of 18 subjects each were assigned to the two cutoff-frequency conditions. Subjects heard 15 sentences in each of the six filter slope conditions. The sentence list-to-condition correspondence was balanced so that each list was heard in each condition an equal number of times, and the order in which conditions were heard was randomized for each subject. Each test sentence was heard only once. Subjects were tested individually in a sound-attenuating booth seated with the experimenter. They first heard the 10 SPIN practice sentences broadband, then in the 6 dB/octave condition (the highest intelligibility condition, based on pilot testing). The practice list was presented again, processed in the same manner as each condition, prior to each set of CID test sentences. Subjects repeated as much of each sentence as they could and were encouraged to guess if unsure of the content. The experimenter controlled the delivery of sen-

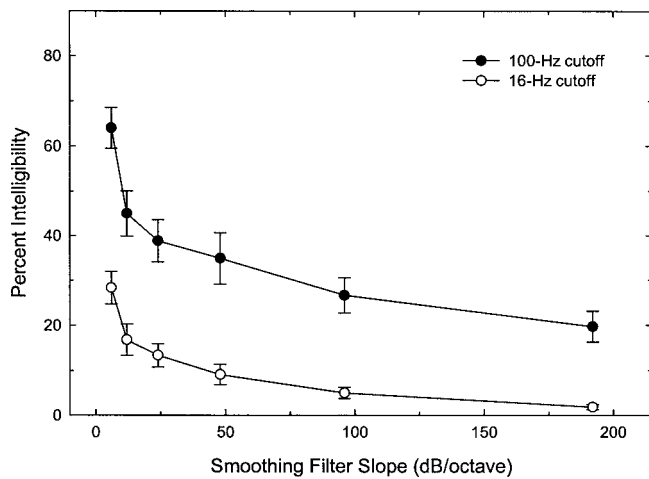


FIG. 2. Intelligibility of CID sentences presented as three amplitude-modulated carriers, as a function of temporal smoothing filter slope at two cutoff frequencies. Shown are means and standard errors for two groups of 18 subjects each.

tences and recorded the number of standard scoring keywords correctly. Only exact matches were accepted.

4. Results

Figure 2 shows performance (percent correct keywords) as a function of smoothing filter slope for the 16- and 100-Hz cutoffs. Intelligibility was highest with the shallowest slope employed and dropped precipitously as slope angle increased.¹ Repeated-measures ANOVAs performed on the 16- and 100-Hz cutoffs indicated significant effects of smoothing filter slope [$F(5,85)=20.04$ and 12.89 , $p < 0.001$]. Tukey posthoc testing indicated that, for both cutoffs, scores at 6 dB/octave were different ($p < 0.05$) from those at all other slopes. Scores at 192 dB/octave were not different than those at 48 dB/octave or above. The intermediate values at 12 and 96 dB/octave were also significantly different from one another.

III. EXPERIMENT 2: SPECTRAL SPECIFICITY OF TEMPORAL RATE INFORMATION

A. Method

Thirty-eight additional listeners were recruited using qualification and compensation procedures employed in the first experiment. Three-band stimuli were created using procedures similar to those of experiment 1, except that temporal extraction and modulation were performed at 400 Hz for one of the spectral channels, and at 16 Hz for the remaining two channels. In addition to these three-band conditions, which provide relatively-low overall intelligibility, four-band conditions were prepared to confirm the results at higher overall levels of performance. These latter conditions were prepared by partitioning the speech at 100–750, 750–1500, 1500–3000, and 3000–8000 Hz and following the same procedures employed to create the three-band stimuli. Because the increased temporal rate was applied to each partition in turn, there were three three-band stimuli and four four-band stimuli. It was decided to employ noise carriers, rather than pure tones in this experiment to ensure that spectral density

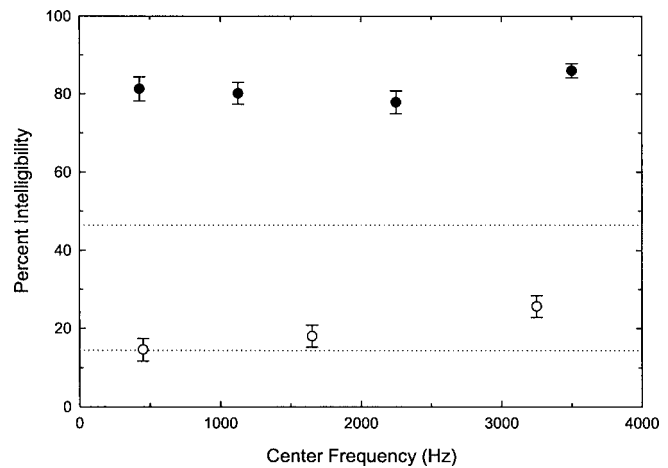


FIG. 3. Intelligibility of CID sentences presented as either three (open symbols) or four (filled symbols) amplitude-modulated noise carriers. Points represent the center frequency of the band having smoothing at 400 Hz, whereas the other bands in the array had smoothing at 16 Hz. Dotted reference lines show intelligibility in corresponding three-band conditions presented to a separate group of listeners in which all channels had smoothing at 16 Hz (lower line) or 400 Hz (upper line).

remained constant across the carriers as temporal rates were differentially manipulated. Temporal information was extracted using half-wave rectification and LP filtering, and used to modulate broadband white noise carriers.² The resulting modulated noises were postfiltered using the same filters used to create the corresponding speech partitions. The amplitude-modulated noise bands were then combined for presentation to listeners.

The different temporal smoothing cutoffs employed for the different component bands caused noticeable phase shifts (time delays) across the constituent bands. To eliminate this asynchrony across channels, temporal extraction was performed using a pair of cascaded fourth-order Butterworth LP filters. The first pass was performed on each rectified speech partition in usual fashion, then a subsequent pass was made on the time-reversed version of this filtered signal. The combination of cascaded fourth-order smoothing was then similar to the eighth-order smoothing found to produce asymptotic performance in experiment 1. It was found that this procedure effectively corrected for the differential filter delays and eliminated the apparent asynchrony across channels.

One group of 18 subjects heard the three-band conditions and another group of 20 subjects heard the four-band conditions (different group sizes were required for proper balancing). Subjects heard 20 sentences in each condition. As before, the sentence list-to-condition correspondence was balanced, conditions were presented in random order, and test sentences were presented only once. Procedures were the same as those employed in experiment 1, except that 10 additional CID sentences, processed in accord with the first-heard condition, were presented as additional practice prior to the first test condition.

B. Results

Figure 3 shows the intelligibility of the three- and four-band conditions as a function of the band having the in-

creased temporal rate. As can be seen, scores in the four-band conditions were similar when each of the individual bands was subjected to an increase in rate. A repeated-measures ANOVA on these conditions was marginally non-significant [$F(3, 57)=2.74, p=0.052$]. However, scores in the three-band conditions were higher when the band having the highest spectral frequency possessed the highest temporal rate. A repeated-measures ANOVA was significant [$F(2, 34)=12.01, p<0.001$], and Tukey posthoc testing indicated that scores were equivalent when either the low- or the mid-frequency band was raised in rate, but that these scores were lower than that obtained when the highest spectral band was raised in rate ($p<0.05$).

Additional data were collected for comparison to the three-band conditions and are also presented in Fig. 3. In these conditions, all bands were smoothed at 16 Hz (lower dotted line) or at 400 Hz (upper dotted line). These data were produced by an additional group of 18 listeners having the same characteristics as those employed in the formal experiments. Fifteen sentences were heard in each condition and all other processing and presentation procedures were the same as those employed previously. Although obtained from a separate group of listeners, these comparison data indicate that the increased temporal rate had little or no effect when presented to only the low- or middle-frequency bands, but that it produced a substantial increase in intelligibility when presented in the higher spectral frequencies. However, it is equally clear that the use of these cues was not restricted exclusively to the higher spectral frequencies, as intelligibility was far higher when all three bands possessed the higher temporal rate.

IV. GENERAL DISCUSSION

Experiment 1 shows that, as with filtering in the spectral domain, information contained within the skirt of the temporal smoothing filter can contribute considerably to the intelligibility of speech signals represented by primarily temporal cues. A comparison between the curves in Fig. 2 indicates that the intelligibility obtained using a 16-Hz cutoff at 6 dB/octave was roughly equivalent to that obtained using an otherwise identical stimulus having a 100-Hz cutoff at 96 dB/octave (trace a horizontal line across curves at approximately 28% intelligibility). The inclusion of additional temporal detail beyond the nominal cutoff is apparent from the upper two panels of Fig. 4, which show temporal patterns extracted at 16 Hz and relatively steep versus shallow slopes. Although not visually identical, the middle and lower panels show some similarity in temporal patterns obtained using the different smoothing parameters that yielded similar intelligibility scores.

In the spectral domain, increases in filter slope beyond several hundred dB/octave can have profound effects on narrow-band sentence intelligibility (Healy, 1998; Warren *et al.*, 2004). For example, the intelligibility reduction shown in Fig. 1 occurred with increases in slopes beyond 100 or 300 dB/octave. In contrast, Fig. 2 shows that the influence of filter slope on temporal smoothing may be constrained to

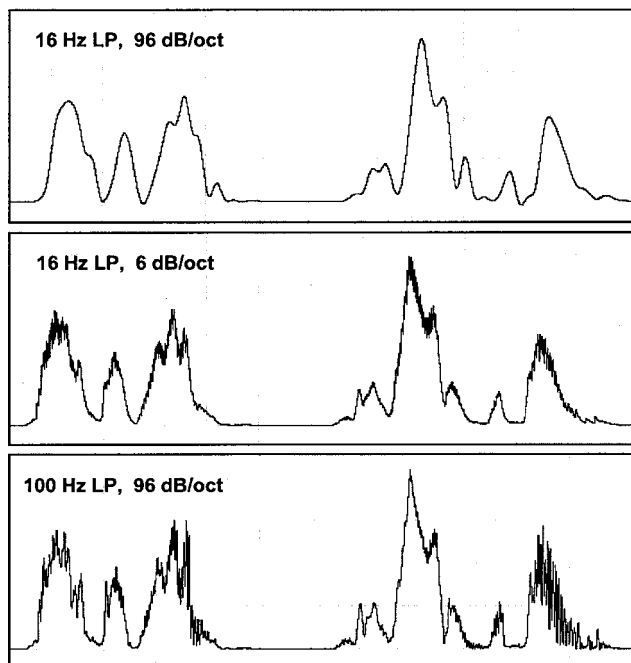


FIG. 4. Temporal patterns corresponding to a pair of CID sentences extracted using the low-pass smoothing parameters indicated. Time divisions are 0.2 s/DIV.

relatively shallow angles—the largest changes in performance were observed between 6 and 48 dB/octave.

In experiment 2, where an increase in temporal rate was applied to individual spectral bands, performance was similar across conditions when the spectrum was represented by four channels. However, when the spectrum was represented more sparsely, intelligibility was increased only when the increased rate was applied to the highest spectral frequencies. This result is in accord with those of Silipo *et al.* (1999) employing lower temporal rates, and those of Lorenzi *et al.* (1999) and Apoux and Bacon (2004) using fixed temporal rates. The indication that higher temporal rates may be of particular significance in higher spectral regions may reflect the larger bandwidths of auditory filters at higher center frequencies.

However, it was also the case that scores were far higher when all three spectral regions were raised in temporal rate, than when any individual band was raised. Thus, it is also apparent that these temporal cues can be effectively processed across the spectrum. Potentially interesting is the fact that a strong synergy appears to exist in which increases in temporal rate were most effective when distributed across all spectral regions, rather than when isolated to one.

The current results have implications for experiments involving vocoder simulations of speech. It is suggested that the restriction of temporal information requires smoothing slopes of at least 48 dB/octave. Further, a better understanding of the spectral specificity of temporal cues has the potential to further our understanding of speech processing and assist the design of more advanced signal processing strategies.

V. CONCLUSIONS

It was found that the slope of the temporal smoothing filter had a large effect on the intelligibility of sentences

represented by a small number of temporal patterns. However, unlike filtering in the spectral domain, the impact on performance was found to be restricted to rather shallow slopes. When an increase in temporal rate was presented to individual regions of the spectrum, performance enhancement was largest in the higher spectral region. However, performance was greatest when these higher-rate cues were distributed across spectral frequencies, indicating that their effective use is not constrained to only high spectral regions.

ACKNOWLEDGMENTS

This work was supported in part by NIDCD Grant No. DC05795. We thank Kimberly Carson for her assistance in testing subjects, and Ken Grant, Christopher Brown, and two anonymous reviewers for comments on an earlier version of this manuscript.

¹Excessively-steep temporal smoothing filters can cause the envelope to become negative and result in overmodulation (see Drullman *et al.*, 1994). To ensure that the current results were not affected in this way, additional stimuli were prepared in which the envelope signals following rectification and LP filtering were subjected to an additional half-wave rectification prior to multiplication with the carriers. This processing left the positive envelope values intact, and so had essentially no effect on these stimuli where overmodulation was generally absent. However, the procedure served to ensure that no negative envelope values or overmodulation existed. No differences were observed for stimuli incorporating this control.

²If temporal rate is assumed to be restricted to half the speech and carrier bandwidth, then rates for the lowest band in the three-band array was limited to 350 Hz, rather than the 400 Hz dictated by LP smoothing. Similarly, the lower two bands in the four-band array were limited to 325 and 375 Hz. However, in additional measurements using these materials and the current three noise-band conditions, intelligibility by NH listeners was found to asymptote at 100 Hz (statistically) or 250 Hz (numerically). Thus, all source and presentation bandwidths employed were sufficiently wide to carry temporal information at rates up to the limits of useful information.

- ANSI (1996). ANSI-S3.6, 1996. "Specifications for audiometers," American National Standards Institute, New York.
- Apoux, F., and Bacon, S. P. (2004). "Relative importance of temporal information in various frequency regions for consonant identification in quiet and in noise," *J. Acoust. Soc. Am.* **116**, 1671–1680.
- Davis, H., and Silverman, S. R. (1978). *Hearing and Deafness*, 4th ed. (Holt, Rinehart, and Winston, New York).
- Dorman, M. F., Loizou, P. C., Fitzke, J., and Tu, Z. (1998). "The recognition of sentences in noise by normal-hearing listeners using simulations of cochlear-implant signal processors with 6-20 channels," *J. Acoust. Soc. Am.* **104**, 3583–3585.
- Dorman, M. F., Loizou, P. C., and Rainey, D. (1997). "Speech intelligibility as a function of the number of channels of stimulation for signal processors using sine-wave and noise-band outputs," *J. Acoust. Soc. Am.* **102**, 2403–2411.
- Drullman, R., Festen, J. M., and Plomp, R. (1994). "Effect of temporal

- envelope smearing on speech reception," *J. Acoust. Soc. Am.* **95**, 1053–1064.
- Faulkner, A., Rosen, S., and Smith, C. (2000). "Effects of the salience of pitch and periodicity information on the intelligibility of four-channel vocoded speech: Implications for cochlear implants," *J. Acoust. Soc. Am.* **108**, 1877–1887.
- Fu, Q.-J., and Shannon, R. V. (2000). "Effect of stimulation rate on phoneme recognition by Nucleus-22 cochlear implant listeners," *J. Acoust. Soc. Am.* **107**, 589–597.
- Fu, Q.-J., Zeng, F.-G., Shannon, R. V., and Soli, S. D. (1998). "Importance of tonal envelope cues in Chinese speech recognition," *J. Acoust. Soc. Am.* **104**, 505–510.
- Grant, K. W., Braida, L. D., and Renn, R. J. (1991). "Single band amplitude envelope cues as an aid to speechreading," *Q. J. Exp. Psychol.* **43**, 621–645.
- Healy, E. W. (1998). "A minimum spectral contrast rule for speech recognition: Intelligibility based upon contrasting pairs of narrow-band amplitude patterns," doctoral dissertation, University of Wisconsin-Milwaukee.
- Horii, Y., House, A. S., and Hughes, G. W. (1971). "A masking noise with speech-envelope characteristics for studying intelligibility," *J. Acoust. Soc. Am.* **49**, 1849–1856.
- Kalikow, D. N., Stevens, K. N., and Elliot, L. L. (1977). "Development of a test of speech intelligibility in noise using sentence materials with controlled word predictability," *J. Acoust. Soc. Am.* **61**, 1337–1351.
- Lorenzi, C., Berthommier, F., Apoux, F., and Bacri, N. (1999). "Effects of envelope expansion on speech recognition," *Hear. Res.* **136**, 131–138.
- Lou, X., and Fu, Q.-J. (2004). "Enhancing Chinese tone recognition by manipulating amplitude envelope: Implications for cochlear implants," *J. Acoust. Soc. Am.* **116**, 3659–3667.
- Nie, K., Barco, A., and Zeng, F.-G. (2006). "Spectral and temporal cues in cochlear implant speech perception," *Ear Hear.* **27**, 208–217.
- Qin, M. K., and Oxenham, A. J. (2003). "Effects of simulated cochlear-implant processing on speech reception in fluctuating maskers," *J. Acoust. Soc. Am.* **114**, 446–454.
- Rosen, S. (1992). "Temporal information in speech: Acoustic, auditory and linguistic aspects," *Philos. Trans. R. Soc. London* **336**, 367–373.
- Shannon, R. V., Galvin, J. J. III, and Baskent, D. (2001). "Holes in hearing," *Journal of the Association for Research in Otolaryngology* **3**, 185–199.
- Shannon, R. V., Zeng, F.-G., Kamath, V., Wygonski, J., and Ekelid, M. (1995). "Speech recognition with primarily temporal cues," *Science*, **270**, 303–304.
- Shannon, R. V., Zeng, F.-G., and Wygonski, J. (1998). "Speech recognition with altered spectral distribution of envelope cues," *J. Acoust. Soc. Am.* **104**, 2467–2476.
- Silipo, R., Greenberg, S., and Arai, T. (1999). "Temporal constraints on speech intelligibility as deduced from exceedingly sparse spectral representations," in *Proceedings of the 6th European Conference on Speech Communication and Technology (Eurospeech-99)*, pp. 2687–2690.
- Van Tasell, D. J., Soli, S. D., Kirby, V. M., and Widin, G. P. (1987). "Speech waveform envelope cues for consonant recognition," *J. Acoust. Soc. Am.* **82**, 1152–1161.
- Warren, R. M., and Bashford, J. A. Jr. (1999). "Intelligibility of 1/3-octave speech: Greater contribution of frequencies outside than inside the nominal passband," *J. Acoust. Soc. Am.* **106**, L47–L52.
- Warren, R. M., Bashford, J. A. Jr., and Lenz, P. W. (2004). "Intelligibility of bandpass filtered speech: Steepness of slopes required to eliminate transition band contributions," *J. Acoust. Soc. Am.* **115**, 1292–1295.
- Xu, L., Thompson, C. S., and Pfingst, B. E. (2005). "Relative contributions of spectral and temporal cues for phoneme recognition," *J. Acoust. Soc. Am.* **117**, 3255–3267.

Singing proficiency in the general population

Simone Dalla Bella^{a)}

Department of Cognitive Psychology, University of Finance and Management in Warsaw, Ul. Pawia 55, 01-030 Warsaw, Poland

Jean-François Giguère and Isabelle Peretz

Department of Psychology, University of Montreal, Montreal, Canada

(Received 7 August 2006; revised 12 November 2006; accepted 22 November 2006)

Most believe that the ability to carry a tune is unevenly distributed in the general population. To test this claim, we asked occasional singers ($n=62$) to sing a well-known song in both the laboratory and in a natural setting (experiment 1). Sung performances were judged by peers for proficiency, analyzed for pitch and time accuracy with an acoustic-based method, and compared to professional singing. The peer ratings for the proficiency of occasional singers were normally distributed. Only a minority of the occasional singers made numerous pitch errors. The variance in singing proficiency was largely due to tempo differences. Occasional singers tended to sing at a faster tempo and with more pitch and time errors relative to professional singers. In experiment 2 15 nonmusicians from experiment 1 sang the same song at a slow tempo. In this condition, most of the occasional singers sang as accurately as the professional singers. Thus, singing appears to be a universal human trait. However, two of the occasional singers maintained a high rate of pitch errors at the slower tempo. This poor performance was not due to impaired pitch perception, thus suggesting the existence of a purely vocal form of tone deafness. © 2007 Acoustical Society of America.

[DOI: 10.1121/1.2427111]

PACS number(s): 43.75.Rs, 43.75.Cd [Diana Deutsch]

Pages: 1182–1189

I. INTRODUCTION

Singing is generally regarded as the privilege of a select few who are widely prized for their skill. Accordingly, most believe that the majority of individuals with vocal training or formal musical education are unable to carry a tune. However, singing is quite natural for humans. Singing is a universal form of vocal expression that transcends places and cultures. Moreover, singing is a group activity that is typically associated with a highly pleasurable experience and thought to promote group cohesion (Mithen, 2006; Wallin *et al.*, 2000).

Singing abilities emerge spontaneously and precociously during development. The first songs are produced at around 1 year of age and, at 18 months, children start to generate recognizable songs (e.g., Ostwald, 1973; see Dowling, 1999, for a review). This precocious emergence of basic singing abilities is reflected in the characteristics of adult singing, which is remarkably consistent both within (Bergeson and Trehub, 2002; Halpern, 1989) and across subjects (Levitin, 1994; Levitin and Cook, 1996) when considering both starting pitch and tempo. Therefore, it is expected that the general population can sing proficiently.

Singing represents one of the richest sources of information regarding the nature and origins of musical behavior because it is a universal and socially relevant activity and it emerges precociously. Yet, surprisingly, sung performance has received relatively little empirical attention (Gabrielsson, 1999; Parncutt and McPherson, 2002). The few studies on

sung performance have mostly targeted professional singing. Differences have been found between professional singers and nonsingers in terms of voice quality (e.g., Sundberg, 1987, 1999). More specifically, partials falling in the frequency range of 2.5–3.0 KHz (the so-called *singer's formant*; see Sundberg, 1987) are much stronger in sung vowels than in spoken vowels; the intensity of the *singer's formant*, the presence of vibrato, and the maximum phonational frequency range increase with musical experience (e.g. Brown *et al.*, 2000; Mendes *et al.*, 2003). Occasional singers have accurate memory for initial pitch and tempo of popular songs but poor vocal pitch matching abilities (Amir *et al.*, 2003; Murbe *et al.*, 2002; Ternstrom *et al.*, 1988). When asked to reproduce single pitches in pitch matching tasks, nonmusicians deviate by 1.3 semitones on average as compared to 0.5 semitones for musicians (Amir *et al.*, 2003; Murry, 1990; Murry and Zwiner, 1991; Ternstrom *et al.*, 1988). These findings may not apply to singing notes in the context of songs. In songs, the melody is highly structured on both pitch and time dimensions, thereby providing multiple musical cues aiding to plan and monitor sung performance. Furthermore, prior studies have focused on pitch accuracy. Yet, time accuracy is also an important characteristic of proficient singing. In sum, there is insufficient information regarding the distribution of singing abilities in occasional singers.

The paucity of research on singing in the general population might be related to the difficulties that are inherent in the analysis of sung performance. The analysis of sung performance is arguably more challenging as compared to the analysis of piano performance, for example, where key strokes can be accurately recorded (in MIDI format) by way of a computer-monitored electronic keyboard. In previous

^{a)}Electronic mail: sdallabella@vizja.pl

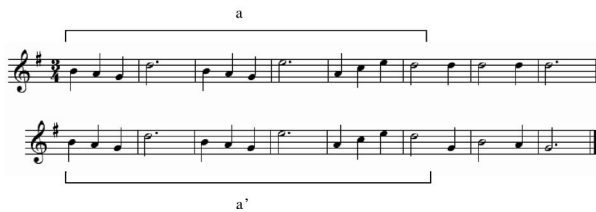


FIG. 1. Refrain of *Gens du Pays*.

studies of sung performance, objective methods based on pitch extraction algorithms have been successfully applied in the analysis of single pitch performance (e.g., Alcock *et al.*, 2000a, b; Amir *et al.*, 2003). However, there is currently no consensus on how to obtain similar objective measures of singing proficiency in sung melodies. In the past, singing accuracy was assessed by expert musicians (e.g., Alcock, 2000a, b; Hebert *et al.*, 2003; but see Murayama *et al.*, 2004). For example, Alcock and collaborators (2000a, b) asked experts to rate singing accuracy separately for pitch and rhythm in healthy and brain-damaged subjects. However, when making judgments, experts are subject to the constraints of both music notation and their perceptual system. Musicians often categorize pitch and duration information with respect to the closest musical value. Moreover, they tend to integrate pitch and time information when embedded in a musical context (Jones and Pfordresher, 1997; Peretz and Kolinsky, 1993). These difficulties might explain the reported discrepancies between raters in their evaluations of singing proficiency (e.g., see Kinsella *et al.*, 1988; Prior *et al.*, 1990). Thus, acoustic-based analyses of sung performance are more likely to yield a reliable measure of singing proficiency than expert judgments.

Such an objective approach was adopted in the present study to examine pitch and time accuracy of sung performance in the general population. To this aim, 62 individuals were asked to sing a well-known Quebec folk tune, “*Gens du pays*” (Gilles Vigneault; see Fig. 1), including 20 nonmusicians who were tested in the laboratory, and 42 individuals who were tested in a public park. A customized computer-guided analysis of sung performance was devised to objectively measure pitch and time accuracy. This technique is based on acoustical segmentation of sung recordings and pitch extraction, and was inspired by recent “query-by-humming” methods that serve to access large electronic musical databases through singing (e.g., Pardo *et al.*, 2004). The analyses yield several measures of pitch and temporal accuracy such as pitch interval deviation and temporal variability (i.e., the coefficient of variation of inter-onset-intervals between sung notes) that are known to be indicative of expert performance (e.g., Repp, 1998; Vurma and Ross, 2006). If indeed singing abilities are poorly developed in the general population, we expect that the vast majority of individuals will sing out-of-tune and have problems keeping time. Alternatively, if singing proficiency is widespread, we expect that singing abilities will be normally distributed, and that the majority of individuals will sing in-tune and in-time.

II. EXPERIMENT 1

A. Method

1. Participants

Twenty individuals (hereafter referred to as *group 1*), ten males and ten females, were recruited from the University of Montreal community. Their age ranged from 19 to 29 ($M = 23.9$ years). Forty-two individuals (*group 2*), 19 males and 23 females, were recruited randomly in a public park. Their age ranged from 18 to 75 ($M = 41.4$ years). Participants from group 1 were nonmusicians and participants from group 2 were not selected for musical training. For the sake of simplicity, participants from groups 1 and 2 are hereafter referred to as *occasional singers*. For comparison, four professional singers ($M = 11$ years of vocal training; range = 8–17 years) and Gilles Vigneault (G.V.), the composer and singer of the target song, participated in the experiment. Participants had no neurological history. Group 1 and the four anonymous singers were compensated for their participation.

2. Material and procedure

Participants were asked to sing the well-known refrain of the song *Gens du pays* (Vigneault and Rochon, 1976), which is typically sung in Quebec to celebrate birthdays. As can be seen in Fig. 1, the refrain is composed of 32 notes with a vocal range of less than one octave and a stable tonal center. Each note is associated with one syllable. The segment *a'* is an exact repetition of *a* and can be used to evaluate pitch stability. The experimenter (Michel) pretended that it was his birthday and that he had made a bet with friends that he could get 100 individuals each to sing the refrain of *Gens du pays* for him on this special occasion. This strategy was effective for the purposes of recruiting the participants that formed group 2. The performances of group 1 subjects and the professional singers were recorded in the laboratory, while G.V.'s performance was recorded in a studio. Group 1 was asked to sing the refrain three times: at the beginning of the experiment (test 1), immediately afterwards (test 2), and one week later (test 3). Only tests 1 and 2 were completed by the four professional singers (eight performances overall). G.V. sang the song twice. Sung performance was recorded at a sampling frequency of 44.1 KHz using a Shure 565SD microphone directly onto a IBM-compatible computer using Cooledit software in the laboratory and using a portable Sony TCD-D10 Pro DAT for group 2, professional singers, and G.V.

Sung renditions of group 1 (test 1) and group 2 were presented in random order to ten nonmusicians who had not participated in the singing session. The peers had to rate each performance on a 10-point scale with 1 indicating “very inaccurate” and 10 “very accurate.”

3. Acoustical analysis of sung performance

In order to compute various measures of pitch and time accuracy, an acoustic-based method was used to analyze the recordings of the sung performances. Acoustical analyses of each sung performance were carried out on the vowel groups (e.g., “i” in “Mi”). Vowel-groups are the best targets for

acoustical analysis because vowels carry the maximum of voicing and stable pitch information (see Murayama *et al.*, 2004). These groups were determined by visual inspection of the waveform and of the spectrogram. The onsets of vowel groups were used to compute *note onset time* and were measured in ms. The median of the fundamental frequencies of the vowel-group was computed with Praat software (Boersma, 2001) using an accurate autocorrelation method (Boersma, 1993) (sampling rate= 100 Hz; Gaussian window= 80 ms) and served to measure *pitch height* (F0 in Hertz). It is noteworthy that pitch extraction based on autocorrelation methods when applied to pitch detection in normal speech is prone to false detections (e.g., octave jumps), for instance in presence of weak fundamental frequencies or strong high harmonics. In the present study, when false pitch detections occurred they were manually corrected.

Note onset time and pitch height were used to obtain various pitch and time variables as described below. These analyses were implemented with Matlab 7.1 software.

3.1. Pitch dimension variables.

Pitch stability is the difference between the produced pitch in the melody segment *a* and in the repetition *a'* (as in Flowers and Dunne-Sousa, 1990). The absolute difference in semitones between the 12 corresponding notes (e.g., note 1 in segment *a* and *a'*, note 2 in segment *a* and *a'*, and so forth) was computed. Pitch stability is the mean of these absolute differences. The larger this mean difference, the less stable is the pitch.¹

Number of pitch interval errors (see Fig. 2) indicates the number of errors in the performance of musical intervals compared to the musical notation. An error was scored when the sung interval was larger or smaller by 1 semitone than the interval prescribed by the notation. This measure was not influenced by absolute pitch level, nor by the size of the deviation.

CORRECT



PITCH INTERVAL ERROR



PITCH INTERVAL + CONTOUR ERROR



TIME ERROR



FIG. 2. Examples of pitch interval error, contour error, and time error.

Number of contour errors (see Fig. 2) refers to the number of changes in pitch directions relative to musical notation. Pitch direction was considered as ascending or descending if the sung interval between two notes was higher or lower by more than 1 semitone. A contour error was counted when the pitch direction deviated from the musical score.

Interval deviation is a measure of the size of the pitch deviation from the score and is calculated by averaging the absolute difference in semitones between the produced intervals and the intervals prescribed by the score. A small deviation reflects high accuracy in terms of relative pitch.

3.2. Time dimension variables.

Tempo was obtained by computing the mean inter-onset-interval (IOI) of the quarter-note.

Number of time errors (see Fig. 2) represents duration deviations from the score. When the duration of the sung note was 25% longer or shorter than its predicted duration based on the preceding note, as prescribed by the musical

TABLE I. Mean values for pitch and time variables for group 1 ($n=60$) at test 1, test 2, and test 3, group 2 ($n=42$), professional singers ($n=8$), and G.V. ($n=4$). *Ns* indicate the number of performances.

Variable	GROUP 1			GROUP 2	SINGERS	G.V.
	Test 1	Test 2	Test 3			
	<i>M</i> (SE)	<i>M</i> (SE)	<i>M</i> (SE)	<i>M</i> (SE)	<i>M</i> (Range)	<i>M</i>
Pitch dimension						
Pitch first note (Hz)						
Males	134.0 (6.6)	135.1 (6.8)	129.3 (4.9)	143.0 (6.5)	165.8 (134.5–199.0)	221.1
Females	252.1 (9.7)	259.7 (8.1)	257.7 (8.8)	234.6 ^a (6.1)	308.9 (276.8–338.3)	...
Pitch stability (semitone)	0.5 ^a (0.1)	0.6 ^a (0.1)	0.6 ^a (0.0)	0.7 ^b (0.3)	0.3 (0.1–0.4)	0.4
No. of coutour errors	0.7 ^b (0.3)	1.2 ^b (0.4)	1.2 ^b (0.3)	2.5 ^b (0.4)	0.0 (0.0)	0.3
No. of pitch interval errors	5.5 ^b (1.2)	4.8 ^b (1.2)	4.4 ^b (1.0)	9.8 ^b (0.8)	0.5 (0.0–2.0)	1.8
Interval deviation (semitone)	0.6 ^b (0.1)	0.6 ^b (0.1)	0.6 ^b (0.1)	0.9 ^b (0.1)	0.3 (0.2–0.4)	0.3
Time dimension						
Tempo (Mean IOI, ms)	275.0 ^b (10.0)	281.0 ^b (12.2)	289.7 ^b (10.4)	239.7 ^b (8.6)	398.8 (366.9–427.6)	338.7
No. of time errors	2.2 (0.5)	1.5 (0.3)	2.2 (0.4)	4.7 ^a (0.5)	0.9 (0–4.0)	2.5
Temporal variability (CV IOIs)	0.12 (0.01)	0.10 (0.01)	0.10 (0.01)	0.17 (0.01)	0.10 (0.06–0.16)	0.16
Rubato	0.6 (0.06)	0.7 (0.05)	0.6 (0.06)	0.6 (0.04)	0.6 (–0.3–1.0)	0.6

^a ± 2 SD from the mean of professional singers

^b ± 3 SD from the mean of professional singers

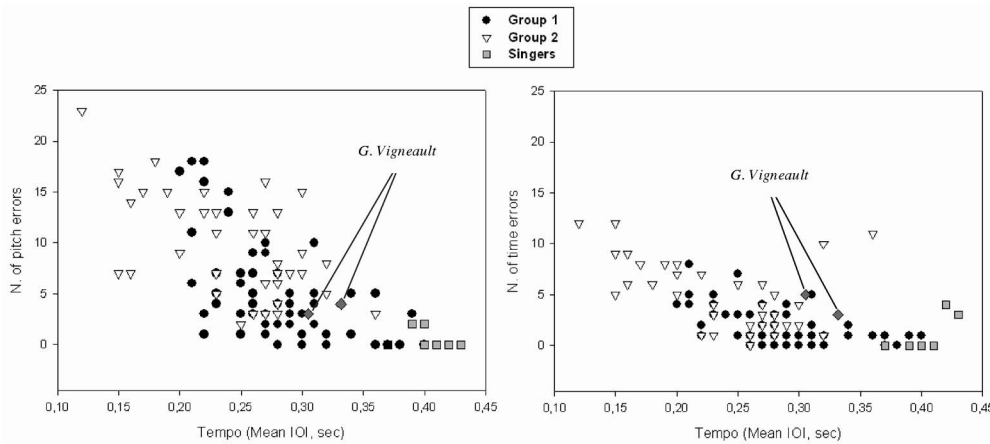


FIG. 3. Number of pitch interval errors and time errors plotted against tempo (i.e., mean quarter-note IOI) for group 1, group 2, professional singers, and G.V.

notation, this was considered as a time error (using a stricter criterion than in piano performance studies; e.g., Drake and Palmer, 2000). The first and last notes were not used to compute time errors.

Temporal variability is the coefficient of variation of the quarter-note IOIs, calculated by dividing the standard deviation of the IOIs by the mean IOI (as in Repp, 1998). This measure of time accuracy is less dependent on tempo than the simple standard deviation of the IOIs.

Rubato is an additional measure of timing consistency. This can be observed, for instance, when a musician increases the tempo at the beginning of a musical phrase and slows down at the end (Todd, 1985). To obtain a measure of Rubato, the quarter-note IOIs for the segment *a* were correlated with the IOIs for segment *a'* (for a similar measure in piano performance, see Timmers *et al.*, 2000). High correlation corresponds to high consistency in the rubato pattern.

B. Results

Means and standard error of pitch and time variables for groups 1 and 2 are reported in Table I. Corresponding measures of singing proficiency of professional singers and for G.V. are also reported for comparison purposes. As shown in Table I, the occasional singers seemed to have less control over pitch relative to time as compared to expert singers. They differed from professionals on all pitch dimension variables, with the exception of the pitch of the first note. In addition, occasional singers tended to produce more pitch intervals that were out-of-key (group 1: 2.72 errors, SE=0.28; group 2: 4.93 errors, SE=0.76) than in-key (group 1: 2.18 errors, SE=0.28; group 2: 4.88 errors, SE=0.75). This trend reached significance in group 1 [one-tailed $t(59) =$

$-1.70, p < 0.05$]. Nevertheless, occasional singers rarely produced pitch intervals that deviated by more than one semitone (see Table II) and made few time errors (Table I). However, they sang, on average, almost twice as fast as professional singers.

This difference in tempo between occasional and professional singers may account for the higher error rates observed in the nonexperts. Fast tempos typically lead to reduced accuracy in piano performance (e.g., see Repp, 1998). To examine this possibility, pitch and time errors were plotted against tempo for all participants. As can be seen in Fig. 3, faster tempi were associated with reduced accuracy, especially on the pitch dimension. Interestingly, the occasional singers who sang at a slow tempo exhibited accuracy comparable to that of professionals. Regression analyses confirmed that tempo accounted for pitch accuracy [pitch stability, $R^2=0.36, F(1,112)=63.94, p < 0.001$; contour errors, $R^2=0.30, F(1,112)=47.13, p < 0.01$; pitch interval errors, $R^2=0.47, F(1,112)=100.07, p < 0.001$; interval deviation, $R^2=0.46, F(1,112)=96.84, p < 0.001$] and time accuracy [time errors, $R^2=0.32, F(1,112)=53.17, p < 0.001$]. Fast singing is also judged to be less accurate than slow singing by the peers [$R^2=0.39, F(1,100)=64.43, p < 0.001$]. Hence, a significant portion of the variability in sung performance may be accounted for by tempo differences. Sung performance was optimal at slow speeds.

The peer ratings did not differ significantly from normality (Kolmogorov-Smirnov test, $p = ns$), as shown in Figs. 4(a) and 4(b), respectively. The peer ratings for the performance of the subjects who were tested in the laboratory (group 1) were higher than those who were tested in a natural setting [group 2; $t(100)=2.87, p < 0.01$]. However, the objective measures of accuracy derived from the acoustical analysis revealed that the general population is not as homogenous as may be inferred from perceptual judgments. A closer look at the distribution of pitch interval errors and time errors [see Figs. 4(a) and 4(b)] reveals that the majority of individuals were fairly in-tune and in-time, while a minority were poor singers. In group 1, 70% committed less than 6 pitch errors and less than 4 time errors, whereas 3% sang clearly out-of-tune, making more than 17.6 pitch errors, which corresponds to 2 standard deviations above the average of both groups. In group 2, accuracy was lower but simi-

TABLE II. Number and percentage of pitch intervals that deviated from the score by a quarter of tone, 1, 2, and 3 semitones in the laboratory setting (group 1) and outdoors (group 2).

Interval deviation from the score	Group 1 <i>n</i> (%)	Group 2 <i>n</i> (%)
>1 quarter of tone	29 (48)	3 (7)
>1 semitone	53 (88)	30 (71)
>2 semitones	60 (100)	41 (97)
>3 semitones	...	42 (100)

larly distributed with 70% making less than 14 pitch errors and less than 7 time errors (i.e., threshold of 2 standard deviations above the average). It is worth noting that poor singers were the fastest singers and were inaccurate in both the pitch and time dimensions. In general, proficiency in pitch and time were correlated; the occasional singers who made more pitch errors were also those making more time errors ($r=0.36$ and 0.37 , $p < 0.01$, for groups 1 and 2, respectively). However, only 15% of pitch and time errors jointly occurred on the same notes.

The data from group 1 were further analyzed so as to assess the consistency across performances, and possible practice effects. No significant effect of time of testing (test 1, 2, and 3) was found for any of the variables. To estimate which parameters were the most stable across repetitions, the mean values for each variable at test 1 were correlated with the corresponding values at test 2 and at test 3. All the variables with the exception of rubato were highly correlated, even when performances were recorded 1 week apart (with r

values between 0.56 and 0.97, $p < 0.01$), showing remarkable consistency in untrained singing. Finally, between-subjects consistency was assessed for absolute pitch and tempo with reference to the most frequently heard version of “Gens du pays,” sung in G Major and with a tempo (mean quarter-note IOI) of 347 ms. This “frequent” version was obtained from six commercial recordings by G.V.² The results reported in Table III show that the untrained population has a good memory for absolute pitch. In the majority of performances (72%), the first note laid within 2 semitones of the original note. In comparison, the tempo was more variable, with only 11% of the performances where the tempo was within 8% of the original tempo.

C. Discussion

Singing proficiency appears to be normally distributed in the general population with a majority of occasional singers being able to sing on time, with few pitch deviations. The pitch deviations were also fairly subtle, typically smaller than a semitone. Thus occasional singers are more accurate when they sing well-known melodies than isolated pitches (Amir *et al.*, 2003; Ternstrom *et al.*, 1988). It is remarkable that the occasional singers were extremely proficient along the time dimension. Although they tended to sing more quickly than professional singers, occasional singers performed as accurately as professionals in terms of regularity, rubato, and time deviations. Finally, the present study showed that occasional singers’ performance is particularly consistent, both between-subjects (mostly for the pitch dimension, as in Levitin, 1994, and Levitin and Cook, 1996) and across repetitions (as in Bergeson and Trehub, 2002).

Given that the occasional singers sang at a faster tempo than professional singers, a speed-accuracy trade-off may be responsible for the observed differences in pitch accuracy between the two groups. If this hypothesis holds true, occasional singers should be able to make minimal to no errors in singing at a slower tempo. We tested this hypothesis in experiment 2.

III. EXPERIMENT 2

A. Method

This follow-up session with 15 participants from group 1 was carried out 3 years following experiment 1. Experi-

TABLE III. Comparison between the pitch of the first note and tempo of performances in groups 1 and 2 and pitch and tempo of the original version of “Gens du Pays”.

Dimension	Group 1 <i>n</i> (%)	Group 2 <i>n</i> (%)
Pitch of the first note		
Same as the original	9 (15)	5 (12)
Within 1 semitone	30 (50)	13 (31)
Within 2 semitones	43 (72)	30 (71)
Tempo		
Within 4% of the actual tempo	5 (8)	0 (0)
Within 8% of the actual tempo	10 (17)	2 (5)

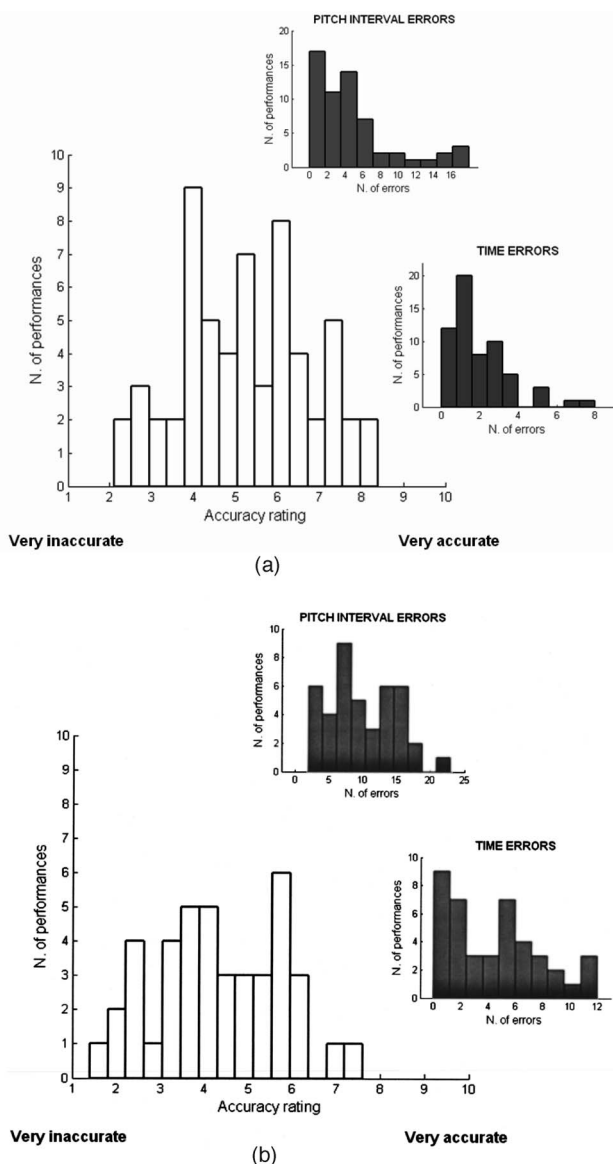


FIG. 4. Peer judgments, objective pitch interval errors and time errors for group 1 (a) and group 2 (b).

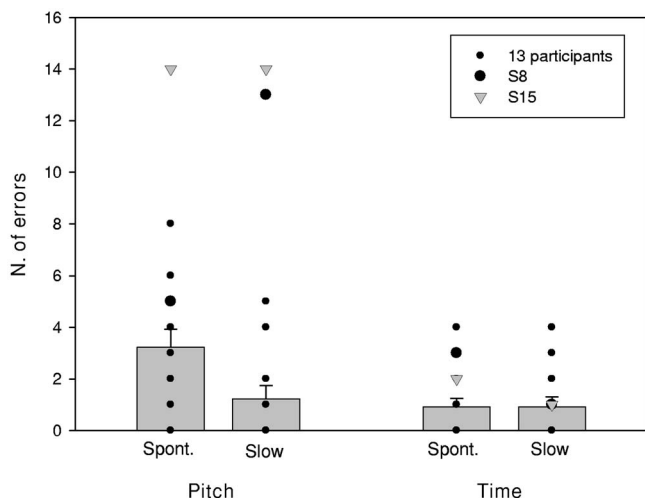


FIG. 5. Number of pitch interval errors and time errors in experiment 2 when singing at spontaneous tempo and slow tempo.

ment 2 involved the same material and procedure as those used in experiment 1. The only difference was that participants were asked to sing *Gens du pays* in two conditions: (1) at a spontaneous tempo as in experiment 1 and (2) at a tempo of 120 beats per min (corresponding to a mean IOI of 500 ms) as marked by a metronome. As soon as the participants felt they could synchronize their performance with the metronome, the latter was turned off and the sung production was recorded.

Eleven participants were further tested for music perception. They were presented with 60 unfamiliar tonal melodies of which half contained a pitch or time error. The task was to press one button when an error was detected and another button when there was no error.

B. Results and discussion

As shown in Fig. 5, all participants succeeded in singing at the imposed tempo (mean IOI=499 ms, SE=7 ms) and making less errors while doing so. There were two notable exceptions. Two participants (S8 and S15) exhibited a large number of pitch interval errors in both the spontaneous and slow tempo conditions and were qualified as poor singers. Their performance will be described in more detail below.

Performance in the spontaneous condition did not differ from that obtained in experiment 1, on all pitch and time variables previously examined [all $t(12)$ tests being n.s.]. As shown in Fig. 5 and Table IV, pitch accuracy markedly improved with slower tempos [pitch interval errors, $t(12)=4.28$, $p<0.01$; pitch stability, $t(12)=2.12$, $p<0.05$; contour errors, $t(12)=2.31$, $p<0.05$; and interval deviation, $t(12)=6.63$, $p<0.01$]. As a result of slowing down, proficiency measures for occasional singers fell within the range exhibited by professional singers. For instance, when singing at slow tempo occasional singers exhibited small pitch interval deviation (i.e., 0.3 semitones), as observed in professional singers. Such interval deviation is acceptable in singing as estimated by expert listeners (Vurma and Ross, 2006). These findings confirm that a speed-accuracy trade-off was

TABLE IV. Mean values for pitch and time variables at the slow tempo for 15 occasional singers re-tested in experiment 2.

Variable	13 singers	S8	S15
	M (SE)	M	M
Pitch dimension			
Pitch stability (semit.)	0.3 (0.0)	0.4	0.4
No. of contour errors	0.2 (0.2)	6.0	6.0
No. of pitch interval errors	1.2 (0.5)	13.0	14.0
Interval deviation (semit.)	0.3 (0.0)	1.0	1.1
Time dimension			
Tempo (Mean IOI, ms)	497.0 (8.7)	494.2	535.1
No. of time errors	0.9 (0.4)	1.0	1.0
Temporal variability (CV IOIs)	0.07 (0.01)	0.07	0.08
Rubato	0.4 (0.01)	0.1	0.9

mostly responsible for the observed differences between occasional singers and professionals in experiment 1.

In contrast, the two poor singers (S8 and S15) maintained a high rate of pitch interval errors when requested to slow down (Fig. 5). Their sung performance was clearly out-of-tune, by producing many intervals that deviated from the score by more than 1 full semitone, while this type of deviation never occurred in the other 13 participants (Table IV). As a result, the poor singers sang mostly out-of-key notes (9 out of 13 errors for S8; 8 out of 14 errors for S15) that often fell on strong beats (51% of the cases). While their singing was out-of-tune, it was in-time. The poor singers did not make more time errors than the other participants (their sung performance can be heard along with representative renditions of the other occasional singers at www.umontreal.brams/peretz). Moreover, their poor vocal control of pitch was not due to a perceptual deficiency. S8 and S15 correctly detected 90% and 96% of pitch deviations in a melodic context. Their performance falls within 2 SD of the mean (88%, SE=1.1) scores obtained by 71 university students (mean age= 26.5 years). That S8 and S15 exhibited a normal perception is consistent with the observation that these subjects were aware that they sang out-of-tune.

IV. GENERAL DISCUSSION

In the present study, we found that the majority of individuals can carry a tune with remarkable proficiency. Occasional singers typically sing in-time but are less accurate in pitch as compared to professional singers. When asked to slow down, occasional singers greatly improve in performance, making as few pitch errors as professional singers. Thus, singing appears to be a widespread skill.

It is noteworthy that time precision in sung performance is well suited for group synchronization. Indeed, choral singing requires time accuracy, precise alignment of note onsets, and rapid adaptation to changes in tempo, as in the case of rubato (e.g., Aschersleben *et al.*, 2002). *Gens du pays* (the Quebec version of *Happy Birthday*) is typically sung in choir. Occasional singers' spontaneous control of time factors in vocal performance is optimal for singing in a group context. If, in addition, singing along imposes a slower

tempo, then the group should sing perfectly in tune. These are the necessary and sufficient conditions for producing a harmonious choral performance, thus making singing a pleasurable experience for everyone.

There were two notable exceptions. Two participants were unable to correct the numerous pitch errors that they made, although they sang in-time and were normal at detecting pitch errors in musical contexts. The inability to sing accurately despite efforts to do so characterizes self-declared tone deaf individuals (Sloboda *et al.*, 2005). Tone deafness is rare, affecting about 4% of the general population (Kalmus and Fry, 1980). To date, tone deafness has been studied and defined in terms of poor perceptual abilities (congenital amusia; see Ayotte *et al.*, 2002; Foxton *et al.*, 2004; Peretz, 2006; Peretz *et al.*, 2002; Peretz and Hyde, 2003). Poor singing, a landmark of this perceptual disorder as well as a selection criterion, is interpreted as a consequence of an impoverished perceptual system. Nonetheless, the present results suggest that poor singing may occur in the presence of normal perception. This possibility finds support in a recent study conducted with poor singers who exhibited pitch production deficits but normal pitch discrimination (Bradshaw and McHenry, 2005). Similarly, brain damage can selectively impair sung performance without affecting perception (Schon *et al.*, 2003). Thus, the present findings suggest that tone-deafness may emerge as a pure output disorder, indicating that there may exist a variety of lifelong musical disorders, just as there are a variety of acquired musical disorders consequent to brain damage (see Stewart *et al.*, 2006, for a recent review).

An acoustically based analysis of sung performance proved to be useful to characterize singing proficiency in the general population. Furthermore, in order to obtain an optimal estimate of singing proficiency, one must control for tempo. As observed here, occasional singers performing at a fast tempo tend to make more errors than professional vocalists. This may lead to erroneously qualifying many occasional singers as poor singers. Hence, acoustically based analyses and tempo control should be adopted by researchers who are interested in the acoustical correlates of accurate singing to ensure a true measure of singing proficiency.

In summary, the present study indicates that singing in the general population is more accurate and widespread than is currently believed. The average person is able to carry a tune almost as proficiently as professional singers. This result is consistent with the idea that singing is a basic skill that develops in the majority of individuals, enabling them to engage in musical activities. In short, singing appears to be as natural as speaking with the added value of promoting social cohesion and activity coordination at a group level (Brown *et al.*, 2004; Peretz, 2006; Wallin *et al.*, 2000).

ACKNOWLEDGMENTS

This research was supported by an International Reintegration Grant (No. 14847) from the European Commission to S.D., by a grant from the Human Frontier Science program and Canadian Institutes for Health Research to I.P., and by a FCAR scholarship to J-F.G. We are particularly grateful to

Michel Jaspas for testing occasional singers from group 2.

¹An additional measure of *intranote pitch stability* was obtained from the SD of the extracted fundamental frequency within a vowel group. Average intranote pitch stability for occasional singers (group 1=4.6 Hz, *SE* =0.2 Hz; group 2=5.9 Hz, *SE*=0.3) was within two standard deviations from the mean of professional singers (average intranote pitch stability= 5.9 Hz, range= 2.4–9.2 Hz). Nonetheless, this measure is difficult to interpret since intranote pitch stability does not distinguish between abnormal pitch fluctuations (e.g., random changes) and deliberate pitch variations for expressive purposes (e.g., vibrato).

²G.V.'s performance recorded for the purposes of our study (see Table I) is very representative of his recordings. Nevertheless, G.V. sang "Gens du pays" in F Major instead of G Major. Since listeners are more likely to be exposed to recordings, we used the frequent version for comparison.

- Alcock, K. J., Passingham, R. E., Watkins, K., and Vargha-Khadem, F. (2000a). "Pitch and timing abilities in inherited speech and language impairment," *Brain Lang* **75**(1), 34–46.
- Alcock, K. J., Wade, D., Anslow, P., and Passingham, R. E. (2000b). "Pitch and timing abilities in adult left-hemisphere dysphasic and right-hemisphere damaged subjects," *Brain Lang* **75**(1), 47–65.
- Amir, O., Amir, N., and Kishon-Rabin, L. (2003). "The effect of superior auditory skills on vocal accuracy," *J. Acoust. Soc. Am.* **113**(2), 1102–1108.
- Aschersleben, G., Stenneken, P., Cole, J., and Prinz, W. (2002). "Timing mechanisms in sensorimotor synchronization," in *Common Mechanisms in Perception and Action, Attention and Performance XIX*, edited by W. Prinz and B. Hommel (Oxford U. P., New York), pp. 227–244.
- Ayotte, J., Peretz, I., and Hyde, K. (2002). "Congenital amusia: a group study of adults afflicted with a music-specific disorder," *Brain* **125**(2), 238–251.
- Bergeson, T. R., and Trehub, S. E. (2002). "Absolute pitch and tempo in mothers' songs to infants," *Psychol. Sci.* **13**(1), 72–75.
- Boersma, P. (1993). "Accurate short-term analysis of the fundamental frequency and the harmonics-to-noise ratio of a sampled sound," *Proceedings of the Institute of Phonetic Sciences (University of Amsterdam)* **17**, 97–110.
- Boersma, P. (2001). "Praat: a system for doing phonetics by computer," *Glot Int.* **5**(9/10), 341–345.
- Bradshaw, E., and McHenry, M. A. (2005). "Pitch discrimination and pitch-matching abilities of adults who sing inaccurately," *J. Voice* **14**(3), 431–439.
- Brown, S., Martinez, M. J., Hodges, D. A., Fox, P. T., and Parsons, L. M. (2004). "The song system of the human brain," *Brain Res. Cognit. Brain Res.* **20**, 363–375.
- Brown, W. S., Jr., Rothmann, H. B., and Sapienza, C. (2000). "Perceptual and acoustic study of professionally trained versus untrained voices," *J. Voice* **14**(3), 301–309.
- Dowling, W. J. (1999). "The development of music perception and cognition," in *The Psychology of Music*, edited by D. Deutsch (Academic, San Diego), pp. 603–625.
- Drake, C., and Palmer, C. (2000). "Skill acquisition in music performance," *Cognition* **74**, 1–32.
- Flowers, P. J., and Dunne-Sousa, D. (1990). "Pitch-pattern accuracy, tonality, and vocal range in preschool children's singing," *J. Res. Mus. Edu.* **38**, 102–114.
- Foxton, J. M., Dean, J. L., Gee, R., Peretz, I., and Griffiths, T. D. (2004). "Characterization of deficits in pitch perception underlying 'tone deafness'," *Brain* **127**, 801–810.
- Gabrielsson, A. (1999). "The performance of music," in *The Psychology of Music*, edited by D. Deutsch (Academic, San Diego), pp. 501–602.
- Halpern, A. R. (1989). "Memory for the absolute pitch of familiar songs," *Mem. Cognit.* **17**(5), 572–581.
- Hebert, S., Racette, A., Gagnon, L., and Peretz, I. (2003). "Revisiting the dissociation between singing and speaking in expressive aphasia," *Brain* **126**(8), 1838–1850.
- Jones, M. R., and Pfordresher, P. Q. (1997). "Tracking melodic events using Joint Accent Structure," *Can. J. Exp. Psychol.* **51**, 271–291.
- Kalmus, H., and Fry, D. B. (1980). "On tune deafness (dysmelodia): frequency, development, genetics and musical background," *Ann. Hum. Genet.* **43**, 369–382.
- Kinsella, G., Prior, M. R., and Murray, G. (1988). "Singing ability after

- right and left sided brain damage. A research note," *J. Appl. Mech. Tech. Phys.* **24**(1), 165–169.
- Levitin, D. J. (1994). "Absolute memory for musical pitch: Evidence from the production of learned melodies," *Percept. Psychophys.* **56**, 414–423.
- Levitin, D. J., and Cook, P. R. (1996). "Memory for musical tempo: Additional evidence that auditory memory is absolute," *Percept. Psychophys.* **58**, 927–935.
- Mendes, A. P., Rothman, H. B., Sapienza, C., and Brown, W. S., Jr. (2003). "Effects of vocal training on the acoustic parameters of the singing voice," *J. Voice* **17**(4), 529–543.
- Mithen, S. (2006). *The Singing Neanderthals* (Harvard U. P., Cambridge, MA).
- Murayama, J., Kashiwagi, T., Kashiwagi, A., and Mimura, M. (2004). "Impaired pitch production and preserved rhythm production in a right brain-damaged patient with amusia," *Brain Cogn* **56**, 36–42.
- Murbe, D., Friedemann, P., Hofmann, G., and Sundberg, J. (2002). "Significance of auditory and kinesthetic feedback to singers' pitch control," *J. Voice* **16**, 44–51.
- Murry, T. (1990). "Pitch-matching accuracy in singers and nonsingers," *J. Voice* **4**, 317–321.
- Murry, T., and Zwiner, P. (1991). "Pitch matching ability of experienced and inexperienced singers," *J. Voice* **5**, 197–202.
- Ostwald, P. F. (1973). "Musical behavior in early childhood," *Dev. Med. Child Neurol.* **15**, 367–375.
- Pardo, B., Shifrin, J., and Birmingham, W. (2004). "Name that tune: A pilot study in finding a melody from a sung query," *J. Am. Soc. Inf. Sci. Technol.* **55**(4), 283–300.
- Parncutt, R., and McPherson, G. E. (2002). *The Science and Psychology of Music Performance: Creative Strategies for Teaching and Learning* (Oxford U. P., New York).
- Peretz, I. (2001). "Brain specialization for music: New evidence from Congenital Amusia," *Ann. N.Y. Acad. Sci.* **930**, 189–192.
- Peretz, I. (2006). "The nature of music from a biological perspective," *Cognition* **100**(1), 1–32.
- Peretz, I., and Hyde, K. (2003). "What is specific to music processing? Insights from congenital amusia." *Trends Cogn. Sci.* **7**(8), 362–367.
- Peretz, I., and Kolinsky, R. (1993). "Boundaries of separability between melody and rhythm in music discrimination: A neuropsychological perspective," *Q. J. Exp. Psychol. A* **46**, 301–325.
- Peretz, I., Ayotte, J., Zatorre, R., Mehler, J., Ahad, P., Penhune, V., and Jutras, B. (2002). "Congenital amusia: A disorder of fine-grained pitch discrimination," *Neuron* **33**, 185–191.
- Prior, M., Kinsella, G., and Giese, J. (1990). "Assessment of musical processing in brain-damaged patients: implications for laterality of music," *J. Clin. Exp. Neuropsychol* **12**(2), 301–312.
- Repp, B. H. (1998). "A microcosm of musical expression. I. Quantitative analysis of pianists' timing in the initial measures of Chopin's Etude in E major," *J. Acoust. Soc. Am.* **104**(2), 1085–1100.
- Schon, D., Lorber, B., Spacal, M., and Semenza, C. (2003). "Singing: A selective deficit in the retrieval of musical intervals," *Ann. N.Y. Acad. Sci.* **999**, 189–192.
- Sloboda, J. A., Wise, K. J., and Peretz, I. (2005). "Quantifying tone deafness in the general population," *Ann. N.Y. Acad. Sci.* **1060**, 255–261.
- Stewart, L., von Kriegstein, K., Warren, J. D., and Griffiths, T. D. (2006). "Music and the brain: disorders of music listening," *Brain* **129**(10), 2533–2553.
- Sundberg, J. (1987). *The Science of the Singing Voice* (Northern Illinois U. P., DeKalb, IL).
- Sundberg, J. (1999). "The perception of singing," in *The Psychology of Music*, edited by D. Deutsch (Academic, San Diego), pp. 171–214.
- Ternstrom, S., Sundberg, J., and Collden, A. (1988). "Articulatory F0 perturbations and auditory feedback," *J. Speech Hear. Res.* **31**, 187–192.
- Timmers, R., Ashley, R., Desain, P., and Heijink, H. (2000). "The influence of musical context on tempo rubato," *J. New Music Res.* **29**(2), 131–158.
- Todd, N. (1985). "A model of expressive timing in tonal music," *Music Percept.* **3**(1), 33–58.
- Vigneault, G., and Rochon, G. (1976). *Gens du pays* (People from the country, Score) (Editions du vent qui tourne, Montreal).
- Vurma, A., and Ross, J. (2006). "Production and perception of musical intervals," *Music Percept.* **23**(4), 331–344.
- Wallin, N. L., Merker, B., and Brown, S. (2000). *The Origins of Music* (MIT P., Cambridge, MA).

A mechanistic analysis of stone fracture in lithotripsy

Oleg A. Sapozhnikov

Department of Acoustics, Physics Faculty, Moscow State University, Leninskie Gory, Moscow, 119992, Russia

Adam D. Maxwell, Brian MacConaghy, and Michael R. Bailey^{a)}

Center for Industrial and Medical Ultrasound, Applied Physics Laboratory, University of Washington, 1013 Northeast 40th Street, Seattle, Washington 98105

(Received 17 July 2006; revised 7 November 2006; accepted 9 November 2006)

In vitro experiments and an elastic wave model were used to analyze how stress is induced in kidney stones by lithotripsy and to test the roles of individual mechanisms—spallation, squeezing, and cavitation. Cylindrical U30 cement stones were treated in an HM-3-style lithotripter. Baffles were used to block specific waves responsible for spallation or squeezing. Stones with and without surface cracks added to simulate cavitation damage were tested in glycerol (a cavitation suppressive medium). Each case was simulated using the elasticity equations for an isotropic medium. The calculated location of maximum stress compared well with the experimental observations of where stones fractured in two pieces. Higher calculated maximum tensile stress correlated with fewer shock waves required for fracture. The highest calculated tensile stresses resulted from shear waves initiated at the proximal corners and strengthened along the side surfaces of the stone by the liquid-borne lithotripter shock wave. Peak tensile stress was in the distal end of the stone where fracture occurred. Reflection of the longitudinal wave from the distal face of the stone—spallation—produced lower stresses. Surface cracks accelerated fragmentation when created near the location where the maximum stress was predicted. © 2007 Acoustical Society of America.

[DOI: 10.1121/1.2404894]

PACS number(s): 43.80.Gx [CCC]

Pages: 1190–1202

I. INTRODUCTION

Despite over 20 years of clinical practice and fundamental research, a complete physical explanation of stone comminution by lithotripsy remains unknown. Incomplete understanding is evidenced by rising retreatment rates despite the release of over 40 lithotripter designs over the history of shock wave lithotripsy (SWL).^{1–3} The goal of this paper is to explain how a specific stone fractures by using a theoretical model to simulate the combined effect of many mechanisms and by using the model and experiment to test the role of individual already-described mechanisms of inducing the stress that leads to stone fracture.

Stone fracture is similar to fracture of any brittle object and can be considered as a process whereby cracks form, grow, and coalesce as a result of internal stresses, in this case, generated by the externally applied lithotripter shock wave (Fig. 1). Cracks are presumed to initiate at locations where the stress exceeds a critical value. Cracks grow and coalesce under the repetitive loading and unloading in a process called dynamic fatigue, and common practice indicates several lithotripter shock waves are required to fracture stones.⁴ Generally, the process of crack growth can be studied using existing methods of fracture mechanics, for instance, using the cohesive zone model.^{5–7} Although the described scenario of fracture is agreed upon, this knowledge in

itself does not help in predicting stone fragmentation without knowing the mechanisms of how appropriate stresses are generated inside the stone.

A. Direct physical mechanisms of shock-wave-induced stress

Several physical mechanisms, i.e., ways stresses leading to stone fracture are generated, have been proposed, but there is no consensus on the roles of these various mechanisms. The two primary mechanisms directly resulting from the shock wave (SW) and investigated here are spallation due to reflections of longitudinal waves within the stone^{8,9} and squeezing due to circumferential stresses generated by shock waves outside the stone.¹⁰

In spallation, the distal surface of a stone in liquid or tissue is an acoustically soft interface, generating a reflected tensile wave from the initially compressive longitudinal shock pulse (Fig. 1) that enters and propagates through the stone.¹¹ With a flat distal surface, spallation yields a maximum tension within the stone where the reflected tensile wave overlaps the negative tail (Fig. 1) of the incident wave; the distance of this maximum from the distal surface, l , is fixed by the pulse length alone: $l = c_l \Delta t / 2$, where c_l is longitudinal wave speed in the stone and Δt is time delay between the positive and negative peaks in the acoustic waveform. For instance, if $c_l = 3 \text{ mm}/\mu\text{s}$ (typical value for kidney stones), then for the waveform of Fig. 1 that has $\Delta t \approx 2 \mu\text{s}$, this formula predicts $l \approx 3 \text{ mm}$, which is close to the experimental observations. The predicted spall-formed failure sur-

^{a)}Electronic mail: bailey@apl.washington.edu

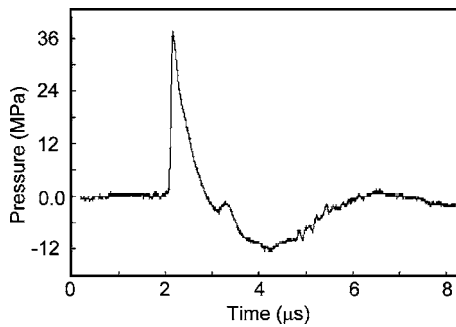


FIG. 1. Shock wave generated by an HM-3-clone lithotripter and measured by PVDF membrane hydrophone in water. An initial positive pressure spike of $1 \mu\text{s}$ is followed by a negative pressure trough of roughly $4 \mu\text{s}$.

face is orthogonal to the shock wave propagation and appears close to the distal surface of the stone. With a curved distal stone surface, the position of the maximum depends on the curvature, and the maximum can be intensified by focusing of the reflected wave.^{12–14}

In squeezing, the shock wave is assumed to be broader but shorter than the stone and travels in liquid along the side surface of the stone creating circumferential stress on the stone.¹⁰ Eisenmenger¹⁰ supposed that the wave velocity in the fluid is much lower than the elastic wave velocities in the stone, i.e., the longitudinal wave moves through the stone leaving the thin shock wave in the fluid encircling and squeezing the stone in a quasi-static manner. As a result, tensile stresses are created near the proximal and distal ends of the stone, which gives rise to a fracture parallel to the wave-propagation direction.

There is experimental evidence for both mechanisms. The spallation mechanism is supported by the fact that generally stones appear to break first in two pieces with the fracture in the distal end of the stone. Figure 2 shows a typical break for a cylindrical U30 model stone.¹⁵ A fracture occurred about one-third of the length from the distal end and has frequently been attributed to spallation.^{8,9,16} A lithotripter designed to emphasize the squeezing mechanism with a broad (less-focused) shock wave that extends laterally well beyond the width of the stone has been shown to be clinically efficacious,¹⁷ and modeling shows squeezing could account for the observed fracturing in half of stones.^{10,18} Nei-



FIG. 2. (Color online) Typical fracture pattern for a U30 model stone treated fixed at the focus of an HM-3 clone lithotripter. The proximal face (left) has cavitation pitting. The stone is fractured in two pieces about $1/3$ of the length from the distal end.

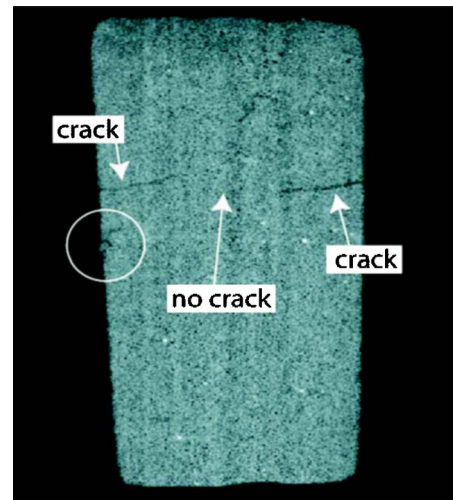


FIG. 3. (Color online) Micro-computed tomography image of a U30 model stone treated in an HM-3-clone lithotripter before the stone fractured in two pieces. Cracks are apparent extending outside of the stone toward the axis of the stone at about $1/3$ of the length from the distal end. Used with permission from Robin Cleveland (Ref. 25).

ther mechanism alone explains both these results, which supports either a combination of these two mechanisms or a separate mechanism.

B. Indirect physical mechanisms of shock-wave-induced stress

In addition to the direct mechanisms, the lithotripter produces cavitation that can generate stress in the stone and cause fracture.¹⁹ Cavitation—of individual bubbles or clusters of bubbles in fluid near the stone surface—creates localized pressure and stress waves that diverge. Localized stress initiated at the stone surface can be created by direct impact of a fluid jet formed by asymmetric bubble or cloud collapse, and stress can be created by SWs generated by asymmetric or symmetric collapse. SWs are generated by the halting of the intruding fluid by the compressed contents of a symmetric bubble or by the water jet forcibly impinging the fluid on the opposite side of an asymmetric bubble. These SWs can have much higher peak pressures than the lithotripter shock wave; however, individual collapse emissions are spherically diverging and lose amplitude rapidly with propagation distance.²⁰ Cavitation, by these mechanisms, induces stress at a localized region on the stone surface.

As with the direct mechanisms, there is substantial evidence cavitation plays a role in stone comminution in SWL. Stones have been shown not to fragment when cavitation is suppressed by static pressure,²¹ viscous fluid,²² or shock wave modification.^{23,24} Pits and fractures in the proximal face of the stone (Fig. 2) have commonly been attributed to cavitation. Here, we focus on the fracture in two pieces at the distal surface. X-ray computed tomography images of U30 model stones treated in a Dornier HM-3-clone lithotripter indicate that these fractures grow from the surface of the stone inward (Fig 3).²⁵ Pishchalnikov *et al.*,²⁶ with a similar HM-3-clone lithotripter, observed not only a substantial jet through a large cavitation cluster on the proximal face of the U30 stone but a ring of bubbles around the stone near the

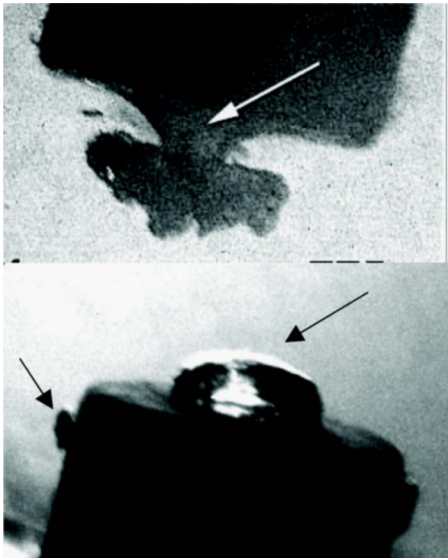


FIG. 4. (Color online) High-speed photography of the cavitation clouds on the proximal end (top) and distal end (bottom) of a U30 stone following passage of a lithotripter SW. Entrained bubbles reveal the fluid jet impinging on the proximal surface as the cloud collapses. A band of bubbles can be seen encircling the stone near where cracks are seen in Fig. 3 and where fracture occurred in Fig. 2. Used with permission from the Journal of Endourology (Ref. 26).

distal end (Fig. 4). The jet was approximately 1 mm in diameter, and other evidence indicates jet velocities can reach 100 m/s.^{27,28} Spherically diverging shock waves resulting from bubble collapse were observed with shadowgraph imaging. Experiments also showed that cracks were generated at the proximal and side surfaces. Sapozhnikov *et al.*²⁹ used the linear elasticity model described in this paper to determine that elastic waves in the stone created a low pressure that encircled the stone near the distal end. This low pressure yielded a particularly long growth and collapse cycle in a single bubble modeled with the Gilmore equation,^{20,30} and was therefore used to explain the existence of the cloud ring encircling the stone. It is not known whether the cavitation collapse on the proximal surface imparts stress that leads to fracture of the distal end or if pitting by the cavitation ring contributes to this fracture.

C. Effort to model stone comminution in SWL

Numerical models reveal information perhaps not detected in experiments and make possible parametric studies of the effect of variables difficult or time-consuming to control in experiments. For example, the following models developed specifically for application to SWL have been used to simulate effects of varying the shock wave delivery rate, numbers of cavitation bubbles, stone shape, stone material, lithotripter waveform, and beamwidth. Tanguay and Colonius³¹ have coupled a prediction of the acoustic field with a model of the bubble cloud behavior near a rigid stone surface, and predicted an optimal shock wave delivery rate. Zabolotskaya *et al.*³² have focused on the bubble-bubble interactions near a rigid stone. Dahake and Gracewski^{12,13} developed a linear elastic model of stress waves within the stone that they tested against spherical and oval model

stones. LeVeque³³ has coupled nonlinear acoustic and nonlinear elastic models in what is called CLAWPACK and has reported initial results of medical shock wave interaction with bones. Cleveland and Sapozhnikov¹⁸ recently modified the linear elastic approach in order to pinpoint the location of maximum stress for comparison with the location of initial fracture in model stones.

D. Scope of this paper

In this paper, action of a shock wave on a stone is studied using a finite difference model in the approximation of linear elasticity, and by visual observation of fracture in U30 model stones. First, the theoretical model is used to describe as a whole the mechanisms involved in producing the maximum stress in the stone. Second, the role of individual mechanisms is tested numerically and experimentally. The end point of the experiments was fracture of the stone into two pieces as shown in Fig. 2 or a predetermined maximum number of SWs without fracture. Location of the calculated maximum stress is compared to the location of fracture determined experimentally, and relative amplitude of the maximum stress is compared to number of SWs to fracture. The scope is restricted to the first fracture into two pieces, not full comminution, of a specific stone model of one shape and composition. If suppressing one mechanism did not cause an increase in the SWs required for fracture, it was interpreted that the mechanism was of lesser importance and could not alone explain the fracture. The following hypotheses were tested.

If spallation is the sole mechanism: Stones will fracture at the distal end as shown in Fig. 2 (Spallation Test 1). Stones of different length will fracture the same distance from the distal end (Spallation Test 2). Blocking transmission of the SW through most of the proximal face will increase the number of SWs to fracture (Spallation Test 3).

If squeezing is the sole mechanism: Blocking transmission of the squeezing wave will increase the number of SWs to fracture (Squeezing Test 1). The shape of the tip or the tail of the stone will not alter the number of SWs to fracture (Squeezing Test 2). Blocking the entire proximal face of the stone will not alter the number of SWs to fracture (Squeezing Test 3).

If cavitation is the sole mechanism: Jet impact will produce high stress in the region of fracture (Cavitation Test 1).

If cracks formed by cavitation are significant in fracture: Stones in a cavitation suppressing medium will have a higher number of SWs to fracture than stones in a cavitating medium (Cavitation Test 2). Stones with surface cracks but in a cavitation suppressing medium will have the same number of SWs to fracture as stones initially without surface cracks in a cavitation supporting medium (Cavitation Test 3).

II. THEORY

A. Description of the model

A linear elastic model was used to simulate the stress wave propagation within a kidney stone. The model is described in the paper by Cleveland and Sapozhnikov.¹⁸ Here,

we summarize the model, list the material properties used, and describe the predicted parameters to be compared to experiment.

Kidney stones exhibit a brittle behavior, i.e., little or no visible plastic deformation precedes the fracture;^{7,34} therefore, linear elasticity is a reasonable model to the point of stone failure. The stone and surrounding liquid are considered as an isotropic medium. The dynamics of such a medium is governed by the equation of motion

$$\rho \frac{\partial v_i}{\partial t} = \frac{\partial \sigma_{ij}}{\partial x_j}, \quad (1)$$

where $i, j=1, 2, 3$, ρ is medium density, $v_i = \partial u_i / \partial t$ are medium velocity components (u_i are displacement vector components), and σ_{ij} are components of stress tensor. In the linear approximation, that is valid for small strains, elastic forces are governed by Hooke's law:

$$\sigma_{ij} = \lambda (\nabla \cdot \mathbf{u}) \delta_{ij} + \mu \left(\frac{\partial u_i}{\partial x_j} + \frac{\partial u_j}{\partial x_i} \right). \quad (2)$$

Here λ and μ are the Lamé constants (μ is also called the shear modulus), and δ_{ij} is the Kronecker delta function. Note that the stress tensor is symmetric: $\sigma_{ij} = \sigma_{ji}$, i.e., only six of the nine tensor components are independent. We suppose that the stone has an axisymmetric shape with the axis oriented along the initial shock wave propagation. It is convenient to use polar coordinates (r, z, θ) , where r and z are the radial and axial distances and θ is the polar angle. Because of the axial symmetry of the problem, the velocity vector has only two components—radial, v_r , and axial, v_z , and only four stress tensor components are nonzero: σ_{rr} , σ_{zz} , $\sigma_{\theta\theta}$, and σ_{rz} . Equations (1) and (2) can be written in the following form suitable for the numerical implementation:

$$\frac{\partial v_r}{\partial t} = \rho^{-1} \left\{ \frac{1}{r} \frac{\partial [r(\sigma_{rr} - \sigma_{\theta\theta})]}{\partial r} + \frac{\partial \sigma_{rz}}{\partial z} + \frac{\partial \sigma_{\theta\theta}}{\partial r} \right\}, \quad (3)$$

$$\frac{\partial v_z}{\partial t} = \rho^{-1} \left\{ \frac{1}{r} \frac{\partial (r\sigma_{rz})}{\partial r} + \frac{\partial \sigma_{zz}}{\partial z} \right\}, \quad (4)$$

$$\frac{\partial \sigma_{rr}}{\partial t} = \lambda \left(\frac{1}{r} \frac{\partial (rv_r)}{\partial r} + \frac{\partial v_z}{\partial z} \right) + 2\mu \frac{\partial v_r}{\partial r}, \quad (5)$$

$$\frac{\partial \sigma_{zz}}{\partial t} = \lambda \frac{1}{r} \frac{\partial (rv_r)}{\partial r} + (\lambda + 2\mu) \frac{\partial v_z}{\partial z}, \quad (6)$$

$$\frac{\partial \sigma_{\theta\theta}}{\partial t} = \lambda \frac{\partial v_z}{\partial z} + (\lambda + 2\mu) \frac{1}{r} \frac{\partial (rv_r)}{\partial r} - 2\mu \frac{\partial v_r}{\partial r}, \quad (7)$$

$$\frac{\partial \sigma_{rz}}{\partial t} = \mu \left(\frac{\partial v_z}{\partial r} + \frac{\partial v_r}{\partial z} \right). \quad (8)$$

When the stone is surrounded by liquid, appropriate boundary conditions should be used for velocities and forces. However, it is more convenient and valid to consider the liquid and stone as one inhomogeneous medium whose parameters ρ , λ , and μ are functions of the spatial coordinates. In this approach there is no need to consider the stone bound-

ary separately, i.e., the boundary conditions are accounted for automatically.¹⁸ This approach also allows introducing inhomogeneity to the stone structure. Here, only uniform U30 stones are modeled and the physical properties are density $\rho = 1700 \text{ kg/m}^3$, longitudinal sound speed $c_l = [(\lambda + 2\mu)/\rho]^{1/2} = 2630 \text{ m/s}$, shear wave speed $c_s = (\mu/\rho)^{1/2} = 1330 \text{ m/s}$, which corresponds to $\lambda = 5.8 \text{ GPa}$, and $\mu = 3.9 \text{ GPa}$. Values for water are $\rho = 1000 \text{ kg/m}^3$, sound speed in liquid $c_l = 1500 \text{ m/s}$, and $\lambda = 2.25 \text{ GPa}$.¹⁸ Water is assumed not to support shear: $\mu = 0$. All calculations are lossless.

To solve Eqs. (3)–(8) in finite differences, the partial differential equations are discretized using a central differencing scheme with staggered grids both in space and in time.^{18,35} Velocity and stress in the stone are initially set to zero. The initial conditions in the liquid correspond to the traveling shock pulse. Although arbitrary initial pressure distribution is possible, in this paper we suppose that the initial pulse is a plane wave. This approximation is supported by the existence of a Mach stem during weak shock focusing in a Dornier HM3 lithotripter.⁴ It is supposed that a lithotripter shock wave is initially located in the liquid 5 mm to the left of the stone and propagates to the right as a plane wave. For such a plane wave, $\sigma_{rr} = \sigma_{zz} = \sigma_{\theta\theta} = -P(t + (z_* - z)/c_l)$, $\sigma_{rz} = 0$, $v_r = 0$, and $v_z = (\rho c_l)^{-1} P(t + (z_* - z)/c_l)$. The acoustic pressure waveform $P(t)$ at the initial position $z = z_*$ was a classic lithotripsy pulse modified with a hyperbolic tangent function to provide a smooth shock front:²⁰ $P(t) = (P_0/2)[1 + \tanh(t/t_s)] \exp(-t/t_L) \cos(2\pi f_L t + \pi/3)$, where P_0 is peak pressure, t_s is the shock front thickness, and $t_L = 1.1 \mu\text{s}$ and $f_L = 83.3 \text{ kHz}$ control the pressure waveform. The wave is an analytical approximation to the measured wave shown in Fig. 1. We used $P_0 = 50 \text{ MPa}$, which is roughly the amplitude produced by our lithotripter,³⁶ and $t_s = 100 \text{ ns}$, which is the rise-time measured *in vivo*.³⁷

Elastic waves in a cylindrical U30 stone with diameter 6.5 mm and length 8.5 mm were modeled. The calculation region was a cylinder of 20 mm diameter and 30 mm length, and calculations were completed before reflections from the region boundary reached the stone. The typical spatial grid step was $h_z = h_r = 50 \mu\text{m}$ and the temporal step was $h_t = 0.5 h_z / c_l \approx 10 \text{ ns}$, which was sufficient to maintain stability and accuracy.

In this paper, the maximum principal tensile stress is the value reported. In the considered axisymmetric case, the three principal stresses are: $\sigma_{I,II} = (\sigma_{zz} + \sigma_{rr}) / 2 \pm \sqrt{((\sigma_{zz} - \sigma_{rr})/2)^2 + \sigma_{rz}^2}$ and $\sigma_{III} = \sigma_{\theta\theta}$. The maximum principal tensile stress $\sigma_{\max} = \max(\sigma_I, \sigma_{III})$ is an appropriate parameter to characterize shock wave impact on kidney stones, because brittle materials, such as kidney stones, are typically weakest in tension. Calculated results reported here show σ_{\max} on a discretized slice of the stone at a snapshot in time, for various subsequent times. The stress σ_{\max} is plotted on a fixed scale blue -70 MPa to red $+70 \text{ MPa}$, where minus indicates compression. In the on-line version color images are used on a scale blue -70 MPa to red $+70 \text{ MPa}$. The stress field at the instant of peak σ_{\max} is referred to as the peak stress field. The field plotted as the maximum tension recorded over the duration of the simulation at each location in the stone is referred to as the max field and indicates where

the highest tension occurred. Other relevant parameters such as maximum strain or maximum shear stress do not produce markedly different stress field maps.¹⁸ To aid interpretation of the results, the divergence of the particle velocity was used to identify waves traveling at the longitudinal wave speed, and the curl of the particle velocity was used to identify waves at the shear wave speed.¹⁸

B. Test of mechanisms

Table I shows the simulated experiments conducted to test the nine hypotheses. Diameter of the cylindrical portion of all stones was 6.5 mm. Acoustically reflective disks and baffles were simulated as pressure release media with low wave velocities: $c_l=3$ m/s and $c_t=1.5$ m/s. For Cavitation Test 1, a 1-mm-diam cylinder of fluid with velocity 100 m/s normal to the stone was modeled impacting the stone. In this case alone, the lithotripter shock wave was not modeled; only the stress induced by direct impact of the fluid jet on the stone was calculated. This jet is a simplified model of the complex cavitation process, but it is intended to give an approximation to the localized stress created in cavitation collapse. Cavitation Test 3 was simulated with the stone in glycerol ($\rho=1260$ kg/m³, $c_l=1980$ m/s) and with the stone in water. Both showed similar stress concentration at the cracks. Results of the stone in water are shown for simpler comparison to the other figures.

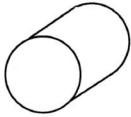
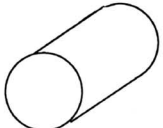
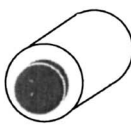
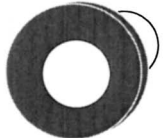
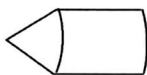

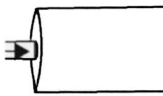
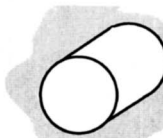
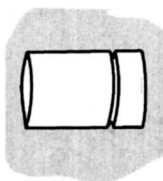
III. MATERIALS AND METHODS

Experiments were conducted in the water bath of a research lithotripter³⁶ modeled after the unmodified (80 nF capacitor) Dornier HM3 electrohydraulic lithotripter (Dornier GmbH, Germany). The reflector was mounted in the tank so that the acoustic axis was horizontal, normal to gravity. Experiments were conducted at 1-Hz repetition frequency and 18 kV charging potential. Room temperature water was filtered through 10 μ m pores before filling the tank and conditioned to 600 μ S/cm and a 25%–30% gas saturation level. Refurbished electrodes (Service Trends, Kennesaw, GA) were used after conditioning with 150 shock waves and were replaced after 2000 shock waves.

Model stones were made from Ultracal-30 (U30) gypsum (United States Gypsum, Chicago, IL). The only modification to the recipe defined by McAteer *et al.*¹⁵ was the use of a plastic mold with pieces that were separated to remove the stones rather than using chloroform to dissolve plastic molds [Fig. 5(a)]. As described previously,¹⁵ the U30 gypsum was mixed for 10 min, poured into molds, and allowed to solidify under water for 24 h. Also as described previously,¹⁵ the gypsum settled some in formation and the lower surface of the stones was slightly harder than the upper surface of the stone. The stones were stored under water and then were removed briefly to place them in the lithotripter bath. Separate stones were dried and resubmerged for 48 h and produced statistically the same results as stones that were never dried. All stones were used within two weeks of preparation.

To test the nine hypotheses listed in Table I, stones of the shapes and dimensions described in Table I were made.

TABLE I. Description and illustration of the numerical tests of the nine hypotheses. Dark objects are acoustically reflective barriers. The proximal face, where the shock wave enters, is circular and on the left facing to different degrees out of the page.

Test	Location and amplitude of σ_{\max} were calculated for	Illustration
Spallation Test #1	stones 6.5 mm in diameter, 8 mm long and cylindrical in shape (standard stones).	
Spallation Test #2	stones of lengths 8-18 mm.	
Spallation Test #3	standard stones with an acoustically reflective disk (1 mm thickness, diameter 4.5 mm) centered on the proximal face of the stone.	
Squeezing Test #1	standard stones with an acoustically reflective disk (1 mm thickness, inner diameter 6.5 mm, outer diameter 25 mm) placed around the proximal face of the stone, leaving the proximal face exposed.	
Squeezing Test #2	standard stones with a conical point on the proximal or distal third of the 8 mm long stone.	
Squeezing Test #3	standard stones with an acoustically reflective disk (1 mm thickness, diameter 6.5 mm) centered on the proximal face of the stone.	
Cavitation Test #1	a water jet (1-mm diameter, 100 m/s velocity) impacting the proximal face of the stone, normal to the face along the axis of the stone.	
Cavitation Test #2	standard stones in glycerol.	
Cavitation Test #3	standard stones in glycerol with a 0.5 mm V-shaped groove encircling the stone either 4 mm, 3 mm or 2 mm from the distal end.	

All cylindrical stones were positioned in the lithotripter with the hard surface (the lower end in preparation) facing the shock source. In Squeezing Test 2, the conical point was the hard surface and pointed either toward or away from the source. In Cavitation Tests 2 and 3, stones were dried for 1 week, placed in 2 mm of glycerol for 1 day to permit wicking into the stone, and then submerged in glycerol for a week. In Cavitation Test 3, a razor blade and a plastic stone holder were used to score a groove encircling stones 2, 3, or

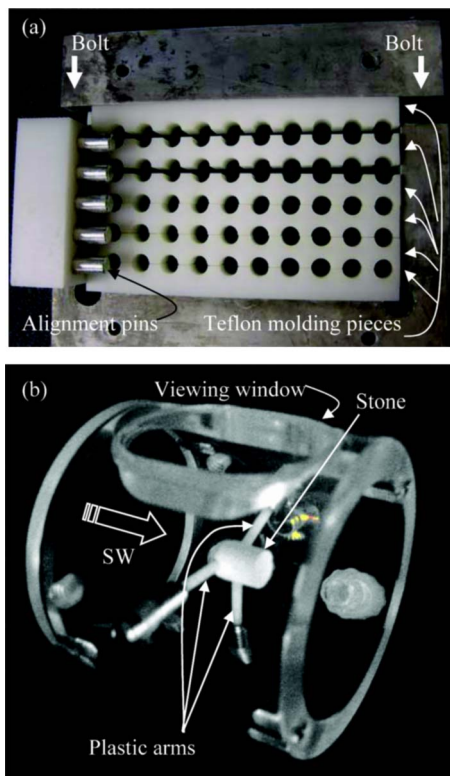


FIG. 5. (Color online) Photographs of the plastic molds used here to form U30 stones (a) and of the holder used to position the stones in the focus of the lithotripter (b). Molds had six white Teflon™ pieces aligned by pins and held in an aluminum frame closed by bolts. The holder had three spring-loaded arms to hold the stone repeatedly but with little interference to the SW.

4 mm from the distal end. The groove was nearly triangular in cross section with a 0.5 mm depth and maximum width of 0.5 mm. In Spallation Test 2 and Squeezing Test 3, the stones were dried for 2 days; a 1-mm-thick corprene disk was glued with epoxy on the proximal face of the stone and allowed to dry for 1 day; and then stone and disk were submerged in water for 1 week. In Squeezing Test 1, a 1-mm-thick corprene baffle was fit without glue around a wet stone. SW pressure transmission through the corprene measured by hydrophone was less than 5%. A number of stones, N , were tested for each experiment, and the number of SWs to fracture were recorded for each stone. Average number for several stones is presented as mean \pm standard deviation.

Stones were fixed axisymmetrically in the acoustic field with the proximal face at the external focus of the lithotripter. The specially designed stone holder was a 5-cm-diam polycarbonate ring with three spring loaded plastic arms that held the proximal edge of the stone with repeatable force [Fig. 5(b)]. The 2-mm-diam arms could be mounted at two positions along the 5 cm length of the holder (4 and 25 mm from the holder aperture). For Cavitation Tests 2 and 3, the holder was capped with foodservice plastic wrap (25 μ m high density polyethylene) and filled with glycerol. Trapped air bubbles were removed through ports in the holder. For the glycerol experiments only, the stone was held with the arms 4 mm from the plastic wrap in an effort to minimize the length of the path through the glycerol, which is more attenu-

ative than water. Glycerol has been used by other researchers to suppress cavitation to investigate comminution mechanisms in SWL.^{20,22}

A CCD camera (Sony CCD-IRIS, Nikon 28-80 lens) mounted outside the acrylic water-filled lithotripter tank recorded movies to laptop computer (ULead card and software, Torrance, CA). The number of SWs to fracture and the position of this fracture along the length of the stone were recorded. The position of the break was also measured from the recovered fragments. The experimental end point was detecting fracture or completing a fixed maximum number of SWs without detecting fracture. The number was fixed for each test but varied from 200 to 250 to 300 between tests. Specific limits are listed with the results.

IV. RESULTS

A. Mechanism described by the numerical model

Figure 6 includes a sequence of images showing the shock-wave-induced maximum principal stress within a U30 stone at specific times. The corresponding time is written in the upper right corner of each frame. At $t=0$ a longitudinal wave propagating in water approaches the stone. Then it enters the stone ($t=1 \mu$ s) and moves ahead of the shock wave in water, because the longitudinal speed in the stone is higher than the sound speed in water. When this longitudinal wave reaches the back end of the stone, it reflects and inverts ($t=4 \mu$ s), creating a thin vertical region of tensile stress indicated by the dashed arrow. This process is called spallation. The region is faint indicating low tensile stress, and the stress does not change greatly over the distal third of the stone. Following the longitudinal wave is a conical wake, compressive in the water and tensile in the stone (marked by arrows at $t=3 \mu$ s) that is generated at the surface of the stone, where the longitudinal wave travels faster than the shear wave in the stone and the sound wave in water and therefore creates a “supersonic” source at the stone surface. Traveling at the sound speed in water along the stone surface and encircling the stone is the shock wave (marked by dotted arrows at $t=1 \mu$ s), and it creates squeezing. The frame at 2μ s yields little time for dynamic wave effects to develop and is therefore the best frame to compare to the static idea of squeezing. In this frame the stress due to squeezing is low amplitude and localized near the surface of the stone. Shear waves generated at the proximal corners of the stone (shown by solid arrows at $t=4 \mu$ s), track the shock wave propagation along the surface of the stone, and focus in the distal half of the stone ($t=5 \mu$ s). Because the shear wave speed in the stone is close to the sound speed in water, the squeezing wave reinforces the shear wave and this shear wave adds to the weaker stress due to spallation to create the highest tensile stress within the stone. The peak σ_{\max} is 100 MPa, is on axis, and is 3.5 mm from the distal surface.

This result of the model can be termed “dynamic squeezing.”¹⁸ Here, the predicted process is labeled “full model.” The peak σ_{\max} occurs 3.5 mm from the distal end on axis. The shortest route to the stress release of the stone surface is in the radial direction. Thus, an orthogonal fracture at 3.5 mm is the most logical interpretation. The modeled

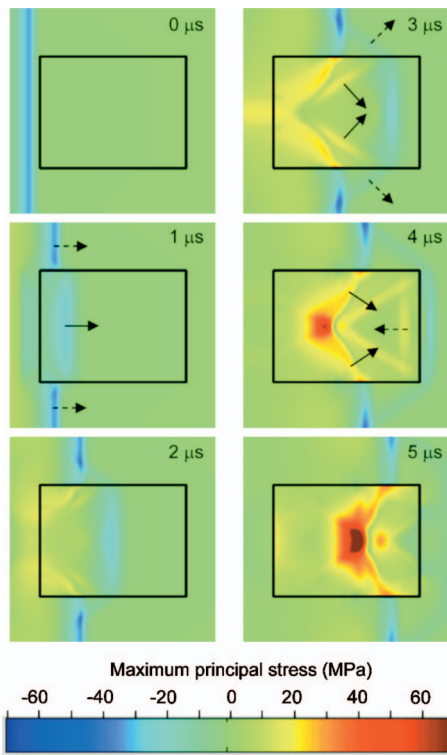


FIG. 6. Calculated results showing the maximum principal stress σ_{\max} in a slice of the stone in a time sequence. The stress σ_{\max} is plotted on a fixed scale blue -70 MPa to red $+70$ MPa, where minus indicates compression. In the on-line version color images are used on a scale blue -70 MPa to red $+70$ MPa. The SW contacts the stone at $t=0$. The arrows in some of the frames indicate direction of propagation of specific waves, with each arrow starting at the corresponding wave front. At $t=1 \mu\text{s}$, the solid arrow represents the compression longitudinal wave in the stone, and two dotted arrows outside the stone show the compression associated with the shock wave propagating in liquid. This wave gives rise to the dynamic squeezing effect. At $t=3 \mu\text{s}$, arrows show two leaky waves that are generated on the stone surface by the longitudinal wave propagating inside the stone: The dotted arrows show the divergent conical wave front of a pressure wave in water and the solid arrow indicates the convergent conical wave front of a shear wave in the stone. At $t=4 \mu\text{s}$, solid arrows start at the wave front of the convergent shear wave that is generated at the proximal corner of the stone and reinforced by the longitudinal wave propagating in water (shown by dotted arrow in $1 \mu\text{s}$ frame), this wave creates the highest tensile stress and can be interpreted as dynamic squeezing. The dotted arrow at $t=4 \mu\text{s}$ shows a longitudinal wave of tension that appears because of reflection of the compression wave from the distal end of the stone; this wave is associated with the “spallation” mechanism. The region of high tension seen at $t=5 \mu\text{s}$ in the central part of the stone is a result of the shear dynamic squeezing wave with little contribution from the longitudinal spallation wave.

time sequence (Fig. 6) illustrates that spallation and squeezing are present, but the shear wave initiated by the corners of the stone and driven by the squeezing wave traveling along the stone (dynamic squeezing) leads to the greatest stress. In the Sec. IV B, tests of the roles of these individual mechanisms and the interpretation of the simulation are reported.

B. Test of mechanisms

The results are summarized in Table II. Data were found to support and to contradict each mechanism. However, the process described by the linear elastic model consistently explained the results.

TABLE II. Summary of results: A plus sign indicates support of a mechanism, and a minus sign indicates contradiction of a mechanism. Results do not support any one of the three mechanisms completely, but the results are consistently explained by the linear elastic model.

Test	Spallation	Squeezing	Cavitation	Full model
Spallation Test 1	+			+
Spallation Test 2	-			+
Spallation Test 3	-			+
Squeezing Test 1	-	+		+
Squeezing Test 2		-		+
Squeezing Test 3		-		+
Cavitation Test 1			-	
Cavitation Test 2			+	
Cavitation Test 3			+	+

If spallation is the sole mechanism, stones will fracture at the distal end as shown in Fig. 2 (Spallation Test 1): All standard stones fractured in two at the distal end (Fig. 2) with what has been termed classic spall fracture or spalling.¹⁶ Standard stones yielded a peak σ_{\max} of 100 MPa, 3.5 mm from the distal surface (modeling), and fractured normal to the cylinder axis after 45 ± 10 SWs ($N=10$) at 3.6 ± 0.2 mm from the distal surface (experiment). Location of fracture agreed well with the location of calculated maximum tension.

This result is the most compelling evidence for spallation. The fracture location is in excellent agreement with the distance $l \approx 3$ mm from the distal end that was predicted for a plane wave in Sec. I. The location is also in good agreement with the broad location of the maximum stress due to spallation seen in the simulation. The region is broad because the negative tail of the shock wave is long.

However, when the model was used to track stress produced only by the longitudinal wave and its reflection, what we have defined as spallation, the maximum tension is much lower, less than 50 MPa. In fact, according to the modeling, the true maximum stress induced by reflection of the longitudinal wave occurs within 1 mm of the distal end and does not exceed 20 MPa. The reason is a shortening of the longitudinal wave due to diffraction at the stone edges. Thus, the full model predicts the location of maximum stress that agrees well with the location of fracture, and the fracture looks like spallation. But the model indicates that the spallation mechanism is not solely responsible and contributes only a small portion of tension where the fracture occurs.

If spallation is the sole mechanism, stones of different length will fracture the same distance from the distal end (Spallation Test 2): Although stones of different lengths broke with classic spall fracture, fracture in longer stones occurred farther from the distal end. The result contradicted spallation. Figure 7 shows the results. Although the predicted location of maximum tension due to spallation is constant in all stone lengths, fracture was farther from the distal end in longer stones. The result that fracture distance increased with stone length was also observed by Xi and Zhong¹⁴ with larger cylindrical stones.

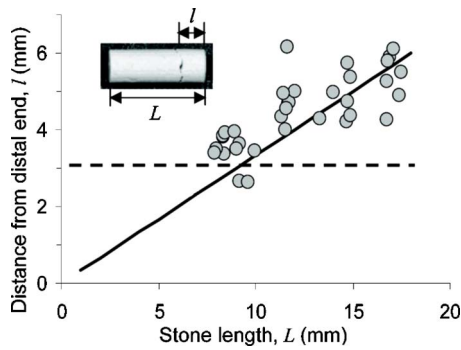


FIG. 7. (Color online) Plot of the distance, l , between the fracture and the distal end vs stone length, L . The fracture occurs farther from the distal end for longer stones whereas spallation should occur repeatedly at the same distance, 3.1 mm, based on only the shock wavelength (dotted line). The solid line corresponds to the distance $l=L/3$.

Figure 7 shows fracture occurred consistently approximately 1/3 of the length from the distal end. Calculated peak σ_{\max} did the same. This one-third point is the location where the shear wave traveling at 1330 m/s meets the reflected longitudinal wave traveling at 2630 m/s. The constructive interference of these two waves produced the peak σ_{\max} as seen in Fig. 6 ($t=5 \mu\text{s}$). The simulations show that both the reflected wave and the focused shear wave maintain a level amplitude for several millimeters around the one-third point.

If spallation is the sole mechanism, blocking transmission of the SW through most of the proximal face will increase the number of SWs to fracture (Spallation Test 3): In the corresponding experiment a 4.5 mm corprene disk was placed on the proximal surface of the stones and prevented the longitudinal SW, responsible for spallation, from entering the stone, yet stone fracture was unchanged with and without the disk, which indicates the fracture mechanism was not spallation. With the shield in place it took 50 ± 20 SWs ($N=8$) to break the stone and the fracture was 3.5 ± 0.1 mm from the distal end, which was not significantly different from the case without the baffle. Comparison of Fig. 6 and the left column of Fig. 8 shows that although the longitudinal wave is attenuated by the small proximal disk, the location and amplitude of peak σ_{\max} were little affected. Calculations, both with and without the baffle, yielded peak σ_{\max} equal to 100 MPa at distance 3.5 mm from the distal end. Based on Spallation Tests 1–3, the fracture in these experiments does not appear to be due to spallation.

If squeezing is the sole mechanism, blocking transmission of the squeezing wave will increase the number of SWs to fracture (Squeezing Test 1): The result of the corresponding test supports squeezing. The baffle ringing the stone's proximal edge blocked the squeezing wave, and the stones did not fracture. The baffle did not cover the proximal or distal faces of the stone but presented a barrier to acoustic waves traveling in the water along the stone. The right column of Fig. 9 shows the calculations. The proximal baffle significantly reduced stress deep in the stone, and the stress produced with the distal baffle was very similar to the case without a baffle (Fig. 6). Correspondingly, no stones with the proximal baffle fractured before the maximum number of applied shock waves, 300, of this experiment ($N=3$). Stones

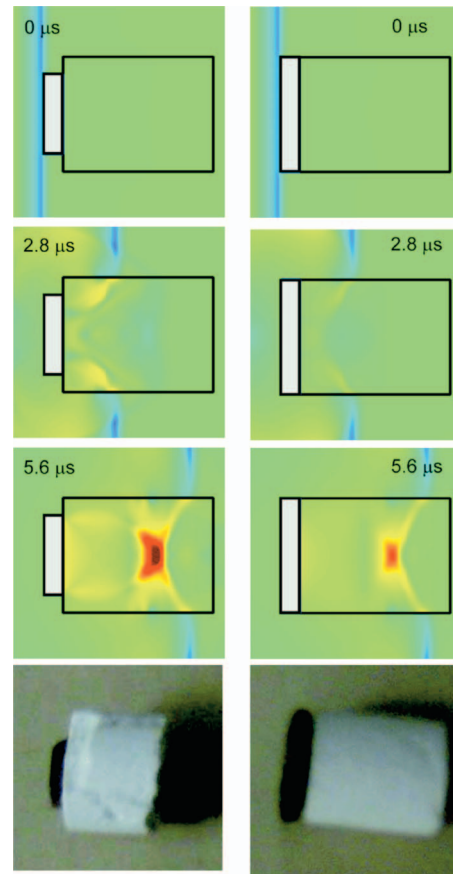


FIG. 8. The stress field calculation for Spallation Test 3 (left) and Squeezing Test 3 (right), where a small reflective disk is positioned on the proximal face of the stone to prevent transmission of the longitudinal wave responsible for spallation from entering the stone. Note no vertical longitudinal wave front is seen entering either stone. When the disk does not cover the proximal edge (disk 4.5 mm diameter, left) the stress pattern and amplitude does not differ significantly from Fig. 6, the maximum stress field without the disk. The calculation indicates spallation does not contribute significantly to the stress in the U30 stone. When the disk covers the entire front surface (disk 6.5 mm diameter, right), stress is still present inside the stone but at reduced amplitude. The result is not explained by static concept of squeezing. The photographs show the fractured stone with the small disk and a still intact stone with the large disk.

broke in 40 SWs with the distal baffle which was not statistically different from the results with no baffle.

The result indicates the squeezing wave is an important contributor; however, the simulations (Fig. 6) indicate that the maximum stress grows over time, which is not what would be expected of the static model of squeezing. Unlike a static field induced by hoop stress, the dynamic stress field in the simulations shows a shear wave generated at the corners of the stone and focusing toward the distal axis of the stone. The shear waves appear to be reinforced by the squeezing wave traveling along the edge of the stone at nearly the same speed as the shear wave speed. Thus, the mechanism is more complicated than and differs from the quasistatic squeezing mechanism proposed by Eisenmenger,¹⁰ but the source is the wave encircling the stone in both cases.

If squeezing is the sole mechanism, the shape of the tip or the tail of the stone will not alter the number of SWs to fracture (Squeezing Test 2): The result of this test did not support squeezing. Although the squeezing wave was little

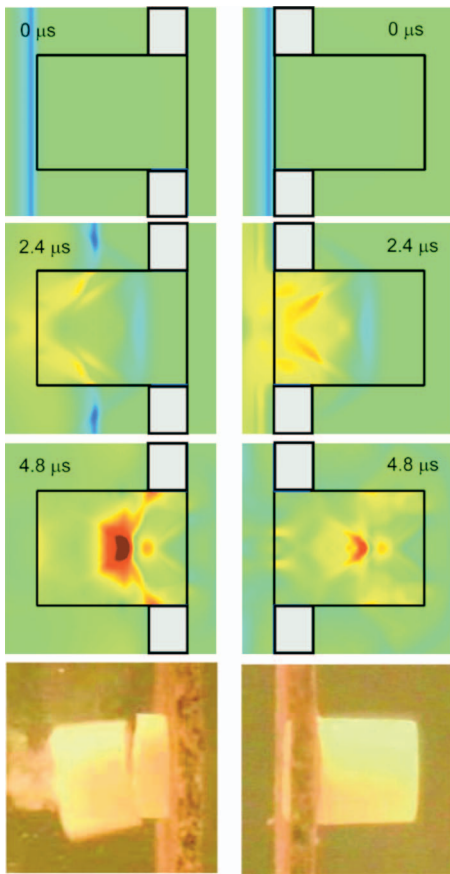


FIG. 9. Comparison of the stress field calculated for Squeezing Test 1 with a reflective baffle around the distal face (left) and proximal face (right) of the stone. The distal baffle case is little different from the no baffle case in Fig. 6. Adding the baffle on the proximal face blocks the squeezing wave and significantly reduces the stress particularly at the distal end of the stone. Thus inhibiting the squeezing wave, for example with a narrow focus, reduces the stress induced in the stone. The images at the bottom are photos of the stones taken during shock wave application. The 1-mm-thick baffle was made of corprene. The photograph on the left was taken at the time of fracture.

changed by the shape of the stone, stones with a proximal conical point required many more SWs to fracture than standard cylindrical stones or stones with a distal point. The stress induced by squeezing in conical stones is the same as in the cylindrical stones since it depends only on the SW amplitude in the water. Figure 10 shows the results of simulation and the images after fracture. With the conical tip on the proximal side, predicted stresses within the stone are very low, and no fracture was observed after 200 SWs ($N=3$), which was the maximum number applied. Although the distal end is cylindrical, the conical tip increases significantly the number of SWs required to fracture the stone. The time sequence of the simulations in Fig. 10 compared to those in Fig. 6 reveals that the tapered conical point did not produce a strong and focused shear wave as was generated at the corners of the blunt end of the cylindrical stone. High stresses were calculated on the distal surface and after ~ 25 SWs a crater 4 mm in diameter and <1 mm deep formed. With the tip on the distal end, high stresses, produced by the shear wave generated at the blunt proximal face, were calculated in the conical region, and the conical section fractured after 40 SWs.

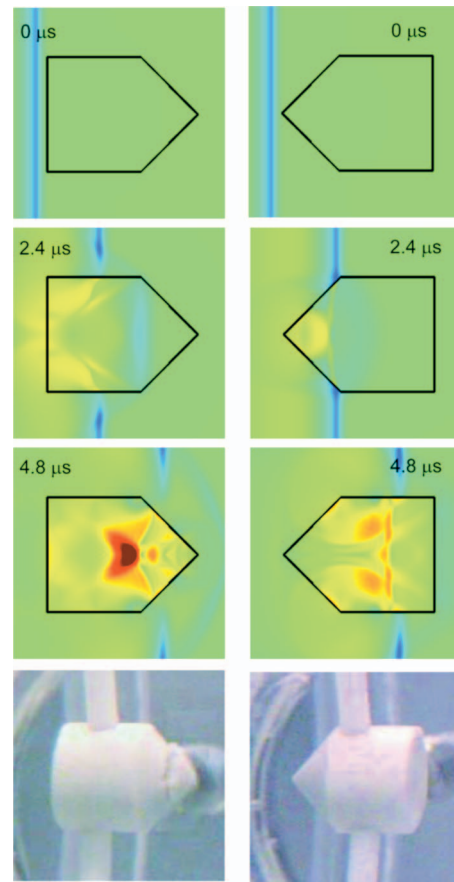


FIG. 10. The stress field calculated for a conical stone with the point distal (left) and proximal (right). The squeezing wave is unaffected in each but the stress is much less with the proximal point. The difference is that the proximal point does not create a strong shear wave, because it does not contain a sharp corner. The result with the distal point is little different from the cylindrical case Fig. 6. Focusing of the shear wave in the cylindrical and the distal conical cases is responsible for the peak tension. The stone in the left photograph shows fracture at the location of σ_{\max} , and the right stone did not fracture.

If squeezing is the sole mechanism, blocking the entire proximal face of the stone will not alter the number of SWs to fracture (Squeezing Test 3): The result of this test did not support static squeezing but supported that the fracture was caused by the shear wave initiated at the proximal corners and strengthened along the side surface of the stone by the liquid-borne lithotripter shock wave. With the whole face covered by a corprene disk, low stresses were predicted in the stone, and stones broke after 212 ± 53 SWs ($N=8$) including three cases where the stone had not broken after 250 SWs, the maximum in this experiment. The distal third of the stone also did not break cleanly from the stone; it splintered into about three pieces. The squeezing wave was largely unaltered as diffraction at the disk is small, but many more SWs were required to fracture the stone, because the shear wave was suppressed.

As a whole, these six tests are in agreement with simulations by the model and the description of the mechanism of creating maximum stress in the stone provided by the model. In the standard stone (Fig. 6, $t=5 \mu\text{s}$), the peak σ_{\max} was in the distal end where the fracture occurred. Stress due to spallation was calculated to be low, but added to the primary

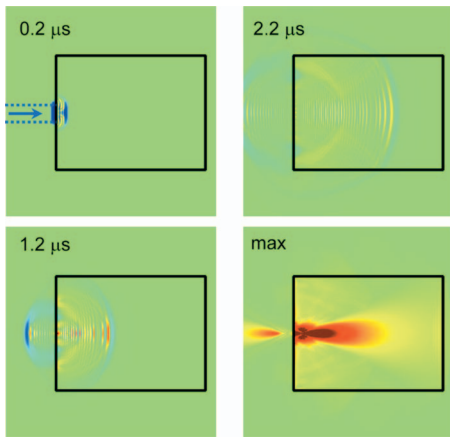


FIG. 11. Maximum principal stress induced by a 1-mm-diam fluid jet impacting upon the U30 stone surface at 100 m/s in a simulation of the fluid jet impact by a collapsing cavitation cloud as seen in Fig. 4(a). It is seen that the jet generates spherically divergent longitudinal (faster) and shear waves (slower) waves in the stone. The bottom-right image represents absolute maximum stress throughout time, the so-called max stress field. Stress is high but localized to the region of impact. Little stress is induced in the distal end where fracture occurred. However, cavitation-induced cracks in the surface may be critical to seeding fracture.

mechanism, which was dynamic squeezing where the shear wave focused from the corner of the proximal face and was reinforced by the squeezing wave. However, cavitation, likely present in the experiment but not present in the model, was not considered.

If cavitation is the sole mechanism, jet impact will produce high stress in the region of fracture (Cavitation Test 1): Although from the first few SWs, experiments showed pits on the proximal and distal surfaces, which is indicative of cavitation, simulation of a cavitation jet impact did not yield high stress at the distal end of the stone where fracture occurred. In Fig. 11 only, the model was used to simulate the force of a 100 m/s water jet (1 mm in diameter) impacting the stone. The result seen in Fig. 11 is that high maximum tension was localized to the region of jet impact. Significant stresses did not appear in the distal portion of the stone except on the distal surface. These distal stresses were due to surface shear waves traveling the surface of the stone and refocusing on the distal surface. As shown previously,^{12,13} the stress of impact in the stone acts as a point source, and losses due to divergence within the stone rapidly weaken the wave. Figure 11 shows some numerical dispersion, and a sufficiently small grid was not obtained to remove it. The dispersion weakens the wave artificially; nevertheless, there was no evidence that further refining the grid would reveal significant stress across the distal third of the stone. From this result, it is apparent cavitation contributes to the pitting erosion on the surface of the stone (Fig. 2) but does not appear to contribute directly or strongly to the fracture, because it induces no strong stress in the region of the crack.

If cracks formed by cavitation are significant in fracture, stones in a cavitation suppressing medium will have a higher number of SWs to fracture than stones in a cavitating medium (Cavitation Test 2): The corresponding experimental results supported that with cavitation suppressed stones took longer to fracture. Standard stones in glycerol required

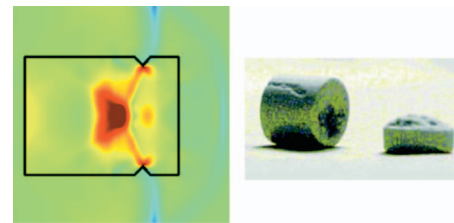


FIG. 12. A stone etched 2 mm from the distal end fractures in a conical shape (right) as illustrated by the modeled peak stress field at $t=5 \mu\text{s}$ (left). Stress concentrations appear at the tip of the etched cracks. The result indicates fractures grow between the point of maximum stress and surface cracks as may be generated by cavitation as illustrated in Fig. 4(b).

127 ± 57 SWs ($N=8$) to break. Vakil *et al.*²² also found many more SWs were required to fracture stones in glycerol. Although the previous test showed the cavitation collapse might not induce significant stresses within the stone, this test result indicates that surface pitting is important in fracture.

If cracks formed by cavitation are significant in fracture, stones with surface cracks but in a cavitation suppressing medium will have the same number of SWs to fracture as stones initially without surface cracks in a cavitation supporting medium (Cavitation Test 3): This test was positive. Stones with the etched band 2 mm from the distal surface required 17 ± 6 SWs ($N=8$) to break in glycerol. The fractures were conical as might be predicted by the calculated peak maximum tensile surface, a two-dimensional view of which is shown in Fig. 12. Thus with cavitation suppressed, the stones did not break unless an etched band (representing cavitation damage) was present, and the fracture pattern was predictable with the model.

When the etched band was placed 3 or 4 mm instead of 2 mm from the distal end, fracture was not as rapid. However in water, 17 ± 8 SWs ($N=5$) were required to break a stone with an etched band at 4 mm, which is not statistically different from the etched stone in glycerol. The sensitivity to location of the etch is likely due to the faster sound speed in glycerol, but the similarity in number of SWs to fracture indicates that glycerol had little effect other than to reduce cavitation. Simulations in glycerol also showed little effect, but a slight reduction in peak σ_{max} due to (1) loss at the slight acoustic impedance mismatch between water and glycerol and (2) the mismatch, and therefore reduced reinforcing, between the sound speed in glycerol and the shear wave speed in the stone.

C. Summary of results

Figures 13 and 14 show a summary of calculated results for some of the cases. Figure 13 shows peak maximum tensile stress that occurred at anytime during the simulation at every point in the field, the max stress field. Figure 14 shows an axial plot of these max stresses. The left column of Fig. 13 and the lines labeled a, b, and d in Fig. 14 show how little the stresses were changed by blocking the longitudinal wave from entering the stone or altering the distal end of the stone. In addition, stress is concentrated at the tips of cracks (top

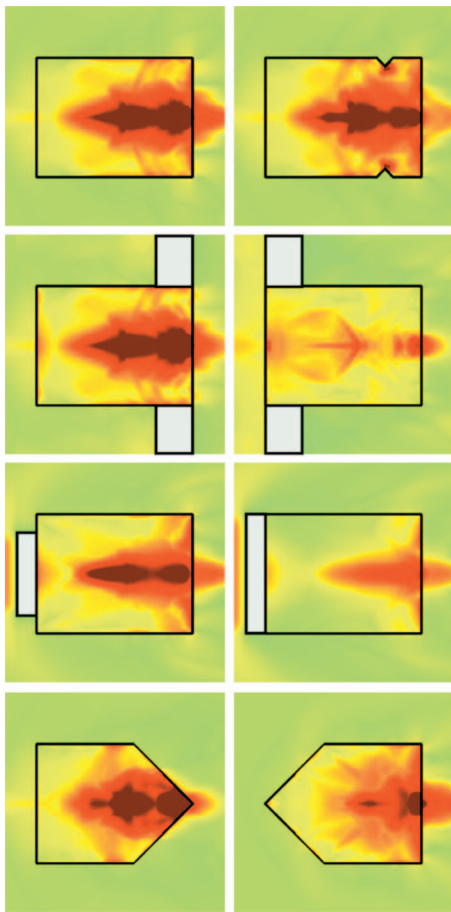


FIG. 13. Distribution of the absolute maximum throughout time of the maximum principal stress (tension) in various test stones. The max stress field is little changed by blocking the longitudinal wave entering the stone or altering the distal end of the stone as in the left column. In addition, stress is concentrated at the tips of cracks (top right). However, blocking the “squeezing” wave or preventing creation of a shear wave at the corners of the proximal face significantly reduces the stress (lower three frames in the right column). In addition, the elastic waves in the stone create high negative pressure (~ 50 MPa) in the liquid near the proximal and distal surfaces of the stone. Cavitation may be expected in these regions and is indeed observed (Ref. 26).

right in Fig. 13). However, the lower three frames in Fig. 13 and the lines labeled c and e in Fig. 14 show how dramatically the stress is reduced by blocking the “squeezing” wave or preventing creation of a shear wave at the corners of the proximal face. The lower right frame in Fig. 13 indicates that the squeezing wave is most important in creating the stress in that although the proximal corners are smooth and not abrupt, high stress is created and occurs near the distal end as the squeezing wave must travel over the length of the stone to generate the reinforcement and focusing.

In addition to the stress field in the stone, the negative pressures in liquid are of interest. The negative pressure of the planar shock wave is -10 MPa and is not particularly noticeable in Fig. 13. Instead the elastic waves in the stone generate negative pressures greater than -10 MPa in the fluid around the stone.²⁶ At the proximal and particularly the distal end of the stones negative pressure near -50 MPa is calculated and this is where particularly large and long-lasting cavitation bubbles are observed (Fig. 4).²⁶ In addition,

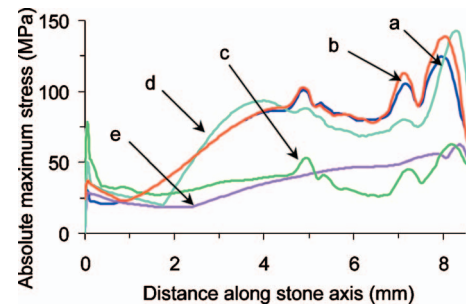


FIG. 14. Distribution of the absolute maximum throughout time of the maximum principal stress (tension) along cylindrical stone axis in various test conditions: (a) standard stone, (b) baffle encircling distal end, (c) baffle encircling proximal end, (d) 4.5 mm disk on the proximal face, and (e) 6.5 mm disk on the proximal face. Blocking the longitudinal wave responsible for spallation only minimally reduces the stress, (d). Blocking generation of the shear wave (e) from the proximal corners of the stone or blocking the squeezing wave (c) that drives the shear wave results in a significant reduction in stress in the stone.

tion, faint but still strong negative pressure can be seen ringing the stone on the distal end, which presumably contributes to the band of bubbles encircling the stone.²⁹

V. DISCUSSION AND CONCLUSIONS

A new mechanistic description of stress and fracture in cylindrical U30 stones in lithotripsy was reported. The description is that shear waves generated at corners in the boundary of the stone are reinforced by the SW in water traveling along the surface of the stone and focus to generate the highest stress in the distal end of the stone. It was argued that a fracture plane results between the maximum stress and the stone surface. The description is the result of calculation based on linear elasticity theory. Although some in the lithotripsy community have been content that energy density (temporal and spatial integral of the pressure squared divided by the focal beam width)³⁸ of the conventional lithotripsy shock wave correlates with stone comminution,¹⁶ this model shows how the energy is applied is important and leads to different mechanisms of action. Long ago, Griffith³⁹ introduced an energy concept to fracture mechanics that we apply here to kidney stones and that states that the fracture growth depends on the elastic energy (associated with tension) applied to the material. However, the important energy is that associated with the tension in the stone and not the initial energy in the shock wave applied to the stone. The tension in the stone was adequately described by the model but is not simply related to the SW energy or energy density: it depends on the shock waveform as shown by Sapozhnikov and Cleveland¹⁸ and on beamwidth as shown here as well. If the beamwidth of the lithotripter is narrower than the stone then dynamic squeezing—the dominant mechanism in this study—cannot contribute.

A series of experiments tested the result of the theoretical model versus already defined mechanisms—spallation, squeezing, and cavitation—of inducing stress in the stone. Some test results could be explained by spallation or squeezing, but other tests could not. The results of the model were consistent with all the tests. A SW beamwidth broader than the stone was critical to maximizing the stress in the stone.

Test results did not support that cavitation on the proximal end generated stress that led to fracture seen on the distal end of the stone. However, results did support that cavitation pitting on the surface led to stress concentrations from which fractures grow. It should be noted that multiple localized stresses resulting from many cavitation bubbles along the surface of the stone as seen in experiments²⁶ were not simulated and could possibly sum to generate considerable stress deep within the stone.

The mechanisms were specifically and rigorously defined. Although the model includes shear in general, the mechanism related to shear discussed here was shear waves generated at the boundary of the stone. Spallation is the creation of tension due by the interference of the longitudinal wave and its inverted reflection. Squeezing is a static concept of stress induced by a narrow band of pressure encircling the stone. Others have dismissed squeezing from outside the stone and attributed comminution entirely to spallation by loosely defining spallation as “shear and tear,”¹⁶ in other words all stress within the stone. However, this broad definition of spallation essentially means the comparison could be restated as stress in the stone is more important than stress outside the stone, which is obvious. Our results with the rigorous definition of the mechanisms show that shear waves reinforced by squeezing and to a small extent constructively interfering with the reflected longitudinal wave lead to the maximum stress. The location of this peak maximum principal tensile stress, not the location of the maximum stress of spallation, agrees with the location of the “spall fracture” or fracture in two at the distal end.

Our experiment was also specific. The end point was the first fracture into two pieces of a specific stone, fixed in a specific position, in specific fluid conditions, in a specific lithotripter. The controlled conditions provided for a careful test of the model and of mechanisms of breakage. The excellent correlation of calculated high stress to few shock waves to fracture and the location of high stress to the location of fracture in these controlled tests gives confidence in the model. From here, the use of the model might be extended.

For example, repeated calculations might be used to simulate the comminution process. (It is important to note here that one case of axisymmetric simulations shown in Figs. 6 and 8–10 takes fewer than 10 min on a 2 GHz personal computer, i.e., the modeling is fairly fast.) Our study neglected how the role of each mechanism may change with repetitive shock waves and stone breakage. Appearance of a crack will reflect the shock wave and prevent its propagation deeper in the stone; the stress distribution would then change. In repetitive SW application, cavitation plays two additional roles. With repetitive shock waves especially at fast clinical rates, bubbles do not have sufficient time to dissolve between consecutive shock waves, and absorption and scattering of the acoustic energy by the bubbles can reduce the pressure that reaches the stone.^{31,40–42} Also, cavitation may play an increasingly important role as stones fragment and become smaller.⁴³ Elastic wave propagation is suppressed as stones approach the size of a wavelength, but surface forces, such as generated by cavitation, are not a function of stone size.¹⁸ However, a series of simulations,

where perhaps the SW amplitude is diminished to simulate shielding and stone size is reduced to simulate fragmentation, may reveal how the dominant mechanism changes during treatment.

The model may be used to test the parameter space of stone material, stone shapes, shock wave beamwidths, and more, in ways not reasonable by experiments. It may be gleaned from our results that the shear wave so important in the cylindrical stone would be less important in the spherical stone because shear waves were generated at sharp edges in the stone boundary. Calculations would be further refined by including a simulation of cavitation activity^{31,32} and fracture dynamics.⁶ Currently, simulation could be useful in treatment planning. For example, focal beamwidth, which is adjustable on some current machines, might be changed based on a diagnostic image of the stone and a calculation of the stress produced in the stone. In the future, real-time imaging and simulation could direct changes to the beamwidth or the shock waveform during treatment.

In summary, it was reported that a theoretical model accurately described the physical mechanism leading to observed stone fracture. None of the specific mechanisms, spallation, squeezing, or cavitation, completely described the fracture. The results of the model were more useful than these descriptors.

ACKNOWLEDGMENTS

The authors would like to thank the many members of the Consortium on Shock Waves in Medicine and the Center for Industrial and Medical Ultrasound for discussions, research help, and guidance on this paper. In particular, we would like to thank Professor James A. McAteer, Dr. Yuriy A. Pishchalnikov, and Professor James C. Williams, Jr. (Indiana University School of Medicine) for guidance in preparing U30 stones, Professor Robin Cleveland for collaboration in developing the numerical code, and Fran Olson for design and fabrication of much of the experimental apparatus. The work was supported by NIH Grant Nos. DK43881 and DK55674, NSBRI Grant No. SMS00402, an NIH Fogarty International Research Collaboration Award, an ONR International Field Office Visiting Scientist grant, a CRDF grant, and RFBF grants.

¹K. Kerbl, J. Rehman, J. Landman, D. Lee, C. Sundaram, and R. V. Clayman, “Current management of urolithiasis: Progress or regress?,” *J. Endourol* **16**, 281–288 (2002).

²A. P. Evan, J. A. McAteer, J. C. Williams, L. R. Willis, M. R. Bailey, L. A. Crum, J. E. Lingeman, and R.O. Cleveland, “Shock wave physics of lithotripsy: Mechanisms of shock wave action and progress toward improved SWL,” in *Textbook of Minimally Invasive Urology*, edited by R. Moore, J. T. Bishoff, S. Loening, and S. G. Docimo (Martin Dunitz, London, 2004), Chap. 28, pp. 425–438.

³J. A. McAteer, J. C. Williams, Jr., M. R. Bailey, R. O. Cleveland, and A. P. Evan, “Strategies for improved shock wave lithotripsy,” *Minerva Urol. Nefrol* **57**, 271–279 (2005).

⁴B. Sturtevant, “Shock wave physics of lithotripters,” in *Smith’s Textbook of Endourology*, edited by A. D. Smith (Quality Medical Publishing, St. Louis, 1996), pp. 529–552.

⁵G. I. Barenblatt, “The mathematical theory of equilibrium cracks in brittle fracture,” *Adv. Appl. Mech.* **7**, 55–129 (1962).

⁶M. Ortiz, “Microcrack coalescence and macroscopic crack growth initiation in brittle solids,” *Int. J. Solids Struct.* **24**, 231–250 (1988).

⁷M. Lokhandwalla and B. Sturtevant, “Fracture mechanics model of stone

- commutation in ESWL and implications for tissue damage," *Phys. Med. Biol.* **45**, 1923–1940 (2000).
- ⁸C. Chaussy, E. Schmiedt, D. Jocham, V. Walther, W. Brendel, B. Forssmann, and W. Hepp, *Extracorporeal Shock Wave Lithotripsy: New Aspects of the Treatment of Kidney Stone Disease*, edited by C. Chaussy (Karger, Basel, 1982).
- ⁹M. Delius, G. Heine, and W. Brendel, "A mechanism of gallstone destruction by extracorporeal shock waves," *Naturwiss.* **75**, 200–201 (1988).
- ¹⁰W. Eisenmenger, "The mechanisms of stone fragmentation in ESWL," *Ultrasound Med. Biol.* **27**, 683–693 (2001).
- ¹¹H. Kolsky, *Stress Waves in Solids* (Dover, New York, 1963).
- ¹²G. Dahake and S. M. Gracewski, "Related articles finite difference predictions of P-SV wave propagation inside submerged solids. I. Liquid-solid interface conditions," *J. Acoust. Soc. Am.* **102**, 2125–2137 (1997).
- ¹³G. Dahake and S. M. Gracewski, "Finite difference predictions of P-SV wave propagation inside submerged solids. II. Effect of geometry," *J. Acoust. Soc. Am.* **102**, 2138–2145 (1997).
- ¹⁴X. Xi and P. Zhong, "Dynamic photoelastic study of the transient stress field in solids during shock wave lithotripsy," *J. Acoust. Soc. Am.* **109**, 1226–1239 (2001).
- ¹⁵J. A. McAteer, J. C. Williams, Jr., R. O. Cleveland, J. Van Cauwelaert, M. R. Bailey, D. A. Lifshitz, and A. P. Evan, "Ultrasound-30 gypsum artificial stones for lithotripsy research," *Urol. Res.* **33**, 429–434 (2005).
- ¹⁶J. J. Rassweiler, G. G. Tailly, and C. Chaussy, "Progress in lithotripter technology," *EAU Update Series* **3**, 17–36 (2005).
- ¹⁷W. Eisenmenger, X. X. Du, C. Tang, S. Zhao, Y. Wang, F. Rong, D. Dai, M. Guan, and A. Qi, "The first clinical results of 'wide focus and low pressure' ESWL," *Ultrasound Med. Biol.* **28**, 769–774 (2002).
- ¹⁸R. O. Cleveland and O. A. Sapozhnikov, "Modeling elastic waves in kidney stones with application to shock wave lithotripsy," *J. Acoust. Soc. Am.* **118**, 2667–2676 (2005).
- ¹⁹L. A. Crum, "Cavitation microjets as a contributory mechanism for renal calculi disintegration in ESWL," *J. Urol. (Baltimore)* **140**, 1587–1590 (1988).
- ²⁰C. C. Church, "A theoretical study of cavitation generated by an extracorporeal shock wave lithotripter," *J. Acoust. Soc. Am.* **86**, 215–227 (1989).
- ²¹M. Delius, "Minimal static excess pressure minimises the effect of extracorporeal shock waves on cells and reduces it on gallstones," *Ultrasound Med. Biol.* **23**, 611–617 (1997).
- ²²N. Vakil and E. C. Everbach, "Transient acoustic cavitation in gallstone fragmentation: A study of gallstones fragmented *in vivo*," *Ultrasound Med. Biol.* **19**, 331–342 (1993).
- ²³M. R. Bailey, "Control of acoustic cavitation with application to lithotripsy," Technical Report No. ARL-TR-97-1, Applied Research Laboratories, The University of Texas at Austin, Austin, TX and Defense Technical Information Center, Belvoir, VA, 1997.
- ²⁴X. F. Xi and P. Zhong, "Improvement of stone fragmentation during shock wave lithotripsy using a combined EH/PEAA shock wave generator—in vitro experiments," *Ultrasound Med. Biol.* **26**, 457–467 (2000).
- ²⁵R. O. Cleveland and J. van Cauwelaert, "Fragmentation mechanisms of kidney stones in shock wave lithotripsy can be detected with microCT X-ray imaging," *Proceedings of the Joint German Convention on Acoustics and Congrès Français d'Acoustique (CFA)*, Strasbourg, France, 2004, edited by D. Cassereau and M. Kob, Vol. 2, pp. 981–982.
- ²⁶Y. A. Pishchalnikov, O. A. Sapozhnikov, J. C. Williams, Jr., A. P. Evan, J. A. McAteer, R. O. Cleveland, T. Colonius, M. R. Bailey, and L. A. Crum, "Cavitation bubble cluster activity in the breakage of kidney stones by lithotripter shock waves," *J. Endourol.* **17**, 435–446 (2003).
- ²⁷J. R. Blake and D. C. Gibson, "Cavitation bubbles near boundaries," *Annu. Rev. Fluid Mech.* **19**, 99–123 (1987).
- ²⁸A. Philipp, M. Delius, C. Scheffczyk, A. Vogel, and W. Lauterborn, "Interaction of lithotripter-generated shock waves with air bubbles," *J. Acoust. Soc. Am.* **93**, 2496–2508 (1993).
- ²⁹O. A. Sapozhnikov, R. O. Cleveland, M. R. Bailey, and L. A. Crum, "Numerical modeling of stresses generated by lithotripter shock wave in cylindrical kidney stone," *Third International Symposium on Therapeutic Ultrasound*, Lyon, France, 2004, pp. 323–328.
- ³⁰F. R. Gilmore, "The growth or collapse of a spherical bubble in a viscous compressible liquid," *California Institute of Technology Report No. 26–4*, 1952, pp. 1–40.
- ³¹M. Tanguay and T. Colonius, "Progress in modeling and simulation of shock wave lithotripsy (SWL)," *Fifth International Symposium on Cavitation (CAV2003)*, Osaka, Japan, 2003, <http://iridium.me.es.osaka-u.ac.jp/cav2003/index1.html>; paper OS-2–1–010. Last viewed 1/19/2007.
- ³²E. A. Zabolotskaya, Yu. A. Ilinskii, G. D. Meegan, and M. F. Hamilton, "Bubble interactions in clouds produced during shock wave lithotripsy," *Proc.-IEEE Ultrason. Symp.* **2**, 890–893 (2004).
- ³³R. J. LeVeque, *Finite Volume Methods for Hyperbolic Problems* (Cambridge University Press, New York, 2002).
- ³⁴F. Ebrahimi and F. Wang, "Fracture behaviour of urinary stones under compression," *J. Biomed. Mater. Res.* **23**, 507–521 (1989).
- ³⁵J. Vireux, "P-SV wave propagation in heterogenous media: Velocity stress finite-difference method," *Geophysics* **51**, 889–901 (1986).
- ³⁶R. O. Cleveland, M. R. Bailey, N. Fineberg, B. Hartenbaum, M. Lokhandwalla, J. A. McAteer, and B. Sturtevant, "Design and characterization of a research electrohydraulic lithotripter patterned after the Dornier HM3," *Rev. Sci. Instrum.* **71**, 2514–2525 (2000).
- ³⁷R. O. Cleveland, D. A. Lifshitz, B. A. Connors, A. P. Evan, L. R. Willis, and L. A. Crum, "*In vivo* pressure measurements of lithotripsy shock waves in pigs," *Ultrasound Med. Biol.* **24**, 293–306 (1998).
- ³⁸International Electrotechnical Committee, "Ultrasonics—pressure pulse lithotripters—characteristics of fields," *IEC Standard No. 61846*, 1998.
- ³⁹A. A. Griffith, "The phenomenon of rupture and flow in solids," *Philos. Trans. R. Soc. London, Ser. A* **221**, 163–198 (1920).
- ⁴⁰R. F. Paterson, D. A. Lifshitz, J. E. Lingeman, A. P. Evan, B. A. Connors, J. C. Williams, Jr., and J. A. McAteer, "Stone fragmentation during shock wave lithotripsy is improved by slowing the shock wave rate: Studies with a new animal model," *J. Urol. (Baltimore)* **168**, 2211–2215 (2002).
- ⁴¹O. A. Sapozhnikov, V. A. Khokhlova, M. R. Bailey, J. C. Williams, Jr., J. A. McAteer, R. O. Cleveland, and L. A. Crum, "Effect of overpressure and pulse repetition frequency on shock wave lithotripsy," *J. Acoust. Soc. Am.* **112**, 1183–1195 (2002).
- ⁴²Y. A. Pishchalnikov, O. A. Sapozhnikov, M. R. Bailey, I. V. Pishchalnikova, J. C. Williams, Jr., and J. A. McAteer, "Cavitation selectively reduces the negative-pressure phase of lithotripter shock pulses," *ARLO* **6**, 280–286 (2005).
- ⁴³S. L. Zhu, F. H. Cocks, G. M. Preminger, and P. Zhong, "The role of stress waves and cavitation in stone comminution in shock wave lithotripsy," *Ultrasound Med. Biol.* **28**, 661–671 (2002).

The freshwater dolphin *Inia geoffrensis geoffrensis* produces high frequency whistles

Laura J. May-Collado^{a)}

Florida International University, Department of Biological Sciences, 11200 SW 8th Street, Miami, Florida 33199 and Universidad de Costa Rica, Escuela de Biología, Apto. 2060 San Pedro, Costa Rica

Douglas Wartzok

Florida International University, Department of Biological Sciences, 11200 SW 8th Street, Miami, Florida 33199

(Received 20 May 2006; revised 31 October 2006; accepted 11 November 2006)

Because whistles are most commonly associated with social delphinids, they have been largely overlooked, ignored, or presumed absent, in solitary freshwater dolphin species. Whistle production in the freshwater dolphin, the boto (*Inia geoffrensis geoffrensis*), has been controversial. Because of its sympatry with tucuxi dolphins (*Sotalia fluviatilis*), a whistling species, some presume tucuxi whistles might have been erroneously assigned to the boto. Using a broadband recording system, we recorded over 100 whistles from boto dolphins in the Yasuní River, Ecuador, where the tucuxi dolphins are absent. Our results therefore provide conclusive evidence for whistle production in *Inia geoffrensis geoffrensis*. Furthermore, boto whistles are significantly different from tucuxi whistles recorded in nearby rivers. The Ecuadorian boto whistle has a significantly greater frequency range (5.30–48.10 kHz) than previously reported in other populations (Peru and Colombia) that were recorded with more bandwidth limited equipment. In addition, the top frequency and the range are greater than in any other toothed whale species recorded to date. Whistle production was higher during resting activities, alone or in the presence of other animals. The confirmation of whistles in the boto has important implications for the evolution of whistles in Cetacea and their association with sociality. © 2007 Acoustical Society of America. [DOI: 10.1121/1.2404918]

PACS number(s): 43.80.Ka [WWA]

Pages: 1203–1212

I. INTRODUCTION

The Amazon River dolphin, or boto, is known to produce a variety of sounds, e.g., echolocation clicks, single intense clicks, jaw snaps, and burst-pulsed sounds (Caldwell and Caldwell 1967, Caldwell *et al.* 1966). Whistles were first reported by Nakasai and Takemura (1975) in Peru and later documented in more detail by Wang *et al.* (1995a, 2001). Whistles have been also reported in the boto from the Orinoco River (Diazgranados and Trujillo 2002). Despite these reports, whistle production in this riverine dolphin has been questioned on the basis that boto distribution overlaps largely with tucuxi dolphins (*Sotalia fluviatilis*), a well documented whistling species. Hence, tucuxi whistles may have been erroneously assigned to the boto (e.g., Podos *et al.* 2002). In fact, it has been suggested that whistles are unique to social delphinids (Herman and Tavolga 1980; Podos *et al.* 2002). Certainly, whistles are best studied in social delphinids, where they are used for various communication purposes such as individual identifiers, coordination of group behavior, and maintenance of group cohesion (e.g., Caldwell and Caldwell 1965; Caldwell *et al.* 1990; Fripp *et al.* 2005; Herzog 2000; Janik 2000; Tyack 1997, 2000; Watwood *et al.* 2004). However, nondelphinid toothed whale species like the Chinese river dolphin *Lipotes vexillifer* (Jing *et al.* 1981;

Xianying *et al.* 1981; Wang *et al.* 1989; Wang *et al.* 2006), the beaked whales of the genus *Berardius* spp (Dawson *et al.* 1998, Rogers and Brown 1999), the narwhal *Monodon monoceros*, and the beluga *Delphinapterus leucas* (e.g., Belikov and Bel'kovich 2001, 2003; Ford and Fisher 1978; Karlsen *et al.* 2002; Shapiro 2006; Sjare and Smith 1986; Watkins *et al.* 1970) are known to produce whistles as well in a variety of contexts.

Here we document whistles and their behavioral context in the boto dolphins of the Yasuní River, Ecuador, and discuss the potential of these signals as communicative signals in this solitary freshwater dolphin.

II. METHODS

A. Study site

The boto is one of the most widely distributed freshwater dolphins. In parts of its distribution it is sympatric with *Sotalia fluviatilis* (da Silva 2002). The boto inhabits principal tributaries of the Amazon River as well as small rivers and lakes across its distribution (da Silva 2002). Since one of the main criticisms of previous work on boto whistles is the presence of *S. fluviatilis* in the area of recordings, it was important for our study to be conducted in areas where only botos were found. We selected the Yasuní River, a tributary of the Napo River, a narrow river that inundates the adjacent forest and lagoons, during the high-water season (Fig. 1). During the low-water season the river becomes narrower and

^{a)}Author to whom correspondence should be addressed. Electronic mail: lmayc002@fiu.edu

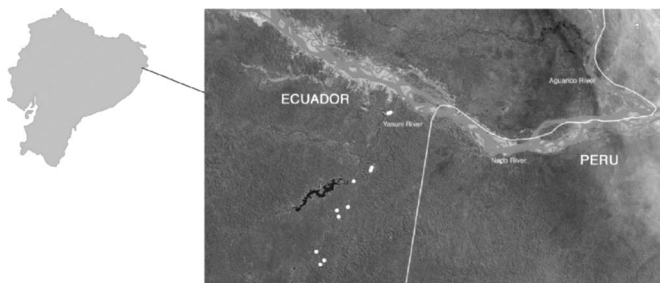


FIG. 1. Map showing the location of the Yasuni River and groups of botos (white dots) recorded during this study.

the lagoons dry out (Galacatos *et al.* 2004), not the type of habitat in which *S. fluviatilis* is known to occur (da Silva 2002).

Overall *S. fluviatilis* is believed to have low population densities in Ecuador (Dekinger 2001, Zapata-Rios and Utreras 2004). While relatively common in the Putumayo and Morona Rivers, local biologists (Zapata-Rios and Utreras 2004, Victor Utreras pers. com. 2006), park rangers, and inhabitants of the area confirm that *S. fluviatilis* is rare in the Yasuní, Napo, and Aguarico rivers, and absent in the Yasuní during the low-water season. Our study took place in the Yasuní River during the low-water season when boto were confined to deeper areas of this narrow river.

We recorded boto dolphins from 14 to 19 August 2005 between 6 a.m. to 6 p.m. In order to decrease chances of encountering (and accidentally recording) *S. fluviatilis* we recorded botos at least 1.5 km away from the point of intersection with the Napo River where the chances to see *S. fluviatilis* may be higher (Zapata-Rios and Utreras 2004). As expected, we observed only botos in the Yasuní River and are thus confident that all the whistles presented in this study correspond exclusively to the boto. To verify this, we compare and contrast boto whistles with 20 whistles recorded from six individuals of *S. fluviatilis* and 13 whistles from one group that contained both species at the intersection between the Napo and the Aguarico rivers, about 14 km downstream from the intersection between Yasuní and the Napo rivers. The 20 whistles recorded from single animals were very similar in contour, time, and frequency parameters to other *S. fluviatilis* populations (e.g., Podos *et al.* 2002, Azevedo and Van Sluys 2005, Wang *et al.* 1995a, 2001). These single animals were recorded near the boat and botos were not present in the area. The other 13 whistles were identical to these in all acoustic parameters therefore they were assigned to *S. fluviatilis*.

B. Whistle definition

To understand the evolutionary history of whistles and the factors that may have influenced their evolution we must first understand their distribution among cetaceans. To do so it is important not to *a priori* bias whistle definition, e.g., by defining them in the context of a behavior that may have much more limited distribution than the sounds themselves. Rather, it seems less presumptuous to define sounds in terms of acoustic parameters. Whistles are tonal sounds produced

by toothed whales. These sounds have a specific acoustic structure that consists of narrowband and frequency modulated sounds (Richardson *et al.* 1995). Whistles may be complex in contour (e.g., sine, convex, concave, upsweep, downsweep) or simply constant in frequency, e.g., *Lagenorhynchus albirostris* (Rasmussen and Miller 2002), *Sotalia guianensis* (Azevedo and Van Sluys 2005) and *Stenella longirostris* (Barzúa-Durán and Au 2002). Often whistle fundamental frequency is below 20 kHz (Richardson *et al.* 1995), but not limited to this range, e.g., Oswald *et al.* (2004) found that *Delphinus delphis*, *Stenella attenuata*, *S. coeruleoalba*, and *S. longirostris* produced whistles with frequencies up to 24 kHz, in *Lagenorhynchus albirostris* whistle fundamental frequency can go up to 35 kHz (Rasmussen and Miller 2002) and up to 41 kHz in *Tursiops truncatus* (Boisseau 2005). Whistles may be continuous or consist of series of breaks and segments (Richardson *et al.* 1995) and contain or not harmonics (Au 2000). Some dolphin species like *S. longirostris* (Lammers and Au 2003) and *L. albirostris* (Rasmussen *et al.* 2006) produce whistles with high order harmonics. Finally, whistles vary greatly in duration. For instance, *Sousa chinensis* whistles can range from 0.01 to 1.3 s (Van Parijs and Corkeron 2001) and in *Tursiops truncatus* from 0.05 to 3.2 s (Wang *et al.* 1995b).

C. Recordings and behavioral observations

Dolphin signals were recorded using a broadband system consisting of a RESON hydrophone (−203 dB re 1 V/μPa, 1 Hz–140 kHz) connected to AVISOFT recorder and Ultra Sound Gate 116 (sampling rate 400–500 kHz 16 bit) that sent the signals to a laptop. Recordings were made continuously. For accompanying behavioral observations, recording sessions were segmented into 3 min intervals. Behavioral observations were made in every other 3 min interval and the predominant behavior during that interval was recorded. Because the river was narrow and relatively shallow, animals were in sight for the observers most of the time. When animals were not in sight during a 3 min scanning period, the behavior was noted as unknown. Only 3 min periods with acoustic and behavioral information were used for the analyses. Five behavioral categories were defined: (1) Feeding/Foraging, when animals were actively searching, pursuing, and/or consuming prey were assigned to this category, (2) Social activities, when dolphins interacted among themselves, e.g., body contact, tail slapping, and animals following the boat or other animals, (3) Traveling, when dolphins were swimming either slowly or fast while maintaining a defined direction, (4) Resting was defined as in Dekinger (2001) were animals showed nondirectional swimming and surfaced regularly at a slow speed or when surfacing occurred in the same area without any abrupt or fast movement, (5) Unknown behavior, was assigned when the animals were not in sight and thus the behavior activity could not be determined.

Group size, group composition, photo-ID, and geographical position data were also collected. Recordings were obtained from 14 to 19 August 2005, giving a total of 214 files recorded (~9 h and 45 min of recorded time). We ana-

TABLE I. Descriptive statistics of boto whistles with comparison to previously published data (in bold values for all 121 whistles and in parenthesis values for 70 whistles with frequency values below 25 kHz for comparison purposes).

	<i>Min F</i> (kHz)	<i>Max F</i> (kHz)	<i>Start F</i> (kHz)	<i>End F</i> (kHz)	<i>Delta F</i> (kHz)	<i>Peak F</i> (kHz)	<i>Duration</i> (s)
This Study							
<i>Mean</i>	14.54 (12.59)	24.71 (19.26)	23.30 (18.49)	15.48 (13.10)	10.18 (6.71)	18.62 (15.36)	0.009 (0.010)
<i>SD</i>	4.32 (3.96)	8.37 (4.0)	8.53 (4.10)	5.70 (4.35)	7.02 (2.47)	6.61 (4.52)	0.011 (0.014)
<i>Range</i>	5.30–26.44 (5.30–21.37)	10.88–48.10 (10.88–24.89)	9.77–48.10 (9.77–24.89)	5.30–42.99 (5.30–24.62)	2.94–34.39 (2.99–16.52)	3.22–48.83 (6.35–22.95)	0.002–0.080 (0.002–0.080)
<i>CV%</i>	29.7 (31.5)	33.9 (20.8)	36.1 (22.1)	38.60 (33.3)	68.9 (36.9)	35.50 (29.5)	128.2 (134.2)
Wang <i>et al.</i> (1995a, 2001) ^a							
<i>Mean</i>	2.54	2.97	2.61	2.86	1.14
<i>SD</i>	0.76	0.84	0.75	0.77	1.01
<i>Range</i>	0.220–4.22	0.5–5.16	0.220–4.22	0.360–4.86	0.16–4.42
<i>CV%</i>	29.88	28.11	28.55	27.01	91.10
Diazgranados and Trujillo (2002)							
<i>Mean</i>
<i>SD</i>
<i>Range</i>	3	13
<i>CV%</i>

^aRecording system with maximum frequency limited to 25 kHz.

lyzed all good quality whistles using the program Raven 1.1 (Cornell Laboratory of Ornithology, New York) with a fast Fourier transform size of 1024 points, an overlap of 50%, and using a 512–522 sample Hann window.

Eight parameters were measured for each whistle: starting frequency (SF), ending frequency (EF), minimum frequency (MinF), maximum frequency (MaxF), delta frequency (DF=MaxF—MinF), peak frequency (PF, measured in the whistle contour where intensity was the highest), duration (s), number of inflection points and contour type. Contour type was categorized as by Azevedo and Simão (2002).

We used SYSTAT® statistical software for descriptive and nonparametric statistics. After testing for normality using the K-S Lilliefors, Skewness, and Kurtosis tests, nonparametric tests were selected to analyze the data. The Kruskal-Wallis test was used to determine if whistle acoustic parameters varied across behavioral states and groups (sightings) and Chi-square one sample test for Goodness of Fit to determine if whistle production rate (No. whistles/min/individual) varied across behaviors. The Kolmogorov-Smirnov test for two independent samples was used to determine if the medians of the acoustical parameters differed between the two species. A multivariate discriminant function analysis was used to classify whistles within and between species. The Jackknife method was used to calculate the percent of correct classification for each species.

III. RESULTS

A total of 121 high quality tonal sounds fitted the definition of “whistles” (see above) until now only described in delphinids and a few other toothed whales. However, these whistles were not produced in bouts as in many delphinid species. They were produced singly and spaced in time. The overall whistle production was 0.015 whistles/min/individual.

Whistle fundamental frequency ranged from 5.30 up to 48.10 kHz and was short in duration (0.002–0.080 s) (Table I, Fig. 2). About half (48%; $n=58$) of the whistles had maximum frequency values above 24 kHz. This demarcation point was chosen because most dolphin whistles reportedly do not go beyond 24 kHz (with the exceptions mentioned earlier) and this is often the upper limit of recording equipment used in many earlier studies. Similarly 42.1% ($n=51$) of beginning frequency, 13.2% ($n=16$) of peak frequency, 5.78% ($n=7$) of end frequency, and 1.65% ($n=2$) of minimum frequency measurements were above 24 kHz.

In terms of whistle contours 95.8% ($n=116$) of the whistles were descending in frequency. Examples of whistle contours produced by botos are shown in Fig. 2 in conjunction with tucuxi whistles for comparison purposes. Only five of all selected whistles had harmonics. The highest frequency harmonic reached 43.5 kHz.

The whistles were recorded during three behavioral categories: slow traveling, feeding, and resting. Although more whistles were produced during travel activities when accounting for time and number of individuals, whistle production was significantly higher during resting activities with 0.24 whistles/min/per individual ($\chi^2=0.50$, $df=1$, $p<0.05$) compared to traveling (0.03) and feeding (0.03). There were no significant differences in the acoustic parameters of whistles across behaviors at p -value 0.05 level (Table II).

Whistles did vary significantly in their acoustic structure across sighted groups (only groups with more than five whistles were compared) for all whistles parameters except delta frequency (Kruskal-Wallis test, $df=8$, $n=121$: MinF $\chi^2=20.31$, $p=0.026$; MaxF $\chi^2=25.46$, $p=0.005$; SF $\chi^2=23.31$, $p=0.010$; EF $\chi^2=23.86$, $p=0.008$; PF $\chi^2=23.28$, $p=0.010$; Duration $\chi^2=25.46$, $p=0.005$, DF $p>0.05$, Table III). Whistle acoustic parameters did not vary significantly when comparing whistles of groups consisting of adults with groups of adults with calves ($p>0.05$).

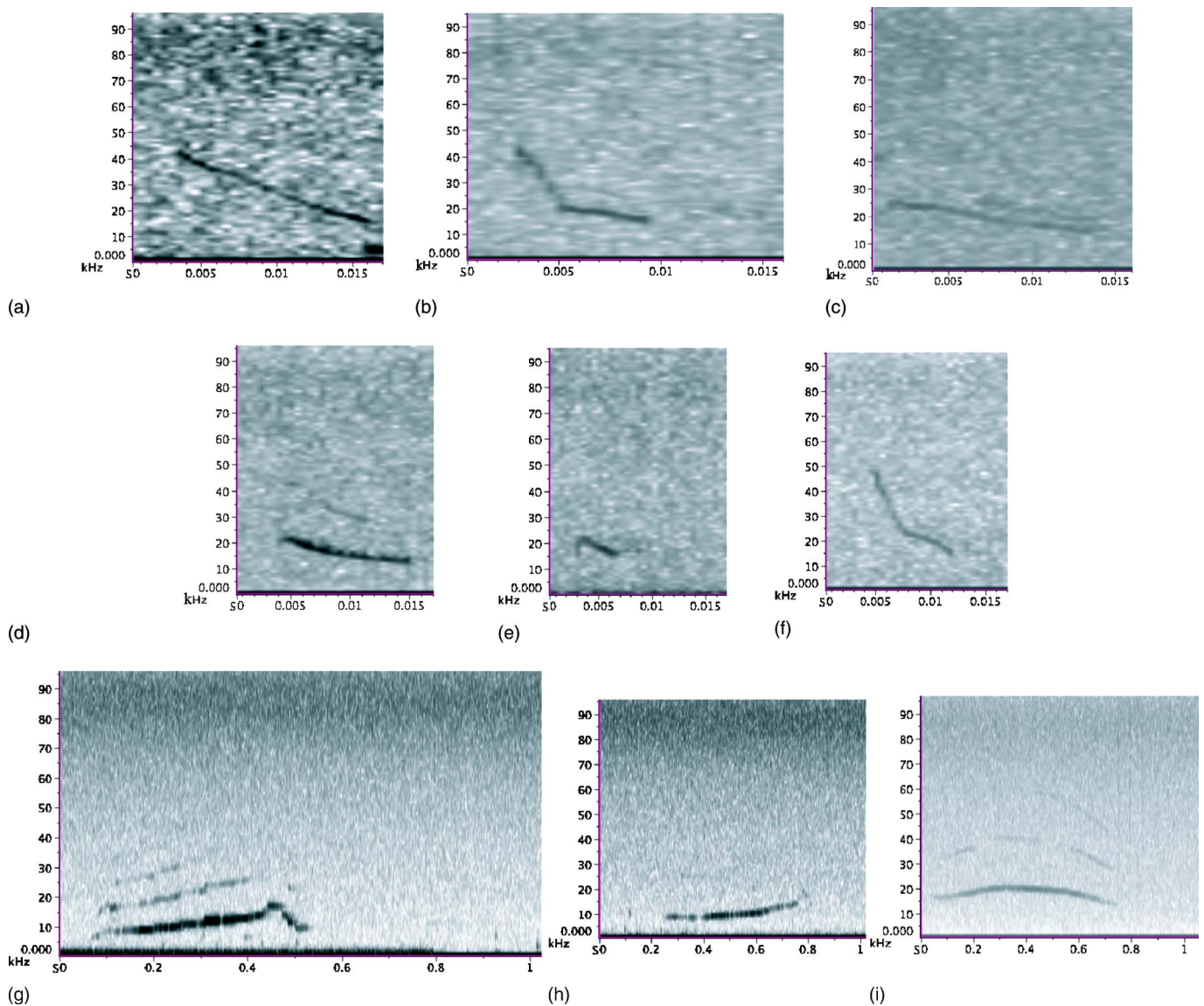


FIG. 2. Examples of whistles (y axis=frequency in kHz, x axis=time in seconds) recorded from *Inia geoffrensis geoffrensis* in the Yasuni River, Ecuador (a)–(f). Examples of whistles recorded from *Sotalia fluviatilis* in the Napo and Aguarico River are given for comparison purposes (h)–(i).

When comparing boto and tucuxi whistles we found significant differences in all whistle parameters medians (MinF Kolmogorov–Smirnov (KS)=0.543, $p < 0.001$; MaxF KS =0.537, $p < 0.001$; DF KS=0.190, $p < 0.001$, SF KS=0.683, $p < 0.001$; EF KS=0.298, $p < 0.001$; PF KS=0.336, $p < 0.001$; Duration KS=0.901, $p < 0.001$). The boto whistles were higher in frequency for all frequency parameters and much shorter in duration than the whistles produced by tucuxis recorded from the Napo and Aguarico rivers (Fig. 3). Tucuxis produced two classes of whistles that can be described as (1) whistles with maximum frequencies below 20 kHz and minimum frequencies below 10 kHz, and (2) whistles with maximum frequencies below 25 kHz and minimum frequencies above 10 kHz (see Fig. 4). Both categories of whistles overlap with boto whistles. Despite this overlap in frequency, the discriminant function analysis correctly classified (based on all acoustical parameters) all boto whistles (100%). Only 15% of the tucuxi whistles were incorrectly classified.

IV. DISCUSSION

Our results confirm previous findings that botos indeed whistle (Wang *et al.* 1995a, 2001, Diazgranados and Trujillo 2002) and suggest that boto whistles are frequency modulated with one of the widest frequency ranges ever reported in a toothed-whale species. Interestingly, the acoustic structure of these whistles is not only distinct from those of the sympatric *S. fluviatilis* but also appears quite distinct from other acoustically known boto populations in Colombia (*Inia geoffrensis humboldtiana*) (Diazgranados and Trujillo 2002) and Perú (*Inia geoffrensis geoffrensis*) (Wang *et al.* 1995a, 2001). However, the comparison between these studies is difficult due to differences in recording equipment as discussed below.

A. Between and within species variation

Boto whistles differ from tucuxi whistles in all their acoustical parameters. As shown in Fig. 4, botos produced

TABLE II. Descriptive statistics for each behavioral class for a total of 121 whistles recorded in relation to their behavioral context (there were not significant differences for any of these parameters across behaviors).

Parameters	Feeding (n=32)	Resting (n=21)	Slow Traveling (n=68)
Min F (kHz)			
(mean±SD)	14.48±4.95	14.59±4.66	14.56±4.39
Range	6.56–21.22	6.26–23.10	5.30–26.44
CV%	28.0	32.0	30.2
Max F (kHz)			
(mean±SD)	25.25±9.28	22.84±6.97	25.03±8.36
Range	11.83–43.68	12.76–41.72	10.88–48.06
CV%	36.8	30.5	33.4
Delta F (kHz)			
(mean±SD)	10.84±7.84	8.25±6.48	10.47±6.77
Range	3.82–28.24	2.99–30.35	2.94–34.40
CV%	72.3	78.6	64.7
Start F (kHz)			
(mean±SD)	22.79±9.06	22.15±7.14	24.43±8.68
Range	11.83–43.68	12.76–41.72	9.77–48.06
CV%	39.7	32.2	35.5
End F (kHz)			
(mean±SD)	16.85±7.85	15.62±5.21	14.80±4.50
Range	7.06–42.98	6.26–26.85	5.30–27.34
CV%	46.6	33.3	30.4
Peak F (kHz)			
(mean±SD)	17.95±4.95	16.15±5.80	18.49±5.75
Range	7.81–27.34	3.22–26.86	6.35–33.69
CV%	27.6	35.9	31.1
Duration (s)			
(mean±SD)	0.006±0.007	0.008±0.008	0.010±0.014
Range	0.002–0.039	0.002–0.039	0.002–0.080
CV%	111.5	103.4	129.4

higher frequency whistles. These whistles are more limited in their contour diversity (95.8% of the whistles were down-sweep) than tucuxi whistles (and those of most other dolphins). Several factors have been proposed to explain interspecific whistle variation including: morphological constraints (Wang *et al.* 1995a, Matthews *et al.* 1999), environment (Wang *et al.* 1995a), sociality (Podos *et al.* 2002), zoogeographical relationships (Steiner 1981), and phylogenetic relationships (Steiner 1981, Wang *et al.* 1995a).

Body size is the most important morphological factor believed to influence signal frequency in animals (Marquet and Taper 1998). Overall, the larger the animal the lower frequency sounds it tends to produce. This is because body size and the size of sound producing organs are often correlated (Fletcher 1992). Some authors (e.g., Wang *et al.* 1995a, Podos *et al.* 2002) have proposed a similar relationship between body size and maximum frequency. However, in the case of cetaceans a recent study showed that when accounting for phylogeny the proposed relationship between body size and maximum frequency disappears (May-Collado *et al.* in press). Thus the fact that botos (~2.6 m, 160 kg) can produce much higher frequency whistles than the smaller tucuxis (~1.52 m, 40 kg) is not counter to any general rule.

It is unlikely that whistle variation is explained by differences in habitat acoustic structure since both species live in very similar environmental conditions. Another proposed factor to explain interspecific whistle variation is zooge-

graphical relations. Steiner (1981) suggested “the degree of differences in the whistle vocalizations among (five dolphin) species closely followed predictions based on classic allopatric/sympatric relations among species.” This idea is congruent with the “species recognition hypothesis” (see Sætre *et al.* 1997) that states that animal vocal acoustic structure has evolved “to” reduce hybridization. Unfortunately, there is very little quantitative information of the extent to which botos and tucuxis are allopatric and sympatric at both spatial and temporal scales to test this idea.

Botos and tucuxis are not closely related (e.g., Hamilton *et al.* 2001, May-Collado and Agnarsson 2006) which could largely explain their differences in whistle structure. However, there is recent evidence that social structure (or at least some components of sociality) could also explain part of this variation. For instance, differences in whistle contour and frequency and time parameters of the distantly related spinner and bottlenose dolphins (e.g., Hamilton *et al.* 2001, LeDuc *et al.* 1999, May-Collado and Agnarsson 2006) have been largely explained in terms of “group fluidity” (a component of sociality) (Barzúa-Durán 2004). Botos and tucuxis are not only more distantly related but also differ even more radically in their social structure. While botos appear to be solitary (Best and da Silva 1993) or at least live in small nonstructured groups (where the strongest social bond appears to be limited to mother and calf) (e.g., Aliaga-Rossel 2002; McGuire and Winemiller 1998), *Sotalia spp.* lives in

TABLE III. Whistle acoustic structure described for each recorded single animal and group.

Groups	Min F (kHz)	Max F (kHz)	Delta F (kHz)	Start F (kHz)	End F (kHz)	Peak F (kHz)	Duration (s)	No. of whistles	No. individuals present	Group composition
G1 Mean±SD	17.20±2.48	30.23±8.28	13.04±7.62	29.63±9.27	17.80±2.60	23.43±4.56	0.006±0.007	6	1	Adult ^a
Range	13.90–20.04	19.71–38.60	3.62–23.27	16.10–38.60	13.9–20.04	17.58–27.34	0.002–0.019			
C.V.%	14.4	27.4	58.4	31.3	14.6	20.0	111.8			
G2 Mean±SD	14.44±4.18	23.68±8.93	9.24±7.56	23.44±9.13	14.53±4.01	17.32±4.69	0.005±0.003	23	3	Adults
Range	7.18–24.90	11.83–43.68	3.82–28.02	11.83–43.68	7.44–21.22	7.81–24.90	0.002–0.017			
C.V.%	27.1	37.7	81.8	38.9	27.6	27.1	76.0			
G3 Mean±SD	16.08±5.03	26.95±7.82	10.87±7.72	26.37±8.22	16.19±5.11	19.03±6.630	0.009±0.015	33	4	3 Adults 1 calf ^b
Range	5.30–26.44	12.58–48.10	2.94–34.39	9.77–48.07	5.30–27.34	3.22–27.83	0.002–0.080			
C.V.%	31.1	29	71.0	31.2	31.6	33.1	156.9			
G4 Mean±SD	14.60±3.22	24.36±6.40	9.77±4.47	24.36±6.40	14.60±3.22	18.80±4.85	0.004±0.002	8	3	2 Adults 1 Juvenile ^c
Range	7.43–17.68	12.07–33.14	4.64–18.14	12.07–33.14	7.43–17.68	9.76–24.41	0.002–0.007			
C.V.%	22.1	26.3	45.7	26.3	22.1	25.8	43.1			
G5 Mean±SD	14.53±3.72	24.39±9.84	9.84±7.89	23.80±10.17	14.66±3.76	17.94±6.35	0.008±0.009	12	3	2 Adults 1 Juvenile
Range	7.85–18.31	10.88–41.44	2.99–25.02	10.84–41.44	7.85–18.31	8.79–33.69	0.002–0.030			
C.V.%	25.6	40.4	80.2	42.7	25.7	35.4	116.2			
G6 Mean±SD	8.92±3.48	16.20±4.07	7.28±1.07	16.03±4.15	8.92±3.48	11.28±3.52	0.026±0.014	9	1	Adult
Range	6.53–17.80	14.13–27.01	6.02–9.21	13.67–27.01	6.53–17.80	7.81–19.53	0.002–0.046			
C.V.%	39.0	25.1	14.8	25.9	39.0	31.2	54.4			
G7 Mean±SD	13.84±4.10	27.89±9.81	14.05±8.09	19.17±6.48	22.56±13.40	18.30±5.35	0.012±0.012	7	2	1 Adult 1 calf
Range	7.06–18.87	13.98–42.99	6.93–28.24	13.98–29.92	7.06–42.99	10.90–21.41	0.002–0.039			
C.V.%	29.6	35.2	57.6	33.8	59.4	29.3	105.3			
G8 Mean±SD	13.83±2.11	21.83±2.36	8.0±2.44	20.51±2.87	14.93±2.22	18.42±2.58	0.010±0.011	7	2	Adults
Range	11.71–16.66	17.11–24.39	4.01–10.98	16.11–23.44	12.7–18.55	14.65–22.95	0.003–0.033			
C.V.%	15.3	10.8	30.6	14	14.9	14	111.9			
G9 Mean±SD	13.98±3.17	26.63±8.06	9.65±7.76	22.63±8.31	15.25±4.51	17.14±4.39	0.007±0.003	13	2	1 Adult 1 calf
Range	9.12–19.60	17.11–41.72	3.45–30.35	16.11–41.72	9.12–26.85	11.23–26.86	0.002–0.012			
C.V.%	22.7	34.1	80.4	36.7	29.6	25.6	45.3			
G10 Median±SD	17.27	34.10	17.98	27.85	23.51	23.9320.51–	0.006	2	2	1 Adult 1 calf
Range	15.53–19.01	28.02–40.18	14.78–21.17	15.53–40.18	19.01–28.02	27.34	0.004–0.008			
C.V.%	14.2	25.2	25.2	62.6	27.1	20.2	47.1			
G11 Mean±SD	12.51	17.66	5.15	16.11	17.66	12.51	0.008	1	1	Adult
Range			
C.V.%			

^aAdult is defined as full sized individuals.

^bCalf is defined as an individual that is less than half the adult's size.

^cJuvenile defined as an individual larger than a calf but not as big as an adult.

structured social groups (Monteiro-Filho 2000). Additionally, May-Collado *et al.* (submitted B) found that whistle complexity—a concept based on whistle mean number of inflection points—may be influenced by group size and social structure (two components of sociality). More specifically, they found that simple whistles (mean number of inflection points equal or below one) were particularly concentrated in “solitary” species while the phylogenetic distribution of complex whistles and social species largely overlap.

Although boto dolphins from the Yasuní River produced whistles with frequency parameters that appear to be far above (5.30–48.10 kHz) the values reported by Wang *et al.* (1995a, 2001) in botos from the Marañon and Tigre Rivers in Peru (0.22–5.16 kHz) and by Diazgranados and Trujillo (2002) in the Orinoco River (3–13 kHz) (Table I) comparisons cannot be done at this point. This is due in part to differences in the recording systems maximum frequency limitations (up to 25 kHz), to the lack of information on several standard acoustic parameters (Diazgranados and

Trujillo (2002), and the uncertainty regarding the assignment of the low frequency whistles to boto dolphins (Wang *et al.* 1995a, 2001). Therefore, until we have full frequency range recordings from other botos populations, comparisons are difficult and speculative.

We limit this part of the discussion to the observed differences among “groups” (note that several of the groups consisted of only one individual) where with the exception for delta frequency, whistle acoustic parameters vary significantly across groups (Table III). In most delphinids within species variation is primarily in duration and modulation (e.g., Wang *et al.* 1995b, Morisaka *et al.* 2005a, 2005b, Barzúa-Dúran and Au 2002, 2004) rather than in frequency as observed in this boto population (also see Azevedo and Van Sluys 2005, Rossi-Santos and Podos 2006 for *Sotalia guianensis*). In part, this variation has been explained as product of adaptation to local ecological conditions (e.g., ambient noise, see Morisaka *et al.* 2005b). It is unlikely that the among group whistle differences observed in this boto population are explained by contrasting habitat acoustic

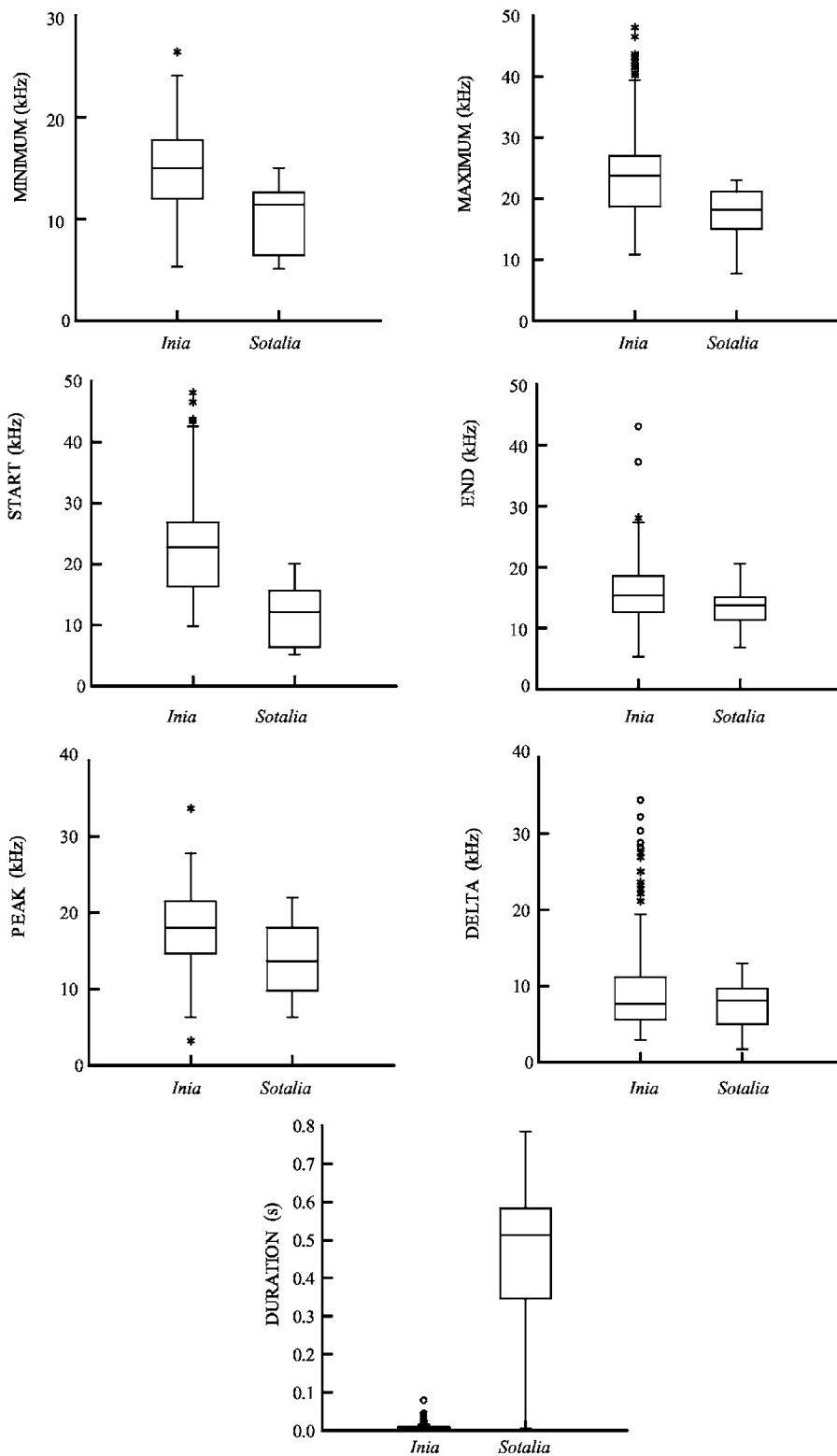


FIG. 3. Distribution of whistle acoustic parameters as a function of dolphin species where * and ° represent outside and far outside values of the 50% central tendency (*Inia*=121 whistles, *Sotalia*=33 whistles).

characteristics alone, since recorded single animals and groups were in the same environment. Furthermore, age composition and behavioral states appear not to influence whistle variation either. However, our sample size is too small and geographically restricted to conclude age and behavior does not have some influence on boto dolphin whistles acoustic structure. In addition to these two factors, others such as genes, gender, and overall inter-individual variation, merit further study.

B. Behavior and communication

Diazgranados and Trujillo (2002) reported that boto whistles were produced within groups that engaged in social and feeding activities. Half of the whistles produced by the botos in this study occurred during traveling activities, but when accounting for time of the encounter and number of individuals present, whistle production was higher during resting activities. In addition, whistles were produced by both solitary and grouped animals.

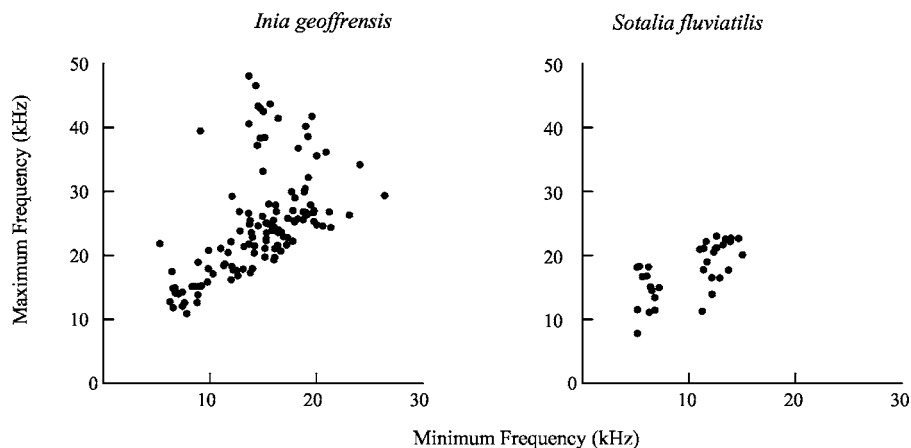


FIG. 4. Plot of maximum versus minimum frequency of all recorded whistles for each species (*Inia*=121 and *Sotalia*=33 whistles).

The closest neighbor maximum distance was found at approximately 0.15–1.5 km, suggesting these animals might be still in acoustic contact. Because of the behavioral context at which most whistles were emitted and the low whistle production, it is possible that whistles in boto dolphins may be used to keep distance between animals, rather than promote social interactions or cohesion among individuals as it occurs in delphinids (e.g., Jones and Sayigh 2002). Assuming cylindrical spreading loss and freshwater absorption at the mean maximum frequency, the boto whistles could propagate as far as 3.3 km before falling below the ambient noise although the actual range will be less depending on channel depth, bottom type, and vegetation (Quitana-Rizzo *et al.* 2006). Wang *et al.* (2006) assuming spherical spreading losses estimated that *Lipotes vexillifer* low frequency whistles (with dominant frequency 5.7 kHz) could propagate in a very calm environment up to 6.6 km, but possibly only 22–220 m considering the noisy conditions of the Yangtze River. The Yasuní River is a very calm environment; unlike the Yangtze River, it is protected and boat traffic is limited to park rangers and scientists.

During the period of this study botos produced whistles randomly and not in bouts as many delphinids species. Based on our data it appears that boto dolphins in Yasuní whistle rarely. Our sample size is too small not only to clearly associate these sounds with the same social contexts as in delphinids but also to determine how frequently botos and other riverine dolphin species generally whistle. Nevertheless, confirming the presence of whistles in botos and other freshwater toothed whales helps illuminate the evolutionary history of whistles, and their relation to sociality—a factor proposed to have shaped the complexity of toothed whale whistles (May-Collado *et al.* submitted B).

V. CONCLUSIONS

This study confirms whistles in the solitary freshwater dolphin *Inia geoffrensis geoffrensis*. The frequency range of boto whistles we document is among the greatest ever reported in a cetacean species. The acoustic structure of these whistles in Ecuadorian botos differs from that of the sympatric *Sotalia fluviatilis* and apparently from conspecific populations from Perú and Colombia. Differences in the acoustic structure of boto and tucuxi whistles may be in large prod-

uct of their distant phylogenetic relationships and their different social structure. Although our study suggests remarkable whistle variation between populations, this may be largely a product of limited recording systems used by previous studies. Finally, although the use of whistles for communication purposes has been largely attributed to social dolphin species, it is possible that botos (even solitary animals) use them to communicate but in the context of keeping distances among animals rather than to promote group cohesion. We propose this based on two observations (1) whistles were produced when the animals were engaged in resting activities, and (2) based on the fact that solitary animals were potentially within acoustic range of each other (estimated maximum of 3.3 km). Finally, better understanding of whistle production in solitary freshwater species will further understanding of the evolutionary history of whistles and their proposed association with sociality.

ACKNOWLEDGMENTS

We thank Ingi Agnarsson, University of British Columbia, Tim Collins, Mike Heithaus, Zhenim Chen, Florida International University, Peter Tyack, WHOI, and two anonymous reviewers for comments and suggestions to this manuscript. Thanks to Maureen Donnelly for her support. Thanks to Alonso Jaramillo Encargado del Parque Nacional Yasuní, Ecuador, Dr. Luis Albuja del Departamento de Ciencias Biológicas de la Escuela Politécnica Nacional, the boat captains Walter Prado and Daniel Contreras, biologists Víctor Utreras and Judith Denking, field assistants Mónica Gamboa-Poveda and Angélica Caiza. Locals Don Segundo, Esturado Hidalgo, and all the park rangers at Yasuní National Park. Recordings were carried out with permission of the Ministerio del Ambiente de la República de Ecuador and the National Park Yasuní (Permit No. 019-IC-FL-PNY-RSO) and authorization from the IACUC committee at Florida International University. This study was funded by Judith Parker Travel Grant, Cetacean International Society, and the Russell E. Train Education Program-WWF to Laura May-Collado.

Aliaga-Rossel, E. (2002). "Distribution and abundance of the river dolphin (*Inia geoffrensis*) in the Tijamuchi River, Beni, Bolivia," *Aquat. Mamm.* **28**, 312–323.

Azevedo, A. F., and Van Sluys, M. (2005). "Whistles of tucuxi dolphins (*Sotalia fluviatilis*) in Brazil: Comparisons among populations," *J. Acoust.*

- Soc. Am. **117**, 1456–1464.
- Azevedo, A. F., and Simão, S. M. (2002). “Whistles produced by marine tucuxi dolphins *Sotalia fluviatilis* in Guanabara Bay, southeastern Brazil,” *Aquat. Mamm.* **28**, 261–266.
- Au, W. W. L. (2000). “Hearing in whales and dolphins: An overview,” in *Hearing by Whales and Dolphins*, edited by W. W. L. Au, A. N. Popper, and R. R. Fay (Springer-Verlag, New York), pp. 1–42.
- Barzúa-Durán, M. C., and Au, W. W. L. (2002). “Whistles of Hawaiian spinner dolphins,” *J. Acoust. Soc. Am.* **112**, 3064–3072.
- Barzúa-Durán, M. C. (2004). “Differences in the whistle characteristics and repertoire of bottlenose and spinner dolphins,” *An. Acad. Bras. Cienc.* **76**, 386–392.
- Barzúa-Durán, M. C., and Au, W. W. L. (2004). “Geographic variations in the whistles of spinner dolphins (*Stenella longirostris*) of the Main Hawaiian Islands,” *J. Acoust. Soc. Am.* **116**, 3757–3769.
- Belikov, R. A., and Bel’kovich, V. M. (2001). “Characteristics of white sea beluga whale (*Delphinapterus leucas*) whistle-like signals,” *XI Session of the Russian Acoustical Society*, Moscow, November 19–23.
- Belikov, R. A., and Bel’kovich, V. M. (2003). “Underwater vocalization of the beluga whales (*Delphinapterus leucas*) in a reproductive gathering in various behavioral situations,” *Oecologia* **43**, 112–120.
- Best, R. C., and da Silva, V. M. F. (1993). “Inia geoffrensis,” *Mammalian Species* **426**, 1–8.
- Boisseau, O. (2005). “Quantifying the acoustic repertoire of a population: The vocalizations of free-ranging bottlenose dolphins in Fiordland, New Zealand,” *J. Acoust. Soc. Am.* **117**, 2318–2329.
- Caldwell, M. C., and Caldwell, D. K. (1965). “Individual whistle contours in bottlenose dolphins (*Tursiops truncatus*),” *Nature (London)* **207**, 434–435.
- Caldwell, M. C., and Caldwell, D. K. (1967). “Intra-specific transfer of information via the pulsed sound in captive odontocete cetaceans,” in *Animal Sonar Systems*, edited by R.-G. Busnel (Jouy-en-Josas, France), Vol. **2**, pp. 879–936.
- Caldwell, M. C., Caldwell, D. K., and Evans, W. E. (1966). “Sounds and behavior of captive Amazon freshwater dolphin, *Inia geoffrensis*,” *Los Angeles County Mus. Cont. Sci.* **108**, 1–24.
- Caldwell, M. C., Caldwell, D. K., and Tyack, P. L. (1990). “Review of the signature-whistle hypothesis for the Atlantic bottlenose dolphin,” in *The Bottlenose Dolphin*, edited by S. Leatherwood and R. R. Reeves (Academic, San Diego), pp. 199–234.
- da Silva, V. M. F. (2002). “Amazon River dolphin (*Inia geoffrensis*),” in *Encyclopedia of Marine Mammals*, edited by W. F. Perrin, B. Wursig, and J. G. M. Thewissen (Academic, San Diego), pp. 18–20.
- Dawson, S., Barlow, J., and Ljungbland, D. (1998). “Sounds recorded from Baird’s beaked whale, *Berardius bairdii*,” *Marine Mammal Sci.* **14**, 335–344.
- Dekinger, J. (2001). “Demographische untersuchung am Amazonasdelphin (*Inia geoffrensis*) in cuyabeno reservat, in Ecuador,” Ph.D. Dissertation, Universitat Bielefeld, Bielefeld, Germany.
- Diazgranados, M. C., and Trujillo, F. (2002). “Vocal repertoire of the freshwater dolphins *Inia geoffrensis* and *Sotalia fluviatilis* in Colombia, South America,” *J. Acoust. Soc. Am.* **112**, 2400.
- Fletcher, N. H. (1992). *Acoustic Systems in Biology*, Oxford University Press, Oxford, England, p. 352.
- Ford, J. K. B., and Fisher, H. D. (1978). “Underwater acoustic signals of the narwhal (*Monodon monoceros*),” *Can. J. Zool.* **56**, 552–560.
- Fripp, D., Owen, C., Quintana-Rizzo, E., Shapiro, A., Buckstaff, K., Janowski, K., Wells, R., and Tyack, P. (2005). “Bottlenose dolphin (*Tursiops truncatus*) calves appear to model their signature whistles on the signature whistles of community members,” *Anim. Cogn.* **8**, 17–26.
- Galacatos, K., Barriga-Salazar, R., and Steward, D. J. (2004). “Seasonal and habitat influences on fish communities within the lower Yasuní River Basin of the Ecuadorian Amazon,” *Environ. Biol. Fishes.* **71**, 33–51.
- Hamilton, H., Caballero, S., Collins, A. G., and Brownell, Jr., R. L. (2001). “Evolution of river dolphins,” *Proc. R. Soc. London, Ser. B* **268**, 549–558.
- Herman, L. M., and Tavolga, W. N. (1980). “The communication systems of cetaceans,” in *Cetacean Behavior: Mechanisms and Functions*, edited by L. M. Herman (Wiley, New York).
- Herzing, D. L. (2000). “Acoustics and social behavior of wild dolphins: Implications for a sound society,” in *Hearing by Whales and Dolphins*, edited by W. W. L. Au, A. N. Popper, and R. E. Fay (Springer, New York), pp. 225–272.
- Janik, V. M. (2000). “Whistle matching in wild bottlenose dolphins (*Tursiops truncatus*),” *Science* **289**, 1355–1357.
- Jing, X., Xiao, Y., and Jing, R. (1981). “Acoustic signals and acoustic behavior of Chinese river dolphin (*Lipotes vexillifer*),” *Sci. Sin.* **2**, 233–239.
- Jones, G. J., and Sayigh, L. S. (2002). “Geographic variation in rates of vocal production of free-ranging bottlenose dolphins,” *Marine Mammal Sci.* **18**, 384–393.
- Karlsen, J. D., Bisther, A., Lydersen, C., Haug, T., and Kovacs, K. M. (2002). “Summer vocalizations of adult male white whales (*Delphinapterus leucas*) in Svalbard, Norway,” *Polar Biol.* **25**, 808–817.
- Lammers, M. O., and Au, W. W. L. (2003). “Directionality in the whistles of Hawaiian spinner dolphins (*Stenella longirostris*): A signal feature to cue direction of movement?” *Marine Mammal Sci.* **19**, 249–264.
- LeDuc, R. G., Perrin, W. F., and Dizon, A. E. (1999). “Phylogenetic relationships among the delphinid cetaceans based on full cytochrome *b* sequences,” *Marine Mammal Sci.* **15**, 619–648.
- Marquet, P. O., and Taper, M. L. (1998). “On size and area: Patterns of mammalian body size extreme across landmasses,” *Evol. Biol.* **12**, 127–139.
- Matthews, J. N., Rendell, L. E., Gordon, J. C. D., and MacDonald, D. W. (1999). “A review of frequency and time parameters of cetacean tonal calls,” *Bioacoustics* **10**, 47–71.21.
- May-Collado, L. J., and Agnarsson, I. (2006). “Cytochrome *b* and Bayesian inference of whale phylogeny,” *Mol. Phylogenet. Evol.* **38**, 344–354.
- May-Collado, L. J., Agnarsson, I., and Wartzok, D. (2006). (in press) “Re-examining the relationship between body size and tonal signals frequency in whales: A comparative phylogenetic approach,” *Marine Mammal Science*.
- May-Collado, L. J., Agnarsson, I., and Wartzok, D. (2006). (B) “Phylogenetic review of tonal sound production in whales in relation to sociality,” (Submitted to *BMC Evol. Biol.*)
- McGuire, T. L., and Winemiller, K. O. (1998). “Occurrence patterns, habitat associations, and potential prey of the river dolphin, *Inia geoffrensis*, in the Cinaruco River, Venezuela,” *Biotropica*. **30**, 625–638.
- Monteiro-Filho, E. L. A. (2000). “Group organization of the dolphin *Sotalia fluviatilis* guianensis in an estuary of southeastern Brazil,” *Ciencia e Cultura J. Braz. Ass. Adv. Sci.* **52**, 97–101.
- Morisaka, T., Shinohara, M., Nakahara, F., and Akamatsu, T. (2005a). “Geographic variations in the whistles among three Indo-Pacific bottlenose dolphin *Tursiops aduncus* populations in Japan,” *Fish. Sci.* **71**, 568–576.
- Morisaka, T., Shinohara, M., Nakahara, F., and Akamatsu, T. (2005b). “Effects of ambient noise in the whistles of Indo-Pacific bottlenose dolphin *Tursiops aduncus* populations in Japan,” *J. Mammal.* **86**, 541–546.
- Nakasai, K., and Takemura, A. (1975). “Studies on the underwater sound. VI. On the underwater calls of freshwater dolphins in South America,” *Bull. Fac. Fish. Nagasaki Univ.* **40**, 7–13.
- Oswald, J. N., Rankin, S., and Barlow, J. (2004). “The effect of recording and analysis bandwidth on acoustic identification of delphinid species,” *J. Acoust. Soc. Am.* **116**, 3178–3185.
- Podos, J., da Silva, V. M. F., and Rossi-Santos, M. R. (2002). “Vocalizations of Amazon river dolphins, *Inia geoffrensis*: Insights into the evolutionary origins of delphinid whistles,” *Ethology* **108**, 601–612.
- Quintana-Rizzo, E., Mann, D. A., and Wells, R. S. (2006). “Estimated communication range of social sounds used by bottlenose dolphins (*Tursiops truncatus*),” *J. Acoust. Soc. Am.* **120**, 1671–1683.
- Rasmussen, M. H., and Miller, L. A. (2002). “Whistles and clicks from white-beaked dolphins (*Lagenorhynchus albirostris* Gray 1846), recorded in Faxaflói Bay, Iceland,” *Aquat. Mamm.* **28**, 78–89.
- Rasmussen, M. H., Lammers, M., Beedholm, K., and Miller, L. A. (2006). “Source levels and harmonic content of whistles in white-beaked dolphins (*Lagenorhynchus albirostris*),” *J. Acoust. Soc. Am.* **120**, 511–517.
- Richardson, W. J., Greene, C. R. J., Malmé, C. I., and Thomsom, D. H. (1995). *Marine Mammals and Noise* (Academic, New York), p. 547.
- Rogers, T. L., and Brown, S. M. (1999). “Acoustic observations of Arnoux’s beaked whale (*Berardius arnuxii*) off Kemp Land, Antarctica,” *Marine Mammal Sci.* **15**, 192–198.
- Rossi-Santos, M. R., and Podos, J. (2006). “Latitudinal variation in whistle structure of the estuarine dolphin *Sotalia guianensis*,” *Behaviour* **143**, 347–364.
- Sætre, G. P., Moum, T., Bures, S., Kral, M., Adamjan, M., and Moreno, J. (1997). “A sexually selected character displacement in flycatchers reinforces premating isolation,” *Nature (London)* **387**, 589–591.
- Shapiro, A. (2006). “Preliminary evidence for signature vocalizations among free-ranging narwhals (*Monodon monoceros*),” *J. Acoust. Soc. Am.* **120**, 1695–1705.
- Sjare, B. L., and Smith, T. G. (1986). “The vocal repertoire of white whales,

- Delphinapterus leucas*, summering in Cunningham Inlet, Northwest Territories," *Can. J. Zool.* **64**, 407–415.
- Steiner, W. W. (1981). "Species-specific differences in pure tonal whistle vocalizations of five western North Atlantic dolphin species," *Behav. Ecol. Sociobiol.* **9**, 241–246.
- Tyack, P. L. (1997). "Development and social functions of signature whistles in bottlenose dolphins *Tursiops truncatus*," *Bioacoustics* **8**, 21–46.
- Tyack, P. L. (2000). "Functional aspects of cetacean communication," in *Cetacean Societies: Field Studies of Dolphins and Whales*, edited by J. Mann, R. C. Connor, P. L. Tyack, and H. Whitehead (The University of Chicago Press, Chicago), pp. 270–307.
- Van Parijs, S. M., and Corkeron, P. J. (2001). "Vocalizations and behaviour of Pacific Humpback dolphins, *Sousa chinensis*," *Ethology* **107**, 701–716.
- Wang, D., Lu, W., and Wang, K. (1989). "A preliminary study of the acoustic behavior of the baiji, *Lipotes vexillifer*," *Occasional Papers of the IUCN Species Survival Commission (SSC) No. 3*, pp. 137–140.
- Wang, D., Würsig, B., and Evans, W. E. (1995a). "Comparisons of whistles among seven odontocete species," in *Sensory Systems of Aquatic Mammals*, edited by R. A. Kastelien, J. A. Thomas, and P. E. Nachtigal (De Spill, Woerden, The Netherlands) pp. 299–323.
- Wang, D., Würsig, B., and Evans, W. E. (1995b). "Whistles of bottlenose dolphins: Comparisons among populations," *Aquat. Mamm.* **21**, 65–77.
- Wang, D., Würsig, B., and Leatherwood, S. (2001). "Whistles of boto, *Inia geoffrensis*, and tucuxi, *Sotalia fluviatilis*," *J. Acoust. Soc. Am.* **109**, 407–414.
- Wang, X., Wang, D., Akamatsu, T., Fujita, K., and Shiraki, R. (2006). "Estimated detection distance of a baiji's (Chinese river dolphin, *Lipotes vexillifer*) whistles using a passive acoustic survey method," *J. Acoust. Soc. Am.* **120**, 1361–1365.
- Watkins, W. A., Schevill, W. E., and Ray, C. (1970). "Underwater sounds of *Monodon* (Narwhal)," *J. Acoust. Soc. Am.* **49**, 595–599.
- Watwood, S. L., Tyack, P. L., and Wells, R. S. (2004). "Whistle sharing in paired male bottlenose dolphins, *Tursiops truncatus*," *Behav. Ecol. Sociobiol.* **55**, 531–543.
- Xianying, J., Youfo, X., and Rongcai, J. (1981). "Acoustic signals and acoustic behavior of the Chinese River Dolphin (*Lipotes vexillifer*)," *Sci. Sin.* **24**, 407–415.
- Zapata-Rios, G., and Utreras, V. B. (2004). "Notes on the distribution of tucuxi, *Sotalia fluviatilis* (Cetacea: Delphinidae), in Ecuadorian Amazonia," *Lat. Am. J. Aquatic Mamm.* **3**, 85–87.

Patterned burst-pulse vocalizations of the northern right whale dolphin, *Lissodelphis borealis*

Shannon Rankin

Southwest Fisheries Science Center, 8604 La Jolla Shores Drive, La Jolla, California 92037

Julie Oswald

Scripps Institution of Oceanography, University of California San Diego, La Jolla, California 92038

Jay Barlow

Southwest Fisheries Science Center, 8604 La Jolla Shores Drive, La Jolla, California 92037

Marc Lammers

Hawaii Institute of Marine Biology, University of Hawaii, Kaneohe, Hawaii 96744

(Received 24 May 2006; revised 4 November 2006; accepted 11 November 2006)

Vocalizations from the northern right whale dolphin, *Lissodelphis borealis*, were recorded during a combined visual and acoustic shipboard survey of cetacean populations off the west coast of the United States. Seven of twenty single-species schools of *L. borealis* produced click and pulsed vocalizations. No whistles were detected during any of the encounters. Clicks associated with burst-pulse vocalizations were lower in frequency and shorter in duration than clicks associated with echolocation. All burst-pulse sounds were produced in a series containing 6–18 individual burst-pulses. These burst-pulse series were stereotyped and repeated. A total of eight unique burst-pulse series were detected. Variation in the temporal characteristics of like units compared across repeated series was less than variation among all burst-pulses. These stereotyped burst-pulse series may play a similar communicative role as do stereotyped whistles found in other delphinid species. © 2007 Acoustical Society of America. [DOI: 10.1121/1.2404919]

PACS number(s): 43.80.Ka, 43.30.Sf [WWA]

Pages: 1213–1218

I. INTRODUCTION

The northern right whale dolphin, *Lissodelphis borealis*, is a slender, elongated delphinid species distinguished by the lack of a dorsal fin and is endemic to the North Pacific. It is one of the more abundant species in its range, which extends from Baja California to Alaska in the eastern Pacific and from Japan to the Aleutians in the western Pacific (Baird and Stacy, 1991). The population size off the west coast of the United States has been estimated as 20 632 (CV=0.26, Barlow, 2003). *Lissodelphis borealis* schools range from single animals to groups of greater than 2000 individuals, with average group sizes of approximately 100–200 animals (Rice, 1998; Jefferson *et al.*, 1994). They often associate with other species, particularly Pacific white-sided dolphins (*Lagenorhynchus obliquidens*).

Despite their relatively high abundance, little is known about the biology, behavior, or vocalizations of *L. borealis*. Vocalizations produced by other delphinids include whistles, burst-pulses, and echolocation clicks (Thomson and Richardson, 1995). The few acoustic recordings of *L. borealis* that have been reported in the literature include all three of these vocalization types (Fish and Turl, 1976; Leatherwood and Walker, 1979). The bulk of the reported vocalizations were echolocation clicks with energy that extended beyond the frequency sensitivity of the recording equipment (40 kHz).

In the fall of 2001, a combined visual and acoustic survey of cetaceans was conducted off the west coast of the United States (Appler *et al.*, 2004). During this survey, twenty single-species groups of *L. borealis* were encoun-

tered. Vocalizations were detected from seven of these groups, providing a unique opportunity to gain insight into the vocal behavior of this species. This paper describes the characteristics of individual vocalizations and series of vocalizations recorded during these seven encounters with *L. borealis*.

II. METHODS

The ORCAWALE 2001 research survey combined visual line-transect and acoustic methods on the NOAA ship R/V *David Starr Jordan* to study cetacean populations within the exclusive economic zone off the west coast of Oregon, California, and Washington. Visual methods consisted of a team of three experienced visual observers searching with “big-eye” 25×150 power binoculars, 7× binoculars, and unaided eye (Appler *et al.*, 2004). All visual sightings were approached for accurate species identification and group size estimation.

A five-element hydrophone array (Sonatech, Inc., Santa Barbara) was towed at a depth of 2–4 m, 200 m behind the ship at 10 knots during daylight hours. The hydrophone array had a flat frequency response from 1.5 to 40 kHz (± 4 dB at -132 dB re 1 ν/μ Pa after internal amplification). Signals from the array were sent through a Mackie CR1604-VLZ mixer for equalization. Vocalizations detected on all hydrophones were recorded to a Tascam DA-38 eight-channel digital recorder (sample rate 48 kHz). Simultaneous (but not continuous) broadband recordings were made directly to a computer hard disk (sample rate 250 kHz) after being filtered

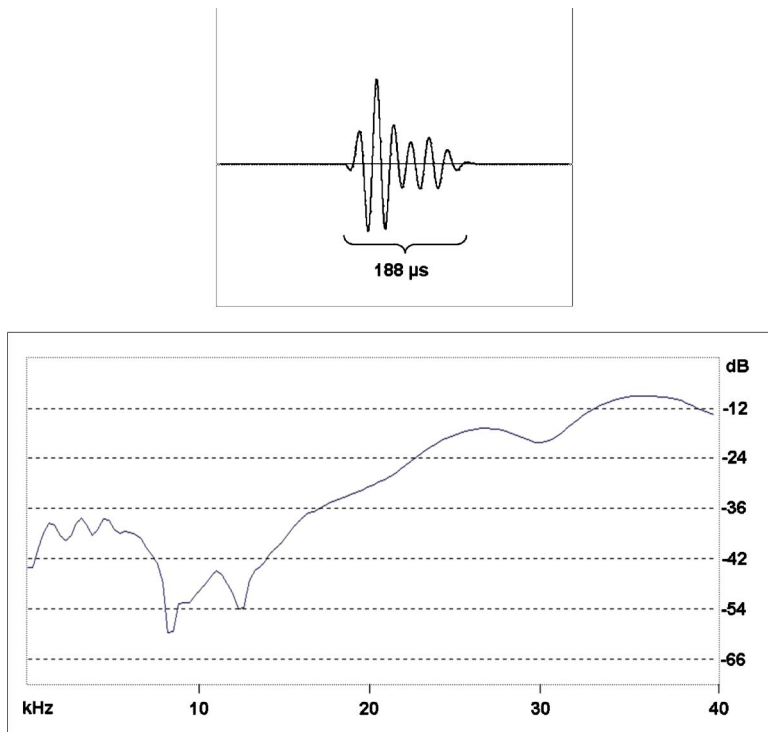


FIG. 1. Waveform and frequency spectrum of *Lissodelphis borealis* echolocation click. Orientation of the sound source relative to the hydrophone is unknown and is likely off-axis. Sample rate 250 kHz, 512 FFT size, 25% overlap.

at the Nyquist frequency (125 kHz) using an Avens Model 4128 band pass filter. Hard disk recordings were digitized using an analog-to-digital conversion card (National Instruments DAQCard-6062E) and automatic recording function within ISHMAEL, a real-time digital signal processing program (Mellinger, 2001).

Only recordings from confirmed single-species groups of *L. borealis* were included in the analysis. In addition, vocalizations were localized using ISHMAEL's beamforming function to ensure that the recorded vocalizations were produced by the observed animals. High quality echolocation click trains and burst-pulses were chosen from broadband digital recordings to examine characteristics of individual vocalizations. Vocalizations were considered to be high quality if they were greater than 9 dB above ambient noise. Given our sampling rate, the Nyquist frequency (125 kHz) greatly exceeded the upper bandwidth of our hydrophone (40 kHz), allowing us to better resolve the waveform of the clicks. However, the sensitivity of our hydrophones drops off dramatically above 40 kHz and it is probable that additional peaks in energy occur above 40 kHz. Individual clicks were measured using a MATLAB signal processing algorithm written by Lammers *et al.* (2004). Variables measured from individual clicks include: Peak frequency (Hz), 3 dB bandwidth (Hz), 10 dB bandwidth (Hz), and click duration (ms). In addition, inter-click interval (ms) and click train duration (ms) were measured from individual burst-pulses.

Individual burst-pulses always occurred in consistent, repeated patterns of six or more burst-pulse units. These repeated burst-pulse series were examined to compare the characteristics of a particular burst-pulse against the same unit in a successive burst-pulse series. Presence of the burst-pulse series was examined using the continuous Tascam recordings, which offered localization options using the phone-pair bearing algorithm in ISHMAEL (Mellinger, 2001).

Measurements of variation for a sample burst-pulse series were taken from the broadband recordings.

III. RESULTS

Twenty single-species schools *L. borealis* were sighted during the ORCAWALE 2001 survey. Vocalizations were recorded from seven of these sightings, including 28 min of broadband digital recordings (250 kHz sample rate) from five sightings and 162 min of Tascam recordings (48 kHz sample rate) from seven sightings. Group sizes of nonvocal sightings of *L. borealis* ranged from 2 to 15 animals ($n=13$, mean=7.2); group sizes of vocal sightings of *L. borealis* ranged from 6 to 63 animals ($n=7$, mean=27.3).

A total of 1142 echolocation clicks were measured from the broadband digital recordings (Table I). Peak frequency of echolocation clicks was 31.3 kHz (SD=3.7 kHz), and the maximum frequency ranged above the 40 kHz high-frequency response of the recording system. The waveform and spectrum of a typical echolocation click is shown in Fig. 1. Mean click duration for echolocation clicks was 0.31 ms (SD=0.08) (Table I).

TABLE I. Summary statistics (mean, standard deviation, minimum, and maximum) for individual echolocation clicks ($n=1,142$) recorded from *Lissodelphis borealis*.

	Peak frequency (Hz)	Bandwidth (Hz)		Click duration (ms)
		3 dB	10 dB	
Mean	31 340	9411	18 891	0.31
Standard Deviation	3660	2895	5198	0.08
Minimum	23 193	4639	8301	0.09
Maximum	41 016	21 729	33 447	0.63

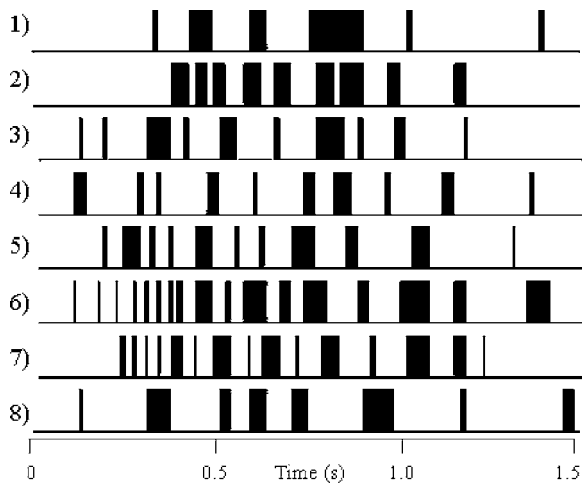


FIG. 2. Graphical representation of eight unique stereotyped burst pulse series encountered during this research. The width of the burst pulse units (black) and intervals (white) are proportional to the durations of each.

A total of 2974 clicks from 129 burst-pulses were measured from the broadband digital recordings (Table II). The mean peak frequency of burst-pulse clicks was 18.2 kHz (SD=5.5 kHz), with a 10 dB bandwidth greater than 22 kHz (mean=22.7 kHz, SD=7.0 kHz). The mean individual click duration was 0.18 ms (SD=0.06). The burst-pulse duration varied from 0.18 to 1.3 s, and burst-pulses were composed of between 2 and 159 individual clicks (Table II).

All burst pulses detected in these recordings occurred in a series, where each series was composed of 6–18 individual burst-pulse units. A total of eight unique stereotyped burst-pulse series were detected during the 162 min of Tascam recordings (Fig. 2), and most series were repeated in succession (Fig. 3). Based on our localizations, we determined that no more than one of the stereotyped burst pulse series was attributed to a single subgroup within a sighting. We could not determine whether the same individual was producing each stereotyped series. Some variation did exist among repetitions and included changes in one or more individual units within the series (Fig. 4).

One repeated burst-pulse series was chosen for closer examination of this variability. Ten units [Figs. 4(a)–4(j)], were present within this stereotyped burst pulse series. Ten variables (Table III) were measured to characterize each unit from up to eight of these repeated series (signal quality did not allow all measurements to be made on all units in each series). Analysis of variance (ANOVA) on each type of mea-

surement indicates that none of the frequency measures (peak frequency, center frequency, and three different measures of bandwidth) varied significantly among the units ($p > 0.05$). Most temporal characteristics (click interval, burst-pulse duration, clicks per burst pulse, and burst-pulse interval) did vary significantly among units ($p < 0.0001$), but click duration did not ($p = 0.066$).

IV. DISCUSSION

The study of broadband clicks produced by free ranging delphinids in offshore habitats is challenging due to the highly directional nature of these sounds as well as bandwidth limitations of recording equipment. Temporal, frequency, and amplitude characteristics of clicks vary depending on the orientation of the animal relative to the hydrophone (Au, 1993). In experiments with captive animals on bite plates it is possible to ensure that signals are recorded on-axis. This is difficult, if not impossible, in free ranging situations due to rapid changes in the orientation of the animals and difficulty in identifying which animal in a group is vocalizing. However, while controlled experiments with trained animals provide important data about signal characteristics and sonar capabilities, they do not allow a full understanding of the function and use of these signals in natural habitats. In addition, passive acoustic techniques are increasingly being utilized as a method to monitor cetacean populations (Goold, 1998; Rankin and Barlow, 2005; Stafford *et al.*, 2001). The ability to identify species based on their vocalizations is imperative in these situations, and this is especially important for species such as *L. borealis* for which very few descriptions of vocalizations exist and the likelihood of a controlled study in captivity is small. Despite the limitations of *in situ* recordings from wild dolphins, these data are essential in learning to distinguish dolphin species using their vocalizations.

A previous description of free-ranging *L. borealis* vocalizations included two types of whistles recorded in the presence of a small group of *L. borealis* (Leatherwood and Walker, 1979). A high frequency whistle at 16 kHz that appears to “blend in” to a burst-pulse vocalization was noted and several lower frequency whistles were also described. The lower frequency whistles are similar to those produced by *Globicephala* spp. (Rendell *et al.*, 1999), a species that *L. borealis* have been known to associate with (Jefferson *et al.*, 1994). In contrast to the findings of Leatherwood and Walker (1979), acoustic monitoring in the presence of twenty sight-

TABLE II. Summary statistics (mean, standard deviation, minimum, and maximum) for individual clicks ($n = 2,974$) in burst-pulses recorded from *Lissodelphis borealis*.

	Peak frequency (Hz)	Click interval (ms)	Bandwidth (Hz)		Click duration (ms)	Burst pulse Duration (ms)	Clicks per burst pulse
			3 dB	10 dB			
Mean	18 196	1.15	10 275	22 702	0.18	26.98	24.6
Standard Deviation	5543	0.4	3157	7025	0.06	25.68	24.6
Minimum	6348	0.28	5127	9277	0.08	1.34	2
Maximum	37 109	6.46	28 564	48 340	0.51	178.62	159

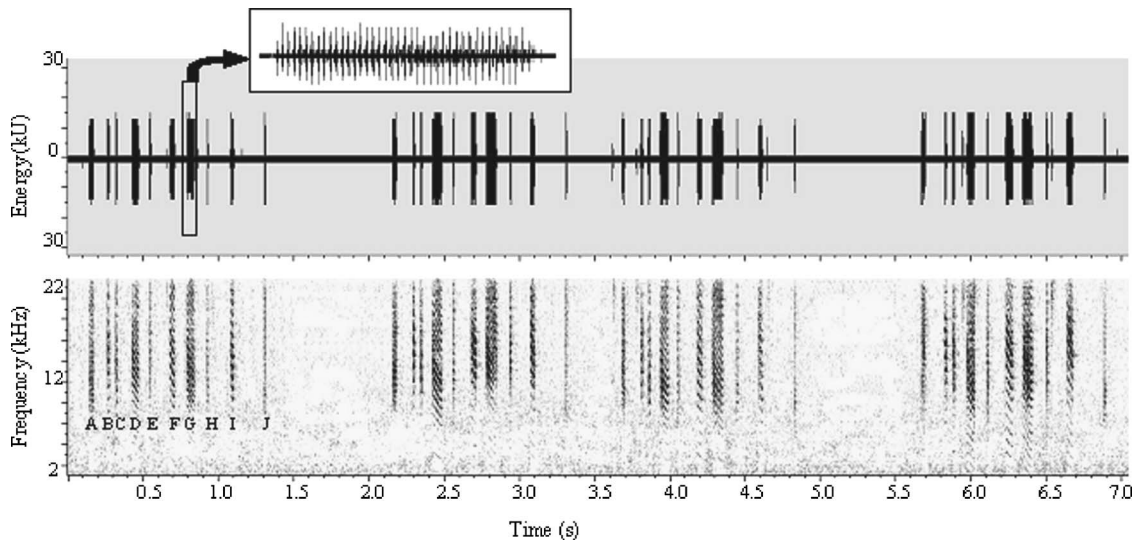


FIG. 3. Waveform and spectrogram of a burst-pulse series repeated four times in succession (Fig. 2, series 4). Inset waveform shows rapid pulsing within individual burst pulses; pulse repetition rate is represented in the frequency banding appearance of the burst pulses in the spectrogram. Individual burst pulse units A–J (Table III) are labeled for the first series. Sampling rate 48 kHz, 512 FFT size, Hann window function.

ings of single-species *L. borealis* schools in this study failed to detect a single whistle. We suggest that the whistles presented in Leatherwood and Walker (1979) may have been produced by another species in the area that was not detected by the research team.

The phylogeny of *Lissodelphis* spp. is not well understood, but they appear to be most closely linked with dolphins of the genus *Lagenorhynchus* and *Cephalorhynchus* under the group Lissodelphinidae (May-Collado and Agnarsson, 2006). *Cephalorhynchus* spp. are not known to produce whistles (Dawson, 1991; Herman and Tavolga, 1980), and a large proportion of the vocalizations recorded in the presence of *Lagenorhynchus* spp. have been click or pulsed sounds. Our research suggests that *Lissodelphis borealis* follows the same trend as other Lissodelphinidae in producing only or predominantly click and pulsed vocalizations.

While bandwidth and logistical constraints in this study prevent detailed descriptions of the click sounds of *L. borealis*,

general trends, and characteristics can be noted. For example, clicks associated with burst-pulses were shorter in duration and had lower peak and center frequencies than those associated with echolocation click trains. This is similar to what has been found in other delphinids and it has been suggested that these burst-pulse sounds may function in communication (Lammers *et al.*, 2004; Dawson, 1991).

The recordings presented in this study allow a general characterization of the vocalizations themselves, but also provide insight into the signaling behavior of *L. borealis*. Previous studies of odontocete vocalizations have found differences in the function of stereotyped calls across taxonomic groups. In dolphins, repeated stereotyped whistles are unique at an individual level (Caldwell *et al.*, 1990; Janik and Slater, 1998; McCowan and Reiss, 2001), while stereotyped discrete calls in *O. orca* are shared between matrilineal groups (Ford, 1991; Miller and Bain, 2000). *P. macrocephalus* codas, on the other hand, appear to function at larger

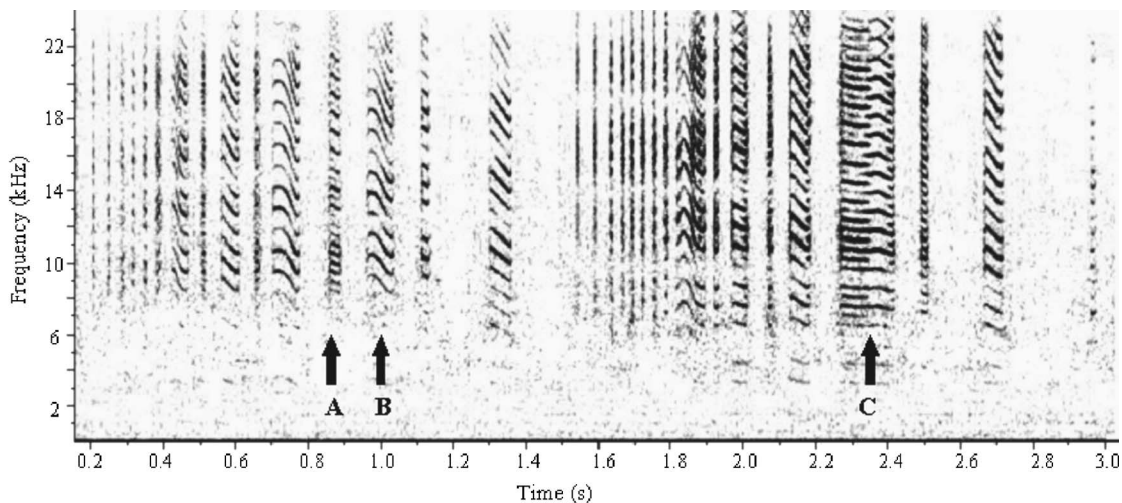


FIG. 4. Variation in burst-pulse series (Fig. 2, series 6). The individual burst-pulse units highlighted by (a) and (b) are replaced by (c) during one of six repeated burst pulse series. Sampling rate 48 kHz, 512 FFT size, Hann window.

TABLE III. Summary statistics for burst-pulse units (identified as A–J) within the repeated burst-pulse series shown in Fig. 1 ($n=8$). The burst-pulse interval is measured from the end of the lettered unit to the beginning of the next lettered unit.

Unit		Sample size	Peak frequency (Hz)	Click interval (ms)	Bandwidth (Hz)		Click duration (ms)	Burst pulse duration (ms)	Clicks per burst-pulse	Burst-pulse interval (s)
					3 dB	10 dB				
A	Mean	6	19 595	1.96	9705	18757	0.16	19.54	9.8	0.115
	Standard Deviation		4867	0.46	1841	5112	0.02	8.23	3.7	0.008
B	Mean	5	17 177	1.10	7707	14 304	0.22	13.18	13.0	0.039
	Standard Deviation		5353	0.75	946	2400	0.08	5.22	2.5	0.004
C	Mean	5	18 804	0.79	8457	16 428	0.18	9.79	12.2	0.085
	Standard Deviation		4958	0.03	1110	2451	0.02	2.17	2.8	0.009
D	Mean	7	17 519	1.13	9449	18 536	0.18	34.84	29.6	0.073
	Standard Deviation		4799	0.18	1131	4119	0.02	14.61	10.8	0.006
E	Mean	8	16 086	0.98	8643	18 811	0.17	9.71	9.1	0.114
	Standard Deviation		5711	0.07	1026	4205	0.02	12.93	11.3	0.007
F	Mean	5	18 165	0.89	8016	15 399	0.20	27.14	31.0	0.071
	Standard Deviation		5559	0.05	1198	2518	0.02	14.57	17.1	0.003
G	Mean	7	17 705	1.11	9161	18 569	0.17	45.74	40.7	0.088
	Standard Deviation		4369	0.10	1061	4178	0.01	12.31	9.3	0.005
H	Mean	7	18 883	1.02	8831	18 248	0.17	11.68	10.7	0.134
	Standard Deviation		6848	0.06	1302	4129	0.02	16.00	13.8	0.013
I	Mean	6	19 152	0.93	7887	16 181	0.19	19.03	20.5	0.209
	Standard Deviation		6873	0.07	883	2961	0.01	10.82	12.0	0.011
J	Mean	6	19 706	1.07	8287	15 675	0.19	13.07	14.0	...
	Standard Deviation		5911	0.18	1157	2330	0.02	13.34	16.3	...

population levels (Watkins and Schevill, 1977; André and Kamminga, 2000). Caldwell and Caldwell (1966) described individual variation in a stereotyped burst-pulse recorded from a captive *Lagenorhynchus obliquidens*, and suggested the existence of a “signature” burst-pulse vocalization. Simple stereotyped burst-pulse vocalizations have also been examined for Risso’s dolphins, *Grampus griseus* (Corkeron and Van Parijs, 2001). However, the repeated series of burst-pulses presented here appear to be complex stereotyped patterning of burst-pulses that has not been previously described in cetaceans.

Each unique burst pulse series detected during this survey were localized to the same subgroup of animals within a sighting. Therefore, a particular burst pulse series was produced by either a single individual or by the different individuals within a given subgroup. Specific burst pulse series were not detected in more than one sighting or more than one subgroup within a sighting. Our research suggests that *L. borealis* do not whistle, and that the stereotyped burst-pulse series that they do produce may serve the same communicative function as the stereotyped whistles produced by other delphinids or the stereotyped discrete calls found in *O. orca*.

While our research presents the existence of repeated patterns of stereotyped burst pulses in *L. borealis*, we can only speculate as to the behavioral function of these vocalizations. Future research should examine these burst pulse series to determine if they are unique to individuals, suggesting the possibility of a behavioral context similar to the repeated stereotyped whistle produced by other small dolphins, or if burst pulse series are shared by other related individuals, suggesting a behavioral context similar to the discrete calls of killer whales.

ACKNOWLEDGMENTS

This research could not have been accomplished without the dedicated efforts of the officers and crew of the R/V *David Starr Jordan*. Many thanks to the field scientists who made ORCAWALE a successful survey, especially Megan Ferguson, Tony Martinez, and Jessica Burtenshaw for their assistance with acoustics. Funding was provided by the U.S. Navy and Southwest Fisheries Science Center.

- André, M., and Kamminga, C. (2000). “Rhythmic dimension in the echolocation click trains of sperm whales: a possible function of identification and communication,” *J. Mar. Biol. Assoc. U.K.* **80**, 163–169.
- Appler, J., Barlow, J., and Rankin, S. (2004). “Marine mammal data collected during the Oregon, California, and Washington line-transect expedition (ORCAWALE) conducted aboard the NOAA ships *McArthur* and *David Starr Jordan*,” July–December 2001. NOAA Tech. Mem. NOAA-TM-NMFS-SWFSC-359. Available from SWFSC, 8604 La Jolla Shores Dr., La Jolla, CA 92037, p. 32.
- Au, W. W. L. (1993). *The Sonar of Dolphins* (Springer-Verlag, Berlin), p. 277.
- Baird, R. W., and Stacey, P. J. (1991). “Status of the northern right whale dolphin *Lissodelphis borealis*, in Canada,” *Canadian Field Naturalist* **105**, 243–250.
- Barlow, J. (2003). “Preliminary estimates of the abundance of cetaceans along the U.S. west coast: 1991–2001,” Southwest Fisheries Science Center Administrative Report LJ-03-03. Available from SWFSC, 8604 La Jolla Shores Dr., La Jolla, CA 92037, p. 31.
- Caldwell, M. C., and Caldwell, D. K. (1966). “Intraspecific transfer of information via the pulsed sound in captive odontocete cetaceans,” in *Animal Sonar Systems: Biology and Bionics*, Vol 2, edited by Rene-Guy Busnel, Symposium of the Animal Sonar System, Frascati, NATO Advanced Study Institute, France, pp. 879–935.
- Caldwell, M. C., Caldwell, D. K., and Tyack, P. L. (1990). “Review of the signature-whistle hypothesis for the Atlantic bottlenose dolphins, *Tursiops truncatus*,” in *The Bottlenose Dolphin*, edited by S. Leatherwood and R. R. Reeves (Academic Press, San Diego), pp. 199–234.
- Corkeron, P. J., and Van Parijs, S. M. (2001). “Vocalizations of eastern

- Australian Risso's dolphins, *Grampus griseus*," Can. J. Zool. **79**, 160–164.
- Dawson, S. M. (1991). "Clicks and communication: The behavioral and social contexts of Hector's dolphins vocalizations," Ethology **88**, 265–276.
- Fish, J. F., and Turl, C. W. (1976). "Acoustic source levels of four species of small whales," Naval Undersea Center Tech. Rep. TP547, pp. 1–14.
- Ford, J. K. B. (1991). "Vocal traditions among resident killer whales (*Orcinus orca*) off Vancouver Island, British Columbia, Canada," Can. J. Zool. **67**, 727–745.
- Goold, J. C. (1998). "Acoustic assessment of common dolphins off the west Wales coast, with perspectives from satellite infrared imagery," J. Mar. Biol. Assoc. U.K. **78**, 1353–1364.
- Herman, L. M., and Tavolga, W. N. (1980). "The communication systems of cetaceans," in *Cetacean behavior: Mechanisms and functions*, edited by L. M. Herman (Wiley, New York), pp. 149–209.
- Janik, V. M., and Slater, P. J. B. (1998). "Context-specific use suggests that bottlenose dolphin signature whistles are cohesion calls," Anim. Behav. **56**, 829–838.
- Jefferson, T. A., Newcomer, M. W., Leatherwood, S., and van Waerebeek, K. (1994). "Right whale dolphins - *Lissodelphis borealis* (Peale, 1848) and *Lissodelphis peronii* (Lacépède, 1804)," in *Handbook of Marine Mammals - Vol. 5: The first book of dolphins*, edited by S. H. Ridgway and S. R. Harrison (Academic, London), pp. 335–362.
- Lammers, M. O., Au, W. W. L., and Aubauer, R. (2004). "A comparative analysis of echolocation and burst-pulse click trains in *Stenella longirostris*," in *Echolocation in Bats and Dolphins*, edited by J. Thomas, C. Moss, and M. Vater (University of Chicago Press), pp. 414–419.
- Leatherwood, S., and Walker, W. A. (1979). "The northern right whale dolphin *Lissodelphis borealis* Peale in the eastern North Pacific," in *Behavior of marine animals, Vol. 3: Cetaceans*, edited by H. E. Winn and B. L. Olla (Plenum, New York), pp. 85–141.
- May-Collado, L., and Agnarsson, I. (2006). "Cytochrome *b* and Bayesian inference of whale phylogeny," Mol. Phylogenet. Evol. **38**, 344–354.
- McCowan, B., and Reiss, D. (2001). "The fallacy of 'signature whistles' in bottlenose dolphins: A comparative perspective of 'signature information' in animal vocalizations," Anim. Behav. **62**, 1151–1162.
- Mellinger, D. K. (2001). ISHMAEL 1.0 User's Guide. NOAA Technical Memorandum OAR PMEL-120, available from NOAA/PMEL, 7600 Sand Point Way NE, Seattle, WA 98115-6349. Miller, P. J. O., and Bain, D. E. (2000). "Within-pod variation in killer whale calls," Anim. Behav. **60**, 617–628.
- Rankin, S., and Barlow, J. (2005). "Source of the North Pacific 'boing' sound attributed to minke whales," J. Acoust. Soc. Am. **118**(5), 3346–3351.
- Rendell, L. E., Matthews, J. N., Gill, A., Gordon, J. C. D., and McDonald, D. W. (1999). "Quantitative analysis of tonal calls from five odontocete species, examining interspecific and intraspecific variation," J. Zool. **249**, 403–410.
- Rice, D. W. (1998). "Marine mammals of the world: Systematics and distribution," Society for Marine Mammalogy, Special Publication Number 4, edited by D. Wartzok, Lawrence, KS.
- Stafford, K. M., Nieuwkerk, S. L., and Fox, C. G. (2001). "Geographic and seasonal variation of blue whale calls in the North Pacific," J. Cetacean Res. Manage. **3**(1), 65–76.
- Thomson, D. H., and Richardson, W. J. (1995). "Marine mammal sounds," in *Marine Mammals and Noise*, edited by W. J. Richardson, C. R. Greene, Jr., C. I. Malme, and D. H. Thomson (Academic, San Diego), pp. 159–204.
- Watkins, W. A., and Schevill, S. E. (1977). "Sperm whale codas," J. Acoust. Soc. Am. **62**, 1485–2490.

Spatial release from masking of aerial tones in pinnipeds

Marla M. Holt^{a)}

Ocean Sciences Department, University of California, Santa Cruz, Long Marine Laboratory,
100 Shaffer Road, Santa Cruz, California 95060

Ronald J. Schusterman

Institute of Marine Sciences, University of California, Santa Cruz, Long Marine Laboratory,
100 Shaffer Road, Santa Cruz, California 95060

(Received 7 August 2006; revised 3 November 2006; accepted 11 November 2006)

In most masking experiments, target signals and sound intended to mask are located in the same position. Spatial release from masking (SRM) occurs when signals and maskers are spatially separated, resulting in detection improvement relative to when they are spatially co-located. In this study, SRM was investigated in a harbor seal, who naturally lacks pinnae, and California sea lion, who possesses reduced pinnae. Subjects had to detect aerial tones at 1, 8, and 16 kHz in the presence of octave bands of white noise centered at the tone frequency. While the masker occurred in front of the subject (0°), the tone occurred at 0, 45, or 90° in the horizontal plane. Unmasked thresholds were also measured at these angles to determine sensitivity differences based on source azimuth. Compared to when signal and masker were co-located, masked thresholds were lower by as much as 19 and 12 dB in the harbor seal and sea lion, respectively, when signal and masker were separated. Masked threshold differences of the harbor seal were larger than those previously measured under water. Performance was consistent with some measurements collected on terrestrial animals but differences between subjects at the highest frequency likely reflect variations in pinna anatomy. © 2007 Acoustical Society of America. [DOI: 10.1121/1.2404929]

PACS number(s): 43.80.Lb, 43.80.Nd, 43.66.Dc [WWA]

Pages: 1219–1225

I. INTRODUCTION

The directional hearing systems of many vertebrates have been shown to enhance the reception of relevant acoustic signals in the presence of noise (NRC, 2003). For example, when a target signal and masker have separate spatial locations, detection and identification of the target signal is improved relative to the condition when the signal and masker are located in the same place. This phenomenon has been termed spatial release from masking (SRM) or spatial unmasking and can significantly increase the detection range of signals such as those of conspecifics, prey, or predators.

In both air and water, pinnipeds (seals, sea lions, and walruses) are often faced with the challenge of detecting socially and reproductively important sounds in a background of ambient noise. Auditory masking in pinnipeds has been relatively well documented in a few species given appreciable concerns regarding ocean noise, human activity, and their potential negative effects on free-ranging marine mammals (Terhune and Ronald, 1975; Turnbull and Terhune, 1990; Turnbull, 1994; Southall *et al.*, 2000; Southall *et al.*, 2003a). In all but one pinniped masking study (Turnbull, 1994), the auditory signals and maskers were spatially coincident despite the fact that in everyday experiences, signals and maskers may take on a vast number of different spatial

configurations relative to each other. In fact, only a handful of masking studies in nonhuman subjects have investigated the effects of SRM.

The earliest work on masking and spatial hearing documented this effect in human subjects wearing earphones by presenting a low frequency signal 180° out of phase between the two ears while the noise masker remained in phase (e.g., Hirsh, 1948; Jeffress *et al.*, 1962). Because interaural phase differences are the dominant spatial cues for azimuth localization at low frequencies, the assumption followed that detection would improve if the signal is spatially separated from the masker (Yost, 1997). Other interaural disparities projected through earphones that resulted in release from masking include onset time and level differences (Colburn and Durlach, 1965; Zerlin, 1966) as well as frequency differences (Robinson, 1971). Thus, from these early studies with humans, a binaural system seemed to have advantages over a monaural one not only for sound localization in the horizontal plane but also for the detection of signals in the presence of noise.

Subsequent investigations have shown that SRM in humans also occurs in “free-field” environments at most frequencies (Santon, 1987; Terhune and Turnbull, 1989; Saberi *et al.*, 1991; Gilkey and Good, 1995). While interaural time cues are important for SRM at azimuth in the case of low frequency signals, monaural spectral cues, which also govern localization in the vertical plane, are the predominant cues necessary for release from masking for high frequency target signals (Gilkey and Good, 1995; Gilkey *et al.*, 1997; Zurek *et al.*, 2004). Furthermore, SRM has been observed for signal and masker configurations spatially separated in the vertical

^{a)}Current address: National Oceanic and Atmospheric Administration, National Marine Fisheries Services, Northwest Fisheries Science Center, 2725 Montlake Blvd. East, Seattle, Washington 98112. Electronic mail: marla.holt@noaa.gov

plane, although the effects tend to be smaller in magnitude than those measured in the horizontal plane (Saberi *et al.*, 1991; Gilkey and Good, 1995). These monaural cues are created by differences in signal to (masking) noise level ratios in frequency dependent ways from both near or “better ear” effects as well as binaural input differences (Shinn-Cunningham *et al.*, 2005).

Measures of spatial release from masking in nonhuman mammals are limited to a few studies including those conducted in air in ferrets (*Mustela putorius*; Hine *et al.*, 1994) and mice (*Mus musculus*; Ison and Agrawal, 1998), and under water in a dolphin (*Tursiops truncatus*; Au and Moore, 1984) and harbor seal (*Phoca vitulina*; Turnbull, 1994). In these studies, when the signal source and masker were located at different points in either the horizontal or vertical plane, masked thresholds were lower in most conditions relative to the condition in which the signal and masker were either spatially co-located or heard monaurally. In the Hine *et al.* (1994) investigation, SRM for low frequencies was due to binaural processing given that monaural conditions abolished the detection advantages of spatially separating the signal and masker. On the other hand, release from masking occurred with high but not low frequencies in mice subjects (Ison and Agrawal, 1998). Likewise, these animals have been shown to localize high but not low frequencies in the horizontal plane, indicating that they cannot use interaural time differences for either auditory process (Ison and Agrawal, 1998). In the underwater marine mammal investigations, it is unclear whether or not performance was influenced by monaural spectral cues, binaural cues, or some combination of both. Turnbull (1994) found that spatial release from masking (threshold differences for co-located versus separated sources) generally grew with increasing spatial separation by up to 4 dB but depended on both test frequency and masker location. Although these threshold differences measured under water were small, those based on interaural cues would likely be greater in air. Given the faster travel time and longer wavelengths of sound in water relative to air, the magnitude of interaural differences as well as monaural spectral cues created by the shadowing effects of the body are diminished in an aquatic medium. For example, pinniped localization acuity, which is based on these two binaural cues, is worse under water than in air by a factor that is predicted based on these propagation differences (Terhune, 1974; Moore and Au 1975; Holt *et al.*, 2004).

Localization performance of most pinnipeds tested in azimuth, including harbor seals and California sea lions (*Zalophus californianus*), is consistent with the duplex theory (low frequencies are localized by interaural time differences and high frequencies by interaural level differences; Strutt, 1907; Terhune, 1974; Moore and Au 1975; Holt *et al.*, 2005). If SRM in the horizontal plane is governed by the same binaural cues that dictate localization performance then it is expected that the effects of SRM will be comparable at the lower and higher frequencies in the harbor seal and California sea lion. Additionally, these effects are expected to be reduced at intermediate frequencies in which both binaural cues are reduced in magnitude. On the other hand, if monaural filtering effects of the external ears, head, and body are

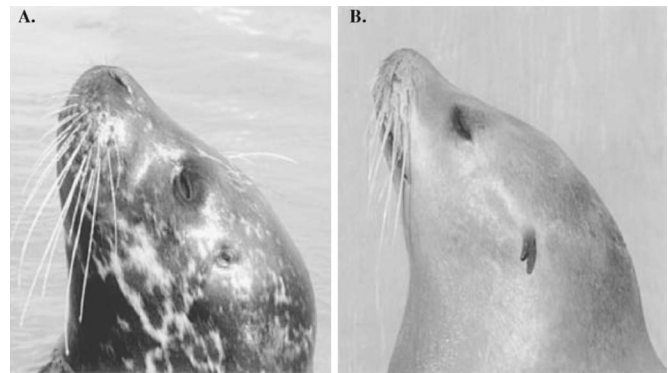


FIG. 1. External ears of the (A.) harbor seal on the left and (B.) California sea lion on the right (see text for discussion).

responsible for SRM at higher frequencies, differences in performance and the extent of SRM between seals and sea lions are expected at these frequencies given that there are considerable variations in the presence and configurations of the external ears between the two pinniped taxa. Figure 1 shows that the harbor seal lacks pinnae while the sea lion possesses pinnae which are considerably reduced in size compared to most terrestrial mammals. Thus, it is hypothesized that if the monaural effects of the external ears (as well as the head and body) rather than interaural level differences are responsible for SRM at high frequencies, then the size of the observed SRM will differ between the two subjects at higher frequencies.

Spatial release from masking in free-ranging animals has important implications for understanding how masking interferes with the reception of important signals, such as intraspecific vocalizations. This is relevant for considering detection in noise from both natural and anthropogenic sources, particularly for directional maskers (see Zurek *et al.*, 2004). For example, masking effects of noise from oil-spill cleanup vessels on the reception of killer whale (*Orcinus orca*) vocalizations was investigated in two trained killer whales. Results showed that masking was reduced when signal and noise sources were separated (Bain and Dahlheim, 1994). Furthermore, spatial release from masking may result in larger detection ranges of calls (e.g., of those enabling female and offspring to reunite) which in turn may have significant consequences for survival and fitness.

In this study, spatial release from masking was investigated in air in two pinniped subjects (a female California sea lion and a male harbor seal) to determine potential detection advantages that might be afforded by free-ranging pinnipeds from this type of auditory process. Both masked and unmasked thresholds were measured for all signal locations to determine what contribution azimuth-dependent hearing sensitivity had on SRM.

II. METHODS

A. Subjects

The subjects were a 17-year-old male harbor seal (Sprouts) and a 20-year-old female California sea lion (Rio). Both subjects were resident animals at Long Marine Laboratory in Santa Cruz, CA and had extensive previous experi-

ence performing sound detection tasks in the presence and absence of masking noise in air (Southall *et al.*, 2003a; Reichmuth Kastak *et al.*, 2004). For the current study, subjects received up to 50% of their daily food totals (2.5–5.5 kg of mixed herring and capelin) during experimental sessions. This study followed the protocols approved by the University of California Chancellor's Animal Research Committee.

In a previous localization investigation, both subjects could localize 1 and 16 kHz tones with equal proficiency, indicating that they both possess comparable abilities to utilize interaural time and level differences. However, both had more difficulty localizing a 8 kHz tone (Holt *et al.*, 2005). Thus, these frequencies were used in this study to determine, if like localization, there exists predictable frequency-dependent effects on SRM performance.

B. Apparatus

Testing occurred in a custom-built $4.0 \times 2.8 \times 2.4$ m double-walled hemi-anechoic chamber (Eckel Industries) as described in Holt *et al.* (2004). All surfaces of the test chamber were lined with acoustic foam wedges except the concrete floor and stainless steel door, which were covered with 2.6 cm neoprene mats. A stationing chin cup made of polyvinyl chloride (PVC) was mounted to the floor and placed 1 m from the sound sources mounted to the wall in front of the chin cup. One rectangular PVC response target (each 11.4×8.9 cm) was also mounted to the floor and spaced to the left side of the chin cup.

C. Stimulus production and equipment

All equipment was controlled by the experimenter in a $1.3 \times 2.8 \times 2.4$ m control room adjacent to the test chamber. The signals were pure tones at 1, 8, and 16 kHz generated and triggered by the experimenter using custom designed LABVIEW™ 6 software and operated by a National Instruments PXI 1010 Chassis and National Instruments 6070E multifunction input/output (I/O) board. The signal duration was 500 ms and was shaped with a linear rise and fall time of 20 ms. The signal was routed to a stepwise attenuator (Hewlett-Packard 350D) and then to a speaker (Morel MDT37 horn tweeter for 1 and 8 kHz or Fostex FT96H horn tweeter for 16 kHz tone) placed at 0° , 45° , or 90° relative the subject's head.

The masker was an octave band of white noise in which the center frequency was set to the target signal. The masker was generated (sampling rate 48 000 Hz, 16 bit resolution) and filtered on a PC laptop using Cool Edit Pro software (Syntrillium). A six second sample of the masker was fed from the sound card output of the laptop to the input channel of a 20 W power amplifier (Radio Shack MPA-40). The masker source was always placed at 0° and was only presented during the trial interval to prevent potential confounding effects of loudness adaptation (Southall *et al.*, 2000). When the signal was projected at 0° , the signal and masker were mixed into the power amplifier and broadcast through the same speaker.

Signal and masker levels were determined using a calibrated free-field microphone (C550H, Josephson Engineering, Santa Cruz, CA) and a spectrum analyzer (SpectraPlus). The sound pressure level of the signal (dB rms re: $20 \mu\text{Pa}$) and noise spectral density level of the masker (dB re: $\mu\text{Pa}^2/\text{Hz}$) were determined at a position corresponding to the center of the subject's head (with the subject removed) for each of the test angles at the beginning and end of each experimental session. Acoustic mapping was performed prior to experimental testing in which received masker and signal levels were measured for each possible source location. For each azimuth location, received levels were mapped at 27 separate positions within a $20 \times 20 \times 20$ cm area surrounding the chin cup of the test apparatus to ensure that signal and masker level variation fell between ± 3 dB. Unmasked sound detection thresholds for each signal location were determined using methods described below. The average masker spectral density level was approximately 5–20 dB above the unmasked threshold for both subjects, a value set by hardware limitations of the experimental setup. These differences were not likely to affect the measured masked thresholds because the signal to noise ratio at masked threshold is generally independent of the masker level (i.e., critical ratios are independent of the masker level, see Fay, 1988).

D. Procedure

A go/no-go procedure was used to determine unmasked and masked thresholds for each subject. A correct response was defined as pressing the response target when a signal was triggered (a hit) and withholding response during trials when no signal was triggered (a correct rejection).

During data collection, subject responses were monitored by the experimenter in the control room via a surveillance camera. Once the animal stationed itself in the chin cup, the trial began with the experimenter illuminating the trial light and, in the case of masked threshold testing, the masking noise was presented. Trial durations were 5 s and signal presentations randomly varied between 1 and 4 s during the trial interval. If a correct response occurred, a digitized whistle bridge was broadcast through a separate speaker (placed on 0° azimuth on the floor), the trial light was turned off, and an assistant sitting in the control room delivered a fish reward via a PVC conduit in front of the subject. Both types of correct responses were given an equal proportion of fish (i.e., a payoff matrix of 1:1). Incorrect responses [responding in the absence of a signal (false alarm) or withholding response during a signal presentation (miss)] were not reinforced. The overall and first order conditional probabilities of signal-present and signal-absent (catch) trials were 0.5 within a testing session. Catch trials were used to monitor false alarm rates in order to maintain comparable response criteria between experimental sessions. Data from sessions were only used if the false alarm rate fell between 5 and 25%. Approximately eight warm-up and cooldown trials were given at the beginning and end of each experimental session in which the signal was approximately 25 dB above

threshold. Warm-up and cooldown trials were used to ensure good stimulus control over the subject's go/no-go behavior but were not included in data analysis.

Two types of psychophysical approaches were used to estimate detection thresholds. To determine a preliminary estimate of both unmasked and masked thresholds, approximately two sessions were conducted using the staircase method (Cornsweet, 1962). For these sessions, signal levels were initially attenuated in 4 dB steps after each correct detection until the first miss. The following signal levels were then adjusted in 2 dB steps (either decreased after a correct detection, or increased after a miss) until nine reversals between misses and hits were conducted. Once a threshold estimate using the staircase method was obtained for a given frequency and signal-masker configuration, method-of-constant stimuli sessions (Stebbins, 1970) were then conducted.

Both unmasked and masked thresholds reported here were estimated only from method-of-constant stimuli sessions. In these sessions, five to six signal levels separated by 2 dB steps around the predicted threshold were presented in random order within the test phase of an experimental session. Performance was pooled across these sessions for each signal level and a 50% correct detection threshold was estimated from signal trial performance using Finney's probit analysis (Finney, 1971). Threshold testing for a particular frequency and condition was completed when the 95% confidence limit of a threshold estimate fell within a ± 3 dB range. This typically required data from two to three experimental sessions, each consisting of approximately 50 trials. Critical ratios were defined as the difference in dB of the masking noise spectrum level at the center frequency of the noise band, measured from the spectral density level of the masker, and the masked threshold sound pressure level.

Testing order for frequencies and locations were randomized to measure thresholds. Unmasked thresholds for each of these signal source locations were first determined. Masked thresholds for each of the signal source locations were then measured. The difference in unmasked and masked thresholds (in dB re: 20 μ Pa) for each signal source location was calculated and masking level differences (MLDs) were computed as defined in Saberi *et al.* (1991):

$$\text{MLD} = [(M_{\theta} - M_{0^{\circ}}) - (U_{\theta} - U_{0^{\circ}})], \quad (1)$$

where $U_{0^{\circ}}$ is the unmasked threshold with the signal projected at 0° , U_{θ} is the unmasked threshold with the signal projected at angle, θ , $M_{0^{\circ}}$ is the masked threshold with the signal projected at 0° , and M_{θ} is the masked threshold with the signal projected at angle θ . These differences were compared to the condition in which the signal and masker were both at 0° . In this way, the effects of varying the spatial configuration of the signal relative to the masker were directly compared to the condition in which the signal and masker were coincident in space while controlling for sensation level effects (Saberi *et al.*, 1991). Note that the sign of MLDs reported here was reversed as in other investigations (e.g. Saberi *et al.*, 1991) and thus, a positive MLD indicates spatial release from masking.

III. RESULTS

Unmasked and masked thresholds and critical ratios for each subject are shown in Table I. Thresholds referenced to those at 0° for each test frequency of the harbor seal and the sea lion are shown in Fig. 2. For the harbor seal, differences of unmasked thresholds at azimuth relative to 0° ranged from -0.6 to -13.1 dB, with the largest differences occurring at the highest test frequency. Differences of masked thresholds at azimuth relative to 0° of this subject ranged from -7.5 to -19.0 dB and were lowest at 90° for all frequencies tested. In contrast, unmasked threshold differences of the sea lion relative to 0° ranged from $+5.0$ to -7.7 dB, with the largest differences occurring at the lowest test frequency. For the sea lion, masked threshold differences relative to 0° ranged from $+1.3$ to -11.7 dB. These differences were lowest at 90° for the 1 and 8 kHz test tones and at 45° for the 16 kHz test tone. For both subjects, Table I shows that critical ratios at 0° for each frequency were in close agreement with those of an earlier study in which the signal and masker were spatially coincident (Southall *et al.*, 2003a).

Masking level differences (MLDs) for each test frequency of the harbor seal and the sea lion are shown in Fig. 3. MLDs of the harbor seal ranged from 0.3 to 6.9 dB and were largest at 90° for the 1 and 16 kHz test tone and at 45° for the 8 kHz tone. In contrast, MLDs of the sea lion ranged from 2.1 to 8.2 dB and were largest at 45° for all three test frequencies, although MLDs at 45° and 90° at 1 kHz were approximately the same.

IV. DISCUSSION

In real world cases, the detection advantages with spatial separation of the signal and the masker are fully described by considering the differences in masked thresholds for co-located versus separated sources. This is because increased sensitivity of a signal from free-field SRM includes both "better ear" effects, that is larger signal to noise ratios at the near ear (Kopco and Shinn-Cunningham, 2003), and monaural and binaural effects that are generated by the relative spatial positions of the signal and masker. Better ear effects may include level gain from filtering mechanisms of the head, torso, and external ears as well as resonance of the ear canal and middle ear structures (Shaw, 1974). These factors may act separately or in combination with one another.

In all conditions in the harbor seal and all but one condition in the sea lion, masked thresholds were lower with spatial separation of signal and masker compared to when they were co-located. Based on previous studies conducted on humans and animals, the largest differences in masked thresholds were expected to occur for the largest separations between signal and masker (i.e., a 90° separation). In most cases, this was observed in both pinniped subjects of this investigation. The average difference in masked threshold from 0° for all frequencies was -10.3 dB for the harbor seal and -6.4 dB for the sea lion. These masked threshold differences were within the range of previous results on humans and other mammals although in some of these studies methodological differences do not justify direct comparisons (Santon, 1987; Terhune and Turnbull, 1989; Saberi *et al.*,

TABLE I. Unmasked and masked thresholds, threshold differences from 0°, masking level differences (MLDs), and critical ratios of each subject for each test condition.

Subject	Frequency (kHz)	Type	Angle (degrees)	Threshold (dB SPL)	Difference from 0°	MLD	Critical ratio
Harbor seal (<i>Phoca</i>)	1	Unmasked	0	10.8	0
	1	Unmasked	45	6.9	-3.9
	1	Unmasked	90	8.4	-2.4
	8	Unmasked	0	-1.8	0
	8	Unmasked	45	-2.4	-0.6
	8	Unmasked	90	-5.0	-3.2
	16	Unmasked	0	24.6	0
	16	Unmasked	45	15.3	-9.3
	16	Unmasked	90	11.5	-13.1
	1	Masked	0	48.6	0	0	17.8
	1	Masked	45	40.8	-7.8	3.9	10.0
	1	Masked	90	39.3	-9.3	6.9	8.5
	8	Masked	0	39.6	0	0	21.4
	8	Masked	45	32.1	-7.5	6.9	13.9
	8	Masked	90	31.1	-8.5	5.3	12.9
	16	Masked	0	59.9	0	0	30.3
	16	Masked	45	50.3	-9.6	0.3	20.7
	16	Masked	90	40.9	-19.0	5.9	11.3
Sea lion (<i>Zalophus</i>)	1	Unmasked	0	40.8	0
	1	Unmasked	45	35.4	-5.4
	1	Unmasked	90	33.1	-7.7
	8	Unmasked	0	9.7	0
	8	Unmasked	45	7.1	-2.6
	8	Unmasked	90	3.6	-6.1
	16	Unmasked	0	13.7	0
	16	Unmasked	45	18.7	5.0
	16	Unmasked	90	18.5	4.8
	1	Masked	0	67.4	0	0	21.6
	1	Masked	45	57.8	-9.6	4.2	12.0
	1	Masked	90	55.7	-11.7	4.0	9.9
	8	Masked	0	57.4	0	0	27.7
	8	Masked	45	50.3	-7.1	4.5	20.6
	8	Masked	90	49.2	-8.2	2.1	19.5
	16	Masked	0	52.5	0	0	28.8
	16	Masked	45	49.3	-3.2	8.2	25.6
	16	Masked	90	53.8	1.3	3.5	30.1

1991; Hine *et al.*, 1994; Gilkey and Good, 1995). As expected, the harbor seal's threshold differences of the present study were larger in air than those previously measured under water when the signal was projected at 0° and the masker azimuth varied between 0° and 90° (Turnbull, 1994). Even relatively small masking level differences resulting from different signal-masker configurations can have significant effects on intraspecific communication ranges. For example, the detection range of a pup call may change on the order of tens of meters or more with a 5 dB detection advantage (assuming a source level around 87 dB and spherical 20 log R spreading loss in ideal conditions; Southall, 2002; 2003b). Because separated pups are more likely to be attacked by other females and even die of starvation if they are orphaned (Reiter *et al.*, 1981), such effects have important fitness consequences on individual pinnipeds.

Masking level differences, as defined in this study (from Saberi *et al.*, 1991), take into account spatial separation of the signal relative to the masker while subtracting out the

sensation level effects of the signal varying in azimuth. For example, unmasked human thresholds of broadband signals are generally lowest at approximately 50° in the horizontal plane (Saberi *et al.*, 1991). In the case of pure tones, unmasked threshold differences relative to 0° vary in azimuth in frequency-dependent ways. These threshold differences tend to be relatively small (less than 5 dB) below 1 kHz but may be as large as -15 dB at higher frequencies (Sivian and White, 1933). In the harbor seal of this study, unmasked as well as masked threshold differences relative to 0° were also largest at the highest test frequency. This was not the case in the sea lion subject, for whom the largest negative unmasked and masked threshold differences occurred at the lowest test frequency. MLDs at the lowest frequency of both subjects were comparable further indicating a similar ability to utilize interaural time cues (Holt *et al.*, 2005). In this study, the masker was always positioned at 0° and thus the differences in relative amplitude spectra of the masker between the two ears are likely to be small in the absence of anatomical asym-

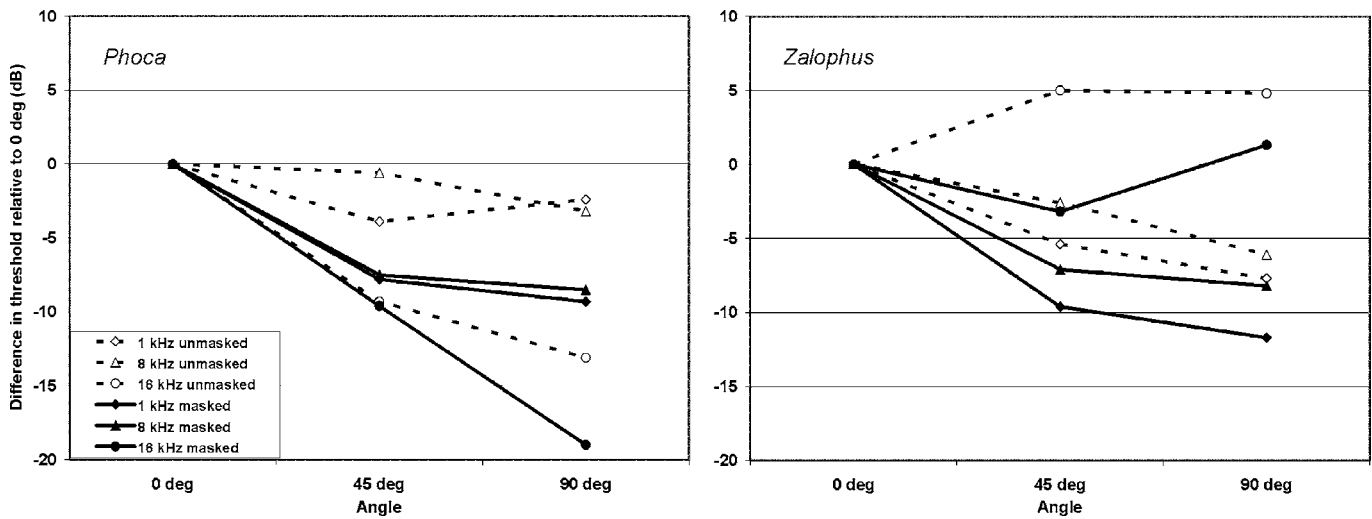


FIG. 2. Unmasked (dashed lines) and masked (solid lines) thresholds relative to those measured at 0° as a function of signal azimuth of the harbor seal (*Phoca*) on the left and the California sea lion (*Zalophus*) on the right.

metry. However, despite subtracting out the unmasked detection advantages of a signal projected to the closer ear, MLDs of both pinniped subjects were generally larger than zero, indicating release from masking that was not solely explained by sensation level effects in azimuth. This was also observed in human subjects detecting broadband signals in which MLDs were as large as approximately 10 dB when the masker was presented at 0° and the signal at 90° (Saber *et al.*, 1991).

Based on the assumption that release from masking at higher frequencies is primarily governed by monaural filtering effects of the pinna (as well as the head), it was expected that SRM would differ between the harbor seal and sea lion at higher frequencies. While there were considerable differences between the two subjects' unmasked and masked thresholds (referenced to 0°) as well as MLDs at 16 kHz, masked thresholds (referenced to 0°) at 8 kHz were similar. This was the case even though the resulting MLDs of the sea lion were almost half of those of the harbor seal at this frequency. It remains in question whether or not the sea lion

pinna functions in similar ways to those of terrestrial mammals for spatial auditory processing. The sea lion pinna is assumed to be primarily adapted to reduce drag for swimming and diving but it is likely that the structure along with the head and torso would provide some filtering effect at both 8 and 16 kHz. Furthermore, differences in body position, head shape, and pinna configuration between the two subjects would likely result in substantial differences in head related transfer functions (i.e., the way that these structures filter sound from source to ear drum). Because performance between the two subjects at 16 kHz showed the most variation, it is likely that SRM at higher frequencies in the horizontal plane is influenced by monaural cues created by these anatomical structures. However, it is possible that differences between the SNRs between the two ears can be quite substantial at high frequencies. It remains unclear at this point what influence binaural effects may have on high frequency SRM in pinnipeds given that monaural masked thresholds were not determined in this investigation to make comparisons with binaural performance.

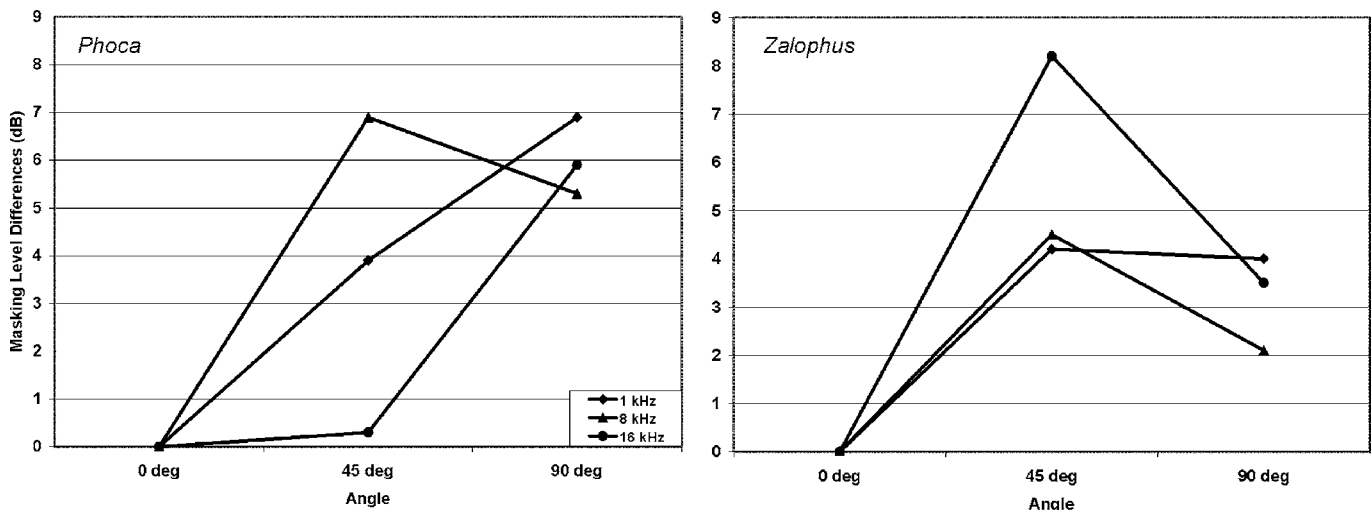


FIG. 3. Masking level differences relative to those measured at 0° as a function of signal azimuth of the harbor seal (*Phoca*) on the left and the California sea lion (*Zalophus*) on the right.

The results of this study illustrate that when signal and masker are spatially separated, hearing sensitivity of pinnipeds in the presence of simultaneous masking noise is enhanced. This improvement in sensitivity was as much as 19 dB in the harbor seal and 12 dB in the sea lion. Signals and maskers may take on an almost infinite number of different spatial configurations relative to each other in the everyday world. Accordingly, this study extends earlier masking work in pinnipeds to more complex auditory scenes and provides results that are important for considering the challenges of detecting biologically significant sounds in a background of noise including those from anthropogenic sources.

ACKNOWLEDGMENTS

This study was conducted under U.S. Marine Mammal Permit No. 0172-1771-00 of the U.S. National Marine Fisheries Service Office of Protected Resources. Funding from the Office of Naval Research (Grant No. N00014-04-1-0284) to David Kastak and Stephen Insley, and the Myers' Oceanographic Trust Fund, the Friends of Long Marine Laboratory, University of California Regents Fellowship Program, and Graduate Assistance in Areas of National Need (GAANN) Doctoral Fellowship Program to M.M.H. made this study possible. The authors thank the dedicated volunteers at Long Marine Laboratory in Santa Cruz, CA, and Colleen Reichmuth Kastak and David Kastak for commenting on earlier versions of this manuscript.

Au, W. W. L., and Moore, P. W. B. (1984). "Receiving beam patterns and directivity indices of the Atlantic bottlenose dolphin *Tursiops truncatus*," J. Acoust. Soc. Am. **75**, 255–262.

Bain, D. E., and Dahlheim, M. E. (1994). "Effects of masking noise on detection thresholds of killer whales," in *Marine Mammals and the Exxon Valdez*, 4th edition, edited by T. R. Loughlin (Academic, San Diego, CA), pp. 243–256.

Colburn, H. S., and Durlach, N. I. (1965). "Time-intensity relations in binaural unmasking," J. Acoust. Soc. Am. **38**, 93–103.

Cornsweet, T. N. (1962). "The staircase method in psychophysics," Am. J. Psychol. **75**, 485–491.

Fay, R. R. (1988). *Hearing in Vertebrates: A Psychophysical Databook* (Hill-Fay, Winnetka, IL).

Finney, D. J. (1971). *Probit Analysis*, 3rd ed. (Cambridge Press, Cambridge).

Gilkey, R. H., and Good, M. D. (1995). "Effects of frequency on free-field masking," Hum. Factors **37**, 835–843.

Gilkey, R. H., Good, M. D., and Ball, J. M. (1997). "The relation between detection in noise and localization in noise in the free field," in *Binaural and Spatial Hearing in Real and Virtual Environments*, edited by R. H. Gilkey and T. A. Anderson (LEA, Mahwah, NJ), pp. 349–376.

Hine, J. E., Martin, R. L., and Moore, D. R. (1994). "Free-field binaural unmasking in ferrets," Behav. Neurosci. **108**, 196–205.

Hirsch, I. J. (1948). "The influence of interaural phase on interaural summation and inhibition," J. Acoust. Soc. Am. **20**, 536–544.

Holt, M. M., Schusterman, R. J., Southall, B. L., and Kastak, D. (2004). "Localization of aerial broadband noise by pinnipeds," J. Acoust. Soc. Am. **115**, 2339–2345.

Holt, M. M., Schusterman, R. J., Kastak, D., and Southall, B. L. (2005). "Localization of aerial pure tones by pinnipeds," J. Acoust. Soc. Am. **118**, 3921–3926.

Ison, J. R., and Agrawal, P. (1998). "The effect of spatial separation of signal and noise on masking in the free field as a function of signal frequency and age in the mouse," J. Acoust. Soc. Am. **104**, 1689–1695.

Jeffress, L. A., Blodgett, H. C., and Deatherage, B. H. (1962). "Masking and

interaural phase. II. 167 cycles," J. Acoust. Soc. Am. **34**, 1124–1126.

Kopco, N., and Shinn-Cunningham, B. G. (2003). "Spatial unmasking of nearby pure-tone target in a simulated anechoic environment," J. Acoust. Soc. Am. **114**, 2856–2870.

Moore, P. W. B., and Au, W. W. L. (1975). "Underwater localization of pulsed pure tones by the California sea lion (*Zalophus californianus*)," J. Acoust. Soc. Am. **58**, 721–727.

National Research Council (NRC) (2003). *Ocean Noise and Marine Mammals* (National Academy Press, Washington, DC).

Reichmuth Kastak, C., Kastak, D., Holt, M. M., Schusterman, R. J., and Southall, B. L. (2004). "Aerial hearing sensitivity in some pinnipeds is comparable to that of humans," J. Acoust. Soc. Am. **115**, 2406.

Reiter, J., Panken, K. J., and Le Boeuf, B. J. (1981). "Female competition and reproductive success in northern elephant seals," Anim. Behav. **29**, 670–687.

Robinson, D. E. (1971). "The effect of interaural signal-frequency disparity on signal detectability," J. Acoust. Soc. Am. **50**, 568–571.

Saberi, K., Dostal, L., Sadralodabai, V. B., and Perrott, D. R. (1991). "Free-field release from masking," J. Acoust. Soc. Am. **90**, 1355–1370.

Santon, F. (1987). "Détection d'un son pur dans un bruit masquant suivant l'angle d'incidence du bruit. Relation avec le seuil de réception de la parole (Detection of a pure sound in the presence of masking noise, and its dependence on the angle of incidence of the noise)," Acustica **63**, 222–228.

Shaw, E. A. G. (1974). "Transformation of sound pressure level from the free field to the eardrum in the horizontal plane," J. Acoust. Soc. Am. **56**, 1848–1861.

Shinn-Cunningham, B. G., Satyavarta, A. I., and Larson, E. (2005). "Bottom-up and top-down influences on spatial unmasking," Acust. Acta Acust. **91**, 967–979.

Sivian, L. J., and White, S. D. (1933). "On minimum audible sound fields," J. Acoust. Soc. Am. **4**, 289–321.

Southall, B. L. (2002). "Northern elephant seal field bioacoustics and aerial auditory masked hearing in three pinnipeds," Unpublished doctoral dissertation, University of California, Santa Cruz, CA.

Southall, B. L., Schusterman, R. J., and Kastak, D. (2000). "Masking in three pinnipeds: Underwater, low-frequency critical ratios," J. Acoust. Soc. Am. **108**, 1322–1326.

Southall, B. L., Schusterman, R. J., and Kastak, D. (2003a). "Auditory masking in three pinnipeds: Aerial critical ratios and direct critical bandwidth measurements," J. Acoust. Soc. Am. **114**, 1660–1666.

Southall, B. L., Schusterman, R. J., and Kastak, D. (2003b). "Acoustic communication ranges for northern elephant seals (*Mirounga angustirostris*)," Aquat. Mamm. **29.2**, 202–213.

Stebbins, W. C. (1970). "Principles of animal psychophysics," in *Animal Psychophysics: The Design and Conduct of Sensory Experiments*, edited by W. C. Stebbins (Appleton-Centru-Crofts, New York), pp. 1–19.

Strutt, J. W. (1907). "On our perception of sound direction," Philos. Mag. **13**, 214–232.

Terhune, J. M. (1974). "Directional hearing of a harbor seal in air and water," J. Acoust. Soc. Am. **56**, 1862–1865.

Terhune, J. M., and Ronald, K. (1975). "Masked hearing thresholds of ringed seals," J. Acoust. Soc. Am. **58**, 515–516.

Terhune, J. M., and Turnbull, S. D. (1989). "Masked threshold changes associated with angular separation of noise and signal sources," Scand. Audiol. **18**, 85–89.

Turnbull, S. D. (1994). "Changes in masked thresholds of a harbor seal (*Phoca vitulina*) associated with angular separation of signal and noise sources," Can. J. Zool. **72**, 1863–1866.

Turnbull, S. D., and Terhune, J. M. (1990). "White noise and pure tone masking of pure tone thresholds of a harbor seal listening in air and under water," Can. J. Zool. **68**, 2090–2097.

Yost, W. A. (1997). "The cocktail party problem: Forty years later," in *Binaural and Spatial Hearing in Real and Virtual Environments*, edited by R. H. Gilkey and T. A. Anderson (LEA, Mahwah, NJ), pp. 329–347.

Zerlin, S. (1966). "Interaural time and intensity difference and the MLD," J. Acoust. Soc. Am. **39**, 134–137.

Zurek, P. M., Freyman, R. L., and Balakrishnan, U. (2004). "Auditory target detection in reverberation," J. Acoust. Soc. Am. **115**, 1609–1620.

Semi-analytical computation of the acoustic field of a segment of a cylindrically concave transducer in lossless and attenuating media

Başak Ülker Karbeyaz^{a)}

Analogic Corporation, 8 Centennial Drive, Peabody, Massachusetts 01960

Eric L. Miller^{b)}

Department of Electrical Engineering and Computer Science, Northeastern University, Boston, Massachusetts 02115

Robin O. Cleveland^{c)}

Department of Aerospace and Mechanical Engineering, Boston University, Boston, Massachusetts 02115

(Received 12 December 2005; revised 16 November 2006; accepted 20 November 2006)

Conventional ultrasound transducers used for medical diagnosis generally consist of linearly aligned rectangular apertures with elements that are focused in one plane. While traditional beamforming is easily accomplished with such transducers, the development of quantitative, physics-based imaging methods, such as tomography, requires an accurate, and computationally efficient, model of the field radiated by the transducer. The field can be expressed in terms of the Helmholtz-Kirchhoff integral; however, its direct numerical evaluation is a computationally intensive task. Here, a fast semi-analytical method based on Stepanishen's spatial impulse response formulation [J. Acoust. Soc. Am. **49**, 1627–1638 (1971)] is developed to compute the acoustic field of a rectangular element of cylindrically concave transducers in a homogeneous medium. The pressure field, for lossless and attenuating media, is expressed as a superposition of Bessel functions, which can be evaluated rapidly. In particular, the coefficients of the Bessel series are frequency independent and need only be evaluated once for a given transducer. A speed up of two orders of magnitude is obtained compared to an optimized direct numerical integration. The numerical results are compared with Field II and the Fresnel approximation. © 2007 Acoustical Society of America.
[DOI: 10.1121/1.2409489]

PACS number(s): 43.80.Vj, 43.20.Fn, 43.20.Rz, 43.20.Bi [TDM]

Pages: 1226–1237

I. INTRODUCTION

Diagnostic ultrasound imaging systems typically employ one-dimensional arrays to form two-dimensional B-scan images. In the axis normal to the image plane, the so-called elevation plane, the elements have a fixed focus that is effected either by the use of elements that are curved or by the use of an acoustic lens. In the image, or scan plane, the elements in the array are electronically steered and focused using delay and sum beamforming. In theory, these arrays are capable of being used for ultrasound computed tomography if the unbeamformed data can be recorded for each element on the array. For ultrasound computed tomography to be effective an accurate physical model of the acoustic field produced by each element of the transducer in the tissue is needed. The field can be expressed in terms of an integral, however, practical computation of the integral is not trivial.

One method that is well suited for evaluating the field of an ultrasound imaging system is the spatial impulse response (SIR). The SIR is defined as the pressure wave at a point in space in response to a velocity impulse on the radiating sur-

face of the transducer.^{1–3} The SIR may be convolved with the time derivative of the normal particle velocity to obtain the time pressure distribution. For ultrasound imaging systems, where short duration pulses are employed, the convolution can be carried out quickly. Exact expressions of the SIR have been calculated for transducers of the following shapes: flat pistons, flat sectors, flat polygons, and spherically focused bowls (or segments thereof). An exact expression for the SIR for the cylindrical elements used in imaging arrays has not been forthcoming. Wu and Stepinski⁴ proposed modeling cylindrically concave elements as a row of narrow strips, which can be considered as planar rectangular transducers whose exact SIRs are available. This technique still results in two integrals, the convolution in time and the summation over the subelements, but has been effectively employed by the Field II program.⁵

One issue with the SIR is that it cannot directly simulate the field in an attenuating medium. Frequency dependent attenuation (and its concomitant dispersion) has a significant impact on ultrasound propagation in the human body. In the SIR approach, attenuation is typically handled by determining the pressure waveform for a lossless medium and then correcting the waveform by applying a filter, the material transfer function⁶ (p. 207), to compensate for attenuation. The implicit assumption is that attenuation and diffraction

^{a)}Electronic mail: bulker@ece.neu.edu

^{b)}Electronic mail: elmiller@ece.neu.edu

^{c)}Electronic mail: robinc@bu.edu

are uncoupled. A time domain method that can be applied to attenuating media is the **discrete representation array modeling** (DREAM) procedure, which models arbitrary transducer surfaces as a discrete number of point sources⁷ and can be used to model power law type attenuating medium as is appropriate for soft tissue. However, DREAM is computationally intensive as it “trades simplicity, clarity, and generality for increased computational time.”⁷

In the frequency domain, the field from an arbitrary flat transducer can be evaluated by means of the angular spectrum technique.⁸ However, the angular spectrum technique is very computationally intensive and for transducer elements that are not flat it is necessary to migrate the source condition to a plane. An alternative frequency domain approach is to employ the Fresnel approximation⁶ (p. 140), which is computationally efficient but restricts the solution to points that are close to the axis and not too close to the transducer.

We seek a rapid method for calculating the spatial response of a cylindrical radiator in lossy media. Our technique was instigated by the work of Theumann *et al.*,⁹ who considered the field inside a cylinder transducer and were able to reduce the surface integral to a single integral in the time domain for which numerical methods were employed to obtain the result. The philosophy here is similar except that the problem is cast in the frequency domain and, for a small cylindrical concave element, a mild approximation to the integrand allows an analytical solution for one of the two integrals to be obtained. The remaining integral is expanded as a truncated series of Legendre polynomials, which are integrated exactly term by term. The resulting response is represented as summation of a small number of Bessel functions and compared to an optimized numerical routine.

II. THEORY: SPATIAL IMPULSE RESPONSE

For a homogeneous fluid medium with a constant sound speed and density, the acoustic field at frequency ω and position \mathbf{r}_p is calculated with the use of the velocity potential $\Phi(\mathbf{r}_p, \omega)$ and imposing the appropriate boundary conditions.^{2,10} For uniform excitation, the normal particle velocity on the transducer surface is independent of the position on the transducer, i.e., $v_o(\omega, \mathbf{r}_t) = v_o(\omega)$ where \mathbf{r}_t is the vector traversing the transducer surface, and the velocity potential is expressed as

$$\Phi(\mathbf{r}_p, \omega) = v_o(\omega) \int_S \frac{e^{-jk|\mathbf{r}_p - \mathbf{r}_t|}}{2\pi|\mathbf{r}_p - \mathbf{r}_t|} dS \quad (1a)$$

$$= v_o(\omega) H(\mathbf{r}_p, k), \quad (1b)$$

where k is the wave number. The integral $H(\mathbf{r}_p, k)$ is the spatial transfer function of the transducer and is the subject of this paper.

In lossless media, k is a real valued quantity equal to ω/c_o , where c_o is the speed of sound. For a lossy medium, an imaginary component is introduced,

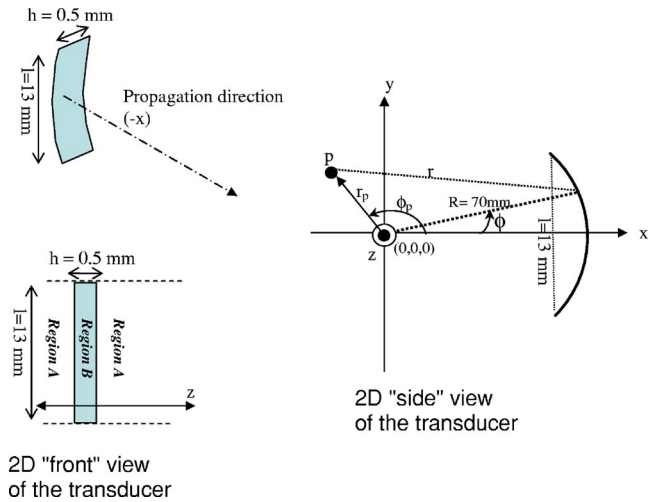


FIG. 1. (Color online) The geometry of the transducer and the coordinate system.

$$k(\omega) = \frac{\omega}{c_o(\omega)} - j\alpha(\omega), \quad (2)$$

where $\alpha(\omega)$ is the frequency dependent attenuation coefficient and $c_o(\omega)$ is the dispersive sound speed that is related to $\alpha(\omega)$ through causality. Closed form expressions for the causality relationship exist for power law attenuation as is appropriate for soft tissue.¹¹

The pressure generated by the transducer at point \mathbf{r}_p is calculated from Eq. (1a) as

$$p(\mathbf{r}_p, \omega) = -j\omega\rho_o\Phi(\mathbf{r}_p, \omega), \quad (3)$$

where ρ_o is the density.

III. SPATIAL TRANSFER FUNCTION FOR THE CYLINDRICAL GEOMETRY

For many commercial transducers, the source surface S is a truncated cylinder with lateral dimensions $l \times h$ and a radius R —see Fig. 1. The focal point of the cylindrical radiator is the origin of the cylindrical coordinates system, and the center of the element is at $(x=R, y=0, z=0)$, where the negative x direction is the principal propagation direction. The quantity r is the distance from a point on the transducer surface (R, ϕ, z) to the observation point $p(r_p, \phi_p, z_p)$. The spatial transfer function for this geometry is then

$$H(\mathbf{r}_p, k) = \int_S \frac{e^{-jkr}}{2\pi r} ds, \quad (4)$$

where S is the radiator surface and $ds = R d\phi dz$. For transducer elements that are many wavelengths in size (as is typical for 1D ultrasound arrays), the kernel of Eq. (4) has a highly oscillatory behavior.

The semi-analytical method (SAM) we have developed to evaluate this oscillatory integral can be summarized as follows: First a change of variable is employed to smooth the oscillations of the kernel, which results in elliptical type integrals in terms of the angle ϕ . For most imaging transducers, ϕ is small (bounded by the half angle of the element) and the elliptical integrals can be approximated by quadratic

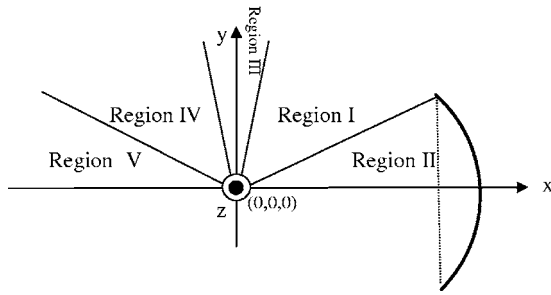


FIG. 2. Schematic showing the segmentation for ϕ_p .

type integrals for which closed form analytical solutions exist. The evaluation of ϕ integrals is carried out by dividing the x - y plane into five regions (Fig. 2). Having reduced the dimension of the integral, the line integral kernels will be expanded as truncated series of Legendre polynomials, which can be integrated exactly term by term. The resulting spatial transfer function will be represented as summation of a small number of Bessel functions. In this section, the initial steps of our algorithm are introduced.

First the variable transformation is carried out by expressing the distance r in Eq. (4) in cylindrical coordinates as

$$r^2 = (r_p \cos(\phi_p) - R \cos(\phi))^2 + (r_p \sin(\phi_p) - R \sin(\phi))^2 + (z_p - z)^2 = M(\phi) + (z_p - z)^2, \quad (5)$$

where $M(\phi) = r_p^2 + R^2 - 2r_p R \cos(\phi) \cos(\phi_p) + \sin(\phi) \sin(\phi_p)$ contains all the ϕ dependent terms. Equation (4) is written explicitly as

$$H(r_p, k) = \frac{1}{2\pi} \int_{-\phi_H}^{\phi_H} \int_{-h/2}^{h/2} \frac{e^{-jk\sqrt{M(\phi) + (z_p - z)^2}}}{\sqrt{M(\phi) + (z_p - z)^2}} R dz d\phi, \quad (6)$$

where $\phi_H = \arcsin(l/2R)$ is the half-angle of the element in the elevation plane with respect to the geometrical focus.

First, to simplify the integral, the element $ds = R d\phi dz$ is expressed as a function of r by eliminating the z dependence. Taking the derivative of both sides of Eq. (5),

$$dz = -\frac{r}{(z_p - z)} dr. \quad (7)$$

The sign of the element dz depends on the value of $z_p - z$ at the observation point. The field point z_p can have values between $[-\infty, \infty]$ but the surface point z is limited to the width of the transducer, h . Mathematically, $(z_p - z) = \sqrt{r^2 - M(\phi)}$ for $z_p > z$ and $-\sqrt{r^2 - M(\phi)}$ for $z_p < z$. Hence the new surface element ds is given as

$$ds = \pm \frac{r}{\sqrt{r^2 - M(\phi)}} R d\phi dr \quad (8)$$

and the correct sign is determined from the observation point and will be discussed below.

The integral now takes the form

$$H(r_p, k) = \frac{R}{2\pi} \int_{-\phi_H}^{\phi_H} \int_{F_1(\phi)}^{F_2(\phi)} E(r, \phi) dr d\phi, \quad (9)$$

where

$$E(r, \phi) = \frac{e^{-jkr}}{\sqrt{r^2 - M(\phi)}}. \quad (10)$$

The functions $F_1(\phi)$ and $F_2(\phi)$ will be discussed below.

The surface S is now a function of r and ϕ , and the new integration limits must be calculated. To express the new integrals, it is convenient to divide the half space in front of the transducer into two regions. Due to the symmetry in x - y and x - z planes of the radiator, the evaluation of $H(r_p, k)$ can be restricted to one quadrant of the y - z plane with $z_p \geq 0$ and $y \geq 0$. The two regions are defined as follows:

Region A ($z_p \geq h/2$): If $z_p > h/2$ (the maximum value of z), then $(z_p - z)$ will always be positive and $ds < 0$. The integral limits for r in Eq. (9) can be found by substituting the limiting values of z , $(-h/2, h/2)$ in Eq. (5), $F_1(\phi) = \sqrt{M(\phi) + (z_p - h/2)^2}$ and $F_2(\phi) = \sqrt{M(\phi) + (z_p + h/2)^2}$.

Region B ($0 \leq z_p < h/2$): If z_p is smaller than the limiting value of z , the integral needs to be segmented into two regions.

- (i) If $-h/2 \leq z \leq z_p$, then $(z_p - z) \geq 0$ and $ds < 0$. Substituting the limiting values of z , $(-h/2, z_p)$, in Eq. (5), the integral limits in Eq. (9) are obtained as $F_1(\phi) = \sqrt{M(\phi)}$ and $F_2(\phi) = \sqrt{M(\phi) + (z_p + h/2)^2}$
- (ii) If $z_p \leq z \leq h/2$, then $(z_p - z) \leq 0$ and $ds > 0$. The limiting values for z are $(z_p, h/2)$ and the new integral is defined with the limits $F_1(\phi) = \sqrt{M(\phi)}$ and $F_2(\phi) = \sqrt{M(\phi) + (z_p - h/2)^2}$

As a result, for this region SIR can be expressed as

$$H = \frac{R}{2\pi} \int_{-\phi_H}^{\phi_H} \left[\int_{\sqrt{M(\phi)}}^{\sqrt{M(\phi) + (z_p + h/2)^2}} E(r, \phi) dr + \int_{\sqrt{M(\phi)}}^{\sqrt{M(\phi) + (z_p - h/2)^2}} E(r, \phi) dr \right] d\phi. \quad (11)$$

All the integrals are of the form shown in Eq. (9) with the limits for the inner r integral given as

$$F_1(\phi) = \sqrt{M(\phi) + A_{z_p}}, \quad (12a)$$

$$F_2(\phi) = \sqrt{M(\phi) + B_{z_p}}; \quad (12b)$$

here A_{z_p} and B_{z_p} represent the region specific constants defined by the z_p value of the observation point.

IV. INTEGRAL EVALUATION

Equation (9) is an elliptical type integral (in terms of ϕ) and we were unable to find an analytical closed form solution. For most imaging transducers the ratio of $l/(2R)$ is small enough that $\cos(\phi)$ can be approximated with $(1 - \phi^2/2)$ and $\sin(\phi)$ with ϕ . For example, the parameters of the transducer used in this study are $R=70$ mm and $l=13$ mm, and $\phi = \arcsin(\frac{13}{140}) \approx 5^\circ$. By means of this smallness approximation, $M(\phi)$ can be described by

$$M(\phi) \approx (r_p^2 + R^2 - 2r_p R \cos(\phi_p)) - (2r_p R \sin(\phi_p)) \phi + (r_p R \cos(\phi_p)) \phi^2. \quad (13)$$

Employing the smallness approximation converts the elliptical integral in Eq. (9) into a quadratic type with respect to ϕ , which has a closed form solution. Therefore, it is necessary to change the order of integration so that the ϕ integral can be calculated. For observation points on the z axis ($r_p=0$) the kernel is independent of ϕ and this transformation cannot be employed. Therefore, the points on the z axis will be handled separately.

For the change of integration the x - y plane is divided into five regions as shown in Fig. 2. Regions II and V correspond to the points inside the cone subtended by the circular boundary of the transducer and its center of curvature. Regions I and IV correspond to the points outside the ray cone, except for a small cone around the y axis, region III. For points close to the y axis, where $\cos(\phi_p) \rightarrow 0$, the coefficient of ϕ^2 in Eq. (13) becomes infinitesimally small and in subsequent steps results in numerical instability. In region III, $\cos(\phi)$ was approximated as unity and the last term in Eq. (13), with the troublesome $\cos(\phi_p)$ term, was dropped. To minimize the error arising from this approximation, a threshold value for ϕ_p was chosen such that $2r_p R \sin(\phi_p) \phi_H > 10^3 (r_p R \cos(\phi_p) \phi_H^2)$. For the type of transducer used in this study, this threshold value, ϕ_t , was $69\pi/140$ and region III was defined between $69\pi/140$ and $(\pi - \phi_t) = 71\pi/140$, which was the symmetric interval with respect to the y axis.

The underlying principle to convert Eq. (9) into line integrals is very similar for all the regions. In this paper, the mathematical details for regions I, II, and III are described. The introduced algebra covers all the mathematical tools needed to obtain the response at any observation point in front of the radiator. The interested reader is referred to Ref. 12 for the mathematical derivations of regions IV and V. The formulas for the spatial transfer functions for all regions are summarized in the Appendix.

A. Case 1: regions I and II $0 \leq \phi_p \leq \phi_t$

In regions I and II, $M(\phi)$, $F_1(\phi)$ and $F_2(\phi)$ are represented by

$$M(\phi) \approx (r_p^2 + R^2 - 2r_p R \cos(\phi_p)) - (2r_p R \sin(\phi_p))\phi + (r_p R \cos(\phi_p))\phi^2 \quad (14a)$$

$$= a + b\phi + c\phi^2, \quad (14b)$$

$$F_1(\phi) \approx \sqrt{a + b\phi + c\phi^2 + A_{zp}}, \quad (14c)$$

$$F_2(\phi) \approx \sqrt{a + b\phi + c\phi^2 + B_{zp}}, \quad (14d)$$

where, to simplify the notation, the equations will be represented in terms of a , b , and c throughout this section. We will first introduce the solution for region I, as it sets the basis for the other solutions. The boundaries between the regions are described in terms of $\tan \phi_p$ and the reasoning behind this choice will be explained in the next section.

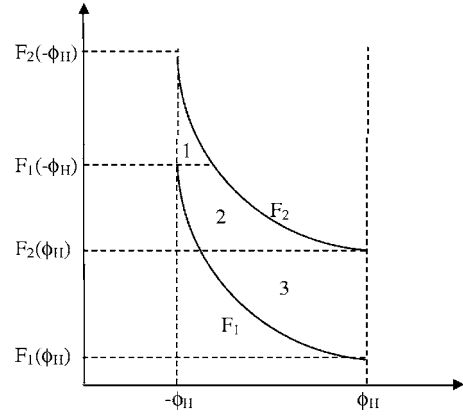


FIG. 3. The limit functions with monotonic decreasing dependence on ϕ .

1. Region I: $\phi_H < \tan \phi_p \leq \tan(\phi_t)$

The region of integration is shown in Fig. 3 and, to facilitate the change of order, it was necessary to divide the integral into three pieces (labeled as 1, 2, and 3 in Fig. 3):

$$\begin{aligned} & \int_{-\phi_H}^{\phi_H} \int_{F_1(\phi)}^{F_2(\phi)} E(r, \phi) dr d\phi \\ &= \int_{F_1(-\phi_H)}^{F_2(-\phi_H)} \int_{(-\phi_H)}^{F_2^{-1}(r)} E(r, \phi) d\phi dr \\ &+ \int_{F_2(\phi_H)}^{F_1(-\phi_H)} \int_{F_1^{-1}(r)}^{F_2^{-1}(r)} E(r, \phi) d\phi dr \\ &+ \int_{F_1(\phi_H)}^{F_2(\phi_H)} \int_{F_1^{-1}(r)}^{\phi_H} E(r, \phi) d\phi dr. \end{aligned} \quad (15)$$

The mapping functions from r to ϕ , which are denoted with $F_1^{-1}(r)$ and $F_2^{-1}(r)$, are not single valued, e.g., $F_1(\phi) = \sqrt{a + b\phi + c\phi^2 + A_{zp}}$, which is a quadratic with two roots. To solve the problem uniquely, the correct root must be picked and this motivates the separation into regions. The derivative of the quadratic term changes sign at $-b/2c = \tan(\phi_p)$. Hence, the boundaries between the regions are described in terms of $\tan(\phi_p)$. For region I, $\tan(\phi_p) > \phi_H$ and the appropriate results are

$$F_1^{-1}(r) = \phi = \frac{-b - \sqrt{b^2 - 4c(a + A_{zp} - r^2)}}{2c}, \quad (16a)$$

$$F_2^{-1}(r) = \phi = \frac{-b - \sqrt{b^2 - 4c(a + B_{zp} - r^2)}}{2c}. \quad (16b)$$

Moreover, in this region, $c > 0$ and the integral with respect to ϕ is given as¹³

$$\int \frac{1}{\sqrt{r^2 - (a + b\phi + c\phi^2)}} d\phi = \frac{1}{\sqrt{c}} \arcsin \left(\frac{-2c\phi - b}{\sqrt{b^2 + 4c(r^2 - a)}} \right), \quad (17)$$

hence Eq. (15) can now be written as

$$\begin{aligned}
& \int_{-\phi_H}^{\phi_H} \int_{F_1(\phi)}^{F_2(\phi)} E(r, \phi) dr d\phi \\
&= \int_{F_1(-\phi_H)}^{F_2(-\phi_H)} e^{-jkr} [\Psi_2(r) - \Psi_3(r)] dr \\
&+ \int_{F_2(\phi_H)}^{F_1(-\phi_H)} e^{-jkr} [\Psi_2(r) - \Psi_1(r)] dr + \int_{F_1(\phi_H)}^{F_2(\phi_H)} \\
&\times e^{-jkr} [\Psi_4(r) - \Psi_1(r)] dr, \tag{18}
\end{aligned}$$

where

$$\Psi_1(r) = -\frac{1}{\sqrt{c}} \arcsin \left(\sqrt{1 - \frac{4cA_{zp}}{b^2 + 4r^2c - 4ac}} \right), \tag{19a}$$

$$\Psi_2(r) = -\frac{1}{\sqrt{c}} \arcsin \left(\sqrt{1 - \frac{4cB_{zp}}{b^2 + 4r^2c - 4ac}} \right), \tag{19b}$$

$$\Psi_3(r) = -\frac{1}{\sqrt{c}} \arcsin \left(\sqrt{\frac{2c\phi_H - b}{b^2 + 4r^2c - 4ac}} \right), \tag{19c}$$

$$\Psi_4(r) = -\frac{1}{\sqrt{c}} \arcsin \left(\sqrt{\frac{-2c\phi_H - b}{b^2 + 4r^2c - 4ac}} \right). \tag{19d}$$

The transfer function in a compact form consists of four line integrals:

$$\begin{aligned}
H &= \frac{R}{2\pi} \left[\int_{F_1(\phi_H)}^{F_1(-\phi_H)} e^{-jkr} [-\Psi_1(r)] dr \right. \\
&+ \int_{F_2(\phi_H)}^{F_2(-\phi_H)} e^{-jkr} [\Psi_2(r)] dr + \int_{F_1(-\phi_H)}^{F_2(-\phi_H)} e^{-jkr} \\
&\times [-\Psi_3(r)] dr + \left. \int_{F_1(\phi_H)}^{F_2(\phi_H)} e^{-jkr} [\Psi_4(r)] dr \right]. \tag{20}
\end{aligned}$$

2. Region II: $\tan \phi_p \leq \phi_H$

When $\tan(\phi_p)$ is smaller than the limiting value of ϕ , the inverse mapping functions $F_1^{-1}(r)$ and $F_2^{-1}(r)$ change sign in the integral interval. Therefore, the integral in Eq. (9) should be decomposed into two parts for a unique representation:

$$\begin{aligned}
\int_{-\phi_H}^{\phi_H} \int_{F_1(\phi)}^{F_2(\phi)} E(r, \phi) dr d\phi &= H_1 + H_2 \\
&+ \int_{-\phi_H}^{\tan(\phi_p)} \int_{F_1(\phi)}^{F_2(\phi)} E(r, \phi) dr d\phi \\
&+ \int_{\tan(\phi_p)}^{\phi_H} \int_{F_1(\phi)}^{F_2(\phi)} E(r, \phi) dr d\phi. \tag{21}
\end{aligned}$$

To obtain H_1 , the algorithm used in region I will be implemented. The limit functions $F_1(\phi)$ and $F_2(\phi)$ are decreasing functions of ϕ and the inverses of the functions are represented with the negative roots, hence the resulting integral

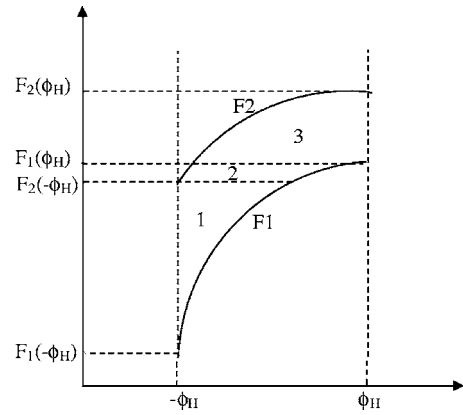


FIG. 4. The limit functions with monotonic increasing dependence on ϕ .

has a form similar to the previous case and can be expressed as

$$\begin{aligned}
H_1 &= \frac{R}{2\pi} \left[\int_{F_1(\phi_1)}^{F_1(-\phi_H)} e^{-jkr} [-\Psi_1(r)] dr \right. \\
&+ \int_{F_2(\phi_1)}^{F_2(-\phi_H)} e^{-jkr} [\Psi_2(r)] dr + \int_{F_1(-\phi_H)}^{F_2(-\phi_H)} e^{-jkr} \\
&\times [-\Psi_3(r)] dr \left. \right] \tag{22}
\end{aligned}$$

where $\phi_1 = \tan(\phi_p)$ and the $\Psi_4(r)$ integral vanishes in this interval.

To calculate H_2 , the same path will be followed with minor modifications. For this case, M and r are the increasing functions of ϕ . The behavior of the limiting functions with respect to ϕ is given in Fig. 4. After algebraic manipulations, the resulting integral can be written as

$$\begin{aligned}
H_2 &= \frac{R}{2\pi} \left[\int_{F_1(\phi_1)}^{F_1(\phi_H)} e^{-jkr} [-\Psi_1(r)] dr \right. \\
&+ \int_{F_2(\phi_1)}^{F_2(\phi_H)} e^{-jkr} [\Psi_2(r)] dr \\
&+ \left. \int_{F_1(\phi_H)}^{F_2(\phi_H)} e^{-jkr} [\Psi_4(r)] dr \right] \tag{23}
\end{aligned}$$

and the $\Psi_3(r)$ integrals vanishes in this interval.

B. Case 2: region III, $\phi_t < \phi_p \leq \pi - \phi_t$

As discussed previously, the approximation $\cos(\phi) \approx 1$ is employed in this region, which is equivalent to setting $c = 0$ in Eq. (14a). The integral is divided up into three pieces as was done for region I [Eq. (15)], where the mapping functions are now

$$F_1^{-1}(r) = \frac{r^2 - a - A_{zp}}{b}, \tag{24a}$$

$$F_2^{-1}(r) = \frac{r^2 - a - B_{zp}}{b}. \tag{24b}$$

The ϕ integrals can be evaluated as follows,

$$\int \frac{1}{\sqrt{r^2 - (a + b\phi)}} d\phi = \frac{2\sqrt{r^2 - (a + b\phi)}}{-b}, \quad (25)$$

and the spatial transfer function for region III is

$$H = \frac{R}{\pi(-b)} \left\{ \int_{F_1(-\phi_H)}^{F_2(-\phi_H)} e^{-jkr} [\sqrt{B_{zp}} - \sqrt{r^2 - (a - b\phi_H)}] dr \right. \\ \left. + \int_{F_2(\phi_H)}^{F_1(-\phi_H)} e^{-jkr} [\sqrt{B_{zp}} - \sqrt{A_{zp}}] dr \right. \\ \left. + \int_{F_1(\phi_H)}^{F_2(\phi_H)} e^{-jkr} [\sqrt{r^2 - (a + b\phi_H)} - \sqrt{A_{zp}}] dr \right\}, \quad (26)$$

with the definitions

$$\Psi_5(r) = \sqrt{r^2 - (a - b\phi_H)}, \quad (27a)$$

$$\Psi_6(r) = \sqrt{r^2 - (a + b\phi_H)}. \quad (27b)$$

The spatial transfer function is expressed in a compact form as

$$H = \frac{R}{\pi(-b)} \left[\int_{F_2(\phi_H)}^{F_2(-\phi_H)} e^{-jkr} [\sqrt{B_{zp}}] dr + \int_{F_1(-\phi_H)}^{F_2(-\phi_H)} e^{-jkr} \right. \\ \left. \times [-\Psi_5(r)] dr + \int_{F_1(\phi_H)}^{F_2(\phi_H)} e^{-jkr} [\Psi_6(r)] dr \right. \\ \left. + \int_{F_1(\phi_H)}^{F_1(-\phi_H)} e^{-jkr} [-\sqrt{A_{zp}}] dr \right]. \quad (28)$$

C. Case 3: on the z axis $r_p=0$

For this case, Eq. (9) is written as

$$H = \frac{R}{2\pi} \int_{-\phi_H}^{\phi_H} \int_{F_1}^{F_2} \frac{e^{-jkr}}{\sqrt{r^2 - M}} dr d\phi, \quad (29)$$

where $M=R^2$ for $r_p=0$, and F_1 and F_2 reduce to $\sqrt{R^2 + (z_p \pm h/2)^2}$ where the sign depends on the region. The integrand is independent of ϕ and Eq. (29) is expressed as

$$H = \frac{R\phi_H}{\pi} \int_{F_1}^{F_2} \frac{e^{-jkr}}{\sqrt{r^2 - R^2}} dr. \quad (30)$$

To remove the singularity caused by $F_1=R$, the integration by parts is employed and Eq. (30) is rewritten as

$$H = \frac{R\phi_H}{\pi} \left[e^{-jkr} \ln(r + \sqrt{r^2 - R^2}) \Big|_{F_1}^{F_2} \right. \\ \left. - \int_{F_1}^{F_2} (-jk)e^{-jkr} \ln(r + \sqrt{r^2 - R^2}) dr \right]. \quad (31)$$

D. Polynomial approximation

The compact expressions for the spatial transfer function of the cylindrical radiator involve line integrals, most of which cannot be computed analytically. The integrals with the nonlinear functions of r can be evaluated using a numerical integration technique such as Gauss quadrature. The

drawback of such a time consuming implementation is that a separate numerical integral routine must be used for each different frequency value.

In this study, a faster approach is introduced. The integrands were expanded as a series of Legendre polynomials. The Legendre polynomials were chosen as the expansion basis functions since the coefficients of the resulting series can be obtained without an integration routine and a closed form solution exists for the exponential integrands found in the expressions here. The resulting spatial transfer function is represented as summation of a small number of Bessel functions.

The normalized Legendre polynomials $\bar{P}_n(x)$ form a complete orthogonal system over the interval $[-1, 1]$. Therefore function $f(x)$ defined in this interval may be expanded in terms of the normalized Legendre polynomials as

$$f(x) = \sum_{n=0}^{n=\infty} a_n \bar{P}_n(x), \quad (32a)$$

where the coefficients a_n are obtained from

$$a_n = \int_{-1}^1 \bar{P}_n(x) f(x) dx. \quad (32b)$$

If $f(x)$ is smooth and well behaved, it can be represented with a truncated series where the upper limit of Eq. (32a) is replaced with N .

It can be shown that the coefficients of the truncated Legendre series are given by¹⁴

$$a_n = \sum_{q=1}^{n+1} W_q \bar{P}_n(\lambda_q) f(\lambda_q), \quad (33)$$

where λ_q are the zeros of the Legendre polynomial of order $N+1$ and W_q are the weights of the Gauss-Legendre quadrature, that is, the coefficients a_n can be obtained without integration.

The application of this series expansion to our algorithm will be as follows. As a general representation, the integrals that one needs to compute can be written as

$$\int_a^b e^{-jkr} \Psi(r) dr = A e^{-jkb} \int_{-1}^1 e^{-jkAx} \Psi(Ax + B) dx \quad (34)$$

with $r=Ax+B$, $A=(b-a)/2$, and $B=(b+a)/2$. The function $\Psi(Ax+B)$ is expanded in terms of the Legendre polynomials

$$\Psi(Ax + B) = \sum_{n=0}^{n=N} a_n \bar{P}_n(x), \quad (35a)$$

and, using the identity¹⁵ [p. 649]

$$\int_{-1}^1 e^{-jkx} \bar{P}_n(x) dx = \sqrt{4n+2} (j)^{-n} j_n(k), \quad (35b)$$

where $j_n(k)$ is the n th order spherical Bessel function, one obtains

$$\int_a^b e^{-jkr} \Psi(r) dr = A e^{-jkB} \sum_{n=0}^N a_n \sqrt{4n+2} (j)^{-n} j_n(Ak). \quad (35c)$$

The resulting summation, Eq. (35c), is valid for any wave number and can be used to evaluate the remaining integrals in Eqs. (20), (22), (23), (28), and (31). From these one can predict the acoustic fields in both lossless and attenuating media.

V. RESULTS

We carried out numerical experiments to verify the SAM introduced in this paper. Using the formulas given in Sec. IV, the spatial transfer function of a cylindrical transducer was calculated and compared with the results of direct numerical integration of Eq. (6) using a brute force quadrature routine. The SAM was also compared to Field II and the Fresnel approximation along the axis of the element and performance analysis is given. The element had lateral dimensions $13 \times 0.5 \text{ mm}^2$, a 70-mm elevation focal length, and a center frequency of 3.5 MHz and was based on a clinical probe (Model 8665, BK Medical, Wilmington, MA). To have a reasonable sized problem the maximum frequency of the signals was limited to 10 MHz.

A. Direct numerical approach (DNA)

A number of direct numerical integration techniques were applied to compute Eq. (6). The Gauss-Legendre quadrature was found to produce the most accurate results in the shortest time compared to other standard integration techniques such as the trapezoidal rule and Simpson's rule.

The 2D numerical routine can be summarized with the following equation:

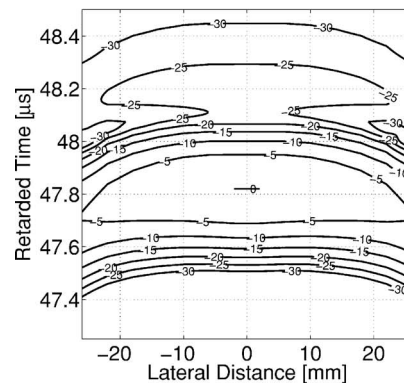
$$H \approx \frac{R}{2\pi} \sum_{n=1}^{\bar{N}} \sum_{u=1}^{\bar{U}} w_n w_u \frac{e^{-jk\sqrt{M(\phi_n) + (z_p - z_u)^2}}}{\sqrt{M(\phi_n) + (z_p - z_u)^2}}, \quad (36)$$

where ϕ_n and z_u denote the abscissas, and w_n , w_u are the weights for ϕ and z , respectively. The number of terms is determined according to the maximum frequency component of the signal. In this study, 2π terms per minimum wavelength were found to be sufficient for an accurate integral evaluation. The number of terms for z was $\bar{U} = \text{round}(2\pi f_{\max} h / c_o)$ and the number of terms for ϕ was $\bar{N} = \text{round}(2R\phi_H \bar{U} / h)$. The routine was implemented in Matlab R14 on a Pentium 4, 3 GHz, 1 GB RAM machine. For the transducer used in this study $\bar{N} = 547$ and $\bar{U} = 21$.

B. Comparison of SAM and DNA

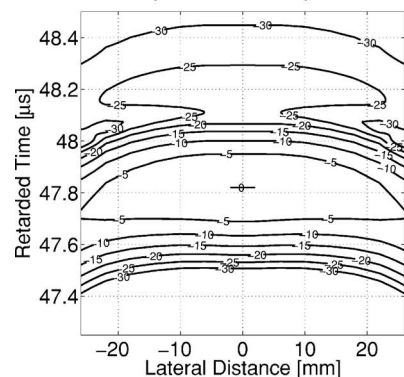
A number of numerical experiments were performed to evaluate the performance of our method. In this study, four comparison results are presented. Figures 5–7 each show contour plots of the envelope of the normalized wave forms for two cases: (a) the simulated response calculated with the semi-analytical method (SAM) introduced in Sec. IV and (b) the simulated response computed with the direct numerical approach (DNA) in Sec. V A without any approximations. The error between the two simulated responses [(a) and (b)]

Simulated Response $x=0\text{mm } y=0\text{mm } 5 \text{ dB lines}$



(a)

Simulated Response II $x=0\text{mm } y=0\text{mm } 5 \text{ dB lines}$



(b)

FIG. 5. Amplitude of envelope of acoustic field at $x=0$ and $y=0$ mm. (a) Fast semi-analytical technique. (b) Direct computational method. Contours are at 5-dB intervals. Retarded time scale: $t_r = t - r^2 / (2Rc_o)$.

and the speed improvement in computation time are the most important parameters to assess the performance of our method. The measures that will be used to compare these two results are defined as follows:

$$\text{Error \%} = 100 \frac{\|\text{SAM} - \text{DNA}\|_2}{\|\text{DNA}\|_2}, \quad (37a)$$

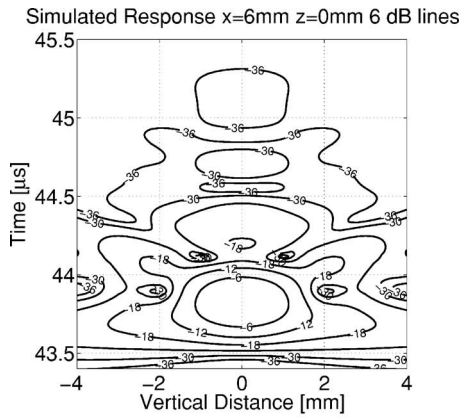
Speed Improvement Ratio

$$= \frac{\text{Total time required to compute DNA}}{\text{Total time required to compute SAM}}. \quad (37b)$$

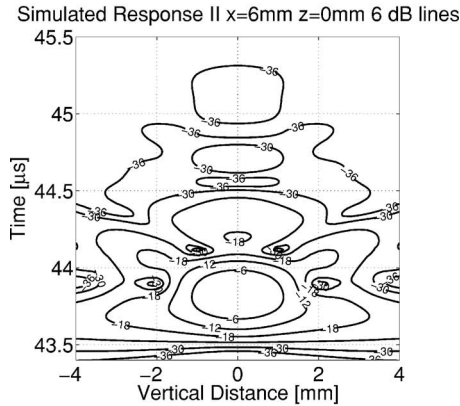
The real valued wave number used in these simulations was equal to ω/c_o , where $c_o = 1500 \text{ m/s}$.

Figure 5 compares the field predictions in the scan plane (z axis) of the transducer element at the elevation focus. In this case, 14 equally spaced observation points are chosen between -26 and 26 mm . The time axis was adjusted to remove the curvature of the wavefronts associated with spreading from the element. This allows for a detailed comparison of the phase fronts. The error between the two simulated responses was $7.5 \times 10^{-5}\%$ and the speed improvement ratio 1355. The total time required to compute SAM was 0.3 s.

In Fig. 6, the off-axis propagation in regions I and II was investigated where the approximation for ϕ had the most significant effect on the results. For this experiment, the ob-



(a)



(b)

FIG. 6. Amplitude of envelope of acoustic field at $x=6$ and $z=0$ mm. (a) Fast semi-analytical technique. (b) Direct computational method. Contours are at 6-dB intervals.

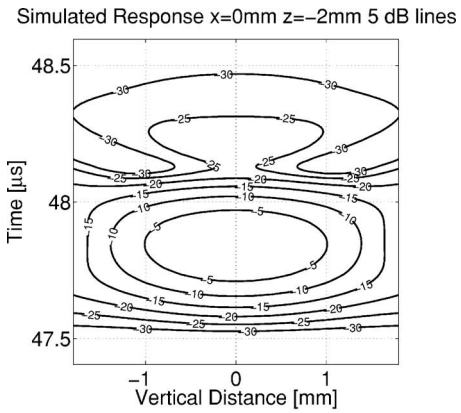
servation points were 6 mm behind the focus and parallel to the y axis. Forty-one equally spaced points were selected between -4 and 4 mm. The error was found to be 0.12% and the speed improvement ratio 225 times. The total time required to compute the SAM was 3.3 s.

Figure 7 shows the acoustic field in region III, on the y axis, for $z_p=-2$ mm. The observation points were selected at 19 equally spaced locations between -1.8 and 1.8 mm. For this region, the error between two simulated responses [(a) and (b)] was found to be 0.07% and the speed improvement ratio 541. The total time required to compute the SAM was 0.7 s.

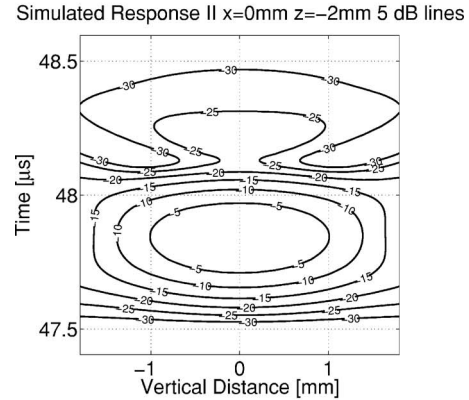
The numerical results presented here were also validated with experimental measurements on the field from a single element of the clinical probe. There was a good agreement confirming that the small half-angle approximation was appropriate for this transducer. The interested reader is referred to Ref. 12 for the comparison results.

C. Attenuating media

A numerical experiment was performed to assess the performance of the method in lossy media. The same experiment described in Fig. 6 was simulated with a complex wave number representing a power law attenuating medium. Attenuation was incorporated into the model by using α_b



(a)



(b)

FIG. 7. Amplitude of envelope of acoustic field at $x=0$ and $z=-2$ mm. (a) Fast semi-analytical technique. (b) Direct computational method. Contours are at 5-dB intervals.

$= 54(\omega/2\pi 3.5 \text{ MHz})^{1.2} \text{ Np/m}$ [which corresponds to $4.7(\omega/2\pi 3.5 \text{ MHz})^{1.2} \text{ dB/cm}$] and is appropriate for tissue.¹² The wave number was defined as

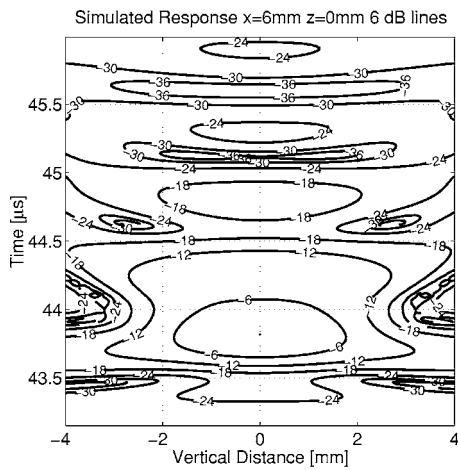
$$k^2(\omega) = \frac{\omega^2}{c_o^2} - j \frac{2\omega\alpha_b(\omega)}{c_o}. \quad (38)$$

The predicted responses obtained with the two different methods are given in Fig. 8. There is an excellent agreement between two results. Quantitatively, the speed improvement ratio is obtained as 225 times and the error between two simulations is 0.08%. The total time required to compute the SAM was 3.6 s.

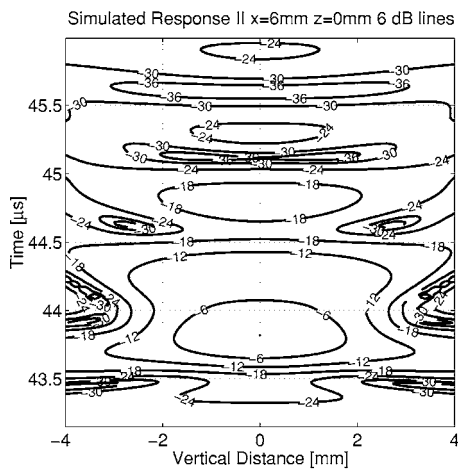
D. Comparison with Field II and the Fresnel approximation

A numerical experiment was performed to compare the performance of the SAM, with the Field II program and calculations based on the Fresnel approximation. The subroutine “`xdc_focused_array`” was used from the Field II package with following parameters: `no_elements = 1`, `width = 5 × 10-4`, `height = 0.013`, `kerf = 1.6667 × 10-4`, `Rfocus = 0.07`, `no_sub_x = 1`, `no_sub_y = 200`, and `focus = [0 0 0.07]`. The Fresnel approximation was implemented in Matlab 6.0.0.88 (R12) using the formula given in Ref. 6 (p. 157, Eq. 6.27b).

Figure 9 shows two plots of the amplitude of the 3.5-MHz component of a pulse as a function of distance along



(a)

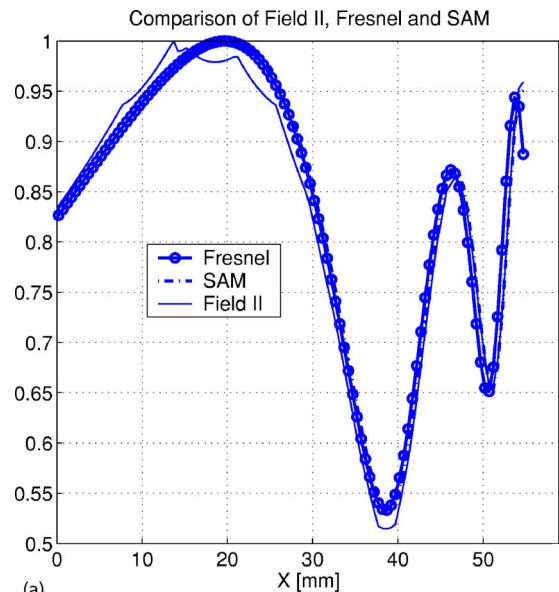


(b)

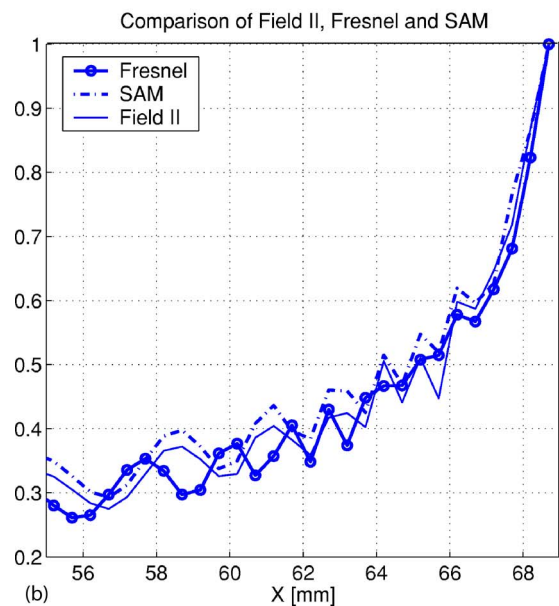
FIG. 8. Amplitude of envelope of acoustic field in lossy medium at $x=6$ and $z=0$ mm. (a) Fast semi-analytical technique. (b) Direct computational method. Contours are at 6-dB intervals.

axis of the element from 0 to 69 mm in 0.5-mm steps. One can see that around the focus of the transducer [Fig. 9(a)] the Fresnel approximation gives an accurate result. However, in the near field [Fig. 9(b)] the paraxial approximation fails to capture the oscillations in the pressure field accurately. In comparison Field II provides accurate results in the near field while showing some discrepancy in the focal region. This is consistent with reports that the SIR employed by Field II can be inefficient in the focal region.⁴

Table I shows a comparison of the total computation time and the estimated error relative to the DNA for Field II, Fresnel, and SAM on a computer with a Pentium 4, 1.6 GHz and 768 MB RAM. It can be seen that the SAM is more accurate than the Fresnel or Field II methods. The Fresnel method was the fastest, as would be expected due to its use of the paraxial approximation. The Field II program appears faster than the SAM, however the bulk of the computations in Field II are carried out in a compiled C-file (Matlab “mex” file), which is inherently faster than the direct Matlab implementation of the SAM (and the Fresnel method). A direct C-implementation of the SAM should lead to at least an



(a)



(b)

FIG. 9. (Color online) Prediction of the amplitude of the 3.5-MHz component along the axis of the transducer. Comparison of Field II, Fresnel, and SAM.

order of magnitude improvement in speed, making it equivalent to Field II, and could potentially be another order of magnitude faster.

VI. CONCLUSION

In this study, a fast method to compute the spatial transfer function of cylindrically concave transducers in lossless

TABLE I. Comparison of Field II, Fresnel, and SAM.

Figure 9(a)	SAM	Fresnel	Field II
Error (%)	0.08	2.10	2.4
Computation time (s)	4.05	0.33	0.22
Figure 9(b)			
Error (%)	1.07	10.58	5.73
Computation time (s)	1.22	0.08	0.22

and attenuating medium was introduced. For cylindrically focused transducers, with small half-angles in the elevation plane, the 2D surface integral was transformed from an elliptic type to a parabolic type. The integrals could be evaluated by reducing the problem to a 1D line integral. The remaining integrand was expressed as a truncated series of Legendre polynomials, from which it was possible to evaluate the line integral as a sum of spherical Bessel functions. The form of the line integrals is such that the coefficients of the Legendre polynomials depend only on geometry and not on frequency. They only need to be calculated once for specific elements and then the response at any frequency can be determined by a summation where the number of terms does not depend on frequency. This contrasts to direct integration approaches, which need to employ finer discretization for higher frequency components.

The method was compared to an optimized numerical method, which evaluated the surface integral directly. The speed of the new algorithm depends on the number of line integrals that need to be evaluated for an observation point. For the specific transducer used in this study, the speed improvement was between 40 and 1400 and the maximum error between two simulations was found to be 0.4%. The semi-analytical frequency domain method can predict the spatial transfer function of a cylindrical radiator in lossy medium simply by adding an imaginary component to the wave number.

In summary, a powerful semi-analytical method has been presented that complements the numerical approaches in the current literature. The approach can predict the acoustic field for a cylindrical concave transducer in attenuating homogeneous media. The approach can be applied to determine the fields in classical beam forming and also for applications such as tomography, which do not employ delay and sum beamforming.

ACKNOWLEDGMENTS

This work was supported in part by CenSSIS (the Center for Subsurface Sensing and Imaging Systems), under the Engineering Research Centers Program of the National Science Foundation (Award No. EEC-9986821). The authors are grateful for technical assistance provided by Dr. Emmanuel Bossy and Ersel Karbeyaz.

APPENDIX: ACOUSTIC FIELD OF A CYLINDRICALLY CONCAVE TRANSDUCER

The type of the integral to be solved here can be expressed in the following form:

$$\frac{R}{2\pi} \int_{-\phi_H}^{\phi_H} \int_{F_1(\phi)}^{F_2(\phi)} \frac{e^{-jkr}}{\sqrt{r^2 - M(\phi)}} dr d\phi, \quad (A1a)$$

where

$$F_1(\phi) = \sqrt{M(\phi) + A_{zp}}, \quad (A1b)$$

$$F_2(\phi) = \sqrt{M(\phi) + B_{zp}}, \quad (A1c)$$

$$M(\phi) = r_p^2 + R^2 - 2r_p R \cos(\phi - \phi_p), \quad (A1d)$$

where A_{zp} and B_{zp} represent the region specific constants defined by the z_p value of the observation point.

1. Case 1: Regions I and II $0 \leq \phi_p \leq \phi_t$

In this region $M(\phi)$, $F_1(\phi)$, and $F_2(\phi)$ are represented by

$$M(\phi) \approx (r_p^2 + R^2 - 2r_p R \cos(\phi_p)) - (2r_p R \sin(\phi_p))\phi \quad (A2a)$$

$$+ (r_p R \cos(\phi_p))\phi^2 \quad (A2b)$$

$$= a + b\phi + c\phi^2, \quad (A2c)$$

$$F_1(\phi) \approx \sqrt{a + b\phi + c\phi^2} + A_{zp}, \quad (A2d)$$

$$F_2(\phi) \approx \sqrt{a + b\phi + c\phi^2} + B_{zp}. \quad (A2e)$$

a. Region I: $\phi_H < \tan \phi_p \leq \tan(\phi_t)$

The expression for the spatial transfer function is given by

$$H = \frac{R}{2\pi} \left[\int_{F_1(\phi_H)}^{F_1(-\phi_H)} e^{-jkr} [-\Psi_1(r)] dr + \int_{F_2(\phi_H)}^{F_2(-\phi_H)} e^{-jkr} [\Psi_2(r)] dr + \int_{F_1(-\phi_H)}^{F_2(-\phi_H)} e^{-jkr} \times [-\Psi_3(r)] dr + \int_{F_1(\phi_H)}^{F_2(\phi_H)} e^{-jkr} [\Psi_4(r)] dr \right], \quad (A3)$$

where

$$\Psi_1(r) = -\frac{1}{\sqrt{c}} \arcsin \left(\sqrt{1 - \frac{4cA_{zp}}{b^2 + 4r^2c - 4ac}} \right), \quad (A4a)$$

$$\Psi_2(r) = -\frac{1}{\sqrt{c}} \arcsin \left(\sqrt{1 - \frac{4cB_{zp}}{b^2 + 4r^2c - 4ac}} \right), \quad (A4b)$$

$$\Psi_3(r) = -\frac{1}{\sqrt{c}} \arcsin \left(\frac{2c\phi_H - b}{\sqrt{b^2 + 4r^2c - 4ac}} \right), \quad (A4c)$$

$$\Psi_4(r) = -\frac{1}{\sqrt{c}} \arcsin \left(\frac{-2c\phi_H - b}{\sqrt{b^2 + 4r^2c - 4ac}} \right). \quad (A4d)$$

b. Region II: $\tan \phi_p \leq \phi_H$

The expression is given as the summation of the two responses:

$$\int_{-\phi_H}^{\phi_H} \int_{F_1(\phi)}^{F_2(\phi)} dr d\phi = H_1 + H_2. \quad (A5)$$

H_1 :

$$H_1 = \frac{R}{2\pi} \left[\int_{F_1(\phi_1)}^{F_1(-\phi_H)} e^{-jkr} [-\Psi_1(r)] dr + \int_{F_2(\phi_1)}^{F_2(-\phi_H)} e^{-jkr} [\Psi_2(r)] dr + \int_{F_1(-\phi_H)}^{F_2(-\phi_H)} e^{-jkr} [\Psi_3(r)] dr \right], \quad (\text{A6})$$

where

$$\phi_1 = \tan(\phi_p). \quad (\text{A7a})$$

H_2 :

$$H_2 = \frac{R}{2\pi} \left[\int_{F_1(\phi_1)}^{F_1(\phi_H)} e^{-jkr} [-\Psi_1(r)] dr + \int_{F_2(\phi_1)}^{F_2(\phi_H)} e^{-jkr} [\Psi_2(r)] dr + \int_{F_1(\phi_H)}^{F_2(\phi_H)} e^{-jkr} [\Psi_4(r)] dr \right]. \quad (\text{A8})$$

2. Case 2: Region III, $\phi_t < \phi_p \leq \pi - \phi_t$

$$H = \frac{R}{\pi(-b)} \left[\int_{F_2(\phi_H)}^{F_2(-\phi_H)} e^{-jkr} [\sqrt{B_{zp}}] dr + \int_{F_1(-\phi_H)}^{F_2(-\phi_H)} e^{-jkr} \times [-\Psi_5(r)] dr + \int_{F_1(\phi_H)}^{F_2(\phi_H)} e^{-jkr} [\Psi_6(r)] dr + \int_{F_1(\phi_H)}^{F_1(-\phi_H)} e^{-jkr} [-\sqrt{A_{zp}}] dr \right], \quad (\text{A9})$$

where

$$\Psi_5(r) = \sqrt{r^2 - (a - b\phi_H)}, \quad (\text{A10a})$$

$$\Psi_6(r) = \sqrt{r^2 - (a + b\phi_H)}, \quad (\text{A10b})$$

$$F_1(\phi) = \sqrt{a + b\phi + A_{zp}}, \quad (\text{A10c})$$

$$F_2(\phi) = \sqrt{a + b\phi + B_{zp}}. \quad (\text{A10d})$$

3. Case 3: Regions IV and V $\pi - \phi_t \leq \phi_p \leq \pi$

$M(\phi)$, $F_1(\phi)$, and $F_2(\phi)$ have the same forms in Sec. IV A as

$$M(\phi) \approx (r_p^2 + R^2 - 2r_p R \cos(\phi_p)) - (2r_p R \sin(\phi_p))\phi \quad (\text{A11a})$$

$$+ (r_p R \cos(\phi_p))\phi^2 \quad (\text{A11b})$$

$$= a + b\phi + c\phi^2, \quad (\text{A11c})$$

$$F_1(\phi) \approx \sqrt{a + b\phi + c\phi^2 + A_{zp}}, \quad (\text{A11d})$$

$$F_2(\phi) \approx \sqrt{a + b\phi + c\phi^2 + B_{zp}}. \quad (\text{A11e})$$

a. Region IV: $\tan \phi_p < -\phi_H$

$$H = \frac{R}{2\pi} \left[\int_{F_1(\phi_H)}^{F_1(-\phi_H)} e^{-jkr} [-\Psi_7(r)] dr + \int_{F_2(\phi_H)}^{F_2(-\phi_H)} e^{-jkr} [\Psi_8(r)] dr + \int_{F_1(-\phi_H)}^{F_2(-\phi_H)} e^{-jkr} \times [-\Psi_9(r)] dr + \int_{F_1(\phi_H)}^{F_2(\phi_H)} e^{-jkr} [\Psi_{10}(r)] dr \right], \quad (\text{A12})$$

where

$$-\phi_H = -\arcsin(l/R), \quad (\text{A13a})$$

$$\phi_H = \arcsin(l/R), \quad (\text{A13b})$$

$$\Psi_7(r) = \frac{1}{\sqrt{-c}} \ln(2\sqrt{-cA_{zp}} + \sqrt{b^2 - 4c(a + A_{zp} - r^2)}), \quad (\text{A13c})$$

$$\Psi_8(r) = \frac{1}{\sqrt{-c}} \ln(2\sqrt{-cB_{zp}} + \sqrt{b^2 - 4c(a + B_{zp} - r^2)}), \quad (\text{A13d})$$

$$\Psi_9(r) = \frac{1}{\sqrt{-c}} \ln(2\sqrt{-c(r^2 - a + b\phi_H - c\phi_H^2)} + 2c\phi_H - b), \quad (\text{A13e})$$

$$\Psi_{10}(r) = \frac{1}{\sqrt{-c}} \ln(2\sqrt{-c(r^2 - a + b\phi_H - c\phi_H^2)} - 2c\phi_H - b). \quad (\text{A13f})$$

b. Region V: $\tan \phi_p \geq -\phi_H$

$$\int_{-\phi_H}^{\phi_H} \int_{F_1(\phi)}^{F_2(\phi)} dr d\phi = H_1 + H_2. \quad (\text{A14})$$

H_1 :

$$H_1 = \frac{R}{2\pi} \left[\int_{F_1^*(\phi_H)}^{F_1^*(\phi_2)} e^{-jkr} [-\Psi_7(r)] dr + \int_{F_2^*(\phi_H)}^{F_2^*(\phi_2)} e^{-jkr} [\Psi_8(r)] dr + \int_{F_1^*(\phi_2)}^{F_2^*(\phi_2)} e^{-jkr} \times [-\Psi_{11}(r)] dr + \int_{F_1^*(\phi_H)}^{F_2^*(\phi_H)} e^{-jkr} [\Psi_{12}(r)] dr \right], \quad (\text{A15})$$

$$F_1^*(\phi^*) = \sqrt{(a - b\phi^* + c(\phi^*)^2) + A_{zp}}, \quad (\text{A16a})$$

$$F_2^*(\phi^*) = \sqrt{(a - b\phi^* + c(\phi^*)^2) + B_{zp}}, \quad (\text{A16b})$$

$$\Psi_{11}(r) = \frac{1}{\sqrt{-c}} \ln(2\sqrt{-c(r^2 - a + b\phi_2 - c\phi_2^2)} - 2c\phi_2 + b), \quad (\text{A16c})$$

$$\Psi_{12}(r) = \frac{1}{\sqrt{-c}} \ln \left(2\sqrt{-c(r^2 - a + b\phi_H - c\phi_H^2)} - 2c\phi_H + b \right), \quad (\text{A16d})$$

$$\phi_2 = -\tan(\phi_p). \quad (\text{A16e})$$

H_2 :

$$H_2 = \frac{R}{2\pi} \left[\int_{F_1(\phi_H)}^{F_1(\phi_2)} e^{-jkr} [-\Psi_7(r)] dr + \int_{F_2(\phi_H)}^{F_2(\phi_2)} e^{-jkr} [\Psi_8(r)] dr + \int_{F_1(\phi_2)}^{F_2(\phi_2)} e^{-jkr} \times [-\Psi_9(r)] dr + \int_{F_1(\phi_H)}^{F_2(\phi_H)} e^{-jkr} [\Psi_{10}(r)] dr \right]. \quad (\text{A17})$$

¹M. Arditi, F. Foster, and J. Hunt, "Transient fields of concave annular arrays," *Ultrason. Imaging* **3**, 37–61 (1981).

²P. R. Stepanishen, "The time-dependent force and radiation impedance on a piston in a rigid infinite planar baffle," *J. Acoust. Soc. Am.* **49**, 841–849 (1971).

³P. R. Stepanishen, "Transient radiation from pistons in an infinite planar baffle," *J. Acoust. Soc. Am.* **49**, 1627–1638 (1971).

⁴P. Wu and T. Stepinski, "Spatial impulse response method for predicting

pulse-echo fields from a linear array with cylindrically concave surface," *IEEE Trans. Ultrason. Ferroelectr. Freq. Control* **46**, 1283–1299 (1999).

⁵J. A. Jensen, "Field: A Program for Simulating Ultrasound Systems," *10th Nordic-Baltic Conference on Biomedical Imaging, Medical & Biological Engineering & Computing*, Vol. **34**, Suppl. 1, Part 1, pp. 351–353 (1996).

⁶T. L. Szabo, *Diagnostic Ultrasound Imaging Inside Out* (Elsevier Academic, Amsterdam, 2004), p. 157.

⁷B. Piwakowski and K. Sbai, "A new approach to calculate the field radiated from arbitrarily structured transducer arrays," *IEEE Trans. Ultrason. Ferroelectr. Freq. Control* **46**, 422–440 (1999).

⁸P. R. Stepanishen and K. C. Benjamin, "Forward and backward projection of acoustic fields using FFT methods," *J. Acoust. Soc. Am.* **71**, 803–812 (1982).

⁹J. F. Theumann, M. Arditi, J. J. Meister, and E. Jaques, "Acoustic fields of concave cylindrical transducers," *J. Acoust. Soc. Am.* **88**, 1160–1169 (1990).

¹⁰G. Tupholme, "Generation of acoustic pulses by baffled plane pistons," *Mathematika* **16**, 209–224 (1969).

¹¹T. L. Szabo, "Time domain wave equations for lossy media obeying a frequency power law," *J. Acoust. Soc. Am.* **96**, 491–500 (1994).

¹²B. U. Karbeyaz, "Modeling and shape based inversion for frequency domain ultrasonic monitoring of cancer treatment," Ph.D. thesis, Northeastern University, Boston, MA.

¹³I. Gradshteyn and I. Ryzhik, *Table of Integrals, Series, and Products* (Academic, New York, 2000).

¹⁴N. S. Bakhvalov and L. G. Vasil'eva, "Evaluation of the integrals of oscillating functions by interpolation at nodes of gaussian quadratures," *USSR Comput. Math. Math. Phys.* **8**, 241–249 (1968).

¹⁵C. A. Balanis, *Advanced Engineering Electromagnetics* (Wiley, New York, 1989).

Method for detecting small changes in vibrotactile perception threshold related to tactile acuity

A. J. Brammer^{a)}

Ergonomic Technology Center, University of Connecticut Health Center, Farmington, Connecticut 06030-2017 and Institute for Microstructural Sciences, National Research Council, Ottawa, Ontario K1A 0R6, Canada

J. E. Piercy

Institute for Microstructural Sciences, National Research Council, Ottawa, Ontario K1A 0R6, Canada

I. Pyykkö

Department of Otorhinolaryngology, Tampere University Hospital, FIN-33521 Tampere, Finland

E. Toppila

Department of Otorhinolaryngology, Tampere University Hospital, FIN-33521 Tampere, Finland and Finnish Institute of Occupational Health, FIN-00250 Helsinki, Finland

J. Starck

Finnish Institute of Occupational Health, FIN-00250 Helsinki, Finland

(Received 21 May 2006; revised 7 November 2006; accepted 9 November 2006)

Two metrics, expressing the *change* in mechanoreceptor-specific vibrotactile thresholds at a fingertip over a time interval of months or years, and the *shift* in threshold from the mean values recorded from the fingertips of healthy persons, have been constructed for thresholds measured from individual fingers. The metrics assume the applicability of the acute adaptation property of mechanoreceptors, which has been confirmed by thresholds obtained from 18 forest workers on two occasions, separated by 5 years. Hence, when expressed in decibels, both threshold changes and threshold shifts may be averaged at frequencies mediated by the same receptor population to improve precision. Differences between threshold changes at frequencies mediated by the same receptor population may be used to identify inconsistent subject performance, and hence potentially erroneous results. For this group of subjects, the threshold changes and threshold shifts at frequencies believed mediated by the slowly adapting type I (SAI) (4 and 6.3 Hz) and rapidly adapting type I (FAI) (20 and 32 Hz) receptors within each finger were correlated. In these circumstances, which may be expected to occur for some work-induced and systemic peripheral neuropathies, both threshold changes and threshold shifts may be summed over SAI and FAI receptors to improve precision, and hence the potential for interpretation. © 2007 Acoustical Society of America. [DOI: 10.1121/1.2404631]

PACS number(s): 43.80.Vj, 43.66.Wv, 43.80.Qf [FD]

Pages: 1238–1247

I. INTRODUCTION

It has been recognized for some time that the sense of touch in the hands is mediated by four populations of mechanoreceptors, which may be differentiated physiologically on the basis of their morphology, and functionally on the basis of their responses to static and dynamic skin indentation (Vallbo and Johansson, 1984; Bolanowski *et al.*, 1988; Verrillo, in press). The slowly adapting type I receptors (SAI) are primarily involved in the detection of surface topography, such as ridges, edges, and curvature. The primary role of the rapidly adapting type I receptors (FAI) is to provide the sensory input necessary to grip and hold objects between the thumb and fingers, which triggers compensatory muscle action in response to the detection of microslips (Johansson and Westling, 1984; Srinivasan *et al.*, 1990). Thus, a loss of

sensory input will impede the performance of this basic manipulative function. The rapidly adapting type II receptors (FAII) are insensitive to static or low frequency skin motion, but are very sensitive to vibration. They can also provide information on distant transient events (Johnson, 2001). A fourth mechanoreceptor population in the fingertips appears to respond primarily to skin stretch, and as such appears little involved in tactile acuity (slowly adapting, type II—SAII). The four receptor populations are associated with distinct anatomical structures in the glabrous skin of the hand: Merkel disks (SAIs), Meissner corpuscles (FAIs), Pacinian corpuscles (FAIIs), and Ruffini endings (SAIIs). Psychophysical techniques for determining the vibrotactile sensitivity of these receptor populations, separately, at the thenar eminence or the fingertips have been described (Bolanowski *et al.*, 1988; Brammer and Piercy, 2000; Gescheider *et al.*, 1985, 2002), and, for the latter, codified in an international standard (ISO 13091-1, 2001).

^{a)}Electronic mail: tony.brammer@nrc-cnrc.gc.ca

The purpose of the present work was to develop a method for detecting small changes in afferent acuity at the fingertips of *individual hands*, as an aid to the diagnosis of peripheral sensory neuropathies. Thus, in a clinical setting, the method is intended to signal a patient's deteriorating acuity, or to follow nerve repair or recovery by monitoring improving acuity. Clearly, such a method would require the availability of a means for noninvasively and rapidly measuring some physiological parameter related to tactile acuity. Vibrotactile perception and other quantitative sensory tests have been explored for this purpose, with apparently limited success (Gerr *et al.*, 1991; Lundborg *et al.*, 1992; Van Boven and Johnson, 1994). However, none to our knowledge have employed a procedure designed to elicit, separately, responses from the different mechanoreceptor populations subserving the sense of touch.

Statistically significant associations between vibrotactile thresholds mediated, separately, by the SAI, FAI, and FAII receptor populations at the fingertips and symptoms of deteriorating tactile acuity evidenced as reports of numbness, difficulty manipulating small objects, and difficulty buttoning clothing have recently been reported in a field study of manual workers (Coutu-Wakulczyk *et al.*, 1997). Based on this link between receptor-specific vibrotactile thresholds and tactile performance, it appeared worthwhile to examine the potential for detecting small changes in mechanoreceptor-specific vibrotactile thresholds to serve as a surrogate for direct measurement of tactile performance. The method described in this paper considers two metrics constructed from mechanoreceptor-specific vibrotactile perception thresholds measured at the fingertips. The first examines the *changes* in mechanoreceptor-specific vibrotactile thresholds over a time interval, and is derived from thresholds determined on two occasions separated by a matter of months, or years. As such it employs the individual as his/her own reference, but will be sensitive to the change in threshold with age. The second examines the persistent *shifts* in threshold from the mean values recorded from the fingertips of healthy persons. This metric assumes that the latter are known for the age of the subject.

In view of the potential confounding of both metrics by aging, it is essential that the effect of aging on the thresholds be mitigated. Two strategies are adopted for this purpose. First, the observed rate of change of receptor-specific vibrotactile threshold with age in healthy persons is used to select those frequencies, and hence the receptor populations, most suitable for analysis. Second, a method for combining thresholds at different stimulus frequencies mediated by the same receptor population is developed to increase the precision of the measurement. It is based on the known neurophysiological and psychophysical properties of mechanoreceptor populations (Vallbo and Johansson, 1984; Johnson, 2001; Verrillo, 1985, in press; Bolanowski *et al.*, 1988; Gescheider *et al.*, 1985, 2002). In particular, the analysis employs the adaptation property of mechanoreceptors whereby in response to a pure-tone, suprathreshold conditioning vibration the vibrotactile threshold at each frequency mediated by a given receptor population is found to change by the same amount (Verrillo and Gescheider, 1977). This result of

a laboratory experiment with trained subjects involved determining their vibrotactile perception threshold at the thenar eminence: first, prior to commencing the 10 min conditioning exposure and second, immediately after the exposure. Justification for applying this acute property of mechanoreceptors to persistent threshold changes, and threshold shifts, is explored by conducting measurements on the hands of forest workers who operate power tools (which produced their "conditioning" exposure), some of whom were known to be experiencing neurological symptoms compatible with reduced tactile acuity (Sutinen *et al.*, 2006).

II. METHOD, APPARATUS, AND SUBJECTS

Two metrics for detecting small alterations in mechanoreceptor-specific vibrotactile thresholds are first developed. In this paper, threshold *changes*, and threshold *shifts*, are ascribed distinct and different meanings. The derivation focuses on the SAI and FAI receptor populations, as these appear to have the most direct link to the dimensions of touch concerning the identification and manipulation of small objects, and their vibrotactile thresholds are less affected by aging than the FAII receptors (Verrillo, in press; Brammer *et al.*, 1993).

A. Changes in a person's mechanoreceptor-specific thresholds with time

In view of the association between vibrotactile thresholds and tactile function, establishing the *change* in mechanoreceptor-specific thresholds that has occurred over a period of time permits, in principle, potential changes in tactile acuity to be followed. The limit of significance of this metric will be related to the test/retest repeatability of threshold measurements, which has been reported for medically screened, healthy male subjects using the apparatus employed in this study (Brammer *et al.*, 1992), and to the change in threshold from aging. The threshold change over a period of time, Δt , at a stimulation frequency, f , can be calculated for each finger from thresholds recorded at that finger at times t_1 and t_2 , $T(f, t_1)$ and $T(f, t_2)$, i.e.,

$$TC_f(\Delta t) = T(f, t_2) - T(f, t_1). \quad (1)$$

In this and all other equations the thresholds are considered to be expressed in decibels (dB), a measure associated with sensation magnitude (Gescheider, 1997).

In psychophysical experiments it has been observed that acute changes in threshold in response to suprathreshold stimuli are the same at all frequencies at which the threshold is mediated by a given receptor population (Verrillo and Gescheider, 1977). If this property of mechanoreceptor populations is assumed to be applicable to persistent threshold changes, then for frequencies f_i at which the threshold is mediated by the same receptor population:

$$TC_{f_i}(\Delta t) \cong TC_{f_{(i+r)}}(\Delta t) \quad \text{for } r = 1, 2, 3, \dots \quad (2)$$

in circumstances in which the *difference* between the threshold changes due to aging at the two frequencies is negligible. The precision of the measure of threshold change may therefore be improved for thresholds recorded at frequencies be-

TABLE I. Mechanoreceptor-specific vibrotactile thresholds for the fingertips of healthy males at age 30, from Brammer *et al.* (1993).

Receptor population	Frequency (Hz)	Mean threshold (dB re 10^{-6} m s $^{-2}$)	Standard deviation (dB)	Change with age (dB/year)
SAI	4	78.8	5.3	0.025
	6.3	83.2	5.3	0.07
FAI	20	92.7	5.3	0.07
	32	100.2	5.3	0.07
FAII	100	110.9	4.5	0.25
	160	110	4.5	0.3

lied mediated by the same receptor population by forming the mean change in threshold for that population. Hence, if vibrotactile thresholds are determined at stimulus frequencies of, say, $f=4$, and 6.3 Hz (believed mediated by SAIs), and 20, and 32 Hz (believed mediated by FAIs), then

$$TC_{SAI} = [TC_4(\Delta t) + TC_{6.3}(\Delta t)]/2, \quad (3)$$

etc., where TC_{SAI} , and TC_{FAI} defined equivalently, are taken to be the mean threshold changes for the SAI and FAI receptor populations, respectively, during the time period Δt .

For time intervals chosen so that aging introduces little difference in the threshold change between frequencies mediated by a given receptor population, analysis of the significance of an observed change in threshold can then be based on the statistical significance of the magnitudes of TC_{SAI} , and TC_{FAI} , derived from published values for the repeatability of threshold determinations. For healthy persons screened for peripheral neuropathies, the test/retest repeatability for receptor-specific thresholds appears to be normally distributed with a standard deviation (s.d.) of close to 2.1 dB (Brammer *et al.*, 1992). Accordingly, in circumstances in which aging-related errors may be neglected, the magnitudes of TC_{SAI} , and TC_{FAI} may be interpreted by reference to a normal distribution with this s.d.

B. Status of a person's mechanoreceptor-specific thresholds relative to expected values

In order to establish whether the thresholds recorded from a subject remain within the range associated with healthy persons, the observed thresholds need to be compared with those recorded from persons medically screened for symptoms of neurological disease, and with no history of exposure of the hands to vibration or to trauma. Thresholds for approximately 100 hands of healthy male Caucasian and Asian professional workers, and Caucasian manual workers, with ages ranging from 25 to 75 years, have been obtained using the apparatus employed in this study (Brammer *et al.*, 1993). Mean values, standard deviations, and the change in mean thresholds with age for these persons are summarized in Table I, and are taken to define normative values of vibrotactile thresholds for the purposes of the present work.

The *shift* in threshold from the mean normal value is first calculated at each measurement frequency, $TS_{f_i}(t)$. Provided the mean normal vibrotactile threshold changes little

during the time interval between measurements, we obtain from Eq. (1):

$$TC_{f_i}(\Delta t) \cong TS_{f_i}(t_2) - TS_{f_i}(t_1). \quad (4)$$

Applying Eq. (2):

$$TS_{f_{(i+r)}}(t_2) - TS_{f_i}(t_2) \cong TS_{f_{(i+r)}}(t_1) - TS_{f_i}(t_1). \quad (5)$$

Thus, a consistent *difference* between threshold shifts at frequencies believed mediated by the same receptor population is expected. The threshold shift may be conveniently expressed in terms of the range in thresholds observed in healthy hands at the same stimulation frequency, which appears to possess a normal distribution when expressed in dB. For this purpose, the range within the Gaussian distribution is expressed in units of the s.d. of the population mean, so that

$$TS_{4(s.d.)} = TS_4(t)/s.d._4, \quad (6)$$

etc., where $s.d._4$, $s.d._{6.3}$, etc., are the standard deviations of the threshold distributions for healthy persons at 4, 6.3 Hz, etc., respectively. In consequence, it is possible to express the magnitude of this metric in terms of probability values for a normal distribution. In this way the magnitude of an observed normalized threshold shift may be interpreted in terms of the probability of a given deviation from the mean value recorded in the hands of healthy persons.

C. Apparatus and measurements

The performance of these metrics has been examined by conducting noninvasive measurements of vibrotactile perception threshold at the fingertips using a tactometer (Brammer and Piercy, 1991; 2001). The apparatus consists essentially of: a stimulator mounted on a vertically adjustable track, with axis of motion in the direction of the track; an arm support on which the hand and forearm rest with palm facing upwards; a vibration sensor, attached to the stimulator, and electronics to record the motion at the surface of the skin, and a computer to administer the stimulus and psychophysical algorithm, calculate perception thresholds and, in the second study, indicate inconsistencies in the performance of the subject during the threshold tracking task (see Sec. IV B).

When the subject was sitting comfortably, the stimulator was positioned so that a 3-mm-diam, cylindrical, flat-ended probe could be lowered onto a fingertip. Once in contact with the skin, a static compressive force of 0.05 N was maintained. No additional stationary surface contacted the fingertip or surrounded the vibrating probe. Pulsed oscillatory stimuli (i.e., tone bursts) were then applied to the skin at amplitudes close to the threshold of perception at frequencies which, together with the stimulator contact conditions, were intended to elicit, separately, responses from one of the following mechanoreceptor populations: SAI or FAI (Brammer and Piercy, 2000; ISO 13091-1, 2001).

The psychophysical test paradigm employed an up-down procedure suitable for applications in the field, where rapid threshold determination is deemed most important. In this paradigm sinusoidal bursts of vibration of constant am-

plitude separated by quiescent periods are applied to the skin at a selected frequency. The bursts were 800 ms in duration at frequencies of 20 Hz and above, and 1.6 s in duration at frequencies of 6.3 Hz and below. The quiescent interval was 0.6 s. Successive bursts initially increase in intensity until the subject signals, by pressing a switch, that the stimulus has been detected. This action defines the first ascending, or “upper” threshold. Successive bursts then decrease in intensity until the subject signals, by releasing the switch, that the stimulus can no longer be felt, so defining the first descending or “lower” threshold. The burst intensity is then, once again, increased. This cycling of burst intensity according to the subject’s response was repeated at least four and up to six times if the ascending and descending thresholds were inconsistent. The mean threshold acceleration is calculated from the arithmetic sum of the sequence of ascending and descending thresholds, each of which are expressed in dB re 10^{-6} m/s^2 . In forming the mean threshold, the values of the first ascending and descending thresholds have been excluded.

The change in stimulus intensity between bursts was fixed at 2 dB during the initial study. During the second study the step size was automatically decreased from 3 dB to a minimum of 2 dB depending on the magnitude of the difference between individual ascending and descending threshold pairs. With the accelerated procedure, the mean vibrotactile threshold at a single stimulus frequency could be determined in about 1 min. The threshold values for healthy males obtained in this way are comparable to those obtained by other techniques (Piercy and Brammer, 2004).

Prior to commencing threshold determinations, each subject was first given at least two trials of the measurement procedure, one for each receptor population. The pulsed nature of the stimulus was described, and the subject was instructed to identify the repeated pattern of stimulus-on, stimulus-off, by observing the cycling on-and-off of a lamp illuminated during presentation of the stimulus. The different sensations experienced from different receptor types during suprathreshold stimulation were described. Measurements commenced when the subject believed he understood the response procedure. Familiarization with the procedure typically took 5 min. Thresholds were determined at the fingertips of digits 3 and 5 of both hands, at frequencies of 4, 6.3, 20, and 32 Hz, and took approximately 45 min. Skin temperature was measured at the fingertips and maintained at at least 27 °C.

The apparatus was calibrated daily before commencing measurements, using a built-in reference signal that generates a known acceleration. Day-to-day variations in calibration were less than 1 dB at all measurement frequencies, and typically less than 0.5 dB.

D. Subjects

Measurements were performed on 18 forest workers, most of whom operated vibrating power tools (chain saws and brush cutters) that produced their “conditioning” vibration exposure. The subjects had no prior experience of vibrotactile testing, and ranged in age from 30 to 56 years, with a

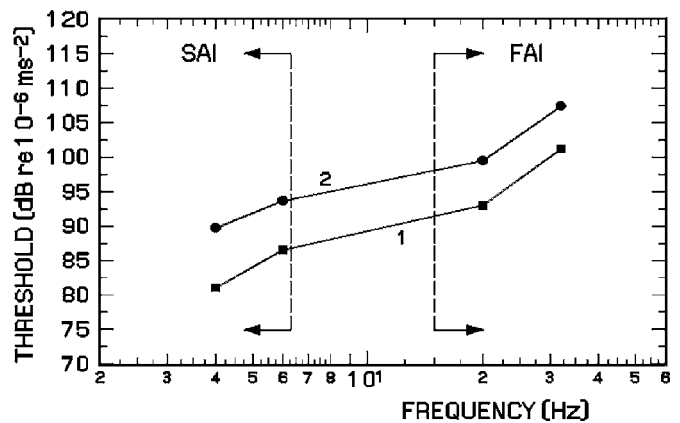


FIG. 1. Vibrotactile perception thresholds at the fingertip of an asymptomatic subject. Study 2 was performed 5 years after study 1.

mean age of 44 years. All gave their informed consent to participate in the experiments, which had received ethics committee approval. Prior to the measurements, which were conducted as part of two health studies separated by 5 years, none of the subjects had engaged in manual work or operated their customary power tools. In consequence, the observed thresholds are believed to be free of any temporary loss in sensation resulting from acute exposure of the hand to intense vibration (Brammer *et al.*, 2006).

III. RESULTS

A. Vibrotactile perception thresholds at different frequencies

A typical pattern of thresholds recorded in the two studies separated by 5 years is shown for one finger of a symptom-free subject in Fig. 1. In this diagram, the approximate boundaries between frequencies believed mediated by different mechanoreceptor populations are indicated by dashed (vertical) lines. The vibrotactile thresholds are expressed as rms accelerations in dB relative to 10^{-6} m/s^2 , following the recommendation of ISO 13091-1 (2001). It is evident by comparing the results at 4 and 6.3 Hz, and those at 20 and 32 Hz, that similar *changes* in threshold occurred in the hand of this subject at thresholds believed mediated by the same receptor population. Clearly, the thresholds at these frequencies have increased in magnitude between the two studies, that is, the sensitivity is reduced with continuing exposure to the conditioning vibration (from power tool operation).

Inspection of Table I shows that the mean age dependence of thresholds will introduce a systematic error of, typically, 0.35 dB when $\Delta t=5$ into the relationship of Eqs. (1) and (4) at frequencies of 6.3, 20, and 32 Hz, and less at 4 Hz. Within the precision of psychophysical measurements, errors of this magnitude can be tolerated. It is thus appropriate to employ the data from these subjects to: (1) examine the assumption underlying the two metrics, and (2) develop ways for identifying inconsistent subject performance, in order to exclude potentially erroneous thresholds and hence inappropriate assessments of tactile performance.

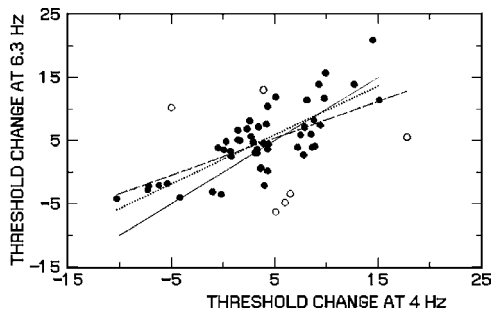


FIG. 2. Scatter plot of threshold changes over 5 years in the same finger at 4 and 6.3 Hz. Data for all subjects. The solid line is the expected relationship between threshold pairs at 4 and 6.3 Hz. A linear regression fit to all data is shown by the dashed line and to data excluding outliers by the dotted line. The outliers excluded from the analysis are shown by open circles (see the text).

B. Changes in threshold between studies

The relationships between the threshold *changes* recorded in each fingertip at 4 and 6.3 Hz, and at 20 and 32 Hz, are shown in Figs. 2 and 3, respectively, for digits 3 and 5 of all subjects (left, and right, hands). The observed threshold changes, when paired by frequencies believed mediated by the same receptor population, form a scatter plot about the relationship: $TC_{f_2}(\Delta t) = TC_{f_1}(\Delta t)$ [see Eq. (2)]. This relationship is plotted as a continuous line in the diagrams. A linear regression fit to all the data is shown by the dashed line which, while similar to that expressing the assumption underlying the method (the continuous line), deviates somewhat in gradient and origin, particularly for the thresholds at 4 and 6.3 Hz (Fig. 2).

There are two potential sources of these deviations. The first is the assumption of the applicability of the acute adaptation property of mechanoreceptor populations in response to a short-duration conditioning stimulus to the persistent changes in threshold observed in this study, and the second is the psychophysical nature of the measurements. Thus, thresholds may be influenced, for example, by a subject's lack of concentration, changing response criterion, or fatigue (Levitt, 1971). To explore further the influences on the relationship between $TC_{f_1}(\Delta t)$ and $TC_{f_2}(\Delta t)$, the modulus of the difference between threshold changes at two frequencies believed mediated by the same receptor population within each

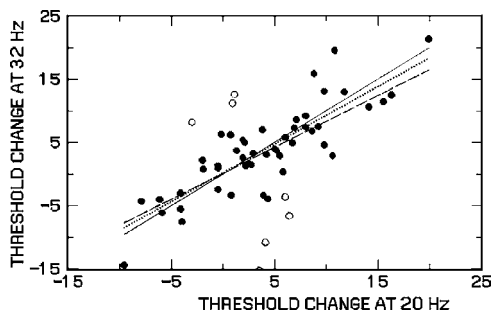


FIG. 3. Scatter plot of threshold changes over 5 years in the same finger at 20 and 32 Hz. Data for all subjects. The solid line is the expected relationship between threshold pairs at 20 and 32 Hz. A linear regression fit to all data is shown by the dashed line and to data excluding outliers by the dotted line. The outliers excluded from the analysis are shown by open circles (see the text).

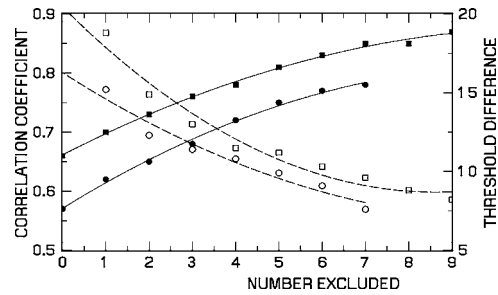


FIG. 4. Pearson correlation coefficient for threshold changes believed mediated by a single receptor population within the same finger expressed as a function of the number of threshold pairs excluded: closed circles—4 and 6.3 Hz, closed squares—20 and 32 Hz. The modulus of the smallest threshold difference excluded is shown on the right ordinate: open circles—4 and 6.3 Hz, open squares—20 and 32 Hz.

finger, i.e., $|TC_{f_1}(\Delta t) - TC_{f_2}(\Delta t)|$, has been used to rank order the outliers in Figs. 2 and 3. The correlation between the remaining pairs of threshold changes has been calculated repeatedly as the most extreme remaining outlier is successively excluded. The results of this calculation are shown in Fig. 4 for the removal of up to nine threshold pairs. The correlation coefficients for the threshold changes believed mediated by the SAI receptors (at 4 and 6.3 Hz) are shown by the closed circles, and for those believed mediated by the FAI receptors (at 20 and 32 Hz) by the closed squares. The corresponding modulus of the smallest difference between threshold changes removed from the calculation, $|TC_{f_1}(\Delta t) - TC_{f_2}(\Delta t)|_{\min}$, is shown by open circles and squares, respectively, and the dashed lines (right-hand scale in Fig. 4). Inspection of Fig. 4 reveals that the correlation between $TC_{f_1}(\Delta t)$ and $TC_{f_2}(\Delta t)$ increases as the initial outliers are excluded, with the rate of increase slowing as the number of outliers removed is increased. Consistent with this trend is a slowing in the reduction in magnitude of $|TC_{f_1}(\Delta t) - TC_{f_2}(\Delta t)|_{\min}$, until a value of threshold change approaching approximately four times the standard deviation for the test/retest repeatability of a threshold measurement is reached (8.3 dB) (Brammer *et al.*, 1992). The influence of outliers exceeding this value of $|TC_{f_1}(\Delta t) - TC_{f_2}(\Delta t)|_{\min}$ can be seen in Figs. 2 and 3, where open circles identify six outliers excluded from the calculation. Linear regression fits to the remaining data are shown by the dotted lines. Comparison between the dashed lines and dotted lines in Figs. 2 and 3 confirms that the regression fits to the data are now closer to the continuous lines expressing the relationship expected between $TC_{f_1}(\Delta t)$ and $TC_{f_2}(\Delta t)$ if the assumption of the applicability of the adaptation property of receptor populations to persistent changes in threshold is valid.

Now the 95% confidence interval for the mean difference between threshold changes recorded at 4 and 6.3 Hz is $-2.15 \leq TC_4(\Delta t) - TC_{6.3}(\Delta t) \leq 0.57$, and for threshold changes recorded at 20 and 32 Hz is $-1.0 \leq TC_{20}(\Delta t) - TC_{32}(\Delta t) \leq 2.06$, for *all* the threshold changes obtained from these subjects. Thus the magnitudes of the threshold changes recorded at the two frequencies believed mediated by the same receptor population are not demonstrably different, as would be expected from the acute adaptation property of mechanoreceptors, and may be taken to confirm the valid-

TABLE II. Change in thresholds believed mediated by the SAI and FAI receptors in digit 3 of the right hand.

Subject	Change in threshold		Mean change in SAI threshold TC _{SAI} (dB)	Mean change in FAI threshold TC _{FAI} (dB)	TC _{sum} (dB)
	At 4 Hz (dB)	At 6.3 Hz (dB)			
1	9.9	15.7	12.8	8.6	21.4
2	3.3	3.6	3.5	-0.6	2.9
3	1.4	6.6	4	3.1	7.1
4	4.3	3.6	4	3.7	7.7
5	-10.3	-4.2	-7.3	-12	-19.3
6	7.9	7.1	7.5	4.5	12
7	5.1	-6.3	R	-5.1	-10.2
8	4	-2.1	1	-4.8	-3.8
9	4.3	0.2	2.3	2.5	4.8
10	3.1	3	3.1	R	6.2
11	2.9	4.7	3.8	3.6	7.4
12	3.4	7.1	5.3	7.7	13
13	14.5	20.9	17.7	R	35.4
14	2.3	6.8	4.6	2.1	6.7
15	2.7	5.6	4.2	14.4	18.6
16	3.6	0.6	2.1	2.3	4.4
17	M	7.5	7.5	10.8	18.3
18	3.9	13	R	5.4	10.8

ity of the basic assumption underlying the method [Eq. (2)]. In addition, identifying pairs of threshold changes for which $TC_{f_2}(\Delta t) \neq TC_{f_1}(\Delta t)$ can now be seen as a way for assessing a subject's performance of the psychophysical task, and hence the presence of one, or more, erroneous thresholds.

The changes in thresholds at stimulation frequencies of 4 and 6.3 Hz are shown in columns 2 and 3 of Table II, respectively, for digit 3 of the right hand of all subjects. For most subjects the threshold changes recorded at the two frequencies tend to be similar in magnitude. However, the magnitude of $|TC_{f_1}(\Delta t) - TC_{f_2}(\Delta t)|$ can be seen to range from 0.1 dB (subject 10) to 11.4 dB (subject 7) in Table II. This is considered sufficient to warrant introducing a limit for the maximum acceptable difference between threshold changes recorded at frequencies believed mediated by the same receptor population, on the expectation from the preceding analysis of outliers that one, or both, of the threshold changes may contain errors. A limit of 8.3 dB would appear appropriate for this purpose, i.e.,

$$|TC_{f_1}(\Delta t) - TC_{f_2}(\Delta t)|_{\max} \leq 8.3. \quad (7)$$

Application of this condition to these subjects, which from the repeatability of threshold determinations is believed to have a (two-sided) probability of occurrence of $p=0.05$, would lead to the rejection of data from 14/140 (10%) of the threshold pairs.

The mean change TC_{SAI} is shown in column 4 of Table II, and excludes data from subjects 7 and 18 (indicated by "R") as the threshold changes failed to satisfy the consistency condition [Eq. (7)]. The mean threshold changes at 20 and 32 Hz within the same fingers, TC_{FAI} , are shown in column 5: data for subjects 10 and 13 have been rejected (R) for the same reason. It is now evident by comparing the results in columns 4 and 5 with those in columns 2 and 3 that the

TABLE III. Correlation between changes in thresholds believed mediated by SAI and FAI receptors, for the right and left hands, for threshold changes satisfying the consistency condition, Eq. (7).

	Digit 3			Digit 5		
	TC _{SAI}	TC _{FAI}	TC _{sum}	TC _{SAI}	TC _{FAI}	TC _{sum}
Right hand						
Digit 3 TC _{SAI}	1					
Digit 3 TC _{FAI}	0.81	1				
Digit 3 TC _{sum}	0.92	0.97	1			
Digit 5 TC _{SAI}	0.47	0.62	0.59	1		
Digit 5 TC _{FAI}	0.53	0.84	0.76	0.78	1	
Digit 5 TC _{sum}	0.53	0.78	0.73	0.93	0.95	1
Left hand						
Digit 3 TC _{SAI}	1					
Digit 3 TC _{FAI}	0.57	1				
Digit 3 TC _{sum}	0.87	0.9	1			
Digit 5 TC _{SAI}	0.75	0.56	0.73	1		
Digit 5 TC _{FAI}	0.66	0.68	0.75	0.89	1	
Digit 5 TC _{sum}	0.72	0.64	0.76	0.97	0.97	1

mean threshold changes believed recorded from *different* receptor populations within the same finger appear to be as consistent as the threshold changes recorded at different frequencies believed mediated by the *same* receptor population for these subjects.

To further explore this observation, Pearson correlation coefficients between the changes in threshold believed mediated by the SAI and FAI receptors within each finger satisfying the consistency condition have been calculated separately for the right and left hands, and are given in Table III. Examination of Table III reveals that the correlation between TC_{SAI} and TC_{FAI} within the same fingertip, for digits 3 and 5 of the right hand, and digit 5 of the left hand, are 0.81, 0.78, and 0.89, respectively. Reference to Fig. 4 reveals that such correlations are indeed equivalent to those recorded at different frequencies within the same receptor population. The correlation between threshold changes believed mediated by the SAI and FAI receptors within digit 3 of the left hand is, however, much lower (0.57). It should be noted that a correlation coefficient of this magnitude was obtained between the threshold changes recorded in each finger at 4 and 6.3 Hz prior to excluding outliers (see the closed circle in Fig. 4 at zero abscissa). Accordingly, at least for these subjects, it appears reasonable to sum the mean threshold changes recorded within the same finger to produce a single-number metric for that finger:

$$TC_{\text{sum}} = TC_{SAI} + TC_{FAI}. \quad (8)$$

While, as expected, the summed mean threshold changes, TC_{sum} , are highly correlated to the threshold changes within the same finger from which they were calculated (see Table III), the correlations between summed mean threshold changes for different digits of the same hand are lower, as are the correlations between summed threshold changes for digits from different hands.

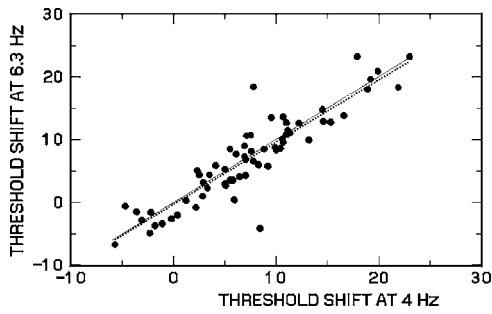


FIG. 5. Scatter plot of threshold shifts from mean normative values recorded in the same finger at 4 and 6.3 Hz. Data for all subjects (study 2). The solid line is the relationship $TS_{6.3}(t_2)=TS_4(t_2)$. A linear regression fit to all data is shown by the dotted line.

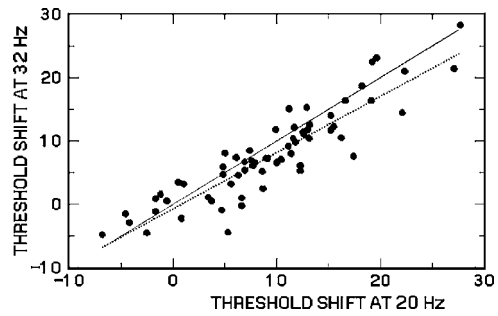


FIG. 6. Scatter plot of threshold changes recorded in the same finger at 20 and 32 Hz. Data for all subjects (study 2). The solid line is the relationship $TS_{32}(t_2)=TS_{20}(t_2)$. A linear regression fit to all data is shown by the dotted line.

C. Shifts in thresholds from expected values

The relationships between the threshold *shifts* recorded in each fingertip at 4 and 6.3 Hz, and at 20 and 32 Hz, are shown in Figs. 5 and 6, respectively, for digits 3 and 5 of all subjects (left, and right, hands). The results are from the second study. The observed threshold shifts, when paired by frequencies believed mediated by the same receptor population (shown by closed circles), again form a scatter plot with the linear regression fit shown by the dotted line in each diagram. Inspection of Fig. 5 reveals that the observed relationship between threshold shifts at 4 and 6.3 Hz in the same finger is almost identical to the continuous line, which has the equation: $TS_{f_2}(t_2)=TS_{f_1}(t_2)$. For all threshold shifts obtained from these subjects, the 95% confidence interval for the mean difference between threshold shifts recorded at 4 and 6.3 Hz is $-0.36 \leq TS_4(t_2) - TS_{6.3}(t_2) \leq 1.12$, indicating that the magnitudes of the threshold shifts at these frequencies in a fingertip are not demonstrably different. Hence, for

thresholds believed mediated by the SAI receptor population, Eq. (5) becomes

$$TS_{f_{(i+r)}}(t) - TS_{f_i}(t) \approx 0. \quad (9)$$

The threshold shifts may thus be averaged in order to improve the precision of the metric, i.e.,

$$TS_{SAI}(t) = [TS_4(t) + TS_{6.3}(t)]/2, \quad (10)$$

where $TS_{SAI}(t)$ is the mean threshold shift at time t .

The observed shift in threshold is shown for each subject in Table IV, for digit 3 of the left hand. The shifts at 4 and 6.3 Hz relative to the mean values recorded at the same frequency in healthy persons are given in columns 2 and 3, respectively. The differences between these threshold shifts range from 0.2 to 4.1 dB (3.9 dB), and are much smaller than the corresponding differences between the threshold *changes* at the same frequencies (see Table II). The mean shift for thresholds believed mediated by the SAI receptors is

TABLE IV. Shifts re normal values of thresholds believed mediated by the SAI and FAI receptors in digit 3 of the left hand (data for study 2).

Subject	Threshold shift		Mean threshold shift for SAI (dB)	Mean SAI shift/s.d. of normals $TS_{SAI(s.d.)}$	Mean FAI shift/s.d. of normals $TS_{FAI(s.d.)}$
	4 Hz (dB)	6.3 Hz (dB)			
1	19.2	19.6	19.4	3.66	3.45
2	9.2	5.8	7.5	1.42	2.04
3	8.3	6	7.15	1.35	1.54
4	6.9	9	7.95	1.5	2.34
5	8.8	8.5	8.65	1.63	1.3
6	5.5	3.6	4.55	0.86	0.4
7	7.6	8.1	7.85	1.48	0.83
8	11.1	11.4	11.25	2.12	1.27
9	-0.2	-2.6	-1.4	-0.26	-0.08
10	6.4	4.1	5.25	0.99	1.55
11	6.1	7.7	6.9	1.3	1.3
12	-4.7	-0.6	-2.65	-0.5	-0.01
13	14.5	14.8	14.65	2.76	3.35
14	13.2	9.9	11.55	2.18	2.22
15	7	6.8	6.9	1.3	1.66
16	5	3	4	0.75	1.06
17	16.6	13.8	15.2	2.87	2.36
18	10	8.4	9.2	1.74	2.75

TABLE V. Correlation between threshold shifts believed mediated by SAI and FAI receptors, for the right and left hands (study 2).

	Digit 3			Digit 5		
	TS _{SAI(s.d.)}	TS _{FAI(s.d.)}	TS _{sum(s.d.)}	TS _{SAI(s.d.)}	TS _{FAI(s.d.)}	TS _{sum(s.d.)}
Right hand						
Digit 3 TS _{SAI(s.d.)}	1					
Digit 3 TS _{FAI(s.d.)}	0.94	1				
Digit 3 TS _{sum(s.d.)}	0.98	0.99	1			
Digit 5 TS _{SAI(s.d.)}	0.89	0.85	0.88	1		
Digit 5 TS _{FAI(s.d.)}	0.93	0.93	0.94	0.87	1	
Digit 5 TS _{sum(s.d.)}	0.94	0.92	0.94	0.97	0.97	1
Left hand						
Digit 3 TS _{SAI(s.d.)}	1					
Digit 3 TS _{FAI(s.d.)}	0.87	1				
Digit 3 TS _{sum(s.d.)}	0.97	0.97	1			
Digit 5 TS _{SAI(s.d.)}	0.87	0.91	0.92	1		
Digit 5 TS _{FAI(s.d.)}	0.85	0.95	0.93	0.97	1	
Digit 5 TS _{sum(s.d.)}	0.87	0.94	0.93	0.99	0.99	1

given in column 4, and the normalized mean threshold shift for this receptor population in column 5, where

$$TS_{SAI(s.d.)} = TS_{SAI}(t)/s.d._{SAI} \quad (11)$$

and $s.d._{SAI}$ is the corresponding standard deviation of the threshold distribution in healthy persons from Table I. It can be seen by reference to column 5 that, for example, the threshold shift of subject 1 was found to be elevated, that is reduced in sensitivity, by 3.66 s.d. from the mean value recorded in the hands of healthy persons. In contrast, the threshold shifts of subjects 9 and 12 were found to be slightly more sensitive than the mean normal value (by 0.26 and 0.5 s.d., respectively).

Reference to Fig. 6 reveals that the threshold shifts at 20 Hz tend to be greater than those at 32 Hz in the same fingertip, with the deviation apparently increasing in magnitude with increasing threshold shift. The 95% confidence interval for the mean difference between the threshold shifts recorded at 20 and 32 Hz is $0.83 \leq TS_{20}(t_2) - TS_{32}(t_2) \leq 2.69$, which does not include the condition expressed by Eq. (9). A more appropriate relationship for these threshold shifts would appear to be

$$TS_{f_2}(t_2) = \alpha TS_{f_1}(t_2) + \beta, \quad (12)$$

where $f_1=20$ Hz, $f_2=32$ Hz, and α and β are constants. For these data, the 95% confidence interval for α is $0.77 \leq \alpha \leq 1.01$ and for β is $-2.22 \leq \beta \leq 0.74$. Thus, although the mean difference between the threshold shifts recorded at the two frequencies differs from zero, the 95% confidence interval for the relationship between the threshold shifts at these frequencies includes the values $\alpha=1$ and $\beta=0$, for which values Eq. (12) becomes identical to Eq. (9). Hence, in view of the relationship found for the SAI receptors [Eq. (9)], it appears appropriate to apply this form of Eq. (12) to the FAI receptors, so that the magnitudes of the threshold shifts recorded at 20 and 32 Hz may also be averaged to improve the precision of the metric.

The normalized mean threshold shift for the FAI receptor population in the same finger, $TS_{FAI(s.d.)}$, estimated in an equivalent manner to $TS_{SAI(s.d.)}$ [see Eq. (11)], is shown in column 6 of Table IV. Note by comparing columns 5 and 6 that, for each subject, the magnitudes of the normalized threshold shifts tend to be similar for thresholds believed mediated by the two receptor populations. Results equivalent to those shown in Table IV have been found in these subjects for digit 5 of the left hand, and digits 3 and 5 of the right hand.

The correlations between the threshold shifts believed mediated by different receptor populations within the same fingertip, and between those in digits 3 and 5 of the same hand, are listed in Table V. Inspection of Table V reveals that the threshold shifts within the same fingertip are closely related, with Pearson correlation coefficients of 0.94, 0.87, 0.87, and 0.97 for digits 3 and 5 of the right and left hands, respectively. Accordingly, at least for our subjects, it appears reasonable to combine the threshold shift recorded at the four frequencies within the same finger (i.e., 4, 6.3, 20, and 32 Hz), to produce a second, single-number metric for that finger. For this reason the summed normalized threshold shift is formed:

$$TS_{sum(s.d.)} = TS_{SAI(s.d.)} + TS_{FAI(s.d.)}. \quad (13)$$

As expected, the summed normalized threshold shifts, $TS_{sum(s.d.)}$, are highly correlated to the normalized receptor-specific threshold shifts within the same finger from which they were calculated (see Table V). The summed normalized threshold shifts in digits 3 and 5 of the same hand are also highly correlated in these workers.

IV. DISCUSSION

A. Threshold changes between studies

The variability of the threshold *changes* recorded at the two frequencies mediated by the same receptor population is worthy of further consideration. The consistency condition

[Eq. (7)] has been introduced to identify, and hence reject, the most inconsistent threshold changes. However, it is worth noting that the 95% confidence interval for the mean difference between the remaining threshold changes at 4 and 6.3 Hz after application of the consistency condition of Eq. (7) is $-2.16 \leq TC_4(\Delta t) - TC_{6.3}(\Delta t) \leq -0.14$. This suggests that a small bias in the threshold changes may have been introduced by the rejection in this case of 6/72 threshold pairs (8.3%). Accordingly, a future analysis may wish to re-examine this approach.

The observation that the threshold changes in this group of subjects appeared to be of similar magnitude at frequencies believed mediated by the SAI and FAI receptor populations within one fingertip could be interpreted that the thresholds were all mediated by the same receptor population, as could occur in hands containing pathological changes. However, recent experiments with healthy subjects using the same apparatus and measurement procedure as in this study have shown that acute threshold changes at 4 and 32 Hz in response to exposure to a pure-tone, or damped sinusoidal conditioning vibration differ substantially, which implies that the thresholds at these frequencies were mediated by different mechanoreceptor populations (Brammer *et al.*, 2006). Thus, while the formation of an overall metric, the summed mean threshold change, TC_{sum} , would appear justified for the neurologic disturbances experienced by the subjects in this study, it cannot be presumed to apply generally. For our subjects, interpretation of the change in threshold can be based on the statistical significance of the magnitude of TC_{sum} as derived from published values for the repeatability of threshold determinations using the same apparatus and measurement procedure.

B. Threshold shifts from expected values

Close inspection of the threshold shifts in Table IV reveals that 9/18 of the differences are less than 2 dB (the smallest step in stimulus magnitude), and 15/18 were less than 3 dB. The consistent resolution of threshold shifts of the order of 2 dB is obtained by averaging repeated determinations of ascending and descending thresholds. A source of error will, however, be introduced by inaccuracies in the values for the thresholds of healthy persons. Such errors would lead to systematic differences between $TS_{f_1}(t_2)$ and $TS_{f_2}(t_2)$. Clearly, from the analysis of the data in Fig. 5, any error in the normative values for thresholds at frequencies of 4 and 6.3 Hz must be less than 0.5 dB, which is within the uncertainty of the psychophysical measurements. The data of Fig. 6 suggest that somewhat larger errors may be present in the normative values for thresholds at 20 and/or 32 Hz. A systematic difference between the threshold shifts recorded at these frequencies would require, however, a nonzero value of β and $\alpha \neq 1$ [Eq. (12)]. While these values cannot be excluded and, by inspection of Fig. 6 with $\alpha \equiv 1$, could lead to $\beta \approx -1$, neither can the values $\beta=0, \alpha=1$, which correspond to $TS_{f_2}(t_2) = TS_{f_1}(t_2)$, as already noted. Values of threshold shift at each frequency were in fact calculated during the

threshold measurements performed in study 2, and employed as an indicator of inconsistent subject performance, using Eq. (9) (Brammer and Piercy, 1995).

The influence of the magnitude of the threshold shift recorded in a finger on its detection may be inferred from the results in Figs. 5 and 6. For the data in Fig. 5, the scatter of the measured values from the values if $TS_{f_2}(t_2) = TS_{f_1}(t_2)$, that is, the deviations from the continuous line, can be seen to be similar in magnitude irrespective of whether the threshold shift being measured is close to zero or not (with the exception of one or two outliers). This suggests that both large and small threshold shifts are being detected in the fingers of these subjects with approximately equal precision. For the data in Fig. 6, the scatter of the measured values displays a tendency to increase with increasing magnitude of the threshold shift, possibly suggesting that smaller threshold shifts are detected more precisely. The effect, if any, is, however, small.

As already described, the metric of threshold shift may be improved for our subjects by forming the summed normalized threshold shift, $TS_{sum(s.d.)}$, and may be interpreted in terms of probability values for the distributions of thresholds obtained from healthy persons.

C. Implications for tactile function

Clearly, whatever is causing the threshold shifts, and threshold changes, appears to be affecting similarly the receptor populations in each digit of our subjects. The sensory and neuromuscular symptoms in these forest workers associated with the threshold shifts and threshold changes will be published elsewhere.

Alterations in receptor-specific vibrotactile thresholds, either over a period of time or with respect to the values found in healthy persons, will reflect changes in the acuity of specific mechanoreceptor populations. The SAI and FAI populations perform well-defined roles in tactile function, as already described, and alterations in their acuity at the fingertips can be expected to impede perception of the surface features of objects, as well as the gripping and holding of small objects. The threshold *changes* observed are considerably in excess of those due to aging. Uncertainties in estimates of “normal” thresholds for healthy persons introduce errors into threshold *shifts*, which have been shown to be negligible for the SAI receptors but cannot be completely discounted for the FAI receptors. Threshold changes avoid this bias by employing the individual as his/her own reference. They involve, however, two measurements, and so are subject to two measurement errors, each of which will be defined by the test/retest repeatability. Thus the two metrics provide related, but different, information with which to assess vibrotactile thresholds, and are subject to somewhat different errors.

V. CONCLUSIONS

Threshold *changes*, and threshold *shifts*, have been constructed from thresholds measured at the fingertips. Both metrics require that thresholds be determined at at least two frequencies mediated by the same mechanoreceptor popula-

tion. The metrics assume the applicability of the adaptation property of mechanoreceptors, which has been confirmed by thresholds obtained from 18 forest workers. Hence, when expressed in dB, both threshold changes and threshold shifts may be averaged at frequencies mediated by the same mechanoreceptor population to improve the precision of the metric for individual fingers. Differences between threshold changes observed at frequencies mediated by the same receptor population may be used to identify inconsistent subject performance, and hence potentially erroneous results.

In this group of subjects, the threshold changes, and threshold shifts, at frequencies believed mediated by the SAI and FAI receptors within each finger were correlated. In these circumstances, which may be expected to occur for some work-induced and systemic peripheral neuropathies, both threshold changes and threshold shifts may be summed over SAI and FAI receptors to improve precision, and hence the potential for interpretation.

ACKNOWLEDGMENTS

The authors wish to acknowledge the provision of financial assistance by the Finnish National Board of Forestry. We greatly appreciated the cheerful support of the staff and interpreters at the Regional Health Clinic at Ämmänsari, Finland. We remain indebted to the forest workers who generously and patiently donated their time.

Bolanowski, S. J., Gescheider, G. A., Verrillo, R. T., and Checkosky, C. M. (1988). "Four channels mediate the mechanical aspects of touch," *J. Acoust. Soc. Am.* **84**, 1680–1694.

Brammer, A. J., Peterson, D. R., Cherniack, M. G., and Diva, U. A. (2006). "Temporary changes in mechanoreceptor-specific vibrotactile perception to stimuli simulating impact power tools," in *Proceedings, Inter-Noise 2006*, Noise Control Foundation, New York.

Brammer, A. J., and Piercy, J. E. (1991). "Measuring vibrotactile perception thresholds at the fingertips of power-tool operators," in *Proceeding of the United Kingdom Informal Group on Human Response to Vibration*, Buxton, United Kingdom, pp. 1–7.

Brammer, A. J., and Piercy, J. E. (1995). "Method and apparatus for identifying vibrotactile perception thresholds of nerve endings with subject inconsistency detection," U.S. Patent 5433211.

Brammer, A. J., and Piercy, J. E. (2000). "Rationale for measuring vibrotactile perception at the fingertips as proposed for standardization in ISO 13091-1," *Arbetslivsrapport* **4**, 125–132 (ISSN 1400–8211).

Brammer, A. J., and Piercy, J. E. (2001). "Vibrotactile perception thresholds: The tactile equivalent of audiometry," *Can. Acoust.* **29**, 14–15.

Brammer, A. J., Piercy, J. E., Nohara, S., and Nakamura, S. (1992). "Repeatability of threshold measurements used to assess sensory changes in the hands," in *Proceedings Inter-Noise 92*, edited by G. A. Daigle and M. R. Stinson, Noise Control Foundation, New York, pp. 1127–1130.

Brammer, A. J., Piercy, J. E., Nohara, S., Nakamura, H., and Auger, P. L.

(1993). "Age-related changes in mechanoreceptor-specific vibrotactile thresholds for normal hands," *J. Acoust. Soc. Am.* **93**, 2361 (A).

Coutu-Wakulczyk, G., Brammer, A. J., and Piercy, J. E. (1997). "Association between a quantitative measure of tactile acuity and hand symptoms reported by operators of power tools," *J. Hand Surg. [Am]* **22A**, 873–881.

Gerr, F., Letz, R., Hershman, D., Farraye, J., and Simpson, D. (1991). "Comparison of vibrotactile thresholds with physical examination and electrophysiological assessment," *Muscle Nerve* **14**, 1059–1066.

Gescheider, G. A. (1997). *Psychophysics: The Fundamentals* (Ehrlbaum, Mahwah, NJ).

Gescheider, G. A., Bolanowski, S. J., Pope, J. V., and Verrillo, R. T. (2002). "A four channel analysis of the tactile sensitivity of the fingertip: Frequency selectivity, spatial summation, and temporal summation," *Somatosen. Mot. Res.* **19**, 114–124.

Gescheider, G. A., Sklar, B. F., Van Doren, C. L., and Verrillo, R. T. (1985). "Vibrotactile forward masking: Psychophysical evidence for a triplex theory of cutaneous mechanoreception," *J. Acoust. Soc. Am.* **78**, 534–543.

ISO 13091-1. (2001). *Mechanical Vibration: Vibrotactile Perception Thresholds for the Assessment of Nerve Dysfunction—Part 1: Methods of Measurement at the Fingertips* (International Organization for Standardization, Geneva).

Johnson, K. O. (2001). "The roles and functions of cutaneous mechanoreceptors," *Curr. Opin. Neurobiol.* **11**, 455–461.

Johansson, R. S., and Westling, G. (1984). "Roles of glabrous skin receptors and sensorimotor memory in automatic control of precision grip when lifting rougher or more slippery objects," *Exp. Brain Res.* **56**, 550–564.

Levitt, H. (1971). "Transformed up-down methods in psychoacoustics," *J. Acoust. Soc. Am.* **49**, 467–477.

Lundborg, G., Dahlin, L. B., Lundström, R., Necking, L. E., and Strömberg, T. (1992). "Vibrotactile function of the hand in compression and vibration-induced neuropathy," *Scand. J. Plast. Reconstr. Surg. Hand Surg.* **26**, 275–279.

Piercy, J. E., and Brammer, A. J. (2004). "Reference vibrotactile perception thresholds at the fingertips of healthy males," *Note Scientifique et Technique NS242*, 199–206 (Institut National de Recherche et de Sécurité, Paris).

Srinivasan, M. A., Whitehouse, J. M., and LaMotte, R. H. (1990). "Tactile detection of slip: Surface microgeometry and peripheral neural codes," *J. Neurophysiol.* **63**, 1323–1332.

Sutinen, P., Toppila, E., Starck, J., Brammer, A. J., Zou, J., and Pyykkö, I. (2006). "Hand-arm vibration syndrome with use of anti-vibration chain saws: 19-year follow-up of forestry workers," *Int. Arch. Occup. Environ. Health* **79**, 665–671.

Vallbo, Å. B., and Johansson, R. S. (1984). "Properties of cutaneous mechanoreceptors in the human hand related to touch sensation," *Hum. Neurobiol.* **3**, 3–14.

Van Boven, R. W., and Johnson, K. O. (1994). "A psychophysical study of the mechanisms of sensory recovery following nerve injury in humans," *Brain* **117**, 149–167.

Verrillo, R. T. (1985). "Psychophysics of vibrotactile stimulation," *J. Acoust. Soc. Am.* **77**, 225–232.

Verrillo, R. T. (in press). "Tactile response to vibration," in *Handbook of Signal Processing in Acoustics*, edited by D. Havelock, S. Kuwano, and M. Vorlander (Springer, New York).

Verrillo, R. T., and Gescheider, G. A. (1977). "Effect of prior stimulation on vibrotactile thresholds," *Sens. Processes* **1**, 292–300.

Erratum: “The acoustic center of laboratory standard microphones” [J. Acoust. Soc. Am. 120(5), 2668–2675 (2006)]

Salvador Barrera-Figueroa^{a)} and Knud Rasmussen^{b)}

Danish Primary Laboratory for Acoustics, Danish Institute for Fundamental Metrology, Matematiktorvet
B307, DK-2800 Lyngby, Denmark

Finn Jacobsen^{c)}

Acoustic Technology, Ørsted•DTU, Technical University of Denmark, Ørsted's Plads B352, DK-2800 Lyngby,
Denmark

(Received 22 November 2006; accepted 25 November 2006)

[DOI: 10.1121/1.2427116]

PACS number(s): 43.38.Kb, 43.58.Vb, 43.20.Rz, 43.10.Vx [AJZ]

There is an error in one of the coefficients in Table I, corrected in the revised table below.

TABLE I. Coefficients of the polynomial approximation of the acoustic center.

LS1	Coeff.	LS2
10.8	a_0	4.6
-2.32	a_1	-0.13
0.317	a_2	-0.052
-0.0268	a_3	0.0055
0.0011	a_4	-0.000224
-1.64e-5	a_5	3.993e-6
---	a_6	-2.573e-8

TABLE II. Alternative coefficients of the polynomial approximation of the acoustic center.

LS1	Coeff.	LS2
10.08	a_0	4.59
-1.302	a_1	-0.115
-0.0375	a_2	-0.0542
0.02676	a_3	0.005678
-0.002792	a_4	-0.0002327
0.00011735	a_5	4.215e-6
-1.744e-6	a_6	-2.78e-8

Alternatively, a slightly different polynomial approximation based on more data can be used. The coefficients of the alternative polynomial approximation are given in Table II.

^{a)}Electronic mail: sbf@oersted.dtu.dk

^{b)}Electronic mail: kr@oersted.dtu.dk

^{c)}Electronic mail: fja@oersted.dtu.dk